



DEBRIS-FLOW HAZARDS MITIGATION: Mechanics, Monitoring, Modeling, and Assessment

Edited by
Jason W. Kean,
Jeffrey A. Coe,
Paul M. Santi, &
Becca K. Guillen

PROCEEDINGS OF THE SEVENTH INTERNATIONAL CONFERENCE ON DEBRIS-
FLOW HAZARDS MITIGATION, GOLDEN, COLORADO, USA, JUNE 10-13, 2019

DEBRIS-FLOW HAZARDS MITIGATION: Mechanics, Monitoring, Modeling, and Assessment

Edited by

Jason W. Kean

US Geological Survey, Golden, Colorado

Jeffrey A. Coe

US Geological Survey, Golden, Colorado

Paul M. Santi

Department of Geology and Geological Engineering
Colorado School of Mines, Golden, Colorado

Becca K. Guillen

Continuing and Professional Education Services
Colorado School of Mines, Golden, Colorado

ASSOCIATION OF ENVIRONMENTAL AND ENGINEERING
GEOLOGISTS SPECIAL PUBLICATION 28

2019



DFHM logo by Alyssa Schwarz

On the Cover: Debris flow at the Chalk Cliffs monitoring site near Nathrop, Colorado. Photo taken by an automated monitoring camera, courtesy of Jeffrey Coe, US Geological Survey.

Authors granted permission to the organizers of the 7th International Conference on Debris-Flow Hazards Mitigation to release (publish) your paper online, with Open Access, on the AEG and Mountain Scholar websites.

Published by the Association of Environmental and Engineering Geologists
Distributed by the Association of Environmental and Engineering Geologists and
Mountain Scholar Digital Collections of Colorado & Wyoming

ISBN: 978-0-578-51082-8

Preface

The Seventh International Conference on Debris-Flow Hazards Mitigation was held in Golden, Colorado June 10-13, 2019. The major objective of the conference was to provide a forum for international researchers, engineers, and policy makers to exchange ideas and promote communication to advance the scientific understanding of debris-flow hazards as well as approaches to assess and mitigate debris-flow risk to infrastructure and people. The conference agenda consisted of 14 keynote presentations, 38 shorter oral presentations, and 86 poster presentations. The conference sessions were preceded by a 1-day field trip to examine 2013 debris flows in Rocky Mountain National Park and followed by a 2-day field trip to the Chalk Cliffs debris-flow monitoring basin near Nathrop, Colorado.

This proceedings volume contains 134 papers from 17 countries that accompanied all three types of presentations. All papers underwent peer review, with each paper receiving at least one technical and one editorial review, and most receiving two technical and two editorial reviews. We acknowledge the critical role that reviewers played in assuring the high-quality of papers in this volume. Reviewer names and affiliations are given on the following pages.

Many people contributed to the success of the conference. The International Organizing Committee provided guidance to the Local Organizing Committee throughout the multi-year preparation period leading up to the conference, as well as assisting with the review process and by serving as session moderators during the conference. The Colorado School of Mines Continuing and Professional Education Services group, led by Melody Francisco and including Becca Guillen, Jennifer Graser, and Andy Ledford, managed the massive job of creating and updating the conference website, corresponding with authors and attendees, wrangling manuscript submission and review logistics, and organizing meeting rooms, housing, and food arrangements for the conference. Emily Bongiovanni, the Colorado School of Mines Scholarly Communications Librarian, assured that this volume was posted on the Mountain Scholar website. Several organizations provided sponsorship through financial support. Their names are provided on the following pages. Our profound thanks goes out to all of these individuals and groups.

The Editors:

Jason W. Kean
US Geological Survey

Jeffrey A. Coe
US Geological Survey

Paul M. Santi
Colorado School of Mines

Becca K. Guillen
Colorado School of Mines

International Organizing Committee

Dieter Rickenmann	Swiss Federal Research Institute WSL, Birmensdorf, Switzerland
Elisabeth Bowman	The University of Sheffield, Sheffield, United Kingdom
Marcel Hürlimann	Universitat Politècnica de Catalunya, Barcelona, Catalunya
Mark Reid	US Geological Survey, Menlo Park, California, USA
Paul Santi	Colorado School of Mines, Golden, Colorado, USA
Yoshifumi Satofuka	Ritsumeikan University, Kyoto, Japan

Local Organizing Committee

Paul Santi	Colorado School of Mines
Jeffrey Coe	US Geological Survey
Jason Kean	US Geological Survey
Jonathan Godt	US Geological Survey

Conference and Proceedings Management Team

Colorado School of Mines, Continuing and Professional Education Services

Melody Francisco	Director
Jennifer Graser	Event Manager
Becca Guillen	Finance & Administrative Manager
Andy Ledford	Webmaster
Ed Mantz	Manager of Program Technology & Services

Reviewers

The editors thank the following people who peer-reviewed manuscripts submitted to the conference:

Kate Allstadt	US Geological Survey (USA)
Muneyuki Arai	Meijo University (Japan)
Katherine Barnhart	University of Colorado (USA)
Rex Baum	US Geological Survey (USA)
Scott Beason	US National Park Service (USA)
Erin Bessette-Kirton	US Geological Survey (USA)
David Bonneau	Queen's University (Canada)
Elisabeth Bowman	The University of Sheffield (United Kingdom)
Miguel Cabrera	Universidad de los Andes (Columbia)
Nancy Calhoun	Oregon Dept. of Geology and Mineral Industries (USA)
Felix Camire	Town of Canmore (Canada)
Kerry Cato	California State University, San Bernardino (USA)
Hua-Yong Chen	Institute of Mountain Hazards and Environment (China)
Jian-Gang Chen	Institute of Mountain Hazards and Environment (China)
Shin-Kyu Choi	Korea Advan. Inst. Science and Tech. (Republic of Korea)
Jeffrey Coe	US Geological Survey (USA)
Velio Coviello	Free University of Bozen-Bolzano (Italy)
Matt Crawford	Kentucky Geological Survey (USA)
Kahlil Fredrick Cui	Institute of Mountain Hazards and Environment (China)
Joanna Curran	Indicator Engineering (USA)
Tim Davies	University of Canterbury (New Zealand)
Alexander Densmore	Durham University (United Kingdom)
Litan Dey	National Cheng Kung University (China)
Vivian Dias	University of São Paulo (Brazil)
Junhan Du	Institute of Mountain Hazards and Environment (China)
Paul Duhart	Servicio Nacional de Geología y Minería (Chile)
Evan Friedman	Lithos Engineering (USA)
Masaharu Fujita	Disaster Prevention Research Institute (Japan)
Joe Gartner	BGC Engineering Inc. (USA)
Jonathan Godt	US Geological Survey (USA)
Christoph Graf	Swiss Federal Institute WSL (Switzerland)
Carlo Gregoretti	University of Padova (Italy)
Xiaojun Guo	Institute of Mountain Hazards and Environment (China)
Norio Harada	Mitsui Consultants Co. (Japan)
Yuji Hasegawa	Hiroshima University (Japan)
Junya Hina	Construction Technology Institute Co. (Japan)
Jacob Hirschberg	Swiss Federal Institute WSL (Switzerland)
Leslie Hsu	US Geological Survey (USA)

Yu-Charn Hsu	National Taiwan University (China)
Hongsen Hu	Institute of Mountain Hazards and Environment (China)
Kaiheng Hu	Institute of Mountain Hazards and Environment (China)
Li-Jeng Huang	National Kaohsiung University Science and Tech. (China)
Yi-Min Huang	Feng Chia University (China)
Johannes Hübl	University Natural Resources and Life Sciences (Austria)
Marcel Hürlimann	Universitat Politècnica de Catalunya (Spain)
Akihiko Ikeda	Sabo & Landslide Technical Center (Japan)
Fumitoshi Imaizumi	Shizuoka University (Japan)
Takahiro Itoh	Nippon Koei Co. (Japan)
Richard Iverson	US Geological Survey (USA)
Mattias Jakob	BGC Engineering Inc. (Canada)
Eranda Jayasekara	University of Peradeniya (Sri Lanka)
Roland Kaitna	University Natural Resources and Life Sciences (Austria)
William Kane	Kane Geotech Inc. (USA)
Jason Kean	US Geological Survey (USA)
Jeffrey Keaton	Wood (USA)
Masato Kobiyama	Federal University of Rio Grande do Sul (Brazil)
Viktorii Kurovskaia	St. Petersburg State University (Russia)
Dominique Laigle	Université Grenoble Alpes (France)
Jeremy Lancaster	California Geological Survey (USA)
Deuk-Hwan Lee	KAIST (Republic of Korea)
Kwangwoo Lee	Korea Railroad Research Institute (Republic of Korea)
Shuai Li	Institute of Mountain Hazards and Environment (China)
Dingzhu Liu	Institute of Mountain Hazards and Environment (China)
Fangzhou Liu	Georgia Institute of Technology (USA)
Jon Major	US Geological Survey (USA)
Tiago Martins	Federal University of São Paulo (Brazil)
Naoki Matsumoto	Nat. Inst. for Land and Infrastructure Management (Japan)
Kevin McCoy	Colorado Geological Survey (USA)
Scott McCoy	University of Nevada, Reno (USA)
Luke McGuire	University of Arizona (USA)
Abigail Michel	US Geological Survey (USA)
Kate Mickelson	Washington Geological Survey (USA)
Ben Mirus	US Geological Survey (USA)
Kuniaki Miyamoto	Nippon Koei Co. (Japan)
Chiara Morstabilini	Maccaferri Innovation Center (Italy)
Robb Moss	California Polytechnic State University (USA)
Naoto Nakamura	CTI Engineering Co. (Japan)
Kana Nakatani	Kyoto University (Japan)
Ba-Quang-Vinh Nguyen	Pukyong University (Republic of Korea)
Petter Nyman	University of Melbourne (Australia)
Nina Oakley	Desert Research Institute (USA)
Takehiro Ohta	Yamaguchi University (Japan)
Rosa Palau	Universitat Politècnica de Catalunya (Spain)
Jefferson Picanço	Unicamp (Brazil)

Marina Pirulli	Politecnico di Torino (Italy)
Guillaume Piton	Université Grenoble Alpes (France)
Sara Rathburn	Colorado State University (USA)
Mark Reid	US Geological Survey (USA)
Francis Rengers	US Geological Survey (USA)
Dieter Rickenmann	Swiss Federal Research Institute WSL (Switzerland)
Yuichi Sakai	University of Tokyo (Japan)
Paul Santi	Colorado School of Mines (USA)
Claudia Vanessa Santos Corrêa	Cemaden (Brazil)
Nicoletta Sanvitale	University of Sheffield (United Kingdom)
Luca Sarno	University of Salerno (Italy)
Katherine Scharer	US Geological Survey (USA)
Manfred Scheikl	ALPINFRA (Austria)
Kevin Schmidt	US Geological Survey (USA)
Vinod Sharma	Geological Survey of India (India)
Stephen Slaughter	Washington Geological Survey (USA)
Joel Smith	US Geological Survey (USA)
Dongri Song	Institute of Mountain Hazards and Environment (China)
Eu Song	Seoul National University (Republic of Korea)
Alex Strouth	BGC Engineering Inc. (USA)
Kiyotaka Suzuki	PASCO Corporation (Japan)
Takuro Suzuki	Forestry and Forest Products Research Institute (Japan)
Brian Swanson	California Geological Survey (USA)
Matt Thomas	US Geological Survey (USA)
Ting-Chi Tsao	Sinotech Engineering Consultants (China)
Haruka Tsunetaka	Forestry and Forest Products Research Institute (Japan)
Taro Uchida	Nat. Inst. for Land and Infrastructure Management (Japan)
Bianca Vieira	University of São Paulo (Brazil)
Thad Wasklewicz	East Carolina University (USA)
Shih-Chao Wei	National Taiwan University (China)
Michaela Wenner	ETH Zürich (Switzerland)
Jia Yang	Institute of Mountain Hazards and Environment (China)
Shun Yang	Institute of Exploration Technology (China)
Kousuke Yoshino	Asia Air Survey Co. (Japan)
Ann Youberg	Arizona Geological Survey (USA)
Sophia Zubrycky	University of British Columbia (Canada)

Keynote Speakers

Some keynote speakers do not have papers in this volume

Processes and Mechanics

Nico Gray (United Kingdom)

Anne Mangeney (France)

Monitoring, Detection, and Warning

Kate Allstadt (USA)

Brian McArdell (Switzerland)

Experiments and Modeling

Liz Bowman (United Kingdom)

Dave George (USA)

The Role of Disturbance

Fumitoshi Imaizumi (Japan)

Luke McGuire (USA)

Case Studies and Hazard Assessments

Jeremy Lancaster (USA)

Alex Densmore (United Kingdom)

Mike Chard (USA)

Mattias Jakob (Canada)

Engineering and Mitigation

Johannes Huebl (Austria)

Ken Ho (China)

Sponsors

The conference was financially supported by:

Access Limited Construction

Association of Environmental and Engineering Geologists

BGC Engineering Inc.

Geobrugg North America

KANE Geotech Inc.

MACCAFERRI Inc

US Geological Survey

Table of Contents

Processes and Mechanics

Numerical investigation of particle size segregation in saturated granular flows using CDF-DEM coupling approach	2
<i>Cui, K.F.E., Zhou, G.G.D.</i>	
Erosion by experimental debris flows: particle size effects	10
<i>Ghasemi, A., Kaitna, R., Fritton, P., Blankenship, B.T., Feng, Q., Denmore, A., de Haas, T., Hill, K.M.</i>	
How does particle-size segregation affect the fluidity of multi-granular debris flows?	18
<i>Hotta, N., Iwata, T., Suzuki, T.</i>	
Valid debris-flow models must avoid hot starts	25
<i>Iverson, R.M., George, D.L.</i>	
The role of topography on the volume of material eroded by debris flows	33
<i>Kudo, T., Uchida, T., Sakurai, W.</i>	
Numerical investigation of deposition mechanism of submarine debris flow	38
<i>Liu, D., Cui, Y., Choi, C.E., Bazai, N.A., Yu, Z., Lei, M., Yin, Y.</i>	
Compressibility of solid phase of debris flow and erosion rate	46
<i>Miyamoto, K., Itoh, T., Kisa, H.</i>	
Commonalities between debris flows and flow failures	54
<i>Moss, R.E.S.</i>	
Soil characteristics of long-traveling landslides and a hybrid model to predict travel distance ...	61
<i>Usuki, N., Toshino, K., Mizuyama, T.</i>	
The research on the movable solid materials under seepage flow effect in debris-flow source area	69
<i>Yang, S., Ou, G., Pan, H., Xie, Z., Yang, D.</i>	

Monitoring, Detection, and Warning

Overcoming barriers to progress in seismic monitoring and characterization of debris flows and lahars	77
<i>Allstadt, K.E., Farin, M., Lockhart, A.B., McBride, S.K., Kean, J.W., Iverson, R.M., Logan, M., Smith, J.B., Tsai, V.C., George, D.L.</i>	

Topographic change detection at Chalk Cliffs, Colorado, USA, using airborne lidar and UAS-based Structure-from-Motion photogrammetry	85
<i>Barnhart, K.R., Rengers, F.K., Ghent, J.N., Tucker, G.E., Coe, J.A., Kean, J.W., Smith, J.B., Staley, D.M., Kleiber, W., Wiens, A.M.</i>	
Forecasting and seismic detection of debris flows in pro-glacial rivers at Mount Rainier National Park, Washington, USA	93
<i>Beason, S.R., Legg, N.T., Kenyon, T.R., Jost, R.P., Kennard, P.M.</i>	
Deciphering sediment dynamics in a debris-flow catchment: insights from instrumental monitoring and high-resolution topography	103
<i>Coviello, V., Theule, J.I., Marchi, L., Comiti, F., Crema, S., Cavalli, M., Arattano, M., Lucía, A., Macconi, P.</i>	
Examining the impact force of debris flow in a check dam from small-flume experiments	111
<i>Eu, S., Im, S.</i>	
The vibrational characteristics of debris flow in Taiwan	116
<i>Huang, Y., Fang, Y., Yin, H.</i>	
Monitoring and modeling of debris-flow surges at the Lattenbach creek, Austria	124
<i>Huebl, J., Arai, M., Kaitna, R.</i>	
Monitoring of rainfall and soil moisture at the Rebaixader catchment (Central Pyrenees)	131
<i>Hürlimann, M., Oorthuis, R., Abancó, C., Carleo, L., Moya, J.</i>	
Debris flow monitoring using load cells and pressure sensors on Sakurajima Island	138
<i>Itoh, T., Fujimura, N., Katou, H., Tagata, S., Mizuyama, T.</i>	
Implementation of an integrated management strategy to deal with landslide triggered debris flows: the Valloire case study (Savoie, France)	146
<i>Laigle, D., Jongmans, D., Liebault, F., Baillet, L., Rey, E., Fontaine, F., Borgniet, L., Bonnefoy-Demongeot, M., Ousset, F.</i>	
Taking the pulse of debris flows: Extracting debris-flow dynamics from good vibrations in southern California and central Colorado	154
<i>Michel, A., Kean, J.W., Smith, J.B., Allstadt, K.E., Coe, J.A.</i>	
Observations on the development and decay processes of debris flows	162
<i>Murasawa, M., Imaizumi, F., Yokota, Y.</i>	
Monitoring of sediment runoff and observation basin for sediment movements focused on active sediment control in Jo-Gan-Ji River	170
<i>Nagayama, T., Furuya, T., Matsuda, S., Itoh, T., Fujita, M., Mizuyama, T.</i>	

Measurements of velocity profiles in natural debris flows: a view behind the muddy curtain	177
<i>Nagl, G., Huebl, J., Kaitna, R.</i>	
Debris-flow early warning system at regional scale using weather radar and susceptibility mapping	184
<i>Palau, R.M., Hürlimann, M., Berenguer, M., Sempere-Torres, D.</i>	
Real-time monitoring of debris-flow velocity and mass deformation from field experiments with high sample rate lidar and video	192
<i>Rengers, F.K., Rapstine, T.D., Allstadt, K.E., Olsen, M., Bunn, M., Iverson, R.M., Kean, J.W., Leshchinsky, B., Logan, M., Sharifi-Mood, M., Obryk, M., Smith, J.B.</i>	
Exploring controls on debris-flow surge velocity and peak discharge at Chalk Cliffs, Colorado, USA	199
<i>Smith, J.B., Kean, J.W., Coe, J.A.</i>	
Dynamic characteristics of extreme superelevation of debris flows observed by laser profile scanners in Sakura-jima volcano, Japan	207
<i>Takahashi, Y., Fujimura, N., Akita, H., Mizuno, M.</i>	
Monitoring and early warning of debris flow in an earthquake impacted area, Baishahe catchment, southwest China	214
<i>Tian, H., Yang, Z., Qiao, J., Shi, L.</i>	
Deciphering debris-flow seismograms at Illgraben, Switzerland	222
<i>Wenner, M., Walter, F., McArdell, B., Farinotti, D.</i>	
 <i>Experiments and Modeling</i>	
Reproducibility of debris-flow fan physical modeling experiments	231
<i>Adams, K., Wasklewicz, T., de Haas, T., Lecce, S., Gares, P.</i>	
Influence of momentum correction factor and friction factor on flow models of debris flow related to flow surface deformation	239
<i>Arai, M.</i>	
Constraining parameter uncertainty in modeling debris-flow initiation during the September 2013 Colorado Front Range storm	249
<i>Baum, R.L., Scheevel, C.R., Jones, E.S.</i>	
An evaluation of debris-flow runout model accuracy and complexity in Montecito, California: Towards a framework for regional inundation-hazard forecasting	257
<i>Bessette-Kirton, E.K., Kean, J.W., Coe, J.A., Rengers, F.K., Staley, D.M.</i>	

Possibilities and limitations for the back analysis of an event in mountain areas on the coast of São Paulo State, Brazil using RAMMS numerical simulation	265
<i>Corrêa, C.V.S., Reis, F.A.G.V., Giordano, L.C., Cabral, V.C., Targa, D.A., Brito, H.D.</i>	
Discrete-element investigation of granular debris-flow runup against slit structures	273
<i>Du, J., Zhou, G.G.D.</i>	
A method for predicting debris-flow occurrence based on a rainfall and sediment runoff model	280
<i>Fujita, M.; Yamanoi, K.; Suzuki, G.</i>	
Seamless numerical simulation of a hazard cascade in which a landslide triggers a dam-breach flood and consequent debris flow	287
<i>George, D.L., Iverson, R.M., Cannon, C.M.</i>	
Woody debris blocking conditions at bridges in mountainous streams	294
<i>Hasegawa, Y., Nakatani, K., Satofuka, Y.</i>	
Flume experiments and numerical simulation focused on fine sediments in stony debris flow	301
<i>Hina, J., Uchida, T., Matsumoto, N., Sakurai, W., Nishiguchi, Y., Murakami, M.</i>	
On the regression of velocity distribution of debris flows using machine learning techniques	307
<i>Huang, L., Hsiao, D.</i>	
Experimental evaluation for peak and temporal changes in debris-flow initiation processes ...	315
<i>Itoh, T., Ikeda, A., Mizuyama, T.</i>	
Correlation between the slump parameters and rheological parameters of debris flow	323
<i>Jan, C., Yang, C., Hsu, C., Dey, L.</i>	
Concentration distribution in debris flow consisting of particles with two different sizes	330
<i>Kida, H., Iwao, M.</i>	
Debris-flow hazard investigation with Kanako-2D in a rural basin, Alto Feliz municipality (Brazil)	338
<i>Kobiyama, M. and Michel, R.D.L.</i>	
Numerical analysis on the behavior of the debris flow and impact force on check dam	346
<i>Lee, K., Jeong, S., Kim, H.</i>	
Impact load estimation on retention structures with the discrete element method	354
<i>Leonardi, A., Calcagno, E., Pirulli, M.</i>	

Debris-flow deposition: effects of fluid viscosity and grain size	361
<i>Li, S., Zhou, G.G.D., Chen, X., Song, D.</i>	
Regional-scale modelling of liquefaction-induced shallow landslides in unsaturated slopes ..	369
<i>Li, X., Song, Z., Lizárraga, J.L., Buscarnera, G.</i>	
Flume experiment on the influence of particle size distribution on sediment capturing efficiency of open-type steel Sabo dams	377
<i>Matsumoto, N., Uchida, T., Sakurai, W., Matsubara, T., Okuyama, R., Hina, J., Satofuka, Y.</i>	
Debris-flow behavior containing fine sediment considering phase shift	385
<i>Nakatani, K., Hasegawa, Y., Asano, Y., Satofuka, Y.</i>	
Long travel distance of landslide-induced debris flows	393
<i>Nishiguchi, Y., Uchida, T.</i>	
Effect of rheological properties on debris-flow intensity and deposition in large scale flume experiment	401
<i>Nguyen, B., Lee, J., Kim, Y., Lee, S., Kwon, T.</i>	
Long travel distance of landslide-induced debris flow	407
<i>Pinzón, G., Cabrera, M.A.</i>	
Small scale debris-flow experiments on run-up height	414
<i>Rickenmann, D., Karrer, T., McArdell, B., Scheidl, C.</i>	
Numerical simulation of debris flows focusing on the behavior of fine sediment	421
<i>Sakai, Y., Hotta, N.</i>	
Optical measurements of velocity and of solid volume fraction in fast dry granular flows in a rectangular chute	429
<i>Sarno, L., Carleo, L., Papa, M.N., Villani, P.</i>	
Debris flow behavior in super- and subcritical conditions	437
<i>Scheidl, C., McArdell, B., Nagl, G., Rickenmann, D.</i>	
Experimental examination for influence of debris-flow hydrograph on development processes of debris-flow fan	443
<i>Tsunetaka, H., Hotta, N., Sakai, Y., Nishiguchi, Y., Hina, J.</i>	
Numerical simulation for evaluating the phase-shift of fine sediment in stony debris flows ...	451
<i>Uchida, T., Nishiguchi, Y., McArdell, B., Satofuka, Y.</i>	
Run out processes of sediment and woody debris resulting from landslides and debris flow...	459
<i>Yamazaki, Y., Egashira, S.</i>	

Comparison of an empirical and a process-based model for simulating debris-flow inundation following the 2010 Schultz Fire in Coconino County, Arizona, USA..... 467
Youberg, A.M., McGuire, L.A.

The Role of Disturbance

The impact of global warming on the formation of debris flows in an alpine region of southeastern Tibet 476
Cui, P, Yang, J., Liu, D.

Relationship between rainfall intensity and debris-flow initiation in a southern Colorado burned area 484
Friedman, E.Q. and Santi, P.M.

Effects of terrain on temporal changes in susceptibility of debris flows and associated hydrogeomorphic processes after forest harvesting 492
Imaizumi, F.

Overview of geotechnical effects of the January 9, 2018, debris-flow and flash-flood disaster in Montecito, California 500
Keaton, J., Oriz, R.M., Turner, B., Alessio, P., Gartner, J., Duffy, J., Parker, G., Smilovsky, D., Watts, T.

The debris flows and mitigation systems after the 2008 Wenchuan earthquake 508
Liu, F., Frost, J.D., Xu, Q., Huang, R.

Looking through the window of disturbance at post-wildfire debris-flow hazards 516
McGuire, L.A., Rengers, F.K., Kean, J.W., Staley, D.M., Tang, H., Youberg, A.M.

Conceptual framework for assessing disturbance impacts on debris-flow initiation thresholds across hydroclimatic settings 524
Mirus, B.B., Staley, D.M., Kean, J.W., Smith, J.B., Wooten, R., McGuire, L.A., Ebel, B.A.

A novel approach for determining risk of water supply disruptions due to post-wildfire debris flows 532
Nyman, P., Yeates, P., Langhans, C., Schärer, C., Noske, P.J., Lane, P.N.J., Haydon, S., Sheridan, G.J.

Rainfall intensity limitation and sediment supply independence of postwildfire debris flows in the western U.S. 539
Santi, P.M., MacAulay, B.

Case Studies and Hazard Assessments

Debris flows in the North Pacolet River valley, Polk County, North Carolina, USA - case studies and emergency response 549
Bauer, J.B., Wooten, R.M., Cattnach, B.L., Fuemmeler, S.J.

Characteristics of debris flows just downstream the initiation area on Punta Nera cliffs, Venetian Dolomites 557
Bernard, M., Berti, M., Crucil, G., Simoni, A., Gregoretti, C.

Characterizing debris transfer patterns in the White Canyon, British Columbia with terrestrial laser scanning 565
Bonneau, M., Hutchinson, D.J., McDougall, S.

Simulation of the debris flow occurred the 15 August 2010 on Rio Val Molinara Creek (northeast Italian Alps) 573
Boreggio, M., Bernard, M., Alberti, R., Gregoretti, C.

Post-fire rockfall and debris-flow hazard zonation in the Eagle Creek fire burn area, Columbia River Gorge, Oregon: A tool for emergency managers and first responders..... 581
Calhoun, N.C., Burns W.J., Hay, S., Staley, D.M., Kean, J.W.

Hydrogeomorphology and steep creek hazard mitigation lexicon: French, English and German 589
Camiré, F., Piton, G., Schwindt, S.

Debris flow in southeast Brazil: susceptibility assessment for watersheds and vulnerability assessment of buildings 597
Vieira, B.C., de Souza, L.M., Alcalde, A.L., Dias, V.C., Bateira, C., Martins, T.D.

Complexity of a debris-flow system at Forest Falls, California 605
Cato, K., Goforth, B.

A 4000-year history of debris flows in north-central Washington State, USA: preliminary results from trenching and surficial geologic mapping at the Pope Creek fan 613
Coe, J.A., Bessette-Kirton, E.K., Slaughter, S.L., Rengers, F.K., Contreras, T.A., Mickelson, K.A., Taylor, E.M., Kean, J.W., Jacobacci, K.E., Hanson, M.A.

Modeling frequent debris flows to design mitigation alternatives 621
Curran, J.C., Flanagan, P.

Application of knowledge-driven method for debris-slide susceptibility mapping in regional scale 629
Das, R., Nandi, A.

Making sense of avulsions on debris-flow fans	637
<i>Densmore, A.L., de Haas, T., McArdell, B., Schuerch, P.</i>	
The morphology of debris-flow deposits from a 1967 event in Caraguatatuba, Serra do Mar, Brazil	645
<i>Dias, V.C., Martins, T.D., Gramani, M.F., Coelho, R.D., Dias, H.C., Vieira, B.C.</i>	
The Santa Lucía landslide disaster, Chaitén-Chile: origin and effects	653
<i>Duhart, P., Sepúlveda, V., Garrido, N., Mella, M., Quiroz, D., Fernández, J., Moreno, H., Hermosilla, G.</i>	
Debris-flow risk management in practice: a New Zealand case study	661
<i>Farrell, J., Davies, T.</i>	
Post-fire debris-flow hazard analysis for interstate 80, Truckee River Canyon, near the California-Nevada state line, USA	669
<i>Felling, G., Myers, A., McCoy, S.W.</i>	
Debris-flow risk assessment and mitigation design for pipelines in British Columbia, Canada	677
<i>Gartner, J.E., Jakob, M.</i>	
An overview of a decade of applied debris-flow runout modeling in Switzerland: challenges and recommendations	685
<i>Graf, C., Christen, M., McArdell, B.W., Bartelt, P.</i>	
Analysis of rainfall and runoff for debris flows at the Illgraben catchment, Switzerland	693
<i>Hirschberg, J., McArdell, B.W., Badoux, A., Molnar, P.</i>	
Debris-flow assessment from rainfall infiltration induced landslide	701
<i>Hsu, Y., Liu, K., Shu, H.</i>	
Study of prediction methods of debris-flow peak discharge	709
<i>Ikeda, A., Mizuyama, T., Itoh, T.</i>	
Debris-flow hazard assessments -- a practitioner's view	716
<i>Jakob, M.</i>	
Evaluation of shallow landslide-triggering scenarios through a physically based approach: A case study from Bulathsinhala area, Sri Lanka	724
<i>Jayasekara, E.I., Weerasekara, N.K., Jayathissa, H.A.G., Gunatilake, A.A.J.K.</i>	
Hydro-meteorological trigger conditions of debris flows in Austria	732
<i>Kaitna, R., Prenner, D., Braun, M., Hrachowitz, M.</i>	

Weather-radar inferred intensity and duration of rainfall that triggered the January 9, 2018, Montecito, California, disaster	740
<i>Keaton, J.R.</i>	
Review of contemporary terminology for damaging surficial processes – stream flow, hyperconcentrated sediment flow, debris flow, mud flow, mud flood, mudslide	748
<i>Keaton, J.R.</i>	
Evaluation of slope stability of Taebaeksan Mountain National Park using detailed soil map	758
<i>Kim, Y., Jun, K., Jun, B., Lee, H., Kim, S., Jang, C.</i>	
Estimation of debris-flow volumes by an artificial neural network model	766
<i>Lee, D., Lee, S., Jeon, J., Park, J., Kim, Y.</i>	
Post-fire debris flows of 9 January 2018, Thomas Fire, southern California: Initiation areas, precipitation and impacts	774
<i>Lukashov, S.G., Lancaster, J.T., Oakley, N.S., Swanson, B.J.</i>	
Debris-flow susceptibility mapping in Colorado using Flow-R: calibration techniques and selected examples	782
<i>McCoy, K.M.</i>	
Landslides and debris flows in volcanic rocks triggered by the 2017 Northern Kyushu heavy rain	790
<i>Ohta, T., Eguchi, S.</i>	
Debris-flow occurrence in granite landscape in south-southeast Brazil	798
<i>Picanço, J., Vieira, B., Martins, T., Gramani, M., Faccuri, G., Silva, M.</i>	
Hillslope evaluation in the vicinity of the Wolsong nuclear power plant after 12th September 2016 Gyeongju earthquake, South Korea	808
<i>Pradhan, A.M.S., Lee, J., Lee, S., Kwon, T., Kim, Y.</i>	
Historical debris-flow occurrence in Rocky Mountain National Park, Colorado, USA	816
<i>Rathburn, S.L., Patton, A.I., Bilderback, E.L.</i>	
Debris-flow initiation promoted by extension of a slow-moving landslide	824
<i>Reid, M.E., Brien, D.L.</i>	
Regional level debris-flow hazard assessment for alpine infrastructure facilities using the 3D numerical high-performance simulation tool FIMT	832
<i>Scheickl, M., Powell, D.</i>	

Using satellite radar interferometry to delineate burn area and detect sediment accumulation, 2018 Montecito disaster, California	840
<i>Smilovsky, D., Keaton, J.R.</i>	
Quantitative risk management process for debris flows and debris floods: lessons learned in Western Canada	847
<i>Strouth, A., McDougall, S., Jakob, M., Holm, K., Moase, E.</i>	
Semi-automated regional scale debris-flow and debris-flood susceptibility mapping based on digital elevation model metrics and Flow-R software	855
<i>Sturzenegger, M., Holm, K., Lau, C., Jakob, M.</i>	
Study on methods for assessing sediment disaster inundation zone in regions with insufficient data: Case study of the Aranayake disaster in Sri Lanka	863
<i>Suzuki, K., Uchida, T., Matsumoto, N., Nakatani, K., Jayathissa, G.</i>	
Application of an MPS-based model to the process of debris-flow deposition on alluvial fans	871
<i>Suzuki, T., Hotta, N., Tsunetaka, H., Sakai, Y.</i>	
Numerical modeling of debris flows and landslides triggered by extreme rainfall event	879
<i>Tsai, Y., Syu, F., Lee, S., Shieh, C.</i>	
Debris-flow building damage level and vulnerability curve – A case study of a 2015 Typhoon event in northern Taiwan	887
<i>Tsao, T., Hsu, C., Yin, H., Cheng, K.</i>	
Estimating mechanical slope stability to predict the regions and ranges of deep-seated catastrophic landslides	895
<i>Yoshino, K., Uchida, T.</i>	
Multi-scale hazard assessment of debris flows in eastern Qinghai-Tibet Plateau area	903
<i>Zou, Q., Cui, P., Zhang, G., Wang, D.</i>	
Preliminary calibration of a numerical runout model for debris flows in Southwestern British Columbia	911
<i>Zubrycky, S., Mitchell, A., Aaron, J., McDougall, S.</i>	
 <i>Engineering and Mitigation</i>	
Predicting debris-flow scour depth downstream from a check dam	920
<i>Chen, H., Chen, Z., Chen, J., Tang, J.</i>	

Debris-flow mitigation measures and an application case in a small-scale watershed in China	928
<i>Chen, J., Chen, X., Zhao, W., You, Y.</i>	
Roles of barrier location for effective debris-flow mitigation: assessment using DAN3D	936
<i>Choi, S., Kwon, T., Lee, S., Park, J.</i>	
Scour and erosion experience with flexible debris-flow nets	941
<i>Feiger, N. and Wendeler, C.</i>	
Steel stakes to capture debris-wood on an impermeable type sabo dam	949
<i>Harada, N. and Satofuka, Y.</i>	
Debris-flow mitigation – research and practice in Hong Kong	957
<i>Ho, K.K.S., Koo, R.C.H., Kwan, J.S.H.</i>	
Flume investigation of the interaction mechanisms between debris flow and slit dams	965
<i>Hu, H.S., Zhou, G.G.D., Song, D.</i>	
Empirical model for assessing dynamic susceptibility of post-earthquake debris flows	973
<i>Hu, K., Wang, Z., Chen, C., Li, X.</i>	
From practical experience to national guidelines for debris-flow mitigation measures in Austria	981
<i>Huebl, J., Nagl, Georg</i>	
Flexible debris-flow nets for post-wildfire debris mitigation in the western United States	988
<i>Kane, W.F., Jones, M.A.</i>	
Laboratory tests of an innovative check dam	996
<i>Morstabilini, C., Boschini, I., Zambrini, F., Menduni, G., Deana, M.L., Zorzi, N.</i>	
Application of an innovative, low-maintenance weir to protect against debris flows and floods in Ottone, Italy device	1004
<i>Morstabilini, C., Deana, M.L.</i>	
Numerical study of debris flows in presence of obstacles and retaining structures: A case study in the Italian Alps	1012
<i>Pirulli, M., Manassero, M., Terriotti, C., Leonardi, A., La Porta, G.</i>	
Design of a debris retention basin enabling sediment continuity for small events: the Combe de Lancey case study (France)	1019
<i>Piton, G., Mano, V., Richard, D., Evin, G., Laigle, D., Tacnet, J., Rielland, P.</i>	

Review of the mechanisms of debris-flow impact against barriers	1027
<i>Poudyal, S., Choi, C.E., Song, D., Zhou, G.G.D., Yune, C.Y., Cui, Y., Leonardi, A., Busslinger, M., Wendeler, C., Piton, G., Moase, E., Strouth, A.</i>	
Small scale impact on rigid barrier using transparent debris-flow models	1035
<i>Sanvitale, N., Bowman, E., Cabrera, M.A.</i>	
Estimation of temporal changes of debris flows and hydraulic model tests of channel works with multi-drop structures	1043
<i>Watabe, H., Ikeshima, T., Nishi, Y., Nagarekawa, Y., Matsuda, S., Nakayama, T., Itoh, T., Mizuyama, T.</i>	
<i>Author Index</i>	1051

Processes and Mechanics

Numerical investigation of particle size segregation in saturated granular flows using CFD-DEM coupling approach

Kahlil F. E. Cui ^{a,b,*}, Gordon G. D. Zhou^{a,b}

^a Key Laboratory of Mountain Hazards and Earth Surface Process/Institute of Mountain Hazards and Environment, Chinese Academy of Sciences (CAS), Chengdu, China

^b University of Chinese Academy of Sciences, Beijing, China

Abstract

Particle size segregation is a common feature in debris-flow deposits and is assumed to develop in a similar way as in dry granular flows where fluid forces are neglected. Solid-fluid coupling however is a defining feature of debris flows and fluid forces must therefore be accounted for in modelling for the segregation that develops therein. This paper presents a numerical investigation of the mechanisms of segregation under the influence of fluid forces. For this, a segment of a fully submerged bi-disperse steady granular flow is simulated using the CFD-DEM method. The solid-fluid interactions come in the form of buoyancy and fluid drag force. It is found that the presence of the fluid generally retards the rate and quality of segregation primarily by promoting the formation of a plug flow in the stream-wise velocity profile. The plug flow region forms at the free surface where it significantly reduces or zeroes out the shear rates thus inhibiting the main mechanisms of segregation, i.e. kinetic sieving and squeeze expulsion, to take place. It is inferred that the rapid shearing that occurs near the base promotes segregation but is unable to proceed towards the free surface due to the presence of the plug flow region that serves as a barrier. The quality of submerged segregation improves at lower angles where the plug flow region is minimized and the usual parabolic shear profile develops.

Keywords: CFD-DEM; interstitial pore fluid; particle size segregation; debris flows; solid-fluid interaction

1. Introduction

Particle size segregation is a prominent physical feature observed in debris-flow deposits (Major 1997) and is believed to have significant effects on the flow's overall dynamics (Johnson et al. 2012, Kokelaar et al. 2014). The head region and the lateral edges are primarily composed of larger and coarser grains while the tail region is mostly composed of fines. Cutting into the deposit, one can observe an inversely graded profile where the large particles rise to the free surface and the fine particles settle at the base. This phenomenon has been well observed in highly sheared dry granular mixtures (e.g. chute flows, rotating drums, heaps and silos) and has been found to be well accounted for by the theories of kinetic sieving and squeeze expulsion (Savage & Lun 1989, Vallance & Savage 2000, Gray & Thornton 2005, Gray & Chugunov 2006). Debris flows however are distinct from other granular and geophysical mass flows due to the active influence of the interstitial fluid on the particle dynamics (Cuossot & Meunier 1995, Iverson 1997).

Physical experiments on segregation (Vallance & Savage 2000, Zanuttigh & Ghilardi 2010, van der Vaart et al. 2015) have been invaluable in characterizing the mechanisms that drive the process and have been instrumental in the development of theories that are able to predict the degree of segregation for different initial conditions (Gray & Thornton 2005, Benjy & Marks 2011, Gajjar & Gray 2014). It is, however, only through computational and numerical simulations of particle interactions that the micro-mechanical origins (i.e. particle scale) of segregation can truly be investigated (Fan & Hill 2011, Hill & Tan 2014, Jing et al. 2017). Recently, particle dynamics simulations have been computationally 'coupled' with fluid dynamics solvers in order to model fluid effects on particle motion and vice

* Corresponding author e-mail address: kfcui@imde.ac.cn

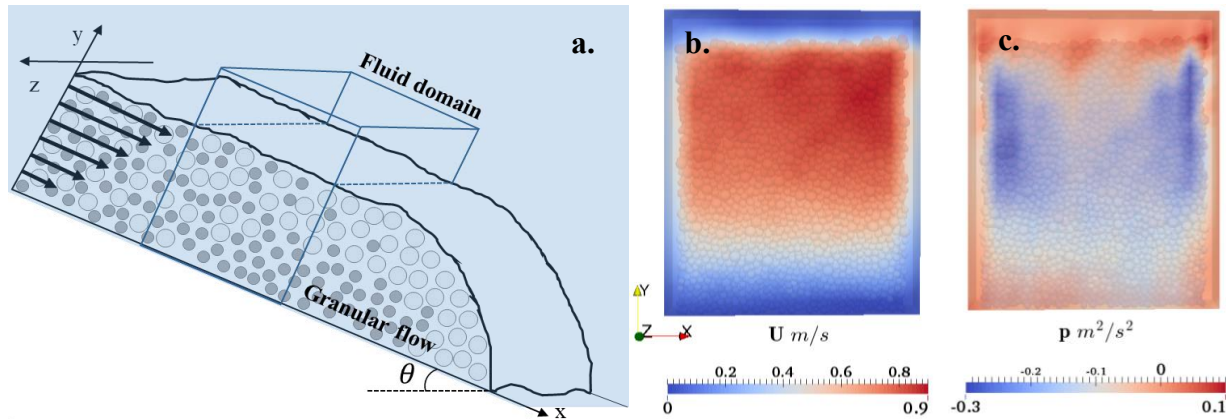


Fig. 1. (a) The conceptual diagram of the system being simulated. Snapshots of the (b) velocity and (c) dynamic pressure distributions of the actual simulation which represents the segment bordered by the cube in (a).

versa. Several works that employ these methods have already demonstrated their effectiveness in providing significant insight to the dynamics of coupled systems ranging from laboratory-scale granular transport (Tsuji et al. 1992), and saturated soil mechanics (Zhao et al. 2014), to landslides (Zhao & Shan 2013, Zhao et al. 2016) and debris flows (Leonardi et al. 2015, Zhao 2017, Li & Zhao 2018).

In this study, we report the results of a series of computational experiments that were aimed to study the development of particle size segregation under the influence of fluid forces. This is to further understand the driving mechanisms responsible for the size re-arrangement observed in natural debris flows. We use the coupled Discrete Element Method – Computational Fluid Dynamics (CFD-DEM) to simulate bi-disperse mixtures of particles ‘flowing’ at different angles of inclination in water. The segregation that develops in the saturated cases are compared with the segregation of dry particles.

2. Methodology

2.1. Definition of the system

The simulation consists of two separate but coupled domains. In the solid domain, the flow of a bi-disperse mixture of solid spheres is simulated using the open-source code ESyS-Particle (Weatherly et al. 2011). Periodic boundaries were set in the stream-wise direction to represent an infinitely long chute. The distance between the span-wise boundaries were set to be small enough for side-wall effects to be negligible (Jop et al. 2005). The floor was roughened by ‘gluing’ a randomized array of small particles to the base; the flow surface was free. The particles were initially set to be randomly mixed. The exact number of small and large particles were calculated according to a volume fraction of 0.5, a large to small particle size ratio of 1.5 and an initial packing volume of $0.3 \times 0.1 \times 0.4\text{m}$ ($L \times W \times H$). Flow was initiated by tilting the xz plane of gravity to the desired inclination angle. It is to be noted that the chosen parameters are highly idealized and do not necessarily reflect natural debris flows which are known to have much wider size distributions and size ratios. The goals of this paper simply focus on the particle scale effects of fluid forces on the particle dynamics that lead to inverse grading and not on the effects of varying these parameters themselves. Hence they will be held constant throughout the study. In particular, the chosen size ratio is relatively small but is sufficient to induce size segregation within a short period of time.

The fluid domain was implemented using the open-source CFD code OpenFOAM. The whole domain was given the material properties of water at 20°C. The domain was uniformly discretized in such a way that at least 5 large particles would fit (Zhao et al. 2014). A free-atmosphere boundary condition (pressure is based on local velocity of adjacent mesh; velocity dynamically changes from zero gradient when there is outflow to having a flux dependence when there is inflow (OpenCFD 2004)) was set at the right, left and top walls, allowing the fluid to freely flow in and out of the domain. A no-slip condition (zero pressure gradient, fixed zero velocity) was set at the bottom wall. For the turbulence, the standard $k - \epsilon$ model is implemented. The complete set of material and system parameters are summarized in Table 1.

The solid domain is positioned completely within the fluid domain. The fluid domain is set to be slightly longer stream-wise since setting both domains to exactly coincide would mathematically result to very sharp fluid pressure

Table 1. CFD-DEM material and simulation parameters

DEM Parameters		CFD Parameters	
Small particle diameter (mm)	10	Fluid density (kg/m ³)	1000
Large particle diameter (mm)	15	Viscosity (Pa.s)	0.001
Number of small particles	5999		
Number of large particles	1777	Simulation Parameters	
Solid volume fraction	0.5	Gravity (m/s ²)	-9.81
Young's modulus (N/m)	1x10 ⁷	DEM time-step (s)	1x10 ⁻⁵
Poisson's ratio	0.3	CFD time-step (s)	1x10 ⁻⁴
Friction angle (°)	30°	Coupling frequency*	10
Linear Damping Coefficient	0.1		
Inclination angle (°)	[22,24,26,30]		

*Coupling frequency pertains to the number of DEM time steps that have to elapse before a single CFD time step.

gradients. Over-all one can imagine the whole simulation to be that of a segment of a submerged bi-disperse debris flow (Fig. 1a). A fully submerged case is chosen since, for now, we only wished to observe the effects of fluid forces on segregation, while avoiding the complications of solving for fluid free surface flows. The fluid is initially static and only flows as a reaction to the particle motion.

Snapshots of the velocity and dynamic pressure distributions are shown in Figs. 1b and c respectively. The highest velocities are observed at the top-right since particle velocities are highest near the free surface for a flow that moves from left to right. Relatively low velocities are measured at the left since that is where the 'new' particles enter whose velocities are impeded by the particles ahead of them. On average, granular flow and fluid velocities are approximately equal. Dynamic pressures fluctuate as a reaction to the random dilation and contraction of the particles within the mixture. The extremely low pressures at the boundaries of the solid domain are due to the velocity differences of the solids and the fluids (Zhao 2016).

2.2. The CFD-DEM method

The CFD-DEM method relies on a message passing algorithm that relays information from the DEM solver to the CFD solver after a pre-defined number of DEM time-steps. The algorithm proposed by Zhao et al. (2014) was used in this study.

The translational and rotational displacements resulting from particle-particle interactions are updated after each numerical time-step, determined after integrating the governing differential equations which are based on Newton's second law of motion. The governing equations for the said trajectories can be written as:

$$m_i \frac{d^2 \mathbf{x}_i}{dt^2} = m_i \mathbf{g} + \sum_c (\mathbf{f}_{nc} + \mathbf{f}_{tc}) + \mathbf{f}_{fluid} \quad (1)$$

$$\mathbf{I}_i \frac{d\boldsymbol{\omega}_i}{dt} = \sum_c \mathbf{r}_c \times \mathbf{f}_{tc} \quad (2)$$

for linear and rotational motions respectively. Here m_i and \mathbf{x}_i are the mass and position of a particle i at a single numerical time-step and \mathbf{g} is the acceleration due to gravity. \mathbf{f}_{nc} and \mathbf{f}_{tc} are the normal and tangential forces defined at a contact point c . A linear spring-dashpot contact model (Cundall & Strack 1979) is used to calculate for the contact forces. \mathbf{I}_i is the moment of inertia of a sphere, $\boldsymbol{\omega}_i$ is the rotational acceleration, and \mathbf{r}_c is the distance between the centers of two contacting spheres.

The final term on the right hand side of Eqn. (1) represents the force exerted by the fluid on particle i . This is called the solid-fluid interaction force (Zhao 2016) and is calculated as the sum of 2 types of fluid forces: the hydrostatic and the hydrodynamic. The hydrostatic forces are represented by buoyancy $f_b^i = -v_{pi} \nabla p$, which is basically a function of the particle volume and the pressure gradient that develops between two adjacent fluid cells. The hydrodynamic forces are born from the relative motion of the solid and the fluid phases and usually come in the form of the drag force which is quantified as:

$$F_{di} = \frac{1}{2} C_d \rho_f \frac{\pi D^2}{4} |\mathbf{U} - \mathbf{V}| (\mathbf{U} - \mathbf{V}) n^{-\chi+1} \quad (3)$$

where:

$$C_D = \frac{24}{Re} (1 + 0.15Re^{0.681}) + \frac{0.407}{1 + \frac{8710}{Re}} \quad (4)$$

$$Re = \rho_f d |\mathbf{U} - \mathbf{V}| / \mu \quad (5)$$

are the drag coefficient and Reynold's number defined at the particle scale respectively. \mathbf{U} and \mathbf{V} are the fluid and particle velocities, ρ_f is the fluid density, and μ is the dynamic viscosity. n is the local porosity while χ is the empirical porosity correction factor calculated as $\chi = 3.7 - 0.65 \exp\left[-\frac{(1.5 - \log_{10} Re)^2}{2}\right]$.

The fluid domain is discretized into 3-dimensional cells where the Navier-Stokes equations are solved using the Finite Volume Method (FVM) (OpenCFD 2004). The mass and momentum continuum equations are written as:

$$\frac{\partial(\rho_f n)}{\partial t} + \nabla \cdot (\rho_f n \mathbf{U}) = 0 \quad (6)$$

$$\frac{\partial(\rho_f n \mathbf{U})}{\partial t} + \nabla \cdot (\rho_f n \mathbf{U} \mathbf{U}) - n \nabla \cdot \boldsymbol{\tau} = -n \nabla p + n \rho_f \mathbf{g} + \mathbf{f}_d \quad (7)$$

where $\boldsymbol{\tau}$ fluid stress tensor calculated via the standard $k - \varepsilon$ turbulent model (Zhao 2016), and p is the fluid pressure. The term $\mathbf{f}_d = \sum_{i=1}^N F_{di} / V_{cell}$ is the drag force per unit fluid volume. The fluid pressures and velocities that are calculated in each cell are used, in turn, to calculate for the interaction forces.

3. Results and discussions

3.1. Post-processing

To calculate for the relevant kinematics of the system, the whole granular flow was divided into bins of fixed dimensions along the flow depth (y -direction). The kinematic properties will be calculated considering the contribution of the part of each particle that falls within a certain bin with height Δy centered at y . The bin height is arbitrarily set to be 1/5 of the small particle diameter. Dry and submerged mixtures flowing at 26° were simulated to provide comparison between the segregation that develops with and without buoyant forces. Submerged mixtures at different angles of inclination were simulated to show how the segregation process varies under different flow conditions.

3.2. Measuring segregation

Segregation is measured as the deviation of the local volume concentration ϕ^n of a certain size species n from the global volume concentration (which is 0.5 at all times) at a height y for a certain time t . This is calculated using the equation proposed by Hill & Tan (2014):

$$S^n(y) = \sqrt{\sum_{j=1}^{N_{bin}} (\phi_j^n(t) - \phi) / (N_{bin} - 1)} \quad (8)$$

where S^n is the segregation of a species and N_{bin} is the number of bins along the y -direction respectively. The higher the value of S^n the better the 'quality' of segregation, where the best case involves a complete separation of small and large particles into two homogeneous layers.

Fig. 2a shows the segregation trends of the large particles of both dry and submerged mixtures. The segregation of the dry mixture (at 26°) shows a rapid increase at the beginning which evens out to a nearly constant value at around 120 seconds. Beyond this point, there is no longer a clear change in the local large particle concentration deviations,

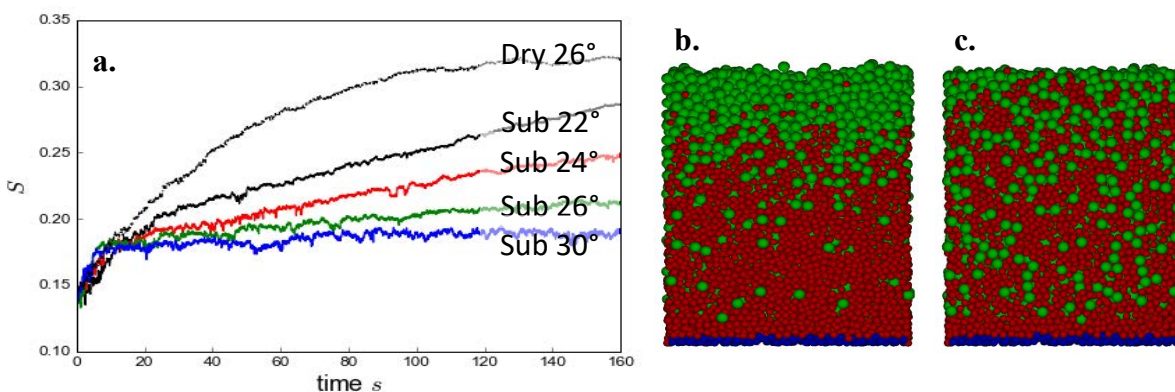


Fig. 2. (a) Segregation of a dry bi-disperse mixture at 26° and submerged mixtures (indicated by the prefix ‘sub’) at different angles of inclination. Snapshots of segregation for a (b) dry and (c) submerged mixture at 26°, 160 seconds.

implying that there is no longer a net flux of large (small) particles to the free surface (base) and segregation has achieved a steady state.

The segregation of submerged mixtures are significantly different. The levels of segregation are lower and slower compared to the dry case. Instead of a parabolic trend, segregation rapidly increases in a linear manner initially for a short period of time before abruptly slowing down. The slow increase continues until the end of the simulation. Segregation steady-state was not achieved except for the mixture flowing down at a 30° angle. This flow was very diffuse – random particle motion dominated – and hence no net upward nor downward flux was able to develop, maintaining a constant concentration deviation until the end.

Segregation is a shear driven process. At higher velocities shear rates are high, more random voids appear for small particles to percolate down to and more inter-particle contacts to hoist large particles up. High velocities will increase random particle motion and create voids that even large particles can fall into, preventing them from segregating up. Flows that are relatively slow result to lower shear rates which also effectively reduce segregation. Simply put, the presence of the fluid slows down the granular flow, reducing local shear rates and consequently slows down segregation. The difference that the presence of fluid makes can be seen when comparing Figs. 2b and c – snapshots of dry and submerged mixtures respectively, both simulated at an inclination angle of 26°; taken at 160 seconds.

3.3. Particle distribution

For a more qualitative assessment of the spatio-temporal development of segregation, phase diagrams representing the solid volume concentrations of large particles ϕ^l for the dry case at 26° (Fig. 3a) and the submerged cases (Figs. 3b-e) at different angles of inclination are presented in the first column of Fig. 3. As in section 3.1, the dry case is simply included for comparison. For the dry case, a thick layer composed of purely large particles is observed at the free surface. One that is dominated by small particles develops at the bottom. The black dashed line near the floor marks the height of the base particles. A blurred transition line develops between these two regions. This area is where both size species co-exist and mix under dynamic equilibrium (cf. Jing et al. 2017). This is usually attributed to diffusivity which prevents the perfect segregation of the two particle species (cf. Vallance & Savage 2000, Gray & Chugunov 2006).

For the submerged case, the large particle layers are noticeably much thinner and take much longer times to develop. Immediately under this layer is a region which, although dominated by large particles, is also sufficiently populated with small particles. This layer continues to thicken over time indicating that large particles still continue to rise from the bottom. Most of these large particles, however, do not continue all the way upwards but instead remain suspended there. This can be seen from the granularity that develops in this region where a certain degree of striation is observed. This indicates that the solid concentrations at a certain height remain constant for prolonged periods of time. All throughout the rest of the flowing body, the mixture is more or less homogenous and a more ‘diffuse’ granularity is observed. This suggests that there is a difference between the flow properties along the height of the flow that, in effect, causes particles to behave differently.

Comparing the phase diagrams of the flows at different angles, it can be seen that the lower the slope angles the better the segregation, and the more the distribution resembles that of the dry case. At low angles (i.e. low velocities; 22° and 24°) the large particles in the stagnant layer accumulate at the beginning but then slowly rise up to be a part of the pure large particle layer. This is accompanied by the continued increase in the thickness of the small particle

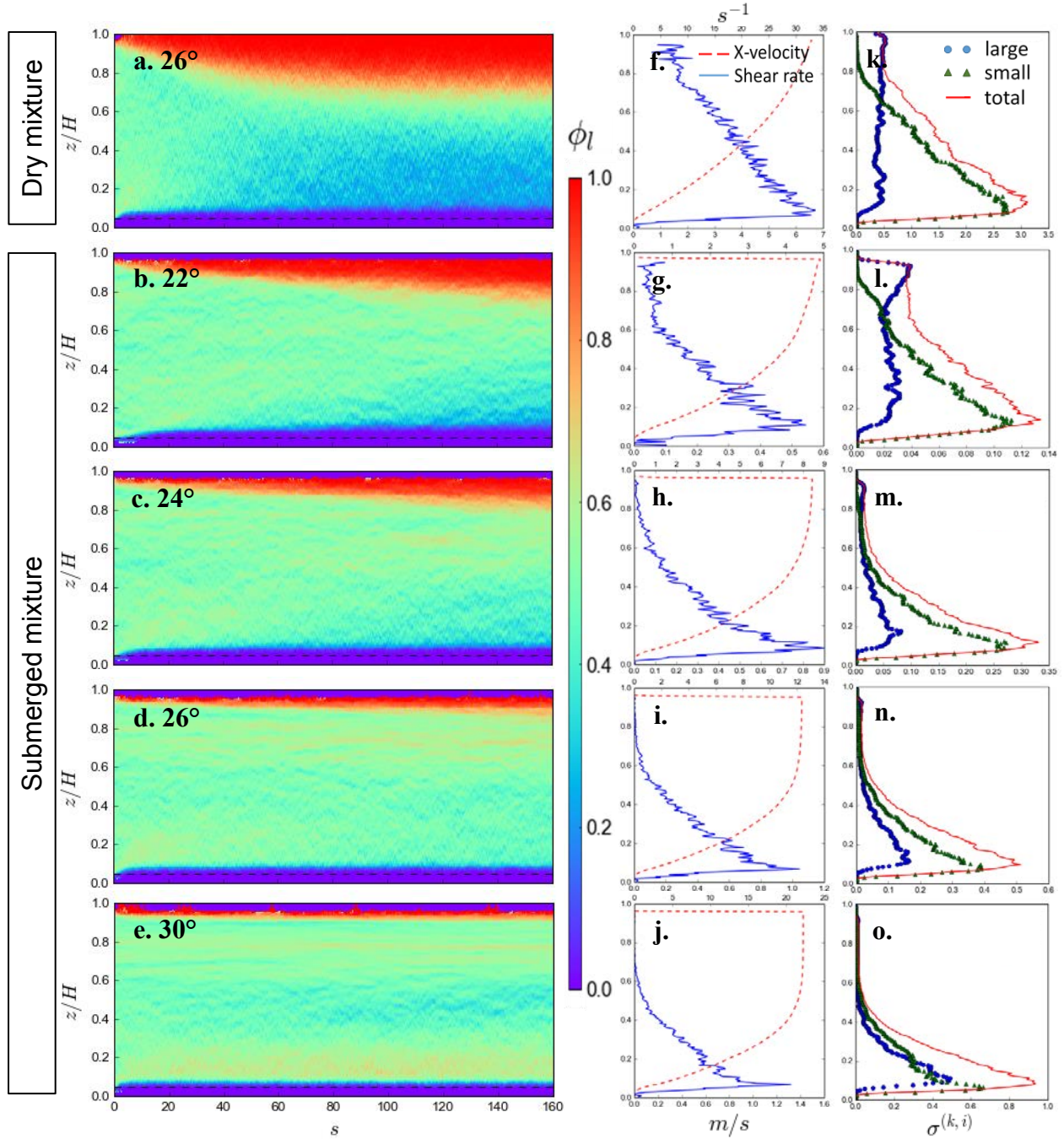


Fig. 3. The solid volume concentration distributions of large particles ϕ^l of (a) a dry bi-disperse mixture at 26° and submerged mixtures for angles (b) 22° , (c) 24° , (d) 26° , and (e) 30° . The stream-wise velocity and shear profiles of the (f) dry and (g-j) submerged mixtures at 160 seconds. The kinetic stress profiles of the (f) dry and (g-j) submerged mixtures at 160 seconds.

layer. This means that although slow, segregation and its primary mechanisms (e.g., kinetic sieving, squeeze expulsion) are still in progress and the inhomogeneities in the flow profile are less pronounced. At higher angles (i.e. higher velocities; 26° and 30°), the striation in the stagnant regions are more pronounced, indicating that almost no relative change in the solid concentration has occurred for long periods of time. The same is also true for the fine particle layer near the base whose thickness has ceased to increase indicating that even the gravity-driven downward percolation of small particles is also inhibited. In addition (especially at an inclination of 30°), distinct layers start to form at the lower regions indicating more pronounced differences in the flow profile along the depth.

3.4. Kinetic properties

To further shed light on the flow properties that are believed to affect the manner of segregation, the kinetic properties of the simulated granular mixtures are evaluated according to their velocity, shear rate and kinetic stress profiles. The kinetic stress is a measure of the degree of individual particle mobility, expressed in terms of their relative velocities to the average velocity of the surrounding particles at the height where they are located. This value is analogous to the granular temperature. Here we calculate the kinetic stress through (Fan & Hill 2011):

$$\sigma_{yy}^{k,n}(y) = \rho_m \phi^n \left(\frac{1}{N} \sum_{i=1}^N \frac{\sum_j (v_{ij}^n - v(y))^2 V_{ij}^n}{\sum_j V_{ij}^n} \right) \quad (9)$$

where v_{ij}^n is the velocity of the volume portion of a certain particle and $v(y)$ is the average velocity of both size species at bin center y . i is the time-step number, of which there are N at which the velocity per bin is averaged, V_{ij}^n is the total volume of a particle specie at y , and ρ_m is the material density.

Figs. 3f and k show the relevant kinetic properties of the dry flow respectively. The measured stream-wise velocity and shear rate profile of the dry case is typical for dry granular flows (cf. Jop et al. 2004). In dry mixtures, the kinetic stress is mostly borne by the small particles and is highest near the base where the shear rate is highest. Large particle kinetic stress is significantly lower and more or less even throughout the flow height.

The flow profiles of the submerged mixture (Figs. 3g-j) exhibit a plug flow near the free surface and a rapid shear at the base. This profile is consistent with the stream-wise flow profiles of submerged (Istad et al. 2004) and even free-surface debris flows (Mainali & Rajaratnam 1994). The kinetic stress magnitudes (Figs. 3l-o) of both small and large particles are lower in the submerged case and are also notably less distinct – both of them show near zero values at the plug flow region and both peak near the base. This implies that the presence of fluid reduces individual particle mobility and does this to the point that individual particle motion for both species are nearly equalized. Relating the inhomogeneity of the kinetic profiles to the concentration profiles in 3.2, one can infer that the particles in the plug flow region almost move as a single block where due to the lack of shearing find it hard to segregate up or down.

Comparing the velocity profiles at different angles, the plug flow region is more pronounced and is wider for higher velocities. The larger the relative velocities of the particles and the surrounding fluid, the greater the opposing drag force and hence when the particles move faster, the greater the drag force they experience from an initially static fluid. When the granular flow is slow, the fluid resistance is less and hence a velocity and shear profile resembling a dry flow can be achieved.

4. Conclusions and outlook

A simple case of a submerged bi-disperse mixture is simulated using the CFD-DEM method to investigate the effects of fluid forces on the development of particle size segregation. From the initial results, it can be seen that the fluid generally retards the degree and rate of segregation. It is inferred that the resistive forces of the fluid create a plug flow region near the free surface wherein the shearing of the particles are greatly reduced to the point that the particles seemingly move as a single block. The reduction of the shearing inhibits the generation of random voids which are essential for small particle percolation downwards and reduces the relative inter-particle motion which necessary for the ‘squeezing’ of the large particles upwards. The shearing that exists in the lower regions continues to promote the aforementioned mechanisms, however, it is supposed that further segregation from this region is suppressed due to the plug flow that develops at the upper regions.

The aforementioned mechanism however still requires a more stringent evaluation which would involve knowing the fluid effects on particle contacts and how the shear profile that develops actually affects the particle trajectory. Further insight can also be gained through the variation of particle parameters such as the size ratio and the density ratio between the solid and the fluid.

Acknowledgements

The authors acknowledge financial support from the Key Research Program of the Chinese Academy of Sciences (grant no.KZZD-EW-05-01) and the CAS-TWAS President’s Fellowship for International PhD students.

References

- Coussot, P., Meunier, M., 1996, Recognition, classification and mechanical description of debris flows: *Earth-Science Reviews* v. 40, p. 209-227
- Cundall, P. A., & Strack, O. D. L., 1979, A discrete numerical model for granular assemblies: *Geotechnique*, v. 29, p. 47-65
- Fan, Y., Hill, K.M., 2011, Theory for shear-induced segregation of dense granular materials: *New Journal of Physics*, v. 13, 095009, doi:10.1088/1367-2630/9/095009.
- Gajjar, P., Gray, J.M.N.T., 2014, Asymmetric flux models for particle-size segregation in granular avalanches: *J. Fluid Mech.*, v. 757, p. 297-329, doi:10.1017/jfm.2014.503.
- Gray, J.M.N.T., Chugonov, V.A., 2006, Particle-size segregation and diffusive remixing in shallow granular avalanches: *J. Fluid Mech.*, v. 569, p. 365-398.
- Gray, J.M.N.T., Thornton, A.R., 2005, A theory for particle size segregation in shallow granular free surface flows: *Proc. R. Soc. A*, v. 461, p. 1477-1473.
- Hill, K.M., Tan, D., 2014, Segregation in dense sheared flows: gravity, temperature gradients, and stress partitioning: *J. Fluid Mech.*, v. 756, 54-88.
- Istad, T., Elverhoi, A., Issler, D., Marr, J.G., 2004, Sub-aqueous debris flow behaviour and its dependence on the sand/clay ratio: a laboratory study using particle tracking: *Marine Geology* v. 213, 415-438. doi:10.1016/j.margeo.2004.10.017
- Iverson, R.M., 1997, The physics of debris flows: *Reviews of Geophysics*, v. 35, no. 3, p. 245-296.
- Jing, L., Kwok, C.Y., Leung, Y.F., 2017, Micro-mechanical origin of particle size segregation: *Phys. Rev. Lett.*, v. 118, 118001, doi:10.1103/PhysRevLett.118001.
- Johnson, C. G., Kokelaar, B.P., Iverson, R.M., Logan, M., LaHusen, Gray, J.M.N.T., 2012, Grain-size segregation and levee formation in geophysical mass flows: *J. Geophys. Res.*, v. 117, F01032.
- Jop, P., Forterre, Y., Poliquen, O., 2005, Crucial role of sidewalls in granular free surface flows: consequences for the rheology: *J. Fluid Mech.* v. 541, p. 167-192. doi:10.1017/S0022112005005987
- Kokelaar, B.P., Graham, R.L., Gray, J.M.N.T., Vallance, J.W., 2014, Fine-grained linings of leveed channels facilitate run-out of granular flows: *Earth and Planetary Science Letters*, v. 385, p. 172-180, doi:10.1016/j.epsl.2013.10.043.
- Leonardi, A., Cabrera, M., Wittel, F., Kaitna, R., Mendoza, M., Wu, W., Herrmann, H., 2015, Granular-front formation in free-surface flow of concentrated suspensions: *Phys. Rev. E.*, v. 92, 052204. doi:10.1103/PhysRevE.92.052204
- Mainali, A., Rajaratnam, N., 1994, Experimental study of debris flows: *J. Hydraul. Eng.*, v. 120, p. 104-123.
- Major, J.J., 1997, Depositional process in large-scale debris-flow experiments: *The Journal of Geology*, v. 105, no. 3, p. 345-366, doi:10.1086/515390.
- Marks, B., Rognon, P., Einav, I., 2011, Grainsize dynamics of poly-disperse granular segregation down inclined planes: *J. Fluid Mech.*, 690, 499-511.
- OpenCFD, 2004, OpenFOAM – The open source CFD toolbox: <http://www.openfoam.com/Othmer>,
- Savage, S.B., Lun, K.K., 1988, Particle size segregation in inclined chute flow of dry cohesion-less granular Solids: *J. Fluid Mech.*, v. 189, p. 311-335.
- Thornton, A.R., Gray, J.M.N.T, Hogg, A.J., 2006, A three-phase mixture theory for particle size segregation in shallow granular free surface flows. *J. Fluid Mech.*, v. 550, p. 1-25.
- Tsuji, Y., Tanaka, T., Ishida, T., 1992, Lagrangian numerical simulation of plug flow of cohesionless particles in horizontal pipe. *Powder Tech.*, v. 71, p. 239-250
- Vallance, J.W., Savage, S.B., 2000, Particle size segregation in granular flows down chutes, in *Proceedings, Rosato, A.D., Blackmore D.L. (eds.) IUTAM Symposium on Segregation in Granular Flows, Solid Mechanics and Its Applications*, v. 81, p. 31-51, doi:10.1007/978-94-015-9498-1_3
- van der Vaart, K., Gajjar, P., Epely-Chauvin, G., Andreini, N., Gray, J.M.N.T., Ancey, C., 2015, Underlying asymmetry within particle size segregation: *Phys. Rev. Lett.*, 114, 238001, doi:10.1103/PhysRevLett.114.238001.
- Weatherly, D., Boros, V., Hancock, W., Abe, S., 2011, ESyS-particle tutorial and user's guide version 2.3.1: *Earth System Science Computational Centre, The University of Queensland*, 152 p.
- Zanuttigh, B., Ghilardi, P., 2010, Segregation process of water-granular mixtures released down a steep chute: *Journal of Hydrology*, v. 391, p. 175-187.
- Zhao, J., Shan, T., 2013, Coupled CFD-DEM simulation of fluid-particle interaction in geo-mechanics. *Powder Technology*, v. 239, p. 248-258.
- Zhao, T., 2017, *Coupled DEM-CFD Analyses of Landslide-Induced Debris Flows*: Singapore, Springer Nature, 220 p.
- Zhao, T., Houlsby, G.T., Utili, S., 2014, Investigation of batch sedimentation via DEM-CFD coupling. *Granular Matter*, 16, 921-932. doi:10.1007/s10035-014-0534-0.
- Zhao, T., Utili, S., Crosta, G.B., 2016, Rockslide and impulse wave modelling in the Vajont Reservoir by DEM-CFD analysis. *Rock Mech. Rock Eng.*, v. 49, p. 2437-2456. doi:10.1007/s00603-015-0731-0

Erosion by experimental debris flows: particle size effects

A. Ghasemi^{a,b}, R. Kaitna^c, P. Fritton^a, B.T. Blankenship^d, Q. Feng^e, A. Densmore^f, T. de Haas^g, K. M. Hill^{a,b*},

^a*Department of Civil, Environmental, and Geo-Engineering, University of Minnesota, Minneapolis 55455 USA*

^b*St. Anthony Falls Laboratory, University of Minnesota, Minneapolis 55455 USA*

^c*Institute of Mountain Risk Engineering, University of Natural Resources and Life Sciences, Vienna, Austria*

^d*Department of Physics and Astronomy, Sewanee University, Sewanee, 37383 USA*

^e*State Key Laboratory of Hydrosience and Engineering, Tsinghua University, Beijing, China*

^f*Department of Geography, Durham University, Durham, UK*

^g*Department of Geosciences, Utrecht University, Utrecht, The Netherlands*

Abstract

The mobilization of surface material by particle-laden flows involves phenomenology that cross multiple scales: particle-scale interactions and mesoscopic stresses have significant implications for landscape evolution and associated hazard mitigation issues. Here, we consider the problem of erosion of bed materials by debris flows – flows of boulders, gravel, sand, fine particles, and fluids – as they entrain soils and rocks from steep hillsides. In this paper we report results from laboratory experiments investigating the effect of changing coarse particle concentration in a dry “debris flow” on the erosion of a bed over which it flows. We find that increasing the fraction of coarse particles in the bed often increases the bed erosion. However, for some systems, the details are noisier and harder to discern. We associate the variable erosion and noisiness in part with the competing dynamics of small scale interactions, such as the coarse grain impacts, and larger scale details, such as those related to angles of repose. We also present preliminary results measuring instantaneous erosion rates and demonstrate that size dependence of the erosion rates can vary considerably from that of the net erosion. We conclude by summarizing some limitations of our experiments and ongoing next steps to address these limitations.

Keywords: debris flows, granular materials, erosion

1. Introduction

Debris flows are massive movers of sediment – boulders, gravel, and sand- and clay-sized particles – from mountainous regions and steep hillslopes to foothills, valleys, and river channels below (Hung, McDougall, Jakob and Bovis, 2005). Along the way, they pose significant hazards to infrastructure and human life, and they determine important details of river channel dynamics to which they supply a substantial amount of sediment. There is significant evidence that changing land use and climate change are increasing debris flow magnitude and frequency (e.g., Stoffel and Beniston, 2006; Jakob and Friele, 2009; Jomelli et al., 2009).

Much of our understanding of debris-flow processes is drawn from experimental studies and limited natural examples. Changing environmental conditions, such as rainfall frequency and magnitude, and variable particle properties limit effectiveness of empirical models based primarily on previous debris flows. A solution to this problem may lie in a more physics-based understanding of the manner in which debris flow composition, interstitial fluid composition, and particles which can vary from one debris flow to the next can affect debris flow behaviors. Understanding the mechanisms that control the rate at which a particular debris flow entrains particles and grows in size is important for predicting their hazard (Godt and Coe, 2007).

In this paper, we focus on the effect of changing the concentration of large particles in an experimental debris flow on net erosion, the difference in bed mass before and after the flow, of a bed of erodible materials (loose

* Corresponding author e-mail address: kmhill@umn.edu

particles rather than bedrock). We also perform a preliminary investigation of the dependence on near-instantaneous bed material erosion rates on large particle concentration in an initial debris flows.

1.1. Field-scale observations of debris flow entrainment

Much of our intuition of debris flow entrainment has historically come from observations of landscape evolution associated with natural debris flows. After a debris flow is initiated, inspection of the steepest part of the canyons indicates that at the steepest slopes, debris flows entrain most loose sediment in their paths and incise into the bedrock itself (e.g. Wieczorek et al., 2000; Stock and Dietrich, 2006). At intermediate slopes debris flows no longer scour down to bedrock, but they typically continue to entrain debris from the channel bed causing granular flows increase considerably in size (e.g., Revellino et al., 2004, Hungr et al., 2005). This paper concerns the dynamics of the entrainment process when the limit to entrainment is set by the details of the flow and the particles in the bed.

Many physical factors influence debris flow entrainment rates under these conditions. In most cases, these have been categorized into one of two mechanisms: (1) an applied shear stress by the flow on the bed that has the potential to accelerate the material into motion and (2) internal forces or stresses within the bed that resist the movement of bed materials into the flow (e.g., Takahashi, 1981; Hungr et al., 2005). In other words, the rapid loading associated with debris flows can entrain particles by increasing the shear loading of the material at the same time it can reduce the internal stress or even induce a liquefaction of the bed material, leading to erosion.

Monitoring stations around the world have produced data that have increased our understanding of key factors in debris flow entrainment. Notably, these include stations in active debris flow sites such as Acquabona Creek in the Dolomites in the Italian Eastern Alps (Berti et al., 1999); Illgraben channel in the Swiss Alps (Berger et al, 2011); Chalk Cliffs study basin in the Sawatch Range, Colorado, USA (McCoy et al., 2012). Berti et al. (2000) used flow height sensors, load cells, and fluid pore pressure sensors buried in the channel bed to understand entrainment dynamics in the Italian Eastern Alps. Their data indicated that the scour rate was proportional to local slope gradient. Berger et al. (2011) used a progressive erodible daisy-chained sensor in conjunction with dynamic load cells measuring downslope and normal stresses, pore pressure sensors video monitors in moderately moist debris flows along the Illgraben channel in a temperate-humid region in the Swiss Alps. They found that entrainment rate increases with both average and fluctuating stresses, and demonstrated that the fluctuations and entrainment rate particularly well-correlated with the highly fluctuating granular front. McCoy et al. (2012) used a comparable situ sensor network to measure related quantities in the Chalk Cliffs study basin of Colorado for dry-to-saturated flows in the typically semi-arid conditions. They found a strong correlation between entrainment and bed-sediment moisture content by comparing time-averaged entrainment rates across all six (dry and saturated) flows. In contrast to the findings of Berger et al. (2011) McCoy et al. (2012) found negligible correlations between stress fluctuations and sediment entrainment, perhaps because of a difference in the nature of the debris flows. The Chalk Cliffs measurements indicated shallow stress fluctuation penetration depths into the bed.

These field studies have demonstrated the importance of bed inclination, moisture level, and dynamics such as shear stress and bed fluctuations. However, investigating the effects of grain size distribution of the debris flow, or of the erodible material, on erosion dynamics is difficult due to the difficulty of systematically isolating the effect of grain sizes, interstitial fluid properties and other factors from one another.

1.2. Previous studies of erosion – laboratory scale

Laboratory investigations can isolate the effects of particle properties, changing interstitial fluid properties, slopes and other parameters from one another. Egashira et al. [2001], Papa et al. [2004], and De Haas and Van Woerkom [<https://doi.org/10.1002/esp.3963>] reported experiments in a laboratory flume designed to study the effect of changing relative size of the particles in the flow and the bed. Egashira, Papa, and colleagues [Egashira et al., 2001 and Papa et al. 2004] both used millimeter-sized particles (from ~ 2 mm to 10 mm) in an experimental flume with an adjustable angle. The flume was designed with a “weir” at the bottom, allowing these researchers to fill the bottom of the downstream end of the flume with particles and provide an erodible bed at a lower angle of inclination. Papa et al. [2004] showed that, for these systems, if both bed and flow particles are of the same size distribution, erosion rates decrease monotonically with increasing particle size. Egashira et al. [2001] demonstrated that, using smaller or equal-sized particles in the flow, the net erosion rate increases with decreasing bed particle size. Egashira, Papa, and colleagues [Egashira et al., 2001 and Papa et al. 2004] predicted theoretically that net erosion rate should scale as d_{flow}/d_{bed} , i.e., the smaller the bed particles relative to the particles in the flow, the larger the erosion rates. While

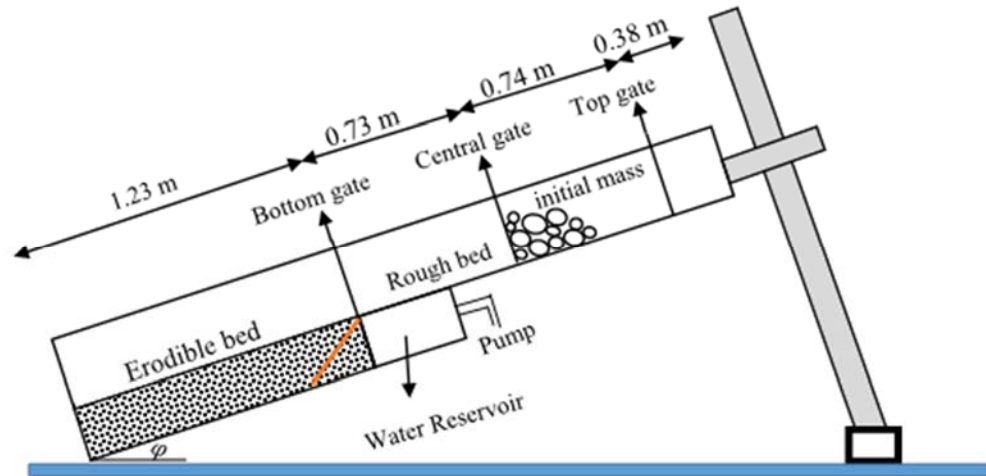


Fig. 1 Sketch of laboratory flume (not to scale).

the results are compelling, typical laboratory experiments such as these suffer the risk of scale-limiting issues, particularly when it comes to particle-fluid flows [e.g., Iverson, 1997].

The well-known United States Geological Survey (USGS) flume [Iverson et al., 2010] provides some best elements of both worlds – those of laboratory experiments and field measurements. At 95 m long and 2 m wide, it is sufficiently big to minimize scaling issues of smaller laboratory experiments. Yet because of its relatively simple (rectangular) channel geometry and extensive instrumentation, it provides a setting that allows for systematic studies primarily only possible in relatively small laboratory flumes. Using these facilities, researchers have been able to isolate a number of important dynamics of debris flows [e.g., Iverson et al., 2010] Notably, Iverson et al. [2011] and Reid et al. [2011] tested the effect of changing volumetric water content of the bed on relative erosion of that bed by a debris flow. To do so, they varied water content from ~ 15% to 30% holding all else constant, including the particles in the bed and flow, i.e., mostly gravel and sand with a small percentage of finer particles. They demonstrated that bed moisture plays an indisputable role in entrainment: the more moisture in the bed, the higher the measured entrainment rates. Further, they showed that higher entrainment rates associated with the higher bed moistures were strongly correlated with higher mobility rates of the debris flows.

1.3. Present studies of erosion – laboratory scale

We developed a laboratory flume, detailed in Section 2, to focus on particular aspects of entrainment rates. In the rest of this paper we present our experimental investigations of the influence of grain size dependence of an initial debris flow on its erosion of materials in the bed over which it flows. To help provide a simple foundation for these studies, we focus on bimodal mixtures in the initial debris flow and use dry particles only for the results described here. We discuss potential issues with these simplifications in the last section of this paper.

2. Experimental set-up

2.1. Experimental equipment

The experiments described herein were performed in our laboratory flume (Fig. 1) fabricated by the University of Minnesota (UMN) College of Science and Engineering (CSE) machine shop, that we designed specifically to study erosion and deposition by model channelized debris flows. The flume channel is approximately 3 m long \times 0.08 m wide. The inclination angle of the flume (ϕ) is adjustable from approximately 0° to 40° .

The upslope ~1.8 m of the flume channel has a rigid rough bed and is approximately 1.8 m long \times 0.15 m deep \times 0.08 m wide. Three release gates are installed along this section of the flume, at 0.38 m, 1.12 m, and 1.84 m from the upstream end. The bed is roughened from 1.12 mm to the end of this upslope region using sandpaper of ~ 1mm roughness elements. For the experiments we report here, we used the central release gate at 1.12 m from the upstream end. (We have found similar results using release gates at 0.38 m from the upstream end as detailed in [Moberly, 2016]). The downslope ~ 1.3 m of the flume has a false bottom, without which is ~ 1.3 m long \times 0.70 m

tall \times 0.15 m high. Both ends of the erodible bed chamber are bounded by a wire mesh of spacing \sim 0.5 mm up to the height of the bottom of the rigid bed (0.15 m high). A ramp installed between the bottom of the rigid bed and the bottom of the erodible bed chamber (inclined \sim 30° from the bed) greatly minimized the scour that otherwise occurred at the upstream end of the erodible bed, and did not otherwise appear to affect the results we present here.

We used three primary pieces of measurement equipment: During the course of each experiment, we made two relatively simple measurements of relevance here: (1) We determined the inclination angle of the flume, ϕ , using a digital level (Husky® accurate to the nearest 0.1°), placed the digital level on the base of the flume, as we inclined the flume. (2) We collected mass measurements of the particles using a digital scale with a resolution of one gram. In addition, we captured high speed videos of the experiments using two Photron high speed cameras, the FASTCAM SA3 and v9.0, both capable of taking slightly higher than 1000 \times 1000 pixel resolution figures at a frequency of 1000 frames per second. Most of the data we present here concerns the total net erosion from the bed associated with each debris flows. In addition, we present some preliminary instantaneous erosion rate data for which we used data from the digital images to track the particles from one image to the next as we describe shortly.

2.2. Bed and debris flow materials

For these experiments, we used two different sizes of near-spherical zirconium silicate beads (Quackenbush, specific gravity \sim 4.0) with diameters of 2.0 mm and 0.8 mm. For both mixtures, we dyed the smaller particles blue using Sharpie ink to enhance differentiation of the two constituents when used together in an experiment. To simplify the experiments for this paper, we used only one type of bead in the bed at the beginning of each experiment and used uniform or bimodal systems in the supply, or initial debris flow, of the same material as the particles in the bed.

2.3. Experimental procedures

To prepare for each experiment, we reset the bed with the flume is in a horizontal position, such that $\phi \approx 0^\circ$ and apply anti-static spray to the flume walls. We place a predetermined mass and mixture of particles in a position upslope of the closed gate to act as the initial debris flow for our experiment. The shape of the conglomerate of particles placed here is similar from one experiment to the next, though, using this release gate, we observed little-to-know difference in net erosion when this was changed [Moberly, 2016]. Next, we place an amount of particles in the erodible bed chamber predetermined to fill the chamber to the top. We use a flat rectangular plastic piece to gently smooth the top of the erodible bed in a way that flattens the surface while minimizing disturbance to the bed beyond the top layer of beads. After this, we incline the flume to a predetermined angle and then secure the flume in place.

To initiate each experiment, we quickly open the gate to allow the initial debris flow material to flow downstream. As the initial debris flow travels over the roughened rigid section of the flume, the particles accelerate, become agitated and spread out due to the interparticle interactions. Once the energized particles reach the stationary erodible bed, they collide with and mobilize initially stationary particles. These mobilized particles, once energized, become part of the energized shearing collisional flow and subsequently mobilize lower, initially stationary particle in the bed. An apparent non-material boundary between moving and stationary particles descends for some time, depending on the experimental conditions (discussed shortly). Then, the process reverses. The bottom-most moving particles slow and stop due to “drag” forces from the particles below them and insufficient mobilizing interactions from the particles above. Then, the particles slightly higher in the bed slow to a stop and so on, until the non-material boundary between moving and stationary particles comes to a rest at the top of the bed. Over the course of an experiment, the bed may increase in height and mass, associated with deposition of some or all of the initial debris flow on and in the bed; the bed height may be lower associated with removal of some of the bed material; or, the bed surface may return to its initial height or mass if no net material was removed from or deposited into the bed.

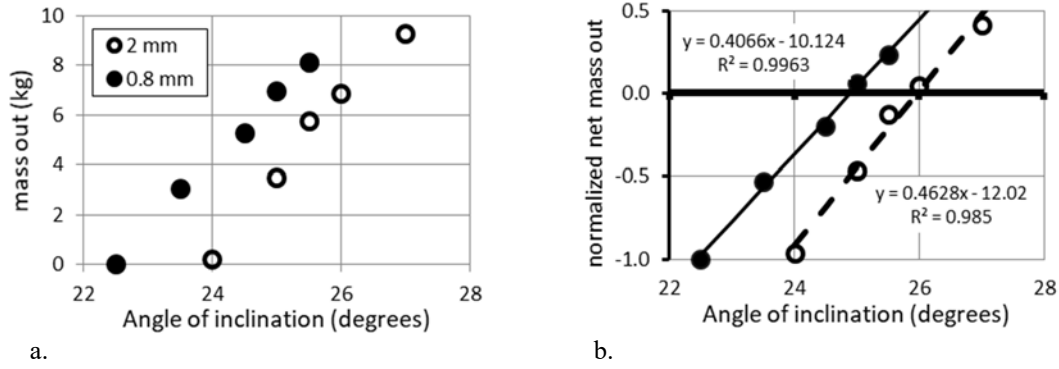


Figure 2: Net eroded mass as a function of bed inclination, ϕ . (a) total mass discharged from the system, m_{out} (b) normalized net mass out, $\tilde{m}_e \equiv (m_{out} - m_{initial})/m_{initial}$. The lines represent linearized least squares fit lines, Eqn. 1: $\tilde{m}_{e,fit} = (\Delta m/\Delta\phi)_{fit} \times (\phi_{fit} - \phi_n)$.

During flow, we monitor the flow, entrainment, and deposition dynamics primarily using one high speed camera, though a second camera catches a wider view and qualitative details over the duration of the experiment. After flow ceases, we weigh the particle that exited the flume during the experiment to calculate a net mass eroded from the bed, and we analysed the digital images to measure the local quasi-instantaneous entrainment rate.

3. Results

3.1. Summary of Experiments

We conducted results for two different sets of experiments. For the first set we performed what we call “uniform particle experiments,” where all particles (in the initial debris flow and in the bed) were the same. We plot the mass that exited the flume (m_{out}) and the normalized net mass eroded ($\tilde{m}_e \equiv (m_{out} - m_{initial})/m_{initial}$), where $m_{initial}$ is the initial debris flow mass, as a function of each inclination angle in Fig. 2(a) and Fig. 2(b), respectively. Table 1 also contains the parameters of the linearized least squares fit shown in Fig. 2(b):

$$\tilde{m}_{e,fit} = \frac{\Delta\tilde{m}_{e,fit}}{\Delta\phi} \times (\phi_{fit} - \phi_n) \quad (1)$$

In this equation, $\Delta\tilde{m}_{e,fit}/\Delta\phi$ and ϕ_n are fit parameters, as we discuss in section 4.

Table 1. Particle properties, input parameters and fit parameters for uniform particle experiments

ρ (kg/m ³)	d (mm)	m_{init} (kg)	m_{bed} (kg)	ϕ (deg)	ϕ_n (deg)	$\Delta\tilde{m}_{e,fit}/\Delta\phi$	R^2	\sqrt{var}
4100	0.8	6.6	17.1	22.5, 23.5, 24.5, 25, 25.5	24.9	0.41	0.996	0.027
4100	2	6.6	17.1	24, 25, 25.5, 26, 27	26.0	0.46	0.985	0.057

In table 2, we present the inputs for our two sets of “mixture erosion experiments”; here, the bed was composed of zirconium silicate of one size (d_b). For these, we varied the percentage of finer and coarser particles in the initial debris flow ($d_{init,f}$ and $d_{init,c}$, respectively). For the coarse bed ($d_b \approx 2.0$ mm), we performed the experiments at the fitted angle for which we found no net erosion for the uniform particle experiments ($\phi \approx \phi_n = 26.0^\circ$), as we discuss in more detail in Section 4. The finer particle bed ($d_b \approx 0.8$ mm) was not stable under the same conditions, so we performed the experiments using a somewhat lower angle than that at which we achieved stability ($\phi = 23.5^\circ < 24.9^\circ = \phi_n$). For the mixture erosion experiments, we plot the dimensionless (total net) erosion, $E_d = m_e/m_{init} = (m_{out} - m_{init})/m_{init}$, vs. percentage of small particles in the initial debris flow in Fig. 3.

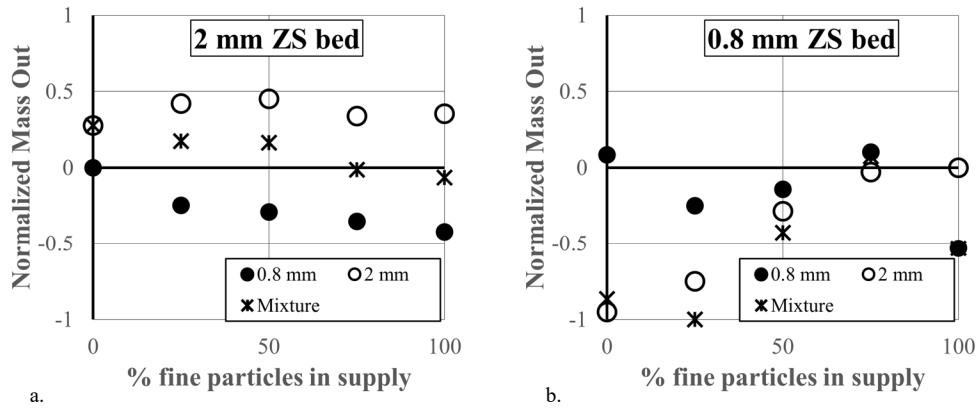


Figure 3 Dimensionless net mass out for each component and mixture $E_{d,i} = m_{e,i}/m_{init}$ (i represents one of the components or the mixture) as a function of concentration of the fine particles in the supply.

Table 2 Input parameters for mixture erosion experiments

Experiment	d_b (mm)	$d_{s,c}$ (mm)	$d_{s,f}$ (mm)	ϕ (deg)	% fine particles by mass in initial debris flow (supply)
0.8 mm ZS bed	0.8	2	0.8	23.5	0, 25, 50, 75, 100
2 mm ZX bed	2	2	0.8	26	0, 25, 50, 75, 100

For one set of our mixture erosion experiments, we performed digital image analysis. We located and tracked nearly all particles in all images taken during an experiment (Fig. 4a). Then we tracked the particles from one image to the next and calculated an average velocity profile (Fig. 4b). From this, we calculated the location of the interface between moving and quasi-stationary particles, i.e., the bed material “entrainment height.” (Fig. 4c). The derivative of this quantity (rate change of entrainment height), shown in Fig. 4d, is a quasi-instantaneous entrainment rate.

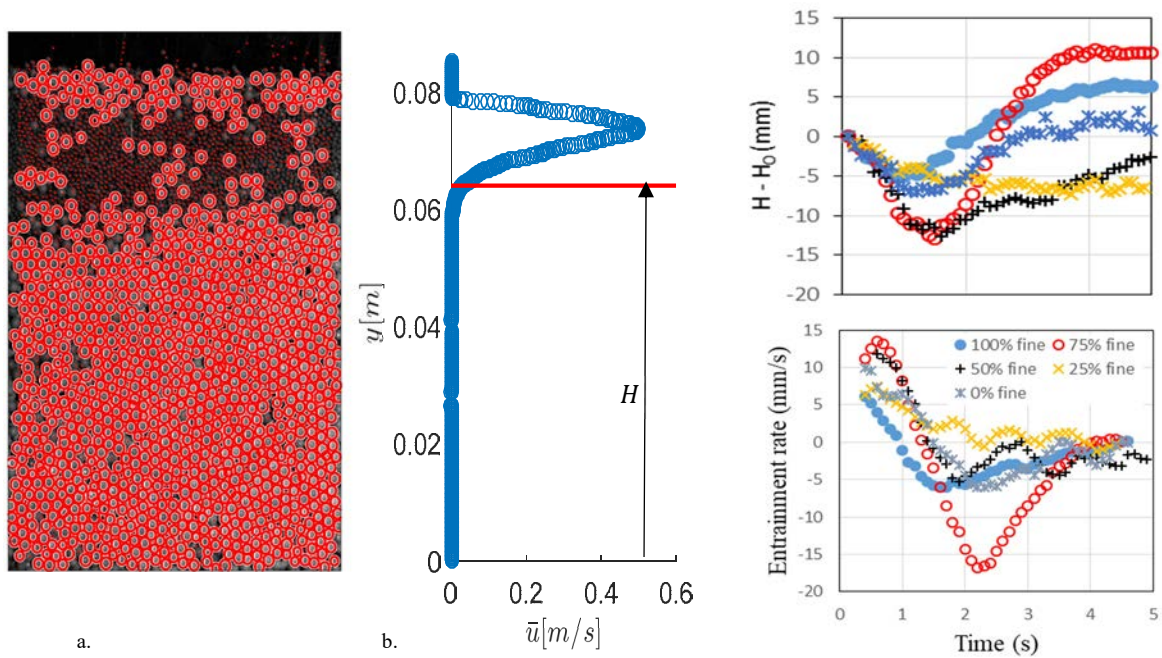


Figure 4 Image analysis results of the experiments for the coarse bed ($d_b \approx 2.0$ mm). (a) illustrates that the fine and coarse particles are detected separately, (b) shows the bulk velocity profile of the flow at an instantaneous time, (c) shows the time series the entrainment height, H , (top) and the entrainment rate (bottom). H_0 is the entrainment height at the initial time.

4. Discussion

The results from our uniform particle experiments presented in Figure 2, i.e., the net erosion, m_e , versus flume inclination angle, ϕ , for each system, show that the total net erosion increases linearly with ϕ , similar to that we found for particles of different materials. The linear relationship between increase in inclination (i.e., slope) angle and erosion highlights the significance of the slope of the debris flow path in determining erosion and deposition patterns [Conway et al. 2010]. We define the fit parameter ϕ_n as the neutral angle for a particular set of particles. This is the fitted value for the flume inclination angle at which erosion $\tilde{m}_e \propto (m_{out} - m_{initial}) = 0$, analogous to the equilibrium angle discussed in Egashira et al. [2001] and Papa et al. [2004]. The fitted slopes of our linear least squares fits, $(\Delta\tilde{m}_{e,fit}/\Delta\phi)$ represents a measure of the sensitivity of the erosion to the deviation of the angle of inclination from the neutral angle. We suspect the variability of this slope from one system to the next is due to a variability of relative roughness of the beads, another surface property, or a relative asphericity of the particles. Although investigating this is beyond the scope of this paper, it is likely important in the context of natural particles that differ more significantly in shape and surface properties and is the topic of future work.

The results from our mixture erosion experiments presented in Figure 3, i.e., $E_{d,i} = (m_{out,i} - m_{init,i})/m_{init}$ vs. percent fine particles, lends more intuition. For the 2 mm ZS bed, $E_{d,mix}$ decreases with increasing fraction of fine particles in the initial debris flow, or supply. This is similar to results we reported previously for other materials. We hypothesize that this is due to the increasing effect of the impact of large particles with their size, increasing their capability to dislodge other particles. In contrast, for our 0.8 mm ZS bed we report here, we note that the coarse particles have a higher value of ϕ_n than the fine particles. We hypothesize that a bulk effect drives this, related to the deposition of the coarse particles on the bed inclined lower than its own ϕ_n . We note that the results for the individual particle sizes varies a bit more. One might expect that the normalized net erosion of one component should be proportional to its representation in the initial flow. However, for the 2 mm ZS bed experiments, $E_{d,f}$ decreases with increase of fine particles, while the normalized net output of the coarse particles $E_{d,c}$ is relatively flat. In the case of the 0.8 mm ZS bed experiments, the normalized net output of the fine particles $E_{d,f}$ increases slightly overall, while $E_{d,c}$ actually *increases* with decreasing representation of coarse particles in the initial debris flow. We suspect that in the case of the erosion behavior of the individual components, complex interparticle interactions including segregation, and disparate momentum and energy exchange may play a role. We believe these details are important in predicting the overall evolution of a debris flow and its deposit and are currently investigating this with a wider variety of mixtures and with particle tracking of the dynamics during the flow. From Fig. 4c we see that the instantaneous entrainment details reveal that intuition we develop from our average entrainment rates do not always provide helpful insights for instantaneous entrainment rates. For example, the case of the highest entrainment rates at a particular time is the case of 75% fine particles, while the net total erosion in this case is among the smallest. More analysis is needed to understand how the instantaneous erosion rates may be related to the net erosion that can be more easily measured in the field.

5. Summary and Future Directions

In this work we investigated the effect of changing the fraction of large particles in a bimodal grain size distribution in an initial debris flow on the erosion of the bed over which it flows. For our systems we found:

- The dependence of the net bed material eroded on the composition in the flow strongly depends on the composition of the bed: (1) When the neutral angle of the bed material is less than that of the initial debris flow, increasing the percentage of larger particles in the bed increases the net erosion of the bed, and (2) When the neutral angle of the bed material is greater than that of the initial debris flow, increasing the percentage of larger particles in the bed appears to have a less systematic effect on the net erosion.
- We hypothesize, based on our average results, that the relationship between coarse particle fraction of the debris flow and bed material erosion is influenced by competing effects at the bulk scale and at the particle scale, including a particle-scale collisional effect on net erosion.
- Instantaneous erosion rates, which determine other dynamics of debris flows, indicate complex dynamics that may include relative segregation that are not accounted for in our current relatively simplistic understanding.

The experiments presented in this paper provide a foundation for the work needed to understand the complexity of the particle size dependence of erosion by debris flows. However, there are still many unanswered questions regarding our mixture-dependent erosion results, including those involving: (1) the presence of moisture; and (2) changing grain size distribution in a more continuous distribution of particle sizes.

Acknowledgements

We gratefully acknowledge the support of this research by the National Science Foundation under the grant EAR-1451957 “Entrainment and Deposition of Surface Material by Particle-Laden Flows: From Laboratory to the Hillslope” and by the US Department of State through the Institute for International Education under the grant “Influences on Natural Resources and Hazard Mitigation under a Changing Climate”. The authors also thank Delaney Kolb for help with the experiments.

References

- Berger, C., McArdell, B.W. and Schlunegger, F., 2011, Direct measurement of channel erosion by debris flows, Illgraben, Switzerland. *Journal of Geophysical Research: Earth Surface*, 116(F1), doi: 10.1029/2010JF001722
- Breien, H., De Blasio, F.V., Elverhøi, A. and Høeg, K., 2008, Erosion and morphology of a debris flow caused by a glacial lake outburst flood, Western Norway. *Landslides*, 5(3), pp.271-280.
- Coe, J.A., Kinner, D.A. and Godt, J.W., 2008, Initiation conditions for debris flows generated by runoff at Chalk Cliffs, central Colorado. *Geomorphology*, 96(3-4), pp.270-297, doi: 10.1016/j.geomorph.2007.03.017
- Conway, S.J., Decaulne, A., Balme, M.R., Murray, J.B. and Towner, M.C., 2010, A new approach to estimating hazard posed by debris flows in the Westfjords of Iceland. *Geomorphology*, 114(4), pp.556-572, doi: 10.1016/j.geomorph.2009.08.015
- Egashira, S., Honda, N. and Itoh, T., 2001, Experimental study on the entrainment of bed material into debris flow. *Physics and Chemistry of the Earth, Part C: Solar, Terrestrial & Planetary Science*, 26(9), pp.645-650, doi: 10.1016/S1464-1917(01)00062-9
- Hungr, O., McDougall, S. and Bovis, M., 2005, Entrainment of material by debris flows. In *Debris-flow hazards and related phenomena* (pp. 135-158). Springer, Berlin, Heidelberg.
- Iverson, R.M., 1997, The physics of debris flows. *Reviews of geophysics*, 35(3), pp.245-296, doi: 10.1029/97RG00426
- Iverson, R.M., Reid, M.E., Iverson, N.R., LaHusen, R.G., Logan, M., Mann, J.E. and Brien, D.L., 2000, Acute sensitivity of landslide rates to initial soil porosity. *science*, 290(5491), pp.513-516, doi: 10.1126/science.290.5491.513
- Iverson, R. M., Logan, M., LaHusen, R. G., & Berti, M. (2010). The perfect debris flow? Aggregated results from 28 large - scale experiments. *Journal of Geophysical Research: Earth Surface*, 115(F3).
- Iverson, R.M., Reid, M.E., Logan, M., LaHusen, R.G., Godt, J.W. and Griswold, J.P., 2011, Positive feedback and momentum growth during debris-flow entrainment of wet bed sediment. *Nature Geoscience*, 4(2), p.116.
- Mangeney, A., Roche, O., Hungr, O., Mangold, N., Faccanoni, G. and Lucas, A., 2010, Erosion and mobility in granular collapse over sloping beds. *Journal of Geophysical Research: Earth Surface*, 115(F3), doi: 10.1029/2009JF001462
- McCoy, S.W., Kean, J.W., Coe, J.A., Tucker, G.E., Staley, D.M. and Wasklewicz, T.A., 2012, Sediment entrainment by debris flows: In situ measurements from the headwaters of a steep catchment. *Journal of Geophysical Research: Earth Surface*, 117(F3), doi: 10.1029/2011JF002278
- Meyer, N.K., Dyrddal, A.V., Frauenfelder, R., Etzelmuller, B. and Nadim, F., 2012, Hydrometeorological threshold conditions for debris flow initiation in Norway, doi: 10.5194/nhess-12-3059-2012
- Papa, M., Egashira, S. and Itoh, T., 2004, Critical conditions of bed sediment entrainment due to debris flow. *Natural Hazards and Earth System Sciences*, 4(3), pp.469-474, doi: 10.5194/nhess-4-469-2004.
- Reid, M.E., Iverson, R.M., Logan, M.A.T.T.H.E.W., LaHusen, R.G., Godt, J.W. and Griswold, J.P., 2011, June. Entrainment of bed sediment by debris flows: results from large-scale experiments. In *Fifth International Conference on Debris-flow Hazards Mitigation, Mechanics, Prediction and Assessment*, edited by: R. Genevois, Hamilton, DL, and Prestinzi, A., Casa Editrice Universita La Sapienza, Rome (pp. 367-374).
- Schuerch, P., Densmore, A.L., McArdell, B.W. and Molnar, P., 2006, The influence of landsliding on sediment supply and channel change in a steep mountain catchment. *Geomorphology*, 78(3-4), pp.222-235, doi: 10.1016/j.geomorph.2006.01.025
- Stock, J.D. and Dietrich, W.E., 2006, Erosion of steepland valleys by debris flows. *Geological Society of America Bulletin*, 118(9-10), pp.1125-1148, doi: 10.1130/B25902.1.

How does particle-size segregation affect the fluidity of multi-granular debris flows?

Norifumi Hotta^{a,*}, Tomoyuki Iwata^b, Takuro Suzuki^c

^a *The University of Tokyo, Japan, 1-1-1 Yayoi, Bunkyo-ku, Tokyo 113-8657, Japan*

^b *Chiba Prefectural Government Office, 1-1 Ichiba-cho, Chuo-ku, Chiba City, Chiba 260-8667, Japan*

^c *Forestry and Forest Products Research Institute, 1 Matsunosato, Tsukuba, Ibaraki 305-8687, Japan*

Abstract

It is essential to consider the fluidity of a debris-flow front when calculating its impact. Here, we flume-tested monogranular and bigranular debris flows, and compared the results to those of numerical simulations. We used sand particles with diameters of 0.29 and 0.14 cm at two mixing ratios, of 50% and 50% (5:5), and 30% and 70% (3:7), respectively. Particle segregation was recorded using a high-speed video camera. We evaluated the fronts of debris flows at 0.5-s intervals. We then numerically simulated one-dimensional debris flows under the same conditions, and we used the mean particle diameter when simulating mixed-diameter flows. For monogranular debris flows, the experimental and simulated results were in good agreement in terms of flow depth, front velocity, and flux, but the bigranular debris flows were not well-simulated; the simulated flow depth was less than that found experimentally, and the front velocity and flux were greater. The differences may be attributable to the fact that the dominant shear stress was caused by the concentration of smaller sediment particles in the lower flow layers; such inverse gradations were detected in the debris flow bodies. In this situation, most shear stress is supported by smaller particles in the lower layers; the debris-flow characteristics become similar to those of monogranular flows. Consequently, the calculated front velocities were underestimated; particle segregation at the front of bigranular debris flows did not affect fluidity either initially or over time.

Keywords: Flume test; Multi-granular debris flow; Numerical simulation; Particle-size segregation

1. Introduction

Stony debris flows have been modeled by reference to internal stresses caused by interactions (such as collision and friction) between particles and the viscosity of pore fluid (Egashira et al., 1997; Takahashi, 2007). Numerical simulations have been used to reproduce and predict debris-flow behaviors (Nakagawa and Takahashi, 1997; Osti and Egashira, 2009). In both laboratory models and numerical simulations, a representative (uniform) particle size is usually assumed, although real-world debris flows include grains of many different sizes associated with inverse gradations and accumulation of large boulders at debris-flow fronts (Stock and Dietrich, 2006; Suwa et al., 2009).

Particle size greatly affects debris-flow fluidity; larger particles impart higher flow resistance (Takahashi, 2007). Hence, the fluidity of the debris-flow front, which is important in terms of impact forces, is affected by both particle size and particle admixing. Accumulation of boulders at the front causes the flow characteristics of that front to differ from those of the main body; these cannot be reflected in numerical simulations employing particles of uniform size.

Here, we flume-tested monogranular and bigranular debris flows and compared the results to those of numerical simulations, to determine the effects of particle segregation on the debris-flow front.

* Corresponding author e-mail address: hotta.norifumi@fr.a.u-tokyo.ac.jp

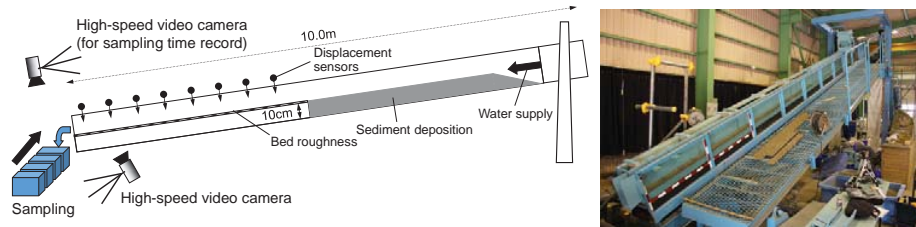


Fig. 1. The experimental setup.

2. Materials and Methods

2.1. Flume test

A channel of variable slope (10 m long and 10 cm wide) with a left-side glass sidewall was used for all experiments (Fig 1). The slope angle was set to 15°. The upper 3.5 m of the channel was filled with sand particles to a depth of 10 cm and connected to a lower stream 10 cm in height; this was a rigid bed 5 m in length to the surface, to which 2.9-mm-diameter sand particles were glued to impart roughness. To prevent overflow, the sand was watered to near-saturation immediately before each test. A steady flow of water (2,000 mL/s) was supplied from the upper end of the channel to generate debris flow by eroding the deposited sand.

Silica sands 0.29- and 0.14-cm in diameter were used; the mixing ratios were 50% and 50% (5:5), and 30% and 70% (3:7) (Table 1). Particle-size distribution affects the flow characteristics of debris flow in several ways. For example, fine sediment and its liquefaction change the fluidity (Nishiguchi et al., 2012; Hotta et al., 2013). In this study, we focused on particle segregation in stony debris flows. Sand particles of 0.29 and 0.14 cm were selected because they have been validated to behave as representative stony debris flows under this experimental setting (Hotta and Miyamoto, 2008; Hotta, 2012). Monogranular debris flows using each particle size, and bi-dispersed mixtures would simplify and clarify the particle segregation process.

Eight ultrasonic displacement sensors (E4C; Omron, Kyoto, Japan) were placed above the channel at 0.5-m intervals from 0.5–4.5 m distant to the downstream end; these monitored flow depth and timing. The temporal data were used to calculate front velocities. A high-speed video camera (EX-F1; Casio, Tokyo, Japan) was placed 0.5 m from the downstream end of the flow and recorded the debris flow from the side at 600 frames/s; we used the resulting images to evaluate the vertical velocity profiles and the locations of the larger (2.9 mm-diameter) particles by tracking the particles through the sequence of images. Five debris-flow samples from the front edges were collected at ca. 0.5 s intervals into a container with five separate rooms (Fig. 1), and one sample was also obtained from the main body at the lower end of the channel. We measured sediment concentrations and particle segregation.

Table 1. The silica sands used in the flume test.

Mixing ratio (0.29 cm : 0.14 cm)	Mean diameter (cm)
10 : 0	0.29
5 : 5	0.22
3 : 7	0.19
0 : 10	0.14

2.2. Numerical simulation

We performed a one-dimensional numerical simulation of debris flow. When modeling debris flows containing particles of two different diameters, we used the mean diameter (Table 1). The equations included a continuity equation for the debris flow, a continuity equation for the sediment, and a momentum equation:

$$\frac{\partial h}{\partial t} + \frac{\partial M}{\partial x} = E \quad (1)$$

$$\frac{\partial(\bar{c}h)}{\partial t} + \frac{\partial(c_t M)}{\partial x} = E c_s \quad (2)$$

$$\frac{\partial M}{\partial t} + \beta \frac{\partial(uM)}{\partial x} = -gh \frac{\partial H}{\partial x} - \frac{\tau_0}{\rho_m} \quad (3)$$

where h is the flow depth, M is the discharge rate per unit width, E is the bed entrainment rate, \bar{c} is the mean cross-sectional sediment concentration, c_t is the transported sediment concentration, c_s is the sediment concentration deposited in the channel, β is a compensation coefficient for momentum, u is the cross-sectional average velocity, g is the acceleration attributable to gravity, H is the elevation of the flow surface ($H = h + z_b$, where z_b is the bed elevation), τ_0 is the shear stress at the bed, and ρ_m is the density of debris flow. \bar{c} and c_t are identical when assuming a uniform profile of sediment concentration. According to our measurements, c_s was 0.60. For τ_0 , Itoh and Miyamoto (2002) developed constitutive equations, as follows:

$$\tau_0 = \tau_{0y} + \rho f_b u^2 \quad (4)$$

$$\tau_{0y} = \left(\frac{\bar{c}}{c_s} \right)^{\frac{1}{5}} (\sigma - \rho) \bar{c} g h \cos \theta \tan \phi_s \quad (5)$$

$$f_b = \frac{25}{4} \{K_g + K_f\} \left(\frac{h}{d} \right)^{-2} \quad (6)$$

$$K_g = k_g \frac{\sigma}{\rho} (1 - e^2) \bar{c}^{\frac{1}{3}} \quad (7)$$

$$K_f = k_f \frac{(1 - \bar{c})^{\frac{5}{2}}}{\bar{c}^{\frac{2}{3}}} \quad (8)$$

where ρ is the density of water, σ is the density of the sediment particles (2.64), θ is the bed slope angle, ϕ_s is the internal friction angle of the sediment particles (34.0°), d is the mean diameter of the sediment particles, k_g is an experimental constant that was reported to be 0.0828 by Miyamoto (1985), according to Itoh et al. (1999) and, e , the coefficient of restitution of sediment particles, is equal to 0.85. k_f is a constant reflecting the interstitial space, which Egashira et al. (1988) evaluated as 0.16. Eqs (1)–(3) can be closed using an entrainment rate equation for E . We used the equation of Egashira et al. (1988):

$$\tan \theta_e = \frac{\bar{c}(\sigma/\rho - 1)}{\bar{c}(\sigma/\rho - 1) + 1} \tan \phi_s \quad (9)$$

$$E = u \tan(\theta - \theta_e) \quad (10)$$

where θ_e is the equilibrium bed slope, which can be calculated based on a given sediment concentration (Takahashi,

1978).

3. Results

3.1. Flow depth and discharge

The experimental and simulated results were in close agreement in terms of the depths of monogranular, but not bigranular, debris flows (Fig 2). The experimental depths of bigranular flows were very similar to those predicted for monogranular flows of the smaller particles (diameter 0.14 cm) regardless of the mixing ratio (5:5 or 3:7 of 0.22- and 0.19-cm-diameter particles; Fig 2bc, respectively). Eqs (4) and (6) show that the flow depth differs by particle size, thus affecting flow resistance. However, the discharges did not differ greatly; the amounts of water supplied were identical. Eq (10), the entrainment rate equation, governing the sediment concentration is implicitly incorporating particle size (Hotta et al., 2015). Experimentally, the discharges of monogranular debris flows of 0.29- and 0.14-cm-diameter particles differed slightly, but calculations did not reveal any distinct difference (Fig 3a). The calculated and experimental data for the 0.14-cm-diameter-particle and mixed-particle debris-flow fronts disagreed (Fig 3b). The discharges were similar at particle mixing ratios of 5:5 and 3:7, as were the flow depths.

3.2. Velocity

The experimental and calculated monogranular debris-flow frontal velocities (both initially and over time) were in good agreement (Fig 4a). However, the experimental frontal velocity of bigranular debris flows were initially that of the 0.29-cm-diameter monogranular flow, and later became that of a debris flow containing particles of diameter equal to the mean of 0.14 and 0.29 cm, regardless of the mixing ratio (Fig 4bc). Fig 5 shows the experimental vertical distributions of particle velocities within bigranular debris flows. The velocities of the 0.14- and 0.29-cm-diameter particles did not differ at the same depth. The velocity profile indicated that the inclination was steeper in the flow body (7.9 and 6.9 s after the front had passed) than at the front (photos taken at 0.3 s; Fig 5a and 5b, respectively).

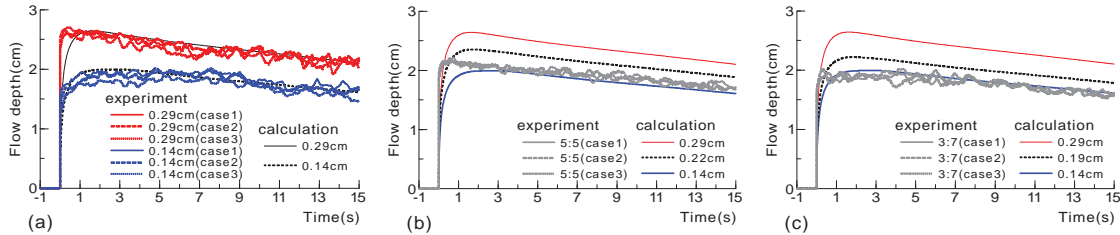


Fig. 2. Debris-flow depths over time of (a) monogranular flows, and (b) and (c), bigranular flows at particle mixing ratios (larger:smaller) of 5:5 and 3:7 respectively, at a point 0.5 m from the downstream end. The experimental flow depths are smoothed using a 0.4-s moving average.

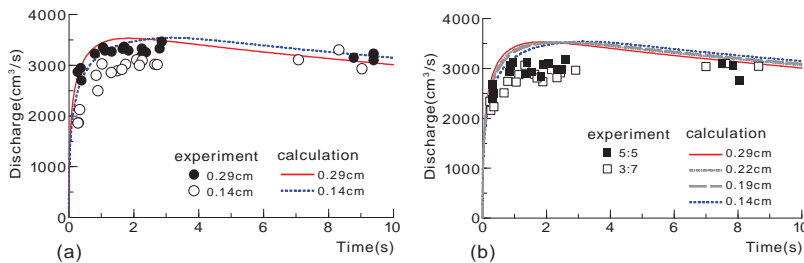


Fig. 3. Debris-flow discharge over time of (a) monogranular flows and (b) bigranular flows.

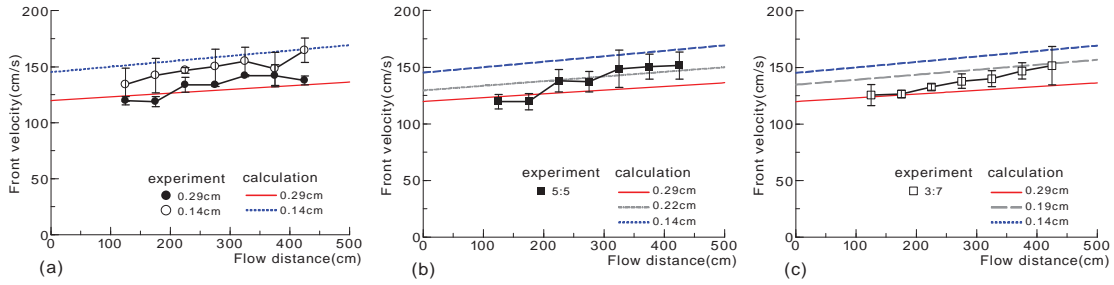


Fig. 4. Debris-flow frontal velocities over time of (a) monogranular flows, and (b) and (c), bigranular flows at particle mixing ratios (larger:smaller) of 5:5 and 3:7 respectively.

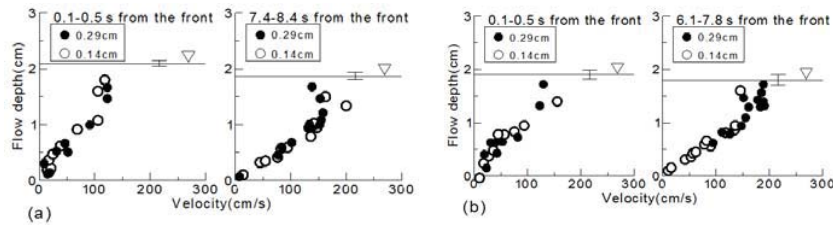


Fig. 5. Comparison between vertical velocity distributions of the front (left) and main body (right) of the debris flow at particle-mixing ratios (larger:smaller) of (a) 5:5 and (b) 3:7. The solid line indicates the average flow depth with error bar of the standard deviation.

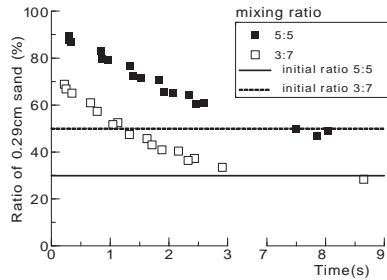


Fig. 6. The experimental particle mixing ratios of the fronts and main bodies of debris flows.

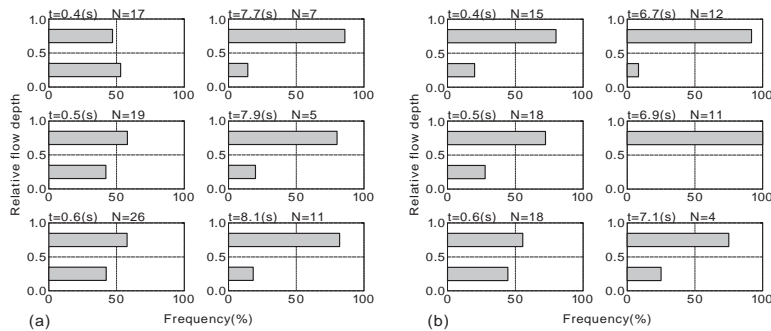


Fig. 7. Frequency distributions of 0.29 cm-diameter particles in the upper and lower layers of the experimental debris flows with particle mixing ratios (larger:smaller) of (a) 5:5 and (b) 3:7. N indicates the number of 0.29 cm-diameter particles in each image taken using the high-speed video camera. The relative flow depth was normalized by the surface level.

3.3. Particle segregation

Experimentally, the larger particles (0.29 cm) accumulated at the front (Fig 6). The extent of accumulation clearly differed by mixing ratio; the flow body retained the initial mixing ratio but inverse grading was apparent. Fig 7 compares large particle accumulation in the upper flow between the front and the main body. The extent of inverse grading was more significant in the main body; small particles thus predominated in the most inclined section of the velocity profile (Fig 5b).

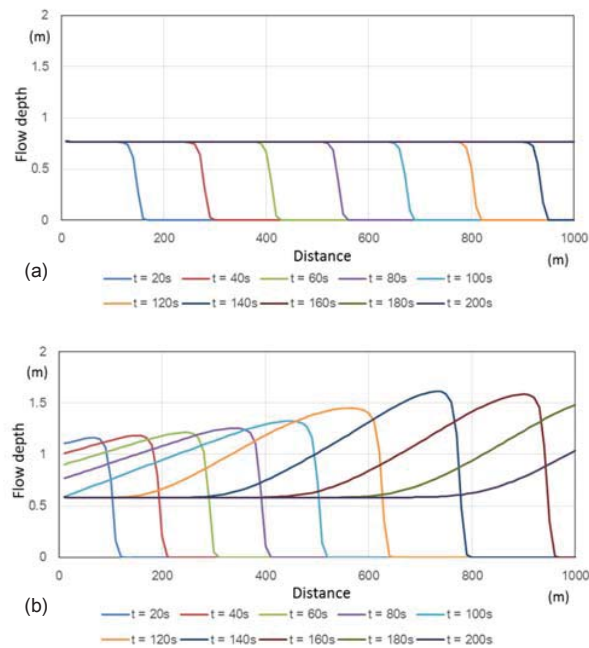


Fig. 8. Simulated profiles of the surges for (a) monogranular and (b) bigranular debris flows. In (b), the mean particle diameter was defined to decrease at the front of the body to simulate particle segregation.

4. Discussion and Conclusion

As shown in Figs 2 and 4, the behavior of bigranular debris flows could not be modeled using the mean particle diameter, whereas the behavior of monogranular flows could. This may be attributable to particle segregation; the uneven distribution of particles renders it inappropriate to use the mean particle diameter when seeking to model fluidity. Particle segregation is initially caused by inverse grading (Fig. 7), as shown in previous reports on bi-dispersed dry granular flow (Goujon et al., 2007) and saturated flow (Yamano and Daido, 1985). Thus, small particles concentrate in the lower layer, characterized by a steeper velocity profile (Fig 5b), suggesting that most shear stress is borne by small particles. This is consistent with the fact that the behavior of bi-granular flows corresponds to that predicted for flows with small particles only, regardless of the mixing ratio, after the flow has developed sufficiently (Fig 2bc). Similar behavior was pointed out by Linares-Guerrero et al. (2007) through numerical simulation, who used the discrete element method to model bi-dispersed dry granular flow.

On the other hand, at the start of the debris flow, when differently sized particles had not yet segregated, the fluidity of bigranular flows was similar to that of a monogranular flow of 2.9-cm-diameter particles (Fig 4bc). Large dispersed particles within the flow body may dominate the internal stress environment, but, as the flow descended, the flow velocity changed to that of a flow of smaller-sized particles (Fig 4bc). Thus, in reality, debris-flow motion, especially that of the front, is not adequately described by numerical simulations featuring a uniformly sized particle.

In a further example, we compare the simulated profiles of the surges for monogranular and bigranular debris flows in Fig 8. The calculation employs the same model as used in Section 2.2 but was applied at a real scale so that we

could clarify the different performances after simulating the distances descended by mono- and bigranular debris flows. In Fig 8b, the frontal accumulation of large boulders is modeled by gradually decreasing the particle size; the larger particles accumulate at the front and the smaller ones accumulate in the main body, and the average particle size is that of a monogranular debris flow (Fig 8a). The monogranular flow exhibits steady motion; the velocity of the mixed-particle flow is lower, in contrast to the observed results (Fig. 4). The flow depth of the bigranular flow increases as the main body catches up to the front, due to the greater velocity of the main body, which consists of smaller particles. This result conflicts with that of the experiment (Fig. 2). Thus, the results of the calculations based on a basic particle-segregation model that simply incorporates the transition of the mean particle size differ markedly from our experimental results.

Particle segregation in a debris flow is not simple. Debris flow fluidity may be controlled by local conditions, such as the vertical distribution of particle sizes, resulting in an uneven structure of internal stresses. Further understanding of particle segregation is needed for better assessment of on-site debris flows that contain a variety of particle sizes.

References

- Egashira, S., Ashida, K., and Sasaki, H., 1988, Mechanics of debris flow in open channel, *in* Proceedings, Japanese Conference on Hydraulics, Japan Society of Civil Engineers, v. 32, p. 485–490. (in Japanese with English summary)
- Egashira, S., Miyamoto, K., and Itoh, T., 1997, Constitutive equations of debris flow and their applicability, *in* Proceedings, International Conference on Debris-Flow Hazards Mitigation, 1st, San Francisco, p. 340–349.
- Goujon, C., Dalloz-Dubrujeaud, B., and Thomas, N., 2007, Bidisperse granular avalanches on inclined planes: A rich variety of behaviors: *The European Physical Journal E* 23, p. 199–215, doi:10.1140/epje/i2006-10175-0.
- Hotta, N., and Miyamoto, K., 2008, Phase classification of laboratory debris flows over a rigid bed based on the relative flow depth and friction coefficients: *International Journal of Erosion Control Engineering*, v. 1, p. 54–61, doi:10.13101/ijece.1.54.
- Hotta, N., 2012, Basal interstitial water pressure in laboratory debris flows over a rigid bed in an open channel: *Natural Hazards and Earth System Sciences*, v. 12, p. 2499–2505, doi:10.5194/nhess-12-2499-2012.
- Hotta, N., Kaneko, T., Iwata, T., and Nishimoto H., 2013, Influence of fine sediment on the fluidity of debris flows: *Journal of Mountain Science*, v. 10, p. 233–238, doi:10.1007/s11629-013-2522-y.
- Hotta, N., Tsunetaka, H., and Suzuki, T., 2015, Interaction between topographic conditions and entrainment rate in numerical simulations of debris flow: *Journal of Mountain Science*, v. 12, p. 1383–1394, doi:10.1007/s11629-014-3352-2.
- Itoh, T., Miyamoto, K., 2002, Study on one dimensional numerical simulation of debris flow, *in* Proceedings, Japanese Conference on Hydraulics, Japan Society of Civil Engineers, v. 46, p. 671–676. (in Japanese with English summary)
- Itoh, T., Egashira, S., Miyamoto, K., Takeuchi, T., 1999, Transition of debris flows over rigid beds to over erodible beds, *in* Proceedings, Japanese Conference on Hydraulics, Japan Society of Civil Engineers, v. 43, p. 635–640. (in Japanese with English summary)
- Linares-Guerrero, E., Goujon, C., and Zenit, R., 2007, Increased mobility of bidisperse granular avalanches: *Journal of Fluid Mechanics*, v. 593, p. 475–504, doi:10.1017/S0022112007008932.
- Mymaoto, K., 1985, Study on the grain flows in Newtonian fluid [Ph.D. thesis]: Ritsumeikan University, 155 p. (in Japanese)
- Nakagawa, H., and Takahashi, T., 1997, Estimation of a debris flow hydrograph and hazard area, *in* Proceedings, International Conference on Debris-Flow Hazards Mitigation, 1st, San Francisco, p 64–73.
- Nishiguchi, Y., Uchida, T., Takezawa, N., Ishizuka, T., and Mizuyama, T., 2012, Runout characteristics and grain size distribution of large-scale debris flows triggered by deep catastrophic landslides: *International Journal of Erosion Control Engineering*, v. 5, p. 16–26, doi: 10.13101/ijece.5.16.
- Osti, R., and Egashira, S., 2008, Method to improve the mitigative effectiveness of a series of check dams against debris flows: *Hydrological Processes*, v. 22, p. 4986–4996, doi: 10.1002/hyp.7118.
- Stock, J. D., and Dietrich, W. E., 2006, Erosion of steepland valleys by debris flows: *Geological Society of America Bulletin*, v. 118, p. 1125–1148, doi:10.1130/B25902.1.
- Suwa, H., Okano, K., and Kanno, T., 2009, Behavior of debris flows monitored on test slopes of Kamikamihorizawa Creek, Mount Yakedake, Japan: *International Journal of Erosion Control Engineering*, v. 2, p. 33–45, doi:10.13101/ijece.2.33.
- Takahashi, T., 1978, Mechanical characteristics of debris flow: *Journal of Hydraulic Division, American Society of Civil Engineering*, v. 104, p. 1153–1169.
- Takashi, T., 2007, *Debris Flow: Mechanics, Prediction and Countermeasures*: Taylor and Francis, Balkema, 448 p.
- Yamano, K., and Daido, A., 1985, The mechanism of granular flow of mixed diameter composed two diameters: *Journal of Japan Society of Civil Engineers*, v. 357, p. 25–34. (in Japanese with English summary)

Valid debris-flow models must avoid hot starts

Richard M. Iverson^{a,*}, David L. George^a

^a*U.S. Geological Survey, 1300 SE Cardinal Ct., Vancouver, WA 98683 USA*

Abstract

Debris-flow experiments and models commonly use “hot-start” initial conditions in which downslope motion begins when a large force imbalance is abruptly imposed. By contrast, initiation of natural debris flows almost invariably results from small perturbations of static force balances that apply to debris masses poised in steep channels or on steep slopes. Models that neglect these static balances may violate physical law. Here we assess how the effects of hot starts are manifested in physical experiments, analytical dam-break models, and numerical models in which frictional resistance is too small to satisfy static force balances in debris-flow source areas. We then outline a numerical modeling framework that avoids use of hot starts. In this framework an initial static force balance is gradually perturbed by increasing pore-fluid pressure that may trigger the onset of debris motion. Subsequent increases in pore-fluid pressure, driven by debris motion, may then reduce the debris frictional strength, leading to high flow mobility.

Keywords: debris flow, numerical model, hot start, initial conditions, dam break, experiments

1. Introduction

Debris flows can begin to move in a variety of ways, but nearly all natural debris flows arise from mechanically balanced initial states in which stationary sediment is poised in steep channels or on steep slopes. The onset of debris-flow motion might entail wholesale landsliding or piecemeal sediment entrainment by running water, but in either case motion of sediment-rich debris begins when a static force balance is slightly perturbed. By contrast, many debris-flow experiments and models use “hot-start” initial conditions in which motion begins when a large force imbalance is abruptly imposed. (The term “hot start” has been used previously to describe tsunami simulations that begin by imposing an instantaneous—thus excessively energetic—uplift of the seafloor (*e.g.*, Grilli *et al.* 2012). We adopt the term here to describe excessively energetic onsets of simulated debris flows.)

One type of hot-start initial condition involves a dam break in which a barrier that impounds debris on a slope is instantaneously or rapidly removed. Instantaneous dam breaks provide important mathematical idealizations because they precisely represent end-member behavior that can be used to test the accuracy of numerical solution techniques (*e.g.*, Mangeney *et al.*, 2000). Rapid—but not instantaneous—dam breaks also serve an important purpose in physical experiments and model testing because they provide a convenient means of creating reproducible debris flows (*e.g.*, Iverson *et al.*, 2010) (Figure 1). On the other hand, use of dam-break initial conditions in simulations of natural debris flows generally involves an unwarranted artifice because it assumes that debris in steeply sloping source areas can remain in place only if held there by an imaginary dam.

An analogous type of hot-start initial condition is used in numerical models that do not explicitly consider a dam but which nevertheless assume that a static debris mass has too little strength to satisfy a static force balance (*e.g.*, Hungr, 1995; Moretti *et al.*, 2015). The modelled debris mass is held in place merely by withholding a computer command, and issuing the command triggers motion of the debris by abruptly imposing a large force imbalance. Like dam-break initial conditions, this type of hot-start initial condition is simple and convenient to use, but it conflicts with evidence from field observations. Moreover, by imposing an instantaneous transition from an equilibrium state to a far-from-equilibrium state without any physical cause, this type of hot-start condition violates physical law.

* Corresponding author e-mail address: riverson@usgs.gov

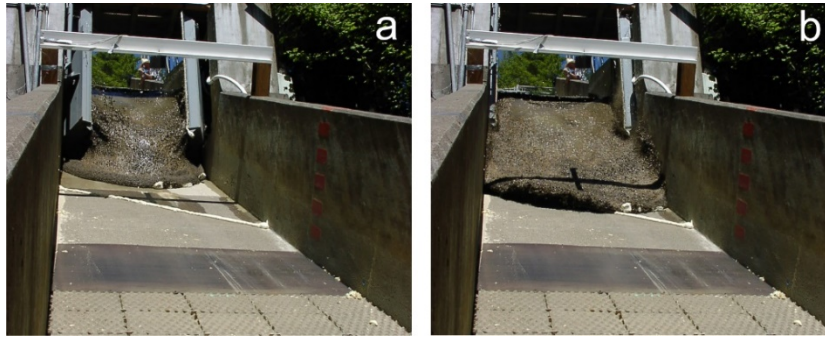


Fig. 1. Sequential photographs of a 10 m³ debris flow discharging through the opening headgate at the U.S. Geological Survey debris-flow flume. (a) photo captured at $t \approx 0.6$ s, and (b) photo captured at $t \approx 0.8$ s, where $t = 0$ denotes the time when the headgate began to open. A shadow visible on the flume bed and debris-flow surface is cast by a crossbar that suspends a laser depth-measurement gauge 2.5 downslope from the headgate.

Some landslide and debris-flow modelers have attempted to rationalize use of hot-start initial conditions by claiming that the physics of motion onset has no consequential effect on debris behavior downslope or downstream (*e.g.*, Aaron *et al.*, 2018). This claim is contradicted not only by qualitative field observations but also by quantitative evidence from physical experiments (*e.g.*, Iverson *et al.*, 1997, 2000) and results of numerical simulations that account for the influence of varying debris porosities on the propensity for debris liquefaction (George and Iverson, 2014; Iverson and George, 2016). Indeed, these studies show that the behavior of debris masses can be extraordinarily sensitive to initial conditions and short-timescale (~ 1 s) dynamics that unfold as downslope motion begins.

In this paper we first examine some implications of hot-start initial conditions and then summarize an alternative modeling approach that avoids hot starts. This approach requires a debris-flow model that uses physical conservation laws, values of material properties, and numerical solution methods that allow statically balanced initial states to persist indefinitely in the absence of force-balance perturbations. A satisfactory model also must account for the effect of external agents such as rainfall in gradually perturbing the static force balance, and for a natural evolution of material strength that occurs as debris begins to move, liquefies, flows downslope, and eventually forms deposits (*e.g.*, Iverson and George, 2014; George and Iverson, 2014).

2. Hot starts in physical experiments

Although hot starts are primarily a property of mathematical models, hot-start initial conditions are also used in physical experiments that involve either dry granular avalanches or wet debris flows suddenly released from behind barriers that impound static material on a slope (*e.g.*, Savage, 1979; Iverson and LaHusen, 1993). These “dam-break” experiments are defensible scientifically because their goal is to abstract and simplify natural phenomena rather than to simulate their full complexity. Nevertheless, a physical dam break can introduce experimental artifacts that must be considered if the purpose of the experiments is to test models that are intended ultimately to explain or simulate the behavior of natural debris flows.

A set of six dam-break debris-flow experiments conducted at the U.S. Geological Survey (USGS) debris-flow flume in June 2016 revealed some important aspects of hot-start flow behavior. In these experiments either 10 m³ or 8 m³ of debris consisting almost entirely of sand and gravel-sized material was initially impounded to a depth of 1.9 m behind a vertical headgate, saturated with water, and then abruptly released on a 31° slope (Figure 1) (Logan *et al.*, 2007, revised 2018; Iverson and Logan, 2017). Opening of the side-by-side doors that formed the steel headgate required ~ 0.8 s and was accompanied by rapid evolution of basal normal stresses, shear stresses, and pore-fluid pressures measured beneath mobilizing debris at locations 2.23 to 2.85 m upslope from the headgate (*e.g.*, Figure 2a and 2b). Although this stress evolution largely mirrored behavior measured in natural, gravity-driven failures of loosely packed wet debris (Iverson *et al.*, 2000), it also showed evidence of experimental artifacts.

One possible artifact resulted from a nearly instantaneous ~ 45 kN force drop that occurred during unlatching of the flume headgate at $t = 0$ s. The abrupt force drop radiated seismic energy into the concrete flume bed and generated conspicuous ~ 10 Hz fluctuations in basal normal stress that persisted until $t \approx 1$ s (*e.g.*, Figure 2a and 2b). These fluctuations may have facilitated the debris liquefaction process, much as cyclic loading can cause liquefaction of saturated soils during earthquakes (*e.g.*, Jefferies and Been, 2016). However, soil liquefaction during earthquakes

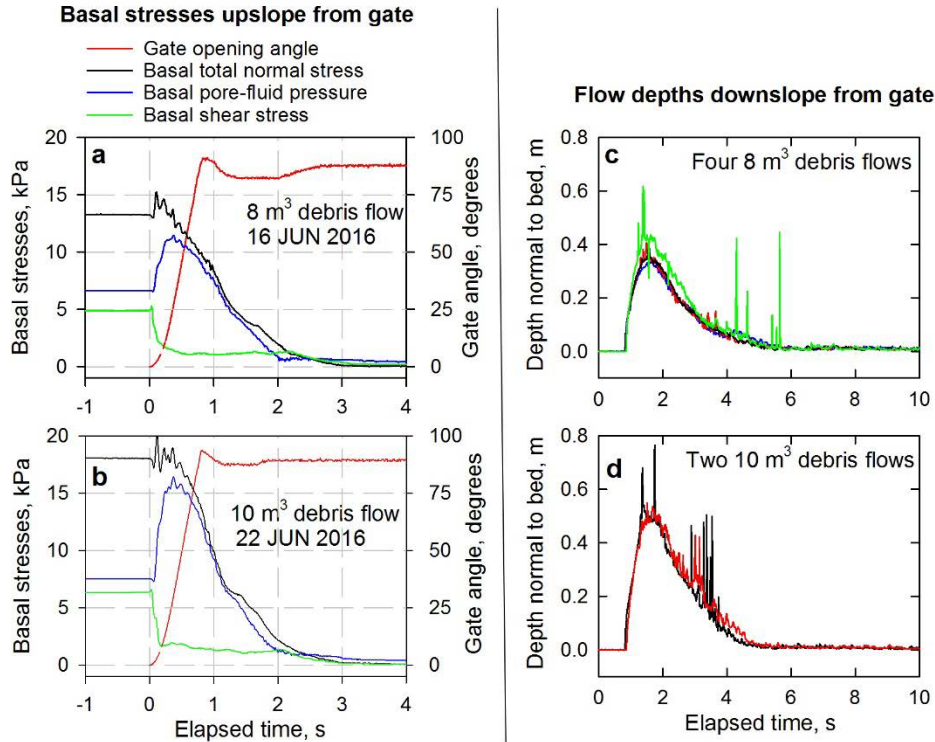


Fig. 2. Graphs of data collected in dam-break debris-flow experiments conducted at the USGS debris-flow flume in June, 2016. (a) and (b) basal stresses measured at locations 2.23 to 2.85 m upslope from the headgate as it opened in two typical experiments. (c) and (d) flow depths measured 2.5 m downslope from the headgate in six experiments. In each graph $t = 0$ denotes the time when the gate began to open.

typically develops over tens of seconds, whereas liquefaction in our experiments was essentially complete within ~ 1 s (as evidenced in Figure 2a and 2b by basal pore pressure becoming nearly equal to the total basal normal stress). Owing in part to this liquefaction, nearly all debris evacuated the area upslope from the headgate within ~ 3 s (Logan *et al.*, 2007, revised 2018). However, we do not know whether similarly rapid liquefaction and debris acceleration would have occurred in the absence of radiation of seismic energy during opening of the headgate.

Despite differences in debris volumes, the six dam-break experiments conducted in June 2016 each produced flow fronts that initially traveled downslope at nearly identical speeds. At a position 2.5 m downslope from the headgate, flow-front arrival times ranged from $t = 0.82$ s to $t = 0.87$ s, where $t = 0$ denotes the time the headgate began to open (Figures 2c and 2d). In comparison, a frictionless point mass released from the base of the headgate at $t = 0$ would have required 0.995 s to travel 2.5 m downslope. Thus, the abrupt release of potential energy associated with collapse of the leading edge of the debris mass during the dam break boosted the speed of the flow fronts. On the other hand, the front speeds measured in the experiments were smaller than the front speeds predicted by analytical models of instantaneous dam breaks, which we consider next.

3. Hot starts in analytical models of instantaneous dam breaks

Exact analytical solutions that describe the start-up behavior of idealized, depth-averaged, dam-break flows illustrate some important mathematical properties of hot starts. We focus on 1-D dam-break solutions aimed at predicting downslope propagation speeds of flow fronts that are resisted by basal Coulomb friction, with a zero-friction case as an end member. Despite the effects of basal friction, these solutions predict flow-front speeds that exceed the speeds of frictionless point masses released from rest at the base of the dam. The high speeds reflect the influence of an idealized dam break in instantaneously converting potential energy to kinetic energy.

The first solution considers a dam that is oriented normal to the bed at $x = 0$ and initially retains an infinite upslope reservoir of debris with uniform thickness h_0 (Figure 3a). At time $t = 0$ the dam vanishes, releasing a flow that descends a uniform slope inclined at an angle θ . Mangeney *et al.* (2000) addressed this problem by generalizing a

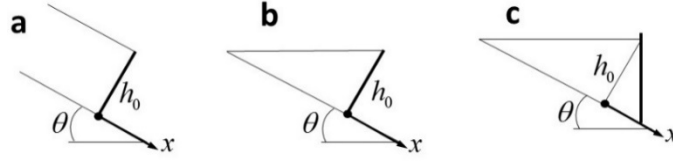


Fig. 3. Schematics illustrating different dam and debris configurations considered in analytical dam-break models. (a) bed-normal dam located at $x=0$ with infinite, rectilinear debris reservoir upslope, (b) bed-normal dam located at $x=0$ with finite, triangular debris reservoir upslope, (c) vertical dam located at $x=h_0 \tan \theta$ with finite, triangular debris mass upslope. In each case the bed-normal thickness of debris at $x=0$ is h_0 .

classical dam-break analysis to obtain a solution for the downslope velocity of the flow front u_f that can be expressed as

$$u_f = Sgt + 2\sqrt{h_0 g \cos \theta} \quad , \quad (1)$$

where g is the magnitude of gravitational acceleration and S is defined as

$$S \equiv \sin \theta - \cos \theta \tan \phi_{bed} \quad . \quad (2)$$

The value of S is proportional to the difference between the downslope gravitational driving force and the upslope resisting force produced by basal Coulomb friction, which depends on the effective basal friction angle ϕ_{bed} .

The two terms on the right-hand side of (1) have distinct physical implications. The term Sgt describes the growth of velocity due to steady downslope acceleration of a Coulomb point mass that begins from a position of rest at the base of the dam (i.e., $u_f = 0$ at $t = 0$). By contrast, the term $2\sqrt{h_0 g \cos \theta}$ describes an instantaneous velocity boost that lacks any dependence on time or frictional resistance. In the case of debris-flow flume experiments with debris initially impounded 1.9 m deep against a vertical dam face on a 31° slope (Figure 1), use of the formula $2\sqrt{h_0 g \cos \theta}$ and the bed-normal debris thickness $h_0 = 1.9 \text{ m} \times \cos \theta = 1.629 \text{ m}$ predicts that a velocity boost of 7.4 m/s applies for all $t > 0$.

The flow-front propagation solution (1) also applies to cases in which the reservoir of debris upslope from a bed-normal dam has a horizontal upper surface and finite length (Figure 3b). This solution can easily be obtained from an analogous dam-break solution for frictionless fluids by inserting (2) in place of $\sin \theta$ in the derivation of Ancy *et al.*, (2008). A key implication of this solution is that the presence of a finite reservoir does not modify the terms Sgt or $2\sqrt{h_0 g \cos \theta}$ in (1). The sum of these terms describes flow-front propagation even after an upslope-traveling wave of disturbance arrives at the upper end of the finite debris reservoir, thereby resulting in downslope motion of the entire mass of debris (Ancy *et al.*, 2008).

If a vertical rather than bed-normal dam impounds a finite mass of debris with a horizontal upper surface, then a different solution describes flow-front propagation following the dam break. In this case the base of the dam is positioned at $x = h_0 \tan \theta$, in which h_0 is the debris thickness measured normal to the bed where $x = 0$ (Figure 3c). Relative to the geometries discussed previously, this geometry better approximates the initial geometry used in our debris-flow flume experiments described in section 2. For this geometry an analytical solution obtained by Fernandez-Feria (2006) describes the dam-break behavior of frictionless fluids, but only for a short time following the dam break (i.e., $t \leq 2\sqrt{h_0/g} \left[\tan \theta / \sqrt{\cos \theta} \right]$, indicating the interval $0 < t \leq 0.53 \text{ s}$ in our debris-flow flume experiments. The solution of Fernandez-Feria (2006) can be generalized to account for the effect of basal Coulomb friction by using (2) in place of $\sin \theta$ in his analysis, thereby yielding the result

$$u_f = Sgt + \frac{\cos \theta}{\tan \theta} gt \quad . \quad (3)$$

This solution implies that the flow front behaves as an accelerating Coulomb point mass that is subject to a persistent force imbalance proportional to $[S + (\cos \theta / \tan \theta)]g$, which exceeds the force imbalance implied in (1). However, the flow-front speed predicted by (3) is not subject to an explicit dependence on h_0 or to a time-independent velocity

boost like that described by the term $2\sqrt{h_0 g \cos \theta}$ in (1). This key difference between (1) and (3) exists because the bed-normal thickness of impounded material adjacent to a vertical dam vanishes for all $\theta > 0$.

Equations (1) and (3) can be used to calculate the theoretical positions of advancing flow fronts for circumstances like those in the debris-flow flume experiments summarized in Figures 1 and 2. Predicted flow-front positions $x_F(t)$ are obtained by integrating the equation $dx_F/dt = u_F$. Use of (1) and the initial condition $x_F(0) = 0$ in this integration yields the prediction

$$x_F = (1/2)Sgt^2 + 2t\sqrt{h_0 g \cos \theta} \quad (4)$$

whereas use of (3) and the initial condition $x_F(0) = h_0 \tan \theta$ yields the prediction

$$x_F = (1/2)[S + (\cos \theta / \tan \theta)]gt^2 + h_0 \tan \theta \quad (5)$$

Inserting $t = 0.5$ s along with the experimental values $\theta = 31^\circ$ and $h_0 = 1.9 \text{ m} \times \cos \theta = 1.629 \text{ m}$ in (4) and (5) yields results that are summarized in Table 1 for limiting cases with no basal friction (i.e., $S = \sin \theta$) and with basal friction that is sufficient to counteract the entire downslope driving force (i.e., $S = 0$). For reference, the table also lists x_F values calculated for a point mass that is released at $x = 0$ and obeys $x_F = (1/2)Sgt^2$. The tabulated values show that the distances of flow-front advance predicted for a bed-normal dam are larger than those predicted for a vertical dam, and that each of these predictions greatly exceeds the prediction for a point mass released at $x = 0$ in the absence of a dam of finite height.

The predicted flow-front arrival time t_F at a specified downslope distance x can be calculated by performing some simple algebraic manipulations of (4) and (5). Table 1 lists t_F values calculated for $x = 2.5$ m. For this location, data collected in our June 2016 debris-flow flume experiments yielded flow-front arrival times with a mean and standard deviation $t_F = 0.846 \pm 0.016$ s (Figure 2c and 2d). All predictions of t_F listed in Table 1 differ significantly from this measured value. Indeed, the most accurate prediction of t_F is provided by the simplest and most naïve model, the frictionless point-mass model. This finding reveals the limitations of hot-start dam-break solutions in evaluating physical scenarios, even if those scenarios are as highly idealized as they are in our dam-break debris-flow experiments.

Table 1. Analytical predictions of flow-front position x_F at $t = 0.5$ s and flow-front arrival time t_F at $x = 2.5$ m.

Basis of prediction	$S = 0$ (maximum friction)		$S = \sin \theta$ (frictionless)	
	x_F at $t = 0.5$ s	t_F at $x = 2.5$ m	x_F at $t = 0.5$ s	t_F at $x = 2.5$ m
equation (4), bed-normal dam	3.70 m	0.338 s	4.33 m	0.306 s
equation (5), vertical dam	2.73 m	0.483 s	3.36 m	0.414 s
point mass with no dam	0 m	∞	0.63 m	0.995 s

4. Hot starts in numerical models of natural debris flows

Rather than simulating dam breaks, numerical models commonly implement hot starts by using a computational artifice in which the specified geometry of an initially static debris mass is intentionally mismatched with the debris frictional resistance. In such models resistance typically is set to a value far smaller than is necessary to statically balance forces in debris-flow source areas, but motion of the modeled debris is held in check by withholding a computer command (e.g., Hungr, 1995; Moretti *et al.*, 2015; Aaron *et al.*, 2017). Then, when a command is issued, the debris mass is instantaneously released with a great excess of net driving force, analogous to launching it downslope with a slingshot.

The implications of this hot-start tactic can be illustrated by considering a very simple model that lies at the quantitative heart of many complicated debris-flow dynamics models. The simple model stipulates that the downslope velocity u of a debris flow's center of mass obeys Newton's second law as summarized by the equation of motion $du/dt = Sg$, which can be rewritten as

$$\frac{du}{dt} = g \sin \theta \left[1 - \frac{\tan \phi_{bed}}{\tan \theta} \right], \quad (6)$$

where ϕ_{bed} is an effective basal friction angle that implicitly accounts for any effects of pore-fluid pressure. For physically valid initial states in which static debris is poised to begin downslope motion, (6) indicates that $\tan \phi_{bed} = \tan \theta$ must be satisfied. This condition places an unambiguous constraint on the value of ϕ_{bed} , yet numerical models that use hot starts ignore this constraint and commonly use values similar to $\tan \phi_{bed} \approx 0.5(\tan \theta)$ instead (e.g., Moretti *et al.*, 2015; Aaron *et al.*, 2017).

The motion predicted by (6) depends strongly on whether there is a small perturbation of a statically balanced initial state (e.g., $\tan \phi_{bed} / \tan \theta = 0.9999$) or a large perturbation like that implied by $\tan \phi_{bed} / \tan \theta = 0.5$. Integration of (6) shows that the predicted instantaneous speed (u) in either case is proportional to $[1 - (\tan \phi_{bed} / \tan \theta)]t$ and that the predicted distance travelled (x) is proportional to $[1 - (\tan \phi_{bed} / \tan \theta)]t^2$. Table 2 lists numerical values of such predictions for motion down a uniform slope inclined at the angle $\theta = 31^\circ$ (the angle of the USGS debris-flow flume).

The results listed in Table 2 illustrate why it is tempting for modelers to use hot-start initial conditions rather than physically valid initial conditions that involve small perturbations of statically balanced initial states. Flow speeds and travel distances obtained by assuming that $\tan \phi_{bed} / \tan \theta = 0.5$ applies may be far more realistic than those obtained by using $\tan \phi_{bed} / \tan \theta = 0.9999$. Indeed, the predictions obtained by using $\tan \phi_{bed} / \tan \theta = 0.9999$ are more suitable for a slowly creeping landslide than for a fast-moving debris flow, whereas those obtained by using $\tan \phi_{bed} / \tan \theta = 0.5$ indicate that after 100 s, a debris flow has traveled nearly 500 m and reached a speed of nearly 10 m/s—values that are quite plausible in many circumstances. However, while the numerical results obtained by using a hot start with $\tan \phi_{bed} / \tan \theta = 0.5$ may seem pleasing, the underlying physics are deeply flawed. The large speeds and travel distances attained by modeled debris flows with $\tan \phi_{bed} / \tan \theta = 0.5$ are merely artifacts of using physically implausible hot-start initial conditions and inappropriate parameter values.

Table 2. Dynamic responses to different perturbations of a balanced initial state, as indicated by solutions of (6).

Elapsed time (s)	Small perturbation, $\tan \phi_{bed} / \tan \theta = 0.9999$		Large perturbation, $\tan \phi_{bed} / \tan \theta = 0.5$	
	Speed, u (m/s)	Distance traveled, x (m)	Speed, u (m/s)	Distance traveled, x (m)
1	1.981e-5	9.906×10^{-6}	0.09906	0.04953
4	7.925e-5	1.584×10^{-4}	0.3962	0.7925
10	1.981e-4	9.906×10^{-4}	0.9906	4.012
20	3.962e-4	3.962×10^{-3}	1.981	19.81
50	9.906e-4	0.02476	4.953	123.8
100	1.981e-3	0.09906	9.906	495.3

5. An alternative to hot starts

Physically valid models of natural debris flows must avoid hot starts, but how can this be accomplished? The basic requirements are that such a model must be compatible with a statically balanced initial state and must simulate an evolution of debris strength that occurs after motion is triggered by a small perturbation of the static balance. A simplistic way to accomplish this goal is through arbitrary adjustments of debris strength. For example, a model might stipulate that the static debris strength decays gradually until downslope motion commences, and that the strength then continues to decline to emulate a transition to a more mobile, flowing state. With a sufficient number of adjustments of flow resistance, this model-tuning approach could yield results that match observations quite precisely. However, such an approach is essentially an elaborate curve-fitting exercise that has no explanatory power and limited value for making useful predictions. It merely mimics observed physical behavior rather than explaining it.

A requisite feature of a physically based debris-flow model that has both explanatory power and value as a predictive tool is that it accounts for natural transitions in debris strength through solution of evolution equations that are integral components of the model. Indeed, the central scientific problem in understanding and predicting the dynamics of landslides and debris flows is to quantify not only the effects but also the physical causes of strength evolution that occurs naturally during downslope motion. As noted by Johnson (1970), the most remarkable property of debris is its ability to flow fluidly in some circumstances and behave almost rigidly in others. From a scientific perspective, this property demands explanation, and not merely emulation.

Our depth-averaged numerical model D-Claw explains and simulates natural transitions in debris strength by solving differential equations that describe evolving distributions of solid volume fraction and pore-fluid pressure. These differential equations are strongly coupled to additional differential equations that describe the evolving distributions of debris mass and momentum (Iverson and George, 2014, 2016; George and Iverson, 2014). The system of coupled equations shows how pore-fluid pressure responds to dilation or contraction of the granular solid phase, such that contractive deformation drives up the fluid pressure. In turn, increases in fluid pressure reduce the intergranular effective normal stress and thereby reduce the effects of intergranular Coulomb friction, which provides most of the resistance to debris motion.

In D-Claw simulations, the highest flow mobility develops when debris becomes fully liquefied (*i.e.*, has zero effective normal stress). In this case the only resistance to motion is provided by viscous shearing of the debris' fluid phase. The lowest degree of mobility develops when all positive pore-fluid pressure has dissipated and the debris behaves as a Coulomb granular solid. The conceptual and mathematical framework of this model generalizes the Coulomb mixture-theory framework presented by Iverson and Denlinger (2001) by accounting for dilatancy and its coupling to debris motion. The D-Claw framework also generalizes some key principles of critical-state soil mechanics (*e.g.*, Wood, 1990) by considering the effects of inertial forces.

D-Claw simulations begin by specifying a statically balanced initial state and then perturbing the static balance by gradually increasing the basal pore-fluid pressure—as might occur naturally in response to rainfall or snowmelt. Pore-pressure increases can be either spatially uniform or nonuniform, but in all cases debris motion begins locally when the pore pressure in some computational cell becomes large enough to destabilize the static force balance there. The local force balance is, however, influenced by lateral stresses imposed by neighboring computational cells. Motion thereby begins in the weakest finite sector of a debris mass, which may or may not set off a chain reaction of motion in adjacent sectors as momentum is transferred from moving debris to static debris. If motion is accompanied by contractive deformation that drives up the pore pressure, then it can instigate a positive feedback process in which further motion yields even higher pore pressure and ultimately leads to liquefaction. If the feedback is strong, a complete transformation from slow, rigid-body motion to highly fluid flow can occur within seconds—leading to a style of debris-flow onset like that observed in physical experiments (*e.g.*, Iverson *et al.*, 1997, 2000).

6. Conclusion

Hot starts arise from use of initial conditions in which a large force balance is abruptly imposed on a static debris mass. Debris-flow models that rely on hot starts to simulate high flow mobility lack a sound scientific basis. Indeed, numerical models that use hot starts impose an instantaneous transition from equilibrium to far-from-equilibrium states, which is inconsistent with physical principles as well as field observations. A possible exception to this inconsistency exists when debris flows are triggered by strong earthquakes, but even in those circumstances, the onset of debris motion begins when a static force balance is infinitesimally violated.

Hot starts can serve useful scientific purposes in other contexts, as when dam-break debris-flow onsets are used to create reproducible experiments or analytical dam-break solutions are used to test the accuracy of computational algorithms. Dam-break behavior nevertheless fails to represent the behavior exhibited during the early stages of motion of most natural debris flows. Indeed, results we report in this paper indicate that analytical dam-break solutions can yield poor predictions of measured flow-front speeds—even under the idealized circumstances of our dam-break debris-flow experiments.

Use of hot starts can be avoided in properly formulated debris-flow models that account rigorously for statically balanced initial states. In these models motion is triggered by an infinitesimal perturbation of the balanced state, but the subsequent force balances and flow accelerations can evolve rapidly during the early stages of motion. Evidence from our debris-flow flume experiments indicates that a requisite feature of these models is representation of the pore-pressure feedback process that allows a nearly rigid granular mass to transition into a flowing, liquefied mass, and then transition back to a nearly rigid mass following pore-pressure dissipation.

Acknowledgements

We thank the many colleagues who participated in USGS debris-flow flume experiments conducted in June 2016. We especially thank Matthew Logan, Chris Lockett, Kelly Swinford, and Kate Allstadt, who played instrumental roles in the experiments. Joe Walder, Luke McGuire, and an anonymous referee provided useful critiques of our manuscript.

References

- Aaron, J., Hungr, O., Stark, T.D., and Baghdady, A.K., 2017, Oso, Washington, Landslide of March 22, 2014: Dynamic Analysis, *J. Geotech. Geoenviron. Eng.*, v. 143, 05017005. doi: 10.1061/(ASCE)GT.1943-5606.0001748.
- Aaron, J., Stark, T.D., and Baghdady, A.K., 2018, Closure to "Oso, Washington, Landslide of March 22, 2014: Dynamic Analysis" by Jordan Aaron, Oldrich Hungr, Timothy D. Stark, and Ahmed K. Baghdady, *J. Geotech. Geoenviron. Eng.*, v. 144, 07018023, doi: 10.1061/(ASCE)GT.1943-5606.0001748.
- Ancey, C., Iverson, R.M., Rentschler, M., and Denlinger, R.P., 2008, An exact solution for ideal dam-break floods on steep slopes. *Water Resources Research*, v. 44, W01430, doi:10.1029/2007WR006353.
- Fernandez-Feria, R., 2006, Dam-break flow for arbitrary slopes of the bottom, *J. Engineering Mathematics*, v. 54, p. 319–331, doi: 10.1007/s10665-006-9034-5.
- George, D.L., and Iverson, R.M., 2014, A depth-averaged debris-flow model that includes the effects of evolving dilatancy. II. numerical predictions and experimental tests, *Proc. Royal Society London, Ser. A*, v. 470, doi: 10.1098/rspa.2013.0820
- Grilli, S.T., Jarris, J.C., Bakhsh, S.T., Masterlark, T.L., Kyriakopolous, C., Kirby, J.T., and Shi, F., 2012, Numerical simulation of the 2011 Tohoku tsunami based on a new transient FEM co-seismic source: comparison to far- and near-field observations, *Pure and Applied Geophysics*, v. 170, 1333-1359. doi: 10.1007/s00024-012-0528-y.
- Hungr, O., 1995, A model for the runout analysis of rapid flow slides, debris flows, and avalanches, *Canadian Geotech. J.*, v. 32, p. 610-623, doi: 10.1139/t95-063.
- Iverson, R. M., and LaHusen, R.G., 1993, Friction in debris flows: Inferences from large-scale flume experiments, *Hydraulic Engineering '93* (Proceedings of the 1993 Conference of the Hydraulics Division of the American Society of Civil Engineers), v. 2, p. 1604–1609, *Am. Soc. of Civ. Eng.*, New York.
- Iverson, R.M., Reid, M.E., and LaHusen, R.G., 1997, Debris-flow mobilization from landslides: *Annual Rev. Earth and Planetary Sciences*, v. 25, p. 85-138.
- Iverson, R.M., Reid, M.E., Iverson, N.R., LaHusen, R.G., Logan, M., Mann, J.E., Brien, D.L., 2000, Acute sensitivity of landslide rates to initial soil porosity, *Science*, v. 290, p. 513-516.
- Iverson, R.M., and Denlinger, R.P., 2001, Flow of variably fluidized granular masses across three-dimensional terrain: 1. Coulomb mixture theory, *J. Geophys. Res. Solid Earth*, v. 106, B1, p. 537-552. doi: 10.1029/2000JB900329.
- Iverson, R.M., Logan, M., LaHusen, R.G., and Berti, M., 2010, The perfect debris flow? aggregated results from 28 large-scale experiments. *J. Geophys. Res. Earth Surface*, v. 115, F03005, doi:10.1029/2009JF001514.
- Iverson, R.M., and George, D.L., 2014, A depth-averaged debris-flow model that includes the effects of evolving dilatancy. I. physical basis, *Proc. Royal Society London, Ser. A*, v. 470, 20130819, doi: 10.1098/rspa.2013.0819
- Iverson, R.M., and George, D.L., 2016, Modeling landslide liquefaction, mobility bifurcation and the dynamics of the 2014 Oso disaster. *Geotechnique*, v. 66, p. 175–187, doi: 10.1680/jgeot.15.LM.004.
- Iverson, R.M., and Logan, M., 2017, Sensor data from debris-flow experiments conducted in June, 2016, at the USGS debris-flow flume, HJ Andrews Experimental Forest, Blue River, Oregon: U.S. Geological Survey Data Release, doi: 10.5066/F7N58JKH.
- Jefferies, M., and Been, K., 2016, *Soil Liquefaction a Critical-state Approach*, 2nd Edition, CRC Press, Boca Raton, Florida, 690 p.
- Johnson, AM., 1970, *Physical Processes in Geology*, Freeman, Cooper and Company, San Francisco, 577 p.
- Logan, M., Iverson, R.M., and Obryk, M.K., 2007 (revised 2018), Video documentation of experiments at the USGS debris-flow flume, 1992-2017. U.S. Geological Survey Open-file Report 2007-1315 (<http://pubs.usgs.gov/of/2007/1315/>).
- Mangeney, A., Heinrich, P., and Roche, R., 2000, Analytical solution for testing debris avalanche numerical models, *Pure and Applied Geophysics*, v. 157, p. 1081-1096.
- Moretti, L., Allstadt, K., Mangeney, A., Capdeville, Y., Stutzmann, E., and Bouchut, F., 2015, Numerical modeling of the Mount Meager landslide constrained by its force history derived from seismic data, *J. Geophys. Res. Solid Earth*, v. 120, p. 2579–2599, doi:10.1002/2014JB011426.
- Savage, S.B., 1979, Gravity flow of cohesionless granular materials in chutes and channels, *J. Fluid Mechanics*, v. 92, p. 53-96, doi: 10.1017/S0022112079000525.
- Wood, D.M., 1990, *Soil Behavior and Critical State Soil Mechanics*, Cambridge University Press, Cambridge, 465 p.

The role of topography on the volume of material eroded by debris flows

Tsukasa Kudo^{a,*}, Taro Uchida^b, Wataru Sakurai^b

^a*Sabo Engineering Corporation, Kawagoe, Japan*

^b*National Institute for Land and Infrastructure Management, Sabo Planning Division, Tsukuba, Japan*

Abstract

Prediction of sediment volume of debris flows is the most important factor for designing debris-flow control structures or estimating debris-flow prone area. It has been considered that debris-flow volume may increase due to erosion at the steep channel. So, clarifying erosion volume (in this study, erosion volume is sediment volume in the channel eroded by debris flow) due to debris flow is a key information to mitigate debris-flow disasters. This study hypothesized that erosion volume might be controlled by topography, because it can be thought that the transport capacity of debris flow increased with the increase of stream bed gradient and contributing area. In Recent field observations by Schürch et al. (2011) supported to this hypothesis and showed a correlation, showing the correlation between flow depth and magnitude of erosion. However, detailed information about spatial pattern of erosion depth due to debris flow is still limited. In this study, spatial pattern measurements of erosion volume due to debris flows for 16 debris flows in Japan. LiDAR data taken before and after the debris flow was used for the comparison. Then, examination of stream bed gradient and drainage area derived from the LiDAR dataset was performed. The study found that erosion volume of debris flow increases as slope of stream bed gradient and drainage area increases. The study proposed methods to predict erosion volume due to debris flow using stream bed gradient and drainage area based on the probabilistic relationship between measured erosion volume and topography. That is, it is considered that the topography derived from LiDAR can be used as one of the indicators used in estimating volume of future debris flow.

Keywords: Debris flow, erosion volume, topography, LiDAR survey

1. Introduction

Many debris flows increase in volume as they travel downstream, enhancing their mobility and hazard (Reid et al., 2016). It is recognized that an increase in debris-flow volume of debris flow can result from diverse physical processes (e.g., Reid et al., 2016). In general, it is recognized that the volume of debris flow should be controlled by sediment transport capacity or removable sediment volume. Removable sediment volume should be determined by both distribution of channel-bed sediment and the range where erosion is expected by debris flow.

This study reports on the relationship between topography and erosion volume of debris flow, using LiDAR data, and proposed methods to predict erosion volume due to debris flow using stream bed gradient and drainage area based on the probabilistic relationship between measured erosion volume and topography.

2. Method

2.1. The debris-flow data

This study focused on 16 debris-flow events that occurred from 2009 to 2014, in Japan (Table. 1). 16 debris flows are classified into 5 location. The data of Minamiuonuma City, Nagiso town and Hofu city is mainly Granite area.

* Corresponding author e-mail address: t_kudou@saboeng.co.jp

The data of Inabe City is mainly limestone area. The data of Aso City is mainly pyroclastic flow deposits area.

2.2. Estimation of sediment volume of debris flow and calculation of topography

The runout path of debris flows was interpreted from aerial photos. Then a survey point was established every 10m in the longitudinal direction of the identified runout path of the debris flow (Fig.1). Additionally, discharged sediment volume due to debris flow was estimated and topography at each survey points was calculated at each survey points using LiDAR dataset (Fig.1). Discharged sediment volume due to debris flow is variation volume estimated every 10m in the longitudinal direction of the runout path using surface changes derived from DEM data. Topography calculated in this study is slope and catchment area. The slope was measured on the average 100m using DEM data before debris flow occurred to longitudinal gradient in the runout path. Similarly, the catchment area was measured upstream area from each survey points using DEM data.

Table 1. Debris flows used in this study

Name	Date of occurrence	Location
Ubasawa	July 29-30, 2011	Minamiuonuma City, Niigata Pref.
Futagosawakawa	July 29-30, 2011	Minamiuonuma City, Niigata Pref.
Garasawakawa	July 29-30, 2011	Minamiuonuma City, Niigata Pref.
Koudanakawa	July 29-30, 2011	Minamiuonuma City, Niigata Pref.
Tsuchisawa	July 29-30, 2011	Minamiuonuma City, Niigata Pref.
Nashisawa	July 8-11, 2014	Minamikido town, Nagano Pref
Nishinokaitogawa	September 16-19, 2012	Inabe City, Mie Pref.
Kotakigawa	September 16-19, 2012	Inabe City, Mie Pref.
Abetanbugawa	July 21, 2009	Hofu City, Yamaguchi Pref.
Yahatadanikeiryu	July 21, 2009	Hofu City, Yamaguchi Pref.
Matsugatanikawa	July 21, 2009	Hofu City, Yamaguchi Pref.
Kamisatogawa	July 21, 2009	Hofu City, Yamaguchi Pref.
Uedaminamigawa	July 21, 2009	Hofu City, Yamaguchi Pref.
Daimongawa	July 11-12, 2012	Aso City, Kumamoto Pref.
Sakanashi area	July 11-12, 2012	Aso City, Kumamoto Pref.
Shioigawa2	July 11-12, 2012	Aso City, Kumamoto Pref.
Shinsyogawa3	July 11-12, 2012	Aso City, Kumamoto Pref.
Doigawa	July 11-12, 2012	Aso City, Kumamoto Pref.

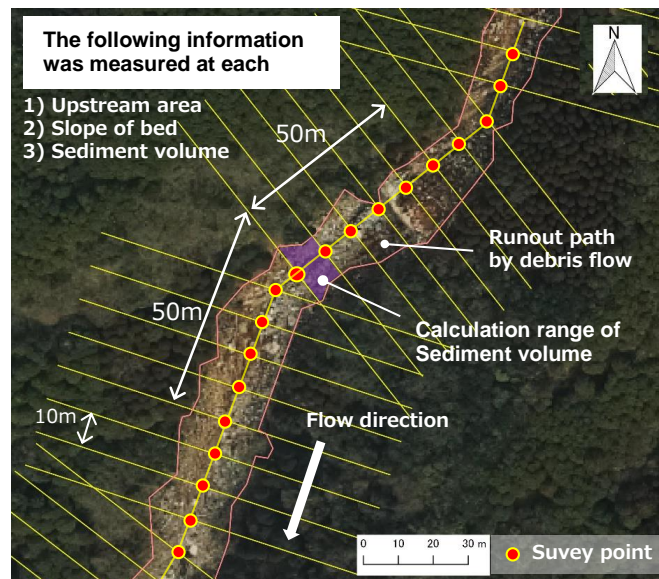


Fig. 1. Example of survey points

2.3. Relationship between topography and sediment volume of debris flow

Topography was classified at each survey points into categories. The slope and catchment area classes were classified based on Fig.2. The slope was classified into 9 every 5° classes and the catchment area was classified into 8 classes per order size. Additionally, the calculated variation volume at survey area was applied to each category. Then, the percentile (10%, 50%, 75%, 90%) of variation volume every 10m in the longitudinal direction of the runoff path using surface changes was calculated in each category (Fig.3).

2.4. Estimation of erosion volume of debris flow based on relationship between topography and sediment volume

This study proposes methods to predict erosion volume due to debris flow using stream bed gradient and catchment area based on the probabilistic relationship between measured erosion volume and topography (that is, probabilistic method in this study). In this study, the 50th percentile (the median) of variation volume for each category obtained from 16 debris-flows data was assumed as standard erosion volume by debris flow occurring at the topographic condition corresponding to each category. Therefore, the 50th percentile calculated in this study is used as estimated erosion volume due to debris flow for each topographic condition. Then a comparison of actual erosion volume with topography was developed using pre-flow and post-flow LiDAR imagery.

3. Results

Fig 2 shows the relationship between catchment area and the slope of the stream bed with the plots classified by erosion or deposition calculated each survey area (Fig.1 purple area). Erosion or deposition were determined based on the variation volume. The plots where erosion dominates is widely distributed regardless catchment area size and stream bed gradient.

Fig 3 shows the relationship between topography and percentile (10%, 50%, 75%, 90%) of erosion volume due to debris flow. For each classified category, erosion and deposition were classified and color coded according to the scale. Place where the number of plots corresponding to the category is less than 1% of the total number of plots is indicated by parenthesized numbers, and places where there is no corresponding plot are indicated by [-].

Looking at the overall trend, in areas where the slope is steep and the catchment area is large, the volume of the eroded sediment tends to be larger than in the area with a low gradient slope and a small catchment area (Fig.3).

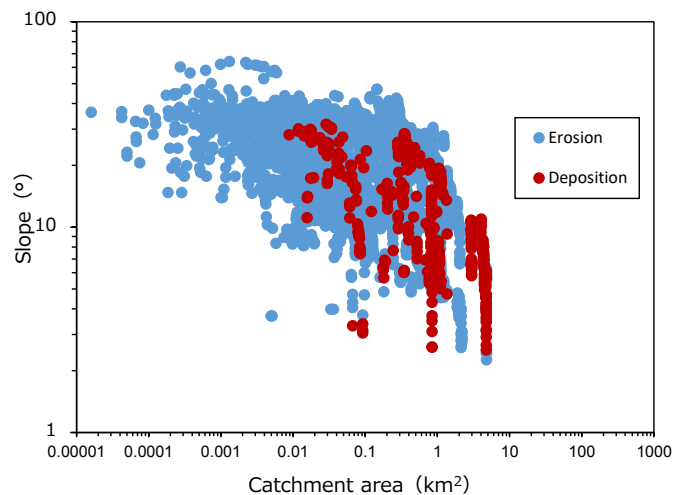


Fig. 2. Relationship between catchment area and slope of bed for each survey points

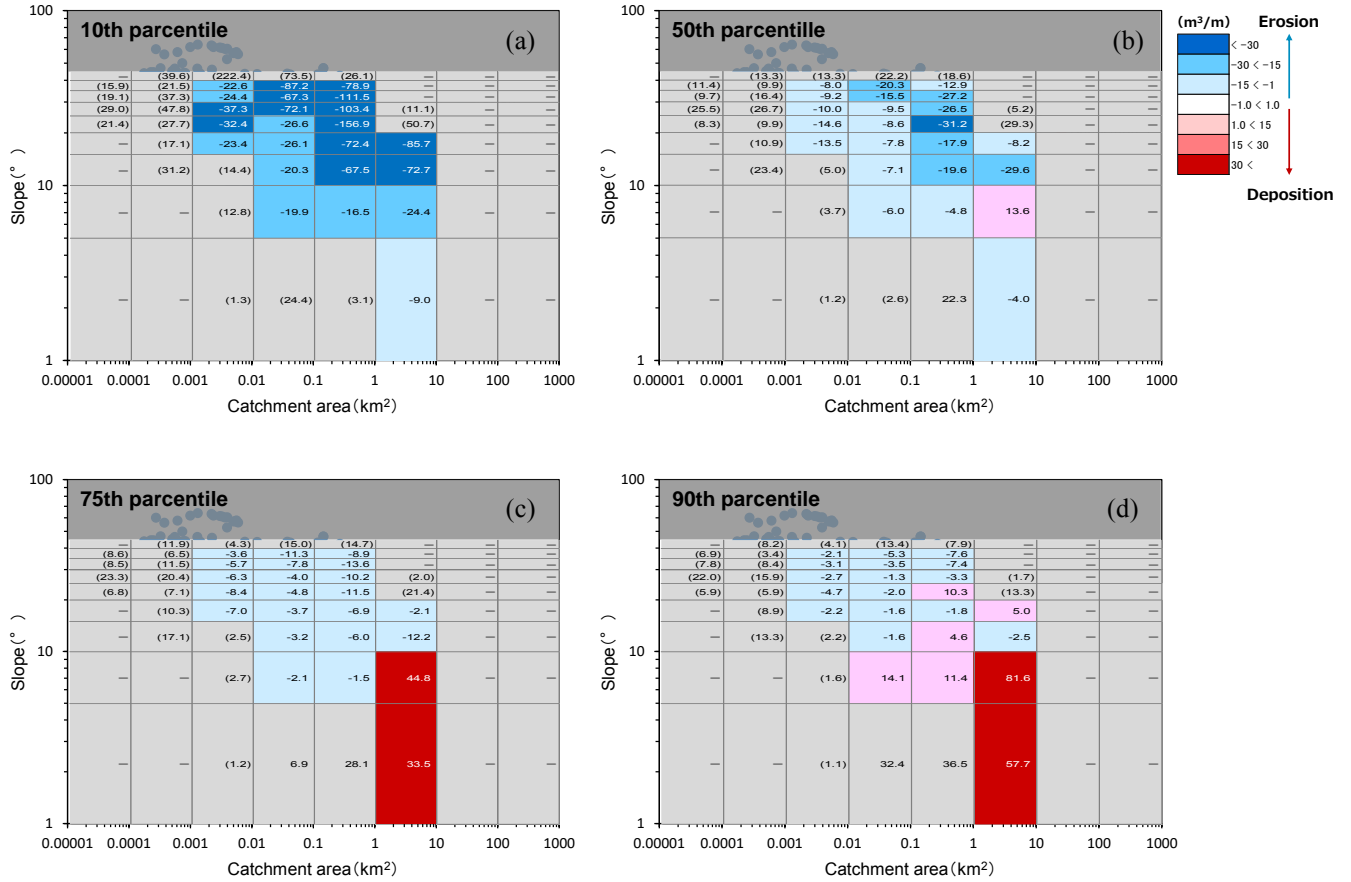


Fig. 3. Relationship between topography and variation volume due to debris flow, (a) 10th percentile of variation volume, (b) 50th percentile of variation volume, (c) 75th percentile of variation volume, (d) 90th percentile of variation volume,

Fig 4 shows example of the result of the relationship between actual sediment volume and estimated sediment volume. There was a clear correlation between actual sediment volume and estimated sediment volume in Koudanakawa02 (Fig 4 (a), orange plots). Although, in Koudanakawa01 (Fig 4 (a), blue plots), the actual sediment volume was about 3 times the estimated value regardless of survey points. Also, in Matsugatanikawa05 (Fig 4 (b), blue plots), the actual sediment volume was about half of the estimated sediment volume.

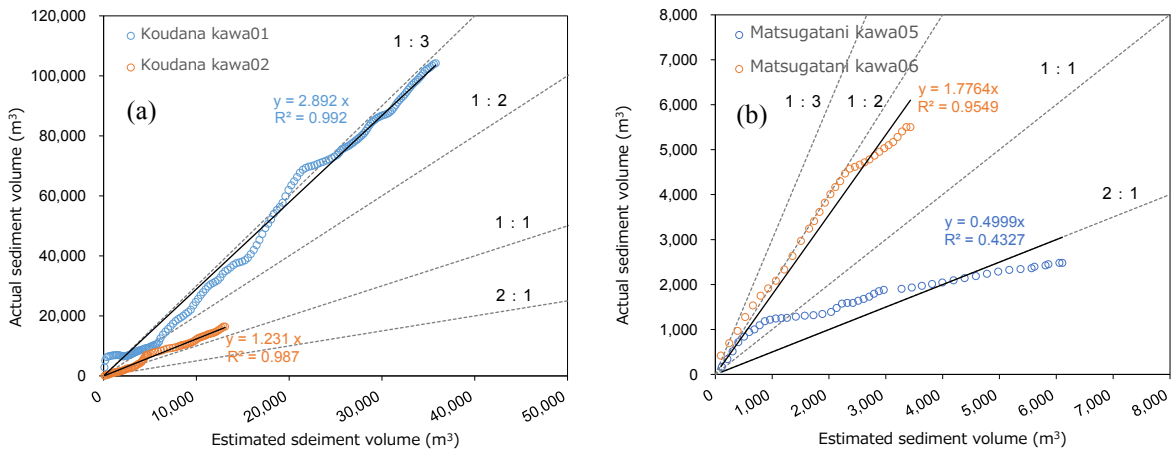


Fig. 4. Relationship between actual sediment volume and estimated sediment volume, (a) Example of Koudanakawa river, (b) Example of Matsugatanikawa river

4. Conclusion

By comparing pre-and post-flow LiDAR imagery, this study found that erosion volume of debris flow increases as slope of stream bed gradient and drainage area increases. Then, An erosion volume prediction was developed using a probabilistic relationship between measured erosion volume and topography. As a result, it is considered that the topography derived from LiDAR can be used as one of the indicators used in estimating volume of future debris flow. On the other hand, there may be a large difference between the actual sediment volume and estimated sediment volume. In this case, it is thought that the debris-flow scale at the start point and distribution of channel-bed sediment are influenced, but detailed analysis is necessary.

References

- Reid, M.E., Coe, J.A., Dianne L., Brien D.L., 2016, Forecasting inundation from debris flows that grow volumetrically during travel, with application to the Oregon Coast Range, USA: *Geomorphology* 273, p.369-411
- Schürch, P., Densmore, A.L., Rosser, N.J., and McArdell, B.W. 2011, Dynamic controls on erosion and deposition on debris-flow fans: *Geology* 39, p.827-830.

Numerical investigation of deposition mechanism of submarine debris flow

Dingzhu Liu^{a,b,*}, Yifei Cui^{c*}, Clarence E. Choi^{c,d}, Nazir Ahmed Bazai^{a,b}, Zhilin Yu^e,
Mingyu Lei^{a,b}, Yanzhou Yin^{a,b}

^aKey Laboratory of Mountain Hazards and Earth Surface Process, Institute of Mountain Hazards and Environment, Chinese Academy of Sciences, Chengdu 610041, China

^bUniversity of Chinese Academy of Sciences, Beijing 100049, China

^cDepartment of Civil and Environmental Engineering, Hong Kong University of Science and Technology, Clear Water Bay, Hong Kong, China

^dThe HKUST Jockey Club Institute for Advanced Study, HKSAR, Hong Kong, China

^eSouthwest Electric Power Design Institute, Chengdu 610021, China

Abstract

Submarine debris flow can damage oil and gas transport pipelines with potentially adverse consequences to the environment and to the industrial activity itself. The deposition process of submarine debris flow, which is related to the flow viscosity, is complex due to the slurry diffusion process that happens during the interaction of water and slurry. In addition, a quantitative characterization of the characterize the flow mechanism as influenced by the material density during the deposition process remains a scientific challenge. To fundamentally understand the mechanisms of solid-fluid interactions in fast-flowing submarine debris flows, a series of three-dimensional (3D) numerical simulations using Computational Fluid Dynamics (CFD) were conducted. The Herschel-Bulkley (HB) model was used to define the submarine slurry's rheological characterization as calibrate through simple rheological experiment. Results reveal that deposition is a mass diffusion process. Shear stress at the bottom and at the top of the slurry leads to velocity differences in the vertical direction which in turn generates a huge vortex, which contributed to a separation of slurry into two parts: the frontal head, and the tail. The velocity difference in vertical direction is helpful for hydroplaning. For higher slurry viscosity case, the flow profile is longer and thicker with a front head that has a lower averaged densities and sharper head angles. In addition, highly viscous slurries have lower average frontal velocities during the deposition process. The mixture density decreases in two stages: quick decreasing stage and stable decreasing stage. In the first stage, the slurry expands quicker than the second stage. Higher viscosities also lead to larger volume expansions which consequently leads to quicker density decrease.

Keywords: Submarine debris flow; Deposition mechanism; Computational fluid dynamics; Volume of fluid; Herschel-Bulkley model

1. Introduction

The construction of offshore infrastructure brings great challenges to the engineers due to the very completed geologic engineering environment in oceans. Specifically, the challenging problem, about the security of pipelines and platforms under the impact of submarine debris flow, are all responsible for the major advances in the understanding of the phenomena of submarine debris flows and their inherent consequences. Submarine debris flow is a kind of catastrophic hazard. That pose great risk to the security and structural integrity of submarine structures such as pipelines and platforms. These events are associated with mass movements that can have a run-out distance of more than 100 km (Locat and Lee, 2002) with a wide coverage area. Subaqueous debris flow is known to travel long distances due to hydroplaning (Mohrig et al., 1998; Piper, 1999) and substantial damages to foundational facilities such as underwater pipelines or cables. An appropriate evaluation of submarine debris flow movements is a major challenge for risk assessment (Locat and Lee, 2002).

Many submarine debris flows are triggered by earthquakes, overloading or are dislodged from steep slopes. (Roberts and Cramp, 1996). Two distinct phenomena can be observed in submarine debris flows: hydroplaning and turbidity currents. Hydroplaning is a thin layer of entrained water at the bottom of the debris flow head which develops due to the influence of bottom friction (Mohrig, 1998) and which usually leads to longer deposition distances (Locat

* Corresponding author e-mail address: yifeicui@ust.hk; liudingzhu@imde.ac.cn;

and Lee, 2002). Turbidity currents are smoke-like sediments dissociated from the debris flow head (Mohrig et al., 2003; Sahaheldin et al., 2000). These phenomena can be observed in both high and low coherent debris flows (Marr 2001). Due to their effects on the flow dynamics and deposition of submarine debris flows, it is important to understand the formation mechanisms of hydroplaning and turbidity current, (Locat and Lee, 2002). The potential damage brought about by these flow events can be calculated by formulas that are functions of the flow velocity, slurry's height, rheology and flow distance (Zakeri, 2009; Haza et al., 2015; Wang, 2016). Iverson (1997) compared flow distance and longitudinal height which are related to the gravitational potential energy and frictional dissipation energy respectively. Results show that the runout distance is highly influenced by different clay and water content. However, these tests were not carried out in a submerged condition. Nonetheless, it could be comprehended that viscosity also influences the energy dissipation process in submarine conditions as well.

Zhu et al. (2013) used two-dimensional (2D) Finite Element Method (FEM) with adaptive mesh technique to simulate large flow deformations and its impact force on submarine pipeline. Results show there is a critical pipe depth at which the where generated drag force is minimum. However, the method is only effective in analysis of specific conditions, and cannot account for hydroplaning, the velocity field that develops, and the turbidity current. Depth Integral Method (DIM) was adopted to simulate landslide flows into the lake (Imran et al., 2001; Marr et al., 2002; Blasio et al., 2004; Sue et al., 2011; Liu et al., 2016). Imran et al. (2001) used a one-dimensional (1D) numerical model to analyze the influence using of different rheological models. Blasio et al. (2004) adopted a 2D numerical model to analyze the mechanisms of hydroplaning. Sue et al. (2011) used this method to analyze tsunamis generated by submarine landslides. Liu et al. (2016) found that bed erosion enhances the damage caused by landslides and increase the possibility of blocking rivers. Pore water pressure has also been found to influences the erosion process.

The algorithms presented are usually two-layer models which assume the interaction between landslides and the ambient water does not involve mass exchange and diffusion. Besides, slurry's morphology and velocity regime cannot be calculated. Smoothed particle hydrodynamics (SPH) coupled with DIM was adopted by Pastor et al. (2009a, 2009b) and Wang et al. (2016) to simulate submarine debris flow. Wang found water depth does not influence flow distance and flow velocity, whereas the friction coefficient and slope influences the maximum velocity and flow distance. This model still cannot calculate the mass diffusion process and hydroplaning's influence was ignored. Gauer et al. (2006) and Zakeri et al. (2009) simulated submarine debris flow movement using Computational Fluid Dynamics (CFD) based on Eulerian-Eulerian multiphase flow theory. Hydroplaning phenomenon was observed although the effects of viscosity were not considered using in detail. Zakeri et al. (2009) used multiple incompressible fluid models in CFX program to analyze the drag force that submarine pipes experience as generated by submarine debris flows. The test conducted a comparison between experimental tests and numerical tests verifying the applicability of a proposed non-Newtonian Reynold's number. Many rheological models were adopted to simulate the rheological characteristics of submarine debris flow: Bingham model (Marr et al., 2002; Pastor et al., 2004; Gauer et al., 2006), Bilinear rheological model (Imran et al., 2001), Power law model (Zakeri et al., 2008) and Herschel-Bulkley model (Imran et al., 2001; Haza et al., 2015). In general, the Herschel-Bulkley model is more adaptive in CFD simulation for the accurate prediction of shear force by instance changing of shear rate (Blasio et al., 2004).

In this study, small-scale tests are carried out using a 3-dimensional (3D) biphasic CFD numerical model. The numerical results bear insight on how viscosity is manifested through the debris flow deposition process.

2. Methodology

2.1. Theory and governing equations

In the current study, the motion of submarine debris material of submarine motion and surrounding water are schematized as two different type of liquid. The Volume of Fluid (VOF) model (Hirt and Nichols, 1981) has been designed for modelling two immiscible fluids phase. The mass continuity of Navier-Stokes equations of submarine flow is shown in Equation 2. Meanwhile, from momentum conservation, the Navier-Stokes equations is expressed in Equation 3, which is a single momentum equation solved throughout the domain, and the resulting velocity field is shared among the phases. Equation 3 is dependent on the volume fractions of all phases through the properties ρ and μ that are calculated from Equation 1.

$$\tilde{\rho} = \sum_{i=1}^3 \alpha_i \rho_i; \tilde{\mu} = \sum_{i=1}^3 \alpha_i \mu_i; \tilde{P} = \sum_{i=1}^3 \alpha_i P_i; \quad (1)$$

$$\tilde{\rho}_i + \nabla(\tilde{\rho}V) = 0 \quad (2)$$

$$(\tilde{\rho}V)_i + \vec{V} \cdot \nabla(\tilde{\rho}V) = -\nabla P + \nabla \cdot [\tilde{\mu}(\nabla\vec{V} + \nabla\vec{V}^T)] + \tilde{\rho}g \quad (3)$$

where i states the i th phases of fluid during the calculation, ρ_i is the density of the i th phase; α_i is the volume fraction of i th phase, μ_i is the i th phase dynamic viscosity, P_i is i th fluid pressure; ∇ is the differential operator given in Cartesian coordinates system; \vec{g} is gravity acceleration; \vec{V} is velocity field.

2.2. Calibration and input parameters

The composition of different percent of kaolin clay and Toyoura sand were adopted in this study. Many composition ratio were adopted, but for the flowability under water, three reliable content were adopted. Three tests were conducted, all of which had water and total mass (sum of the mass of kaolin and sand) contents of 50%. sand mass content is 37.5%, 25% and 12.5% in different experiment. After thoroughly mixing, three different slurries with different densities (as shown in Table1) were produced. The rheological respective characteristics were measured using an (Anton Paar Physica MCR301) rheometer. The measured shear stress-strain rate behaviours of the three different samples are shown in Figure 1. Both non-linear rheological models, Power Law, and Herschel-Buckley Model are used to fit the experimental data. The most obvious difference is Power Law Model without yield stress, which influences mechanics during deposition. The Power Law Model and Herschel-Bulkley Model are expressed in Equation 4 and 5, respectively. According to comparison results, Herschel-Bulkley model is more reliable compared with Power Law, and yield stress should be considered.

$$\tau = K\dot{\gamma}^n \quad (4)$$

$$\tau = \tau_c + K\dot{\gamma}^n \quad (5)$$

where τ is shear stress; τ_c is critical shear stress; $\dot{\gamma}$ is shear rate; K and n are adjustment coefficients according to fitted data. The fitting results is shown in Table 2. It is found that all the fitting coefficient is larger than 0.99 for Herschel-Buckley Model, which validate the selection. According to comparison results, the Herschel-Bulkley model best represents the materials' rheology

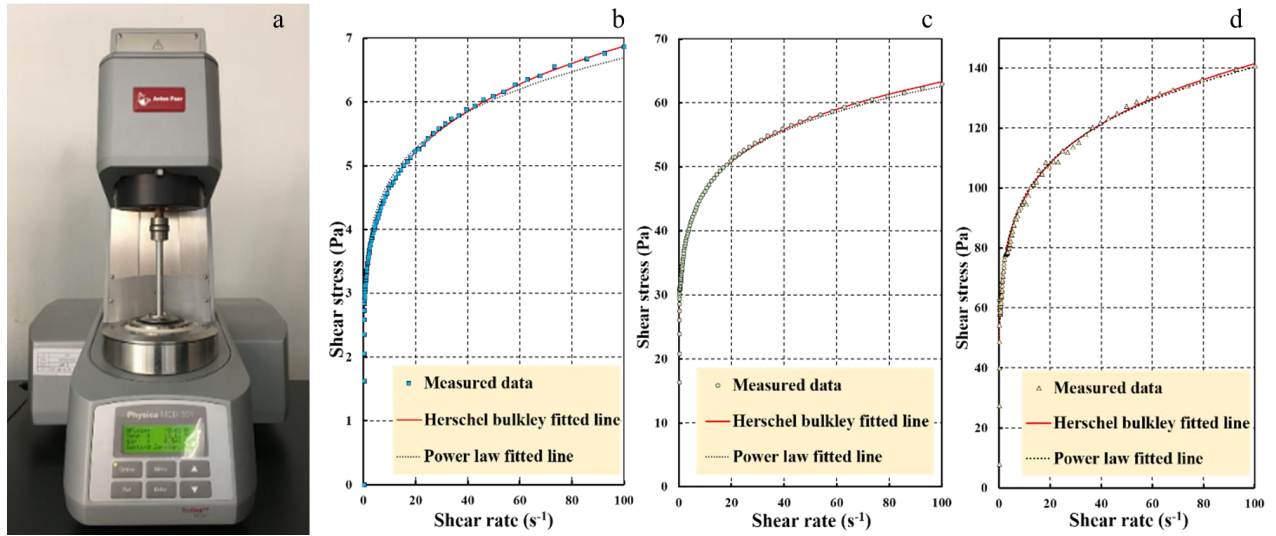


Fig. 1. (a) Rheometer (Anton Paar Physica MCR301); (b) rheological data fitting of RD = 1.406; (c) rheological data fitting of RD = 1.419; (d) rheological data fitting of RD = 1.431; RD means relative density.

Table 1. Rheological fitting (RD means relative density)

Test ID	Density (kg/m ³)	R ² of Herschel Bulkley model (%)	R ² of Power Law model (%)
RD = 1.406	1406	99.34	98.34
RD = 1.419	1419	99.13	98.66
RD = 1.431	1431	99.11	97.88

Table 2. Input data of Herschel Bulkley Model

Test ID	τ_c	K	n
RD = 1.406	1.501	1.863	0.231
RD = 1.419	5.031	29.303	0.149
RD = 1.431	9.307	57.803	0.179

2.3. Domain and boundary conditions

The model was built and meshed in the Gambit 2.4.6b and then transferred into Ansys before the start of calculation. The volume of the storage (0.009 m³) and debris transportation channel is much smaller compared to the water tank (0.6m³). In order to increase the calculation accuracy, the mesh size in the slurry domain (Fig.2 domain a-b-c-d) was set to be as 0.001 m, 0.002 m in the transportation channel (Fig.2 domain b-d-f-e) 0.002 m in the storage (Fig.2 domain g-a-b-h). The mesh size of other remaining domains are 0.020 m. The side view of the model is shown in Figure 2. A total of 1.33 Million meshes were generated in high quality with a value of 0.946 as reported in Ansys Fluent (quality number close to 1 correspond to high quality, the range is between 0 and 1). The boundary condition between water and the wall interface is set as non-slip. This mean that fluid has zero velocity relative to the boundary, consistent to what is observed in experiments (Gue, 2012; Elverhoi et al., 2010).

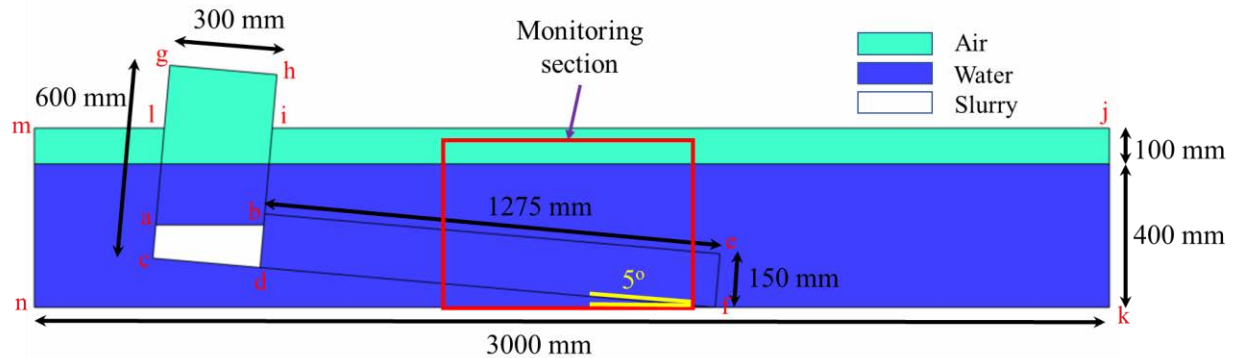


Fig.2. Side view of the 3D Numerical model setup

2.4. Numerical simulation program

Three series of numerical simulations were carried out using different rheological parameters, which were listed in Table 2. The debris slurry is assumed as an incompressible flow. A Pressure-based solver of pressure-velocity coupling algorithm is used to solve the coupled formula of the VOF model. Semi-Implicit Method for Pressure-Linked Equations-Consistent (SIMPLEC) algorithm was adopted to solve this problem with the aims of achieving relative quick convergence. The time step was set as 0.001s determined using von Neumann stability method (Anderson and Wendt, 1995). Maximum iterations were set as 30 steps for calculation convergence and autosave per 100 steps. The acceleration due to gravity is 9.81 m/s² in all the tests. This model includes three phases: air, water, and slurry. Air and water properties are shown in Table.3.

Table 3. Physical character of air and water phase

Fluid Phase	Density (kg/m^3)	Viscosity ($\text{kg}/(\text{m} \cdot \text{s})$)
Air	1.225	1.003×10^{-3}
Water	988.2	1.789×10^{-5}

3. Interpretation of results

Figure 3 (a) shows the deposition process of submarine debris flow with $RD = 1.419$. as can be seen, it reflects the deposition process of submarine debris flow. During deposition, as the slurry mixes with the surrounding water, its average water decrease. The mixing process is dominated by the shear stress in the interface of slurry and water. In the head of debris flow, instability between slurry and water would generate a vortex, one part of vortex is in mixed slurry and another part is in pure water area (Fig.3 (b)). The vortex would separate the debris flow into two parts: the tail part which develops like a triangle and a front part which is like a quadrilateral during deposition. In the vertical direction of frontal head, velocity in the middle part of slurry is larger than the bottom part and interface, where the shear stress is higher. The higher velocity area would absorb water into the slurry's head as shown in Fig.3 (b) which promotes the decreasing of density. Apart from this, higher velocity in the middle layer generate hydroplaning in the front most point at which slurry is lifted by the surrounding water (Fig.3). Furthermore, the velocity difference in the vertical direction elongates and deepen the front head.

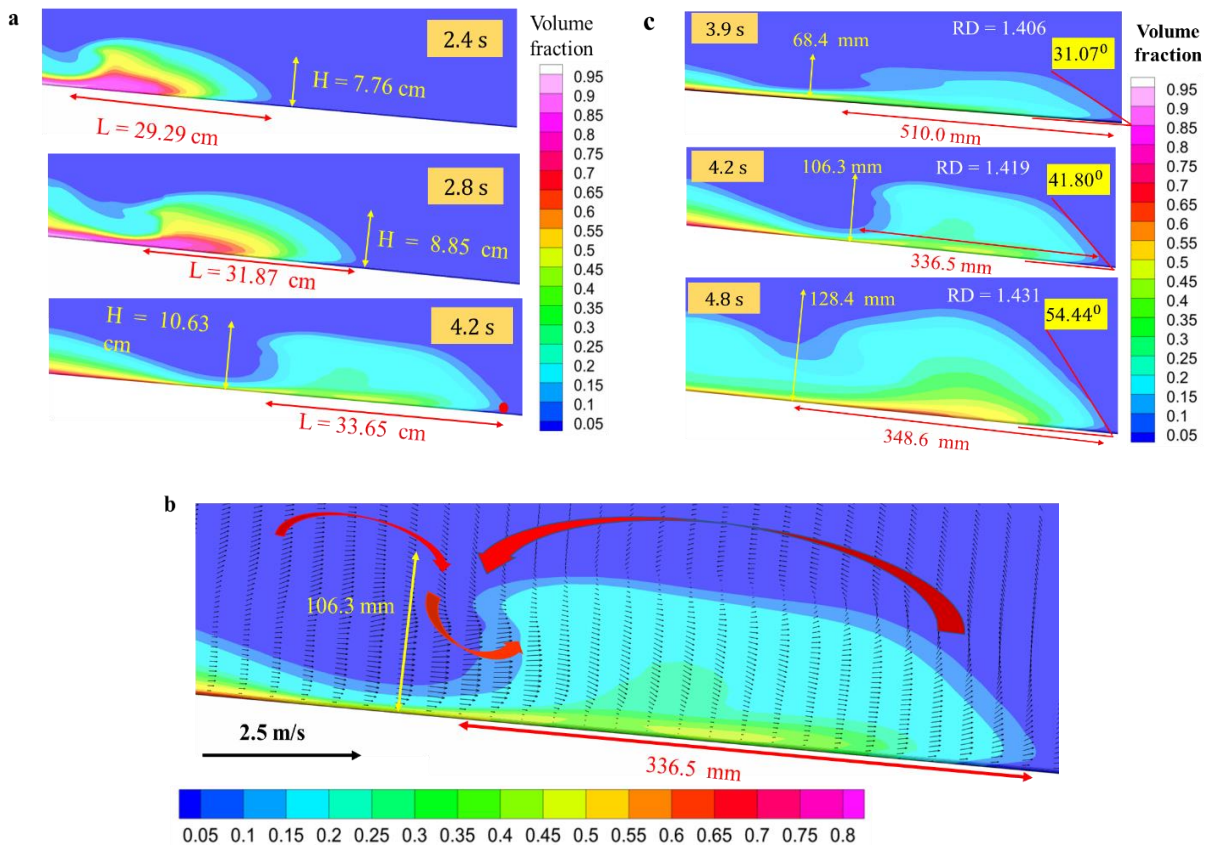


Fig.3. shows the mixing that happens during submarine debris flow deposition (a) the mixture at different times of test for a relative density = 1.419; (b) Flow regime of relative density = 1.419 at 4.2 s; (c) Flow profiles that slurries flow to the end of the channel for different densities.

Denser slurries flow slower than low-density slurries., The time that slurry reach the tail of the channel from the gate opening are 3.9 s, 4.2 s, and 4.8 s respectively. Figure 3 (c) shows the density profile at the time the front head reaches channel's end. High-density slurry flows are thicker both at the front part and at the tail due to high coherency

and viscosity. Higher yield stresses and viscosities generally lead to thicker slurries which can retain their thicknesses. Higher viscosities are related to higher shear stresses at the bottom, interface, and body. This is the reason why the case shows lower fluidity and thicker flow profile. This also leads to a sharper angle at the front head and tail part as well. Sharper angles correspond to lower velocity differences at the vertical section. The ratio of the middle layer's velocity over the distance of the middle layer to bottom is lower than high density case.

For higher density condition, slurry expanded into larger domain, density decreasing process were considered, the averaged density of slurry was calculated from Equation 6, the calculate domain is the mesh that volume fraction of slurry more than 0. The average density is calculated as:

$$\rho(t) = \frac{\sum_{i=1}^N (\alpha_{si} V_i \rho_s + \alpha_{wi} V_i \rho_w)}{\sum_{i=1}^N V_i} \quad (6)$$

where α_{si} is the volume fraction of slurry in mesh i ; α_{wi} is the volume fraction of water in mesh i ; ρ_s is density of slurry; ρ_w is density of water; V_i is volume of mesh i ; the mesh i is a mesh that volume fraction higher than 0.

Figure 4 shows that the averaged density of the slurry decreasing during deposition. This decrease involves two stages. In the first stage (before 2.4 s), the decreasing ratio for each test is higher than the second stage (after 2.4 s). During deposition process, the density decrease ratio (calculated as from Equation 7) of the high-density condition drops quicker than lower-density condition. Compared with the low-density slurry, the decreasing ratio of the high-density slurry is higher in the first stage and lower in the second stage. All these data are concluded in Table.4. The decrease in the density is related to the domain expansion of the slurry which is influenced by the mixtures' rheological characteristics. In the first stage, high viscosity is related to higher shear stress which leads to thicker flows, which creates a larger vortex which results to a higher and larger mixture domain. From these results, high-density slurries expand quicker than low-density slurries. As shown in figure 3 (c), the size of the slurry of the high-density condition is bigger than the low density case. In the second stage, the value of density decreasing ratio is very close, which consequently related to a low decreasing ratio. According to the different expanding ratios, the slurry expands in a relatively manner, which then becomes a stable mass diffusion at the second stage that the slurry. This stage would continue till the end of deposition. The violent expansion at the first stage only lasts for a short time, but it is very important in deposition process.

$$\text{decreasing ratio} = \frac{\text{initial density of this stage} - \text{ending density of this stage}}{\text{slurry density}} \quad (7)$$

where slurry density is the density of slurry before deposition; initial density of this stage means the value of the beginning of this stage; ending density of this stage means the density of the end of this stage.

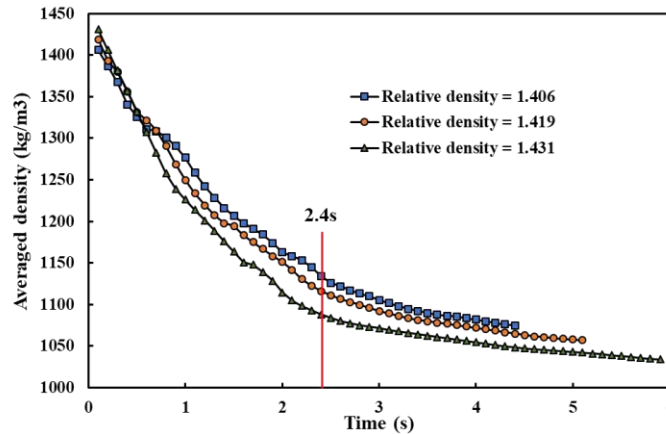


Fig.4. Averaged density decreases during deposition

Table 4. Averaged density decreasing ratio of each test in every stage

Test ID	Decreasing ratio in stage 1	Decreasing ratio in stage 2
RD = 1.406	19.33	4.21
RD = 1.419	21.35	4.16
RD = 1.431	23.97	3.78

4. Conclusion

In this study, three numerical analyze were carried out to study the deposition mechanism of submarine debris flows. The deposition process is a process of mass diffusion. In the head of debris flow, shear stress in the interface of slurry and water would generate a huge vortex that separate the debris flow into two parts. This vortex also promotes mass diffusion of the debris flows. High density slurries have higher viscosities, yield shear stresses, and coherency which leads to sharper heads, thicker depths, and larger vortices which are generated by higher shear stress at the interface. The higher velocity layer in the middle part of the slurry enhances the hydroplaning which in turn increase the fluidity of the slurry. Averaged density decrease includes two stages. Density decreases quickly in the first stage in which mass strongly diffuses. In contrast, density decreases slower in the second stage. The quick expansion of deposition happened in short period and stable expansion would last for a long time until the end of deposition.

5. Acknowledgments

The authors would like to thank the National Natural Science Foundation of China (5170091039), the Hong Kong Research Grants Council (IGN15EG03), and the Key Research Program of Frontier Sciences, CAS (No. QYZDY-SSW-DQC006) for their generous support. The authors would also like to thank the theme-based research grant T22-603/15N and general research fund 16209717 of the Hong Kong Research Grants Council. The authors are grateful for financial sponsorship from the Opening Fund of State Key Laboratory of Hydraulics and Mountain River Engineering (SKHL1609) and the support of the HKUST Jockey Club Institute for Advanced Study.

References

- Anderson, J. D., & Wendt, J., 1995, Computational fluid dynamics: New York: McGraw-Hill. ANSYS Inc. ANSYS Fluent, v.206, p. 1-3.
- De Blasio, F. V., Engvik, L., Harbitz, C. B., & Elverhøi, A., 2004, Hydroplaning and submarine debris flows: *Journal of Geophysical Research: Oceans*, 109(C1), doi:10.1029/2002JC001714.
- Elverhøi, A., Breien, H., De Blasio, F. V., Harbitz, C. B., & Pagliardi, M., 2010, Submarine landslides and the importance of the initial sediment composition for run-out length and final deposit. *Ocean Dynamics*, v.60, no. 4, p. 1027-1046, doi: 10.1007/s10236-010-0317-z.
- Gauer, P., Elverhøi, A., Issler, D., & De Blasio, F. V., 2006, On numerical simulations of subaqueous slides: back-calculations of laboratory experiments of clay-rich slides: *Norsk Geologisk Tidsskrift*, v.86, no.3, p. 295.
- Gue, C. S. (2012). Submarine landslide flows simulation through centrifuge modelling [Ph.D. thesis]: Cambridge, University of Cambridge, 33 p.
- Haza, Z.F., Hamonangan, I.S., 2015, On the Numerical Simulations of Drag Forces Exerted by Subaqueous Mudflow on Pipeline: A Laboratory Experiment Assessment. *Proceeding of the 14th International Conference on QIR*, p.181-185.
- Hirt, C. W., & Nichols, B. D., 1981, Volume of fluid (VOF) method for the dynamics of free boundaries: *Journal of computational physics*, v.39, no.1, p. 201-225.
- Imran, J., Harff, P., Parker, Gary., 2001, A numerical model of submarine debris flow with graphical user interface: *Computer & Geosciences*, 27, p. 717-729, doi:org/10.1016/S0098-3004(00)00124-2.
- Iverson, R. M., 1997, The physics of debris flows: *Reviews of geophysics*, v.35, no.3, p. 245-296, doi: 10.1029/97RG00426.
- Liu, W., & He, S., 2016, A two-layer model for simulating landslide dam over mobile river beds: *Landslides*, v.13, no.3, p. 565-576, doi: 10.1007/s10346-015-0585-2.
- Locat, J., & Lee, H. J., 2002, Submarine landslides: advances and challenges: *Canadian Geotechnical Journal*, v.39, no.1, p. 193-212, doi: 10.1139/T01-089.
- Marr, J. G., Elverhøi, A., Harbitz, C., Imran, J., & Harff, P., 2002, Numerical simulation of mud-rich subaqueous debris flows on the glacially active margins of the Svalbard-Barents Sea: *Marine Geology*, v.188, no.3-4, p. 351-364, doi: 10.1016/S0025-3227(02)00310-9.
- Mohrig, D., & Marr, J. G., 2003, Constraining the efficiency of turbidity current generation from submarine debris flows and slides using laboratory experiments. *Marine and Petroleum Geology*, v.20, no.6-8, p. 883-899, doi:10.1016/j.marpetgeo.2003.03.002.
- Mohrig, D., Ellis, C., Parker, G., Whipple, K. X., & Hondzo, M., 1998, Hydroplaning of subaqueous debris flows: *Geological Society of America Bulletin*, v.110, no.3, p. 387-394, doi: 10.1130/0016-7606(1998)110<0387:HOSDF>2.3.CO;2.
- Pastor, M., Quecedo, M., González, E., Herreros, M. I., Merodo, J. F., & Mira, P., 2004, Simple approximation to bottom friction for Bingham fluid depth integrated models: *Journal of Hydraulic Engineering*, v.130, no.2, p. 149-155, doi: 10.1061/(ASCE)0733-9429(2004)130:2(149).

- Pastor, M., Blanc, T., & Pastor, M. J., 2009, A depth-integrated viscoplastic model for dilatant saturated cohesive-frictional fluidized mixtures: application to fast catastrophic landslides: *Journal of Non-Newtonian Fluid Mechanics*, v.158, no.1-3, p. 142-153, doi: 10.1016/j.jnnfm.2008.07.014.
- Pastor, M., Haddad, B., Sorbino, G., Cuomo, S., & Drempetic, V., 2009, A depth-integrated, coupled SPH model for flow-like landslides and related phenomena: *International Journal for numerical and analytical methods in geomechanics*, v.33, no.2, p. 143-172, doi: 10.1002/nag.705.
- Piper, D. J., Cochonat, P., & Morrison, M. L., 1999, The sequence of events around the epicentre of the 1929 Grand Banks earthquake: initiation of debris flows and turbidity current inferred from sidescan sonar: *Sedimentology*, v.46, no.1, p. 79-97, doi: 10.1046/j.1365-3091.1999.00204.x.
- Roberts, J. A., & Cramp, A., 1996, Sediment stability on the western flanks of the Canary Islands: *Marine Geology*, v.134, no.1-2, p. 13-30, doi: 10.1016/0025-3227(96)00021-7.
- Salaheldin, T. M., Imran, J., Chaudhry, M. H., & Reed, C., 2000, Role of fine-grained sediment in turbidity current flow dynamics and resulting deposits: *Marine Geology*, v.171, no.1-4, p. 21-38, doi: 10.1016/S0025-3227(00)00114-6.
- Sue, L. P., Nokes, R. I., & Davidson, M. J., 2011, Tsunami generation by submarine landslides: comparison of physical and numerical models: *Environmental fluid mechanics*, v.11, no.2, p. 133-165, doi: 10.1007/s10652-010-9205-9.
- Wang, Z., Li, X., Liu, P., & Tao, Y., 2016, Numerical analysis of submarine landslides using a smoothed particle hydrodynamics depth integral model: *Acta Oceanologica Sinica*, v.35, no.5, p. 134-140, doi: 10.1007/s13131-016-0864-3.
- Zakeri, A., Høeg, K., & Nadim, F., 2009, Submarine debris flow impact on pipelines—Part II: Numerical analysis: *Coastal engineering*, v.56, no.1, p. 1-10, doi:10.1016/j.coastaleng.2008.06.005.
- Zhu, H., Qi, X., Lin, P., & Yang, Y., 2013, Numerical simulation of flow around a submarine pipe with a spoiler and current-induced scour beneath the pipe: *Applied Ocean Research*, 41, p. 87-100, doi: 10.1061/(ASCE)GM.1943-5622.0000054.

Compressibility of solid phase of debris flow and erosion rate

Kuniaki Miyamoto^{a,*}, Takahiro Itoh^b, Hiroshi Kisa^c

^aResearch and Development Center, Nippon Koei Co., Ltd., 2304 Inarihara, Tsukuba 300-1259, Japan

^bCenter for Advanced Research and Development, Nippon Koei Co., Ltd., 2304 Inarihara, Tsukuba 300-1259, Japan

^cResearch Center for Advanced Research and Development, Nippon Koei Co., Ltd., 2304 Inarihara, Tsukuba 300-1259, Japan

Abstract

The change in sediment concentration of debris flow causes erosion and sedimentation of the solid phase of debris flows. Moreover, the changing affects the mobility of the flow. Therefore, knowledge of the mechanism of the changing is important to understand the mechanism of debris flow. The changing can be considered as compressibility of the flow of the solid phase. We developed a constitutive equation set of debris flow by concerning energy dissipation. A part of the energy dissipation is due to inelastic collision of particles. This process must be compressible. Therefore, we reinvestigate the process of the inelastic collisions and the effect to the compressibility. As the result, we lead internal energy to control the compressibility and so-called erosion rate equation. According to the erosion rate equation, it depends on bed gradient and energy loss gradient. A flume test is conducted to evaluate the erosion rate equation. by using a prismatic steep slope channel, which inclination is set at 12 degrees. By comparison of experimental result with the erosion rate equation, it is found that the difference between energy gradient and bed gradient to control the erosion/deposition is not so large. It means that the erosion/deposition might be very much sensitive against the unbalance of the energy gradient and bed gradient.

Keywords: Debris flow; Erosion rate, Compressibility; Flume tests

1. Introduction

Theoretical research of constitutive equations for debris flow can be categorized as (1) to define stress tensor to be satisfied mathematical requirement of tensor (Goodman & Cowin, 1972; Savage and Jeffrey, 1981; Jenkins and Savage, 1983; Iverson et al., 2001), (2) to define stress tensor based on momentum exchange, that is, interaction force, at the collisions (Bagnold, 1954; Hashimoto et al., 1983; Takahashi, 1980 & 1991) and (3) to define stress tensor by solving a simultaneous equation set of mass, momentum and kinetic energy conservation in accordance with continuum physics (Miyamoto, 1985; Egashira et al., 1997).

These theories are employed to explain the characteristics of the flow such as the resistance of the flow, sediment concentration and the transport rate of the sediment. However, in the process to derive the constitutive equations, the change in sediment concentration is not taken into account. Therefore, the simulation of the flow accompanied with changing in sediment concentration is somehow technical. We usually employ another equation to govern the change in sediment concentration. The changing causes bed aggradation and degradation. Therefore, erosion rate equation is usually introduced instead of the changing of sediment concentration. There are several researches on erosion rate (e.g., Takahashi, 1991, 2007; Egashira et al., 2001; Takahama et al., 2003). Those equations for bed entrainment are proposed conceptually.

Miyamoto (1985) discussed on the energy dissipation rate due to collision of neutral suspended particles in a simple shear flow by introducing inelasticity of particles to describe constitutive equation. In the process to derive it, it was needed to introduce the changing in sediment concentration at the instance of a collision and in a period from a collision to next collision. It means that the process must be basically compressible. Therefore, it could be applied to the changing process of sediment concentration.

* Corresponding author e-mail address: a8562@n-koei.co.jp

We modify the energy conservation law, so as to investigate the changing of sediment concentration and the erosion/deposition rate. A flume test to investigate the erosion rate using a prismatic steep slope channel with 12 degrees is also newly conducted. The erosion rate will be evaluated by the moving down velocity of upstream end of bed sediment which is parallelly set to the flume bed.

2. Governing Relationships of Compressibility and Erosion Rate

2.1. Governing relationships of compressibility

In the solid and liquid mixture flow, kinetic energy conservation equation is described as,

$$\frac{dK}{dt} + Ku_{i,i} = \rho_m g_i u_i + (u_i \sigma_{ij})_j - \Phi, \quad K = \frac{1}{2} \rho_m u_i u_i \quad (1)$$

where, K is the kinetic energy, t is the time, u_i is the velocity, i and j are the coordinate/components (=1 to 3), ρ_m is the averaged mass density of flow field, g_i is the acceleration of gravity, σ_{ij} is the stress tensor, “ $,i, ,j$ ” mean the partial difference operator and Φ is the energy dissipation. Notations of i and j obey the Einstein’s summation convention.

Equation (1) and mass and momentum conservation equations yield the following formula for energy dissipation.

$$\Phi = \frac{1}{3} \sigma_{ii} u_{j,j} + s_{ij} d_{ij} \quad (2)$$

where,

$$s_{ij} \equiv \frac{1}{2} (\sigma_{ij} + \sigma_{ji}) - \frac{1}{3} \sigma_{kk} \delta_{ij}, \quad d_{ij} \equiv \frac{1}{2} (u_{i,j} + u_{j,i}) - \frac{1}{3} u_{k,k} \delta_{ij}$$

Equation (2) means that energy dissipation rate is divided into deviatoric and isotropic parts. where, δ_i is the Kronecker’s delta

Figure 1 is a schematic view of the work rate and energy dissipation rate during a collision to next collision in simple shear flow proposed by Miyamoto (1985) and Egashira et al. (1997). In the figure, W is the work by stress and u_i' is the fluctuation component of velocity of solid particle. The space occupied by a particle is shrinking at an instance of collision and is expanding during a period from a collision to next collision. In the simple shear flow, the macroscopic flow field is incompressible. That is, both changings in occupied space by a particle, shrinking and expanding, are in balance. Moreover, in a simple shear flow, work rate by stress, dW/dt , and energy dissipation rate Φ must be in balance. That is, it must satisfy,

(Continuity in the flow field)

$$u_{i,i}' + n \frac{\Delta V}{V} = 0 \quad (3)$$

(Energy conservation law)

$$\frac{dW}{dt} + \Phi = 0. \quad (4)$$

in which, n is the number of the collision in a unit time, V is the space occupied by a particle, and ΔV is the volumetric change after particle to particle collision and takes negative value. The work rate and energy dissipation rate Φ in Eq. (4) is expressed by using intergranular pressure p_s and expanding/shrinking rate, $u_{i,i}$, $\Delta V/V$, as follows.

$$\frac{dW}{dt} = -p_s u_{i,i}', \quad \Phi = -p_s n \frac{\Delta V}{V} \quad (5)$$

Equation (4) can be enhanced to compressible flow field. When we note the energy dissipation rate in compressible state Φ_T , Eq. (4) is re-written as,

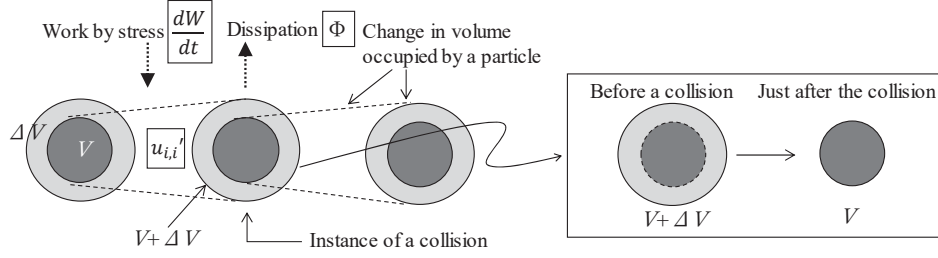


Fig. 1. Schematics of changes in space occupied by a particle and energy flow due to collisions

$$\frac{dW}{dt} + \Phi_T = 0. \quad (6)$$

Equation (5) is also rewritten as

$$\frac{dW}{dt} = -p_s u'_{i,i} = -p_s \left\{ (u'_{i,i} + n \frac{\Delta V}{V}) - n \frac{\Delta V}{V} \right\} = -p_s (u'_{i,i} + n \frac{\Delta V}{V}) + p_s n \frac{\Delta V}{V}. \quad (7)$$

$$\Phi_T = -\frac{dW}{dt} = p_s (u'_{i,i} + n \frac{\Delta V}{V}) + \Phi. \quad (8)$$

The second term in brackets of right side of Eq. (8) must be equal to divergence of the macroscopic flow field, that is,

$$u'_{i,i} + n \frac{\Delta V}{V} = u_{i,i} \quad (9)$$

When we introduce Φ_i as follows, we can define something like an internal energy, E_i , too,

$$\Phi_i \left(= \frac{dE_i}{dt} \right) \equiv p_s u_{i,i}, \quad (10)$$

and Φ_T is expressed by sum of internal energy changing rate and energy dissipation rate, as follows.

$$\Phi_T = \Phi_i + \Phi. \quad (11)$$

Herein, Φ_i depend on the divergence of flow field, so that E_i is reversible energy because the value of E_i increases as positive divergence, and E_i decreases as negative divergence.

The continuity equation of flow field is expressed by using sediment concentration in the sediment-water mixture layer as follows,

$$\frac{dc}{dt} + c u_{i,i} = 0 \quad (12)$$

where, c is the volumetric concentration. Eq. (12) can be re-written as

$$u_{i,i} = -\frac{1}{c} \frac{dc}{dt} = -\frac{d}{dt} (\log c). \quad (13)$$

Substituting of Eq. (13) into Eq. (10) yields

$$\Phi_i = \frac{dE_i}{dt} = -p_s \frac{d}{dt} (\log c). \quad (14)$$

Using the condition that $c = c^* \rightarrow E_i = 0$ in Fig. 2, integration of Eq. (14) along the plane, $p_s = \text{constant}$, yields

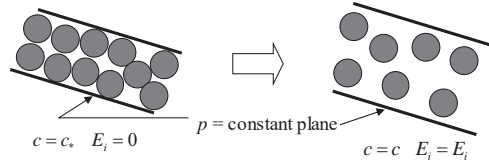


Fig. 2. Schematics of flow field

$$E_i = -p_s \log\left(\frac{c}{c^*}\right). \quad (15)$$

E_i depends on concentration profile. Sediment concentration profile depends on bed gradient. In following discussion, we assume that the sediment moving layer does not reach to the flow surface. It means that the gradient is relatively gentle, it must be less than 10 to 12 degrees. We also assume that the sediment concentration in sediment moving layer is as shown in Fig. 3, That is, the concentration at the bed is c^* , and 0 at the surface of sediment moving layer, and the profile is linear. It yields the average sediment concentration over the sediment moving layer, c_s , should be equal to $c^*/2$. And, it must be noted that $E_i = 0$ at the bed.

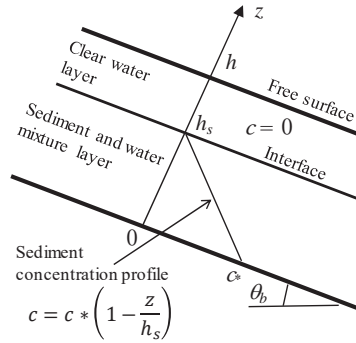


Fig. 3. Schematics figure of debris flow with two-layer, sediment moving layer and clear water layer

Pressure profile with a linear profile of sediment concentration in the sediment moving layer is expressed as

$$p_s = c_s s \rho g h_s \left(1 - \frac{z}{h_s}\right)^2 \cos \theta_b, \quad s = \frac{\sigma}{\rho} - 1. \quad (16)$$

where, σ is the mass density of sediment, that is solid phase, ρ is the mass density of clear water, that is liquid phase, z is the vertical axis normal to the bed, h_s is the thickness of sediment and water mixture layer and θ_b is the bed slope.

Substituting of Eq. (16) to Eq. (15) and integrating it over the depth, E_i of the flow, E_{iT} , is obtained as follows.

$$E_{iT} = \frac{1}{9} c_s s \rho g h_s^2 \cos \theta_b \quad (17)$$

2.2. Equations for erosion rate

From Eq. (17), erosion rate can be derived. The time differential of the E_{iT} , Eq. (17), is

$$\frac{dE_{iT}}{dt} = \frac{2}{9} c_s s \rho g h_s \cos \theta_b \frac{dh_s}{dt} = \frac{2}{9} c_s s \rho g h_s \cos \theta_b \left(\frac{\partial h_s}{\partial t} + u_{st} h_{s,t}\right). \quad (18)$$

Herein, the bed elevation changing, that is erosion/deposition rate, is expressed by using the continuity relation for solid phase, as follows.

$$\frac{\partial h_s}{\partial t} + (h_s u_{si})_i = -\frac{c_s}{c_s} \frac{\partial z_b}{\partial t} \quad (19)$$

where, z_b is the bed elevation and u_{si} is the velocity of sediment that is solid phase.

Substituting of Eq. (19) into Eq. (18) under the assumption of slow and gentle changing of the flow, $u_{si} h_{s,i} \cong 0$, the relationship between the changing of E_{iT} and the bed elevation changing is expressed as

$$\frac{dE_{iT}}{dt} = \Phi_i \cong -\frac{2}{9} c_s s \rho g h_s \cos \theta_b \frac{c_s}{c_s} \frac{\partial z_b}{\partial t} = -\frac{4}{9} c_s s \rho g h_s \cos \theta_b \frac{\partial z_b}{\partial t} \quad (20)$$

The work rate, that is shown in Eq. (6), in the energy conservation law in compressible flow can be expressed by using bed gradient as

$$\frac{dW}{dt} \cong \int_0^{h_s} (1 + c_s s) \rho g \sin \theta_b u_s dz. \quad (21)$$

From Eq. (6), therefore, Φ_T can be evaluated as

$$\Phi_T \cong (1 + c_s s) \rho g h_s \sin \theta_b \bar{u}_s. \quad (22)$$

where, \bar{u}_s is the representative velocity in the sediment moving layer. Equation (11) corresponds to real energy dissipation, Φ , and that in in Eq. (5) can be expressed by using energy slope, $\sin \theta_e$,

$$\Phi \cong (1 + c_s s) \rho g h_s \sin \theta_e \bar{u}_s. \quad (23)$$

From Eq. (11), Φ_i is derived as follows.

$$\Phi_i = \Phi_T - \Phi = (1 + c_s s) \rho g h_s \bar{u}_s (\sin \theta_b - \sin \theta_e) \quad (24)$$

Then, substituting of Eq. (24) into Eq. (20) yields the following deposition rate equation.

$$\frac{\partial z_b}{\partial t} = -\frac{9}{4} \frac{(1+c_s s)}{c_s s} \bar{u}_s \frac{(\sin \theta_b - \sin \theta_e)}{\cos \theta_b}. \quad (25)$$

Introducing an approximation, $\theta \cong \theta_b \cong \theta_e$, yields

$$\frac{\partial z_b}{\partial t} = -\frac{9}{4} \frac{(1+c_s s)}{c_s s} \bar{u}_s (\tan \theta_b - \tan \theta_e). \quad (26)$$

3. Flume Tests and Those Results

To evaluate the characteristics of erosion rate equation, a flume experiment was conducted. The flume dimensions are around 8 m in length, 10 cm in width and 40cm in depth. Bed slope of the flume is 12 degrees. Sediment is set on the bed with longitudinally constant thickness, 10 cm, and is saturated. Only clear water is supplied steadily at 1.0 l/s from upstream end on the saturated sediment. A permeable weir is set at the downstream reach. The value of equilibrium flux sediment concentration correspond to bed gradient 12 degree is 0.220 (e.g., Egashira et al., 1997). The physical property of the sediment is as follows: d_{60} is 1.47 mm, $d_{max}=4.75$ mm, $\sigma/\rho= 2.63$, $\phi_s= 36.9$ degrees and $c_s=0.547$, where d_{60} is the 60% diameter, d_{max} is the maximum diameter of sediment and ϕ_s is the interparticle friction angle.

Figure 4 shows temporal changes of flux sediment concentration at downstream end. Herein, time “0” is the time that clear water was sullied at the upstream end. In the figure, equilibrium flux sediment concentration (0.220) is also shown. This figure shows that equilibrium state is established for around 80 sec. since the flow is reaching to downstream end. Fig. 5 shows temporal changes of longitudinal bed shapes and the time evolution of upper end of movable bed. In Fig. 5 (a), coordinate x is set along to the flume bed. From Fig. 5 (b), the velocity of erosion of upper end along to the flume bed, u_b , is obtained and is almost constant, $u_b = 0.052$ m/s. If the velocity of erosion along to

the flume bed is the same over the bed, bed profile is not change. If the profile is maintained, transforming coordinate from x to X , $X = x - u_b \Delta t$, $\Delta t = t_0 - t$, all of bed profiles must be plotted in one line. Fig. 6 is the result of the transformation. The reference time, t_0 , in Fig. 6 is 47 s, and it is found that all of bed profiles fall on the same line.

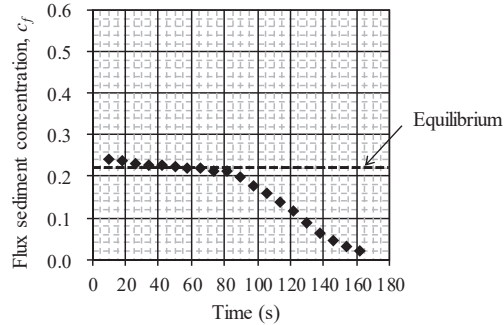


Fig. 4. Temporal changes of flux sediment concentration measured at downstream end

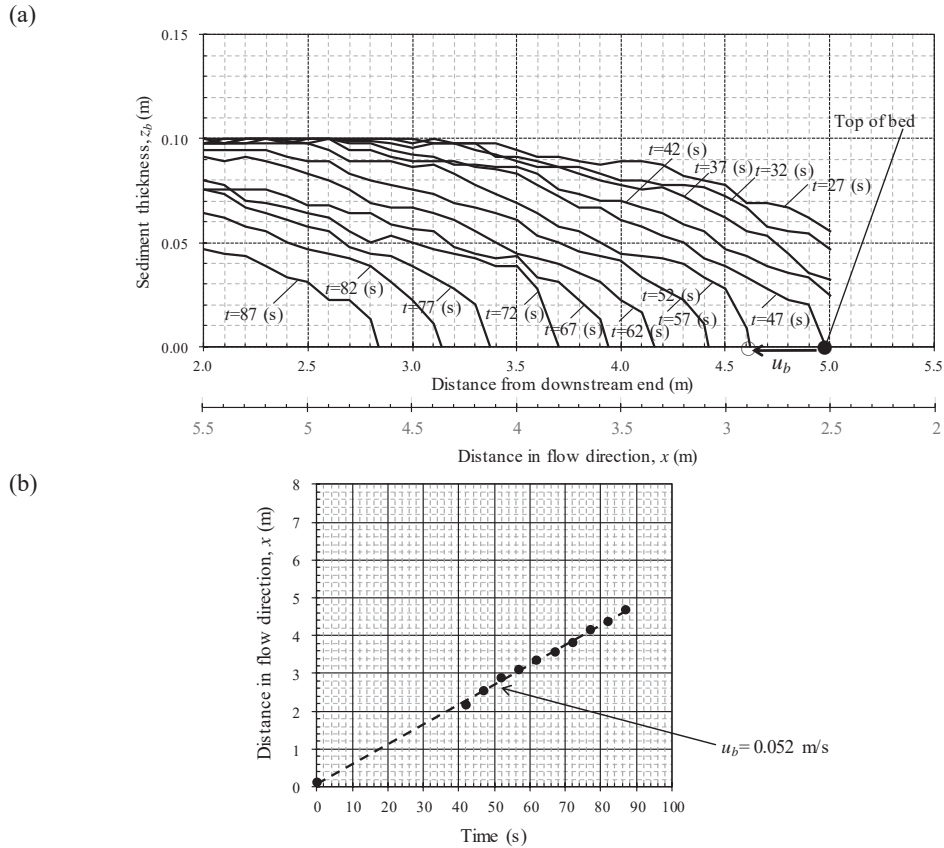


Fig. 5. (a) Temporal changes of longitudinal bed shapes and (b) Time evolution of upper end point of movable bed

Present tests were carried out for bed erosion over the constant sediment thickness on the rigid bed. In case of erosion of sediment on the rigid bed as shown in Fig. 7, the erosion rate is schematically expressed as

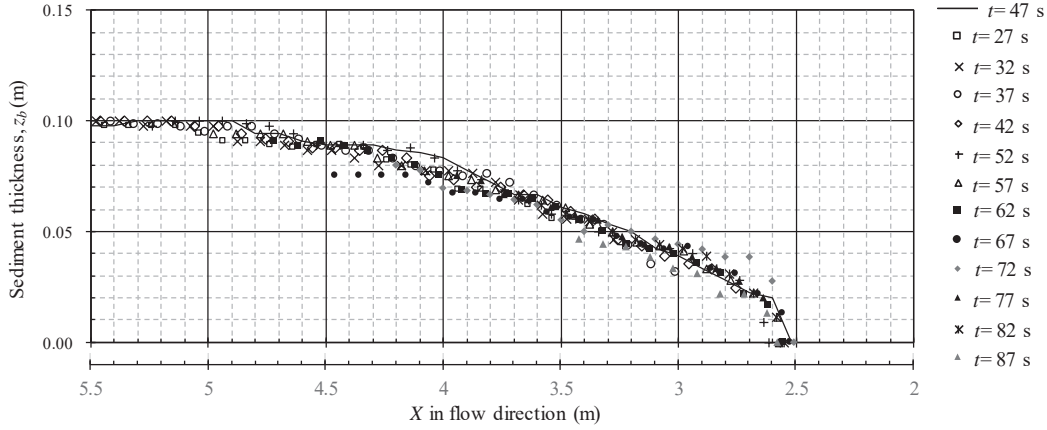


Fig. 6. Longitudinal bed shapes obtained by transformed distance in flow direction

$$\frac{\partial z_b}{\partial t} = -u_b \tan(\theta_\infty - \theta_b). \quad (27)$$

where, u_b is the erosion rate along the direction of rigid bed slope with θ_∞ .

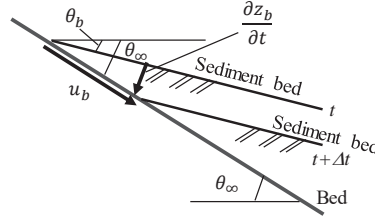


Fig. 7. Schematics of bed erosion

Relation between θ_e and θ_b as shown in Fig. 7 is discussed using flume data for u_b , \bar{u}_s , and proposed erosion rate, Eq. (26). Substituting of Eq. (27) into Eq. (26) yields

$$\frac{u_b}{\bar{u}_s} = \frac{9(1+c_s s) \tan \theta_b - \tan \theta_e}{4 c_s s \tan(\theta_\infty - \theta_b)}. \quad (28)$$

Introducing following approximations, $\tan(\theta_\infty - \theta_b) \cong \tan \theta_\infty - \tan \theta_b$, $\tan \theta_b - \tan \theta_e \cong \tan(\theta_b - \theta_e)$, Eq. (28) is also expressed

$$\frac{u_b}{\bar{u}_s} = \frac{9(1+c_s s) \tan \theta_b - \tan \theta_e}{4 c_s s \tan \theta_\infty - \tan \theta_b} \quad \text{or} \quad \frac{u_b}{\bar{u}_s} = \frac{9(1+c_s s) \tan(\theta_b - \theta_e)}{4 c_s s \tan(\theta_\infty - \theta_b)} \quad (29)$$

If the bed erosion can be progressed with maintaining of the bed shape, the bed erosion rate along the direction of θ_∞ , $u_b(x)$, can take constant value. Supposing that \bar{u}_s takes constant value over the bed, the following takes constant values.

$$\frac{\tan \theta_b - \tan \theta_e}{\tan(\theta_\infty - \theta_b)} \cong \frac{\tan \theta_b - \tan \theta_e}{\tan \theta_\infty - \tan \theta_b} \cong \frac{\tan(\theta_b - \theta_e)}{\tan(\theta_\infty - \theta_b)} \quad (30)$$

When the constant value of u_b/\bar{u}_s is obtained by flume tests, Eq. (30) can be determined experimentally. To evaluate the relation in Eq. (30), u_s must be known in addition to u_b . The flow surface velocity, u_w , is measure instead

of u_s . And u_b/u_w takes almost constant value $1/27$ to $1/28$ ($\cong 1/30$). Free surface velocity u_w is larger than u_s , then u_b/u_w is smaller than u_b/u_s . Supposing $u_s \cong u_w/2$, $u_b/u_s \cong 1/15$ is satisfied, and then the value of Eq. (30) takes constant value about 0.01. This means that the difference of bed gradient and energy gradient is extremely smaller than the difference of two angles θ_∞ and θ_b , and is less than $0.01 \tan \theta_\infty$. Consequently, θ_e is almost same as θ_b , and the state is close to equilibrium. It means that small difference of energy gradient with bed gradient, such as disturbance, leads to relatively erosion/sedimentation. Therefore, we may find easily anti-dune formation under equilibrium state.

4. Conclusions

The constitutive equation of the erosion rate is newly derived based on the energy conservation law considering the compressibility of solid phase, and the erosion rate is evaluated by flume tests.

- (1) Erosion rate, Eq. (26), is derived based on energy conservation law focused on compressibility of flow field. We investigate the effect of the inelasticity to the flow and define some “internal energy” to control the compressibility. The time differential of the depth integrated internal energy, and difference between the time differential and work rate yield erosion rate by using continuity of solid phase in the sediment moving layer. The ratio of erosion rate to the flow velocity of sediment moving layer is proportional to difference between bed slope and equilibrium bed slope.
- (2) Flume tests are carried out using a prismatic steep slope channel of 12 degrees in slope. Erosion rate is evaluated by erosion of bed sediment around upstream reach of parallelly deposited sediment to the flume bed in steady flow. A speed of the upper endpoint of movable bed, u_b , due to erosion process is almost constant, and longitudinal bed shape during erosion process keeps the shape. Then, by using moving coordinate with u_b in flow direction, the bed profile has similarity in geometry.
- (3) In comparison of experimental data with the erosion rate equation, energy gradient is not so much different with bed gradient. It means that small disturbance in energy gradient may cause something like anti-dune formation.

As future issues, we need to investigate the longitudinal bed profile, sedimentation process as well as more cases of erosion.

Acknowledgements

Authors would like to thank members of the Research and Development Center of Nippon Koei Co. Ltd., for conducting present flume tests and collecting the experimental data.

References

- Bagnold, R. A., 1954, Experiments on gravity-free dispersion of large solid spheres in Newtonian fluid in under shear: *Proceedings of Royal Society of London*, A225, p. 49-63.
- Egashira, S., Miyamoto, K., and Itoh, T., 1997, Constitutive equations of debris flow and their applicability, in *Proceedings C-L. Chen (ed.), 1st International Conference of Debris-flow Hazards Mitigation: Mechanics, Prediction, and Assessment*: San Francisco, ASCE, p. 340-349.
- Egashira, S., Honda, N., and Itoh, T., 2001, Experimental study on the entrainment of bed material into debris flow: *Journal of Physics and Chemistry of the Earth, Part C*, v. 26, no. 9, p. 645-650.
- Goodman, M. A., and Cowin, S. C., 1972, A continuum theory for granular materials: *Archive for Rational Mechanics and Analysis*, 44, Springer, p. 249-266.
- Hashimoto, H., and Tsubaki, T., 1983, Reverse grading in debris flow: *Proc. JSCE*, 336, p. 75-84 (in Japanese).
- Iverson, R. M., Denlinger, R. P., 2001, Flow of variably fluidized granular masses across three-dimensional terrain 1. Coulomb mixture theory: *Journal of Geophysical Research*, 106 B1, p. 537-552.
- Jenkins, J. T. and Savage, S. B., 1983, A theory for the rapid flow of identical, smooth, nearly elastic particles: *Journal of Fluid Mechanics*, 130, p. 187-202.
- Miyamoto, K., 1985, Study on the grain flows in Newtonian fluid [Ph. D. thesis]: Ritsumeikan University (in Japanese).
- Savage, S. B., and Jeffrey, D. J., 1981, The stress tensor in a granular flow: *Journal of Fluid Mechanics*, 110, p. 252-272.
- Takahama, J., Fujita, Y., Hachiya, K., and Yoshino, K., 2003, Application of two layer simulation model for unifying debris flow and sediment sheet flow and its improvement, in *Proceedings Rickenmann & C-L. Chen (ed.), Debris-flow Hazards Mitigation: Mechanics, Prediction, and Assessment*: Davos, Switzerland, Sep. 10-12, Millpress, Rotterdam, p. 515-526.
- Takahashi, T., 1980, Debris flow on prismatic open channel: *Journal of Hydraulic Engineering*, ASCE, 106, HY3, p. 381-396.
- Takahashi, T., 1991, Debris flow: Monograph series (International Association for Hydraulic Research): Rotterdam, Brookfield, A.A. Balkema, 165 p.
- Takahashi, T., 2007, Debris flow -Mechanics, Prediction and Countermeasures: Leiden, Taylor & Francis/Balkema, 448 p.

Commonalities between debris flows and flow failures

Robb Eric S. Moss, Ph.D., P.E., F.ASCE ^{a,*}

^aProf. Dept Civil and Environmental Engineering, Cal Poly, San Luis Obispo, CA 93401

Abstract

Debris flow and flow failure are terms used to describe large displacement slope failures. The initiation or triggering often differs due to the nature and state of the material, but once triggered these two failure mechanisms both tend to behave like a Bingham plastic exhibiting a yield strength and a strain-rate dependent strength. In this paper the rheology of these failures is examined and compared to field data and lab data to find commonalities. A future goal is to move towards a common definition of the physics and a joint empirical database for improved statistics and predictive models. The authors own field investigations in Chile and lab investigations using shake table experiments will be reviewed along with studies by other researchers.

Keywords: flow failure; debris flow; liquefaction; residual strength; steady state; critical state; mine tailings; colluvium

1. Introduction

Debris flows and flow failures are both forms of particulate behavior that result in flows with large runout distances, ranging from 10's to 1000's of meters (Hung, 1995; Iverson, 1997; Yazdi & Moss, 2015). Debris flow typically describes failure of a naturally deposited heterogeneous coarse grained material (e.g., colluvium) that has been triggered by a high intensity rainfall event or other mechanism resulting in rapid flow-type behavior. Flow failure typically describes failure of a man-made material (e.g., mine tailings) or uniform natural material (e.g., sand) that has been triggered statically or seismically resulting in rapid flow-type behavior. In both failure mechanisms the bulk soil/rock mass fluidizes, resulting in low shear strength and little resistance to deformation. Triggering of these failure mechanism can come about in many different ways, and the runout is a function of several specific mass and intergranular conditions, but the flow phase of these failures are physically the same. In this paper the commonalities and differences of debris flows and flow failures are explored to arrive at some understanding of the physics. Then some recent studies are discussed that evaluate the flow characteristics of fluidized particulate material.

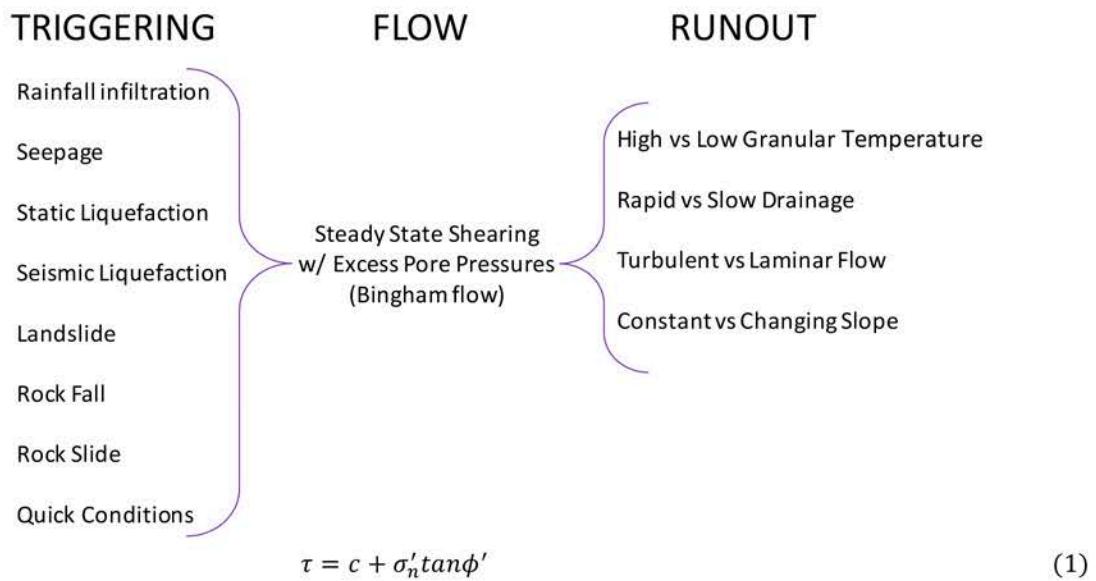
2. Flow Commonalities

Debris flows and flow failures can be triggered in a number of different ways, and can exhibit different amounts of runout, but both failures have similar flow characteristics (Iverson et al., 1997; Sassa, 2000; Kramer, 1988; Hung, 1995). Figure 1 shows a schematic separating the triggering, from the flow, and the runout. The following discussion will define these terms and their physics.

The flow phase of both debris flows and flow failures can be characterized as steady state shearing with excess pore pressures (Figure 2a). Steady state meaning that the critical void ratio ($e_{critical}$) has been reached where no further contraction or dilation is needed to continue shearing the soil (Schofield & Wroth, 1968) at a residual shear strength ($\tau_{residual}$). With the addition of excess pore pressures the soil can exhibit flow-like behavior.

This behavior is consistent for both uniform (e.g., beach sand) and non-uniform (e.g., colluvium) materials. The shear strength (τ), or the shear stress at which the soil “fails”, is generally defined by the contributions of any cohesion (c) and stress dependent (σ'_n) inter-particle friction (ϕ') as shown in Equation 1 (Terzaghi, 1951). In the case of granular material, the cohesion term is often negligible.

* Corresponding author: rmoss@calpoly.edu



The stress dependence is influenced by the pore pressure (u) as shown in Equation 2 (Terzaghi, 1951) where (σ'_n) is the normal effective stress and (σ_n) is the normal total stress. Pore pressures will increase to the point that the frictional forces are reduced below some threshold, allowing the soil to flow.

$$\sigma'_n = \sigma_n - u \tag{2}$$

Sufficiently sheared particulate materials approach a steady state response regardless of if they have the capacity to initially dilate or contract (Figure 2a). Once steady state is achieved and if excess pore pressure are sufficient the material can approach a flow threshold. The threshold to flow is often represented in terms of non-Newtonian flow as shown in Figure 2b. If we restrict flow to laminar conditions (Reynolds number, $R_e < 5$) then we can treat the fluid as visco-plastic (i.e., Bingham plastic). The characteristic of a non-Newtonian fluid like a Bingham plastic is that it has

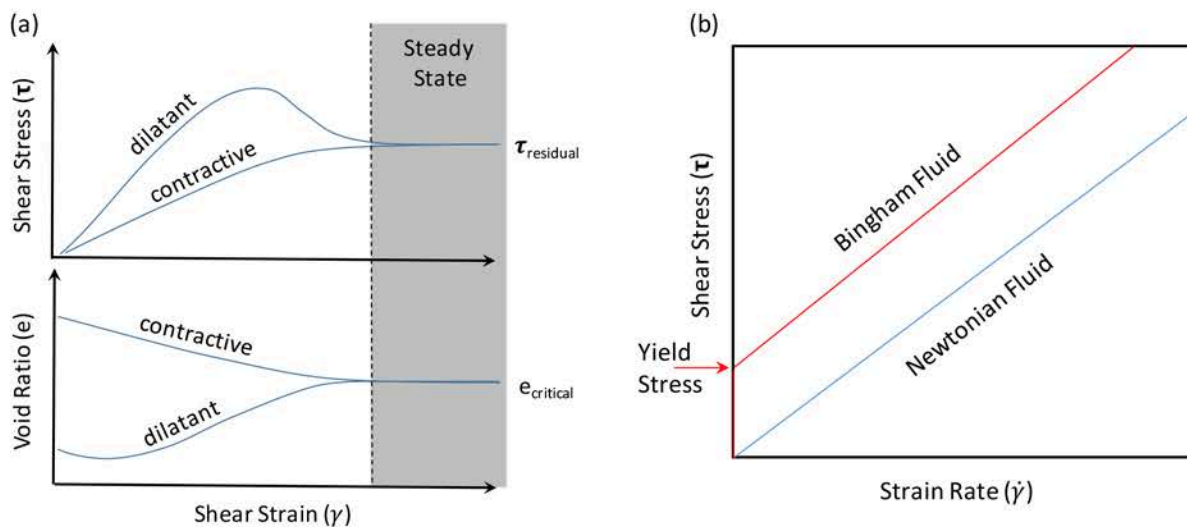


Figure 2. (a) Qualitative plot of dilatant and contractive behaviour of granular soils when subjected to shearing. Sufficient shearing will result in a steady state response at a critical void ratio and a residual shear strength. (b) Diagram showing Newtonian and Non-Newtonian fluid response to strain rate. A non-Newtonian fluid such as a Bingham fluid will deform after the shear stress exceeds a material specific yield stress.

some limiting yield strength followed by a strain rate ($\dot{\gamma}$) dependent shear strength. This behavior is typically explained in a physical manner by stating that the fluid has particles that provide some limiting stress threshold.

3. Triggering and Runout Dissimilarities.

If flow can be posited as the same for debris flows and flow failures, what of the triggering and runout? Here the two failure mechanisms differ greatly. The triggering can come about in many different ways, all resulting in steady state behavior with excess pore pressures. Whether the material starts out as dilatant colluvium (Anderson and Sitar, 1995) or contractive mine waste (Bryant, Duncan, and Seed, 1983) the steady state flow behavior can be described the same. Figure 3 is a conceptual summary of lab tests showing both contractive and dilatant materials achieving the critical state line.

Runout distance from a hazard perspective is an important parameter to be able to forecast. Unfortunately the complexity of the physics has so far rendered this a daunting task (Lucia, Duncan, and Seed, 1981; Jeyapalan, Duncan, and Seed, 1983a and b; Bryant, Duncan, and Seed, 1983; Hungr, 1995; Iverson et al., 2010). The duration in which the material remains in a fluidized state is a primary variable that controls runout distance. This is influenced by any change in slope, two dimensional effects of topography, the presence of an impeding or impermeable layer above/below the fluidized soil, if the flow is behavior is laminar or turbulent, the granular “temperature” or granular kinetics, and possibly other variables. Granular temperature (Iverson, 1997) is a term that describes behavior of heterogeneous particle sized materials that during flow tend to translate potential energy (slope) into kinetic energy (relative particle dilation) that results in continued capacity of the material to contract and generate more excess pore pressures. Hungr (1995) proposed a model that has been shown to capture runout for flow failures in tailings material adequately for most simple 2D situations based on back-analysis of field case histories. More complex geometries and source materials have not been as well captured.

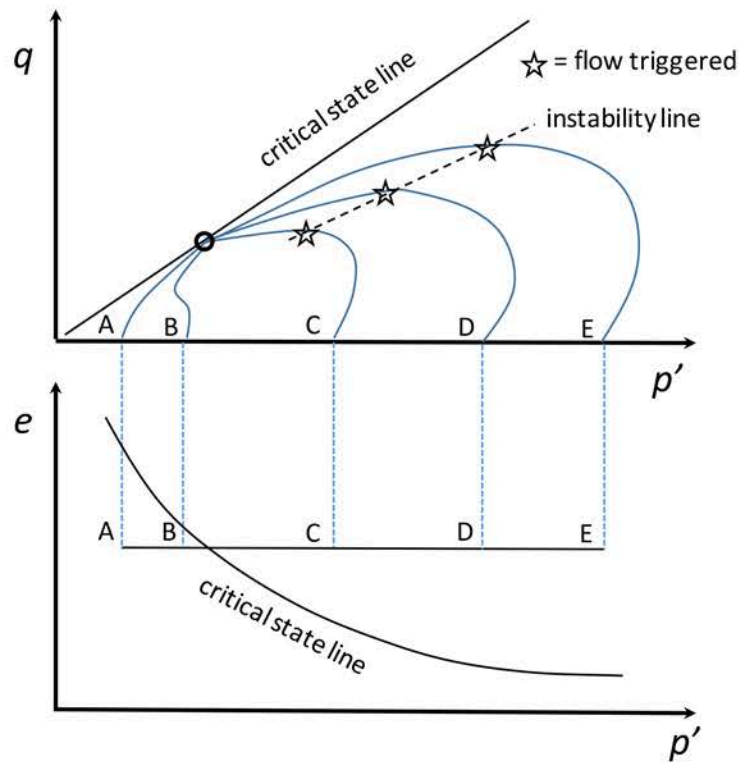


Figure 3. Triggering of flow liquefaction with respect to the critical state line (after Kramer, 1996; Lade, 1999). The top plot shows soil triaxial test results plotted as mean effective stress (p') versus deviatoric stress (q). The bottom plot shows the same results plotted against void ratio (e). All samples achieved steady state “failure” at the critical state line but flow liquefaction occurred along the instability line in contractive soil prior to steady state.

4. Lab and Field Measurements

Two recent studies, supervised by the author, on flow failure and steady state response are described here. The first is a full scale laboratory experiment that captured the residual strength of liquefied soil (Honnett, 2018). In this test a large flexible bucket (1.5 m high by 2.3 m diameter) containing loose saturated Monterey sand was placed on a 10 ton shake table and excited with a harmonic motion at its resonant frequency to induce seismic liquefaction. During liquefaction, in addition to acceleration and pore pressure measurements, a T-bar was pulled through the liquefied soil to measure the steady state shear strength. Prior research (Randolf and Houlsby, 1984; Tokpavi et al., 2008 and 2009) has shown that in a laminar state the flow can be characterized by a closed form solution using a cylinder which the T-bar mimics. Other table top and centrifuge experiments have attempted similar residual strength measurements (de Alba and Ballesterro, 2006; Dewoolkar et al., 2016). The shake table results show that for loose ($e > e_{crit}$) uniform sand at a low confining stress of 0.1 atm the steady state residual strength is roughly 1.4 kPa, with a cone penetration resistance of $q_{c1} \approx 0.2$ MPa. Full details on this study are currently under review for publication elsewhere, but the thesis work can be accessed online (Honnette, 2018).

The second study is a field investigation on a seismic induced flow failure from the 2010 M8.8 Chile earthquake (GEER, 2010). Strong ground shaking caused the liquefaction and subsequent flow failure of a tailings dam of mine waste at a defunct gold mine. The 25m high embankment experienced liquefaction at its base resulting in a runout of up to 350 m on shallow slopes. This failure was investigated thoroughly (Moss et al., 2018) and used to develop a detailed case history for future reference (Gebhart, 2017). The failed slope was evaluated against engineering runout distance methods and was back-analyzed to determine an estimate of the steady state residual strength. Here the confining stress conditions were roughly 2 atm and the estimated liquefied residual strength was 8.3 kPa. The soils were measured as contractive ($e < e_{crit}$) based on low cone penetration resistance ($q_{c1} \approx 1.3$ MPa) with respect to Yazdi and Moss (2015) as shown in Figure 4a. Figure 4b shows the results from these investigations plotted against a revised plot of penetration resistance versus liquefied residual strength. The red star is this particular case history with respect to the known database of flow failures (Weber et al., 2015). It should be noted that the analytical “dam break” solution by Hungr (1995) provides an excellent estimate of the observed runout distance of 350 m for this particular failure.

A different study on debris flows was carried out by McKenna et al. (2014). This table top experiment focused on a range of materials that could fail in a debris flow and characterized their properties. The authors used a test mold where the prepared samples could be saturated. The mold is then quickly removed to horizontally load and fail the

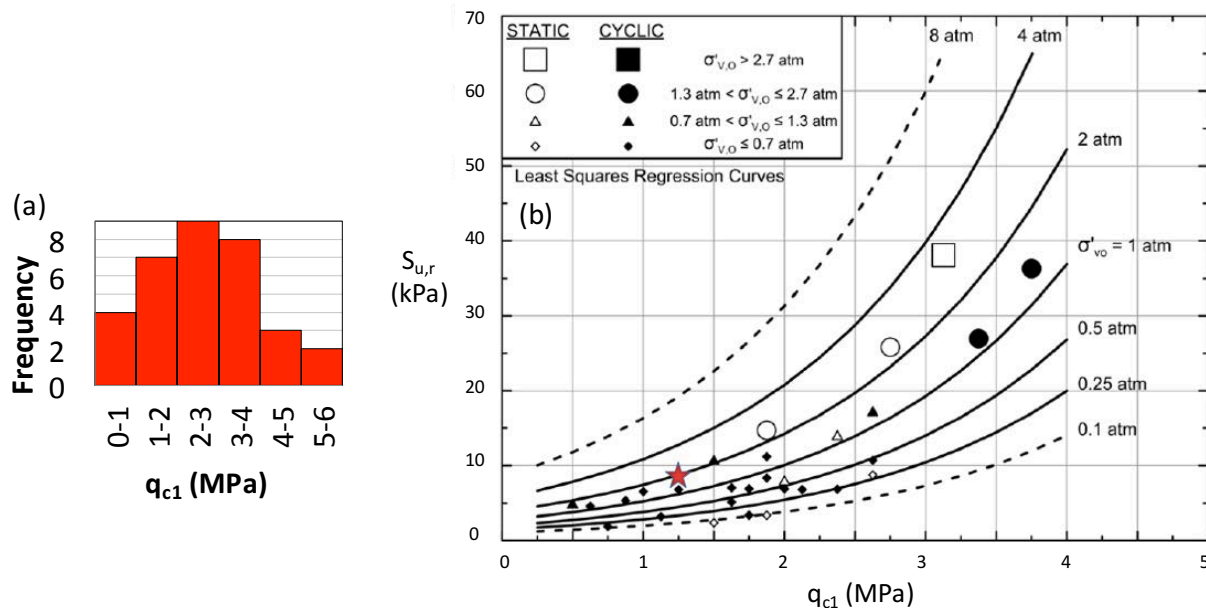


Figure 4. (a) Histogram of cone penetration resistance (q_{c1}) values of flow failure case histories from the Olson & Stark (2002) database (after Yazdi and Moss, 2016). (b) Plot (revised after Weber et al., 2015) correlating penetration resistance to the liquefied residual strength. Red star shows the location of the Las Palmas tailings dam flow failure.

soil in a radial pattern for capturing the failure mode and subsequent deformations. The results generally agreed with large flume experiments (Iverson et al., 2000; Logan and Iverson, 2009). Some of the test results that are pertinent to this discussion are that the density, and hence the void ratio, dictated whether the soil sample would fail as a flow ($e > e_{crit}$) or as a slide ($e < e_{crit}$). [Note: $\rho_d = \rho_s / (1 + e)$ dry density is equal to the density of the solids divided by one plus the void ratio, and $\rho_{sat} = (\rho_s + \rho_w e) / (1 + e)$ saturated density is equal to the density of solids plus the density of water times the void ratio divided by one plus the void ratio]. Soils that were initially dilatant were capable of dilating past critical state rendering them susceptible to flow during subsequent loading. Failure velocity increased with permeability, and loose soils ($e > e_{crit}$) exhibited higher failure velocities. The analytical “dam break” solution of Hungr (1995) is used here to back-calculate the liquefied residual strength of the samples that were observed to have failed in flow. The equation for “dam break” when rearranged and solved for the liquefied residual strength is:

$$s_{u,r} = 4 \left(\frac{\gamma H_o^2 \frac{x_o}{2} x_f - \frac{9}{16} \gamma H_o^2 x_o^2}{x_o^2 x_f - x_f^3} \right) \quad (3)$$

where $s_{u,r}$ is the liquefied residual strength (kPa), γ the unit weight (kN/m³), H_o the initial height of the “dam” material (m), x_o the initial length of the “dam” material (m), and x_f the runout distance of the flow failure (m). In this simplified solution the initial slope is treated as vertical and the runout shape is treated as a parabola. The liquefied residual strength values from these table top tests at essentially zero confining stress show an average of roughly 6.5 kPa, with a low of 1.7 kPa and a high of 11.9 kPa. The samples are from slope failures sites that covered a range of source materials from gravels to sands (both with fines content) and are representative of the *in situ* field gradations. The liquefied residual strength values from these debris flow materials are in agreement with those observed in tailings flow failure materials and in clean sand liquefaction tests discussed previously.

5. Discussion

In cases of flow failure and debris flows the density or void ratio with respect to the critical density or critical void ratio is a primary controlling variable of flow-like behavior. The *in situ* properties of soil are regularly estimated in engineering situations using cone penetration measurements that are statistically related to engineering properties. Contractive soils exhibit a positive state parameter:

$$\psi = e - e_{crit} \quad (4)$$

For clean sands the state parameter can be estimated using an empirical relationship as found in (Robertson and Cabal, 2014):

$$\psi = 0.56 - 0.33 \log Q_{tn,cs} \quad (5)$$

where $Q_{tn,cs}$ is the stress corrected cone tip resistance of a clean sand, similar to the curves in in Figure 4b but in dimensionless form. So for sandy soils, if they are sufficiently contractive and fully saturated, then flow is the likely failure mechanism which can be forecast using cone penetration measurements.

Fluvially deposited gravels, cobbles, boulders, usually exhibit dilatant behavior due to the nature of the particles and the high energy depositional environment that formed the units. Dilatant material can be pushed into a contractive state by changes in stress as seen in Figure 3 and also to steady state by constant shearing. The propensity for these materials to fail in a debris flow is harder to predict because the flow behavior occurs after large strains and post-peak-strength failure. Here granular kinetics (i.e., granular temperature) is thought to increase the void ratio and the contractive-ness of the material as it tumbles downslope, thereby producing high excess pore pressures and flow condition.

Dry colluvially deposited gravels, cobbles, boulders can exhibit contractive behavior because of the low energy depositional environment that formed these units and therefore can be susceptible to flow type failure when saturated during intense rainfall. Here penetration measurements are not viable because of large particle sized material, but geophysical measurements may be. In soil liquefaction a shear wave velocity of less than roughly 180

m/s (Kayen et al., 2013) is indicative of a contractive soil and subsequent field testing may be useful in refining this value for soils with large particle sizes (e.g., boulders, cobbles, gravels).

As in all these cases the saturation level and contractive behavior are key in determining the likelihood of triggering, post-liquefaction residual strength, and propensity for flow failure.

6. Summary

Presented here are some thoughts on the different phases of flow failures and debris flows, which defines different regions of physics of these failures. Steady state flow with excess pore pressures has been observed to be in common between flow failures and debris flows. The physics of this phase is examined using conceptualized lab results to understand the stress-strain response. Empirical studies of flow failures and debris flows were also examined and the liquefied residual strength were shown to be in rough agreement supporting the argument that this phase is common. Some suggestions were offered as to how best to identify the hazard for different field conditions. The overall goal here is to foster further discussion of their commonalities and to help push hazard mitigation of debris flows and flow failures forward.

Acknowledgements

The author's research on the Chilean flow failure was supported by NRC, SWRI, and CalTrans through the PEER NGL program. The initial investigations of the Chilean flow failure were supported by GEER and NSF. The author's shake table experiments were supported in part by NavFac.

References

- Anderson, S. A., and Sitar, N. 1995, Analysis of rainfall-induced debris flows. *Journal of Geotechnical Engineering*, 121(7), 544-552.
- Bryant, S. M., Duncan, J. M., & Seed, H. B. 1983, Application of tailings dam flow analyses to field conditions. Report UCB/GT/83-03, Department of Civil Engineering, University of California, Berkeley, Calif.
- de Alba, P., and Ballesterio, T. P. 2006, "Residual strength after liquefaction: A rheological approach." *Soil Dyn. Earthquake Eng.*, 26(2-4), 143-151.
- Dewoolkar, M., Hargy, J., Anderson, I., de Alba, P., and Olson, S.M. 2016, "Residual and Postliquefaction Strength of a Liquefiable Sand." *J. Geotech. Geoenviron. Eng.*, 142(2): 04015068.
- Gebhart, T. 2016, Post-Liquefaction Residual Strength Assessment of the Las Palmas, Chile Tailings Failure. Thesis in partial fulfillment of MS degree. Cal Poly, San Luis Obispo, CA.
- GEER. 2010, Geo-Engineering Reconnaissance of the February 27, 2010 Maule, Chile Earthquake. GEER Association Report No. GEER-022. Berkeley, CA.
- Honnette, T. 2018, Measuring Liquefied Residual Strength using Full-Scale Shake Table Cyclic Simple Shear Tests. Thesis in partial fulfillment of MS degree. Cal Poly, San Luis Obispo, CA.
- Hung, O. 1995, "A model for the runout analysis of rapid flow slides, debris flows, and avalanches." *Canadian Geotechnical Journal*, 32, 610-623.
- Iverson, R.M., 1997, The physics of debris flows: Reviews of Geophysics, v. 35, p. 245-296, doi:10.1029/97RG00426.
- Iverson, R.M., 2005, Regulation of landslide motion by dilatancy and pore pressure feedback: *Journal of Geophysical Research*, v. 110, F02015, doi:10.1029/2004JF000268.
- Iverson, R.M., and Denlinger, R.P., 2001, Flow of variably fluidized granular masses across three-dimensional terrain: 1. Coulomb mixture theory: *Journal of Geophysical Research*, v. 106, p. 537-552, doi:10.1029/2000JB900329.
- Iverson, R.M., and LaHusen, R.G., 1989, Dynamic pore- pressure fluctuations in rapidly shearing granular materials: *Science*, v. 246, p. 796-799, doi:10.1126/science.246.4931.796.
- Iverson, R.M., Reid, M.E., Iverson, N.R., LaHusen, R.G., Logan, M., Mann, J.E., and Brien, D.L., 2000, Acute sensitivity of landslide rates to initial soil porosity: *Science*, v. 290, p. 513-516, doi:10.1126/science.290.5491.513.
- Jeyapalan, J. K., Duncan, J. M., & Seed, H. B. 1983, Analyses of flow failures of mine tailings dams. *Journal of Geotechnical Engineering*, 109(2), 150-171.
- Jeyapalan, J. K., Duncan, J. M., & Seed, H. B. 1983, Investigation of flow failures of tailings dams. *Journal of geotechnical engineering*, 109(2), 172-189.
- Kayen, R., Moss, R. E. S., Thompson, E. M., Seed, R. B., Cetin, K. O., Kiureghian, A. D., Tanaka, Y., & Tokimatsu, K. 2013, Shear-wave velocity-based probabilistic and deterministic assessment of seismic soil liquefaction potential. *Journal of Geotechnical and Geoenvironmental Engineering*, 139(3), 407-419.
- Kramer, S. L. 1988, Triggering of liquefaction flow slides in coastal soil deposits. *Engineering Geology*, 26(1), 17-31.
- Kramer, M. G. 1996, *Geotechnical earthquake engineering*. Upper Saddle River, NJ: Prentice Hall.
- Lade, P. V. 1999, Instability of granular materials. In *Physics and mechanics of soil liquefaction* (eds P. V. Lade and J. A. Yamamuro), pp. 3-16. Rotterdam: Balkema.
- Logan, M., and Iverson, R.M., 2007, revised 2009. Video documentation of experiments at the USGS debris-flow flume 1992-2006 (amended to include 2007-2009): U.S. Geological Survey Open-File Report 2007-1315, v. 1.1, <http://pubs.usgs.gov/of/2007/1315/>.

- Lucia, P.C., Duncan, J.M., and Seed, H.B. 1981, Summary of research on case histories of flow failures of mine tailings impoundments. Proc. Mine Waste Disposal Technology. Bureau of Mines, Pittsburgh, PA. Informational Circular, 8857. 46-53.
- Moss, R.E.S., Gebhart, T.R., Frost, D.J., and Ledezma, C. 2018, Flow Failure Case History of the Las Palmas, Chile, Tailings Dam. PEER Report No. XXXX. Berkeley, CA.
- Yazdi, J. S., & Moss, R. E. S. 2016, Nonparametric liquefaction triggering and postliquefaction deformations. *Journal of Geotechnical and Geoenvironmental Engineering*, 143(3), 04016105.
- Randolph, M. G., and Houlsby, G. T. 1984, "The limiting pressure on a circular pile loaded laterally in cohesive soil." *Geotechnique*, London, England, 34(4), 613-623.
- Robertson, P., and Cabal, K. 2014, *Guide to Cone Penetration Testing*, 6th ed. Gregg Drilling and Testing, Signal Hill, CA.
- Schofield, A., & Wroth, P. 1968, *Critical state soil mechanics* (Vol. 310). London: McGraw-Hill.
- Stewart, D.P., and Randolph, M.F. 1994, "T-Bar Penetration Testing in Soft Clay." *J. Geotech. Engrg.*, 120(12): 2230-2235.
- Terzaghi, K. (1951). *Theoretical soil mechanics*. Chapman And Hall, Limited.; London.
- Tokpavi, D., L., Magnin, A., and Jay, P. 2008, "Very slow flow of Bingham viscoplastic fluid around a circular cylinder." *Journal of Non-Newtonian Fluid Mechanics*, 154, 65-76.
- Tokpavi, D., L., Jay, P., Magnin, A., and Jossic, L. 2009, "Experimental study of the very slow flow of a yield stress fluid around a circular cylinder." *Journal of Non-Newtonian Fluid Mechanics*, 164, 35-44.

Soil characteristics of long-traveling landslides and a hybrid model to predict travel distance

Nobuhiro Usuki^{a,*}, Kousuke Yoshino^b, & Takahisa Mizuyama^c

^aAsia Air Survey Co., Ltd, 29F, OAP Tower 1-8-30, Tenmabashi Kita-ku, Osaka 530-6029, Japan

^bAsia Air Survey Co., Ltd., 3F., Ozone Front Building 3-15-58 Osone, Kita-ku, Nagoya-shi, Aichi 462-0825, Japan

^cNational Graduate Institute for Policy Studies, 7-22-1, Roppongi Minato-ku, Tokyo 106-8677, Japan

Abstract

When landslides liquefy and sediment movement takes on characteristics of a debris flow, travel distance increases, expanding the range of potential damage. Clarifying the liquefaction mechanism for such phenomena and predicting travel distance are important for evaluating hard and soft measures for controlling landslide damage. The authors have compiled data on landslide travel distance in Japan, used the travel coefficient (Tr) to classify movement of landslide soil masses, and investigated the relationship between landslide movement and soil characteristics with the goal of clarifying the liquefaction mechanism. These results were used to analyze the soil characteristics of long-traveling landslides. The hybrid model developed by Satofuka (2004) was used as a liquefaction model and sensitivity analysis was conducted for the model parameters. Model validity was evaluated by comparing the simulated and actual sediment flow, deposition, and displacement velocity of a landslide that occurred in Niigata Prefecture in March 2004.

Keywords: long-traveling landslide, soil properties of landslides, simulation, hybrid model

1. Introduction

In previous analyses of major landslides that have occurred in Japan, as an index of travel distance, the authors used the travel coefficient ($Tr = L2/L1$), where $L1$ is the horizontal distance from the top of a landslide to the toe of the surface of rupture and $L2$ is the horizontal distance from the toe of the surface of rupture to the toe of the displaced soil mass. Along with defining long-traveling landslides as those with $Tr \geq 0.5$, which have a cumulative frequency of approximately 20% (Fig. 1(a)), landslides were classified into the following three cases based on the travel coefficient and condition of the displaced soil mass. The authors showed that the travel coefficient for a completely liquefied landslide is on the order of $Tr \geq 0.5$ (Fig. 1(b)) (Usuki and Mizuyama, 2011).

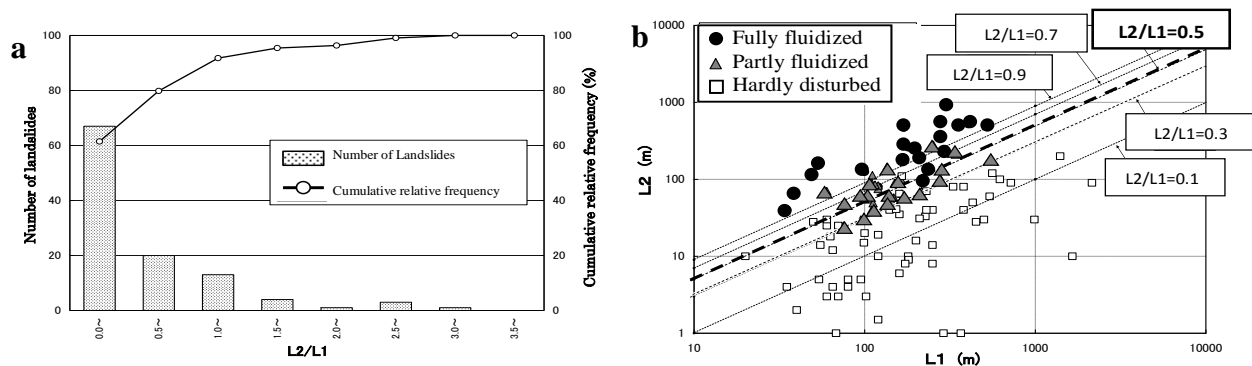


Fig. 1. (a) Histogram of the travel coefficient (Tr) of landslides; (b) Relationship between travel distance and original horizontal distance of landslides (Usuki and Mizuyama, 2011)

* Corresponding author e-mail address: usu.usuki@ajiko.co.jp

- (1) landslide soil masses and surfaces with little disturbance ($Tr < 0.3$)
- (2) landslide soil masses with lightly disturbed surfaces (partially liquefied $0.3 \leq Tr < 0.9$)
- (3) landslide soil masses violently disturbed with soil masses not retaining their original form (completely liquefied $Tr \geq 0.5$)

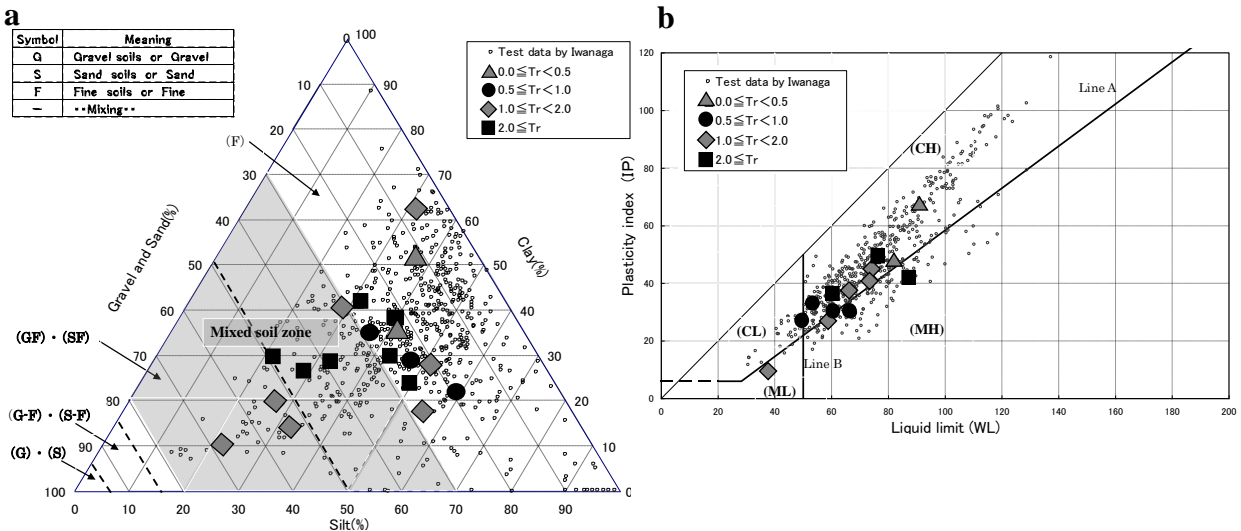
While factors including landslide volume, soil water content, and gradient of the terrain are believed to control the movement type of landslide soil masses, in terms of soil quality, soil masses of landslides with large travel coefficients were found to contain relatively large proportions of sand and gravel in addition to clay and silt. In terms of particle size distribution, the soils had mixed soil composition. We believe that the soil characteristics of these mixed soils will provide insight into understanding the liquefaction mechanism of landslides with long travel distances. In this paper, we report the results of our investigation of the soil characteristics of long traveling landslides and the validity of hybrid model simulations.

2. Soil Characteristics of Long-traveling Landslides

Given that the physical properties of soil vary with various factors including particle size distribution and water content, mechanical testing is needed to evaluate soil characteristics. The ability to estimate mechanical properties of soils from factors such as particle size distribution is also important. One method for estimating the mechanical properties of soils is the engineering classification method based on the Unified Soil Classification System of Japan. Iwanaga (1983) developed particle size distribution–plasticity diagrams based on the soil quality data of soil masses for 130 landslide sites in Niigata Prefecture, a region of Japan where landslides frequently occur. The authors analyzed the relationship between travel coefficients and soil characteristics of the sliding soil masses for 16 cases where the particle size distribution-plasticity diagrams from Iwanaga also existed.

2.1. Particle size distribution and fine particle content

As can be seen in Fig. 2(a), most of Iwanaga’s data (1983) are distributed in the fine soil (F) region of the soil texture triangle with a large proportion clay and silt. In contrast, soils from landslides with large travel coefficients tend to be distributed near the boundary between the fine soil (F) region and the gravel and fine soil (GF) region, which contains large proportions of gravel and sand, to the sand and fine soil (SF) region. The particle size distribution of soils with $R \geq 1.0$ tend to fall in the central region with sand, gravel, silt and clay content greater than 20%. Travel coefficient increases as the gravel and sand content rises above 20% and decreases when the sand and gravel content rises above 50%.



Kitago (1973) conducted consolidated undrained triaxial compression tests for saturated soils with various proportions of sand and clay, with the goal of evaluating the effect of the sand and clay content (proportion) on consolidation characteristics, pore-water pressure at time of shearing, shearing deformation characteristics, and

strength constants: the results show that the boundary between the sand region and the intermediate region is associated with a fine particle content of 20 to 30%, while the boundary between the clay region and the intermediate region was associated with a fine particle content of 60 to 70%. Mixed soils in the intermediate region with fine particle content greater 40% were found to behave similarly to cohesive soils, and a transition state between sandy soils and cohesive soils was reported to exist near 30% fine particle content. The fine particle content (R) was defined as follows:

$$\text{Fine particle content(R)} = \frac{\text{Fine grain dry weight}}{(\text{Fine grain} + \text{Coarse fraction}) \text{ Dry weight}} \times 100 \quad (1)$$

Fine grain : Soil particles of 75 μm or less

Given that soil particle densities typically fall within a range of 2.6 to 2.8 g/cm³ (no moisture), content defined by mass and content defined by volume do not differ substantially. Accordingly, here we assess content defined by mass. In terms of fine particle content, soil masses of landslides with $\text{Tr} \geq 1.0$ are distributed in or near the boundary of the mixed soil region. The soil texture is classified as mixed soil comprising intermediate particles falling into the sand and clay categories.

Omine (1993) investigated the effect of particle size on the stress and deformation behavior of mixed soils containing sand and clay of greatly differing particle sizes: the results show that as the fine particle content decreases, the angle of internal friction increases and approaches the value for coarse particles only. Conversely, the angle of internal friction decreases for mixed soils with high fine particle content, meaning that disruption of soil masses may proceed readily in such soils.

In previous work (Usuki and Mizuyama, 2011), we tested the strength of 4 sample soils prepared to have different particle size distributions (fine particle contents of 90%, 75%, 45% (mixed soil), or 10%). For a single axis compression test, the deformation coefficient (E50) indicating ease of soil deformation was smallest for the mixed soil region sample. Testing after 48-h immersion showed that the cohesion of the mixed-soil sample declines by about 60% from an original value of 23.9 to 15.1 kN/m². Furthermore, in triaxial compression tests, mixed-soil samples from a depth of 5 to 10 m from the surface near the sliding surface of the landslide were found to have the lowest shear strength among all the samples. In mixed soils, soil strength declines as the fine particle content increases. This point should be considered when evaluating the role of soil characteristics in liquefaction mechanisms of long-traveling landslides and setting simulation.

2.2. Plasticity diagram

In Fig. 2(b), much of Iwanaga and Nozaki's data (1983) is distributed in the high-plasticity clay (CH) region of cohesive soils while data for low-plasticity clay (CL) and low-plasticity silt (ML) soil regions are rare. Line A shows the boundary for high-plasticity clay (CH) and high-plasticity silt (MH) regions and represents the water content range of the plastic state. Above the A line, the range of water content expands, indicating the prominence of clay properties. Also, the B line located at the liquid limit $\text{WL} = 50$ shows the magnitude of compressibility, with deformation occurring more readily in soils located right of the B line. Soils from landslides with large travel coefficients are distributed slightly above the A line and, as a whole, near the B line; thus, it is evident that the water content range in the plastic state is relatively large, that compressibility is high, and that the soils are readily deformed. Generally, as the clay content decreases, the liquid limit declines and the region near the B-line is approached; thus, in soils associated with landslides with large travel coefficients, although clay is present, silt, sand, and gravel content tends to be high.

3. Liquefaction Mechanisms of Long-Traveling Landslides and Evaluation of the Simulation Model

3.1. Liquefaction mechanism

Starting from the assumption that the surface of the landslide becomes highly disturbed in the transition from partially to completely liquified, disruption of the soil mass progresses from near the liquified layer inside the landslide. The landslide moves as the soil mass near the bottom of the main body is gradually incorporated into the liquified layer that has been formed. Eventually, the surface soil mass of the landslide is incorporated into the liquified layer and the surface of the landslide becomes highly disturbed. Based on consideration of soil properties

and other factors, if the landslide soil mass is assumed to be adequately saturated, the following liquefaction mechanism can be inferred for long-traveling landslides (Fig. 3).

- (1) The landslide begins with displacement of the slide surface.
- (2) Disruption of the landslide soil mass progresses due to the loading and deformation caused by displacement.
- (3) A liquefied layer is created in the lower area of the soil mass where displacement begins.
- (4) The liquefied layer develops (expands) by incorporating the disrupted soil mass. In cases where the liquefied layer does not develop, the upper part of the soil mass remains disturbed, and the landslide stops without complete liquefaction.
- (5) When an adequate amount of water is supplied (including the interior of the landslide soil mass), the liquefied layer develops until the entire soil mass is incorporated into the liquefied layer and the landslide becomes completely liquefied.
- (6) The original structure of soil mass becomes completely disturbed through the disruption of the soil mass and incorporation into the liquefied layer.

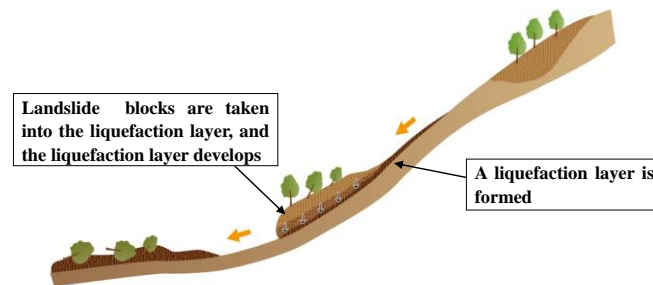


Fig. 3. liquefaction mechanism of Long-Traveling Landslide

If the landslide soil mass is adequately saturated and there is no substantial change in the terrain conditions such as the gradient, disruption of the landslide soil mass progresses. Regarding the development of the liquefied layer, decreased soil strength due to particle size distribution of mixed soil is believed to be one factor that determines a larger travel coefficient.

When the particle size distribution of the landslide soil mass is in the mixed soil region, from a soil mechanics standpoint, the soil mass is readily disrupted and easily incorporated into the liquefied layer. Given that this soil region is distributed along the A line of the plasticity diagram, the soil is more readily liquefied as the natural water content ratio increases, and the accompanying change in volume tends to be large.

During prolonged snow melt or rainfall periods, the degree of water saturation of the landslide soil mass increases and is assumed to be near the liquid limit. If the soil is liquefied, the particle volume ratio changes and void ratio increases. If the soil mass begins to slide under these conditions, disruption of the soil mass further increases the void ratio. These voids become filled with not only liquefied clay and silt but, also, with gravel and sand, causing the liquefied layer to develop further to a state close to a debris flow, thereby increasing the travel coefficient.

3.2. Hybrid model selection

With regard to the soil mass liquefaction mechanism, the D-Claw model (George and Iverson, 2014) and other models have been proposed to describe the process from landslide onset to liquefaction based on rising pore water pressure and soil particle dilatancy. Here, from the travel coefficient-dependent classification of landslide movement type presented in this study, we identified the hybrid model for debris flow from slope collapse as a model that could express the liquefaction mechanism described above and evaluated its applicability to long-traveling landslides. Based on previous research on debris from a collapsing soil and sand slope, Satofuka (2004) divided the soil mass from a collapsing hillside into several blocks that flow downslope on top of the liquified layer (Fig. 4(a),(b)).

The soil mass comprised an upper unsaturated soil part and the lower saturated soil part. The saturated soil erodes due to shear stress, and the mixture of eroded soil, sand, and water form a liquefied layer. To estimate the distance traveled by the debris from the collapsed slope, it is necessary to track the rigid motion of the unsaturated soil and to analyze the motion of the liquefied material as a continuous body. Accordingly, a flood model of debris flow based on the finite difference method was combined with a Lagrangian analysis method for the movement of the soil mass to construct a 2-dimensional hybrid debris flow model. The hybrid model for debris flow from a collapsing soil and

sand slope represents the soil mass as several cylinder blocks (For calculation, approximate to a hexagon) and assumes that the saturated layer flows after being incorporated into the liquefied layer. In our research, we assumed that the liquefaction mechanism for long-traveling landslides involves formation of a liquefied layer, with the low soil strength of mixed soil leading to progressive disruption of the soil mass after initial displacement. The disrupted soil mass is incorporated into the liquefied layer as flow continues. Complete liquefaction is defined as the state in which the liquefied layer incorporates the entire soil mass including the surface layer. Partial liquefaction is defined as the state in which this process stops before the landslide surface is incorporated into the liquefied layer. This process is essentially the same as the liquefaction mechanism assumed by the hybrid model.

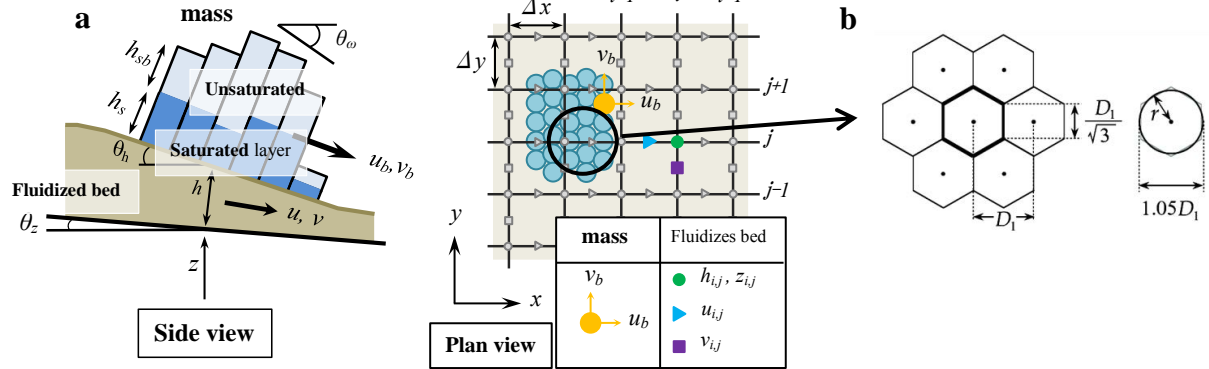


Fig. 4. (a) Hybrid model; (b) Cylinder model of the soil mass (Satofuka, 2004)

4. Sensitivity Analysis of Hybrid Model Parameters

4.1. Parameter sensitivity analysis

The slopes of many locations where long-traveling landslides have occurred are relatively gentle with gradients ranging from 10 to 30°. For parameter sensitivity analysis, we constructed a continuous slope with gradients of 0.5°, 5°, and 10° (Fig. 5(a)). This flatter slope, rather than a deep valley terrain, was also chosen to enable confirmation of the spread of the soil mass block as well as the downslope travel distance. The calculation mesh consisted of 10 × 10 m squares in both x and y directions. The time step for calculations was 0.1 s; the radius of the cylindrical block bases as well as the initial distance between cylindrical block centers D1, D2 (Distance at which the attractive force of the cylinder block is maximum) and D3 (The critical distance at which the attractive force of the cylinder block does not act) were the same values used in Satofuka (2004). These values were 4.85m, 9.24m, 9.70m and 10.16m, respectively. Also, the landslide soil mass or liquefied layer debris concentration was 0.54, deposition layer concentration was 0.6, the Manning roughness coefficient was 0.04, specific gravity of soil particles was 2.65, the dynamic friction coefficient between soil mass and river bed μ_m was 0.5.

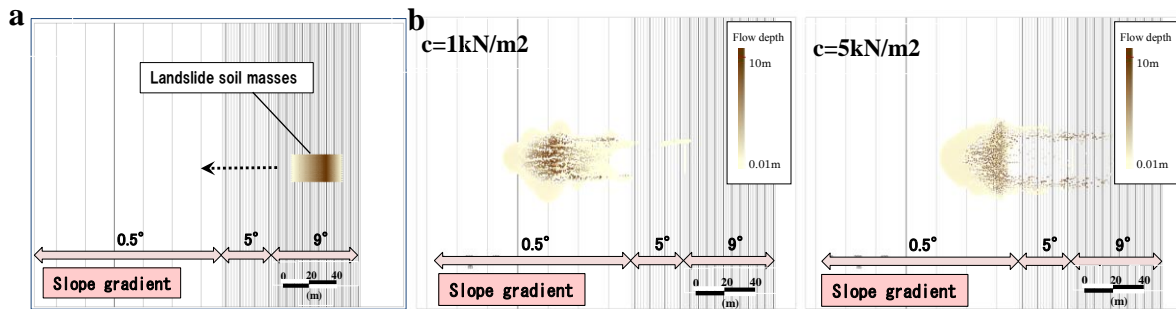


Fig. 5. (a) Slope model; (b) Calculation results with varying cohesion strength

Parameter sensitivity analysis was conducted for 5 parameters: angle of internal friction, cohesion, particle diameter, erosion rate coefficient, and saturation. The base conditions for each parameter were as follows: internal friction angle, $\theta = 10^\circ$; cohesion, $c = 5 \text{ kN/m}^2$; particle diameter, $d = 10 \text{ cm}$; erosion rate coefficient, $\beta = 0.13$; and saturation $s_b = 1.0$. Calculations were performed while varying each parameter (internal friction angle 5°, 10°, 15° and 30°; cohesion 1, 5, 10, and 20 kN/m^2 ; particle diameter 1, 10, and 100 cm; erosion rate coefficient $\beta = 0.06, 0.13,$

0.24, 1.20; degree of saturation of the unsaturated layer $s_b = 0.1, 0.5, 1.0$). Results of the sensitivity analysis show that the parameters with a large influence on travel distance were cohesion, particle diameter and erosion rate coefficient. Travel distance increased with decreasing cohesion; and cohesion influenced the spread (degree of dispersion) of the cylindrical blocks (Fig. 5(b)). Particle diameter and erosion rate coefficient were found to affect the liquefied layer, with decreasing particle diameter and increasing erosion rate coefficient being associated with greater travel distance due to their contribution to development of the liquefied layer.

4.2. Parameter review

Cohesion varied widely depending on the condition of cohesive soil (from extremely soft to hard or consolidated) from several kN/m^2 to greater than 200 kN/m^2 . That said, soil is assumed to approach a near fluid state with saturation near 1.0 during rains or snowmelt periods. Furthermore, the Road Earthwork Temporary Guidelines (March 1999, Japan Road Association) assumes a cohesion of less than 12 kN/m^2 for extremely soft soil conditions approaching fluid state. Based on the above, when cohesion is less than 12 kN/m^2 , the internal friction angle, which was shown to have negligible impact by the parameter sensitivity analysis, is set to a general value of $\phi = 35^\circ$; the erosion rate coefficient is set to $\beta = 0.12$ as a guide, and saturation degree is set to $s_b = 1.0$, taking into account the fact that rain and snowmelt periods are contributing factors to landslides. Particle diameter is set based on the local field conditions.

5. Hybrid Model Simulation of a Long-traveling Landslide

5.1. Simulated landslide

A long-traveling landslide occurred in Nagaoka, Niigata Prefecture on March 1, 2004 (Fig. 6). The landslide comprised an area of $110,000 \text{ m}^2$ (length 450 m, width 250 m) and approximate volume of $1,650,000 \text{ m}^3$. Geologically, the base comprised green tuff with alternating layers of sandstone and mudstone. The average gradient from the end of the landslide to the confluence of the Nishitani River was 8° , which is a gradual slope. Part of the landslide engulfed driftwood as it flowed down and deposited earth and sand ranging from 4 to 10 m thickness. In constrained areas, we observed sand and mud deposits up to 10 m in thickness. Also, in wider areas of the basin, there was evidence that the soil mass had spread laterally and deposited material. Very little evidence of piling up caused by debris flow-like braided flow was observed. The landslide soil mass was displaced approximately 550 m from the starting point, and the movement type was completely liquefied (travel coefficient $Tr = 1.2$). In terms of particle size distribution, the soil consisted of 70% fine particle material and was classified in the mixed soil region. In the plasticity diagram, the liquid limit was $WL = 74.9$, and the plasticity limit was $IP = 44.4$, corresponding to the region slightly above the A line and near the B line. The mixed soil would be expected to readily liquefy and to be readily deformable when the natural water content ratio increases.

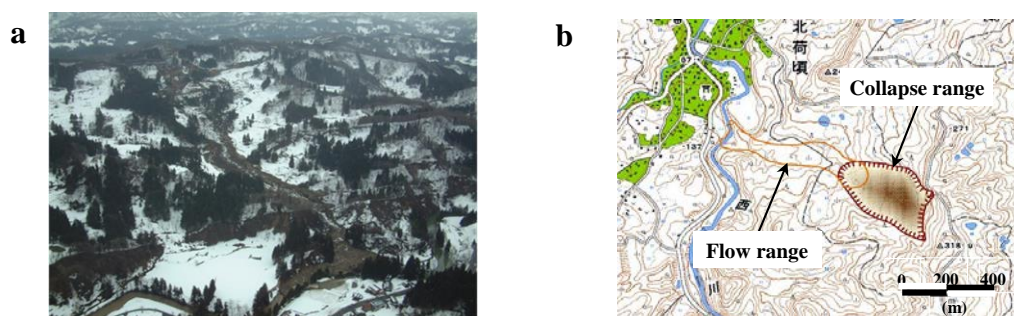


Fig. 6. (a) Long-Traveling Landslides occurred in Niigata Prefecture; (b) Movement range of landslide

5.2. Parameter

The calculation mesh consisted of squares measuring 10 m in both x and y directions. The time step for calculations was 0.1 s, and the radius of the cylindrical block bases, the initial distance between cylindrical block centers $D1$, $D2$ and $D3$ were the same values used in the Satofuka (2004) study. The calculation parameters are

shown in Table 1. As the daily average temperatures during the second half of February were high and snowmelt progressed continuously, the water content of the soil mass was assumed to be high, and the degree of saturation (s_b) of the unsaturated zone was set to 1.0. Soil and sand cohesion (C_b) was set to 5 kN/m², considering the meteorological conditions and the extremely saturated state of the soil. Table 1 lists the set values of the simulation parameters. Also, as gravel ranging from about 1 to 5 cm to about 10 cm was found in the landslide soil mass, an average particle diameter of 10 cm was used.

Table 1. Parameter settings

Item	Setting value
Calculated mesh	dx=dy=10m
Radius of lumps	4.85m
Sediment concentration of the fluidized bed	0.54
Sedimentary soil concentration	0.6
Average grain diameter	10cm
Manning roughness coefficient	0.04
Density of pore fluid	1,000kg/m ³
Density of soil grain	2,650kg/m ³
Dynamic friction coefficient	0.5
Angle of internal friction	35°
Cohesion	5kN/m ²
Saturation degree of unsaturated moiety	1.0

5.3. Flow Range and Deposition

Although some of the simulation results for flow width exceed the observed flow range, in general the results were a good fit (Fig. 7(a)). The dark areas in Fig. 7(a) indicate thick cylindrical blocks (soil masses). Cylindrical blocks are thicker in narrow terrain, whereas cylindrical block thickness varies and is generally thinner in wider terrain. The simulation accurately reproduced actual deposition trends, as shown in Fig. 7(b),(c). For points where an actual deposition depth of approximately 8 m was observed, the simulation indicated deposition depths between 5 to 10 m. The simulation indicated erosion of 10 to 20 m at the top of the landslide, which is on the same order as the height of the main scarp. The simulation accurately reproduced the distance traveled, flow, and deposition by the landslide.

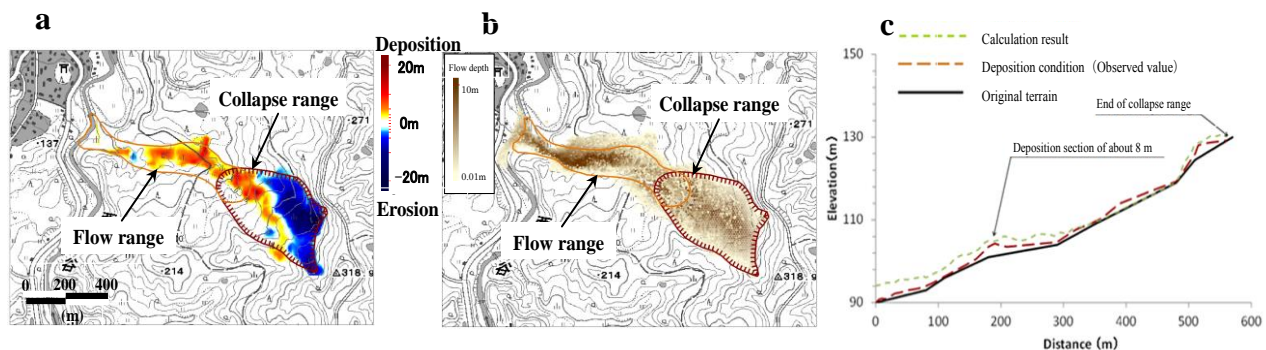


Fig. 7. (a) Calculation result (fluctuation amount); (b) Calculation result (flow depth) ; (c) Calculation result (longitudinal section)

5.4. Soil mass displacement velocity

The simulation results are shown as a time series in Fig. 8. The time taken for the soil mass to move 550 m from initial displacement to the confluence of Nishitani River was about 200 s. The average simulated velocity was 2.75 m/s. As there were no witnesses who observed the landslide flow conditions, the actual velocity is unknown. A fallen tree was found during the field investigation. Some of these trees were taken up by landslide clumps and were disturbed, but also those carried in the state of standing trees above the landslide were confirmed; thus, we believe the displacement velocity was relatively slow, on the order of several m/s, which is similar to simulation result.

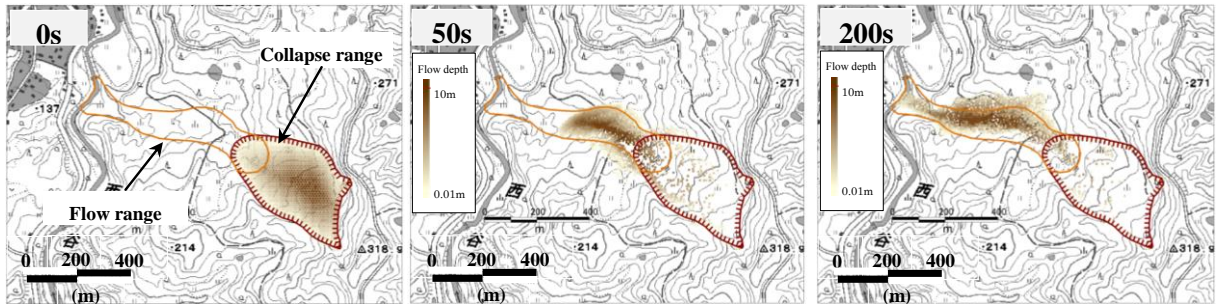


Fig. 8. Range of landslide (time series)

5.5. Applicability of the hybrid model for prediction of travel distance and other factors for long traveling-distance landslides

The simulation, adjusted based on the results of the parameter sensitivity analysis, accurately reproduced the March 2004 landslide that occurred in Nagaoka, Niigata Prefecture in terms of soil mass flow, deposition trends, travel distance, and estimated displacement velocity. One advantage of the hybrid model over conventional methods for predicting landslide travel distance is the ability to simulate movement through complex terrain. Given the ability to estimate flow range, deposition conditions, travel distance, and displacement velocity, the hybrid model method is expected to prove useful in producing hazard maps and facility planning that takes into account soil movement.

6. Future Issues

In addition to investigating movement-related aspects of long traveling landslides such as occurrence, flow, and deposition, it will be necessary to collect soil samples, conduct mechanical and other soil tests, and perform statistical analyses of the relationship between motion type and soil quality. These studies will be especially important to deepen our understanding of the relationship between the characteristics of mixed soils and liquefaction mechanisms relevant to landslides and to incorporate these soil characteristics in hybrid models for predicting travel distance of soil masses in landslides. Such models will be useful in developing hazards maps and in designing emergency measures when advanced warnings of landslides are observed.

References

- George, D.L., and Iverson, R.M., 2014, A depth-averaged debris-flow model that includes the effects of evolving dilatancy: II. Numerical predictions and experimental tests, *Proceedings of the Royal Society A*, doi:10.1098/rspa.2013.0820.
- Hsü, K.j., 1975, Catastrophic debris streams generated by rockfalls., *Geol.Soc.Amer.Bull.*, Vol.86, p.129-140.
- Hsü, K.j., 1978, Albert Heim: Observation on landslides and relevance to modern interpretation., in Voight, B., ed., *Rockslides and Avalanches*, Vol.1, p.71-93.
- Iverson, R.M., 1997, Debris-flow mobilization from land-slides, *Annual Review of Earth and Planetary Sciences*, Vol.25, p.85-138.
- Iwanaga, S. and Nozaki, T., 1983, Characteristics of Soils in the Landscape-prone Areas of Niigata Prefecture, *Journal of Japan Landslide Society*, Vol. 20, No. 2, p. 5–14. (in Japanese)
- Omine, K. and Ochiai, H. and Yoshida, N., 1993, Strength Properties of Sand-Clay Mixed Soils Based on Soil Structure, *Doboku Gakkai Ronbunshu*, Issue 467, p. 55–64. (in Japanese)
- Satofuka, Y., 2004, Numerical Simulation of the Debris Flow at the Atsumari River, Minamata City, 2003, *Proceedings of Hydraulic Engineering*, Vol. 48, p. 925–930. (in Japanese)
- Scheidegger, A. E., 1973, On the prediction of the reach and velocity of catastrophic landslide., *Rock mechanics*, Vol.5, p.231-236.
- Takahashi, T., 2000, Initiation and flow of various types of debris flow., *Proc. 2nd Inter. Conf. on Debris Flow Hazard Mitigation*, Balkema, p.15-25.
- Usuki, N., Tanaka, Y. and Mizuyama, T., 2006, Investigation of Distribution of long-traveling landslides, *Disaster Mitigation of Debris Flows Slope Failures and Landslides*, p.101-112.
- Usuki, N. and Mizuyama, T., 2009, Study on the actual behavior and soil quality of long-traveling landslides, *Asia-Pacific Symposium on New Technologic for Prediction and Mitigation of Sediment Disasters*, p.86-87.
- Usuki, N. and Mizuyama, T., 2011, Soil properties and fluidity of long-traveling landslides, *5th International Conference on Debris-Flow Hazards Mitigation, Mechanics, Prediction, and Assessment*, p.787-795.

The research on the movable solid materials under seepage flow effect in debris-flow source area

Shun Yang^{a,*}, Guo-qiang Ou^b, Hua-li Pan^b, Zhong-sheng Xie^a, Dong-xu Yang^a

^a Technical Center for Geological Hazard Prevention and Control, CGS, Institute of Exploration Technology, CAGS, Chengdu 611734, China

^b Institution of Mountain Hazard and Environment, CAS, Key Laboratory of Mountain Hazards and Surface Processes, CAS, Chengdu 610041, China

Abstract

Solid materials distributed on the surface of watershed transform to debris flow under seepage flow effect is one of the most common disaster type in the mountainous area, especially in the Longmen Fault regions, China. The high frequency of debris-flow event takes a big menace to local people's safety of life and properties directly, as well as the reconstruction work. Currently, more theory and experiment researches are concentrated on solid materials instability mechanism, debris-flow initiation, movement process of slope-gully system, but fewer research are focused on the moveable critical condition of solid materials under hydrodynamic condition as seepage flow and surface flow. Thus, based on the mechanical balance, through define the theory of the movable solid materials firstly. Then, take a comparison with traditional terms as loosen solid materials, dynamic reserves and efficient solid materials, it found that solid materials move or not is a mechanical problem rather than traditional definition. Thirdly, on the condition of saturated seepage flow, according to setting up geological model and taking mechanical analysis, it gained dynamical formula and resistance formula respectively, then, give confined parameters, it found a liner distribution of dynamical value and resistance value versus depth when the geology model is homogeneous and the seepage flow saturated in whole layer.

Key words: Debris-flow Area; Seepage Flow Effect; Solid Materials

1. Introduction

Debris flow is a flow of a sediment–water mixture driven by gravity, which related to factors as geological tectonics, topographical conditions, hydrology and human engineering et al (Zhou et al., 1991; Xu, 2010). It has been reported that in over 70 countries in the world and often causes 5 severe economic losses and human casualties annually, which seriously retarding social and economic development (Degetto et al., 2015; McCoy et al., 2012; Hu et al., 2016; Cui et al., 2011; Dahal et al., 2009; Liu et al., 2010). According to Takahashi, The mechanical triggers of debris flows can be classified into three types, namely erosion by surface runoff, transformation from landslides, and collapse of debris dams (Takahashi, 2007). Through different water content before debris-flow initiation, Brand et al concluded that the thinner layer failure by rainfall infiltration which result in the weight increasing and the minor of the matrix suction (Brand, 1981). With the different water content between debris-flow initiation and failure, Johnson definite movable index MI (Johnson, 1984), based on the MI, Ellen put forward the index as AMI and set standard as $AMI > 1$, the debris is easily flow along the gully, while the $AMI < 0.45$, it could not form debris flow (Ellen et al., 1987). Similarly, Takahisa through carried out experiments, it got that when the ratio of $l/h < 4.0$, the landslide materials could not move as debris flow, while the ratio of $l/h > 7.5$, it easily to form debris flow (Takahisa, 1981). Generally, the gravity and hydrodynamic are the mainly driven forces to form debris flow (Howard, 1988; Hongey et al., 2006). With numerous experiments and field survey, it also found that the pore water pressures increased while the loose solid materials moved with surface water, which lead to liquefaction (Wang et al., 2003; Iverson et al., 2004). Based on laboratory experiments and field observations, Wang based on fluid mechanics

* Corresponding author e-mail address: yangshun09@foxmail.com

theory, obtained a flow movement equation for the deposit surface and shear stress, but those equations ignored the influence of the pore water pressure on the shearing strength and parameters that could change with time (Wang et al., 1990).

As is known to all, loosen solid materials is one of the essential condition of debris-flow formation, for the numerous solid materials in the watershed, how many solid materials would form the debris flow and how the debris flow moving is also the question. As to the volume calculation, currently most calculations mainly lie in statistics. Actually, plenty of debris-flow researchers carried out numerous studies on debris volume research, such as the volume and distribution of loosen solid materials, traditional concept of effective solid materials (Qiao et al., 2012; Tang et al., 2011; Zhou et al., 1991), those researches take a positive effect for debris-flow prevention and reconstruction post-earthquake. However, most of those methods are mainly based on the field survey and statistics, lack of physical and mechanical meaning. Thus, based on the analysis of debris-flow formation, it can conclude that loosen solid materials whether move or not under hydrodynamic condition in source district is decided by dynamic force and resistance which is a physical and mechanical problem, rather than broadly qualitative description, that is the movable solid materials problem (Yang et al., 2014).

In this context, the study is on condition of mechanical equilibrium principle, definite the movable solid materials of debris-flow source area first, which articulate the movable characteristics of solid materials under hydrological condition in debris-flow source area. Secondly, take a contrast with available traditional definition as dynamic reserve, effective solid materials and movable solid material. Last, take saturated seepage flow as an example, through build geological model and mechanical analysis, to test and verify the formulas by experiment. The research provides a quantitative calculation method of the loose solid materials in the shallow landslide areas, which can favor for the design of the small watershed debris-flow prevention.

2. Definition of the movable solid materials

2.1 Definition

Currently, most solid materials calculation in the small watershed are statistics and estimation, the direct question of those method could cause the error of statistics is between 70 to 150 percent. As to the debris-flow check dam design, the unreasonable loose solid materials volume can result in high cost or low prevent ability. Therefore, based on the Yang's research (Yang et al., 2014), it proposed the concept of critical movable solid materials, which can be definite that when the composition force of hydrologic and the gravity components is larger than the resistant, the critical thickness is the cross point beneath the surface slope, as seen in Fig 1.

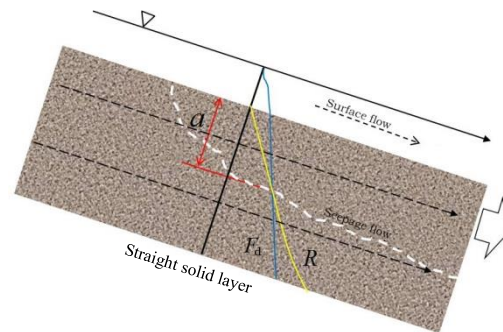


Fig. 1. General map of the movable solid materials

When $Fd < R$, the whole layer of loosen solid materials is in stable state. When $Fd = R$, the layer of loosen solid materials is in critical state. While $Fd > R$, the loosen solid materials within the critical depth would lose failure, seen formula (1) as follows. In summary, the movable solid materials is the solid materials within the critical depth when $Fd = R$.

$$\text{Critical fomula of movable solid materials} = \begin{cases} Fd < R & \text{stable state} \\ Fd = R & \text{critical state} \\ Fd > R & \text{fail to move} \end{cases} \quad (1)$$

2.2 Contrast among movable solid materials and traditional conception

As to debris-flow prevention design, the volume of loose solid materials is one of the most important parameters. Many researcher focused on the solid materials condition of debris flow, numerous researches are mainly using loosen solid material, dynamical reserve and effective solid materials et al., but the research method lies in quantitative description, field survey and experiences calculation. The contrast between movable solid materials and traditional concept is seen in Table 1.

Table 1. The contrast between movable solid materials and traditional conception

	The Movable Solid Materials	Loosen Solid Material	Dynamical Reserve	The Effective Solid Materials
Concept	When the sum of the hydrological force and gravity component equal to the resistance, the solid within the critical depth	Loosen solid materials distributed in the widely surface	The potential solid materials to form debris flow in source area	loosen solid materials of slope and gully bank fail to move by water saturation and scour, especially to join the next debris flow's solid materials
Volume calculation method	Calculation by mechanical model	Estimate the area and depth in debris-flow watershed	Investigate the area and depth of the potential debris-flow watershed	Estimate the area and depth
Mechanical meaning	Mechanical equilibrium	none	none	none

Solid material is a defined qualitative concept in traditional statement, but what kind of loosen content will form debris flow under hydrologic condition still not appeared in literatures so far. In practical application, mostly loosen solid materials volume calculation is by field survey estimation. As to debris-flow dynamical reserve, which is loosen solid materials volume calculated by measuring length, width and estimated potential thickness, the problem is the estimated thickness originated from investigating outside and there is none practical meaning, actually, the thickness should be controlled by mechanical properties of solid materials. The effective solid materials is just defined as solid materials which joined in the debris flow under water effect, this concept did not applied in actual example currently.

Whether the loosen solid materials on the slope is move or not and how many solid materials could be arised by the rainfall is a mechanical problem, which should be decided by its propulsion and resistance. The dynamic propulsion is mainly including seepage flow and surface flow's component, gravity component, as to rainfall debris-flow pattern, the dynamic propulsion could be calculated by rainfall, runoff and convergence under a certain rainfall frequency. The resistance is constituted of cohesion, friction and shear resistance among particles. The concept of movable solid materials is just based on the mechanical balance, which possess clear physical meaning and distinguished from traditional definition essentially.

3. The Movable Research under Saturated Seepage Flow

3.1 Geology model

It is known to all that the deposition mode and the amount of loosen solid materials in the debris-flow watershed affect the thickness of solid materials. The mechanical characteristics, the longitudinal slope and the difference of hydrodynamic effect also determined the thickness. As to the movable solid materials which is controlled by the relationship among the slope angle, hydrodynamic, gravity and resistance. When the resultant of hydrodynamic component and gravity component is larger than the resistance, the solid materials fail to move and even form debris flow finally.

Water is the essential parts of debris flow, which are mainly come from rainfall and ground water. The movement forms lie in saturated seepage flow/ non-saturated flow and surface flow. As to saturated seepage flow condition, take the loose solid materials firstly, the geology model as Fig. 2 shown.

Geology model conditions described as follows.

- The particles are the heterogeneous anisotropy; the porosity of the detrital grain layer is n .
- The thickness is D , slope angle is θ .
- Surface water thickness is H , when none of surface water, $H=0$.
- The bottom plate is impermeable and the whole layer distributes saturated seepage.

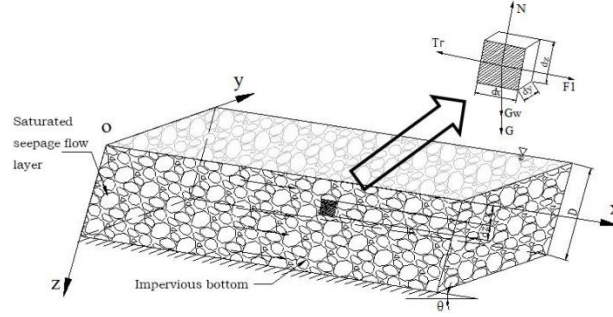


Fig. 2 The general view of geo-model under saturated seepage flow condition

3.2 Mechanical analysis

When the slope angle is less than the repose angle of deposition, the loosen solid materials stay in a stable state. But with a certain hydrodynamic of seepage and surface flow's effect, the balance would be disturbed and the deposited loosen solid materials would fail to move in debris flow. The seepage force and the drag force by surface flow are the mainly hydrodynamic form, the formulas see as following.

The seepage force is related to hydraulic gradient, the formula is seen (2).

$$F_1 = \gamma_w j V \quad (2)$$

where γ_w is water density, j is hydraulic gradient, $j = \Delta h / \Delta L$, Δh is water head difference or head loss, ΔL is seepage path, $\Delta h = \Delta z + \Delta p / \gamma_w + (\Delta u)^2 / 2g$, Δz is the position head difference, $\Delta p / \gamma_w$ is pressure head difference, $(\Delta u)^2 / 2g$ is flow velocity head difference.

With saturated seepage flow, select a micro-element body $dx dy dz$ along slope incline direction of any depth to take mechanical analysis. It found that the micro-element are mainly suffered gravity, seepage force and shear resistance of particles et. al, as Fig 2 shown.

3.3 Gravity of soil and water dG

At any depth z , the saturated slope layer dG can be expressed by formula (3).

$$dG = \gamma_{sat} \frac{z}{\cos\theta} dx dy \quad (3)$$

where γ_{sat} is the saturated density of slope layer, $dx dy$ is the bottom area of micro-element body, θ is the slope angle of geology model.

Therefore, the component force of the saturated layer in x direction can be expressed as formula (4).

$$dG_x = \gamma_{sat} z \tan\theta dx dy \quad (4)$$

Component force in z direction is seen formula (5)

$$dG_z = \gamma_{sat} z dx dy \quad (5)$$

The gravity dG_w of micro-element body

From the mechanical analysis, the gravity dG_w of the micro-element body can be expressed as formula (6).

$$dG_w = \gamma_{sat} dV \quad (6)$$

where dV is the volume of micro-element body, $dV = dx dy dz$, dz is the thickness of micro-element body.

The gravity component in x direction of micro-element body is seen formula (7).

$$dG_{wx} = \gamma_{sat} \sin \theta dV \quad (7)$$

The gravity component in z direction of micro-element body is seen formula (8).

$$dG_{wz} = \gamma_{sat} \cos \theta dV \quad (8)$$

Seepage flow dF_1

The seepage flow dF_1 in x direction of micro-element body is seen formula (9).

$$dF_1 = \gamma_w j dV \quad (9)$$

where γ_w is water density, j is hydraulic gradient, $j = \Delta h / \Delta L$, Δh is water head difference or head loss, ΔL is seepage path, $\Delta h = \Delta z + \Delta p / \gamma_w + (\Delta u)^2 / 2g$, Δz is the position head difference, $\Delta p / \gamma_w$ is pressure head difference, $(\Delta u)^2 / 2g$ is flow velocity head difference. On considering of low flow velocity in saturated layer, set the flow velocity head difference minimum. Another point is micro-element body is parallel with slope debris layer, then presume the water pressure in upstream slide is equal to the downstream slide, thus neglect the water pressure head. dV is the volume of micro-element body. Therefore, the formula (9) can be set as formula (10).

$$dF_1 = \gamma_w \sin \theta dx dy dz \quad (10)$$

Shear resistant $d\tau_r$ among particles

During seepage process, the particle framework prevents the water flow across the porosity among the particles. It set the framework as high dense of debris, and then at random depth of z, the shear resistant among particles can be expressed as formula (11).

$$d\tau_r = (\gamma_s - \gamma_w)(1 - n) \cos \theta dx dy dz \quad (11)$$

where γ_s is soil particles density, n is porosity, θ is slope angle, dV is the volume of micro-element body, $dV = dx dy dz$, dz is the thickness of micro-element body.

As formulas ahead, the dynamic force along slope direction is including seepage force and the gravity component, which can be expressed as the formula (12).

$$dF_d = \gamma_w \sin \theta dx dy dz + \gamma_{sat} z \tan \theta dx dy + \gamma_{sat} \sin \theta dx dy dz \quad (12)$$

The force in z direction is mainly composed of gravity component, which is expressed as formula (13).

$$d\sigma = \gamma_{sat} z dx dy + \gamma_{sat} \cos \theta dx dy dz \quad (13)$$

The pore water pressure is seen formula (14)

$$dp = \gamma_w z dx dy \quad (14)$$

Combined with the Mohr-Coulomb criterion, the resistant formula in x direction of micro-element body can be expressed by formula (15).

$$dR = c + (d\sigma - dp) \tan \varphi + d\tau_r \quad (15)$$

Therefore, the formula (12) and (15) are the dynamic expression and resistance expression respectively, which locate at the depth of z and the saturated seepage flow in the whole layers. Among it, formula (12) is constitute of seepage force, the gravity component of soil in x direction and the micro-element gravity component. Formula (15) is mainly composed of cohesion, friction in deposit layer and the shear resistant among the particle.

From those two formulas, it can get the stress distribution of the micro-element body under saturated seepage flow of the dynamic and resistance vertical in slope direction respectively. From the formula (12) and (15), the dynamic force and the resistance varied with slope angle, soil strength and porosity of layer et. cl. The depth z is the

variable, the micro-element body thickness is dz , it assumes the micro-element thickness is the characteristics particle size d_{50} of the deposit layer, it also grants the bottom area of micro-element is $dA = dx dy = 1$, therefore, the dynamic formula and the resistance formula can be expressed as formula (16) and (17) as follows.

$$F_d = (\gamma_w + \gamma_{sat}) \sin \theta d_{50} + \gamma_{sat} z \tan \theta \tag{16}$$

$$R = c + [\gamma_{sat} \cos \theta \tan \varphi + (\gamma_s - \gamma_w)(1 - n) \cos \theta] d_{50} + (\gamma_{sat} - \gamma_w) z \tan \varphi \tag{17}$$

The porosity and the density are constant when the slope layer is constituted of homogeneous isotropic particles. Thus, the dynamic force and the resistant varied in linear with depth in z direction. While the slope material is composed of heterogeneous particles, the density and the porosity changed with depth, thus the dynamic force and the resistant shown nonlinearity with depth in z direction. Therefore, take the homogeneous isotropic particle layer as example, set the parameters as seen in Table 2. It can get the force distribution map of dynamic and resistant along z direction under fixed condition, seen Fig. 3.

Table 2. The parameters of deposit under saturated seepage flow condition

Layer	Slop angle	θ	$^\circ$	12
Deposition Particles	Porosity	n	-	0.3
	Characteristic particle size	d_{50}	mm	3
	Cohesion	c	kPa	0
	Internal friction angle	φ	$^\circ$	30
	Particle density	γ_s	kN/m ³	22.3
Saturated Seepage Flow	Water density	γ_w	kN/m ³	10
	Saturated density	γ_{sat}	kN/m ³	18.4
	Flow discharge	Q	ml/s	440

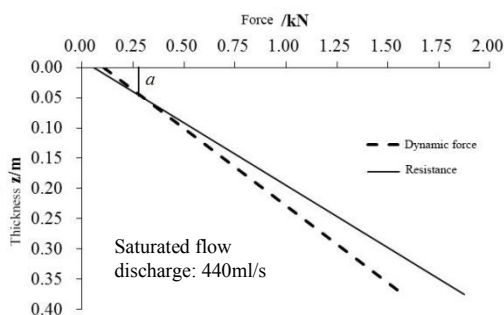


Fig. 3 The stress distribution of movable solid materials under saturated seepage flow

From Fig.3, the dynamic force and resistant of movable solid materials under saturated seepage flow show linear distribution, it also get that the critical thickness a of the homogenous layers is about 5 cm when the seepage flow discharge is 440 ml/s. Actually, with increasing of flow discharge, the critical movable thickness will exceed 5 cm, which will initiate more solid materials.

4. Discussion and Conclusions

4.1 Discussion

Actually, loosen solid materials initiated by rainfall and surface water has been researched widely (Takahashi, 2007), which classified as landslide transforming type and water erosion type. On considering with hydraulic theory, it set up dynamic force and resistant formulas in saturated seepage condition which mainly composed of gravity component and pore water pressure. Actually, pore water pressure is a variable parameter in different position and is difficult to obtain, because of the spatial location easily changing in the loosen materials layer during the failure process. Thus, the model posed in the paper is also need to be improved in the future research.

4.2 Conclusion

Water is one of the most essential compositions for debris-flow formation. The research posed a concept of the movable solid materials in mechanics firstly. Then take the contrast between the new concept and other traditional terms in definition, calculation method and mechanics meaning aspects, it easily got that the movable solid material whether move or not under hydrodynamic condition are a mechanical problem, rather than traditional definition and estimation. Thirdly, take saturated seepage flow as example, through built geology model and carried mechanical analysis, set up the dynamic force and resistant formulas in fixed condition, through set confined parameters, it got a liner distribution of the two formulas with depth increasing when the geology model is homogenous and the seepage flow saturated in whole deposit layer. The next step is to verify the formulas based on experiment and field observation.

Acknowledgements

This work was financed by the National Nature Science Foundation of China (Grant no: 41502330 and 51679229) and China Geological Survey Project (Grant no: DD20160251 and DD20190643).

References

- Brand E W., 1981, Some thoughts on rainfall induced slope failures, in Proceedings of 10th International Conference on Soil Mechanics and Foundation Engineering, p. 373–376.
- Cui P., Hu K H., Zhuang J Q., Yang Y., Zhang J., 2011, Prediction of debris-flow danger area by combining hydrological and inundation simulation methods: *Journal of Mountain Science*, v. 8(1), p. 1-9, doi: 10.1007/s11629-011-2040-8.
- Dahal R K., Hasegawa S., Nonomura A., Yamanaka M., Masuda T., Nishino K., 2009, Failure characteristics of rain fall-induced shallow landslides in granitic terrains of Shikoku Island of Japan: *Environmental geology*, v. 56(7), p. 1295-1310, doi: 10.1007/s00254-008-1228-x.
- Degetto M., Gregoretti C., Bernard M., 2015, Comparative analysis of the differences between using LiDAR contour-based DEMs for hydrological modeling of runoff generating debris flows in the dolomites: *Frontiers in Earth Science*, v. 3, p. 21, doi: 10.3389/feart.2015.00021.
- Ellen S D., Fleming R W., 1987, Mobilization of debris flows from soil slips, San Francisco Bay region, California. *Debris flows/avalanches: Processes, recognition, and mitigation: Geological Society of America, Reviews in Engineering Geology*, p. 31-40.
- Wang G H., Kyoji Sassa., 2003, Pore-pressure generation and movement of rainfall-induced landslides: effects of grain size and fine-particle content: *Engineering Geology*, v. 69, p. 109-125, doi: 10.1016/S0013-7952(02)00268-5.
- Hongey C., Simon D., Yi-Guan C., 2006, Recent rainfall-induced landslides and debris flow in northern Taiwan: *Geomorphology*, v. 77, p. 112-125, doi: 10.1016/j.geomorph.2006.01.002.
- Howard A D., McLane C F., 1988, Erosion of cohesionless sediment by groundwater seepage: *Water Resources Research*, v. 24(10), p. 1659-1674, doi: 10.1029/WR024i010p01659
- Hu W., Dong X J., Wang G H., van Asch T W J., Hicher P Y., 2016, Initiation processes for run-off generated debris flows in the Wenchuan earthquake area of China: *Geomorphology*, v. 253, p. 468–477, doi: 10.1016/j.geomorph.2015.10.024.
- Iverson R M., Schaeffer D G., 2004, Regulation of landslide motion by dilatancy and pore-pressure feedback: AGU Fall Meeting. AGU Fall Meeting Abstracts, p. 273-280.
- Johnson, A.M., 1984, Debris flow, in Brunsten, D., *Slope instability: New York, John Wiley & Sons*, p.257-361.
- Liu J F., You Y., Chen X Z., Fan J R., 2010, Identification of potential sites of debris flows in the upper Min River drainage, following environmental changes caused by the Wenchuan earthquake: *Journal of Mountain Science*, v. 3, p. 255-263. doi: 10.1007/s11629-010-2017-Z.
- McCoy S W., Kean J W., Coe J A., Tucker G E., Staley D M., Wasklewicz W A., 2012, Sediment entrainment by debris flows: In situ measurements from the head waters of a steep catchment: *Journal of Geophysical Research*, v. 117, F03016. doi: 10.1029/2011JF002278.
- Qiao J P., Huang D., Yang Z J., Meng H J., 2012, Statistical method on dynamic reserve of debris flow's source materials in meizoseismal area of wenchuan earthquake region: *The Chinese Journal of Geological Hazard and Control*, v. 23(02), p 1-6, doi: 10.3969/j.issn.1003-8035.2012.02.001.
- Takahisa M., 1981, An intermediate phenomenon between debris flow and bed load transport: erosion and sediment transport in pacific rim steep lands, I.A.H.S. Publ. No. 132 (Christ church).
- Takahashi, T., 2007, *Debris Flow: Mechanics, Prediction and Countermeasures: Taylor and Francis Group, London, UK*, p. 33–101.
- Tang C., Li W L., Ding J., Huang X C., 2011, Field investigation and research on giant debris flow on August 14, 2010 in Yinxiu town, epicenter of Wenchuan Earthquake: *Earth Science-Journal of China University of Geosciences*, v. 36(1), p. 172-180, doi: 10.3799/dqkx.2011.018.
- Wang Z Y., Zhang X Y., 1990, Initiation and laws of motion of debris flow, in Proceedings of the International Symposium on the Hydraulics and Hydrology of Arid Lands in conjunction with the 1990 National Conference on Hydraulic Engineering, San Diego, California, 30 July–3 August, p. 596–601.
- Xu Q., 2010, The 13 August 2010 catastrophic debris flows in Sichuan province: characteristics, genetic mechanism and suggestions, *Journal of Engineering Geology*, v. 18(5), p. 576- 608, doi: 1004- 9665/2010/18(5) 059613.
- Yang S., 2014, Study on the movable critical model of solid materials under hydro-dynamical condition in debris flow area: *University of Chinese Academy of Sciences*, p. 2-4.
- Zhou B F., Li D J., Luo D F., 1991, *Manual of Debris Flow Prevention: Beijing, Science Press*, p. 2-3.
- Zhou B F., Li D J., Luo D F., 1991, *Debris Flow Solid Materials Reserves: Beijing, Science Press*, p. 32-36.

Monitoring, Detection and Warning

Overcoming barriers to progress in seismic monitoring and characterization of debris flows and lahars

Kate E. Allstadt,^{a*} Maxime Farin^c, Andrew B. Lockhart^b, Sara K. McBride^d, Jason W. Kean^a, Richard M. Iverson^b, Matthew Logan^b, Joel B. Smith^a, Victor C. Tsai^c, David George^b

^aU.S. Geological Survey, Geologic Hazards Science Center, Golden, CO, ^bU.S. Geological Survey Cascades Volcano Observatory, Vancouver, WA, ^cCalifornia Institute of Technology, Pasadena, CA, ^dU.S. Geological Survey Earthquake Science Center, Menlo Park, CA

Abstract

Debris flows generate seismic signals that contain valuable information about events as they unfold. Though seismic waves have been used for along-channel debris-flow and lahar monitoring systems for decades, it has proven difficult to move beyond detection to more quantitative characterizations of flow parameters and event size. This is for two primary reasons: (1) our limited understanding of how the radiated wavefield relates to debris flow characteristics and dynamics, and (2) difficulties quantifying the effects of heterogeneous shallow earth structure on the observed wavefield. The latter issue, essentially our inability to sufficiently separate seismic path effects from source information, is a barrier to improving our understanding of the first issue. We review the progress that has been made toward establishing the theory, models and methods required to use seismic observations to make quantitative measurements of flows and summarize the practical, social, and scientific barriers to progress. We discuss some specific ongoing efforts to overcome some of these barriers, with a focus on how we are using large-scale seismic experiments at the U.S. Geological Survey debris-flow flume to develop methods for directly measuring path effects and to develop and validate theoretical debris flow seismicity models.

Keywords: debris flows; lahars; seismology; monitoring

1. Introduction

A debris-flow warning system must provide four pieces of information: (1) *if an event is coming*, (2) *what areas might be inundated*, (3) *when will it arrive*, and (4) *what to do*. The latter three require flow modeling and close collaboration between scientists and public officials, but the first of these is currently possible using just seismic methods. Seismic methods bring advantages to debris-flow monitoring and research. Seismic waves are generated by interactions between the flow and the substrate and contain information about flow dynamics. Unlike most non-seismic instruments that provide point measurements (flow depth sensors, force plates) (e.g., Arattano et al., 2008), seismic signals are generated by the entire proximal flow. One of the biggest advantages is that seismic methods allow one to make precisely timed remote observations of debris-flow processes while they are occurring, day or night. Seeking to take advantage of these benefits, many debris-flow monitoring sites have incorporated seismic methods for research and monitoring (e.g., Galgaro et al., 2005; Suwa et al., 2011; Kean et al., 2015), and seismically based lahar (volcanic debris flow) detection systems have been used to protect lives at volcanoes worldwide for decades (e.g., Hadley and LaHusen, 1995; Marcial et al., 1996; Lavigne et al., 2000; Andrade et al., 2006; Leonard et al., 2008; Pulgarin et al., 2015).

Existing operational seismic monitoring systems are relatively simple and qualitative and are used sparingly because they can be expensive to install and maintain. The majority, whether primarily for research or warning, are along-channel, meaning one or more sensors are located within tens to hundreds of meters of the channel of interest. Amplitude-based along-channel systems detect seismicity generated by flows as they pass, sometimes to trigger alerts based on a threshold duration or other signal characteristics. Typically, multiple sensors are deployed at different distances along the channel to provide redundancy and for velocity estimates. Average velocities can be estimated by

* Corresponding author e-mail address: kallstadt@usgs.gov

cross-correlating the seismic envelopes to get the time offset and dividing the along-channel distance between sensors by that time (Marchi et al., 2002). Along-channel systems require instrumentation for each monitored drainage. Depending on circumstances, seismic and/or infrasound instrumentation may be augmented with additional methods such as rain gauges, cameras, tripwires or flow depth gauges.

In an ideal world, we would be able to detect flows and use the seismic signal to obtain an estimate of the evolving basal stresses and relate those to flow characteristics such as flow depth, discharge rate, velocity, and particle concentration. In turn, we could use the flow characteristics to estimate the hazard a particular flow may pose to downstream populations. In the decades since its initial development, the utility of seismic monitoring methods for debris-flow detection has been limited due, in part, to barriers related to unknowns in seismic path effects and theoretical debris-flow seismicity models.

In the following sections, we review the current state of debris-flow seismic monitoring, investigate the barriers to expanding seismic monitoring capabilities into a more quantitative realm, and discuss some work underway by the U.S. Geological Survey (USGS) and collaborators to try to overcome some of these barriers.

2. Background

Debris flows exert forces on the channel bed and channel walls that vary in time and space, generating seismic waves (Moretti et al., 2012). These basal and lateral forces relate to the flow properties. Time-averaged mean normal force relates most closely to flow depth and flow density, whereas the fluctuating forces are more correlated with other flow properties such as grain diameter, average flow velocity, and average particle impact forces (Iverson, 1997; McCoy et al., 2013; Hsu et al., 2014). At high frequencies, the seismic signal is often modeled as the result of a series of individual random particle impacts (e.g., Kean et al., 2015; Lai et al., 2018). Much of the seismic energy radiated by surface sources such as debris flows propagates as surface waves (Sánchez-Sesma et al., 2011). At typical along-channel recording sites high frequency (5-100s Hz) energy dominates (Allstadt et al., 2018). Higher frequency surface waves with their shorter wavelengths propagate in the shallowest and typically most attenuating layers—dissipating the energy over relatively short distances. This is why along-channel seismic monitoring is the dominant form of monitoring—more distant stations may record nothing above the ambient noise level for many flows, especially given that ambient noise may be elevated during flow events due to storm noise.

Seismic signals carry information about the source process through frequency, amplitude, and polarization variations with time. To recover information about the source, we need to be able to correct for alterations to that signal caused by attenuation and scattering (path effects). Geophysical field methods can be used to estimate the relevant elastic parameters of the ground so that these path effects can be modeled and removed. However, this can be costly, uncertain, nonunique, and low resolution. Our inability to easily and accurately correct for path effects is one of the main barriers to progress in this field. We also do not know whether it is even possible to uniquely obtain parameter estimates even if the basal stresses are perfectly known, though previous studies have found relationships between fluctuating basal forces and some flow parameters (McCoy et al., 2013; Hsu et al., 2014).

Though many studies have investigated relations between seismic signal characteristics and debris-flow characteristics, there is no concise, uniform, quantitative summary. This is because many different flow parameters can contribute to basal stresses, and because path effects are so difficult to separate from source effects. However, generally, when recorded at near-source along-channel sites, amplitudes are higher when (1) the flow passes closest to the station (Marcial et al., 1996; Arattano et al., 2008; Cole et al., 2009); (2) the flow height/discharge/wetted area is greater (Marcial et al., 1996; Marchi et al., 2002; Doyle et al., 2010; Kean et al., 2015); (3) the particle concentration is greater (Lavigne et al., 2000; Doyle et al., 2010); (4) particle size is greater (Arattano and Moia, 1999; Vázquez et al., 2016); and (5) the flows move over bedrock or compact sediment rather than loose sediment (Cole et al., 2009; Kean et al., 2015).

3. Overcoming Barriers

As outlined above, we already have the capability to use debris-flow seismicity for practical and research purposes. However, many existing methods are qualitative and have significant limitations. In this section, we will discuss some of the barriers that are hindering the use of seismic monitoring for more quantitative purposes. We focus first on work the USGS and collaborators are doing to overcome two scientific barriers: our inability to account for path effects and our lack of theoretical debris-flow seismicity models. We address both issues using large-scale seismic experiments that we conducted in 2016 at the USGS debris-flow flume near Blue River, Oregon, USA. The flume is a 95-m long, 2-m wide, 1.2-m deep concrete channel that has been used for decades to study debris-flow dynamics (Iverson et al., 2010). In 2016, we conducted experiments in which saturated material was suddenly released from behind a 2-m high

gate. The flume has a constant slope of 31° until 74 m downslope from the gate, where it begins to curve and then finally flatten to about 2° where it reaches a large runout pad. Distances along the flume bed are gauged by their downslope distance in meters from the gate, with the gate at $x=0$ m.

The experiment setup for 2016 is shown in Fig. 1a. Further details and data can be found in Iverson and Logan (2017) and Allstadt (2016). For brevity, here we focus on just one experiment, a release of 10 m^3 of water-saturated sand and gravel on 23 June 2016. We use data from a broadband seismometer, E03, located at $x\approx 32\text{ m}$ $\sim 4\text{ m}$ away from the flume, and basal normal and shear stress data recorded by force plates mounted flush with the bed of the flume about 5 m from E03. A screenshot of this experiment is shown in Fig. 1c; full videos of the experiment are available in Logan et al. (2018).

3.1. Path effects

We established earlier that path effects are one of the biggest barriers to quantitative use of seismic recordings of debris flows and that although geophysical imaging methods are helpful, they are not always feasible. In the flume experiments, we instead directly measure the path effects by recording the seismic response at a given station location to an impulse source that we control at a specific source location. The impulse response is known as a Green's function. The earthquake community has used "empirical Green's functions" (EGFs) for decades, but they typically consider source to station distances of up to hundreds of kilometers and thus usually use naturally generated sources like small earthquakes or ambient noise (Hartzell, 1978). For the shorter distances and higher frequencies we consider for debris flows, it is practical to generate our own forces using a sledgehammer that measures impact force (force hammer) at closely spaced source locations along the flow channel. While hammer sources are commonly used for seismic imaging, the distinction here is that we actually measure the time series of forces imparted on the ground and use the amplitude information of the source. While, to our knowledge, our approach is distinct for debris flows, similar approaches have been used on a larger scale for lahars (Walsh et al., 2016).

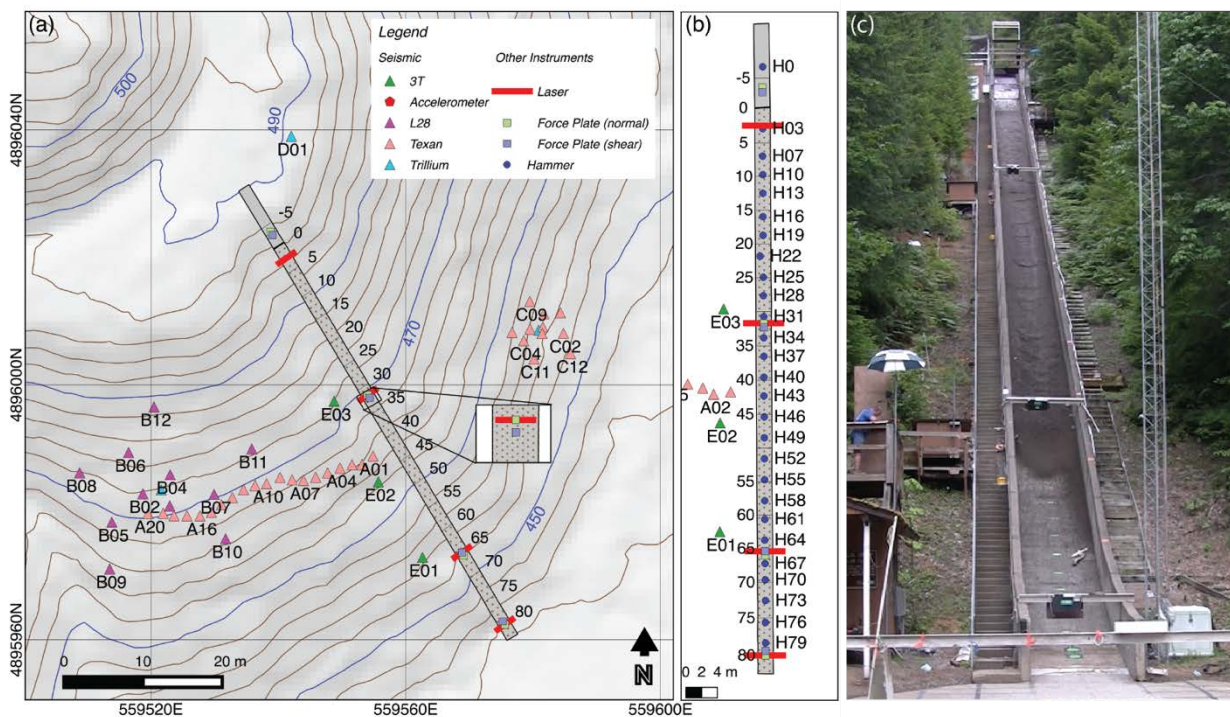


Fig. 1 (a) Map of USGS debris-flow flume showing seismic station locations, distances along flume, camera, laser, and force plate locations. Elevations are in meters above sea level, contour interval is 2 m. Numbers along flume indicate distance from flume gate in meters. (b) Hammer blow locations shown along length of flume, labeled with H, relative to other nearby flume instrumentation. (c) Image of 23 JUN 2016 experiment at $t=9\text{ s}$. Map coordinate system is NAD 1983, UTM Zone 10N.

During the 2016 flume experiments, we used a 5.4 kg sledge force hammer (PCB Piezotronics Model 086D50) to hit specific hammer locations (Fig. 1b) and recorded the resulting force time series and seismic signals on nearby sensors on GPS-timed RT-130 digitizers to ensure time synchronization. We impacted each hammer location at least

five times normal to the bed, using a cement block that interlocks with the bump pattern on the bed of the flume to protect the fragile flume bed tiles. We compute EGFs for each hammer location-station pair by deconvolving the force-time series recorded by the hammer from the waveform of each individual blow to remove the hammer impulse. The hammer impulse has a non-negligible duration, so this is needed in order to best approximate a Dirac delta function (impulse of zero duration, infinite amplitude) of 1 Newton-sec. We then stacked this result for all five hammer blows at each location to augment the signal and reduce noise. Since flows also impart shear forces, shear EGFs are also needed to completely explain the observed wavefield (Aki and Richards, 2002). However, shear forces were difficult to generate on the steep flume. By comparing the shear and normal EGFs for hammer locations on flat ground where we could generate shear forces by hitting the side of the block weighted down by a person, we found that the normal EGFs were very similar in amplitude, phase, and frequency content to the shear EGFs for station E03 below 50 Hz; so we directly substitute normal EGFs for shear ones for this simple analysis. The validity of this simplification for other station-hammer location pairs requires further investigation in the future.

To test how well our EGFs capture the path effects, we forward model the vertical component seismogram at E03 using the shear and normal force plate data from $x=32$ m and the EGFs for E03 (Fig. 2a) and compare the result to the actual recorded signal. In the time domain, the recorded seismic signal is equal to the convolution of the source-time series and the Green's function between that source location and the seismic station (Aki and Richards, 2002). Therefore, we need to convolve the force time series experienced at each section of the bed of the flume with the corresponding EGFs. Both the forcing and the EGFs are continuous functions in reality, but we have discrete hammer locations (~ 3 m apart) and we only have the actual source function for one point. Therefore, we need to manipulate the force plate data and distribute it in a realistic way to make it better represent the forcing of a continuous flow. We explain how this is done in Fig. 2g and the corresponding caption. Though we do the simulation at all frequencies up to the Nyquist frequency, we focus on trying to reproduce the observed signal in the band of 15-35 Hz in order to avoid the flume structural resonance that occurs at ~ 45 Hz and because, as noted earlier, normal EGFs only provide a good approximation of the shear EGFs at frequencies < 50 Hz.

We compare the result of this simulation to the actual recorded signal in Fig. 2b-2f. Comparing to the full synthesis (Fig. 2f) shows that the signal is similar in character and frequency content but slightly overestimated in amplitude. We note that the best overall fit is the signal that neglects the shear forces (Fig. 2e). This may occur because grain collisions with the upslope faces of the bumps on the force plates may result in some conversion of shear or normal energy into the orthogonal component. However, this hypothesis requires a more detailed investigation. We can obtain a fit almost as good if we only use the single EGF with the highest amplitudes (H28 in this case) (Fig. 2d). The downside is that this underestimates the signal as the flow approaches the station because the signal can only start once the flow front actually reaches H28. Our ability to fairly closely reproduce the characteristics of the observed seismic wavefield at E03 using just the EGFs and force plate data confirms that the EGFs do capture the path effects with relatively high fidelity and relate closely to the fluctuating basal forces. There are many possible uses for this approach, and we are only beginning to explore practically how these EGFs can be used inversely to estimate fluctuating boundary stresses from recorded seismic signals.

3.2. Theoretical debris-flow seismicity models

The next major barrier to obtaining quantitative information from seismic signals of debris flows is a lack of a theoretical framework for the generation of debris-flow seismicity. Models are needed to relate seismic amplitudes to specific source parameters and are also needed to understand the degree to which it is possible to actually constrain such parameters from the seismic wavefield. A few simple theoretical models have been proposed recently, though none have yet been independently validated. Kean et al. (2015) proposed a seismic model for debris flows occurring at Chalk Cliffs, Colorado, but since they did not know the ground parameters, they could only compute the relative change of seismic power between two debris flows at the same site. Lai et al. (2018) proposed a physical model for debris-flow seismic power in which they stochastically model the individual impacts of particles in the main flow front, but the model only considers that the main flow front generates seismic waves, and many orders of magnitude uncertainty are dependent on knowing the elastic parameters of the ground.

Debris flows often consist of chains of surges of differing flow characteristics (e.g., Vázquez et al., 2016) and even a single surge can have spatially variable characteristics (Iverson, 1997) that are not modeled by either of the two aforementioned models. A new theoretical model that expands on the Lai et al. (2018) model will enable us to account for the entire typical structure of a debris-flow surge, each with differing impact rates and grain size distributions. The modeled flow is led by a saltating front, followed by a snout lip where rocks fall from the flow onto the bed, then a coarser-grained snout and the main flow front. Several of these debris-flow surge sequences could be chained together to simulate the series of surges typical in reality. Though such a model is still a simplified version of reality,

preliminary comparison with data from debris-flow flume experiments, using the EGFs described above as the source of the impulses, suggests that the modeled power spectral density (PSD) matches the observed PSD when flow velocities are steady (Farin, written communication, 2018). While the model does not account for natural complexities and variations, it provides a starting point upon which to build more complex models.

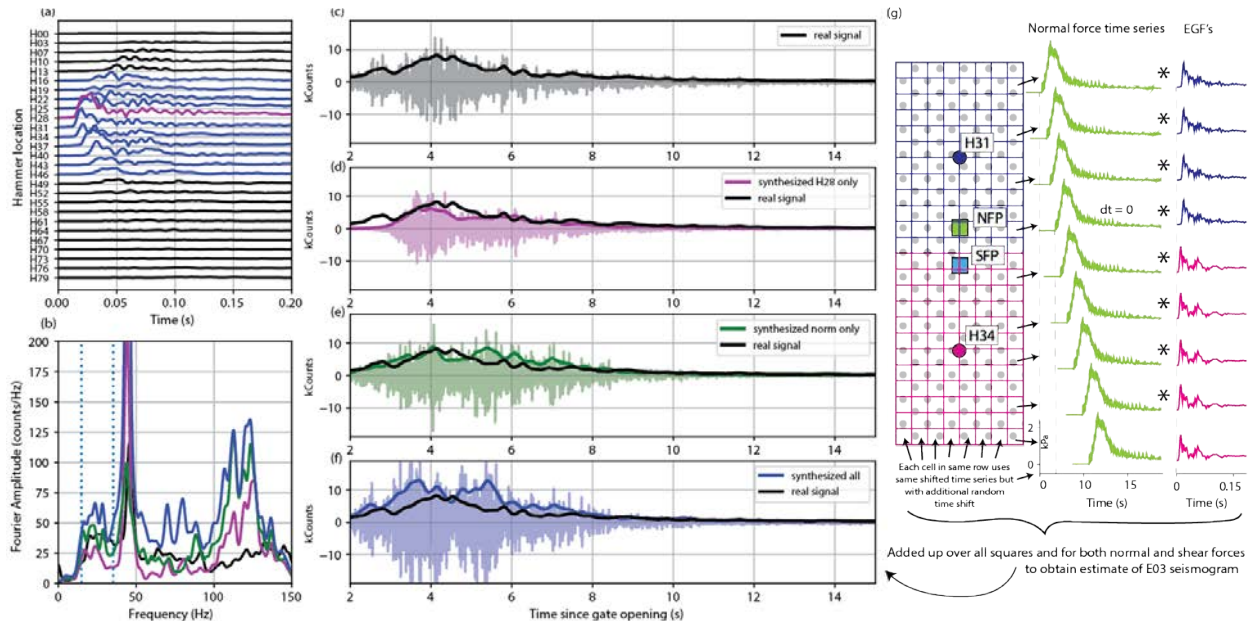


Fig. 2) Forward modeling of vertical seismic signal at E03 for the 23 JUN 2016 10 m³ flume experiment. (a) Record section of normal force EGFs for vertical component of E03, blue colors indicate hammer locations used in full synthesis, magenta color indicates dominant hammer location (H28). (b) Smoothed Fourier spectra of real and three different synthesized waveforms, colors labeled at right, dashed lines indicate bandpass filter limits applied to waveforms in c-f. (c) Actual recorded signal at E03 (gray) and smoothed envelope (black), (d) Synthesized waveform and envelope using just the H28 hammer location, (e) same for just the normal component of force for H16-H46, (f) same as E but including shear component. (g) Schematic of method for synthesizing the signal showing a section of the flume around the force plates at $x=32$ m, NFP is normal force plate, SFP is shear force plate. The flume bed is discretized into 25 cm squares (same size as force plates because this is the dimension over which basal forces is measured and scale of measurement controls the observed fluctuating forces (Iverson, 1997; Hsu et al., 2014)). Each bed square is represented by the EGF of the closest force plate location (blue or pink for H31 or H34, in schematic). The forcing time from the force plate is shifted for each row by dt , which equals the arrival time at the force plate minus the flow front arrival time at the row (derived from video). For each element of each row, an additional randomized time shift is added from a gaussian distribution (mean=0, stdev=0.5 s) to best reflect the poor spatial correlation and randomness of basal forces of real flows. We then convolve the shifted force-time series with the EGF for the corresponding hammer location and add the result up over all bed elements.

3.3. Event size estimation and inundation modeling

The main weakness of many warning systems is event size estimation. Size is a crucial factor in determining how far a debris flow will travel and whether or not it is likely to inundate populated areas downstream. Size also affects velocity (Iverson, 1997), and thus influences our ability to estimate when the flow will arrive. These are all critical pieces of information for warning systems. The crux of the issue is that there is so far no universal way to relate high-frequency seismic amplitudes to flow depth, discharge, or volume based on seismic methods alone.

For this reason, at present, seismic methods are almost always combined with other instrumentation that can help constrain event size such as flow depth gauges, cameras, tripwires, and pendulums (e.g., Arattano et al., 2008). Each of those instrumentation types comes with its own issues and limitations. In the future, a combination of the EGF approach and the theoretical models discussed earlier could be part of the solution, but none of the existing models have a direct relationship with flow depth, discharge, or volume, and many different factors contribute. This may be a fundamental limitation of seismic methods, though many of the contributing factors do relate to event size (e.g., wetted area relates to flow depth and channel geometry, larger events are often faster and have larger clasts); so the task may not be insurmountable.

For drainages with repeated events, some researchers have used past events to calibrate detection algorithms by correlating seismic amplitudes with discharge rates empirically (e.g., Lavigne et al., 2000; Galgaro et al., 2005; Andrade et al., 2006). But these calibrations are typically specific to a single monitoring site, flow regime, and size range and they provide order of magnitude estimates, at best. Empirical methods are of little help when installing a

system on a new drainage in a new location with different path effects, channel morphology, bed conditions, and flow characteristics, all of which control the amplitude and frequency content of the signals that ultimately are recorded at a monitoring site. Even if we could perfectly associate a recorded seismic signal with a discharge rate, the discharge at a specific location and time is not necessarily proportional to the entire flow volume. Using seismic methods to measure velocity and other factors that control inundation limits downstream may be a better (or complementary) proxy for size than measuring discharge or flow height at a single point.

If a debris flow is detected and its relevant characteristics determined, the next step is taking that information and estimating how far the flow will travel, what areas it will inundate, and when. This requires accurate flow modeling and inundation modeling abilities—a complex topic that is far beyond the scope of this paper. For brevity, we note that our ability to model debris flows and inundation accurately and rapidly is limited but improving (e.g., Iverson and George, 2014; Bessette-Kirton et al., this issue). The relevant point here is that seismic monitoring can provide crucial model input information and constraints at one or more locations along the flow's path.

3.4. Costs and distributed methods

Cost often comes into play when deciding whether to monitor for debris flows and how. Installing an expensive, drainage-specific monitoring system when debris-flow hazard is commonly widely distributed over many drainages and varies with time and conditions (fire, antecedent precipitation, post-earthquake) is not often a priority outside of volcanic settings. Even in volcanic settings, the requirement of installing a monitoring system on each populated drainage can be cost prohibitive and may require that difficult choices be made. To reduce the number of systems required, monitoring is often installed far downstream after several drainages have coalesced. This reduces the total number of systems required but also reduces the warning times.

More distributed methods that are not channel-specific could provide greater value. Several methods have been proposed and demonstrated, such as those that use amplitude source location methods applied to existing distributed seismic monitoring networks (Kumagai et al., 2009; Walter et al., 2017), and those that use array methods to track moving sources (Almendros et al., 2002), but due to the rapid attenuation of high frequency energy, they are most practical for larger, more energetic flows.

3.5. Social factors and warning times

Many critical social and cultural aspects of warning system development are commonly overlooked or considered to be separate from the geophysical issues. These include determining channels for appropriate delivery of messages, message development, warning times, relationships with local officials and emergency managers, as well as language and culture (Grasso and Singh, 2011). Composition of messaging to address protective actions is a challenge specific to recipient locations and available warning times and requires development as well as testing. Best practice in alerts and warnings in text messages ideally should contain the following: who is sending it, what the hazard is, and brief instructions as to what to do (Bean et al., 2015; Ripberger et al., 2015). After this brief message is sent, follow up messages should also be sent to provide more information to people about the situation (Liu et al., 2017). Further complexities exist in terms of what to tell people when the outcome is still uncertain, particularly if good predictive models are not available and the limitations are not well communicated to decision makers. Media and social media are now often used quickly to distribute warning messaging and information about debris flows and lahars (Becker et al., 2017). Given our emerging technologies, more could be done to alert people and inform them of evolving situations, and the involvement of geoscientists who are familiar with the capabilities, limitations, and uncertainties of the information such systems can provide is necessary from the beginning.

One issue that requires close collaboration between geoscientists and social scientists is determining what potential warning times may be and what the best actions are given that time window. In some situations, it may not be possible for a detection system to provide meaningful warning time to a population. This problem should be fully understood by civil authorities before planning such a system to avoid dangerously unrealistic expectations. Because non-volcanic debris flows travel shorter distances in general, warning times can be on the order of a few minutes. The same can be true for areas close to the source for volcanic lahars. When warning times are short, the best approach may sometimes be to simply automatically close roads or hiking trails to keep people from entering harm's way (Badoux et al., 2009) or to provide procedures and trainings that are specific to the setting (Leonard et al., 2008). The key is to provide enough specific actionable information that is possible in the time window available. Since most non-volcanic debris flows are triggered by storms, forecast-based methods which can cover wider areas and give warning times of up to several days (e.g., NOAA-USGS Debris Flow Task Force, 2005) are often preferred where feasible, though they come with a trade-off of the risk of false alarms. The same is true of lahars triggered by precipitation or volcanic activity:

evacuations can take place days in advance if the hazard and risk is well known (e.g., Pulgarin et al., 2015; Capra et al., 2018), and this is preferable over warnings issued after an event is already underway. Unheralded lahars, on the other hand, such as those initiated by landslides or outburst floods, are a primary target of event warning systems. Runout distances of lahars can exceed 100 km, and populations often are far from the source area. Therefore, warning times can be on the order of an hour, and rapid evacuations are often part of the plan. Even with longer warning times, public education, training, and drills are required to make this a feasible approach. For example, the town of Orting, Washington, USA, holds monthly siren tests and annual lahar evacuation drills (cityoforting.com) to prepare for potential unheralded lahars from Mt. Rainier.

4. Conclusions

In conclusion, seismic debris-flow monitoring has already been used successfully for decades for both research and early warning systems. However, our existing capabilities are relatively qualitative, primarily because of difficulties accurately accounting for path effects at the high frequencies typically recorded and due to a lack of theoretical models. While just a start, undertaking studies focused on overcoming these barriers will enable seismic debris-flow monitoring to be used in a more quantitative manner. These methods must then be implemented, validated, and updated for natural monitoring sites. Furthermore, if these systems are to be used to issue warnings, they must be integrated with other important system components such as event size and inundation modeling, social factors, cost-benefit analysis, and warning time analysis.

Acknowledgements

We thank Aaron Rinehart, Chris Lockett, Kelly Swinford, Francis Rengers, Liz Westby, and Luke McGuire for contributing to the 2016 flume experiments. MF and VCT acknowledge support from NSF grant EAR 1558479. Any use of trade, firm, or product names is for descriptive purposes only and does not imply endorsement by the U.S. Government.

References

- Aki, K., and Richards, P.G., 2002, *Quantitative Seismology*, 2nd Ed.: Mill Valley, California, University Science Books.
- Allstadt, K., 2016, Seismic signature of debris flume experiments: International Federation of Digital Seismograph Networks, doi:10.7914/SN/ZK_2016.
- Allstadt, K.E., Matoza, R.S., Lockhart, A.B., Moran, S.C., Caplan-Auerbach, J., Haney, M.M., Thelen, W.A., and Malone, S.D., 2018, Seismic and acoustic signatures of surficial mass movements at volcanoes: *Journal of Volcanology and Geothermal Research*, v. 364, p. 76–106, doi:10.1016/j.jvolgeores.2018.09.007.
- Almendros, J., Chouet, B., and Dawson, P., 2002, Array detection of a moving source: *Seismological Research Letters*, v. 73, p. 153–165, doi:10.1785/gssrl.73.2.153.
- Andrade, D. et al., 2006, Lahar early warning systems based on acoustic flow monitors in Ecuador, *in* *Cities on Volcanoes 4*, Quito, Ecuador.
- Arattano, M., Marchi, L., Arattano, M., and Marchi, L., 2008, Systems and Sensors for Debris-flow Monitoring and Warning: *Sensors*, v. 8, p. 2436–2452, doi:10.3390/s8042436.
- Arattano, M., and Moia, F., 1999, Monitoring the propagation of a debris flow along a torrent: *Hydrological Sciences Journal*, v. 44, p. 811–823.
- Badoux, A., Graf, C., Rhyner, J., Kuntner, R., and Mc Ardell, B.W., 2009, A debris-flow alarm system for the Alpine Illgraben catchment: design and performance: *Natural Hazards*, v. 49, p. 517–539, doi:10.1007/s11069-008-9303-x.
- Bean, H., Sutton, J., Liu, B.F., Madden, S., Wood, M.M., and Mileti, D.S., 2015, The study of mobile public warning messages: A research review and agenda: *Review of Communication*, v. 15, p. 60–80.
- Becker, J.S., Leonard, G.S., Potter, S.H., Coomer, M.A., Paton, D., Wright, K.C., and Johnston, D.M., 2017, Organisational Response to the 2007 Ruapehu Crater Lake Dam-Break Lahar in New Zealand: Use of Communication in Creating an Effective Response:
- Bessette-Kirton, E.K., Kean, J.W., Coe, J.A., Rengers, F.K., and Staley, D.M., this issue, An evaluation of debris-flow runout model accuracy and complexity in Montecito, CA: Towards a framework for regional inundation-hazard forecasting: 7th International Conference on Debris-Flow Hazards Mitigation.
- Capra, L., Coviello, V., Borselli, L., Márquez-Ramírez, V.-H., and Arámbula-Mendoza, R., 2018, Hydrological control of large hurricane-induced lahars: evidence from rainfall-runoff modeling, seismic and video monitoring: *Natural Hazards and Earth System Sciences*, v. 18, p. 781–794, doi:https://doi.org/10.5194/nhess-18-781-2018.
- Cole, S.E., Cronin, S.J., Sherburn, S., and Manville, V., 2009, Seismic signals of snow-slurry lahars in motion: 25 September 2007, Mt Ruapehu, New Zealand: *Geophysical Research Letters*, v. 36, p. L09405, doi:10.1029/2009GL038030.
- Doyle, E.E., Cronin, S.J., Cole, S.E., and Thouret, J.-C., 2010, The coalescence and organization of lahars at Semeru volcano, Indonesia: *Bulletin of volcanology*, v. 72, p. 961–970.
- Galgaro, A., Tecca, P.R., Genevois, R., and Deganutti, A.M., 2005, Acoustic module of the Acquabona (Italy) debris flow monitoring system: *Natural Hazards and Earth System Science*, v. 5, p. 211–215.
- Grasso, V.F., and Singh, A., 2011, Early warning systems: State-of-art analysis and future directions: Draft report, UNEP, v. 1.
- Hadley, K.C., and LaHusen, R., 1995, Technical Manual for the Experimental Acoustic Flow Monitor: U.S. Geological Survey Open-File Report 95-114, https://pubs.usgs.gov/of/1995/0114/report.pdf.
- Hartzell, S.H., 1978, Earthquake aftershocks as Green's functions: *Geophysical Research Letters*, v. 5, p. 1–4, doi:10.1029/GL005i001p00001.
- Hsu, L., Dietrich, W.E., and Sklar, L.S., 2014, Mean and fluctuating basal forces generated by granular flows: Laboratory observations in a large vertically rotating drum: *Journal of Geophysical Research: Earth Surface*, v. 119, p. 1283–1309.

- Iverson, R.M., 1997, The physics of debris flows: Reviews of Geophysics, v. 35, p. 245–296, doi:10.1029/97RG00426.
- Iverson, R.M., and George, D.L., 2014, A depth-averaged debris-flow model that includes the effects of evolving dilatancy. I. Physical basis: Proc. R. Soc. A, v. 470, p. 20130819, doi:10.1098/rspa.2013.0819.
- Iverson, R.M., and Logan, M., 2017, Sensor data from debris-flow experiments conducted in June, 2016, at the USGS Debris-flow Flume, HJ Andrews Experimental Forest, Blue River, Oregon, doi:10.5066/F7N58JKH.
- Iverson, R.M., Logan, M., LaHusen, R.G., and Berti, M., 2010, The perfect debris flow? Aggregated results from 28 large-scale experiments: Journal of Geophysical Research: Earth Surface, v. 115, p. F03005, doi:10.1029/2009JF001514.
- Kean, J.W., Coe, J.A., Coviello, V., Smith, J.B., McCoy, S.W., and Arattano, M., 2015, Estimating rates of debris flow entrainment from ground vibrations: Geophysical Research Letters, v. 42, p. 2015GL064811, doi:10.1002/2015GL064811.
- Kumagai, H., Palacios, P., Maeda, T., Castillo, D.B., and Nakano, M., 2009, Seismic tracking of lahars using tremor signals: Journal of Volcanology and Geothermal Research, v. 183, p. 112–121.
- Lai, V.H., Tsai, V.C., Lamb, M.P., Ulizio, T.P., and Beer, A.R., 2018, The Seismic Signature of Debris Flows: Flow Mechanics and Early Warning at Montecito, California: Geophysical Research Letters, v. 45, p. 5528–5535, doi:10.1029/2018GL077683.
- Lavigne, F., Thouret, J.-C., Voight, B., Young, K., LaHusen, R., Marso, J., Suwa, H., Sumaryono, A., Sayudi, D.S., and Dejean, M., 2000, Instrumental lahar monitoring at Merapi Volcano, Central Java, Indonesia: Journal of Volcanology and Geothermal Research, v. 100, p. 457–478, doi:10.1016/S0377-0273(00)00151-7.
- Leonard, G.S., Johnston, D.M., Paton, D., Christianson, A., Becker, J., and Keys, H., 2008, Developing effective warning systems: Ongoing research at Ruapehu volcano, New Zealand: Journal of Volcanology and Geothermal Research, v. 172, p. 199–215, doi:10.1016/j.jvolgeores.2007.12.008.
- Liu, B.F., Wood, M.M., Egnoto, M., Bean, H., Sutton, J., Mileti, D., and Madden, S., 2017, Is a picture worth a thousand words? The effects of maps and warning messages on how publics respond to disaster information: Public Relations Review, v. 43, p. 493–506.
- Logan, M., Iverson, R.M., and Obryk, M.K., 2018, Video Documentation of Experiments at the USGS Debris-Flow Flume 1992–2017 (ver 1.4, January 2018): U.S. Geological Survey Open-File Report, v. 2007–1315, doi:https://doi.org/10.3133/ofr20071315.
- Marchi, L., Arattano, M., and Deganutti, A.M., 2002, Ten years of debris-flow monitoring in the Moscardo Torrent (Italian Alps): Geomorphology, v. 46, p. 1–17, doi:10.1016/S0169-555X(01)00162-3.
- Marcial, S.S., Delos Reyes, P.J., Chu, A.V., and Solidum, R.U., 1996, Instrumental lahar monitoring of Mt. Pinatubo, in Newhall, C.G. and Punongbayan, R.S. eds., Fire and Mud: Eruptions and Lahars of Mt. Pinatubo, Seattle and London, University of Washington Press, p. 1015–1022, https://pubs.usgs.gov/pinatubo/index.html.
- McCoy, S.W., Tucker, G.E., Kean, J.W., and Coe, J.A., 2013, Field measurement of basal forces generated by erosive debris flows: Journal of Geophysical Research: Earth Surface, v. 118, p. 589–602.
- Moretti, L., Mangeney, A., Capdeville, Y., Stutzmann, E., Huggel, C., Schneider, D., and Bouchut, F., 2012, Numerical modeling of the Mount Steller landslide flow history and of the generated long period seismic waves: Geophysical Research Letters, v. 39, p. L16402, doi:10.1029/2012GL052511.
- NOAA-USGS Debris Flow Task Force, 2005, NOAA-USGS Debris-Flow Warning System—Final Report: U.S. Geological Survey Circular 1283, 47 p., https://pubs.usgs.gov/circ/2005/1283/ (accessed October 2018).
- Pulgarin, B., Cardona, C., Agudelo, A., Santacoloma, C., Calvache, M., Murcia, C., Cuéllar, M., Medina, E., Balanta, R., and Calderón, Y., 2015, Erupciones Recientes del Volcán Nevado del Huila: Lahares Asociados y Cambios Morfológicos del Glaciar: Bol Geológico, v. 43, p. 75–87.
- Ripberger, J.T., Silva, C.L., Jenkins-Smith, H.C., and James, M., 2015, The influence of consequence-based messages on public responses to tornado warnings: Bulletin of the American Meteorological Society, v. 96, p. 577–590.
- Sánchez-Sesma, F.J., Weaver, R.L., Kawase, H., Matsushima, S., Luzón, F., and Campillo, M., 2011, Energy partitions among elastic waves for dynamic surface loads in a semi-infinite solid: Bulletin of the Seismological Society of America, v. 101, p. 1704–1709.
- Suwa, H., Okano, K., and Kanno, T., 2011, Forty years of debris flow monitoring at Kamikamihorizawa Creek, Mount Yakedake, Japan, in 5th international conference on debris-flow hazards mitigation: mechanics, prediction and assessment. Casa Editrice UniversitaLa Sapienza, Roma, p. 605–613.
- Vázquez, R., Suriñach, E., Capra, L., Arámbula-Mendoza, R., and Reyes-Dávila, G., 2016, Seismic characterisation of lahars at Volcán de Colima, Mexico: Bulletin of Volcanology, v. 78, p. 8.
- Walsh, B., Jolly, A.D., and Procter, J.N., 2016, Seismic analysis of the 13 October 2012 Te Maari, New Zealand, lake breakout lahar: Insights into flow dynamics and the implications on mass flow monitoring: Journal of Volcanology and Geothermal Research, v. 324, p. 144–155, doi:10.1016/j.jvolgeores.2016.06.004.
- Walter, F., Burtin, A., McArdell, B.W., Hovius, N., Weder, B., and Turowski, J.M., 2017, Testing seismic amplitude source location for fast debris-flow detection at Illgraben, Switzerland: Natural Hazards and Earth System Sciences, v. 17, p. 939–955, doi:https://doi.org/10.5194/nhess-17-939-2017.

Topographic change detection at Chalk Cliffs, Colorado, USA, using airborne lidar and UAS-based Structure-from-Motion photogrammetry

Katherine R Barnhart^{a,b*}, Francis K. Rengers^c, Jessica N. Ghent^d, Gregory E. Tucker^{a,b},
Jeffrey A. Coe^c, Jason W. Kean^c, Joel B. Smith^c, Dennis M. Staley^c, William Kleiber^e,
Ashton M. Wiens^e

^aUniversity of Colorado, Department of Geological Sciences, UCB 399, Boulder, CO 80309, USA

^bUniversity of Colorado, Cooperative Institute for Research in Environmental Sciences, UCB 216, Boulder, CO 80309, USA

^cU.S. Geological Survey, Landslide Hazards Group, 1711 Illinois St., Golden, CO 80401, USA

^dFront Range Community College, 3645 W 112 Ave, Westminster, CO 80031, USA

^eUniversity of Colorado, Department of Applied Mathematics, UCB 526, Boulder, CO 80309, USA

Abstract

The Chalk Cliffs debris-flow site is a small headwater catchment incised into highly fractured and hydrothermally altered quartz monzonite in a semiarid climate. Over half of the extremely steep basin is exposed bedrock. Debris flows occur multiple times per year in response to rainstorm events, typically during the summer monsoon season. The frequency of debris flows, and the uniformity of the underlying rock, make Chalk Cliffs an ideal study catchment for translating mechanistic understanding of natural debris flows to other sites. A 2008 National Center for Airborne Laser Mapping (NCALM) airborne lidar survey provides baseline topography for the site; however, heretofore there has been no systematic effort to collect repeat topography of the entire site. Starting in May 2018, we made repeat surveys of the basin with an unmanned aircraft system (UAS). The UAS-based imagery was processed into (x, y, z) point clouds using Structure-from-Motion (SfM) photogrammetry. We georegistered the point clouds using 12 ground control points placed within and around the study basin. In this study we compare the lidar with one SfM point cloud to assess topographic change over a 10-year time period. The difference map provides observational data relevant to understanding sediment provenance and transport at the Chalk Cliffs. The difference image indicates erosion of colluvial surfaces, with limited deposition in the survey area. Some colluvial hillslopes show spatially uniform erosion while others experienced concentrated erosion of up to 3 m depth over a 10-year period.

Keywords: Structure-from-Motion, topographic difference map, Chalk Cliffs

1. Introduction

Debris flows are water-laden slurries of soil and rock that move rapidly through channels in steep landscapes, and present hazards to human life, infrastructure, and property. Debris flows are among the most dangerous and frequent natural hazards—once initiated, a debris flow can continue to travel over shallow terrain, extending the hazard from steep regions to areas adjacent to the mouths of canyons and near valley bottoms. Progressive entrainment of debris through surface water runoff and bulk failure of debris are the two main mechanisms for the initiation of debris flows (Coe et al., 2008; Kean et al., 2013). Here, we apply Structure-from-Motion (SfM) to create 3D point clouds using images taken using an unmanned aircraft system (UAS). The SfM point clouds are then compared with an aerial lidar

* Corresponding author e-mail address: katherine.barnhart@colorado.edu

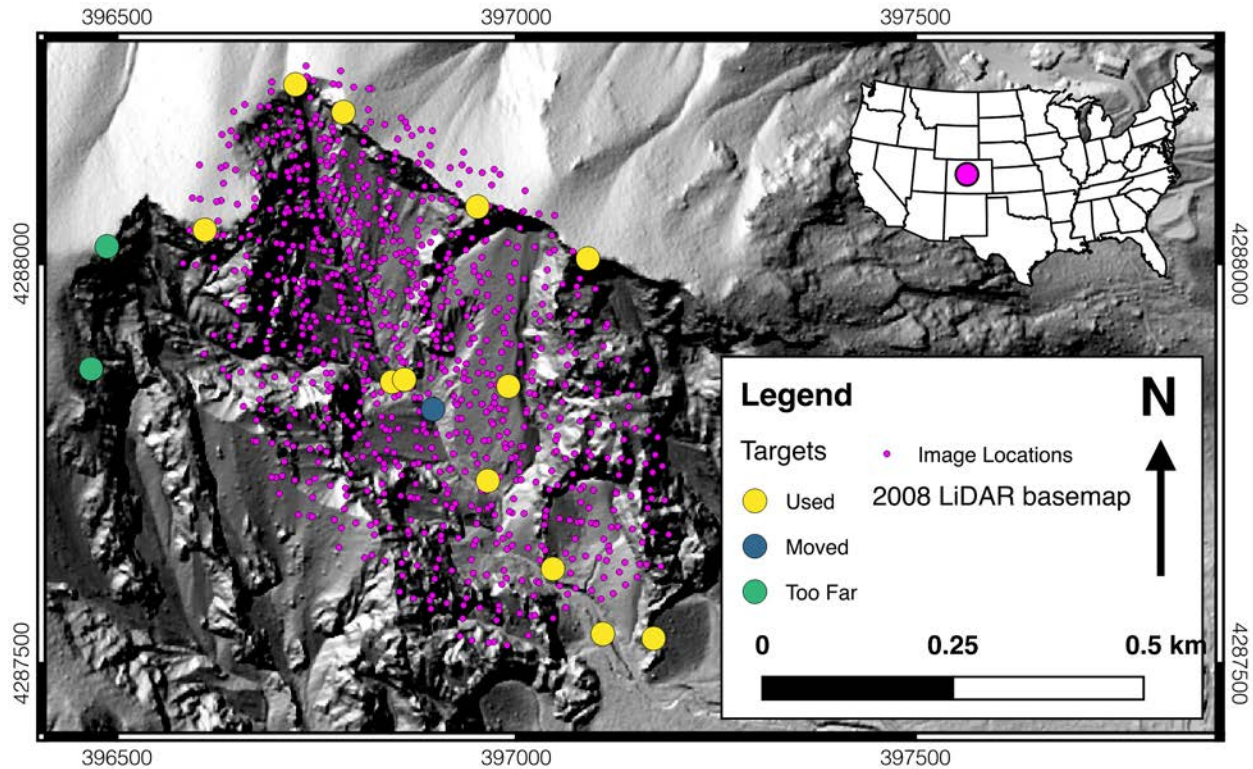


Fig 1. Field site map showing the location of ground control targets (large dots) and image locations (small dots) over the 2008 lidar basemap. The image locations are the (x, y) positions of the UAS at the time each image was taken. Map coordinate system is WGS84 UTM zone 13N.

survey (ALS) dataset taken in 2008 in order to construct a topographic difference map at a debris-flow site in central Colorado, USA.

SfM uses a set of overlapping photographs, taken from different locations, to generate 3D models without prior knowledge of image position, image look angle, or matching feature locations across image pairs (Snavely et al., 2006; 2007; 2008; James and Robson, 2012; Fonstad et al., 2013). Differencing the resulting point cloud with existing ALS provides for a topographic difference map that can be used to identify dominant geomorphic processes operating in the basin. After describing the geologic setting and the methods of data collection and processing, we describe the results of the change detection in the context of debris-flow processes.

2. Geologic Setting

The Chalk Cliffs site is a 0.37 km²-sized drainage basin incised into highly fractured and hydrothermally altered quartz monzonite in a semiarid climate (Sharp, 1970; Coe et al., 2008). The basin is located on the southeastern corner of Mount Princeton in Colorado's Sawatch Range (Fig 1). Starting in 2004, the U.S. Geological Survey (USGS) established a monitoring site in the Chalk Cliffs basin (Coe et al., 2008). Over half of the basin is exposed bedrock, and gradients in the basin are steep—ranging from 5° to 60° in the channels, 25° to 40° on colluvial slopes, and 40° to vertical on bedrock slopes (McCoy et al., 2010). Debris flows occur one to four times per year in response to rainstorm events, usually during the summer monsoon season between May and September (Dillon and Grogger, 1982; Mortimer, 1997). An airborne lidar survey flown on October 7th, 2008, provides baseline topography (National Center for Airborne Laser Mapping, 2008). This ALS point cloud covers 55 km² with a total point density of 5.74 pts/m² and a ground point density of 3.6 pts/m². Additionally, there have been occasional Terrestrial Laser Scanner surveys at the site (McCoy et al., 2010; Staley et al., 2011).

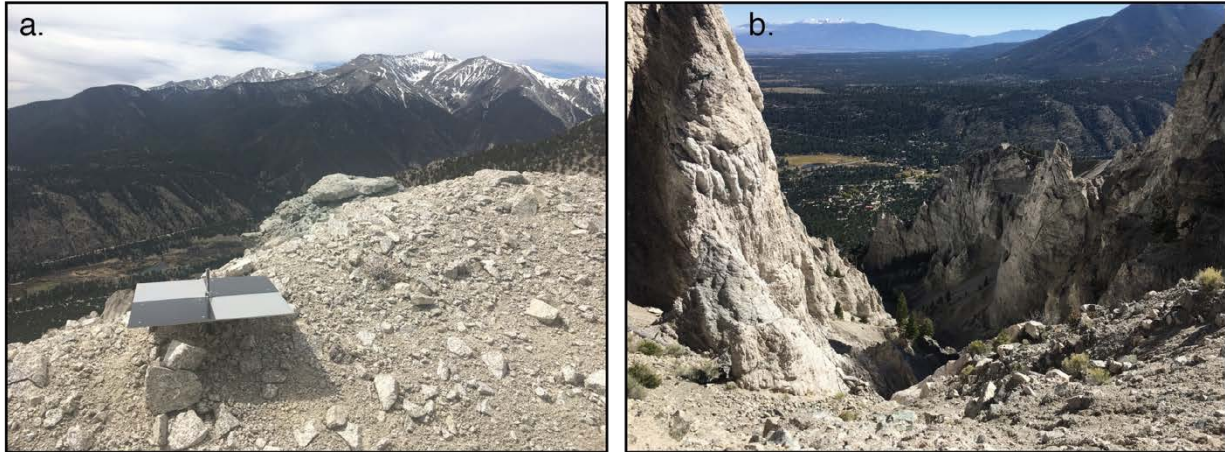


Fig 2. (a) View of ground control point (GCP) RD2 at the site. Each GCP is 16 inches square and is attached to rebar. (b) Field photo showing view of basin from UAS survey point. Photo credit for both images: Katherine Barnhart.

3. Methods

3.1. Ground Control Point Placement

In order to construct a georeferenced SfM point cloud of Chalk Cliffs, ground control points (GCPs) were required to be placed within the study basin (James and Robson, 2012). We constructed permanent GCPs (Fig 2a) and placed 15 of them in and around the study basin on May 5, 2017 (Fig 1, Table 1). The location of the center of each GCP was determined using survey-grade GPS equipment. GPS observations were processed using GNSS Solutions software by Magellan into WGS84 (G1150) latitude, longitude and ellipsoid height and UTM zone 13N easting, northing, and NAVD88 orthometric height above mean sea level (using GEOID09). Errors reported by GNSS Solutions are ± 1 cm in all three directions.

3.2. Unmanned Aircraft Surveying

We undertook repeat UAS surveys of the Chalk Cliffs basin in the summer of 2018. We visited the site 10 times over this period. In this work, we only focus on the visit from June 18th. This date was chosen because it was the first set of flights to be fully processed from images to a georeferenced point cloud.

We used a DJI Phantom 4 Pro with the onboard stock camera and GPS. We programmed the mission flight paths using the MapsMadeEasy (MME) iPad software. The UAS was programmed to fly at a constant elevation above the ground surface (represented in MME by Shuttle Radar Topography Mission elevation data). The UAS was programmed to fly one multi-battery double-grid mission at 400 ft above ground level (AGL) over most of the Chalk Cliffs basin with the camera pointed at nadir and one multi-battery single-grid mission at 250 ft AGL over the interior of the eastern and southern portions basin with the camera pointed 15° off-nadir (photo locations shown in Fig 1). Flight speed and photo triggering were set to ensure 85% overlap, 80% sidelap, and motion blur of less than 0.1 pixel. The camera was set to engage autofocus only once at the beginning of each flight (above the take-off point and at cruising altitude), to take photos in RAW mode (DNG file format), and to use auto exposure settings. The number of flights necessary to accomplish the same mission depends on the wind speed during the flights. On June 18th, the basin survey required 10 flights and approximately 3 hours. The June 18th, 2018, UAS mission resulted in a total of 909 images.

We were not able to fly over the entirety of the upper western portion of the basin because it would require the UAS to fly in an area that is occluded from view from the take-off location. Even though we did not fly over the entirety of this part of the basin, tie point identification and error reduction still yielded a sufficient number of matched points to reconstruct the topography in this area. We posit that this occurred because of the high level of overlap and side lap used in the UAS survey plan.

Table 1. Location of ground control points at study site.

Point Name	UTM zone 13N Easting (m)	UTM Zone 13N Northing (m)	Orthometric (NAVD88) Height above mean sea level (m)	WGS84 Longitude	WGS84 Latitude	Ellipsoid Height (m)	Comments
T3	396844.354	4287852.198	2777.991	106° 11' 12.57469"	38° 43' 59.95738"	2763.751	Used
T4	396859.901	4287855.177	2773.339	106° 11' 11.93252"	38° 44' 00.06053"	2759.098	Used
T9	396895.794	4287817.972	2759.541	106° 11' 10.42620"	38° 43' 58.86887"	2745.299	Moved
DT1	397172.146	4287531.326	2685.091	106° 10' 58.82899"	38° 43' 49.68735"	2670.836	Used
DT2	397108.508	4287537.005	2673.035	106° 11' 01.46722"	38° 43' 49.84486"	2658.782	Used
DT3	397046.074	4287618.310	2697.428	106° 11' 04.09608"	38° 43' 52.45583"	2683.178	Used
DT4	396964.370	4287728.544	2726.193	106° 11' 07.53850"	38° 43' 55.99704"	2711.947	Used
DT5	396990.221	4287846.686	2807.117	106° 11' 06.53131"	38° 43' 59.83986"	2792.872	Used
RD1	397089.690	4288006.511	3050.903	106° 11' 02.49786"	38° 44' 05.06562"	3036.657	Used
RD2	396951.457	4288071.344	3052.344	106° 11' 08.25705"	38° 44' 07.11047"	3038.103	Used
RD3	396783.498	4288189.678	3042.692	106° 11' 15.27604"	38° 44' 10.87807"	3028.458	Used
RD4	396723.543	4288224.254	3026.432	106° 11' 17.77750"	38° 44' 11.97431"	3012.200	Used
RD5	396609.904	4288042.318	3142.828	106° 11' 22.38566"	38° 44' 06.02529"	3128.597	Used
RD6	396487.367	4288021.633	3165.115	106° 11' 27.44894"	38° 44' 05.30268"	3150.888	Too Far
RD7	396467.437	4287868.513	3093.844	106° 11' 28.19178"	38° 44' 00.32779"	3079.616	Too Far

3.3. Structure-From-Motion Photogrammetry Processing

All 909 photos were imported into Agisoft PhotoScan Pro (version 1.4.3). Images were imported in RAW format and no image preprocessing was done. Image quality was checked using Photoscan, and images with quality values of less than 0.7 were discarded. The remaining 899 photos were aligned with settings of 60,000 key points, 0 tie points (which means all are kept), highest accuracy, generic preselection, and reference preselection. Adaptive camera model fitting was turned off. This resulted in the creation of 3.4 million tie points. We then performed the first two of three steps of gradual selection on the tie points: reconstruction uncertainty and projection accuracy. In this process, we followed the recommendations of the USGS National Unmanned Aircraft Systems Project Office (National Unmanned Aircraft Systems Project Office, 2017) developed in collaboration with Tom Noble (Breithaupt et al., 2004; Thoeni et al., 2014; Matthews et al., 2016; Warrick et al., 2017; Sherwood et al., 2018, Noble, *oral communication*, 2018).

The first step, reconstruction uncertainty, removes tie points with poor geometry. We removed tie points with a reconstruction uncertainty value of 15 or above and then re-ran camera optimization. Note that none of the gradual selection metric values have units. In the second step, we removed tie points with bad projection accuracy (values above 3) associated with tie points with pixel matching errors. After the first two steps of gradual selection, the locations of the GCP targets were imported into PhotoScan. We used the WGS84 zone 13 N UTM easting and northing and the WGS84 ellipsoidal height as the reference frame. Each of the 13 used targets were hand-marked in each of the photographs. We estimated a marker placement uncertainty of 0.1 pixels. After the markers were placed, we performed the final step of gradual selection: reprojection error. In this step, tie points that have bad pixel residual errors are removed. We removed points down to a reprojection error level of 0.3. At the end of gradual selection, the original 3.4 million tie points were reduced to a set of 1.2 million. Even though we had not flown over the entirety of the western portion of the basin, we were able to get sufficient tie points with good characteristics to reconstruct the topography in much of this area.

We explored how increasing the number of GCPs influenced the check point root mean squared error (RMSE) by undertaking the error reduction process for multiple sets of GCPs. We found that the check point RMSE (1σ) of our results was 4 cm. This magnitude is similar to that identified in similar studies (Warrick et al., 2017).

Finally, we built a dense cloud on the medium quality setting and exported it as a LAZ file. This created a point cloud with 47 million points each of which have an (x, y, z) as well as red, blue, and green (RGB) color attributes (Fig 3b). The RGB color is based on the pixel values of the original images. The point cloud covers an area of ~ 0.75 km² and has a point density of ~ 70 pts/m².

3.4. Lidar point cloud reprojection

The ALS point cloud has a horizontal reference system of NAD83 UTM zone 13N and a vertical reference system of NAVD88 based on GEOD03. To perform change detection between the ALS and the SfM point cloud, we converted the ALS dataset to the SfM point cloud reference frame. We used NOAA's VDATUM program to convert the lidar to WGS84 (G1150) UTM zone 13N horizontal reference frame and the WGS84 (G1150) ellipsoidal height vertical reference frame.

3.5. SfM point cloud tree removal

SfM point clouds are based on optical imagery, and thus they create (x, y, z) points that represent the surface of trees in the surveyed area. Unlike lidar, SfM does not see *through* trees and there are no "ground" points within the footprint of each tree. Thus, we needed a suitable approach for the separation of "ground" and "tree" point returns in the SfM point cloud. We determined RGB and whole-point cloud-based classification methods to be insufficient to differentiate between shady rock crevices and trees. As an alternative, we identified the following method, which was successful at removing trees from the SfM point cloud. Starting with the entire 2008 ALS dataset (all returns), we reset the "ground/other" classification and reclassified points into ground/vegetation/unclassified using LAStools (LAStools, 2018). We then examined all the vegetation points in the context of the SfM cloud and manually added additional points where the SfM point cloud shows that a tree is present, but the lidar has no vegetation points. The x and y coordinates of this "tree-only" point cloud were then buffered by 3.5 m and merged in order to create the tree mask shown in Fig 3a. We tried smaller buffer sizes but found that 3.5 m was the minimum distance required to remove the trees. Finally, we removed all points from the SfM cloud that had (x, y) coordinates within the tree mask. Areas covered by the tree mask were not considered in the change detection analysis.

3.6. Difference Construction

Next, we performed a change detection analysis between the tree-removed SfM cloud with the ground-only version of the 2008 lidar available through OpenTopography using the Multiscale Model to Model Cloud Comparison (M3C2) plugin in CloudCompare (Lague et al., 2013). This approach is suitable for comparing two point clouds, particularly when they have different point densities. As the lidar has a ground point density of 3.6 pts/m² and the SfM cloud has a density of ~70 pts/m², we used all of the lidar ground points as the core points for M3C2. We used a value of 3 m for the projection scales, a max depth of 30 m, and multi-scale calculation of the normal (min=1, step=0.5, max=5 m). We estimate our limit of detection (LoD) as the independent combination of normally distributed uncertainties in the SfM point cloud (1 σ =5 cm), the ALS (1 σ =10 cm), and the GCP locations (1 σ =1 cm). This yields a combined 1 σ LoD of 11 cm. Plan-view and perspective views of the M3C2 distance are presented in Fig 3.

3.7. Calculation of basin-averaged erosion rate

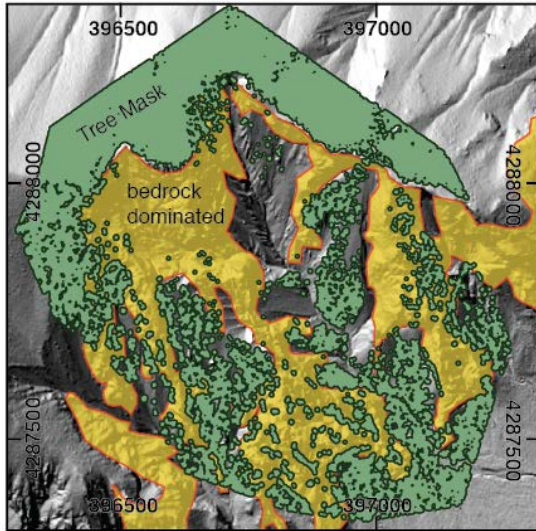
We estimated the basin-averaged erosion rate by exporting the M3C2 difference point cloud from CloudCompare to a GeoTIFF raster at a horizontal scale of 1 m. After clipping the M3C2 difference to area inside the basin, we calculate an average erosion depth of 0.02 m over the 10-year baseline. Given the basin area of 0.37 km³, this average erosion depth corresponds to an average volumetric sediment export of 750 m³ per year.

4. Results and Discussion

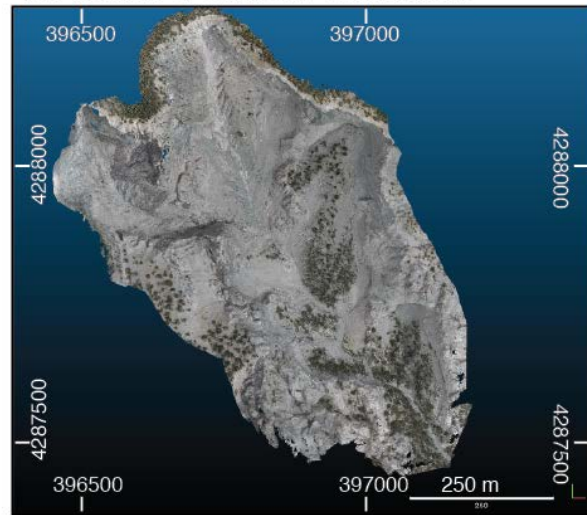
The results of the October 2008–June 2018 lidar-SfM topographic difference highlight active geomorphic processes. In many areas of the basin, the difference image indicates up to 3 m of erosion (Figs 3 and 4). Given the RMSE of ~10 cm, we cannot expect to resolve centimeter-scale changes in elevation; however, much of the basin has experienced topographic change in excess of our detection limit. Therefore, we have focused on changes to the colluvial regions of the study area.

There are three main types of colluvial surfaces within the surveyed area. First are surfaces that have not eroded or aggraded at levels beyond our limit of detection over the ten-year period. Many of these surfaces (such as the one

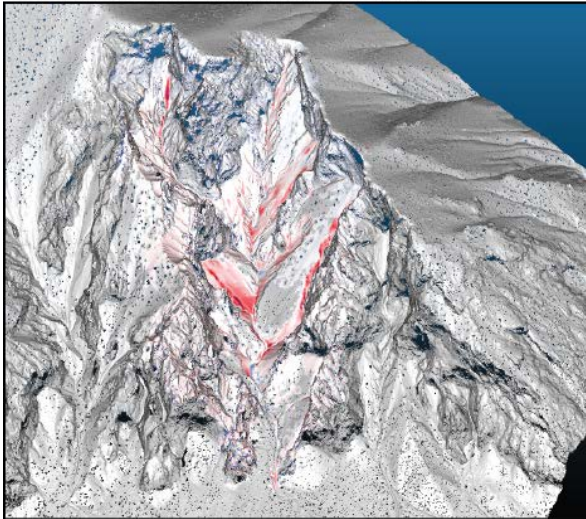
a. Plan view of tree mask and bedrock dominated areas



b. Plan view of SfM point cloud in RGB



c. Oblique view of M3C2 difference



d. Plan view of M3C2 difference

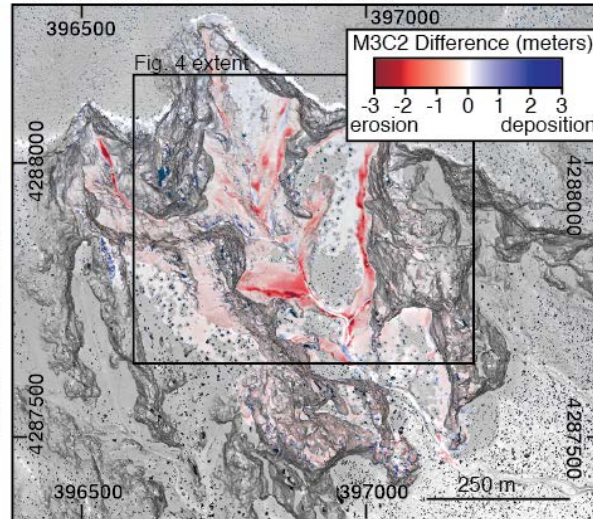


Fig 3. Results of SfM construction and M3C2 differencing. Shaded relief map derived from 2008 ALS. (a) shows the tree mask (green) and the areas dominated by bedrock (yellow). Areas with no color in (a) are neither tree covered nor dominated by bedrock. Areas covered by the tree mask were excluded from the change detection analysis. (b) and (d) show look down views of the basin in true-color (RGB) and as a shaded relief with M3C2 difference overlain, respectively. (c) shows a perspective view of the basin. The extent of Fig 4 shown in panel d.

labeled “stable colluvial surface” in Fig 4) are tree covered—where the trees are present, we are not able to assess topographic change. However, away from trees, the estimated topographic difference on this surface is within ± 11 cm (below our LoD). Second are colluvial surfaces above the main cliff band, which have eroded slightly (0.2–0.3 m of erosion) and relatively uniformly. The stable colluvial surface labeled in Fig 4 has a slope of $\sim 34^\circ$ while the slope above the cliff band is slightly steeper ($\sim 36^\circ$). The final type of colluvial surface has spatially variable erosion likely due to erosion by concentrated surface runoff. Fig 4 shows two examples of this sort of surface: the margins of the stable colluvial surface, and the surface labeled “A.” The pattern of erosion in this second example of an eroding surface is shown as an example of “firehose impact” erosion described by Coe et al. (2008, their Fig 9).

In both channels in the upper portion of the study basin, it appears that erosion of the channel has occurred. The condition of the beds of these channels during the lidar flight is unknown, making estimation of channel bedrock lowering difficult. Thus, we are unable to determine how much of the ~ 3 m of erosion in the upper west part of the channel is due to the evacuation of sediment, the erosion of bedrock, and the plucking of large blocks. The channel

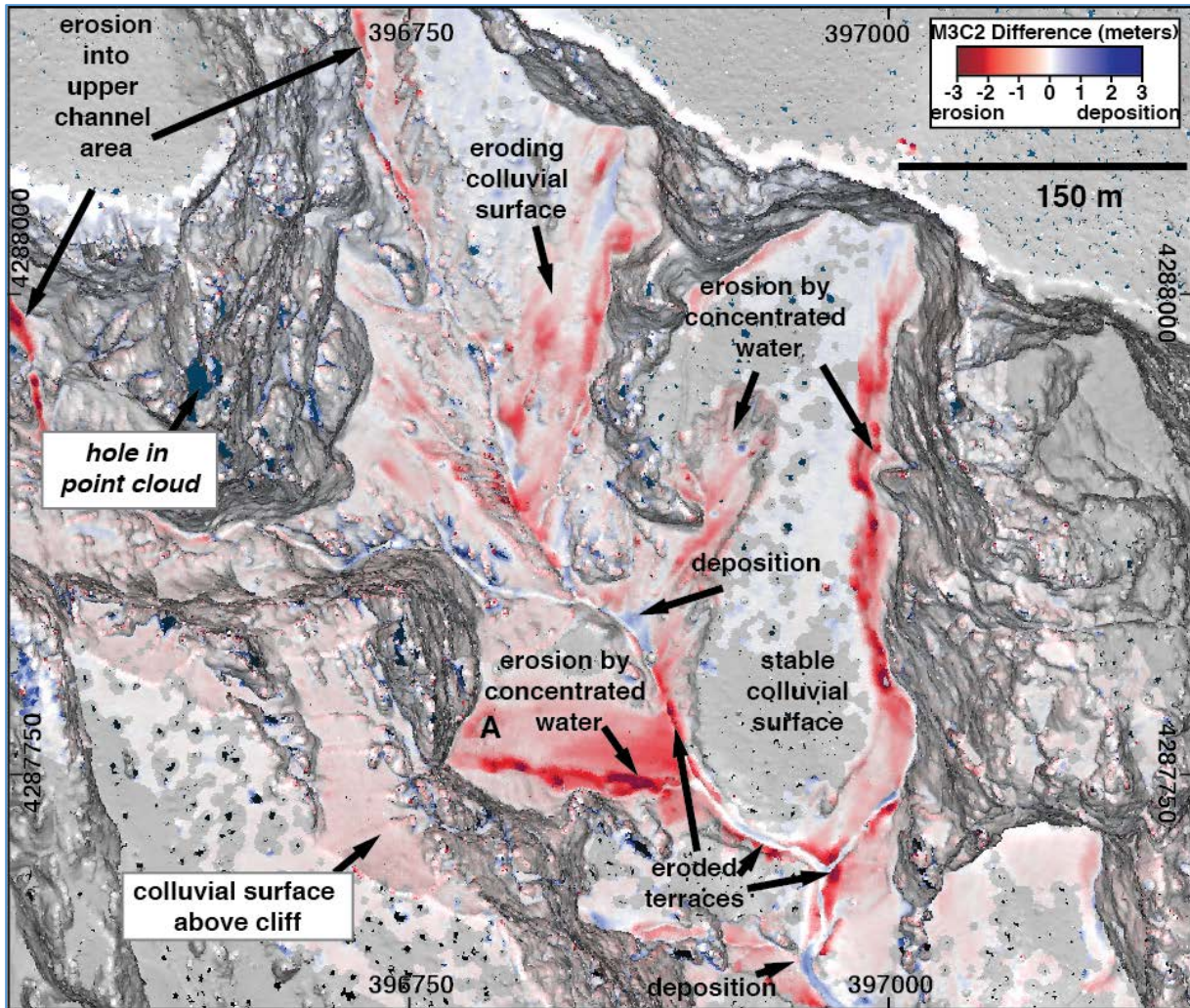


Fig 4. Shaded relief map of the site colored by M3C2 difference and annotated with features in the difference map.

thalweg has been observed in the field to alternate between periods when bedrock is exposed (commonly after debris flows), and periods when the channel is filled with sediment (between debris flows). Elsewhere in the basin, the channel shows patterns of erosion, no change, and deposition. Deposition may be associated with areas of temporary sediment storage in lower-gradient channel segments (Kean et al., 2013). Elsewhere in the basin there is extensive erosion of the terraces adjacent to the channels.

5. Conclusions

Here, we have demonstrated that SfM and lidar can be used in combination to identify topographic change over a 10-year period at an active debris-flow site. Patterns of topographic change in the Chalk Cliffs basin are dominated by erosion of colluvial surfaces. The combined geomorphic processes yield a basin-averaged erosion rate of 0.002 m per year and a sediment export rate of 750 m³ per year. Along the channel thalweg, we are unable to attribute topographic change to specific geomorphic process. Comparing two SfM point clouds, each with extensive optical imagery, will be able to pinpoint the evolution of sediment coverage within the channel thalweg.

Acknowledgements

KRB was supported by NSF Grant EAR-1725774. JNG was supported during a Research Experience for Community College Students internship by NSF-EAR 1757930 and by NSF EAR-1450409 (to GET). Additional funding for this work was provided by a University of Colorado Innovative Seed Grant Program proposal to WK. KRB thanks Rachel Glade, Charlie Shobe, Matt Rossi, Robert Anderson, Nadine Reitman, Charlie Shobe, and Margaux Mouchene for assistance in the field, Tom Noble and Chris Sherwood for help with Agisoft PhotoScan best practices, and Frontier Ranch Young Life Camp for access to the site through their property. The lidar data were accessed through OpenTopography. Lidar data acquisition and processing completed by the National Center for Airborne Laser Mapping (NCALM - <http://www.ncalm.org>). NCALM funding provided by NSF's Division of Earth Sciences, Instrumentation and Facilities Program. EAR-1043051. We thank the editors, one anonymous reviewer, and Erin Bessette-Kirton for comments that improved the quality of the manuscript. Any use of trade, firm, or product names is for descriptive purposes only and does not imply endorsement by the U.S. Government.

References

- CloudCompare (version 2.9.1) [GPL software]. (2018). Retrieved from <http://www.cloudcompare.org/>
- Breithaupt, B.H., Matthews, N.A., and Noble, T.A., 2004, An Integrated Approach to Three-Dimensional Data Collection at Dinosaur Tracksites in the Rocky Mountain West: *Ichnos*, v. 11, p. 11–26, doi: 10.1080/10420940490442296.
- Coe, J.A., Kinner, D.A., and Godt, J.W., 2008, Initiation conditions for debris flows generated by runoff at Chalk Cliffs, central Colorado: *Geomorphology*, v. 96, p. 270–297, doi: 10.1016/j.geomorph.2007.03.017.
- Dillon, G.D., and Grogger, P.K., 1982, Mudflows of Mt. Princeton/Chalk Creek, Chaffee County, Colorado: *Geological Society of America Abstracts with Programs* 14 (6) 309.
- Fonstad, M.A., Dietrich, J.T., Courville, B.C., Jensen, J.L., and Carbonneau, P.E., 2013, Topographic structure from motion: a new development in photogrammetric measurement: *Earth Surface Processes and Landforms*, v. 38, p. 421–430, doi: 10.1002/esp.3366.
- James, M.R., and Robson, S., 2012, Straightforward reconstruction of 3D surfaces and topography with a camera: Accuracy and geoscience application: *Journal of Geophysical Research*, v. 117, p. F03017, doi: 10.1029/2011JF002289.
- Kean, J.W., McCoy, S.W., Tucker, G.E., Staley, D.M., and Coe, J.A., 2013, Runoff-generated debris flows: Observations and modeling of surge initiation, magnitude, and frequency: *Journal of Geophysical Research-Earth Surface*, v. 118, p. 2190–2207, doi: 10.1002/jgrf.20148.
- Lague, D., Brodu, N., and Leroux, J., 2013, Accurate 3D comparison of complex topography with terrestrial laser scanner: Application to the Rangitikei Canyon (NZ): *ISPRS Journal of Photogrammetry and Remote Sensing*, v. 82, p. 10–26, doi: 10.1016/j.isprsjprs.2013.04.009.
- LAStools, (2018) "Efficient LiDAR Processing Software", obtained from <http://rapidlasso.com/LAStools> October 2018.
- Matthews, N., Noble, T.A., and Breithaupt, B.H., 2016, Close-Range photogrammetry for 3D ichnology: the basics of photogrammetric ichnology, in Falkingham, P.L., Marty, D., and Richter, A. eds., *Dinosaur tracks-Next Steps*, Bloomington, Indiana University Press, p. 29–55.
- McCoy, S.W., Kean, J.W., Coe, J.A., Staley, D.M., Wasklewicz, T.A., and Tucker, G.E., 2010, Evolution of a natural debris flow: In situ measurements of flow dynamics, video imagery, and terrestrial laser scanning: *Geology*, v. 38, p. 735–738.
- Mortimer, P., 1997, Stratigraphic and rheologic analysis of debris flow deposits in Chalk Creek Canyon, Colorado. Thesis for distinction in Geology, Colorado College, 99 p.
- National Center for Airborne Laser Mapping, 2008, San Isabel NF, CO: Debris Flow Mechanics and Landscape Evolution, doi: 10.5069/G9TX3C9D.
- National Unmanned Aircraft Systems Project Office, 2017, Unmanned Aircraft Systems Data Post - Processing Structure - Photogrammetry from - Motion, p. 1–21, <https://uas.usgs.gov/pdf/PhotoScanProcessingDSLRLMar2017.pdf>.
- Sharp, W.N., 1970, Extensive zeolitization associated with hot springs in central Colorado: U.S. Geological Survey Professional Paper 700-B, p. B14–B20.
- Sherwood, C.R., Warrick, J.A., Hill, A.D., Ritchie, A.C., Andrews, B.D., and Plant, N.G., 2018, Rapid, Remote Assessment of Hurricane Matthew Impacts Using Four-Dimensional Structure-from-Motion Photogrammetry: *Journal of Coastal Research*, v. 346, p. 1303–1316, doi: 10.2112/JCOASTRES-D-18-00016.1.
- Snaveley, N., Garg, R., Seitz, S.M., and Szeliski, R., 2008, Finding paths through the world's photos: *ACM Transactions on Graphics (TOG)*, v. 27, p. 15, doi: 10.1145/1399504.1360614.
- Snaveley, N., Seitz, S.M., and Szeliski, R., 2007, Modeling the World from Internet Photo Collections: *International Journal of Computer Vision*, v. 80, p. 189–210, doi: 10.1007/s11263-007-0107-3.
- Snaveley, N., Seitz, S.M., and Szeliski, R., 2006, Photo tourism: exploring photo collections in 3D: *ACM, exploring photo collections in 3D*, v. 25, p. 835–846, doi: 10.1145/1141911.1141964.
- Staley, D.M., Wasklewicz, T.A., Coe, J.A., Kean, J.W., McCoy, S.W., and Tucker, G.E., 2011, Observations of debris flows at Chalk Cliffs, Colorado, USA: Part 2, Changes in surface morphometry from terrestrial laser scanning in the summer of 2009 (R. Genevois, D. L. Hamilton, & A. Prestinini, Eds.): *Debris-flow Hazards Mitigation, Mechanics, Prediction, and Assessment*, p. 759–768, doi: 10.4408/IJEGE.2011-03.B-083.
- Thoeni, K., Giacomini, A., Murtagh, R., and Kniest, E., 2014, A comparison of multi-view 3D reconstruction of a rock wall using several cameras and a laser scanner: *Proceedings of the International Archives of the Photogrammetry, Remote Sensing and Spatial Information Sciences 2014 ISPRS Technical Commission V Symposium*, v. XL-5, p. 573–580.
- Warrick, J.A., Ritchie, A.C., Adelman, G., Adelman, K., and Limber, P.W., 2017, New Techniques to Measure Cliff Change from Historical Oblique Aerial Photographs and Structure-from-Motion Photogrammetry: *Journal of Coastal Research*, v. 331, p. 39–55, doi: 10.2112/JCOASTRES-D-16-00095.1.

Forecasting and seismic detection of debris flows in pro-glacial rivers at Mount Rainier National Park, Washington, USA

Scott R. Beason^{a,*}, Nicholas T. Legg^b, Taylor R. Kenyon^a,
Robert P. Jost^a, and Paul M. Kennard^a

^aU.S. National Park Service, Mount Rainier National Park, 55210 238th Ave E, Ashford, WA 98304

^bWolf Water Resources, 1001 SE Water Ave, Suite 180, Portland, OR 97214

Abstract

The glaciated Mount Rainier volcano in Southwestern Washington State (USA) has a rich history of outburst floods and debris flows that have adversely impacted infrastructure at Mount Rainier National Park in the 20th and 21st century. Retreating glaciers leave behind vast amounts of unconsolidated till that is easily mobilized during high precipitation intensity fall storms and during outburst floods during warm summer months. At least 60 debris flows and outburst floods have been documented between 1926 and 2017 at Mount Rainier. Debris-flow activity has led to the closure of campgrounds and visitor destinations, which has limited visitor access to large swaths of the park. After a relative lull in activity between 2006 and 2014, the historically debris-flow-prone South Tahoma Glacier released two separate sequences of debris flows in 2015, possibly signaling a reawakening in activity. The August 13, 2015 debris flow was especially well documented by park visitors, seismographs and, most interestingly, a soundscape monitor which recorded an anomalous decrease in river noise prior to the arrival of the first debris flow. The seismograph near Tahoma Creek accurately recorded the passage of each debris-flow surge. Using the day of and historic antecedent weather conditions on past debris-flow days, we have developed a debris-flow hazard model to help predict those days with a higher relative hazard for debris-flow activity park-wide based on prevailing and forecasted weather conditions. Debris flows are detected in near-real-time using the USGS Real-time Seismic Amplitude Measurement (RSAM) tool. If an event is detected, we can then provide alerts to employees and visitors working and recreating in the areas downstream to evacuate. Our goal is to accurately forecast the hazard of a debris flow up to seven days ahead of time and then use RSAM to detect debris flows within minutes of their genesis.

Keywords: Debris flows; outburst floods; hazard mitigation and monitoring; hazard forecasting; Real-time Seismic Amplitude Measurement

1. Introduction

Mount Rainier is a 4,392 m (14,410 ft) stratovolcano located in southwest Washington State, USA, approximately 70 km (43 mi) southeast of Tacoma and 90 km (56 mi) south-southeast of Seattle (Fig. 1). The volcano occupies most of the 956 sq. km (369 sq. mi) Mount Rainier National Park (MORA) and is visible from much of western Washington State. MORA has been episodically active in the last 500,000 years, including at least 10-12 eruptions in the last 2,600 years (Sisson and Vallance, 2009). Eruptions have initiated large lahars that have inundated areas of the Puget lowland as far as 100 km (62 mi) from the volcano (Crandell, 1971). Because of its far-reaching lahar hazards MORA has a “very high” threat and ranks as the third most hazardous volcano in the nation (Ewert et al., 2008).

Debris flows initiated during intra-eruptive periods at MORA are generally much smaller in magnitude and impact than the large lahars that have occurred during eruptive periods (Pierson and Scott, 1985; Vallance and Scott, 1997; Vallance, 2005). This species of debris flow is initiated when surges of water recruit additional sediment and transform into slurries of coarse sediment (Scott et al., 1995). These surges originate from within a glacier, referred to as glacial outburst floods, or during periods of intense and prolonged precipitation. Debris flows of this type attenuate rapidly and the deposits are often reworked by subsequent event runoff, leaving them nearly identical to overbank flood deposits. Sometimes, these debris flows often go unnoticed in remote reaches of the park. Understanding the initiation

* Corresponding author e-mail address: Scott_Beason@nps.gov

characteristics and thus cataloging all events at MORA is one of the prime motivating factors in the development of the real-time detection efforts described in this paper.

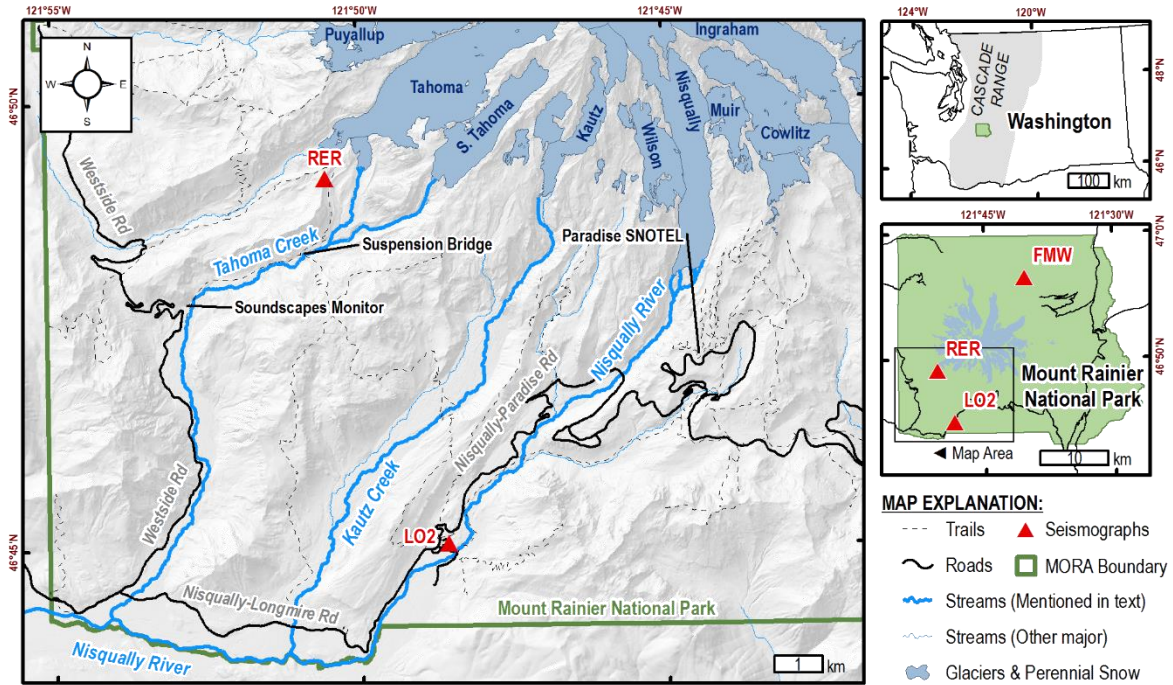


Fig. 1. Location map of the southwest side of Mount Rainier National Park in Washington State, USA. RER, LO2 and FMW refer to the Emerald Ridge, Longmire, and Mt. Fremont seismographs, respectively. Locations listed in text are shown on the detail map.

The glaciers in MORA are one of the strongest controlling influences on the park landscape. MORA has 29 named glaciers which cover a total of $78.76 \pm 1.11 \text{ km}^2$ ($30.41 \pm 0.43 \text{ mi}^2$), and encompass a total volume of $3.22 \pm 0.31 \text{ km}^3$ ($0.77 \pm 0.07 \text{ mi}^3$) as of 2015 (Beason, 2017; George and Beason, 2017). Studies show that the glacial ice on MORA has decreased in area by 39.1% from 1896 to 2015 ($0.44 \text{ km}^2 \cdot \text{yr}^{-1}$ avg.), and in volume by 45% from 1896 to 2015 ($0.02 \text{ km}^3 \cdot \text{yr}^{-1}$) (Driedger and Kennard, 1986; George and Beason, 2017). Glacial recession contributes to increases in glacial melt runoff and, through mechanisms not yet understood, subglacial water storage, both of which have been observed to cause glacial outburst floods and many of the debris flows recorded in the park. As such, quantifying changes in these glaciers and the impacts of newly uncovered glacial sediment stockpiles must be considered if we are to understand the hazards discussed here.

2. Brief history of debris flows at Mount Rainier

The first recorded debris flow in the park occurred in the Nisqually watershed on October 16, 1926. This event was initiated by the first heavy rain at the end of the summer season (Richardson, 1968). Prior to the event it was noted that there was 33 cm (13 in) of snow at Paradise on October 13, all of which had melted by October 16. After this melt, a warm rain event brought in 9.9 cm (3.9 in) of rain on the day of the 16th. Between 1932 and 1976, at least six outburst floods or debris flows occurred in the Nisqually River, originating from the Nisqually Glacier. Most of these events were induced by precipitation, which varied from 6-25 cm (2.4-9.9 in). Four of the events occurred in October and two occurred in June and July. On October 14, 1932, visiting engineers from the Bureau of Public Lands witnessed a precipitation-induced debris flow, described as “a wall of water 25 ft high and 125 ft wide” and “similar to a huge mixture of concrete except darker in color” (Richardson, 1968). The force of this event moved the entire old Nisqually Glacier Bridge over 0.8 km (0.5 mi) downstream from its original location. Some of the debris-flow events were well witnessed, including the October 25, 1955 and July 3, 1976 events (Samora and Malver, 1996; Richardson, 1968). An event in 1955 had six pulses in 45 minutes, had an estimated velocity of $6.1 \text{ m} \cdot \text{s}^{-1}$ and a discharge of $2000 \text{ m}^3 \cdot \text{s}^{-1}$, and

was estimated to be 70% sediment by volume (Richardson, 1968). This event also led to the construction of the current tall Nisqually Glacier Bridge that exists to this day.

There are an additional five events cataloged on the Nisqually during the park's history which behave similarly to the events listed, but were much smaller and had negligible impacts on park infrastructure. These five data points contain three glacial outbursts and two "other hydrologic events." Two of the outburst floods are wet events that were preceded by notably intense rainfall in a short period beforehand, with the other being a dry event that took place in July. Of these, only the dry event was noted to have multiple surges. The "other hydrologic events" were noted for increases in stream stage, but not significant enough to cause any lasting damage to infrastructure or mobilize mass wasting events. The most recent event recorded in the Nisqually River was a precipitation initiated outburst flood on October 27, 2012 (Beason, 2012), which caused a 1 m (3 ft) increase in river stage at Longmire, approximately 7.9 km (4.9 mi) downstream of the glacier.

2.1. 1947 Kautz Mudflow

The largest recorded debris-flow event in the history of MORA is the 1947 Kautz Mudflow, which had an estimated volume of $3.8 \times 10^7 \text{ m}^3$. In the 24 hours prior to the event, 15 cm (5.9 in) of heavy rain and high freezing levels were seen in the Kautz watershed (Driedger and Fountain, 1989). These conditions resulted in the collapse of the lower 1.6 km (1 mi) of the Kautz Glacier and a rapid release of water stored within the glacier (Scott et al., 1995). The surge of water entrained glacial outwash material transforming into a clay-poor debris flow. Placement of the Kautz mudflow deposits occurred over several days and included multiple pulses of water. Debris flows were noted in other drainages during this event, including the Nisqually River.

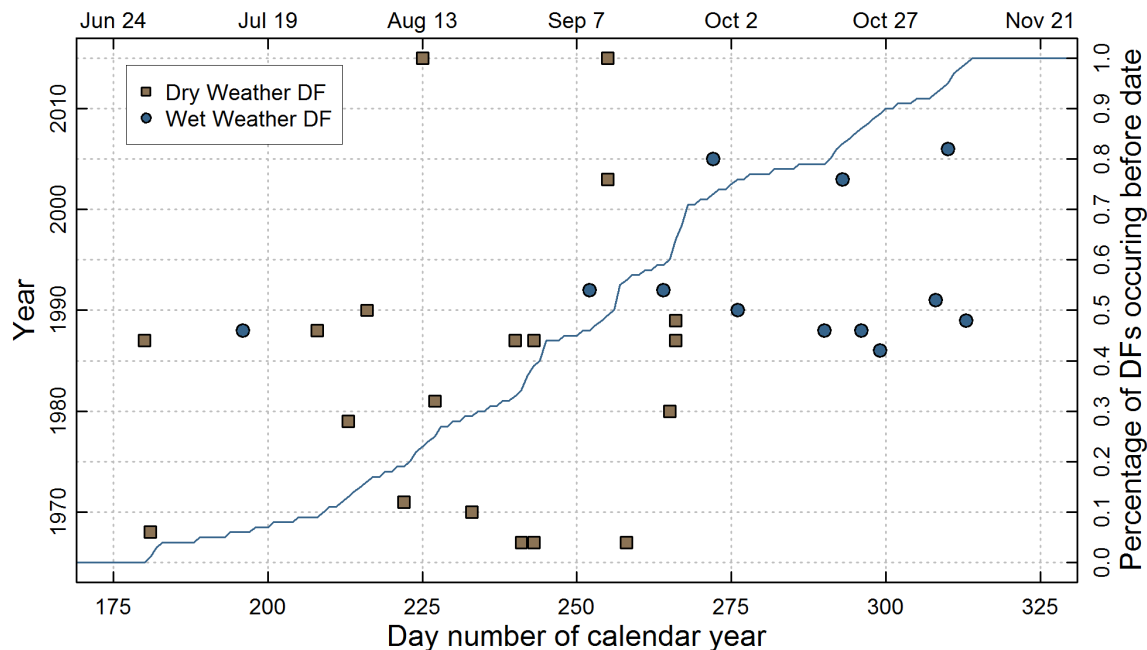


Fig. 2. Seasonal timing of debris flows in Tahoma Creek from 1967 to 2015. Dry weather flows refer to those not induced by heavy precipitation.

2.2. South Tahoma Glacier activity

Recent debris-flow activity began in the Tahoma Creek valley during the summer of 1967. The summer of 1967 was noted as exceptionally warm and dry. On August 29, a short-lived outburst flood destroyed a footbridge 1.9 km (1.2 mi) below the South Tahoma Glacier. The stream rose about 0.5 m (1.5 ft) at the Tahoma Creek Campground, ~5.6 km (3.5 mi) downstream of the glacier. Two days later an outburst flood roared down Tahoma Creek (Richardson, 1968). Fortunately, the campground was already closed due to fire danger.

Between 1967 and 2015, at least 31 distinct events have occurred (Fig. 2). Walder and Driedger (1994a) note that the record for debris flows in Tahoma Creek does have some gaps, specifically between 1967 and 1985. This is due

to poor record-keeping during this time. Crandell (1971) notes that “Floods not associated with rainfall also moved down the [Tahoma Creek] valley from time to time during the summer of 1968.” Walder and Driedger (1994a) note that debris flows from the years of 1971 to 1985 are described “only sketchily” in park records. Debris flows that occurred between 1986 and 1992 are well documented, largely owing to increased awareness among NPS staff (Walder and Driedger, 1994a).

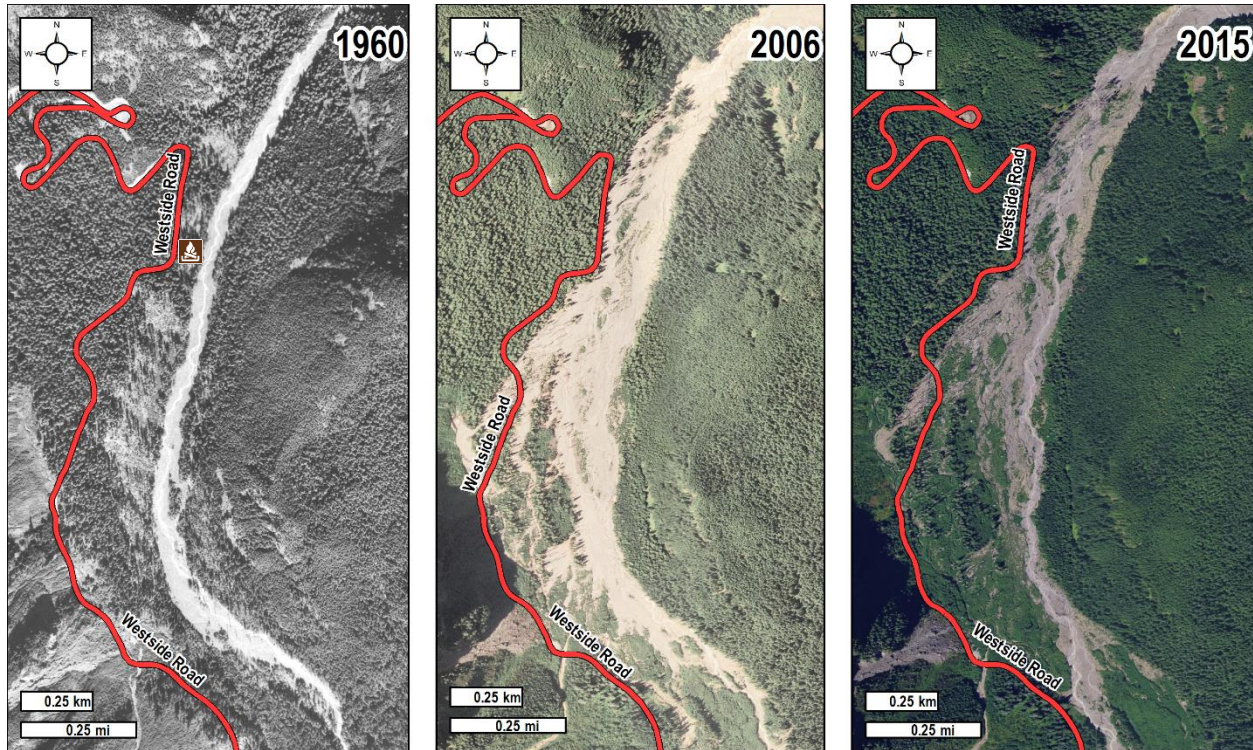


Fig. 3. Aerial photos from 1960, 2006, and 2015 showing the westward lateral migration of Tahoma Creek along the West Side Road due to debris-flow activity. Brown campfire sign in 1960 image indicates approximate position of former Tahoma Creek Campground.

The cumulative impact of over 30 debris flows in less than half a century and a major flood event in 2006 (Bullock et al., 2007) has been remarkable to the built infrastructure in the Tahoma Creek valley. The 24 km (15 mi) West Side Road was closed to vehicular traffic at mile post 3 in 1988. The sudden increase in debris-flow deposition forced the westward lateral migration and avulsion of Tahoma Creek, completely decimating an old-growth forest in the process (Fig. 3). Portions of the West Side road in Fig. 3 have had to be repaired numerous times due to the combined effects of debris flows and seasonal floods. The reduction in vehicular traffic and thus foot traffic on the West Side Road lead to a rapid and dramatic decrease to the recreational use of the trails and campgrounds on this side of the park since the late 1980s.

3. Debris flows in 2015 – Direct Observations and Monitoring Results

After a lull in debris-flow activity in the Tahoma Creek basin between 2006 and 2015, four separate debris-flow sequences occurred between 09:49 AM - 12:44 PM PDT (16:49 - 19:44 UTC) on 13 August 2015 (dry season). Each individual sequence was identified in seismic records from the Emerald Ridge (RER) seismograph, located near Tahoma Creek (Fig. 4; location in Fig. 1). This event is the best documented debris flow in the park’s history. Seismic monitors, a soundscape monitor, and stream gages downstream all recorded data relevant to each debris-flow surge, while numerous park visitors, volunteers and employees all witnessed and photographed the event. Several visitors, including a geology professor at Pacific Lutheran University, recorded photos and videos of individual flows. A park volunteer in the upper Tahoma Creek basin accurately recorded and documented hyperconcentrated flow surges after the four debris flows (not recorded on the seismograph); recording a total of 12 individual hyperconcentrated flows.

The first debris flow issued by the South Tahoma Glacier was witnessed by visitor Croil Anderson. Anderson described the event as being “louder than a jet” at a distance of 2.5 km (1.5 mi) from the glacier (Anderson, personal communication, 2015). Anderson also stated that the first debris flow was an “incredibly large surge of black water, ice and rock” from the terminus. Claire Todd, a geology professor from Pacific Lutheran University, was on the Tahoma Creek suspension bridge as the DF 2a and 2b moved down the watershed (Fig. 4). When arriving at the bridge she noted “a very high water/mud mark on wall of channel” quickly followed by a “loud roar and terrific ground shaking” (Todd, personal communication, 2015). Continuing to observe the scene she noted “a ~1.5 m boulder is exposed in the channel” as the flow passes, and within another minute “roar and shaking resumes, a second flow passes, just as thick as the first -completely obscuring the large boulder again.” Professor Todd witnessed the wave pass “exposing all of the large boulder again.” Lastly she recorded “a thin flow of hyperconcentrated water is passing... and a view upstream shows another low wave of hyperconcentrated flow approaching,” noting that “these minor flows are not producing the roar or shaking that the first two offered.”

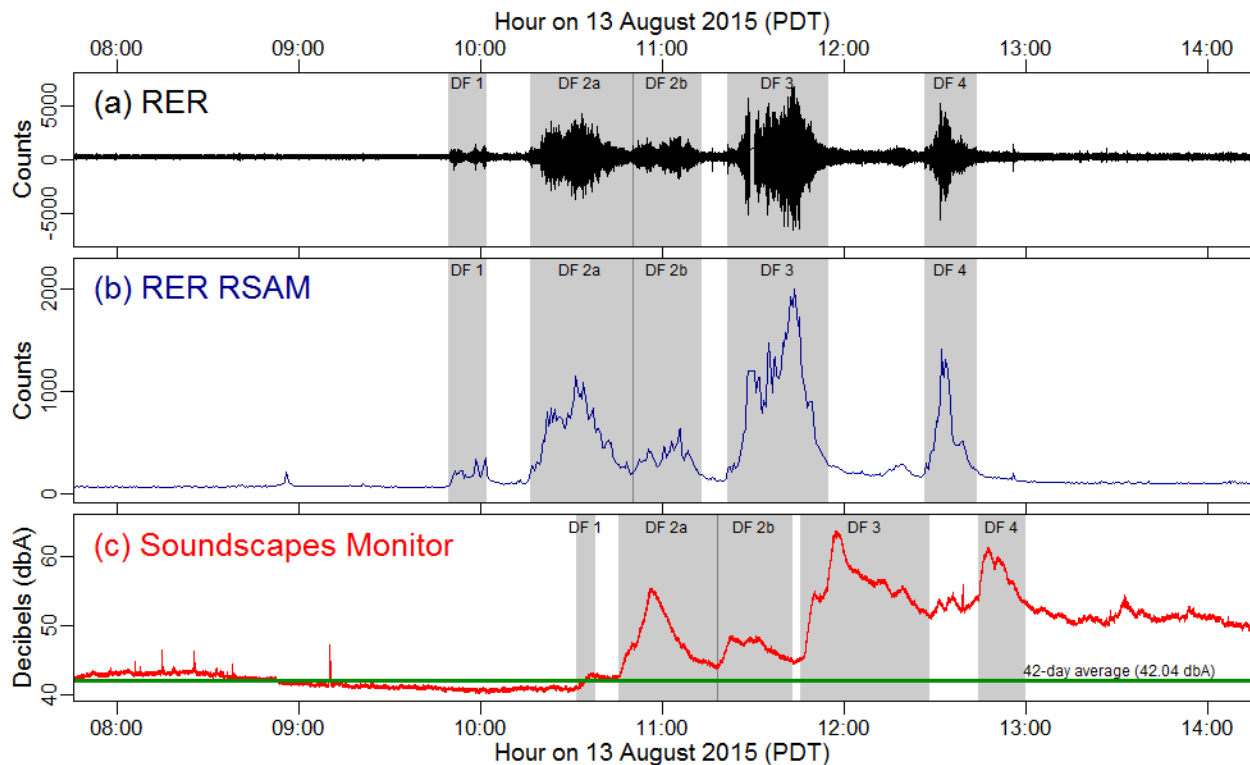


Fig. 4. Comparison of waveforms from (a) Emerald Ridge seismograph (RER), (b) Real-time Seismic Amplitude Measurement of the Emerald Ridge Seismograph (RER RSAM), and (c) Tahoma Creek Soundscape Monitor during the 13 August 2015 debris flow sequence. RER and RER RSAM are computed at the same geographic location, whereas the soundscapes monitor was approximately 3.7 km (2.3 mi) downstream, which accounts for the lag in arrival times for that instrument. The green line in plot (c) is the 42-day background average of 42.04 dbA.

The Emerald Ridge seismograph (RER, Fig. 1) is located approximately 1 km (0.6 mi) from Tahoma Creek and accurately recorded the passage of each debris-flow surge. Using the seismic data as an input, after the event, we calculated the USGS Real-time Seismic Amplitude Measurement (RSAM) signature (Fig. 4) (Endo and Murry, 1991). RSAM summarizes seismic activity for characterizing a volcano’s changing seismicity in real time. We use it to downsample the seismic signal to an average amplitude over a set time, in this case, 30 seconds. The combination of the seismic data and RSAM calculations (Fig. 4 (b)) show the passage of each debris-flow surge clearly.

One of the most interesting findings from the August 13 debris-flow sequence is the analysis of the soundscapes data in Fig. 4 (c). The soundscapes monitor is a research effort by the National Park Service to understand the natural and unique soundscape of the park (NPS, 2018). Equipment emplaced along Tahoma Creek in 2015 fortuitously recorded the background noise on the months prior to and day of the debris flow. The monitor recorded an anomalous decrease in river noise from the background level approximately 1.5 hours before the arrival of the first debris-flow

surge. Each successive surge was recorded and the river was relatively louder after the last debris-flow surge. This coincides with visual observations that the river was flowing much more vigorously after the event than before.

Park staff became aware of the debris-flow event at 12:02 PM when park volunteer Yonit Yogev called the MORA dispatch center on the radio reporting an outburst flood at Tahoma Creek trailhead. Yogev described the event as “telltale sounds of a rumbling train, a huge amount/sounds of trees, and a huge amount of water coming over the road out of the creek bed” (Yogev, personal communication, 2015; NPS Dispatch Records). A park visitor, Zachary Jones, videoed the passing debris-flow surge (DF 3 in Fig. 4) with his cellphone which provided visual evidence of the flow.

Based on all observations and data observed from this event, we postulate that this event began as a physical blockage in the normal discharge of the glacier, perhaps as either a collapse of ice within the glacier or a small landslide just downstream of the glacier. This is evidenced by the anomalous and steady decrease in river noise from the soundscapes monitor just before 09:00 AM, showing that the total input to the river had dropped below the normal background level.

4. Debris-flow hazard forecasting

The impetus for generating the debris-flow hazard forecast is to avoid having park staff and visitors in debris-flow-prone areas when likely events could occur – like those conditions seen on 13 August 2015. The debris-flow hazard forecasting approach at MORA is based on two separate models combined, which have different variables for dry, warm weather debris flows and cool, wet weather debris flows. The full model is shown in Appendix A.

4.1. Cool, wet weather debris flows

In recent decades, warm rain storms occurring with low snowpack have been anecdotally associated with debris flows on MORA. These storm and debris-flow events typically occur in late fall, when “Atmospheric River” storms bring intense tropical moisture from mid-latitudes and drop voluminous rain high on the volcanic flanks (Neiman et al., 2008). Prior to this study there had been no systematic characterization of debris flow occurrence with respect to meteorological and antecedent hydrologic conditions. In practice, such a characterization could be paired with weather forecasts and in-situ monitoring to classify current debris-flow hazards. This specific phase of our study focused on characterization of past storms and their associated debris-flow potential.

Past debris-flow events were compiled from multiple sources and included in our analysis if the debris flow’s timing was known within a day, was associated with measurable precipitation, and occurred within the monitoring record of the snow telemetry (SNOTEL) station at Paradise (NRCS Site 679, elevation 1,640 m) on the southern flank of MORA. Debris-flow sources include Walder and Driedger (1994a), Walder and Driedger (1994b), Walder and Driedger (1995), Driedger and Fountain (1989), and Copeland (2009). This SNOTEL station lies at the lower elevation range of mapped drainage networks and gullies identified as having high potential for debris-flow initiation using slope-drainage area thresholds (Legg et al., 2014). This station broadly characterizes precipitation, temperature, and antecedent snowpack in the elevation band of potential debris-flow generation on MORA’s flanks. For each debris-flow event, precipitation, temperature, and snowpack measurements were compiled for 1-, 3-, and 15-day periods on and prior to the day of the debris flow. These metrics were also compiled for all monthly maximum precipitation events for the full SNOTEL record to compare the known debris-flow producing storms to the broader population of storms.

This data compilation effort resulted in a total of eleven debris-flow producing storms that occurred between 1979 and 2014. All eleven storms had daily average temperatures above freezing, and all but two events had daily average temperatures above 40° Fahrenheit. Based on a typical vertical lapse rate of 5.5°C/1,000 m, a temperature of 40°F at the SNOTEL station indicates temperatures above freezing for the full elevation band of high hazard gullies, suggesting rainfall and potential surficial runoff generation in the zone of likely debris flow initiation. All debris-flow producing storms also had limited antecedent snowpack, suggesting antecedent snowpack inhibits debris-flow generation by limiting runoff and/or stabilizing surficial colluvium. Additionally, there were negligible reductions in snowpack in the 3 days leading up to the eleven debris-flow events, suggesting snowmelt-derived runoff as an unlikely ingredient for debris-flow generation.

Precipitation quantities were further compared to an intensity-duration threshold for the nearby Seattle, Washington area developed by Chleborad et al. (2006), which is based on 3-day and 15-day cumulative precipitation totals in inches. Initial comparisons to this landslide threshold found that eight of the eleven known debris flow producing storms exceeded the Seattle threshold; however, 247 of 376 monthly maximum storms (without known debris flows) from 1979-2014 also plotted above the threshold. These results suggest landslide threshold alone is a poor predictor

of debris flow potential on MORA. To explore potential refinements to the model, we then removed monthly maximum storms with greater than 5” SWE and/or 3-day average temperatures less than freezing. In the remaining group, 33 monthly maximum (non-debris flow producing) storms exceeded the Seattle threshold, in addition to the 8 debris flow-producing storms. These numbers indicate ~20% (8 of 41) of these storms (with above-freezing temperatures and low snowpacks, while exceeding Seattle threshold) generated debris flows. A similar calculation utilized a temperature threshold of 40°F instead of 32° and revealed that 5 of 14 storms (36%) storms exceeding the Seattle threshold produced debris flows. The increased proportion of debris flow producing storms indicate warm temperatures (i.e. high freezing levels) are indeed a requirement for debris flow generation. Overall, these results highlight the need for temperature and snowpack information to be coupled with landslide thresholds in order to increase predictive capability of our wet debris flow model.

The above analysis informed development of a simple decision tree approach to hazard classification as a planning tool for MORA (Legg, 2015). The approach uses 3-day precipitation and temperature forecasts in concert with measurements of SWE and 15-day precipitation totals to classify and forecast debris flow hazards into low, medium and high hazard categories over a coming 3-day period. More broadly, this effort represents an example of hazard forecasting in an alpine setting where seasonal temperature and snow fluctuations are major drivers of debris-flow potential.

4.2. Dry, warm weather debris flows

The method for forecasting dry weather debris flows is an expansion of Legg’s (2015) model. A total of 35 debris-flow events which occurred in a dry season (i.e., no rain and relatively warm temperatures [average high temperature of ~65°F]) were compiled from the various sources mentioned in Section 4.1. From that list, antecedent weather information for the day of event and the days leading up to the event itself were calculated from the Paradise SNOTEL station and other weather sources in the vicinity. A Monte Carlo analysis was completed on each weather variable to determine its relative importance to the overall detection of a debris flow. Once the relative weighting of each variable was completed, all days in the historic record were run to determine the debris flow hazard scores on those days (this includes the wet weather debris flows) (Table 1).

Table 1. Performance of current debris-flow hazard model based on all available weather data for the period of 1917-2017 at the Paradise SNOTEL station. Event type categories are split out on known debris flow and outburst flood days from the historic record. The undefined category means that weather conditions were not available to adequately calculate the debris-flow hazard score for that day.

Event Type	Model Type	Low	Medium	Medium High	High	Very High	Undefined
Debris Flow (N = 42)	Wet:	0	0	1	12	-	0
	Dry:	3	4	6	11	5	0
	TOTAL:	3	4	7	23	5	0
Outburst Flood (N = 8)	Wet:	2	0	0	0	-	0
	Dry:	3	1	0	1	1	0
	TOTAL:	5	1	0	1	1	0
Debris Flow + Outburst Flood (N = 50)	Wet:	2	0	1	12	-	0
	Dry:	6	5	6	12	6	0
	TOTAL:	8	5	7	24	6	0
No Debris Flow or Outburst Flood (N = 31,647)	Wet:	12,633	980	539	1083	-	942
	Dry:	11,608	984	618	1001	540	719
	TOTAL:	24,241	1,964	1,157	2,084	540	1,661
TOTAL:		24,249	1,969	1,164	2,108	546	1,661
		76.50%	6.21%	3.67%	6.65%	1.72%	5.24%

The specific variables of interest for the dry side of the model are: P_{18} , or 18-day precipitation total at Paradise, which is necessary to determine whether to run the dry side or wet side of the model; T_{max} , which is the maximum daily temperature observed at Paradise; $T_{max\ Percentile}$, which is the maximum temperature expressed as a percentile based on the historic maximum temperatures (1917-2017); $DSOSP$, which is “days since zero snow pack”, a relative variable used to determine when debris source areas will be snow free – for the model, this variable is assumed as days since July 11th, which is the average “melt out” date at Paradise in the historic (1917-2017) record; $DD32_{18}$, or the 18-

day cumulative degree days above freezing; P_3 , or the 3-day precipitation total, a key dry-weather variable defined by Walder and Driedger (1994a); and SWE , or snow water equivalent. Each variable is given a numeric score between 1 and 5 (see Appendix A) and the debris-flow hazard score is calculated by the model when it is run.

At this time, the method is still being refined as more data is uncovered about the antecedent weather conditions and as more debris flows occur in the park. Additionally, an improved Monte Carlo approach is being undertaken to improve the model. The performance of the model for all available dates between 1917 and 2017 is shown in Table 1. In general, those days with a debris flow or outburst flood from the historic record should have a higher score, whereas those days with no event should have a lower score for the model to be considered truly calibrated successfully.

4.3. Combination forecast and data sources

The combination forecast (Appendix A) utilizes both the wet and dry sides into a simple decision tree based on calculated weather factors. Weather information is downloaded every hour from the DarkSky.net API. DarkSky provides a free ensemble forecast for individual locations throughout the park that is easily incorporated into the debris-flow hazard model. Every four hours, these weather variables and antecedent weather observations are automatically compiled based on the wet or dry forecast and then run through the decision tree algorithm (Appendix A). A qualitative score (Low, Medium, Medium High, High, or Very High) is generated for the day of interest and next seven days. This is then reported on a website for monitoring and decision-based analysis by park staff. Hazard scores are tied to weather forecasts and will change as forecasts are updated. While this process is automated, park staff still must monitor the model every day to determine the future relative risk for debris flow activity.

5. Real-time debris flow monitoring

The final piece in the debris-flow hazard system at MORA is the ability to detect debris flows as they occur. As shown in Section 3, debris flows like those in 2015 have a seismic and RSAM signature that is distinctive. With assistance from the University of Washington's Pacific Northwest Seismic Network (UW PNSN), seismic data is run through the USGS RSAM program and binned into 30 second values. At five-minute intervals, an automated computer script then downloads the RSAM values and runs through the data file looking for a "debris-flow-like signature." A debris flow signature is defined as an increasing signal above a set point over a set amount of time. If these values are exceeded, an alert is sent out to park staff for analysis and hazard notification via cellphone text messages and emails.

As an example, at the Emerald Ridge (RER) seismograph, the relevant variables are an RSAM value greater than 500 counts for over 5 minutes with a RSAM value that is increasing (slope > 0.030), on average, over those 5 minutes. Using this definition, three of the four debris flows on 13 August 2015 (2a/2b, 3 and 4) and an additional debris flow that occurred in Tahoma Creek on 12 September 2015 (not discussed in this paper) would have been detected with this system. Additionally, this system would have detected the second debris flow on August 13th at roughly 10:20 am, almost a full two hours before park staff were alerted to the event on the radio.

Real-time debris-flow monitoring via the RSAM system is currently being run on the Emerald Ridge (RER) seismograph (Puyallup, Tahoma and South Tahoma Glaciers), Mt. Fremont (FMW) seismograph (Emmons, Inter, and Winthrop Glaciers), and Longmire (LO2) seismograph (Kautz, Nisqually, Pyramid, Success, Van Trump, and Wilson Glaciers). Most of the major glacial streams at MORA now have some sort of seismic monitoring; those without, with the exception of the Carbon Glacier, do not have extensive infrastructure development in their watershed boundaries.

The overall performance value of the RSAM system in detection of debris flows is not yet available since the park has yet to experience a confirmed debris flow since the system's inception. There have been several false positive readings, almost exclusively due to wind noise (especially at RER). Local, regional, and teleseism earthquake events are such short period and punctuated that they are excluded in the analysis and rarely generate alerts. When false positives have been detected, staff is able to quickly analyze real-time seismic data to determine if the event is truly a debris flow or some other event. In this sense, the system is semi-automated and still requires human intervention in order to take the step from an alert generation to an alert being broadcast to the field. Lastly, we are not yet able to co-locate exact drainages where a debris flow due to a paucity of seismic stations. However, a strong signal in one seismograph and relatively weak signals in others (as was the case in the August 2015 event) can help determine a narrower geographic location of the event. Future seismic implementation at MORA is being planned in the next five years which will help the co-location ability of this system.

6. Conclusions

Mount Rainier is an environment that is ideally suited for debris-flow genesis and has a rich history of these events. With our work, we have been successful in providing a forecast for debris-flow hazard based on past antecedent weather conditions on prior debris-flow days up to seven days in advance. We then can detect individual debris flows using in situ seismometers and the RSAM system. As glaciers continue to retreat, new sediment sources will be exposed to annual storms and occasional outburst floods – all of which will continue the threat of debris flows to downstream areas. The forecasting and detection systems we have in place now are in their infancy and will be further refined as more events occur. Additional seismic installations planned in the next decade at MORA will only improve these systems and will provide better warning to park staff and visitors working and recreating at the park.

Acknowledgements

This work is greatly indebted to the following individuals for their observations, photos, videos, and assistance during and after the 2015 debris flows, including, but not limited to: Anthony "Scott" Anderson, Croil Anderson, Jenni Chan, Carolyn Driedger, Maxine Dunkleman, Terry Flower, Jeff Gardner, Sara Hall, Mitch Haynes, Steve Hughes, Zachary Jones, Dave Keltner, Paul Kennard, Glenn Kessler, Rebecca Lofgren, Steve Malone, Kendra Martinez, Seth Moran, Dave Morgan, Casey Overturf, Heather Rogers, Heather Sharp, Kurt Spicer, Trisha Stanfield, Karen Thompson, Claire Todd, Dave Turner, and Yonit Yogev. Finally, thank you to Kate Allstadt and Abigail Michel who provided critical review to this manuscript prior to submission.

References

- Beason, S.R., 2017, Change in glacial extent at Mount Rainier National Park from 1896-2015: National Park Service Natural Resource Report NPS/MORA/NRR—2017/1472, 98 p.
- Beason, S.R., 2012, Small glacial outburst flood occurs on Mount Rainier – October 27, 2012: Science Brief, National Park Service, 3 p.
- Bullock, A.B., Bacher, K., Baum, J., Bickley, T., and Taylor, L., 2007, The flood of 2006: 2007 update: Unpublished report, Mount Rainier National Park, 43 p.
- Chleborad, A.F., Baum, R.L., and Godt, J.W., 2006, Rainfall thresholds for forecasting landslides in Seattle, Washington, area – exceedances and probability: U.S. Geological Survey Open-File Report 2006-1064, 31 p., doi: 10.3133/ofr20061064.
- Copeland, E.A., 2009, Recent periglacial debris flows from Mount Rainier, Washington [M.S. Thesis]: Oregon State University, 139 p.
- Crandell, D.R., 1971, Postglacial lahars from Mount Rainier volcano, Washington: U.S. Geological Survey Professional Paper 677, 75 p, doi: 10.3133/pp677.
- Driedger, C.L., and Fountain, A.G., 1989, Glacier outburst floods at Mount Rainier, Washington state, U.S.A., *Annals of Glaciology*, v. 13, p. 51-55, doi: 10.3189/S0260305500007631.
- Driedger, C.L., and Kennard, P.M., 1986, Ice volumes on Cascade Volcanoes: Mount Rainier, Mount Hood, Three Sisters, and Mount Shasta: U.S. Geological Survey Professional Paper 1365, 38 p, doi: 10.3133/pp1365
- Endo, E.T. and Murry, T.L., 1991, Real-time seismic amplitude measurement (RSAM): A volcano monitoring and prediction tool: *Bulletin of Volcanology*, v. 53, no. 7, p. 533-545, doi: 10.1007/BF00298154.
- Ewert, J.W., Difenbach, A.K., and Ramsey, D.W., 2018, 2018 update to the U.S. Geological Survey national volcanic threat assessment: U.S. Geological Survey Scientific Investigations Report 2018-5140, 40 p, doi: 10.3133/sir20185140.
- George, J.L., and Beason, S.R., 2017, Dramatic changes to glacial volume and extent since the late 19th century at Mount Rainier National Park, Washington, USA: Poster #158-6, *Geological Society of America Abstracts with Programs*, v. 49, no. 6, doi: 10.1130/abs/2017AM-299694.
- Legg, N.T., 2015, An assessment of hazards from rain-induced debris flows on Mount Rainier: Unpublished internal document, Mount Rainier National Park, 30 p.
- Legg, N.T., Meigs, A.J., Grant, G.E., and Kennard, P.M., 2014, Debris flow initiation in proglacial gullies on Mount Rainier, Washington: *Geomorphology*, v. 226, p. 249-260, doi: 10.1016/j.geomorph.2014.08.003.
- National Park Service, 2018, Mount Rainier Soundscapes [Online]: Accessed from <https://www.nps.gov/mora/learn/nature/soundscapes.htm>.
- Neiman, P.J., Ralph, F.M., Wick, G.A., Kuo, Y.H., Wee, T.K., Ma, Z., Taylor, G.H, and Dettinger, M.D., 2008, Diagnosis of an intense atmospheric river impacting the Pacific Northwest: Storm summary and offshore vertical structure observed with COSMIC satellite retrievals: *American Meteorological Society Monthly Weather Review*, v. 136, no. 11, p. 4398-4420, doi: 10.1175/2008MWR2550.1.
- Pierson, T.C., and Scott, K.M., 1985, Downstream dilution of a lahar: Transition from debris flow to hyperconcentrated streamflow: *Water Resources Research*, v. 21, p. 1511-1524, doi: 10.1029/WR021i010p01511.
- Richardson, D., 1968, Glacier outburst floods in the Pacific Northwest: U.S. Geological Survey Professional Paper 600-D, p. 79-86.
- Samora, B.A., and Malver, A., 1996, Inventory of information on glaciers in Mount Rainier National Park: Unpublished report, Mount Rainier National Park, 417 p.
- Scott, K.M., Vallance, J.W., and Pringle, P.T., 1995, Sedimentology, behavior, and hazards of debris flows at Mount Rainier, Washington: U.S. Geological Survey Professional Paper 1547, 56 p, doi: 10.3133/pp1547
- Sisson, T.W., and Vallance, J.W., 2009, Frequent eruptions of Mount Rainier over the last ~2,600 years: *Bulletin of Volcanology*, v. 71, no. 6, p. 595-618, doi: 10.1007/s00445-008-0245-7.

Vallance, J.W., 2005, Volcanic debris flows in Jakob, M., and Hungr, O., eds., Debris-flow hazards and related phenomena: Springer Praxis Books, Springer, Berlin, Heidelberg, p. 247-274, doi: 10.1007/b138657.

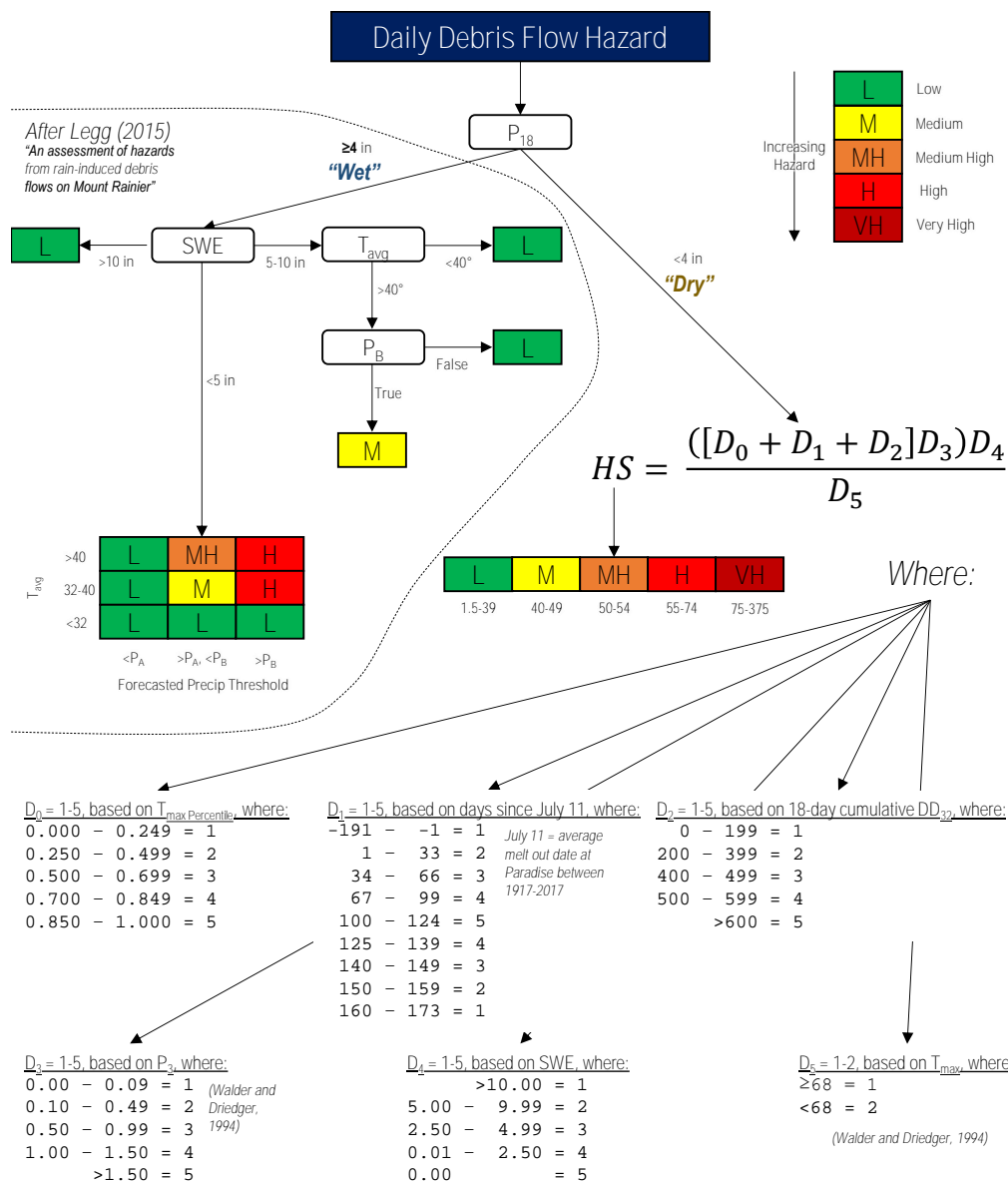
Vallance, J.W., and Scott, K.M., 1997, The Osceola Mudflow from Mount Rainier: Sedimentology and hazard implications of a huge clay-rich debris flow: Geological Society of America Bulletin, v. 109, no. 2, p. 143-163, doi: 10.1130/0016-7606(1997)109<0143:TOMFMR>2.3.CO;2

Walder, J.S. and Driedger, C.L., 1995, Frequent outburst floods from South Tahoma Glacier, Mount Rainier, U.S.A.: Relation to debris flows, meteorological origin and implications for subglacial hydrology: Journal of Glaciology, v. 41, no. 137, 11 p., doi: 10.3189/S0022143000017718

Walder, J.S. and Driedger, C.L., 1994a, Geomorphic change caused by outburst floods and debris flows at Mount Rainier, Washington, with emphasis on Tahoma Creek Valley: U.S. Geological Survey Water-Resources Investigations Report 93-4093, 100 p, doi: 10.3133/wri934093.

Walder, J.S. and Driedger, C.L., 1994b, Rapid geomorphic change caused by glacial outburst floods and debris flows along Tahoma Creek, Mount Rainier, Washington, U.S.A.: Arctic and Alpine Research, v. 26, no. 4, p. 319-327, doi: 10.2307/1551792.

Appendix A. Debris flow hazard forecast model at Mount Rainier



Variables:

DD_{32} = Degree day above 32°F (dimensionless)

P_A = Precipitation threshold A, $P_3 = 2.5 - 0.67P_{15}$

P_B = Precipitation threshold B, $P_3 = 4.5 - 0.67P_{15}$

P_3 = 3-day (D1-D3) cumulative precipitation at Paradise (in)

P_{15} = 15-day cumulative precipitation at Paradise prior to 3-day period (D4-D18) (in)

P_{18} = 18-day cumulative precipitation at Paradise (in)

SWE = Snow water equivalent at Paradise (in)

T_{avg} = Average temperature at Paradise (°F)

T_{max} = Maximum temperature at Paradise (°F)

$T_{max\ Percentile}$ = Maximum temperature as a percentile compared to the historic temperature (1917-2017), (dimensionless)

Deciphering sediment dynamics in a debris-flow catchment: insights from instrumental monitoring and high-resolution topography

Velio Coviello^{a,*}, Joshua I. Theule^b, Lorenzo Marchi^c, Francesco Comiti^a, Stefano Crema^c, Marco Cavalli^c, Massimo Arattano^c, Ana Lucía^d, Pierpaolo Macconi^e

^aFree University of Bozen-Bolzano, Faculty of Science and Technology, Italy

^bTerrAlp Consulting, St Martin d'Uriage, France

^cResearch Institute for Geo-hydrological Protection, National Research Council, Italia

^dCenter for Applied Geoscience, Eberhard Karls Universität Tübingen, Germany

^eCivil Protection Agency, Autonomous Province of Bozen-Bolzano, Italy

Abstract

In mountainous catchments, the quantification of sediment yield is of paramount relevance for land-use planning and design of sediment control structures. However, deciphering the contribution of the different sediment transport processes (debris flows, debris floods and bedload transport) is often challenging as they are strongly controlled by basin morphometry, hydrological regime, and sediment supply. Therefore, long-term instrumental monitoring through catchment-scale sensor networks can provide precious information, especially if coupled with high-resolution topographical surveys. The Gadoria catchment, located in the eastern Italian Alps, offers the possibility to perform a systematic monitoring of sediment transport processes. This catchment typically features several low-magnitude flood episodes and a few debris-flow events per year, from late spring to early fall. Starting from 2011, various instruments mainly devoted to debris-flow detection (geophones, video cameras, flow stage sensors) have been installed along the main channel, just upstream of a retention basin. High-resolution topographical surveys of the retention basin are carried out each year, at the beginning and at the end of the summer season and after debris-flow events. Rainfall is measured in the intermediate part of the catchment and in the headwaters, while PIT-tracing of bedload was performed in the main channel. In this work, we present the reconstruction of the sediment dynamics at the catchment scale during the 2014 and 2015 monitoring seasons. Instrumental monitoring was used to estimate the contribution of the different flow processes, and data from topographical surveys to quantify the transported volumes. Results show that (i) coarse sediment yield is driven by sporadic debris flows while flood events allow the continuous fine-sediment migration along the channel network; (ii) volume estimations may be significantly different – up to 30% lower - if performed through a DEM of Difference (DoD) analysis of the retention basin or by analysing monitoring data; (iii) a multi-parametric monitoring is needed to decipher sediment dynamics at catchment scale.

Keywords: bedload transport, debris flows, monitoring, rainfall, topographic survey

1. Introduction

In Alpine valleys, the sediment supply to the channel network is typically episodic and it is controlled by the interaction between geomorphic conditions and hydrological processes (Benda and Dunne, 1997). The upstream edge of the fans acts as bedload traps, creating longitudinal discontinuities in sediment transport and causing large-scale aggradation of sediment (Hoffman and Gabet, 2007). Massive, impulsive sediment inputs – typical of debris flows and floods occurring in steep channels – can alter water and sediment continuity along the channel network, by determining large-scale bed aggradation, confluence migration, and channel obstructions with the formation of temporary lakes and fan-delta systems (Brardinoni et al., 2018). Understanding the effect of debris flows and bedload on channel topography and the quantification of sediment yield is of paramount relevance for hazard assessment and design of

* Corresponding author e-mail address: velio.coviello@unibz.it

mitigation measures. However, the sediment cascade associated with debris flows and bedload events and their relative yields at the catchment scale has been rarely addressed.

In recent years, the increase of topographic instrument automation and resolution significantly improved the cost-effectiveness of multi-temporal analysis of Digital Elevation Models (DEMs). The geomorphic changes associated with erosion/deposition processes can be quantified through DEM of Difference (DoD) grids, where the elevation difference between old and new surfaces represents a measure of net sediment transport (Schürch et al., 2011; Theule et al., 2015; Cavalli et al., 2017). However, discriminating the contribution of the different sediment transport processes (namely debris flows vs bedload) and the effects of multiple flow events is often challenging. Thus, long-term instrumental monitoring of sediment fluxes through catchment-scale sensor networks can provide precious information, especially if coupled with high-resolution topographical surveys (McCoy et al., 2010; Comiti et al., 2014). To this aim, the Gadria catchment (eastern Italian Alps) offers the opportunity to understand the main processes driving the sediment supply at the catchment scale thanks to the intense, ongoing monitoring activities. In this paper, we focus on two years (2014–2015) for which frequent field surveys were available.

2. Methods

2.1. The study site

The Gadria catchment is located in the Venosta Valley, eastern Italian Alps, and belongs to the Adige river basin. At the retention basin, it has a drainage area of 6.3 km² and ranges in elevation from 1,394 to 2,945 m a.s.l. The Gadria is underlain by paragneiss and ortogneiss lithologies, result of Permian and Cretaceous matamorphisms. Sediment produced by the weathering of these highly fractured rocks and thick Quaternary deposits fills the channel networks through a number of mechanisms including shallow debris slides, rockfalls, and dry raveling on the steep slopes (Figure 1a). These colluvial processes dominate the upper and intermediate sections of the basin, and the presence of steep channels sets the perfect conditions for chronic debris-flow activity. The Gadria catchment is characterized by dry inner-Alpine climate, with mean annual precipitation of 480 mm in the Venosta valley floor (station of Laas-Lasa, 863 m a.s.l., period 1989–2012), due to the sheltering effect of the mountainous ranges to southerly and northerly winds. Mean annual precipitation increases with altitude, with 662 mm measured at a rain gauge located at 1,754 m a.s.l. (period 1993–2012).

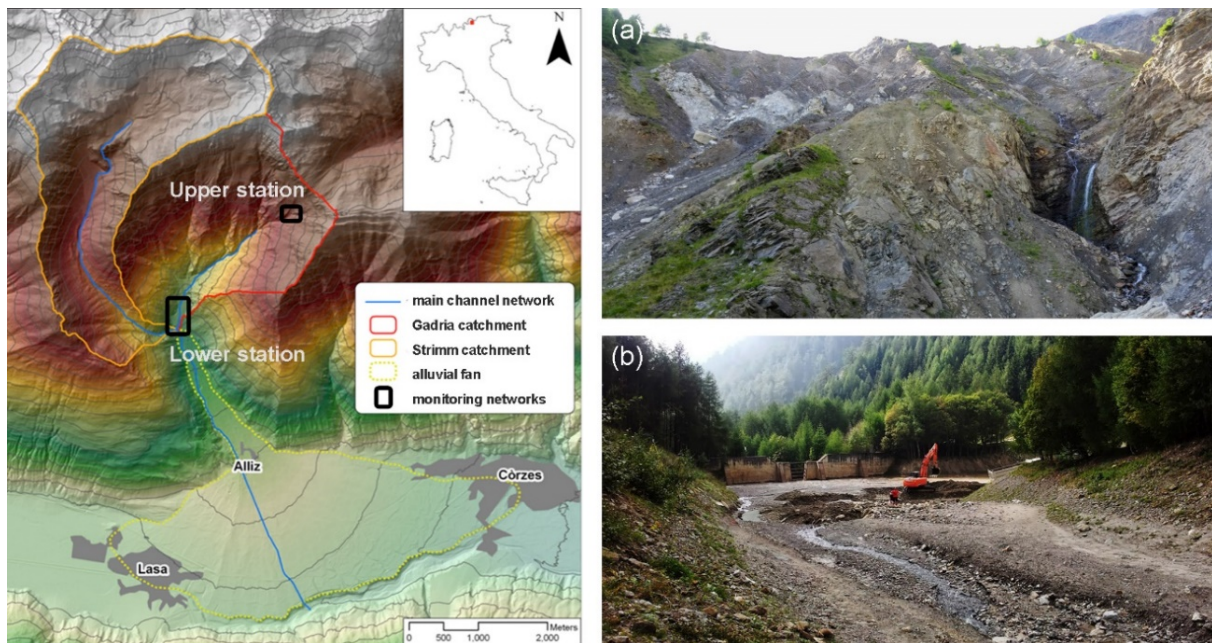


Fig. 1. The Gadria instrumented catchment, the adjacent Strimm catchment and the alluvial fan; the black frames highlight the location of the upper and lower monitoring sites at Gadria. (a) View of the main sediment source areas monitored with the upper station; (b) the retention basin located at the outlet of the catchments.

The catchment is characterized by a high degree of sediment connectivity and a sediment yield of about $5,200 \text{ m}^3 \text{ km}^{-2} \text{ y}^{-1}$ was estimated for the period 2005-2011 (Cavalli et al., 2017). A retention basin was constructed in the 1970s to protect settlements located on the Gatria fan (Figure 1b). This basin is periodically emptied, but some residual risk still exists as extremely large debris flows could exceed its capacity.

2.2. Instrumental monitoring

At Gatria, the first downstream monitoring station (*lower station*) was equipped in 2011 close to the alluvial fan apex, at an elevation of about 1,400 m a.l.m. (Comiti et al., 2014). This installation was designed for the measurement of basic debris-flow variables, the characterization of flow dynamics, and the development of early warning systems. The station is composed of three video cameras framing channel and retention basin, four vertical geophones (10 Hz) placed along the left channel bank, two in the ground and two on the wing of the check-dam, and two stage sensors at the same cross sections where the geophones are installed (Figure 2). In 2013, the geophone array was extended in the upstream direction with three additional geophones (Coviello et al., 2015). This latter geophone network recorded the seismic data that are analyzed in the present work. One rain-gauge and an additional stage sensor are located about 500 m upstream, at an elevation of 1500 m a.s.l.. The video footage has been used to assess the surface velocity of debris flows through the application of the large-scale particle image velocimetry technique (Theule et al., 2018).

The upstream monitored area (*upper station*) is located in the upper basin, at an elevation of about 2,200 m a.l.m., with the objective of monitoring initiation conditions and triggering processes. A number of instruments have been installed during the last years: rain-gauges, rain-triggered video cameras, piezometers, and erosion probes. Recently, a new geophone network composed of three 4.5 Hz vertical sensor was installed on a ridge separating two steep channels of the upper basin to detect incipient sediment motion related to debris flow initiation.

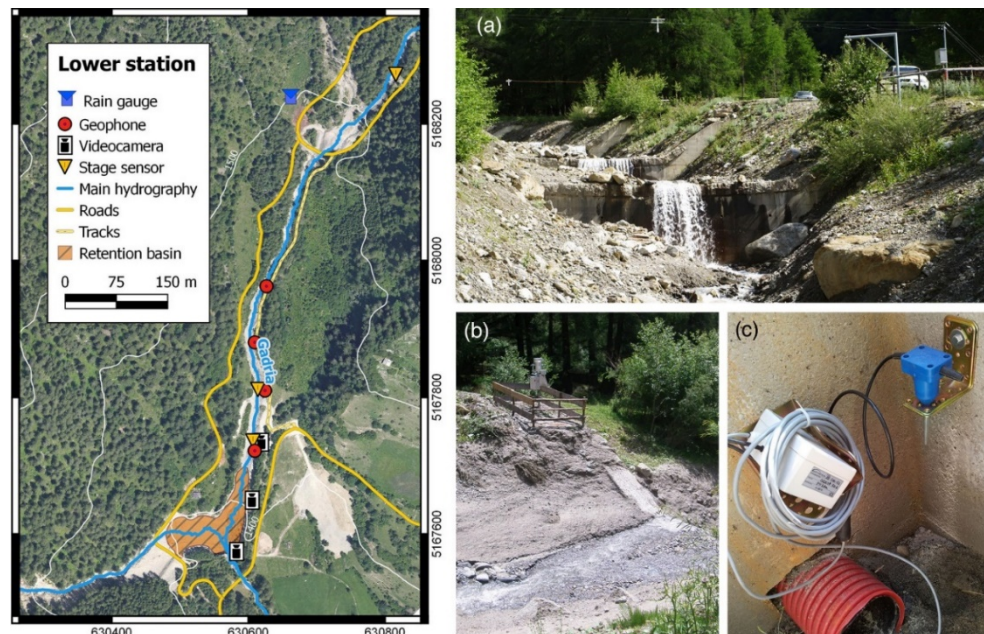


Fig. 2. The lower station of Gatria: (a) view of the channel in the upstream direction, two stage sensors, and one video camera are visible; (b) geophone recording unit and channel conditions right after a debris flow; (c) detail of one of the vertical 10-Hz geophones.

2.3. Topographical surveying and PIT-tracing

Repeated topographic surveys of the retention basin at the beginning of the debris-flow season and after each debris flow were carried out by terrestrial laser scanning (TLS) from 2011 to 2013. Afterwards, the Structure from Motion (SfM) photogrammetry (using Agisoft Photoscan Professional) was adopted because of its field efficiency and spatial coverage. From 2013 to 2015, an operator took photos from a 6-m extendable pole at 1 frame per second while walking along the channel banks (Figure 3a). Since 2015, photos are taken from helicopter covering the retention basin,

channel, and source areas and also from a drone for just the retention basin. Painted reference points were appropriately distributed around the sediment trap and channels and were surveyed with the total station and differential GPS (dGPS). For DoD analysis, CloudCompare freeware was used to further align both TLS and SfM point clouds by using the iterative closest point algorithm. This was applied to unchanged permanent features resulting in root mean square errors of 21 cm for older TLS comparisons (volume uncertainty for the retention basin of $\pm 740 \text{ m}^3$), 2 cm for extendable pole SfM ($\pm 100 \text{ m}^3$) and 9 cm for helicopter SfM ($\pm 450 \text{ m}^3$) for the general retention basin area. 10-cm DEMs were developed and their differences were used for measuring the volumes in the retention basin (Figure 3b).

In the main channel, 280 passive integrated transponders (PITs) were installed in 2014 and their positions measured using dGPS, with the aim to contrast incipient motion and transport distances between debris flows and bedload events. Their grain-size ranges from small cobbles to boulders and their percent embeddedness were estimated in the field. They were distributed throughout the channel from entrainment reaches, transport reaches and the reach before the sediment trap. Field checks and antennae surveys took place after floods with bedload transport and after debris flows.

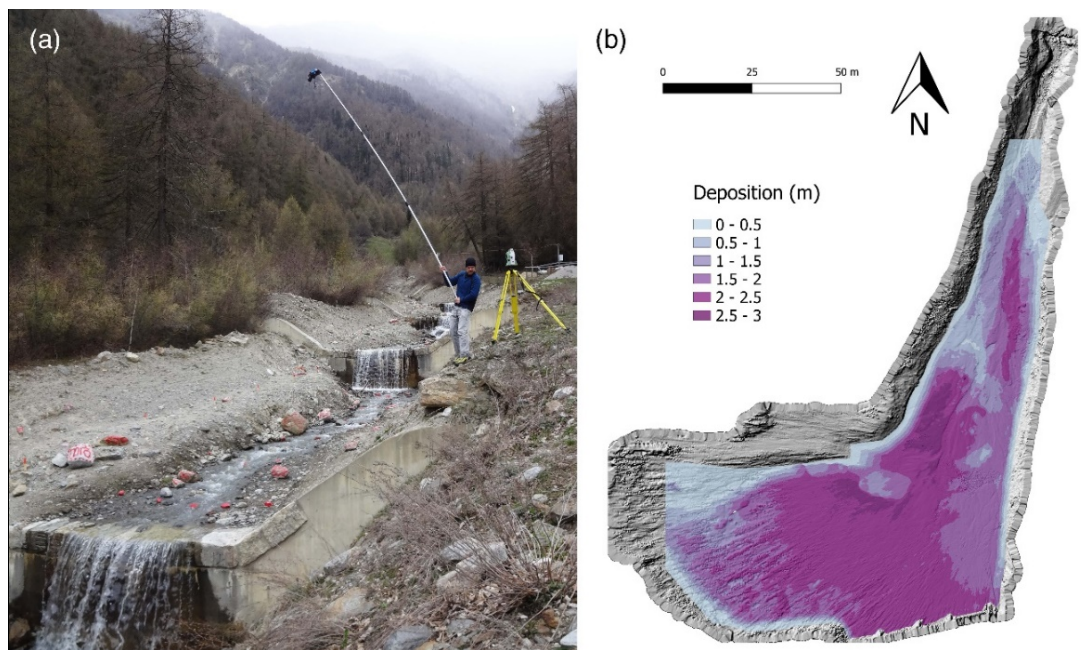


Fig. 3. (a) Photogrammetric surveying of the main channel with the 6-m extendable pole; (b) DoD of the retention basin from two photogrammetric surveys carried out in April and August 2014.

3. Results and discussion

3.1. Catalog of flow events

Several flow processes occurred at Gatria in 2014 and 2015 (Table 1). Complete information on the debris flows that occurred in this period was already available (Theule et al., 2018). We constructed the event catalog of floods featuring bedload transport analyzing the seismic dataset gathered at the lower monitoring station. Compared to debris flows, seismic signals produced by floods present significantly longer durations and lower amplitude peaks (Coviello et al., 2015; Mao et al., 2009; Bel, 2017). Flood events were identified by analyzing 140 days of continuous seismic recordings from the geophone network installed at the lower station. In two years, nine flood events were detected using an intensity-duration threshold (amplitude above the long-time-average of the seismic signal for at least 10 minutes). The event detection was validated through the manual inspection of the video frames, when available, and with the analysis of rainfall events recorded at the upper station. An image every 5 minutes was recorded by the video camera framing the channel in the upstream direction (from 4 June to 18 July 2014 and from 1 May to 23 October 2015). In addition, four additional flood events with bedload transport were identified by inspecting the images recorded in the periods of time lacking seismic records. Finally, two snow-melt induced bedload events (20 and 21 May 2015) were directly observed in the field (with bedload measured by portable traps).

Table 1. Debris flows and flood events with bedload transport detected at the lower station of Gatria in 2014 and 2015 and dates of topographic surveys of the sediment trap carried out during the monitoring seasons (in italics). Peak times correspond to the amplitude peaks of the seismic signal. Bedload events identified only with images and rainfall data are marked with *.

Date (dd.mmm.yy)	Typology	Peak time (hh.mm UTC)	Duration (min)
<i>9.May.14</i>	<i>PIT survey</i>	-	-
<i>10.Apr.14</i>	<i>topographic survey</i>	-	-
05.Jun.14	bedload	05:00*	> 120
09.Jun.14	bedload	05:00*	> 120
29.Jun.14	bedload	18:00	360
<i>2.Jul.14</i>	<i>PIT survey</i>	-	-
08.Jul.14	bedload	14:55	360
13.Jul.14	bedload	20:30*	> 180
15.Jul.14	debris flow	17:13	26
<i>19.Jul.14</i>	<i>PIT survey</i>	-	-
21.Jul.14	bedload	07:45	360
24.Jul.14	bedload	13:32	120
13.Aug.14	bedload	12:00	180
<i>18.Aug.14</i>	<i>topographic survey</i>	-	-
<i>18.Apr.15</i>	<i>topographic survey</i>	-	-
20.May.15	bedload	-	> 600
21.May.15	bedload	-	600
06.Jun.15	bedload	15:23	> 240
08.Jun.15	debris flow	17:16	50
<i>10.Jun.15</i>	<i>topographic survey</i>	-	-
16.Jun.15	bedload	8:30*	> 240
29.Jul.15	bedload	15:00	180
04.Aug.15	bedload	18:40	> 300
07.Aug.15	bedload	21:20	> 180

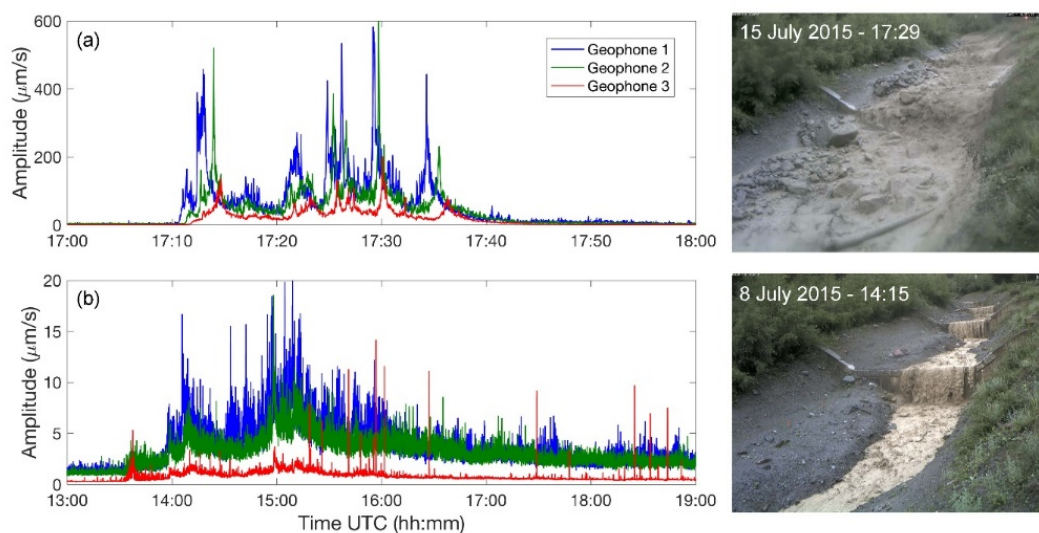


Fig. 4. Geophone signals of the debris flow that occurred on 15 July 2015 (a) and of the flood event that occurred on 8 July 2015 (b). Amplitude and duration of the debris flow are one order of magnitude greater than the ones of the flood event.

3.2. Particle motion

In 2014, three surveys of PITs positions were carried out on 9 May, 2 July and 19 July. In the time interval 9 May - 2 July three flood events featuring bedload transport were observed, while in the following time interval (2 - 19 July) two floods and one debris-flow event occurred (Table 1). Therefore we can surely attribute the displacement lengths measured in the first time interval to bedload transport. The log-log plot of travel distance versus grain size diameter shows an inverse correlation for the particles transported during the first, bedload-only period (Figure 5). On the contrary, no clear relationship can be detected for the second period when a debris flow occurred, as it could be anticipated based on the transport *en masse* of sediment by debris flows (Theule et al., 2015). Thus, in second time interval, the longer displacement lengths are produced by the debris flow of 15 July 2014. Indeed, PIT-tags measurements in debris-flow channels are probably mainly useful to analyze the variability in clast entrainment (e.g., based on clast position along cross-sections and thus on the experienced shear stress) rather than transport distances. In addition, PIT-tracing installation is very resource-intensive, as well as their manual surveying is time-consuming and the recovery rate can be very low. The 2014 debris flow had a 29 percent recovery rate due to the depth of the pit tag deposits, which we assume are mostly buried in the sediment trap. However, more significant results could be achieved if the travel distance of the tagged particles is measured in a debris-flow channel which is not ending in a sediment trap like the Gatria (see Bel, 2016). In fact, here the maximum travel distance (slightly smaller than 1400 m) is close to the distance between the most upstream transect equipped with PIT tags and the retention basin (Figure 5).

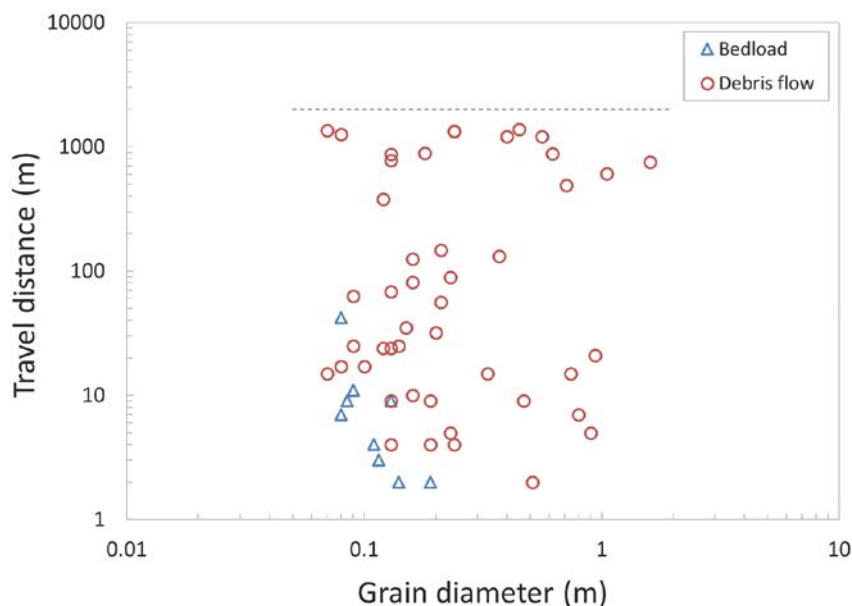


Fig. 5. PIT-tracing at Gatria in 2014, from 9 May to 2 July (only bedload transport observed) and from 2 July to 19 July (one debris flow). The upper travel-distance limit (dashed-line) is the distance between the most upstream transect equipped with PIT tags and the retention basin.

3.3. Sediment volumes

The volume of sediment deposited in the retention basin by each debris flows was determined by two topographic surveys carried out at the beginning of the debris-flow season and after the debris flow (Table 2). Video recordings and post-event observations, show that the trapping efficiency of the basin (ratio of sediment volume retained to the total incoming sediment) is below 100% (Comiti et al., 2014). We estimate that from 10% to 20% of sediment flowed through the slit opening of the retention check dam. In addition, also bedload transport contributes to the sediment yield, as well as to the erosion of deposits, in both the retention basin and the channel network (Figure 6). In particular, eight flood events occurred in the Gatria catchment in the period between the two surveys in 2014, and three in 2015.

We calculated the volume of debris flows using data from the monitoring station. The velocity of each debris-flow surge was estimated considering the mean propagation velocity of each front as the ratio of the distance between two equipped cross-sections (75 m) to the time interval between the arrival of the debris-flow surge at the two stations

(Arattano et al., 2015). The discharge of each debris flow wave is computed as the product of surge velocity by the flow's cross-sectional area, estimated using the flow stage measurement. This is the main source of uncertainty of this method, as the cross-sectional area may change during a single debris flow due to erosion/deposition processes. The method is also very sensitive to the choice of the hydrometric zero adopted to perform the calculations. Finally, the bulked volume carried by each surge was calculated as:

$$Volume = v \cdot \int_{t_0}^{t_e} A(t) dt \quad (1)$$

where $A(t)$ is the cross-sectional area at the time t ; v is flow velocity of the surge; t_0 and t_e represent the initial and final time of the surge, respectively.

Table 2. Debris-flow events that occurred at Gatria from 2011 to 2015, volumes computed using stage sensor measurements integrated in time are compared with DoD of the retention basin.

Date (dd.mmm.yy)	Debris-flow peak discharge (m ³ /sec)	Debris-flow volume (m ³)	Time interval DoD	DoD (m ³)	Reference
05.Aug.11	11	2 400	June - September 2011	2000	Comiti et al., 2014
18.Jul.13	80	10 000	June 2011 (empty trap) - August 2013	8100	Arattano et al., 2015
15.Jul.14	26	11 600	April - August 2014	10400	This study
08.Jun.15	27	12 600	April - June 2015	9850	This study

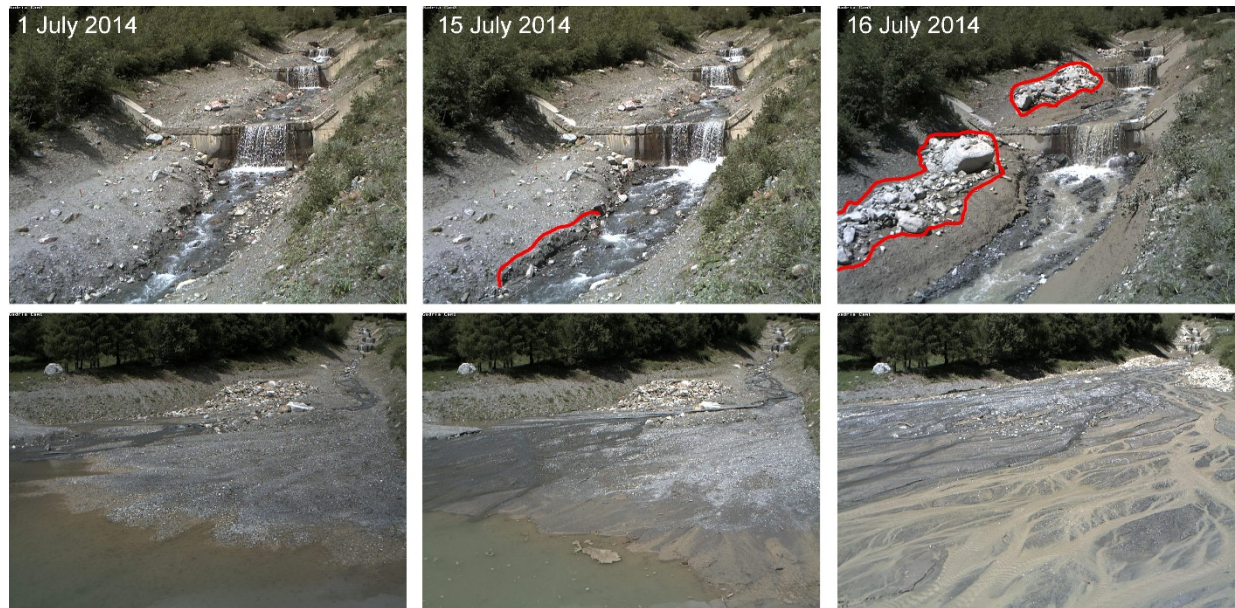


Fig. 6. Channel and retention basin conditions on 1 July, 15 July (after three flood events) and 16 July 2014 (after a debris-flow event). Erosion of fine to medium-size material due to floods and coarse deposits produced by the debris flow in the main channel are highlighted.

Volume estimations may significantly differ if performed through the DoD of the retention basin or with instrumental measurements carried out with the use of flow stage data (Table 2). Estimates deriving from topographic surveys resulted constantly lower, with differences that may reach 30% of their value. This is consistent with the observed outflow of the suspended sediment through the check dam during the tail of each debris-flow events. In the neighboring Strimm catchment, a bedload yield of 200 m³ yr⁻¹ was observed during two years of PIT-tracing carried out from 2011 to 2013 (Dell'Agnese et al., 2015), which also contributes to the filling-up of the retention basin. Neglecting the contribution of the Strimm, a sediment yield of about 1,900 m³ km⁻² y⁻¹ was calculated based on DoD analysis in the period of time 2014-2015, which is largely dominated by debris-flow processes considering both

preliminary estimates for bedload virtual velocities and debris-flow volumes stemming from Eq. 1. The sediment yield value is significantly lower than the estimation made for the time period 2005-2011 ($5,200 \text{ m}^3 \text{ km}^{-2} \text{ y}^{-1}$), during which much larger debris-flow events were observed (Cavalli et al., 2017).

4. Conclusions

We constructed the event catalog of debris flow and flood events with bedload transport by analyzing the monitoring dataset (geophone data, video images) gathered at Gadria, eastern Italian Alps. Topographic surveys of debris-flow deposits provide volume estimations significantly lower - up to 30% - than those obtained through instrumental measurements carried out with the use of hydrograph data. Sediment yield of about $1,900 \text{ m}^3 \text{ km}^{-2} \text{ y}^{-1}$ is estimated for the investigated period (2014-2015), a value significantly lower than the one previously estimated in a wider time interval affected by larger events. Sediment yield is dominated by debris flows, whereas the contribution of flood events featuring bedload transport is apparently very minor and mostly relative to the gravel and small cobbles fractions only, based on preliminary data from travel distances of PIT-tagged clasts. Longer periods of observations are nonetheless needed to identify the factors (e.g., climate) that control sediment yield variability over time.

Acknowledgements

The Gadria monitoring station is managed by the Civil Protection Agency of the Autonomous Province of Bozen-Bolzano. Funding for this research came from the Kinoflow project, funded by the Autonomous Province of Bozen-Bolzano. The current research at Gadria is supported by the SEDIPLAN-r project (Sediment budgeting and planning for rivers in South-Tyrol: from hazard mitigation to environmental restoration) - European Regional Development Fund, and by the EARFLOW project, funded by the MAECI - Ministero degli Affari Esteri e della Cooperazione Internazionale and the AMEXCID - Agencia Mexicana de Cooperación Internacional para el Desarrollo.

References

- Arattano, M., Bertoldi, G., Cavalli, M., Comiti, F., D'Agostino, V., and Theule, J., 2015, Comparison of Methods and Procedures for Debris-Flow Volume Estimation, *in* Lollino, G., Arattano, M., Rinaldi, M., Giustolisi, O., Marechal, J.-C., and Grant, G.E. eds., *Engineering Geology for Society and Territory*, Springer International Publishing, p. 115–119, doi:10.1007/978-3-319-09054-2_22.
- Bel, C., 2017, Analysis of debris-flow occurrence in active catchments of the French Alps using monitoring stations, PhD thesis, Université Grenoble Alpes, France.
- Benda, L., and Dunne, T., 1997, Stochastic forcing of sediment routing and storage in channel networks: *Water Resources*, v. 33, p. 2865–2880, doi:10.1016/j.rmed.2004.03.018.
- Brardinoni, F., Picotti, V., Maraio, S., Paolo Bruno, P., Cucato, M., Morelli, C., and Mair, V., 2018, Postglacial evolution of a formerly glaciated valley: Reconstructing sediment supply, fan building, and confluence effects at the millennial time scale: *GSA Bulletin*, v. 130, p. 1457–1473, doi:10.1130/B31924.1.
- Cavalli, M., Goldin, B., Comiti, F., Brardinoni, F., and Marchi, L., 2017, Assessment of erosion and deposition in steep mountain basins by differencing sequential digital terrain models: *Geomorphology*, v. 291, p. 4–16, doi:10.1016/j.geomorph.2016.04.009.
- Comiti, F. et al., 2014, A new monitoring station for debris flows in the European Alps: first observations in the Gadria basin: *Natural Hazards*, v. 73, p. 1175–1198, doi:10.1007/s11069-014-1088-5.
- Coviello, V., Arattano, M., and Turconi, L., 2015, Detecting torrential processes from a distance with a seismic monitoring network: *Natural Hazards*, v. 78, p. 2055–2080, doi:10.1007/s11069-015-1819-2.
- Dell'Agnese, A., Brardinoni, F., Toro, M., Mao, L., Engel, M., and Comiti, F., 2015, Bedload transport in a formerly glaciated mountain catchment constrained by particle tracking: *Earth Surface Dynamics*, v. 3, p. 527–542, doi:10.5194/esurf-3-527-2015.
- Hoffman, D.F., and Gabet, E.J., 2007, Effects of sediment pulses on channel morphology in a gravel-bed river: *Bulletin of the Geological Society of America*, v. 119, p. 116–125, doi:10.1130/B25982.1.
- Mao, L., Cavalli, M., Comiti, F., Marchi, L., Lenzi, M.A., and Arattano, M., 2009, Sediment transfer processes in two Alpine catchments of contrasting morphological settings: *Journal of Hydrology*, v. 364, p. 88–98, doi:10.1016/j.jhydrol.2008.10.021.
- McCoy, S.W., Kean, J.W., Coe, J.A., Staley, D.M., Wasklewicz, T.A., and Tucker, G.E., 2010, Evolution of a natural debris flow: In situ measurements of flow dynamics, video imagery, and terrestrial laser scanning: *Geology*, v. 38, p. 735–738, doi:10.1130/G30928.1.
- Schürch, P., Densmore, A.L., Rosser, N.J., Lim, M., and Mcardell, B.W., 2011, Detection of surface change in complex topography using terrestrial laser scanning: Application to the Illgraben debris-flow channel: *Earth Surface Processes and Landforms*, v. 36, p. 1847–1859, doi:10.1002/esp.2206.
- Theule, J.I., Crema, S., Marchi, L., Cavalli, M., and Comiti, F., 2018, Exploiting LSPIV to assess debris-flow velocities in the field: *Natural Hazards and Earth System Sciences*, v. 18, p. 1–13, doi:10.5194/nhess-18-1-2018.
- Theule, J.I., Liébault, F., Laigle, D., Loye, A., and Jaboyedoff, M., 2015, Channel scour and fill by debris flows and bedload transport: *Geomorphology*, v. 243, p. 92–105, doi:10.1016/j.geomorph.2015.05.003.

Examining the impact force of debris flow in a check dam from small-flume experiments

Song Eu^a, Sangjun Im^{a,*}

*^aDepartment of Forest Sciences, College of Agriculture and Life Sciences, Seoul National University,
1 Gwanak-ro, Gwanak-gu, Seoul, 08826, Korea, Republic of.*

Abstract

Debris flow is one of the most hazardous disasters in mountain regions of Korea. Rainfall-induced debris flows have occurred more frequently during past decades due to climate changes. Especially, its threat on many lives and properties in urban or suburban areas have increased. To control debris-flow disaster, check dams have been constructed in forest watersheds since 1985. Although check dams that recently constructed in Korea are expected to function as debris-flow barriers, impact force has not been considered during design procedure. For effective structure design regarding debris-flow disaster, estimation of debris-flow impact force is necessary. Meanwhile, it is well known that impact force is closely related to the flow characteristics of debris flow. In this study, small flume experiments were conducted to analyze the influence of flow characteristics to impact force of debris flow. Flume slope, total volume, and viscosity of mixture were selected as experiment variables. As a result, faster flow velocity was observed on steeper channel slope and larger mixture volume condition. In terms of viscosity, sediment-water mixture flowed faster as the viscosity becomes lower. The effect of flume slope on flow velocity was different as the viscosity of mixtures. However, flowing depth was correlated only to total mixture volume. Impact force was positively correlated to flow velocity and flow depth. By comparing various impact force estimation model, the hydrodynamic model has been selected for the best method to appropriately calculate the design impact force for check dams in small forested watersheds.

Keywords: Debris flow; Impact force; Flume experiment; Structure Design

1. Introduction

Debris flow is one of the most hazardous disaster in a forested mountain area in the Republic of Korea. Most debris-flow disasters that occurred in Korea were induced by severe rainfall (Woo et al., 2014). Due to climate change, debris-flow events have been increased last decades. Especially, the debris-flow hazard in urban areas nearby mountainous regions has become increased (Yoon et al., 2017). To prevent huge damage to lives and properties in an urban area due to these disasters, many debris-flow control structures, such as check dam or erosion control dam, have been implemented.

Structural mitigation is one of the most typical approaches to prevent damages from debris-flow disaster (Hübl et al., 2009). In Korea, more than 11,000 of check dams have been installed since 1985 (KFS, 2017). Recently, these structures are expected to function as debris-flow barriers or breakers that need to endure debris-flow impact force directly. Thus, it is necessary to consider the effect of debris-flow impact force on check dam during designing.

To apply debris-flow impact force to check dam design, appropriate impact force estimation is important. Through several pioneer studies (Hung et al., 1984; Armanini, 1997; Proske et al., 2011), it is well known that debris-flow impact force is closely related to debris-flow behavior. Based on this relationship, many researchers have conducted flume experiments to develop a model for impact force estimation (Moriguchi et al., 2009; Scheidl et al., 2013), and suggested several models for impact force estimation, such as hydraulic static or dynamic models (Hung et al., 1984; Armanini, 1997).

* Corresponding author e-mail address: junie@snu.ac.kr

In this study, we conducted small-scale flume experiment to analyze the relationship between flow behavior and corresponding impact force. Flume experiments were conducted with various sets of the sediment composition, slope, and water-sediment mixture volume. With measured flow characteristics and impact force, we derived impact force estimation model that is most appropriate to explain our data.

2. Materials and Methods

2.1. Sediment mixtures

As shown in Table 1, we used various combination of sediment mixture that consisted of gravel, sand, clay, and water. During the preparation of mixtures, we applied four different mixing ratios to analyze the effect of viscosity on flow behavior. Also, we tried to use three different total mixture volume because the volume condition is one of the most effective factors controlling flow depth. The average density of mixtures was $1669.39 \text{ kg m}^{-3}$, and it was not significantly different between experimental conditions.

Table 1. Overview of mean (\pm standard deviation) sediment mixture properties. “A, B, and C” mean different volume conditions (about 8,400, 11,200, and 14,000 cm^3 , respectively), and “A’, B’, C’, and D’” mean different clay contents (about 21%, 25%, 29%, and 32% of total weight, respectively).

Category	Total volume (cm^3)	Total weight (g)	Density (kg m^{-3})	Composition of each material			
				Water (cm^3)	Clay (g)	Sand (g)	Gravel (g)
A-A'	5026.27 ± 91.97	8399.66 ± 1.15	1671.71 ± 30.24	3000	1799.61 ± 0.90	1799.88 ± 0.56	1800.17 ± 0.57
A-B'	5042.95 ± 56.89	8400.15 ± 2.97	1665.93 ± 18.55	3000	2099.82 ± 2.85	2100.23 ± 0.18	1200.09 ± 0.22
A-C'	5016.54 ± 119.68	8400.37 ± 0.78	1675.50 ± 40.46	3000	2400.22 ± 0.74	2400.07 ± 0.15	600.07 ± 0.11
A-D'	5075.64 ± 78.87	8400.55 ± 0.67	1655.47 ± 25.39	3000	2700.45 ± 0.68	2700.10 ± 0.34	0
B-A'	6734.43 ± 63.74	11200.45 ± 0.39	1663.31 ± 15.68	4000	2400.27 ± 0.30	2400.11 ± 0.15	2400.08 ± 0.11
B-B'	6601.20 ± 170.48	11200.37 ± 0.54	1697.87 ± 44.57	4000	2800.22 ± 0.51	2800.09 ± 0.13	1600.07 ± 0.16
B-C'	6598.00 ± 114.05	11199.95 ± 1.74	1697.98 ± 29.12	4000	3200.16 ± 0.79	3200.05 ± 0.89	799.74 ± 0.34
B-D'	6625.76 ± 122.30	11200.69 ± 0.87	1691.05 ± 31.27	4000	3600.37 ± 0.43	3600.32 ± 0.70	0
C-A'	8334.82 ± 116.74	14002.96 ± 3.26	1680.39 ± 23.61	5000	3000.06 ± 1.31	3001.60 ± 1.94	3001.30 ± 1.55
C-B'	8373.84 ± 61.93	14000.39 ± 3.63	1672.01 ± 12.34	5000	3499.75 ± 3.16	3500.59 ± 0.69	2000.05 ± 1.16
C-C'	8384.82 ± 148.30	13999.29 ± 3.58	1670.12 ± 29.59	5000	3997.64 ± 3.40	4001.12 ± 1.72	1000.52 ± 1.12
C-D'	8557.15 ± 246.76	13996.97 ± 21.82	1637.04 ± 49.59	5000	4499.57 ± 9.77	4497.40 ± 19.69	0

2.2. Small-scale flume experiment

The flume apparatus used in this study (Fig.1) was 2.4 m in length including 0.4 m of sediment storage. The cross section was 0.2 m in width and 0.3 m in height. Although the slope of this flume can be changed from 20° to 40° manually, we applied four slope conditions: 25°, 30°, 35°, and 40°. Between slope conditions, 35° and 40° of channel slope seem to be steep than general slope observed at channelized debris flow. However, initial part of debris flow in Korea is generally steeper than 30° and reach 40° in some case. Thus, we included those gradients of channel in experiments. In terms of measuring devices, we used two video cameras; one was installed in front of the flume to measure flow velocity, and the other was implemented beside the flume to measure flow depth. To measure the impact force of simulated debris flow, the load cell (MNC-100L, CAS), which is connected to data logger (CI-201A, CAS), was installed 0.1 m backside from the outlet.

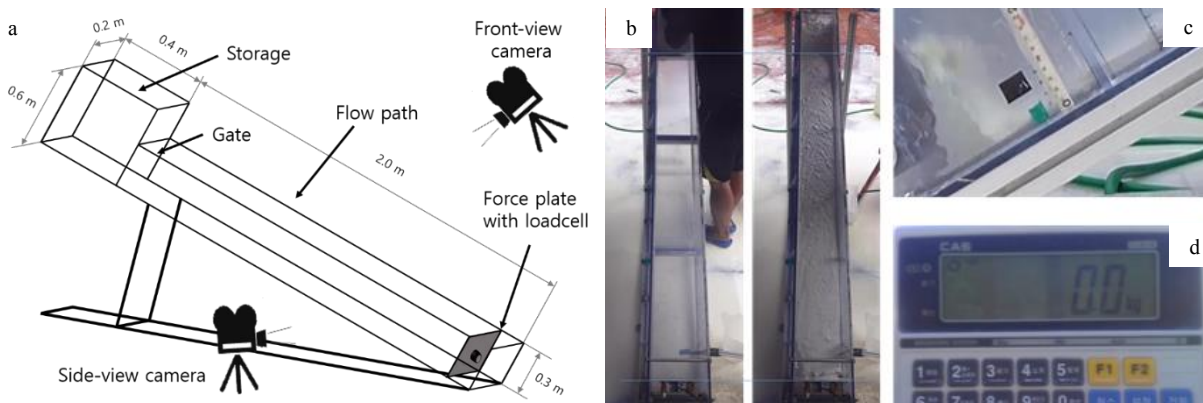


Fig. 1. (a) Experimental flume and setting up of measuring instrument, and examples of actual experiments: (b) an image from the frontal camera for flow velocity, (c) an image from the side camera for flow depth, and (d) an image of the data logger.

2.3. Experimental procedure

In each experiment, the sediment-water mixture is preliminary mixed using a mixer drill, total volume and weight of which are measured in that time. Then, the mixture was pulled in the storage, and kept being mixed just before opening the gate to minimize deposition of sediments. After the mixture prepared, the gate is opened immediately, and flow behavior (average velocity and flow depth) and impact force are measured. While conducting total sets of experiments, we carried out five replications in every combination of sediment mixture and the slope condition. After finishing experiments, flow velocity and depth were accurately calculated by analyzing the video images. By comparing each experimental condition with corresponding flow behavior, the effect of mixing ratio, total volume, and slope on flow characteristics were examined. To analyze the relationship between impact force and flow behavior, we synchronized the change of impact force and flow behavior. Then, we statistically analyzed maximum impact force, which is the maximum logged value in the data logger, and flow behavior at the time.

3. Results and Discussion

3.1. Flow behavior

As a result, flow velocity increased when the inclination of the flume increased, or the clay contents decreased (Fig. 2a). Especially, flow velocity of sediment mixture that has lower clay contents increased more drastically. Also, the effect of volume on velocity was significant; the larger mixture volume showed faster flow velocity (Fig.2b).

Higher clay contents induced stronger shear stress in the flow body, so the flow velocity tends to decrease in same slope condition. On the other hands, in steep slope condition, the difference of velocity between sediments mixture is much smaller. Assuming that simulated debris flow in this study as Bingham fluid or Herschel-Bulkley fluid (Takahashi, 2014), it seems that the acceleration of flow body is large enough to ignore yield strength of viscous debris

flow. In terms of volume, the larger volume means greater acceleration, so debris flow can move to downward much faster.

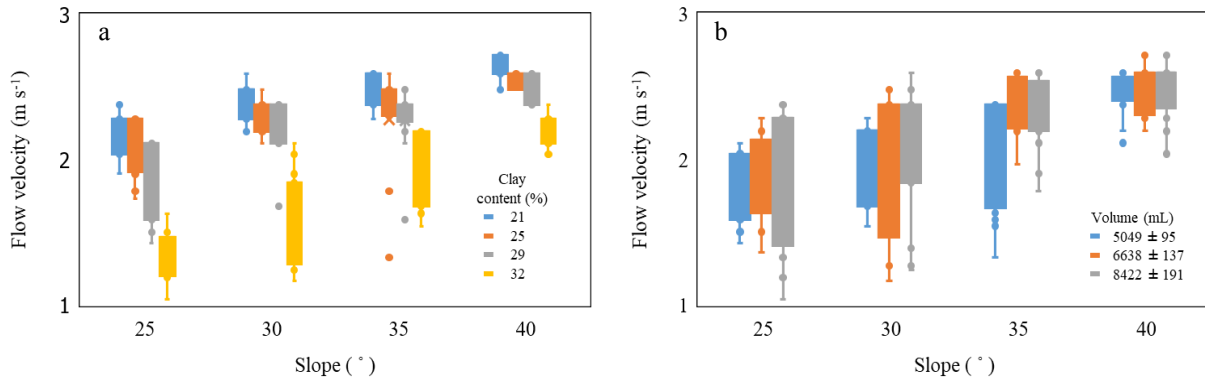


Fig. 2. The change of flow velocity according to (a) clay contents, and (b) mixture volume, as slope condition change

Flow depth was significantly correlated with mixture volume while there was no change of flow depth along slope condition (Fig. 3a). It can be interpreted that the initial volume of mixture affects flow depth dominantly than other factors. Although clay contents seemed to affect flow depth, it was not significantly different between mixture volumes (Fig. 3b).

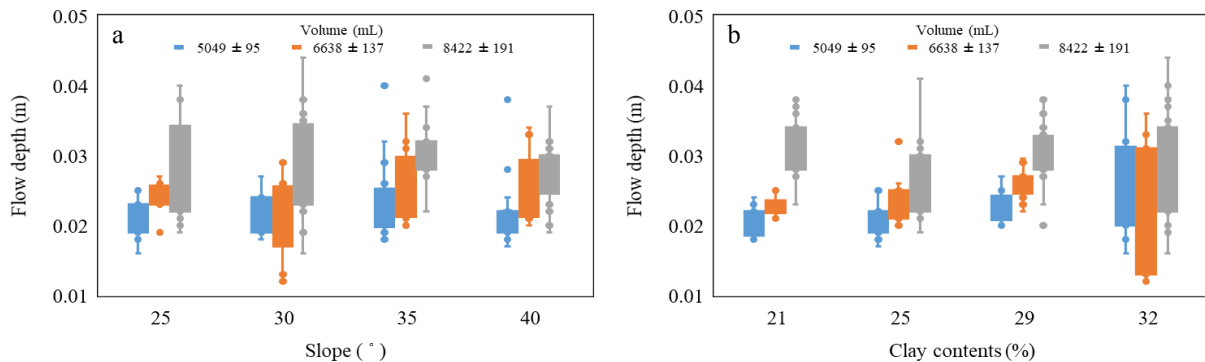


Fig. 3. The change of flow depth according to (a) flume slope, and (b) clay content, as total mixture volume change

3.2. Impact force estimation

Fig. 4 shows the analysis result of the relationship between impact force and flow velocity. Flow velocity is positively correlated to impact force, and the relationship between flow depth and impact force was also significant. With flow velocity and flow depth from flume experiments, the impact force of debris flow is well explained by hydrodynamic model (Scheidl et al., 2013). The general form of hydrodynamic model is as the following equation,

$$p_{peak} = a\rho v^2 hw \quad (1)$$

where p_{peak} is the maximum impact force (kN); ρ is the density of sediment-water mixture (kg m^{-3}); v is the flow velocity (m s^{-1}); h is the flow depth (m); w is the width of the channel (m); a is dynamic coefficient (dimensionless). Although several properties, such as the density of mixtures, are change in time and space, we used those values measured during the mixture preparation due to difficulty of installation of measuring instruments that can simultaneously measure the change of mixture property, such as density.

In terms of coefficient “ a ”, several researchers have suggested the value of a . According to Proske et al. (2011), previous studies generally have reported this value between 1.0 and 2.5. When calculating coefficient “ a ” using the

results of flume experiment and equation (1), coefficient of this research was 2.07 ± 1.38 . Especially, About 68% of calculated “a” were 1-3 in Froude number that ranged from 2 to 6, which is similar to Proske et al. (2011).

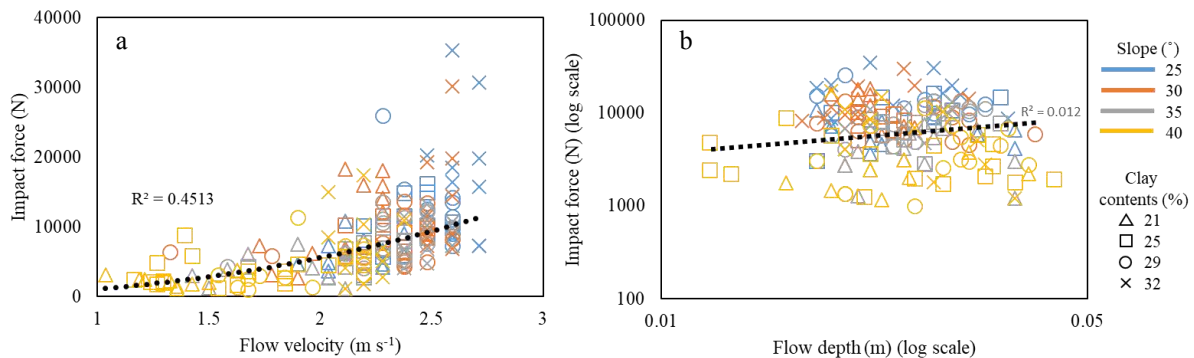


Fig. 4. The relationship between the impact force and the flow behavior; (a) flow velocity; (b) flow depth.

4. Conclusion

In this study, we conducted small-scale flume experiments to understand flow characteristics and impact force of debris flow. The flow characteristics was closely related to slope condition, sediment mixture composition, and total mixture volume. The flow velocity increased as flume slope increased, and sediment viscosity decreased caused by low clay contents. The flow depth becomes deeper in larger volume of mixtures. The impact force of debris flow was positively correlated to both the flow velocity and the flow depth, and it can be well explained by the hydrodynamic model. Using the hydrodynamic model, coefficient “a” was calculated about 2 with Froude number ranging from 2 to 6.

Acknowledgements

This study was carried out with the support of ‘R&D Program for Forest Science Technology (Project No. 2017061B10-1919-AB01)’ provided by Korea Forest Service(Korea Forestry Promotion Institute).

References

- Armanini, A., 1997, On the dynamic impact of debris flows, *in* Armanini, A., and Michiue, M., eds, *Recent Developments on Debris Flows: New York*, Springer Berlin Heidelberg, p. 208-226.
- Hübl, J., Suda, J., Proske, D., Kaitna, R. and Scheidl, C., 2009, Debris flow impact estimation. *in* Proceedings of the 11th International Symposium on Water Management and Hydraulic Engineering, Ohrid, Macedonia, September 2009, Volume 1: Skopje, University od Ss Cyril and Methodius, Faculty of Civil Engineering, p. 1-5.
- Hungr, O., Morgan, G. and Kellerhals, R., 1984, Quantitative analysis of debris torrent hazards for design of remedial measures: *Canadian Geotechnical Journal*, v. 21, no. 4, p. 663-677, doi: 10.1139/t84-073.
- Korea Forest Service, 2017, Check Dam Installation Status, http://www.forest.go.kr/newkfsweb/html/HtmlPage.do?pg=/lsls/UI_LSIS_1000_050101.html&orgId=lsls&mn=KFS_02_06_05_07_01, Accessed 31 October 2018.
- Moriguchi, S., Borja, R., Yashima, A. and Sawada, K., 2009, Estimating the impact force generated by granular flow on a rigid obstruction: *Acta Geotechnica*, v. 4, no. 1, p. 57-71, doi: 10.1007/s11440-009-0084-5.
- Proske, D., Suda, J. and Hübl, J., 2011, Debris flow impact estimation for breakers: *Georisk-Assessment and Management of Risk for Engineered Systems and Geohazards*, v. 5, no. 2, p. 143-155, doi: 10.1080/17499518.2010.516227.
- Scheidl, C., Chiari, M., Kaitna, R., Mullegger, M., Krawtschuk, A., Zimmermann, T. and Proske, D., 2013, Analysing Debris-Flow Impact Models, Based on a Small Scale Modelling Approach: *Surveys in Geophysics*, v. 34, no. 1, p. 121-140, doi: 10.1007/s10712-012-9199-6.
- Takahashi, T., 2014, *Debris flow: mechanics, prediction and countermeasures*: Boca Raton, Florida, CRC Press, p.572.
- Woo, C., Kwon, H., Lee, C. and Kim, K., 2014, Landslide hazard prediction map based on logistic regression model for applying in the whole country of south Korea: *Journal of Korean Society of Hazard Mitigation*, v. 14, no. 6, p. 117-123, doi: 10.9798/KOSHAM.2014.14.6.117.
- Yoon, S., Jang, S., Rhee, J. and Cho, J., 2017, Analysis of Future Extreme Rainfall Under Climate Change Over the Landslide Risk Zone in Urban Areas: *Journal of the Korean Society of Hazard Mitigation*, v. 17, no. 5, p. 355-367, doi: 10.9798/KOSHAM.2017.17.5.355.

The vibrational characteristics of debris flow in Taiwan

Yi-Min Huang^{a,*}, Yao-Min Fang^b, Hsiao-Yuan Yin^c

^aDept. of Civil Engineering, Feng Chia University, 100 Wenhwa Rd., Taichung, 407, Taiwan, R.O.C.

^bGIS Research Center, Feng Chia University, 100 Wenhwa Rd., Taichung, 407, Taiwan, R.O.C.

^cSoil and Water Conservation Bureau, No.6, Guanghua Rd., Nantou City, Nantou, 540, Taiwan, R.O.C.

Abstract

Debris flows have become a common disaster in Taiwan in recent years since the impacts of extreme weathers has been aggravated. To protect people from the debris-flow disasters, a monitoring and warning system was developed by Soil and Water Conservation Bureau (SWCB) in Taiwan. The rainfall-based criteria are used in Taiwan for debris flow warning. Different to rainfall measurement, the ground surface vibrational signal from a debris flow has been studied more widely in recent years. Sensors of geophone (short period seismograph) and broadband seismograph are commonly used for debris flow monitoring. In this paper, the signal analysis of debris flows was performed by calculating the vibrational energy. The comparison of the analysis results indicated that when the energy ratios of at least two of the axes are greater than 1.12, a debris flow is highly likely to occur. The starting point in the increasing trend of vibrational energy implied the possible warning time point for debris flow. Vibration examples of debris flow and earthquakes were also compared in this paper.

Keywords: debris flow; vibrational energy; signal analysis; geophone

1. Introduction

According to World Bank reports (Dilley et al., 2005), Taiwan is classified as a high-risk area of many types of natural hazards. Among the natural hazards, the slope-related hazards, landslides and debris flows, are the two most serious disasters to people in Taiwan (Huang et al., 2016). With the increasing impacts of climate change and extreme weathers, Taiwan has suffered more from seasonal heavy rainfalls and typhoons than usual. To protect people from the impacts of debris flows, Taiwan government, Soil and Water Conservation Bureau (SWCB), started to build debris-flow monitoring stations and a warning system since 2002. Currently there are 19 debris-flow monitoring stations in Taiwan. Most of the stations are located in central Taiwan.

The warning system developed by SWCB for debris-flow disasters was primarily based on the estimation and prediction of rainfalls. The warning model was derived from researches in which the rainfall was widely used as the major triggering factor for debris flows (Jan et al., 2003; Jan and Lee, 2004; Lee 2006). The measurement of rainfall, however, is an indirect measurement of debris flows (Huang et al., 2013). The rainfall warning is useful for disaster response but usually results in "false alarms". Another measurement used to identify the occurrence of debris flows was to apply geophone (short period seismograph) and broadband seismograph (Chu et al., 2014; Huang et al., 2012), which are direct measurements of debris flows (Huang et al., 2013). Geophones and broadband seismographs detect the ground surface vibrations generated by the movement of a mixture of rocks, gravels, and soil within a debris flow. The vibration signals of debris flows cases in Shenmu, Taiwan, were used and analyzed in this paper to discuss the characteristics of debris flows. The energy of debris-flow vibrational signals was the focus of discussion in this paper.

* Corresponding author e-mail address: ninerh@mail.fcu.edu.tw

2. Study Area and Case Histories

The Shenmu Debris-Flow Monitoring Station is located at the Shenmu Village in central Taiwan, where debris flows frequently occur (Lee et al., 2014). The local village is adjacent to the confluence of three high-potential debris-flow torrents: Aiyuzi Stream (DF226), Huosa Stream (DF227) and Chushuei Stream (DF199). Table 1 summarizes the environment of the Shenmu area and Fig. 1 shows the terrain of the three aforementioned streams. The length of streams and catchment areas are summarized in Table 2, as well as the landslide areas at Shenmu area after 2009. In Shenmu, the debris flows commonly occur at the Aiyuzi Stream due to its shorter length and large landslide area located in its upstream (Huang et al., 2013). Some of the debris flows that happened in the Aiyuzi Stream, along with other debris flows that transpired in the Shenmu area, were considered for this paper. Table 3 contains a list of debris-flow occurrences in the Shenmu area.

Table 1. Environment of Shenmu Monitoring Station (Huang, et al., 2013)

Location	Shenmu Village, Nantou County	Debris Flow No.	DF199, DF227, DF226
Catchment	Zhuoshui River	Streams	Chusuei, Huosa, Aiyuzi
Debris Flow Warning Threshold	250 mm	Hazard Type	Channelized debris flow
Monitored Length	5.518 km	Catchment Area	7,216.45 ha (Shenmu)
Geology	Neogene sedimentary rock	Slope at Source	30~50°
Landslide area	Large, $1\% \leq$ landslide ratio $\leq 5\%$	Sediment	Average debris material size: 3''-12''
Vegetation	Natural woods, medium sparse	Damaged by	debris, overflow
Engineering Practice	None	Priority of Mitigation	High
Station Elevation	1,187 m	Coordinate (TWD97)	X: 235367 Y: 2602749
Protected Targets	Residents > 5 households	Facility	Transportation roads, bridges
		school	

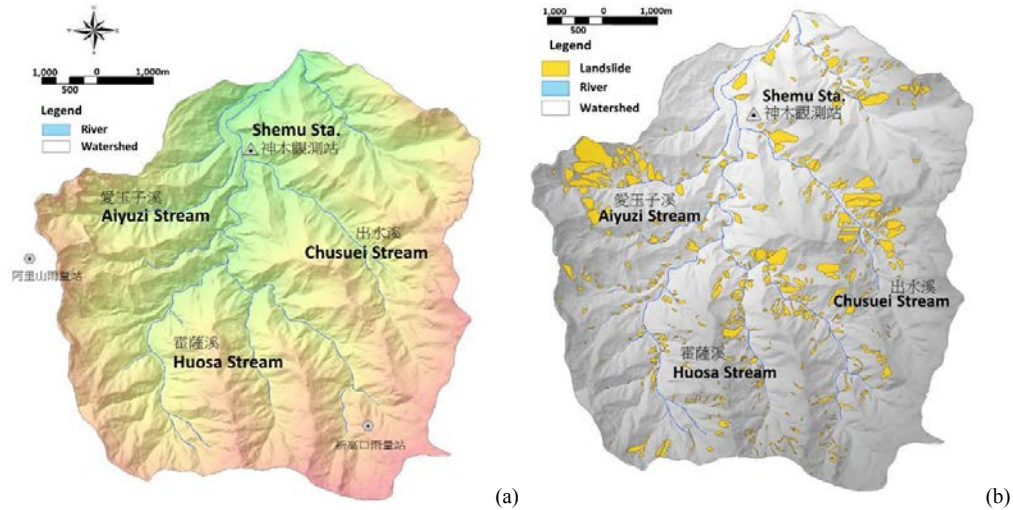


Figure 1. The terrain (a) and landslide areas (b) of Shenmu area. (Lei et al., 2014)

Table 2. The landslide area in Shenmu after 2009 (Huang, et al., 2013)

Debris Flow No.	Stream	Length (km)	Catchment Area (ha)	Landslide Area (ha)
DF199	Chusuei Stream	7.16	861.56	33.29
DF227	Huosa Stream	17.66	2,620	149.32
DF226	Aiyuzi Stream	3.30	400.64	99.85

Table 3. Debris flow hazard history of Shenmu (after Huang, et al., 2013)

Date	Event	Location (stream)	Occurrence	Hazard Type
2004/6/11	-	Aiyuzi	16:42	debris flow
2004/7/2	Typhoon Mindulle	Aiyuzi	16:41	debris flow
2005/7/19	Typhoon Haitang	Chusuei, Aiyuzi	-	flood
2005/8/4	Typhoon Matsa	Chusuei, Aiyuzi	-	flood
2005/9/1	Typhoon Talim	Chusuei, Aiyuzi	-	flood
2006/6/9	0609 Rainfall	Chusuei, Aiyuzi	about 08:00	debris flow
2007/8/13	0809 Rainfall	Chusuei	-	flood
2007/8/18	Typhoon Sepat	Chusuei	-	flood
2007/10/6	Typhoon Krosa	Chusuei	-	flood
2008/7/17	Typhoon Kalmaegi	Chusuei	-	flood
2008/7/18	Typhoon Kalmaegi	Aiyuzi	-	flood
2009/8/8	Typhoon Morakot	Chusuei, Aiyuzi, Huosa	08:00 (landslide) 16:57 (debris flow)	landslide, debris flow
2010/9/19	Typhoon Fanapi	Huosa	-	flood
2011/7/13	-	Aiyuzi	14:33	debris flow
2011/7/19	0719 Rainfall	Aiyuzi	03:19	debris flow
2011/11/10	1110 Rainfall	Aiyuzi	13:17	debris flow
2012/5/4	0504 Rainfall	Aiyuzi	15:56 16:09	debris flow
2012/5/20	-	Aiyuzi	8:15	flood
2012/6/10	0610 Rainfall	Aiyuzi	10:34 15:14	debris flow
2012/6/11	0610 Rainfall	Chusuei	17:08	flood
2013	0517 Rainfall	Aiyuzi	07:02 (May 19)	debris flow
2013	Typhoon Saulik	Aiyuzi	06:54 (July 13)	debris flow
2013	Typhoon Trami	Aiyuzi	22:41 (Aug. 21)	flood
2014	0520 Rainfall	Aiyuzi	12:53 (May 20)	debris flow
2017/6/01	0601 Rainfall	Aiyuzi	11:40 (June 02)	debris flow

3. Shenmu Debris-Flow Monitoring Station

The Shenmu monitoring station includes sensors and instruments including a rain gauge, water level meter, wire sensor, soil water moisture sensor and CCD camera. The station has a data center to receive and transmit debris-flow information from the site to the emergency operation center (EOC). Fig. 2 shows the monitoring layout at Aiyuzi Stream and the other two streams. Among these sensors, the rain gauges measure the rainfall, a major cause of debris flow, in real-time manner and are usually used for warning criteria. The wire sensors, geophones and broadband seismographs function as indicators when a debris flow actually occurs. Unlike the other sensors, the CCD camera is used for identifying, in real-time, if a triggered warning is a "false alarm" or a real debris flow. The camera is also used to capture images of the debris flow.



Figure 2. Shenmu Debris-Flow Monitoring Station, Shenmu, Nantou, Taiwan.

4. Characteristics of Vibration Signals

The events in Table 4 were used for signal analysis and discussion in this paper. Two earthquake events were included in order to compare the signal characteristics with those of debris flows. The signal was studied and analyzed by means of time-series data (original velocity records), Fast Fourier Transform (FFT), and Gabor Transform (Huang et al., 2016). Typical vibrational signal in the time-domain is illustrated in Fig. 3. The vibrational signal of Hualien Earthquake event is shown in Fig. 4. It is noted that the signal patterns of debris flow and earthquake are different. Earthquake signals had more apparent and intensive responses than a debris flow in the low frequency range (i.e., less than 5 Hz). This is because an earthquake usually generates stronger energy and the vibration propagates a longer distance than a debris flow.

Table 4. Events selected for analysis.

Year	Event	Max. hourly rainfall (mm)	Flow speed (m/s)	Warning announced*	Debris flow arrived**	Debris Flow?	Debris Flow Scale	Used for analysis (G or BS)****
2011	1110 Rainfall	17	1.77	13:18	13:29	Y	medium	G
2012	0504 Rainfall	11.5	NA	NA	16:09	Y	small	G
2013	0517 Rainfall	45.5	NA	NA	07:02	Y	medium	G
2013	0530 Heavy Rainfall	15	~1.0	NA	~15:24	Y	small	BS
2013	Typhoon Saulik	51.5	8.52	6:47	6:54	Y	large	G & BS
2014	0520 Heavy Rainfall	39.5	4.87	NA***	12:53	Y	medium to large	G & BS
2017	0211 Tainan 2/11 Earthquake ^a (01:12)	NA	NA	NA	NA	N	NA	G
2018	0206 Hualien 2/06 Earthquake ^b (23:50)	NA	NA	NA	NA	N	NA	G&BS

*, **: the time recorded based on the geophone at the upper stream of Aiyuzi River. ***: communication unstable, no records.

****: G for geophone (GS-20 DX) and BS for broadband seismograph (Yardbird DF-2)

a: epicenter at (22.87N, 120.14E), M=5.7 (Richter scale), distance to Shenmu station is about 103,394 m.

b: epicenter at (24.10N, 121.73E), M=6.2 (Richter scale), distance to Shenmu station is about 109,231 m.

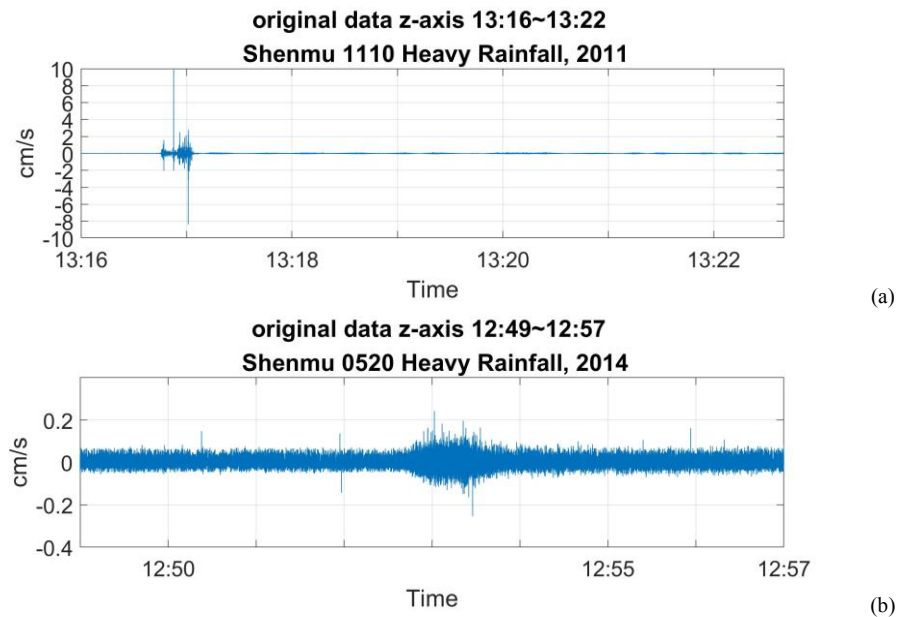


Fig. 3. Comparison of original signals of geophone. (a) Nov. 10, 2011 (b) 0520 Rainfall (after Huang et al., 2017).

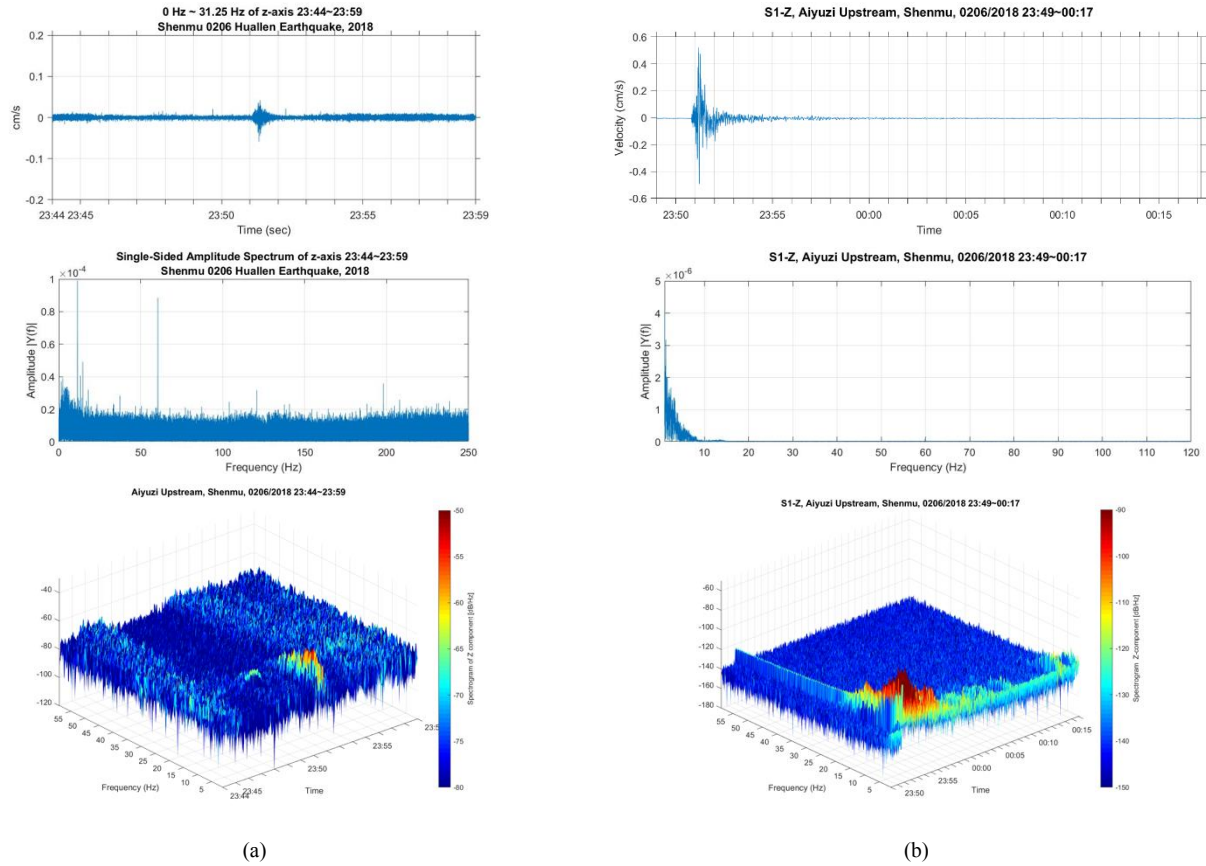


Fig. 4. Vibration signals of 0206 Hualien Earthquake at Aiyuzi stream, Shenmu (a) geophone (b) broadband seismograph

The vibrational signal of ground surface is used for debris flow monitoring more widely than before in recent years. The major goal is to understand the characteristics of debris-flow signals and to be used for debris flow warning if possible. For this attempt, Huang et al. (2017) studied the in-situ data and pointed out that the intensity of frequency of 0~10 Hz reflects longer periods of signals observed usually a few minutes earlier than debris flows reached the location of geophones in some cases. However, the capability of capturing the low frequencies requires expensive high-resolution sensors, and this may not applicable in most cases. Therefore, another approach of estimating the energy of signals was tried and proposed to help debris flow early warning. Fig. 5 shows the energy per second estimated from the vibrational signals and energy per minute for signals of 0~31.25 Hz. It is obvious from the figure that peaks are at time close to the arrival of debris flow (jumps in the figure), in both time series of signal and energy. Also, the energy increases before reaches the peak. This finding provides a hint to determine if a debris flow is coming by calculating the change of vibrational energy with time. The energy change, i.e., the energy ratio in this study, was estimated by simply comparing the current vibrational energy with the background average value. The background average energy was defined as the average energy of all available data before the time point after which the vibrational energy started to rise clearly. For the purpose of early warning, different time steps of 10, 20, and 30 second were used to calculate the energy ratio.

Table 5 shows the accumulated signal energy ratios from signals of 0~31.25 Hz and original signals. The higher ratios in the table indicated larger debris-flow scale, which was compliance with observations. The ratio of accumulated energy also implies that when the energy ratios of X, Y, Z axes are all or two of them greater than 1.12, a debris flow is highly likely to occur. Fig. 6 shows examples of vibrational energy of different time steps. It is noted that there is an increasing path of energy in all time-step estimates. The increasing path is useful to determine the tuning time point on which the early warning is based. Compared to the debris flow events, there were peaks of the vibrational signal energy of earthquakes (Fig. 6), but these are “lonely” peaks, indicating an abrupt jump without an increasing trend in time. The case of 0517 Rainfall in 2013, however, is an exception that has energy ratios of about

1.0, different to others in Table 5. This can be explained by the signal data in which there is no obvious peak in the energy time series (Fig. 7).

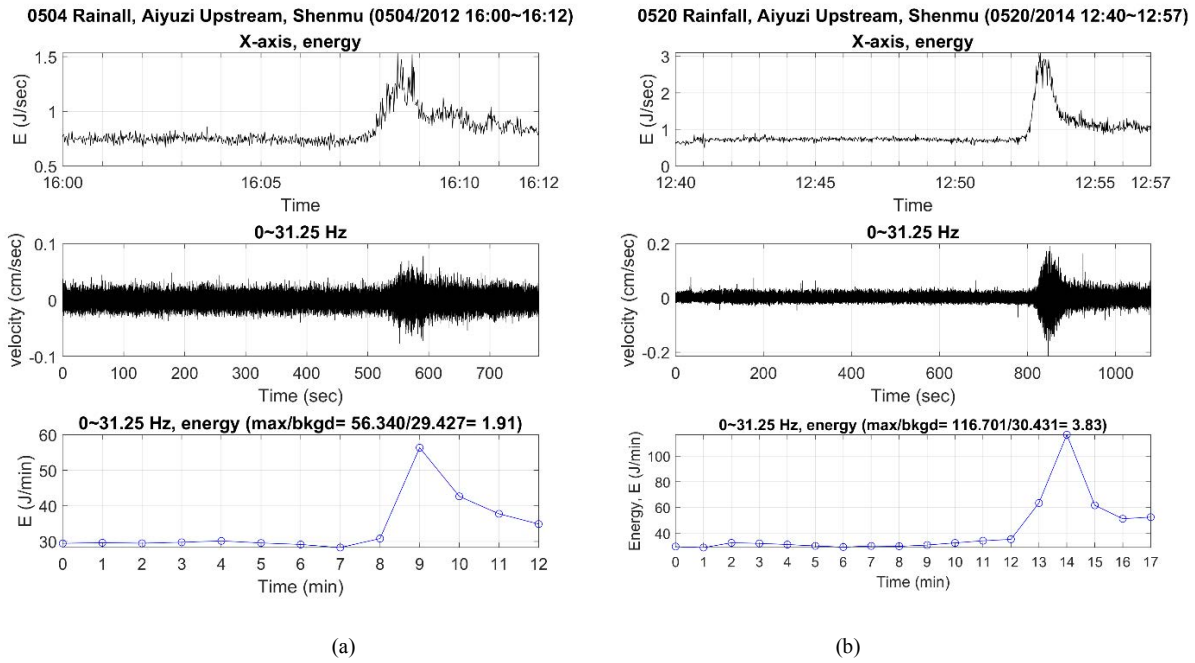


Fig. 5. Energy of vibrational signals (a) 0504 Rainfall in 2012 (b) 0520 Rainfall in 2014.

Table 5. Accumulated Signal Energy Ratio (geophone at Aiyuzi upstream, Shenmu)

Year	Event (date)	0~31.25 Hz Energy		0~250 Hz Energy Ratio*, per time step			
		Ratio*, per min.	axis	10 sec	20 sec	30 sec	
2011	1110 Rainfall (11/10)	X**	2.70	X	9.49	5.95	4.08
		Y**	3.52	Y	19.92	11.42	7.80
		Z**	2.40	Z	4.94	3.43	2.38
2012	0504 Rainfall (5/04)	X	1.91	X	1.67	1.65	1.60
		Y	1.21	Y	1.15	1.13	1.12
		Z	1.03	Z	1.03	1.03	1.03
2013	0517 Rainfall (5/17)	X	1.01	X	1.01	1.01	1.01
		Y	1.07	Y	1.07	1.04	1.01
		Z	1.03	Z	1.11	1.05	1.02
2013	Typhoon Saulik (07/13)	X	284.91	X	176.06	163.72	143.78
		Y	255.05	Y	142.53	122.82	123.89
		Z	105.10	Z	60.80	56.53	63.48
2014	0520 Heavy Rainfall (05/20)	X	3.83	X	3.83	3.83	3.70
		Y	2.45	Y	2.46	2.43	2.35
		Z	6.01	Z	6.02	5.96	5.91
2017	Tainan Earthquake (02/11)	X	1.54	X	2.16	1.67	1.48
		Y	1.24	Y	1.38	1.21	1.19
		Z	1.47	Z	1.79	1.49	1.33
2018	Hualien Earthquake (02/06)	X	3.16	X	3.25	2.48	2.30
		Y	1.69	Y	1.78	1.53	1.55
		Z	2.51	Z	2.45	2.04	2.05

*Energy Ratio = max. value / background value **X and Y axes are plane directions perpendicular and parallel to the flow directions, respectively, and Z axis is the vertical direction perpendicular to X-Y plane.

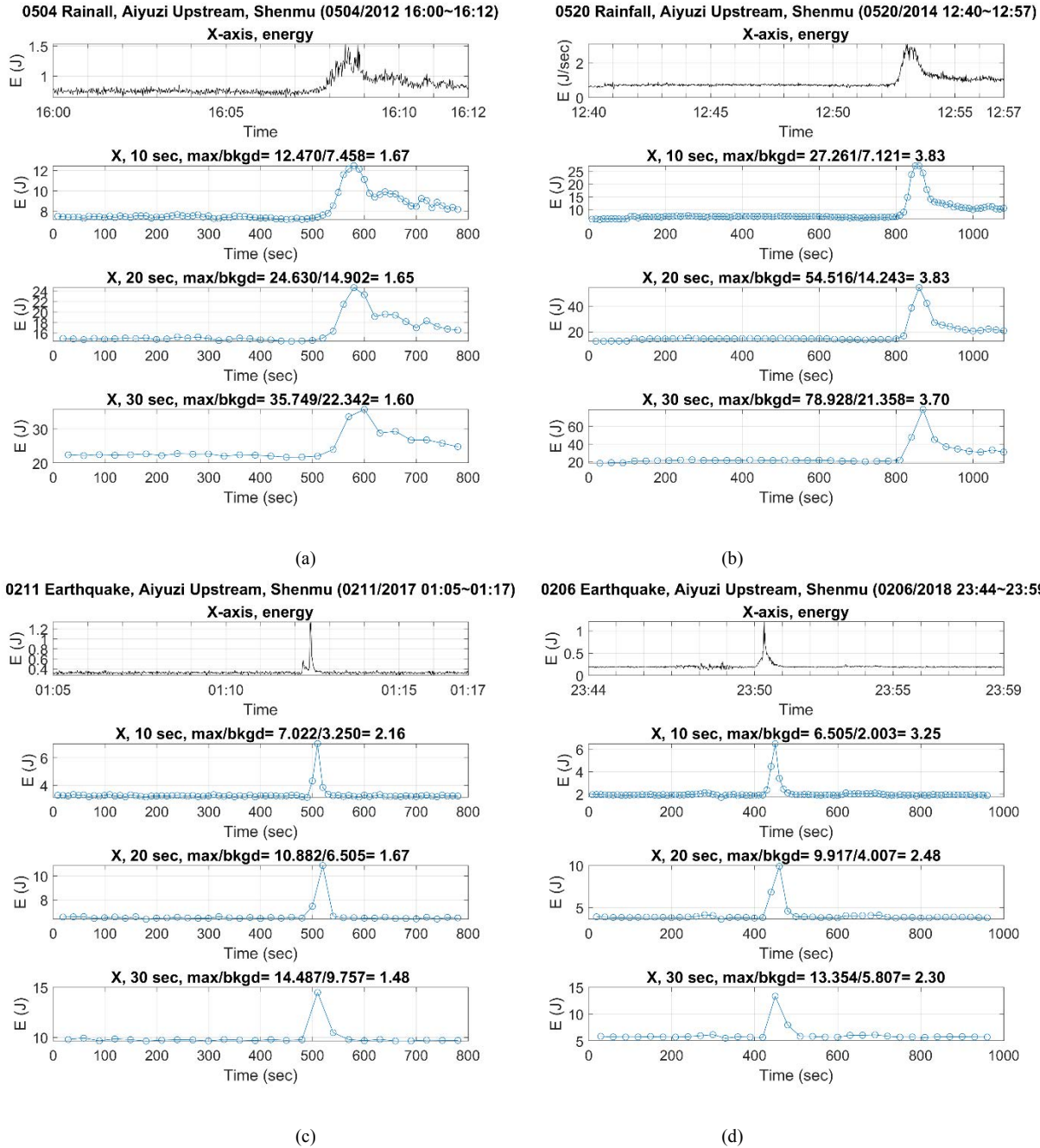


Fig. 6. Signal energy of study cases. (a) 0504 Rainfall, 2012 (b) 0520 Rainfall, 2014 (c) 0211 Tainan Earthquake, 2017 (d) 0206 Hualien Earthquake, 2018

5. Conclusion

This study evaluated the vibration signals of debris flows and earthquakes observed in Shenmu area. The characteristic frequency of debris flow is in the range of 0~31.25 Hz. In contrast with the debris flow, the characteristic frequency of earthquake is in the lower range of 0~10 Hz. The cumulative signal energy intensity was studied and found to be useful in determine the status of debris flow. A debris flow was highly likely to occur when the energy ratio of axes (X, Y, Z) are or two of them greater than 1.12, based on the cases in this paper. It is also noted that the increasing path of accumulated energy based on different time steps was useful to determine the turning time point.

The findings of energy ratio, in association with frequency characteristics, was practically promising for debris flow monitoring.

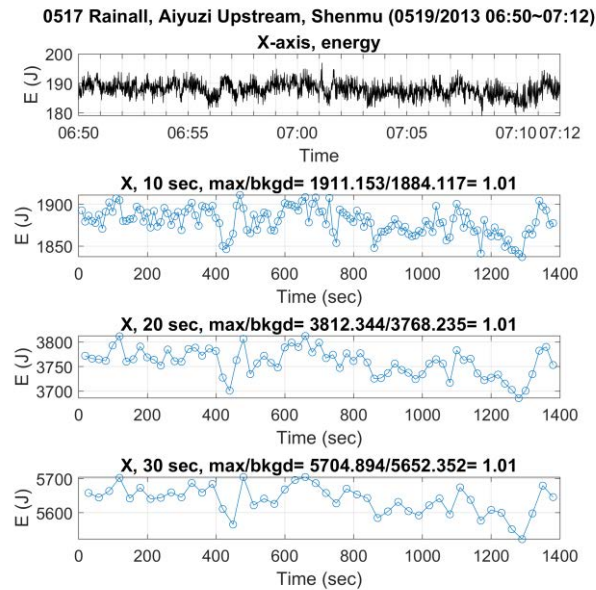


Fig. 7. Signal energy of 0517 Rainfall, 2013

Acknowledgements

This research was partly supported by the Soil and Water Conservation Bureau, Council of Agriculture, Executive Yuan, Taiwan. Thanks to Gau-Hao Huang, Chun-Ju Wang, and all other people providing help on this study.

References

- Dilley, Maxx; Chen, Robert S.; Deichmann, Uwe; Lerner-Lam, Arthur L.; Arnold, Margaret; Agwe, Jonathan; Buys, Piet; Kjevstad, Oddvar; Lyon, Bradfield; Yetman, Gregory. 2005. Natural disaster hotspots: A global risk analysis (English). Washington, DC: World Bank.
- Fang, Y.M. et al., 2008, Analysis of Debris Flow Underground Sound by Wavelet Transform-A Case Study of Events in Aiyuzih River, Journal of Chinese Soil and Water Conservation, CSWCS, 39(1), p. 27-44.
- Huang, Y.M., Chen, W.C., Fang, Y.M., Lee, B.J., Chou, T.Y., Yin, H.Y., 2013, Debris Flow Monitoring – A Case Study of Shenmu Area in Taiwan, Disaster Advances, 6(11), p. 1-9.
- Huang, Y.M., Chu, C.R., Fang, Y.M., Tsai, M.C., Lee, B.J., Chou, T.Y., Lee C.Y., Chen, C.Y., and Yin, H.Y., 2016, Characteristics of debris flow vibration signals in Shenmu, Taiwan, in Proceedings, Interpraevent International Symposium 2016, Lucerne, Switzerland.
- Huang, Y.M., Fang, Y.M., Chou, T.Y., Lee C.Y., Yin, H.Y., 2017, The Vibration Signal Analysis of Debris Flow in Taiwan, in Proceedings, 5th International Conference on Geotechnical Engineering for Disaster Mitigation and Rehabilitation, Taipei, Taiwan, Sep. 13-14.
- Jan, C.D., Lee, M.H., Huang, T.H., 2003, Effect of Rainfall on Debris Flows in Taiwan, in Proceedings of the International Conference on Slope Engineering, Hong Kong, 2, p. 741-751.
- Jan, C.D. and Lee, M.H., 2004, A Debris-Flow Rainfall-Based Warning Model, Journal of Chinese Soil and Water Conservation, CSWCS, 35(3), p. 275-285.
- Lei, T.-C., Huang, Y.-M., Lee, B.-J., Hsieh, M.-H., Lin, K.-T., 2014, Development of an Empirical Model for Rainfall-induced Hillside Vulnerability Assessment- A Case Study on Chen-Yu-Lan Watershed, Nantou, Taiwan, Natural Hazards, 74(2), pp. 341-373.
- Lee, M.H., 2006, A Rainfall-Based Debris Flow Warning Analysis and Its Application, [Ph.D. Thesis]: National Cheng Kung University, Taiwan.
- Lee, B.J. et al., 2015, The 2015 On-site Data gathering and Monitoring Station Maintenance Program, Project Report, Soil and Water Conservation Bureau, 476 p.

Monitoring and modeling of debris-flow surges at the Lattenbach creek, Austria

Johannes Huebl^a, Muniyuki Arai^b, Roland Kaitna^{a,*}

^a University of Natural Resources and Life Sciences, Peter Jordanstr. 82, 1190 Vienna, Austria

^b Mejo University, Adress, Japan

Abstract

Debris-flow events are often comprised by a sequence of surges, sometimes termed roll waves. The reason for this surging behavior is still a matter of debate. Explanations include the growth of hydraulic instabilities, periodic sediment deposition and release, or grain size sorting. Also, the shape and the velocity of single surges and the implications for hazard mitigation are hard to predict. Here we present results of several years of monitoring debris-flow events at the Lattenbach creek (AUT). The monitoring system includes radar sensors for measuring flow depth at different locations along the channel, as well as a 2-D rotational laser sensor installed over a fixed cross-section that yields a 3-D surface model of the passing debris-flow event. We find that the debris flows at Lattenbach creek exhibited surges for each observed event. The celerity of the surges were up to twice as high as the front velocity. Often, the first surges had highest flow depth and discharge, and showed an irregular geometry. Video recordings reveal that this might be connected to the presence of large boulders and woody debris. On the contrary, the shape of the surges in the second half of the flow, which carried smaller grain sizes and less woody debris, were rather regular and showed a striking geometric similarity, but still high velocities. We tested a recently derived wave equation based on hydraulic theory and found that the shape of these regular roll waves can be reasonably reproduced by that model. The results of our monitoring efforts aim to improve our understanding of the surging behavior of debris flows and provide data for model testing for the scientific community.

Keywords: debris-flow surges, roll waves, 2-D laser, wave equation

1. Introduction

Debris flows are commonly described as one or more surges of unsorted sediment and water, sometimes having steep, granular front followed by an more dilute body (e.g. Stiny, 1910; Pierson 1986; Marchi et al., 2002; McArdeell et al., 2007; McCoy et al., 2013; Okano et al., 2012; Comiti et al., 2014). A hydraulic approach to explain the development of several surges is based on the observation that in steady uniform flows small perturbations can amplify without external forcing to create roll waves when a certain flow intensity threshold is exceeded (Dressler, 1949). Concepts based on hydraulic theory were applied to Newtonian (Dressler, 1949), non-Newtonian (e.g. Ng and Mei, 1994; Zanuttigh and Lamberti, 2007; Longo, 2011; Arai et al., 2013), and granular flows (e.g. Forterre and Pouliquen, 2003; Di Cristo et al., 2009).

Another explanation for the development of surges in flowing debris is connected to the two-phase nature of debris flows. By dynamic grain size segregation (Johnson et al., 2012), patches of coarse sediment might develop. These regions of higher flow resistance progressively grow to form wave fronts, which ultimately might de-couple from the flow ahead. Iverson et al. (2010) described this mechanism for roll waves developing during large-scale debris-flow experiments.

In natural channels, surge development might also be connected to discrete sediment input from landslides or bank failure, and/or channel bed erosion. In a study combining high-resolution hydrologic and geomorphic monitoring data

* Corresponding author e-mail address: roland.kaitna@boku.ac.at

in a recently burned watershed, McGuire et al. (2017) conclude that the mechanism for debris-flow surge initiation is likely connected to en-mass failure of sediment stores that were periodically deposited in the channel during a storm event (cf. the sediment capacitor model of Kean et al., 2013).

Independent of the initiation mechanism surges traveling downstream typically show non-equal velocities (“celerities”) and are often faster than the mean velocity of the debris flow, which is close to the front velocity. Therefore fast surges may cannibalize slow ones and eventually may overtake the front of the flow. This leads to a continuous change of the stage hydrograph. Field data on surge development, surge celerities and shapes are rare (cf. review by Zanuttigh and Lamberti, 2007), and there are also only few approaches to model the downstream deformation of single waves (Arai et al., 2014). In this contribution we present and analyze monitoring data of observed debris flows from 2015 to 2017 at Lattenbach creek, Austria.

2. Study area

The Lattenbach creek is a tributary to the Sanna river in the western part of Austria (Tyrol province). The Lattenbach drains an area of about 5.3 km², flows through the village of Grins and confluences with the Sanna river at the community Pians (Fig 1a). The watershed is located at the transition between the so-called crystalline Alps and limestone formation of the northern Alpine chain. This tectonically heavily stressed and rugged terrain has deep seated landslides, constantly feeding the channel with fresh sediment. This geomorphological activity is expected to be connected to the frequent occurrence of debris flows in the watershed.

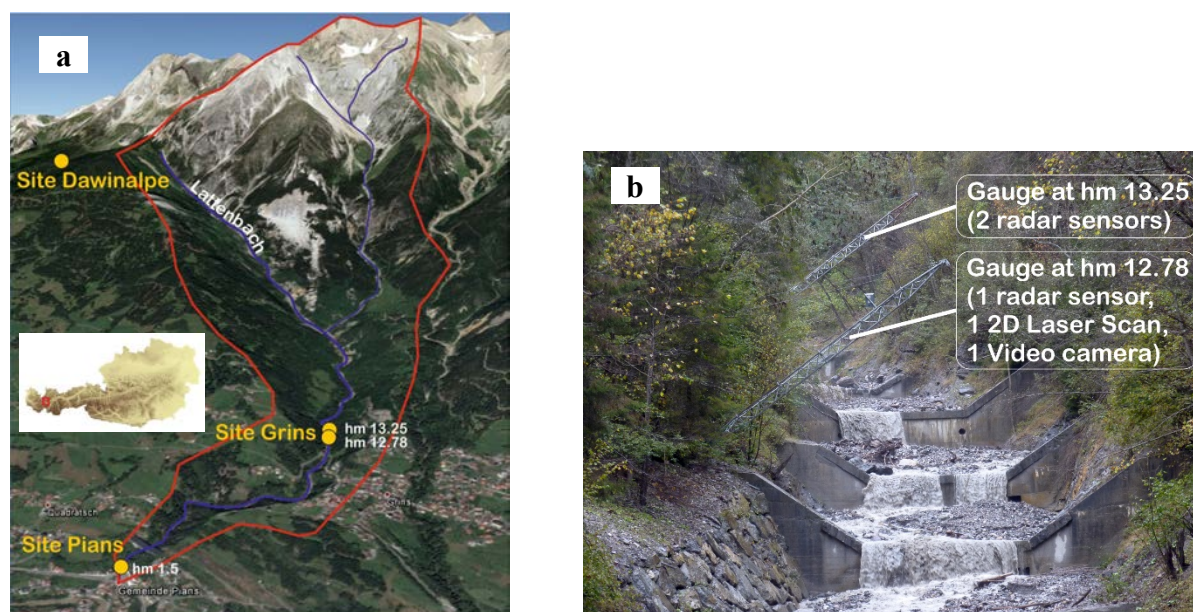


Fig. 1. (a) Overview and location of the study site Lattenbach; (b) photo of the monitoring site Grins.

3. Methods

A meteorological station is located around 300 m west of the Lattenbach catchment at an altitude of 1820 m a.s.l. The measured parameters at site Dawinalpe include temperature, humidity, radiation, snow height, and rainfall. Rainfall data was recorded at an interval of 10 min. A channel monitoring system was installed at two locations at the lower reach of the channel. Over the years several modifications were made to improve the system. Here we describe the most recent configuration. Site Grins (Fig 1b) is located about 1.3 km upstream of the confluence with the Sanna river at the end of a reach of check dams and consists of two radar distance sensors (S1 and S2) for measuring flow height (type Vegapuls WL 61, accuracy +/- 2 mm), a rotational laser scanner (type Sick LMS511-20190, accuracy +/- 3 %), and a digital video camera (type Mobotix M16). The measurement frequency of the radar sensors is 2 Hz and

that of the rotational laser scanner 36 kHz, with a rotation rate of 25 per second. The laser scanner data was binned at 0.25° intervals and averaged over five consecutive rotations, yielding five data points per bin per second. After transformation into Cartesian coordinates, mean values over one second were computed for better visualization. The distance between S1 and S2 is 47 m. Since all sensors are located at the overflow section of a check-dam, channel erosion is limited to the height of temporary minor deposits from fluvial bedload transport. The laser sensor is installed at the same location as the upstream sensor S1. At the channel banks additionally seismic sensors (types Sercel SG-5, Lennartz electronics LE-IDV; sampling rate 100 Hz) were installed.

To record the wave deformation over an extended distance, site Pians was installed 1.14 km downstream of station Grins, at a location 0.15 km upstream of the confluence with the Sanna river. Only one flow depth sensor S3 (type Sommer UPM-10, accuracy ± 10 mm) with a measurement frequency of 2 Hz and a digital video camera (type Mobotix M16) was installed. The monitoring system is triggered when one of three conditions are met: a voltage signal from a ripcord upstream of the station Grins, a seismic threshold at Grins, or a flow depth threshold 0.5 m at S1. The front velocity and the celerity of single surges was estimated by manually determining the travel time of the front and the peaks of the surges between sensors S1 and S2. Additionally, surface velocity was measured with a high-frequency Doppler radar system (HF radar, IBTP Koschuch), which was tested and described in Huebl et al. (2018). Based on the fixed cross-section shape, measured hydrograph and estimated front and surge velocities, the discharge and the total volume have been estimated.

4. Results

4.1. Debris flows 2015-2017

Between 2015 and 2017 six debris-flow events were registered, with two events occurring on the same day (August 9th, 2015). All of the events were triggered by convective rainfall events, with (measured) precipitation durations at site Dawinalpe between 30 and 120 minutes and precipitation sums between 4 and 24 mm (Fig 2). All of the events displayed several surges, with a maximum of more than 50 surges for the event on September 10th, 2016. For three out of six events the maximum peak discharge was associated with the first surge and were estimated with 47, 60, and 65 m³/s. The maximum observed peak discharge was registered for the event in 2016, with 143 m³/s, exceeding the engineering design discharge of the 150 year flood event (~ 30 m³/s) more than four times. We do not find a correlation between rainfall volume and total event volume.

4.2. Debris-flow event on September 10th, 2016

For the debris-flow event in 2016 we counted more than 50 surges. The combined information of cross-sectional flow depth variations (3-D hydrograph, Fig 3) and surface velocity with time shows that a sequence of very irregular surges with a wide variety of surface velocities ($t \sim 3250 - 3900$ sec) is followed by a period of relative regular surges with velocities around 8 m/s and inter-surge velocities < 1 m/s ($t \sim 3900 - 4330$). The time refers to the start of data recording at around 6:00 pm. The debris-flow event lasted another 30 minutes with some minor surges and generally a more uniform flow depth and surface velocity as shown in Fig 3.

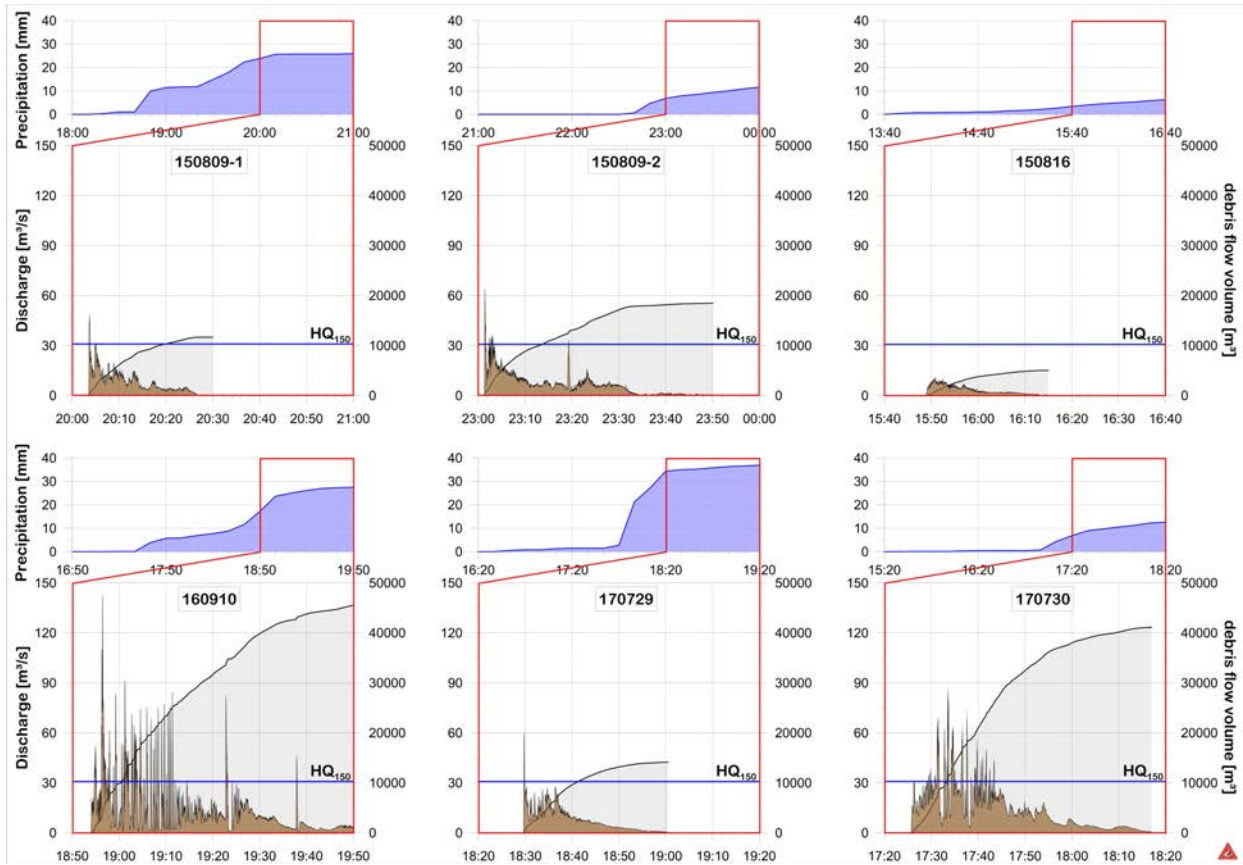


Fig. 2. Overview of debris-flow stage hydrographs, recorded rainfall sums and calculated cumulative debris-flow volumes at the Lattenbach creek for the period 2015-2017. The value of $HQ_{150} = 30 \text{ m}^3/\text{s}$ is based on an engineering hydrological assessment by public authorities.

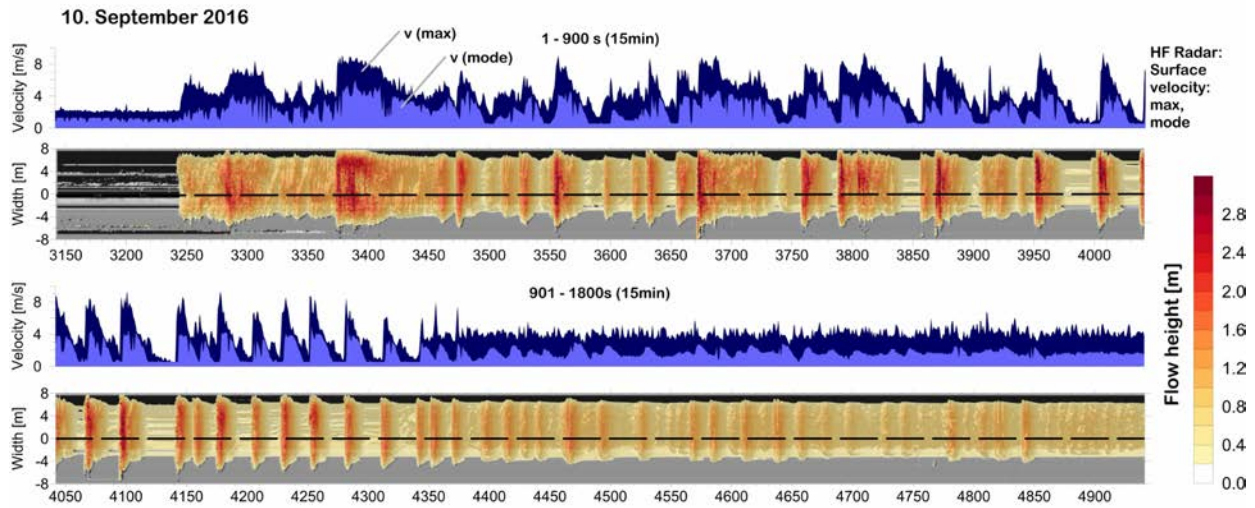


Fig. 3. 3-D hydrograph and surface velocity of surges of the debris-flow event at Lattenbach on September 10th, 2016.

In Fig 4 we compare the hydrographs measured at site Grins (S1) with the hydrograph measured at site Pians (S3), which is 1.14 km downstream of Grins. The mean travel time of the front was about 4 min and 16 sec, yielding a mean front velocity of 4.5 m/s. The manually derived celerity of the surges at site Grins varied between 4 and 12 m/s (Fig 4a). It is interesting to see that the fast moving surges eventually merged with preceding slower ones, leading to one big first surge that seemed to be slightly detached from the rest of the flow (Fig 4a-b). The tail of the flow again displays rather regular surges, but with a reduced number. The generally high flow height at site Pians can be explained by the bedrock reach at Pians, which is much more narrow compared to the cross section at site Grins. To test the self-similarity of the shapes of surges we overlaid the regular, non-coalescing surges in the back of the flows at both sites. We find that surges after a longer travel distance are more similar than the ones at the upper station (Fig4 c-d). We speculate that this might be connected to internal flow dynamics of the very fine grained flows rather than external forcing, e.g. from lateral or basal sediment input.

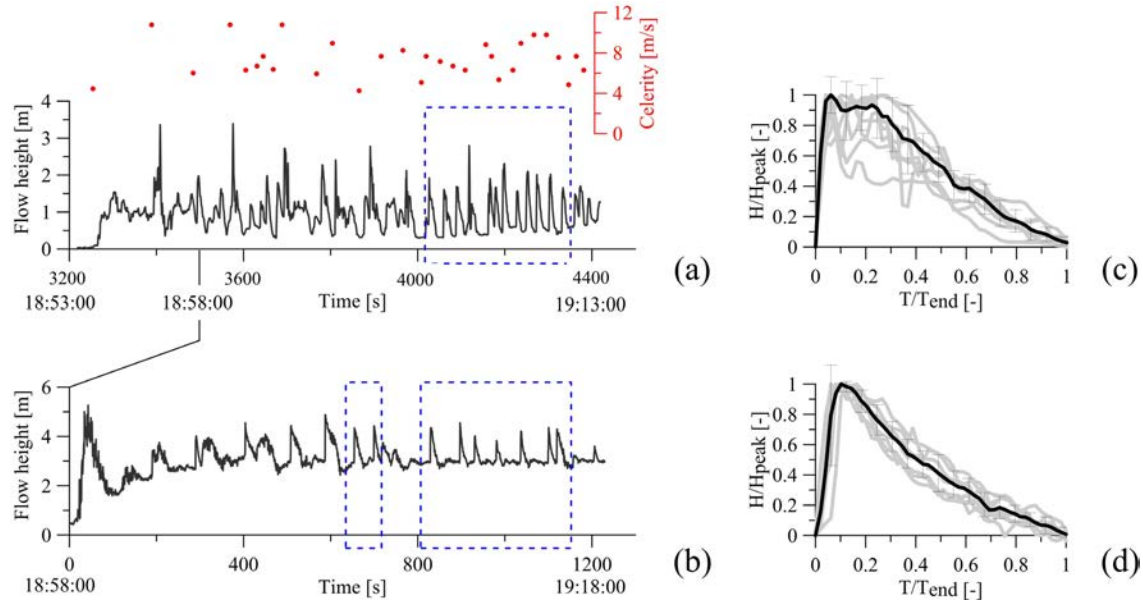


Fig. 4. Stage hydrographs of the debris-flow event at Lattenbach on September 10th, 2016, at the site Grins (a) and the site Pians (b); blue boxes mark the surges used to calculate average normalized surges at site Grins (c) and site Pians (d).

5. Discussion

We tested whether the shape of the visually undisturbed (non-coalescing) surges in the back of the flow can be modelled by hydraulic theory. For this, we compared the non-dimensional shape of the surges with a recently developed wave equation for roll wave deformation. The derivation of the equation goes beyond this contribution. A summary of the model can be found in Arai et al. (2014) as well as in the proceeding of this conference. For the simplified case of a linear velocity profile the wave equation reads

$$\frac{\partial \eta'}{\partial \tau'} + \frac{3}{2} \eta' \frac{\partial \eta'}{\partial \xi'} = \mu \frac{\partial^2 \eta'}{\partial \xi'^2} \quad (1)$$

where η' is the dimensionless variance of the mean flow height (i.e. $\eta' = 0$ equals mean flow height), ξ' is a dimensionless coordinate traveling with the mean wave celerity (i.e. $\xi' = 0$ is the center of the surge, $\xi' > 0$ is towards the front, and $\xi' < 0$ is towards the tail), τ' is the dimensionless time, and μ is a measure for the mean flow velocity. In this equation, all information on flow resistance is packed into the information of mean flow height and mean flow velocity, and therefore does not require a pre-defined rheologic flow model. Fig 5 shows a comparison of the model predictions with the observed surges displayed in Fig 4c. We see a reasonable agreement between the model and the observation; however, we must note that the variations of the observed surges at Grins are high compared to a later state of the event as observed at site Pians (data from site Pians could not be used for comparison with the model, because the no velocity measurements are available).

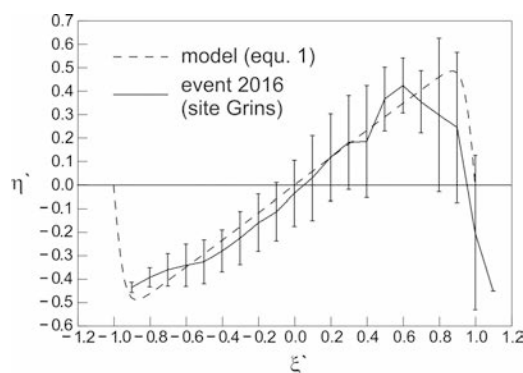


Fig. 5. Comparison of the normalized waves recorded at Lattenbach on September 10th, 2016, at the site Grins with model predictions using Equation 1. Parameters η' and ξ' are as explained in the text; the flow is from left to right.

6. Conclusions

In this contribution we presented monitoring data of debris flows occurring from 2015 to 2017 at the Lattenbach creek, AUT. In total six events were recorded with event volume of $\sim 45,000$ m³. Though there was a significant variation of event volumes, velocities, and water content (visually assessed from videos), the events showed some common features. All events were triggered by short, intensive rainfalls, all events occurred as a sequence of several surges, and 5 out of 6 events exceeded the engineering design water discharge with a return period of 150 years. A rotational laser scanner together with a high-frequency Doppler radar were successfully tested and the data will be further analyzed. The events with a large event volume showed irregular surges at the front of the flow, which were associated with large boulders and woody debris. At a later stage the surges appeared more regular and were used for comparison with predictions from a new wave equation from hydraulic theory. All surges had higher velocities (celerities) than the front. For the largest event (2016) we observed a significant transformation of the hydrograph over a distance of more than 1 km resulting in a very large frontal surge and a reduced number of smaller surges.

Acknowledgements

We thank Fritz Zott for realizing and maintaining the monitoring site, Georg Nagl for field support and Andreas Schimmel for processing the laser data.

References

- Arai, M., Huebl, J., and Kaitna, R., 2013, Occurrence conditions of roll waves for three grain-fluid models and comparison with results from experiments and field observation: *Geophysical Journal International*, v. 195(3), p. 1464-1480, doi:10.1093/gji/ggt352.
- Arai, M., Huebl, J., and Kaitna, R., 2014, A wave equation of intermittent flow with sediment on inclined channel and experimental and observed results: *Proceedings of the International Symposium Interpraevent Pacific Rim 2014*, Nov. 25-28, 2014, Nara, JP.
- Comiti, F., Marchi, L., Macconi, P., Arattano, M., Bertoldi, G., Borga, M., et al., 2014, A new monitoring station for debris flows in the European Alps: first observations in the Gadria basin: *Natural Hazards*, v. 73(3), p. 1175-1198, doi:10.1007/s11069-014-1088-5.
- Di Cristo, C., Iervolino, M., Vacca, A., and Zanuttigh, B., 2009, Roll-waves prediction in dense granular flows: *Journal of Hydrology*, v. 377(1), p. 50-58, doi:10.1016/j.jhydrol.2009.08.008.
- Dressler, R. F., 1949, Mathematical solution of the problem of roll-waves in inclined open channels: *Communications on Pure and Applied Mathematics*, v. 2(2-3), p. 149-194, doi:10.1002/cpa.3160020203.
- Forterre, Y., and Pouliquen, O., 2003, Long-surface-wave instability in dense granular flows: *Journal of Fluid Mechanics*, 486, 21-50, doi:10.1017/s0022112003004555.
- Huebl, J., Schimmel, A. and Koschuch, R., 2018, Evaluation of Different Methods for Debris Flow Velocity Measurements at the Lattenbach Creek, in: Yamada, T. et al., eds., *INTERPRAEVENT 2018 in the Pacific Rim Symposium proceedings*, p. 2-8.
- Iverson, R. M., Logan, M., LaHusen, R. G., and Berti, M., 2010, The perfect debris flow? Aggregated results from 28 large-scale experiments: *Journal of Geophysical Research: Earth Surface*, v. 115(F3), doi:10.1029/2009JF001514.
- Johnson, C., Kokelaar, B., Iverson, R., Logan, M., LaHusen, R., and Gray, J., 2012, Grain-size segregation and levee formation in geophysical mass flows: *Journal of Geophysical Research: Earth Surface*, v. 117(F1), doi:10.1029/2011JF002185.

- Kean, J. W., McCoy, S. W., Tucker, G. E., Staley, D. M., and Coe, J. A., 2013, Runoff-generated debris flows: Observations and modeling of surge initiation, magnitude, and frequency: *Journal of Geophysical Research: Earth Surface*, v. 118(4), p. 2190–2207, doi:10.1002/jgrf.20148.
- Longo, S., 2011, Roll waves on a shallow layer of a dilatant fluid: *European Journal of Mechanics-B/Fluids*, v. 30(1), p. 57–67, doi:10.1016/j.euromechflu.2010.09.001.
- Marchi, L., Arattano, M., and Deganutti, A. M., 2002, Ten years of debris-flow monitoring in the Moscardo Torrent (Italian Alps): *Geomorphology*, v. 46(1), p. 1–17, doi:10.1016/S0169-555X(01)00162-3.
- McArdell, B. W., Bartelt, P., and Kowalski, J., 2007, Field observations of basal forces and fluid pore pressure in a debris flow: *Geophysical Research Letters*, v. 34(7), doi:10.1029/2006GL029183.
- McGuire, L. A., Rengers, F. K., Kean, J. W., and Staley, D. M., 2017, Debris flow initiation by runoff in a recently burned basin: Is grain-by-grain sediment bulking or en-masse failure to blame? *Geophysical Research Letters*, doi:10.1002/2017GL074243.
- Ng, C. O., and Mei, C. C., 1994, Roll waves on a shallow layer of mud modelled as a power-law fluid: *Journal of Fluid Mechanics*, v. 263, p. 151–184.
- Okano, K., Suwa, H., and Kanno, T., 2012, Characterization of debris flows by rainstorm condition at a torrent on the Mount Yakedake volcano, Japan: *Geomorphology*, v. 136(1), p. 88–94.
- Stiny, J., 1910, *Die Muren* [Debris flows]: Wagner, Innsbruck.
- Pierson, T., 1986, Flow behavior of channelized debris flows, Mount St. Helens, Washington, in Abrahams, A.D., ed., *Hillslope processes*, Allen and Unwin, London, p. 269–296.
- Zanuttigh, B., and Lamberti, A., 2007, Instability and surge development in debris flows: *Reviews of Geophysics*, v. 45(3), doi:10.1029/2005rg000175.

Monitoring of rainfall and soil moisture at the Rebaixader catchment (Central Pyrenees)

Marcel Hürlimann^{a,*}, Raül Oorthuis^a, Clàudia Abancó^{a,b}, Luigi Carleo^c, José Moya^a

^a Department of Civil and Environmental Engineering, UPC BarcelonaTECH, Jordi Girona 1-3, 08034 Barcelona, Spain

^b Institut Cartogràfic i Geològic de Catalunya, Parc de Montjuïc, 08038 Barcelona, Spain

^c Department of Civil Engineering, University of Salerno, Via Giovanni Paolo II 132, 84084 Fisciano, Italy

Abstract

The instrumental monitoring of torrential catchments is a fundamental research task and provides necessary information to improve our understanding on the mechanisms of debris flows. While most monitoring sites include meteorological sensors and analyze the critical rainfall conditions, only very few contain soil moisture measurements. In our monitoring site, the Rebaixader catchment, 11 debris flows and 24 debris floods were detected during the last nine years. Herein, the initiation mechanisms of these torrential flows were analyzed focusing on the critical rainfall conditions and the soil water dynamics. Comparing the temporal distribution of both rainfall episodes and torrential flows, the Kernel density plots showed maximum values for rainfalls at the beginning of June, while the peak for torrential flows is at July 20th. This means that highest probability of debris flows and debris floods triggering is about 1.5 months later than the one of rainstorms in the catchment. Thus, the antecedent rainfall and especially the soil moisture conditions may influence the triggering of torrential flows. In a second step, a new updated rainfall threshold was proposed including total rainfall duration and mean intensity. The analysis of soil moisture data was more complicated and no clear trends were observed in the dataset. Therefore, additional data has to be recorded in order to quantitatively analyze the role of soil moisture on the triggering of flows and for the definition of thresholds. Some preliminary results show that the soil moisture at the beginning of a rainfall event affects the maximum increase of soil moisture, while a slight trend was visible comparing the initial soil moisture with the necessary rainfall amount to trigger a torrential flow.

Keywords: monitoring; rainfall infiltration; soil moisture; threshold; Pyrenees

1. Introduction

Detailed data recorded at catchments with monitoring systems are necessary to improve our knowledge about the triggering mechanisms of debris flows and other torrential processes. Herein, we present data recorded at the Rebaixader torrent, where torrential activity is high and a comprehensive time series on the initiation of debris flows and debris floods is available. In this study, we distinguish between the torrential flows using the classification of Hungr et al. (2001, 2014).

There are three principal approaches to monitor and analyze debris-flows triggering. The most common approach focuses on rainfall measurements and generally defines thresholds for debris-flow triggering (e.g. Abancó et al., 2016; Bel et al., 2017; Coe et al., 2008; Deganutti et al., 2000). The second approach analyses the soil water dynamics by recording moisture and/or pore water pressure in natural slopes of the catchment (e.g. Comiti et al., 2014) or in the channel bed (McCoy et al., 2012). The third approach investigates the channel discharge (e.g. Gregoretti et al., 2016).

The present investigation focuses on the rainfall and the soil moisture measured at the Rebaixader catchment. The rainfall time-series covers the last 10 debris flow seasons (2009 to 2018), while the soil moisture records started in

* Corresponding author e-mail address: marcel.hurlimann@upc.edu

2013. The main objective of the study is to improve our understanding on the initiation mechanisms of debris flows and debris floods. A secondary goal includes the definition of critical values or thresholds that are necessary information for the launch of early warning or alarm systems.

2. The Rebaixader monitoring site

2.1. Settings

The Rebaixader monitoring site is located in a small first order basin at the Southern Central Pyrenees, which shows a typical morphology of a torrential system (Fig. 1) developed in an old glacial valley. The catchment drains an area of 0.53 km²; the altitude ranges from 1350 m asl at the fan apex up to 2475 m asl at the highest peak. The debris flows and debris floods initiate in a steep bare scarp with a badland-like morphology and progresses to the channel zone. This latter is 150 m long and has a mean slope of 21°. At the bottom of the slope, the fan has area of 8.4 Ha and an average slope of 18°.

The bedrock consists of Palaeozoic slates and phyllites formed during Hercynian orogeny (Muñoz, 1992), while the soils include colluvium and glacial deposits. The main scarp is located in a thick lateral till, which consists of sandy gravels, and provides almost unlimited sediment availability.

The climate conditions are affected by three principal factors: i) the west winds from the North-Atlantic, ii) the vicinity of the Mediterranean Sea; and, iii) the orographic effects of the Pyrenean mountain range. In the Pyrenees, the most common triggering rainfalls are on one side short duration and high intensity convective summer storms, and on the other side long-lasting rainfalls with moderate intensity during autumn (Hürlimann et al., 2003).

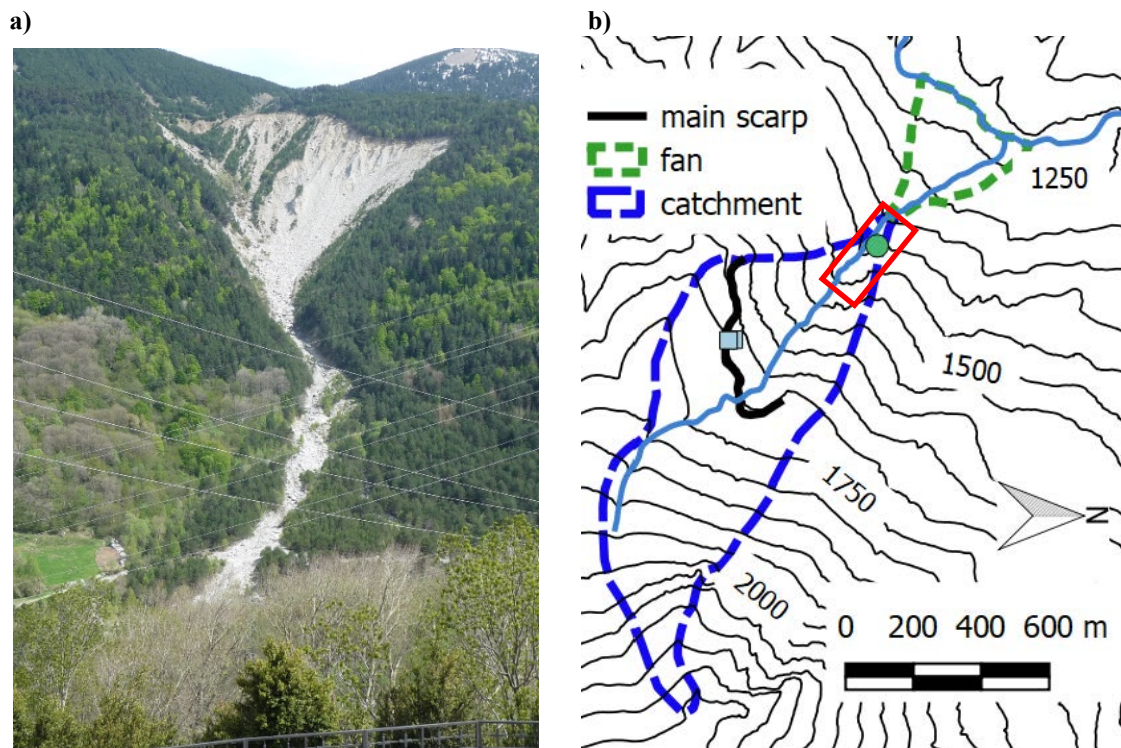


Fig. 1. The Rebaixader monitoring site. (a) General view of the catchment with the open scarp, where the debris flows and debris floods initiate. (b) Situation of the monitoring stations used in this study (green dot indicates the rain gauge, light blue squares represent the infiltration stations and the red rectangle specifies the area where the sensors of the flow detection station are installed).

2.2. Monitoring description

The monitoring in the Rebaixader torrent started in summer 2009 and includes at the moment five different stations. In this study, we used records of the two meteorological stations METEO-CHA and METEO-TOP, two infiltration stations (INF-SCARP1 and INF-SCARP2) and the FLOW-WR station, which detects and identifies the different torrential flows (Fig. 1).

The principal rain gauge is METEO-CHA, which is installed in the lower part of the catchment. It is a standard tipping bucket rain gauge with a resolution of 0.2 mm (until 2015, the resolution was 0.1 mm). The rain gauge METEO-TOP was temporarily installed just above the main scarp and not used in this study. The infiltration stations are built in a steep (30–40°) bare slope at the highest part of the open scarp, which is actually stable but very close to the most active portion of the initiation zone. They consist of eight soil moisture sensors (Decagon 10HS) and two water potential sensors (Decagon MPS-2). This set-up is totally different to other sites in the literature, where soil moisture and pore water pressure are measured in the channel bed (McCoy et al., 2012). All of the monitoring stations have a sampling rate of 5 minutes.

The most important part of the monitoring system forms the FLOW-WR station, which detects and allows classifying the flows. Sensors in this station include five geophones, one ultrasonic device, one radar sensor and one video camera. All these devices are located in the channel reach or at the highest part of the fan (Fig. 1) and register the data at 1 Hz. Detailed information on the monitoring system is available in Hürlimann et al. (2014).

3. Analysis of the rainfall data

Between July 2009 and September 2018 a total of 11 debris flows and 24 debris floods were observed. Rainfall data from METEO-CHA are available for all events except one debris flows, which was measured by METEO-TOP. Moreover, 446 rainfall episodes that did not trigger any important torrential flow were selected. Rainfall parameters like duration (D), total rainfall (P_{tot}), mean intensity (I) and maximum intensity for different durations (e.g. $I_{\text{max}_5\text{min}}$ for 5 minute), were evaluated. An important and critical task during the rainfall analysis is the definition of the total rainfall duration. Herein, this parameter was determined by the condition that no rainfall was observed one hour before and after the episode.

In the first step, the rainfall events were analyzed searching for seasonal or cyclic patterns using Kernel density plots. The Kernel density is a method to estimate the density of a sample smoothly by removing the dependence of the end points of histogram bins centering the blocks at each data point (Duong, 2001). The temporal distribution of all the 481 rainfall episodes (both triggering torrential flows or not) is plotted in Figure 2a. The results show that the highest density for the rainfall episodes is at 14:00 UTC and between April and July, with a maximum at June 5. If this density plot is compared with the one of debris flows and debris floods occurrence (Fig. 2b), some interesting facts can be observed. First of all, the maximum Kernel density for the triggering of torrential flows is shifted 45 days to July 20 and the range of high density values is between June and August. In contrast, the maximum density of a trigger is approximately at the same hour as for the rainfall episodes (13:00 UTC). The difference of the temporal occurrence between rainfall and triggering of torrential flows (about 1.5 months) may be associated with the effects of antecedent rainfall and the soil moisture evolution during late spring and early summer. The importance of antecedent rainfall and the corresponding increase of soil moisture has been reported many times in debris-flow and landslide research (Gregoretto and Dalla Fontana, 2007; Wieczorek and Glade, 2005), but until now no clear relation between antecedent rainfall and debris-flow triggering was observed at Rebaixader (Abancó et al., 2016). Nevertheless, a possible effect of snowmelt cannot be neglected for debris flows that occur in late spring or early summer (Hürlimann et al., 2010; Abancó et al., 2016). It must be stated that additional information of rainfall (intensity, duration or total rainfall) was not incorporated in the density plot. However, the measurements gathered at Rebaixader confirm the hypothesis that debris flows are generally triggered in summer by convective rainstorms of short duration and high intensity, while long-lasting rainfalls during spring normally not provoke events (Hürlimann et al., 2014).

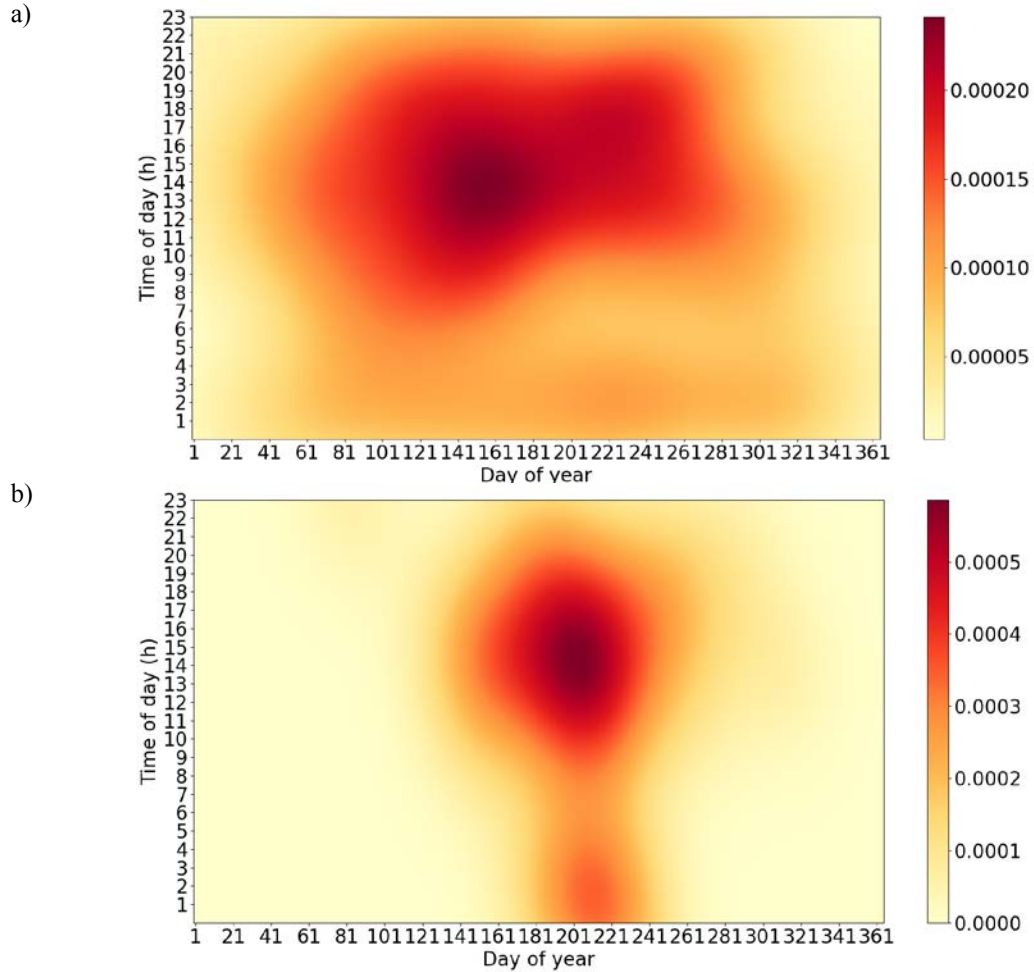


Fig. 2. Temporal distribution of rainfall and torrential activity. Kernel density plots of 481 rainfall episodes (a) and 35 debris-flow or debris-flood events (b).

In the second step, the rainfall threshold for the triggering of torrential flows was assessed. Abancó et al. (2016) already proposed two thresholds for the data registered during 2009 and 2014. The present dataset includes additional records of the last four years. Therefore, the threshold for the relation between total duration and the mean intensity was reconsidered and updated. The new threshold line was defined applying the following procedure: first, a power-law trend line was fitted using the data of the 11 debris-flow triggering rainfalls. Then, the scale parameter defined in the previous step was reduced, keeping constant the exponent, until all the debris flows were located above the threshold line. The new updated threshold can be expressed by

$$I = 11 D^{-0.74} \quad (1)$$

, where I is the mean intensity (in mm/hours) and D is the duration (in hours) of the rainfall events. Although the rainfall events, which triggered debris floods, were not used to define the threshold, it is noteworthy that most of them are located above the threshold. Indeed, only four debris floods (usually of small volume) did not fulfill the threshold condition.

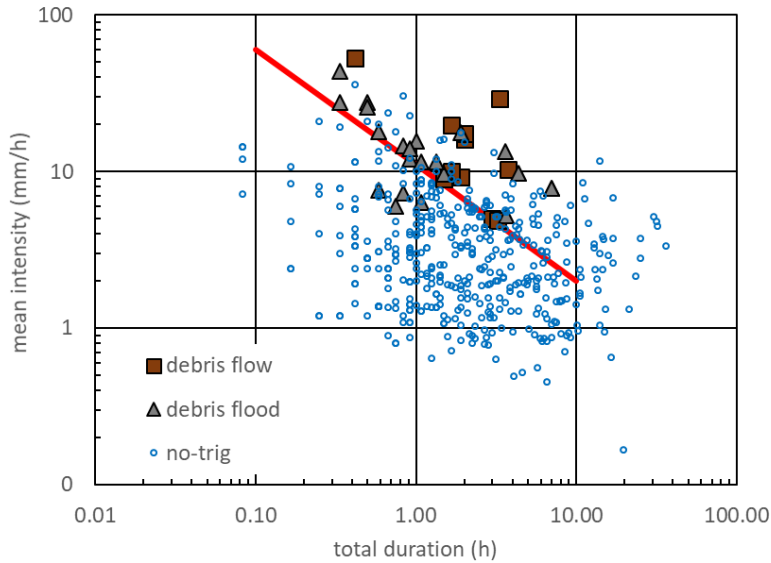


Fig. 3. Relation between total rainfall duration and mean intensity for debris flows/debris floods triggering and non-triggering (no-trig) events. The resulting threshold is illustrated by the red line and expressed in Eq. (1).

4. Analysis of the soil moisture data

The analysis of the soil moisture due to rainfall infiltration focuses on the station with the longest record (INF-SCARP1). Figure 4 shows two examples of the soil moisture response during rainfalls that produced torrential flows. The soil moisture is given by the volumetric water content (VWC) and is measured at three different depths (-15, -30 and -50 cm). The first case shows the fast response and sharp increase of the VWC at the three depths due to a short and intense rainstorm ($P_{tot} = 15.8$ mm in 3.3 h) that triggered a large debris flow of about 10000 m³. The second example illustrates the soil moisture response during a rainfall with a longer duration and smaller intensity ($P_{tot} = 54.5$ mm in 7h), which triggered two debris floods with a total volume of about 2000 m³. In this case, the VWC slowly increased during about 2 – 3 h and maximum values were generally lower than in the first example, although the total rainfall is more than three times higher. A significant time lag occurred between the start of the rainfall and the increase of VWC.

Unfortunately, soil moisture measurements are not available for all the debris flows and debris floods occurred in the site. Technical problems have been occurring many times, since maintenance is complicated in such a remote high-mountain environment and because processes like soil thawing and freezing, rock falls and other slope instabilities are very common. Nevertheless, a complete record of rainfall and soil moisture is available for seven of the torrential events (three debris flows and four debris floods). Figure 5 shows the soil moisture values measured at -30 cm at INF-SCARP1. The seven events are compared with soil moisture data from non-triggering rainfalls, which were selected for I_{max_5min} -values larger than 35 mm/h.

The relation between the initial VWC before the rainfall and the increment of VWC due to the rainfall is presented in Figure 5a. A tentative trend is observed for the rainfalls that triggered torrential flows: a larger increase of soil moisture was measured when the soil was dryer at the beginning of the rainfall. In addition, maximum rainfall intensity recorded in 5 min were compared with the initial VWC (Figure 5b). A slight trend might be identified, which show that smaller rainfall is needed to trigger debris flows when the initial VWC is higher. Such a pattern was already observed during a rainfall analysis in Italy (Gregoretto and Dalla Fontana, 2007).

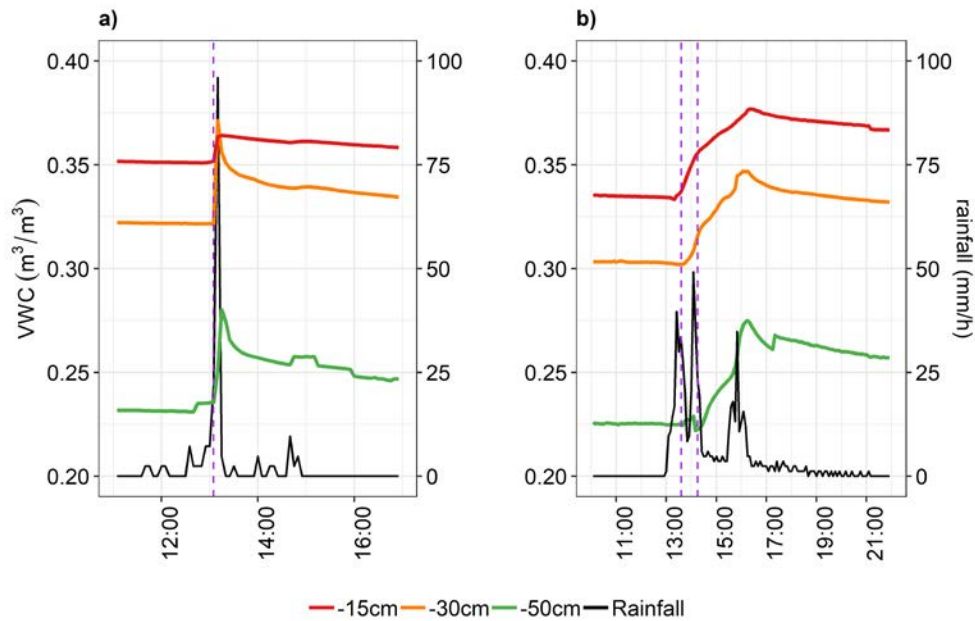


Fig. 4. Relation between rainfall and volumetric water content of the soil (VWC) during the triggering of torrential flows. Examples of 2013 July 17th debris flow (a) and 2013 June 5th debris floods (b). VWC is measured at the three different depths of station INF-SCARPI. Vertical dashed lines indicate the moment of peak discharge observed at the FLOW-WR monitoring station.

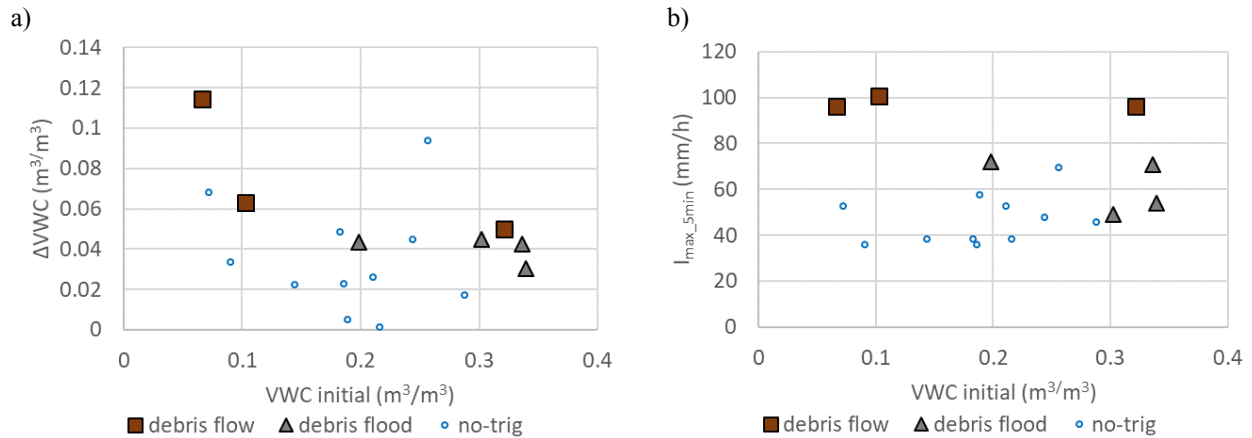


Fig. 5. Comparison between rainfall and soil moisture corresponding to debris flows/debris floods triggering and non-triggering (no-trig). (a) Relation between initial volumetric water content (VWC initial) and the increment in volumetric water content (ΔVWC). (b) Relation between initial VWC and maximum rainfall intensity for 5 min duration (I_{max_5min}).

5. Conclusions

Monitoring data on debris-flow triggering has been recorded in the Rebaixader catchment since 2009. A total of 11 debris flows and 24 debris floods were detected during this period. In this work, we focused on the initiation mechanisms of these torrential flows by analyzing the critical rainfall conditions and the soil moisture related to water infiltration into the soil.

The results show that most of the torrential flows in the test site occurred in summer (between June and August) and at around 13:00 UTC. In contrast, the highest probability of rainstorms is about 1.5 months earlier (between April and July), which supports the hypothesis that antecedent rainfall, snowmelt and/or soil moisture conditions are important for debris-flow triggering. The intensity and duration of rainfall is not included in this analysis, but previous studies at Rebaixader showed that most debris flows are provoked by short and intense rainstorms in summer, while spring rainfalls of lower intensity and longer duration normally do not trigger debris flows. In addition, a new updated threshold was defined including total duration and mean intensity of the rainfalls.

Regarding the soil water dynamics, the VWC changes during rainstorms were analyzed. Preliminary results show that a higher soil moisture increment is produced when the soil is dryer at the beginning of a rainstorm. Comparing rainfall and soil moisture measurements, the data indicate that the maximum 5 minutes rainfall intensities required for the triggering of torrential flows are generally larger than the non-triggering rainfalls, as it could be expected. Moreover, it seems that the initial soil moisture content affects the values of the triggering rainfalls and smaller rainfall amounts are necessary to trigger a torrential flow when soil moisture content is higher at the beginning of the rainstorm. However, a complete data set is available only for a small number of events. Therefore, additional data are necessary to confirm the former hypothesis and to define threshold values of soil moisture causing torrential flows.

Acknowledgements

The study is funded by the national research project called “Slope mass-wasting under climate change (SMuCPHy)” granted by the Spain Government (project reference number BIA 2015-67500-R) and co-funded by AEI/FEDER, UE and the EC H2020 project ANYWHERE (DRS-01-2015-700099).

References

- Abancó, C., Hürlimann, M., Moya, J. and Berenguer, M., 2016, Critical rainfall conditions for the initiation of torrential flows. Results from the Rebaixader catchment (Central Pyrenees): *J. Hydrol.*, p. 541, 218–229, doi:10.1016/j.jhydrol.2016.01.019.
- Bel, C., Liébault, F., Navratil, O., Eckert, N., Bellot, H., Fontaine, F. and Laigle, D., 2017, Rainfall control of debris-flow triggering in the Réal Torrent, Southern French Prealps: *Geomorphology*, 291, p. 17–32.
- Coe, J. A., Kinner, D. A. and Godt, J. W., 2008, Initiation conditions for debris flows generated by runoff at Chalk Cliffs, central Colorado: *Geomorphology*, 96(3–4), p. 270–297.
- Comiti, F., Marchi, L., Macconi, P., Arattano, M., Bertoldi, G., Borga, M., Brardinoni, F., Cavalli, M., D’Agostino, V., Penna, D. and Theule, J., 2014, A new monitoring station for debris flows in the European Alps: first observations in the Gadria basin: *Nat. Hazards*, 73(3), p. 1175–1198, doi:10.1007/s11069-014-1088-5.
- Deganutti, A. M., Marchi, L. and Arattano, M., 2000, Rainfall and debris-flow occurrence in the Moscardo basin (Italian Alps), *in* Proceedings, Debris-Flow Hazards Mitigation: Mechanics Prediction and Assessment, Taipei, Taiwan, Balkema, p. 67–72.
- Duong, T., 2001, Notes of seminar at Weatherburn Lecture Series for the Department of Mathematics and Statistics, University of Western Australia, 24th May 2001
- Gregoretto, C. and Dalla Fontana, G., 2007, Rainfall threshold for the initiation of debris flows by channel bed failure of the Dolomites, *in* Proceedings, Debris-Flow Hazards Mitigation: Mechanics Prediction and Assessment. Chengdu, China, Millpress, p. 11–21.
- Gregoretto, C., Degetto, M., Bernard, M., Crucil, G., Pimazzoni, A., De Vido, G., Berti, M., Simoni, A. and Lanzoni, S., 2016, Runoff of small rocky headwater catchments: Field observations and hydrological modeling: *Water Resour. Res.*, 52(10), p. 8138–8158, doi:10.1002/2016WR018675.
- Hungr, O., Evans, S. G., Bovis, M. J. and Hutchinson, J. N., 2001, A review of the classification of landslides of the flow type: *Environ. Eng. Geosci.*, 7(3), p. 221–238.
- Hungr, O., Leroueil, S. and Picarelli, L., 2014, The Varnes classification of landslide types, an update: *Landslides*, 11(2), p. 167–194, doi:10.1007/s10346-013-0436-y.
- Hürlimann, M., Corominas, J., Moya, J. and Copons, R., 2003, Debris-flow events in the Eastern Pyrenees. Preliminary study on initiation and propagation, *in* Proceedings, Debris-Flow Hazards Mitigation: Mechanics Prediction and Assessment, Davos, Switzerland, Millpress, p. 115–126.
- Hürlimann, M., Abancó, C. and Moya, J., 2010, Debris-flow initiation affected by snowmelt. Case study of the Senet monitoring site, Eastern Pyrenees, *in* Proceedings, Mountain Risks: Bringing Science to Society, Florence, Italy, p. 81–86.
- Hürlimann, M., Abancó, C., Moya, J. and Vilajosana, I., 2014, Results and experiences gathered at the Rebaixader debris-flow monitoring site, Central Pyrenees, Spain: *Landslides*, 11, p. 939–953.
- McCoy, S.W., Kean, J.W., Coe, J.A., Tucker, G.E., Staley, D.M., and Wasklewicz, T.A., 2012, Sediment entrainment by debris flows: In situ measurements from the headwaters of a steep catchment: *J. Geophys. Res.* 117, F03016.
- Muñoz, A., 1992, Evolution of a continental collision belt: ECORS-Pyrenees crustal balanced cross-section, *in* Thrust Tectonics, edited by McClay, K. R. ed., Thrust Tectonics, Chapman & Hall, pp. 235–246., Chapman & Hall.

Debris-flow monitoring using load cells and pressure sensors on Sakura-jima Island

Takahiro Itoh^{a,*}, Naoki Fujimura^b, Hitoshi Katou^c, Satoshi Tagata^d, Takahisa Mizuyama^e

^a Center for Advanced Research and Development, Nippon Koei Co., Ltd., 2304 Inarihara, Tsukuba 300-1259, Japan

^b Volcano and Debris Flow Research Team, Public Works Research Institute, 1-6 Minamihara, Tsukuba 305-8516, Japan

^c Nara Prefectural Office, 30 Ohji-cho, Nara 630-8501, Japan

^d Nippon Koei Co., Ltd., 1-14-6 Kudan-kita, Chiyoda-Ku, Tokyo 102-8539, Japan

^e National Graduate Institute for Policy Studies (GRIPS), 22-1 7Chome Roppongi, Minato-Ku, Tokyo 106-0032, Japan

Abstract

Numerous debris flows have recently taken place frequently in Sakura-jima Island located at southwest in Japan due to rainfall events after ash deposition due to volcanic activities since 2010. Debris-flow measurement system with loadcell and pressure sensor (DFLP) had been applied for debris-flow monitoring (Osaka et al., 2014). In present study, a modified monitoring DELP system using load cells and a stainless-steel plate is employed. Mass density and sediment concentration are calculated using data obtained by the DFLP system and data measured by ultrasonic level meter and surface velocity by of image analyses of CCTV camera. (Results) Temporal changes of specific weight, sediment concentration and sediment volume of debris-flow in Nojiri and Arimura Rivers in 2014 were well measured using DFLP system. Sediment concentration and specific weight were calculated in both rivers, and there are at least 10 data in Arimura River and 8 data in Nojiri River for calculations of temporal changes of mass density and sediment concentration since 2012 and 2014, respectively. Averaged sediment concentration near peak discharge are calculated as 0.441 in Arimura River and 0.279 in Nojiri River, respectively. However, values of calculated concentration do not always take correlation with rainfall depth before debris-flow occurrences. Data analyses continuously need by more data collections of debris-flow events.

Keywords: Debris flow; DFLP; Sakura-jima, Loadcell, Sediment Concentration, Specific Weight

1. Introduction

Numerous debris flows have recently taken place frequently in Sakurajima Island, which is located at southern-west in Japan, due to rainfall events after deposition of volcanic ash by volcanic activities since 2010, and the number of debris-flow occurrences has been gradually increasing though volcanic activities were active in 1980s there and the number of debris-flows occurrences decreased in 1990s to 2000s due to decrease of volcanic activities. The numbers of debris-flow occurrences are counted by the numbers of disconnected wire sensors. Many kinds of measurements have been carried out to evaluate flow characteristics of debris flows. In those monitoring, temporal changes of flow depth, discharge and bed profiles tried to be collected using ultrasonic sensors and video camera, and profiles of bed elevations were also monitored along the channel for longitudinal deposition and near river mouth in the sea using a sounding machine, that was for measuring bed elevation due to debris-flow deposition under the sea, to evaluate sediment runoff volume from river mouth. Sediment in debris-flow bodies was measured using a sampler box produced by an iron bucket. However, it was quite difficult to obtain continuous data for sediment discharge and the runoff volume due to debris flows.

A modified debris-flow measurement system with loadcell and pressure sensor (DFLP) system, which is firstly installed in Switzerland (McArdell et al., 2007), using load cells and an iron plate was installed to evaluate flow characteristics of debris flows at the Arimura River No. 3 sabo dam in June in 2012 (Osaka et al., 2014). After the

* Corresponding author e-mail address: a6556@n-koei.co.jp

installation in Arimura River, a system with small size of loadcell and iron plate without accuracy change of measurements was discussed for easier maintenance, and the newly modified three systems with an iron plate (1 m in width and 1 m in length) were installed transversely at the No. 1 sabo dam in Nojiri River in March in 2013.

In present study, temporal changes of specific weight, sediment concentration and sediment volume of debris flow using DFLP systems in Nojiri and Arimura Rivers in 2014 were shown because of well measured data using DFLP system. Sediment concentration and specific weight were calculated in both rivers, and there are at least 10 data in Arimura river and 8 data in Nojiri river for calculations of temporal changes of mass density and sediment concentration since 2012 and 2014, respectively. Averaged sediment concentration near peak discharge are calculated as 0.441 in Arimura River and 0.279 in Nojiri River, respectively.

2. Installation and modification of the DFLP

Figures 1 to 4 show plan view and longitudinal bed profiles of Noji river and Arimura River, respectively. Nojiri River is southern-west area in Sakurajima, and is with a watershed area 2.99 km², bed slope 4.5 % measured from top of river to the river mouth and flow width 13.2 m at the Nojiri No. 1 sabo dam (see Figs. 1 and 2). Arimura River is in southern-east area in Sakurajima with a watershed area 1.35 km², bed slope 19% and flow width 20.5 m at the Arimura No. 3 sabo dam (see Figs. 3 and 4), though the information is shown in previous research (Osaka et al., 2014).

Herein, in Arimura and Nojiri Rivers where debris flows take place frequently, the number of debris-flow occurrences in Arimura River exceeds 6 per year: e.g., 6 times in 2010, 6 times in 2011 and 9 times in 2012, and in Nojiri River exceeds 10 per year, e.g., 18 times in 2010, 10 times in 2011, 21 times in 2012 and 18 times in 2013 in Nojiri River. In Arimura river, debris-flow measurement system with loadcell and pressure sensor (DFLP) system was installed in June in 2012, and ultrasonic velocity meter was also set up in 2013 (Osaka et al., 2014). Measurements using a DFLP system on the bed can obtain temporal changes of data without disturbing debris-flow body. Flow discharge and depth are measured by image analyses of CCTV or ultra-sonic wave meter. Data sampling and collections system are introduced in the literature (Osaka et al., 2014).

In Nojiri River, after the installation in Arimura River in 2012, a system with small size of loadcell and iron plate without accuracy change of measurements was discussed for easier maintenance against mechanical troubles and the newly modified three systems with an iron plate (1 m in width and 1 m in length) was developed and installed transversely at the No. 1 sabo dam in March in 2013, as shown in a picture in Figure 1.

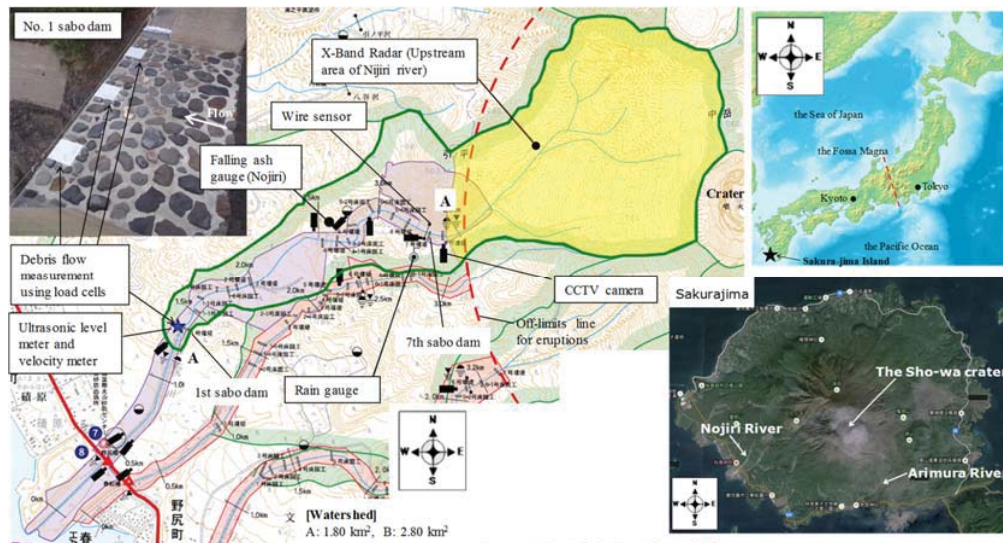


Fig. 1. Plan view of Nojiri River basin and installed various sensors for debris-flow monitoring (Osaka et al., 2014)

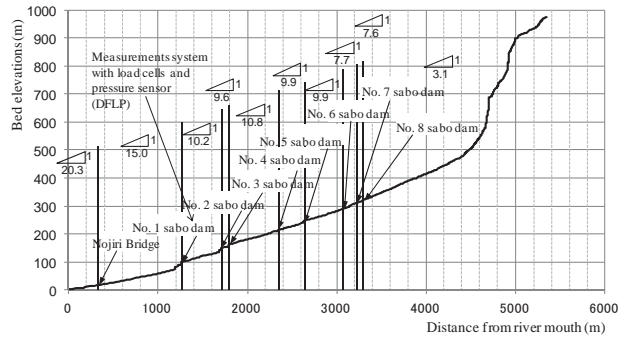


Fig. 2. Longitudinal bed profile of Nojiri River

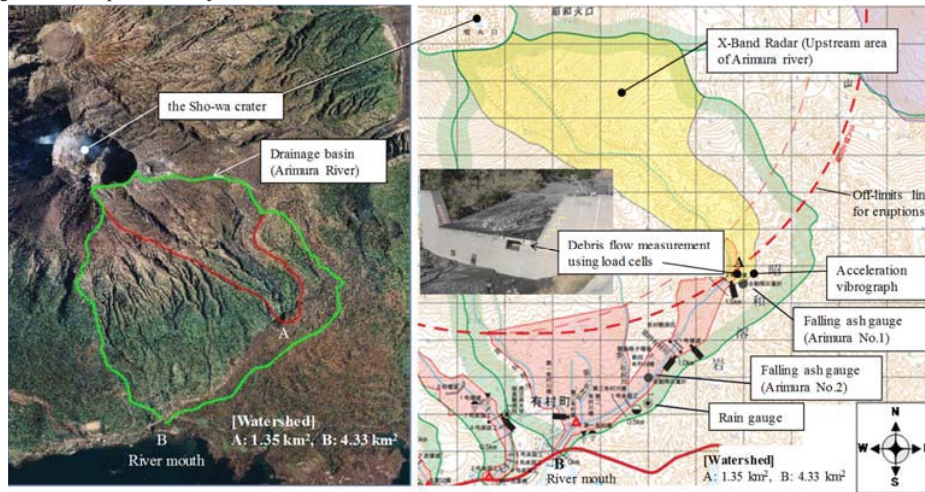


Fig. 3. Plan view of Arimura River basin and installed sensors for debris-flow monitoring (Osaka et al., 2014)

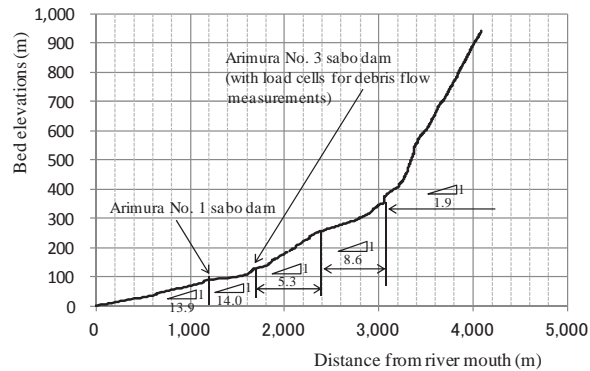


Fig. 4. Longitudinal bed profile of Arimura River

3. Typical debris flows monitored by the DFLP

3.1. Temporal changes of flow discharge, weight and pressure

Many sensors have been installed (see Figures 1 and 3) to measure occurrence and runoff of debris flow, and those are as follows: Rain gauge on the bed, X-band MP Radar, ultrasonic water level meter, wire sensor, falling ash gauge, acceleration vibrograph (in only Arimura River) and CCTV camera in Arimura and Nojiri River. In Sakurajima Island, the number of debris-flow occurrences are counted by the numbers of disconnected wires of wire sensor and wires are

installed at the position of 60 cm, 120 cm and 180 cm on the bed surface to define debris-flow magnitude. In Arimura River, debris flow took place 13 times in 2014, and debris flows with middle magnitude were observed on June 27th, July 30th, August 29th and November 1st, among these events debris flows on June 27th were observed by the DFLP systems. While, in Nojiri River, debris flow took place 17 times in 2014, and debris flows with middle magnitude were observed on May 14th, June 21st, June 27th, July 9th, August 1st and November 1st. Debris flows on June 21st and 27th were measured by three DFLP systems in Nojiri River. In Arimura River, debris flows are observed by the DFLP system as shown in Figure 3, and sediment concentration of both coarse sediment and suspended & liquid phase can be estimated by data measured by the DFLP system and calculations (Osaka et al., 2014) as shown in Figure 5.

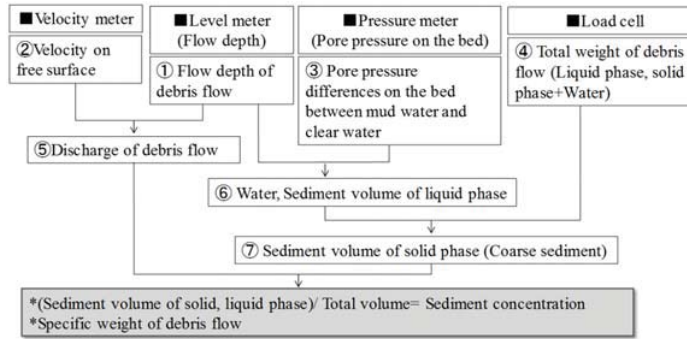


Fig. 5. Flow chart for calculations of mass density and sediment concentration using data obtained by the DFLP system (Osaka et al., 2014)

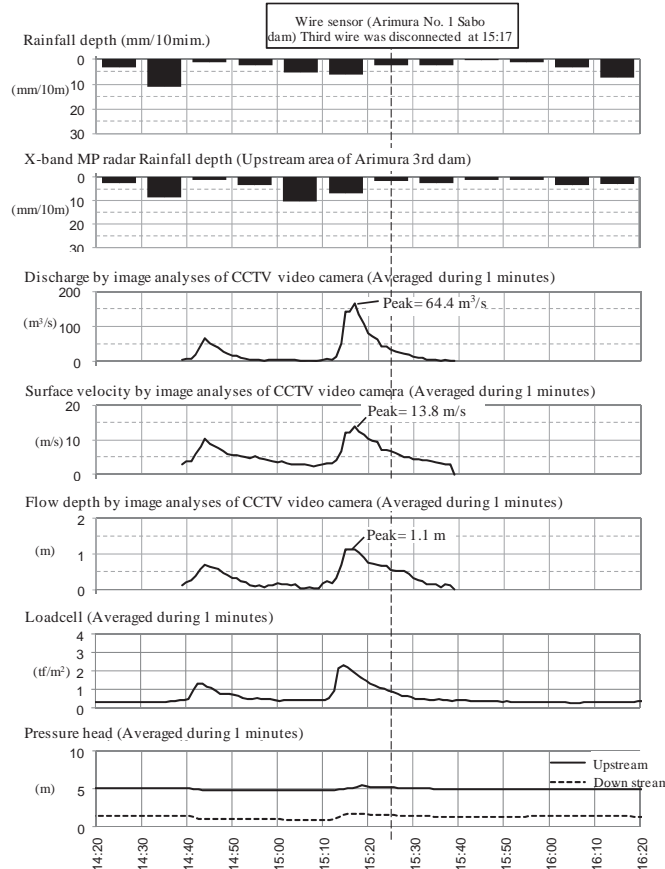


Fig. 6. Temporal changes of rainfall depth, flow discharge, surface velocity and flow depth, and weight and pressure head on the bed, observed at Arimura River (Debris-flow events on 27th June in 2014)

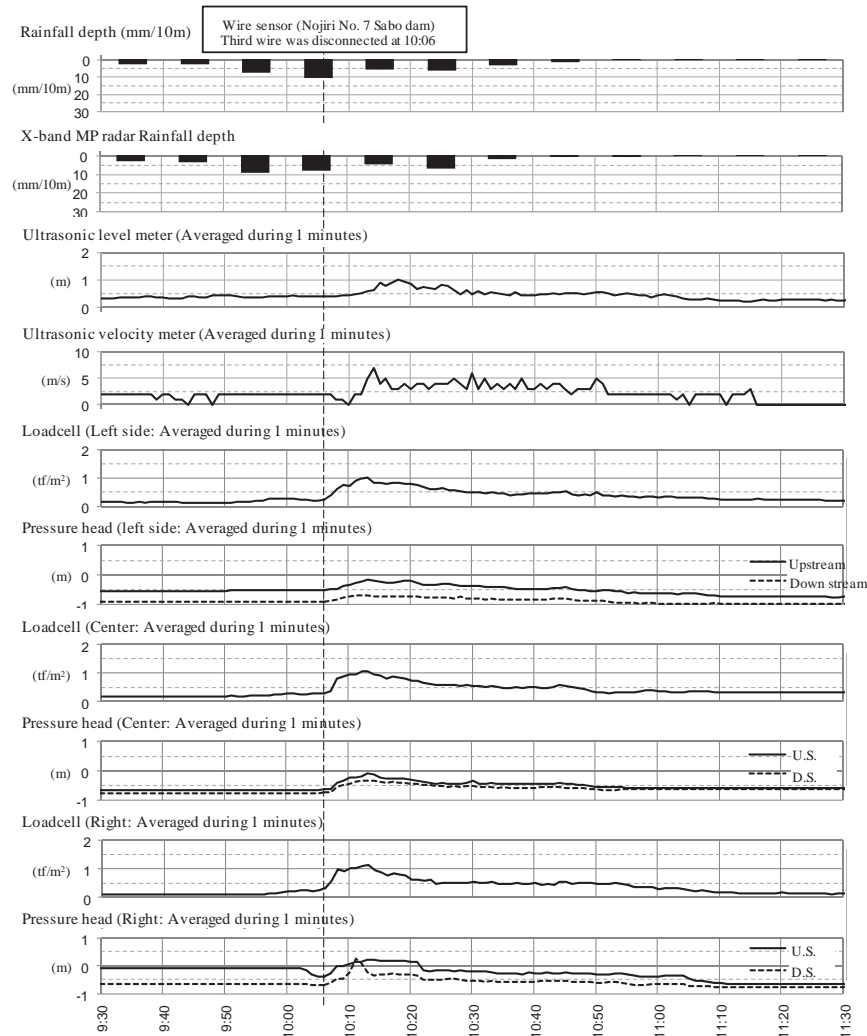


Fig. 7. Temporal changes of rainfall depth, surface velocity and flow depth measured by ultra-sonic meters, pressure head and weight on the bed by the DFLP system in Nojiri River (Debris-flow events on 27th June in 2014)

In present paper, monitored data and the related knowledge are introduced for debris-flow events measured well by the DFLP system in 2012 to 2015. In debris-flow events on 27th June in 2014, two debris-flow surges were observed with magnitude of $64.4 \text{ m}^3/\text{s}$ in peak discharge, 1.1 m in a depth and 13.8 m/s in surface velocity at Arimura River, because the flow width was not full in spill way of the sabo dam (around 4 m). Debris flows with one surge took place with magnitude of 1.0 m in peak flow depth at Nojiri River in the day. The velocity and flow depth are analyzed by image analyses of CCTV video camera in Arimura River, and by data of CCTV video camera and ultrasonic meter in Nojiri River.

Figure 6 shows temporal changes of rainfall depth, surface velocity and flow discharge, as well as pressure head and weight on the bed, which are observed at Arimura River. Figure 7 shows temporal changes of rainfall depth, surface velocity and flow depth measured by ultra-sonic meters, pressure head and weight by the DFLP system at Nojiri River. In addition, two pressure gauges on the iron plate are set longitudinally with 50 cm in a distance, and the pressure differences are measured though the value of zero for each pressure meter is moving before events. Those debris surges can be observed well, and temporal changes of those data are compared with time of disconnected wires. Wire sensors are at downstream of the monitoring section in Arimura River and, whereas, wire sensors are at upstream

of the monitoring section in Nojiri River. Differences between arrival time of peak values and disconnected time of wire appear clearly, and travel time of debris flow is also measured with several sensors.

3.2. Specific weight and sediment concentration

Temporal changes of specific weight, sediment concentration and sediment volume of debris flow using data obtained by DFLP systems are calculated as flow chart shown in Figures 5, in Nojiri and Arimura Rivers in 2014, because of well measured data using DFLP system. Detail explanation for calculations of specific weight and sediment concentration are introduced in Osaka et al. (2014). Specific weight is the ratio of mass density of debris flow to clear water without a dimension and sediment concentration is volumetric concentration.

The bed slope at the Nojiri No. 7 sabo dam test site is 1/7.6 (7.50 degrees) and the supposed equilibrium sediment concentration for the bed slope is 0.147 for a specific weight of 2.65 and an interparticle friction angle of the sediment particles of 34 degrees. The bed slope at the Arimura No. 3 sabo dam is 1/5.3 (10.7 degrees) and recently 1/14 (4.1 degrees). The supposed equilibrium sediment concentration for the bed slope is 0.235 and 0.0721, respectively, for same values of physical parameters of sediment particles in Nojiri River.

Figures 8 (a) to (b) are calculation data for sediment concentration, specific weight of debris flow, and sediment discharge rate for events on June 27th, 2014 in Arimura River. Figures 9 (a) to (c) also show calculation data in Nojiri River.

In Arimura River, sediment concentration and specific weight are calculated as 0.463 and 1.76, respectively, on June 27th, 2014, and sediment discharge is totally calculated as 46,073 m³ in total surges and 22,656 m³ in second surge as shown in Figures 8. Temporal changes of specific weight and sediment concentration can be calculated during debris flow events using DFLP system. In addition, data for sediment concentration of debris flow is obtained by eight debris-flow events, and the averaged sediment concentration, which is averaged near peak of debris-flow surge, is 0.441 during June in 2012 to September 2016 in Arimura River (see Table 1).

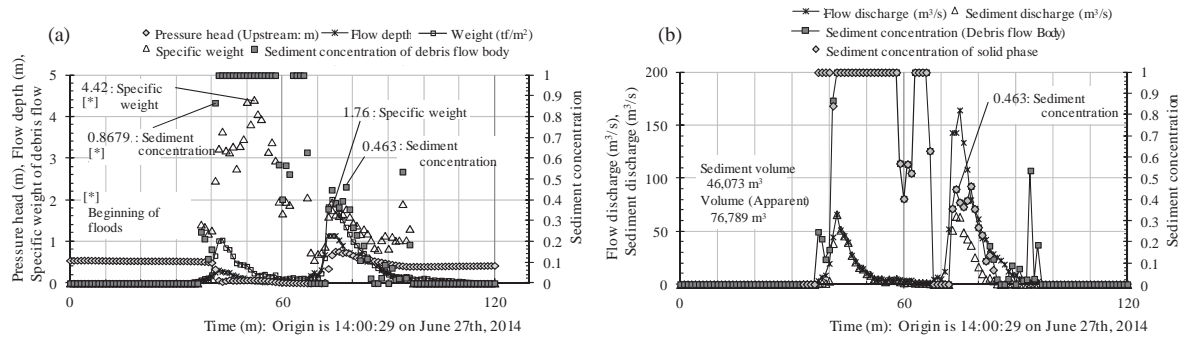


Fig. 8. Calculated sediment concentration, specific weight of debris flow, and sediment discharge rate for events on June 27th, 2014 in Arimura River

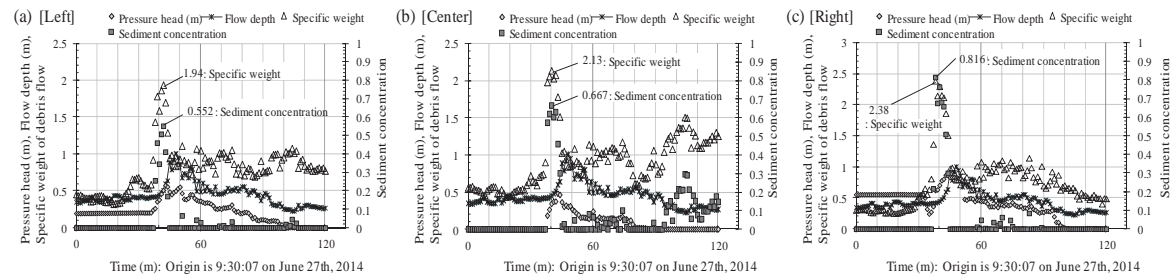


Fig. 9. Calculated sediment concentration and specific weight of debris-flow measured at left, center and right side, respectively (Debris-flow events on June 27th, 2014 in Nojiri River)

In Nojiri River, sediment concentration and specific weight (Fig. 9) were calculated such as 0.552 (left side), 0.667 (center), 0.816 (right side) and 1.94 (left side), 2.13 (center), 2.38 (right side), respectively, in Nojiri River (on 27th in June, 2014). Effects of channel shifting on mass density and sediment concentration are clearly shown in measurements in Nojiri River, though the characteristics could depend on flow magnitude of debris flow. Sediment volume for solid and liquid phase is calculated using data in Figure 9. Total runoff sediment volume is 1,920 m³, and sediment volume of solid and liquid phase are estimated 1,781 m³ and 139 m³, respectively. Moreover, averaged near peak of debris-flow surge, is 0.279 during June in 2014 to June 2016 in Nojiri River (see Table 1).

Table 1 lists calculated sediment concentration near peak stage by the DFLP system at Arimura River. Disconnected wire, accumulated rainfall depth and rainfall depth during 10 minutes before debris-flow occurrences are also listed in the table. Table 2 lists calculated sediment concentration and so on at Noriji No. 1 sabo dam like Table 1. Sediment concentration seems to be independent on rainfall intensity in Arimura and Nojiri River.

Table 1. Sediment concentration of debris flow calculated by DFLP at Arimura No. 3 sabo dam

Time (y/m/d)	Disconnected wire (1st, 2nd, 3rd)	Sediment concentration near peak stage	Rainfall depth (mm) (*)	Rainfall depth during 10 min. (mm) (**)
2012/6/15	2	0.290	39.0	14.0
2012/6/21	1	0.371	122	10.0
2014/6/27	3	0.288	34.0	11.0
2014/8/1	2	0.295	21.0	15.0
2014/8/29	2	0.515	13.0	6.00
2015/6/3	2	0.491	52.0	7.00
2015/6/11	2	0.554	10.0	9.00
2015/6/14	2	0.551	23.0	7.00
2016/6/27	1	0.654	86.0	12.0
2016/9/20	2	0.402	74.0	16.0
Average	-	0.441	39.3	9.88

(*) Accumulated rainfall before debris-flow occurrences

(**) Maximum rainfall depth during 10 minutes before debris-flow occurrences (mm)

Table 2. Sediment concentration calculated by DFLP at Nojiri No. 1 sabo dam

Time (y/m/d)	Disconnected wire (1st, 2nd, 3rd)	Sediment concentration near peak stage	Rainfall depth (mm) (*)	Rainfall depth during 10 min. (mm) (**)
2014/6/21	2	0.156	12.0	5.0
2014/6/27	1	0.191	55.0	10.0
2015/3/19	3	0.435	16.0	6.0
2015/4/6	1	0.371	8.00	7.0
2015/6/6	2	0.187	24.0	7.0
2016/4/21	2	0.182	15.0	8.0
2016/6/19	2	0.270	42.0	19.0
2016/6/27	2	0.443	82.0	12.0
Average	-	0.279	23.0	7.00

(*) Accumulated rainfall before debris-flow occurrences

(**) Maximum rainfall depth during 10 minutes before debris-flow occurrences (mm)

Estimated sediment concentration counts solid and liquid (mud) phase, and the value does not seem to be equal to the equilibrium sediment concentration of solid phase, that is coarse component of sediment. The bed slope at the Nojiri No. 7 sabo dam is 1/7.6 (7.50 degrees) and the supposed equilibrium concentration for coarse component of sediment is 0.147 for the bed slope, and the values of 0.235 and 0.0721 are also supposed respectively for the bed slope at the Arimura No. 3 sabo dam is 1/5.3 (10.7 degrees) and recently 1/14 (4.1 degrees). Meanwhile, averaged value of calculated sediment concentration is 0.279 and 0.441, respectively, using the DFLP system. Those values are almost twice than those of estimation by the equilibrium concentration for coarse components, and we need evaluate whether those differences are caused by liquid phase (mud), other factors and so on.

4. Conclusions

Debris-flow measurement system with loadcell and pressure sensor (DFLP system) are developed by modification of the DFLP proposed firstly in Switzerland, to almost directly measure temporal changes of debris flows. In Nojiri and Arimura Rivers in Sakurajima Island, DFLP systems were installed in March of 2013 and June of 2012, respectively. Temporal changes of debris-flow quantities need to be evaluated through stable measurement method such as direct measurements using the DFLP system, because of evaluation for internal flow structures of debris-flow surges. Several typical debris flows were measured by present methods. Results obtained using the DFLP in present study are summarized as follows.

- (1) Mass density and sediment concentration are calculated using data obtained by the DFLP system and data measured by ultrasonic level meter and surface velocity by of image analyses of CCTV camera. There are at least 10 data in Arimura River and 8 data in Nojiri River for calculations of temporal changes of mass density and sediment concentration since 2012 and 2014, respectively. Especially, coarse components (solid phase) and liquid phase of debris flows can be estimated by calculations using the DFLP system, and those mass density and sediment concentration are calculated.
- (2) Estimations for sediment concentration for each event are compared to rainfall values such as the accumulated rainfall before debris-flow occurrences and maximum rainfall depth during 10 minutes before debris-flow occurrences. Averaged value of calculated sediment concentration is 0.279 and 0.441 based on measured data obtained from DFLP systems in Nojiri No. 1 sabo dam and Arimura No. 3 sabo dam, respectively.
- (3) However, values of calculated concentration do not always take correlation with rainfall depth before debris-flow occurrences. Data analyses continuously need by more data collections of debris-flow events.

Acknowledgements

Authors should be thankful for Osumi Office of River and National Highway, Kyushu Regional Development Bureau, Ministry of Land in Japan (MLIT) for useful advice on monitoring data for present research.

References

- Itoh, T., Mizuyama, T., and Tagata, S., 2017, Direct debris flow monitoring using load cell systems in Sakurajima Island, in Proceedings, 37th IAHR World Congress: Kuala Lumpur, Malaysia, August 13 to 18, p. 1142-1150.
- McArdell, B. W., Bartelt, P., and Kowalski J., 2007, Field observations of basal forces and fluid pore pressure in a debris flow: Geophysical Research Letters, 34, L07406.
- Osaka T., Utsunomiya R., Tagata S., Itoh T., and Mizuyama T., 2014, Debris flow monitoring using load cells in Sakurajima Island, in Proceedings (edited by Fujita, M. et al.), Interpraevent 2014 Pacific Rim: Nara, Japan, November 25 to 28, O-14.pdf in DVD.

Implementation of an integrated management strategy to deal with landslide triggered debris flows: the Valloire case study (Savoie, France)

Dominique Laigle^{a,*}, Denis Jongmans^b, Frédéric Liebault^a, Laurent Baillet^b, Etienne Rey^c, Firmin Fontaine^a, Laurent Borgniet^d, Mylène Bonnefoy-Demongeot^a, Frédéric Ousset^a

^aUniv. Grenoble Alpes, IRSTEA, ETNA, Saint Martin d'Hères, 38402, France

^bUniv. Grenoble Alpes, ISTerre, CNRS, Grenoble, 38000, France

^cGéolithe SA, Crölles, 38920, France

^dUniv. Grenoble Alpes, IRSTEA, LESSEM, Saint Martin d'Hères, 38402, France

Abstract

The Rieu Benoît is a debris-flow-prone catchment located in Valloire (Savoie, France). In 2011, a lateral landslide was detected about 600 m upstream of the fan apex where houses are present. This landslide has evolved slowly since 2011 but is likely, in case of rapid collapse, to provide up to 150,000 to 200,000 m³ of material to the channel and generate intense debris flows thus threatening human settlements on the fan and in the Valloire ski resort. This paper presents a contribution to the definition of a protection strategy based on the principle that a catastrophic evolution of the landslide can be detected sufficiently in advance to set up an effective alert procedure. Such early warning system can be designed provided (i) the landslide is instrumented to properly detect its evolution and characterize the volumes likely to mobilize into debris flows, this is carried out using photogrammetric, seismic, and electrical techniques; (ii) the interaction between the landslide and the channel is observed and sufficiently understood, this is carried out using a time-lapse camera taking a picture every two hours and at higher frequency once a flow is detected by a geophone; (iii) subsequent debris flows are observed and characterized in terms of flow thickness and velocity, this is carried out at a monitoring station located at the fan apex and equipped with a radar flow stage sensor and three geophones; (iv) consequences on urbanized areas are evaluated *a priori* on the basis of scenarios, this is carried out by simulating the spreading of debris flows for different volumes and material properties. The final step consists in building alert and evacuation procedures in collaboration with local authorities.

Keywords: debris flow, landslide, monitoring, hazard assessment, risk protection

1. Introduction

The Rieu Benoît is a 6.3 km² debris flow-prone catchment located in Valloire (Savoie, France). Elevations range between 1,540 and 3,037 m a.s.l. The Rieu Benoît is a tributary of the Valloire mountain river which flows across the city and has the capacity to propagate debris flows triggered in its tributaries. Significant events were recorded in 1682, 1934, 1935, 1982, 2006, 2008, 2009 and 2011. In 2011 a lateral landslide (Fig 1.a) was detected about 600 m upstream of the fan apex where houses, buildings and roads are present (Fig 1.b). This landslide has evolved slowly since 2011 but is likely, in case of rapid collapse, to provide up to 150,000 to 200,000 m³ of material to the channel and generate intense debris flows thus threatening human settlements on the stream fan and in the Valloire ski resort. A scientific study was initiated in the aim of defining a protection strategy based on the concept of integrated management of natural risks. This strategy is based on the principle that a catastrophic evolution of the landslide could be detected sufficiently in advance to set up an effective alert procedure. Before setting such a procedure, we

* Corresponding author e-mail address: dominique.laigle@irstea.fr

need to better understand and quantify all factors potentially contributing to the debris-flow triggering. In particular, in the case of a landslide triggering, it is critical to unravel the various cascading effects that can lead to increased risk to the population. This paper focuses on the methodology and monitoring techniques used to address these questions about the physical processes at work in the considered catchment.

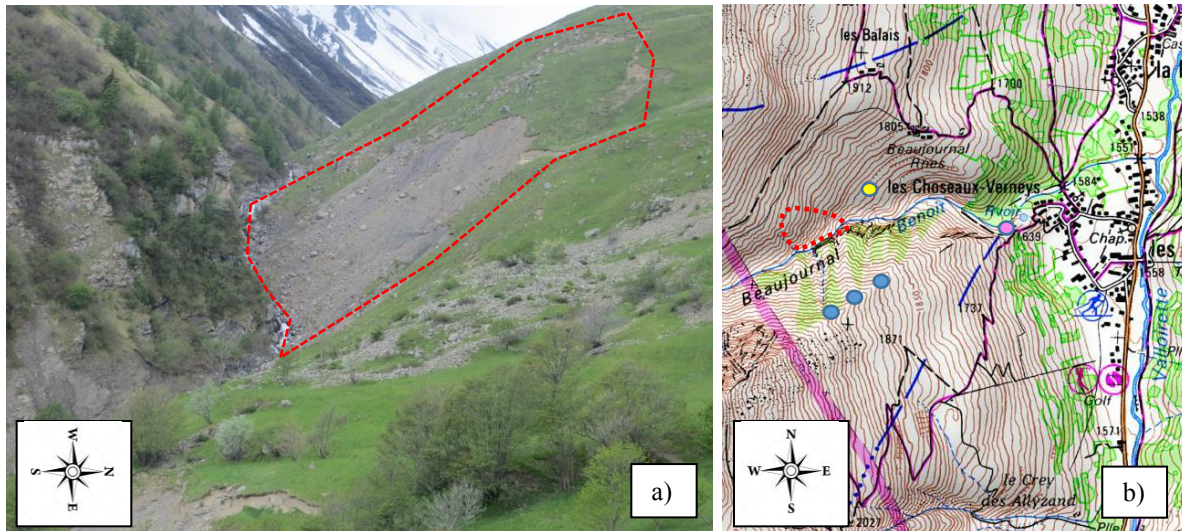


Fig. 1. (a) picture of the stream channel and approximate delineation of the landslide (red dashed line); (b) local topographic map with the downstream part of the Rieu Benoît stream including the alluvial fan and position of human settlements. The position of the lateral landslide is given by the red dotted line. Pictures for the photogrammetry study were taken from the positions marked by the blue dots (see section 3.1.). The yellow dot gives the position of the permanent observation station (see section 4.1.). The pink dot gives the position of the monitoring station (see section 5.).

2. Objectives and methodology

Our main goal is to analyze the possible cascading effects leading to an increase of the debris-flow risk. This can be achieved by considering the following points:

- Debris flows can be initiated in the upper part of the catchment, we must thus consider them independently of the landslide. This study will be mainly based on a Lidar survey covering the whole catchment, which will be used to characterize all the areas of active erosion and to analyze the connectivity of these areas with the hydrographic network. We supplement this analysis with information on past events from historical archives.
- We need to characterize the landslide and, in particular, its volume and conditions of collapse in order to create scenarios of future evolution (see section 3.)
- We need to analyze precisely the processes at the contact between the landslide and the stream channel. This area has already been recognized as a key-point of debris-flow triggering for the reasons developed in section 4.
- Because of the complexity of cascading processes, one can hardly deduce the flow characteristics (depth, velocity, discharge...) immediately upstream of the areas at stake only from consideration of the triggering conditions. Thus, we considered monitoring the flows at the apex of the stream fan. This point will be presented in section 5.
- It is only when we understand the exact impact on urbanized areas that we can set up efficient alert systems and procedures. Our strategy consists in establishing a series of hazard maps based on forecast scenarios of evolution of the landslide. This point will be presented in section 6.

3. Landslide monitoring

Before setting a permanent station to monitor the landslide evolution (Larose et al., 2015; Bottelin et al., 2013; Colombero et al., 2017), we performed preliminary photogrammetric and geophysical studies in order to estimate the landslide activity and the potential unstable volume, respectively.

3.1. Photogrammetric study

We performed two photogrammetric surveys in 2015 and 2018 to estimate the activity of the landslide. Pictures were taken from three sites located in the opposite side of the thalweg and represented by blue dots in Fig 1.b. Each pixel of the photos represents a 3 cm x 3 cm surface of the terrain and the elevation, measured with a RTK GPS, is known with a precision of 4 to 6 cm. On Fig 1.a, we can clearly see the headscarp and the lower gully. The difference between 2015 and 2018 surveys (Fig 2.) reveals maximum motions of 1.5 m, with erosion zones mainly located at the top of the gullied area and, to a lesser extent, at the headscarp. No massive motion is observed and the material moved over three years is estimated at 230 m³.

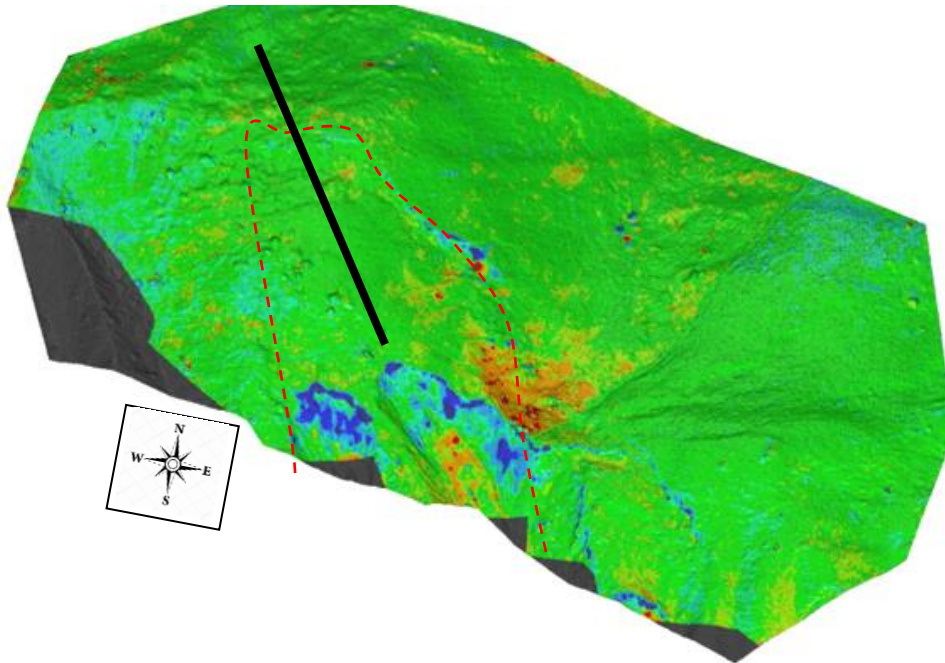


Fig. 2. Difference between the November 2015 and July 2018 photogrammetric surveys. Red: accumulation. Blue: erosion. The maximum motion is 1.5 m and the displaced volume is estimated at 230 m³. The red dashed line gives an approximate delineation of the landslide. The black line marks the position of the seismic tomography profile (see section 3.2.)

3.2. Geophysical investigation

A geophysical campaign including seismic and electrical tomography profiles was carried out in July 2018 with the aim of determining the geological structure of the slope and the prone-to-move volume. Fig 3. shows the seismic image (P-wave velocity) obtained along the slope (black line in Fig 2.). The analysis of both electrical and seismic results has led to the detection of three layers: (1) a thin, low-velocity (300-600 m/s) layer of grass cover and colluvium, (2) a 20-m-thick till layer with a velocity ranging from 800 m/s to 1,000 m/s, (3) a high-velocity (from 2,000 m/s to 2,800 m/s) layer, probably corresponding to the weathered bedrock. The permeable till layer is drained and the water table is low, probably located close to the interface with the bedrock.

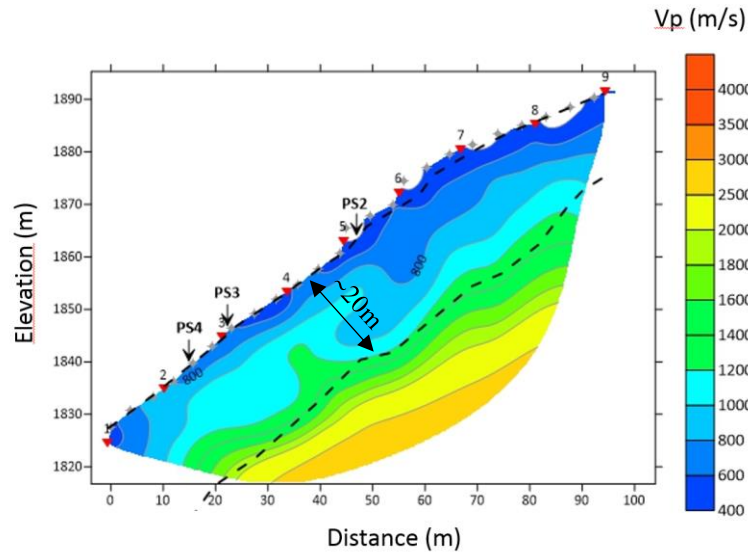


Fig. 3. Seismic tomography profile (P-wave velocity) performed along the slope (black line in Fig 2.) in the upper part of the landslide (over the gullied area).

The landslide develops in the till layer with a rupture surface (bottom of the layer) located at about 20 m below the surface (Fig 3.). From this observation, we estimate that the maximum volume of the prone-to-move material is between 150,000 and 200,000 m³. By creating different landslide scenarios, we will be able to estimate the soil volume that could reach the thalweg and generate debris flows.

4. Monitoring the landslide – stream channel interaction

The contact zone between the landslide and the stream channel is of particular interest for several reasons. The slope gradient of the stream channel is higher in this area compared to values observed upstream and downstream. The destabilization of this section by erosion could lead to the release of substantial quantities of solid material, independently of the landslide activity. Additionally, it could destabilize the bottom of the landslide and trigger its collapse. In the absence of significant erosive processes of the streambed, the collapse of the landslide would provide large quantities of solid material in this area, which are likely to be remobilized by water or debris flows coming from the upstream part of the catchment. For these reasons, it was decided to specifically monitor this area by combining two techniques: permanent observation using a camera and quantitative evaluation by comparison of DEMs obtained by Lidar surveys before and after some substantial activity is detected by the camera.

4.1. Permanent observation station

The permanent station was installed on the North bank of the stream, about 50 m above the channel. Its position is given by the yellow dot in Fig 1.b. It is mainly composed of a camera (Canon Rebel T6[®]) aimed upstream toward the base of the landslide, and a time-lapse controller (DigiSnap Pro[®]) taking a picture every two hours in normal conditions. The camera is installed on a mast, protected by a waterproof box and electric power is supplied by a solar panel (Fig 4.a). The pictures (Fig 4.b) are locally stored in full resolution and some of them are compressed and transferred using the GPRS network. The pictures are regularly visually checked to detect signs of morphological (erosion/deposition) evolution in this area. Additionally, to enhance the temporal resolution during an event, the camera is triggered by an external input based on a geophone sensor. This geophone, installed near the stream on a lateral bank, measures the vertical ground displacement speed. The geophone signal is digitalized and processed by an Arduino Nano[®] and triggers the camera every 4 seconds if it overcomes a calibrated threshold. More technical information is available in Piton et al. (2018).

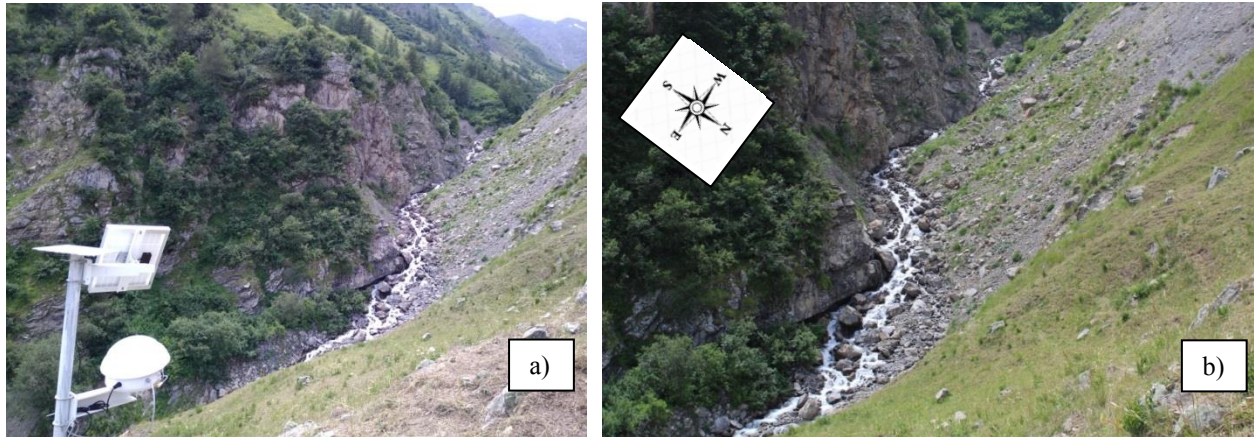


Fig. 4. (a) The permanent observation station installed about 50 m above the stream channel on the left bank and pointing upstream. Its position is given by the yellow dot in Fig. 1.b; (b) Example of a picture shot by the camera, the gullied part of the landslide can be seen on the top right side of the picture

4.2. Lidar survey of the landslide – stream channel interaction area

The direct observation of the landslide – stream channel area helps detecting processes but is not sufficient to quantify them. In that aim, we acquire a series of high-resolution DEMs of the area of interest: one initial DEM acquired in July 2018 used as a reference and one DEM each time movements are detected. Comparison of the DEMs will provide a basis for quantification. Such strategy requires acquisition techniques that can be quickly deployed. For this reason, we have chosen to carry out surveys with the help of a drone (Escadrone SIX 3[®], Fig 5.a) equipped with a Lidar (YellowScan Surveyor Ultra[®]). A 3D representation of the initial DEM, which has a resolution of one point every 0.1 m, is given in Fig 5.b.

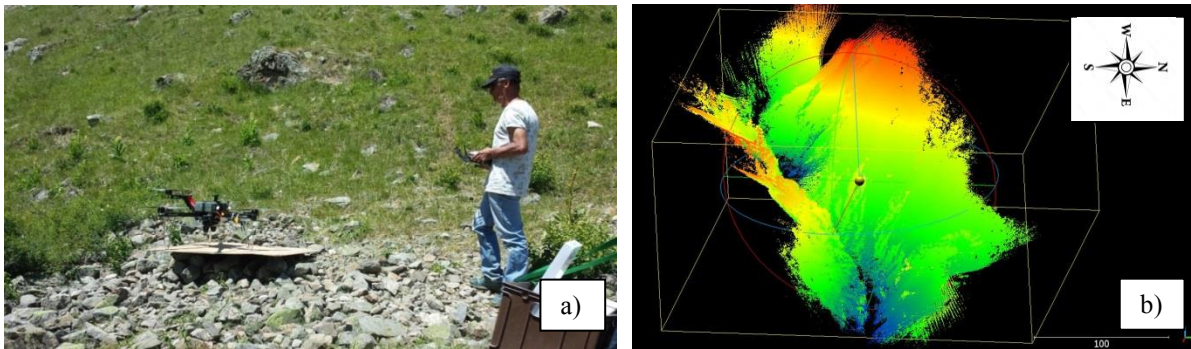


Fig. 5. (a) operating the drone; (b) 3D representation of the initial DEM acquired in July 2018 by the Lidar installed under the drone

5. Monitoring floods and debris flows at the fan apex

The main threat on human settlements comes out of the flows that are likely to reach the Rieu Benoît alluvial fan and the Valloirette downstream. Characteristics of the floods and debris flows in this area can hardly be deduced from the consideration of triggering processes only. That is why we decided to install a monitoring station at the fan apex with the objective to directly measure flow depths and velocities and to discriminate between floods with bedload transport and debris flows (Fontaine et al., 2017). The monitoring station (Fig 6.) is set up at the outlet of the gorge overhanging the fan (pink dot in Fig 1.b). It is equipped with a tipping bucket rain gauge, a radar flow stage sensor and a set of three vertical geophones, about 100 m away. Data are recorded by an environmental datalogger (Campbell Scientific CR1000X[®]) powered by a solar panel, and are stored in a SD card (Bel et al., 2017). Thanks to

the geophones located along the channel at a known distance, we can assess the velocity of the debris-flow front on the basis of the phase shift between the peak intensities of vibrations detected by each instrument (Arattano & Marchi, 2005). Flow stage and conditioned seismic signal are sampled at a 20-Hz frequency. Rainfall is totalized over a 5-min period.



Fig. 6. Flow monitoring station located at the fan apex (pink dot in Fig 1.b) with: rain gauge, solar panel and flow stage sensor on cables; all devices are connected to a datalogger.

6. Debris-flow event scenarios and associated hazard maps

As the volume of material mobilized during a single event cannot be known long before the debris flow triggers, the adopted strategy consists in building a series of scenarios and analyzing the respective possible consequences on urbanized areas. In practice, the consequences of each scenario, and, in particular, the affected area, are assessed with the help of the 2D numerical model Lave2D (Rickenmann et al., 2003) dedicated to the computation of debris-flow spreading. This model is based on shallow-water equations and on the assumption that the mechanical properties of the flowing material are properly represented by a Herschel-Bulkley rheological model, which is reasonable on this site. Each scenario will be defined as a set of input parameters: the total debris-flow volume, the peak discharge at the fan apex and the rheological parameters – yield stress, density and consistency. Simulations will be carried out on a high-resolution 1 m x 1 m DEM based on an airborne Lidar survey.

Fig 7. gives a preliminary example of such computation (with no practical pertinence), using a rough DEM and for a debris-flow volume of 50,000 m³. The recent acquisition of a precise DEM based on a Lidar survey will improve the assessment of the affected areas related to debris-flow scenarios. Once all hazard maps are available, we can quickly and easily estimate the downstream consequences of any collapse or triggering process observed upstream and we can define protection measures accordingly.

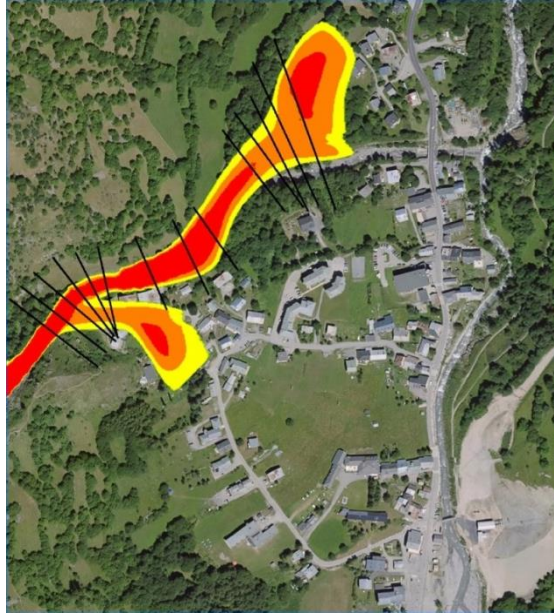


Fig. 7. Tentative example of computation of the area affected by debris flows for a single scenario, this example of a 50,000 m³ debris-flow spreading computed using a rough DEM is given for illustrative purpose only.

7. Conclusions

We have presented the principles of a protection strategy based on the concept of integrated management of natural risks and its application on the Rieu Benoît catchment, Valloire municipality, Savoie, France. The main threat on this site results from the recent activation of a lateral landslide which is likely to drastically increase the intensity of phenomena in this debris-flow-prone catchment. We have mainly presented the monitoring activity developed to improve understanding of the cascading effects, which, from a landslide collapse, may lead to debris-flow spreading in the urbanized areas of the Valloire ski resort. This study will help defining event scenarios and assessing the corresponding hazards more accurately. The next steps will consist in: 1) defining the features of a permanent alert system to be installed and transferred to the local municipality, and 2) collaborating with the local municipality to define a crisis management plan (information, warning, evacuation of the population...).

Acknowledgements

This work is part of the projects SIMOTER 1 and 2 funded by the European Union under the ERDF – POIA program and by the French government under the FNADT – CIMA program. The authors would like to thank the Valloire municipality for their cooperation in this study.

References

- Arattano, M., and Marchi, L., 2005, Measurements of debris-flow velocity through crosscorrelation of instrumentation data: *Natural Hazards and Earth System Sciences*, v. 5, no. 1, p. 137-142, doi: 10.5194/nhess-5-137-2005.
- Bel, C., Liebault, F., Navratil, O., Eckert, N., Bellot, H., Fontaine, F., and Laigle, D., 2017, Rainfall control of debris-flow triggering in the Réal torrent, Southern French Alps: *Geomorphology*, v. 291, p. 17-32, doi: 10.1016/j.geomorph.2016.04.004.
- Bottelin, P., Jongmans, D., Baillet, L., Lebourg, T., Hantz, D., Lévy, C., Le Roux, O., Cadet, H., Lorier, L., Rouiller, J.-D., Turpin, J., and Darras, L., 2013, Spectral Analysis of Prone-to-fall Rock Compartments using Ambient Vibrations: *Journal of Environmental and Engineering Geophysics*, v. 18, no. 4, p. 205-217, doi: 10.2113/jeeg18.4.205.
- Colombero, C., Baillet, L., Comina, C., Jongmans, D., and Vinciguerra, S., 2017, Characterization of the 3-D fracture setting of an unstable rock mass: From surface and seismic investigations to numerical modeling: *Journal of Geophysical Research: Solid Earth*, v. 122, no. 8, p. 6346–6366, doi: 10.1002/2017JB014111.

- Fontaine, F., Bel, C., Bellot, H., Piton, G., Liebault, F., Juppet, M., and Royer, K. , 2017, Suivi automatisé des crues à fort transport solide dans les torrents. Stratégie de mesure et potentiel des données collectées, *in* Monitoring en milieux naturels – Retours d’expériences en terrains difficiles: Collection EDYTEM no 19, p. 213-219. (in French).
- Larose, E., Carrière, S., Voisin, C., Bottelin, P., Baillet, L., Guéguen, P., Walter, F., Jongmans, D., Guillier, B., Garambois, S., Gimbert, F., and Massey, C., 2015, Environmental seismology: What can we learn on earth surface processes with ambient noise?: *Journal of Applied Geophysics*, v. 116, p. 62-74, doi: 10.1016/j.jappgeo.2015.02.001.
- Piton, G., Fontaine, F., Bellot, H., Liébault, F., Bel, C., Recking, A., and Hugerot, T., 2018, Direct field observations of massive bedload and debris-flow depositions in open check dams, *in* Proceedings, River flow 2018 conference, E3S Web of Conferences 40,03003, p. 1-8, doi: 10.1051/e3sconf/20184003003
- Rickenmann, D., Laigle, D., McArdell, B. W., and Hübl, J., 2006, Comparison of 2D debris-flow simulation models with field events: *Computational Geosciences*, v. 10, no. 2, p. 241-264, doi: 10.1007/s10596-005-9021-3.

Taking the pulse of debris flows: extracting debris-flow dynamics from good vibrations in southern California and central Colorado

Abigail Michel ^{a,b,*}, Jason W. Kean ^a, Joel B. Smith ^a, Kate E. Allstadt ^a, and Jeff A. Coe ^a

^a*U.S. Geological Survey, 1711 Illinois St, Golden, CO 80401, USA*

^b*now at B3, 518 17th St, Suite 1400, Denver, CO, 80202, USA*

Abstract

The destructive nature of debris flows makes it difficult to quantify flow dynamics with direct instrumentation. For this reason, seismic sensors placed safely away from the flow path are often used to identify the timing and speed of debris flows. While seismic sensors have proven to be a valuable tool for event detection and early warning, their potential for identifying other aspects of debris flows (such as sediment concentration) is less studied. Here, we use two monitoring sites to investigate the extent to which debris-flow dynamics can be decoded from ground vibrations. One site is a bedrock channel in a steep semiarid basin in central Colorado (Chalk Cliffs), and the other is in a debris-flow channel incised in alluvium in a recently burned area in southern California (Van Tassel). At both sites, seismic data are measured with geophones (4.5 Hz) mounted next to the channels and sampled at high frequencies (500-1000 Hz). Independent constraints on flow dynamics are provided by laser distance meters to record flow stage (at 10 Hz) and high-definition video cameras to record flow velocity and qualitative estimates of sediment concentration. The observed debris flows at Chalk Cliffs typically consist of a series of short-duration (~30 second) surges with total durations of <40 minutes and have coarse-grained fronts and fluid-rich tails. In contrast, the events at Van Tassel are longer duration flows (>40 minutes) that begin as debris flows and transform into more steady debris floods. The arrangement of sensors at both sites allows us to identify correlations between vertical ground velocity, frequency, flow stage, and qualitative estimates of sediment concentration.

Keywords: debris flow; flood; seismic; ground vibrations; post-wildfire; channel; frequency; spectrum; Colorado; California

1. Introduction

Debris flows and landslides generate seismic signals as they move downslope, which can be used to detect the event and provide early warning for communities downstream (e.g., Arattano, 1999; Hürlimann et al., 2003; LaHusen, 2005; Allstadt, 2013). A debris flow is a fast-moving flow, which carries a large amount of fine to coarse sediment downstream in steep mountainous areas. Debris flows may mobilize from the failure of a discrete landslide (e.g., Iverson, 1997), or they can be triggered by runoff and associated sediment entrainment (e.g., Coe et al., 2008). Runoff-generated debris flows, which are the focus here, typically occur in semiarid areas with abundant loose sediment situated downslope of low-permeability surfaces, such as bedrock in alpine areas or water-repellent soil in recent burn areas (Kean et al., 2013). Regardless of the style of initiation, the fast-moving and destructive nature of debris flows makes them difficult to monitor. Geophones, which can measure the ground vibrations produced by debris flows, are a robust monitoring tool because they can be placed a safe distance away from the flow path. Using seismic signals to understand debris-flow and sediment transport processes requires an understanding of how the seismic waves are generated. Quantitative models have developed specifically for bedload in rivers (e.g., Govi et al., 1993; Burtin et al., 2008; Tsai et al., 2011; Gimbert et al., 2014; Roth et al., 2016), but the equivalent for debris-flow processes is in its infancy (Huang et al., 2007; Kean et al., 2015; Lai et al., 2018; Allstadt et al., 2019). Here, we use ground vibrations created by debris flows at two sites with different flow and geologic characteristics to help extract information on flow dynamics that is not available from other instrumentation (e.g., stage sensors and videos) and to better understand the relation between a flow and the seismic signal it generates.

* Corresponding author e-mail address: abigailmichel7@gmail.com

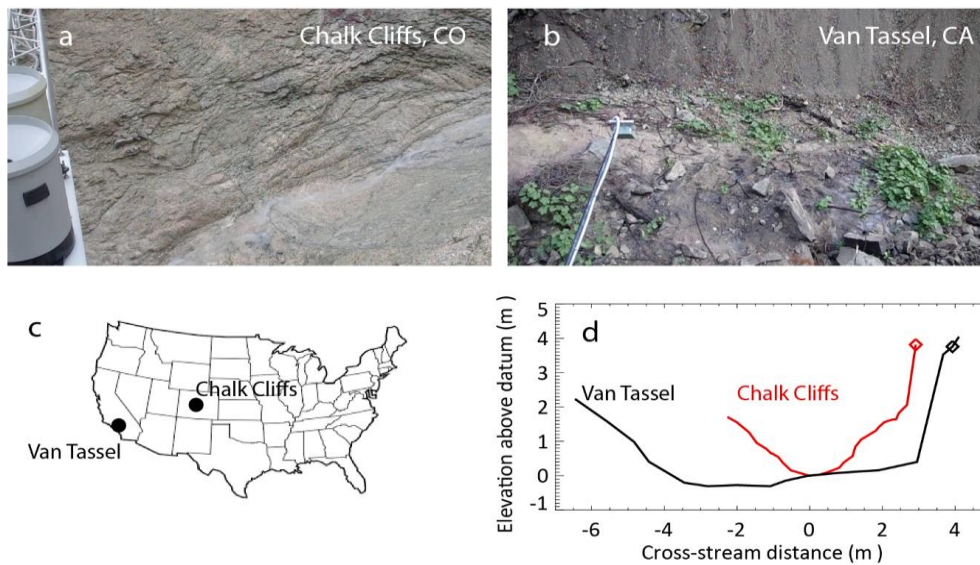


Fig. 1. Views from the banks of (a) the bedrock channel at Chalk Cliffs (5.5-m long reach), CO, and (b) the sediment covered channel at Van Tassel, CA (9.3-m long reach). (c) Locations of both study sites. (d) Cross section of Chalk Cliffs channel (red) and Van Tassel channel (black) at monitoring site locations. Diamonds show the locations of the geophones in the cross section.

2. Study Sites

The two study sites (Fig. 1 and Table 1) have semiarid climates and debris flows that are primarily triggered by runoff and associated sediment transport. One site is a narrow bedrock channel at the outlet of a 0.06 km² alpine basin in central Colorado (Chalk Cliffs), and the other site is a wider sediment-covered channel at the outlet of a recently burned 4 km² basin in southern California (Van Tassel). Although the two locations have similar debris-flow initiation processes, the two sites have substantially different drainage areas, channel dimensions, and geologic materials, and thus, have different flow characteristics and seismic signals. Both Van Tassel and Chalk Cliffs have similar instrumentation (described below) with high-frequency data recorded during rainstorms.

2.1. Van Tassel, California

The Van Tassel site is in the Angeles National Forest within the granitic San Gabriel Mountains in southern California. Most of the drainage area above the station was burned at moderate and high severity by the Fish fire, which began on June 20, 2016. Wildfires temporarily alter the hydrologic response of a watershed by decreasing the infiltration capacity of the soil and making soils easier to erode (Moody et al., 2013). These changes greatly increase the susceptibility of steep basins to debris flows for several years after the fire (Cannon et al., 2010). Between the fire and the first winter rainstorm in December 2016, the channels above the Van Tassel basin were loaded with dry ravel from the steep (>35°) burned hillslopes. The dry ravel further increased the sediment cover at the station (Fig. 1b). We analyze the first two flow events after the fire. The first event on December 16, 2016, was a debris flow (sediment concentration >40%), and the second event on January 20, 2017, was a debris flood (sediment concentration between 10% and 40%) (Fig. 2).

2.2. Chalk Cliffs, Colorado

Chalk Cliffs is in the Sawatch Range of the Rocky Mountains in central Colorado. The cliffs are a band of hydrothermally altered quartz monzonite that is highly fractured. Additionally, the area has very sparse vegetation cover and 60% of the drainage is exposed bedrock (Coe et al., 2008). The slopes in the basin are very steep, with colluvium slopes ranging from 25° to 40° and bedrock slopes ranging from 40° to almost vertical (Coe et al., 2008). Several debris flows occur each year between May and October, when intense rainfall produces runoff from the steep slopes that entrain loose channel material accumulated from winter rockfall. The debris flows at Chalk Cliffs are short

in duration (<40 min) compared to Van Tassel and generally contain a series of surges (~30 seconds each). The channel at the monitoring station is typically covered with sediment from the beginning of the summer until debris flows scour the channel to bedrock by mid-summer. The sediment cover has a strong damping effect on the debris-flow ground vibrations (Kean et al., 2015). Here, we focus on two events when the channel had a bare bedrock bed, to contrast the signals with the sediment-covered Van Tassel channel (Fig. 1a, 1b).

Table 1. Summary of site characteristics

Site Characteristics	Van Tassel	Chalk Cliffs
Setting	Recent burn area	Alpine
Drainage area	4 km ²	0.06 km ²
Channel width	7 m	3 m
Channel slope	7° (over 30 m)	17° (over 42 m)
Channel material	Sediment covered (Alluvium)	Exposed bedrock (Quartz monzonite)
Debris-flow duration	>40 min	<40 min with ~30 sec surges

3. Measurement Methods and Data Analysis

The debris-flow monitoring systems at Van Tassel and Chalk Cliffs are similar and record high-frequency data when a rainfall threshold is exceeded. The instrumentation at each site includes a rain gage, multiple geophones, a laser distance meter to measure flow stage, and a high-definition video camera to record flow characteristics and velocity. Rainfall is measured using a tipping-bucket rain gage, installed near the channel cross sections, and sampled every 2 seconds. Rainfall data are used to calculate 5-minute peak rainfall intensities (I_5), which have been closely correlated with debris flows in both study settings (Kean et al., 2013). Both sites use 4.5 Hz geophones connected to a seismic data recorder. Both seismic stations are digitized at a high gain of 32, have 629,327 counts per volt, and a geophone sensitivity of 32 v/m/s. At Van Tassel, there are three single-channel geophones mounted vertically along the channel and sampled at a rate of 500 Hz. At Chalk Cliffs, there are two triaxial geophones that are sampled at a rate of 1000 Hz. In this analysis, we focus on the records from a single vertical geophone at each site, which is located on the side of the channel at the same cross section where stage is measured (Fig. 1d). Laser distance meters are used to measure flow stage at both sites. They are suspended ~3 m above the channels and sampled at a rate of 10 Hz. The Chalk Cliffs laser is installed on a bridge section directly over the channel (Fig. 1a). Distance measurements are converted to flow stage above the bedrock channel bed. To avoid the possibility of being destroyed by large flows, the laser distance meter at Van Tassel was not mounted directly over the channel. Instead, the Van Tassel laser is suspended at an angle on the side of the channel (Fig. 1b). Flow stage at Van Tassel is estimated by multiplying the laser distance measurements by the cosine of the shot angle. High-definition cameras at both locations are used to record information on flow type and velocity during daytime events (see Smith et al., 2019). Video and seismic recording is triggered using a rainfall threshold. At Van Tassel, there is a single camera mounted on the side of the channel. At Chalk Cliffs, there are two cameras, one located at the bridge cross section at the channel (view in Fig. 1a) and another on the opposite side of the basin with a broader view of the channel (view in Fig. 2a and 2b). We use the videos and their audio to interpret how the flow characteristics, such as sediment concentration, vary with time and as a timeline of events to compare to seismic observations.

From each site, two events with different levels of sediment concentration were chosen for analysis. A low-water content (sediment-rich) debris flow at Chalk Cliffs occurred on August 4, 2017, and was triggered by a rainstorm with a peak I_5 of 20 mm/hr. The surges are typical at the site and consist of coarse-grained fronts and fluid-rich tails lasting less than a minute in duration (Fig. 2a). A second more watery debris flow at Chalk Cliffs occurred a day later, on August 5, 2017, when rainfall intensities were much greater ($I_5 = 80$ mm/hr) than the previous day. This debris flow lasted approximately 13 minutes and contained a series of sediment-rich surges embedded within a steadier, more watery flow. This event also had a higher peak surge velocity (7.2 m/s) than the previous day (2.6 m/s) (Fig. 2b). The maximum grain sizes in the August 5 debris flow (~0.3 m, Fig. 2a) were also larger than on August 4 (~0.1 m, Fig. 2b). At Van Tassel, the first event was a debris flow that occurred on December 16, 2016, during the first major

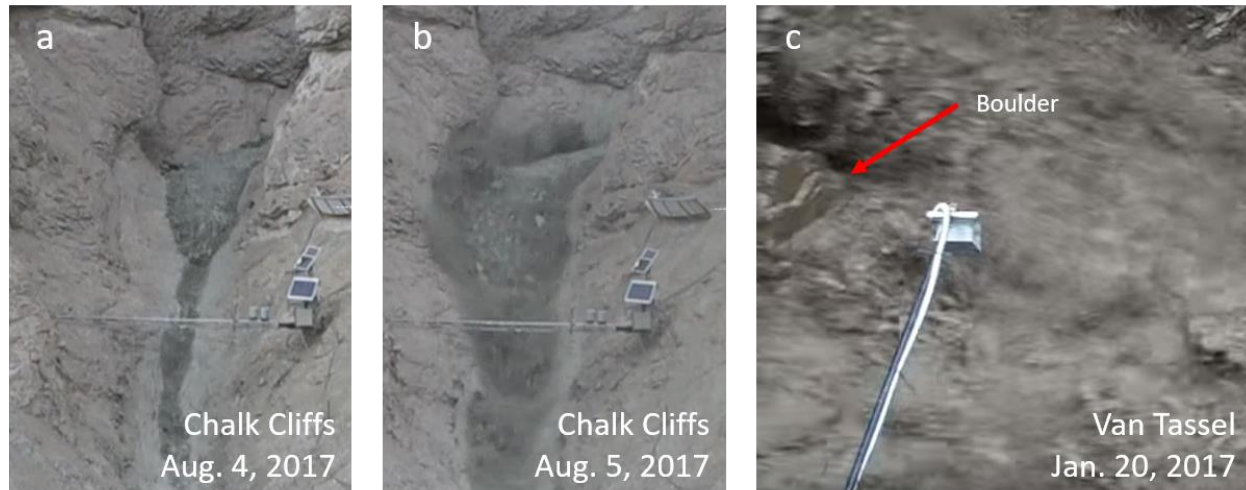


Fig. 2. (a) Low-water content debris flow at Chalk Cliffs on August 4, 2017; (b) High-water content debris flow at Chalk Cliffs on August 5, 2017; (c) Debris flood at Van Tassel on January 20, 2017. A ~ 1 -m diameter boulder can be seen in the left of the image. An image of the December 16, 2016 debris flow at Van Tassel is not available because the event occurred at night.

rainstorm after the fire, with a peak I_5 of 60 mm/hr. The event occurred at night, and the video images were too dark to interpret. Although video cannot confirm the flow was a debris flow, we assume it was a debris flow based on the characteristics of the flow-stage time series, which show an abrupt rise in stage similar in shape to surge fronts measured in other post-fire debris flows in southern California (Kean et al., 2011). The second event at Van Tassel was a debris flood that occurred on January 20, 2017, following the third major rainstorm after the fire ($I_5 = 40$ mm/hr). This flow lasted approximately 40 minutes, had a flow velocity of approximately 5 m/s, and transported ~ 1 -m diameter boulders (Fig. 2c) and large woody debris.

For each event, the seismic records were corrected to physical units of vertical ground velocity (V) and plotted with flow stage. Vertical ground velocity was determined from a function of the recorded counts, gain, and sensitivity of the geophone and digitizer. Spectrograms were then created with a 5-s window and were normalized by their respective absolute maximums. Most of the periods with high seismic power were correlated with times of high stage. However, raindrop impacts also contributed to the seismic signal at both sites with comparable amplitudes as vibrations generated by the flows. We isolated the seismic signature of rainfall impacts by analyzing the geophone time series during the intense triggering rainfall that occurred before the arrival of the flows. The timing of this rainfall noise was closely correlated with the time stamps of rain gage bucket tips. We found that rainfall impacts generally create high-frequency seismic energy on our sensors ($\sim >30$ Hz), whereas the seismic signal of the flows produced energy at both low and high frequencies ($\sim <30$ Hz and $\sim >30$ Hz, respectively). To remove rainfall noise, we applied a lowpass Butterworth, zero-phase filter to the geophone signals with a cutoff frequency of 30 Hz. After applying the filter and examining the time series of each event, it was clear that most of the effect from the rainfall had been removed while the low-frequency signal from the flows remained (Fig. 3b and 3d).

3.1. Low-water content debris flow at Chalk Cliffs on August 4, 2017

The first event consists of two 30-second surges about 1 min and 15 sec apart from each other (Fig. 3a and 3b). The spectrogram shows three identifiable peaks in amplitude (Fig. 3a). The first peak is an impact from a rock rolling down the channel, as confirmed in the video. The following two peaks in amplitude are broader and correspond to the two surges, labeled as high sediment concentration flows. The ground velocity time series displays an increase in V that tapers to a lower V as the surge passes the station (Fig. 3b). Surges often identified in debris flows are commonly characterized by a sediment-rich front followed by a water-rich tail. Surge fronts generally exert forces orders of magnitude greater and flow heights significantly higher than the rest of the flow (Iverson, 1997). The impacts of the

large grain sizes that have accumulated at the front of the surges produce the peak amplitudes, and the amplitudes diminish as the flow tail passes the station (Huang et al., 2007).

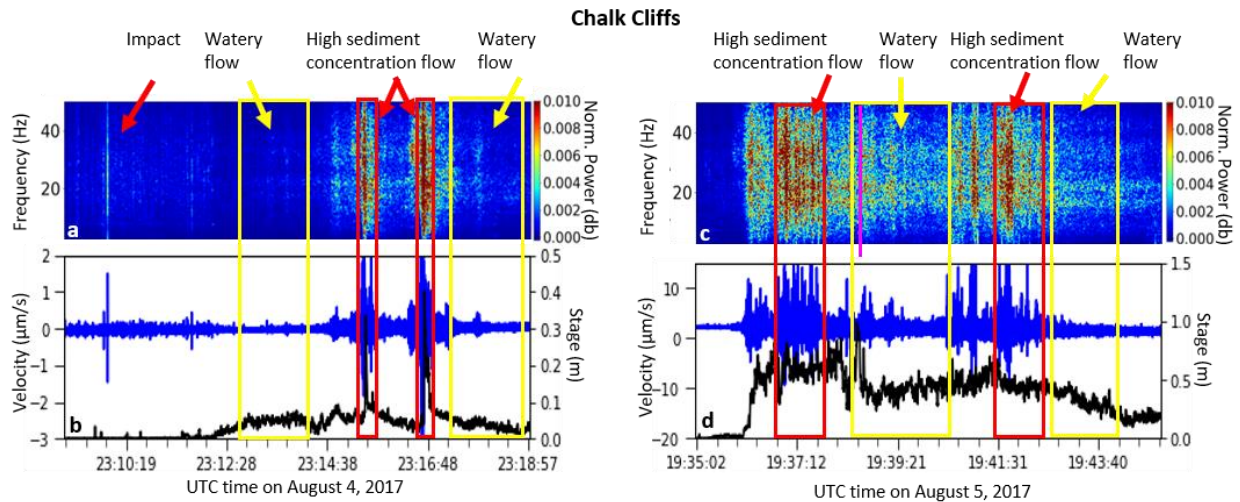


Fig. 3. Chalk Cliffs ground vibrations and flow stage for (a and b) low-water content debris flow on August 4, 2017, and (c and d) high-water content debris flow on August 5, 2017. (a and c) Normalized spectrograms of ground velocity. (b and d) Time series of lowpass filtered ground velocity (blue) and flow stage (black).

3.2. High-water content debris flow at Chalk Cliffs on August 5, 2017

The second event at Chalk Cliffs is a larger event, both in maximum V as well as flow heights (Fig. 3c and 3d). The time series shows periods of high ground motion velocity are longer in duration than the first event. The maximum flow height reaches 1 m, double the height of the flow of the other event. Although this debris flow was larger, similar characteristics to the previous day's event are visible in both the time and frequency domain. Short surges are identified within the larger flow by correlating values of high stage, high V , and high energy in the frequency domain (indicating a large amount of debris). Another good indicator of the surge is the sudden peak in ground velocity that slowly tapers, as seen in the previous event. The watery tail at the end of the surge has higher amplitude V than the tail of the previous event, suggesting that later tail had greater flow velocity and sediment concentration. The video shows that the high flow depths transport a larger variation in grain sizes in comparison to the event from the previous day. Unlike the first event at Chalk Cliffs, the highest amplitudes in V ($t = \sim 19:37:12$ and $\sim 19:41:43$) do not coincide with the peak stage ($t = 19:38$). This difference suggests that the flow during the peak stage had slightly lower sediment concentrations than at other times during the flow.

3.3. Debris flow at Van Tassel, December 16, 2016

The first major rainstorm after the fire produced a debris flow at Van Tassel (Fig. 4a and 4b). At the start of the flow, there are several short impulsive signals in the amplitude (duration < 1 s) that correspond to a broad range of frequencies and high power in the spectrogram. Two possibilities for the source of the impulsive signals are thunder and impacts from large clasts, which have been shown by Hsu et al. (2011) and McCoy et al. (2013) to create large excursions from the mean normal force. Audio from the nighttime video footage did not record any thunder. We therefore interpret the brief spikes in V , which have high power across a broad frequency range, to be impacts from large clasts in the flow (labeled as "impacts" in Fig. 4a). Two minutes after the beginning of the flow, the stage time series ends, because mud splatter covered the laser. Five minutes after the beginning of flow, there are two 90-second periods of high power (labeled "High sediment concentration flow" in Fig. 4a). The power is greatest at the beginning of the period and gradually tapers with time. We interpret these periods to be pulses of high sediment concentration with large clasts. Unlike the two events at Chalk Cliffs, the high amplitude V is sustained for a long period of time (as opposed to occurring briefly during surges), suggesting that the first flow at Van Tassel had high sediment concentrations during most of the flow. It is not until around 11:38 UTC that a signal suggesting a watery tail arrives

as evidenced by the lack of high power in the spectrogram, but we cannot confirm with the video because this event occurred at night.

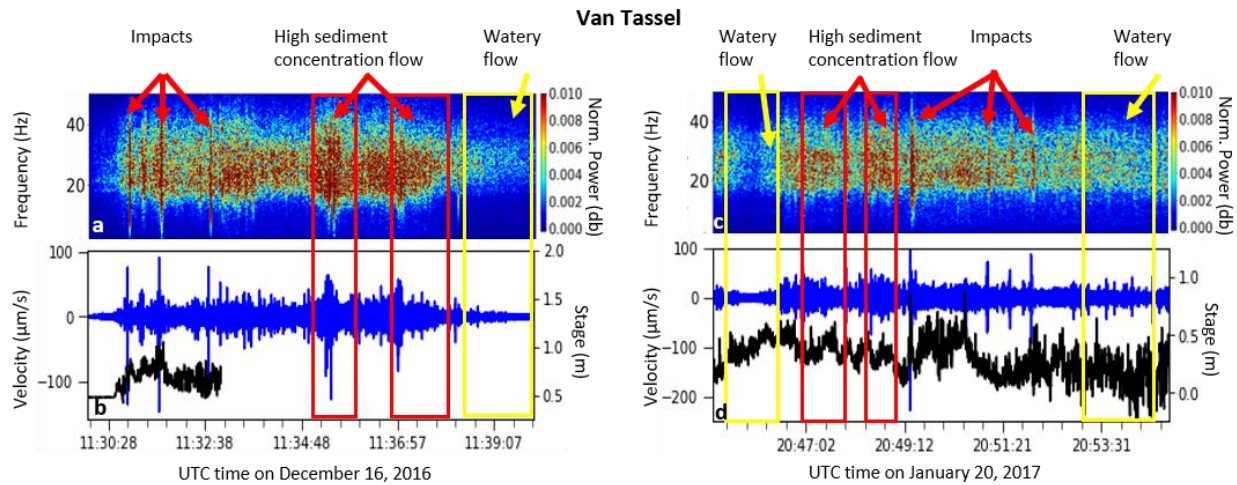


Fig. 4. Van Tassel ground vibrations and flow stage for (a and b) debris flow on December 16, 2016, and (c and d) debris flood on January 20, 2017. (a and c) Normalized spectrograms of ground velocity. (b and d) Time series of lowpass filtered ground velocity (blue) and flow stage (black).

3.4. Debris flood at Van Tassel, January 20, 2017

Based on video observations, the second event at Van Tassel was a debris flood (Fig. 4c and 4d). The flow lasted for over 40 minutes, although we focus our analysis on the 10 minutes around the time of peak flow. Despite the fact the flow has lower sediment concentrations than a debris flow, the time series of V resembles patterns like the Chalk Cliffs surges, displaying periodic peaks in V that gradually taper. Along with these surges, large spikes in V with high power across the frequency domain indicate that there were periodic large impacts from boulders such as the one seen in Fig. 2c.

Like the first event at Van Tassel, the flow has high vertical ground velocities and high power distributed throughout much of the flow, showing debris is consistently being transported. However, the event on January 20 also has periods of low power within the spectra during times of high stage (labeled watery flow in Fig. 4c and 4d). We interpret these periods as times when the flood had much lower sediment concentrations than times when the spectra had high power.

4. Discussion and Conclusions

Comparison of the events at the two field sites with different sediment concentrations has shown that a significant amount of information can be derived from near-channel ground vibrations. At Chalk Cliffs, we observed that a flow in a bare bedrock channel produced a seismic signal with a broad frequency range (5 Hz to 400 Hz), whereas the sediment-covered channel at Van Tassel had a limited frequency range, with similar low-frequency characteristics but much lower peak frequencies (5 Hz to 100 Hz). The effect of sediment cover on the frequency content is best seen in the unfiltered spectrograms shown in Fig. 5. In a previous study conducted by Kean et al. (2015), it was observed that the maximum amplitude of V recorded from ball drop tests on loose sediment was orders of magnitude smaller than the maximum amplitude of V recorded on bare bedrock. For this reason, the difference of frequency bands seen between the two sites is thought to be due to the bare bedrock channel of Chalk Cliffs as compared to the dampening that occurred from the sediment-covered channel of Van Tassel. Additional differences between the ground vibration response at the two sites may be due to differences in flow speed, channel gradient, grain size distribution, instrument response, and seismic attenuation between the two sites. We also found that rainfall was an important source of seismic noise at high frequencies. For this reason, it was important to remove the rainfall signal using a lowpass filter to isolate the signal from the flow. In addition, we were able to infer times where large debris such as boulders or trees were transported within the flow by using the deviations from the average frequencies. The large impacts (Figs. 3 and 4)

stand out as an impulse on the time-series signal and in the spectrogram and are especially clear during periods of lower sediment concentration.

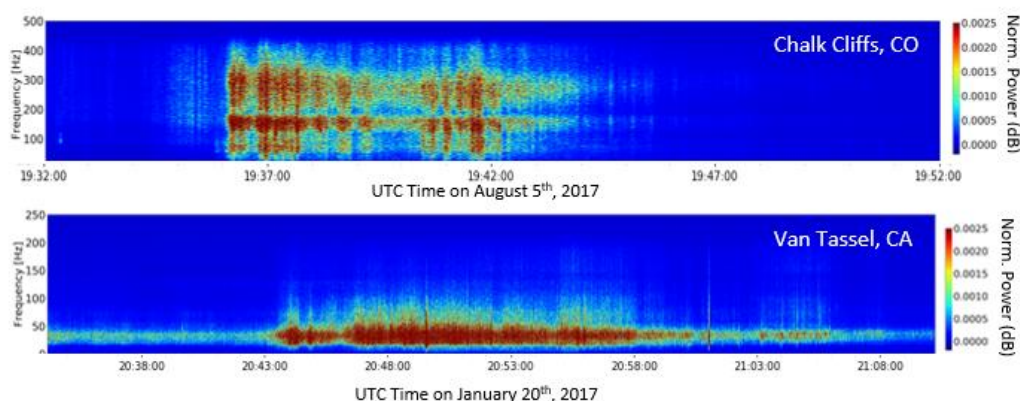


Fig. 5. Comparison of unfiltered spectrograms for events at Chalk Cliffs (bedrock channel) and Van Tassel (sediment-covered channel). The presence of loose sediment on the bed of the Van Tassel channel substantially damps the high-frequency vibrations relative to Chalk Cliffs.

All four events had substantial contrasts in relative frequency amplitudes between times of high-sediment concentration flows and low-sediment concentration flows. These contrasts are well illustrated by the amplitude spectrums of ground velocity during 15-s time windows in each event (Fig. 6). Flow periods with higher sediment concentrations (orange lines) have greater ground velocity amplitudes than flows with lower sediment concentrations (blue lines), though these comparisons are not normalized by stage or flow velocity.

Our observations show that complementary observations of flow stage, video, and ground vibrations reveal a more complete picture of debris-flow and debris-flood dynamics than can be obtained with a single style of measurement. Moreover, the combination of sensors provides measurement redundancy that can fill gaps in observation when one sensor does not work (such as when a laser is destroyed or splattered with mud, or a nighttime event that cannot be observed with video). However, much additional work is needed to move beyond the qualitative observations of sediment concentration presented here to quantitative estimates of sediment volumes and grain size. Our data show that one challenge to making quantitative measurements of sediment concentration is the different seismic properties of the channel bed (i.e., the seismic properties of loose bed sediment versus bedrock and attenuation and scattering of the signal between station and source), which can vary during a flow. Emerging theory, such as Lai et al. (2018), and laboratory-style observations, such as Allstadt et al. (2019) are providing new insights into the seismic signature of debris flows that should further unlock the potential for seismic measurements to aid the understanding of debris-flow dynamics.

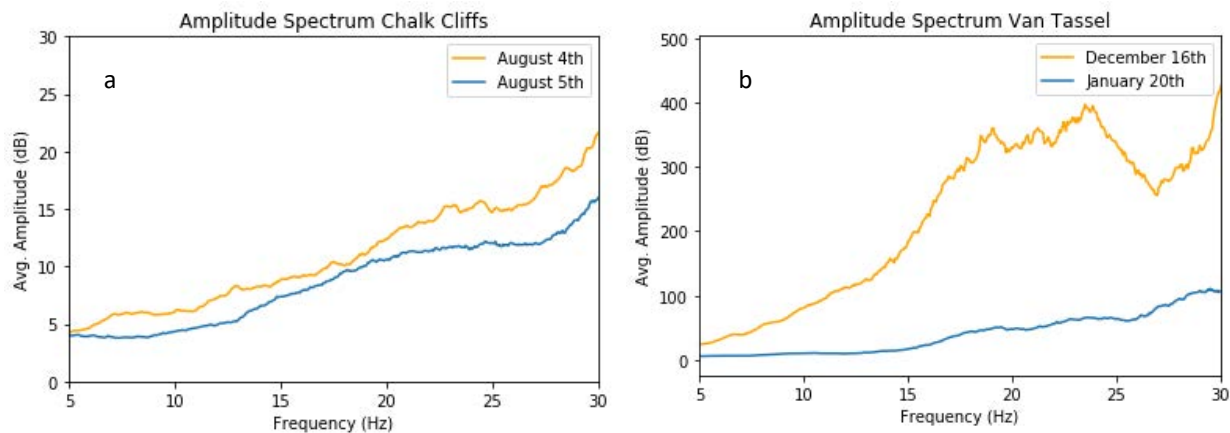


Fig. 6. Comparison of amplitude spectrums in 15-s time slices of ground velocity during flows with comparatively lower (orange) and higher (blue) water contents at (a) Chalk Cliffs and (b) Van Tassel. The events and time windows are: Chalk Cliffs low-water content debris flow on August 4, 2017, 23:16:38 to 23:16:53 (a, orange); Chalk Cliffs high-water content debris flow on August 5, 2017, 19:39:45 to 19:40:00 (a, blue); Van Tassel debris flow on December 16, 2016, 11:35:15 to 11:35:30; and Van Tassel debris flood on January 20, 2017 (b, blue). Amplitude spectrums are averaged over a 0.2-s window.

Acknowledgements

We thank Michaela Wenner, Corina Cerovski-Darriau, and an anonymous reviewer for thoughtful comments that improved the paper.

References

- Allstadt, K., 2013, Extracting source characteristics and dynamics of the August 2010 Mount Meager landslide from broadband seismograms, *J. Geophys. Res. Earth Surf.*, v. 118, p. 1472–1490, doi:10.1002/jgrf.20110.
- Allstadt, K.E., Farin, M., Lockhart, A.B., McBride, S.K., Kean, J.W., Iverson, R.M., Logan, M., Smith, J.B., Tsai, V.C., and George, D., 2019, Overcoming barriers to progress in seismic monitoring and characterization of debris flows and lahars, this volume.
- Arattano, M., 1999, On the use of seismic detectors as monitoring and warning systems for debris flows, *Nat. Hazards*, v. 20, p. 197–213.
- Barrière, J., Oth, A., Hostache, R., and Krein, A., 2015, Bed load transport monitoring using seismic observations in a low-gradient rural gravel bedstream, *Geophys. Res. Lett.*, v. 42, p. 2294–2301, doi:10.1002/2015GL063630.
- Burtin, A., Bollinger, L., Vergne, J., Cattin, R., and Na'be'lek, J.L., 2008, Spectral analysis of seismic noise induced by rivers: A new tool to monitor spatiotemporal changes in stream hydrodynamics, *J. Geophys. Res.*, v. 113, B05301, doi:10.1029/2007JB005034.
- Cannon, S.H., Gartner, J.E., Rupert, M.G., Michael, J.A., Rea, A.H., and Parrett, C., 2010, Predicting the probability and volume of postwildfire debris flows in the intermountain western United States, *Geol. Soc. Am. Bull.*, v. 122, p. 127–144.
- Coe, J., Kinner, D., and Godt, J., 2008, Initiation conditions for debris flows generated by runoff at Chalk Cliffs, central Colorado. *Geomorphology*, 10.1016/j.geomorph.2007.03.017.
- Díaz, J., Ruíz, M., Crescentini, L., Amoroso, A., and Gallart, J., 2014, Seismic monitoring of an alpine mountain river, *J. Geophys. Res. Solid Earth*, v. 119, p. 3276–3289, doi:10.1002/2014JB010955.
- Gimbert, F., Tsai, V.C., and Lamb, M.P., 2014, A physical model for seismic noise generation by turbulent flow in rivers, *J. Geophys. Res. Earth Surf.*, v. 119, p. 2209–2238, doi:10.1002/2014JF003201.
- Hsu, L., Finnegan, N.J., and Brodsky, E.E., 2011, A seismic signature of river bedload transport during storm events, *Geophys. Res. Lett.*, v. 38, L13407, doi:10.1029/2011GL047759.
- Huang, C.-J., Yin, H.-Y., Chen, C.-Y., Yeh, C.-H., and Wang, C.-L., 2007, Ground vibrations produced by rock motions and debris flows, *J. Geophys. Res.*, v. 112, F02014, doi:10.1029/2005JF000437.
- Hürlimann, M., Rickenmann, D., and Graf, C., 2003, Field and monitoring data of debris-flow events in the Swiss Alps, *Can. Geotech. J.*, v. 40, p. 161–175.
- Iverson, R.M., 1997, The physics of debris flows, *Reviews in Geophysics*, v. 35, no. 3, p. 245–296.
- Kean, J.W., Staley, D.M., and Cannon, S.H., 2011, In situ measurements of post-fire debris flows in Southern California: Comparisons of the timing and magnitude of 24 debris-flow events with rainfall and soil moisture conditions, *J. Geophys. Res.*, v. 116, F04019, doi:10.1029/2011JF002005.
- Kean, J.W., Coe, J.A., Coviello, V., Smith, J.B., McCoy, S.W., and Arattano, M., 2015, Estimating rates of debris flow entrainment from ground vibrations, *Geophys. Res. Lett.*, v. 42, doi:10.1002/2015GL064811.
- Kean, J.W., McCoy, S.W., Tucker, G.E., Staley, D.M., and Coe, J.A., 2013, Runoff-generated debris flows: Observations and modeling of surge initiation, magnitude, and frequency, *J. Geophys. Res. Earth Surf.*, v. 118, p. 2190–2207, doi:10.1002/jgrf.20148.
- Lai, V.H., Tsai, V.C., Lamb, M.P., Ulzio, T.P., and Beer, A.R., 2018, The seismic signature of debris flows: Flow mechanics and early warning at Montecito, California, *Geophysical Research Letters*, v. 45, no. 11, doi: 10.1029/2018GL077683.
- McCoy, S.W., Tucker, G.E., Kean, J.W., and Coe, J.A., 2013, Field measurement of basal forces generated by erosive debris flows, *J. Geophys. Res. Earth Surf.*, v. 118, p. 589–602, doi:10.1002/jgrf.20041.
- Moody, J.A., Shakesby, R.A., Robichaud, P.R., Cannon, S.H., and Martin, D.A., 2013, Current research issues related to post-wildfire runoff and erosion processes, *Earth Sci. Rev.*, v. 122, p. 10–37, doi:10.1016/j.earscirev.2013.03.004.
- Roth, D.L., Brodsky, E.E., Finnegan, N.J., Rickenmann, D., Turowski, J.M., and Badoux, A., 2016, Bed load sediment transport inferred from seismic signals near a river, *J. Geophys. Res. Earth Surf.*, v. 121, p. 725–747, doi:10.1002/2015JF003782.
- Roth, D.L., Finnegan, N.J., Brodsky, E.E., Rickenmann, D., Turowski, J.M., Badoux, A., and Gimbert, F., 2017, Bed load transport and boundary roughness changes as competing causes of hysteresis in the relationship between river discharge and seismic amplitude recorded near a steep mountain stream, *J. Geophys. Res. Earth Surf.*, v. 122, p. 1182–1200, doi:10.1002/2016JF004062.
- Schmandt, B., Aster, R.C., Scherler, D., Tsai, V.C., and Karlstrom, K., 2013, Multiple fluvial processes detected by riverside seismic and infrasound monitoring of a controlled flood in the Grand Canyon, *Geophys. Res. Lett.*, v. 40, p. 4858–4863, doi:10.1002/grl.50953.
- Smith, J.B., Kean, J.W., and Coe, J.A., 2019, Exploring controls on debris-flow surge velocity and peak discharge at Chalk Cliffs, Colorado, USA, this volume.
- Tsai, V.C., Minchew, B., Lamb, M.P., and Ampuero, J., 2012, A physical model for seismic noise generation from sediment transport in rivers. *Geophys. Res. Lett.*, v. 39, L02404, doi:10.1029/2011GL050255.

Observations on the development and decay processes of debris-flows

Masaki Murasawa , Fumitoshi Imaizumi, Yushi Yokota

Affiliation, Faculty of Agriculture, Shizuoka University, 836, Ohya, Kita-ku, Shizuoka City, 422-8529, Japan

Abstract

It is important to understand the development and decay processes of debris-flows in order to plan effective debris-flow countermeasures. However, few studies have successfully observed the development and decay processes of debris-flows. This study aimed to reveal changes in characteristics of debris-flow surges as they flow down, based on observation using time lapse cameras installed at multiple sites along a debris-flow torrent in the upper Ichinosawa catchment within the Ohya landslide, central Japan. Observation results showed that debris-flow surge volume and flow velocity tended to increase in the section just below their initiation point. In the subsequent section, debris-flow surges tended to maintain their volume and flow velocity while descending. Increases in flow velocity were observed in sections with a fixed bed, the channel bed consists of exposed bedrock with no sediment cover. Debris-flow surge volume and velocity tended to decrease in these sections, in which channel gradient decreases abruptly. These observation results can be explained by the theory of equilibrium concentration, which states that sediment concentration in the flow approaches the equilibrium concentration given from the channel gradient by the erosion and deposition of sediment. At the same time, small debris-flow surges tended to terminate with a short travel distance, which cannot be explained fully by the theory of equilibrium concentration.

Keyword: Ohya landslide; observation; development and decay; the equilibrium concentration; fixed bed

1. Introduction

Debris-flows cause severe natural disasters due to their high velocity, and destructive power. It is important to understand the development and decay processes of debris-flows in order to plan effective debris-flow countermeasures. To clarify these processes, laboratory experiments have been conducted and developed the models based on physical flow mechanisms (Egashira et al., 1986; Iverson, 1997; Suzuki et al., 2009). One of representative models is the theory of equilibrium concentration, which states that sediment concentration in the flow approaches the equilibrium concentration given from the channel gradient by the erosion and deposition of sediment (Takahashi, 1977; Imaizumi et al., 2017; Lazoni et al., 2017).

Field observations are another approach to understand the behaviors of debris-flows, and have been conducted in many countries including China (Chu et al., 2011), Italy (Arattano et al., 2012), Japan (Okano et al., 2009; Suzuki and Suzuki, 2009), Switzerland (Berger et al., 2010). These studies have confirmed that debris-flows consist of multiple surges (Abanó et al., 2014; Imaizumi et al., 2016), and a surge frequency near the initiation zones of debris-flows is usually higher than that observed downstream (Kean et al., 2013). However, most of these observations have been conducted in the transportation and deposition zones, while observations on the changes of characteristics of debris-flows at multiple sites in the initiation zones are scarce (Arattano et al., 2012; McCoy et al., 2012). These observations are needed in order to reveal the development processes of debris-flows and verify the correspondence with the theories.

In this study, field observations of debris-flows were made using time-lapse cameras at multiple sites along a debris

* Corresponding author e-mail address: m.murasawa45@gmail.com

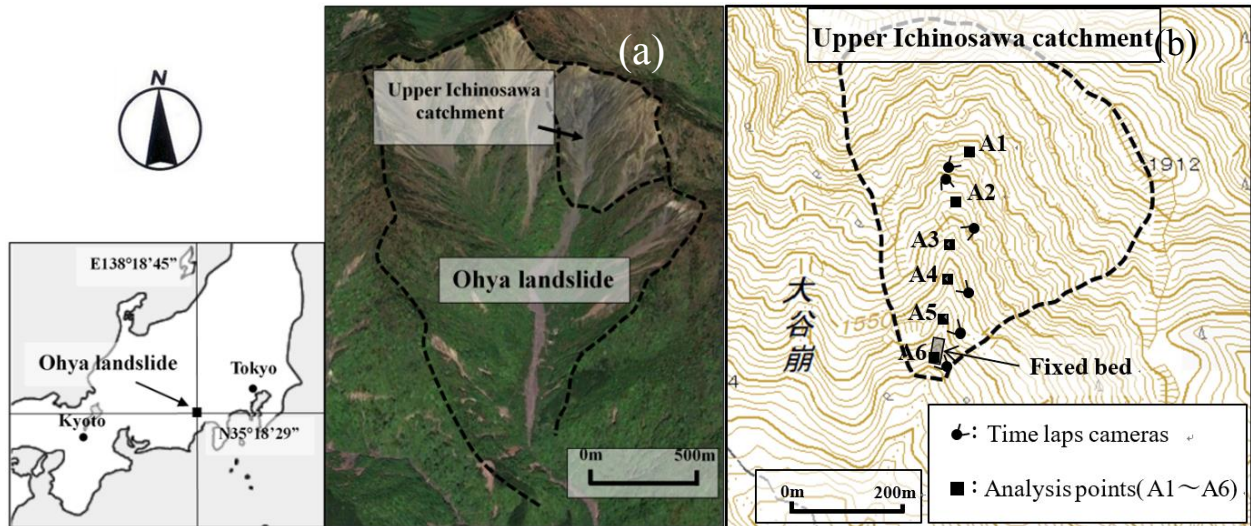


Fig. 1. Map of the Ohya landslide and the upper Ichinosawa catchment. (a) Satellite image of the Ohya landslide (Google Earth). (b) Topographic map of the upper Ichinosawa catchment showing locations of the time laps cameras and analysis points

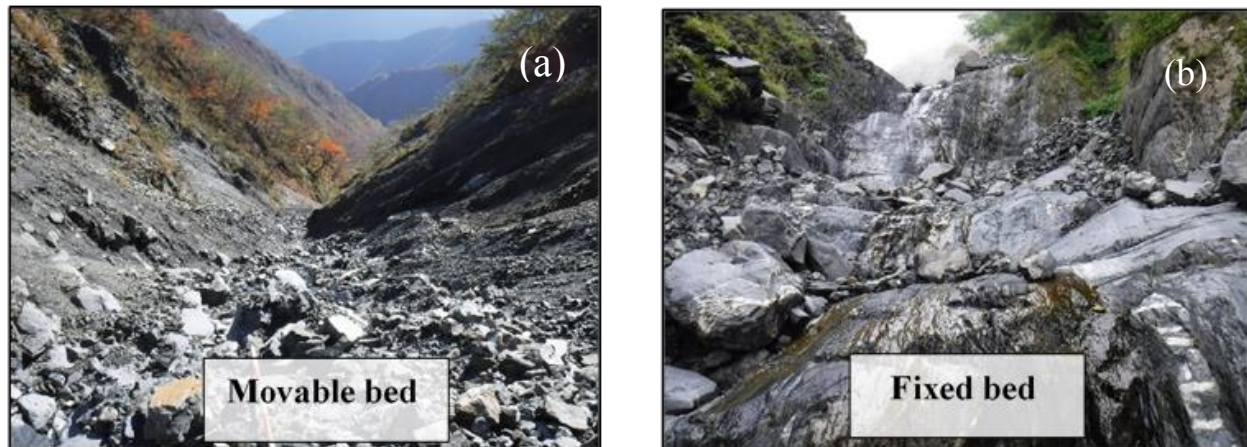


Fig. 2. Photograph of the channel bed in the upper Ichinosawa catchment. (a) The movable bed in the section between A3 and A4. (b) The fixed bed in the section between A5 and A6.

flow torrent in the upper Ichinosawa catchment within the Ohya landslide, which is the one of the most active debris-flow initiation zones in Japan. The aim of this study is to observe the changes of characteristics of debris-flow surges, as they flow downstream after their initiations. We also compare the observation results with the theory of debris-flow mechanics.

2. Study area

The Ohya landslide is located in the Southern Alps, central Japan (Fig. 1a). The Ohya landslide, which is in the headwaters of the Abe river flowing in Shizuoka prefecture, was formed by an earthquake in 1707 (Tuschia and Imaizumi, 2010). The horizontal area is about 1.8 km² and the height difference is about 800 m. The geological unit belongs to Tertiary strata which consists of sandstone, shale and their alternation. It is fractured by two faults existing on both sides of the Ohya landslide.

The upper Ichinosawa catchment is located in the northern part of the Ohya landslide (Fig. 1). This area is an initiation zone of debris-flows, where three or four debris-flows occur every year triggered by heavy rainfall during rainy season (June to July) and autumn typhoon season (late August to early October). The horizontal area is approximately 0.20 km², the total length of the channel is approximately 500 m, and the average gradient of the channel is 30°. There is a little vegetation due to the harsh environmental conditions, and most of the slope is scree

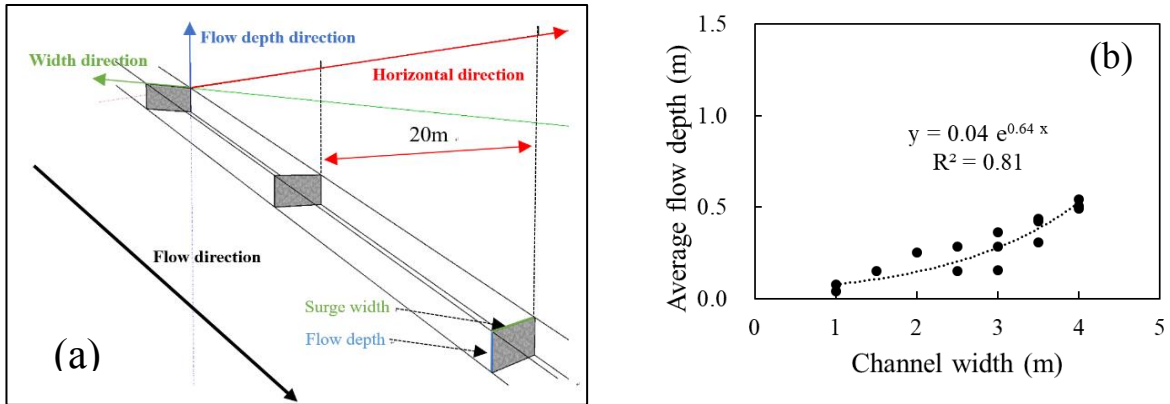


Fig. 3. Calculation method of volume of debris-flow surges. (a) Schematic diagram of debris-flow surge approximated to multiple truncated square pyramids. (b) Relationship between the channel depth and average flow depth in the section between A1 and A2.



Fig. 4. Image of the channel in the section between A4 and A5 before and during debris-flow event. Red rectangles in the image show the location where the surge width was measured. (a) The channel before debris-flow event. A pole at the center of image indicates 3 m. (b) The channel during debris-flow event captured by a time-laps camera.

and rock outcrop. Sediment on the channel bed, which was supplied from the outcrops by freeze-thaw weathering in winter, is several metres thick in some sections (Imaizumi et al., 2006, 2017). Most of the channel bed in the upper Ichinosawa is the movable bed, which is covered by erodible sediment (Fig. 2a). However, in the section between A5 and A6, the channel bed is a fixed bed, where the bedrock is exposed without sediment cover (Fig. 1b and 2b).

3. Methodology

3.1 Instrumentation

Six time-lapse cameras (TLC200pro, Brinno, Taipei City, Taiwan) with a frame rate of 15 s were installed in this study to interpret volume and runoff timing of debris-flow surges (Fig. 1b). The analysis points A1~A6 were set in the imaging range of cameras. The volume and flow velocity of the front of each surge were analyzed at each analysis point. In this study, the movements of sediment, which did not pass through two or more analysis points, were excluded from the analysis, because the changes in their flow characteristics cannot be interpreted.

Semiconductor-type water pressure sensor (S&DLmini, OYO, Tokyo, Japan) was installed at A6 analysis point to record hydrostatic pressures with a logging interval of 1 min, with an accuracy of $\pm 3\%$. A tipping bucket rain gauge (LR5061, HIOKI, Ueda City, Japan) was also installed at A4 analysis point to record rainfall with a logging interval of 1 min.

3.2. Calculation method of volume of debris-flow surges

The volume of the debris-flow surge was estimated by approximating the shape of the surge as a series of truncated square pyramids. To obtain the volume of each truncated square pyramid, we set rectangles, of which width and height are the surge width and average flow depth, respectively, with intervals of 20 m (horizontal distance) from the front to the tail of the surge (Fig. 3a). The surge width was measured by comparing the length of 3 m pole in the image, which was taken on a day without debris-flow, with the width of debris-flow in images taken by the time-lapse cameras during debris-flow event (Fig. 4). The average flow depth was calculated by applying the surge width to the equations which represent the relationship between the channel width and the average flow depth obtained by measurement of cross-sectional topography at several points within each channel section before the debris-flow event (On September 5, 2016; Fig. 3b). The volume of each debris-flow surge, which was obtained by adding the volume of all truncated square pyramids, was calculated when head of the surge passed each analysis point. The volumes at the A6 analysis point could not be calculated, because of the long section outside the imaging range of the time-lapse camera.

3.3. Calculation method of flow velocity of debris-flow surges

The mean velocity of the debris-flow surge front between adjacent analysis points was obtained by their distance divided by the time lag of the passages of the surge front between the two analysis points. This mean velocity was taken as the flow velocity of the surge front at the down-site analysis point. The velocity was calculated when surges passed each analysis point.

4. Results

4.1 Debris-flow surges observed on 8 September 2016

A debris-flow was observed in the upper Ichinosawa catchment on 8 September 2016 (Fig. 5). The debris-flow surges occurred intensively in the three periods (8:30 ~ 9:00, 10:30 ~ 11:30, 15:30 ~ 16:00). Total of 21 surges passed through two or more analysis points (Fig. 6). Surges initiated mainly in the section upstream from the A1 analysis point (9 surges) and in the section between A2 and A3 (7 surges). According to this result, the following analyses of the changes in volume and flow velocity were conducted by classifying surges into two groups depending on their initiation positions

4.2. Changes in volume of debris-flows surges with distance downstream

The surges initiated in the section upstream from A1 tended to increase their volumes in the section between A1 and A3, which is just below their initiation points. Development of the surge volume stopped below the A3 analysis point (Fig. 7a and 7b). In the section between A4 and A5, where the channel gradient decreases rapidly from approximately 30 ° to 25 ° (Fig. 7c), they tended to decrease their volume. The small surges stopped in this section

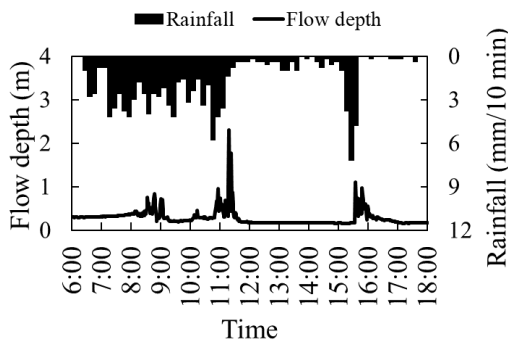


Fig. 5. Hyetohydrograph on 8 September 2016.

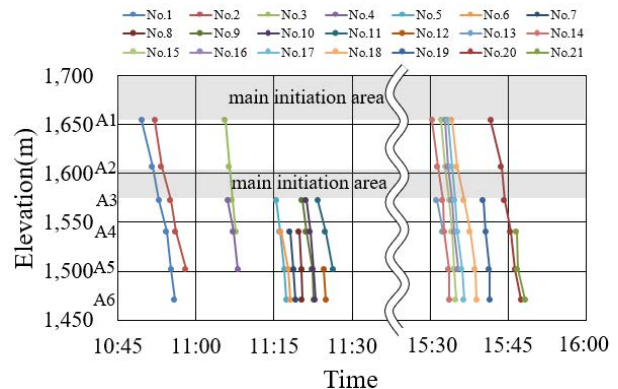


Fig. 6. Arrival time of surges at each analysis point.

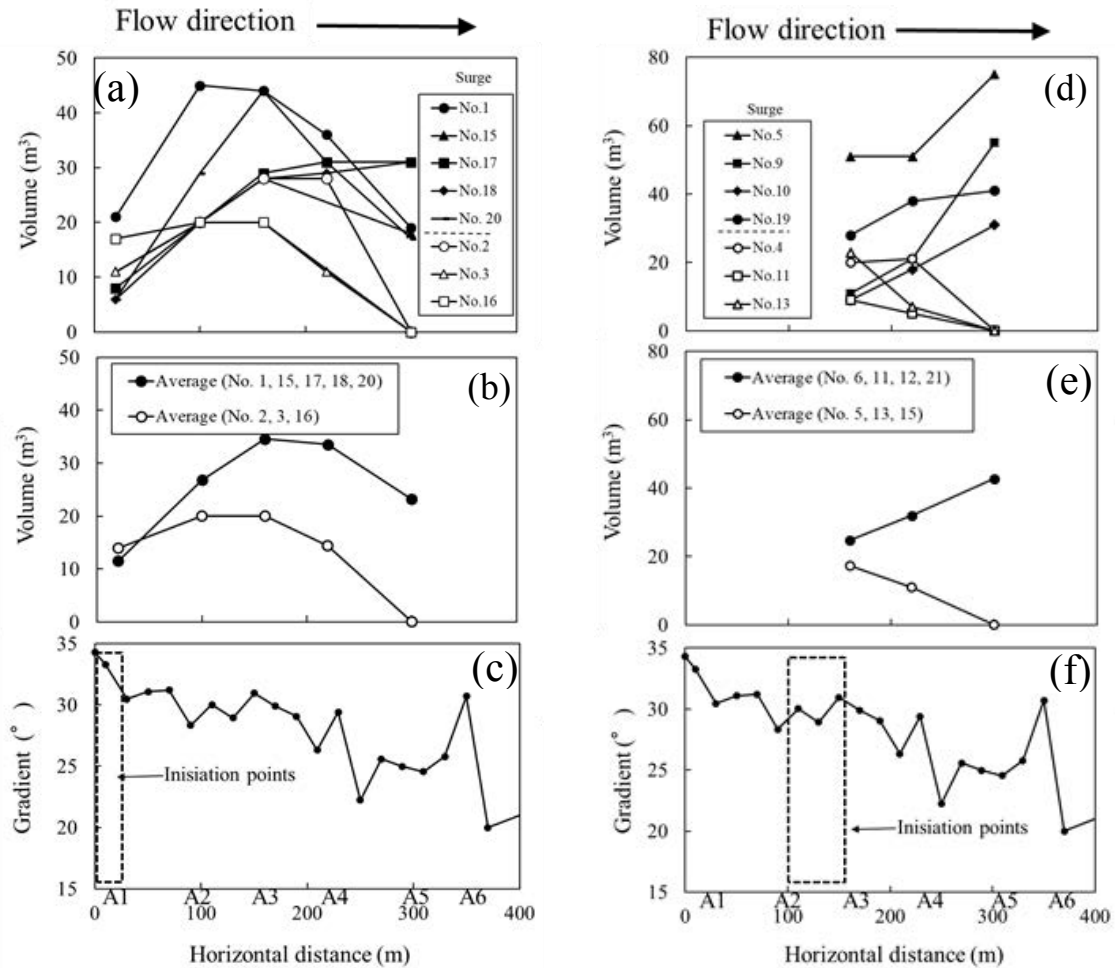


Fig. 7. Changes in volume of debris-flow surges as they flowed downstream. (a) Surges that initiated in the section upstream from A1. The black symbols are the volume of the surges which did not stop in the section between A4 and A5, the white symbols are that of the surges which stopped in this section. (b) Average volume of the surges that initiated in the section upstream from A1. (c) The channel gradient in the study area. The black rectangle indicates the initiation points of the surges that initiated in the section upstream from A1. (d) Surges that initiated in the section between A2 and A3. (e) Average volume of the surges that initiated in the section between A2 and A3. (f) The channel gradient in the study area. The black rectangle indicates the initiation points of the surges that initiated in the section between A2 and A3.

(white symbols in Fig. 7a and 7b). Half of the surges, which initiated in the section between A2 and A3, increased their volumes in the section between A3 and A5, which is also just below their initiation point (black symbols in Fig. 7d and 7e). The other surges continued to decrease their volume throughout their traveling, and stopped in the section between A4 and A5 (white symbols in Fig. 7b and 7e).

4.3. Changes in flow velocities of debris-flow surge fronts with distance downstream

The surges that initiated in the section upstream from A1 tended to increase their velocity in the section between A1 and A3, which is just below their initiation points (Fig. 8a and 8b). Most of these surges stopped accelerating in the subsequent sections. The surges that did not stop in the section between A4 and A5 tended to increase their velocity rapidly in the section between A5 and A6, in which the channel bed is fix bed (black symbols in Fig. 8a and 8b). Half of the surges that initiated in the section between A2 and A3 also increased their velocity in the section just below their initiation points and the section between A5 and A6 (black symbols in Fig. 8d and 8e). The other surges continued to decrease their velocity throughout their traveling, and stopped in the section between A4 and A5 (white symbols in Fig. 8d and 8e).

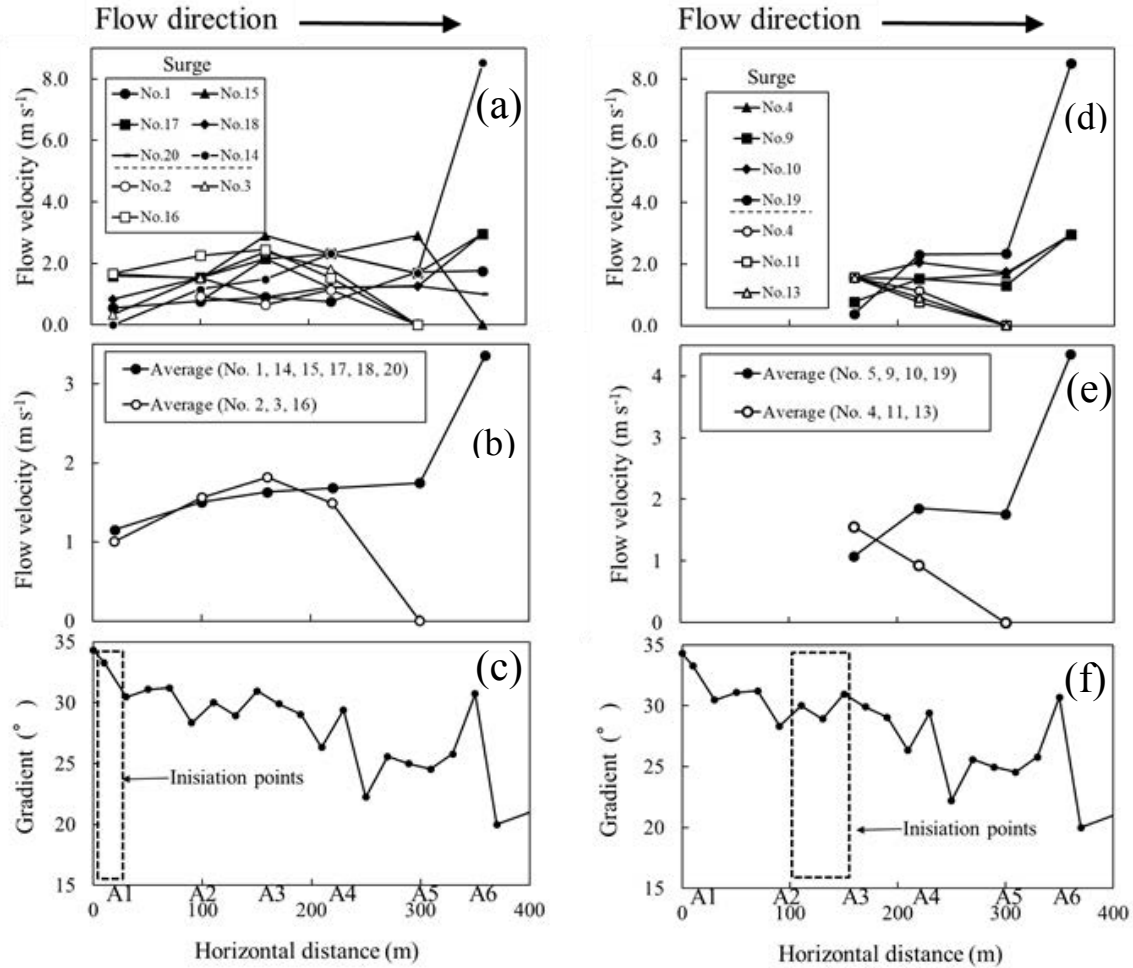


Fig. 8. Changes in flow velocity of debris-flow surges as they flowed downstream. (a) Surges that initiated in the section upstream from A1. The black symbols are the flow velocity of the surges which did not stop in the section between A4 and A5, the white symbols are that of the surges which stopped in this section. (b) Average velocity of the surges that initiated in the section upstream from A1. (c) The channel gradient in the study area. The black rectangle indicates the initiation points of the surges that initiated in the section upstream from A1. (d) Surges that initiated in the section between A2 and A3. (e) Average velocity of the surges that initiated in the section between A2 and A3. (f) The channel gradient in the study area. The black rectangle indicates the initiation points of the surges that initiated in the section between A2 and A3

5. Discussion

5.1. Changes in volumes of debris-flow surges with distance downstream

The volume of surges changes by erosion and deposition of sediment (Takahashi, 1977; Hungr et al., 2005). The processes of erosion and deposition by debris-flows can be explained by the equilibrium concentration, which is the sediment concentration of debris-flows when they are in steady state under the given channel gradient. The equilibrium concentration is given by the balance between the shear stress coming from slope direction component of gravity force and the shear resistance, which are both static forces. The equilibrium concentration is expressed as a function of the channel gradient as follows.

$$G = \{c(\sigma - \rho) + \rho\}gh \sin \theta \quad (1)$$

$$\tau = c(\sigma - \rho)gh \cos \theta \tan \phi \quad (2)$$

$$G = \tau \quad \therefore \quad c_e = \frac{\rho \tan \theta}{(\sigma - \rho)(\tan \phi - \tan \theta)} \quad (3)$$

where G is the shear stress at the bottom of the debris-flow surge, τ is the shear resistance, g is the gravity acceleration, h is the flow depth, e is the sediment concentration, c_e is the equilibrium concentration, ρ is density of water, σ is the density of sediment particles, θ is the channel gradient, ϕ is the internal friction angle. Takahashi (1977) explained that the sediment concentration in the flow approaches the equilibrium concentration by erosion and deposition of sediment. That is, when the sediment concentration in the flow is lower than the equilibrium concentration, the surge erodes sediment on the channel bed until their sediment concentration reach the equilibrium concentration. After the sediment concentration in the flow become equivalent to the equilibrium concentration, the surge is in steady state and stops eroding sediment. On the contrary, when the sediment concentration in the flow is higher than the equilibrium concentration, the surge deposits sediment.

In the section just below their initiation points, the debris-flow surges, which are considered to be in the early stage of development with low sediment concentration (Takahashi, 1977), actively eroded sediment and increased their volume (Fig. 7a, b, d, and e). As a result, surges are considered to have approached the equilibrium concentration. Surges stopped eroding and maintain their volumes in the subsequent section, because the sediment concentration in the surges likely reached the equilibrium concentration (Fig. 7a and b). Then, surges deposited the sediment and decreased their volume in the section between A4 and A5 where the channel gradient decreases rapidly (Fig. 7a, b, and c). In this section, the sediment concentration in the flow likely exceeded the equilibrium concentration, because the equilibrium concentration became lower due to decreases in the channel gradient. In contrast, surges with comparatively small volume stopped in the section between A4 and A5 without the control of sediment concentration by deposition of sediment (white symbols in Fig. 7a, b, d, and e). In addition, some surge started to deposit their sediment just after their initiation, (white symbols in Fig. 7d and e). These surges are assumed to have high sediment concentrations from their initial stage.

5.2. Changes in flow velocity of debris-flow surges with distance downstream

In the sections where the debris-flow surges are accelerating, the shear stress at the bottom of the surge exceeds the shear resistance. On the contrary, in the section where the surges are decelerating, the shear resistance is higher than the shear stress. Equations (1) and (2) indicate that the shear resistance increases as the sediment concentration in the surge increases and its increase rate exceeds that of the shear stress. Equation (3) indicates that the shear resistance balances with the shear stress at bottom of the mass when the sediments concentration reaches the equilibrium concentration (Takahashi, 1977).

Therefore, in the section just below their initiation points, surges, which eroded sediment actively because of the lower sediment concentrations than the equilibrium concentration, accelerated as they flowed down (Fig. 8a, b, d, and e). Such surges stopped acceleration in the subsequent sections because the sediment concentration likely reached the equilibrium concentration (Fig. 8a and 8b). Then, surges tended to rapidly increase their flow velocity in the section between A5 and A6, where the channel bed is fixed bed (Black symbols in Fig. 8a, b, d, and e). In this section, the sediment concentration in the flow likely became lower than the equilibrium concentration, because there is no erodible sediment although the equilibrium concentration became higher due to the increase in the channel gradient (Fig. 8c and 8f). As another factor for the rapid increase in the flow velocity in this section, it is thought that shear resistance at the bottom of the flow decreased because of the smoother surface of the fixed bed compared with that of the movable bed (Fig. 2) (Suzuki et al., 2003). In contrast, surges with comparatively small volume continued deceleration and stopped with a short travel distance without deposition of sediment, which decreases sediment concentration (white symbols in Fig. 8a, b, d, and e). Such behaviors of small surges in their terminal stage cannot be explained by the relationship between the shear stress and the shear resistance at the bottom of the flow.

6. Conclusion

To clarify the changes in the characteristics of debris-flow surges as they flow down, field observations using time laps-cameras was conducted at multiple sites along the debris-flow torrent in the upper Ichinosawa catchment. The results of our observations are summarized below.

- Debris-flow surges increased their volume and velocity in the section just below their initiation points, and maintained them in the subsequent section.
- Debris-flow surges decreased their volume in the section where the channel gradient decreases rapidly, and surges with a comparatively small volume stopped there.
- Debris-flow surges increased their velocity rapidly in the fixed bed.

These results of our observations are consistent with the theory of the equilibrium concentration. In contrast, the theory of the equilibrium concentration cannot fully explain the observation that surges with a small volume stopped and deposited all sediment with a short travel distance. In addition, some surges lost volume and velocity in their initial stage.

References

- Arattano, M., Marchi, L., and Cavalli, M., 2012, Analysis of debris flow recordings in an instrumented basin: confirmations and new findings: *Natural Hazards and Earth System Science*, 12, p. 679–686, <https://doi.org/10.5194/nhess-12-679-2012>.
- Abancó, C., Hürlimann, M., and Moya, J., 2014, Analysis of the ground vibration generated by debris-flow and other torrential processes at the Rebaixader monitoring site (Central Pyrenees Spain): *Natural Hazards and Earth System Sciences*, 14, p. 929–943. <https://doi.org/10.5194/nhess-14-929-2014>.
- Berger, C., McARDell, B. W., Fritschi, B., and Schlunegger, F., 2010, A novel method for measuring the timing of bed erosion during debris flows and floods: *Water Resources Research*, 46, W02502, doi:10.1029/2009WR007993.
- Cui, P., Hu, K., Zhuang, J., Yang, Y., and Zhang, J., 2011, Prediction of debris-flow danger area by combining hydrological and inundation simulation methods: *Journal Mountain Sciences*, 8, p. 1–9, <https://doi.org/10.1007/s11629-011-2040-8>.
- Egashira, S., Ashida, K., and Sasaki, H., 1988, Mechanics of debris-flow in open channel: *Proceedings of the Japanese Conference on Hydraulics*, 33, p. 485–490. [In Japanese with English abstract.]
- Hungr, O., S. McDougall, and M. Bovis, 2005, Entrainment of material by debris-flows: in *Debris-flow Hazards and Related Phenomena*, edited by M. Jakob and O. Hungr, pp. 135–158, Springer, Berlin.
- McCoy, S. W., Kean, J. W., Coe, J. A., Tucker, G. E., Staley, D. M., and Wasklewicz, T. A., 2012, Sediment entrainment by debris-flows: In situ measurements from the headwaters of a steep catchment, *Journal of Geophysical Research*, 117, F03016, doi:10.1029/2011JF002278
- Imaizumi, F., Sidle, R. C., Tsuchiya, S., and Ohsaka, O., 2006, Hydrogeomorphic processes in a steep debris flow initiation zone: *Geophysical Research Letters*, 33, L10404, <https://doi.org/10.1029/2006GL026250>.
- Imaizumi, F., Tsuchiya, S., and Ohsaka, O., 2016, Behavior of boulders within a debris flow initiation zone: *International Journal of Erosion Control Engineering*, 9, p. 91–100, <https://doi.org/10.13101/ijece.9.91>.
- Imaizumi, F., Hayakawa, Y. S., Hotta, N., Tsunetaka, H., Ohsaka, O., Tsuchiya, S., 2017, Relationship between the accumulation of sediment storage and debris-flow characteristics in a debris-flow initiation zone, Ohya landslide body, Japan: *Natural Hazards and Earth Science Systems*, 17, p. 1923–1938.
- Iverson, R.M., 1997, The physics of debris-flows: *Reviews of Geophysics*, 35, p. 245–296.
- Kean, J. W., McCoy, S. W., Tucker, G. E., Staley, D. M., and Coe, J.A., 2013, Runoff-generated debris flows: Observations and modeling of surge initiation, magnitude, and frequency: *Journal of Geophysical Research*, 118, 2190–2207, <https://doi.org/10.1002/jgrf.20148>.
- Lanzoni, S. Gregoretto, C., and Stancanelli, L. M., 2017, Coarse-grained debris-flow dynamics on erodible beds. *Journal of Geophysical Research: Earth Surface*, 122, p. 592–614. <https://doi.org/10.1002/2016JF004046>.
- Okano, K., Suwa, H., and Kanno, T., 2009, Rainstorm control of scale and type of debris-flows at Kamikamihorizawa Creek of Mount Yakedake, Japan: *Journal of the Japan Society of Erosion Control Engineering*, v. 62, no. 4, p. 3–10. [In Japanese with English abstract].
- Suzuki, Y., and Suzuki, T., 2009, Observation system of debris-flow on Kitamata valley of the Name river, *Journal of the Japan Society of Erosion Control Engineering*, v. 61, no. 6, p. 43–46. [In Japanese with English abstract.]
- Suzuki, T., Hotta, N., and Miyamoto, k., 2003, Influence of riverbed roughness on debris-flows: *Journal of the Japan Society of Erosion Control Engineering*, v. 56, no. 2, p. 5–13. [In Japanese with English abstract.]
- Suzuki, T., Hotta, N., and Miyamoto, k., 2009, Numerical simulation method of debris-flow introducing the non-entrainment erosion rate equation, at the transition point of the riverbed gradient or the channel width and in the area of sabo dam: *Journal of the Japan Society of Erosion Control Engineering*, v. 63, no. 3, p. 14–22. [In Japanese with English abstract.]
- Takahashi, T., 1977, A mechanism of occurrence of mud-debris-flows and their characteristics in motion: *Annals of the Disaster Prevention Research Institute, Kyoto University*, 20(B-2), p. 405–435. [In Japanese with English abstract.]
- Tsuchiya, S., and Imaizumi, F., 2010, Large sediment movement caused by the catastrophic Ohya-kuzure landslide: *Journal of Disaster Science*, No. 5, Vol. 3, p. 257–263.

Monitoring of sediment runoff and observation basin for sediment movements focused on active sediment control in Jo-Gan-Ji River

Takahiko Nagayama ^{a,*}, Tomohiko Furuya ^a, Satoru Matsuda ^a, Takahiro Itoh ^b,
Masaharu Fujita ^c, Takahisa Mizuyama ^d

^a NIPPON KOEI Co., Ltd, 1-43, Eki Nishihon-machi 5-chome, Kanazawa-shi, Ishikawa 920-0025 JAPAN

^b NIPPON KOEI Co., Ltd, 2304 Inarihara, Tsukuba, Ibaraki 300-1259 JAPAN

^c Disaster Prevention Research Institute, Kyoto University, Gokasho, Uji, Kyoto 611-0011 JAPAN

^d National Graduate Institute For Policy Studies (GRIPS), 7-22-1 Roppongi, Minato-ku, Tokyo 106-8677, Japan

Abstract

Continuously measuring sediment runoff along multiple sections of the Jo-Gan-Ji River is necessary to understand both the propagation of sediment as well as the changing of grain sizes in order to appropriately evaluate sediment yielding from debris flows temporally and spatially. The present study proposes a combination of sediment monitoring tools and appropriate equipment to identify various sediment transport modes from wash load to bedload in mountainous torrents. As a result of monitoring runoff volume and grain sizes, sediment management can be achieved. In the Jo-Gan-Ji River basin in Japan, temporal and longitudinal sediment runoff has been measured continuously since the 1990's. Previous studies help determine the proper instrumentation suite for this type of sediment runoff monitoring. Bedload is measured with a Reid-type bedload slot sampler and by use of the hydrophone to survey acoustic waves. In addition, hydrophones and a velocity meter (vertically installed on a side wall) are used to quantify suspended loads. A turbidity meter is also used to measure wash load. Propagation of sediment particles can be observed during flooding in mountainous torrents. Specifically, bedload discharge rates of each particle are evaluated using of the hydrophone. Monitoring of the Jo-Gan-Ji river also identifies inactive bedload movements such as large boulders. Previous installations of this type monitoring equipment make it clear that the destructive nature of bedload collisions indicate a need for robust instruments. Alternate instrumentation methods, that are robust, are explored here. Moreover, in order to actively control sediment runoff in flooding, we developed a sabo dam with shutter and pilot operations that activate during flooding. Differences of those sediment transport characteristics with/without the shutter also shown through the sediment monitoring along the Jo-Gan-Ji River.

Keywords: sediment monitoring; Japanese pipe hydrophone; bedload monitoring tools; sediment management; sabo dam with shutter

1. Introduction

Sediment runoff due to floods has been continuously monitored in a small basin in a mountainous region of Japan since the 1990s to evaluate runoff properties as well as administer watershed management. Several sensors are used for this monitoring including a Japanese hydrophone, turbidity meter, pressure sensor for flow depth, bedload slot, etc. (e.g., U.S. Geological Survey, 2010). However, there are only a few examples for longitudinal measurements along a main river with a length > 10km. In the basin where sediment yield is continuously active, detection for sediment movement/runoff through monitoring is necessary for reduction of disaster. For this reason, it is necessary to rapidly monitor river channel conditions by using both longitudinal and temporal measurement tools to appropriately evaluate continuous sediment runoff and sediment sorting.

For the purpose of sediment control in basin management, information on sediment runoff and water flow in mountainous torrents has attempted to be collected using various sensors to continuously measure bedloads, suspended loads, turbidity, flow depth and so on. Relationships found through monitoring between bedload/wash loads and water

* Corresponding author e-mail address: a4619@n-koei.co.jp

runoff show that there is a discontinuous relationship between sediment and water runoff in mountainous regions. This further shows that direct monitoring and evaluation of suspended loads and bedloads is still quite difficult. Several members of Kyoto University, Japan have reviewed passive and direct sediment monitoring methods in mountainous regions (in Japan and abroad) and have tried to develop previous methods of evaluating sediment runoff. The following instruments were selected as a suitable monitoring apparatus: a set of pipe-hydrophones for bed loads, pressure sensors for the flow depth, turbidity meters for wash loads and an electro-magnetic velocity meter on the bed for bed shear stress (Mikami et al., 2014). These instruments are installed in several sections of the upstream reach of the Jyo-Gan-Ji River.

In Jo-Gan-Ji River, longitudinal sediment monitoring for various wide sediment transport modes (from wash load) to bed load is carried out using preferable sensors for measuring sediment movement, focused on sediment discharge rates for each component of grain size. Moreover, those sensors are robust to protect from sediment collision by large boulders. In the Jo-Gan-Ji River basin, a sabo dam with a shutter is proposed and installed for smoothing sediment runoff with open-type concrete slit dam. An effective control of sediment runoff is attempted using of the silt dam along with sediment monitoring tools and sensors. The results are an active sediment management system in the basin. In the present study, monitoring data and trial runs with a shutter on the dam are shown for management of water and sediment runoff in a mountainous basin. Sabo dam (a dam with a movable shutter) is an effective tool in the basin when combined with the applied monitoring system.

2. Bed load to wash load and related hydraulic quantities monitoring

2.1. Study basin and installed sensors for monitoring

The monitoring system installed in the Jyo-Gan-Ji River, prepared by the Tateyama Sabo Office, consists of a data collection network and an optical cable network. Temporal and longitudinal monitoring for water and sediment runoff is conducted continuously to evaluate the spreading of sediment discharge, the effects of sabo facilities, and the confluence of tributaries on the sediment runoff.

Fig. 1 shows the observation stations in the Jyo-Gan-Ji River, and Fig. 2 are the longitudinal bed profiles of the river. Sabo dams and weirs are indicated from (A) to (F) in Fig. 1. Because sabo facilities work well for maintaining bed elevation, from a macroscopic view the longitudinal bed profiles are almost level. The optical network for monitoring data collection has been set up in the basin and data is collected at the Sabo Office (Mikami et al., 2014).

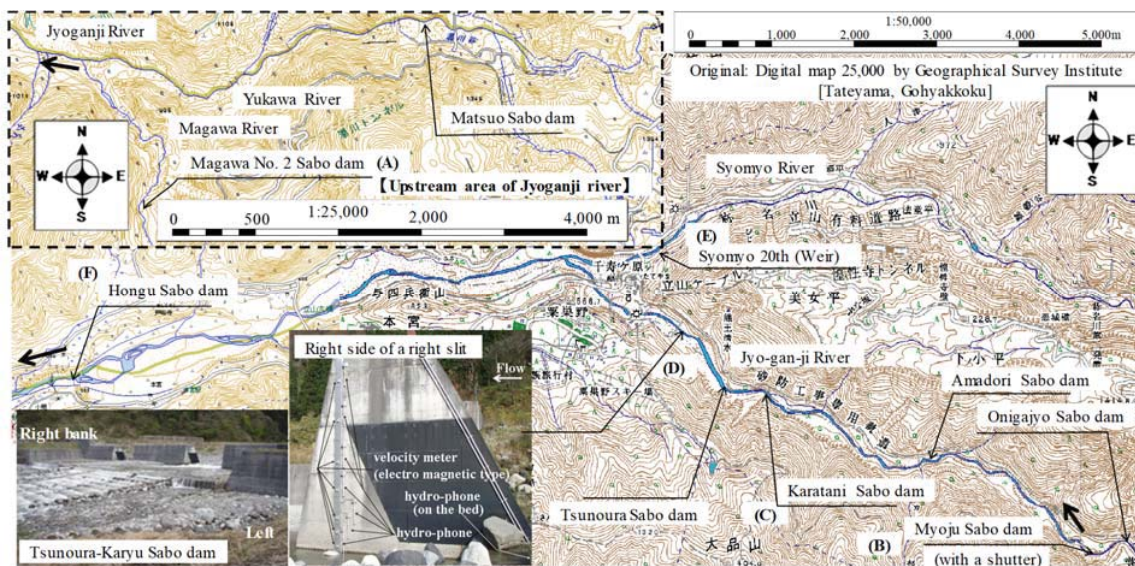


Fig. 1. Observation station in Jyo-Gan-Ji River

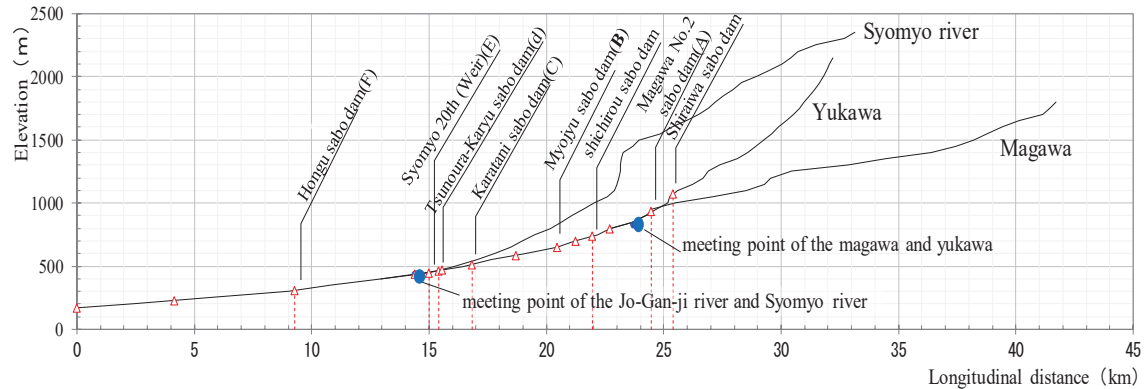


Fig. 2. Longitudinal bed profile of Jo-Gan-Ji River

2.2. Measured data

Bed load monitoring at the Hongu sabo dam ((F) in Fig.1) using a Japanese pipe hydrophone and pressure meter for the flow depth started on 15th of December in 2009. Modified measurements using the pipe hydrophone for bedload, pressure meter for flow depth and turbidity meter for wash load began on the 17th December in 2012. At the Hongu sabo dam, flow width is 52 m and bed slope is 1/90(0.0111). Water discharge is calculated using a relationship between flow depth, H , and discharge, Q , estimated by surface velocity measurements in floods ($H-Q$ curve). Bed sediment has a wide range of diameters: $d_{60}=30$ mm and $d_{95}=150$ mm. At the Tsunoura-Karyu sabo dam ((D) in Fig. 1), concentrated monitoring has been conducted at the slit part in right bank site of the sabo dam since June of 2001 (U.S. Geological Survey, 2010). The watershed area of the dam is 139.49 km² and the bed slope near the dam is 1/56(0.0179), which is measured in 2007. In the Tsunoura-Karyu sabo dam, monitoring of water and sediment started with a combination of Reid-type bedload slot, a flow depth meter, and a pipe hydrophone. Temporal changes indicated around 70 events that occurred between the installation in June of 2001 until March of 2013. Rainfall is measured at Senjyu-ga-hara Station. The monitoring was started using the pipe hydrophone and pressure meter for the flow depth. In January of 2008, a Reid-type bedload slot was installed to obtain the correlation between impulses of the Japanese pipe hydrophone and bedload discharge recorded by the bedload slot. At this station, flow width is 110 m and bed sediment also has a wide range of diameters: $d_{60}=20$ mm and $d_{95}=200$ mm.

Fig. 3 shows the calibration line between impulses by Japanese pipe hydrophone and bedload discharge measured by the bedload slot at the Tsunoura-Karyu sabo dam. This relationship is used of estimation for bedload discharge at several observatories in the Jo-Gan-Ji River. Several equilibrium bedload formulas for d_{60} are compared with previously measured data (e.g., Japan Society of Civil Engineering, 1999). Fig. 4 shows the relationship between water discharge and bedload discharge at Hongu sabo dam. Water discharge is calculated using the $H-Q$ curve and bedload discharge is calculated using Fig. 3. Fig. 3 is the correlation between the amount of sediment transport measured by the bedload slot and the impulse number of the Japanese hydrophone. Fig. 5 shows the relationship between water discharge and fine components of sediment discharge measured by a turbidity meter at several observatories in the Jo-Gan-Ji River. The two dashed lines identify the range of fine components of sediment discharge in Japan (Japan Society of Civil Engineering, 1999) to compare to the monitored data in the Jo-Gan-Ji River. Although fine components of sediment discharge have large values, bedload transportation is not active because there has not been a large magnitude of sediment yielding as a result of large events, such as a landslide and a debris flow, in the past 50 years.

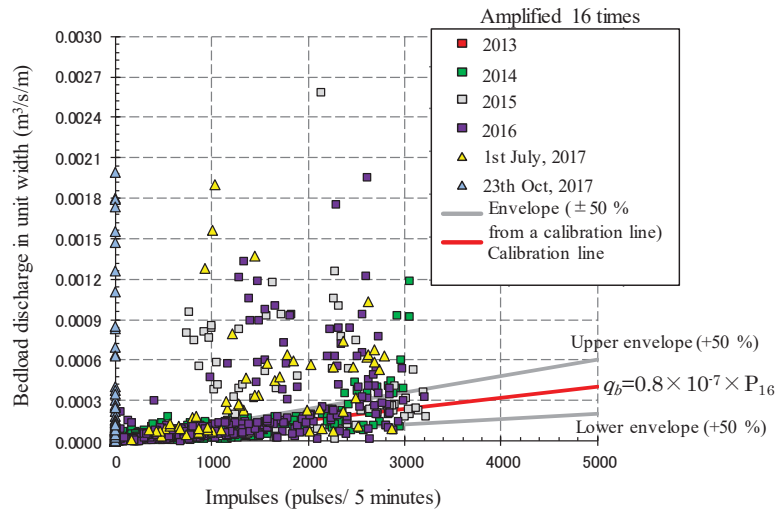


Fig. 3. Calibration line between impulses by Japanese pipe hydrophone and bed load discharge measured by a bedload slot

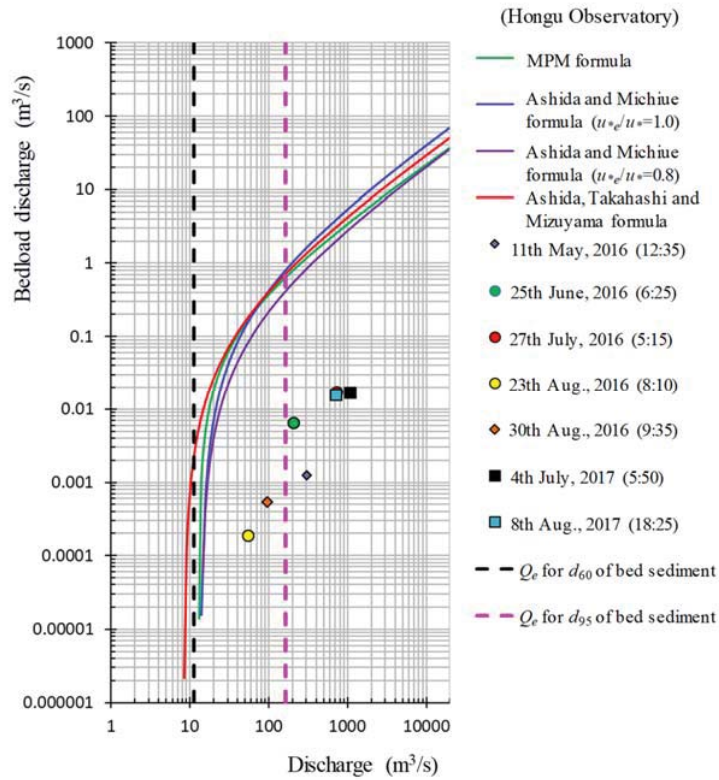


Fig. 4. Relationship between water discharge and bedload discharge

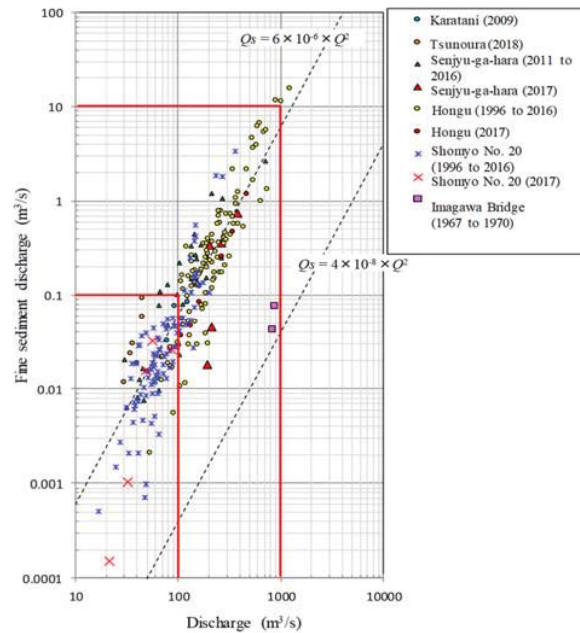


Fig. 5. Relationship between water discharge and fine components of sediment discharge measured by a turbidity meter

2.3. Development of robust sensors in mountainous region

Continuous longitudinal sediment observation such as bedload and wash load started in Jo-Gan-Ji River since 2013. However, damage to sensors often occurred, especially the Japanese pipe hydrophone, which has a pipe of 3 mm thickness. As a result, continuous measurements of bedload discharge could only be obtained in small/medium sized floods. During large-sized floods, pipes on the bed surface experience physical damages such as indentation and deformation.

In order to prevent the Japanese pipe hydrophone from having physical damage during continuous bedload monitoring, two different robust solutions were compared. One is thick pipe (e.g., 10.2 mm) and the other is a plate-type (thickness is 12 mm), ideally to help withstand heavy collisions by large boulders. Figs. 6 show the relationships between impulses recorded by the robust-type hydrophones (thick pipe and plate) and the bedload discharge measured by the bedload slot. The data is measured at the Tsunoura-Karyu sabo dam (D) in Fig. 1). A similar correlation was found between the bedload discharge measured in the bedload slot and the standard type of hydrophone (thickness is 3 mm), but there is variation at the small impulse number. These data show that it is difficult to measure sediments of small particle size. for that reason, impulses from the hydrophone must be measured with a higher amplification than that of standard type of hydrophone (thickness is 3 mm). More data collection is needed for further discussion of general applicability using robust-type hydrophones.

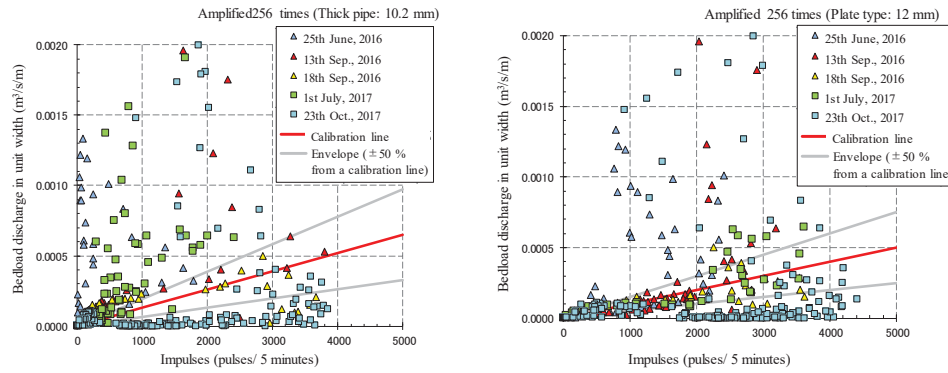


Fig. 6. Relationship between impulses by robust type hydrophone and bed load discharge measured by bedload slot, (a) Thick pipe; (b) Plate type

3. Effective sediment control tool and their applicability

3.1. Installation of sabo dam with a shutter

A sabo dam with a shutter is installed in the middle region of the Jo-Gan-Ji River ((B) in Fig. 1). The purpose of the shutter is to actively control sediment runoff during floods. The shutter has a structure in which the lower part of the slit dam is opened and closed by oil hydraulic pressure, as shown in Fig. 7. The slit with a shutter has two important roles, one being sediment runoff control, and the other being shutter movement control.

Trial operations have been conducted by floods, and the preferable timing of the shutter operation is found through trial operations.

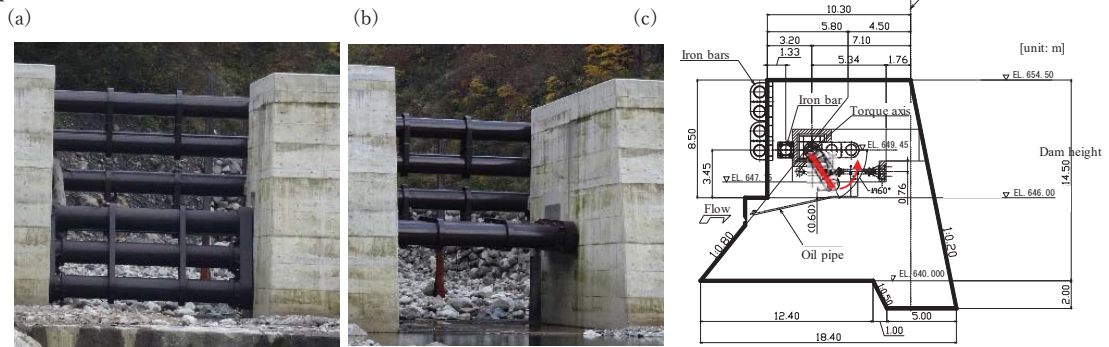


Fig. 7. A shutter at Myoju sabo dam ; (a) closed; (b) open in usual operation ; (c) longitudinal structure of a shutter

3.2. Trial control with a shutter and its sediment control

In 2016, we started pilot operations by measuring sediment traps. As a result of when shutter operation was performed in the latter half of the flood, sediment transport was controlled. Floods large enough for significant sediment transport were observed twice, once on July 27th, 2016 and again on July 4th, 2017, because sensors for water and sediment measurement are longitudinally installed along the Jyo-Gan-Ji River. When both of these floods occurred, the shutter responded appropriately and closed. Sediment transport after installation, sediment transport was first observed on July 27th, 2016, as shown in Fig. 8. Several amplifier such as 16,64,256 and 1024 times the Japanese pipe hydrophone detected movements of sediment articles during the flood. Low magnitude of the amplifier can detect coarse sediment particles. As shown in Fig.8, coarse and fine bedload articles take characteristics temporal changes of impulses in the increasing/decreasing stage of the flood. As the beginning of the flood, bedload discharge decreases, and then the value took almost constant. After operation of a shutter at the Myoju sabo dam, coarse components of bedload decreased. And then fine component of bedload also decreased gradually in the decreasing

stage of the flood. The rapid sediment run-off can be controlled by the shutter operation. Moreover, when focusing on the flow depth and impulses of the Japanese pipe hydrophone, the sediment transportation is delayed after the shutter operation at the Karatani sabo dam, which is located downstream of the Myoju sabo dam, as shown in (C) in Fig.1. As shown in Fig.8, sediment transportation can be detected between Myoju sabo dam and Karatani sabo dam, focused gradually on the shapes of temporal changes of impulses by hydrophones.

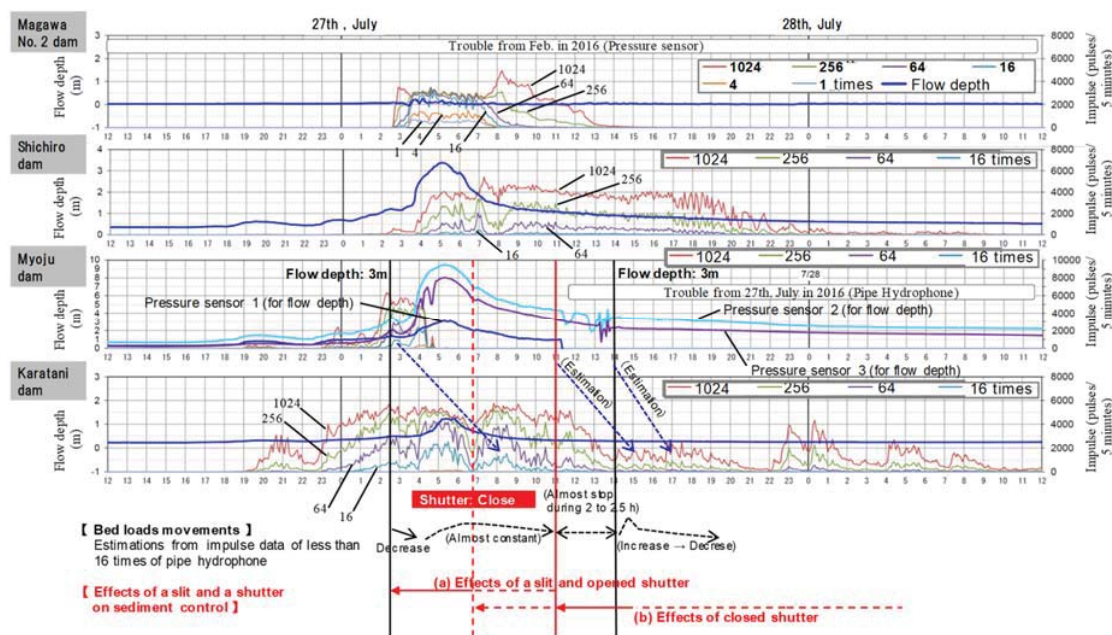


Fig. 8. Effects of shutter operation on longitudinal sediment transportation

Along with this, the operation of opening the shutter can be triggered in a stage of lower water level. However, in order to decide to trigger the opening of the shutter, further test operations must be conducted as well as water use downstream must be considered. Therefore, the preferable timing of closing and opening operations without adverse effects will be addressed in the future.

4. Conclusion

In the Jo-Gan-Ji River Basin, continuous sediment monitoring is performed longitudinally and temporally. Sediment runoff monitoring is performed simultaneously with hydrological monitoring. Present bed conditions do not allow for significant sediment runoff because of bed armor and large gravels. On the other hand, during floods, large components of bed sediment are transported along the river, including wash load and suspended load. Robust solutions tried to be conducted for the Japanese hydrophone against heavy collisions by large boulders. Those trials will be continued for further discussions of general applicability.

For the purpose of actively controlling the sediment transport during floods, a sabo dam with a shutter is proposed and the effective control function is evaluated through the test operation. The preferable timing of the shutter operation can be evaluated using longitudinal sediment monitoring with passive sensors for bedload to wash load measurements.

References

- Japan Society of Civil Engineering, 1999, Handbook of Hydraulic Engineering, Maruzen (in Japanese).
- Mikami, K., Koshino, M., Okui, J., Nagayama, T., Tagata, S., Miyamoto, K., Fujita, M., Itoh, T and Mizuyama, T., 2014, Install of a Movable shutter in Myo-Jyu Sabo Dam and Longitudinal Bedload Monitoring in Jyo-Gan-Ji River, Proceedings of the Interpraevent 2014 Pacific Rim (edited by Fujita, M. et al.), November 25-28, Nara, Japan, 2014, P-36.pdf in DVD.
- U.S. Geological Survey, 2010, Bedload-Surrogate Monitoring Technologies, Scientific investigations Report 2010-5091, 37p.

Measurements of velocity profiles in natural debris flows: a view behind the muddy curtain

Georg Nagl^a, Johannes Huebl^a, Roland Kaitna^{a,*}

^a University of Natural Resources and Life Sciences, Peter Jordanstr. 82, 1190 Vienna, Austria

Abstract

The internal deformation behavior of natural debris flows is of interest for model development and model testing for debris-flow hazard mitigation. Up to now, only a few attempts were made to measure velocity profiles in natural debris flows due to low predictability and high destructive power of these flows. In this contribution we present recent advances of measuring in-situ velocity profiles together with flow parameters like flow depth, basal normal stress, and pore fluid pressure. For that a fin-shaped monitoring barrier was constructed in the Gadoria creek (IT), laterally carrying an array of paired conductivity sensors. We present results from two debris-flow events with volumes of around 5,000 m³ each. Compared to the first event on July 10th, 2017, the second event on August 19th, 2017, was visually more liquid. Both debris flows exhibited significant longitudinal changes of flow properties like flow depth and density. The liquefaction ratios reached values up to unity in some sections of the flows. Velocity profiles for the July event were mostly concave up, while the profiles for the more liquid event in August were linear to convex. Though limited by boundary roughness at the wall and occasional sediment deposition on the force plates and pressure sensors, these measurements gain new insights of the dynamics of real-scale debris flows.

Keywords: velocity profile, pore fluid pressure, Gadoria valley

1. Introduction

The high volumetric content of sediment together with grain sizes ranging over several orders of magnitudes, and velocities sometimes exceeding 10 m/s, form a challenging task to measure velocity profiles in natural debris flows. However, observations under natural conditions avoid all scaling effects and would provide some indication of the constitutive flow behavior of the mixture, which we regard as useful for model development and testing.

Measurements of experimental velocity profiles in natural sediment-water mixtures are rare, but mostly show a strong dependence on material composition (Arai and Takahashi, 1983; Mainali and Rajaratnam, 1994; Johnson et al., 2012; Kaitna et al., 2014), which has also been observed in artificial solid-fluid mixtures (SanVitale et al., 2011; Chen et al., 2017). For natural flows measurements of mean velocity and surface velocity are available (Berti et al., 1999; Genevois et al., 2000; Marchi et al., 2002). Indication of the internal deformation behavior were derived from paired shear force measurements on a vertical side wall side at the Illgraben test site in Switzerland (Walter and McArdell, 2015). The importance of non-hydrostatic fluid pressure that reduces the shear resistance in debris-flow mixtures has been shown by different authors (e.g. Pierson, 1986; Iverson and LaHusen, 1989; Iverson, 1997; Major, 2000; Kaitna et al., 2014; Kaitna et al., 2016) and has also been measured in the field (McArdell et al., 2007; McCoy et al., 2010; McCoy et al., 2013).

Herein, we present first results of our efforts to measure the internal deformation behavior in natural debris flows at a monitoring station at the Gadoria creek, IT. We first give an overview of the test site and the installed setup. Subsequently we show measurements of velocity profiles, normal stresses, flow depth and basal pore fluid pressure, and close with a short discussion of the outcomes and the limitations.

* Corresponding author e-mail address: roland.kaitna@boku.ac.at

2. Method

2.1. Field site

The catchment of the Gadria creek is located in the Vinschgau valley in South Tyrol, Italy, and occupies an area of 6.3 km². The highest point of the catchment is at 2,945 m a.s.l. and the confluence with the receiving river Etsch. With 1-2 debris flows per year in the recent years, the area was considered to be well suited for debris-flow monitoring (Comiti et al., 2014). The steep terrain, frequent thunderstorm events as well as metamorphic rock and thick glacier deposit ensure sufficient quantity of material to be mobilized and transported. Since the last ice-age, the Gadria creek developed a large fan, which is mainly used for agriculture and settlement. At the apex of the fan, at 1,390 m a.s.l., a slit check dam was built, providing a retention capacity of around 40,000 to 60,000 m³. Just upstream of the retention area, a monitoring station was installed by the Torrent Control Service of South Tyrol in cooperation with the Free University of Bozen-Bolzano in 2011 with two radar sensors for flow depth, rain gauges, geophones and three cameras (Comiti et al., 2014), Fig 1a). In 2016 the test site was extended with a sensor-equipped debris-flow breaker (“monitoring barrier”) to measure impact pressures and investigate the process/barrier/ground interaction. In the course of the construction, also force plates, fluid pressure sensors, and a velocity profiler have been installed.

2.2. Barrier

The monitoring barrier is located 200 m upstream to the retention basin at an altitude of 1,400 m a.s.l. The mean channel slope is 6° at the position of the barrier. The construction consists of two concrete parts, the barrier itself and an unconnected traverse check-dam in front of the barrier flush to the ground. For measuring normal stress and shear stress two force plates were installed on the traverse check-dam, one in front of the barrier and the second one two meter aside, both set to a sampling frequency of 2,400 Hz. The barrier is combined of a single concrete fin-shaped element in the middle of the channel connected to a foundation plate (Fig 1b).

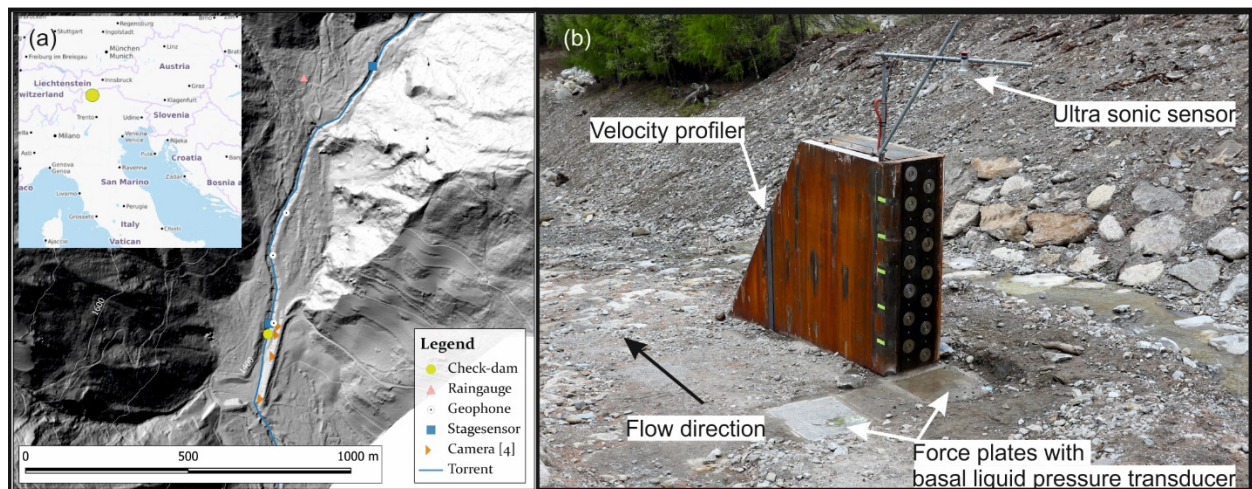


Fig 1. (a) Study site of the Gadria torrent in South Tyrol, Italy; (b) Monitoring barrier with measurement system.

2.3. Monitoring system

Two quadratic force plates of 1 m² were attached to the transverse check-dam. Each force plate is supported by four load pins with a maximum capacity of 10 kN each. In the middle of each force plate a pressure sensor is installed. Each sensor consists of a pressure transducer connected to a reservoir filled with hydraulic oil. The top of the sensor (flush with the force plate) is sealed with a thin silicone membrane and protected with two steel meshes of 0.5 and 2 mm grid sizes, similar as used in rotating drum experiments by Kaitna et al. (2014). Two ultra-sonic sensors for the flow depth measurement were installed above each force plate. The sampling frequency of the ultra-sonic sensors and the pressure transducer was set to 100 Hz. The velocity profiler is situated on the orographically left side of the barrier

3 m behind the front to minimize the disturbance of the passing material, but still capable to capture a maximum flow height of 1.8 m. The profiler consists of eleven sensors at different heights (levels). The first level is located at 18 cm above the concrete bed; the next levels are equally stepped at 15 cm distance. Each velocity sensor consists of a pair of conductivity sensors at a distance of 6 cm apart. The normalized sensor signals were cross-correlated to determine the velocity of passing debris (Nagl and Huebl, 2017). The size of a moving correlation window for set to 1 second (2,400 data points) and the window was moved with a step size of 100 data points. Results with a correlation coefficient < 0.8 and unrealistic accelerations from adjacent values were excluded from further analysis (see discussion in Kern et al., 2010; Kaitna et al., 2014). Finally, a digital video system equipped with an infrared spot was installed on the orographic left side of the channel, which enabled us to assess the surface velocity near the profiler by particle tracking. Two data acquisition systems are integrated at the top of the barrier. First, a QuantumX HBM data acquisition system is in use to acquire signals from the load cells on the front of the barrier (impact measurements) with a sampling rate set to 19,200 Hz. The second system, which records the sensors described herein, is a MGCplus HBM data acquisition system with a sampling rate set to 2,400 Hz. Except for the velocity profiles, all signals were filtered with a Butterworth low-pass 500 Hz. The complete setup is powered by an uninterruptible power supply system (UPS).

3. Results

3.1. Event July 10th, 2017

On 10th of July 2017, a debris flow was triggered by intense rainfall. The front velocity was about 1 m/s and the maximum flow depth of around 1 m (Fig 2). Video recordings reveal that the flow had a steep bouldery front with rocks of around 0.5 m in diameter, followed by a mud rich tail with some boulders immerse in the flow. The main surge was followed by small waves. The complete event lasted around 240 seconds (4 minutes) and had a total volume of about 5,000 m³.

The normal stress σ_N reached values up to 18,000 N/m² and the basal pore fluid (P) pressure peaks only slightly lower (Fig 2). The liquefaction ratio ($LR = P/\sigma_N$) were therefore very high throughout the flow and reached values close to unity at the tail. For comparison, an equivalent clear water pressure calculated from flow depth, the density of water (1,000 kg/m³) and the gravitational acceleration is peaks at about 9,000 N/m². Hence, except for the very front of the flow, an excess pore water pressure was observed during the whole event duration.

For the duration of the first surge, the median of the velocity profiles from the profiler exhibit a concave up form. The numbers Fig 2b-d are the number of successful correlations (see section 2). The independently derived surface velocity is in the same range but slightly higher as the uppermost velocity of the profiler. This might be connected to the non-existing effect of wall friction, as surface velocities were derived at some distant from the barrier. The 10/90 percentile of the box-whisker plot shows the highest variability on the upper levels. A closer look into the small waves, present a convex form of the velocity profile. Taking all velocity profiles into consideration, a concave up form exhibits.

3.2. Event 19th of August 2017

The second event on August 19th, 2017, resulted again from heavy rainfall and started as a sediment-laden flash flood with woody debris, and developed into a debris flow with a less pronounced peak with a maximum flow depth of 1.8 m and a velocity of 4 m/s (Fig 3a). The event consists of two main surges with no characteristic bouldery front; the second surge was characterized by six small waves. A muddy rich tail with no visible boulders finalized the debris flow. The complete event lasted 1,600 seconds (~ 27 minutes). A log clogged the force plate in front of the barrier and affected the measurement of this force plate. The second force plate aside of the barrier measured normal stresses up to 36,000 N/m² at the first surge.

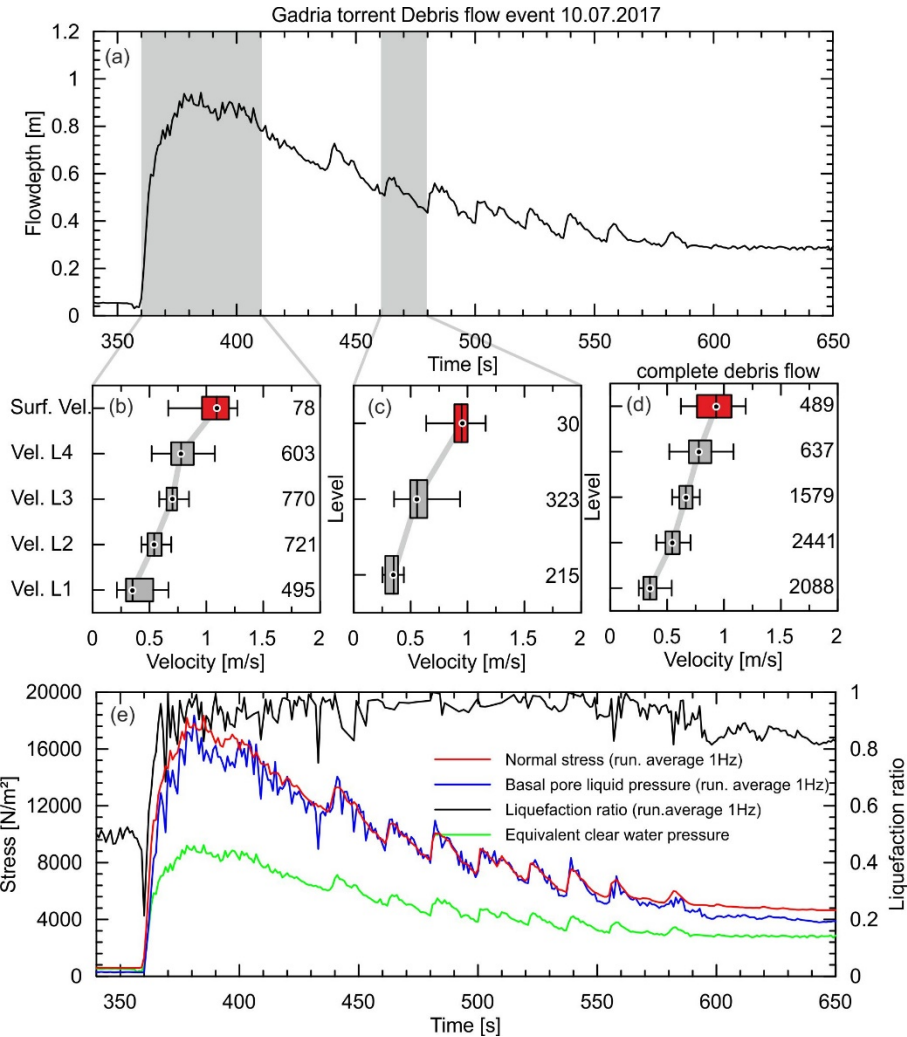


Fig 2. Data of the debris flow from July 10th, 2017. (a) Flow depth [m] of the ultra-sonic sensor of the force plate 1 aside the barrier. (b) Velocity profile of the first surge (360-410 sec.) (c) Velocity profile of a small wave (460-480 sec.) (d) Collective velocity profile of the complete debris flow, (e) normal stress (red line), basal pore liquid pressure (blue line), liquefaction ratio (black line), and equivalent clear water pressure (green line) in running average values of 1Hz.

Here, the basal pore liquid pressure achieved values to 20,000 N/m², and as a result, a liquefaction ratio reached values of 0.5 to 0.6. At the first surge, the equivalent clear water pressure was similar to the basal pore liquid pressure; at the second surge, an excessive pore pressure was observed, but did not reach values as observed for the flow on July 10th. We find a linear to slightly convex velocity profile for the first surge and for the complete event from the profiler (Fig 3b and Fig 3d). Surface velocity values are not yet available. For the fast flowing and rather liquid middle part of the event (Fig 3c), the derived velocity profiles shows a clear convex profiles, with very low velocities at the base, indicating that material that eventually would deposit was overridden by a surge from behind, similar as for the small wave in the first event. For the average profile of the complete flow the lowest level shows very few (124, compared to 3910 in the level above), but surprisingly high values compared to the upper layers. Here, close to the base, material might have decelerated, eventually deposited and remobilized. In that case, the correlation coefficient decreases and when the velocity approaches zero, ultimately no cross-correlation is possible. This missing information of very low, respectively zero velocity values, over a long reference period yields biased median values towards higher velocities.

4. Discussion

The velocity profiles shown here represent the original results from the monitoring barrier. Despite the fact that differences of velocities over the height are larger than the scatter of the data, the derived data, several sources of uncertainties have to be considered: (1) Firstly, there are uncertainties that are connected to shortcomings of the experimental field setup. That is, we unavoidably measure velocities of particles passing and probably sliding along a rigid wall, i.e. there is the effect of wall friction (cf. Jop et al., 2005; Kaitna et al., 2014). Additionally, we measure only particle velocity and not fluid velocity and the geometry of the paired conductivity sensors captures only flow variations in flow direction. (2) Secondly, there are uncertainties associated with the data analysis. For example, the choice of a threshold for the correlation coefficient is to some extent arbitrary. We tried to avoid misleading correlation results by defining a high correlation coefficient of 0.8. Another source of error arises from the comparison of velocities derived from the profiler with a surface velocity derived from video recordings. Due to the resolution of the camera, we cannot derive surface velocities at the boundary of the barrier, but only in a region some 5-20 cm distant. Additionally, we found that for natural flows, including large boulders and woody debris, deposition pattern may influence the flow along the barrier as can be seen for the second event in August 2017, where surface velocity was often smaller than the velocities at the barrier.

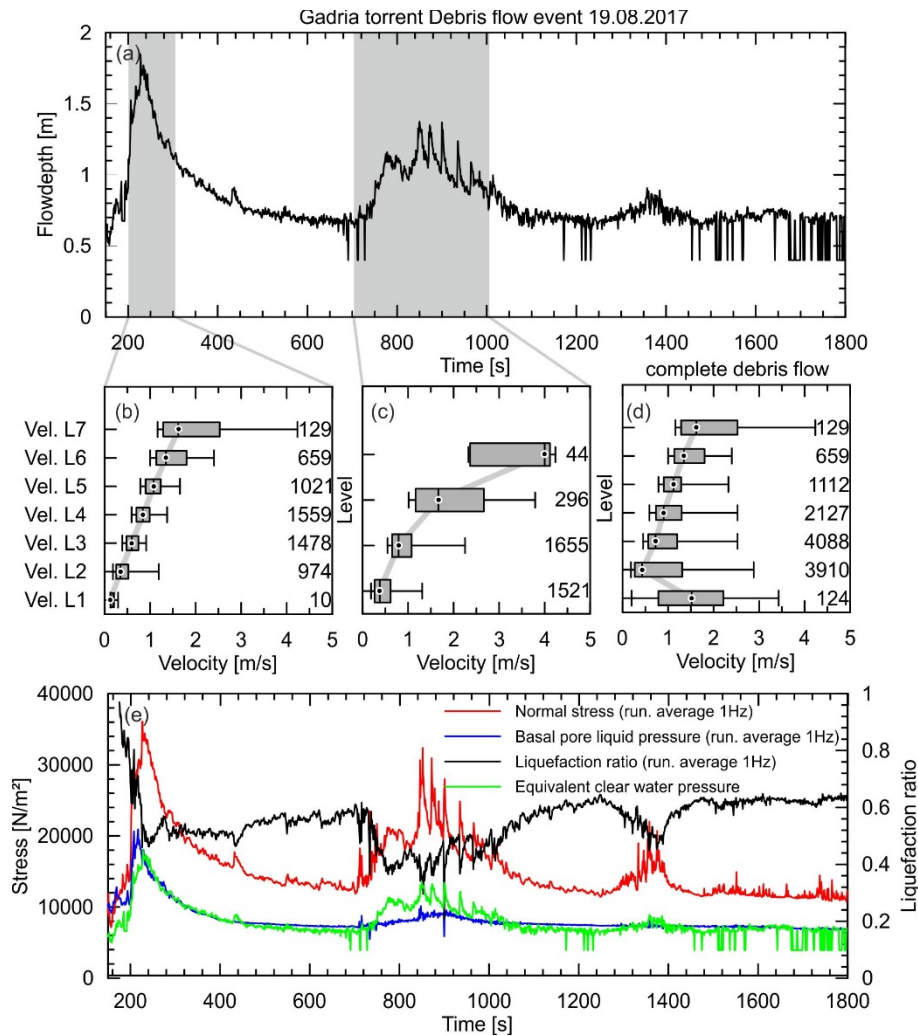


Fig. 3. Data of the debris flow from August 19 2017 (a) Flow depth [m] of the ultra-sonic sensor of the force plate 1 aside the barrier. (b) Velocity profile of the first surge (200-300 sec.). (c) Velocity profile of the second surge (700-1000 sec.). (d) Collective velocity profile of the complete debris flow, (e) normal stress (red line), basal pore liquid pressure (blue line), liquefaction ratio (black line), and equivalent clear water pressure (green line) in running average values of 1Hz.

5. Conclusion

Two debris flows were observed in the Gadria torrent in South Tyrol in the year 2017 by the new monitoring barrier. Additionally to the internal velocity profile, the normal stress, basal liquid pore pressure, and the flow depth were recorded. The minimum temporal resolution for the velocity profiles at this stage is around 1 second. Our measurements demonstrate that natural debris flows undergo different states of deformation during the flow and indicate no constant velocity profile throughout the flow. Velocity profiles are strongly affected by surges and deposition of material between surges. We assume that the general shape of the derived profiles may be representative for the respective section of the flow, but there are several sources of errors that might affect the results. We think that especially the connection between excess pore liquid pressure and the velocity profiles need to be further investigated.

Acknowledgements

Friedrich Zott deserves all the credits for the installation of the monitoring system. We thank Pierrepaolo Macconi and Lea Gasser for logistic and field support in all situations and all helping parties in this project. The monitoring barrier has been conducted through a cooperation of the Department of Civil Protection of the Autonomous Province of Bozen-Bolzano in Italy and the University of Natural Resources and Life Science, Vienna.

References

- Arai, M., and Takahashi, T., 1983, A method for measuring velocity profiles in mud flows, *in* Proceedings 20th International Congress, International Association for Hydraulic Research, Volume 3: Moscow, Russia, p. 279–286.
- Berti, M., Genevois, R., Simoni, A., and Tecca, P. R., 1999, Field observations of a debris flow event in the Dolomites: *Geomorphology* v. 29(3-4), p. 265–274, doi:10.1016/S0169-555X(99)00018-5.
- Chen, H., Hu, K., Cui, P., and Chen, X., 2017, Investigation of vertical velocity distribution in debris flows by PIV measurement: *Geomatics, Natural Hazards and Risk*, v. 8 (2), p. 1631–1642, doi:10.1080/19475705.2017.1366955.
- Comiti, F., Marchi, L., Macconi, P., Arattano, M., Bertoldi, G., Borga, M., et al., 2014, A new monitoring station for debris flows in the European Alps. First observations in the Gadria basin: *Natural Hazards*, v. 73(3), p. 1175–1198, doi:10.1007/s11069-014-1088-5.
- Genevois, R., Tecca, P. R., Berti, M., and Simoni, A., 2000, Debris-flows in the dolomites: experimental data from a monitoring system *in* Wieczorek, G. F., Naeser, N.D., eds.: *Debris Flow Hazard Mitigation: Mechanics, Prediction and Assessment*: Taipei, Taiwan, p. 283-292.
- Iverson, R. M., 1997, The physics of debris flows: *Reviews of Geophysics* v. 35(3), p. 245–296.
- Iverson, R. M., and Lahusen, R. G., 1989, Dynamic pore-pressure fluctuations in rapidly shearing granular materials: *Science (New York, N.Y.)* v. 246 (4931), p. 796–799, doi:10.1126/science.246.4931.796.
- Johnson, C. G., Kokelaar, B. P., Iverson, R. M., Logan, M., Lahusen, R. G., and Gray, J. M. N. T., 2012, Grain-size segregation and levee formation in geophysical mass flows: *Journal of Geophysical Research*, v. 117 (F1), doi:10.1029/2011JF002185.
- Jop, P., Forterre, Y., and Pouliquen, O., 2005, Crucial role of sidewalls in granular surface flows. Consequences for the rheology: *Journal of Fluid Mechanics*, v. 541, p. 167, doi:10.1017/S0022112005005987.
- Kaitna, R., Dietrich, W. E., and Hsu, L., 2014, Surface slopes, velocity profiles and fluid pressure in coarse-grained debris flows saturated with water and mud: *Journal of Fluid Mechanics*, v. 741, p. 377–403, doi:10.1017/jfm.2013.675.
- Kaitna, R., Palucis, M. C., Yohannes, B., Hill, K. M., and Dietrich, W. E., 2016, Effects of coarse grain size distribution and fine particle content on pore fluid pressure and shear behavior in experimental debris flows: *Journal of Geophysical Research: Earth Surface*, v. 121(2), p. 415–441, doi:10.1002/2015JF003725.
- Kern, M. A., Bartelt, P. A., and Sovilla, B., 2010, Velocity profile inversion in dense avalanche flow: *Annals of Glaciology*, v. 51 (54), p. 27–31, doi:10.3189/172756410791386643.
- Mainali, A., and Rajaratnam, N., 1994, Experimental Study of Debris Flows: *Journal of Hydraulic Engineering*, v. 120, p. 104–123.
- Major, J. J., 2000, Gravity-driven consolidation of granular slurries: implications for debris-flow deposition and deposit characteristics: *Journal of Sedimentary Research*, v. 70 (1), p. 64–83.
- Marchi, L., Arattano, M., and Deganutti, A. M., 2002, Ten years of debris-flow monitoring in the Moscardo Torrent (Italian Alps): *Geomorphology*, v. 46(1-2), p. 1–17, doi:10.1016/S0169-555X(01)00162-3.
- McArdell, B. W., Bartelt, P., and Kowalski, J., 2007, Field observations of basal forces and fluid pore pressure in a debris flow: *Geophysical Research Letters*, v. 34(7), p. 171, doi:10.1029/2006GL029183.
- McCoy, S. W., Kean, J. W., Coe, J. A., Staley, D. M., Wasklewicz, T. A., and Tucker, G. E., 2010, Evolution of a natural debris flow. In situ measurements of flow dynamics, video imagery, and terrestrial laser scanning: *Geology*, v. 38(8), p. 735–738, doi:10.1130/G30928.1.
- McCoy, S. W., Tucker, G. E., Kean, J. W., and Coe, J. A., 2013, Field measurement of basal forces generated by erosive debris flows: *Journal of Geophysical Research: Earth Surface*, v. 118(2), p. 589–602, doi:10.1002/jgrf.20041.
- Nagl, G., and Hübl, J., 2017, A Check-Dam to Measure Debris Flow-Structure Interactions in the Gadria Torrent. *in* Mikoš, M., Vilímek, V., Yin, Y., Sassa, K., eds.: *Advancing Culture of Living with Landslides*. Cham: Springer International Publishing, p. 465–471.
- Pierson, T. C., 1986, Flow behaviour of channelized debris flows, Mount St. Helens, Washington. *in* A. D. Abrahams, eds.: *Hillslope processes*. Boston: Allen & Unwin, p. 269–296.
- Sanvitale, N., Bowman, E. T., and Genevois, R., 2011, Experimental measurements of velocity through granular-liquid flows, *in* Genevois, R., Hamilton, D.L., and Prestininzi, A., eds.: *Proceedings of the 5th International Conference on Debris-flow Hazards Mitigation: Mechanics*,

Prediction and Assessment. Italian Journal of Engineering Geology and Environment. Casa Editrice Universita La Sapienza, Rome, Italy. 2011.

Walter, F., and McArdell, B., 2015, What is the velocity profile of debris flows?: Abstract, European Geosciences Union 2015-12815, 2015, v. 17, European Geosciences Union, General Assembly 2015. Vienna, 2015.

Debris-flow early warning system at regional scale using weather radar and susceptibility mapping

Rosa M Palau^{a,b,*}, Marcel Hürlimann^b, Marc Berenguer^a, Daniel Sempere-Torres^a

^aCenter of Applied Research in Hydrometeorology, Universitat Politècnica de Catalunya, Jordi Girona 1-3 (C4), Barcelona 08034, Spain

^bDivision of Geotechnical Engineering and Geosciences, Department of Civil and Environmental Engineering, Universitat Politècnica de Catalunya, Jordi Girona 1-3 (D2), Barcelona 08034, Spain

Abstract

Risk mitigation for debris flows at regional scale is a challenge. Early warning systems are helpful in depicting the time and the location of future debris flows so that emergency responders can act in advance before the disaster takes place. Herein we present a prototype real-time regional early warning system for rainfall induced shallow landslides and debris flows for the region of Catalonia (northeastern Spain). The model issues a warning level combining susceptibility information and real-time rainfall triggering conditions obtained from weather radar observations and forecasts. Susceptibility maps have been derived using a fuzzy-logic approach and two input variables, terrain slope and land cover. These maps have been obtained using (i) grid cells of different resolutions, and (ii) physical catchments (of first order) as terrain units. Although high resolution grid-cell maps show a more accurate representation of susceptibility over the region, maps based on catchments are more intuitive and better characterize the area affected by future debris flows. Rainfall triggering conditions are assessed by means of probabilistic intensity-duration thresholds obtained from literature. Finally, we have validated the early warning system and tested its performance for some important events from the last ten years that were either monitored in specific catchments, or were reported in unmonitored catchments. In general, the system has been able to satisfactorily forecast the time of occurrence of most of the analyzed past debris-flow events.

Keywords: Debris flow; Early Warning System, Susceptibility map; Rainfall thresholds; Weather radar; Catalonia

1. Introduction

Debris flows represent an important hazard in mountainous regions and can cause substantial economic and human losses. Although debris flows are not as widely reported in Catalonia (northeastern Spain) as in other regions, they still represent a significant hazard (Portilla et al., 2010; Raïmat et al., 2010; Abancó, 2013; Palau et al., 2017).

Rainfall is the most important debris-flow trigger in Catalonia. Intense rainfall events are expected to increase in frequency due to climate change (Gariano and Guzzetti, 2016). In such a context, strategies to reduce the risk by increasing awareness, and preparedness of communities living at areas that may be affected must be developed (UNISDR, 2015; Alcántara-Ayala et al., 2017). Early warning systems help us anticipate the risk prior to the event, in order that emergency strategies could be adopted in advance.

The majority of early warning systems focus on rainfall induced shallow landslides and debris flows on natural slopes (Aleotti, 2004; Chen and Lee, 2004; Baum and Godt, 2010). Most of them use rainfall inputs obtained from rain gage data. However, the density and temporal resolution of rain gage networks is usually low and landslide triggering rainfalls tend to be underestimated (Marra et al., 2014). The main advantage of radar data is its high temporal and spatial resolution (of the order of one kilometer and up to five minutes). Only in few early warning systems radar measurements have been adopted instead; e.g. Japan (Osanaï et al., 2010), Southern California (NOAA-USGS Debris Flow Task Force, 2005) and the Pyrenees (Berenguer et al., 2015).

* Corresponding author e-mail address: palau@crahi.upc.edu

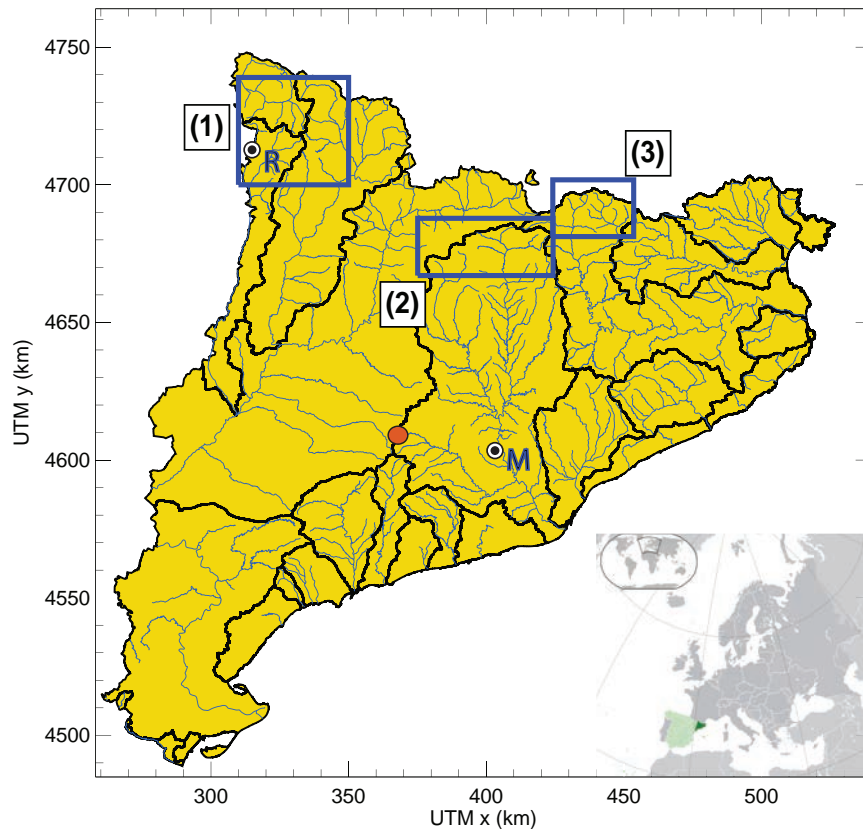


Fig. 1. Overview map of the Catalonia region. The Rebaixader Catchment (R) and Montserrat (M) locations are marked with a concentric black circle. The orange circle represents the location of the radar. The zones of the inventories used for the susceptibility maps are delimited by the blue rectangles.

The terrain predisposing factors can be considered by means of landslide susceptibility maps. The majority of them are raster maps (Carrara et al., 2007; Kirschbaum et al., 2016; Bee et al., 2018; Wilde et al., 2018), but some use other terrain units as hydrological catchments (Cannon et al., 2004; Carrara et al., 2007; Chevalier et al., 2013; Hürlimann et al., 2016; Krøgli et al., 2017). Choosing the most appropriate susceptibility terrain unit requires considering several factors and is not always trivial.

The main aim of this work is to present an updated version of the early warning system of Berenguer et al., (2015) for the Catalan Pyrenees. The new version of the early warning system covers the entire Catalonia region, uses an updated susceptibility map and a new approach to define the critical rainfall. The effect of using different terrain map units for the susceptibility classification is also introduced. Finally, the early warning system has been run for the summer season of 2010 (April to October) using radar Quantitative Precipitation Estimates (QPE) and validated for some recorded events occurred in specific catchments.

2. Methodology

The prototype early warning system presented herein uses information on debris-flow susceptibility and rainfall observations. These two inputs are combined in real-time to obtain a qualitative warning level (very low, low, moderate or high).

2.1. Susceptibility assessment

In this work, two terrain features were seen as the most important in order to derive the susceptibility map of Catalonia: slope and land cover. To calibrate and validate the susceptibility model, information on past debris-flow and shallow landslide events contained in the inventories of three zones of the Catalan Pyrenees is introduced. Slope

accounts for the topography of the terrain. Land cover accounts for the terrain resistance parameters. Additionally, we attempted to use the geology map to provide some information about the surface deposits, but this information showed no clear skill in characterizing landslide susceptibility.

The susceptibility class is calculated for each of the terrain units using a fuzzy logic classifier (Mendel, 1995). The classifier requires membership functions for each variable, that were obtained based on expert criteria. Then, a weight is assigned to each variable. In our case, we have defined four classes: “very low”, “low”, “moderate” and “high” susceptibility. Therefore, for each variable there are four membership functions, one for each susceptibility class. The membership degree to each susceptibility class is calculated for each of the terrain units as the weighted average of the membership degrees for the two variables. The susceptibility class having higher membership degree is assigned to each terrain unit.

The last step of the susceptibility assessment is the validation of the resulting susceptibility maps. Receiver Operating Characteristics (ROC) curves have been calculated (Fawcett, 2006), and the area under the curve (AUC) is the metrics used to assess the model performance.

2.2. Analysis of triggering rainfalls

For the purpose of this work, rainfall inputs are obtained from the observations of the CDV C-band radar of the Meteorological Service of Catalonia (SMC) with the chain of algorithms of the Integrated Tool for Hydrometeorological Forecasting (EHIMI, Corral et al., 2009). This tool includes the correction of the beam-blockage effect, ground clutter elimination, identification of the type of precipitation, extrapolation of elevated reflectivity measurements to surface and conversion of reflectivity to rain-rate. The rainfall products used here consist of real-time 30-min radar rainfall accumulations with a spatial resolution of one kilometer. Additionally, radar-based nowcasts (Berenguer et al., 2011) could be included to increase the lead-time.

To assess if a given rainfall event has the potential of triggering a debris flow, the global probabilistic rainfall intensity-duration percentile thresholds obtained by (Guzzetti et al., 2008) have been adapted. The thresholds represent the percentile of past shallow landslides and debris flows triggered by a given rainfall intensity and duration. Using them, four rainfall hazard levels have been defined: “very low”, “low”, “moderate” and “high” (see Figure 2). If a set of more local rainfall thresholds is available, they could be easily adapted in the LEWS.

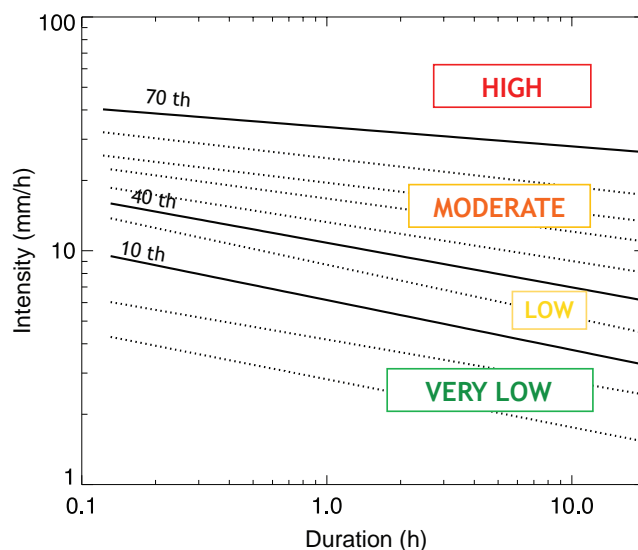


Fig. 2. Rainfall intensity-duration thresholds adapted from Guzzetti et al. (2008) and selected rainfall hazard levels. The continuous lines represent the 10th, 40th and 70th percentiles of rainfall that were selected as thresholds.

2.3. Combination of susceptibility and rainfall: Issuing a warning level

In the current configuration, susceptibility information is a static input in the early warning system, while the radar-based rainfall estimates are updated every 30 minutes.

The combination of the four susceptibility classes and the four rainfall hazard classes is done by means of a warning level matrix (Figure 3). The columns of the warning level matrix represent the susceptibility and the rows represent the rainfall hazard. The combination of each susceptibility class with each rainfall hazard class results in a warning level, which again is of four classes: “very low”, “low”, “moderate” and “high”.

The final result is presented in the form of a warning level map assessing the possibility of having a debris flow in each terrain unit for every time-step.

		Susceptibility			
		Susceptibility Very Low	Susceptibility Low	Susceptibility Moderate	Susceptibility High
Rainfall hazard level	Rain Very Low	VL	VL	VL	L
	Rain Low	VL	L	L	M
	Rain Moderate	VL	L	M	H
	Rain High	L	M	H	H

Fig. 3. Warning level matrix. Rows represent rainfall hazard level, columns represent susceptibility class. VL states for very low, L for low, M for moderate and H for high warning level.

3. Analyzing the influence of the terrain unit

A terrain unit is a portion of the terrain that can be distinguished from the terrain units around it because of its properties (Hansen, 1984). It should maximize internal homogeneity and enhance heterogeneity between different terrain units (Guzzetti et al., 2005). Choosing an appropriate terrain unit requires considering the studied phenomena, the available datasets, the resolution, the quality of the results and the final purpose of the susceptibility map among other factors.

As part of this work, we are studying the applicability of the early warning system to different terrain units. Herein we will examine the possible advantages and limitations of using (i) first order catchments (Strahler, 1957), (ii) and 30 m resolution grid-cells.

Since debris flows are transported along channels, the initiation, transportation and deposition zones coincide with the area defined by hydrological catchments. The majority of debris-flow events were recorded in first order basins. Such catchments located at the headwaters are usually steeper and generally have higher susceptibility than higher order catchments. For this reason, we have set up the early warning system using a susceptibility map based on first order basins.

Both maps shown in Figure 6 have approximately the same percentage of moderate and high warning level terrain units: 38% and 58% respectively in the case of first order basins, and 38% and 52% in the case of 30 m resolution grid-cells. However, the number of terrain units classified as very low and low susceptibility is somewhat different. 8% of the pixel-based map is classified as very low and 2 % as low susceptibility, whereas the first order basins map has no terrain unit with very low susceptibility and classifies only a 4% of terrain units as having low susceptibility. As a result, the number of warnings issued when using the basin-based susceptibility map will probably be higher than when using the pixel-based susceptibility map.

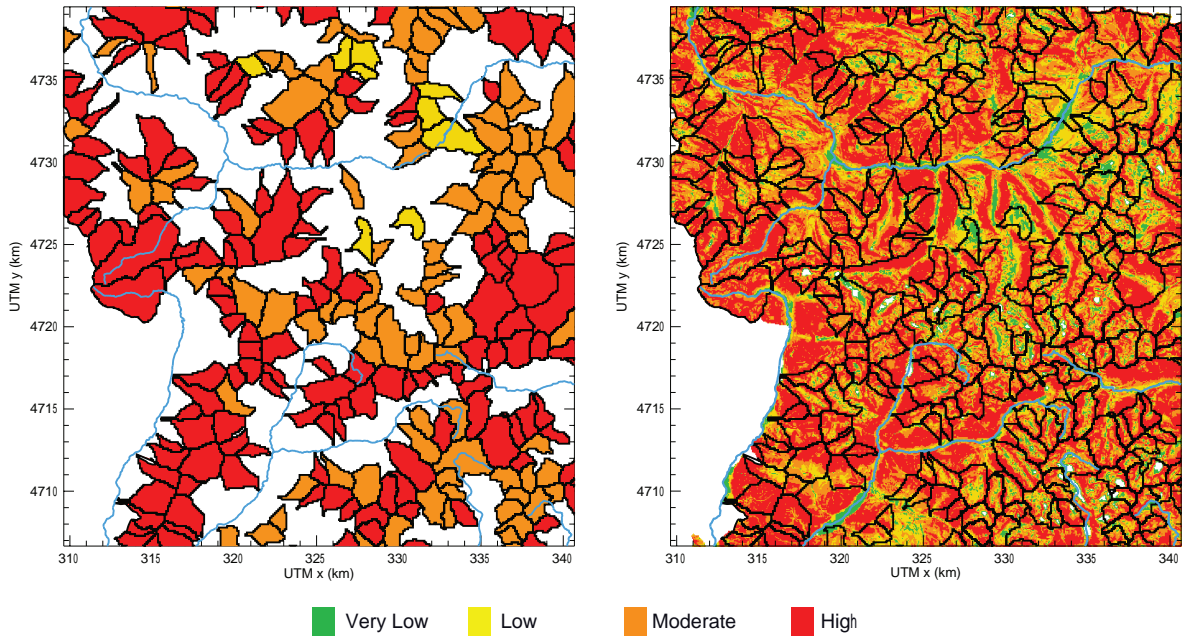


Fig. 6. Preliminary results of susceptibility mapping. a) Map based on first order basins for the NW-Catalonia region, b) map based on 30 m resolution grid cells for the same region.

Maps based on grid-cells have the advantage of covering the entire analysis domain but unlike first order basins lack of physical meaning. For this reason, early warning system results will be easier to interpret when using the susceptibility map based on first order basins.

Another important aspect when thinking on the implementation of the susceptibility map into the proposed real-time early warning system is the required computational time required to compute a time-step over the region of Catalonia. A priori it seems that the 30 m resolution grid-cell configuration will be more computationally demanding than the configuration based on first order catchments.

4. Results

First, we have generated a susceptibility map for the Catalonia region based on first-order basins and run the prototype early warning system for a period of seven months in 2010. The early warning system outputs have been checked for recorded events in monitored and unmonitored catchments. All the recorded events are associated with a moderate or high warning levels, and coincide with intense rainfall episodes.

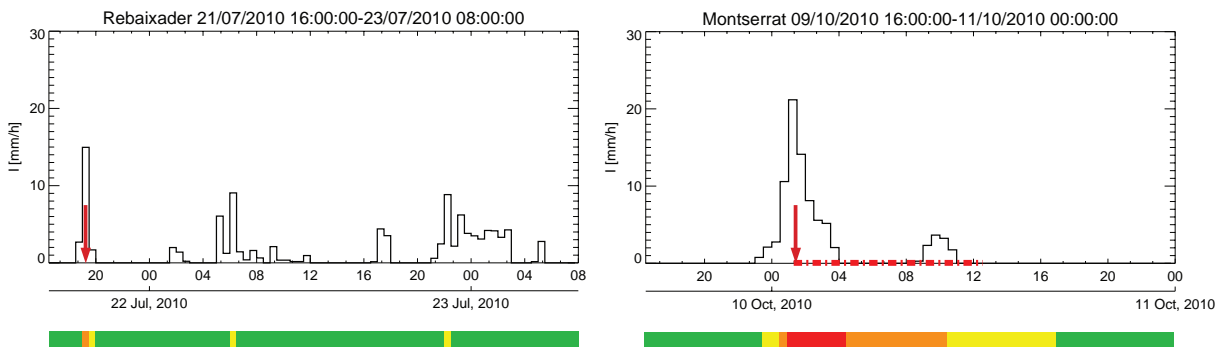


Fig. 4. Output of the early warning system for a debris-flood event in the Rebaixader catchment and a debris-flow event in Montserrat. The black line shows the evolution of the rainfall intensity in the catchment, and the color bar indicates the warning level diagnosed with the warning system. Green, yellow, orange and red correspond, respectively, to “very low”, “low”, “moderate” and “high” warning level. The red arrows represent the time the Rebaixader monitoring station recorded the debris flow and when the event was reported at Montserrat. The discontinuous red line represents the period of time road and railway remained closed.

This is the case for the events shown in Figure 4. The first case corresponds to the event that occurred on 21 July 2010 at the Rebaixader catchment. A debris-flow monitoring system has been running in this catchment since 2009 (Hürlimann et al., 2014) and recorded a debris-flood event at 19:05. The early warning system issued a moderate warning level for the same time. Figure 4 (right) shows the case of the 09-10 October 2010 at the Montserrat basin. In this case the exact time of the debris-flow event is unknown. However, a road and a railway were blocked by a debris flow and remained closed on 10 October 2010 from approximately 01:00 to 12:00, coinciding with the time when the system issues moderate and high warning levels.

Many debris-flow events happen in remote areas and are not recorded. Thus, one of the challenges in the evaluation of the early warning system performance is the correct determination of the total number of false alarms and misses. The number of days with moderate and high warning level has been counted for every first order basin (Figure 5). Results for monitored and unmonitored catchments where debris flows have been reported are promising. Four events were recorded at the Rebaixader monitoring site, and the prototype LEWS issued a total of five days with moderate or high warning. However, in Montserrat only one event was reported, but seven days presented a moderate or high warning.

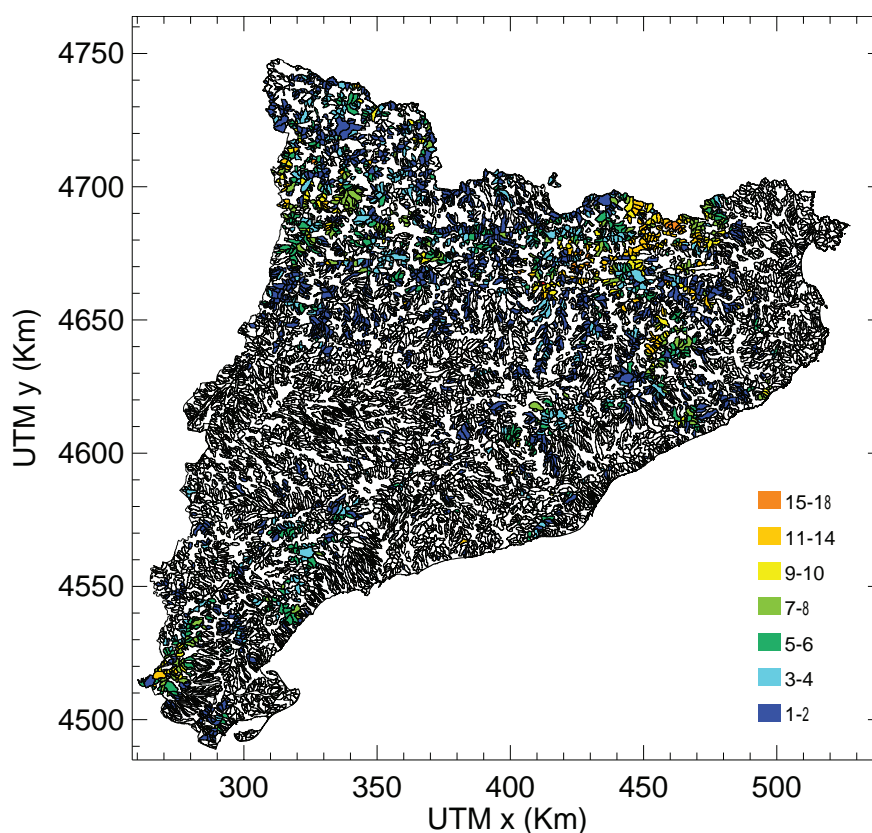


Fig. 5. Number of days with moderate or high warning level for each of the first order catchments between April and October 2010.

5. Conclusions

Early warning systems constitute a useful tool for the mitigation of debris-flow and debris-flood impacts. The methodology proposed herein presents a regional scale early warning system. The presented early warning model makes use of only two input parameters. A susceptibility map accounting for the terrain predisposing factors, and the triggering rainfall that is assessed by means of weather radar observations and probabilistic rainfall thresholds. The output of the early warning system is a warning level (very low, low, moderate and high) that is computed for each terrain unit by means of a warning level matrix.

We have implemented the early warning system for the Catalonia region using a susceptibility map based on first order basins and ran it for a seven-month period in 2010. An important challenge in this domain is the correct

determination of the number of false alarms and misses. Most debris-flow events happen in remote areas and many are unreported. Therefore, the evaluation of the performance of the early warning system is challenging.

The influence of terrain map units on the early warning system performance is an interesting topic. We have presented preliminary results comparing susceptibility maps based on first order basins and 30 m resolution grid-cells. On the one hand, the interpretation of the early warning system seems easier using susceptibility maps based on first order basins. On the other hand, the analysis area is not completely covered. Another drawback is that considering the terrain land cover variability is difficult. As a result, the susceptibility tends to be higher. The implementation of the susceptibility map of 30 m resolution pixels into the early warning system would cover the entire domain, account for land cover variability and provably issue higher resolution warnings. However, it would complicate the interpretation of the outputs and require more computational resources. Although using first order basins may seem better, choosing the best mapping unit requires implementing the two susceptibility maps into the early warning system and consider the performance of both configurations.

Finally, in the context of an Early Warning System, extending the lead time is fundamental to enable efficient emergency management. In real time, it will thus be advisable to extend the series of radar observations with high-resolution rainfall forecasts (such as radar-based rainfall nowcasts).

Acknowledgements

This work has been done in the framework of the EC H2020 project ANYWHERE (DRS-01-2015-700099) and the Spanish project SMuCPhy (BIA 2015-67500-R). The first author is supported by a grant from the Secretaria d'Universitats i Recerca del Departament d'Empresa i Coneixement de la Generalitat de Catalunya.

References

- Abancó, C., 2013, Monitoring and geomorphologic characterization of debris flows at catchment scale: TDX (Tesis Doctorals en Xarxa), p. 177pp, <http://www.tdx.cat/handle/10803/128677> (accessed October 2018).
- Alcántara-Ayala, I., Murray, V., Daniels, P., and McBean, G., 2017, International Council for Science (ICSU)-On the future challenges for the integration of science into international policy development for landslide disaster risk reduction: Advancing Culture of Living with Landslides, v. 5, p. 1–557, doi:10.1007/978-3-319-53483-1.
- Aleotti, P., 2004, A warning system for rainfall-induced shallow failures: Engineering Geology, v. 73, p. 247–265.
- Baum, R.L., and Godt, J.W., 2010, Early warning of rainfall-induced shallow landslides and debris flows in the USA: Landslides, v. 7, p. 259–272, doi:10.1007/s10346-009-0177-0.
- Bee, E., Pennington, C., Dashwood, C., and Lee, K., 2018, Creating a national scale debris flow susceptibility model for Great Britain: Geophysical Research Abstracts, v. 20, p. 7939.
- Berenguer, M., Sempere-Torres, D., and Hürlimann, M., 2015, Debris-flow forecasting at regional scale by combining susceptibility mapping and radar rainfall: Natural Hazards and Earth System Science, v. 15, p. 587–602, doi:10.5194/nhess-15-587-2015.
- Berenguer, M., Sempere-Torres, D., and Pegram, G.G.S., 2011, SBMcst - An ensemble nowcasting technique to assess the uncertainty in rainfall forecasts by Lagrangian extrapolation: Journal of Hydrology, v. 404, p. 226–240, doi:10.1016/j.jhydrol.2011.04.033.
- Cannon, S.H., Gartner, J.E., Rupert, M.G., and Michael, J.A., 2004, Emergency assessment of debris-flow hazards from basins burned by the Cedar and Paradise Fires of 2003, southern California, doi:10.3133/ofr20041011.
- Carrara, A., Crosta, G., and Frattini, P., 2007, Comparing models of debris-flow susceptibility in the alpine environment: Geomorphology, v. 94, p. 353–378, doi:10.1016/j.geomorph.2006.10.033.
- Chen, H., and Lee, C.F., 2004, Geohazards of slope mass movement and its prevention in Hong Kong: Engineering Geology, v. 76, p. 3–25, doi:10.1016/j.enggeo.2004.06.003.
- Chevalier, G., Medina, V., Hürlimann, M., and Bateman, A., 2013, Debris-flow susceptibility analysis using fluvio-morphological parameters: Application to the Central-Eastern Pyrenees: Natural Hazards, v. 67, p. 213–238, doi:DOI 10.1007/s11069-013-0568-3.
- Fawcett, T., 2006, An introduction to ROC analysis: Pattern Recognition Letters, v. 27, p. 861–874, <http://www.scopus.com/inward/record.url?eid=2-s2.0-33646023117&partnerID=40&md5=61763f4a8bb45525c553958e3a2cd8d1>.
- Gariano, S.L., and Guzzetti, F., 2016, Landslides in a changing climate: Earth-Science Reviews, v. 162, p. 227–252, doi:10.1016/j.earscirev.2016.08.011.
- Guzzetti, F., Peruccacci, S., Rossi, M., and Stark, C.P., 2008, The rainfall intensity-duration control of shallow landslides and debris flows: An update: Landslides, v. 5, p. 3–17, doi:10.1007/s10346-007-0112-1.
- Guzzetti, F., Reichenbach, P., Cardinali, M., Galli, M., and Ardizzone, F., 2005, Probabilistic landslide hazard assessment at the basin scale: Geomorphology, v. 72, p. 272–299.
- Hansen, M.J., 1984, Strategies for classification of landslides, in Brunnsden, D. ed., Slope Instability, Chichester, John Wiley, p. 1–25.
- Hürlimann, M., Abancó, C., Moya, J., and Vilajosana, I., 2014, Results and experiences gathered at the Rebaixader debris-flow monitoring site, Central Pyrenees, Spain: Landslides, v. 11, p. 939–953, <http://link.springer.com/article/10.1007/s10346-013-0452-y>.
- Hürlimann, M., Lantada, N., Gonzalez, M., and Pinyol, J., 2016, Susceptibility assessment of rainfall-triggered flows and slides in the Central-Eastern Pyrenees, in Aversa, S., Cascini, L., Picarelli, L., and Scavia, C. eds., XII Int. Symposium on Landslides and Engineered Slopes, Naples, CRC Press, p. 1129–1136.

- Kirschbaum, D., Stanley, T., and Yatheendradas, S., 2016, Modeling landslide susceptibility over large regions with fuzzy overlay: *Landslides*, v. 13, p. 485–496, doi:10.1007/s10346-015-0577-2.
- Krøgli, I.K., Devoli, G., Colletuille, H., Sund, M., Boje, S., and Engen, I.K., 2017, The Norwegian forecasting and warning service for rainfall- and snowmelt-induced landslides: *Natural Hazards and Earth System Sciences Discussions*, p. 1–34, doi:10.5194/nhess-2017-426.
- Marra, F., Nikolopoulos, E.I., Creutin, J.D., and Borga, M., 2014, Radar rainfall estimation for the identification of debris-flow occurrence thresholds: *Journal of Hydrology*, v. 519, p. 1607–1619, doi:10.1016/j.jhydrol.2014.09.039.
- Mendel, J.M., 1995, Fuzzy Logic Systems for Engineering : A tutorial: *Proceedings of the IEEE*, v. 83, p. 345–377, doi:10.1109/5.364485.
- NOAA-USGS Debris Flow Task Force, 2005, NOAA-USGS Debris-Flow Warning System - Final Report, doi:10.3133/cir1283.
- Osanai, N., Shimizu, T., Kuramoto, K., Kojima, S., and Noro, T., 2010, Japanese early-warning for debris flows and slope failures using rainfall indices with Radial Basis Function Network: *Landslides*, v. 7, p. 325–338, doi:10.1007/s10346-010-0229-5.
- Palau, R.M., Hürlimann, M., Pinyol, J., Moya, J., Victoriano, A., Génova, M., and Puig, C., 2017, Recent debris-flows in the Portainé catchment (Eastern Pyrenees, Spain). Analysis of monitoring and field data focussing on the 2015 event: *Landslides*, v. 14, p. 1161–1170, doi:10.1007/s10346-017-0832-9.
- Portilla, M., Chevalier, G., and Hürlimann, M., 2010, Description and analysis of major mass movements occurred during 2008 in the Eastern Pyrenees: *Nat. Hazards Earth Syst. Sci.*, v. 10, p. 1635–1645, doi:10.5194/nhess-10-1635-2010.
- Raïmat, C., Luis, R., and Wendeler, C., 2010, Behaviour of VX barriers and initial results from the pioneer monitoring station in Erill & Portainé/Spain, http://www1.geobruigg.com/contento/Portals/35/media/Techdok_Debflow_Portainé_en.pdf (accessed July 2016).
- Strahler, A.N., 1957, Quantitative Analysis of Watershed Geomorphology: *EOS, Transactions - American Geophysical Union*, v. 38, p. 913–920, doi:10.1029/tr038i006p00913.
- UNISDR, 2015, Sendai Framework for Disaster Risk Reduction, *in* Third United Nations World Conference on Disaster Risk Reduction, p. 1–25, doi:A/CONF.224/CRP.1.
- Wilde, M., Günther, A., Reichenbach, P., Malet, J.-P., and Hervás, J., 2018, Pan-European landslide susceptibility mapping: ELSUS Version 2: *Journal of Maps*, v. 14, p. 97–104, doi:10.1080/17445647.2018.1432511.

Real-time monitoring of debris-flow velocity and mass deformation from field experiments with high sample rate lidar and video

Francis K. Rengers^{a,*}, Thomas D. Rapstine^{a,b}, Kate E. Allstadt^a, Michael Olsen^c, Michael Bunn^c, Richard M. Iverson^d, Jason W. Kean^a, Ben Leshchinsky^c, Matthew Logan^d, Mahyar Sharifi-Mood^c, Maciej Obryk^d, Joel B. Smith^a

^aU.S. Geological Survey, 1711 Illinois St, Golden 80401, USA

^bColorado School of Mines, 1500 Illinois St, Golden 80401, USA

^cOregon State University, 140 Peavy Hall, 3100 SW Jefferson Way, Corvallis, 97331, USA

^dU.S. Geological Survey, 1300 SE Cardinal Ct # 100, Vancouver, WA 98683, USA

Abstract

Debris flows evolve in both time and space in complex ways, commonly starting as coherent failures but then quickly developing structures such as roll waves and surges. These processes are readily observed, but difficult to study or quantify because of the speed at which they occur. Many methods for studying debris flows consist of point measurements (e.g., of flow height or basal stresses), which are inherently limited in spatial coverage and fail to fully capture the spatiotemporal evolution of a flow. In this study, we use terrestrial lidar to measure debris-flow profiles at high sample rates to examine debris-flow movement with high temporal and spatial precision and accuracy. We acquired measurements during gate-release experiments at the USGS debris-flow flume, a unique experimental facility where debris flows can be simulated at a large scale. In this study, the laser scanner was placed at the bottom of the steep flume and recorded topography of the entire flume bed and debris flow at a rate of 60 Hz along a narrow profile (~1mm in width), providing a detailed, two-dimensional cross-section of the debris flow through time. The high-resolution profiles enabled us to quantify flow front and surge velocities of the debris flow and provide an unprecedented record of the development and evolution of the flow structure over time. The profiles also preserve a record of the highly variable deposition pattern of the debris flow on a downstream fan with a time resolution of hundredths of a second. In addition, video imagery from the experiment was used to track debris-flow movement through time. By acquiring high-resolution topographic data and video imagery during a controlled experiment, we have been able to obtain unusually complete quantitative measurements of debris-flow movement. Such measurements may help constrain future modeling efforts.

Keywords: Debris flow; lidar;

1. Introduction

Debris flows are rapidly deforming mixtures of sediment and water that can lead to dramatic geomorphic change (e.g. Stiny, 1910, Anderson et al., 2015) as well as the destruction of life and infrastructure (Costa, 1984). Because these hazardous phenomena can be so deadly, it is important to understand the fundamental physical processes that govern debris-flow initiation, movement, and deposition. Much progress has been made on understanding debris-flow physics through numerous experiments at the USGS debris-flow flume over many years (Iverson et al., 2010).

Debris-flow experiments in a large-scale flume can reproduce much of the behavior of natural debris flows (Iverson et al., 2010), which allows for the quantification of physical parameters that are difficult to measure in natural events. Such measurements are crucial for informing debris-flow models (George and Iverson, 2014; Iverson and George, 2014). However, even in a controlled flume setting, monitoring the continuous evolution of debris-flow movement is

* Corresponding author e-mail address: frengers@usgs.gov

a challenge. In past flume experiments at the USGS debris-flow flume, mounted sensors at several discrete points (as many as six in some experiments) were used to measure flow properties. These fixed sensors measured the flow timing and depth, which provided an estimate of flow velocity between fixed points. Herein we use lidar data and video imagery to show continuous flow dynamics of an experimental debris flow as it moves down a flume.

In this study, we used a terrestrial lidar unit as a line-scanner to acquire a full longitudinal profile of the surface of a debris flow at snapshots taken every 0.017 s (~60 Hz) as it traveled from the release point to the deposition point at the base of the flume. This suite of topographic data records the continuous evolution of the center of the debris-flow surface as it moves downstream. In addition, we used video to identify the flow front based on color differences between the flume surface and the debris-flow body. Results from this video image analysis agree well with the lidar data, suggesting that in future studies video data could be used to extract important flow characteristics.

2. Methods

Lidar data were obtained during a flume experiment on May 25, 2017 (Logan et al., 2018) using a Riegl VZ-400 terrestrial lidar scanner (Fig 1). A custom C++ program, Drive VZ-400 (Olsen et al., 2012) was used to operate the scanner and to fix a vertical profile with a vertical field of view of 44 degrees, to measure the entire flume and runoff path. Horizontal angles along that profile were within a total spread of only 0.13 degrees as a result of the angular precision and leveling capabilities of the scanner. The laser resolved a complete swath of the flume every 0.017 s. A general 3D survey of the flume with multiple scan positions was conducted before the flume experiment and georeferenced into UTM coordinates using survey control targets positioned along the flume (Fig. 1) that were linked to ground control points with a total station. Another custom program was written in C++ using the RivLib Library (Riegl, 2017) to interface with the raw scan data stream to extract the time stamp, x, y, and z coordinates of each laser observation at a desired time range, time interval, and vertical angle resolution for analysis. The program also applies the scanner position and orientation (e.g., leveling) information such that the data can be georeferenced. Finally, the program organizes the lidar points into laser swaths that are uniquely numbered.

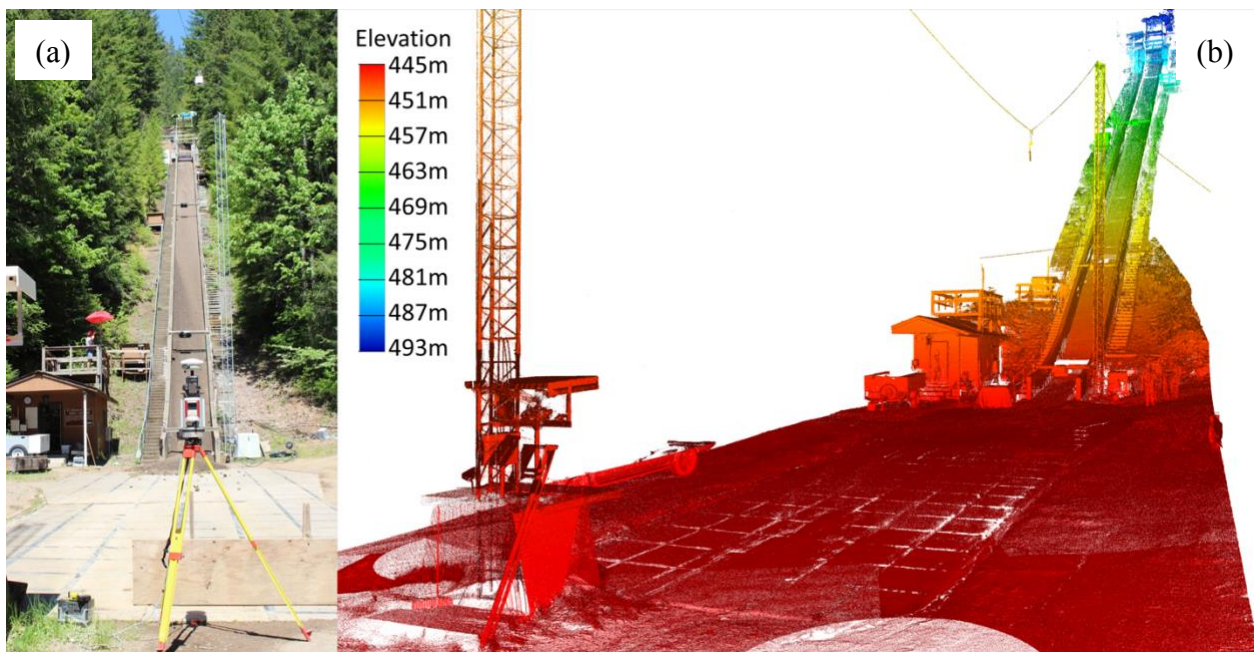


Fig. 1 (a) View of the lidar scanner at the base of the flume; (b) Lidar data showing the flume. Colors denote the elevation in meters.

The flow front was identified from the lidar data through time by tracking changes in height relative to the initial bed height. For each unique lidar swath, we used the lidar point data to interpolate z values (defined as the vertical

direction parallel to gravity) to evenly spaced points along the flume axis every 1 cm. The flow front could be tracked by calculating the change in z values (z_{diff}) from each new lidar swath versus the original bed elevation, using

$$z_{diff} = z_i - z_{bed} \quad (1)$$

where i is the line swath iteration that represents all of the points obtained during a 0.017 s lidar scan.

In addition, we compared the lidar data with videos taken at 60 frames per second (the same sampling rate as the lidar) during the debris-flow experiments to extract further information about the flow movement. Flow-front velocity was estimated by observing the change in pixel color along the flume axis during a video of the debris flow. Surveyed points along the flume axis were visible in the video and provided geometric information for correcting video perspective. We assigned each surveyed point to a pixel location in each video frame by manually picking point pixel locations along the flume axis. These pixel locations and surveyed positions were used to derive a conversion from distance in pixels to distance in meters along the flume axis. For each video frame, pixel color values were extracted along the flume axis between known points using a Bresenham March analysis algorithm, which resulted in an array of colors corresponding to distances down flume (Bresenham, 1965). For a given frame, the array of colors quantifies the appearance of the flume axis at a specific moment in time. Each color array from a single video frame was used to construct a row of the image in Fig. 2a. The process is repeated for all video frames to generate each row of Fig. 2a. The rows of the image in Fig. 2a collectively show how the appearance of the debris flow evolves in time and space.

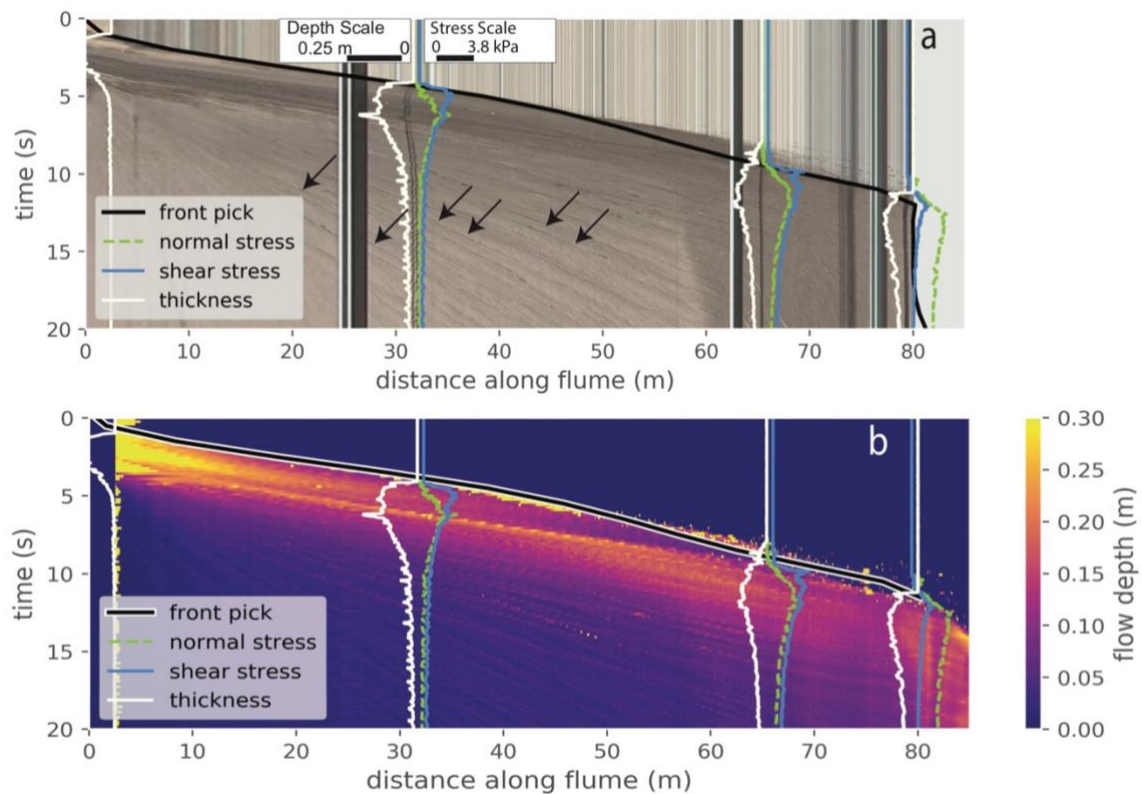


Fig. 2. (a) Colored pixels extracted from video imagery and plotted as function of time and distance along the flume axis. Basal normal stress, basal shear stress, and laser-based flow thickness data are overlaid at the fixed cross sections where they were measured. Note, for display purposes, stress curves increase to the right and the thickness curves increase to the left. These measurements follow the methods described in Iverson et al. (2010). The vertical black lines with white trim are beams across the flume. Black arrows indicate roll waves. The black line is an interpolated cubic spline fit to the flow front. (b) Flow depth measured from lidar swaths plotted a function of time and distance along the flume axis. The flow depth displayed is equal to the flow height above the flume bed, and for clarity the color scale is saturated at 0.3 m. The horizontal black line with white trim is the interpolated cubic spline fit to the flow front in (a).

The video was transformed to show the color of the flow along the flume for each frame (Fig. 2a). Fig. 2a is similar to a shot gather typically generated when processing seismic data; however, instead of sampling a seismic wavefield we sample the appearance of the debris flow. We therefore refer to Fig. 2a as a flow gather. The speed, character, and evolution of flow events are readily observed within the flow gather. For comparison and clarity, we represent the lidar data in the same image format (Fig. 2b) and observe the change in flow height as a function of time and distance along flume. We manually picked the front arrival time on the flow gather image and interpolated between front positions using a cubic spline (Fig. 2a solid black line). Using this flow front line (Fig. 2a solid black line), we estimated the front position, velocity, and acceleration (not shown) of the debris flow as a function of time and space. In addition, we applied the flow front line, without modification, to the lidar-derived flow gather (Fig. 2b) in order to show that there is little misfit, and therefore similar velocities are estimated from the two different methods.

3. Results and Discussion

The high-frequency lidar data allowed for the identification of the debris-flow front as a function of time (Fig. 3). The debris flow had a steep front, and during the early stages of motion the front was not the deepest portion of the flow (Fig. 3c). As the flow progressed downstream the larger cobbles moved to the front of the flow, and this grain segregation appeared to begin around 16 m from the debris-flow release gate (Fig. 4). At ~16 m the flow height is obscured by bouncing particles (Fig. 4b). As the flow neared the end of the flume, the leading cobbles were moving ahead of a steep front (Fig. 3d-f), which was followed by a tail that stretched behind it for tens of meters.

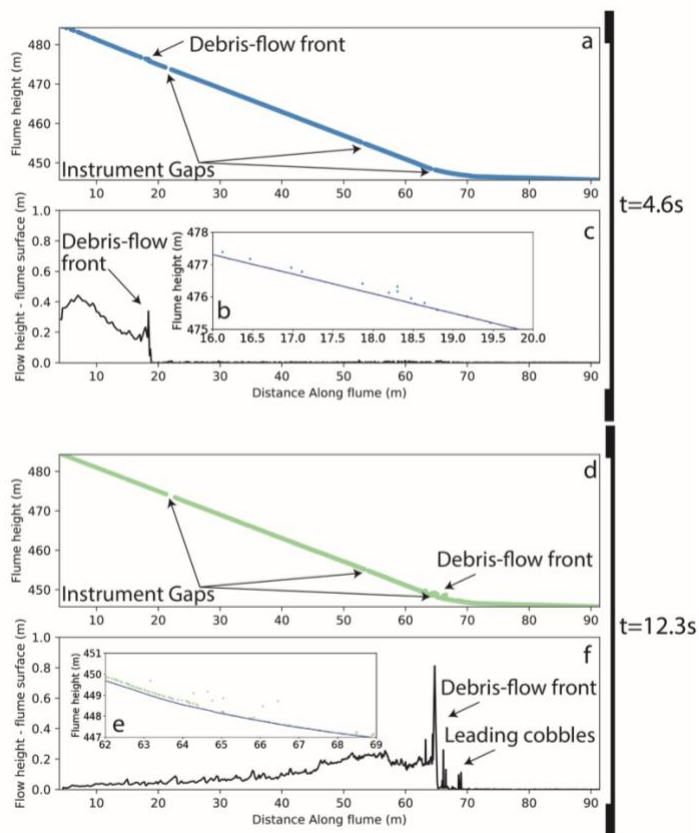


Fig. 3. (a) Lidar points showing debris-flow front moving down the flume (time = 4.6 seconds or lidar swath 300); (b) inset showing an enlarged view of the debris-flow front in (a) where the solid blue line shows the debris flow base; (c) difference between the debris height and the underlying flume; (d) lidar points showing debris-flow front moving down the flume at a later time (time = 12.3 seconds or lidar swath 800); (e) inset showing an enlarged view of the debris-flow front in (d) where the solid blue line shows the debris-flow base, and (f) difference between the debris height and the underlying flume.

The front arrival time derived from video and lidar agree with one another and with auxiliary data for the basal normal and shear stresses (Fig. 2). For example, the measured stress and thickness have a value of zero for times before the flow front is observed, and then abruptly increase at the time when the flow front crosses the sensor (Fig. 2a). This parity in time between the measured flow front at the three fixed sensors and the flow gather suggested the reliability of the flow gather to accurately record timing. The flow gather also reveals flow dynamics; for example, the spectral differences between the water/mud of roll waves and the roll wave shadow highlights the wave depth (Fig. 2a).

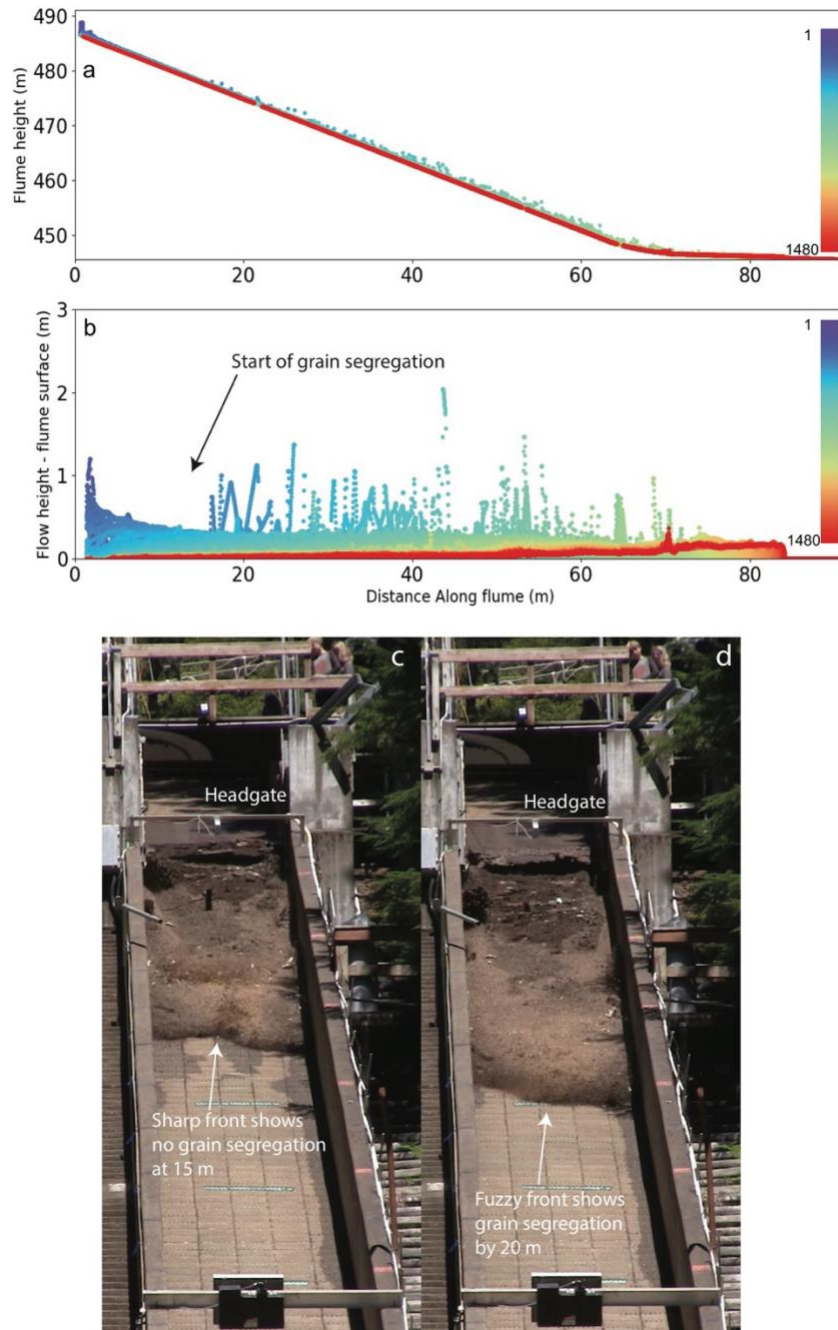


Fig. 4. (a) Lidar swaths over a 22.5 second interval (1480 total swaths subsampled by 10) where cool colors represent the position of the flow at earlier times and warm colors show later times. (b) Flow depth (i.e. the flow elevation subtracted from the flume surface elevation) with respect to distance along the flume. Grain segregation occurs 16 m downstream of the flume gate, indicated by dots showing bouncing particles. (c) Video still showing sharp front before grain segregation at 15 m. (d) Video still showing full grain segregation by 20 m from the gate.

Using the video-derived flow gather, we estimated flow velocities from the slope of the flow front with a cubic spline (black line on Fig. 2a). The cubic spline (Fig. 2a) reduces noise from the individual pixels in the flow gather and allows us to perform a first derivative on a continuous function to estimate the velocity (Fig. 5). The velocity plot shows an initial acceleration as the flow moves away from the gate and achieves an initial peak velocity of 10.7 m/s in the first few seconds (Fig. 5). The velocity subsequently decreases before increasing again to 7.3 m/s. The second peak occurs at 10 seconds when the flow is approximately 78 m from the headgate and on the flat portion of the flume. This double peak is an artefact of the gate release (Iverson and George, 2019).

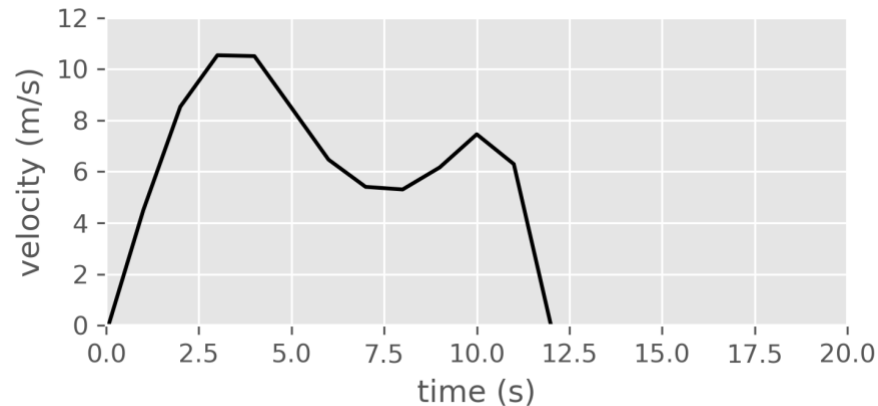


Fig. 5. Flow front velocity evolution derived from the flow gather. The flow front reached the base of the flume in ~12 seconds and achieved a peak velocity near 11 m/s.

4. Conclusions

In this study we used a terrestrial lidar unit and video imagery to track a debris flow during a flume experiment every 0.017 s. These data reveal the evolution of a debris-flow surface as it is released by a gate and moves down the flume. These data allow us to quantify aspects of the flow through time such as the velocity of the flow front and the position along the flume, particularly when coarse and fine grains begin to segregate. This study demonstrates the utility of continuous measurements and highlights the potential of video imagery to reproduce measurements similar to lidar data. Moreover, the flow gather images produced by the videos, quantitatively show dynamics of the debris flows such as the timing and velocity of roll waves.

Acknowledgements

Any use of trade, firm, or product names is for descriptive purposes only and does not imply endorsement by the U.S. Government.

References

- Anderson, S.W., Anderson, S.P., and Anderson, R.S., 2015, Exhumation by debris flows in the 2013 Colorado Front Range storm: *Geology*, no 43, v. 5, p. 391-394, doi.org/10.1130/G36507.1
- Bresenham, J.E., 1965, Algorithm for computer control of a digital plotter: *IBM Systems Journal*, no. 1, v. 4, p. 25-30.
- Costa, J.E., 1984, Physical geomorphology of debris flows. in Costa J.E., Fleisher P.J. eds., *Developments and Applications of Geomorphology*: Springer, Berlin, Heidelberg, p. 268-317.
- George, D.L., and Iverson, R.M., 2014, A depth-averaged debris-flow model that includes the effects of evolving dilatancy. II. Numerical predictions and experimental tests: *Proc. R. Soc. A*, no. 470, v. 2170, p. 20130820, doi.org/10.1098/rspa.2013.0819.
- Iverson, R.M., Logan, M., LaHusen, R.G., and Berti, M., 2010, The perfect debris flow? Aggregated results from 28 large-scale experiments: *Journal of Geophysical Research: Earth Surface*, no.115, v. F3, doi.org/10.1029/2009JF001514.
- Iverson, R.M., & George, D.L., 2014, A depth-averaged debris-flow model that includes the effects of evolving dilatancy. I: Physical basis. *Proc. R. Soc. A*, no. 470, v., 2170, p. 20130819, dx.doi.org/10.1098/rspa.2013.0819.

- Iverson, R.M., & George, D.L., 2019, Valid debris-flow models must avoid hot starts, this volume.
- Logan, M., Iverson, R.M., and Obryk, M.K., 2018, Video documentation of experiments at the USGS debris-flow flume 1992–2017 (ver 1.4, January 2018): U.S. Geological Survey Open-File Report 2007–1315, <https://doi.org/10.3133/ofr20071315>.
- Olsen, M.J., Butcher, S., and Silvia, E.P., 2012, Real-time change and damage detection of landslides and other earth movements threatening public infrastructure: OTREC Final Report 2011-22 and ODOT Final Report RS 500-500, 80p.
- Riegl Laser Measurement Systems, GmbH, 2017, RiVLib <http://www.riegl.com/index.php?id=224> (accessed April 6, 2017).
- Stiny, J., 1910, Die Muren: Verlag der Wagner'schen Universitäts-buchhandlung. Innsbruck: 139 p.

Exploring controls on debris-flow surge velocity and peak discharge at Chalk Cliffs, Colorado, USA

Joel B. Smith^a, Jason W. Kean^a, Jeffrey A. Coe^a

^a*U.S. Geological Survey, Box 25046 MS 966, Denver 80225, U.S.A.*

Abstract

We present a series of debris-flow events and use combined sensor and video data to explore how sediment concentration and triggering rainfall intensity affect the velocity and discharge of debris-flow surges generated by surface-water runoff. We analyze an initial data set of 49 surges from four debris-flow events recorded by a monitoring system at Chalk Cliffs, Colorado, and compare measurements of surge height, velocity, peak discharge, triggering rainfall intensity, and qualitative estimates of sediment concentration. Measurements of sediment concentration and velocity were obtained using an automated camera system with a high resolution and frame rate. We find that the triggering rainfall intensity of the debris flows, which affects the sediment-to-water ratio, is a strong control on surge velocity and peak discharge. While surges with high and low sediment concentrations both exceed the peak discharge of water-only flow, fluid-rich surges generated by high rainfall intensities have much greater velocities and peak discharges than sediment-rich surges generated by lower rainfall intensities. These observations suggest that rainfall intensity may be an important predictive variable in empirical relationships for estimating the velocity and peak discharge of runoff-generated debris flows, which are common in alpine areas and burned steplands.

Keywords: debris flow; monitoring; velocity; entrainment; flow depth

1. Introduction

Debris flows have long been recognized as a significant hazard in steep watersheds, and methods to estimate their velocity and peak discharge are needed for quantifying the risk to infrastructure (e.g., Hungr et al., 1984). Empirical relations derived from monitoring data and field and laboratory observations are frequently used to estimate the velocity and peak discharge of debris flows (e.g., Rickenmann, 1999). Observations of debris-flow properties have come from a diverse set of observations made worldwide (e.g., Pierson, 1985; Davies, 1990; Suwa et al., 1993; Iverson, 1997; Hürlimann et al., 2003, Arattano and Marchi, 2005). Advancements in sensors and computing technologies have made it easier to monitor debris flows, and the number of sites making direct measurements of debris-flow dynamics is growing worldwide (e.g., Imaizumi et al., 2005; Huang et al., 2007; McCoy et al., 2010; Kean et al., 2011; Navratil et al., 2013; Comiti et al., 2014; Hürlimann et al., 2014; Cui et al., 2018; Schimmel et al., 2018; and others in this volume). Even with this large body of existing knowledge, a broad spectrum of flow types exists due to differences in topography, triggering conditions, sediment availability, grain-size distribution, boundary conditions, and flow density. This variability makes it very difficult to predict debris-flow dynamics in a given watershed.

Monitoring debris-flow events with automated equipment can provide the information to define rainfall intensity-duration thresholds and relations between debris-flow velocity, flow depth, peak discharge, and volume. However, monitoring remains challenging and expensive due to the hazardous and destructive nature of debris flows. Even when the equipment is working, the complexity and variability of debris flows make interpreting instrumental data challenging. Auxiliary data from video recorded by automated systems can clarify the interpretation of debris-flow dynamics. For example, video can help differentiate debris flows from floods, and estimate sediment concentrations

* Corresponding author e-mail address: jbsmith@usgs.gov

and grain sizes. Additionally, data extraction from video footage is becoming easier due to the advent of methods for image analysis, such as particle image velocimetry (PIV).

Here, we use observations of flow stage, rainfall intensity, and video recorded in a small basin in central Colorado (Fig. 1) to identify the controls on velocity and peak discharge of debris-flow surges triggered by surface-water runoff. Video is used to estimate both the sediment concentration and height (thickness) of the surges. This work is a first step towards a long-term goal of defining empirical relations for velocity and discharge for runoff-generated debris flows, which are common in alpine areas and burned steeplands.

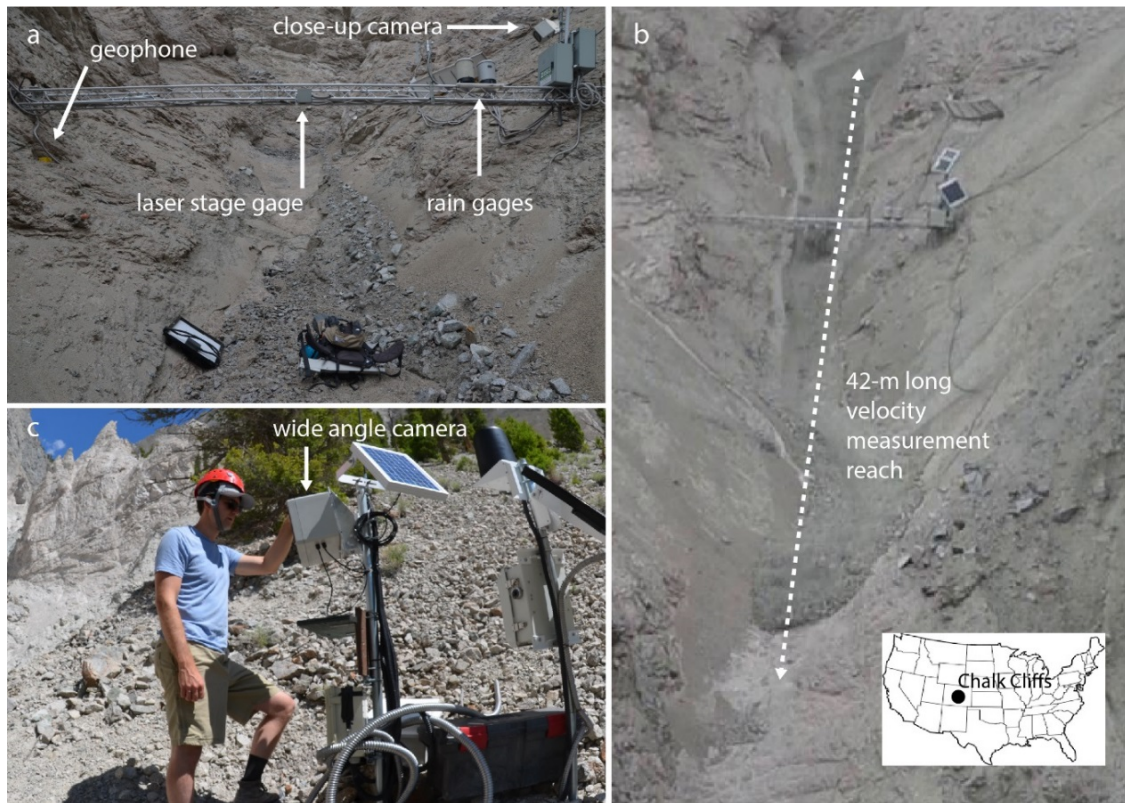


Fig. 1. Instrumentation to measure debris-flow surge characteristics. (a) Detailed view of the monitoring system to measure debris-flow depth, rainfall, and ground vibrations; (b) Camera view of 42-m long reach used to measure surge velocity and sediment concentrations; and (c) Automated camera system used for the 42-m long reach.

2. Study site

The Chalk Cliffs is a natural laboratory to study debris flows, and a monitoring program for associated mass movement research was established in 2002 (Coe et al., 2008). The Chalk Cliffs are located at the base of Mt. Princeton in the Sawatch Range of the Rocky Mountains, in central Colorado. The cliffs are composed of highly fractured, hydrothermally altered quartz monzonite (Miller, 1999), which gives the Cliffs their characteristic look of white “chalk.” The average slope of the 42-m reach of channel by the upper monitoring station is 17° (Fig. 1). The drainage area above the station is 0.06 km^2 . Bedrock with slopes greater than 25° is exposed in 60% of the entire Chalk Cliffs basin. Sparsely vegetated colluvium with slopes less than 25° covers the remaining area. The relatively large amount of exposed bedrock promotes rapid surface-water runoff during rainstorms that entrains channel sediment and initiates debris flows. An annual monsoon pattern of high-intensity summer thunderstorms and the substantial supply of sediment derived from the hydrothermally altered bedrock produce an average of about four debris flows per year.

Since 2002, a range of automated monitoring equipment has been added to study various aspects of debris-flow dynamics (e.g., McCoy et al. 2010, 2012, 2013; Kean et al., 2013, 2015). The components of the monitoring system are shown in Fig. 1. The primary data acquisition hub is located on a 6-m long aluminum truss bridge spanning the channel. The enclosure houses a datalogger, cellular modem, and power system. A laser stage gage, directed slope normally, and a pair of siphoning tipping-bucket rain gages are mounted on the bridge, approximately 3 m above the

approximate center of the channel. The datum of the stage gage is the elevation of the bedrock channel bed beneath the gage. Other instrumentation installed, but not included in this paper, includes geophones, force plate, rock temperature profilers, pyranometers, a close-up video camera, and a dedicated seismic logging system and geophones (see Michel et al., this volume, for a description of the debris-flow induced ground vibrations at the site). The wide-angle camera shown in Fig. 1c is triggered by a rainfall threshold, and its (cropped) field of view is shown in Fig. 1b.

Debris-flow surges at Chalk Cliffs can vary greatly in flow depth, frequency, sediment concentration, and flow velocity (Fig. 2). This variability is correlated with rainfall intensity, which affects the sediment-to-water ratio in the debris flow. Rainstorms with peak 5-minute rainfall intensity (I_5) less than ~ 30 mm/hr typically trigger a series of small, slow-moving, and sediment-rich debris-flow surges (Fig. 2a). These surges have a characteristic granular snout and more watery tail. Debris flows triggered by intermediate rainfall intensity ($\sim 30 < I_5 < \sim 80$ mm/hr) also typically have a granular snout and watery tail but have higher water content and are thicker and faster moving than debris flows triggered at low rainfall intensity. High rainfall intensity ($I_5 > \sim 80$ mm/hr) triggers the largest and fastest moving debris flows at the site. Debris flows triggered by high rainfall intensity typically have fewer surges than debris flows triggered by lower rainfall intensities. Surges triggered by high rainfall intensity are typically followed by a sustained period of high, fast-velocity flow. In general, the grain size of the sediment in each Chalk Cliffs flow varies proportionally with the initiating rainfall intensity.

Sediment availability, which changes over the summer debris-flow season, also affects surge characteristics. Early season debris flows (May-June) typically have more sediment available in the channel than debris flows occurring later in the summer (Coe et al., 2008). During some years with frequent rainstorms, the material available for debris flows is flushed from the basin upstream of the station, resulting in late season water floods. When accumulated bed sediment is present, it not only provides more potential debris for entrainment, but the accumulated material changes channel geometry such that, in the case of v-shaped sections in bedrock, “flatter” flows are produced, as well as a lesser thickness for any given flow volume.



Fig. 2. Representative examples of debris-flow surges with different sediment concentrations estimated qualitatively from video. (a) High-sediment (Low-water) concentration; (b) Intermediate-sediment concentration; and (c) Low-sediment (high-water) concentration. In general, sediment concentrations decrease with increasing rainfall intensity.

3. Data Collection and Processing

We used an automated video camera (Fig. 1c) system (1280 x 720 pixels, 24 frames per second) to determine the mean front velocity, define qualitative sediment concentrations, and estimate the stage of the base of the flow for determining peak flow height (surge thickness). We used a laser distance sensor to take stage measurements at 10 Hz, and rainfall was measured by a siphoning rain gage at 1-minute intervals.

Flow velocity was calculated by recording the travel time of a debris-flow surge between two known points whose along-flow travel distance was derived from a site survey. To minimize error, these points were chosen to be 42 m apart, and spanned a straight, relatively uniform reach of channel. Peak flow height was estimated at the bridge station located in the middle of the reach (Fig. 1b).

Sediment concentrations were determined qualitatively and assigned three different levels: high-sediment (low-water) concentration, intermediate, and low-sediment (high-water) concentration. These terms are used in a relative sense, as all the surge fronts recorded in this study have sediment concentrations high enough to be classified as debris flows. Furthermore, the flows characterized as low-sediment concentration have the largest volumes and carry the largest grains. The sediment concentration levels were determined based on inspection of video imagery (e.g., Fig. 2) and stage time series. For example, the presence of splashing in the video was used to identify fluid-rich flows. In addition, high-frequency variability in the laser stage measurements also indicated the flows had higher water content than the fluid-poor (high-sediment) surges, which did not exhibit high-frequency stage fluctuations (see also Kean et al., 2013).

We estimated peak-flow height (surge thickness) by differencing the elevation (stage) of the flow surface from the elevation of the base of the flow. The laser distance meter accurately measures the elevation of the flow surface; however, the base of the flow was estimated. The base of the flow does not always correspond to the elevation of the bedrock channel due to the periodic presence of bed sediment beneath the flow. The level of bed sediment changes with time due to erosion or deposition by flows. We estimated the base of flows in two ways based on erosional or depositional characteristics of each flow. Erosional flow events are characterized by high-velocity surges that progressively decrease in peak stages as bed material is entrained by the flow (Fig. 3a). For simplicity, we estimated the base of the erosional flows using the debris-flow entrainment rates measured at the site by McCoy et al. (2012), which found that dry beds erode at a rate of 0.035 m/s. Ground vibrations could also be used to estimate the base of the flow using a more complicated analysis (Kean et al., 2015). For depositional events, we used a combination of video and stage measurements to estimate the base of the flow (Fig. 3b). Video was used to identify times in between surges when there was negligible flow, and the stage at this time was used to represent the elevation of stationary bed sediment. We linearly interpolated an estimate of the base of the flow between times when the bed level could be identified from the video (Fig. 3b).

We calculated peak discharge for each surge by multiplying the measured surge velocity over the 42-m reach by the cross-sectional area of the surge at its peak height. The cross-sectional area was defined by (1) the elevation of the flow surface, (2) estimated base of the flow, and (3) a surveyed channel cross-section that defined the lateral boundaries of the flow when used with the elevation of the flow surface. To evaluate the amplification of surface-water discharge by debris-flow sediment, we used the runoff coefficient of the “rational method” to evaluate the ratio of peak discharge to the water discharge supplied by rainfall (e.g., Chow et al., 1988). This non-dimensional ratio is often used to evaluate the peak water discharge in small basins. The runoff coefficient is defined by the equation $Q_p / (I_5 A_b)$, where Q_p is the peak discharge, I_5 is peak 5-minute rainfall intensity, and A_b is the area of the basin (0.06 km²). The theoretical upper limit in the runoff coefficient for steady rainfall and water-only discharge is 1; however, the runoff coefficient for debris flows can greatly exceed 1 due to the addition of sediment and the unique flow dynamics of debris-flow surges, which amplify peak flows relative to water (Hung, 2000; Kean et al., 2016).

We estimated the volume of each debris-flow event (sediment and water) by integrating the discharge time series over the duration of the flow. We used the measured velocity of the surge front to represent the velocity of the complete surge (i.e., surge front and tail) and determined a time series of flow cross-sectional area using the same method to determine the cross-sectional area at the time of peak flow.

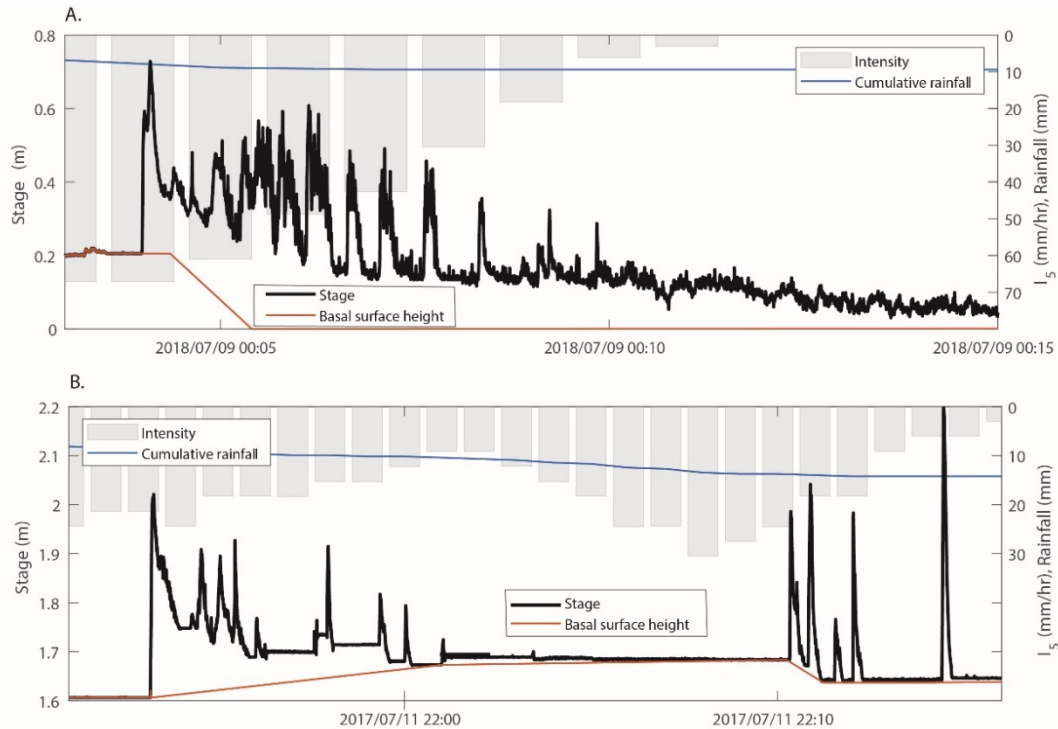


Fig. 3. Time series of flow stage (black), estimated base level of flow (red), 5-minute rainfall intensity (grey), cumulative rainfall (blue) for (a) an erosional debris-flow event on July 9, 2018 and (b) a depositional debris-flow event on July 11, 2017.

4. Results and Discussion

We examined an initial data set of four debris-flow events (including a total of 49 surge fronts) from 2017 and 2018 (Table 1) to identify possible controls on debris-flow surge velocity and peak discharge. Analysis of additional events recorded at the site is planned. Time series of two of the events are shown in Fig. 3. Both events were the first events of their respective season and flow over an initially sediment-covered bed. It is notable that a significant amount of material accumulated in the monitoring reach prior to the 2017 season (~ 1.6 m depth of sediment, Fig. 3b). Twelve of the 20 surge fronts, from July 11, 2017, were omitted from our results since an incised channel in the sediment redirected the surge fronts away from the stage sensor (i.e., camera footage indicated that the height measurements were unreliable). This accumulated material was entrained during a large event on July 14, 2017. The July 14, 2017 event is included in the results since it was uncommon to have rain from an extremely intense thunderstorm fall on such a large amount of accumulated sediment. Unfortunately, several of the surges overtopped the laser distance sensor and coated it in an opaque slurry of fine material. As a result, measurements of surge properties for this event are only available for the time when the laser was working, and the estimated total volume is a minimum. The fourth event analyzed occurred on August 14, 2018, on a bare bedrock channel. This event, which occurred late in the debris-flow season, was fluid rich and had few coarse-grained surge fronts. With the exception of the July 11, 2017 event, all of the analyzed debris flows were erosive.

Table 1. Summary of debris-flows properties from this study.

Date	Volume (m ³)	Q_{peak} (m ³ /s)	peak I_5 (mm/hr)	# of surges	Cumulative rainfall (mm)
11 July 2017	420	4.2	30	20	14
14 July 2017	5,700	46	110	13	37
9 July 2018	330	3.8	67	10	10
14 Aug 2018	1,600	5.1	73	6	21

For the years that we included in this study (2017-2018), the first flows of the summer season (July 11, 2017, and July 9, 2018) were dominated by surge fronts with high-sediment concentrations, whereas later events in the season (July 14, 2017, and August 14, 2018) had more fluid-rich surges. The increased water content of the later season debris flows was likely because they were triggered by higher intensity rainstorms, and because there was less sediment available due to sediment export by the first flows of the season.

Measured surge velocity and peak discharge appear to be correlated with both peak rainfall intensity and sediment concentration (Fig. 4). High flow velocities and peak discharges are generally associated with high rainfall intensities and fluid-rich surges, whereas low flow velocities and peak discharges are associated with low rainfall intensities and high sediment concentration surges. Furthermore, the vertical clustering suggests that v is independent of h at a given h , with water content or sediment concentration having a strong influence.

In Figure 4, we compared the velocity and peak flow thickness data with two other relations sometimes used to estimate flow velocity: the critical Froude number and the Manning equation. Estimates of velocity based on a critical Froude number are used to estimate water velocity in steep channels (e.g., Grant, 1997) given by the equation $v = \sqrt{gh}$, where v is velocity, g is acceleration of gravity, and h is peak flow thickness. Manning's equation, which is also used to estimate turbulent water velocity, is given by the equation $v = (1/n)h^{2/3}S^{1/2}$, where n equals the roughness coefficient, and S is the channel slope. Rickenmann (1999) showed that a Manning's roughness coefficient of 0.1 provided a reasonable match to a variety of debris-flow observations. The fit of the data-derived best-fit line shown in Fig. 4a suggests the relationship between velocity and peak discharge at the Chalk Cliffs site falls in between these two estimates. Variability in the debris-flow observations may also be influenced by other factors, such as changing cross-sectional flow geometry as the result of variable bed sediment cover. Figure 4b indicates a correlation between peak discharge (a function of cross-sectional flow area) and surge thickness.

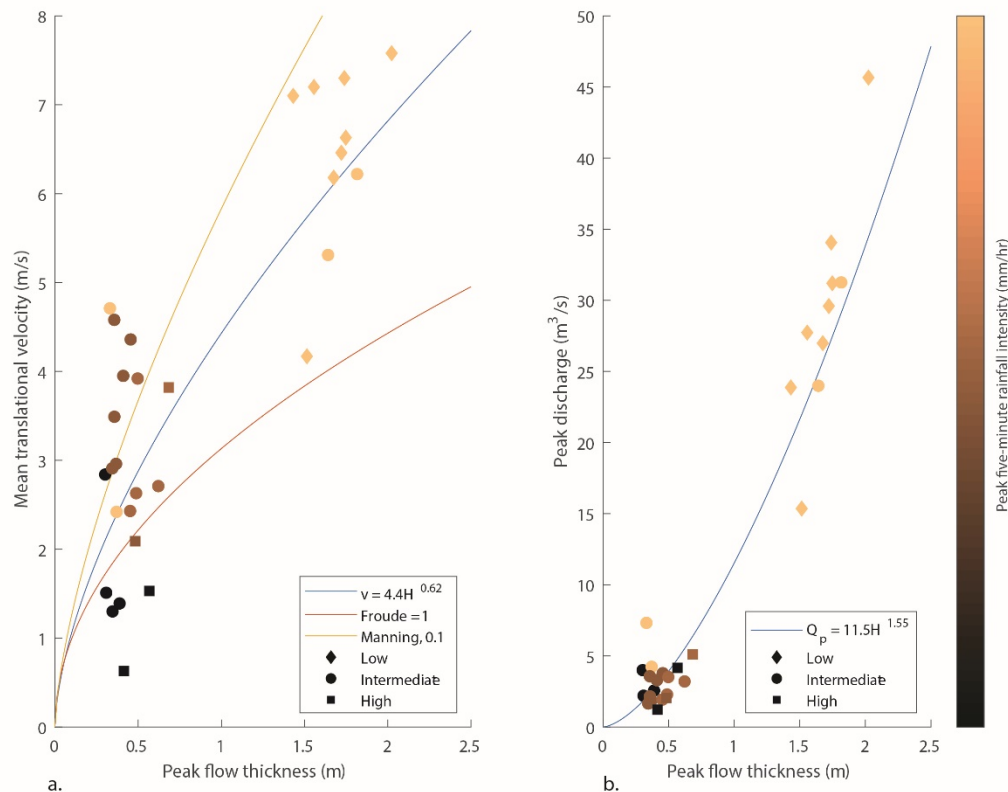


Fig. 4. Relations between (a) peak flow thickness and flow velocity and (b) peak flow thickness and peak discharge. Data points are color coded by 5-minute rainfall intensity, and the symbols for each data point are classified according to three levels of sediment concentration. Mean translational velocity is the time taken by the flow front to move between two known locations.

The difference in the distributions in the runoff coefficient (Q_p/I_5A) for flows with low- and high-sediment concentrations further highlights the control of water content (and indirectly rainfall intensity) on the peak discharge of debris flows (Fig. 5). While the median of both distributions exceeds the theoretical limit of water flow, the runoff coefficient of low sediment concentration flows is multiple times greater than the runoff coefficient of high-sediment concentration flows.

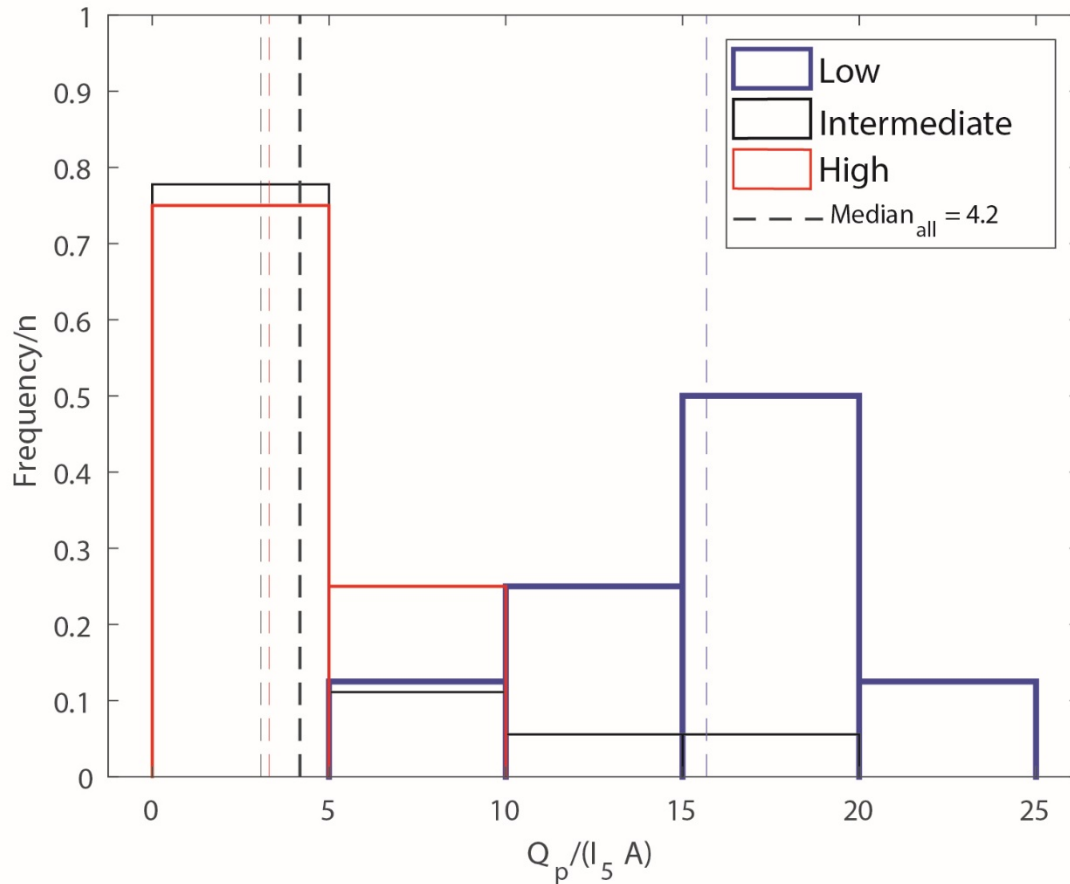


Fig. 5. A histogram showing the frequency distribution of normalized peak discharge (i.e., the runoff coefficient) for flow surges with low-, intermediate-, and high-sediment concentration. The light, dashed lines show the median coefficient values of the concentration groups.

5. Conclusion

We have presented a set of debris-flow height, velocity, qualitative sediment concentration, and rainfall intensities from the Chalk Cliffs debris-flow monitoring site. We have shown that these data can be used to improve, on a site-by-site basis, empirical debris-flow velocity-height relationships. Although these data can contribute to enhanced understanding of the debris-flow dynamics, the hazardous conditions of the monitored basin challenge system reliability, and the difficulties associated with accurate data interpretation benefit from validation and cross-correlation of multiple sensors—especially video.

These data have shown that empirical relationships for debris flows provide a fair approximation of debris-flow magnitudes. However, other factors not taken into account in this study, such as pre-event sediment availability and its moisture levels and grain size provide an additional opportunity for monitoring that could lead to more accurate debris-flow height and velocity predictions. Over time, as more debris-flow events are added to a database, we are

hopeful that new correlations considering bed sediment heights, and/or the integration of tiered rainfall thresholds, may serve to further refine the predictive ability and utility of existing empirical debris-flow relationships.

Acknowledgements

We thank Rex Baum, Erin Bessette-Kirton, and Akihiko Ikeda for providing reviews that improved the clarity of this paper.

References

- Arattano, M., and Marchi, L., 2005, Measurements of debris flow velocity through cross-correlation of instrumentation data: *Natural Hazards and Earth System Science*, Copernicus Publications on behalf of the European Geosciences Union, v. 5 no. 1, p. 137-142
- Chow, V. T., Maidment, D. R., and Mays, L. W., 1988, *Applied Hydrology*: New York, McGraw-Hill, 572 p.
- Coe, J. A., Kinner, D. A., and Godt, J. W., 2008, Initiation conditions for debris flows generated by runoff at Chalk Cliffs, central Colorado: *Geomorphology*, v. 96, no. 3–4, p. 270–297, doi:10.1016/j.geomorph.2007.03.017.
- Comiti, F., Marchi, L., Macconi, P., Arattano, M., Bertoldi, G., Borga, M., Brardinoni, F., Cavalli, M., D’Agostino, V., Penna, D., Theule, J., 2014, A new monitoring station for debris flows in the European Alps: First observations in the Gadria basin: *Natural Hazards*, v. 73, no. 3, doi: 10.1007/s11069-014-1088-5.
- Cui, P., Guo, X., Yan, Y., Li, Y., Ge, Y., 2018, Real-time observation of an active debris flow watershed in the Wenchuan earthquake area: *Geomorphology*, Volume 321, p. 153-166, doi.org/10.1015/j.geomorph.2018.08.024.
- Davies, T.R.H. 1990, Debris-flow surges—Experimental simulation: *Journal of Hydrology*, New Zealand, vol. 29, no. 1, p. 18–46, www.jstor.org/stable/43944650.
- Grant, G.E., 1997, Critical flow constrains flow hydraulics in mobile-bed stream: A new hypothesis: *Water Resources Research*, v. 33, p. 349–358, doi:10.1029/96WR03134.
- Huang, C.-J., Yin, H.-Y., Chen, C.-Y., Yeh, C.-H., and Wang, C.-L., 2007, Ground vibrations produced by rock motions and debris flows: *Journal of Geophysical Research*, v. 112, no. F02014, doi:10.1029/2005JF000437.
- Hungr, O., 2000, Analysis of debris flow surges using the theory of uniformly progressive flow: *Earth Surface Processes and Landforms*, v. 25, p. 483–495.
- Hungr, O., Morgan, G.C., and Kellerhals, R., 1984, Quantitative analysis of debris torrent hazards for design of remedial measures: *Canadian Geotechnical Journal*, v. 21, p. 663–677.
- Hürlimann, M., Rickenmann, D., and Graf, C., 2003, Field and monitoring data of debris-flow events in the Swiss Alps, *Canadian Geotechnical Journal*, v. 40, p. 161–175.
- Hürlimann, M., Abancó, C., Moya, J., Vilajosana, I., 2014, Results and experiences gathered at the Rebaixader debris-flow monitoring site, Central Pyrenees, Spain: *Landslides*, v. 11, p. 939, doi.org/10.1007/s10346-013-0452-y.
- Imaizumi, F., Tsuchiya, S., and Ohsaka, O., 2005, Behaviour of debris flows located in a mountainous torrent on the Ohya landslide, Japan, *Canadian Geotechnical Journal*, v. 42, no. 3, doi: 10.1139/t05-019.
- Iverson, R. M. 1997, The physics of debris flows: *Rev. Geophysics* v. 35, no. 3, p. 245–296.
- Kean, J.W., Staley, D.M., and Cannon, S.H., 2011, In situ measurements of post-fire debris flows in southern California: Comparisons of the timing and magnitude of 24 debris-flow events with rainfall and soil moisture conditions: *Journal of Geophysics Research*, v. 116, no. F04019, doi:10.1029/2011JF002005.
- Kean, J.W., McCoy, S.W., Tucker, G.E., Staley, D.M. and Coe, J.A., 2013, Runoff-generated debris flows: Observations and modeling of surge initiation, magnitude, and frequency: *Journal of Geophysics Research Earth Surfaces*, v. 118, p. 2190–2207, doi:10.1002/jgrf.20148.
- Kean, J.W., Coe, J.A., Coviello, V., Smith, J.B., McCoy, S.W., and Arattano, M., 2015, Estimating rates of debris flow entrainment from ground vibrations: *Geophysical Research Letters*, v. 42, no. 15, 6365-6372, doi: 10.1002/2015GL064811.
- Kean, J.W., McGuire, L.A., Rengers, F.K., Smith, J.B., and Staley, D.M., 2016, Amplification of post wildfire peak flow by debris: *Geophysical Research Letters*, v. 43, p. 8545–8553, doi: 10.1002/2016GL069661.
- McCoy, S.W., Kean, J.W., Coe, J.A., Staley, D.M., Wasklewicz, T.A., and Tucker, G.E., 2010, Evolution of a natural debris flow: In situ measurements of flow dynamics, video imagery, and terrestrial laser scanning: *Geology*, v. 38, no. 8, p. 735–738, doi:10.1130/G30928.1.
- McCoy, S.W., Kean, J.W., Coe, J.A., Tucker, G.E., Staley, D.M., and Wasklewicz, T.A., 2012, In situ measurements of sediment entrainment from the headwaters of a steep catchment: *Journal of Geophysics Research: Earth Surface*, v. 117, no. F03016, doi:10.1029/2011JF002278.
- McCoy, S.W., Tucker, G.E., Kean, J.W., and Coe, J.A., 2013, Field measurement of basal forces generated by erosive debris flows, *Journal of Geophysics Research: Earth Surface*, v. 118, doi:10.1002/jgrf.20041.
- Miller, M.G., 1999, Active breaching of a geometric segment boundary in the Sawatch Range normal fault, Colorado, USA: *Journal of Structural Geology*, v. 21, p. 769-776
- Navratil, O., Liébault, F., Bellot, H., Travaglini, E., Theule, J., Chambon, G., Laigle, D, 2013, High-frequency monitoring of debris-flow propagation along the Réal Torrent, southern French Prealps: *Geomorphology*, v. 201, no. 1, doi:10.1016/j.geomorph.2013.06.017.
- Pierson, T.C., 1985, Initiation and flow behavior of the 1980 Pine Creek and Muddy River lahars, Mount St. Helens, Washington: Boulder, Colorado, Geological Society of America Bulletin, v. 96, p. 1056–1069.
- Rickenmann, D., 1999, Empirical relationships for debris flows, *Natural Hazards*, v. 19, no. 47. doi.org/10.1023/A:1008064220727.
- Schimmel, A., Hübl, J., McArdeil, B.W., and F. Walter, 2018, Automatic identification of alpine mass movements by a combination of seismic and infrasound sensors: *Sensors*, v. 18, no. 5, doi:10.3390/s18051658.
- Suwa, H., Okunishi, K., and Sakai, M., 1993, Motion, debris size and scale of debris flows in a valley on Mount Yakedake, Japan, *Proceedings of Sediment Problems: Strategies for Monitoring, Prediction and Control*, Yokohama: International Association of Hydrological Services, no. 217, p. 239–247.

Dynamic characteristics of extreme superelevation of debris flows observed by laser profile scanners in Sakura-jima volcano, Japan

Yuya Takahashi^{a,b,*}, Naoki Fujimura^a, Hiromi Akita^a, Masaki Mizuno^a

^aPublic Works Research Institute, 1-6 Minamihara, Tsukuba-shi, Ibaraki-ken, 305-8516, Japan

^bCTI Engineering Co., Ltd., 1047-27 Onigakubo, Tsukuba-shi, Ibaraki-ken, 300-2651, Japan

Abstract

Supercritical flows in natural open channel show very complicated behavior due to shockwaves, roll waves, and superelevations. Traces of debris flows often show large difference in height at inner and outer sides of curved channels, and not only that, superelevation of debris flow is larger than that of pure water. This behavior of debris flow may cause underestimation of channel section design or unexpected bank erosion. Therefore, accumulation of observation data is important to estimate hydraulic characteristics of debris flows at curved channels. We conducted continuous field observations at Sakura-jima volcano, Japan, introducing laser profile scanners (LPSs) to acquire surface geometry of debris flows, especially superelevation at curved channels. The LPS can measure distance from sensor to obstacles with sufficiently high resolution to document superelevations and spillway flow profiles both in space and time on a survey line. A debris flow that occurred at Arimura River, Sakura-jima volcano on January 17, 2018 is well documented by LPSs. Data from the debris flow compared with coefficient in current model, which indicates traction/viscosity and potential superelevation of the debris-flow front is under-predicted assuming the flow is super-critical pure water flow.

Keywords: Debris Flow; Field observation; Laser Profile Scanner; Superelevation

1. Introduction

Sediment-laden floods, such as debris flow, often cause devastating damages to human properties and lives, so that it is necessary to prevent them from plunging into residential area. Therefore, estimation of hydraulic characteristics of debris flows, such as velocity, flow depth, etc., is an important goal to prepare appropriate countermeasures to protect at-risk residential areas. In particular, superelevation of debris flow at curved channels can trigger unexpected flooding. Thus, observation of actual behavior of debris flows is important. However, field measurement of physical state of debris flows is technically difficult because of the very high momentum of flows and hazardous risks at channels. Hence, the parameters for designing mitigation structures are mostly based on post-event field investigations or laboratory experiments.

Discussions on superelevation of debris flows started in the early 1980's. Ashida et al. (1981) discussed amplification of roll waves along the outer wall and reduction of superelevation in curves and downstream tangents based on free vortex assumption and described derivation of analytical solution of static state superelevation of super critical flow in rectangular channel. Mizuyama et al. (1981) introduced correction factor α to the formula mentioned above to express superelevation of debris flows in steep and curved channels based on laboratory experiments. Ikeya et al. (1982) investigated trace of actual debris flows and found that the correction factor $\alpha \cong 10$ if the river slope is 16 degrees, which support the experimental results by Mizuyama et al. (1981). Hungr et al. (1984) summarized Mizuyama et al. (1981) and Ikeya et al. (1982) and recommended to use $\alpha = 5$ to calculate superelevation for design and $\alpha = 2.5$ to calculate velocity from superelevation data. Mizuno (2004) conducted experiments introducing a flume with two consecutive bending curves and marked that the correction factor of debris flow is larger than that of

* Corresponding author e-mail address: yy-takahashi@ctie.co.jp

pure water. Scheidl et al. (2015) conducted laboratory experiments and discussed estimation of debris-flow velocity from superlevation and relationship between the correction factor and Froude number. Those discussions of superlevation are mostly based on laboratory experiments and there is no report of detailed field observation, yet.

On the other hand, LiDAR technologies are now popular and used for various field measurements. Application of LiDAR sensor to measure debris-flow characteristics can be found for example in Yoshinaga et al. (2017) and Takahashi et al. (2018). In this article, we analyzed data from field observation conducted with a laser profile scanner (LPS) installed at a volcanic area in Japan. The objective of the field observation is to capture the detailed behavior of actual debris flow in the curved channel in order to assess accuracy of correction factor used to model potential superlevation with a given velocity.

2. Method

2.1. Observation site

The Arimura River is on the Sakura-jima volcano (Fig. 1 (a)), which is one of the most active volcanoes in the world and its highest peak rises to 1,117 m (3,665 ft) above sea level. The Arimura River flows from south edge of the Minami-dake crater through the southeast slope of the volcano and on to the Kagoshima Bay. The river channel curves rightward along the northwest-facing Showa lava cliff (Fig. 1 (b)) and is dry most of the time through the year except rainfall events. The observation site is at the Arimura 3rd check dam installed in the Arimura River. Catchment area of the check dam is 1.55 km² and the channel is curving at upstream of the check dam. Channel length from the edge of the crater to the check dam is 2.5 km and relief ratio is 0.36. Compactness coefficient at the catchment area is 1.62. The check dam is unmanaged type and behind the check dam is full of sediment. Sedimentation gradient of channel above the check dam is 3.4 degrees.

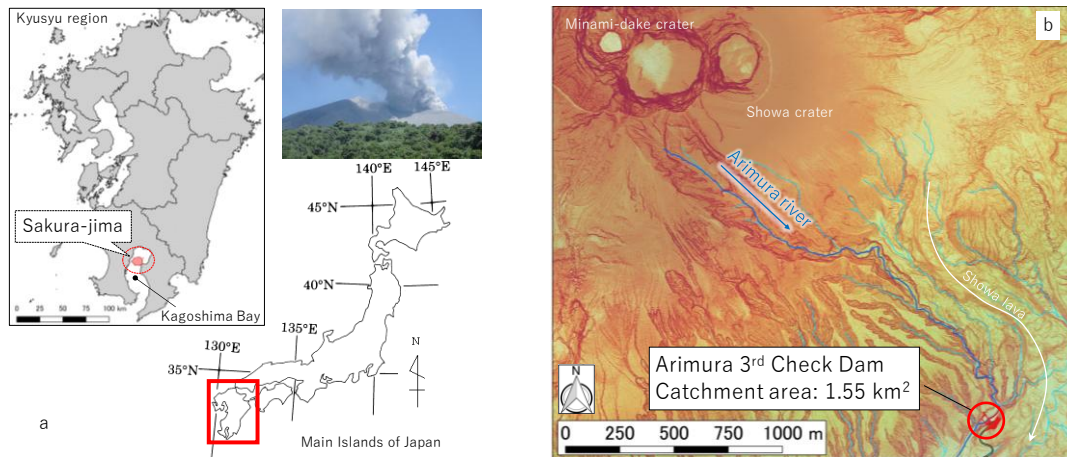


Fig. 1. (a) Location map of Sakura-jima volcano; (b) Topographic map of Arimura river basin

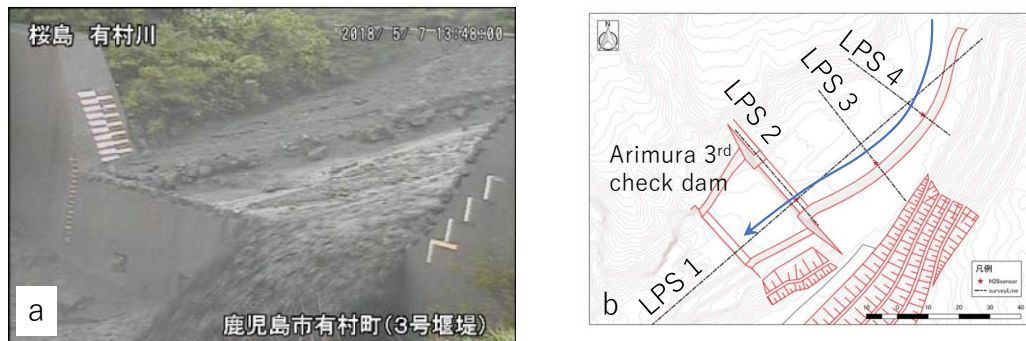


Fig. 2. (a) CCTV image of debris flow at the Arimura 3rd check dam; (b) Survey lines of LPSs

Table 1. Specification of LPS

Model	UXM-30LXH-EWA Hokuyo Automatic Co., Ltd.
Power Source	DC24V, 250mA
Light Source	Semiconductor laser diode $\lambda = 905$ nm
Scanning range	0.1 to 80 m
Scanning accuracy	± 50 mm
Angular resolution	Approx. 0.125 deg.
Scanning angle	190 deg. 1,520 steps
Scanning time	50 ms/scan, 20Hz
Inter face	Ethernet 100BASE-TX
Ambient temperature	-10 to 50 deg. C
Weight	Approx. 1,200 g

Because of volcanic activities such as denudation and volcanic ash falls, debris flows repeatedly occur in the basin. Average number of debris-flow occurrence in the basin is 7.5 times per year in past 10 years. CCTV image of debris flow at the Arimura 3rd check dam is shown in Fig. 2 (a).

2.2. Observation device

To observe the surface profile of debris flows, four LPSs were installed around the Arimura 3rd check dam, and the survey lines of the LPSs are illustrated in Fig. 2 (b). The LPS can scan distances from the sensor to obstacles with 0.125 degrees pitch in range of 190 degrees on a single line during each scan and the scan rate is 20 scans per second. The surface profiles captured by LPSs are converted into a Cartesian coordinate system to evaluate horizontal and vertical change of surface profiles and 20 scans are averaged to investigate 1 second averaged surface profile. The detail specification of the LPS is shown in Table 1. LPSs 1 and 2 are installed perpendicular to each other above the check dam to observe longitudinal and cross-sectional profiles of dropping debris flows from the spillway, respectively, and LPSs 3 and 4 are installed upstream of the check dam across a curved segment of the river channel to evaluate superelevation from cross-sectional profiles.

2.3. Evaluation procedure of observed debris flow

Superelevation of debris flow in a curved channel with a radius of curvature R was proposed by Mizuyama et al. (1981) as follows;

$$\Delta h = \alpha \frac{bv}{gR} \quad (1)$$

where Δh , b , v and g are superelevation, flow width, flow velocity and gravitational acceleration respectively (Fig. 3(a)) and α is a correction factor for debris flows. If the flow is super-critical pure water, $\alpha = 1$. The radius R is measured from drawing sheet of the bank protection on left bank of the Arimura river and is 78 m. The channel width b is measured from cross-sectional data from LPS. The flow velocity v is estimated from longitudinal surface profile of the debris-flow surface as it spilled over the check dam, as scanned by LPS 1. Estimation of flow velocity of debris flow was proposed in Yoshinaga et al. (2017) as follows;

$$v = 0.6 \frac{L}{k} \frac{g}{2(H + h_e)} \quad (2)$$

where L , H and h_e are horizontal drop length from spill way of the check dam, vertical drop length from spill way to test height and exit flow depth at spill way respectively. The coefficient k expresses relationship between exit flow depth and critical depth, and the value is 1.312 according to Hong et al. (2010). Schematic image of dropping debris flow is illustrated in Fig. 3(b).

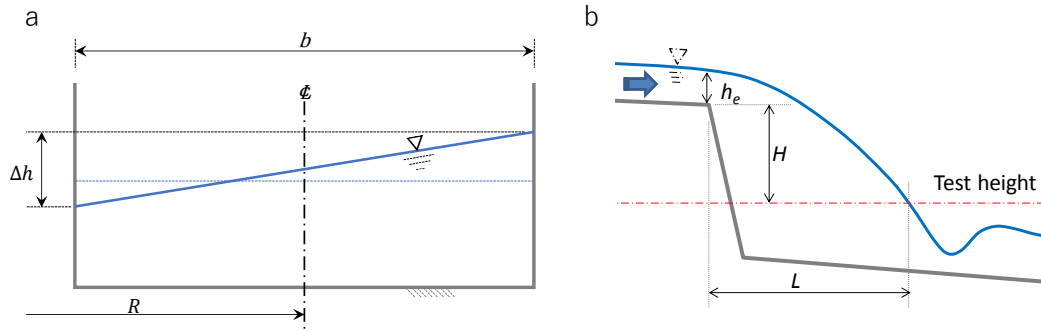


Fig. 3. (a) Schematic image of superlevation in rectangular channel with a radius R ; (b) Schematic image of dropping debris flow at check dam

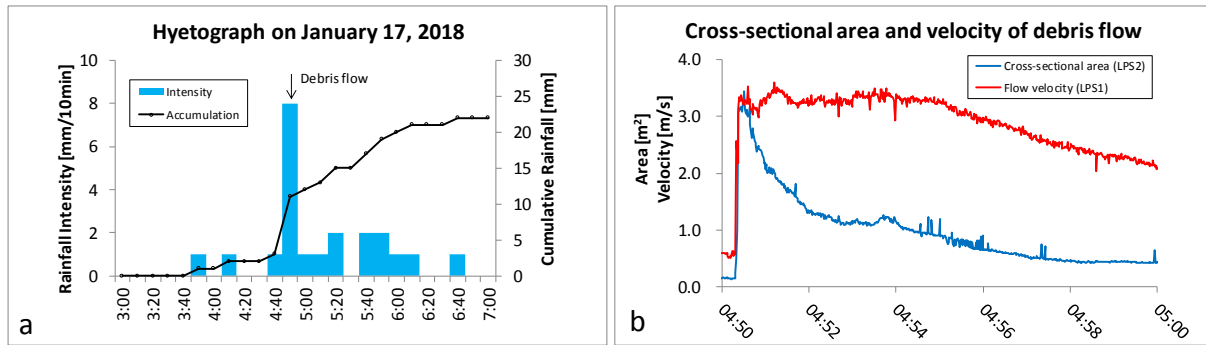


Fig. 4. (a) Hyetograph on January 17, 2018 at Arimura river; (b) Cross-sectional area and velocity of debris flow at Arimura 3rd check dam

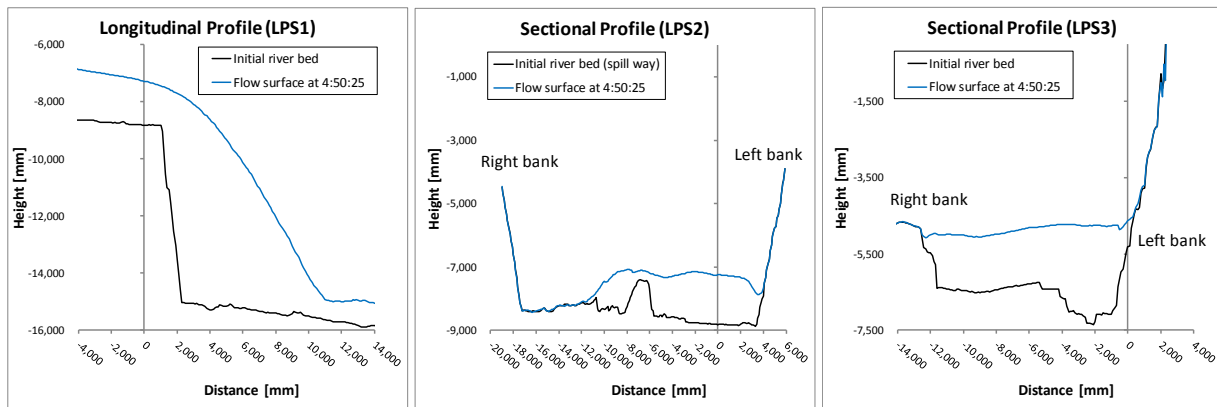


Fig. 5. Observed profiles of debris flow on January 17, 2018 captured by LPSs

3. Results

3.1. Observed debris flow

A debris flow occurred in the early morning (before the sun rise) of the January 17, 2018 and the flow geometry was clearly captured by LPSs 1, 2 and 3. Data from LPS 4 contain noise and a surface profile could not be obtained. The rainfall was triggered by the passage of the cold front and the debris flow was the first event after September 22, 2017. The cumulative rainfall was 22 mm and the highest 10-minute rainfall intensity was 8 mm/10 min (Fig. 4 (a)). Maximum flow depth was 1.6 m at spill-way of the Arimura 3rd check dam according to the observations at LPS 1. The surface profiles of the debris flow around the peak discharge are plotted in Fig. 5.

3.2. Investigation of hydraulic characteristics

The flow velocity is estimated by Equation (2) from free falling drop profile at check dam captured by LPS 1. Horizontal drop length and exit flow depth at spill way are evaluated from the observation of LPS1. The debris flow shows sudden peak at the front of the flow and the velocity at peak was estimated 3.3 m/s. Temporal change of the velocity estimated by data from LPS 1 and observed cross-sectional area at the spill way captured by LPS 2 are plotted in Fig. 4 (b). From Fig. 4 (b), cross-sectional area shows a sharp peak at the front of debris flow, but the velocity plot shows a plateau during about 5 minutes from the front. Normally, the flow velocity is a function of hydraulic radius according to Manning's formula, but the velocity at the front of the debris flow estimated by Equation (2) does not follow the formula. This means the front of the debris flow is subjected to a higher traction force and viscosity in comparison with the tailing flow.

Temporal changes of cross-sectional surface profiles of the debris flow captured by LPS 3 are shown in Fig. 7. Superelevation of the debris flow is clearly observed in the first 12 seconds. The observed superelevation of debris flow is 2.18 m at the front and diminishes rapidly.

4. Discussion

Sequential surface profiles observed at LPS 3 were compiled every 3-seconds and used to investigate superelevation characteristics of the January 17 debris flow. For comparison, the superelevation expected based on Equation 1 was also calculated assuming the correction factor is equal to 1. The observed superelevation and estimated superelevation based on Equation 1, are compared in Fig. 6, along with the observed flow velocity and width. The observed flow shows a relatively large superelevation of the flow surface between the inner and outer banks of the curved channel during the first 12 seconds of the flow, and then diminishes over the next 6 seconds to the value estimated with Equation 1. In contrast, the superelevation estimated from Equation 1 does not show a larger superelevation for the surge front.

The maximum value of superelevation from observation is 2.18 m; by contrast the estimated value is 0.19 m. At this time, the correction factor should be 11.5.

Our observation suggests that superelevation at the front part of debris flows exceeds estimation based on the static state assumption. Because of dynamic behavior of the front part of debris flows, rectilinear motion is the dominant flow process. Consequently, debris flows can run farther up the side bank of a channel than currently estimated.

5. Conclusion

From our observations, the dynamic behavior of a debris flow was captured clearly with very high resolution both in space and time. Using observed data, we can evaluate hydraulic characteristics, such as velocity and superelevation. Observation of debris flows in the real world is still rare and behavior of flow differs according to characteristics of the flow, such as size of grains and density, thus additional observations will be necessary.

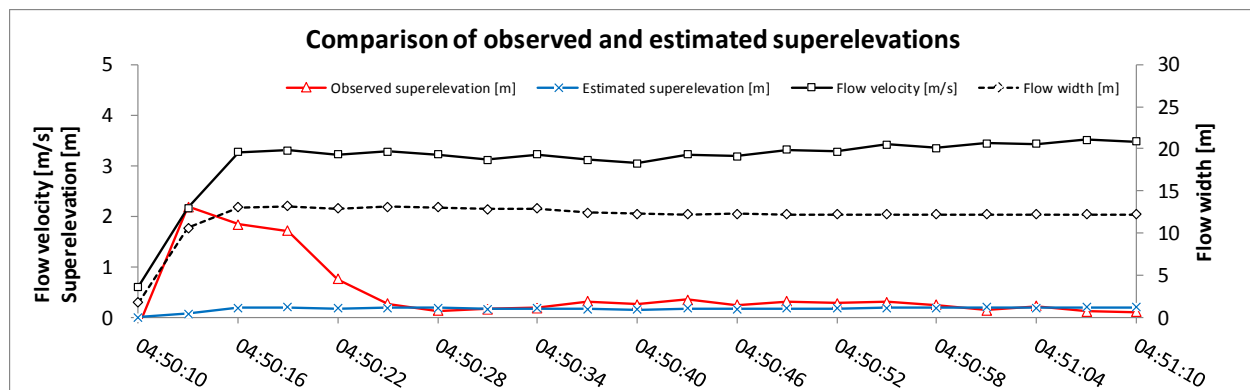


Fig. 6. Comparison of superelevations observed at LPS 3 from January 17 debris flow with superelevations estimated based on Equation 1 ($\alpha = 1$)

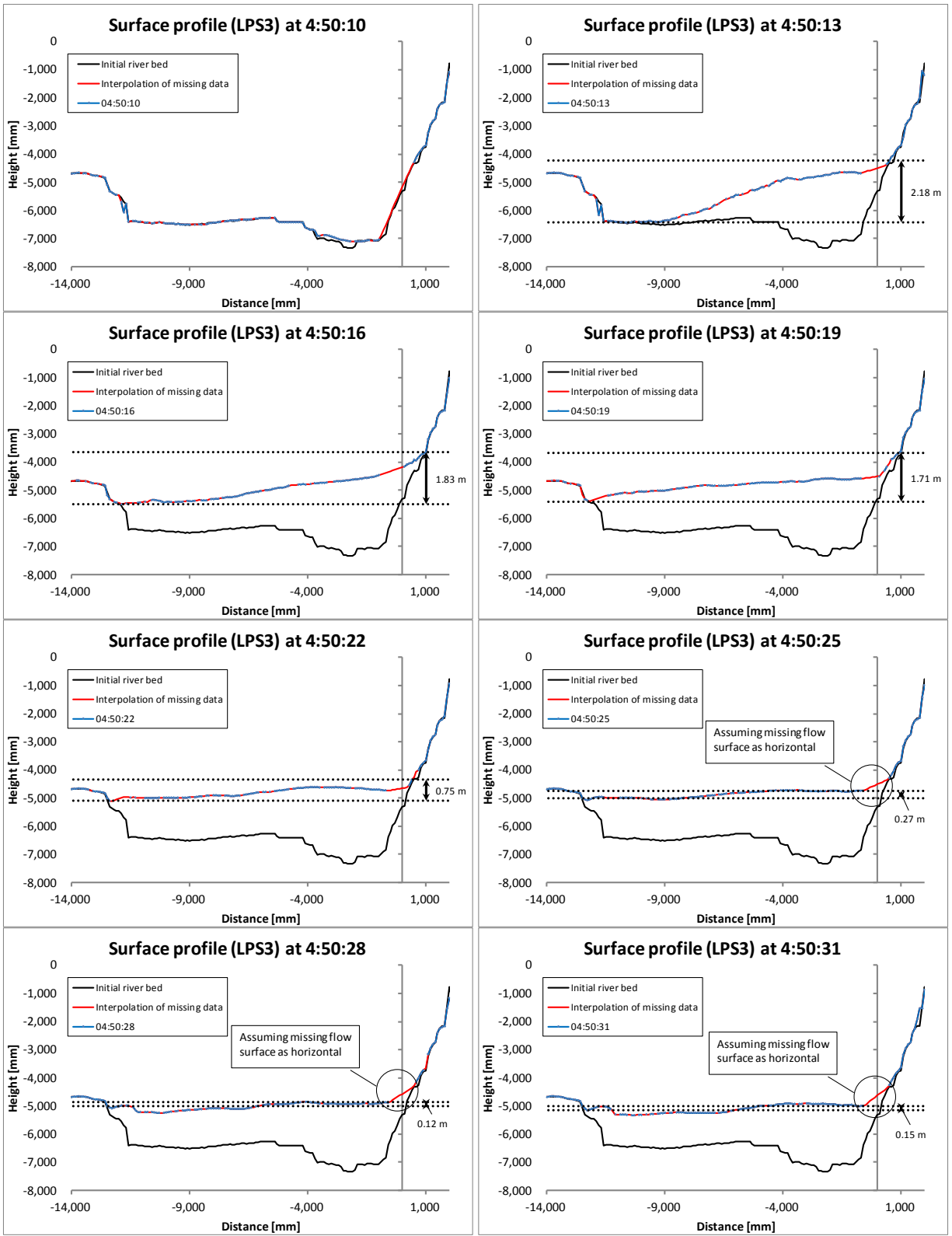


Fig. 7. Time change of sectional surface of debris flow on January 17, 2018 captured by LPS 3

Acknowledgements

The authors thank to Osumi office of rivers and highways for generous support of our research activities at Arimura River.

References

- Ashida, K., Takahashi, T., and Arai, M., 1981, Study on debris flow control (2) —Debris flow in bends of rectangular section—: DPRI Annuals, no. 24B-2, p. 251–263.
- Hong, Y.M., Huang, H.S., Wan, S., 2010, Drop characteristics of free-falling nappe for aerated straight-drop spillway: Journal of hydraulic research, v. 48:1, p. 125–129, doi: 10.1080/00221680903568683.
- Hungr, O. and Morgan, G. C., 1984, Quantitative analysis of debris torrent hazards for design of remedial measures, Canadian Geotechnical Journal, v. 21, p. 663–677, doi: 10.1139/t84-073.
- Ikeya, H. and Uehara, S., 1982, Debris flow in S-shaped channel curves, Japanese Civil Engineering Journal, no. 24–12, p. 645–650.
- Mizuno, H., 2004, Experimental study on a estimating method for velocity of debris flow in bending curves: Journal of the Japan Society of Erosion Control Engineering, v. 57, no. 4, p. 56–59.
- Mizuyama, T., and Uehara, S., 1981, Debris flow in steep slope channel curves: Civil Engineering Journal, no. 23–5, p. 243–248.
- Scheidt, C., McArdell, B.W., and Rickenmann, D., 2015, Debris-flow velocities and superelevation in a curved laboratory channel: Canadian Geotechnical Journal, no. 52(3), p. 305–317, doi: 10.1139/cgj-2014-0081.
- Takahashi, Y., Fujimura, N., and Mizuno, H., 2018, Evaluation of hydraulic characteristics from observation of surface profiles of debris flows: Proceedings of INTERPRAEVENT2018, p. 116–117.
- Yoshinaga, S., Shimizu, T., Mizutani, T., Takahashi, Y., Fujimura, N., Izumiya, and H., Ishizuka, T., 2017, A method for measuring nappe distance and depth of debris flow using laser range finder and application to estimate debris flow velocity: Journal of the Japan Society of Erosion Control Engineering, v. 70, no. 1, p. 46–53.

Monitoring and early warning of debris flow in an earthquake impacted area, Baishahe catchment, southwest China

Hongling Tian^{a,b,*}, Zongji Yang^{a,b}, Jianping Qiao^{a,b}, Lili Shi^c

^a Key Laboratory of Mountain Hazards and Earth Surface Processes, Chinese Academy of Sciences, #.9, Block 4, Renminnanlu Road, Chengdu 610041, China

^b Institute of Mountain Hazards and Environment, Chinese Academy of Sciences, #.9, Block 4, Renminnanlu Road, Chengdu 610041, China

^c Chengdu Geo-environment monitoring station, 69, Shuxiuxilu Road, Chengdu 610042, China

Abstract

After 10 years of the Wenchuan earthquake of China, the post-seismic landslides are turning weak. However, the debris flows in earthquake-stricken area continue to be threat. In order to reduce the risk from debris flows in this region, we discuss the operation of an alert system, monitoring objectives, and early-warning policies. Three gullies in the Baishahe catchment, Dujiangyan, Southwest China were selected and rain-gauge, tilt-sensor, mud-meter and ground acoustic meter combined to a warning system in April, 2014. The data collected from these events shows changes in susceptibility levels and triggering rainfall complicating the application of a fixed rainfall threshold for any alert system.

Keywords: Warning system, debris flow, susceptibility, monitoring

1. Introduction

It has been 10 years since the Wenchuan Ms 8.0 earthquake, occurred on 12 May 2008 in the Sichuan Province of China (Zhang et al., 2014). The post-seismic landslides frequency and the intensity is less than before (Fan et al., 2018; Chigira et al., 2010). However, huge amounts of loose material still remain on steep hillsides or in gullies. Heavy rain has on several occasions, mobilized this debris into debris flows and that has impacted infrastructure and local people. In the beginning years following the earthquake, debris flows caused significant loss of life (Zhang et al., 2016) such as the catastrophic rockslide-debris flow at Sanxi village, Dujiangyan, near the epicentre in 2013, where 166 people were killed (Yin et al., 2016).

Compared to the shallow landslide and flooding, debris flow often causes greater losses and casualties, thus these hazards often catch the public attention and thus require mitigation measure in the susceptible area by the governmental authorities. Monitoring is critical to providing insight into the processes that initiate debris flows and control their growth and travel, which can be used to develop mitigative strategies (Angeli et al., 2000). Many monitoring systems were built in the disaster prone area (Tian et al., 2013).

The objective of the debris flow monitoring systems described in this paper is to provide alerts of the occurrence of debris flow. A successful debris flow monitoring system consist of three parts. The fore-end including the right sensors and their arrangement, data acquisition and data routing. The middle part is data communication system. And the rear-end is the data proceeding and disaster judging. Most important to an alert system is not just instruments on the ground, but require that information be delivered to those that need it and that people at risk know what protective actions to take. Whereas some system only relies on rain gauge, and simply release signal of rainfall. With the development of sensor and network technology, current monitoring system seldom only rely on single parameter. Wireless sensor network and Internet of Things (short as IoT) improve the performance of monitoring system greatly (Hongling et al., 2012; Rosi et al., 2011).

* Corresponding author e-mail address: thl@imde.ac.cn

2. Key issues for debris flow monitoring and early-warning system

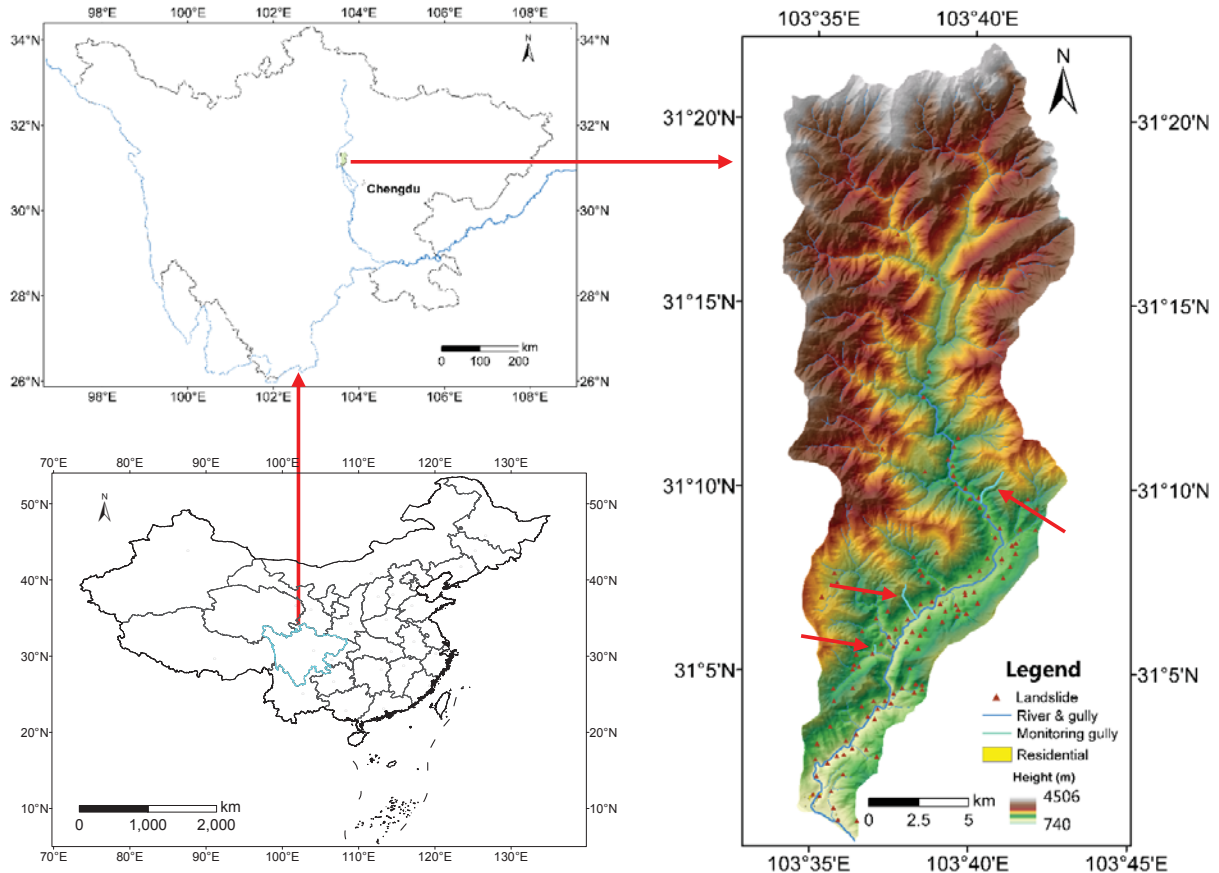
To monitoring a debris flow and employ an early-warning system, there are some important technique issues should settle beforehand, here the after-disaster-alert actions are not involved.

Where will a debris flow will occur, when will a debris flow occurs, what is the magnitude of the coming debris flow, how long will a debris flow continue; it also means how long the warning system is valid, where the monitoring sensors should be employed.

These five questions should settle before a debris flow early-warning system plan begin.

3. Location and description of study area

An early-warning system was built in Baishahe catchment, Dujiangyan city, Southwest China. The Baishahe catchment (Fig 1) is 364km², located in the middle of Longmen Shan fault, about 25 km from the location of the epicenter of the Wenchuan earthquake. The research area is a low susceptibility area of landslide before the earthquake. But the circumstance changed greatly since the giant earthquake in 2008. There are 6119 landslides including 199 debris flow gullies in this area were identified from Quickbird imagery from 2010 and 2011 (Fig 2) (Wang, 2018). With heavy rains, dense intensive debris flow struck local resident frequently in summer of 2009, 2010, 2013.



Three monitoring gullies in right map: Yindongzi, Gangou, Guoquanyan. (from north to south)

Fig. 1. Baishahe catchment and the distribution of landslides triggered by the Wenchuan earthquake

An earthquake-triggered landslide hazard zoning map (Fig 3) were completed by using the contributing weight

model (wang, et al. 2010). There are 10s of gullies in the middle reaches which were near to residential areas or tourist places. 3 most dangerous gullies were selected in different susceptibility levels as monitoring targets (Fig 4). All of these gullies generated debris flows in the summer of 2013 and abundant loose material can be found in these gullies (Yang, et al. 2011) (table 1).

Table 1. Facts of 3 monitoring gullies

Gully name	Loose material volume ($\times 10^4\text{m}^3$)	Length of master gully (km)	Drainage area (km^2)	Relative height difference (m)
Yindongzi	35.93	2.50	2.2	980
Gangou	35.24	1.972	1.12	490
Guoquanyan	4.0	0.89	0.15	272

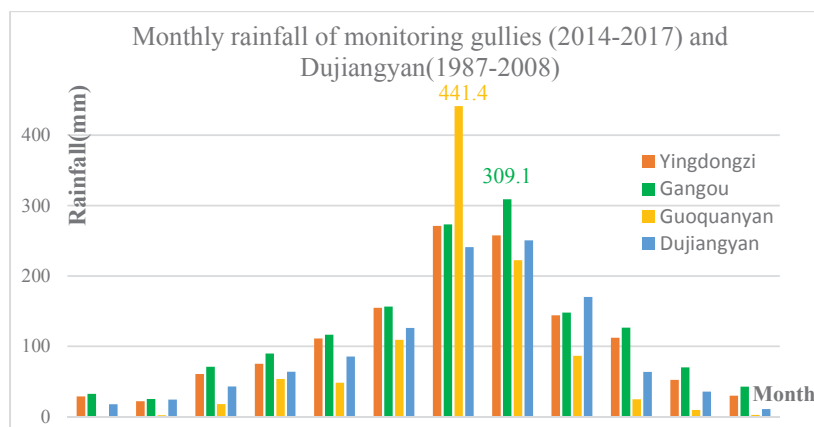


Figure 2. Monthly precipitation of monitoring gullies and Dujiangyan

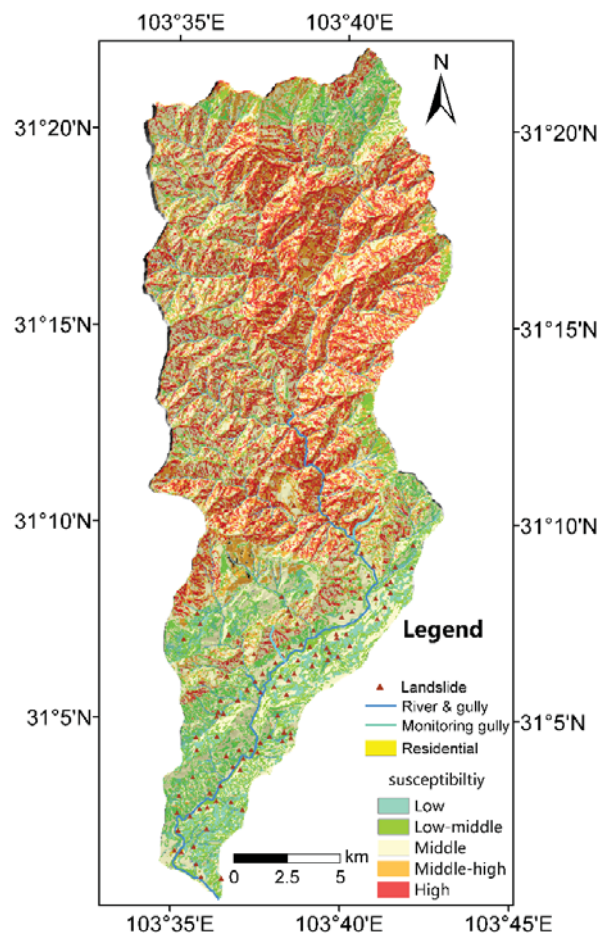


Figure 3. Susceptibility zonation of Baishahe catchment (Wang, 2018)

4. Monitoring system and alert policy

Rainfall, topography, lithology affect which types of debris flows occur in different locales (Drew et al 2009). Most debris flow warning systems keep watching on these factors or part of them. Although some monitoring system using similar factors even the same type sensor, the accuracy of their alerts have big difference. We found that the phenomenon of the debris flow process and its position, the movements on the bank slope is important for early warning.

Here we propose a multi-sensor step-inspection approach based on the hydrological process of the debris flow. The first step is observing the rainfall using rain gauges, the second is measuring the soil moisture of the bank slope, the third step is to observing the water flow in the gully, the fourth step is obtaining information on the vibrations generated by collisions among boulders and the stream bank. The final step is video recordings to observe debris flow passage.

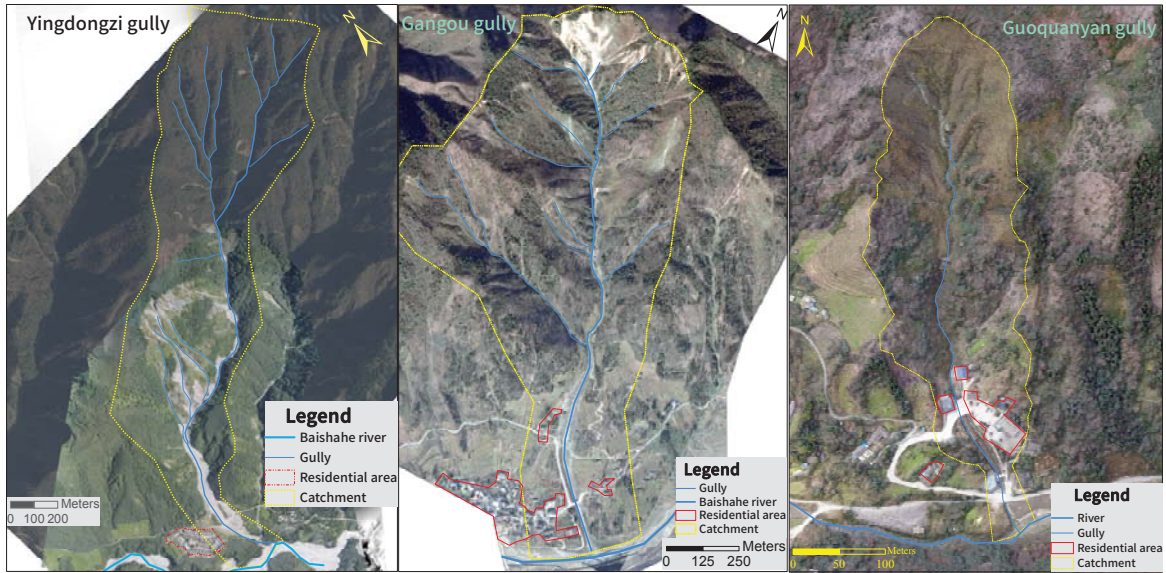


Figure 4. Monitoring gullies in Baishahe catchment

In the 3 selected gullies, the demonstration warning systems were installed in May, 2014. These warning systems not only monitoring the debris flow, but also monitoring the movements on the slope, such as rockfall and landslide.

Three types of sensors were chosen for the purpose of obtaining information to support early-warning.

- Hydrological sensor such as rain gauges, soil moisture meter, mud-level meter
- Slope deformation or contact sensor such as tilt sensors, ground acoustic meters and trip wires
- video cameras.

Except the video camera, other sensors were installed in the circulating zone to the formation zone of a gully (Fig 5). Thus, much information before a debris-flow forming can be get. Not only the flow in the gully but also the slope movements can be obtained, we can release alert of the slope's movement before the debris flow initial.

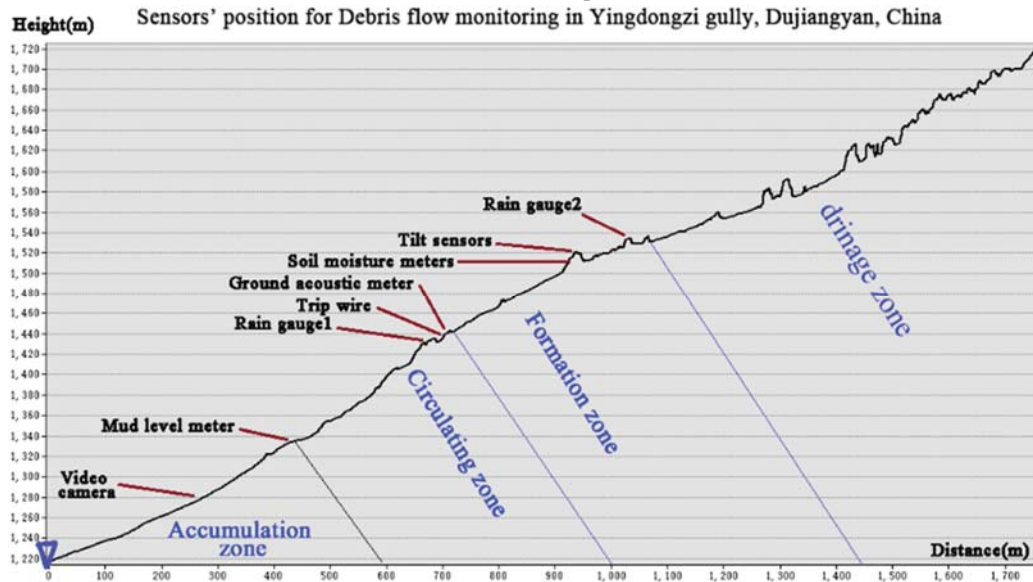


Figure 5. Example of Sensors position in Yindongzi gully in profile view (other gullies monitored in the similar manner)

5. Debris flow and related landslide events during the monitoring duration

A heavy rainstorm hit the Baishahe area since 6:00am, in July 9, 2013. The total rainfall was 564.8mm and the duration was 72 hours, and the maxim rainfall intensity was 35.3mm/h. This rainstorm caused a wide range of landslides and debris flows in the Baishahe river, including the three selected gullies. This made the Baishahe area lack of disasters in the following seasons.

After the monitoring system began to work, there are still few events occurred, only two debris-flow events and one rockfall was recorded.

5.1. Rock fell in July 6, 2014 Gangou gully

There is no rain or earthquake at that time, a tilt sensor recorded the rockfall occurred at 9:10 on the right bank; the sensor was damaged at 11:40 (Fig 6).

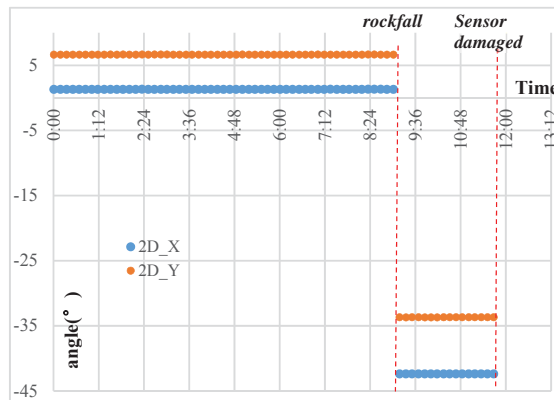


Fig 6. Rock fall in July 6, right bank of Gangou gully

5.2. Debris flow in Aug 28, 2017, Yindongzi gully

A heavy rain event occurred on Aug 28, 2017(Fig 7), which caused a debris flow in Yindongzi gully. The trip-break and ground acoustic meter both detected the debris flow passage. The alert released to the local government, together with the effective disaster education, this event did not bring casualty at all. However, the trip wire, mud-level meter, ground acoustic meter was all damaged or buried by the debris.

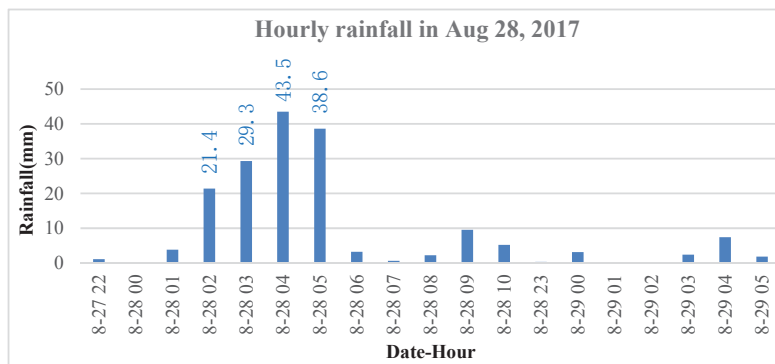


Fig 7. Hourly accumulated precipitation of Yindongzi gully

5.3. Debris flow in Jun 26, 2018, Yindongzi gully

A similar event repeated in June 26, 2018(Fig 8), a debris flow occurred in Yindongzi gully. There is no

casualty also.

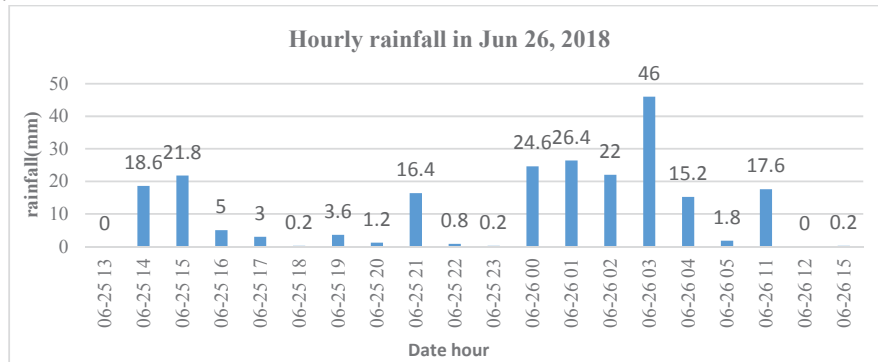


Fig 8. Hourly precipitation of Yindongzi gully in Jun 26, 2018.

6. Conclusions

With four years monitoring, this monitoring system release three warning signals to the local government. Some conclusions drew from the experience here:

- The monitoring experience shows that the selection of the monitoring object by susceptibility is valid. The three monitoring gullies' behaviour reflect their susceptibility level. Yingdongzi gully in high level zone occurred 2 debris flow events, Gangou gully in middle zone occurred rock fall event, Guoquanyan gully in low level zone with no disaster.
- Besides the rainfall, slope movement and phenomenon of debris flowing play important roles in debris flow early-warning.
- the formation zone and circulating zone is good to install monitoring sensors to catch the early change of the debris flow.

Acknowledgement

The paper was financially supported by the National Natural Sciences Foundation of China (41471429), The National Key Research and Development Program of China(2017YFC1502502), Key Technology Talent Program, CAS.

The monitoring work and research also received help from The Field Observation and Research Base of Geological Hazards in Chengdu Earthquake Disturbed Area of Longmen Mountain.

We thank for the reviewer who gave us detailed advices, constructive comments and linguistic assistance to this paper.

References

- Angeli, M. G., A. Pasuto and S. Silvano, 2000, A critical review of landslide monitoring experiences: *Engineering Geology*, v.55: p.133-147.
- Chigira, M., X. Wu, T. Inokuchi and G. Wang, 2010, Landslides induced by the 2008 Wenchuan earthquake, Sichuan, China: *Geomorphology*, v.118, p.225-238.
- Drew, B., and Marwan, A. H., 2009, Debris flow initiation and sediment recharge in gullies: *Geomorphology*, v109, p.122-131.
- Fan, X., C. H. Juang, J. Wasowski, R. Huang, Q. Xu, G. Scaringi, C. J. van Westen and H.-B. Havenith, 2018, What we have learned from the 2008 Wenchuan Earthquake and its aftermath: A decade of research and challenges: *Engineering Geology*, v.241, p.25-32.
- H. Tian, M. Wang, Z. Yang and J. Qiao, 2013, Multiple Predict Landslides in Giant Earthquake Struck Region: A Case Study in Chengdu, China. Earthquake-Induced Landslides, in Proceedings, the International Symposium on Earthquake-Induced Landslides, Kiryu, Japan, 2012. K. Ugai, H. Yagi and A. Wakai. Berlin, Heidelberg, Springer Berlin Heidelberg: p.989-996.
- Hongling, T., Jianping Q., UCHIMURA T., and Lin, W., 2012, Monitoring on Earthquake Induced Landslides - A case study in northwest Chengdu, China: *Geotechnical Engineering Journal of the SEAGS & AGSSEA*, V.43, p.71-74.
- Rosi, A., M. Berti, N. Bicocchi, G. Castelli, A. Corsini, M. Mamei and F. Zambonelli, 2011. Landslide monitoring with sensor networks: experiences and lessons learnt from a real-world deployment: *International Journal of Sensor Networks*, v.10, p.111-122.
- Yang C., Chen N. Deng M., 2011, Assessment on Debris-flow Hazard Based on the Volume of Debris – A Case study in the Baishahe River, Dujiangyan: *Research of Soil and Water Conservation*, v.18: p.25-31

- Yin, Y., Y. Cheng, J. Liang and W. Wang 2016, Heavy-rainfall-induced catastrophic rockslide-debris flow at Sanxicun, Dujiangyan, after the Wenchuan Ms 8.0 earthquake: *Landslides*, v.13: p.9-23.
- Wang M., 2018, Research on Landslide hazard zoning and raining threshold in Baishahe catchment in Jianping Qiao, eds., *Research on Monitoring and Early warning of Rainfall-induced Landslide and Debris Flows*: Beijing, Science Press, p.105-127.
- Wang M., Qiao J., He S., 2010, GIS-based earthquake-triggered landslide hazard zoning using contributing weight model: *Journal of Mountain Science*, v.7, p.339-352.
- Zhang, S., L. Zhang, S. Lacasse and F. Nadim, 2016, Evolution of Mass Movements near Epicenter of Wenchuan Earthquake, the First Eight Years: *Scientific Reports*, v.6, p.36154.
- Zhang, Y., Y. Cheng, Y. Yin, H. Lan, J. Wang and X. Fu, 2014, High-position debris flow: A long-term active geohazard after the Wenchuan earthquake: *Engineering Geology*, v.180, p.45-54.

Deciphering debris-flow seismograms at Illgraben, Switzerland

Michaela Wenner^{a,b,*}, Fabian Walter^a, Brian McArdell^b, Daniel Farinotti^{a,b}

^aLaboratory of Hydraulics, Hydrology and Glaciology (VAW), ETH Zurich, Hönggerbergstrasse 26, 8093 Zürich, Switzerland

^bSwiss Federal Institute for Forest, Snow and Landscape Research (WSL), Zürcherstrasse 111, 8903 Zürich, Switzerland

Abstract

Mass wasting, such as rockfalls, landslides and debris flows in steep mountain terrain, has a high destructive potential, and plays a key role in both erosion and landscape evolution. As an alternative to many conventional approaches, seismology allows monitoring of such mass movements at safe distances, provides estimates of event location and timing, and can give insights into dynamics and rheology granular flows. Here, we analyze seismic data recorded during the 2017 and 2018 debris-flow seasons at Illgraben, a steep canyon located in Switzerland. Yearly precipitation is controlled by summer rainstorms with high rainfall intensity during which mass wasting including rock-slope failure and debris flows occur regularly. The frequent debris-flow occurrence (on average three events per year) makes the Illgraben an ideal site for cross-validating a seismically-derived event catalog of mass movements with “ground-truth data”, such as digital terrain models, flow depths estimates and other in-torrent measurements. We present seismic frequency characteristics of the Illgraben debris-flow series and investigate how the seismic signature depends on actual debris-flow characteristics, such as grain sizes, and on propagation effects of the generated seismic waves. Whereas these two effects are usually difficult to separate, the source component contains valuable information on the flow’s material composition. Stations that are close to the torrent, we find that dominant frequencies in the recorded signal reflect the distance to the dominant source. For one particular station, this is shown on recordings of several events, where a dominant frequency of about 5.5 Hz indicates the passing of the flow at a 48m check dam. Power spectral densities at that instance give an estimate of the particle content of the debris flow. We also find that a jump in dominant frequency does not necessarily reflect the location of the flow front. Seismic studies of debris-flow dynamics and material composition should therefore not be limited to entire debris-flow seismograms, but instead focus on individual time windows and consider different sensors separately. The presented analysis underlines the use of seismic data in torrent and landscape studies.

Keywords: seismology, spectral characteristics, monitoring, debris flow

1. Introduction

In mountainous areas, mass movements such as debris flows are a significant threat to infrastructure, properties and human life. Monitoring of debris-flow prone catchments is essential to improve our understanding of debris-flow dynamics, and needed for both designing mitigation measures and damage reduction. Standard granular flow models for debris flows assume a shallow propagating mass, in which the rheology is described by an effective friction (Mangeney-Castelnau et al., 2005; Mangeney et al., 2007; Christen et al., 2010). Field measurements are essential to constrain this effective friction and other parameters, including erosion, flow depth and flow density. Classical monitoring techniques, like radar altimeters, aerial imagery and geophones within the torrent, can give information about onset time, flow depth, discharge and erosion or deposition areas. However, they offer no direct measurements of flow characteristics such as effective friction and material density (for an overview in debris-flow monitoring instrumentation see Arattano & Marchi, 2008).

In recent years, seismology has evolved into a standard tool to study mass movements and their dynamics at high temporal resolution (Larose et al., 2015; Allstadt et al., 2018). Seismic signals generated by such events are often classified into low and high frequency content. The low frequency signal (< 10 s) is modelled by the elastic response

* Corresponding author e-mail address: wenner@vaw.baug.ethz.ch

the earth to acceleration and deceleration of the bulk mass of the flow (e.g. Ekström & Stark, 2013). In contrast, higher frequency signals (> 1 Hz) are generated by collisions of grains within the flow, and their impacts on the bed. For smaller scale mass movements, the force that is exerted on the earth is often too small to generate detectable low-frequency elastic waves. In contrast, high frequency signals can be recorded in such cases, and are used to study rockfalls and rock avalanches in both volcanic (e.g. Norris, 1994; Hibert et al., 2011; Hibert et al., 2017) and mountainous areas (eg. Deparis et al., 2008 ; Vilajosana et al., 2008; Dammeier et al., 2011; Burtin et al., 2014; Dietze et al., 2017; Provost et al., 2017) or snow avalanches (eg. Suriñach et al., 2005, Heck et al., 2018). Such signals are typically emergent with dominant frequencies of 5–10 Hz and no distinguishable seismic phases. Signal durations vary between seconds to several tens of seconds, depending on the type of movement. Consisting of numerous and overlapping individual particle-bed and inter-particle collisions, source models of the high frequency mass movement signals are far more complicated than the low frequency component of the signal, and are hence less understood.

Recently, Kean et al. (2015) and Lai et al. (2018) adapted a model of fluvial bedload transport to explain the high-frequency seismic spectrum of debris flows in sediment-filled channels, and during a debris flow in California, respectively. The model explains the seismic signal in terms of instantaneous Hertzian impacts of bedload particles on the ground. In this way, the impact force generating seismic waves results from a change in the particles' linear momentum (impulse), which is two times the product of the particle's initial mass and velocity (Tsai et al., 2012). To simplify the model for debris flows, these impacts are integrated over the boulder-rich flow front.

The adapted Tsai et al. (2012) model makes assumptions for particle velocities and seismic path effects describing the propagation of seismic waves from the river bed to a recording unit. Importantly, the calculated seismic spectrum is influenced by the poorly constrained grain size distributions of moving particles, as well as seismic velocities and attenuation of ground substrate influence. Nevertheless, the model explains observed seismic frequency spectra for bedload transport (Burtin et al., 2008). For debris flows, the model proposes that spectral amplitudes are primarily influenced by the grain sizes of the boulder-rich debris-flow front. Furthermore, the peak frequencies are controlled by the source-receiver distance, with higher (lower) peak frequencies indicating shorter (longer) distances between flow front and seismometer. By analysing peak frequencies at different time steps, Lai et al. (2018) propose that one can estimate location and velocity of the flow (Lai et al., 2018). Kean et al. (2015) used their adapted model to invert for sediment cover, and to estimate entrainment rates that compare well with observations.

Here, we study the high frequency content of seismic signals recorded at the debris-flow prone Illgraben torrent, located in Switzerland. This torrent is one of the most active catchments in the Alps (Hürlimann et al., 2003), producing several debris flows per year. In 2017 and 2018, we recorded a total of seven debris flows of different volumes, flow velocities and material composition. We relate spectral characteristics of the debris-flow seismograms to flow-receiver distances, and to topographic features within the torrent. The results show that the spectrum (1) cannot be analyzed as a whole, but has to be segmented in time in order to elucidate characteristics of the debris flow and (2) has to be treated independently for each sensor since the latter are sensitive to different stages of the debris flow.

2. Study site

The Illgraben catchment, located in the southwest of Switzerland, spans from its highest point, the Illhorn (2716 m asl), down to the Rhône Valley where its main torrent, the Illbach, flows into the Rhône River (610 m asl). Past activity within the 9.5 km² catchment and 5 km long torrent produced a large fan with a radius of about 2 km and a volume of about 500 x 10⁶ m³ (Hürlimann et al., 2003; McArdell et al., 2007). Illgraben is characterized by a complex geology, with the northwest Illhorn face and the head of the trunk channel being dominated by highly fractured quartzite, and the southeast facing slope of the catchment mostly consisting of limestone (Schlunegger et al., 2009; Bennett et al., 2012). The fractured quartzite with erosion rates of tens of centimeters per year is the main contributor to the sediment transported via debris flows (Bennett et al., 2012). Precipitation patterns during summer are characterized by storms, with rainfall intensities of up to several tens of mm/h, and a duration of half an hour to one hour (Hürlimann et al., 2003). In such events, sediment deposited at the head of the trunk channel is mobilized by water gathered along the steep (> 40 degrees) slopes (McArdell et al., 2007). This produces on average 3–5 debris flows per year that contribute significantly to the sediment discharge of the Rhône River (Schlunegger et al., 2009). Typical events have volumes around 20,000 m³ and velocities 3–4 m/s, and transport blocks up to several meters in diameter. In contrast, some events have lower concentration of sediment and fewer such large particles and are more appropriately classified as “debris floods” (e.g. Pierson & Costa, 1987). After a large (3 x 10⁶ m³) rock avalanche in 1961 in the upper catchment, a 48 m tall check dam (CD1, Figure 1) was built within the channel to stabilize the deposit and to prevent large debris

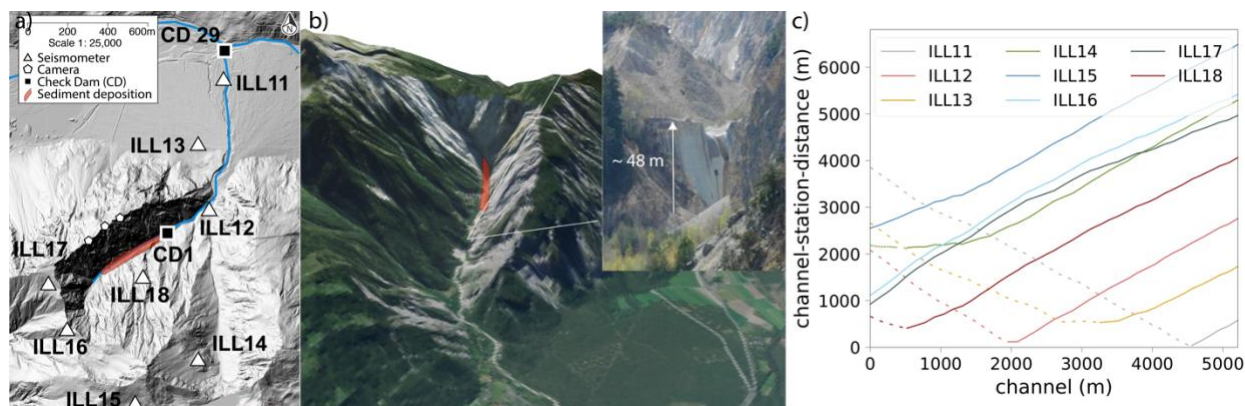


Fig. 1. (a) Overview of the Illgraben catchment and the instrumentation installed during the debris-flow season (June-August) 2018. Seismometer locations (white triangles), the area of sediment supply for the debris flows (shaded red area), and the position of the 48 m tall check dam 1, and check dam 29 (black squares) are depicted (b) 3D orthophoto with sediment deposition area in red and check dam 1 shown on a photo. (c) Channel-receiver distances for all seismic stations installed in 2018. The y-axis represents the distance whereas the x-axis marks the position along the channel (origin at the head of the catchment; 5000m corresponds to the Illbach inflow into the Rhône river). Dashed (continuous) lines show the section where the flow is approaching (moving away from) the station.

flows (Hürlimann et al., 2003). Further downstream along the torrent, 29 additional check dams of several meters height were built to minimize vertical and lateral erosion, thereby stabilizing the channel at the present location. With these measures, most debris flows no longer leave the channel, and damage to infrastructure is rare. To our knowledge, the Illgraben carries little or no discharge in the summer between debris flows, and therefore considerable recreational activity takes place near and in the channel. For this reason, an early warning system was installed in 2000. It is maintained by the Swiss Federal Institute for Forest, Snow and Landscape research (WSL) and consists of radar flow-depth sensors and geophone sensors to provide automatic detection of flows. Upon detection, acoustic alarms are activated and information is sent to local authorities. The data from the early warning system complements the existing scientific observation station (no warnings are generated) which consists of radar, laser and ultrasonic flow stage sensors at selected check dams, geophones mounted on the downstream facing wall of check dams, as well as video cameras and a 2m x 4m force plate (McArdell et al., 2007; Badoux et al., 2009). Recently, geophone and infrasound sensors have additionally been installed on the fan to increase early warning capabilities (Schimmel et al., 2018; Marchetti et al., 2019). An additional seismic network was installed throughout the Illgraben catchment between May and September in both 2017 and 2018 (Figure 1). This network recorded seven debris flows, and consisted of eight stations with real-time data transfer via the mobile phone network. The interstation distance of the network is about 1.5 km, with an aperture of 5.5 km. Most stations operate with a Lennartz-1s sensor that has a flat response between 1-100 Hz and a sampling rate of 100 Hz. Station ILL11 is equipped with a Trillium compact sensor with a low-frequency corner at 120 seconds.

3. Data: Debris-flow seismograms

During the monitoring period in 2017, three large ($> 25,000 \text{ m}^3$) debris flows occurred, with one flow of $\sim 100,000 \text{ m}^3$ (Table 1). In 2018 four events were recorded. After the destruction of the force plate in July 2016, volume and flow depth are estimated at the instrumented wall, CD 29 (Figure 1), situated about 10 m upstream of the location of the force plate (Berger et al., 2011). Due to the irregularity of the cross-section shape and the variability in the direction of the approaching flow at this location, flow depths tend to be over-estimated when compared to values previously reported at the force plate. Flow velocity is calculated from the travel time between in-torrent sensors along the channel as described in Schlunegger et al. (2009). As discussed in Section 5, video footage and power spectral densities of the signals suggest a relatively large water content without a boulder-rich front for the first two events in 2018.

Figure 2a shows the seismogram of a debris flow recorded on August 8, 2018. The signal shows the emergent onset and dominant frequencies above 5 Hz, typical for mass movements. The signal emerges from the background noise at a time that depends on the distance between the debris-flow front and the recording station (Walter et al., 2017). For the shown event, amplitudes at different stations vary between $1.5 \times 10^{-3} \text{ ms}^{-1}$ at station ILL11, and $2 \times 10^{-6} \text{ ms}^{-1}$ at

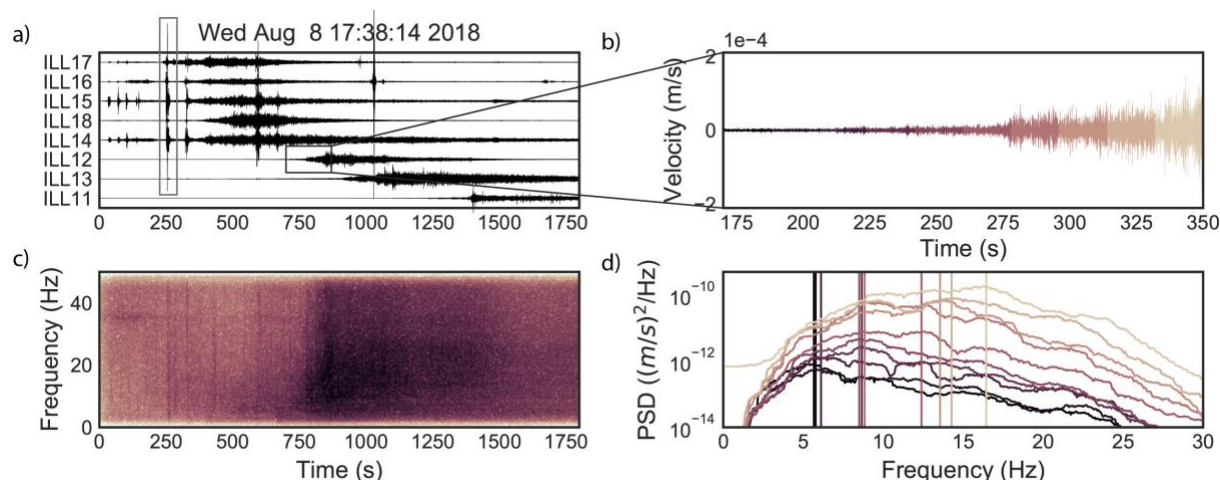


Fig. 2. (a) Seismogram of August 8, 2018 debris flow recorded on all stations of the network. Amplitudes were normalized for each station. Impulsive signals (grey rectangle) are of atmospheric origin (thunderstorm). (b) Close up of onset of the debris-flow signal on station ILL12. Note the emergent onset over several tens of seconds. (c) Spectrogram of signal recorded at station ILL12. The colors show the energy of the frequencies at each time step in decibel, where darker colors represent a higher energy. (d) Spectra of ten time-windows of 18 seconds corresponding to the color-coded waveform in (b). The spectra are smoothed with a 1 Hz running average. The vertical lines mark the peak amplitude of the spectral power.

ILL16. High amplitude impulsive signals on some stations within the network are of atmospheric origin, generated by thunder, and not directly related to the debris-flow signal (Marchetti et al., 2019).

Between debris flows, seismic background noise at Illgraben is dominated by several almost discrete frequency bands (Fig. 3). Between 1 and 5 Hz, anthropogenic noise is present showing diurnal variation, as well as lower energy on both weekends and public holidays compared to work days. Though strong, this signal is unlikely to affect seismic detectability of debris flows (Walter et al., 2017). Another distinct frequency band of noise is found at about 15 Hz. Within this band, an abrupt decrease in power can be observed at the end of June of both 2017 and 2018. We suggest that this could either be related to water discharge in the catchment due to snow melt, or to a change in hydropower operations at a dam 3 km away from the seismic station.

Here we concentrate on the frequency spectrum of the signal directly before and during the debris-flow events. We focus on station ILL12, because its near-torrent location implies a large range of distances to the flow front, both up and down-stream (Figure 1c). Such distance variations are particularly important for investigating variations in frequency signature (Lai et al., 2018). The goal is, to separate source and path effects on the frequency content of the signal, to constrain source mechanisms.

4. Peak frequency migration

For all 2017 and 2018 debris flows we computed the frequency spectrum for signal bins of 5 s with an overlap of 2.5 s. Figure 2c shows a close up of the initiation of the debris flow on August 8, 2018, with Figure 2d showing the corresponding color-coded spectra. As expected, the spectra show a peak migration from about 5.5 Hz towards higher frequencies for the flow front approaching station ILL12.

Table 1 Characteristics of the seven debris flows recorded in 2017 and 2018 (n.a. denotes that estimates are not yet available for 2018). “CD1” stands for “check dam 1”.

Date	Arrival time CD1 (UTC)	Volume (m ³)	Velocity (m/s)	Flow depth (m)
2017-05-29	16:58:31	100000	6.7	4.8
2017-06-03	23:27:38	25000	5.1	3.3
2017-06-14	19:30:48	35000	7.1	3.4
2018-06-11	10:46:39	35000	7.0	3.5
2018-06-12	18:29:16	n.a.	n.a.	n.a.
2018-07-25	16:56:40	< 50000	4.69	2.0
2018-08-08	17:49:25	< 100000	6.70	n.a.

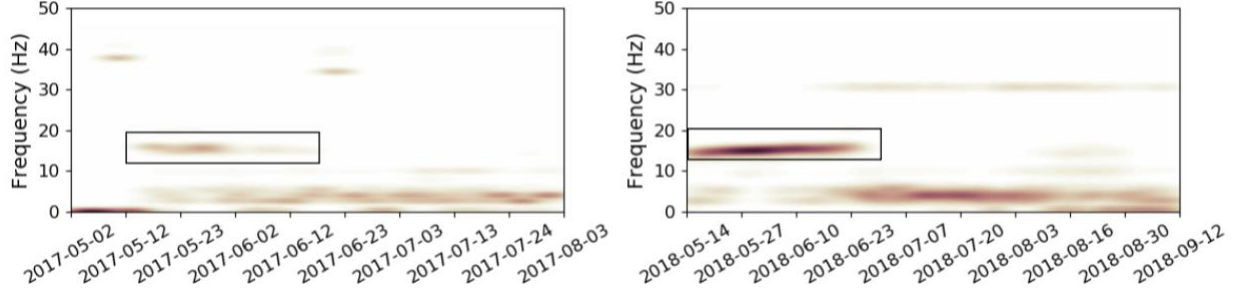


Fig. 3. Density plot of peak frequencies at station ILL12 for both 2017 and 2018. The rectangles mark a discrete noise band at about 15 Hz. The noise-source stops in June for both years. We suggest this to be either related to snow melt or to a change in nearby hydropower operations.

Figure 4a shows the peak frequencies at each time step for all recorded events. As a result of the broadband nature of the debris-flow seismograms, peak frequencies are difficult to identify in conventional spectrograms (Figure 2b). Only peak frequencies corresponding to a spectral power above $1 \times 10^{-13} \text{ ms}^{-2} \text{ Hz}^{-1}$ were plotted, to eliminate low energy background noise caused by anthropogenic and discharge-related seismicity. In-torrent geophone-counts at CD1 of the August 8, 2018 event are shown additionally. The geophones, which measure the vertical velocity of ground vibration, start recording when the front of the debris flow reaches the check dam. The signal is represented as impulses that exceed a certain threshold (e.g. McArdell et al., 2007). In Figure 4a, all events were aligned according to the first recording of the geophone impulses, hence the arrival of the flow at CD1. The 48 m drop at CD1 leads to a shift in dominant frequencies from pre-event noise bands of 1-5Hz and 15Hz to about 5.5 Hz for all events and an overall increase in spectral power (Figure 4a, dashed black line). Observations of flow over CD1 are not available, however, given that debris-flow velocities are relatively large, it is likely that the flow is largely detached from the face of the spillway and that it resembles free-fall conditions. Note that with the imposed energy threshold, the two small events of June 2018 do not emerge from the background noise. After the flow fronts pass CD1 and the 48 m free fall, the dominant frequencies rise to around 15 Hz when directly passing the station. After the initial rise, dominant frequencies shift between 12 and 25 Hz, but no time-dependent pattern can be observed (Figure 4a, dotted black line). In contrast to the frequency domain, the signal of the free fall cannot be distinguished from background noise in the time domain as has been observed at other sites (Coviello et al., 2015; Schimmel et al., 2018).

The evolution from low to higher peak frequencies can also be observed at station ILL11 and ILL13 (Appendix A). The stations have a minimum distance to the channel of 30 and 700 m, respectively. ILL18, which is closest to the initiation area of the flow, does not show a clear pattern in dominant frequencies. This can be explained by signal mixing of noise sources that are close to this station (i.e. precipitation and runoff concentration from the slopes, discharge, and 48 m channel step at CD1). For stations farther away from the channel, no pattern in dominant frequencies can be observed either. Specifically, stations that are farther away than 1 km from the channel (ILL14, 15, 16, 17) do not capture the peak frequency migration. For these stations, the 48 m free fall at CD1 may be too far to generate a signal that dominates over other seismic sources at the head of the trunk channel, closer to the stations.

5. Debris-flow characteristics from seismic signals

Next, we investigate the origin of the frequency signature of the flows in order to connect the findings with flow characteristics. The model by Lai et al. (2018), predicts the following power spectral density P as a function of frequency f of the seismic signal generated by the boulder-rich debris-flow front:

$$P \approx 1.9 LWD^3 u^3 \times \frac{f^{3+5\xi}}{v_c^5 r_0} e^{-\frac{8.8 f^{1+\xi} r_0}{v_c Q}} \quad (1)$$

L and W are the debris-flow head length and width, respectively, D is the 94th percentile of the grain size diameter, u is the flow velocity, and r_0 is the average distance between the debris-flow front and the receiver. Equation 1 shows, that the peak frequency is mostly dependent on the distance between source and receiver. The amplitude of the signal, however, linearly scales with the length and the width of the debris-flow front, as well as with the third power of particle size and flow velocity.

Using values of 500 ± 100 m/s for Rayleigh-wave phase velocity v_c , 60 ± 10 for the quality factor Q , and 0.417 ± 0.05 for ξ (Tsai et al., 2012; Burtin et al., 2014; Burtin et al., 2016; Lai et al., 2018), Equation (1) places the sources of the

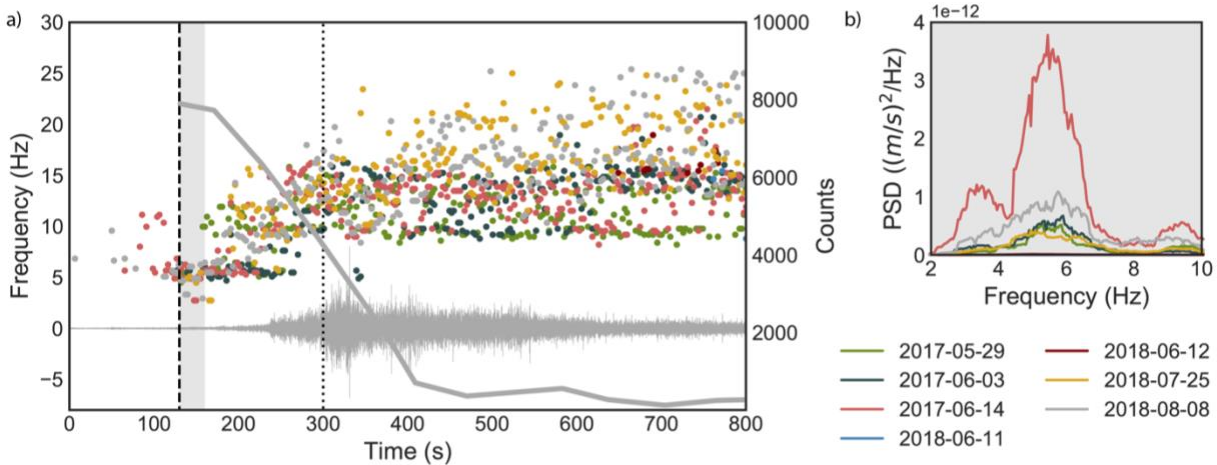


Fig. 4. (a) Peak frequencies for all events in 2017 and 2018, binned for time steps of 2.5 s (dots), together with geophone counts recorded at CD1 for August 8, 2018 event (grey line). The grey signal shows the waveform of the August 8, 2018 event recorded on station ILL12. The events were aligned according to the onset of the geophone measurements at CD1. The peak frequencies are plotted for power spectral densities that exceed $1 \times 10^{-13} (ms^{-1})^2 Hz^{-1}$. The shaded area shows the time span used to calculate the spectra in (b). The dashed line marks the onset of the geophone recordings at CD1 and the corresponding frequency drop to 5.5 Hz. The dotted line marks the approximate passage of the debris flow at ILL12 which corresponds to a change in frequency pattern. Note the increase in dominant frequencies after the passage of CD1 until passing station ILL12. (b) Spectra of all events 30 seconds after passing CD1. The spectra are smoothed with a 1 Hz running average. The June 14, 2017 event clearly shows the highest power spectral density at that time.

two dominant frequency bands of 5.5 Hz and 15 Hz at distances of about 1100 ± 500 m and 300 ± 150 m from ILL12, respectively. This corresponds to the distance between (a) the station and CD1, and (b) the smallest distance between the station and the channel, which lies for both cases within the uncertainties. Due to model simplifications and poorly constrained site effects, the distance is only a rough estimate. Nevertheless, it suggests that the main sources for the seismic waves recorded at ILL12 are the flow over the spillway at CD1 and the processes that happen at small distances from the station. Lai et al. (2018) use the continuous increase in peak frequencies to estimate flow velocity. At Illgraben, the two distinct dominant sources inhibit estimation of flow velocity, as the jump in frequency reflects the time when the dominance of the two signals changes, rather than a location of the flow front.

Next, we compare the different event spectra recorded at Station ILL12 when the flow fronts pass CD1 (Fig. 4b). The spectra are computed over 30s, and a running average of 1 Hz was applied. We assume that at these time intervals, the signals are dominated by seismic waves generated by boulder impacts at the base of the 48 m free fall at CD1. At this moment, projectile motion of the boulders implies that vertical flow (impact) velocities are the same for all events. Length of the front and width are therefore expected to be similar, assuming that the flow front impact lasts longer than the 30 s-long time window used to calculate the spectra. To only concentrate on the 5.5 Hz signals generated at CD1, the signal was filtered between 3 and 10 Hz. According to Equation (1), differences in spectra, in particular spectral amplitudes, are then attributable to grain size differences. The largest amplitude of power spectral density is generated by the event on June 14, 2017. Unfortunately, no video material is available for this event since it happened at night. Therefore, a cross validation to check whether the largest power is generated by larger boulder size in the debris-flow front, is not possible. When comparing the debris flow on May 29, 2017 with other events, one can observe that the energies are similar to the events on July 25 and August 8 in 2018. The videos indicate the presence of large boulders in all three flows, but a quantitative statement on the 94th percentile of the particle sizes is difficult. The small events in June 2018 show the lowest spectral energies, which suggests that particle sizes for these flows are substantially smaller than for other events. Analysis of the videos for the 2018 events has not yet been completed, but preliminary analysis suggests that these events might be debris floods rather than debris flows.

6. Conclusion

The source mechanism of seismic signals of debris flows is strongly dependent on particle sizes and topographic features of the flow path. Seismic studies of debris-flow dynamics and material composition should therefore not focus on the entire (temporally averaged) debris-flow seismograms, but on individual time windows. The spectral content of the signal can be dominated by large topographical features, such as the free fall behind a check dam in our case.



Fig. 5. Pictures of five debris flows at check dam 29 at the lowermost part of the torrent. Pictures of the events of June 3 and June 14, 2017 do not give any insight on particle sizes, as they happened during night time. The pictures in the first row show the large event on May 29, 2017 (left), and the event on August 8, 2017 (right) that has been used as an example in Fig. 2.

Large uncertainties of the seismic properties of the torrent catchment's sub-surface inhibit accurate models of the seismic propagation between flow front and recording unit. This complicates the interpretation of seismograms in terms of flow properties.

Acknowledgements

The project is funded by WSL's strategic initiative Climate Change Impacts on Alpine Mass Movements (CCAMM). FW's salary was funded by the Swiss National Science Foundation (GlaHMSeis Project PP00P2_157551). The municipality of Leuk and Anniviers generously provided permission and assistance for the seismometer deployment. We thank the Swiss Seismological Service who supported the project with seismic stations, real time data transfer and archiving facilities as well as manpower in the field. Alexandre Badoux and Christoph Graf assisted in the field campaign planning. We also thank the VAW and WSL personal, especially Martin Funk, for technical and scientific input and support in the field. The authors are grateful to Kate Allstadt and Velio Coviello for detailed and constructive reviews.

Online content

The data and code that was used in this study are available in the `deciphering_debris-flow_seismograms` git repository, https://github.com/michaelawenner/deciphering_debris-flow_seismograms

References

- Allstadt, K. E., Matoza, R. S., Lockhart, A., Moran, S. C., Caplan-Auerbach, J., Haney, M., ... & Malone, S. D., 2018, Seismic and acoustic signatures of surficial mass movements at volcanoes: *Journal of Volcanology and Geothermal Research*, v. 364, p. 76-106.
- Arattano, M., & Marchi, L., 2008, Systems and sensors for debris-flow monitoring and warning: *Sensors*, v. 8(4), p. 2436-2452.
- Badoux, A., Graf, C., Rhyner, J., Kuntner, R., & McArdell, B. W., 2009, A debris-flow alarm system for the Alpine Illgraben catchment: design and performance: *Natural hazards*, v. 49(3), p. 517-539.
- Bennett, G. L., Molnar, P., Eisenbeiss, H., & McArdell, B. W., 2012, Erosional power in the Swiss Alps: characterization of slope failure in the Illgraben: *Earth Surface Processes and Landforms*, v. 37(15), p. 1627-1640.
- Berger, C., McArdell, B. W., & Schlunegger, F., 2011, Direct measurement of channel erosion by debris flows, Illgraben, Switzerland: *Journal of Geophysical Research: Earth Surface*, v. 116(F1).
- Burtin, A., Bollinger, L., Vergne, J., Cattin, R., & Nábělek, J. L., 2008, Spectral analysis of seismic noise induced by rivers: A new tool to monitor spatiotemporal changes in stream hydrodynamics. *Journal of Geophysical Research: Solid Earth*, v. 113(B05301).
- Burtin, A., Hovius, N., McArdell, B. W., Turowski, J. M., & Vergne, J., 2014, Seismic constraints on dynamic links between geomorphic processes and routing of sediment in a steep mountain catchment: *Earth Surface Dynamics*, v. 2(1), p. 21-33.
- Burtin, A., Hovius, N., & Turowski, J. M., 2016, Seismic monitoring of torrential and fluvial processes: *Earth Surface Dynamics*, v. 4(2), p. 285-307.
- Christen, M., Kowalski, J., & Bartelt, P., 2010, RAMMS: Numerical simulation of dense snow avalanches in three-dimensional terrain: *Cold Regions Science and Technology*, v. 63(1-2), p. 1-14.
- Coviello, V., Arattano, M. and Turconi, L., 2015, Detecting torrential processes from a distance with a seismic monitoring network: *Natural Hazards*, v. 78(3), p. 2055-2080.

- Dammeier, F., Moore, J. R., Haslinger, F., & Loew, S., 2011, Characterization of alpine rockslides using statistical analysis of seismic signals: *Journal of Geophysical Research, Earth Surface*, v. 116(F4), p. 1-19.
- Deparis, J., Jongmans, D., Cotton, F., Baillet, L., Thouvenot, F., & Hantz, D., 2008, Analysis of rock-fall and rock-fall avalanche seismograms in the French Alps: *Bulletin of the Seismological Society of America*, v. 98(4), p. 1781-1796.
- Dietze, M., Turowski, J. M., Cook, K. L., & Hovius, N., 2017, Spatiotemporal patterns, triggers and anatomies of seismically detected rockfalls: *Earth Surface Dynamics*, v. 5(4), p. 757.
- Ekström, G., & Stark, C. P., 2013, Simple scaling of catastrophic landslide dynamics: *Science*, v. 339(6126), p. 1416-1419.
- Heck, M., Hammer, C., Herwijnen, A. V., Schweizer, J., & Fäh, D., 2018, Automatic detection of snow avalanches in continuous seismic data using hidden Markov models: *Natural Hazards and Earth System Sciences*, v. 18(1), p. 383-396.
- Hibert, C., Mangeney, A., Grandjean, G., & Shapiro, N. M., 2011, Slope instabilities in Dolomieu crater, Réunion Island: From seismic signals to rockfall characteristics: *Journal of Geophysical Research, Earth Surface*, v. 116(F4), p. 1-18.
- Hibert, C., Mangeney, A., Grandjean, G., Peltier, A., DiMuro, A., Shapiro, N. M., ... & Kowalski, P., 2017, Spatio-temporal evolution of rockfall activity from 2007 to 2011 at the Piton de la Fournaise volcano inferred from seismic data: *Journal of Volcanology and Geothermal Research*, v. 333, p. 36-52.
- Hürlimann, M., Rickenmann, D., & Graf, C., 2003, Field and monitoring data of debris-flow events in the Swiss Alps: *Canadian geotechnical journal*, v. 40(1), p. 161-175.
- Kean, J. W., Coe, J. A., Coviello, V., Smith, J. B., McCoy, S. W., & Arattano, M., 2015, Estimating rates of debris flow entrainment from ground vibrations: *Geophysical Research Letters*, v. 42(15), p. 6365-6372.
- Lai, V. H., Tsai, V. C., Lamb, M. P., Ulizio, T. P., & Beer, A. R., 2018, The Seismic Signature of Debris Flows: Flow Mechanics and Early Warning at Montecito, California: *Geophysical Research Letters*, v. 45(11), p. 5528-5535, doi: 10.1029/2018GL077683.
- Larose, E., Carrière, S., Voisin, C., Bottelin, P., Baillet, L., Guéguen, P., ... & Gimbert, F., 2015, Environmental seismology: What can we learn on earth surface processes with ambient noise?: *Journal of Applied Geophysics*, v. 116, p. 62-74.
- Mangeney-Castelnau, A., Bouchut, F., Vilotte, J. P., Lajeunesse, E., Aubertin, A., & Pirulli, M., 2005, On the use of Saint Venant equations to simulate the spreading of a granular mass: *Journal of Geophysical Research, Solid Earth*, v. 110(B9).
- Mangeney, A., Tsimring, L. S., Volfson, D., Aranson, I. S., & Bouchut, F. (2007). Avalanche mobility induced by the presence of an erodible bed and associated entrainment. *Geophysical Research Letters*, 34(22), doi: 10.1029/2007GL031348.
- Marchetti, E., Walter, F., Barfucci, G., Genco, R., Wenner, M., Ripepe, M., et al., 2019, Infrasound array analysis of debris flow activity and implication for early warning: *Journal of Geophysical Research: Earth Surface*, v. 124, doi: 10.1029/2018JF004785.
- McArdell, B. W., Bartelt, P., & Kowalski, J., 2007, Field observations of basal forces and fluid pore pressure in a debris flow: *Geophysical Research Letters*, v. 34(7), doi: 10.1029/2006GL029183.
- Norris, R. D., 1994, Seismicity of rockfalls and avalanches at three Cascade Range volcanoes: Implications for seismic detection of hazardous mass movements: *Bulletin of the Seismological Society of America*, v. 84(6), p. 1925-1939.
- Pierson, T. C., & Costa, J. E., 1987, A rheologic classification of subaerial sediment-water flows. Debris flows/avalanches: process, recognition, and mitigation: *Reviews in Engineering Geology*, v. 7, p. 1-12.
- Provost, F., Hibert, C., & Malet, J. P., 2017, Automatic classification of endogenous landslide seismicity using the Random Forest supervised classifier: *Geophysical Research Letters*, v. 44(1), p. 113-120.
- Schimmel, A., Hübl, J., McArdell, B. W., & Walter, F., 2018, Automatic Identification of Alpine Mass Movements by a Combination of Seismic and Infrasound Sensors: *Sensors*, v. 18(5), p. 1658.
- Schlunegger, F., Badoux, A., McArdell, B. W., Gwerder, C., Schnydrig, D., Rieke-Zapp, D., & Molnar, P., 2009, Limits of sediment transfer in an alpine debris-flow catchment, Illgraben, Switzerland: *Quaternary Science Reviews*, v. 28(11-12), p. 1097-1105.
- Suriñach, E., Vilajosana, I., Khazaradze, G., Biescas, B., Furdada, G., & Vilaplana, J. M., 2005, Seismic detection and characterization of landslides and other mass movements: *Natural Hazards and Earth System Science*, v. 5(6), p. 791-798.
- Tsai, V. C., Minchew, B., Lamb, M. P., & Ampuero, J. P., 2012, A physical model for seismic noise generation from sediment transport in rivers: *Geophysical Research Letters*, v. 39(2), doi: 10.1029/2011GL050255.
- Vilajosana, I., Suriñach, E., Abellán, A., Khazaradze, G., García, D., & Llosa, J., 2008, Rockfall induced seismic signals: case study in Montserrat, Catalonia: *Natural Hazards and Earth System Sciences*, v. 8(4), p. 805-812.
- Walter, F., Burtin, A., McArdell, B. W., Hovius, N., Weder, B., & Turowski, J. M., 2017, Testing seismic amplitude source location for fast debris-flow detection at Illgraben, Switzerland: *Natural Hazards and Earth System Sciences*, v. 17(6), p. 939-955.

Appendix A. Signals at other seismic stations

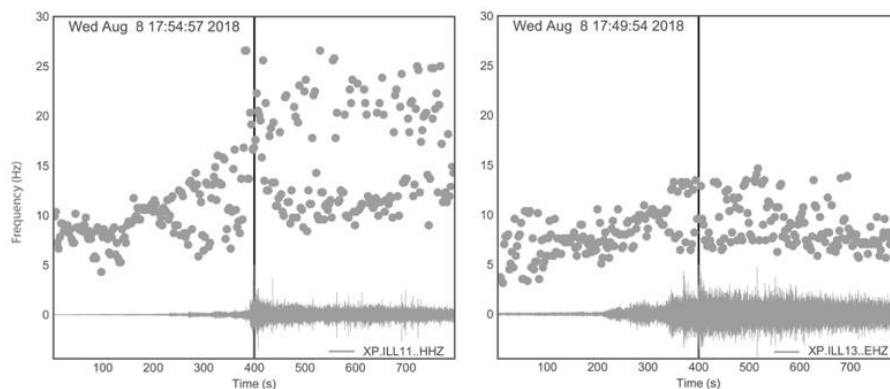


Fig. A1. Seismic signal and corresponding dominant frequencies of the August 8, 2018 event recorded at stations ILL11 and ILL13.

Experiments and Modeling

Reproducibility of debris-flow fan physical modeling experiments

Kailey Adams^{a,*}, Thad Wasklewicz^b, Tjalling de Haas^c, Scott Lecce^b, Paul Gares^b

^a Department of Earth Sciences, Montana State University, P.O. Box 173480, Bozeman, MT 59717-3480, USA

^b Department of Geography Planning and Environment, East Carolina University, Greenville, NC 27858, USA

^c Faculty of Geoscience, Universiteit Utrecht, Heidelberglaan 2, 3584 CS Utrecht, the Netherlands

Abstract

Debris-flow fans are common in steep mountainous terrain. The complexity of these environments makes it difficult to be onsite at the time of the debris flow, which has led many researchers to turn to physical models. While physical models have played an integral role in unraveling how alluvial fans have been developed, little work has been done to test and validate the approaches and results reported in physical models. Here, we replicated a debris-flow physical model developed at Utrecht University in a laboratory at East Carolina University (ECU). The ECU physical modeling experiment was done in an independent laboratory from the original study and was conducted with different equipment and different operators. Sediment size and water volume varied slightly from the original experiments. Fifty-six debris flows were released to form the ECU fan. Each debris flow was recorded with video. Terrestrial laser scanning recorded the topographic changes on the ECU fan throughout the experiment. Despite sediment size and water volume differences, ECU's physical model replicated the autogenic processes promoting flow avulsion patterns in a debris-flow fan with simulated unlimited accommodation space (the trap door in feeder channel and table edge did confine the maximum extent the fan could grow). These results corroborate previous findings from the Utrecht fan and support the repeatability of processes from the different models despite differences in the materials used as the debris-flow medium. Reproducibility also permits future collaborative efforts to run multiple concurrent physical modeling experiments to increase the sample size of the study populations on debris-flow processes and resulting forms.

Keywords: debris flow; runoff; alluvial fan; digital elevation model; autogenic processes

1. Introduction

Physical modeling is by no means a novel approach in alluvial fan research and can be traced back to the seminal works of Hooke (1967; 1968; Hooke and Rohrer, 1979) and Schumm (1977; Schumm et al., 1987). Early small-scale physical experiments demonstrated many of the fundamental features and processes (i.e., avulsions, lateral migration, channel entrenchment, channelization, and sheetflow) present in natural alluvial fans. Findings from the early experiments were often compared to field evidence, but the experiments themselves were not directly scalable to any specific natural alluvial fans. Paola et al. (2009) later showed that the morphodynamics active on experimental and real-world surfaces are often scale independent, which in turn has allowed many studies to invoke a similarity of processes and form approach to physical modeling. These findings provide a subsequent means to validate some of the earlier assertions made about the relations of natural alluvial fans and fans generated from physical model experiments.

A recent proliferation of studies using physical models has led to the observation of a wide array of processes and features on alluvial fans (Kim and Paola, 2007; Kim and Jerolmack, 2008; van Dijk et al., 2008, 2009, 2012; Hoyal and Sheets, 2009; Clarke et al., 2010; Reitz et al., 2010; Reitz and Jerolmack, 2012; Hamilton et al., 2013; Clarke, 2015; Eaton et al., 2017). While many studies have focused on fluvial processes, recent work has started to emphasize debris flow fan development (de Haas et al., 2015, 2016; 2018a). Significant advances have been made within this body of literature, but to date, little effort has been made to independently test the repeatability of results from physical models. This is a critical step in the progression of the field because not only are scientists verifying results and

* Corresponding author e-mail address: kailey.adams@student.montana.edu

methods, but validation of methods and findings permit researchers to address more in-depth questions. If physical models produce similar outcomes, then multiple concurrent simulations can be performed to expand the ability of scientists to provide deeper understandings of fan development. Multiple simulations run concurrently in various labs means more samples can be used to either refute or advance our current understanding of how processes and forms are changing, which has both scientific and applied implications. Here, we replicate the specification and procedures of a debris-flow fan physical modeling experiment described in de Haas et al. (2016) and qualitatively and quantitatively determine if the experimental details of the fans that develop and the findings are reproducible.

1.1. Prior physical modeling results from Utrecht experiments

De Haas et al. (2015; 2016; 2018a) designed and built an experimental debris-flow flume in which they examined runout, depositional mechanisms, deposit morphology and the impact of debris-flow magnitude-frequency distributions and autogenic processes on avulsion and debris-flow fan development in a setting with unlimited accommodation space. Details of the flume dimensions, operations, and data recording for the original simulations are thoroughly described in de Haas et al. (2015, 2016) and are described below, as our own experiment is designed to reproduce the original physical model and the debris-flow fan experiment of de Haas et al (2016). Therefore, our review touches on the key methodological and scientific findings from the experiments as they are critical from a comparative standpoint.

De Haas et al. (2016) found that debris-flow fans developing under constant formative processes evolve through phases of autogenic channelization, backfilling, and avulsion (Fig. 1). Fan development is limited by maximum possible debris-flow length, which depends on debris-flow volume and composition. Individual debris flows alternate between channelized within coarse-grained levees, resulting in distal deposition, and unchannelized forming short and wide deposits with limited runout. As flows become progressively short and wide they backfill the active channel by upstream migration of depositional lobes, until the channel is completely filled, and the flows avulse to a topographically favorable pathway. The characteristic fan shape is developed over multiple avulsion cycles that are driven by topographic compensation as the fan avulses toward the steepest flow path. The findings provide valuable insights into the processes governing the autogenic formation of debris-flow fans.

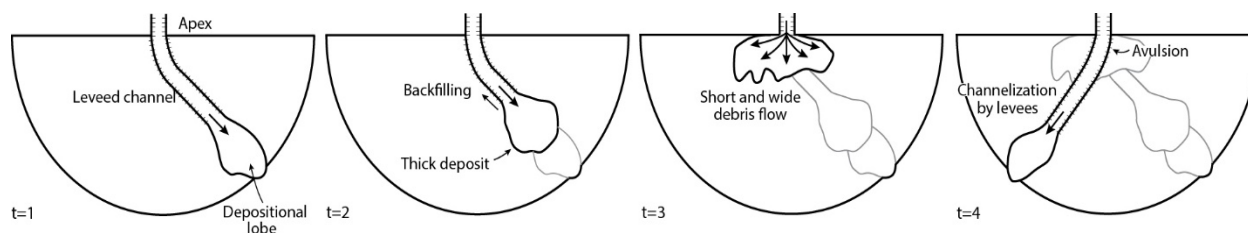


Fig. 1. Schematic of the autogenic cycle on a debris-flow fan (after De Haas et al., 2016). The presence of a channel results in distal deposition. Distal deposition reduces the distal channel gradient and flows start to retrograde over multiple debris flows. Flows become progressively short and wide, backfilling the channel. The next debris flows avulse and form a new channel along a topographically more favorable pathway.

2. Methods

2.1. Physical model

In the ECU experiment, a mixing tank agitates and releases a debris flow into a 2 m long flume, replicating a feeder channel positioned at a 30° angle and then onto the outflow plain (1.8 m by 1.8 m) (Fig. 2). Each debris flow mixture consisted of 1,650 g water, 288 g kaolinite clay, 1,010 g fine sand, 2,837 g coarse sand, and 865 g gravel. The sediment-water mixture varies slightly from de Haas et al. (2016) in that our debris-flow mixture contains 150 g more water. Additional water leads to longer runout and larger fans to enhance the potential for measuring multiple avulsions. The addition of 150 g of water was also validated by testing other sediment ratios and water volumes to determine which combination yielded morphologically and morphometrically similar results to de Haas et al. (2016).

Experimental fans were formed over many individual flows, which is consistent with alluvial fan development in natural settings. Each debris flow was created using the following process: (1) each portion of the debris mixture was weighed; sediment was roughly mixed by hand to ensure that clay did not stick to sides of the mixing bucket; (2) the

sediment mixture was poured into the opening of the mixing tank, followed by the water; (3) the total debris mixture was manually agitated for approximately 20 seconds; (4) the mixing tank gate was opened pneumatically via a manually operated switch; (5) debris was released into the flume and transported onto the outflow plain; (6) 1.5 seconds after the gate was opened, a hatch located in the bottom of the flume 0.75 m from the apex of the fan opened, preventing debris flow tailwater from entering the outflow plain and obscuring fan morphometry; and (7) the debris-flow deposits were allowed to dry for 2-3 hours with one portable fan directed at the fan apex and another directed at the active fan section.

2.2. Data recording techniques

A Leica P40 laser scanner in a nadir-looking position was placed above the outflow table (Fig. 2) and recorded high-resolution topography (3 mm horizontal point spacing) after every debris flow. Four black and white targets were affixed at each corner of the outflow table and four additional targets were dispersed evenly on the walls of the laboratory (Fig. 2). The nadir-looking positioning of the scanner allowed a single scan position per debris flow. Targets located on the corners of the outflow plain and laboratory walls were used in the registration process. All registration was conducted within Leica's Cyclone software in order to resolve any differences in the non-fixed scanner location and provide a consistent coordinate system relative to the first scan position.

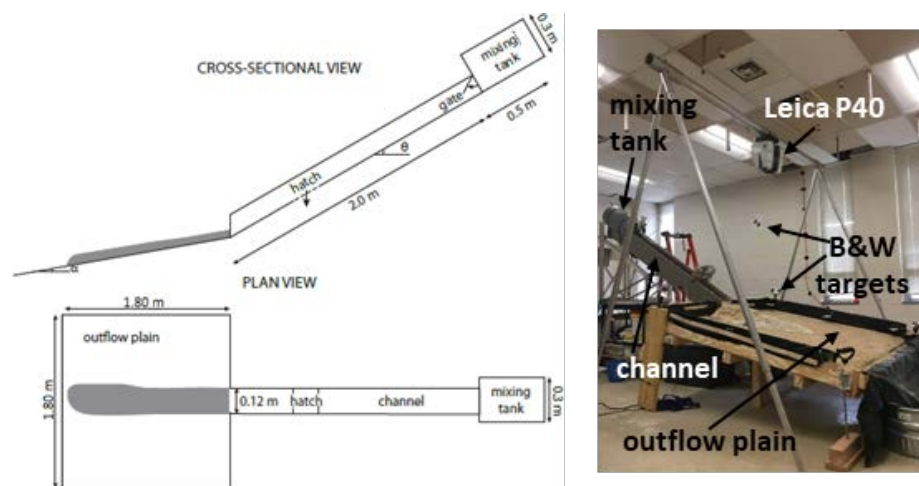


Fig. 2. Sketch of experimental laboratory setup [left, adapted from de Haas et al. (2016)] and picture of ECU laboratory setup (right).

2.3. Data processing and analysis

All analyses were conducted in ArcGIS. Registered point clouds were processed into 3 mm digital elevation models (DEMs) using LAStools (cf. Staley et al., 2014). DEMs were used to measure debris flow slope, thickness, and length. Fan slope was measured from the fan apex to the maximum active debris flow extent. Debris flow length was measured from the apex to the maximum flow runout position. Average debris-flow thickness was derived from elevation differences between pre- and post-topographic surfaces following the methodology of Wheaton et al. (2010). Outlines of individual debris flows were digitized from the topographic change detection (TCD) and subsequently used to extract elevations from the TCDs. This step was necessary to ensure that only elevation changes resulting from debris flows were included in calculations. Extracted elevations were then averaged to calculate average debris-flow thickness.

3. Results

3.1. Morphometric characterization of flows and fan

The experimental debris-flow fan was developed from 56 individual debris flows and the fan shape evolved as a result of two avulsion cycles. The experiment was terminated after flow 56 as debris backfilled the feeder channel and

debris flows could no longer reach the outflow plain. Debris-flow fan evolution occurred as a result of channelization, backfilling, and avulsion. These phases of development result directly from autogenic cycles as no external forcing mechanism was introduced over the duration of this experiment.

During channelization, flows were characterized by progressively longer deposits constrained by coarse-grained levees and punctuated by thick depositional lobes (Fig. 3A, Fig. 4A). Conversely, flows became increasingly short and wide during the backfilling phase (Fig. 3B, Fig. 4B). Average flow thickness ranged between approximately four and ten millimeters with no discernable correlation between flow thickness and autogenic phases.

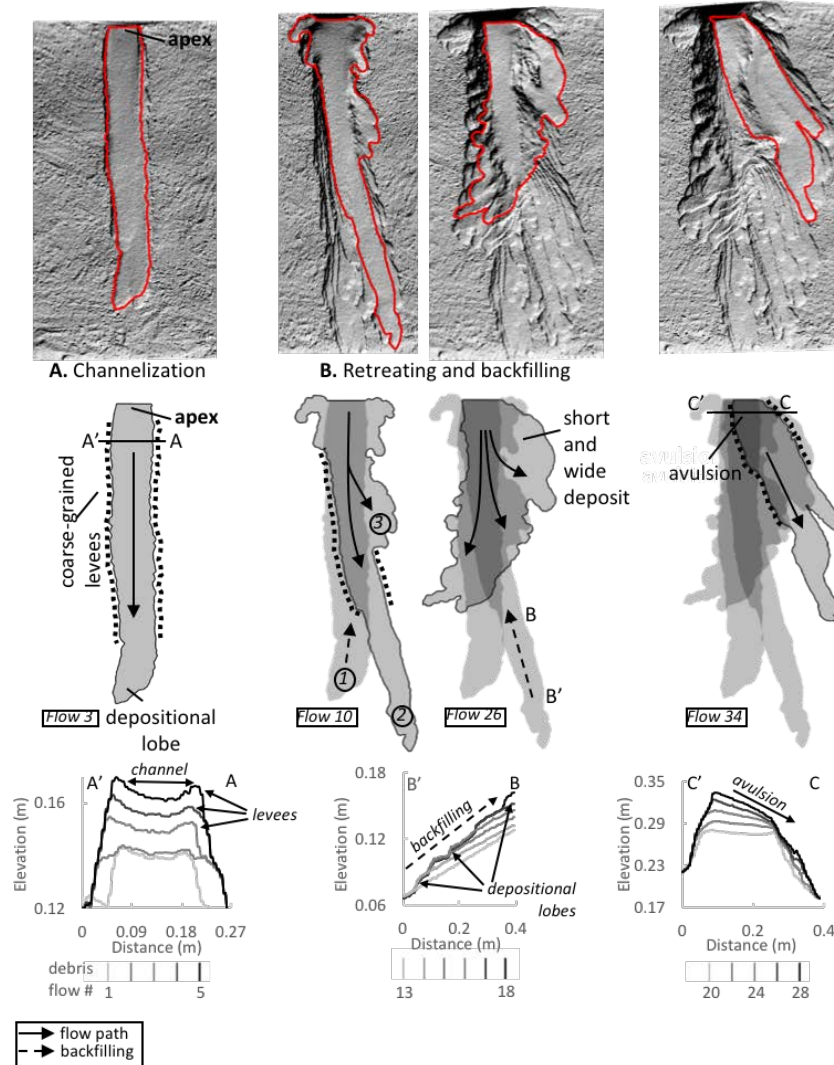


Fig. 3. Diagram showing the avulsion cycle of our experimental debris-flow fan and hillshades of selected debris flows (top panels). Three main processes characterize the avulsion cycles. First (A), flows are channelized between coarse-grained levees, punctuated by thick depositional lobes. Debris-flows retreat and backfill (B), ultimately resulting in short and wide deposits. Channel backfilling can occur multiple times over the course of one avulsion cycle [e.g., (B) channel (1) backfills as flow is diverted to channel (2). Channel (2) backfills as flow is diverted to newly forming channel (3)]. The channel is completely filled, and the fan avulses (C), whereby flow is diverted toward the steepest flow path and the cycle begins again. Cross sections (bottom panel) demonstrate the processes of the avulsion cycle illustrated and labeled in the middle panel.

The final fan surface was primarily covered by stacked depositional lobes and coarse-grained levees. Fan slope ranged between 6° and 20° , averaging approximately 12° (Fig. 4C). Fan slope varied with autogenic phases and between autogenic cycles. During the first cycle, channel slope generally increased as flows were channelized and decreased during backfilling. One exception, however, occurred during the phase of backfilling prior to the first avulsion (flows 21 – 28) when fan slope increased and decreased several times before the fan avulsed. Fan slope

during the second autogenic cycle was roughly constant throughout channelization and decreased during backfilling before the fan avulsed again (Fig. 4C).

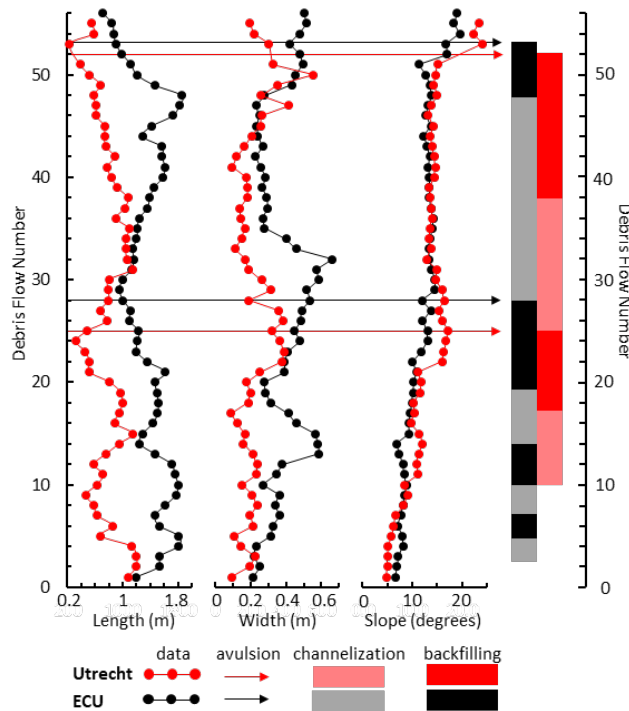


Fig. 4. Summary of debris-flow characteristics for the Utrecht and ECU fans. Light and dark boxes indicate phases of channelization and backfilling, respectively. Flow channelization starts at flow 2 in ECU fan and flow 10 in Utrecht fan. Arrows indicate instances of avulsion. (a) Debris-flow length measured from apex to maximum runout length. (b) Debris-flow width measured at the widest point of the flow. (c) Average fan slope measured along the active channel.

3.2. Autogenic behavior as reflected in deposition patterns

Both avulsion cycles observed on our experimental debris-flow fan exhibited flow channelization and channel backfilling. Fan avulsions occurred along the steepest flow path. First and second autogenic cycles were similar in length, consisting of 26 and 25 individual debris flows, respectively (Fig. 4). Minimum and maximum flow widths, lengths, and thicknesses were similar between the two distinct avulsion cycles. Additionally, debris-flow lengths and widths were inversely related, oscillating between long and narrow during phases of channelization and short and wide during phases of channel backfilling.

The phases of autogenic debris-flow fan evolution observed on our fan are demonstrated particularly well over the course of the first avulsion (Fig. 3). Flow channelization and channel backfilling alternated three times prior to the first fan avulsion phase at flow twenty-eight (Fig. 4). Flow channelization can be seen to develop as a result of constraining, coarse-grained lateral levees. Channel backfilling is shown as debris flows get progressively shorter, limited by the previous flow's thick, depositional lobe. The fan avulsion phase develops as the channel near the fan apex is backfilled and steepened until flow is preferentially diverted to the steepest flow path.

The major differences observed between the first and second autogenic cycles are in the number and length of sets of flow channelization and backfilling. The first autogenic cycle was initiated during flow three when flow was channelized following the first two debris flows. The first autogenic cycle consisted of three sets of channelization and backfilling. The second autogenic cycle exhibited only one set of channelization and backfilling. Following avulsion during flow twenty-eight, debris flows became progressively longer and slowly migrated from the left side of the fan. The sustained period of channelization observed during the second autogenic cycle compared to the first can be explained by debris-flow interaction with antecedent topography whereby debris flows preferentially deposited in topographically low areas. This resulted in debris flows that were progressively longer as previous deposit morphology guided, and effectively channelized, flow to the distal fan. Despite the channelizing effect of antecedent topography, individual flows in the second autogenic cycle still exhibited lateral levees typical of channelized flows.

4. Discussion

4.1. Replicability of debris flow physical models

The results of our experimental debris-flow fan are very similar to those reported in de Haas et al. (2016) despite the differences in experimental design. Both fans experienced two full autogenic avulsion cycles driven by phases of channelization, backfilling, and avulsion in a similar number of debris flows (55 and 56, respectively, Fig. 4). During these phases, both fans grew in length through flow channelization and expanded laterally as a result of preferential deposition toward the steepest flow path and topographically low areas. Individual debris flows on the ECU fan displayed the same morphology corresponding with these phases as those on the Utrecht fan (de Haas et al., 2016; Fig. 5). Additionally, all flows had well-defined depositional lobes; long, narrow flows constrained by coarse-grained lateral levees characterizing phases of channelization; and short, wide flows dominating during phases of backfilling. These experimentally observed patterns of debris-flow evolution also mimic those observed on natural debris flow fans (e.g., Suwa and Okuda, 1983; Imaizumi et al., 2016; Wasklewicz and Scheinert, 2016; de Haas et al., 2018b).

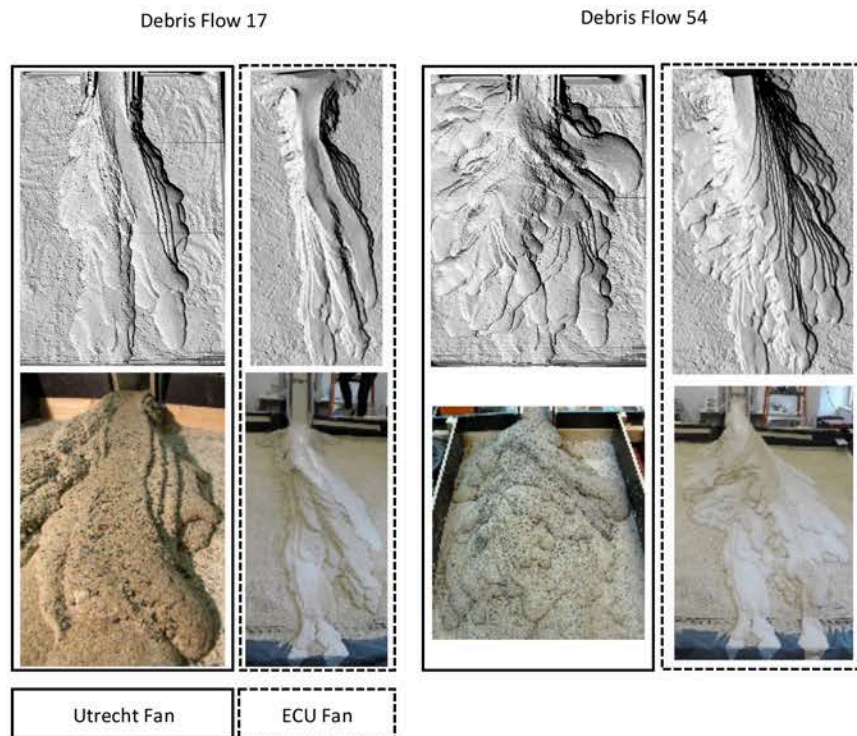


Fig. 5. Examples of fan morphology similarities between the Utrecht and ECU fans. Hillshades (top panel) and pictures (bottom panel) of debris flow numbers seven and fifty-four for the Utrecht and ECU fans.

The major differences between our results and those reported in de Haas et al. (2016) are the observed flow lengths, fan slopes, and deposit thicknesses. ECU debris flows were longer, fan slopes were gentler, and debris-flow deposits were less thick than those measured on the Utrecht fan. All of these differences can be attributed to the larger volume of water used to make the debris flows in the ECU fan. This assertion has been clearly articulated in previous research and graphically displayed in Fig. 6 of de Haas et al. (2015). Regardless of the aforementioned differences associated with the larger volume of water used in the ECU fan, the processes driving autogenic evolution of both debris-flow fans were the same and both fans were formed by morphologically similar debris flows.

4.2. Implications of the debris-flow physical model replicability for alluvial fan evolution

Our experiment provides a successful independent test of the results identified in de Haas et al. (2016). Reproducibility is clearly achieved here as we designed our own physical model in a different lab, used different researchers to conduct the experiments, and the media used (water and sediment) varied slightly from the original

design. All of these items meet the widely accepted standard for observation conditions having independent measurement in a different test/measurement facility with different operators using different equipment (ISO, 2017). The implications of these results are several fold. Church et al. (2017) highlighted the importance of reproducibility in the field of Earth sciences as a vital component preventing incorrect or biased inferences. Our findings provide strong support for the physical modeling methods presented by de Haas et al. (2016) and corroborate the role of autogenic processes in promoting flow avulsion that lead to semi-conical form of debris-flow fans with “unlimited” accommodation. Our findings provide further support to the broader literature for autogenic controls on alluvial fan development, especially as they relate to debris-flow fan formation in unlimited accommodation space. The achievement of reproducing the equipment, methods and findings of de Haas et al. (2016) speak broadly to the credibility of the approach to capturing 4D information on the debris flows and debris-flow fan dynamics, which provides greater confidence for the employment of this approach to advance science.

The ability to reproduce this type of experiment with an independent test also has implications for moving forward with physical modeling. This opens the opportunity to run large-scale experiments at many institutions and produce a large sample size. Information gathered from numerous simulations as opposed to a single simulation lends itself to unravelling process-form relations with a much greater degree of certainty because the scientific research would be based on multiple repeated results. This will provide the potential to advance conceptual and theoretical scientific knowledge and lead to more authoritative scientific communications. Advances might come in the areas of bajada development or limited accommodation space, impacts of base-level lowering, and interactions between endogenic and autogenic processes. There will also be opportunities to simulate multiple scenarios in landscape evolution. This would involve starting models at various evolutionary stages, or slightly modifying the flow characteristics or materials to examine how these differences would impact the outcome. What would normally take months or years to accomplish could be done in a matter of a month or less with multiple cooperative labs simulating the various aspects of the experiment. The ability to develop simulations in this fashion will provide a deeper understanding of the processes driving long-term landform and landscape development as well as begin to incorporate the role of and the impacts on humans in these experimental settings, in particular how built structures modify and are in turn impacted by debris flows. The ability to test multiple scenarios simultaneously would also provide scientists with the ability to inform numerical modeling and corroborate results that will assist the numerical modeling community to advance more rapidly. This synergy opens opportunities for integrative research whereby multiple labs could work cooperatively integrating numerical and physical models in a manner that could lead to greater insights into bajada formation, role of base-level in fans, external and internal factors leading to fan forms and how fans impacted humans living on and adjacent to fans.

5. Conclusions

The use of physical models to study processes acting on the Earth’s surface has helped to advance our knowledge of a myriad of geomorphological, scientific, and engineering questions. However, heretofore independent physical modeling experiments of debris-flow fans have seldom been designed with the goal of reproducing or validating the previous modeled experiments. Our findings, based upon a physical debris-flow fan model designed by and the associated experimental results reported in de Haas et al. (2016), provide clear evidence for the reproducibility of the previous simulations, despite experimental design differences. Our debris-flow fan evolved by channelization, backfilling, and avulsion of many individual debris flows, displaying the same scale-independent morphology of natural debris-flow fans. These results not only corroborate previous findings specific to autogenic debris-flow fan evolution, but they speak to the importance and value of replicating physical modelling experiments. The ability to reproduce physical modelling experiments could foster collaborations between research scientists from different laboratories internationally to advance theoretical and applicable knowledge.

Acknowledgements

We would like to extend our thanks to Gene Oakley, Trades Technician in the Department of Physics at ECU, for his invaluable design and machining of the ECU mixing tank, support, pneumatically driven gate, and flume. This experiment could not have been accomplished without his expertise and craftsmanship. William Holland, Electronics Specialist in the Department of Physics at ECU, helped with the electronics and timer for the hatch in the flume. We would also like to thank Mr. Rob Howard, research scientist in the Department of Geography, Planning and

Environment at ECU, for his assistance with data collection logistics. The space, computing, data storage, and funding for this research were supplied by the Terrain Analysis Lab (TAL) at ECU.

References

- Church, M.A., Dudill, A.R., Frey, P., and Venditti, J.G., 2017, Testing Reproducibility in Earth Sciences. In AGU Fall Meeting Abstracts.
- Clarke, L.E., 2015, Experimental alluvial fans: Advances in understanding of fan dynamics and processes. *Geomorphology*, v. 244, p. 135-145.
- Clarke, L., Quine, T., and Nicholas, A., 2010, An experimental investigation of autogenic behaviour during alluvial fan evolution. *Geomorphology*, v. 115, p. 278-285.
- de Haas, T., Braat, L., Leuven, J.R., Lokhorst, I.R., and Kleinhans, M.G., 2015, Effects of debris flow composition on runout, depositional mechanisms, and deposit morphology in laboratory experiments. *Journal of Geophysical Research: Earth Surface*, v. 120, no. 9, p. 1949-1972.
- de Haas, T., van den Berg, W., Braat, L., and Kleinhans, M.G., 2016, Autogenic avulsion, channelization and backfilling dynamics of debris - flow fans. *Sedimentology*, vol. 63, no. 6, p. 1596-1619.
- de Haas, T., Kruijt, A., and Densmore, A.L., 2018a, Effects of debris-flow magnitude-frequency distribution on avulsions and fan development. *Earth Surface Processes and Landforms*, v. 43, p. 2779 - 2793.
- de Haas, T., Densmore, A.L., Stoffel, M., Suwa, H., Imaizumi, F., Ballesteros-Cánovas, J. A., and Wasklewicz, T., 2018b, Avulsions and the spatio-temporal evolution of debris-flow fans. *Earth-Science Reviews*, v. 177, p. 53-75.
- Eaton, B., MacKenzie, L., Jakob, M. and Weatherly, H., 2017, Addressing Erosion Hazards due to Floods on Fans: Physical Modelling and Application to Engineering Challenges: *Journal of Hydraulic Engineering*, v. 143, no. 8, p. 0401721.
- Hamilton, P., B., Strom, K., and Hoyal, D., 2013, Autogenic incision-backfilling cycles and lobe formation during the growth of alluvial fans with supercritical distributaries. *Sedimentology*, v. 60, p. 1498-1525.
- Hooke, R.L., 1967, Processes on arid-region alluvial fans. *The Journal of Geology*, p. 438-460.
- Hooke, R.L., 1968, Steady-state relationships on arid-region alluvial fans in closed basins. *American Journal of Science*, v. 266, no. 8, p. 609-629.
- Hooke, R.B., and Rohrer, W.L., 1979, Geometry of alluvial fans: Effect of discharge and sediment size. *Earth Surface Processes*, v. 4, no. 2, p. 147-166.
- Hoyal, D.C.J.D., and Sheets, B.A., 2009, Morphodynamic evolution of experimental cohesive deltas. *Journal of Geophysical Research: Earth Surface*, v. 114(F2).
- Imaizumi, F., Trappmann, D., Matsuoka, N., Tsuchiya, S., Ohsaka, O., and Stoffel, M., 2016, Biographical sketch of a giant: deciphering recent debris-flow dynamics from the Ohya landslide body (Japanese Alps). *Geomorphology*, v. 272, p. 102-114.
- ISO, 2017, Guidance for the use of repeatability, reproducibility and trueness estimates in measurement uncertainty evaluation. ISO 21748:2017, International Organization for Standardization, p. 38.
- Kim, W., and Paola, C., 2007, Long-period cyclic sedimentation with constant tectonic forcing in an experimental relay ramp. *Geology*, v. 35, no. 4, p. 331-334.
- Kim, W., and Jerolmack, D.J., 2008, The pulse of calm fan deltas. *The Journal of Geology*, v. 116, no. 4, p. 315-330.
- Paola, C., Straub, K., Mohrig, D., and Reinhardt, L., 2009, The "unreasonable effectiveness" of stratigraphic and geomorphic experiments. *Earth-Science Reviews*, v. 97, no. 1, p. 1-43.
- Reitz, M.D., Jerolmack, D.J., and Swenson, J.B., 2010, Flooding and flow path selection on alluvial fans and deltas. *Geophysical Research Letters*, v. 37, no. 6., p. Citation L06401.
- Reitz, M.D., and Jerolmack, D.J., 2012, Experimental alluvial fan evolution: Channel dynamics, slope controls, and shoreline growth. *Journal of Geophysical Research: Earth Surface*, v. 117(F2).
- Schumm, S.A., 1977, *The Fluvial System*. John Wiley and Sons, New York.
- Schumm, S.A., Mosley, P.M., and Weaver, P.H., 1987, *Experimental Fluvial Geomorphology*. John Wiley & Sons, New York.
- Staley, D.M., Wasklewicz, T.A. and Kean, J.W., 2014, Characterizing the primary material sources and dominant erosional processes for post-fire debris-flow initiation in a headwater basin using multi-temporal terrestrial laser scanning data. *Geomorphology*, v. 214, p. 324-338.
- Suwa, H., and Okuda, S., 1983, Deposition of debris flows on a fan surface, Mt. Yakedake, Japan. *Zeitschrift für Geomorphologie NF Supplementband 46*, p. 79-101.
- Van Dijk, M., Postma, G., and Kleinhans, M.G., 2008, Autogenic cycles of sheet and channelised flow on fluvial fan-deltas. *River, Coastal, and Estuarine Morphodynamics*: London, Taylor and Francis Group, p. 823-828.
- Van Dijk, M., Postma, G., and Kleinhans, M.G., 2009, Autocyclic behaviour of fan deltas: an analogue experimental study. *Sedimentology*, v. 56, no. 5, p. 1569-1589.
- Van Dijk, M., Kleinhans, M.G., Postma, G., and Kraal, E., 2012, Contrasting morphodynamics in alluvial fans and fan deltas: effect of the downstream boundary. *Sedimentology*, v. 59, no. 7, p. 2125-2145.
- Wasklewicz, T., and Scheinert, C., 2016, Development and maintenance of a telescoping debris flow fan in response to human-induced fan surface channelization, Chalk Creek Valley natural debris flow laboratory, Colorado, USA. *Geomorphology*, v. 252, p. 51-65.
- Wheaton, J.M., Brasington, J., Darby, S.E., and Sear, D.A., 2010, Accounting for uncertainty in DEMs from repeat topographic surveys: improved sediment budgets. *Earth Surface Processes and Landforms*, v. 35, no. 2, p. 136-156.

Influence of momentum correction factor and friction factor on flow models of debris flow related to flow surface deformation

Muneyuki Arai^{a,*}

^aDepartment of Civil Engineering, Meijo University, Tempaku-ku, Nagoya, 468-8502, Japan

Abstract

Intermittent debris-flow surges may be considered as roll wave phenomenon of shallow water flow that naturally develop in the mountain basins. The shape of the water surface with discontinuous depth change is one manifestation of flow wave phenomena. Here we obtained a wave equation representing the wave phenomenon of shallow water flow by using the Laplace equation, the bottom condition, a surface conservation condition, a flow surface fluctuation condition, and the perturbative expansion method. The derived equation is a kind of KdV-Burgers equation in which a nonlinear term includes a momentum correction factor β , a dissipation term includes a friction factor f' and a third term does not include either dispersion terms. The derived equation offers an explanation of the discontinuity of the water surface in shallow water flow that may be useful for debris flow modeling.

Keywords: Intermittent debris-flow surges, roll waves, KdV-Burgers equation, friction factor, flow model

1. Introduction

The intermittent surge phenomenon in steep mountain channels has been observed in China for more than 20 years (DPRI, et.al., 1999). In recent years many intermittent surge flows have been also recorded in the European Alps using advanced systems (Huebl and Kaitna, 2010). Based on hydraulic theory these intermittent surges can be modeled as a kind of roll wave that emerge from flow instabilities (Arai, Huebl and Kaitna, 2013). In a pioneering study Dressler (Dressler, 1949) first showed that an occurrence condition of roll waves in shallow water can be derived from the divergence condition of the water surface equation. Early studies were directed to laminar flows that were easy to analyze, and subsequently Needham (Needham and Merkin, 1984) and Merkin (Merkin and Needham, 1986) also analyzed turbulent flows. In addition, Sandro (Sandro, 2011) studied roll waves of non-Newtonian, dilatant fluid flows. Arai et.al. (2013) studied the occurrence condition roll wave for arbitrary flow models.

Kadomtsev-Petriashvili (Kadomtsev and Petviashvili, 1970) derived a KdV wave equation with surface tension taking into account the wave motion of the shallow water flow. This equation is called the Kadomtsev-Petriashvili equation, or the KP equation. However, Miles (1976) pointed out the need for consideration of the bottom friction. Hunter and Verden-Broke (1983a) also pointed out that this equation is not valid for a long wave situation. Arai (2017) provides a wave equation considering a long wave situation including bottom friction in shallow water flow.

In this study, a wave equation is derived including the momentum correction factor β and the friction factor f' , which expresses the characteristics of the respective constitutive fluid model, and clarify how β and f' are involved in the wave equation.

2. Governing Equations

In the following the derivation of a wave equation for (surging) flow with a sudden depth change in an inclined channel is summarized. The fluid is assumed incompressible and non-rotational, thus $\text{div } \vec{v} = 0$, $\text{curl } \vec{v} = 0$. The velocity

* Corresponding author e-mail address: arai@meijo-u.ac.jp

potential ϕ is defined in flow direction x , y and the flow depth takes the direction y (Fig. 1). Consequently the Laplace equation is given with

$$\phi_{xx} + \phi_{yy} = 0 \quad (1)$$

In the following, expressions of differentiation are indicated by subscripts, for example, $\partial^2\phi/\partial x^2 = \phi_{xx}$.

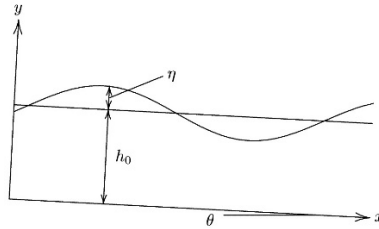


Fig. 1. Coordinate system

Equation (1) is obtained from uncompressed and non-rotating conditions of the fluid. Using the Laplace equation for the governing equation means that the flow field is a potential flow.

For the condition at the flow bottom ($y = -h_0$), the vertical velocity component v is 0 at the bottom,

$$v = \phi_y = 0, \quad (y = -h_0). \quad (2)$$

The condition under which the deformation of the water surface coincides with the movement of a water volume element on the surface is represented by the expression $D(y - \eta)/Dt = 0$, where $\eta(x, t)$ is the fluctuation component from the average water depth h_0 , D is the differential sign, and t is time. It is $dy/dt = v = \phi_y$ from the flow velocity v in the y direction, and $dx/dt = u = \phi_x$ from the flow velocity u in the x direction. From these, the expression $D\eta/Dt = \partial\eta/\partial t + \partial\eta/\partial x dx/dt = \eta_t + \eta_x\phi_x$ can be obtained. The condition that the deformation of the water surface coincides with the movement of the water volume element on the surface is given by the following equation:

$$\phi_y - \eta_t - \phi_x\eta_x = 0, \quad (y = 0). \quad (3)$$

The Bernoulli equation is subsequently used for modeling the water surface fluctuation condition in the derivation of the wave equation in the shallow water. The wave equation is obtained by using the water surface fluctuation conditions based on the motion equation for shallow water flow. However, the resulting expression is not ideal to discuss the differences in for different fluid models. Here, the wave equation is obtained by using the water surface fluctuation condition including the momentum correction coefficient β and the friction factor f' which expresses the characteristics of an arbitrary fluid model as shown in the following equation.

$$\phi_t + \frac{1}{2}(2\beta - 1)(\phi_x)^2 - g \sin \theta x + g \cos \theta h + \frac{f' u_0}{2 h_0} \phi + (\beta - 1) \frac{u_0}{h_0} \int \phi_x \eta_x dx = 0 \quad (4)$$

In this wave equation, β : momentum correction factor, f' : friction factor, g : acceleration due to gravity, θ : slope angle of the channel, and $h = h_0 + \eta$: depth of flow. The first term on the left side represents the velocity potential in dependence of time, the second the kinetic energy, the third is the potential energy, the fourth is the specific energy of the flow surface, the fifth is the loss of energy due to basal friction, and the sixth term is the additional energy fluctuation depth including a non-uniform velocity profile. The momentum correction factor β and the friction factor f' characterize the flow mechanics.

In a uniform rectangular cross section with channel width B wider than the water depth h , the one dimensional motion and mass conservation equation for shallow water flows considering sudden water surface fluctuations are as follows.

$$u_t + \beta u u_x - (\beta - 1) \frac{u}{h} h_t - g \sin \theta + g \cos \theta h_x + \frac{f' u^2}{2 h} = 0 \quad (5)$$

$$h_t + (hu)_x = 0 \quad (6)$$

On left side of Equation (5), the first term is an acceleration term, the second an advection term, the third a velocity distribution term, the fourth a gravity force term, the fifth a gradient surface term and the sixth term represents friction at bottom.

Special consideration is given to the sixth term u^2/h . Here, the depth h and the velocity u are denoted as $h = h_0 + h'$, $u = u_0 + u'$, where, h_0 is the mean depth, u_0 is the mean velocity, and h' and u' are fluctuating components of h_0 and u_0 . h' and u' are much smaller than h_0 and u_0 , and are regarded as $(h'/h_0)^2 \ll 1$, $(u'/u_0)^2 \ll 1$ and $h'/h_0 - u'/u \ll 1$. From these considerations, u^2/h can be approximated as follows.

$$\frac{u^2}{h} = \frac{u_0}{h_0} u \quad (7)$$

Substituting Equation (6) into the third term on the left side of Equation (5) and substituting Equation (7) for the sixth term yields,

$$u_t + \frac{1}{2}(2\beta - 1)(u^2)_x - g \sin \theta + g \cos \theta h_x + \frac{f' u_0}{2 h_0} u + (\beta - 1) \frac{u_0}{h_0} u h_x = 0 \quad (8)$$

It is $u = \phi_x$ from the velocity potential ϕ . ϕ has continuity for x and t , and it is $u_t = (\phi_x)_t = (\phi_t)_x$. Also, from $h = h_0 + \eta$, it is $h_x = \eta_x$. Considering these, integration of Equation (8) for x yields,

$$\phi_t + \frac{1}{2}(2\beta - 1)(\phi_x)^2 - g \sin \theta x + g \cos \theta h + \frac{f' u_0}{2 h_0} \phi + (\beta - 1) \frac{u_0}{h_0} \int \phi_x \eta_x dx = E_0 \quad (9)$$

Here, E_0 is an integral constant. E_0 represents the potential ϕ as a reference, and when $E_0 = 0$ is given as the initial condition, it becomes Equation (4).

3. Derivation of Wave Equation by Reductive Perturbation Method

3.1. Non-dimensional basic equations and perturbation expansion

Let the representative length be the mean depth h_0 , and the representative velocity be the phase velocity v_{p0} of the Gerdner-Morikawa(G-M) transformation of Equation (10).

$$\xi = \epsilon^{1/2}(x - v_{p0}t), \quad \tau = \epsilon^{3/2}t \quad (10)$$

ϵ is a minute parameter in the perturbation development. From these, we define dimensionless variables as follows and prime the dimensionless variables.

$$\phi' = \phi/(h_0 v_{p0}), \quad x' = x/h_0, \quad y' = y/h_0, \quad t' = (v_{p0}/h_0)t, \quad \eta' = \eta/h_0. \quad (11)$$

And the dimensionless variables ξ' , τ' of ξ , τ are as follows.

$$\xi' = \epsilon^{1/2}(x' - t'), \quad \tau' = \epsilon^{3/2}t' \quad (12)$$

Therefore, the dimensionless equations of Equation (1) to (4) are

$$\phi'_{x'x'} + \phi'_{y'y'} = 0, \quad (13)$$

$$\phi'_{y'} = 0, \quad (y' = -1), \quad (14)$$

$$-\phi'_{y'} + \eta'_{t'} + \phi'_{x'} \eta'_{x'} = 0, \quad (y' = 0), \quad (15)$$

$$\phi'_{\tau'} + \frac{1}{2}(2\beta - 1)(\phi'_{x'})^2 - c_0'^2 \tan \theta x' + c_0'^2(1 + \eta') + \frac{f'}{2}u_0'c_0'\phi' + (\beta - 1)u_0'c_0' \int \phi'_{x'} \eta'_{x'} dx' = 0 \quad (16)$$

Here,

$$u_0' = u_0/c_0, \quad c_0' = c_0/v_{p0}, \quad c_0 = \sqrt{gh_0 \cos \theta}. \quad (17)$$

Furthermore, the dimensionless variable of the perturbation expansion is defined as

$$\eta' = \eta/h_0, \quad \eta^{(1)} = \eta^{(1)}/h_0, \quad \eta^{(2)} = \eta^{(2)}/h_0, \quad \dots, \quad (18)$$

$$\phi' = \phi/(h_0 v_{p0}), \quad \phi^{(1)} = \phi^{(1)}/(h_0 v_{p0}), \quad \phi^{(2)} = \phi^{(2)}/(h_0 v_{p0}), \quad \dots. \quad (19)$$

The dimensionless perturbation expansion of η' and ϕ' is expressed as

$$\eta' = \epsilon \eta^{(1)}(\xi', \tau') + \epsilon^2 \eta^{(2)}(\xi', \tau') + \dots, \quad (20)$$

$$\phi' = \epsilon^{1/2} \phi^{(1)}(\xi', y', \tau') + \epsilon^{3/2} \phi^{(2)}(\xi', y', \tau') + \dots. \quad (21)$$

Also, the Taylor expansion by Boussinesq on ϕ' in neighborhood η' of $y' = 0$ is

$$\phi'(\xi', \eta', \tau') = \phi'(\xi', 0, \tau') + \eta' \phi'(\xi', 0, \tau')_{y'} + \frac{\eta'^2}{2} \phi'(\xi', 0, \tau')_{y'y'} + \dots. \quad (22)$$

From these, the perturbation expansions of the dimensionless fundamental equations are expressed as follows.

The Laplace expression of Equation (13) is

$$\phi'_{x'x'} + \phi'_{y'y'} = \epsilon^{3/2} \phi'^{(1)}_{\xi'\xi'} + \epsilon^{5/2} \phi'^{(2)}_{\xi'\xi'} + \dots + \epsilon^{1/2} \phi'^{(1)}_{y'y'} + \epsilon^{3/2} \phi'^{(2)}_{y'y'} + \dots = 0. \quad (23)$$

The bottom condition of Equation (14)

$$\phi'_{y'} = \epsilon^{1/2} \phi'^{(1)}_{y'} + \epsilon^{3/2} \phi'^{(2)}_{y'} + \dots = 0. \quad (24)$$

A flow surface condition of Equation (15)

$$\begin{aligned} -\phi'_{y'} + \eta'_{\tau'} + \phi'_{x'} \eta'_{x'} &= -\phi'_{y'} - \epsilon^{1/2} \eta'_{\xi'} + \epsilon^{3/2} \eta'_{\tau'} + \epsilon \phi'_{\xi'} \eta'_{\xi'} \\ &= -\epsilon^{1/2} \phi'^{(1)}_{y'} - \epsilon^{3/2} \eta'^{(1)}_{\xi'} \phi'^{(1)}_{y'y'} - \dots - \epsilon^{3/2} \phi'^{(2)}_{y'} - \epsilon^{5/2} \eta'^{(1)}_{\xi'} \phi'^{(2)}_{y'y'} - \dots - \epsilon^{5/2} \phi'^{(3)}_{y'} - \epsilon^{7/2} \eta'^{(1)}_{\xi'} \phi'^{(3)}_{y'y'} - \\ &\dots - \epsilon^{3/2} \eta'^{(1)}_{\xi'} - \epsilon^{5/2} \eta'^{(2)}_{\xi'} - \dots + \epsilon^{5/2} \eta'^{(1)}_{\tau'} + \epsilon^{7/2} \eta'^{(2)}_{\tau'} + \dots + \epsilon^{5/2} \phi'^{(1)}_{\xi'} \eta'^{(1)}_{\xi'} + \epsilon^{7/2} \phi'^{(1)}_{\xi'} \eta'^{(2)}_{\xi'} + \dots = 0 \end{aligned} \quad (25)$$

The condition of the water surface fluctuation in Equation (16) can be expressed as

$$\begin{aligned} \phi'_{\tau'} + \frac{1}{2}(2\beta - 1)(\phi'_{x'})^2 - c_0'^2 \tan \theta x' + c_0'^2 + c_0'^2 \eta' + \frac{f'}{2}u_0'c_0'\phi' + (\beta - 1)u_0'c_0' \int \phi'_{x'} \eta'_{x'} dx' \\ = -\epsilon \phi'^{(1)}_{\xi'} - \epsilon^2 \phi'^{(2)}_{\xi'} - \dots + \epsilon^2 \phi'^{(1)}_{\tau'} + \epsilon^3 \phi'^{(2)}_{\tau'} + \dots + \frac{1}{2}(2\beta - 1) \left\{ \epsilon^2 (\phi'^{(1)}_{\xi'})^2 + 2\epsilon^3 \phi'^{(1)}_{\xi'} \phi'^{(2)}_{\xi'} + \right. \\ \left. \epsilon^4 (\phi'^{(2)}_{\xi'})^2 + \dots \right\} - c_0'^2 \tan \theta x' + c_0'^2 + c_0'^2 (\epsilon \eta'^{(1)} + \epsilon^2 \eta'^{(2)} + \dots) + \frac{f'}{2}u_0'c_0' \left\{ \epsilon^{1/2} \phi'^{(1)} + \right. \\ \left. (\epsilon^{3/2} \eta'^{(1)} + \epsilon^{5/2} \eta'^{(2)} + \dots) \phi'^{(1)}_{y'} + \dots + \epsilon^{3/2} \phi'^{(2)} + (\epsilon^{5/2} \eta'^{(1)} + \epsilon^{7/2} \eta'^{(2)} + \dots) \phi'^{(2)}_{y'} + \dots + \epsilon^{5/2} \phi'^{(3)} + \right. \end{aligned}$$

$$\left(\epsilon^2 \eta'^{(1)} + \epsilon^2 \eta'^{(2)} + \dots \right) \phi'_{y'}^{(3)} + \dots \Big\} + (\beta - 1) u_0' c_0' \left\{ \epsilon^2 \int \phi'_{\xi'}^{(1)} \eta'^{(1)}_{\xi'} d\xi' + \epsilon^3 \int \phi'_{\xi'}^{(1)} \eta'^{(2)}_{\xi'} d\xi' + \epsilon^3 \int \phi'_{\xi'}^{(2)} \eta'^{(1)}_{\xi'} d\xi' + \epsilon^4 \int \phi'_{\xi'}^{(2)} \eta'^{(2)}_{\xi'} + \dots \right\} = 0. \quad (26)$$

3.2. ϵ -order equations in perturbation expansions and derivation of wave equation

A necessary condition to satisfy the perturbation expansion equation of the basic equation is to satisfy homogeneous equations concerning the same order of ϵ . Therefore, the equations for same order of ϵ are as follows.

1) $O(\epsilon^0)$ order;

$$\tan \theta = \frac{1}{x'} \quad (27)$$

2) $O(\epsilon^{1/2}, \epsilon^1)$ order;

Homogeneous equations of the order of $\epsilon^{1/2}$ and ϵ^1 are as follows from Equation (23) to (26).

From Equation (23), (24), (25),

$$\phi'_{y'y'}^{(1)} = 0, \quad \phi'_{y'}^{(1)} = 0, (y' = -1), \quad \phi'_{y'}^{(1)} = 0, (y' = 0), \quad (28), (29), (30)$$

and from Equation (26),

$$-\phi'_{\xi'}^{(1)} + c_0'^2 \eta'^{(1)} + \frac{f'}{2} u_0' c_0' \phi'^{(1)} = 0. \quad (31)$$

3) $O(\epsilon^{3/2}, \epsilon^2)$ order;

Homogeneous equations of the order of $\epsilon^{3/2}$ and ϵ^2 are as follows.

From Equation (23), (24), (25),

$$\phi'_{\xi'\xi'}^{(1)} + \phi'_{y'y'}^{(2)} = 0, \quad \phi'_{y'}^{(2)} = 0, (y' = -1), \quad -\eta'^{(1)} \phi'_{y'y'}^{(1)} - \phi'_{y'}^{(2)} - \eta'_{\xi'}^{(1)} = 0, (y' = 0), \quad (32), (33), (34)$$

and from Equation (26),

$$-\phi'_{\xi'}^{(2)} + \phi'_{\tau'}^{(1)} + \frac{1}{2} (2\beta - 1) \left(\phi'_{\xi'}^{(1)} \right)^2 + c_0'^2 \eta'^{(2)} + \frac{f'}{2} u_0' c_0' \left(\eta'^{(1)} \phi'_{y'}^{(1)} + \phi'^{(2)} \right) + (\beta - 1) u_0' c_0' \int \phi'_{\xi'}^{(1)} \eta'^{(1)}_{\xi'} d\xi' = 0. \quad (35)$$

4) $O(\epsilon^{5/2}, \epsilon^3)$ order;

Homogeneous equations of the order of $\epsilon^{5/2}$ and ϵ^3 are as follows.

From Equation (23), (24),

$$\phi'_{\xi'\xi'}^{(2)} + \phi'_{y'y'}^{(3)} = 0, \quad \phi'_{y'}^{(3)} = 0, (y' = -1), \quad (36), (37)$$

from Equation (25),

$$-\eta'^{(2)} \eta'_{y'y'}^{(1)} - \eta'_{y'y'}^{(2)} - \phi'_{y'}^{(3)} - \eta'_{\xi'}^{(2)} + \eta'_{\tau'}^{(1)} + \phi'_{\xi'}^{(1)} \eta'_{\xi'}^{(1)} = 0, \quad (38)$$

and from Equation (26),

$$-\phi'_{\xi'}^{(3)} + \phi'_{\tau'}^{(2)} + (2\beta - 1) \phi'_{\xi'}^{(1)} \phi'_{\xi'}^{(2)} + c_0'^2 \eta'^{(3)} + \frac{f'}{2} u_0' c_0' \left(\eta'^{(2)} \phi'_{y'}^{(1)} + \eta'^{(1)} \phi'_{y'}^{(2)} + \phi'^{(3)} \right) + (\beta - 1) u_0' c_0' \left\{ \int \phi'_{\xi'}^{(1)} \eta'^{(2)}_{\xi'} d\xi' + \int \phi'_{\xi'}^{(2)} \eta'^{(1)}_{\xi'} d\xi' \right\} = 0. \quad (39)$$

In this case, the equation of ϵ relating to the water surface fluctuation and Equations relating to $\eta^{(1)}$ are obtained using Equations (27) to (39). Equation (27) represents the relationship of the slope gradient and is not used in the derivation of $\eta^{(1)}$. Also, the equation relating to $\eta^{(1)}$ is obtained from Equation (28) to (38), and therefore Equation (39) is not used.

Equation (31) is an approximate expression and transposes terms as follows:

$$\phi'_{\xi'}^{(1)} - \frac{f'}{2} u_0' c_0' \phi'^{(1)} = c_0'^2 \eta'^{(1)} \tag{40}$$

This is the first order differential equation of ξ' with respect to $\phi'^{(1)}$. Solving $\phi'^{(1)}$ for ξ' yields

$$\phi'^{(1)} = e^{-h} \left[\int e^h c_0'^2 \eta'^{(1)} d\xi' + C \right], \quad \text{here, } h = \int \left(-\frac{f'}{2} u_0' c_0' \right) d\xi' = -\frac{f'}{2} u_0' c_0' \xi',$$

where, C is the integral constant.

In the target flow, the friction factor $f' \ll 1$. u_0' corresponds to the Froude number when the phase velocity v_{p0} equals the wave velocity of the long wave and is $10 > u_0' \geq 1$ in the target flow. c_0' is $c_0' \approx 1$ when the phase velocity v_{p0} is close to the wave velocity of the long wave. The possible range of the value of ξ' is $\xi' = 0 \sim 1$ for one wavelength. Hence, since $(f'/2)u_0'c_0'\xi' \ll 1$, we can regard $e^{|h|} \approx 1$. From these, the approximate solution of Equation (40) is

$$\phi'^{(1)} \approx \int c_0'^2 \eta'^{(1)} d\xi' + C$$

The derivative for ξ' in the above equation is as follows.

$$\phi'_{\xi'}^{(1)} = c_0'^2 \eta'^{(1)} \tag{41}$$

This is an approximate expression of Equation (31). From this, Equation (41) is used instead of Equation (31). From the above relational equations, we obtain the equation of $\eta'^{(1)}$. The derivation process is very complicated and therefore only the results are shown.

Here, $\eta'^{(1)}$ is represented by η' .

$$\eta'_{\tau'} + \frac{1}{2} \{ (2\beta + 1)c_0'^2 + (\beta - 1)u_0'c_0' \} \eta' \eta'_{\xi'} - \frac{1}{4} \left(\frac{1}{c_0'^2} - \frac{1}{2} \right) f' u_0' c_0' \eta'_{\xi' \xi'} + \frac{1}{2} \left(\frac{2+c_0'^4}{2c_0'^2} - \frac{3}{2} \right) \eta'_{\xi' \xi' \xi'} = 0. \tag{42}$$

Equation (42) is a type of KdV-Burgers equation. From this result, it can be seen that the momentum correction factor β indicating the influence of the flow velocity distribution is related to the nonlinear term of the second term, and the friction factor f' is related to the dissipation term of the third term. In addition, the coefficient of the dispersion term of the fourth term does not include β and f' , which means that the dispersion term is not influenced by the flow velocity distribution and flow resistance.

4. Discussion

From the results obtained above we conclude that different flow resistance laws result in different predictions for the surge waveform development. Here we investigate the outcomes for the laminar and the turbulent flow laws, as well as situation of a linear velocity profile. For laminar flow the momentum correction factor β is about $\beta = 1.2$ and for turbulent flows $\beta = 1.1$. In case the flow velocity distribution is linear, $\beta = 1$, the coefficient of the nonlinear second term on the left side of Equation (42) reduces to $(3/2)c_0'^2$. The waveform of the discontinuous water depth change is formed when the phase velocity v_{p0} is the long wave velocity c_0 , that is, $c_0' = c_0/v_{p0} = 1$. At this time, the ratio r_β between the coefficient of the nonlinear term of the second term on the left side of the Equation (42) and the case of $\beta = 1$ is

$$r_\beta = \frac{1}{3}\{(2\beta + 1) + (\beta - 1)u_0'\} \tag{43}$$

At $v_{p0} = c_0$, u_0' means Froude number. The waveform of roll wave is generated when the phase velocity v_{p0} is the long wave velocity $v_{p0} = c_0$. Therefore, the Froude number is $F_r = 1$, or in the vicinity thereof. Fig.2 shows the relationship between r_β and β in Equation (43) in the case of $u_0' = 1.0$ and 1.2 corresponding to the Froude number. From this result, within the range of $\beta = 1.0 \sim 1.2$, the nonlinear term of the Equation (42) has the same degree of change as $\beta = 1$, and the influence of β is small. As will be described later, in the Burgers equation where the waveform of the roll wave is formed, the coefficient of the nonlinear term does not affect its waveform formation. That is, β does not influence the formation of the roll wave form.

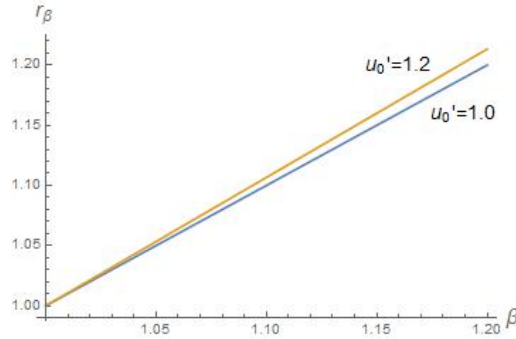


Fig. 2. Relation between r_β and β

When the phase velocity v_{p0} is the wave velocity c_0 of the long wave, that is, $c_0' = 1$, the coefficient of the fourth term of Equation (42) becomes 0, and the dispersion term is ignored. Hence,

$$\eta'_{\tau'} + \frac{1}{2}\{(2\beta + 1) + (\beta - 1)u_0'\}\eta'\eta'_{\xi'} - \frac{1}{8}f'u_0'\eta'_{\xi'\xi'} = 0 \tag{44}$$

The friction factor f' in the third term on the left side is a function of water depth. When water depth is taken constant f' is an average constant value. The composition formula of the flow model is usually obtained in a state of steady and uniform flow. However, it is not clear how these expressions can be applied in a situation where the water depth violently fluctuates like a roll wave. For this reason, we use a Vedernikov type resistance law to understand the influence on waveform formation due to the difference in resistance law rather than using individual rheology models. This equation is a generalized expression of a Chezy type equation, a Manning equation, a laminar flow equation and the like. The flow velocity U is expressed by

$$U^a = r_v R^{(1+b)} \sin \theta, \tag{45}$$

here, U = velocity, R = hydraulic radius, r_v = coefficient, and a, b = constant value. The constants a and b are expressed as $a = 2, b = 0$ in the case of the Chezy equation, $a = 2, b = 1/3$ in the case of Manning expression, $a = 1, b = 1$ in the case of the laminar flow law. The friction factor f' can be expressed by the following equation using Equation (45).

$$\frac{f'}{2} = \frac{u_*^2}{u_0^2} = r_v^{-2/a} g(\sin \theta)^{1-2/a} h_0^{1-2(1+b)/a} \tag{46}$$

where, $u_* = \sqrt{gh_0 \sin \theta}$ and $R \approx h_0$. Substituting Equation (46) into Equation (44) and transforming the equation we find

$$\eta'_{\tau'} + a_1 \eta'\eta'_{\xi'} = \mu \eta'_{\xi'\xi'}, \tag{47}$$

where,

$$a_1 = \frac{1}{2}\{(2\beta + 1) + (\beta - 1)u_0'\}, \quad \mu = \frac{1}{8}f'u_0' = \frac{1}{4}r_v^{-\frac{2}{a}}g(\sin \theta)^{1-\frac{2(1+b)}{a}}u_0'. \quad (48), (49)$$

Equation (47) is a type of Burgers equation and the solution of the Burgers equation is well established. The relationship of β and f' in equation (47) will be described below.

From the Cole-Hopf transformation, the nonlinear Burgers equation is transformed into a linear heat conduction equation that can be solved. Then, the solution is obtained by inverse transformation of Cole-Hopf transformation to yield solution of the original Burgers equation. The Cole-Hopf transform is defined as follows using $z(\xi', \tau')$.

$$\eta' = -\frac{2}{a_1}\mu(\ln z)_{\xi'} = -\frac{2}{a_1}\mu\frac{1}{z}z_{\xi'} \quad (50)$$

Using this Cole-Hopf transformation, Equation (47) becomes a thermal conduction equation of the following equation.

$$z_{\tau'} = \mu z_{\xi'\xi'} \quad (51)$$

In the above equation, a_1 in Equation (47) disappears and only μ remains. μ represents the thermal conductivity or diffusion coefficient of the conduction equation. From this, it can be shown that the friction factor f' represents the rate of change of the waveform shape.

In order to find the relationship between the momentum correction factor β and the friction factor f' , a simple analysis example will be shown. We describe the analytic solution under the fixed boundary condition and the sinusoidal initial condition in period $2l(-l \leq \xi' \leq l)$. The boundary condition is $\eta' = 0$ at $\xi' = -l, \xi' = l$ respectively. That is,

$$\eta'(-l, \tau') = 0, \quad \eta'(l, \tau') = 0 \quad (52)$$

As shown in Fig. 3, the initial condition is a sinusoidal wave of amplitude a_0 and period $T = 2l$. That is,

$$\eta'(\xi', 0) = \frac{a_0}{2}\sin(2\pi\xi'/T) = \frac{a_0}{2}\sin(\pi\xi'/l) \quad (53)$$

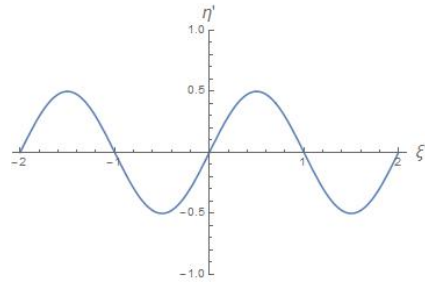


Fig. 3. The initial condition of η'

When the initial condition of Equation (53) is transformed by Cole-Hopf transformation Expression (50), it is as follows

$$z(\xi', 0) = \exp\left(\frac{lr}{\pi} \cos \frac{\pi\xi'}{l} + \frac{lr}{\pi}\right), \quad \text{where, } r = \frac{1}{2a_1\mu} \frac{a_0}{2} \quad (54), (55)$$

The boundary condition is given by $\xi' = -l, \xi' = l$ in Equation (54). That is,

$$z(-l, 0) = z(l, 0) = 1 \quad (56)$$

For the initial condition of Equation (54), (55), and the boundary condition of Equation (56), we can solve the heat conduction Equation (51) using a Fourier series expansion and obtain the solution of Equation (47) from the inverse transformation of Cole-Hopf transformation as follows.

$$\eta'(\xi', \tau') = \left[\frac{a_0}{2r} \sum_{n=1}^{\infty} \left\{ \frac{n\pi}{l^2} \int_{-l}^l \exp\left(\frac{lr}{\pi} \cos \frac{\pi v}{l} + \frac{lr}{\pi}\right) \cos \frac{n\pi v}{l} dv \right\} \sin\left(\frac{n\pi \xi'}{l}\right) e^{-\lambda_n^2 \tau'} \right] \times \left[e^{\frac{lr}{\pi}} J_0\left(\frac{lr}{\pi}\right) + \sum_{n=1}^{\infty} \left\{ \frac{1}{l} \int_{-l}^l \exp\left(\frac{lr}{\pi} \cos \frac{\pi v}{l} + \frac{lr}{\pi}\right) \cos \frac{n\pi v}{l} dv \right\} \cos\left(\frac{n\pi \xi'}{l}\right) e^{-\lambda_n^2 \tau'} \right]^{-1} \quad (57)$$

where, $\lambda_n = \frac{\sqrt{\mu n \pi}}{l}$, ($n = 1, 2, \dots$), $J_0(\cdot)$: 1st kind Bessel function (58)

Equation (57) represents the deformation process of the water surface deformation η' with time evolution τ' . Since the initial magnitude a_0 and the period T cannot be theoretically determined, the case of $a_0 = 1, l = 1$ will be described as a calculation example. Also, there is a limit to the deformation of η' due to time evolution, and its shape is retained in later time evolution after that. Fig.4 shows the case of $r = 3, 30$ for the dimensionless time $\tau' = 3$. The horizontal axis is ξ' and the vertical axis is η' . The waveform of the rounded shape in the figure is the case of $r = 5$ and the triangular waveform is the calculation result in the case of $r = 30$. r is related to a_1 and μ as shown in Equation (55). a_1 and μ are related to β and f' as shown in Equation (48) and (49). Therefore, when the value of r is small, a_1 and μ have large values. Conversely, when r is large, a_1 and μ have small values. That is, when the friction factor f' is small, at the same time development τ' , the waveform of the discontinuous water depth change is obtained. However, when f' has a large value, we find that the discontinuous shape waveform does not develop. As in this analysis example, the influence due to the difference in the fluid model is related to the deformation rate of the fluid accompanied by the flow and the magnitude of the energy dissipation, meaning that it influences the deformation process with time.

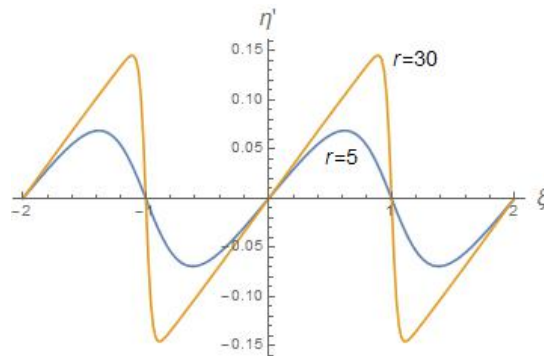


Fig. 4. Calculation example of η' ($a_0 = 1, l = 1, \tau' = 3, r = 3, r = 30$)

5. Conclusions

In this contribution a wave equation is presented to model the water surface variation in shallow fluid flows, allowing for predicting the development of roll wave in an inclined channel. Since the model was derived as a general equation including a momentum correction factor β and a friction factor f' , it can be applied to different flow models, which might be therefore be useful for debris flow applications. Through concrete analysis examples of the Burgers equation which can express discontinuous water depth change in the derived wave equation, β and f' showed to influence waveform formation. Although β does not contribute much to the deformation of the waveform, f' is related to the deformation rate, f' develops to a discontinuous water depth change when f' is small, but does not develop when f' is large. These things mean the following. The flow surface shape with discontinuous depth change of intermittent debris-flow surge is not directly influenced by the fluid model of debris-flow, but is affected by the value of friction factor f' based on the fluid model. In other words, when f' becomes small, that is, when r of equation (55) exceeds 30, irrespective of the difference in fluid model, the flow is a surge flow with discontinuous depth change.

Acknowledgements

I would like to thank Professor Johannes Huebl, Dr. Roland Kaitna of University of Natural Resources and Life Sciences Vienna (Boku) and Professor Hajime Nakagawa of Kyoto University in carrying out this research. And this work was supported by the Research Institute for Mathematical Sciences, a Joint Usage/Research Center located in Kyoto University.

References

- Arai M., Huebl J. and Kaitna R., 2013, Occurrence conditions of roll waves for three grain-fluid models and comparison with results from experiments and field observation, *Geophysical Journal International*, Vol.195, Issue 3, pp.1464-1480 (doi:10.1093/gji/ggt352).
- Arai, M., 2017, Wave equation and Some solutions on intermittent debris flow, *International Journal of Erosion Control Engineering*, Vol.10, No.1, pp.39-46.
- Disaster Prevention Research Institute, Kyoto University, and Institute of Mountain Hazards and Environment, Chinese Academy of Sciences and Ministry of Water Conservancy, 1999, Japan-China Joint Research on the Mechanism and the Countermeasures for the Viscous Debris Flow, 206p.
- Dressler, R. F., 1949, Mathematical solution of the problem of roll-waves in inclined open channels, *Communication on Pure and Applied Mathematics*, Vol.II, No.2/3.
- Huebl J. and Kaitna R., 2010, 1999 Sediment delivery from the Lattenbach catchment by debris floods and debris flows, *Abstracts of European Geosciences Union General Assembly 2010*, EGU2010-10585.
- Hunter, J. K. and Vanden-Brock, J. M., 1983a, Solitary and periodic gravity-capillary waves of finite amplitude, *J. Fluid Mech.*, 134, 205-19.
- Kadomtsev, B. B. and Petviashvili, V. L., 1970, On the stability of solitary waves in weakly dispersive media, *Dokl. Akad. Nauk. SSSR*, 192, 753-6(1970), *Sov. Phys. Dok.*, 15, 539-41.
- Merkin, J. H. and Needham, D. J., 1986, An infinite period bifurcation arising in roll waves down an open inclined channel, *Proc. R. Soc. London*, A405, pp.103-116.
- Miles, J. W., 1976, Korteweg-de Vries equation modified by viscosity, *Phys. Fluids*, 19, 1063. Sandro, L., 2011, Roll waves on a shallow layer of a dilatant fluid, *European Journal of Mechanics B/Fluids*, 30, pp.57-67.
- Needham, D. J. and Merkin, J. H., 1984, On roll waves down an open inclined channel, *Proc. R. Soc. London*, A394, pp.259-278.

Constraining parameter uncertainty in modeling debris-flow initiation during the September 2013 Colorado Front Range storm

Rex L. Baum^{a,*}, Caroline R. Scheevel^{a,b}, Eric S. Jones^a

^a*U.S. Geological Survey, Box 25046, M.S. 966, Denver, Colorado 80225, USA*

^b*Present address: BGC Engineering Inc., 701 12th Street, Suite 211, Golden, Colorado 80401, USA*

Abstract

The occurrence of debris flows during the September 2013 northern Colorado floods took the emergency management community by surprise. The September 2013 debris flows in the Colorado Front Range initiated from shallow landslides in colluvium. Most occurred on south- and east-facing slopes on the walls of steep canyons in crystalline rocks and on sedimentary hogbacks. Previous studies showed that most debris flows occurred in areas of high storm-total rainfall and that strength added by tree roots accounts for the low number of landslides in densely forested areas. Given the lack of rainfall thresholds for debris flow occurrence in northern Colorado, we want to parameterize a numerical model to assess potential for debris flows in advance of heavy rainfall. Natural Resources Conservation Service (NRCS) soil mapping of the area, supplemented by laboratory testing and field measurements, indicates that soil textures and hydraulic properties of landslide source materials vary considerably over the study area. As a step toward modeling storm response, available soil and geologic mapping have been interpreted to define zones of relatively homogeneous properties. A new, simplified modeling approach for evaluating model input parameters in the context of slope and depth of observed debris flow source areas and recorded debris-flow inducing rainfall helps narrow the range of possible parameters to those most likely to produce model results consistent with observed debris flow initiation. Initial results have narrowed the strength parameters to about one third of possible combinations of cohesion and internal friction angle and narrowed hydraulic conductivity to a range spanning slightly more than one order of magnitude.

Keywords: Debris flow; Rainfall-induced landslides; Numerical models; Parameter uncertainty; Colorado Front Range

1. Introduction

Since the 1970s, approaches for debris flow warning have relied on empirical rainfall thresholds (Guzzetti et al., 2008; Baum and Godt, 2010). Empirical thresholds are limited by the availability and completeness of records of past rainfall and debris-flow occurrence. In recent years, efforts have been undertaken to derive warning thresholds for landslides and debris flows using process-based models to overcome this limitation, especially for areas where debris flows occur infrequently (Godt et al., 2008; Thomas et al., 2018). Although geologists have known for decades (Hansen, 1976) where to expect debris flows in the Colorado Front Range, this risk was not well appreciated by residents and government officials. They were thus unprepared when rainfall on 9–13 September 2013 triggered at least 1,138 debris flows in a 3430 km² area of the Colorado Front Range (Coe et al., 2014). Debris flows occurred over an extremely broad range of elevation, geology, and ecosystems. The 2013 debris-flow event makes the Front Range area a prime candidate for testing warning approaches using process-based models, due to the scarcity of historical data for developing empirical thresholds and the geologic, topographic, and ecosystem diversity of the affected area. This paper explores approaches for narrowing parameter uncertainty for such models.

* Corresponding author e-mail address: baum@usgs.gov

2. Study area

The September 2013 debris flows in the Colorado Front Range initiated from shallow landslides in colluvium (Coe et al., 2014). Most occurred on south- and east-facing slopes on the walls of steep canyons in crystalline rocks and on sedimentary hogbacks. Slopes at the source areas ranged from 26° to 43°. Only 3% of the slides initiated in channels, whereas 48% initiated on open slopes and 49% in swales. An area of about 1350 km² in the northern part of the Colorado Front Range (Fig. 1) was selected for more detailed analysis and numerical modeling (Alvioli and Baum, 2016a, 2016b). This area encompasses three-fourths of the September 2013 debris flows. The area spans five ecosystem zones (Coe et al., 2014), and the dominant vegetation is coniferous forest. Vegetation density, soil development, and regolith production are dependent on slope aspect, particularly on north- versus south-facing slopes in the montane zones. North-facing slopes have a higher density of trees and more leached, colder soils than south-facing slopes (Birkeland et al., 2003; Coe et al., 2014). Rengers et al. (2016) showed that most debris flows occurred in areas of low tree density and high storm-total rainfall. McGuire et al. (2016) concluded that strength added by tree roots, rather than rainfall interception or permeability differences between densely and sparsely forested slopes, accounts for the low number of landslides in densely forested areas.

Field observations in the study area indicate that most debris-flow source areas have thin colluvium or regolith, commonly <1 m, but as deep as 5 m (Coe et al., 2014). Regolith in source areas at higher elevations in the western part of the study area was commonly 3-5 m deep. Large areas of exposed bedrock also exist throughout the area.

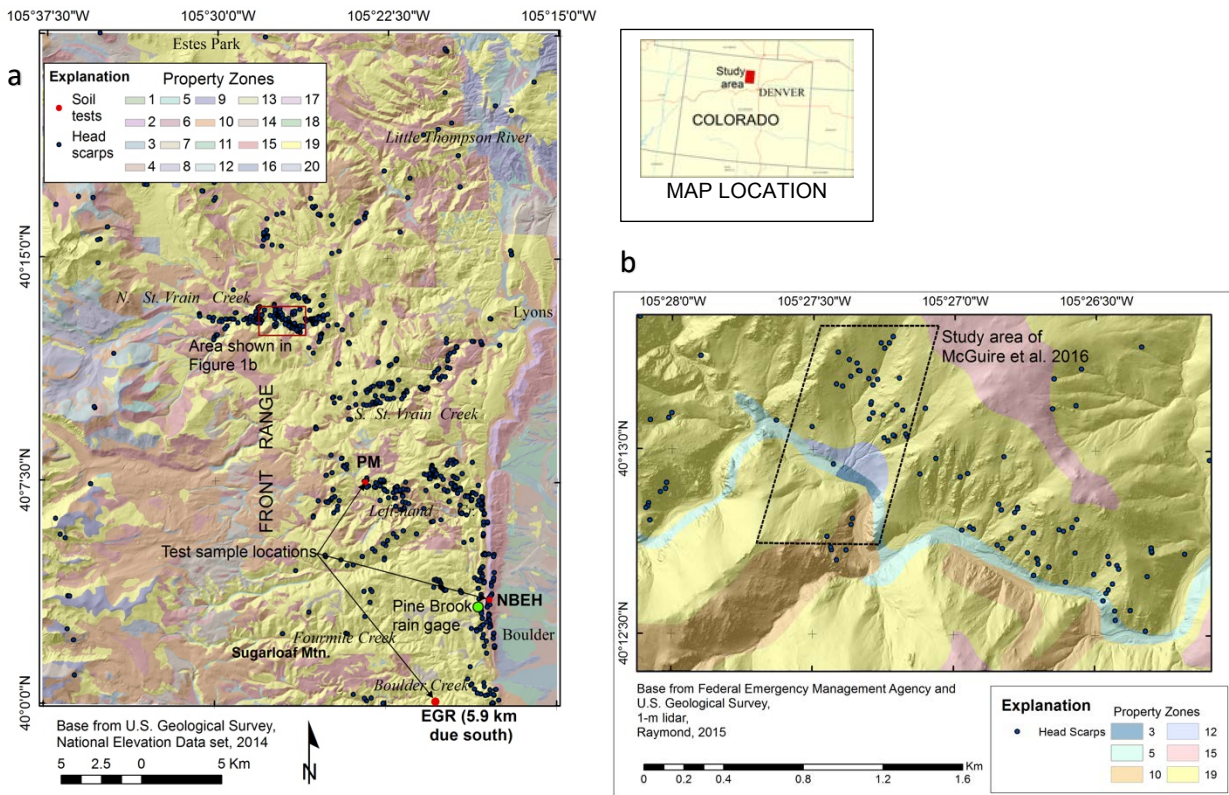


Figure 1. Maps of study area. (a) Map showing debris flow head scarps, sample and test locations (EGR, East of Gross Reservoir; NBEH, North Boulder East Hogback; PM, Porphyry Mountain), and property zones (areas where model parameters fall in specific ranges, see Table 1). Map area is the same as that used by Alvioli and Baum (2016a). (b) Map showing detail of study area (see red rectangle in a).

The entire study area (Fig. 1a) is too large to depict at a scale suitable for describing parameter variability and uncertainty; so a smaller area of high landslide density is depicted in Fig. 1b. It is a subset of the study area chosen to illustrate parameter variability in an area of steep canyon walls underlain by crystalline bedrock. South-facing slopes are grassy and covered with a smooth blanket of colluvium everywhere except on rugged rock outcrops jutting from the canyon walls. In the focus area, interquartile depth to bedrock on steep slopes ranged from 0.43 to 0.61 m on south-

facing slopes and 0.48 to 0.73 m on forested north-facing slopes (McGuire et al., 2016). The bedrock weathers to porous, permeable, gravelly, sandy loam.

3. Methods

Methods were developed for this study with the goal of defining parameter distributions that could be used in a spatially distributed process-based model such as TRIGRS (Baum et al., 2010; Alvioli and Baum, 2016a, 2016b). Sampling and testing properties of materials in a statistically valid manner over a large geographic area is time-consuming and costly. Therefore, considering the spatial variability of surficial deposits and weathered bedrock throughout the study area, we wish to define ranges of parameters that can result in similar outcomes for a set of modeled sequences of events that simulate rainfall conditions that either have or have not historically resulted in debris flows. For purposes of this study, model parameters were assigned to categories affecting either infiltration and pore pressure rise or slope stability. Parameters controlling the infiltration process vary with depth below the ground surface and include hydraulic properties of the soil: the hydraulic conductivity, K_s , porosity, n , parameters describing the shape of the soil-water characteristic curve, including the height of capillary rise, α , as well as the rate at which water is supplied at the ground surface. Ground deformation leading to slope instability is linked to rainfall infiltration through induced pore pressure rise and a common input parameter, depth to bedrock, where strength increases and K_s decreases. Parameters controlling slope stability include depth, pore pressure, slope angle, density, and the soil strength and deformation properties. The following paragraphs describe methods used to define map units (property zones) that have relatively uniform parameters for the purpose of modeling rainfall infiltration and initiation of shallow landslides on steep hillsides.

Soil mapping and databases published by the U.S. Department of Agriculture's Natural Resources Conservation Service (NRCS) indicate a significant range in the textures (particle-size distributions) and hydraulic properties of soils in the study area (USDA, 2005). In addition, detailed geologic mapping of the area provides lithologic information that can be used to extrapolate characteristics of thin soils present in areas mapped by the NRCS as exposed bedrock from nearby areas mapped as soil and underlain by similar bedrock. In previous studies (Godt et al., 2008), incorporating the spatial distribution of soil types and properties into models of infiltration and slope stability has improved their accuracy and is likely to do so in the Front Range study area as well.

3.1. Field and Laboratory testing

Disturbed and minimally disturbed samples of silty gravelly sand and gravelly fine sand were collected at two sites underlain by igneous intrusive rock (EGR and PM, Fig. 1a). Field-measured bulk density was used to reconstitute disturbed samples to field density for testing. The Colorado School of Mines and U.S. Geological Survey joint geotechnical laboratory conducted direct-shear tests using a procedure described by Likos et al. (2010). Values of α and K_s were measured using the TRIM method (Wayllace and Lu, 2012; Lu and Godt, 2013). Mini Disk infiltration tests for K_s were conducted at EGR and PM and at a site underlain by sedimentary rock (NBEH, Fig1a, Table 2).

3.2. Spatial distribution of the hydraulic and soil strength parameters

The TRIGRS program requires several input parameters to model infiltration and slope stability. The parameters can be assigned to zones or areas expected to have relatively homogeneous parameters based on geologic or soil mapping. For the purpose of testing performance of the parallel code, Alvioli and Baum (2016a) kept the number of input parameters to as few as possible, because assigning the study area to a large number of zones with different hydromechanical properties would greatly increase the complexity of the model but have little impact on the time required for program execution. The present study explores how the variability of landslide source materials and uncertainty in hydromechanical properties of those materials affects the accuracy of model results. The complex geologic history of the study area has resulted in a wide range of bedrock and soil types and debris flows initiated in colluvial soils formed on nearly every geologic unit in the Front Range (Coe et al., 2014).

We tried four different strategies to define property zones for modeling rainfall infiltration and slope stability. The first strategy, using USDA (2005) soil maps to define zones proved unsuccessful because many locations where dense clusters of debris flows initiated were mapped as unweathered bedrock (UWB). Most USDA soil map units are associated with grain size distribution, hydraulic properties, and other useful soil characteristics in the accompanying database; however, UWB is not. Thus, subsequent strategies focused on developing a consistent methodology for

assigning soil characteristics to UWB. Two different strategies for iteratively assigning properties to UWB from neighboring soil map units failed due to the prevalence of UWB in the study area. The fourth, successful, strategy used published geologic mapping (Cole and Braddock, 2009) with the soil maps to define property zones based on generalized lithologies (Table 1). This strategy followed seven basic steps:

- Generalize geologic map units to clay/mud rocks (Cm), sandstone (S), metamorphic (M), igneous (I), Quaternary overburden (Q), and water.
- Find the intersection of soil polygons with the dominant underlying bedrock lithology.
- Find the modes and map-area weighted average for each (soil, rock) combination's attributes.
- Use soil texture (grain-size distribution) and hydraulic attributes from USDA (2005) to define zones. Specific criteria for sorting soils into zones were Unified Soil Classification System (USCS, see Lambe and Whitman, 1969) designation, hydraulic conductivity magnitude, K_s , and difference between saturated water content, θ_s , and water content at 15 bars suction, θ_{15} . The value of θ_{15} is taken as a proxy for the residual water content, θ_r .
- If soil map unit does not have associated property values, as with many UWB units, assign values as if they are poorly graded or silty gravels; UWB was dominantly granite and other crystalline rocks, but included sandstone and other sedimentary rocks as well.
- Assign texturally named soil map units that do not have associated property values that overlie one lithology to similarly named soils with properties overlying another similar lithology.
- Remaining soil polygons not assigned by the previous six steps (mainly moraines and associated floodplain and hillside areas) were lumped into a final zone (zone 20, Table 1).

This procedure resulted in 20 zones. Ranges (soil classification, hydraulic conductivity) or means (θ_s - θ_r) of relevant parameters were summarized from the properties of soil map units merged into each zone (Table 1). Properties not found in the USDA (2005) soil database were estimated based on texture and comparison with measured parameters. Inverse height of capillary rise, α (see Table 1), was estimated based on soil texture and descriptive statistics compiled by Carsel and Parish (1988). The ranges of soil strength parameters, cohesion, c' , and angle of internal friction, ϕ' , both for effective stress (Table 1), were estimated by comparing USCS texture class with average values tabulated at <http://www.geotechdata.info/parameter/parameter.html> (accessed 10/30/2018) and verified in text books (Hough, 1969; Lambe and Whitman, 1969; Terzaghi et al., 1996).

3.3. Infiltration and slope stability model initial and boundary conditions

The TRIGRS model assumes a steady background flux and initial water-table depth, d , to determine the infiltration initial condition. Infiltration boundary conditions are specified flux at the ground surface and an impermeable boundary, representing the low-permeability bedrock, at depth Z_{max} . The slope-stability initial condition is a factor of safety, F_s , greater than 1 and the slope-stability boundary conditions are a stress-free ground surface and a sliding surface parallel to the ground surface at some depth, $Z \leq Z_{max}$. A few measurements are available to constrain infiltration initial conditions. Coe et al. (2014) noted that 75-85 mm of rain fell September 9-11, 2014, during the 50 h preceding the beginning of moderate to intense rainfall. This followed about two weeks of dry weather. Soil moisture data from a site on a ridge extending east from Sugarloaf Mountain (west of Boulder, Fig. 1a) indicate soil saturation in the upper 30 cm of soil ranged from 30 to 60 percent in gravelly-sandy soil on September 11 before intense debris-flow triggering rainfall (Ebel et al., 2015). The observed level of soil saturation is consistent with what would be expected from the September 9-11 rainfall. The thin colluvial deposits drain rapidly so $d = Z_{max}$ (initial water table at the impermeable basal boundary) is assumed.

To aid rapid interpretation of model results, we applied the TRIGRS model to synthetic grids in which each row of the slope grid has incrementally (0.5°) higher slope angle and each column of the soil depth grid has incrementally (0.1 m) greater depth. This grid configuration made it possible to evaluate model performance throughout the range of observed source-area slopes and depths for a large number of parameter permutations using a small grid of 60×50 grid cells (Fig. 2b). The model was first used (Stage 1) to find ranges of strength parameters that result in stability (as measured by the factor of safety, F_s , with $F_s > 1$) for dry soil conditions and instability ($F_s < 1$) for extreme wet conditions. Subsequently, the model was used to predict pore-pressure rise and F_s for different combinations of hydraulic parameters and storm rainfall (Stage 2). The two model stages are intended to find likely combinations of parameters that can explain the observed pattern of debris-flow occurrence for use in probabilistic assessment (Canli et al., 2018).

3.4. Estimation of colluvium depth

Three methods were used to estimate depth of colluvial deposits from exposures in landslide scars (Fig. 2a): (1) Direct measurements were made in the field during the weeks and months following the event. (2) Estimates were made from terrestrial photography of landslides that were not accessible on the ground but could be viewed and photographed from a nearby location. (3) Anderson et al. (2015) measured landslide source area depths using elevation differences between pre-event and post-event airborne lidar. Slope angle for sources measured by (1) and (2) were obtained from a 10-m U.S. Geological Survey digital elevation model of the study area.

Table 1. Estimated parameter ranges in property zones (Fig. 1)

[See Fig. 1 for locations of property zones. Abbreviations of parent rock types, Cm, clay/mud rocks; S, sandstone; M, metamorphic; I, igneous; Q, Quaternary deposits. Unified Soil Classification System (USCS) symbols, CL, low-plasticity clay; GC, clayey gravel; GM, silty gravel; GP, poorly graded gravel-sand mixtures; GW, well-graded gravel-sand mixtures; ML low-plasticity silts and fine sands; SM, silty sand. Dual USCS symbols indicate a range of classes, rather than a borderline classification. -- not available]

Zone number (Fig. 1)	Number of debris flow source areas	Parent rock group	USCS symbols	Hydraulic conductivity, K_s , (ms^{-1})	Inverse capillary rise, α (m^{-1})	Saturated minus residual water content, $\theta_s - \theta_r$ (%)	Angle of internal friction for effective stress, ϕ' , (degrees)	Cohesion for effective stress, c' (kPa)
1	0	Cm/Q/S	CL	$1 \times 10^{-7} - 1 \times 10^{-6}$	0.4 - 3.4	11.5	27 - 35	5 - 20
2	9	Cm/I/Q/S	GM-ML	$1 \times 10^{-6} - 1 \times 10^{-5}$	1.5 - 5.7	12.1	27 - 41	0 - 20
3	0	I/M/Q/S	ML	$1 \times 10^{-6} - 1 \times 10^{-5}$	1.5 - 5.7	24.8	27 - 41	0 - 20
4	0	Cm/I/Q/S	CL-ML	$1 \times 10^{-7} - 1 \times 10^{-6}$	1.5 - 5.7	29.5	27 - 41	5 - 20
5	5	Cm/I/M/Q	ML-GM	$1 \times 10^{-6} - 1 \times 10^{-5}$	1.5 - 5.7	31.5	27 - 41	0 - 20
6	0	S	ML	$1 \times 10^{-6} - 1 \times 10^{-5}$	1.5 - 5.7	36	27 - 41	0 - 20
7	0	I	ML	$1 \times 10^{-6} - 1 \times 10^{-5}$	1.5 - 5.7	44.8	27 - 41	0 - 20
8	0	I/M/Q/S	GM-SM	$1 \times 10^{-6} - 1 \times 10^{-5}$	3.8 - 11.2	9.9	27 - 40	0
9	1	I/M/Q/S	GM-SM	$1 \times 10^{-6} - 1 \times 10^{-5}$	3.8 - 11.2	15.0	27 - 40	0
10	135	Cm/I/M/Q/S	SM-ML	$1 \times 10^{-6} - 6 \times 10^{-4}$	3.8 - 11.2	19.4	30 - 41	10 - 20
11	0	Cm/I/M/Q/S	GM-GC	$1 \times 10^{-5} - 1 \times 10^{-4}$	0.4 - 3.4	17.1	28 - 40	0 - 20
12	2	I/M/Q/S	GM-GC	$1 \times 10^{-6} - 1 \times 10^{-5}$	0.4 - 3.4	27.9	28 - 40	0 - 20
13	0	Cm	SM	$1 \times 10^{-5} - 1 \times 10^{-5}$	0.4 - 3.4	35.8	30 - 35	0 - 20
14	9	Cm/I/M/Q/S	GM	$1 \times 10^{-5} - 1 \times 10^{-4}$	3.8 - 11.2	12.9	30 - 40	0
15	64	Cm/I/M/Q/S	GM	$4 \times 10^{-6} - 6 \times 10^{-4}$	3.8 - 11.2	18.8	30 - 40	0
16	0	Cm/Q/S	GW	$1 \times 10^{-5} - 1 \times 10^{-4}$	11.6 - 17.4	24.1	33 - 40	0
17	0	Q	GM	$1 \times 10^{-6} - 1 \times 10^{-5}$	1.5 - 5.7	16.5	30 - 40	0
18	0	Cm	ML	$1 \times 10^{-6} - 1 \times 10^{-6}$	1.5 - 5.7	33.4	27 - 41	0 - 20
19	634	Cm/I/M/S	GP-GM	$1 \times 10^{-5} - 7 \times 10^{-4}$	1.5 - 17.4	30	30 - 44	0
20	0	I/M/Q	GP-GM	$1 \times 10^{-5} - 1 \times 10^{-4}$	1.5 - 17.4	--	30 - 44	0

4. Results

4.1. Property zone distribution

Fig. 1a shows the property zones in the entire study area, and Table 1 lists the characteristics of each zone. Zone boundaries are irregular and show evidence of mismatch at the boundaries of individual soil surveys used in compiling the final map. Debris flows occurred in only 8 of the 20 zones, and most were concentrated in only 3 zones. Most zones included multiple underlying rock types despite similarity in soil texture based on grain-size distribution. Fig. 1b shows a more detailed map of property zones in a subset of the study area.

Table 2. Measured parameters from test sites (Fig. 1a)

[See Fig. 1a for test and sample locations, EGR, East of Gross Reservoir; NBEH, North Boulder East Hogback; PM, Porphyry Mountain. Unified Soil Classification System (USCS) symbols, GM, silty gravel; GP, poorly graded gravel sand mixtures. -- not available]

Sample number	USCS symbol	Hydraulic conductivity, K_s , (ms ⁻¹) (Mini Disk)	Inverse capillary rise, α (m ⁻¹) drying, wetting	Angle of internal friction for effective stress, ϕ' , (degrees)	Cohesion for effective stress, c' (kPa)
EGR1	GP-GM	9.8×10^{-6} - 1.0×10^{-4}	3.5, 8.0	29	4
NBEH1	ML-SM	8.7×10^{-7}	--, --	--	--
PM1	GM	1.0×10^{-5} - 3.2×10^{-5}	4.1, 7.7	46	0
PM2	GP-GM	3.9×10^{-6} - 4.8×10^{-5}	3.5, 3.5	31-36	11-13

4.2. Parameter ranges

Landslide source materials from areas underlain by crystalline rock are primarily poorly sorted, coarse sand to silty sand, containing abundant gravel-, cobble-, and boulder-sized rock fragments. In the USCS (Lambe and Whitman, 1969; Terzahi et al., 1996), these materials typically classify as poorly graded gravel-sand mixtures (GP) and silty gravels (GM). Landslide source materials from areas underlain by sedimentary rock range from medium silty sand (SM) to clayey silt (ML), and may contain gravel-, cobble-, and boulder-sized rock fragments. Table 1 lists soil classifications and estimated ranges of model parameters for modeling infiltration and slope stability in the study area. Values of K_s and θ_s - θ_r in Table 1 are reported ranges of soil map units (USDA, 2005) composing each zone. The most common values of K_s for zones 10 and 15 range from 1.4×10^{-5} - 4.2×10^{-5} m/s. Ranges of α are $\alpha \pm s_\alpha$ (α is the mean and s_α is the standard deviation) tabulated by Carsel and Parish (1988) for representative soil textures. Cohesion listed in Table 1 is soil cohesion. Measured values of K_s in the database fall within the order of magnitude range listed in Table 1. Based on previous studies elsewhere, McGuire et al. (2016) estimated apparent cohesion attributable to roots in grassland areas of the Front Range at ~1.6–2.1 kPa and ~2.8–6.2 kPa in pine and fir forests on north-facing hillsides. McGuire et al. (2016) measured strength parameters on well-graded sand from sites (Fig 1b) underlain by crystalline rock $\phi' = 29^\circ$ - 31° , $c' = 0$ kPa.

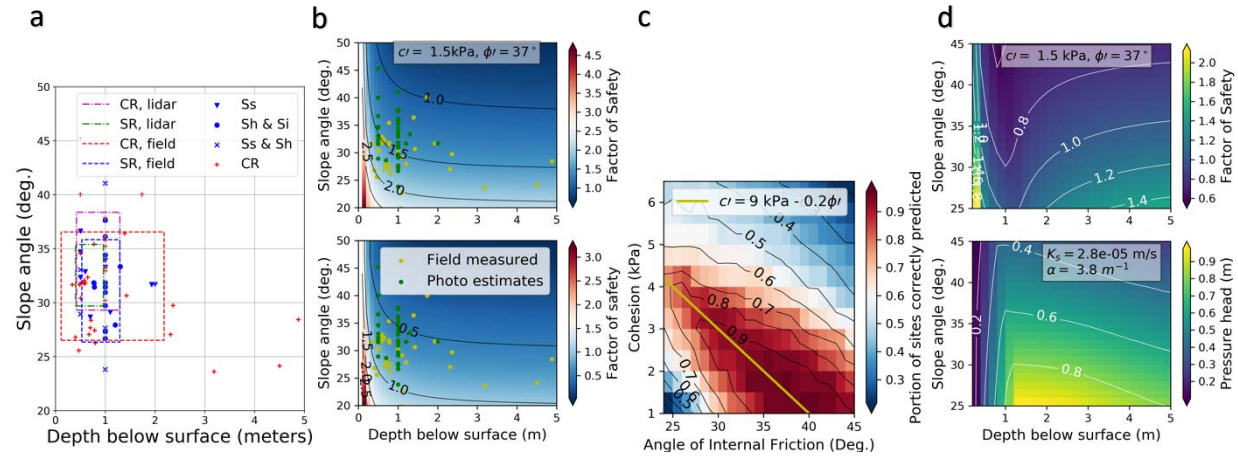


Fig. 2. (a) Observed landslide depths and slopes. Boxes outline ranges one standard deviation about the mean. Points from U.S. Geological Survey field measurements and photographic estimates. Lidar ranges from Anderson et al. (2015). Symbols, CR, crystalline rock; SR, sedimentary rock; Ss, sandstone; Sh, shale; Si, siltstone. (b) Plots comparing factor of safety F_s , to source-area slope and depth for cohesion, c' , and angle of internal friction, ϕ' , both for effective stress. Upper and lower plots show dry and wet end-members: upper, F_s for dry soil, lower, F_s for saturated soil with the water table at the ground surface and seepage parallel to the slope. (c) Plot showing fraction of sites where $F_s > 1$ for dry conditions and $F_s < 1$ for water table at the ground surface. Yellow line is trend of c' - ϕ' combinations that correctly predict F_s for more than 80% of measured source areas. (d) Plot of F_s for a specific set of parameters and rainfall hydrograph (Coe et al., 2014).

4.3. Colluvium depth

Colluvial deposits in the study area are thin. Estimates of colluvial thickness obtained from debris-flow source areas cluster between 0.4 and 1.3 m (Fig. 2a). The few deposits thicker than 2 m vertically were on slopes flatter than 30°. Central tendencies of measurements obtained by field surveys and lidar were similar (Fig. 2a).

4.4. Model results

Model Stage 1 tested 420 combinations of c' (1.0–6.5 kPa, in 0.5 kPa increments) and ϕ' (25°–45°, in 1° increments) for the synthetic terrain described previously. Results for a single combination of c' and ϕ' is shown in Fig. 2b. These tests showed that about one third of the c' and ϕ' combinations predicted $F_s > 1$ for dry conditions and $F_s < 1$ for wet conditions for 70% or more of the observed source-area depths and slopes (Fig 2c). Combinations that correctly predicted more than 80% of the observed values clustered along a line, $c' = 9 \text{ kPa} - 0.2\phi'$, $25^\circ < \phi' < 45^\circ$ (yellow line, Fig. 2c). Combinations of low friction angle and low cohesion predicted a high percentage of slopes with $F_s < 1$ for dry conditions. Similarly, combinations of high friction angle and high cohesion predicted a high percentage of slopes with $F_s > 1$ for wet conditions; consistent with the findings of McGuire et al. (2016) for apparent cohesion due to roots.

Model Stage 2, though still preliminary, has narrowed the range of feasible hydraulic parameters from that listed in Table 1. Both c' and ϕ' were held constant ($c'=1.5 \text{ kPa}$ and $\phi'=37^\circ$), a combination that correctly predicted more than 90 percent of observed debris-flow source depths and slopes (Fig. 2c), while K_s and α varied. Values listed in Table 1 and the soil map databases (USDA, 2005) for the three zones having the greatest number of debris-flow sources (zones 10, 15, and 19) guided selection of ranges for testing K_s (1.4×10^{-6} – $7.0 \times 10^{-4} \text{ m/s}$, in uneven increments) and α (1.5, 3.8, 7.5, and 11.2 m^{-1}). For our model, heavy rainfall of varying intensity associated with occurrence of the debris flows was represented by a 31-hour hydrograph of hourly rainfall for the Pine Brook gage (Fig. 1a, Coe et al., 2014). The model was tested using 12 combinations of K_s and α to explore their limits in predicting debris flow initiation for the storm. Model results showed that combined high values of K_s ($> 7.0 \times 10^{-5} \text{ m/s}$) and α ($\geq 7.5 \text{ m}^{-1}$) drained too freely to produce sufficient rise in pressure head to cause instability, whereas reducing α to 3.8 m^{-1} produced instability on slopes as low as 28° in a narrow range centered on 0.5 m depth. Combinations of low values of K_s ($1.4 \times 10^{-6} \text{ m/s}$) and α (1.5 m^{-1}) produced considerable pore pressure rise and instability at depths $< 2 \text{ m}$, but could not predict instability at depths of 3–5 m (Fig 2b). Intermediate values, of K_s ($2.8 \times 10^{-5} \text{ m/s}$) and α (3.8 m^{-1}) produced the most successful predictions of slope instability, 85% of the observed debris-flow source depth-slope combinations (Fig. 2d).

5. Discussion and Conclusion

The NRCS soil maps and databases (USDA, 2005) contain sufficient data on soil grain-size distribution, plasticity, and soil-water properties to serve as a starting point for defining input parameters for modeling rainfall-induced debris-flow initiation. Intersecting soil map units with geologic map units proved useful in extrapolating soil data into areas mapped as UWB. Knowledge gained from fieldwork and laboratory testing of a few specimens from debris-flow source areas in locations having a large proportion of exposed bedrock further aided interpretation of soil mapping in the UWB areas and assignment of parameter ranges (Table 1). The property zones provide constraints that can improve accuracy in modeling debris-flow initiation. So likewise, spatially distributed rainfall inputs and improved models of soil depth (Baum, 2017) would likely reduce the areas of false positives in model output. Obtaining sufficient measurements of slope and depth of debris-flow sources to have a statistically meaningful distribution is critical to the success of our approach to constraining model input parameter ranges. Agreement between depth distribution obtained by fieldwork (including many where depth was estimated from close-range photography) and that obtained by differencing pre- and post-event lidar (Anderson et al., 2015) boosts our confidence that the distribution is representative of debris-flow sources throughout the study area (Fig. 2b).

We have developed a simplified approach to defining ranges of input parameters that result in successful predictions for modeling landslide and debris-flow initiation. Preliminary results indicate that using a synthetic depth and slope grid to compute F_s for possible ranges of parameters and comparing the results with observed source area depths and slopes can effectively narrow the range of strength parameters needed to predict debris flow initiation. Combinations that correctly predicted more than 80% of the observed values clustered in a narrow range along, $c' = 9 \text{ kPa} - 0.2\phi'$, $25^\circ < \phi' < 45^\circ$ (Fig. 2c). Likewise, applying this approach to modeling rainfall infiltration and resulting pressure head rise and change in factor of safety can effectively narrow the range of soil water parameters. For our study area,

preliminary results cluster in the ranges $1.4 \times 10^{-6} \leq K_s \leq 2.8 \times 10^{-5}$ and $1.5 \leq \alpha \leq 7.5$. Parameter ranges determined by modeling (Fig. 2c, 2d) are consistent with those determined by laboratory testing (Table 2) and estimated based on texture for property zones where significant numbers of debris flows initiated (Table 1).

Acknowledgements

Jeff Coe, Jason Kean, and Francis Rengers (all U.S. Geological Survey [USGS]) shared depth measurements from debris-flow source areas. Cassandra Lindsey (Colorado Geological Survey) and Ben Mirus (USGS) helped with fieldwork. York Lewis (formerly Colorado School of Mines) performed laboratory testing and helped with fieldwork. Karen Olson helped with formatting. This paper benefited from constructive reviews by Francis Rengers and two anonymous referees. Any use of trade, firm, or product names is for descriptive purposes only and does not imply endorsement by the U.S. Government.

References

- Alvioli, M., and Baum, R.L., 2016a, Parallelization of the TRIGRS model for rainfall-induced landslides using the message passing interface: *Environmental Modelling & Software*, v. 81, p. 122-135, doi:10.1016/j.envsoft.2016.04.002.
- Alvioli, M., and Baum, R.L., 2016b, Serial and parallel versions of the Transient Rainfall Infiltration and Grid-Based Regional Slope-Stability Model (TRIGRS): U.S. Geological Survey software release, <https://doi.org/10.5066/F7M044QS>.
- Anderson, S.W., Anderson, S.P., and Anderson, R.S., 2015, Exhumation by debris flows in the 2013 Colorado Front Range storm: *Geology*, v. 43, no. 5, p. 391-394, <https://doi.org/10.1130/G36507.1>.
- Baum, R.L., 2017, Effects of topographic data quality on estimates of shallow slope stability using different regolith depth models, *in* De Graff, J.V., and Shakoor, Abdul, eds., *Landslides—Putting Experience, Knowledge and Emerging Technologies into Practice*, Proceedings of the 3rd North American Symposium on Landslides: Association of Environmental and Engineering Geologists Special Publication 27, ISBN: 978-0-9897253-7-8, p. 807-818.
- Baum, R.L., and Godt, J.W., 2010, Early warning of rainfall-induced shallow landslides and debris flows in the USA: *Landslides*, v. 7, p. 259–272, doi: 10.1007/s10346-009-0177-0.
- Baum, R.L., Godt, J.W., and Savage, W.Z., 2010, Estimating the timing and location of shallow rainfall-induced landslides using a model for transient, unsaturated infiltration: *Journal of Geophysical Research, Earth Surface*, v. 115, F03013, doi:10.1029/2009JF001321.
- Birkeland, P.W., Shroba, R.R., Burns, S.F., Price, A.B., and Tonkin, P.J., 2003, Integrating soils and geomorphology in mountains—An example from the Front Range of Colorado: *Geomorphology*, v. 55, p. 329–344, doi: 10.1016/S0169-555X(03)00148-X.
- Canli, E., Mergili, M., Thiebes, B., and Glade, T., 2018, Probabilistic landslide ensemble prediction systems: lessons to be learned from hydrology: *Natural Hazards and Earth Systems Science*, v. 18, p. 2183-2202, <https://doi.org/10.5194/nhess-18-2183-2018>.
- Carsel, R.F., Parish, R.S., 1988, Developing joint probability distributions of soil water retention characteristics: *Water Resources Research*, v. 24 no. 5, p. 769-775.
- Coe, J.A., Kean, J.W., Godt, J.W., Baum, R.L., Jones, E.S., Gochis, D.J., and Anderson, G.S., 2014, New insights into debris-flow hazards from an extraordinary event in the Colorado Front Range: *GSA Today*, v. 24, no. 10, p. 4-10, doi:10.1130/GSATG214A.1.
- Cole, J.C., and Braddock, W.A., 2009, Geologic map of the Estes Park 30' × 60' quadrangle, north-central Colorado: U.S. Geological Survey Scientific Investigation Map 3039, scale 1:100,000, 56 p. pamphlet.
- Ebel, B.A., Rengers, F.K. and Tucker, G.E., 2015, Aspect-dependent soil saturation and insight into debris-flow initiation during extreme rainfall in the Colorado Front Range: *Geology*, v. 43, no. 8, p. 659–662.
- Godt, J.W., Baum, R.L., Savage, W.Z., Salciarini, D., Schulz, W.H., and Harp, E.L., 2008, Transient deterministic shallow landslide modelling—Requirements for susceptibility and hazard assessments in a GIS framework: *Engineering Geology*, v. 102, no. 3-4, p. 214- 226, DOI: 10.1016/j.enggeo.2008.03.019.
- Guzzetti, F., Peruccacci, S., Rossi, M., and Stark, C.P., 2008, The rainfall intensity-duration control of shallow landslides and debris flows—an update: *Landslides*, v. 5, no. 1, p. 3–17. doi: 10.1007/s10346-007-0112-1.
- Hansen, W.R., 1976, Geomorphic constraints on land development in the Front Range Urban Corridor, Colorado, in Coates, D.R., ed., *Urban Geomorphology*: Geological Society of America Special Paper 174, p. 85–109.
- Hough, B.K., 1969, *Basic Soils Engineering*, 2nd Ed.: New York, The Ronald Press Co., 634 p.
- Lambe, T.W., and Whitman, R.V., 1969, *Soil Mechanics*: New York, Wiley, 553 p.
- Likos, W.J., Wayllace, A., Godt, J., and Lu, N., 2010, Modified direct shear apparatus for unsaturated sands at low suction and stress: *Geotechnical Testing Journal*, v. 33, no. 4, p. 286-298, <https://doi.org/10.1520/GTJ102927>.
- Lu, N. and Godt, J.W., 2013, *Hillslope Hydrology and Stability*: New York, Cambridge, 437 p.
- McGuire, L.A., Rengers, F.K., Kean, J.W., Coe, J.A., Mirus, B.B., Baum, R.L. and Godt, J.W., 2016, Elucidating the role of vegetation in the initiation of rainfall-induced shallow landslides—Insights from an extreme rainfall event in the Colorado Front Range: *Geophysical Research Letters*, v. 43, p. 9084–9092, doi:10.1002/2016GL070741.
- Rengers, F., McGuire, L., Coe, J., Kean, J., Baum, R., Staley, D. and Godt, J., 2016, The influence of vegetation on debris-flow initiation during extreme rainfall in the northern Colorado Front Range: *Geology*, v. 4, no. 10, p. 823-826, doi:10.1130/G38096.1.
- Terzaghi, K., Peck, R.B., and Mesri, G., 1996, *Soil Mechanics in Engineering Practice*, 3rd Ed.: New York, Wiley, 549 p.
- Thomas, M.A., Mirus, B.B., and Collins, B.D., 2018, Identifying physics-based thresholds for rainfall-induced landsliding: *Geophysical Research Letters*, v. 45, no. 18, p. 9651-9661, doi: 10.1029/2018GL079662.
- USDA, 2005, *Natural Resources Conservation Service*. Tech. Rep. United States Department of Agriculture.
- Wayllace, A. and Lu, N., 2012, A transient water release and imbibitions method for rapidly measuring wetting and drying soil water retention and hydraulic conductivity functions: *Geotechnical Testing Journal*, v. 35, no. 1, p. 103-117, <https://doi.org/10.1520/GTJ103596>.

An evaluation of debris-flow runout model accuracy and complexity in Montecito, California: Towards a framework for regional inundation-hazard forecasting

Erin K. Bessette-Kirton^{a,*}, Jason W. Kean^a, Jeffrey A. Coe^a, Francis K. Rengers^a, and Dennis M. Staley^a

^aU.S. Geological Survey, Box 25046, MS 966, Denver, CO 80401, USA

Abstract

Numerous debris-flow inundation models have been applied retroactively to noteworthy events around the world. While such studies can be useful in identifying controlling factors, calibrating model parameters, and assessing future hazards in specific study areas, model parameters tailored to individual events can be difficult to apply regionally. The advancement of debris-flow modeling applications from post-event model validation of individual case studies to pre-event forecasting that can be implemented rapidly and at regional scales is critical considering the fatalities and extensive infrastructure damage caused by debris flows that inundated a developed fan in Montecito, California, following heavy rain on 9 January 2018. In this study, we evaluated the tradeoffs between model accuracy and simplicity in the context of the need for a framework that can be used in conjunction with initiation models and storm predictions for rapid, large-scale inundation hazard mapping as a component of post-fire debris-flow hazard assessments. We used numerical (FLO-2D) and empirical (LAHARZ) models to simulate debris flows from one of the drainages upstream of Montecito that was burned in the Thomas fire in December 2017 and compared model results with field observations and building damage assessments collected immediately following the event. Initial testing demonstrated that LAHARZ can simulate channelized flow but is not able to replicate flow bifurcations or avulsions, which are critical aspects of flows travelling over populated fans. FLO-2D simulations matched well with observed inundation area data, but variably under- and overpredicted inundation height, deposit depth, and velocity. We found that FLO-2D and LAHARZ had true positive rates of 0.84 and 0.6, respectively, and both models had similar false positive rates (0.3 and 0.35, respectively). Our model evaluation framework allowed us to compare model results with detailed field observations and will serve as a platform for more extensive model testing in the future.

Keywords: post-fire debris flows; debris-flow inundation; runout modeling; FLO-2D; LAHARZ

1. Introduction

The 9 January 2018 Montecito, California, debris-flow event was triggered by a deluge of rain (peak 5-minute rainfall intensity exceeding 150 mm/hr) over several catchments of the Santa Ynez Mountains that had been burned by the Thomas fire several weeks prior (National Weather Service, 2018; Kean et al., in press). Debris flows initiated from burned source areas, and major flows ran out along Montecito, Oak, San Ysidro, Buena Vista, and Romero Creeks, subsequently inundating communities residing on alluvial fans downstream of the mountain front, causing 23 fatalities and damaging over 400 structures (Kean et al., in press). While tools exist to quickly assess the likelihood and potential volume of debris flows within burned areas (Gartner et al., 2014; Staley et al., 2017), debris-flow runout models that can be implemented rapidly over large areas (tens to hundreds of basins) with variable terrain are not currently available. Prior to the Montecito debris-flow event, the U.S. Geological Survey (2018) determined that there was a high probability of debris flows initiating from the basins upstream of Montecito. However, the large number of fatalities and widespread infrastructure damage from debris-flow inundation on the alluvial fan downstream of the

* Corresponding author e-mail address: ebessette-kirton@usgs.gov

source areas burned by the Thomas fire underscore the importance of an operational capability to predict debris-flow inundation areas and flow characteristics (e.g., depth and velocity).

Numerous empirical and physically based runout models exist and have been used to simulate debris flows in diverse settings around the world. Runout models are often back-calibrated to well-studied debris flows (e.g., O'Brien et al., 1993; Rickenmann et al., 2006; Hungr and McDougall., 2009) and in some cases have been used as forecasting tools in regional hazard assessments (e.g., Horton et al., 2013). Complex debris-flow processes are a result of varying material composition and water content, physical interactions between the solid and fluid phases of flow, and changes in material properties during an event (e.g., Rickenmann et al., 2006; Iverson and George, 2014). Empirical models do not inherently capture the physical processes of debris flows, and the complexities of debris flows preclude single-phase physical models from comprehensively capturing the processes at work. Nevertheless, the success of such models at predicting the inundation area and flow characteristics of debris flows renders them useful for practical applications (Hungr and McDougall, 2009). A few studies have used runout modeling to assess inundation of post-fire debris flows (Bernard, 2007; Cannon et al., 2010; McCoy et al., 2016), but more extensive model testing and calibration is needed to meet the need for regional runout forecasting on urbanized fans.

In this paper, we apply two runout models at Montecito and develop a framework with which to evaluate models for use in post-fire debris-flow hazard assessments. As a starting point, we used the empirical model, LAHARZ (Schilling, 1998), and FLO-2D, a widely used two-dimensional, finite difference model (O'Brien et al., 1993), to simulate debris flows along one of the drainages inundated during the Montecito debris-flow event (San Ysidro Creek). We then compared model results with field data collected by Kean et al. (2019) during the first 12 days after the event. A wealth of detailed field data provided a unique opportunity to evaluate the ability of runout models to predict inundation area, flow depth, deposit thickness, and velocity. We compare results from both models by assessing model accuracy and utility for timely and efficient debris-flow inundation forecasting. This paper serves as a starting point for more extensive runout model testing and calibration for application to post-fire debris-flow hazard assessments in the future.

2. Setting

Montecito is located 8 km east of Santa Barbara, California on a populated piedmont plain at the foot of the Santa Ynez Mountains (Fig. 1a). San Ysidro Creek spans approximately 3 km between the mountain front and the Pacific Ocean, intersecting State Route 192 and Highway 101. A topographic high resulting from the Mission Ridge fault zone (Fig. 1a) separates steeply sloping alluvial landforms to the north from more gently sloping alluvial landforms near the coast (Kean et al., in press). San Ysidro Creek is deeply incised at its intersection with the Mission Ridge fault zone but is less confined elsewhere on the piedmont. The basin upstream from the head of the fan at San Ysidro Creek covers an area of 7.6 km² and is characterized by steeply dipping Eocene bedrock units (Dibblee, 1966). During the Thomas fire, 85% of the study basin was burned at moderate to high severity (Kean et al., in press; Fig. 1b). Prior to the 9 January 2018 rainfall event, the U.S. Geological Survey (2018) predicted a 69% probability of debris flows from the San Ysidro Creek basin for a design rainstorm of $I_{15} = 24$ mm/hr.

During the rainstorm on 9 January 2018, debris flows on San Ysidro Creek yielded a total sediment volume of about 297,000 m³ (Kean et al., in press). Observations of debris-flow source areas by Kean et al. (in press) indicated that debris flows initiated from water runoff and hillslope erosion, as is common in post-fire debris flows (Fig. 1b). Debris flows inundated the entirety of San Ysidro Creek and avulsed in several places, resulting in a 500-meter wide flow path in some areas (Fig. 1a). Large flow avulsions occurred upstream of the Mission Ridge fault zone and at the distal end of the fan. Additionally, flow bifurcated approximately 0.7 km downstream of the mountain front and traveled in a southwest direction away from San Ysidro Creek, along El Bosque Road (Fig. 1a). Debris-flow deposits consisted of large boulders (up to 4.3 m in diameter) supported by a silty sand matrix (Kean et al., in press). Boulders were deposited along the entire length of San Ysidro Creek, with an especially high concentration of boulders in the avulsion north of the Mission Ridge fault zone (Fig. 1c). The flows on San Ysidro Creek resulted in damage to at least 163 structures and complete destruction of an additional 92 structures (CAL Fire, 2018).

Field mapping and observations by Kean et al. (2019) provide a wealth of data to compare with runout model results. We used measurements of inundation height from field observations (n=115) and building impact analyses (n=157), sediment depth from field observations (n=107), and flow velocity from building impact analyses (n=83) to compare with model results. The locations of field measurements (blue) and building damage assessments (red) are shown in Fig. 1a.

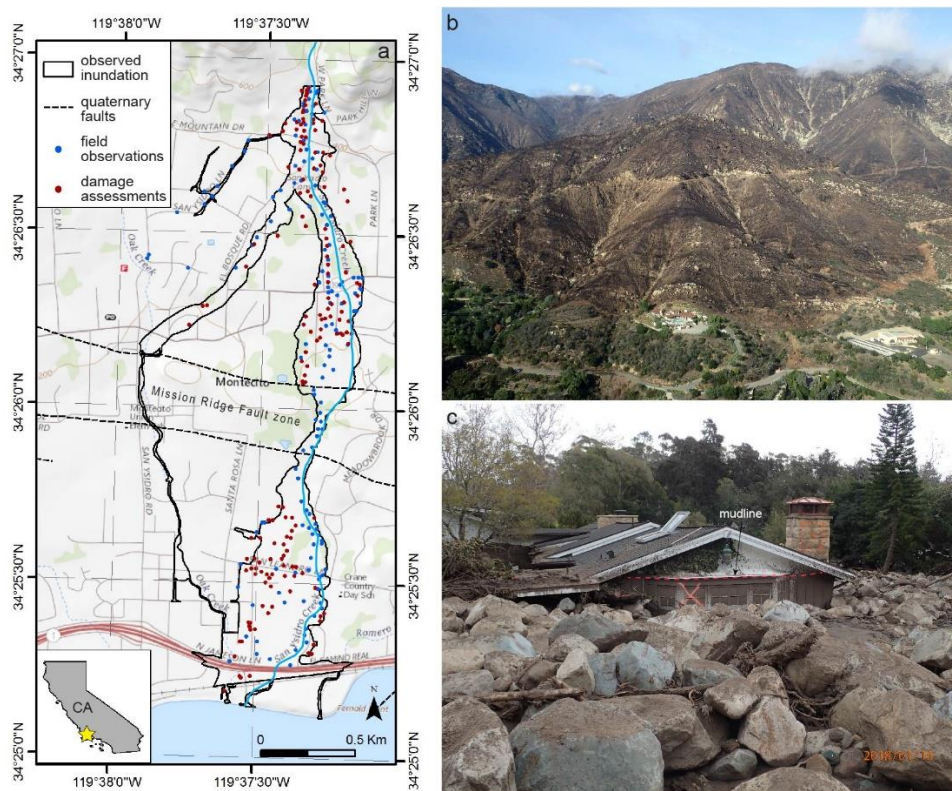


Fig 1. a) Map of the area inundated by debris flows along San Ysidro Creek in Montecito, CA, showing the locations of field observations (blue) and damage assessments (red) used for comparison with model results. b) Aerial view of the burned debris-flow source areas above Montecito (photo credit: Dennis Staley). c) Boulder-rich debris-flow deposits surrounding a damaged house along San Ysidro Creek (photo credit: Jeffrey Coe). The inundation height of debris flows is evident from the mudline on the house.

3. Methods

To systematically compare model results, we held input data equal for both models whenever possible. As detailed in the following sections, this is inherently difficult when comparing multiple models because of differences in the input data and parameters required for each. A 5-meter resolution (resampled from 3.05 m) pre-event digital elevation model was used as the topographic surface in both models. For each model, we used an input sediment volume of 297,000 m³. Differing input requirements necessitated us to vary the implementation of a fixed input sediment volume, as described in the following sections. Since the purpose of preliminary testing was to compare the strengths and shortcomings of each model for use in post-fire debris-flow hazard assessments, we performed initial calibration runs for FLO-2D but did not execute exhaustive parameter sensitivity and optimization analyses.

LAHARZ uses empirical equations for cross-sectional (A) and planimetric area (B) as functions of volume (V) to delineate debris-flow inundation areas on a given topographic surface (Schilling, 1998; Griswold and Iverson, 2008). Iverson et al. (1998) and Griswold and Iverson (2008) derived sets of empirical equations from statistical analyses of lahar, debris flow, and rock-avalanche runout paths. We implemented the empirical equations for both lahars and debris flows on San Ysidro Creek by applying a sediment volume of 297,000 m³ at a point location, which we chose as the outlet of the San Ysidro Creek basin at the head of the fan (Table 1).

FLO-2D is a two-dimensional finite difference model that utilizes a quadratic rheologic model to simulate water and mudflows over floodplain and alluvial fan surfaces (O'Brien et al., 1993). FLO-2D requires an input hydrograph, which is bulked with a given volumetric sediment concentration (C_v) for mud and debris-flow simulations. The timing of debris flows closely followed the peak in rainfall intensity (Kean et al., in press), so we modeled the shape of the hydrograph based on the observed hyetograph of rainfall intensity. We interpolated 15-minute rainfall intensity data from two rain gages that lie to the east and west of San Ysidro Creek (KTYD, 5 km west and Doulton Tunnel, 5.3 km east) to estimate the rainfall rate within the study basin. We accounted for infiltration by using a version of the Green-Ampt infiltration model, as described in Rengers et al. (2016), to extract water from the hyetograph during the

storm. To parameterize the infiltration equation, we used a hydraulic conductivity of 15 mm/hr (the geometric mean of the saturated hydraulic conductivity obtained from field measurements; Kean et al., in press), a pressure head of 1 mm (a commonly observed value after wildfire; Ebel and Moody, 2016), and estimated porosity and initial water content values of 0.5 and 0.2, respectively. The resulting rainfall intensity time-series, corrected for the estimated infiltration rate, was then multiplied by the total basin area to estimate a discharge hydrograph (m^3/s). We scaled the discharge hydrograph given our prescribed input sediment volume ($297,000 \text{ m}^3$) and assuming $C_v = 0.6$ (which is consistent with field observations). The resulting input hydrograph, which yields a water volume of $198,000 \text{ m}^3$ and a total volume (water plus sediment) of $495,000 \text{ m}^3$, was applied at the basin-outlet point.

In FLO-2D, surface roughness is prescribed by Manning's n -value, which we set as either $n = 0.04$ or $n = 0.1$ in accordance with recommended values from previous studies (e.g., Bertolo and Wieczorek, 2005; Rickenmann et al., 2006). For the simulation of debris flows, FLO-2D requires input values for the resistance parameter for laminar flow (K), and the specific gravity (S_G), yield stress (τ_y), and viscosity (η) of the water-sediment mixture. τ_y and η vary with C_v and are determined using a set of equations with empirically determined coefficients (O'Brien et al., 1993). As recommended, we used $K = 2285$ for urban areas (FLO-2D Software, Inc., 2017). We calculated S_G by using a rock density of 2650 kg/m^3 and accounting for the proportion of water in the material, as defined by C_v . We performed initial calibration runs by varying n and using high, medium, and low values of τ_y and η from the range of values available in literature (e.g., Bertolo and Wieczorek, 2005; Rickenmann et al., 2006). The values of n , τ_y , and η that best fit the observed inundation area of debris flows in San Ysidro Creek are listed in Table 1. In addition to inundation area, FLO-2D outputs inundation height, deposit depth, and velocity (Table 1).

Table 1. Model inputs, parameters, and outputs for FLO-2D and LAHARZ, where C_v is volumetric sediment concentration, n is Manning's n -value, K is the resistance parameter for laminar flow, S_G is specific gravity, τ_y is yield stress, η is viscosity, A is inundated cross-sectional area, B is inundated planimetric area, and V is volume.

Model	Volume configuration	Input volume	Parameters	Outputs
FLO-2D	Hydrograph with specified C_v	297,000 m^3 of sediment, 198,000 m^3 of water, $C_v = 0.6$	$n = 0.04$, $K = 2285$, $S_G = 1.99$ $\tau_y = 1000 \text{ Pa}$, $\eta = 100 \text{ Pa}\cdot\text{s}$	Inundation area, inundation height, deposit depth, velocity
LAHARZ debris flow	Point source	297,000 m^3	$A = 0.1V^{2/3}$, $B = 20V^{2/3}$	Inundation area
LAHARZ lahar	Point source	297,000 m^3	$A = 0.05V^{2/3}$, $B = 200V^{2/3}$	Inundation area

4. Results

The area inundated by each model is shown in comparison to the observed debris-flow inundation area along San Ysidro Creek in Fig. 2. Dark blue represents the area that was correctly predicted by the model (true positive area), while light blue represents the area that was falsely inundated by the model (false positive area). Conversely, the area that was inundated but is not captured by the model (false negative area) is shown by the striped area. To compare between models, we divided the true positive, false positive, and false negative areas by the total observed inundation area to obtain the true positive rate (TPR), false positive rate (FPR), and false negative rate (FNR), respectively (Fig. 2). We also calculated the threat score (TS; e.g., Staley et al., 2017) for each model, which is defined as TPR divided by the sum of TPR, FPR, and FNR (Fig. 2).

In addition to assessing the overall proportion of inundated area captured by each model, we calculated the observed and modeled inundation areas in 10 equally sized rectangular zones that encompass the total area inundated by debris flows along San Ysidro Creek (Fig. 3a). Observed and modeled inundation areas as a function of downstream distance (d) are shown in Fig. 3b, where d was measured as the difference in northing from the basin outlet point to the center of each zone. The total runout distance for each model was found by calculating the difference in northing between the basin outlet point and the farthest extent of inundation. The resulting root-mean-square errors (RMSE) for runout distance (E_R) and inundation area (E_A) normalized by the total observed runout distance and inundation area, respectively, are listed in Table 2.

We compared measurements of inundation height, deposit depth, and velocity with FLO-2D model results at the field observation and damage-assessment points shown in Fig. 1 (Fig. 4). To assess the correlation between observations of flow characteristics and model results, we divided the observed inundation area into four zones (Fig.

4a). Figs. 4b-d show the correlation between measured and modeled inundation height, deposit depth, and velocity, respectively, where the coloration of data points corresponds to the deposit zone in which the measurement was located. We assessed inundation height (Fig. 4b) by comparing model results with 115 field observations and 157 building damage assessment measurements (Kean et al., 2019). Similarly, we used 107 deposit depth field measurements and 83 velocity measurements calculated from building damage assessments. The RMSE of FLO-2D model results for inundation height (E_H), deposit depth (E_D), and flow velocity (E_V) are listed in Table 2.

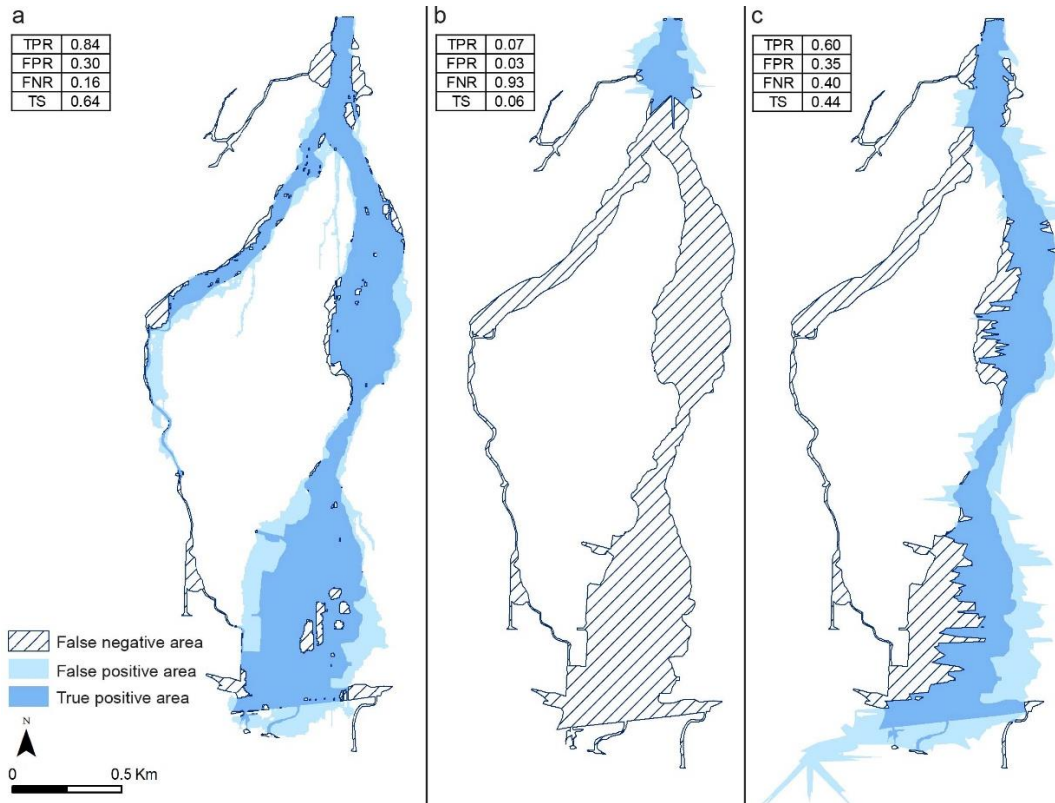


Fig. 2. Modeled inundation area from a) FLO-2D, b) LAHARZ debris flow, and c) LAHARZ lahar, showing the true positive area (dark blue), false positive area (light blue), and false negative area (striped) resulting from each model run, in comparison to the mapped inundation area of debris flows on San Ysidro Creek (Kean et al., 2019; Fig. 1). True positive rate (TPR), false positive rate (FPR), and false negative rate (FNR) are defined as the true positive, false positive, and false negative areas divided by the observed inundation area, respectively. Threat score (TS) is defined as TPR divided by the sum of TPR, FPR, and FNR.

5. Discussion

Debris-flow runout model accuracy is imperative to hazard assessments because of the consequences associated with either under- or overpredicting both debris-flow inundation and flow characteristics. Receiver operating characteristic (ROC) analyses show that FLO-2D models inundation area most accurately (Fig. 2), with the highest TPR and TS, and the lowest FPR and FNR. However, a TS of 0.64 indicates that the FLO-2D model could still be improved. Our analysis of inundation area as a function of d (Fig. 3) shows that the inundation area modeled by FLO-2D is underpredicted in the first 300 m downstream of the basin outlet point but is overpredicted elsewhere. Nonetheless, the similarity in shape of the FLO-2D and observed series (Fig. 3b), indicates that the model correctly predicts relative changes in inundation area with d and the fit could likely be improved with further calibration.

The LAHARZ debris flow model substantially underpredicts the observed inundation area (FNR=0.93; Fig. 2b) and has a runout distance that is only 15% of the observed runout distance. The modeled inundation area from LAHARZ lahar fits the observed data better than does LAHARZ debris flow, but the inundation area is still substantially underpredicted (FNR=0.4), especially in places where the flow avulses from the main channel (Fig. 4a, zones 2 and 4). Additionally, LAHARZ lahar overpredicts the total runout distance (Table 2). The discrepancy between the results of the LAHARZ models reflects differences in the coefficients that are used for each flow type, which are

derived from empirical data showing that debris flows generally have a higher sediment concentration than lahars (Iverson et al., 1998). The underprediction of inundation area highlights the inability of LAHARZ to simulate avulsions. Similarly, LAHARZ does not predict the bifurcation of flow at El Bosque Road (Fig. 1a), which is an important aspect of debris-flow inundation on populated alluvial fans. The inability of LAHARZ to simulate flow bifurcation and avulsions indicates that the use of empirical equations may not be sufficient to accurately represent the complex physical process of debris flows traveling through built environments. The discrepancies between the results of the LAHARZ models and the observed inundation area demonstrate that, as indicated by previous work (Bernard, 2007; Magirl et al., 2010), the empirical coefficients used in LAHARZ should be modified if the model is utilized for post-fire debris-flow hazard assessments in the future.

Table 2. FLO-2D and LAHARZ runout (R) and inundation area (A) results, model errors, and runtimes. Errors are expressed as the root-mean-square errors of runout distance (E_R), inundation area (E_A), inundation height (E_H), deposit depth (E_D), and flow velocity (E_V). Model results are compared with field data and building damage assessments from the Montecito debris-flow event along San Ysidro Creek (Kean et al., 2019). E_R and E_A are listed as percentages of the total observed runout distance and inundation area, respectively. LAHARZ does not output inundation height, deposit depth or flow velocity.

Model	R (m)	A (m ²)	E_R	E_A	E_H	E_D	E_V	Model Runtime
FLO-2D	3,280	1,076,827	2.0%	2.2 %	0.97	0.65	0.92	41 minutes
LAHARZ debris flow	493	89,535	85.3%	10.7%	--	--	--	0.5 seconds
LAHARZ lahar	3,498	890,596	4.5%	4.1%	--	--	--	4 seconds

The ability to model flow characteristics in addition to inundation area is important because of the implications that inundation height, deposit depth, and flow velocity have on the physical harm and damage to infrastructure that debris flows can inflict. Furthermore, predictions of flow characteristics are critical for predictive-damage assessments (e.g., Kean et al., in press). Comparisons of observed data and modeled inundation height and deposit depth from FLO-2D show that, in general, both metrics were underpredicted on the upper half of the alluvial fan (zones 1 and 2) but were overpredicted on the lower half of the fan (zones 3 and 4; Fig. 4). Modeled velocities were also overpredicted on the lower half of the fan (zone 4; no observed data exist for zone 3), while modeled velocities in zones 1 and 2 were both under- and overpredicted. Inconsistent under- and overpredictions in different deposit regions likely indicate discrepancies between modeled and actual physical processes and rheological parameters. For example, FLO-2D is intended for the modeling of hyper-concentrated sediment flows, and the rheologic model used to simulate debris flows does not account for the influence of coarse sediment (gravel, cobbles, and boulders; FLO-2D Software, Inc., 2015), which, as shown in Fig. 1c, was an important component of debris flows along San Ysidro Creek.

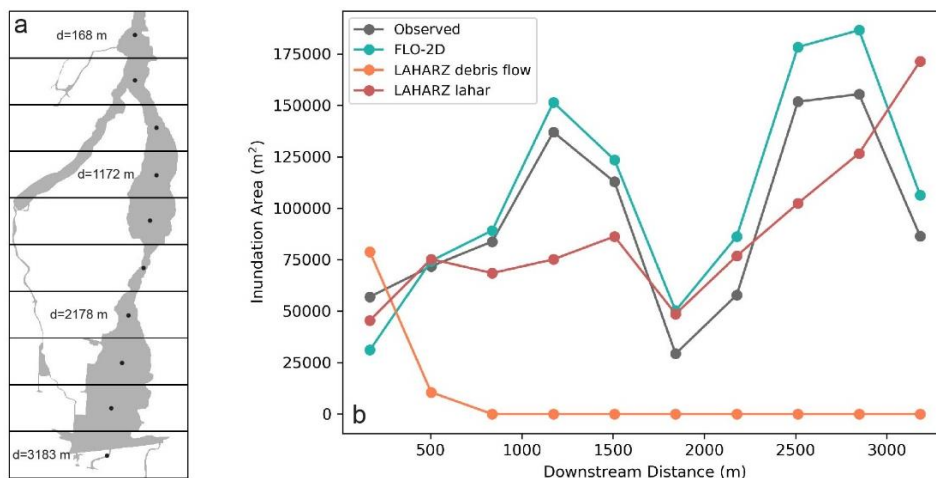


Fig. 3. a) Diagram showing the 10 zones used to compare modeled and observed inundation area. b) Observed and modeled inundation area in each zone plotted as a function of downstream distance at the center of each segment (d).

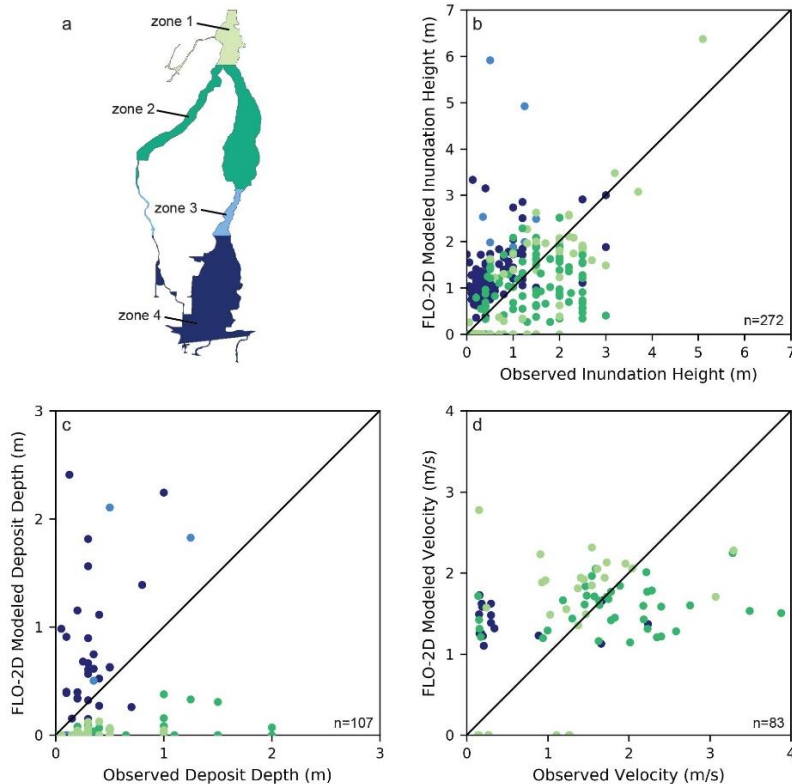


Fig. 4. a) Zones used to assess observed measurements and FLO-2D model results for b) inundation height, c) deposit depth, and d) velocity. Velocity measurements were derived from building impact analyses (see Kean et al. (in press) for details). The coloration of points corresponds to their location in zones 1-4.

The San Ysidro Creek basin was one of 1738 basins that were analyzed in the U.S. Geological Survey's post-fire debris-flow hazard assessment for the Thomas fire (U.S. Geological Survey, 2018). In this context, a debris-flow runout model that can be used as a predictive tool for post-fire debris-flow hazard assessments must have flexibility for use in variable settings (e.g., channelized, urbanized fans), while also being computationally efficient. LAHARZ took several seconds to run simulations on San Ysidro Creek, which is over 2000 times faster than the runtime for FLO-2D (41 minutes; Table 2). While LAHARZ runs very quickly and could likely be applied efficiently to tens or hundreds of drainages, the model is primarily intended for settings where flow is channelized (Schilling, 1998), and hence, accuracy is limited in areas with minimal channel confinement. FLO-2D is capable of modeling debris flows in both channelized and non-channelized settings and can be customized to simulate infrastructure components (e.g., culverts, debris-retention basins) and transient surface properties (FLO-2D Software, Inc., 2017). While this flexibility is advantageous, the need to set numerous adjustable parameters requires time-consuming calibration and is difficult without a priori knowledge of the parameter values that are valid in certain regional or geomorphic settings. Predetermined parameterization and the development of design storms based on robust back-calibration to past events in a given area could be used to improve the efficiency of employing FLO-2D for forecasting, but the application to large, multi-basin areas would still require substantial computing time and user analysis.

6. Conclusion

Detailed field data collected after the Montecito debris-flow event enabled us to make comprehensive quantitative comparisons between observations and modeled results. Preliminary debris-flow runout model testing demonstrated that a model applied to post-fire debris-flow hazard assessments must be able to simulate both channelized and non-channelized flows on fans. Comparisons of observed data and model runs show that LAHARZ does not replicate flow bifurcations or avulsions and is not well-suited for use in non-channelized settings. Additionally, new empirical coefficients may be necessary for post-fire debris flows in southern California. FLO-2D simulations matched well with observed inundation area data, but variably under- and overpredicted inundation height, deposit depth, and

velocity in different areas. More extensive model calibration could be used to improve FLO-2D model results, and parameterization based on flow characteristics could be used to improve the potential for use in predictive damage assessments. In the future, testing should assess the accuracy and efficiency of other widely used runout models that could be coupled with existing post-fire debris-flow hazard assessments to better inform local government agencies and emergency managers prior to imminent precipitation events.

Acknowledgements

We thank Matthew Thomas and two anonymous reviewers for their insightful reviews of our paper. Any use of trade, firm, or product names is for descriptive purposes only and does not imply endorsement by the U.S. Government.

References

- Bernard, D., 2007, Estimation of inundation areas of post-wildfire debris flows: Master's Thesis, Colorado School of Mines, Department of Geology and Geological Engineering, 77 p.
- Bertolo, P. and Weiczorek, G.F., 2005, Calibration of numerical models for small debris flows in Yosemite Valley, California, USA: *Natural Hazards and Earth Systems Science*, v. 5, p. 993-1001, doi: 10.5194/nhess-5-993-2005.
- CAL Fire 2018, Damage Inspection Database: California Department of Forestry and Fire Protection, Office of the State Fire Marshall, DINS GIS data, GIS file dated 26 April 2018.
- Dibblee, T.W., Jr., 1966, Geology of the central Sana Ynez Mountains, Santa Barbara County, California: California Division of Mines and Geology Bulletin 186, 99 p.
- Cannon, S.H., Gartner, J.E., Rupert, M.G., Michael, J.A., Staley, D.M., and Worstell, B.B., 2010, Emergency assessment of postfire debris-flow hazards for the 2009 Station fires, San Gabriel Mountains, southern California: U.S. Geological Survey Open-File Report 2009-1227, 27 p.
- Ebel, B.A., and Moody, J.A., 2017, Synthesis of soil-hydraulic properties and infiltration timescales in wildfire-affected soils: *Hydrological Processes*, v. 31, no. 2, p. 324-340, doi:10.1002/hyp.10998.
- FLO-2D Software, Inc., 2017, FLO-2D Reference Manual, Build No. 17: <https://www.flo-2d.com/download>.
- FLO-2D Software, Inc., 2015, Simulating Mudflows: White Paper, <https://www.flo-2d.com/download>.
- Gartner, J.E., Cannon, S.H., and Santi, P.M., 2014, Empirical models for predicting volumes of sediment deposited by debris flows and sediment-laden floods in the transverse ranges of southern California: *Engineering Geology*, v. 176, p. 45-56, doi: 10.1016/j.enggeo.2014.04.008.
- Griswold, J.P. and Iverson, R.M., 2008, Mobility Statistics and Automated Hazard Mapping for Debris Flows and Rock Avalanches (ver. 1.1, April 2014): U.S. Geological Survey Scientific Investigations Report 2007-5276, 59 p.
- Horton, P., Jaboyedoff, M., Rudaz, B., and Zimmermann, M., 2013, Flow-R, a model for susceptibility mapping of debris flows and other gravitational hazards at a regional scale: *Natural Hazards Earth Systems Science*, v. 13, p. 869-885, doi: 10.5194/nhess-13-869-2013.
- Hungr, O. and McDougall, S., 2009, Two numerical models for landslide dynamic analysis: *Computers & Geosciences*, v. 35, p. 978-992, doi:10.1016/j.cageo.2007.12.003.
- Iverson, R.M., Schilling, S.P., and Vallance, J.W., 1998, Objective delineation of lahar-inundation hazard zones: *Geological Society of America Bulletin*, v. 110, no. 8, p. 972-984, doi:10.1130/0016-7606(1998)110<0972:ODOLIH>2.3.CO;2.
- Iverson, R.M. and George, D.L., 2014, A depth-averaged debris-flow model that includes the effects of evolving dilatancy. I. Physical basis: *Proceedings of the Royal Society A*, v. 470, no. 20130819, doi:10.1098/rspa.2013.0819.
- Kean, J.W., Staley, D.M., Lancaster, J.T., Rengers, F.K., Swanson, B.J., Coe, J.A., Hernandez, J.L., Sigman, A.J., Allstadt, K., and Lindsay, D.N., *in press*, Inundation, flow dynamics, and damage in the 9 January 2018 Montecito Debris-Flow Event, California, USA: Opportunities and challenges for post-wildfire risk assessment.
- Kean, J.W., Staley, D.M., Lancaster, J.T., Rengers, F.K., Swanson, B.J., Coe, J.A., Hernandez, J.L., Sigman, A.J., Allstadt, K., and Lindsay, D.N., 2019, Debris-flow inundation and damage data from the 9 January 2018 Montecito Debris-Flow Event, U.S. Geological Survey data release, doi:10.5066/P9JQU0E.
- Magirl, C.S., Griffiths, P.G., and Webb, R.H., 2010, Analyzing debris flows with the statistically calibrated empirical model LAHARZ in southeastern Arizona, USA: *Geomorphology*, v. 119, no. 1, p. 111-124, doi:10.1016/j.geomorph.2010.02.022.
- McCoy, K., Krasko, V., Santi, P., Kaffine, D., and Reffennack, S., 2016, Minimizing economic impacts from post-fire debris flows in the western United States: *Natural Hazards*, v. 83, no. 1, p. 149-176, doi: 10.1007/s11069-016-2306-0.
- National Weather Service, 2018, Flash Flood & Debris Flow Event Montecito, California January 9, 2018, National Weather Service Los Angeles/Oxnard CA: <https://www.arcgis.com/apps/MapJournal/index.html?appid=541c23aa483b48978d1bc9904a6fb14d>.
- O'Brien, J.S., Julien, P.Y., and Fullerton, W.T., 1993, Two-dimensional water flood and mudflow simulation: *Journal of Hydraulic Engineering*, v. 119, no. 2, p. 244-261.
- Rengers, F., McGuire, L., Kean, J.W., Staley, D.M., and Hobley, D., 2016, Model simulations of flood and debris flow timing in steep catchments after wildfire: *Water Resources Research*, v. 52, no. 8, p. 6041-6061, doi:10.1002/2015WR018176.
- Rickenmann, D., Laigle, D., McArdeall, B.W., and Hübl, J., 2006, Comparison of 2D debris-flow simulation models with field events: *Computational Geosciences*, v. 10, p. 241-264, doi:10.1007/s10596-005-9021-3.
- Schilling, S.P., 1998, LAHARZ: GIS programs for automated mapping of lahar-inundation hazard zones: U.S. Geological Survey Open-File Report 98-638, 80 p.
- Staley, D.M., Negri, J.A., Kean, J.W., Laber, J.L., Tillery, A.C. and Youberg, A.M., 2017, Prediction of spatially explicit rainfall intensity-duration thresholds for post-fire debris-flow generation in the western United States: *Geomorphology*, v. 278, p. 149-162, doi:10.1016/j.geomorph.2016.10.019.
- U.S. Geological Survey, 2018, Emergency assessment of post-fire debris-flow hazards, 2017 Thomas Fire: https://landslides.usgs.gov/hazards/postfire_debrisflow/detail.php?objectid=178.

Possibilities and limitations for the back analysis of an event in mountain areas on the coast of São Paulo State, Brazil using RAMMS numerical simulation

Claudia Vanessa dos Santos Corrêa^{a,*}, Fábio Augusto Gomes Vieira Reis^b, Lucília do Carmo Giordano^b, Victor Carvalho Cabral^b, Débora Andrade Targa^b, Hermes Dias Brito^b

^a*Cemaden (National Center for Monitoring and Early Warning for Natural Disaster), Dr. Altino Bondensan Road 500, São José dos Campos 12247-016, Brazil*

^b*UNESP (São Paulo State University), Institute of Natural Sciences and Technology, 24-A Avenue 1515, Rio Claro 13506-900, Brazil*

Abstract

Debris flows are mass movements that develop along drainage networks and involve generally dense fluids, composed of materials of different grain sizes, as well as woods and variable amounts of water, identified as natural processes that constitute the dynamics and the modeling of the landscape. The areas most susceptible to the occurrence of these processes in Brazil are in the foothills of the Serra do Mar, Serra da Mantiqueira and the Serra Geral, and on the north coast of São Paulo State. In 03/18/1967 there was an important landslide and debris-flows which affected the region of Caraguatatuba and São Sebastião. In this area, there is a pipeline network associated with Petrobras Treatment Units, other enterprises, structures and a large urban area in growth. The aim of this work is to show the results of the back-analysis of the debris-flow events that occurred in 1967 in a mountain area in the Serra do Mar in Caraguatatuba region (São Paulo State, Brazil) with RAMMS numerical simulation, using calibrated input parameters. The inputs were viscosity, DEM, landslide scars as release areas, the density of the debris-flow material, duration of debris-flow process and orthophoto. The modeling results were compared with the deposit area mapped in aerial photos, which was established zones of iso-thickness of the materials. The results showed a good correlation between the area and thickness of deposition modeled and observed. Moreover, the fieldwork and the retro-analysis studies revealed that the Serra do Mar debris flows have a predominantly granular rheological flow and the modeling results showed that the deposition zones are given preferably in regions with slope less than 5°.

Keywords: Numerical simulation; RAMMS model; Serra do Mar; Brazil

1. Introduction

Debris flows are rapid downslope, gravity-driven movements of materials behaving as, highly viscous, dense and concentrated to hyperconcentrated fluids. Debris-flow processes can comprise large volumes of soils, blocks of rocks, wood and other plant materials, man-made structures, and varying amounts of water. Often initiated by heavy rainfall and/or landslides, debris-flows process commonly develop along steep talwegs and deposit in flat areas (Selby, 1993; Hutter et al., 1994; Takahashi, 2014; Kang and Lee, 2018). They are characterized by the long range, high speed, high peak flow, high erosion capacity, impact force and for this they constitute an important risk factor for the population (Begueria et al., 2009; Kang and Lee, 2018).

Mathematically, debris flows can be described as a one-phase fluid composed by an interstitial liquid and by a granular fluid that constitutes the solid phase and has proper rheological properties (Iverson, 1997; Rosatti and Begnudelli, 2013; Liu et al., 2017). This represents a simplification of a debris-flow process where the main components are water and solid material consisting of a wide range of grain sizes (Rickenmann et al., 2006). Thus,

* Corresponding author e-mail address: claudia.correa@cemaden.gov.br

several numerical models have been elaborated in the last years, to measure, identify, predict and monitor debris-flow processes with more accuracy, as FLO-2D, KANAKO 2D and MassMov2D (Pudasaini, 2005; Wu et al., 2012). One of these models is RAMMS (Rapid Mass Movement Simulation), which uses a single-phase model, that doesn't distinguish between fluid and solid phases and the material is modeled as a bulk flow. This model describes the frictional behavior of debris-flows movement using the Voellmy relation (Christen et al., 2010).

The most susceptible areas to debris-flow processes in Brazil are located in the southeastern in the SW-NE oriented foothills of Serra do Mar, Serra da Mantiqueira and Serra Geral. In the city of Caraguatatuba (São Paulo State), one of the most expressive brazilian mass movements event occurred in 1967, triggered by heavy rains. It is estimated that a huge volume of earth material and over 30,000 trees descended the Serra do Mar slopes of the and reached the city, totally or partially destroying 400 houses, and killing 120 people (Gomes et al., 2008a).

Studies involving modeling of debris flows both, retro- and forward analysis are still very rare in Brazil. The pioneering work of Alvarado (2006) used of the Discrete Element Method (DEM) to simulate debris-flow process and in the last years Lopes and Riedel (2007), Gomes et al. (2008b), Polanco (2010), Bueno et al. (2013), Gomes et al. (2013), Sakai et al. (2013), Silva et al. (2013), Conterato (2014), Pelizoni (2014), Rocha et al. (2014), Sancho (2016), and Silva-Filho (2016) also included in their scope studies of brazilian debris-flow cases involving mathematical modeling.

Thus, the aim of this work is to show the results of modeling of a debris-flow process occurred in 1967 in a mountain area in the Serra do Mar in Caraguatatuba region (São Paulo State, Brazil) with RAMMS numerical simulation, using parameters calibrated as input, obtained by retro-analysis of the event. In the last years, there has been an increase in the occurrence of these phenomena in Brazil, which demands a better understanding of their conceptual model. In the Serra do Mar region there is a pipeline network associated with Petrobras Treatment Units, roads, industries and a large urban area in growth, which increases the risk factor for debris-flow movements.

1.1. Study area

The study area is the Santo Antônio river basin (Fig 1), inserted in the Serra do Mar mountain range, an escarpment area on the eastern margin of the Brazilian highlands, which has been known to be the most landslide and debris flows prone location in Brazil, due to the local hot and humid climate and its long slopes (Cruz, 1974; Lacerda and Silveira, 1992; Cruz, 2000; Cerri et al., 2018). The region has as a humid tropical climate with dry season. Rainfall is concentrated during summer, which amounts for 70% of the annual total, while winter months (June to August) are characterized as the dry season, with monthly precipitation around 100 mm. The annual precipitation ranges from 1,784 to 2,000 mm and the annual average temperature is 27°C (Cruz, 1974; Seluchi et al., 2011).

The Santo Antônio river basin, which has an area of 37.5 km², extending from the Serra do Mar escarpments to alluvial and coastal plains, the Caraguatatuba urban area. The most upstream portions of the catchment are characterized by particularly steep slopes, while the downstream areas are very flat area (Fig 2), where urbanization is still expanding (Sakai, 2014).

The geology encompasses neoproterozoic rocks, such as to gneisses, migmatites, migmatitic gneisses, granites, schists and quartzites, with a predominant NE-SW structural orientation (Almeida, 1964; Chieregati et al., 1982; Cerri et al., 2018). The lower section of the Santo Antônio Basin is composed of unconsolidated sediments such as sands, silts, clays and fluvial gravels, as well as colluvial sediments and beach, marine and fluvial-marine deposition sands (Chieregati et al., 1982).

1.2. The 03.18.1967 event

The occurrence of the 1967 event in Caraguatatuba is related to the incidence of high rainfall rates that affected the region in March of the same year. So, about 945.9 mm were recorded in this month, from that, 260 mm and 325 mm were recorded on 17th and 18th, respectively. In the day of the event, 585 mm accumulated in 48 hours (IPT, 1988).

Landslides began on the morning of March 18th and were gradually occurring until the afternoon, a period that registered its most critical phase, in a generalized and simultaneous manner, particularly on slopes steeper than 22° (Cruz, 1990; Gramani, 2001) (Fig 3).

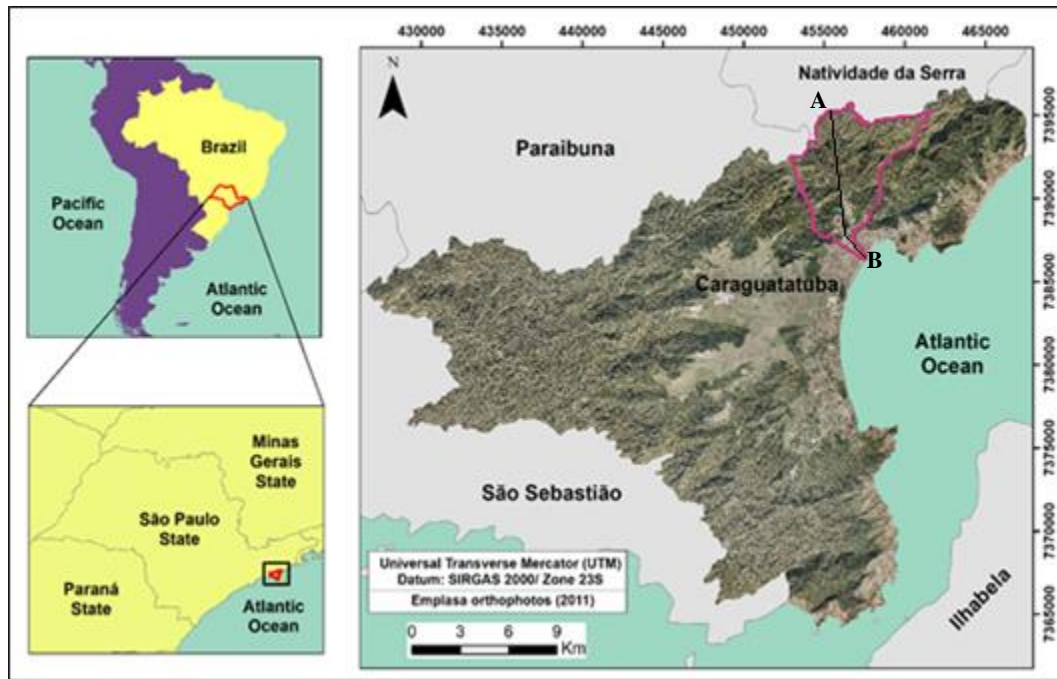


Fig. 1. Location map of the study area. The Santo Antônio basin is marked on pink. The A-B section represents the profile path (Fig 2).

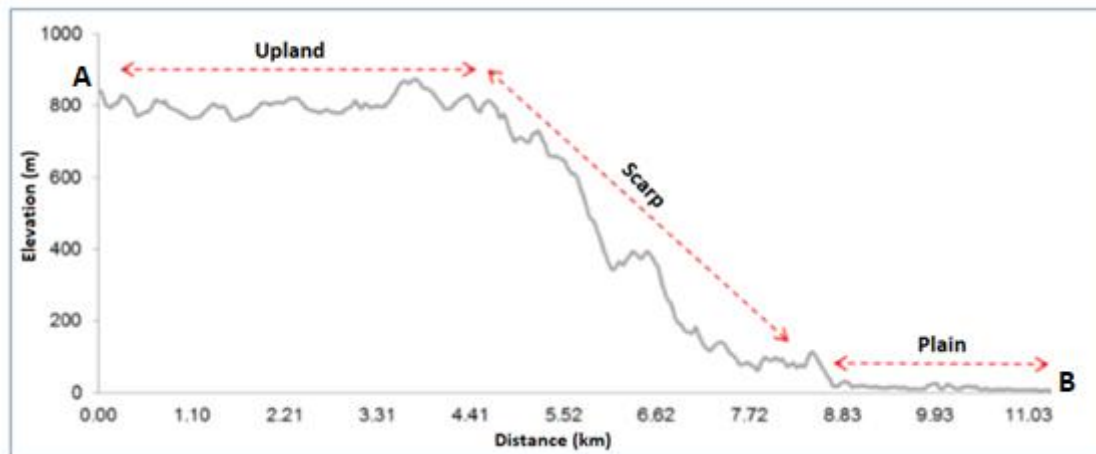


Fig. 2. Topographic profile of Santo Antônio Basin. The relief in the catchment is compartmentalized in upland, escarpment, and plain, whose associated features are mamelonized hills, predominantly retilized slopes, and flat areas, respectively (Cruz, 1974). Adapted from Nery (2016).

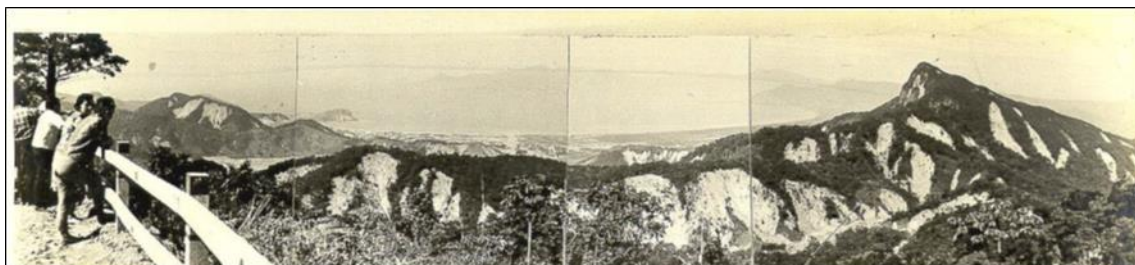


Fig. 3. Landslide scars on the Serra do Mar slopes in the Santo Antônio basin. The photo was taken from a belvedere on the Tamoios Highway, main access road of the plateau to the coast, one month after the occurrence of the events of 03/18/1967. Landslide scars are mainly distributed on slopes with slopes greater than 22°. Photograph by Cruz (1974).

Around 4:15 pm, after the material mobilized by the landslides converged almost simultaneously to the main drainages of the mountainous region and were channeled, causing debris-flow process, that transported a great amount of earth and biomass. After 5 pm, in the final section of the river, next to the coast, the processes of mud flow and mud flood began, so that the material mobilized by these processes accumulated in a bridge of the Santo Antônio River and caused its disruption, which promoted a flood in the whole plain of the river with lots of mud and logs, reaching the urban area and the beach, where drainage flows into the sea (Cruz, 1974) (Fig 4). In the fieldwork

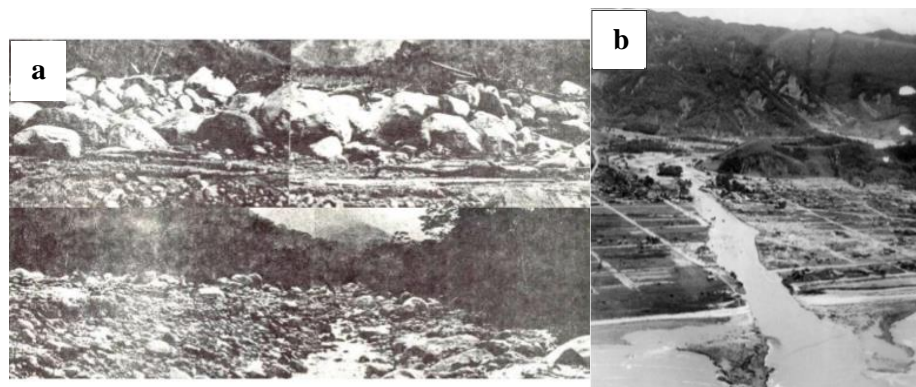


Fig. 4. Mud flow, mud flood and debris flows of 03/18/1967 in the Santo Antônio basin in Caraguatatuba. (a) Blocks mobilized during the process, near the landslides, in the tributary channels and in the middle section of the main river of the Santo Antônio basin. In the fieldworks, the block deposits also were observed in the middle section of the main channel. (b) Aerial view of the escarpments with the landslide scars and the plain with mud flow and mud flood processes. Photographs by Cruz (1974) and municipal archives of Caraguatatuba.

1.3. The RAMMS model

RAMMS (Rapid Mass Movement Simulation) is a numerical 2D simulation model developed by the WSL Institute for Snow and Avalanche Research SLF and the Swiss Federal Institute for Forest, Snow and Landscape Research WSL. The physical model of RAMMS uses the Voellmy-Salm continuous flow model (Salm et al., 1990; Salm, 1993) based on Voellmy friction law (1955) and describes debris-flow processes as a continuous model of medium depth. This model divides the frictional resistance into two parts: a dry-Coulomb type friction (coefficient μ) that scales with the normal stress and a velocity-squared drag or viscous-turbulent friction (coefficient ξ). Thus, the friction resistance S (Pa) is defined as

$$S = \mu \rho H g \cos(\varnothing) + \frac{\rho g U^2}{\xi} \quad (1)$$

where ρ is the density, g the gravitational acceleration, \varnothing the slope angle, H the flow height and U the flow velocity. The normal stress on the running surface, $\rho H g \cos(\varnothing)$, can be summarized in a single parameter N . RAMMS uses a single-phase model, so we cannot distinguish between fluid and solid phases and the material is modeled as a bulk flow. Regarding the entrainment of bed materials, the version v1.5 does not consider the erosion effect, so it is not possible to predict the increase in volume of the debris-flow material as it travels along the channel.

The input parameters of RAMMS are the total volume of the debris flow and the resistance parameters μ and ξ . As output data, the program provides values (for each grid cell) of flow height, flow velocity, flow pressure, impact forces, as well as profiles of height, velocity and flow pressure at certain locations for projecting structures (Bartelt et al., 2013).

2. Materials and methods

2.1. Back-analysis studies of the 03/18/1967 debris flows

The back-analysis studies included the historical retrieval of the variables that involved the debris-flow processes in the Santo Antônio basin in March 1967, the extraction of the landslide scars and the mapping of the deposits and their respective thicknesses (Gregoretto et al., 2016). The main causes of occurrence of the event were investigated through bibliographical research on reference works, including photographic and cartographic registration.

For the landslides scars extraction aerial photos in 1: 25,000 scale with 1.5 x 1.5 m spatial resolution of the VASP (São Paulo Airway) aerial photogrammetric survey were selected for the respective procedures. The extraction was performed using photointerpretation techniques in a GIS environment so that the size, the vegetation, the texture and shape were the criteria considered to the identification (Loch, 1984; Marchetti and Garcia, 1986; Barlow et al., 2003; Guzzetti et al., 2012). The mapping of the debris-flow deposits and their respective thicknesses was also carried out in the GIS environment using photointerpretation techniques (Vandine, 1985; Van Steijn, 1996), complemented information from bibliographical data and fieldwork.

2.2. Debris-flow modeling RAMMS

Prior to numerical modeling in RAMMS, the program input parameters were listed and modified according to the model needs. Thus, the topographic data from the DEM was converted to ASCII format. Moreover, the calculation domain and the release area were transformed to the shapefile format and the release height was inserted in the program/ imported of the shapefile attribute table of the release areas. The information about debris flow duration, the material density and μ/ξ parameters were obtained from bibliographical data (Table 1).

The modeling step in the RAMMS version 1.5 program was performed through the establishment of a simulation routine, based on different release heights, material density, and viscosity (ξ).

3. Results and Discussion

Before the modelling in the RAMMS program, the input parameters were adjusted according to the its requirements (Table 1).

Table 1. Input parameter, data source and numerical parameter required in the RAMMS model

Input	Source	Numerical parameter
Topographic data	DEM in 1:10,000 scale, from 1979	Grid of 8 m
Release area	Landslide scars from aerial photos (1973)	-----
Release height	Back-analysis (Fúlfaro et al. 1976; Massad et al., 1997; Massad, 2002) and fieldwork observations	1.0 m
		1.3 m
Calculation domain	Santo Antônio basin with 600 meters buffer	-----
Debris flow duration	Back-analysis (Gramani, 2001)	45 min (2,700 s)
Material density	Back-analysis (Fúlfaro et al., 1976; Listo and Vieira, 2015)	Fúlfaro et al. (1976) – 1.8 ton/m ³ (1,800 kg/m ³)
		Listo and Vieira (2015) – 1,800 kg/m ³ , 1,900 kg/m ³ e 2,000 kg/m ³
μ (dry-Coulomb type friction coefficient)	Back-analysis / $\tan(\alpha)$ (α is the slope angle in the deposition zone)	0,05 [-] (slope angle in the deposition zone (2.9°) was obtained by photointerpretation analysis in the debris flow deposit)
ξ (viscous-turbulent friction coefficient)	Back-analysis (flow characteristics described by Cruz (1974), Fúlfaro et al. (1976) and Gramani (2001)) and empirical tests	100, 130, 160, 190 and 200 m/s ²

From the presented inputs, the simulations routine conducted in the program was based on the different thicknesses of the landslide scars, material density, and viscosity (Table 2).

Table 2. Simulation routines in the RAMMS model

		Release height 1 meter					Release height 1.3 meters				
		100	130	160	190	200	100	130	160	190	200
ξ (m/s ²)											
Material density (kg/m ³)	1,800	S-1	S-2	S-3	S-4	S-5	S-16	S-17	S-18	S-19	S-20
	1,900	S-6	S-7	S-8	S-9	S-10	S-21	S-22	S-23	S-24	S-25
	2,000	S-11	S-12	S-13	S-14	S-15	S-26	S-27	S-28	S-29	S-30

In general, the simulations of the different scenarios showed that the materials mobilized by the landslides in the escarpments of the tributaries of the Santo Antônio river were channeled in the thalwegs and advanced downstream, where slopes lower than 5° prevail (Fig. 5). The mud flow and mud flood processes, which occurred after the debris flow and caused the rupture of a bridge in the Santo Antônio River, were not simulated.

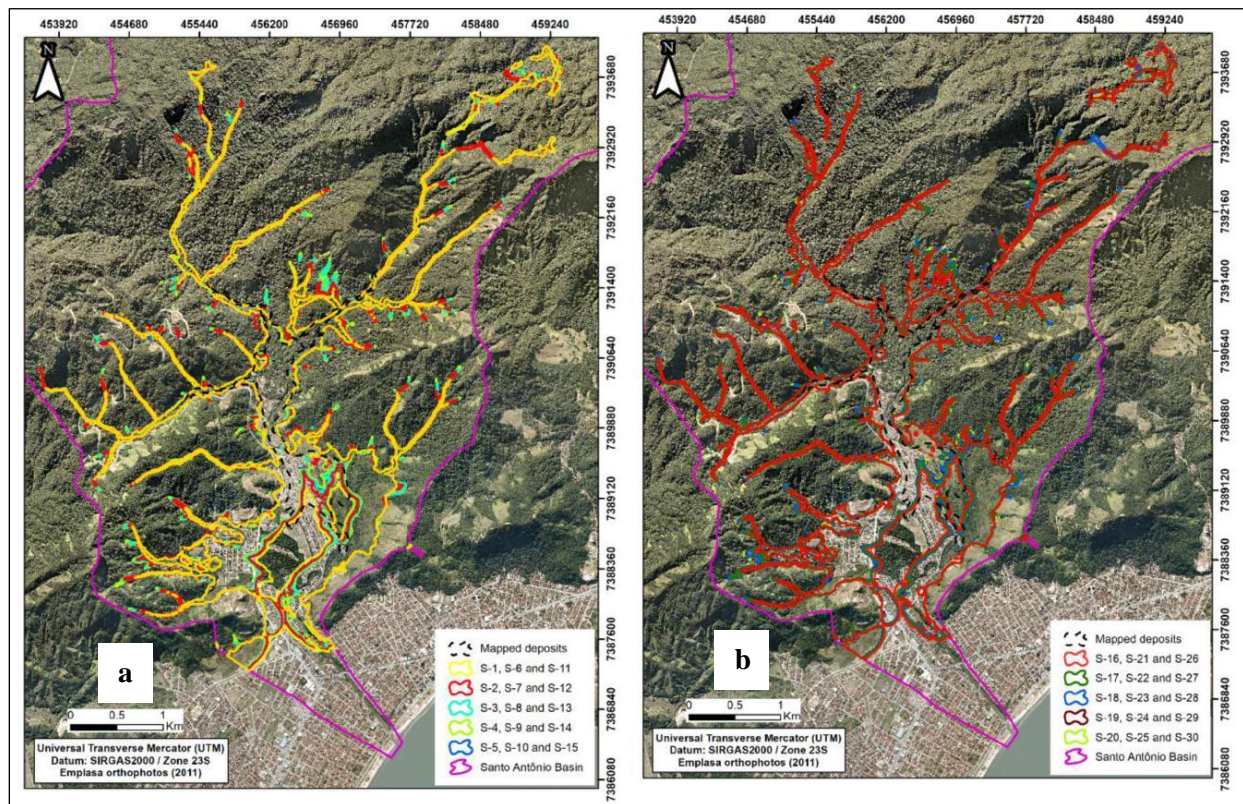


Fig. 5. (a) Spatial distribution of the debris-flow deposits produced by the RAMMS model from release height of 1.0 meter vs. deposits mapped on 1973 aerial photographs in the retro-analysis step and (b) debris-flow deposits resulting from RAMMS model for release height of 1.3 meters.

The debris-flow fan could not be represented by the simulations due to the Digital Elevation Model used, dating from 1979 (IGC, 1979), 12 years after the event. Consequently, the DEM does not represent the conditions of relief before the debris flow. Thus, noticeable differences are observed in the Santo Antônio river thalweg, which was originally meandering, and after the event, whose date is not precise, underwent a process of channelization. The limitation of DEM is because there are no older topographical bases for the place, since the first aerophotogrammetric surveys in the region date back to 1974 and correspond to the 1:50,000 scale. It was decided not to use them because the elaboration of a DEM from these data would hinder and reduce the quality of the simulations in the model.

Although the mapped deposit considered aerial photographs of 1973, 6 years after the event, it is notorious that the debris-flow deposit area that the limitation of the DEM (based on 1979 topographic data) influenced the result calculated by the model, especially in relation to the river Santo Antonio in plain area, which was channeled some

years after the 1967 event. Hussin et al. (2012), when performing debris-flow modeling in the French Alps in 2003, also verified that changes in channel morphology directly influence the results produced in the simulations in the RAMMS.

4. Conclusions

Even though the simulations have not been able to adequately reproduce the geometry of the debris-flow deposits related to the 1967 event in the Santo Antônio basin, they suggest that future debris-flow events are unlikely to form debris cones due to the channeling of the Santo Antônio river. Results of the retro-analysis and modeling showed that the areas of deposition of the debris-flow process to the place are preferably in regions of low slope ($<5^\circ$).

Acknowledgements

The authors would like to thank the Brazilian research agencies: Agência Nacional do Petróleo/ Programa de Recursos Humanos (ANP/ PRH-05) and Conselho Nacional de Desenvolvimento Científico e Tecnológico (CNPq). We also thank the Laboratório de Geologia de Engenharia e Meio Ambiente (GEMA), Centro de Geociências Aplicadas ao Petróleo (Unespetro) and Department of Geosciences (University of Tübingen/ Germany) for technical and scientific support.

References

- Almeida, F.F.M., 1964, Fundamentos Geológicos do Relevo Paulista: Boletim do Instituto de Geografia e Geologia, v. 4, p. 169-263.
- Alvarado, L.A.S., 2006, Simulação bidimensional de corridas de detritos usando o Método de Elementos Discretos [Ph.D. thesis]: Rio de Janeiro, PUC-RJ, 154 p.
- Barlow, J., Martin, Y., Franklin, S.E., 2003, Detecting translational landslide scars using segmentation of Landsat ETM+ and DEM data in the northern Cascade Mountains, British Columbia: Canadian Journal of Remote Sensing, v. 29, p. 510-517, doi: 10.5589/m03-018.
- Bartelt, P., Buehler, Y., Christen, M., Deubelbeiss, Y., Graf, C., McArdeell, B.W., Salz, M., Schneider, M., 2013, RAMMS - A modelling system for debris flows in research and practice: Davos, WSL Institute for Snow and Avalanche Research SLF, User Manual v.1.5 / Debris flow.
- Beguerra, S., Van Asch, T.W.J., Malet, J.P., Grondahl, S., 2009, A GIS-based numerical model for simulating the kinematics of mud and debris flows over complex terrain: Natural Hazards and Earth System Sciences, v. 9, p. 1897-1909, doi: 10.5194/nhess-9-1897-2009.
- Bueno, K.E.M., Siefert, C.A.C., Santos, I., 2013, Modelagem simplificada para previsão do alcance de fluxo de detritos na bacia hidrográfica do rio Gigante – Serra do Mar Paranaense, in Proceedings, Simpósio Brasileiro de Geografia Física e Aplicada, 15th, Vitória: Vitória, Brazil.
- Cerri, R.I., Reis, F.A.G.V., Gramani, M., Rosolen, V., Luvizotto, G.L., Giordano, L.C., Gabelini, B.M., 2018, Assessment of landslide occurrences in Serra do Mar mountain range using kinematic analyses: Environmental Earth Sciences, v. 77, no. 9, doi: 10.1007/s12665-018-7508-1.
- Chierigati, L.A.; Theodorovicz, A.M.G.; Theodorovicz, A.; Menezes, R.G.; Chiodi-Filho, C.; Ramalho, R., 1982, Projeto folhas Natividade da Serra e Caraguatutuba: Relatório Final: São Paulo, Companhia de Pesquisa de Recursos Minerais, Diretoria da Área de Pesquisas. Superintendência Regional de São Paulo, v. 1, 158 p., <http://rigeo.cprm.gov.br/xmlui/handle/doc/6948>.
- Christen, M., Kowalski, J., Bartelt, P., 2010, RAMMS: Numerical simulation of dense snow avalanches in three-dimensional terrain: Cold Regions Science and Technology, v. 63, p. 1-14, doi: 10.1016/j.coldregions.2010.04.005.
- Conterato, L., 2014, Uso do programa RAMMS na modelagem de corridas de detritos e previsão de áreas atingidas: estudo do caso de Quitite-Papagaio [Ph.D. thesis]: Porto Alegre, Federal University of Rio Grande do Sul, 188 p.
- Cruz, O., 1974, A Serra do Mar e o Litoral na Área de Caraguatutuba-SP: Contribuição à Geomorfologia Litorânea Tropical [Ph.D. thesis]: São Paulo, São Paulo University (USP), 181 p.
- Cruz, O., 2000, Studies on the geomorphic processes of overland flow and mass movements in the Brazilian geomorphology: Revista Brasileira de Geociências, v. 30, p. 504-507.
- Fúlfaro, V., Ponçano, W.L., Bistrichi, C.A., Stein, D.P., 1976, Escorregamentos de Caraguatutuba: expressão atual, e registro na coluna sedimentar da planície costeira adjacente in Proceedings, Congresso Brasileiro de Geologia de Engenharia, 1st, Volume 2: Rio de Janeiro, Brazil, p.341-346.
- Gomes, C.L.R., Ogura, A.T., Gramani, M.F., Corsi, A.C., Alameddine, N., 2008a, Retro-análise da corrida de massa ocorrida no ano de 1967 nas encostas da Serra do Mar, vale dos rios Camburu, Pau D' Alho e Canivetal, município de Caraguatutuba - SP: quantificação volumétrica dos sedimentos depositados nas planícies de inundação, in Proceedings, Congresso Brasileiro de Geologia de Engenharia e Ambiental, 12th, November 2008: Recife, Brazil.
- Gomes, R.A.T., Guimarães, R.F., Carvalho, A.O. Jr., Fernandes, N.F., Vargas, E.A. Jr., Martins, E.A., 2008b, Identification of the affected areas by mass movement through a physically based model of landslide hazard combined with an empirical model of debris flow: Natural Hazards, v. 45, p. 197-209, doi: 10.1007/s11069-007-9160-z.
- Gomes, R.A.T., Guimarães, R.F., Carvalho, A.O. Jr., Fernandes, N.F., Vargas, E.A. Jr., 2013, Combining Spatial Models for Shallow Landslides and Debris-Flows Prediction: Remote Sensing, v. 5, p. 2219-2237, doi: 10.3390/rs5052219.
- Gramani, M.F., 2001, Caracterização geológica-geotécnica das corridas de detritos (“Debris Flows”) no Brasil e comparação com alguns casos internacionais [M.Sc. thesis]: São Paulo, São Paulo University (USP), 372 p.

- Gregoretti, C., Degetto, M., Boreggio, M., 2016, GIS-based cell model for simulating debris flow runout on a fan: *Journal of Hydrology*, v. 534, p. 326–340, doi: 10.1016/j.jhydrol.2015.12.054.
- Guzzetti, F., Mondini, A.C., Cardinali, M., Fiorucci, F., Santangelo, M., Chang, K.T., 2012, Landslide inventory maps: new tools for an old problem: *Earth Science Reviews*, v. 112, p. 42–66, doi: 10.1016/j.earscirev.2012.02.001.
- Hussin, H.Y., Quan-Luna, B., Van Westen, C.J., Christen, M., Malet, J.P., Van Asch, Th.W.J., 2012, Parameterization of a numerical 2-D debris flow model with entrainment: a case study of the Faucon catchment, Southern French Alps: *Natural Hazards and Earth System Sciences*, v. 12, p. 3075–3090, doi: 10.5194/nhess-12-3075-2012.
- Hutter, K., Svendsen, B., Rickenmann, D. 1994, Debris-flow modeling: A review: *Continuum Mechanics and Thermodynamics*, v. 8, p. 1–35, doi: 10.1007/BF01175749.
- IPT-Instituto de Pesquisas Tecnológicas, 1988, Estudos da instabilização de encostas da Serra do Mar na Região de Cubatão, objetivando a caracterização do fenômeno “corrida de lama” e a prevenção de seus efeitos, São Paulo: IPT report, n. 25258.
- Iverson, R.M., 1997, The physics of debris flows: *Reviews of geophysics*, v. 35, p. 245–296, doi: 10.1029/97RG00426.
- Kang, S., Lee, S.R., 2018, Debris flow susceptibility assessment based on an empirical approach in the central region of South Korea: *Geomorphology*, v. 308, p. 1–12, doi: 10.1016/j.geomorph.2018.01.025.
- Lacerda, W.A., Silveira, G.C., 1992, Características de resistência ao cisalhamento e de compressibilidade dos solos residuais e coluvionares da encosta do Soberbo, RJ *in* Proceedings, COBRAE, 1st, Rio de Janeiro, Volume 1: ABMS/ABGE, p. 445–461.
- Listo, F.D.L.R., Vieira, B.C., 2015, Influência de Parâmetros Geotécnicos e Hidrológicos na Previsão de Áreas Instáveis a Escorregamentos Translacionais Rasos Utilizando o Modelo Trigrs: *Revista Brasileira de Geomorfologia*, v. 16, p. 485–500, doi: 10.20502/rbg.v16i3.665.
- Loch, C., 1984, A interpretação de imagens aéreas: noções básicas e algumas aplicações nos campos profissionais: Florianópolis, Brazil, Série didática, Editora da UFSC, 86 p.
- Lopes, E.S.S., Riedel, P.S., 2007, Simulação de corrida de detritos na bacia do Rio das Pedras que afetou a Refinaria Presidente Bernardes em Cubatão-SP, São José dos Campos: INPE ePrint: sid.inpe.br/mtcm17@80/2007/06.28.12.48.
- Liu, W., Siming, H.E., Ouyang, C., 2017, Two-dimensional Dynamics Simulation of Two-phase Debris Flow: *Acta Geologica Sinica (English Version)*, v. 91, p. 1873–1883, doi: 10.1016/j.compfluid.2012.10.006.
- Marchetti, D.A.B., Garcia, G.J., 1986, Princípios de fotogrametria e fotointerpretação: São Paulo, Nobel, 257 p.
- Massad, F., 2002, Corridas de massas geradas por escorregamentos de terra: relação entre área deslizada e a intensidade de chuva *in* Proceedings, Congresso Brasileiro de Mecânica dos Solos e Geotecnia, 12th, Volume 2: São Paulo, Brazil, p. 1223–1234.
- Massad, F., Cruz, P., Kanji, M., 1997, Comparison between estimated and measured debris flow discharges and volume of sediments *in* Proceedings, Pan-American Symposium on Landslides, 2nd: Rio de Janeiro, Brazil: p. 213–222.
- Nery, T.D., 2016, Dinâmica das corridas de detritos no Litoral Norte de São Paulo [Ph.D. thesis]: São Paulo, São Paulo University (USP), 164 p.
- Pelizoni, A.B., 2014, Análise de fluxos de detritos na região serrana fluminense [M.Sc. thesis]: Rio de Janeiro, Federal University of Rio de Janeiro (UFRJ), 141 p.
- Polanco, L.S.E., 2010, Correlações empíricas para fluxo de detritos [M.Sc. thesis]: Rio de Janeiro, Federal University of Rio de Janeiro (UFRJ), 110 p.
- Pudasaini, S.P., Wang, Y., Hutter, K., 2005, Modelling debris flows down general channels: *Natural Hazards and Earth System Science*, v. 5, p. 799–819.
- Rickenmann, D., Laigle, D., McArdell, B., Hübl, J., 2006, Comparison of 2D debris-flow simulation models with field events: *Computational Geosciences*, v. 10, p. 241–264, doi: 10.1007/s10596-005-9021-3.
- Rocha, H.L., Kobiyama, M., Michel, G.P., 2014, Aplicação do modelo FLO-2D para simulação de fluxos de detritos na bacia do rio Cunha, Rio dos Cedros/SC *in* Proceedings, Encontro Nacional de Engenharia de Sedimentos, 11th, João Pessoa, December 2014: João Pessoa, Brazil.
- Rosatti, G., Begnudelli, L., 2013, Two-dimensional simulation of debris flows over mobile bed: Enhancing the TRENT2D model by using a well-balanced generalized Roe-type solver: *Computer and Fluids*, v. 7, p. 179–195, doi: 10.1016/j.compfluid.2012.10.006.
- Salm, B., 1993, Flow, flow transition and runout distances of flowing avalanches: *Annals of Glaciology*, v. 18, p. 221–226, doi: 10.3189/S0260305500011551.
- Salm, B., Burkard, A., Gubler, H., 1990, Berechnung von Fliesslawinen: eine Anleitung für Praktiker mit Beispielen: Davos, Institut für Schnee- und Lawinenforschung SLF Mitteilung 47, Eidgenössische.
- Sakai, R.O., 2014, Estudo do impacto de Debris flows: caso da Bacia do Rio Santo Antônio em Caraguatuba (Brasil) [M.Sc. thesis]: São Paulo, São Paulo University (USP), 236 p.
- Sakai, R.O., Cartacho, D.L., Arasaki, E., Alfredini, P., Pezzoli, A., Sousa-Júnior, W.C., Rosso, M., Magni, L., 2013, Extreme Events Assessment Methodology Coupling Debris Flow, Flooding and Tidal Levels in the Coastal Floodplain of the São Paulo North Coast (Brazil): *International Journal of Geosciences*, v. 4, p. 30–38, doi: 10.4236/ijg.2013.45B006.
- Sancho, A.M.V., 2016, Análise dinâmica de fluxos de detritos em regiões tropicais [M.Sc. thesis]: Rio de Janeiro, PUC-RJ, 160 p.
- Selby, M.J., 1993, Hillslope: materials and process. Oxford University Press, Oxford, 142 p.
- Seluchi, M.E., Chou, S.C., Gramani, M., 2011, A case study of a winter heavy rainfall event over the Serra do Mar in Brazil: *Geofísica internacional*, v. 50, p. 41–56.
- Silva, J.A.P., Viera, L.C.L.M., Cintra, D.T., Lira, W.W.M., 2013, Desenvolvimento de metodologia para simulação de corrida de detritos utilizando o método dos elementos discretos *in* Proceedings, Congresso Brasileiro de Pesquisa e Desenvolvimento em Petróleo e Gás, 7th, Aracaju, October 2013: Aracaju, Brazil.
- Silva-Filho, J.W.P., 2016, Simulação e caracterização de corridas de detritos através do Método dos Elementos Discretos [M.Sc. thesis]: Maceió, Federal University of Alagoas (UFAL), 104 p.
- Takahashi, T., 2014, Debris flow: mechanics, prediction and Countermeasures, London: Taylor & Francis Group, 572 p.
- Van Steijn, H., 1996, Debris-flow magnitude-frequency relationships for mountainous regions of Central and Northwest Europe: *Geomorphology*, v. 15, p. 259–273, doi: 10.1016/0169-555x(95)00074-f.
- Vandine, D.F., 1985, Debris flows and debris torrents in the Southern Canadian Cordillera: *Canadian Geotechnical Journal*, v. 22, p. 44–68, doi: 10.1139/t85-006.
- Wu, Y.-H., Liu, K.-F., Chen, Y.-C., 2012, Comparison between FLO-2D and Debris-2D on the application of assessment of granular debris flow hazards with case study: *Journal of Mountain Science*, v. 10, p. 293–304, doi: 10.1007/s11629-013-2511-1.

Discrete-element investigation of granular debris-flow runup against slit structures

Junhan Du ^{a,b*}, Gordon G.D. Zhou ^{a,b}

^a Key Laboratory of Mountain Hazards and Earth Surface Process/Institute of Mountain Hazards and Environment, Chinese Academy of Sciences (CAS), Chengdu, China

^b University of Chinese Academy of Sciences, Beijing, China

Abstract

Runup of granular debris flows against slit dams on slopes is a complex process that involves deceleration, deposition and discharge. It is imperative to understand the runup mechanism and to predict the maximum runup height for the engineering designs and hazards mitigation. However, the interaction between granular flows and slit dams, which affects the runup height significantly, is still not well understood. In this study, a numerical investigation of granular debris flow impacting slit dams by the discrete element method (DEM) was then conducted. The influence of the opening size of slit dams characterizing by the relative post spacing $R=b/d$ (b : post spacing; d : particle diameter) on runup height was studied. Numerical study illustrates that there is a critical value of relative post spacing (R_c): within the critical value, the maximum runup height is insensitive to the relative post spacing; once b/d exceeds the critical value, the maximum runup height decreases rapidly as the relative post spacing increases.

Keywords: Granular debris flow; soil/structure interaction; discrete element method

1. Introduction

Granular debris flows comprise a wide range of particle sizes (Jakob et al., 2005), surging down slopes in response to gravitational attraction (Iverson et al., 1997). Due to the high mobility and huge entrained solid volume (Shen et al., 2018), granular debris flows can potentially result in disastrous consequences to downstream human lives and facilities (Hung et al., 1984). To mitigate such destructive hazards, slit structures such as slit dams (Watanabe et al., 1980) and an array of baffles (VanDine et al., 2012) are often strategically installed along the predicted flow path because such structures are effective in impeding flow mobility and dissipating flow energy (Choi et al., 2014a). Granular debris flows impact rigid structures and transfer momentum vertically into runup, potentially overtopping the obstacles (Ng et al., 2016). Design of structural countermeasures requires estimates of runup height to prevent overtopping downstream (Chu et al., 1995). However, runup of debris flows against obstacles is a complex process that involves a combination of flow deceleration and redirection that challenges the ability of physically based debris flow models to calculate the maximum runup heights accurately (Iverson, 2016).

In this study, a discrete-element investigation of granular debris flows impacting a slit structure under varying Froude conditions (N_{Fr}) and relative post spacing (b/d) was carried out. The runup mechanisms of granular flows in different Froude condition were observed. The influence of flow regime and relative post spacing on runup height was elaborated.

* Corresponding author e-mail address: spardadevil@vip.qq.com

2. Discrete element method

2.1. Numerical model setup

The 3-D particulate flow code EDEM (TranscenData, 2007) is adopted to simulate the dynamics of granular flow in this study. In the DEM, contact forces and displacements of a stressed assembly of particles are found by tracing the movement of individual particles. Discrete elements displace independently of each other and interact at contacts between particles and boundaries. The particle motion of each discrete element is calculated from forces acting on it by Newton's law of motion and finite displacements of discrete elements are computed progressively during the simulation (Ng et al., 2013).

Figure 1 show a plan view and a side view of the numerical model setup, respectively. Planar rigid geometry is constructed to model the channel bed and the slit dam. The sidewalls adopt the periodic boundaries condition (PBC) which is applied along the flow direction and spans the width of the channel ($w=200$ mm). The PBC is required to eliminate the unrealistic particle arrangement at the wall boundary caused by the constraint of particle sizes in discrete element simulations (Rapaport, 2004). Slit dam with rigid barriers and an adjustable opening b is positioned downstream of the flows. The rigid barriers are set to $H=2000$ mm in perpendicular height, which is high enough to avoid potential overflows so that the maximum runup height can be captured.

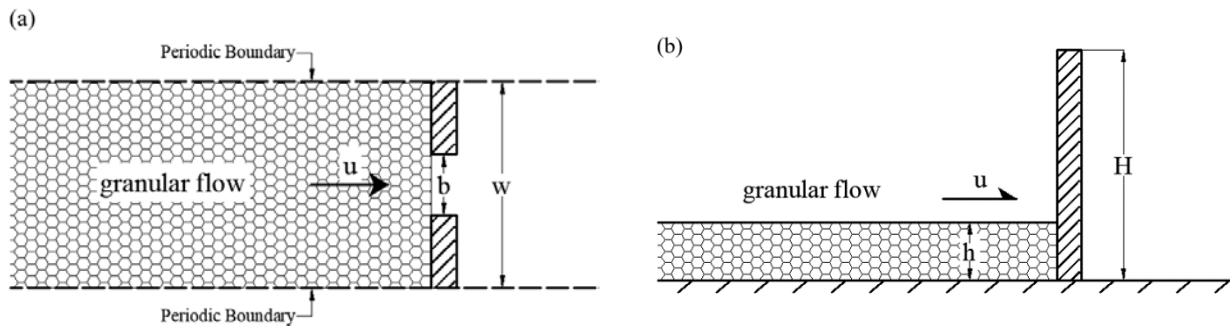


Fig. 1. Numerical model: (a) plan view; (b) side view

2.2. Input parameters

The granular flow is composed of an assembly of 30000 rigid spherical particles with a uniform diameter of 0.01 m. According to the commonly used values in numerical simulations of granular medium, the material density of each particle is 2630 kg/m³ and the material shear modulus is set to be 24,000 MPa. The contact friction angle of discrete elements is set as 35° (Pudasaini et al. 2005; Pudasaini and Hutter 2007; Mancarella and Hungr 2010; Ng et al. 2013; Choi et al. 2014b; Law et al. 2015). The interface friction angle is set as 16.6° which is consistent with the values adopted by Choi et al. (2016) in laboratory tests. Based on field and laboratory tests (Azzoni and Freitas 1995; Robotham et al. 1995; Chau et al. 2002), the coefficient of restitution is set as 0.5. Details of the input parameters are given in Table 1.

Table 1. DEM input parameters

Input parameter	Value
Number of discrete elements	30000
Particle diameter (m)	0.01
Density (kg/m ³)	2630
Total mass (kg)	41.4
Shear Modulus (MPa)	24000
Discrete element/wall friction	0.3
Discrete element friction	0.6
Rolling friction coefficient	0.01
Coefficient of restitution	0.5

The numerical study is divided into two stages: preparation stage and impact stage. In the preparation stage, a steady granular flow with a uniform depth is prepared right behind the slit dam. The initial flow depth h is fixed at 50 mm, which is 5 times the particle diameter. In the impact stage, initial velocities ranging from 0.38m/s to 5.7m/s are uniformly applied to the assembly of particles in order to obtain incoming flows with different flow regimes (Froude condition). The Froude number of the approach granular flow is set between the range of 0.5 and 7.5 which is consistent with the Froude number range of the reported channelized debris flow ranging from 0.5 to 7.6 based on field observations (Hübl et al. 2009; Scheidl et al. 2013; Cui et al. 2015). Gravitational acceleration (9.81m/s²) acts downward along the vertical direction. The channel inclination is fixed as 20° to supply the acceleration along the flow direction during the runoff process. Slit dams with relative post spacings (b/d) ranging from 2 to 12 were constructed and the transverse blockage ranged (R) from 10% to 60%. A control test without opening was also conducted for reference.

3. Interpretation of DEM results

3.1. Granular flows runoff mechanism

Froude number (N_{Fr}) which indicates the ratio of inertial force to gravitational force can capture the bulk characteristics of a flowing medium. Subcritical and supercritical flow conditions are characterised with Froude numbers less and greater than unity, respectively (Choi et al., 2015a). Figure 2 shows a side view of the impact and runoff process of subcritical flow ($N_{Fr}=0.5$) and supercritical flow ($N_{Fr}=6.5$), respectively. At $t = 0$ s, both subcritical and supercritical flows approach the barrier with an identical flow height (Fig.2 a1 and b1). For subcritical flow, a typical pile up mechanism can be observed; at $t = 0.1$ s, granular flow impacts the barrier, most particles in front of the flow deposits behind the rigid barrier, forming a ramp-like dead zone at the base of the barrier while a small amount of particles pass through the opening (Fig.2 a2). As subsequent flow material impacts the existing deposits, the pile up continues to develop and the dead zone expands upward (Fig.2 a3). Thereafter, the dead zone continues to thicken until the arrest of granular motion for all particles (Fig.2 a4 and a5). Numerical simulation results indicate that the subcritical granular flow exhibits a distinct pile up characteristics which is consistent with Armanini et al.(2011) and Choi et al. (2015b).

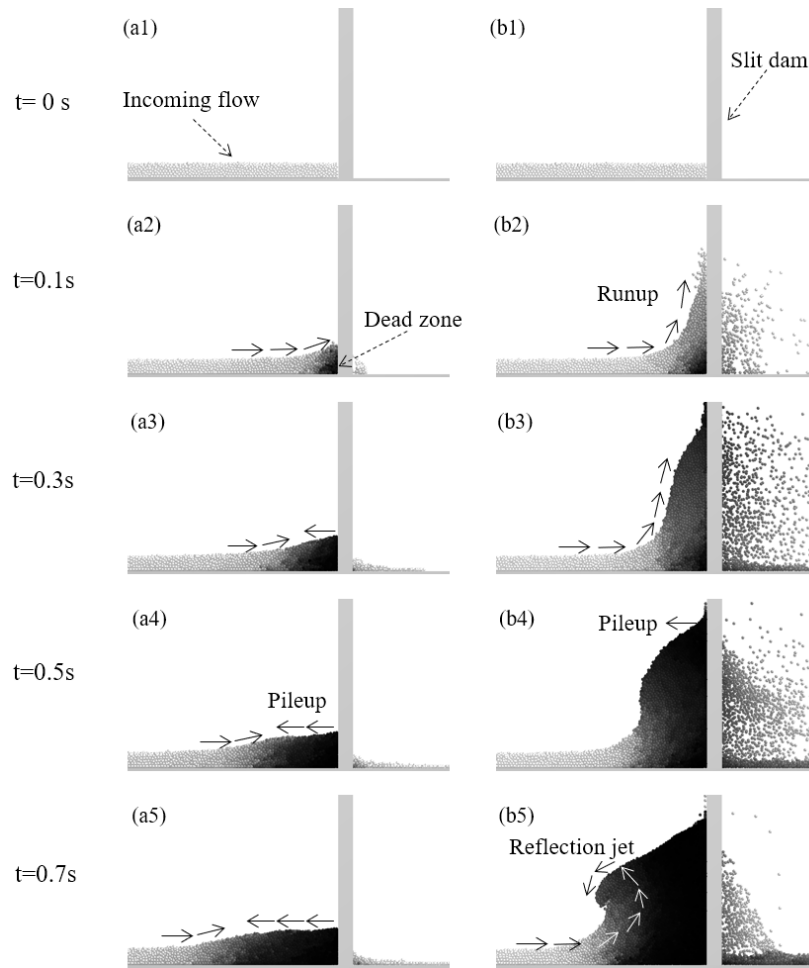


Fig. 2. Simulated flow kinematics for subcritical flow (a1-a5) and supercritical flow (b1-b5), $b/d=2.0$. The color of particles denotes the velocity of particles and the darker the color, the lower the velocity.

Supercritical granular debris flow resulted in a combination of a vertical jet runup and a pileup mechanism. At $t = 0.1$ s, a distinct upward jet along the barrier forms as the supercritical flow impacts the slit-dam (Fig. 2 (b2)). Such a runup mechanism is more reminiscent of the vertical jet mechanism described by Armanini et al. (2011) and Choi et al. (2015b) for liquid flows and is consistent with Ng et al. (2017) for granular flows of large glass particles. Subsequently, runup continues to develop and the runup height keeps increasing. Simultaneously, a large number of particles discharge the spacing and discharge dispersedly in a downstream jet. (Fig. 2 (b3)). When the maximum runup height is reached, the runup process ceases. Concurrently, the pileup process begins: the dead zone keeps thickening while its height remains unchanged (Fig. 2 (b4)). The numerical simulation results demonstrate that the runup mechanism between subcritical and supercritical granular flows are quite different, subcritical granular flows only exhibit a pileup mechanism while supercritical flows show a combination of vertical jet runup and pileup mechanism.

In this numerical study, the incoming flow is homogeneous, steady and uniform so that the runup height grows without intense fluctuation and the secondary wave phenomenon reported by Iverson(2016) is not observed. Figure 3(a) shows the time series of runup heights in simulations of different flow regimes (Froude numbers). For the flows of low Froude numbers(e.g. $N_{Fr}<3.5$), the runup height reaches its peak values rapidly and then almost maintains a constant level. For the flows of high Froude numbers s(e.g. $N_{Fr}>5.5$), the runup height increases over time until the maximum runup height is reached. This increase is non-linear that the growth rate varies in different periods. At first, the runup heights increase rapidly and the growth rate reach its peak value as the flow front impacts the dam. Thereafter, the growth rate decreases over time meanwhile the runup process tends to rest gradually. After reaching the peak value, the runup heights decrease slowly and then maintains a constant level, indicating that the pile up process is underway.

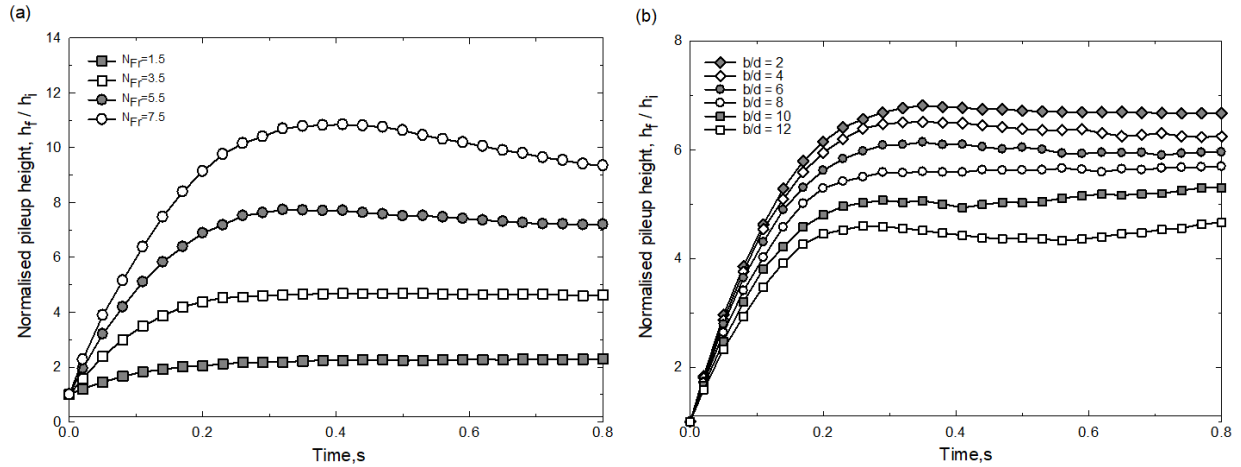


Fig. 3. Evolution of the runup height. (a) $b/d=2.0$, (b) $N_{Fr}=4.5$, zero time corresponds to the time instance at which the flow front reaches the dam.

Figure 3(b) shows the time series of runup heights in different relative post spacings. Numerical simulation results reveal that the evolutions of runup height in different relative post spacings share the similar tendency: the runup height increases over time to peak value then almost keeps a constant level. The relative post spacing controls the peak value that the higher the relative post spacing, the lower the maximum runup height. And the runup height in higher relative post spacings tend to reach its peak value earlier, indicating that the slit size affect the runup processes of granular flows against slit dams.

3.2. Influence of the relative post spacing on runup height

Figure 4 shows the relationship between the normalized maximum runup heights and relative post spacings. The numerical simulation results are compared with experimental data (Choi et al., 2016), which has the similar configurations in channel geometry, granular material property and slit structure type while Froude numbers are no more than 2.3.

In low Froude number conditions, the runup heights of numerical study are very close to the values measured by Choi et al. (2016). The results show that the normalized maximum runup height is not strongly influenced by the relative post spacing. This is because stable arches can easily form at the slit, provided that the Froude number of the incoming flow is low ($N_{Fr} \leq 3.5$). In this case, there is no significant difference between slit dams of different slit sizes since the stable arches can block the outlet and halt the flows. When the Froude number is high, supercritical flows with high velocities can break arches easily. Pardo and Sáez (2014) observed that the arch strength evidently depends on its length: shorter arch is generally stronger since higher contact stresses can be sustained in constrictions. The length of arch is directly related to the relative post spacing and the probability of formation of stable arches decreases as b/d increases (Janda et al., 2008). In this case, the relative post spacings affect the runup height significantly. In general, the maximum runup height declines as the b/d increases. Numerical results show that there is a critical value of relative post spacing (R_c): within the critical value, the maximum runup height is insensitive to the relative post spacing; once b/d exceeds the critical value, the maximum runup height decreases rapidly as the relative post spacing increases. Such a critical value has been studied in many previous works and it is noted that it does not exist an exact value for R_c (Zuriguel et al., 2005; Janda et al., 2008).

As shown in Figure 4, the numerical results can be interpreted by dividing two zones. Zone I ($b/d \leq R_c$, in grey): the runup heights of granular flows against slit dams maintain a constant level within a critical range of the relative post spacing. The R_c decreases with the increase of N_{Fr} , so that Zone I shrinks as the Froude number of incoming flows increases; Zone II ($b/d \geq R_c$, in white): the relative post spacing has a significant effect on runup heights that the maximum runup height decreases rapidly as the b/d increases. Zone II expands as N_{Fr} increases and eventually spans the full range of the relative post spacing ($N_{Fr}=7.5$). In this case, the arching structures no longer work and the runup height decreases monotonically as the relative post spacing increases. According to these results, engineers anticipating a dense granular debris flow can safely use the principle in this study to estimate the height required for the slit-dam to avoid dangerous overtopping.

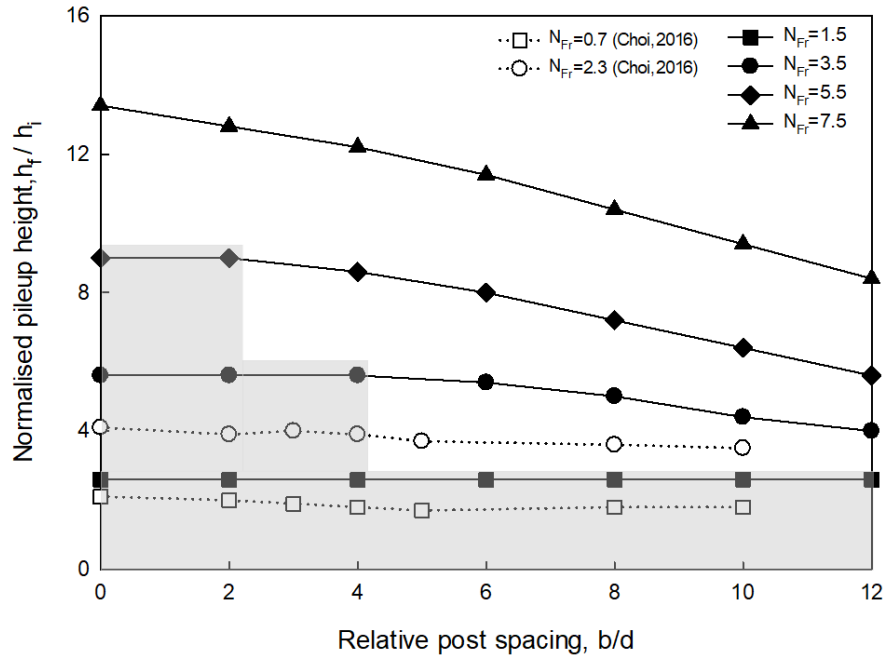


Fig. 4. Relationship between runup height and relative post spacing (Zone I: gray region; Zone II: white region).

4. Conclusions

A numerical study of granular debris flows impacting slit dams by discrete method was conducted. The numerical results were compared with the analytical models and the experimental data. From the initial results, it can be observed that the subcritical granular flows resulted in a typical pile up mechanism, whereas supercritical flows led to a combination of vertical jet runup and pile up mechanism. The relative post spacing of slit dams could affect the runup height. There is a critical value of relative post spacing (R_C): within the critical value, the maximum runup height is insensitive to the relative post spacing; once b/d exceeds the critical value, the maximum runup height decreases rapidly as the relative post spacing increases.

Acknowledgement

The authors acknowledge financial support from the Key Research Program of the Chinese Academy of Sciences (grant no.KZZD-EW-05-01).

References

- Armanini, A., Larcher, M., Odorizzi, M., 2011, Dynamic impact of a debris flow front against a vertical wall. In Proceedings of the 5th International Conference on Debris-Flow Hazards Mitigation: Mechanics, Prediction and Assessment, Padua, Italy, p. 1041-1049, doi:10.4408/IJEGE.2011-03.B-113.
- Azzoni, A., & De Freitas, M. H., 1995, Experimentally gained parameters, decisive for rock fall analysis: Rock mechanics and rock engineering, v. 28, p. 111-124.
- Chau, K. T., Wong, R. H. C., & Wu, J. J., 2002, Coefficient of restitution and rotational motions of rockfall impacts: International Journal of Rock Mechanics and Mining Sciences, v. 39, p. 69-77, doi:10.1016/S1365-1609(02)00016-3.
- Choi, C. E., Ng, C. W. W., Song, D., Kwan, J. H. S., Shiu, H. Y. K., Ho, K. K. S., & Koo, R. C. H., 2014a, Flume investigation of landslide debris-resisting baffles: Canadian Geotechnical Journal, v. 51, p. 540-553, doi:10.1139/cgj-2013-0115.
- Choi, C. E., Ng, C. W. W., Law, R. P., Song, D., Kwan, J. S. H., & Ho, K. K. S., 2014b, Computational investigation of baffle configuration on impedance of channelized debris flow: Canadian Geotechnical Journal, v. 52, p. 182-197, doi:10.1139/cgj-2013-0157.
- Choi, C. E., Ng, C. W. W., Au-Yeung, S. C. H., & Goodwin, G. R., 2015a, Froude characteristics of both dense granular and water flows in flume modelling: Landslides, v. 12, p. 1197-1206.
- Choi, C. E., Au-Yeung, S. C. H., Ng, C. W. W., & Song, D., 2015b, Flume investigation of landslide granular debris and water runup mechanisms: Géotechnique Letters, v. 5, p. 28-32, doi:10.1680/geolett.14.00080.

- Choi, C. E., Goodwin, G. R., Ng, C. W. W., Cheung, D. K. H., Kwan, J. S., & Pun, W. K., 2016, Coarse granular flow interaction with slit structures: *Géotechnique Letters*, v. 6, p. 267-274, doi:10.1680/jgele.16.00103.
- Chu, T., Hill, G., McClung, D. M., Ngun, R., & Sherkat, R., 1995, Experiments on granular flows to predict avalanche runup: *Canadian Geotechnical Journal*, v. 32, p. 285-295, doi:10.1139/t95-030.
- Cui, P., Zeng, C., & Lei, Y., 2015, Experimental analysis on the impact force of viscous debris flow: *Earth Surface Processes and Landforms*, v. 40, p. 1644-1655.
- Hübl, J., Suda, J., Proske, D., Kaitna, R., & Scheidl, C., 2009, September, Debris flow impact estimation. In Proceedings of the 11th international symposium on water management and hydraulic engineering, Ohrid, Macedonia, p. 1-5.
- Hungr, O., Morgan, G. C., & Kellerhals, R., 1984, Quantitative analysis of debris torrent hazards for design of remedial measures: *Canadian Geotechnical Journal*, v. 21, p. 663-677, doi:10.1139/t84-073.
- Iverson, R. M., 1997, The physics of debris flows. *Reviews of geophysics*, v. 35, p. 245-296, doi:10.1029/97RG00426.
- Iverson, R. M., George, D. L., & Logan, M., 2016, Debris flow runup on vertical barriers and adverse slopes: *Journal of Geophysical Research: Earth Surface*, v. 121, p. 2333-2357.
- Jakob, M., Hungr, O., & Jakob, D. M., 2005, *Debris-flow hazards and related phenomena*, Vol. 739, Berlin: Springer.
- Janda, A., Zuriguel, I., Garcimartín, A., Pugnali, L. A., & Maza, D., 2008, Jamming and critical outlet size in the discharge of a two-dimensional silo: *Europhysics Letters*, v. 84.
- Law, R. P. H., Choi, C. E., & Ng, C. W. W., 2015, Discrete-element investigation of influence of granular debris flow baffles on rigid barrier impact: *Canadian Geotechnical Journal*, v. 53, p. 179-185, doi:10.1139/cgj-2014-0394.
- Mancarella, D., & Hungr, O., 2010, Analysis of run-up of granular avalanches against steep, adverse slopes and protective barriers: *Canadian Geotechnical Journal*, v. 47, p. 827-841, doi:10.1139/T09-143.
- Ng, C. W. W., Choi, C. E., & Law, R. P., 2013, Longitudinal spreading of granular flow in trapezoidal channels: *Geomorphology*, v. 194, p. 84-93, doi:10.1016/j.geomorph.2013.04.016.
- Ng, C. W. W., Song, D., Choi, C. E., Liu, L. H. D., Kwan, J. S. H., Koo, R. C. H., & Pun, W. K., 2016, Impact mechanisms of granular and viscous flows on rigid and flexible barriers: *Canadian Geotechnical Journal*, v. 54, p. 188-206, doi:10.1139/cgj-2016-0128.
- Ng, C. W. W., Choi, C. E., Liu, L. H. D., Wang, Y., Song, D., & Yang, N., 2017, Influence of particle size on the mechanism of dry granular run-up on a rigid barrier: *Géotechnique Letters*, v. 7, p. 79-89.
- Pardo, G. S., & Sáez, E., 2014, Experimental and numerical study of arching soil effect in coarse sand. *Computers and Geotechnics*, v. 57, p. 75-84, doi:10.1016/j.compgeo.2014.01.005.
- Pudasaini, S. P., Hsiau, S. S., Wang, Y., & Hutter, K., 2005, Velocity measurements in dry granular avalanches using particle image velocimetry technique and comparison with theoretical predictions: *Physics of Fluids*, v. 17, doi:10.1063/1.2007487.
- Pudasaini, S. P., & Hutter, K., 2007, *Avalanche dynamics: dynamics of rapid flows of dense granular avalanches*. Springer Science & Business Media.
- Rapaport, D. C., & Rapaport, D. C. R., 2004, *The art of molecular dynamics simulation*. Cambridge university press.
- Scheidl, C., Chiari, M., Kaitna, R., Müllegger, M., Krawtschuk, A., Zimmermann, T., & Proske, D., 2013, Analysing debris-flow impact models, based on a small scale modelling approach: *Surveys in Geophysics*, v. 34, p. 121-140.
- Shen, W., Zhao, T., Zhao, J., Dai, F., & Zhou, G. G., 2018, Quantifying the impact of dry debris flow against a rigid barrier by DEM analyses: *Engineering Geology*, v. 241, p. 86-96, doi:10.1016/j.enggeo.2018.05.011.
- VanDine, D. F., 1996, Debris flow control structures for forest engineering. Res. Br., BC Min. For., Victoria, BC, Work. Pap., v. 8.
- Watanabe, M., Mizuyama, T., & Uehara, S., 1980, Review of debris flow countermeasure facilities: *Journal of the Japan Erosion Control Engineering Society*, v. 115, p. 40-45.
- Zuriguel, I., Garcimartín, A., Maza, D., Pugnali, L. A., & Pastor, J. M., 2005, Jamming during the discharge of granular matter from a silo: *Physical Review E*, v. 71, 051303, doi:10.1103/PhysRevE.71.051303.

A method for predicting debris-flow occurrence based on a rainfall and sediment runoff model

Masaharu Fujita^{a,*}, Kazuki Yamanoi^b, Gota Suzuki^c

^a*Disaster Prevention Research Institute, Yokooohji, Fushimi-ku, Kyoto 612-8235, Japan*

^b*Institute of Physical and Chemical Research, 7-1-26 Minatogima-minamimachi, Chuo-ku, Kobe, Hyogo 650-0047, Japan*

^c*Graduate School of Engineering, Kyoto University, Yokooohji, Fushimi-ku, Kyoto 612-8235, Japan*

Abstract

Based on a basin scale rainfall runoff model, we proposed a prediction method of debris-flow occurrence on steep mountain slopes related to hydrological processes such as the rainfall infiltration, the surface flow and the slope stability. For example, in one case that the soil layer is unsaturated and a landslide does not occur in the slope even though the groundwater level rises in the slope soil layer during a rainfall event, it is unlikely for a debris flow to occur on the slope. However, if the soil layer is more unstable due to fully saturation and a surface flow also takes place on the slope, the possibility of debris-flow occurrence gets much higher. According to such a consideration, the slope conditions on hydrological processes during heavy rainfalls were classified into six patterns. For these patterns, the possibility of debris-flow occurrence was investigated qualitatively. Then, SiMHiS (Storm Induced Multi-Hazards Information Simulator) by Yamanoi and Fujita was employed as a rainfall runoff model. A slope stability model has been already installed in SiMHiS. Therefore, this model can simulate the time variations of the safety factors for landslides as well as the saturation degrees and the hydrographs of the surface flow for the slopes. SiMHiS was applied to the sediment disasters due to a heavy rainfall in July 2017 in the Akatani river basin to examine the occurrence patterns of debris flow. Also, the differences in the occurrence patterns were shown for other two rainfall events. Using the simulation result on the safety factor, the saturation degree and the surface flow discharge, it was noted whether debris flows took place or not, and the debris-flow occurrence patterns on the slopes in the basin could be identified.

Keywords: debris flow; rainfall runoff model; basin scale; occurrence process of debris flow; sediment disaster

1. Introduction

An empirical approach to predicting debris-flow occurrence is a standard method for practical applications. A warning system based on a critical rainfall is used worldwide for road risk management for sediment disasters and a warning alert for the debris-flow occurrence is issued using a rainfall monitoring system. There are also theoretical approaches, but the theoretical research has so far focused on the mechanisms of debris flows and has not discussed the debris-flow process as one of the components in a rainfall runoff system. Therefore, the critical rainfall for debris-flow occurrence cannot be found from a previous theoretical research. Because debris flows as well as floods in a basin are typical phenomena in the hydrological process in the basin, they should be analyzed with a basin scale rainfall runoff model

Previous studies on debris flows have shown that there are several processes of debris-flow occurrence. The sediment deposits in a steep channel with a gradient of more than 15 degrees could be an original source of debris flows. In a steep mountain slope, sediment movement such as landslides and slope erosion could initiate debris flows. The debris flow occurs related to the variables in the hydrological process on the slope such as the slope stability, the saturation degree and the surface flow. The processes of debris-flow occurrence are thought to be different depending

* fujita.masaharu.5x@kyoto-u.ac.jp

on the features of hydrological processes. At a heavy rainfall event, the time variations of the safety factor on landslide in the slopes as well as the time variations on the saturation degree and the surface flow discharge on the slopes are different each other. The different hydrological processes create different patterns of debris-flow occurrence. In this paper we focus on this point and try to classify the debris-flow occurrence patterns into six typical cases. For each case, the possibility of debris-flow occurrence is discussed qualitatively. Although this method cannot provide a triggering condition such as a critical rainfall, the risk of debris-flow occurrence can be evaluated on the basin scale.

The above-mentioned idea is specifically indicated for the Akatani river basin which had severe sediment disasters in July 2017. To analyze hydrological process on the slopes, SiMHIS (Storm Induced Multi-Hazards Information Simulator) by Yamanoi and Fujita was employed. A slope stability model as well as a rainfall runoff model is installed in this model. Therefore, this model can simulate the time variation of the safety factors on landslides, the saturation degrees and the surface flow discharges in the hydrological processes for the slopes. Using the simulation result, we can note whether debris flows take place or not in the basin and identify possible occurrence patterns.

2. Patterns of Debris-Flow Occurrence

2.1. Indices on debris-flow occurrence

It is well known that the critical slope for debris-flow occurrence is around 15 degrees and there are several processes of debris-flow occurrence. An initiation of debris flow on a slope is generally a massive movement of slope soil layer such as a landslide. This initial massive movement transitions into a debris flow by erosion of the slope soil. This is one of the typical processes of debris-flow occurrence. Safety factor (S_F) on massive movement (landslide) expresses the stability of slope soil layer. If the soil layer is stable ($S_F > 1$), debris flows unlikely occur. If $S_F = 1$, the soil layer on the critical sliding surface is in a critical unstable situation. If $S_F < 1$, the slope soil on the critical sliding surface is accelerated to the downstream. If a critical condition of landslide is reached before the slope soil is fully saturated with water, after this stage the soil layer on the critical sliding surface could be accelerated because the subsequent rainfall decreases the safety factor more. It is thought that these situations have a different potential for debris-flow occurrence. The safety factor decreases with an increase in a ground water level. As a result, the landslide occurrence risk changes with the ground water level. However, even though a surface flow occurs on the saturated slope soil layer, the surface flow only slightly lowers the safety factor because the surface flow is rather shallow. This means the safety factor of the slope soil layer with a surface flow is almost kept at the safety factor for the full saturation condition without surface flow.

A hydrograph (Q_{sur}) of surface flow on the slope and the saturation degree of the slope soil (S_r) are important factors on the erosion of slope soil. If the surface flow discharge is large and the saturation degree is almost 100%, the erosion is very active. This means these two variables are other factors related to the potential of debris-flow occurrence. According to the above-mentioned consideration, the safety factor (S_F), the saturation degree of the slope soil on the critical sliding surface (S_r) and the surface flow discharge (Q_{sur}) are used as the indices that influence the debris-flow occurrence.

2.2. Process of debris-flow occurrence and the patterns

Each slope has a different time variation of S_F , S_r and Q_{sur} during a heavy rainfall event. Therefore, the timing when the slope soil layer enters an unstable condition and the timing when the slope soil layer is fully saturated with water are different for every slope. Also, the hydrograph of the surface flow at full saturation is different for every slope. Considering the features of the variations, the slope conditions on the hydrological process are classified into six cases as shown in Fig. 1.

In Fig. 1 two stages during a rainfall event are shown. *Pattern 1* shows that the slope soil layer is stable during the rainfall event even if the ground water level rises in the soil layer. No debris flow takes place under this condition. However, if the soil layer is saturated (right figure) and a surface flow occurs, gully erosion easily takes place. *Pattern 2(a)* shows that the soil layer is saturated with water around at the peak rainfall ($S_r = 1.0$) and at the same time S_F decreases to around 1.0. The critical sliding surface appears and the soil layer on the critical surface is attained in unstable. A surface flow simultaneously appears on the slope, but S_F is not significantly reduced because the surface flow depth is rather shallow. However, the possibility of debris flow is high because the erosion by the surface flow is more active than *Pattern 1*. *Pattern 2(b)* is similar with *Pattern 2(a)*, but the critical condition of landslide appears after the peak rainfall. The surface flow discharge, therefore, is small and the possibility of debris-flow occurrence is

lower than *Pattern 2(a)*. *Pattern 3* shows that S_r is less than 1.0 even at the critical condition of landslide and S_r remains less than 1.0 during the rainfall event. In this case the unsaturated slope soil layer is accelerated, but it is thought that the unsaturated soil is difficult to fluidize and cannot transition to a debris flow. *Pattern 4(a)* shows that the safety factor reaches to 1.0 even at $S_r < 1.0$. After this stage, the increase in S_r due to the subsequent rainfall reduces the safety factor more and the soil layer is accelerated. In this case a surface flow acts on the surface of the soil layer fully saturated with water. The potential of debris-flow occurrence is thought to be very high because the surface flow acts on the accelerated and saturated soil layer. *Pattern 4(b)* is similar with *Pattern 4(a)*. However, a surface flow on the saturated soil layer is very small. The possibility of debris flow is lower than *Pattern 4(a)*, but higher than *Pattern 2(b)* because the saturated soil layer is accelerated. The occurrence of these patterns is dependent on the slope angle, the properties of the soil layer and rainfall condition, but the possible patterns could be qualitatively classified.

Comparing six patterns, *Pattern 4(a)* has a highest potential of debris-flow occurrence. *Pattern 2(a)* has a second highest potential. Then, *Pattern 4(b)* and *Pattern 2(b)* follow *Pattern 2(a)*. *Pattern 3* has rather low potential of debris-flow occurrence. This is a quantitative evaluation and a qualitative model is necessary to obtain the criteria on debris-flow occurrence.

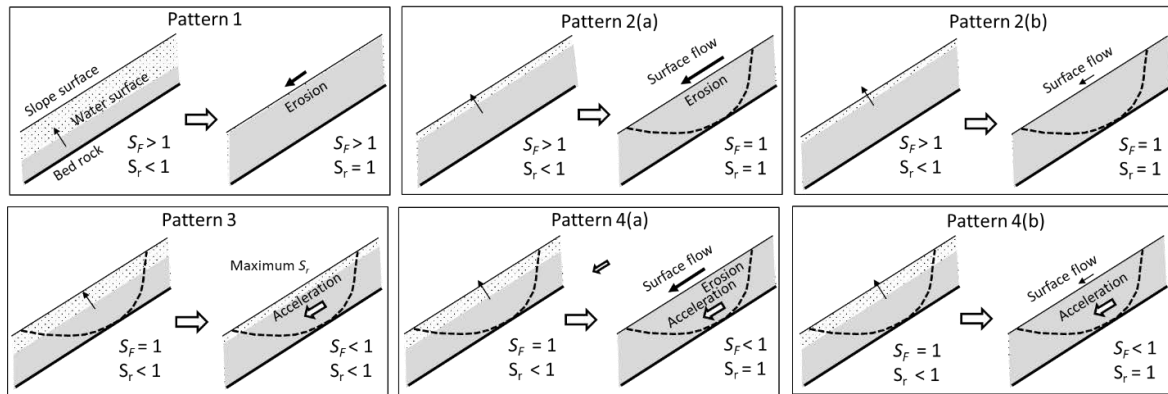


Fig. 1. Occurrence patterns of debris flows

3. Employed Model

3.1. SiMHIS (Storm Induced Multi Hazard Information Simulator)

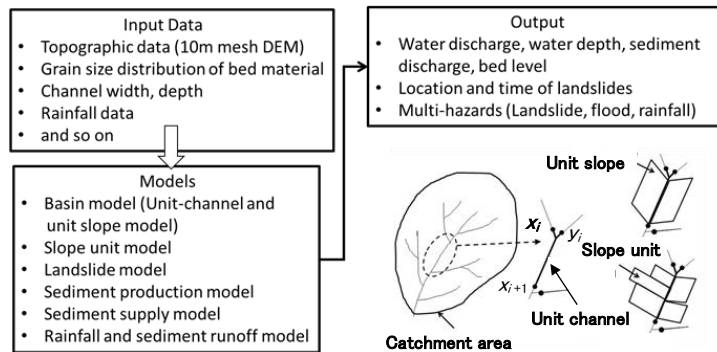


Fig. 2. Outline of SiMHIS

The time variations of S_F , S_r and Q_{sur} in slopes are necessary to detect whether a debris flow occurs or not, and to identify which occurrence pattern takes place in the slope. Yamanoi and Fujita (2014) have developed SiMHIS that analyzes rainfall runoff, slope stability and sediment transport on a basin scale. SiMHIS consists of a basin model, a landslide model and a rainfall-sediment runoff model and so on as shown in Fig.2. The basin model creates a network consists of unit slopes and unit channels using a DEM. This model has been proposed by Egashira and Matsuki (2000). Fig.2 shows a schematic view of channel network. A unit channel is a straight uniform channel between a confluence and the next confluence. A unit slope is assumed a rectangular inclined plane. The angle is calculated as an averaged

angle of the actual slopes and the area is determined so that those projection areas to plain are equal. Rainfall runoff is simulated for the channel network with unit slopes by means of a kinematic wave model. Unit slopes have rather large scales for landslide simulation. Therefore, Chen and Fujita (2014) have divided a unit slope into several slope units with a real slope scale and proposed the following landslide model. In the model, a critical water content of landslide in a slope unit, W_{cr} , is determined beforehand based on a seepage analysis and a slope stability analysis. A water content in each slope unit, W , is calculated by the seepage flow analysis. If $W > W_{cr}$ in a slope unit, it is identified that a landslide occurs on the slope unit at the location and the timing. The safety factor ($S_f = W_{cr}/W$) is calculated with such a physical based simple method. SiMHIS can provide also the saturation degree of each slope unit, S_r , and analyze the surface flow discharge Q_{sur} . SiMHIS can also simulate the sediment runoff after the landslide, but in this study, we only simulate the landslides and the rainfall runoff in a basin.

3.2. Application basin

A heavy rainfall occurred on the north part of Kyushu Island, Japan in July 2017. The cumulative precipitation was more than 800 mm in a local area. A large number of landslides occurred in the basins and a large amount of sediment resulted in the severe sediment deposition in the downstream area. The sediment deposition made the flood inundation much larger. In the mountain area the debris flows caused severe sediment disasters. Fig.3 shows the Akatani river basin which suffered from severe sediment disasters and the locations of landslides and the inundation area investigated by Geospatial Information Authority of Japan. Landslides occurred almost in all mountain areas and the inundation extended very widely along the Akatani River. Because a large cumulative precipitation as well as a high intensity affected the basin, almost all the landslides were carried downstream as debris flows. A few landslides remained near the slope.

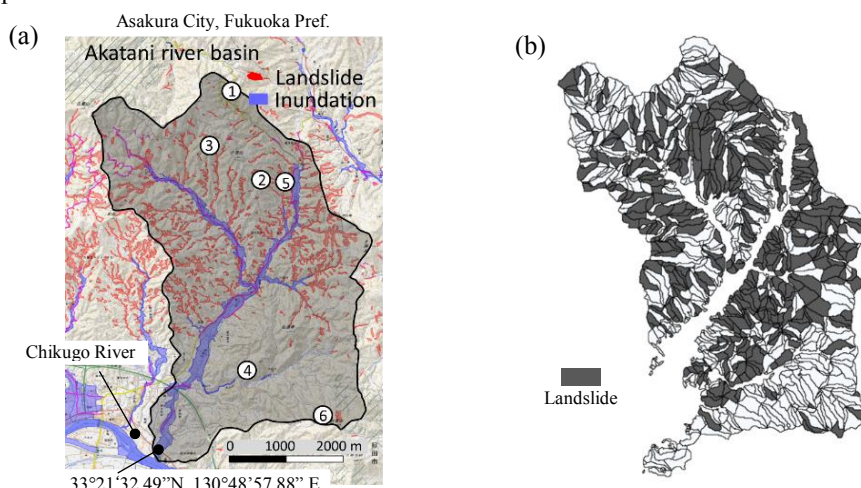


Fig.3. (a) Akatani river basin and the location of landslides due to the rainfall in July 2017(Geospatial Information Authority of Japan), (b) Simulation result of the landslides

It is assumed that the thicknesses of soil layers of the unit slopes and the slope units are 2 m and 1m, respectively, and the permeability of slope soil layer is 3.5×10^{-5} m/s. The porosity of the slope soil material is 0.5. The rainfall intensity distribution (Rain A) provided by Japan Meteorological Agency was used for the simulation. The rainfall conditions at Slope 1 to 6 in Fig.3 (a) are shown in Fig.4 (a) to (f). Other two rainfalls were used to compare the difference in the landslide occurrence and the debris-flow occurrence pattern. Rain B has a same rainfall duration as Rain A, but with half the intensity. Rain C has a same rainfall intensity, but the duration is half of Rain A.

This model has several parameters such as permeability of the soil layer, the porosity and the friction angle of the soil to be identified, but it is difficult to adjust the values to explain the actual phenomena. In this paper a standard value for each parameter or surveyed value is used as mentioned above and the critical safety factor is adjusted to express the actual landslide locations. As a result, the critical safety factor S_{Fcr} is found to be 0.925. Fig.2(b) shows the distribution of simulated landslide locations. The number of landslides looks larger than the actual one, but the agreement between the locations of simulated landslides and the actual ones is acceptable.

4. Results and Discussion

4.1. Simulation results

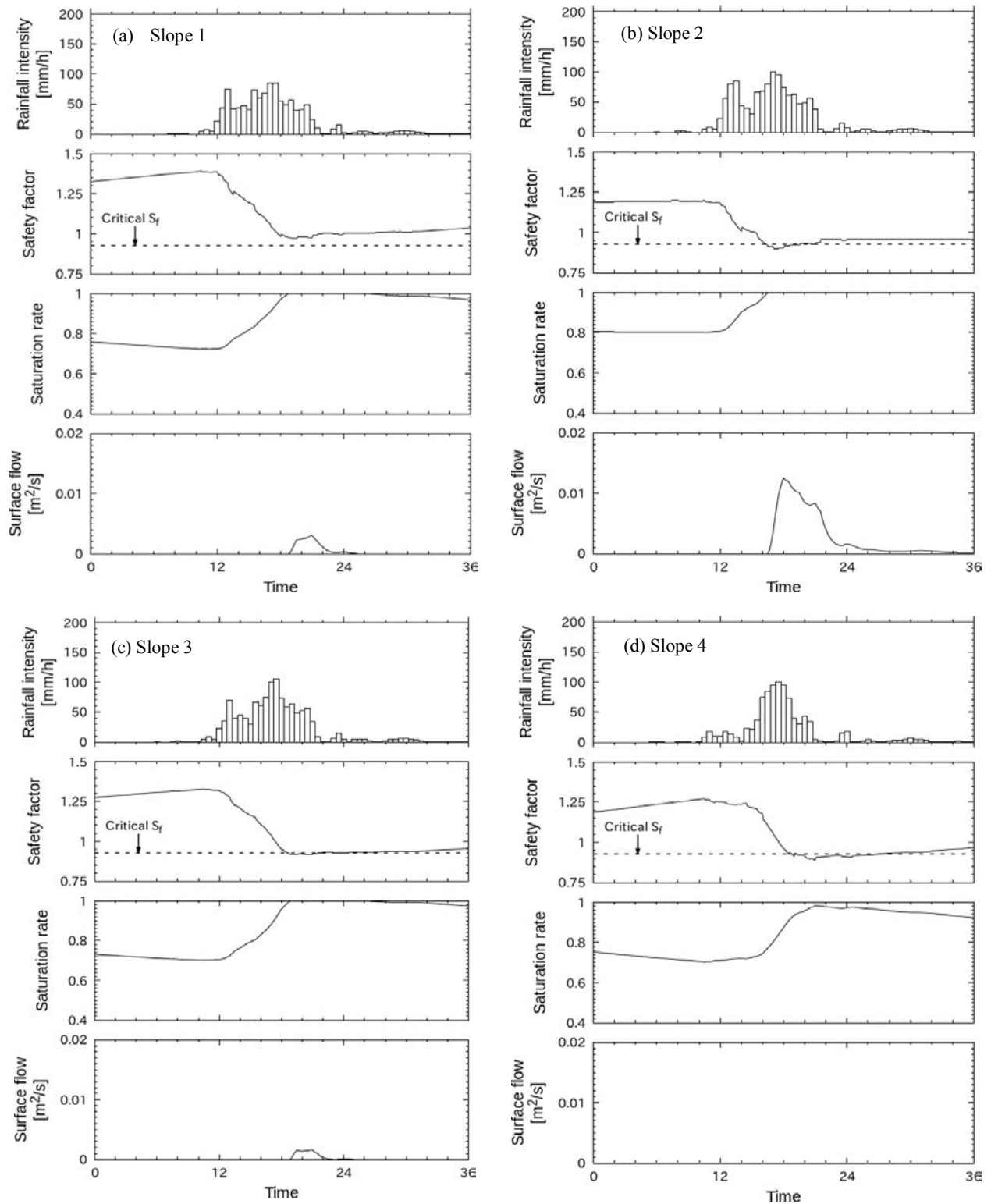


Fig. 4. (a)-(d) Time variations of rainfall intensity, safety factor, saturation degree and surface flow discharge (Slopes 1, 2,3 and-4)

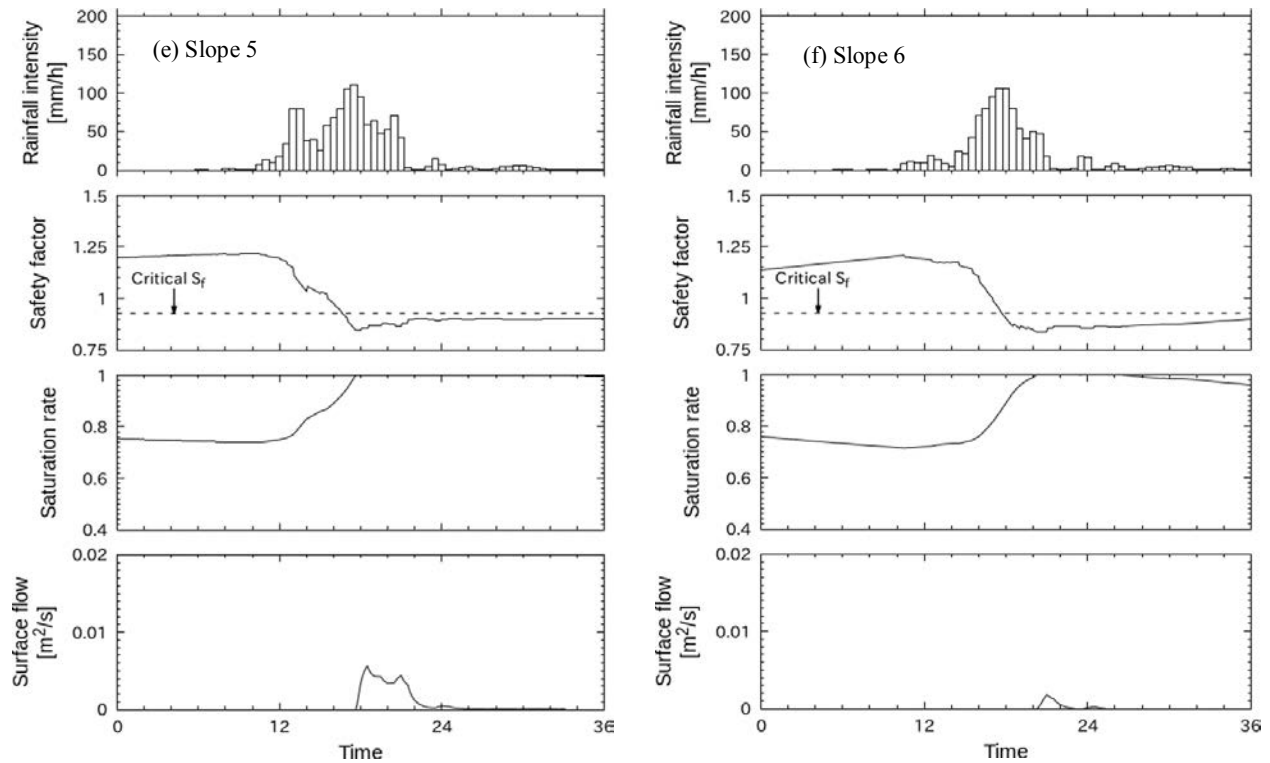


Fig.4. (e)-(f) Time variations of rainfall intensity, safety factor, saturation degree and surface flow discharge (Slopes 5 and 6)

Fig.4 (a) shows the simulation result on the change of S_F , S_r and Q_{sur} with time at Slope 1 in Fig.3 (a). S_F is larger than S_{Fcr} during Rain A. This is a typical case of *Pattern 1*. After the peak rainfall intensity, the slope soil layer is saturated with water and the surface flow takes place on the slope. It is predicted that gully erosion is active. Fig.4 (b) shows the simulation result for Slope 2. S_F reaches to S_{Fcr} after first peak of rainfall intensity but before second peak. At the same time the slope soil layer is saturated with water. Both conditions of $S_F=1.0$ and $S_r=1.0$ are satisfied at the same time before the peak of the rainfall intensity, and the surface flow discharge is large. It is evaluated that this is a case of *Pattern 2(a)* with high potential of debris-flow occurrence. Fig.4 (c) shows the simulation result for Slope 3. S_F reached to S_{Fcr} after the peak of rainfall intensity. At that time the slope soil layer was saturated with water. The timing when S_F reached 1.0 is later than at Slope 2. Also, the surface flow discharge on the slope is very small. This is a typical case of *Pattern 2(b)* with the third highest potential of debris-flow occurrence. Fig.4 (d) shows the simulation result for Slope 4. This situation indicates *Pattern 3* where the unsaturated soil is accelerated. The possibility of debris-flow occurrence is rather low. Fig.4 (e) shows the simulation result for Slope 5. S_F reaches to S_{Fcr} before the peak of the rainfall intensity. At that time the slope layer is not saturated with water, but fully saturated after two hours. The surface flow with large water discharge acts on the saturated soil layer. This is a typical case of *Pattern 4(a)* with a highest potential of debris-flow occurrence. Fig.4 (f) shows the simulation result for Slope 6. S_F reaches S_{Fcr} after the peak of rainfall intensity. This situation indicates *Pattern 4(b)* where the unsaturated slope soil is accelerated and is saturated in 3 hours, but the surface flow discharge is low. The possibility of debris flow is high.

4.2. Distribution of debris-flow occurrence patterns

Fig.5 (a) shows the distribution of debris-flow occurrence patterns in the Akatani river basin for Rain A. *Pattern 4(a)* with highest potential of debris-flow occurrence occupied 13.3 % of the land area. Percentages of *Patterns 2(a)* and *4(b)* with the second highest potential are 2.6% and 21.1%, respectively. These two patterns occupied 23.7% of the land area. Percentage of *Pattern 2 (b)* with the third highest potential is 62.0%. Percentage of *Pattern 3* is 1.0%. The traces of landslide mass movement in an aerial photograph show most landslides seem to have transitioned into debris flow. A few landslides remained near the slope. Therefore, it is thought that *Patterns 4(a), 2(a), 4(b), 2(b)* generate debris flows.

Rain B has a same rainfall duration with Rain A, but the intensity is half of Rain A. Fig.5(b) show the distribution of debris-flow occurrence patterns for Rain B. A few landslides occur because lower rainfall intensity reduces the landslide occurrence. Rain C has a smaller cumulative precipitation than Rain A, but the rainfall intensity is same as Rain A. Therefore, many landslides occur as shown in Fig.5(c). However, the debris-flow occurrence patterns are dominantly *Pattern 3* and *Pattern 4* (b). Particularly, half of the landslides has *Pattern 3*. The slope soil layer become unstable and accelerated, but it can be saturated with water because of lower cumulative precipitation.

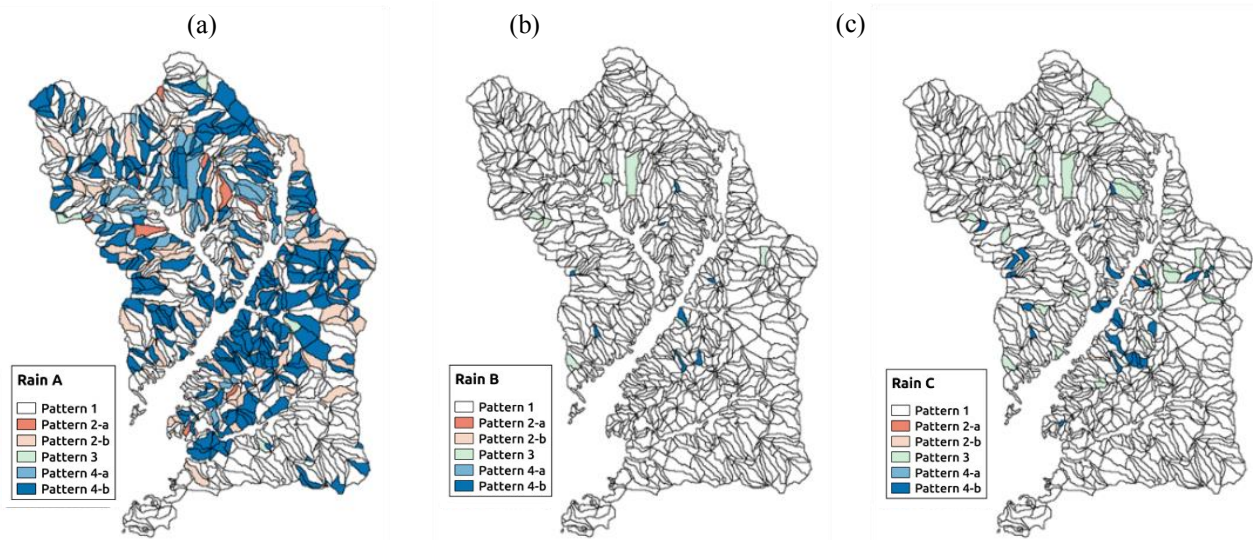


Fig.5. (a)-(c) Distributions of debris-flow occurrence patterns for Rain A, B and C

5. Conclusion

Debris flows occur from hydrological processes on mountain slopes such as rainfall infiltration and surface flow on the slopes. The slope stability is also related to the initiation of debris flow. Therefore, the time variations of the saturation degree and the safety factor of slope soil layer, as well as the hydrograph of surface flow on the slopes, are very important indices. In this study, the difference of the features of the variations was investigated, and the patterns of the variations were clarified. Considering the relation between the patterns and debris-flow occurrence, the possibilities of debris-flow occurrence were qualitatively evaluated. A rainfall runoff model was applied to an actual river basin that experienced severe sediment disasters to verify effectiveness of this idea. The changes of the safety factor and the saturation degree and the hydrograph of surface flow were simulated to identify the patterns. Because the actual rainfall was very heavy, it was evaluated that most of the landslides transitioned into debris flows. This result agreed with the actual situation. It was evaluated that half of the landslides did not transition into debris flows if the duration of the rainfall was reduced to half of the actual rainfall with the same rainfall intensity. Using this method, it may be possible to identify the processes of debris-flow occurrence after landslides. However, in order to confirm the effectiveness of this method, it is necessary to apply this method to other sediment disasters.

References

- Egashira, S., and Matsuki, K., 2000, Method for predicting sediment runoff caused by erosion of stream channel bed, Annual Journal of Hydraulic Engineering, JSCE, v.44, p.735-740.
- Chen-Yu Chen and Fujita, M., 2014, A method for predicting landslides on a basin scale using water content indicator, Journal of Japan Society of Civil Engineering, Ser. B1 (Hydraulic Engineering), v.70, n.4, p. 113-118.
- Yamanoi, K. and Fujita M., 2016, Risk estimation of multiple hazards related to sediment and water disasters occurring in heavy rainfall, Journal of Japan Society of Civil Engineers, Ser. B1 (Hydraulic Engineering), v.72, n.4, p. I_1291-I_1296.

Seamless numerical simulation of a hazard cascade in which a landslide triggers a dam-breach flood and consequent debris flow

D.L. George^{a,*}, R.M. Iverson^a, C.M. Cannon^{a,b}

^a*U.S. Geological Survey, 1300 SE Cardinal Ct. 100, Vancouver, WA 98683, U.S.A.*

^b*U.S. Geological Survey, 2130 SW 5th Ave, Portland, OR 97201, U.S.A.*

Abstract

Numerical simulations of hazard cascades downstream from moraine-dammed lakes commonly must specify linkages between models of discrete processes such as wave overtopping, dam breaching, erosion, and downstream floods or debris flows. Such linkages can be rather arbitrary and can detract from the ability to accurately conserve mass and momentum during complex sequences of events. Here we describe an alternative methodology in which we use high-resolution lidar topography and 2-D, two-phase conservation laws to seamlessly simulate all stages of a hazard-cascade that culminates in a debris flow. Our simulations employ our depth-integrated numerical model D-Claw to evaluate hazards from prospective breaching of a moraine dam that impounds Carver Lake on the eastern flank of South Sister volcano in central Oregon, USA. We simulate a “worst-case scenario” sequence of events that begins with a hypothetical 1.6 million m³ landslide that originates near the summit of South Sister and enters Carver Lake. Wave generation and displacement of lake water then leads to dam overtopping, breach erosion, and a downstream debris flow that funnels into Whychus Creek and eventually reaches the community of Sisters, Oregon, about 20 km away. Notably, our simulations predict that much of the debris is directed away from Sisters as a result of natural avulsion and flow diversion that occurs near the head of a low-gradient alluvial fan upstream from Sisters. Consequently, predicted hazards to downtown Sisters are less severe than those predicted by 1-D shallow-water simulations of a Carver Lake dam breach that were performed in the 1980s.

Keywords: debris-flow modeling; lake-outburst floods; two-phase modeling; Carver Lake; South Sister volcano.

1. Introduction

D-Claw is a software package that we developed primarily for simulating landslides and debris flows, but it can also be applied to a wider class of problems that involve water bodies as well as grain-fluid mixtures. The depth-averaged model describes the temporal and spatial evolution of flow thickness, velocity, solid and fluid volume fractions, and basal pore-fluid pressure (Iverson and George, 2014; George and Iverson, 2014). However, in the limit of vanishing solid volume fraction, D-Claw's model equations reduce to the shallow water equations, allowing the simulation of water waves or overland flooding in a way similar to that of models developed specifically for those applications (*e.g.*, Berger et al., 2011). We have recently exploited this property and used D-Claw to simulate cascading natural hazards, such as tsunamis generated by subaerial landslides (George et al., 2017), glacial lake-outburst floods, and overland floods that entrain debris. For these applications we can seamlessly employ D-Claw without needing to specify interaction terms or couple disparate models and software. This approach ensures accurate conservation of mass and momentum throughout the cascade of processes.

* Corresponding author e-mail address: dgeorge@usgs.gov



Figure 1. Southwest-looking Google Earth imagery showing the location of the community of Sisters, Oregon, in relation to Carver Lake and South Sister volcano.

In a recent study, we used D-Claw to model a hypothetical outburst flood from a moraine-dammed lake on the east side of South Sister volcano near the town of Sisters, Oregon, USA. The hypothetical landslide begins near the summit of South Sister and enters Carver Lake, where it generates large waves that overtop the moraine dam. Because D-Claw can model the erosion and entrainment of basal sediment, the subsequent dam breaching process occurs spontaneously, leading to lake drainage and downslope floods and debris flows. Owing to spreading and avulsion of the modeled flow in a system of distributary channels on the alluvial fan upstream from Sisters, the predicted hazard to the community is less severe than was predicted by 1-D shallow-water computations performed in the 1980s (Laenen et al., 1987), as the 1-D modeling does not make possible the direct modeling of stream bifurcation, but rather requires the primary flood channel to be chosen *a priori*.

2. Hazards Downstream from Carver Lake, Oregon

Carver Lake is a moraine-dammed lake on the eastern flank of South Sister volcano in central Oregon, USA (Figures 1 and 2). The lake sits approximately 20 km upstream from the community of Sisters, Oregon, located in the valley below. The outlet channel of Carver Lake is a small tributary of Whychus Creek, which flows through downtown Sisters.

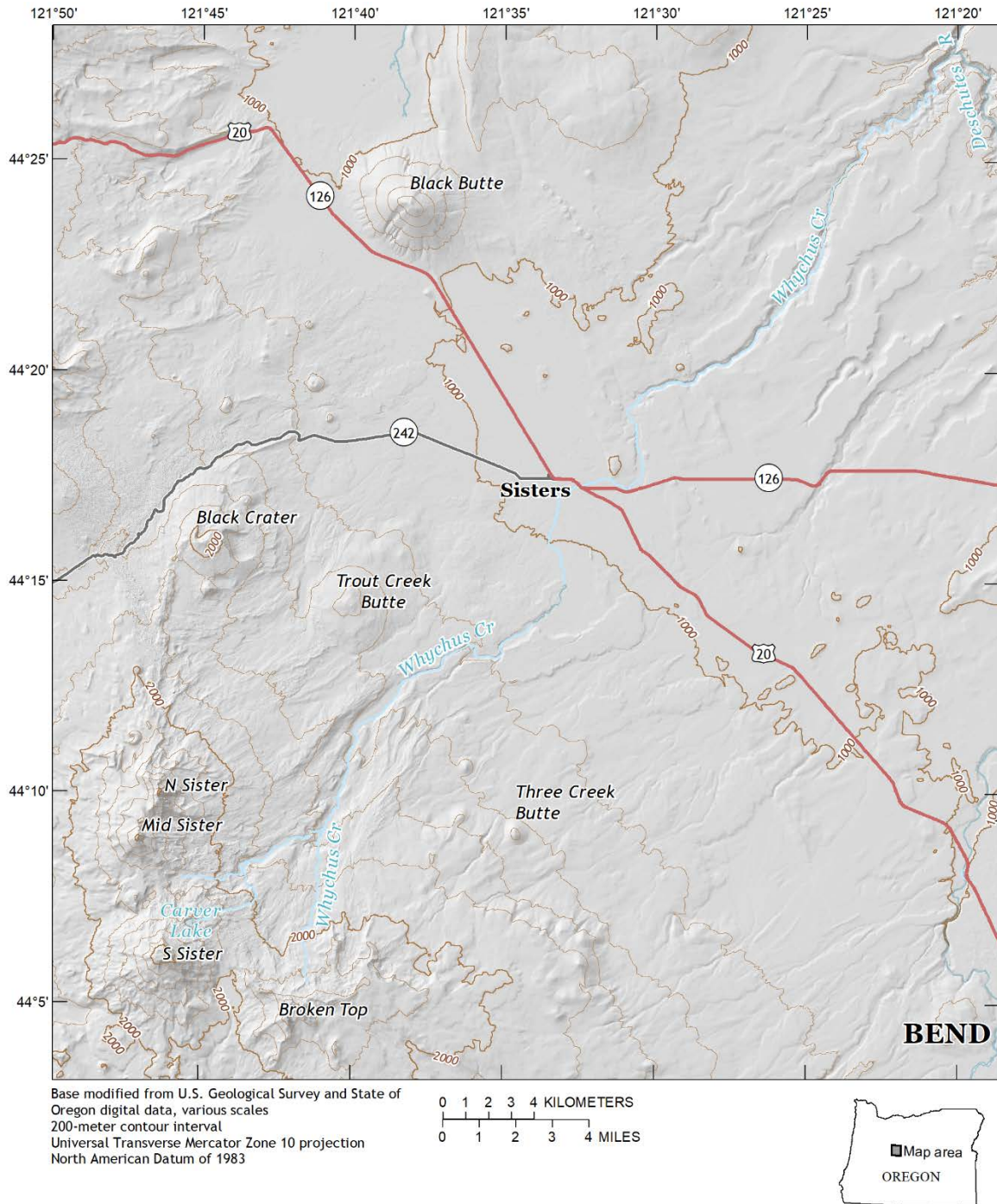


Figure 2. Map showing the location of Carver Lake (near southwest corner) and Sisters, Oregon.

In the 1980s, concern was raised regarding the flooding risk posed to the Sisters community, should a moraine-dam failure lead to an outburst flood from Carver Lake. Modeling conducted at the time utilized 1D shallow-water equations and suggested that, in the event of complete lake drainage, the flooding hazard could be substantial (Laenen et al., 1987). Because of recent advances in flood and debris-flow modeling capabilities, there has been interest by community members to reassess this hazard with more sophisticated methods.

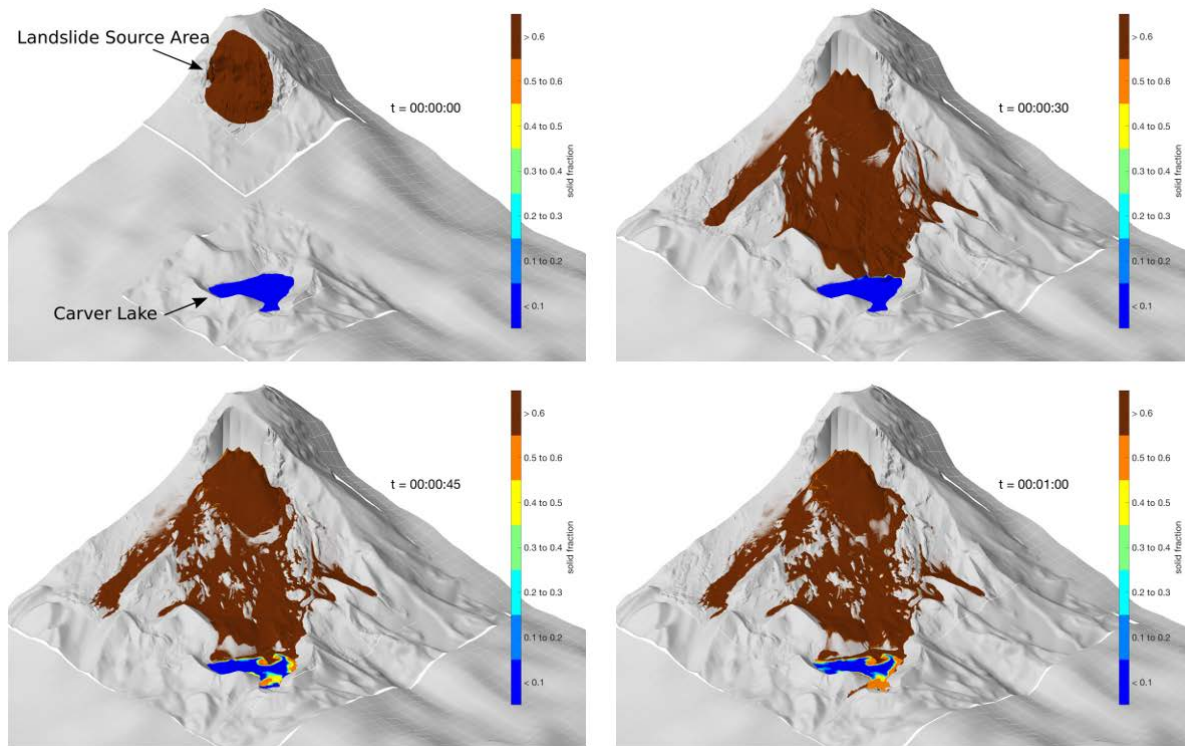


Figure 3. West-looking oblique perspective of the failure and evolution of the simulated landslide mass which inundates Carver Lake and generates waves that overtop the moraine dam. The wave action at the dam begins to erode channel material. Shading indicates the solid volume fraction, m , which varies from 0 (pure water) to ~ 0.6 (dense granular-fluid mixture). The area depicted is $\sim 3 \times 3 \text{ km}^2$.

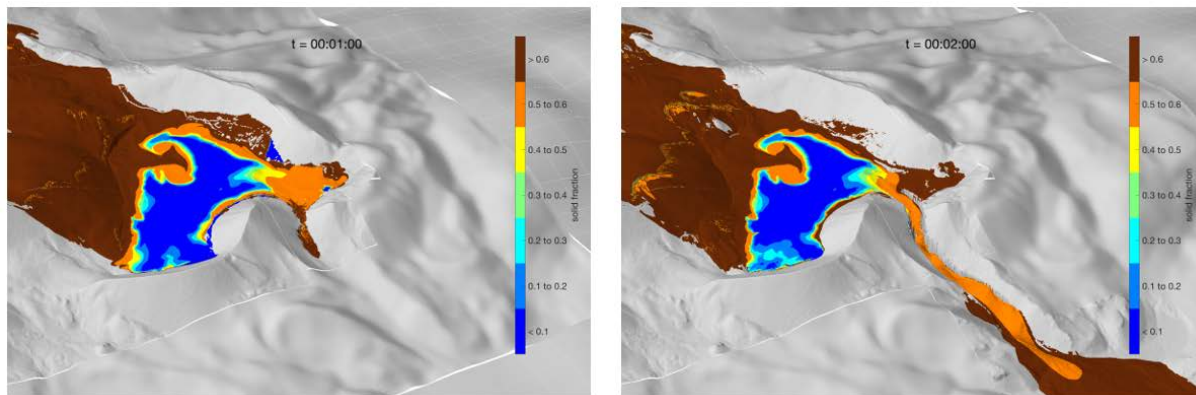


Figure 4. North-looking oblique perspective of wave generation, overtopping and erosion of the moraine dam that leads to a downstream debris flow. Shading indicates the solid volume fraction, m , which varies from 0 (pure water) to ~ 0.6 (dense granular-fluid mixture). The evolving values of m reveal the mixing and nature of the downstream flow. Area shown is $\sim 1.5 \times 1.5 \text{ km}^2$.

There is consensus among geologists and engineers who have visited Carver Lake (*e.g.*, Laenen et al., 1987; O'Connor et al., 2001) that the moraine dam appears stable to spontaneous failure, and that a failure would most likely require overtopping waves generated by a landslide entering the lake. We therefore used D-Claw to simulate scenarios in which a landslide originates on the slopes of South Sister above Carver Lake. All subsequent processes (*e.g.*, wave generation, dam overtopping, erosion, downstream flooding and debris flows) were simulated seamlessly. That is,

dam failure and flooding were not specified by the model set-up. Assumptions only about the landslide size and location and the erodibility of the dam material were explicitly prescribed.

3. Modeling

3.1 Model Set-Up

D-Claw simulations were performed on a large domain (approximately 50 km by 50 km), which included the summit of South Sister in the southwest corner and extended northward beyond the community of Sisters. High-resolution lidar topography (approximately 1 m) from 2017 was available throughout the domain, but required some manual modifications due to recent channel alterations near Sisters, which occurred as part of an ecological restoration project. Due to D-Claw's use of adaptive mesh refinement (AMR), model resolution varied dynamically as flows evolved, but 1 m resolution was retained in the valley surrounding Sisters.

A hypothetical landslide source geometry encompassing 1.6 million cubic meters of material was constructed by first creating transects running longitudinally along the length of the hypothetical basal failure surface, in the form of logarithmic spirals, near the summit of South Sister volcano and extending downslope toward Carver Lake. A continuous basal surface was then constructed by interpolating the transects with a triangulated network. The transects were constructed such that the failure surface had prescribed scarp and toe inclination angles. The specific geometry was chosen with the goal of creating a large enough landslide to significantly displace the water in Carver Lake, yet conform reasonably to the local topography. Computations were initialized in D-Claw with a solid volume fraction, $m=0.62$, within the landslide source area and throughout the rest of the computational domain, except for within Carver Lake (Figure 3).

Our DEM was modified to include Carver Lake bathymetry collected in the field in 2016. The D-Claw simulation was initialized with pure water ($m = 0$) above the bathymetry of Carver Lake, and below a horizontal lake surface with an elevation determined from field surveys. This resulted in a lake volume of 1.4 million cubic meters.

A region beginning near the upstream face of the moraine dam and extending downstream from the lake outlet was initialized with potentially erodible material occupying depths approximately 20 meters below the current DEM topography, and extending for approximately 300 meters downstream along the drainage channel. The erodible material was assumed to be a saturated granular-fluid mixture with the same material properties as the surrounding material, but was subject to entrainment under the physical constraints identified by Iverson and Ouyang, 2015, where the basal stress jump and a tunable coefficient is used to define the entrainment rate. The channel geometry was chosen based on current topography and slope gradients.

3.2 Model results

At the start of the D-Claw simulation, the pore-fluid pressure acting on the base of the landslide mass was manually raised until failure commenced locally at the weakest location. The manual manipulation then ceased and D-Claw's evolution equations dictated the failure process and coupled evolution of pore pressure.

After failure commenced, the landslide material became nearly liquefied and accelerated downslope, eventually inundating Carver Lake (Figure 3). The model equations led to mixing of material and generation of impulse waves in the lake. The waves eventually overtopped the crest of the dam, eroding bed material in the process, leading to channel excavation. The positive feedback loop of dam and channel erosion led to further flooding and lake drainage. After approximately 5 minutes simulated time the lake evacuation stabilized, leading to a mixture of landslide material and fluid stranded in the lake bed (Figure 3). The flow downstream of the dam had the characteristics of a debris flow, with $m = 0.5 - 0.6$ (Figure 4).

The D-Claw simulation continued to resolve the downstream flood and debris flow as it descended the lower flanks of South Sister volcano. By utilizing AMR, grid efficiency was greatly enhanced by only resolving parts of the domain with active flow (*c.f.* (Berger et al., 2011)).

The debris flows and flooding were primarily confined to the Wychus Creek drainage for an approximately 15 km reach downstream of Carver Lake, where the creek is deeply incised for much of its path.

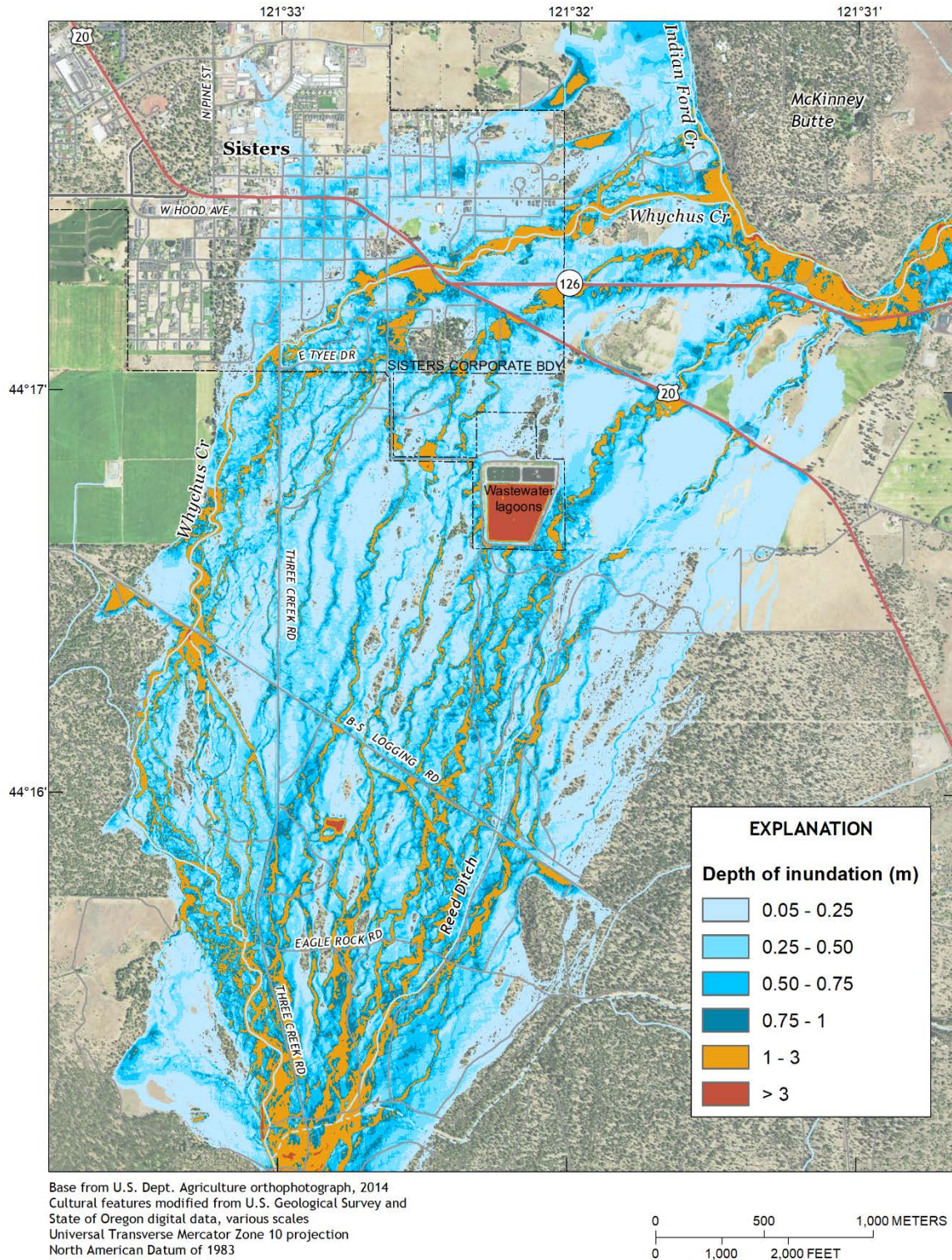


Figure 5. D-Claw results showing the flood and debris-flow inundation in the alluvial fan surrounding Sisters. Shading indicates the maximum depth observed at any location for the duration of the simulation.

Several kilometers upstream of the community of Sisters, Whychus Creek debouches onto an alluvial fan with low relief and a system of (now dry) distributary channels. When the modeled flow reached this point after

approximately 1 hour, it immediately overtopped the low banks of the main branch of Whychus Creek, spreading into the distributory channels. The flow continued to spread widely across the alluvial fan, eventually inundating Sisters (Figure 5). However, due to the spreading, the depth of the flow in the main channel was reduced significantly, presumably lessening the flood risk posed to the more densely populated area of Sisters adjacent to the main channel. The results contrasted with early 1-D simulations performed in the 1980's, which assumed that most of the flow was confined to the channel.

4. Conclusions

Dam-break outburst floods and other phenomena that involve grain-fluid mixtures (*e.g.*, landslides, debris flows, dam breaches and bed-material entrainment) interacting with bodies of water, pose modeling challenges due to the multi-physics nature of the cascading hazards. Coupling disparate models together is less than desirable, due to implementation difficulties and model inaccuracy from *ad hoc*, non-conservative, coupling assumptions.

We used D-Claw to seamlessly model a hypothetical landslide and the resulting cascade of lake inundation, wave generation, dam overtopping, breach growth and downstream debris flow. The modeling approach requires only initial conditions and material parameters for the landslide material, water, and erodible bed material with no explicitly specified coupling assumptions. Obtaining high-resolution results with such simulations also requires use of high-resolution digital topographic data, such as the lidar data we utilized in this study.

Compared to earlier studies employing 1-D equations and coarse topography, our modeling suggests a strikingly different result for our test case involving inundation near Sisters, Oregon. Owing in part to the use of 2-D equations as well as high-resolution lidar topography, our results suggest that flow avulsion and diversion on the alluvial fan surrounding Sisters would lead to a less severe flood hazard to the community.

References

- Berger, M.J., George, D.L., LeVeque, R.J., and Mandli, K.T., 2011, The GeoClaw software for depth-averaged flows with adaptive refinement. *Advances in Water Resources*, 34:1195-1206.
- George, D.L., and Iverson, R.M., 2014, A depth-averaged debris-flow model that includes the effects of evolving dilatancy. II. Numerical Predictions and experimental tests. *Proc. R. Soc. A*, 470(2170).
- George, D.L., Iverson, R.M. and Cannon, C.M., 2017, New methodology for computing tsunami generation by subaerial landslides: application to the 2015 Tyndall Glacier landslide, Alaska. *Geophys. Res. Lett.*, 44(14):7276-7284.
- Iverson, R.M. and George, D.L., 2014, A depth-averaged debris-flow model that includes the effects of evolving dilatancy. I. Physical basis. *Proc. R. Soc. A*, 470(2170).
- Iverson, R.M. and Ouyang, C., 2015, Entrainment of bed material by earth-surface mass flows: review and reformulation of depth-integrated theory. *Reviews of Geophysics*, 53.
- Laenen, A., Scott, K.M. Costa, J.E. and Orzol, L.L., 1987, Hydrologic hazards along Squaw Creek from a hypothetical failure of the glacial moraine impounding Carver Lake near Sisters, Oregon. Open-file report 87-41, U.S. Geological Survey.
- O'Connor, J.E., Hardison, J.H., and Costa, J.E., 2001, Debris flows from failures of Neoglacial-age dams in the Three Sisters and Mount Jefferson wilderness areas, Oregon, U.S. Geological Survey Professional Paper 1606, U.S. Geological Survey.

Woody debris blocking conditions at bridges in mountainous streams

Yuji Hasegawa^{a,*}, Kana Nakatani^b, Yoshifumi Satofuka^c

^aGraduate School of Integrated Arts and Sciences, Hiroshima University, 1-7-1 Kagamiyama, Higashi Hiroshima, Hiroshima 7398251, Japan

^bGraduate School of Agriculture, Kyoto University, Oiwake-cho, Kitashirakawa, Sakyo-ku, Kyoto 6068502, Japan

^cDepartment of Civil Engineering, Ritsumeikan University, 1-1-1 Noji-higashi, Kusatsu, Shiga 5258577, Japan

Abstract

When debris flows occur, bridges in mountainous streams may become dangerous when blocked by woody debris. When bridges are blocked with accumulated woody debris, high flow depths can cause the flow to spread widely. However, not all bridges become blocked with woody debris. Many studies have examined bridges blocked with woody debris for gentle slopes, but few studies have been conducted on steep mountain streams with supercritical flow. To better understand the interaction of woody debris and bridges across steep streams, we conducted laboratory experiments using one-pier bridge model and considered factors for the blockage of bridges by woody debris. We used straight rectangular channel flume 7 m in length, 0.3 m width, and with a variable slope. We supplied steady water from upstream end. We supplied woody debris model to the upstream end of the flume at approx. 1 second. We set the bridge model 1.5 m upstream from the downstream end of the flume. We used ABS plastic material with a specific weight of 1.05 for the experimental woody debris. We varied the flume slope, water discharge, supply of woody debris, length of wood, height of bridge piers and Froude number. When the woody debris reached the bridge model, the total time of woody debris to pass through became longer from the supplied upstream condition due to rotational motion and diffusion. Because the total time changed, the amount of woody debris per unit time at the bridge was smaller than supplied condition. When examining the blocking conditions, we applied the woody debris condition at bridge model. From the results, we proposed methods to estimate the threshold condition of woody debris blocking at bridge from dimensional analysis. We applied parameters combining the experimental conditions of the bridge model, woody debris model, and hydraulic conditions, as well as the amount of woody debris per unit time required for bridge blocking.

Keywords: woody debris, channel experiment, bridge, accumulation, dimensional analysis

1. Introduction

It is known that woody debris enhances the damage of sediment-related disasters when it accumulates and blocks bridges (Abbe and David, 2003; Bilby and Ward, 1991; Ishikawa et al., 1989). In Japan, hillslope works consisting of steel pipes have been installed to trap woody debris (Mizuyama et al., 1991). However, compared to sediment countermeasures, such as the widely constructed sabo dams in Japan, countermeasures for woody debris are insufficient. Furthermore, it has been reported that closed type sabo dams, especially which have been filled with sediment, hardly capture woody debris. Therefore, even on channels with sabo dams, the transport and potential damage by woody debris must be considered.

Previous studies on woody debris have focused on mild slope sections with subcritical flow conditions (e.g., Adachi and Daido, 1957; Nakagawa et al., 1994). However, few studies have been conducted on steep sections of mountain rivers with supercritical flow. Understanding the accumulation processes requires consideration of the three-dimensional motion of woody debris. Numerical simulation is suitable for predicting flood damage caused by woody debris accumulation. Recently, discrete particle methods and horizontal two-dimensional analysis methods have been proposed to model the dynamics of woody debris (e.g., Gotoh et al., 2007; Shimizu and Osada, 2007). Both types of

* Corresponding author e-mail address: y-hasegawa@hiroshima-u.ac.jp

studies track the movement of woody debris using Lagrangian methods. However, those models focus on a limited domain in time and in space, and practical models for analyzing the long reaches of mountain rivers have not yet been developed.

The blocking of bridges by woody debris is similar to the blocking of open steel sabo dams by debris flows. The blocking of sabo dams by sediment is a complicated three-dimensional process, which often requires stochastic methods to represent. However, Satofuka and Mizuyama (2005) have proposed a practical model describing an open steel sabo dam's sediment trap function with an approximate equation. Here, we aim to develop a similar practical model describing the accumulation and blocking of bridges by woody debris. To propose a practical model, we need to identify the necessary conditions for woody debris accumulation and bridge blocking. It is known that the woody debris accumulation on bridges is influenced from the amount of wood per unit time arriving at bridge, but few studies have been conducted (Braudrick et al., 1997). In this study, we conducted channel experiments on woody debris accumulation and bridge blocking, and also applied dimensional analysis to identify the critical conditions of bridge blocking.

2. Experimental Outline

We conducted experiments using a rectangular channel 7-m long and 0.3-m wide. We attached approximately 0.7-mm diameter uniform particles on the riverbed to create a rough surface. We observe the flow conditions on the right side of the channel. The bridge model was placed 1.5 m from the downstream end of the flume. The pier of the bridge was placed in the center of the channel. We used three different bridge heights H_b (0.05, 0.07, 0.09 m height from river bed to bridge girder). The girder width was 0.2 m, the girder thickness was 0.02 m, the handrail height was 0.03 m, the pier diameter was 0.02 m, and the spacing between the pier and channel side wall was 0.14 m. Water was supplied at a steady state. We adjusted the water discharge to achieve a uniform flow depth at the bridge that did not exceed the depth of the bridge deck. Experimental woody debris was made from ABS resin with specific gravity of 1.05.

We modeled woody debris as a log and did not consider roots and branches. We used cylindrical round bars of length l 0.15, 0.175, 0.2, 0.3 m and diameter 0.03 m. Woody debris was supplied to the flow 5.5 to 6.0 m upstream from the bridge model in 1 second. The amount of supplied woody debris Q_{d1} condition at upstream was changed from 20 to 250 logs/s with 10 logs/s interval. The initial pulse of woody debris diffused as it flowed downstream. But it flowed almost in a steady state within the range of 1-m upstream from the bridge. From experimental observations, we identified the process by which woody debris accumulated and blocked the bridge. First the frontal part of woody debris arrived at the bridge, and the following woody debris within the range of 1-m upstream from the bridge caused blocking. We measured the number of woody debris pieces and the average woody debris velocity in the range of 1-m upstream from the bridge. The amount of woody debris per unit time, Q_{d2} , was obtained from the moving volume and speed of the woody debris. In this experiment, Q_{d2} was considered as the supply amount. We counted and measured woody debris from the video. The discharge of woody debris varied slightly with time. We defined Q_{d2} as discharge when more than half of the woody debris was within the 1-m reach upstream of the bridge. As a result, Q_{d2} ranged from 6.5 to 130.1 logs/s. Fig.1 shows the outline of the experimental channel and bridge model. Fig.2 shows an image of the experimental channel and woody debris blocking the bridge. Table 1 lists the experimental conditions. We conducted the experiment multiple times under the same conditions, for a total of 359 experimental runs.

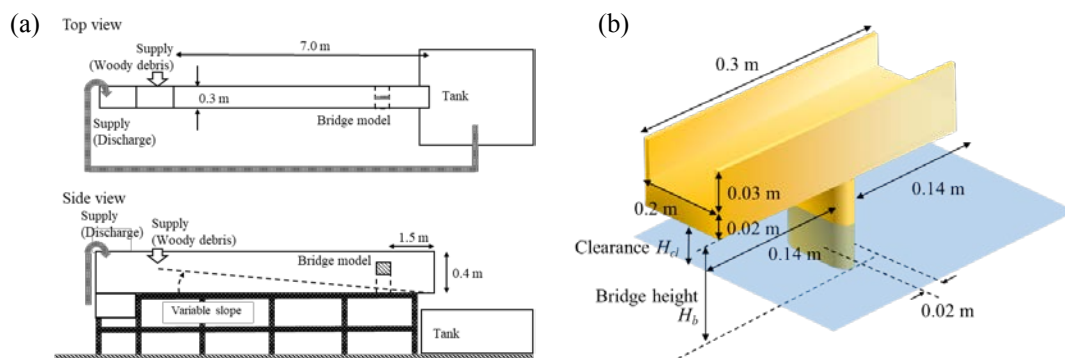


Fig. 1. (a)Outline of the experimental channel and (b)bridge model

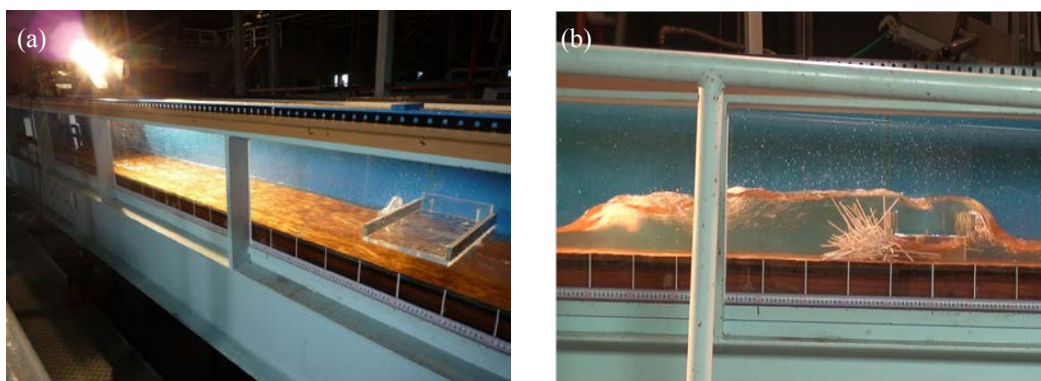


Fig. 2. (a) Experimental channel and (b) woody debris blocking at bridge

Tabel 1. Experimental conditions and cases

Case	Channel slope i	Discharge Q (m^3/s)	Woody debris length l (m)	Woody debris from upstream side (logs /s)	discharge	Bridge Height H_b (m)	Fr
1-1	1/20	0.0141	0.2	20~250		0.05	3.09
1-2	1/30	0.0115					2.52
1-3	1/40	0.0099					2.17
2-1	1/40	0.0047	0.2			0.05	2.07
2-2		0.0099					2.17
2-3		0.0141					2.20
3-1	1/40	0.0141	0.15			0.05	2.20
3-2			0.175				
3-3			0.2				
3-4			0.3				
4-1	1/40	0.0141	0.2			0.05	2.20
4-2						0.07	
4-3						0.09	

* Case1-3 and Case2-2 or Case2-3 and Case3-3 and Case4-1 are same condition

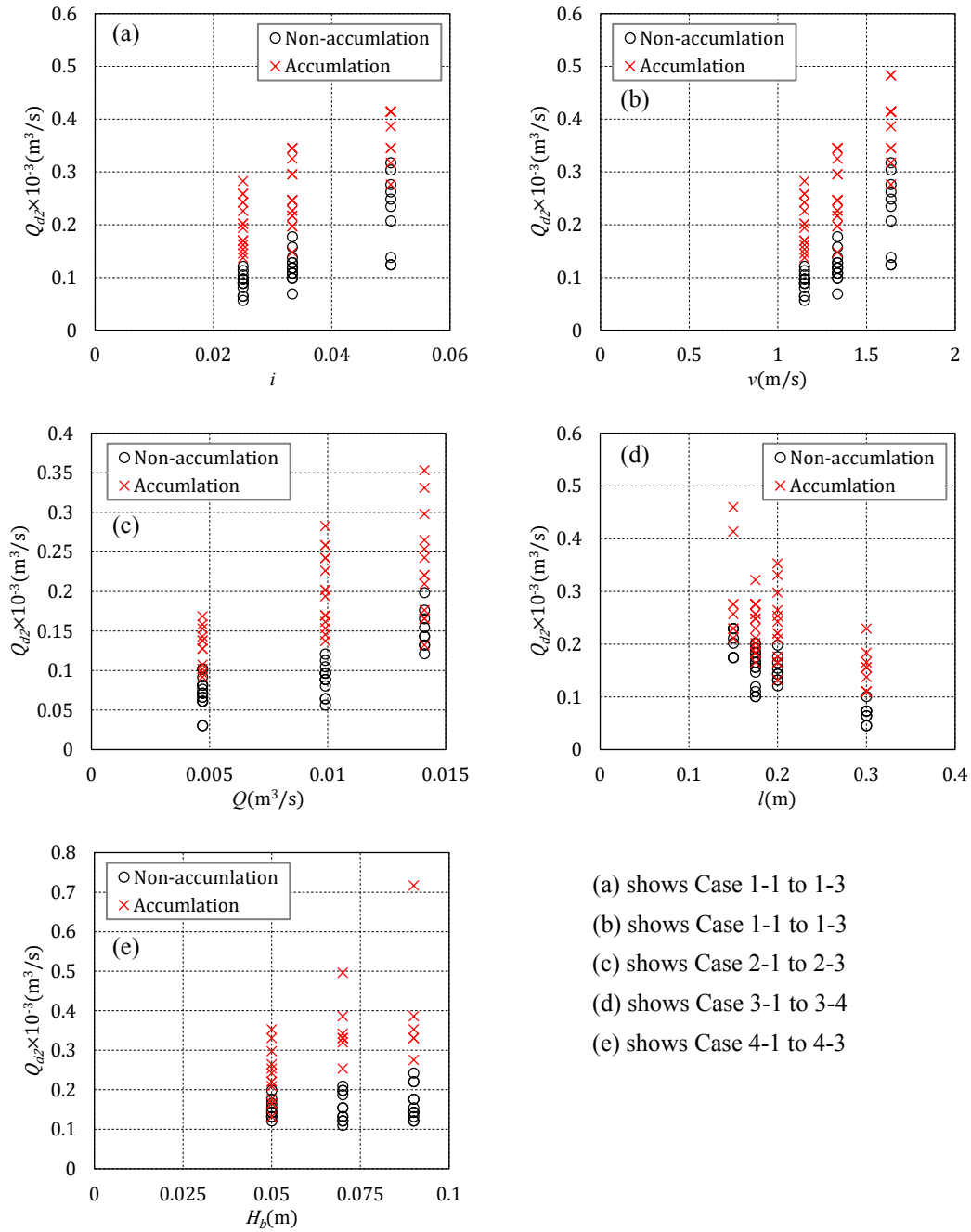
3. Experimental Results

3.1. Woody debris discharge and other factors effecting bridge blocking

Fig.3 shows the results of woody debris accumulation and bridge blocking. The “o” symbol in the figure indicates woody debris that passed the bridge without accumulating, and the “x” symbol indicates woody debris accumulated at the bridge and caused a dam-up on the upstream side. We eliminated the case when woody debris was caught temporarily on the bridge and flowed out.

Fig.3a shows the relationship between the channel slope i and the amount of woody debris per unit time (hereafter, call as woody debris discharge) Q_{d2} . Fig.3b shows the relationship between the flow velocity v and woody debris discharge Q_{d2} . Fig. 3a and 3b shows Case 1-1 to 1-3. In steep slope cases, the Q_{d2} required to cause accumulation was large. Cases 1-1 to 1-3 were conducted in same flow depth, and Q_{d2} required to accumulate at the bridge increased as the velocity increased. The minimum Q_{d2} for woody debris to accumulate at the bridge was linearly related to the riverbed gradient and to flow velocity. The required Q_{d2} to accumulate at the bridge varied in steep slope conditions.

Fig.3c (Case 2-1 to 2-3) shows the relationship between the supplied water discharge Q and the woody debris discharge Q_{d2} . When water discharge was large, Q_{d2} required to cause accumulation was large. In the same slope



(a) shows Case 1-1 to 1-3
 (b) shows Case 1-1 to 1-3
 (c) shows Case 2-1 to 2-3
 (d) shows Case 3-1 to 3-4
 (e) shows Case 4-1 to 4-3

Fig. 3. Results on woody debris accumulation and bridge blocking

conditions, the flow depth became high when discharge was large, and the clearance H_{cl} between the flow surface and the bridge girder became small. The clearance H_{cl} was 0.014 m in maximum water discharge condition and was 0.032 m in minimum water discharge condition. However, the diameter D of the woody debris was 3 mm is small compared to the clearance. Therefore, in this study, the effect of clearance H_{cl} seemed to be rather small. The required Q_{d2} to accumulate at the bridge varied in maximum water discharge conditions.

Fig.3d (Case 3-1 to 3-4) shows the relationship between the woody debris length l and the woody debris discharge Q_{d2} . When the length l was long, the probability that woody debris was caught by bridge pier increased. Therefore, accumulation seemed to occur in smaller woody debris discharge conditions compared to shorter length conditions.

The ratio of the opening width of the bridge (distance between bridge pier and side wall: w) and woody debris length l , was related to the accumulation results due to wood length difference. This trend matched the recent studies. The required Q_{d2} to accumulate at the bridge varied in shorter woody debris length conditions.

Fig.3e (Case 4-1 to 4-3) shows the relationship between the bridge pier height H_b and the woody debris discharge Q_{d2} . Compared to other factors, we could not identify a significant trend. But when pier height H_b was shorter, the required Q_{d2} to accumulate at the bridge became slightly smaller. Recent studies reported that woody debris accumulation and blocking at bridges in steep slope mountainous rivers was affected by three-dimensional motion of the wood. Therefore, ratios $H_b/(h+D)$ or H_{cl}/D appear to be related to the probability that woody debris caught by the bridge pier and accumulates on bridge. The required Q_{d2} to accumulate at the bridge varied in shorter bridge pier height conditions.

3.2. Threshold conditions for bridge blocking by woody debris

Based on the trends in experimental results, we considered that the following three conditions affect bridge blocking by woody debris: (1) hydraulic conditions described by parameters Q , h and i ; (2) the probability that woody debris would be caught by the bridge pier, which is described by the parameter w/l ; and (3) the probability that woody debris would be caught by bridge girder, which is described by the parameters $H_b/(h+D)$ and H_{cl}/D . Therefore, we examined variables combining the three conditions' parameters. Furthermore, we found that woody debris discharge Q_{d2} also effects the bridge blocking, so we proposed new variables that have the same dimension with Q_{d2} . Here, we should take into account for cases when woody debris was caught temporarily on the bridge and flowed out, because those cases help identify the boundary between blocking occurrence and non-occurrence conditions. We also defined the temporal blocking condition as blocking and found the smallest woody debris discharge Q_{dlim} to cause blocking in each condition. When multiple results exist in same case, we used the average value.

From the experiments results, we considered the variables $w/l \cdot Q \cdot H_b/(h+D)$ and $w/l \cdot Q \cdot H_{cl}/D$. Fig.4 shows the relationship between Q_{dlim} and the variables $w/l \cdot Q \cdot H_b/(h+D)$, $w/l \cdot Q \cdot H_{cl}/D$, $w/l \cdot Q \cdot H_b/(h+D) \cdot i$, and $w/l \cdot Q \cdot H_b/(h+D) \cdot i^{0.5}$. The straight line in the figure shows the boundary of accumulation at bridge. The line in each figure was drawn by least squares method.

Comparing the variables $w/l \cdot Q \cdot H_b/(h+D)$ and $w/l \cdot Q \cdot H_{cl}/D$, $w/l \cdot Q \cdot H_b/(h+D)$ showed good relation to the boundary line. Focusing on variables $w/l \cdot Q \cdot H_{cl}/D$, D became small value for H_{cl} , and H_{cl}/D showed less influence than w/l and Q . Therefore, conditions with large H_{cl} deviated from the boundary line. In Fig.4a, results for steep conditions also deviated from the boundary line. To take into account of the effects of slope, next we considered the variable $w/l \cdot Q \cdot H_b/(h+D)$ multiplied by slope. Here, only the $i=1/20$ condition deviated from the boundary line. Therefore, in order to reduce the slope influence and achieve a better linear relationship, we multiplied the variable $w/l \cdot Q \cdot H_b/(h+D)$ by $i^{0.5}$. This combination of variables resulted in the closest relation to the boundary line. We obtained the relation $Q_{dlim} = \alpha \cdot w/l \cdot Q \cdot H_b/(h+D) \cdot i^{0.5}$ as the threshold of woody debris discharge Q_{dlim} required to accumulate on the one-pier bridge with two spans. Here, α is an experimental coefficient, 0.11 in this experiment.

Fig.5 shows the relationship between the woody debris blocking threshold $Q_{dlim}/(Q+Q_{dlim})$ and the blocking safety factor for woody debris discharge Q_{d2}/Q_{dlim} . Results showed that most of the blocking occurred when the safety factor was equal or larger than 1. And the boundary of occurrence and non-occurrence of the bridge blocking were shown to be around a safety factor of 1. However, some results had blocking occur when the safety factor was less than 1, and it is important to understand what the factors were that caused this condition. From experimental observations, we found several factors. There were some conditions in which there were a large number of pieces of woody debris oriented nearly perpendicular to the flow direction. In these situations, there were a large number of pieces of woody debris that collided with the bridge pier. And there were also conditions that during the experiment, in which woody debris was concentrated for a short time. We need to consider how these conditions have affected for blocking boundary in future studies.

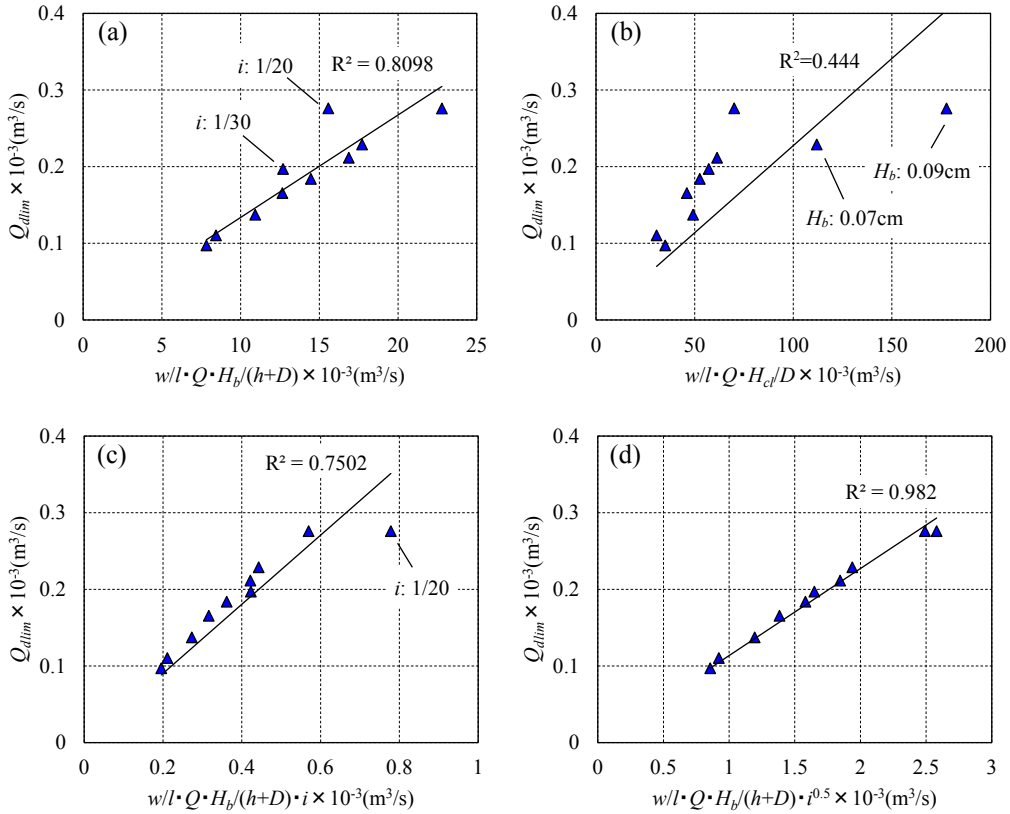


Fig. 4. Relationship between the variable i and woody debris discharge: the boundary line in each figure was drawn by least squares method using the result plots

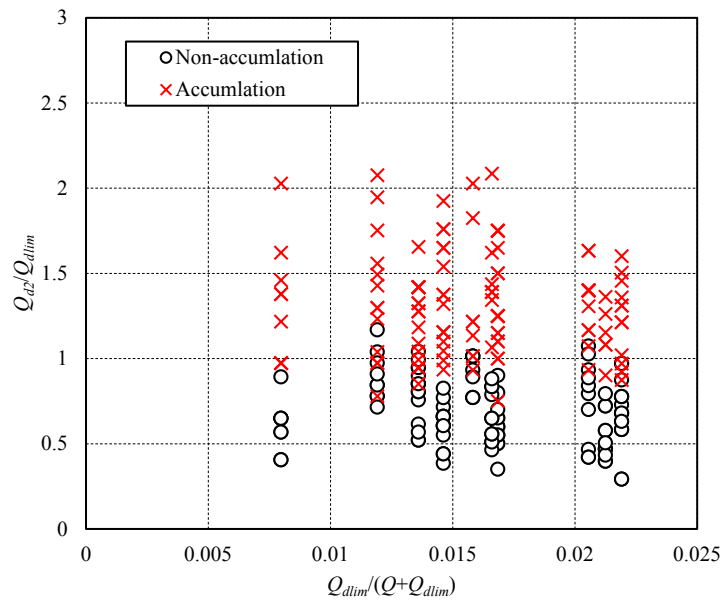


Fig. 5. Relationship between the woody debris concentration and the threshold for blocking

4. Conclusion

In this study, we conducted channel experiments focusing on the amount of woody debris per unit time and examined the necessary conditions for wood accumulation at bridges. The diffusion of woody debris may have been due to the rotation of logs caused by the cross-stream variation in flow velocity. It seemed to happen due to rotation and flow velocity distribution at transverse direction. Using the results, we identified the necessary conditions for woody debris to accumulate at bridges from the relationship between the amount of woody debris per unit time and combinations of the following variables: the woody debris length, diameter, pier height, distance between the pier and sidewall, water depth, flow velocity, and slope.

We did not clearly find a relation between the bridges clearance and the diameter of woody debris in this study. The specific gravity of coniferous trees is different from broad-leaved tree. Therefore, the type of wood may cause a different trend for accumulation at bridges and relationships between bridge clearance and log diameter.

Although we focused on a bridge model with one pier, bridges with no piers or two piers are common. We will consider bridge geometries in the future studies. Furthermore, we obtained a method to estimate woody debris accumulation and bridge blocking, but there is some variability around the threshold for woody debris accumulation. Therefore, we need to analyze the results and the process in more detail. Finally, when considering countermeasures for woody debris, the most important condition will be the amount of woody debris. However, it is difficult to estimate and know the exact amount at the present time. Recently, we are able to obtain and apply high resolution DEM or Lidar data in a mountainous area. Therefore, we can apply those data and also analyze data from field observations to estimate the accumulation of woody debris in a natural river. Combining our results with other studies may eventually lead to methods to predict woody debris hydrographs and design effective countermeasures.

References

- Abbe, T.B., and David, R.M., 2003, Patterns and processes of wood debris accumulation in the Queets river basin, Washington, *Geomorphology*, 51, p. 81-107.
- Adachi, S., and Daido, A., 1957, Experimental study on washed timbers, *Kyoto university Disaster Prevention Research Institute Annuals*, v. 1, p. 41-49 (Japanese with English abstract).
- Bilby, R.E., and Ward, J.W., 1991, Characteristics and function of large woody debris in streams draining old-growth, clear-cut, and second-growth forests in Southwestern Washington, *Canadian Journal of Fisheries and Aquatic Sciences*, v. 48, p. 2499-2508.
- Braudrick, C.A., Grant, G.E., Ishikawa, Y., and Ikeda, H., 1997, Dynamics of wood transport in streams: A flume experiment, *Earth surface processes and landforms*, v. 22, p. 669-683.
- Gotoh, H., Ikari, H., Tetsuo, S. and Oku, K., 2007, 3D simulation of blocking of bridge in mountain stream by drift wood, *Journal of Hydraulic Engineering, JSCE*, v. 51, p. 835-840 (Japanese with English abstract).
- Ishikawa, Y., Mizuyama, T., and Fukuzawa, M., 1989, Generation and flow mechanisms of floating logs associated with debris Flow, *Journal of the Japan Society of Erosion Control Engineering*, v. 42, no.3, p. 4-10 (Japanese with English abstract).
- Mizuyama, T., Ishikawa, Y., and Fukuzawa, M., 1991, A study on mechanisms of movement and accumulation of floating logs and their countermeasures, *Report of PWRI*, v. 183, p. 71-156 (Japanese).
- Nakagawa, H., Inoue, K. and Ikeguchi, M., 1994, Numerical simulation of the driftwood behavior (3)-Analysis considering the dynamics of the rotational motion of the driftwood-, *Kyoto university Disaster Prevention Research Institute Annuals*, no. 37 (B-2), p.1-15 (Japanese with English abstract).
- Satofuka, Y., and Mizuyama, T., 2005, Numerical simulation on debris flow control by a grid dam, *Journal of the Japan Society of Erosion Control Engineering*, v. 57, no. 6, p. 21-27 (Japanese with English abstract)
- Shimizu, Y., and Osada, K., 2007, Numerical experiments on accumulation process of driftwoods around piers by using a dem-flow coupling model, *Journal of Hydraulic Engineering, JSCE*, v. 51, p. 829-834 (Japanese with English abstract).

Flume experiments and numerical simulation focused on fine sediments in stony debris flow

Junya Hina^{a*}, Taro Uchida^b, Naoki Matsumoto^b, Wataru Sakurai^b, Yuki Nishiguchi^c,
Masato Murakami^c

^aCTI Engineering, Co., Ltd., 1-6-7 Doshucho, Chuo-ku, Osaka, Osaka 5410045, Japan

^bNational Institute for Land and Infrastructure Management, 1 Asahi, Tsukuba, Ibaraki 3050804, Japan

^cCTI Engineering, Co., Ltd., 1047-27 Onigakubo, Tsukuba, Ibaraki 3002358, Japan

Abstract

In stony debris flow, it has been considered that the gravels move like laminar flow, but the interstitial water behave as turbulent flow. Moreover, fine particles can behave with the interstitial water as fluid and many previous studies call this process of fine sediment as shifting solid phase to fluid phase, “phase-shift”. Phase-shifted sediment affect the fluidity of debris flow. Therefore, it is necessary to consider fine sediments behavior to describe run-out processes of debris flow. However, the hydraulic conditions that fine sediment can behave as a fluid are not well understood. Here, we analyzed this hydraulic condition through flume experiments and numerical simulations. We examined effects of grain size distribution on the equilibrium sediment concentration, which has been defined as the sediment concentration that in which there is neither erosion nor deposition on the experimental flume bed. We found that for the same hydraulic conditions the equilibrium sediment concentration differed due to variations in the grain size distribution. Based on these experimental results, we tested the following three models for describing the conditions that fine sediment can behave as a fluid. First, we fixed fine sediment concentration in interstitial fluid (Model 1), then, we fixed the maximum diameter of phase-shifted sediment (D_c) (Model 2). In Model 3, D_c is assumed to be variable according to the ratio of the friction velocity to the settling velocity of D_c . As the result, the experimental relationship between grain size distribution and longitudinal gradient of deposited sediment surface under steady-state condition can be described by using the Models 2 and 3, but Model 1 could not describe.

Keywords: debris flow, simulation model, fine sediments

1. Introduction

Debris flow is a mixture of water and high concentrations of sediment. It can cause serious damage to downstream houses and human lives. It is important to predict the area of inundation and depth of sedimentation for mitigating debris-flow disasters. Numerical models tested with flume experiments can be used to help make these predictions. In stony debris flow, it has been considered that the gravels move like laminar flow, but the interstitial water behave as turbulent flow (Takahashi, 2004). Moreover, fine particles mixed with the interstitial water can behave as a fluid (Takahashi, 1977). We call the process of fine sediment shifting from a solid phase to a fluid phase, “phase-shift”. Phase-shifted sediment affects the fluidity of debris flow. Therefore, it is necessary to consider the effects of fine sediments on the run-out processes of debris flow.

In the previous numerical analyses considering phase-shift sediment, a method of setting the interstitial fluid density to a certain fixed value larger than the pure water and a method of setting the maximum diameter of phase-shifted sediment (D_c) (Nishiguchi, 2014) has been used. It is necessary to set the interstitial fluid density and the particle diameter of D_c at which phase-shift occurs so that the calculation result fits the actual result. On the other hand, studies using flume experiments have shown that the grain size distribution affects the equilibrium concentration of debris flow (Hasegawa et al., 2013) and D_c is larger as the ratio of friction velocity of debris flow to

* Corresponding author e-mail address: jny-hina@ctie.co.jp

settling velocity of D_c (Nakatani et al., 2018). However, the hydraulic conditions that fine sediment can behave as fluid are not well understood. Here, we analyzed this hydraulic condition through flume experiments and numerical simulations.

2. Hypotheses

2.1. Hypotheses about phase-shift

It is assumed that the phase-shift of the fine sediments occurs because some of the sediment in the debris flow is incorporated into the interstitial fluid by the turbulent stress of the interstitial fluid. In this study, we defined that phase-shifted sediment is “fine sediment”. The maximum diameter of the fine sediment is “ D_c ”, and we assume that all sediment smaller than D_c flows as part of the interstitial fluid. Then, the interstitial fluid density of the debris flow is expressed by the equation (1).

$$\rho_m = \sigma \frac{C_f}{1-C_c} + \rho_w \left(1 - \frac{C_f}{1-C_c}\right) \quad (1)$$

$$C = C_f + C_c \quad (2)$$

where ρ_m is interstitial fluid density of the debris flow, σ is mass of sediment, C_f is fine sediment concentration, C_c is coarse sediment concentration, ρ_w is water density, C is total sediment concentration.

We use three models to describe sediment phase shift. In Model 1, the interstitial fluid density, i.e., the fine sediment concentration in interstitial fluid, assumed to be constant, regardless of grain size distribution of the debris flow. In Model 2, the maximum diameter of phase-shifted sediment (D_c) remained constant in time and space. This assumption is based on the concept proposed by Nishiguchi (2014). Thus, the interstitial fluid density varied with grain size distribution and total sediment (coarse and fine sediment) concentration. In Model 3, we assumed that D_c varies with the ratio of the friction velocity of the debris flow to the settling velocity of D_c . D_c increases as the ratio of the friction velocity of the debris flow to the settling velocity of D_c increases (Nakatani et al., 2018). Thus, in Model 3, the interstitial fluid density varied with not only grain size distribution and total sediment concentration, but also hydraulic condition. This relationship is described by the following three equations:

$$u_* = \alpha w_s \quad (3)$$

$$u_* = \sqrt{g h \tan\theta_w} \quad (4)$$

$$w_s = \left(\sqrt{\frac{2}{3} + \frac{36\nu^2\rho}{sgD_c^3(\sigma-\rho)}} - \sqrt{\frac{36\nu^2\rho}{sgD_c^3(\sigma-\rho)}} \right) \sqrt{\left(\frac{\sigma}{\rho} - 1\right) g D_c} \quad (5)$$

where u_* is friction velocity, α is coefficient, w_s is settling velocity, g is gravitational acceleration, h is flow depth, $\tan\theta_w$ is water surface gradient, ν is kinematic viscosity coefficient, σ is mass density of sediment.

2.2. Numerical simulation model

We used the debris-flow simulator, Kanako LS (Uchida et al., 2013) to describe the relationship between grain size distribution and longitudinal gradient of deposited sediment surface of flume experiments under steady-state condition (see section 3.1). We used the three different models to set the interstitial fluid density in Kanako-LS. In this numerical simulation model, the equilibrium concentrations of the debris flow and immature debris flow are calculated by the equations (6) and (7).

$$C_\infty = \frac{\rho_m \tan\theta_w}{(\sigma - \rho_m)(\tan\theta - \tan\theta_w)} \quad (6)$$

$$C_\infty = 6.7 \left\{ \frac{\rho_m \tan\theta_w}{(\sigma - \rho_m)(\tan\theta - \tan\theta_w)} \right\}^2 \quad (7)$$

where C_∞ is equilibrium concentration, ϕ is friction angle.

3. Methods

3.1. Experiment and analysis methods

We analyzed the results of previous debris-flow flume experiments (Shima et al., 2014). The experimental flume is a straight rectangular channel with a width of 10 cm and a length of 7 m. The gradient of the flume can be adjusted from 5 degrees to 15 degrees. Coarse sediments are supplied from the upstream end of the flume by a hopper and water and fine sediments are circulated by a pump for circulation to constantly supply water and sediments (Fig. 1a). A plate with a height of 20 cm is installed at the downstream end of the flume. Moreover, the supplied sediment was deposited upstream from the plate, and we measured water surface gradient to clarify the longitudinal gradient of the deposited sediment surface was measured by the ultrasonic sensor. Using 4 types of mixed particle size materials (fig. 1b), 56 cases with different flume gradient (5-15 degrees), flow rate (0.75-2.5 ℓ /sec) and sediment concentration (6.2-29.8 %) were conducted.

In this study, we assumed that once the deposited sediment surface became steady-state condition, the sediment concentration in debris flow became the equilibrium concentration that in which there is neither erosion nor deposition on the experimental flume bed. So, we hypothesized the sediment concentration of debris flow can be calculated using the equilibrium concentration theories of (1), (2), (6) and (7). We set C_f to describe relationship between total sediment concentration and water surface gradient using equations (6) and (7).

3.2. Calculation conditions

Calculation conditions, such as supply flow rate, grain size distribution of materials, supply sediment concentration, flume gradient, width and length, were set to the same values as the experimental conditions. The simulation was run until the plate installed at the downstream end of the flume filled up and the flow upstream stabilized. Furthermore, reproducibility was evaluated for each model by comparing the observed and calculated longitudinal gradient of the deposited sediment surface under steady-state condition.

We set fluid density, D_c -diameter, and α in equation 3 set for Models 1, 2 and 3, respectively. We used several values for each parameter (Table 1).

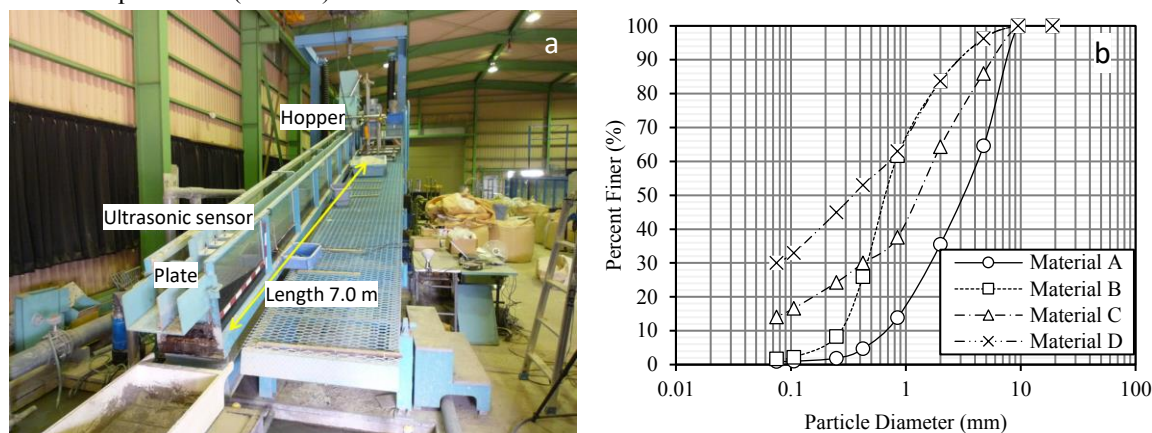


Fig. 1. (a) Grain size distribution and (b) flume of the experiments of Shima et al. (2014)

Table 1. Calculation conditions

Model	Method	Setting value
1	fixing interstitial fluid density (ρ_m)	$\rho_m = 1.05, 1.10, 1.15 \text{ g/cm}^3$
2	fixing the maximum diameter of phase-shifted sediment (D_c)	$D_c = 0.2, 0.425, 0.9 \text{ mm}$
3	Varying D_c according to the ratio of friction velocity of flow to settling velocity of D_c (α)	$\alpha = 3$

4. Results

4.1. Analysis results of experiments

The interstitial fluid density estimated by equations (6) and (7) increased from Material A to Material D (Fig. 2). D_c estimated by grain size distribution of the materials, equations (1) and (2) roughly decreased from Material A to Material D (Fig. 2). However, the estimated values of the interstitial fluid density and D_c fluctuated even same material. This result shows that the condition of the phase-shift does not depend only on the grain size distribution of the debris flows.

Next, the relationship between D_c and the ratio of friction velocity during experiment to settling velocity of D_c is shown in Fig. 3. D_c tends to decrease as the ratio of the friction velocity to settling velocity of D_c is larger, and the friction velocity and settling velocity of D_c are distributed in the range of approximately 2 to 13. Furthermore, in the range where D_c is larger than 0.3 mm, the ratio of the friction velocity to settling velocity of D_c is 2 to 4 regardless of grain size distribution of materials.

4.2. Calculation results

As a result of calculation in Model 1, the gradient of deposited sediment surface in the equilibrium state is roughly 0.8 to 1.6 times (correlation coefficient 0.29) with respect to the experiment result in the case of $\rho_m=1.05 \text{ g/cm}^3$, 0.7 to 1.5 times (correlation coefficient 0.61) in the case of $\rho_m=1.10 \text{ g/cm}^3$, 0.6 to 1.3 times (correlation coefficient 0.54) in the case of $\rho_m=1.15 \text{ g/cm}^3$ (Fig.4). When the density was set to $\rho_m=1.10 \text{ g/cm}^3$, the experiment result could be relatively well reproduced by calculation, however it is not possible to express the difference in the grain size distribution of debris flows, so the concentration of fine sediments can not be calculated appropriately.

Second, as a result of calculation in Model 2, the sediment gradient in the equilibrium state is roughly 1.0 to 1.3 times (correlation coefficient 0.63) with respect to the experiment result in the case of $D_c=0.2 \text{ mm}$, 0.9 to 1.2 times (correlation coefficient 0.91) in the case of $D_c=0.425 \text{ mm}$, 0.7 to 1.1 times (correlation coefficient 0.78) in the case

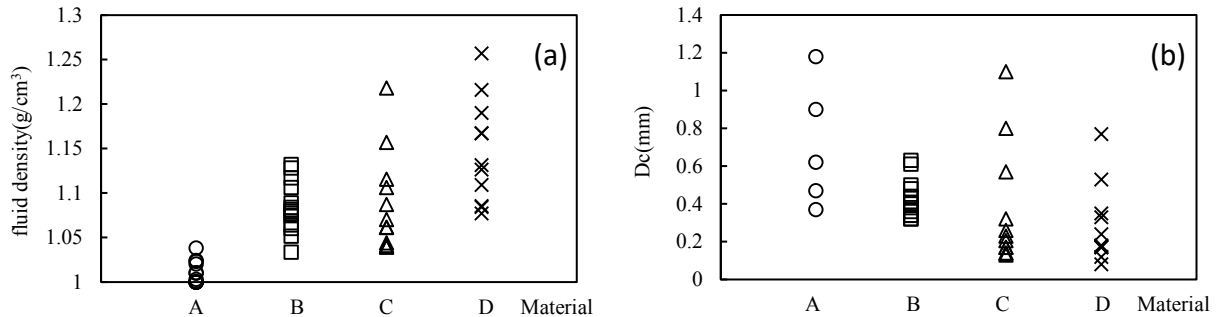


Fig. 2. (a) Estimated result of interstitial fluid density; (b) estimated result of D_c based on analysis results of experiments

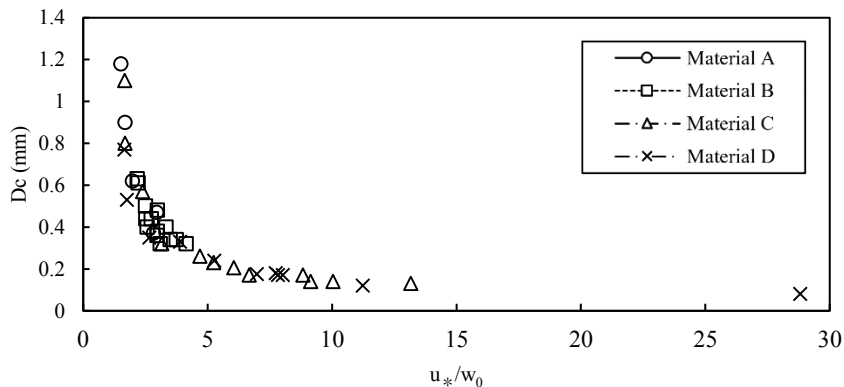


Fig. 3. The relationship D_c and the ratio of friction velocity to settling velocity of D_c

of $D_c=0.95$ mm (Fig.5). When the density was set to $D_c=0.425$ mm, the experiment result could be well reproduced by calculation.

Third, in Model 3, the gradient of deposited sediment surface in the equilibrium state is roughly 0.9 to 1.2 times (correlation coefficient 0.91) with respect to the experiment result (Fig. 6). Model 3 was able to reproduce the experiment result better by calculation.

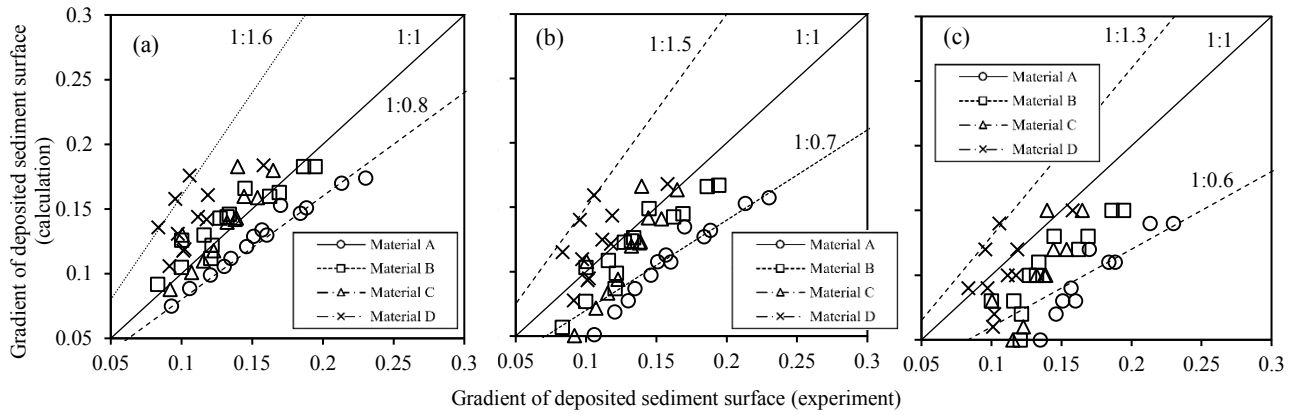


Fig. 4. Relationship between observed and calculated longitudinal gradient of deposited sand surface using Model 1: (a) $\rho_m=1.05$ g/cm³; (b) $\rho_m=1.10$ g/cm³; (c) $\rho_m=1.15$ g/cm³

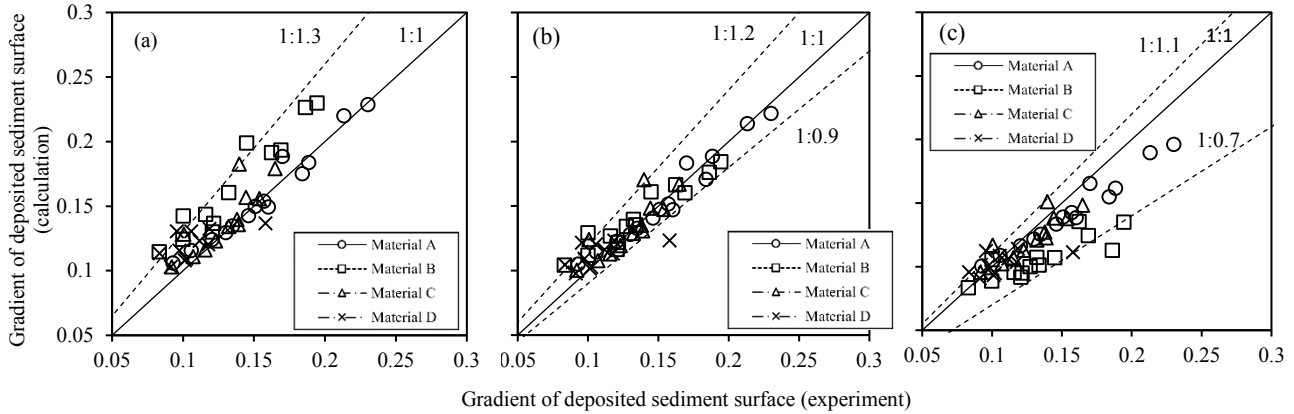


Fig. 5. Relationship between observed and calculated longitudinal gradient of deposited sand surface using Model 2: (a) $D_c=0.2$ mm; (b) $D_c=0.425$ mm; (c) $D_c=0.95$ mm

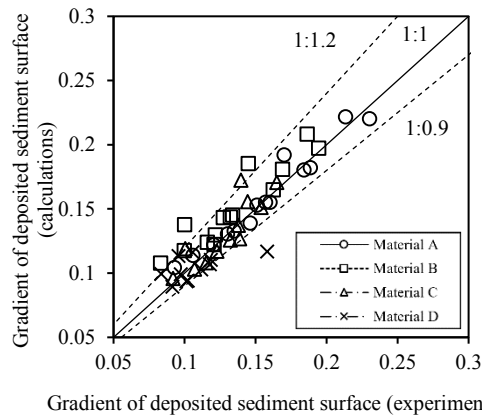


Fig. 6. Relationship between observed and calculated longitudinal gradient of deposited sand surface using Model 3

5. Conclusion

We tested following three models for describing condition that fine sediment can behave as fluid through the comparison between results of flume experiment and numerical simulation. First, we assumed constant fine sediment concentration in interstitial fluid (Model 1). Then, we fixed the maximum diameter of phase-shifted sediment (D_c) (Model 2). In Model 3, D_c is assumed to be variable according to the ratio of the friction velocity to the settling velocity of D_c . As the result, the experimental relationship between grain size distribution and longitudinal gradient of deposited sediment surface under steady-state condition can be described by using the Models 2 and 3, but Model 1 could not describe. In particular, Model 3 is expected to be versatile simulation model because it does not depend on the change in D_c due to the scale and the particle size of debris flow.

Acknowledgements

We are grateful to MLIT Fujigawa Sabo Office for giving very valuable data on flume experiments.

References

- Hsegawa, Y., Sugiura, N., Okamoto, A., Uchida, T., Hayashi, S., Niwa, S., Suzuki, T., 2013, Experiment on the influence of fine sediment on equilibrium concentration of debris flow: Outline of the 62nd Sabo study meeting presentation, B, pp.118-119. (in Japanese)
- Nakatani, K., Furutani, T., Hasegawa, Y., Kosugi, K., Satofuka, Y., 2018, Investigation on the influence and its factors on the debris flow behaviors of fine sediment: Journal of Erosion Control Engineering, no. 70, v. 6, p.3-11. (in Japanese)
- Nishiguchi, Y., 2014, Study on numerical simulation method of debris flow caused by deep collapse: Kyoto University thesis. (in Japanese)
- Shima, H., Mistunaga, T., Moriya, T., Ooura, J., Uchida, T., Suzuki, T., Kuroda, A., Hasegawa, Y., 2014, Method for calculating debris flow equilibrium concentration including fine sediment: Outline of the 63rd Sabo study meeting presentation, A, pp.118-119. (in Japanese)
- Takahasi, T., 1977, A mechanism of occurrence of mud-debris flows and their characteristics in motion: Kyoto University Disaster Prevention Research Institute Annuals, Vol.20, B-2, p.405-435. (in Japanese)
- Takahasi, T., 2004, A mechanism of debris flow and measures: Kinmiraisya, p.40. (in Japanese)
- Uchida, T., Nisiguchi, Y., Nakatani, K., Satofuka, Y., Yamakoshi, T., Okamoto, A., and Mizuyama, T., 2013, New numerical simulation procedure for large-scale debris flows (Kanako-LS): International Journal of Erosion Control Engineering, Vol.6, No.2, pp.58-67.

On the regression of the velocity distribution of debris flows using machine learning techniques

Li-Jeng Huang^{a,*}, Dar-Horng Hsiao^a

^aDepartment of Civil Engineering, National Kaohsiung University of Science and Technology, 807 Kaohsiung, Taiwan, R.O.C.

Abstract

Five machine learning techniques— classical nonlinear regression (NLR), multi-layer perceptrons (MLP), support vector machines (SVM) with radial-basis function (RBF) kernel, k nearest neighbour (k NN) and decision tree (DT) schemes— were applied for regression of velocity distribution along the depth of debris flows by using experimental data of steady uniform open-channel flows. Programs coded in Python and package *scikit-learn* were developed for machine learning analyses. Experimental results of two cases conducted and published by Matsumura and Mizuyama (1990) were adopted for training and prediction curves of the velocity distributions using the five different machine learning techniques. Three theoretical formulas were employed for comparison and investigation, the power-law derived by Takahashi (1978) based on Bagnold dilatant flow, theory modified by Matsumura and Mizuyama (1990), and the two-region formula derived by Su et al. (1993). R -squared scores for each case were calculated to check the fitness of the machine learning results to the experimental data and then to verify the fitness of the theoretical formulas to the machine learning predictions. The quantified results revealed that machine learning schemes provide powerful approaches for building prediction models for velocity distribution of debris flows.

Keywords: data analysis; debris flows; machine learning; nonlinear regression; velocity distribution

1. Introduction

Disasters caused by debris flows often occur in Japan, Taiwan and elsewhere in the world (Takahashi, 1977; Jan, 2000). Development of the disaster prevention techniques is based on the understanding and analysis of the mechanical characteristics of debris flow. Debris flows are inherently non-Newtonian flows from the viewpoints of fluid mechanics, in which the rheological behavior is highly nonlinear and complicated.

Many flow models have been proposed for analysis of the mechanical characteristics of debris flows. Among them, the following models are useful and significant: the dilatant fluid model initiated by Bagnold (1954) and extended by Takahashi (1977, 1978); the Bingham fluid model, and the pseudo- or generalized visco-plastic fluid models proposed by Chen (1986), O'Brien and Julien (1988), Chen et al. (1991), and Julien and Lan (1991); the Prandtl mixing-length model employed by Matsumura and Mizuyama (1990); the modified turbulent flow model proposed by Yu and Chen (1990); the mixed-layer model proposed by Su et al. (1993); and the two-layer model, proposed by Ho (1997) in which an inertia sub-region and a viscous sub-region exist.

Conversely, machine learning and artificial intelligence technologies have been developed widely during the past decades (Muller and Guido, 2017; Bonaccorso, 2017). Among these schemes the supervised learning algorithms employed for regression can be applied for the prediction of flow velocity profiles.

In this study we applied five machine learning schemes, i.e., classical nonlinear regression (NLR), multi-layer perceptrons (MLP), support vector machines (SVM) with radial-basis function (RBF) kernel, k nearest neighbour (k NN) and decision tree (DT) schemes to predict the velocity profiles of debris flows using the experimental data from the study of Matsumura and Mizuyama (1990). Two objectives were emphasized in this investigation: (1) to check the fitness of the five machine learning techniques to the experimental data; and (2) to compare the fitness of three theoretical formulas to the machine learning predictions.

* Corresponding author e-mail address: ljhuang@nkust.edu.tw

2. Some Supervised Machine Learning Techniques for Regression

The prediction of velocity profile for a debris flow is in general a nonlinear regression problem due to the inherent non-Newtonian characteristics of the debris flow. Regression problems pertain to supervised learning because of the existence of targets of value type for training data. The relationship between velocity (the target), u , and depth (the data), y , can be expressed as follows:

$$u = f(y) \quad (1)$$

where f is in general a non-linear function. Some researchers have attempted to derive the relationship based on mechanics of debris flows, including the equations of continuity, momentum, energy and the kinematics of non-Newtonian flows in which some special term such as Bagnold stress term was introduced (Takahashi, 1978; Matsumura and Mizuyama, 1990; Su et al., 1993). However, there are some parameters that make theoretical analyses difficult to be applied to practical cases, for example, the constant a in three theoretical formulas and mixing lengths present in the turbulence flow models.

In the following sections we summarize the five machine learning techniques used in this study for regression of Eq. (1) that is obtained from experimental data, especially those developed and provided in *scikit-learn* package (Scikit-learn.org, 2018):

2.1. Nonlinear Regression (NLR)

In this scheme a power-law form of the nonlinear relation can be expressed as

$$u(y) = c y^n \quad (2)$$

This equation can be transformed into a linear one by taking the natural logarithm on both sides. Then we obtain

$$\ln u = \ln c + n \ln y = A + BY \quad (3)$$

After the linear regression analysis we can obtain the two parameters: $c = e^A$, $n = B$. The approach is direct and simple and the obtained value n in the power-law can be compared with theoretical results. In the *scikit-learn* package, *LinearRegression* class can be imported to solve Eq. (3).

2.2. Neural Network Using MLPs

Multi-layer perceptron (MLP), such as the *MLPRegressor* class in *scikit-learn* package, can be employed for conducting regression of a nonlinear function by training from input data to target values by constructing a specific neural network topology along with, input, output and hidden layers using different activation (transfer) functions. The errors are resolved using the back-propagation scheme. Some activation functions usually employed are as follows: (1) sigmoid (logistic); (2) tanh; and (3) relu. Parameters such as the learning rate, momentum factor, and iteration number can be adjusted.

2.3. SVM with RBF Kernel

An SVM is a powerful tool that is employed for classification and regression problems (linear or nonlinear). The concept is to search for the separation boundary for classification problem and the fitting curve for regression problem based on the so-called supporting vectors. Various kernel functions can be used, among which the Gaussian (RBF) kernel function is often employed. In the *scikit-learn* package, the *SVR* class can be employed for regression analysis.

2.4. *kNNs*

The *kNN*, such as the *KNeighborsRegressor* class in the *scikit-learn* package, is a non-parametric technique in which the predicted value of a point is obtained by taking the simple average or weighted average using inverse of distance of values of the *k* nearest neighbors. This algorithm is very simple.

2.5. *DT*

A *DT* is also a famous non-parametric supervised learning scheme that is used for classification and regression. In this method, the dataset is continuously partitioned into smaller subsets as the size of a tree is increased, and the final result is a tree with decision nodes and leaf nodes. The partitioning process is repeated until the criterion is satisfied. The aim is to create a model that predicts the value of target by learning simple decision rules inferred from the data features. In the *scikit-learn* package, the *DecisionTreeRegressor* class can be imported for analysis.

2.6. *Pros and Cons*

The pros and cons of the above five machine learning techniques are summarized and compared in Table 1 when they are applied for nonlinear regression. Moreover, the coefficient of determination, R^2 , used for measurement index for all machine learning algorithms, is defined as follows:

$$R^2 = 1 - \frac{SS_{res}}{SS_{total}} \quad SS_{total} = \sum_{i=1}^N (u_i - \bar{u})^2, \quad SS_{res} = \sum_{i=1}^N (u_i - \hat{u}_i)^2 \quad (4)$$

Here R^2 is a statistical measure that represents the portion of the variance for a dependent variable that is explained by an independent variable. The value of R^2 approaches 1.0 implies good fitness.

Table 1. Summary of the pros and cons of the five machine learning techniques employed in this study

	<i>NLR</i>	<i>MLP</i>	<i>SVM</i>	<i>kNN</i>	<i>DT</i>
Pros	<ul style="list-style-type: none"> • non-linear models • can obtain analytical curve 	<ul style="list-style-type: none"> • Capability to learn non-linear models 	<ul style="list-style-type: none"> • Memory efficient • Versatile in usage of kernel functions 	<ul style="list-style-type: none"> • non-parametric method • simple 	<ul style="list-style-type: none"> • Data scaling not required. • Simple • Robustic
Cons	<ul style="list-style-type: none"> • requires to assume the form of function 	<ul style="list-style-type: none"> • Local minimum problem • Including Many parameters • Scaling sensitive 	<ul style="list-style-type: none"> • SVMs do not directly provide probability estimates 	<ul style="list-style-type: none"> • Prediction curve is not smooth 	<ul style="list-style-type: none"> • May be unstable • Prediction curve is not smooth

3. Typical Theoretical Formulas for the Velocity Profiles of Debris Flows

(1) *Takahashi (1978)*: Based on the dispersive stress concept proposed by Bagnold, the velocity can be expressed as

$$u(y) = \frac{2}{3d_s} \frac{1}{\lambda} \sqrt{\frac{g \sin \theta}{a \sin \phi} [C_d + (1 - C_d) \frac{\rho_f}{\rho_s}]} \cdot [h^{3/2} - (h - y)^{3/2}] \quad (5)$$

(2) *Matsumura and Mizuyama (1990)*: By adding the Reynolds turbulent stress to the theory provided by Takahashi, the following can be obtained:

$$u(y) = \frac{2}{3d_s} \sqrt{\frac{\rho_d g \sin \theta}{a \sin \phi \rho_s \lambda^2 + \rho_f \left(\frac{1-C_d}{C_d}\right)^{2/3}}} \cdot [h^{3/2} - (h-y)^{3/2}] \quad (6)$$

(3) *Mixed-layer theory* (Su et al., 1993): Considering two layers, visco-layer and inertia layer, exist in the profile, the velocity distributions in each layer and interface can be derived as follows:

(a) Within the visco-layer:

$$u_{VL}(y) = \sqrt{\frac{\rho_d g \sin \theta}{a \sin \phi \rho_s h_V d_s^2 \lambda^2}} \cdot \left[\frac{\pi h^2}{16} - \frac{h-2y}{4} \sqrt{y(h-y)} - \frac{h^2}{8} \sin^{-1} \frac{h-2y}{h} \right] \quad 0 \leq y \leq h_{BL} \quad (7a)$$

(b) On the interface:

$$u_{Inter} = u_{VL}(y = h_{VL}) \quad (7b)$$

(c) Within the inertia layer:

$$u_{IL}(y) = u_{Inter} + \frac{2}{3} \sqrt{\frac{\rho_d g \sin \theta}{a \sin \phi \rho_s d_s^2 \lambda^2 + \rho_f \zeta^2 d_s^2 \lambda^2}} \cdot [(h-h_{BL})^{3/2} - (h-y)^{3/2}] \quad h_{BL} \leq y \leq h \quad (7c)$$

In the above equations, the height of the visco-layer can be deduced as follows:

$$\frac{h_{VL}}{h} = \frac{3 - \sqrt{9 - 12 \left[\frac{\rho \tan \theta - (\rho_s - \rho) C_d (\tan \phi - \tan \theta)}{\rho_d \tan \theta} \right]}}{2} \quad (7d)$$

Some important parameters are defined in Table 2.

4. Application of Five Machine Learning Techniques to Regression of the Velocity Profiles for Debris Flows

4.1. Collection of Experiment Data

We used the experimental results of the study conducted by Matsumura and Mizuyama (1990) and summarized by Su et al. (1993) as listed in Table 2. Matsumura and Mizuyama (1990) employed natural sand ($\rho_s = 2.65 \text{ g/cm}^3$) and conducted the flow experiments on a channel with dimensions $7 \text{ cm} \times 30 \text{ cm} \times 500 \text{ cm}$ ($W \times H \times L$).

Table 2. Data for debris-flow experiments conducted by Matsumura and Mizuyama (1990)

Case	Material Characteristics			Experimental Conditions				Mixing Layer Parameters			
	Density g/cm^3	Internal Friction Angle ϕ (deg)	d_{50} (cm)	Bed Slope θ (deg)	Debris-Flow Height (cm)	Averaged Concentration	Shear Velocity U^* (cm/s)	λ	a (VL)	a (IL)	h_{VL}
1-1	2.65	38	0.30	15	3.5	0.348	21.4	4.32	0.15	0.15	0.55
1-2	2.65	38	0.30	15	3.4	0.348	21.3	4.21	0.08	0.07	0.57

4.2. Nonlinear Regression Using Machine Learning Techniques

In this study, we used Python 3.6 and the associated package *scikit-learn* for conducting regression of experimental data of the debris flows. The training data are presented in Table 3. The imported and called functions employed in each machine learning schemes are presented as follows:

```
LinearRegression(),\
MLPRegressor(hidden_layer_sizes=(20,), activation='logistic', solver='adam', alpha=0.001, batch_size='auto',\
learning_rate='constant', learning_rate_init=0.01, max_iter=5000, random_state=0, tol=0.0001, momentum=0.),\
SVR(kernel='rbf', gamma=1.0, C=1),\
KNeighborsRegressor(5),\
DecisionTreeRegressor(max_depth=3)]
```

Table 3. Training data using machine learning techniques for debris-flow experiments conducted by Matsumura and Mizuyama (1990)

Case 1-1 (N = 34)		
Training Data (X)	Depth y/h	0.18; 0.16; 0.21; 0.18; 0.20; 0.22; 0.32; 0.24; 0.34; 0.41; 0.37; 0.38; 0.48; 0.40; 0.50; 0.53; 0.52; 0.54; 0.56; 0.65; 0.63; 0.82; 0.82; 0.64; 0.66; 0.67; 0.92; 0.76; 0.82; 0.86; 0.87; 1.00; 0.98; 0.97
Target (y)	Velocity u/U^*	1.20; 1.40; 1.40; 1.50; 1.60; 1.70; 2.00; 2.50; 2.90; 3.20; 3.20; 3.40; 3.50; 3.90; 4.00; 4.30; 4.40; 5.00; 5.10; 5.80; 5.80; 5.80; 6.00; 6.50; 6.50; 6.60; 7.50; 7.50; 7.60; 7.70; 8.00; 8.30; 8.40; 8.50
Case 1-2 (N = 38)		
Training Data (X)	Depth y/h	0.16; 0.18; 0.20; 0.22; 0.26; 0.23; 0.20; 0.26; 0.27; 0.29; 0.29; 0.40; 0.38; 0.37; 0.48; 0.44; 0.52; 0.46; 0.53; 0.48; 0.54; 0.60; 0.70; 0.71; 0.76; 0.77; 0.70; 0.76; 0.82; 0.83; 0.80; 0.79; 0.84; 0.98; 0.94; 0.84; 0.99; 0.88
Target (y)	Velocity u/U^*	1.00; 1.20; 1.60; 1.60; 1.60; 1.80; 2.00; 2.00; 2.10; 2.00; 2.80; 3.00; 3.20; 3.30; 3.60; 3.70; 4.00; 4.40; 4.40; 4.60; 4.90; 5.80; 5.80; 6.00; 6.10; 6.30; 6.40; 6.80; 7.00; 7.30; 7.40; 7.50; 7.70; 8.00; 8.20; 8.40; 8.80; 8.90

The regression results obtained using the five schemes are plotted in Fig. 1 and Fig. 2 for case 1-1 and case 1-2, respectively. In these plots the R^2 scores are presented (in the upper left corner) to depict the measure of fitness of the machine learning results to the experimental data. In the *NLR* scheme the value of the power law n was obtained. The value of n was 1.07 and 1.13 for case 1-1 and case 1-2, respectively, and the theoretical value was $n = 3/2 = 1.5$. Moreover, all the results predicted by the five machine learning schemes fit well with the original data because their R^2 scores are all near one. Note that although we can adjust some parameters in each scheme to obtain higher scores over-fitting should be avoided. The first row of Tables 4 and 5 present the averaged R^2 scores.

4.3. Comparative Study on the Prediction of Velocity Profiles Using the Theoretical Formulas

We attempted to employ the five machine learning schemes to compare the fitness of velocity predictions by using the three theoretical formulas, Eq. (5), (6) and (7a-d). Here the reference bases are the machine learning results because they have been verified to have good fitness to the experimental data and can be considered to be valid velocity profiles for case 1-1 and case 1-2. The R^2 scores $R_T^2, R_{MM}^2, R_{SLC}^2$ shown in the bottom left corners depict the measure of fitness of theoretical formulas obtained from Takahashi (1978), Matsumura and Mizuyama (1990), and Su et al. (1993), respectively. In the second, third and fourth row of Table 4 and Table 5, the values for each machine learning scheme and averaged R^2 scores are also summarized. We can see that all these values depict good fitness. However, among them, formulas proposed by Matsumura and Mizuyama (1990), Eq. (6), and by Su et al. (1993), Eq. (7a-d), present relatively higher fitness than that by Takahashi (1978), Eq. (5). However, we should emphasize that these analysis results are obtained based on the experimental data set we used.

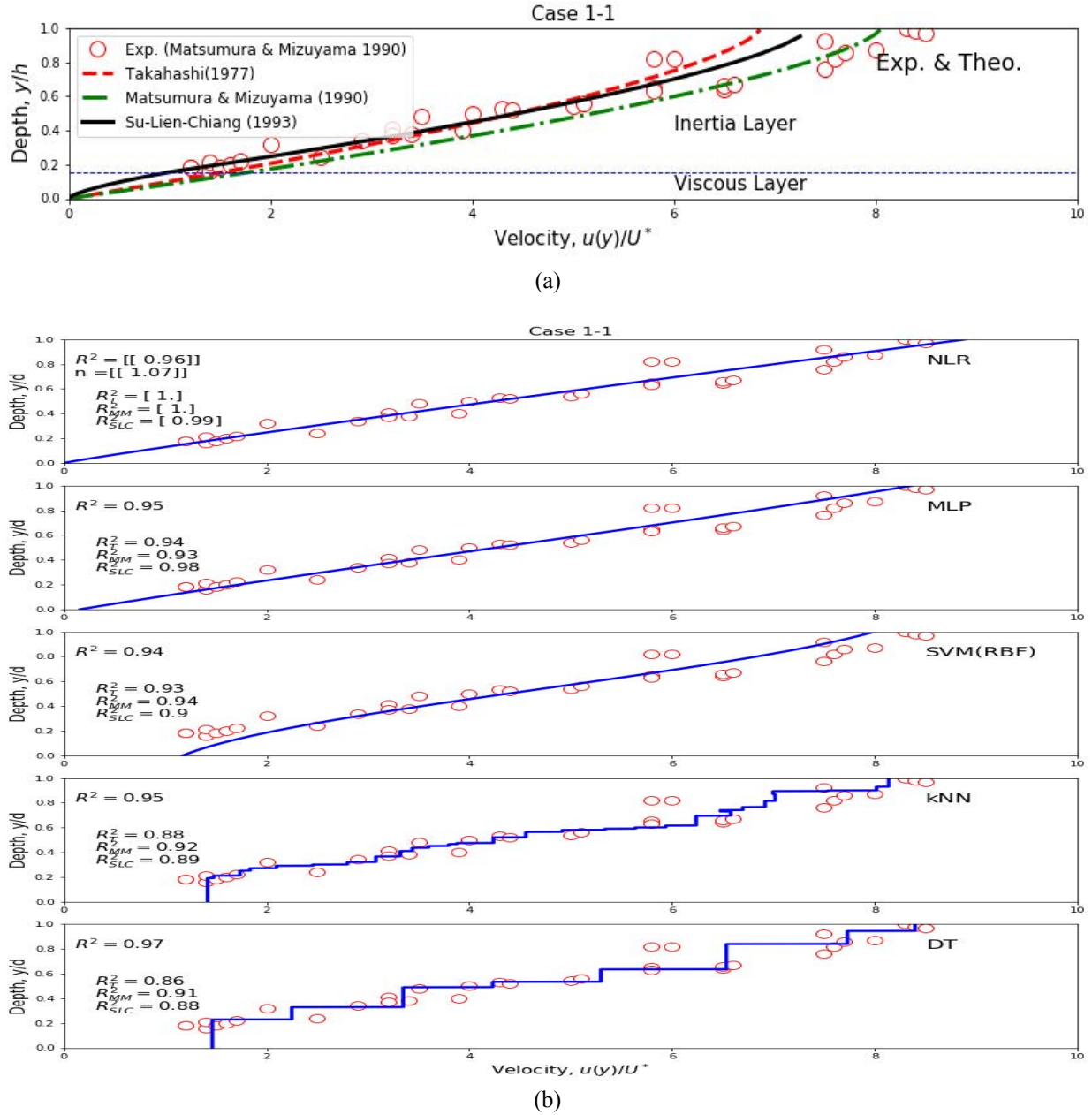
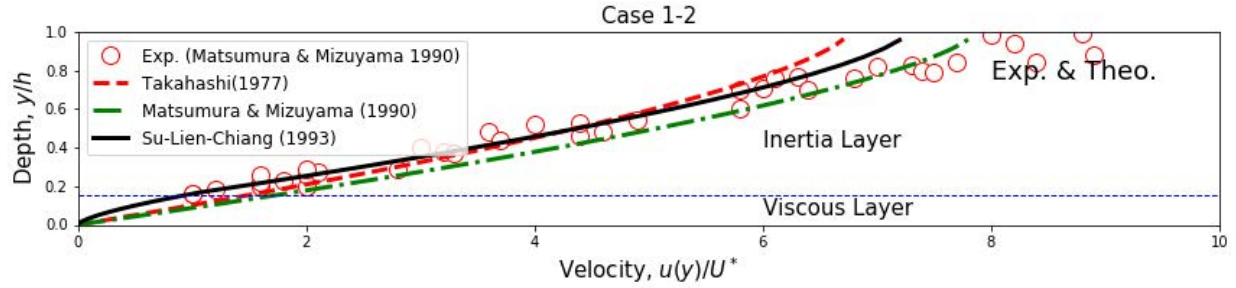


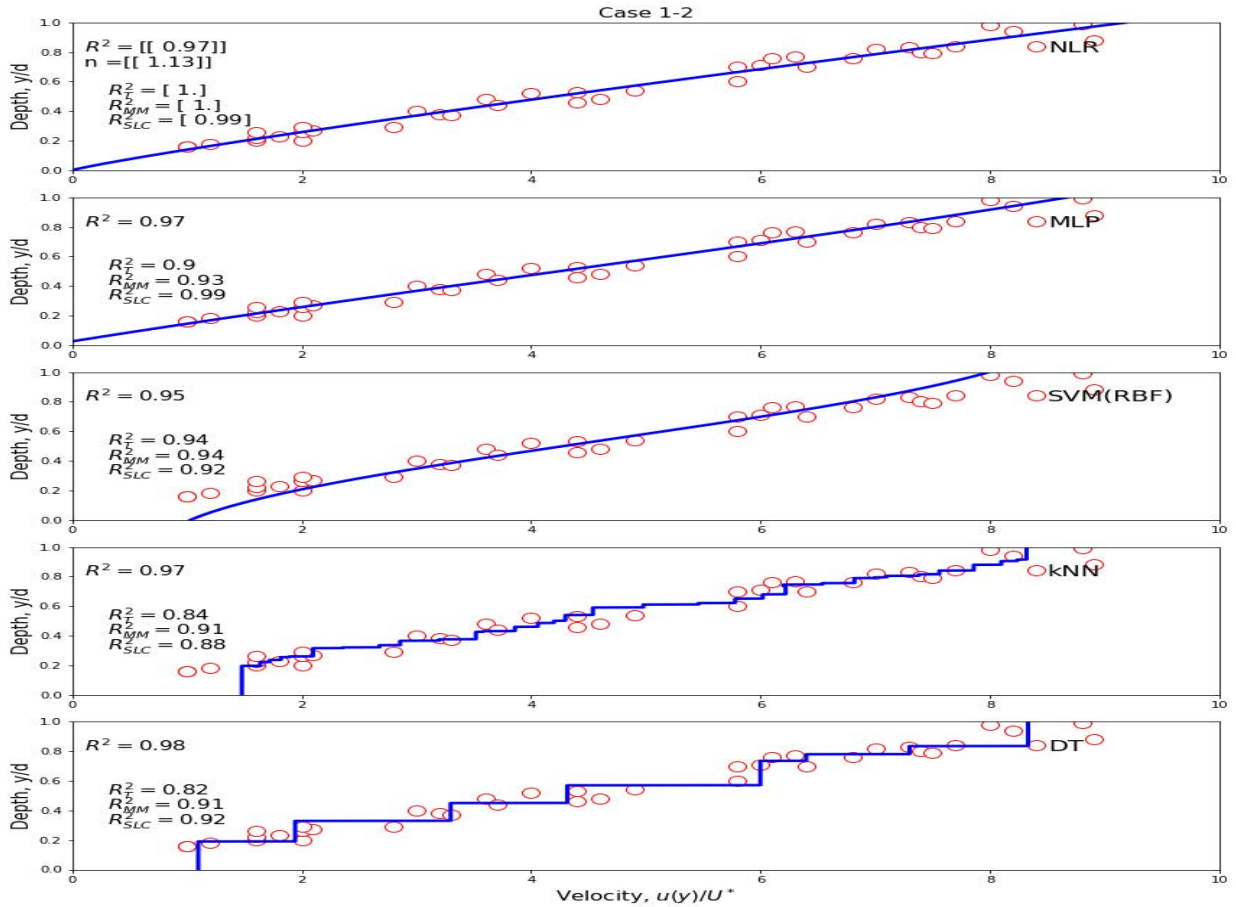
Fig. 1. Velocity profiles of debris flow in case 1-1 (a) experimental data and theoretical predictions; (b) experimental data and machine learning predictions

Table 4. R^2 score of the experimental data and the three theoretical results predicted by the five machine learning algorithms

Algorithms	NLR	MLP	SVM (RBF)	kNN (k=5)	DT	Ave.
Experiment	0.96	0.95	0.94	0.95	0.97	0.954
Takahashi (1978)	1.0	0.94	0.93	0.88	0.86	0.922
Matsumura & Mizuyama (1990)	1.0	0.93	0.94	0.92	0.91	0.94
Su et al. (1993)	0.99	0.98	0.90	0.89	0.88	0.928



(a)



(b)

Fig. 2. Velocity profiles of debris flow in case 1-2 (a) experimental data and theoretical predictions; (b) experimental data and machine learning predictions

Table 5. R^2 score of the experimental data and the three theoretical results predicted by the five machine learning algorithms

Algorithms	<i>NLR</i>	<i>MLP</i>	<i>SVM (RBF)</i>	<i>kNN (k=5)</i>	<i>DT</i>	Ave.
Experiment	0.97	0.97	0.95	0.97	0.98	0.968
<i>Takahashi (1978)</i>	1.0	0.9	0.94	0.84	0.82	0.90
<i>Matsumura & Mizuyama (1990)</i>	1.0	0.93	0.94	0.91	0.91	0.938
<i>Su et al. (1993)</i>	0.99	0.99	0.92	0.88	0.92	0.94

5. Concluding Remarks

Data analysis was conducted on using five machine learning technologies, namely, NLR, MLPs, SVM with RBF kernel, kNN and DT schemes, to predict debris-flow velocity profiles of the experimental data presented by Matsumura and Mizuyama (1990). The results are:

- (1) Machine learning schemes offer systematic and convenient ways to predict the velocity profile of debris flow by using experimental data. The schemes can achieve good fitness without requiring any physical characteristics and assumptions that are usually employed in the derivation of a theoretical formula. This is a process of description and prediction of data from data.
- (2) In the NLR analysis we obtained the power-law values n to be 1.07 and 1.13 for case 1-1 and case 1-2, respectively. Both these are smaller than those used in theoretical formulas ($n = 3/2 = 1.5$). The NLR model can be revised using more experimental cases, and some assumptions in theoretical formulas can be re-examined.
- (3) The three theoretical predictions depicted good fitness. Among them, the results by Matsumura and Mizuyama (1990) and Su et al. (1993) presented relatively higher fitness than that by Takahashi (1978) in the analysis of the data sets used in this study.

References

- Bagnold, R. A., 1954, Experiments on a gravity-free dispersion of large solid spheres in a Newtonian fluid under shear, *Proceeding of Royal Society of London, Ser. A*, 225, p. 49-63.
- Bonaccorso, G., 2017, *Machine learning algorithms*, Packt Publishing.
- Chen, C. L., 1986, Generalized Visco-Plastic Modeling of Debris Flow, *J. of Hydraulic Engineering*, 114(3), p. 237-258.
- Chen, C.L., Lin, C. H. and Jan, C. D., 1991, Rheological model for ring-shear type debris flows. *Proceeding. of the 5th International Sediment Conference.*, (5), p. 1-8.
- Ho, M. L., 1997, Study on initiation mechanism and blocking structures of debris flows. [Ph.D Thesis]: Institute of Civil Engineering, National Taiwan University (in Chinese).
- Huang, L. J., 2001, Introduction to theory and practice of debris-flow hazards mitigation, Chuan-Hwa Publishing Ltd., Taiwan, R.O.C. (in Chinese).
- Jan, C. D., 2000, Introduction to debris flows, Science and Technology Books Company, Taiwan, R. O. C. (in Chinese).
- Julien, P. Y. and Lan, Y., 1991, Rheology of hyperconcentrations. *J. of Hydraulic Engineering.*, 117, p. 346-353.
- Matsumura, K. and Mizuyama, T., 1990, Experimental study on mechanism of debris flow using light materials. *Shin-Sabo*, 43(1), p. 16-22. (In Japanese).
- Muller, A. C. and Guido, S., 2017, Introduction to machine learning with Python, O'Reiley, Media, Inc.
- O'Brien, J. S. and Julien, P. Y., 1988, Laboratory analysis of mud flow properties. *J. of Hydraulic Engineering*, 114(8), p. 877-887.
- Scikit-learn.org, 2018, User's guide of *scikit-learn*: https://scikit-learn.org/stable/user_guide.html (accessed October 2018).
- Su, C. G., Lien, H. P. and Chiang, Y. C., 1993, Study on the velocity distribution of debris flow. *J. Chinese Soil & Water Conservation*, 24(1), p. 75-82. (in Chinese)
- Takahashi, T., 1977, A mechanism of occurrence of mud-debris flow and their characteristics in motion, *Annuals, Disaster Prevention Reserach Institute.*, Tokyo University, 20B(2), p. 405-435 (in Japanese).
- Takahashi, T., 1978, Mechanical characteristics of debris flow. *J. of Hydraulic Division, ASCE*, 104(HY8), p. 1153-1169.
- Yu, F. C. and Chen, C. G., 1990, Basic study on the debris flow: (II) preliminary study on the flow velocity of debris flow. *J. Soil & Water Conservation*, 21-22(2), p. 115-142. (in Chinese)

Appendix A. Nomenclature

- u : Velocity of debris flow
- \bar{u} : Averaged value of velocity of all samples
- u_i : Velocity of the i -th sample point
- \hat{u}_i : Predicted velocity of the i -th sample point
- X : Training data in machine leaning schemes
- y : Depth of debris flow; target value in machine learning schemes

Experimental evaluation of peak and temporal changes in debris-flow initiation processes

Takahiro Itoh^{a,*}, Akihiko Ikeda^b, Takahisa Mizuyama^c

^aCenter for Advanced Research and Development, Nippon Koei Co., Ltd., 2304 Inarihara, Tsukuba 300-1259, Japan

^bSabo & Landslide Technical Center, 2-7-5 Hirakawa cho, Chiyoda-ku, Tokyo 102-0093, Japan

^cNational Graduate Institute for Policy Studies (GRIPS), 22-1 7Chome Roppongi, Minato-Ku, Tokyo 106-0032, Japan

Abstract

Saturated sediment water mixture flow can move as landslide if the vertical sediment concentration is constant and the value takes a maximum sediment concentration, c^* , which is sediment concentration in the non-flowing layer in sediment deposition. The flow is debris flow over the rigid bed and the flow can change as debris flow with vertical sediment concentration distribution if the saturated flow reaches downstream reach, where bed inclination is around 17 to 18 degrees. The thinking proposes that it is important to know transition process in between saturated landslide and debris flows in evaluating peak and temporal changes of debris flows in initiation processes for debris-flow mitigation in planning and design of sabo dam, because the transition process can be explained by a relation between bed slope and depth-averaged sediment concentration (e.g., Takahashi 1991). In present study, important knowledge for estimating peak discharge is discussed using experimental data obtained by present flume tests. Flume tests are carried out using prismatic open channel which is set 22 degrees and around 18 degrees at downstream end. Sediment is deposited parallelly to the flume bed and water is supplied steady at upstream end, and the transition of between saturated landslide to debris flow is produced. Two kinds of sediment deposition depth and length are specified in the present tests, and temporal changes of debris flow are measured using side view of digital video camera and debris-flow runoff at downstream end of the flume. The data shows that peak discharge rate of debris flow depends on sediment volume during debris-flow running from the up to the downstream reach, and that entrained sediment volume by a debris flow will be determined by erosion capacity during a debris-flow surge.

Keywords: Debris flow; Peak discharge; Initiation process; Flume tests

1. Introduction

Estimation and prediction peak discharge of debris flow are important matters, and there are a lot of researches from experimental, numerical and field investigation approaches related to the debris-flow initiation (e.g., Takahashi, 2007; Rickenmann, 2016). Saturated sediment deposited parallelly on the bed can be stable in the region that bed slope is less than 17 to 18 degrees ($= \theta_*$), because volumetric sediment concentration of sediment layer takes vertically uniform value of maximum sediment concentration, c^* , which is sediment concentration in the non-flowing layer in sediment deposition, over the θ_* of bed slope.

The sediment mass with constant thickness moves totally due to the driving force reduced by yield stress, if bed slope takes over the θ_* . This means that the peak discharge and temporal shape of debris flow can be estimated in the region that bed slope is less than θ_* , if the hydrograph of debris flow at the section of θ_* of bed slope, because the trigger of the debris flow can be evaluated. Previous study (Ou et al., 1993) introduced the spreading of debris-flow surge over the movable bed slope of θ_* , and the longitudinal shape and spreading characteristics of the debris flow. However, the peak discharge of the debris flow was not discussed in the literature, though the debris mass shape takes longitudinally triangle with similarity shape.

* Corresponding author e-mail address: a6556@n-koei.co.jp

In present studies, following experimental approaches try to be conducted, based on the meaning of the bed slope of θ_* , to discuss estimation of peak discharge of debris flow triggered in the steep region over the θ_* of bed slope: (1) Flume tests over the bed slope of θ_* , (2) Dimensional analyses of peak discharge and total volume of the debris-flow surge. Additionally, several data and related discussions are shown in present studies.

2. Flume tests

2.1. Experimental flume, hydraulic and sediment condition

Figure 1 shows experimental flume: around 8 m in length, 10 cm in width and 40cm in depth. Bed slope of the flume is set as 22 degrees and the bed slope is saturated sediment on the bed can be transported with c_* of sediment concentration. Sediment is deposited on the bed with longitudinally constant depth, D_p , and clear water is supplied from upstream end on the saturated sediment. A weir is set at the downstream reach and the bed slope there is set as 18 degrees after debris flow passing.

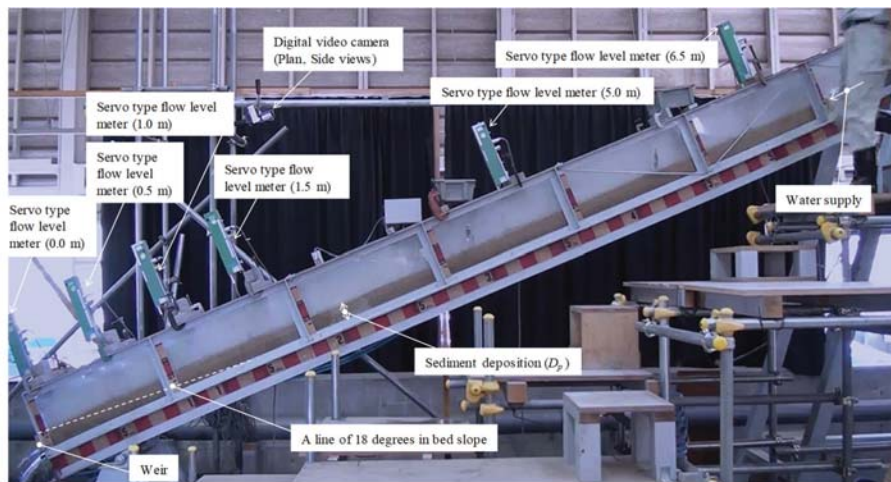


Fig. 1. Experimental flume

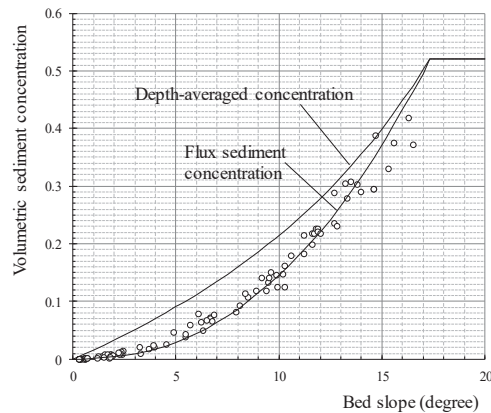


Fig. 2. Relation between equilibrium bed slope and sediment concentration (e.g., Egashira et al. 1997)

Figure 2 shows relation between equilibrium bed slope and sediment concentration in the steady and uniform debris flow (e.g., Egashira et al., 1997). In the figure, two lines are draw and those are depth-averaged sediment concentration and flux sediment concentration, respectively. The value of sediment concentration can be supposed as c_* along the flume in the present flume tests, and the value of sediment concentration less than c_* can be measured at the

downstream end of the flume. Sand particles are used in the flume test with almost uniform sand in diameter, and those have physical values as follows: d_{60} is 1.4 mm, $d_{max}=2.0$ mm, $\sigma/\rho=2.66$, $\phi_s=35.9$ degrees, $k=0.657$ cm/s and $c^*=0.514$, where d is the diameter of sand particles, σ is the mass density of sand, ρ is the mass density of water, ϕ_s is the interparticle friction angle and k is the permeability of sand measured by the constant head permeability test. Herein, the value of c^* is measured with uniform sand particles for present tests, and the value is usually less than that of spherical particles.

Table 1 shows experimental conditions and results that are described below. In the table, Q_u is the supplied water discharge rate, Q_d is the seepage flow water discharge in the sediment deposition layer to be saturated condition, D_p is the thickness of sediment deposition on the flume, L is the length of sediment deposition, Q_p is the peak discharge rate measured at the downstream end, T_d is the flowing duration of debris-flow surge and ΣQ is the total volume of debris-flow surge. In present flume tests, following results are shown for discussions.

- 1) Two kinds of the deposition length
- 2) Two kinds of the depth of sediment deposition on the flume
- 3) Three patterns of combinations of the length and the deposition thickness: $(L, D_p) = (6.5\text{m}, 0.1\text{ m}), (6.5\text{m}, 0.05\text{m})$ and $(3.25\text{m}, 0.05\text{m})$.

Table 1. Experimental runs and results

Run No.	D_p (cm)	L (m)	$D_p L$ (m ²)	Q_u (l/s)	Q_d (l/s)	Q_p (l/s)	T_d (s)	ΣQ (l)
027	10	6.5	0.650	0.5	0.15	5.62	23	42.6
034	10	6.5	0.650	0.5	0.15	8.54	17	48.6
035	10	6.5	0.650	0.5	0.15	9.52	18	62.2
042	5	6.5	0.325	0.25	0.075	6.21	12	16.4
043	5	6.5	0.325	0.25	0.075	5.15	12	31.7
045	5	3.25	0.163	0.25	0.075	4.86	14	21.7
048	5	3.25	0.163	0.25	0.075	3.42	9	18.1

2.2. Measurements

In the present flume tests, several values of hydraulic parameters are measured as follows. At the downstream end, water and sediment discharge are sampled by buckets, and the sediment concentration is calculated. Duration of measurement using a bucket is set around 2 seconds because accuracy of sampling at least is kept for data collections.

From side wall, free surface and bed of debris flows are taken by digital camera, and digital images are taken from overhead view. Longitudinal profiles of bed and free surface are obtained by image analyses using image data for bed and free surface variations from the plan and longitudinal views.

Longitudinally, servo-type level meters are set at the sections 0, 0.5, 1.0, 1.5, 5.0, 6.5 m from downstream end of flume, and temporal changes of free surface of debris-flow body are measured. Measured data of free surface level at 0 m (H) are correlative relation with sampled discharge (Q) at downstream end (H - Q relation), and temporal changes of discharge there are calculated using the relations, because sampling by buckets can obtain temporally discrete data during several seconds and cannot obtain continuously temporal changes of outlet discharge of debris flow. The method using the H - Q relation with a servo-type level meter at downstream end of the flume can obtain temporal and continuous outlet discharge through the flume end.

3. Estimation of peak discharge

Experimental data are shown for the combinations of the length, L , and the depth, D_p , of sediment deposition on the flume: $(L, D_p) = (6.5\text{m}, 0.1\text{ m}), (6.5\text{m}, 0.05\text{m})$ and $(3.25\text{m}, 0.05\text{m})$. Table 2 is the ratio of peak to inlet discharge measured at downstream end, and shows differences of measured value for peak discharge, Q_p . In the table, Q_{p-b} is the measurement by buckets and the Q_p is the calculation by the correlation (H - Q relation) between free surface level, H , by servo-type level meter (at 0 m) and discharge by buckets. The calculations can estimate well the peak value of discharge, though calculations are interpolation of direct measurement by buckets. Figure 3 shows temporal changes of discharge, sediment runoff and flux sediment concentration, for Run 035, 042, 045.

In present data, the value of Q_p is applied for calculations using the correlation of $H-Q$ relation. The sediment concentration, c , takes almost the value of c_* in the beginning stage of sediment runoff at downstream end. The duration

Table 2. Ratio of peak to inlet discharge measured at downstream end

Run No.	D_p (cm)	L (m)	$D_p L$ (m ²)	Q_d (l/s)	Q_u (l/s)	Q_{p-b} (l/s)	Q_p (l/s)	Q_p/Q_u (bucket, Servo)
027	10	6.5	0.650	0.15	0.5	5.3	5.62	10.6, 11.8
034	10	6.5	0.650	0.15	0.5	6.12	8.54	12.2, 17.1
035	10	6.5	0.650	0.15	0.5	5.81	9.52	11.6, 19.0
042	5	6.5	0.325	0.075	0.25	6.21	4.54	18.2, 19.4
045	5	3.25	0.163	0.075	0.25	4.86	3.71	14.8, 19.4

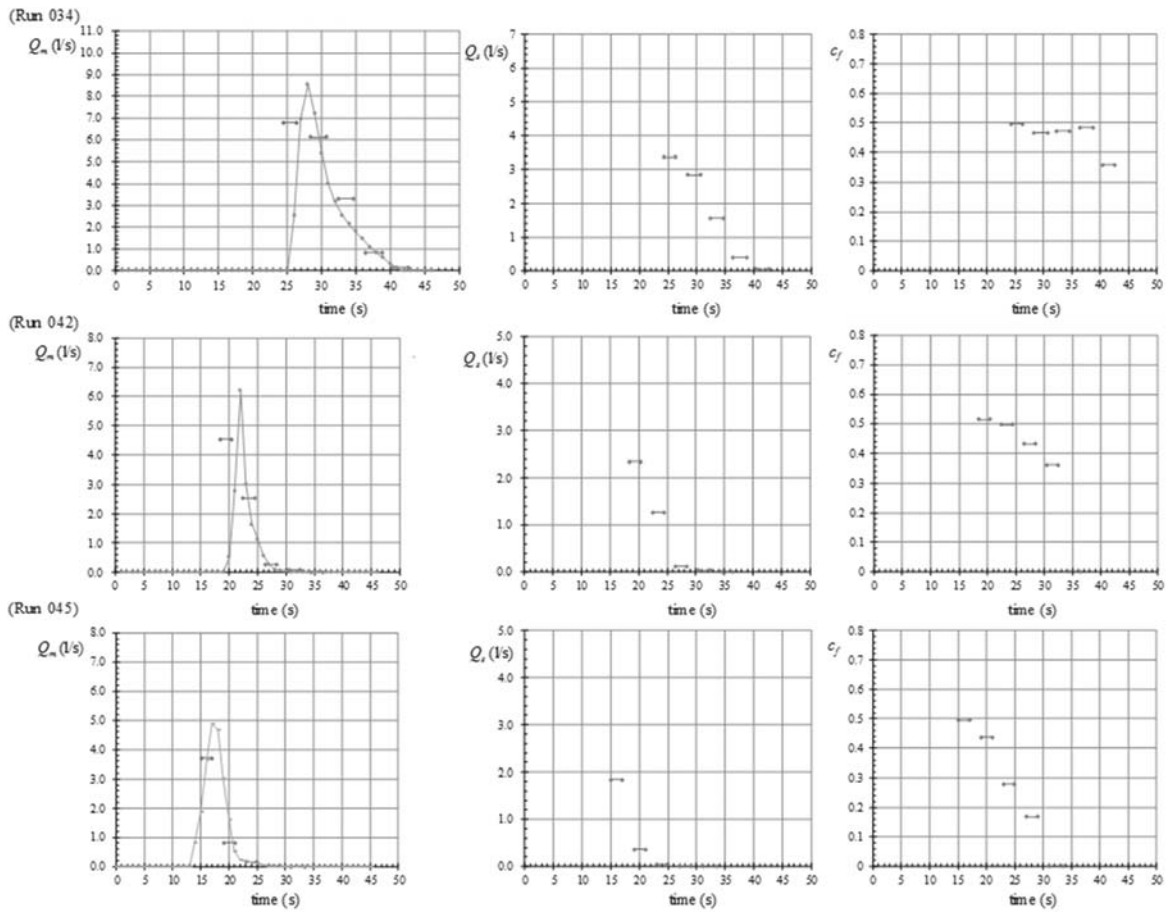


Fig. 3. Temporal changes of discharge, sediment runoff and flux sediment concentration, for Run 035, 042, 045

of $c=c_*$ becomes short due to decrease of sediment volume ($D_p L$). Temporal changes and peak value of debris flow have interesting characteristics.

Herein, Takahashi (1991, 2007) shows the ratio of peak to inlet water discharge from upstream reach using bore spreading and mass conservation relation for debris mass entrainment.

$$\frac{Q_p}{Q_{in}} = \frac{c_*}{c_* - c_{\infty}}, \quad c_{\infty} = \frac{\tan \theta}{(\sigma/\rho - 1)(\tan \phi_s - \tan \theta)} \quad (1)$$

where Q_{in} is the inlet clear water discharge from upstream reach over the bed and c_{∞} is the equilibrium sediment concentration, that is determined by mass density of sediment, σ , and mass density of water, ρ , interparticle friction angle of sediment particles, ϕ_s , and bed slope, θ , and the formula is described in the literature (e.g., Takahashi, 1991). Herein, substituting several values into the equation of c_{∞} yields 18.4 degrees for the value of θ_s : $\sigma/\rho = 2.66$, $c_s = 0.514$ and $\phi_s = 35.9$ degrees for physical parameters of experimental sand particles. The peak discharge, Q_p , in present tests cannot be calculated using Eq. (1), because the sediment concentration is supposed as c_s and the value in Eq. (1) takes infinity. Present data needs to be evaluated experimentally.

Except data of Run 027, the ratio of peak to inlet water discharge is 17.1 to 24.8, and those averaged value (peak ratio) is almost 20. Those mean that peak discharge of debris flow is determined by bed sediment volume, and that peak ratio has almost similarity to the ratio of debris-flow volume to bed sediment volume, if bed sediment is almost entrained to debris-flow body.

Figure 4 shows temporal changes of longitudinal profiles of free surface and bed elevation for Run 034, 042, 045. Herein, the experimental condition of Run 035 is same as that of Run 034. Longitudinal shape of debris flow is almost triangle and those temporal shape are almost similar each other as pointed by Ou et al. (1993), though bed elevation of the frontal part is affected by frontal parts of debris flow. Figure 5 shows spreading of frontal part from up to downstream along the flume. In the figure, the points "A", "B" and the pass line from "A" to "B" are shown for

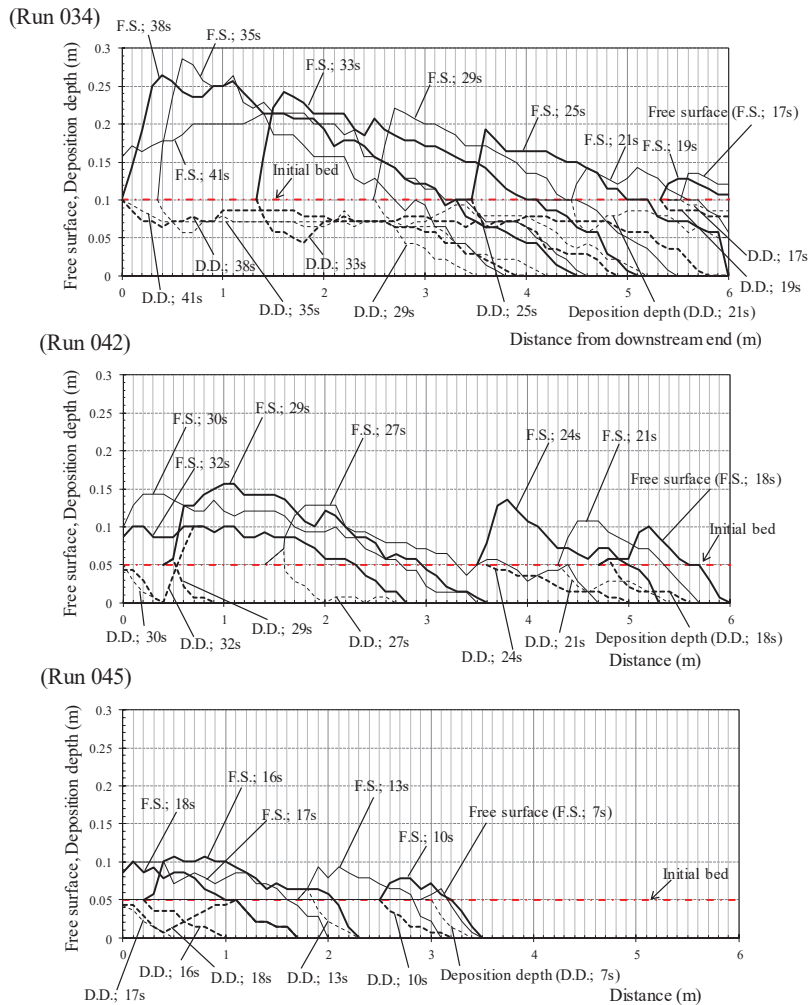


Fig. 4. Temporal changes of longitudinal profiles of free surface and bed elevation obtained by Run 034, 042 and 045

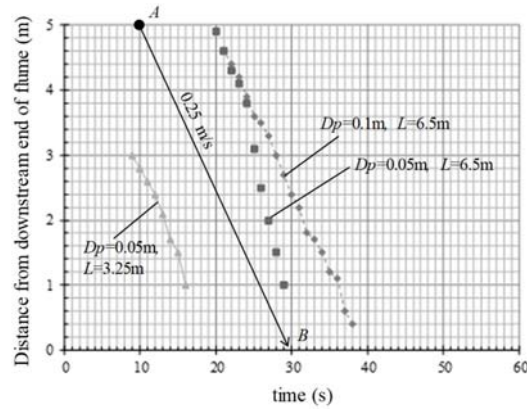


Fig. 5. Spreading of frontal part from up to downstream along the flume

understanding the spreading velocity. The spreading velocity is almost 0.25 m/s, except Run 042, because occurrences of some velocity acceleration. In Run 042 ($D_p = 0.05$ m, $L = 6.5$ m), the spreading velocity takes almost 0.5 m/s and the speed seems to be changed by increase debris entrainment due to imbalance saturation in deposition layer, D_p , as shown in data during 24s to 27s in Fig. 4.

Let us discuss estimations of peak discharge debris flow with steeper inclination than that of θ^* for $c=c^*$. The value of θ^* in Fig. 2 is around 17 degrees, as described in Introduction. The peak discharge of debris flow, Q_p , can be expressed dimensionally using the total volume of debris-flow surge, V , in case of mass movement for saturated bed sediment. The discharge of debris flow is calculated by the production of the cross section, A , and depth-averaged flow velocity, v . Peak discharge, Q_p , can be also expressed as;

$$Q_p = Av \quad (2)$$

The cross section, A , can be expressed using the co-efficient of cross-sectional shape and the thickness of debris deposition, D .

$$A = k_B D^2 \quad (3)$$

where, k_B is the co-efficient of cross-sectional shape of the area.

The flow depth, h , can be expressed using the thickness of debris deposition.

$$h = k_D D \quad (4)$$

where, k_D is the co-efficient of the ratio of flow depth to sediment deposition thickness.

In debris flows, velocity co-efficient, v/u_* , is proportional to relative flow depth, h/d (e.g., Takahashi 2007; Egashira et al. 1997);

$$\frac{v}{u_*} \propto \frac{h}{d} \Rightarrow \frac{v}{u_*} = k_v \frac{h}{d} \quad (5)$$

where, k_v is co-efficient of velocity factor, d is the diameter of bed sediment and debris flow and u_* is the shear velocity defined as;

$$u_* = \sqrt{gh \sin \theta} \quad (6)$$

where, g is the gravity acceleration.

Substitution of Eqs. (3) to (6) into Eq. (2) yields the following relation for peak estimation.

$$Q_p = f\left(\theta, \frac{h}{d}, k \dots\right) D^{5/2} \tag{7}$$

In addition, the total volume of debris-flow surge, V , can be proportional to D^3 , because the length of debris flow is almost 5 to 10 times to debris mass height according to empirical knowledges (e.g., Ashida et al. 1986) supposing the flow width can be proportional to the thickness of debris deposition, D , and Eq. (7) is re-written as follows,

$$Q_p = f\left(\theta, \frac{h}{d}, k \dots\right) V^{5/6}. \tag{8}$$

The relation between the peak discharge of debris flow, Q_p , and debris-flow volume can be the power law and the value of Q_p is proportional to the power of 5/6 for debris-flow volume, V . The peak discharge in the reach of $\theta > \theta_*$ can be estimated dimensionally, in case of saturated bed sediment.

Figure 6 shows relation between peak discharge and debris-flow volume obtained by present flume tests. The power lines of 5/6 (=0.833) are drawn in the figure, with some range from maximum to minimum of discharge. The data shows that peak discharge has similarity to debris-flow volume of flow body, and the peak value can be estimated by debris-flow volume and bed sediment volume in case of debris flow with entrained all bed sediment in saturate condition.

Figure 7 shows the relation between relative longitudinal volume and relative peak discharge of debris flow. The relative sediment volume is obtained by calculation of the longitudinal area at downstream end of the flume, as shown in Fig. 4. The value of $D_p L$ means the total volume of bed deposition on the bed in the initial stage. The relative peak discharge is defined as the ratio of the peak to inlet discharge from upstream end.

Experimental data shows that the relative peak discharge increases due to the longitudinal area of debris flow at the downstream end and the relation between relative longitudinal volume and relative peak discharge of debris flow can be determined uniquely, though data collections needs to be continued. The results emphasize that the peak

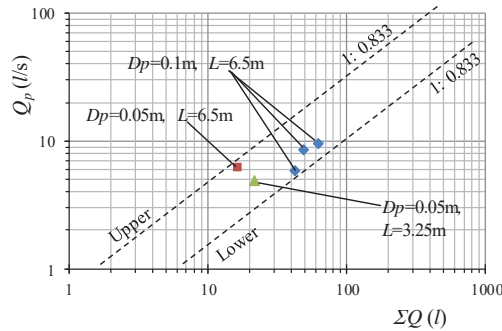


Fig. 6. Relation between peak discharge and debris-flow volume obtained by present flume tests

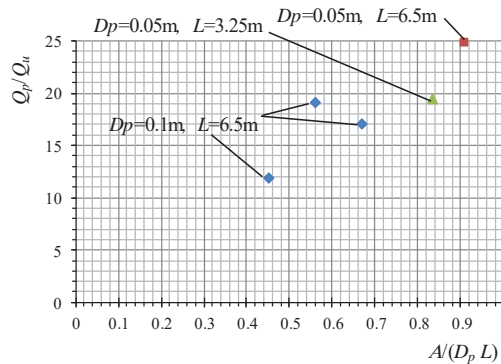


Fig. 7. Relation between relative longitudinal volume and relative peak discharge of debris flow

discharge can be estimated experimentally, in case that saturated bed sediment is transported perfectly to downstream, when bed slope is over θ_* of bed slope for $c = c_*$ (17 to 18 degrees in bed slope). Present results emphasize that peak and temporal shape of debris flows can be determined using some methods such as numerical simulation from the section that $c = c_*$ (17 to 18 degrees in bed slope), if the specific shape of debris flow is uniquely determined in the region between $c = c_*$ and $c < c_*$ through present data and future experimental data collections.

4. Conclusions

In present flume tests, peak discharge rate of debris flow over steep slope channel that is over θ_* of bed slope is experimentally discussed and those are summarized as follows.

(1) Peak discharge of debris flow, Q_p , can be estimated using total volume of a debris-flow surge, V , in dimensional analysis, under the condition that bed slope is around over 17 to 18 degrees and bed sediment is fully saturated. The peak discharge is proportional to the power of 5/6 for total volume of a debris flow, V . The relation is confirmed using present experimental data.

(2) Longitudinal shape of debris flow over the bed in case of $c = c_*$ is triangle and the debris mass increases with longitudinal similarity shape. The results support the previous report (Ou et al., 1993).

(3) Peak value and temporal changes of debris flow are discussed experimentally in the region between $c = c_*$ and $c < c_*$ in sediment concentration, c , because the peak value cannot be evaluated by theoretical consideration (e.g., Takahashi, 1991) in case of $c = c_*$. Those quantities can be evaluated using longitudinal shape of debris mass and potential volume of bed sediment.

Acknowledgements

The authors would like to thank members of the Sabo Technical Center and Nippon Koei Co. Ltd., for doing the flume tests and collecting the experimental data.

References

- Ashida, K. and Egashira, S., 1986, Running-out processes of the debris associated with the Ontake landslide: *Natural Disaster Science*, v. 8, no. p. 63-79.
- Egashira, S., Miyamoto, K., and Itoh, T., 1997, Constitutive equations of debris flow and their applicability, In *Proceedings by C-L. Chen (ed.), Debris-flow Hazards Mitigation: Mechanics, Prediction, and Assessment: Proceedings of 1st International Conference*, San Francisco, ASCE, p.340-349.
- Ou, C., Kobashi, S., and Mizuyama T., 1993, Development processes of debris-flow: *Journal of the Japan Society of Erosion Control Engineering*, p.11-20 (in Japanese with English abstract).
- Rickenmann, D., 2016, *Methods for the quantitative assessment of channel processes in torrents (Steep streams)*: London, Taylor & Francis/Balkema, 133 p.
- Takahashi, T., 1991, *Debris flow: Monograph series (International Association for Hydraulic Research)*: Rotterdam, Brookfield, A.A. Balkema, 165 p.
- Takahashi, T., 2007, *Debris flow: Mechanics, Prediction and Countermeasures*: Leiden, Taylor & Francis/Balkema, 448 p.

Correlation between the slump parameters and rheological parameters of debris flow

Chyan-Deng Jan^a, Chih-Yuan Yang^b, Ciao-Kai Hsu^c, Litan Dey^{b*}

^aProfessor, Department of hydraulic and ocean engineering, Tainan-701, Taiwan

^bPh.D. student, Department of hydraulic and ocean engineering, Tainan-701, Taiwan

^cM.S. student, Department of hydraulic and ocean engineering, Tainan-701, Taiwan

Abstract

Rheological characteristics are important information for understanding or simulating debris-flow movement. Debris-flow movements involves complex and heterogeneous material with grain size distributions ranging from silt to large rocks. Conventional rheometers are usually limited to measure the rheological parameters of debris-flow of fine particles. Slump-tests has been used to evaluate the flow behaviour of fresh concretes which allow the tested concrete slurries to have larger particles. In this study, the relationship between the parameters obtained from rheometer measurements and slump tests for debris-flow slurries with/without big particles were investigated. At the initial stage, we used fine-sediment slurries to conduct rheological experiments to find the relationship between the parameters obtained from the rheometer measurements and slump tests. The rheological parameters of slurries were measured using the 'Brookfield DV-III rheometer'. The rheological behavior of the slurry samples used in this study follow the Bingham fluid model. Rheological parameters (i.e., yield stress and viscosity) are affected by the concentration of slurry, indicating that the higher the concentration, the greater the value of the rheological parameters. Slump test was then conducted using the same material samples prepared for rheometer test and the slumped height and spreading diameter of the tested sample were measured. The result shows that the slump height ratio and spreading ratio of the tested slurry decrease with the increase of slurry sediment concentration. Experimental sediment slurry samples were prepared by mixing coarse sands of about 1 mm in diameter. Our results show that the parameters obtained by rheometer measurements are closely related with those by slump tests for the slurries used in this study, indicating that there is a high potential to evaluate rheological parameters of debris-flow using a slump test as an alternative method.

Keywords: Slump test; Bingham model; rheological parameters; and slump parameters.

1. Introduction

Rheology is a science that deals with the study of fluid and deformation behavior of fluid. When an external force is applied to a body (solid, liquid or gas), it leads to the movement of the body from its original position towards the down slopes or cause a change in its original shape (Malkin and Isayev, 2006). The study of rheology is important in debris-flow as well as in many industries such as paints, polymers, printing inks, paper coatings, ceramics, cosmetics, food systems, pharmaceutical and agrochemical formulation, concrete related constructions company, and liquid detergents (Tadros, 2010). The researchers have been suggested numerous techniques to measure the rheology of concrete, concentrated suspensions, thickened tailings and paste fill, which behave as viscoplastic fluids (Bird et al., 1983; Utracki, 1988; Nguyen and Boger, 1992; Schramm, 2000). Nguyen and Boger (1992) mentioned two main methods of rheology measurements; namely direct and indirect methods. In the indirect methods, yield stress can be obtained from the shear stress vs. shear rate graph by extrapolating and in the direct methods the yield stress can be obtained under static conditions (which also known as true yield stress). Debris-flow is usually treated as the movement of a continuum for simplicity, in spite of the existence of solid particles in it. To simulate the debris-flow both in field and in laboratory, we use partial differential equations with some rheological parameters. Selecting suitable rheological model and its associated parameters are very important in debris-flow simulation (Arattano et al., 2006, Jan and Shen, 1997). Iverson (2003) observed that the debris-flow behavior can changes with the changes of

* Corresponding author e-mail address: litanwre@gmail.com

particle concentration in the mixtures. He also mentioned that Coulomb mixture theory is a good alternative which can represent the inconstant solid-fluid interaction in a heterogeneous mixture.

The rheological behaviors of sediment-slurry mixtures are depended on sediment concentration, sediment type, and particle size distribution. Many researchers have shown that the high concentration slurry mixture could be treated as a Bingham fluid having yield stress and viscosity parameters (Chu, 1983; Fei, 1981 and 1983; Iverson, 2003; Jan et al., 2009, 2011, & 2018; Major and Iverson, 1999; Wu, 1981). Most poorly sorted, naturally debris-flow mixtures are composed of a fluid phase of water and fines (clay and silt), and a granular phase of sand and gravel (Rodine, 1974; Hampton, 1975; Pierson, 1981). The clay and much of the silt are considered to be an intrinsic part of the fluid because they usually will not settle out of suspension during a natural flow event (Tan, 1985; Davies, 1986); sand and gravel, on the other hand, might or might not be carried in suspension by a particular flow. With increasing amounts of silt or clay, sediment-slurry mixtures may acquire a yield strength. Mixtures that contain largely silt acquire a yield strength in the range of 30-35% of volume concentration (Qian et al., 1980). Clay-rich mixtures may exhibit yield strength at volume concentrations as low as 10% or less (Hampton, 1975; Wan, 1982; Yang and Zhao, 1983). Conventional rheometers are usually limited to measure the rheological behavior parameters of debris-flow with fine particles.

The slump measurement using slump test is widely used for measuring the workability of concrete due to its simplicity. In this test, the concrete will collapse or flow if the yield stress is exceeded and will stop when the stress is below the yield stress. Therefore, the slump test is associated to the measurement of yield stress (Ferraris and Larrard, 1998) and spreading distance. Some researchers have used the finite element method to simulate the slump test (Mori and Tanigawa, 1992) assuming that concrete follows the Bingham model. The slump heights were used to measure the viscosity and workability of the mixtures. When the slump height is large, the mixtures holds a small yield stress, and small slump height specifies a large yield stress of the mixture. In this paper, efforts were given on the potential of application of slump test to measure the rheology of sediment-slurry mixtures.

The applicability of slump test to measure rheological parameters of kaolin slurry, slurry with added coarse particles were studied and found a linear relation between rheological parameters and slump parameters (Jan et al., 2009, 2011, 2018). In the present study, the experiments were conducted in two phase: firstly, sediment mixture was used as the tested material and a traditional rheometer was used to measure its rheology. In the second stage, the same sediment mixture was used as the testing materials and its flow behavior were measured by a slump cone instead of a rheometer. The main objective of this study objective is to find the correlation between the rheological parameters and slump parameters, so as to evaluate the potential of using slump test to assess the rheological parameters.

2. Materials and methods

In this study, the tested slurries were the mixtures of fine sediments taken from a reservoir deposition. The sediments have a median diameter of 0.0036 mm and the particle size distribution is shown in Fig. 1. We proportioned those sediment materials into five kinds of slurries having sediment concentrations of 25%, 27.5%, 30%, 32.5% and 35%, respectively. The slurry of sediment concentration 30% was used to mix with different amounts of coarse particles having diameter approximately 1 mm to form five kinds of slurry-gravel mixtures having total sediment concentration of 30%, 40.5%, 44%, 47.5% and 51%, respectively. Those fine-sediment slurries and the slurries with coarse particles (simply named slurry-gravel mixtures herein) were used in the rheological experiments and slump tests.

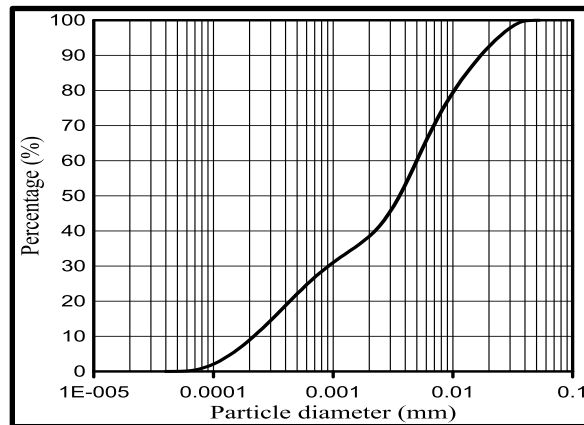


Fig. 1. Particle size distribution of fine-sediment slurry

Rheological experiments in this study were conducted to understand the variation of shear stress of sediment-slurry mixtures with different volume concentration under low shear rates (i.e., $< 20 \text{ s}^{-1}$). Based on the measured shear stress, the yield stress and viscosity coefficient of sediment material were calculated to investigate the relationship between the yield stress and viscosity coefficient under the varying concentration of sediment-slurry mixtures. The details experimental procedure and considerations has been described elaborately by Jan *et al.* (2011 and 2018)

3. Methodology

In this study, the Bingham fluid model, having two parameters (i.e., the yield stress and viscosity), was used to simulate the rheological behavior of the slurries and the slurry-gravel mixtures,

$$\tau = \tau_B + \mu_B \dot{\gamma} \quad (1)$$

where τ_B is the yield stress and μ_B is the Bingham viscosity, and $\dot{\gamma}$ is the shear rate. The rheological curves of slurries were measured using the 'Brookfield DV-III rheometer' and were shown in Fig. 2b.

The slope of each trend line in the shear stress vs shear rate graph represents the coefficient of viscosity. The plots of Bingham viscosity vs volume concentration and the yield stress vs volume concentration have been constructed as shown in Figs. 3a & b. Later on the rheological parameters will be compared with slump parameters obtained from the slump tests to find the correlation.

A self-made cylindrical slump cone (mould) having top inner diameter of 50 mm, bottom inner diameter of $D_0=100$ mm, and height of $H_0=150$ mm was used in the slump tests and slump heights and spreading diameters under different conditions of slurries were measured. The experimental setup is shown in Fig 2c. The slump height and spreading diameter were normalized as the ratio of the slump height to the initial height of tested sample (it equals the height of slump cone), and the ratio of the spreading diameter to the bottom inner diameter of the mould. The normalized terms are known as slump height ratio (H_r) and spreading diameter ratio (D_r), which are shown in equations 2 & 3.

$$H_r = \Delta H / H_0 \quad (2)$$

$$D_r = \Delta D / D_0 \quad (3)$$

Using the above calculated values the correlations of shear stress and viscosity with the slump height ratio and spreading diameter ratio were determined, respectively. After having the rheological parameters and slump parameters from the experimental results, the plots between the rheological parameters (the yield stress and viscosity) and slump parameters (the slump height ratio and spreading diameter ratio) were compared to assess their relationships.

4. Results and discussion

4.1. Rheological parameters

As shown in Fig. 2b, it is clear that the shear stress is linearly related with the shear rate, and this phenomenon indicates that the slurries used in the present study can be treated as Bingham fluids. The shear rate of the reservoir sediments is 20 s^{-1} or less than 20 s^{-1} (Fig. 2b) and the shear stress is about 7.5 to 10 Pa for sediment volume concentration of 25%. Similarly, the range of shear stress at volume concentrations of 27.5%, 30%, 32.5% and 35% are 14~19.1 Pa, 21.9~28.9 Pa, 35.9~50.9 Pa, and 47.4~85.3 Pa, respectively, as shown in Fig. 2b.

The experimental results in Fig 3a, explain that when coarse particles are present in the fine sediment slurry, the yield stress of that slurry become less compared to that mixtures of only fine sediment under same sediment concentration. This phenomenon was also observed by Philips and Davies (1991) and Major and Pierson (1992). The viscosity coefficient of slurry gravel mixtures also shows the similar trend as shown in Fig 3b. The reason behind this characteristic could be the development of stress and viscosity in sediment slurry containing coarse particles is much slower than the development in fine sediment slurry due to high frictional resistance (Major and Iverson, 1999). Therefore, the rheology of the sediment slurry could vary widely depending on the particle size present in the slurry.

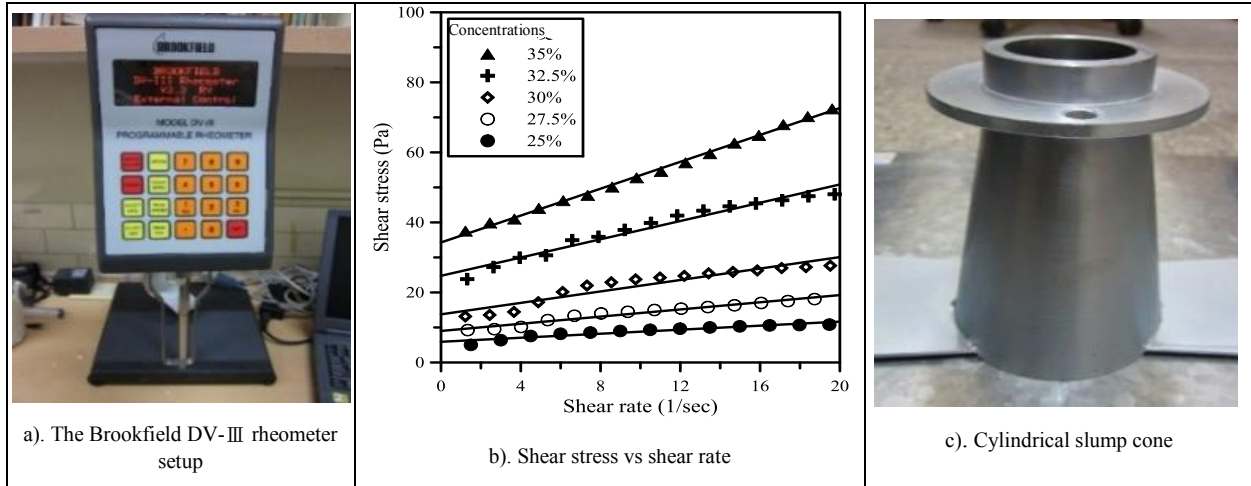


Fig. 2: Rheometer and cylindrical mould used in this study

4.2. Slump test

The slump height ratios and spreading diameter ratios of the results of slump tests under different slurry conditions were presented in Figs. 4a & b. As shown in these figures, the slump height ratio and spreading diameter ratio sharply decreases with the increase of slurry sediment concentration. When different amounts of coarse particles mixed with the fine-sediment slurry of concentration 30% to form slurry-gravel mixtures, the decreasing rates of both ratios of slump height and spreading diameter against total sediment concentrations of the slurry-gravel mixtures are much smaller than those obtained from the fine sediment slurries. This indicates that fine sediments (clays) and coarse particles (sands or gravels) play different roles in the rheology of sediment slurries. The former provides friction and cohesion, while the latter majorly provides friction only. The content of fine sediments plays more sensitive roles in the rheological behavior of slurry due to cohesions between fine particles.

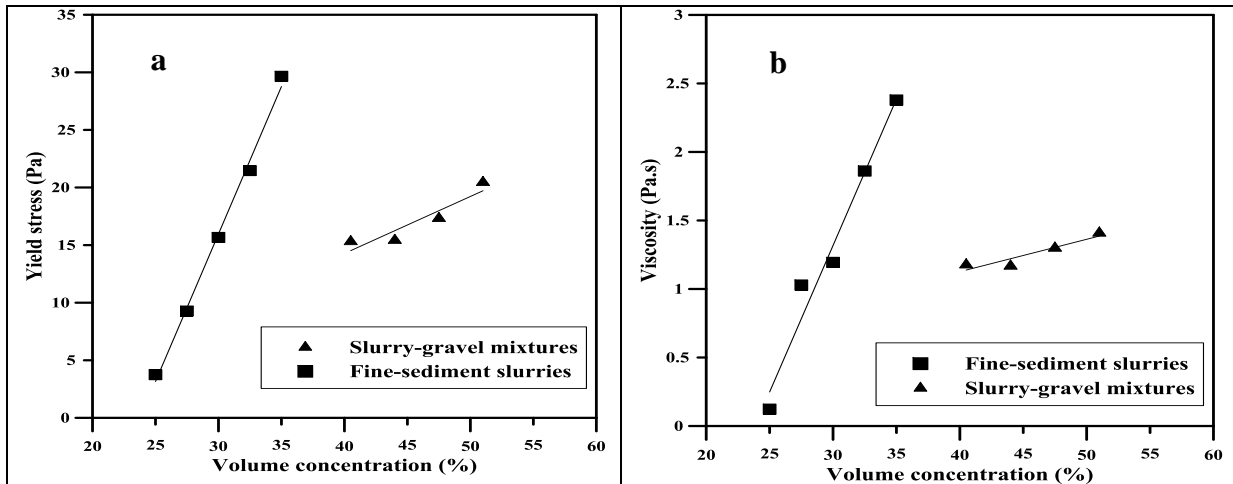


Fig. 3: Relationships of rheological parameters and sediment concentrations of slurries

4.3 Correlation between rheological and slump parameters

The rheological parameters (the yield stress and viscosity) obtained from rheometer measurements, slump parameters (slump height ratio and spreading diameter ratio) obtained from slump tests for fine-sediment slurries, and slurry-gravel mixtures used in this study were compared as shown in Fig. 5. In the above rheological and slump parameters models analysis, the values of R^2 for the relation of parameters of fine-sediment slurries ranges from 0.85 to 0.99. The R^2 values greater than 0.7 are considered as strongly correlated (Moore et al. 2013), as a result it implies that the rheological parameters are strongly related to slump parameters.

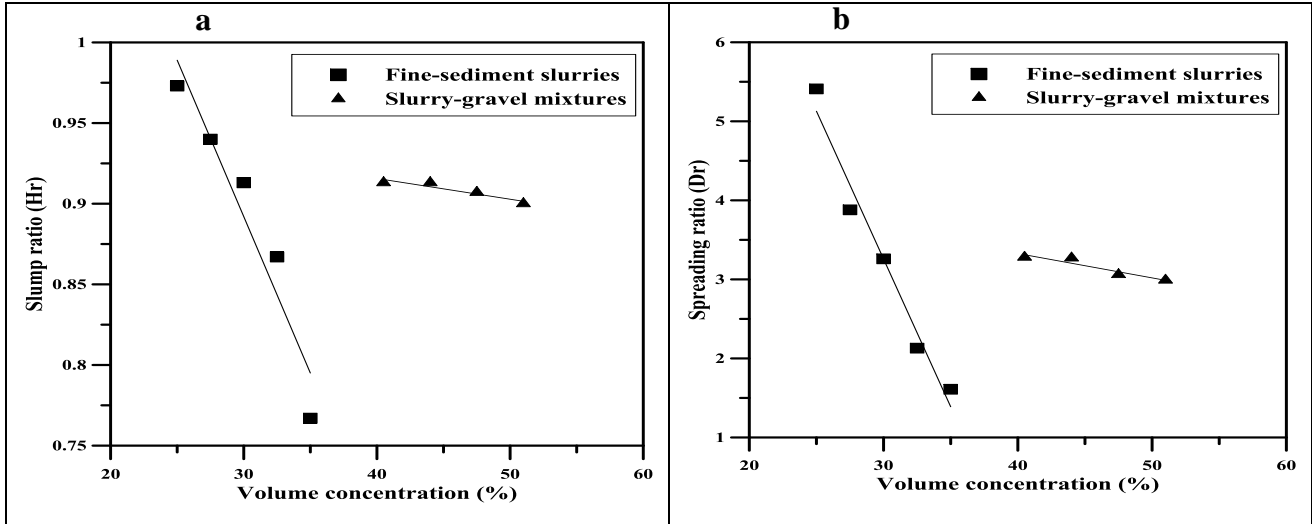


Fig. 4. (a) Slump height ratio vs. concentrations; (b) Spreading ratio vs. concentrations

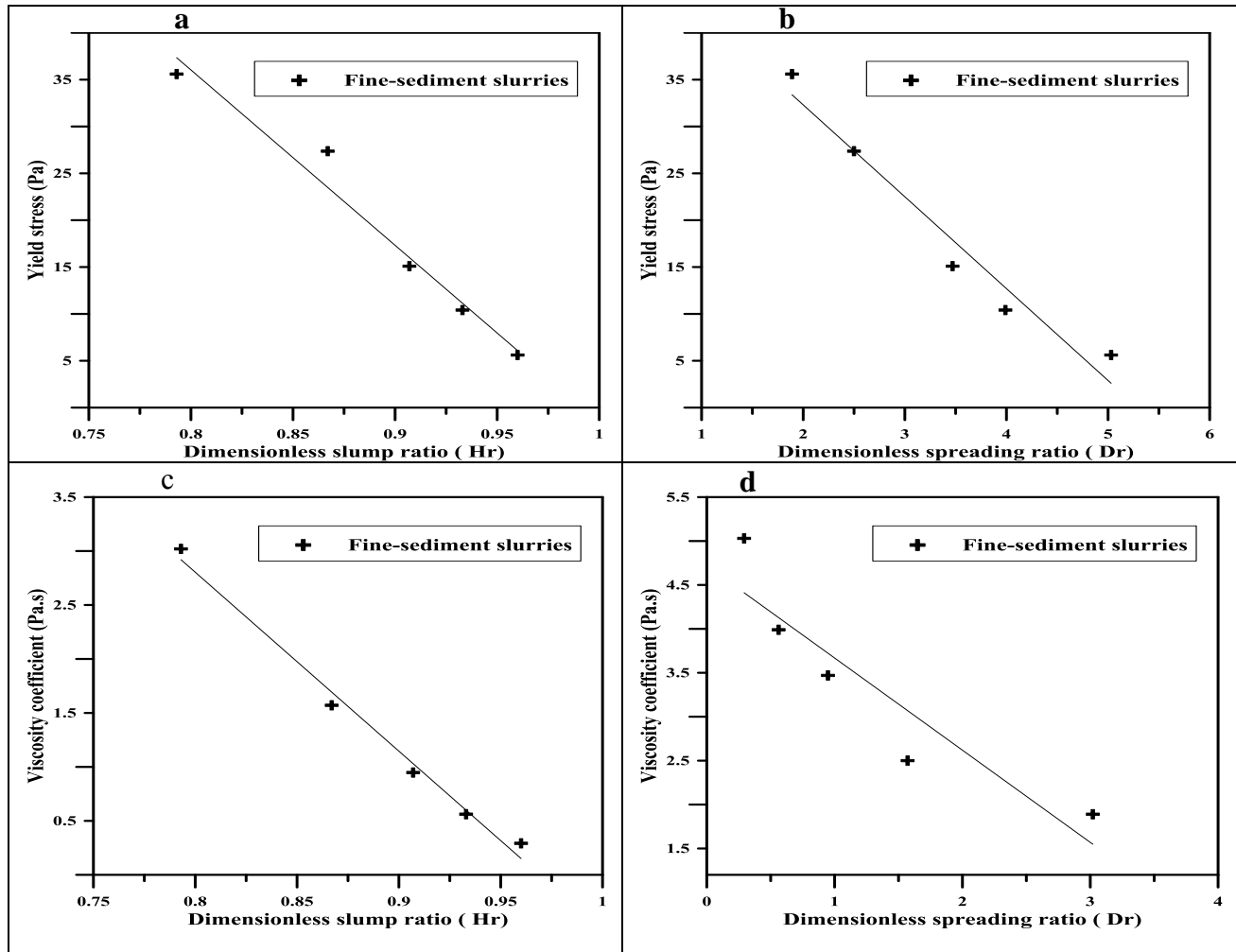


Fig. 5. (a) Yield stress vs. slump height ratio; (b) Yield stress vs. spreading diameter ratio; (c) Viscosity coefficient vs. slump height ratio; (d) Viscosity coefficient vs. spreading diameter ratio.

Table 1: Relations among the rheological and slump parameters of fine-sediment slurries

Relation model	Model coefficients (a, b)	Coefficient of determination R ²
$\tau_B = a + bH_r$	185.78, -187.18	0.97
$\tau_B = a + bD_r$	51.92, -9.8	0.96
$\mu_B = a + bH_r$	16.07, -16.58	0.99
$\mu_B = a + bD_r$	4.71, -1.05	0.85

5. Conclusions:

This study conducted rheological experiments and slump tests of sediment slurries that have Bingham fluid behaviour, to explore the correlation between the rheological parameters and slump parameters. Looking at the experimental results, we conclude:

1. The slurry-gravel mixtures and fine-sediment slurry mixtures at low shear rates ($< 20 \text{ s}^{-1}$) exhibit the characteristics of Bingham fluid.
2. The rheological parameters (the yield stress and Bingham viscosity) are affected by the sediment concentration in the slurry as well as by sediment size distribution. The higher the concentration, the greater the value of rheological parameters.
3. With increasing the sediment concentration of the tested slurry using slump test, the values of slump height ratio and spreading diameter ratio are gradually decreasing. Under the same total concentration, the slurry mixed with coarse particles spread slower and shorter than fine sediment slurry.
4. Among the slump parameters, spreading of slump or slump diameter is more sensitive to rheology measurement.
5. The rheological parameters are well related with slump parameters, and this indicates that there is a high potential to evaluate rheological parameters of debris-flow using a slump test as an alternative method.

Acknowledgements

The authors would like to thank the Ministry of Science and Technology, Taiwan (MOST 107–2221-E-006-029-MY3) for its financial support on this experimental study.

References:

- Bird, R. B., Gance, D., and Yarusso, B. J., 1983, The rheology and flow of viscoplastic materials. Review of chemical engineering. Vol. 1.
- Chu, J., 1983, Basic characteristics of sediment-water mixture with hyper concentration. Proceedings of 2nd International Symposium on River Sedimentation, Nanjing, China, pp. 265-273 (in Chinese with abstract in English).
- Costa, J.E., Jarrett, R.D., 1981, Debris-flows in small mountain stream channels of Colorado and their hydrologic implications. Bull Assoc. of Engin. Geol., 18 (3): 309-322.
- Dai, J., W. Chen, and Zhou, B., 1980, An experimental study of slurry transport in pipes, in River Sedimentation, edited by B. Li, pp. 195–204, Guanghai, Beijing.
- Davies, T.R.H., 1986, Large debris-flows. a macro viscous phenomenon. Acta Mechanica, 63: 161-178.
- Fei, X., 1981, Bingham yield stress of sediment-water mixture with hyper-concentration. J. of Sediment Research, Beijing, China, No.3: 19-28 (in Chinese with abstract in English).
- Fei, X., 1983, Grain composition and flow properties of heavily concentrated suspensions. In: Proceedings of 2nd International Symposium on River Sedimentation, Water Resources ffield Electrical Power Press, Nanjing, China, pp.307-308.
- Ferraris, C.F., and Larrard, F.D., 1998, Testing and Modelling of Fresh Concrete Rheology, NISTIR 6094.
- Fink, J.H., Malin, M.C., D'alli, R.E., and Greeley, R., 1981, Rheological properties of mudflows associated with the Spring 1980 eruptions of Mount St Helens Volcano, Washington. Geophys. Res. Letters, 8(1): 43-46.
- Hampton, M.A., 1975, Competence of fine grained debris-flows. J. Sediment Petrol. 45 (4) 835-844.
- Iverson, R. M., 2003, The debris-flow rheology myth, in Debris-flow Hazards Mitigation: Mechanics, Prediction, and Assessment, vol. 1, edited by D. Rickenmann and C. L. Chen, pp. 303–314, Millpress, Rotterdam, Netherlands.
- Jan, C.D., and Shen, H.W., 1997, Review dynamic modelling of debris-flows. Lecture Notes in Earth Sciences, 64: 93-116.
- Jan, C.D., Chang, Y.W., Kao, F.H., and Lo, W.C., 2009, Effects of solid particles on the rheo-logical parameters of Bingham Fluid. Journal of Chinese Soil and Water Conservation, 40(1), 95-104. (in Chinese).
- Jan, C.D., Kuo, F.H., and Chang, L.Y., 2011, An Experimental Study on the Time-dependent Rheological Parameters for Kaolin Slurries. Journal of Chinese Soil and Water Conservation, 42 (3):196-206. (in Chinese)
- Jan, C.D., Hsu C.K., and Yang C.Y., 2018, Study on Rheological Experiments and Slump Tests of Kaolin Slurries. Journal of Chinese Soil and Water Conservation (in Chinese, accepted on Feb. 7.

- Johnson, A.M., and Hahn, P.H., 1970, Mobilisation of debris-flows. *Zeitschrift für Geomorph. Suppl.*, 9: 168-186.
- Kang, Z., and Zhang, S., 1984, An analysis of sediment transport by debris-flows in the Jiangjia Gully, Yunnan. In: *Catchment experiments in Fluvial Geomorphology*. Proc. LG. U. commission meeting, Exeter and Huddersfield (98). Ed. T.P. Burt and D.E. Walling. Geo Books Northwest 1984. pp. 477-488.
- Li, Jian, and Luo, Defu., 1981, The formation and characteristics of mudflow and flood in the mountain area of the Dachao River and its prevention. *Z. Geomorph. NF.*, 25 (4): 470-484.
- Li, J., Yuan, J., Cheng, B., and Luo, D., 1983, The main features of the mudflow in Jiang-Jia Ravine. *Z. Geomorph. N. F.* 27 (3): 325-341.
- Lowe, D.R., 1982, Sediment gravity flows II. Depositional models with special reference to the deposit of high density turbidity currents. *J. Sediment Petrol.*, 52 (1): 279-297.
- M. Arattano, L. Franzi, and L. Marchi, 2006, Influence of rheology on debris-flow simulation. *Natural Hazards and Earth System Sciences*, 6, 519–528
- Major, J. J., and R. M. Iverson 1999, Debris-flow deposition: Effects of pore-fluid pressure and friction concentrated at flow margins, *Geol. Soc. Am. Bull.*, 111(10), 1424–1434
- Malkin, A.Y., Isayev, A.I., 2006, *Rheology: Concepts, Methods and Applications*. Chem Tec Publishing, Toronto, Canada.
- Mansfield, C.F., 1985, Modelling Newtonian fluids and Bingham plastics. *Journal of Geological Education*, 33 : 97-100.
- Mitschka, P., 1982, Simple conservation of Brookfield R.V.T. readings into viscosity functions. *Rheologica Acta*, 21, 207-209.
- Mori, H., and Tanigawa, Y., 1992, Simulation methods for fluidity of fresh Concrete, *Memoirs of the School of Engineering, Nagoya University* 44, 71–133.
- Moore, D. S., Notz, W. I., and Flinger, M. A., 2013, *The basic practice of statistics* (6th ed.). New York, NY: W. H. Freeman and Company. Page (138).
- Nguyen, Q. D., and Boger, D. V., 1992, Measuring the flow properties of yield stress fluids. *Annual Review of Fluid Mechanics*, 24.
- Phillips, C. J., and T. R. H. Davies, 1991, Determining rheological parameters of debris-flow material, *Geomorphology*, 4, 101-110.
- Pierson, T.C., 1981, Dominant particle support mechanisms in debris-flows at Mt Thomas, New Zealand, and implications for flow mobility. *Geol. Soc. Am. Bull.*, 96 (1056-1069).
- Qian, Y., Yang, W., Zhao, W., Cheng, X., Zhang, L. and Xu, W., 1980, Basic characteristics of flow with hyper-concentration of sediment. In: *Proc. of the Int. Syrup. on River Sedimentation*, pp 175-184, Chinese Society Hydraulic Engineering, Beijing, China, 1980.
- Rodine, J.D., 1974, Analysis of the mobilization of debris-flows. Ph.D. dissertation, Stanford University, Stanford, California, 226 p
- Schramm, G., 2000, *A Practical Approach to Rheology and Rhometry*. Thermo Haake Rheology, Karlsruhe.
- Shen, S., and Xie, S., 1985, Structure mode and rheological property of mud debris-flow. In. *proc. of the Int. Symposium. on Erosion, debris-flow and disaster prevention*, Tsukuba, Japan, 227-230.
- Tadros, T.F., 2010, *Rheology of Dispersions: Principles and Applications*, first ed. Wiley-VCH.
- Tan, B., 1985, The activity of debris-flow in Chinese loess region and its prevention. *Proc. Int. Syrup. on Erosion, Debris-flow and Disaster Prevention*, Tsukuba, Japan. 187-190.
- Utracki L. A., 1988, *The rheology of two phase flows*. Rheological Measurement. London: Elsevier.
- Wan, Z., 1982, Bed material movement in hyper-concentrated flow'. Institute of hydrodynamics and hydraulic engineering, Technical University of Denmark. Series Paper No.31.
- Wu, J., 1981, A preliminary study on the static shear stress of debris-flow slurry. *Journal of Sediment Research*, Beijing, China, No.4, pp. 38-49 (in Chinese with English abstract).
- Yang, W., and Zhao, W., 1983, An experimental study of the resistance to flow with hyper-concentration in rough flumes. In: *Proc. of the 2nd Int. Syrup. on River Sedimentation*, Engl. Sum. pp 54-55, Water Resources and Electrical Power Press, Nanjing, China, 1983.
- Zhang, X., Liu, T., Wang, Y., and Luo, J., 1985, The main features of Debris-flows and Control structures in Hunshui Gully, Yuannan Province, China. In. *Proc., of the Int. Symp on Erosion, Debris-flow and Disaster Prevention*, Tsukuba, Japan, pp 181-186.

Concentration distribution in debris flow consisting of particles with two different sizes

Hiroshi Kisa^{a,*}, Iwao Miyoshi^b

^a Nippon Koei Co., Ltd, 2304, Inarihara, Tsukuba, Ibaraki 3001259, Japan

^b Kyoto Prefectural University, 1-5 Nakaragi-cho, Shimogamo, Sakyo-ku, Kyoto-shi, Kyoto 6068522, Japan

Abstract

Debris flows contain solid particles of various sizes. The gaps between large particles contain fine-grained sediment, and this is known to maintain high pore pressures. Inverse grading in which large particles become increasingly concentrated towards the surface of the flow is also known to occur. Therefore, to determine the flow behavior, it is important to clarify the grain-size distribution for not only large particles, but also fine sediment in the depth direction of the flow. In the present study, we generated a debris flow by eroding riverbed material consisting of large particles and fine-grained sediment in an experimental flume, and measured the concentration of different sized particles in layers at three different depths. The test results showed that the highest concentration of large particles was in the middle layer. The highest concentration of fine-grained sediment was in the bottom layer, and this concentration decreased towards the surface of the flow. Inverse grading was observed from the bottom layer to the middle layer; however, no noticeable inverse grading occurred from the middle layer to the upper layer. The reason for this kind of concentration distribution is considered to be that there was insufficient turbulence in the gaps between large particles in the bottom layer, and so fine-grained sediment settled, while in the upper layer, interstitial turbulent stress developed and fine-grained sediment was dispersed. We calculated the concentration distribution of fine-grained sediment from the middle to the upper layer on this basis, and the results were in general agreement with the measured distribution in the dispersion region.

Keywords: Debris flow; Concentration distribution; Fine sediment; Gaps between coarse particles; Dispersion

1. Introduction

Debris flows contain solid particles with a wide range of sizes. This may include fine sediment that can influence the flow characteristics of the debris flow. Some of the fine sediment distributed in the gaps between large particles is thought to change to a fluid phase (e.g., Hotta et al., 2012). Maintenance of high pore pressures caused by the existence of fine sediment in the fluidized layer influence the size and flow characteristics of debris flows (e.g., Iverson et al., 2010). Also, it has been noted that fine sediment influences so-called inverse grading, by which large particles are concentrated towards the surface of the flow, and that when the concentration of fine sediment in the lower layer becomes high, it affects the flow characteristics (Iwata et al., 2013). Therefore, we decided that evaluating concentration distribution of fine sediment in the depth direction of the flow is important in predicting the behavior of debris flows. The intensity of pore-fluid turbulence is considered to influence the suspension of fine sediment in the gaps between coarse particles (e.g., Takahashi et al., 1990). The gap size varies in the depth direction of the flow depending on the size and concentration distribution of coarse particles. Therefore, Takahashi et al. (1990) suggested that the grain size and concentration of suspended fine sediment in the gaps between coarse particles may vary in the depth direction. However, as far as the authors are aware, there have been no studies in which the fine sediment distribution has been measured from the bed to the water surface for a real debris flow, since this is difficult to accomplish. Therefore, in the present study, we conducted a debris-flow flume experiment to determine the concentration distribution of fine sediment in the gaps between coarse particles. The flow in this study was a so-called “stony debris flow”, which is one of the flows classified as inertial debris flows by Takahashi (2007),

* Corresponding author e-mail address: a6460@n-koei.co.jp

and the pore fluid contained a high concentration of very fine particles.

In this study, drawing on prior knowledge (e.g., Iwata et al., 2013), we assumed that in the lower layer, which contains a high concentration of fine sediment due to inverse grading, this sediment is not suspended in the pore fluid, but bears skeletal stresses. In contrast, in the surface layer, we assumed that the fine sediment is in suspension in the pore fluid due to turbulent diffusion. We considered the mixing scale for turbulent diffusion of fine sediment in this region to be governed not by the mixing length on the depth scale, but by the size and concentration of coarse particles. This is an important concept in this study, and based on this, we investigated the mechanism responsible for the concentration distribution of fine sediment in the top layer using a combination of calculations and experiments. We conducted an experiment on mixed-size debris flowing downward over an erodible bed composed of fine sediment and coarse particles. The fine sediment used in the experiment had maximum and minimum grain sizes of approximately 1/7th and 1/50th of the size of the coarse particles, respectively. We obtained the concentration distribution of fine sediment and coarse particles in three different layers in the depth direction. The concentration distributions by grain size were simply determined from the velocity distribution and three sets of experimental data: the transport concentration for the entire flow and two local transport concentrations at different heights.

2. Methods

An open-channel flume made of transparent acrylic and measuring 800 cm long, 8 cm wide, and 10 cm deep, as shown in Figure 1a, was used in the experiment. The flume gradient (θ) was set at 14° . There were roughness strips on the flume bed in the 740 cm long section from the flume upstream end. This section was an erodible bed covered with a water-saturated solid material with a fine-to-coarse sediment mixing ratio of 1:1. The 30 cm section from the flume downstream end was a rigid bed. Glass beads used as coarse particles were stuck to this section of the flume bed. The rigid bed section was 3 cm higher than the flume bed in the erodible bed section. There was a sampler at the downstream end of the flume. The sampler was equipped with a single separation board running parallel to the flume bed. The sampler was capable of collecting all of the debris flow during the sampling period, or the flow that passed over the separation board, which could be set at any height (Figures 1b and 1c).

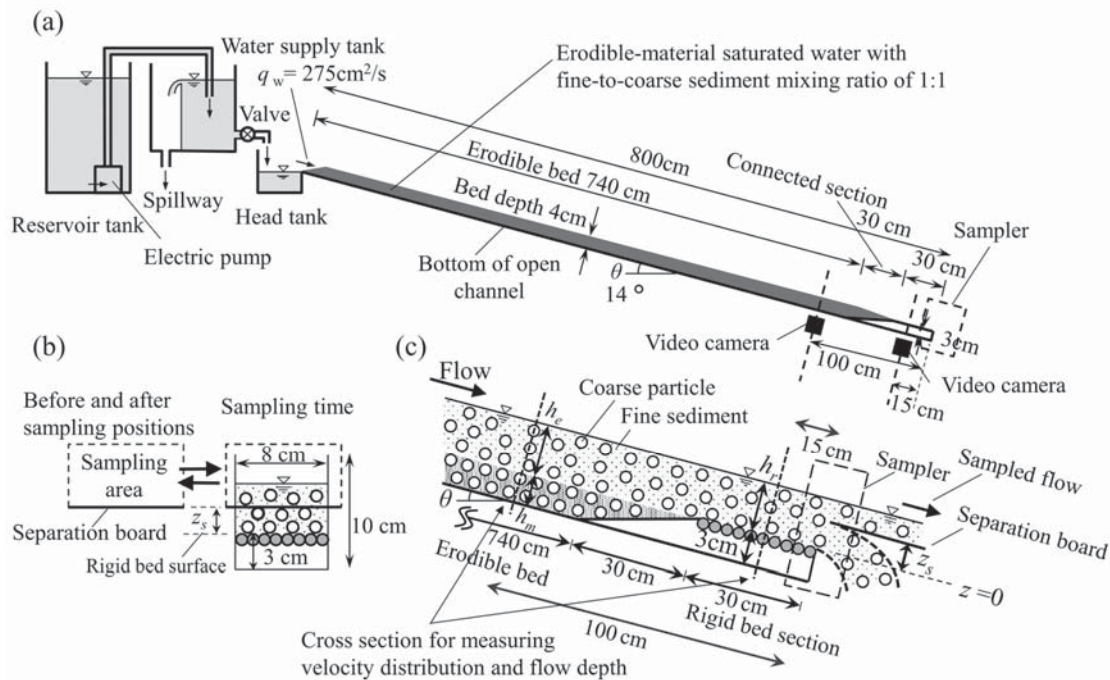


Fig. 1. (a) Side view of debris flow experimental flume (before generating a debris flow by eroding the bed material); (b) Cross section of end of flume; (c) Side view of lower part of flume (during sampling)

Table 1. Materials used in erodible bed experiments

Case No.	Diameter of fine sediment particles	Density of fine sediment particles	Diameter of coarse particles	Density of coarse particles	Fine-to-coarse sediment mixing ratio	Internal friction angle for mixed materials
Case 1	0.21 mm (0.11-0.3 mm)	2.58 g cm ⁻³	10 mm	2.49 g cm ⁻³	1:1	40.5°
Case 2	0.64 mm (0.42-0.85 mm)	2.58 g cm ⁻³	10 mm	2.49 g cm ⁻³	1:1	41.5°
Case 3	1.43 mm (0.85-2.0 mm)	2.55 g cm ⁻³	10 mm	2.49 g cm ⁻³	1:1	43.3°
Case 4	0.21 mm (0.11-0.3 mm)	2.58 g cm ⁻³	5 mm	2.54 g cm ⁻³	1:1	39.5°

For simplicity, this study examined debris flows consisting of two different particle sizes (coarse particles and fine sediment). Table 1 shows the experimental conditions. The grain diameter of the fine sediment (d_f) was 0.21, 0.64, or 1.43 mm, while the coarse particles were spherical glass beads with diameters (d_c) of 10 or 5 mm. The experiment was carried out according to the following procedure. Fine sediment and coarse particles were mixed at a volume ratio of 1:1 and deposited to a height of 4 cm from the flume bed. A small quantity of water was supplied from the flume upper end to saturate the solid material. Then, a constant water flow was supplied from the upstream end at a flow rate per unit width of 275 cm²/s to generate a debris flow by eroding the bed material. The flow was collected using the sampler for approximately 1 s immediately after the flow depth in the measurement cross section in the erodible bed section h_e , shown in Figure 1c, became steady. The flow in the measurement cross section in the erodible bed section and in the rigid bed section was filmed from the side of the flume using a video camera. From these videos, the flow depth and coarse particle velocity distribution were identified in each measurement cross section. The surface of the rigid bed was set as the origin ($z=0$) for measuring the flow depth and coarse particle velocity distribution in the measurement cross section in the rigid bed section (Figures 1b and 1c).

The experiment was repeated three times under the same conditions (Run 1, Run 2 and Run 3). In Run 1, the entire fluidized layer was collected. In Run 2, the installation height of the separation board z_s was set at h_a , approximately one third of the mean flow depth in the rigid bed section h_r measured in Run 1, and the debris flow passing over the separation board was collected. In Run 3, the installation height of the separation board z_s was set at h_b , approximately two thirds of the mean flow depth in the rigid bed section h_r measured in Run 1. The entire volume of the debris flow, the fine sediment volume, and the coarse particle volume collected in Run 1, Run 2, and Run 3 were measured, and the transport concentration in Run 1 and the local transport concentration in Runs 2 and 3 were obtained. The concentration distributions by grain size were simply determined from the velocity distribution in the rigid bed section and the three sets of experimental data using Equations (1) to (6). The velocity distribution in the rigid bed section was used as the overall velocity distribution. The local transport concentrations in the upper layer were the measured values $C_{f\ upper}$ and $C_{c\ upper}$.

$$C_{f\ upper} = C_{f3} \int_{h_b}^{h_r} u dz / \int_{h_b}^{h_r} u dz \quad (1)$$

$$C_{f\ middle} = (C_{f2} \int_{h_a}^{h_r} u dz - C_{f3} \int_{h_b}^{h_r} u dz) / \int_{h_a}^{h_b} u dz \quad (2)$$

$$C_{f\ lower} = (C_{f1} \int_0^{h_r} u dz - C_{f2} \int_{h_a}^{h_r} u dz) / \int_0^{h_a} u dz \quad (3)$$

$$C_{c\ upper} = C_{c3} \int_{h_b}^{h_r} u dz / \int_{h_b}^{h_r} u dz \quad (4)$$

$$C_{c\ middle} = (C_{c2} \int_{h_a}^{h_r} u dz - C_{c3} \int_{h_b}^{h_r} u dz) / \int_{h_a}^{h_b} u dz \quad (5)$$

$$C_{c\ lower} = (C_{c1} \int_0^{h_r} u dz - C_{c2} \int_{h_a}^{h_r} u dz) / \int_0^{h_a} u dz \quad (6)$$

Here, $C_{f\ upper}$, $C_{f\ middle}$ and $C_{f\ lower}$ are the fine sediment concentrations in the upper layer ($h_b < z \leq h_r$), middle layer ($h_a < z \leq h_b$), and lower layer ($h_0 < z \leq h_a$) of the debris flow, respectively. $C_{c\ upper}$, $C_{c\ middle}$ and $C_{c\ lower}$ are the coarse particle concentrations in the upper, middle, and lower layers, respectively. C_{f1} is the transport concentration of fine sediment

collected in Run 1, and C_{f2} and C_{f3} are the local transport concentrations of fine sediment collected in Runs 2 and 3, respectively. C_{c1} is the transport concentration of coarse particles collected in Run 1, and C_{c2} and C_{c3} are the local transport concentrations of coarse particles collected in Runs 2 and 3, respectively. z is the height from the top surface of the rigid bed, and u is the flow velocity at a height z . The sum of the fine sediment concentration c_f and the coarse particle concentration c_c is taken to be the solid particle concentration c .

3. Results

The flow depth in the measurement cross section in the erodible bed section increased instantly after the arrival of the flow, and under all experimental conditions, the flow depth reached a maximum in roughly 1 s. The video footage confirmed that the debris flow moved in a stratified manner in the measurement cross section in both the erodible bed section and the rigid bed section, without any notable switching of position of coarse particles between top and bottom. It also confirmed that the bed depth in the measurement cross section in the erodible bed section (h_m) was almost 3 cm during the sampling period. Figure 2a shows an example of the measured velocity distribution in the rigid bed section. Taking the flow velocity at a height $z=0$ to be $u=0$, approximate values for the velocity distribution were determined and used to calculate the concentration distribution. We decided that the debris flow generated in this experiment was a stony debris flow in the inertial regime on the rigid bed, so the approximation was based on a 3/2 power law for dilatant fluids (e.g., Takahashi et al., 2007). The coefficient A was calculated for each case in order to minimize the sum of the absolute differences between the measured coarse particle velocity and the velocity approximated using Equation (7).

$$u = A\{1 - (1 - z/h_r)^{3/2}\} \tag{7}$$

Here, u is the flow velocity at a height z from the rigid bed, A is a coefficient, and h_r is the mean flow depth measured in Run 1. Figure 2b shows an example of the measurement results for the transport concentration.

Figure 3 shows the concentration distributions for fine sediment and coarse particles in the upper, middle, and lower layers of the debris flow in the lower end of the flume, obtained from Equations (1) to (6). The mean cross-sectional concentration of all solid particles was lowest in Case 3 at 0.43, and highest in Case 1 at 0.53. Except in Case 1, the concentration of fine sediment was highest in the lower layer, followed by the middle layer, and then the upper layer. The concentration of coarse particles tended to be high in the middle layer in each case.

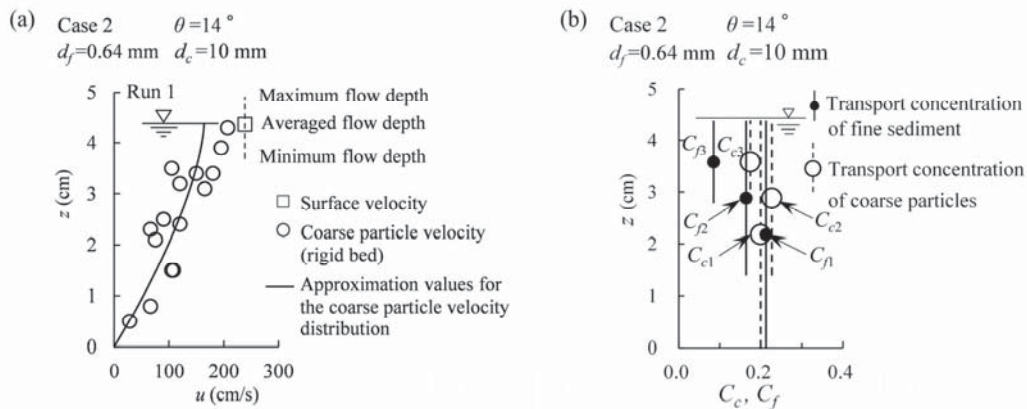


Fig. 2. (a) Example velocity distribution for coarse particles; (b) Example transport concentration of fine sediment and coarse particles

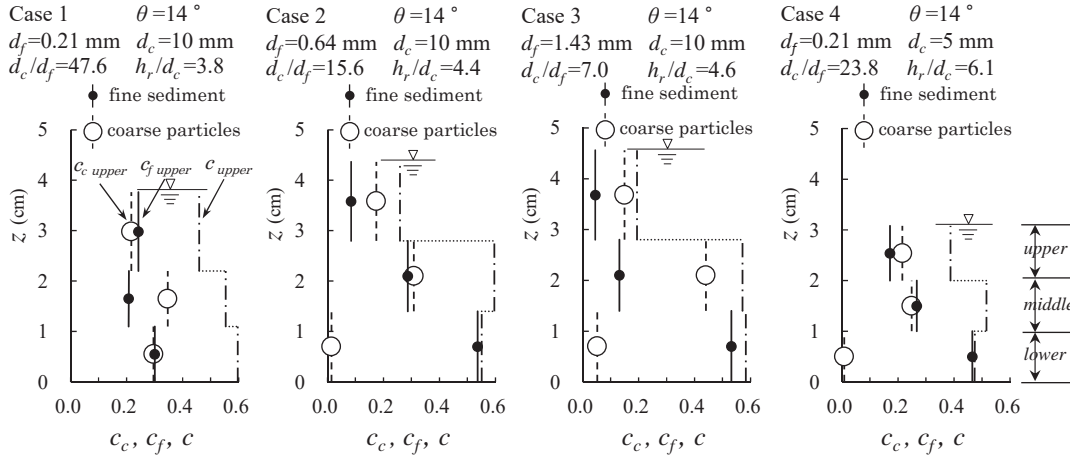


Fig. 3. Concentration distribution of fine sediment and coarse particles

4. Discussion

Inverse grading from the lower layer to the middle layer was observed in the grain-size distributions. However, in the upper and middle layers, the coarse particles and fine sediment were mixed, and inverse grading was not as apparent as in the middle and lower layers. In other words, for the fine sediment, the concentration in the lower layer was high due to inverse grading, but the fraction of fine sediment particles was distributed similarly in the upper and middle layers. Only in Case 1 were the coarse particles and fine sediment in a mixed state in all layers. The concentration of fine sediment in the gaps between coarse particles was found for the lower, middle, and upper layer using:

$$c_f' = c_f / (1 - c_c). \quad (8)$$

Here, c_f' is the concentration of fine sediment in the gaps between coarse particles, c_f is the concentration of fine sediment, and c_c is the concentration of coarse particles.

Figure 4 shows the concentration distributions for fine sediment in the gaps between coarse particles in the debris flow determined using Equation (8). The concentration in the upper layer $c_f'_{upper}$ was lowest in Case 3 at 0.05, and highest in Case 1 at 0.31. The smaller the grain size of the fine sediment d_f , the higher the concentration of fine sediment in the upper layer $c_f'_{upper}$. Meanwhile, the concentration in the lower layer $c_f'_{lower}$ was high in all cases, but was lowest in Case 1 at 0.43, and highest in Case 3 at 0.56.

This study examined equations for calculating the concentration distribution of fine sediment in the gaps between coarse particles in debris flow. The concentrations of coarse particles and fine sediment in the depth direction of the flow were obtained. Therefore, we next examined equations for estimating the concentration distribution of fine sediment based on the coarse particle concentration distribution and velocity distribution at heights. The turbulent stress τ_f acting on the pore fluid between coarse particles was calculated using (Egashira et al., 1989; Takahashi, 2007):

$$\tau_f = \rho l^2 (du/dz)^2. \quad (9)$$

Here, ρ is the fluid-phase density of the debris flow, while l is the mixing length of the debris flow and represents the scale of the gap between coarse particles, and du/dz is the velocity gradient. The concentration distribution for fine sediment in the gaps between coarse particles is given by Equation (10), by analogy with theories on suspended sediment in rivers that deal with floating and settling of sand particles (e.g., Rouse, 1937; Ashida et al., 1970).

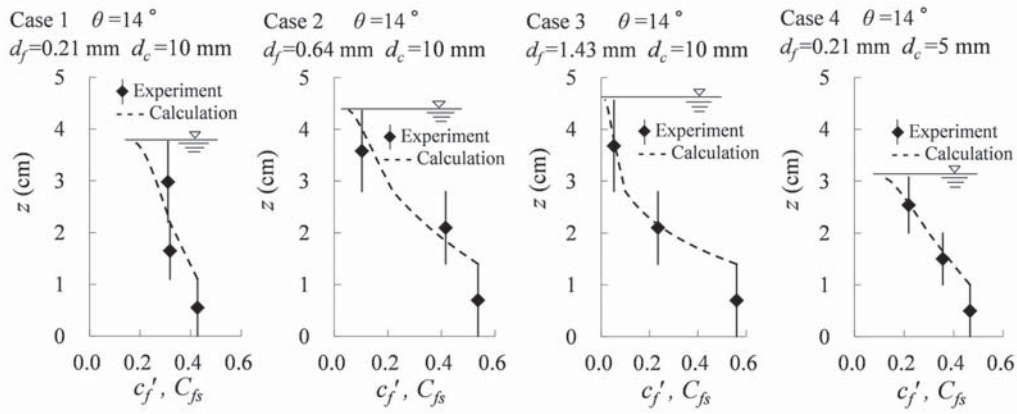


Fig. 4. Fine sediment concentration in gaps between large particles (solid vertical lines) and calculated concentration distribution of fine-grained sediment from intermediate to top layer (dashed lines)

$$\frac{c_{fs}}{c_{fsa}} = \exp \left[- \int_a^z \left\{ \frac{w_0 \cos \theta}{l^2 (du/dz)} \right\} dz \right] \quad (10)$$

Here, z is height from the bed in the depth direction of the flow, C_{fs} is the concentration of fine sediment in the gaps between coarse particles at a height z , C_{fsa} is the concentration of fine sediment in the gaps between coarse particles at a height a , which is the height of the supply source of fine sediment, and w_0 is the settling velocity of fine sediment.

The parameters were determined as follows. First, the reference plane height and reference plane concentration were considered. In the experiment in this study, there was inverse grading from the lower layer to the middle layer, and in the lower layer, the coarse particle concentration was low and the fine sediment concentration was high. Previous research on mixed-size debris flow indicated that in flows with high concentrations of fine sediment in the lower layer due to inverse grading, the fine sediment is subject to inter-particle stress (Iwata et al., 2013). In the mixed-size debris flow examined in this study, it was assumed that in the lower layer where the concentration of fine sediment was high, the fine sediment primarily bore inter-particle stress, and no turbulence developed in the pore fluid. It was assumed that while fine sediment settled towards the lower layer under the influence of size segregation, fine sediment was diffused from the boundary between the lower and middle layers to the upper layer due to stress caused by fluid turbulence in the gaps between coarse particles. Therefore, for convenience, the reference plane height a was taken as the height of the boundary between the lower layer and the middle layer h_a . Also, for convenience, the reference plane concentration at that height C_{fsa} was assumed to be the measured concentration of fine sediment in the gaps between coarse particles in the lower layer $c'_{f, lower}$. The settling velocity of the fine sediment w_0 was determined using the settling velocity equation proposed by Rubey (1933), and was found to be 2.6 cm/s for a fine-sediment grain diameter d_f of 0.21 mm, 7.2 cm/s for a d_f of 0.64 mm, and 11.6 cm/s for a d_f of 1.43 mm. The mixing length was determined using (Egashira et al., 1989):

$$l = \sqrt{k_f} \left(\frac{1-c_c}{c_c} \right)^{\frac{1}{3}} d_c. \quad (11)$$

Here, c_c is the concentration of coarse particles, d_c is the coarse particle diameter, and k_f is an empirical constant with a value of 0.16 (Egashira et al., 1997).

The coarse particle concentration obtained from the debris-flow experiment was substituted for the concentration of coarse particles c_c in the middle and upper layers. The velocity gradient du/dz was determined at 1-mm intervals in the z -direction from the approximate velocity distribution for coarse particles, and substituted into Equation (10). Although the values obtained using Equation (10) are in fact based on experimentally measured values for the height of the reference plane, the concentration of fine sediment in the gaps between coarse particles at a given height and

the velocity gradient, we still refer to them as “calculated values”.

In this way, the concentration distribution for fine sediment in the gaps between the coarse particles from the boundary between the lower and middle layers ($z=h_a$) to the water surface ($z=h_r$) was calculated, and is indicated by the dashed lines in Figure 4. The trends in concentration and distribution were compared with the measured values for the middle and upper layers. For the fine sediment, there was reasonable agreement between the calculated and measured values. This suggests that the fine sediment in mixed-size debris flow is not only segregated towards the bed due to inverse grading, but is also distributed up to the vicinity of the water surface under the influence of turbulent diffusion in the gaps between coarse particles. Also, because the higher the fine sediment concentration in the upper layer, the higher the concentration of coarse particles in the upper layer, it is possible that the fine sediment in the upper layer behaved as a fluid phase due to pore fluid turbulence, so that high pore pressures maintained.

Our explanation of why the coarse particles and fine sediment were in a mixed state in all layers only in Case 1 of the four experimental cases is as follows. We consider the high concentration of fine sediment in the gaps between coarse particles in the upper layer to be primarily due to the fact that the fine sediment had the smallest grain size, meaning that the settling velocity was low and the conditions made it easy for the fine sediment to float up to the vicinity of the water surface. It is possible that because the concentration of fine sediment in the gaps between coarse particles in the upper layer was high, the pore pressure was also high. Consequently, the concentration of coarse particles was high, and grains with two different sizes were mixed. When the concentration of coarse particle increases, the mixing length in Equation (11) becomes shorter. Although the grain size in the fine sediment is small, there may be an upper limit to the concentration of fine sediment in the upper layer due to the high concentration of coarse particle. In the lower layer, we suggest that the similar concentration of coarse particles and fine sediment results from the fact that coarse particles sank from the middle layer to fill the spaces formed by diffusion of fine sediment from the lower layer to the layer adjacent to the water surface.

5. Conclusions

In this study, we considered the concentration distribution of fine sediment in a mixed-size debris flow to be influenced by turbulent stress in the fluid in the gaps between coarse particles. Through an open-channel flume experiment on debris flow with two different particle sizes, consisting of coarse particles and fine sediment, we obtained the concentration distributions by grain size in three layers. The main conclusions that we reached in this study are as follows:

(1) The debris flow generated in this experiment moved in a stratified manner without any notable switching of position of coarse particles between top and bottom. We assumed that the debris flow generated in this experiment was a stony debris flows in the inertial regime.

(2) The concentration distributions by grain size showed that inverse grading occurred from the lower layer to the middle layer, and the fine sediment concentration was highest in the lower layer. However, inverse grading was not apparent from the middle layer to the upper layer, and the fine sediment as a proportion of the solid particles in the upper layer was similar to that in the middle layer.

(3) In the surface layer of the debris flow in this experiment, we assumed that the fine sediment is in suspension in the pore fluid due to turbulent diffusion. We considered the mixing scale for turbulent diffusion of fine sediment in this region to be governed not by the mixing length on the depth scale, but by the size and concentration of coarse particles.

(4) When the lower layer with a high concentration of fine sediment was assumed to be the supply source of suspended fine sediment, the measured concentration distribution of fine sediment was generally explained by the formula proposed in the present study. This suggests that this distribution is influenced by diffusion due to stress caused by turbulence of fluid in the gaps between coarse particles, which is evaluated by the size, concentration, and velocity gradient of coarse particles.

As described above, we examined a method for estimating the concentration distribution for fine sediment in the gaps between coarse particles in layers where turbulence develops in the pore fluid, and the experimental and calculated results were in reasonable agreement. The concentration of fine sediment at a specific height in a debris flow can therefore potentially be quantitatively evaluated from the coarse particle size, coarse particle concentration, velocity distribution, the settling velocity of fine sediment, the height of the supply source of fine sediment and the concentration of fine sediment in the gaps between coarse particles at a given height. It should be pointed out that the measurement error for the local transport concentration is unclear for the sampling method using a separation board in the case of large particles, and this is one of the issues that should be addressed in a future study.

References

- Egashira, S., Ashida, K., Yajima, H., and Takahama, J., 1989, Constitutive equations of debris flow: Disaster Prevention Research Institute Annuals, Kyoto University, no. 32, B-2, p.487-501 (in Japanese with English abstract).
- Egashira, S., Miyamoto, K., and Itoh, T., 1997, Constitutive equations of debris flow and their applicability: 1st International Conference on Debris-Flow Hazards Mitigation, ASCE, p.340-349.
- Hotta, N., Kaneko, T., Iwata, T., and Nishimoto, H., 2013, Influence of fine sediment on the fluidity of debris flows: Journal of Mountain Science, v. 10, no. 2, p. 233–238.
- Iverson, R.M., Logan, M., LaHusen, R.G., and Berti, M., 2010, The perfect debris flow? Aggregated results from 28 large-scale experiments: Journal of Geophysical Research, v. 115, F03005, p. 1-29.
- Iwata, T., Hotta, N., and Suzuki, T., 2013, Influence of particle-size segregation in multi-granular debris flow on the fluidity: Journal of the Japan Society of Erosion Control Engineering, v. 66, no. 3, p. 13-23 (in Japanese with English abstract).
- Rouse, H., 1937, Modern conception of fluid turbulence: Transactions of the ASCE, v. 102, p. 463-543.
- Rubey, W.W., 1933, Settling velocities of gravel, sand, and silt particles: American Journal of Science, v. 25, no. 148, p. 325-338.
- Takahashi, T., 2007, Debris Flow, Mechanics, Prediction and Countermeasures, Balkema, Proceedings and Monographs in Engineering, Water and Earth Sciences, Taylor & Francis Group, London, UK, 448 p.
- Takahashi, T., Nakagawa, H., and Harada, T., 1990, Prediction of debris flow generated by erosion of steep well-graded sediment mixture bed: Disaster Prevention Research Institute Annuals, Kyoto university, no. 33, B-2, p.443-456 (in Japanese with English abstract).

Debris-flow hazard investigation with Kanako-2D in a rural basin, Alto Feliz municipality (Brazil)

Masato Kobiyama^{a,*} and Rossano Dalla Lana Michel^a

^a*Hydraulic Research Institute (IPH), Federal University of Rio Grande do Sul(UFRGS), Bento Gonçalves Avenue, Porto Alegre/RS – 91501-970, Brazil*

Abstract

Mountainous regions of Brazil, especially where rural families live, need to be assessed for debris flow. Though debris flows rarely occur in this country, they have caused serious damages including human losses. Computational modeling of debris flows is an important tool to develop hazard maps and to improve the understanding of debris-flow mechanisms, since observed occurrences are rare. Therefore, the objective of the present study was to evaluate the potential for debris flows in a small rural basin (0.712 km²), in the municipality of Alto Feliz, Rio Grande do Sul state (Brazil), by using the Kanako-2D model which was calibrated with another debris flow in the same region. We simulated three scenarios by altering the debris volume and consequently the hydrograph (peak flow and peak time). All the scenarios show that debris flows would impact an existing rural house, even with the smallest potential debris volume. The modeled erosion and deposition areas along the debris flow are similar, with the magnitudes (depths) of erosion and deposition being different among the scenarios. In general, in each transversal section, the most pronounced point of erosion or deposition is almost always at the thalweg location. Along the stream channel, deposition was greatest upstream of an abrupt reduction in slope. The formation of a natural dam is observed at the channel junctions where erosion and deposition alternatively took place. Because of the investigation of the potential of debris flows, the simulation results were not compared with the actual occurrence in the present study. However, the present study could show that computational modeling of debris flow is very important for localities where debris flow occurs and that the debris-flow hazard map is useful for land-use planning.

Keywords: Debris flows; Kanako-2D; Southern Brazil.

1. Introduction

In Brazil, ecotourism, construction of small hydropower plants, and establishment of water supply systems in headwater areas, have caused increased infrastructure development in mountainous regions. Increased occupation of mountain regions without adequate management has caused an increase in the frequency and magnitude of debris-flow disasters, especially in the last decade (Kobiyama et al., 2019). Under these circumstances, preventive measures based on scientific investigations are necessary to reduce the disasters. Numerical modeling is a useful tool for investigating the mechanism of debris flow and measures, such as hazard mapping and alert system implementation that can improve safety (Jacob and Hungr, 2005; Takahashi, 2007).

Debris flows usually occur in mountains regions and are rarely observed. Since they occur suddenly, it is very difficult to monitor and record them. After the scientific observation with continuous photos reported by Okuda et al. (1977), many photos and videos of debris flows have been captured around the world. However, the number of these materials that demonstrate debris flows in Brazil is small.

Hence the investigation of debris flow with numerical models should be carried out in Brazil. Among various computational models in the world, the Kanako-2D (Nakatani et al., 2008) has been applied to several areas and situations. The Kanako-2D was initially developed to evaluate the check-dams' influences on debris flow

* Corresponding author e-mail address: masato.kobiyama@ufrgs.br

propagation. However, it has been increasingly used for mapping areas susceptible to these events. Its good performance was confirmed by Michel and Kobiyama (2016), Paixão and Kobiyama (2017) and Kobiyama et al. (2018) that constructed hazard maps and visually compared with real occurrence of debris flows. Therefore, the objective of the present study was to investigate the potential of debris flows in a rural area of the Alto Feliz municipality, Rio Grande do Sul state, Brazil, by using this model calibrated by Kobiyama et al. (2018) that investigated a large debris flow which occurred in this region in December 2000. Note that at that time the debris flow caused the deaths of four peoples. In this municipality there are many places susceptible to debris flows, which has increased the worries of local inhabitants about the debris flows. Thus, it is thought that the investigation of the potential of debris flow by using the calibrated numerical model is useful for understanding the future disasters.

2. Materials and methods

2.1. Study area

The study basin (0.712 km²) is located within the Jaguar basin which is a rural area of Alto Feliz municipality, southern Brazil (Fig. 1). Elevation ranges from 290 m to 670 m. The Alto Feliz region has historically suffered from hydrological disasters, including flash flood and mass movement. In 2000 the Jaguar basin was damaged by an extreme rainfall event, which triggered several landslides that became debris flows (Michel, 2015).

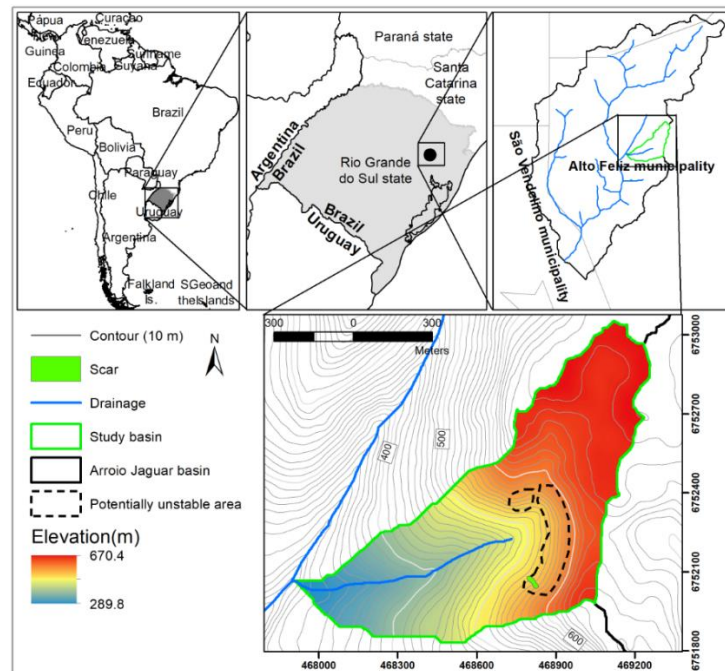


Fig. 1. Location of the study area

The study area is characterized by a mountainous landscape with steep hillslopes and vegetation consisting of native forest and eucalypt reforestation. Geologically it is located on the escarpment of the Serra Geral formation (basalt) (Viero and Silva, 2010). The predominant soils on hillslopes and near river networks are entisols and ultisols, respectively (Flores et al., 2007).

2.2. Kanako-2D

Kanako-2D (Nakatani et al., 2008) is a physically-based computational model and has a graphical interface, which allows the graphical modification of input parameters. The basic equations of the model are based on the theory established by Takahashi and Nakagawa (1991) and are shown below:

- Continuation equation for the total volume of debris flow:

$$\frac{\partial h}{\partial t} + \frac{\partial uh}{\partial x} + \frac{\partial vh}{\partial y} = i \quad (1)$$

- Continuation equation for determining the debris flow of the k -th grade of particle i :

$$\frac{\partial C_k h}{\partial t} + \frac{\partial C_k u h}{\partial x} + \frac{\partial C_k v h}{\partial y} = i_k C_* \quad (2)$$

- Equation of momentum in x and y -axis:

$$\frac{\partial(u,v)}{\partial t} + u \frac{\partial(u,v)}{\partial x} + v \frac{\partial(u,v)}{\partial y} = g \sin \theta_{(wx,wy)} - \frac{\tau_{(x,y)}}{\rho h} \quad (3)$$

- Equation to determining change in bed surface elevation:

$$\frac{\partial z}{\partial t} + i = 0 \quad (4)$$

where h is the flow depth; u and v are the velocities in the x and y -axis, respectively; C_k is the k -th sediment concentration by volume; z is the bed elevation; t is the time; i is the erosion/deposition velocity; i_k is the k -th erosion/deposition velocity; g is the gravitational acceleration; ρ is the interstitial fluid density; θ_{wx} and θ_{wy} are the flow surface gradient (in x and y -axis respectively); C_* is the sediment concentration in movable bed layer; τ_x and τ_y are the riverbed shearing stresses in the x and y -axis, respectively.

2.3. Input data

The present study considered three different scenarios for a debris flow simulation. There is a landslide scar mapped by the CPRM in the study area and this scar's area was used to construct Scenario 1. Scenario 2 adopted the mean area between Scenarios 1 and 3, for comparison. Scenario 3 considered that all areas determined as unstable in the basin by Michel (2015) collapse at the same time. Thus, it can be said that Scenario 3 is the largest possible event for the basin. According to Michel (2015) which carried out the field survey, the mean soil depth in this basin is 2 m. Then, this value was adopted and considered constant for all scenarios. Table 1 shows the values of the input parameters common to all scenarios. These values are similar to those used by Kobiyama et al. (2018) that calibrated this model to one debris flow whose locality is very near to the present study area.

Table 1. Kanako-2D input parameters common to all simulations

Parameter	Unity	Value
Mass density of bed surface	kg/m ³	2650
Mass density of fluid phase	kg/m ³	1000
Concentration of movable bed	m ³ / m ³	0.65
Manning's roughness coefficient	s/m ^{1/3}	0.03
Coefficient of erosion rate	-	0.0007
Coefficient of deposition rate	-	0.05
Diameter of material	m	0.45
Internal friction angle	°	37
Minimum flow depth	m	0.01
Minimum depth at the front of debris flow	m	0.01
Concentration of material	m ³ / m ³	0.5

The debris flow propagation input is a hydrograph which is set at the upper part of channel (1D system). This hydrograph was constructed by following the triangle hydrograph theory of Whipple (1991), where the ascension duration is 1/3 of the total time. The hydrograph peak discharge was calculated using the formula proposed by Rickenmann (1999). The values of input parameters in each scenario are shown in Table 2. Scenario 1 supposed that the smaller unstable area (930 m²) marked in Fig 1 suffers from shallow landslide and causes debris flow. Scenario 3 considered that the total unstable area (44062 m²) marked in Fig. 1 generates landslide. Then Scenario 2 treated half of volume of Scenario 3. Therefore, three scenarios have the same hydrograph-form but the different magnitudes.

Table 2. Parameters variation in each case

Parameter	Unity	Value		
		Scenario 1	Scenario 2	Scenario 3
Sediment volume	m ³	1860.01	44,062.05	88,124.1
Peak discharge	m ³ /s	52.9	738.7	1,316.02
Peak time	s	23.3	39.8	44.7

One of the main bases for the debris flow propagation in the model is topographic data, which were extracted from a digital elevation model (DEM) with a spatial resolution of 2.5 m, obtained from the Brazilian Geological Survey (CPRM). Since the present study treated the potential of debris flow, the year of the DEM construction is out of question.

2.4. Model application

According to Nakatani (2008), Kanako-2D simulates debris flow in the channel with one-dimensional equations (1D) and propagation and deposition with two-dimensional equations (2D). The outputs of simulations were: flow depth, material concentration, velocity in the two dimensions, bed surface altitude and deposition thickness, in each configured time interval. The present study focused on changes in deposit thickness with time.

The simulation result is limited, because the limit of the matrix size that can be used as the elevation model is restricted to 500 x 500 pixels. In the present study, the time interval for calculation was 0.01 s and the simulation time was one hour, in order to ensure that at the end of the simulations there would be no further changes on the bed of the modeled area.

In the study basin, the possible propagation channel was not observed on field. It implies the possibility to have various courses. Hence, the propagation area in one-dimension was minimized (only two pixels with 5m x 5m) and the two-dimension calculation area was maximized, because of the restricted pixels.

3. Results and discussion

Fig. 2 shows the results of three simulated scenarios, which allows the comparison between the flow propagation in each case. The whiter color presents the larger thickness of the deposition layer, meanwhile, the blacker the more erosion in all the scenarios. Due to the model spatial limitation, the flows propagated to exceed the maximum simulation area. However, it did not cause the difficulty to analyze the phenomena, because the very small volume reached the final pixel of simulations.

Scenario 1 represents propagation of the smallest volume, which results in a smaller deposit extent and also a smaller difference between the maximum erosion and maximum deposition (Fig. 2a). In Scenario 3, which has a volume of material that is 47 times than Scenario 1, the difference between the maximum erosion and the maximum deposition is approximately 10 m (Fig. 2c). All the scenarios indicate that an existing house inside the study basin would be affected by a debris flow, regardless of the propagated volume. It is noted that the largest depth of erosion was 2 m due to the fact that this was the maximum depth of soil configured in the model.

Fig. 2d shows the locations at which the cross sections were made along the longitudinal profile of the debris flow travel path. Fig. 3 shows the longitudinal profile along the river thalweg before and after the debris flow occurrence in Scenario 3. In the upstream portion the largest change in the riverbed was a deposition of 7.98 m. This large deposition resulted from the entrance of debris in the channel in the upper part of the thalweg and also from the abrupt change of slope of the thalweg that is present approximately at the altitude of 400 m (Fig. 3).

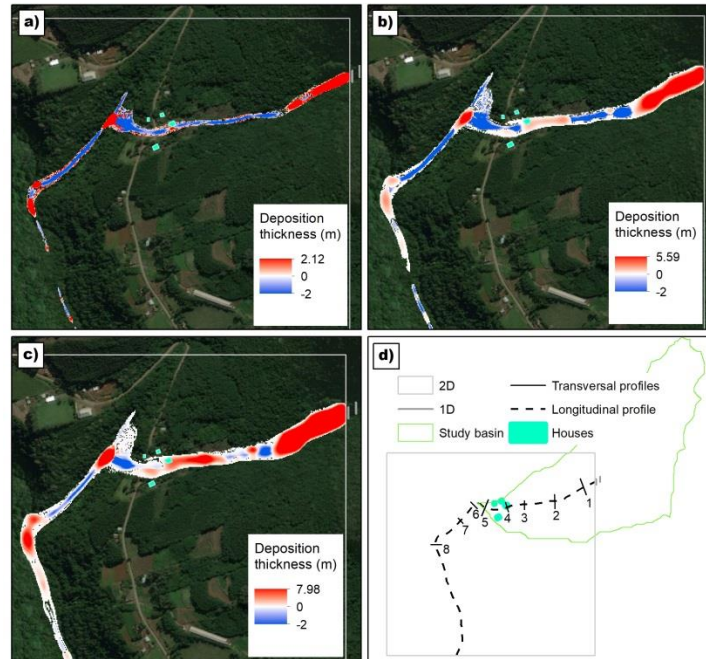


Fig. 2. Results of simulations: a) Scenario 1; b) Scenario 2; c) Scenario 3; and d) cross-sections localities.

It is apparent along the longitudinal profile that there is a semi-regular occurrence of erosion and deposition of debris, which are presented in agreement with the abrupt or smooth variations of channel slope, respectively. The portions of the flow with higher deposition are in the intervals with lower slope along the channel.

Other accumulation points of material are in sections 6 and 8. These two sections are located in a neatly embedded channel and there is accumulation of material, even with the propagation of a low volume in the debris flow. Precisely for this reason, these places possess the potential for natural dams to form.

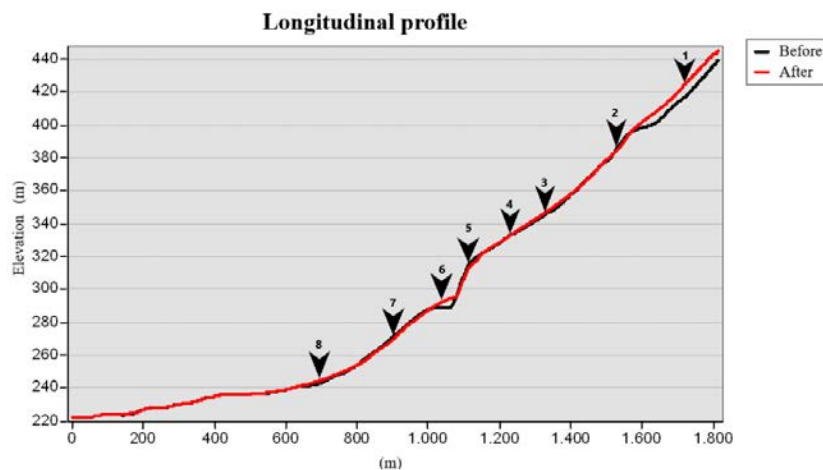


Fig. 3. Debris flow longitudinal profile. After and before Scenario 3.

Fig. 4 shows changes in profiles at 8 cross-sections, whose locations are indicated in Fig. 3, before and after debris-flow occurrence of Scenario 3. The profiles are distributed along the river, perpendicular to the thalweg. Note that the profile is viewed in the upstream direction. Deposition occurred at cross-sections 1, 3, 4, 6 and 8, while

erosion occurred at cross-sections 2, 5 and 7 (Fig. 4). At cross-section 4 the arrow indicates the location of a residence near the channel, demonstrating that the residence is susceptible to debris flow impacts in the future.

The deposition forms a normal pattern, with higher deposition rates upstream, and lower rates further downstream. Besides, the deposition surface is approximately parallel to the horizontal line. The surfaces formed by erosion present a “V” shape.

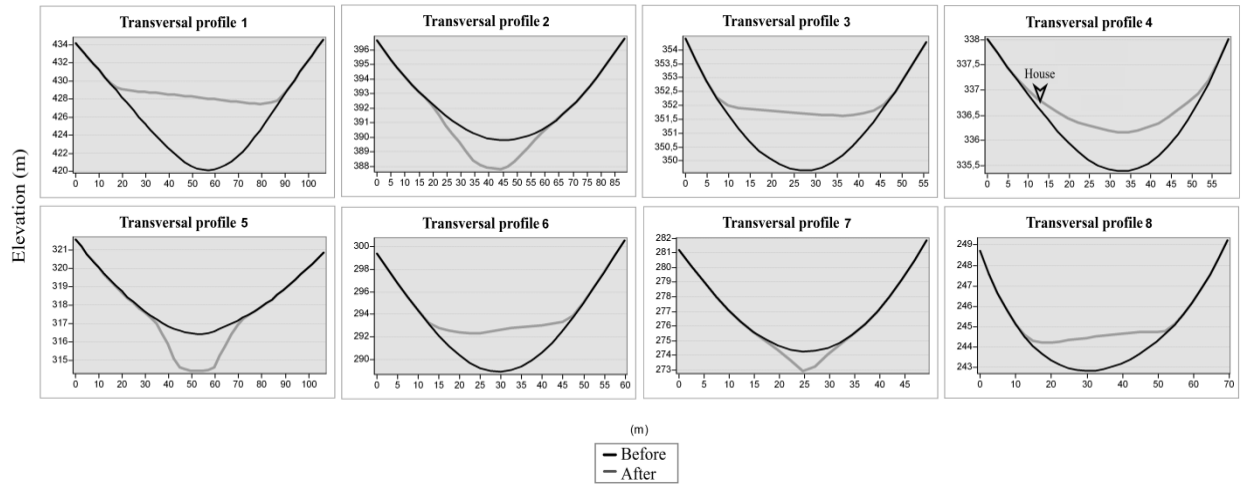


Fig. 4. Transversal sections to debris flow. After and before at the Scenario 3.

Near cross-section 6 there is a confluence (Fig. 2). Fig. 5 demonstrates the erosion and deposition dynamics at the confluence during different time steps. Just after the confluence point, the deposition process is more predominant meanwhile just before the confluence erosion dominates. After reaching the confluence point, the debris flow propagation generated a backwater processes in the direction of the affluent upstream. At the time step 1800 s, the influence area along the affluent stream reached about 100 m. As the debris flow dynamics is very complex at the confluence, more detailed analyses should be numerically done in a future study. Though the simulation results are nor confirmed on field, the local inhabitant should recognize the possibility that at the confluence point a part of debris flow go upstream.

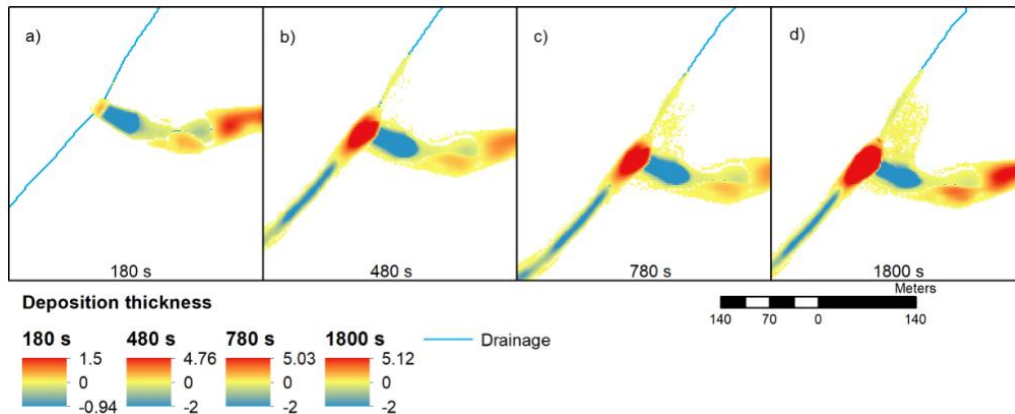


Fig. 5. Detailed results of simulation at the confluence: a) 180 s; b) 480 s; c) 780 s; and d) 1800 s.

In case of the context of the alert system, it is very important to know the speed of the debris flow. In order to observe this speed, the flow propagation features at the different time-steps are demonstrated in Fig. 6. By using each runout map in Fig. 6, the mean speeds of the debris flow through its evolution on time were estimated (Table

3). Though the speed is slightly reduced along the downstream displacement, the reduction rate is not exactly linear to the time or to displacement.

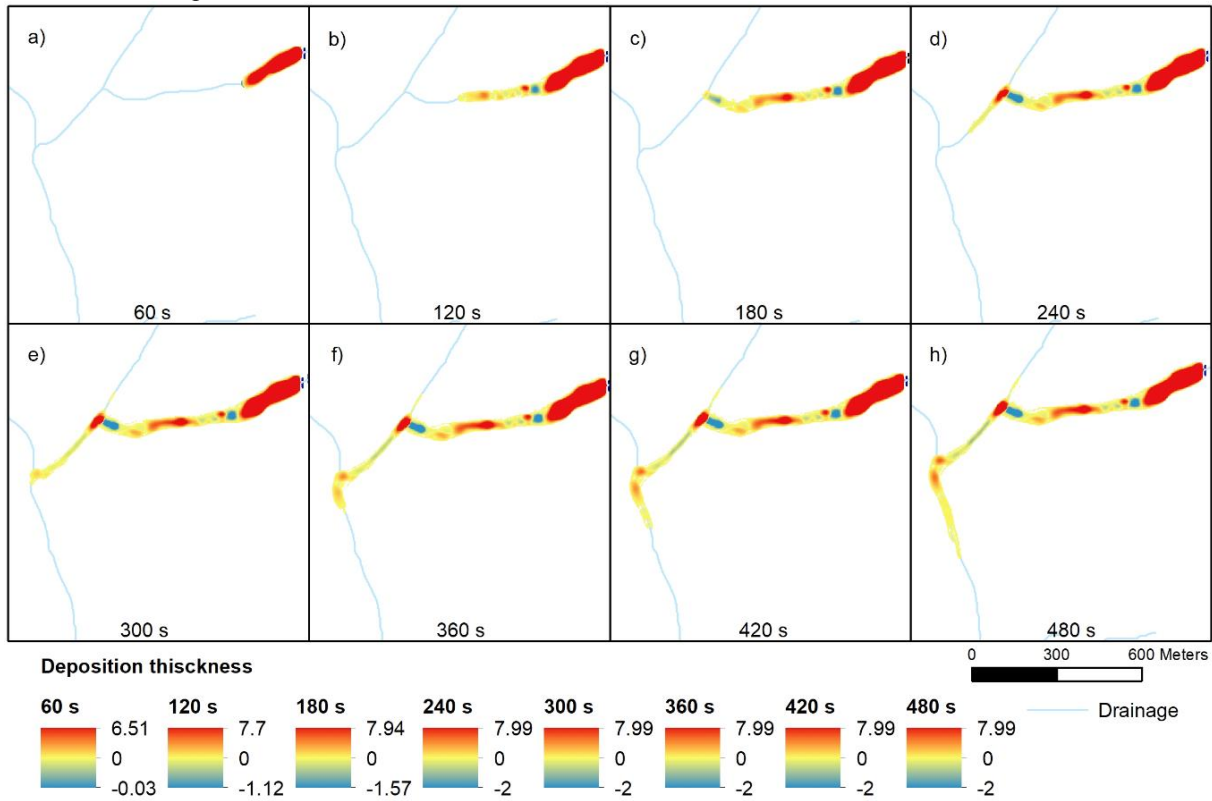


Fig. 6. Temporal evolution of the debris flow: a) 0 s to 60 s; b) 60 s to 120 s; c) 120 s to 180 s; d) 180 s to 240 s; e) 240 s to 300 s; f) 300 s to 360 s; g) 360 s to 420 s; and h) 420 s to 480 s.

Table 3. Displacement and speed variations of the debris flow over the time.

Time interval (s)	L (m) (horizontal variation)	ΔS (m) (vertical variation)	Displacement (m)	Mean speed (m/s)
0 - 60	242.69	42.91	246.45	4.11
60 - 120	306.92	59.29	312.59	5.21
120 - 180	198.36	47.32	203.93	3.40
180 - 240	190.4	24.25	191.94	3.20
240 - 300	151.03	20.16	152.37	2.54
300 - 360	91.87	4.44	91.98	1.53
360 - 420	79.85	3.13	79.91	1.33
420 - 480	144.27	2.39	144.29	2.40

4. Conclusions

Computational modeling of the debris flows is an important tool to make hazard maps of this phenomenon and also to comprehend its occurrence mechanism. This importance should be emphasized in countries which have rare occurrence of debris flow and suffer from large damages due to this phenomenon. Therefore, the present study applied the Kanako-2D model to a small basin, the majority of which is covered by forest and characterized by the mountains environment in the municipality of Alto Feliz, southern Brazil.

By changing the debris volume and consequently the hydrograph (peak discharge and peak time), three scenarios were simulated. Regardless of the scenarios, the hazard maps generated with all scenarios show that the debris flow would destroy an existing rural house. Though the localities of erosion and deposition in the stretch of the debris flow are similar among the scenarios, their magnitudes (depths) of erosion and deposition were different among them. In general, at each cross-section, the most pronounced local of erosion or deposition is almost always the thalweg location.

Numerical modeling research allowed the recognition of debris flow dynamics at confluence as well as flow speed. Though the comparison between numerical simulation results and field observation of actual occurrences is essential for debris-flows studies, only computational investigation also has its own importance because the phenomenon is comparative rare. In this sense, the Kanako-2D model remains very useful especially in Brazil.

Acknowledgments

The authors thank the CNPq and the PROPESQ-UFRGS for providing scholarships and the CAPES-ANA (Programa Pró-Recursos Hídricos, chamada 16/2017, Finance Code 001) for a scientific project which supported the execution of the present study. Special thanks are due to one anonymous reviewer to significantly develop the present study.

References

- Flores, C.A., Pötter, R.O., Fasolo, P.J.; Hasenack, H., and Weber, E., 2007, Levantamento semidetalhado de solos: Região da Serra Gaúcha - Rio Grande do Sul, Porto Alegre: UFRGS/Embrapa Clima Temperado.
- Jacob, M., and Hungr, O. (eds.), 2005, Debris-flow hazards and related phenomena, Berlin: Springer-Verlag, 739p.
- Kobiyama, M., Michel, R.D.L., Paixão, M.A., and Michel, G.P., 2018, Small fish-pond design for debris flow disaster measure with Kanako-2D, In: Proceedings of INTERPRAEVENT 2018, held in Toyama, Japan, 1-4 October, 2018. p.264-269.
- Kobiyama, M., Michel, G.P., and Goerl, R.F., 2019, Proposal of debris flow disasters management in Brazil based on historical and legal aspects, *International Journal of Erosion Control Engineering*, (in press).
- Michel, G.P., 2015, Estimativa da profundidade do solo e seu efeito na modelagem de escorregamentos, Porto Alegre: Universidade Federal do Rio Grande do Sul, PhD dissertation, 164 p.
- Michel, G.P., and Kobiyama, M., 2016, Mapeamento de áreas susceptíveis a fluxos de detritos por meio de modelagem computacional, In: Ladwig, N.I. and Schwalm, H. (Org.) Planejamento e gestão territorial: Hidrografia e sustentabilidade. Florianópolis: Insular, p.71-89.
- Nakatani, K., 2008, GUI Equipped user friendly debris flow simulator “Kanako 2D (Ver.2.02)” handy manual, Kyoto: Laboratory of Erosion Control/Kyoto University, 44p.
- Nakakita, K., Wada, T., Satofuka, Y., and Mizuyama, T., 2008, Development of “Kanako 2D (Ver.2.00),” a user-friendly one- and two-dimensional debris flow simulator equipped with a graphical user interface, *International Journal of Erosion Control Engineering*, v.1, n.2, p.62-72.
- Okuda, S., Suwa, H., Okunishi, K., Nakano, K., and Yokoyama, K., 1977, Synthetic observation on debris flow. Part 3. Observation at valley Kamikamihorizawa of Mt. Yakedake in 1976, *Annuals DPRI*, v.20B-1, p.237-263.
- Paixão, M.A., and Kobiyama, M., 2017, Efeito do tamanho dos sedimentos sobre a área atingida por fluxos de detritos: Estudo de caso da bacia do arroio Böni, Serra Gaúcha, *Ciência e Natura*, v.39, n.2, p.299-307.
- Rickenmann, D., 1999, Empirical Relationships for Debris Flows, *Natural Hazards*, v.19, n.1, p.47-77.
- Takahashi, T., 2007, *Debris Flow: Mechanics, Prediction and Countermeasures*, Leiden: Taylor and Francis/ Balkema, 448p.
- Takahashi, T., and Nakagawa, H., 1991, Prediction of stony debris flow induced by severe rainfall, *Journal of the Japan Society of Erosion Control Engineering*, v.44, n.3, p.12-19. (in Japanese with English abstract).
- Viero, A.C., and Silva, D.R.A. (org.), 2010, *Geodiversidade do estado do Rio Grande do Sul*, Porto Alegre: CPRM.
- Whipple, K.X., 1992, Predicting debris-flow runout and deposition on fans: the importance of the flow hydrograph, *IAHS Publication*, v.209, p.337-345.

Numerical analysis on the behavior of debris flows and impact force on check dams

Kwangwoo Lee^{a,*}, Sangseom Jeong^b, Hyunki Kim^a

^a Advanced Infrastructure Research Team, Korea Railroad Research Institute, 176, Cheoldobangmulgwan-ro, Uiwang-si, 16105, Korea

^b Department of Civil and Environmental Eng., Yonsei University, 50, Yonsei-ro, Seodaemun-gu, Seoul, 03722, Korea

Abstract

Debris flows with high velocity may have enormous impact forces on obstacles in their flow paths. It is necessary to install protective structures, such as check dams that slow down or interrupt the debris flows from affecting adjacent infrastructure and residential communities. The impact forces of debris flows on check dams are an essential factor in hazard mitigation evaluation and design of check dams. To accurately evaluate the impact force of debris flows on the check dams, a numerical model that takes into account the fluid-solid interactions is needed. In this study, the large deformation analysis, which is the coupled Eulerian-Lagrangian (CEL) technique, was applied to evaluate the behavior of the debris flows and the impact force on the check dams, simultaneously. The numerical method was validated using published data on laboratory experiments. A series of numerical analyses were performed to evaluate the significant influencing factor on the dynamic impact force of debris flows, such as the flow velocity and the thickness of sedimentation. Based on the results of these analyses, it was observed that the dynamic impact force of debris flows on the check dams is significantly dependent on the velocity of the debris flows. In addition, the debris flows are gradually accumulated towards the top of the check dams after the debris flows first contacts the check dams, thereby the position of the dynamic load acting on the check dams is increased.

Keywords: Debris flows; Check dams; Impact force; Large deformation analysis

1. Introduction

Debris flows are one of the most catastrophic natural hazards because of the high economic losses and human casualties that they cause. Debris flows with a large mass and high velocity can apply tremendous impact forces on an obstacle in its flow path. The magnitude of debris-flows impact depends primarily on the velocity, height of debris flows and the sediment. In order to protect humans and infrastructures against debris flows, two different types of debris-flow models, process and impact model, are necessary (Proske et al., 2011). The initiation of debris flows can occur through a variety of processes as they descend the watershed by entraining sediment, mobilization of separate landslides and high concentration of surface water flow (Godt and Coe, 2007). As shown in Fig. 1, to reduce the immediate risk of both hazard and vulnerability, two different types of debris-flow models which are process model and impact model are necessary.

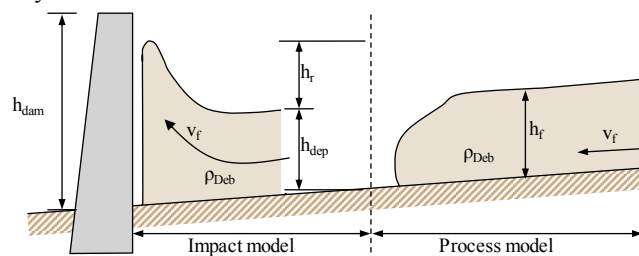


Fig. 1. Combination of process model and impact model for debris flows

* Corresponding author e-mail address: kwoo.alpha@gmail.com

In this study, large deformation analysis for debris flows was conducted by using coupled Eulerian- Lagrangian (CEL) technique in ABAQUS. This rigorous FE analysis method can indicate both, the potential influence of debris flows and the estimation of dynamic impact force on check dams. This method could be used to hazard mitigation evaluation and the design of the check dams.

2. Numerical method

2.1. Coupled Eulerian and Lagrangian method

The coupled Eulerian-Lagrangian (CEL) analysis, one of the large deformation analysis method, combines the advantages of the Eulerian and Lagrangian methods to model large-deformation problems in geomechanics (Qiu et al., 2011). There is no limit to the range or on terrain, so it is suitable for evaluating the movement of debris flows at high velocity. In Lagrangian analysis, the nodes of the Lagrangian mesh move together with the material. The main advantage of a Lagrangian formulation is that the interface between the two parts is precisely defined and traced. However, large deformations within the target region will lead to hopeless mesh tangling in a Lagrangian reference frame. In Eulerian analysis, a Eulerian reference mesh which remains undistorted is required to trace the motion of the material in the Eulerian domain. The materials can move freely through the Eulerian mesh. The Eulerian reference frame prevents the mesh distortion on the target. However, loses the precise interface description provided by the Lagrangian formulation. The coupled Eulerian-Lagrangian (CEL) method captured the advantage of the Lagrangian and Eulerian methods. A significant benefit of the coupled Eulerian-Lagrangian method is that there is no requirement to generate a conforming mesh for the Eulerian region. The general contact algorithm does not require contact between the Eulerian elements and Lagrangian elements. The Lagrangian part can move through the Eulerian region without resistance until the Eulerian element filled with the material (Qiu et al., 2011). Numerical stability is guaranteed by the introduction of the critical time interval size that is approximately proportional to the smallest element length and inversely proportional to the square root of the elastic stiffness of the material. A convergence study of the combined effects of mesh density and velocity is needed into a well-designed verification for each particular problem to achieve a suitable compromise between accuracy in the quasistatic response and computational efficiency (Wang et al., 2015). High-quality results require a fine mesh due to the difficulties in modeling interfaces between materials. The movement of the material properties within the Eulerian region can be determined as the volume ratio, the Eulerian volume fraction (EVF) of each element. Each Eulerian element has represented a percentage, which the portion of that element filled with a material. As shown in Fig. 2, when the Eulerian elements filled with a material, EVF is 1, whereas when there is no material in part, EVF is 0.

0.0	0.0	0.0	0.0	0.0	0.0
0.0	0.32	0.91	0.91	0.32	0.0
0.0	0.91	1.0	1.0	0.91	0.0
0.0	0.91	1.0	1.0	0.91	0.0
0.0	0.32	0.91	0.91	0.32	0.0
0.0	0.0	0.0	0.0	0.0	0.0

Fig. 2. Eulerian volume fraction (EVF)

2.2. Geometry and boundary condition

The analysis of the debris flows is composed of the soil layer, bedrock, structures which are dams or building, and void area. Lagrangian elements are applied to relatively hard bedrock components and structures. Eulerian elements

are applied to the erodible soil layer and the debris flows. A typical 3D coupled Eulerian-Lagrangian (CEL) analysis geometry for the dynamic impact force on check dams is depicted in Fig. 3. The initial debris-flow volume was 3 m^3 ($3 \text{ m} \times 1 \text{ m} \times 1 \text{ m}$) and 35° in inclination angle, and the transportation area was defined as 10 m in length and 20° in inclination angle. The deposition area was set to 5 m to confirm the arrival velocity and shape of the debris flows. The thickness of bedrock was defined as 0.5 m . The dams were modeled as 1.5 m high, 1 m wide, and 0.5 m thick. This interpretation consists of the Lagrangian part and Eulerian part. The Eulerian area is divided into three parts: the initial debris flows, the erodible soil layer, and the void layer where the debris flows. The check dams and bedrock were considered as a Lagrangian domain. The boundary conditions of the check dams are defined only on the bottom, and the displacements in all directions are fixed. The only loading condition considered in this analysis was gravity in the z-direction.

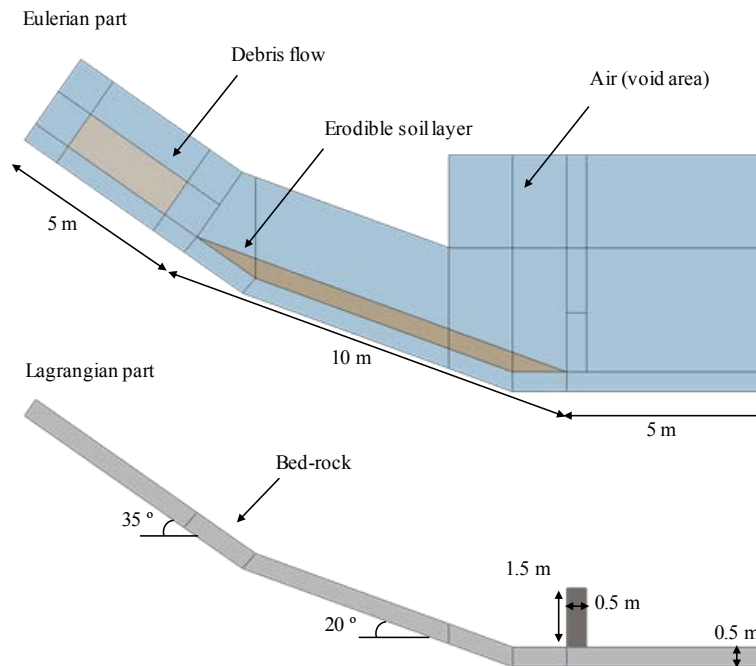


Fig. 3. Idealized numerical model for impact on debris-flows barrier

3. Validation of numerical technique

3.1. Numerical modeling

The applicability of the coupled Eulerian-Lagrangian (CEL) method to the analysis of debris flows was verified in comparison with laboratory tests. Some researcher conducted flume experiment to investigate the behavior of debris flows and impact forces acting on check dams. To verify the proposed method for the debris flows analysis with dynamic impact force, the laboratory tests (Moriguchi et al., 2009) was chosen. The analytical results were compared with the velocity and shape of the debris flows as well as the impact force measured by the load cell. The physical laboratory modeling of debris flows was performed at different slopes and measure the impact force exerted by this material on a fixed rigid wall. Fig. 4 shows a schematic view of the flume with a sand box and impact force measuring instrument. The surface of the flume was coated with the same sand to provide surface friction. The flume was designed with a length of 1.8 m and a width of 0.3 m , and the slope was designed to be adjustable from 45° to 65° . In this study, 45° , 55° , 60° and 65° experiments were selected for validation. The geometry of the analysis is depicted in Fig. 5. The Flume and measurement instrument were modeled using Lagrangian elements and the initial volume of

debris and are modeled using Euler elements. In this analysis, only gravity in the z-direction is defined as the only loading condition. The dry sand is suddenly released at $t = 0$ s, and then it slides down the slope hitting the rigid wall. Boundary conditions were set on the floor space to fix all displacements in the x, y, and z directions and for the size space to fix only displacements in the x, and y directions. The mesh of the debris flows and flume domain consists of 8-noded Eulerian brick elements (EC3D8R) and 8-noded Lagrangian brick elements (C3D8R), respectively. The mesh dimensions of both the Lagrangian element and the Eulerian element were set to $0.01 \times 0.01 \times 0.01$ m.

The constitutive behavior of sand is modeled with an elastic-perfectly plastic model with Mohr-Coulomb failure criterion. The properties required for the analysis used the values given in the reference paper (Moriguchi et al. (2009)). In order to the analysis, the necessary properties were estimated based on the proposed property values, and the values required for the analysis were estimated based on the given values.

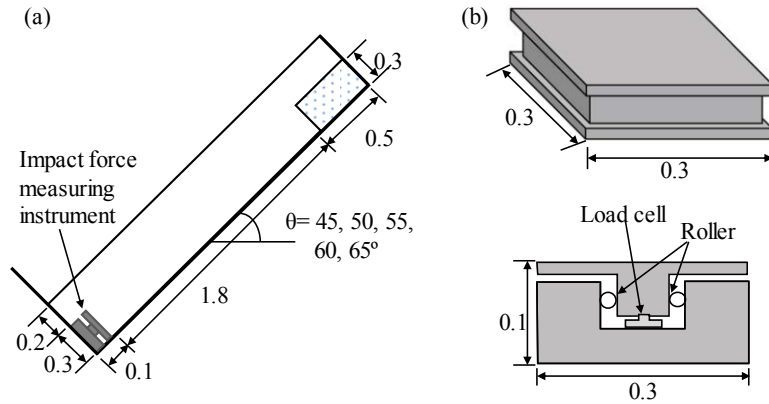


Fig. 4. (a) Schematic illustration of slope model; (b) impact force measuring instrument (Moriguchi et al., 2009)

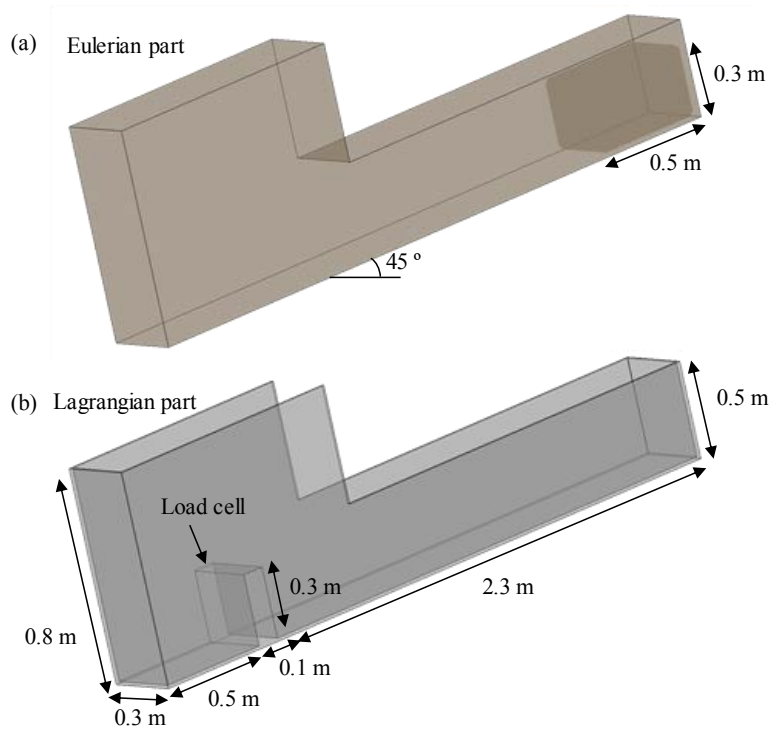


Fig. 5. Geometry used in 3D FE analysis (Moriguchi et al., 2009)

3.2. Compare with laboratory and analysis results

Fig. 6 shows the experimentally and numerically observed free surface configurations on a flume inclined at $\theta = 45^\circ$ at different time instants ($T = 0.4$ sec, $T = 0.8$ sec, $T = 1.2$ sec, $T = 1.6$ sec). To make the free surface more visible, a red outline was drawn on the surface of the sand at each snapshot. The last two snapshots show the debris flows overtopping the wall. The debris-flow accelerates and elongates while descending the slope. When debris flows reach the load cell, the debris flows are deviated upwards, parallel to the wall, with the formation of a bulge, and it subsequently decelerates. The simulated results capture the experimentally observed flow behavior which flows velocity and shape of debris flows.

In the CEL analysis, the total impact force is the value of the contact force at the contact surface between the Lagrangian part and Eulerian part. The total impact force was calculated as the sum of the normal forces on the structure ($0.3 \text{ m} \times 0.3 \text{ m}$). Fig.7 compares the experimental and numerical results with the time-varying impact force. In an experiment with a slope angle of 60, the impact force on the measuring instrument increases rapidly to the maximum value of 0.42 kN at $t = 0.85\text{s}$, and after the peak, the force decreases to the quasi-static value which is the maximum value of the experiment with the slope angle of 45 degrees. The simulated results firmly agree with the laboratory test results, which indicates that the applied method is appropriate for simulating debris-flow impact force on check dams.

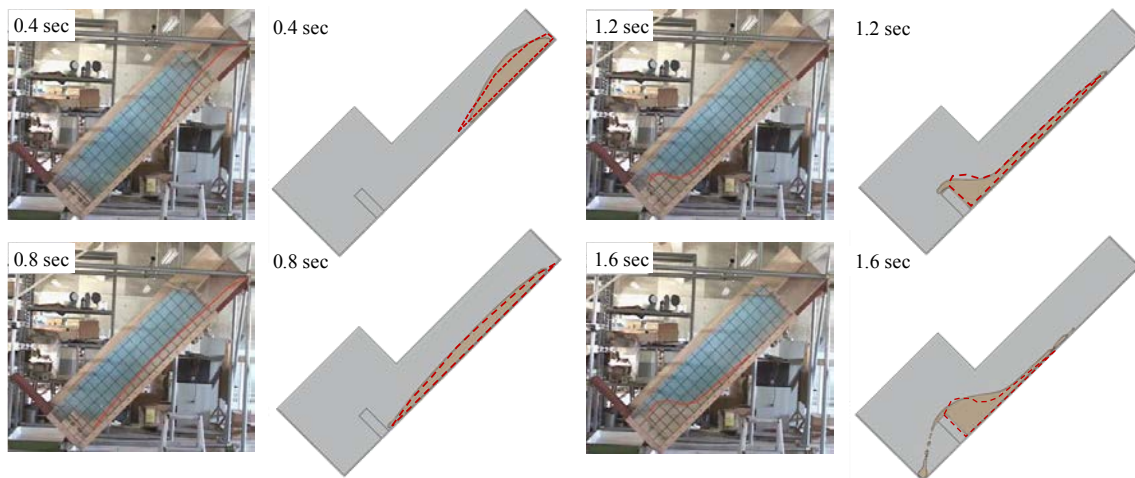


Fig. 6. Analysis results of the height and shape of the debris flows (Moriguchi et al., 2009)

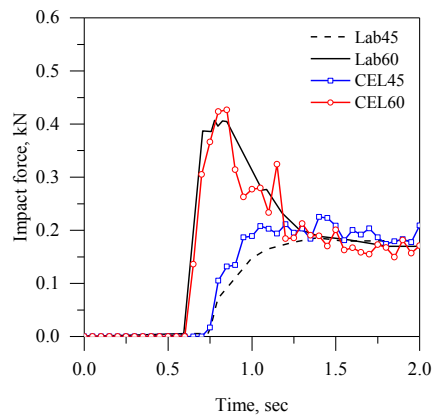


Fig. 7. Comparison between laboratory experiments and simulated impact force

4. Numerical analysis

4.1. Velocity

The impact force exerted by a debris flows on a fixed structure depends on the debris-flow height and velocity, as well as on the density of the flowing mixture. In this study, a series of analysis was conducted to confirm the effect of the velocity of debris flows on the impact force acting on the check dams. The inclination angle of slope was determined as 10, 15, 20, 25°. Fig. 8 presents the results of the shape and velocity vector of debris flows in the analysis. The debris flows from the initial part flowed down onto the ground layer. Fig.9 shows the time histories of impact force for each of the four inclination angle of slope. It can be seen that the peak and residual force are similar for the angle of slopes 10 ° and 15 °. However, in the angle of slopes 20 ° and 25 °, maximum forces are generated by debris flows and then converge to residual values. As a result, the increase in the magnitude of the debris flows reaching the check dams is causing more damage.

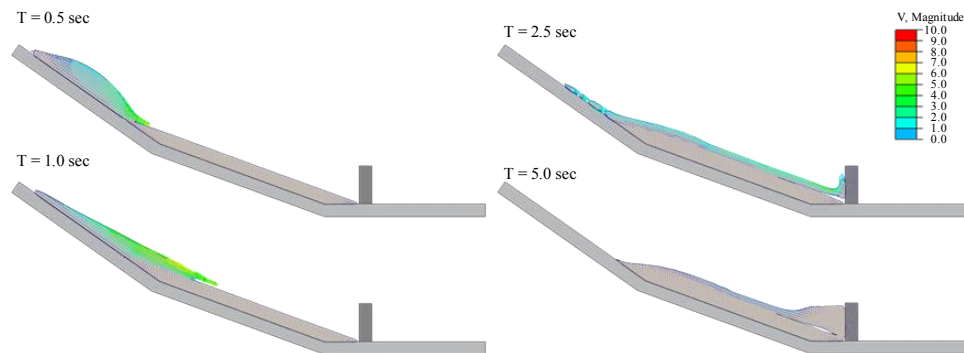


Fig. 8. Velocity vectors for debris-flow impact without entrainment

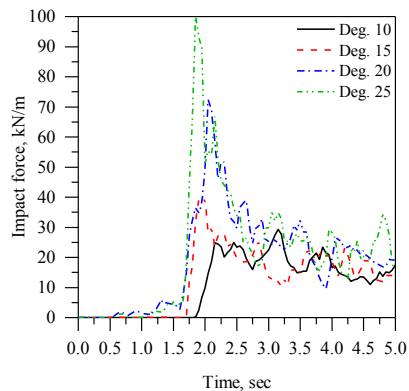


Fig. 9. Time history of impact force for various inclination angle

4.2. Thickness of sedimentation

In a closed-type check dams, erodible sediment is moved down by sediment transport and accumulates behind the barrier. The debris flows have a static behavior similar to that of the deposited debris flows and imparts a static pressure normal to the barrier after the initial dynamic impact. The total impact force consists of a dynamic impact force from the moving debris flows and a static force from the deposited debris-flow material acting as earth pressure due to the gravity. The deposited materials behind a barrier play an essential role in the dynamic load transfer process (Tiberghien

et al. 2007). As shown in Fig. 10 (a), to confirm the influence of the deposited debris, a series of numerical analysis were carried out with sediment thicknesses of 0.0 m, 0.5 m, 1.0 m, and 1.5 m. Fig. 10 (b) shows result of numerical analysis. The debris-flow momentum was delivered to the check dams during the first impact, and immediately forming a deposited static zone directly behind the barrier. The remaining debris flows over the deposited material and collides with the check dams at a higher elevation after a run-up process. This result agrees with the experimental results obtained by Tiberghien et al. (2007). Therefore, various loading conditions should be considered to verify the stability of check dams.

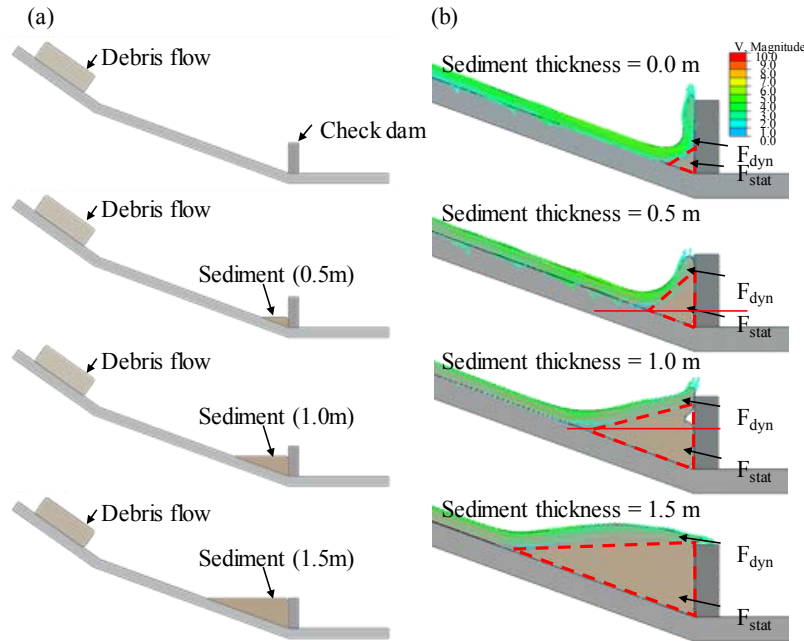


Fig. 10. (a) Case study of sediment thickness; (b) Depositional shape of debris flows

5. Conclusions

In this study, the impact force of debris flows on check dams was evaluated by using Coupled Eulerian-Lagrangian (CEL) take into account the fluid-solid interactions. A series of rigorous numerical analyses were performed to examine the significant influencing factor on the dynamic impact force of debris flows. The results of this investigation are summarized below.

1) The primary objective of this study was to analyzed the behavior of debris flows with impact force on check dams using the large deformation FE analysis technique of a coupled Eulerian-Lagrangian (CEL) technique. The analytical method was validated using published data on laboratory experiments (Moriguchi et al. 2009). This study clearly shows that the analysis result is in good agreements with the chosen laboratory data.

2) Based on the analysis results, it was observed that the dynamic impact force of debris flows on check dams is significantly dependent on the inclination angle and the thickness of sedimentation. In the analysis taking into account the effects of slope, the peak and residual force are similar for the angle of slopes 10° and 15° , but in the angle of slopes 20° and 25° , maximum forces are generated by debris flows and then converge to residual values.

3) The debris flows are progressively impounded upstream of the check dams after the first contact of the debris flows to the check dams. The debris-flow momentum was transferred to the check dams during the first impact, instantly forming a deposited static zone immediately behind the barrier. The remaining debris flows then rode over the deposited material to hit the check dams at a higher elevation after a run-up process. Therefore, various loading conditions should be considered to verify the stability of check dams.

Acknowledgements

This research was supported by Basic Science Research Program through the National Research Foundation of Korea (NRF) funded by the Ministry of Education (No. 2018R1A6A1A08025348), and Main Project of Korea Railroad Research Institute (No. PK1902A2).

References

- Abaqus, 2013, Abaqus user's and theory manuals. Version 6.13. Rhode Island: Hibbitt, Karlsson and Sorensen, Inc.
- Godt, J. W., and Coe, J. A., 2007, Alpine debris flows triggered by a 28 July 1999 thunderstorm in the central Front Range, Colorado: *Geomorphology* v. 84(1-2), p. 80-97.
- Moriguchi, S., Borja, R.I., Yashima, A., and Sawada, K., 2009, Estimating the impact force generated by granular flow on a rigid obstruction: *Acta Geotechnica*, v. 4, p. 57-71.
- Proske, D., Suda, J., and Hübl, J., 2011, Debris flows impact estimation for breakers: *Georisk*. V. 5, p. 143-55.
- Qiu, G., Henke, S., and Grabe, J., 2011, Application of a Coupled Eulerian-Lagrangian Approach on Geomechanical Problems Involving Large Deformations: *Computers and Geotechnics*, v. 38, p. 30-39.
- Tiberghien, D., Laigle, D., Naaim, M., Thibert, E., and Ousset, F., 2007, Experimental investigations of interaction between mudflow and an obstacle: *Debris-flow hazards mitigation: mechanics, prediction and assessment*, Millpress, Rotterdam.
- Wang, D., Bienen, B., Nazem, M., Tian, Y., Zheng, J., Pucker, T., and Randolph, M. F., 2015, Large deformation finite element analyses in geotechnical engineering: *Computers and Geotechnics*, v. 65, p. 104-114.

Impact load estimation on retention structures with the discrete element method

Alessandro Leonardi^{a,*}, Ezio Calcagno^a, Marina Pirulli^a

^a *Politecnico di Torino, Corso Duca degli Abruzzi 24, 10121 Turin, Italy*

Abstract

The design of countermeasures such as barriers and filter dams needs an accurate estimation of the impact load. However, debris flows typically contain poorly sorted grains, whose size can span several orders of magnitude. Large grains can induce impulsive loads on a barrier, and potentially clog the openings designed to induce self-cleaning after an event. The current modeling techniques, mostly based on continuum-based depth-integrated approximations, cannot accurately describe these mechanisms, and analytical approaches often fail to tackle this complexity. In an effort to reproduce a realistic impact load, a sample flow composed of grains is reproduced with a three-dimensional model based on the Discrete Element Method (DEM). The mass impinges upon a barrier with a prescribed velocity. The barrier design is inspired by a monitored dam built on a catchment located in the Italian Alps, which features multiple outlets. The grains can clog the outlets, forming frictional arches. The load pattern on the barrier is analyzed in terms of single-grain impact and of collective behaviors. The impulse transferred by the granular mass to the structure is then used as input for a structural analysis of the barrier through a Finite Element analysis. The results highlight how frictional chains can induce loads that are substantially different from those determined by standard analytical approaches.

Keywords: Debris flow; Discrete element method, Flow-structure interaction; Hazard mitigation

1. Introduction

One of the methods to reduce risk associated with flow-like landslides is the construction of baffles (Law et al., 2015), deflectors (Ng et al., 2017b), or slit dams (Zhou et al., 2018). When installed immediately downstream from a catchment area, barriers are effective in breaking the energy of the flow early on, reducing its erosive power and effectively controlling the volume of large sediments transported. When sediments of different size are present, as is typical in debris flows, the barrier should retain the largest sediments (Piton and Recking, 2016). However, it is often preferable to avoid complete obstruction of the channel, in order to allow the regular flux of small sediments to occur in normal conditions. This is achieved by prescribing one or more outlets in the barrier (Marchelli et al., 2018a), whose size is designed as a function of the dimension of the minimum grain that should be retained.

A more rational evaluation of the impact force is a long-standing problem for the design of retention structures (Hungar and Jakob, 2015). The single cost of an experiment discourages the exploration of multiple geometries or conditions, and small-scale physical modeling suffers from scaling issues (Iverson, 2015). A cost-effective approach is to apply monitoring stations on existing barriers, in order to evaluate their performance, possibly both in vulnerability reduction and in robustness of the barrier design (Kwan et al., 2014).

The test case in exam is the sectional dam shown in Fig. 1(a), located in the municipality of St. Vincent, eastern Italian Alps. It consists of a concrete wall with multiple steel beams protruding from the top. Each beam has an IPE-type section (c), and is equipped with a strain gauge (a,c) to monitor the dam by recording the strain at the base of the steel beams. The dam is hit every summer from multiple stony debris flows, and is designed to retain the coarsest

* Corresponding author e-mail address: alessandro.leonardi@polito.it



Fig 1. Illustration of the sectional dam used as study case, respectively before (a) and after (b) the collapse happened on 20/07/2014; (c) the cross section of the steel beams. The pictures are courtesy of Regione Autonoma Valle d'Aosta.

fraction of the grains. After every major event, the reservoir behind the dam is emptied in order to restore functionality. The dam dramatically collapsed during an event occurred in 2014, see Fig. 1(b). A discussion followed on the actual reason that induced the collapse. When activated by an impact, the sensors typically record compression (negative strain). However, it is not uncommon for sensors to record positive tension. This is puzzling, as it was originally believed that all sensors would only register compression when activated, since they are located on the side of the beam that does not face the flow.

In order to give an interpretation to the signals recorded on site, we use in this work the discrete element method (DEM). We evaluate the type of load exerted on the barrier, assuming the barrier itself is hit by a single surge of monodisperse grains. The output is plugged into a finite-element model (FEM) of the barrier as a time-history of external actions. A dynamic analysis is then performed, studying how the bending moments at the base of the beams evolve. The strain at the base is then compared to the site recordings.

2. Numerical model

The numerical procedure is outlined in Fig. 2(a). The debris flow is modelled with the DEM, which allows to obtain a time-history of load patterns on the barrier. The barrier itself is modelled as an elastic body with a FEM model, where the forces recorded in the DEM simulation are used as a set of external loads. This allows to compute the stress and strain fields on the barrier, and compare them to the data obtained from the monitored dam.

2.1. Discrete load model with DEM

We compute the load on the barrier using a simplified approach, where the debris flow is simulated as a collection of spherical particles of mean diameter $d_f = 0.2$ m. Moreover, the actual material composition is complex, including grains with different size and shape immersed in a liquid (Kaitna et al., 2016; Leonardi et al., 2018).

The debris flows recorded in St. Vincent are frequently multi-surge events. These surges can occur within minutes or separated by few hours. As a consequence, it is common that a second surge impacts the barrier before the first is removed. They impinge on the lowest portion of the barrier with a relatively high speed and belatedly on the upper portion, usually with a lower speed due to the barrier having already reduced the momentum of the flow at that point. In the DEM model, we simplify this scenario by considering only the upper half of the barrier, i.e. only the metal bars plus a portion of the concrete dam, for a total height of $h = 2.5$ m. We simulate only a total width of $w = 3i$, where $i = 2.5d_f = 0.5$ m is the spacing between two beams. We further consider that the particles reach the upper portion of the barrier with a homogeneous speed (Calvetti et al., 2018), see the example of Fig. 2(b). In spite of these assumptions, the model is able to capture many relevant aspects of the problem, as will be apparent in the following chapters.

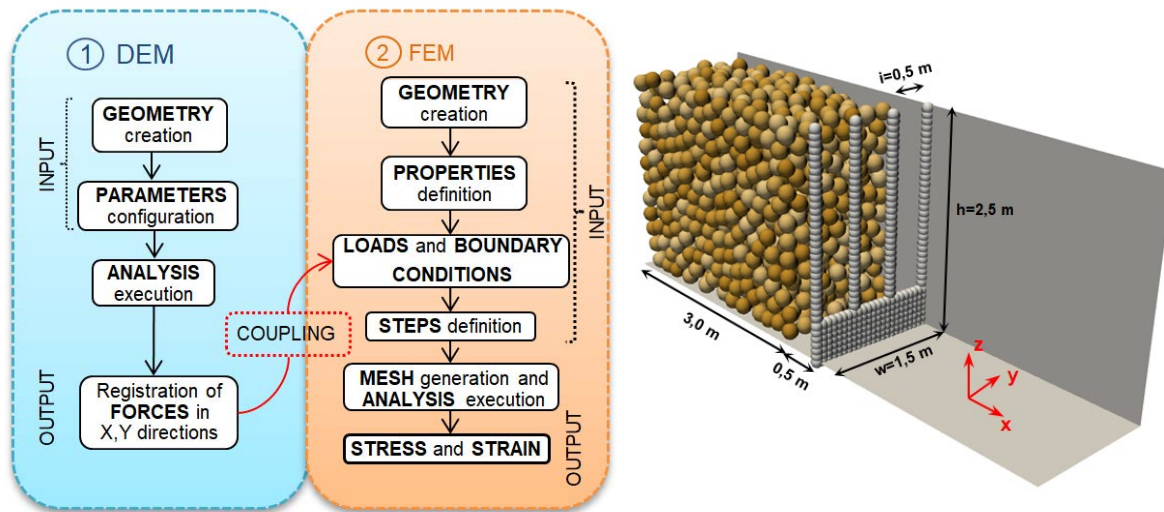


Fig. 2. (a) outline of the DEM-FEM model; (b) initial setup of the DEM simulation, with the discretization of the dam using spherical particles.

The DEM model employed for this study is implemented in the code by Leonardi et al. (2015; 2016). A Herzian contact model is used in the normal direction and the tangential contact model presented in Marchelli et al. (2018b) reproduces frictional effects. The numerical parameters used in this work are collected in Table 1. For their physical and numerical explanation, please refer to Marchelli et al. (2018b). The barrier is represented using an agglomeration of fixed spheres of constant diameter $d_b = 0.135$ m, overlapping by $d_b/2$. This greatly simplifies the computation of contact forces, as the same algorithm managing contact dynamics between the grains can be used to track the interactions with the barrier too.

Table 1. Parameters for the DEM flow model

DEM parameters	Value
Density ρ [kg/m ³]	2630
Diameter d_f [m]	0.2
Young modulus E [Pa]	$1.2 \cdot 10^9$
Poisson ratio ν [-]	0.2
Restitution coefficient ξ [-]	0.8
Tangential damping coefficient α_t [-]	0.5
Friction coefficient μ_s [-]	0.6
Rolling coefficient μ_r [-]	0.07
Mean particle diameter d [m]	0.2

Each of the barrier spheres registers a time-history of forces transmitted by the flow. Three samples of typical records are shown in Fig.3. The force is initially transmitted by quick impulsive loads (type A, red), whose direction is mainly aligned with the channel longitudinal direction, x . However, the grain size is large enough to induce jamming at the outlets. Therefore, immediately after the dynamic phase has finished, the grains jam and the load reduces to the transmission of the grains self-weight. However, the formation of the deposit is not immediately stable, and multiple ruptures and reorganization of the grains are observed for a relatively long period of time. This progressive clogging of the barrier causes a type of load that is semi-permanent (type B, blue), with every contact between barrier and grains transmitting a portion of the deposit weight through a frictional arch. The arches transmit a load both in direction x and in direction y . Therefore, strong force components F_y are registered at this stage. The deposit instabilities cause oscillations of the load, and also additional sharp impulses. Finally, after jamming is complete, some sensors register a final stationary load in both direction, due to the attainment of a stable jamming configuration of the deposit (type C, green).

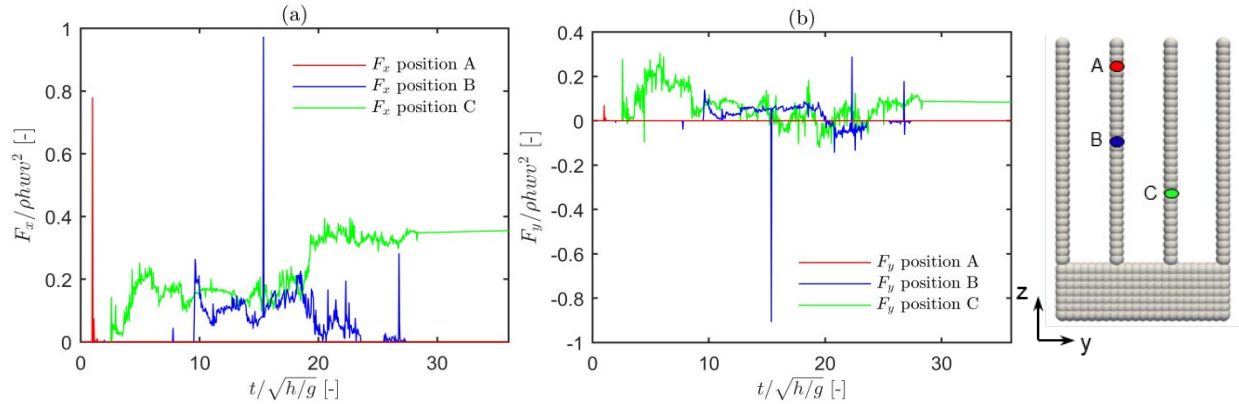


Fig. 3. Three sample loads registered at different locations on the barrier: (a) streamwise component F_x ; (b) transversal component F_y .

2.2. Dynamic analysis of barrier response with a FEM model

The dynamic response of the barrier is obtained by assembling an FEM model (ABAQUS, www.3ds.com). The concrete basement is modelled using 3D brick elements, and the metal bars using 1D beams. The beams, as in the actual barrier, continue inside the basement for 1 m. Along this length, the beams lie embedded within the bricks, i.e. displacement of the beams is limited by the stiffness of the host material (Tabatabaei et al., 2014). Rotational degrees of freedom are instead simply constrained. The beams section is an IPE270, as in St. Vincent. The forces recorded with the DEM using the barrier sensors are given to the FEM model as point loads with a time-history of intensity. Therefore, 30 point loads are active for each beam. The concrete basement is modeled with fixed joint constraints on the base and edges. The material parameters are given in Table 2.

The stress-strain evolution over time is obtained through an explicit dynamic analysis with the central-difference rule. The system is overdamped, with damping factors set in order to reproduce the effects of the surrounding flow. During impact, the beams are surrounded by stony debris, which quickly dissipate the inertial load due to dynamic effects. Every 0.05 s the state of the system is saved for postprocessing.

Table 2. Parameters for the FEM model

FEM parameters	Value	
Materials	Concrete	Steel
Density ρ [kg/m ³]	2500	7850
Young modulus E [Pa]	$3.0 \cdot 10^{10}$	$2.1 \cdot 10^{11}$
Poisson ratio ν [-]	0.15	0.3
Damping factor α [-]	100.0	100.0
Damping factor β [-]	$1.0 \cdot 10^{-8}$	$1.0 \cdot 10^{-8}$

3. Reconstruction of the load patterns

Though the numerical workflow described in the previous section, the reaction in the barrier can be directly linked to specific stages of the interaction. Three instances are described in Fig. 4. In the first row, the stress field on the steel beams is reconstructed, and the beams themselves are depicted at the deformed state, with a displacement magnification of $2.5 \times$. The second row shows the velocity of the particles close to the outlets, which allows to infer the dynamic state of debris mass at the same instant. Finally, the third row shows the in-plane component of the forces transmitted by the flow to the structure at that instant.

The beams have a much higher moment of inertia in direction x , see Fig. 1(c), and therefore exhibit reduced bending when loaded normally to the dam. The moment of inertia resisting bending in direction y is lower, therefore even a small in-plane force induces a significant bending, as can be observed at $t = 0.3$ s and $t = 19.0$ s. The first column in the figure corresponds to the dynamic impact ($t=0.3$ s). At this instant jamming is not complete. There is a diffuse

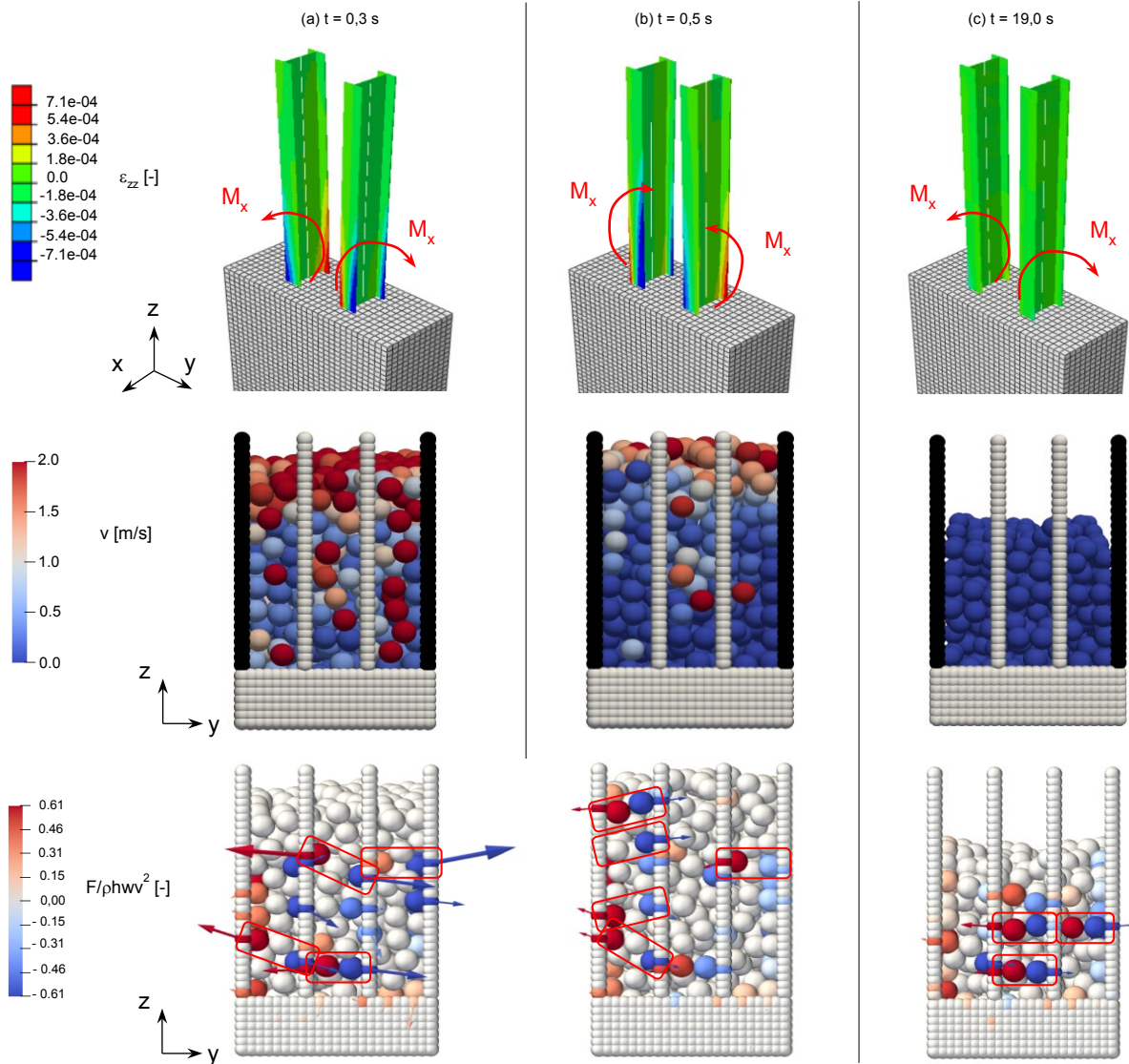


Fig. 4. Schematic of the mechanism of force transmission to be barrier, and corresponding strain field on the beams. A few granular arches are highlighted with red boxes.

outflow of material, but the central outlet already sees the formation of two granular arches that induce diverging loads on the beams (highlighted with red boxes in the figure). Therefore, the bending moments M_x at the base have opposite signs. Note that the bending moments M_y , conversely, are always positive.

On the second column is the interaction at $t = 0.5$ s. At that instant, jamming has completed and the lowest portion of the grains is not moving. The system is however not stable yet, and collapses are still occurring. Specifically, the figure shows that the central outlet is active, while the lateral ones are stable (Marchelli et al., 2018a). Consequently, the lateral outlets have more active arches than the central one (see the multiple red boxes in the figure), and exert a stronger in-plane load to the beams. This leads to a switch of the sign of M_x compared to the previous instant, which induces a converging deformation of the beams. The final, stationary configuration is shown at time $t = 19.0$ s on the third column. Here, the statistical process of particle rearrangement has terminated with strongest loads in the central outlet, overall similar to the one of the first column, and with diverging moments on the beams.

4. Interpretation of the strain signals measured on site

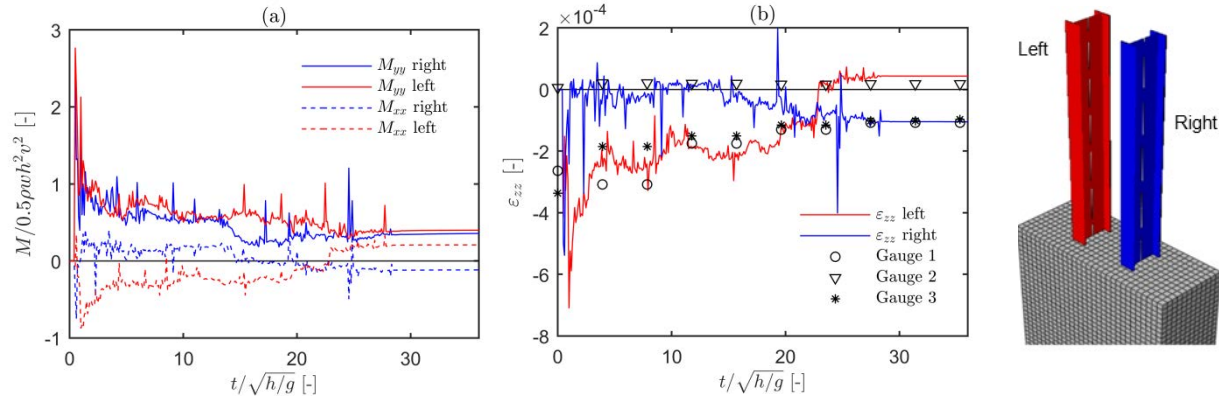


Fig. 5. Time-history of (a) the bending moment registered at the beam junction with the concrete basement, and (b) corresponding strains registered at the location where the strain gauges are installed.

The 3D nature of the barrier-flow interaction determines spurious stresses, which had not been accounted for in the barrier design. This observation provides an interpretation for the counterintuitive stresses recorded on the instrumented dam. Assuming the only actions are the bending moments on x and y , the strain at the instrument location can be estimated by using the simple formula for asymmetric bending

$$\epsilon_{zz} = \frac{M_x}{I_x} d_x + \frac{M_y}{I_y} d_y, \quad (1)$$

where (d_x, d_y) is the distance of the gauges from the section centers, see Fig. 1(c). The recorded moments are shown in Fig. 5(a). The moments in y are always positive and induce a compression (negative) strain. On the other hand, the moments in x do not have a preferential direction, and often switch from positive to negative and vice versa during the simulation. This corresponds to the statistical configuration of the in-plane loads due to the frictional arches, as shown with Fig. 4.

The bending moments in the two directions have the same order of magnitude, however the inertia moment in x is much smaller than the one in y . Therefore, the main factor that determines amplitude and sign of ϵ_{zz} is M_x , rather than M_y . This is confirmed by the FEM computations of ϵ_{zz} , shown in Fig. 5(b). The figure also shows three typical signals taken from the recording at St.Vincent. Notwithstanding the many simplifications adopted in the procedure, the model is able to capture the order of magnitude of the recorded strains. Moreover, it is able to explain the positive components registered by some sensors, e.g. Gauge 2 in Fig. 5(b).

5. Conclusions and outlook

We apply a numerical framework for the estimation of impact forces, and resulting reaction, exerted by a debris flow on a retention barrier. The framework employs the DEM for the simulation of the flow, and for recording the load pattern over the whole barrier. A FEM model processes the recorded load and perform a dynamic analysis of the structure response. The model describes how the flow interacts with the barrier through the formation and ruptures of frictional arches. This determines a type of load in the barrier that has a strong in-plane (transversal) component in addition to the more intuitive component orthogonal to the wall. The results are in excellent agreement with the type of signal recorded on site.

The analysis leads to two prescriptions for the design and monitoring of this type of barrier. Firstly, an effective monitoring system should be designed to give information at two locations on the same section, in order to infer the actual load from strain measurement. Most importantly, the stiffness of the structural element should always be prescribed as symmetrical, in order to cope with the in-plane component of the load. Assuming the load on the barrier to be orthogonal, as suggested by multiple codes and guidelines, might lead do grossly under designed barriers.

In this work, a simple one-way coupling has been implemented for the computation of forces. However, the large deformations of the beams probably alter the jamming mechanisms (Marchelli and De Biagi, 2018). To assess the feedback mechanism, a two-way coupling will be implemented in the future.

References

- Calvetti, F., di Prisco, C. G., and Vairaktaris, E., 2015, Impact of dry granular masses on rigid barriers. *IOP Conference Series: Earth and Environmental Science*, v. 26, no. 1, 012036, doi: 10.1007/s11440-016-0434-z.
- Hungr, O., and Jakob, M., 2005, *Debris-flow Hazards and Related Phenomena*, Springer-Verlag Berlin Heidelberg, doi: 10.1007/b138657.
- Iverson, R. M., 2015, Scaling and design of landslide and debris-flow experiments: *Geomorphology*, v. 244, p. 9–20, doi: 10.1016/j.geomorph.2015.02.033.
- Kaitna, R., Palucis, M. C., Yohannes, B., Hill, K. M., and Dietrich, W. E., 2016, Effects of coarse grain size distribution and fine particle content on pore fluid pressure and shear behavior in experimental debris flows: *Journal of Geophysical Research: Earth Surface*, v. 121, no. 2, p. 415–441, doi: 10.1002/2015JF003725.
- Kwan, J. S. H., Chan, S. L., Cheuk, J. C. Y., and Koo, R. C. H., 2014, A case study on an open hillside landslide impacting on a flexible rockfall barrier at Jordan Valley, Hong Kong: *Landslides*, v. 11, no. 6, p. 1037–1050, doi: 10.1007/s10346-013-0461-x.
- Law, P. R. H., Choi, C. E., and Ng, W. W. C., 2015, Discrete-element investigation of influence of granular debris flow baffles on rigid barrier impact: *Canadian Geotechnical Journal*, v. 7, p. 1–7, doi: 10.1139/cgj-2014-0394.
- Leonardi, A., Cabrera, M., Wittel, F. K., Kaitna, R., Mendoza, M., Wu, W., and Herrmann, H. J., 2015, Granular-front formation in free-surface flow of concentrated suspensions: *Physical Review E - Statistical, Nonlinear, and Soft Matter Physics*, v. 92, no. 5, 052204, doi: 10.1103/PhysRevE.92.052204.
- Leonardi, A., Wittel, F. K., Mendoza, M., Vetter, R., and Herrmann, H. J., 2016, Particle-Fluid-Structure Interaction for Debris Flow Impact on Flexible Barriers: *Computer-Aided Civil and Infrastructure Engineering*, v. 31, no. 5, p. 323–333, doi: 10.1111/mice.12165.
- Leonardi, A., Pokrajac, D., Roman, F., Zanello, F., and Armenio, V., 2018, Surface and subsurface contributions to the build-up of forces on bed particles: *Journal of Fluid Mechanics*, v. 851, p. 558–572, doi: 10.1017/jfm.2018.522.
- Marchelli, M., Leonardi, A., and Pirulli, M., 2018a, The clogging mechanism of debris-flow material in the multiple outlets of sectional barriers: *Geingegneria Ambientale e Mineraria*, v. 153, no. 1, p. 78–85.
- Marchelli, M., Leonardi, A., and Pirulli, M., 2018b, On the efficiency of slit dams in retaining granular flows: *Géotechnique*, doi: 10.1680/jgeot.18.p.044 (in press).
- Marchelli, M., and De Biagi, V., 2018, Dynamic effects induced by the impact of debris flows on protection barriers: *International Journal of Protective Structures*, v. 10, no. 1, p. 1–12, doi: 10.1177/2041419618798378.
- Ng, C. W. W., Choi, C. E., Goodwin, G. R., and Cheung, W. W., 2017, Interaction between dry granular flow and deflectors: *Landslides*, v. 14 no. 4, p. 1375–1387, doi: 10.1007/s10346-016-0794-3.
- Pirulli, M., Barbero, M., Marchelli, M., and Scavia, C., 2017, The failure of the Stava Valley tailings dams (Northern Italy): numerical analysis of the flow dynamics and rheological properties: *Geoenvironmental Disasters*, v. 4, no. 1, p. 1–15, doi: 10.1186/s40677-016-0066-5.
- Piton, G., and Recking, A., 2016, Design of Sediment Traps with Open Check Dams. I: Hydraulic and Deposition Processes: *Journal of Hydraulic Engineering*, v. 142, no. 2, 04015045, doi: 10.1061/(ASCE)HY.1943-7900.0001048.
- Tabatabaei, S. A., Lomov, S. V., and Verpoest, I., 2014, Assessment of embedded element technique in meso-FE modelling of fibre reinforced composites: *Composite Structures*, v. 107, p. 436–446, doi: 10.1016/j.compstruct.2013.08.020.
- Zhou, G. G. D., Hu, H. S., Song, D., Zhao, T., and Chen, X. Q., 2018, Experimental study on the regulation function of slit dam against debris flows: *Landslides*, v. 16, no. 1, p. 75–90, doi: 10.1007/s10346-018-1065-2.

Debris-flow deposition: effects of fluid viscosity and grain size

Shuai Li^{a,*}, Gordon G. D. Zhou^a, Xiaoqing Chen^a, Dongri Song^a

^a Key Laboratory of Mountain Hazards and Earth Surface Process, Institute of Mountain Hazards and Environment, Chinese Academy of Sciences, No.9 Section 4, South RenMin Road, Chengdu 610041, China

Abstract

Debris flows in mountainous regions are of great concern because they present a serious threat to the residents and infrastructures in downstream areas as a result of their long runout distances. However, the mechanisms of debris-flow runout are still unclear because of many factors influencing debris-flow mobility. This study focuses on two major factors, namely, particle size and slurry viscosities. A series of experimental model tests were conducted in a rectangular inclined flume connected to a final horizontal plain. Results reveal that the debris-flow mobility is significantly influenced by the slurry viscosities. The runout distance initially increases and then decreases as the slurry viscosities increase. Also, runout distance for debris flows contain large particle sizes is longer than that of debris flows contain small particle sizes. The depositional widths are almost unchanged in the experimental test, which suggests that the debris flows are constrained by the fixed channel boundaries. The results of this study can improve the understanding the behavior and the deposition features of debris flows.

Keywords: Debris flow; Flume experiments; Runout distance; Fluid viscosity; Grain size

1. Introduction

Debris flows are reported to destroy infrastructures and surrounding environment and threaten the local residents in mountainous areas (D'Agostino et al. 2013; Kim and Paik 2015). Given that the dynamics processes of debris flows are difficult to predict (Iverson, 1997), as an alternative, debris-flow deposit was used to infer debris-flow mechanisms. Thus, the debris-flow deposit is critical to enhance the mitigation of debris flows and to protect downstream facilities (Iverson et al. 2010; Shu et al. 2015).

Flume experiments are widely adopted in the development of debris-flow research, as reproducible experiments can be carried out with specific boundary conditions, relatively cheaply and quickly. Quantitative flume modelling studies have been conducted to predict debris-flow runout distance. These researches were mainly focused on topography (i.e., the length, width and slope; e.g., Hürlimann et al., 2008; D'Agostino et al., 2010; Scheidl and Rickenmann, 2010), volume of mass (e.g., Iverson et al., 1998; Berti and Simoni, 2007; Zhou et al. 2016), and sediment composition (e.g., Major and Iverson, 1999; Hürlimann et al., 2015; Haas et al., 2015). However, the effect of grain sizes and viscosities on debris-flow deposit morphology was less investigated, although they have a profound effect on debris-flow dynamics and runout distance. Haas et al. (2015) reported that sediment composition is a key variable that influenced the runout distance, deposition area, levee height, lobe height, and lobe width of the deposited sediments. Although debris-flow deposits have been studied for many years, the deposition mechanisms and morphology are still poorly understood.

Therefore, an improved understanding of the factors control deposit morphology is essential for significant progress in deposition mechanisms of debris flows. This work aims to address this need by undertaking laboratory experiments exploring this phenomenon. Here, a series of flume tests were carried out to discern the effects of particle sizes and interstitial fluid viscosities on the deposit length and width.

* Corresponding author e-mail address: lishuai@imde.ac.cn

2. Experimental Method

2.1. Flume modelling

The laboratory experiments were conducted in a flume 0.30 m wide and 0.35 m deep, with a flow travel distance of 5 m over a fixed roughness bed on an inclined angle of 30° to the horizontal (Figure 1). The flume slope of 30° was chosen to study the flow of realistic debris flows, since most of the debris flows with typical slope angles between 20°-45° (Hungri et al. 2001), and steep enough for the mixtures to flow down. A tank (1.0 m long, 0.3 m wide and 0.8 m deep) was installed at the head of the channel. The tank was fitted with a vertical locked gate which contains the mixtures in a wedge-shaped space. The gate was opened in a direction perpendicular to the inclined bottom of the flume. The flume bed and horizontal run-out fan were roughed by gluing glass beads (2 mm in diameter) to the surface. Debris-flow kinematics was captured using cameras (SONY FDR-AX40, 1440×1080 pixels, 25 fps) installed on crossbeams over the channel, side and frontage of channel, and top of deposit fan.

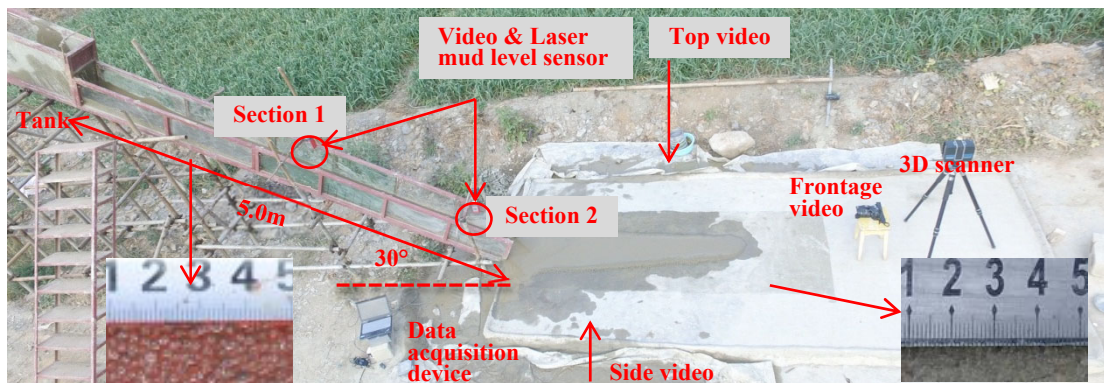


Fig. 1. Schematic diagram of the experimental setup.

The interstitial fluid was designed with mixture of water and sediments of less than 1.0 mm. The sediments were sampled from the natural deposition fans of Jiangjia Gully. Figure 2 shows the grain size distribution (GSD) of the sediments (< 1.0 mm). Viscosity was varied through adjusting the sediments content in the debris-flow experiments. Rheological tests were performed with the roughened concentric cylinder system of an Anton Paar Physica MCR301 rheometer. In order to eliminate the interference of particle shape on the debris-flow deposits, spherical glass beads with 2 mm and 4 mm in diameter were used as granular material. The test program is summarized in Table 1. The concentration of sediments (<1 mm) was ignored when we calculate the solid concentration ($C_s = 0.5$, refers to debris flow samples prepared before the experiment). Here, we choose the sediment <1 mm as part of the fluid phase while consider the particles large than 2 mm as solid phrase. The standard for distinguishing solid and liquid phases is a controversial topic. The conclusions reached by various scholars are also different, for example, 0.025mm (Yang et al., 2014) and 0.0625mm (Iverson, 2014). There is no generally accepted standard at present. The reason why we do this is based on the consideration of solid-liquid boundary particle size according to Wang et al. (2001).

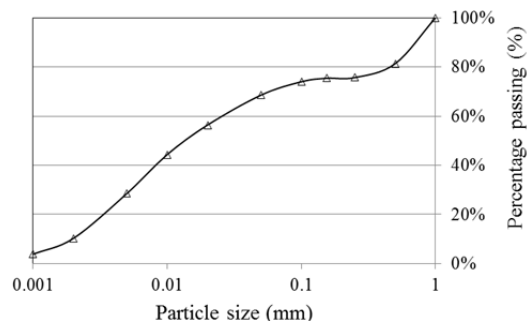


Fig. 2. Cumulative grain-size distribution (GSD) of the particle (<1.0mm).

Table 1. Experimental tests program.

Test ID	Interstitial fluid viscosity μ (Pa·s)	glass bead diameter d (mm)	Solid fraction C_s	Debris-flow density ($\times 10^3$ kg/m ³)
1	0.0042	2	0.5	1781.152
2	0.0045	2	0.5	1794.310
3	0.0047	2	0.5	1803.597
4	0.0060	2	0.5	1813.332
5	0.0066	2	0.5	1823.548
6	0.0068	2	0.5	1839.852
7	0.0075	2	0.5	1883.251
8	0.0081	2	0.5	1919.882
9	0.0218	2	0.5	1962.512
10	0.0289	2	0.5	2012.748
11	0.1780	2	0.5	2072.824
12	0.3808	2	0.5	2145.945
13	0.0041	4	0.5	1781.152
14	0.0046	4	0.5	1803.597
15	0.0061	4	0.5	1823.548
16	0.0067	4	0.5	1851.437
17	0.0071	4	0.5	1883.251
18	0.0079	4	0.5	1919.882
18	0.0216	4	0.5	1962.512
20	0.0255	4	0.5	2012.748
21	0.1797	4	0.5	2072.824
22	0.3814	4	0.5	2145.945

2.2. Debris flow scaling

A comparison of dimensionless numbers was used to provide a quantitative analysis of debris-flow scaling relationships. There are three important stresses that govern the motion of a debris flow, specifically inertial, frictional, and viscous stresses (Iverson 1997; Iverson and Denlinger 2001; Parsons et al. 2001; Hsu et al. 2008; Zhou and Ng 2010). Inertial forces arise from short-term collisions between solid grains, frictional forces are associated to enduring contacts between grains, and viscous forces are controlled by viscosity of the pore fluid (slurry) and relative shearing between the solid and fluid phases (Stancanelli et al. 2015). The relative importance and dominance between these forces are characterized by the Bagnold number N_{Bag} , Savage number N_{Sav} , and Friction number N_{Fric} . The N_{Bag} defines the ratio of inertial to viscous forces and is given as follows:

$$N_{\text{Bag}} = \frac{C_s \rho_s \delta^2 \dot{\gamma}}{(1 - C_s) \mu} \quad (1)$$

where δ is the characteristic grain size of the sediments in the debris flow; ρ_s is density of the solids (2750 kg/m³, Zhou and Ng 2010); μ is the interstitial fluid viscosity; C_s is the volumetric solid fraction, and $\dot{\gamma}$ is the shear rate and it can be approximately estimated by:

$$\dot{\gamma} = \frac{v}{h} \quad (2)$$

The N_{Sav} is the ratio of grain inertial to contact frictional forces and is given as follows:

$$N_{\text{Sav}} = \frac{\rho_s \delta^2 \dot{\gamma}^2}{(\rho_s - \rho_f) g h \tan \phi} \quad (3)$$

where ϕ is the friction angle between grains (30° for the granular materials, Zhou and Ng 2010); and ρ_f is the density of the fluid (assumed to be 1000 kg/m^3).

The ratio of grain-contact to fluid viscous stresses is defined as the Friction number, N_{Fric} :

$$N_{\text{Fric}} = \frac{C_s (\rho_s - \rho_f) gh \tan \phi}{(1 - C_s) \dot{\gamma} \mu} \quad (4)$$

These dimensionless numbers enable comparisons of the relative importance of the aforementioned stresses at different scales and link experimental observations with physical stresses (Haas et al. 2015; Iverson 2015).

Table 2 illustrates the dimensionless numbers of debris-flow experiments in this study. Additionally, Table 3 shows the dimensionless parameters in experimental debris flows of different scales and recorded in nature. This includes a comparison between the values obtained from experiments of Haas et al. (2015), which were conducted at a miniature scale (2 m flume), the small-scale experimental values from this study (5 m flume), the large-scale experimental values from the USGS flume (90 m flume; Iverson, 1997), and values from typical of natural debris flows (Haas et al., 2015). The values of this study are generally within the range of values expected for experimental and natural debris flows.

Table 2. Dimensionless parameters of present debris-flow experiments.

solids density kg/m ³	solid fraction	fluid density kg/m ³	characteristic grain size m	flow height m	shear rate	fluid viscosity pa s	friction angle	Bagnold Number	Savage Number	Friction Number
2500	0.5	1062.30	0.002	0.052	48.08	0.00417	0.52	115.24	0.05	2111.09
2500	0.5	1088.62	0.002	0.048	52.08	0.00451	0.52	115.56	0.07	1634.56
2500	0.5	1107.19	0.002	0.048	62.50	0.00468	0.52	133.61	0.10	1295.12
2500	0.5	1126.66	0.002	0.045	68.89	0.00601	0.52	114.60	0.14	845.26
2500	0.5	1147.10	0.002	0.044	70.45	0.00658	0.52	107.05	0.15	727.13
2500	0.5	1179.70	0.002	0.042	71.43	0.00678	0.52	105.37	0.16	648.62
2500	0.5	1266.50	0.002	0.04	72.50	0.00751	0.52	96.48	0.19	512.92
2500	0.5	1339.76	0.002	0.041	68.29	0.00806	0.52	84.75	0.17	489.60
2500	0.5	1425.02	0.002	0.04	72.50	0.02176	0.52	33.32	0.22	154.38
2500	0.5	1525.50	0.002	0.041	68.29	0.02894	0.52	23.60	0.21	114.52
2500	0.5	1645.65	0.002	0.048	54.17	0.17801	0.52	3.04	0.13	24.09
2500	0.5	1791.89	0.002	0.064	31.25	0.38080	0.52	0.82	0.04	21.57
2500	0.5	1062.30	0.004	0.049	69.39	0.00411	0.52	674.92	0.48	1398.29
2500	0.5	1107.19	0.004	0.048	68.75	0.00462	0.52	595.69	0.50	1193.04
2500	0.5	1147.10	0.004	0.043	81.40	0.00612	0.52	531.96	0.80	661.40
2500	0.5	1202.87	0.004	0.042	78.57	0.00672	0.52	467.67	0.80	584.37
2500	0.5	1266.50	0.004	0.038	78.95	0.00715	0.52	441.77	0.94	470.43
2500	0.5	1339.76	0.004	0.039	79.49	0.00792	0.52	401.30	0.99	406.95
2500	0.5	1425.02	0.004	0.038	78.95	0.02157	0.52	146.37	1.08	135.83
2500	0.5	1525.50	0.004	0.04	77.50	0.02546	0.52	121.76	1.09	111.89
2500	0.5	1645.65	0.004	0.049	53.06	0.17968	0.52	11.81	0.47	24.87
2500	0.5	1791.89	0.004	0.064	28.13	0.38136	0.52	2.95	0.12	23.93
2500	0.5	1062.30	0.002	0.048	68.75	0.00421	0.52	163.30	0.12	1350.36
2500	0.5	1147.10	0.002	0.041	78.05	0.00620	0.52	125.84	0.19	648.99
2500	0.5	1266.50	0.002	0.039	84.62	0.00748	0.52	113.05	0.26	430.22
2500	0.5	1425.02	0.002	0.038	86.84	0.02016	0.52	43.08	0.33	132.17
2500	0.5	1525.50	0.002	0.041	78.05	0.02458	0.52	31.75	0.27	117.95
2500	0.5	1645.65	0.002	0.051	54.90	0.17810	0.52	3.08	0.12	25.24

Table 3. Dimensionless parameters of small-scale, large-scale and natural debris flows.

Dimensionless number	Small-scale flume (This study)	Very small-scale (Haas <i>et al.</i> 2015)	USGS Large-scale (Iverson, 1997)	Typical natural debris flows (Haas <i>et al.</i> 2015)
N_{Bag}	0.8-675	37-1589	400	$1-10^8$
N_{Sav}	0.5-1.1	0.17-2.25	0.20	$10^{-7}-1$
N_{Fric}	21-2112	141-2760	2000	$1-10^5$

3. Results

3.1. Deposit Morphology

The debris-flow deposit morphology was assessed using measurements taken during the experiments, including length and width data. Observations were also made associated to the debris-flow deposit shapes. There was, however, considerable variation in deposit shapes (Figure 3). It demonstrates the presence of lateral levees in the majority of the debris-flow deposits, formed by the shouldering apart of the coarse front by the saturated debris-flow tail. However, the high-viscosity (e.g. 0.3808 Pa·s) debris-flow deposits appeared to lack distinct grain-size segregation and lateral levees. This is due to a change in the rheology of the flow as viscosity varied.

The authors did not measure the rheology of debris flows in the deposit fan, and therefore, we can only speculate about the processes that caused deposition in present experiments. However, observations of the different deposit morphology, suggest that deposition in most of our experimental debris flows is mainly influenced by viscosities. Increasing viscosities reduced permeability and diffusivity, preventing pore fluid from escaping the mixture. As a result, we visually observed that debris flow deposits with high viscosities retained excess pore fluid pressure for long times and needed a long time to consolidate.

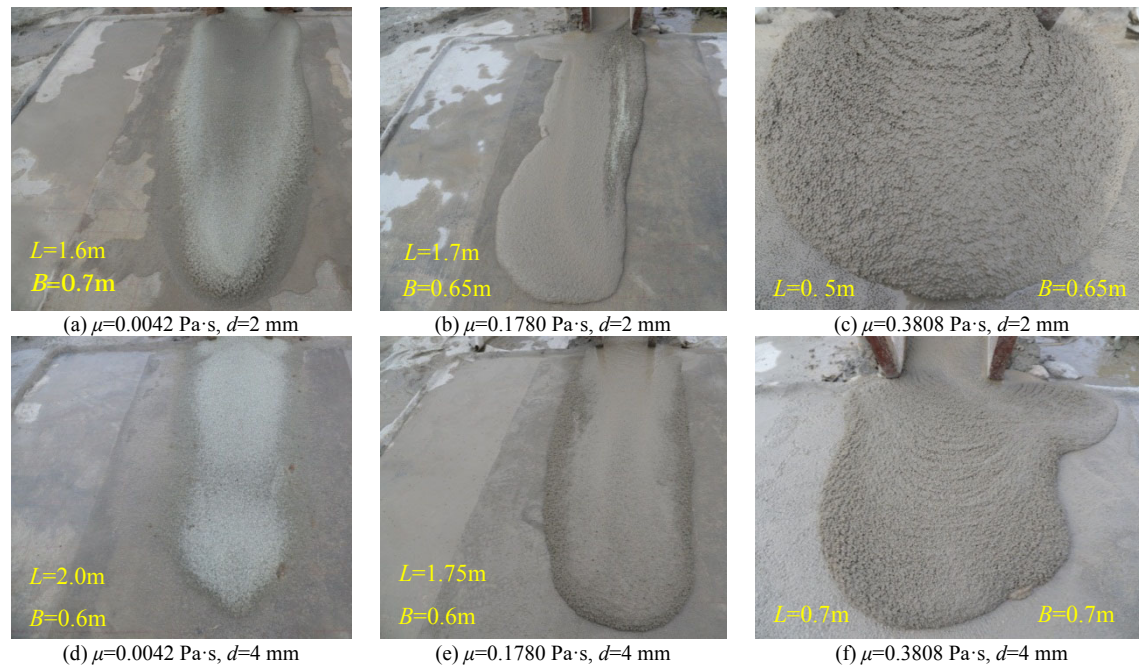


Fig. 3. Examples of debris-flow deposits, showing the varied deposit shapes produced.

For all experiments carried out within different interstitial fluid viscosities (0.0042-0.3808 Pa·s) and solid sizes (2.0 mm and 4.0 mm), the lengths of the debris-flow deposits varied considerably (from 0.5m to 2.0m), whereas less variation in the maximum width of deposits. The average deposits width across all experiments was 0.7 ± 0.1 m. This may suggest that interstitial fluid viscosity and solid size were not the most factors determining the lateral spreading of the deposit, as there was little variation between and within experiment subsets.

3.2. Effects of viscosity on debris-flow deposit

Figure 4 shows the relationships between interstitial fluid viscosity and runout distance, maximum deposit width, and debris-flow velocity, all of which are considered to be key indicators of debris-flow behaviour.

Runout distance was initially increased and then decreased with the increasing of viscosities, within a distance ranging from 0.43 m to 2.50 m. It seems that an optimum interstitial fluid viscosity for debris-flow runout. The results suggest that a small change in debris-flow viscosity can sufficient to alter the rheology of the flow, and hence impact upon debris-flow dynamics. These results are as expected, as viscosity is included in the denominator for calculating Bagnold number and Friction number (Eqs. (1) and (4)). Therefore, viscosities have an obvious influence on debris-flow behaviour, and then affecting the deposit morphology.

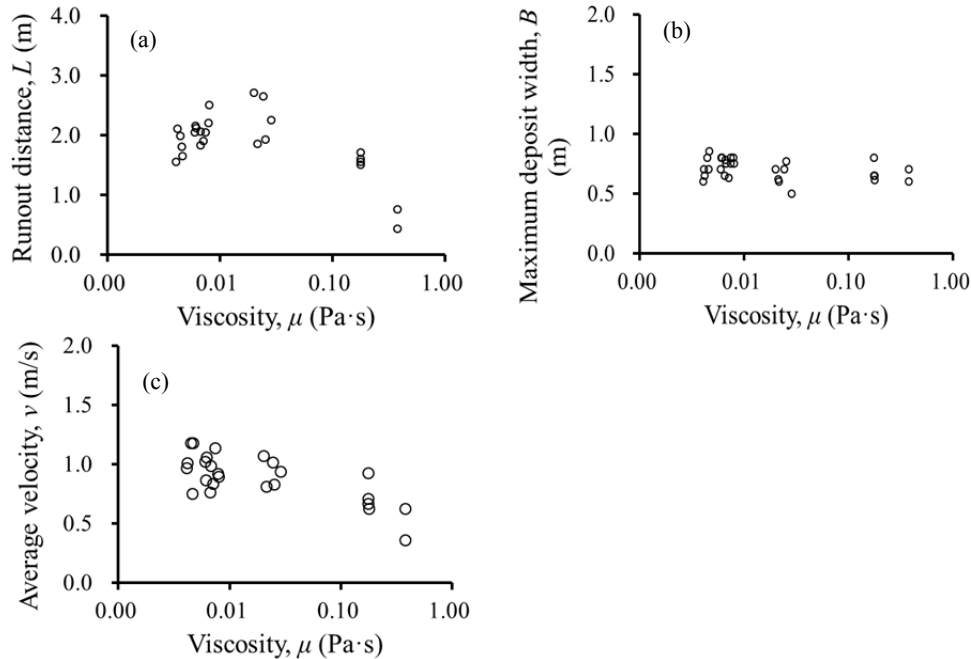


Fig. 4. Relationships between interstitial viscosity and (a) runout distance, (b) maximum deposit width, and (c) average velocity in deposit fan.

The statistically significant relationship of viscosity with maximum deposit width is unambiguous, which reflects the unimportance of viscosity in influencing the lateral spreading of debris-flow deposits. This indicates that channel width may be a control factor on the lateral spreading of debris flows because the flume width kept constant in this study. Velocity was inversely proportional to viscosity, most likely because viscous resistance is increasingly developed in high viscous debris flows.

3.3. Effects of grain size on debris-flow deposit

The effects of grain sizes on debris-flow deposits can be seen in Figure 5. There are some differences in runout distance between the debris-flow experiments within different grain sizes. The debris flows contain 4 mm particles have a longer runout length than debris flows contain 2 mm particles. This is because the resistance-driven force ratio of a solid particle flowing along an inclined slope is dependent on $1/\delta$ (δ is the characteristic particle diameter, d_{50}), which governs flow mobility (Zhou et al. 2016). This implies that larger coarse particles exhibit greater mobility. Furthermore, larger particle sizes led to larger Bagnold number (inertial-viscous ratio) and Savage number (inertial-friction ratio), as particle size is included in the numerator for calculating those two dimensionless numbers. Because of the dimensionless numbers provide insight into the debris-flow dynamics, which highlight larger particle lead to longer runout distance. However, the maximum deposit width varied slightly between the 2 mm particles-contained debris flows and 4 mm particles-contained debris flows.

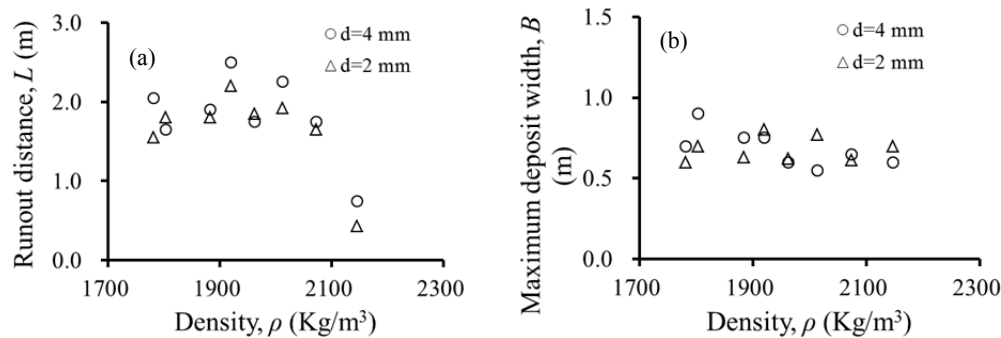


Fig. 5. Relationships between grain size and (a) runout distance and (b) maximum deposit width.

4. Conclusions

This study provides an improved understanding of the deposit morphology of debris flows. More specifically, the effects of fluid viscosities and grain sizes are examined. Key findings can be drawn as follows:

(1) The deposit morphology of debris flows in present experiments exhibited characteristics typical of natural debris flows; these included coarse-grained snouts and lateral margins, saturated tails, and surge flows.

(2) The geometry of debris-flow deposits is strongly controlled by viscosities and grain sizes. Debris-flow runout initially increases and then decreases with an increase in viscosities. There is an optimum interstitial fluid viscosity for maximum runout. An increase in grain sizes enhances runout, most likely because of lower resistance-driven force.

(3) The viscosity and grain size were statistically significant in determining the values for Bagnold, Savage, and Friction numbers, and as these numbers describe the flow dynamics, it is expected that variations in grain size and viscosity result in variations in debris-flow behavior and, as a result of this, in variations in deposit morphology.

Acknowledgements

The research reported in this manuscript is funded by the Chinese Scholarship Council (Grants No. 201804910306), the Science and Technology Service Network Initiative (Grant No. KFJ-STZ-ZDTP-015), the Natural Science Foundation of China (Grants No. 11672318 and 41731283), the CAS “Light of West China” Program (Grant No. Y6R2220220), and the China Postdoctoral Science Foundation (grant 2016M602716).

References

- Berti, M., and Simoni, A., 2007, Prediction of debris flow inundation areas using empirical mobility relationships: *Geomorphology*, v. 90, no.1, p. 144–161. doi:10.1016/j.geomorph.2007.01.014
- D’Agostino, V., Cesca M., Marchi L., 2010, Field and laboratory investigations of runout distances of debris flows in the Dolomites (Eastern Italian Alps): *Geomorphology*, v. 115, no.3, p. 294–304. doi:10.1016/j.geomorph.2009.06.032
- D’Agostino, V., Bettella, F., and Cesca, M., 2013, Basal shear stress of debris flow in the runout phase: *Geomorphology*, v. 201, p. 272–280. doi:10.1016/j.geomorph.2013.07.001p.
- Haas, T., Braat, L., Leuven, J. R., Lokhorst, I. R., and Kleinhans, M. G., 2015, Effects of debris flow composition on runout, depositional mechanisms, and deposit morphology in laboratory experiments: *Journal of Geophysical Research: Earth Surface*, v. 120, p. 1949–1972. doi:10.1002/2015JF003525
- Hsu, L., Dietrich, W.E., and Sklar, L.S., 2008, Experimental study of bedrock erosion by granular flows: *Journal of Geophysical Research: Earth Surface*, v. 113, F02001. doi:10.1029/2007JF000778
- Hungr, O., Evans, S. G., and Hutchinson, I., 2001, A review of the classification of landslides of the flow type: *Environmental & Engineering Geoscience*, v. 7, no.3, p. 221–238. doi:10.2113/gsegeosci.7.3.221
- Hürlimann, M., McArdell, B.W., and Rickli, C., 2015, Field and laboratory analysis of the runout characteristics of hillslope debris flows in Switzerland: *Geomorphology*, v. 232, p. 20–32. doi:10.1016/j.geomorph.2014.11.030
- Hürlimann, M., Rickenmann, D., Medina, V., and Bateman, A., 2008, Evaluation of approaches to calculate debris-flows parameters for hazard assessment: *Engineering Geology*, v. 102, p. 152–163. doi:10.1016/j.enggeo.2008.03.012
- Iverson, R.M., 1997, The physics of debris flows: *Reviews of geophysics* v. 35, no.3, p. 245–296. doi:10.1029/97RG00426
- Iverson, R.M., 2015, Scaling and design of landslide and debris-flow experiments: *Geomorphology*, v. 244, p. 9–20. doi:10.1016/j.geomorph.2015.02.033
- Iverson, R.M., and Denlinger, R.P., 2001, Flow of variably fluidized granular masses across three-dimensional terrain: 1. Coulomb mixture

- theory: *Journal of Geophysical Research: Solid Earth*, v. 101, no.B1, p. 537-552. doi:10.1029/2000JB900329
- Iverson, R. M., Logan, M., LaHusen, R. G., and Berti, M., 2010, The perfect debris flow? Aggregated results from 28 large-scale experiments: *Journal of Geophysical Research: Earth Surface*, v. 115, F03005. doi:10.1029/2009JF001514
- Iverson, R.M., Schilling, S.P., and Vallance, J.W., 1998, Objective delineation of lahar-hazard zones downstream from volcanoes: *Geological Society of American Bulletin*, v. 110, p. 972–984. doi:10.1130/0016-7606(1998)110<0972:ODOLIH>2.3.CO;2
- Kim, Y., and Paik, J., 2015, Depositional characteristics of debris flows in a rectangular channel with an abrupt change in slope: *Journal of Hydro-environment Research*, v. 9, no.3, p. 420-428. doi:10.1016/j.jher.2015.01.001
- Major, J.J., and Iverson, R.M., 1999, Debris-flow deposition: Effects of pore-fluid pressure and friction concentrated at flow margins: *Geological Society of America Bulletin*, v. 111, no.10, p. 1424–1434. doi:10.1130/0016-7606(1999)111<1424:DFDEOP>2.3.CO;2
- Parsons, J.D., Whipple, K.X., and Simoni, A., 2001, Experimental study of the grain-flow, fluid-mud transition in debris flows: *The Journal of Geology*, v. 109, no.4, p. 427-447. doi:10.1086/320798
- Scheidl, C., and Rickenmann, D., 2010, Empirical prediction of debris-flow mobility and deposition on fans: *Earth Surface Processes and Landforms*, v. 35, no.2, p. 157–173. doi:10.1002/esp.1897
- Shu, A. P., Tang, C., Zhang, X., Shao, S. D., and Yang, K., 2015, Deposition morphology of non-homogeneous debris flow and its energy characteristics: *Journal of mountain science* v. 12, no.5, p. 1157-1168. doi:10.1007/s11629-014-3188-9
- Stancanelli, L.M., Lanzoni, S., and Foti, E., 2015, Propagation and deposition of stony debris flows at channel confluences: *Water Resources Research*, v. 51, p. 5100-5116. doi:10.1002/2015WR017116
- Wang Y., Zhan Q., Yan Y. Structure and rheological properties of debris flow: Changsha: Hunan Science and Technology Press, 2001, 5-7.
- Yang H, Wei F, Hu K, and Wang, C., 2014, Determination of the suspension competence of debris flows based on particle size analysis: *International Journal of Sediment Research*, v. 29, no.1, p. 73-81.
- Zhou, G.G.D., and Ng, C.W.W., 2010, Dimensional analysis of natural debris flows: *Canadian Geotechnical Journal*, v. 47, no.7, p. 719-729. doi:10.1139/T09-134
- Zhou, G.G.D., Wright, N. G., Qicheng, S., and Qipeng, C., 2016, Experimental Study on the Mobility of Channelized Granular Mass Flow: *Acta Geologica Sinica (English Edition)*, v. 90, no.3, p. 988-998. doi:10.1111/1755-6724.12739

Regional-scale modelling of liquefaction-induced shallow landslides in unsaturated slopes

Xiang Li^a, Zhichen Song^b, José J. Lizárraga^{a*}, Giuseppe Buscarnera^a

^aNorthwestern University, 633 Clark Street, Evanston 60208, USA

^bCentral South University, Shaoshan South RD, Changsha 410075, China

Abstract

Regional modelling of rainfall-induced landslide triggering poses several technical challenges. These events can originate from a number of hydro-mechanical processes, such as soil-strength degradation, development of localized zones of pore-water pressures, liquefaction, among others. At the same time, the interplay between the spatial variability of topographic attributes, soil properties and transient infiltration can lead to a widespread distribution of distinct slope failure mechanisms across the same landscape. To this aim, this contribution describes a simulation platform for the efficient generation of storm-induced, landslide susceptibility maps in which different slope instability mechanisms can be considered. The framework relies on a vectorized finite element (FE) algorithm that performs fully-coupled simulations of transient infiltration in unsaturated soils, while input and output processing stages are linked to a Geographical Information System. To illustrate the capabilities of the proposed framework, the role of several hydro-mechanical processes on the inception of slope instability are first explored (i.e., coupled flow-deformation analyses, constitutive couplings). After this, results of regional-scale simulations are presented, where it is shown that such considerations can affect the computed spatio-temporal patterns of landslide triggering. Lastly, approaches to incorporate uncertainty of input data into landslide susceptibility zonation by using spatially-correlated random fields are discussed. The proposed framework provides an important step towards the development of robust, physically-based models for regional landslide hazard assessment.

Keywords: flowslides; shallow landslides; infiltration; distributed modelling; spatial uncertainty

1. Introduction

During the last decades, analyses of landslide hazard zonation on urban areas have gained considerable attention (Guzzetti et al., 1999). Indeed, the advent of Geographical Information Systems (GIS), advances in computational resources and remote-sensing technologies have opened new avenues for the development of data-driven, physically-based models of regional landslide forecasting. Such models aim to infer and analyze the factors responsible for slope instabilities across a geological setting by combining principles of hydrology and mechanics (Montgomery and Dietrich, 1994; Baum et al., 2010; Milledge et al., 2014). Among their key challenges is the ability to incorporate advanced features of soil-moisture interactions (i.e. coupled flow soil-deformation processes, inelastic soil response, layered profiles) and uncertainty quantification into a unified framework.

This contribution presents a versatile computational platform for regional analyses of shallow-landslide susceptibility. To provide description of its functionality, a well-documented series of rainfall-induced landslides in volcanic soils is used as a background case study. The paper is structured in three parts, namely, i) a presentation of the model equations; ii) examples of regional-scale landslide triggering zonation; iii) modelling spatial uncertainty of input properties. Details of specific implementation procedures are shown in other references. Here, the aim is to provide an overall description of the current model capabilities and discuss future areas of improvement.

* Corresponding author e-mail address: jjlizarraga@u.northwestern.edu

2. Governing equations

2.1. Field equations

The discussion is focused on shallow unsaturated sloping ground. For an infinite slope, in the absence of variations of body forces, the balance of linear momentum for an incremental loading process is given by:

$$\frac{\partial \dot{\sigma}}{\partial z} = 0, \quad \frac{\partial \dot{\tau}}{\partial z} = 0 \quad (1)$$

where σ and τ represent the total normal and shear stresses, respectively, z is the coordinate in the direction normal to the slope and the upper dot denotes rate terms. Balance of water mass in the presence of constant air pressure leads to:

$$S_r \dot{\varepsilon} + n \frac{\partial S_r}{\partial h} \dot{h} - \frac{\partial}{\partial z} \left(K \frac{\partial h}{\partial z} \right) - \frac{\partial K}{\partial z} \cos \alpha = 0 \quad (2)$$

where S_r is the degree of saturation, ε is the normal strain, n is the porosity, h is the pressure head (negative values representing suction), K is the hydraulic conductivity, and α is the slope angle. The mechanical behaviour of the soil skeleton is here hypothesized to be governed by the effective stress σ' :

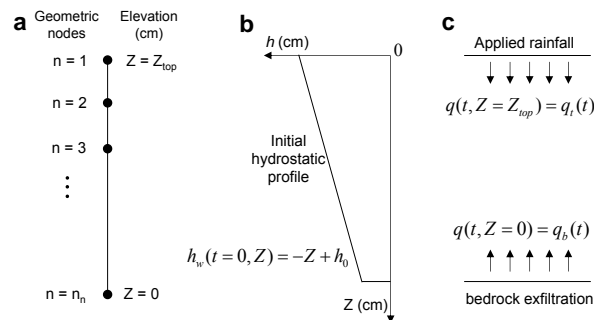
$$\sigma = \sigma' + \chi_k (\gamma_w h) \quad (3)$$

where γ_w is the unit weight of water, and χ_k is an effective stress parameter. A constitutive relationship of the soil skeleton is required to complete the problem formulation. While general inelastic constitutive laws written in incremental form can be used, linear elasticity is used here for illustrative purposes i.e., $\dot{\sigma}' = E \dot{\varepsilon}$, $\dot{\tau} = G \dot{\gamma}$ where E and G are material constants. Additionally, constitutive relationships for the hydraulic variables are required i.e., $S_r = F_w(s)$, $K = F_k(s)$ where $s = \gamma_w h$ is the matric suction, while F_w and F_k are functions known as the *Water Retention Curve* (WRC) and *Hydraulic Conductivity Function* (HCF), respectively. Substituting them into (1) and (2) and imposing appropriate initial and boundary conditions completes the initial boundary-value problem (IBVP) to solve.

3. Analyses of single slopes

3.1. Effects of soil deformability on infiltration analyses

nt
 }-
 ie
 on



F

Consider first the case of constant rainfall rate $q = K$, in which the role of soil deformations is neglected (i.e., rigid soil skeleton). The computed profiles of h are shown in Fig. 2a with continuous lines, while time histories at two different locations are shown in Fig. 2b. As expected, the pressure head increases during the infiltration process, such that at a depth of $z = 4$ m an increment of $\Delta h = 2$ m is computed after 30 hrs.

To analyze the role of soil deformability, a linear elastic model is used to characterize the mechanical behavior of the soil. In this case, the reduction of pressure head driven by the infiltration process causes a decrease of the effective stress, hence promoting swelling and lower values of h when compared against the rigid case. In other words, soils that expand upon wetting hinder the development of high pore pressures during infiltration. Alternatively, soils that compact upon infiltration are detrimental for slope stability, in that they can cause elevated values of h . The role of such effects can be modeled by introducing an additional elastic modulus that controls the amount of compaction upon changes of suction (Wu et al., 2016). This illustrated in Fig 2, where an increment of $\Delta h = 2.5$ m at $z = 4$ m is computed after 30 hrs. Such examples highlight the importance of modelling the role of coupled hydro-mechanical processes into slope stability analyses.

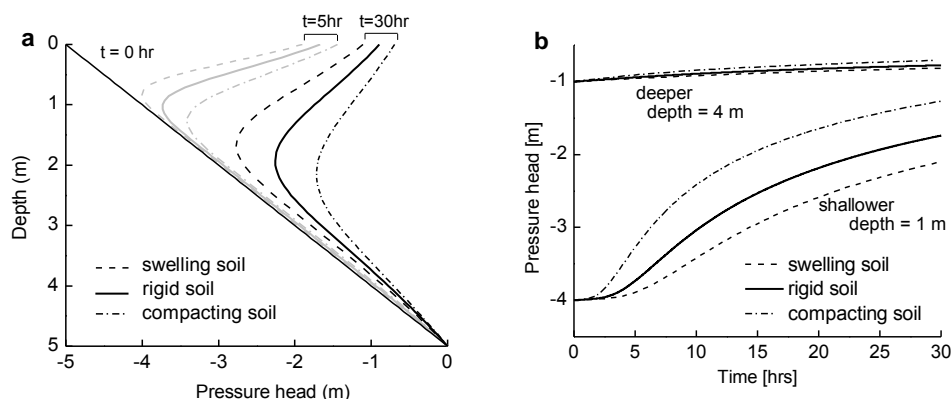


Fig. 2. Comparison of model simulations using different soil deformability properties: (a) profiles and (b) time histories of pressure head.

3.2. Modelling flowslide susceptibility

Debris flows can be the outcome of different mechanisms. For instance, they can originate from marginally stable slopes that start to move when driving forces overcome their soil frictional resistance. As they propagate downslope, they can grow in size by entraining sediments and water (Iverson, 2014).

The inception of soil failure due sharp fluid pressurization can also promote the spontaneous acceleration of soil masses (a phenomenon known as soil liquefaction) even before the entrainment of sediments (Dawson et al., 1998). Indeed, full or partial liquefaction in granular soils is among the key factors responsible for highly mobile landslides, which are referred as flowslides when liquefaction takes place directly at the source (Hungr et al., 2001). Such definition is adopted in this work.

Soil liquefaction is an unstable process that is highly dependent on the hydro-mechanical properties of the material. For example, it is well known that soils that dilate upon shearing are less prone to liquefaction than those that contract (Jefferies and Been, 2015). Similarly, materials that compact upon wetting, such as residual soils, loess and volcanic materials, also display susceptibility to liquefy due to their high capability to retain pore water and their loose internal packing (Picarelli et al., 2008). Thus, defining landslide triggering thresholds that explicitly incorporate such features of soil behavior into slope stability analyses can be useful for enhanced landslide hazard modeling platforms.

A possible approach was proposed by Lizárraga and Buscarnera, 2017. In summary, failure thresholds were derived by analyzing the soil response within an unsaturated shallow slope under two scenarios: uncoupled *drained* response (where failure conditions are referred to as slips) and coupled failures driven by the pressurization of pore water and soil plastic response (referred to as flowslides). A simple rigid-plastic constitutive law was used. Particularly, the response of the soil was modelled with a non-associated flow rule based on logarithmic expressions of yield function and plastic potential, as well as through an exponential hardening law dependent on plastic strains and suction. In this way, conditions that reflect instability (i.e., a mathematical singularity of the equations) were expressed explicitly in terms of soil properties, eventually casting them into the following safety factors (FS):

$$FS_{SLIPS} = \frac{\tan \alpha}{\tan \phi'} \left(1 + \frac{\chi_k s}{\sigma} \right), \quad FS_{FLOWS} = \frac{\tan \alpha}{\tan \phi^{LQ}} \left(1 + \frac{\chi_k s}{\sigma} \right) \chi_w \quad (4)$$

At zero suction, FS_{SLIPS} converges to the classical definition of FS for saturated infinite slopes. The coefficient χ_w is a function of the deformation/wetting properties of the unsaturated soil (Lizárraga and Buscarnera, 2017). Depending on the prevailing hydrological state, overburden stress, and deformability properties, the onset of flowslides can indeed anticipate the initiation of slips throughout the duration of the infiltration process.

The above set of FS were calibrated by using data of unsaturated volcanic soils that were involved in a series of rainfall-induced flowslides (Greco et al., 2010). For instance, Fig. 3a and 3b shows the calibration of hydrologic functions by using Gardner's exponential functions for the WRC and HCF, respectively. A detailed description of the calibration procedures for the mechanical parameters can be found in Lizárraga and Buscarnera, 2017.

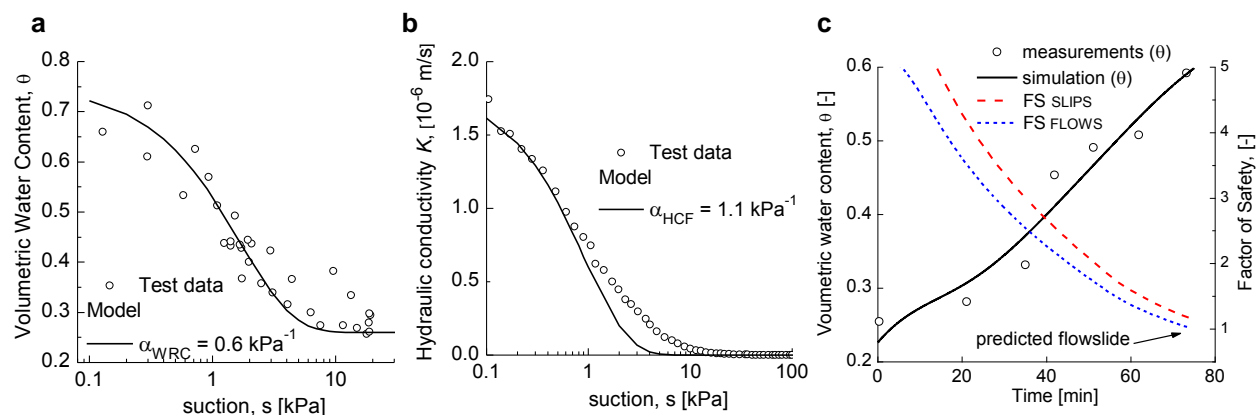


Fig. 3. Calibration of adopted hydrological models. (a) Water Retention Curve; (b) Hydraulic Conductivity Function; (c) Results of numerical simulation. The model captures the variation of volumetric water content and the onset of a flowslide ($FS_{FLOWS} < 1$) by the end of the test.

The performance of the calibrated FS was tested against results of highly-monitored flume tests that displayed different failure mechanisms upon infiltration. For instance, Fig. 3c shows a comparison between values of volumetric water content θ measured during a test (open circles) and FE simulation (thicker, black continuous line). Additionally, the evolution of both sets of FS are plotted. Note that values of FS_{FLOWS} are in close proximity to unity by the end of test (where a flowslide was detected). In other words, the calibrated model was able to satisfactorily reproduce the hydrologic behavior of slope and the onset of a flowslide event. It is worth noting that slips were observed to occur in other flume tests in which the same soil was used, but the material was deposited at different levels of porosity and initial degrees of saturation, thus highlighting the possible coexistence of such mechanisms under field conditions. Further details of the model performance can be found in Lizárraga and Buscarnera, 2017.

4. Regional analyses of landslide susceptibility

The solution of the coupled system of PDE has been implemented into a spatially-distributed modelling framework for regional landslide assessment. Specifically, the FE algorithm has been vectorized such that parallel simulations of coupled infiltration analyses can be performed simultaneously under a wide variety of model conditions. Such simulations are then linked to a Geographical Information System (GIS) platform to generate maps of landslide susceptibility over duration of a storm event. This allows the incorporation of different constitutive models, coupled-flow deformation analyses, layering, and distinct initial and boundary conditions, into a unified computational platform thus providing a versatile tool for regional landslide susceptibility. Details of the implementation procedures can be found in Lizárraga and Buscarnera (2018).

The proposed methodology was applied to a series of landslides that occurred Campania (southern Italy). On May 4-5 of 1998, more than a hundred of shallow landslides occurred over an area of 60 km², after more than 40 hr of continuous rainfall. Most events were characterized as flowslides able to propagate downslope for several km, thus causing extensive damage and loss of life on the surrounding urban centers (Fig. 4). Detailed analyses of the meteorological aspects of the event, geological and geotechnical characteristics of the deposits and field monitoring

studies have been widely documented elsewhere (Cascini et al., 2008; Crosta and Dal Negro, 2003; Guadagno et al., 2005).

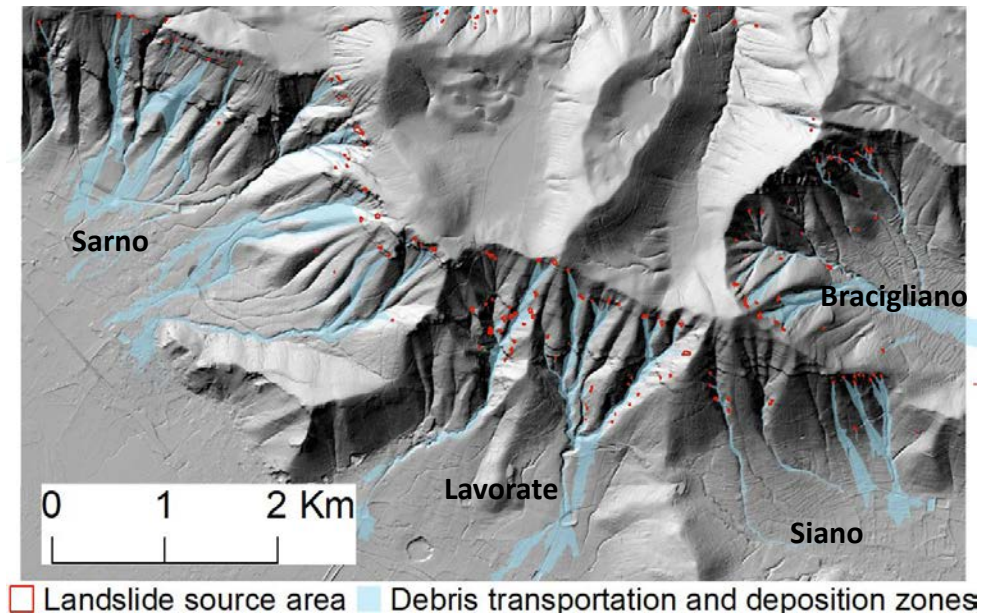
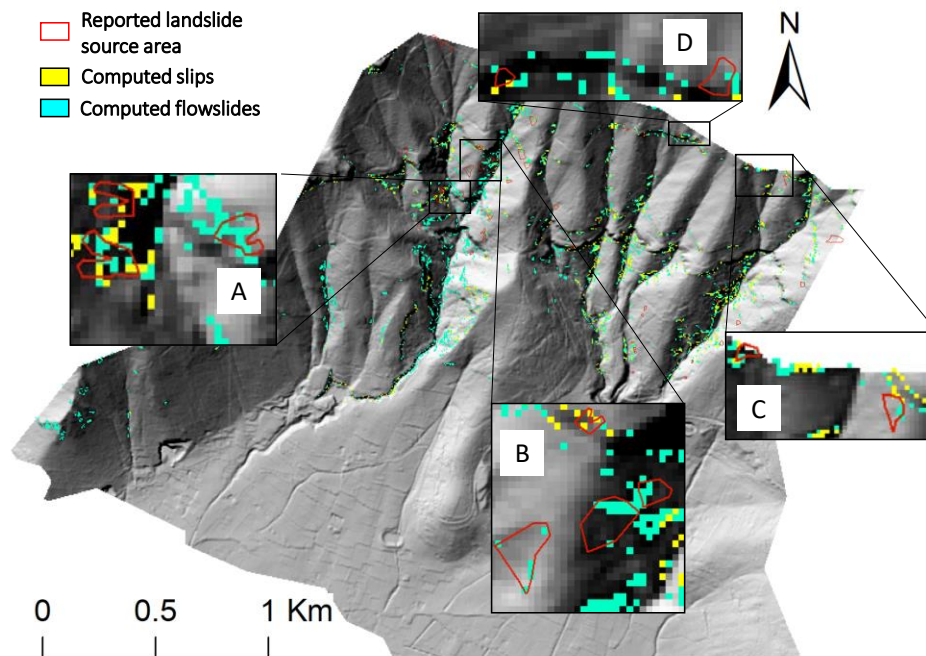


Fig. 4. Spatial distribution of shallow landslides in Campania (Southern Italy) after the rainfall events of 1998.

An example of model application for the municipality of Lavarate (south central sector of Fig. 4) is shown below. The spatial distribution of computed slips and flowslides by the end of the storm provides a reasonable agreement with the documented landslide source areas. Indeed, the ratio of successful prediction versus overpredicted areas is approximately 10, which is an improvement over previous studies performed in the same region (Sorbino et al., 2010).



The temporal evolution of computed unstable area is shown in Fig 6. The upper continuous line reflects the cumulative fraction of computed unstable area accounting for both failure mechanisms, while the lower curve provides the partition between each failure mode. The first unstable slopes are computed at $t = 24$ hr and are classified as slips. After this, flowslides begin to appear around $t = 30$ hr. The performance of the computations improves over time, however, with the model predicting a marked increase in the rate of slope failures after $t = 34$ hr, i.e. much closer to the temporal interval of reported failures for this site.

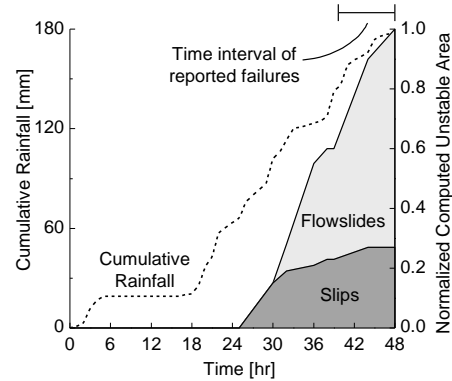


Fig. 6. Cumulated rainfall and temporal evolution of computed unstable area.

The above results were based on the assumption of vertical homogeneous slopes. Further improvements on model performance can be obtained by introduced the effect of layering. Examples of such application can be found in Lizárraga and Buscarnera, 2018.

5. Modelling spatial uncertainty in regional landslide hazard assesment

The model allows to incorporate the role of spatial uncertainty of input data on landslide susceptibility. Specifically, physical properties can be treated as spatially-correlated random fields (RF) with prescribed statistical attributes. In this manner, Monte Carlo simulations are performed for each realization and the results are aggregated and visualized in terms of maps of probability of landslide triggering that evolve over the duration of the storm. In the following, such approach is applied over a subsector located in the Siano municipality (south eastern corner of Fig. 4). Consider first Fig. 7 which shows three distinct realizations of RF of saturated hydraulic conductivity K_s , characterized by the same probability density function (*pdf*), but different levels of spatial correlation distance δ .

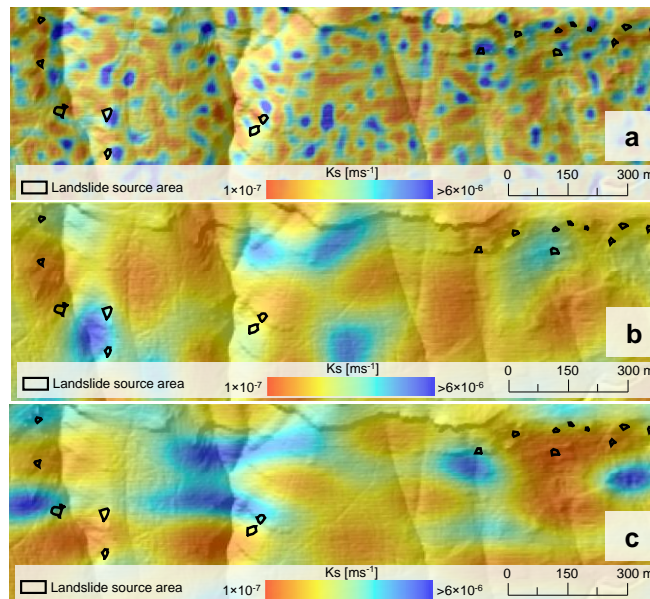


Fig. 7. Examples of random field realizations of K_s using a lognormal distribution (gaussian parameters mean = standard deviation = $1 \times 10^{-6} \text{ ms}^{-1}$) (a) isotropic correlation distance $\delta = 10$ m; (b) $\delta = 30$ m; (c) anisotropic spatial correlation with $\delta x = 60$ m and $\delta y = 30$ m.

This parameter controls the variability of K_s as a function of proximity (Fenton and Griffiths, 2008). For instance, lower values of δ promotes the development highly-heterogeneous scenarios (Fig. 7a), and conversely, higher spatial correlation result in more homogeneous conditions (Fig. 8b). It is also possible to develop RF with anisotropic spatial correlation (Fig. 8c, $\delta x > \delta y$). In other words, in order to model the spatial uncertainty of a physical variable, one must specify not only its *pdf*, but also its degree of spatial variability.

The computed maps of probability of landslide triggering (p_f) using 100 Monte Carlo samples and a value of $\delta x = \delta y = 30$ m are shown in Fig. 8a and 8b for $t = 32$ and 40 hr, respectively. For comparison, the reported landslide source areas were superposed (white hollow polygons). Note that as time progresses, areas with high levels of p_f (red zones) start to spread across the landscape. By $t = 40$ hr, most of the reported landslide source areas either coincide or are in the vicinity of cells with very high p_f , thus suggesting that the computations are in good agreement with the reported evidence.

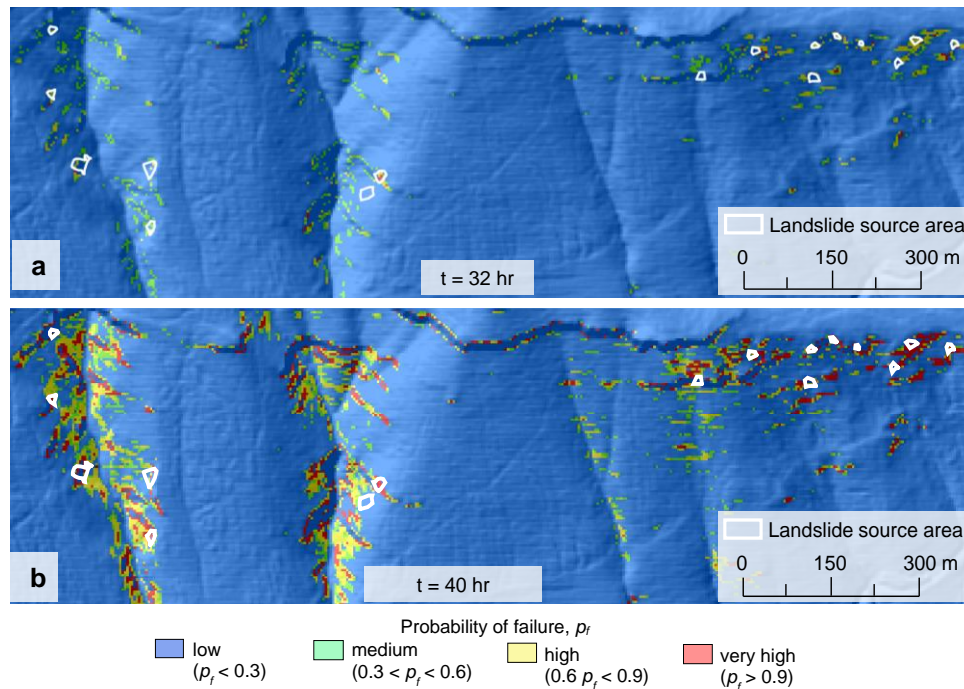


Fig. 8. Computed maps of probability of failure (a) $t = 32$ hr. and (b) $t = 40$ hr.

6. Conclusions

This contribution has described an integrated computational framework for regional assessment of rainfall-induced landslide triggering. The model relies on a vectorized numerical solver capable to perform multiple coupled flow-deformation analyses in unsaturated slopes under different conditions. The simulations are linked to a GIS platform to generate output maps of landslide susceptibility over the duration of a storm event.

Approaches to model flowslide triggering in terms of soil properties have been highlighted, and examples of application at both local and regional scales have been described. Additionally, a methodology to incorporate the role of spatial uncertainty of physical properties in the model simulations was presented, thus allowing the model outputs to be expressed in terms of probability of landslide triggering.

The proposed simulation platform fosters the use of laboratory data, georeferenced field measurements, and recent advances in stochastic and geomechanical modelling to construct an integrated virtual platform for regional landslide hazard assessment.

Acknowledgements

This work was supported by Grant No. CMMI-1324834 awarded by the US National Science Foundation

References

- Baum, R.L., Godt, J.W. and Savage, W.Z., 2010, Estimating the timing and location of shallow rainfall-induced landslides using a model for transient, unsaturated infiltration: *Journal of Geophysical Research: Earth Surface*, 115, no. F3, doi:10.1029/2009JF001321.
- Cascini, L., Cuomo, S. and Guida, D., 2008, Typical source areas of May 1998 flow-like mass movements in the Campania region, Southern Italy. *Engineering Geology*, 96(3-4), p. 107-125, doi:10.1016/j.enggeo.2007.10.003.
- Crosta, G.B. and Dal Negro, P., 2003, Observations and modelling of soil slip-debris flow initiation processes in pyroclastic deposits: the Sarno 1998 event. *Natural Hazards and Earth System Science*, 3(1/2), p. 53-69, doi:10.5194/nhess-3-53-2003.
- Dawson, R.F., Morgenstern, N.R. and Stokes, A.W., 1998, Liquefaction flowslides in Rocky Mountain coal mine waste dumps. *Canadian Geotechnical Journal*, 35(2), p. 328-343, doi:10.1139/t98-009.
- Fenton G.A., and Griffiths, V.D., 2008, Risk assessment in geotechnical engineering. John Wiley & Sons, doi:10.1002/9780470284704.
- Greco, R., Guida, A., Damiano, E. and Olivares, L., 2010, Soil water content and suction monitoring in model slopes for shallow flowslides early warning applications. *Physics and Chemistry of the Earth, Parts A/B/C*, 35(3-5), p. 127-136, doi:10.1016/j.pce.2009.12.003.
- Guadagno, F.M., Forte, R., Revellino, P., Fiorillo, F. and Focareta, M., 2005, Some aspects of the initiation of debris avalanches in the Campania Region: the role of morphological slope discontinuities and the development of failure. *Geomorphology*, 66(1-4), p. 237-254, doi:10.1016/j.geomorph.2004.09.024.
- Guzzetti, F., Carrara, A., Cardinali, M. and Reichenbach, P., 1999, Landslide hazard evaluation: a review of current techniques and their application in a multi-scale study, Central Italy. *Geomorphology*, 31(1), p.181-216, doi:10.1016/S0169-555X(99)00078-1.
- Hungr, O., Evans, S.G. and Hutchinson, I., 2001, A Review of the Classification of Landslides of the Flow Type. *Environmental & Engineering Geoscience*, 7(3), p. 221-238, doi:10.2113/gseegeosci.7.3.221.
- Iverson, R.M., 2014, Debris flows: behaviour and hazard assessment. *Geology today*, 30(1), p. 15-20, doi:10.1111/gto.12037.
- Jefferies, M. and Been, K., 2015, Soil liquefaction: a critical state approach. CRC press, doi:10.4324/9780203301968.
- Lizárraga, J.J. and Buscarnera, G., 2017, Safety factors to detect flowslides and slips in unsaturated shallow slopes. *Géotechnique*, 68(5), p. 442-450, doi:10.1680/jgeot.17.T.003.
- Lizárraga, J.J. and Buscarnera, G., 2018, Spatially distributed modeling of rainfall-induced landslides in shallow layered slopes. *Landslides*, p. 1-11, doi:10.1007/s10346-018-1088-8.
- Milledge, D.G., Bellugi, D., McKean, J.A., Densmore, A.L. and Dietrich, W.E., 2014, A multidimensional stability model for predicting shallow landslide size and shape across landscapes. *Journal of Geophysical Research: Earth Surface*, 119(11), p. 2481-2504, doi:10.1002/2014JF003135.
- Montgomery, D.R. and Dietrich, W.E., 1994, A physically based model for the topographic control on shallow landsliding. *Water resources research*, 30(4), p. 1153-1171, doi:10.1029/93WR02979.
- Picarelli, L., Olivares, L. and Avolio, B., 2008, Zoning for flowslide and debris flow in pyroclastic soils of Campania Region based on “infinite slope” analysis. *Engineering Geology*, 102(3-4), p. 132-141, doi:10.1016/j.enggeo.2008.03.015.
- Sheng, D., Sloan, S.W., Gens, A. and Smith, D.W., 2003, Finite element formulation and algorithms for unsaturated soils. Part I: Theory. *International journal for numerical and analytical methods in geomechanics*, 27(9), p. 745-765, doi:10.1002/nag.295.
- Sorbino, G., Sica, C. and Cascini, L., 2010, Susceptibility analysis of shallow landslides source areas using physically based models. *Natural hazards*, 53(2), p. 313-332, doi:10.1007/s11069-009-9431-y.
- Wu, L.Z., Selvadurai, A.P.S., Zhang, L.M., Huang, R.Q. and Huang, J., 2016, Poro-mechanical coupling influences on potential for rainfall-induced shallow landslides in unsaturated soils. *Advances in water resources*, 98, p. 114-121, doi:10.1016/j.advwatres.2016.10.020.

Flume experiment on the influence of particle size distribution on sediment capturing efficiency of open-type steel Sabo dams

Naoki Matsumoto^a, Taro Uchida^a, Wataru Sakurai^a, Tomoo Matsubara^b,
Ryosuke Okuyama^b, Junya Hina^b and Yoshifumi Satofuka^c

^aNational Institute for Land and Infrastructure Management, 1 Asahi Tsukuba, Ibaraki 305-0804, Japan

^bCTI Engineering, Co., 1047-27 Onigakubo Tsukuba, Ibaraki 300-2651, Japan

^cRitsumeikan University, 1-1-1 Nozohigashi Kusatsu, Shiga 525-8577, Japan

Abstract

The purpose of this study is to clarify the influence of particle size distribution on the sediment capturing effect of open-type steel Sabo dams constructed in the sediment sheet flow section. First, we conducted a flume experiment in order to clarify the minimum boulder size contributing to blockage (flume gradient was 5 °). Based on the result, we set the particle size distribution for a flume experiment to clarify the effect of particle size distribution on the sediment capturing effect of the open-type steel Sabo dams in the sediment sheet flow section. We found that the minimum boulder size contributing to blockage is 1/3 to 1/2 of the individual grid width. We tested the volumetric effects of sediment larger than the minimum boulder size on sediment capturing efficiency through its contribution to blockage. In addition, we defined the value obtained by dividing the blockage-contributing sediment volume per unit area by the average particle size as "dimensionless sediment volume contributing to blockage". We found that this "dimensionless sediment volume contributing to blockage" and sediment capture rate have a logarithmic approximation relationship. Thus, this value can be expected as a new index for setting the individual grid width of the open-type steel Sabo dams.

Keywords: sediment sheet flow; flume experiment; open-type steel Sabo dams; boulder size distribution; dimensionless sediment volume contributing to blockage

1. Introduction

In Japan, as a countermeasure against debris flow, it is recommended to construct open-type steel Sabo dams that trap not only sediment but also driftwood. When planning open-type steel Sabo dams, setting the individual grid width is one of the important considerations. In Japan, the individual grid width is set at 1.0 times the sediment of 95% particle diameter as per guidelines(National Institute for Land and Infrastructure Management). Although it is known that boulders smaller than the individual grid width block individual grids due to arching, there is little knowledge of the boulder size contribution to blockage and the influence of particle size distribution on open-type steel Sabo dams installed in the sediment sheet flow section.

So, in this study, we conducted a flume experiment to clarify the effect of particle size distribution on the sediment capturing effect of open-type steel Sabo dams in the sediment sheet flow section, and organize the relationship between particle size distribution and sediment captured rate. The names of the various parts of an open-type steel Sabo dam are as shown in Fig.1(a).

* Corresponding author e-mail address: matsumoto-n92ta@mlit.go.jp

2. Outline of experiment

2.1. Equipment and conditions

The water flume used in this study was a straight rectangular water flume with a length of 10 m, a width of 30 cm, a height of 50 cm, and a channel slope of 5 ° (Fig. 1(b)). The water flume floor was fixed. Also, a roughness plate with experimental sediment (Fig. 2(a)) was affixed to the water flume floor. Mixed sand, 95% of which had a particle diameter of 32 mm and 50% a particle diameter of 8 mm, was used as the test sediment so that the maximum particle size was about 1 m when the model scale was set to 1/30. In addition, an open-type steel Sabo dam was installed at a point 2.25 m from the downstream end of the water flume. In order to analyze the effect of backwater and grid area on the sediment capturing performance of open-type Sabo dams, we prepared two kinds of open-type Sabo dams with different opening widths (Fig. 2(b),(c)). In addition, the individual grid width was set to 95% particle diameter 1.0 times for both horizontal and vertical intervals based on Japanese guidelines.

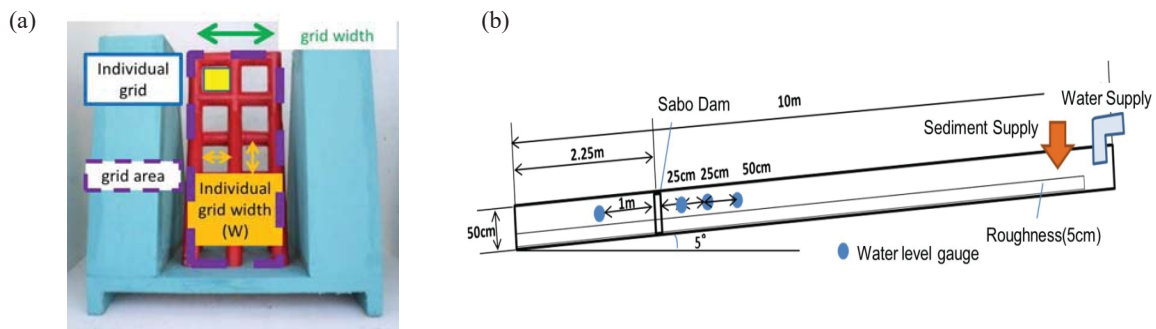


Fig. 1. (a) Names of parts of an open-type steel Sabo dam; (b) Water flume

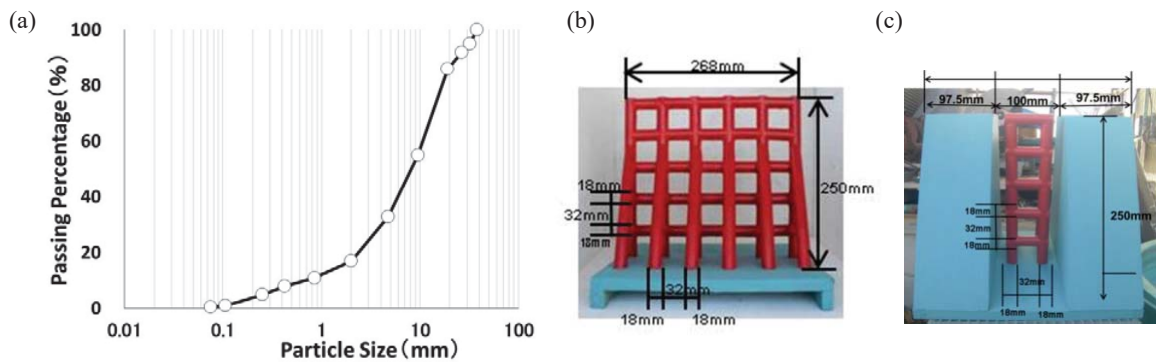


Fig. 2. (a) Particle size distribution; (b) Full-open-type Sabo dam model; (c) Partially-open type Sabo dam model

2.2. Experimental method

For water and sediment supply methods, water was supplied from the upstream end of the water flume and the amount of supply water was controlled by programming the opening and closing of the electrically operated valve. Based on the set hydrograph, the sediment was supplied manually according to the equilibrium sediment amount calculated by the gradual equation (Ashida et.al., 1978). The hydrograph was rectangular with a stable flow rate of sediment and water at 18 l/sec for a duration of 5.5 minutes (Fig. 3(a)). In addition, the amount of sediment was supplied so that the sediment gradient was equal to the capacity (321 liter) when accumulated at 2/3 the gradient of the original riverbed. At the downstream end of the water flume, the outflow flow rate to the downstream and the

discharge sediment volume were collected at intervals of 30 to 60 seconds and measured. The experimental situation was recorded on video from the side wall of the water flume and the deposited sediment situation was measured.

2.3 Preliminary experiment for identifying the minimum particle size capable of blocking the opening section

This study aimed to investigate the influence of the particle size distribution constituting the sediment sheet flow on the sediment capturing performance of open-type steel Sabo dams. Therefore, the particle size distribution was set after identifying the minimum particle diameter that closes the grid area. First, we removed the sand of coarse particles so that the maximum sizes of the experimental sediment shown in Fig. 2(a) were 9.5 mm and 19 mm. We carried out preliminary experiments to supply water and sediment from the upstream of the water flume and to check whether or not the sediment blocked the open-type steel Sabo dam. Judgement was based on whether or not the lowermost stage of the dam was blocked. We supplied water and sediment under the conditions shown in Fig. 3(a). We halted supply when it was confirmed that the lowest stage was assuredly blocked. Also, even in the case where the lowest stage was not blocked, we halted supply after 4 minutes, which was adequate time to supply the amount of sediment equivalent to the planned deposited sediment volume. Preliminary experiment cases are shown in Table 1. In Cases 1 and 2, 3 minutes after the start of supply, we confirmed that the lowest stage of the Sabo dam was surely blocked. On the other hand, in Cases 3 and 4, we confirmed that, even 4 minutes after the start of supply, the lowest stage of the Sabo dam was not blocked at all. From the above results, in this study, we treated grain sizes of 9.5 mm to 19 mm or more as the particle sizes contributing to the blockage of open-type steel Sabo dams (hereinafter referred to as "blockage-contributing particle size").

Table1. Preliminary experimental case

CASE	Maximum Particle Size	Dam-type
1	19mm	Full-open type
2	19mm	Partially-open type
3	9.5mm	Full-open type
4	9.5mm	Partially-open type

2.4 Setting of particle size distribution in this experiment

Using the particle size distribution shown in Fig. 2(a) as the basic pattern, we set three particle size distributions in which the ratio of the blockage-contributing particle size was changed. The concept of setting the particle size distribution is as follows.

- (1) 95% of the particles of the basic pattern are 32 mm in diameter and contribute 45% to the blockage.
- (2) Since individual grids can be blocked by one particle of 32 mm or more in diameter, the proportion of the blockage-contributing particle size changes according to the reduction ratio of the sediment amount of 32 mm or more. For example, in Pattern 1, since the sediment of 32 mm or more in diameter was reduced to 0.83% (reduction ratio: 0.166), the blockage-contributing particle size was set to 7.5% ($= 0.45 \times 0.166$).
- (3) Regarding Patterns 2 and 3, an amount of sediment having a particle size of 32 mm or more, capable of closing all individual grids of a Sabo dam was set. If it is assumed that one particle of 32 mm or more in diameter is simply a sphere, in order to block individual grids, 0.0171 l ($= 17.1 \text{ cm}^3$) of sediment is required. Since the full-open type steel Sabo dam has 25 individual grids, 0.428 l ($= 0.0171 \times 25$) is necessary. Also, assuming the porosity to be 0.6, 0.71 l ($= 0.428 / 0.6$) of sediment is required. Since this is 0.2% ($= 0.71 / 321$) (reduction ratio: 0.04) of the supplied sediment volume, the overall proportion of the blockage-contributing particle size is about 2% ($= 0.45 \times 0.04$). Similarly, Pattern 3 was determined.

Based on (1) to (3) above, the particle size ratio and the particle size distribution are shown in Fig. 3(b) and Fig.4(a). Fig. 4(b) is an enlargement of the passing percentage of 80-100%.

2.5 Experimental cases

Based on 2.2, 2.3 and 2.4, a total of 7 experimental cases combining the particle size distribution of Fig. 3(b) and the Sabo dam model of Fig. 2(b),(c) were set (Table.2).

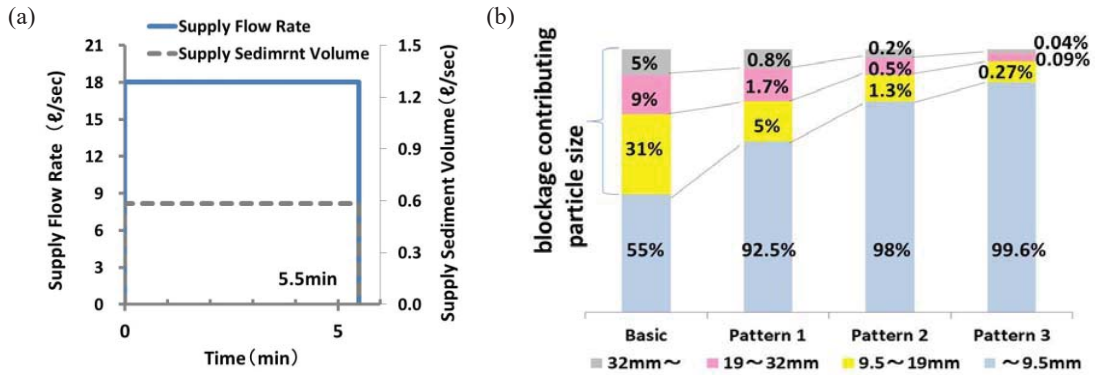


Fig. 3. (a) Hydrograph and sedigraph; (b) Particle size ratio

Table 2. Experimental cases

CASE	Particle Size Ratio	Dam-type
Basic	Basic	Full-open type
1	Pattern 1	Full-open type
2	Pattern 1	Partially-open type
3	Pattern 2	Full-open type
4	Pattern 2	Partially-open type
5	Pattern 3	Full-open type
6	Pattern 3	Partially-open type

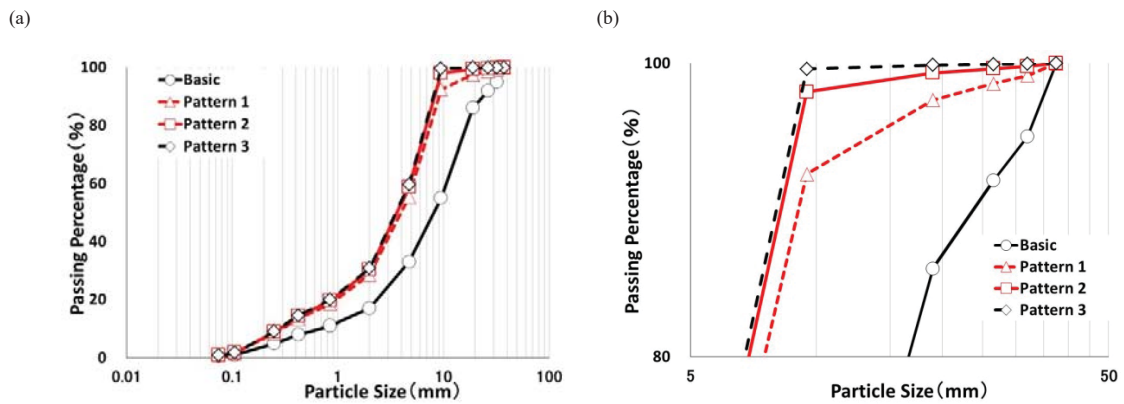


Fig. 4. (a) Particle size distribution of the main experimental sediment; (b) Particle size distribution enlarging 80-100%

3. Results

3.1. Sediment captured rate

The sediment captured rate is the ratio of the amount of sediment captured by the Sabo dam (sediment captured volume) to the supplied sediment volume (Fig. 5(a)). The amount of sediment captured by the Sabo dam was calculated by subtracting the amount of sediment discharged from the supplied sediment volume to the downstream of the Sabo dam. As for the Basic Case and Cases 1, 2, and 4, since the sediment captured rate is 88 to 94%, it can be seen that most of the supplied sediment was captured by the Sabo dam. On the other hand, in Case 5, since the sediment captured rate is 16%, it can be seen that much of the sediment flowed out downstream without being captured by the Sabo dam.

Next, we focused on the difference in dam-type. The sediment captured rate of full-open type dam is 92% for Case 1, 70% for Case 3, and 16% for Case 5. The sediment captured rate decreases as the sediment volume of blockage-contributing particle size (hereinafter referred to as "blockage-contributing sediment volume") decreases. Meanwhile, the sediment captured rate of the partially-open type dam is 89% for Case 2, 88% for Case 4, and 76% for Case 6. Case 6 with the smallest blockage-contributing sediment volume has a lower sediment captured rate than the other cases (Cases 2 and 4).

We then focused on the difference in blockage-contributing sediment volume. Cases 1 and 2 with large blockage-contributing sediment volume had almost equal sediment captured rates. On the other hand, in Cases 3 - 6 with small blockage-contributing sediment volume, the partially-open dam of Cases 4 and 6 had a larger sediment captured rate than the full-open dam of Cases 3 and 5. Especially, in Cases 5 and 6 with smallest blockage-contributing sediment volume, the partially-open dam of Case 6 captured about 5 times more sediment volume than the full-open dam of Case 5.

3.2. Sediment deposition process

Fig.5(b) plots the sediment-deposited height at a point 25 cm upstream of the dam, taken from video image. In the Basic Case and Cases 1, 3, and 5 of the full-open dam, the sediment reached the Sabo dam immediately after the start of the experiment in each case. Also, in the Basic Case, Case 1, and Case 3, the sediment-deposited height reached 25 cm of the dam height after the experiment was completed. In other words, this means that the Sabo dam is full of sediment. Also, in the Basic Case, the sediment-deposited height reached 14 cm at 60 seconds and 18.6 cm at 120 seconds after the start of supply. In Case 1, the sediment-deposited height reached 11.6 cm at 60 seconds and 17.3 cm at 120 seconds after the start of supply. In Case 3, the sediment-deposited height reached 9.3 cm at 60 seconds and 11.6 cm at 120 seconds after the start of supply. As can be seen from the above, the sediment-deposited speed tends to be slower as the blockage-contributing sediment volume becomes smaller. That is, it can be seen that it takes a long time for the dam to fill up with sediment. On the other hand, Case 5 with the smallest blockage-contributing sediment volume was about 10 cm in sediment-deposited height after the experiment.

In Cases 2, 4, and 6 with the partially-open dam, sediment was deposited while forming sediment shoulders in each case. Also, in all cases, the sediment-deposited height reached 25 cm of the dam height after the experiment was completed. However, in Cases 2 and 4, the sediment shoulder reached the dam 90 seconds after the start of supply, whereas Case 6 was 120 seconds after the start of supply. In Cases 2 and 4, the sediment-deposited height reached 25 cm of the dam height at 240 seconds after the start of supply, whereas Case 6 was 300 seconds after the start of supply. As a result, it can be said that it takes a long time for the dam to fill up with sediment when the blockage-contributing sediment volume becomes less than 2% as in Case 6.

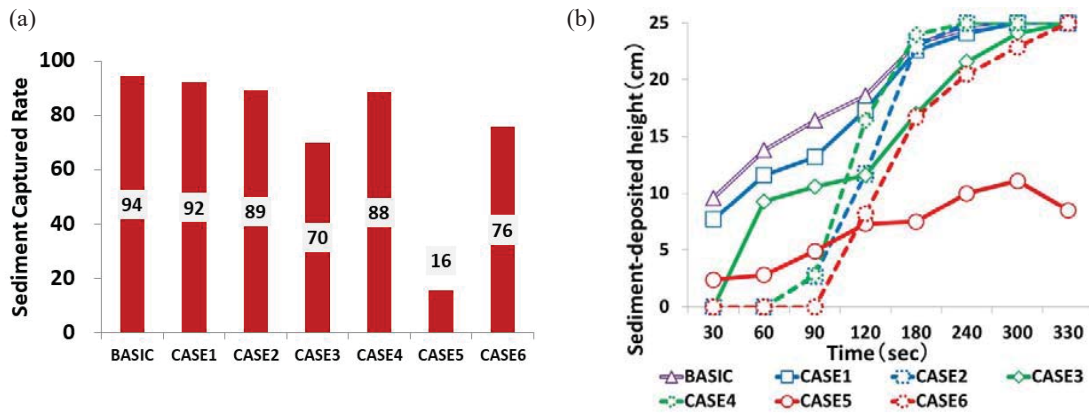


Fig. 5. (a) Sediment captured rate (Numbers in bars refer to the percent captured.); (b) Sediment-deposited height

4. Discussion

4.1. Distance between steel pipes ratio and sediment captured rate

In this study, we conducted flume experiments on the influence of particle size distribution on sediment capturing performance of open-type steel Sabo dams. We first considered the relationship between the ratio of the individual grid width to a certain particle size (hereinafter referred to as " $D_{[particle\ size]}/W$ ") and the sediment captured rate. For example, in Japan, the individual grid width is set at 1.0 times the 95% particle diameter (D_{95}/W). Fig.6 (a) shows the relationship between D_{95}/W and the sediment captured rate. In this study, the 95% particle diameter is 32 mm for the Basic Case, 24.5 mm for Cases 1 and 2, 9.13 mm for Cases 3 and 4, and 8.94 mm for Cases 5 and 6. Also, in the same figure, the past experimental results are also plotted for comparison (Ashida et al., 1987; Takahara et al., 2007; Horiuchi et al., 2009; Nakatani et al., 2015). When the D_{95}/W is about 1, the sediment captured rate is 80% or more in all cases, but it can be seen that the sediment captured rate largely varies when the D_{95}/W is larger than 1.5. Also, in this study result, it was confirmed that the sediment captured rate greatly differs from 10 to 90% or more. Next, Fig.6 (b) shows the relationship between D_{80}/W and the sediment captured rate. The sediment captured rate is 80% or more until the D_{80}/W is about 2.0, but it can be seen that the sediment captured rate largely varies when the D_{80}/W is larger than 2.0. As a result, there is no noticeable correlation between the $D_{[95\ or\ 80]}/W$ and the sediment captured rate.

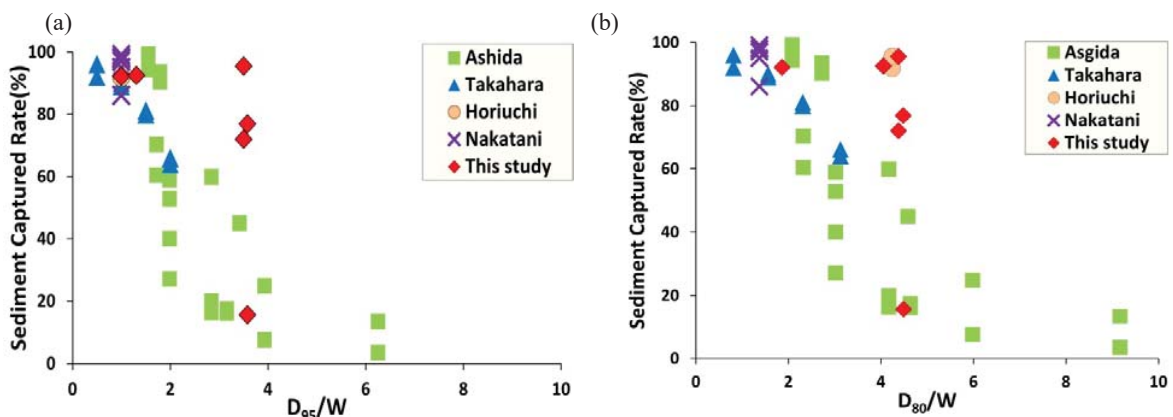


Fig. 6. (a) D_{95}/W and sediment captured rate; (b) D_{80}/W and sediment captured rate

4.2. Blockage contributing sediment volume and sediment captured rate

Next, we consider the relationship between the blockage-contributing sediment volume and the sediment captured rate. Cases 1 and 2, Cases 3 and 4, and Cases 5 and 6 are the experimental cases with the same blockage-contributing sediment volume. From Fig. 5 (a), the sediment captured rates of Cases 1 and 2 are 92% and 89% respectively, which are almost equal. The sediment captured rates of Cases 3 and 4 are 70% and 88% respectively, while a somewhat narrow type of Sabo dam shows a high sediment captured rate. The sediment captured rates of Cases 5 and 6 are 16% and 76% respectively, which are largely different. As a result, there is no noticeable correlation between the blockage-contributing sediment volume and the sediment captured rate.

4.3. Dimensionless blockage-contributing sediment volume and sediment captured rate

It was found that there is no significant correlation between the $D_{[95 \text{ or } 80]}/W$ and the blockage-contributing sediment volume and the sediment captured rate. Here, we consider the relationship between sediment captured rate for grid area and blockage-contributing sediment volume. The grid area is a value obtained by multiplying the area of an individual grid of the Sabo dam by the area of all individual grids.

It is reasonable to consider the blockage-contributing sediment volume per unit area (blockage-contributing sediment volume / grid area). However, it is more convenient to make it dimensionless if we also look into application on site. However, if we actually design an open-type Sabo dam, it would be more useable if we made it dimensionless. Therefore, we define the value obtained by dividing the blockage-contributing sediment volume per unit area by the average particle size as "dimensionless blockage-contributing sediment volume".

Fig.7 and Fig.8 show the contribution of dimensionless blockage-contributing sediment volume and the sediment captured rate. Fig.7 shows a case where sediment having a particle diameter of 1/2 or more of the individual grid width is set as the blockage-contributing particle size and the dimensionless blockage-contributing sediment volume was calculated. Also, Fig. 8 shows a case where sediment having a particle diameter of 1/3 or more of the distance between steel pipes is set as the blockage-contributing particle size and the dimensionless blockage-contributing sediment volume was calculated. Like 4.1, in the same figure, the past experimental results are also plotted for comparison. From both figures, there is a tendency to increase logarithmically between the dimensionless blockage-contributing sediment volume and the sediment captured rate.

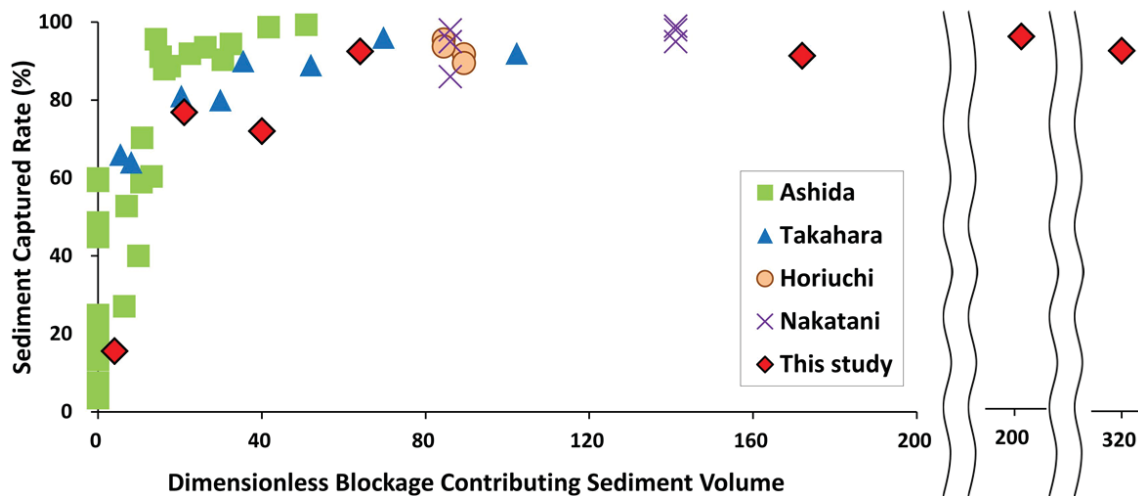


Fig. 7. Dimensionless blockage-contributing sediment volume (1/2) and sediment captured rate

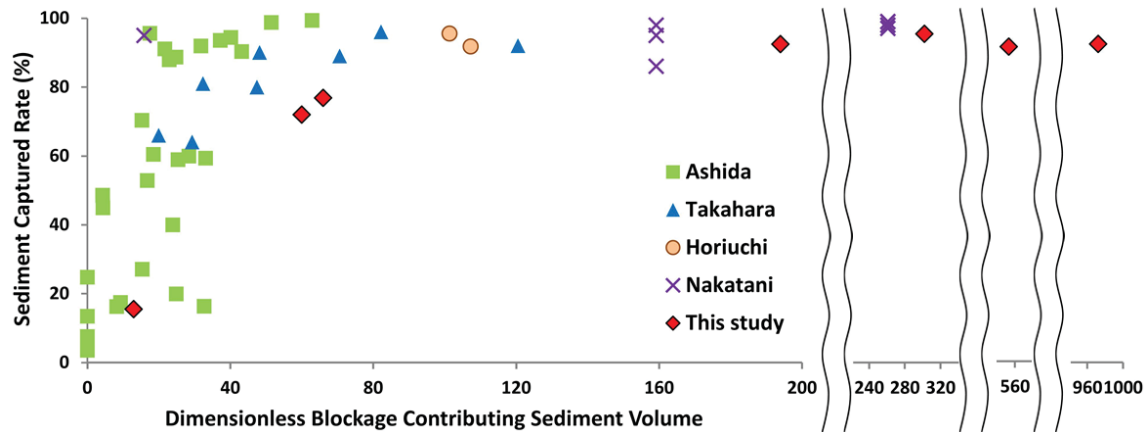


Fig.8. Dimensionless blockage-contributing sediment volume (1/3) and sediment captured rate

Conclusions

In this study, we conducted flume experiments on the effect that differences in particle size distribution have on the sediment capturing effect of the open-type steel Sabo dams in the sediment sheet flow section, and obtained the following results.

- (a) The individual grid width of open-type Sabo dams is set with $D_{95 \text{ or } 80}/W$. When D_{95}/W is set to 1.0 of Japan's setting standard, sufficient sediment capturing performance can be expected. On the other hand, it was confirmed that the sediment captured rate greatly varies when the distance between steel pipes ratio is 1.5 or more. In addition, it was confirmed that even when the individual grid width was set based on the D_{80}/W , there was a variation in sediment captured rate.
- (b) "Dimensionless blockage-contributing sediment volume", which is a value obtained by dividing the blockage-contributing sediment volume by the grid area, and the sediment captured rate were found to be logarithmically correlated. That is, it appears that the "dimensionless blockage-contributing sediment volume" may be effective for setting the individual grid width.

References

Ashida, K., Egashira, S., Kurita, M., and Aramaki, H., 1987, Debris flow control with grid dam: Prevention research institute annals, v.30.B-2, p.441-456.

Ashida, K., Takahashi, T., and Mizuyama, T., 1978, Study on bed load equations for mountain streams: Journal of the Japan Society of Erosion Control Engineering, v.30, no.4, p.9-17.

Horiuchi, S., Akanuma, J., Ogawa, K., Kuraoka, S., Sugiyama, M., Morita, T., Itoh, T., and Mizuyama, T., 2009, Hydraulic model tests for evaluating sediment control function with a grid-type high dam in a straight flume: Journal of the Japan Society of Erosion Control Engineering, v.62, no.2, p.29-36.

Nakatani, K., Mizuyama, T., and Satofuka, Y., 2015, Considerations on sediment capture function of open-type Sabo dams according to catchment characteristics: Presentation paper of Sabo landslide technology research results report meeting, p.73-101.

National Institute for Land and Infrastructure Management Sabo Planning Division Sabo Department., 2016, Manual of technical standards for establishing Sabo master plan for debris flow and driftwood: Technical Note of NILIM, No.904.

National Institute for Land and Infrastructure Management Sabo Planning Division Sabo Department., 2016, Manual of technical standards for designing Sabo facilities against debris flow and driftwood: Technical Note of NILIM, No.905.

Takahara, T. and Matsumura, K., 2007, Evaluation of sediment trap ability based on sediment made and members distance: Journal of the Japan Society of Erosion Control Engineering, v. 60, no.4, p.55-60.

Debris-flow behavior containing fine sediment considering phase shift

Kana Nakatani^{a,*}, Yuji Hasegawa^b, Yusuke Asano^a, Yoshifumi Satofuka^c

^a Graduate School of Agriculture, Kyoto University, Oiwake-cho, Kitashirakawa, Sakyo-ku, Kyoto 6068502, Japan

^b Graduate School of Integrated Arts and Sciences, Hiroshima University, 1-7-1 Kagamiyama, Higashi Hiroshima, Hiroshima 7398251, Japan

^c Department of Civil Engineering, Ritsumeikan University, 1-1-1 Noji-higashi, Kusatsu, Shiga 5258577, Japan

Abstract

Recent observations have shown that debris flows containing fine particles in volcanic regions exhibit greater mobility compared to stony debris flows. Recent researches have described that greater mobility occurred from fine sediment phase shift from solid phase to fluid phase in debris flow. In Japan, debris-flow research and sabo or erosion control planning widely apply the equilibrium concentration methods proposed by Takahashi. For considering fine sediment phase shift with the equilibrium method, it is proposed to set high fluid density. However, the mechanism of phase shift and behaviours of debris flows with fine sediment, are not fully understood. In this study, we conducted hydraulic experiments with sediment particles of two different diameters, defined as fine sediment and coarse sediment. We applied the equilibrium methods and took into account the increased fluid phase density due to the sediment phase shift to fluid. From the results, we found that part of the fine particles contribute to the increase in the fluid phase density. When conducting experiments, not only fine sediment, but some parts of coarse sediment behaved as a fluid. For considering the shift of sediment to fluid phase in debris flows, we presumed that the flow turbulence in debris flow affected. Regarding the sediment concentration, higher total sediment (coarse and fine) concentration increased the fluid phase density. A larger ratio of coarse sediment increased the fluid phase density more than when sediment contained only fine particles. It was speculated to occur from the flow turbulence owing to the mixture condition. Cases with smaller total sediment discharge showed higher fluid phase density though in same sediment concentration. We also found that the larger dimensionless tractive force showed a smaller ratio behaving as fluid phase, which was in contrast with the trends in recent studies.

Keywords: debris flow, fine sediment, phase shift, laboratory experiment

1. Introduction

Debris flows occur due to various phenomena including landslides, river bed erosion, and landslide dam outbursts (e.g., Iverson, 1997; Takahashi, 1991). Damage from debris flows is serious due to their high mobility. In Japan, many debris flows occurred in Hiroshima Prefecture in 2014 and in 2018 (Kaibori et al., 2018). Reports show that the sediment particle distribution in these debris flows was wide ranging from fine particles to large boulders, as shown in Fig.1. There are many studies on debris flows but most of them are focused on the stony debris flows with large sediment particles, in particular, on the concentration of coarser particles in the front of the flow (e.g., Wada et al., 2015). In Aso (Kumamoto Prefecture, Japan), debris flows containing high concentrations of fine particles occurred in 2012. They showed high mobility, and the sediment deposition extended outside of the debris-flow-risk designated areas, reaching to mild-slope areas with slopes less than 2 degrees (Ministry of Land, Infrastructure, Transport and Tourism, 2014). These debris-flow characteristics are different from what is typical for stony debris flows.

In Japan, the equilibrium concentration equation (Takahashi, 1991) appears widely in studies on debris flows and on countermeasure planning using sabo (sedimentation and erosion control) works. To be applicable to debris flows containing fine sediments, the methods should consider the change of phase by fine sediment to fluid phase (e.g. Uchida et al., 2013). It is confirmed that setting higher fluid density in the method described higher mobility of debris

* Corresponding author e-mail address: kana2151@kais.kyoto-u.ac.jp

flows containing fine sediment. Some studies have proposed that fine sediment should be taken into interstitial fluid turbulence to cause phase shift by fine sediment to fluid phase (e.g. Nishiguchi et al., 2011; Hotta and Miyamoto, 2008). Furthermore, some experiment results showed not only fine sediments, but part of the coarse sediment, behaved as a fluid (Nakatani et al., 2018). However, the mechanism and behaviors of debris flows with fine sediments, and also the method needed to estimate the proper fluid density, are not clear.

In this study, we focused on debris flows composed of sediment particles with two different diameters: defined as fine sediment and coarse sediment, and conducted hydraulic experiments. We also considered the effect of the sediment concentration, the mixing ratio of different sized particles, the hydraulic conditions, and the turbulence intensity on debris-flow behavior and fluid phase density.



Fig. 1. Debris flow that occurred in the 2014 Hiroshima sediment disaster

2. Methods

2.1. Laboratory experiment methods

The experimental setup is shown in Fig. 2a. The experimental channel is a rectangular straight open channel 5-m long and 10-cm wide with a variable slope. In this study, we set the flume angle for each cases not to cause larger gap than 3 degrees from equilibrium state slope angle. We supplied constant water from the upstream tank. For the sediment supply, we used two hoppers. The first hopper supplied fine sediment and was positioned set 450 cm upstream from the downstream end. The second hopper supplied coarse sediment and was positioned set 400 cm upstream from the downstream end. We set fine sediment hopper at upstream side because smaller particle requires more time and space to mix with water comparing to larger particle.

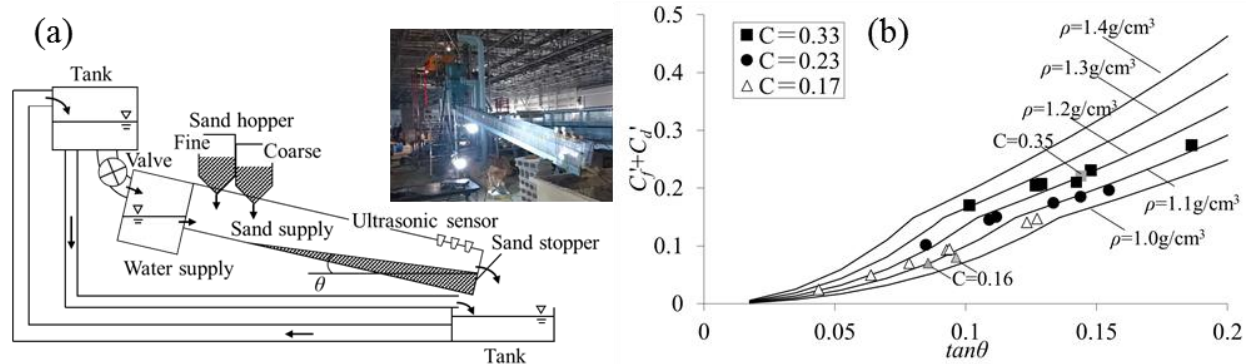


Fig.2. (a) Experimental flume setup and (b) results showing the relationship between slope and solid phase sediment concentrations (legend C describes the supplied total sediment concentration)

We used two types of uniform sediment particles: 0.13 mm as fine sediment and 2.81 mm as coarse-grained sediment. The sediment density σ was 2.61 g/cm³, and internal friction angle of the sediment ϕ was 35 deg. We conducted 23 cases, as shown in Table 1 (left 5 elements showing experiment conditions). We placed a high-speed camera (Ex-F1, Casio, Japan) with 300 fps at 50 cm upstream from the downstream end of the flume. We measured the flow depth from video because ultrasonic sensor could not distinguish riverbed deposition. We defined riverbed where soil particles did not move. In Case 16, the condition was rather unstable compared to other cases, and we could not determine a flow depth.

Table 1. Experiment conditions and results

Case	Experiment conditions (5 elements)				Results (5 elements)					
	Supplied water	Supplied sediment (fine)	Supplied sediment (coarse)	Sediment concentration	Ratio of fine and coarse sediment	Deposit slope θ	Flow depth h	Ratio of fine sediment behave as fluid phase	Ratio of coarse sediment behave as fluid phase	Fluid phase density ρ
	cm ³ /s	cm ³ /s	cm ³ /s	$C_f + C_d$	$C_f : C_d$	deg.	cm	C_f'' / C_f	C_d'' / C_d	g/cm ³
1	1500	370	370	0.33	1:1	10.56	1.6	0.34	0	1.12
2	1500	150	150	0.17	1:1	7.03	2.2	0.35	0	1.05
3	1500	150	300	0.23	1:2	8.19	1.4	0.58	0	1.09
4	1000	300	0	0.23	3:0	8.80	2.0	0.15	(only C_f)	1.07
5	1000	165	330	0.33	1:2	7.22	1.6	1.00	0.07	1.25
6	1000	250	250	0.33	1:1	7.28	1.3	0.75	0	1.25
7	1000	100	200	0.23	1:2	6.23	1.3	1.00	0.05	1.16
8	1000	150	150	0.23	1:1	7.61	1.6	0.49	0	1.11
9	1000	70	140	0.17	1:2	4.48	1.3	1.00	0.36	1.17
10	1000	100	100	0.17	1:1	5.30	1.3	0.93	0	1.14
11	1000	90	120	0.17	3:4	5.36	1.3	1.00	0.01	1.13
12	600	100	200	0.33	1:2	7.35	1.0	1.00	0.05	1.25
13	600	150	150	0.33	1:1	5.79	0.9	0.96	0	1.31
14	600	90	90	0.23	1:1	6.38	0.8	0.69	0	1.15
15	600	60	60	0.17	1:1	2.50	1.0	1.00	0.75	1.24
16	600	300	0	0.33	3:0	8.41	-	0.30	(only C_f)	1.21
17	600	40	80	0.17	1:2	7.25	1.35	0.42	0	1.04
18	600	70	110	0.23	7:11	4.85	1.45	1.00	0.28	1.23
19	600	50	70	0.17	5:7	3.65	1.1	1.00	0.53	1.20
20	555	200	100	0.35	2:1	8.2	1.2	0.56	0	1.27
21	600	200	100	0.33	2:1	8.1	1.1	0.55	0	1.25
22	1550	200	100	0.16	2:1	4.9	3.5	0.87	0	1.16
23	1550	100	200	0.16	1:2	5.5	3.5	1.00	0.21	1.13

(- is showing the case flow depth could not measure)

At 15 cm, 30 cm, and 45 cm upstream from the downstream end of the flume, we set three ultrasonic sensors (from upstream, we called as No.1-No.3) with 50 Hz resolution (E4SC-DS30, Omron, Japan) and measured the flow surface slope from the flow surface height. At the downstream end, we installed 10 cm height sand stopper to cause deposition. For the initial condition, we set the sediment deposition as horizontal state for 10 cm height at downstream end to provide a movable bed condition. We supplied water and sediment for approximately 120 seconds, which was sufficient time for the deposit slope angle became stable.

We assumed equilibrium flow conditions were achieved when ultrasonic sensors showed the same value for 10 seconds. Each sensor measurement of the flow surface height and slope was calculated as the average value from three sensors. Using average slope from sensor No.1-No.2 and No.2-No.3, we also checked there was not significant difference with No.1-3. Here, we used the flow surface slope angle θ as river bed slope angle assuming that in the equilibrium state, the river bed slope and surface flow slope expected to become equal. Applying the supplied sediment concentration and the results of slope angle, we calculated fluid phase density using the equilibrium concentration method described in the next section.

2.2. Methods for estimating the fluid phase density

Different phases of debris flow are shown in Fig. 3. Fig.3a shows no phase shift conditions, so all the sediments behave as solid phase. Fig.3b shows that part of the fine sediment behaves as fluid phase, as reported in recent studies (e.g., Uchida et al., 2013). Fig.3c shows the fine sediment and part of the coarse sediment also behaving as fluid phase. Equation (1) shows the total sediment concentration C containing coarse sediment and fine sediment. Equation (2) shows the constitution of fine sediment considering different phases.

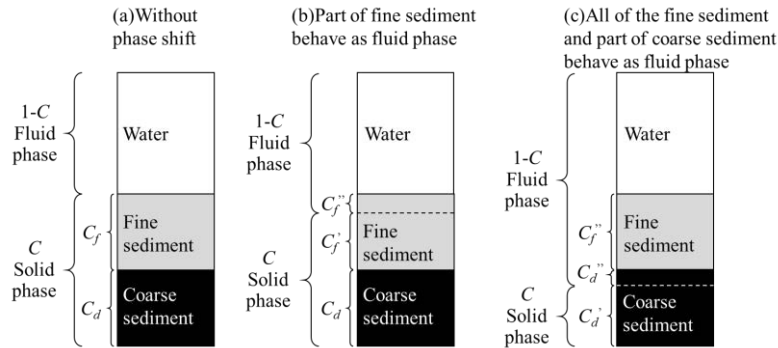


Fig. 3. Images of phases in debris flow (a) no phase shift, (b) part of fine sediment behaves as fluid phase, (c) all the fine sediment and part of the coarse sediment behaves as fluid phase.

$$C = C_d + C_f \tag{1}$$

$$C_f = C_f' + C_f'' \tag{2}$$

where C_d is the coarse sediment concentration, C_f is the fine sediment concentration, C_f' is the fine sediment concentration that behaves as solid phase, and C_f'' is the fine sediment concentration that behaves as fluid phase.

As in recent studies and in Fig. 3b, when considering fine sediment in debris flows behaving as solid and fluid phases, the following equation describes the fluid phase density ρ considering phase shift:

$$\rho = \frac{(1-C)\rho_w + C_f'' \cdot \sigma}{(1-C) + C_f''} \tag{3}$$

where σ is the mass density of the sediment and ρ_w is the mass density of pure water.

When applying the sediment concentration and the slope from our experiments, we can calculate the fluid phase density ρ using the equilibrium concentration method (Takahashi, 1991) for debris flow (equation 4) and for sediment sheet flow (equation 5). Applying equation (4) or equation (5) depends on the flow characteristics, especially on the degree of slope.

$$C_\infty = \frac{\rho \tan \theta}{(\sigma - \rho)(\tan \phi - \tan \theta)} \quad (\theta_x \leq \theta) \tag{4}$$

$$C_\infty = 6.7 \left\{ \frac{\rho \tan \theta}{(\sigma - \rho)(\tan \phi - \tan \theta)} \right\}^2 \quad (1.8 \leq \theta \leq \theta_x) \tag{5}$$

where C_∞ is the equilibrium concentration, θ is the slope angle, and ϕ is internal friction angle of the sediment.

When calculating the equilibrium concentration, we changed the fine sediment concentration behaving as fluid phase C_f'' , also changing the fluid phase density ρ , and repeated the calculation until the values of both equations for (3) and (4), or (3) and (5) became equal. After achieving equal values, we defined the fluid phase density ρ considering the fine sediment phase shift. And we also defined the solid phase sediment concentration excluding the concentration of the fine sediment behaving as fluid phase C_f'' .

We used the flow surface slope angle θ assuming that in the equilibrium state, the river bed slope and surface flow slope expected to become equal. Here, θ_x is the angle transition from debris flow to sediment sheet flow: $\rho = 1.0$

g/cm^3 and $\theta_x = 7.81$ deg. In the original equilibrium concentration, it is known that a discontinuous boundary occurs between debris flow (equation 4) and sediment sheet flow (equation 5) when the value of ρ changes from 1.0 g/cm^3 . Therefore, we applied this method to set the continuous boundary, changing θ_x as proposed in recent studies (e.g., Suzuki et al., 2013).

When the calculated fluid density ρ became larger than the condition under which all the fine sediment behaved as fluid phase, we assumed that part of the coarse sediment also behaved as fluid phase, as shown in Fig. 2c. In that case, the coarse sediment concentration C_d is as defined in equation (6) and the solid phase sediment C_{solid} is as defined in equation (7), as follows

$$C_d = C_d' + C_d'' \quad (6)$$

$$C_{solid} = C_d' + C_f' \quad (7)$$

where C_d' is the coarse sediment concentration that behaves as solid phase, and C_d'' is the coarse sediment concentration of that which behaves as fluid phase. In Fig. 2c, the right argument of equation (7) C_f' will be zero.

2.3. Experimental conditions

In Table 1, the left 5 elements show the experimental conditions and the right 5 elements show the experiment results. From Case 1–19, we set the supplied sediment concentration ($C_f + C_d$) as 0.33, 0.23, or 0.17, and changed the water supplied to $1500 \text{ cm}^3/\text{s}$, $1000 \text{ cm}^3/\text{s}$, or $600 \text{ cm}^3/\text{s}$. We also changed the ratio of fine sediment and coarse sediment (f:c), focusing in particular, on 1:1 and 1:2. In Case 20–23, we set the total supplied sediment to $300 \text{ cm}^3/\text{s}$, and changed the sediment concentration and particle size supply ratio.

3. Results And Discussion

In Fig. 2b, the graph shows the slope on the horizontal axis acquired from the result, and the calculated sediment concentration behaving as solid phase ($C_f' + C_d'$) on the vertical axis. The plots shown in the legend describe the total supplied sediment concentration ($C_f + C_d$). In the figure, the equilibrium concentration equations are also described, showing the change in the fluid phase density ρ from 1.0 g/cm^3 to 1.4 g/cm^3 .

From the results, all cases showed higher sediment concentration than expected with equilibrium concentration equations with fluid phase density $\rho = 1.0 \text{ g/cm}^3$. When the supplied sediment concentration was small, the fluid phase density ρ became small. When the supplied sediment concentration was constant, and the slope $\tan\theta$ was small, the fluid phase density ρ became large. From Table 1 (right 5 elements showing results) and Fig. 2b results, the supplied sediment concentration, and also the ratio of fine to coarse sediments suggested to affect the fluid phase density. This shows that the presence of coarse sediment influences the phase shift.

3.1. Factors affecting phase shift

Fig. 4 shows the experimental results for the debris flow phases: the upper part shows the effect of discharge and the lower part shows the effect of the particles and water ratio. Only the cases in which the supplied sediment ratio (fine to coarse: f:c) was (1:1) or (1:2) are described. The bar charts distinguished with a dotted line shows cases with the same supplied sediment concentration and the supplied sediment ratio f:c. For Case 23, the supplied concentration was 0.16, but it was placed with cases in which the concentration was 0.17.

All cases showed a phase shift to fluid phase for the fine sediment. In cases 5, 7, 9, 11, 12, 15, 18, 19, and 23, not only all the fine sediment, but also part of the coarse sediment was presumed to behave as fluid phase. In Case 15 and 19, more than half of the coarse sediment was presumed to behave as fluid phase. The supplied sediment concentration C was 0.17, the supplied sediment discharge was the smallest ($120 \text{ cm}^3/\text{s}$), and the ratio of fine to coarse sediment (f:c) was (1:1) and (5:7), respectively. However, when the supplied sediment concentration was $C = 0.17$, the supplied sediment discharge was $120 \text{ cm}^3/\text{s}$, and the ratio of fine to coarse sediment was (1:2); Case 17 did not show coarse sediment behavior as fluid phase. In the cases which coarse sediment behaving as fluid phase, the proportion of the coarse sediment was larger than that of the fine sediment, except for Case 15. Therefore, it is suggested that the mixture ratio of fine and coarse sediment affect the phase shift. On the other hand, the fluid phase density ρ became larger

than 1.25 g/cm^3 when the supplied sediment concentration was $C = 0.33$ (in Cases 5, 6, 12, and 13). Thus, the supplied sediment concentration and supplied sediment discharge indicated to affect the phase shift.

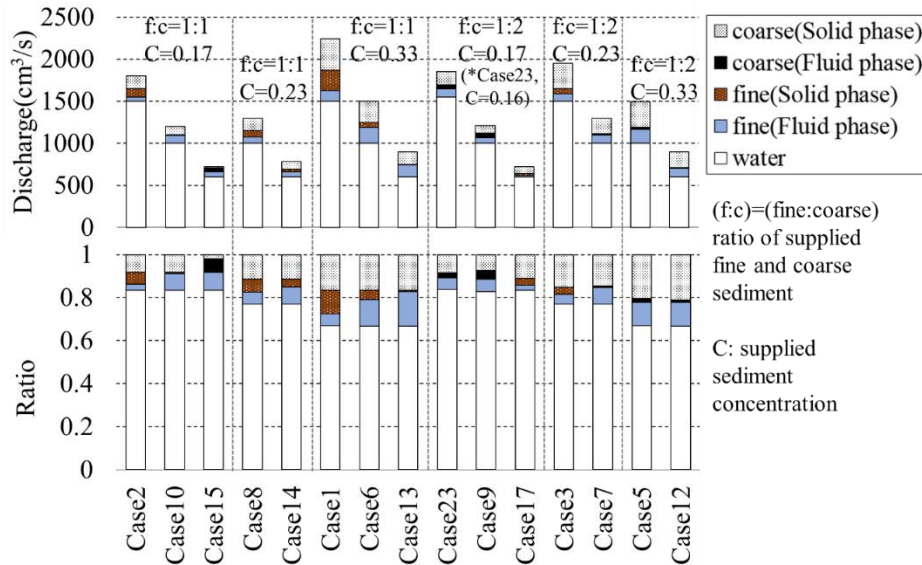


Fig. 4. Experimental results when the sediment supply fine-to-coarse ratio (in graph, shown as f:c) was 1:1 or 1:2

At the same sediment concentration, the space around sediment particles in debris flow becomes small when the sediment discharge is small. Generally, turbulence in debris flow occurs more easily when the space around sediment particles is large. And it is presumed that turbulence causes sediment phase shift from solid to fluid more easily (e.g. Nakatani et al., 2018). However, in our experiment, some case results showed a different trend. When the supplied fine-sediment discharge was large, the space around fine sediment particle became large, but showed lower fluid phase density indicating that there was difficulty completing the phase shift. This trend was especially clear in cases with the fine to coarse particle ratio of 1:1 (e.g., when the supplied sediment concentration C was 0.33: cases 1, 6, and 13).

When assuming that the space size around sediment particles in debris flow had become larger than the turbulence intensity influence range, we could explain the phenomenon that cases with large supplied fine sediment discharge resulted in lower fluid phase density indicating difficulty causing the phase shift. However, the cases in which the supplied sediment concentration $C = 0.33$ and the ratio of fine to coarse sediment was 1:2 (cases 5 and 12) showed almost the same fluid phase density, even though the supplied sediment discharge became large. In cases 5 and 12, it is suggested that the space size around sediment became close to the upper limit of the turbulence intensity influence range. On the other hand, when $C = 0.17$ and the ratio of fine to coarse sediment was 1:2 (cases 9 and 17), when the supplied sediment discharge was large, higher fluid phase density occurred which matches to the general approach. Here, it is presumed that the influence range of turbulence intensity influence was related to the amount of space around the sediment particles in debris flow, which can be considered from the supplied sediment discharge.

3.2. Considering the phase shift from turbulence

In our study, we did not acquire turbulence intensity directly from experiment results. Therefore, we focused on the turbulent mixing length as a factor related to the sediment mobility in debris flows to consider the turbulence intensity. It is influenced by kinetic energy dissipation due to the interstitial fluid turbulence in debris flow. Referring to a previous study (Egashira et al., 1986), we defined the turbulent mixing length l as follows:

$$l = \sqrt{k_f} \left(\frac{1 - C_{solid}}{C_{solid}} \right)^{\frac{1}{3}} d \quad (8)$$

where k_f is the coefficient, $\sqrt{k_f} = 0.5$ from previous studies, and d is for the diameter of the sediment particles behaving as solid phase.

Fig. 5a shows the l/d , ratio of turbulent mixing length and sediment diameter on the horizontal axis. The vertical axis shows ρ/ρ_w , a non-dimensional parameter calculated by dividing fluid phase density ρ by the density of pure water ρ_w . In the graph, the plots show the supplied sediment concentration and supplied sediment discharge. From the results, when l/d becomes large, ρ/ρ_w also becomes large. When the supplied sediment concentration C is high, l/d becomes small and ρ/ρ_w becomes large. Regarding the different supplied sediment concentrations C , the inclination of the relationship between l/d and ρ/ρ_w becomes steep when C is high. Calculating l/d from equation (8), it is assumed that when the sediment concentration C becomes higher, l/d becomes smaller and turbulence is less likely to occur. However, in our study, when sediment concentration C became higher, l/d became lower, but showing larger ρ/ρ_w and turbulence was more likely to occur.

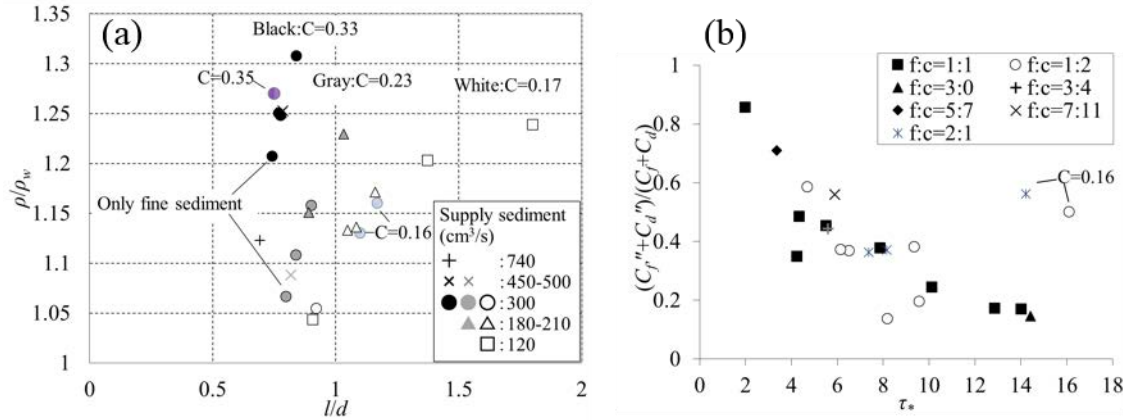


Fig. 5. Results (a) showing the relationship between the ratio of turbulent mixing length and diameter, and ρ/ρ_w , (b) showing the relationship between the dimensionless tractive force τ_* and ratio of sediment acting in fluid phase

With the same supplied sediment concentration C , cases with smaller supplied sediment discharge showed larger l/d and ρ/ρ_w , and cause a greater shift in the sediment phase to fluid phase. The previously noted trend was clear in Case 13, $C = 0.33$ and supplied sediment was 300 cm³/s; in Case 18, $C = 0.23$ and supplied sediment was 180 cm³/s; and in Case 15, $C = 0.17$ and supplied sediment was 120 cm³/s. With $C = 0.33$, Case 1 showed the smallest l/d and ρ/ρ_w , which was also the largest supplied sediment discharge case. This was an example to show that larger sediment discharge was presumed to inhibit turbulence and the phase shift. The second smallest l/d and ρ/ρ_w with $C = 0.33$ was Case 16 for which the supplied sediment was 300 cm³/s, case including only fine sediment. Except for Case 16, the next larger l/d and ρ/ρ_w with $C = 0.33$ was for supplied sediment of 500 cm³/s and then for 300 cm³/s. Therefore, this also matches the trend that smaller sediment discharge shows larger l/d and ρ/ρ_w and causes more phase shift. When $C = 0.23$, Case 4 had the smallest l/d and ρ/ρ_w , the supplied sediment discharge was 300 cm³/s, case including only fine sediment. Except for Case 4, Case 3 was the largest supplied sediment discharge with 450 cm³/s, showing the smallest l/d and ρ/ρ_w for $C = 0.23$. With $C = 0.17$, except for the smallest l/d and ρ/ρ_w in Case 17, the trend shows smaller supplied sediment discharge cases with larger l/d and ρ/ρ_w . In Fig. 5a, the supplied concentration of $C = 0.35$ is only one plot, but it matches the trend that when the concentration becomes large, l/d is lower and ρ/ρ_w is higher. For $C = 0.16$, two plots in Fig. 5a show trend similar to that for the $C = 0.17$ cases.

Next, we considered the indicator for turbulence intensity applying the dimensionless tractive force τ_* , which is widely used as a parameter for sediment movability on riverbeds given by the equation

$$\tau_* = \frac{\rho_w h \sin \theta}{(\sigma - \rho_w) d_f} \quad (9)$$

Fig. 5b shows the dimensionless tractive force τ_* on the horizontal axis. The vertical axis shows $(C_f + C_d)/(C_f + C_d)$, the ratio of sediment that behaves as fluid phase. From these results, when τ_* becomes large, the ratio of sediment behaving as fluid phase becomes small. This trend was different from those of recent studies using similar parameters u_*/w_0 for the indicator of sediment mobility, ratio of friction velocity u_* , and settling velocity w_0 . In a recent study (Nakatani et al., 2018), when u_*/w_0 became large, the ratio of sediment behaving as fluid phase became larger. The difference occurred because the supplied sediment discharge was fixed in the recent study. However, in the current

study, we applied several conditions of supplied sediment discharge. Therefore, with high sediment concentrations and also large supplied discharge conditions, it is assumed that river-bed shear force to which sediment particles are exposed while flowing, and the energy loss due to particle collision, become larger. This results in lower mobility, and in lower fluid density. In cases with smaller sediment concentration ($C = 0.16$), the two plots in Fig. 5b show rather large ratios compared with other cases with higher sediment concentrations.

4. Conclusions

In this study, we conducted hydraulic experiments with sediments of two different particle diameters, defined as fine sediment and coarse sediment. We applied equilibrium methods and also took into account the contribution of the sediment to the increase in the fluid phase density due to sediment phase shift to fluid phase. From the results, all the cases showed a shift of fine sediment to fluid phase. Furthermore, in some cases, not only fine sediments, but some part of the coarse sediments as well, indicated to behave as fluid phase. Sediment phase shift presumed to happen because of flow turbulence resulting from the factors sediment concentration, mixture of particles of different sizes, and the supplied sediment discharge. Higher total sediment concentration, and a higher proportion of coarse sediment (rather than only the fine particle content), indicated to increase the fluid phase density. Cases with smaller total sediment discharge showed higher fluid phase density in same concentration. In this study, we focused on turbulent mixing length as turbulence intensity, and found that higher sediment concentration cases showed smaller turbulent mixing length, but also showed higher fluid density. We also found that larger dimensionless tractive force linked to smaller ratios of particles behaving as fluid phase. This was opposite the trends in other recent studies. For future studies, we will aim to measure turbulence intensity from experiments to consider further mechanism of phase shift.

On the other hand, some studies claim that the sediment will not behave as either fluid or solid phase in debris flows (e.g. Sakai et al, 2016). We will consider it from different aspects such as applying resistance coefficients. In future work, we aim to propose a method for estimating the sediment phase shift to fluid phase, and apply these results in realistic debris flow simulations containing fine sediments, for more effective planning of countermeasure projects.

Acknowledgements

The study was supported by JSPS KAKENHI Grant No. 15K16312, Grant-in-Aid for Young Scientists (B). For the channel experiments, we used the facilities in the Ujigawa Hydraulics Laboratory of Disaster Prevention Research Institute, Kyoto University (Ujigawa Open Laboratory).

References

- Egashira, S., Ashida, K., Yajima, H. and Takahama, J., 1989, Constitutive equations of debris flow, Kyoto University Disaster Prevention Research Institute Annuals, v.32, B-2, p.487-499 (Japanese with English abstract).
- Hotta, N. and Miyamoto, K., 2008, Phase classification of laboratory debris flows over a rigid bed based on the relative flow depth and friction coefficients, International Journal of Erosion Control Engineering, v. 1, no. 2, p. 54-61.
- Iverson, R.M., 1997, The physics of debris flows, Reviews of Geophysics, AGU Publications, 35, p.245-296.
- Kaibori, M., Hasegawa, Y., Yamashita, Y., Nakatani, K., et al., 2018, Sediment related disaster due to heavy rainfall in Hiroshima Prefecture in July, Journal of the Japan Society of Erosion Control Engineering, v.71, no.4, p.49-60 (Japanese with English abstract).
- Ministry of Land, Infrastructure, Transport and Tourism, Water and Disaster Management Bureau, Sabo Division, 2014, Meeting Materials for Strengthening Countermeasures against Sediment Disasters, Subcommittee for structural countermeasures (in Japanese) http://www.mlit.go.jp/river/sabo/dosya_kyouka/140207_hard/140207_hard_shiryo01.pdf (accessed Nov 2018).
- Nakatani, K., Furuya, T., Hasegawa, Y., Kosugi, K. and Satofuka, Y., 2018, Study on fine sediment phase change factors and influence on debris flow behavior, Journal of the Japan Society of Erosion Control Engineering, v.70, no.6, p.3-11 (Japanese with English abstract).
- Nishiguchi, Y., Uchida, T., Tamura, K. and Satofuka, Y., 2011, Prediction of run-out process for a debris flow triggered by a deep rapid landslide, Proceedings of 5th Debris Flow Hazard Mitigation Conference, p.477-485. doi: 10.4408/IJEGE.2011-03.B-053
- Sakai, Y., Hotta, N. Hasegawa, Y. and Nakatani, K., 2016, The model calculation of the velocity of steady-state debris flow containing finer sediment, Abstract EP21C-0887 presented at 2016 Fall Meeting, AGU, San Francisco, California, 12-16 December.
- Suzuki, T., Uchida, T. and Okamoto, A., 2013, Resolution of the discontinuity with the changes of sediment transport form in numerical simulation, Journal of the Japan Society of Erosion Control Engineering, v.66, no.2, p.21-30 (Japanese with English abstract).
- Takahashi, T., 1991, Debris Flow. Balkema, Rotterdam, 165p.
- Uchida, T., Nishiguchi, Y., Nakatani, K., Satofuka, Y., Yamakoshi, T., Okamoto, A. and Mizuyama, T., 2013, New Numerical Simulation Procedure for Large-scale Debris Flows (Kanao-LS), International Journal of Erosion Control Engineering v. 6, no. 2, p.58-67.
- Wada, T., Furuya, T., Nakatani, K., Satofuka, Y. and Mizuyama, T., 2015, Experimental study on the concentration of coarser particles at the frontal segment of a debris flow, International Journal of Erosion Control Engineering, v.8, no.2, p.20-30.

Effect of rheological properties on debris-flow intensity and deposition in large scale flume experiment

Ba-Quang-Vinh Nguyen^a, Ji-Sung Lee^a, Yun-Tae Kim^{a*},
Seung-Rae Lee^b, Tae-Hyuk Kwon^b

^a Dept. of Ocean Engineering, Pukyong National Univ., Busan, Republic of Korea

^b Dept. of Civil and Environmental Engineering, KAIST, Daejeon, Republic of Korea

Abstract

Debris flows are one of the most serious hazards in the mountainous areas. To assess and mitigate the debris-flow hazard, debris-flow intensities and deposition on fans must be estimated. Rheological properties including yield stress and viscosity are major parameters to describe and predict behaviors of debris flow. In the present study, the effect of rheological properties on debris-flow intensities and deposition on fans of natural clay was investigated using large scale flume experiments. The experimental device employed in the tests consists of a tilting flume with an inclination 17°, on which a steel tank with a removable gate was installed. A final horizontal plane works as the deposition area. Natural soil samples of different water contents were tested. Rheological properties of soil mixtures were obtained from vane-rheometer tests. Non-linear regression analysis was used to assess the effect of yield stress and viscosity on debris-flow velocity, runout distance, deposited area and deposited volume. We found that the relationship between surface velocity profile and horizontal distance was complicated and could be expressed by sixth order polynomial function. Mean velocity, runout distance, deposited area decreased following a power law with an increase in yield stress and viscosity. Empirical equations were proposed to estimate these properties. The results of laboratory tests compared reasonably well with the results from numerical analysis. The results indicated that yield stress and viscosity play a significant role in the behavior of debris flow.

Keywords: Debris-flow intensities; debris-flow deposition; flume test; rheological properties.

1. Introduction

A debris flow is a moving mass of loose mud, sand, soil, rock, water and air that travels down a slope under the influence of gravity. High velocities and deposition on debris-flow fan are a hazard to residential areas. On July 27, 2011, a large catastrophic debris flow occurred in Seoul in Korea, this debris flow event caused the deaths of 49 people and affected 125,000 people. Therefore, the evaluation of debris-flow intensities and their deposition on fans are a key requirement to reduce the risk from debris flow. The debris-flow intensities can be expressed through velocity and runout distance. The deposition on fan can be represented by deposited area and deposited volume. Until now, many researchers have focused on the estimation and assessment of velocity, runout distance and volume of debris flow. The velocity and runout distance of a debris flow can be assessed via two methods including: theoretical methods (Hungr et al. 1984, Cannon and Savage 1988, Van Gassen and Cruden 1989, Takahashi 1991, Hungr 1995, VanDine 1996, Iverson 1997, Rickenmann 2005, Armanini et al. 2009) established mass and momentum conservation equations using the depth-integrated method based on the continuum theory; empirical methods estimated debris-flow properties using regression analysis based on data from field observatory or flume experiment (Hungr et al. 1984, Johnson 1984, Ikeya 1989, Corominas 1996, Rickenmann 1999, Chen and Jan 2000, Marchi and D'Agostino 2004). The key steps in theoretical methods are the selection of parameters that can be difficult to accurately estimate, such as rheological properties, flow depth, flow velocity along the channel, etc...; while the formulas obtained from

* Corresponding author e-mail address: yuntkim@pknu.ac.kr

empirical methods are limited to specific regions or flow conditions. In addition, the above studies have not considered clearly the effect of soil properties: grain size, clay fraction, water content, solid volumetric concentration, yield stress and viscosity on debris-flow behavior. From this point, this paper assess the effect of rheological properties on velocity, runout distance and deposition on fan of debris flow using the series of large scale flume experiment with natural clay at different water contents. Rheological properties of natural clay including yield stress and viscosity were obtained by large scale vane rheometer test. We compared results of flume tests with analysis using the BING numerical model. The results indicate that rheological properties like yield stress and viscosity play an important role in debris-flow behavior.

2. Materials and Methods

The laboratory tests were carried out using natural clay were collected from Miryang and Hwangnyeong mountains in Korea. Both soils in Miryang and Hwangnyeong mountains were classified as well graded sand-clay (SW-SC) with particle size distribution curve is shown in Fig. 1. In the laboratory tests, water content of material sample ranges from 48.9% to 83.2% in flume experiments and from 36% to 59% in vane rheometer tests as presented in Table 1. A series of large scale vane rheometer test and flume experiments were carried out to assess the effect of debris-flow rheological properties on velocity, runout distance and deposition on fan. A woody flume with a cross section is a isosceles trapezoid, with 4 m long and was adjusted to a slope angle of 17° for this set of experiments (Fig. 2). Then, the results of laboratory tests were compared with the results from simulations using Bing model. BING is a one-dimensional model for simulating the flow of debris flows. The governing equations are integral forms obtained from the slender flow approximations typical in the application of Boundary Layer Theory. Slope angle is assumed to be sufficiently small to allow the approximations $\sin\theta \approx \tan\theta \approx S$ and $\cos\theta \approx 1$; here S is bed slope. The general formulation used in BING is described in Imran et al. (2001). It is based on the formulation for a Bingham slurry. The numerical formulation is the Lagrangian scheme.

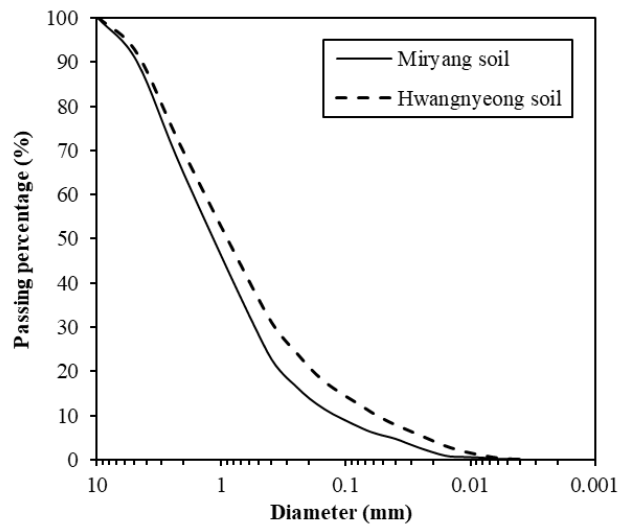


Fig. 1. Particle size distribution curve of soil sample

Table 1. List of the experiments of flume test and vane rheometer test

Soil	Flume experiment		Vane rheometer test	
	No.	Water content (w, %)	No.	Water content (w, %)
Miryang	1	48.9	1	36.4
	2	49.1	2	37.2
	3	56.8	3	40.9
	4	68.5	4	44.6
			5	49.0
Hwang- nyeong	1	51.5	1	44.7
	2	63.8	2	46.8
	3	67.3	3	49.8
	4	75.4	4	54.6
	5	79.1	5	59.3
	6	83.2		

3. Results and Discussion

3.1. Rheological properties

Fig. 3 presents a series of flow curves of the experimental results for Miryang soil (Fig. 3a) and Hwangnyeong soil (Fig. 3b) at different water content. All soil mixtures have a non-Newtonian fluid behavior. Experimental results showed that shear stress increased as shear rate increased at given water content. The test results are consistent with the results reported by Scotto Di Santolo et al. (2010), Jeong (2010), Kang (2016) and Nguyen et al (2018). Fig. 4a expresses the influence of water content on the yield stress (τ_y , Pa) for Miryang soil and Hwangnyeong soil. As water content increases an exponential decrease in the yield stress is observed. This relationship is in line with the experimental results of Kang (2016) and Nguyen et al. (2018). Fig. 4b shows the relationship between plastic viscosity and water content of soil materials in Miryang and Hwangnyeong mountains. An increase in water content is accompanied by an exponential decrease in the plastic viscosity (η , Pa.s) of all the tested soil mixtures, which is in line with the results obtained in a study of Ghezzehei and Dani (2001), Parsons et al. (2001), Kang (2016) and Nguyen et al. (2018). From these results, the yield stress and viscosity of soil mixtures used in the flume experiments were calculated from Fig. 4.

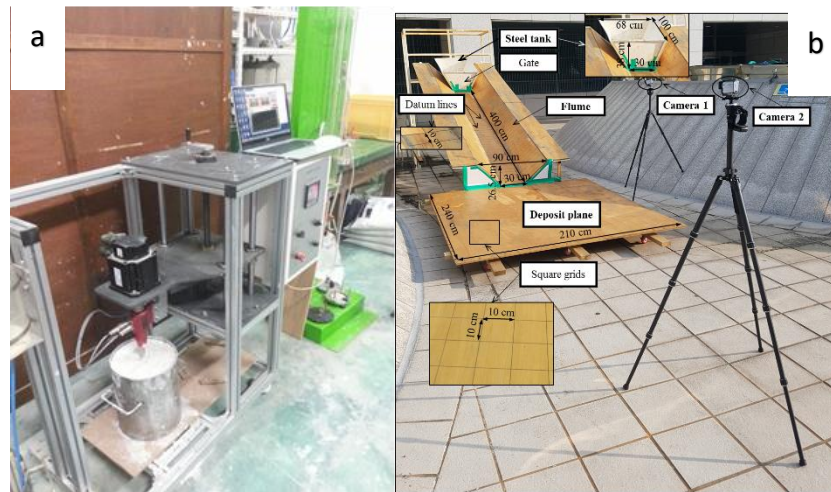


Fig. 2. (a) The large scale vane rheometer (Kang and Kim, 2016); (b) The large scale flume experimental device

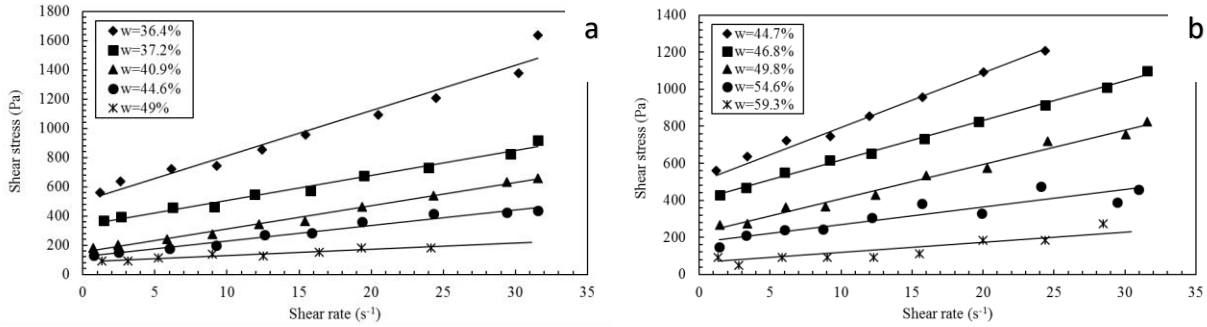


Fig. 3. Fitting rheological models obtained from experimental results at the different values of water content (a) Miryang natural clay; (b) Hwangnyeong natural clay

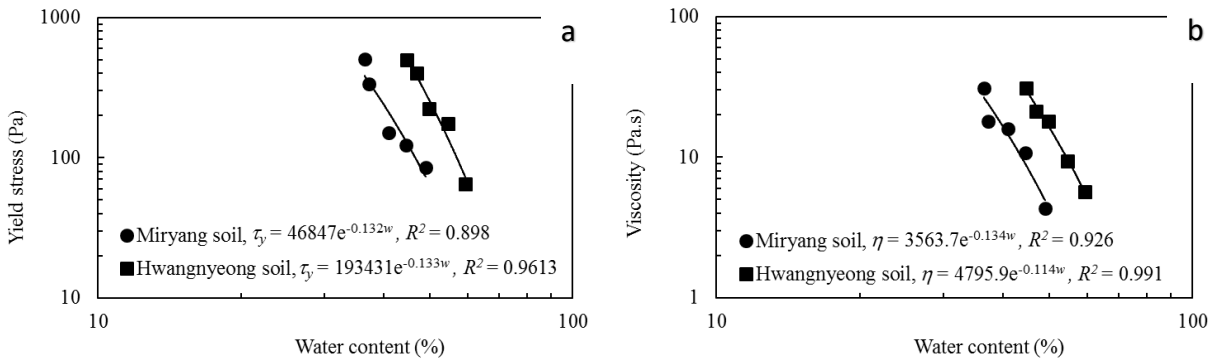


Fig. 4. Relationship between rheological properties and water content (a) Yield stress; (b) Viscosity

3.2. The effect of rheological properties on debris-flow properties

Fig. 5 shows front velocity profile of debris flow versus distance from the gate with different water content for Miryang soil (Fig. 5a) and Hwangnyeong soil (Fig. 5b). The sixth order polynomial function is a regression line of the front velocity profile with $R^2 > 0.7$. The front velocity can be described through three phases including: Phase 1, front velocity increases linearly with time and the rate of increase slightly depends on the rheological properties; Phase 2, the velocity increases to reach peak value. This value increase when water content increases. Location to reach peak front velocity also depends on water content. This result indicates that the peak velocity was very sensitive to the change of rheological properties of debris-flow material; Phase 3, front velocity decreases from peak then it increases again to reach another high value. Finally, it decreases to zero at the end of deposition area. The results of flume experiment were also compared with velocity profile obtained from BING simulation (Fig. 6). There were differences in the shape of experimental front velocity profiles from those of the BING model. In the Bing model, the velocity profile can be divided to two phase: firstly, velocity increases linearly to archive a peak value; secondly, the velocity decreases from peak value to zero at the end of deposition area. However, the effect of rheological properties on front velocity was clearly observed with the rate of increase of front velocity and the peak velocity increases with a decrease in values of the rheological properties-namely, viscosity and yield stress. These results indicate that front velocity of debris flow behaved in a complex manner with time and was very sensitive to the change of rheological properties.

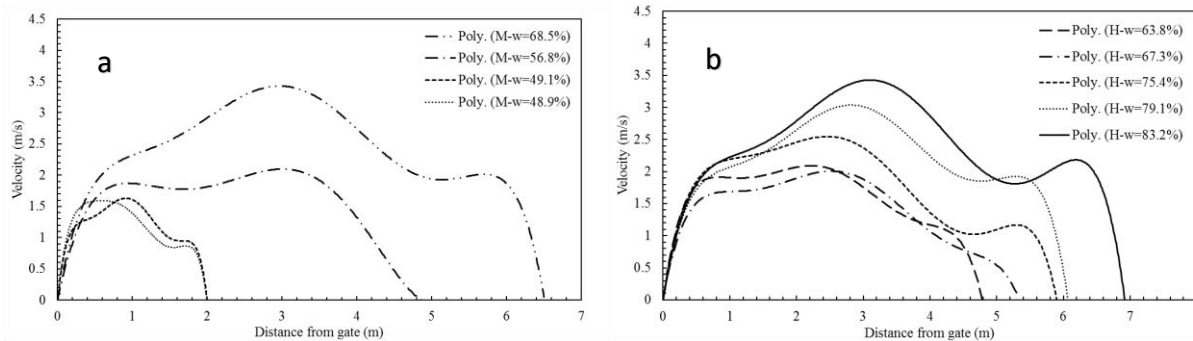


Fig. 5. Regression curve of front velocity profile of debris flow versus distance from gate at different water content (a) Miryang natural clay; (b) Hwangnyeong natural clay

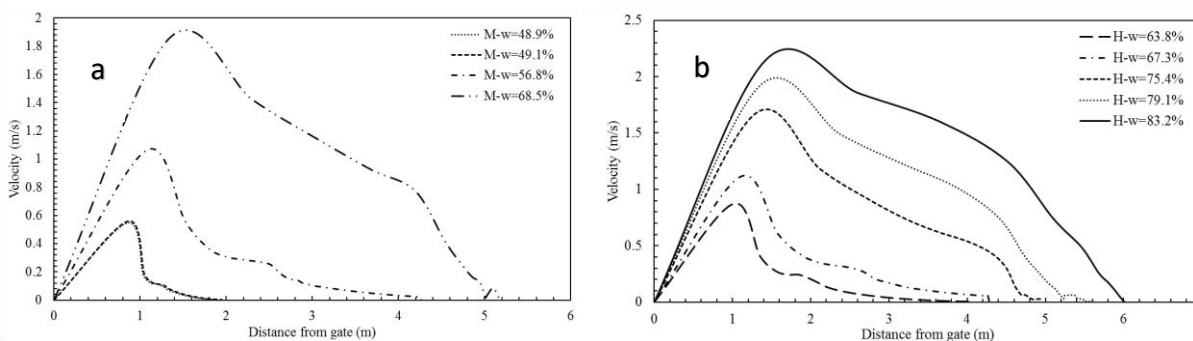


Fig. 6. Front velocity profile of debris flow versus distance from gate at different water content obtained from BING simulation (a) Miryang natural clay; (b) Hwangnyeong natural clay

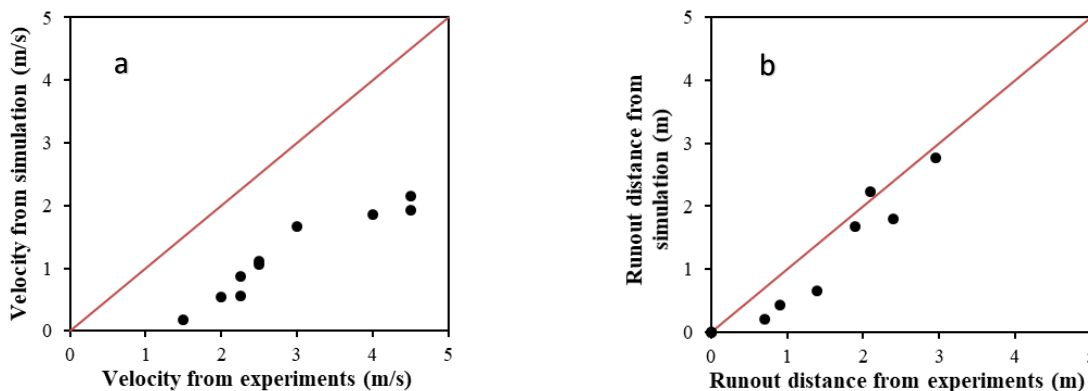


Fig. 7. Correlation between experiments and numerical simulation (a) Maximum velocity; (b) Runout distance

Fig. 7 presents the correlation of results between flume experiments and numerical simulation. Fig. 7a shows maximum velocity correlation between experiments and simulation with correlation coefficient is 0.827. Fig. 7b shows runout distance correlation between experiments and simulation with correlation coefficient is 0.937. There are underestimations in simulation results compared with experiment results. It could be explain as follows: in flume experiment, there is the change in viscosity of debris-flow material due to deposition on the flume during flow process, while in numerical simulation, Bing model could not consider this phenomenon.

Fig. 8 expresses the relationship between yield stress, viscosity and maximum front velocity (v_{max} , m/s) on the flume in a 3D-coordinate system. An increase in yield stress and viscosity is accompanied by an exponential decrease in the maximum front velocity, which is in line with the results obtained in a study of Ilstad et al. (2004) and Breien

et al. (2007). These studies had not presented directly the relationship between average front velocity of debris flow and rheological properties but, they assessed the effect of clay fraction in debris-flow material on front velocity of debris flow using laboratory flume experiments. In general, the velocities of debris flow are decreasing with increasing in clay content of soil sample. Fig. 8 also shows the comparison between the results from laboratory experiments and the results from BING simulation. The results from numerical simulation also expresses the effect of yield stress and viscosity on front velocity following an exponential fit.

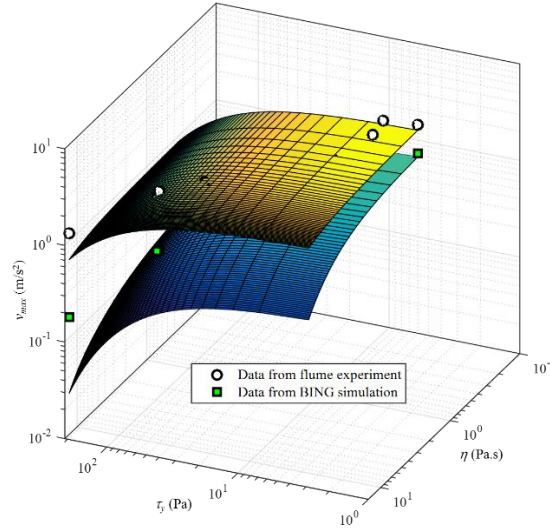


Fig. 8. Relationship between front velocity and yield stress, viscosity based on laboratory experiments and BING simulations

The relationship between runout distance (R , cm) and yield stress and viscosity is reported in Fig. 9. It can be observed that runout distance exponentially decreases with an increase in yield stress and viscosity. This result is consistent with the conclusion obtained in a study of D'Agostino et al. (2010) that reported the effect of solid volume concentration of debris-flow material on travel angle of debris flow. Hurlimann et al. (2015) also presented the relationship between runout distance and water content of soil mixture based on flume experiments. In general, runout distance increases when water content increases. Fig. 9 also shows the comparison between the results from laboratory experiments and the results from BING simulation. The results from numerical simulation also express the effect of yield stress and viscosity on runout distance following an exponential relationship.

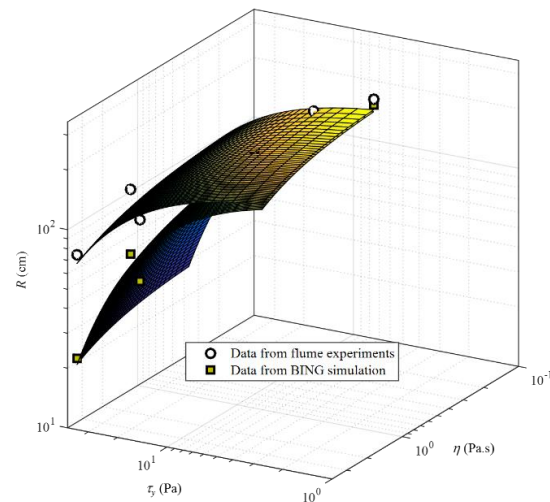


Fig. 9. Relationship between runout distance and yield stress, viscosity based on laboratory experiments and BING simulations

Fig. 10 expresses the relationship between yield stress, viscosity and deposited area (A , m²) in a 3D-coordinate system. An increase in yield stress and viscosity is accompanied by an exponential decrease in deposited area and deposited volume, which is in line with the results obtained in the studies of Ilstad et al. (2004) and Hurlimann et al. (2015). Ilstad et al. (2004) reported the influence of clay content of the material on deposition thickness of debris flows, such that the deposit thickness increases as clay fraction decreases. Hurlimann et al. (2015) also presented the relationship between deposited area and water content of the soil mixture. In general, deposited area increases when water content increases.

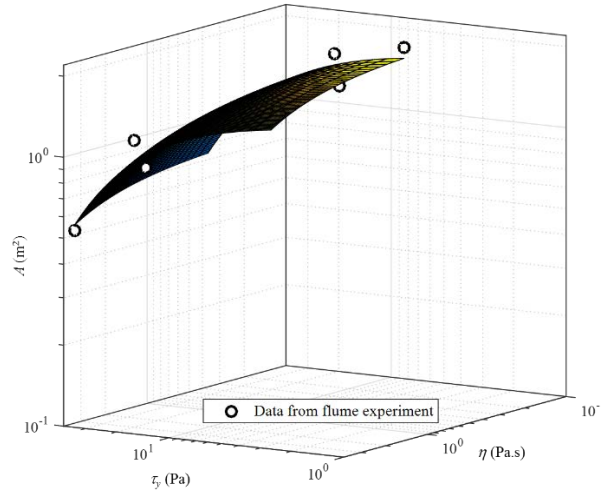


Fig. 10. Relationship between deposited area and yield stress, viscosity obtained from laboratory experiments

Average front velocity, runout distance and deposited area of debris flow can be calculated from best fit equation from Fig. 8, 9 and 10; as follows:

$$v_{max} = 3.840e^{-0.007\tau_y - 0.023\eta}, R^2 = 0.808 \quad (1)$$

$$R = 296.9e^{-0.030\tau_y - 0.104\eta}, R^2 = 0.903 \quad (2)$$

$$A = 2.260e^{-0.027\tau_y - 0.103\eta}, R^2 = 0.861 \quad (3)$$

It is noted that front velocity, runout distance and deposited area are more sensitive to the change of viscosity than the change of yield stress.

4. Conclusions

Several series of large size vane rheometer tests and large scale flume experiments were carried out in order to evaluate the effect of both yield stress and viscosity on the debris-flow intensities and deposition on fan. The following conclusions were drawn from the experimental test results: The front velocity profile could be described through three phases: Phase 1, front velocity increased linearly with time and the rate of increase was slightly dependent on rheological properties; Phase 2, the velocity increased to reach peak value at the middle of debris flow. This value increased when yield stress and viscosity decreased. The location of the peak front velocity also depend on the yield stress and viscosity; Phase 3, front velocity decreases from peak then it increases again to reach another high value. Finally, it decreases to zero at the end of deposition area. An increase in yield stress and viscosity was accompanied by an exponential decrease in the maximum and maximum front velocity. The maximum front velocity on the flume were more sensitive to the change of viscosity than the change of yield stress. Runout distance exponentially decreased with an increase in yield stress and viscosity and was more sensitive to the change of viscosity than the change of yield stress. Deposited area exponentially decreased with an increase in yield stress and viscosity, and was more sensitive to the change of viscosity than the change of yield stress.

Acknowledgements

This research was supported by a basic research grant from the National Research Foundation of Korea (NRF), funded by the Ministry of Education, Science and Technology (grant no. 2018R1D1A1B07049360), from the National Research Foundation of Korea (NRF), funded by the Korea government (grant no. 2018R1A4A1025765) and by funding from the Brain Korea 21 Plus (BK 21 Plus) initiative.

References

- Armanini, A., Fraccarollo, L., and Rosatti, G., 2009, Two-dimensional simulation of debris flows in erodible channels: *Computers & Geosciences*, v. 35(5), p. 993-1006.
- Breien, H., Pagliardi, M., De Blasio, F. V., Issler, D., and Elverhoi, A., 2007, Experimental studies of subaqueous vs. subaerial debris flows—velocity characteristics as a function of the ambient fluid: *Submarine Mass Movements and Their Consequences*, p. 101-110.
- Cannon, S. H., and Savage, W. Z., 1988, A mass-change model for the estimation of debris-flow runout: *The Journal of Geology*, v. 96(2), p. 221-227.
- Chen, J. C., and Jan, C. D., 2000, Debris flow occurrence probability on hillslopes, *Proceedings of Debris Flow Mitigation: Mechanics, Prediction and Assessment*.
- Corominas, J., 1996, The angle of reach as a mobility index for small and large landslides: *Canadian Geotechnical Journal*, v. 33(2), p. 260-271.
- D'Agostino, V., Cesca, M., and Marchi, L., 2010, Field and laboratory investigations of runout distances of debris flows in the Dolomites (Eastern Italian Alps): *Geomorphology*, v. 115(3), p. 294-304.
- Gassen, W. V., and Cruden, D. M., 1989, Momentum transfer and friction in the debris of rock avalanches: *Canadian Geotechnical Journal*, v. 26(4), p. 623-628.
- Ghezzehei, T. A., and Or, D., 2001, Rheological properties of wet soils and clays under steady and oscillatory stresses: *Soil Science Society of America Journal*, v. 65(3), p. 624-637.
- Hungr, O., Morgan, G. C., and Kellerhals, R., 1984, Quantitative analysis of debris torrent hazards for design of remedial measures: *Canadian Geotechnical Journal*, v. 21(4), p. 663-677.
- Hungr, O., 1995, A model for the runout analysis of rapid flow slides, debris flows, and avalanches: *Canadian Geotechnical Journal*, v. 32(4), p. 610-623.
- Hürlimann, M., McArdell, B. W., and Rickli, C., 2015, Field and laboratory analysis of the runout characteristics of hillslope debris flows in Switzerland: *Geomorphology*, v. 232, p. 20-32.
- Ikeya, H., 1989, Debris flow and its countermeasures in Japan: *Bulletin of the International Association of Engineering Geology*, v. 40(1), p. 15-33.
- Ilstad, T., Elverhoi, A., Issler, D., and Marr, J. G., 2004, Subaqueous debris flow behaviour and its dependence on the sand/clay ratio: a laboratory study using particle tracking: *Marine Geology*, v. 213(1), p. 415-438.
- Imran, J., Harff, P., and Parker, G., 2001, A numerical model of submarine debris flow with graphical user interface: *Computers & geosciences*, v. 27(6), p. 717-729.
- Iverson, R. M., 1997, The physics of debris flows: *Reviews of geophysics*, v. 35(3), p. 245-296.
- Jeong, S. W., 2010, Grain size dependent rheology on the mobility of debris flows: *Geosciences Journal*, v. 14(4), p. 359-369.
- Johnson, A. M., 1984, Debris flow: Slope instability.
- Kang, H. S., 2016, Physical vulnerability assessment of buildings considering rheological properties of debris flow and rainfall return period, Doctor thesis, Department of Ocean Engineering, Pukyong National University, Korea.
- Marchi, L., and D'Agostino, V., 2004, Estimation of debris-flow magnitude in the Eastern Italian Alps: *Earth Surface Processes and Landforms*, v. 29(2), p. 207-220.
- Nguyen, V. B. Q., Kang, H. S., and Kim, Y. T., 2018, Effect of clay fraction and water content on rheological properties of sand–clay mixtures: *Environmental Earth Sciences*, v. 77(16), p. 576.
- Parsons, J. D., Whipple, K. X., and Simoni, A., 2001, Experimental study of the grain-flow, fluid-mud transition in debris flows: *The Journal of Geology*, v. 109(4), p. 427-447.
- Rickenmann, D., 1999, Empirical relationships for debris flows: *Natural hazards*, v. 19(1), p. 47-77.
- Rickenmann, D., 2005, Runout prediction methods: In *Debris-flow hazards and related phenomena*, p. 305-324.
- Scotto di Santolo, A., Pellegrino, A. M., and Evangelista, A., 2010, Experimental study on the rheological behaviour of debris flow: *Natural Hazards and Earth System Sciences*, v. 10(12), p. 2507-2514.
- Takahashi, T., 1991, *Debris Flow: IAHR Monograph Series*, AA Balkema: Rotterdam. Doi. org/10.1201/9780203946282.
- VanDine, D. F., 1996, Debris flow control structures for forest engineering. *Res. Br., BC Min. For., Victoria, BC, Work. Pap.*, 8, 1996.

Long travel distance of landslide-induced debris flows

Yuki Nishiguchi^{a,*} and Taro Uchida^b

^a CTI Engineering, Co., Ltd., 1047-27, Onigakubo, Tsukuba, Ibaraki 300-2651, Japan

^b National Institute for Land and Infrastructure Management, 1 Asahi, Tsukuba, Ibaraki 305-0804, Japan

Abstract

Large-scale landslides often induce debris flows and cause serious damage to humans. These events typically have water contents in the landslide mass less than 60 % and sediment concentrations more than 40 %. In spite of high sediment concentrations, landslide-induced debris flows can runout long distances. For large-scale stony debris flows, many previous studies have suggested that coarse gravels behave as a solid phase, whereas fine particles with interstitial water can behave as a fluid phase. We hypothesized this fine sediment might be one of the key processes controlling the long travel distances of landslide-induced debris flows. Here we assumed that the maximum diameter of the fine sediment behave as a fluid phase should vary depending on the friction velocity of the debris flow and the settling velocity of sediments. We conducted detailed field surveys for four landslide-induced debris flows and applied our numerical simulation model to describe the travel distance of the debris flows. Our results show that, if we set the ratio of the friction velocity of debris flow to the settling velocity of sediments around 1 to 4, the simulated travel distance agreed well with our studied four debris flows. We also confirmed that, while the total volume or mean sediment diameter of debris flows varied between study cases, the variability of ratios was small. We believe that our new method and the information it provides, may be helpful for predicting the future risk from the landslide-induced debris flows.

Keywords: debris flow, numerical simulation, travel distance; fine sediment

1. Introduction

Debris flows induced by large-scale landslides have sometimes runout long distances (e.g., Nishiguchi et al., 2012). Nishiguchi et al. (2011) studied the relationship between the travel distance of landslide (L) and the maximum height between landslide scar and deposited area (H) of 10 Japanese debris flows caused by deep-seated rapid (catastrophic) landslides. The ratios of H to L were ranging from 0.11 to 0.35 and smaller than that for shallow landslide and small-scale debris flows. Similar processes have been studied in the last several decades in the world (e.g., Iverson et al., 2015). These long travel distanced debris-flows have serious impacts on human life and infrastructure. Therefore, in this study, we focused these large-scale debris-flow travelled relatively long distance.

It is important to identify large debris flow hazard areas. In large-scale stony debris flows, other researches considered that the gravels move like laminar flow, but the interstitial water behaves as turbulent flow (e.g., Takahashi, 2009; Hotta, 2012). Moreover, fine particles can behave within the interstitial water as a fluid and many previous studies call this process of fine sediment as shifting from solid phase to fluid phase (e.g., Iverson, 1997; Hotta, 2012). We refer to it as “phase-shift”. Based on this phase-shift concept, Nishiguchi et al. (2014) proposed a maximum diameter of sediments that behave like a fluid as D_c and confirmed that if we use best-fit D_c , the long travel distance of several past debris flows can be described by numerical simulations. However, the problem remains of that how to determine the parameter of D_c in the simulations given D_c should be variable in time and space, yet Nishiguchi et al. (2014) assumed D_c to be constant in their simulations.

Here we developed a program in which the maximum diameter of phase-shifted sediment is varied depending on hydraulic conditions. Also, we conducted numerical simulations for landslide-induced debris flows with long runout and verified the applicability of our model.

* Corresponding author e-mail address: nishiguchi@ctie.co.jp

2. Simulation model

2.1. Phase-shift concept

Uchida et al. (2013) assumed that sediments can be classified into two groups (fine and coarse) by sediment diameter and defined the critical diameter of the sediment (D_c) as the smallest diameter that behaves as a solid in a debris flow. That is, they proposed that sediments larger than D_c move as solids, while those smaller than D_c behave as fluids in a debris flow. Here, we have adopted this concept to describe the phase shift of fine sediment. So, we defined the solid concentration of debris flow as the concentration of the sediment larger than D_c in debris flow. Also, we defined the representative grain diameter of the solid sediment as the mean diameter of the sediment larger than D_c . In addition, we calculated the interstitial fluid density (ρ) as follows.

$$\rho = \rho_s \cdot C_f / (1 - C) + \rho_w (1 - C_f / (1 - C)) \quad (1)$$

where C is the concentration of total sediment in debris flow, C_f is the concentration of phase-shifted sediment in a debris flow, ρ_w is pure water density and ρ_s is the solid density of the sediment.

Nishiguchi et al. (2014) assumed that fine particles can be physically suspended due to riverbed shear stress in a debris flow and showed that the settling velocities of best-fit D_c were lower than the friction velocities of the debris flow from the simulation results of past debris flows. Then, we propose that D_c varies depending on the ratio of settling velocity of D_c to friction velocity of the debris flow (α) as follows.

$$u_* > \alpha w_k \quad (2)$$

where u_* is friction velocity of the debris flow, w_k is settling velocity of diameter of d_k and α is a coefficient. α is assumed to be constant in time and space. Here we calculated u_* for each time and space using the flow depth and longitudinal gradient as follow. This means that u_* should varied in time and space, indicating that because the D_c varied with the u_* , the D_c was also varied in time and space.

We considered friction velocity and settling velocity can be calculated from riverbed shear stress and the equation of Rubey, respectively. The friction velocity (u_*) can be calculated from riverbed shear stress as

$$u_* = \sqrt{ghI}, \quad (3)$$

where I is the slope angle and h is flow depth of a debris flow. According to Rubey (1933), settling velocity can be expressed as follows.

$$w_k = \sqrt{sgd_k} \cdot \left(\sqrt{\frac{2}{3} + \frac{36v^2}{sgd_k^3}} - \sqrt{\frac{36v^2}{sgd_k^3}} \right) \quad (4)$$

$$s = \rho_s / \rho - 1 \quad (5)$$

where v is kinematic viscosity of the fluid (0.01 cm²/s), s is submerged density of sediment, d_k is particle diameter, g is gravitational acceleration. Therefore, the behaviors of debris flow should be affected by friction velocity through change of fluid density and sediment diameter of solid phase due to phase-shift of fine sediment.

2.2. Simulation model

Kanako-LS, developed by Uchida et al. (2013), can describe a variety of sediment transport processes ranging from stony debris flow to bed load transport. In the model, the equations for momentum, continuity, riverbed deformation, erosion/deposition rate, and riverbed shear stress are based on previous studies by Takahashi and colleagues (e.g., Takahashi and Nakagawa, 1991; Takahashi, 2009). Kanako-LS can describe the phase-shift effect, but D_c is assumed to be constant in both space and time, regardless of solid sediment concentrations and flow

condition, such as debris flow, sediment sheet flow, or ordinary turbulent water flow.

In this study, we modified the two-particle model of Kanako-LS to a multi-particle model and introduced our assumption of determining D_c , which varies depending on hydraulic condition as described in section 2.1.

3. Method

3.1. Study sites

The study sites (referred to as Sites A–D) are located in Japan. These debris flows occurred between 2003 and 2015 (Table 1). All studied debris flows were triggered by heavy rainstorms and were caused by a deep-seated rapid landslide. These depths of landslides were around 20 m, 10 m, 45 m and 15 m at Sites A–D, respectively.

We obtained the elevations of the land surface after the debris flows from prefecture LiDAR data for Sites A, C and D at a resolution of 1 m, 1 m and 2 m, respectively. For Site B, we obtained the results of field survey measurements. The landslide volumes (including the volume of the voids) determined from these topographic data ranged from 1.9×10^4 to 2.7×10^5 m³ and the extent of travel of the debris flow ranged from 0.6–2.1 km. Maximum erosion depths at Sites A, B and C were around 5, 7 and 3 m, respectively, whereas there were no eroded areas at Site D.

We evaluated the grain size distribution of the debris flows using sieve tests, cross-sectional photographs of the deposits, and grain size distributions obtained from field measurements. Mean diameters of debris flow sediment for Sites A–D were 251, 600, 140, 735 mm, respectively.

3.2. Data preparation for numerical simulation

The longitudinal profiles of the riverbed that we used for the numerical simulations were set based on topographic data acquired before the debris flow events. The widths of the debris flows were determined as the averages of the riverbed widths before and after the debris flow. The initial depths of the movable bed layer were determined as the maximum erosion depth. Therefore, we set this variable to 5, 7, 3, and 0 m for Sites A, B, C, and D, respectively. Site B contained one grid-type sabo dam at 280 m below the landslide that was effectively blocked by the rocks and sediments of the debris flow. Therefore, we included a closed-type sabo dam in this simulation.

We assumed that the soil and weathered bedrock of the landslide material were fully saturated by water. We used water content of the landslide mass based on measured porosity data of 0.34 and 0.49 for Site A and Site C, respectively. We did not have porosity data at sites B and C; therefore, we used the data collected for Site A.

To create the input hydrographs at the lower end of landslide scar, we used the method proposed by Nishiguchi et al. (2013), who assumed that the relationship between velocity and flow depth could be described by Takahashi's theory (Takahashi, 2004) and assumed that the longitudinal length of the debris flow at the lower end of landslide scar was the same as that of the landslide scar. Peak discharges of hydrographs for Sites A–D were estimated as about 4300, 1800, 3900 and 5400 m³/s, respectively.

We used the particle size distribution of the debris flows measured in the field. Parameters of sediment density,

Table 1. Studied debris flows

Site	Date	Total volume of landslide *	Total volume of debris flow *	Travel distance	Distance of eroded section	Maximum erosion depth	Mean diameter of debris flow sediment
A	2003/7	43,000 m ³	31,000 m ³	1.6 km	0.8 km	5 m	251 mm
B	2007/7	19,000 m ³	19,000 m ³	0.6 km	0.15 km	7 m	600 mm
C	2015/7	91,000 m ³	91,000 m ³	1.1 km	0.25 km	3 m	140 mm
D	2005/9	520,000 m ³	272,000 m ³	2.1 km	0 km	0 m	735 mm

* including volume of the voids

Table 2. Parameters for the simulations

Parameters	Value
Water density	1,000 kg/m ³
Sediment density	2,650 kg/m ³
Volumetric sediment concentration in the riverbed	0.65
Coefficient of riverbed roughness	0.06
Coefficients of erosion rates	0.0007
Coefficients of deposition rates	0.05

Table 3. Simulation cases

Case	Diameter of fine sediments of fluid phase
Case1	All sediments are regarded as solid phase.
Case2	$\alpha = 4$ in Equation (2).
Case3	$\alpha = 1$ in Equation (2).

sediment concentration of riverbed, coefficients of erosion rates and deposition rates were set to 2,650 kg/m³ and 0.65, 0.0007 and 0.05, respectively (Table 2).

3.3. Simulation cases

To test the effect of the magnitude of phase-shift on the propagation processes of a debris flow, we assumed three different condition of phase-shift. In Case 1, we assumed that all sediments were treated as a solid phase. In Cases 2 and 3, the ratio of settling velocity of D_c to friction velocity of the debris flow (α) were 4 and 1 in the debris flow.

4. Results

In Case 1, the simulated travel distances from the lower ends of the landslide scars to the lower ends of the debris-flow deposits were less than half of the observed travel distances (Fig. 1). The lower ends of the landslide scars are zero of x-axis in Fig.1. If we consider the phase-shift of fine sediment in Cases 2 and 3, the simulated travel distances of the debris flows increased; the distances of eroded section at Sites A, B and C also increased. As the critical ratio of settling velocity of phase-shifted sediment to friction velocity of debris flow (α) decreased, simulated travel distance of the debris flows increased.

Comparing simulated results with observations, little agreement was found when all sediments are regarded as solids (Case1). The simulated travel and erosion distances matched our observations well when α was 1 (Case3) at Sites A and B, and when α was 1 or 4 at Site C (Fig.1). Although the calculated elevation riverbed change agreed well with the observed river bed change at 0–1200 m from the landslide scar in Site D, the calculated travel distance of the debris flow was shorter than observed. This might mean that α should be set as less than 1 in Site D to reproduce the observed travel distance.

Fig.2 (a) shows the relation between mean sediment diameter of debris flow sediment and α for simulations with a good match to observations for Sites A-D and Fig.2(b) shows the relation between total volume of debris flow and α . Although the mean sediment diameter and total volume of debris flow varied between study cases, α ranged from 1 to 4 and the variability of α was small. It means that phase-shifted sediment was variable in time and space and our assumption, in which D_c varies depending on the ratio of settling velocity of D_c to friction velocity of the debris flow, was effective in predicting the particle size of phase-shifted sediment.

5. Concluding remarks

We introduced the concept that the diameter of phase-shifted sediment is variable depending on friction velocity of a debris flow, which represents riverbed shear stress of a debris flow in our numerical simulations, then examined the applicability of our method to a variety of large-scale debris flows. As a result, we showed that, although their volumes and topography were diverse, the simulated results for these debris flows reproduced well the observed erosion and deposition patterns, if we set the ratio of friction velocity of debris flow to settling velocity of sediments as around 1 to 4 to account for phase-shift effects. Thus, we believe that our new method may be helpful for predicting the future risk from the long travel distance of landslide-induced debris flows.

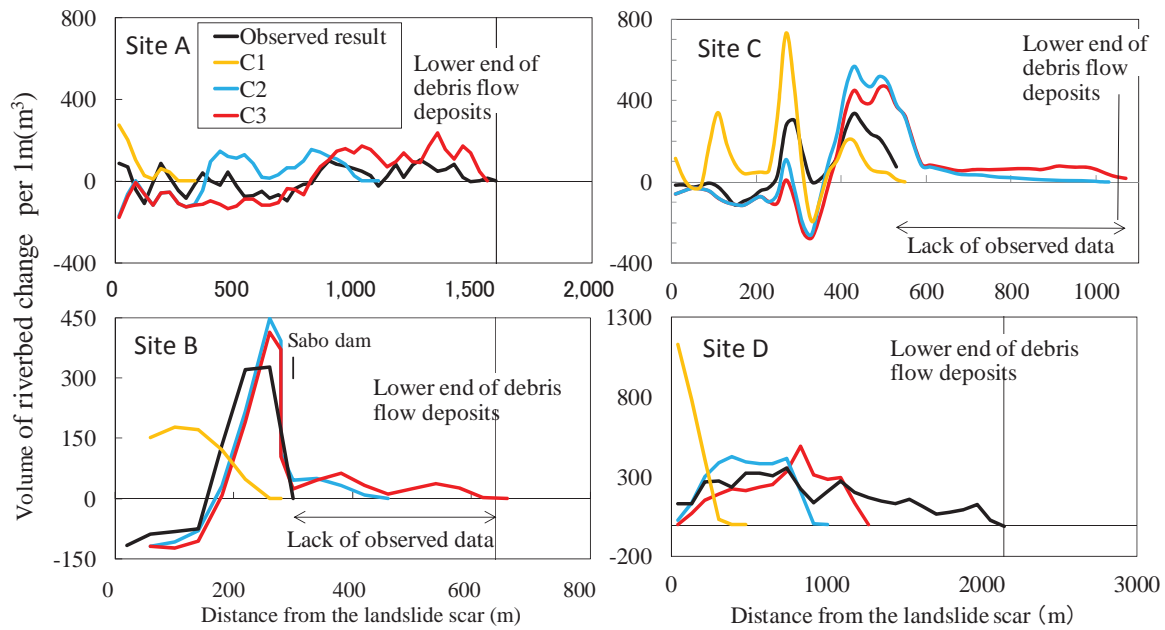


Fig. 1. Simulated Case1, Case2 and Case3 and observed riverbed change at Site A-D

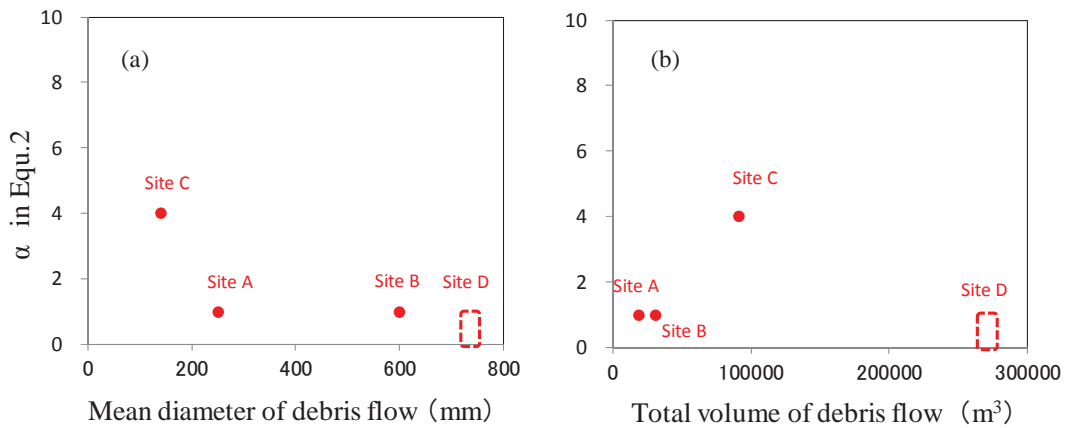


Fig. 2. (a) Relationship between mean sediment diameter of debris flows and α providing a good match to observations; (b) Relationship between total volume of debris flow and α providing a good match to observations

References

- Hotta, N., 2012, Basal interstitial water pressure in laboratory debris flows over a rigid bed in an open channel: *Nat. Hazards Earth Syst. Sci.*, v.12, p.2499–2505, doi:10.5194/nhess-12-2499-2012.
- Iverson, R. M., 1997, The physics of debris flows: *Rev. Geophys.*, v.35, no.3, p.245–296, doi: 10.1029/97RG00426.
- Iverson, R. M., et.al., 2015, Landslide mobility and hazards: implications of the 2014 Oso disaster: *Earth and Planetary Science Letters*, v.412, p.197–208, doi: 10.1016/j.epsl.2014.12.020.
- Nishiguchi, Y., Uchida, T., Ishizuka, T., Satofuka, Y. and Nakatani, K., 2013, Numerical simulation of debris flows induced by deep-seated catastrophic landslide: 12th International Symposium on River Sedimentation, Kyoto, p.119-127.
- Nishiguchi, Y., Uchida, T., Satofuka, Y., Nakatani, K. and Mizuyama, T., 2014, Controlling Factors of Phase-shift of Fine Sediment in Large-scale Debris flows, in *Proceedings of INTERPRAEVENT International Symposium 2014*, Nara, p.640-647, http://www.interpraevent.at/palm-cms/upload_files/Publikationen/Tagungsbeitraege/2014_1_640.pdf.
- Nishiguchi, Y., Uchida, T., Takezawa, N., Ishizuka, T. and Mizuyama, T., 2012, Runout characteristics and grain size distribution of large-scale debris flows triggered by deep catastrophic landslides: *International Journal of Erosion Control Engineering*, v.5, p.16–26, doi:10.13101/ijece.5.16.
- Rubey W.W., 1933, Settling velocities of gravel, sand and silt particles: *American Journal of Science*, v.25, p. 325-338, doi:10.2475/ajs.s5-25.148.325.
- Takahashi T., 2004, Mechanics and countermeasure of debris flow: *Kinmirai-sha*, 432 p.
- Takahashi T., 2009, A Review of Japanese Debris Flow Research: *International Journal of Erosion Control Engineering*, v.2, no. 1, p.1-14, doi:10.13101/ijece.2.1.
- Takahashi, T. and Nakagawa, H., 1991, Prediction of stony debris flow induced by severe rainfall: *Journal of the Japan Society of Erosion Control Engineering*, v.44, no.3, p.12–19, doi:10.11475/sabo1973.44.3_12.
- Uchida, T., Nishiguchi, Y., Nakatani, K., Satofuka, Y., Yamakoshi, T., Okamoto, A. and Mizuyama, T., 2013, New Numerical Simulation Procedure for Large-scale Debris Flows (Kanako-LS): *International Journal of Erosion Control Engineering*, v.6, p.58-67, doi:10.13101/ijece.6.58.

Submerged planar granular column collapse: Fluid fluxes at the collapsing granular front

Gustavo Pinzón^a, Miguel Angel Cabrera^{a,*}

^aUniversidad de los Andes, Carrera 1 Este No. 19^a-40, Bogotá, 111711, Colombia

Abstract

Understanding of particle-fluid interactions in a kinematic system is of great importance in the assessment and mitigation of natural mass flows (i.e., debris flows, submarine landslides, pyroclastic density currents). Previous research has pointed on the crucial role of the solid packing fraction in the motion of saturated and submerged granular systems. However, issues in understanding the role and dominance of particle-fluid interactions in transitional granular flows remain a work in progress. The granular column collapse allows a simplification of the complex dynamics observed in those systems, in which a granular assembly is organized with a given aspect ratio, between its initial height and initial width ($a=H_0/R_0$), and let to collapse by self-weight onto a horizontal surface. This work presents a new approach to study submerged granular columns through the use of a modified planar model, incorporating a novel gate mechanism that does not interact with the surrounding fluid nor the granular media. Dye fluid is added to visualize the behaviour of the fluid enclosing the granular mass. Experimental results allow the formulation of an interaction mechanism between the particles and the surrounding fluid, identifying the fluid inflow into the column at release, followed by an recirculating outflow during the column spreading. These fluxes between the mobile mass and the fluid result in vortices next to the surface, entraining particles and mixing the surrounding fluids. The insights and conclusions gained in this research can be applied to the development and validation of analytical and numerical models studying the motion of immersed granular flows.

Keywords: Granular column; granular flows; physical modeling; submarine landslides

1. Introduction

Submarine landslides can generate tsunamis (Ivanova et al., 2018), damage submarine infrastructure (Harbitz et al., 2013) and even induce coastal geomorphological changes (Dawson, 1994). Recent studies have found that the coupled motion of submarine landslides has a strong link with the initial volume packing fraction (Rondon et al., 2011), presenting a dilatant behaviour when densely packed and a contractant behaviour when loosely packed. However, it is yet not clear the mechanism controlling the momentum exchange between the particulate media and surrounding fluid during failure. In this paper, we address the momentum exchange originated in a submerged granular column collapse.

The granular column collapse is an ideal model to reproduce transitional granular flows on a small scale (both in dry and submerged conditions), where a granular column is quickly released over a horizontal surface and led to collapse by self-weight (Lajeunesse et al., 2004; Lube et al., 2004). In the current paper, a submerged granular system with the addition of dyed fluid is studied in a planar 2D model. The granular mass is characterized by its initial height H_0 and horizontal length R_0 , related by the aspect ratio $a=H_0/R_0$. Two aspect ratios ($a=0.85$ and $a=2.63$) are used to analyze the behaviour of the surrounding fluid during collapse.

* ma.cabrera140@uniandes.edu.co

2. Planar granular column setup

A dry planar model, similar to a Hele-Shaw cell, is introduced by Lacaze et al. (2008) with a thickness varying from 1.2 to 1.8 particle diameters. This configuration provides an easy measurement of the internal deformation and kinematic field during collapse. In their configuration, a top-swinging gate is employed as the opening mechanism. However, if such a mechanism is to be employed in submerged conditions, the gate motion will generate secondary fluxes that would interact with the overall collapse dynamics. This paper presents a similar setup adapted to the submerged case condition with an alternative opening mechanism. In this model, the top-swinging gate is replaced by a sliding gate moving in a plane perpendicular to the particles plane of motion, guaranteeing that all particles are released simultaneously and that no additional fluxes are generated (see Fig. 1).

Figure 1 presents a sketch of the experimental setup. The experimental setup is composed of two Plexiglass (PMMA) square windows of 450 mm side and 10 mm thick. A cell gap of 2.4 mm lies between them and a 2 mm thick PMMA hollow square with an inner length of 390 mm. To limit leakages in the model perimeter, pieces of paperboard are added in between the PMMA windows and the hollow square. The paperboard pieces are moistened to diminish their potential absorption and prevent leakages. The opening mechanism is operated by a 4 bar linear pneumatic actuator. A high-intensity LED panel of 4000 lm backlights the model. A Mikrotron MotionBLITZ Cube 4 camera records the granular column collapse at a frame rate of 800 fps and with a resolution of 720 px by 530 px.

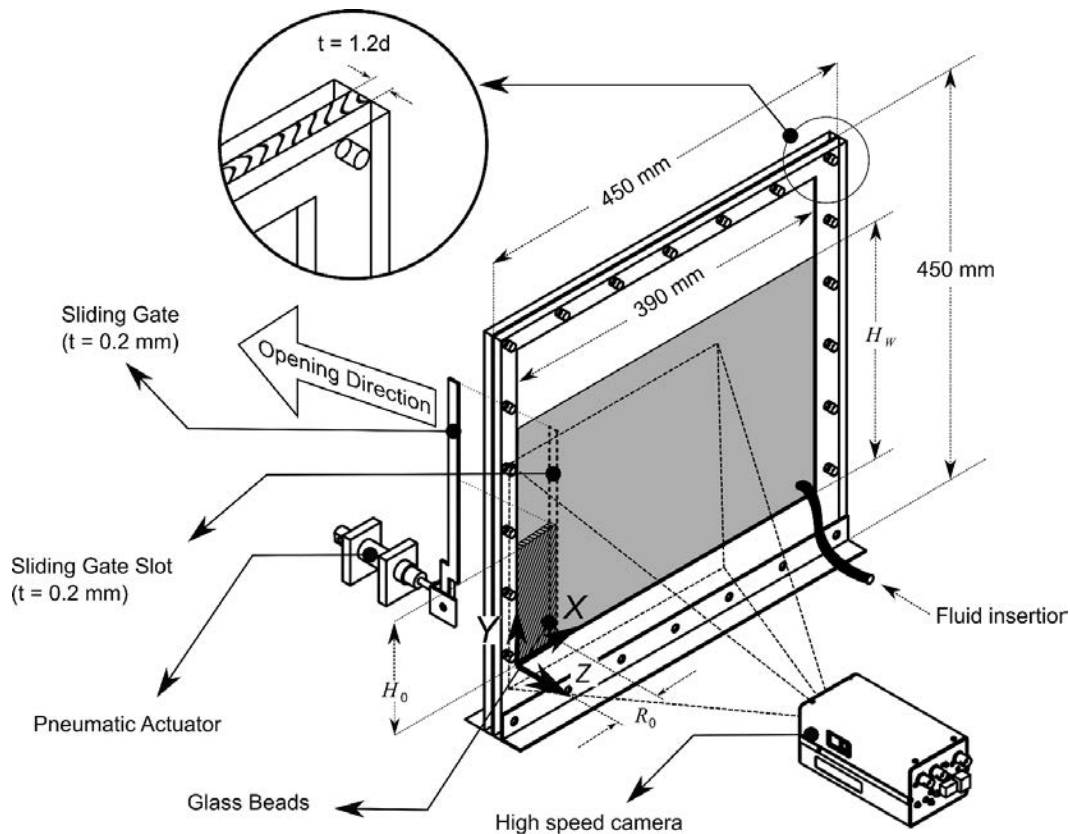


Fig. 1. Sketch of the granular column setup

Experiments are performed with 2 mm diameter ceramic beads with a particle density of $\rho_p = 3600 \text{ kg/m}^3$, manufactured by Sigmund-Lindner GmbH. The particles present a repose angle of $28.15^\circ \pm 0.75^\circ$, measured inside the experimental setup by releasing the particles in free-fall and under dry conditions. To prevent leaks in the sliding gate slot, petroleum-jelly seal is applied in the sliding gate, taking care that none of it gets inside the slot. The granular column is build up to a desired initial height H_0 and the fluid is injected into the model. A slow fluid injection is performed, ensuring that no air bubbles remain trapped inside the granular body. The fluid used in this work is

composed of a mixture of deionized water with regular soap in a volume ratio of 40:1. Fluid is added until it reaches a height of 50 mm above the granular column. The sliding gate is connected to the pneumatic actuator and the illumination system is turned on, along with the camera and pressure system. At this point a dye is added using a needle through a compartment in the upper part of the experimental setup (see Fig. 2). The dye solution is made of 100 ml of whole milk and 10 ml of rubbing alcohol. Once the dye reaches the bottom of the model and stabilize, the opening mechanism is activated and the camera records the movement of the granular mass. In this paper, we explore the collapse dynamics of short and tall columns at aspect ratios of $a=0.85$ and $a=2.63$, respectively. The following sections present the main results on the interaction of the granular column collapse and the surrounding fluid.

3. Results and discussion

The submerged granular column is released evenly and quickly through its height with the occurrence of minimal droppings at the gate slice. The column collapse starts with the release of single particles on the column's vertical free-face and the formation of a curved wedge at its bottom-right corner. For the aspect ratio of $a=0.85$, the wedge crosses the granular column and emerges at near its surface-mid-width, transitioning into a shallow flow over the collapsed material, up to five particles thick, and deposits into a trapezoidal shape (see Fig. 2 (a-e)). For the aspect ratio of $a=2.63$, the wedge extends through the full column width curving up to the column's top-left corner, releasing groups of free falling particles (see Fig. 2(g)) and transitioning into a slightly thicker flow over the collapsed material, up to ten particles thick, and deposits into a triangular shape (see Fig. 2 (f-j)). The single particles ejected from the collapsing mass decelerate and swirl, in a counterclockwise motion, until returning to the moving mass at a position behind from their release point (Topin et al., 2011).

Following the work of Courrech du Pont et al. (2003) the Stokes number St (Eq. 1) and the fluid-grain density ratio χ (Eq. 2) can be used in the classification of a mass flow within three main flow regimes: free-fall regime, viscous regime, and inertial regime. Considering the particle parameters described above and assuming a fluid density of $\rho_f=1000 \text{ kg/m}^3$ and fluid viscosity of $\mu_f=0.001 \text{ Pa}\cdot\text{s}$, the current set of experiments result in $St \approx 17.9$ and $\chi \approx 1.9$, falling into the inertial regime. Mass flows in the inertial regime are understood to be controlled by gravity and fluid drag, approaching a limit velocity when the equilibrium between these two quantities is reached.

$$St = \frac{1}{18\sqrt{2}} \frac{(\rho_p \Delta \rho g d^3)^{1/2}}{\mu_f} \quad (1)$$

$$\chi = \left(\frac{\rho_p}{\rho_f} \right)^{1/2} \quad (2)$$

Figure 3 presents the propagation of the granular front in time for the two aspect ratios being studied. On it, the collapse dynamics can be divided into three phases: first, an acceleration phase initiates after the column is released; then, the front propagation reaches a constant-velocity phase; and finally, a deceleration phase transits the column motion until deposition. The instantaneous front position (R_i) is measured directly from the digital images and the time collapsing time (t_f) is taken as the time lasted until the column reached its final front position (R_f). Unlike dry granular flows, the front spreads as an interconnected mass (see Fig. 2), without releasing particles during its spreading (Pinzon and Cabrera, 2018). The collapsing time t_f is 0.8 s and 1.7 s for the short and tall columns, respectively.

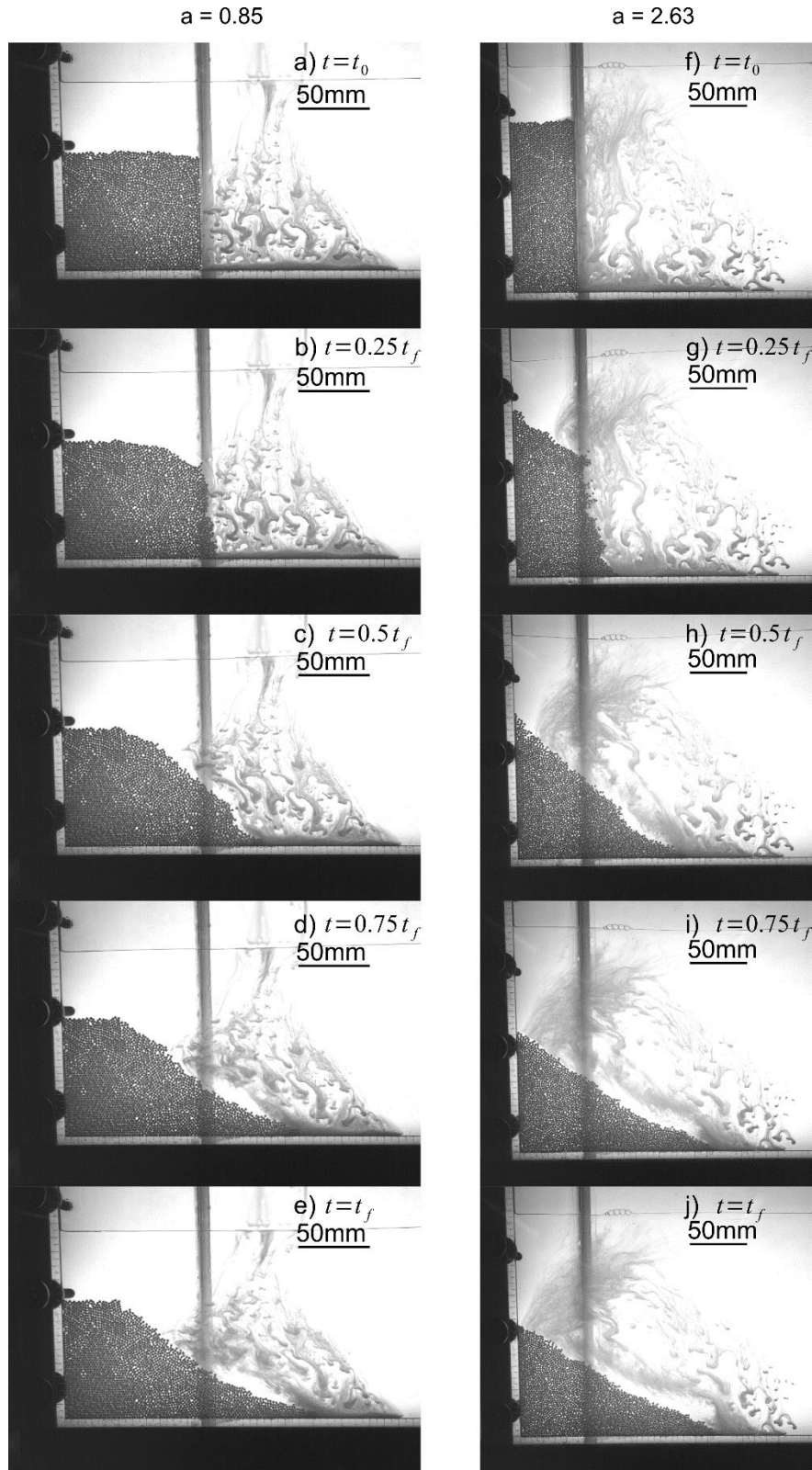


Fig. 2. Snapshots of the submerged column collapse. (a) to (e) short column with initial aspect ratio $a = 0.85$; (f) to (j) tall column with initial aspect ratio $a = 2.63$.

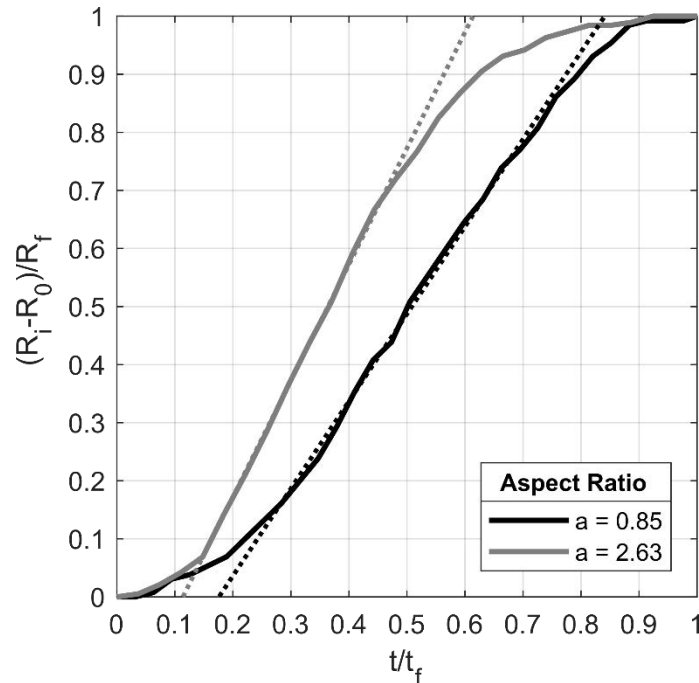


Fig. 3 Normalized lateral displacement of the granular front vs time. The dashed line marks the zone where the front presents a steady lateral propagation.

Figure 3 shows that the short column accelerates for a longer period of its total collapsing time, while the deceleration phase starts earlier on the tall column. However, the duration of the acceleration phase is on both cases close to 0.25 s, being in agreement with the observations of Bouguin and Lacaze (2018) for submerged columns in water. Moreover, the constant-velocity phase occurs in an equivalent time fraction of $0.4 t_f$ on both cases but relates to different durations. In this region, the front propagation velocity is 0.35 m/s and 0.42 m/s for short and tall columns, respectively.

After the column release, the water free-surface above the column is dragged-down, up to 4 mm and 10 mm for the short and tall columns, respectively, and waves sideways. Thanks to the dyed fluid, it is possible to visualize the flow patterns generated from the interaction of the granular column collapse with the surrounding fluid. Note that no secondary flows being induced by the gate opening are observed, being one of the main advantages of the current experimental setup.

Rondon et al. (2011) found that the deposit morphology of a submerged granular column is mainly controlled by the initial volume packing fraction, resulting in short runout (R_f) for initially dense columns and viceversa. In their analysis, dense columns would dilate at the column release, inducing an inflow of fluid into the newly form voids and then reaching an equilibrium between the system dilation speed and viscous drag. For the current experimental setup, a rather dense assembly is obtained, being controlled by the cell gap and the system configuration alignment (Lévy et al., 2018). In our experiments, the momentum exchange mechanism between particles and fluid can be identified at the same three phases described in Fig. 3.

Figure 4 presents the mean velocities of the fluid next to the granular column at release and within the acceleration phase. These flow velocities are computed with the particle image velocimetry (PIV) technique implemented in PIVlab (Thielicke and Stamhuis, 2014) and correspond to the mean velocities along the x-axis of the bottom-half and top-half of the initial column height (hollow and filled markers, respectively). Mean negative velocities, within the coloured region, represent fluid motion pointing into the granular column. The short column presents fluid motion predominantly in the collapse direction at release and transits into a slight inflow at its bottom marked up by the hollow markers errorbars (see Fig. 4(a)). The tall column presents an oscillating inflow through the column height,

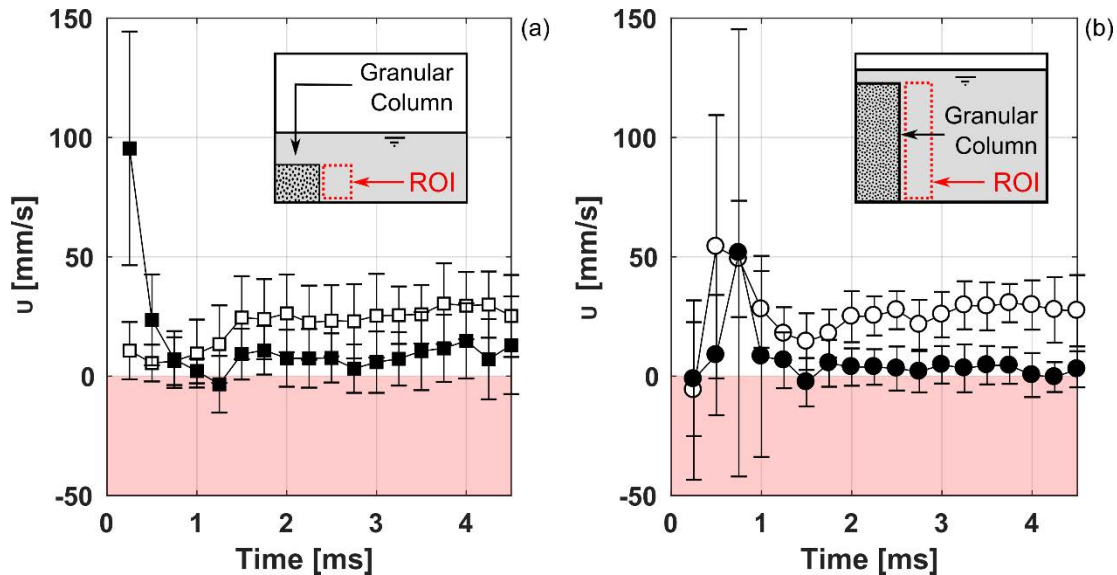


Fig. 4. Mean fluid front velocity at release and within the region of interest (ROI) marked in the inset for (a) $a=0.85$; (b) $a=2.63$. Hollow and filled markers represent the mean velocities along the x-axis of the bottom-half and top-half of the initial column height, respectively

immediately after release, and then dissipates moving predominantly in the collapse direction on top and presenting fluid inflow next to the column's bottom.

At the constant-velocity phase, three simultaneous movements occur: the fluid next to the granular column front i) fills the moving particles at its base, ii) is pushed upwards at its mid-height, and iii) moves against the collapse direction at its top. This motion pattern results in vortices that spin the ejected particles in a counterclockwise direction and explain the formation of the dye-free zone parallel to the granular surface (observed in Fig. 2(c) and 2(h)). The generation of this zone is formed from the fluid that is dragged from within the column and then flows out the granular assembly at this phase.

At the decelerating phase, some dye reached the deposit top and starts to settle while being moved by the remaining inertia from the momentum transfer described in the previous phase. Note that at this phase most of the dye is mixed and diffuse during the collapse.

4. Conclusions

The collapse of a submerged granular column is studied in a planar configuration, testing short and tall columns made of densely packed ceramic beads, immersed in a solution of deionized water and regular soap. The fluid motion next to the column is visualized with the addition of a dye solution.

Our experiments agree on the deposition patterns between short and tall columns (i.e., trapezoidal and triangular deposits, respectively) and can be classified as submerged granular flows within the inertial regime. In this regime, the collapse phases (e.g., acceleration, constant-velocity, and deceleration) are clearly identified from the motion of the granular column spreading, and are linked with the interaction mechanism between grains and surrounding fluid. This mechanism is observed on both column's aspect ratios, starting with an inflow of fluid next to the column's free-vertical face associated with the dilation of the granular assembly. This inflow is overcome by the moving granular media, entraining fluid at its base and pushing fluid out at its surface. These fluxes between the collapsing granular media and the surrounding fluid result in vortices next to the surface, entraining particles and mixing the surrounding and interstitial fluids. This mechanism complements the current understanding of mass flows in submerged conditions and provides an opportunity for analytical and numerical verification.

Further work would extend on this visualization advantages, studying the coupling between particles and fluid as a function of the column aspect ratio, fluid viscosity, and level of saturation. These extensions would set the validation case for the development of numerical approaches studying the motion of immersed granular flows.

Acknowledgements

We are grateful to Daniel Osorio for his assistance in the execution of the experiments. This research was funded by the Early-stage Researcher fund (FAPA) under the Grant No. PR.3.2016.3667.

References

- Ivanova, A. A., Kulikov, E. A., Fine, I. V., and Baranov, B. V., 2018, Generation of a Tsunami from the Submarine Landslide Near the East Coast of Sakhalin Island: *Moscow University Physics Bulletin*, v. 73, no 2, p. 234-239.
- Harbitz, C. B., Løvholt, F., and Bungum, H., 2014, Submarine landslide tsunamis: how extreme and how likely?: *Natural Hazards*, v. 72, no 3, p. 1341-1374.
- Dawson, A. G., 1994, Geomorphological effects of tsunami run-up and backwash: *Geomorphology and Natural Hazards*, p. 83-94.
- Rondon, L., Pouliquen, O., and Aussillous, P., 2011, Granular collapse in a fluid: role of the initial volume fraction: *Physics of Fluids* v. 23, no 7, p. 073301.
- Lajeunesse, E., Mangeney-Castelnau, A., and Vilotte, J. P., 2004, Spreading of a granular mass on a horizontal plane: *Physics of Fluids*, v. 16, no 7, p. 2371-2381.
- Lube, G., Huppert, H. E., Sparks, R. S. J., and Hallworth, M. A., 2004, Axisymmetric collapses of granular columns: *Journal of Fluid Mechanics*, v. 508, p. 175-199.
- Lacaze, L., Phillips, J. C., and Kerswell, R. R., 2008, Planar collapse of a granular column: Experiments and discrete element simulations: *Physics of Fluids*, v. 20, no 6, p. 063302.
- Topin, V., Dubois, F., Monerie, Y., Perales, F., and Wachs, A., 2011, Micro-rheology of dense particulate flows: Application to immersed avalanches: *Journal of Non-Newtonian Fluid Mechanics*, v. 166, no 1-2, p. 63-72.
- Courrech du Pont, S., Gondret, P., Perrin, B., & Rabaud, M., 2003, Granular avalanches in fluids: *Physical review letters*, v. 90, no 4, p. 044301.
- Pinzon, G., and Cabrera, M. A., 2018, Planar Granular Column Collapse: A Novel Releasing Mechanism, in *Proceedings of China-Europe Conference on Geotechnical Engineering*. Springer, Cham. p. 591-596.
- Bougouin, A., & Lacaze, L., 2018, Granular collapse in a fluid: Different flow regimes for an initially dense-packing: *Physical Review Fluids*, v. 3, no 6, p. 064305.
- Lévay, S., Fischer, D., Stannarius, R., Szabó, B., Börzsönyi, T., and Török, J., 2018, Frustrated packing in a granular system under geometrical confinement: *Soft matter*, v. 14, no 3, p. 396-404.
- Thielicke, W., and Stamhuis, E. J., 2014, PIVlab-towards user-friendly, affordable and accurate digital particle image velocimetry in MATLAB: *Journal of Open Research Software*, v. 2.

Small scale debris-flow experiments on run-up height

Dieter Rickenmann ^{a,*}, Tobias Karrer ^{a,b}, Brian McArdell ^a, Christian Scheidl ^c

^aSwiss Federal Research Institute WSL, Zuercherstrasse 111, Birmensdorf CH-8903, Switzerland

^bIUB Engineering AG, Heinrichstrasse 147, Zürich CH-8005, Switzerland

^cUniversity of Natural Resources and Life Sciences, Vienna A-1190, Austria

Abstract

We studied the run-up behavior of debris flows in a small-scale experimental flume using various material compositions, approach flow velocities, and geometries of the obstacle. The experiments were performed with a straight and 4 m to 6 m long flume channel with a circular cross-section of 15 cm top width. The debris flows were released from a head tank. We used three debris-flow mixtures, three channel slopes and either a vertical wall or an adverse slope of 30° as an obstacle. Additional tests were performed using water without sediment. The inclined channel was followed by a 30 cm long horizontal transition reach. Immediately upstream and along this reach we measured the shape of the approaching debris-flow surge with four laser sensors, and determined also the approach flow velocity and depth. The run-up conditions were recorded with a high-speed video camera. The measured run-up conditions were compared with four different theoretical models. The observed run-up conditions differed to some extent between debris-flow mixtures and clear water flows, and there were also some differences among the debris flow mixtures depending on the relative proportion of coarse particles. The observed run-up heights were generally within the range predicted by the theoretical models, but none of them appears to be universally applicable to the entire range of investigated flow conditions. The commonly used energy principle is not always a conservative method to estimate run-up heights, as has been reported in previous studies.

Keywords: debris flow; experiment; run-up height; flow velocity

1. Introduction and theoretical models

Debris-flow run-up on obstacles in their path has a great practical relevance. For a number of applications the flow velocity of a debris flow is one of the key parameters. Owing to the extreme nature of this process, direct measurements in the field are challenging. One important problem in engineering practice is the estimation of run-up height of debris flows against obstacles in their paths. If no direct measurements are possible, characteristics of debris flow events can be estimated based on post-event field investigations (Scheidl et al., 2015). In the specific case of velocity estimation such field investigations can be based on geological deposits on banks (Scheidl et al., 2015) and flow marks on trees, rocks or walls. In bigger events run-up trimlines at adverse slopes can be used. These post facto estimates of debris flow speeds are only useful, if the models that relate flow speeds to run-up heights are well-founded (Iverson et al., 2016). Unfortunately this is not always the case.

The goal of this study is to systematically investigate the run-up height on obstacles and find a relation to debris-flow parameters. To reach this goal several small-scale laboratory experiments were conducted. The debris-flow velocities as well as the run-up heights were measured independently. The measured flow properties of the incoming flow were used as input to theoretical models, and the predicted run-up heights were then compared with the measured run-up heights.

The (frictionless) Point Mass (PM) model, based on the energy principle and a complete conversion of kinetic energy into potential energy, is the most commonly used to predict debris-flow run-up height against vertical walls

* Corresponding author e-mail address: dieter.rickenmann@wsl.ch

(Kwan, 2012; Choi et al., 2015). The PM model used here is formulated for a fluid element moving on top (at the surface) of the approach flow to the obstacle. We note that Iverson et al. (2016) used a modified version of the PM model without adding the approach flow depth h_1 to the final run-up height H . The frictionless Finite Mass (FM) Model is derived by a mechanical energy balance for a finite mass, as presented by Iverson et al. (2016). Also here, a complete conversion of kinetic energy into potential energy is assumed, but the model is formulated with respect to the center of the finite mass, and a uniform vertical distribution of the mass in its final position (at the vertical wall) is assumed.

Theoretical runout models for mass flows against obstacles (dams) with adverse slopes were developed for snow avalanches, debris flows, and rapid landslides (e.g., Takahashi and Yoshida, 1979; Mancarella and Hungr, 2010), and this model was called Smooth Momentum Flux (SMF) model. So far the SMF model was always formulated and tested on obstacles perpendicular to an inclined channel. Iverson et al. (2016) modified the SMF equation in three key aspects. First, it is assumed that all incoming flow momentum is redirected upslope by centripetal forces that act on the foot of the adverse slope. Second, the focus is on basal flow resistance caused exclusively by Coulomb friction. Third, a more precise treatment of the effects of longitudinal pressure gradients is considered.

One significant recognition from recent research is that the behavior of avalanches impacting a dam can be characterized by shock waves. This approach was first described by Hákonardóttir et al. (2003) and tested for avalanches, steady water flows and granular flows. It was again reported in Jóhannesson et al. (2009) (avalanches) and by Choi et al. (2015), who investigated the run-up mechanism for pure water and supercritical sand flows. Here a generalized version of the Momentum Jump (MJ) approach proposed by Iverson et al. (2016) is used, which accounts for the possibility of non-hydrostatic longitudinal normal stresses and/or a jump in the flow bulk density from upstream to downstream of the jump.

The four theoretical models are summarized in the Table 1 below, where the run-up height H (presented in non-dimensional form as H/h_1) is given as a function of the approach flow depth h_1 and approach flow velocity v_1 and further parameters for. These are g = gravitational acceleration, $Fr_1 = v_1/(gh_1)^{0.5}$ = Froude number (of the approach flow), κ = earth pressure coefficient, θ = angle of adverse slope, and ϕ_e = basal friction angle. Iverson et al. (2016) noted that the MJ Model (Table 1) can be rearranged with the only dependent variable (H/h_1) in the form of a cubic equation.

Table 1. Four theoretical run-up height models that were used for comparison with the experimental results. The models are as presented in Iverson et al. (2016), except for the PM model for which we added the approach flow depth h_1 to obtain the final run-up height H . For the FM, SMF, and MJ models, equal densities $\rho_1 = \rho_2$ are assumed, where ρ_1 refers to the density of the flow before the obstacle and ρ_2 to that in the run-out or run-up zone.

<i>Model equation</i>	<i>Model name</i>	<i>Short name</i>
$\frac{H}{h_1} = 1 + \frac{v_1^2}{2gh_1} = 1 + \frac{Fr_1^2}{2}$	Point Mass	PM
$\frac{H}{h_1} = 1 + \frac{v_1^2}{gh_1} = 1 + Fr_1^2$	Finite Mass	FM
$\frac{H}{h_1} = \frac{\left(Fr_1 + \frac{\kappa}{2} \frac{1}{Fr_1} \cos^3 \theta \right)^2}{\left(1 + \frac{\tan \phi_e}{\tan \theta} \right)}$	Smooth Momentum Flux	SMF
$\frac{H}{v_1^2/g} = \frac{2}{\kappa} \left(\frac{H}{h_1} \right) + \frac{1}{Fr_1^2}$	Momentum Jump	MJ

There are two important limitations associated with our study presented here. First, the experiments were performed at a very small scale, which makes it difficult to compare them with natural debris flows (Iverson, 2015). Second, the analytical models considered in Table 1 are based on the assumption of steady, uniform incoming flow;

this has to be kept in mind for our comparison of the experimental observations with the analytical model predictions.

2. Experiments and measurements

The experiments were conducted at the Swiss Federal Institute for Forest, Snow and Landscape Research WSL in Birmensdorf. A schematic overview of the flume and the instrumentation layout is presented in Fig. 1. The flow is started from a reservoir with a gate which can be rapidly opened to initiate a dam-break-like release of the sediment mixture. The reservoir empties into a 60 cm long acceleration section, in which the rectangular cross section smoothly transitions to a semi-circular cross section of the main flume. This main part of length L (s. also below) consists of a flexible plastic half-pipe with a diameter of 0.17 m mounted on a wooden supporting construction and aligned with wooden retaining walls alongside of the plastic half-pipe. The surface of the flume is covered with 40-grid aluminum oxide carbide sandpaper (P40, 1960 siarexx) providing a uniform basal friction layer. At the downstream end the flume bed begins to flatten. In this bend section, 0.22 m long, the flume bed is covered with duct tape (tesa®extra Power Universal) in order to minimize the hydraulic energy losses. The transition from a uniformly sloped, semicircular channel to a horizontal, rectangular outlet does not follow a well-defined geometrical shape but great care was taken to establish a smooth changeover. The flume ends on a planar formwork panel. Vertically placed acrylic sidewalls channel the debris flows on the flat runout surface, 0.24 m long, and help them maintain high speeds as they cross the horizontal runout surface and encounter obstacles. Two geometries of obstacles were used: an adverse slope inclined at 30°, and a vertical wall (inclined at 90°), and both obstacles were 0.8 m wide. In every case there was a gap of 0.05 m in flow direction between the acrylic sidewalls and the beginning of the obstacle. Three different channel inclinations were used to vary the approach flow velocity v_1 in front of the obstacle: 20° and 25° with a flume length $L = 6$ m, and 40° with $L = 4$ m.

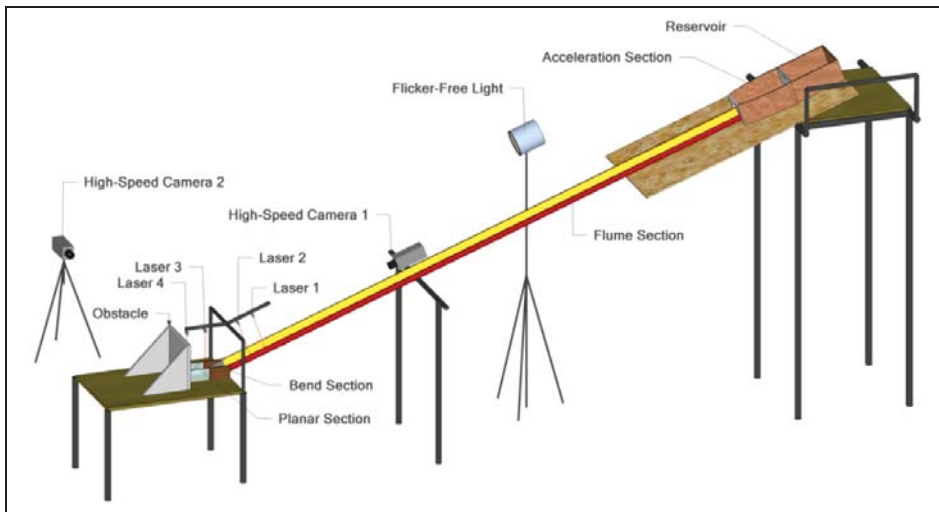


Fig. 1. Schematic view of experimental set-up and the instrumentation layout.

Three sediment-water mixtures with different grain size distribution were used. The experimental mixtures used in this study (A, B and C) are similar to those described in Scheidl et al. (2015) and fit in the large variability of grain size distributions of field debris-flow samples. Scheidl et al. (2015) and Scheidl et al. (2013) provide a comparison between mixtures A, B, C and sediment mixtures used in other studies. The mixtures are based on combinations of loam, crushed stone and water. Four different crushed stone fractions from the KIBAG Kies Stadel AG (Windlach, Switzerland) were used. The loam was imported from the clay pit of Stoob (Austria), a village well known for pottery art. The result of a mineral analysis revealed, that the loam consists of 26 % clay, 60 % silt and 14 % sand. Further the analysis showed that the clay fraction of the loam ($< 2\mu\text{m}$) contains 22 % illite, 24 % kaolinite and 53 % smectite. Smectite is a swellable clay mineral, which counteracts phase separation for a longer time period

(Scheidl et al., 2013). The mass contribution of each grain size fraction and of the water is given in Table 2. The total weight of each experimental mixture was kept constant at 12 kg. All the mixtures were composed of 60 volume-percent (vol.%) or 73 weight-percent (wt.%) of sediment (loam and crushed stone) and 40 vol.% of (or 27 wt.%) of water. This results in a total volume of approximately 8.1 dm^3 experimental debris flow mass with a bulk density of $\rho_{df} = 1484 \text{ kg/m}^3$. The characteristics of the experimental debris mixtures are given in Table 3 which includes also information on the grain size distributions.

The instrumentation layout includes four laser devices at the lower end of the channel to determine flow depth and front velocity. They were mounted directly above the channel with the same inclination as the channel (Fig. 1). Two high speed cameras (monochrome, 800×600 pixels, up to 500 frames per second) were mounted to capture the run-up process. One was installed at the side, perpendicular to the flow axis, and the other one captured a frontal view of the run-up. They were triggered with a capacitive proximity switch at the gate in the moment of the gate opening. The lasers recorded flow depths over a time interval of 20 s with an additional pre-trigger of 1 s. The raw data contained a lot of noise and scattered signal due to the wet surface of the channel and the debris flow. For that reason, all raw data was initially filtered. A moving median filter based on a running window of 80 points removed random effects and the signal noise. The measurement frequency of the laser devices is 2 kHz, hence a moving median over 80 points basically averages measurements over a time duration of $1/25 \text{ s}$. The laser devices were calibrated at the beginning of each day. The flow observed at the section of laser 4 was sometimes already influenced by the run-up process ca. 5.5 cm downstream. Some further pre-processing of the laser data was needed to find a robust method to determine reliable values of flow depth and flow velocity before the impact of the flow with the obstacle. If possible the flow depth measured by laser 4 was used as input parameter h_1 for the theoretical models, otherwise the flow depth measured by laser 3 was used as input parameter h_1 . The approach flow velocity was determined from the time difference of characteristic positions of the front between two laser cross-sections close to the obstacle.

Table 2. Proportions of the crushed particle fractions used to prepare the sediment mixtures (s. also Table 3).

Mixture	Water [kg]	Loam [kg]	Crushed stone fraction			
			0-2 mm [kg]	2-4 mm [kg]	4-8 mm [kg]	8-11 mm [kg]
A	3.20	2.52	2.52	2.00	0.88	0.88
B	3.20	2.21	2.21	1.75	1.32	1.32
C	3.20	1.89	1.89	1.50	1.76	1.76

Table 3. Characteristics of sediment mixtures used for the experiments. d_{xx} is the sediment particle diameter for which xx% of the mass of is finer. (The mixtures are similar as those used by Scheidl et al., 2015).

Mixture	d_{30} [mm]	d_{50} [mm]	d_{90} [mm]	W [vol.%]	ρ_{df} [kg/m ³]	Total mass [kg]
A	0.1	0.8	4.9	40	1484	12
B	0.2	1.2	5.9	40	1484	12
C	0.4	1.8	6.9	40	1484	12

3. Results and discussion

3.1. Run-up against adverse slope

The normalized run-up heights H/h_1 are shown as a function of the approach flow Froude number Fr_1 in Fig. 2 for the experiments with a 30° adverse slope. Also shown are the normalized run-up heights predicted by the four models listed in Table 1 (whereby the MJ Model equation was solved for the dependent variable H/h_1). We cannot observe a clear stratification of the experimental data, except for a slight tendency of mixture A with the finest sediment to plot at the lower range of the data (for a given Froude number). The FM model provides the most conservative estimate of run-up height (upper bound of theoretical models) for values of Fr_1 larger than 2, and all

experiments resulted in run-up heights smaller than predicted by this model. If the MJ model is assumed to be valid for the experiments, then different earth pressure coefficients κ would be required for different ranges of the Froude number Fr_1 for a best fit with the data, with an approximate value of $\kappa \approx 1.0$ for Fr_1 smaller than about 2.8, and $\kappa \approx 0.4$ for Fr_1 larger than about 2.8 (Fig. 2). The SMF model (which may be appropriate for the run-up against an inclined obstacle) approximately fits the experiments for $\kappa \approx 1.0$ and a basal friction angle ϕ_b between 30° and 40° in the case of Fr_1 larger than about 3, and for $\kappa \approx 1.0$ and $\phi_b \approx 10^\circ$ in the case of Fr_1 smaller than about 3. For comparison, the results from the water experiments are included in a separate plot (inset in Fig. 2); these data are in reasonable agreement with the PM model.

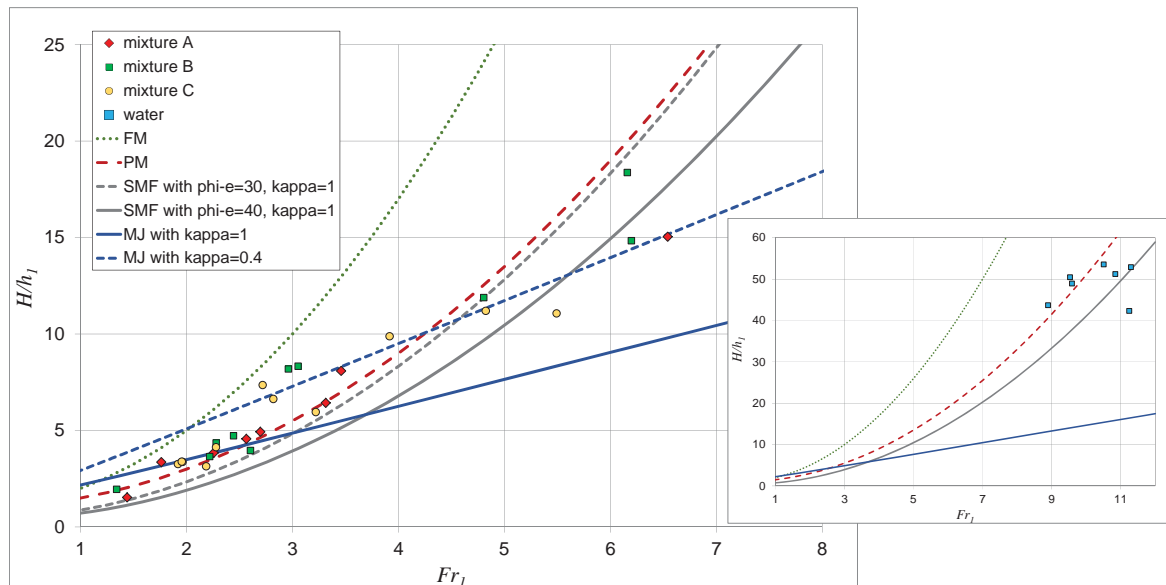


Fig. 2. Run-up heights against an inclined wall (adverse slope of 30°), comparison of experimental results with theoretical models. For the FM, SMF and MJ models equal densities $\rho_1 = \rho_2$ are assumed before and at the obstacle. The inset shows results for the clear water experiments.

3.2. Run-up against vertical wall

For the experiments with a vertical wall as obstacle (i.e. a 90° adverse slope), the normalized run-up heights H/h_1 are shown as a function of the approach flow Froude number Fr_1 in Fig. 3. Also shown are the normalized run-up heights predicted by the four models listed in Table 1 (whereby the MJ Model equation was solved for the dependent variable H/h_1). Again, we cannot observe a clear stratification of the experimental data; in this case, however, there is again a tendency of mixture A with the finest sediment to plot at the lower range of the data for Fr_1 smaller than about 4, whereas the mixture A data tend to plot at the upper range of the data for Fr_1 between 6 and 8. Both the FM and the SMF models (SMF with $\kappa = 1.0$ and $\phi_b = 40^\circ$) appear to provide the most conservative estimate of run-up height (upper bound of theoretical models) for values of Fr_1 larger than about 2, and are closer to the experimental data only for values of Fr_1 between about 1 and 3. The MJ model (which may be appropriate for the run-up against a vertical wall) provides a reasonable fit to the experiments for $\kappa \approx 1.0$ and Fr_1 smaller than about 2.4, and for $\kappa \approx 0.5$ and Fr_1 larger than about 2.4. For comparison, the results from the water experiments are included also here in a separate plot (inset in Fig. 3); in this case the PM model appears to provide an upper limit for the water data.

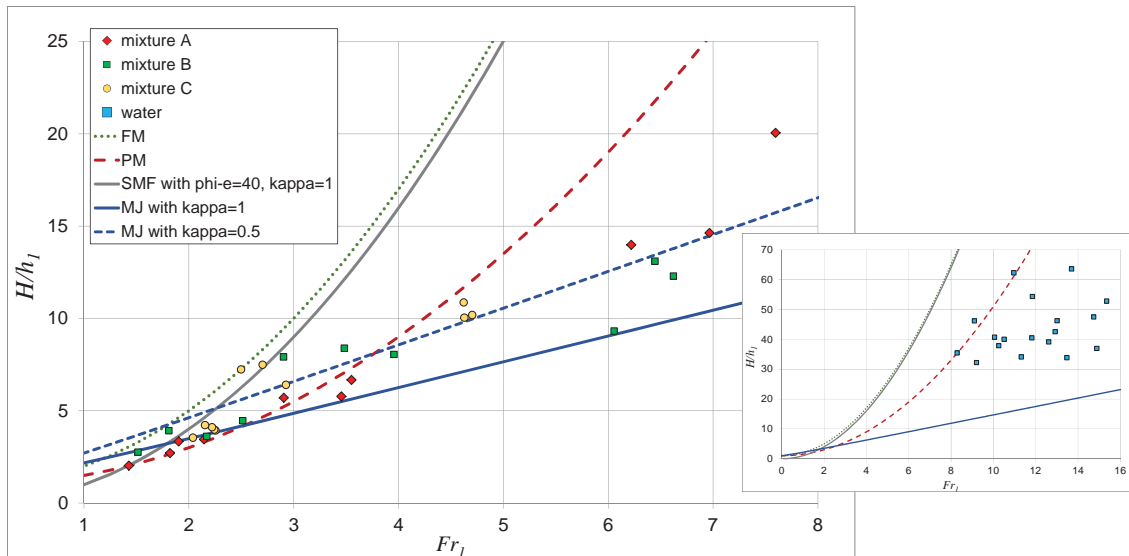


Fig. 3. Run-up heights against a vertical wall (adverse slope of 90°), comparison of experimental results with theoretical models. For the FM, SMF and MJ models equal densities $\rho_1 = \rho_2$ are assumed before and at the obstacle. The inset shows results for the clear water experiments.

3.3. Discussion

One may argue that run-up on an adverse slope (Fig. 2) is best described by gradual deceleration and smooth transfer of mass and momentum from the body to the flow head, as reflected by the SMF model. Our experimental results indicate that an increasing basal friction angle ϕ_b would be necessary for increasing Froude number or flow velocities to provide a reasonable fit with the SMF model prediction (if we neglect possible discrepancies due to the steady, uniform flow assumption for the analytical models). This may appear to be counterintuitive at first sight (since a "dilatation" effect might be expected for higher granular temperatures) and indicates a possible limitation of the SMF model. If we assume, however, that the friction force in the run-up zone is governed by a velocity-squared dependent, Chezy-like friction term (as in the Voellmy fluid model often used for debris flows), then a resulting increase of the total friction with increasing velocity can be justified (note that the approach flow depths h_1 varied much less in our experiments than the approach flow velocity v_1).

A common observation for both the adverse slope (Fig. 2) and the vertical wall experiments (Fig. 3) is that for an approximate agreement of the experimental data with the MJ model an earth pressure coefficient κ smaller than 1 would be required for Fr_1 values larger than about 2.5 to 2.8, whereas a value $\kappa \approx 1$ appears to be appropriate for smaller Froude numbers. This finding is somewhat counterintuitive, as a larger longitudinal compression of the flow requires larger κ values in the range of passive earth pressure coefficients (Hungri, 1995), and a larger longitudinal compression of the flow may be expected for our debris-flow experiments with higher Froude numbers.

However, it should be kept in mind that the comparison of our run-up heights with the analytical models represents a simplification in view of the unsteady and non-uniform approach flow to the obstacle in the experiments. Iverson et al (2016) found that the SMF model yielded predictions of relative run-up heights that were broadly in agreement with results of more accurate simulations with a numerical model; however, the SMF model yielded relative run-up heights that were generally too small if $Fr_1 = 1$ and too large if $Fr_1 = 5$, while they were more accurate if $Fr_1 = 3$. For our experiments with an adverse slope of 30° as obstacle, there is a qualitatively somewhat similar comparison in the sense that the SMF model (with $\kappa = 1$) underestimates the data for smaller Fr_1 and overestimates for larger Fr_1 values.

It is somewhat surprising that MJ model is not in agreement with the clear water experiments for the vertical wall case (although the relative disagreement is less than for the adverse slope case). Concerning the other vertical wall experiments (Fig. 3), we observed a qualitative difference in the run-up behavior depending on flow velocity (or Froude number). For smaller Fr_1 values, sediment tended to pile up in form of a ramp in front of the obstacle, which helped redirect some incoming flow momentum upward. This tendency was more pronounced for the coarser

mixtures B and C that promoted the formation of static deposits, and this could partially explain why these mixtures lead to higher run-up measurements than mixture A, for Froude numbers smaller than about 4. This piling up of sediments in front of the obstacle producing a ramp may also be a reason why the SMF model (with $\phi_c = 40^\circ$ and $\kappa = 1$) may reasonably well describe the debris flow experiments lower Fr_1 numbers (1 to 3). This piling up of sediments in front of the obstacle producing a ramp also occurred for the adverse slope experiments for smaller Froude numbers. For the adverse slope experiments and larger Froude numbers, deflection of flow when encountering the obstacle was observed.

An important limitation of our study is the fact that our experiments involved a very small scale compared to natural events. According to Iverson (2015), miniaturized debris flows exhibit disproportionately large effects of viscous shear resistance and cohesion as well as disproportionately small effects of excess pore-fluid pressure that is generated by debris dilation or contraction.

4. Conclusions

While run-up on an adverse slope is best described by gradual deceleration and smooth transfer of mass and momentum from the body to the flow head, run-up against a vertical barrier is dominated by an abrupt and complete stoppage of the incoming flow. This leads to a rapid upward jump in the surface elevation of the approach flow, and to a shock wave travelling upstream. The experimental results reveal that the run-up mechanism is strongly dependent on incoming flow conditions. Supercritical watery flows resulted in a vertical jet mechanism, granular dry flows resulted in a pile-up mechanism instead of a distinct run-up. The observed run-up heights were generally within the range predicted by the theoretical models, but none of them appears to be universally applicable to the entire range of investigated flow conditions. The commonly used energy principle is not always a conservative method to estimate run-up heights.

References

- Choi, C.E., Au-Yeung, S.C.H., Ng, C.W.W., and Song, D., 2015, Flume investigation of landslide granular debris and water runoff mechanisms: *Geotechnique Letters*, v. 5, p. 28–32, doi:10.1680/geolett.14.00080.
- Kwan, J.S.H., 2012, Supplementary Technical Guidance on Design of Rigid Debris-resisting Barriers: GEO Report No. 270, Geotechnical Engineering Office, Hong Kong, https://www.cedd.gov.hk/eng/publications/geo_reports/doc/er270/er270links.pdf.
- Hákonardóttir, K. M., Hogg, A., and Jóhannesson, T., 2003, A laboratory study of the interaction between supercritical, shallow flows and dams: Icelandic Meteorological Office, Vedurstofa Islands, <http://www.vedur.is/media/vedurstofan/utgafa/greinargerdir/2003/03038.pdf>.
- Hungr, O., 1995, A model for the runout analysis of rapid flow slides, debris flows, and avalanches: *Canadian Geotechnical Journal*, v. 32, p. 610–623, doi:10.1139/t95-063.
- Mancarella, D., and Hungr, O., 2010, Analysis of run-up of granular avalanches against steep, adverse slopes and protective barriers: *Canadian Geotechnical Journal*, v. 47, p. 827–841, doi: 10.1139/T09-143.
- Iverson, R.M., 2015, Scaling and design of landslide and debris-flow experiments: *Geomorphology*, v. 244, p. 9–20, doi:10.1016/j.geomorph.2015.02.033.
- Iverson, R.M., George, D.L., and Logan, M., 2016, Debris flow runup on vertical barriers and adverse slopes: *Journal of Geophysical Research, Earth Surface*, v. 121, p. 2333–2357, doi:10.1002/2016JF003933.
- Jóhannesson, T., Gauer, P., Issler, P., Lied, K. (eds.) 2009, The design of avalanche protection dams: recent practical and theoretical developments: European Commission Directorate for Research, Brussels, Project Report EUR 2339, http://www.preventionweb.net/files/10851_avalanche-protection.pdf.
- Scheidl, C., Chiari, M., Kaitna, R., Müllegger, M., Krawtschuk, A., Zimmermann, T., and Proske, D., 2013, Analysing debris-flow impact models, based on a small scale modelling approach: *Surveys in Geophysics*, v. 34, p. 121–140, doi:10.1007/s10712-012-9199-6.
- Scheidl, C., McArdell, B.W., and Rickenmann, D., 2015, Debris-flow velocities and superelevation in a curved laboratory channel: *Canadian Geotechnical Journal*, v. 52, p. 305–317. doi:10.1139/cgj-2014-0081.
- Takahashi, T., and Yoshida, H., 1979, Study on the deposition of debris flows, Part 1—Deposition due to abrupt change of the bed slope [in Japanese with English abstract]: *Annals of the Disaster Prevention Research Institute, Kyoto Univ., Japan*, 22 B-2.

Numerical simulation of debris flows focusing on the behavior of fine sediment

Yuichi Sakai^{a,*}, Norifumi Hotta^a

^a*Graduate School of Agricultural and Life Sciences, The University of Tokyo, Tokyo, Japan*

Abstract

Debris flows generally includes a wide range of grain sizes, in which fine sediment behaves as a fluid phase rather than as a solid phase and enlarges the pore fluid density. Although in existing models fine sediment constantly behave as fluid phase from initiation to deposition, previous researches have reported that behavior of fine sediment can vary through debris-flow propagations depending on the kinematic conditions (i.e., relation of turbulence and the settling velocity of the particles). To test the effects of this transitional behavior of fine sediment and compare with existing models, we conduct numerical simulations of debris flows with bidisperse granular materials, employing two models for the behavior of small particles: (i) all small particles constantly behave as a fluid phase (Model I); and (ii) the ratio of small particles behaving as a fluid phase varies depending on the kinematic conditions (Model II). In the simulations, we used an inclined channel with erodible bed at the upper stream end of the reach, where debris flows initiate by supplying water. Varying the inclination from 15° to 20°, we measured the time series of discharges, flow depths, sediment concentrations and pore fluid densities at the downstream end. Hydrographs of the two models are significantly different at higher slopes, with a sharp peak at the front of debris flows in Model I and relatively moderate peak in Model II. These differences are caused by higher pore fluid densities from the front to the tail of debris flows in Model I, in contrast to lower pore fluid densities in Model II, where not all of small particles behave as a fluid phase. This infers that discharge rate of debris flows can be overestimated especially at higher slopes if the transitional behavior of fine sediment is not considered.

Keywords: debris flow; numerical simulation; fine sediment; pore fluid density; hydrograph

1. Introduction

Debris flows are mixtures of water and sediment descending steep slopes in mountainous regions: these phenomena can cause severe damage to human life and property. Numerical simulations of debris flows have been used to prevent and mitigate sediment disasters related to debris flows. Previous studies have explored the numerical simulation of debris flow using flow resistance formula (Iverson, 1997) and entrainment rate equations (Iverson and Ouyang, 2015), which reflect the physical characteristics of the flow. Flow resistance formula are derived based on the constitutive equations for debris flows, which are modeled under the assumption that sediment particles are of uniform grain size (Takahashi, 1991; Egashira et al., 1997; Berzi and Jenkins, 2008). The performance of these numerical simulation models has been validated by laboratory measurements of the characteristics of monogranular debris flows, and good agreement with the calculation results has been reported (Egashira et al., 2001; Berzi and Larcan, 2013).

In contrast, natural debris flows comprise a wide range of grain sizes, from clay and silt to boulders (Coe et al., 2008): this variation partly determines flow characteristics such as the segregation of coarse grains to the flow surface (Takahashi et al., 1992) and the suspension of fine sediment in pore fluid (Iverson, 1997; Kaitna et al., 2016). The pore fluid of debris flows can be made turbulent by strong shear of coarse sediment particles (Hotta, 2011), such that fine sediment may contribute to the pore fluid as a fluid phase (Hotta et al., 2013). Thus, numerical simulations of natural debris flows must take into account the increase in pore fluid density that can result from the suspension of fine sediment (Osti et al., 2004; Osti and Egashira, 2008). In early simulations, pore fluid density was generally assumed

* Corresponding author e-mail address: sakai@fr.a.u-tokyo.ac.jp

to be constant throughout debris-flow propagation, in the absence of clear selection criteria to determine pore fluid density. Recently, numerical simulations of *in situ* debris flows containing fine sediment have considered the critical diameter of the sediment particles, below which sediment particles contributes to a fluid phase, accordingly varying the pore fluid densities through debris flow propagations (Nishiguchi et al., 2011; Uchida et al., 2013). This have led to a higher reproducibility of the propagation behavior of such debris flows.

Although introducing the critical diameter made it clearer how to set the pore fluid density, fine sediment behaving as a fluid phase was determined simply by a given grain size. However, recent research from laboratory experiments using bidisperse granular materials has shown that fine sediment does not necessarily behave as a fluid phase (Hotta et al., 2013), or rather, the behavior of fine sediment depends on the kinematic conditions, i.e. the ratio of shear or turbulent velocity to the settling velocity of fine sediment (Nakatani et al., 2018; Sakai et al., 2019). In other word, this implies that the behavior of the fine sediment is not simply determined by the grain size, and fine sediment may behave as a solid or fluid phase depending on the kinematic conditions even with the same grain size.

In this study, we constructed a numerical simulation model incorporating these fine sediment behaviors and tested its performance for debris flows with bidisperse granular materials, comparing with the numerical simulation based on the existing method in which fine sediment behaving as a fluid phase was determined simply by a given grain size.

2. Numerical simulation of debris flows focusing on fine sediment behavior

2.1. Governing equations for debris flows consisting of bidisperse granular materials

The one-dimensional behavior of debris flows consisting of bidisperse granular materials is described based on the following governing equations, i.e., continuity equations for debris flow with large and small particles and the momentum equation for debris flow:

$$\frac{\partial h}{\partial t} + \frac{\partial M}{\partial x} = E \quad (1)$$

$$\frac{\partial(C_L h)}{\partial t} + \frac{\partial(C_L M)}{\partial x} = E(1-r)C_* \quad (2)$$

$$\frac{\partial(C_S h)}{\partial t} + \frac{\partial(C_S M)}{\partial x} = ErC_* \quad (3)$$

$$\frac{\partial M}{\partial t} + \beta \frac{\partial(uM)}{\partial x} = -gh \frac{\partial H}{\partial x} - \frac{\tau_0}{\rho_m} \quad (4)$$

where t is time, x is the coordinate axis along the flow direction, h is the flow depth, M is the discharge rate at a unit width, E is the entrainment rate at the bed, C_L and C_S are the depth-averaged sediment concentration of large and small particles in the cross section, C_* is the concentration of the sediment mixture in the channel deposits, r is the ratio of entrained small particles to the entrained bidisperse granular mixture, β is the momentum correction factor, u is the depth-averaged velocity, g is the acceleration due to gravity, H is the elevation of the flow surface, τ_0 is the shear stress at the bed, and ρ_m is the density of the debris flow.

There are several existing resistance formula and entrainment rate equations of debris flows. The flow resistance formula proposed by Egashira et al. (1997) is employed for τ_0 :

$$\tau_0 = \tau_{0y} + \rho f_b u^2 \quad (5)$$

$$\tau_{0y} = \left(\frac{C_d}{C_*}\right)^{\frac{1}{5}} (\sigma - \rho) C_d g h \cos \theta \tan \phi_s \quad (6)$$

$$f_b = \frac{25}{4} \left\{ k_g \frac{\sigma}{\rho} (1 - e^2) C_d^{\frac{1}{3}} + k_f \frac{(1 - C_d)^{\frac{5}{3}}}{C_d^{\frac{2}{3}}} \right\} \left(\frac{h}{d}\right)^{-2} \quad (7)$$

where ρ is the density of the pore fluid, σ is the density of the sediment particles, C_d is the concentration of sediment particles behaving as a solid phase, θ is the bed inclination, ϕ_s is the internal friction angle of the sediment particles, k_g is a constant (= 0.0828), e is the coefficient of the restitution of the sediment particles, k_f is the constant relating to interstitial space, and d is the representative diameter of particles in sediment mixture.

The entrainment rate equation proposed by Egashira et al. (2001) is employed for E :

$$E = u \tan(\theta - \theta_e) \quad (8)$$

$$\tan \theta_e = \frac{C_d(\sigma/\rho - 1)}{C_d(\sigma/\rho - 1) + 1} \tan \phi_s. \quad (9)$$

Equation (8) employs the concept of equilibrium bed slope θ_e for a given sediment concentration expressed in Eq. (9), where erosion and deposition are balanced. The surface position of the river bed varies through erosion and deposition such that slope θ approach θ_e .

In this framework, the suspension of small particles affects the flow resistance and entrainment rate through the changes in the sediment concentration behaving as solid phase, the pore fluid density and the representative diameter. Details of this point are discussed in the next section.

2.2. Models for the behavior of fine sediment

As coarse sediment contributes to inter-particle stress, fine sediment contributes to the stress on the pore fluid, increasing its density. Among bidisperse granular materials containing large particles that constantly behave as a solid phase, small particles can behave as both a solid and a fluid phase. Thus, modeling the behavior of small particles may affect the overall results of numerical simulations. In this study, we defined two models for the behavior of small particles: (i) all small particles constantly behave as a fluid phase (Model I); and (ii) the ratio of small particles behaving as a fluid phase varies depending on the kinematic conditions (Model II) (Fig. 1). In Model II, the sediment concentration of small particles (C_s) is divided into that behaving as a fluid phase (C_f) and a solid phase ($C_s - C_f$).

Model I reflects the conventional treatment of fine sediment, with the threshold decided simply by the grain size. In Model I, the pore fluid density ρ and representative diameter d are expressed as $\rho_{Model\ I} = \rho_w (1 - C)/(1 - C_L) + \sigma C_s/(1 - C_L)$ and $d_{Model\ I} = d_L$, where C is the sediment concentration of the bidisperse granular mixture ($C_L + C_s$) and ρ_w is the density of water.

Model II adopts the concept that the behavior of small particles depends on the kinematic conditions, i.e., the ratio of shear velocity $u_* = \sqrt{gh \sin \theta}$ or turbulent velocity of the pore fluid $v_t = 5/2 \sqrt{k_f} ((1 - C_L)/C_L)^{1/3} u_* d_L/h$ to the settling velocity of small particles $w_s = ((1 - C)/(1 - C_L))^n w_o$, where n is an empirically determined exponent (for simplicity, $n = 4$ in this study) and w_o is the terminal settling velocity of a single particle. v_t is derived from the constitutive equations of Egashira et al. (1997), which assume that the mixing length contributing to the Reynolds stress is defined by the scale of the pore space between particles.

Through flume tests with bidisperse granular materials, Sakai et al. (2019) derived linear-regression based relationships between the behavior of small particles and the kinematic conditions, u_*/w_s or v_t/w_s , using the blending factor α , which is defined as $f_{ex} = (1 - \alpha)f_{cal:Model\ 1} + \alpha f_{cal:Model\ 2}$ through the comparison between the experimental and theoretical friction coefficients of steady-state debris flows. The experimental friction coefficient of debris flows is $f_{ex} = 2gh \sin \theta / u^2$ and the theoretical friction coefficients for Models 1 and 2 in Sakai et al. (2019) are $f_{cal:Model\ 1} = 25/(2\rho_m)K(\rho_w, C)(h/d_m)^{-2}$ and $f_{cal:Model\ 2} = 25/(2\rho_m)K(\rho_f, C_L)(h/d_L)^{-2}$, where $K(\rho, C_d)$ is the function of the pore fluid density and concentration of sediment particles behaving as a solid phase, the volume-averaged diameter of bidisperse granular mixtures $d_m = (d_L C_L + d_s C_s)/(C_s + C_L)$ and the pore fluid density with all small particles suspended $\rho_f = \rho_w (1 - C)/(1 - C_L) + \sigma C_s/(1 - C_L)$. In Models 1 and 2, all small particles behave as solid and fluid phases, respectively (see Sakai et al. (2019) for further details). The relationships between α and u_*/w_s or v_t/w_s are expressed as follows:

$$\alpha = 0.0175 u_*/w_s - 0.0374 \quad (10)$$

$$\alpha = 0.0167 v_t/w_s - 0.0457. \quad (11)$$

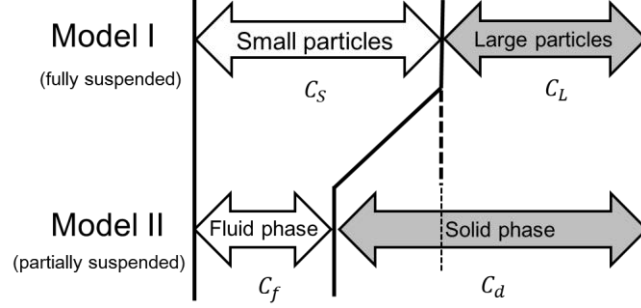


Fig. 1. Conceptual diagram of Models I and II for the behavior of small particles.

As seen from the definition, α cannot be used directly to calculate the fraction of small particles behaving as a fluid phase, such as $C_f = \alpha C_S$. To do so, we need to derive the relationship between α and α' define α' as the ratio of sediment particles behaving as a fluid phase to all small particle. The definition of α can be approximated as follows under the assumption that the friction coefficient is less sensitive to the changes of the pore fluid density and sediment concentration behaving as solid phase in the function $K(\rho, C_d)$ compared to the change of the representative diameter, i.e., $K(\rho, C_L) \approx K(\rho, C_d)$:

$$f_{ex} = (1 - \alpha)f_{cal:Model 1} + \alpha f_{cal:Model 2} = \frac{25}{2\rho_m} \left\{ (1 - \alpha)K(\rho_w, C) \left(\frac{h}{d_m}\right)^{-2} + \alpha K(\rho_f, C_L) \left(\frac{h}{d_L}\right)^{-2} \right\} \quad (12)$$

$$\approx \frac{25}{2\rho_m} \frac{K(\rho_f, C_L)}{h^2} \left\{ (1 - \alpha) \left(\frac{C_L d_L + C_S d_S}{C_L + C_S}\right)^2 + \alpha d_L^2 \right\}.$$

Using α' , Eq. (12) is rewritten as

$$f_{ex} = \frac{25}{2\rho_m} \frac{K(\rho, C_d)}{h^2} \left(\frac{C_L d_L + (1 - \alpha') C_S d_S}{C_L + (1 - \alpha') C_S} \right)^2. \quad (13)$$

Using Eqs. (12) and (13) under the assumption $K(\rho_f, C_L) \approx K(\rho, C_d)$, we obtain the following relationship between α and α' :

$$\alpha' = 1 - \frac{d_L - D}{D - d_S} \frac{C_L}{C_S} \quad (14)$$

$$D = \frac{\sqrt{(1 - \alpha) (C_L d_L + C_S d_S)^2 + \alpha (C_L + C_S)^2 d_L^2}}{C_L + C_S}. \quad (15)$$

Thus, the concentration of sediment particles behaving as a fluid phase C_f and solid phase C_d are expressed as

$$C_f = \alpha' C_S \quad (16)$$

$$C_d = C_L + C_S - C_f \quad (17)$$

and the density of the pore fluid ρ and the representative diameter d are

$$\rho_{Model II} = \rho_w \frac{1 - C_d - C_f}{1 - C_d} + \sigma \frac{C_f}{1 - C_d} \quad (18)$$

$$d_{Model II} = \frac{d_L C_L + d_S (C_S - C_f)}{C_d}. \quad (19)$$

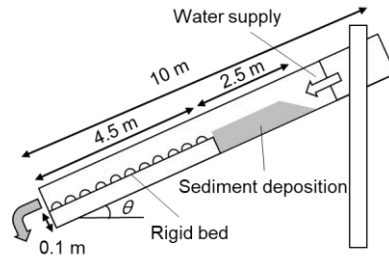


Fig. 2. Schematic diagram of the channel used in Sakai et al. (2019).

Table 1. Physical parameters used in the numerical simulation.

Density of water: ρ_w (g/cm ³)	1.00
Density of sediment particles: σ (g/cm ³)	2.60
Internal friction angle of the sediment particles: ϕ_s (°)	38.5
Coefficient of the restitution of the sediment particles: e	0.85
Concentration of the sediment mixture in the channel deposition C_*	0.70
Constant relating to interstitial space: k_f	0.08

2.3. Numerical conditions

Numerical simulations were using the flume test configuration used by Sakai et al. (2019), as shown in Fig. 2. The channel was 10 m in length and 0.1 m wide. At 4.5 m from the downstream end, the channel floor was raised to a height of 10 cm, and 2.9-mm grains were glued to the rigid bed to provide bed roughness. Sediment comprising bidisperse granular mixtures was deposited upstream of the rigid bed to the height of the bed roughness surface to form an erodible bed. We selected bidisperse granular mixtures of 2.9-mm and 0.11-mm grains at a mixing ratio of 4:1 for the deposited materials at the upper stream. The maximum sediment concentration of the flowing particles was set to the value of the concentration of the sediment deposition at the channel deposition. Small particles are assumed to behave as solid phase when they are deposited and can behaves as fluid phase only after entrainment into the flow. For the erosion process, r is assumed to be the same value as the ratio of small particles to the deposited bidisperse granular mixtures. The inclination of the channel was 15° in the original literature; however, we varied this inclination from 15° to 20° for sensitivity analysis. Water was supplied from the upstream end at the constant rate of 3,000 cm³/s for 20 s. At the downstream end, we measured a time series of discharges, flow depths, pore fluid densities, and sediment concentration of bidisperse granular mixtures, small particles, and small particles behaving as a fluid phase. We applied a leapfrog scheme for calculations on a staggered grid, with a temporal resolution of 0.0005 s and spatial resolution of 0.5 cm. The physical parameters used in the numerical simulation are listed in Table 1.

3. Results and Discussion

The calculations by Models I and II were compared to test their performance and investigate the sensitivity, showing the calculated results for channel inclinations of 15° and 20° as representative cases in this section. The time series of discharges calculated by Models I and II are compared in Fig. 3, where both models showed sharper peaks at higher inclinations. Model I showed the highest peak among the three calculated results at all inclinations, followed by Model II with u_* / w_s . Model II with v_t / w_s exhibited lower peak discharges and relatively smoother changes between peaks, which occurred later than those of the other two model results. Differences in the calculated hydrographs between Model I and Model II with v_t / w_s were larger at higher slopes. Since the amount of water supplied was constant, differences between hydrographs are mainly attributed to differences in the degree of entrainment from upstream sediment deposition, which is affected by pore fluid density through changes in the equilibrium slope in Eq. (9).

The time series of flow depths calculated by Models I and II are compared in Fig. 4. Although the timing of the peaks in Model I and Model II with u_*/w_s were different from those of Model II with v_t/w_s , their overall performance was relatively close in contrast to that of the discharge results.

Figure 5 shows the time series of pore fluid density calculated by Models I and II. Pore fluid density had the highest values at the flow front, and then decreased with density of water. This result corresponds to the trend in discharge, which also had a peak at the flow front. In Model II with v_t/w_s , pore fluid density was small compared to that in Models I and II with u_*/w_s at an inclination of 15° , whereas this difference became small at higher slopes. The maximum value of the pore fluid densities reached about 1.5 g/cm^3 , which are achieved when the sediment concentration of bidisperse granular materials becomes its maximum value and all small particles included in them behaves as a fluid phase, as shown in the calculation by Model I with an inclination of 20° .

Since pore fluid densities directly corresponds to the behavior of small particles, the ratio of small particles behaving as a fluid phase should be investigated. Fig. 6 shows the time series of concentrations of sediment mixtures, small particles, and small particles behaving as a fluid phase. This indicates that the behavior of small particles estimated by Model II varies with debris flow propagations.

The difference between Models I and II is detected in the above calculations, especially at higher slopes. Model I may have overestimated the hydrograph compared to Model II because not all small particles actually behave as a fluid phase (Sakai et al., 2019). Model II performed better than Model I, but exhibited different performance depending on the kinematic conditions, i.e., u_*/w_s or v_t/w_s . Model II with u_*/w_s and v_t/w_s have several advantages and disadvantages. Although u_*/w_s is easily incorporated into the model by the simple expression u_* , it is important to remember that u_* reflect the external stress exerted on debris flow and does not directly reflect the Reynolds stress, which lead to the suspension of small particles in the pore fluid. In contrast, v_t strictly reflects the Reynolds stress of the pore fluid. For this reason, Model II with v_t/w_s seems to be a stricter model; however, it should be noted that v_t can exhibit unstable behavior when the sediment concentration approaches zero, as seen from its expression.

To investigate the sensitivity of u_* and v_t , the time series of u_* and v_t calculated by Model II with u_*/w_s and v_t/w_s are compared in Fig. 7, which shows opposite trends in u_* and v_t . This results is attributed to the flow depths at which u_* and v_t exhibit opposite behavior: u_* corresponds directly to the flow depth, whereas v_t corresponds inversely to the flow depth. The flow depth was most sensitive to u_* and v_t , and the sediment concentration has relatively little effect on v_t . The sharp peak of v_t at the debris flow front is also attributed to small flow depth values. These behavior of u_* and v_t in turn affect pore fluid density through the suspension of small particles.

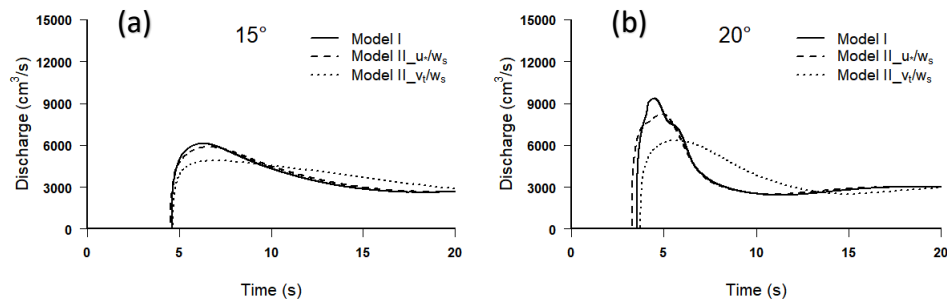


Fig. 3. Time series of discharges calculated by Models I and II (u_*/w_s and v_t/w_s) for channel inclinations of (a) 15° and (b) 20° .

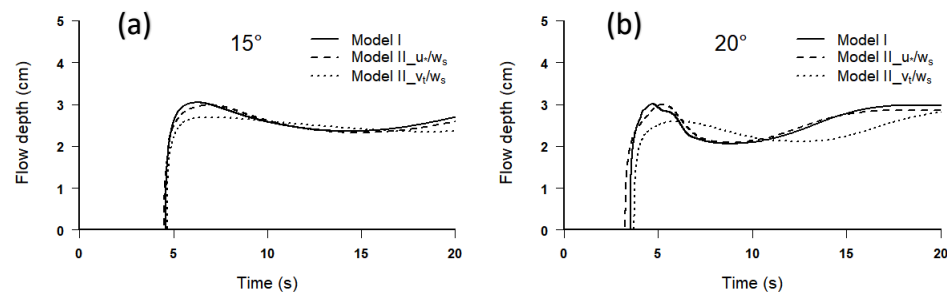


Fig. 4. Time series of flow depths calculated by Models I and II (u_*/w_s and v_t/w_s) for channel inclinations of (a) 15° and (b) 20° .

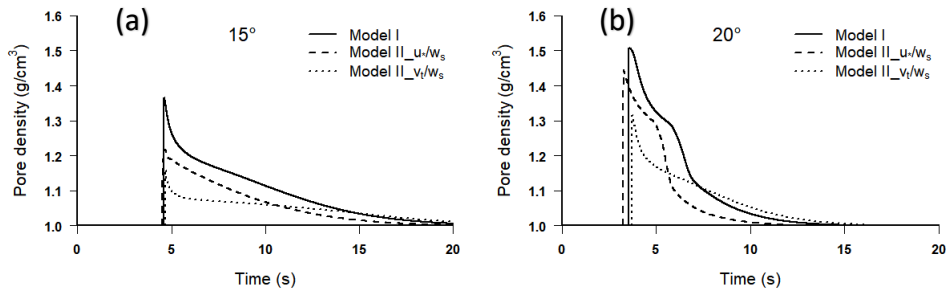


Fig. 5. Time series of pore fluid density calculated by Models I and II (u_*/w_s and v_t/w_s) for channel inclinations of (a) 15° and (b) 20°.

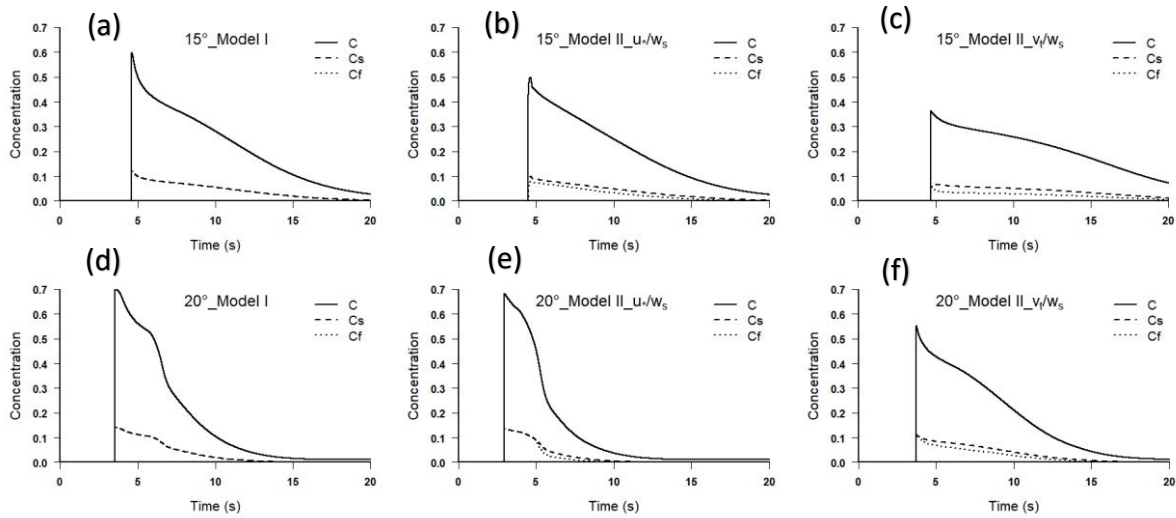


Fig. 6. Time series of concentrations of sediment mixture, small particles, and sediment particles behaving as a fluid phase calculated by Models I and II (u_*/w_s and v_t/w_s): (a) 15°, Model I; (b) 15°, Model II, v_t/w_s ; (c) 15°, Model II, u_*/w_s ; (d) 20°, Model I; (e) 20°, Model II, u_*/w_s ; (f) 20°, Model II, v_t/w_s .

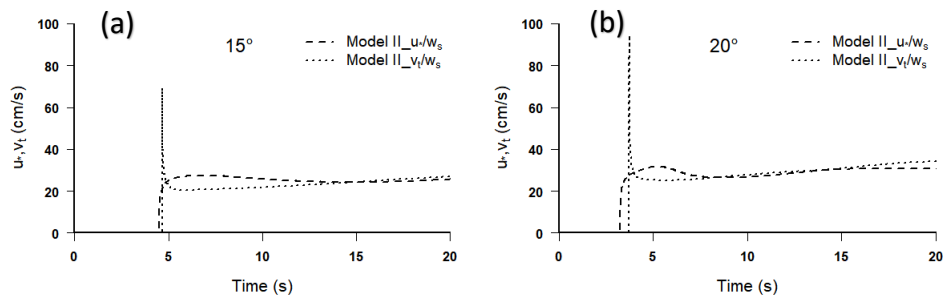


Fig. 7. Time series of u_* and v_t calculated by Model II (u_*/w_s and v_t/w_s) for channel inclinations of (a) 15° and (b) 20°.

4. Conclusion

In this work, we constructed numerical simulation model of debris flows focusing on the transitional behavior of fine sediment and compared its performance with existing models. We conducted numerical simulations of debris flows with bidisperse granular materials, employing two models for the behavior of small particle. Hydrographs of the two models were significantly different at higher slopes, with a sharp peak at the front of debris flows in Model I results and a relatively moderate peak in those of Model II. These differences are caused by higher pore fluid densities from the front to the tail of debris flows in Model I, in contrast to the lower pore fluid density observed in the Model

II results, where not all small particles behaved as a fluid phase. These results indicate that the debris flow discharge rates can be overestimated especially at higher slopes, if the transitional behavior of fine sediment is not appropriately considered.

The sensitivity analysis conducted in this study addressed relatively limited conditions, such that further investigation may be needed to decide whether u_*/w_s or v_t/w_s in Model II leads to better performance. This study focused only on the erosion process; however, the deposition process should be also investigated in future studies.

Acknowledgements

This work was partly supported by Grant-in-Aid for JSPS Fellows Grant Number 17J08424 and by a grant from the Ministry of Land, Infrastructure, Transport and Tourism, Japan.

References

- Berzi, D., and Jenkins, J. T., 2008, A theoretical analysis of free-surface flows of saturated granular-liquid mixtures: *Journal of Fluid Mechanics*, v. 608, p. 393–410, doi:10.1017/S0022112008002401.
- Berzi, D., and Larcan, E., 2013, Flow resistance of inertial debris flows: *Journal of Hydraulic Engineering*, v. 139, no. 2, p. 393–410, doi: 10.1061/(ASCE)HY.1943-7900.0000664.
- Coe, J. A., Kinner, D. A., and Godt, J. W., 2008, Initiation conditions for debris flows generated by runoff at Chalk Cliffs, central Colorado: *Geomorphology*, v. 96, p. 270–297, doi:10.1016/j.geomorph.2007.03.017.
- Egashira, S., Miyamoto, K., and Itoh, T., 1997, Constitutive equations of debris flow and their applicability, *in Proceedings, 1st Int. Conf. on Debris Flow Hazards Mitigation: Mechanics, Prediction, and Assessment*, C. L. Chen, ed.: ASCE, New York, p. 340–349.
- Egashira, S., Honda, N., and Itoh, T., 2001, Experimental study on the entrainment of bed material into debris flow: *Physics and Chemistry of the Earth (C)*, v. 26, no. 9, p. 645–650.
- Hotta, N., 2011, Pore water pressure distributions of granular mixture flow in a rotating mill, *in Italian Journal of Engineering Geology and Environment*, R. Genevois, D. L. Hamilton, and A. Prestininzi, eds.: Sapienza Universita Editrice Univ. Press, Rome, Italy, p. 319–330.
- Hotta, N., Kaneko, T., Iwata, T., and Nishimoto, H., 2013, Influence of fine sediment on the fluidity of debris flows, *Journal of Mountain Science*, v. 10, no. 2, p. 233–238, doi: 10.1007/s11629-013-2522-y.
- Iverson, R. M., 1997, The physics of debris flows, *Review of Geophysics*, v. 35, no. 3, p. 245–296.
- Iverson, R. M. and Ouyang, C., 2015, Entrainment of bed material by Earth-surface mass flows: Review and reformulation of depth-integrated theory: *Review of Geophysics*, v. 53, p. 27–58, doi:10.1002/2013RG000447.
- Kaitna, R., Palucis, M. C., Yohannes, B., Hill, K. M., and Dietrich, W. E., 2016, Effects of coarse grain size distribution and fine particle content on pore fluid pressure and shear behavior in experimental debris flows: *Journal of Geophysical Research: Earth Surface*, v. 121, p. 415–441.
- Nakatani, K., Furuya T., Hasegawa Y., Kosugi K., and Satofuka, Y., 2018, Study on fine sediment phase change factors and influence on debris flow behavior: *Journal of the Japan Society of Erosion Control Engineering*, v. 70, no. 6, p. 3–11. (in Japanese with English summary)
- Nishiguchi, Y., Uchida, T., Tamura, K., and Satofuka, Y., 2011, Prediction of run-out process for a debris flow triggered by a deep rapid landslide, *in Italian Journal of Engineering Geology and Environment*, R. Genevois, D. L. Hamilton, and A. Prestininzi, eds.: Sapienza Universita Editrice Univ. Press, Rome, Italy, p. 477–485.
- Osti, R., and Egashira, S., 2008, Method to improve the mitigative effectiveness of a series of check dams against debris flows: *Hydrological Processes*, v. 22, p. 4986–4996, doi: 10.1002/hyp.7118.
- Osti, R., Egashira, S., and Itoh, T., 2004, Prediction of 1999-San Julian debris flows based on dependent and independent occurrences: *Annual Journal of Hydraulic Engineering*, JSCE, v. 48, p. 913–918.
- Sakai, Y., Hotta, N., Kaneko, T., and Iwata, T., 2019, Effects of grain-size composition on flow resistance of debris flows: behavior of fine sediment: *Journal of Hydraulic Engineering*, v. 145, no. 5, doi: 10.1061/(ASCE)HY.1943-7900.0001586.
- Takahashi, T., 1991, *Debris flow*, Balkema, Rotterdam, Netherlands.
- Takahashi, T., Nakagawa, H., Harada, T., and Yamashiki, Y., 1992, Routing debris flows with particle segregation: *Journal of Hydraulic Engineering*, v. 118, no. 11, p. 1490–1507, doi:10.1061/(ASCE)0733-9429(1992)118:11(1490).
- Uchida, T., Nishiguchi, Y., Nakatani, K., Satofuka, Y., Yamakoshi, T., Okamoto, A., and Mizuyama, T., 2013, New numerical simulation procedure for large-scale debris flows (Kanako-LS), *International Journal of Erosion Control Engineering*, v. 6, no. 2, p.58–67.

Optical measurements of velocity and of solid volume fraction in fast dry granular flows in a rectangular chute

L. Sarno^{a,*}, L. Carleo^a, M. N. Papa^a, P. Villani^{a,b}

^aDepartment of Civil Engineering, University of Salerno, Via Giovanni Paolo II, 132, 84084 Fisciano, Italy

^bCUGRI, University Consortium for Research on Major Hazards, Salerno, Italy

Abstract

Geophysical flows, like avalanches and debris flows, are characterized by the gravity-driven motion of a granular medium immersed in an interstitial fluid. To better understand their dynamics, laboratory investigations represent invaluable tools and are essential to study several peculiar features (e.g. the effects of fixed boundaries, non-local momentum exchanges, segregation effects) that are difficult to isolate at the field scale. An experimental study on dry granular flows in a chute geometry is reported. Different basal conditions are investigated by varying the bed roughness. Several flow rates are investigated by adjusting the inflow boundary condition. By employing two high-speed cameras and particle image velocimetry (PIV) technique, accurate velocity measurements (typical error ≈ 0.004 m/s) could be obtained at sidewall and free surface. An innovative stochastic-optical method [Sarno et al., *Granul. Matter*, 2016], which exploits highly controlled illumination conditions guaranteed by a flickering-free planar lamp, allowed to obtain reliable volume fraction profiles (typical error ≈ 0.025). The method uses a transfer function, numerically determined on random grain distributions of known volume fraction. This function stochastically relates the near-wall volume fraction with a measurable quantity, named *two-dimensional volume fraction* and accessible by binarization of digital pictures, taken by a high-speed camera. The combined knowledge of velocity and volume fraction fields allowed a detailed description of the rheological behavior of channelized granular flows and of the effects of the flume boundaries. The superposition of different flow regimes is revealed by different shapes of velocity and volume fraction profiles along the flow depth. It emerges that frictional momentum exchanges increase at the expense of collisional mechanisms with increasing depth. This behavior appears related to the sidewall resistances and to the increasing normal pressures.

Keywords: granular flows; volume fraction; sidewall friction; boundary conditions; rheological stratification.

1. Introduction

Granular materials are ubiquitously involved in hazardous geophysical phenomena, such as debris flows and avalanches. Yet, to date several aspects of their dynamics remain not completely understood. Beside theoretical and field-scale investigations (e.g. Iverson and Vallance, 2001; Medina et al., 2008; Kuo et al., 2009; Iverson and George, 2014; Sarno et al., 2017; Papa et al., 2018), laboratory experiments on granular media still represent an extraordinary tool to get insight into the granular dynamics (e.g. GDR Midi, 2004; Sarno et al., 2011a; Baker et al., 2016; Sarno et al., 2018a). Granular flows exhibit a rich variety of flow regimes, ranging from a *solid-like* behavior in the case of slow deformations and frictional dissipation mechanisms to a *gas-like* behavior in the case of large deformations and strong collisions among grains. An intermediate regime, frequent in geophysical flows and known as *dense-collisional*, is characterized by the coexistence of collisional and frictional mechanisms. To date, a unified constitutive law capable of reliably describing all these flow regimes is lacking. Moreover, some peculiarities of the granular dynamics, such as the effects of fixed boundaries (e.g. Jop et al., 2005; Sarno et al., 2011b), the occurrence of a rheological stratification (e.g. Armanini et al., 2005; Sarno et al., 2014) and non-local momentum exchange mechanisms (e.g. Mills et al., 1999; Pouliquen and Forterre, 2009) still require efforts to be properly described.

The flow velocity and solid volume fraction fields represent crucial quantities to be investigated in laboratory. In particular, the volume fraction is coupled with the rheological behavior of the granular medium in free-surface flows where a stress-free boundary condition occurs at the free surface. While optical techniques for measuring the flow

* Corresponding author e-mail address: lsarno@unisa.it

velocity (e.g. particle image velocimetry, PIV, and particle tracking velocimetry, PTV) have reached a certain maturity (e.g. Jesuthasan et al., 2006; Sarno et al., 2018b), the reliable estimation of the volume fraction is much more challenging. For obtaining reliable velocity measurements, in the present work we employed a multi-pass PIV approach (Sarno et al., 2018b) by using the open-source code PIVlab (Thielicke and Stamhuis, 2014). Conversely, the stochastic-optical method (SOM) by Sarno et al. (2016) is employed for estimating the sidewall volume fraction.

We present an extensive experimental campaign on steady dry granular chute flows with various basal surfaces. Sarno et al. (2018a) recently reported an investigation on chute flows with chute inclination angle of 30° , where a rich variety of velocity profiles, depending on the roughness of the basal surface and also on the flow depth, was observed. As an extension of the work by Sarno et al. (2018a), here we report new experiments, performed with the same apparatus but with the higher chute inclination angle of 35° . Moreover, different from Sarno et al. (2018a), we obtained not only the velocity measurements but also reliable measurements of the sidewall volume fraction, which are particularly useful for better understanding the granular flow dynamics. The employment of several bed surfaces allowed to investigate different basal kinematic boundary conditions (KBC): namely, slip KBC, no-slip KBC and also an intermediate no-slip KBC where grain rolling and saltations are made possible by the low bed roughness. We anticipate that the shapes of the velocity profiles, observed by Sarno et al. (2018a), are only partially observed in this new campaign. In fact, owing to the increased bed slope, the lower creep flow rarely occurs. Conversely, basal grain saltations and rolling significantly influence the flow dynamics.

2. Experimental setup and measuring methods

The apparatus consists of a 2-m long Plexiglas chute with a rectangular cross section of width 8cm (i.e. ≈ 24 grain diameters). For all experiments the chute inclination, α , is set equal to 35° . The granular material is made of acetal-polymeric (POM) spheroidal beads with mean diameter $d=3.3\text{mm}$, internal angle of friction of $\approx 27^\circ$ and coefficient of restitution of ≈ 0.83 (Sarno et al., 2018a). The upper part of the channel is used as a reservoir and is equipped with an external hopper (capacity 40l) (Fig. 1a). The granular material is allowed to flow down the chute through an adjustable gate, so that different flow rates could be studied. The investigated range of gate openings is from 5cm to 14cm. An intermediate steady state, lasting several seconds, was observed in all experiments.

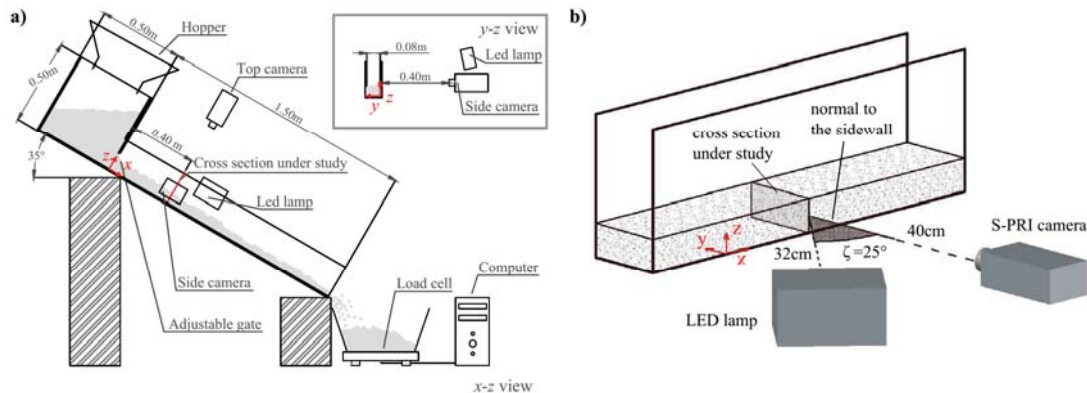


Fig. 1. (a) Experimental apparatus (chute inclination angle $\alpha=35^\circ$); (b) position of the LED lamp

Several basal surfaces with different roughness were investigated: (1) smooth Bakelite surface (S) with a characteristic length of the roughness $\ll 10\mu\text{m}$; (2) different sandpaper linings with characteristic lengths of the roughness of $162\mu\text{m}$ (P100 FEPA/ISO 6344), $269\mu\text{m}$ (P60), and $425\mu\text{m}$ (P40); (3) *granular* basal surface (G), made up by randomly gluing the same POM beads on the smooth bed surface (characteristic length of roughness $d/2=1.65\text{mm}$).

The instrumentation is composed of the following devices: a load-cell placed at the outlet for the estimation of the mass flow rate, two high-speed cameras, a high-brightness flickering-free LED lamp. The camera model AOS S-PRI was placed aside the channel to measure sidewall velocity and volume fraction at the cross section under study, located 40cm downstream the inflow gate (cf. Fig. 1). The second camera (model AOS Q-PRI) was located above

the free surface to measure the free-surface velocity profile at the same cross section ($x=40\text{cm}$). For reliable PIV analyses and volume fraction estimations, the cameras' sampling rate was set to 1 kHz. The LED lamp (mod. PhotoSonics MultiLED-LT) was located aside the channel at a distance of 32cm. The angle of incidence of light, ζ , with the respect to the normal to the side wall was carefully adjusted and set equal to 25° (Fig. 1b). The position of the lamp and, especially, the choice of ζ is crucial for reliable volume fraction measurements (Sarno et al., 2016).

Thanks to the open-source code PIVlab (Thielicke and Stamhuis, 2014), a window deformation multi-pass particle image velocimetry (PIV) approach is adopted for velocity measurements at the sidewall and at the free surface. In classical fluid mechanics the PIV is a well-established technique, based on the maximization of the discrete cross-correlation function between two frames delayed by a short time interval. Nonetheless, some specific measures need to be adopted to reliably extend the PIV approach to granular flows (e.g. Eckart et al., 2003; Sarno et al., 2018b). As highlighted by Sarno et al. (2018b), the employment of the window deformation approach is crucial to reduce gradient-bias errors in case of highly sheared flows, which is a frequent case in granular flows. As well, the multi-pass approach, which uses a progressive refinement of the interrogation window to obtain a high spatial resolution without loss-of-pairs errors, is particularly useful in granular flow applications. We employed the same PIV settings of Sarno et al. (2018a), to which we refer the reader for further details. According to the theoretical accuracy of PIVlab reported to be <0.02 pixel/frame (Thielicke and Stamhuis, 2014) and by also considering the specific image scales of the video-recordings, the PIV accuracy is ≈ 0.004 m/s and ≈ 0.002 m/s at the sidewall and at the free surface, respectively.

The measurement of the volume fraction is obtained by using the stochastic-optical method (SOM) proposed by Sarno et al. (2016), to which we refer the reader for details. This method, thanks to a highly-controlled illumination, allows the estimation of the near-wall volume fraction, c_{3D} , from a measurable quantity called *two-dimensional volume fraction*, c_{2D} . With reference to a given interrogation window Δ on the measuring wall, this quantity is defined as the ratio of the overall area of the projections on Δ of all the illuminated and visible surface elements belonging to the grains and the total area of Δ . A stochastic transfer function between c_{3D} and c_{2D} is found through several Monte Carlo simulations, reproducing random grain dispersions with different volume fractions

$$c_{3D} = f(c_{2D}, \zeta) = a(\zeta) \exp(b(\zeta) c_{2D}), \quad (1)$$

where a and b are parameters depending on ζ . A local binarization formula, requiring the calibration of one threshold parameter, is employed for estimating c_{2D} from gray-scale images. The method was extensively validated by Sarno et al. (2016) on random dispersions of POM beads immersed in a water-sucrose solution. The best accuracy was found with angles of incidence of light, ζ , between 20° and 40° . In the present investigation we chose $\zeta = 25^\circ$ with zero tilt of the lamp with respect to the z direction (cf. Fig. 1b). Different from Sarno et al. (2016), rectangular interrogation windows of dimensions $1d$ and $16d$ in the z and x directions, respectively, are employed. Such interrogation windows are also designed to have a 50%-overlap along z , so as to get a spatial resolution of the measurements equal to $d/2$ along the flow depth. The accuracy of the method was verified by validation on random granular dispersions of known volume fraction and a root mean square error (RMSE) on c_{3D} of ≈ 0.025 was obtained. Additional inaccuracies might arise near the free surface, due to the fact that the binarization algorithm struggles to identify the illuminated and visible elements whenever the background is visible. To reduce such errors, a white-noise background, with a similar brightness of POM grains but distinguishable from them, is employed.

3. Results and discussion

By comparing the experiments with the same gate opening, we preliminarily observed that the runs on different sandpaper linings always exhibit a no-slip basal KBC and very similar velocity and volume fraction profiles. It indicates that the flow dynamics is weakly influenced by changes of the basal roughness within the range [$162\mu\text{m}$, $425\mu\text{m}$]. For brevity, we chose only to present the experiments carried out on sandpaper P40. Conversely, for ease of comparison, in Fig. 2 we report the longitudinal velocity profiles, u_x , at the sidewall, previously obtained by Sarno et al. (2018a) with $\alpha=30^\circ$ and on analogous bed surfaces of those employed in the new experimental campaign ($\alpha=35^\circ$).

The list of experiments with $\alpha=35^\circ$ is reported in Tab. 1. The mass flow rate, Q_m , and the flow depth, h , in Tab. 1 are obtained by two subsequent averages: the time-averages in a time interval of 1s within the steady state, are subsequently ensemble-averaged over four repetitions of the same experiment. As well, the velocity and volume fraction profiles, reported in Fig. 2 and hereafter, are obtained by time- and ensemble-averaging.

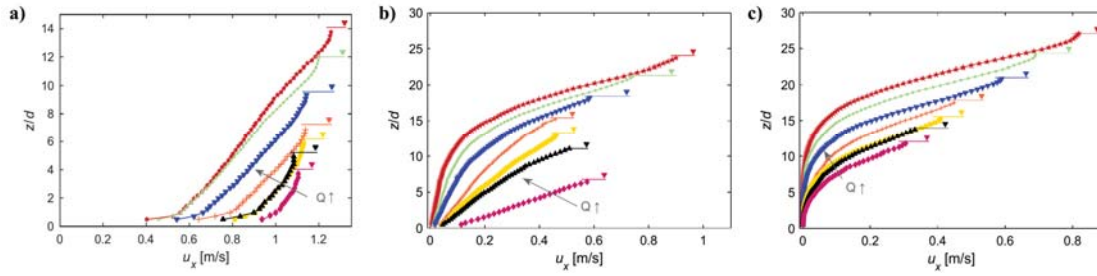


Fig. 2. Sidewall u_x velocity profiles obtained by Sarno et al. (2018a) with $\alpha=30^\circ$. (a) Bakelite (S), (b) sandpaper (P40), (c) grain surface (G)

Table 1. List of the experiments carried out by employing a chute inclination angle of 35°

Exp. ID	Gate opening [m]	Basal surface	Q_m [g/s]	h [m]
Exp-5S	0.05	Bakelite (S)	1084	0.009
Exp-6S	0.06	Bakelite (S)	1417	0.012
Exp-7S	0.07	Bakelite (S)	1725	0.016
Exp-8S	0.08	Bakelite (S)	2124	0.020
Exp-10S	0.10	Bakelite (S)	2717	0.027
Exp-12S	0.12	Bakelite (S)	3332	0.034
Exp-14S	0.14	Bakelite (S)	4243	0.044
Exp-5P40	0.05	Sandpaper (P40)	858	0.018
Exp-6P40	0.06	Sandpaper (P40)	1146	0.021
Exp-7P40	0.07	Sandpaper (P40)	1440	0.023
Exp-8P40	0.08	Sandpaper (P40)	1799	0.027
Exp-10P40	0.10	Sandpaper (P40)	2353	0.035
Exp-12P40	0.12	Sandpaper (P40)	2819	0.042
Exp-14P40	0.14	Sandpaper (P40)	3399	0.050
Exp-5G	0.05	Grain (G)	773	0.019
Exp-6G	0.06	Grain (G)	1038	0.023
Exp-7G	0.07	Grain (G)	1297	0.027
Exp-8G	0.08	Grain (G)	1555	0.031
Exp-10G	0.10	Grain (G)	2263	0.040
Exp-12G	0.12	Grain (G)	2635	0.050
Exp-14G	0.14	Grain (G)	3066	0.059

Good experimental repeatability is obtained by controlling the relative air humidity ($>60\%$), so as to avoid significant electrostatic forces among grains and chute boundaries. The PIV measurements at the free surface showed roughly parabolic transverse velocity profiles with minima at the sidewalls, which confirms the non-negligible sidewall friction. This trend is generally observed in all experiments, regardless the bed roughness.

The runs on smooth Bakelite (S) exhibit a slip basal KBC with negligible grain rolling. The longitudinal velocity, u_x , and the volume fraction, c_{3D} , profiles at the sidewall are reported in Fig. 3, while the shear rate, $\partial_z u_x$, is shown in Fig. 6a. Few measurement points immediately below the free surface are chosen not to be reported in Fig. 3, since velocity and c_{3D} inaccuracies might have occurred there due to strong oscillations of the free surface. Conversely, though a further investigation is planned, we do not believe that drag effects due to air at the free surface are relevant in this experimental campaign, especially considering that the flow velocities at the free surface are relatively small ($<2\text{m/s}$). Due to large slip velocities, the u_x profiles are much blunter than those observed on the same S bed with $\alpha=30^\circ$ (cf. Fig. 2a). By considering the additional information of the c_{3D} profiles (Fig. 3b), three regions could be

identified: (1) a $\approx 1d$ -thick region, near the basal surface, where c_{3D} is relatively small (≈ 0.3 - 0.5) and increases with z : in this region the shear rate, $\partial_z u_x$, is of order of 15 - 25s^{-1} (Fig. 6a) and is larger than in the rest of the flow domain; (2) an intermediate region, only noticeable if h is high enough, where c_{3D} shows an approximately constant value (slightly less than 0.6) and u_x is approximately linear with a shear rate of $\approx 10\text{s}^{-1}$ (Fig 6a); (3) a $\approx 2d$ - $4d$ -thick upper region, where c_{3D} decreases and u_x increases less than linearly with z .

The small values of c_{3D} in the $1d$ -thick region near the bed are mainly caused by the fact that the fixed surface prevents grain interlocking. Conversely, the very large values of $|\partial_z c_{3D}|$, which occur near the free surface and may appear unphysical, are mainly caused by the fact that the background becomes occasionally visible due to grain saltations and, thus, the time-averaged c_{3D} rapidly decreases with z . In case of small flow depths, the u_x profile exhibits a Bagnold-like scaling (Bagnold, 1954), i.e. a $3/2$ -power law with z , in the entire profile, suggesting that the flow regime is mainly collisional (Sarno et al., 2018a). When h increases, the effects of the sidewall friction and, possibly, also the occurrence of non-local momentum exchanges, causes a progressive linearization of the velocity profiles, so that a convex shape of u_x can be only observed in the upper region where the flow regime is collisional and the sidewall resistances become negligible. The observed behavior of u_x is in substantial agreement with the previous experiments with $\alpha=30^\circ$ (cf. Fig. 2a) and suggests the occurrence of a rheological stratification, which is further confirmed by the volume fraction measurements.

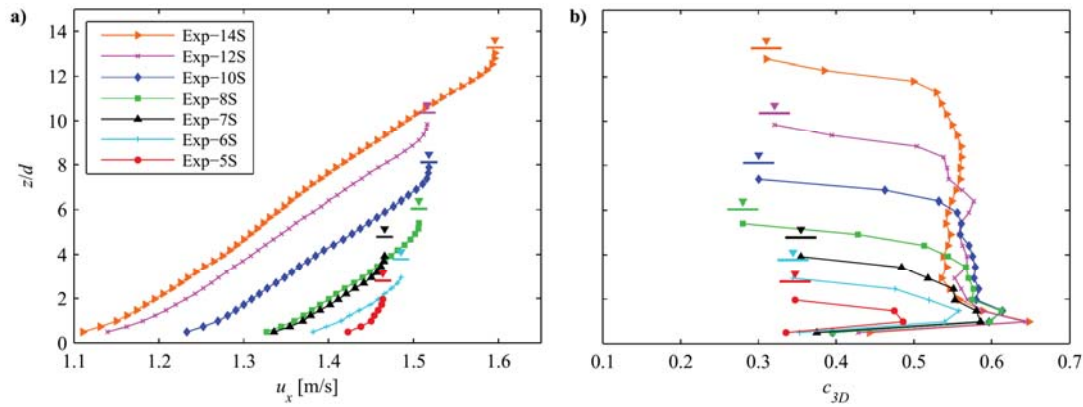


Fig. 3. Experimental profiles obtained on the smooth Bakelite bed (S). (a) Longitudinal velocity profiles, u_x ; (b) volume fraction profiles, c_{3D}

Different basal KBCs were observed by increasing the basal roughness. Fig. 4 reports the experimental profiles of u_x and c_{3D} , obtained on the sandpaper bed (P40). The related shear rate profiles are shown in Fig. 6b. In this case, different from the Bakelite bed, the roughness is large enough to inhibit grain sliding: namely a no-slip KBC occurs. Yet, since the characteristic length of roughness ($425\mu\text{m}$) is still significantly smaller than the grain size, noticeable grain rolling and saltation at the basal surface are observed, especially for experiments with low h . Such phenomena are progressively inhibited by increasing h due to the increase of the normal pressures. The magnitude of grain rolling and saltation is stronger to that previously observed with $\alpha=30^\circ$. By analyzing the fluctuation velocities, it was clear that basal rolling and saltation represent a source of fluctuation kinetic energy that diffuses from $z=0$ toward the flow domain and, thus, increases the collisional character of the flow. As highlighted by Sarno et al. (2018a), the KBC at the bed is not only influenced by the basal angle of friction between but also by the characteristic length of the roughness, which influences the fluctuation velocities. Moreover, some influence to the fluctuation velocity at the bed could be also due to the shape of the roughness, which merits further investigation.

As a consequence, a rheological stratification slightly different from the smooth bed can be observed in Fig. 4. In the lower zone (approx. $1d$ -thick), c_{3D} is very small and $\partial_z u_x$ is quite high (Fig. 6b). From the lower to the central zone, c_{3D} increases for all experiments. Yet, it becomes approximately constant at ≈ 0.6 , only in the experiments with high h (i.e. Exp-10P40, Exp-12P40 and Exp-14P40). In the same intermediate region, the u_x profiles mainly exhibit a Bagnold grain-inertial convex shape, instead of the linear shape observed on the S bed. An approximately linear behavior of u_x (cf. Fig. 6b) can be barely observed only in the three experiments with highest h . This finding can be explained by the fact that the basal roughness causes stronger grain velocity fluctuations, which propagate in the intermediate region. By comparing the experiments on sandpaper with those on smooth bed with similar h , it

emerges that such a higher grain collisionality induces a more persistent Bagnold shape of the u_x profiles. Moreover, it should be noted that the convex velocity profiles are notably different from those observed with $\alpha=30^\circ$ on the same bed surface (P40), which are either linear or even concave in their lower zone (cf. Fig. 2b). This discrepancy is clearly due to the slightly different basal KBC, induced by the higher chute slope. Only if the h becomes significantly high, so that the sidewall friction increases and also the basal grain saltations are inhibited by the pressure, the character of the velocity profiles shifts from convex to approximately linear, indicating the onset of frictional mechanisms within the lower part of the flow domain. Analogous to the S bed (cf. Fig. 3), a mainly collisional layer, with a convex u_x profile and rapidly decreasing c_{3D} , takes place immediately below the free surface.

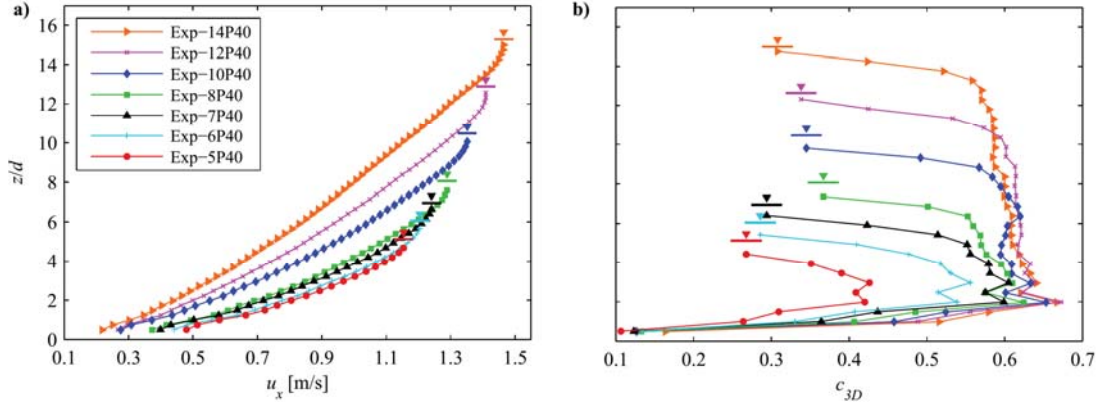


Fig. 4. Experimental profiles obtained on the sandpaper bed (P40). (a) Longitudinal velocity profiles, u_x ; (b) volume fraction profiles, c_{3D}

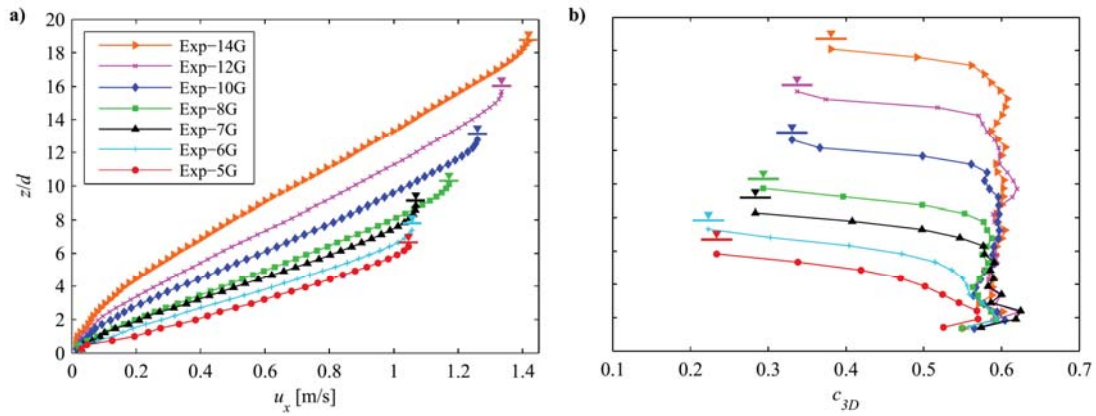


Fig. 5. Experimental profiles obtained on the grain basal surface (G). (a) Longitudinal velocity profiles, u_x ; (b) volume fraction profiles, c_{3D}

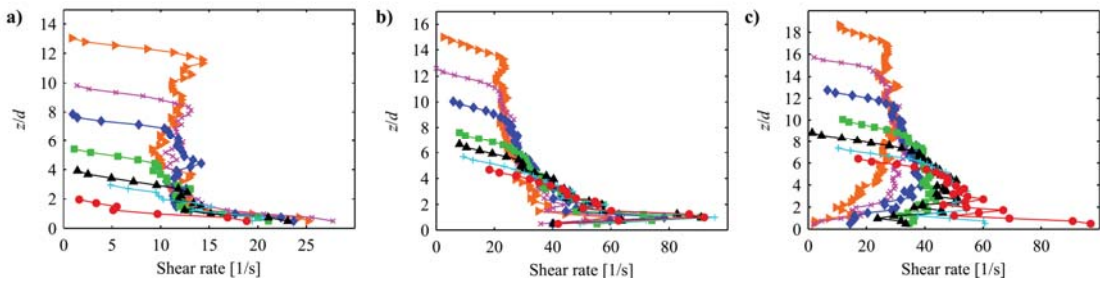


Fig. 6. Experimental profiles of the shear rate, $\partial_z u_x$. (a) smooth Bakelite (S); (b) sandpaper (P40); (c) grain basal surface (G)

Finally, the experimental results on the granular bed (G), are reported in Figs. 5 and 6c. Similar to the P40 bed, a no-slip KBC is guaranteed by the high basal friction. Yet, different from the sandpaper bed, in this case the roughness is high enough that the grain rolling and saltations are almost completely inhibited. In fact, the grains tend to interlock with the bumpy granular bed. As a consequence, a very weak grain rolling is observed only in the case of small flow depths (i.e. runs Exp-5G and Exp-6G), while in all other experiments a no-slip KBC with no rolling occurs. By comparing Fig. 5a with Fig. 2c, it can be noted that the increased chute slope does not allow the formation of a lower creep flow, characterized by very small velocities and a concave shape of the u_x profile.

Nonetheless, owing to the interlocking between the grains and the basal surface, for all experiments the volume fraction c_{3D} reaches the asymptotical value of ≈ 0.6 soon above the fixed bed. The c_{3D} profiles are almost constant along the entire flow depth, except near the free surface. For small enough values of h (i.e. Exp-5G, Exp-6G and Exp-7G), the shape of the u_x profile is weakly convex, analogous to the case of sandpaper bed.

When h increases, and, consequently, also the pressures and the sidewall resistances become larger, the u_x profile exhibits a progressive concave shape in its lower region and an approximately linear shape in an upper intermediate region (cf. Fig. 6c). In these cases, the behavior of the lower layer can be regarded as the onset of the creep flow regime (cf. Fig. 2c), which, however, cannot fully develop, due to the higher slope and, consequently, higher active forces. In this lower zone, frictional momentum exchanges among the grains start to become prevalent with respect to collisions, thanks to the confining effects of the normal pressures and of the sidewall resistances. Analogous to that already observed on different beds and in the experimental dataset with $\alpha=30^\circ$ (Fig. 2), an upper almost collisional layer of thickness of few grain diameters, where the u_x profile shows a convex shape and c_{3D} rapidly decreases with z , occurs in all experiments on G bed. This finding suggests that the flow dynamics near the free surface is scarcely influenced by the roughness of the basal surface if h is high enough. Finally, it is worth underlining that the general shape of the c_{3D} profiles is common to all the investigated beds: near the bed $\partial_z c_{3D} > 0$, while $\partial_z c_{3D} \leq 0$ along the rest of the flow depth. This finding is in agreement with other works on dry granular flows (e.g. Ancey, 2001), while it differs from some investigations on liquid-granular mixtures, where also the case $\partial_z c_{3D} > 0$ was observed along the flow depth due to the other dissipation mechanisms related to the interstitial fluid (e.g. Egashira et al., 2001).

4. Conclusion

In this work we systematically studied the effects of the basal surface on the dynamics of granular flows in a rectangular chute. As an extension of the work by Sarno et al. (2018a), a higher chute inclination angle of 35° was investigated to determine the influence of larger active forces on the basal KBC. Moreover, in this experimental campaign we provided not only the flow velocity measurements but also estimations of the volume fraction by using the SOM method (Sarno et al., 2016). The comparisons of the velocity and volume fraction profiles indicate that different flow regimes coexist along the flow depth.

For all investigated basal surfaces, a Bagnold-like shape of the velocity profile is generally observed, if the flow depth is small enough. As the flow depth increases, the velocity profile becomes approximately linear in its intermediate part and, for the case of granular bed (G), even weakly convex in the lower zone. It suggests the occurrence of a rheological stratification, where the lower region is governed by frictional exchange mechanisms and the upper region is more collisional. Yet, owing to the larger bed slope with respect to the dataset reported by Sarno et al. (2018a), no fully-developed creep flow could be observed in the case of the granular bed.

In the whole dataset we observed similar behaviors of the volume fraction profiles. Small values of volume fraction occur near the fixed bed in both smooth Bakelite and sandpaper basal surface, while relatively larger values are observed in the case of the bumpy grain bed. In the regions where the velocity profiles exhibit a convex shape, the volume fraction is typically smaller than 0.6. Conversely, the volume fraction is found to exhibit an approximately constant value close to ≈ 0.6 , where a linear velocity profile occurs. In the experiments on sandpaper beds, interestingly, we observed that the Bagnold convex shape of the velocity profiles persists also in the presence of relatively high flow depths. This finding seems to be due to grain rolling and saltations at the basal surface, made possible by the roughness much smaller than the grain diameter and by the increased acting forces, in turn due to the larger bed slope. Such a complex no-slip KBC, allowing basal grain rolling and saltations, seems responsible for an increase of the grain collisionality also in the upper regions of the flow domain. Immediately below the free surface, a prevalently collisional layer with rapidly decreasing volume fraction and convex velocity profiles is observed in all experiments, independent from the kind of basal surface.

From these experimental findings it emerged that the granular flow dynamics and the occurrence of stratified flow regimes depend on the basal roughness and sidewall resistances but it is also crucially governed by the active forces due to the bed slope. Further laboratory investigations with larger bed slopes and on bed surfaces with intermediate roughnesses could be useful to better understand the flow regimes, and, the behavior of the fluctuation velocities at the bed. Moreover, a further investigation on the scale effects of this laboratory study, especially those ones due to rate-dependent dissipations, could be useful to extend the experimental findings to field-scale applications.

Acknowledgements

The authors thank V. D'Avino for help in the experimental campaign given during his traineeship at the University of Salerno. The authors are also grateful to N. Immediata for valuable assistance in experimental design.

References

- Ancey, C., 2001, Dry granular flows down an inclined channel: Experimental investigations on the frictional-collisional regime: *Physical Review E*, v. 65, no. 1, 011304, doi:10.1103/PhysRevE.65.011304.
- Armanini, A., Capart, H., Fraccarollo, L., and Larcher, M., 2005, Rheological stratification in experimental free-surface flows of granular-liquid mixtures: *Journal of Fluid Mechanics*, v. 532, p. 269-319, doi:10.1017/S0022112005004283.
- Bagnold, R. A., 1954, Experiments on a gravity-free dispersion of large solid spheres in a Newtonian fluid under shear: *Proceedings of the Royal Society A*, v. 225, no. 1160, p. 49-63, doi:10.1098/rspa.1954.0186.
- Baker, J., Gray, N., and Kokelaar, P., 2016, Particle size-segregation and spontaneous levee formation in geophysical granular flows: *International Journal of Erosion Control Engineering*, v. 9, no. 4, p. 174-178, doi:10.13101/ijece.9.174.
- Eckart, W., Gray, J.M.N.T., and Hutter, K., 2003, Particle Image Velocimetry (PIV) for granular avalanches on inclined planes, *in* Hutter, K., Kirchner, N., eds., *Dynamic response of granular and porous materials under large catastrophic deformations: Lecture notes in applied and computational mechanics*, v. 11, Springer, Berlin, p. 195-218, doi:10.1007/978-3-540-36565-5_6.
- Egashira, S., Itoh, T., and Takeuchi, H., 2001, Transition mechanism of debris flows over rigid bed to over erodible bed: *Physics and Chemistry of the Earth, Part B: Hydrology, Oceans and Atmosphere*, v. 26, no. 2, p. 169-174, doi:10.1016/S1464-1909(00)00235-5.
- Iverson, R. M., and Vallance, J. W., 2001, New views of granular mass flows: *Geology*, v. 29, no. 2, p. 115-118. doi:10.1130/0091-7613(2001)029<0115:NVOGMF>2.0.CO;2.
- Iverson, R. M., and George, D. L., 2014, A depth-averaged debris-flow model that includes the effects of evolving dilatancy. I. Physical basis: *Proceedings of the Royal Society A*, v. 470, no. 2170, 20130819, doi:10.1098/rspa.2013.0819.
- Jesuthasan, N., Baliga, B. R., and Savage, S. B., 2006, Use of particle tracking velocimetry for measurements of granular flows: review and application: *KONA Powder and Particle Journal*, v. 24, p. 15-26, doi:10.14356/kona.2006006.
- Jop, P., Forterre, Y., and Pouliquen, O., 2005, Crucial role of sidewalls in granular surface flows consequences for the rheology: *Journal of Fluid Mechanics*, v. 541, p. 167-192, doi:10.1017/S0022112005005987.
- Kuo, C. Y., Tai, Y. C., Bouchut, F., Mangeney, A., Pelanti, M., Chen, R. F., and Chang, K. J., 2009, Simulation of Tsaoling landslide, Taiwan, based on Saint Venant equations over general topography: *Engineering Geology*, v. 104, no. 3-4, p. 181-189, doi:10.1016/j.enggeo.2008.10.003.
- Medina, V., Hürlimann, M., and Bateman, A., 2008, Application of FLATModel, a 2D finite volume code, to debris flows in the northeastern part of the Iberian Peninsula: *Landslides*, v. 5, no. 1, p. 127-142, doi:10.1007/s10346-007-0102-3.
- MiDi, G. D. R., 2004, On dense granular flows: *European Physical Journal E*, 14(4), 341-365, doi:10.1140/epje/i2003-10153-0.
- Mills, P., Loggia, D., and Tixier, M., 1999, Model for a stationary dense granular flow along an inclined wall: *Europhysics Letters*, v. 45, no. 6, 733, doi:10.1209/epl/i1999-00229-y.
- Papa, M., Sarno, L., Vitiello, F., and Medina, V., 2018, Application of the 2D Depth-Averaged Model, FLATModel, to Pumiceous Debris Flows in the Amalfi Coast: *Water (Switzerland)*, v. 10, no. 9, 1159, doi:10.3390/w10091159.
- Pouliquen, O., and Forterre, Y., 2009, A non-local rheology for dense granular flows: *Philosophical Transactions of the Royal Society A*, v. 367, no. 1909, p. 5091-5107, doi:10.1098/rsta.2009.0171.
- Sarno, L., Papa, M.N., and Martino, R., 2011a, Dam-break flows of dry granular material on gentle slopes, *in* *Proceedings of the 5th International Conference on Debris-Flow Hazards Mitigation*, Padua, Italy, June 2011, p. 503-512, doi:10.4408/IJEGE.2011-03.B-056.
- Sarno, L., Martino, R., and Papa, M. N., 2011b, Discussion of "Uniform flow of modified bingham fluids in narrow cross sections" by A. Cantelli: *Journal of Hydraulic Engineering*, v. 137, no. 5, p. 621, doi:10.1061/(ASCE)HY.1943-7900.0000238.
- Sarno, L., Carravetta, A., Martino, R., and Tai, Y.-C., 2014, A two-layer depth-averaged approach to describe the regime stratification in collapses of dry granular columns: *Physics of Fluids*, v. 26, no. 10, p. 103303, doi:10.1063/1.4898563.
- Sarno, L., Papa, M.N., Villani, P., and Tai, Y.-C., 2016, An optical method for measuring the near-wall volume fraction in granular dispersions: *Granular Matter*, v. 18, no. 4, doi:10.1007/s10035-016-0676-3.
- Sarno, L., Carravetta, A., Martino, R., Papa, M. N., and Tai, Y. C., 2017, Some considerations on numerical schemes for treating hyperbolicity issues in two-layer models: *Advances in water resources*, v. 100, p. 183-198, doi:10.1016/j.advwatres.2016.12.014.
- Sarno, L., Carleo, L., Papa, M.N., and Villani, P., 2018a, Experimental investigation on the effects of the fixed boundaries in channelized dry granular flows: *Rock Mechanics and Rock Engineering*, v. 51, no. 1, p. 203-225, doi:10.1007/s00603-017-1311-2.
- Sarno, L., Carravetta, A., Tai, Y.-C., Martino, R., Papa, M.N., and Kuo, C.-Y., 2018b, Measuring the velocity fields of granular flows – Employment of a multi-pass two-dimensional particle image velocimetry (2D-PIV) approach: *Advanced Powder Technology*, v. 29, no. 12, p. 3107-3123, doi:10.1016/j.apt.2018.08.014.
- Thielicke, W., and Stamhuis, E.J., 2014, PIVlab—Towards user-friendly, affordable and accurate digital particle image velocimetry in MATLAB: *Journal of Open Research Software*, v. 2, no.1, doi:10.5334/jors.bl.

Debris-flow behavior in super- and subcritical conditions

Christian Scheidl ^{a,*}, Brian McArdell ^b, Georg Nagl ^a, Dieter Rickenmann ^b

^aUniversity of Natural Resources and Life Sciences, Vienna A-1190, Austria

^bSwiss Federal Research Institute WSL, Zuercherstrasse 111, Birmensdorf CH-8903, Switzerland

Abstract

Observations of debris-flow events all over the world cover a wide range of phenomenologically similar processes, consisting of different concentrations of water, fine and coarse sediment, and frequently wooden debris. For this reasons, empirically derived coefficients to be used in prediction models to estimate debris-flow dynamics often show a wide degree of scatter. Two of such empirically derived concepts, originally developed for pure water flows, are presented in this study, showing similar deviations from hydrostatic stress assumption in subcritical flow conditions. The first concept is used to estimate debris-flow velocities, based on superelevation data. Based on our experimental results as well as observations from real debris-flow events at the field monitoring station at Illgraben (canton Valais, Switzerland) we show that the empirical coefficient used in the superelevation equation to account for non-Newtonian flow effects correlates with the Froude number – the dimensionless ratio between gravitational and inertia forces in the flow. Interestingly, a similar relationship – the second concept presented – has been found in recent studies to estimate the maximum impact pressure of a debris-flow event. Our results suggest that for debris flows and decreasing Froude numbers inertia forces become more important and the hydrostatic pressure distribution may be an unrealistic assumption for empirically based prediction models in subcritical conditions.

Keywords: Froude dependency, superelevation, impact estimation, earth pressure, debris-flow behaviour

1. Introduction

The dynamic behavior of debris flows is mainly driven by its water content, the ratio of fine to coarse particles in the flow, and possibly also the degree of agitation induced by the interaction of the flow with the rough channel bed. Iverson (1997), for instance, proposed different dimensionless parameters referring to the various stresses (solid grain shear and normal stress, fluid shear and normal stress, and solid-fluid interaction stress) that characterize the flowing mixture. These controlling factors are variable within any given flow and between individual debris-flow events, but all over the world the term debris flow is widely used to describe a broad range of phenomenologically similar processes. This lead, for instance, to a substantially variability of data on viscosities of debris-flow events in nature (Cui et al., 2005; Tecca et al., 2003), and empirically derived coefficients, which are used in prediction models to estimate for instance maximum impact forces of debris flows, show a wide degree of scatter - although a physically correct concept for its development may be assumed.

For this study we use the Froude number – the dimensionless ratio between gravitational and inertia forces in the flow - to characterize different debris-flow behaviors. In this context, two concepts to derive dynamic characteristics of debris-flow events are analyzed more closely. Originally developed for pure water flows, the first concept to be considered, concerns the estimation of maximum flow velocities based on superelevation information. The other concept, estimation of the maximum impact pressure of a debris-flow event, is an important design parameter for many protection structures. However, with both concepts it is difficult to account for the full range of flow conditions of debris flows.

* Corresponding author e-mail address: christian.scheidl@boku.ac.at

2. Bulk mixture variability and flow conditions

2.1. Superelevation

Numerous studies have shown that the destructive power of debris flows is proportional to the flow velocity (Armanini, 1997; Bugnion et al., 2011; Scheidl et al., 2013). A possible approach to estimate (maximum cross-sectional mean) flow velocities of debris flows (for a given event) is based on the vortex equation by using superelevation marks. Superelevation can be observed in curved channels, where the flow-height at the inner bend is lower than the flow-height at the outer bend (Figure 1).

However, to apply the vortex equation also to Non-Newtonian fluids, the vortex formulae was modified by introducing a correction factor. This correction factor can be expressed with equation (1), where R_c denotes the centerline radius of the bend, g^* the slope normal component of gravity, Δh denotes superelevation, B accounts for the channel width and v is the flow velocity.

$$k = \frac{R_c g^* \Delta h}{B v^2} \quad (1)$$

Several studies comparing experimental or observed superelevation data with estimated velocities suggest a wide range of values for the correction factor k - accounting for the viscosity, vertical sorting and the boundary effects in bends for debris flows (e.g.: Hungr et al., 1984; VanDine, 1996; Bulmer et al., 2002; Prochaska et al., 2008). Based on small-scale experiments, Scheidl et al. (2014) analyzed debris-flow velocities in a curved flume and back-calculated correction factors for more than 150 experimental debris-flows. They measured superelevation and investigated the influence of different material mixtures as well as bend geometries. The flume investigations were conducted using a flexible plastic half-pipe, mounted on a wooden plane construction. Two different bend radii (1.0 m and 1.5 m) with a bend angle of 60° were implemented. The total length of the flume, of about 8 m, was covered with 40 grit silicon carbide sandpaper, reflecting a constant basal friction layer. To account for the complexity of a debris-flow process, four different material mixtures based on four different grain size distributions, were defined.

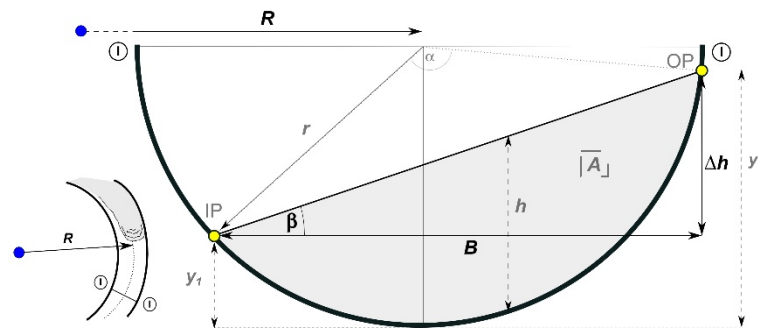


Fig. 1. Illustration of parameters used for estimating debris-flow velocities based on superelevation, modified after Scheidl et al. (2014).

Scheidl et al. (2014) found systematic deviations of observed superelevation heights as compared to those estimated by applying the simple vortex equation for a Newtonian fluid, and these deviations appeared to be a function of the Froude number, $F = v/\sqrt{gh}$. The experimental results suggest that superelevation of debris flows cannot be solely described with approaches from the pure water hydraulics. This is also confirmed by an analysis of superelevation data from real debris-flow events observed at the Illgraben (Valais, CH), and back-calculated correction factors for these events presented below.

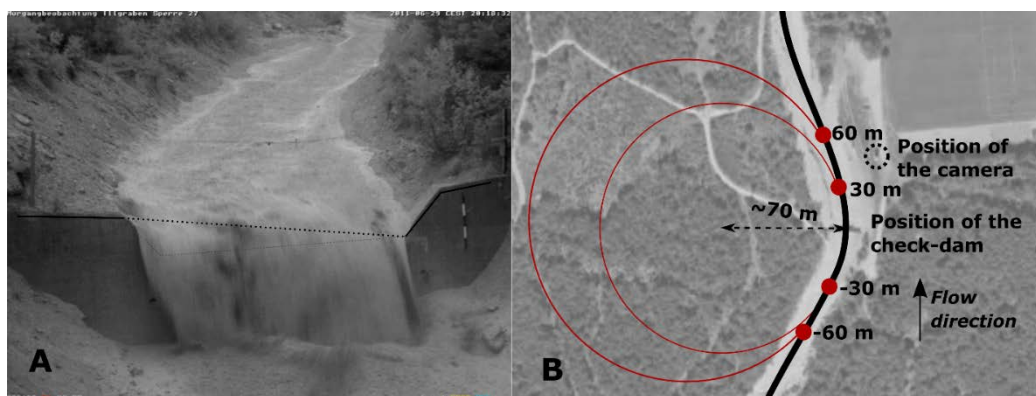


Fig. 2. Superelevation observation from a real debris-flow event at the Illgraben. A) Maximum superelevation of the debris-flow event at the Illgraben on June 29, 2011. B) The relevant curve radius R_c were determined based on circular arcs fit to sets of points marked on the bend, following a method proposed by Prochaska et al. (2008).

For this purpose, video recordings of debris-flow events were analyzed at a location where the flow passed over a check dam, which served as the basis for the determination of the event-related superelevation height (Fig. 2A and B). The relevant curve radius R_c to be used in equation (1), is estimated based on a method proposed by Prochaska et al. (2008). For field analyzes, they recommend the channel curve to be approximated by three points at intervals of 30 m, 60 m or 90 m (Fig. 2B). The determination of the maximum flow velocities v for the respective events is based on the time of maximum flow intensity according to geophone recordings. The maximum flow height h was determined from radar measurements perpendicular to the check-dam crown. From this, the Froude numbers F of the respective events could be determined. Figure 3 (left panel) shows the relation between correction factors k and Froude numbers F for all experiments of Scheidl et al. (2014) and for superelevation data based on real debris-flow events observed at the Illgraben monitoring station. The regression model (black line) is based on the experimental data of Scheidl et al. (2014) and follows a power law model ($R^2 = 0.77$):

$$k = 4.4F^{-1.2} \quad (2)$$

2.2. Impact modelling

Interestingly, a similar relationship with the Froude number has been found for the empirical pressure coefficient a of the general form of the dynamic impact model:

$$a = \frac{p}{\rho v^2} \quad (3)$$

where p is the impact pressure, ρ is the debris-flow density and v are the approach flow velocity. For clear water a has been found to be between 1 and 2 (Watanabe and Ikeya, 1981). However, numerous studies suggest that a can vary significantly for debris flows, depending on the flow type. Watanabe and Ikeya (1981), for example, estimated $a = 2.0$ for laminar flow and fine-grained material. Egli (2005) proposed values up to $a = 4.0$ for coarse material. Zhang (1993) recommended values of a between 3.0 and 5.0, based on field measurements of over 70 debris flows. Based on laboratory impact measurements on flexible debris-flow barriers, Wendeler et al. (2007) list up scaled field values of a between 0.7 and 2.0. For granular debris flows, theoretical considerations by Coussot (1997) result in values of $a = 5$ to $a = 15$. A similar range of a values was proposed for debris flows by Daido (1993).

Cui et al. (2015) fitted the pressure coefficient a as a power law function to the Froude number F , based on their experiments and experiments conducted by Hübl and Holzinger (2003); Scheidl et al. (2013), Tiberghien et al. (2007) as well as estimations of field events of Costa (1984) and Zhang and Yuan (1985):

$$a = 5.3F^{-1.5} \quad (4)$$

Considering both the hydrostatic pressure and the hydrodynamic pressure of a debris-flow impact, Vagnon and

Segalini (2016) as well as Wang et al. (2018) showed that the total pressure coefficient a' follows the general form of:

$$a' = \beta F^{-2} + c \quad (5)$$

In equation (5) the static impact coefficient \square denotes the exceedance from the hydrostatic pressure whereas the dynamic impact coefficient c acts as a drag coefficient depending on v^2 . Wang et al. (2018) propose $\square = 3.8$ and $c = 0.8$, according to the experimental results.

3. Results and Discussion

Empirically derived coefficients, back-calculated from the simple equations to (i) estimate debris-flow velocity based on superlevation (left) and (ii) predict maximum impact pressures (right), as a function of the corresponding Froude numbers, are shown in Figure (3). It must be noted that there is some spurious correlation between the coefficients and the Froude number determined from debris-flow experiments and field observations.

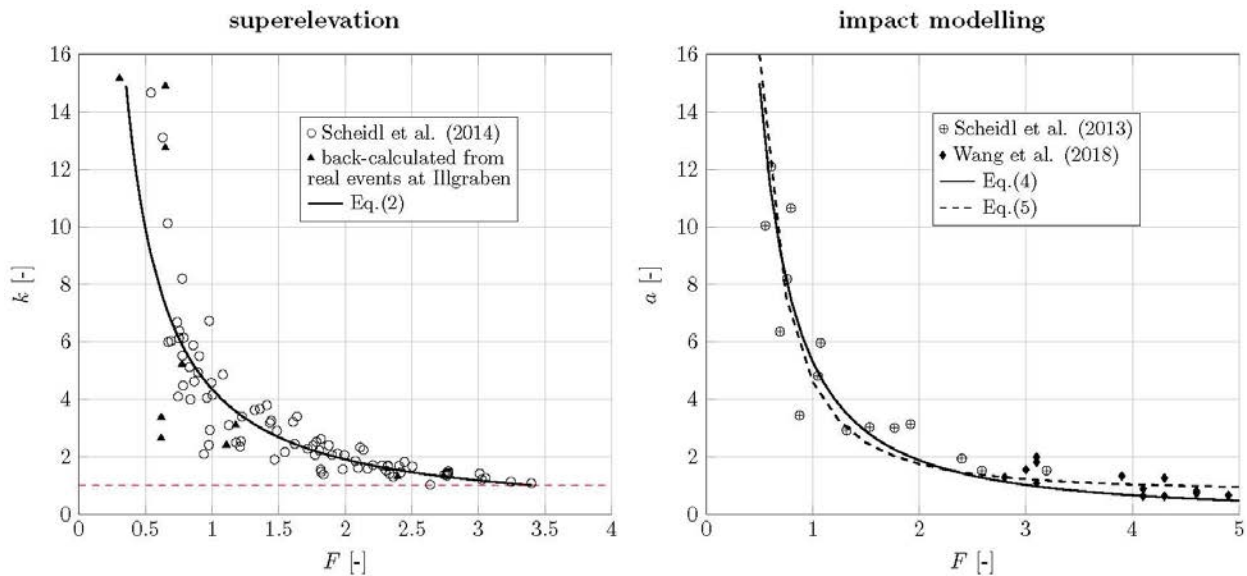


Fig.3. Relation of empirical derived coefficients of modified prediction models to estimate debris-flow velocity (left) and debris-flow impact pressure (right) and Froude number. Left: The empirical correction factors k of the vortex equation (eq.1) are based i) on superlevation experiments from Scheidl et al. (2014) and ii) from superlevation field investigations at the debris-flow monitoring station at Illgraben (CH). The horizontal dashed line shows a constant relation of $k = 1$ with the Froude number as expected for clear water flows. The black line indicates the power model (eq. 2) based on the superlevation experimental data of Scheidl et al. (2014). Right: The prediction of the empirical coefficient a of the impact model (eq. 3) is based on the power model (eq.4) as proposed by Cui et al. (2015) and on the general form (eq. 5), accounting also for hydrostatic pressure with $\beta = 3.8$ and $a = 0.8$. Additionally the experimental data of Scheidl et al. (2013) and Wang et al. (2018) are included.

The results in the context of superlevation estimates indicate that the vortex equation (1) together with correction factors of $1 < k < 5$ might be considered for supercritical flow. However, secondary flow or spiral flow phenomena in the lateral direction could limit the estimation of the maximum front velocity based on superlevation, because the vortex equation is derived to apply only for conditions where no cross-wave disturbance patterns within the bend section is produced.

For subcritical flow conditions the correction factor determined from the flume experiments shows a higher deviation in comparison to a pure Newtonian fluid, which is also confirmed by field observations from real events at Illgraben. We assume that for subcritical flow conditions the mixture properties and the internal flow mechanism result in an enhanced deviation from the simple force balance considering only hydrostatic and centrifugal forces in the superlevation equation for Newtonian fluids. Considering a debris flow as a single phase (bulk) mixture, one possibility to account for the deviation in subcritical conditions was proposed by Scheidl et al. (2014) who assumed a

correction factor k_{ep} to be a function of active and passive earth pressure as well as inundated flow heights on the inner (y_1) and outer (y_2) sides of the curve :

$$k_{ep} = \left[K_p + (K_p - K_a) \left(\frac{y_2^2}{y_2^2 - y_1^2} - 1 \right) \right]^{-1} \quad (6)$$

Equation (7) is based on a force balance approach and on the assumption of a rectangular cross section. K_p and K_a denote the passive, respectively active earth pressure coefficient. However, the results of the experiments and from field observations suggest higher variability of induced anisotropic stress distributions in the bulk mixture of debris flows for subcritical flow regimes.

The power law models to describe the empirical pressure coefficient a , and the total pressure coefficient a' , respectively, as a function of the Froude number, closely match. This implies that the general form of eq. (7) can be used in subcritical as well as in supercritical flow conditions to predict the total pressure coefficient. However, Wang et al. (2018) used also the grain Reynolds number (N_R) as well as the modified Savage number (N_{Sav}) (e.g. Iverson, 1997) to distinguish between different debris-flow types for impact pressure estimations. Based on experiments, they found the dynamic impact model (eq. 4) only applicable for debris flows with $N_R > 1$ and $N_{Sav} < 0.002$, characterized either as dilute and turbulent or dense and steady debris-flow type. Both types have been indicated by Wang et al. (2018) to behave like fluids, and the related experiments were associated with Froude numbers > 2 . For debris-flow types with grain Reynolds numbers and Savage numbers different from the thresholds given above, Wang et al. (2018) suspect debris flows not to behave fluid-like - discarding the dynamic impact model given in eq. (4).

Similar to the coefficient k , determined from superelevation experiments, the hydrodynamic impact coefficients a and a' show a comparable variation with the Froude number. Higher deviation of both impact coefficients can be observed for low Froude numbers, hence for subcritical flow conditions. Following the general equation (5), prediction of the pressure coefficient a' for Froude conditions $F < 1$ is mainly influenced by the hydrostatic term (β), accounting for the exceedance from the hydrostatic pressure. Considering debris flows as single-phase flows and applying a similar approach as assumed for the derivation of equation (3) or proposed by Vagnon and Segalini (2016) we can rewrite equation (5) tentatively replacing a^* by the passive earth pressure coefficient K_p :

$$K_p = F^{-2} + c \quad (7)$$

The passive earth pressure coefficient is the ratio between bed-normal and bed-parallel (longitudinal) stresses within the bulk mixture. According to Savage and Hutter (1989) and modified by Hungr (2008) this ratio can be described by:

$$K_p = 2 \left[\frac{1 + \sqrt{1 - \cos^2 \varphi_i (1 + \tan^2 \varphi_e)}}{\cos^2 \varphi_i} \right] - 1 \quad (8)$$

In equation (8), φ_i denotes the internal friction angle and φ_e , the basal friction angle, is modified by Hungr (2008) to account for the rotation of principal stresses in spreading flows. If φ_i as well as φ_e get zero, then $K_p = 1$, reflecting hydrostatic conditions. proposed Static impact coefficients (β in eq. 5, respectively K_p in eq. 7) have been proposed by Lichtenhahn (1973), ranging from 2.8 – 4.4. Armanini (1997) stated a static impact coefficient of 5, and based on miniaturized tests, Scotton and Deganutti (1997) found values between 2.5 and 7.5. This is in accordance of passive earth pressure values proposed by Hungr (1995) for numerical 1-d modelling of debris-flow propagation.

He proposed passive earth pressure values up to 5.0. The dependence of a^* and possibly K_p with the Froude number, as stated by equation (7), seems also to be in line with the superelevation analysis from Scheidl et al. (2014). Based on the theoretical Smooth Momentum Flux model to estimate run-up heights, Rickenmann et al. (this proceeding) observed a tendency for lower K_p values with increasing F – values.

4. Conclusions

Our results suggest that for debris flows and decreasing Froude numbers inertia forces become more important, and the evolution of internal stresses governing deformation is largely dominated by constitutive stress conditions of the bulk mixture -- as an effect of rheological characteristics. For both presented concepts, applicable to derive

dynamic characteristics of debris-flow events, it seems that hydrostatic pressure distribution may be unrealistic when dealing with the flow of granular material that has internal strength due to its frictional nature (Savage and Hutter 1989).

References

- Armanini, A., 1997, On the dynamic impact of debris flows, in: *Recent Developments on Debris Flows*, in Armanini, A., and Michiue, M., eds., Lecture Notes in Earth Sciences, Springer-Verlag Berlin Heidelberg, p. 208–226.
- Bugnion, L., McArdell, B., Bartelt, P., and Wendeler, C., 2012, Measurements of hillslope debris flow impact pressure on obstacles: *Landslides*, v. 9, p. 179–187, doi: 10.1007/s10346-011-0294-4.
- Bulmer, M.H., Barnouin-Jha, O.S., Peitersen, M.N., and Bourke, M., 2002, An empirical approach to studying debris flows: Implications for planetary modelling studies: *Journal of Geophysical Research*, v. 107, p. 1–16. doi: 10.1029/2001/B001531.
- Costa, John E., 1984, Physical Geomorphology of Debris Flows, in Costa, J. E., and Fleisher, P.J. eds., *Developments and Applications of Geomorphology*, Springer-Verlag Berlin Heidelberg, p. 268–317.
- Cui, P., Chen, X., Waqng, Y., Hu, K., and Li, Y., 2005, Jiangia Ravine debris flows in southwestern China, in Jakob, M., and Hungr, O., eds., *Debris-Flow Hazards and Related Phenomena*, Springer-Verlag Berlin Heidelberg, p. 565–594.
- Cui, P., Zeng, C., and Lei, Y., 2015, Experimental analysis on the impact force of viscous debris flow: *Earth Surfaces Processes and Landforms*, v. 40, p. 1644–1655, doi: 10.1002/esp.3744.
- Egli, T., 2005, *Wegleitung Objektschutz gegen gravitative Naturgefahren: Vereinigung Kantonaler Feuerversicherungen (VKF)*, Bern, p. 105.
- Hübl, J., and Holzinger, G., 2003, *Entwicklung von Grundlagen zur Dimensionierung kronenoffener Bauwerke für die Geschiebewardirtschaftung in Wildbächen. Kleinmassstäbliche Modellversuche zur Wirkung von Murbrechern: WLS Report, no. 50 vol. 3*, Institut of Mountain Risk Engineering.
- Hungr, O., 2008, Simplified models of spreading flow of dry granular material: *Canadian Geotechnical Journal*, vol. 45, p. 1156–1168, doi:10.1139/T08-059.
- Hungr, O., 1995, A model for the runout analysis of rapid flow slides, debris flows, and avalanches: *Canadian Geotechnical Journal*, vol. 32, p. 610–623, doi: 10.1139/t95-063.
- Hungr, O., Morgan, G.C., and Kellerhals, R., 1984, Quantitative analysis of debris torrent hazards for design of remedial measures: *Canadian Geotechnical Journal*, vol. 21, p. 663–677, doi: 10.1139/t84-073.
- Iverson, R.M., 1997, The Physics of Debris Flows: *Reviews of Geophysics*, vol. 35, p. 245–296, doi: 10.1029/97RG00426.
- Lichtenhahn, C., 1973, *Die Berechnung von Sperren in Beton und Eisenbeton: Kolloquium über Wildbach-Sperren: Mitteilungen der Forstlichen Bundesanstalt Wien*, p. 91–127.
- Prochaska, A., Santi, P., Higgins, J., and Cannon, S., 2008, A study of methods to estimate debris flow velocity: *Landslides*, vol. 5, p. 431–444, doi: 10.1007/s10346-008-0137-0.
- Savage, S.B., Hutter, K., 1989, Motion of a finite mass of granular material down a rough incline: *Journal of Fluid Mechanics*, vol. 199, p. 177–215, doi: 10.1017/S00222112089000340.
- Scheidl, C., Chiari, M., Kaitna, R., Müllegger, M., Krawtschuk, A., Zimmermann, T., and Proske, D., 2013, Analysing debris-flow impact models, based on a small-scale modelling approach: *Surveys in Geophysics*, vol. 34, p. 121–140, doi: 10.1007/s10712-012-9199-6.
- Scheidl, C., McArdell, B.W., and Rickenmann, D., 2014, Debris-flow velocities and super-elevation in a curved laboratory channel: *Canadian Geotechnical Journal*, vol. 52, p. 1–13, doi: 10.1139/cgj-2014-0081.
- Scotton, P., and Deganutti, A., 1997, Phreatic line and dynamic impact in laboratory debris flow experiments, in Chen, C.L. ed., *Proceedings of the 1st International Conference on Debris-Flow Hazards Mitigation: Mechanics, Prediction and Assessment*, p. 777–786.
- Tecca, P.R., Galgano, A., Genevois, R., and Deganutti, A., 2003, Development of a remotely controlled debris flow monitoring system in the Dolomites (Acquabona, Italy): *Hydrological Processes*, vol. 17, p. 1771–1784, doi: 10.1002/hyp.1212.
- Tiberghien, D., Laigle, D., Naaim, M., Thibert, E., Ousset, F., 2007, Experimental investigation of inter-action between mudflow and obstacle, in Cui, P., and Cheng, Ch., eds., *Proceedings of the 4th International Conference on Debris-Flow Hazards Mitigation: Mechanics, Prediction and Assessment*, p. 281–292.
- Vagnon, F., and Segalini, A., 2016, Debris flow impact estimation on a rigid barrier: *Natural Hazards and Earth System Sciences*, vol. 16, p. 1691–1697, doi: 10.5194/nhess-16-1691-2016.
- VanDine, D.F., 1996, *Debris flow control structures for forest engineering: Ministry of Forest Research Program, Victoria, British Columbia*.
- Wang, Y., Liu, X., Yao, C., Li, Y., Liu, S., and Zhang, X., 2018, Finite Release of Debris Flows around Round and Square Piers: *Journal of Hydraulic Engineering*, vol. 144, p. 06018015, doi: 10.1061/(ASCE)HY.1943-7900.0001542.
- Watanabe, M., and Ikeya, H., 1981, Investigation and analysis of volcanic mud flows on Mt Sakurajima, Japan, in, *Erosion and Sediment Transport Measurement, Proceedings of the Florence Symposium*, IAHS Publ. 133, p. 12.
- Wendeler, C., Volkwein, A., Denk, M., Roth, A., and Wartmann, S., 2007, Field measurements used for numerical modelling of flexible debris flow barriers, in Cui, P., and Cheng, Ch., eds., *Proceedings of the 4th International Conference on Debris-Flow Hazards Mitigation: Mechanics, Prediction and Assessment*.
- Zhang, S., 1993, A Comprehensive Approach to the Observation and Prevention of Debris Flows in China, *Natural Hazards*, vol. 7, p. 1–23, doi: 10.1007/BF00595676.
- Zhang, S., and Yuan, J., 1985, Impact force of debris flow and its detection: *Memoirs of Lanzhou Institute of Glaciology and Cryopedology, Chinese Academy of Sciences*, p. 269–274.

Experimental examination for influence of debris-flow hydrograph on development processes of debris-flow fan

Haruka Tsunetaka^{a,*}, Norifumi Hotta^b, Yuichi Sakai^b, Yuki Nishiguchi^c, Junya Hina^c

^aForestry and Forest Products Research Institute, Matsunosato 1, Tsukuba 305-8687, Japan

^bGradual School of Agricultural and Life Sciences, The University of Tokyo, Bunkyo-ku Yayoi -1-1-1, Tokyo 113-8657, Japan

^cConstruction Thecnology Institute Co., Ltd., Onigakubo 1047-27, Tsukuba 300-2651, Japan

Abstract

In order to assess the influence of different flow hydrographs on fan development processes, we carried out flume tests using a sloped channel (15°, 10 cm wide) with a deposition area (slope decreases from 12° to 3° at a rate of 3° per m). The channel was filled with 0.12 m³ of sediment materials. Debris flows were generated by the entrainment of filled sediment via a steady water flow (0.003 m³/s). We used two types of water supply systems: single surge (60 second duration) and double surge (first surge lasting 50 seconds followed by a second surge with 45 second duration). For the double surge system, there was a 60 second pause in water supply between two surges. Fan formation processes in the deposition area were captured on video, and synchronized interval photography (1 second intervals) using three digital cameras. Time-series changes in fan topography were detected using Structure from Motion photogrammetry (SfM), while flow directions were detected using Particle Image Velocimetry (PIV). The results demonstrate that the flows of single surge cases produced asymmetric fans that inclined to one side due to an increase in the runout distance of the continuing flow. In contrast, the first surge of the double surge cases produced fans that were relatively symmetric. Despite this, the second surge continuously changed flow direction while stopping in the deposition area, and covered the symmetric surge produced by the first surge. Consequently, the final topography of double surge cases was highly variable, despite having the same water supply conditions.

Keywords: Debris-flow fan; Flume test; SfM-MVS; PIV

1. Introduction

Debris-flow deposition plays a critical role in debris-flow fan development (De Haas et al., 2018) and has been linked to many debris-flow disasters (Dowling and Santi, 2014). The ability to estimate and predict debris-flow deposition in the vicinity of the outlet of the feeder channel is important to prevent debris-flow disasters and to interpret the long-term sedimentation regime on alluvial fans. Numerical simulations based on the governing equation of debris flow can be an effective means to estimate the magnitude and extent of deposition. A comparison between the results from simulations and flume tests has demonstrated that simulations can account for almost all of the deposition range of debris-flow fan (e.g., Nakagawa and Takahashi, 1997).

Almost all of these simulations have focused on the occurrence of single debris-flow. However, recent field observations (Pederson et al., 2016), flume tests (De Haas et al., 2016), and numerical simulations (Chen et al., 2017) revealed debris-flow surges on alluvial fans are altered by existing topography. Therefore, in the case where multiple surges had intermittently descended, there is the possibility that the varying fan topography would be produced because of topographic differences resulting from the deposition of the previous surges.

However, direct field measurement of debris-flow rate and fan formation processes are difficult due to the low frequency of debris flows and their destructive power. Accordingly, the influence of debris-flow hydrograph in accordance with the number of surges on fan formation processes has not been fully understood. In this study, we examine the changes in topography and flow directions on the fan with differences in the debris-flow hydrograph, based on the comparison of fan formation processes between single or double debris-flow surges.

* Corresponding author e-mail address: tsunetakaharuka@ffpri.affrc.go.jp

2. Methods

We identified differences in the debris-flow fans among cases based on flume test results, using Structure from Motion - Multi View Stereo (SfM-MVS) and Particle Image Velocimetry (PIV).

2.1. Flume test setting

The flume channel used for the experiments was 8 m long and 10 cm wide with a 15° slope. The dimensions are approximately one-hundredth of real-life debris-flow torrents in scale (Fig. 1). The deposition area was located at the end of the channel (Fig. 1a), and the slope decreases from 12° to 3° at a rate of 3° per meter (Fig. 1b). Square grid lines (20 cm × 20 cm) were drawn in the deposition area in order to measure the runout distance and inundation range (Fig. 1a).

The section in the lower end of the channel (7 m long) was filled with 0.12 m³ of sediment particles (Fig. 1b). The deposition depth was set between 0 to 0.2 m to be smoothly connected at the upper and lower end of deposits. Consequently, the slope of the initial bed changed at the lower end of deposits from 15° (in the channel) to 12° slope (in the deposition area). The filled sediment consisted of multi-granular particles (2.14 to 7 mm in size), and the D_{50} was approximately 3.7 mm. We generated debris flows through entrainment of the filled sediment using steady water flow supplied from the top of the channel. The flow rate was set at 0.003 m³/s.

Two types of water supply systems, single surge and double surge, were employed to compare the influence of debris-flow hydrograph. There is a time lag between the start of overflow and the valve closing because the water supply was controlled by the opening and closing of a valve. For the single surge system, the water was supplied 60 seconds after the start of overflow from the top of the channel. Consequently, a single debris-flow surge was generated. For the double surge system, the water was supplied 50 seconds after the overflow, and again after a 60 second pause in water supply, the valve was opened for 45 seconds. As a result, the two surges descended with an interval of approximately 65 seconds.

2.2. Measurement contents and SfM-MVS, PIV

Four digital single-lens reflex cameras (DSLRs) were installed approximately 2.5 m above the point where the bed slope changed from 9° to 6° to capture the development of the debris-flow fans through photographs and video footage (Fig. 1b). Three of the DSLRs (D5100, Nikon Co.) were automatically synchronized using the remote shutter. The photographs were captured with 1-second intervals. Video footages of the fan formation process of the debris flow were acquired using an additional DSLR set at 60 fps (K-3 ii, Ricoh Co.).

The average velocity of the surge front, from the end of the flume to the stoppage in the deposition area, was measured via the video footage. Assuming that the end of the channel is 0 m, the runout distance of the surge front was read from the video footage. The amount of time required to reach this distance was used to measure the travel time. The average velocity was calculated by dividing the distance by the travel time.

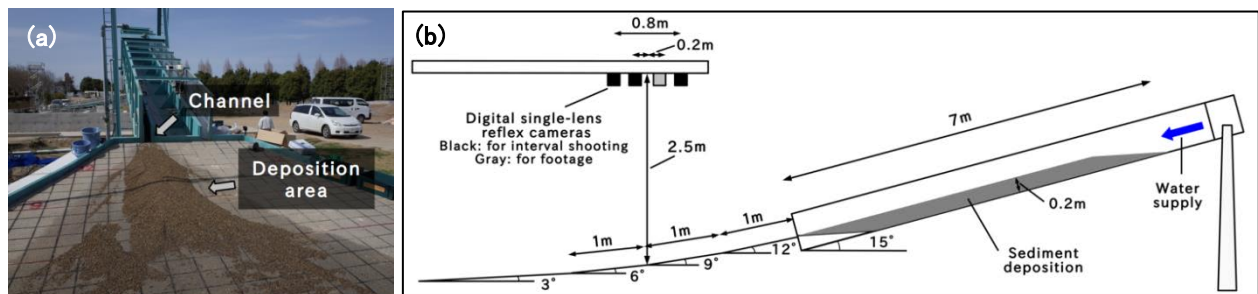


Fig. 1. Experimental setup. (a) View of the channel. (b) Setting of channel and equipment.

We created high-definition digital surface models (DSM) of the debris-flow fan using SfM-MVS software (PhotoScan Professional, Agisoft LLC) from three synchronized photographs. The resolution of the DSMs was set at 1.5 mm, based on the average density of the point cloud. Georeferences were performed using local geographic coordinates of outcropped intersection points of grid lines in the deposition area. In order to test and validate the accuracy of the DSMs, we directly measured the depth of the fan at each intersection point of the deposition area to compare with the DSMs at the end of the experiment.

PIV was used to detect the main flow direction during the fan formation process. We estimated the vectors of surface velocity by the cross-correlation analysis using pairs of photographs (with 1/60-s intervals) extracted from the video footages.

3. Results

The first surge produced symmetrical deposition ranges similarly among cases (Fig. 2). The runout of the first surge continued for approximately 30 seconds. The deposition depth of the fan at that time was almost similar to the single surge system (Fig. 3). In contrast, the second surge produced fans that were asymmetrical and had different topography among cases (Figs. 4 and 5), due to the differences in inundation and deposition processes.

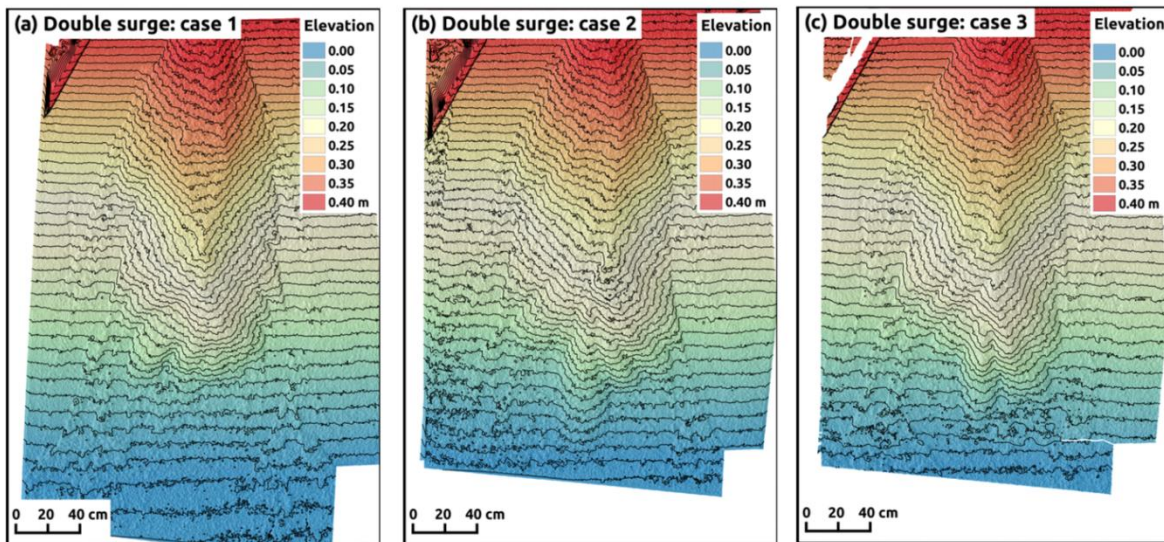


Fig. 2. DSMs of double surge cases after deposition of first surge. (a) case 1. (b) case 2. (c) case 3. Color of the legend indicates elevation when the elevation of the area with a slope of 6° is 0 (3 m from the end of upper channel). The contour interval is 1 cm.

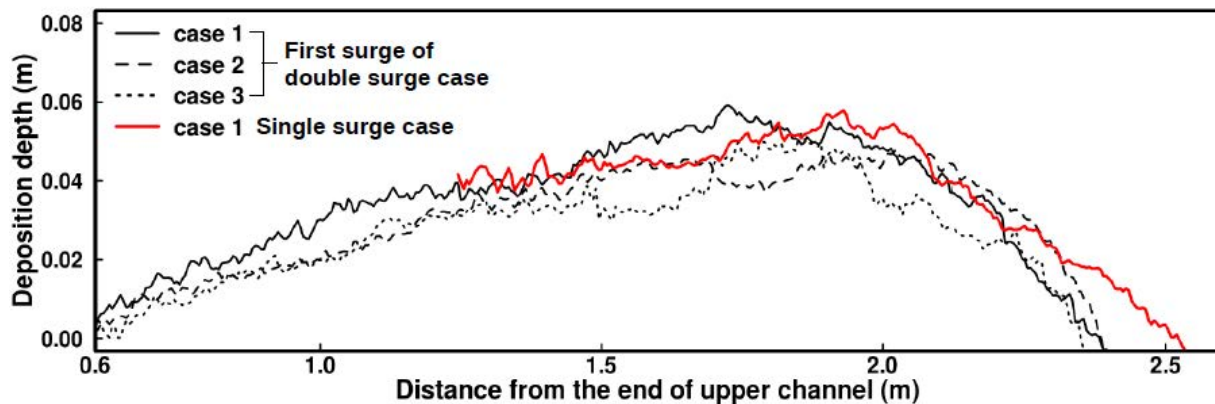


Fig. 3. Comparison of the deposition depths at the center of the fans. The black lines indicate the deposition depths of the fans produced by the first surge. The solid red line indicates the deposition depth of the single surge case after 30 seconds from the start of the run out.

Although the fans tended to bank to the right side in all single surge cases (Fig. 6), the deposition distances reached further downstream and had a greater area compared with those of the double surge cases (Figs. 2-5). Along the edge of the flow path, topography similar to a natural levee was produced, and the bed slope of the path was consistent at approximately 6 degrees.

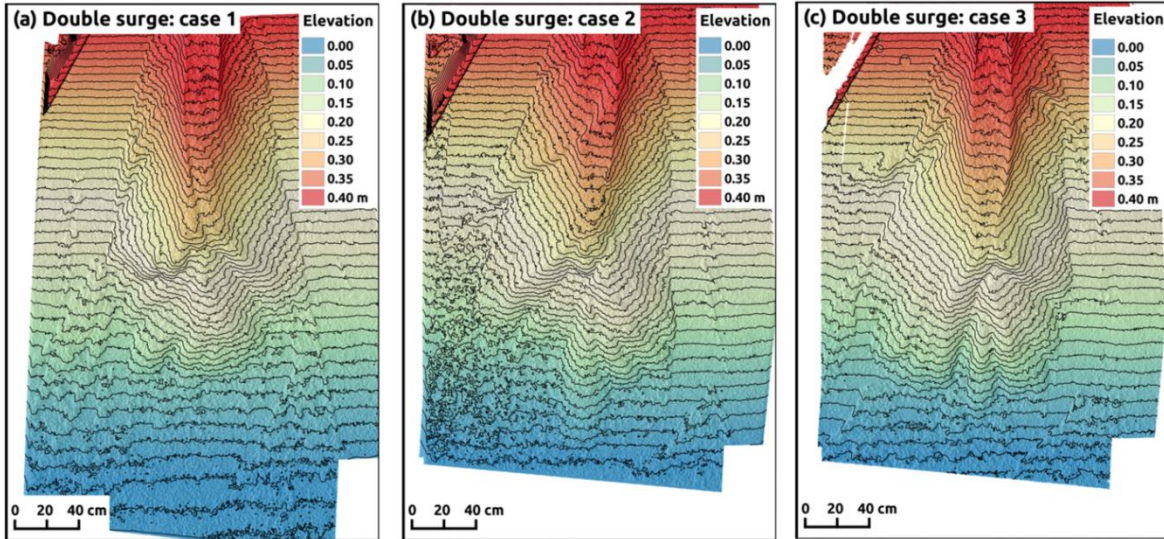


Fig. 4. DSMs of double surge cases after deposition of second surge. (a) case 1. (b) case 2. (c) case 3.

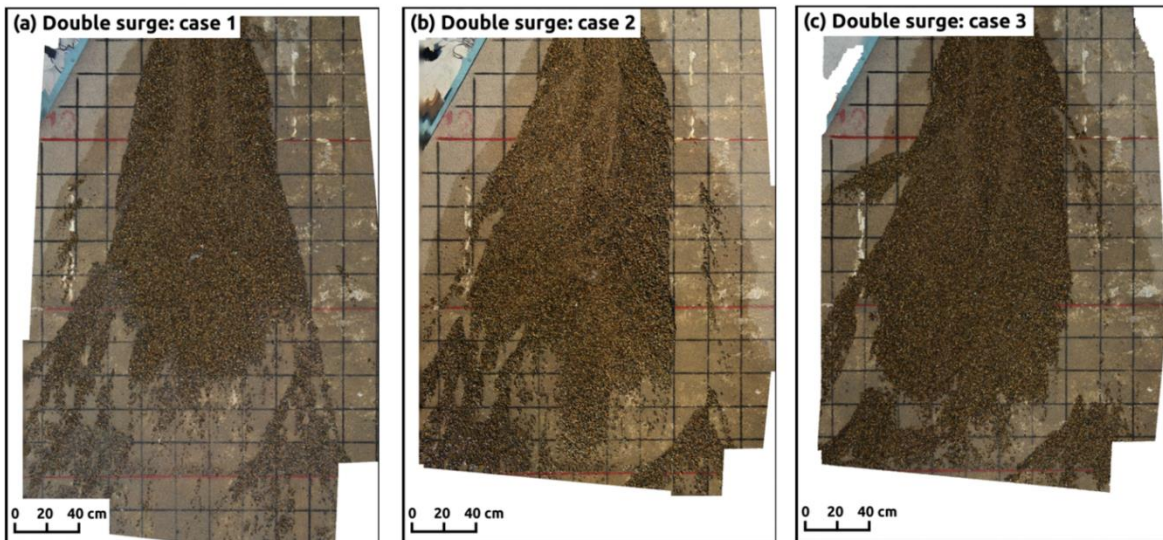


Fig. 5. Photographs of double surge cases after deposition of second surge. (a) case 1. (b) case 2. (c) case 3.

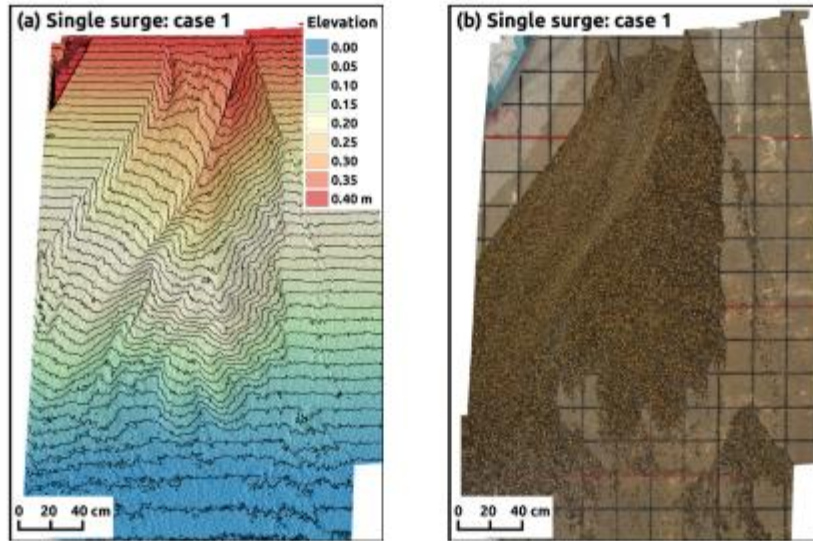


Fig. 6. SfM-MVS results of single surge cases after finish of surge deposition. (a) DSM. (b) Ortho photograph.

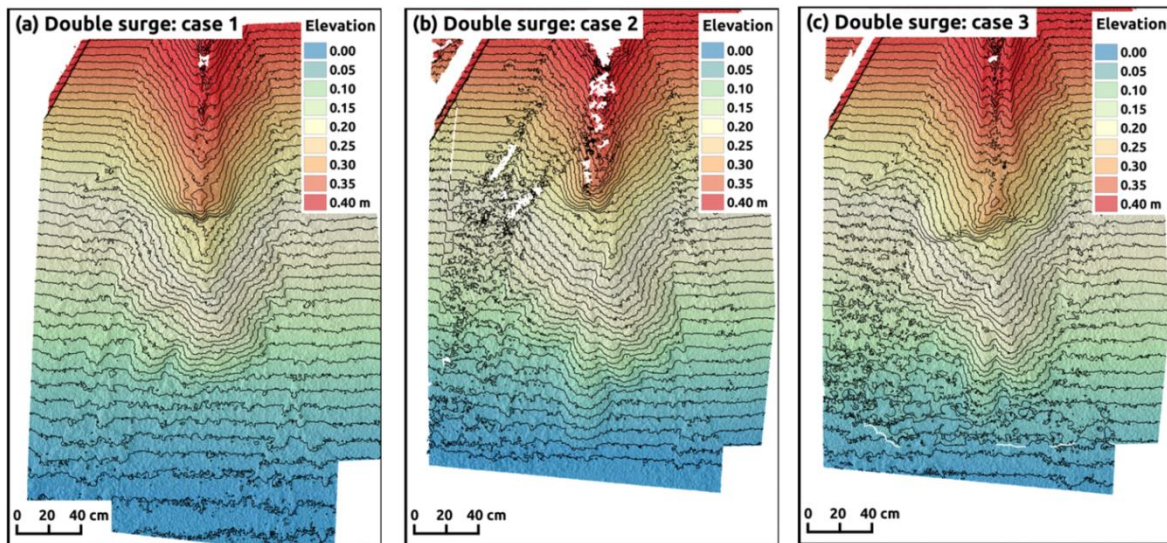


Fig. 7. DSMs of double surge cases after 10 seconds from the start of runout of second surge. (a) case 1. (b) case 2. (c) case 3.

For the double surge cases, the time-series changes in flow path direction of the second surge were different among the cases. The results of SfM-MVS showed that in all cases, the front of the second surge stopped approximately 1.2 m downstream from the outlet of the channel, and above the fan produced by the first surge (Fig. 7). After this stoppage, the flow following the front changed their direction of descent. Fourteen seconds after the start of the runout of the second surge, the flow descended with a right side in cases 1 and 2 (Figs. 8a, b), whereas the flow descended with a left bank in case 3 (Fig. 8c).

The avulsion processes in the flow paths continued and progressed with differentiation in topography. After 4 seconds, the flow directions were changed again in cases 1 and 3 (Figs. 9a, c), whereas the flow continued to descend to the right side in case 2 (Fig. 9b). Consequently, the final topography of the fan inclined to the left bank in case 1 (Fig. 4a), and the right bank in cases 2 and 3 (Figs. 4b, c).

The difference in runout distance of the first surge front between the single and double surge cases was up to 0.2 m (Fig. 10a). However, the difference between the first and second surge for the double surge cases was more significant, with the first surge and the second surge at around 2.8 m and 1.2 m, respectively. Through this decrease in the runout distance, almost all sediment from the second surge deposited upstream at a point where the bed slope changed 6 to 3 degrees. The travel time of the first surge was approximately 6 seconds, whereas the travel time of the second surge was 2 seconds longer at 8 seconds (Fig. 10b). Correspondingly, the velocity of the first surge front was approximately 0.4 m/s, and the velocity of the second surge was 0.18 m/s, less than half of that of the first surge (Fig. 10c).

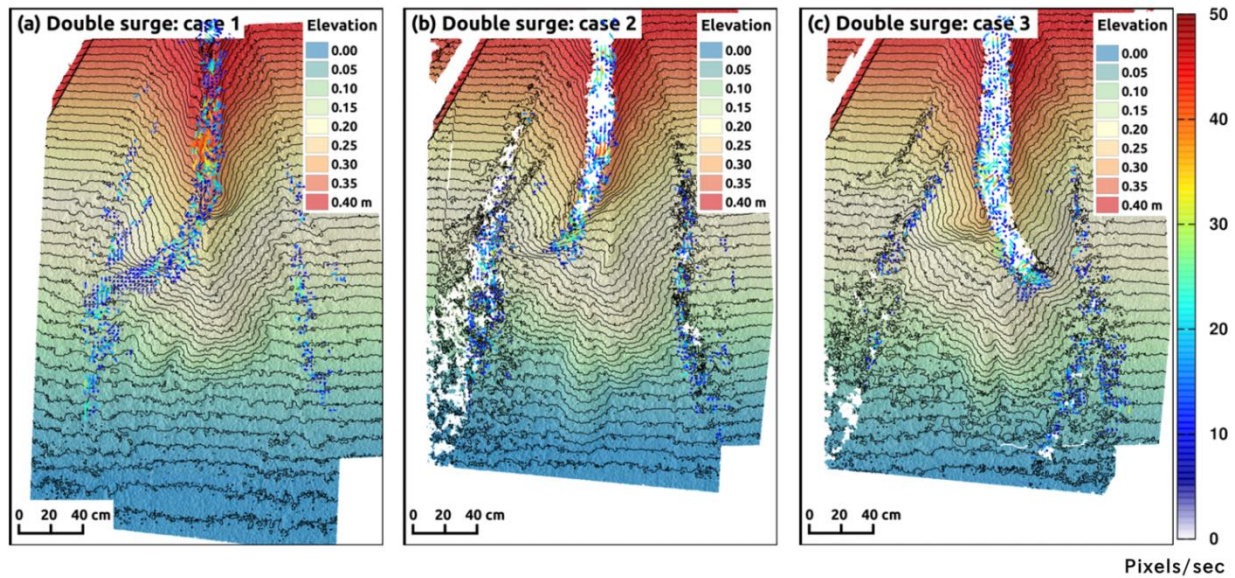


Fig. 8. DSMs of double surge cases after 14 seconds from the start of runout of second surge. (a) case 1. (b) case 2. (c) case 3. Arrows indicate estimated vectors for velocity of debris-flow surface.

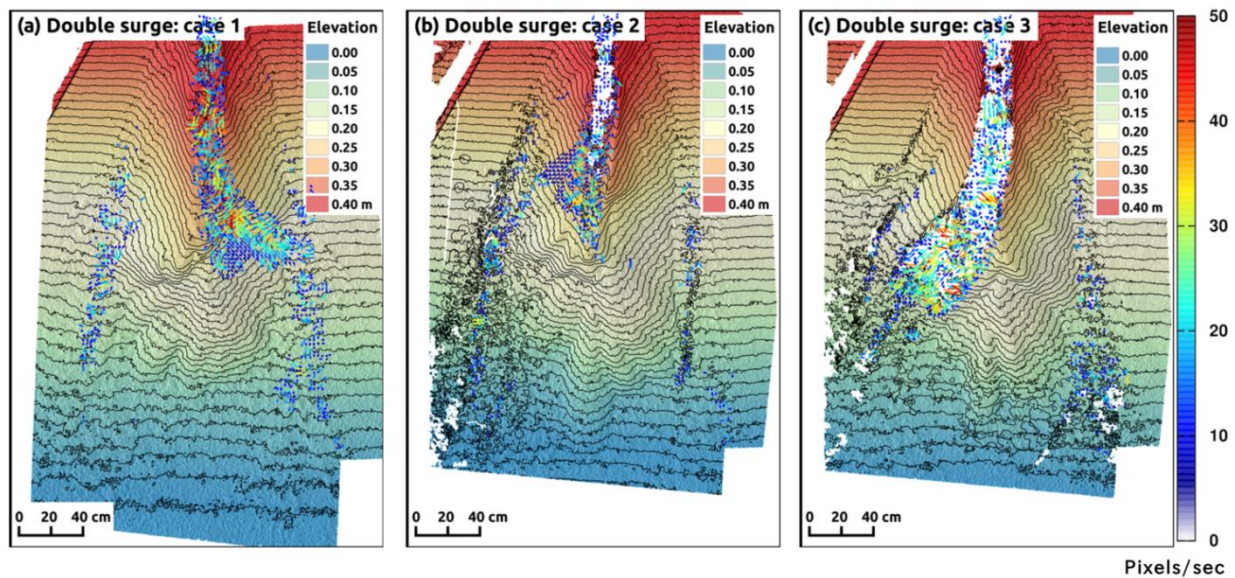


Fig. 9. DSMs of double surge cases after 18 seconds from the start of runout of second surge. (a) case 1. (b) case 2. (c) case 3.

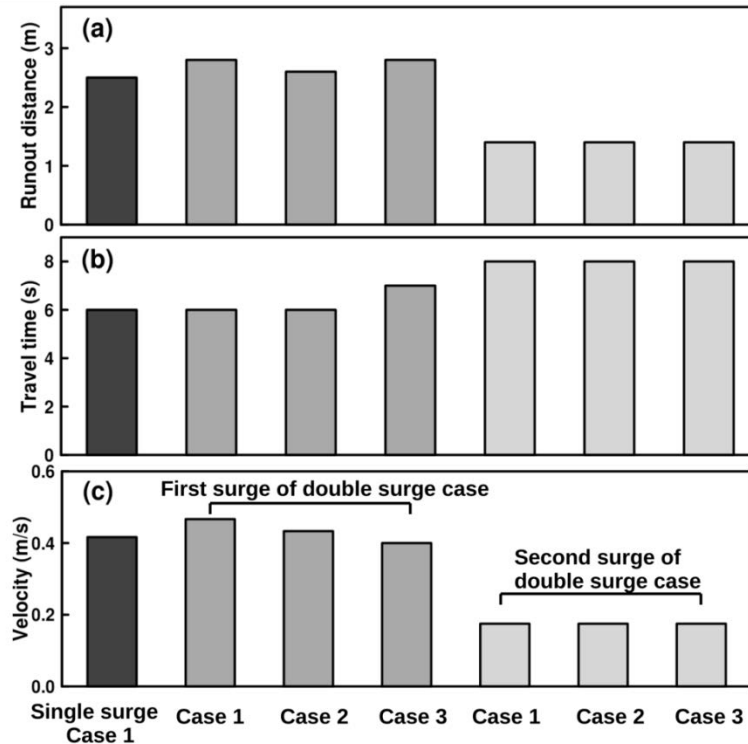


Fig. 10. Characteristics of surge front. (a) Runout distance from the end of upper channel. (b) Travel time from start of run out to stop of front. (c) Average velocity.

4. Discussion

The travel distance of the second surge decreased in the double surge system. A larger amount of sediment tended to deposit in the upper and middle portion of the fan when compared to the fan produced by the single surge system. There is a clear indication of backfilling of the channel after the deposition of materials from the initial surge.

In debris-flow mechanics, sediment deposition has been described by the deposition (entrainment) rate equations (Takahashi, 2007). Several deposition rate equations have been proposed (e.g., Takahashi and Kuang, 1986; Egashira et al., 2001; Suzuki et al., 2011). Although the parameters involved in evaluating deposition rate are different among these equations, these equations were based on the concept that the current flow state is transitional to the equilibrium state. Here, the equilibrium state is the state where both deposition and entrainment do not occur due to the steady flow condition (Takahashi, 2007). The flow direction of the single surge cases was fixed due to the development of the channel, with a relatively consistent bed slope surrounded by topographies similar to natural levees. Running through this channel, sediments reached and deposited further downstream compared to the double surge cases. These results indicate that the continuing flow was able to reach further downstream due to the prevention of deposition by the equilibrium bed slope formed by the continuous flow in the fixed channel.

In contrast, the travel distance of the second surge was short, where sediment was deposited upstream with a thick depth. This result implies that the deposition and stoppage of the second surge were induced by the factor differed from the transition from the current flow state to the equilibrium state in the single surge cases. De Haas et al. (2016, 2018) indicated that the low-gradient zones produced by the deposition of previous surges progress the backfilling of channels. Although the runout of the first surge continued for approximately 30 seconds, the deposition depth of the fan at that time was almost similar for all cases. Therefore, the difference in the slope of the fan was small between the single surge and double surge systems until 30 seconds after the start of the runout. This result implies that the deposition of the second surge was affected by not only the slope of the fan but also the condition produced by the intermittency of the surges.

In the double surge cases, there was no surface flow on the fan produced by the first surge when the second surge that was generated by second water supply reached the deposition area. In other words, the surface was in a state

that was almost unsaturated. On the unsaturated bed, the deposition of flow is accelerated through the increase in the shear resistance stress due to the decrease in the pore-fluid pressure at the boundary between the bottom of the flow and the bed surface (Gonda, 2009). Similar deposition patterns induced by unsaturated deposits had been reported before in a field survey (Staley et al., 2011). Therefore, the deposition of the second surge may be caused by the unsaturated fan. The decrease in flow velocity at the front of the second surge also supports the notion that the flow stoppage and deposition was due to the increased resistance on this unsaturated bed.

Importantly, the flow direction shifted through the topographic changes in the fan due to the stoppage of the second surge front. Therefore, the final deposition range of the fan differed among the double surge cases. This result implies that the deposition range may be different among debris-flow where there had been multiple intermittent surges flowing down, even where the hydrograph is similar. This indicates there is a possibility that accurate numerical simulation of the deposition range cannot be achieved even where the correct observed debris-flow hydrograph is being used. Therefore, the representation of the saturation condition in deposition layers needs consideration in order to simulate the fan development process accurately.

5. Conclusion

This study demonstrated that double surge cases produce different fan morphology among cases, due to the differences in inundation and deposition range of the second surge. This implies that the unsaturated surface condition of the fan produced by the first surge led to a change in the deposition range of the second surge. These results indicate that a change in the saturated condition of the bed surface induces differentiation in fan morphology. Therefore, examination of characteristics of the fan and surge affecting saturation, such as surge duration and grain-size distribution, is necessary for understanding flow deposition. Additionally, the elucidation of the mechanism of entrainment and deposition of debris flow in relation to the degree of saturation in the bed would be the key to the development of more accurate numerical simulations of debris flow.

Acknowledgements

The research is supported by JSPS KAKENHI Grant Number 18J01961.

References

- Chen, H.X., Zhang, L.M., Gao, L., Yuan, Q., Lu, T., and Xiang, B., 2017, Simulation of interactions among multiple debris flows: *Landslides*, v. 14, no. 2, p. 595–615.
- De Haas, T., Van Den Berg, W., Braat, L., and Kleinhans, M.G., 2016, Autogenic avulsion, channelization and backfilling dynamics of debris flow fan: *Sedimentology*, v. 63, no. 6, p. 1596–1619.
- De Haas, T., Densmore, A.L., Stoffel, M., Suwa, H., Imaizumi, F., Ballesteros-Cánovas, J.A., and Wasklewicz, T., 2018, Avulsions and the spatio-temporal evolution of debris-flow fans: *Earth-Sciences Reviews*, v. 177, p. 53–75.
- Dowling, C.A., and Santi, P.M., 2014, Debris flow and their toll on human life: a global analysis of debris-flow fatalities from 1950 to 2011: *Natural Hazards*, v. 71, p. 203–227.
- Egashira, S., Honda, N., and Itoh, T., 2001, Experimental study on the entrainment of bed material into debris flow: *Physics and Chemistry of the Earth, Part C: Hydrology, Ocean and Atmosphere*, v. 26, p. 645–650.
- Gonda, Y., 2009, Function of a debris-flow brake: *International Journal of Erosion Control Engineering*, v. 2, no. 1, p. 15–21.
- Nakagawa, H., and Takahashi, T., 1997, Estimation of a debris flow hydrograph and hazard area: *in Proceedings of 1st International Conference, Debris Flow Hazards Mitigation/Mechanics, Prediction, and Assessment*, p. 64–73.
- Pederson, C.A., Santi, P.M., and Pyles, D.R., 2015, Relating the compensational stacking of debris-flow fans to characteristics of their underlying stratigraphy: *Geomorphology*, v. 248, p. 47–56.
- Staley, D.M., Wasklewicz, T.A., Coe, J.A., Kean, J.W., McCoy, S.W., and Tucker, G.E., 2011, Observations of debris flows at Chalk Cliffs, Colorado, USA: Part 2, changes in surface morphometry from terrestrial laser scanning in the summer of 2009: *in Proceedings of 5th International Conference, Debris Flow Hazards Mitigation/Mechanics, Prediction, and Assessment*, p. 759–768.
- Suzuki, T., Hasegawa, Y., Mizuno, H., and Osanai, N., 2011, Numerical simulation method of debris flow introducing the non-entrainment erosion rate equation, at the transition point of the riverbed gradient or the channel width and in the area of sabo dam: *in Proceedings of 5th International Conference, Debris Flow Hazards Mitigation/Mechanics, Prediction, and Assessment*, p. 615–622.
- Takahashi, T., and Kuang, S.F., 1986, Formation of debris flow on varied slope bed: *Annals of the Disaster Prevention Research Institute, Kyoto University*, v. 29, no. B-2, p. 345–359. (In Japanese with English summary)
- Takahashi, T., 2007, *Debris Flow: Mechanics, Prediction and Countermeasures*: Taylor and Francis, Balkema. pp 448.

Numerical simulation for evaluating the phase-shift of fine sediment in stony debris flows

Taro Uchida^{a,*}, Yuki Nishiguchi^b, Brian W. McArdell^c and Yoshifumi Satofuka^d

^aNational Institute for Land and Infrastructure Management, 1 Asahi, Tsukuba, Ibaraki 305-0804, Japan

^bCTI Engineering, Co., Ltd., 1047-27, Onigakubo, Tsukuba, Ibaraki 300-2651, Japan

^cWSL Swiss Federal Research Institute, CH-8903, Birmensdorf, Switzerland

^dRitsumeikan University, Kusatsu, Shiga, 525-8577, Japan

Abstract

To predict hazard-endangered areas and debris-flow velocity, a variety of physically-based numerical simulation models have been developed. In these models, the relatively large sediment particles such as boulders move as a laminar flow, but the interstitial fluid between sediments behaves like a turbulent flow. Moreover, several recent models assumed that fine sediments act as a fluid. This behavior of fine sediment is referred to as the “phase-shift” of fine sediment. However, because it is difficult to observe the phase-shift of fine sediment in the field, adequate data on the phase-shift of debris flow are still lacking. In the last two decades, intensive monitoring for debris flow has been conducted all over the world, and observations have dramatically increased. For example, in the Illgraben catchment, Switzerland, observations of bulk density, pore pressure, flow depth, front velocity, and temporal and spatial patterns of erosion due to debris flows are available. So, we used these data for model input conditions. We applied the numerical simulation model Kanako-LS to evaluate the phase-shift concept for describing a variety of debris flow properties and behaviors at the Illgraben, Switzerland. Here we successfully describe a variety of observed debris flow behaviors, such as erosion and deposition pattern and shape and velocity of debris-flow fronts. However, if we ignored effects of phase-shift, the deposition volume was overestimated and flow velocity was underestimated.

Keywords: debris-flow; numerical simulation; input condition; hazard map; Aranayake disaster

1. Introduction

Stony (boulder-rich) debris flow have been described as consisting of two phases, the fluid and solid phase (e.g., Takahashi, 1991). Some researchers suggested that coarse sediment in stony debris flow move in a laminar manner, but interstitial fluid between sediment behaves like a turbulent flow (e.g., Takahashi, 1991). If a grain remains suspended for a period of time that exceeds the duration of a debris flow as a result of the viscous resistance of water only, it may act as part of the fluid (e.g., Iverson, 1997). In this study, this behavior of the fine sediment refers to “phase-shift” of fine sediment.

It has been considered that all of sediments often behave likes fluid in mud flow and rock avalanches (e.g., Hunger and Evans, 2004; Hotta and Miyamoto, 2008). Moreover, several researchers proposed two layers (i.e., the liquefied layer at the bottom and the solid layer at the surface flow) concept to describe long runout landslide (e.g., Iverson et al., 2015). This concept also hypothesized that all of sediments in bottom layer should be liquefied. In contrast to these concepts, we assumed that a part of sediments move as fluid and mixed two phases, solid and fluid, in the same layer.

The phase-shift of fine sediment might enhance the fluidity of debris flow due to reducing grain contact forces (e.g., Iverson and George, 2014; Iverson et al., 2010; de Haas et al., 2015). Moreover, it can be thought that the phase-shift of fine sediment increases the mass density of the interstitial fluid and enhances the transport capacity of stony debris flows (e.g., Nishiguchi et al., 2011). This effect of fine sediment on debris flow transport capacity has been tested in laboratory experiments. These experiments have shown that the greatest sediment transport capacity occurs in the

* Corresponding author e-mail address: uchida-t92rv@mlit.go.jp

debris flows that contain fine sediment (e.g., Hotta et al., 2013). Furthermore, several numerical simulation models describing fine sediment as fluid have been proposed (e.g., Nishiguchi et al., 2011; Uchida et al., 2013; Iverson and George, 2014).

However, previous numerical simulations mainly focused on only debris-flow travel distance and/or erosion and deposition patterns, because of lack of field data. Thus, effects of a phase-shift on flow properties, such as flow velocity, have not been fully examined. The objective of this study is to test effects of phase-shift on erosion/deposition patterns and flow velocity of debris flows by composing data from observation stations with simulation results. Herein, we applied a numerical simulation that included effects of phase-shift for describing not only erosion and deposition patterns, but also flow velocity and sediment concentration of debris flow in Illgraben, Switzerland, where one of most intensive debris flow monitoring sites in the world (e.g., McArdell et al., 2007; 2016; Berger et al., 2011).

2. Methods

2.1. Study site and data

The Illgraben catchment is located in southwest Switzerland. The active part of the catchment on the north face of Illhorn mountain has an area of 4.5 km² and is underlain by sedimentary rocks which weather to produce quartzite and dolomite boulders up to several meters in diameter, as well as some clay-size particles. The Illgraben debris-flow observation station was installed in 2000 to monitor debris flow activity. The station includes a large force plate (McArdell et al., 2007) that was installed at check dam 29 (Fig. 1). The force plate consists of a 2-m long, 4-m wide, three ton steel structure, installed flush with the base of the concrete check dam, which has a trapezoidal cross-sectional shape. A normal force transducer is installed under each corner and the forces are summed and recorded at 2 kHz. A laser sensor mounted on the road bridge above the force plate measures the distance to the top of the flow. McArdell et al. (2007) calculated the bulk density of debris flows using data of normal stress and flow depth. Furthermore, Berger et al. (2011) observed timing of erosion at the riverbed about 90 m upstream from the check dam 29.

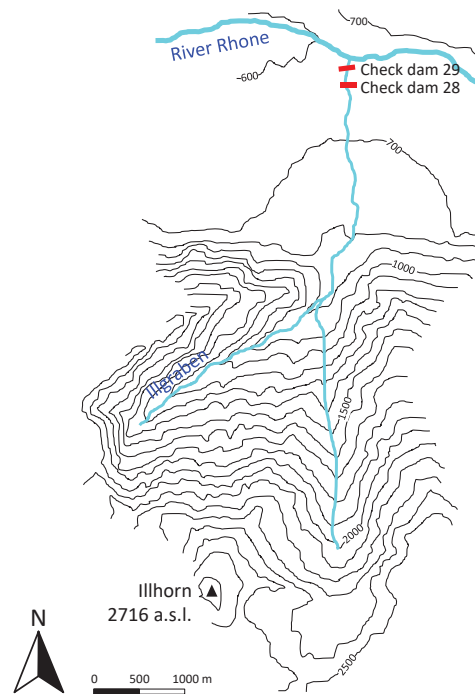


Fig. 1. Topographic map of Illgraben, Switzerland.

Many debris flows have been observed in Illgraben (e.g., McArdell et al., 2007; 2016; Berger et al., 2011). In this study, we focused on a debris flow that occurred on 1 July, 2008, because it is one of the most well-documented debris flows at the site to date. For 2008 debris flow, Berger et al. (2011) reported the peak flow discharge of 89 m³/s at check dam 29. Observed bulk density ranged from 1200 to 2000 kg/m³ (Berger et al., 2011). Berger et al. (2011) indicated that averaged density for the front part of debris flow (i.e., from the front arrival to 25 s after it) was relatively high, around 1800 kg/m³. The bulk density of the debris flow tail (i.e., about 100 s after the front arrival) was about 1300 kg/m³. The width of channel where erosion or deposition occurred ranged from 6 to 16 m.

2.2. Numerical simulation model

We applied our original 1D numerical simulation model, Kanako-LS, which was developed to include the process of phase shift (Uchida et al., 2013). The Kanako-LS model was based on the Kanako model developed by Nakatani et al. (2007) who modelled debris-flow properties, such as equilibrium concentration (i.e., the concentration that results in neither erosion of the bed nor deposition onto the bed), riverbed shear stress, and erosion and deposition rates using Takahashi's stony debris-flow theories (see Takahashi, 1991).

In Kanako-LS, the effect of "phase-shift" on debris-flow dynamics was modelled. We assumed that sediments can be classified into two groups (fine and coarse) on the basis of sediment diameter, and defined the critical diameter of the sediment (D_c) as the smallest diameter that behaves as a solid. That is, they proposed that sediments larger than D_c move as solids, while those smaller than D_c behave as fluids. So, sediment concentration for all sediments (C_s), i.e., coarse and fine sediments was described by coarse sediment concentration (C_c) and fine sediment concentration (C_f) as follow.

$$C_s = C_c + C_f \quad (1)$$

Moreover, we assumed that the mass density of interstitial fluid (ρ) can be described as

$$\rho = \sigma \frac{C_f}{1 - C_c} + \rho_w \left(1 - \frac{C_f}{1 - C_c} \right) \quad (2)$$

where σ is the mass density of the sediment and ρ_w is the mass density of clear water.

In Kanako-LS, the continuity equations for the total volume of debris flow and the entrained (removable) bed sediment are

$$B \frac{\partial h}{\partial t} + \frac{\partial uhB}{\partial x} = iB \quad (3)$$

$$\frac{\partial z}{\partial t} + i = 0 \quad (4)$$

where h is the flow depth, u is the flow velocity, B is the flow width, x is the horizontal distance, t is time, i represents the erosion and deposition velocity, and z is the height of the riverbed. Moreover, two continuous equations for fine and coarse sediments were derived.

Erosion

$$B \frac{\partial C_c h}{\partial t} + \frac{\partial C_c uhB}{\partial x} = i C_{*ic} B \quad (5)$$

$$B \frac{\partial C_f h}{\partial t} + \frac{\partial C_f uhB}{\partial x} = i C_{*if} B \quad (6)$$

Deposition

$$B \frac{\partial C_c h}{\partial t} + \frac{\partial C_c u h B}{\partial x} = i C_{*dc} B \quad (7)$$

$$B \frac{\partial C_f h}{\partial t} + \frac{\partial C_f u h B}{\partial x} = i C_{*df} B \quad (8)$$

where C_{*ic} and C_{*if} are the concentrations of coarse and fine sediments in the initial mobile layer of the riverbed, respectively, and C_{*dc} and C_{*df} are the concentrations of coarse and fine sediments in the deposited layer of the riverbed, respectively.

We also applied the equations 9 and 10 for calculation of erosion and deposition rate respectively.

$$i = \delta_e \frac{C_\infty - C_c}{C_{*i} - C_\infty} \frac{q}{d} \quad (9)$$

$$i = \delta_d \frac{C_\infty - C_c}{C_{*d} - d_c} \frac{q}{d_c} \quad (10)$$

where δ_e and δ_d is the coefficient for the erosion and deposition velocity, respectively, C_{*i} is the sediment concentration in the initial entrained (removable) bed sediment, q is the flow rate per unit width, d is the representative sediment, including both coarse and fine sediments, diameter of riverbed, and d_c is the representative sediment diameter of coarse sediments.

We used three different equilibrium sediment concentration theories in terms of water surface gradient. We used the debris-flow theory for steep water surface, the sediment sheet flow theory for intermediate gradient water surface, and the bedload theory for gentle water surface (Uchida et al., 2013).

The momentum equation adopted is the same as that used in the original Kanako scheme

$$\frac{\partial u}{\partial t} + u \frac{\partial u}{\partial x} = -g \frac{\partial H}{\partial x} - \frac{\tau_h}{\rho h} \quad (15)$$

where H is the height of the water surface ($H = z + h$), g is the gravitational acceleration, and τ_h is the riverbed shearing stress. Based on the original Kanako scheme, we used three different flow resistance theories in terms of flow conditions to calculate the riverbed shearing stress (τ_h) (Uchida et al., 2013). We defined three flow conditions, as debris flow, sediment sheet flow, and ordinary turbulent water flow. We classified these flow conditions on the basis of the coarse sediment concentration (C_c).

2.3. Parameter setting

In this study, we simulated for the section between check dams 28 and 29, because detailed data about erosion and deposition patterns reported by Berger et al. (2011) were available. We assumed the input hydrograph and bulk density at check dam 28 should be similar to observed hydrograph and bulk density at check dam 29, since the distance between check dams 28 and 29 is only 140 m and erosion and deposition between check dams 28 and 29 was not obvious. Based on the observed flow depth at check dam 29, we assumed a triangle shape as input hydrograph at the check dam 28. We set the duration of debris flow at 3000s and the peak discharge at 89 m³/s, which appeared 21s after the front of debris flow.

Based on the observations of Berger et al. (2011), we set three bulk densities (ρ_m) as the averaged density of tail part of flow (1300 kg/m³), entire debris flow (1500 kg/m³) and the front part (1800 kg/m³), respectively. In this study, we ignored the temporal change in bulk density at check dam 28. We set bulk densities of water and sediment at 1000 and 2600 kg/m³, respectively, and we fixed the total sediment concentration, including both coarse and fine sediments, at 18.8, 31.3, and 50 % for $\rho_m=1300, 1500$ and 1800 kg/m³, respectively (Table 1).

We did not have data on ratio of fine sediment that was present in the fluid phase. Thus, we simply set two phase-shift ratios, i.e., the ratio of phase-shifted fine sediment volume to total sediment volume (Table 1). In cases 1a-c, we assumed that effects of phase-shift were negligible. So, we considered that all of sediment behaved as solid phase (coarse sediment). In cases 2a-c, we assumed that 70 % of sediment phase-shifted and behaved as fluid phase. Other parameter values are summarized in Table 2.

Table 1. Numerical simulation cases

Case	Bulk density [kg/m ³]	C_s	PR	C_c	C_f	ρ [kg/m ³]	C_f'
Case 1a	1300	0.188	0.000	0.188	0.000	1000	0.000
Case 1b	1500	0.313	0.000	0.313	0.000	1000	0.000
Case 1c	1800	0.500	0.000	0.500	0.000	1000	0.000
Case 2a	1300	0.188	0.700	0.056	0.132	1223	0.139
Case 2b	1500	0.313	0.700	0.094	0.219	1387	0.242
Case 2c	1800	0.500	0.700	0.150	0.350	1659	0.412

C_s ; total sediment, including both coarse and fine, concentration, PR Phase-shift ratio ($=C_f/C_s$),

C_c ; coarse sediment concentration, C_f Fine sediment concentration,

ρ ; density of interstitial fluid, C_f' Fine sediment concentration in interstitial fluid ($=C_f/(1-C_c)$)

Table 2. Parameter values

Parameters	Symbol	Value	Unit
Mass density of pure water	ρ_w	1000	kg m ⁻³
Mass density of sediment	σ	2600	kg m ⁻³
Sediment concentrations in the initial mobile layer of the riverbed	C_{*i}	0.65	-
Sediment concentrations in the deposited layer of the riverbed	C_{*d}	0.65	-
Coefficient for erosion velocity	δ_e	0.0007	-
Coefficient for deposition velocity	δ_d	0.05	-
Friction angle of sediment	$\tan\phi$	0.7	-
Gravitational acceleration	g	9.8	m s ⁻²
Manning's coefficient	n	0.045	s m ^{-1/3}
Depth of removable materials on initial riverbed		1.3	m
Time step for calculation	-	0.005	s

3. Results

3.1. Erosion and deposition pattern

Berger et al. (2011) conducted topographic survey before (17 June, 2008) and after (4 July, 2008) our studied debris at the section between check dams 28 (upstream) and 29. This survey showed that erosion dominated at the upper section of survey area (downstream of check dam 28), while deposition occurred at the lower section (upstream of check dam 29) (Fig. 1). Maximum measured erosion and deposition depths were around 1.1 and 0.9 m.

In contrast, if we assumed no phase-shift conditions (Cases 1), obvious deposition occurred at the section between check dams 28 and 29 (Fig. 2). Deposition volume became large, because the input sediment concentration became large (Fig.2a). Although if we input the lowest observed sediment concentration (case 1a), the deposition depth was around 12 m at the downstream of check dam 28, although the observed maximum deposited depth was 0.9 m. In case 1c, the riverbed was elevated more than 30 m at the downstream of check dam 28.

In the phase-shift case, the deposition depth became dramatically smaller. In case 2a ($C_s=0.188$), deposition occurred in almost the entire section. In the lower part of the section (i.e., more than 90 m away from the check dam), the deposition depth was relatively large (0.5-0.8 m), compared with the upper part (~0.3 m). While, in case 2b ($C_s=0.313$), the deposition was dominant in the lower part of the section, but the erosion was dominant in the upper section. In case 2c ($C_s=0.500$), the riverbed was eroded in the entire section. The erosion depth in the upper part was around 0.4-0.7m, while, in the lower part was around 0.1-0.4 m. The patterns from case 2c are well agreed well with

the observations. In conclusion, we successfully model the observed erosion and deposition pattern, although we have to fine tune the phase-shift ratio.

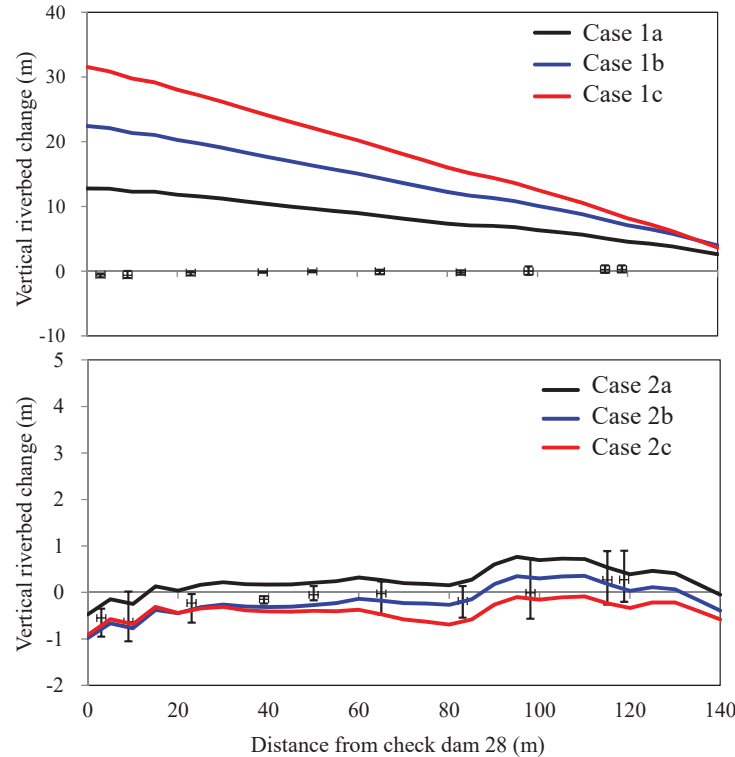


Fig. 2. Simulated elevation change due to debris flow. Positive and negative change indicate deposition and erosion, respectively. Observed data were compiled based on the Figures 10 and 11 of Berger et al. (2011). Plots indicate mean value and the upper and lower ends of error bars indicate maximum and minimum on the cross sections.

3.2. Front shape and velocity of the debris flow

Berger et al. (2011) showed temporal change in longitudinal profile of the surface of the debris flow immediately upstream of the front of debris flow at the section between check dams 28 and 29 (Fig. 1). They reported the longitudinal profile of debris flow front for 10 seconds after the front arrived at check dam 28. Thus, here we compared the calculated longitudinal profile of debris flow front with the observed profiles. Since the observed bulk density of the debris flow front ranged from 1700 to 2000 kg/m³, we focused on the cases that the bulk density was 1800 kg/m³ (i.e., cases 1c and 2c) (Fig. 3).

The front velocity in case 2c is greater than that of case 1c, indicating that the front velocity increased with an increase in the phase-shift ratio. This suggests that the flow resistance became small as the phase-shift ratio became large (Fig. 3). Moreover, the calculated longitudinal surface angle of debris-flow front became gentle as the phase-shift ratio increased. The front velocity of phase-shift condition was 1.5 times greater than that of no phase-shift condition.

The front shape and velocity of case 2c agreed well with observations. However, if we ignored effects of phase-shift of fine sediment, the front height and velocity were underestimated (Fig. 3).

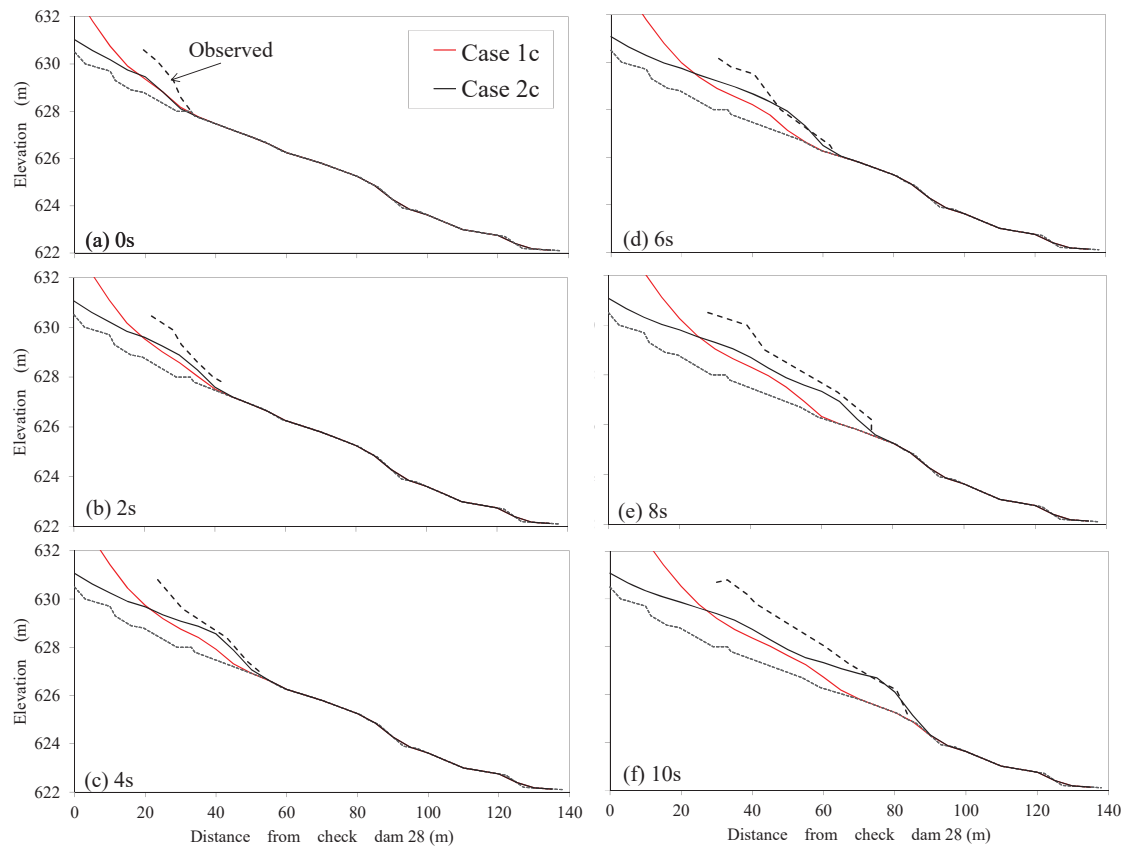


Fig. 3. Simulated front shape of debris flow. Observed data was compiled based on Figure 4 of Berger et al. (2011).

4. Discussion and conclusions

In this study, we test the applicability of numerical simulation models for describing not only erosion and deposition patterns, but also front shape and velocity and the effect of the phase-shift of fine sediment on deposition depth and flow velocity of the July, 2008 debris flow at Illgraben, Switzerland. We applied the numerical simulation model Kanako-LS to test the phase-shift concept on a well-documented dataset from the Illgraben debris-flow observation station. We successfully modeled the observed erosion and deposition pattern, and the front shape and velocity of the debris flow, although we have to fine tune the phase-shift ratio (i.e., ratio of fine sediment to the total sediment, which behaves as a fluid).

We showed that the phase-shift ratio has an extremely large impact on the erosion and deposition pattern. If we ignored effects of phase-shift, the deposition depth was more than 10 times larger than observed. This suggests that the effect of phase-shift on equilibrium concentration is very large. On the contrary, the influence of the phase-shift ratio on the front velocity was relatively small. When the phase shift was considered, the observed front velocity was 1.4 times larger than when the phase-shift effect was neglected. This suggests that the effect of phase shift on flow resistance is relatively small, but still significant.

Additionally, we showed that the numerical simulation of debris-flow runout could be effective for predicting not only erosion and deposition patterns, but also flow-front velocity. This demonstrates that numerical simulation of debris flow should be effective for prediction of not only potential affected area, but also the force acting on structures, such as houses, infrastructure, and structural countermeasures. If we don't have any ground truth data, we have to predict phase-shift ratio (e.g., Nishiguchi and Uchida, 2019). We consider that the phase-shift ratio should be controlled by both hydraulic condition of debris flow, such as flow depth etc. and particle size distribution of sediment

in debris flow. So, we need more study for clarifying relationship between the phase-shift ratio, hydraulic condition and particle size distribution.

References

- Berger, C., McARDell, B.W., and Schlunegger, F., 2011, Direct measurement of channel erosion by debris flows, Illgraben, Switzerland: *Journal of Geophysical Research-Earth Surface*, v. 116, doi: 10.1029/2010JF001722.
- de Haas, T., Braat, L., Leuven, J.R.F.W., Lokhorst, I.R., and Kleinhans, M.G., 2015, Effects of debris flow composition on runout, depositional mechanisms, and deposit morphology in laboratory experiments: *Journal of Geophysical Research-Earth Surface*, v.120, p.1949–1972, doi: 10.1002/2015JF003525.
- Hotta, N., and Miyamoto, K., 2008, Phase classification of laboratory debris flows over a rigid bed based on the relative flow depth and friction coefficients: *International Journal of Erosion Control Engineering*, v.1, p.54-61, doi: 10.13101/ijece.1.54.
- Hotta, N., Kaneko, T., Iwata, T., and Nishimoto, H., 2013, Influence of fine sediment on the fluidity of debris flows: *Journal of Mountain Science*, v.10, p.233-238, doi: 10.1007/s11629-013-2522-y
- Hungr, O., and Evans, S., 2004, Entrainment of debris in rock avalanches: An analysis of a long run-out mechanism: *Geological Society of America Bulletin*, v.116, p.1240-1252, doi: 10.1130/B25362.1.
- Iverson, R.M., 1997, The physics of debris flows: *Reviews of Geophysics*, v.35, p.245–296, doi: 10.1029/97RG00426
- Iverson, R.M., Logan, M., LaHusen, R.G., and Berti, M., 2010, The perfect debris flow? Aggregated results from 28 large scale experiments, *Journal of Geophysical Research-Earth Surface*, v.115, doi: 10.1029/2009JF001514.
- Iverson R.M., and George, D.L., 2014, A depth-averaged debris-flow model that includes the effects of evolving dilatancy. I. Physical basis: *Proceedings of the Royal Society of London, Ser. A*, v.470, doi: 10.1098/rspa.2013.0819
- Iverson, R.M., George, D.L., Allstadt, K., Reid, M.E., Collins, B.D., Vallance, J.W., Schilling, S.P., Godt, J.W., Cannon, C.M., Magirl, C.S., Baum, R.L., Coe, J.A., Schulz, W.H., and Bower, J.B., 2015, Landslide mobility and hazards: implications of the 2014 Oso disaster: *Earth and Planetary Science Letters*, v.412, p.197-208, doi: 10.1016/j.epsl.2014.12.020.
- McArdell, B.W., Bartelt, P., and Kowalski, J., 2007, Field observations of basal forces and fluid pore pressure in a debris flow: *Geophysical Research Letters*, v.34, L07406, doi: 10.1029/2006GL029183.
- McArdell, B.W., 2016, Field measurements of forces in debris flows at the Illgraben: Implications for channel-bed erosion: *International Journal for Erosion Control Engineering*, v.7, 194-198, doi: 10.13101/ijece.9.194.
- Nakatani, K., Satofuka, Y., and Mizuyama, T., 2007, Development of 'KANAKO', a wide use debris flow simulator equipped with GUI: *Proceedings of 32nd Congress of IAHR, Venice, Italy, CD-ROM*, 10p, A2, c-182.
- Nishiguchi, Y., Uchida, T., Tamura, K. and Satofuka, Y., 2011, Prediction of run-out process for a debris flow triggered by a deep rapid landslide: *Proceedings of 5th Debris Flow Hazard Mitigation Conference*, p.477–485, doi: 10.4408/IJEGE.2011-03.B-053.
- Nishiguchi, Y., and Uchida, T., 2019, Lonmg travel distance of landslide induced debris flow: *Proceedings of 7th Debris Flow Hazard Mitigation Conference*, (in this volume).
- Takahashi, T., 1991, *Debris flow*. Balkema, Rotterdam, 165p.
- Uchida, T., Nishiguchi, Y., Nakatani, K., Satofuka, Y., Yamakoshi, T., Okamoto, A., and Mizuyama, T., 2013, New Numerical Simulation Procedure for Large-scale Debris Flows (Kanako-LS): *International Journal of Erosion Control Engineering*, v.6, p.58-67, doi: 10.13101/ijece.6.58

Run out processes of sediment and woody debris resulting from landslides and debris flow

Yusuke Yamazaki^{a,b*}, Shinji Egashira^a

^aInternational Centre for Water Hazard and Risk Management/Public Works Research Institute, 1-6, Minamihara, Tsukuba-shi, 305-8516, Japan

^bPublic Works Research Institute, 1-6, Minamihara, Tsukuba-shi, 305-8516, Japan

Abstract

Process of sediment and woody debris transport generated by landslides and debris flows are simulated numerically using the depth-integrated two-dimensional forms for mass and momentum conservation equation with Egashira et al., (1997)'s formulas for resistance law and erosion-deposition formulas. In order to discuss woody debris behavior, a convection equation is formulated with erosion-deposition term where the yield of woody debris takes place proportionally to sediment erosion and deposition. A small drainage basin located within Akatani River basin of the Fukuoka Prefecture of Japan, where a large number of landslides and debris flows with woody debris occurred during a heavy rainfall event in 2017, is selected for this study. The numerical solution reproduced the spatial distribution of erosional area and depositional area, and run out volume of sediment at the outlet of the valley. The solution also reproduced the spatial distribution and run out volume of woody debris.

Keywords: landslide; debris flow; sediment and woody debris run out; numerical modeling

1. Introduction

Sediment and woody debris transported by shallow landslides and debris flow associated with heavy rainfalls change river courses and riverbeds drastically in mountainous drainage basins. In addition, accumulated woody debris at bridges causes upstream flood inundation. The amount of the transported sediment and woody debris sometimes becomes extremely large and this damages lives and assets severely. The flood and sediment disasters occurred in the northern Kyushu, 2017 and in Iwate Prefecture, 2016 are the examples which show the fact that a large amount of sediment and woody debris caused severe disasters.

This study formulates processes of yield and transport of sediment and woody debris resulting from landslides and debris flows. A soil block released by a landslide associated with heavy rainfall will fluidize when internal strain energy of the soil block due to boundary shear exceeds a certain threshold value (Ashida et al., 1984). When the soil block satisfies the threshold conditions, the soil block change into debris flows easily on its run out process. The mobility of debris flow is influenced by the fine sediment fraction of debris flow material. A mass density of pore fluid will increase because fine sediment behaves as a fluid phase. In addition, numerous woody debris is produced by a landslide and debris flow and part of woody debris deposit with sediment transported by debris flow (Mizuyama et al., 1985, Ishikawa et al., 1989).

Numerical models which deal with debris flow as continuum body are proposed (Medina et al., 2008, Armanini et al., 2009, Hussin et al., 2012, Frank et al., 2015). In the numerical model, bed shear stress and sediment entrainment play important role in characterizing run out processes of debris flow. Bed shear stress is composed of terms for Coulomb friction and turbulent friction. Coulomb friction is evaluated by internal friction angle, sediment concentration, but sometimes coulomb friction as it is omitted. The sediment entrainment is evaluated by mainly empirical method or method which is based on local equilibrium.

* Corresponding author e-mail address: yamazaki-y575bs@pwri.go.jp

Characteristics of debris flow such as flow depth, velocity, sediment consecration, and bed elevation are determined by solutions obtained from mass and momentum conservation equation of debris flow as well as bed sediment. This study proposes convection and storage equations of woody debris with a term for yield and deposition by using the erosion and deposition formula of debris flows. This study applied those equations to one of a small drainage basin of Akatani River drainage basin in Fukuoka Prefecture where many landslides and debris flows occurred from the heavy rainfall in 2017, and discusses the suitability of the equations and run out processes of the sediment and woody debris.

2. Governing equations for debris flow with woody debris

The sediment on mountain slope is composed of particles of various sizes. In this study, sediment is divided into fine sediment and coarse sediment by a threshold size, because the fine sediment influences the mobility of debris flow as suggested before. When the sediment is saturated with water and starts to fluidize, fine sediment and coarse sediment stay as solid status, and the pores are saturated with water. When the sediment fluidizes, coarse sediment behaves as solid phase and fine sediment and water behave as a fluid phase. In the erosion process on a river bed, the coarse sediment is entrained in debris flow body as a solid and the fine sediment as a fluid with water in pores. In the deposition process, the fluid composed of water and fine sediment is entrained into pores formed by deposition of coarse sediment. Thus, the different mass conservation equations are formulated in the erosion and the deposition processes for the total flow body and the coarse and fine sediment (Egashira et al., 2016):

In the erosion process:

$$\frac{\partial h}{\partial t} + \frac{\partial uh}{\partial x} + \frac{\partial vh}{\partial y} = \frac{E}{c_*} \quad (1)$$

$$\frac{\partial \gamma c_c h}{\partial t} + \frac{\partial \gamma c_c uh}{\partial x} + \frac{\partial \gamma c_c vh}{\partial y} = p_c E \quad (2)$$

$$\frac{\partial c_f(1 - c_c)h}{\partial t} + \frac{\partial c_f(1 - c_c)uh}{\partial x} + \frac{\partial c_f(1 - c_c)vh}{\partial y} = p_f E \quad (3)$$

In the deposition process:

$$\frac{\partial h}{\partial t} + \frac{\partial uh}{\partial x} + \frac{\partial vh}{\partial y} = \frac{E}{c_{*D}} \quad (4)$$

$$\frac{\partial \gamma c_c h}{\partial t} + \frac{\partial \gamma c_c uh}{\partial x} + \frac{\partial \gamma c_c vh}{\partial y} = E \quad (5)$$

$$\frac{\partial c_f(1 - c_c)h}{\partial t} + \frac{\partial c_f(1 - c_c)uh}{\partial x} + \frac{\partial c_f(1 - c_c)vh}{\partial y} = (1/c_{*D} - 1)c_f E \quad (6)$$

in which t is the time, h is the depth of debris flow, x and y are the directions of orthogonal coordinate system, u and v are the depth-averaged velocity of x and y directions, respectively, E is the erosion-deposition rate, c_* is the volumetric concentration of sediment on the mountain slope and river bed, c_c is the concentration of coarse sediment, c_f is the concentration of fine sediment, p_c is the composition rate of coarse sediment, p_f is the composition rate of fine sediment, and γ is the correction parameter for the sediment transport. The erosion-deposition rate is defined by (Egashira et al., 2001) as follows:

$$\frac{E}{\sqrt{u^2 + v^2}} = c_* \tan(\theta - \theta_e) \quad (7)$$

$$\tan \theta_e = \frac{(\sigma/\rho - 1)c_c}{(\sigma/\rho - 1)c_c + 1} \tan \phi \quad (8)$$

$$\rho = (\sigma - \rho_w)c_f + \rho_w \quad (9)$$

in which θ is the local gradient, θ_e is the equilibrium gradient of debris flow, σ is the mass density of sediment, ρ is the mass density of the mixture of fine sediment and water, ϕ is the internal friction angle, and ρ_w is the mass density of water.

2.1. Momentum conservation equation of debris flow

The momentum conservation equation of debris flow is described as follows (Egashira, 2007),

$$\frac{\partial uh}{\partial t} + \frac{\partial \beta uuh}{\partial x} + \frac{\partial \beta vuh}{\partial y} = -gh \frac{\partial H}{\partial x} - \frac{\tau_{bx}}{\rho_m} \quad (10)$$

$$\frac{\partial vh}{\partial t} + \frac{\partial \beta uvh}{\partial x} + \frac{\partial \beta vvh}{\partial y} = -gh \frac{\partial H}{\partial y} - \frac{\tau_{by}}{\rho_m} \quad (11)$$

in which β is the correction parameter for momentum, g is the acceleration of gravity, H is the elevation of debris flow surface, τ_{bx} and τ_{by} are the x, y component of bed shear stress, and ρ_m is mass density of debris flow body. The mass density of debris flow body is described as follows:

$$\rho_m = (\sigma - \rho)c_c + \rho \quad (12)$$

Bed shear stress τ_{bx} and τ_{by} , are defined by (Miyamoto and Ito, 2002, Egashira, 2007) as follows:

$$\tau_{bx} = \tau_b u / \sqrt{u^2 + v^2} \quad (13)$$

$$\tau_{by} = \tau_b v / \sqrt{u^2 + v^2} \quad (14)$$

in which τ_b is the bed shear stress and described as follows:

$$\tau_b = \tau_y + \rho f_b (u^2 + v^2) \quad (15)$$

in which τ_y is the yield stress, f_b is the friction factor. The yield stress τ_y and the friction factor f_b are described as follows:

$$\tau_y = \left(\frac{c_c}{c_*}\right)^{1/5} (\sigma - \rho)c_c gh \cos \theta \tan \phi \quad (16)$$

$$f_b = \frac{25}{4} (f_d + f_f) \left(\frac{h}{d}\right)^{-2} \quad (17)$$

in which f_d and f_f are defined as follows:

$$f_d = k_d (\sigma / \rho) (1 - e^2) c_c^{1/3} \quad (18)$$

$$f_f = k_f (1 - c_c)^{5/3} / c_c^{2/3} \quad (19)$$

in which e is the restitution coefficient 0.85 in the case of natural sands, and k_d and k_f are the universal constants specified as $k_d = 0.0828$ and $k_f = 0.16$. In case of gentle slope or large relative depth or turbulent flow, f_d is evaluated as follows (Julien and Paris, 2010):

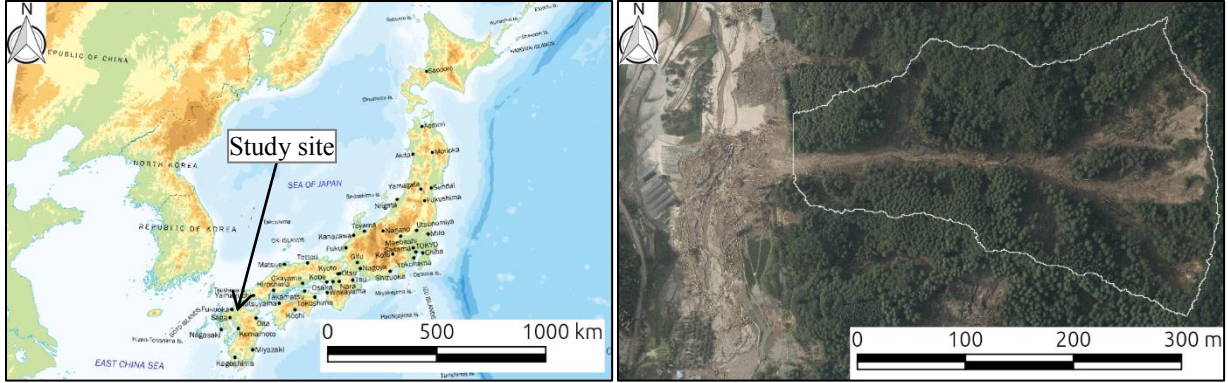


Fig. 1. (a) Location of the drainage basin; (b) Aerial photograph the drainage basin after heavy rainfall.

$$\frac{25}{4} (f_d + f_f) \left(\frac{h}{d}\right)^{-2} \leq 1 / \left\{ A_r - \frac{1}{\kappa} + \frac{1}{\kappa} \ln \frac{h}{\kappa_s} \right\}^2 \quad (20)$$

$$f_b = 1 / \left\{ A_r - \frac{1}{\kappa} + \frac{1}{\kappa} \ln \frac{h}{\kappa_s} \right\}^2 \quad (21)$$

in which $A_r = 8.5$, $\kappa = 0.4$, and κ_s is the roughness.

2.2. Mass conservation equation of woody debris

Assuming the yield and deposition of woody debris are in proportion to erosion and deposition of debris flow, convection equation of woody debris in debris flow and storage equation of woody debris on river bed are described as follows:

In the erosion process:

$$\frac{\partial c_{drf} h}{\partial t} + \frac{\partial c_{drf} u h}{\partial x} + \frac{\partial c_{drf} v h}{\partial y} = E \frac{S}{D} r \quad (22)$$

$$\frac{\partial S}{\partial t} = -E \frac{S}{D} r \quad (23)$$

In the deposition process:

$$\frac{\partial c_{drf} h}{\partial t} + \frac{\partial c_{drf} u h}{\partial x} + \frac{\partial c_{drf} v h}{\partial y} = E c_{drf} r \quad (24)$$

$$\frac{\partial S}{\partial t} = -E c_{drf} r \quad (25)$$

in which c_{drf} is the concentration of woody debris of debris flow body, d_{drf} is the average diameter of trees, r is correction factor, and S is the volume of deposition of woody debris on the river bed per unit area. In the erosion process, $r = 1$. In the deposition process, when $h \geq d_{drf}$, $r = 1$, and when $h < d_{drf}$, $r = 0$. In this study, we assume that woody debris does not influence the mass and momentum of debris flow.

3. Yield and run out of sediment and woody debris by heavy rainfall in 2017

A heavy rainfall event occurred in the northern Kyushu in July 2017. Landslides and debris flows extensively occurred, resulting in a drastic topographical change along Akatani channel. We selected a small drainage basin

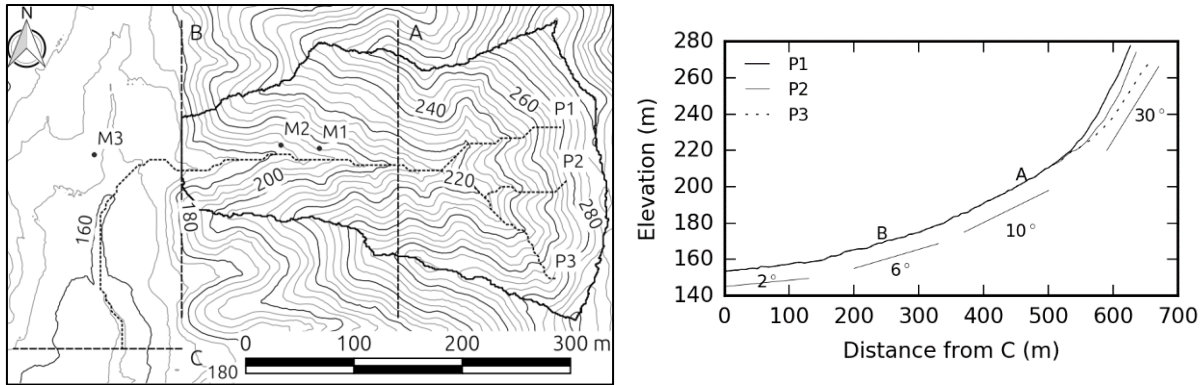


Fig. 2. (a) Topography of the drainage basin; (b) Longitudinal profiles of [P1, P2 and P3]indicated in Figure. 2. (a).

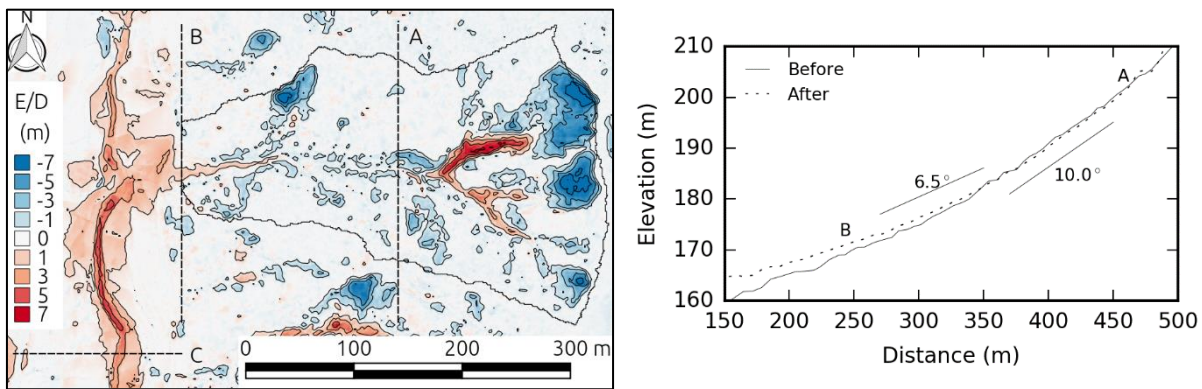


Fig. 3. (a) Changes in elevation before and after the heavy rainfall; (b) Longitudinal profile of stream channel between section A and B.

from Akatani River basin to investigate yield and run out of sediment and woody debris based on field surveys, aerial photographs, and elevation data taken by laser from airplane before and after the event. Fig.1 (a) shows the location of the target drainage basin site in Fukuoka Prefecture of Kyushu, Japan. The area of the drainage basin is 6.7 ha and covered with coniferous trees. The maximum 24-hour rainfall was 450 mm and the maximum hourly rainfall was 100 mm around the drainage basin, based on the radar of Japan Meteorological Agency (Yamazaki et al., 2018). Fig. 1 (b) shows the aerial photograph of the drainage basin after the heavy rainfall. The photograph shows a run out mark of sediment in the upper and middle of the valley and deposition of sediment and woody debris in and around the outlet of the valley. Those depositions in their run out paths are assumed to be formed by the sediment and woody debris due to erosion by landslides and debris flows. In this valley, the deposition in the run out paths is assumed to be partly transported by flood water of main channel. A detailed investigation is required for the volume of transportation to the downstream. A number of trees per unit area, locations and lengths of woody debris are investigated by counting tree crowns of conifers on this aerial photograph.

Fig. 2 (a) and (b) show the topography of the drainage basin before the heavy rainfall and longitudinal profile along the stream segments P1, P2, and P3 shown in Fig.2 (a). The longitudinal profile indicates the gradient of the slopes where landslides occurred is around 30 degrees. The gradient of the stream bed from the confluence point of P1, P2, and P3 to cross section B ranges from 10 to 6. Sediment deposits were collected at M1, M2, and M3 in Fig. 2 (a). These samples were sieved in the laboratory. The result of the sieving is shown in Fig. 4 (a).

Fig. 3 (a) shows changes in elevation before and after the heavy rainfall. This study classifies these areas where elevation decreased as erosional areas, and these areas where elevation increased as depositional area. Based on the elevation change, the volume of sediment yield and deposition within the drainage basin is estimated at 59,000 m³ from the erosional area and the volume of deposition is estimated at 12,000 m³ from the depositional area. Because the volume of sediment transport from the drainage basin is calculated as the sum of the volume of elevation change

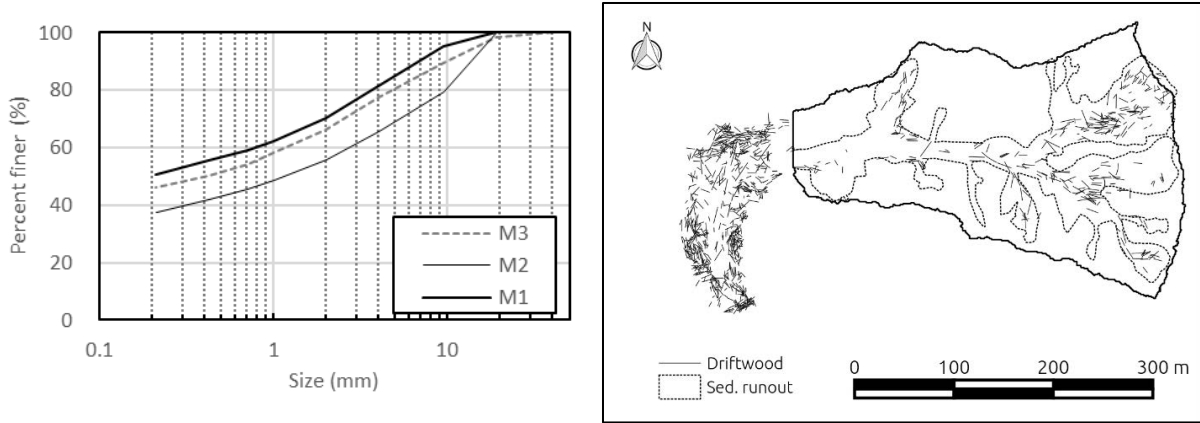


Fig. 4. (a) Grain size distribution of soil samples; (b) Spatial distribution of woody debris and area of sediment run out.

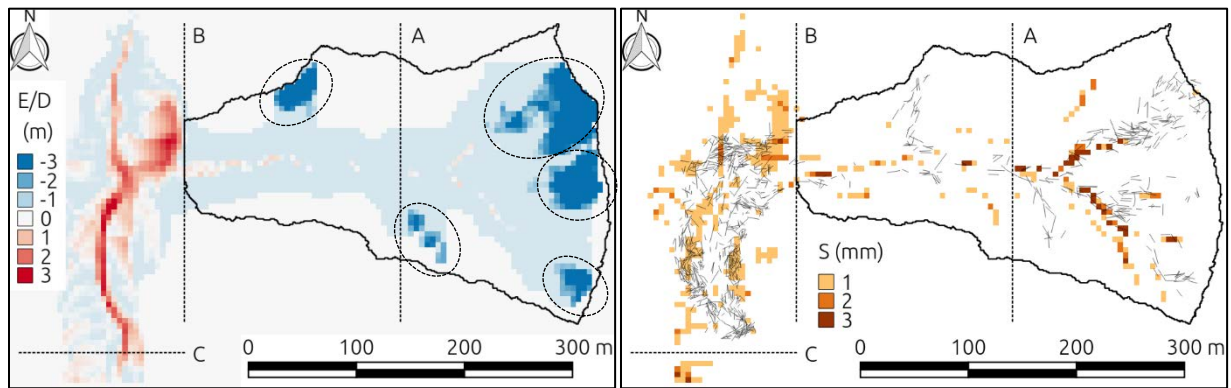


Fig. 5. (a) Simulated erosion and deposition area; (b) Simulated spatial distribution of woody debris deposition with the overlay of measured woody debris.

on erosional area and depositional area, the volume of sediment transport is estimated at 47,000 m³. The deposition in the area between cross section A and B is 23,000 m³. Sediment run out from the drainage basin to the mainstem may be estimated around 24,000 m³. A section of streambed from 350 m to 450 m in Fig. 3 (b) is eroded and depth is 0.5 m. A section from 350 m to the outlet of the valley is a deposited area and the gradient of the deposited area is around 6.5 degrees.

Fig. 4 (a) shows the grain size distribution of soil samples of a mountain slope taken at M1, M2, and M3 displayed in Fig. 2 (a). Although M3 locates in the center of the mainstem, the sample is taken from a large soil lump attached to root zone of a tree which is estimated to be originally located in the mountain slopes. Here, a soil particle with a diameter less than 0.2 mm which is generally called as wash load is treated as a fine sediment which behaves as a fluid in a debris flow. The grain size distribution shows p_f ranges from 0.3 to 0.5. The topographical gradient of deposition on stream bed from 250 m to 450 m after the heavy rainfall ranges from 6 to 10 degrees (Fig. 3 (b)). The equilibrium gradient of debris flow calculated by the equation (8) becomes $\theta_e = 10.3, 8.0, 6.1$ degrees when $p_f = 0.3, 0.4, 0.5$ with soil physical parameter described in section 4. This supports the validity of the equation.

Fig. 4 (b) shows the locations and lengths of the woody debris investigated on the aerial photograph and the region where sediment transports occurred by landslides and debris flows. Woody debris heavily accumulated around the outlet of the drainage basin and slightly deposited in the stream channel within the drainage basin. Run out volume of the woody debris is estimated as follows. A calibrated number of trees per unit area is 0.09 based on the aerial photograph. The average height and the average breast high diameter (diameter at 1.2 m) are 30 m and 0.3 m, respectively based on the field survey heavily empirical. Assuming a shape of a tree is a cone, a volume of a tree is 0.77 m³. Ignoring leaves and small branches of trees, the volume of trees per unit area is 668 m³/ha. The eroded area is 1.58 ha. Assuming woody debris is yielded in erosion area, the volume of woody debris yield becomes 1055

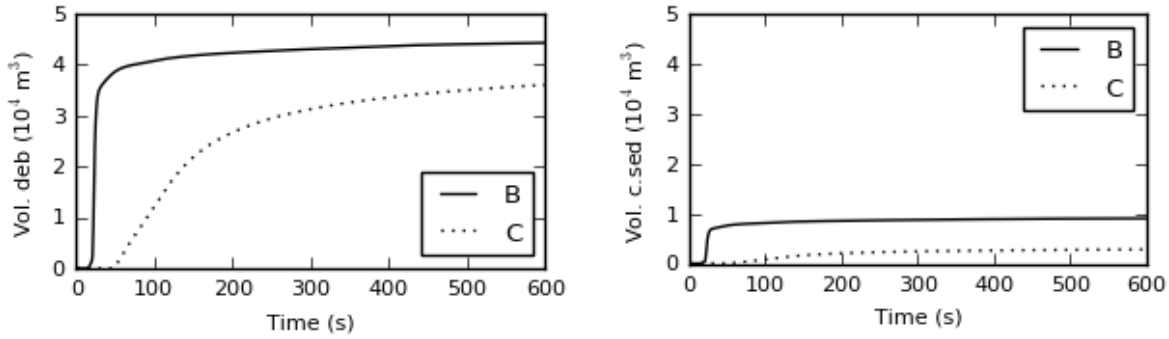


Fig. 6. (a) Temporal changes in run out volume of debris flow; (b) Temporal changes in run out volume of coarse sediment (without pore).

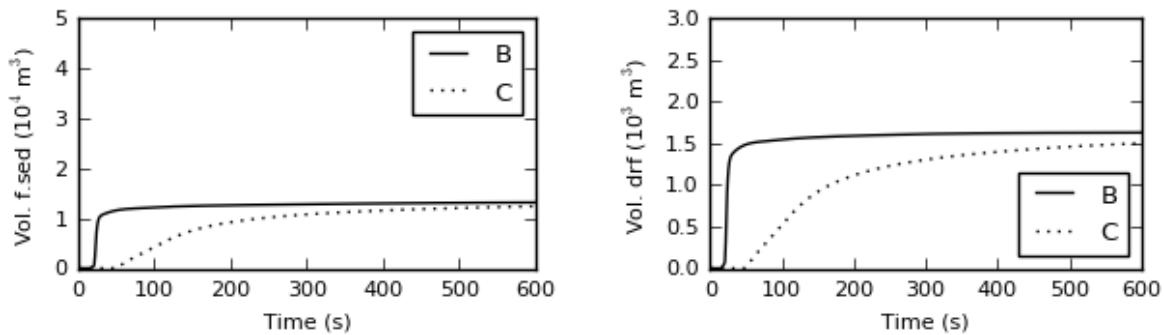


Fig. 7. (a) Temporal changes in run out volume of fine sediment (without pore); (b) Temporal changes in run out volume of woody debris.

m³. The remaining woody debris within the drainage basin is 70 m³. The run out volume of woody debris from the drainage basin is 985 m³. The deposition of woody debris around the outlet of the drainage basin is 120 m³, then the volume of woody debris supply to the mainstem is estimated at 865 m³.

4. Transport processes of sediment and woody debris estimated by numerical simulation

To investigate the transport processes of sediment and woody debris, the governing equation of debris flow and convection and storage equation of woody debris are solved numerically.

Condition and setting for the simulation are as follows. The initial condition of surface soil layer is saturated with water, and the area marked by dotted circle becomes fluidized with $h = E$ shown in Fig.3 (a), $c_c = p_c c_*$, $c_f = p_f c_*$, $u = 0$, $v = 0$ when $t = 0$. Potential erosion depth of area is set to 0.5 m. Size of grid cells is 5 m. Physical constants are set as follows, $g = 9.8 \text{ m/s}^2$, $\sigma = 2650 \text{ kg/m}^3$, $\rho_w = 1000 \text{ kg/m}^3$, $\phi = 37^\circ$, $e = 0.85$, $p_f = 0.4$, and $p_c = 0.6$.

Fig. 5 (a) shows the simulated spatial distribution of erosion and deposition of sediment and Fig. 5 (b) shows the simulated spatial distribution of woody debris storage expressed by height. Although the deposition of sediment around upper stream area of cross section A is simulated less than the estimation by using elevation data, the trend of the spatial distribution of erosion and deposition simulated by this study looks similar to the estimation by elevation data. Assuming sediment yield volume is the total amount of the volume of erosion area multiplying that erosion height, the sediment yield volume is 53,000 m³, and volume without pore of coarse sediment is 19,000 m³ and the volume of fine sediment is 13,000 m³ because $c_* = 0.6$, $p_c = 0.6$, $p_f = 0.4$. The trend of spatial distribution of woody debris deposition is similar to that of the spatial distribution obtained from the aerial photograph (Fig. 5 (b)). A volume of the woody debris deposition within the drainage is 7 m³.

Fig. 6 (a) shows the temporal changes in the accumulated volume of debris flow passing the cross section B and C. It indicates the debris flow reached at the outlet of the drainage basin in 15 seconds, and 90% of the total volume of

debris flow run out in 100 seconds. The volume of debris flow at the cross section B is 44,200 m³ (@ $t=600$ s in Fig. 6 (a)). Debris flow temporarily staying around the area between cross section B and C, flows to the lower reaches crossing section C. Fig. 6 (b) and Fig. 7(a) show accumulated run out volume of coarse sediment and fine sediment without pore at the cross section B and C. The volume without pore of coarse and fine sediment at cross section B is 9,070 m³ and 12,170 m³, respectively. The deposition volume without pore of coarse and fine sediment around outlet is estimated at 6,230 m³ and 750 m³, respectively based on the difference in the value of cross section B and C. Sediment supply from the drainage basin to the mainstem is estimated at 2,840 m³ and 11,420 m³, respectively. This indicates 70 % of coarse sediment remain within the drainage basin, on the other hand, 90 % of fine sediment run out from the drainage basin to the mainstem.

Fig. 7 (b) shows temporal changes in the accumulated volume of woody debris. Run out volume at the outlet is 1,630 m³, deposition at the outlet is 130 m³, and supplying to the mainstem is 1,500 m³.

5. Conclusion

This study proposed convection and storage equations with a term for yield and deposition to describe transport process of woody debris using the erosion and deposition equation of debris flows. The proposed equations for woody debris and governing equations were applied to a small drainage basin which experienced heavy rainfall in 2017. The result shows the equations reproduced the actual process of yield and run out of sediment and debris flows well. It is estimated by this study that 70 % of run out coarse sediment deposit around the outlet of the drainage basin and 90 % of fine sediment run out into the main stem, which is difficult to estimate by using only aerial photographs and elevation data. It is estimated that 90 % of woody debris flows into the mainstem while the rest remains within the drainage basin and is deposited around the outlet. Although r still needs to be discussed, this study is expected significantly to contribute to flood disaster and risk research in the middle and lower reaches from the perspective of considering the sediment and woody debris supply.

References

- Ashida, K., Egashira, S., Ohtsuki, H., 1983, Dynamic behavior of a soil mass produced by slope failure, Disaster Prevention Research Institute Annals, v.26, B-2, pp.315-327 (in Japanese)
- Armanini, A., Fraccarollo, L., Rosatti, G., 2009, Two-dimensional simulation of debris flows in erodible channels. *Comput., Geosci.*, 35, pp.993–1006
- Egashira, S., 2007, Review of research related to sediment disaster mitigation, *Journal of Disaster Research*, v.2, 1, pp.11-18
- Egashira, S., Honda N., Ito T., 2001, Experimental study on the entrainment of bed material into debris flow, *Phys. Chem. Earth (C)*, v.26, 9, pp.645-650
- Egashira, S., Miyamoto, K., Ito T., 1997, Constitutive equations of debris-flow and their applicability, *Proceeding of 1st International Conference on Debris-flow Hazards Mitigation*, C. L. Chen (Eds), ASCE pp.340-349
- Egashira S., Takebayashi H., Yorozuya A., 2016, Influence of fine sediment on runout process of debris flow, *Joint Workshop of 2016 International Debris-Flow Workshop and 6th International Workshop of Multi-modal Sediment Disasters*, A-12
- Frank, F., McArdell, B.W., Huggel C., Vieli. A., 2015, The importance of entrainment and bulking on debris flow runout modeling: examples from the Swiss Alps. *Nat. Hazards Earth Syst. Sci.* 15, pp.2569-2583
- Hussin, H. Y., Quan Luna, B., Van Westen, C. J., Christen, M., Malet, J. P., van Asch, T. W., 2012, Parameterization of a numerical 2-D debris flow model with entrainment: a case study of the Faucon catchment, Southern French Alps. *Natural Hazards and Earth System Sciences*, 12, 10, pp.3075-3090
- Ishikawa, Y., Mizuyama, T., Fukuzawa, M., 1989, Generation and flow mechanisms of floating logs associated with debris flow, *Journal of the Japan Society of Erosion Control Engineering*, v. 42, 3, pp.4-10 (in Japanese)
- Julien P. Y., Paris A., 2010, Mean velocity of mudflows and debris flows, *Journal of Hydraulic Engineering*, v. 136, 9, pp.676-679
- Medina, V., Hurlimann, M., and Bateman, A., 2008, Application of FLATModel, a 2d a finite volume code to debris flows in the northeastern part of the Iberian peninsula. *Landslide* 5, pp.127–142
- Miyamoto, K. and Ito T., 2002, Numerical simulation method of debris flow introducing the erosion rate equation, *Journal of the Japan society of erosion control engineering* vol.55, no.2, pp. 24-35 (in Japanese)
- Mizuyama T., Ohba, A., Manzen, H., 1985, Production and transport of woody trash and logs associated with debris flow occurrence, *Journal of the Japan Society of Erosion Control Engineering*, v. 38, 1, pp.2-6 (in Japanese)
- Takahashi, T., 1977, A mechanism of occurrence of mud-debris flows and their characteristics in motion, *Disaster Prevention Research Institute Annals*, v. 20, B-2, pp.405-435 (in Japanese)
- Yamazaki, Y., Egashira, S., Nagumo, N., 2018, Method to predict sediment runoff resulting from landslides and debris flows, *The 9th International Conference on Scour and Erosion*, The 9th International Conference on Scour and Erosion, pp.683-688

Comparison of an empirical and a process-based model for simulating debris-flow inundation following the 2010 Schultz Fire in Coconino County, Arizona, USA.

Ann M. Youberg^{a,*}, Luke A. McGuire^b

^aUniversity of Arizona, Arizona Geological Survey, 1955 E 6th St, Tucson 85721, USA

^bUniversity of Arizona, Department of Geological Sciences, 1040 E. 4th Street, Tucson 85721, USA

Abstract

The importance of understanding the extent of areas threatened by post-wildfire debris flows cannot be overstated, as illustrated by the post-Thomas Fire flows through Montecito, California, in January 2018. Methods and models developed by the U.S. Geological Survey to identify burned basins at risk of producing post-wildfire debris flows are well established, effective and commonly used. In contrast, there is no similarly established methodology for delineating debris-flow hazard zones downstream of basins prone to producing post-fire debris flows. Understanding potential inundation zones is critical for protecting human life, property and infrastructure. Recently, some communities and local government agencies have begun assessing potential risks from post-wildfire hazards before an area burns (pre-fire hazard assessments). These assessments utilize modeled burn severity maps and existing methodologies to identify basins likely to generate post-fire debris flows should the basins burn. In most studies, however, there have been no attempts to delineate hazard zones downstream of the basins that could produce post-fire debris flows. This information is critical for identifying mitigation opportunities and for establishing emergency evacuation routes and procedures. Here, we report on work using a newly developed process-based model and an empirical model, Laharz using two different sets of mobility coefficients, to assess debris-flow runout from a recently burned basin. The actual extent of debris-flow runout is known, which allows us to compare model performance. Laharz is efficient for assessing large areas but requires the user to select the location of deposition *a priori*, and mobility coefficients for post-fire debris flows have not yet been developed. Laharz did not adequately predict the downstream extent of deposition using either set of mobility coefficients. The process-based model using two sets of parameters, friction angle, ϕ , and ratio of pore fluid pressure to total basal normal stress, λ , provided a range of results. The simulation using parameters $\lambda = 0.8$ and $\phi = 0.35$ provided the best match between mapped and modeled deposits and provided a better estimate of inundation relative to Laharz. This two-model approach is helpful for assessing the shortcomings and benefits of each model, and for identifying the next steps needed for developing a method to identify post-fire debris-flow hazard zones before a fire begins.

Keywords: Wildfires; debris flows; inundation modeling; Arizona

1. Introduction

Increasing wildfire size and severity across the western U.S. and continued encroachment into the wildland-urban interface place more people, property, and infrastructure at risk from post-wildfire hazards. Extensive research efforts focused on post-wildfire debris flows have led to an improved understanding of initiation mechanisms (e.g. Kean et al., 2013; McGuire et al., 2017), the development of objectively-defined rainfall-intensity duration thresholds (Staley et al., 2013; Staley et al., 2017), and new logistic regression models to predict debris-flow probability and volume (Gartner et al., 2014; Staley et al., 2016). As such, it is possible to identify burned basins at risk of producing post-wildfire debris flows. These methods are now being employed to identify, proactively, basins that are at risk of producing post-fire debris flows should a fire occur (Tillery et al., 2014; Tillery and Haas, 2016; Staley et al., 2018). While these studies provide valuable information, there is also a need for local governments and communities to

* Corresponding author e-mail address: ayouberg@email.arizona.edu

identify post-wildfire hazard zones downstream of burned areas for planning and mitigation purposes. For example, a series of devastating post-fire debris flows and floods from the 2010 Schultz Fire in Coconino County, Arizona (Figure 1; Youberg et al., 2010), caused significant impacts to homes and infrastructure, the loss of one life, and economic impacts to the greater Flagstaff area between \$133 and \$147 million (Combrink et al., 2013). To help prevent similar situations in other areas of the county, Coconino County Public Works conducted a pre-fire assessment of post-fire hazards in areas not yet burned by wildfires (Loverich et al., 2017).

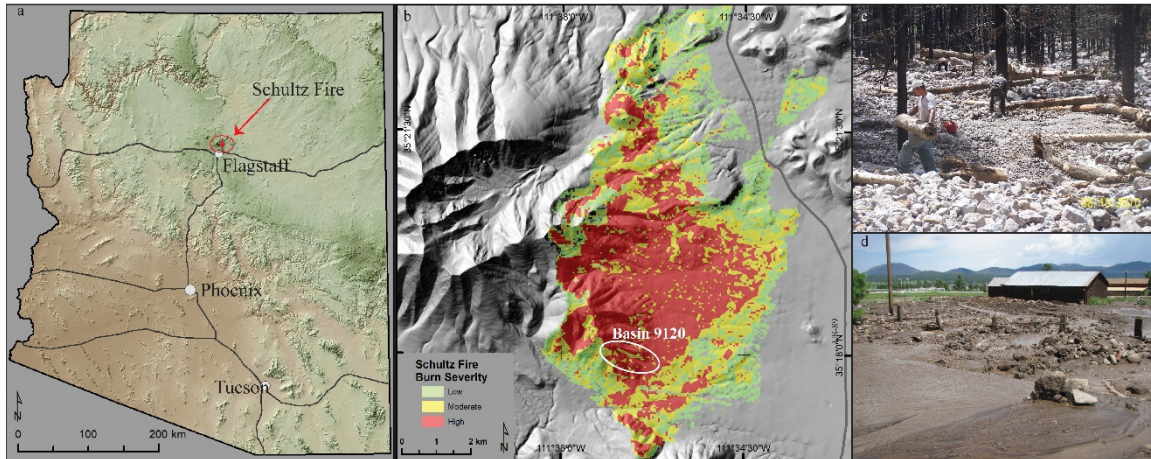


Figure 1. 2010 Schultz Fire location map (a) and burn severity with location of study basin (b). Post-Schultz Fire removal of debris-flow deposits from channels on forest (c; photo: M. Nabel) and debris-laden flows in a subdivision below the burn area (d; photo: A. Youberg).

One of the goals of the Coconino County pre-fire study was to delineate potential debris-flow hazard zones, based on a reasonable wildfire scenario, to identify mitigation opportunities that would reduce impacts from the aftermath of wildfires. A challenge with this study was selecting an appropriate model to assess debris-flow inundation that adequately balanced model complexity with available information. While more detailed, physically based models might have provided better approximations of debris-flow behavior and inundation zones, time and resource constraints, data limitations, and the size of the study areas precluded the use of these models. In addition, few, if any, models have been developed for, calibrated, or tested on post-fire debris flows. Unlike debris flows mobilized from shallow landslides, post-fire debris flows are frequently triggered when runoff concentrates in steep channels (Meyer and Wells, 1997; Kean et al., 2011). As such, post-fire debris-flow surges are often embedded within, and interact with, water-dominated flows. The resulting implications for debris-flow mobility are not clear.

The empirical, volume-driven Laharz model (Iverson et al., 1998; Schilling, 2014) was selected to simulate post-fire debris-flow inundation for the Coconino County study. This model was selected because modified mobility coefficients had been developed for Arizona debris flows (Magirl et al., 2010) and the model could be further tested with data of mapped post-Schultz Fire flow deposits (Youberg, 2017). Laharz, in its current form, requires the user to determine where deposition will begin and, because it simply deposits flow across the topography based on volume and mobility coefficients, it does not accurately reflect flow behavior. Based on Laharz results from the Schultz burn area, this model was deemed acceptable for the Coconino County study. We revisit this issue because better methodologies for assessing and delineating potential inundation zones are needed for upcoming pre-fire hazard assessments. In this study, we use Laharz and a process-based model to assess debris-flow runout from a recently burned basin. The actual extent of debris-flow runout is known, which allows us to compare model performance and assess the utility of the two modelling approaches.

2. Study Area

In June 2010, the small but severe Schultz Fire burned 6100 ha on the eastern slopes of the San Francisco Peaks northeast of Flagstaff, Arizona (Figure 1). This wind-driven fire burned 60% of the area within the first 24 hours with the majority of the fire area burned at moderate (27%) to high (40%) severity on moderate to very steep slopes (Figure 1; USDA Forest Service, 2010). The fire was followed by a wetter than average monsoon which resulted in numerous

debris flows, extensive flooding, the destruction of a city waterline, damage to homes and other infrastructure, and the loss of one life (Youberg et al., 2010). Reconnaissance fieldwork was conducted in August and September 2010 to document which storms and basins produced debris flows (Youberg, 2015) and to map and classify deposits as debris flow, flood, or reworked/mixed (i.e. deposits with debris-flow characteristics - unsorted, snouts, levees - reworked by hyper-concentrated and flood flows) (Youberg, 2017). The modeling efforts in this study focus on basin 9120, which produced debris flows on June 20 and August 16, 2010, and numerous floods throughout the summer (Youberg et al., 2010). The mapped reworked/mixed deposit (Figure 1, orange polygons) may have initially been emplaced during the first debris-flow event, June 20, and subsequently reworked. The mapped debris-flow deposits (Figure 1, dark brown polygons) were likely emplaced during the second debris-flow event, August 16. Debris-flow volume estimates for basins in the Schultz Fire burn area ranged from 1000 m³ to 14,000 m³ but were most frequently 3000 m³ and averaged 5000 m³ (Youberg, 2015).

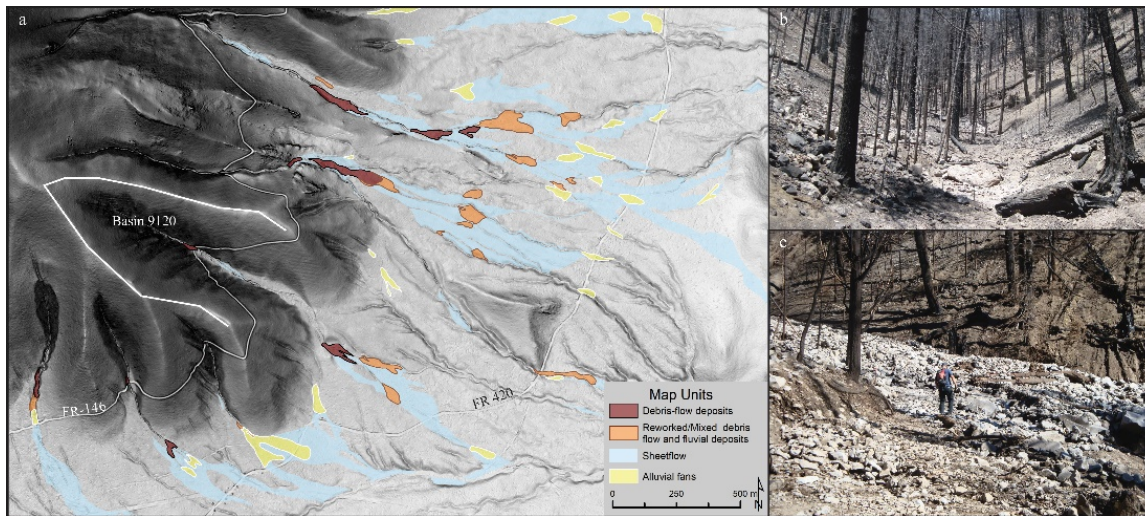


Figure 2. Debris flow (dark brown), reworked/mixed (orange), alluvial (yellow) deposits, and sheetflow areas (light blue) mapped during August and September 2010 (a) (from Youberg, 2017). Basin 9120 on June 29, 2010, looking upstream from FR 146 (b), when it was an unincised swale (Photo: City of Flagstaff), and on August 4, 2010, looking NE from FR 146 (c) with debris-flow deposits on and above the road (Photo: City of Flagstaff). Below the road, the channel is incised 2-3 m.

3. Methods

3.1. Laharz modeling

Laharz is a volume-driven empirical model first developed to identify potential hazard zones from volcanic lahars (Iverson et al., 1998), and later modified to include rock avalanches and worldwide debris flows (Griswold and Iverson, 2008), and saturation-induced debris flows in Arizona (Magirl et al., 2010). Laharz uses digital topography and two volume-based flow equations with mobility coefficients, α_1 and α_2 , to define inundation of cross-sectional area, A , and planimetric area, B (Table 1), occupied by the flow as it moves down the channel until the volume is exhausted (Schilling, 2014). The mobility coefficients are statistically derived from past debris-flow inundation data of high-flow marks (e.g. scouring, strandlines, log jams) and runout (e.g. snouts, levees) (Griswold and Iverson, 2008). Here, we calculated and assessed results using both worldwide and modified Arizona mobility coefficients.

Table 1. Laharz coefficients for two different mobility characteristics. Volumes modeled were 1,000, 3,000 and 5,000 m³.

Mobility coefficients, x and y	Cross-sectional area, $A = \alpha_1 V^{2/3}$	Planimetric area, $B = \alpha_2 V^{2/3}$
Worldwide (Griswold and Iverson, 2008)	0.1	20
Arizona (Magirl et al., 2010)	0.1	40

Simulations were run to assess inundation downstream of basin 9120 with deposition beginning where the channel debouches onto the piedmont at approximately 444832 m E and 3906084 m N (Figure 3a). Debris-flow volumes of 1000 m³, 3000 m³ and 5000 m³ were chosen based on previous mapping (Youberg, 2015) and expected debris-flow volumes from 1- to 2-year precipitation (Youberg, 2017). The digital topography (1 m) was derived from airborne lidar collected in 2012. We selected this post-event topography as the available pre-event digital topography was of poor quality and hydrologically incorrect (drainages didn't follow actual topography). The extent and locations of modeled deposition and mapped deposits, which reflect geomorphic conditions after the second set of debris-flow-producing storms on August 16, 2010, were assessed using two different metrics. First, we computed the percentage of aerial overlap between modeled and mapped deposits. Second, to assess differences between observed and modeled runout potential, we report the distance between the base of the modeled deposit and the base of the mapped deposits.

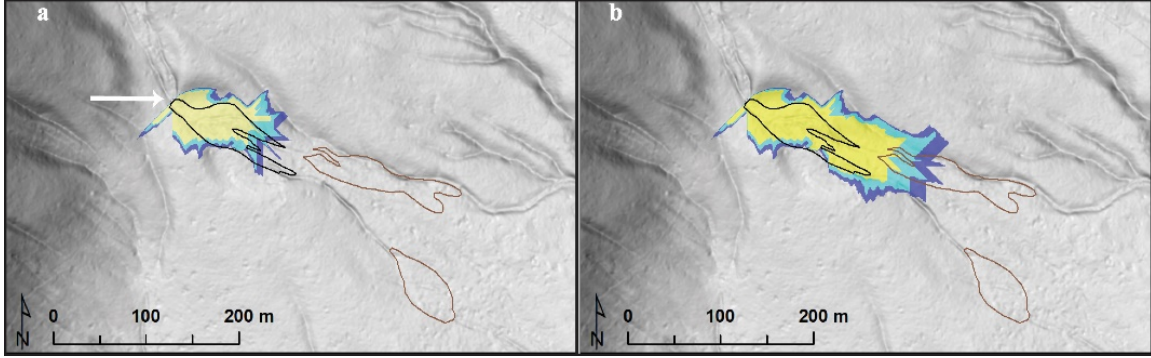


Figure 3. Laharz results for volumes of 1000 m³ (yellow), 3000 m³ (light blue), and 5000 m³ (dark blue) using the equations for worldwide (WW) debris flows (a) and the modified Arizona (AZ) equations (b). Black line is a debris-flow deposit, and brown lines are reworked/mixed debris-flow deposits reworked by hyperconcentrated and flood flows. The white arrow indicates where deposition begins in the model runs.

3.2. Process-based debris flow routing model

The debris flow routing model is based on a set of conservation laws for mass and momentum in a 3D depth-averaged framework, similar to that used by Denlinger and Iverson (2001). The governing equations are given by,

$$\frac{\partial h}{\partial t} + \frac{\partial(hu)}{\partial x} + \frac{\partial(hv)}{\partial y} = 0 \quad (1)$$

$$\frac{\partial(hu)}{\partial t} + \frac{\partial}{\partial x} \left(hu^2 + \frac{1}{2} g_z^2 h \right) + \frac{\partial}{\partial y} (huv) = g_x h - sgn(u)(1 - \lambda) g_z h \tan \phi - \frac{2uv_f \mu}{\rho h} \quad (2)$$

$$\frac{\partial(hv)}{\partial t} + \frac{\partial}{\partial x} (hvu) + \frac{\partial}{\partial y} \left(hv^2 + \frac{1}{2} g_z^2 h \right) = g_y h - sgn(v)(1 - \lambda) g_z h \tan \phi - \frac{2vv_f \mu}{\rho h} \quad (3)$$

where h is flow depth, u and v represent velocity in the x and y directions respectively, g_x , g_y , and g_z are the components of gravitational acceleration in the x , y , and z , directions, $\lambda = p_b / \rho g_z h$ is the ratio of the pore fluid pressure (p_b) to the total basal normal stress, ϕ is the bed friction angle, and μ is the pore fluid viscosity. The flow resistance is dominated in most cases by the second term on the right-hand side of equations (2) and (3), which represents the effects of friction modified by pore fluid pressure. The viscous resistance, represented by the third term on the right-hand side of equations (2) and (3), is generally small in comparison. Here, we assume a pore fluid viscosity of $\mu = 0.1$ Pa s, consistent with muddy water (e.g. Denlinger and Iverson, 2001). The governing equations are solved using a Godunov-type finite volume method, where the numerical fluxes are computed with the Harten-Lax-vanLeer-Contact (HLLC) approximate Riemann solver (e.g. Toro, 2013) and source terms are treated explicitly. Additional details on the numerical solution, including a thorough description of the flux computations, can be found in McGuire et al. (2016).

The ratio of the pore fluid pressure to the total basal normal stress, λ , is held fixed throughout each simulation although its value does vary among simulations. In reality, the pore fluid pressure will change with time throughout the flow event. Here, rather than reconstructing detailed dynamics of a flow event, we instead seek to simulate debris-flow runout following wildfire using a simplified process-based routing model with a minimal number of parameters.

Results from this model can then be used to assess the benefits and weaknesses of employing Laharz and to provide guidance for moving forward with refining the process-based model.

Debris-flow runout simulations were performed using the routing model at basin 9120 (Figure 2). For all simulations, a static volume of debris was initialized in a channel reach defined between points 444539 m E - 30906328 m N and 44698 m E - 3906274 m N (Figure 4a). This particular reach was chosen since it is near the bottom of the study basin, but the banks of the channel are still defined. Thus, it was possible to initialize the debris-flow volume within the channel, where post-fire debris flows typically initiate, in a channel section where we can reasonably assume that the debris flow was no longer entraining a substantial amount of material, and had likely achieved its final volume at that point in the basin. The debris flow moves from its static initial position once the simulation begins and is routed downslope to its final stopping point. Simulations were run with two different volumes, 1000 m³ and 5000 m³, as well as for two different values of λ ($\lambda=0.65$ and $\lambda=0.8$) and two different friction angles ($\phi=30^\circ$ and $\phi=35^\circ$) for a total of eight simulations.

4. Results

4.1. Laharz

Laharz runs were conducted using the worldwide debris-flow equations (Griswold and Iverson, 2008) and the modified Arizona equations (Magirl et al., 2010) with volumes of 1000 m³, 3000 m³ and 5000 m³ (Table 1). The Arizona model more reasonably captures the mapped debris-flow deposit and begins to encompass the reworked/mixed deposit, while the worldwide model more dramatically underestimated the runout distance (Table 2, Figure 3).

4.2. Process-based debris flow routing model

Debris-flow runout varies considerably among simulations due to changes in the friction angle, ϕ , and the ratio of pore fluid pressure to total basal normal stress, λ (Figure 4). In cases where $\lambda=0.65$, the debris flow spreads out of the channel and runout is severely underestimated regardless of whether $\phi=30^\circ$ or $\phi=35^\circ$. Increasing λ leads to a decrease in the effective normal stress and a corresponding increase in flow mobility, as expected. Varying the friction angle from $\phi=35^\circ$ to $\phi=30^\circ$ increases the runout distance of the leading edge of the flow by roughly 400 m. Choosing $\lambda=0.8$ and $\phi=35^\circ$ results in the best match between the modeled and mapped deposits. Although volume clearly affects deposit thickness, it has minimal impacts on flow mobility at our study site.

5. Discussion

Laharz with the Arizona mobility coefficients appears to better capture the extent of the mapped debris-flow deposit (Figure 3, black line) and begins to capture the reworked/mixed deposit (Table 2, Figure 3, brown lines), however neither set of mobility coefficients result in a simulation that fully captures the downstream extent of reworked/mixed deposits. There may be several reasons for this. First, mobility coefficients developed from and for post-fire debris flows may provide better results. Second, mapped debris-flow and reworked/mixed deposits were likely deposited during two different storms and thus may be difficult to reproduce by assuming they were emplaced at the same time. Lastly, we route the debris flows over post-event topography due to the poor quality of pre-event DEMs, which has potential implications for debris-flow spreading and runout. As such, model results reflect those expected under current topographic configurations rather than topography at the time of the flows.

A drawback of using Laharz is that users are required to define where deposition begins, which is difficult to estimate, especially given the dramatic geomorphic changes typical of the disturbed post-fire environment. In the Coconino County study, this problem was addressed by modeling a wide range of volumes (half-order magnitudes from 10³ to 10⁵ m³), and selecting multiple deposition points using channel gradients and potential fan avulsion areas (Youberg, 2017). Results were then combined and generalized to create debris-flow hazard zones (first-order approximations) in each pilot study area (Loverich et al., 2017).

The benefit of using a process-based routing model is that the deposition location does not need to be defined *a priori*. A debris-flow initiation location is still needed, but it may be possible to estimate initiation locations within a watershed using a hydrologic model and critical discharge thresholds required for bed failure (Gregoretti and Fontana, 2008). The major uncertainties associated with the routing model used here include the friction angle and the ratio of pore fluid pressure to total basal normal stress. Runout extent and deposit shape were quite variable due to changes in

the friction angle, ϕ , and the ratio of pore fluid pressure to total basal normal stress, λ (Figure 4). Note that post-fire topography was also used with this model which likely influenced lateral spread and runout patterns. In all cases when $\lambda = 0.65$, regardless of friction angle, the model overestimated lateral spread and severely underestimated debris-flow runout (Table 2). The simulations for both volumes using $\lambda = 0.8$ and $\phi = 0.35$ provided the best match between mapped and modeled deposits and performed better than other model configurations and Laharz (Table 2, Figure 4). A challenge in using a process-based routing model, even one with a minimal number of parameters as presented here, is that the results can be sensitive to small changes of parameters. Both $\lambda = 0.65$ and $\lambda = 0.8$ are reasonable choices, given that pore fluid pressures are likely high initially (i.e. $\lambda=0.9$) and then decay with time (e.g. Denlinger and Iverson, 2001), yet they result in very different inundation predictions. Using $\lambda = 0.8$ is consistent with a debris flow that maintains high pore fluid pressure throughout the entirety of its runout. The fact that simulations assuming high pore fluid pressures perform the best could be a result of the interaction between the debris flows and the surrounding water-dominated flow. Here, however, we only simulate the debris flow and neglect the water-dominated flow that the debris flow was likely embedded in.

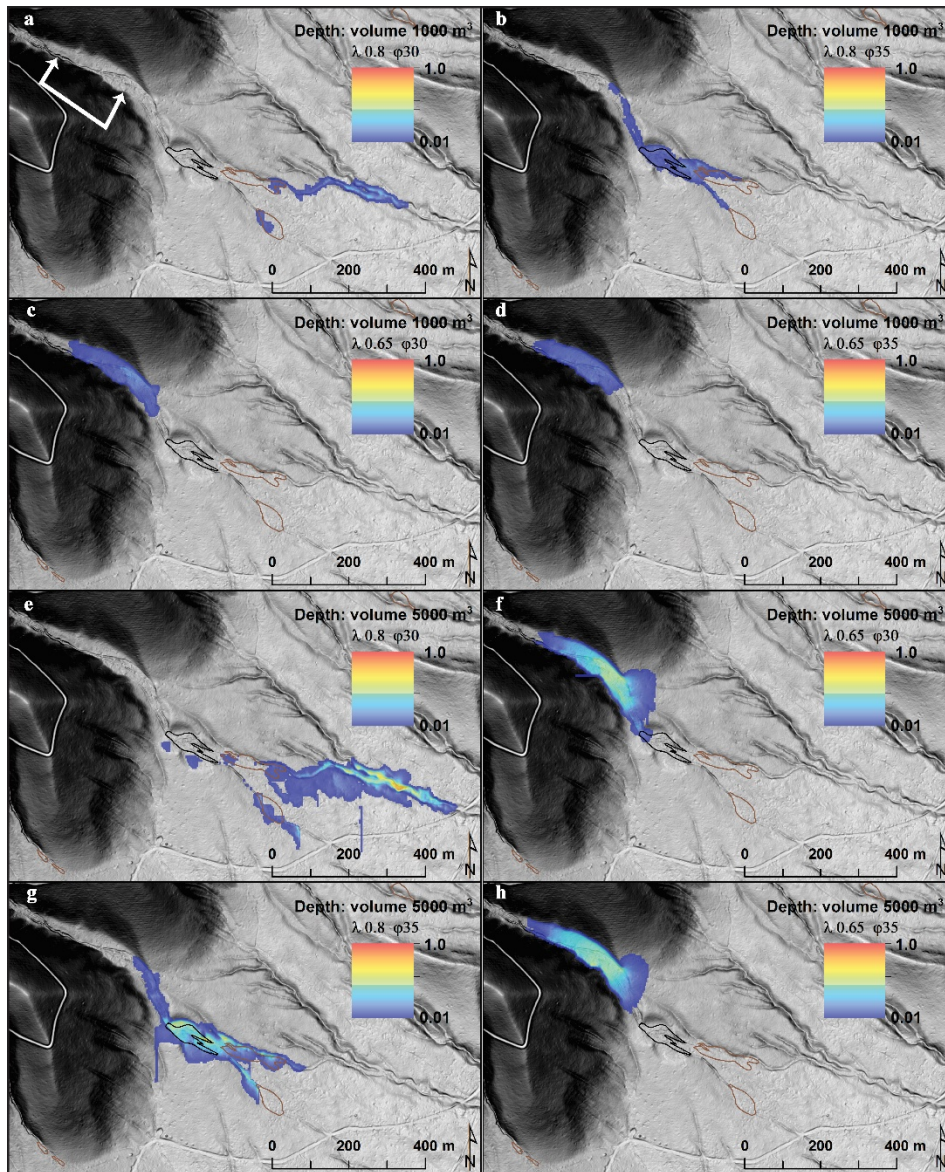


Figure 4. Results from the 8 process-based model runs for various values of λ and ϕ as well as total flow volumes of 1000 m³ (a, d, b, e) and 5000 m³ (c, f, g, h). White line with arrows in (a) shows the model initiation reach.

While the process-based debris-flow model is generally more complex and time consuming to run compared with Laharz, it may provide results that more accurately reflect debris-flow behavior and it is possible to constrain certain parameters (e.g. friction angle) given knowledge of debris-flow constituents (Table 2). Hence, there is potential for using the process-based routing model described here to develop inundation zones, particularly when there is not an immediate time constraint posed by an impending rainstorm (i.e. pre-fire assessments of post-fire hazards), if λ and φ can be sufficiently constrained. Given the spread in inundation scenarios simulated by the model for relatively narrow parameter ranges ($0.65 < \lambda < 0.8$, $30^\circ < \varphi < 35^\circ$), studies that help to identify typical parameter values for post-fire debris flows would aid in limiting the number of simulations required for sensitivity analyses.

Table 2. Metrics used to compare model results with mapped deposits. The downstream extent of modeled deposits is compared with the downstream extent of mapped debris-flow (column 2) and reworked/mixed flow (column 3) deposits. Negative numbers indicate modeled deposits stop upslope of the downstream extent of the mapped deposits. The percent-area overlap between modeled deposits with mapped debris-flow (column 4) and reworked/mixed (column 5) deposits provides another assessment of each model

Process-Based Model	Average distance upstream (-) / downstream (+) from base of modeled deposits to		Percent area overlap between modeled deposit and mapped deposits	
	Base of mapped debris-flow deposit	Base of mapped rework/mixed deposit	Mapped debris-flow deposit	Mapped reworked/mixed deposits
depthV1k $\lambda 0.80 \varphi 30$	516	320	0%	23%
depthV1k $\lambda 0.80 \varphi 35$	137	-77	98%	20%
depthV1k $\lambda 0.65 \varphi 30$	-203	-285	0%	0%
depthV1k $\lambda 0.65 \varphi 35$	-272	-309	0%	0%
depthV5k $\lambda 0.80 \varphi 30$	475	263	0%	42%
depthV5k $\lambda 0.80 \varphi 35$	156	-12	100%	57%
depthV5k $\lambda 0.65 \varphi 30$	-112	-324	13%	0%
depthV5k $\lambda 0.65 \varphi 35$	-179	-353	0%	0%
Laharz Model				
AZ_V1k	28	157	89%	3%
AZ_V3k	99	163	95%	11%
AZ_V5k	68	113	98%	20%
WW_V1k	-56	-254	67%	0%
WW_V3k	-40	-239	82%	0%
WW_V5k	-35	-234	89%	0%

6. Conclusions

The two-model approach presented here is helpful for assessing the shortcomings and benefits of empirical and process-based debris-flow inundation models, and for identifying the next steps needed for developing a method to identify post-fire debris-flow hazard zones before a fire begins. While Laharz is efficient for assessing inundation over large areas, especially under data limitations and constraints of time and resources, it requires the user to reasonably determine the location of deposition *a priori*. Also, mobility coefficients for post-fire debris flows have not yet been developed. A new version of Laharz is under development, and will allow the user to identify initiation areas and channel-slope thresholds below which deposition begins (Reid et al., 2016; D. Brien, personal communication). Once mobility coefficients for post-fire debris flows are developed, Laharz may more adequately represent post-fire debris-flow inundation zones. The process-based routing model, using two sets of parameters, provided quite variable results. Nevertheless, results using $\lambda = 0.8$ and $\varphi = 0.35$ provided a reasonable match between mapped and modeled deposits. Future work with this model could focus on identifying the typical range of key parameters for post-fire debris flows, such as ratio of pore fluid pressure to total basal normal stress (λ), that could be used for developing plausible inundation zones. Mapped deposits from the Schultz Fire and other fires could be used to help develop Laharz mobility coefficients and constrain the range of parameters needed for process-based routing models for post-fire debris flows in Arizona.

Acknowledgements

We would like to thank two anonymous reviewers for thoughtful reviews that improved the quality of this manuscript. This work was partially supported by the Arizona Geological Survey, University of Arizona.

References

- Combrink, T., Cothran, C., Fox, W., Peterson, J., and Snider, G., 2013, A full cost accounting of the 2010 Schultz Fire: Ecological Restoration Institute, Northern Arizona University, 44 p.
- Denlinger, R.P., and Iverson, R.M., 2001, Flow of variably fluidized granular masses across three-dimensional terrain: 2. Numerical predictions and experimental tests: *Journal of Geophysical Research: Solid Earth*, v. 106, no. B1, p. 553-566. doi:10.1029/2000JB900330.
- Gartner, J.E., Cannon, S.H., and Santi, P.M., 2014, Empirical models for predicting volumes of sediment deposited by debris flows and sediment-laden floods in the transverse ranges of southern California: *Engineering Geology*, v. 176, no. 0, p. 45-56. <http://dx.doi.org/10.1016/j.enggeo.2014.04.008>.
- Gregoretti, C., and Fontana, G.D., 2008, The triggering of debris flow due to channel-bed failure in some alpine headwater basins of the Dolomites: analyses of critical runoff: *Hydrological Processes*, v. 22, no. 13, p. 2248-2263.
- Griswold, J.P., and Iverson, R.M., 2008, Mobility Statistics and Automated Hazard Mapping for Debris Flows and Rock Avalanches [electronic resource] (version 1.0 ed.): Reston, Virginia, U.S. Geological Survey, p. 59.
- Iverson, R.M., Schilling, S.P., and Vallance, J.W., 1998, Objective delineation of lahar-inundation hazard zones: *Geological Society of America Bulletin*, v. 110, no. 8, p. 972-984. 10.1130/0016-7606.
- Kean, J.W., McCoy, S.W., Tucker, G.E., Staley, D.M., and Coe, J.A., 2013, Runoff-generated debris flows: Observations and modeling of surge initiation, magnitude, and frequency: *Journal of Geophysical Research: Earth Surface*, p. 2013JF002796. 10.1002/jgrf.20148.
- Kean, J.W., Staley, D.M., and Cannon, S.H., 2011, In situ measurements of post-fire debris flows in southern California: comparisons of the timing and magnitude of 24 debris-flow events with rainfall and soil moisture conditions: *J. Geophys. Res.*, v. 116, no. F4, p. F04019. 10.1029/2011jgrf002005.
- Loverich, J.B., Youberg, A.M., Kellogg, M.J., and Fuller, J.E., 2017, Post-wildfire debris-flow and flooding assessment: Coconino County, Arizona: Arizona Geological Survey Open-File Report OFR-17-06, 63 p.
- Magirl, C.S., Griffiths, P.G., and Webb, R.H., 2010, Analyzing debris flows with the statistically calibrated empirical model LAHARZ in southeastern Arizona, USA: *Geomorphology*, v. 119, no. 1-2, p. 111-124. DOI: 10.1016/j.geomorph.2010.02.022.
- McGuire, L.A., Kean, J.W., Staley, D.M., Rengers, F.K., and Wasklewicz, T.A., 2016, Constraining the relative importance of raindrop- and flow-driven sediment transport mechanisms in postwildfire environments and implications for recovery time scales: *Journal of Geophysical Research-Earth Surface*, v. 121, no. 11, p. 2211-2237. 10.1002/2016jgrf003867.
- McGuire, L.A., Rengers, F.K., Kean, J.W., and Staley, D.M., 2017, Debris flow initiation by runoff in a recently burned basin: Is grain-by-grain sediment bulking or en masse failure to blame?: *Geophysical Research Letters*, v. 44, no. 14, p. 7310-7319. 10.1002/2017GL074243.
- Meyer, G.A., and Wells, S.G., 1997, Fire-related sedimentation events on alluvial fans, Yellowstone National Park, U.S.A.: *Journal of Sedimentary Research*, v. 67, no. 5, p. 776-791.
- Reid, M.E., Coe, J.A., and Brien, D.L., 2016, Forecasting inundation from debris flows that grow volumetrically during travel, with application to the Oregon Coast Range, USA: *Geomorphology*, v. 273, p. 396-411. <http://dx.doi.org/10.1016/j.geomorph.2016.07.039>.
- Schilling, S.P., 2014, Laharz_py—GIS tools for automated mapping of lahar inundation hazard zones, U.S. Geological Survey Open-File Report 2014-1073, p. 78.
- Staley, D., Kean, J., Cannon, S., Schmidt, K., and Laber, J., 2013, Objective definition of rainfall intensity–duration thresholds for the initiation of post-fire debris flows in southern California: *Landslides*, v. 10, p. 547-652. 10.1007/s10346-012-0341-9.
- Staley, D.M., Negri, J.A., Kean, J.W., Laber, J.L., Tillery, A.C., and Youberg, A.M., 2017, Prediction of spatially explicit rainfall intensity–duration thresholds for post-fire debris-flow generation in the western United States: *Geomorphology*, v. 278, p. 149-162. <http://dx.doi.org/10.1016/j.geomorph.2016.10.019>.
- Staley, D.M., Negri, J.A., Kean, J.W., Laber, J.M., Tillery, A.C., and Youberg, A.M., 2016, Updated logistic regression equations for the calculation of post-fire debris-flow likelihood in the western United States, U.S. Geological Survey Open-File Report 2016-1106, p. 13.
- Staley, D.M., Tillery, A.C., Kean, J.W., McGuire, L.A., Pauling, H.E., Rengers, F.K., and Smith, J.B., 2018, Estimating post-fire debris-flow hazards prior to wildfire using a statistical analysis of historical distributions of fire severity from remote sensing data: *International Journal of Wildland Fire*, v. 27, no. 9, p. 595-608. <https://doi.org/10.1071/WF17122>.
- Tillery, A.C., and Haas, J.R., 2016, Potential postwildfire debris-flow hazards—A prewildfire evaluation for the Jemez Mountains, north-central New Mexico 2016-5101 [Report].
- Tillery, A.C., Haas, J.R., Miller, L.W., Scott, J.H., and Thompson, M.P., 2014, Potential postwildfire debris-flow hazards—A prewildfire evaluation for the Sandia and Manzano Mountains and surrounding areas, Central New Mexico: Reston, VA, U.S. Geological Survey Scientific Investigations Report 2014-5161, p. 24 p. with appendix.
- Toro, E.F., 2013, Riemann solvers and numerical methods for fluid dynamics: a practical introduction, Springer.
- USDA Forest Service, 2010, Schultz Fire Burned Area Emergency Response Report, USDA Forest Service, Coconino National Forest, unpublished report, p. 167.
- Youberg, A., Koestner, K.A., and Neary, D.G., 2010, Wind, rain and floods: a case study of the June 2010 Schultz Wildfire, Flagstaff, Arizona: *Arizona Geology*, v. 40, no. 3, p. 1-6.
- Youberg, A.M., 2015, Geodatabase of Post-Wildfire Study Basins: Assessing the predictive strengths of post-wildfire debris-flow models in Arizona, and defining rainfall intensity-duration thresholds for initiation of post-fire debris flow.: Digital Information Series DI-44: Tucson, AZ, Arizona Geological Survey, p. geodatabase, excel workbook, report 10.
- Youberg, A.M., 2017, Coconino County Post-Wildfire Flood and Debris Flow Risk Assessment, Post-Wildfire Debris Flow Risk Assessment Summary, in *Arizona Geological Survey: Tucson, Arizona, Arizona Geological Survey*, v. Post-Wildfire Debris-Flow and Flooding Assessment: Coconino County, Arizona, no. OFR-17-06 Appendix E, p. 20.

The Role of Disturbance

The impact of global warming on the formation of debris flows in an alpine region of southeastern Tibet

Peng Cui^{a,b}, Jia Yang^{a,c,*}, Dingzhu Liu^{a,c}

^aKey Laboratory of Mountain Hazards and Surface Process, Institute of Mountain Hazards and Environment, Chinese Academy of Sciences, China

^bCAS Center for Excellence in Tibetan Plateau Earth Sciences, China

^cUniversity of Chinese Academy of Sciences, China

Abstract

Debris flows are one of the typical mountain hazards in the Qinghai Tibet Plateau, and they are also one of the most active and harmful hazards in the southeast of Tibet. Different from the formation mechanism of debris-flow hazard at low altitude, the debris flows in this alpine region are caused by the coupling of glacier movement, snow melting, and precipitation. To get the meteorological conditions in formation area of debris flows at the time of disaster occurrence, the daily temperature and precipitation in the areas near glacier tongues were obtained from the method of Anulspin and optimized TRMM data to analyze the influence of meteorological conditions on the formation of debris flows, and the ten mega debris flows that occurred after 1980 in Guxiang, Peilong and Tianmo drainage basins in southeastern Tibet were selected as research samples. The results show that the values of climate extremes during the year and the month when most hazards occurred were obviously greater than at other times. In addition, we developed a hazards identification model $T_{D-year} = s + 3.1775\alpha$ (where s represents accumulated snow water equivalents in basin and α is the rise rate of accumulated temperature) through a combination of the accumulated snow water equivalents and the rise rate of accumulated temperature ($> 0^{\circ}\text{C}$) in the areas near glacier tongues. The threshold of annual climate (T_{D-year}) for identifying the occurrence of mega debris-flow hazard was determined as 5.46. The threshold was also verified by three debris-flow events that occurred in other basins (Zhamu, Bianche and Jiaqinbu) in 2007. Moreover, in terms of meteorological condition before the debris flows, the cumulative precipitation and average temperature in the areas near glacier tongues prior to the first five mega debris flows occurrence matched the formula $T_{D-day} = P_{Acc30} \times T_{Ave30}^{2.903}$ (where P_{Acc30} is the cumulative precipitation and T_{Ave30} is average temperature for 30 days), and all the values of T_{D-day} calculated from the subsequent five debris flows exceeded the threshold (155287), which means that the model was satisfactory for predicting the occurrence of mega debris flows in this region.

Keywords: Mega debris flows; Global warming; Climatic conditions; Alpine region

1. Introduction

Global warming has accelerated the melting of more accumulated snow and glaciers in the Tibetan Plateau (Alexander et al., 2006; Yao et al., 2012; IPCC, 2013; Pepin et al., 2015). The increase in water from melting, a key triggering factor for debris-flow hazard in the area, reduces the shearing resistance of the material resulting in an increase in mobility, which greatly increases the potentiality of a variety of mountain hazards, including debris-flow hazard. Moraine deposits can easily be entrained into debris flows with the coupling effects of rainstorms, ice avalanches, glacier movement, and melt water,

On global scale, there is a correlation between increases in global temperature and the scale and numbers of debris-flow events (Choi et al., 2009; Cui and Jia, 2015). On regional scale, debris-flow hazard can be related to the availability of glacier melt water and the topography of the area (Cui et al., 2010). Understanding debris-flow hazard processes in the region is important for the mitigation of geohazards in mountainous terrains, and for infrastructure development and protecting human lives and properties. The topic is also a frontier scientific issue for multiple hazard processes, as well as disaster forecasting in a complex environmental background.

* Corresponding author e-mail address: 8394186@163.com

In this paper, we studied the triggering conditions for ten mega debris flows that occurred after 1980 in Guxiang, Peilong and Tianmo drainage basins in the alpine region of southeastern Tibet (Fig.1). We analyzed these debris flows using long-time scale climatic data and meteorological conditions before the mega debris-flow occurrence.

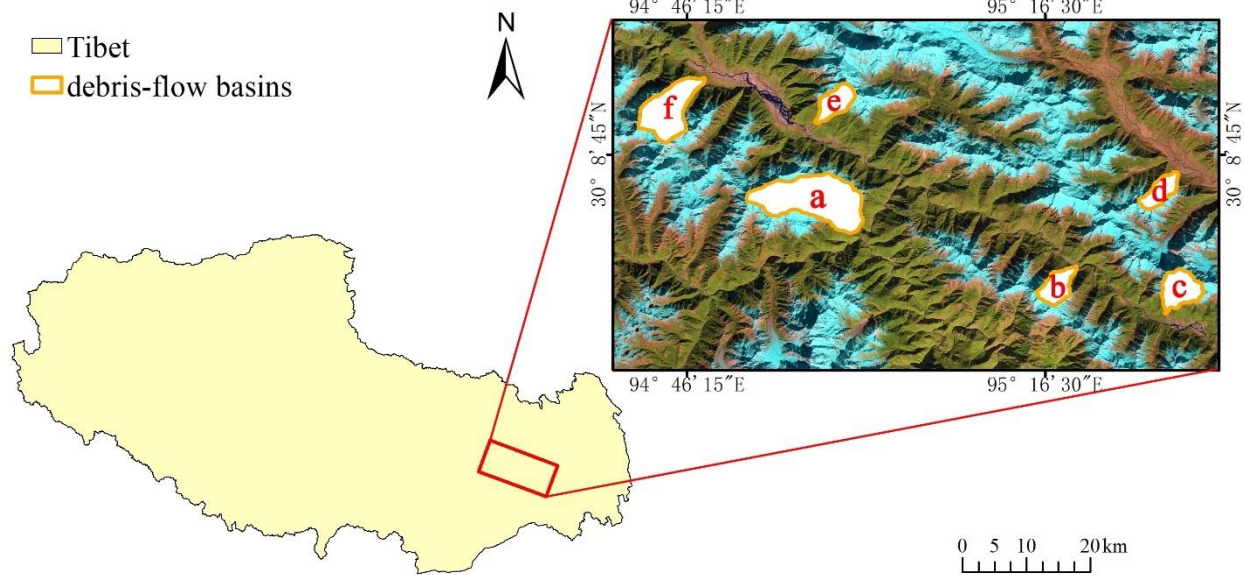


Fig. 1. Location of Peilong (a), Tianmo (b), Guxiang (c), Bianche (d), Zhamu (e), Jiaqinbu (f) drainage basins in southeastern Tibet

2. Climate background for debris-flow occurrence

2.1 The method of principal components extraction from climate data

Sixteen extreme temperature indices and five extreme precipitation indices, recommended by the Expert Team on Climate Change Detection and Indices (ETCCDI), were calculated, and the variation and abrupt characteristics of these indices in southeastern Tibet over the past 50 years were analyzed (Table 1).

Because of the large number of extreme climate indices, which is not conducive to the overall analysis of regional climate change, the method of Principal Component Analysis (PCA) was used to reduce sixteen extreme temperature indices to three principal components (Y_1, Y_2, Y_3) using equation (1), also transformed five extreme precipitation indices to one principal component (Y) using equation (2).

$$\begin{aligned}
 Y_1 &= 0.29 \times X_1 + 0.29 \times X_2 - 0.26 \times X_3 + 0.29 \times X_4 - 0.27 \times X_5 + 0.27 \times X_6 \\
 &\quad + 0.26 \times X_7 + 0.25 \times X_8 + 0.22 \times X_9 + 0.20 \times X_{10} + 0.25 \times X_{11} - 0.24 \times X_{12} \\
 &\quad - 0.28 \times X_{13} + 0.20 \times X_{14} + 0.27 \times X_{15} - 0.06 \times X_{16} \\
 Y_2 &= 0.16 \times X_1 - 0.24 \times X_2 + 0.33 \times X_3 - 0.11 \times X_4 - 0.05 \times X_5 + 0.26 \times X_6 \\
 &\quad - 0.12 \times X_7 - 0.01 \times X_8 + 0.21 \times X_9 + 0.11 \times X_{10} + 0.21 \times X_{11} - 0.06 \times X_{12} \\
 &\quad + 0.24 \times X_{13} + 0.30 \times X_{14} - 0.03 \times X_{15} + 0.68 \times X_{16} \\
 Y_3 &= -0.09 \times X_1 + 0.02 \times X_2 + 0.08 \times X_3 + 0.16 \times X_4 + 0.20 \times X_5 + 0.11 \times X_6 \\
 &\quad + 0.23 \times X_7 - 0.31 \times X_8 + 0.35 \times X_9 - 0.50 \times X_{10} + 0.15 \times X_{11} + 0.38 \times X_{12} \\
 &\quad - 0.06 \times X_{13} + 0.42 \times X_{14} - 0.02 \times X_{15} - 0.18 \times X_{16}
 \end{aligned} \tag{1}$$

where X_1 is the daily maximum temperature, X_2 is the daily minimum temperature, X_3 is the cold night frequency, X_4 is the warm night frequency, X_5 is the cold day frequency, X_6 is the warm day frequency, X_7 is the warmest night temperature, X_8 is the coldest night temperature, X_9 is the warmest day temperature, X_{10} is the coldest day temperature, X_{11} is the warm spell duration indicator, X_{12} is the ice days, X_{13} is the frost days, X_{14} is the summer days, X_{15} is the length of growing season, X_{16} is the diurnal temperature range.

$$Y = 0.45 \times X_1 + 0.48 \times X_2 + 0.39 \times X_3 + 0.44 \times X_4 + 0.46 \times X_5 \quad (2)$$

where X_1 is the annual total precipitation from wet days, X_2 is the very wet day precipitation (>95th), X_3 is the annual maximum 1-day precipitation, X_4 is the annual maximum consecutive 5-day precipitation, X_5 is the Number of heavy precipitation days ($\geq 10\text{mm}$).

2.2 Analysis of extreme climate anomalies

Table 1 shows that the abnormal state of annual climate extremes when ten mega debris flows occurred in southeastern Tibet. It can be seen that high annual temperature and high annual precipitation are conducive to the occurrence of mega glacial debris flows.

At the monthly scale of climate, air temperatures showed a higher value when 90% of debris flows occurred (Table 2).

Table 1. Abnormal state of annual climate extremes when debris flow occurred in southeastern Tibet ("+" indicates a high level, which means a higher value than the average in the past five years; "-" indicates a low level, which means a lower value than the average in the past five years)

	the year of hazard occurrence	Extreme temperature	Extreme precipitation
Peilong	1983	+	-
Peilong	1984	+	+
Peilong	1985	-	+
Peilong	2007	+	+
Guxiang	2004	+	+
Guxiang	2005	+	-
Tianmo	2007	+	+
Tianmo	2010	+	+

Table 2. Abnormal state of monthly climate extremes when debris-flow hazard occurred in southeastern Tibet ("+" indicates a high level, which means a higher value than the average of the same month in the past five years; "-" indicates a low level, which means a lower value than the average of the same month in the past five years)

	the month of hazard occurrence	Extreme temperature
Peilong	Jul-1983	+
Peilong	Aug-1984	-
Peilong	Jun-1985	+
Peilong	Sep-2007	+
Guxiang	Sep-2004	+
Guxiang	Jul-2005	+
Guxiang	Aug-2005	+
Tianmo	Sep-2007	+
Tianmo	Jul-2010	+
Tianmo	Sep-2010	+

3. Climatic characteristics prior to debris-flow occurrence

3.1 Determination of the key factors at annual scale

The snow cover in Tibet reaches its peak in January every year, followed by snow melt through springtime. If temperatures rise quickly, snow melts rapidly. In addition, new snowfall during the springtime can add additional water to the basins and increase the probability of debris-flow hazard during the snow accumulation and melting processes.

In order to accurately describe the coupling of climate and surface environment on the formation of debris flows, we studied five mega debris-flow events occurred after 2000 in three typical glacial debris-flow basins (Peilong, Guxiang and Tianmo, see in Fig.2) in southeastern Tibet. The daily temperature data in the areas near glacier tongues (glacier activity region, also debris-flow initiation region, see the areas shaded in light blue in Fig.2) was interpolated by the method of Anusplin (Hock, 2003; Hijmans et al., 2005; Hutchinson, 1991; Hutchinson and Xu, 2013) to characterize the active state of glacier melting indirectly. In addition to glacial activity, snow melting also provides a great deal of water for triggering mega debris flows. We calculated the cumulative snow-water equivalent to describe the active state of snow melting in Tianmo, Guxiang and Peilong basins prior to the occurrence of debris flows from the MODIS snow products (Hall et al., 2002; Tekeli et al., 2005; Hall et al., 2006; Gafurov et al., 2009; Morriss et al., 2016) and the passive microwave remote sensing data-SSM/I (Derksen et al., 1998; Che et al., 2004; Tong et al., 2010; Stigter et al., 2017).

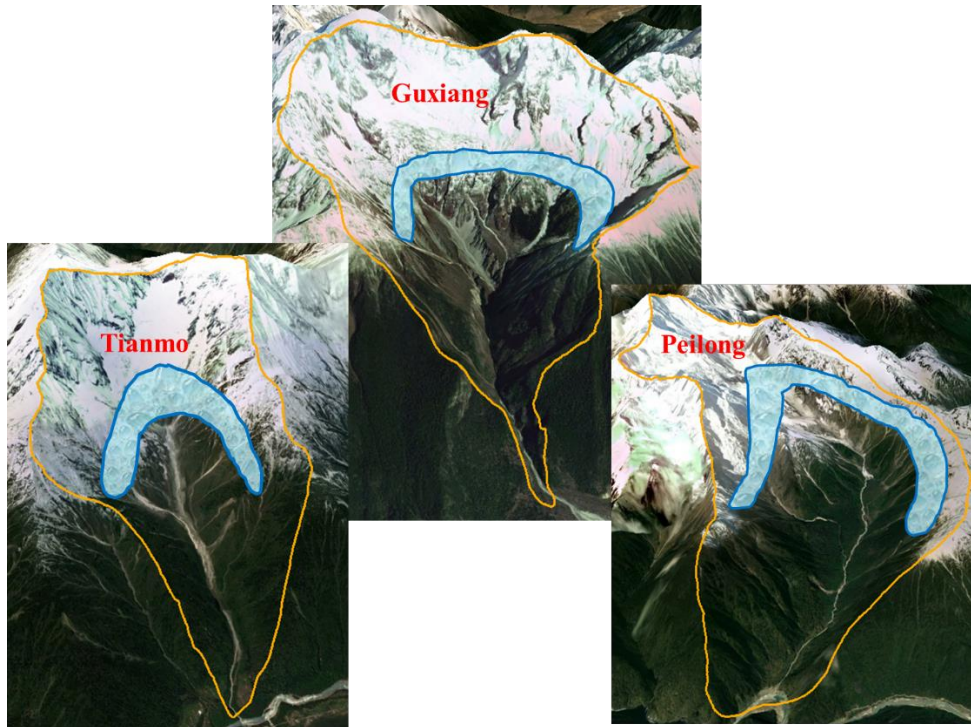


Fig. 2. Definition of glacier activity regions (areas shaded in light blue) in the debris-flow basins studied

Table 3. The rising rate of air temperature in °C during the year prior to debris-flow occurrence in Peilong, Guxiang and Tianmo basins shown in Fig.2 (the value of rising rate calculating explained in Fig.3)

	Time	Rising rate prior to debris-flow occurrence	Rising rate during the same period of no hazard occurrence
Peilong	Sep-2007	1.4379	1.6745
Guxiang	Sep-2004	1.5982	1.5564
Guxiang	Jul-2005	1.5366	1.6236
Tianmo	Sep-2007	1.5964	1.7285
Tianmo	Jul-2010	1.5103	1.6053

Taking the Fig.3 as an example, the larger rising rate of cumulative temperature ($>0^{\circ}\text{C}$) in the areas near glacial tongues, and the faster melting rate of glacier.

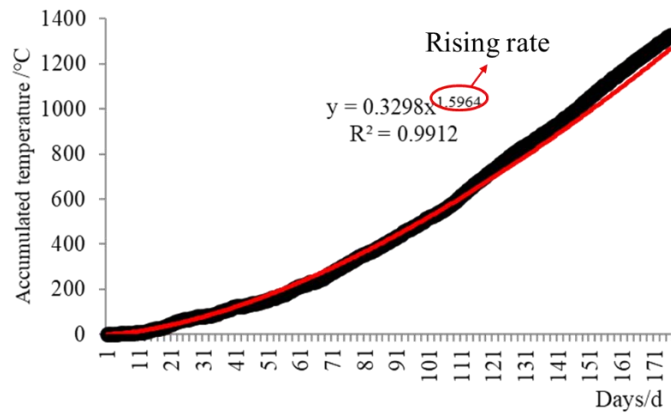


Fig. 3. Rising rate of accumulated temperature in the year prior to debris-flow occurrence (the black points represent the cumulative value of accumulated temperature from the first day in January to the time when hazard occurrence; the red line is the fitting trend of all black points.).

The cumulative snow-water equivalent (Kodama et al., 1979; Gao et al., 2010; Alonsogonzález et al., 2018) from January to the time when hazards occurrence was calculated for the Guxiang, Tianmo and Peilong basins using equation (3). In addition, we defined the snow water equivalent (SWE) coefficient (the cumulative SWE was normalized by dividing newly accumulated snow volume by the area of each basin) in this paper, which eliminated the effect of area differences among different basins.

$$\text{SnowMass}_{\text{accum}} = \sum_{i=1}^{\text{days}-1} (\Delta\text{SWE}_i) \quad (3)$$

where $\text{SnowMass}_{\text{accum}}$ is the total volume of newly accumulated snow, days is the number of newly accumulated snow days, ΔSWE is the volume of newly accumulated snow per day.

3.2 Analysis of the climate characteristics at annual scale

An optimal threshold line (defined by equation 4) can be found by comparing the rising rate of accumulated temperature and the SWE, which effectively separates periods of debris-flow hazard and periods of no hazard. The threshold value is 5.46 (Fig.4a).

$$T_{D\text{-year}} = s + 3.1775\alpha \quad (4)$$

where $T_{D\text{-year}}$ is the threshold determination model by annual climatic characteristics, s is SWE coefficient (normalized value of the cumulative SWE), and α is the rising rate of accumulated temperature in debris-flow initiation region.

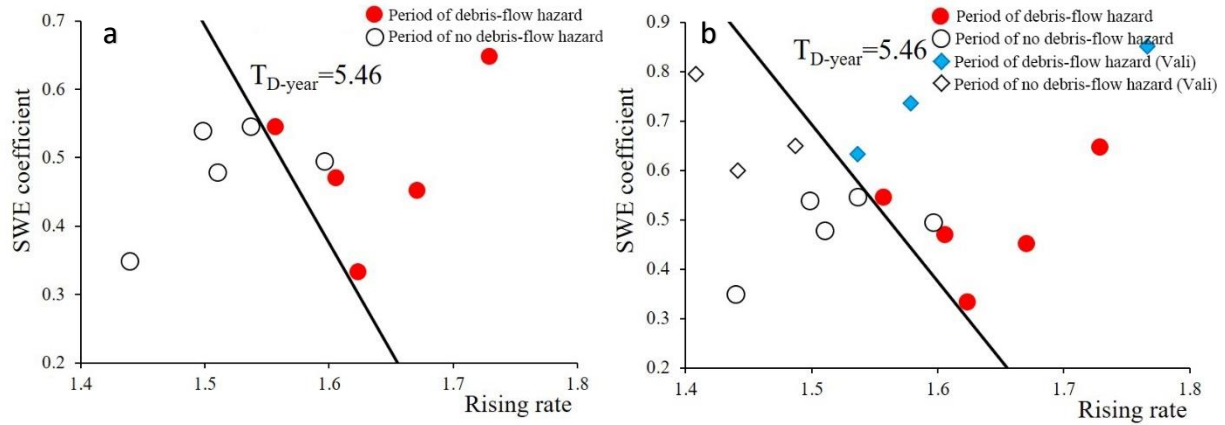


Fig. 4. (a)The rising rate of accumulated temperature and SWE coefficient during the period of debris-flow hazard and the period of no debris-flow hazard; (b) ‘vali’ means that we validate the model by the other three debris-flow basins (Zhamu, Bianche, Jiaqinbu, see Fig. 1.) during the period of debris-flow hazard and the period of no debris-flow hazard.

The rising rate of accumulated temperature and the SWE coefficient when the debris-flow hazard occurred in Zhamu, Bianche and Jiaqinbu (Fig.1) in 2007 were calculated to validate the threshold model (Fig.4b), Results showed that the threshold line also effectively separates the model value in Zhamu, Bianche and Jiaqinbu basins during the period of debris-flow hazard and the period of no debris-flow hazard in terms of annual climatic change.

4. Short-term meteorological characteristics prior to debris-flow occurrence

4.1 Extraction of daily temperature and precipitation for 30-day period prior to debris flows

The formation of debris flows is influenced not only by the annual climatic characteristics, but also by the meteorological conditions in the 30-day period prior to the events. By using the method of Anusplin (Hock, 2003; Hijmans et al., 2005; Hutchinson, 1991; Hutchinson and Xu, 2013) and optimized TRMM data, the 30-day meteorological conditions (temperature and precipitation) prior to the ten mega debris flows occurrence in the Peilong, Guxiang, and Tianmo basins were estimated (Table 4).

Table 4. 30-day temperature and precipitation prior to these ten debris flows

	The time of debris-flow occurrence	30-day average temperature prior to debris-flow hazard (°C)	30-day accumulated precipitation prior to debris-flow hazard (mm)
Peilong	1983/7/28	13.36	99.24
	1984/8/23	11.76	132.45
	1985/6/18	10.02	193.70
	2007/9/4	12.83	97.77
Guxiang	2004/9/7	13.20	88.14
	2005/7/30	14.02	82.13
	2005/8/6	13.50	91.42
Tianmo	2007/9/4	13.09	93.40
	2010/7/25	14.31	108.23
	2010/9/4	13.11	103.37

4.2 Analysis of the meteorological characteristics at daily scale

A threshold model was established by using the 30-day average temperature and accumulated rainfall of the five glacial debris flows with the earliest dates of occurrence (equation 5), and the value of threshold is 155287 (Fig.5a). The model results (T_{D-day}) from the subsequent five debris-flow events were calculated, and the values were greater than 155287 (Fig.5b), which means that the model successfully predicted the occurrence of mega debris flows in the region.

$$T_{D-day} = Acc_{30} \times T_{Ave30}^{.903} \quad (5)$$

where T_{D-day} is the threshold model determined by meteorological characteristics prior to hazards, Acc_{30} is the 30-day accumulated rainfall in debris-flow initiation region prior to hazards. T_{Ave30} is the 30-day average temperature in debris-flow initiation region prior to hazards .

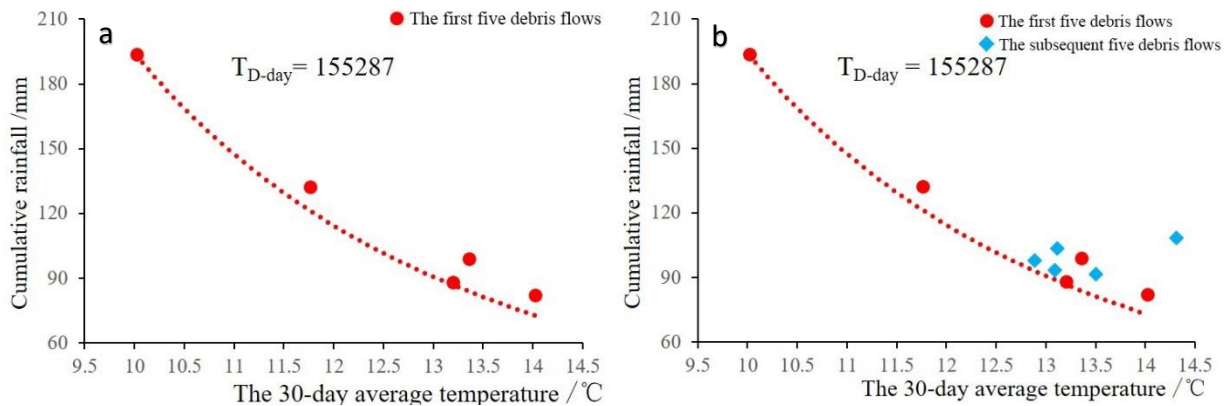


Fig. 5. (a) Meteorological conditions in the areas near glacier tongues in the 30 days prior to the first five mega debris flows; (b) validation of model using five subsequent debris flows

5. Conclusion and discussion

This paper innovatively obtained the change of air temperature and precipitation in debris-flow initiation region by using the method of Anusplin and optimized TRMM data, which were used to describe the climatic conditions conducive to the formation of debris-flow hazard from different time scales, and build the corresponding threshold models. Although we use redundant samples of debris-flow hazard to validate these models we built, and the results showed that the threshold line of model could effectively separates the model value in the validation sample debris-flow basins (Zhamu, Bianche and Jiaqinbu) during the period of debris-flow hazard and the period of no debris-flow hazard.

However, there are still some space to revise and upgrade the research conclusions in this paper:

- 1) At present, we only use the changes of temperature and SWE to describe the active state of the glacier and snow indirectly in debris-flow basins, and cannot quantify the water supplied from of glacier or snow melting, which is not conducive to set up a quantitative equation to describe the initiation process of debris-flow hazard.
- 2) For getting the climatic condition conducive to trigger a mega debris-flow hazard, there are a small number of mega glacial debris-flow samples in southeastern Tibet since 1980 we collected to reduce the impact of the strong earthquakes happened in Motuo in 1950 ($M > 8$) on providing a lot of fresh loose materials for debris-flow drainage basins. It is necessary to collect more samples of debris-flow hazard to validate or optimize the model in this paper.

Acknowledgements

This research was supported by the key project (41190084) and the key international collaborative project (41520104002) of the Natural Science Foundation of China.

References

- Alonso González, E., Lópezmoreno, J., Gascoin, S., et al., 2018, Daily gridded datasets of snow depth and snow water equivalent for the Iberian Peninsula from 1980 to 2014, *Earth System Science Data*, v. 1, p. 1–24.
- Alexander, L.V., Zhang, X., Peterson, T.C., Caesar, J., Gleason, B., Tank, A., Haylock, M., Collins, D., Trewin, B., Rahimzadeh, F., Tagipour, A., Kumar, K., Revadekar, J., Griffiths, G., Vincent, L., Stephenson, D., Burn, J., Aguilar, E., Brunet, M., Taylor, M., New, M., Zhai, P., Rusticucci, M., Vazquez, J., 2006. Global observed changes in daily climate extremes of temperature and precipitation. *J Geophys Res-Atmos* v. 111, p. 1042–1063.
- Choi, G., Collins, D., Ren, G.Y., Trewin, B., Baldi, M., Fukuda, Y., Afzaal, M., Pianmana, T., Gomboluudev, P., Huong, P., Lias, N., Kwon, W., Boo, K., Cha, Y., Zhou, Y., 2009, Changes in means and extreme events of temperature and precipitation in the Asia-Pacific Network region, 1955–2007, *International Journal of Climatology*, v. 29, p. 1906–1925.
- Che, T., Xin, L., Gao, F., 2004, Estimation of Snow Water Equivalent in the Tibetan Plateau Using Passive Microwave Remote Sensing Data (SSM/I). *Journal of Glaciology and Geocryology*, v. 3, p. 364–368.
- Cui, P., Dang, C., Cheng, Z., 2010, Debris flows resulting from glacial-lake outburst floods in Tibet, China, *Physical Geography*, v. 31, p. 508–527.
- Cui, P., Jia, Y., 2015, Status and prospect of study on mountain hazards in Tibetan Plateau, *National Science Review*, v. 2, p. 397–402.
- Derksen, C., Ledrew, E., Goodison, B., 1998, SSM/I derived snow water equivalent data: The potential for investigating linkages between snow cover and atmospheric circulation, *Atmosphere*, v. 2, p. 95–117.
- Gafurov, A., Bárdossy, A., 2009, Cloud removal methodology from MODIS snow cover product, *Hydrology and Earth System Sciences*, v. 7, p. 1361–1373.
- Gao, Y., Xie, H., Lu, N., et al., 2010, Toward advanced daily cloud-free snow cover and snow water equivalent products from Terra-Aqua MODIS and Aqua AMSR-E measurements, *Journal of Hydrology*, v. 1, p. 23–35.
- Hall, D., Riggs, G., Salomonson, V., et al., 2002, MODIS snow-cover products, *Remote Sensing of Environment*, v. 1, p. 181–194.
- Hall, D., Riggs, G., Salomonson V., 2006, MODIS snow and sea ice products, Tsinghua University Press [Beijing] and Springer Verlag GmbH [Berlin] Co published, p. 154–181.
- Hock, R., 2003, Temperature index melt modelling in mountain areas. *Journal of Hydrology*, v. 1, p. 104–115.
- Hijmans, R., Cameron, S., Parra, J., et al., 2005, Very high resolution interpolated climate surfaces for global land areas, *International Journal of Climatology*, v. 25, p. 1965–1978.
- Hutchinson, M., 1991, The application of thin-plate smoothing splines to continent-wide data simulation, *Data Assimilation Systems*, v. 27, p. 104–113.
- Hutchinson, M., Xu, T., 2013, Anusplin version 4.4 user guide, The Australian National University [Canberra].
- Intergovernmental Panel on Climate Change (IPCC) (2013) *Climate Change, 2013, The Physical Science Basis, Contribution of Working Group I to the Fifth Assessment Report of the Intergovernmental Panel on Climate Change*, Cambridge University Press [Cambridge], p. 1535.
- Kodama, M., Nakai, K., Kawasaki, S., et al., 1979, An application of cosmic-ray neutron measurements to the determination of the snow-water equivalent, *Journal of Hydrology*, v. 1, p. 85–92.
- Morriss, B., Ochs, E., Deeb, E., et al., 2016, Persistence-based temporal filtering for MODIS snow products. *Remote Sensing of Environment*, v. 175, p. 130–137.
- Pepin, N., Bradley, R., Diaz, H., Baraer, M., Caceres, E.B., Forsythe, N., Fowler, H., Greenwood, G., Hashmi, M.Z., Liu, X.D., Miller, J.R., Ning, L., Ohmura, A., Palazzi, E., Rangwala, I., Schonher, W., Severskiy, I., Shahgedanova, M., Wang, M.B., Williamson, S.N., Yang, D.Q., Grp, M.R.I.E.W., 2015, Elevation-dependent warming in mountain regions of the world, *Nature Climate Change*, v. 5, p. 424–430.
- Stigter, E., Wanders, N., Saloranta, T., et al., 2017, Assimilation of snow cover and snow depth into a snow model to estimate snow water equivalent and snowmelt runoff in a Himalayan catchment, *Cryosphere*, v. 4, p. 1647–1664.
- Tekeli, A., Zuhail, A., Sormanc, A., et al., 2005, Using MODIS snow cover maps in modeling snowmelt runoff process in the eastern part of Turkey, *Remote Sensing of Environment*, v. 2, p. 216–230.
- Tong, J., Déry, S., Jackson, P., et al., 2010, Snow distribution from SSM/I and its relationships to the hydroclimatology of the Mackenzie River Basin, Canada, *Advances in Water Resources*, v. 6, p. 667–677.
- Yao, T.D., Thompson, L., Yang, W., Yu, W., Gao, Y., Guo, X., Yang, X., Duan, K., Zhao, H., Xu, B., Pu, J., Lu, A., Xiang, Y., Kattel, D., Joswiak, D., 2012, Different glacier status with atmospheric circulations in Tibetan Plateau and surroundings, *Nature Climate Change*, v. 2, p. 663–667.

Relationship between rainfall intensity and debris-flow initiation in a southern Colorado burned area

Evan Q. Friedman^{a,*}, Paul M. Santi^b

^aLithos Engineering, 1360 South Wadsworth Boulevard, Lakewood 80232, United States

^bColorado School of Mines, 1500 Illinois Street, Golden 80401, United States

Abstract

Wildfire impacts on vegetation, soils, and resulting hydrologic processes often result in debris-flow activity in mountainous areas, particularly in response to intense rainfall events that follow. Rainfall thresholds for debris-flow initiation in burned areas have been studied in a variety of settings. It has been proposed that short duration, high-intensity rainfall events are responsible for debris-flow initiation in burned areas. The timing of these responses relative to rainfall intensity peaks is not well understood, leaving uncertainty regarding the duration of intense rainfall necessary to trigger debris flows, which is pertinent to debris-flow initiation thresholds and processes, as well as potential risk mitigations. This study evaluates timing of debris-flow initiation relative to various periods of rainfall intensity at a burned area in Colorado. Detailed local monitoring data from the first intense rainfall events following the 2010 Medano Fire are presented and provide insight into temporal correlations between rainfall intensity peaks and debris-flow initiation. Findings indicate that flow arrivals were within approximately 10 minutes after the beginning of periods of peak short duration rainfall intensity and as soon as 6 minutes after the first rainfall of a storm event was recorded, suggesting that short periods of intense rainfall were responsible for initiation. Tests for equality of variances and means indicated that rainfall intensity values of up to 1-hour duration differentiated between storms that triggered debris flows and those that did not, while average storm intensity did not distinguish between them. The return intervals of storms that triggered debris flows in the Medano Fire burned area burned areas evaluated was as low as 2 years; however, short-period rainfall intensity within the triggering storms were similar in magnitude and correlated temporally with debris flows.

Keywords: debris-flow initiation; rainfall intensity-duration; wildfire burned area

1. Introduction

Debris and sediment-laden flows are often observed in mountainous burned areas in response to rainstorms shortly after wildfires. Their increase in frequency can be attributed to increases in runoff and erosion of material affected by the fire, which are most dramatic in the year or two following the fire (Cannon and Gartner, 2005). As vegetation recovers, and as the supply of ash and soil affected by the fire is eroded away, debris-flow activity generally decreases over time. Monitoring of rainfall and debris-flow activity in the initial years following a wildfire provides insight into the rainfall conditions and processes responsible for debris-flow initiation, as well as the recovery of the burned area and resulting decrease in debris-flow activity.

The investigation discussed herein includes evaluation of rainfall conditions and debris-flow responses using instrumented monitoring data from a wildfire burned area in Colorado. Instrumentation was installed within the Medano Fire burned area for monitoring as part of a research investigation by the authors.

* Corresponding author e-mail address: evan@lithoseng.com

2. Background

2.1. Precedent for debris-flow initiation mechanisms in wildfire burned areas

In basins burned by wildfire in the intermountain western US, debris flows and floods are often triggered by short-duration convective thunderstorms (Cannon, 2001; Cannon et al., 2003; Cannon and Gartner, 2005; Cannon et al., 2008). Wildfires change the infiltration characteristics and erodibility of soils through alteration of physical properties and enhancement of water repellency (Cipra et al., 2003; Parise and Cannon, 2011). Removal of vegetation and consumption of organic litter and duff by severe wildfire reduces rainfall interception and transpiration, exposes bare soil to raindrop impact, and reduces storage capacity. Effects of fire-induced changes include decreased infiltration, increased overland flow, runoff in channels, and movement of soil. These changes in hydrologic response are generally accompanied by a lowering of the intrinsic threshold of erosion (Moody and Martin, 2001; Schumm, 1973) that changes the geomorphic response of a burned watershed.

The generation of debris flows can generally be attributed either to runoff and scour processes, or to slope failures that mobilize sediment to a channel (Cannon, 2001; Cannon et al., 2003; Parise and Cannon, 2011). Studies have shown that the majority of debris flows in burned areas are initiated by progressive bulking of storm runoff with eroded material, as opposed to slope failure (Cannon, 2001; Cannon et al., 2003; Santi et al., 2008). Santi et al. (2008) found that the majority of material in debris flows in burned areas in the intermountain western U.S. came from channel erosion and incision, with an average of only 3% from hillslope erosion. Cannon et al. (2003) found that debris flows in burned areas were initiated in incised channel reaches through excavation of stepped plunge pools that contribute episodic fluxes of sediment and concluded that this process appears necessary to entrain sufficient material in runoff to impart debris-flow characteristics. This process, referred to as progressive sediment bulking, involves the increase in sediment load and thus density of runoff by erosion and entrainment of soil and ash. Flooding that occurs in response to intense rainfall and concentrated runoff leads to scour, sediment-laden flows, and debris flows when a supply of erodible material is available. The latter phase of sediment-laden flooding prior to debris-flow initiation is commonly referred to as hyper-concentrated flooding. In this paper hyper-concentrated and debris flows are considered to be part of the same process of progressive sediment bulking that generates debris flows. The timing of these hydrologic and geomorphic responses relative to rainfall intensity peaks is pertinent to the timing of debris-flow initiation by runoff and progressive sediment bulking.

2.2. Medano Fire burned area

The Medano Fire occurred in June and July of 2010, burning approximately 6000 acres, mainly within the Great Sand Dunes National Park and Preserve in south-central Colorado (Figure 1). The wildfire occurred almost entirely within the Medano Creek Watershed, on the west side of the northern Sangre de Cristo Mountain Range. Medano Creek flows from headwaters in at Medano Lake, on Mount Herard (4069 meters elevation), through a wide upper basin and into a narrow canyon between Mt. Herard to the north and Mt. Zwischen (3659 meters elevation) to the south. The creek emerges from the canyon, crosses over the range bounding Sangre de Cristo Fault, and runs between the range front and the Great Sand Dunes complex. The portions of the upper Medano Creek Watershed burned by the fire are underlain primarily by gneissic bedrock and igneous intrusions, along with various surficial deposits (Johnson et al., 1989). The large deposit of eolian sand at the Great Sand Dunes complex plays a role in the morphology and sediment transport processes of the Medano Creek Watershed. The prevailing westerly winds transport sand up into the watershed and over basin divides. The sand mantles the lee hillslopes of the watershed and collects in its drainage network, especially on the western end, near the dune complex.

The Medano Fire occurred near the end of the summer rainfall season, and the low-intensity rainstorms that followed triggered few minor, ashy sediment-laden floods carrying primarily fine sand. The spring, summer, and fall of 2011 provided an ideal opportunity to monitor flood and debris-flow activity in response to the first intense storms since the fire. Beginning in July 2011, approximately one year after the fire, a series of short-duration and high-intensity convective thunderstorms delivered rain to the watershed, triggering ashy, sandy sediment-laden floods, hyper-concentrated flows, and debris flows.

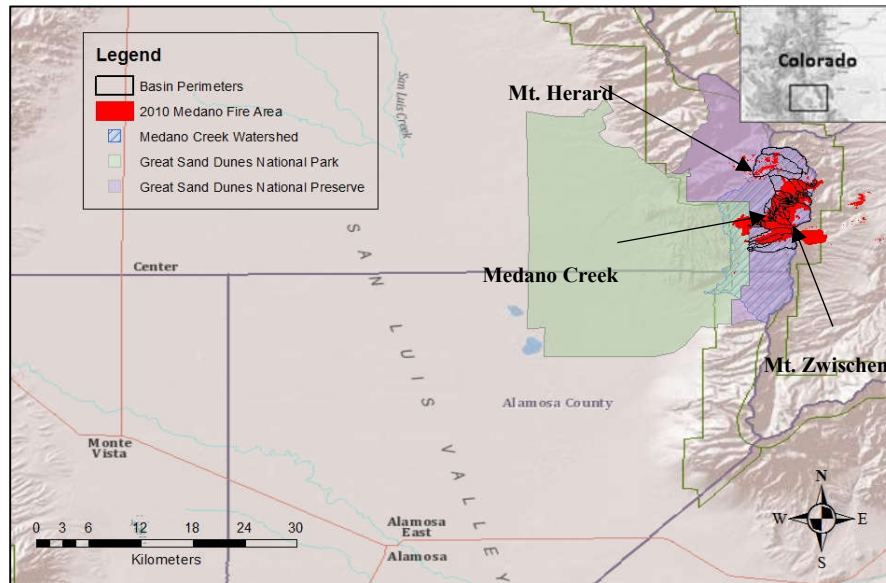


Fig.1. Map of the Medano Fire at Great Sand Dunes National Park and Preserve, Colorado (National Park Service, 2004; National Park Service, 2009).

3. Instrumented Debris-Flow Monitoring

This research includes instrumented monitoring and field mapping of geomorphic response to rainfall events in the severely burned basins of Medano Creek Watershed. Analysis of rainfall characteristics and temporal correlation with pressure transducer records from nearby channels provided insight into the relationship of rainfall intensity to debris-flow initiation by runoff.

The purpose of the study was to integrate rainfall data, debris-flow and flood timing information, and observations of geomorphic response in order to characterize the rainfall conditions responsible for debris-flow initiation in the severely burned alpine basins of Medano Creek Watershed, as well as the timing of these flow events relative to rainfall intensity peaks. This data was used to define a rainfall intensity threshold for debris-flow response, and to compare the timing of peak rainfall intensity to that of sediment-laden- and debris-flow occurrence.

3.1. Methods

A variety of methods have been utilized for instrumented monitoring of debris flows over the last 30 or more years (Itakura et al., 2005; Arratano and Marchi, 2008). The pressure transducer has been successfully used as a low cost and reliable instrumented method to detect debris-flow occurrence (McCoy et al., 2011; Kean et al., 2011; Kean et al., 2012). In this study, unvented pressure transducers and rain gauges were installed to measure the timing of hyper-concentrated- and debris-flow responses relative to rainfall intensity peaks. Rain gages and pressure transducers installed in several low order tributary channels recorded the first major rainfall events of the summer following the fire and resulting runoff responses. Monitoring identified the relative timing of flows with respect to rainfall intensity peaks and allowed calculation of threshold rainfall intensity for debris-flow occurrence. Tributary basins were selected for instrumentation based on debris-flow hazard models (Friedman and Santi, 2014), mapping by Robert Kirkham, field observation of debris-flow deposits, and exposure of bedrock in which to install pressure transducers. Three basins were initially chosen for instrumentation based on these criteria, and a fourth basin later instrumented.

3.2. Monitoring results

Forty-seven individual storms were recorded in the instrumented basins during the monitoring period. Defining criteria for a storm event included a minimum of 0.5 mm rainfall and no more than one hour between rain gauge bucket tips. Figure 2 shows peak intensities of rainfall for various time periods, and average intensity, plotted against the storm durations.

During two recorded storm events, on August 22 and August 28, the peak hourly rainfall intensity measured on the installed rain gauges exceeded 18.9 mm, the magnitude of the 2-year, 1-hour storm (Miller et al., 1973). During the August 28 storm event, the peak hourly rainfall was 26.0 mm, equal to the 5-year, 1-hour storm. These two storm events produced the greatest total rainfall and average rainfall intensity of any recorded storms.

Based on field observations and monitoring records, flows occurred in basins 7, 24, 25, and 32 during the August 22 storm, and in basins 7, 12, 15, 23, 24, and 25 during the August 28 storm. Pressure transducers captured flows in basins 24 and 32 during the August 22 storm event. However, data recorded on pressure transducers in basin 7 during the August 22 flow event and in basins 7 and 24 during the August 28 flow events was not retrieved before the data logger's memory capacity was exceeded and the data overwritten. Figure 3 shows the relative timing of debris flows with respect to peak rainfall for the recorded events data. The precipitation data for the basin 32 flow is from the nearest rain gauge at that time, located in basin 16 approximately 1.2 km from the basin 32 pressure transducer, at a similar elevation. No rain gauge was installed in basin 32 at the time of the event on August 22. The precipitation data for the basin 24 flow is from the nearest rain gauge, in basin 24 approximately 30 meters from the pressure transducer.

One additional flow occurred in basin 32, presumably during one of several storm events on July 11, 28, 29, or August 14; however, no pressure transducer data was recorded during this time period and a site visit was not made between the storm events to confirm the flow timing. Flows also occurred in basin 7, presumably during at least one other storm event on July 11 and/or July 29; however, the pressure transducer was lost in the flow event, thus no data was recovered, and a site visit was not made between the storm events to confirm the flow timing. No flows were observed or recorded in basin 16.

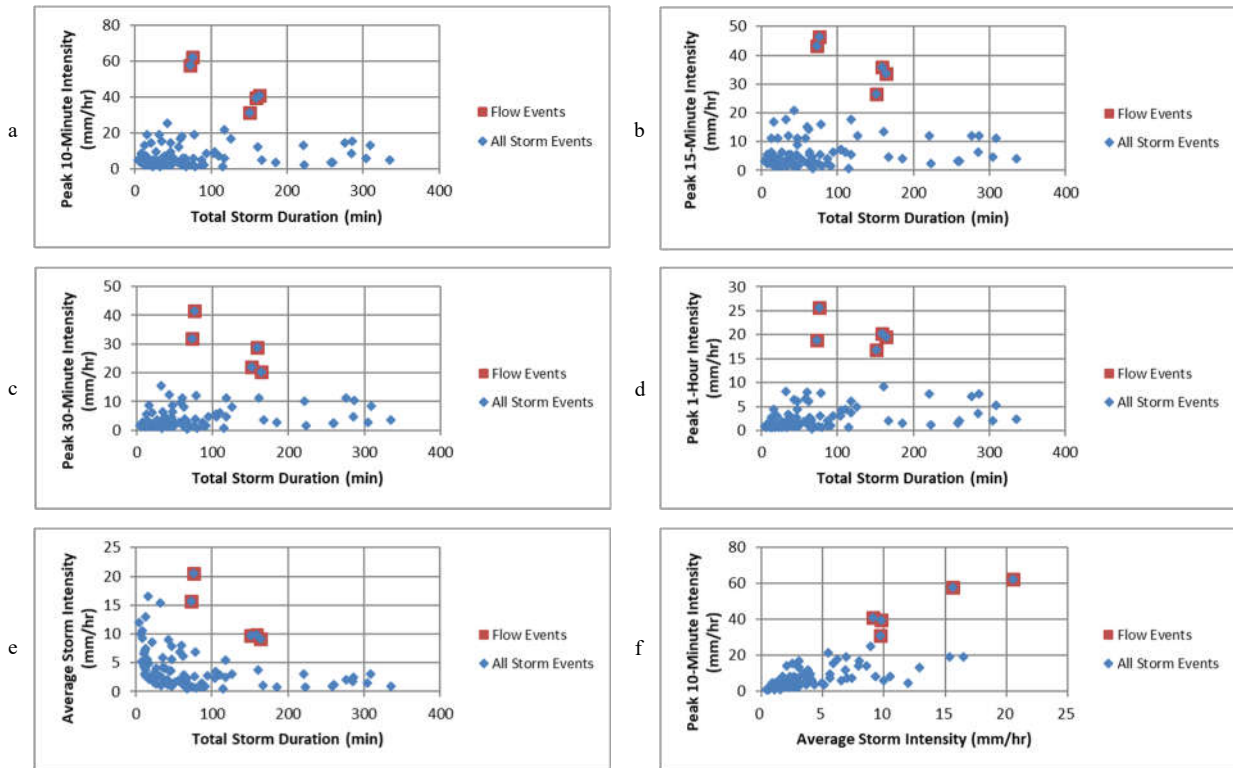


Fig. 2. 10-minute, 15-minute, 30-minute, 1-hour, and average storm rainfall intensity (a, b, c, d, and e, respectively) plotted against duration for all storms recorded during the monitoring period and the subset of flow-triggering storms. (f) Relationship between peak 10-minute intensity and average storm intensity.

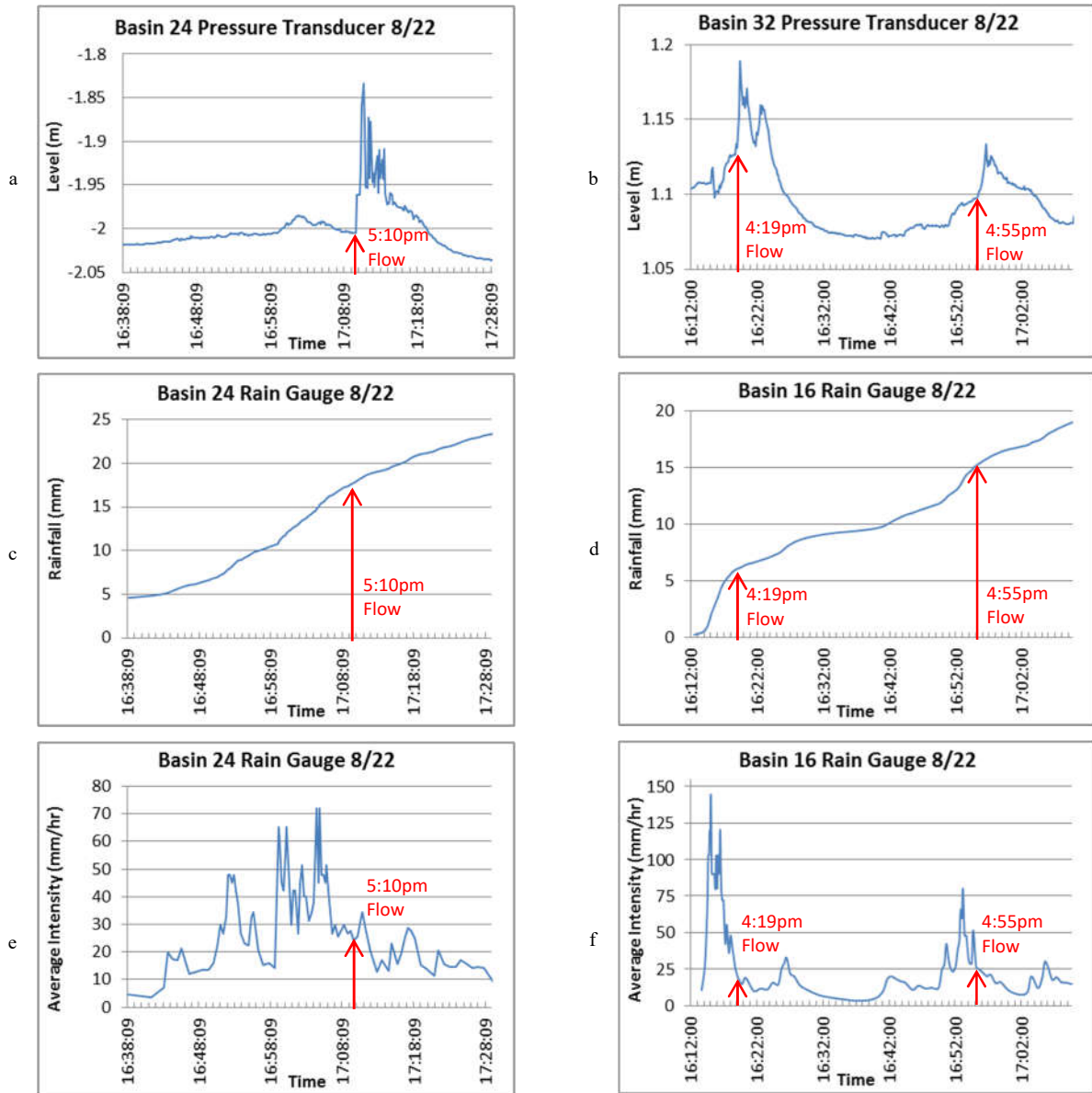


Fig. 3. Pressure transducer level (a and b), cumulative rainfall (c and d), and instantaneous average intensity (e and f) versus time in basins 24 and 16/32, respectively. Red arrows indicate timing of flow arrivals at pressure transducers in basins 24 and 32.

4. Discussion

4.1. Rainfall intensity thresholds for debris-flow initiation

Intensity of rainstorms recorded on rain gauges often varied between basins during the same event. In several of the July storms, significant rain events recorded on one gauge were not recorded at all on another gauge. This indicates that some intense storm cells that trigger debris flows in the study area are small enough to affect only portions of the Medano Creek watershed. Field observations and data suggest that many storms tend to be centered either over Mt. Zwischen to the south of Medano Creek or Mt. Herard to the north (Figure 1). However, the large storm on August 22 had similar intensity and duration on all three rain gauges. The storm on August 28 had similar intensity on two of the rain gauges in basins 7 and 24, but much lower intensity in basin 32, in the upper elevations of the Medano Creek Watershed.

The total rainfall amounts recorded during the largest storm events in the watershed, on August 22 and 28, were both 26.0 mm in basin 24, which recorded greater rainfall amounts than the other rain gauges in both events. The storm of August 22 had a total duration of 159 minutes, while that of the August 28 storm was 74 minutes. The maximum 1-hour rainfall intensity within the August 28 storm was 25.6 mm/hr, roughly equal to the magnitude of the 5-year return interval, 1-hour storm for the area (Miller et al., 1973). Debris-flow responses in the vicinity of the basin 24 rain gauge included events in two basins during the August 22 storm and in four basins during the August 28 storm. Average rainfall intensity was greater during the August 28 storm than the August 22 storm, as were peak 1-hr, 30-min, 15-min, 10-min, and instantaneous rainfall intensities (Table 1). The 1-hr peak rainfall intensity values for these two storms are between the magnitude of the 2- and 5-year return intervals for the area, while the 30-, 15-, and 10-min peak intensities for the storms are all approximately equal to or less than the 2-year return interval (Miller et al., 1973; Arkell and Richards, 1986).

Table 1. Total storm duration and rainfall intensity measures for August 22 and 28 storms, recorded in basin 24.

Storm Date	Duration (minutes)	Average Storm Intensity (mm/hr)	Peak Hourly Intensity (mm/hr)	Peak 30-min Intensity (mm/hr)	Peak 15-min Intensity (mm/hr)	Peak 10-min Intensity (mm/hr)	Peak Instantaneous Intensity (mm/hr)
8/22/12	159	9.8	20.2	28.8	36.0	39.6	72.0
8/28/12	76	20.5	25.6	41.6	46.4	62.4	144.0

Storm intensity-duration plots in Figure 2 suggest that short duration (10-minute to 1-hour) peak rainfall intensity values distinguish between storms with positive and negative debris-flow responses. Figure 2 shows significant overlap in average intensity values of storms that trigger debris flows and those that do not, while there is no overlap in the peak rainfall intensity values for any of the short period (10-minute to 1-hour) of measurement evaluated. Tests for equality of variances and means between sample sets of storms with positive and negative debris-flow response for logarithmic transformations of all measures of intensity indicated that average storm intensity is the only measure for which the two data sets are equal at $\alpha = 0.05$. The lower right graph in Figure 2 shows the relationship between peak 10-minute rainfall intensity and average storm intensity. It is apparent from this plot that less than half of the storms above a minimum threshold value of average storm intensity (8.9 mm/hr) triggered debris flows, whereas all of the storms above a minimum threshold value of peak 10-minute rainfall intensity (25.2 mm/hr) triggered debris flows. The differences in values of peak instantaneous rainfall intensity (defined as the amount of rainfall per bucket tip divided by the time between bucket tips) between storms with positive and negative debris-flow responses is much larger than that of any other intensity measure (Table 2). The magnitude of peak instantaneous rainfall intensity for storms that triggered debris flows ranged between approximately 72.0 mm/hr to 144.0 mm/hr, while the maximum instantaneous intensity of storms that did not trigger debris flows was approximately 40.0 mm/hr.

Table 2. Various rainfall intensity measures for storms that define the threshold for debris-flow initiation.

	Average Storm Intensity (mm/hr)	Peak Hourly Intensity (mm/hr)	Peak 30-min Intensity (mm/hr)	Peak 15-min Intensity (mm/hr)	Peak 10-min Intensity (mm/hr)	Peak Instantaneous Intensity (mm/hr)
Minimum of Debris Flow Storms	9.1	16.8	20.4	26.4	31.2	72.0
Maximum of No Debris Flow Storms	16.5	9.2	15.6	20.8	25.2	40.0
Difference	-7.4	7.6	4.8	5.6	6.0	32.0

Based on the data collected for this study, we propose that short-duration peaks of intense rainfall within a storm event are responsible for triggering debris flows in this setting. While average rainfall intensity over the full duration of storm events has been correlated to debris flow initiation in past studies, we suggest that the average rainfall intensity

for an entire storm does not accurately represent the critical threshold intensity for debris-flow initiation by runoff. Within a given debris flow triggering storm, substantial rainfall may occur after the debris flow initiates, which is figured into the average rainfall intensity of the event though it may not have contributed to debris-flow initiation. Recent work by Staley et al. (2017) also found that short duration (15-minute) peak intensity correlated strongly with debris flow occurrence.

A rainfall intensity-duration threshold for Medano Creek Watershed in the first year following the Medano Fire is presented in Figure 4. Each storm event recorded is represented by data points for peak intensities of different durations within the storm. The Medano Fire threshold is similar to other published thresholds from Colorado burned and unburned areas (Cannon et al., 2008) at short durations (approximately 5 to 20 minutes).

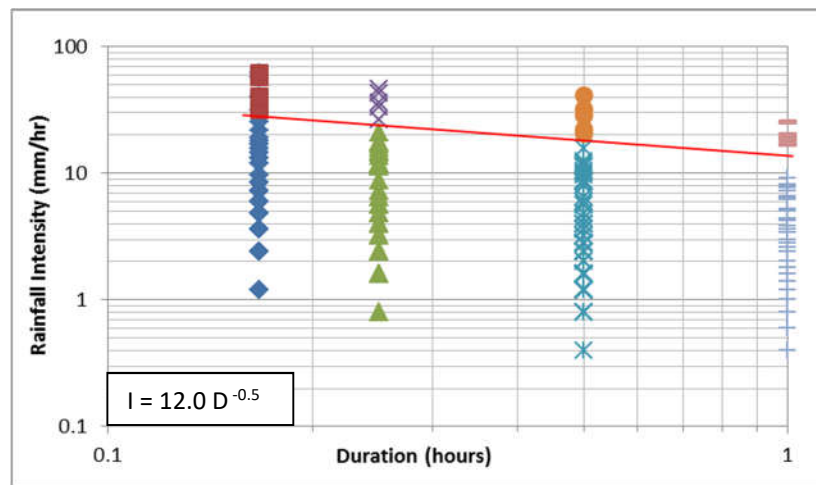


Fig. 4. Rainfall intensity-duration threshold for debris-flow initiation at the Medano Fire (red line) drawn between intensity values of storm events that triggered debris flows (above) and those that did not (below), calculated for various durations of rainfall within the storms.

4.2. Timing of rainfall and debris flows

Comparison of rainfall hydrographs with plots of pressure transducer recordings (Figure 3) from flow events during the August 22 storm, in basins 24 and 32, shows the relative timing of rainfall to flows for these basins. In basin 24, the storm began at approximately 4:16 pm, and the peak 10-minute intensity (39.6 mm/hr) period of the storm began at approximately 4:59 pm. Rainfall intensity peaked at approximately 5:05 pm, with an instantaneous value of 72.0 mm/hr. A flow arrival was recorded near the bottom of the basin at approximately 5:10 pm, approximately 5 minutes after the peak instantaneous rainfall intensity. The flow was recorded near the end of the peak 10-minute rainfall intensity period of the storm, after 17.8 mm of total rainfall over the previous 54 minutes (19.8 mm/hr), of which 6.6 mm had fallen during the 10 minutes prior to the arrival of the flow (39.6 mm/hr).

In basin 16, rainfall began at approximately 4:12 pm on August 22 and the peak 10-minute intensity (40.8 mm/hr) period coincided with the start of the storm. Rainfall intensity peaked at approximately 4:15 pm, at an instantaneous value of 144.0 mm/hr. At approximately 4:18 pm, only 3 minutes after the peak instantaneous rainfall, a small flow arrival was recorded on the pressure transducer near the outlet of basin 32. The flow was initiated during the peak 10-minute intensity period, after a total of approximately 5.2 mm of rainfall over the first 5 minutes of the storm (62.4 mm/hr). The antecedent rainfall prior to the event was minimal (approximately 0.8 mm in the previous week) and a flow was recorded within 6 minutes after the start of the storm, suggesting that the flow occurred in direct response to this short period of high intensity rainfall. A smaller flow was recorded in basin 32 later in the storm, at approximately 4:55 pm. This flow was recorded approximately 43 minutes into the storm, after a total of approximately 15 mm of rainfall (20.9 mm/hr), immediately following another peak in rainfall intensity during which approximately 3.0 mm of rain fell in within a 5-minute period (37.9 mm/hr).

These examples support the concept that short periods (as little as 5 minutes) of high intensity rainfall are responsible for debris-flow initiation in severely burned areas, which agrees with findings of Kean et al. (2011), who found that the peak 5-minute intensity was the rainfall intensity measurement best cross-correlated temporally with peak flow stage in post wildfire floods and debris flows.

5. Conclusions

- Hyper-concentrated flows and debris flows occurred in 7 tributary basins of Medano Creek Watershed (7, 12, 15, 23, 24, 25, and 32) in response to multiple storm events throughout July and August of 2011.
- Tipping bucket rain gauges and unvented pressure transducers were found to be a useful way to monitor rainfall and associated hydrologic response in basins within the burned area of Medano Creek Watershed.
- Peak rainfall intensity values for periods of 10, 15, 30, and 60 minutes during storm events distinguish between populations of positive and negative debris-flow responses, whereas average storm intensity values do not.
- Recorded flow initiations occurred within periods of peak 10-minute rainfall intensity, and correlate temporally with peak 5-minute and instantaneous rainfall intensity values, occurring less than 6 minutes after onset of peaks.
- An intensity-duration threshold for debris-flow initiation in the Medano Fire burned area during 2011 was defined as $I = 12.0D^{-0.5}$, which is within the range of other published values for burned areas in the western U.S.

Acknowledgments

This study was supported by the National Science Foundation under Grant No. EAR-1118056 and by the United States Geological Survey (USGS). The authors are grateful for assistance from Andrew Valdez and Fred Bunch of the Great Sand Dunes National Park and Preserve; support and guidance from Sue Cannon, Joe Gartner, and Jason Kean of the USGS Hazards Science Center; and fieldwork contributions by Bob Kirkham and Dan Pratt.

References

- Arkell, R.E., Richards, F., 1986, Short duration rainfall relations for the Western United States: Preprint Volume of the Conference on Climate and Water Management: American Meteorological Society, p. 136-141.
- Arratano, M., Marchi, L., 2008, Systems and sensors for debris-flow monitoring and warning: *Sensors*, v. 8, p. 2436-2452.
- Cannon, S.H., 2001, Debris flow generation from recently burned watersheds: *Environmental and Engineering Geoscience*, v. 7, no. 4, p. 321-341.
- Cannon, S.H., Gartner, J.E., Parrett, C., Parise, M., 2003, Wildfire-related debris-flow generation through episodic progressive sediment bulking processes, western USA, in Rickenmann, D., Chen, C.L., eds., *Debris-Flow Hazards Mitigation: Mechanics, Prediction, and Assessment*: Rotterdam, Millpress, p. 71-82.
- Cannon, S.H., Gartner, J.E., 2005, Wildfire-related debris flow from a hazards perspective, in Hungr, O., Jacob, M., eds., *Debris-Flow Hazards and Related Phenomena*: Chichester, Springer-Praxis Books in Geophysical Sciences, p. 321-344.
- Cannon, S.H., Gartner, J.E., Wilson, R.C., Bowers, J.C., Laber, J.L., 2008, Storm rainfall conditions for floods and debris flows from recently burned areas in southwestern Colorado and southern California: *Geomorphology* v. 96, p. 250-269, doi 10.1016/j.geomorph.2007.03.019.
- Cipra, J.E., Kelly, E.F., MacDonald, L., Norman, J., 2003, Part 3: Soil Properties, Erosion, and Implications for Rehabilitation and Aquatic Ecosystems: USDA Forest Service Gen. Tech. Rep. RMRS-GTR-114, p. 204-219.
- Friedman, E.Q., Santi, P.M., 2014, Debris-Flow hazard assessment and validation following the Medano Fire, Great Sand Dunes National Park and Preserve, Colorado: *Landslides*, v. 11, p.1093-1113, doi 10.1007/s10346-013-0462-9.
- Itakura, Y., Inaba, H., Sawada, T., 2005, A debris-flow monitoring devices and methods bibliography: *Natural Hazards and Earth System Sciences*, v. 5, p. 971-977.
- Johnson, B.R., Bruce, R.M., Lindsey, D.A., 1989, Geologic map of the Medano Pass Quadrangle and part of the Liberty Quadrangle, Alamosa, Huerfano, and Saguache Counties, Colorado: U.S. Geological Survey Miscellaneous Field Studies Map MF-2089, scale 1:24000.
- Kean, J.W., Staley, D.M., Cannon, S.H., 2011, In-situ measurements of post-fire debris flows in southern California: Comparisons of the timing and magnitude of 24 debris-flow events with rainfall and soil moisture conditions: *J. Geophys. Res.*, v. 116.
- Kean, J.W., Staley, D.M., Leeper, R.J., Schmidt, K.M., Gartner, J.E., 2012, A low cost method to measure the timing of post-fire flash floods and debris flows relative to rainfall, *Water Resources Research*, v. 48.
- McCoy, S.W., Coe, J.A., Kean, J.W., Tucker, G.E., Staley, D.M., Wasklewicz, T.A., 2011, Observations of debris flows at Chalk Cliffs, Colorado, USA: Part 1, in-situ measurements of flow dynamics, tracer particle movement and video imagery from the summer of 2009: *Italian Journal of Engineering Geology and Environment*, v. 1, p. 65-75, doi 10.4408/IJEGE.2011-03.B-078.
- Miller, J.F., Frederick, R.H., Tracy, R.J., 1973, *Precipitation-Frequency Atlas of the Western United States*, NOAA Atlas 2, Volume III-Colorado: National Weather Service.
- Moody, J.A., Martin, D.A., 2001, Initial hydrologic and geomorphic response following a wildfire in the Colorado Front Range: *Earth Surface Processes and Landforms*, v. 26, p. 1049-1070, doi 10.1002/esp.253.
- Parise, M., Cannon, S.H., 2011, Wildfire impacts on the processes that generate debris flows in burned watersheds: *Nat. Hazards*, doi 10.1007/s11069-011-9769-9.
- Santi, P.M., deWolfe, V.G., Higgins, J.D., Cannon, S.H., Gartner, J.E., 2008, Sources of debris flow material in burned areas: *Geomorphology* v. 96, p. 310-321, doi 10.1016/j.geomorph.2007.02.022.
- Schumm, S.A., 1973, Geomorphic thresholds and the complex response of drainage systems, in Morisawa, M., ed., *Fluvial Geomorphology*: Binghamton, State University of New York, p. 299-310.
- Staley, D.M., Negri, J.A., Kean, J.W., Laber, J.L., Tillery, A.C., Youberg, A.M., 2017, Prediction of spatially explicit rainfall intensity-duration thresholds for post-fire debris-flow generation in the western United States. *Geomorphology*, 278, 149-162. <http://dx.doi.org/10.1016/j.geomorph.2016.10.019>.

Effects of terrain on temporal changes in susceptibility of debris flows and associated hydrogeomorphic processes after forest harvesting

Fumitoshi Imaizumi^a

^a*Faculty of Agriculture, Shizuoka University, 836 Ohya, Suruga, Shizuoka 422-8529, Japan*

Abstract

Forest harvesting is one of the most common and significant land cover changes and largely affects hydrogeomorphic processes in mountainous areas. Many studies have reported the direct impacts of forest harvesting on the susceptibility of slopes to landslides and surface erosion. However, ambiguity still remains in the impacts of forest harvesting on the occurrence of debris flows in channel. The impact of forest harvesting on the susceptibility of torrents to debris flows and associated hydrogeomorphic processes was interpreted in the Sanko catchment, central Japan, where the forest management record dates back to 1912. In order to clarify the contribution of landslides on the initiation of debris flows, landslides were classified into three types based on the termination point of the landslide sediment. Effects of terrain on the susceptibility of debris flows coming directly from landslides and those caused by mass movement of channel deposits were analyzed separately using aerial photographs taken in nine different years. Impact of forest harvesting on debris-flow occurrence was greatest in forest stands that were clearcut 1 to 10 yr earlier, with progressively lesser impacts continuing up to 25 yr after harvesting. The frequency of debris flows, which came directly from landslides, showed a similar time variation to that of landslides. A higher ratio of landslides turned directly into debris flows in steeper channel sections than in gentler channel sections. Angle of the landslide-channel junction also affected the ratio of landslides turning into debris flows. Debris flows caused by mass movement of channel deposits during high streamflow events also frequently occurred within 25 yr of clearcutting, possibly associated with active sediment supply from hillslopes by the landslide. Debris flows classified into this type were mostly initiated in channel sections steeper than 20°. Therefore, the effect of forest harvesting on debris flow susceptibility is variable depending on catchment terrain. Field monitoring showed that volume and spatial distribution of channel deposits, which affects bedload rate, depends on debris flow history in the catchment. Suspended sediment rate was also affected by debris flow and landslide history, because debris flows create sources of suspended sediment, such as bare areas along channel banks. Therefore, the impacts of debris flows on hydrogeomorphic processes after forest harvesting likely continue beyond the decline in debris flow and landslide frequency, due to changes to the sediment storage and sediment source by the occurrence of debris flows.

Keywords: Forest harvesting; Debris flow; Landslide

1. Introduction

The occurrence of debris flows, which cause severe sediment disasters all over the world, is controlled by sediment and water supply from hillslopes into channels (Bovis and Jakob, 1999; Imaizumi et al., 2017). Forest harvesting is one of the most common and significant land cover changes and largely affects hydrogeomorphic processes on mountain hillslopes (Ueno et al., 2015; Borrelli et al., 2017). Although many studies have reported the direct impacts of forest harvesting on the susceptibility of slopes to landslides and surface erosion (Imaizumi et al., 2008; Goetz et al., 2015), ambiguity still remains in the impacts of forest harvesting on the occurrence of debris flows (May, 2002; Jakob et al., 2005). Increases in the landslide frequency on hillslopes affects debris flows originating directly from landslides (Imaizumi et al., 2007). Additionally, changes in the sediment and water supply caused by forest harvesting

* Corresponding author e-mail address: imaizumi@shizuoka.ac.jp

possibly alters the frequency of debris flows triggered by streamflow erosion of channel deposits. Understanding of the susceptibility of debris flows triggered by each mechanism after forest harvesting is important in reducing the risk of sediment disasters by the forest management.

The predominant type of sediment transport process is highly affected by channel gradient. Debris flows are predominant in steep channel sections (e.g., >15 degrees), while bedload transport is predominant in gentler channel sections (VanDine, 1985; Imaizumi et al., 2007). Thus, increases in the sediment supply rate into channel networks does not simply increase debris-flow frequency in gentler channels. Impacts of forest harvesting on the occurrence of debris flows need to be evaluated under the consideration of catchment topography.

Occurrence of debris flows does not only directly alter channel topography (e.g., Imaizumi et al., 2017), it also creates possible sediment sources for fluvial processes by erosion of channel banks and deposition of unstable sediment within the channel (Imaizumi et al., 2012). Therefore, the impact of a debris flow on hydrogeomorphic processes after forest harvesting possibly continue beyond the decline in debris flow and landslide frequency.

The aim of this study is to clarify the effects of forest harvesting on the susceptibility of debris flows and associated hydrogeomorphic processes. Occurrence of debris flows and landslides were interpreted using aerial photographs for the Sanko catchment, central Japan, where forest harvesting and replanting have been conducted for over 100 years (Imaizumi et al., 2008; 2012). Effects of harvesting on the occurrence of debris flows were evaluated by analyses of the forest management history and the topography using GIS. Field surveys were also conducted to reveal the volume of sediment storage (i.e., channel deposits and landslide sediment in this study) in the basin and sediment transport activity by fluvial processes including bedload and suspended sediment transport.

2. Study Site

The Sanko catchment is an 8.50 km² basin which forms the headwaters of the Kanno River, a tributary of the Kumano River, central Japan (Fig. 1). The area is underlain by the Cretaceous Shimanto belt comprised of sandstone and claystone. Sandstone dominates surface geology and is relatively homogeneous throughout the catchment. Elevation of the catchment ranges from 750 to 1372 m a.s.l. Despite the east of the catchment being slightly steeper than other portions, hillslope gradient is relatively homogeneous throughout the catchment with a mean of 34°. Channel gradients are 1.5–5° in the main stream (Kanno River), and 5–35° in the tributaries. All channels in the subcatchments are deeply incised with narrow riparian areas (ranging from 5 to 10 m wide). Soil depth is shallow (typically ranging from 0.5 to 1.0 m) because of the steep terrain.

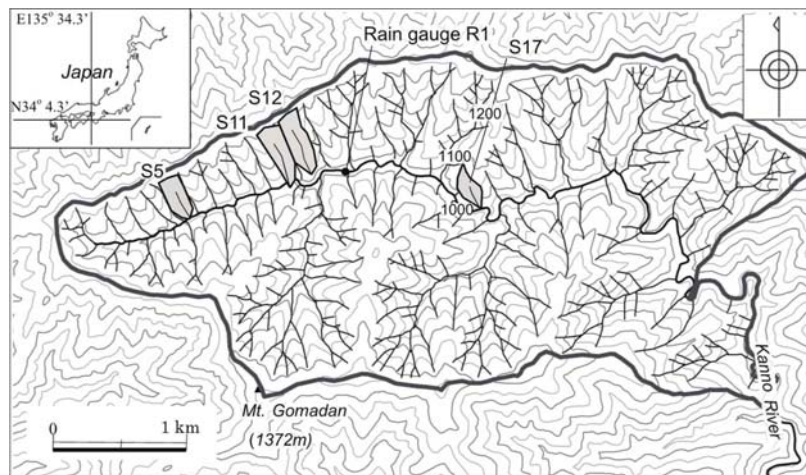


Fig. 1. Topographic map and stream network for the Sanko Catchment, Japan, with the location of the four surveyed sub-catchments shaded and labelled.

Mean annual rainfall measured at Kyoto University's Wakayama Forest Research Station located about 3 km west of Sanko catchment is 2500 mm (Imaizumi, 2008). Heavy rainfall events (i.e., total storm rainfall > 100 mm) occur during the Baiu rainfall front (June and July) and in the typhoon season (from late August to early October). Snowfall

occurs at higher elevations within the catchment, but precipitation in winter (from December to February) is only about 10% of total annual precipitation. Annual maximum snow depth is generally <20 cm, and snow usually melts within one week.

About 95% of the Sanko catchment has been converted to industrial managed forest (largely Japanese cedar with minor amounts of Japanese cypress); the remainder is secondary broadleaf forests, forest roads, and log landings where debris flows and landslides were not interpreted in this study because of their different geographic positions. Clearcutting has been the only harvesting method used in the catchment, and replanting typically occurs one or two years after logging. In the Sanko catchment, forest records (harvesting and replanting) are available from 1912. Because timber harvesting is typically confined to within individual subcatchments, both the clearcutting and replanting periods are almost the same throughout each subcatchment (Imaizumi et al., 2008). Thus, changes in the frequency of debris flows related to forest age (and elapsed time after clearcutting and replanting) can be analyzed in the Sanko catchment. Since only skyline logging, which transports harvested logs by suspending them using a thick metal cable, was conducted, we expect that timber removal practices did not affect the occurrence of landslides.

We monitored bedload and suspended sediment transport in four selected subcatchments (S5, S11, S12, and S17; Fig. 1) with different histories of forest harvesting and mass movements (Table 1) (Imaizumi et al., 2012). Drainage area of these subcatchments ranges from 3.2 to 7.1 ha. Mean channel gradient was similar amongst the four headwater channels (ranging from 24° to 29°). Several landslides were identified based on aerial photo observations and field surveys in each subcatchment. Catchments S5 and S12 experienced the most recent debris flows during a typhoon on June 21, 2004 (total precipitation 171 mm at the Gomadan observation station located at the south end of the Sanko catchment).

Table 1. Topography, histories of mass movements, and sediment source in the four surveyed subcatchments (partly from Imaizumi et al. 2012).

Subcatchment	Drainage area (ha)	Year of last planting	Year of last debris flow	Number of landslides	Volume of sediment storage in the system (m ³)	Bare area along channel (m ²)
S5	3.97	1973	2004	2	13	768
S11	6.52	1970	1989	9	254	141
S12	7.13	1988	2004	4	185	47
S17	3.15	1915	Before 1964	2	28	6

3. Methodology

Monochrome aerial photographs for nine different years (1964, 1965, 1967, 1971, 1984, 1989, 1994, 1998, and 2003) and color aerial photographs for 1976 were used to assess the location of mass movements (i.e., debris flows, landslides) in the Sanko catchment. Mass movements were identified by stereo photograph pairs and mapped on 1:5000 forest management maps. Most of the aerial photographs were taken in March (before the Baiu season), thus almost all of the mass movements (i.e., landslides and debris flows) identified by aerial-photo stereographs likely occurred prior to December of the previous year. Newly occurred mass movements were identified by comparing successive aerial photographs. All mass movements on hillslopes, mainly characterized as shallow translational landslides, were designated as landslides and all in-channel mass movements were designated as debris flows. Landslides initiating from forest roads were excluded from assessment in this study in order to clarify the impact of clearcutting and subsequent forest regeneration on landslide occurrence. Channel reaches affected by debris flows were interpreted based on continuous loss of artificial trees along channels, because artificial trees are not planted in the riparian areas and are not by damaged by runoff events without debris flow. Landslides were classified into 3 groups based on the descent of the landslide sediment: landslides terminating on hillslopes (Type A, Fig. 2a), landslides whose sediment immediately stops at the junction with a channel (Type B, Fig. 2b), and landslides which turned into debris flows (Type C, Fig. 2c). In addition to debris flows originating directly from landslides without termination of the sediment, debris flows triggered by erosion of landslide sediment, which was deposited during previous rainfall events, are included in Type C if the landslide and the debris flow occurred in the same photograph period. These two types of debris flows were grouped in this study because of the difficulty in classification of the two types based on aerial photographs. Average channel gradient within 20 m below the landslide-channel junction of Types B and C landslides were calculated from a 5 m resolution DEM, which was constructed from airborne LiDAR data by

Geospatial Information Authority, Japan. The angle between landslide and channel at the junction of Types B and C landslides were also measured on GIS (θ in Fig 2b).

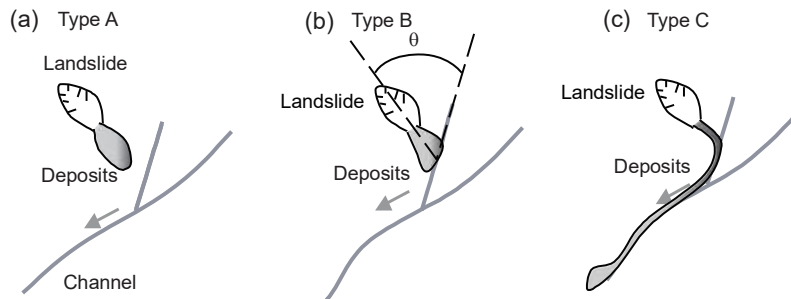


Fig. 2. Classification of landslides based on the descent of landslide sediment. Concept of the channel junction angle is illustrated as θ in (b).

Volumes of 11 landslide scars, including their initiation and transport zones, were measured in the field to develop an approximate volume–area relationship for landslides within the catchment (Imaizumi et al., 2008). This relationship was used to estimate the volume of all landslides from landslide area measured in GIS. Volume of landslide sediment reaching channels was estimated from the total volume of Type B and C landslides multiplied by the ratio of total landslide sediment that reached channels. The ratio of sediment reaching channels was obtained in the Miyagawa river basin, central Japan, which has similar topographic, geological, and climate conditions to the Sanko catchment (Imaizumi and Sidle, 2007).

In the four selected subcatchments (S5, S11, S12, S17), we observed bedload transport rate in the period June 25 to September 26, 2005, by weighing sediment stored behind a weir at the lowermost part of each subcatchment (Imaizumi et al., 2012). We interpreted volume of detached sediment (hereafter sediment storage) stored across the four subcatchments. Length and width of individual sediment deposits (i.e., channel deposits and landslide sediment) were measured by tapes and stadia rods (Imaizumi and Sidle, 2012) in all four subcatchments. We also measured depth of deposits at many points (usually about ten points per individual deposit) by inserting a sharp metal rod to bedrock. Volume of individual deposits was obtained from the area of deposits multiplied by its average depth. Total volume of sediment deposits in each subcatchment was obtained from the total volume of all sediment deposits in the catchment. Interpretation of the sediment storage volume was conducted only at the beginning of the monitoring period under the assumption that the temporal changes in the storage volume are negligible, because volume of sediment loss by bedload transport was several orders lower than that in the storage volume (see next chapter). Size of the bare area, which is the area with exposed soil due to the removal of vegetation by recent debris flows, was also measured along the channels.

4. Results

4.1. Debris-flow frequency after forest harvesting

A total of 133 debris flows originated in the period 1964 to 2002, including 74 debris flows that were directly initiated by landslides and 59 debris flows that were caused by mobilization of channel deposits or bank failures. Frequency of debris flows initiated by landslides was greatest 1-5 yr after clearcutting and decreased with increasing forest age. The impact of forest harvesting continued up to 25 yr after forest harvesting. The frequency of landslides showed a similar time variation to those of debris flows originating directly from landslides. Temporal changes in the frequency of debris flows caused by the mass movement of channel deposits showed a similar trend to those initiated by landslides.

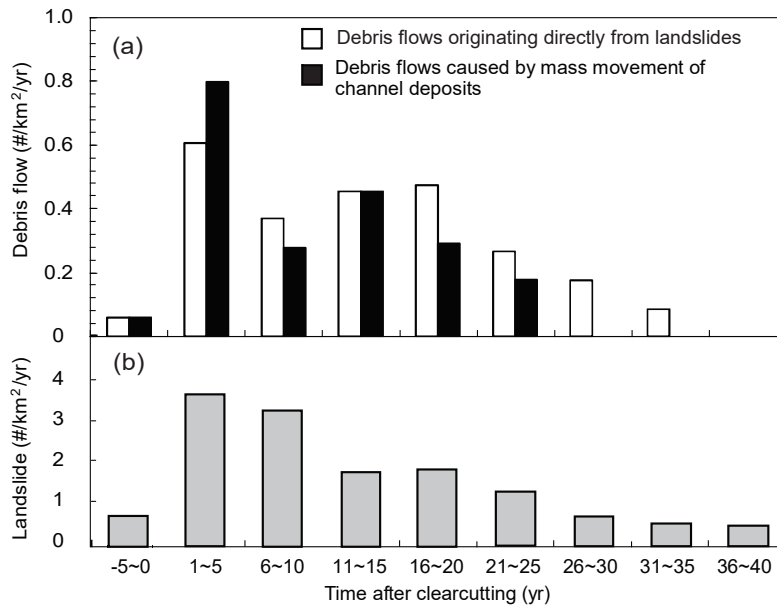


Fig. 3. Temporal changes in debris-flow and landslide frequency after clearcutting (modified from Imaizumi et al., 2008). (a) Debris-flow frequency. (b) Landslide frequency.

4.2. Debris flows originating directly from landslides

Debris flows rarely occur from deposits of type A landslides because the amount of overland flow on hillslope (maximum of several millimeters) is likely not sufficient for the mobilization of deposits. In addition, not all of the landslides that reached channel networks turned into debris flows (Fig. 3). Ratio of landslides that turned into debris flows, which was obtained by the number of Type C landslides divided by the total number of Type B and C landslides (Fig. 2), was higher in steeper channels (Fig. 4). Only 25% of landslides turned into debris flows in the channel sections gentler than 20°, while 86% of landslides turned into debris flows in the channel sections steeper than 35°. Another important factor affecting the occurrence of debris flows originating directly from landslides is channel-junction angle of the landslide (Fig. 2b). A higher ratio of landslides turned into debris flows in the case of smaller channel-junction angles (Table 2). No landslides turned into debris flows in the case of channel-junctions > 90°.

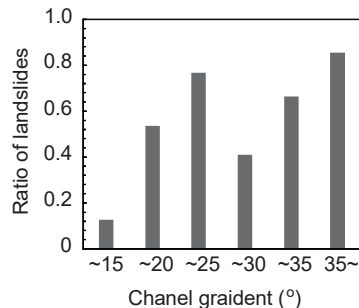


Fig. 4. Ratio of landslides that turned into debris flows in each channel gradient class.

Table 2. Effect of channel junction angle on ratio of landslides that turned into debris flows.

Channel junction angle (°)	Number of debris flows	Ratio of landslides that turned into debris flows
0~45	100	0.68
45~90	45	0.13
90~	8	0

4.3. Debris flows caused by mass movement of channel deposits

Landslides on the hillslope do not only directly turn into debris flows, but also supply large volumes of sediment into channel networks. Volume of landslide sediment reaching channels, which is considered an important material for debris flows caused by the mass movement of deposits within the channel, was largest just after harvesting, with progressively lesser volume continuing up to 30 yr after harvesting (Fig. 5). Channel gradient is also an important factor controlling initiation points of debris flows caused by mass movement of channel deposits. Initiation points of fifty debris flows (91% in number) was in channel sections steeper than 20°, while only five debris flows initiated in channel sections gentler than 20°.

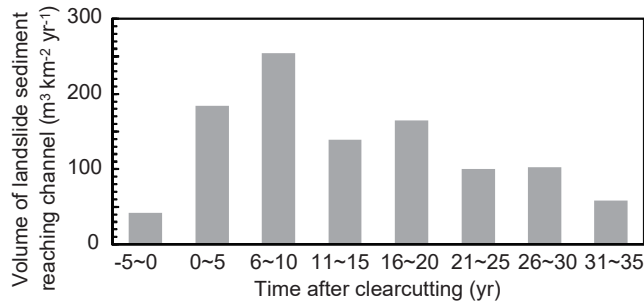


Fig. 5. Temporal changes in the volume of landslide sediment reaching channel after forest harvesting.

4.4. Impact of debris flows on fluvial processes in harvested areas

Initiation of debris flows and landslides largely changes the volume of sediment storage, which is a potential source of future fluvial sediment transport, in the basin. Volume of sediment storage in catchment S5, in which a large part of the sediment storage had been discharged from the system by a debris flow in 2004, was lowest among the four surveyed subcatchments (Table 1). On the contrary, volume of sediment storage in S12 was much higher, despite a debris flow also occurring in the catchment at the same time as in S5. This is because the debris flow in S12 left a large volume of sediment within the system. Volume of sediment storage in catchment S11, within which nine landslides were identified, was highest among the four subcatchments.

Debris flows also form bare areas, which are potential sources of suspended sediment, along channels. The size of the bare area in S5, in which a debris flow in 2004 severely eroded the channel bank, was the largest among the four subcatchments.

Weight of bedload had a positive relationship with the volume of sediment storage in the subcatchments (Fig. 6). Weight of bedload was high (>3000 kg) in the subcatchments with a large volume of sediment storage (S11 and S12), and was significantly lower (<300 kg) in the subcatchments with a small volume of sediment storage (S5 and S17). Suspended sediment rate also varied among subcatchments (Imaizumi et al., 2012). Suspended sediment rate was highest in S5, in which wide bare areas were formed by debris flow erosion.

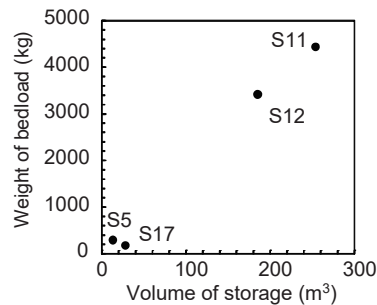


Fig. 6. Comparison of volume of sediment storage (i.e., channel deposits and landslide sediment) in the system and weight of bedload trapped by weirs.

5. Discussion

Temporal changes in the frequency of debris flows showed a similar time variation to that of landslides (Fig. 3), implying that frequency of landslides affects that of debris flows in the harvested area. Previous experimental and field-based studies showed that increases in landslide frequency after forest harvesting is highly affected by decreases in the root strength of harvested trees (Sidle, 1992; Imaizumi et al., 2008). Debris flows originating from landslides increased as the number of landslides reaching channels increased (Fig. 3a). In addition to increases in the number of debris flows originating directly from the landslide without termination of the sediment, increases in the number of debris flows triggered by erosion of in-channel landslide sediment, which was deposited during previous rainfall events, possibly affected increases in this debris-flow type. Ratio of landslides that turned into debris flows was small in gentle channel sections ($< 15^\circ$; Fig. 4). This agrees with previous studies that debris-flow initiation zones are generally located in steep channel sections (VanDine, 1985; Imaizumi et al., 2017). Another factor affecting initiation of the debris flow originating directly from a landslide is the angle at landslide-channel junction; ratio of landslides directly turning into debris flows is smaller if the angle is larger (Table 2). Benda (1990) also reported that many debris flows terminate at channel junctions with a large angle.

Water and sediment supply are needed for the occurrence of debris flows caused by the mass movement of channel deposits (Imaizumi et al., 2017). Many mountainous basins are characterized as supply limited (weathering limited) basins, in which the occurrence of debris flows is controlled by the volume of debris-flow material in the system (Bovis and Jakob, 1999). Increases in the volume of sediment supply into channel networks by high landslide activity in the forest just after harvesting likely facilitated the occurrence of debris flows in such supply limited channels (Fig. 5). Another potential factor affecting the debris flows caused by the mass movement of channel deposits is changes in the rainfall-runoff process on hillslopes, which controls water discharge in channels. However, difference in the rainfall-runoff characteristics was not clear among basins with different forest ages in the Sanko catchment (Imaizumi et al., 2012).

Occurrence of debris flows, facilitated by forest harvesting, affects fluvial processes in the channel (Imaizumi et al., 2012). Volume of sediment storage, which is largely variable by deposition and erosion of sediments by debris flows, affected bedload transport rate in the basin (Fig. 6), while size of bare areas formed by debris-flow erosion affects suspended sediment rate (Table 2). Therefore, the impact of debris flows on fluvial processes in the harvested areas likely continues for a longer period after decreases in the debris-flow activities.

6. Summary and Conclusion

In order to clarify the impact of forest harvesting on debris flow and related hydrogeomorphic processes, aerial photograph interpretations and field surveys were conducted in the Sanko catchment, central Japan, where forest harvesting records are available from 1912. Our study showed that temporal changes in the debris flow frequency after forest harvesting is closely related to the occurrence of landslides accelerated by root decay following forest harvesting. Frequency of debris flows originating directly from landslides increases just after forest harvesting. Frequency of debris flows caused by the mass movement of channel deposits was increased following increases in the sediment supply from hillslopes into channel networks by landslides. Thus, the impact of harvesting on the occurrence of landslides is essential to explain the impact of harvesting on the occurrence of debris flows. Ratio of landslides directly turning into debris flows is affected by the channel gradient and junction angle with channels. Initiation of this type of debris flow is also affected by channel gradient. Consequently, the impact of forest harvesting on the occurrence of debris flows is highly affected by the terrain in the basin. The junction angle between hillslope and channel in headwaters is usually smaller than that in lower channel reaches. In addition, channel gradient is steeper in headwaters. Therefore, forest harvesting in headwaters should be conducted carefully in order to prevent sediment disasters following harvesting.

Field monitoring showed that the volume of channel deposits, which affects bedload rate, depends on debris flow and landslide histories in the catchment. Suspended sediment rate was also affected by debris flow history, because debris flows create sources of suspended sediment, such as bare areas along channel banks. Therefore, the impacts of debris flows on hydrogeomorphic processes after forest harvesting likely continue beyond the decline in landslide and debris flow frequency, due to changes to the sediment storage and sediment source by the occurrence of debris flows.

Acknowledgements

This study was supported by JSPS Grant Numbers 18H02235, 18K18917, and 17H02029. Professors Naoko Tokuchi, Nobuto Ohte, and Keitaro Fukushima kindly provided us with data on forest harvesting in the Sanko catchment. We appreciate Sanko Forestry, the owner of Sanko catchment, for allowing us access to the site and permission to conduct field surveys. Staff in Wakayama Forest Research Station kindly supported our study in the remote mountain area. Gratitude is also expressed to previous members of the Slope Conservation Section at the Disaster Prevention Research Institute, Kyoto University (Roy C. Sidle, Toshitaka Kamai, Takashi Gomi, Sohei Kobayashi, Rieko Kamei, and the other colleagues and students) for helping with this study.

References

- Benda, L. E. and Cundy T. W., 1990, Predicting deposition of debris flows in mountain channels: *Canadian Geotechnical Journal*, v. 27, p. 409-417.
- Bovis, M. J., and Jakob, M., 1999, The roll of debris supply conditions in predicting debris flow activity: *Earth Surface Processes and Landforms*, v. 24, p. 1039–1054. [https://doi.org/10.1002/\(SICI\)1096-9837\(199910\)24:11<1039::AID-ESP29>3.0.CO;2-U](https://doi.org/10.1002/(SICI)1096-9837(199910)24:11<1039::AID-ESP29>3.0.CO;2-U)
- Borrelli, P., Panagos, P., Märker, M., Modugno, S., and Schütt, B., 2017, Assessment of the impacts of clear-cutting on soil loss by water erosion in Italian forests: First comprehensive monitoring and modelling approach: *Catena*, v. 149, p. 770–781, <https://doi.org/10.1016/j.catena.2016.02.017>.
- Goetz, N., Guthrie, R. H., and Brenning, A., 2015, Forest harvesting is associated with increased landslide activity during an extreme rainstorm on Vancouver Island, Canada: *Natural Hazards and Earth System Sciences*, v. 15, p. 1311–1330, doi:10.5194/nhess-15-1311-2015.
- Imaizumi, F., and Sidle, R. C., 2007, Linkage of sediment supply and transport processes in Miyagawa Dam catchment, Japan: *Journal of Geophysical Research: Earth Surface*: v. 112, F3, <https://doi.org/10.1029/2006JF000495>.
- Imaizumi, F., and Sidle, R. C., 2012, Effect of forest harvesting on hydrogeomorphic processes in steep terrain of central Japan: *Geomorphology*, v. 169, p. 109-122.
- Imaizumi, F., Sidle, R.C., and Kamei, R., 2008, Effects of forest harvesting on the occurrence of landslides and debris flows in steep terrain of central Japan: *Earth Surface Processes and Landforms*, v. 33, p. 827-840.
- Imaizumi, F., Sidle, R. C., Tsuchiya, S., and Ohsaka, O., 2006, Hydrogeomorphic processes in a steep debris flow initiation zone: *Geophysical Research Letters*, v. 33, L10404, <https://doi.org/10.1029/2006GL026250>.
- Imaizumi, F., Hayakawa, Y. S., Hotta, N., Tsunetaka, H., Ohsaka, O., and Tsuchiya, S., 2017, Relationship between the accumulation of sediment storage and debris-flow characteristics in a debris-flow initiation zone, Ohya landslide body, Japan: *Natural Hazards and Earth System Sciences*, v. 17, p. 1923–1938. <https://doi.org/10.5194/nhess-17-1923-2017>
- Jakob, M., Bovis, M., and Oden, M., 2005. The significance of channel recharge rates for estimating debris-flow magnitude and frequency: *Earth Surface Processes and Landforms*, v. 30, p. 755–766.
- May, C.L., 2002, Debris flows throughout different forest age classes in the central Oregon coast range: *Journal of American Water Resource Association*, v. 38, p. 1097–1113.
- Sidle R.C., 1992., A theoretical model of the effects of timber harvesting on slope stability: *Water Resource Research*, v. 28, p. 1897–1910. doi: 10.1029/92WR00804
- Ueno, K., Kurobe, K., Imaizumi, F., and Nishii, R., 2015, Effects of deforestation and weather on diurnal frost heave processes on the steep mountain slopes in south central Japan. *Earth Surface Processes and Landforms*: v. 40, p. 2013–2025, doi: 10.1002/esp.3776.
- VanDine, D. F., 1985, Debris flows and debris torrents in the southern Canadian Cordillera: *Canadian Geotechnical Journal*, v. 22, p. 44–62. <https://doi.org/10.1139/t85-006>

Overview of geotechnical effects of the January 9, 2018, debris-flow and flash-flood disaster in Montecito, California

Jeffrey Keaton^{a,*}, Richard M. Ortiz^b, Benjamin Turner^c, Paul Alessio^d, Joseph Gartner^e, John Duffy^f, Grace Parker^g, Danielle Smilovsky^h, and Taylor Watts^g

^aWood, 6001 Rickenbacker Rd, Los Angeles 90040, USA

^bLettis Consultants International, Inc., 1550 Harbor Blvd, West Sacramento 95691, USA

^cDan Brown and Associates, Inc., San Luis Obispo 93401, USA

^dUniversity of California Santa Barbara, Santa Barbara 93106, USA

^eBGC Engineers, Inc., Vancouver, Canada; ^fYeh and Associates, United States

^gUniversity of California, Los Angeles, United States; ^hWood, United States

Abstract

A strong winter storm moved across slopes above Montecito recently burned by the December 2017-January 2018 Thomas Fire, producing disastrous debris flows and flash flooding that killed 23 people, injured many others, and damaged or destroyed residential buildings and community infrastructure. Prior to the event, the National Weather Service issued a flash flood watch, forecasting periods of intense precipitation that had the potential to produce debris flows below recently burned slopes. The Geotechnical Extreme Event Reconnaissance (GEER) Association formed a team to document some of the effects of the Montecito disaster within San Ysidro creek and on bridges along State Route 192, which included geologists, engineers, and a graduate student with a background in public health. The Santa Ynez Mountains are comprised of steeply dipping Tertiary sedimentary rocks that include thick-bedded durable sandstone, with interbeds of shale, claystone, and silty sandstone, which weather to bouldery and cobbly clayey and silty sand sediments. The drainage basins have large upper subbasins separated from the coastal plain where Montecito is located by narrow steep-sided canyons. Alluvial fan deposits on the coastal plain contain boulders of local historic debris flow deposits. The debris flows overwhelmed debris-catch basins at the mouths of canyons and the shallow channels where homes and community infrastructure had been built. The debris flows damaged or destroyed the bridges observed for this study. Stream channels were blocked by accumulated boulder and woody debris in a number of locations during the debris flow event, which diverted flows away from the channels and onto adjacent land with residential and commercial developments. Above-grade stream crossings of some utility pipelines, including water supply, were on the upstream sides of the larger bridges, in part because of difficult and expensive excavation into bouldery alluvial-fan deposits. The flows also ruptured a natural gas pipeline and the leaking gas ignited, causing fire damage during the flood event. Damage in Montecito occurred to property adjacent to the five major stream channels, but life in all parts of the community, and to the region, was severely disrupted, highlighting the need for consideration of potential impacts from rare and extreme geologic processes in land-use decisions and infrastructure design.

Keywords: *Montecito; Debris-flow, Flash-flood; GEER; Geotechnical effects; Post-fire*

1. Introduction

The Thomas Fire burned approximately 113,000 hectares between December 4, 2017 and January 20, 2018, making it, at the time, the largest fire in California's history (InciWeb, 2018). Los Padres National Forest mobilized a Burn Area Emergency Response (BAER) team within the first week of the fire to assess soil burn severity and subsequently partnered with the California Watershed Emergency Response Team (WERT; covers land outside the national forest) to develop debris flow and flooding hazard maps to be issued to counties and other agencies (USDA-Forest Service, 2018 and WERT, 2018).

* Corresponding author e-mail address: jeff.keaton@woodplc.com

A storm system moving east during the evening of January 8, 2018 and early morning hours of January 9, 2018 produced short periods of rainfall intensities on the order of 7.6-15.2 centimeters per hour over the freshly burned slopes, triggering debris flows in several drainages that resulted in 23 fatalities and widespread destruction to homes, businesses, and infrastructure in Montecito, California. Boulders exceeding six meters in diameter and woody debris including mature trees were transported by the debris flows.

Montecito is an unincorporated community in Santa Barbara County located between the Pacific Ocean to the south and the Santa Ynez Mountains to the north, a distance of approximately 3.2 kilometers. This narrow strip of land on which the community is built is itself an accumulation of debris flow deposits and other alluvial and colluvial sediments derived from the mountains to the north (Dibblee and Ehrenspeck, 1986). US Highway 101 runs parallel to the coastline in an approximately east-west direction, and State Route (SR) 192 runs east-west about 2.4 kilometers inland (north) (Fig. 1). At the time of the debris flows, a mandatory evacuation order had been issued for areas of Montecito north of SR 192, and a voluntary evacuation order had been issued for the remainder of Montecito south of SR 192. These evacuation orders extended west towards Santa Barbara and east to the City of Carpinteria. The evacuation orders were issued because the forecasted rainfall intensities of 12.7 to 38.1 mm/h exceeded the predicted debris flow triggering threshold of 28 mm/h (1.1 in./h) (USDA-Forest Service, 2018).

Significant and destructive debris flows occurred in the Montecito Creek, San Ysidro Creek, Buena Vista Creek, and Romero Creek drainages (Fig. 1). Additional debris flows and flooding occurred to the east, affecting the Carpinteria; however, damage was minimal compared to Montecito. In response to the event, GEER initiated a formal response effort including field reconnaissance and interpretation of remote sensing data. The primary reconnaissance effort consisted of two days of field observations on January 29-30, 2018 by a six-person team that focused primarily on the San Ysidro Creek drainage. This was preceded by observations of damaged bridges on SR 192 on January 18, 2018 by B. Turner and by additional geologic observations in the affected drainages by P. Alessio. In addition to field observations, team members collected burn intensity data on the Thomas Fire and precipitation data from the January 8-9, 2018 storm, and analyzed remote sensing data to assess burn extent and sediment erosion and accumulation.

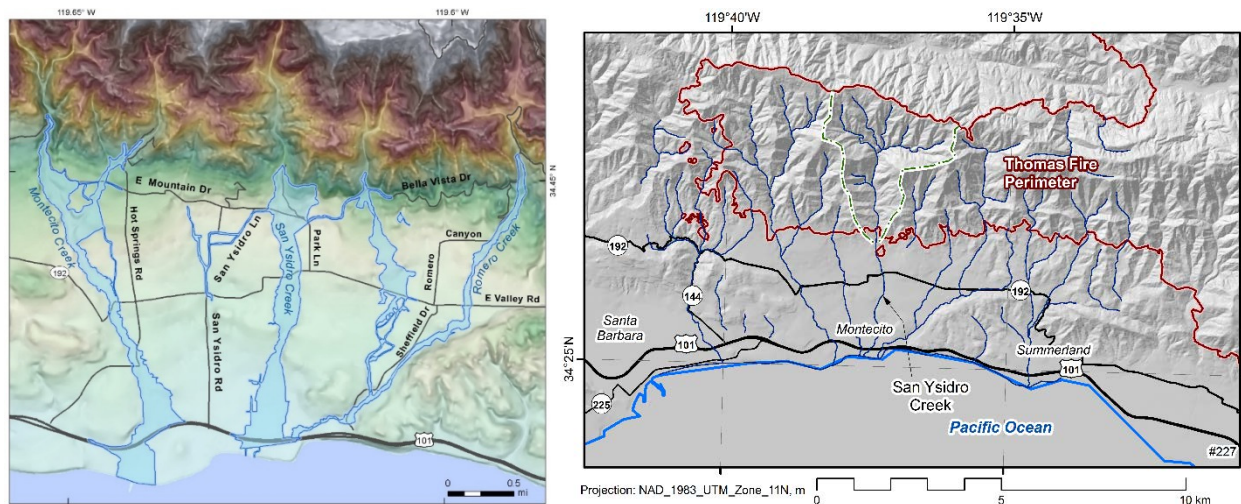


Fig. 1. Location map of Montecito area drainages impacted by debris flows on January 9, 2018, shown on hillshade with extent of debris flows, as mapped by CalFire, outlined in blue (left). Hillshade image with Thomas Fire perimeter and San Ysidro Creek drainage basin (right).

2. Background

GEER is comprised of volunteer members of the engineering, engineering geology, and earth science community and includes members from both the public and private sectors. Based on recommendations from the GEER Steering Committee, a GEER Team will respond to geotechnical extreme events to conduct reconnaissance and document observations. The ultimate purpose for a GEER team is to prepare a report documenting their observations, which can be used by others to advance research and improve engineering practice (<http://www.geerassociation.org/about-geer>).

3. Montecito GEER Team

The Montecito GEER team was comprised of a combination of geologists, engineers, and graduate students. The Montecito team featured two co-leaders: Dr. Jeff Keaton of Wood was a member of the GEER steering committee and organized the team and investigated the rain fall intensity associated with the storms that lead to the debris flows. The second co-lead was Dr. Ben Turner of Dan Brown and Associates, PC., who lead the field reconnaissance team and the drafting of the reconnaissance report. The remainder of the team was composed of Paul Alessio, Ph.D. candidate in earth science at U.C. Santa Barbara, Richard Ortiz, CEG, Senior Engineering Geologist at Lettis Consultants International, Inc, John Duffy, Engineering Geologist at Yeh and Associates, Inc., Grace Parker and Taylor Watts, graduate students at U.C. Los Angeles, Danielle Smilovsky, Remote Sensing Scientist at Wood, and Dr. Joseph Gartner, geologist at BCG Engineers. The field team was composed of a subset of the Montecito GEER team and included Dr. Turner (GEER Team co-lead), Mr. Alessio, Mr. Ortiz, Mr. Duffy, Ms. Parker and Ms. Watts.

4. Observations

Twenty days after the Montecito debris flows, the Montecito GEER team mobilized and made observations over the course of two days of reconnaissance on January 29-30, 2018. The observations made by the team were focused on the impacts the debris flows had on existing infrastructure, such as debris-catch basin, roads, and bridges. At the time of the GEER reconnaissance, recovery and rebuilding activities were already underway, including the removal of much of the debris from the entire length of the San Ysidro creek channels and debris-catch basins. Observations by the GEER team were limited to the San Ysidro Creek drainage and condition of bridges along SR 192.

4.1. Debris-Catch Basins

Large amounts of sediment, woody debris, and large boulders were observed within and upstream of the debris-catch basin located at the base of the range front approximately 360 meters upstream of E. Mountain Drive (Fig. 2). Heavy equipment had removed the majority of boulders and sediment from the basin at the time of observation, but material was still present and stockpiled along the margins of the basin (Fig. 3a and 3b). The culvert for the basin was reinforced concrete pipe and was damaged and undermined on the downstream end of the culvert (Fig. 4a and 4b). This basin became filled with debris and spilled over the top and along the margins of San Ysidro Creek during the debris-flow event (Fig. 2).



Fig. 2. Google Earth images of the San Ysidro debris-catch basin at the mouth of the range front approximately 360 meters upstream of East Mountain Drive. Image date April 14, 2017 (left); January 12, 2018 (right). © Google Earth (both images).

4.2. Roads and Bridges

Impacts to roadway infrastructure due to direct inundation of debris were significant, and resulting highway closures affected the entire southern California region for weeks. Road closures were primarily due to debris deposits on the

roadway surface that made passage impossible; closures due to damage to roadway surfaces and structures such as bridges constituted a significantly smaller portion of the impact. US Highway 101, the main north-south thoroughfare along the Pacific Coast, was closed for 13 days (January 9-21, 2018.) while; approximately 76,000 cubic meters of material up to 3.6 meters thick was removed by Caltrans crews working 24/7 (Ferreira and Holden, 2018). At the time of the GEER reconnaissance, many primary and secondary roads in the impacted areas had been cleared of enough debris to allow access into individual properties and across major stream crossings at safe locations (Fig. 5).



Fig. 3. (a) View downstream showing remaining sediment, boulders, and woody debris within San Ysidro creek debris basin during clean out operations. (b) Cross stream view of debris basin outlet and stock pile of boulders removed from San Ysidro creek debris basin during clean out operations.



Fig. 4. (a) Upstream view of San Ysidro creek debris-catch basin culvert, showing damage sustained during the January 9, 2018 debris flow event. (b) Detail view of damage to culvert.

Dr. B. Turner performed a reconnaissance-level inspection of the State Route (SR) 192 bridges through Montecito on January 18, 2018. He traversed SR 192 from west to east and observed bridges at Montecito Creek, San Ysidro Creek, and Romero Creek. Each of these bridges are single-span, simply supported concrete girder structures with rectangular channel openings on the order of 4.5 to 7.5 meters wide and 3 to 4.5 meters tall (Fig. 6). The Romero Creek Bridge is an exception; the channel opening is arch shaped. It is not clear if the Romero Creek Bridge structure is a true arch or is actually a simply-supported span with an architectural arch finish for aesthetic purposes (Fig. 7). Anecdotal reports from Caltrans employees indicate these bridges were constructed in the first half of 20th century.

Initial inspection of the bridges following the event revealed that the upstream openings of the bridges were clogged with woody debris, typically up to the deck level. It is notable that each of these bridges was likely the first significant channel constriction encountered by the respective debris flows and a significant amount of woody debris had accumulated on the leading edge as the debris flow travelled through the burned source area towards SR 192. Sediment deposits consisting of a primarily sand-sized soil matrix with cobbles and boulders up to approximately 4.5 meters in diameter then accumulated upstream, on top of, and laterally relative to this woody debris jam.



Fig. 5. View north of E. Valley Lane, approximately 150 meters south of State Route 192, showing the condition of cleared secondary roads at the time of the GEER reconnaissance.



Fig. 6. Montecito Creek Bridge at SR 192, January 18, 2018. Note lack of scour behind/below abutment wingwalls. Significant amounts of debris had been removed from the channel at the time of this photo.



Fig. 7. Looking downstream at Romero Creek Bridge, SR 192. Photo January 18, 2018.

While guardrail on the upstream and downstream edges of the bridge decks were completely destroyed, the overall level of damage to the bridges along SR 192 was remarkably low in light of the degree of damage to surrounding residential structures. The most significant damage occurred to the girders on the upstream edges of the bridges and consisted of cracked/spalled concrete, exposed steel reinforcement and residual flexural deformation (Fig. 8). Scour behind the upstream abutment wingwalls was notably absent which may also have been due to the woody debris jam acting as a buffer against sediment and flood water with otherwise significant scour potential.

The East Mountain Road bridge crossing San Ysidro Creek was completely destroyed during the event (Fig. 9), although the circumstances of the destruction are uncertain because an explosion occurred when a natural gas pipeline

that also crossed the creek at the bridge location exploded. It is unclear whether or not this explosion occurred during or after the debris flow, and therefore uncertain whether the bridge succumbed to loads imposed by the debris flow, forces of the explosion, or a combination thereof.



Fig. 8. Damaged girder and utilities, upstream side of Montecito Creek bridge at SR 192. Note exposed girder reinforcement consists of embedded steel beam section and continuously twisted steel bar; steel beam sections exhibit residual curvature.



Fig. 9. Abutments of former East Mountain Road bridge at San Ysidro Creek, January 30, 2018. Burned vegetation due to fire associated with gas line explosion.

4.3. Stream Channels

Prior to the debris flow event, San Ysidro creek was heavily vegetated (Fig. 2) and confined within relatively narrow and entrenched channel, with suburban development along the margins of the channel from the canyon mouth to the Pacific Ocean (Fig. 1). The action of the debris flow removed the majority of the existing vegetation and scoured the channels an unknown amount (Fig. 10a and 10b). A significant amount of accumulated debris had been removed from the San Ysidro Creek channel along its entire length from canyon mouth to the ocean by the time the GEER Montecito team was able to gain access and complete the reconnaissance. The majority of the remaining debris was still in-place beyond the channel margins downstream of the locations where the flow became blocked or constricted, such as at bridge crossings. The debris flow avulsed, overtopped the channel margins, and flowed into the surrounding neighborhoods built upon floodplain surfaces, where the majority of catastrophic damage occurred (Fig. 11a and 11b).

4.4. Utility Infrastructure

The Montecito debris flows affected all major utilities services within the areas of impact. The water transmission and distribution system for the Montecito Water District was significantly damaged during the debris flow event, including multiple breaks of the Highline (Fig. 12) and Jameson Pipeline transmission mains and the destruction of many fire hydrants.



Fig. 10. (a) Looking upstream from SR 192 bridge at San Ysidro Creek, pre-event. Google Maps Street View image taken May 2016 (© Google). (b) Post-event photo taken from same location as Fig. 10a on January 18, 2018. Note a significant amount of debris had already been removed from stream channel.



Fig. 11. (a) accumulated debris flow deposit and intact structure on East Valley Lane approximately 360 meters downstream of the point of debris flow avulsion from San Ysidro Creek channel at SR 192 bridge and 277 meters due west of the San Ysidro Creek channel. Note prominent mudline, this home was located along the western margin of the debris flow deposit. (b) accumulated debris flow deposit and partially destroyed structure on East Valley Lane approximately 165 meters downstream of the point of debris flow avulsion from San Ysidro Creek channel at SR 192 bridge and 135 meters due west of San Ysidro Creek channel. This home was located within the direct flow path of the debris flow after the flow overtopped the San Ysidro Creek channel.



Fig. 12. Downstream view of temporary repair of the “Highline” water main by Montecito Water District. Sections of the previously buried water main were exposed due to channel scour during the debris flow event within San Ysidro Creek.

The primary impact to Southern California Edison infrastructure was the toppling of power poles within the footprint of the debris flow, which led to downed power lines and transformers throughout the impacted area. The GEER Montecito team observed many field technicians from the Southern California Gas Company working to restore service to the residential distribution network within the footprint of the debris flow. One large diameter gas transmission line was observed cut and capped within an open excavation adjacent to East Mountain Road approximately 50 meters west of San Ysidro creek and likely was an intact section of the gas pipeline that ruptured, exploded, and destroyed the East Mountain Road bridge (Fig. 9).

5. Conclusions

- The existing debris-catch basins were overwhelmed by the high volume of large woody debris and boulder-size materials that were transported downstream by the Montecito debris flows.
- Bridges crossing creek channels acted as artificial choke points that clogged with debris and subsequently blocked flow and led to stream channel avulsion by the debris flow, which resulted in damage to structures within the footprint of the debris flow.
- Primary and secondary roads experienced minor damage but acted as flow paths for the debris flow into neighborhoods adjacent to stream channels downstream of avulsion points.
- Above ground and buried utilities were both damaged or destroyed by the debris flows. Utility lines that were hung under bridges were consistently damaged or destroyed along the entire flow paths of the debris flow.

Acknowledgements

The Geotechnical Extreme Events Reconnaissance (GEER) Association, supported by the U.S. National Science Foundation (NSF), organizes the response of the geoengineering community to earthquakes and other natural disasters such as floods, landslides, tsunamis, etc. GEER members donate their time, talent, and resources to collect time-sensitive and potentially perishable field observations and data of the effects of extreme events. The GEER Association web site, which contains additional information, may be found at: www.geerassociation.org.

This material is based upon work supported by the National Science Foundation under Grant No. CMMI 1266418. Any opinions, findings, and conclusions or recommendations expressed in this material are those of the authors and do not necessarily reflect the views of the National Science Foundation.

Mr. Ortiz would like to thank Lettis Consultants International, Inc. for providing the funding for his participation in the GEER Montecito reconnaissance and to develop this and other associated publications and presentations.

References

- Dibblee, T.W., and Ehrenspeck, E.H., 1986, Geologic map of the Santa Barbara quadrangle, Santa Barbara County, California. Dibblee Geological Foundation, Map DF-06, 1:24,000 Scale.
- Ferreira, G., and Holden, L., 2018, "Hwy. 101 reopens through Montecito — a day ahead of schedule." *San Luis Obispo Tribune*, 21 January 2018. Last accessed 18 February 2018. Available: <http://www.sanluisobispo.com/news/local/article195864849.html>
- InciWeb, 2018, Thomas Fire Incident Information. Incident Information System, National Wildfire Coordinating Group Available: <https://inciweb.nwcg.gov/incident/5670/>. Last accessed: 14 February 2018.
- USDA – Forest Service, 2018, Thomas Burned Area Report. United States Department of Agriculture Reference FSH 2509.13 Available: <https://www.fs.usda.gov/detail/lpnl/home/?cid=fseprd570093>. Last accessed: 15 February 2018.
- WERT, 2018, Thomas Fire Watershed Emergency Response Team Final Report. CalFire and California Geological Survey. Available: http://cdfdata.fire.ca.gov/admin8327985/cdf/images/incidentfile1922_3383.pdf. Last accessed: 19 February 2019.

Debris flows and mitigation systems after the 2008 Wenchuan earthquake

Fangzhou Liu^{a,*}, J. David Frost^a, Qiang Xu^b, Runqiu Huang^b

^a*School of Civil and Environmental Engineering, Georgia Institute of Technology, Atlanta, GA, USA*

^b*State Key Laboratory of Geohazard Prevention and Geoenvironment Protection, Chengdu University of Technology, Chengdu, Sichuan, China*

Abstract

Poorly sorted loose granular materials deposited by the coseismic landslides in the 2008 Wenchuan Earthquake provided abundant source material for debris flows to occur during saturation and agitation by rainfall as well as surface and groundwater flow. Debris flows in southwest China are concentrated in the annual monsoon season when substantial precipitation occurs and have resulted in catastrophic damage to downstream regions. With debris-flow susceptibility increasing in regions affected by mega-earthquakes, mitigation systems are considered as critical infrastructures, the performance and resilience of which are vital to the local communities. In this paper, we present 1) the analysis on rainfall intensity-duration (*I-D*) thresholds, Rainfall Index (*RI*), Rainfall Triggering Index (*RTI*) and characteristics of the debris flows that occurred in the gullies located in three watersheds affected by the Wenchuan Earthquake, and 2) the evaluation of the performance of both conventional and some novel mitigation systems deployed in these gullies. Sharp decreases in the associated rainfall thresholds were found in the gullies after the earthquake; however, the level of increase in the rainfall thresholds is highly site- and system-dependent. Most of the existing debris-flow mitigation systems exhibited fair performance yet insufficient resilience to the impact. Notwithstanding the large amount of source materials available to be mobilized in debris flows and the intense surface run-off, many conventional mitigation structures required constant maintenance after each event and even reconstruction after the monsoon season.

Keywords: Debris flow; Mitigation system; Rainfall thresholds; Wenchuan Earthquake; Resilience

1. Introduction

The 2008 Wenchuan Earthquake (M_w 7.9) occurred in Sichuan province, China on May 12, 2008. The long-lasting ground motion and the substantial amount of energy released at a shallow focal depth (15-20 km) resulted in one of the deadliest and costliest seismic event in China (Huang and Fan, 2013); it claimed 87,145 lives (including 17,923 reported missing) and resulted in 374,643 injuries (National Development and Reform Commission, 2008). The severe damage was intensified by the coseismic geohazards; the coseismic landslides have caused more than 30,000 fatalities, exceeding 1/3 of the total fatalities of the earthquake (Fan et al., 2018). Various estimations on the number of geohazards are reported in previous literature following study of the earthquake. Huang and Li (2009) reported more than 1,200 geohazards that were posing direct risks to downstream communities in Sichuan Province. Gorum et al. (2011) mapped about 60,000 landslide scarps. Dai et al. (2011) and Parker et al. (2011) have separately reported more than 50,000 coseismic geohazards in their studies.

The coseismic landslides and the subsequent debris flows represent a post-earthquake instability process (Huang and Fan, 2013; Zhang et al., 2014). Debris flow is the sudden downward surge of saturated and poorly sorted sediments under gravitational forces (Iverson, 1997); it poses significant risks to downstream communities as a large amount of landslide deposit becomes the source material for rainfall-induced debris flow, which can increase the magnitude through progressive entrainment during the movement (Iverson et al., 2011; Cui et al., 2013). A significant increase

* Corresponding author e-mail address: fangzhou.liu@gatech.edu

in debris flow was observed after the Wenchuan Earthquake, and can be attributed to the increase in sediment flux caused by coseismic landslides (Huang and Fan, 2013; Guo et al., 2016); similar changes were found after the 1999 Chi-Chi Earthquake (Jan and Chen, 2005).

The increase in debris-flow events is reflected by comparing the pre- and post-earthquake rainfall thresholds in the corresponding regions. In this paper, the changes of the rainfall thresholds, including the rainfall intensity-duration ($I-D$), Rainfall Index (RI), and Rainfall Triggering Index (RTI), after the earthquake are reviewed and analyzed for the quake-stricken region. Emphasis in the analysis is placed on three catchments with debris-flow mitigation systems implemented between 2010 and 2012, with the aim of using different rainfall thresholds: 1) to assess the long-term impacts of earthquake on debris flows, and 2) to compare the performance and resilience of the conventional and novel mitigation systems in the region.

2. Study Area

The Wenchuan Earthquake originated along the Longmen Mountain Fault zone with a length of 300-500 km and a width of 50 km between the Sichuan Basin and the eastern margin of the Tibetan Plateau (Shen et al., 2009), as illustrated in Fig 1. The autochthon of Longmen Mountain Fault zone encompasses the Proterozoic granite massifs, unconformably overlapped the Lower and Middle Jurassic strata, Cretaceous strata, and deformed Paleozoic sediments with Quaternary alluvium extended to the rheologically strong lithosphere of the Sichuan Basin (Burchfiel et al., 2008; Wang et al., 2011). The steep margin of the Tibetan Plateau is intensely dissected by the tributaries of the Yangtze River (Ouimet et al., 2007), shaping one of the most mountainous regions for human settlement in China. The main surface rupture is along the Yingxiu-Beichuan Fault (YBF) and the Jiangyou-Guanxian Fault (JGF) with lengths of 240 km and 72 km, respectively.

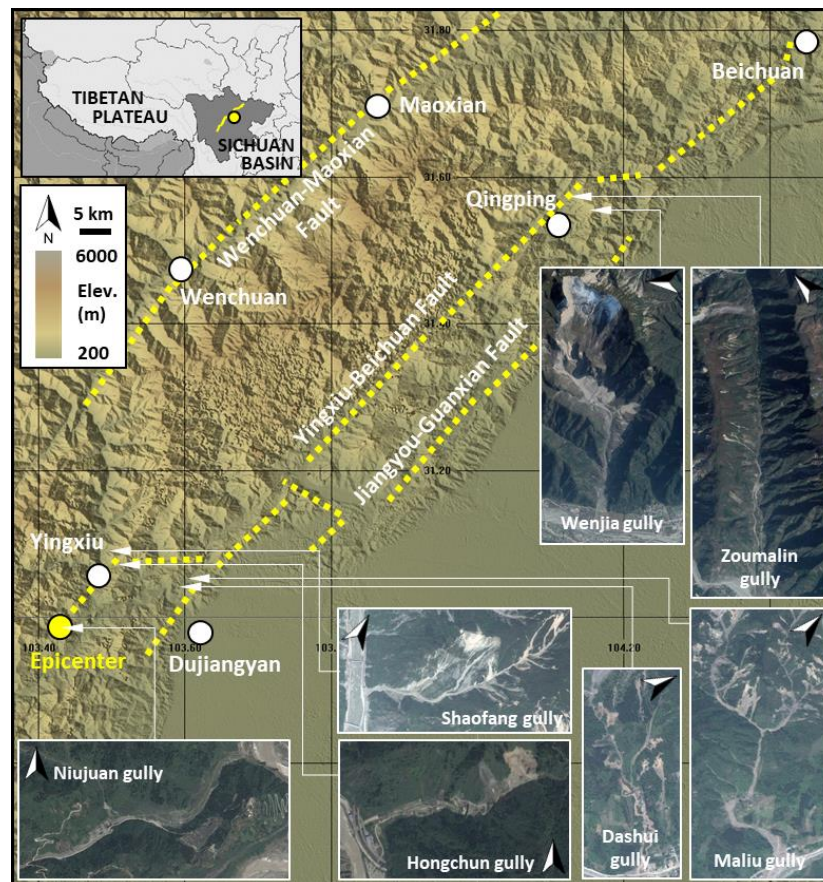


Fig. 1. Tectonic and geomorphic settings of the 2008 Wenchuan Earthquake (ASTER image). The Longmen Mountain Fault zone is located between the Tibet Plateau and the Sichuan Basin (upper left). Satellite images of catchment areas of some representative gullies in the study area are shown (Google Earth image). The epicenter and the main ruptures of the earthquake are highlighted.

The study area includes the watersheds of Qingping, Yingxiu, and Dujiangyan (Fig. 1); these regions contain a more detailed collection of pre-/post-earthquake as well as pre-/post-mitigation records, of rainfall and debris to assess the impacts of earthquake and debris flows. The region is incised by the waterways of the Mianyuan River (Qingping), the Min River (Yingxiu), and the Longxi River (Dujiangyan), which resulted in a relative elevation of 770–4000 m in the study area. The study area comprises a complex lithological assemblage, including mainly 1) shale, sandstone, and limestone in Qingping, 2) granite, limestone, and sandstone in Yingxiu, and 3) granite, sandstone, and mudstone in Dujiangyan. The annual average precipitation in Qingping, Yingxiu and Dujiangyan is 1086 mm, 1253 mm, and 1135 mm, respectively. Rainfall concentrates in the monsoonal season between June and August, with typically 60%–80% of the annual precipitation of the study area.

Numerous destructive debris flows occurred immediately after the earthquake during the monsoonal seasons of 2008 and 2009, including the debris flows in the Wenjia gully in Qingping and in the Weijia gully that buried part of the ruins of Beichuan town. Many debris-flow mitigation systems that were being designed or implemented at the time followed the conventional design specifications which later proved to be insufficient for debris flows after an earthquake due to high sediment flux (Xu et al., 2012). The intense precipitation during August 12–13, 2010, triggered debris flows in more than 80 gullies in the study area, including 20 in Qingping, 21 in Yingxiu, and 44 in Dujiangyan. The debris flows caused fatalities and resulted in damage to the post-earthquake reconstruction process (Tang et al., 2012; Xu et al., 2012; Huang and Li, 2014). The debris flows also destroyed many conventional mitigation systems, which exclusively consisted of a large number and variety of concrete check dams and channels that were inadequately designed. The basic characteristics of the mitigated gullies in the study area are shown in Table 1.

Table 1. The basic geometry of the gully and the estimated amount of the source materials for the debris flow with mitigation system (re-)implemented after August 13, 2010.

Gully	Length (km)	Height (km)	Catchment Area (km ²)	Loose deposit volume (before August 2010) ($\times 10^6$ m ³)*	Loose deposit volume (after August 2010) ($\times 10^6$ m ³)
Hongchun	3.6	1.29	5.35	3.58	3.1
Shaofang	1.85	1.1	1.5	2.52	2.23
Niujuan	3.9	1.78	10.7	7.89	7.43
Maliu	1.59	0.95	1.98	-	8.14
Dashui	0.88	0.32	0.45	-	2.7
Wenjia	3.25	1.52	4.5	80.6	74.5
Zoumalin	3.5	0.59	5.7	4.37	3.26

Note: the estimated volume of source material before August 2010 may not represent the total volume of loose deposit after the earthquake due to subsequent debris flows without detailed records in literature.

3. Rainfall Threshold and Mitigation Systems

3.1. Pre-/Post-earthquake I-D thresholds

Prior to the earthquake, rainfall data for gullies that were susceptible to debris flows were typically collected by the nearby rain gauge without the systematic frameworks of an Early Warning System (EWS) for debris flows. The studies on pre-earthquake debris flows in the region commonly rely on distant rain gauges that may not be at the comparable elevation or the same side of the ridge, as indicated by Guo et al. (2016).

A rainfall threshold represents the minimum precipitation required to trigger a debris flow, slope failure, or shallow landslide. Typical approach includes rainfall intensity-duration relationship that can be expressed as $I = \alpha D^{-\beta}$, where I is the mean rainfall intensity (mm/hr), D is the rainfall duration (hr), and α and β are empirical coefficients (Caine, 1980). However, a single critical rainfall parameter, such as peak rainfall intensity or daily cumulative rainfall, has the tendency to overestimate debris-flow occurrence for mitigated gullies (Liu et al., 2017), and thus additional rainfall threshold parameters are employed to better characterize the critical conditions and the variations after implementing the mitigation system. The Rainfall Index (RI) is defined as $R_d I_{max}$ (Chen et al., 2013), where R_d is the daily cumulative rainfall and I_{max} is the peak rainfall intensity. The Rainfall Triggering Index (RTI) is expressed as the product of $R_d I_{max}$, where R_t is the 7-day antecedent rainfall. The RTI has been used to establish probability of debris flow occurrences in prediction models (Jan et al., 2002; Jan and Lee, 2004; Huang et al., 2015).

Guo et al. (2016) summarized the I - D thresholds and duration that triggered debris flows between 2008 and 2013 for the entire region that was impacted by the Wenchuan Earthquake. Ma et al. (2017) studied the debris-flow events between 2008 and 2013 and summarized a more watershed-scale regional I - D threshold. These rainfall thresholds are compared with some proposed global and regional thresholds, as shown in Fig 2.

A pre-earthquake I - D threshold for the entire region is not available for the Wenchuan Earthquake; but the post-earthquake I - D thresholds are significantly lower than the global or regional thresholds included in this study, which implies a possible severe impact caused by the earthquake. The gradual increase in the I - D thresholds between 2008 and 2013 indicates a decreasing susceptibility to debris flow at a regional scale since the earthquake. Notwithstanding the sediment influx caused by the subsequent geohazards after the earthquake (Huang and Fan, 2013; Huang and Li, 2014), the recovery of the I - D thresholds can be largely ascribed to the decrease of the overall loose materials, as they were entrained and removed by previous debris flows from the gullies. The watershed I - D thresholds are considerably higher than the regional thresholds (Fig. 2); it is postulated that the study on these watersheds were affected by the implementation of debris-flow mitigation systems.

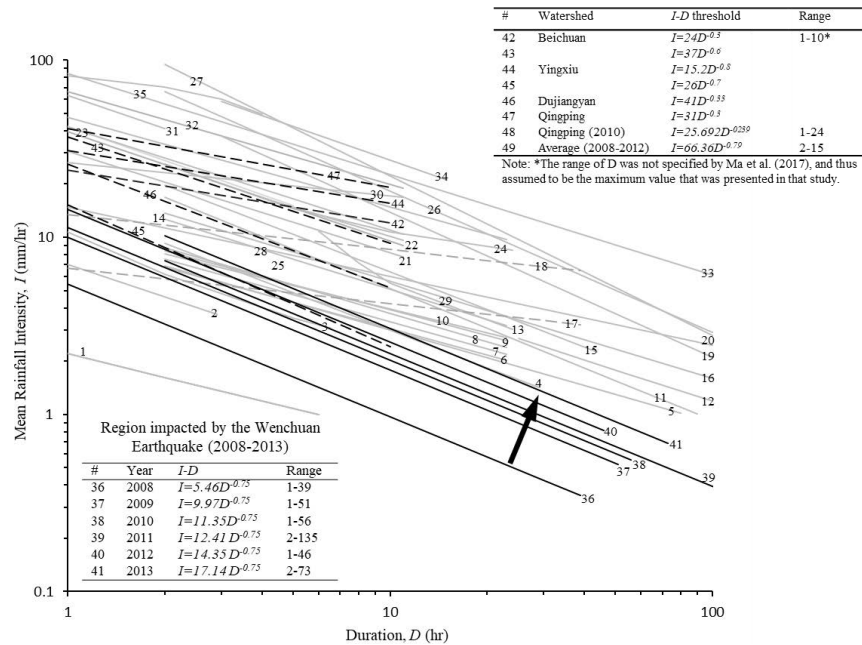


Fig. 2. Global and regional mean rainfall I - D thresholds for debris flows proposed in previous literatures (references see Liu et al., 2017). The regional I - D thresholds for the Wenchuan Earthquake impacted area are highlighted; the watershed I - D thresholds are marked by dash lines. The sharp decrease in thresholds #17 and #18 represents the changes after the 1999 Chi-Chi Earthquake.

3.2. Conventional mitigation systems

The mitigation systems implemented in the representative gullies are discussed and the effects on rainfall thresholds are analyzed. The discussion focuses on the design and performance of mitigation systems implemented after August 2010. An Early Warning Systems (EWS) was implemented for each mitigated gully; it is designed to better collect rainfall and erosion data and monitoring the debris flow events. The conventional mitigation systems in the studied gullies are typically deigned with concrete check dams and drainage channels.

3.2.1. Yingxiu

The heavy rainfall event on May 17, 2008, July 23, 2009, and May 29, 2010 induced numerous landslides, rockfalls, and debris flows. The extreme rainfall event on August 12-14, 2010 caused severe damage to the reconstruction of Yingxiu with urban flood inundation, which resulted from the blockage of the Minjiang River due to the debris flows that occurred in the Hongchun gully, Shaofang gully, and the adjacent gullies. The precipitation reached 163 mm in 2 hours on the morning of August 14, 2010; it triggered debris flows around 3:00 AM local time. The volume of debris

from the Hongchun gully was estimated as 7.5×10^5 (Huang and Li, 2014), and the level of flood was 2-3.5 m in Yingxiu and remained in the area for more than 7 days (Tang et al., 2011). The mitigation system in Hongchun gully was completed before the monsoon season of 2011, and was comprised of a large concrete check dam at the exit of the gully with a drainage channel, and 3 small check dams along the gully. The high slope gradient of the Shaofang gully posed challenges to the design of the mitigation system; it consisted of 3 large check dams and a short drainage channel to divert the debris flow into the Minjiang River to reduce damage to the roadway. The epicenter of the Wenchuan Earthquake is located in the Niujuan gully, in which abundant loose materials were deposited by the coseismic landslide. A total of 8 check dams were implemented, of which half are for the branches to prevent sediment supply into the main gully, with a drainage channel to guide the debris flows.

3.2.2. *Qingping*

A large amount of loose sediment was deposited by coseismic landslides in the Zoumalin gully, with no prior reports of debris flows before the Wenchuan Earthquake. The conventional mitigation system consists of 7 large check dams and 4 drainage channels in the branches with small sectional barriers, and an additional 3 barriers. The intense rainfall events on August 17, 2012 and July 8, 2013 resulted in two large-scale debris flows. The debris flow in 2012 filled most of the basins of the check dams and blocked the drainage channels (Fig 4a and 4b); the basins were subsequently emptied. The debris flow in 2013 overflowed the check dams and caused damage to the community.

3.2.3. *Dujiangyan*

The source material in the gullies of the Dujiangyan watershed were mainly deposited by the coseismic landslides of the Wenchuan Earthquake. The peak hourly rainfall on August 12-14, 2010 was 75 mm, with a high 2-hr cumulative precipitation of 128.3 mm. A large-scale debris flow occurred in Maliu and Dashui gully on August 13 and 18 during intense rainfall, which have collectively mobilized more than $10 \times 10^6 \text{ m}^3$ of loose sediments. The mitigation system in the Maliu gully comprises 7 check dams, with the aim of preventing sediments from reaching downstream, as the exit was close to a temporary settlement for residents of Longchi town that were severely damaged by the earthquake. The volume of the remaining loose materials in the Dashui gully is less compared to other gullies after August 2010, and therefore, the design of the mitigation system was modified to include only 2 larger check dams (height > 13 m) with a drainage channel at the exit of the gully.

3.3. *Novel mitigation system*

A novel mitigation system was subsequently designed and implemented in the gully (Fig. 3), as discussed in detail in Liu et al. (2017). The new system integrates three key elements, i.e. the water-sediment segregation (water control), source material stabilization (sediment control), and channelized erosion prevention (erosion control), with the aim of minimizing surface run-off by separating the fluid and solid components of the debris flow. The sediment control and erosion control focus on the mid-/down-stream of the gully where a large amount of loose materials can be entrained by a debris flow originating from the up-stream. The water-sediment segregation system is shown in Fig. 4; the debris-flow breaker consists of 4 arrays of steel fins aligned perpendicular to the dominant flow direction. In the event of overflowing of check dams #4 and #5, the sediment basin reduces the dynamic impact by permitting settlement of larger boulders and rocks. The breaker system enables rapid drainage of surface runoff through the drainage tunnel, which in turn, prevents erosion and mobilization of the loose particles in the mid- and down-stream. Fluid and small-scale sediment removed from the bulk of the debris flow are drained through the drainage tunnel and discharged to branch #1. Therefore, the debris flow can be contained within a certain branch or a small area, to prevent entrainment of the loose materials in the mid-stream of the gully.

3.4. *Pre-/Post-mitigation rainfall thresholds*

The rainfall parameters associated with the pre-/post-mitigation debris flows in the studied gullies are summarized in Table 4. The variations in the number and volume of the debris flows as well as the associated rainfall thresholds are of direct interest in evaluating the performance of the mitigation system. Since no known debris flows existed in these gullies before the earthquake, the rainfall data prior to the earthquake cannot be identified for many of the studied gullies (Fig. 5). However, the increased number of debris flows is prominent, and decreased abruptly with sharp

increases in the critical rainfall parameters after implementation of the mitigation system, as demonstrated by the Wenjia gully. Although the interplay between rainfall and debris flows are complex and dynamic, plotting the occurrences in such fashion offers an intuitive representation on the variations in the number of debris-flow events and rainfall thresholds. Notwithstanding the difficulties in comparing the pre-/post-mitigation rainfall parameters due to the lack of data, the proposed rainfall parameters can serve as an effective factor to evaluate the performance of the system, as demonstrated by changes of the critical rainfall condition of the Wenjia gully case.

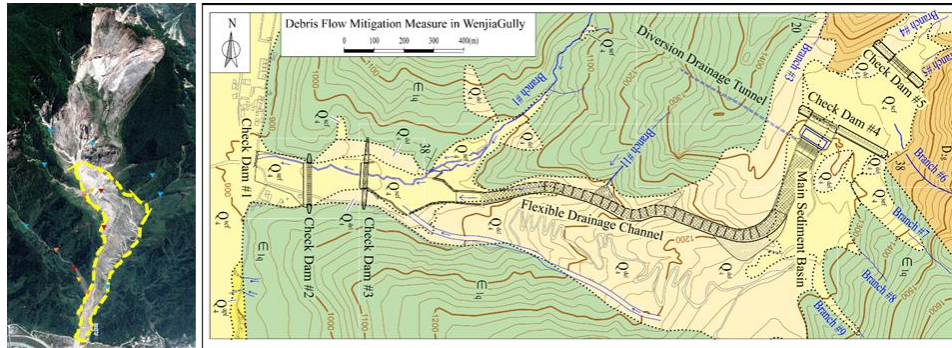


Fig. 3. The debris flow mitigation system in the Wenjia Gully. The midstream section consists of a flexible drainage channel. Three check dams were constructed in the downstream of the gully. A large number and variety of sensors were installed in the gully and/or its catchment, including the rain gauges (blue), deposit thickness gauges (red), piezometers (orange), and video cameras (yellow) (after Liu et al., 2017).

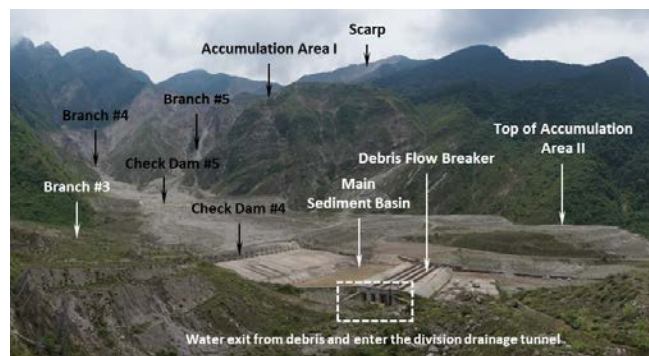


Fig. 4. An overview of the water-sediment segregation system formed by a sediment basin and a breaker system. The drainage conduits are underneath the steel fins of the debris flow breaker, and connects to the drainage tunnel.

4. Concluding Remarks

A typical problem for the design of a mitigation system in a gully that was impacted by a major seismic event is that a large amount of loose materials is deposited by coseismic landslides, and thus debris flows in such a gully is almost inevitable under heavy rainfall. In this paper, we summarize the debris-flow events after the 2008 Wenchuan Earthquake in the entire region emphasizing three watersheds. The study area contains gullies that are extremely susceptible to debris flows under rainfall, and demonstrated significant decreases in the critical rainfall condition. Discussion focused on the design and implementation of mitigation systems, and employs rainfall parameters to evaluate the performance of the systems. The study proposed to use pre-/post-mitigation rainfall parameters to evaluate the performance of the system as indicated by the Wenjia gully mitigation system.

Acknowledgements

The financial support for the first author was also provided by the Elizabeth and Bill Higginbotham Professorship at the Georgia Institute of Technology. Authors are grateful to the data collection conducted by the field team at the State Key Laboratory of Geohazard Prevention and Geoenvironment Protection (SKLGP) at the Chengdu University of Technology.

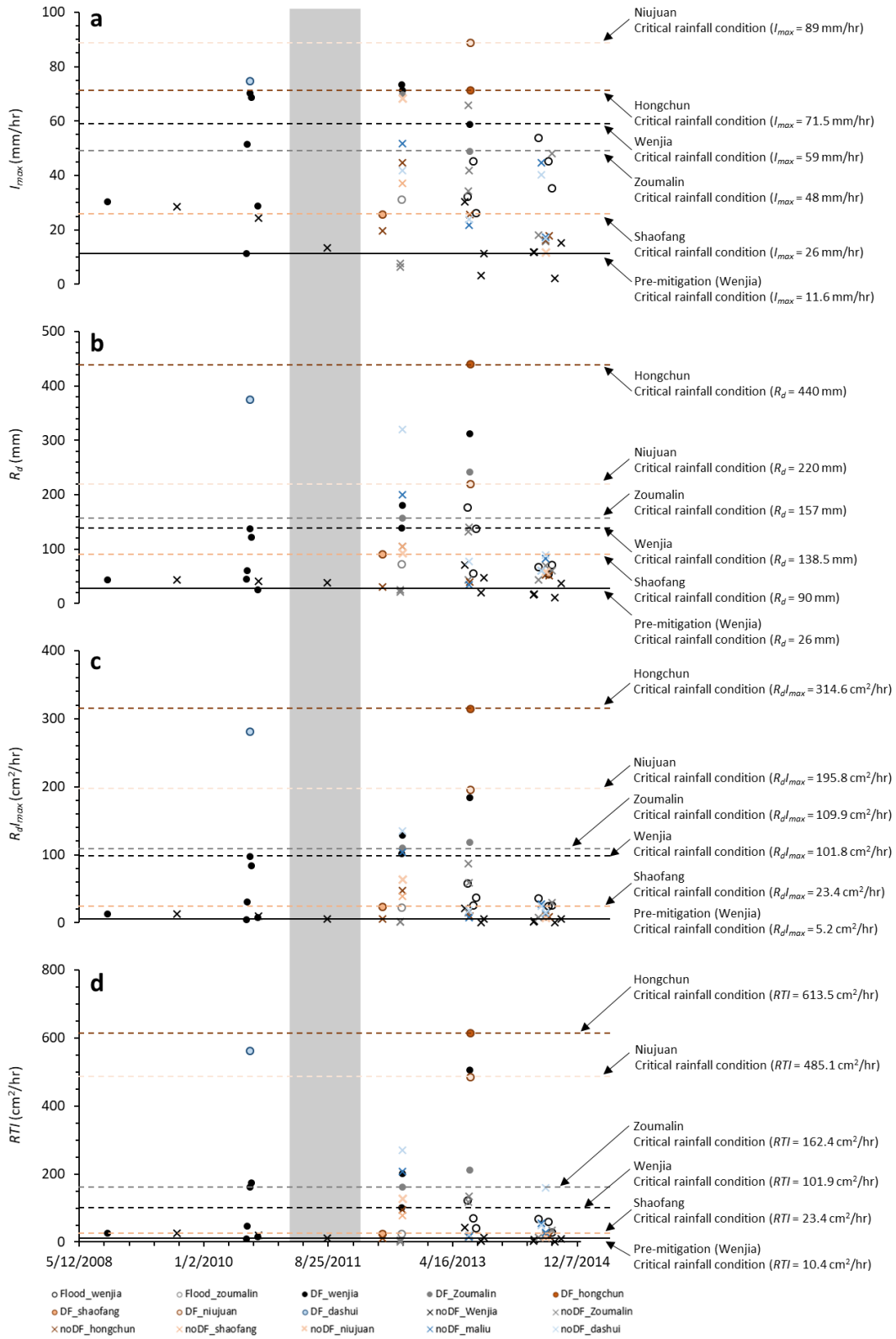


Fig. 6. The variations in the rainfall parameters contributing to the pre- and post-mitigation debris flows in the studied gullies. The gray region represents the period of the construction of the mitigation system, during which no dataset was collected systematically, and thus not included in the analysis.

References

- Burchfiel, B.C., Royden, L.H., van der Hilst, R.D., Hager, B.H., Chen, Z., King, R.W., Li, C., Lü, J., Yao, H., and Kirby, E., 2008, A geological and geophysical context for the Wenchuan earthquake of 12 May 2008, Sichuan, People's Republic of China: *GSA Today*, v. 18, p. 4, doi:10.1130/GSATG18A.1.
- Chen, J.C., Jan, C.D., and Huang, W.S., 2013, Characteristics of rainfall triggering of debris flows in the Chenyulan watershed, Taiwan: *Natural Hazards and Earth System Science*, v. 13, p. 1015–1023, doi:10.5194/nhess-13-1015-2013.
- Cui, P., Zhou, G.G.D., Zhu, X.H., and Zhang, J.Q., 2013, Scale amplification of natural debris flows caused by cascading landslide dam failures: *Geomorphology*, v. 182, p. 173–189, doi:10.1016/j.geomorph.2012.11.009.
- Dai, F.C., Xu, C., Yao, X., Xu, L., Tu, X.B., and Gong, Q.M., 2011, Spatial distribution of landslides triggered by the 2008 Ms 8.0 Wenchuan earthquake, China: *Journal of Asian Earth Sciences*, v. 40, p. 883–895, doi:10.1016/j.jseaes.2010.04.010.
- Fan, X., Juang, C.H., Wasowski, J., Huang, R., Xu, Q., Scaringi, G., van Westen, C.J., and Havenith, H.-B., 2018, What we have learned from the 2008 Wenchuan Earthquake and its aftermath: A decade of research and challenges: *Engineering geology*, v. 241, p. 25–32.
- Gorum, T., Fan, X., van Westen, C.J., Huang, R.Q., Xu, Q., Tang, C., and Wang, G., 2011, Distribution pattern of earthquake-induced landslides triggered by the 12 May 2008 Wenchuan earthquake: *Geomorphology*, v. 133, p. 152–167, doi:10.1016/j.geomorph.2010.12.030.
- Guo, X., Cui, P., Li, Y., Ma, L., Ge, Y., and Mahoney, W.B., 2016, Intensity-duration threshold of rainfall-triggered debris flows in the Wenchuan Earthquake affected area, China: *Geomorphology*, v. 253, p. 208–216, doi:10.1016/j.geomorph.2015.10.009.
- Huang, R., and Fan, X., 2013, The landslide story: *Nature Geoscience*, v. 6, p. 325–326, doi:10.1038/ngeo1806.
- Huang, J., Ju, N.P., Liao, Y.J., and Liu, D.D., 2015, Determination of rainfall thresholds for shallow landslides by a probabilistic and empirical method: *Natural Hazards and Earth System Science*, v. 15, p. 2715–2723.
- Huang, R., and Li, W., 2009, Analysis of the geo-hazards triggered by the 12 May 2008 Wenchuan Earthquake, China: *Bulletin of Engineering Geology and the Environment*, v. 68, p. 363–371.
- Huang, R., and Li, W., 2014, Post-earthquake landsliding and long-term impacts in the Wenchuan earthquake area, China: *Engineering Geology*, v. 182, p. 111–120.
- Iverson, R.M., 1997, The Physics of Debris Flows: Reviews of geophysics, v. 35, p. 245–296.
- Iverson, R.M., Reid, M.E., Logan, M., LaHusen, R.G., Godt, J.W., and Griswold, J.P., 2011, Positive feedback and momentum growth during debris-flow entrainment of wet bed sediment: *Nature Geoscience*, v. 4, p. 116–121, doi:10.1038/ngeo1040.
- Jan, C., and Chen, C., 2005, Debris flows caused by Typhoon Herb in Taiwan, in *Debris-Flow Hazards and Related Phenomena*, Springer, p. 539–563.
- Jan, C.D., and Lee, M.H., 2004, A debris-flow rainfall-based warning model: *J Chin Soil Water Conserv.*, v. 35, p. 275–285.
- Jan, C., Lee, M., and Huang, T., 2002, Rainfall Threshold Criterion for Debris-Flow Initiation: National Cheng Kung University, p. 9104–9112.
- Liu, F.Z., Xu, Q., Dong, X.J., Yu, B., Frost, J.D., and Li, H.J., 2017, Design and performance of a novel multi-function debris flow mitigation system in Wenjia Gully, Sichuan: *Landslides*, v. 14, p. 2089–2104.
- Ma, C., Wang, Y., Hu, K., Du, C., and Yang, W., 2017, Rainfall intensity–duration threshold and erosion competence of debris flows in four areas affected by the 2008 Wenchuan earthquake: *Geomorphology*, v. 282, p. 85–95.
- National Development and Reform Commission, 2008, The state overall planning for post-Wenchuan Earthquake restoration and reconstruction.
- Ouimet, W.B., Whipple, K.X., Royden, L.H., Sun, Z., and Chen, Z., 2007, The influence of large landslides on river incision in a transient landscape: Eastern margin of the Tibetan Plateau (Sichuan, China): *Geological Society of America Bulletin*, v. 119, p. 1462–1476, doi:10.1130/B26136.1.
- Parker, R.N., Densmore, A.L., Rosser, N.J., de Michele, M., Li, Y., Huang, R., Whadcoat, S., and Petley, D.N., 2011, Mass wasting triggered by the 2008 Wenchuan earthquake is greater than orogenic growth: *Nature Geoscience*, v. 4, p. 449–452, doi:10.1038/ngeo1154.
- Shen, Z.-K., Sun, J., Zhang, P., Wan, Y., Wang, M., Bürgmann, R., Zeng, Y., Gan, W., Liao, H., and Wang, Q., 2009, Slip maxima at fault junctions and rupturing of barriers during the 2008 Wenchuan earthquake: *Nature Geoscience*, v. 2, p. 718–724, doi:10.1038/ngeo636.
- Tang, C., Van Asch, T.W.J., Chang, M., Chen, G.Q., Zhao, X.H., and Huang, X.C., 2012, Catastrophic debris flows on 13 August 2010 in the Qingping area, southwestern China: The combined effects of a strong earthquake and subsequent rainstorms: *Geomorphology*, v. 139–140, p. 559–576, doi:10.1016/j.geomorph.2011.12.021.
- Tang, C., Li, W., Ding, J., and Huang, C., 2011, Field Investigation and Research on Giant Debris Flow on August 14, 2010 in Yingxiu Town, Epicenter of Wenchuan Earthquake: *Earth Science*, v. 36, p. 172–180 (in Chinese).
- Wang, Q., Qiao, X., Lan, Q., Freymueller, J., Yang, S., Xu, C., Yonglin, Y., Xinzha, Y., Tan, K., and Chen, G., 2011, Rupture of deep faults in the 2008 Wenchuan earthquake and uplift of the Longmen Shan: *Nature Geoscience*, v. 4, p. 634–640, doi:10.1038/ngeo1210.
- Xu, Q., Zhang, S., Li, W.L., and Van Asch, T.W.J., 2012, The 13 August 2010 catastrophic debris flows after the 2008 Wenchuan earthquake, China: *Natural Hazards and Earth System Science*, v. 12, p. 201–216, doi:10.5194/nhess-12-201-2012.
- Zhang, L.M., Zhang, S., and Huang, R.Q., 2014, Multi-hazard scenarios and consequences in Beichuan, China: The first five years after the 2008 Wenchuan earthquake: *Engineering Geology*, doi:10.1016/j.enggeo.2014.03.020.

Looking through the window of disturbance at post-wildfire debris-flow hazards

Luke A. McGuire^{a,*}, Francis K. Rengers^b, Jason W. Kean^b, Dennis M. Staley^b, Hui Tang^a, Ann M. Youberg^c

^aUniversity of Arizona, Department of Geosciences, 1040 E 4th St, Tucson, AZ 85721, USA

^bU.S. Geological Survey, 1711 Illinois St., Golden, CO 80401, USA

^cUniversity of Arizona, Arizona Geological Survey, 1955 E 6th St., Tucson, AZ 85721, USA

Abstract

The extreme heat from wildfire alters soil properties and incinerates vegetation, leading to changes in infiltration capacity, ground cover, soil erodibility, and rainfall interception. These changes promote increases in runoff and sediment transport that increase the likelihood of runoff-generated debris flows. Over a period of several years, referred to as the window of disturbance, the landscape recovers and wildfire-induced changes become less accentuated. Debris flows are most common in the year immediately following wildfire, but changes in the likelihood and magnitude of debris flows throughout the window of disturbance are not well constrained. Assessing debris-flow hazards throughout the post-wildfire recovery period is complicated, in part, by the myriad of wildfire-induced changes and their nonlinear relationships with sediment transport and runoff generation processes. In this study, we combine measurements of soil hydraulic properties with vegetation survey data and numerical modeling to understand how debris-flow threats are likely to change in steep, burned basins during the first two years of recovery. We focus on documenting recovery following the 2016 Fish Fire in the San Gabriel Mountains, CA, USA and demonstrate how a numerical model can be used to predict temporal changes in debris-flow properties and initiation thresholds within that region. Substantial increases in sorptivity, which represents the capillarity contribution to infiltration, and reductions in the percentage of bare soil occurred during the first 18 months following the Fish Fire. Numerical modeling suggests that these changes lead to a roughly 40% increase in the 15-minute rainfall intensity-duration threshold associated with debris-flow initiation as well as more than a three-fold decrease in debris-flow volume from post-fire year 1 to post-fire year 2. These results provide valuable constraints on changes in debris-flow thresholds within the San Gabriel Mountains as well as a general framework for exploring the impact of changing vegetation and soil hydraulic properties on debris flow magnitude and susceptibility.

Keywords: debris flow, wildfire, recovery, threshold, infiltration

1. Introduction

Wildfire is a well-documented catalyst for change in hydrologic and geomorphic systems (e.g. Shakesby and Doerr, 2006). Post-wildfire reductions in infiltration capacity (Ebel and Moody, 2017) and canopy interception (Stoof et al., 2012) promote increased runoff. Increased runoff combined with the effects of lower critical thresholds for sediment entrainment (Moody et al., 2005) and a high percentage of bare soil lead to a substantial increase in debris-flow likelihood after a wildfire. Post-wildfire debris flows are triggered when runoff concentrates in steep channels and mobilizes large volumes of sediment, in contrast to debris flows that initiate from shallow landslides (e.g. Meyer and Wells, 1997; Cannon et al., 2008; Gabet and Bookter, 2008; Kean et al., 2011). With few exceptions (e.g. Cannon et al., 2008), previous work has focused on the threats posed by runoff-generated debris flows in the first year following disturbance by wildfire, but the extent to which debris flow hazards persist into subsequent years is not well understood.

Rainfall intensity-duration (ID) thresholds are commonly used to assess post-wildfire debris-flow potential, with debris flows often initiating once a critical rainfall intensity is exceeded (Cannon et al., 2008; Staley et al., 2013).

* Corresponding author e-mail address: lmcguire@email.arizona.edu

Staley et al. (2017) recently developed an empirical model to predict debris-flow likelihood as a function of terrain attributes, soil burn severity, and rainfall intensity (averaged over 15, 30, or 60 minutes). However, it is not clear how rainfall ID thresholds change with time following wildfire because data regarding debris-flow occurrence are most common in the first post-wildfire year and because there is no clear connection between the magnitude of empirically

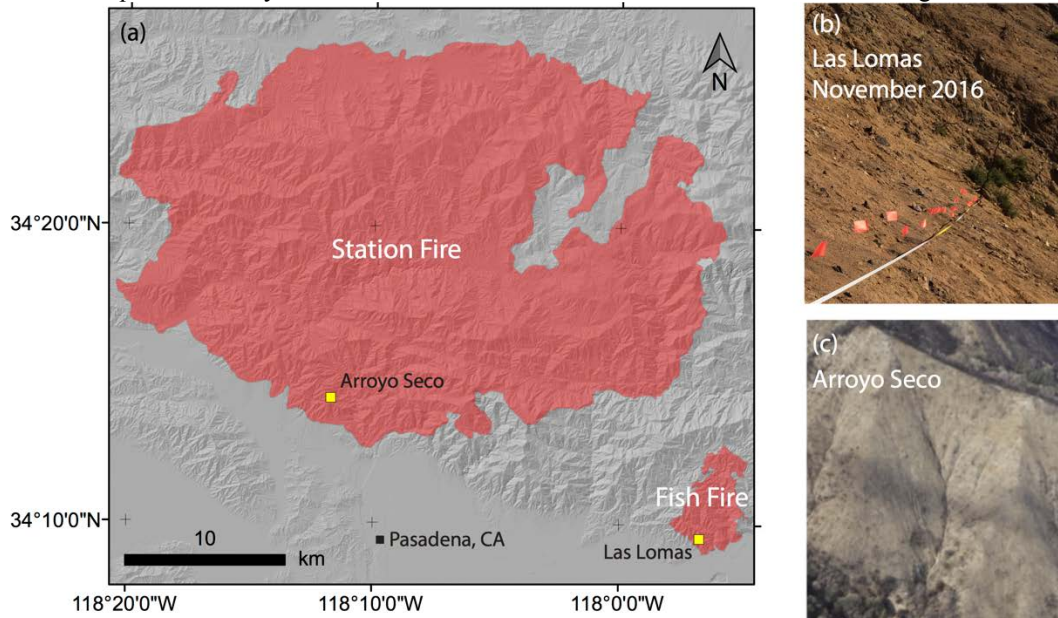


Fig. 1. (a) Overview of study area; (b) Photo looking across the hillslope along a transect at the Las Lomas site where infiltration measurements were conducted. (c) Aerial photo of the Arroyo Seco watershed following the 2009 Station Fire.

derived rainfall ID thresholds and the hydrologic and geomorphic variables that are changing as the landscape recovers. Since runoff is a necessary condition for most post-wildfire debris flows, it is critical to understand how wildfire-driven changes to soil infiltration capacity change with time since burning and how the magnitude of those changes translates into changes in debris-flow potential. Post-wildfire reductions in infiltration capacity are often attributed to increased soil water repellency (Shakesby and Doerr, 2006), which may persist for up to five years but typically decays over timescales of 1-2 years (e.g. Larsen et al., 2009). The percentage of bare soil, which is initially high following wildfire and decays as vegetation recovers, is also likely to be a key factor in determining debris-flow potential since bare soil on hillslopes is particularly vulnerable to erosion. Hillslope erosion can account for a substantial amount of the sediment within post-wildfire debris flows in certain cases (e.g. Smith et al., 2012; Staley et al., 2014) and contribute to sediment bulking in the channel that increases flow depth and discharge.

Given measurements of how wildfire-affected variables change over time, such as ground cover and soil hydraulic properties, physically-based models have the potential to be used to quantify the corresponding changes in debris-flow response. In this study, we utilize the numerical model developed by McGuire et al. (2017), which represents the coupled processes of runoff, sediment transport, and debris-flow initiation, to assess changes in debris-flow ID thresholds and debris-flow magnitude within an 18-month period following wildfire in the San Gabriel Mountains, CA, USA. We make use of data from two study areas, referred to as Las Lomas and Arroyo Seco, both of which are located in the San Gabriel Mountains and have produced numerous debris flows following wildfire. Although the two study sites were burned at different times and in different fires (Figure 1), we utilize them as representative sites for debris-flow prone headwater basins in the San Gabriel Mountains. Data from the Las Lomas study site are used to quantify changes in soil hydraulic properties and canopy/ground cover with time following wildfire. Changes in soil hydraulic properties were quantified at Las Lomas through in situ measurements throughout an 18-month period following the 2016 Fish Fire. Canopy and ground cover were negligible at the start of the study period and were quantified through a field survey 18 months after the Fish Fire. These measurements are then used as inputs for a numerical model in conjunction with a high resolution digital elevation model (DEM), obtained at the nearby Arroyo Seco site (which was the focus of intensive debris-flow monitoring following the 2009 Station Fire), to simulate debris-flow initiation during different stages of recovery. Here, we report on the measured changes at Las Lomas and a series

of simulations designed to assess how debris-flow response is likely to change in the San Gabriel Mountains from the first to second year after the wildfire.

2. Study Area

The Fish Fire, which started on 21 June 2016, burned 4253 acres of the Angeles National Forest in the San Gabriel Mountains near Los Angeles, CA (Figure 1). The wildfire burned mainly in rugged terrain with steep hillslopes dominated by chaparral vegetation. Soils in the area are generally thin (0.5-1 m), rock outcrops are common, and a highly weathered layer of saprolite is occasionally exposed on the hillslopes (Staley et al., 2014). Repeat measurements of soil hydraulic properties were conducted on a roughly 40-degree hillslope, which we will refer to as the Las Lomas study site, in an area that experienced moderate-to-high soil burn severity during the Fish Fire. No vegetation canopy remained and all litter and duff at the surface had been consumed by the wildfire. The hillslope is located in the upper portion of a 0.12 km² basin that drains into the Las Lomas debris basin. A series of rainstorms between December 2016 and February 2017 incised a network of rills through the study area and produced a number of debris flows and floods at the outlet of the drainage basin.

The Arroyo Seco site, also located in the San Gabriel Mountains in an area dominated by chaparral vegetation, is a small drainage basin (0.012 km²) that burned at moderate-to-high severity in the 2009 Station Fire. A number of runoff-generated debris flows were observed in the first winter following the fire (Kean et al., 2011). A DEM derived from terrestrial laser scanner (TLS) surveys performed by Staley et al. (2014) following the first post-wildfire rainstorms provides high-resolution topographic data that are ideal for detailed simulations of runoff and debris flow initiation.

3. Methods

3.1. Field measurements following the Fish Fire

Field saturated hydraulic conductivity (K_s) and sorptivity (S) were determined through in situ measurements conducted with a mini disk tension infiltrometer. The tension infiltrometer has a disk with a radius of 2.25 cm. The suction head was set to 1 cm for all measurements. Measurements were made during site visits to the Las Lomas study area (burned in the 2016 Fish Fire) in September 2016, November 2016, January 2017, February 2017, July 2017, and March 2018. Measurements were performed every 1 meter along a 20 meter transect that extended in the cross-slope direction, with the exception of those made in September 2016. When time permitted, additional measurements were made on the hillslope in the vicinity of the established transect. In September 2016, the transect had not yet been established and measurements were made in nearby areas burned at moderate-high severity.

A total of 26, 35, 28, 40, 21, and 21 infiltration measurements were made during the site visits in September 2016, November 2016, January 2017, February 2017, July 2017, and March 2018, respectively. During each measurement, the total volume of water infiltrated is tracked as a function of time and must later be post-processed to infer field saturated hydraulic conductivity (K_s) and sorptivity (S) (e.g. Zhang, 1997). Estimates of K_s and S were derived using the methods described by McGuire et al. (2018). The wetting front suction head (h_f), a parameter in the Green-Ampt infiltration model, can then be estimated as (Ebel and Moody, 2016) $h_f = S^2/2K_s\theta_s$, where θ_s denotes the volumetric water content at saturation.

In March 2018, we conducted a vegetation survey on a hillslope adjacent to the infiltration transect using the point-intercept method (e.g. Crocker and Tiver, 1948). A measuring tape was extended between two control points marked with steel rebar. The distance between the two control points was 20.8 meters. Every 20 cm along the transect (for a total of 105 measurements), we sighted directly down toward the surface with a laser pointer and recorded the first obstacle that intercepted the light. The laser either hit the vegetation canopy, bare soil, litter, or a rock. Litter was classified as any loose plant material on the soil surface. Any sediment with a diameter greater than 5 mm was classified as rock cover. If the laser hit any portion the canopy, the maximum height of that vegetation was recorded.

3.2. Numerical model

The numerical model represents fluid flow using the shallow water equations, which contain additional source terms to account for changes in flow resistance as a function of sediment concentration (McGuire et al., 2016; 2017). Infiltration is modeled with the Green-Ampt equation, using estimates of K_s and h_f obtained from field measurements. Hydraulic roughness was taken into account using a depth-dependent Manning friction coefficient (Mugler et al.,

2011). Debris-flow resistance is represented using a Coulomb friction approach (e.g. Iverson and Denlinger, 2001) where the effective basal normal stress is modified by pore fluid pressure within the flow. In all simulations, the ratio of pore fluid pressure to total basal normal stress (λ) was set to a constant value of $\lambda=0.65$.

The Hairsine-Rose (HR) model (Hairsine and Rose, 1992a; 1992b) was used to account for sediment entrainment and deposition, as described in detail by McGuire et al. (2016). In the HR model, particles can be detached and entrained into the flow via raindrop impact or flow-driven detachment. The rate at which sediment is detached by raindrops is a function of flow depth, rainfall intensity, and raindrop diameter while the rate of flow-driven sediment detachment is a function of stream power. Since the canopy and ground cover (e.g. litter) can shield the underlying soil from raindrop impact, changes in ground and canopy cover will also influence the rate of raindrop-driven sediment detachment (e.g. McGuire et al., 2016).

3.3. Debris-flow simulations at Arroyo Seco

For model simulations, we applied the vegetation and hydrologic measurements from the Fish Fire to the nearby Arroyo Seco drainage basin (Figure 1) because a high-resolution DEM was available for that site. Although Arroyo Seco was not burned during the Fish Fire, it is representative of headwater areas within the San Gabriel Mountains where post-wildfire debris flows tend to initiate and its steepness is similar to other debris-flow producing basins in the San Gabriel Mountains (Kean et al., 2011). The small size of the basin makes it possible to perform a larger number of simulations, and we coarsened the DEM from 2 cm (Staley et al., 2014) to a grid spacing of 37.5 cm to further increase computational efficiency. Runoff is driven by a family of idealized rainstorms, with peak 15-minute rainfall intensities (I_{15}^p) varying from 20 mm/h to 60 mm/h in increments of 2.5 mm/h (Figure 2).

All simulations were performed using the same parameters and model setup as reported in McGuire et al. (2016) unless otherwise noted (Table 1). McGuire et al. (2016) calibrated the HR sediment transport parameters at the Arroyo Seco site by comparing simulated erosion patterns to those generated from repeat TLS surveys (Staley et al., 2014). The roughness coefficient was set to a value of $n_0=0.05 \text{ s m}^{-1/3}$, which is in range of calibrated roughness values for recently burned, low-order drainage basins in the San Gabriel Mountains (Rengers et al., 2016). The fraction of bare soil exposed to raindrop impact is assumed to be 1.0 in the first year following the fire based on field observations of negligible vegetation and litter cover (Figure 1). Infiltration rates were computed for year 1 using the K_s and h_f values obtained in September 2016 and November 2016, while K_s and h_f values obtained in July 2017 and March 2018 were used for year 2. Each pixel within the computational domain was randomly assigned a value from the measured distribution of K_s and h_f . Due to the number of pixels in the computational domain, we found that differences among simulations performed with different realizations of K_s and h_f were not significant.

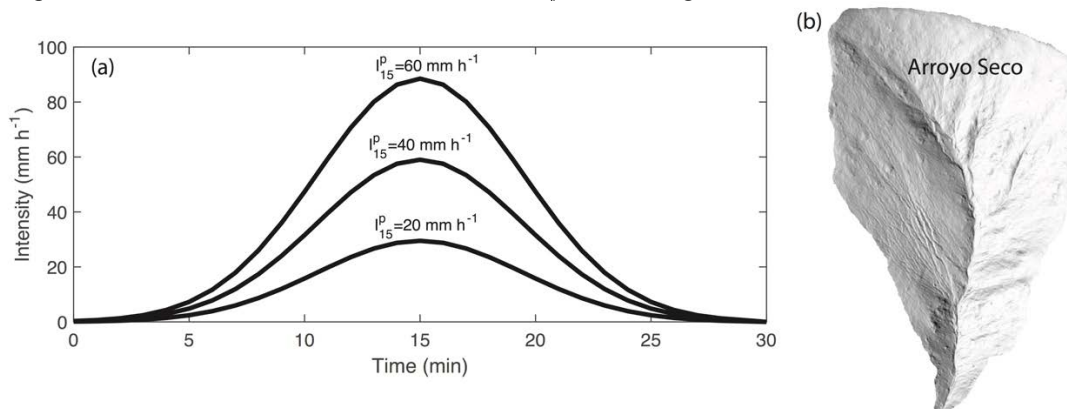


Fig. 2. (a) Designed rainstorms used for simulations at Arroyo Seco. For display purposes only 3 curves are shown; however, for modeling we used curves with peak 15-minute rainfall intensity (I_{15}^p) varying from 20-60 mm h⁻¹ in intervals of 2.5 mm h⁻¹; (b) Shaded relief map of Arroyo Seco.

A total of 19 simulations, each driven by one of the 19 different rainstorms (Figure 2a), were performed using the measured infiltration and vegetation characteristics from the first post-wildfire year. A second set of 19 simulations were performed using the measured infiltration and vegetation characteristics from the second post-wildfire year. Lastly, we performed a final set of simulations using measured soil hydraulic properties from year 2 and vegetation

characteristics (i.e. 100% bare ground) consistent with year 1. The goal of these simulations was to quantify the relative impact of vegetation recovery and soil recovery on post-wildfire debris flows. Flow depth, discharge, and sediment concentration at the basin outlet were recorded in all cases to assess differences among simulations. Debris flows were identified at the outlet of the basin based on exceedance of a sediment concentration threshold of 40%. Flows with a sediment concentration (c) less than 40% were classified as floods. The total volume of sediment exiting the basin, total volume of debris flows (i.e. flows with $c > 40\%$) leaving the basin, and peak debris flow discharge at the outlet were stored for each simulation.

Table 1. Model parameters used for simulations of runoff, sediment transport, and debris flow initiation at the Arroyo Seco site. Notation follows McGuire et al. (2016). When appropriate, values for year 1 and year 2 are both presented and separated by commas. Median values are reported for K_s and h_f .

Parameter name (symbol)	Units	Value	Source
Roughness coefficient (n_o)	$s\ m^{-1/3}$	0.05	Calibrated
Raindrop detachability (a_o)	$kg\ m^{-2}\ s^{-1}$	9000	Calibrated
Raindrop redetachability (a_{o0})	$kg\ m^{-2}\ s^{-1}$	410000	Calibrated
Fraction of effective stream power (F)	-	0.0065	Calibrated
Fraction canopy cover	-	0, 0.29	Measured
Fraction bare soil	-	1, 0.63	Measured
Field saturated hydraulic conductivity (K_s)	$mm\ h^{-1}$	17, 13	Measured
Wetting front suction head (h_f)	m	0.005, 0.022	Measured

4. Results

4.1. Changes in soil hydraulic properties and ground cover

Repeat field measurements of soil hydraulic properties reveal a change in sorptivity (S) between February 2017 and July 2017, which corresponds to a time period of 8 to 13 months after the wildfire (Figure 3). As a result, the median wetting front suction head (h_f) increased with time from roughly 0.001 m in September 2016 to 0.021 m by March 2018. In contrast, field saturated hydraulic conductivity (K_s) appears to be relatively constant with time following the wildfire (Figure 3). The first and third quartiles of K_s in year 1 are 9 mm/h and 33 mm/h, respectively, whereas they are 5 mm/h and 30 mm/h in year 2. The fraction of bare soil decreased from 1.0 immediately following the wildfire to 0.63 in March 2018, after 18 months of recovery. The reduction in bare ground was primarily due to an increase in canopy cover fraction from approximately 0 to 0.29. The fractions of litter (0.07) and rock cover (0.01) were relatively minor. Although the recovering vegetation may be effective at reducing direct raindrop impact on the soil surface, it likely had a minimal ability to intercept and store water since the average vegetation height was less than 10 cm.

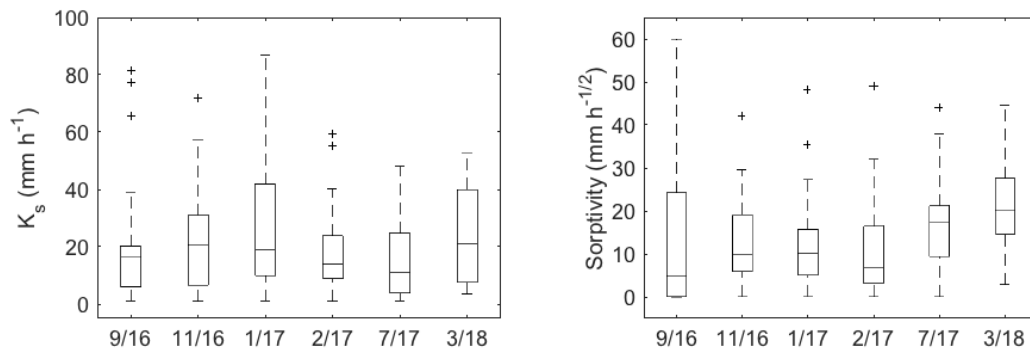


Fig. 3. (a) Field saturated hydraulic conductivity (K_s) and (b) sorptivity (S) derived from field measurements at different times following the June 2016 Fish Fire.

4.2. Simulations of erosion and debris flows

Debris flows initiated in response to lower intensity rainstorms in year 1 relative to year 2 (Figure 4). The first sign of debris flow activity at the lower outlet (i.e. debris flow volume greater than 5 m^3) during year 1 occurs in response to the designed rainstorm with a peak I_{15} of 27.5 mm/h whereas storms during year 2 with a peak I_{15} less than 37.5 mm/h do not produce any debris flows at the outlet. In the theoretical case where vegetation recovery is neglected in year 2 and only changes in infiltration capacity are taken into account, a peak I_{15} of at least 35 mm/h is required to initiate debris flows.

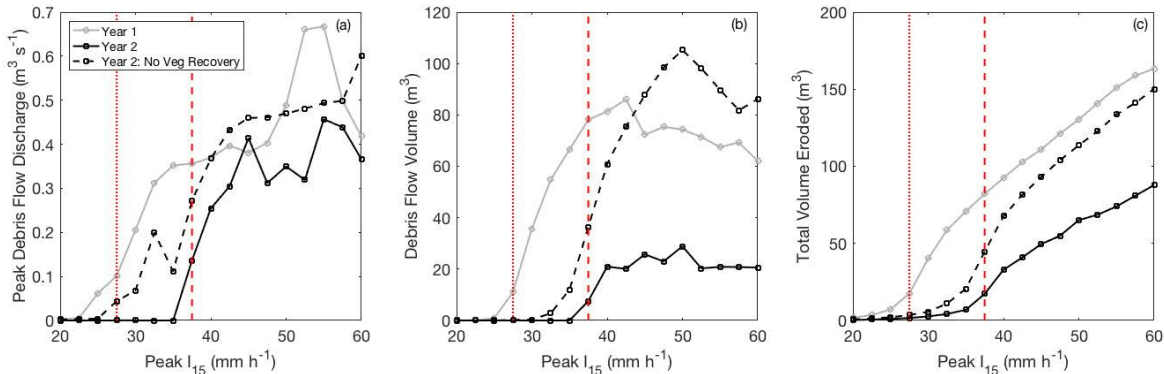


Fig. 4. Model simulations of (a) debris-flow discharge, (b) debris-flow volume, and (c) total volume eroded at the basin outlet as a function of rainfall intensity. Vertical lines indicate model-derived thresholds for year 1 (dotted line) and year 2 (dashed line). (a) Peak debris flow discharge and (c) total sediment volume eroded generally increase with peak I_{15} and are highest in the first year following the fire. (b) Debris flow volumes are limited at higher rainfall intensities due to the increased amount of water runoff, which can reduce sediment concentrations in the flow.

The peak discharge of debris flows generally increases with peak I_{15} and decreases from year 1 to year 2, though peak flow depths (Figure 5) and discharges (Figure 4a) are sometimes comparable between years 1 and 2. Debris-flow volume initially increases with peak I_{15} and then remains constant (year 2) or decreases slightly (year 1). The total volume of sediment eroded, however, continues to increase with peak I_{15} . Debris flow-volumes and total sediment eroded for a given rainstorm are higher in year 1, as expected, with the exception of the case where the site experiences high-intensity rainfall and vegetation recovery is neglected during year 2 simulations.

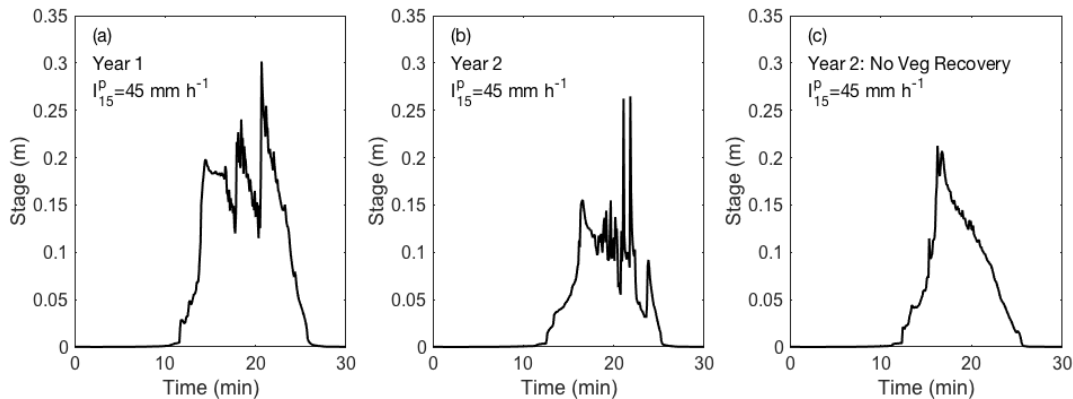


Fig. 5. Model simulations of flow stage at the Arroyo Seco basin outlet under conditions consistent with (a) post-wildfire year 1, (b) post-wildfire year 2, and (c) post-wildfire year 2 where we assume that the vegetation did not recover (i.e. canopy and litter cover are negligible).

5. Discussion

Simulations of erosion and debris-flow initiation suggest that there should be a substantial increase in rainfall ID thresholds between the first and second year after a wildfire as well as decreases in expected debris flow volume due to changes in soil hydraulic properties. Simulations do not take into account the reductions in sediment supply that are likely to have occurred in the time between the first and second year after a wildfire. Results reported here can therefore

be viewed as conservative, with even greater increases in ID thresholds and reductions in volume being likely if sediment supply is reduced in subsequent years from erosion occurring during year 1.

Thresholds of 27.5 mm/h and 37.5 mm/h can be inferred from simulations for years 1 and 2, respectively. The regional I_{15} threshold for debris flow initiation in the San Gabriel Mountains is 19 mm/h (Staley et al., 2013). The difference between the regional threshold and the value derived here could result from basin-specific morphological properties that influence debris flow thresholds (e.g. Staley et al., 2017), uncertainties associated with measured soil hydraulic properties, or from the choice of the designed rainstorm. Increases in the threshold rainfall intensity from 27.5 mm/h in year 1 to 37.5 mm/h year 2 can be attributed to both the increase in h_f and a decrease in percent bare ground. Increases in h_f lead directly to decreases in runoff. Low values of sorptivity (and therefore h_f) in the year immediately following wildfire are consistent with a recent compilation of soil hydraulic properties from burned soils (Ebel and Moody, 2017), which suggests that sorptivity rather than K_s may be more consistently affected by wildfire. Decreases in percent bare ground lead to less hillslope erosion, which subsequently decreases the amount of sediment transported into the channel network (where debris flows are likely to form) and reduces the sediment bulking processes that can increase flow depths and discharges. However, since simulations that neglect vegetation recovery still suggest a 7.5 mm/h increase in the 15-minute rainfall ID threshold, we conclude that changes in infiltration capacity have a greater impact on temporal variations in the rainfall ID threshold relative to changes in percent bare ground.

Simulations also offer insight into how debris flow magnitude can be expected to change with rainfall intensity and time since burning. Simulations indicate that debris-flow volume increases, up to a point, with increasing I_{15} (Figure 4). Gartner et al. (2014), in contrast, found that debris-flow volumes increase monotonically with I_{15} based on a large dataset of estimated volumes from post-wildfire debris flows throughout the Transverse Ranges of southern CA. The difference between our model results and field observations could be partly due to the definition of debris flow employed here, which requires that the sediment concentration exceed 40%. As I_{15} increases, the modeled erosion volumes increase monotonically but debris-flow volumes remain steady or decrease due to increased water runoff, which can dilute portions of the flow to sediment concentrations less than 40%. Since debris flow volumes estimated in the field are based on the amount of sediment deposited in debris basins or estimates of erosion occurring during debris-flow-producing rainstorms (e.g. Gartner et al., 2014), they may include sediment transported through a combination of water-dominated flood, debris flood, and debris-flow mechanisms. Regardless, it is clear that debris flow volumes appear to change more dramatically (i.e. a factor of roughly 3) between year 1 and year 2 compared to the I_{15} rainfall threshold (Figure 4), which increases by approximately 40%. Note that the high debris-flow volumes simulated in year 2 during a case with no vegetation recovery likely exceed those predicted for year 1 due to the fact that increased water runoff in year 1 will dilute some of the flows so that they have a concentration less than the critical value of 40%.

While we focus on a particular geographic region, the San Gabriel Mountains in southern CA, the modeling framework presented here can be used in combination with estimates of post-wildfire infiltration rates from other regions (e.g. Moody et al., 2009; Nyman et al., 2011; Robichaud et al., 2016) to quantify the impact of changing soil hydraulic properties on debris-flow magnitude and initiation thresholds. Similarly, satellite-derived metrics of vegetation recovery, such as the enhanced vegetation index (e.g. Kinoshita and Hogue, 2011), could be used to drive temporal changes in percent ground cover within the model framework. Developing relationships between measurable hydrologic variables, ground cover characteristics, and debris flow properties is a necessary first step towards assessing how debris flow threats are likely to evolve with time following wildfire in different geographic regions.

Conclusions

Disturbance following wildfire leads to an increased potential for runoff-generated debris flows. The hazards posed by debris flows decrease with time following wildfire as soils and vegetation recover. In this study, we monitored changes in soil hydraulic properties and percent bare ground at a site in southern California and used a numerical model to determine how temporal changes in these two variables affect debris flow volumes and initiation thresholds. Simulations suggest that the threshold I_{15} rainfall intensity that triggers debris flows at our study site in the San Gabriel Mountains will increase by approximately 40%, from 27.5 mm/h to 37.5 mm/h. In addition, if debris flows do initiate in the second post-wildfire year, simulations indicate they will be roughly three times smaller (even if sediment supply does not decrease between year 1 and year 2). Although we focus here on post-wildfire debris flows, the methodology used to assess changes in runoff-generated debris flow susceptibility could be applied in other settings, including rocky alpine regions, where runoff-generated debris flows may occur.

Acknowledgements

We would like to thank Petter Nyman and Joe Gartner for thoughtful reviews that improved the quality of this manuscript. This work was supported by the U.S. Geological Survey (USGS) Landslide Hazards Program. Any use of trade, product, or firm names is for descriptive purposes only and does not imply endorsement by the U.S. Government. Code for the numerical model used in this study is available through the Community Surface Dynamics Modeling System (CSDMS) model repository.

References

- Cannon, S.H., Gartner, J.E., Wilson, R.C., Bowers, J.C. and Laber, J.L., 2008, Storm rainfall conditions for floods and debris flows from recently burned areas in southwestern Colorado and southern California: *Geomorphology*, v. 96, no. 3-4, 250-269.
- Crocker, R.L. and Tiver, N.S., 1948, Survey methods in grassland ecology: *Grass and Forage Science*, v. 3, no. 1, 1-26.
- Iverson, R.M. and Denlinger, R.P., 2001, Flow of variably fluidized granular masses across three-dimensional terrain: 1. Coulomb mixture theory. *Journal of Geophysical Research: Solid Earth*, v. 106 (B1), 537-552.
- Ebel, B.A. and Moody, J.A., 2017, Synthesis of soil-hydraulic properties and infiltration timescales in wildfire-affected soils: *Hydrological processes*, v. 31, no. 2, 324-340.
- Gabet, E.J. and Bookter, A., 2008, A morphometric analysis of gullies scoured by post-fire progressively bulked debris flows in southwest Montana, USA: *Geomorphology*, v. 96, no. 3-4, 298-309.
- Gartner, J.E., Cannon, S.H. and Santi, P.M., 2014, Empirical models for predicting volumes of sediment deposited by debris flows and sediment-laden floods in the transverse ranges of southern California: *Engineering Geology*, v. 176, 45-56.
- Hairsine, P.B. and Rose, C.W., 1992a, Modeling water erosion due to overland flow using physical principles: 1. Sheet flow: *Water resources research*, v. 2, no. 1, 237-243.
- Hairsine, P.B. and Rose, C.W., 1992b, Modeling water erosion due to overland flow using physical principles: 2. Rill flow: *Water resources research*, v. 28, no. 1, 245-250.
- Kean, J.W., Staley, D.M., and Cannon, S.H., 2011, In situ measurements of post-fire debris flows in southern California: Comparisons of the timing and magnitude of 24 debris-flow events with rainfall and soil moisture conditions: *Journal of Geophysical Research*, v. 116, F04019, 10.1029/2011JF002005.
- Kinoshita, A.M. and Hogue, T.S., 2011, Spatial and temporal controls on post-fire hydrologic recovery in Southern California watersheds: *Catena*, v. 87, no. 2, 240-252.
- Larsen, I.J., MacDonald, L.H., Brown, E., Rough, D., Welsh, M.J., Pietraszek, J.H., Libohova, Z., de Dios Benavides-Solorio, J. and Schaffrath, K., 2009, Causes of post-fire runoff and erosion: water repellency, cover, or soil sealing?: *Soil Science Society of America Journal*, v. 73, no. 4, 1393-1407.
- Meyer, G.A. and Wells, S.G., 1997, Fire-related sedimentation events on alluvial fans, Yellowstone National Park, USA: *Journal of Sedimentary Research*, v. 67, no. 5, 776-791.
- McGuire, L.A., Kean, J.W., Staley, D.M., Rengers, F.K., and Wasklewicz, T.A., 2016, Constraining the relative importance of raindrop- and flow-driven sediment transport mechanisms in post-wildfire environments and implications for recovery time scales: *Journal of Geophysical Research: Earth Surface*, 10.1002/2016JF003867
- McGuire, L.A., Rengers, F.K., Kean, J.W. and Staley, D.M., 2017, Debris flow initiation by runoff in a recently burned basin: Is grain- by- grain sediment bulking or en masse failure to blame?: *Geophysical Research Letters*, v. 44, no. 14, 7310-7319.
- McGuire, L.A., Rengers, F.K., J Kean, J.W., Staley, D.M. and Mirus, B.B., 2018, Incorporating spatially heterogeneous infiltration capacity into hydrologic models with applications for simulating post-wildfire debris flow initiation: *Hydrological Processes*, 10.1002/hyp.11458.
- Moody, J.A., Smith, J.D. and Ragan, B.W., 2005, Critical shear stress for erosion of cohesive soils subjected to temperatures typical of wildfires: *Journal of Geophysical Research: Earth Surface*, v. 110, F1.
- Moody, J.A., Kinner, D.A. and Úbeda, X., 2009, Linking hydraulic properties of fire-affected soils to infiltration and water repellency: *Journal of Hydrology*, v. 379, no. 3-4, 291-303.
- Mügler, C., Planchon, O., Patin, J., Weill, S., Silvera, N., Richard, P. and Mouche, E., 2011, Comparison of roughness models to simulate overland flow and tracer transport experiments under simulated rainfall at plot scale: *Journal of Hydrology*, v. 402, no. 1-2, 25-40.
- Nyman, P., Sheridan, G.J., Smith, H.G., and Lane, P.N., 2011, Evidence of debris flow occurrence after wildfire in upland catchments of south-east Australia: *Geomorphology*, v. 125, no. 3, 383-401. 2000.
- Rengers, F.K., McGuire, L.A., Kean, J.W., Staley, D.M., and Hobbey, D., 2016, Model simulations of flood and debris flow timing in steep catchments after wildfire: *Water Resources Research*, v. 52, 6041–6061, doi:10.1002/2015WR018176.
- Robichaud, P.R., Wagenbrenner, J.W., Pierson, F.B., Spaeth, K.E., Ashmun, L.E. and Moffet, C.A., 2016, Infiltration and interrill erosion rates after a wildfire in western Montana, USA: *Catena*, v. 142, 77-88.
- Shakesby, R.A. and Doerr, S.H., 2006, Wildfire as a hydrological and geomorphological agent, *Earth-Science Reviews*, v. 74, no. 3-4, 269-307.
- Smith, H.G., Sheridan, G.J., Nyman, P., Child, D.P., Lane, P.N., Hotchkis, M.A. and Jacobsen, G.E., 2012, Quantifying sources of fine sediment supplied to post-fire debris flows using fallout radionuclide tracers: *Geomorphology*, v. 139, 403-415.
- Staley D.M., Kean, J.W., Cannon, S.H., Laber, J.L., and Schmidt, K.M., 2013, Objective definition of rainfall intensity-duration thresholds for the initiation of post-fire debris flows in southern California: *Landslides*, v. 10, 547-562. doi:10.1007/s10346-012-0341-9
- Staley, D.M., Wasklewicz, T.A. and Kean, J.W., 2014, Characterizing the primary material sources and dominant erosional processes for post-fire debris-flow initiation in a headwater basin using multi-temporal terrestrial laser scanning data: *Geomorphology*, v. 214, 324-338.
- Staley, D.M., Negri, J.A., Kean, J.W., Laber, J.L., Tillery, A.C., and Youberg, A.M., 2017, Prediction of spatially explicit rainfall intensity-duration thresholds for post-fire debris-flow generation in the western United States: *Geomorphology*, v. 278, 149-162
- Stoof, C.R., Vervoort, R.W., Iwema, J., Elsen, E., Ferreira, A.J.D. and Ritsema, C.J., 2012, Hydrological response of a small catchment burned by experimental fire: *Hydrology and Earth System Sciences*, v. 16, no. 2, 267-285.
- Zhang, R., 1997, Determination of soil sorptivity and hydraulic conductivity from the disk infiltrometer: *Soil Science Society of America Journal*, v. 61, no. 4, 1024-1030.

Conceptual framework for assessing disturbance impacts on debris-flow initiation thresholds across hydroclimatic settings

Benjamin B Mirus^{a,*}, Dennis M. Staley^a, Jason W. Kean^a, Joel B. Smith^a, Rick Wooten^b,
Luke A. McGuire^c, Brian A. Ebel^d

^aU.S. Geological Survey, Landslide Hazards Program, PO Box 25046, M.S. 966, Denver, CO 80225, USA

^bNorth Carolina Geological Survey, Department of Environmental Quality, 2090 U.S. Highway 70, Swannanoa, NC, USA

^cUniversity of Arizona, Department of Geosciences, 1040 East 4th Street, Tucson, AZ 85721, USA

^dU.S. Geological Survey, Water Cycle Branch, PO Box 25046, M.S. 410, Denver, CO 80225, USA

Abstract

The destructive and deadly nature of debris flows has motivated research into empirical rainfall thresholds to provide situational awareness, inform early warning systems, and reduce loss of life and property. Disturbances such as wildfire and land-cover change can influence the hydrological processes of infiltration and runoff generation; in steep terrain this typically lowers empirical thresholds for debris-flow initiation. However, disturbance impacts, and the post-disturbance recovery may differ, depending on the severity, nature, extent, and duration of the disturbance, as well as on the prevailing hydroclimatic conditions. Thus, it can be difficult to predict impacts on debris-flows hazards in regions where historically such disturbances have been less frequent or severe. Given the increasing magnitude and incidence of wildfires, among other disturbances, we seek to develop a conceptual framework for assessing their impacts on debris-flow hazards across geographic regions. We characterize the severity of disturbances in terms of changes from undisturbed hydrologic functioning, including hillslope drainage and available unsaturated storage capacity, which can have contrasting influences on debris-flow initiation mechanisms in different hydroclimatic settings. We compare the timescale of disturbance-recovery cycles relative to the return period of threshold exceeding storms to describe vulnerability to post-disturbance debris flows. Similarly, we quantify resilience by comparing the timescales of disturbance-recovery cycles with those of disturbance-recurrence intervals. We illustrate the utility of these concepts using information from U.S. Geological Survey landslide monitoring sites in burned and unburned areas across the United States. Increasing severity of disturbance may influence both recovery timescales and lower the return period for debris-flow inducing storms, thus increasing the vulnerability to disturbance-related hazards while also decreasing system resilience. The proposed conceptual framework can inform future data acquisition and model development to improve debris-flow initiation thresholds in areas experiencing increasingly frequent, severe, and even overlapping landscape disturbances.

Keywords: disturbance; hydrologic thresholds; rainfall threshold; debris flows; wildfire; resilience; vulnerability

1. Introduction

Debris flows are a particularly damaging and deadly category of landslides, which move rapidly down steep slopes and channel networks (Iverson, 1997; Coe et al., 2008). Investigations of hydrologically triggered debris flows often focus on the historical rainfall conditions measured during widespread landsliding events, which has facilitated the development of critical rainfall intensity-duration (ID) thresholds for situational awareness (Caine, 1980; Keefer et al., 1987; Kean et al., 2011; Jakob et al., 2012). These ID thresholds are a simple empirical proxy for the complex hydrological processes of infiltration, drainage, and runoff, which influence the force imbalance that triggers failures (Lu and Godt, 2013; Sidle and Ochiai, 2013). Despite recent efforts to develop hydro-meteorological thresholds that incorporate these processes (Mirus et al., 2018; Bogaard and Greco, 2018), empirical ID thresholds are constrained to a specific geographic area and, within this area, limited to hillslopes with similar hydrologic conditions (Guzzetti et al., 2008; Baum and Godt, 2010). As a consequence, such thresholds are stationary and non-transferrable to different regions, as they do not account for the dynamic influence of climate and land-use changes or other disturbances.

* Corresponding author e-mail address: bbmirus@usgs.gov

In zero-order basins that are typical of debris-flow source areas, the balance between rainfall input via infiltration, unsaturated soil storage, drainage, and runoff is controlled by soil-hydraulic properties, climate, topography, and land cover (Mirus and Loague, 2013; Sidle et al., 2018). Landscape disturbances can influence this hillslope water balance by abruptly changing these properties and process thresholds, which impacts hydrologic functioning (Ebel and Mirus, 2014; Mirus et al., 2017a). One important hydrologic function in soil-mantled hillslope environments is balancing drainage and storage to maintain slope stability (Mirus et al., 2017b). Efficient subsurface drainage during large storm events can limit slope failures, but slopes must also store some water between storms to support transpiration by vegetation, whose root strength reinforces slopes.

A wide variety of land-cover disturbances can influence the hillslope water balance across various landscapes and hydroclimatic settings in different ways. Wildfires reduce infiltration capacity, thereby increasing the likelihood of runoff-generated debris flows during relatively moderate rainfall events (Cannon, 2001; Staley et al., 2013). Following the recovery of soils impacted by wildfire, the lack of vegetation can increase the potential for landslides due to reduced root reinforcement or decreased interception and transpiration. Deforestation and road construction also limit root reinforcement and impact subsurface drainage, which can increase landslide susceptibility during prolonged storms (Swanson et al., 1975; Mirus et al., 2007). Previous landslides are another type of disturbance that influence the potential for further slope failures. Debris flows that evacuate mobile material can decrease the potential for a subsequent landslide until the source material is replenished (Imaizumi et al., 2015). However, when failed earth materials are not completely evacuated a positive feedback cycle of repeated landsliding or catastrophic debris flows may result (Iverson et al., 2015; Mirus et al., 2017b; Samia et al., 2017; Morino et al., 2018).

The area of the Earth's surface affected by wildfire and vegetation clearing is likely to continue rising (Cannon and DeGraaf, 2009; Mirus et al., 2017a), as is the frequency of extreme storm events. In this context, we propose a generalized conceptual framework for understanding disturbance impacts on associated debris-flow hazards. Our approach relates the transient changes caused by disturbances to the underlying hydrologic processes that trigger debris flows by relating the hillslope storage-drainage concept from disturbance hydrology (Ebel and Mirus, 2014) to the hydrologic cause-trigger concept proposed for improving hydrologic process representation in landslide early warning thresholds (Bogaard and Greco, 2018).

2. Contrasting Debris-Flow Initiation Mechanisms

Debris flows involve substantial water contents with entrained sediment to maintain high pore-water pressures that enhance mobility (Iverson, 1997), and thus they are largely associated with rainfall triggering events. The high risk typically associated with debris flows has prompted an abundance of studies to identify critical rainfall thresholds for specific regions or conditions. However, when investigating the regional variations between rainfall triggering events, it becomes apparent that different underlying hydrological processes may dominate, depending on the hydroclimatic setting. In some regions, debris flows are associated with prolonged heavy rainfall, where steady infiltration into water-logged soils results in catastrophic and widespread slope failures (Crosta and Dal Negro, 2003; Coe et al., 2014; Wooten et al., 2016). In contrast, debris flows are also triggered in arid or semiarid settings and in areas disturbed by wildfire after only a brief period of higher rainfall intensity without distinct correlation to the initial moisture conditions (Cannon, 2001; Kean et al., 2011; Staley et al., 2013). These contrasting rainfall-triggering conditions reflect different hydrological processes and corresponding debris-flow initiation mechanisms (Cannon et al., 2001), which may also exhibit different geomorphic features (Morino et al., 2018; Staley et al., 2019). However, both initiation mechanisms tend to require steep terrain with available mobile regolith.

In the case of wildfires, changes in near-surface hydraulic properties promote infiltration excess runoff (Moody et al., 2013), which can trigger rapid mobilization of available sediment and debris in stream channels within burn affected areas (Kean et al., 2013). This frequent phenomenon across arid and semiarid regions of the western United States has informed the development of short-duration rainfall intensity thresholds and other empirical metrics for rapid burn-area hazard assessments (Cannon et al., 2011; Staley et al., 2013). This empirical approach has been used in conjunction with quantitative precipitation forecasts to provide situational awareness of potential hazards in advance of incoming storms across the western United States (Oakley et al., 2017; Staley et al., 2017). Subsequent research has focused on distributed numerical models parameterized with measured (or measurable) soil properties to simulate the coupled surface and subsurface hydrological processes in burned areas (Ebel et al., 2016; McGuire et al., 2018). In southern California a more simplified process-based model of infiltration-excess runoff also compares well to measured debris-flow timing (Rengers et al., 2016).

Recent fires in more humid regions in Oregon and North Carolina created a need for U.S. Geological Survey (USGS) post-fire hazard assessments that were developed with the same empirical methods that assumes infiltration-excess runoff (https://landslides.usgs.gov/hazards/postfire_debrisflow/). Neither the empirical approach nor process-based modeling of post-fire debris flows have been rigorously evaluated in these humid settings, so it remains unclear how broadly transferrable either approach is to these types of environments where wildfire is typically infrequent and less severe. In Australia, the enhancement of post-fire runoff response correlates with aridity (Van der Sant et al., 2018), which indicates that the post-disturbance impacts are strongly related to hydroclimatic setting. In the semiarid western U.S. streamflow has increased significantly following wildfire, but in the humid southeast no change in streamflow was observed following prescribed fires, because they are characterized by low fire severity and generally cover less than 20% of a basin, a critical threshold for fire impacts on streamflow (Hallema et al., 2018). Thus, wildfire and other disturbances may not have a universal impact on debris-flow hazards across different geographic regions.

3. Monitoring Post-Disturbance Hydrologic Response

Limited observations of pre-and-post disturbance conditions is a major challenge in disturbance hydrology (Ebel and Mirus, 2014; Mirus et al., 2017a). Fortunately, three USGS landslide monitoring sites in western North Carolina with similar instrument configurations (<https://usgs.gov/natural-hazards/landslide-hazards/monitoring>) provide an opportunity to directly examine the impacts of wildfire on hillslope hydrologic response in steep terrain that is particularly prone to debris flows. In 2016, prolonged drought contributed to numerous wildfires in the southern Appalachian Mountains. The Poplar Cove monitoring site was burned by the Knob Fire in November 2016, while the Mooney Gap and Bent Creek sites were not directly impacted by the various wildfires in the region. At Poplar Cove the duff groundcover and understory vegetation were largely incinerated, but the soils were relatively undisturbed and the larger trees on the hillslope survived the fire (Fig. 1). Site visits to the nearby Party Rock, Chimney Tops II, Rock Mountain, Tellico, and Maple Springs fires in North Carolina, Tennessee, and Georgia confirmed that the limited impacts of relatively low burn severity observed at Poplar Cove were common across the southern Blue Ridge physiographic province of the Appalachian region.



Fig. 1. The Poplar Cove monitoring site before and after the November 2016 Knob Fire: (a) during summer 2014, and (b) on March 9, 2017.

Regrettably, some of the instrumentation at Poplar Cove was damaged by the Knob Fire, and instruments at Mooney Gap were disturbed by wildlife following the fire, so the otherwise continuous data were disrupted for several months until we repaired the instruments during a site visit in early March 2017. Despite this data loss, comparison of the hillslope hydrologic response time series for shallower soil moisture and deeper pore-water pressure from all three sites before and after the wildfire reveals no clear impacts on infiltration events during the fall and winter months when soils remain wetter (Fig. 2). Similarly, field observations during the site visit did not reveal impacts on hydrophobicity or infiltration capacity. During the transition from spring to summer, when increased evapotranspiration rates lead to gradual and sustained drying, the pore pressures and soil water contents at Poplar Cove displayed similar drainage to the other two sites in the year before the fire. After the fire, deeper pore-water pressures at Poplar Cove exhibit a prolonged drainage that is likely the result of decreased interception and lower transpiration by the canopy and understory vegetation in the disturbed area. Considering that debris flows in the southern and central Appalachians are often infiltration triggered during hurricanes and tropical storm events in the summer and early fall, this delayed drainage has potentially important implications for slope stability.

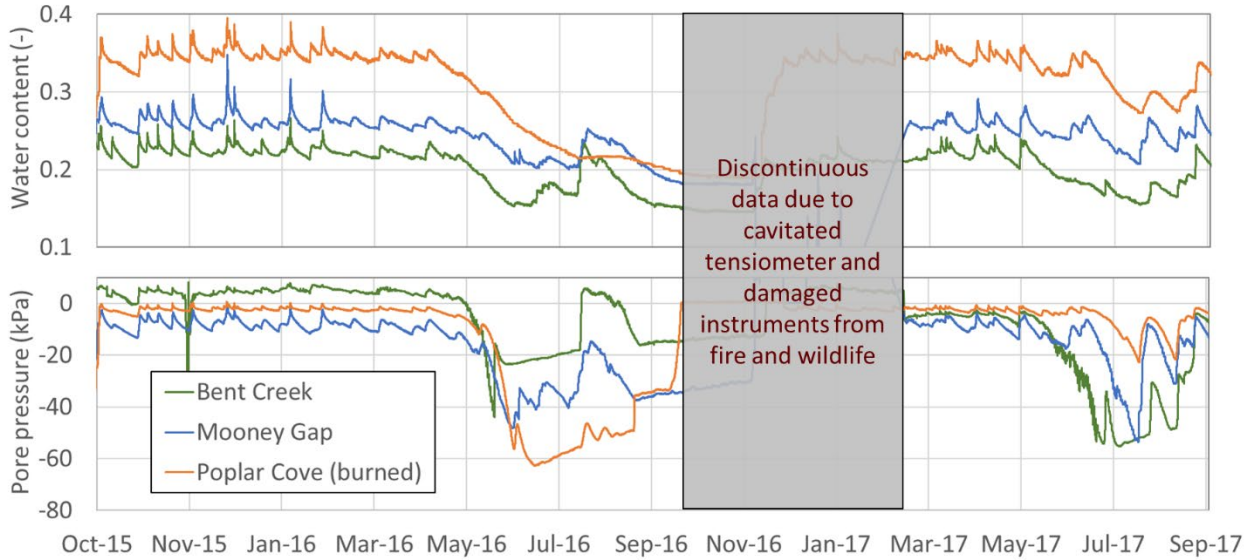


Fig. 2. Time-series of tensiometer measured pore-water pressures at the burned (Poplar Cove, orange line) and unburned (Mooney Gap, blue line; Bent Creek, green line) sites in western North Carolina, measured before and after the November 2016 Knob Fire. Instruments at Poplar Cove and Mooney Gap were damaged during and shortly after the wildfire, which disrupted continuous data collection through March 9, 2017.

Despite the temporary increase in susceptibility to infiltration-triggered debris flows during the early-mid summer of 2017, there were no reports of debris flows in the numerous burn areas since the 2016 wildfires. This lack of reported debris flows is not entirely consistent with our measured rainfall relative to the 15-minute rainfall thresholds indicating 50% probability of runoff-generated debris flows calculated for the USGS post-fire hazard assessments (Fig. 3). However, these thresholds assume the infiltration-excess runoff mechanism triggers debris flows, rather than subsurface pore-pressure development. In contrast, hillslope hydrologic monitoring data suggest that antecedent soil moisture is affected by the fire rather than infiltration rates. Therefore, a more complex conceptual model may be needed to fully assess post-disturbance impacts on hydrologic response and debris-flow hazards. For either runoff or infiltration triggered debris-flow initiation mechanisms, the extent of the impacts of wildfire disturbance were not sufficiently severe to lower debris-flow initiation thresholds to levels below the measured storms in 2016-2017.

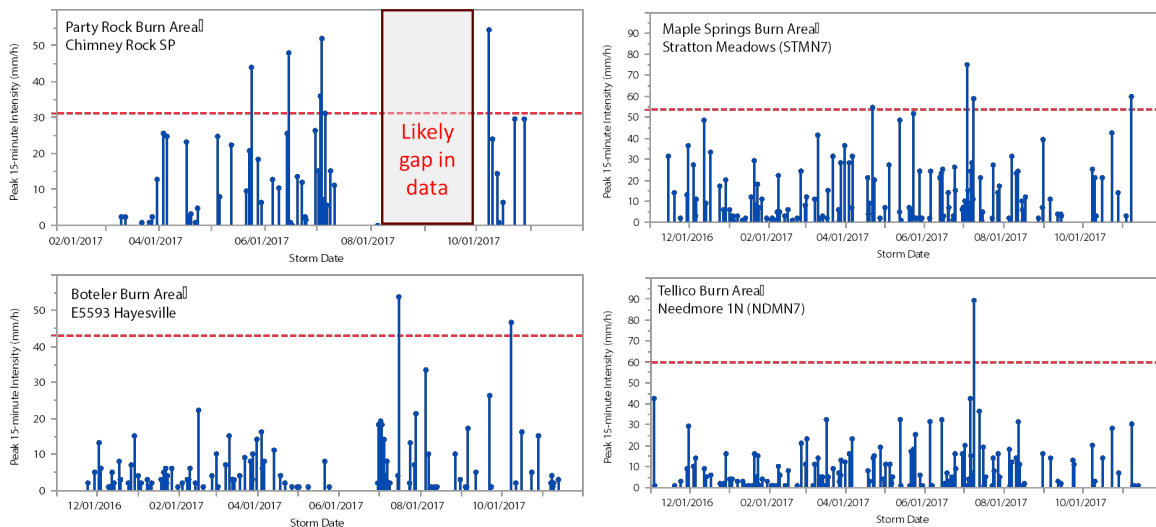


Fig. 3. Time-series of 15-minute peak rainfall intensity measured in areas that burned in November 2016 across North Carolina, relative to USGS calculated thresholds for 50% probability of post-fire debris flows (dashed red line). Gap in data at Chimney Rock fire likely due to clogged rain gage.

4. Disturbance Severity and Recovery of Hydrologic Function

Disturbances are abrupt, but inherently transient phenomena; following a disturbance, hydrologic functioning of a landscape generally recovers or shifts to a new equilibrium (Ebel and Mirus, 2014). When assessing the impacts of disturbances on debris-flow hazards, the magnitude of the disturbance impacts as well as the timescales of the disturbance-recovery cycle and disturbance recurrence interval are relevant.

After several years, soil hydraulic properties altered by wildfire gradually return towards pre-disturbance conditions (McGuire et al., 2016; Ebel and Martin, 2017; Chandler et al., 2018), vegetation canopy regrows, and evapotranspiration recovers (Poon and Kinoshita, 2015; Kinoshita and Hogue, 2018). Similarly, several years after timber harvesting forests regrow and establish some root strength to stabilize slopes, though long-term impacts of anthropogenic disturbances may persist for centuries (Schmidt et al., 2001). Landslide deposits also recover from the disturbance impacts through the processes of pedogenesis, bioturbation, and revegetation (Mirus et al., 2017b), though indications are the timescale of recovery may take several decades (Samia et al., 2017).

The magnitude of disturbance impacts, which influences changes in hydrologic function from the pre-disturbed (or normal) to the disturbed state, can be conceptualized in terms of changes that promote either runoff connectivity or available subsurface storage (Ebel and Mirus, 2014). Runoff generation mechanisms include those governed by the ratio of unsaturated storage capacity versus the cumulative storm totals (i.e. subsurface stormflow and saturation excess overland flow), and the ratio of infiltration capacity to rainfall intensity (i.e. infiltration excess overland flow) (Mirus and Loague, 2013). Similar hydrologic end-members of limited infiltration capacity and limited unsaturated storage can represent the continuum of disturbance impacts on debris-flow initiation potential. Assuming hillslope systems evolve within their hydroclimatic setting to drain water during typical storm events, and also retain water between storms to support vegetation, one can characterize how disturbances contribute to a hillslope water imbalance.

Both of these contrasting impacts can decrease the factor of safety for debris-flow initiation, but in opposite ways, which is demonstrated for burned and unburned sites in different hydroclimatic settings (Fig. 4). In southern California, increased burn severity promotes connectivity of infiltration-excess runoff generated on hillslopes into sediment-laden channels where debris flows initiate (McGuire, et al. 2018), but vegetation recovers rapidly increasing transpiration and root strength. In contrast, a landslide on the coastal bluffs of Puget Sound in Washington reduced subsurface drainage relative to neighboring vegetated hillslopes, which creates a storage imbalance that promoted prolonged susceptibility to recurring slope failures (Mirus et al., 2017b). Our North Carolina monitoring data reveal that for the low severity burn, the disturbed landscape retains more moisture (Fig. 3) and remains more susceptible to infiltration-triggered debris flows during the subsequent hurricane season. The conceptual diagram relating these cases in Fig. 4 illustrates how shifts in hydrologic processes due to the immediate impacts of wildfire may differ with hydroclimatic settings, but also that different disturbances can result in similar decreases in factor of safety with variable recovery timescales and trajectories.

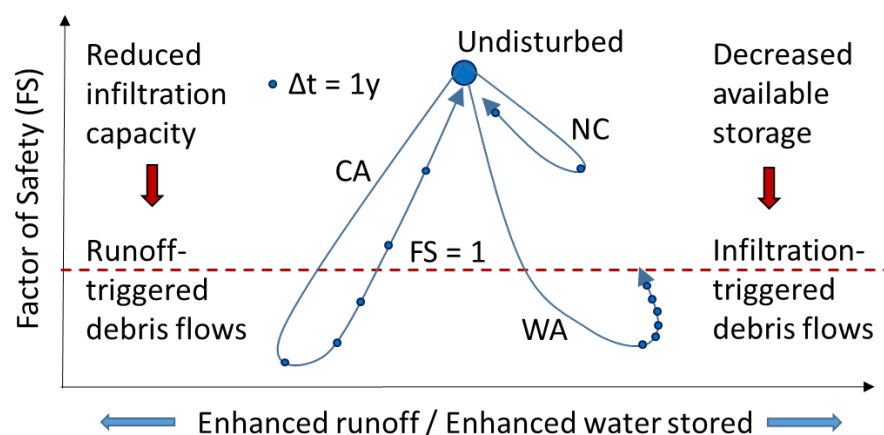


Fig. 4. Conceptual diagram of disturbance impacts on runoff connectivity versus available subsurface storage, and the resulting changes in factor of safety. In undisturbed settings water retention and drainage are balanced to maintain slope stability for a typical storm event (large circle). In different post-disturbance environments changes in hydrologic function reduce factor of safety and recovery rates depending on the hydroclimatic settings (blue arrows): California wildfire, (CA), North Carolina wildfire (NC), and Washington landslide disturbance (WA).

5. Vulnerability and Resilience to Disturbances of Different Magnitude

For a given site or area, the timescale of the disturbance-recovery cycle for a different type and/or severity of disturbance is important for assessing temporal persistence of elevated debris-flow hazards. The vulnerability to post-disturbance debris flows is related to the return period of the corresponding triggering storm event, and the resilience is related to the recurrence interval for the disturbance of interest. A disturbed system where the recovery time is much slower than the recurrence interval for triggering storm event is highly vulnerable to debris flows, whereas a system that recovers rapidly or infrequently experiences potential triggering events is less vulnerable. A system where the recovery time is slower than the return period of the disturbance will experience ongoing disturbance impacts, whereas a resilient system will tend to recover faster than the recurrence interval of the disturbance. The potential utility of these concepts is illustrated in Fig. 5 with the three example disturbances from monitoring sites in southern California, western North Carolina, and Puget Sound, Washington. These concepts in Fig. 5 can also be expressed as non-dimensional ratios to quantitatively define vulnerability and resilience. Disturbance magnitude is more difficult to quantify, but it could be expressed as the ratio of change in hydrologic function from the original, undisturbed state.

Burn severity is one proxy for disturbance magnitude that dominates the likelihood of debris flows in empirical models (Staley et al, 2013) and is conceptually related to the changes in hydrophobicity and other hydraulic properties in process-based models (McGuire et al., 2018; Rengers et al., 2016). Wildfire with moderate to high burn severity on steep terrain will drastically lower the 15-minute rainfall intensity associated with runoff-triggered debris flows. In the Western U.S., the severity of wildfire impacts on hydraulic properties and the frequent recurrence of moderate intensity rainfall events means that post-fire debris flows are likely to occur before the system can recover. In southern California wildfire recurrence interval is on the order of several decades, post-fire recovery is on the order of several years, and the return period of a critical storm for post-fire debris flows is on the order of every year or less. Therefore, areas that do burn are quite likely to experience post-fire debris flows prior to recovery. Thus, within this framework Southern California is classified as system that is resilient, but vulnerable to runoff-triggered post-fire debris flows. However, the decay in water repellency varies and recovery timescale of other soil hydraulic properties and vegetation following wildfire varies by region (Dyrness, 1976; Wondzell and King, 2003; Larsen et al., 2009).

In North Carolina, even low-severity wildfire is infrequent and repeated site visits to burn areas in 2017 and 2018 confirmed that the understory vegetation and duff layer recovered rapidly due to the uniform distribution of rainfall throughout the year. These observations combined with minimal differences between burned and unburned hydrologic response only two years after the Knob Fire suggests that the southern Appalachians are not particularly vulnerable, and also quite resilient to post-fire debris flows. During a typical year in Puget Sound, multiple landslide-triggering storms occur along the coastal bluffs between December and April, but insufficient data exists to distinguish between storms that trigger repeated failures versus those that initiate new failures. Assuming a 25-year recovery time determined for first-time landslides elsewhere (Samia et al., 2017), the Puget Sound system is highly vulnerable and not particularly resilient to landslide disturbances. Of course, changes in climate can impact the recurrence interval and recovery timescale of disturbances such as wildfire, as well as the return period for a storm of given intensity or duration, all of which could also be accommodated within the vulnerability and resilience conceptual framework. For example, shorter return periods of severe storms and increased frequency of wildfire would result in more vulnerable and less resilient systems, respectively.

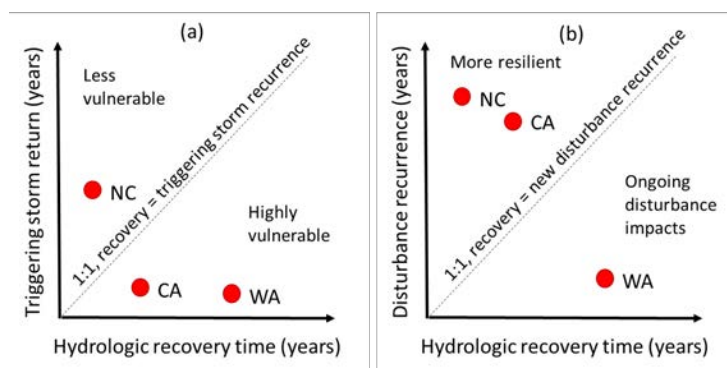


Fig. 5. Plots comparing the timescales of disturbance-recovery cycles for NC, CA, and WA, relative to the (a) return period of a post-disturbance debris-flow triggering storm to illustrate the concept of vulnerability, and (b) recurrence interval of the same disturbance to illustrate resilience.

6. Conclusions

We propose a conceptual framework to assess possible variability in how disturbances impact hydrologic process and corresponding debris-flow initiation thresholds across different geographic regions. Increases or decreases in hillslope runoff connectivity or subsurface drainage provide a metric for assessing the magnitude of disturbance impacts on two contrasting debris-flow initiation mechanisms. These qualitative concepts can be related to quantitative measurements of changes in infiltration or available soil moisture storage capacity in undisturbed and post-disturbance settings, and the corresponding reduction in rainfall triggering conditions for a given hydroclimatic setting. The timescales of the disturbance-recovery cycle relative to the return period for corresponding debris-flow triggering storm and recurrence interval for that disturbance provide metrics for assessing the vulnerability versus the resilience of the system. Examples from USGS monitoring sites in contrasting disturbed settings across the U.S. illustrate the utility of this conceptual framework for understanding how disturbances may impact debris flow hazards. In the context of climate and land-use change, and increasing wildfire disturbances, this conceptual framework can inform future data collection efforts and improved modeling of thresholds for post-disturbance debris-flow hazards.

Acknowledgements

The North Carolina sites were installed with support of NASA Grant No. NNX12AO19G awarded to Ning Lu in cooperation with the USGS at sites facilitated by the USDA-Forest Service including the Coweeta Hydrologic Laboratory and the Bent Creek Experimental Forest, and Chimney Rock State Park. Bart Cattanaich (NCGS), Jenn Bauer (ALC), and Stephen Fuemmeler (ALC), contributed to thoughtful discussions about wildfire disturbances in North Carolina. Thanks to the two anonymous reviewers and Dennis Hallema (USDA-Forest Service) who provided thoughtful and constructive feedback on earlier versions of this paper.

References

- Baum, R.L., and Godt, J.W., 2010, Early warning of rainfall-induced shallow landslides and debris flows in the USA: *Landslides*, v. 7, p. 259-272, doi:10.1007/s10346-009-0177-0.
- Bogaard, T.A., and Greco, R., 2018, Invited perspectives. A hydrological look to precipitation intensity duration thresholds for landslide initiation: proposing hydro-meteorological thresholds: *Nat. Hazards Earth Syst. Sci.*, v. 18, P. 31-19, doi:10.5194/nhess-2017-241.
- Caine, N., 1980, The rainfall intensity-duration control of shallow landslides and debris flows: *Geografiska Annaler*, v. 62(1/2), p. 23-27, doi:10.2307/520449.
- Cannon, S.H., and DeGraff, J., 2009. The increasing wildfire and post-fire debris-flow threat in Western USA, and implications for consequences of climate change, *in* Sassa, K., and Canuti, P., eds., *Landslides — Disaster Risk Reduction*. Springer, Berlin Heidelberg, p. 177–190.
- Cannon, S.H., 2001, Debris-flow generation from recently burned watersheds: *Environmental and Engineering Geoscience*, v. 7, p. 321–341.
- Cannon, S.H., Kirkham, R.M., and Parise, M., 2001, Wildfire-related debris-flow initiation processes, Storm King Mountain, Colorado: *Geomorphology*, v. 39, p. 171-188.
- Cannon S.H., Boldt, E., Laber, J., Kean, J.W., and Staley, D.M., 2011, Rainfall intensity–duration thresholds for postfire debris-flow emergency-response planning: *Natural Hazards*, v. 59(1), p. 209–236.
- Chandler, D.G., Cheng, Y., Seyfried, M.S., Madsen, M.D., Johnson, C. E., and Williams, C. J., 2018, Seasonal wetness, soil organic carbon and fire influence soil hydrological properties and water repellency in a sagebrush-steppe ecosystem: *Water Resources Research*, v. 55, p. 8514-8527, doi:10.1029/2017WR021567.
- Coe, J.A., Kinner, D.A., and Godt, J.W., 2008, Initiation conditions for debris flows generated by runoff at Chalk Cliffs, central Colorado: *Geomorphology*, v. 96, p. 270–297, <https://doi.org/10.1016/j.geomorph.2007.03.017>.
- Coe, J.A., Kean, J.W., Godt, J.W., Baum, R.L., Jones, E.L., Gochis, D.J., and Anderson, G.S., 2014, New insights into debris-flow hazards from an extraordinary event in the Colorado Front Range: *GSA Today*, v. 24(10), p. 4-10, doi: 10.1130/GSATG214A.1.
- Crosta, G.B., and Dal Negro, P., 2003, Observations and modelling of soil slip-debris flow initiation processes in pyroclastic deposits: the Sarno 1998 event: *Natural Hazards and Earth Systems Science*, v. 3, p. 53–69.
- Dymess, C., 1976, Effect of Wildfire on Soil Wettability in the High Cascades of Oregon: USDA, Forest Service Research Paper PNW 202, 18 p.
- Ebel, B.A., and Mirus, B.B., 2014, Disturbance Hydrology: Challenges and Opportunities: *Hydrological Processes*, doi:10.1002/hyp.10256.
- Ebel, B.A., and Martin D.A., 2017, Meta-analysis of field-saturated hydraulic conductivity recovery following wildland fire: Applications for hydrologic model parameterization and resilience assessment: *Hydrological Processes*, 31, 3682–3696, doi:10.1002/hyp.11288.
- Ebel, B. A., F.K. Rengers, and G.E. Tucker (2016) Observed and simulated hydrologic response for a first-order catchment during extreme rainfall three years after wildfire disturbance, *Water Resources Research*, 52, 1-23, doi: 10.1002/2016WR019110.
- Guzzetti, F., Peruccacci, S., Rossi, M., and Stark, C. P., 2008, The rainfall intensity-duration control of shallow landslides and debris flows: An update: *Landslides*, v. 5(1), p. 3-17, doi:10.1007/s10346-007-0112-1.
- Hallema, D.W., Sun, G., Caldwell, P.V., Norman, S.P., Cohen, K.C., Liu, Y., Bladon, K.D., and McNulty, S.G., 2018, Burned forests impact water supplies: *Nature Communications*, doi:10.1038/s41467-018-03735-6.
- Imazumi, F., Sidle, R.C., Togari-Ohta, A., Shimamura, M., 2015, Temporal and spatial variation of infilling processes in a landslide scar in a steep mountainous region, Japan: *Earth Surface Processes and Landforms*, v. 40, p. 642–653, doi:10.1002/esp.3659.

- Iverson, R.M., 1997, The physics of debris flows: Review of Geophysics, v. 3, p. 245-296.
- Iverson, R.M., George, D.L., Allstadt, K., Reid, M.E., Collins, B.D., Vallance, J.W., Schilling, S.P., Godt, J.W., Cannon, C.M., Magirl, C.S., Baum, R.L., Coe, J.A., Schulz, W.H., and Bower, J.B., 2015, Landslide mobility and hazards: Implications of the 2014 Oso disaster: Earth and Planetary Science Letters, doi:10.1016/j.epsl.2014.12.020.
- Jakob, M., Owen, T., and Simpson, T., 2012, A regional real-time debris-flow warning system for the District of North Vancouver, Canada: Landslides, v. 9, p. 165–178, doi:10.1007/s10346-011-0282-8.
- Kean, J.W., Staley, D.M., and Cannon, S.H., 2011, In situ measurements of post-fire debris flows in southern California: Comparisons of the timing and magnitude of 24 debris-flow events with rainfall and soil moisture conditions: Journal of Geophysical Research, v. 116, F04019. doi:10.1029/2011JF002005.
- Kean, J.W., McCoy, S.W., Tucker, G.E., Staley, D.M., and Coe, J.A., 2013, Runoff-generated debris flows: Observations and modeling of surge initiation, magnitude, and frequency: Journal of Geophysical Research: Earth Surface, v. 118, p. 2190–2207, doi:10.1002/jgrf.20148.
- Keefer, D.K., Wilson, R.C., Mark, R.K., Brabb, E.E., Brown, W.M., Ellen, S.D., Harp, E.L., Wieczorek, G.F., Alger, C.S., and Zarkin, R.S., 1987, Real-time landslide warning during heavy rainfall: Science, v. 238(4829), p. 921–925, doi:10.1126/science.238.4829.921.
- Kinoshita, A.M., and Hogue, T.S., 2015, Increased dry season water yield in burned watersheds in Southern California: Environmental Research Letters, v. 10(1), 014003, doi:10.1088/1748-9326/10/1/014003.
- Larsen, I. J., MacDonald, L. H., Brown, E., Rough, D., Welsh, M. J., Pietraszek, J. H., Libohova, Z. Benavides-Solorio, J.D., Schaffrath, K. (2009). Causes of post-fire runoff and erosion: water repellency, cover, or soil sealing?. Soil Science Society of America Journal, v. 73(4), p. 1393-1407.
- Lu, N., and Godt, J.W., 2013, Hillslope hydrology and stability. Cambridge, UK: University Press. <https://doi.org/10.1017/CBO9781139108164>
- McGuire, L.A., Kean, J.W., Staley, D.M., Rengers, F.K., and Wasklewicz, T.A., 2016, Constraining the relative importance of raindrop- and flow-driven sediment transport mechanisms in post-wildfire environments and implications for recovery time scales: Journal of Geophysical Research: Earth Surface, doi:10.1002/2016JF003867.
- McGuire, L.A., Rengers, F.K., Kean, J.W., Staley, D.M. and Mirus, B.B., 2018, Incorporating spatially heterogeneous infiltration capacity into hydrologic models with applications for simulating post-wildfire debris flow initiation: Hydrological Processes, doi:10.1002/hyp.11458.
- Mirus, B.B., and Loague, K., 2013, How Runoff Begins (and Ends): Characterizing hydrologic response at the catchment scale: Water Resources Research, doi:10.1002/wrcr.20218.
- Mirus, B.B., Ebel, B.A., Loague, K., and Wemple, B.C., 2007, Simulated effect of a forest road on near-surface hydrologic response: Redux: Earth Surface Processes and Landforms, doi:10.1002/esp.1387.
- Mirus, B.B., Ebel, B.A., Mohr, C., and Zegre, N., 2017a, Disturbance Hydrology: Preparing for an Increasingly Disturbed Future: Water Resources Research, WRCR22964, doi:10.1002/2017WR021084.
- Mirus, B.B., Smith, J.B., and Baum, R.L., 2017b, Hydrologic Impacts of Landslide Disturbances: Implications for Remobilization and Hazard Persistence: Water Resources Research, WRCR22885, doi:10.1002/2017WR020842.
- Mirus, B.B., Becker, R.E., Baum, R.L., and Smith, J.B., 2018, Integrating real-time subsurface hydrologic monitoring with empirical rainfall thresholds to improve landslide early warning: Landslides, doi:10.1007/s10346-018-0995-z.
- Moody, J.A., Shakesby, R.A., Robichaud, P.R., Cannon, S.H., and Martin, D.A., 2013, Current research issues related to post-wildfire runoff and erosion processes: Earth-Science Reviews, doi:10.1016/j.earscirev.2013.03.004
- Morino, C., Conway, S.J., Balme, M.R., Hillier, J., Jordan, C., Saemundsson, Th, and Argles, T., 2018, Debris-flow release processes investigated through the analysis of multi-temporal LiDAR datasets in north-western Iceland: Earth Surface Processes and Landforms, doi:10.1002/esp.4488.
- Oakley, N.S., Lancaster, J.T., Kaplan, M.L., and Ralph, F.M., 2017, Synoptic conditions associated with cool season post-fire debris flows in the Transverse Ranges of southern California: Natural Hazards, 2017, Volume 88, Number 1, Page 327 DOI: 10.1007/s11069-017-2867-6
- Poon, P.K., and Kinoshita, A.M., 2018, Spatial and temporal evapotranspiration trends after wildfire in semi-arid landscapes: Journal of Hydrology, v. 559, p. 71-83, doi:10.1016/j.jhydrol.2018.02.023.
- Rengers, F.K., McGuire, L.A., Kean, J.W., Staley, D.M., and Hobbey, D., 2016, Model simulations of flood and debris flow timing in steep catchments after wildfire: Water Resources Research, v. 52, p. 6041–6061, doi:10.1002/2015WR018176.
- Samia, J., Temme, A., Bregt, A., Wallinga, J., Guzzetti, F., Ardizzone, F., and Rossi, M., 2017, Do landslides follow landslides? Insights in path dependency from a multi-temporal landslide inventory: Landslides, v. 14, p. 547–558, doi:10.1007/s10346-016-0739-x.
- Schmidt, K., Roering, J.J., Stock, J.D., Dietrich, W.E., Montgomery, D.R., and Schaub, T., 2001, The variability of root cohesion as an influence on shallow landslide susceptibility in the Oregon Coast Range: Can. Geotech. J., v. 38(5), p. 995–1024, doi:10.1139/cgj-38-5-995.
- Sidele, R.C., and Ochiai, H., 2013, Landslides: processes, prediction, and land use. Washington, DC: American Geophysical Union. doi:10.1029/WM018.
- Sidele, R.C., Gomi, R., and Tsukamoto, Y., 2018, Discovery of zero-order basins as an important link for progress in hydrogeomorphology: Hydrological Processes, v. 32, p. 3059-3065, doi:10.1002/hyp/13246.
- Staley D.M., Kean, J.W., Cannon, S.H., Laber, J.L., and Schmidt, K.M., 2013, Objective definition of rainfall intensity-duration thresholds for the initiation of post-fire debris flows in southern California: Landslides v. 10, p. 547-562, doi:10.1007/s10346-012-0341-9.
- Staley, D.M., Negri, J.A., Kean, J.W., Laber, J.L., Tillery, A.C., and Youberg, A.M., 2017, Prediction of spatially explicit rainfall intensity–duration thresholds for post-fire debris-flow generation in the western United States: Geomorphology, v. 278, p. 149-162, doi:10.1016/j.geomorph.2016.10.019.
- Staley, D.M., Kean, J.W., Jackson, M., 2019, Post-Fire Debris-Flow Early Warning: The Case for Forecast-Based Warning Systems, in this issue.
- Swanson, F.J. and Dyrness, C.T., 1975, Impact of clear-cutting and road construction on soil erosion by landslides in the western Cascade Range, Oregon: Geology, v. 3, p. 393–396.
- Van der Sant, R.E., Nyman, P., Noske, P.J., Langhans, C., Lane, P.N.J., and Sheridan, G.J., 2018, Quantifying relations between surface runoff and aridity after wildfire: Earth Surface Processes and Landforms, doi:10.1002/esp.4370.
- Wondzell and King, 2003, Postfire erosional processes in the Pacific Northwest and Rocky Mountain regions: Forest Ecology and Management, v. 178(1–2), p. 75-87.
- Wooten R.M., Witt, A.C., Miniati, C.F., Hales, T.C., and Aldred, J.L., 2016, Frequency and Magnitude of Selected Historical Landslide Events in the Southern Appalachian Highlands of North Carolina and Virginia: Relationships to Rainfall, Geological and Ecohydrological Controls, and Effects, in Greenberg, C.H., and Collins, B.S., eds., Natural Disturbances and Historic Range of Variation, Managing Forest Ecosystems, doi:10.1007/978-3-319-21527-3_9.

A novel approach for determining risk of water supply disruptions due to post-wildfire debris flows

Petter Nyman^{a,*}, Peter Yeates^c, Christoph Langhans^b, Cristine Schärer^c, Philip J Noske^a, Patrick NJ Lane^a, Shane Haydon^d, Gary J Sheridan^a

^aThe University of Melbourne, Baldwin Spencer Building, Parkville, VIC 3010, Australia

^bNetherlands Environmental Assessment Agency (PBL), The Hague, 2594 AV, The Netherlands

^cHydronumerics Pty Ltd, 03/757 Bourke St, Docklands, VIC 3008, Australia

^dMelbourne Water Corporation, 990 La Trobe Street Melbourne, VIC 3001, Australia

Abstract

Forested catchments are critical to water supplies in major cities around the world. As wildfire and extreme rainfall become more frequent, water supply systems are facing an increasing threat of contamination from erosion. In southeast Australia debris flows are particularly problematic because they produce sediment loads that are likely to impact water treatability to the point where water supply interruptions are likely. Assessing the threat of water supply interruptions and evaluating mitigation options is complex, because there are many factors that affect the treatability of the water. For example, the magnitude, frequency and spatial extent of debris flows, entry points of sediment into reservoirs, particle size distribution of sediment, reservoir hydrodynamics, and location of the potable water offtake are factors likely to determine to how debris flows translate to treatability of water at the offtake. In this paper we couple a post-fire debris-flow model with a reservoir hydrodynamic model to estimate the probability and duration of water contamination in a water supply catchment burned by wildfire. Central to this paper is the technique of coupling two models into a risk framework that gives probabilities to the number of days that sediment concentration thresholds for water treatment are exceeded at the offtake. The work is set in the Upper Yarra catchment, which supplies a major reservoir for the city of Melbourne (population ~ 4M). The results show that wildfires pose a substantial threat with relatively high likelihood (exceedance probability between 0.2 and 0.5) for water supply interruptions in the order of several months to a year. The cost of such interruptions could be > AU\$100 million. The framework presented provides a direct link between geophysical models and metrics that are used by water supply authorities in strategic planning around resource allocation and cost-benefit analysis of alternative mitigation options.

Keywords: Post-wildfire debris flows; water quality; reservoir hydrodynamics; water supply; treatability; risk assessment

1. Introduction

The threats to water supply systems from post-wildfire erosion are a concern in fire-prone and mountainous catchments (Bladon et al., 2014; Martin, 2016; Smith et al., 2011). In the southeast (SE) Australian uplands, large impacts on water quality after fire are often attributed to post-fire debris flows (Nyman et al., 2011). These extreme erosion events produce sediment loads that are 1-2 orders of magnitude higher than other post-fire erosion processes and are therefore likely to result in sediment concentrations that exceed treatability thresholds in water supply systems. There are numerous examples in the region of major impacts on reservoir water quality and water supply systems due to post-fire debris flows (Smith et al., 2011; White et al., 2006). The risk to water supply systems is difficult to predict with uncertainties in the hydro-geomorphic response models, propagation of sediment within the reservoir, and stochastic variation in fire and rainfall (Nyman et al., 2013). However, with the future likelihood of increased extreme fire-inducing weather (Dowdy, 2017; Westerling et al., 2006) and increasing rainfall intensities (Guerreiro et al., 2018) the demand for predictive models is becoming pressing.

There are numerous uses for models that predict water quality impacts. On an operational level, models that reveal spatial variation in the erosion susceptibility provide catchment managers with a means to prioritize risk mitigation through fuel reduction or post-wildfire response. In such cases, spatial mapping of erosion risk in a relative sense (e.g. Sheridan et al., 2009) may be sufficient to provide effective tools for allocating resources and mitigating risk in the areas of the catchment that are most likely to be producing sediment. When developing strategic plans and making decisions about the future management of a water resource, the demands on predictive models increase. For instance, a water supply agency may want to determine if there is a case for upgrading water treatment capability or adjusting the water supply network to reduce the likelihood of water supply interruptions

*Corresponding author e-mail address: nymanp@unimelb.edu.au

due to wildfires. In this setting, a detailed understanding of risk is required for cost-benefit analysis to inform decisions about such investments.

Here we present a novel approach for predicting risk associated with post-fire debris flows in water supply systems. In the context of post-fire erosion, the term risk is often used loosely to describe an approach in which models provide a basis for identifying threats (e.g. Hosseini et al., 2018; Sheridan et al., 2009). With our modeling approach described in this paper we define risk to water supply as the ‘probability of a consequence’ (Aven, 2011), where the consequence is the number of days that sediment concentration of water at the reservoir offtake exceeds water treatment capacity. This study focuses on water quality impacts on reservoirs in SE Australia, but the approach is generally applicable to other landscapes where post-fire debris flows occur in catchments upstream of water supply reservoirs (e.g. Gartner et al., 2014; Riley et al., 2013; Staley et al., 2016)

2. Study Area

The study was carried out in the Upper Yarra catchment, which is located ~100km east of Melbourne in SE Australia and flows into a 200 GL reservoir that is central to the potable water supply to more than 4 million people. The reservoir also receives transfers from the larger nearby Thomson Reservoir. Unfiltered water from the Upper Yarra reservoir is then transferred to smaller off-stream storages before treatment and supply into the metropolitan distribution network. The hydrodynamics of the reservoir is governed by strong summer thermal stratification and complete winter mixing. During stratification, inflow intrusions typically form distinct layers of neutrally buoyant ingress that can travel the length of the reservoir (8 km), typically in the upper strata, in as little as 6 days, offering very limited dilution of the flows and short response times for avoiding or managing the potential for extraction of poor-quality water. Once at the dam wall, the rapid mixing of sediment in the water column means that there are limited opportunities to mitigate water supply disruptions by adjusting the depth of the water offtake.

The ~ 337 km² Upper Yarra catchment includes mixed species of dry Eucalyptus forests at lower elevations and on equatorial facing slopes, wet forests dominated by Mountain Ash (*Eucalyptus regnans*) at higher elevations, and damp mixed species forest in intermediate locations. The relief is 850 m and based on the Köppen classification the climate is temperate with no distinct dry season and mild to warm summers. Annual rainfall at the reservoir dam wall is ca 1100mm yr⁻¹. At the catchment divide, the rainfall is ~1700 mm yr⁻¹. The geology is predominantly sedimentary, and the soils are typically clay loams.

3. Methods

3.1. Overview

The model includes two components for predicting the probability of interruption to water supply from post-fire debris flows. One component predicts fine sediment (silts and clays; particle diameter < 0.02 mm) delivery from debris flows in headwaters (above second-order drainages), while the other predicts the propagation of fine sediment towards the water offtake after it has been delivered into the reservoir. The two models are coupled conceptually in a risk framework, which presents outputs from the two models in terms of the probability and duration of water contamination events that exceed the treatment threshold (Fig 1). The model was implemented in the Upper Yarra catchment to evaluate risk after a high fire-severity scenario, which was sourced from fire severity distributions during the Black Saturday Wildfires of 2009. The problem is broken up into several components:

- Estimating the magnitude of sediment delivery from debris flows given rain storms of different annual exceedance probabilities (AEPs).
- Modelling the propagation of pollutant plumes through the reservoir for different sediment input scenarios.
- Defining the sediment concentration thresholds for water treatment and delivery.

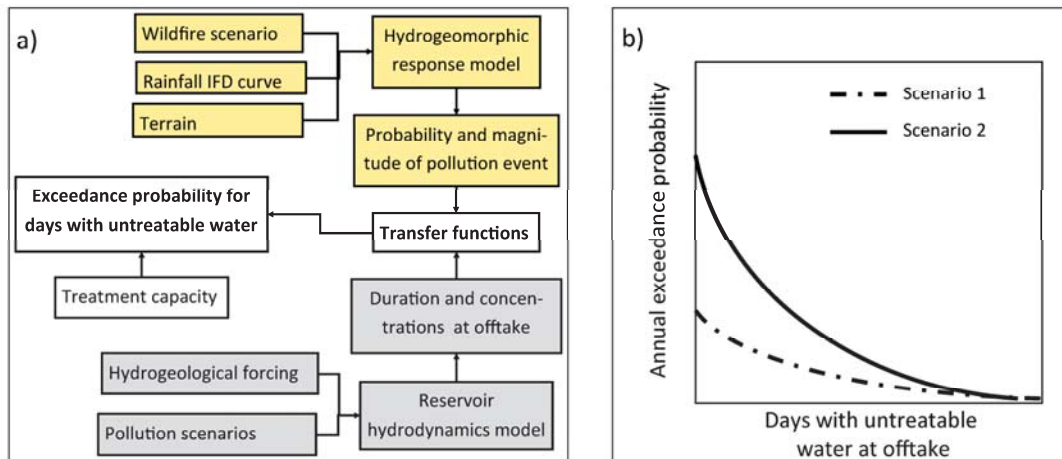


Fig. 1. (a) Model overview showing the workflow for producing a risk metric from transfer functions that couple an erosion model with a reservoir hydrodynamics and reservoir sediment transport model. (b) Example of the final risk metrics which is the probability of consequence. The probability of a range of sediment input events was calculated using a debris-flow response model coupled with storm cells with known AEP from a radar archive. The propagation of sediment from input locations to the reservoir offtake was then modelled using a range of the possible sediment input scenarios.

3.2. Debris-flow response model

The probability of initiating a post-fire debris flow depends on catchment attributes, fire severity and local rainfall regime. The model of post-fire debris flow-initiation is described in detail by Langhans et al. (2016). The slope must be steep enough, with sufficient available sediment on the hillslopes, and the soils must be sufficiently impermeable. Debris flow probability model input parameters are derived only from the zero-order convergent basins (~ 2 ha) of each headwater catchment, as these are the potential debris-flow initiation areas (Cannon et al., 2001). The critical rainfall intensity required to initiate a debris flow in each headwater depends on fixed properties such as slope, and other properties that depend on soil and fire severity, which vary in space and time. The probability of initiating a debris flow depends on the probability of receiving a rainfall event that exceeds critical 12-minute rainfall intensity thresholds (I_{12}) in each zero-order basin. Storm cells obtained from an archive of radar rain fields were simulated at random locations within the catchment. The probability of each rainfall event is based on the intensity-frequency-duration (IFD) rainfall statistics for the headwater location provided by the Bureau of Meteorology (BOM).

The magnitude (load in Mg) of a debris flow once it is initiated depends principally on the slope of the catchment and on the amount of runoff and sediment available for erosion, which is often strongly related to the catchment area. Here we predict the volume of the debris flow (once initiated) using a slope-area landscape analysis described in Nyman et al. (2015). Volumes of debris flow were calculated for each headwater individually at the outlet of first-order streams. The models estimate debris-flows volumes based on characteristics of only the zero- and first-order basins with the outlets located at the point where second-order streams begin. Scour or deposition of sediments in channels between the outlet of first-order streams and the reservoir are neglected. During implementation of the model with simulated storms, all the loads from first-order catchments were accumulated for cases where rainfall intensities exceeded debris-flow thresholds.

The particle size distribution of sediment delivered by debris flows (Table 1) were calculated from size distribution data collected from hillslopes, colluvium, and channels where post-fire debris flows have occurred in the past (Nyman, 2013). For particles with diameter (D) < 1 mm, the distribution was obtained with a laser particle size analyzer. For $D \geq 1$ mm, the distribution was obtained by sieving ($30 \text{ mm} > D \geq 1$) and visual assessment ($D \geq 30 \text{ mm}$). When calculating the particle size distribution at the outlet of headwaters, the particle size distribution was summed by weighting the source distributions (hillslopes vs colluvium) by their relative contribution to the total volume.

Table 1. Particle size of debris-flow material from (Nyman, 2013)

Particles	Size range [mm]	Proportion [%]
>Sand	$D > 2$	62
Sand	$2 > D \geq 0.02$	16
Silt	$0.02 > D \geq 0.002$	14
Clay	$D < 0.002$	8

3.3. Propagation of pollutant plumes within the reservoir

The three-dimensional Aquatic Ecosystem Model (AEM3D) is a coupled hydrodynamics and water quality (including sediments) model that was used to simulate the propagation of the sediment plume through the Upper Yarra reservoir. AEM3D is built on a finite volume numerical grid scheme (Hodges et al., 2000) that solves the unsteady, viscous Navier-Stokes equations for incompressible flow. The model was forced using meteorological data collected from a weather station moored near the dam wall and inflow and outflow monitored by the Melbourne Water Supervisory Control and Data Acquisition (SCADA) system. Thermistor chain data from the same mooring and boat deployed conductivity-, temperature- and depth- (CTD) profiles have been used in previous studies to calibrate the model. The post-fire debris-flow sediment loads (in Mg) were input into the model at four locations around the perimeter of the reservoir that have high probabilities of generating debris flows after fire. Particle densities used in the model are rock/gravel = 2.22 g cm^{-3} and primary soil particles ($D < 0.02 \text{ mm}$) = 2.65 g cm^{-3} . The number of days with untreatable water at the water offtake was calculated assuming a sediment concentration threshold of 5 mg L^{-1} .

4. Results

4.1. Debris-flow response model

Rainfall thresholds for post-fire debris flows (I_{12}) range from ~ 50 to $>250 \text{ mm h}^{-1}$ (Fig 2a). The headwaters with lower rainfall thresholds are located near the reservoir at lower elevations where the mean annual precipitation is lower and where infiltration rates are lower. The rainfall thresholds in the upper region of the catchment are very high ($> 250 \text{ mm h}^{-1}$), and therefore highly unlikely to produce debris flows. Annual exceedance probabilities (AEPs) range from ~ 0.5 for $I_{12} = 50 \text{ mm h}^{-1}$ to < 0.01 for $I_{12} > 250 \text{ mm h}^{-1}$. The modelled clay loads from individual headwaters ranged from 5.5 to 398 Mg with a median of 62 Mg (Fig 2b).

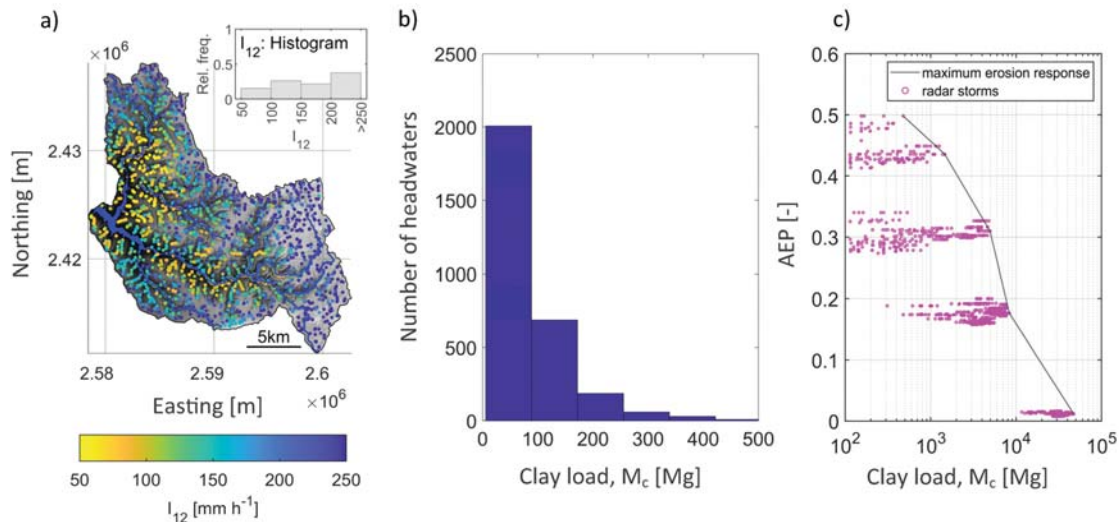


Fig. 2. (a) Rainfall thresholds for post-fire debris flows in the Upper Yarra catchment (b) Distribution of clay loads, M_c , expected from individual first-order headwaters in the case of a debris flow. (c) Annual exceedance probability (AEP) of clay loads inputs to reservoir from debris flows after high-severity fire.

When simulating debris-flow response, the spatial variation in I_{12} means that the probability distribution of clay loads is very sensitive to where storms are located. The distributions of AEPs are shown for locations that are centered on cells in a 10 x 10 grid (grid cells = 3 x 3 km) over the catchment area (Fig 2c). The mass of clay, M_c , from debris flows entering the reservoir for a given storm varies depending on where the storm is located. For an AEP of ~0.3 the M_c ranges from 100 Mg to 5000 Mg depending on where the storm is located. The magnitude of spatial variation in probabilities decrease with the AEP of the rainstorm.

4.2. Propagation of pollutant plumes within the reservoir

The propagation of clay-sized particles to the reservoir offtake was not very sensitive to where sediment was input to the reservoir (Fig 3). For sediment classes greater than clay-sized, deposition on the reservoir bed occurred before they reached the offtake. Within clay-sized particles, it is the very fine fraction ($D < 0.001$ mm) that contribute to suspended sediment concentration at the offtake. Thus, the impact of an erosion event on concentration at the offtake is highly sensitive to the particle size distribution of the sediment delivered to the reservoir. The number of days exceeding a treatment threshold depends on the clay load, with clay loads of about 8000 Mg causing between 450 to 550 days exceeding 5 mg L^{-1} and clay loads of about 1000 Mg causing about 75 to 100 days exceeding 5 mg L^{-1} . The relation is non-linear with the duration of exceedance increasing at a slower rate when at high input loads (Fig 3).

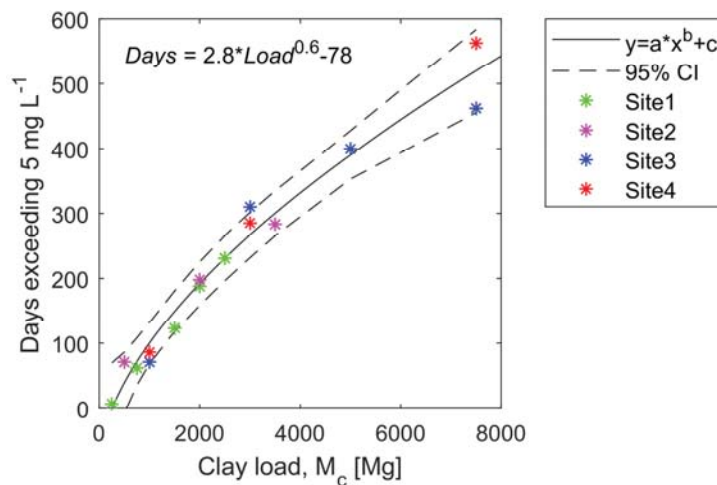


Fig. 3. The relation between days of suspended sediment exceeding 5 mg L^{-1} and input of clay at different sites (1-4) around the Upper Yarra reservoir.

4.3. Probability of consequence

Combining the results in Fig 2c and Fig 3 gives a distribution of probabilities for days of interrupted supply (Fig 4). The distributions are different depending on where in the catchment the storm cells are centered. However, all distributions are equally likely. Thus, the maximum impact shown in solid black line in Fig 4 is the most relevant one because that represents the highest risk to reservoir water quality. The duration of undeliverable water for exceedance probabilities of 0.5, 0.4, 0.3, 0.2 and 0.1, marked with arrows in Fig 4, are 15, 130, 320 and 450 and 900 days, respectively. When centered on an erosion hotspot, a storm with an AEP of ~0.3 will produce about 2000 Mg of clay from debris flows. This equates to ~30 times the median clay load (i.e. 62 Mg) from debris-flow producing headwaters.

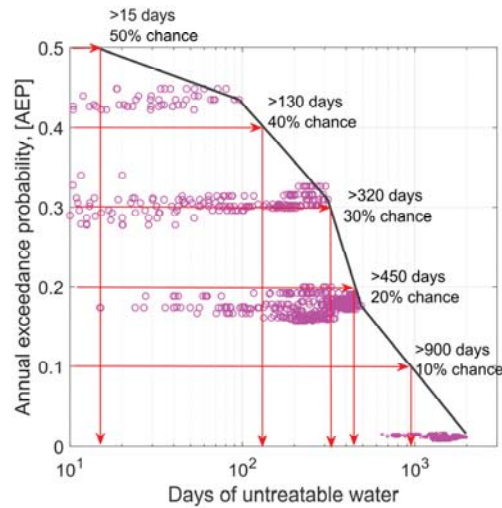


Fig. 4. Annual exceedance probabilities (AEPs) for days of undeliverable water. Based on results in Fig 2c and Fig 3. The scatter plot is the number of days that water exceeds treatability threshold for storms cells with different exceedance probabilities. The variation stems from storm cells being centered on different locations in the catchment. The solid black line is the AEP when storms are centered at a location most susceptible to debris flows.

5. Discussion

Using a novel method for quantifying water quality risk we estimate that a high severity wildfire in the Upper Yarra catchment can lead to water supply interruptions lasting for periods of months to years. The debris-flow susceptibility is spatially variable within the catchment, with hotspots on the eastern flank of the northern reservoir arm representing highest risk. These areas receive lower annual rainfall and have soil properties that are more likely to produce runoff than the those in high rainfall areas at higher elevation. This pattern stems from the way in which infiltration is parametrized in the debris-flow response model, where aridity and fire severity are both causing variation in infiltration (Langhans et al., 2016; Van der Sant et al., 2018).

Much of the risk in Upper Yarra catchment can be attributed to a very small area. Thus, mitigation efforts can be highly targeted at specific areas of the water supply catchment. Possible means for risk mitigation could be fuel reduction burning in these areas to reduce fire intensity in the event of a wildfire. Post-wildfire hillslope treatments such as mulching or small check dams may also be possible mitigation options, to reduce loads and increase debris-flow thresholds. In other water supply catchments, such as the Thomson Reservoir further to the east, the area of dry forest is much larger, and it is likely that the risk will be distributed more broadly.

Future work will include using different fire severity distributions in the model to evaluate the how risk can be mitigated with fuel treatment. By modifying fire severity, it is possible to determine the cost and benefits of carrying out planned (or controlled) burning within the catchment. Model outputs are very sensitive to how storms are modelled, and future work may focus on other methods to model storms. In this paper we have used rain fields from radar to simulate possible erosion scenarios given storms with different return intervals. Using design storms and depth area reduction factors to simulate storms is another way of representing storms. Other approaches are available. There may be opportunities for instance to simulate designs storms using a 2D stochastic rainfall generators (e.g. Peleg et al., 2017). In future modelling efforts, the uncertainty stemming from rainfall, fire severity distributions and the two major model components will be quantified to give some error bounds on the predictions in Fig 4.

The model was developed using the Upper Yarra catchment (and reservoir) as a case study. However, the approach of linking reservoir hydrodynamics with an event-based erosion model to quantify risk is generally applicable and could be applied to debris-flow prone water supply catchments elsewhere. The approach can be easily adapted to operate with debris-flow models that have been developed for other hydro-geomorphic settings (e.g. Gartner et al., 2014).

Acknowledgements

The work is funded by ARC Linkage grant LP150100654, Melbourne Water Corporation and the Victorian Department of Environment, Land, Water and Planning (DELWP).

References

- Aven, T., 2011, On some recent definitions and analysis frameworks for risk, vulnerability, and resilience: *Risk Analysis*, v. 31, no. 4, p. 515-522, doi:10.1111/j.1539-6924.2010.01528.x.
- Bladon, K. D., Emelko, M. B., Silins, U., and Stone, M., 2014, Wildfire and the Future of Water Supply: *Environmental Science & Technology*, v. 48, no. 16, p. 8936-8943, doi:10.1021/es500130g.
- Cannon, S. H., Kirkham, R. M., and Parise, M., 2001, Wildfire-related debris-flow initiation processes, Storm King Mountain, Colorado: *Geomorphology*, v. 39, no. 3-4, p. 171-188, doi:10.1016/S0169-555X(00)00108-2.
- Dowdy, A. J., 2017, Climatological Variability of Fire Weather in Australia: *Journal of Applied Meteorology and Climatology*, v. 57, no. 2, p. 221-234, 10.1175/JAMC-D-17-0167.1
- Gartner, J. E., Cannon, S. H., and Santi, P. M., 2014, Empirical models for predicting volumes of sediment deposited by debris flows and sediment-laden floods in the transverse ranges of southern California: *Engineering Geology*, v. 176, p. 45-56, doi: 10.1016/j.enggeo.2014.04.008.
- Guerreiro, S. B., Fowler, H. J., Barbero, R., Westra, S., Lenderink, G., Blenkinsop, S., Lewis, E., and Li, X.-F., 2018, Detection of continental-scale intensification of hourly rainfall extremes: *Nature Climate Change*, doi:10.1038/s41558-018-0245-3.
- Hodges, B., Imberger, J., Saggio, A., and Winters, K. B., 2000, Modeling basin-scale internal waves in a stratified lake: *Limnology And Oceanography*, v. 45, no. 7, p. 1603-1620, doi: 10.4319/lo.2000.45.7.1603.
- Hosseini, M., Nunes, J. P., Pelayo, O. G., Keizer, J. J., Ritsema, C., and Geissen, V., 2018, Developing generalized parameters for post-fire erosion risk assessment using the revised Morgan-Morgan-Finney model: A test for north-central Portuguese pine stands: *CATENA*, v. 165, p. 358-368, doi:10.1016/j.catena.2018.02.019.
- Langhans, C., Smith, H. G., Chong, D. M. O., Nyman, P., Lane, P. N. J., and Sheridan, G. J., 2016, A model for assessing water quality risk in catchments prone to wildfire: *Journal of Hydrology*, v. 534, p. 407-426, doi:10.1016/j.jhydrol.2015.12.048.
- Martin, D. A., 2016, At the nexus of fire, water and society: *Philosophical Transactions of the Royal Society B: Biological Sciences*, v. 371, no. 1696, p. 20150172, doi:10.1098/rstb.2015.0172.
- Nyman, P., 2013, Post-fire debris flows in southeast Australia: initiation, magnitude and landscape controls [Ph.D. Thesis]: Melbourne University of Melbourne, 214 p.
- Nyman, P., Sheridan, G. J., and Lane, P. N., 2013, Hydro-geomorphic response models for burned areas and their applications in land management: *Progress in Physical Geography*, v. 37, no. 6, p. 787-812, doi:10.1177/0309133313508802.
- Nyman, P., Sheridan, G. J., Smith, H. G., and Lane, P. N. J., 2011, Evidence of debris flow occurrence after wildfire in upland catchments of south-east Australia: *Geomorphology*, v. 125, no. 3, p. 383-401, doi:10.1016/j.geomorph.2010.10.016.
- Nyman, P., Smith, H. G., Sherwin, C. B., Langhans, C., Lane, P. N. J., and Sheridan, G. J., 2015, Predicting sediment delivery from debris flows after wildfire: *Geomorphology*, v. 250, p. 173-186, doi:10.1016/j.geomorph.2015.08.023.
- Peleg, N., Faticchi, S., Paschalis, A., Molnar, P., and Burlando, P., 2017, An advanced stochastic weather generator for simulating 2-D high-resolution climate variables: *Journal of Advances in Modeling Earth Systems*, v. 9, no. 3, p. 1595-1627, doi:10.1002/2016MS000854.
- Riley, K. L., Bendick, R., Hyde, K. D., and Gabet, E. J., 2013, Frequency-magnitude distribution of debris flows compiled from global data, and comparison with post-fire debris flows in the western U.S.: *Geomorphology*, v. 191, no. 0, p. 118-128, doi: 10.1016/j.geomorph.2013.03.008.
- Sheridan, G., Lane, P., Smith, H., and Nyman, P., 2009, A rapid risk assessment procedure for post-fire hydrologic hazards: 2009/10 fire season: Technical Report for the Victorian Department of Sustainability and Environment, Melbourne, Australia, ISBN 9780734041470, 20 p.
- Smith, H. G., Sheridan, G. J., Lane, P. N. J., Nyman, P., and Haydon, S., 2011, Wildfire effects on water quality in forest catchments: A review with implications for water supply: *Journal of Hydrology*, v. 396, no. 1-2, p. 170-192, doi:10.1016/j.jhydrol.2010.10.043.
- Staley, D. M., Negri, J. A., Kean, J. W., Laber, J. L., Tillery, A. C., and Youberg, A. M., 2016, Prediction of spatially explicit rainfall intensity-duration thresholds for post-fire debris-flow generation in the western United States: *Geomorphology*, v. 278, p. 149-162, doi: 10.1016/j.geomorph.2016.10.019.
- Van der Sant, R., Nyman, P., Noske, P., Langhans, C., Lane, P., and Sheridan, G., 2018, Quantifying relations between surface runoff and aridity after wildfire: *Earth Surface Processes and Landforms*, doi:10.1002/esp.4370.
- Westerling, A. L., Hidalgo, H. G., Cayan, D. R., and Swetnam, T. W., 2006, Warming and earlier spring increase western US forest wildfire activity: *Science*, v. 313, no. 5789, p. 940-943, doi: 10.1126/science.1128834.
- White, I., Wade, A., Worthy, M., Mueller, N., Daniell, T., and Wasson, R., 2006, The vulnerability of water supply catchments to bushfires: Impacts of the January 2003 wildfires on the Australian Capital Territory: *Australian journal of water resources* v. 10, no. 2, p. 1-16, doi: 10.1080/13241583.2006.11465291.

Rainfall intensity limitation and sediment supply independence of post-wildfire debris flows in the western U.S.

Paul M. Santi^{a,*}, Blaire MacAulay^b

^aColorado School of Mines, 1500 Illinois St., Golden, CO 80401, USA

^bBaseline Water, #7, 3800-19 Street NE, Calgary, AB T2E 6V2, CANADA

Abstract

This work explores two hypotheses related to post-wildfire debris flows: first, that they are rainstorm-intensity limited and not rainstorm-volume limited, and second, that they are not sediment-supply limited. The first hypothesis suggests that it is common to generate more than enough water to account for the volume in the debris flow, but to actually produce a debris flow the water must be delivered in sufficiently large doses. This is demonstrated by a dataset of 44 debris flows from eight burned areas in California, Colorado, and Utah. Assuming that a debris flow is composed of 30% water and 70% solids, these events were generated during rainstorms that produced an average of 17 times as much water as necessary to develop a debris flow. Even when infiltration is accounted for, the rainstorms still generated an overabundance of water. Intensity-dependence is also shown by a number of cases where the exact timing of debris flows can be pinpointed and are contemporaneous with high intensity bursts of rainfall. The hypothesis is also supported by rainfall intensity-duration thresholds where high volume storms without high intensity bursts do not generate debris flows. The second hypothesis, that of sediment-supply independence, is supported by data indicating the dramatic increase in volume of flows that occur directly after wildfire, as opposed to flows in unburned terrain. Also, repeated flows within short time intervals are only possible with an abundance of channel sediment, dry ravel, and bank failure material that can be mobilized, and field observations confirm these sediment sources, even directly after a debris-flow event.

Keywords: water; intensity; sediment; balance

1. Introduction

Because debris flows are usually triggered by rainfall events, there is often an implicit assumption that their generation is rainfall-limited. Along the same lines, the scouring of debris-flow channels during the event may be interpreted to limit the supply of sediment for future flows in the same channel. The purpose of this study is to demonstrate that neither of these limitations applies to post-wildfire debris flows in particular settings, such as the Western United States. Rainfall is still necessary, and sediment must be available to be mobilized into the flow, but the thresholds can be shown to be quite low, which is why post-wildfire debris flows are common, they are larger than flows in unburned areas, and they can occur repeatedly in the same channels. Rainfall limitations are explored through water-balance calculations to demonstrate how rainstorms are partitioned into debris flows, infiltration, and runoff. Sediment supply is investigated through volume comparisons of burned and unburned source areas, field measurement of sediment sources, and records of repeated flows.

2. Data sources

Our data for rainfall limitation can be found in Gartner (2005); however, portions of the data set are also available in Cannon et al. (2008) and Cannon et al. (2003). The data set contains field measurements from 44 drainage basins with post-wildfire debris flows, including debris-flow volume, basin area, aerial extent of burn severity, total rainfall,

* Corresponding author e-mail address: psanti@mines.edu

rainfall duration, and storm rainfall intensity. The total rainfall amount (mm) for each basin was estimated using inverse distance weighting techniques based on the values of proximal rain gauges (Gartner, 2005). The basins were burned in eight different wildfires in Colorado, California, and Utah. The average size of the study basins is approximately 1 km², however, basin area ranged from 0.01 km² to 4.1 km². Topography ranges from steep, rugged slopes to more gentle gradients (Cannon et al. 2008). Vegetation consists of juniper, shrublands, aspen, fir, grasslands, conifers, and chaparral (Cannon et al., 2008). The climate in the western United States is characterized by very dry, semi-arid periods followed by episodic intense rainfall. Summers are hot and dry, winters are cool and potentially wet (Moody and Martin, 2001; Cannon et al. 2008). The Colorado basins consist of sedimentary interbedded sandstone, siltstone, and conglomerate; the California basins consist of coarse crystalline igneous rocks (Cannon et al. 2008); and the Utah basins consist generally of “quartzite, sandstone, siltstone, schist, gneiss, and amphibolite” intruded by dikes and overlain by limestone and shale (McDonald and Giraud, 2002).

The data for sediment supply can be found in Santi et al. (2008) and Santi and Morandi (2013), consisting of debris-flow volume measurements with associated measurements of in-channel, sheetwash, and rill contributions for the Santi et al. (2008) dataset. The study basins are located primarily in Colorado, California, and Utah, although Santi and Morandi (2013) also include data for comparison from Italy, British Columbia (Canada), Washington state (USA), and several other Western U.S. states.

3. Conceptual model

The analysis of rainfall limitations is done through a water balance calculation, where each drainage basin is idealized as a two-layer system, with ash overlying the soil column (this is a common simplification, used for example in Moody et al., 2009; Woods and Balfour, 2012; and Bodi et al., 2011). Kinner and Moody (2010) suggest the two-layer system exists because of the capillary barrier effect. This effect occurs because ash has much higher hydraulic conductivity and infiltration capacity than the underlying soil (Moody et al., 2009; Gabet and Bookter, 2011; Bodi et al., 2011). Kinner and Moody (2010) note this barrier effect is most enhanced under dry conditions. This model was also confirmed by Ebel et al. (2012), who measured soil water content profiles at a recently burned site and found that almost no water infiltrated below the ash layer.

Because of the high initial infiltration capacity of the ash, we have assumed that 100% of the rainfall will infiltrate the ash layer until it reaches saturation, and any additional rainfall will run off. This is a “fill and spill” infiltration model, where the capacity is not time variant, rather than a Hortonian model that includes time-variable infiltration (Gabet and Bookter, 2011). The effects of evaporation and transpiration were not included due to the short duration of each rainfall event.

Topography plays a significant role in runoff generation, and is undoubtedly a factor for the study basins, which generally have greater than 30-50% slope (Gartner 2005). As a conservative approach, however, the model used in this study does not include the effects of topography, so the actual runoff is expected to be larger than the calculated runoff.

Based on this model, the water balance equation, where each value is a volume over the entire drainage basin, is:

$$\text{Rainfall} = \text{Debris flow water content} + \text{Ash infiltration} + \text{Unburned soil infiltration} + \text{Overland flow} \quad (1)$$

Each of these parameters is described in detail below. For some less-constrained input variables, a range of values is given so that both high overland flow and low overland flow end members can be calculated.

Rainfall is calculated as the total storm rainfall (measured in proximal rain gauges) multiplied by the drainage basin area.

Debris-flow water content can be calculated under the assumption that a debris flow, by definition, contains approximately 20-40% water (Pierson and Costa 1987, Phillips and Davies 1991). If the material contains less than 20% water, then it is a form of rigid mass wasting; if it is above 40% water, it is termed “hyper-concentrated flow” (Phillips and Davies, 1991). Therefore, for the data used in this study, water content of the debris flow is calculated as 20% (high overland flow end member) or 40% (low overland flow end member) of the total volume of the debris-flow deposit.

Ash infiltration is calculated as the product of ash porosity, ash thickness, and burned area within each basin. While ash porosity has been measured as high as 67% (Woods and Balfour 2010) to 83% (Cerdeira and Doerr 2008), this is immediately post-wildfire, and the ash quickly compresses to a lower porosity. We have used a range of 20-30%

porosity (representing high and low overland flow end members, respectively), which matches observations of other researchers and is close to and slightly larger than field capacity of 0.12-0.24 measured by Ebel (2013).

Ash thickness of 10 mm was assumed, based on similar field thickness measurements by Kinner and Moody (2012) and Ebel et al. (2012). The 10 mm assumption is also in agreement with the values used for controlled ash placement in test plots by Gabet and Sternberg (2008), Woods and Balfour (2010), and Bodi et al. (2011). Ash may be thicker than 10 mm after wildfire in more heavily forested areas, such as the pine and juniper areas in Colorado and Utah, but the low tree density and patchy vegetation may result in a lower average thickness, so the assumption of 10 mm is considered reasonable.

The ash infiltration calculation also assumes that ash is present over the entire burned portion of the basin, and ash is not present in the unburned portion. There are possibly burned areas with insignificant ash thickness that are not accounted for in our calculation.

Unburned soil infiltration is expected in unburned portions of the basin. We estimated this infiltration using USDA Natural Resources Conservation Service (NRCS) runoff curves (USDA, 1986). For this calculation, the following assumptions were made:

- Antecedent Moisture Condition II (this is average soil moisture. AMC I – dry soil – may apply directly following the wildfire, but general conditions were assumed to better match with AMC II),
- Hydrologic Soil Groups B, C, and D (representing a range of soil types from fine to sandy textures and slow to high infiltration rates), and
- Hydrologic Condition Poor to Fair (poor is <30% ground cover and fair is 30-70% ground cover).

For Colorado and Utah, these conditions produce a range of Runoff Curve Numbers, CN, from 71-93. For California the CN range is 67-89. Runoff Curve Numbers may be converted to potential maximum retention, S (in inches), with the equation (from Chow et al., 1988):

$$S = 1000/CN - 10 \quad (2)$$

S may then be used to calculate expected runoff, P_e , with the equation (from Chow et al., 1988):

$$P_e = (P - 0.2S)^2 / (P + 0.8S) \quad (3)$$

Where P is cumulative rainfall in inches.

While the range of S values (calculated from CN) is given for statewide location, the P_e values are calculated for each basin depending on the cumulative rainfall measured in that basin or in nearby rain gauges.

Overland flow is calculated from Equation 1 as the difference in the measured rainfall and the calculated infiltration. A range of values is presented, with both low and high overland flow estimations.

4. Results of water balance calculation

Figures 1 and 2 show the final water balance calculation for each basin, where each component (debris flow, infiltration, and overland flow) is represented as a percentage of the total rainfall on the basin. The Low Overland Flow Calculation (Figure 1) assumes the maximum infiltration values for both burned and unburned areas and assumes debris-flow water content of 40%. The High Overland Flow Calculation (Figure 2) assumes minimum infiltration values and debris-flow water content of 20%.

There is excess rainfall in the form of overland flow runoff for all basins except four in Figure 1 (Haflin, Basin 23, Root Creek, and Coal Seam G) and except for one in Figure 2 (Basin 23). Most basins show a significant excess of water, with substantial overland flow. The amount of overland flow is highest for the California basins (Janet Creek J3 through El Capitan II, which are shown on the right side of these graphs).

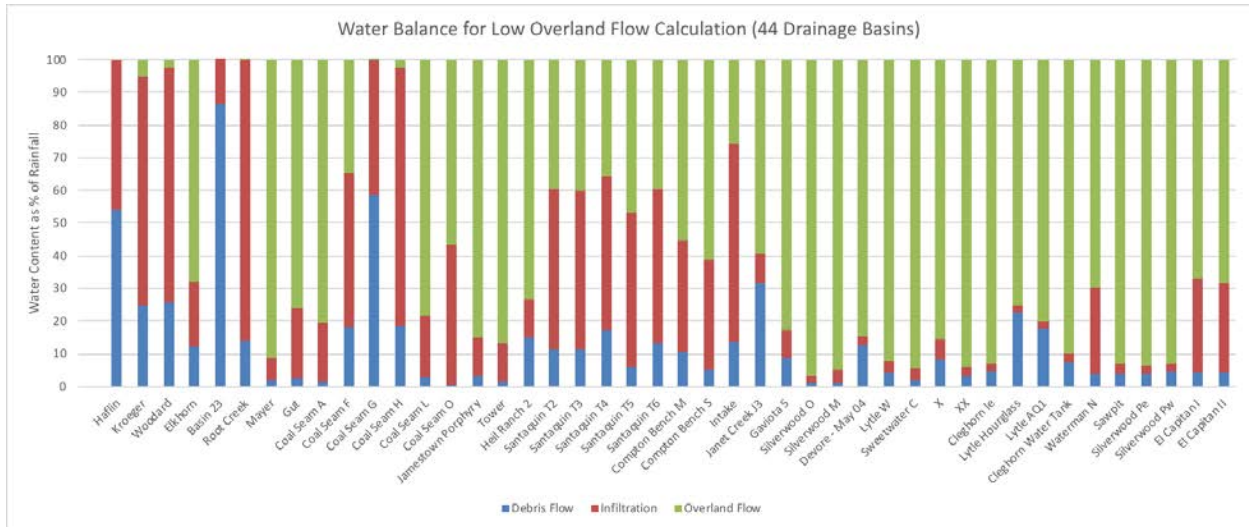


Fig. 1. Results of water balance calculation for Low Overland Flow assumptions.

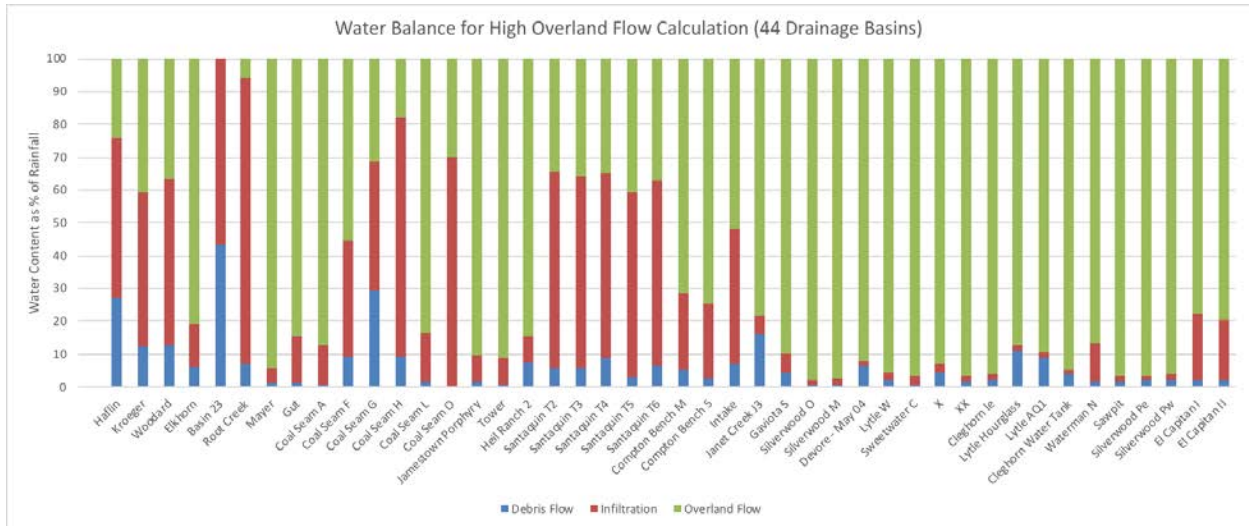


Fig. 2. Results of water balance calculation for High Overland Flow assumptions.

The amount of water incorporated into the debris flows is much less than the amount available in each rainstorm. Assuming an average proportion of water in the debris flow (30%, which is mid-range of the low and high values of 20% and 40% used in the calculation), only a median of 5.9% of the rainstorm water is incorporated into debris flows, with the remainder either infiltrating or exiting as overland flow. This is 1/17th of the available water, and this small fraction verifies that the debris flows are not rainstorm volume limited. The amount of water in debris flows is shown on Figure 3.

5. Rainfall intensity limitations

While rainfall volume can be shown not to limit debris-flow occurrence, a dependence on rainfall intensity can also be demonstrated. Figure 4, from Friedman and Santi (this volume) and Friedman (2012), shows the close time proximity between rainfall intensity bursts (zones of increased slope on the rain gauge cumulative rainfall curves) and the pressure spikes recorded in the nearby pressure transducers. In this study, pressure transducers were drilled into bedrock in the drainage channel to measure debris flows overriding them, and rain gauges were placed within tens of

meters of the pressure transducers (Basin 24) or were in adjacent canyons (Basin 16, located 1.1 km from the Basin 32 pressure transducer). These data show debris-flow response within a few minutes of rainfall intensity bursts. Similar short lag times have been measured by other researchers as well (e.g., Coe et al., 2008).

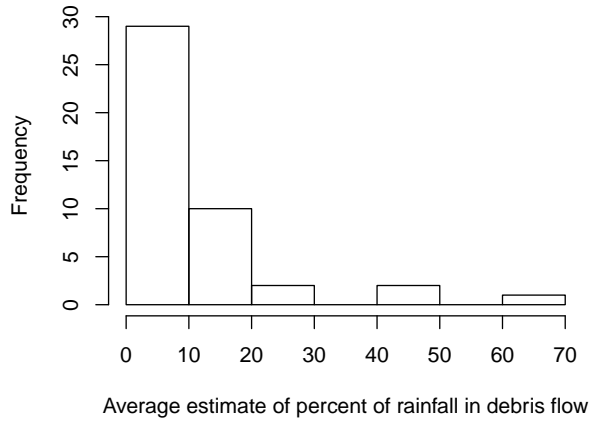


Fig. 3. Histogram of percent of storm rainfall incorporated into debris flow for each watershed, assuming the debris flow is composed of 70% solids and 30% water. In very few cases does the debris flow entrain more than 20% of the available water.

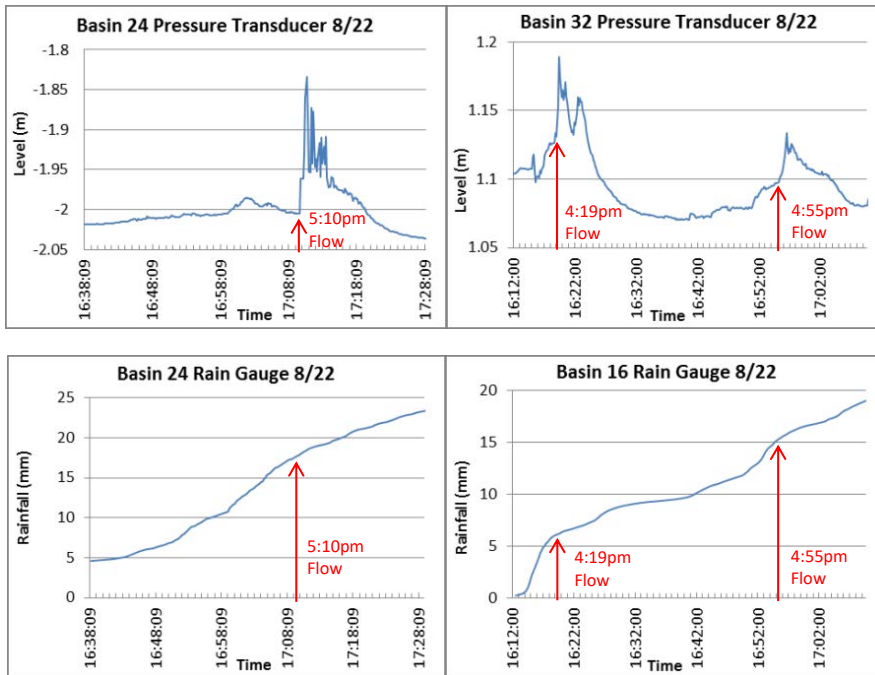


Fig. 4. Example of short lag time between rainstorm intensity burst (zones of increased slope of the cumulative rainfall curves shown in blue on the bottom graphs) and debris-flow generation (spikes on the pressure transducers shown in blue on the upper graphs). Note that the rain gauge for Basin 24 was located within meters of the pressure transducer, but the rain gauge in Basin 16 was located 1.1 km from the pressure transducer in Basin 32.

Rainfall intensity dependence for debris-flow initiation has also been well established through rainfall intensity-duration threshold graphs, where local data can be used to construct thresholds dividing storms that produce debris flows from those that do not. An example is shown on Figure 5, which summarizes the thresholds from numerous locations (with those from burned areas shown in color). It is possible to have rainstorms that generate large amounts of total amounts of water (long duration storms) that do not have sufficient intensity to trigger debris flows.

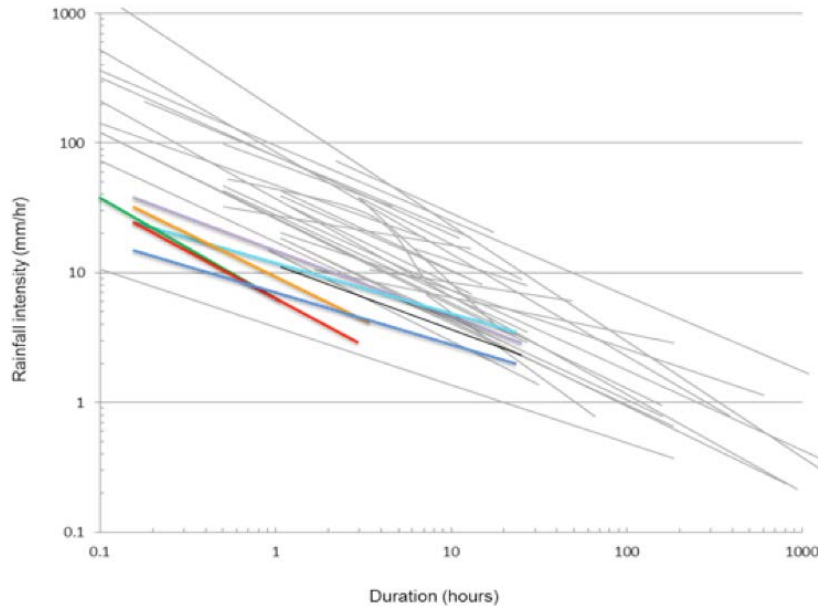


Fig. 5. Compilation of measured intensity-duration thresholds for debris-flow generation at various unburned (gray lines) and burned (colored lines) locations (from Cannon and DeGraff, 2009). Burned areas have lower threshold storms to trigger debris flows, but for all cases it is possible to have long duration storms producing large cumulative rainfall that do not generate debris flows because of low rainfall intensity.

6. Sediment supply independence

Three lines of evidence demonstrate that post-wildfire debris flows are not sediment supply limited. The first is the multi-fold increase in volume of debris flows following wildfire. Santi and Morandi (2012) compared the volumes of debris produced from a large dataset of western US debris flows, including 274 events from recently burned areas (within one year), 162 events from recovering basins (one to ten years after wildfire), and 216 events from areas that are unburned or fully recovered (ten years after wildfire). They showed that the area yield rate (debris-flow volume divided by basin area) was doubled for burned areas. When they used cluster analysis to subdivide the data into areas of similar basin size, channel length, and channel gradient, they showed that burned areas had an even higher difference in debris-flow volume, ranging from 2.7 to 5.4 times the volumes produced by unburned areas.

The amount of sediment produced by these debris flows is substantial, and it has been shown that the majority of it comes from channel scour as water moves down-canyon. Santi et al. (2008) measured incremental debris production from the channel and surrounding hillside for sections of the drainage channel extending from zero-order channels near the top of the drainage basin to the canyon mouth of the at the bottom of the basin. An example of their data is shown on Figure 6. Based on data from 46 debris flows, they showed that hillslope and rill erosion accounted for an average of only 3% of the final debris volume, but channel scour accounted for nearly the entire remainder of the volume. Sediment in the channel accumulates through normal weathering and sedimentation processes, strongly supplemented during and after the fire by dry ravel (Swanson, 1981; Wells, 1987; Florsheim et al., 1991; Schmidt et al., 2011). This produces a sediment-filled channel with ample material to be incorporated into a debris flow by channel scour. In some cases, a debris flow may scour to bedrock, but at many locations sediment remains in the channel (Figure 7) and may be incorporated into subsequent flows. Furthermore, post-debris flow channel banks are over-steepened from scour, and these banks frequently fail, recharging the sediment supply for future flows (Figure 8).

Finally, multiple debris-flow events have been observed in the same canyon over short time frames indicating that the supply of sediment is not easily exhausted. For example, Gartner, et al. (2004) provides a database of post-wildfire debris flow and flood events in the Western US, noting at least eight locations where repeated debris flows occur in the same drainage basin within days to months of each other. Cannon and Gartner (2005) note that “basins with thin colluvial covers and minimal channel-fill deposits generally produce debris flows only in response to the first significant rainfall of the season. Basins with thick channel-fill deposits ... frequently produce numerous debris flows throughout the rainy season.”

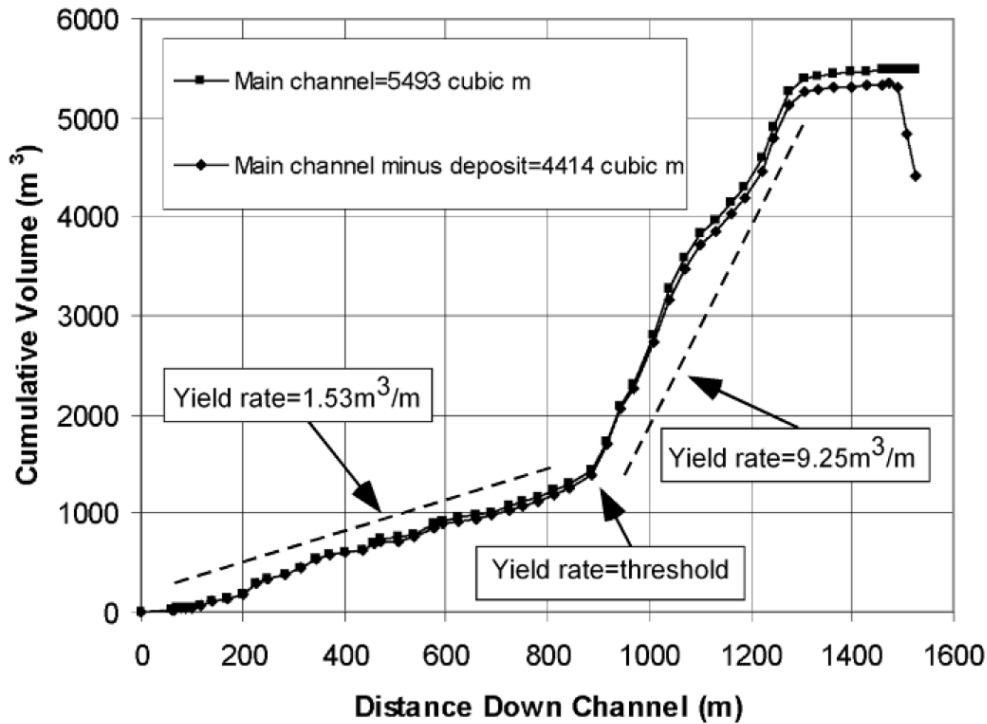


Fig. 6. Measurement of incremental debris production using multiple channel cross-sections (from Santi et al., 2008). Channel yield rate, calculated as the volume of debris produced per unit channel length, is the slope of the graph at any point.



Fig. 7. Channel scour from a debris flow, with remaining sediment that can be incorporated into successive debris flows.



Fig. 8. Failure of channel banks that have been over-steepened by recent debris-flow scour. This process quickly adds new sediment to the channel that can be incorporated into successive debris flows (photograph by Rich Giraud, Utah Geological Survey).

7. Conclusions

Using conservative assumptions for infiltration and debris-flow water content, there is excess water from rainfall in nearly every analyzed drainage basin that produces significant overland flow runoff during debris-flow generating storms. This means that for post-wildfire settings, at least in the Western US and perhaps other semi-arid mountainous or Mediterranean climates, debris flows are not rainfall volume limited. The model for debris-flow generation then becomes a system where there is ample surface water flow both before and after the debris flow, and that the debris flow is triggered not by reaching a threshold total water volume or saturation, but by reaching a threshold rainfall intensity. The limiting factor for triggering debris-flow behavior of the fluid runoff is the dynamics of the pulse of water and entrained sediment. Furthermore, the supply of sediment in drainage channels is substantial, producing much larger debris flows than pre-fire, and the supply of sediment is capable of producing repeat events in the same channel, at least until vegetation recovers enough to temper the overland flow or until smaller rainstorms move sediment through the system by fluvial transport.

References

- Bodi, M.B., Mataix-Solera, J., Doerr, S.H., and Cerda, A., 2011, The wettability of ash from burned vegetation and its relationship to Mediterranean plant species type, burn severity and total organic carbon content, *Geoderma*, v. 160, pp. 599-607.
- Cannon, S.H., and DeGraff, J., 2009, The increasing wildfire and post-fire debris-flow threat in Western USA, and implications for consequences of climate change: Landslides- Disaster Risk Reduction, K.Sassa, P. Canuti (eds.). Springer-Verlag Berlin Heidelberg, 2009.
- Cannon, S.H., Gartner, J.E., Wilson, R.C., Bowers, J.C. and Laber, J.L., 2008, Storm rainfall conditions for floods and debris flows from recently burned areas in southwestern Colorado and southern California. *Geomorphology*, v. 96, pp. 250-269.
- Cannon, S.H., Gartner, J.E., Holland-Sears, A., Thurston, B.M. and Gleason, J.A., 2003, Debris-flow response of basins burned by the 2002 Coal Seam and Missionary Ridge fires, Colorado. in Boyer, D.D., Santi, P.M., and Rogers, W.P., eds., *Engineering Geology in Colorado—Contributions, Trends, and Case Histories: Association of Engineering Geologists Special Publication 14*, Colorado Geological Survey Special Publication 55, on CD-ROM.
- Cannon, S.H. and Gartner, J.E., 2005, Wildfire-related debris flow from a hazards perspective. In: Jakob, M., Hungr, O. (Eds.), *Debris-Flow Hazards and Related Phenomena: Praxis*. Springer, Berlin Heidelberg, pp. 363–385.
- Cerda, A. and Doerr, S.H., 2008, The effect of ash and needle cover on surface runoff and erosion in the immediate post-fire period. *Catena*, v. 74, pp. 256-263.
- Chow, V.T., Maidment, D.R. and Mays, L.W., 1988, *Applied Hydrology*, McGraw-Hill, Inc., New York, 572 p.
- Coe, J.A., Kinner, D.A., Godt, J.W., 2008, Initiation conditions for debris flows generated by runoff at Chalk Cliffs, central Colorado, *Geomorphology*, v. 96, p. 270-297.
- Ebel, B. A., 2013, Wildfire and aspect effects on hydrologic states after the 2010 Fourmile Canyon Fire, *Vadose Zone Journal*, v. 12, doi:10.2136/vzj2012.0089.
- Ebel, B.A., Moody, J.A. and Martin, D.A., 2012, Hydrologic conditions controlling runoff generation immediately after wildfire. *Water Resources Research*, v. 48, W03529.
- Florsheim, J.L., Keller, E.A. and Best, D.W., 1991, Fluvial sediment transport following chaparral wildfires, Ventura County, southern California. *Geol. Soc. Am. Bull.*, v. 103, 504–511.
- Friedman, E.Q. and Santi, P.M., 2019, Relationship between rainfall intensity and debris-flow initiation in a southern Colorado burned area, 7th International Conference on Debris-Flow Hazards Mitigation, pp. XX-XX.
- Friedman, E.Q., 2012, Debris-flow hazard assessment and monitoring within the 2010 Medano Fire burn area, Great Sand Dunes National Park and Preserve, Colorado, unpublished MS thesis, Colorado School of Mines, 104 p.
- Gabet, E.J. and Bookter, A., 2011, Physical, chemical and hydrological properties of ponderosa pine ash. *International Journal of Wildland Fire*, v. 20, pp. 443-452.
- Gabet, E.J. and Sternberg, P., 2008, The effects of vegetative ash on infiltration capacity, sediment transport, and the generation of progressively bulked debris flows. *Geomorphology*, v. 101, pp. 666-673.
- Gartner, J.E., 2005, Relations between wildfire related debris-flow volumes and basin morphology, burn severity, material properties and triggering storm rainfall. Masters of Arts Thesis, Department of Geography, University of Colorado.
- Gartner, J.E., Bigio, E.R. and Cannon, S.H., 2004, Compilation of post wildfire runoff-event data from the Western United States; USGS OFR; 2004-1085.
- Kinner, D.A. and Moody, J.A., 2010, Spatial variability of steady-state infiltration into a two-layer soil system on burned hillslopes. *Journal of Hydrology*, v. 381, pp. 322-332.
- McDonald, G.N. and Giraud, R.E., 2002, September 12, 2002, fire-related debris flows east of Santaquin and Spring Lake, Utah. Utah Geological Survey. Available online at: <http://geology.utah.gov/online/techrpt/santaquin0902.pdf>. Accessed Nov. 5th, 2012.
- Moody, J.A., Kinner, D.A., and Ubeda, X., 2009, Linking hydraulic properties of fire-affected soils to infiltration and water repellency. *Journal of Hydrology*, v. 379, pp. 291-303.
- Moody, J.A. and Martin, D.A., 2001, Initial hydrologic and geomorphic response following a wildfire in the Colorado front range. *Earth Surface Processes and Landforms*, v. 26, pp. 1049-1070.
- Phillips, C.J. and Davies, T.R.H., 1991, Determining rheological parameters of debris flow material. *Geomorphology*, v. 4, pp. 101-110
- Pierson, T.C. and Costa, J.E., 1987, A rheologic classification of subaerial sediment-water flows. *Geological Society of America Reviews in Engineering Geology*, v. 7, pp. 1-12.
- Santi, P.M. and Morandi, L., 2013, Comparison of debris-flow volumes from burned and unburned areas. *Landslides*, v. 10, pp. 757-769.
- Santi, P.M., deWolfe, V.G., Higgins, J.D., Cannon, S.H., and Gartner, J.E., 2008, Sources of debris flow material in burned areas, *Geomorphology* v. 96, pp. 310-321.
- Schmidt, K.M., Hanshaw, M.N., Howle, J.F., Staley, D.M., Stock, J.D., and Bawden, G.W., 2011, Hydrologic conditions and terrestrial laser scanning of post-fire debris flows in the San Gabriel Mountains, CA, USA, *Proceedings, 5th International Conference on Debris-flow Hazards Mitigation: Mechanics, Prediction and Assessment*. June 14-17, 2011, Padua, Italy.
- Swanson, F. J., 1981, Fire and geomorphic processes. In: Mooney, H. A., Bonnicksen, T. H., Christensen, N. L., Lotan, J. E., and Reiners, W. A. (Eds.), *Fire Regimes and Ecosystem Properties*. United States Department of Agriculture, Forest Service General Technical Report WO-26, 401-420.
- United States Department of Agriculture, 1986, *Urban hydrology for small watersheds (PDF)*. Technical Release 55 (TR-55) (Second ed.). Natural Resources Conservation Service, Conservation Engineering Division.
- Wells, W.G., 1987, The effect of fire on the generation of debris flows in southern California. In Costa, J.E. and Wieczorek, G.F., eds., *Debris Flows/Avalanches: Process, Recognition, and Mitigation*, GSA Reviews in Engineering Geology, v. 7, 105-113.
- Woods, S.W. and Balfour, V.N., 2012, The effects of soil texture and ash thickness on the post-wildfire hydrogeological response from ash-covered soils. *Journal of Hydrology*, v. 393, pp. 274-286.

Case Studies and Hazard Assessments

Debris flows in the North Pacolet River valley, Polk County, North Carolina, USA - case studies and emergency response

Jennifer B. Bauer ^{a*}, Richard M. Wooten^b, Bart, L. Cattanach^b, Stephen J. Fuemmeler^a

^a*Appalachian Landslide Consultants, PLLC, PO Box 5516 Asheville, NC 28813, USA*

^b*North Carolina Geological Survey, 2090 US 70 Hwy, Swannanoa, NC 28778, USA*

Abstract

The North Pacolet River valley is incised into the Blue Ridge Escarpment (BRE) near Tryon in southwestern North Carolina. The BRE is a mountain front that marks the change from the mountainous Blue Ridge physiographic province to the lower, rolling topography of the foothills zone of the Piedmont provinces. This escarpment is often comprised of steep slopes with exposed bedrock cliffs and shallow colluvial soils. The down slope sides of the escarpment have evidence of past slope movements in the form of large scale deposits, debris fans, talus slopes, and dormant debris slides. Debris flows have been documented along the BRE in multiple past storm events including those in 1916, 1940, 1996, and 2004. On May 18, 2018, debris flows again initiated near the top of the BRE slopes and travelled down to the North Pacolet River valley floor during heavy rains on soils with high antecedent moisture contents. At least 27 debris flows were initiated, travelling up to ~966 meters (~3,170 feet) down drainages below. At least 6 homes were damaged or destroyed and one fatality occurred due to these debris flows. Main highways, interstates, and multiple private roads were covered by the debris. Appalachian Landslide Consultants, PLLC (ALC) and the North Carolina Geological Survey (NCGS) responded to this emergency situation in order to provide Polk County Emergency Management information about the stability of the slopes before the arrival of Tropical Depression Alberto just 9 days after the May 18 rains. During this reconnaissance, ALC and the NCGS identified areas of potential instability in the coming rains. County Emergency Management used this information when deciding to issue a voluntary evacuation recommendation to the people of the North Pacolet River valley. This paper discusses the findings of the reconnaissance mapping, as well as a general overview of the integration of geological information into emergency response and preparation.

Keywords: debris flow; North Carolina; Blue Ridge Escarpment, landslide, natural hazards identification, management policy

1. Introduction

On May 18, 2018, the North Pacolet River valley (Pacolet Valley), on the Blue Ridge Escarpment near Tryon, in Polk County, North Carolina, received as much as 20 cm (8 inches) of rain in just a few hours (NCEI, 2018b). These heavy rains triggered numerous small and large slope movements, particularly impacting communities near U.S. Highway 176 and Warrior Drive. “One 59-year-old woman died when her garage collapsed as she was trying to flee her home. Her husband was swept into Highway 176 but survived with mostly minor injuries” (NCEI, 2018b). These landslide events impacted all who lived in the Pacolet Valley, as the Highway was closed for several days while mud from the debris flows was removed. Some people in the community whose homes were damaged were not able to return for several months. Other homes were completely destroyed and dismantled by the owners. These events occurred nine days before Subtropical Depression Alberto was forecast to hit the same area.

* Corresponding author e-mail address: Jennifer@appalachianlandslide.com

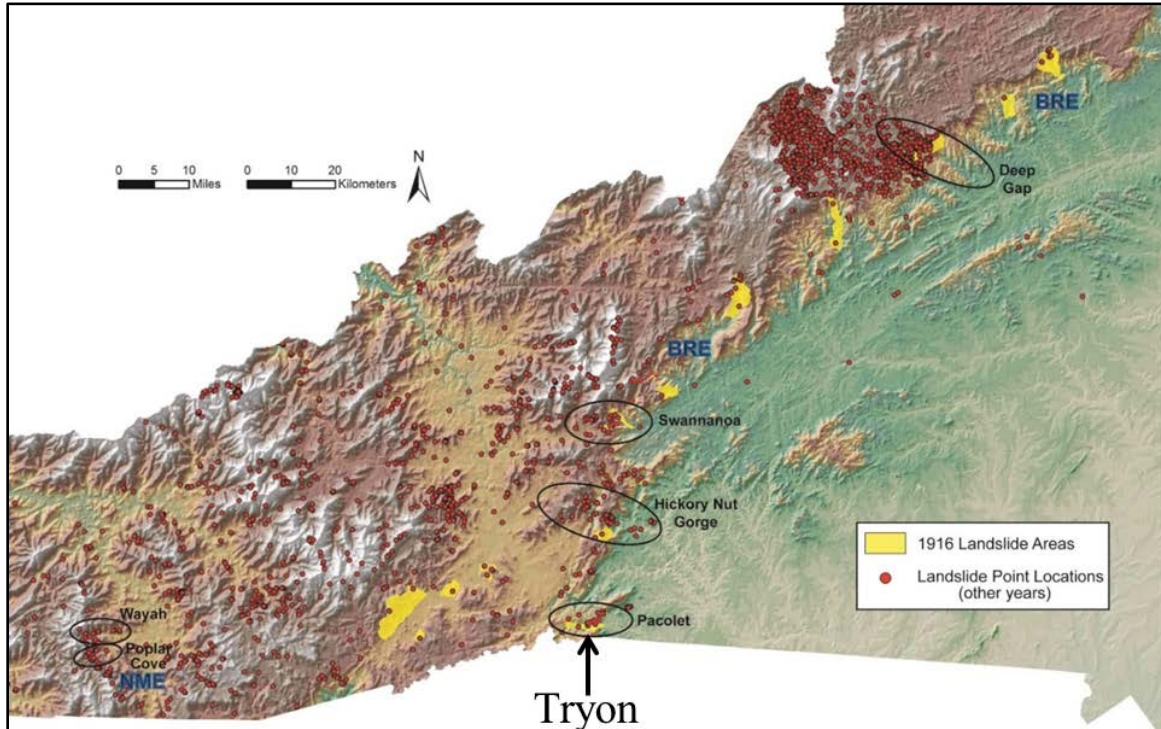


Fig. 1. Hillshade map of Western North Carolina. Ellipsoids define erosional reentrants into high relief areas. Blue Ridge Escarpment extends from the southern to northern border of North Carolina, separating the mountains from the piedmont. Landslide locations from the NC Geological Survey geodatabase are indicated as yellow polygons for 1916 landslide areas, and red points for all other mapped landslide locations.

While these damaging debris flows took residents by surprise, there is evidence that debris flows have been taking place in this valley and similar topographic regions in North Carolina for quite some time. During reconnaissance mapping of the 2018 debris flows, previous slope movement deposits were identified, but dates were not determined. Many homes had been built on debris deposits or close to streams draining the steep slopes above. Landslide susceptibility maps are not available for Polk County, and people in the valley were not aware of these hazards.

1.1. Geomorphic Location

The North Pacolet River valley is a reentrant incised into the regional landform known as the Blue Ridge Escarpment (BRE) (Fig. 1). The BRE is a high relief, erosional feature that extends from northeast Georgia to northwest Virginia, which generally corresponds with the Eastern Continental Divide, and marks the boundary between the Blue Ridge Mountains and the rolling foothills of the Piedmont physiographic province to the east (Wooten et al, 2016). Landslides, particularly rapid to extremely rapid-moving debris flows and slides, have been recorded along the Blue Ridge Escarpment in multiple storms in historic times. “Heavy rainfall, when combined with the high-relief areas of certain landforms and erosional reentrants into them, are more prone to debris flow activity,” (Wooten et al, 2016) (circled areas in Fig 1). This is especially the case with high antecedent soil moisture conditions. In the past 102 years, there have been four scenarios where back-to-back, major storms within 6-20 days of each other triggered debris flows in WNC (July 15-16 1916; August 1940; September 2004, May-June, 2018). The May-June, 2018 storms triggered landslides along the Blue Ridge Escarpment and other areas in surrounding counties.

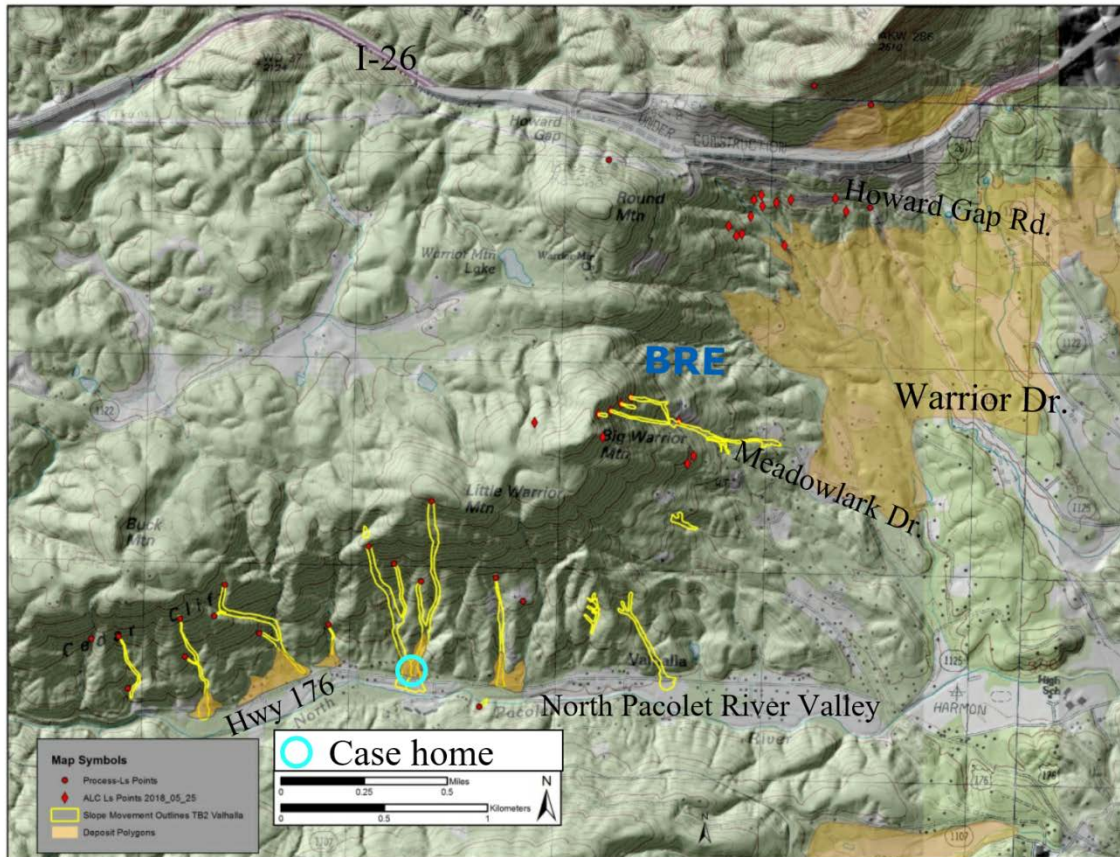


Fig. 2. 2004 hillshade draped with Saluda 1:24,000 quadrangle topographic map. Debris flow outlines are yellow polygons, red points are slope movement initiation zone locations; tan polygons are slope movement deposits. Data from NCGS and ALC geodatabases, 11/01/2018. Home location of Mr. and Mrs. Case is highlighted.

1.2. Summary of events of May, 2018

On the evening of May 18, 2018, heavy rains inundated the Pacolet Valley and surrounding area, triggering debris flows, other types of slope movements, and flooding in the area. The home of Mr. and Mrs. Case was initially hit by a debris flow from the eastern drainage above their home (Fig 2, Fig 3). The Cases tried to get out of their home at that time, but Mrs. Case was not able to due to health complications. Mr. Case assisted Mrs. Case into a detached garage next to the home. He then left, wading through the mud trying to get help, when a second debris flow from the western drainage behind the home hit the garage (Fig 3). Mr. Case tried to get back to the house to get to his wife, but was unable to do so. Early the morning of May 19, Polk County Emergency Management (EM) requested assistance from North Carolina Geological Survey (NCGS) to determine if slopes above the home were stable enough for crews to get to Mrs. Case. Sadly, she was not alive when crews were able to access the garage.

During the following days, NCGS geologists surveyed the damage throughout the valley, assisted by volunteers from Appalachian Landslide Consultants, PLLC (ALC) and former members of the NCGS landslide mapping team. ALC and NCGS geologists spoke to individual members of the community whose homes, property, and/or roads had been damaged by debris flows, and investigated the potential debris-flow source areas upslope of some of the affected properties. The NCGS and ALC participated in Emergency Management meetings, passing on information gathered in the field. The NC Forest Service provided a helicopter flight so geologists could view the extent of the damage and potential remaining source areas from the air.



Fig. 3. (a) Georegistered 2018 UAV Image from the NC Geodetic Survey. Original location of Case home and detached garage outlined in black. (b) Georegistered 2018 Aerial Image from the NC Forest Service. Two debris flows that merged at the base of Little Warrior Mountain at the Case home location along Highway 176.

The week following the debris-flow events, Subtropical Depression Alberto was forecast to bring significant rains to the same region along the Blue Ridge Escarpment. EM requested that the NCGS and ALC provide locations that remained unstable, which they provided in GIS format. Meteorologists from the National Weather Service in Greenville-Spartanburg, SC came up to survey the damage with the NCGS and to participate in EM meetings to assist in preparations for additional rain. Based on information from the geologists and meteorologists, EM decided to issue a voluntary evacuation for the entire Pacolet Valley and Warrior Drive area during Subtropical Depression Alberto. Bobby Arledge, Polk County Emergency Management Director issued a statement saying “The county has been surveyed by professional geologists and these storms will further destabilize areas that have experienced above average rainfall and potentially cause further landslides. A heightened level of concern exists for residents in and around areas that have already experienced land movement” (Tryon Daily Bulletin, 2018).

Rainfall from Subtropical Depression Alberto spanning from May 26-31, 2018 totaled over 18 cm in the Tryon, NC area (7 inches), contributing to continued sliding of unstable areas and erosion (NWS, 2018a). Two news media personnel were killed during these rains when a tree fell on their vehicle on Hwy 176.

2. Data Collection

2.1. Data collection

In the days after the May 18 debris-flow events, data collection was initially targeted to capture GPS locations of debris deposits that had damaged or destroyed homes or roadways. To assist a client, ALC, along with a local grading contractor, hiked to the source area of a coalescing debris flow that impacted homes and roads along

Meadowlark Drive. Most of the other data collection was along Hwy 176 in the Pacolet Valley, or along Howard Gap Road. At the request of a landowner trying to decide if she should evacuate her horses from her farm, ALC and NCGS geologists noted impacts along a trail above her home below the heavily-damaged Howard Gap Road and Warrior Drive.

Several times within the weeks after the May 18 and Alberto events, NCGS geologists went back to the Pacolet Valley to gather more detailed information about debris-flow tracks and characteristics and debris deposits. ALC geologists evaluated another site off of Meadowlark Drive for a client concerned about their driveway. Data was collected in an ArcGIS geodatabase of points, lines, and polygons (Fig 2). Point locations were taken for slope movement initiation locations and for field data collection locations. Lines were used to indicate extents of ground rupture (i.e. tension cracks and scarps). Data for slope movement outlines, delineating the extents of the debris flows or debris slides, were collected as polygon features. These features were mapped either from field observations, aerial photographs (see below), or a combination of the two. Polygons were also used to delineate extents of debris deposits, either from field observation, or remote sensing of a 2004 lidar-derived digital elevation model (6 meter horizontal pixel resolution).

2.2. Aerial photographs

Many types of aerial photographs were taken of the valley and the debris flow features. Multiple photos were taken from a digital camera and smartphone cameras from the North Carolina Forest Service (NCFS) helicopter. Video was also taken with a GoPro™ camera. The Broad River Fire Department and the North Carolina Geodetic Survey captured photos of some of the debris flow locations with an unmanned aerial vehicle (UAV). Unfortunately, orthophotos were not taken immediately after the debris-flow events; however, orthophotos taken during the following leaf-off season greatly aided mapping efforts. Select UAV and NCFS photographs were georeferenced and used for drawing slope movement outlines or areas of impact.

3. Findings

3.1. Debris-flow characteristics

Twenty seven debris flows were cataloged in the geodatabase, although several others remain uncatalogued because they were difficult to delineate through the tree cover. Nineteen debris flow initiation zones were explored in more detail either by foot or via aerial photographs. The dominant initiation zone scenario was one where shallow colluvial soil less than 1.5 meters (5 feet) thick slid, and then flowed off of competent bedrock (stained-state to fresh on the Unified Rock Classification System scale), where groundwater was flowing at the interface of the two. However, there were also examples of debris flows initiating within boulder- and cobble-filled colluvial soil, and residual soil. The common finding was groundwater flow at or near the failure surfaces.

Many of the debris flows on these steep slopes started upslope of the prominent rock cliff, marking the upper edge of the BRE. Most started in concave hollows where water was converging, and most flowed down drainages. Springs were noted just upslope of the cliffs within the debris-flow tracks that were walked. The lengths of the debris flows catalogued range from 966 meters (3170 feet) to 40 meters (130 feet). The depths of these debris flows exceeded 3.6 meters (12 feet) in some areas, based on mudlines and nick marks on standing trees, see Fig 4. The approximate average width of the debris-flow tracks themselves is around 17 meters (56 feet), ranging from 7.6 meters (25 feet) to 30 meters (100 feet). The volumes of material that flowed down the slope have not been calculated to date.

One debris flow that initiated on a convex slope was observed to flow through the trees, rather than uprooting them. This debris flow did not travel far, and spread its deposit out across the convex slope. Another debris flow upslope of Interstate 26 flowed through the trees, and onto the interstate, blocking traffic and creating a traffic control issue for Emergency Management, while they were experiencing the torrential rains, flooding, and landslides.



Fig. 4. Downstream view of debris flow in the Meadowlark Drive area. Tree nick marks can be observed twice as high as the height of the worker by the tree, approximately 3.6 meters high (12 feet).

3.2. Debris deposit characteristics

Many of the debris flows deposited material in areas where prior slope movement deposit material was observed or mapped using a lidar-based digital elevation model. In some locations, pre-existing deposits were incised during the May 2018 event (Fig 2). Many of the homes that were damaged were constructed on these past debris flow deposits.

Debris deposits consisted of silt, sand, gravel, cobbles and boulders. 2018 debris also included woody debris, and in some cases, debris from structures. In the main Pacolet Valley, debris flows tended to stay within the drainages all the way down to the valley bottom. On Meadowlark Drive, several roads and culverts had been placed to access homes on the middle part of the mountain. The debris flows took out these roads in some cases, and blocked culverts in others. Where culverts were blocked, debris was diverted across and down the paved road, and off the embankment side. One home in particular received up to 3.6 meters (12 feet) of mud in the lower driveway. Another home was somewhat protected by a large van parked between the house and the slope that the debris flowed down. The van diverted the mud around the home along the ditch and driveway on both sides, instead of into it.

3.3. Other landslides

There were many (perhaps dozens) of other types of slope movements observed during the aerial reconnaissance flight and while driving the roads. Many of the road cut failures were debris slides or rock/weathered rock slides. Most of these road cut or fill slope landslides have not yet been documented, and therefore are not discussed in detail here.

3.4. Unstable locations and communication

After the initial May 18 landslide events, EM asked NCGS and ALC geologists to provide them with locations of unstable soil that could mobilize during rainfall from Subtropical Depression Alberto. Geologists identified several locations, many of which included fill slopes that had been damaged or destroyed. The sides of the fill along the drainages had been over-steepened by the scour of the debris flows, and loose, unstable slide blocks remained. Because of the remaining dense tree vegetation, and the narrowness of the debris-flow tracks in many areas, it was

difficult to identify all of the potential log jams or blocks of loose soil from the helicopter reconnaissance flight. Two impoundments for ponds or sediment retention structures were identified as potentially unstable locations to monitor. Geologists recommended that anyone living downslope of the areas that were identified, as well as any areas that had experienced previous debris flow activity, evacuate during Alberto. In addition, they recommended that anyone who lived in the valley that was impacted evacuate, due to the potential for additional road damage preventing emergency rescue.

After hearing these recommendations from geologists and other members of the emergency response team, and the predicted rain amounts from the NWS meteorologists, the County Emergency Manager issued a voluntary evacuation recommendation for several of the communities in Polk County.

4. Conclusions

4.1. Debris flows

The May 18 landslide event is the latest in a long history of slope movements in the Pacolet Valley and along the Blue Ridge Escarpment. The exposed bedrock near the top of the ridge is likely evidence of past initiation zones, too steep for vegetation to regrow. Slope movement deposits at the base of the slope indicate past movement events, and now have an additional layer of debris on them, where it has not yet been removed. There were numerous landslides reported along the Saluda Railroad grade on the south side of the Pacolet River valley during the 1916 storm (Southern Railway Company, 1917). The Atlanta Journal Constitution, July 18, 1916 reported 'landslides from the mountains buried the road for long distances' on the Saluda-Tryon Road (current-day Howard Gap Road). Additionally, the NC Department of Transportation had landslide problems during construction of I-26 on the Saluda grade in 1968 (NCGS geodatabase, 2018).

Debris flows from the May 18 event are evidence that although their source areas can be relatively narrow and shallow, they can, nonetheless, cause significant damage and even fatalities because of long run out distances and proximity of residences to the drainages. Intense rainfall was the trigger for these debris flows, where surface or groundwater contributed to destabilizing the relatively shallow colluvial and organic soil on top of the bedrock. Debris flows that started on concave slopes and travelled down drainages had the longest run out distances, compared to debris flows on convex slopes.

4.2. Communication

This event is an example of two communication scenarios: 1) post-May 18 emergency management and pre-Alberto planning and 2) pre-May 18 awareness and preparedness. In scenario one, there was open communication among a vast number of interdisciplinary professionals. Emergency Managers were relying on the geologists and others on the ground for updates on slope stability. Geologists were relying on emergency responders, the NC Forest Service, and others for assistance with evaluation. Landowners were providing access to geologists, the Red Cross, and others assessing damage. Many partners played a role in helping evaluate the current situation, responding to it appropriately, and providing recommendations to best prepare for the predicted upcoming additional heavy rains. However, it became obvious that having tools, such as debris flow susceptibility maps indicating potential source areas and potential debris flow pathways would have assisted in making evacuation decisions.

In the second scenario, pre-May 18 awareness and preparedness, it is clear that the communication in this scenario was not sufficient. Many of the people living in the Pacolet Valley and at the base of the BRE were not aware that they were in the path of debris flows. They did not know that the small stream behind their home could become a raging torrent of mud, rocks, and trees that could destroy their homes. Slope movement deposits that are obvious to a trained geologist's eye looked like nice relatively flat home sites with pretty boulders to the untrained eye. Local citizens did not have this information because the valley had not been evaluated, mapped and modeled. Without this prior work, potential hazards could not have been communicated thoroughly and effectively and therefore, no evacuations were called-for.

4.3. Future work

Recognizing the importance of landslide mapping information to residents of mountainous areas, the North Carolina legislature reallocated funding to the NCGS to re-start a landslide mapping program that was de-funded in 2011. The intention of the funding is to provide maps for the mountainous areas that do not currently have landslide maps (Macon, Watauga, Buncombe, and Henderson Counties were mapped previously by the NCGS, a portion of Haywood County, and all of Jackson County were mapped by ALC). Communication about landslide hazards will be an important component to the landslide mapping program. As the May 18 event in the Pacolet Valley exemplifies, mapping + communication and awareness can save lives.

Acknowledgements

The authors would like to thank the residents of the Pacolet Valley for sharing their stories, heartbreaks, and community during the days and months following the May 18 event. They would also like to thank the Polk County Emergency Management, the National Weather Service Greenville-Spartanburg office, the NC Forest Service, and the NC Geodetic Survey for sharing information and data during this event response. Nick Bozdog, Sierra Isard, and Rebecca Latham assisted with post-event data collection.

References

- Atlanta Journal Constitution staff reporters, July 18, 1916: Atlanta Journal Constitution.
- National Centers for Environmental Information (NCEI), 2018a, Record of Climatological Observations, Station: Tryon NC US USC00318744, May 01-31, 2018 daily precipitation: <https://www.ncdc.noaa.gov/cdo-web/quickdata> (accessed November 2018).
- National Centers for Environmental Information (NCEI), 2018b, Storm Events Database, Polk County, Valhalla, 05/18/2018 Debris Flow, National Oceanic and Atmospheric Administration: <https://www.ncdc.noaa.gov/stormevents/eventdetails.jsp?id=758860> (accessed November 2018).
- North Carolina Geological Survey (NCGS), 2018, Landslide geodatabase: unpublished Geographic Information System data, personal communication November 2018.
- Southern Railway Company, 1917, The Floods of July 1916 – How the Southern Railway Organization Met an Emergency: The Southern Railway Company, 130p.
- Tryon Daily Bulletin staff reporters, 2018, Polk asking two additional neighborhoods to evacuate ahead of Sunday's storm: <https://www.tryondailybulletin.com/2018/05/27/polk-officials-recommending-voluntary-evacuation-of-portions-of-county-ahead-of-forecasted-storm/> (accessed November 2018).
- Wooten R.M., Witt A.C., Miniati C.F., Hales T.C., Aldred J.L., 2016, Frequency and Magnitude of Selected Historical Landslide Events in the Southern Appalachian Highlands of North Carolina and Virginia: Relationships to Rainfall, Geological and Ecohydrological Controls, and Effects, *in* Greenberg C. H., Collins B. S. eds, Natural Disturbances and Historic Range of Variation, Managing Forest Ecosystems, Volume 32: Switzerland, Springer International Publishing, p. 203-262, doi: 10.1007/978-3-319-21527-3_pp. 203-262 (available at https://www.srs.fs.usda.gov/pubs/chap/chap_2015_miniat_001.pdf accessed March 2019).

Characteristics of debris flows just downstream the initiation area on Punta Nera cliffs, Venetian Dolomites

Martino Bernard^a, Matteo Berti^b, Giacomo Crucil^c, Alessandro Simoni^b, Carlo Gregoretti^{a,*}

^aDepartment Land Environment Agriculture Forestry - University of Padova, Viale dell'Università 16, Legnaro 35134, Italy

^bDepartment of Biological, Geological and Environmental Sciences - University of Bologna, Piazza di S. Donato 1, Bologna 40126, Italy

^cGeorges Lemaître Centre for Earth and Climate Research – Université Catholique de Louvain, Louvain-la-Neuve 40126, Belgium

Abstract

The Pieves de ra Mognes fan at the base of the Punta Nera cliffs, in the Venetian Dolomites (Italy), has been subject to debris flow activity for decades. Until recently, these debris flows never reached the National Road 51 on the valley bottom. Debris flows usually initiated at the base of an incised rocky channel in the Punta Nera cliffs where runoff is delivered to loose scree deposits of the fan. The main debris flow channel is strongly incised at the apex of the fan and splits into several minor channels at lower elevations. During the autumn 2014 and May 2016, two cliff collapses produced large debris deposits. Since then, the frequency of debris flows increased considerably because of the availability of debris deposits at very steep slope that lowered the runoff discharge needed for the debris flow initiation. In a few cases, debris flows that initiated in the rocky channel reached and interrupted the National Road 51, about 2 km downstream the well-known touristic village of Cortina d'Ampezzo. On July 2016, a monitoring station was placed at the beginning of the debris flow channel just downstream the base of the rocky channel. In the period between July and -September, the monitoring station recorded six debris flow events. Analysis of these data is used to describe the characteristics of debris flow initial routing. Moreover, we use video image analysis to investigate the velocity and depth of the surge from the 5 August 2016 event.

Keywords: runoff-generated debris flows; initiation area; front velocity; flow depth.

1. Introduction

Several adjacent debris-flow catchments parallel the south side of the Boite Valley, in the Venetian Dolomites, Northeast Italy. The debris-flow channels incise the dolomitic bedrock in their upper part and transition to run over the scree deposits at lower elevations (Gregoretti et al., 2016). High intensity rainfalls of short duration (typically < 1 h) produce abundant runoff which entrain loose debris along the channel forming solid-liquid surges that route downstream as debris flows (Berti and Simoni, 2005; Gregoretti and Dalla Fontana, 2008; D'Agostino et al., 2010, Gregoretti et al., 2019). The debris flows initiated by the entrainment of solid material into runoff, are named runoff-generated debris flows (Kean et al., 2013). These debris flows are widespread in Alps (Theule et al., 2012; Navratil et al., 2013; Tiranti and Deangeli, 2015) and other contexts (Coe et al., 2008; Hurlimann et al., 2014; Imazumi et al., 2006; Kean et al., 2011; Okano et al.; 2012; Ma et al., 2018). Nevertheless, due to poor accessibility monitoring systems in the initiation area of debris-flow catchments are rare. Instrumented sites include those described by Berti et al. (1999), McCoy et al. (2012), Kean et al., (2013), Navratil et al., (2013) and Hurlimann et al. (2014). Field observations of the debris-flow initiation are very important to understand its dynamic and models testing.

In the Autumn of 2014 and May 2016, two rockfall events deposited approximately 100.000 cubic meters of debris in the headwater basin of the Punta Nera debris-flow catchment. The rockfalls were possibly favoured by climate

* Corresponding author e-mail address: carlo.gregoretti@unipd.it

change that, at higher altitudes, can cause permafrost melting in this area (Boeckli et al., 2012). They caused a dramatic increase in the frequency and magnitude of debris flows because their deposits, positioned on slopes averaging 40 degrees can be easily entrained by runoff caused by unexceptional rainfall events. We installed a monitoring system downstream the rocky cliffs where the debris-flow channel is stable, with the purpose of observing the debris flow characteristics during the initial stages.

2. Materials and methods

2.1. The study site

In dolomitic areas, abundant coarse hillslope sediment is commonly found at the toe of rocky cliffs. Debris-flow channels origin where the bedrock surfaces deliver surface runoff, at the outlet of chutes incised into the cliffs. Debris flows initiate along such talus-incised channels following intense rainfall and determine the progressive erosion and deepening of the channels. Sediment recharge mechanisms include rock fall, dry ravel processes, channel-bank failures

The Punta Nera basin includes the cliffs of Punta Nera peak (2847 m a.s.l.) and the Piées de ra Mognes fan (Fig. 1a and Fig. 2) and is dominated in its upper part by the dolomitic cliffs belonging to the “Dolomia Principale” Formation of Triassic age (Fig. 2). It is located on the left side of the Boite Valley in the Venetian Dolomites (northeast Italy, see the inset of Fig. 2). The upper rocky headwater basin is incised by a very steep channel (about 40°) ending with a chute delivering runoff discharge to the apex of the Piées de ra Mognes fan (Fig. 1a and Fig. 2). The debris flow-channel begins at the chute and 400 m further downstream, splits into multiple channels (Fig. 2). In this area, channel avulsion is common due to debris-flow deposits often clogging the channel.

Before 2014, debris flows used to initiate downstream the rocky chute along the talus-incised channel and exhibited poor mobility with most of the sediment depositing at elevations ranging between 1500 and 1300 m a.s.l. Cliff collapses occurred between 2014 and 2016 (Fig. 1a), deposited a large amount of loose unconsolidated debris along the rocky channel in the headwater basin. Such deposits resting on slopes at or in excess of 40° were easily entrained by runoff, triggering debris-flow mass transport phenomena that propagated downstream along the debris-flow channel located on the fan (Fig. 1b).

This explains the notable increase of debris-flow events since June 2015. For the first time, in the last few decades, debris flows repeatedly reached and blocked the National Road 51. Local authorities consequently built road defense structures in the form of a series of retaining basins (Fig. 2). We installed a monitoring system at short distance from the fan apex where the debris-flow channel is deeply incised and avulsion is unlikely (Fig. 1b and Fig. 2), at the purpose of observing the debris flow characteristics shortly after its initiation.

In the last decade, the occurrence of cliff collapses and large rockfalls notably increased in the Alpine region, likely due to thermoclastism and permafrost melting whose action is intensifying due to the increase of average temperatures caused by global climate change. These phenomena commonly affect reliefs higher than 2500 m a.s.l. (Cremonese et al., 2011) as in the case of the Punta Nera Peak. Similar evidences include the rockfall occurred on November 2014 on the dolomitic massif Mount Antelao, located just few kilometers south of Punta Nera. It deposited a large amount of debris on a rocky sloping plateau that was mobilized on August 2015 by abundant runoff descending from the overhanging cliffs, producing a debris flow whose magnitude (about 100000 m³) has never been reported in the historical records for the specific catchment (Gregoretto et al., 2018).

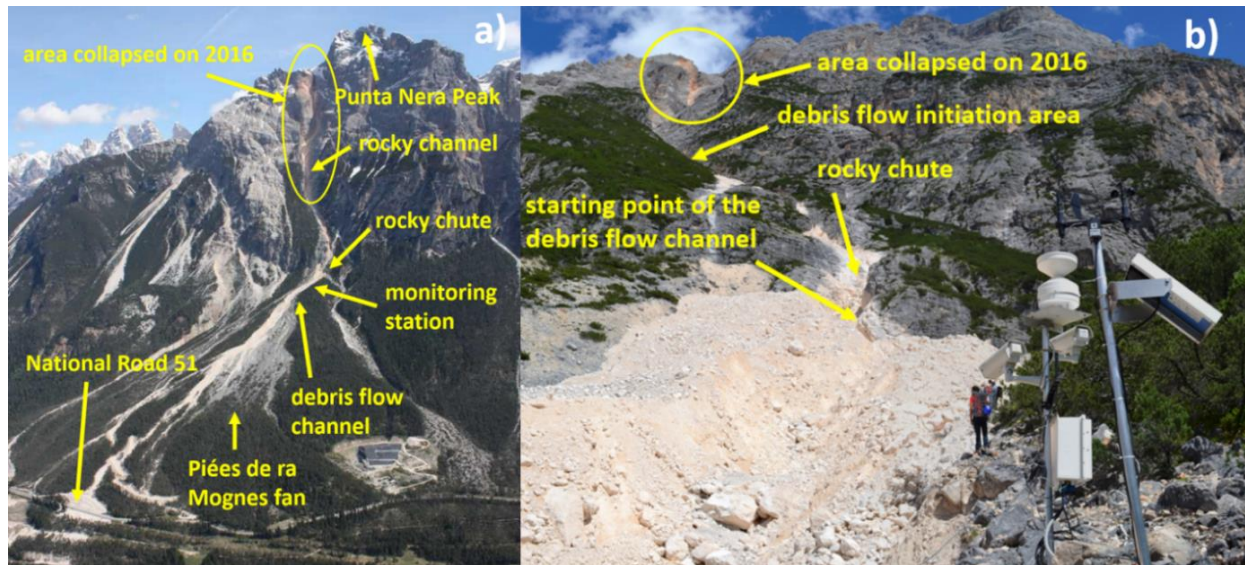


Fig. 1. Frontal view of the Punta Nera rocky cliffs and Piées de ra Mognes fan (a) and the initial reach of the debris-flow channel downstream of the rocky chute with the monitoring station installed at 1515 m a.s.l. (b).

2.2. The monitoring station

Debris-flow initiation is expected to happen upstream or downstream the bedrock – scree transition, so we installed the monitoring station, in this area on the left bank of the debris-flow channel (Fig. 1b). The monitoring station is a programmable data-logger that acquires data from a rain gauge, anemometer, two pressure transducers buried in the channel 7 m apart and two time-lapse cameras that record images to a memory card (frequency: 0.5 s⁻¹). The monitoring station is powered by a battery and a solar panel. Data are acquired every 5 min (normal mode). When the rainfall intensity exceeds 6 mm/h, the system switches to “event” mode and acquires data every five seconds; the time-lapse cameras are also triggered and capture images for two hours. The time-lapse cameras frame different scenes: one frames upstream to record the routing of the debris flow along the chute and the upper reach of the channel; the other frames the channel downstream with the intent to calculate flow depths and velocity. Several targets were placed on the opposite bank of the cameras to provide scale and framing.

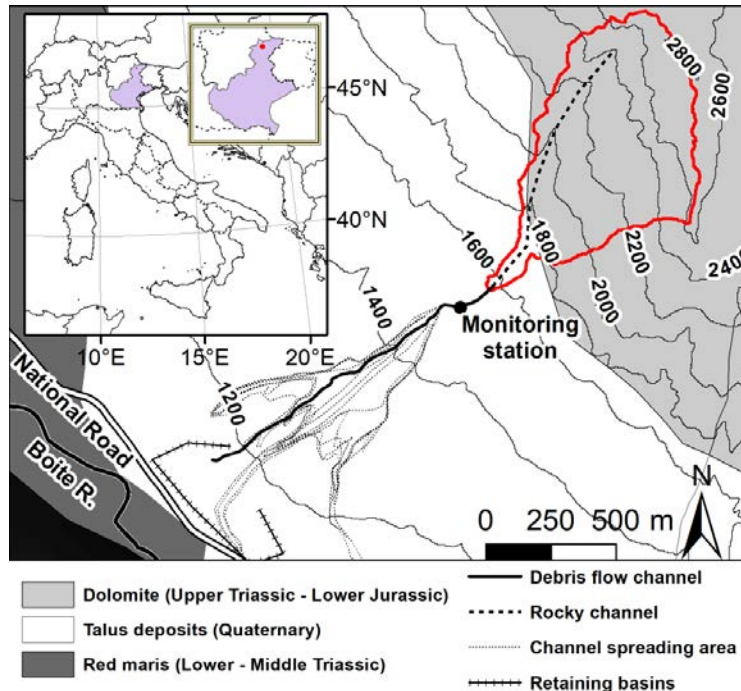


Fig. 2. Schematic geological map of the studied area showing instrumentation and main morphological features. Red line denotes the boundaries of the basin where runoff is simulated.

3. General characteristics of the occurred debris-flow events

During the period from 17 July to 29 September 2016, six debris flows and six runoff events occurred, four debris flows occurred during daylight, one at dusk and one during the night (no time-lapse video). In two cases, the debris-flow events were preceded by water runoff.

3.1. Observed behavior of the debris flows during their initial stages

The debris flows that occurred during daylight consisted of a series of solid-liquid surges. The majority of surges flowed down the channel in unsteady flow conditions. In some cases, incoming surges overtook those preceding. In other cases, surges or their rear part stopped in the channel and their deposits were totally or partially re-mobilized by incoming surges and/or by runoff that infiltrated the deposit. We distinguish two re-mobilization mechanisms to the in-channel deposits. The first mechanism is due to entrainment and is observed when a sediment-laden water flow overtops a deposit and progressively erodes the material owing to the exerted shear stress. The second mechanism is a sliding failure and is observed when seepage of incoming runoff infiltrates the deposit increasing pore pressures and exerting a drag force within it (i.e. the seepage force). A similar mechanism was proposed for the mobilization of sediments accumulated to form a dam at Chalk Cliff (Colorado) by Kean et al. (2013). The two mechanisms can act together, due to the action of runoff, when loose deposits are present along bottom of the channel. The surges arriving from the rocky channel are typically composed of cobbles, gravel and sand. In the initiation area, the debris-flow surges can erode the channel banks inducing local failures that supply additional debris for entrainment. Samples of surge deposits upstream of the monitoring station indicate scarce or no fine fraction (silt and clay); however, fines are present in the channel bank samples and in surge deposits sampled further downstream.

3.2. The debris flows occurred on 5 August 2016

On 5 August 2016 two debris-flow events occurred, separated by runoff. The first from 9:14 to 9:58, the second from 18:00 to 18:05. The first event was composed of fourteen surges, while the latter event, initially a unique surge,

switched to two surges because the surge tail stopped in-channel and after two minutes was subsequently re-mobilized by the action of runoff that infiltrated the deposit.

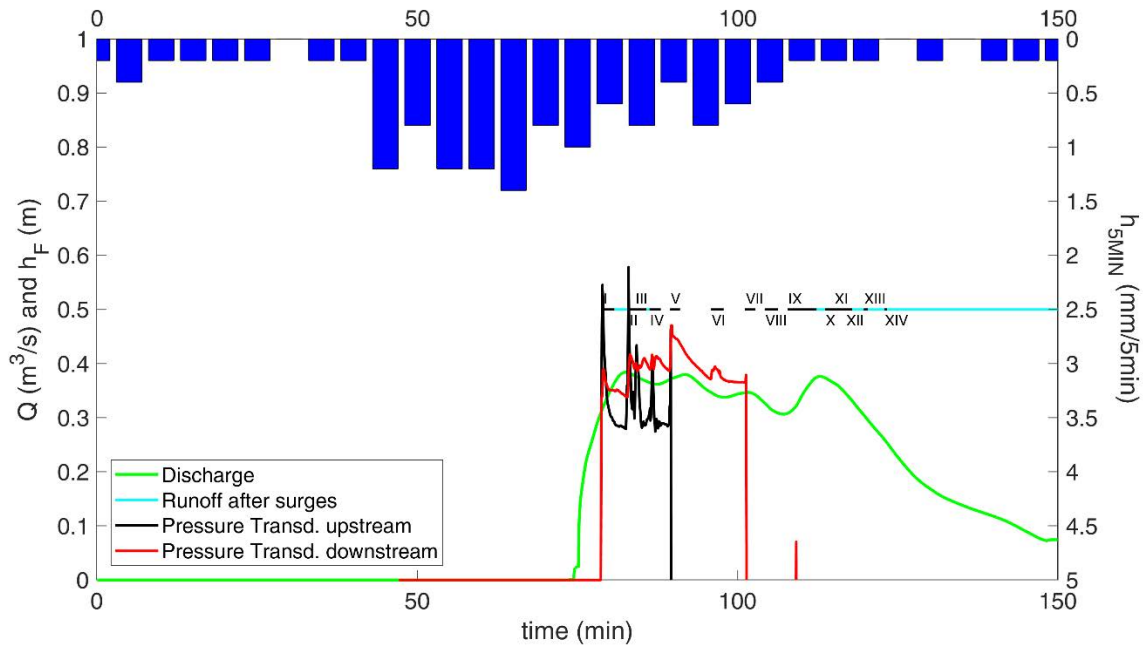


Fig. 3. Measured and simulated data of the debris-flow event occurred in the morning of August 5. The timing of observed debris-flow surges (roman numbers) is compared to pore pressures (h_F) measured in the channel bed and simulated runoff discharge (Q). Blue bars represent the 5 min rainfall (h_{5MIN}).

The surges are described in Table 1 (time of occurrence, duration and some of the characteristics) and Figure 3 graphs the sampled rainfalls, the simulated runoff, and the pressure head measured by the two transducers. Runoff was simulated at the transition between the rocky channel and the debris-flow channel (see Fig. 2) using the model proposed by Gregoretti et al. (2016) for headwater rocky basins, and tested against discharge measurements taken in a basin 8 km north with similar geologic and morphologic characteristics. The simulated discharge exhibits a rapid raise to peak ($\sim 0.4 \text{ m}^3/\text{s}$) followed by a nearly constant plateau, and after 40 minutes, it slowly decreases. Surge I is close to the peak of runoff (i.e. it coincides with the end of the sudden hydrograph growth) confirming the results of Rengers et al. (2016) who demonstrated that the runoff model can provide the timing of debris-flow surge close to the initiation area. Gregoretti et al. (2016) also obtained similar results in the two basins of Acquabona and Rovina di Cancia that share similar geologic and geomorphologic features with the Punta Nera basin. In the present case (Figure 3), the simulated runoff hydrograph nicely fit the timing of occurrence of the debris-flow surges. The last minor surges (XIII and XIV) are observed to travel down the channel at the beginning of the progressive hydrograph decrease when, probably, the discharge is no longer sufficient to mobilize sediment. This result confirms the model capabilities and indicates that the continue action of runoff higher than a certain critical threshold is required to maintain the mobility of debris-flow surges, as also observed by Capra et al., (2018) for lahars.

In between each of the 14 surges (Table 1), water runoff is observed in the channel except between surges IV-IX when the debris-flow surge IV stopped blocking the channel. The deposit remained stable despite incoming surges and infiltrating water until surges VIII and IX progressively entrained the material. Conversely, during the second event, the debris material deposited during the first surge was re-mobilized by runoff, generating the second surge. In this case, the simulated runoff intensity was larger (not shown here for brevity).

Pore water pressures measured in the channel bed during the first event correlates very well with the arrival of the debris-flow surges: they quickly raise up to the peak during the passage of the front and then gradually decrease. The two transducers were swept away during the passage of surges V and VIII, both transporting boulders of size larger than 2 m. Front velocity and flow depth were estimated by image analysis of the time-lapse videos. Cross sections of the channel together with the position targets were surveyed by Real-Time Kinematic GPS (RTK-GPS). The surveys

allow for the computation of the distances (along and normal to the flow direction) needed in the image analysis to fix the position of the surge front at different time steps and the quote of the surface of the surge with respect to the bottom. The flow depth is estimated in a fixed position located 2 m downstream of the upstream pressure transducer. The average velocity of the front is estimated during its advancement from the position where flow depth is estimated, so that the first estimate coincides with the fixed position. Both flow depth and front velocity can be estimated until the front is in view of the camera, for a time interval of about ten seconds.

Figure 4 shows the estimates of the front velocity and debris-flow surge depth together with the pore pressures measured by the transducers. Front velocity ranges between 1 and 2 m/s. Flow depth is increasing during the passage of surges II and V because these fronts have an elongated shape. The short time interval of measure prevents any other consideration about flow depth. Conversely, flow depth is rather constant for surge IV, suggesting that in this case conditions close to the uniform flow are attained. Pressure heads tend to increase rapidly only after the front arrival (see Figures 3 and 4) except for surge IV, when they remain nearly constant. This could mean that, in general, the front is not saturated and it is dominated by collisional and frictional stresses. Berti et al., (2000) and McArdell et al., (2007) observed similar effects, also explained as incomplete saturation of the front. In the case of the surge IV, maybe the interstitial fluid could be negligible.

Table 1. The surges of the two debris-flow events occurred on 5 August 2016 with their description (R = runoff after the surge; F = surge followed by another one; * bed returned to the topographical condition preceding the first surge routing).

n. surge	Time of occurrence (h:m:s)	Duration (sec)	Characteristics of the surge
I	9:13:50 R	116	Front composed by gravel without boulders
II	9:17:50 F	68	Front with boulders of size > 2 m
III	9:18:58 R	108	Front composed by gravel without boulders
IV	9:21:16	106	Front with boulders of size > 2 m; deposit on the bed
V	9:24:26	96	Front and body rich of boulders with size > 2 m; deposit on the bed
VI	9:30:50	120	Front and body rich of boulders with size > 2 m; deposit on the bed
VII	9:36:14	94	Front and body rich of boulders with size > 2 m; deposit on the bed
VIII	9:39:14	124	Front and body rich of boulders with size > 2 m; small erosion of the bed
IX	9:42:48 R	272	Front and body rich of boulders with size > 2 m; large erosion of the bed*
X	9:48:40 F	70	Front with boulders of size > 2 m
XI	9:50:04 R	84	Front composed by gravel without boulders
XII	9:51:54 R	60	Front composed by gravel without boulders
XIII	9:54:42 R	38	Front composed by gravel and cobbles
XIV	9:57:54 R	26	Front with boulders of size > 2 m
I	17:00:25 R	78	Front with boulders of size > 2 m
II	17:04:11 R	58	Solid-liquid surge restarted by runoff as in Kean et al., (2013)

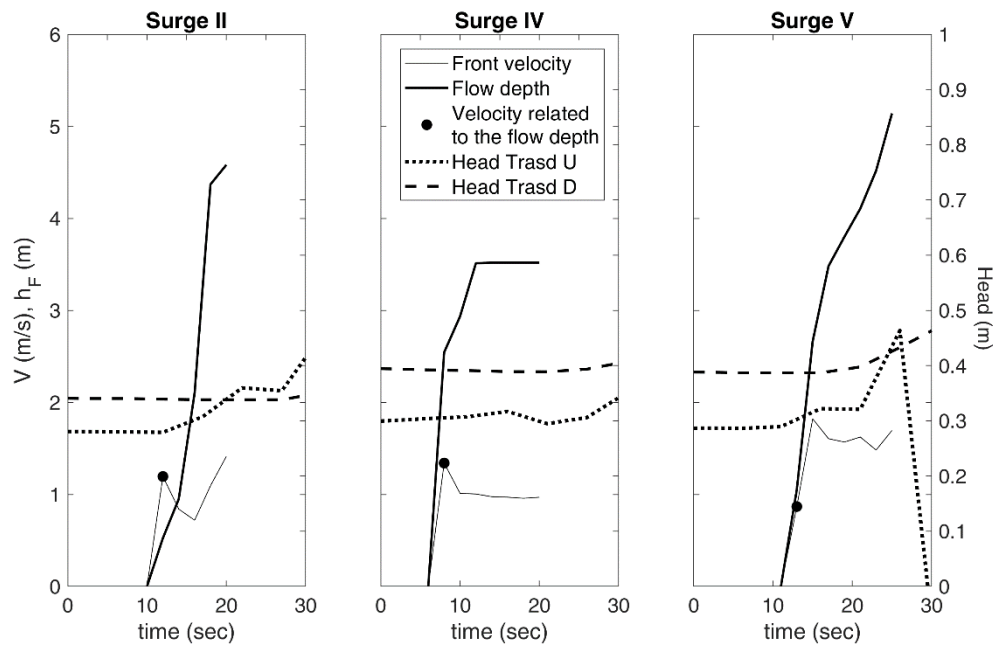


Fig. 4. Estimates of front propagation velocity (V) and flow depth (h_F) compared to measures of pore water pressures (Head) debris flow surges II, IV and V.

4. Discussion and Conclusions

Two cliff collapses, occurred between November 2014 and 2016, deposited a large amount of debris in the rocky headwater basin of Punta Nera. In particular, the material deposited along the main bedrock-incised steep ($> 40^\circ$) channel was subject to frequent rainfall-induced mobilization. Since June 2015, debris-flow activity increased in frequency and magnitude. Multiple events reached the National Road along the valley bottom causing repeated interruptions whereas the Punta Nera debris flow has no record of such events.

Monitoring activities began in 2016 and focused on the debris-flow channel at short distance from the fan apex. Our data document that the debris-flow initiation occurs in the headwater rocky basin and involves the recent rockfall deposits. Debris-flow events arrive at the outlet of the rocky basin with a substantial solid concentration and surging behaviour. It is our belief that prior to the rockfall episodes, debris-flow activity was much less intense because debris was scarce in the steep headwater basin and events used to initiate at the fan apex where the slope is lower ($\sim 25^\circ$) and the channel is incised in talus deposits. Aerial photographs confirm that before 2015, debris-flow events at Punta Nera were rare and much less mobile depositing debris at 1300 m or higher.

The rockfalls triggered an abrupt change in the regime of the Punta Nera debris-flow catchment. Such modification that can be interpreted as accidental or related to the general temperature increase due to the global climate change. In fact, unusually high temperatures favour thermoclastism and permafrost melting which promote instability at high elevation in the Alpine region (Boeckly et al, 2011; Cremonese et al., 2011). Such effect may influence the behaviour of an increasing number of first-order alpine catchments in the near future.

Monitoring activities provided also other more specific information. During the summer of 2016, we documented six debris flows. All of them were composed of solid-liquid surges that in some cases merged, in some cases stopped along the channel to be re-mobilized by incoming surges or by the action of water runoff.

The comparison between the water discharge simulated by an hydrologic model, specifically developed for headwater rocky basin (Gregoretto et al., 2016), measured pore water pressures in the channel bed and image-derived flow properties yields good results in terms of timing. Observed arrival and propagation of the solid-liquid surges correspond to the simulated peak water discharge. Whenever the simulated water discharge drops significantly, the flow becomes turbulent and sediment transport is greatly reduced. Measures of pore fluid pressure on the channel bottom show that the surge front is less saturated than the body and that collisional-frictional forces dominate the flow.

Acknowledgements

We would like to thank the Regole d'Ampezzo Association for the permission to install the monitoring station and the help provided during field work. The authors also thank the reviewers for the useful comments and suggestions that helped to improve the work.

References

- Berti, M., Genevois, R., Simoni, A., and Tecca, P.R., 1999, Field observations of a debris flow event in the Dolomites: *Geomorphology*, v. 29, p. 265–274, doi:10.1016/S0169-555X(99)00018-5.
- Berti, M., Genevois, R., LaHusen, R.G., Simoni, A., and Tecca, P.R., 2000, Debris flow monitoring in the Acquabona watershed on the Dolomites (Italian alps): *Physics and Chemistry of the Earth, Part B: Hydrology, Oceans and Atmosphere*, v. 25, p. 707–715, doi:10.1016/S1464-1909(00)00090-3.
- Berti, M., and Simoni, A., 2005, Experimental evidences and numerical modelling of debris flow initiated by channel runoff: *Landslides*, v. 2, p. 171–182, doi:10.1007/s10346-005-0062-4.
- Boeckli, L., Brenning, A., Gruber, S., and Noetzli, J., 2012, A statistical approach to modelling permafrost distribution in the European Alps or similar mountain ranges: *The Cryosphere*, v. 6, p. 125–140, doi:10.5194/tc-6-125-2012.
- Capra, L., Coviello, V., Borselli, L., Márquez-Ramírez, V.-H., and Arámbula-Mendoza, R., 2018, Hydrological control of large hurricane-induced lahars: evidence from rainfall-runoff modeling, seismic and video monitoring: *Natural Hazards and Earth System Sciences*, v. 18, p. 781–794, doi:10.5194/nhess-18-781-2018.
- Coe, J.A., Kinner, D.A., and Godt, J.W., 2008, Initiation conditions for debris flows generated by runoff at Chalk Cliffs, central Colorado: *Geomorphology*, v. 96, p. 270–297, doi:10.1016/j.geomorph.2007.03.017.
- Cremonese, E. et al., 2011, Brief Communication: “An inventory of permafrost evidence for the European Alps”: *The Cryosphere*, v. 5, p. 651–657, doi:10.5194/tc-5-651-2011.
- D’Agostino, V., Cesca, M., and Marchi, L., 2010, Field and laboratory investigations of runout distances of debris flows in the Dolomites (Eastern Italian Alps): *Geomorphology*, v. 115, p. 294–304, doi:10.1016/j.geomorph.2009.06.032.
- Gregoretti, C., and Dalla Fontana, G., 2008, The triggering of debris flow due to channel-bed failure in some alpine headwater basins of the Dolomites: analyses of critical runoff: *Hydrological Processes*, v. 22, p. 2248–2263, doi:10.1002/hyp.6821.
- Gregoretti, C., Degetto, M., Bernard, M., Crucil, G., Pimazzoni, A., De Vido, G., Berti, M., Simoni, A., and Lanzoni, S., 2016, Runoff of small rocky headwater catchments: Field observations and hydrological modeling: *Water Resources Research*, v. 52, p. 8138–8158, doi:10.1002/2016WR018675.
- Gregoretti, C., Degetto, M., Bernard, M., and Boreggio, M., 2018, The Debris Flow Occurred at Ru Secco Creek, Venetian Dolomites, on 4 August 2015: Analysis of the Phenomenon, Its Characteristics and Reproduction by Models: *Frontiers in Earth Science*, v. 6, p. 80, doi:10.3389/feart.2018.00080.
- Gregoretti, C., Stancanelli, L.M., Bernard, M., Boreggio, M., Degetto, M., and Lanzoni, S., 2019, Relevance of erosion processes when modelling in-channel gravel debris flows for efficient hazard assessment: *Journal of Hydrology*, v. 568, p. 575–591, doi:10.1016/j.jhydrol.2018.10.001.
- Hürlimann, M., Abancó, C., Moya, J., and Vilajosana, I., 2014, Results and experiences gathered at the Rebaixader debris-flow monitoring site, Central Pyrenees, Spain: *Landslides*, v. 11, p. 939–953, doi:10.1007/s10346-013-0452-y.
- Imaizumi, F., Sidle, R.C., Tsuchiya, S., and Ohsaka, O., 2006, Hydrogeomorphic processes in a steep debris flow initiation zone: *Geophysical Research Letters*, v. 33, p. n/a-n/a, doi:10.1029/2006GL026250.
- Kean, J.W., Staley, D.M., and Cannon, S.H., 2011, In situ measurements of post-fire debris flows in southern California: Comparisons of the timing and magnitude of 24 debris-flow events with rainfall and soil moisture conditions: *Journal of Geophysical Research*, v. 116, p. F04019, doi:10.1029/2011JF002005.
- Kean, J.W., McCoy, S.W., Tucker, G.E., Staley, D.M., and Coe, J.A., 2013, Runoff-generated debris flows: Observations and modeling of surge initiation, magnitude, and frequency: *Journal of Geophysical Research: Earth Surface*, v. 118, p. 2190–2207, doi:10.1002/jgrf.20148.
- Ma, C., Deng, J., and Wang, R., 2018, Analysis of the triggering conditions and erosion of a runoff-triggered debris flow in Miyun County, Beijing, China: *Landslides*, v. 15, p. 2475–2485, doi:10.1007/s10346-018-1080-3.
- McArdell, B.W., Bartelt, P., and Kowalski, J., 2007, Field observations of basal forces and fluid pore pressure in a debris flow: *Geophysical Research Letters*, v. 34, p. L07406, doi:10.1029/2006GL029183.
- McCoy, S.W., Kean, J.W., Coe, J.A., Tucker, G.E., Staley, D.M., and Wasklewicz, T.A., 2012, Sediment entrainment by debris flows: In situ measurements from the headwaters of a steep catchment: *Journal of Geophysical Research: Earth Surface*, v. 117, p. n/a-n/a, doi:10.1029/2011JF002278.
- Navratil, O., Liébault, F., Bellot, H., Travaglini, E., Theule, J., Chambon, G., and Laigle, D., 2013, High-frequency monitoring of debris-flow propagation along the Réal Torrent, Southern French Prealps: *Geomorphology*, v. 201, p. 157–171, doi:10.1016/j.geomorph.2013.06.017.
- Okano, K., Suwa, H., and Kanno, T., 2012, Characterization of debris flows by rainstorm condition at a torrent on the Mount Yakedake volcano, Japan: *Geomorphology*, v. 136, p. 88–94, doi:10.1016/j.geomorph.2011.04.006.
- Rengers, F.K., McGuire, L.A., Kean, J.W., Staley, D.M., and Hobley, D.E.J., 2016, Model simulations of flood and debris flow timing in steep catchments after wildfire: *Water Resources Research*, v. 52, p. 6041–6061, doi:10.1002/2015WR018176.
- Theule, J.I., Liébault, F., Loye, A., Laigle, D., and Jaboyedoff, M., 2012, Sediment budget monitoring of debris-flow and bedload transport in the Manival Torrent, SE France: *Natural Hazards and Earth System Sciences*, v. 12, p. 731–749, doi:10.5194/nhess-12-731-2012.
- Tiranti, D., and Deangeli, C., 2015, Modeling of debris flow depositional patterns according to the catchment and sediment source area characteristics: *Frontiers in Earth Science*, v. 3, p. 1–14, doi:10.3389/feart.2015.00008.

Characterizing debris transfer patterns in the White Canyon, British Columbia with terrestrial laser scanning

David A. Bonneau^{a,*}, D. Jean Hutchinson^a, Scott McDougall^b

^aDepartment of Geological Sciences and Geological Engineering - Queen's University, 36 Union Street, Kingston, ON K7L 3N6, Canada

^bDepartment of Earth, Ocean and Atmospheric Sciences – University of British Columbia, 2207 Main Mall, Vancouver, BC V6T 1Z4, Canada

Abstract

In the Thompson-Fraser Rail Corridor in Interior British Columbia, the Canadian National (CN) rail line traverses several alluvial fans, which are subject to occasional debris flows. Debris flows pose a significant geohazard due to the combination of high flow velocities, large impact forces, long runout distances and poor temporal predictability. When a debris flow occurs, the cost of repairs, maintenance, and construction along these single-track railway lines is compounded by the fact that these activities also impede the flow of rail traffic, which has financial repercussions for the operators. As a result, it is vital to be able to identify and prioritize the slopes that pose the greatest hazard to the rail lines. A thorough understanding of the geohazards present on site is an essential component of risk assessment. The Canadian Railway Ground Hazard Research Program (RGHRP) was established in 2003 with the aim of better understanding the natural hazards impacting railway operations across Canada. The present study is part of this initiative and focuses on an active site called the White Canyon, which is located 275 kilometers northeast of Vancouver, BC. In this study, we use terrestrial laser scanning (TLS) and panoramic imagery datasets to analyze the debris recharge patterns that develop between debris flows in a select channel in the White Canyon. TLS scans taken before and after the events provide insight into the volumes of material mobilized and how we can leverage this series of TLS data to give insight into the amount of debris accumulating in the channels prior to failure. The temporal data acquisition rate was found to have a significant influence on the amount of movement that can be interpreted from the TLS change detection analysis and panoramic images. Therefore, the temporal data acquisition rate is key consideration when using TLS to support the determination of accurate return periods on debris flows.

Keywords: Terrestrial Laser Scanning; Channel Recharge

1. Introduction

Over the past decade, the use of remote sensing technologies for the monitoring of landslides and rock slope instabilities has increased dramatically (Jaboyedoff et al. 2012; Abellán et al. 2014; Telling et al. 2017). Airborne Laser Scanning (ALS) and Terrestrial Laser Scanning (TLS) have increased the spatial coverage and density of available datasets through non-selective sampling of millions or even billions of survey points to produce 3D point clouds. Advances in new algorithms for point cloud comparison and acquisition have improved the level of detection to mm-scale using advanced temporal filtering techniques and continuous TLS data acquisition (Kromer et al. 2015, 2017; Williams et al. 2018).

Remote sensing techniques have been used to characterize and monitor the transport of debris in steep channels and processes occurring on alluvial fans. In Switzerland, both ALS (Bennett et al., 2013) and TLS (Oppikofer, 2009; Schürch et al., 2011) have been applied to document movements occurring in the Illgraben debris-flow channel. ALS or TLS have been used to monitor volumes of sediment moving in channels in the Manival Torrent, in France (Theule et al., 2012), the Glyssibach and Glattbach channels in Switzerland (Scheidl et al., 2008), and the Chalk Cliffs in the USA (McCoy et al., 2010; Staley et al., 2011; Scheinert, 2012). Wasklewicz and Hattanji (2009) use cross-sections derived from TLS scans to investigate changes in channel shape and dimensions following a debris flow in the Ashio

* Corresponding author e-mail address: david.bonneau@queensu.ca

Mountains in Japan. In almost all studies, the methodology of performing change detection has been primarily restricted to Digital Elevation Model (DEMs) of Difference (DoD). A DoD is used to quantify the volumetric change between two DEMs. The process involves subtracting the two digital elevation models from one another and then with subsequent error analysis, real topographic changes can be distinguished (Williams, 2012). DoDs are restricted to quantifying change in a single vector direction (vertical), as opposed to methods like Multiscale Model to Model Cloud Comparison (M3C2) (Lague et al., 2013). Schürch et al. (2011) address issues arising from DEM generation on complex surface geometry with abrupt changes in slope, aspect, local surface roughness and high local relief. In their study, they present a method to quantify volumetric uncertainty in change detection specific to data from terrestrial laser scanning in a 300 m reach of the Illgraben.

As a component of the Canadian Railway Ground Hazard Research Program (RGHRP), TLS and other remote sensing techniques have been applied to monitor active rock slopes in the Thompson-Fraser Rail Corridor in Interior British Columbia (BC), Canada. The White Canyon located just outside the community of Lytton, BC, has been a central focus of this research effort. Over the 5+ years of TLS monitoring at the White Canyon, several debris flows have occurred on this active slope. In a few cases, these events have overwhelmed mitigation and have directly impacted the track. These events disrupt the safe operation of rail traffic through this major transportation corridor. As noted by Jakob et al. (2016), the most significant contributor to debris flow occurrence is a supply of readily erodible material, often created by rockfalls and other types of landslides. Additionally, May (2002) notes that as the channel length increases, the relative contribution of the initial failure volume decreases. In other words, the total debris-flow volume approaches more closely the volume of entrained sediment and depends strongly on the length of channel travelled by the debris flow. Therefore, understanding the processes and time-frame that recharge debris to the channel is crucial for evaluating debris-flow hazard.

The aim of this study is to present a methodology to monitor the spatial and temporal accumulation of debris on a slope with terrestrial laser scanning. This methodology will help evaluate the recharge threshold for debris flow initiation as suggested by the supply-limited threshold proposed by Jakob (1996). The supply-limited threshold indicates that a debris flow will occur when a precipitation threshold is exceeded provided sufficient debris is present in the channel. In addition, the work also supports considerations for evaluating return periods on debris flows with remote sensing approaches.

2. Study Site

The steep slopes of the White Canyon (50.266261° , -121.538943°), located 5 km northeast from the community of Lytton, BC, near the confluence of the Thompson and Fraser Rivers, present geohazards to the safe operation of the Canadian National (CN) mainline (Fig 1a). Rockfalls and rockslides contribute to the production of debris which accumulates in channels (Bonneau and Hutchinson, 2017; van Veen et al., 2017). Dry granular flows and debris flows facilitate the transport of debris downslope, which can result in consequences that range from minimal maintenance and repair of warning systems, to complete closure and rebuilding of the impacted rail lines and most unfortunately, the loss of life. The consequence of repairs, maintenance, and construction along single-track railway lines is compounded by the fact that during any such activity the flow of traffic is impeded or stopped.

Differential erosion of the White Canyon has formed a morphology that is highly complex and consists of vertical spires and deeply incised channels (Fig 1b). The Canyon spans approximately 2.2 km between Mile 093.1 and 094.6 of the CN Ashcroft subdivision. The active portion of the Canyon reaches up to 500 m in height above the railway track. Two short portals (tunnels) mark the entrances to the Canyon. A third portal is located in the middle of the Canyon which separates the eastern and western portions of the Canyon.

The dominant geological unit in the White Canyon is the Lytton Gneiss. The Lytton Gneiss is composed of a quartzofeldspathic gneiss with amphibolite bands, containing massive quartzite, gabbroic and amphibolite intrusions. Two sets of dykes have intruded the Lytton Gneiss. The first dyke set consists of tonalitic intrusions that are believed to be related to the emplacement of the Mt. Lytton Batholith (Brown, 1981). The second dyke set is a series of dioritic intrusions that cross cut the Lytton Gneiss and tonalitic dykes. These dioritic intrusions are believed to be part of the Kingsville Andesites (Brown, 1981). All of these units contribute to the production of material to the debris channels, and the dykes provide geometric controls on flow of material toward the rail line.

For this study, the focus will be on a specific channel in the eastern section of the Canyon. The selected channel is highlighted in red in Fig 1. The channel is approximately 450 m in length and has an average slope angle of 35 degrees (Fig 1c). Draped mesh and a ditch protect the rail line at the base of the channel. Due to the vantage of the TLS system in the survey design, a portion of the ditch is occluded in the TLS scans.

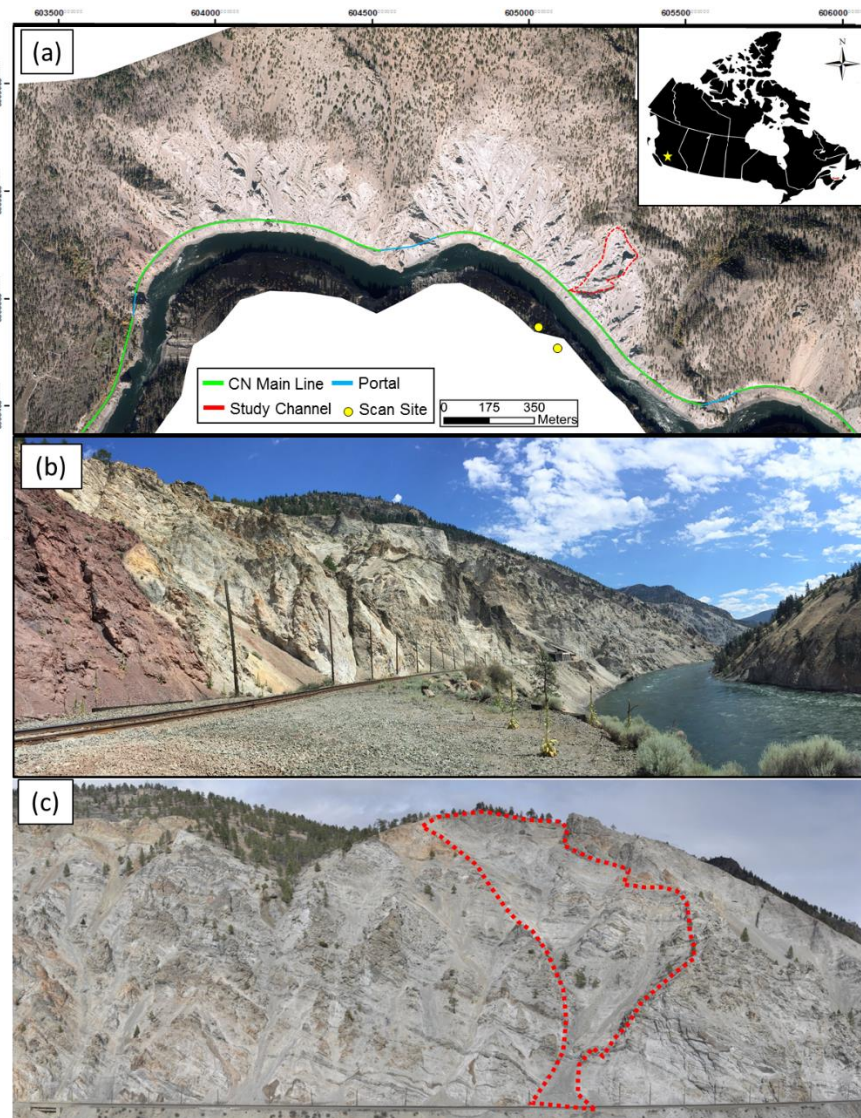


Fig. 1. (a) Map view of an October 2015 orthophoto of the White Canyon and location map; (b) August 2016 panoramic photograph taken from track level at the western end of the canyon displaying the complex morphology of the White Canyon; (c) April 27, 2017 photograph looking North across the Thompson River at the channel being analyzed in this study. The channel is highlighted in the red dashed line.

3. Methods

3.1. Remote sensing datasets

Terrestrial laser scans (TLS) were taken with an Optech Illris 3D-ER scanner. The Optech Illris is a time-of-flight terrestrial laser scanning system that utilizes a 1,535 nm (infrared) wavelength. The reported instrumental accuracy of the Optech Illris 3D-ER is 0.008 m in horizontal and vertical directions with a 0.007 m accuracy in range at a distance of 100 m (Optech, 2014).

For this study, seven TLS scans were taken approximately every two to three months from two scan positions across the Thompson River (Fig. 1A). These two scan positions were used for all TLS scan acquisitions. The baseline scan being taken in November 2014 and the last scan used in this study was taken in May 2016. All TLS scans, with an

average point spacing of 10 cm, were first parsed using the Optech Parsing software. Once parsed, vegetation, slide-detector fences and mesh were all manually removed from the point clouds. After the scans were cleaned, they were aligned to the baseline scan using the Polyworks ImAlign module. The alignment process was completed in two steps; 1) a coarse point picking of common geometric features in each scan, and 2) an iterative closest point algorithm for fine alignment (Besl and McKay, 1992). The standard deviation for alignments varied from 0.018 to 0.025 in the summer months, and 0.035 to 0.05 m in the winter months. The higher standard deviations corresponded to the winter scans where there is a higher amount of humidity in the air and possibly water on the slope surface which have all been noted to influence the alignment process (Abellán et al., 2014). To compute the changes between sequential TLS scans, the limit of detectable change must be specified. The limit of detection (LOD) can be defined based on the registration error (Abellán et al., 2014). In this study, we take two times the standard deviation (95% confidence interval) of the registration error to define the LOD. This limit equates to approximately 5 cm in the summer months and 7 to 10 cm in the winter months. The higher limit of detection in the winter months correspond to a higher standard deviation in the registration error (alignment).

High-resolution digital images were taken with Nikon D800 and D7200 DSLR cameras. The DSLR cameras were mounted on a Gigapan robotic head and equipped with a Nikkor 135mm 2/f prime lens. For each TLS scan location, a swath of overlapping photographs were additionally captured using the described setup. After the photos were captured they were then stitched together using Gigapan Stitch software to generate high-resolution panoramic images. These panoramic images were used for verification of all changes seen in the change maps and visual inspection of the slope.

3.2. Debris monitoring methodology

Figure 2 displays a visual representation of the methodology developed. At Time 1 (T1), a preliminary TLS scan of the channel is completed. The volume of debris in the channel is at this point unknown. However, preliminary estimates of the volume of channel material can be made utilizing approaches developed by Jakob et al., (2005). Locations in the channel where debris is accumulating can also be documented from visual inspection of the panoramic imagery. Subsequently at T2, a debris flow has occurred and scoured the channel to bedrock at select locations along the channel length. With an additional TLS scan and panoramic imagery, the channel bed and geometry can be captured. Locations of exposed bedrock along the channel length are first confirmed with the panoramic imagery and these locations within the TLS scans are stored to generate a bedrock baseline model of the channel. The orientations and spacing of discontinuities in the rockmass can be assessed using the TLS scan and panoramic imagery. The lithology of the channel bedrock can also be mapped from photographs. The areas of exposed bedrock within the channel serve as the baseline for subsequent monitoring. As time progresses (T3), the channel bed begins to recharge with debris from rockfall and rockslides. Debris from accumulations on benches moves into the main channel. When a scan taken at T3 is compared to the bedrock baseline model (T2), volume estimates demonstrate the spatial and temporal location of debris accumulating in the channel. These estimates are all confirmed with visual inspection of the panoramic imagery. Finally, a debris flow occurs at T4. Comparing a TLS scan captured after the debris flow to the bedrock baseline (T2) permits the calculation of the degree of entrainment and bedrock incision.

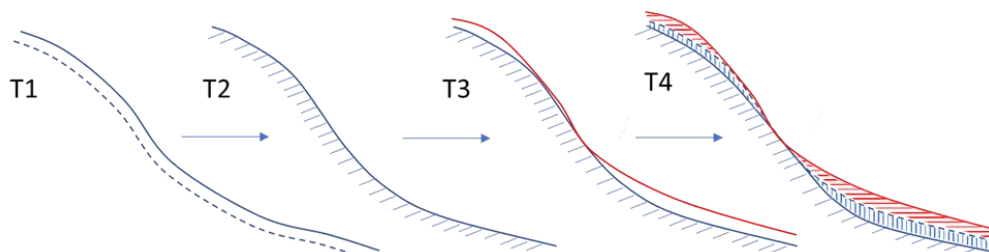


Fig. 2. Overview of the proposed recharge monitoring methodology. T1 – baseline scan of channel. T2 – debris flow has occurred and scoured channel to bedrock. T3 – channel begins to recharge from rockfall and rockslides. T4 – debris flow occurs. Using the T2 baseline, the degree of debris and bedrock incision can be calculated for T4.

3.3. Change detection methodology and volumetric analysis

Multiscale Model to Model Cloud Comparison (M3C2) (Lague et al., 2013), a vector-based change detection algorithm, was used for all change detection computations used in this study. M3C2 does not require mesh generation and operates directly on point clouds. For further details on M3C2, readers are referred to Lague et al. (2013).

All volume calculations were completed in CloudCompare. To compute the volume, CloudCompare first generates rasters in a user defined projection direction. After this process is completed, the contributions of each cell are summed together. The contribution is the volume corresponding to the cell footprint multiplied by the difference in heights between sequential 3D models. To calculate the volumes, areas of change, based on the limit of detection and confirmation of changes within the panoramic imagery, were first segmented out using the segmentation tool in CloudCompare. The area of change was translated to align with one of the principal axes of the scene orientation. This ensured that the projection direction would correspond to the change direction, to minimize the potential for over or underestimation of the volume.

4. Results and Discussion

Using the debris monitoring methodology and panoramic imagery described above, the spatial and temporal accumulation of debris was able to be monitored within the study period. Over the course of the study, two debris flows occurred which scoured the channel to bedrock in several locations along the channel length. These scour locations were confirmed with visual inspection of the panoramic photographs. The first debris-flow occurred between November 2014 and February 2015 (Fig. 3A) while the second event occurred between February 2016 and May 2016. The first debris flow had an estimated volume of approximately 135 m³. The second debris flow had an estimated volume of approximately 120 m³. Although these volumes are relatively small, they represent an operational challenge for CN with substantial financial repercussions for each hour the rail line is out of service. Both events deposited levees in some locations along the channel length. In addition, in-channel deposits were observed in the panoramic imagery in both events. Inspecting the levees of the debris-flow deposit in the panoramic imagery, the outer extents of the levees displayed a concentration of coarse clasts, where the orientation of apparent long-axis of some of the clasts, was parallel to flow direction. Both debris-flow events overwhelmed draped mesh, installed immediately upslope of the rail line, and filled the ditch adjacent to the rail line.

Between February 2015 (after the first debris flow) and February 2016, the channel was replenished with debris from rockfalls and granular flows which moved debris from directly below the cliffs into the channel. Several rockfalls were detected from the analysis of sequential scans leading up to the second debris-flow event. We estimated the calculated in-channel stored debris for each of the scan dates used in this analysis as shown in Fig 4. The maximum estimated volume accumulated prior to each debris flow event was approximately 150 m³.

The channel can be classified as a weathering-limited system (supply-limited) following Jakob's (1996) definition. The definition indicates that a debris flow will occur when a precipitation threshold is exceeded provided sufficient debris is present in the channel. It should be noted that the intrinsic precipitation threshold is constant throughout time in Jakob's model. Brayshaw and Hassan (2009) presented an updated model of sediment recharge, whereby the threshold value for debris-flow initiation is dependent on the volume of sediment in the gully channel, hence on sediment recharge rate and time since last debris flow. A debris flow occurrence resets the volume threshold value to a lower level. Volumetric analysis before and after each debris flow event can provide insight into the amount of material mobilized. However, the TLS scans were taken approximately every 3 months. As a result, we cannot assess whether any additional debris was deposited into the channel prior to the debris flow occurring. In addition, the volumes of material mobilized and deposited do not always match up, due to fact that CN removes debris that is deposited on the track to allow operation of the trains. Furthermore, the TLS scanning survey setup from across the river results in the occlusion of part of the ditch. Moving forward, a 4D monitoring system, which provides near real-time data, such as proposed by Cucchiaro et al. (2018) (SfM) or Kromer et al. (2017) (TLS), would provide great insight into the rate of debris accumulation. This would provide engineers with information about the volume of in-channel stored debris to permit forward modelling under a variety of different precipitation scenarios.

The temporal sampling interval has a significant influence on the amount of change detected (Fig. 3a & 3c.). If only the first and last scans are analyzed, the intermittent change that occurred between these dates is not detected and is overprinted by apparent larger scale movements within the debris (Fig. 3c). Change detection between the first and last scans, misses the second debris-flow event entirely. This has significant implications for assessing the return period

and trying to establish a frequency-magnitude relationship for the channel (Jakob et al., 2016). Therefore, decreasing the time between scans should help refine the movements and recharge occurring in the channel.

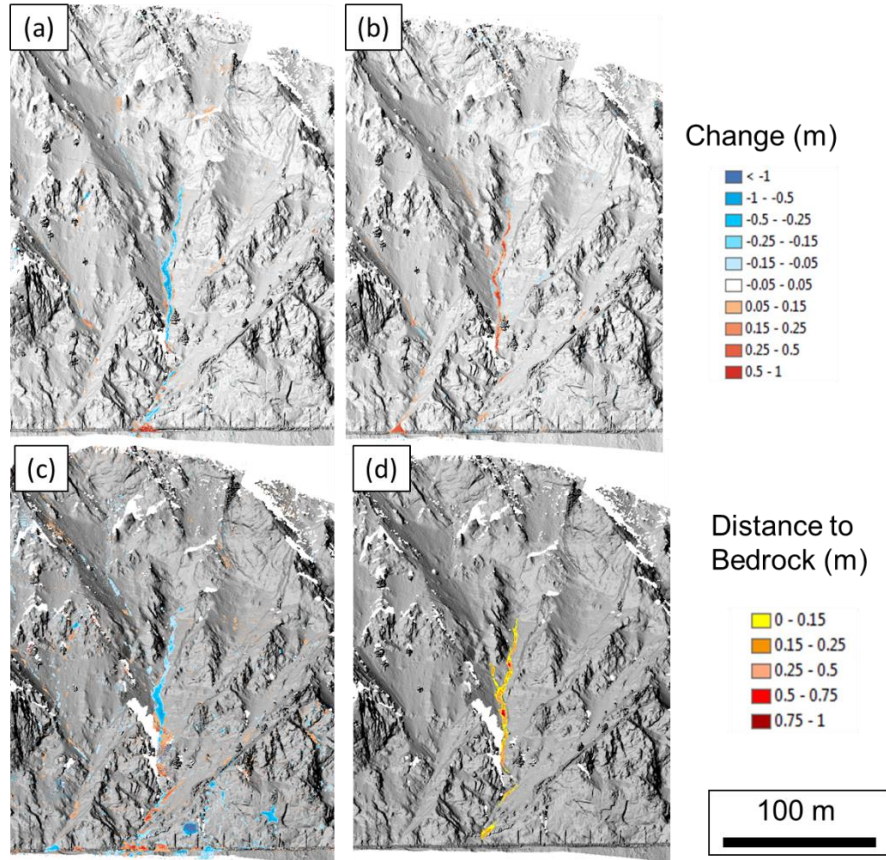


Fig. 3. (a) Change map between scans taken on November 4th, 2014 and February 18th, 2015; (b) Change map between scans taken on February 18th, 2015 and June 9th, 2015. Note that the levees have collapsed and the channel has begun to recharge; (c) Change map between scans taken on November 4th, 2014 (first scan) and May 6th, 2016; (d) Estimated spatial in-channel stored debris accumulation for the scan taken on June 9th, 2015.

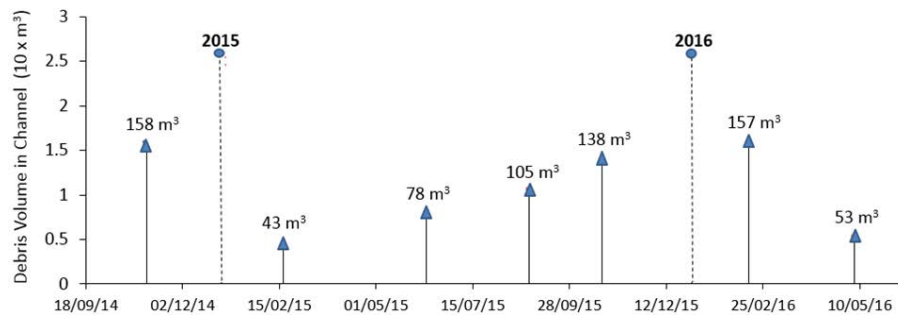


Fig. 4. Estimated in-channel stored debris volumes for each scan date. Volumes are measured using the proposed methodology.

5. Conclusions and Future Work

The use of remote sensing techniques, such as sequential TLS scanning and panoramic photography, offers the ability to document changes occurring on the slope over time, including the volume and size of material moving or accumulating and the time-period over which the activity is occurring. This study has demonstrated that terrestrial laser scanning can be implemented to successfully monitor the spatial and temporal accumulation of debris on a geometrically complex slope.

From an operational standpoint, the results of the current study can be integrated into engineering risk decision making for maintenance planning. The current study demonstrates the ability to document when, where and how much debris is stored in locations along the channel length. Integrating this knowledge into maintenance planning would allow operators to clear ditches or debris build-up behind draped mesh to ensure there is sufficient capacity for future debris-flows.

This study has demonstrated that the temporal data acquisition rate has a significant influence on the amount of movement that can be interpreted from the TLS change detection analysis and panoramic images. During larger scanning intervals, larger debris movements was shown to overprint smaller magnitude debris movements that are occurring in this active channel in the White Canyon. Therefore, the temporal acquisition interval is a component that must be considered when considering survey design for a monitoring program. More frequent scanning or moving towards a near real-time monitoring system is proposed to capture the timing of channel recharge to better establish if the selected channel follows Jakob's (1996) or Brayshaw and Hassan's (2009) debris recharge model. Furthermore, more frequent scanning would capture the small magnitude events which will help to refine the cumulative frequency magnitude curves that can be generated and, in turn, improve the design of mitigation measures.

Acknowledgements

This research was funded by the Natural Sciences and Engineering Research Council of Canada (NSERC) Discovery and CRD grants held by D. Jean Hutchinson and by the Canadian Railway Ground Hazards Research Program (CN Rail, CP Rail, Transport Canada, Geological Survey of Canada). Support was also provided to David A. Bonneau by the NSERC's Graduate Scholarship Program. Past and present Queen's RGHRP team members are gratefully acknowledged with help with data collection. Kumsheen Rafting Resort is also acknowledged for providing logistical support and site access.

References

- Abellán, A., Oppikofer, T., Jaboyedoff, M., Rosser, N.J., Lim, M., and Lato, M.J., 2014, Terrestrial laser scanning of rock slope instabilities: Earth Surface Processes and Landforms, v. 39, p. 80–97, doi:10.1002/esp.3493.
- Besl, P., and McKay, N., 1992, A Method for Registration of 3-D Shapes: IEEE Transactions on Pattern Analysis and Machine Intelligence, v. 14, p. 239–256, doi:10.1109/34.121791.
- Bonneau, D.A., and Hutchinson, D.J., 2017, Applications of Remote Sensing for Characterizing Debris Channel Processes, in De Graff, J. V. and Shakoor, A. eds., Landslides: Putting Experience, Knowledge and Emerging Technologies into Practice., Roanoke, USA, Association of Environmental & Engineering Geologists (AEG), p. 748–759.
- Brayshaw, D., and Hassan, M.A., 2009, Debris flow initiation and sediment recharge in gullies: Geomorphology, v. 109, p. 122–131, doi:10.1016/j.geomorph.2009.02.021.
- Brown, D.A., 1981, Geology of the Lytton Area, British Columbia: Carleton University.
- Cucchiari, S., Cavalli, M., Vericat, D., Crema, S., Llana, M., Beinat, A., Marchi, L., and Cazorzi, F., 2018, Monitoring topographic changes through 4D-structure-from-motion photogrammetry: application to a debris-flow channel: Environmental Earth Sciences, v. 77, p. 632, doi:10.1007/s12665-018-7817-4.
- Jaboyedoff, M., Oppikofer, T., Abellán, A., Derron, M.H., Loye, A., Metzger, R., and Pedrazzini, A., 2012, Use of LIDAR in landslide investigations: A review: Natural Hazards, v. 61, p. 5–28, doi:10.1007/s11069-010-9634-2.
- Jakob, M., 1996, Morphometric and Geotechnical Controls of Debris Flow Frequency and Magnitude in Southwestern British Columbia: University of British Columbia, 1-232 p., doi:10.14288/1.0087740.
- Jakob, M., Bovis, M., and Oden, M., 2005, The significance of channel recharge rates for estimating debris-flow magnitude and frequency: Earth Surface Processes and Landforms, v. 30, p. 755–766, doi:10.1002/esp.1188.
- Jakob, M., Holm, K., and McDougall, S., 2016, Debris-Flow Risk Assessment: Oxford University Press, v. 1, 1-41 p., doi:10.1093/acrefore/9780199389407.013.37.
- Kromer, R.A., Abellán, A., Hutchinson, D.J., Lato, M., Chanut, M.A., Dubois, L., and Jaboyedoff, M., 2017, Automated terrestrial laser scanning with near-real-time change detection - Monitoring of the Séchilienne landslide: Earth Surface Dynamics, v. 5, p. 293–310,

- doi:10.5194/esurf-5-293-2017.
- Kromer, R., Abellán, A., Hutchinson, D., Lato, M., Edwards, T., and Jaboyedoff, M., 2015, A 4D Filtering and Calibration Technique for Small-Scale Point Cloud Change Detection with a Terrestrial Laser Scanner: *Remote Sensing*, v. 7, p. 13029–13052, doi:10.3390/rs71013029.
- Lague, D., Brodu, N., and Leroux, J., 2013, Accurate 3D comparison of complex topography with terrestrial laser scanner: Application to the Rangitikei canyon (N-Z): *ISPRS Journal of Photogrammetry and Remote Sensing*, v. 82, p. 10–26, doi:10.1016/j.isprsjprs.2013.04.009.
- May, C.L., 2002, Debris flows through different forest age classes in the Central Oregon Coast Range: *Journal of the American Water Resources Association*, v. 38, p. 1097–1113, doi:10.1111/j.1752-1688.2002.tb05549.x.
- McCoy, S.W., Kean, J.W., Coe, J.A., Staley, D.M., Wasklewicz, T.A., and Tucker, G.E., 2010, Evolution of a natural debris flow: In situ measurements of flow dynamics, video imagery, and terrestrial laser scanning: *Geology*, v. 38, p. 735–738, doi:10.1130/G30928.1.
- Optech, 2014, ILLRIS Summary Specification Sheet.:
- Scheidt, C., Rickenmann, D., and Chiari, M., 2008, The use of airborne LiDAR data for the analysis of debris flow events in Switzerland: *Natural Hazards and Earth System Science*, v. 8, p. 1113–1127, doi:10.5194/nhess-8-1113-2008.
- Scheinert, C.R., 2012, Debris Flow Fan Evolution, Chalk Creek Natural Debris Flow Laboratory, Colorado: East Carolina University.
- Schürch, P., Densmore, A.L., Rosser, N.J., Lim, M., and Mcardell, B.W., 2011, Detection of surface change in complex topography using terrestrial laser scanning: Application to the Illgraben debris-flow channel: *Earth Surface Processes and Landforms*, v. 36, p. 1847–1859, doi:10.1002/esp.2206.
- Staley, D.M., Wasklewicz, T.A., Coe, T.A., Kean, J.W., McCoy, S.W., and Tucker, G.E., 2011, Observations of debris flows at Chalk Cliffs, Colorado, USA: Part 2, changes in surface morphometry from terrestrial laser scanning in the summer of 2009: 5th International Conference on Debris-Flow Hazards Mitigation: Mechanics, Prediction and Assessment., Padua, Italy, June 14-17, p. 759–768, doi:10.4408/IJEGE.2011-03.B-083.
- Telling, J., Lyda, A., Hartzell, P., and Glennie, C., 2017, Review of Earth science research using terrestrial laser scanning: *Earth-Science Reviews*, v. 169, p. 35–68, doi:10.1016/j.earscirev.2017.04.007.
- Theule, J.I., Liébault, F., Loye, A., Laigle, D., and Jaboyedoff, M., 2012, Sediment budget monitoring of debris-flow and bedload transport in the Manival Torrent, SE France: *Natural Hazards and Earth System Science*, v. 12, p. 731–749, doi:10.5194/nhess-12-731-2012.
- van Veen, M., Hutchinson, D.J., Kromer, R., Lato, M., and Edwards, T., 2017, Effects of sampling interval on the frequency - magnitude relationship of rockfalls detected from terrestrial laser scanning using semi-automated methods: *Landslides*, p. 1–14, doi:10.1007/s10346-017-0801-3.
- Wasklewicz, T.A., and Hattajji, T., 2009, High-resolution analysis of Debris Flow-induced channel changes in a headwater stream, ashio mountains, Japan*: *Professional Geographer*, v. 61, p. 231–246, doi:10.1080/00330120902743225.
- Williams, R.D., 2012, DEMs of Difference: *Geomorphological Techniques*, v. 2, p. 1–17, doi:2047-0371.
- Williams, J.G., Rosser, N.J., Hardy, R.J., Brain, M.J., and Afana, A.A., 2018, Optimising 4-D surface change detection: an approach for capturing rockfall magnitude–frequency: *Earth Surface Dynamics*, v. 6, p. 101–119, doi:10.5194/esurf-6-101-2018.

Simulation of the debris flow occurred the 15 August 2010 on Rio Val Molinara Creek (northeast Italian Alps)

Mauro Boreggio^a, Martino Bernard^a, Ruggero Alberti^b, Carlo Gregoretti^{a*}

^aDepartment Land Environment Agriculture and Forestry, University of Padova, Viale dell'Università 16, Legnaro 35134, Italy

^bDepartment Forests and Wildlife, Autonomous Province of Trento, via G. B. Trener 3, Trento 38121, Italy

Abstract

On the early morning of 15 August 2010, a runoff-generated debris flow routed along the Rio Val Molinara Creek and inundated the village of Baselga di Piné (Autonomous Province of Trento, northeast Italy) with about 50000 m³ of debris. Post-event field surveys allowed both the identification of the initiation area, and the estimate of the average erosion-deposition depths on different zones of the affected area. On one hand, the map of erosion-deposition depths along the Rio Val Molinara Creek was obtained by subtracting the corresponding pre- and post-event DEMs elevation values, interpolated by using the LiDAR data of two aerial surveys carried out in 2007 and 2011, respectively. On the other hand, the map of debris deposits on the inhabited fan was obtained by integrating the direct post-event field estimates and photo interpretation. In the research, the studied debris-flow event was simulated from the triggering to the inundation through a models cascade, which relies on the sequential application of rainfall-runoff, triggering, and routing models. After that, the routing model results were compared with the observed erosion-deposition pattern in order to assess the reliability of the proposed approach. In detail, the runoff was simulated in the initiation area and then used for building the solid-liquid hydrograph. After that, the solid-liquid hydrograph was routed downstream by means of a bi-phase GIS-based cell model, previously parametrized by using approximately the same values employed for the back-analysis of two debris-flow events occurred in the Dolomites (northeast Italian Alps). The comparison between the observed and simulated erosion-deposition depths and volumes is quasi-satisfactory. This is an important research outcome since the reliability of both debris-flow hazard assessments and risk analyses based on routing models relies on the trustworthiness of model simulations. In addition, due to the scarcity of pre- and post-event topographic surveys, the map of erosion-deposition depths might become a precious data source for testing the predictive capability of debris-flow routing models proposed in the literature by other authors.

Keywords: debris flows; routing modeling; integrated hazard assessment approach

1. Introduction

On the early morning of 15 August 2010, a very high intensity rainstorm hit the Dosso di Costalta Ridge (northeast Italian Alps), with a cumulative rainfall depth of about 130 mm in four hours and a half (return period larger than 100 years). At an altitude of about 1300 m a.s.l., the generated runoff triggered a debris flow that routed the Rio Val Molinara Creek before inundating the village of Baselga di Piné with about 50000 m³ of debris (Fig. 1).

Runoff-generated debris flows are a common natural hazard both in the Alps (e.g., Berti and Simoni, 2005; Theule et al., 2012; Navratil et al., 2013; Degetto et al., 2015; Tiranti and Deangeli, 2015) and in other mountainous regions worldwide (e.g., Coe et al, 2008; Hurlimann, 2014; Imazumi, 2006; Kean et al., 2011; Okano et al.; 2012; Ma et al., 2018). These phenomena, due to their magnitude and unpredictability, have a high socio-economic impact (Fuchs et al., 2007; Thiene et al., 2017), that is growing with the increase of both human activities and their occurrence rate (Stoffel and Beninston, 2006; Bollschweiler and Stoffel, 2010). Therefore, the protection of inhabited areas and infrastructures from debris flows is becoming a crucial task for a safe and sustainable development of mountain regions.

* Corresponding author e-mail address: carlo.gregoretti@unipd.it

Useful tools for assessing both the hazard and the effectiveness of defense plans are the numerical models for simulating a debris flow at the event-scale (i.e., from the runoff to the routing). At this purpose, Gregoretto et al. (2019) proposed the integrated modeling of all involved physical processes (i.e., rainfall-runoff, triggering, and routing) by a models cascade, for an effective reproduction of a debris-flow event. In detail, for rainfall-runoff and triggering simulations they used models able to simulate the runoff at the initiation area and to provide the corresponding solid-liquid hydrograph. After that, for simulating the routing of the solid-liquid mixture, they employed a bi-phase GIS-based cell model capable to simulate both the erosion and deposition processes. It is worth pointing out that only routing models which are able to simulate both erosion and deposition should be used for such a type of analysis (e.g., Brufau et al., 2000; Chen et al., 2006; Medina et al., 2008; Armanini et al., 2009; Hussin et al., 2012; Frank et al., 2015; Cuomo et al., 2016). As a matter of fact, the sediment entrainment along the channel can be regarded as the main contributor to the overall transported sediment volume, thus influencing both the extension and the height of debris deposits on the fan (Iverson et al., 1998; Rickenmann, 1999; Santi et al., 2008; Reid et al., 2016).

The object of this paper is the application of the integrated approach for debris-flow hazard assessment proposed by Gregoretto et al. (2019) in the different geologic and morphologic context of the Rio Val Molinara basin, by considering the debris-flow event there occurred on 15 August 2010. In detail, the entire debris-flow process is reproduced through a models cascade (i.e., the sequential application of rainfall-runoff, triggering, and routing models), and then the routing modeling outcomes are compared with the observed erosion-deposition pattern.

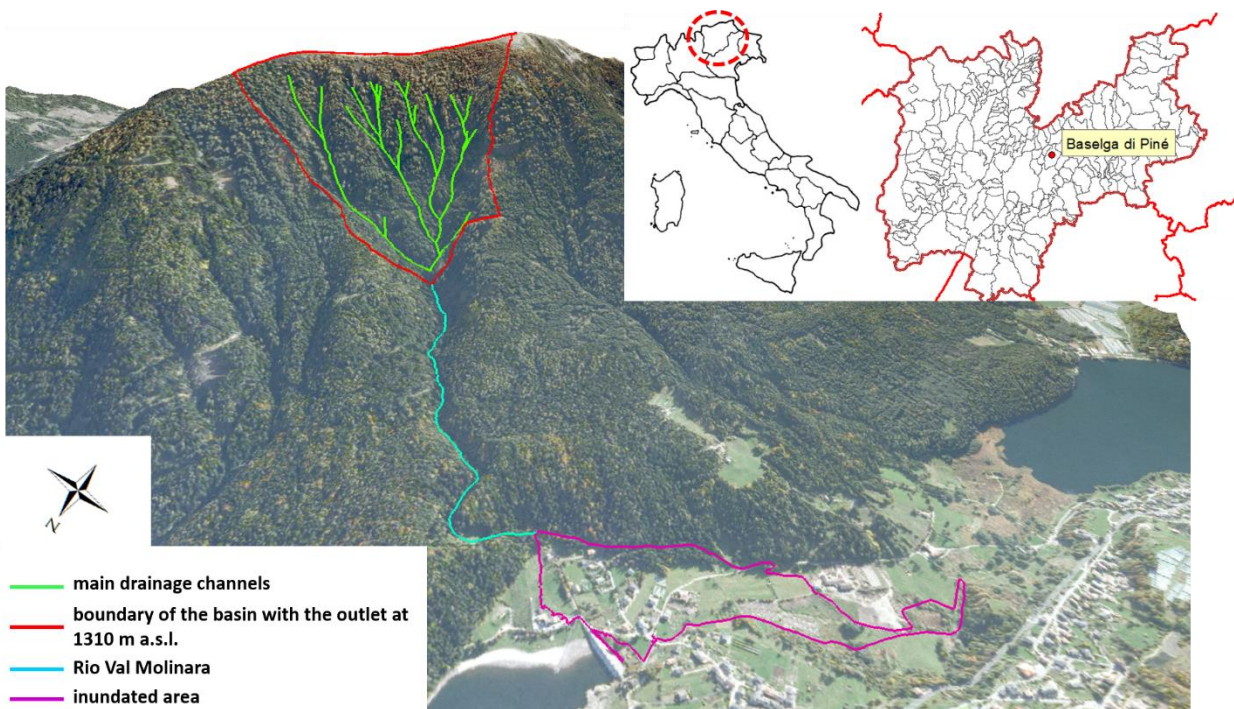


Fig. 1. Aerial view of the study area.

2. Material and methods

2.1. The study site

The Rio Val Molinara basin is located on the west-northwest side of the forested slope descending from the Dosso di Costalta Ridge (altitude of about 1950 m a.s.l., Fig. 1). In the upper part of the basin, four steep headwater channels (average slope of about 30°) incise the underlayer (Gargazzone Formation) just below the ridge line, before joining at an altitude of about 1300 m a.s.l.. From this point to the fan apex, the bed slope angle of the Rio Val Molinara Creek (1.2 km length) progressively diminishes from an average of about 15° to 10°. The main channel is characterized by a narrow v-shaped valley, with banks bordered by very steep and wooded slopes that have the major control over the debris recharge of the channel bed. Further downstream, the fan where the village of Baselga di Piné was built, has an

area of 0.12 km², with a mean slope of about 10° that represents a typical value for debris flows-generated alluvial fans.

Noteworthy, until the August 2010, the Rio Val Molinara basin did not experienced meaningful alluvial events in the 150-200 years before. Therefore, according to Bovis and Jakob (1999), it can be regarded as a supply-limited basin. Only after the 2010 debris-flow event an artificial debris retention basin (about 15000-20000 m³ in volume) equipped with a filtered check dam was built at the fan apex.

2.2. Post-event field surveys and debris-flow event

Post-event field surveys carried out on 17-18 August 2010 allowed the identification of the zone where the solid-liquid surge formed. In detail, it is the area just downstream the confluence of the four steep headwater channels (Fig. 1), where the Rio Val Molinara Creek experienced meaningful erosion processes (depths up to 5-6 m). Furthermore, during the field surveys point estimates of the average erosion-deposition depths were also carried out both in the inundated fan and along the Rio Val Molinara Creek.

The analysis of the 5-minutes rainfall data collected by the rain gauge of the Sant'Orsola station (3.5 km away in the southeast direction) highlights that the rainstorm that triggered the debris-flow event (cumulative rainfall depth of 127.7 mm in four hours and a half) was composed of two bursts of 46.6 mm and 32.2 mm in 70 and 45 minutes, respectively (Fig. 2). The corresponding 5-minutes rainfall peak intensities were equal to 4.6 mm (0.92 mm in one minute) and 6.4 mm (1.28 mm in one minute), respectively.

Once triggered, the routing solid-liquid surge entrained a significant amount of sediment before reaching the fan apex, by exposing the bedrock in a number of channel reaches. Along with the channel bed scouring, another relevant sediment source for the 2010 debris-flow event was represented by the channel banks failure and undercutting (Fig. 3).

After reached the fan apex, the flow spilled out of the channel and flooded the entire village of Baselga di Piné (Fig. 1 and Fig. 3). The volume of deposited sediments was approximately 50000 m³, with depths up to 2-3 m in the central-upper part of the fan. Overall, the event caused significant damage to infrastructures and houses, but without human being lost.

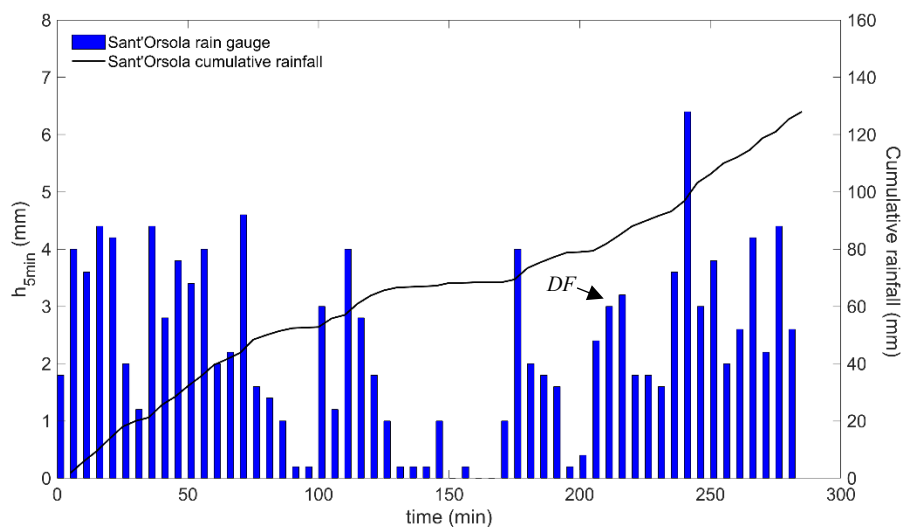


Fig.2. Recorded 5-minutes rainfall data (DF: debris-flow occurrence).

2.3. Topographic data and erosion-deposition maps

The available topographic data include the pre- and post-event 1-meter resolution DEMs, interpolated by using the LiDAR data of two aerial surveys carried out in 2007 and 2011, respectively. Furthermore, real-time kinematic GNSS measurements were acquired along the Rio Val Molinara Creek in 2016 by using a TOPCON GRS-1 dual frequency ground receiver, in order to map the rocky outcrops exposed by the 2010 debris-flow event. It should be noted that due to the vertically extensive and narrow valley walls, the altimetric error of the GNSS measurements was noticeable.

For this reason, this topographic dataset cannot be used to assess the vertical accuracy of the pre- and post-event LiDAR-derived DEMs. Therefore, after a preliminary planimetric alignment check, we evaluated the “relative” accuracy of the two gridded surfaces by comparing the elevations of areas not affected by the occurred debris flow, and that do not experienced meaningful geomorphologic changes in the considered period (e.g., stable roads and paths, walls, and dams). The median of “vertical errors” resulted -0.05 m, and it was eliminated by means of a 2.5D calibration procedure (i.e., a rigid translation in the Z dimension of the post-event LiDAR-derived DEM).

After the vertical alignment of DEMs, the map of erosion-deposition depths along the Rio Val Molinara Creek was obtained by first subtracting the corresponding pre- and post-event elevation values, and then thresholding the derived DEM of Difference map by using a minimum level of detection (e.g., Lane et al., 2003; Wheaton et al., 2010; Milan et al., 2011) equal to ± 0.35 m*. As a matter of fact, in attempting DEMs subtraction exercises it is essential to take into proper account the inherent uncertainties of the differenced gridded surfaces in order to distinguish any detectable signal (e.g., significant geomorphological changes) from the noise. On the other hand, the map of the deposition pattern on the fan was produced by integrating the direct post-event field estimates and photo interpretation of post-event terrestrial and aerial images. In fact, all debris deposits in the inhabited fan were immediately removed by the Torrent and Erosion Control Service of the Autonomous province of Trento, thus not allowing a direct spatially distributed estimate of the deposition depths through DEMs differencing. For this reason, in the research we carefully recognized six homogenous areas where the estimated deposition depth ranges in a defined interval, and we associated with them their algebraic mean. The Figure 3 depicts the observed erosion-deposition pattern for the two areas.

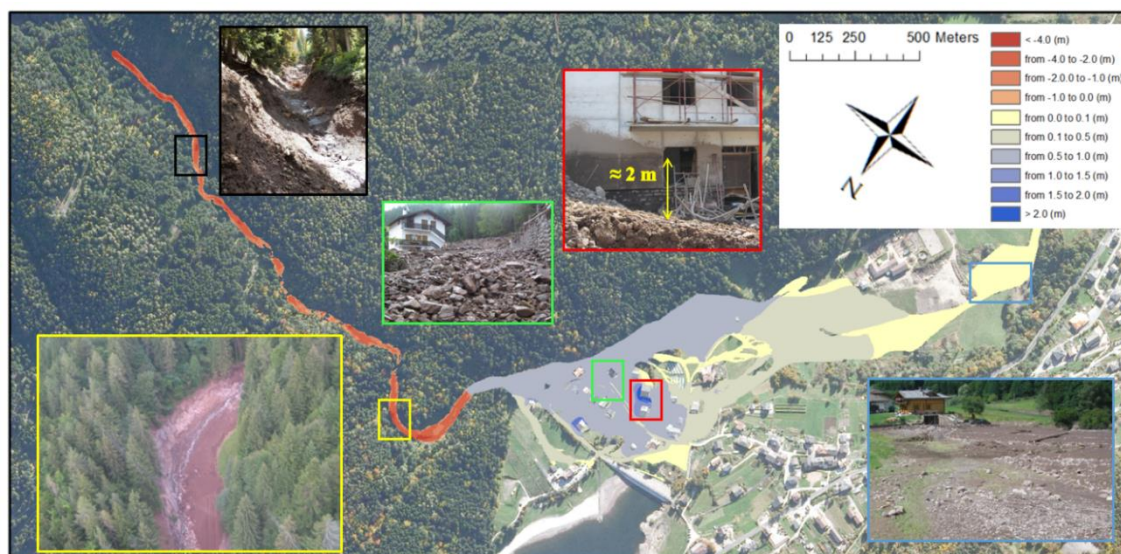


Fig.3. Map of the observed erosion-deposition depths along the Rio Val Molinara Creek and on the inhabited fan.

The estimated total volume of eroded sediment downstream the initiation area is equal to 28120 ± 4218 m³, with a corresponding mean (standard deviation) and maximum scour depth equal to 0.29 (± 0.85) and 6.01 m, respectively. On the other hand, the estimated total volume of deposited sediment on the fan is equal to 47600 m³, with a corresponding minimum and maximum average depth equal to 0.05 and 2.25 m, respectively. It should be noted that according to Gregoretti et al. (2019) the dry bed concentration C^* (i.e., the ratio between the solid and total volume of the dry undisturbed sediment) of the entrained material along the main channel (equal to 0.75 (-)) is different from that of the debris deposit on the fan (equal to 0.62 (-)). Therefore, for the mass balance, the sediment volume entrained in or upstream the initiation area can be estimated in about 11250 m³, by assuming a C^* equal to 0.75 (-). It represents the total sediment volume of the flow descending from the four headwater channels, which triggered the Rio Val Molinara debris flow. Noteworthy, the presence of meaningful vertical discrepancies between the compared DEMs in the upper part of the basin (probably due to a poor LiDAR systems calibration, such as inaccurate determination of

* This value was calculated by taking the sum in quadrature of the pre- and post-event LiDAR-derived DEMs vertical error. Due to the lack of ground reference values, it was estimated equal to 0.25 m for both the gridded surfaces, according to e.g. Cilloccu et al. (2009) and Molina et al. (2014).

boresight angles and offsets between instruments) did not allow the direct estimate of the triggering sediment volume through DEMs differencing.

3. Integrated simulation of the occurred debris flow

The simulation of the occurred debris flow at the event-scale is carried out through the integrated approach proposed by Gregoretti et al. (2019). In detail, all involved physical processes (i.e., the runoff production, the sediment entrainment with the solid-liquid surge formation, and its downstream routing) are simulated in series by means of a models cascade as it follows.

3.1. Runoff production and solid-liquid surge formation

The rainfall-runoff is simulated by means of the hydrological model developed by Gregoretti et al. (2016). In detail, the model initially evaluates the excess rainfall by coupling the SCS-CN method with a simplified hortonian law. After that, it routes the effective rainfall to the catchment outlet by using a land use-dependent constant velocity along slope flow paths and the matched diffusivity kinematic-wave model proposed by Orlandini and Rosso (1996) along the channel network. The simulated hydrograph of the runoff at the triggering section is shown in Figure 4a. The simulated runoff peak discharge is equal to $6.50 \text{ m}^3/\text{s}$, with a corresponding liquid volume of 60500 m^3 . Noteworthy, the employed parameters of the rainfall-runoff model are those used by Gregoretti et al. (2016).

The hydrograph of the corresponding solid-liquid surge in the initiation area is then determined by summing the triggering sediment volume (estimated through mass balance in about 11250 m^3 , see Section 2.3) to the hydrograph of the runoff contributing to the surge (equal to 34919 m^3). It represents the runoff with discharge values larger than the critical discharge for debris-flow occurrence (Q_{crit} , Fig. 4a). In the research, Q_{crit} (equal to $0.44 \text{ m}^3/\text{s}$) is computed according to the relation proposed by Gregoretti and Dalla Fontana (2008), based on the channel bed slope angle (equal to 21°) and the mean sediment grain size (equal to 0.11 m) of the debris material in the initiation area. As shown in Figure 4b, the shape of the solid-liquid surge hydrograph is assumed triangular, with a linear decreasing sediment concentration from the front to the flow tail. The simulated solid-liquid surge peak discharge is equal to $8.15 \text{ m}^3/\text{s}$, with a corresponding debris-flow volume of 46169 m^3 . Furthermore, the estimated front sediment concentration is equal to $0.27 (-)$, with an average of $0.18 (-)$.

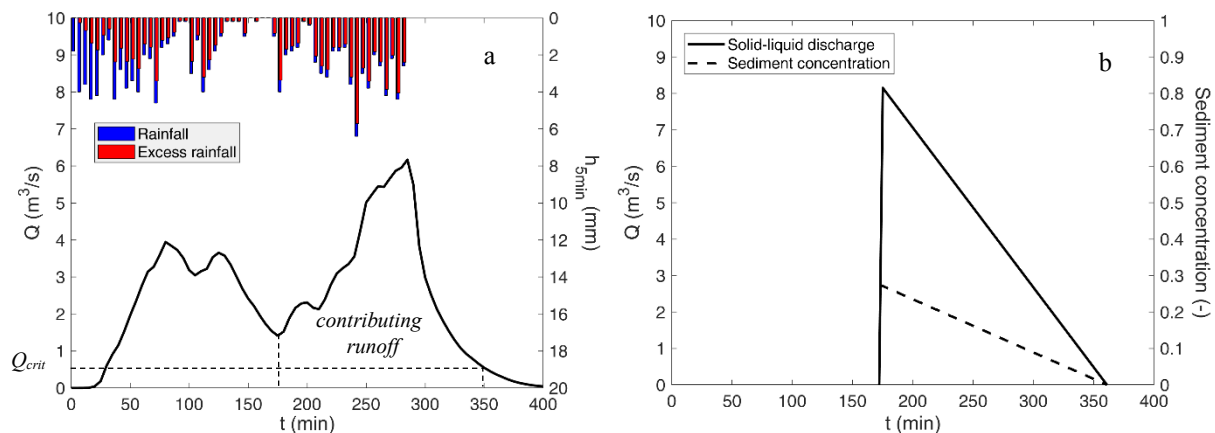


Fig. 4. Simulated hydrograph of the runoff (a), and corresponding simulated solid-liquid one (b).

3.2. Solid-liquid surge routing

The employed bi-phase GIS-based cells routing model is that of Gregoretti et al. (2019). It simplifies the momentum equation according to the kinematic wave approximation, which is usually assumed valid in debris-flows routing modeling since they generally propagated along steep channels (e.g., Arattano and Savage, 1994; Di Cristo et al., 2014). In detail, in the case of gravity-driven flows, the momentum equation is that of uniform flow in a likewise Chezy form with a dimensionless conductance coefficient C . Conversely, in the case of flows along adverse slopes,

the momentum equation is that of broad-crested weir. The deposition and entrainment processes are simulated through a modified version of the Egashira et al. (2001) equation for the rate of change of bed elevation, by assuming as controlling factors the flow velocity (U) and the channel bed slope angle (\mathcal{G}). In particular, the erosion occurs when both the flow velocity and the channel bed sloping exceed the user-defined limiting values U_{LIM-E} and \mathcal{G}_{LIM-E} , respectively. Likewise, the deposition occurs when both the flow velocity and the channel bed sloping are smaller than the user-defined limiting values U_{LIM-D} and \mathcal{G}_{LIM-D} , respectively. The mass balance (total and solid) at the DEM cell scale allows the closure of the equations system, which are solved with an explicit scheme subject to the Courant-Friedrichs-Lewy convergence condition.

For the modeling of the solid-liquid surge routing, the pre-event DEM was adjusted by reporting both the buildings and the obstacles (e.g., dry stone walls) that were present at the time of August 2010, and by removing the artifacts common in LiDAR-derived digital models (e.g., flow obstructions at road crossings). Furthermore, the values of the conductance coefficient C were set equal to 4 (-) and 2 (-) along the Rio Val Molinara Creek (where the flow was channelized) and on the deposition area (where the flow spread in several directions), respectively. It should be noted that these values are smaller than those used by Gregoretti et al. (2018, 2019) for the back-analysis of the debris-flow events occurred on 18 July 2009 and the 4th of August 2015 at Rovina di Cancia and at Ru Secco Creek (Mount Antelao, Venetian Dolomites). Likewise, the parameters governing the erosion (\mathcal{G}_{LIM-E}) and deposition (\mathcal{G}_{LIM-D}) processes were respectively set equal to 13° and 12° , which are smaller than the values used by Gregoretti et al. (2018, 2019). These choices are justified after considering the debris material of the Rio Val Molinara channel bed and of the corresponding deposits. As a matter of fact, the visual analysis of post-event terrestrial photos highlighted the presence of no-negligible quantities of lime and clay. Therefore, the value $C = 5$ (-), which is suitable for a granular and channelized debris flow, might not be reliable due to the different flow behaviour.

The Figure 5 shows the simulated erosion-deposition pattern. The comparison of the routing simulation results with the observations (Fig. 3) highlights that the main features of the observed erosion-deposition pattern are quite well reproduced by the simulation, both along the Rio Val Molinara Creek and on the alluvial fan. Actually, both the observed meaningful channel bed scouring and deposition pattern appear adequately reproduced by the cell model, in terms of both extension and spatial trend. It is worth noting that the simulated deposition processes along the Rio Val Molinara Creek are mainly due to a poor topographic characterization of the real channel morphology. As a matter of fact, the erosion-deposition processes are modeled by assuming the flow velocity and the channel bottom slope as controlling factors, which in turn depend on the channel morphology. Furthermore, during the occurred debris-flow event, local low magnitude deposition processes took place also along the Rio Val Molinara Creek (see insert in Fig. 5). However, due to the small deposition depths, these geomorphologic changes cannot be captured through DEMs differencing.

Overall, the simulated volumes compare well with the observed ones. In detail, the simulated erosion volume along the Rio Val Molinara Creek (24440 m^3) is similar to that observed (28120 m^3), with about 90% of it (22490 m^3) modelled in the area with observed erosion. On the other hand, also the simulated deposition volume on the fan (41748 m^3) is nearly equal to the observed one (47627 m^3), with about 90% of it (38359 m^3) modelled in the area with observed deposition. Likewise, the simulated deposition area on the fan (94370 m^2) compares well with the observed one (110402 m^2). Overall, these results can be regarded as satisfactorily when the cell model is used at forecasting purposes.

4. Conclusion

The 15th of August 2010 a runoff-generated debris flow routed along the Rio Val Molinara Creek and inundated the village of Baselga di Piné with about 50000 m^3 of debris. In the research, the occurred debris-flow event was simulated from the triggering to the inundation through an integrated approach, which relies on the sequential application of rainfall-runoff, triggering, and routing models. After that, the routing model results were compared with the observed erosion-deposition pattern in order to assess the reliability of the proposed approach.

Overall, the main features of the observed erosion-deposition pattern are quite well reproduced by the routing simulation. In fact, both the observed meaningful channel bed scouring and deposition pattern appear adequately reproduced by the cell model, in terms of both extension and spatial trend. Furthermore, also the simulated erosion-deposition volumes and areas compare well with the observed ones. These results appear satisfactorily when the cell model is used at forecasting purposes, and they also show the possibility of using the model itself in environment

contexts different from the Dolomites, where the channels bed is covered by granular material. Nevertheless, deepen investigations have to be carried out.

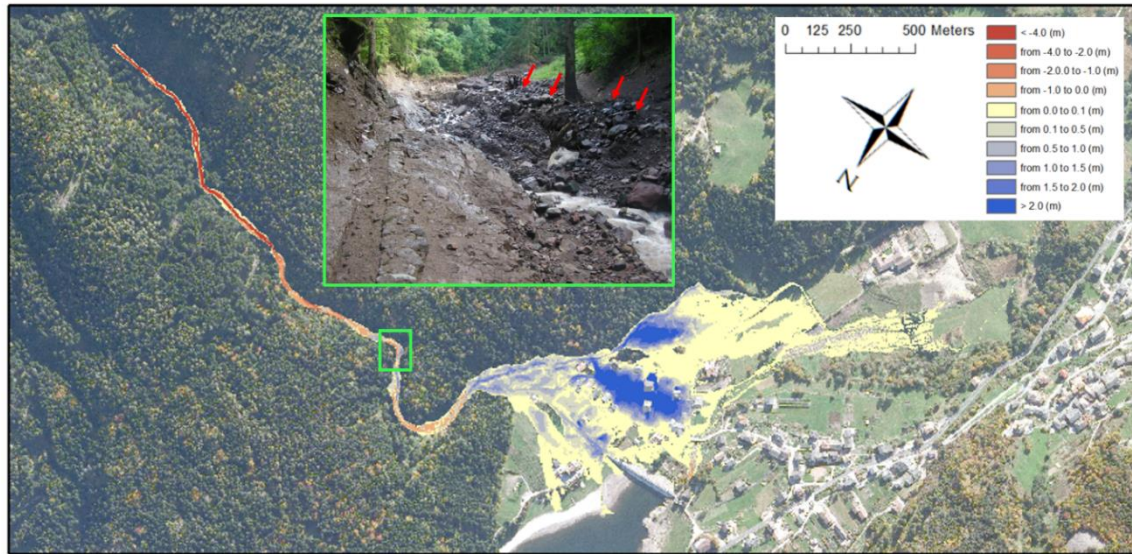


Fig.5. Map of the simulated deposition and erosion depths (insert: red arrows on low magnitude later debris deposits).

Acknowledgements

Authors wish to thank the Autonomous Province of Trento that provided the LiDAR data, the rainfall data, and the post-event photos. The authors also thank the anonymous reviewers for the useful comments and suggestions that helped to improve the manuscript.

References

- Arattano, M., and Savage, W.Z., 1994, Modelling debris flows as kinematic waves: *Bulletin of the International Association of Engineering Geology*, v. 49, p. 3-13, doi:10.1007/BF02594995.
- Armanini, A., Fraccarollo, L., and Rosatti, G., 2009, Two-dimensional simulation of debris flows in erodible channels: *Computer Geosciences*, v. 35, p. 993-1006, doi:10.1016/j.cageo.2007.11.008.
- Berti, M., and Simoni, A., 2005, Experimental evidences and numerical modelling of debris flow initiated by channel runoff: *Landslides*, v. 2, p. 171-182, doi:10.1007/s10346-005-0062-4.
- Bollschweiler, M., and Stoffel, M., 2010, Changes and trends in debris-flow frequency since AD 1850: results from the Swiss Alps: *The Holocene*, v. 20, p. 907-916, doi:10.1177/0959683610365942.
- Bovis, M., and Jakob, M., 1999, The role of debris supply conditions in predicting debris flow activity: *Earth Surface Processes and Landforms*, v. 24, p. 1039-1054, doi:10.1002/(SICI)1096-9837(199910)24:11<1039::AID-ESP29>3.0.CO;2-U.
- Brufau, P., Garcia-Navarro, P., Ghilardi, P., Natale, L., and Savi, F., 2000, 1-d mathematical modelling of debris flow: *Journal of Hydraulic Research*, v. 38, p. 435-446, doi:10.1080/00221680009498297.
- Cilloccu, F., Dequal, S., Brovelli, M., Crespi, M., and Lingua, A., 2009, Ortoimmagini 1:10.000 e modelli altimetrici: *Linee Guida. C.I.S.I.S. - Centro Interregionale per i Sistemi informatici, geografici e statistici, Roma*, 149 p.
- Coe, J.A., Kinner, D.A., and Godt, J.W., 2008, Initiation conditions for debris flows generated by runoff at Chalk Cliffs, central Colorado: *Geomorphology*, v. 96, p. 270-297, doi:10.1016/j.geomorph.2007.03.017.
- Cuomo, S., Pastor, M., Capobianco, V., and Cascini, L., 2016, Modelling the space-time bed entrainment for flow-like landslide: *Engineering Geology*, v. 212, p. 10-20, doi:10.1016/j.enggeo.2016.07.011.
- Di Cristo, C., Iervolino, M., and Vacca, A., 2014, Applicability of kinematic, diffusion and quasi-steady dynamic wave models to shallow mudflows: *Journal of Hydrologic Engineering*, v. 19, p. 956-965, doi:10.1061/(ASCE)HE.1943-5584.0000881.
- Egashira, S., Honda, N., and Itoh, T., 2001, Experimental study on the entrainment of bed material into debris flow: *Physics and Chemistry of the Earth*, v. 26, p. 645-650, doi:10.1016/S1464-1917(01)00062-9.
- Frank, F., McArdell, B., Huggel, C., and Vieli, A., 2015, The importance of entrainment and bulking on debris flow runout modeling: examples from the Swiss Alps: *Natural Hazards and Earth System Sciences*, v. 15, p. 2569-2583, doi:10.5194/nhess-15-2569-2015.
- Fuchs, S., Heiss, K., and Huebl, J., 2007, Towards an empirical vulnerability function for use in debris flow risk assessment: *Natural Hazards and Earth System Sciences*, v. 7, p. 495-506, doi:10.5194/nhess-7-495-2007.

- Gregoretti, C., and Dalla Fontana, G., 2008, The triggering of debris flow due to channel-bed failure in some alpine headwater basins of the Dolomites: analyses of critical runoff: *Hydrological Processes*, v. 22, p. 2248-2263, doi:10.1002/hyp.6821.
- Gregoretti, C., Degetto, M., Bernard, M., Crucil, G., Pimazzoni, A., De Vido, G., Berti, M., Simoni, A., and Lanzoni, S., 2016, Runoff of small rocky headwater catchments: Field observations and hydrological modeling: *Water Resources Research*, v. 52, p. 8138-8158, doi:10.1002/2016WR018675.
- Gregoretti, C., Degetto, M., Bernard, M., and Boreggio, M., 2018, The debris flow occurred at Ru Secco Creek, Venetian Dolomites, on 4 August 2015: analysis of the phenomenon, its characteristics and reproduction by models: *Frontier in Earth Sciences*, v. 6, p. 80, doi:10.3389/feart.2018.00080.
- Gregoretti, C., Stancanelli, L., Bernard, M., Degetto, M., Boreggio, M., and Lanzoni, S., 2019, Relevance of erosion processes when modelling in-channel gravel debris flows for efficient hazard assessment: *Journal of Hydrology*, v. 569, p. 575-591, doi:10.1016/j.jhydrol.2018.10.001.
- Hurlimann, M., Abanco, C., Moya, J., and Vilajosana, I., 2014, Results and experiences gathered at the Rebaixader debris-flow monitoring site, Central Pyrenees, Spain: *Landslides*, v. 11, p. 939-953, doi:10.1007/s10346-013-0452-y.
- Hussin, H., Quan Luna, B., Van Westen, C., Christen, M., Malet, J., and van Asch, T., 2012, Parameterization of a numerical 2-d debris flow model with entrainment: a case study of the faucon catchment, southern french alps: *Natural Hazards and Earth System Sciences*, v. 12, p. 3075-3090, doi:10.5194/nhess-12-3075-2012.
- Imaizumi, F., Sidle, R.C., Tsuchiya, S., and Ohsaka, O., 2006, Hydrogeomorphic processes in a steep debris flow initiation zone: *Geophysical Research Letters*, v. 33, L10404, doi:10.1029/2006GL026250.
- Iverson, R.M., Schilling, S.P., and Vallance, J.W., 1998, Objective delineation of lahar-hazard zones downstream from volcanoes: *Geological Society of America Bulletin*, v. 110, p. 972-984, doi:10.1130/0016-7606(1998)110<0972:ODOLIH>2.3.CO;2.
- Kean, J.W., Staley, D.M. and Cannon, S.E., 2011, In situ measurements of post-fire debris flows in Southern California: Comparison of the timing and magnitude of 24 debris flows events with rainfall and soil moisture conditions: *Journal of Geophysical Research*, v. 116, F04019, doi:10.1029/2011JF002005.
- Lane, S.N., Westaway, R.M., and Hicks, D.M., 2003, Estimation of erosion and deposition volumes in a large, gravel-bed, braided river using synoptic remote sensing: *Earth Surface Processes and Landforms*, v. 28, p. 249-271, doi:10.1002/esp.483.
- Ma, C., Deng, J., and Wang, R., 2018, Analysis of the triggering conditions and erosion of a runoff-triggered debris flow in Miyun County, Beijing, China: *Landslides*, v. 15, p. 2475-2485, doi:10.1007/s10346-018-1080.
- Medina, V., Hurlimann, M., and Bateman, A., 2008, Application of flatmodel, a 2d a finite volume code to debris flows in the northeastern part of the Iberian peninsula: *Landslides*, v. 5, p. 127-142, doi:10.1007/s10346-007-0102-3.
- Milan, D.J., Heritage, G.L., Large, A.R.G., and Fuller, I.C., 2011, Filtering spatial error from DEMs: implications for morphological change estimation: *Geomorphology*, v. 125, p. 160-171, doi:10.1016/j.geomorph.2010.09.012.
- Molina, J.L., Gonzalves, P.R., Molina, C., Aguilera, D.G., and Espejo, F., 2014, Gomatic methods at the service of water resources modelling: *Journal of Hydrology*, v. 509, p. 150-162, doi:10.1016/j.jhydrol.2013.11.034.
- Navratil, O., Liebault, F., Theule, J., Bellot, H., Travaglini, E., Chambon, G., Laigle, D., 2013, High frequency monitoring of debris flows propagation along the real torrent, southern french alps: *Geomorphology*, v. 201, p. 157-171, doi:10.1016/j.geomorph.2013.06.017.
- Okano, K., Suwa, H., and Kanno, T., 2012, Characterization of debris flows by rainstorm condition at a torrent on the Mount Yakedake volcano, Japan: *Geomorphology*, v. 136, p. 88-94, doi:10.1016/j.geomorph.2011.04.006.
- Orlandini, S., and Rosso, R., 1996, Diffusion wave modeling of distributed catchment dynamics: *Journal of Hydrologic Engineering*, v. 1, p. 103-113, doi:10.1061/(ASCE)1084-0699(1996)1:3(103).
- Reid, M.E., Coe, J.A., and Dianne, L.B., 2016, Forecasting inundation from debris flows that grows volumetrically during travel, with application to the Oregon Coast Range, USA: *Geomorphology*, v. 273, p. 396-411, doi:10.1016/j.geomorph.2016.07.039.
- Rickenmann, D., 1999, Empirical relationships for debris flows: *Natural Hazards*, v. 19, p. 47-77, doi:10.1023/A:1008064220727.
- Santi, P.M., deWolfe, V.G., Higgins, J.D., Cannon, S.H., and Gartner, J.E., 2008, Sources of debris flow material in burned areas: *Geomorphology*, v. 96, p. 310-321, doi:10.1016/j.geomorph.2007.02.022.
- Stoffel, M., and Beniston, M., 2006, On the incidence of debris flows from the early Little Ice Age to a future greenhouse climate: a case study from the Swiss Alps: *Geophysical Research Letters*, v. 33, L16404, doi:10.1029/2006GL026805.
- Theule, J.I., Liebault, F., Loye, A., Laigle, D., and Jaboyedoff, M., 2012, Sediment budget monitoring of debris flow and bedload transport in the Manival Torrent, SE France: *Natural Hazard Earth Sciences*, v. 12, p. 731-749, doi:10.5194/nhess-12-731-2012.
- Thiene, M., Shaw, W.D., and Scarpa, R., 2017, Perceived risks of mountain landslides in Italy: stated choices for subjective risk reductions: *Landslides*, v. 14, p. 1077-1089, doi:10.1007/s10346-016-0741-3.
- Tiranti, D., and Deangeli, C., 2015, Modeling of debris flow depositional patterns according to the catchment and sediment source area characteristics: *Frontier in Earth Science*, v. 3, p. 8, doi:10.3389/feart.2015.00008.
- Wheaton, J.M., Brasington, J., Darby, S.E., and Sear, D.A., 2010, Accounting for uncertainty in DEMs from repeat topographic surveys: improved sediment budgets: *Earth Surface Processes and Landforms*, v. 35, p. 136-156, doi:10.1002/esp.1886.

Post-fire rockfall and debris-flow hazard zonation in the Eagle Creek fire burn area, Columbia River Gorge, Oregon: A tool for emergency managers and first responders

N.C. Calhoun^{a,*}, W.J. Burns^a, S. Hay^b, D.M. Staley^c and J.W. Kean^c

^a*Oregon Department of Geology and Mineral Industries, 800 NE Oregon St, Portland, OR 97232, USA*

^b*Oregon Department of Transportation, 123 NW Flanders St, Portland, OR 97209, USA*

^c*Geological Hazards Science Center, U.S. Geological Survey, 1711 Illinois St, Golden, CO 80401, USA*

Abstract

The Eagle Creek Fire burned 48,832 acres (196 km²) of steep, heavily forested terrain along the Columbia River Gorge, Oregon, from September 2nd to November 30th, 2017. The Columbia River Gorge is a critical lifeline for Oregon and Washington, including Interstate Highway 84 (I-84), State Route 14 (SR-14), commercial train lines, a shipping corridor, major pipelines, and hydroelectric dams. The Gorge is also a major tourist destination and home to thousands of permanent residents. Before the Eagle Creek Fire, there was significant landslide and debris-flow hazard in the Gorge due to the steep topography and high annual precipitation (>254 cm). More than 80 landslides have been recorded in the Gorge during the last ~100 years, with 58 of these recorded in the exceptionally wet and stormy winters of 1996 and 1997. Several of these landslides damaged property, temporarily closed I-84, and interrupted train and ship traffic. There is some uncertainty on the degree to which the fire will enhance debris-flow susceptibility, because the climate, terrain and geology is different from the regions where most post-fire debris-flow research has been conducted. A large portion of the Columbia River Gorge National Scenic Area, including popular hiking trails, remains closed 18 months after the fire, and the Historic Columbia River Highway was closed for 14 months after the fire. In the aftermath of the Eagle Creek Fire, emergency managers and first responders identified the critical need for a post-fire landslide response plan and hazard map. To help meet this need, the Oregon Department of Transportation, the Oregon Department of Geology and Mineral Industries, and the U.S. Geological Survey created a landslide hazard map that combined knowledge of pre-fire landslide activity and post-fire debris-flow susceptibility. We describe how this map was created and briefly touch on how this map was integrated into the post-fire response planning.

Keywords: post-fire debris flows; Columbia River Gorge; landslide hazard maps; Oregon; Eagle Creek

1. Introduction

The effect of wildland fires on the landscape can last decades, and have a direct influence on soils, plants, animals, and humans (e.g., Brown et al., 2000). An important secondary hazard created by wildfires is the increased susceptibility of steep slopes to flooding and debris flow during rain storms. The risk of post-fire flooding and debris flow is especially high along the wildland-urban interface, as seen in 2018 with the destructive Montecito debris flows in southern California (WERT, 2018) and many other instances in the western United States (e.g., Cannon and DeGraff, 2009). Over the last two decades, scientists have been studying the secondary impact of increased landslide hazard following wildfires (e.g., Cannon et al., 2010; Staley et al., 2016). Most of these studies have been undertaken in regions with relatively dry climates, which also experience intense bursts of precipitation, such as southern California and the intermountain West. In dry-climate regions, wildfire typically reduces the infiltration capacity of the soil, such that moderate intensity rainstorms can initiate debris flows through processes that result from runoff

* Corresponding author e-mail address: nancy.calhoun@oregon.gov

generation during moderately intense rainfall (Cannon, 2001, Kean et al., 2011, Kean et al., 2013). Post-fire debris-flow generation in wetter climates like the Pacific Northwest is not well understood because the soils in the region tend to have very high infiltration capacities that limit overland flow even after fire (Wondzell and King, 2003; Jackson and Roering, 2009). By combining the known areas of debris-flow deposits with the highest hazard tributary segments and basins, we account for the initiation, transport and depositional area of potential erosion-related debris flows in the Columbia River Gorge in Oregon.

1.1. Study Area

The Columbia River Gorge (CRG) is steep, heavily forested, and characterized by cliffs and flanking talus slopes, ranging in elevation from ~5,000 ft (1525 m) asl at the high point to the Columbia River at about 12 ft (3.7 m) asl. The study area is the extent of the Eagle Creek Fire (Fig. 1). The region receives >100 inches (>254 cm) of precipitation annually with most falling as rain between October and May (PRISM, 2004). The Miocene-aged Eagle Creek Formation, consisting of fluvial conglomerate and andesitic lahar deposits, is the oldest exposed geologic unit along the Oregon side of the Columbia River Gorge. Cliff-forming Columbia River Basalt Group flow sequences of the Grande Ronde, Wanapum, and Saddle Mountains Basalt, also Miocene in age, unconformably overlie the Eagle Creek Formation (Tolan and Beeson, 1984).

The CRG is a critical multimodal lifeline for Oregon and Washington, including Interstate (I-84) and State Route (SR-14), commercial train lines, and commercial shipping. There are also major hydroelectric dams and electric transmission in this corridor (Fig. 1; Wang and Chaker, 2004). The study area, within the CRG, also has approximately 1,400 permanent residents (U.S. Census, 2010), living in approximately 810 buildings (Microsoft building footprint data, 2018). The area is also a major tourist attraction for Portland and the Pacific Northwest, featuring the Columbia River Gorge National Scenic Area.

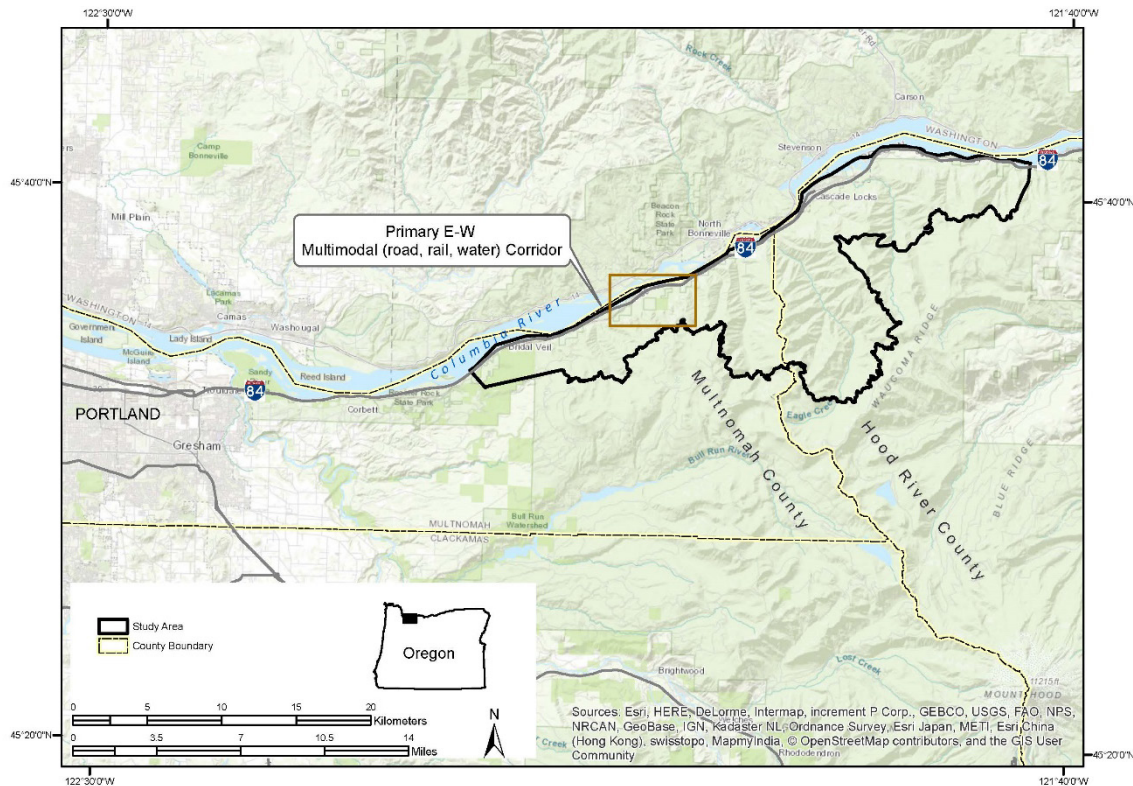


Fig. 1. Study area in the Columbia River Gorge, with the Columbia River dividing Washington State to the north, encompassing the Eagle Creek burn area and downslope infrastructure. I-84 and the rail lines here in the CRG are the primary access through the Cascade Range; the next closest pass is 150 miles to the north via I-90 and ~500 miles to the south via I-80 in Sacramento, CA, through the Sierra Nevada. Note brown box outlining Dodson-Warrendale fan, seen in Fig. 2.

Landslides are a chronic hazard in the CRG. More than 80 landslides have occurred in the study area portion of the CRG during the last ~100 years, with 58 of these recorded in the exceptionally wet and stormy winters of 1996 and 1997 (Burns et al., 1998; Burns and Lindsey, 2017; Burns and Watzig, 2017). Several of these landslides can be seen in an aerial photo of the Dodson-Warrendale area from 2000 (Fig. 2a), and debris flows in this area have damaged property and forced the closure of the rail lines, I-84, and shipping lanes. A 2001 event closed I-84 for 12 days (Wang and Chaker, 2004). Due to the Eagle Creek Fire, related damage, and potential hazards related to rockfall and debris flows, significant road segments were closed from September 2017–November 2018 and much of the recreational area of the Columbia River Gorge National Scenic Area remains closed as of February 2019.

The Eagle Creek Fire engulfed 48,832 acres (196 km²) within the Columbia River Gorge, beginning September 2nd, swiftly growing to the west then east, driven by unfavorable, strong winds (Schnackenberg, 2017). The Eagle Creek burn was deemed 100% contained by November 30th, 2017. Fig. 2b illustrates the variability of burn intensity and a visual perspective of the Columbia River Gorge and the Dodson-Warrendale area.

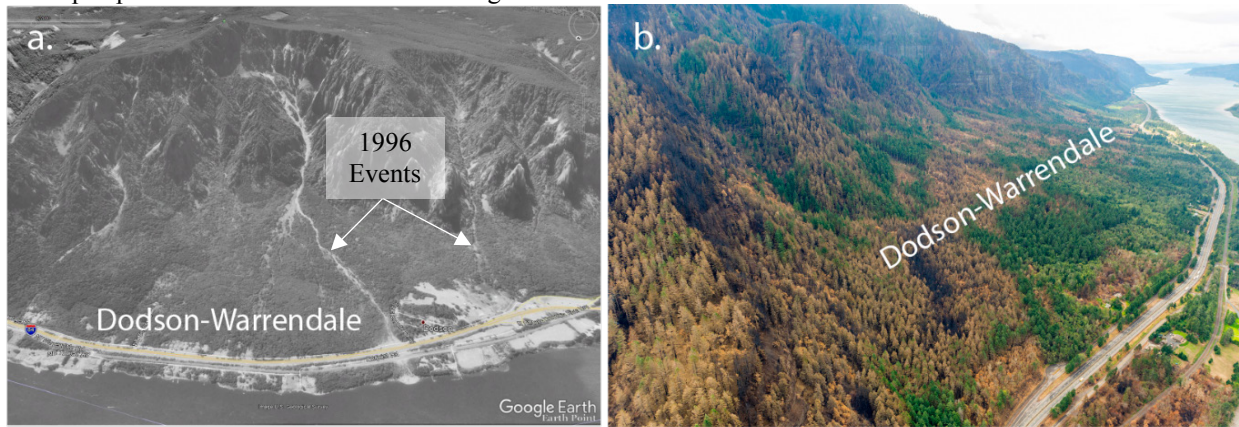


Fig. 2. (a) Aerial photograph from year 2000 draped over topography from Google Earth, at an oblique angle looking south. Several debris-flow tracks from the winter of 1996 are evident (Burns et al., 1998), with I-84 in the foreground. (b) An oblique photograph of the Dodson-Warrendale fan taken September 26th, 2017, looking eastward. The variability of the burn intensity of Eagle Creek Fire is evident, with black- to yellow-scorched trees interspersed with green. I-84 is the highway on the right side of the photograph. (Image provided by ODOT Photo/Video).

An estimated 45% of the area had high or moderate soil burn severity (Fig. 3; Schnackenberg, 2017). The map shown in Fig. 3 was created immediately after the fire by a U.S. Forest Service Burn Area Emergency Response (BAER) team using Landsat satellite imagery products, such as the Burned Area Reflectance Classification (BARC), and field verification. The satellite imagery was analyzed by remote sensing specialists to estimate soil burn severity comparing near-infrared and mid-infrared bands (Parsons et al., 2010). The satellite estimate of burn severity was then field checked by the BAER team soil scientists (Parsons et al., 2010; Schnackenberg, 2017).

In the aftermath of the Eagle Creek Fire, local and regional scientists from the Oregon Department of Transportation (ODOT), Oregon Department of Geology and Mineral Industries (DOGAMI), and the U.S. Geological Survey (USGS), alerted emergency managers and the public of the potential for increased rockfall and debris flows because of the burn. Emergency managers and first responders then identified a critical need for a post-fire landslide response plan and a generalized hazard map. In this paper, we describe how we created the post-fire rockfall and debris-flow hazard map in the Eagle Creek burn area, and briefly touch on how this map was integrated into the post-fire response planning.

2. Methods

In order to make a hazard map for the Eagle Creek burn area, we relied on the established methods of the USGS post-fire debris flow model (Gartner et al., 2014; Staley, et al., 2016, 2017) and the existing landslide inventory created for Multnomah County (Fig. 4, Burns and Lindsey, 2017), which includes historical landslide points and deposits, and prehistoric landslide deposits, mapped at 1:8,000 scale. The landslide inventory includes shallow (<3 m) and deep (>3 m) deposits, rockfall talus and debris flow fans, of different ages and certainty levels, though we extracted debris flow fans and rockfall talus polygons only. We also completed new preliminary landslide inventory mapping (rockfall talus and debris-flow fans only) in the Hood River County portion of the study area. Observations from emergency managers

and first responders identified a need for a combined hazard map that included both datasets in one map, generalized enough for quick decision making and without the need for expert interpretation.

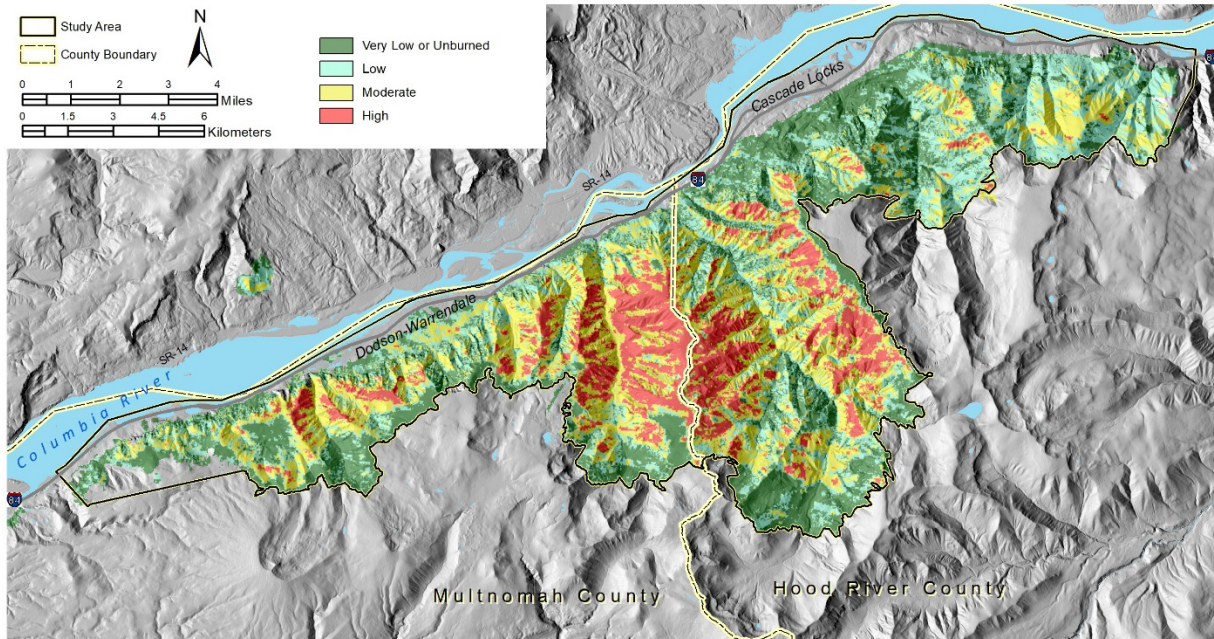


Fig. 3. Soil burn severity map and extent of the Eagle Creek burn (Schnackenberg, 2017), modified to include our study area polygon and 1-m lidar hillshade. See Fig. 1 for study area location.

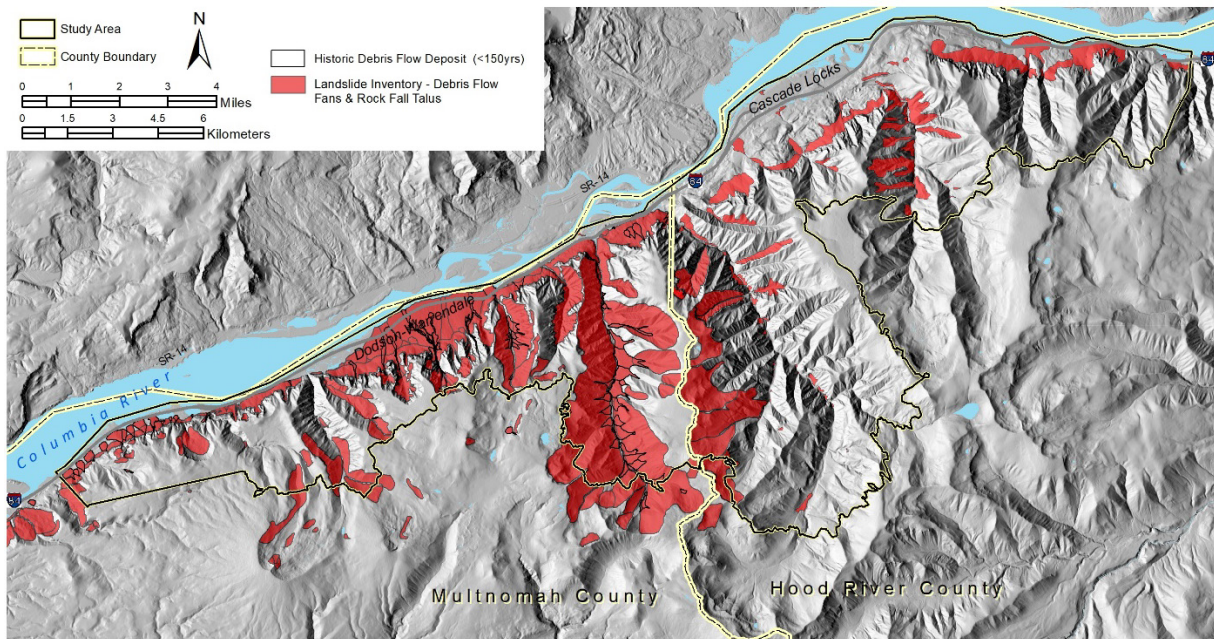


Fig.4. Rockfall and debris-flow fan deposits extracted from Burns and Lindsey (2017) in Multnomah County, with newly delineated rockfall and debris-flow fans in western Hood River County. The black outlines denote historical debris-flow deposits, meaning movement occurred in the last 150 years. See Fig. 1 for study area location.

The post-fire landslide hazard map combines lidar-derived 1-m cell size bare earth DEM as base data from the Oregon Lidar Consortium (DOGAMI, 2009), published landslide inventory (Fig. 4, Burns and Lindsey, 2017), post-

fire debris-flow hazard assessment data (Fig. 5; USGS, 2017) and unpublished remote sensing-based mapping of rockfall and debris-flow fan areas in western Hood River County (Fig. 4), digitized by the author specifically for this hazard map.

We used the combined hazard attribute in the USGS post-fire debris-flow hazard assessment, which includes both probability and volume. The USGS models use basin morphology, burn severity, soil properties and rainfall characteristics to estimate the statistical likelihood (Staley et al., 2016) and potential volume (Garter et al., 2014) of debris flows in response to a storm of a given rainfall intensity. We used the combined hazard for the most intense design storm in the USGS hazard assessment, which had a 15-minute peak rainfall intensity of 40 mm/hr, corresponding to a 5-year recurrence interval based on the methods of Arkell and Richards (1986).

The USGS combined hazard map does not, however, identify zones of potential debris-flow inundation, because an operational tool for rapid post-fire runout prediction does not exist. To estimate zones of potential debris-flow inundation, we used a combination of (1) geomorphic evidence of deposition based on the landslide, rockfall, and fan mapping described above, and (2) enlarged (buffered) versions of the "watch stream" segments that are included in the USGS hazard assessments. "Watch streams" are defined as large trunk streams (drainage area $>8 \text{ km}^2$), which may experience extensive flooding and the effects of debris flow in the drainage network upstream of the watch stream. We merged these datasets into the final post-fire landslide hazard zones defined as low, moderate, and high susceptibility within a geographic information system (GIS).

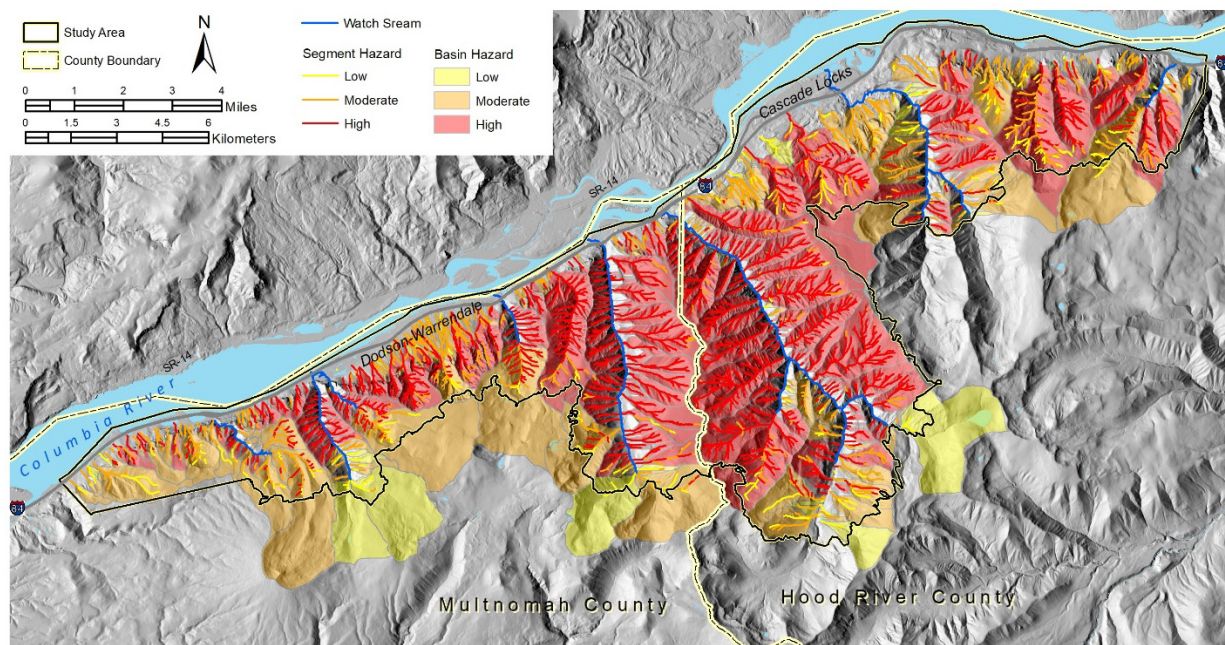


Fig. 5. Debris-flow estimates of combined hazards of both the stream segments and basin scales, from the USGS post-fire debris flow model, for a given peak 15-minute rainfall intensity of 40 mm/hr. Data accessed via the USGS Post-Fire Debris Flow Hazards under the Landslide Hazards Program (USGS, 2017). See Fig. 1 for study area location.

The inputs to the three hazard zones are as follows:

High Zone

- *Rockfall and debris-flow fan deposits*: Extracted from landslide inventory maps (Burns and Lindsey, 2017); deep- and shallow-landslide polygons excluded from hazard map input.
- *Buffered Moderate and High Hazard Stream Segments*: Combined hazard attribute of stream segments, with associated buffer: high with 100 ft (30 m) buffer and moderate with 75 ft (23 m) buffer. We selected different buffer distances for moderate and high hazard stream segments based on measured channel widths for streams in this area. The high hazard stream segment buffer of 100 ft (33 m) was determined from measured mean stream width in the upper, smaller tributaries.
- *High Hazard Basins*: Combined hazard attribute for basin-scale analysis: all high hazard basins included (with no buffer).

- *Buffered Watch Streams*: Watch stream segments were buffered 200 ft (65 m) for entire length, based on measured channel widths for large trunk streams in this area.
- *Manual Revisions*: Revisions of merged datasets to include isolated areas not included but surrounded entirely or mostly by other high hazard data inputs and small-scale linework alterations, to better align with 1-meter resolution topography.

Moderate Zone

- We buffered the high-hazard zone by 200 ft (65 m).

Low Zone

- Areas within the study area boundaries that were not included in moderate or high zones.

The post-fire rockfall and debris-flow hazard map (Fig. 6) is intended to be used by the emergency managers and first responders for the affected area as a tool for choosing operation centers, safe rally points for officers, and similar needs. We do not expect an event where the entire high-hazard zone has landslides at the same time throughout the zone. Instead, the map identifies the most likely areas where landslides may occur and areas where landslides are very unlikely.

3. Results

The final post-fire debris-flow and rockfall hazard map for the Eagle Creek burn area highlights the widespread high hazard, narrow bands of moderate hazard and isolated areas of low hazard near the Columbia River and atop the flat plateau above the gorge (Fig. 6). Human modification of slopes, such as road construction and associated grading, as well as mitigation efforts, such as rockfall fences and jersey barriers, are not considered in these maps, but may affect the hazard.

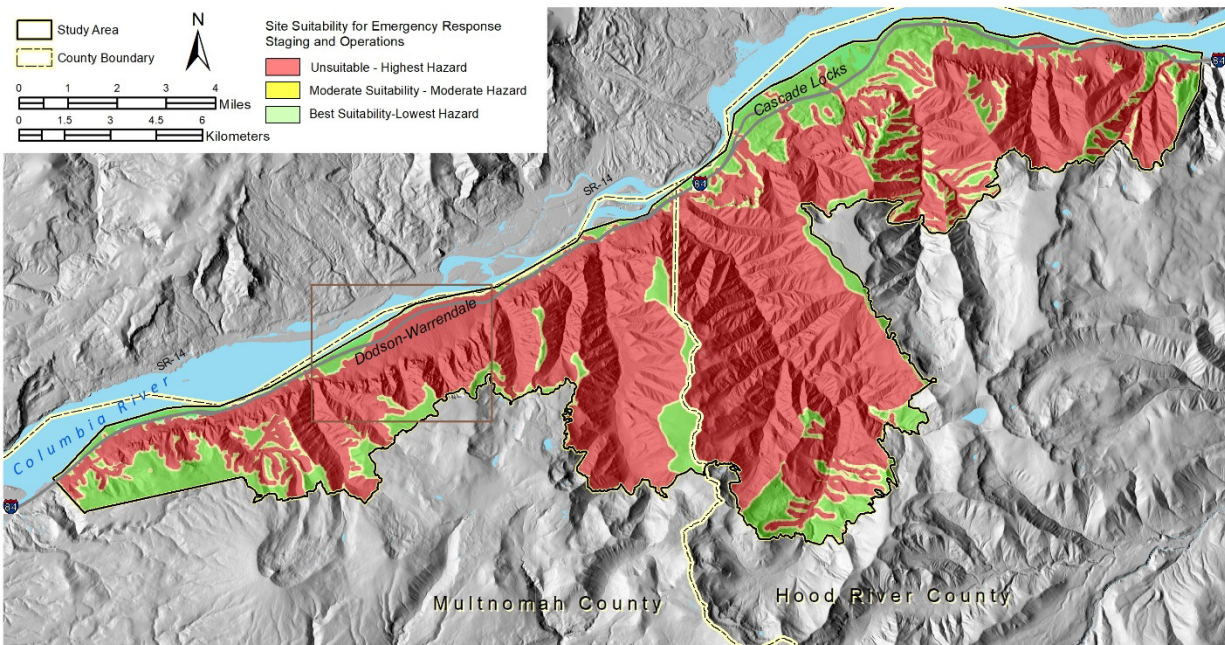


Fig. 6. Post-fire rockfall and debris-flow hazard map created for local first responders and emergency managers. As is evident, much of the upper basins are included in their entirety, because of the steep, confined channels and rockfall hazards along slopes. See Fig. 1 for study area location. Note brown box outlining Dodson-Warrendale fan, seen in Fig. 7. See Fig. 1 for study area location.

4. Discussion and Conclusions

The Eagle Creek Fire garnered local, regional, and national attention during the fall of 2017, with dramatic images of tall Douglas Firs on steep slopes, engulfed in large flames. At several of the post-fire planning meetings hosted by the U.S. Forest Service and others attention turned from the fire hazard to the looming wet season and the post-fire

landslide hazard and associated risk. The goal of the post-fire landslide hazard map was to modify existing landslide hazard data for the Columbia River Gorge into a usable, safety-driven hazard map.

Debris flows are an existing and recurrent hazard in the CRG. A closer view of historical debris-flow deposits from the landslide inventory (Burns and Lindsey, 2017) are shown in Fig. 7 (see also Fig. 2). The unincorporated communities of Dodson-Warrendale have experienced debris flows in the past, and, as is shown in the hazard map, are at continued risk after the fire. The landslide inventory of debris-flow deposits (fans) and rockfall talus slopes likely record thousands of years of debris flow and rockfall accumulation (Burns and Lindsey, 2017). Since the Eagle Creek Fire, frequent rock raveling and isolated, small rockfall events have been observed. As of February 2019, there have been no major debris flows since the fire; however, there have been seven small shallow landslides.

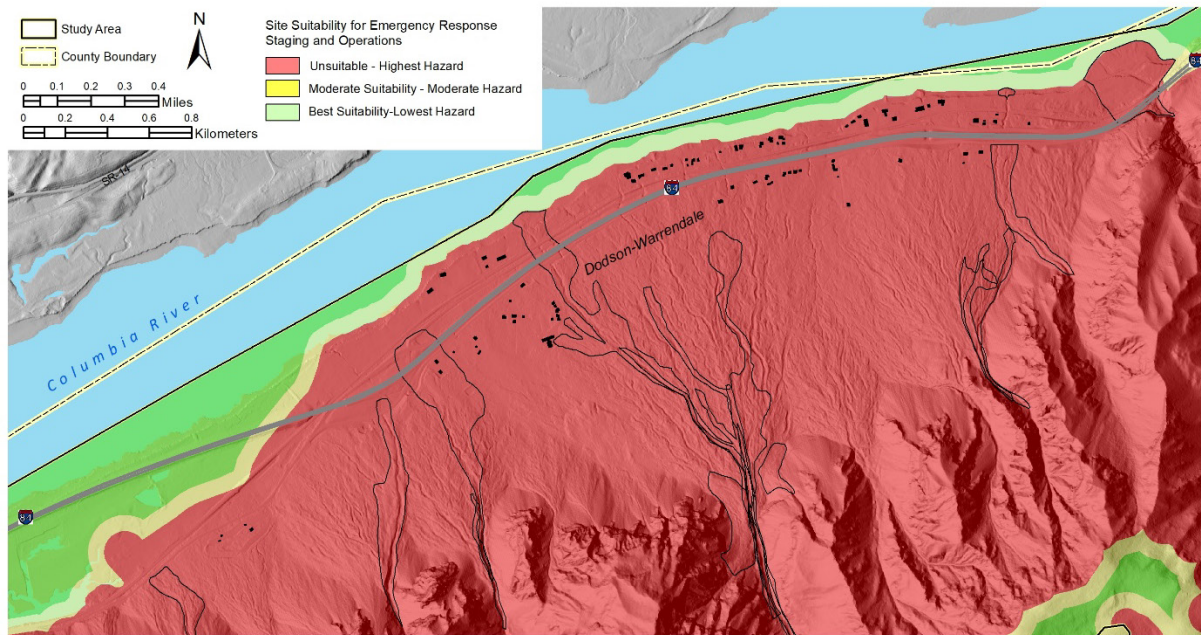


Fig. 7. A closer view of the hazard zonation, in an area with repeated historical debris flows (delineated in black lines) and exposed buildings in the unincorporated communities of Dodson-Warrendale and Interstate Highway 84. See Fig. 6 for study area location (brown box).

Extensive research around the USA demonstrates that wildfires increase debris-flow susceptibility and magnitude (e.g., Cannon et al., 2010). By combining the best available data, we include the area of likely origin, transport and potential depositional areas for debris flows and rockfall in the burn area. USGS empirical models for debris-flow likelihood (Staley et al., 2016) and volume (Gartner et al., 2014) are based on data mostly from semiarid regions of southern California and the intermountain West. Most of the debris flows in the USGS database were triggered in the first two years after the fire by runoff and associated erosion, not debris flows mobilized from shallow landslides. Shallow landsliding may be the more likely mode of slope failure in the wetter Eagle Creek burn area, and the time window of increased susceptibility may last up to 10 years (like the window of disturbance for an unburned but clear-cut slope). Although the USGS models have not been developed or tested with data from the Pacific Northwest, we consider our results to be valid in an ordinal sense (i.e., for identifying areas with high, moderate, and low susceptibility), because the USGS models correctly identify areas with both steep slopes and moderate to high burn severity, two factors that strongly affect slope stability regardless of the style of landslide initiation or duration of vegetation recovery.

The Eagle Creek rockfall and debris-flow hazard map highlights the near-term, secondary impacts of potential rockfall and debris flows in the Columbia River Gorge within the Eagle Creek burn area. The overlap of highly burned soils, slope steepness, existing rockfall talus and debris flow-fans, result in widespread high hazard throughout the footprint of the Eagle Creek burn. The central portion of the study area, along the steep cliffs of the Columbia River Gorge, and in the upper steep watersheds, the high-hazard zone is nearly ubiquitous.

This hazard map was created in response to requests and questions from local first responders and emergency managers, and attempts to create generalized, conservative high and moderate hazard areas to avoid in times of wet

weather. This map highlights a few areas of low hazard that may be secure as a base for operations if a debris flow occurred and rescue operations were to commence. The hazard map also alerts the city of Cascade Locks where potential danger along water bodies and streams may be concentrated within city limits.

Acknowledgements

This work was supported in part by the U.S. Geological Survey Landslide Hazard Program. We would like to acknowledge the feedback and participation of the Multnomah County Sheriff's Office, Portland OR National Weather Service Forecast Office, as well as many other agencies that collaborated for the Eagle Creek Land Movement Table Top Exercise and Workshop, led by Multnomah County Emergency Management. We also want to thank reviewers J. McLaughry, K. Schmidt, and K. Mickelson for their helpful reviews that improved the manuscript. Any use of trade, firm, or product names is for descriptive purposes only and does not imply endorsement by the U.S. Government.

References

- Arnell, R.E., and Richards, F., 1986, Short duration rainfall relations for the western United States, Conference on Climate and Water Management, August 4-7, Asheville, N.C., American Meteorological Society, Boston, MA.
- Brown, J.K., and Smith, J.K., eds., 2000, Wildland fire in ecosystems: Effects of fire on flora. General Technical Report RMRS-GTR-42-vol. 2. Ogden, UT: U.S. Department of Agriculture, Forest Service, Rocky Mountain Research Station. 257 p.
- Burns, S.F., Burns, W.J., James, D.H., and Hinkle, J.C., 1998, Landslides in the Portland, Oregon metropolitan area resulting from the storm of February 1996: Inventory map, database, and evaluation: Portland, Oregon, Portland State University, Metro Contract 905828.
- Burns, W.J., and Lindsey, K.O., 2017, Landslide inventory of eastern Multnomah County, Open-File report O-17-03.
- Burns, W.J., and Watzig, R., 2017, Statewide landslide information database for Oregon, release 3 (SLIDO 3.0). Oregon Department of Geology and Mineral Industries.
- Cannon, S., Bigio, E. and Mine, E., 2001, A process for fire-related debris flow initiation, Cerro Grande fire, New Mexico, Hydrological Processes, v. 15, p. 3011-3023. <https://doi.org/10.1002/hyp.388>.
- Cannon, S.H., and DeGraff, J.V., 2009, The increasing wildfire and post-fire debris-flow threat in western USA, and implications for consequences of climate change, in Sassa, K., and Canuti, P., eds., Landslides—Disaster risk reduction: Berlin, Heidelberg, Springer, p. 177–190.
- Cannon, S.H., Gartner, J.E., Rupert, M.G., Michael, J.A., Rea, A.H., and Parrett, C., 2010, Predicting the probability and volume of postwildfire debris flows in the intermountain western United States., Geological Society of America Bulletin, 122 (1-2), 127-144, doi: 10.1130/B26459.1.
- Gartner, J.E., Cannon, S.H., and Santi, P.M., 2014, Empirical models for predicting volumes of sediment deposited by debris flows and sediment-laden floods in the transverse ranges of southern California, Engineering Geology, v. 176, p. 45-56, doi:10.1016/j.enggeo.2014.04.008.
- Kean, J. W., Staley, D.M., and Cannon, S.H., 2011, In situ measurements of post-fire debris flows in southern California: Comparisons of the timing and magnitude of 24 debris-flow events with rainfall and soil moisture conditions, Journal of Geophysical Research, v. 116, F04019, doi: 10.1029/2011JF002005.
- Kean, J.W., McCoy, S. W., Tucker, G.E., Staley, D.M., and Coe, J.A., 2013, Runoff-generated debris flows: Observations and modeling of surge initiation, magnitude, and frequency, J. Geophys. Res. Earth Surf., v. 118, p. 2190–2207, doi:10.1002/jgrf.20148.
- Jackson, M. and Roering, J.J., 2009, Post-fire geomorphic response in steep, forested landscapes: Oregon Coast Range, USA. Quaternary Science Reviews, v. 28 (11-12), p. 1131-1146.
- Microsoft, US Building Footprints, 2018, GitHub, <https://github.com/Microsoft/USBuildingFootprints>. (accessed July 2018).
- Oregon Department of Geology and Mineral Industries (DOGAMI), 2009, Hood to coast project 2007, Oregon Lidar Consortium, distributed by Oregon Department of Geology and Mineral Industries Lidar Program airborne lidar survey, <https://gis.dogami.oregon.gov/maps/lidarviewer/>
- Parsons, A., Robichaud, P.R., Lewis, S.A., Napper, C., and Clark, J.T., 2010, Field guide for mapping post-fire soil burn severity, General Technical Report RMRS-GTR-243, Fort Collins, Co: U.S. Dept. of Agriculture, Forest Service, Rocky Mountain Research Station, 49 p.
- PRISM Climate Group, Oregon State University, <http://prism.oregonstate.edu>, created 4 Feb 2004 (accessed September 2018).
- Schnackenberg, L., 2017, Burned area emergency response summary – Eagle Creek fire, October 10, 2017, Columbia River Gorge National Scenic Area.
- Staley, D.M., Negri, J.A., Kean, J.W., Laber, J.L., Tillery, A.C., and Youberg, A.M., 2016, Updated logistic regression equations for the calculation of post-fire debris-flow likelihood in the western United States: U.S. Geological Survey Open-File Report 2016-1106.
- Staley, D.M., Negri, J.A., Kean, J.W., Laber, J.L., Tillery, A.C., Youberg, A.M., 2017, Prediction of spatially explicit rainfall intensity-duration thresholds for post-fire debris-flow generation in the western United States. Geomorphology, v. 278, p. 149-162, doi: 10.1016/j.geomorph.2016.10.019.
- Tolan, T.L. and Beeson, M.H., 1984, Exploring the Neogene history of the Columbia River: Discussion and geologic field trip guide to the Columbia River Gorge, Part 1. Discussion, Oregon Geology, v. 46, p. 87-95.
- USGS, 2017, Emergency assessment of post-fire debris-flow hazards, Eagle Creek fire (Columbia River Gorge National Scenic Area, OR, https://landslides.usgs.gov/hazards/postfire_debrisflow/detail.php?objectid=130 (accessed October 2018).
- U.S. Census, 2010.
- Wang, Y., and Chaker, A., 2004, Geologic hazards study for the Columbia River transportation corridor. Oregon Department of Geology and Mineral Industries, OFR O-04-08.
- WERT, 2018, Thomas fire watershed emergency response team – Final report, CA-VNC-103156, http://cdfdata.fire.ca.gov/incidents/incidents_details_info?incident_id=1922 (accessed October 2018).
- Wondzell, S.M., and King, J.G., 2003, Postfire erosional processes in the Pacific Northwest and Rocky Mountain regions. Forest Ecology and Management, v. 178, n. 1-2, p. 75-87.

Hydrogeomorphology and steep creek hazard mitigation lexicon: French, English and German

Félix Camiré^{a,*}, Guillaume Piton^b, Sebastian Schwindt^c

^a *Town of Canmore, Canmore, Canada*

^b *Univ. Grenoble Alpes, IRSTEA, ETNA, Grenoble, France*

^c *Univ. California at Davis, Department of Land, Air and Water Resources, Davis, CA, United States of America*

Abstract

Geoscientists, researchers and engineers study and work on similar projects all over the world. The exchange of information between colleagues of different countries who work on homologous projects or in similar fields requires a common technical vocabulary. Differences in the usage of technical terms and their varying definitions in different regions of the world may constrain the transfer of knowledge, for example in guidelines. Translations of technical papers and of presentations are particularly complicated and troublesome. Moreover, writers waste valuable time when they try to find proper technical terms in a different language. This is currently the case in the fields of fluvial geomorphology and steep creek hazard mitigation since several countries are active in these domains. Papers, guidelines, and policies are published in several languages, such as Japanese, Italian, French, German, English, Korean, Chinese and Spanish. International delegates are also submitting papers to journals, presenting and participating at conferences that are predominantly in English. Finally, working groups with multinational participants have been formed to advance research and transfer of knowledge in fluvial geomorphology and steep mountain creek hazard mitigation. Therefore, standardization and better definitions of technical terms are required. We propose in this paper a lexicon of French, English and German technical terms, and their definitions, related to the fields of fluvial geomorphology and steep mountain creek hazard mitigation. This paper focuses on the most important terms. In the future, other languages and supplemental terms could be added to this document with the help of other contributors.

Keywords: debris flow; debris flood; hydrogeomorphology; hazard; mitigation; torrent; mountain river; steep mountain creek;

1. Introduction

International scientific and technical exchanges play a key role, at least since the 19th century, in sharing good practices, lessons learned from past events and recent results in natural hazards, risk management and mitigation (Piton et al., 2017). New concepts regularly emerge and technical jargons continuously evolve. Therefore, to properly understand the specialized literature, updated glossaries and lexicons acknowledging the current state of definitions and vocabulary are required (e.g. Hungr et al., 2014). Such documents should, if possible, be multilingual to ease sharing of knowledge published abroad. Table 1 shows some topics with wide audiences that have already been covered. To our knowledge, FAO (1981) is the last published multilingual lexicon dedicated to torrent control and debris-flow hazard mitigation. However, some terms are somewhat outdated, and some recent ones are missing.

This paper lists the existing multilingual glossaries partially related to torrent control, and then reviews frequently used terms in hazard mitigation of steep mountain creeks, as well as their uses and definitions in English, French and German. The terms are presented and explained in a summary table with links to publicly available dictionaries or papers.

Finally, this paper uses terms “torrent”, “mountain river” and “steep mountain creek” interchangeably. Their meaning is the same, however their uses are regional; different countries or areas will usually employ only one of the three terms.

Table 1. Non-exhaustive list of existing multilingual glossaries or lexicons related to hydrogeomorphic hazards

* Corresponding author e-mail address: fcamire@canmore.ca

Lexicon / Glossary	Covered topics	Languages	Weblink, Source
FAO	Torrent control	EN.; FR.; DE.; IT.; ES.	http://www.fao.org/docrep/006/AD076F/AD076f00.htm , (FAO, 1981)
ICOLD	Dams, dikes, hydraulic structures	EN.; FR.; DE.; IT.; NL., ES.; PT.; SI.; SE.	http://www.icold-cigb.net/GB/dictionary/dictionary.asp
ISSMGE	Soil mechanics	EN.; FR.; DE.; IT.; ES.; PT.; JA.; RU.; CN., etc.	https://www.issmge.org/lexicon
OFEV	Flood protection	EN.; FR.; DE.; IT.; ES.; PT.; etc.	https://www.termdat.bk.admin.ch
REFORM	River restoration	EN.; FR.; DE.; IT.; GR., CZ., ES., PL.	http://wiki.reformrivers.eu/index.php/Multilingual_glossary
UNISDR	Disaster risk reduction	EN.; FR.; ES.; RU.; AR.; ZH.	https://www.unisdr.org/we/inform/terminology
WP/WLI	Landslides	EN.; FR.; DE.; ES.; RU.; ZH.	http://www.cgs.ca/pdf/heritage/Landslide%20Glossary.pdf
WSL	Dendrochronology	EN.; FR.; DE.; IT.; ES.; PT.; RU.	https://www.wsl.ch/dendro/products/dendro_glossary/index_EN

2. Review method

This paper is much shorter than the FAO (1981) book that constitutes its main reference source. The book includes the following: an index, 156 pages of English, French and German definitions, translations of key terms in Italian and Spanish, and sketches of structures and processes. The book would deserve a complete update since some terms have new synonyms and new ones have been introduced. Moreover, the update should include a user-friendly online version, along with translation in Japanese, Chinese and other relevant languages.

For the sake of conciseness, this paper covers only a selection of the terms that are believed to be the most frequently used in debris-flow hazard mitigation. Table 2 presents selected terms, frequent synonyms, concise definitions, and the main source of information. The reader interested in other terms, not covered in this paper, can browse the FAO's web version (link available in Table 1).

Table 2. Lexicon table, alphabetical ordering of the English terms

English terms, Synonym, Definition (source)	Termes français, Synonyme, Définition (source)	Deutsche begriffe, Synonym, Definition (quellen)
<i>Aggradation, Silting</i> : Accumulation of sediment in a channel or upstream of a structure (adapted from 1).	<i>Atterrissement, aggradation, engraissement</i> : ensemble des alluvions déposées dans un tronçon naturel ou en amont d'un ouvrage (1).	<i>Auflandung</i> : Hebung des Flussbetts durch Sedimentablagerungen (3).
<i>Alluvial cone, Debris cone, Alluvial fan</i> : A fan- or cone-shaped deposit of sediment crossed and built-up by steep mountain creeks (adapted from Wikipedia).	<i>Cône de déjection</i> : Zone où les matériaux se déposent au débouché du torrent dans la vallée et relief formé par leur accumulation (1).	<i>Schwemmkegel</i> : Ablagerungskegel am unteren Ende eines <i>Wildbaches</i> , der sich in Tälern bildet. Die Ablagerungen entstehen, da das verrignerte Sohlgefälle im Unterlauf einen Rückgang der <i>Geschiebetransportkapazität</i> verursacht, d.h., das <i>Gleichgewichtsgefälle</i> verändert sich.
<i>Anchoring, keying</i> : The attachment or inseting of a channel structure into the bed or bank of a stream to prevent its by-passing (1)	<i>Ancrage</i> : Liaison d'un ouvrage avec les berges et le lit par insertion profonde et solide faisant obstacle au contournement et au déchaussement par affouillement de l'ouvrage (1).	<i>Verankerung</i> : Die Verankerung eines hydraulischen Bauwerks oder Schutzbauwerks im angrenzenden Terrain ist notwendig um die Bauwerksstabilität zu garantieren (2).
<i>Avulsion, outflanking</i> : The breaking through of the banks of a stream thus forming a new channel, mostly observed on fans (1).	<i>Changement de lit, bifurcation de lit, avulsion</i> : Abandon par un cours d'eau de son lit antérieur et formation d'un nouveau chenal, principalement observés sur les cônes de déjections.	<i>Gerinnesprung, Avulsion, Gerinneverlagerung</i> : Natürliche, sprunghafte Verlagerung eines alluvialen Flussbettes. Vornehmlich bei Überschreiten des bettbildenden Hochwassers in alluvialen Wildbächen zu beobachten (3).
<i>Bedload/sediment transport</i> : Coarse sediment transport by rolling and sliding on the bottom of the bed due to the force of water (1).	<i>Charriage</i> : Transport de sédiments grossiers sur le fond du lit par roulage et glissement sous la force exercée par l'eau.	<i>Geschiebetransport</i> : Sediment, das auf oder Flussbett durch den Abfluss transport wird (5).
<i>Bedload transport capacity</i> : Maximum amount of sediment of a given grain size distribution that a stream can transport in traction as bedload (Hickin, 1995).	<i>Capacité de transport par charriage</i> : Charge solide maximale d'un écoulement donnée et d'un mélange sédimentaire donné, transporté par charriage.	<i>Geschiebetransportkapazität</i> : Hydraulisch bedingte maximaler Geschiebetransport. In Wildbächen ist der Geschiebetransport meist begrenzt durch die Sedimentzuflussrate. Bei Murgängen kann jedoch die hydraulische Transportkapazität zum limitierenden Faktor werden (typische Gefahrensituation).
<i>Block ramps (structured / unstructured)</i> : Fish-friendly alternative hydraulic structure to drops and sills for the stabilization of river beds that are created with tightly packed blocks (large rocks) or dispersed block clusters (adapted from 8).	<i>Rampe / seuil / radier en blocs / enrochements</i> : Ouvrage de stabilisation du lit des rivières alternatifs aux seuils subverticaux, visant à faciliter la montaison des poissons et constitués de blocs libres organisé en densité et rugosité plus ou moins fortes.	<i>(Aufgelöste) Blockrampe</i> : Künstlicher Gerinnesprung gestaltet durch grobe Blöcke, die so angeordnet sind, das aquatische Lebewesen passieren können (8).
<i>Bypass channel, Diversion works / structure</i> : A diversion channel through which surplus flood water may be diverted around an area to be protected (1).	<i>Canal de décharge, Ouvrage de dérivation</i> : Ouvrage assurant la chenalisation des écoulements excédentaires pour les détourner d'une zone à protéger.	<i>Entlastungskanal / Entlastungsgerinne</i> : Künstliches Parallelgerinne zur Erhöhung der Abflusskapazität.
<i>Canyon, Gorge, Narrows</i> : Narrow passageway of a torrential stream as it passes between canyon walls (1).	<i>Gorge</i> : Nom parfois donné au lit d'écoulement d'un torrent lorsqu'il est creusé entre des berges abruptes (1).	<i>Schluchtstrecke</i> : Steile Abflusssektion, die durch Felshänge und anstehenden Fels in der Gerinnesohle geprägt ist (2).
<i>Channel bed</i> : It is the channel bottom of a stream or creek, the physical confine of the normal water flow.	<i>Lit mineur</i> : Espace d'écoulement normal des eaux.	<i>Gerinnebett, Flussbett</i> : Ständig überflossene Fläche.

Table 2. (Continued)

English terms, Synonym, Definition (source)	Termes français, Synonyme, Définition (source)	Deutsche begriffe, Synonym, Definition (quellen)
<i>Channel cleaning, dredging:</i> Removal of debris and bedload from a channel (1).	<i>Curage du lit:</i> Enlèvement des matériaux encombrant localement le lit d'un torrent (1).	<i>Räumung des Abflussprofils:</i> Unterhaltsmaßnahme, bei der Abflusshindernisse (Pflanzen, Sedimentablagerungen und Schwemmholz oder anderes Treibgut) aus dem <i>Flussbett</i> entfernt werden (3).
<i>Check dam, Solid body dam, Chute structure:</i> Transverse structure to stabilize and consolidate a creek channel or to retain debris (adapted from Moase, 2017).	<i>Barrage de correction torrentielle:</i> Ouvrage établi en travers du lit d'un torrent ou d'un ravin en vue de stabiliser son lit, consolider ses berges ou retenir des sédiments.	<i>Wildbachsperre:</i> Künstliche Querbauwerke in Wildbächen um den Sedimentrückhalt und die Gerinnestabilität zu fördern (2).
<i>Concrete/grouted stone-pitching, grouted riprap wall:</i> Stonework made of very large rocks, which have not been cut to shape, that are grouted together.	<i>Mur/perré de maçonnerie de pierre dégrossies :</i> Ouvrage en maçonnerie de pierres anguleuses brutes liées au mortier (1).	<i>Zementmörtelmauer:</i> Mit Zement verstärktes Mauerwerk.
<i>Danger event/flood/level, :</i> Extreme event/flood/level conditions over which structure's safety is no longer guaranteed (CFBR, 2013).	<i>Crue/événement de danger :</i> Crue/événement au-delà duquel la stabilité de l'ouvrage n'est plus garantie.	<i>Gefahrenhochwasser:</i> Die Bauwerksstabilität ist nicht garantiert für Abflüsse, die höher als das Gefahrenhochwasser sind.
<i>Debris flood:</i> It is a very rapid flow of water, heavily charged with debris, in a steep channel (Hungar et al., 2014)	<i>Charriage hyperconcentré,</i> Écoulement de biphase très chargé en sédiment, capable de mobiliser de gros blocs de façon épars, écoulement potentiel par bouffées mais sans front granulaire.	<i>Rutschung / Hangsturz:</i> Zweiphasiger, intensiver Abgang von Sediment und Wasser in steilem Gelände (2).
<i>Debris flow:</i> It is a relatively rapid to extremely rapid movement of a single phase of saturated non-plastic debris in a steep channel, showing a steep front partially granular and usually generating strong entrainment of material and water from the flow path (adapted from Hungar et al., 2014).	<i>Lave torrentielle:</i> Écoulement relativement rapide et par bouffées d'un mélange monophasique de sédiments, blocs, eau et éventuellement de flottants dans les chenaux raides. Présence d'un front raide, souvent granulaire, au grand pouvoir érosif, générant un recrutement de matériaux du lit le long de sa propagation.	<i>Murgang:</i> Mischung aus Wasser und Sediment, das plötzlich mobilisiert wird, wobei der Sedimentanteil mindestens 10 % beträgt (2).
<i>Design event/flood/level:</i> The events/floods/level adopted for the design of a comprehensive hazard mitigation system, i.e., in torrent control context, events for which the efficacy of hazard mitigation regarding downstream assets should be maximum.	<i>Èvènement/Crue/cote de projet, de protection:</i> Crues/événements adoptés pour dimensionner un dispositif de protection ; dans le contexte des risques torrentiel, événements pour lesquels l'efficacité de protection des enjeux aval doit être maximale.	<i>Projektwassermenge, Dimensionierungshochwasser:</i> Hochwasserabfluss, der der Bemessung von Schutzbauwerken zugrunde liegt (3).
<i>Diversion dyke:</i> A structure in the creek to divert some of the high-water flow or debris (1).	<i>Digue de dérivation / déviation:</i> Digue construite obliquement dans le lit d'un torrent et destinée à dévier les laves torrentielles et les crues (1).	<i>Ablenkdam, Leitdam:</i> Hydraulisches Bauwerk zur Ableitung von Wasser (3).
<i>Dyke, Levee, Training wall:</i> Structure built parallel to channel banks to limit flooding potential.	<i>Digue longitudinale:</i> Ouvrage parallèle à l'axe d'un cours d'eau ayant pour objet de limiter le débordement par-dessus les berges.	<i>Deich, Längsdamm:</i> Länglicher Damm, der parallel zu einem Fließgewässer als Hochwasserschutzmaßnahme gebaut ist.

Table 2. (Continued)

English terms, Synonym, Definition (source)	Termes français, Synonyme, Définition (source)	Deutsche begriffe, Synonym, Definition (quellen)
<i>Drainage</i> : Process of removing water from slopes, hillsides, i.e. topography with relief, to stabilize it or protect crops (1).	<i>Drainage</i> : Collecte et évacuation hors d'une zone menacée des eaux excédentaires imprégnant une portion de versant au détriment de sa stabilité ou de ses cultures (1).	<i>Entwässerung</i> : Überbegriff für die Abführung von Wasser.
<i>Drainage basin, Watershed, Catchment</i> : The whole area having a common outlet for its surface runoff and groundwater flows (1).	<i>Bassin versant</i> : Zone d'alimentation des écoulements souterrains et de ruissellement drainé par un exutoire donné.	<i>Einzugsgebiet</i> : Abgegrenztes Gebiet, aus dem sämtliches Wasser an einem Punkt stammt (4).
<i>Dry stone apron, Artificial armoring</i> : Protective lining or coatings for channels, below structures and streambanks, either stones, concrete or gabion-baskets (adapted from 1).	<i>Pavage artificiel, Radier en enrochements/pierres de taille</i> : Revêtement du lit d'un torrent en pierres brutes ou taillées, béton armé ou gabions.	<i>Künstliche Deckschicht</i> : Manuel (künstlich) gestaltete Deckschicht eines Flussbetts, die aus Grobgestein besteht, welches nicht durch den Abfluss mobilisiert werden kann.
<i>Equilibrium bed slope / profile</i> : The slope or the profile of a channel which attains equilibrium, where aggradation and erosion are in balance (adapted from 1).	<i>Pente de compensation ou d'équilibre</i> : Pente d'un lit torrentiel permettant d'équilibrer dépôt et érosion liées aux apports amont (adapté de 1).	<i>Gleichgewichtsgefälle</i> : Stabiles Sohlgefälle, dass sich einstellt, wenn die Geschiebezufuhr und die Geschiebetransportkapazität eines Flussabschnitts gleich groß sind.
<i>Floodplain</i> : The land area under water during floods (1)	<i>Lit majeur, Plaine d'inondation</i> : Espace recouvert par les hautes eaux.	<i>Flussaue</i> : Angrenzende Flächen oberhalb des Flussbetts. Geprägt durch wechselnde Wasserführung (überschwemmt bei Hochwasser).
<i>Hazardous event/flood/level, Routine event/flood/level</i> : Events at which infrastructures and assets become endangered, usually close to the bank-full discharge. Torrential control structures should generally be activated when the hazardous flood discharge is exceeded (Schwindt et al., 2018a).	<i>Évènement/crue/cote de plein bord, de limite de débordement</i> : Événements générant des niveaux d'écoulement atteignant la limite haute des berges et donc la limite de début des inondations, généralement crue à partir de laquelle les ouvrages de protection doivent commencer à fonctionner.	<i>Sicherheitsabfluss</i> : Entspricht dem Hochwasserabfluss, ab dem Schutzbauwerke aktiviert werden müssen um Infrastruktur zu schützen (6)
<i>Landslide</i> : It is the movement of a mass of rock, debris, or earth down a slope (USGS definition).	<i>Glissement de terrain</i> : Déplacement d'une masse de terrain par glissement sur une pente sous l'action de la pesanteur (1).	<i>Rutschung</i> : Plötzliches Abgleiten von Hängen oder Böschungen.
<i>Log jam, Large wood jam, Driftwood accumulation</i> : Accumulation of woody debris that partly or completely blocks the flow of water in a streambed, channel or structure.	<i>Embâcle, Accumulation de flottants</i> : Obstruction partielle ou totale de l'écoulement par accumulation de matériaux flottants et de sédiment.	<i>Eisstau</i> : Rückstau gebildet durch Eisblöcke.
<i>Morphologically significant flood</i> : Event generating non-negligible geomorphological changes of the bed due to sediment transport.	<i>Crue morphogène</i> : Crue générant des modifications non négligeables de la morphologie du lit par transport sédimentaire.	<i>Bettbildendes Hochwasser</i> : Entspricht dem Hochwasserabfluss, der die <i>Deckschicht</i> eines Flussbetts aufreißen und umbilden kann.
<i>Mountain river, Steep mountain creek, Torrent</i> : A mountain stream which is prone to flood, debris flood and debris flow.	<i>Torrent</i> : Petit cours d'eau de montagne, temporaire ou permanent, à forte pente et à crues violentes et subites, au débit liquide et solide très variable, subissant épisodiquement des crues morphogènes majeures (1).	<i>Wildbach</i> Steiler Bach in Gebirgsregionen mit einem Sohlgefälle von mehr als 0.2 % (9).

Table 2. (Continued)

English terms, Synonym, Definition (source)	Termes français, Synonyme, Définition (source)	Deutsche begriffe, Synonym, Definition (quellen)
<i>Mud flow, Hyper-concentrated flow:</i> Very muddy debris flow-like event involving significantly greater water content relative to the source material (Hungar et al., 2014).	<i>Coulée boueuse, Lave torrentielle boueuse:</i> lave torrentielle constitué d'une part importante de matériaux terreux.	<i>SchlammLawine:</i> Ähnlich einem Murgang.
<i>Natural channel bed armoring, Natural bedload pavement:</i> The coarse stone channel bed pavement where arrangement of bedload particles due to natural sorting leaves a pavement of coarser size (adapted from 1).	<i>Pavage naturel:</i> Consolidation naturelle du lit d'un torrent résultant d'un arrangement par le courant des matériaux grossiers arrangés conjointement en surface, les matériaux fins ayant été entraînés (adapté de 1).	<i>Natürliche Deckschicht:</i> Grobmaterial eines Flussbetts, dass nur durch <i>bettbildende Hochwasser</i> mobilisiert werden kann. Natürliche Deckschichten treten typischerweise in Flüssen mit regelmäßigem Abfluss und regelmäßigen kleineren Hochwassern auf.
<i>Open check dam, Debris retention basin/structure, sediment trap, Torrential barrier, SABO dam, Permeable check dam:</i> A dam constructed with large openings so as to retain only large woods, larger debris and the largest bedload, for the most part (1).	<i>Plage de dépôt, Dépotoir, Barrage filtrant.</i> Barrage muni de larges ouvertures permettant de ne retenir que les matériaux grossiers et le bois d'embâcle (1).	<i>Geschiebesammler:</i> Dolensperre mit großen Öffnungen für den Rückhalt von Grobmaterial (2).
<i>Retention check dam:</i> Check dam whose function is to definitively trap a maximum amount of sediment in its backfilling reach (Piton et al., 2017).	<i>Barrage de rétention, Barrage de retenue sédimentaire:</i> Barrage bâti spécifiquement pour piéger définitivement un volume maximum de sédiments dans sa zone d'atterrissement.	<i>Rückhaltesperre:</i> Dient dem Rückhalt von Sediment oder Schwemmholz bei Hochwasser (2)
<i>Retention basin, Debris-flood retention structure, Flood control dam:</i> Dry dam or similar structure designed to retain water and debris in order of reducing the peak flow during a flood event.	<i>Bassin de rétention, Barrage écrêteur de crue:</i> Bassin qui vise à stocker, temporairement un certain volume d'eau, de sédiments et de flottants, de façon à diminuer le débit de pointe de la crue aval.	<i>Rückhaltebecken:</i> Trockendamm für den Rückhalt von Geschiebespitzenabflüssen und Murgängen.
<i>Rill erosion:</i> Small cut into a slope caused by surface runoff (1).	<i>Griffe d'érosion:</i> Incision peu profonde provoquée par le ruissellement; première phase de l'érosion linéaire (1).	<i>Rillenerosion:</i> Erosionsrillen (Furchen) entstehen durch abfließendes Wasser (1).
<i>Riprap:</i> Large rock, or other material, used to armor shorelines, streambeds, bridge abutments, pilings and other structures against scour and erosion.	<i>Enrochements:</i> Protection d'un ouvrage ou d'une berge contre l'affouillement par accumulation artificielle de gros blocs (1).	<i>Blocksatz:</i> Meist unbearbeitete, grobe Steinblöcke zur Sohl- oder Uferstabilisierung (10)
<i>Safety check event/flood, maximum water level:</i> Events/floods that can be transferred by the structure and its spillway under the maximum water level, i.e., with sufficient freeboard to consider the structure failure very unlikely (CFBR, 2013).	<i>Evènement/crue/cote de sureté:</i> Evènements/crués qui peuvent être transférées par un ouvrage et ses évacuateurs de crues sous la cote de sureté, i.e., avec une revanche suffisante pour considérer la ruine de l'ouvrage très improbable.	<i>Höchsthochwasser:</i> Das größte Hochwasser, dem ein Bauwerk standhalten muss unter Berücksichtigung eines Freibords (vertikaler Abstand zwischen dem Höchsthochwasserspiegel und der Oberkante des Bauwerks); siehe auch: "Höchstes jemals gemessenes Hochwasser" HHQ oder "Rechnerisch höchster Hochwasserabfluss" RHHQ.
<i>Siltation slope:</i> The predictable angle of slope for siltation, for example for the sediment deposition behind a structure (1).	<i>Pente d'atterrissement:</i> Pente prévisible d'un dépôt de matériaux dans une section donnée du lit d'un torrent, par exemple en amont d'un ouvrage (1).	<i>Verlandungsgefälle:</i> Sohlgefälle, dass sich oberhalb eines Querbauwerks (oder natürlichem Abflusshindernis) einstellt (3).

Table 2. (Continued)

English terms, Synonym, Definition (source)	Termes français, Synonyme, Définition (source)	Deutsche begriffe, Synonym, Definition (quellen)
<i>Sluice, slot, slit</i> : An opening in a structure which may be regulated to allow water passage (adapted from 1).	<i>Pertuis</i> : ouverture ménagée dans le corps d'un barrage pour assurer le passage des eaux et des matériaux charriés de petite dimension (adapté de 1).	<i>Durchlass, Dole</i> : Öffnung in einer Wildbach- oder Rückhaltesperre (2).
<i>Stone masonry wall</i> : A stone wall having a masonry work with mortar (1).	<i>Mur/perré en maçonnerie de mortier</i> : Ouvrage en maçonnerie de pierres liées au mortier (1).	<i>Zementmörtelmauer</i> : Mit Zement verstärktes Mauerwerk.
<i>Stone-pitching, Boulder-size stone wall</i> : Stonework made of very large (boulder-size) rocks which have not been cut to shape (1).	<i>Mur/perré de maçonnerie cyclopéenne</i> : Ouvrage constitué de blocs de forte taille non taillés (1).	<i>Zyklopenmauer</i> : Natursteinmauer bestehend aus unregelmäßig großen und unterschiedlich geformten Blöcken, die sorgfältig angeordnet sind (7).
<i>Stone wall, Rustic stone wall</i> : Stone wall construction, stacking without mortar or other binding material (1).	<i>Mur/perré en pierres sèches</i> : Ouvrage constitué de pierres assemblées à la main sans mortier (1).	<i>Trockenmauer</i> : Naturstein bestehend aus unregelmäßigen Blöcken, die lokal verfügbar sind (10).
<i>Structural bedload</i> : bedload transport associated with bed remobilization (Piton and Recking, 2017).	<i>Structural bedload</i> : transport par charriage associé à la remobilisation du lit.	<i>Sohlgeschiebe</i> : Transportiertes Geschiebes, dass der Gerinnesohle entstammt.
<i>Structure by-passing, Outflanking</i> : During a flood, flows pass beyond the limits of a structure, causing erosion usually on the side (adapted from FEMA).	<i>Contournement</i> : Érosion des berges latérales d'un ouvrage résultant en le passage des écoulements sur le côté plutôt que sur l'ouvrage.	<i>Seitenerosion</i> : Aushöhlung der seitlichen Verankerung einer Bauwerks durch Hochwasser.
<i>Toe scouring, Under-mining, Plunge pool action</i> : Degradation of the streambed at the foot of the structure due to the water and chute action.	<i>Affouillement, Sous-cavage</i> : Creusement du lit pied d'un ouvrage par l'effet de la chute d'eau sur l'ouvrage.	<i>Kolk / Auskolkung</i> : Erosion am Fuße eines Bauwerks (2).
<i>Torrent control, Steep creek mitigation</i> : Various engineering and biological measures carried out in a steep mountain creek and its watershed to control the processes and therefore provide protection against erosion, sedimentation and runoff (adapted from 1).	<i>Correction d'un torrent</i> : Ensemble des travaux ayant pour objet, dans un bassin versant torrentiel, de réduire, en luttant contre l'érosion des versants et des berges, la production d'alluvions, et d'en contrôler la circulation et le dépôt.	<i>Flusskorrektur</i> : Oberbegriff für technische Eingriffe in Wildbächen und Flüssen.
<i>Travelling bedload</i> : Bedload transport rapidly transported in a paved reach, with little or no local morphological effect (Piton and Recking, 2017)	<i>Travelling bedload</i> : transport par charriage traversant un tronçon pavé avec un effet morphogène local nul ou marginal.	<i>Laufgeschiebe</i> : Transportiertes Geschiebe, dass sich nicht ablagert und von seitlichen Zuflüssen / Sedimentablagerungen genährt wird
<i>Weir, Sill, Grade control structure, Chute structure</i> : A low submerged structure built across the creek to control erosion of the channel bed. A weir is usually described for small barrier for diverting or controlling water (adapted from 1).	<i>Seuil</i> : barrage de correction torrentielle de faible hauteur, éventuellement calée au niveau du fond du lit pour éviter de futures incisions (adapté de 1).	<i>Schwelle</i> : Niedriges Querbauwerk zur Sohlstabilisierung. Wegen der Unterbrechung der Gerinnekontinuität sollten Blockrampen bevorzugt eingesetzt werden (3).
<i>Woody debris</i> : Logs, whole trees, and other timber debris transported by floods, which can form into a log jam (1).	<i>Bois d'embâcle, Gros bois flottants</i> : Éléments ligneux transportés par les hautes eaux susceptibles de provoquer des embâcles, accumulations.	<i>Schwemmholz</i> : Holz, dass von der Strömung eines Fließgewässers mitgerissen wird. Umschließt Bäume, einzelne Stämme, Äste und Wurzeln.

Référence : (1) FAO, 1981; (2) Bergmeister et al., 2009; (3) Willi et al., 2001; (4) DIN 4049-1, 1992; (5) Einstein, 1950; (6) Schwindt et al., 2018b; (7) Spycher, 2000; (8) Tamagni, 2013; (9) Wohl, 2000; (10) Zeh, 2007.

3. Discussion and conclusion

Table 2 intends to capture the most common synonyms, definitions and translations for each term presented in this lexicon. However, not everyone will accept the chosen terms and their prioritization in this lexicon. There are simply too many different definitions and possible uses of the same terms. As an example, one term can refer to slightly different structure types in different countries. Discussion and feedback are encouraged to improve this lexicon. More terms should be added and could be translated into other languages. Finally, an online storage platform, for a growing lexicon, should be planned to ensure easy access by all interested party. Our references include such pertinent online dictionaries as, for instance, the Swiss “Termdat” database (Swiss Federal Administration, 2018).

Standardization and definition of technical terms commonly used in the fields of fluvial geomorphology and steep mountain creek design and risk mitigation is required. This lexicon is a first step in that direction, with some of the most commonly used terms included, and it may provide a good base for a long-term project that could include more terms in more languages.

Acknowledgements

The work of Guillaume Piton was funded by the H2020 project NAIAD [grant no. 730497] from the European Union’s Horizon 2020 research and innovation program. The authors would like to thank an anonymous reviewer and Jeffrey Keaton for their review comments.

References

- Bergmeister, K., Suda, J., Hübl, J., and Rudolf-Miklau, F., 2009, *Schutzbauwerke gegen Wildbachgefahren: Grundlagen, Entwurf und Bemessung, Beispiele*: Ernst & Sohn, Berlin, Germany, 211 p.
- CFBR, 2013, *Recommandations pour le dimensionnement des évacuateurs de crues de barrages (Dam spillway design guidelines)*: Comité Français des Barrages et Réservoirs, Recommandations du groupe de travail sur les évacuateurs de crues, Le Bourget du Lac, France 326p.
- DIN 4049-1, 1992, *Hydrology: basic terms*: Deutsches Institut für Normung E. V. (German National Standard), Standard 1992-12.
- Einstein, H.A., 1950, *The Bed-Load Function for Sediment Transport in Open Channel Flows*: Washington, D.C., Technical Bulletin 1026, USDA Soil Conservation Service, 71 p.
- FAO, 1981, *Torrent control terminology - French, German, English, Spanish, Italian*: Food and Agriculture organization of the United Nations, FAO Conservation guide 6, Rome, Italy. 156p.
- Hickin, E.J., 1995, *River Geomorphology*: Chichester, England, International Association of Geomorphologists, no. 2, , Wiley, 233 p.
- Hungr, O., Leroueil, S., and Picarelli, L., 2014, *The Varnes classification of landslide types, an update*: *Landslides* 11, p. 167–194, doi:10.1007/s10346-013-0436-y.
- Moase, E.E., 2017, *Guidance for debris-flow and debris-flood mitigation design in Canada* [Msc Thesis]: Vancouver, Simon Fraser University, 227 p.
- Piton, G., Carlados, S., Recking, A., Liebault, F., Tacnet, J.M., Kuss, D., Quefféléan, Y., and Marco, O., 2017, *Why do we build check dams in Alpine streams? An historical perspective from the French experience*: *Earth Surface Processes and Landforms* 42, p. 91–108, doi:10.1002/esp.3967.
- Piton, G., and Recking, A., 2017, *The concept of travelling bedload and its consequences for bedload computation of mountain streams*: *Earth Surface Processes and Landforms* 42, p. 1505–1519, doi:10.1002/esp.4105.
- Schwindt, S., Franca, M.J., Reffo, A., and Schleiss, A.J., 2018a, *Sediment traps with guiding channel and hybrid check dams improve controlled sediment retention: Natural Hazards and Earth System Science* 18, p. 647–668, doi:10.5194/nhess-18-647-2018.
- Schwindt, S., Franca, M.J., and Schleiss, A.J., 2018b, *Teildurchgängige Geschiebesammler für sicheren Rückhalt [Partially permeable sediment traps for safe bed load retention]*: *Wasserwirtschaft* 108, p. 18–23, doi:10.1007/s35147-018-0026-y.
- Spycher, H., 2000, *Die Ausgrabungen Solothurn / «Roter Turm» von 1960/1961*: *ADSO* 5, p. 7–21.
- Swiss Federal Administration, 2018, *Termdat*: Bern, Switzerland.
- Tamagni, S., 2013, *Unstructured block ramps*: Zürich, Switzerland, Laboratory of Hydraulics, Hydrology and Glaciology (VAW), VAW Mitteilung Nr. 223, p.271
- Willi, H.P., Jordan, J.P., Roth, U., and Frei, B., 2001, *Hochwasserschutz an Fließgewässern [Flood protection at rivers]*: Bern, Switzerland, Federal Office for Water and Geology (FOWG), 72 p.
- Wohl, E., 2000, *Mountain rivers*: Washington, D.C., Water Resources Monograph, Book 14, American Geophysical Union, 320 p.
- Zeh, H., 2007, *Soil Bioengineering - Construction Type Manual*: Zürich, Switzerland, European Federation for Soil Bioengineering.

Debris flows in southeast Brazil: susceptibility assessment for watersheds and vulnerability assessment of buildings

Bianca Carvalho Vieira*^a, Luzia Matos de Souza^a, Ana Luiza Alcalde^a,
Vivian Cristina Dias^a, Carlos Bateira^b, Tiago Damas Martins^c

^a University of São Paulo, Avenida Professor Lineu Prestes, 338, São Paulo, 05508000, Brazil

^b Riskam, CEG, ULisboa/FLUP, UP

^c Federal University of São Paulo, Avenida Jacu-Pêssego, 2630, São Paulo, 08260001, Brazil

Abstract

Debris flows is one of the primary mass movement processes in the Serra do Mar, a system of escarpments and mountains that stretches more than 1,500 km in south and southeast of Brazil. Usually, these processes cause environmental and social damages. On March 1967 only one small city was affected by 947 mm, with 115 mm on the 17th and 420 mm on the 18th and triggered numerous landslides and debris flows with the great mobilization of material, reaching a 15 km radius, causing approximately 440 fatalities. Approximately 50 years later, another city, located in the same mountain range, was affected by cumulative rainfall of 150 mm/6 hours causing deaths and houses destroyed and structural damage to bridges. Thus, the objective of this work was to evaluate of vulnerability to debris flows in some watersheds located in two cities of the Serra do Mar affected in 1967 and 2014, respectively. For this purpose, some procedures were defined: (a) the evaluation of the vulnerability of buildings, considered, for instance, the number of floors, the presence of broad terraces, large doors, windows and high walls surrounding the buildings. (b) elaboration of indicators and maps of vulnerability that consider the hazard properties, the exposure, preparedness and prevention of elements at risk; (c) elaboration of indicators and map of risk perception. The results show 38 areas with vulnerable construction to debris flows: 8%-high; 70%-medium; 22%-low vulnerability of buildings. As preliminary results, an inventory of damages was provided from the sectors of the affected districts and preliminary mapping of the debris flow.

Keywords: Serra do Mar, Brazil, Morphometric Parameters, PTVA, Vulnerability

1. Introduction

Debris flows is one of the primary mass movement processes in the Serra do Mar, associated with the rainy season between December and March when 60% of the annual average precipitation of 3,300 mm occurs. The Serra do Mar is a mountain range that extends for about 1,500 km along the south and southeast coast of Brazil. The region has great economic importance since it is crossed by the major land transportation network that connects the city of São Paulo to other large metropolitan areas, as well as to the port of Santos. According to Almeida (1953), the Serra do Mar is one of the most relevant orographic features in the Atlantic coast of the South American continent, and it is known for having the most “Tormented” relief in Brazil due to its steep slopes, tectonic processes, and faults. It is an outstanding feature in the Brazilian terrain for its grand geomorphological features and its role on human occupation from the colonial period to present. Since the 1960s, catastrophic important events were recorded, resulting in millions of dollars in economic loss, thousands of fatalities and homelessness. Several events are remarkable in Brazilian history, particularly in the years 1966, 1967, 1985, 1988, 1995, 2008, 2009, 2010, 2011 and 2014 (Table 1). Thus, the objective of this work was to evaluate the vulnerability of debris flows in some watersheds located in two cities of the

* Corresponding author e-mail address: biancacv@usp.br

Serra do Mar, affected in 1967 and 2014, respectively.

Table 1: Occurrences of mass movements (landslides and debris flows) in the Serra do Mar, highlighting the events studied in this paper.

Year	LOCATION (STATE)	Rain	Area (Km ²)/Speed (m/s)/Volume (m ³)	LOSSES (n° deaths); other damage
1928	Monte Serrate (SP)	649 mm/Jan and 564 mm/Feb.	Vol: > 1x10 ⁵	(60); destruction of Santa Casa
1958	Monte Serrate (SP)	373 mm/24 h	-	(43); destruction of 100 houses
1966	Rio de Janeiro (RJ)	> 250 mm/<12 h	-	(>230)
1967	Serra das Araras (RJ)	275 mm/24 h	Vol: > 10x10 ⁶	(1200); > 100 houses destroyed, damage to highways, destruction of the hydroelectric plant
	Caraguatatuba (SP)	580 mm/48 h	Vol: > 7.6x10 ⁶	(120); 400 houses destroyed, damage to highways
1971	Santos-Jundiá Railway (SP)	-	Vol: 1x10 ⁵ (estimated)	Steel viaduct destroyed, works for slope stabilization
1974	Tubarão (SP)	394 mm/ 72 h 742 mm/16 days	-	(195); urban area flooded
1975-1976	Grota Funda (SP)	-	S:8.4/Vol: > 10x10 ⁶	Pillars of railway bridge damaged
1976	Cachoeira River (SP)	276 mm/24 h	A:4/Vol: 1x10 ⁵	Flooding for industries, two rock-filled and earth-filled dams was built
1985	Cubatão (SP)	380 mm/48 h	-	(10)
1988	Petrópolis (RJ)	145 mm/24 h	-	(171); 5,000 displaced, 1,100 homes interdicted
	Rio de Janeiro (RJ)	-	-	(~300); destruction of dozens of homes
1994	Cubatão (SP)	60 mm/24 h	A:2.64/S:10 Vol: 3x10 ⁵	Flooding of Petrobrás Refinery, interruption of operations and clean-up (US\$44 mil)
1996	Cubatão (SP)	-	A: 2.64/S: > 10 Vol.: 1.6x10 ⁴	Clean-up works
	Oswaldo Cruz Highway (SP)	10 mm/10 min 442 mm/13 h	-	Highway damaged, works for slope stabilization, water capture station affected
	Papagaio River Basin (RJ)	202 mm/24 h	A: 2.13/Vol.: 9x10 ⁴	(1); hundreds of houses destroyed
	Quitite River Basin (RJ)	202 mm/24 h	A: 2.53 Vol.: 4x10 ⁴	houses destroyed
	Rio de Janeiro (RJ)	301 mm/72 h	-	(54)
1999	Anchieta Highway (SP)	128 mm/24 h 274 mm/72 h	Vol.:3x10 ⁵	200 m of the affected area, traffic stopped for several weeks, water capture station affected
2001	Rio de Janeiro, Petrópolis (RJ)	300 mm/24 h	-	(40);164 wounded
2002	Petrópolis (RJ)	-	-	(88)
2008	Santa Catarina (SC)	720 mm/72 h	-	(135); 80,000 displaced/homeless, 85 municipalities in state of emergency
2010	Angra dos Reis (RJ)	143 mm/24 h	-	(53)
	Rio de Janeiro	120 mm/24 h	Vol: 680 m ³	(253) 1,410 displaced, 368 homeless
2011	Rio de Janeiro	-	-	-
	Córrego Dantas (stream) (RJ)	269 mm/72 h	A: 52	(429); 3,220 disappeared, 2,031 homeless, displaced, and many economic losses,
	Córrego Vieira (stream) (RJ)	269 mm/72 h	A: 33	
	Córrego da Posse (stream) (RJ)	92.6 mm/72 h	A: 12	(343); 9,110 disappeared, homeless, 6,727 displaced and numerous losses
	Córrego do Cuiabá (stream) (RJ)	35.8 mm/72 h	A: 36	(71); 6,223 disappeared, homeless, 191 displaced and numerous losses
Antonina (PR)	-	-	(4)	
2013	Córrego do Pilões (stream) (SP)	23 mm/10 min 115 mm/1 h 273 mm/09 h	-	Damage to the water reservoir, chlorine cylinders, and road service station destroyed
	Petrópolis (RJ)	-	-	(31); 4,000 displaced
2014	Itaóca	150 mm/6 hours	-	Structural damage to bridges, destroyed houses, two disappeared and 25 death

Source: adapted from Vieira e Gramani (2015). A = Area (Km²), S = Speed (m/s) and Vol = Volume (m³)

2. Methods

We selected eight basins in two areas of the Serra do Mar affected by intense rainfall, triggering shallow landslides, debris flows, mudflows, and flash floods. Area 1 (A1) is in the northern portion of the Serra do Mar and Area 2 (A2) south of this escarpment in the State of São Paulo (Fig. 1). In A1 five basins were selected (Massaguaçu, Guaxinduba, Santo Antonio, Ribeirão da Aldeia, and Pau d'alho) with and without records deposits of the debris flows generated in 1967. In this area the mass movements were triggered by intense rainfall events during the summer of 1966/1967 (Fig. 2); rain occurred almost every day that summer and reached 945.6 mm by March 1967. The 535-mm rainfall recorded on the 17th and 18th of that month as responsible for the occurrence of hundreds of shallow landslides and debris flows; these events left their mark on the landscape and can still be seen today in the extensive deep scars on the slopes and large deposits of blocks in the slope ruptures (De Ploey and Cruz 1979).

Approximately 50 years later, on 2014, another city, Itaóca, located in the same orographic feature was affected by cumulative rainfall of 150 mm/6 hours causing deaths with houses destroyed and structural damage to bridges (Fig. 2). In this area we selected three basins more: two basins with records of landslides and debris flows (Palmital 1 and Gurutuba) and a third basin, with similar morphological characteristics, on the other hand, without any record of any landslide or debris flows registered.

It was evaluated the influence of all 8 morphometric parameters to debris flows in the 8 basins, however in only one of them, the Guaxinduba, it was possible to estimate the vulnerability of the constructions to debris flows using the PTVA method.

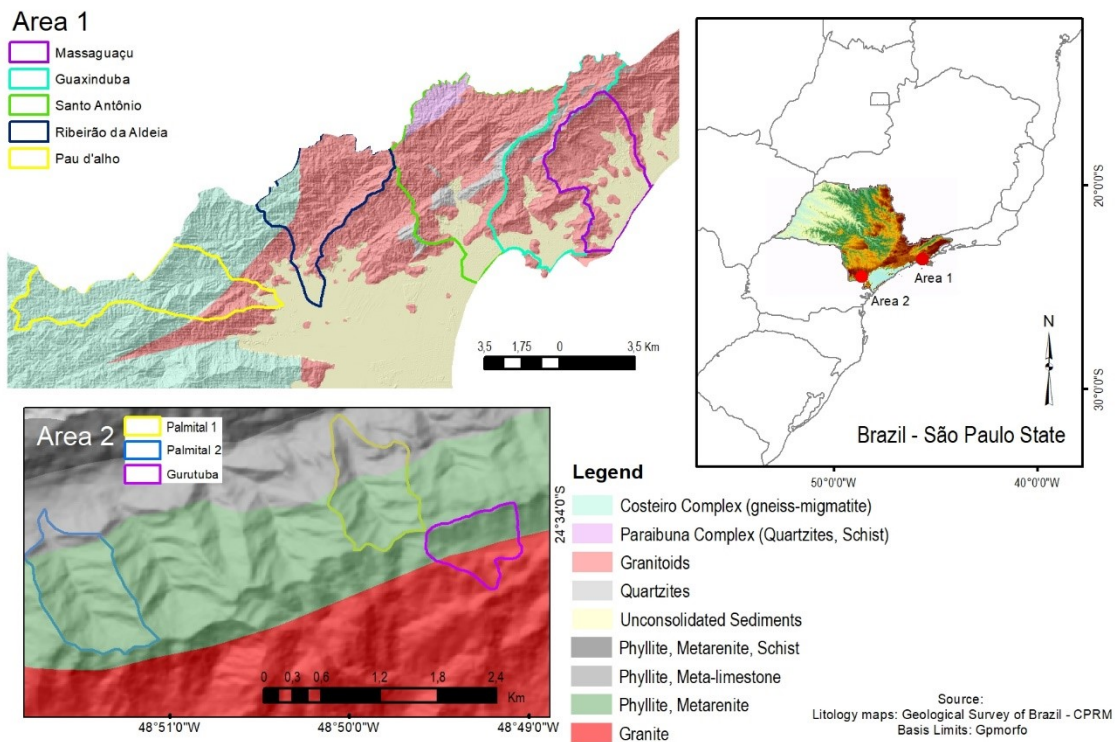


Fig. 1. Location of the eight basins in the Serra do Mar, State of São Paulo.



Fig. 2. (A, B) Mass movements in the Serra do Mar, Caraguatatuba, on March 1967 (C, D) and Itaóca municipality on January 2014. Source: Marcelo Gramani; Municipal Archive Caraguatatuba

2.1 Morphometric parameters

Morphometric parameters have been used by some authors to evaluate the susceptibility of basins to debris flows, because some of these parameters, like drainage channel and slope curvature, sediment availability, shape and area of the basin can influence in the dynamics of the debris flows, including their range, the disposal of the deposits and their magnitude of destruction.

The morphometric parameters used (Drainage Density; Ruggedness Index; Circularity Index; Relief Ratio; Drainage Hierarchy; Slope Mean Channel; Curvature Concave) were defined from literature (Augusto Filho, 1993; De Scally et al., 2001; Jakob, 2005; Chen and Yu, 2011; Dias et al., 2016). The mapping of those parameters derived from two sets of elevation data, one a topographic map (1:10,000 scale) and SRTM (1 arc-sec). The litho structural data were obtained from the geologic map from Brazilian's Geologic Service (Fig. 2).

The debris flows mapping was carried out using the research made by Cruz (1974) as a base, interpretation of aerial photographs in scale 1:25.000 and satellite images, fieldwork, where were collected the characteristics of the deposits. The information was spatialized using the location and characteristics of the deposits, being elaborated a classification of the deposits based in boulders size - "Small, Medium, Large and Very Large," based on the classification proposed by Stoffel (2010). For the delimitation of the deposits, we made a 50meters buffer in the drainage, relating the location of the boulders with the drainages that could have transported and deposited the boulders. We also used the altimetry where the boulders are located and its proximity to slopes as criteria for the mapping.

2.2 PTVA Method

For the vulnerability, the PTVA (Papathoma Tsunami Vulnerability Assessment) method developed by Papathoma-Köhle (2016) was used. Then, two classes of criterion were selected: the constructive itself (building material, the presence of high walls, number of floors, the presence of large doors and windows) and the surrounding of the

constructions (presence of vacant lots or wide-open area, the presence of blocks and their dimensions and proximity of buildings). Subsequently, the method of Multicriteria Evaluation (Voogd, 1983) was applied using a simple linear transformation to count each criterion and assign the weights. The weights were organized according to their importance for the application of the mitigation measures by the public power, as stated by Papathoma and Dominey - Howes (2003). This is the following assignment: Construction material (weight 7), High walls (weight 6), Presence of large / wide doors and windows (weight 5), Large land / wasteland (weight 4), Number of floors, Presence of blocks (weight 2) and Size of blocks (weight 1). In front of the counting and the assigning of weights, the vulnerability was calculated with the sum of the multiplication of each weight by the standardized count of each criterion. Thus, the final vulnerability was divided by the sum of the weights to be expressed in the scale of 0 to 1.

3. Results

3.1 Susceptibility / Morphometric Parameters

Considering the morphometric parameters and the morphology of debris flows deposits, all eight basins presented favorable conditions for debris flows (Table 1). There were high values of Drainage Density (Dd), mainly the Area 2 (A2) and the Guaxinduba basin of Area 1 (A1), where large blocks were also identified and the highest values of the Roughness Index (Ri), indicating its high sediment yield potential, along with the Palmital 1 and Gurutuba (A2) basins.

Table 1: Morphometric Parameters of the five basins in Area 1 and three basins in Area 2, with predominant lithology. Legend: Area (km²); Drainage Density (Dd) (km/km²); Ruggedness Index (Ri) (m/km); Circularity Index (Ci) (km²/km²); Relief Ratio (Rr); Drainage Hierarchy (Dh); Slope Mean Channel (Smc); Cc (Curvature Concave). In highlight = Critical values.

Area	Basin	Area	Dd	Ri	Ci	Rr	Dh	Smc	Cc	Lithology (>50%)
1	Massaguaçu	20,5	1,7	1,6	0,55	132	3°	10°	-	Granitoids
	Guaxinduba	24,1	3,4	3,4	0,25	78	4°	10°	26%	Granitoids
	Aldeia	22,3	2,4	2,6	0,43	112	4°	11°	30%	Granitoids
	S. Antônio	40,0	2,2	2,0	0,43	94	5°	11°	20%	Granitoids Quartzites
	Pau d'alho	23,0	2,2	2,2	0,28	91	4°	14°	29%	Complex (gneiss-migmatite)
2	Palmital 1	0,8	7,7	3,8	0,61	299	3°	22°	25%	Phyllite, Metarenite
	Palmital 2	1,0	5,2	2,7	0,62	252	3°	23°	30%	Phyllite, Metarenite
	Gurutuba	0,5	5,1	8,7	0,42	170	2°	29°	27%	Phyllite, Metarenite /Granite

According to the Circularity Index (Ci), all basins have a more elongated shape (Ci <0.5), except Palmital 1 and Palmital 2, where the large and extra-large rock block deposits were identified, especially the Guaxinduba and Pau d'alho basins (Fig. 3B). According to literature, this elongated shape is more favorable to deflagration of debris flows in steep landscaping slopes (Crozier, 1986). However, two basins (Santo Antonio and Aldeia) presented a circular shape as well large deposits related to previous debris flows (Fig.3A). Although all basins show high values of Relief Ratio (Rr), indicating a significant potential of transport and flows, those with higher volumes of deposits had the lowest values of this index (Santo Antonio, Pau d'alho and Guaxinduba).

The Gurutuba basin (A2) has critical values in all morphometric parameters, where, in its lower portion, the large debris flows with large size deposits were mapped and the high destructive power (Fig. 3) and rapid flash floods that reached elevations between 1.90 and 2.60 m, destroying about 15 buildings.

The Palmital 1 and Palmital 2 basin, which also present critical values in all morphometric parameters, are tributaries of the Palmital river basin, wherein 2014, recorded mudflows and flash floods. All these basins drain into

neighborhoods and districts of two cities (Itaóca and Apiaí) with urban and rural occupations, crops fields and forest.

In 2014 this area was affected by debris flows, mudflows and flash floods that destroyed more than 500 buildings, 300 people homeless and 25 people killed (Gramani and Arduin, 2015, Matos et al., 2016).



Fig. 3. Deposits in Santo Antônio basin (A), Pau d'alto basin (B), mudflows and flash floods in Itaóca city from 2014. Source: Itaoca municipality.

3.2 Vulnerability

Regarding the vulnerability 38 part of the basin were mapped (Fig. 4) with high (8%), average (70%) and low (22%) vulnerability and with a variation of 30% between the lowest vulnerability and the highest one. The high vulnerabilities (76% to 85%) are concentrated in the northern and central portions. Mean vulnerabilities (66% to 75%) are predominant and well distributed, with low vulnerabilities (55% to 65%) concentrated in the central and southern portions.

There was a variation of about 30% of the lowest vulnerability (55%) and the highest vulnerability (83%), as a result of the variation in the conditions of the vulnerability criteria. Some criteria were more important for the increase of the final vulnerability, like lack of high walls involving the constructions, presence of blocks in the surroundings and proximity of the constructions mapped with open lands. On the other hand, other criteria contributed to the reduction of vulnerability: masonry constructions, distance from vacant lots such as fields or vacant lots and absence of previous blocks of races.

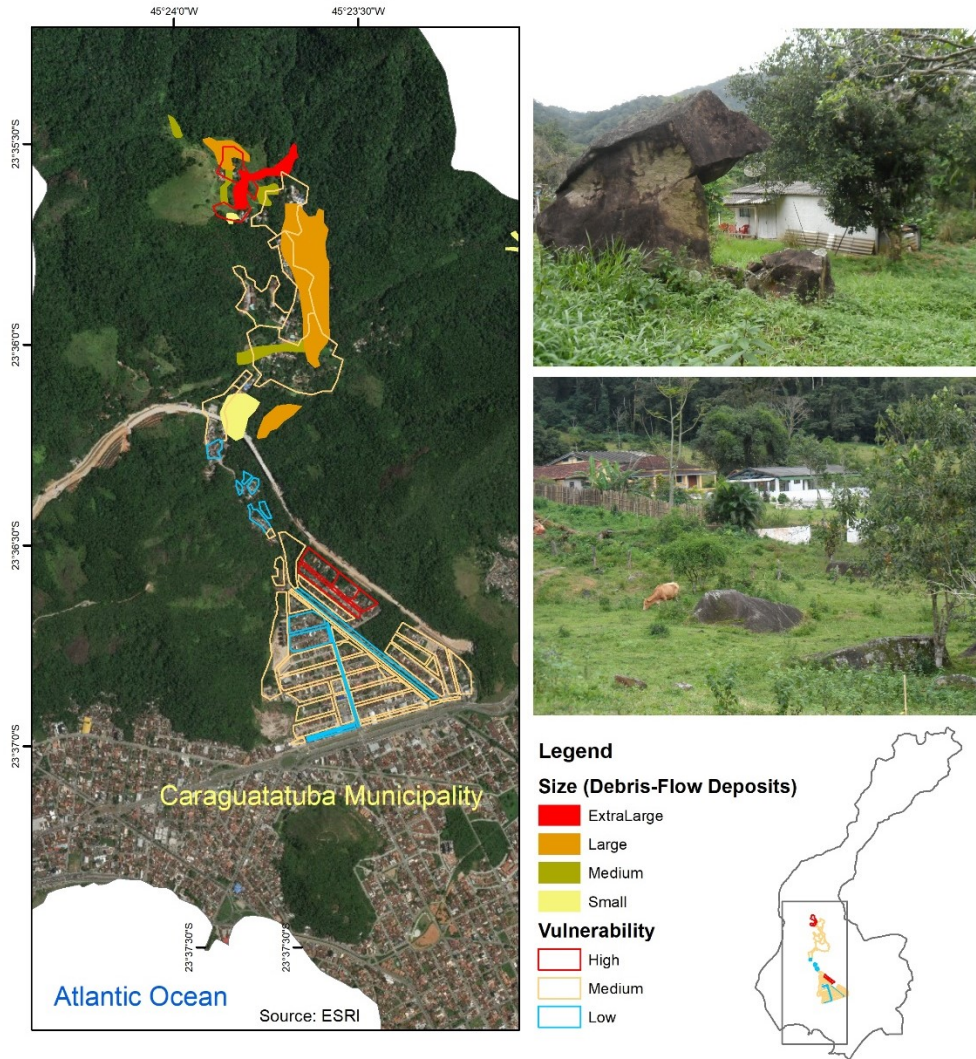


Fig. 4. Vulnerability map of buildings.

4. Conclusions

- No criterion was determinant in the final classification of the vulnerability and the result depends on the variation of a set of criteria that tends to increase or reduce the final vulnerability. In general, the condition of the constructions that most increased the vulnerability met the following criteria: 1) absence of high walls involving construction, 2) the presence of blocks in the surroundings, 3) proximity to buildings mapped with open land, and 4) buildings with only one floor
- There are still few studies on the spatialization, identification, and evaluation of the magnitude of debris flows in Brazil at basin scales. Thus, it is believed that these studies can contribute to future work that aims to identify the potential of watersheds in the generation of debris flows.
- It was not possible in this work to associate the susceptibility and the vulnerability for all analyzed basins. Future works will produce new maps of the deposits seeking to identify this association.

Acknowledgments

The authors thank the reviewers, the São Paulo Research Foundation (FAPESP), the Coordination for the Improvement of Higher Education Personnel (Capes) and Institute of Technological Research of the State of São Paulo (IPT) for partial financial support for this research and Graduate Program in Physical Geography, University of São Paulo.

References

- Almeida, F. F. M., 1953, Considerações sobre a geomorfogênese da Serra de Cubatão. Boletim Paulista de Geografia, São Paulo, v. 15, p. 3-17.
- Augusto Filho, O., 1993, O estudo das corridas de massa em regiões serranas tropicais: um exemplo de aplicação no município de Ubatuba, SP. Congr. Bras. Geol. Eng., 7, Poços de Caldas. ABGE. V2, p. 63 – 70.
- Chen, C.Y. e Yu, F. C., 2011, Morphometric analysis of debris flows and their source areas using GIS. *Geomorphology*, 129, 387 – 397.
- Crozier, M.J. 1986, Landslides: causes, consequences and environment. Croom Helm, 252p.
- Cruz, O., 1974, A Serra do Mar e o litoral na área de Caraguatuba – SP. Contribuição à geomorfologia litorânea tropical. Tese de Doutorado. IG – Série Teses e Monografias nº 11, 181p
- Cruz, O., 1990, Contribuição geomorfológica ao estudo de escarpas da Serra do Mar. *Revista do IG* 11, p. 9 – 20.
- De Ploey Y, Cruz O., 1979, Landslides in the Serra do Mar, Brazil. *Catena* 6: 111 -122p. DOI: 10.1016/0341-8162(79)90001-8
- De Scally, F., Slaymaker, O. e Owens, I., 2001, Morphometric controls and basin response in the Cascade Mountains. *Geografiska Annaler*, 83 A (3), p. 117 – 130.
- Dias, V. C., Vieira, B. C. e Gramani, M. F., 2016, Parâmetros morfológicos e morfométricos como indicadores da magnitude das corridas de detritos na Serra do Mar Paulista. *Confins [Online]*, 29, p. 1 – 18.
- Gramani, M. F.; Arduin, D. H., 2015, Morfologia da drenagem dos depósitos de debris flow em Itaóca, São Paulo. In: 15º Congresso Brasileiro de Geologia de Engenharia e Ambiental (CBGE), Bento Gonçalves (RS) ISBN: 078-85-7270-069. Anais, 10, p., 2015
- Jakob, M., 2005, Debris-flow hazard analysis. In: *Debris-flow hazards and related phenomena* (Eds. Jakob, M. and Hungr, O.) Springer, p. 442 – 474.
- Matos, L., Ferreira, C., Bateira, C., e Vieira, B., 2018. Avaliação das Construções Danificadas por Corridas de Detritos e Inundações Bruscas no Vale do Ribeira (SP) em 2014. *Revista Do Departamento De Geografia, (spe)*, 57-67. <https://doi.org/10.11606/rdg.v0ispe.144423>
- Papathoma, M., Dominey, H. D., Zong, Y., and Smith, D., 2003, Assessing Tsunami vulnerability, an example from Herakleio, Greece. *Natural Hazards and Earth System Sciences*, Vol. 3, 377–389, 2003.
- Papathoma-Köhle, M.: Vulnerability curves vs. vulnerability indicators: application of an indicator-based methodology for debris-flow hazards, 2016 *Nat. Hazards Earth Syst. Sci.*, 16, 1771-1790, <https://doi.org/10.5194/nhess-16-1771-2016>
- Stoffel, M., 2010, Magnitude-frequency relationships of debris Flow – A case study based on field survey and tree-ring records. *Geomorphology*, 116, p. 67 – 76.
- Vieira, B. C.; Gramani, M. F., 2015, Serra do Mar: the most “tormented” relief in Brazil. In: *Landscapes and Landforms of Brazil*, World Geomorphological Landscapes (Ed. Vieira, B. C.; Salgado, A. A. R. e Santos, L. J. C.). Springer, p. 285 – 297.
- Voogd, H. 1983, *Multicriteria Evaluation for Urban and Regional planning*. ISBN 085086 1063. Pion Limited, London p.357, 1983.

Complexity of a debris-flow system at Forest Falls, California

Kerry Cato^{a*}, Brett Goforth^b

^a *Department of Geological Sciences, California State University, San Bernardino, 5500 University Parkway, San Bernardino, CA 92407, US*

^b *Department of Geography, California State University, San Bernardino, 5500 University Parkway, San Bernardino, CA 92407, US*

Abstract

Historical patterns of debris flows have been reconstructed at the town of Forest Falls in the San Bernardino Mountains using a variety of field methods (mapping flow events after occurrence, dendrochronology evidence, soil chrono sequences). Large flow events occur when summer thunderstorms produce brief high-intensity rainfall to mobilize debris, however the geomorphic system exhibits properties of non-linear response rather than being a single-event precipitation-driven process. Previous studies contrasted the relative water content of flows generated by varying intensity summer thunderstorms to model factors controlling their velocity and pathway of deposition. We hypothesize that variation in sediment discharge also results from complexity in this geomorphic system, and this paper presents ongoing empirical field studies focused on sources of complexity in three formative components of recently monitored debris-flows at Snow Creek Canyon: 1) thresholds of sediment delivery from sources at the higher reaches of bedrock canyons; 2) storage effects in sediment transport down the bedrock canyons; and 3) feedbacks in deposition and transport of sediment as flows from the bedrock canyon collect into a single active channel on a fan landform downslope. An example of the first component occurred in March 2017, when snow melt generated a rapid translational landslide/debris slide of about 80,000 m³; this sediment was deposited in the bedrock canyon, but moved no further down-gradient. A second component has been observed when accumulation of meta-stable sediments in the active channel remain in place until fluvial erosion or subsequent debris flow created dynamic instability to mobilize the mass downslope. The third component occurred in the active channel where low-water content debris flows deposited sediments that filled the channel, raising the channel grade level to levy elevation, allowing for subsequent spread of non-channelized flows onto the fan and new scouring channel pathways down fan. Assessment of spatial and temporal complexities in a debris-flow system can improve risk prediction.

Keywords: debris flows; hyperconcentrated flows; debris-flow system

1. Introduction

Debris flows entail considerable spatial and temporal uncertainties that complicate efforts to predict hazards. Geomorphic systems that exhibit non-linear dynamics are said to be ‘complex’ and multiple sources of complexity have been recognized in geomorphology studies (Temme et al. 2015, Murray and Fonstad 2007, Phillips 2003). This paper reports an ongoing empirical field study to explore sources of complexity in a debris-flow system spanning from a canyon catchment to fan landform, located in the Transverse Range of Southern California.

1.1 Site Description

The Transverse range is a west-east oriented mountainous physiographic region of California associated with the transform boundary of the Pacific and North American tectonic plates (Harden 1998). The San Andreas Fault Zone makes the “Big Bend” step-over in Southern California, resulting in regional transpressional tectonic stress which has uplifted the San Bernardino Mountains (Yule and Sieh 2003). The study site is Snow Creek Canyon (Lat. 34.0669° N, Long. 116.9103° W), located on Yucaipa Ridge at the southeastern escarpment of the San Bernardino Mountains in the San Bernardino National Forest (place names after GNIS 2018).

Snow Creek Canyon originates on the north side of Yucaipa Ridge at 2,657 m, and flows into Mill Creek at 1,663 m elevation, over a horizontal distance of 2.6 kilometers. Snow Creek flows through the community of Forest Falls, among several other drainages that form a bajada along the base of Yucaipa Ridge. The bajada trends downhill

* Corresponding author e-mail address: kerry.cato@csusb.edu

in a northward direction to the grade level of Mill Creek Valley (Fig. 1a and 1b). The California Geological Survey and County of San Bernardino classified the northern and southern flanks of Mill Creek Valley as a landslide hazard zone (Tan, 1990; San Bernardino County, 2010). The only ingress to the town is along Valley of the Falls Drive, a two-lane paved, county-maintained road built upon the bajada and intersected by numerous active flow channels.

Forest Falls has a Mediterranean-type climate with warm, dry summers and cold, wet winters. Yucaipa Ridge results in significant orographic enhancement of precipitation. Winter season precipitation occurs during the passage of mid-latitude cyclones, and summer monsoonal rainfall occasionally occurs in thunderstorms with brief intense showers. Flood-intensity rain events infrequently occur in late summer or fall if the region is impacted by the remnants of a dissipating tropical cyclone, as well as in winter if a Pacific atmospheric river circulation pattern develops. A 12-year record of precipitation (2006-2018) is provided by the San Bernardino County Flood Control District that has operated a remote automated weather station (RAWS) with tipping-bucket rain gauge for alert of hazardous rainfall atop Yucaipa Ridge at 2753 m elevation (San Bernardino County Flood Control District, Meteorological Sensor ID: 2900). The rain gauge registers a mean annual precipitation of $85.8 \text{ cm} \pm 24.9 \text{ SD}$ for the October to September hydrologic year. Approximately 84% of precipitation occurs from October through June. On average, the wettest month of the year is December (21.7 cm) and the driest month is June (0.4 cm).

Historically, the study site has experienced several debris and hyper-concentrated flows. Within the last two decades, debris and hyper-concentrated flows have damaged structures, caused one fatality, and produced numerous closures of the only road into this valley (Morton et al., 2008); these flows occurred during summer months. The area has also experienced extensive tectonic activity with the Mission Creek Fault, a part of the San Andreas Fault zone, mapped across the bedrock portion of the Snow Creek channel and the Mill Creek Fault (North Branch of the San Andreas Fault) is concurrent with the main drainage of the valley of which Snow Creek is a tributary (Fig. 1, USGS, 2002). The tectonism not only produces uplifting mountains, and hence source of the debris, but surface faulting and intense shaking has created a highly fractured, and in some cases deeply weathered, rock mass.

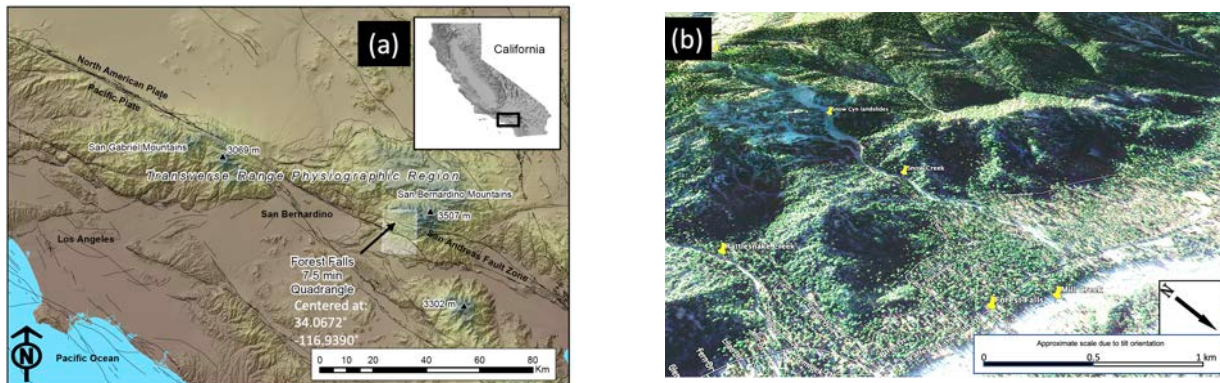


Fig. 1. (a) Map showing Forest Falls location between two strands of the San Andreas Fault in the San Bernardino Mountains of Southern California. (b) Aerial photo showing Snow Canyon, the community of Forest Falls, and nearby features (source: modified from Google Earth Pro, 2018).

1.2 The 2017 and 2018 Mass Movements and Flows

On February 17, 2017, the first of two mass-wasting episodes occurred in the upper reaches of Snow Creek Canyon (Fig. 2a). Less than two months later, a second mass movement occurred in the same area of Snow Creek Canyon (Fig. 2b). These events occurred as seasonal temperatures produced melting of the snow pack on these slopes. From photographs and videos taken by a telephoto lens about 1-1/2 kilometers away in Mill Creek Canyon, and subsequent inspection of the debris slide, the mass movements appeared to be translational landslide movements of intact bedrock with a colluvial veneer. Some detrital material was deposited at the base of the approximate 45 to 50-degree side slope, and at the surface this consists of 1 to 3-meter diameter angular boulders. However, an interesting aspect of this mass movement was the accompanying rapid sediment runout that extended 600 to 700 meters downslope within the narrow bedrock canyon. This runout episode was fortuitously captured on video. Based on the video, the mass of clastic material moved in a fluid manner, at a velocity on the order of 100-140 km/hr, and sediment clasts and sediment waves reached heights estimated of up to 50 meters (Prochaska et al., 2008). The bedrock slope was observed to ravel small amounts of sediment during the following three relatively abnormally dry seasons

(summer 2017, Fall 2017, and winter 2018). However, most of the debris deposited in the canyon from the two mass movement events has remained stationary and has not been remobilized.

About a year and a half later, on August 16, 2018, an intense precipitation cell over Yucaipa Ridge dropped over 5 cm of rain in a 2-hour period. The runoff from this storm produced a hyper-concentrated mudflow that forced closure of Valley of the Falls Road as approximately 0.1 to 0.25 meters of sediment covered the road. Post flow inspection of the fan upstream of the road showed that the sediment produced channel filling and channel avulsion. This sediment was ultimately deposited into the Mill Creek drainage. The sediment source for the flow is not obvious but is thought to be primarily from the scarred area of the 2017 mass wasting event, and material that accumulated 600 to 700 meters downstream from that event having fines flushed from debris interstices.

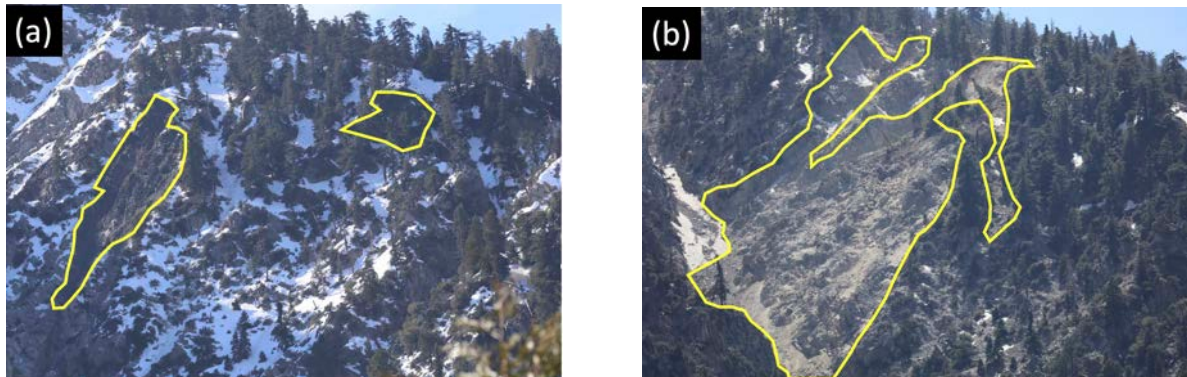


Fig. 2. (a) Mass wasting area in Slide Canyon after first episode (on February 17, 2017); area of movement outlined in yellow. (b) Second movement event in Slide Canyon (about 2 months later). Trees on slide mass are approximately 25 meters high. (Photo source: McIntosh, 2017).

1.3 Empirical approaches to study sources of complexity in the Snow Canyon Debris-Flow System

For almost two decades, the damaging effect of Snow Creek canyon debris flows on the Forest Falls community has been recognized, with the primary causative mechanism attributed to high-intensity summer storms on Yucaipa Ridge. However, the non-linear dynamics of 2017-18 flow events suggests this debris-flow system also functions with multiple sources of complexity. This paper hypothesizes that complexities occur in 3 system components that we describe to guide ongoing empirical field study of the debris-flow system, including: storage effects in episodic sediment loading from bedrock landslide events; sediment storage thresholds and flow movement triggering in the narrow channel; and sediment transport across the alluvial fan in a complex channel filling, cutting, and avulsion process of feedbacks. A Geographical Information System (GIS) modelled dimensions of the catchment source area for debris flow generation. The catchment area of Snow Creek Canyon was analysed from a 10 m cell resolution Digital Elevation Model (DEM) downloaded from the National 3D Elevation Program (USGS 2018), and processed with ArcMap 10.3 software (ESRI, Redlands, CA). The ‘surface tool’ in ArcMap Spatial Analyst derived slope angles of each grid cell. The ‘watershed tool’ was used to delineate the planimetric area of the catchment upstream from a fan apex pour-point. The ‘stream order’ tool was used to determine the rank of trunk stream channel at the fan apex using a 1,000 grid cell flow accumulation rule. The ‘surface volume’ tool in ArcMap 3D Analyst was used to compute a 2D projected area encompassed by the catchment, and a 3D surface area of the canyon slopes.

2. Previous Studies

This paper uses creek names shown on the U.S Geological Survey 7.5' Forest Falls quadrangle (after GNIS 2018), which is consistent with current US Forest Service and local emergency response usage. The names “Snow Creek Canyon” and “Rattlesnake Canyon” have been used interchangeably on some publications.

Previous research concluded that, cumulatively, debris-flow events in Snow Canyon and Rattlesnake Canyon occur on average every 3.5 years with some years having two episodes. This average was based on documented events since 1951 and tree ring data over the past 300 years (Morton et al., 2001; Morton et al., 2008; Turk et al., 2008), which documented 15 large-scale debris-flow events up to 2008.

The active channel of Snow Creek is presently located on the eastern side of the fan. The age of fan surface deposits generally increases from east to west across the landform, as evidenced by chronosequence studies of soil development, and tree-ring age dates of surface deposits (Morton et al., 2008; Turk et al., 2008). The west edge of

the fan is bounded by an inactive debris-flow channel that is cutoff by the active channel at the fan apex. These studies indicate that debris flows are distributed across the fan over time, and identify a need for higher resolution study of how channel pathways change.

3. System Components Operating in Snow Creek Canyon

Three components are observed to operate in different areas of Snow Creek Canyon and each appears to have its own controls, but inputs and thru-puts may link the components or only influence that component. The components include: 1) sediment delivery from source at the higher reaches of bedrock canyons; 2) sediment transport down the bedrock canyons; and 3) deposition and transport of sediment on and across the debris-flow fan.

Our GIS model indicates that Snow Creek Canyon has local relief of 862 m from fan apex (1795 m) to the crest of the highest headwall at Yucaipa Ridge (2657 m), over a total length of 1.6 km horizontal distance (53.8% gradient). Slope angles of DEM grid cells range from 2.7° to 69.5°, with mean of 39.8° (Fig 4b). Although the catchment encompasses 67.2 ha of planimetric area upstream from the fan apex, the 3D surface model provides an estimate that 93.6 ha of surface area covers the steep slopes within this canyon. The trunk channel of this catchment ranks as a 2nd order stream by tributary accumulation of flow from >10 ha drainage area on these slopes, and has a nearly linear drainage pattern. Below the fan apex at the base of the canyon, the trunk channel spans a horizontal distance of approximately 530 m with an average gradient of 17.2% (Fig 4b). The channel makes an s-turn from 317 m to 342 m below the fan apex and is the location of the levee breaches during recent flows.

3.1 Sediment delivery from source at the higher reaches of the bedrock canyon

The Winter-Spring 2017 mass wasting event in Snow Creek Canyon occurred on the west canyon wall, at an elevation of 2347 m. A variety of geological and meteorological conditions may have contributed to the mass wasting event including, rock weathering, steep terrain inducing rock fall, high precipitation rates, tectonic activity, and warm temperatures that produced rapid snow melt.

The rocks are mapped Mesozoic quartz monzonite and Precambrian gneiss (Dibblee, 1964; Gutierrez, 2010). These rocks were observed to be highly fractured and weathered. The walls of Snow Canyon are steep, ranging from 50 degrees to near vertical. The area of movement is a mapped landslide complex with slopes in the failure area at 50-55 degrees. A colluvial layer 1-2 meters thick overlies a highly fractured bedrock mass (Fig 3a and 3b). The mass movement occurred on a plane that is oriented subparallel to the valley wall. At the base of the slope, the block size of the angular boulders ranges from 1.5 to 3.5 meters. By contrast, at the toe of the debris runout located 600-700 meters downslope, the block diameter of the angular boulders exposed at the surface was 0.6 to 1.5 meters. While material size is obviously sorted with distance from the slide area, the rapid and violent nature of this event is also thought to have produced a rapid breakdown of particle sizes. This was most likely enhanced by the rock mass's in situ fracturing and weathering. And even further downstream on the alluvial fan surface, clast diameters range from 10 cm to 0.5 meters along with a considerable sand and silt-sized fraction.

This location is an extremely active tectonic zone. The Mission Creek Fault (aka., North Branch of the San Andreas fault) is about 0.50 km from the Snow Canyon mass movement episode (USGS, 2002). At the bottom of the valley, nearer the Forest Falls community, the Mill Creek fault is about 2.5 km to the north. The main South Branch of the San Andreas fault, located approximately 3.5 km south of upper Snow Canyon, trends along the south side of the Yucaipa Ridge. According to the California Geological Survey's Alquist-Priolo Earthquake Fault Zone maps, all three of the above-mentioned faults are considered potentially active during the Holocene period (CGS, 1974). However, another related factor, seismic shaking is an ongoing process and this topographic high would amplify any seismic shaking at the site. For example, since February 12, 2017, there have been 24 documented earthquakes greater than M2.5 within a 20 km radius of Snow Canyon. According to the USGS Earthquake Hazards program, a magnitude 3.4 earthquake occurred on February 10th, less than one week prior to the Snow Canyon mass movement event, approximately 8 km southwest of the site.

Data obtained from the Yucaipa Ridge rainfall gauging station shows Forest Falls having received 0.81 m of precipitation from October 23, 2016 to February 18, 2017 (San Bernardino County Flood Control District, 2017). In the preceding weeks prior to the mass wasting event there were no recorded precipitation events; however, the warm temperatures during this time melted much of the snow pack and this runoff could have facilitated movement. Note the difference in snow coverage shown in photographs on Figures 2a and 2b.

Based on our observations and conclusions by O'Keefe, 2017, the 2017 Snow Canyon mass wasting event appears to combine aspects of the flow and slide mechanisms, including flow as a debris avalanche (Cruden and

Varnes, 1996). Summerfield (1991) notes that debris avalanches often begin as landslides and historically, the documented major mass wasting episodes in Forest Falls have been classified as debris flows and debris avalanches. Prior to 1999, Forest Falls experienced 11 debris flows and during July 1999 a debris flow and debris avalanche occurred at Snow Creek, east of Snow Canyon (Morton and Hauser, 2001). The California Geological Survey and San Bernardino County have classified the northern and southern mountains of Mill Creek Valley, surrounding Forest Falls and encompassing Snow Canyon, as a landslide hazard zone.

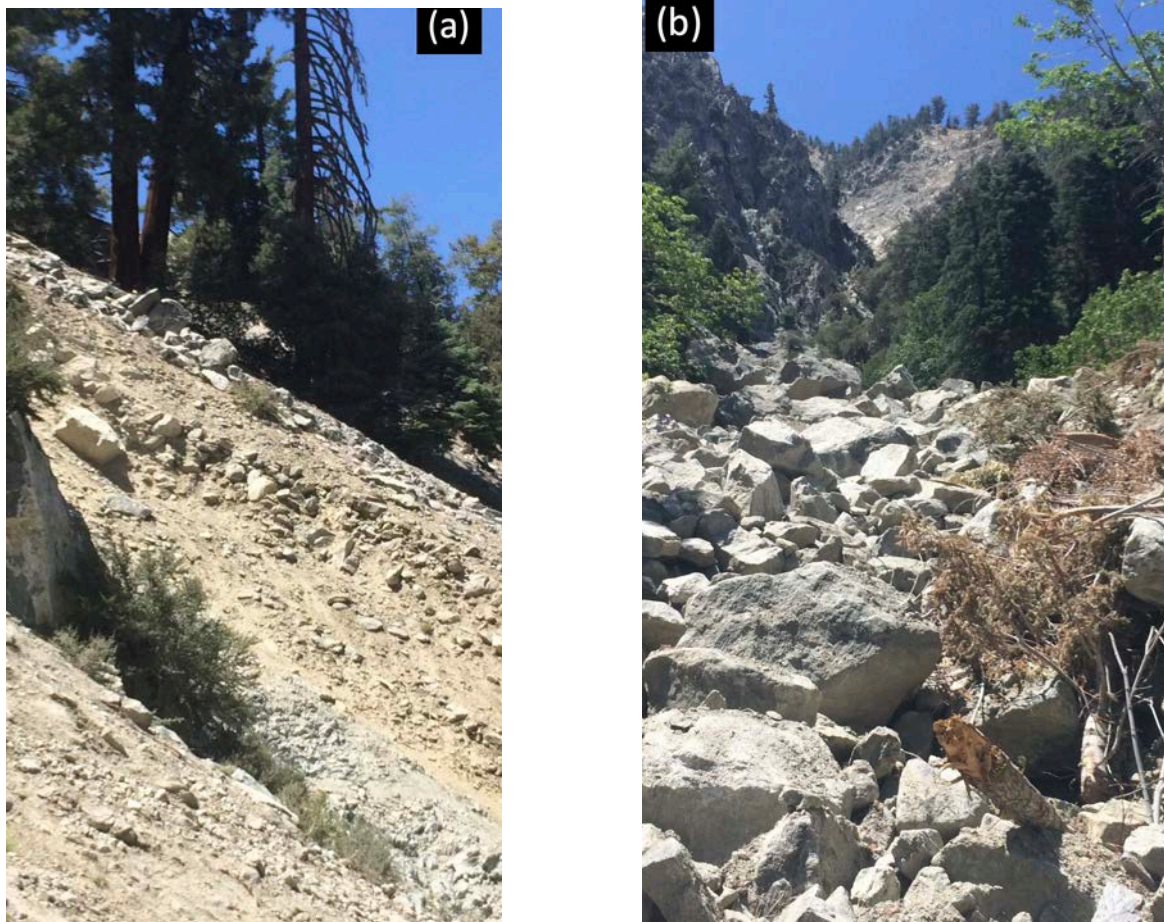


Fig. 3. (a) Source area of mass wasting taken in May 2017, about 2 months after last movement occurred. Rock mass structure is evident, as is moderate to high degree of weathering. Slope orientation is approximately 50 degrees; (b) Trees and large boulders were mobilized by the Winter-Spring 2017 mass wasting event. The landslide source area is several hundred meters upslope from this location. Angular boulder diameters range from 0.2 to 2.0 meters in diameter.

3.2 Sediment storage and transport down the bedrock canyons

Less information is known about this part of the system than of the two other components because it is easily overlooked as an independent component of the process mode. More attention is given to the upslope mass movement that produces the sediment or the downslope alluvial fan. Had it not been for the unique opportunity of the photo and video documentation of this event, we could have also overlooked its importance; however, the fact that all of the sediment produced in the Winter-Spring 2017 mass wasting event was stored in this section, suggests it should not be overlooked. At very least, the amount of sediment stored and estimating its control on groundwater flow within this sediment mass pose intriguing questions.

We are in the process of quantifying the 2017 sediment that was deposited within this bedrock channel segment. Our pre-flow aerial photography is not high enough resolution to use as a base. We are currently using a LIDAR base obtained in 2016 that has been recently made available as our pre-flow base (NCALM, 2014). For post flow, will be using new sUAV LIDAR once it becomes operational or sUAV conventional photography. For both, the steep topography in the area has created logistical obstacles. For obtaining information on groundwater flow

within the deposited sediment and how this sediment may be remobilized into an active debris or hyper-concentrated flow can at this time only be estimated or modelled hydrologically.

At this point we know that the estimated 120,000 cubic meters that moved in the 2017 event was stored within the bedrock channel area from the slide mass site to a distance downstream 600-700 m. In August 2018, a hyper-concentrated sediment flow was produced on the fan and extended onto Valley of the Falls Drive. The volume estimate for this sediment was not able to be accurately determined as precise depth and sediment extent records were not recorded. However, based on crude sediment depths, we roughly estimate that about 15,000 cubic meters of sediment was deposited on and downstream of the road. This combined with the sediment estimates that mapping of alluvial fan surface mapping determined, which was on the order of 10,000 cubic meters, then the total amount of sediment mobilized during event was on the order of about 120,000 cubic meters. This would leave about 95,000 cubic meters of sediment, produced by the 2017 mass wasting event, still stored within the bedrock channel segment.

From a risk standpoint at this time, we can only speculate about the amount of sediment or debris that another intense rainstorm could possibly produce. For example, will a repeat storm again produce another hyper-concentrated flow of relatively fine-grained sediment? Or did the August 16, 2018 storm runoff remove all loose, available stored sediment? At what point will the coarser material be mobilized? Does the coarser material currently exist in a meta-stable state with only the fine material able to be mobilized by fluid flow? What is its threshold trigger? For example, could the coarser material only be mobilized into a true debris flow only episodically, say when another large mass wasting event produces enough kinetic energy (i.e., bull-dozing driving force) to physically mobilize this material (as opposed to mobilization by hydraulic forces alone)?

3.3 Sediment deposition and transport of sediment on and across the debris-flow fan

Open traverse surveys of topography on the fan were recorded using submeter precision global positioning system (GPS) roving receivers (Trimble GEO7x with Zephyr antenna, ArcPad 10 software). The GPS positional data (x,y,z) were recorded only if a real-time differential correction was obtained and the 3D position dilution of precision (PDOP) was < 3.0 . Elevation (z) was calibrated using the GEOID03 model offset of -30.414 m reported by the National Geodetic Survey at the latitude and longitude coordinates of Forest Falls CA relative to height above the WGS84 ellipsoid (NGS 2017, 2018).

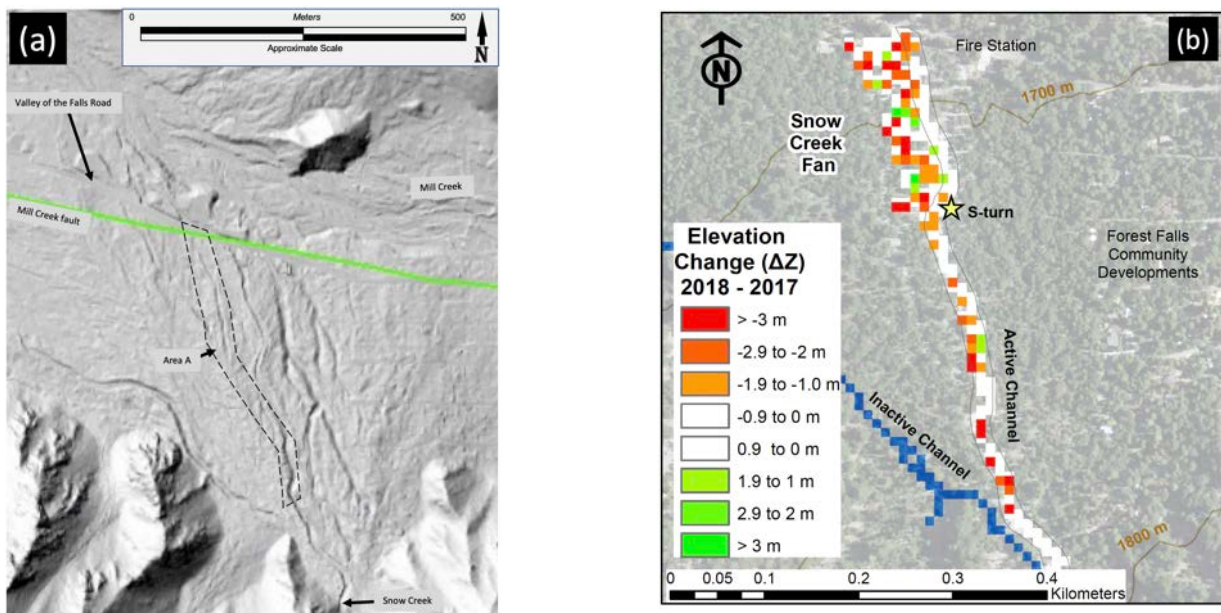


Fig. 4. LIDAR imagery of Snow Creek and alluvial fan. (a) Entire system downstream of mass movement area with features annotated. Area A is the channel where sUAV point cloud imagery was acquired that shows the channel changes produced by the August 16, 2018 hyper-concentrated flow (b) Enlarged area from Fig 4a that shows close up of alluvial fan channels.

A total of 3,022 GPS survey points were recorded across the fan on September 23, 2017. This procedure was repeated on September 28, 2018 to record 2,362 GPS survey points over the active channel and extent of debris flow. Only GPS survey points with Estimated Positional Error (EPE) ≤ 1 m were used for geospatial analysis of the fan

surface elevation change. This resulted in use of 2,002 points (66.2%) from the 2017 survey, and 2,113 points (89.4%) from the 2018 survey. This GNSS data for both years was exported to ArcMap and converted into 10 m cell grids using the ‘Point to Raster’ tool that averaged all elevations within each cell. The Spatial Analyst ‘Raster Calculator’ tool was used to compute the difference in elevation (ΔZ) for 2018 minus 2017. Cells with negative values of -1 m or more indicate areas where net erosion exceeded the range of GPS measurement imprecision (figure of ΔZ). Likewise, positive values greater than 1 m indicate where net deposition measurably occurred. Taken together, our GPS surveying, sUAV photography, and analysis of existing LIDAR across the fan provide multiple lines of evidence that deposition appears to be shifting in a westward direction by spread of non-channelized flows onto the fan. At the same time, there has been significant fluvial erosion by new scouring of channel pathways down fan in a process of channel avulsion below where the active channel was overtopped by bedload accumulation.

4. Discussion of system

Previous work had concluded that summer monsoon rainfall events on Yucaipa Ridge were the hydraulic driving force that produced debris flows. For example, including the 1999 and 2016 debris and hyper-concentrated flows, Forest Falls has experienced 13 debris flows since 1951. However, monsoonal storms occur much more frequently than do documented debris incidents. Based on observations of the 2017 mass wasting event, where sediment was observed to accumulate within the middle portion of the bedrock channel, and then where an August 2018 monsoonal event created a hyper-concentrated flow that mobilized about 25,000 cubic meters, we observed that a large percentage of the coarse-grained material boulders and clasts remain as a meta-stable sediment plug in the middle channel. What is unknown is what type of an event will be required to mobilize the larger volume and larger diameter material into a presumed true debris flow.

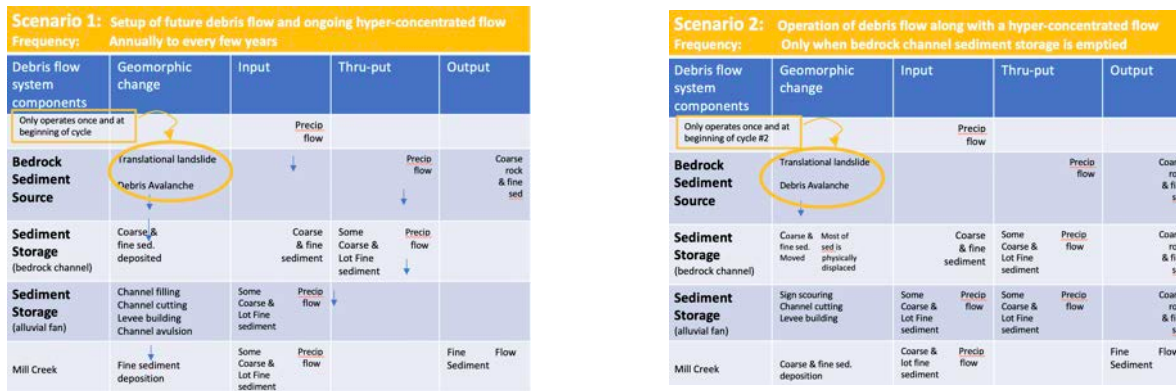


Fig. 5. Some event causes the coarse sediment stored in the middle section (the bedrock channel) to become mobilized and transported downslope. These two possible scenarios are possible models for the complex controls that operate to control the type and volume of flow that may occur in Snow Creek canyon and alluvial fan.

5. Conclusions & Recommendations for Future Research

Sediment loads contained within the debris-flow system at Forest Falls are produced in multiple non-linear components of erosion, transport, and deposition. We identify a need to quantify ‘thresholds’ of rainfall intensity required for sediment mobilization, recognizing that ‘storage effects’ occur in bedrock canyons and active drainage channels which accumulate significant loads of sediment mobilized by antecedent mass-movement processes, as well as from deposits of smaller water-limited debris flows that traveled short distances. Debris flows from the canyon deposited sediments that aggraded within the active drainage channel and breached the active channel levy, allowing for subsequent spread of non-channelized flows onto the fan. A ‘feedback’ process of channel avulsion progressed in subsequent flow events that eroded new channel pathways down fan. Field investigations and monitoring will progress to gather data that will build a model of these complexities. Existing and future imagery such as LIDAR, InSAR, and conventional aerial photography are being analysed through the use of Point Cloud software to quantify baseline geomorphic conditions and provide measurements of event-specific changes. Possible future work is:

- The amount of sediment stored in the bedrock channel needs to be quantified. LIDAR and InSAR may allow more precise calculations so the hypotheses developed can be tested.
- The amount and location of sediment that is stored on the alluvial fan. The forested nature of this geomorphic

surface has limited the use of historic stereo photography or new high resolution sUAV photography for this purpose. LIDAR and InSAR may provide the ability for this purpose.

A sediment budget to determine how much sediment is being produced in which area, where it is being temporarily being stored, and how much sediment passes through the system.

- The locations where individual mass-wasting and debris-flow events are triggered needs to be determined with higher spatial and temporal resolution. A time series of such data could potentially be useful to provide a statistical frequency distribution for occurrences of sediment mobilization, contrast different scales of flow events, as well as to determine the flow distances contained within this system. An array of field instrumentation may be useful, such as infrasound acoustic sensors for mass-wasting events and geophones for ground vibration detection caused by debris flows (after Hurlimann et al. 2003, Abanco et al. 2014, Havens et al. 2014), and could be calibrated with events documented by the aerial surveys and GPS surveys.

References

- Abanco, C., Hurlimann, H., and Moya, J., 2014, Analysis of the ground vibration generated by debris flows and other torrential at the Rebaixader monitoring site, central Pyrenees, Spain, *Natural Hazards and Earth System Sciences*, v. 14, p. 929-943, doi:10.5194/nhess-14-929-2014
- California Geologic Survey (CGS), 1974, Special Study Zone (Alquist-Priolo Earthquake Fault Zone Map), SW ¼ San Gorgonio Mountain Quadrangle (15-minute series); CGS formerly known as the California Division of Mines and Geology).
- Cruden, D.M., and Varnes, D.J., 1996, *Landslide Types and Processes: Landslides Investigation and Mitigation*, Transportation Research Board Special Report 247, 36 p.
- Dibblee, T.W., compiler, 1964, *The San Gorgonio Mountain Quadrangle, San Bernardino and Riverside Counties, California: U.S. Geological Survey, Miscellaneous Geologic Investigations Map I-43*, scale 1:62,500, 1 sheet.
- GNIS 2018. U.S. Board on Geographic Names, U.S. Geological Survey, Geographical Names Information System. <https://geonames.usgs.gov/domestic/index.html> (Accessed 13 Nov 2018).
- Google Earth Pro, 2018, Forest Falls, 34.071852°, -116.913594, accessed October 2018. <http://www.google.com/earth/index.html>.
- Gutierrez, C., Bryant, W., Saucedo, G., and Wills, C., compilers, 2010, *California Geological Survey 150th Anniversary Geologic Map of California*, scale 1:750,000, 1 sheet.
- Harden, D. 1998. *California Geology*. Prentice-Hall, New Jersey.
- Havens, S., Marshall, H., Johnson, J., Nicholson, B., 2014, Calculating the velocity of a fast-moving snow avalanche using an infrasound array, *Geophysical Research Letters*, v. 41, p. 6191–6198, doi:10.1002/2014GL061254
- Hurlimann, M., Rickenmann, D., and Graf, C., 2003, Field and monitoring data of debris-flow events in the Swiss Alps, *Canadian Geotechnical Journal*, v. 40, p. 161-175, doi: 10.1139/T02-087
- McIntosh, Tom, 2017, Personal Communication, Forest Falls, California resident.
- Morton, D.M. and Hauser, R.M., 2001, A Debris Avalanche at Forest Falls, San Bernardino County, California, July 11, 1999: U.S. Geological Survey Open File Report 01-146, <https://pubs.usgs.gov/of/2001/0146/pdf/of01-146.pdf>.
- Morton, D.M., Alvarez, R.M., Ruppert, K.R., and Goforth, B., 2008, Contrasting rainfall generated debris flows from adjacent watersheds at Forest Falls, southern California, USA: *Geomorphology*, v. 96, p. 322-338, doi: 10.1016/j.geomorph.2007.03.021.
- Murray, B., and Fonstad, M., 2007, Preface: complexity (and simplicity) in landscapes, *Geomorphology*, v. 91, p. 173-177, doi:10.1016/j.geomorph.2007.07.011
- National Center for Airborne Laser Mapping (NCALM) Seed, 2014, NCALM Seed- Airborne Laser Swath Mapping (ALSM) survey of the San Andreas Fault (SAF) system of central and southern California, Data archived at [Opentopography.org](http://opentopo.org): <http://opentopo.sdsc.edu/raster?opentopoID=OTSDEM.052016.26911.1>
- NGS 2017, 2018. National Geodetic Survey, Online computation page for GEOID03 GEOID height. Accessed Sept. 23, 2017 and Sept. 28, 2018. https://www.ngs.noaa.gov/cgi-bin/GEOID_STUFF/geoid03_prompt1.prl
- O’Keefe, K., 2017, Characterization of the Winter-Spring 2017 mass movement episode in Snow Canyon, Forest Falls, San Bernardino County, California: Unpublished Undergraduate Research Project, Dept. of Geological Sciences, California State University, Spring 2017, 29p.
- Phillips, J.D. 2003. Sources of non-linearity and complexity in geomorphic systems: *Progress in Physical Geography*, v. 27, p.1-23, doi: 10.1191/0309133303pp340ra
- Prochaska, A.B., Santi, P.M., Higgins, J.D., and Cannon, S.H., 2008, A study of methods to estimate debris flow velocity, *Landslides*, v. 5, p. 431-444, doi: 10.1007/s10346-008-0137-0.
- San Bernardino County, 2010, San Bernardino County General Plan, Geologic Hazard Overlays: Accessed online: <http://cms.sbcounty.gov/lus/Planning/ZoningOverlayMaps/GeologicHazardMaps.aspx> .
- San Bernardino County Flood Control District, Meteorological Sensor ID: 2900, 2017,; online access: <http://www.sbcounty.gov/dpw.pwg/alert/reports.html> .
- Summerfield, M.A., 1991, *Global Geomorphology*, England: Pearson Education Limited, p. 167-174.
- Tan. S.S., compiler, 1990, *Landslide Hazards in the Yucaipa and Forest Falls Quadrangles, San Bernardino County, California, Landslide Hazard Identification Map No. 18: Division of Mines and Geology*, scale 1:24,000, 2 sheets.
- Temme, A., Keiler, M., Karssenber, D., and Lang, A., 2015, Complexity and non-linearity in Earth surface processes: concepts, methods, and applications: *Earth Surface Processes and Landforms*, v. 40, p. 1270-1274, doi: 10.1002/esp.3712
- Turk, J.K., Goforth, B.R., Graham, R.C., and Kendrick, K.J., 2008, Soil morphology of a debris flow chronosequence in a coniferous forest, southern California, USA: *Geoderma*, v. 146, p. 157-165, doi: 101016/j.geoderma.2008.05.012.
- U.S. Geological Survey, 2002, Quaternary Fault and Fold Database for the United States: <https://earthquake.usgs.gov/hazards/qafaults/> .
- U.S. Geological Survey, 2018. National Map Server. <https://www.usgs.gov/core-science-systems/ngp/tnm-delivery/gis-data-downloadOnline> (Accessed 2 Nov 2018)
- Yule, D., and K. Sieh. 2003. Complexities of the San Andreas fault near San Gorgonio Pass: implications for large earthquakes. *Journal of Geophysical Research* 108 (B11): 2548.

A 4000-year history of debris flows in north-central Washington State, U.S.A.: preliminary results from trenching and surficial geologic mapping at the Pope Creek fan

Jeffrey A. Coe^{a,*}, Erin K. Bessette-Kirton^a, Stephen L. Slaughter^b, Francis K. Rengers^a, Trevor A. Contreras^b, Katherine A. Mickelson^b, Emily M. Taylor^a, Jason W. Kean^a, Kara E. Jacobacci^b, Molly A. Hanson^c

^aU.S. Geological Survey, Denver Federal Center, Denver, CO 80225, U.S.A.

^bWashington Department of Natural Resources, Washington Geological Survey, 1111 Washington St. SE, Olympia WA 98504 U.S.A.

^cU.S. Forest Service, Okanogan-Wenatchee National Forest, 215 Melody Lane, Wenatchee, WA 98801 U.S.A.

Abstract

Long-term records of the magnitude and frequency of debris flows on fans are rare, but such records provide critical information needed for debris-flow hazard and risk assessments. This study explores the history of debris flows on a fan with seasonally inhabited cabins at Pope Creek along the Entiat River about 48 km upstream from the town of Entiat, Washington. Motivation for this study was provided by the Duncan Fire, a wildfire which burned the Pope Creek basin in 2014 and resulted in debris flows and water-dominated floods on the fan between August 2014 and October 2016. We excavated and mapped seven 6-m long (2.4-m deep) trenches, mapped deposits on the surface of the fan, and constrained the ages of deposits using radiocarbon dating and the computer program OxCal. Preliminary results indicate that there have been at least 10 debris-flow events (DFEs) since 4000 cal yr BP. The mean recurrence interval between events was 433 +/-44 years, but intervals range from 724 to 20 years. The four most recent events have the shortest recurrence intervals. The largest event had an estimated sediment volume of 97,000 m³ and occurred at about 285 cal yr BP (1665 AD) during the Little Ice Age. The most recent debris-flow event that was triggered by rainstorms following the Duncan Fire was about 8x smaller than the largest event. These results may indicate that the largest DFE was triggered by an exceptional meteorological event that occurred during a cool, wet time, and that smaller DFEs were triggered by less exceptional meteorological events that occurred following wildfires.

Keywords: debris flow; fan; magnitude; frequency; Washington State

1. Introduction

In most parts of the world, debris-flow frequency and magnitude relations, and changes in those relations due to wildfires, are poorly documented, but are critical for hazard and risk assessments. Debris-flow frequency and magnitude relations are poorly documented because of a scarcity of systematic trenching studies of debris-fan deposits. In the western United States, existing studies of natural exposures of fan stratigraphy show an increase in fire-related sedimentation events (floods and debris flows) during warm climatic conditions and multidecadal droughts (e.g., Pierce and Meyer, 2008; Frechette and Meyer, 2009).

In this paper, we present preliminary results from a systematic study of debris-flow deposits on a debris fan in an area susceptible to wildfires in central Washington State. We studied the debris flows by mapping deposits on the fan surface, and by mapping and dating debris-flow stratigraphy in seven ~2.4-m deep trenches distributed across the fan. We used dated deposits to model debris-flow recurrence intervals for 4000 cal yr BP and compared our results to available climate and fire histories in central Washington.

* Corresponding author e-mail address: jcoe@usgs.gov

2. Setting

The debris-fan that we studied is at the mouth of Pope Creek, a tributary to the Entiat River in the Okanogan-Wenatchee National Forest (Fig. 1). The Pope Creek fan and basin cover areas of 0.2 km² and 9.1 km², respectively. Relief from head of basin to the toe of the fan at the edge of the Entiat river is 1,340 m. The basin is underlain by an Eocene-age biotite and hornblende-biotite granodiorite within the Duncan Hill Pluton (Tabor et al., 1987). The fan and river valley were mapped by Tabor et al. (1987) as Holocene and Pleistocene alluvium ranging from poorly-sorted sandy gravelly sand on the fan, to moderately-sorted cobbly gravel along the river.

The geologic history of the study area is complex. The area is on the east side of the volcanically active Cascades Range about 45 km southeast of the Glacier Peak volcano. Pumaceous tephra is present in the Pope Creek basin and most likely originated from an eruption of Glacier Peak between 11,000 and 13,000 years ago (Porter, 1978). The area is also near the western edge of the Okanogan ice lobe of the Pleistocene Cordilleran continental ice sheet, but just outboard from the area that was glaciated (e.g., Balbas et al., 2017). Alpine glacial drift has been mapped in isolated parts of the Entiat Valley near Pope Creek (Haugerud and Tabor, 2009).

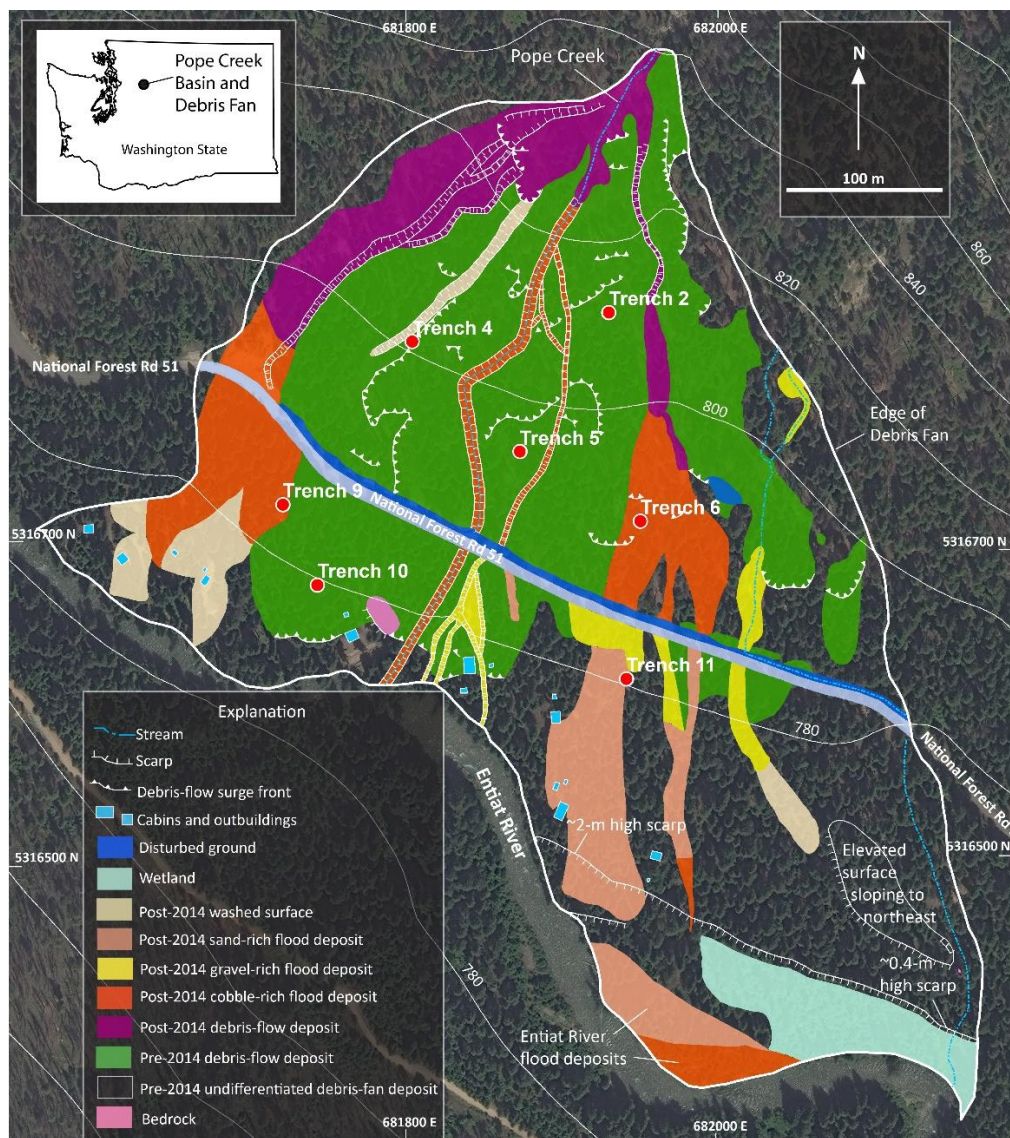


Fig. 1. Map of the Pope Creek debris fan showing surficial geology mapped in 2017, location of trenches excavated in 2017, and location of cabins and outbuildings near the Entiat River. Trenches 1, 3, 7, 8, and 12 were not excavated, and are therefore not shown here. All post-2014 deposits are part of debris-flow event 10 (DFE10). Coordinates of tick marks are UTM, zone 10, meters. Elevation data are from the National Elevation Dataset (NED, USGS, 2018), contour interval is 20 m. Small inset map shows the location of the fan and basin in Washington State.

The Entiat River basin has a long history of destructive wildfires and subsequent floods and debris flows including events in the 1970s (e.g., Perkins et al., 1971; Klock and Helvey, 1976; Woodsmith et al., 2004), 2014 (Duncan Fire, Burned Area Emergency Response, 2014), and 2015 (Wolverine Fire, Burned Area Emergency Response, 2015). After a wildfire in 1970, debris flows in June 1972 destroyed private cabins and killed four people on the Preston Creek fan in the Entiat Valley (Klock and Helvey, 1976). At the Pope Creek fan, there are records from two historical debris-flow events, one on May 19, 1995 (U.S. Bureau of Reclamation, 2009) that was not related to a wildfire, and another following the Duncan Fire which burned in July and August, 2014. The 1995 event deposited boulders and large woody debris at the head of the fan, and finer sediment on lower parts of the fan, including on National Forest Road 51, and near private, seasonally occupied cabins located on the periphery of the fan near the Entiat River. The post-2014 debris-flow event deposited material on the fan in a similar manner to the 1995 event.

The Duncan Fire burned about 65 percent of the Pope Creek basin at moderate to high soil-burn severity (Burned Area Emergency Response, 2014). Prior to the Duncan Fire, a mixed conifer forest blanketed the basin and fan, with ponderosa pine, grand fir, silver fir, and mountain hemlock trees in the basin, and ponderosa pine on the fan. This vegetation regime is classified by the U.S. Forest Service as Pacific Northwest forested, mixed conifer, eastside mesic. For this vegetation regime, the Forest Service Fire Effects Information System gives mean fire return intervals as 200 yrs, 150 yrs, and 40 yrs for stand replacement, mixed, and surface fire-severity classes, respectively (U.S. Forest Service, 2018). There is not a correlation between soil-burn severity and fire-severity classes (e.g., Safford et al., 2007).

3. Methods

During field work in the spring and summer of 2017, we mapped deposits on the surface of the Pope Creek fan, and excavated and mapped seven trenches in the fan. We identified deposits on the fan surface and then mapped deposit boundaries on a June 2016 Digital Globe WorldView-2 image. Trenches were about 6 m long, 2.4 m (8 ft) deep, and had two 1.2 m (4 ft) high walls separated by a 1.2 m (4 ft) wide bench. At each trench, we mapped and described deposits, flagged unit contacts using nails and flagging, surveyed the position (UTM zone 10 coordinates and elevation above mean sea level in m) of all flagged nails using a total station surveying unit, and collected charcoal samples for radiocarbon dating. Charcoal samples were all detrital charcoal, meaning that the charcoal was not created in-situ, but instead was transported to its deposition location from an upstream location either on the fan or in the basin, and thus provided maximum ages for the deposits.

We interpreted deposits as debris-flow deposits or flood (water-dominated) deposits based on sedimentological characteristics. Debris-flow deposits were unsorted, matrix-supported deposits that contained randomly oriented clasts (cobbles and boulders). Flood deposits were sorted, clast supported, contained layers, and were generally finer grained than debris-flow deposits.

From surface and subsurface exposures, we documented that the Pope Creek fan is dominated by debris flows rather than floods, but, we also know from observations of debris-flow events in multiple locations that individual events often have both debris flow and flood components, both in time and in space. Previous investigations have shown that there can be debris flows and/or floods over periods of years to possibly decades that leave sedimentologically identical deposits that cannot be distinguished from one another in cross section unless there are soil horizons visible between the deposits (see Major, 1997 for additional details). To account for such uncertainties, throughout this paper, we use the term debris-flow event (DFE) to describe historical and pre-historic flow events on the fan. A single DFE can include one or more flows that cannot be distinguished from one another, either on the fan surface, or in stratigraphic sections. We identified 10 DFEs at Pope Creek, with the oldest designated as DFE1 and the youngest as DFE10. An individual DFE can contain both debris-flow deposits and flood deposits on different parts of the fan surface, or at single locations. Flows on the fan after the Duncan Fire (Post-2014 DFE10, Fig. 1) are useful to illustrate this point. In DFE10, there were multiple flows following the 2014 Duncan Fire that were indistinguishable from one another on the fan surface and in trenches. Additionally, DFE10 had debris flow and flood components (Fig. 1), with debris-flow deposits near the head of the fan, and flood deposits on the middle and lower parts of the fan.

Soil horizons can be useful to distinguish DFEs because they indicate hiatuses in the debris-flow depositional cycle. For soil descriptions, we used the nomenclature of Schoeneberger et al. (2012). Specifically, we described A, B, and C soil horizons. An A horizon is organic matter and mineral-rich material that accumulates at or near the land surface. A B horizon underlies an A horizon and is different from the original parent material because of an

accumulation of secondary material, color, or structures (aggregation of soil particles). A C horizon is a subsurface horizon and can be like or unlike the material from which the soil formed. C horizons lack properties of A and B horizons. At the Pope Creek fan, C horizons are the parent material from which the A and B horizons formed. In some cases, because of a lack of adequate time and/or climatic conditions, there are C horizons at Pope Creek that never had A and B horizons form. Additionally, it is possible that some C horizons had A and/or B horizons at one point in time that were locally scoured away by subsequent floods and debris flows.

We submitted 17 charcoal samples for accelerator mass spectrometry (AMS, ^{14}C) dating to the Woods Hole Oceanographic Institute (16 samples) and Beta Analytic, Inc. (1 sample). Prior to submittal, we removed inorganic sediment and any organics from modern plant roots and dried the samples by heating them in an oven at 50°C for 2 hours.

We identified and correlated DFEs (Fig. 2) using soils and radiocarbon dates as constraints. To model the timing of DFEs from radiocarbon dates, we used OxCal radiocarbon calibration and analysis software version 4.3.2 (Bronk Ramsey, 2009, 2017) and the IntCal13 calibration curve of Reimer et al. (2013). OxCal is a Bayesian analysis tool that probabilistically models the timing of undated DFEs by incorporating the time distributions of all available chronological constraints (^{14}C dates from charcoal in our case). Oxcal produces a probability density function (PDF) for each undated event. We modeled the maximum ages for the deposition of DFEs (i.e., the age of fires that created the charcoal) using OxCal *R_Date* commands for units with single charcoal samples, OxCal *R_Date* and *Phase* commands for units with multiple charcoal samples, and *Date* commands for ages of the individual DFEs (see Lienkaemper and Bronk Ramsey, 2009, and DuRoss et al., 2011 for additional details regarding these OxCal commands). Our modelling provides mean values and 95% confidence interval bands for the maximum ages of DFEs.

We estimated volumes for each DFE based on our observations of the post-2014 DFE10 event. We used the percentage of the fan area covered by DFE10 (19%) and the number of trenches where deposits from DFE10 were exposed (2) to establish an equation to estimate the sediment volume (V) of DFE10, and the other nine DFEs:

$$V = MT * TE * PF * TA \quad (1)$$

where MT is the mean thickness (m) of DFE deposits from map and/or trench exposures, TE is the number of trenches where DFE deposits are exposed, PF is 0.095, which is the estimated percentage (9.5%, 19%/2 based on DFE10) of the fan that is covered for each trench where DFE deposits are exposed, and TA is 204000, which is the total area of the fan (m^2). For DFE10 (the post-2014 event), MT was based on about 10 natural exposures as well as trench exposures. For all pre-2014 DFEs, MT was estimated from trench exposures alone. This approach for calculating DFE volumes relies on an assumed positive correlation between the percentage of fan area covered by a DFE, and the number of trenches where the DFE is exposed. An additional assumption is that all DFEs would have a similar pattern of deposition to that of DFE10. For example, if a pre-2014 DFE primarily transported material down a single channel and into the Entiat River, rather than spreading across the fan in multiple depositional “fingers” as DFE10 did, then our method for estimating volume would underestimate the volume of the event, or we would simply not see the event in our limited number of trenches. The obvious limitation of our methodology is that it yields rough volume estimates that are subject to refinement as additional trench data become available, or if better subsurface mapping methodologies are used at the fan.

4. Results

Our surficial map of the fan (Fig. 1) distinguishes two ages of material: pre-2014 material that is boulder-rich debris-flow deposit, and post-2014 (DFE10) material that was deposited in 2 or 3 separate flows that the U.S. Forest Service documented as occurring between August 2014 and October 2016. DFE10 had both debris-flow and flood deposits and had an estimated sediment volume of $12,000 \text{ m}^3$ (Table 1). The pre-2014 material can be broken into DFEs based on exposures in trenches and from radiocarbon dates (see Fig. 2).

Trench exposures reveal a total of 10 DFEs in the last 4000 years (Fig. 2). The timing of DFEs 10 and 9 are from historical records. The ages of DFEs 8–6 are well constrained both spatially and temporally because of the presence of buried A and B soil horizons, as well as an abundance of radiocarbon dates. The ages and spatial correlations between trenches for DFEs 5–1 are poorly constrained because of a general lack of soils and sparse availability of radiocarbon dates. The average thicknesses of individual DFEs range from 0.1 to 1.1 m (Table 1).

Estimated sediment volumes of DFEs ranged from 2,000 m³ (DFE9) to 97,000 m³ (DFE7, Table 1). We estimate that the largest DFE in the 4000-year period of record (DFE7) covered about 48% of the total fan area (Table 1).

The modelled ages for each DFE are shown in Figure 3. DFEs had a mean recurrence interval of 433 +/- 44 years for the 4000-year period of record. However, over the last 300 years, DFEs seem to be occurring more frequently, with mean recurrence intervals for the last 4 DFEs (DFEs 10-7) ranging from about 260 to 20 years (Fig. 3). We suspect that this observation is an artifact because we have good soil, radiocarbon, and historical constraints for the last several hundred years that allow us to better distinguish DFEs compared to the rest of the period of record. The largest DFE in the period of record, DFE7, occurred about 285 +/-98 cal yr BP (1665 AD).

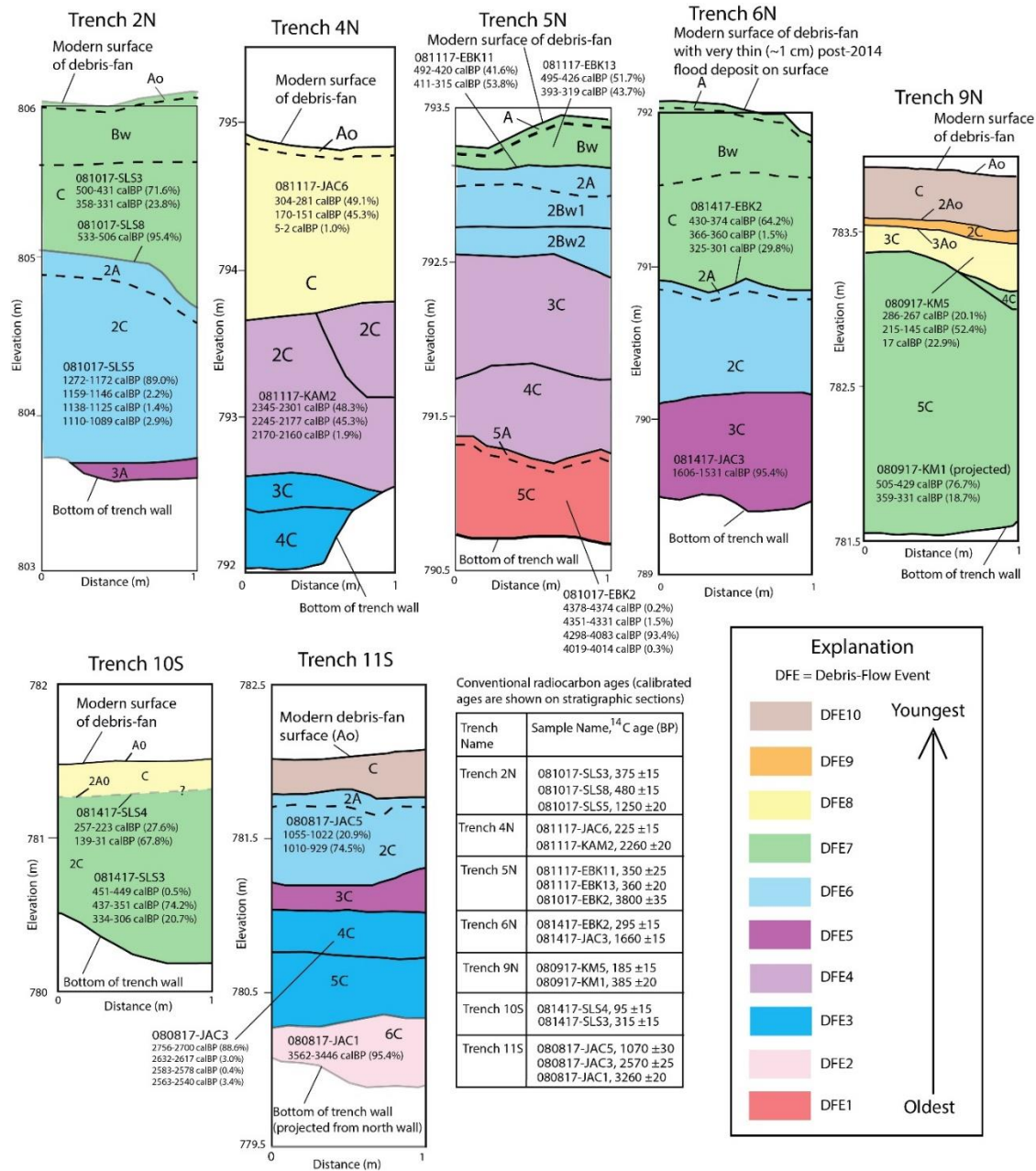


Fig. 2. One-meter wide sections showing stratigraphy exposed in each trench shown in Figure 1. “N” and “S” in trench names refers to north and south walls, respectively. Correlation of debris-flow events (DFEs) between trenches is shown with colors. Soil designations shown in individual sections refer to A, B, and C soil horizons used to correlate deposits between trenches. Conventional radiocarbon ages are shown in the table and calibrated ages are shown in stratigraphic sections. Correlations of older deposits (DFEs 1-5) were difficult because of poor soil and radiocarbon constraints. These correlations are subject to revision as additional radiocarbon dates become available in the future.

Table 1. Estimated areas and sediment volumes for debris-flow events. Estimates are based on measurements of DFE10 which covered 19% of the total fan area and was exposed in two of the seven trenches. Average thickness of DFE10 was estimated from both surface and subsurface (i.e., trench) mapping. All other average thickness estimates were made from multiple measurements in trenches alone. Total fan area is 204,000 m². If deposits from a debris-flow event were exposed in all seven trenches, we estimate that the event would have covered 67% of the fan.

Debris-Flow Event	Number of trenches where DFE is present	Estimated average thickness (m)	Estimated percentage of total fan area covered by the deposits	Estimated area covered by the deposits (m ²)	Estimated sediment volume (m ³)
DFE10	2	0.3	19.0	39,000	12,000
DFE9	1	0.1	9.5	19,000	2,000
DFE8	3	0.5	28.5	58,000	29,000
DFE7	5	1.0	47.5	97,000	97,000
DFE6	4	0.7	38.0	78,000	54,000
DFE5	3	0.3	28.5	58,000	17,000
DFE4	2	1.1	19.0	39,000	43,000
DFE3	2	0.7	19.0	39,000	27,000
DFE2	1	0.3	9.5	19,000	6,000
DFE1	1	0.5	9.5	19,000	10,000

By combining the modelled ages (Fig. 3) and estimated volumes (Table 1) for DFEs over the last 4000 years, we defined a magnitude/frequency relation for debris-flow events on the fan (Fig. 4). This relation shows that the annual probability of DFEs exceeding 1000 m³ is about 0.3 percent, whereas the annual probability for events exceeding 90,000 m³ is about 0.03 percent. This relation is based on the entire period of record and assumes stationarity in climate over the period of record. Stationarity is the concept that climate and other natural systems fluctuate within an unchanging envelope of variability (e.g., see Milly et al., 2008 for details). Climate change is altering the range of historical climate variability (i.e., temperatures and precipitation) and is expected to render the stationarity assumption invalid (Milly et al., 2008). Our magnitude/frequency relation (Fig. 4) does not account for a change in climate stationarity that could be related to the observed increase in DFE frequency over the last several hundred years.

5. Discussion

Wildfires increase the susceptibility of hillslopes to debris flows (e.g., Cannon and Gartner, 2005), but meteorological events trigger the flows. Based on the prevalence of charcoal in our trenches, wildfires have repeatedly burned the Pope Creek basin during the last 4000 years. For the vegetation assemblage that existed at Pope Creek prior to the Duncan Fire, the estimated mean return period for surface fires and stand replacement fires are 40 and 200 years, respectively (U.S. Forest Service, 2018). The surface fire interval is about an order of magnitude less than our mean debris-flow recurrence interval (433 years), whereas the stand replacement interval is about half of our debris-flow interval. In addition to the post-Duncan fire DFE (DFE10), past fires have undoubtedly contributed to other DFEs at Pope Creek. However, the resolution of our data does not allow us to establish a direct link between the timing of fires and debris flows at Pope Creek.

Our records of climatic variations in the Holocene that could influence the magnitude and frequency of fires and meteorological events are similarly crude. Available climate data for our 4000-year period of record come from two sources, radiocarbon-dated pollen records from multiple sites in Washington State (e.g., Whitlock, 1992), and historical records of world-wide climate anomalies such as the Medieval Warm Period and the Little Ice Age (e.g., Broecker, 2001). Pollen records reveal broad changes in temperature and precipitation during the Holocene. In general, these records (e.g., Prichard et al, 2009; Mack et al., 1979) indicate a shift from warm dry conditions in the mid Holocene (~8000 to ~4500 cal yr BP) to cool moist conditions in the late Holocene (~4500 cal yr BP to Present). All of our DFEs occurred in this cooler, moister time period. The Medieval Warm Period

and the Little Ice Age are warmer and cooler periods that are overprinted on this overall period of cool moist conditions.

The largest debris-flow event in our record (DFE7, Table 1) occurred during the Little Ice Age and the 2nd largest event (DFE6, Table 1) occurred at the end of the Medieval Warm Period or in the transition period between the Medieval Warm period and the Little Ice Age (Figure 3). The significance of the largest event occurring during the Little Ice Age is unclear. However, there is about an 8x difference in size between DFE7 and the size of the event that we know is related to wildfire (DFE10). If we speculate a little, this difference may indicate that the largest DFE was triggered by an exceptional meteorological event that occurred during a cool wet time period, and that smaller DFEs were triggered by less exceptional meteorological events that occurred closely following wildfires.

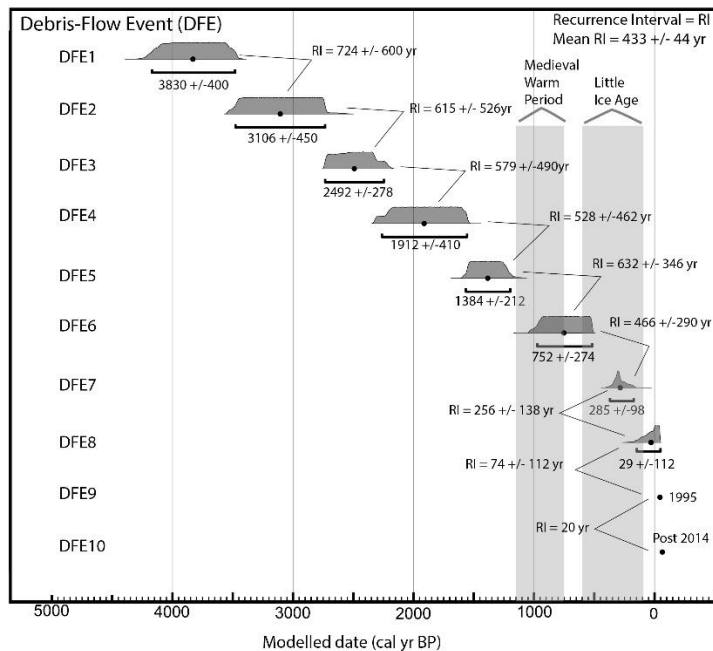


Fig. 3. Probability (PDFs) for the time of debris-flow events (DFEs) on the fan. BP is "Before Present" with "Present" (0 on the x-axis) defined as 1950 AD. PDFs were modeled using the *Date* command in OxCal. Mean values are shown as small black circles. Horizontal bars under each PDF show 2σ ranges. Recurrence intervals between DFEs are the time periods between mean values. Times of the Medieval Warm Period (1150-750 cal yr BP, 800-1200 AD) and Little Ice Age (600-90 cal yr BP, 1350-1860 AD) are from Broecker (2001).

6. Conclusions

We mapped and trenched a small debris-flow fan in central Washington State and found evidence of 10 debris-flow events in the last 4000 years. We used radiocarbon dates from trenches in the program OxCal to model the ages and recurrence intervals between debris-flow events. The mean recurrence interval is 433 years, but intervals range from 724 to 20 years. The four most recent events have the shortest recurrence intervals. The largest event, with an estimated sediment volume of 97,000 m³, occurred at about 285 cal yr BP (1665 AD) during the Little Ice Age. The most recent debris-flow event that was triggered by rainstorms following a wildfire in 2014 was about 8x smaller than the largest event. These results may indicate that the post-fire debris-flow event was triggered by a rainstorm with a relatively small (short) return period compared to the meteorological event that triggered the largest debris flow.

Acknowledgements

We thank the U.S. Forest Service for granting permission for our work at the Pope Creek fan; Jay and Diane Batchelor of Batchelor Excavation for their professional excavation of the trenches; Chris DuRoss and Alan Nelson

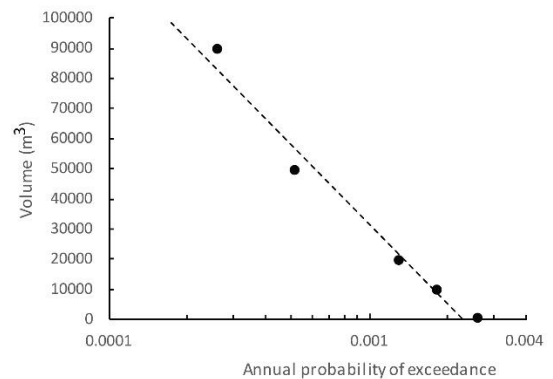


Fig. 4. Annual probability of exceedance for debris-flow event volumes on the Pope Creek fan derived from data in Table 1 using the Poisson probability model and methods described in Coe et al. (2004).

for providing expert advice regarding the use of OxCal; and Kate Scharer, Alex Densmore, and Dennis Staley for their constructive reviews. Any use of trade, firm, or product names is for descriptive purposes only and does not imply endorsement by the U.S. Government.

References

- Balbas, A.M., Barth, A.M., Clark, P.U., Clark, J., Caffee, M., O'Connor, J., Baker, V.R., Konrad, K., and Bjornstad, B., 2017, ¹⁰Be dating of late Pleistocene megafloods and Cordilleran Ice Sheet retreat in the northwestern United States: *Geology*, v. 45, no. 7, p. 583-586.
- Broecker, W.S., 2001, Was the Medieval Warm Period global?: *Science*, v. 291, no. 5508, p. 1497-1499. doi: 10.1126/science.291.5508.1497
- Bronk Ramsey, C., 2009, Bayesian analysis of radiocarbon dates: *Radiocarbon*, v. 51, no. 1, p. 337-360.
- Bronk Ramsey, C., 2017, Methods for Summarizing Radiocarbon Datasets: *Radiocarbon*, 59(2), p. 1809-1833.
- Burned Area Emergency Response, 2014, BAER analysis summary: Duncan Fire 09/08/2014, 11 p.
- Burned Area Emergency Response, 2015, BAER analysis briefing: Wolverine Fire 2015, 4 p.
- Cannon, S.H. and Gartner, J.E., 2005, Wildfire-related debris flow from a hazards perspective: Chapter 15 *in*: Jakob, M. and Hungr, O. eds., *Debris flow hazards and related phenomena: Praxis*, Springer, Berlin, Heidelberg, p. 363-385.
- Coe, J.A., Michael, J.A., Crovelli, R.A., Savage, W.Z., Laprade, W.T., Nashem, W.D., 2004, Probabilistic assessment of precipitation-triggered landslides using historical records of landslide occurrence, Seattle, Washington: *Environmental & Engineering Geoscience*, v. 10, p. 103-122.
- DuRoss, C.B., Personius, S.F., Crone, A.J., Olig, S.S., and Lund, W.R., 2011, Integration of paleoseismic data from multiple sites to develop an objective earthquake chronology: Application to the Weber segment of the Wasatch Fault Zone, Utah: *Bulletin of the Seismological Society of America*, v. 101, no. 6, p. 2765-2781.
- Frechette, J.D. and Meyer, G.A., 2009, Holocene fire-related alluvial-fan deposition and climate in ponderosa pine and mixed conifer forests, Sacramento Mountains, New Mexico, USA: *The Holocene*, v. 19, no. 4, p. 639-651.
- Haugerud, R. A., and Tabor, R. W., 2009, Geologic map of the North Cascade Range, Washington: U.S. Geological Survey Scientific Investigations Map 2940, 2 sheets, scale 1:200,000; 2 pamphlets, 29 p. and 23 p.
- Klock, G.O. and Helvey, J.D., 1976, Debris flows following wildfire in north central Washington: *Proceedings of the Third Interagency Sedimentation Conference*, Denver, CO, pp. 9.
- Lienkaemper, J.L. and Bronk Ramsey, C., 2009, OxCal: versatile tool for developing paleoearthquake chronologies- a primer: *Seismological Research Letters*, v. 80, no. 3, p. 431-434. doi:10.1785/gssrl.80.3.431
- Mack, R.N., Rutter, N.W., Valastro, S., 1979, Holocene vegetation history of the Okanogan Valley, Washington: *Quaternary Research*, v. 12, no. 2, p. 212-225.
- Major, J.J., 1997, Depositional processes in large-scale debris-flow experiments: *The Journal of Geology*, v. 105, p. 345-366.
- Milly, P.C.D., Betancourt, J., Falkenmark, M., Hirsch, R.M., Z.W. Kundzewicz, Lettenmaier, D.P., & Stouffer, R.J. 2008, Stationarity is Dead: Whither Water Management?: *Science*, v. 319, p. 573-574.
- Perkins, R.F., Woodard, R.A., and Ryan, T.P., 1971, Operational report of rehabilitation of the north central Washington fires: Wenatchee National Forest report, U.S. Department of Agriculture, 33 p.
- Pierce, J. and Meyer, G., 2008, Long-term fire history from alluvial fan sediments: the role of drought and climate variability, and implications for management of Rocky Mountain forests: *International Journal of Wildland Fire*, v. 17, p. 84-95.
- Porter, S.P., 1978, Glacier Peak tephra in the north Cascade Range, Washington: stratigraphy, distribution, and relationship to late-glacial events: *Quaternary Research*, v. 10, p. 30-41.
- Prichard, S.J., Gedalof, Z., Oswald, W.W., and Peterson, D.L., 2009, Holocene fire and vegetation dynamics in a montane forest, North Cascade Range, Washington, USA: *Quaternary Research*, v. 72, p. 57-67.
- Reimer, P. J., Bard, E., Bayliss, A., Beck, J. W., Blackwell, P. G., Bronk Ramsey, C., Grootes, P. M., Guilderson, T. P., Hafliðason, H., Hajdas, I., Hatté, C., Heaton, T. J., Hoffmann, D. L., Hogg, A. G., Hughen, K. A., Kaiser, K. F., Kromer, B., Manning, S. W., Niu, M., Reimer, R. W., Richards, D. A., Scott, E. M., Southon, J. R., Staff, R. A., Turney, C. S. M., and van der Plicht, J., 2013, IntCal13 and Marine13 Radiocarbon Age Calibration Curves 0-50,000 Years cal BP: *Radiocarbon*, v. 55, no. 4, p. 1869-1887.
- Safford, H.D., Miller, J., Schmidt, D., Roath, B., Parsons, A., 2007, BAER soil burn severity maps do not measure fire effects to vegetation: a comment on Odion and Hanson (2006): *Ecosystems*, v. 11, no. 1, p. 1-11. doi: 10.1007/s10021-007-9094-z
- Schoeneberger, P.J., Wysocki, D.A., Benham, E.C., and Soil Survey Staff, 2012, Field book for describing and sampling soils, Version 3.0: Natural Resources Conservation Service, National Soil Survey Center, Lincoln, Nebraska.
- Tabor, R.W., Frizzell, V.A., Jr., Whetten, J.T., Waitt, R.B., Swanson, D.A., Byerly, G.R., Booth, D.B., Hetherington, M.J., Zartman, R.E., 1987, Geologic map of the Chelan 30-minute by 60-minute quadrangle, Washington: U.S. Geological Survey Miscellaneous Investigation Series Map I-1661, scale 1:100,000.
- U.S. Bureau of Reclamation, 2009, Entiat tributary assessment, Chelan County, Washington: U.S. Bureau of Reclamation Technical Services Section, Denver, CO, 92 p., 8 appendices. <https://www.usbr.gov/pn/fcrps/ce/wash/entiat/tribassmt/entiattribassmt.pdf>, last accessed October 2018.
- U.S. Forest Service, 2018, Fire regimes of the conterminous United States: U.S. Forest Service Fire Effects Information System (FEIS) web site, https://www.fs.fed.us/database/feis/fire_regime_table/PNVG_fire_regime_table.html#NorthwestForested, last accessed October 2018.
- U.S. Geological Survey, 2018, National Elevation Dataset (NED): <http://nationalmap.gov/elevation.html>, last accessed September 2018.
- Whitlock, C., 1992, Vegetational and climatic history of the Pacific Northwest during the last 20,000 years: implications for understanding present-day biodiversity: *The Northwest Environmental Journal*, v. 8, p. 5-28.
- Woodsmith, R.D., Vache, K.B., McDonnell, J.J., and Helvey, J.D., 2004, Entiat Experimental Forest: catchment-scale runoff data before and after a 1970 wildfire: *Water Resources Research*, v. 40, W11701, doi:10.1029/2004WR003296.

Modeling frequent debris flows to design mitigation alternatives

Joanna Crowe Curran^{a*}, Pat Flanagan^a

^aIndicator Engineering, 7511 Greenwood Ave N #605, Seattle, WA 98103 USA

Abstract

Debris flows are a common problem in Western Washington State. One persistent location of debris flows is Slide Ridge. Glacial till deposits erode in debris flows which travel to Lake Chelan, passing through the community of Shrine Beach in Washington State. In the early 1990s an unlined debris channel was constructed from the apex of Slide Ridge to Chelan lake and a large debris basin was constructed on the upslope side of the road crossing. Every 1-2 years there is a flow large enough to fill the basin, pass over the road to continue downstream to Lake Chelan, and the road is left covered in debris. The largest debris flows since 2003 have volumes estimated to be between 803 m³ to 9863 m³. Samples show the sediment is 85% gravels and dominated by angular cobbles. A number of models are being tested for their ability to predict future debris-flow volume, maximum debris-flow height, and runout distance. Results of the modeling will be used to design and evaluate mitigation measures that include the installation of grates, nets, altering the road configuration, and combination of these measures.

Keywords: debris flow; Cascades; debris channel; mitigation

1. Introduction

Slide Ridge basin is a steep mountainous catchment with rock outcrops split by numerous scree (loose rock) slopes and very sparse areas of soil or vegetation. Based on cursory inspection, the upslope rocks are highly fractured, unstable and are frequently mobilized into debris flows. The occurrence of debris flows in the area has a long history and the GLO maps (circa 1890's) call out the area as "Rock Slide 1000 ft deep". Over geologic time, debris flows have transported sediment from the upper reaches and built an alluvial fan to Lake Chelan. The downstream area of the fan and lakefront have been developed in recent decades despite the prevalence of debris flows. With increased development, the occurrence of road closure due to debris-flow deposition became an issue. The road provides the only year-round access to properties located uplake along the south/west shore.

Debris flows were unmanaged on Slide Ridge until the 1990s. Following a sequence of large debris flows that took multiple paths down the alluvial fan and caused a significant amount of property damage, the County developed an Environmental Impact Statement and options for debris-flow mitigation. The EIS called for construction of a debris flow channel on Slide Ridge to funnel future debris flows to a depositional basin upslope of the road, a culvert under the road to allow for debris passage without overtopping the road, and earthen check dams in the upslope channel to reduce the debris volume transported downstream. These features were built and have been maintained since 1994, but the incidence of debris deposition on the road and around downslope properties has continued. The debris basin was built with 3058.2 m³ (4000 yd³) capacity, and the largest recorded debris-flow volume was 12156.4 m³ (15900 yd³) in 2005.

This presentation presents the results of a mitigation alternatives evaluation for Slide Ridge. The history of the ridge and debris flows were investigated and aided by a large debris flow occurring during the study time frame. Field data collected following this debris flow were combined with historical data to calibrate a DFLOWZ model. This model was used to predict deposition from a range of different debris-flow volumes, including volumes larger than

* Corresponding author e-mail address: crowecurran@gmail.com

any previously recorded, under a range of mitigation alternatives. Alternatives were developed with the goal of reducing or eliminating road closures, reducing the required maintenance, and reducing the public safety hazard. Alternatives included increasing the size and/ or number and location of debris basins, installing a herringbone style debris breaker, and altering the defined debris-flow channel geometry and slope to increase the volume transported into the lake during a debris flow. This presentation focuses on how the alternatives have been selected and analyzed.

2. Site

Lake Chelan is located on the eastern side of the Cascade Range in Washington State. The lake has an upper and lower basin connected by a constricted, shallow reach known as the Narrows. The upper basin, Wapato Basin, was carved by the Chelan glacier and the lower basin, Lucerne Basin, by the Okanogan-Columbia Valley lobe of the Cordilleran Ice Sheet (Kendra and Singleton, 1987). The lake drains to the Columbia River.

Slide Ridge is on the southwest side of Lake Chelan immediately downstream of the Narrows. It is a steep, mountainous catchment of coarsely crystalline granites, schists, and gneisses with well developed jointing. Vegetation is sparse, and outcrops are separated by scree slopes. Debris flows have built an alluvial fan over time, and many historic remnant channels and flow deposits are visible across the fan. Large debris-flow events have deposited sediment into Lake Chelan over time. In 1967, bathymetry measurements identified 45 m of sediment accumulation in the channel center, and it was inferred to have originated with flows off Slide Ridge (Whetten, 1967). Shoreline bathymetry from 1987 were used to estimate the off-shore slope at 11%. LiDAR was collected over the study area in May, 2018.

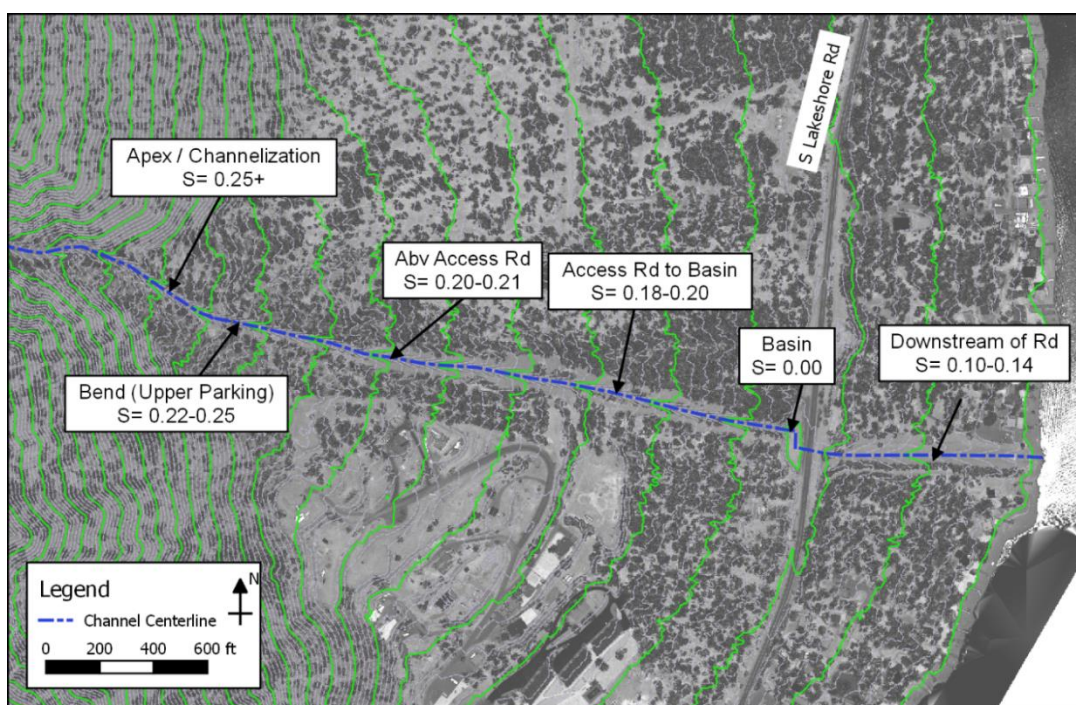


Fig. 1. Channel slopes based on 2018 Lidar for Slide Ridge debris channel.

The existing Slide Ridge geometry channelizes the debris flows from the apex to efficiently convey flows to S Lakeshore Road. Above the apex the upper basin slopes are 45 degrees or more and rapidly contribute water and debris down a dendritic series of steep channels. There is a 30-foot high rock step in the main flow path of this system where the “channel” generally begins. From this step to the apex, hill slopes vary dramatically throughout the year as small events deposit debris and large events scour and transport the debris downstream. Using this surface, measured hillslopes measured from the 2018 LiDAR ranged from 25 to 40% from the step to the apex (Figure 1). The channelization begins at the apex, with a levee attached to the left/north valley wall. The slopes for the channelization gradually decrease from 25% at the apex to 18% above the debris basin as shown in Fig. . The channel slope locally

increases to an average of 22% leading into the debris basin, which is flat. Debris flows entering the basin must turn right/south 90 degrees, travel across the flat basin, then turn 90 degrees through a constrictive 2 m (H) by 3.2 m (W) (6.2 ft (H) by 10.5 ft (W)) corrugated culvert. The bottom of the basin is about 4.3 meter (14 ft) below the road surface. This geometry has effectively conveyed small debris flows to the basin, but also encouraged large debris flow deposition over the road.

3. Debris-Flow History

The recent history of debris-flow timing and volumes have been documented locally since the 1970s. In 1972 a large debris flow scoured a channel 4.6-6.1 meter (15-20 ft) deep along the upper hillslope. As this flow traveled downstream, it spread out and deposited among homes and damaging properties downslope of Lakeshore Road. A broad channel was constructed between the road and lake in response with side levees to contain future flows. The channel downstream of the road has slopes ranging from 14% at the upstream end near the culvert outlet to 8-10% at the lake.

In 1990 two large debris-flow events overwhelmed the downstream channel, depositing on the road and houses. A larger mitigation effort was deemed necessary as development around the Lake continued, and in 1994, the deep and narrow debris channel with levees was constructed from the apex to the road to constrain debris flows and convey them down the constructed channel corridor. Plowed earth check dams were included in the upper channel. A debris basin was built on the upstream side of the road with a 3058.2 m³ (4000 yd³) capacity. A culvert ran under the road with the plan that debris could pass through the culvert and continue downslope to Lake Chelan. This system remains in place. The channel sections vary in size upstream and downstream of the road. The upstream channel section is confined with a bottom width of 4.3-6.1 meter (14 to 20 ft), steep side slopes, 10.7-13.7 meter (35 to 45 ft) top width and depths of 4.3-5.5 meter (14 to 18 ft). The downstream channel is broader with a bottom width of 12 to 20 feet, gradual side slopes, 55 to 80 feet top width and depths of 2.4-3 meter (8 to 12 ft). Channel and basin are cleaned of sediment and the earthen check dams are re-built following debris flows.

Debris-flow volumes overwhelm the basin capacity every few years, requiring road closure, emergency county excavation of the road, and typically contracted excavation of large debris volumes deposited in the basin and channel. The County recorded volumes for those debris flows requiring basin clean outs for the past 15 years. There are 8 recorded events, and it is suspected that many smaller events occurred within this time period that were not recorded. The volumes recorded reflect only the amount deposited on the road and in the basin. We were able to visit the site within days of the 2017 debris-flow event.

Based on our observations, survey, and field measurements following this event, we estimate an additional 764.6 m³ (1000 yd³) of debris/sediment deposited in and around the debris basin that is in addition to the reported volume for basin clean out. Therefore, this estimate has been used to increase volumes from the historic record to account for the entire debris-flow volume (Table 1).

Table 1. Historic debris-flow volumes reported at Lakeshore Road since 2003. Dates were estimated based on available background data (rainfall records, photos), and may not be the exact date of debris flow for all events.

Year	Date	Estimated total volume (m ³)	Estimated total volume (yd ³)
2003	Nov. 11	8,594	11,240
2005	May 10	12,156	15,900
2006	June 11	4,293	5,615
2010	Aug. 3	8,410	11,000
2011	June 10	7,454	9,750
2014	June 13	2,600	3,400
2015	Dec. 9	803	1,050
2017	Oct. 22	7,034	9,200

4. Hydrologic Analysis

Gage records of rainfall intensity and duration in the vicinity of Slide Ridge were analyzed to determine if a correlation exists between observed rainfall and debris-flow volumes. Although there are three nearby rain gages, there is considerable spatial variability in local storm events. The rain gages have varying record lengths, and the longest had recorded data as far back as the 2003 event. Storm data from the dates when large debris flows were documented were used to develop rainfall threshold curves to estimate when a debris flow is likely to occur. A separate threshold curve was created for each gage due to spatial variability in rainfall patterns (Figure 2). Seven of the eight documented debris flows were well represented by the data. The 2011 event was poorly recorded and may have been a more localized thunderstorm.

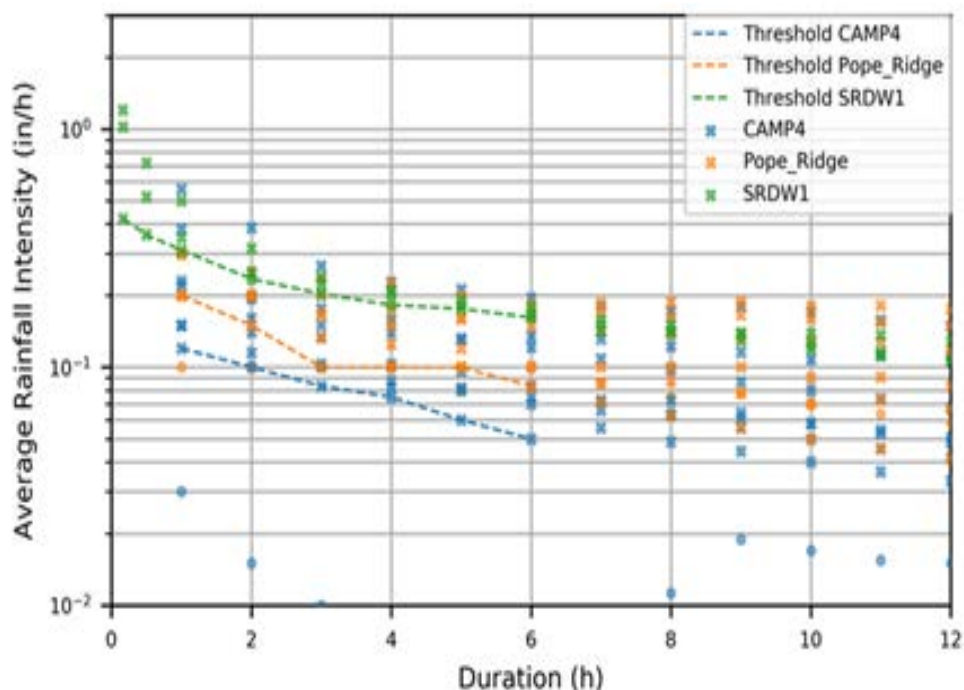


Fig. 2. Duration plot of debris flow events for all 3 rain gages. Historic debris flow events are shown as x. The calculated minimum rainfall thresholds for each gage are shown as dashed lines.

Spearman and Pearson tests showed the 2-hour rainfall duration had the highest statistical correlation between debris flow and rainfall events. A regression curve was fit to the rain gage data for the 2-hour rainfall intensities to provide an approximation of debris-flow volume for predicted average 2-hour rainfall intensities (Figure 3). While highly speculative, this correlation enables managers to begin planning debris-flow mitigation measures.

5. Debris-Flow Characteristics

Field investigations were conducted in 2017 and 2018 to collect sediment samples and evaluate the debris channel. Sediment samples were collected from multiple locations in the defined debris channel (Figure 4). The first site visit was 2 days after the October 2017 event. Samples were collected from the debris slurry downslope of the road (SR1) and in the channel area upstream of the debris basin (SR2). Water contents were measured by weight at 8.2% water for the main part of the debris flow (SR2) and 17.2% water in the runout slurry sample (SR1). The SR1 sample was a suspended liquid, and the SR2 sample from the debris flow was deformable under body weight even with the presence of large angular cobbles. The combination of low water content, silts, and cohesive sediments created the slurry capable of transporting 3 to 4-foot boulders downslope. Three additional samples were collected during a second visit in December, 2017. The full debris channel was investigated during this visit and samples were taken at the apex (SR5), and at major slope breaks on the upper slope (SR3, SR4). There was an abundance of boulders that are commonly 3 to 4 feet in diameter were abundant in the area and evidenced periodic mobilization by debris flows. The

matrix of smaller sediment sizes was saved from these samples and sieved (Figure 5). Samples SR3-5 indicate the matrix in the upper slope area was composed of approximately 10% sand.

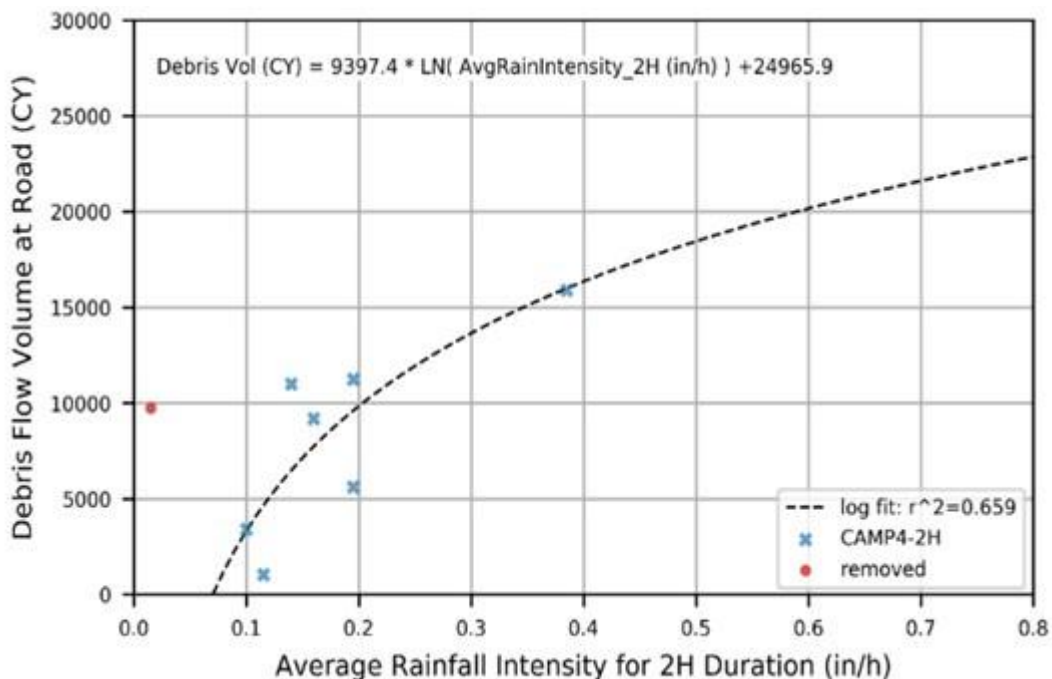


Fig. 3. Regression equation for Slide Ridge debris-flow volume based on Camp4 rain gage intensity (at 2 hour duration). The 2011 event did not appear to be captured by the Camp4 gage and was removed from the fit.

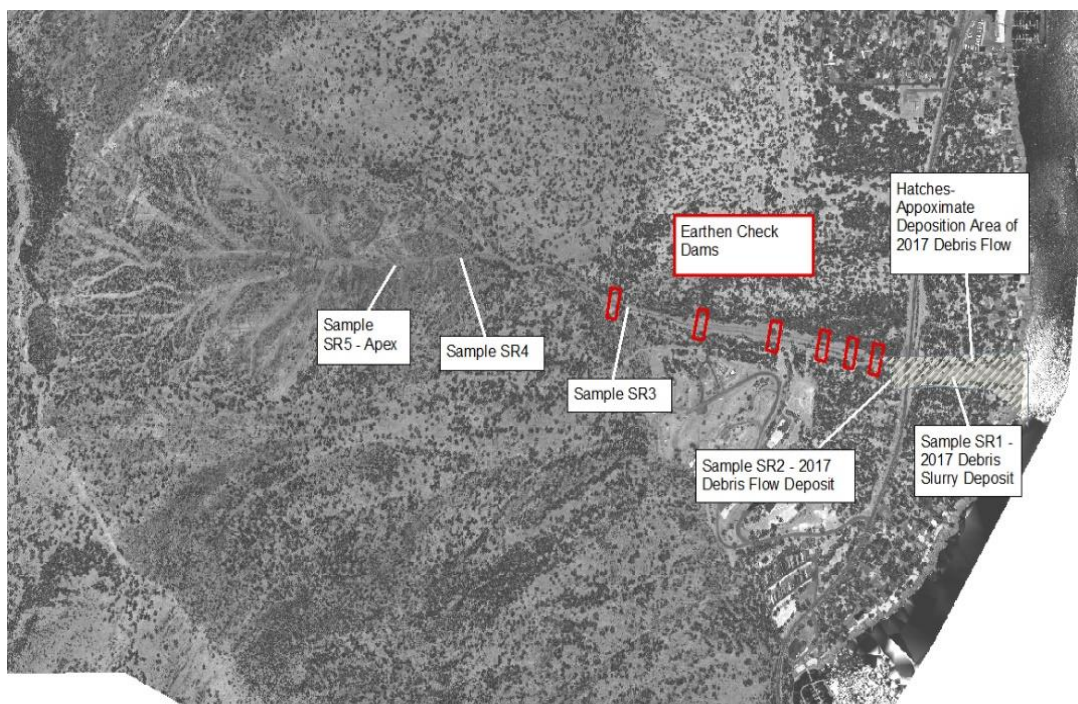


Fig. 4. Locations of sediment samples (call out boxes), earthen check dams (red rectangles), and deposition from the 2017 debris flow on Slide Ridge (grey hatch marks). The background image is the 2018 LiDAR of the site.

The runout length of a debris flow is highly dependent on the water content in the debris-flow front (aka debris-flow snout) and the grain sizes within the debris. Observation and sediment samples indicate that for Slide Ridge the grain size distribution will remain relatively constant. The water content and debris volume will vary with event and act as the main controls over run out lengths and widths. Evidence of rapidly deposited debris snouts were apparent throughout the upper debris channel for flows that did not travel to Lake Chelan. Deposition on the reach between the road and the lake evidenced continued movement of the smaller gravels that had been part of the larger debris-flow matrix. The combination of slope break and culverted basin immediately upstream of the lower reach acted to arrest movement of the largest boulders. Maximum gravel sizes downslope of the road reach 0.5 meter. The debris slurry is much more mobile and extends beyond boundaries of debris deposition. Following the 2017 event, slurry had filled open space in the debris basin, flowed down the road and side ditches, and flows past the debris deposition and into the Lake. It is suspected that slurries associated with large debris events follow this general pattern with a large amount flowing into the Lake.

The earthen dams constructed in the debris channel act as accumulation points for small debris flows and normal bedload transport events that occur between large debris-flow events. Sediment deposits immediately upstream of these dams were observed during field reconnaissance. These check dams may be mobilized during large debris events, adding to debris-flow bulking with distance downslope.

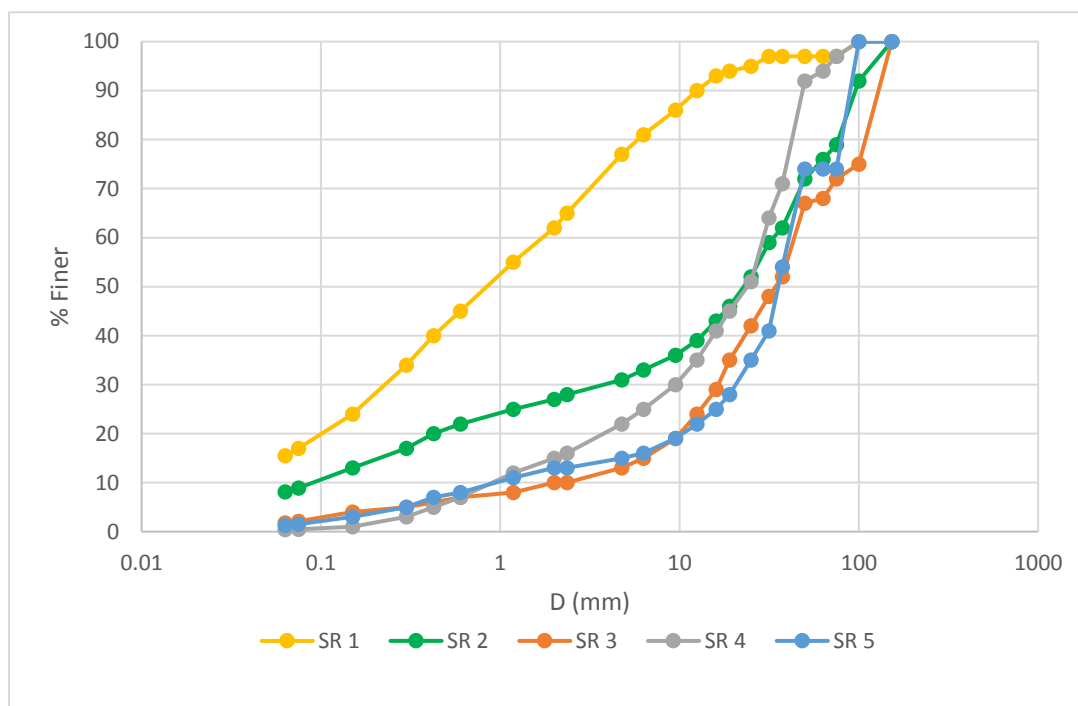


Fig. 5. Grain size distributions for slide ridge samples SR1 to SR5. Samples SR1 and SR2 were taken 2 days after a large debris flow in October, 2017. SR1 is from the debris-flow slurry. SR2 is debris deposited at the road. Samples SR3, SR4, and SR5 were taken from the upper debris channel in December, 2017.

6. Debris-Flow Model

Data were used to calibrate the debris-flow model DFLOWZ. The DFLOWZ model is used to simulate runout length and area for given debris volume events. This information will help determine a mitigation strategy that can reduce maintenance in the future. The model predicts debris-flow runout length and area with a maximum uncertainty of 3 that can be improved upon with calibration data. The model is fully described in Berti and Simoni (2007), Simoni, Mammoliti, and Berti (2011), and Berti and Simoni (2014). We employed the version DFLOWZ_J. Calibration parameters are used to adjust the cross-sectional and planimetric depositional areas for a given debris-flow volume and path. The grain size distribution and water content are used as guides in setting the calibration parameters.

The model was calibrated to within 10% of the documented depositional area and volume from the October 2017 event. The measured grain size and water content were used to guide the calibration. Water content was the least constrained parameter and was the focus of the calibration. Grain size information was assumed to be constant between model runs, while event volume is varied to simulate historic or recurrence interval debris flows. The model does not simulate the slurry deposition downstream of the main debris deposit. Once calibrated to the 2017 event, the model was used to simulate the depositional area and depths associated with the past debris flows documented in Table 1. This was done to evaluate the severity of these debris flows, including when and where debris deposits extended outside the defined channel area. These results were compared to historical photos and evaluated by County staff familiar with the area to provide a qualitative model check. The model calibration was refined using information gained on the past flows.

7. Mitigation Alternatives

The calibrated model was used to aid in conceptual evaluation of mitigation options. Debris flows of larger volume were simulated to predict runout pattern and volume. These present a ‘worst case’ scenario useful when considering possible mitigation and changes in current management practices at the Slide Ridge site. As described above, the existing system is effective at causing debris deposition at the road crossing, however the existing basin is undersized and debris frequently deposits on the road. Alternatives were developed with the goal of reducing or eliminating road closures, reducing required maintenance, and reducing the public safety hazard. A number of alternatives were investigated, and the most promising were to increase debris retention on the channel slope, alter the water content of the debris flow to arrest downstream movement of the largest boulders, and to alter debris channel geometry and slope to increase the volume of debris transported into the lake.

Trapping and storing the debris flow in a retention basin is a proven management technique to trap debris where it can then be more easily hauled away after a debris flow. The existing basin could be lowered to provide additional volume. A large debris basin could be added into the existing system anywhere upstream of S Lakeshore Road. Locating a debris basin below the apex is a typical management strategy as it allows debris flows to be captured from a known location, without relying on the conveyance channel to contain all events. The debris-flow volumes would require that the basin either be very large, or a series of smaller basin be constructed. In either case there is a large disruption to an already unstable slope with little vegetation.

As an alternative to retaining all the debris during an event, systems have been designed that capture only the largest particles allowing the remaining debris flow to have increased water and sand content. Such a system could result in longer runout distances for the remaining debris flow. Installation of the herringbone style debris breaker detailed in Xie et al. (2016, 2017) could be placed in the upstream channel or at the existing basin. The system would arrest the movement of the larger particles in the flow while allowing the smaller gravels to transport downstream in a slurry with a now relatively larger water content. Therefore the grain size distribution of the debris was adjusted to represent an artificially increased water volume. A rough estimate is that about 3058 m³ (4,000 yd³) of 0.3 meter or larger material would reach the road during a 100-year event. If that amount were extracted and retained, the remaining debris would be much more likely to be conveyed to the lake.

An alternative to convey the entire debris flow to the lake in an unlined channel was evaluated. The evaluation included frequent reference to the October 2017 event and historic performance. Different system geometries were evaluated using the DFLOWZ model, following an empirical technique presented by Rickenmann (1999) and with consideration of site geometric constraints. The debris-flow model was applied to determine how debris flows would deposit in the reach from the existing basin to the lake if there were a debris channel for that distance. To simulate this, the current debris basin and road were removed from the model surface. A new debris channel was graded to have a consistent slope from the end of the current channel (just upstream of the existing debris basin) to the lake. Channel slopes of 12% and 14% were tested. The 14% slope is the same as the slope immediately downstream of the road. The slope quickly lessens as the channel approaches the lake and a 12% slope was also tested.

A number of scenarios were tested in the debris-flow model for runout pattern and length. The effectiveness of the alternatives was determined from the ability of the alteration to maintain the debris flow within a contained channel, the relative amount of debris transported to the lake, and the height of the debris at the site of the road. Channelizing the debris flow downstream of the road crossing aiding in transport to the lake. It was quickly found that a channel lined with berms would be necessary to prevent debris deposits from extending into properties near the lakefront while conveying debris to the lake. Different berm and channel geometries were tested, and berm heights over 6 feet did not increase the amount of deposition in the lake. The width of the berm had a greater influence than height on the elevation

of the debris deposits. Berms widths up to 75 feet reduced the height of the deposit at the road. Debris-flow runout length was not found to be sensitive to the channel slope. Altering the slope between 12% and 14% had little influence on the area covered by debris deposition. Debris volumes up to 7646 m³ (10000 yd³) were contained within the area of the channel for all scenarios. Deposition became significant when the debris volume exceeded 15291 m³ (20000 yd³).

8. Summary

Debris flows are a common on Slide Ridge, on the shores of Lake Chelan in Washington State. Glacial till deposits continue to generate debris flows that travel to Lake Chelan, passing through the community of Shrine Beach. In the early 1990s an unlined debris channel was constructed from the apex of the ridge to Chelan lake and a large debris basin was constructed on the upslope side of the road crossing. Every 1-2 years there is a flow large enough to fill the basin, pass over the road to continue downstream to Lake Chelan, and the road is left covered in debris. Debris deposits are 85% gravels and dominated by angular cobbles. Field data were collected and used to calibrate a DFLOWZ model of the system. Modeling enabled formation and testing of a number of mitigation alternatives.

The analysis of mitigation alternatives for debris flows on Slide Ridge in Washington State is under refinement. While a large number of alternatives mitigation options exist, those deemed most appropriate for Slide Ridge included expanding the system of debris storage upslope, increasing conveyance of debris to Lake Chelan through slope and debris channel manipulation, and installation of a herringbone style debris breaker to arrest movement of the largest boulders while increasing relative water content in the debris flow.

Acknowledgements

We thank Paula Cox and Chelan County for the funding and interest in this topic. We also thank Anne Streufert, Jason Peng, and Bob Kimmerling for their conversation and contributions to the progression of this work. The comments of two anonymous reviewers also helped improve the manuscript.

References

- Berti M., and Simoni A., 2014, DFLOWZ: a free program to evaluate the area potentially inundated by a debris flow: *Computers & Geosciences*, v. 67, p. 14-23.
- Berti, M., and Simoni, A., 2007, Prediction of debris flow inundation areas using empirical mobility relationships: *Geomorphology*, v. 90, p. 144-161, doi:10.1016/j.geomorph.2007.01.014.
- Chelan County, 1993, Final Environmental Impact Statement for Chelan County Public Works Slide Ridge Control Channel. Prepared by Hammond, Collier & Wade – Livingstone Associates, Inc., 186 p.
- GeoTerra Inc., 2018, LiDAR Technical Report: Slide Ridge Lidar. Flown on June 8, 2018.
- GLO, compilers, 1895, Map of Township No 28N, Range 21E, Willamette Meridian, Washington: General Land Office Map from October 9, 1895.
- Kendra, W., and Singleton, L., 1987, Morphometry of Lake Chelan: Water Quality Investigations Report. Washington State Department of Ecology Report No. 87-1, 40 p.
- Mastin, M.C., Konrad, C.P., Veilleux, A.G., and Tecca, A.E., 2016, Magnitude, frequency, and trends of floods at gaged and ungaged sites in Washington, based on data through water year 2014 (ver 1.2, November 2017): U.S. Geological Survey Scientific Investigations Report 2016–5118, 70 p., <http://dx.doi.org/10.3133/sir20165118>.
- Pierson, T.C., 1986, Flow Behavior of Channelized Debris Flows, Mount St. Helens, Washington: *Hillslope Processes*, p 269-296.
- Rickenmann, D., 1999, Empirical relationships for debris flows: *Natural hazards*, v. 19, p.47-77.
- Simoni, A., Mammoliti, M., and Berti, M., 2011, Uncertainty of debris flow mobility relationships and its influence on the prediction of inundated areas: *Geomorphology*, v. 132, p. 249–259, doi:10.1016/j.geomorph.2011.05.013.
- Van Asch, T.W., Tang, C., Alkema, D., Zhu, J. and Zhou, W., 2014, An integrated model to assess critical rainfall thresholds for run-out distances of debris flows: *Natural hazards*, v. 70, p. 299-311.
- Whetten, J.T., 1967, Lake Chelan, Washington: Bottom and sub-bottom topography: *Limnology and Oceanography*, v. 12, p.253-259.
- Xie, T., Wei, F., Yang, H., Gardner, J.S., Xie, X., Dai, Z. and Jiang, Z., 2016, Calculation of the separation grid design length in a new water-sediment separation structure for debris flow defense: *Bulletin of Engineering Geology and the Environment*, v. 75, p.101-108.
- Xie, T., Wei, F., Yang, H., Gardner, J.S. and Xie, X., 2017, A design method for a debris flow water-sediment separation structure: *Engineering Geology*, v. 220, p.94-98.

Application of knowledge-driven method for debris-slide susceptibility mapping in regional scale

Raja Das^{a*}, Arpita Nandi^a

^aEast Tennessee State University, 1276 Gilbreath Dr, Johnson City, TN 37614, USA

Abstract

Debris-slides are a frequent hazard in fragile decomposed metasedimentary rocks in the Anakeesta rock formation in Great Smoky Mountain National Park. The spatial distribution of an existing debris-slide area could be used to prepare susceptibility map for future debris-slide initiation zones. This work aims to create a debris-slide susceptibility map by using a knowledge-driven method in a GIS platform in Anakeesta formation of Great Smoky Mountain National Park. Six geofactors, namely, elevation, annual rainfall, slope curvature, landcover, soil texture and various slope failure modes were used to create the susceptibility map. Debris-slide locations were mapped from the satellite imagery, previous studies, and field visits. A Weighted Overlay Analysis was performed in order to generate the final susceptibility map, where individual classes of geofactors were ranked and were assigned weights based on their influence on debris-slide. The final susceptibility map was classified into five categories: very low, low, moderate, high and very high susceptible zones. Validation of the result shows very high category predicted ~10%, high and moderate categories predicted 75.5% and ~14.5% of the existing debris-slide pixels respectively. This study successfully depicts the advantage and usefulness of the knowledge-driven method, which can save considerable amount of time and reduce complicated data analysis unlike statistical or physical based methods. However, the accuracy of the model highly depends on the researcher's experience of the area and selection of respective geofactors.

Keywords: Debris-slide Susceptibility; Heuristic; Weighted Overlay Analysis; Great Smoky Mountain National Park.

1. Introduction

Debris-slides are fast movements of earth materials, which occur including subarctic regions (Rapp and Stromquist, 1976) and humid tropics (Simonett, 1970). Debris-slides are common in the Appalachian Valley and Ridge, and Blue Ridge physiographic provinces of the United States (Bogucki, 1976). Van Westen (1993) discussed that under the presence of favorable causal and triggering factors, such as earthquakes and extreme rainfall, most of the mountainous terrains are susceptible to slope failure. The same was pointed out by Bogucki (1976), who found that a combination of Appalachian slope and rainfall has eroded the mountains by several thousand noticeable debris-slides. About 2000 slides have formed in Georgia, North Carolina, Tennessee, Kentucky, West Virginia, and Virginia and as many as 200 deaths that may have been caused directly by slide activity from 1940 to recent (Scott 1972, Wooten, et al., 2016). Additionally, these events have caused damage to homes, property and road networks, and have had major impacts on federal lands.

It is important to develop a detailed understanding of the causes and mechanisms of debris-slide events for better prediction and risk assessment. One of the preliminary steps to evaluate events and predict future slide related hazards is to develop debris-slide susceptibility maps (Pradhan, 2011). These maps are used to identify zones that are prone to mass failures depending on the geofactors that have caused the slides in past. Presumably, the same factors would cause the slides in future (Varnes, 1978; Carrara et al., 1995; Guzzetti et al., 1999). Geographic Information Systems (GIS) provides a powerful tool to analyze spatial hazard related data, and hence, it has become indispensable tool for regional slope failure hazard and risk analysis. Several authors have applied different methods to map slope failure susceptibility and hazard (e.g., Nandi and Shakoor, 2010; Pradhan, 2011; Lee and Pradhan, 2007). Regional slope failure mapping is generally grouped into three categories: (i) heuristic or knowledge-driven methods (ii) data-driven methods and (iii) physically based models. The heuristic methods are again divided into direct or indirect methods. A direct heuristic method deals with detailed field investigation of area's geomorphology, geology, and hydrology

*Corresponding authors e-mail address: dasr01@etsu.edu, nandi@etsu.edu

(Brabb, 1984). The accuracy of the method is highly dependent on the experience of the investigator and the precision level of the work (Ghosh et al., 2013). On the other hand, the indirect heuristic methods are based on assigning some weights or rating to the individual geofactors according to their importance, which is solely decided by the investigator, based on similar existing research (Hansen, 1984; Varnes, 1984).

Data-driven methods are mostly statistical, which include bivariate and multivariate analysis and are primarily based on the observed data of landslides and relevant spatial geofactors (Nandi and Shakoor, 2010; Ghosh et al., 2013). In these methods, several causative factors for debris-slides are integrated with the slide inventory to statistically model the relationship between the geofactors and slope failure. (Van Westen, 1993). Nandi and Shakoor (2017) used the same approach to study debris-slide susceptibility in Little Pigeon River (WPLPR) watershed in the southern Appalachian Mountains, where debris-slide locations were identified from aerial photographs, and satellite images. Topographical, bedrock geology, and hydrological data were collected, processed, and constructed into a spatial database using GIS. Logistic regression model was used to evaluate the role of these factors in controlling debris-slide susceptibility. While the method was rigorous and powerful, the limitations of the method were (i) time consuming and not recommended for urgent projects, and (ii) rock discontinuity data were not used as input variable. Therefore, the objective of this research is to include bedrock discontinuity data that play crucial role in controlling the debris-slide events in the form of rock kinematical index, and create a knowledge-driven susceptibility model for predicting the spatial probability of debris-slide initiation zones.

2. Study area

The study was conducted in the Anakeesta rock formation in the Upper West Prong Little Pigeon River watershed (WPLPR), Great Smoky Mountain National Park, TN. The elevation of the study area ranges from 1105 m to 2010 m. Temperature in Great Smoky Mountains varies from -2.22°C (28°F) to 31.11°C (88°F) at the base and -7.2°C (19°F) to 18.33°C (65°F) at the ridges. The area receives annual rainfall of 1397mm (55 inches) at the base and 2159 mm (85 inches) at the highest point of the park. The rainfall increases with increase in the elevation and is highest at the Anakeesta formation. Torrential rainfall associated with severe thunderstorms and hurricanes are the main triggering factors for debris-slide in the study area (Bogucki, 1976; Clark, 1987).

Geologically Anakeesta formation is characterized by fine grained dark colored sedimentary and metasedimentary rock having craggy pinnacle structure i.e., needle-shaped rock faces and steep slopes. The dark color of the rocks is mainly due to presence of graphite and some part of the formation exhibits rusty orange color due to presence of iron sulfide minerals mainly pyrite. The main rock types include phyllite, chloritoid slate, graphitic and sulfidic slate, feldspathic sandstone, laminated metasilstone and coarse grained metagraywacke (Southworth et al., 2012). Different sets of discontinuities exist in form of joints, fractures and to some extent as cleavage, which enhance the weathering along these discontinuity planes.

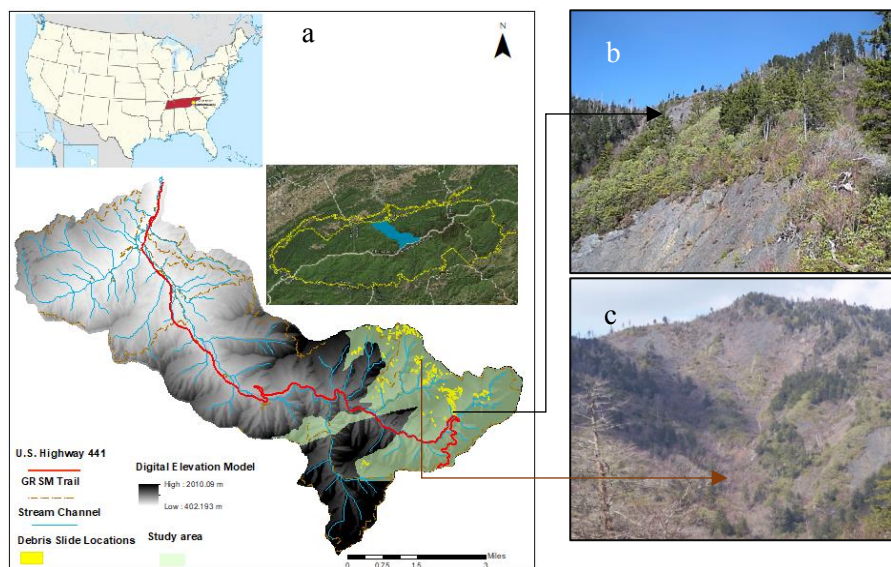


Fig. 1. Study area (a), Debris-slide initiation zones photos in Anakeesta Formation (b, c). [Photo courtesy: Greg Hoover (b) gosmokies.knoxnews.com (c)]

3. Methodology

The present study used both digital data and field investigation. A flow chart in Fig. 2, provides a step by step process of the methodology.

3.1. Digital Data

In order to create the debris-slide susceptibility map, six geofactors, namely, elevation, rainfall accumulation, soil texture, landcover, slope curvature, and various bedrock discontinuity layers responsible for slope failures were used. Elevation and slope curvature maps were derived from LiDAR Digital Elevation Model (DEM) of 0.76m spatial resolution. The LiDAR DEM for Tennessee is available at TNGIS website (<http://www.tngis.org/>). Soil texture, landcover and rainfall accumulation maps were collected from the National Park Service's database (<https://irma.nps.gov/DataStore/Search/Quick>) (Fig.3.a-e). Debris-slide initiation locations were digitized from historical to recent aerial photos and satellite imageries, and about 30% of the locations were confirmed during field studies. The debris-slide initiation locations were used to evaluate the suitability of susceptibility analysis.

3.2. Field investigation and Kinematical index

Geometrical relationship between orientations of the topographic slope and geological discontinuities play important role in controlling the slope instability in an area, which is known as rock kinematics. Slope instability analysis based on this mutual relationship is known as rock kinematic analysis. Factors like topographic slope angle and aspect, internal friction angle of the rock and orientation of geological discontinuities combined with each other control slope stability within a rock mass. Depending upon the number of geological discontinuities and their orientations with the topography, three different modes of rock failure can occur (i) Planar (ii) Wedge (iii) Topple (Eq. 1 and 2) (Ghosh et al., 2010). The kinematical index layer was prepared using the geometric relationship between geological discontinuities and the topographic slope angle and direction (Fig. 3f). From field mapping and previous work, structural orientations (dip angle and dip direction) of a total of 313 discontinuities were used in the study. The internal friction angle (ϕ) of the bedrock was estimated from Rock Mass Rating system data collected in the field (Bieniawski, 1989). Topographic slope angle (θ) was obtained from the LiDAR DEM, dip/plunge angle (β) and direction of discontinuities were obtained by plotting the structural data in Stereonet 10 software (Allmendinger et al., 2012). Subsequently, the following equations were used in ArcGIS to spatially detect the areas where slope failures were kinematically possible (Ghosh et al. 2010):

$$\phi \leq \beta \leq \theta \text{ (for Plane and Wedge Failure)} \quad (1)$$

$$\theta \geq [\phi + (90^\circ - \beta)] \text{ (for Topple Failure)} \quad (2)$$

Eleven combinations of planer, wedge and topple failures were possible in the study area that produced 11 different kinematic layers susceptible to failure. The wedge type of failures were dominant in the study area, and were more prevalent in bedding ($52^\circ \rightarrow 151^\circ$) and Joint1 ($50^\circ \rightarrow 255^\circ$) governed discontinuities. All layers were ranked based on presence of actual debris-slide initiation location, and the ranked layers were combined into one kinematic index layer. A detailed description of the preparation of composite kinematic index layer is presented in a forthcoming paper (Das, et al., in preparation).

A Weighted Overlay Analysis was performed to generate the debris-slide susceptibility map, using a heuristic approach. Weighted Overlay Analysis tool is available in the Spatial Analyst extension in ArcGIS 10.5. All geofactor layers were converted into raster format and rescaled to 0.76-m grid size before the susceptibility analysis. Based on the field studies and prior knowledge of the study area, the individual classes of the geofactors were ranked and the relative weights were assigned to each individual geofactor. The weights represented the degree of influence of individual geofactors in producing debris-slides in the region on a scale of 0 to 100 that added up to 100%. Table 1 summarizes the different geofactors and their corresponding weighting that were used in the susceptibility analysis.

Table 1. Summary table of the geofactors.

Geofactor	Source	Average (Range)	Weight
Elevation	Digital Elevation Model	1526 m (1105m – 2010m)	30
Rainfall	National Park Services	2051mm (1854mm– 2159mm)	25
Soil	National Park Services	Channery loam, Channery silt loam, Loam, Slide area, Peat, Very Channery loam	15
Kinematical Index	Digital elevation model and Lithological map (National Park Service)	5.68 (0 - 57.95)	15
Landcover	National Park Services	Barren land, Deciduous forest, Developed Open space, Developed low intensity, Developed medium intensity, Evergreen Forest, Mixed Forest, Shrub	10
Curvature	Digital Elevation Model	-6.62 (-6839 to + 11380)	5

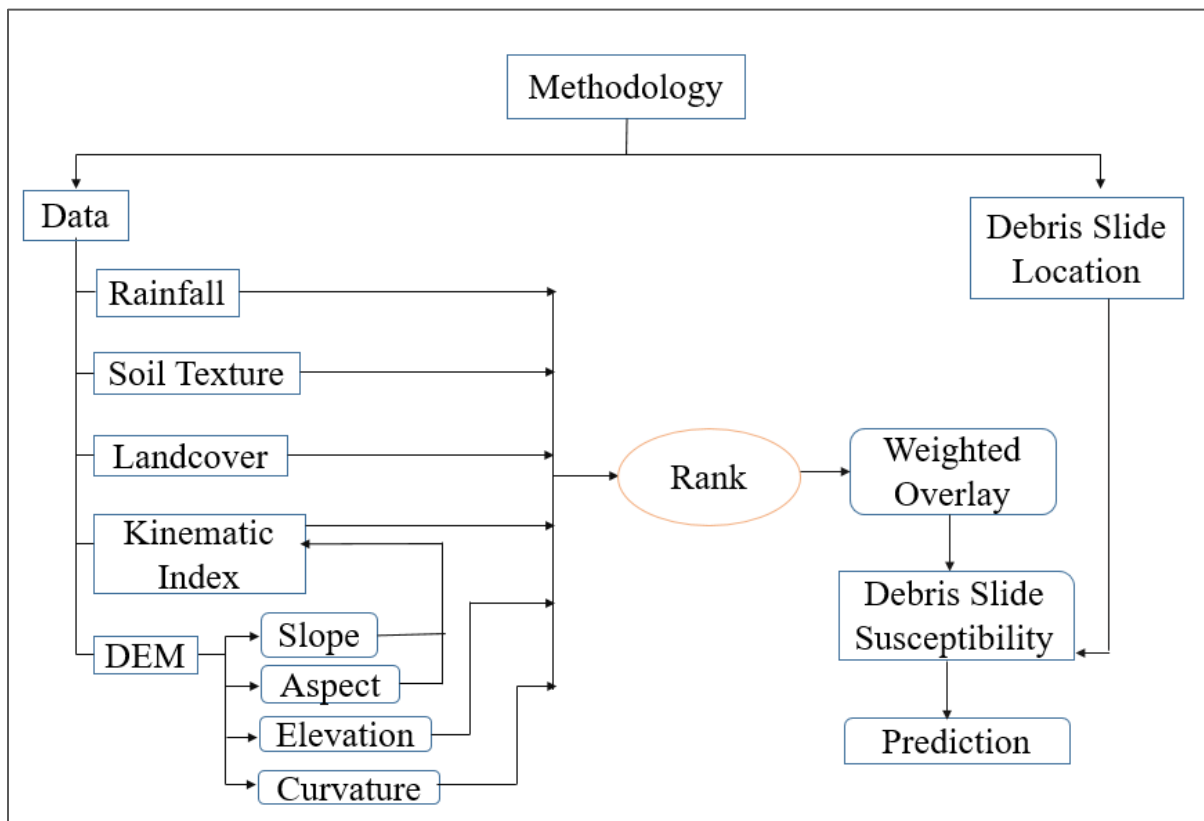


Fig. 2. Flow chart of the methodology.

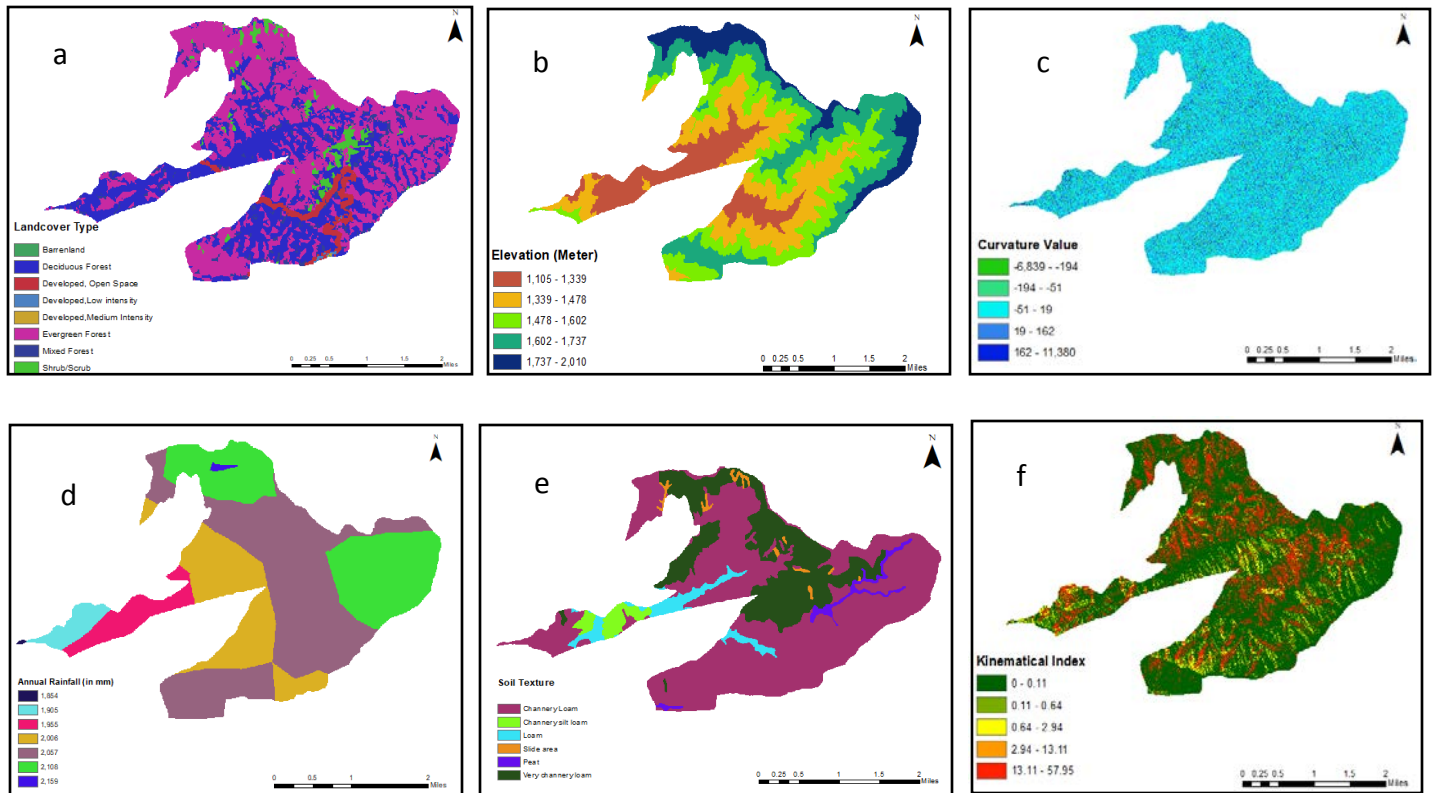


Fig. 3. (a) Landcover Map; (b) Elevation Map; (c) Curvature Map; (d) Annual Rainfall Map; (e) Soil Texture Map; (f) Kinematical Index Map.

4. Result

In the study area, there were 256 debris-slide initiation zones (Fig. 1a). Majority of debris-slides were present in the Newfound Gap and Mt. LeConte areas in the northeastern corner. The elevation of the area ranged from 1105 m to 2010 m with a mean of 1526.64 m (Fig. 3b), rainfall varies from 1854.2 mm to 2159 mm (Fig. 3d) and curvature ranged from -6839.87 to +11380 having mean of -6.62 (Fig. 3c) (Table 1). The negative curvature value stands for upwardly convex surface and positive value indicates concave surface at that cell.

The debris-slide initiation zone susceptibility map from the Weighted Overlay Analysis were classified into: very low, low, medium, high, and very high susceptibility categories (Fig. 4). Only 0.03 % and 9% of the total map area were located under very low and low susceptibility zone, respectively. When the area was compared with the actual debris-slide initiation zones, these areas exhibited no trace of past or recent slide activities. Medium susceptibility zone occupies 43.43% of the study area and predicted 14.44 % of actual debris-slide occurrence zones. High susceptibility zone represented the largest area in the map (45.43%) and accounted for 75.53 % slides in the study area. Very high susceptibility covered only 2% of the total study area; however, it predicted nearly 10% of the known slide locations (Fig. 5).

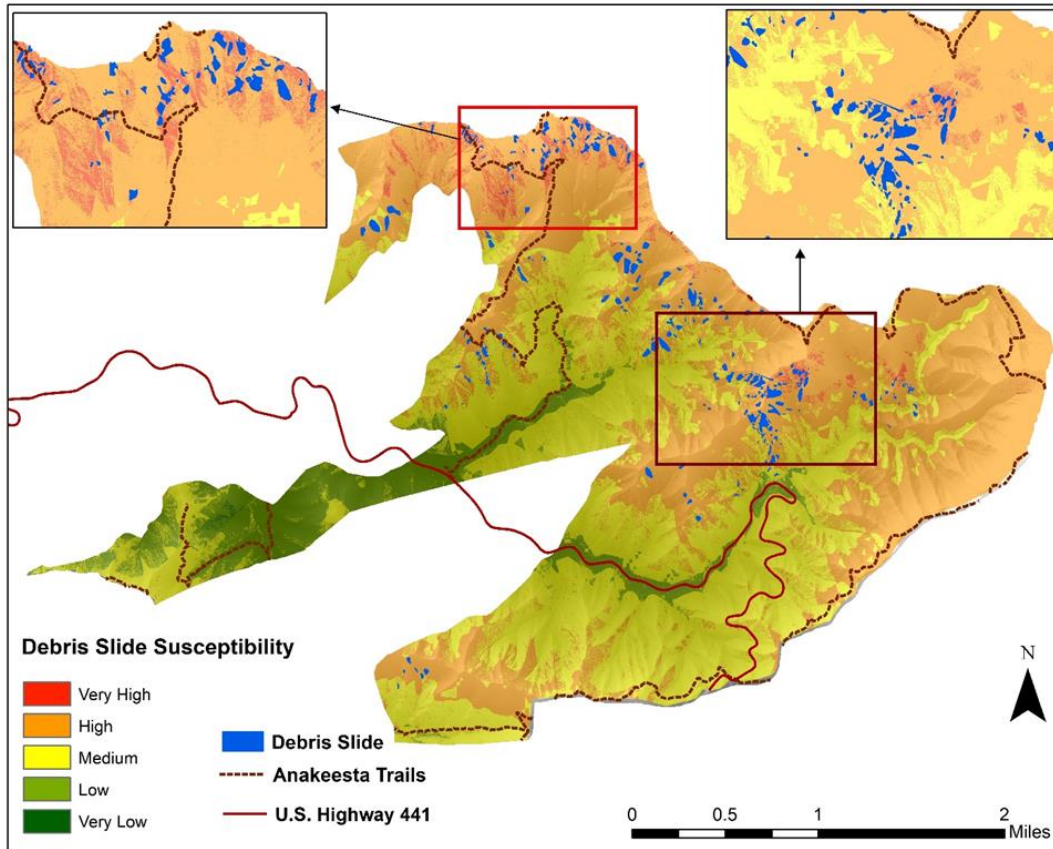


Fig. 4. Debris-slide susceptibility map.

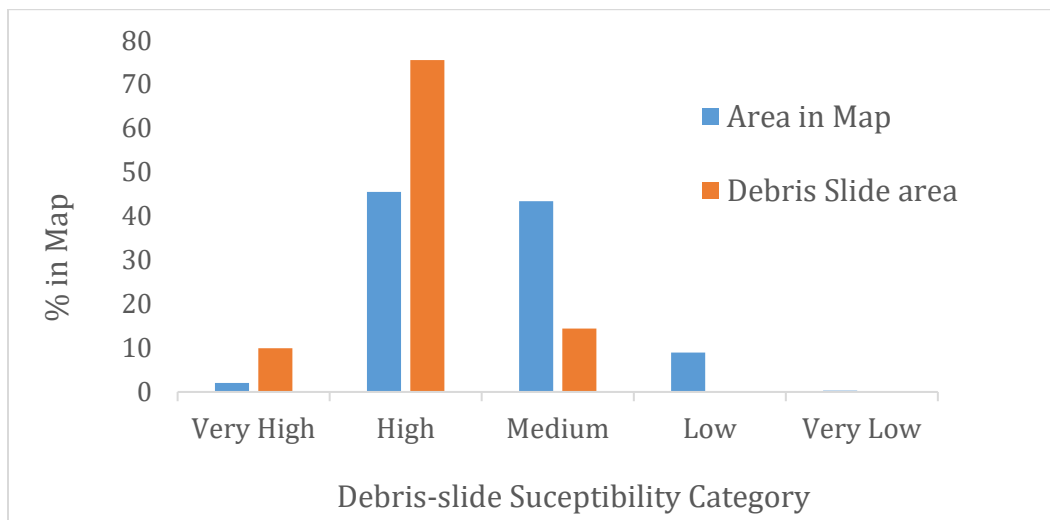


Fig. 5. Debris-slide susceptibility zones compared to the known slide initiation areas.

5. Discussion

Anakeesta ridge in the northeastern part of the study area has experienced failures in the past and is expected to experience failures under the present climatic, geological, and hydrological conditions. Failures in high elevation, and high rainfalls area support the finding. On the other hand, the very channery loam soil texture seems to have a positive correlation with debris-slide initiation zones, which are subangular, blocky, and friable earth materials derived from weathering of phyllitic Anakeesta formation. Evergreen forest and shrub are the dominant vegetation in the area and

show strong spatial relation with debris-slides. Curvature does not reveal any trend with the initiation of slides. Debris-slides could be found in both concave and convex surfaces. The field study and spatial analysis suggested the presence of kinematically triggered failures due to movement of geological discontinuities within bedrock. The investigation also suggested that initial wedge failures dominated the slides on steeper slopes and these slides were eventually converted into debris flows with increasing water content, and soil/decomposed plant/broken rock debris as they moved along existing drainage channels. The present drainage channels were probably paleo debris flow channels, but they were not studied during this research.

The model predicted the existing debris-slides with high accuracy, where 86% of the known slides were situated in high and very high susceptibility categories. However, this study focused on rapid analysis using a heuristic approach. Success of a heuristic model relies on the expert's opinion and selection of incorrect geofactors and assigning inappropriate weighting can lead to erroneous results. Future work will apply data-driven statistical-based approaches like logistic regression or artificial neural networks to model the debris-slide susceptibility and compare the results with the heuristic approach used in the existing study. The study used 256 debris-slide initiation zones; however the dates of failure were unknown, therefore, several thunderstorms and hurricanes induced debris-slides could not be studied. That hindered the spatio-temporal probability analysis of debris-slides in the area. In the future, a time-stamped debris-slide inventory should be generated in order to provide a complete spatio-temporal hazard analysis of the area.

6. Conclusion

This paper successfully demonstrated the usefulness of the heuristic model or knowledge-driven method in order to rapidly generate debris-slide susceptibility map. This study also introduced a kinematical index layer, which is a new addition, and could be included as one of the structural geology based geofactors for debris-slide susceptibility modelling. A satisfactory result was achieved by using this new variable. Validation of the model shows most of the debris-slides (86%) were located in the very high and high susceptible zones. Therefore, it can be concluded that the geofactors used in this study were appropriate with the region's conditions and most likely to be important for predicting debris-slides in the study area.

7. Acknowledgement

The authors would like to gratefully acknowledge the United States National Park Service for the permission to carry out field investigation in the Great Smoky Mountain National Park. A special thanks to DFHM7 organizing committee for selecting our article and the department of Geosciences, East Tennessee State University for providing us all the essentials to accomplish this work.

References

- Allmendinger, R. W., Cardozo, N. C., and Fisher, D., 2012, *Structural Geology Algorithms: Vectors & Tensors*: Cambridge, England, Cambridge University Press, 289 pp.
- Bogucki, D.J., 1976, Debris Slides in the Mt. Le Conte Area, Great Smoky Mountains National Park, U.S.A., *Geografiska Annaler: Series A, Physical Geography*, 58:3, 179-191, doi:10.1080/04353676.1976.11879937.
- Brabb, E.E., 1984, Innovative approaches to landslide hazard mapping. 4th International Symposium on Landslides, Toronto 1,307-324.
- Carrara A., Cardinali M., Guzzetti F., Reichenbach P. (1995) Gis Technology in Mapping Landslide Hazard. In: Carrara A., Guzzetti F. (eds) *Geographical Information Systems in Assessing Natural Hazards. Advances in Natural and Technological Hazards Research*, vol 5. Springer, Dordrecht.
- Clark, G.M., 1987, Debris slide and debris flow historical events in the Appalachians south of the glacial border: *Geological Society of America, Reviews in Engineering Geology*, Volume VII, p. 125-137.
- Ghosh, S., Das, R., Goswami, B., 2013, Developing GIS-based techniques for application of knowledge and data-driven methods of landslide susceptibility mapping. *Indian Journal of Geosciences* 67 (3-4), 249-272.
- Ghosh, S., Günther, A., Carranza, E. J., Westen, C.J. & Jetten, V.G., 2010, Rock slope instability assessment using spatially distributed structural orientation data in Darjeeling Himalaya (India). *Earth Surface Processes and Landforms*. 35. 1773 – 1792, doi:10.1002/esp.2017.
- Guzzetti, F., Carrara, A., Cardinali, M., Reichenbach, P., 1999, Landslide hazard evaluation: a review of current techniques and their application in a multi-scale study, Central Italy. *Geomorphology* 31, 181–216.
- Hansen A., 1984, Landslide hazard analysis. In: Brunsden, D. & Prior, D.B. (Eds.), *Slope Instability*, John Wiley and Sons, New York, pp. 523-602.
- Nandi, A., Shakoor, A., 2010, A GIS-based landslide susceptibility evaluation using bivariate and multivariate statistical analyses. *Engineering Geology* 110, 11–20, doi:10.1016/j.enggeo.2009.10.001.
- Nandi, A., Shakoor, A., 2017, Predicting Debris Flow Initiation Zone Using Statistical And Rock Kinematic Analyses, A Case Study From West Prong Little Pigeon River, TN, 3rd North American Symposium on Landslides, p. 912-922.

- Pradhan, B., 2011, Use of GIS-based fuzzy logic relations and its cross application to produce landslide susceptibility maps in three test areas in Malaysia. *Environmental Earth Sciences*, 63(2), 329–349.
- Rapp, A., Stromquist, L., 1976, Slope Erosion Due to Extreme Rainfall in the Scandinavian Mountains, *Geografiska Annaler: Series A, Physical Geography*, 58:3, 193-200, doi:10.1080/04353676.1976.11879938.
- Scott, R.C., 1972, The geomorphic significance of debris avalanching in the Appalachian Blue Ridge Mountains [Ph.D. thesis]: Athens, University of Georgia, 185 p.
- Simonett, D. S., 1970, The role of landslides in slope development in the high rainfall tropics: Final report, Office of Naval Research, Geography Branch, 583(11), NR 389–133, 24 p.
- Southworth, Scott, Schultz, Art, Aleinikoff, J.N., and Merschat, A.J., 2012, Geologic map of the Great Smoky Mountains National Park region, Tennessee and North Carolina: U.S. Geological Survey Scientific Investigations Map 2997, one sheet, scale 1:100,000, and 54-p. pamphlet. (Supersedes USGS Open-File Reports 03–381, 2004–1410, and 2005–1225.)
- Lee, S., Pradhan, B., 2007, Landslide hazard mapping at Selangor, Malaysia using frequency ratio and logistic regression models. *Landslides* 4, 33–41, doi:10.1007/s10346-006-0047-y.
- Varnes, D.J., 1978, Slope movements types and processes. *In: Landslides: Analysis and Control*, R.L. Schuster and R.L. Krizek (eds.), Special Report 176. Transportation Research Board, National Academy of Sciences, Washington, D.C., 11-33 p.
- Varnes, D.J., 1984, IAEG Commission on Landslides and other Mass-Movements, *Landslide Hazard Zonation: a review of principles and practice*. UNESCO Press, Darantiere, Paris, 61 p.
- Van Westen, C.J., 1993, Application of Geographical Information System to landslide hazard zonation. ITC Publication no. 15, ITC, Enschede, The Netherlands, 245 pp.
- Wooten, Richard M.; Witt, Anne C.; Miniati, Chelcy F.; Hales, Tristram C.; Aldred, Jennifer L., 2016, Frequency and magnitude of selected historical landslide events in the southern Appalachian Highlands of North Carolina and Virginia: relationships to rainfall, geological and ecohydrological controls, and effects. *In: Greenberg, Cathryn H.; Collins, Beverly S. editors. Natural Disturbances and Historic Range of Variation*. Springer International Publishing, p. 203-262, doi:10.1007/978-3-319-21527-3_9.

Making sense of avulsions on debris-flow fans

Alexander L. Densmore^{a,*}, Tjalling de Haas^b, Brian McArdell^c, Peter Schuerch^d

^a Institute of Hazard, Risk, and Resilience and Department of Geography, Durham University, Durham DH1 3LE, UK

^b Department of Physical Geography, Utrecht University, 3584 CB Utrecht, The Netherlands

^c Swiss Federal Institute for Forest, Snow, and Landscape Research WSL, CH-8903 Birmensdorf, Switzerland

^d geosfer ag, CH-8570 Weinfelden, Switzerland

Abstract

Avulsions remain a critical but understudied aspect of debris-flow fans and flow hazard. A substantial body of work on fluvial systems provides a conceptual framework for understanding avulsions, but equivalent research on debris-flow systems has lagged behind. A small but growing set of field examples and analogue experiments shows that many, but not all, avulsions on debris-flow fans follow a relatively predictable ‘avulsion cycle’ that consists of (1) deposition of debris-flow material in the active channel, (2) backstepping of deposition toward the fan apex in one or more small- to medium-sized surges or flows, and (3) avulsion during a subsequent larger surge or flow that leaves the channel and establishes a new pathway down the fan. Debris flows tend to occupy persistent pathways on the time scale of individual flows, but over longer time scales (perhaps greater than ~5-20 flows, based on very limited data) flows tend to avulse to fill topographic lows, leading to compensational behavior. Avulsions may be encouraged by sequences of small- to medium-sized flows followed by a large flow, and discouraged by sequences of large flows in succession, although this idea remains speculative and needs to be tested. Avulsion frequency is important for understanding flow hazard but is poorly constrained, and cannot yet be predicted as a function of either flow or catchment characteristics. The advent of new, high-resolution topographic data from fan surfaces, coupled with methods to estimate the timing and abandonment of deposition on a wide range of fans, should allow us to begin to make some initial estimates of avulsion frequency and to understand the key controls on the timing and pattern of avulsions.

Keywords: debris flows; fans; avulsions; avulsion frequency; hazard

1. Introduction

Debris-flow fans are semi-conical landforms that grow by the deposition of sediment in repeated flows from a mountain catchment. They are ubiquitous in high-relief areas around the world, and because of their relatively low surface slopes they are commonly used for settlement, agriculture, or other human activities. The construction of a debris-flow fan, however, requires that the locus of deposition must shift over time in order to fill the available accommodation. These episodic shifts in the position of the active channel are called avulsions.

Avulsions are critical events in the evolution of a debris-flow fan, and are important for several reasons. First, they control how sediment is distributed across the fan surface. Switching of the active channel between different pathways creates a small number of distinct sectors on the fan surface (Fig. 1). Each of these sectors records debris-flow activity during a particular period of time and over a number of flows (e.g., Schumm et al., 1987; Duehnforth et al., 2007; Schuerch et al., 2016). The sectors thus serve as an archive of past flow size and behavior, and potentially of the environmental conditions under which the flows occurred (d’Arcy et al., 2017). The intervals between avulsions set the period of time recorded by each sector, which can be as long as tens of thousands of years (e.g., Whipple and Dunne, 1992; Duehnforth et al., 2007; 2017).

* Corresponding author e-mail address: a.l.densmore@dur.ac.uk

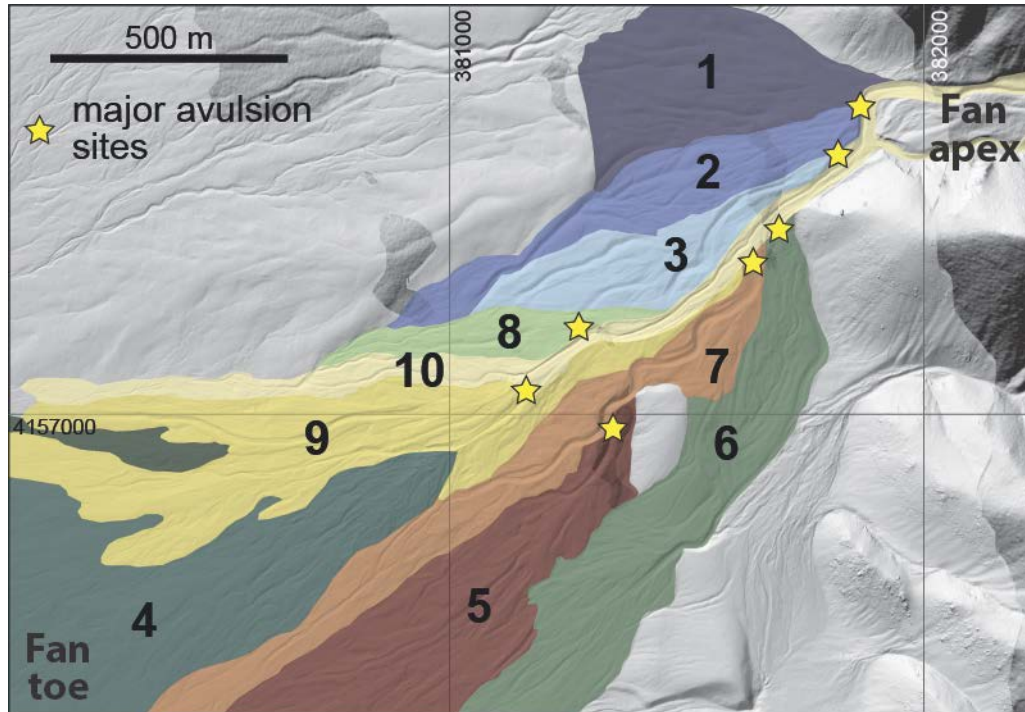


Fig. 1. Sectors on the Straight Canyon debris-flow fan, Chalfant Valley, California, USA, labelled from 1 (oldest) to 10 (youngest, the active channel). Flows travel from right to left across the fan. Stars show locations of major avulsions between sectors.

Second, the frequency of avulsions also determines the persistence of transport pathways (Jerolmack and Paola, 2007; Straub et al., 2009) and thus the architecture of the developing fan stratigraphy (Pederson et al., 2015). Finally, avulsions are also a key determinant of debris-flow hazard. Debris flows that leave the main channel pose the greatest threat to people and infrastructure, because mitigation measures such as check dams are usually applied only to the presently-active channel. Any migration of debris-flow activity outside of the main channel will thus bypass those mitigation measures and threaten other parts of the fan surface.

Despite this importance, avulsions on debris-flow fans have received little research attention. There are some documented examples in the literature, but very few systematic studies of avulsion location, trigger, mechanism, or frequency. This may in part be due to the long time periods between flows in many settings, which make direct observations of avulsions very rare (de Haas et al., 2018a). In addition, there are few debris-flow fans worldwide where debris-flow deposition in space and time has been monitored (e.g., Suwa and Okuda, 1983; Wasklewicz and Scheinert, 2016; Imaizumi et al., 2016) or reconstructed (e.g., Stoffel et al., 2008; Schuerch et al., 2016).

Here, we draw together findings from recent work on debris-flow avulsions and identify some key research priorities that must be tackled in order to understand the full role of avulsions in debris-flow hazard and fan development. For a wider review of debris-flow avulsions, we refer interested readers to de Haas et al. (2018a).

2. Fluvial context

Avulsions have long been recognised as a key element in fan development, irrespective of the sediment transport process. Dutton (1880) wrote eloquently about avulsions in describing the deposition of alluvial sediments at the ‘gate’ or mouth of a mountain catchment:

“When the stream is progressively building up its bed outside of the gate, it is obvious that it cannot long occupy one position; for if it persisted in running for a very long time in one place it would begin to build an embankment. Its position soon becomes unstable, and the slightest cause will divert it to a new bed which it builds up in turn, and which in turn becomes unstable and is also abandoned. The frequent repetition of these shiftings causes the course of the stream to vibrate radially around the gate as a center, and in the lapse of ages it builds up a half-cone, the apex of which is at the gate. The vibration is not regular, but vacillating, like a needle in a magnetic storm; but in the long run, and after very many shiftings, the stream will have swept over a whole semicircle with approximately equal and

uniform results.” (Dutton, 1880, pp. 220-221)

Much of our understanding of avulsions has been derived through observations of fluvial systems, and it is instructive to review some of that work here. Mohrig et al. (2000) showed that avulsions in ancient river deposits were linked to the aggradation of the river system by approximately one channel depth above the surrounding floodplain. We can define an avulsion frequency f_A as the rate of avulsion per unit time; Jerolmack and Mohrig (2007) argued that f_A should scale with mean channel depth \bar{h} , sediment aggradation rate v_A , and the number of active channels N as:

$$f_A = \frac{v_A N}{\bar{h}} \quad (1)$$

Reitz and Jerolmack (2012) proposed an alternative approach to estimate f_A based on channel geometry and the sediment supply rate, building on earlier work by Bryant et al. (1995):

$$f_A = \frac{Q_s}{\left[hBr(t) + \frac{\theta}{6} \Sigma \Delta yr^2(t) \right]} \quad (2)$$

where Q_s is the sediment supply rate, B is the channel width, $r(t)$ is the fan radius as a function of time, θ is the width of a channel lobe, and $\Sigma \Delta y$ is the total vertical aggradation at the fan apex since a fan sector was last active.

Studies of natural and laboratory fluvial fan systems have documented the sequence of events in a typical ‘avulsion cycle’ (e.g., Schumm, 1987; Hoyal and Sheets, 2009; Reitz and Jerolmack, 2012; Ganti et al., 2016): an upstream-propagating wave of in-channel deposition and backfilling, followed by overbank flooding and a ‘searching phase’ during which several new channel pathways may be active, followed by concentration of flow into a new channel. Jerolmack and Paola (2007) argued that avulsions are steered by the presence of abandoned channels on the fan surface, leading to persistent re-occupation of a small number of sediment transport pathways. Straub et al. (2009) termed such behavior ‘persistent’ or ‘anti-compensational’, in contrast to ‘compensational’ behavior in which the channel avulses frequently to fill the topographically-lowest part of the fan surface.

While these studies provide a useful framework and show how avulsion frequency might scale with different measures of a sedimentary system, it is not clear how applicable they are to debris-flow fans. Field observations show that channel beds on debris-flow fans can be super-elevated by 2-5 channel depths or more above the surrounding fan surface (de Haas et al., 2019), so direct application of equation (1) may be limited. The episodic nature of debris flows and the capacity for flows to both erode and deposit sediment on a fan surface (e.g., Schuerch et al., 2011) complicate the definition of a sediment aggradation rate except over long time periods. For the moment, therefore, an expression for avulsion frequency f_A that is relevant for debris-flow fans remains a research priority.

3. Field observations

Field observations of avulsions have tended to focus on individual events, such as the major avulsion that occurred in 1984 on the Dolomite Canyon fan, California, USA, as documented by Blair and McPherson (1998). There, the initial flow surges formed a complex of levee and lobe deposits along the active channel pathway. The boulder-rich front of a large subsequent surge then blocked the channel near the fan apex and diverted the flow by an angle of about 70° into a new pathway.

To identify some common elements of debris-flow avulsions, de Haas et al. (2018a) assembled observations from 16 fans worldwide for which the spatio-temporal evolution of debris-flow activity could be determined. They noted that avulsions often, but not always, occurred in response to the deposition of debris-flow lobes that formed sediment ‘plugs’ (Fig. 2) within the active channel (e.g., Whipple and Dunne, 1992). These avulsions were often preceded by a sequence of small- to medium-size flows, and were most likely to occur when plugs were deposited in locations from which alternative pathways could be easily accessed by future flows. Plug formation was more likely in smaller flows or those with limited mobility. This overall pattern mimics in some way the avulsion cycle observed on fluvial fans – in particular, the role of small flows in setting the conditions for a subsequent avulsion, as argued by Field (2001) – although the processes involved in the individual phases are quite distinct.

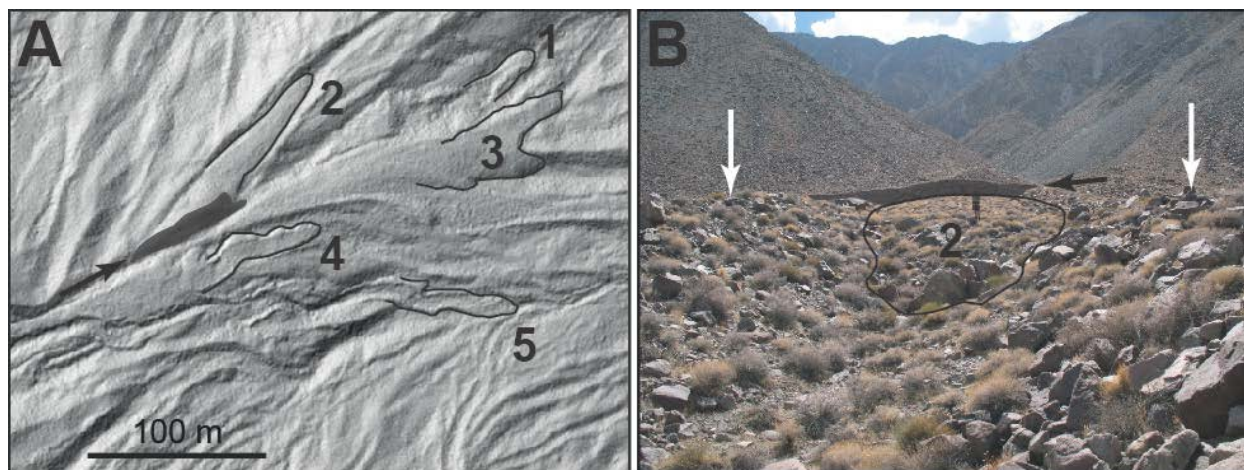


Fig. 2. (A) Shaded-relief image of the proximal part of a small debris-flow fan in Saline Valley, California, USA, showing a sequence of individual debris-flow lobes numbered 1-5 from oldest to youngest. Relative ages are based on cross-cutting relationships. Dark grey shaded area show left-lateral levee deposited after abandonment of lobe 2; black arrow shows flow direction. Image derived from Lidar topographic data with 0.5 m cell size. (B) Field photograph of lobe 2 from panel (A), outlined in black. Flow was toward the camera; note the figure on the lobe for scale. White arrows indicate the crests of the channel-margin levees. This lobe filled and blocked the active channel, forcing an avulsion to the east; a subsequent flow has deposited a lateral levee across the head of the channel (highlighted in dark grey), forcing its abandonment. Black arrow shows flow direction during subsequent levee deposition, as in panel (A).

De Haas et al. (2018a) noted that, unlike on fluvial fans (e.g., Ganti et al., 2016), very large flows (that is, those in the tail of the volume distribution) can have highly variable roles in avulsions. Large debris flows can spill out of the active channel and excavate a new channel or re-occupy an older abandoned channel. Sequences of large flows, however, may be more likely to erode the existing channel, enlarging it and thus making avulsion less likely, especially if the rate of bed entrainment depends on some measure of boundary shear stress (Schuerch et al., 2011; Iverson, 2012; Iverson and Ouyang, 2015). Large flows can also split among multiple channels, depositing material over a large area of the fan surface and increasing the likelihood of future avulsion (de Haas et al., 2018a).

Over sequences of ~5-20 flows, de Haas et al. (2018a) showed that the locus of deposition often tends to shift toward the topographically lowest areas of the fan. This indicates that flow pathways can persist over short time scales of a few flows, but tend toward compensational behavior over longer time scales, as seen in other sedimentary systems (e.g., Straub et al., 2009; van Dijk et al., 2016). A tendency toward long-term compensational behavior was also observed by Pederson et al. (2015), who demonstrated that deposition on three well-exposed debris-flow fans was intermediate between random and fully compensated over sequences of 22-28 individual beds. They inferred that compensational behavior and more frequent avulsions were likely to be enhanced by thick, wide, coarse-grained flows with high clay contents, arguing that such flows can more easily fill topographic lows and form thick deposits that will steer subsequent flows toward other areas of the fan (e.g., Whipple and Dunne, 1992).

4. Analogue experiments

To explore the link between the distribution of flow sizes and avulsion behavior, de Haas et al. (2018b) ran a series of analogue debris-flow experiments in a small laboratory flume and tank. This work built on earlier experiments in the same flume by de Haas et al. (2016), who constructed a model fan with a sequence of 55 flows, each with a total flow mass of ~6.5 kg. De Haas et al. (2018b) ran two additional experiments under identical conditions; however, rather than keeping the flow mass constant, the mass of each flow was chosen from a steep- or shallow-tailed double Pareto mass distribution. The mass of each flow in the two additional experiments ranged up to ~13 kg, although the mean flow mass in all three experiments was the same. All flows had an identical grain-size mixture and a water content of 44% by volume (see de Haas et al., 2016, for materials and methodology).

All three experiments showed broadly similar avulsion cycles that consisted of channel establishment, backstepping of deposition toward the fan apex, a ‘searching phase’ during which deposition spread across the proximal fan, and avulsion toward a new topographically-favorable sector. Comparable behavior was observed in analogue experiments by Schumm et al. (1987). In detail, however, the different flow mass distributions led to markedly-different avulsion mechanisms. A uniform flow mass distribution led to regular avulsion cycles in which backstepping deposition proceeded from fan toe to apex before avulsion occurred. In contrast, a steep-tailed

distribution, corresponding to a narrow range of flow masses, led to two additional avulsion mechanisms: large events that could overtop existing channels and occupy new pathways, and sequences of small flows that led to plugging of only the proximal part of the active channel. A shallow-tailed distribution, with a wide range of flow masses, also showed these additional avulsion mechanisms, although the more frequent large flows excavated the main channel and made avulsions less common.

While these results are based on a small number of experiments and do not consider other factors that may be important, such as variations in flow mobility due to grain size or water content, they suggest that sequences of several small- to medium-sized flows may be critical in forcing avulsion in a subsequent larger flow – as observed, for example, on the Kamikamihori fan in Japan (Suwa and Okuda, 1983). The experimental results also highlight a major difference between the fluvial avulsion cycle and that observed on debris-flow fans: backfilling and channel plugging need not proceed up the entire fan surface in order to force avulsion on debris-flow fans, as is often the case on fluvial fans, but can be limited to a key reach or even a single point. This makes debris-flow avulsions harder to anticipate than their fluvial counterparts, and calls for research on likely avulsion locations.

5. Research priorities

In this final section, we summarise some of the key research priorities that would help to develop a more complete picture of avulsion.

5.1. Avulsion mechanisms and triggers

The avulsion cycle model outlined above predicts that avulsions should be enhanced by particular sequences of flow volumes – especially those in which a series of small- to medium-sized flows that partly or fully block the channel are followed by a large flow that triggers avulsion. As estimates of debris-flow volume are accumulated at more and more observation stations (e.g., McArdell et al., 2007), it should be possible to begin to relate the sequencing of flow volumes to the temporal evolution of bed elevation in different settings. It would also be useful to look for evidence of ‘pre-conditioning’ of an active channel for avulsion – e.g., via channel blockage in key locations on a fan, perhaps where channel incision into the fan surface is minimal and where there are abandoned channels that could form new flow pathways after an avulsion.

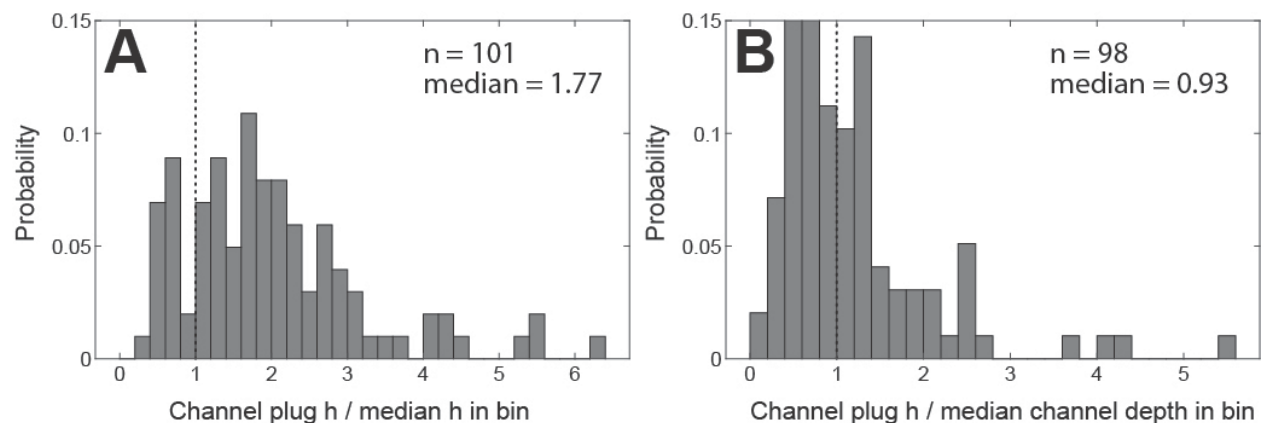


Fig. 3. Characteristics of debris-flow depositional lobes that form channel plugs on fans in Saline Valley. (A) Histogram of channel plug thickness. Values are binned at 50 m radial distance intervals from the fan apex and normalized by median lobe thickness within each bin. Most channel plugs that have triggered avulsion are thicker than the median lobe within that distance bin. (B) Histogram of channel plug thickness. Values are normalized by median channel depth within the same 50 m bins. Note similarity between plug thickness and median channel depth.

Some additional understanding of the formation of channel plugs can be gained by examining the characteristics of flow deposits that have triggered avulsions in the past. Measurements of channel depths and debris-flow depositional lobe thicknesses on fans in Saline Valley, California, USA (Fig. 2) from high-resolution Lidar topography (de Haas et al., 2019) show that depositional lobes that have plugged channels and triggered avulsions tend to be substantially thicker than the median lobe thickness at the same radial position on the fan (Fig. 3A), and to have thicknesses that are comparable to the median channel depth at the same radial position (Fig. 3B). While perhaps not surprising, this result confirms that plugs must fill a substantial portion of the available channel in order

to force avulsion, and that channel plugging, rather than aggradation above the floodplain (e.g., Mohrig et al., 2000), is the key avulsion mechanism at this site. Avulsions can still be forced by plugs which are thinner than the median lobe thickness (Fig. 3A) or channel depth (Fig. 3B), but they are the exception. Similar measurements from other fan settings would be helpful in elucidating the sequence of events involved in channel plugging and avulsion.

5.2. Avulsion size and location

The impact of an avulsion on a fan surface depends on three factors: the size of the flow, the radial position at which the avulsion occurs, and the ‘opening angle’ between the old and new flow pathways. One reasonable measure of avulsion size is the incremental area of fan surface that is inundated after the avulsion, such that full resurfacing of the fan will occur once those incremental areas sum to the total fan area (e.g., Cazanacli et al., 2002). This measure, however, ignores the fact that a large opening angle can pose a hazard to infrastructure that is far from the old pathway, especially if mitigation measures are concentrated close to the active channel. Thus, an alternative measure of avulsion size M_a could be the product of the opening angle D_{az} , normalized by the total angle described by the fan, and the radial distance of the avulsion site from the fan toe D_r , normalized by the fan length (Fig. 4). M_a thus varies between 0 (no avulsion) and 1 (an avulsion at the apex from one fan margin to the other), and provides a way of comparing the potential impacts of avulsions that occur at different locations on the fan.

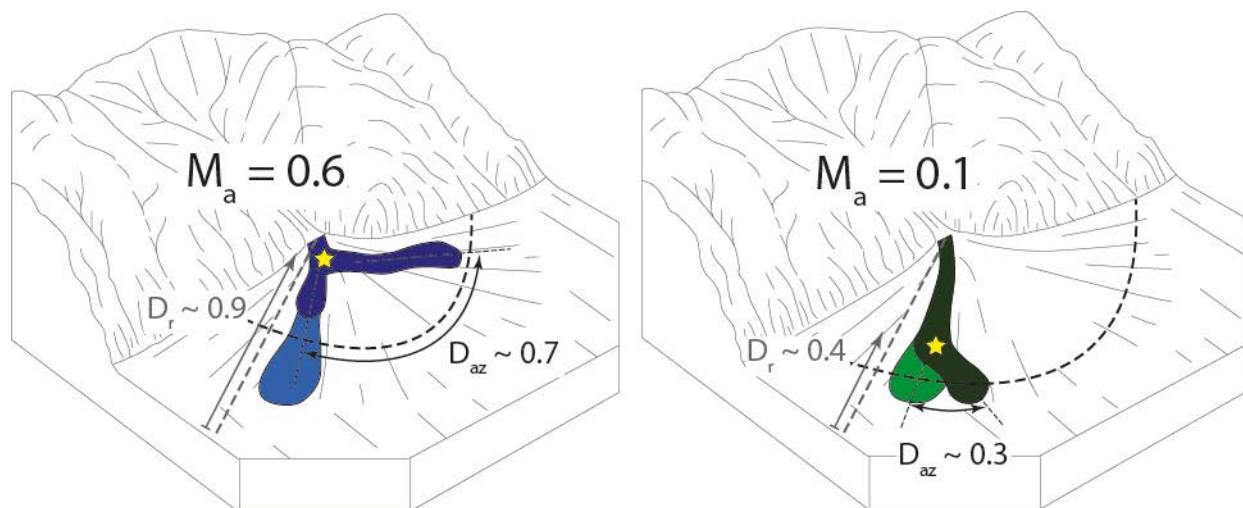


Fig. 4. Schematic of avulsion size M_a as a product of the normalized opening angle D_{az} and the normalized radial position D_r .

Jerolmack and Paola (2007) showed that avulsion sizes in their experiments (measured in terms of the length of new channel created) followed an exponential distribution. They demonstrated that there was no binary distinction between ‘nodal’ avulsions that occur at the fan apex and ‘local’ avulsions that occur elsewhere; instead, the former are simply less frequent. Field observations by de Haas et al. (2018a) tend to support that continuum, with avulsions possible at all radial positions on a fan surface. Field observations by Pederson et al. (2015) and experimental work by de Haas et al. (2018b) both suggest, however, that flows become more compensational, and avulsions thus somewhat more likely, on the distal parts of the fan surface – perhaps driven by down-fan decreases in channel depth that outweigh down-fan decreases in lobe thickness (Whipple and Dunne, 1992). It may thus be possible to identify avulsion ‘hotspots’ by comparing the thickness of typical debris-flow depositional lobes with typical channel depths; as both of these quantities vary down-fan, avulsions should be more common in areas where lobes can more easily fill and block the channel network. These observations also suggest that avulsions with high M_a – those that occur near the apex and have wide opening angles – should be comparatively rare events.

5.3. Avulsion frequency

We currently have no capacity to predict the occurrence or frequency of avulsions on debris-flow fans, meaning that our understanding of avulsion occurrence is almost entirely reactive. A major research priority is therefore to compile sufficient information on avulsion occurrence and timing to enable first-order comparison with channel and flow characteristics, sediment supply, and fan climatic and tectonic setting. De Haas et al. (2018a) reviewed the

available data on historically-active debris-flow fans, and showed that documented avulsions occurred approximately every 3-8 flows. It is worth bearing in mind that those fans were specifically studied because of their frequent flow activity, and they are not necessarily representative of avulsion frequency on less-active fans.

Over the longer term, fans show evidence of switching between different sectors on a range of time scales: for example, sectors on the Illgraben fan in Switzerland are typically active for $\sim 10^2$ yr (Schuerch et al., 2016), but sectors on fans in Owens Valley, California, may be active for $\sim 10^3$ - 10^4 yr (Duehnforth et al., 2007; Le et al., 2007; d'Arcy et al., 2015). There are still relatively few well-dated fan surfaces worldwide for which the timing of sector activity and abandonment can be estimated. The explosion in the practicability of surface dating by analysis of *in-situ* cosmogenic radionuclides over the last 20 years, however, means that it is now more feasible than ever to generate quantitative fan-surface age estimates (e.g., Ivy-Ochs et al., 2013).

At the same time, fan sector identification is typically based on both quantitative and qualitative measures of fan surface topography, including such diverse observations as surface roughness at various scales, channel cross-cutting relationships, downlapping or onlapping relationships, relative weathering of surficial materials, soil development, and vegetation growth. Despite some efforts to quantify these measures (e.g., Frankel and Dolan, 2007), division of the fan surface into discrete sectors remains an uncertain and somewhat ambiguous exercise. Thus, while there is clearly a need for more fan-surface chronologies, we also suggest that attention should be given to the ways in which fan sectors are formed and abandoned, and the implications of these processes for the fidelity with which fan surfaces record avulsions.

5.4. Numerical modelling of avulsions

A promising approach for exploring the controls on avulsion frequency is through the numerical modelling of repeated flows and the concomitant evolution of fan surface topography. McDougall (2017), in a thorough review of landslide and debris-flow runout models, pointed out that predicting the occurrence, location, and impacts of avulsion in numerical flow models remains a major outstanding challenge. While existing flow models can simulate flow paths given some assumptions about initial flow volume and entrainment or deposition along the flow path (e.g., Frank et al., 2015), it is difficult even *a posteriori* to simulate major avulsions due to the need to model the dynamic feedbacks between entrainment or deposition, changes in the channel bed topography, flow volume, and flow behaviour. Recognition of other possible flow paths, for example due to the presence of abandoned channels on the fan surface, is not sufficient; avulsion into those paths requires filling of the active channel, routing of material down the new pathway, and sufficient excavation of the new channel to ensure that it is maintained in subsequent surges or flows. While runout models are typically used to reconstruct the pathways of individual debris flows, there has also been much less attention devoted to modelling the impact of series of flows on a fan surface; thus, the suggestion by de Haas et al. (2018b) that the sequence of flow sizes, as well as the sizes themselves, may be important for triggering avulsion remains untested by independent observations. Finally, fan surface models require sufficient field data to allow testing and evaluation – especially high-resolution topographic data that can resolve individual channels and lobes, as well as repeat imagery of fan surfaces that can be used to identify avulsion occurrence and magnitude. We therefore close by calling for concerted research effort toward the development of numerical approaches that can simulate avulsions and thus the spatial evolution of debris-flow hazard over sequences of multiple flows.

Acknowledgements

This work was supported by the Netherlands Organisation for Scientific Research (NWO) Rubicon grant 019.153LW.002, and by the US State Department Global Innovation Initiative program. We thank Kimberly Hill, Nick Rosser, Miriam Duehnforth, and Anne Kruijt for discussions and support. Jon Major and an anonymous referee provided constructive comments that helped to improve the clarity of the manuscript.

References

- Blair, T.C., and McPherson, J.G., 1998, Recent debris-flow processes and resultant form and facies of the Dolomite alluvial fan, Owens Valley, California: *Journal of Sedimentary Research*, v. 68, p. 800-818.
- Bryant, M., Falk, P., and Paola, C., 1995, Experimental study of avulsion frequency and rate of deposition: *Geology*, v. 23, p. 365-368.
- Cazanacli, D., Paola, C., and Parker, G., 2002, Experimental steep, braided flow: application to flooding risk on fans: *Journal of Hydraulic Engineering*, v. 128, p. 322-330.

- D'Arcy, M., Roda-Boluda, D.C., Whittaker, A.C., and Carpineti, A., 2015, Dating alluvial fan surfaces in Owens Valley, California, using weathering fractures in boulders: *Earth Surface Processes and Landforms*, v. 40, p. 487-501.
- D'Arcy, M., Roda-Boluda, D.C., and Whittaker, A.C., 2017, Glacial-interglacial climate changes recorded by debris flow fan deposits, Owens Valley, California: *Quaternary Science Reviews*, v. 169, p. 288-311.
- De Haas, T., Berg, W., Braat, L., and Kleinhans, M.G., 2016, Autogenic avulsion, channelization and backfilling dynamics of debris-flow fans: *Sedimentology*, v. 63, p. 1596-1619.
- De Haas, T., Densmore, A.L., Stoffel, M., Suwa, H., Imaizumi, F., Ballesteros-Cánovas, J.A., and Wasklewicz, T., 2018a, Avulsions and the spatio-temporal evolution of debris-flow fans: *Earth-Science Reviews*, v. 177, p. 53-75.
- De Haas, T., Kruijff, A., and Densmore, A.L., 2018b, Effects of debris-flow magnitude-frequency distribution on avulsions and fan development: *Earth Surface Processes and Landforms*, v. 43, p. 2779-2793.
- De Haas, T., Densmore, A.L., den Hond, T., and Cox, N.J. (2019) Fan-surface evidence for debris-flow avulsion mechanisms and probabilities, Saline Valley, California. *Journal of Geophysical Research-Earth Surface*, in press.
- Duehnforth, M., Densmore, A.L., Ivy-Ochs, S., Allen, P.A., and Kubik, P.W., 2007, Timing of debris-flow fan aggradation and incision on Shepherd and Symmes Creek fans, Owens Valley, California, deduced from cosmogenic ¹⁰Be: *Journal of Geophysical Research-Earth Surface*, v. 112, doi:10.1029/2006JF000562.
- Duehnforth, M., Densmore, A.L., Ivy-Ochs, S., Allen, P.A., and Kubik, P.W., 2017, Early to Late Pleistocene history of debris-flow fan evolution in western Death Valley (California) using cosmogenic ¹⁰Be and ²⁶Al: *Geomorphology*, v. 281, p. 53-65.
- Dutton, C.E., 1880, Report on the Geology of the High Plateaus of Utah: Washington, D.C., U.S. Government Printing Office, 305 p.
- Field, J., 2001, Channel avulsion on alluvial fans in southern Arizona: *Geomorphology*, v. 37, p. 93-104.
- Frank, F., McArdell, B.W., Huggel, C., and Vieli, A., 2015, The importance of entrainment and bulking on debris flow runout modelling: examples from the Swiss Alps: *Natural Hazards and Earth System Sciences*, v. 15, p. 2569-2583.
- Frankel, K.L., and Dolan, J.F., 2007, Characterizing arid region alluvial fan surface roughness with airborne laser swath mapping digital topographic data: *Journal of Geophysical Research-Earth Surface*, v. 112, F02025, doi:10.1029/2006JF000644.
- Ganti, V., Chadwick, A.J., Hassenruck-Gudipati, H.J., and Lamb, M.P., 2016, Avulsion cycles and their stratigraphic signature on an experimental backwater-controlled delta: *Journal of Geophysical Research-Earth Surface*, v. 121, doi:10.1002/2016JF003915.
- Hoyal, D., and Sheets, B., 2009, Morphodynamic evolution of experimental cohesive deltas: *Journal of Geophysical Research-Earth Surface*, v. 114, doi:10.1029/2007JF000882.
- Imaizumi, F., Trappmann, D., Matsuoka, N., Tsuchiya, S., Ohsaka, O., and Stoffel, M., 2016, Biographical sketch of a giant: deciphering recent debris-flow dynamics from the Ohya landslide body (Japanese Alps): *Geomorphology*, v. 272, p. 102-114.
- Iverson, R.M., 2012, Elementary theory of bed-sediment entrainment by debris flows and avalanches: *Journal of Geophysical Research-Earth Surface*, v. 117, F03006, doi:10.1029/2011JF002189.
- Iverson, R.M., and Ouyang, C., 2015, Entrainment of bed material by Earth-surface mass flows: review and formulation of depth-integrated theory: *Reviews of Geophysics*, v. 53, p. 27-58.
- Ivy-Ochs, S., Duehnforth, M., Densmore, A.L., and Alfimov, V., 2013, Dating fan deposits with cosmogenic radionuclides, in Schneuwly-Bollschweiler, M., Stoffel, M., and Rudolf-Miklau, F., eds., *Dating Torrential Processes on Fans and Cones*, *Advances in Global Change Research*, v. 47, p. 243-263.
- Jerolmack, D.J., and Paola, C., 2007, Complexity in a cellular model of river avulsion: *Geomorphology*, v. 91, p. 259-270.
- Jerolmack, D.J., and Mohrig, D., 2007, Conditions for branching in depositional rivers: *Geology*, v. 35, p. 463-466.
- Le, K., Lee, J., Owen, L.A., and Finkel, R., 2007, Late Quaternary slip rates along the Sierra Nevada Frontal Fault zone, California: slip partitioning across the western margin of the eastern California Shear Zone – Basin and Range Province: *Geological Society of America Bulletin*, v. 119, p. 240-256.
- McArdell, B.W., Bartelt, P., and Kowalski, J., 2007, Field observation of basal forces and fluid pore pressure in a debris flow: *Geophysical Research Letters*, v. 34, doi:10.1029/2006GL029183.
- McDougall, S., 2017, 2014 Canadian Geotechnical Colloquium: Landslide runout analysis – current practice and challenges: *Canadian Geotechnical Journal*, v. 54, p. 605-620.
- Mohrig, D., Heller, P.L., Paola, C., and Lyons, W.J., 2000, Interpreting avulsion process from ancient alluvial sequences: Guadalupe-Matarranya System (northern Spain) and Wasatch Formation (western Colorado): *Geological Society of America Bulletin*, v. 112, p. 1787-1803.
- Pederson, C.A., Santi, P.M., and Pyles, D.R., 2015, Relating the compensational stacking of debris-flow fans to characteristics of their underlying stratigraphy: implications for geologic hazard assessment and mitigation: *Geomorphology*, v. 248, p. 47-56.
- Reitz, M.D., and Jerolmack, D.J., 2012, Experimental alluvial fan evolution: channel dynamics, slope controls, and shoreline growth: *Journal of Geophysical Research-Earth Surface*, v. 117, doi:10.1029/2011JF002261.
- Schuerch, P., Densmore, A.L., Rosser, N.J., and McArdell, B.W., 2011, Dynamic controls on erosion and deposition on debris-flow fans: *Geology*, v. 39, p. 827-830.
- Schuerch, P., Densmore, A.L., Ivy-Ochs, S., Rosser, N.J., Kober, F., Schlunegger, F., McArdell, B.W., and Alfimov, V., 2016, Quantitative reconstruction of late Holocene surface evolution on an alpine debris-flow fan: *Geomorphology*, v. 275, p. 46-57.
- Schumm, S.A., Mosley, M.P., and Weaver, W., 1987, Alluvial fans, in Schumm, S.A., Mosley, M.P., and Weaver, W., eds., *Experimental Fluvial Geomorphology*, p. 281-350.
- Stoffel, M., Conus, D., Grichting, M.A., Lièvre, I., and Maître, G., 2008, Unraveling the patterns of late Holocene debris-flow activity on a cone in the Swiss Alps: chronology, environment and implications for the future: *Global and Planetary Change*, v. 60, p. 222-234.
- Straub, K.M., Paola, C., Mohrig, D., Wolinsky, M.A., and George, T., 2009, Compensational stacking of channelized sedimentary deposits: *Journal of Sedimentary Research*, v. 79, p. 673-688.
- Suwa, H., and Okuda, S., 1983, Deposition of debris flows on a fan surface, Mt. Yakedake, Japan: *Zeitschrift fuer Geomorphologie NF Supplementband*, v. 46, p. 79-101.
- Van Dijk, W., Densmore, A.L., Singh, A., Gupta, S., Sinha, R., Mason, P., Joshi, S., Nayak, N., Kumar, M., Shekhar, S., Kumar, D., and Rai, S.P., 2016, Linking the morphology of fluvial fan systems to aquifer stratigraphy in the Sutlej-Yamuna plain of northwest India: *Journal of Geophysical Research-Earth Surface*, v. 121, doi:10.1002/2015JF003720.
- Wasklewicz, T., and Scheinert, C., 2016, Development and maintenance of a telescoping debris flow fan in response to human-induced fan surface channelization, Chalk Creek Valley Natural Debris Flow Laboratory, Colorado, USA: *Geomorphology*, v. 252, p. 51-65.
- Whipple, K.X., and Dunne, T., 1992, The influence of debris-flow rheology on fan morphology, Owens Valley, California: *Geological Society of America Bulletin*, v. 104, p. 887-900.

The morphology of debris-flow deposits from a 1967 event in Caraguatatuba, Serra do Mar, Brazil

Vivian Cristina Dias^{a,*}, Tiago Damas Martins^b, Marcelo Fischer Gramani^c, Rebeca Durço Coelho^{a,c}, Helen Cristina Dias^{a,c}, Bianca Carvalho Vieira^a

^aUniversity of Sao Paulo, Avenida Professor Lineu Prestes, 338, Sao Paulo, 05508000, Brazil

^bFederal University of Sao Paulo, Avenida Jacu-Pêssego, 2630, Sao Paulo, 08260001, Brazil

^cInstitute for Technological Research of Sao Paulo State, Avenida Prof. Almeida Prado 532 - Prédio 59, Sao Paulo, 05508901, Brazil

Abstract

Morphological characteristics of debris-flow deposits are a fundamental part of the field study of the process. The deposits show aspects related to flow dynamics, which reflects its main mechanics and enables the correct identification of process. Occurrences of debris flows are quite common in Brazil, especially in the Serra do Mar region, located at the southern/southeastern coast of the country. Geological and geomorphological characteristics and high rainfall indexes contribute to high susceptibility of the process in the region. In one of those occurrences, in the summer of 1967, the city of Caraguatatuba was intensely affected by high rainfall far above the average, with maximum values in between the 17th and 18th of March (586 mm/48h), which triggered landslides and debris flows that destroyed the city. In this way, the goal of this research was the morphological characterization and identification of debris-flow deposits from the 1967 event, in Caraguatatuba, Serra do Mar/Brazil. To achieve this goal, the following steps were made: a) selection of watersheds hit by debris flows; b) mapping of the debris-flows deposits in field surveys; and c) identification of morphological characteristics of deposits, applying field records. The results showed that the deposits mapped presented common characteristics described in literature as typical of debris flows, highlighting the presence of inverse grading, lateral levees and large boulders. The watersheds showed differences related to morphology types of deposits, indicating the influence of its characteristics in deposition. Those results contribute to the study of debris flow, mostly to identification of susceptible areas but also to mitigation actions promoted by the government, aiming to improve land use planning, avoiding occupation of those areas by population.

Keywords: geomorphology; mass movement; hydrogeomorphic processes; mapping; tropical environment.

1. Introduction

Debris flows are among the mass movements with the highest destructive power due to their capability to transport high volume of several types of material (e.g. boulders, organic matter) through long distances in high velocities. When debris flows reach areas of lower relief, where people and infrastructure are concentrated, they commonly cause social and economic damage, including casualties.

In the southern and southeastern region of Brazil, the occurrences of debris flow are common, which causes destruction and damage to local infrastructure, homelessness and a higher number of deaths (Vieira and Gramani, 2015). By being a process with a long time return and for the lack of risk mapping and government support, the population occupies susceptible areas, constructing its houses in deposits from past events or using it with landscaping purposes, ignoring the risk to new occurrences. In Brazil, the primary historic debris flows which caused casualties include: Caraguatatuba in 1967 with 120 fatalities; Santa Catarina in 2008 with 135 fatalities; Rio de Janeiro Mountain Region in 2011 with more than 1.000 fatalities; and Itaoca in 2014 with 25 fatalities (Jones, 1973; Avelar *et al.* 2011; Kobiyama and Michel, 2014; Matos, *et al.*, 2017; Dias *et al.*, 2016a; Dias *et al.*, 2016b; Gramani and Martins, 2016; Picanço *et al.*, 2016; Gomes, 2016; Dias, 2017; Côrrea, 2018).

Identification of debris-flow deposits is an important determinant of areas susceptible to debris flow. Identifying distinctive sedimentary features that show flow dynamics, such as inverse grading, lack of sorting and large

* Corresponding author e-mail address: vivian.cristina.dias@usp.br

boulders, differentiates debris-flow deposits from other deposits, like floods or debris floods. (Johnson, 1970; Costa, 1984; Jakob, 2005; Welsh and Davies, 2010).

Characterization of debris-flow deposits can contribute to a better understanding of the process, in addition to serving as a support to the government in preventive and mitigative measures in susceptible areas. Therefore, the aim of this research was identification and characterization of debris-flow deposits in the city of Caraguatuba, related to the 1967 event.

2. Study Area

The city of Caraguatuba is located on the southeastern Brazilian shore, (São Paulo State), in a mountainous region named “Serra do Mar” (Fig. 1). Due to its geological, geomorphological and climatic characteristics, the occurrence of landslides and debris flow is frequent in Serra do Mar. However, despite the high susceptibility and occurrence of fatal debris flow, the area is densely populated with none or little control from authorities, which contribute to higher risk of new fatalities (Matos, 2017).

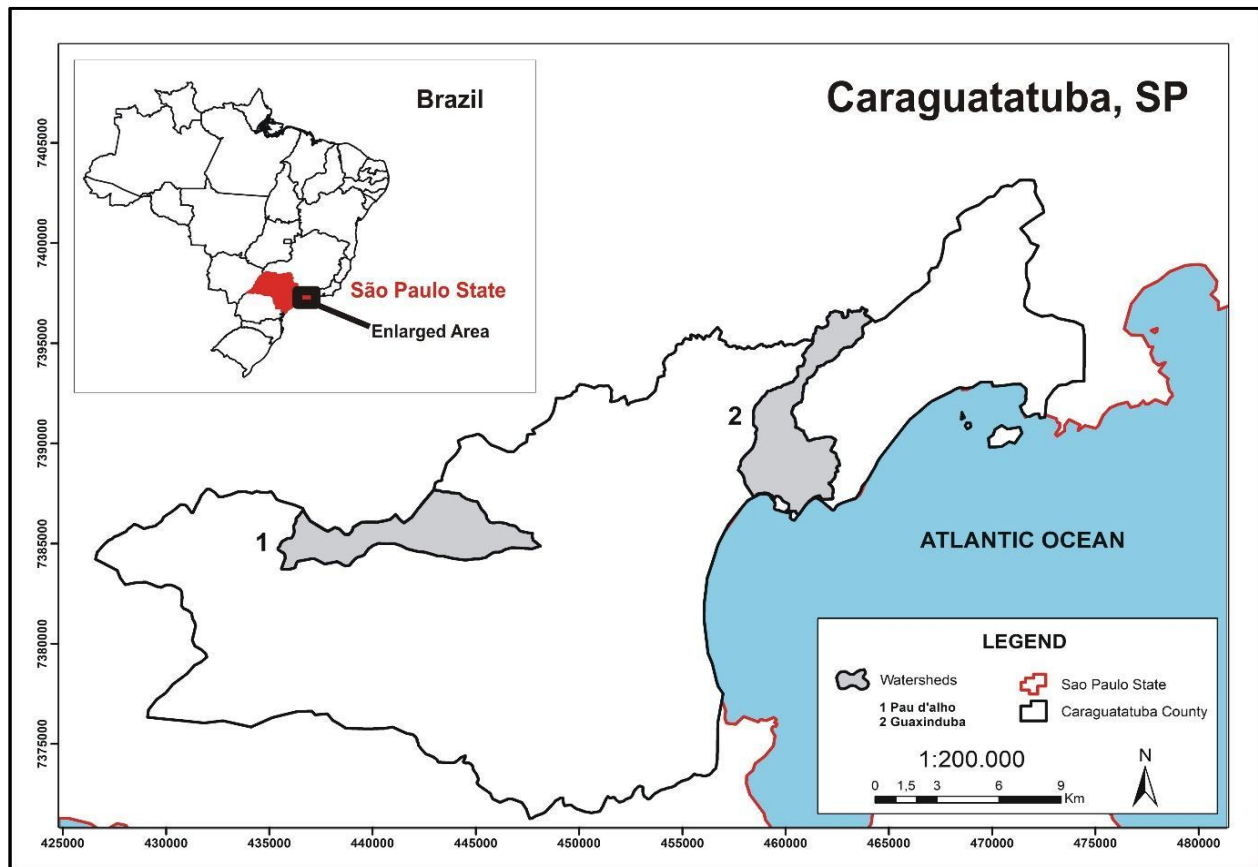


Fig. 1. Location of the study area and the watersheds Pau d'alho (1) and Guaxinduba (2).

Rainfall volumes among the summer season between 1965 – 2011 shows a high rate, typical of the region, however, in the summer of 1966-1967 an unusual rainfall volume affected the city, when the total rainfall exceeded 1.400 mm (Fig. 2), with critical values on March 16th and 17th when it rained about 548 mm/48h, triggering landslides and debris flows. Several watersheds were hit, including Santo Antônio, Guaxinduba, Pau d'alho,

Canivetal and Camburu. The events devastated the city, destroying urban infrastructure, including the main highway to the city, displacing 400 people and causing 120 fatalities (Fig. 3) (Cruz, 1974; De Ploey and Cruz, 1979; Dias *et al.*, 2016). More than 50 years after, the area affected has been re-occupied by population, who ignore the evidence of the debris flows which is still visible in the landscape.

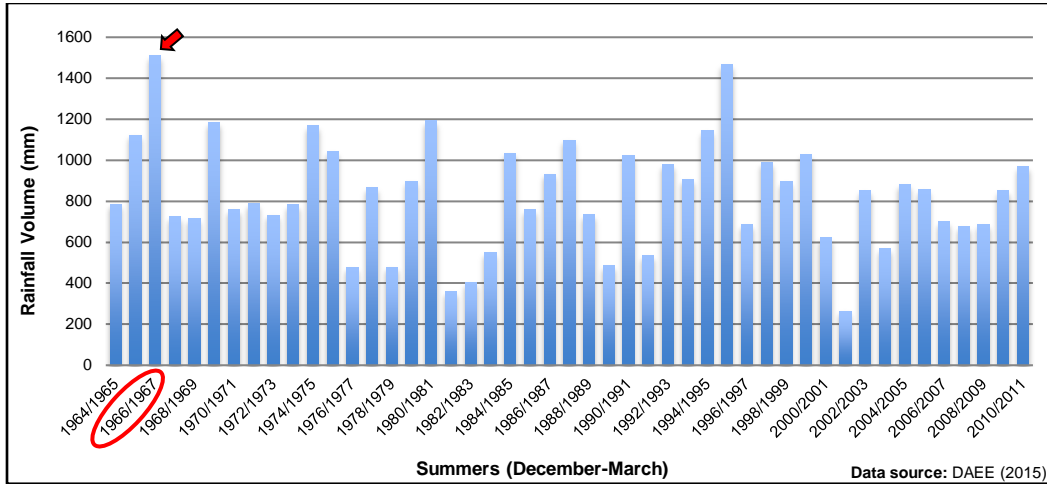


Fig. 2. Total rainfall in the summers of 1965 – 2011 in Caraguatatuba, Brazil, highlighting the summer of 1966 – 1967. Source: Dias *et al.*, 2016b.

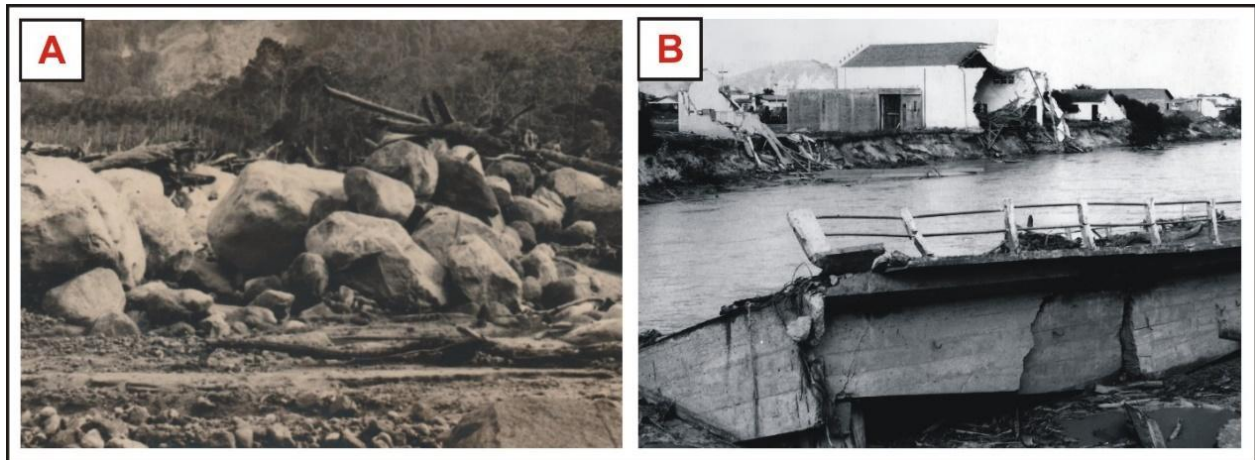


Fig. 3. (a) Debris-flow deposits (boulders size: approx. > 10 meters of diameter) and (b) part of a bridge destroyed in the 1967 event, in Caraguatatuba, SP. Source: (a) Cruz (1974); (b) Public Archive of Caraguatatuba.

3. Methods

3.1. Selection of watersheds hit by debris flows

The selection of watersheds was based on the geomorphological mapping presented by Cruz (1974; 1990), in which identified the areas affected by landslides and debris flows soon after the 1967 event. The affected areas present differences concerning occupation and magnitude of the processes. Thus, the watersheds selected are Guaxinduba and Pau d'algo (Fig. 1). Guaxinduba is a densely occupied area and is near the urban center of the county. Pau d'algo is located within a privately-owned farm. Both watersheds are identified by Cruz's map as areas where debris flows occurred, but without information regarding morphology of deposits (e.g. size, morphological features).

3.2. Mapping of debris-flow deposits

The mapping of debris-flow inundated area was made using the geomorphological map from Cruz (1974; 1990) in which the author identified mass movements occurrences in general, without specifying the typology. With this map, it was possible identifying watersheds where debris flows gone through, as well deposition areas. The map was treated on *Geographical Information System (GIS)* to locate and delimitate the inundated area of debris flows in each watershed. After the digital treatment, field surveys were made to confirm the location of the hit areas and if the characteristics of the deposits correspond to the process analyzed. It was collected information about location, access, size and typology of the deposits.

3.1. Identification of the morphological characteristics of deposits

We characterized the morphological features of deposits during field surveys, including location information (e.g., altitude, coordinate, access, occupation) and features of the deposit (e.g., size, morphological characteristics, presence of large woody debris). First, it was verified if the areas indicated by Cruz (1974;1990) as from debris flows shows characteristics indicated in literature as typical from the deposition of the process, such as lack of sorting, lateral levees and large boulders (Johnson, 1970; Costa, 1984; Eisbacher and Clague, 1984; Ujueta and Mojica, 1995; Jakob, 2005; Takahashi, 2007; Welsh and Davies, 2010). After that, the location of deposits visited in the field was overlaid with the digitized mapping from Cruz (1974; 1990) in GIS and new cartographic products were generated with that information.

4. Results and Discussion

Results showed that both watersheds exhibit morphology typical of debris-flow deposition, as mentioned in literature, highlighting deposits with inverse grading features and lack of sorting in sediments, one of the main characteristics indicated as typical from debris flows (Ujueta and Mojica, 1995; Jakob, 2005; Takahashi, 2007; Welsh and Davies, 2010). However, the deposits are distinct in each watershed. Guaxinduba watershed exhibits deposits with inverse grading, lack of sorting, and very large boulders. No lateral levees or organic matter were found (Fig. 4).

The main body of the deposit is in the central area of the watershed where the largest boulders are located, which are currently used in landscaping. It is an area very much modified and occupied; however, evidences of the 1967 disaster are still visible in the landscape, indicating the susceptibility of the area and the potential risk that residents are subjected to.

Pau d'algo watershed shows more preserved deposits, with features of inverse grading, sediments with lack of sorting and predominance of lateral levees along the main channel (Fig. 5). No large boulders or presence of organic matter were found.

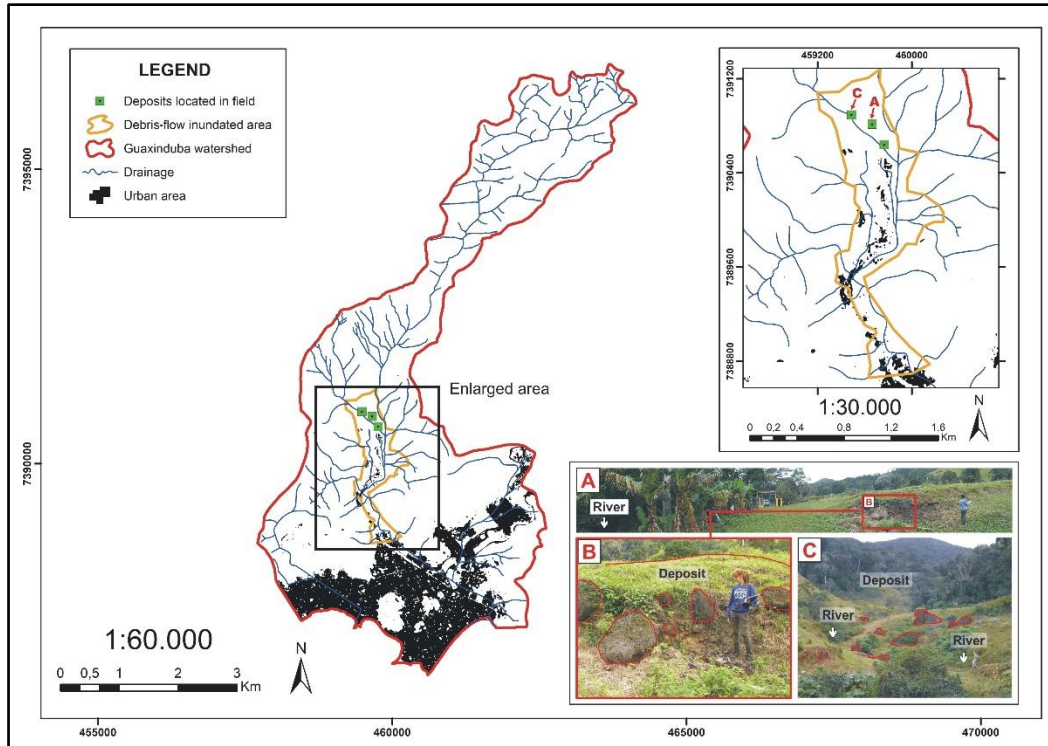


Fig. 4. Debris-flow deposits in Guaxinduba watershed. The inundated area is from digitized of the mapping made by Cruz (1974; 1990). Pictures A and C are identified in the enlarged area, near the urban areas.

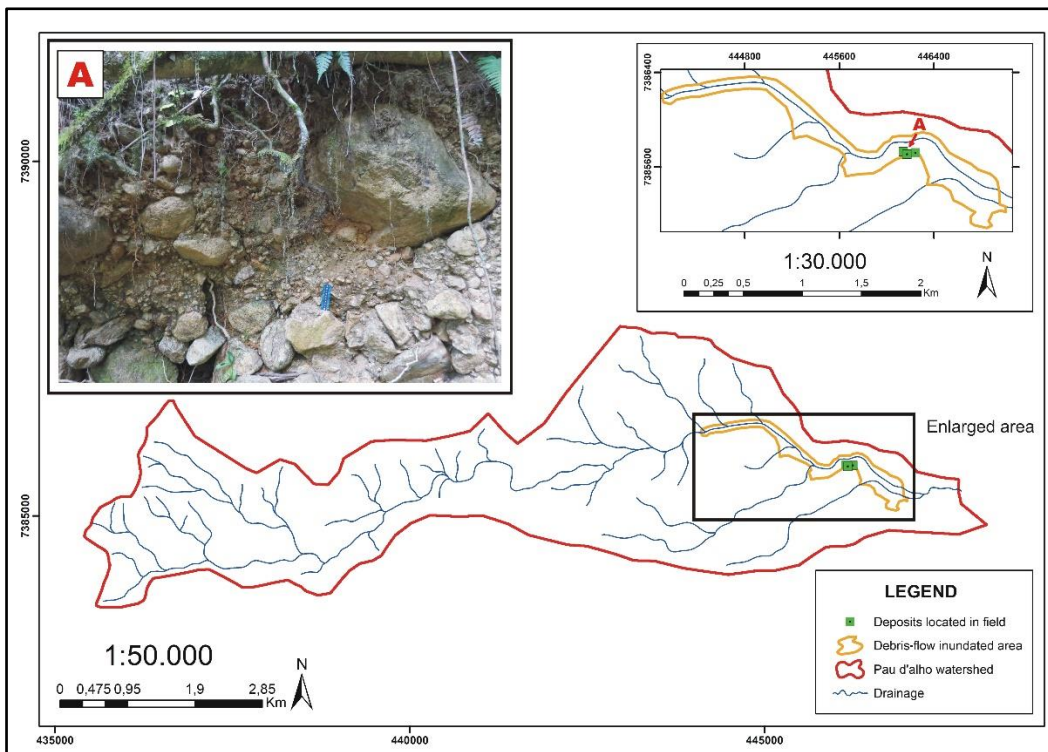


Fig. 5. Debris-flow deposits in Pau d'algo watershed. The inundated area is from digitized of the map made by Cruz (1974; 1990).

By comparison with Guaxinduba watershed, Pau d'algo has no residential occupation, only pasture areas. There are also buildings to support farm activities and employees, and infrastructure (e.g. roads and powerlines). All main activities of the farm are established on the flat zones, distant from deposits and steep areas.

Other differences were observed between the two watersheds, beside the occupation. In Pau d'algo, inside the farm area, was installed the Gas Treatment Unit (UTGCA), from PETROBRAS, responsible to process the natural gas that will be distributed to the domestic market. The construction of the unit was carefully planned considering the susceptibility of the area to the occurrence of debris flows, as shown in the report made by the IPT (2006) (Institute for Technological Research of São Paulo State). Thus, preventive measures were made aiming to mitigate damages, such as the elevation of part of the structure, to avoid debris, and the construction of a barrier.

This demonstrates a difference in the evaluation and precautions taken in each watershed against debris-flow hazards. The Guaxinduba population occupies an area without mitigation measures or governmental planning and is centered among previous debris-flow deposits. Some houses use the large boulders of the debris-flows deposits as part of their construction (Fig. 6b), in Pau d'algo, the risk of new occurrences was a worry before the UTGCA installation, aiming to mitigate damages and loss due the occurrence of debris flows (Fig. 6a).



Fig. 6. (a) The Gas Treatment Unit (UTGCA), from PETROBRAS installed in Pau d'algo watershed, with precautionary measures to debris-flows damage, as the elevation of the pipes (left) and culverts to withstand debris-flow passage (right); (b) boulder used as part of the construction of a wall from a house, in Guaxinduba watershed.

5. Conclusion

This work showed the characteristics of debris-flow deposits in two watersheds from the city of Caraguatatuba/SP (Guaxinduba and Pau d'Alho) from the 1967 event. The features found in the deposits correspond with the main aspects related to the occurrence of debris flows, such as inverse grading and lack of sorting, which validate and complement the geomorphological mapping made after the event, in 1974.

Also, the results show differences related to the occupation and preventive actions in watersheds despite both being susceptible to the occurrence of debris flows and still had evidences from past events in the landscape. In spite of being a very occupied area, Guaxinduba doesn't have any structure or precautions aiming to mitigate damages. In comparison, Pau d'Alho is a farm area, without residents, however, the recent installation of a natural gas treatment unit (UTGCA) included debris-flow mitigation design and construction.

Thus, with this work it was possible to characterize the morphology of debris-flows deposits in both watersheds, as well as the locating debris-flow deposits from the 1967 event and characterizing the risk to the local population and infrastructure. This study contributes to the understanding of debris flows in Brazil and may promote mitigation actions to be included through land use planning and the population living in areas susceptible to debris flows.

Acknowledgements

We gratefully acknowledge support for this project from São Paulo Research Foundation (FAPESP); Coordination for the Improvement of Higher Education Personnel (CAPES); National Council for Scientific and Technological Development (CNPq); Institute for Technological Research of São Paulo State (IPT), the Graduate Program in Physical Geography from University of São Paulo (USP); and the Research Group GPMorfo. The authors specially thank the revisors, for correction and improvement this manuscript.

References

- Avelar, A. S.; Coelho Netto, A. L.; Lacerda, W. A.; Becker, L. B.; Mendonça, M. B., 2011, Mechanisms of the Recent Catastrophic Landslides in the Mountainous Range of Rio de Janeiro, Brazil, *in: The Second World Landslide Forum, 2011, Roma. Landslide Science and Practice. Berlin: Springer-Verlag. vol4. p. 265-270.*
- Costa, J. E., 1984, Physical geomorphology of debris flows, *in: Costa, J. E., and Fleisher, J. P., eds., Developments and applications of geomorphology: New York: Springer-Verlag. p. 268 – 317.*
- Cruz, O., 1974, A Serra do Mar e o litoral na área de Caraguatatuba – SP. Contribuição à geomorfologia litorânea tropical. [PhD thesis]: IG – Série Teses e Monografias nº 11, 181p.
- Cruz, O., 1990, Contribuição geomorfológica ao estudo de escarpas da Serra do Mar. *Revista do IG 11, p. 9 – 20.*
- Corrêa, C. V. S., 2018, Modelagem morfométrica para avaliação da potencialidade de bacias hidrográficas a corridas de detritos: proposta aplicada em Caraguatatuba (SP) e São Sebastião (SP). [PhD Thesis]: Universidade Estadual Paulista, Instituto de Geociências e Ciências Exatas, Rio Claro, 2018, 278p.
- De Ploey, J. and Cruz, O., 1979, Landslides in the Serra do Mar, Brazil. *Catena 6: p. 111 – 122.*
- Dias, V. C.; Viera, B. C.; and Gramani, M. F., 2016a, Parâmetros morfológicos e morfométricos como indicadores da magnitude das corridas de detritos na Serra do Mar Paulista. *Confins [Online], 29, 2016, p. 1 – 18.*
- Dias, H. C.; Dias, V. C.; and Vieira, B. C., 2016b, Landslides and morphological characterization in the Serra do Mar, Brazil, *in: Landslides and Engineered Slopes. Experience, Theory and Practice – AVERSA et al. (Eds), p. 831 – 836.*
- Dias, V. C., 2017, Corridas de detritos na Serra do Mar Paulista: Parâmetros morfológicos e índice de potencial de magnitude e suscetibilidade. [Master dissertation]: Universidade de São Paulo, São Paulo, 129p.
- Eisbacher, G. H. and Clague, J. J., 1984, Destructive mass movements in high mountains: hazard and management. *Geological Survey of Canada, 230 p.*
- Gramani, M. F. and Martins, V. T. S., 2016, Debris flows occurrence by intense rains at Itaoca city, São Paulo, Brazil: field observations. *Landslides and Engineered Slopes. Experience, Theory and Practice. DOI: 10.1201/b21520-120.*
- Gomes, M. C. V., 2016, Influência dos movimentos de massa nas taxas de denudação a longo-termo da Serra do Mar/SP. [PhD thesis]: Universidade de São Paulo, São Paulo, 153p.
- Instituto de Pesquisas Tecnológicas – IPT, 2006, Análise de risco de processos de movimentos de massa e estudos para determinação da cota máxima de inundação para subsidiar a escolha entre as alternativas locais 3A, 4A e 4B da Unidade de Tratamento de Gás do gasoduto Mexilhão, Caraguatatuba, SP. *Relatório Técnico N° 90 p. 643 – 205.*
- Jakob, M., 2005, Debris-flow hazard analysis. *in Jakob, M. and Hungr, O., eds., Debris-flow hazards and related phenomena: Springer, p. 442-474.*
- Johnson, A. M., 1970, Physical Processes in Geology. A method for interpretation of natural phenomena – intrusions in igneous rocks, fractures and folds, flow of debris and ice. *Freeman, Cooper & Company, San Francisco, Califórnia. 577 p.*
- Jones, F., 1973, Landslides of Rio de Janeiro and the Serra das Araras Escarpments, Brazil. *U. S. Geological Survey Professional Paper 697. United States Government Printing Office, Washington, 49p.*

- Kobiyama, M. and Michel, G. P., 2014, Bibliografia dos trabalhos de fluxos de detritos ocorridos no Brasil no período de 1949-2014. Trabalho Técnico GPDEN, n° 01, 15p.
- Matos, L. J.; Vieira, B. C.; and Ferreira, C. J., 2017, Avaliação da Vulnerabilidade das Construções às Corridas de Detritos por meio do método PTVa (Papathoma Tsunami Vulnerability Assessment). Boletim Paulista de Geografia v. 97, p. 42-65.
- Picanço, J. L.; Tanaka, M. J.; Costa, V. V.; Luiz, E. F. O.; Lopes, A. B. B.; Afonso, F. K.; Pimenta, V., 2016, Debris flow hazard zonation in Serra da Prata range, Paraná State, Brazil: Watershed morphometric constraints. *in: Landslides and Engineered Slopes. Experience, Theory and Practice – AVERSA et al. (Eds)*, 7p.
- Takahashi, T., 2007, Debris Flow: mechanics, prediction and countermeasures. Taylor & Francis Group, London, UK. 439 p.
- Ujueta, G. and Mojica, J., 1995, Fotointerpretacion y observaciones del flujo de escombros de Noviembre 13 de 1985 en Armero (Tolima, Colombia). Geologia Colombiana, 1, p. 5 – 25.
- Vieira, B. C. and Gramani, M. F., 2015, Serra do Mar: the most “tormented” relief in Brazil. *in: Vieira, B. C.; Salgado, A. A. R. and Santos, L. J. C., eds., Landscapes and Landforms of Brazil, World Geomorphological Landscapes: Springer*, p. 285-297.
- Welsh, A. and Davies, T., 2010, Identification of alluvial fans susceptible to debris-flow hazards. *Landslides* 8: 183. <https://doi.org/10.1007/s10346-010-0238-4>.

The Santa Lucía landslide disaster, Chaitén-Chile: origin and effects

Paul Duhart^a, Violchen Sepúlveda^a, Natalia Garrido^a, Mauricio Mella^a, David Quiroz^a,
Javier Fernández^a, Hugo Moreno^a, Gonzalo Hermosilla^a

^a*Servicio Nacional de Geología y Minería, Avenida Santa María 0104, Santiago 7520405, Chile.*

Abstract

On December 16, 2017, a rockslide was triggered in the headwaters of the Burrito River (Chaitén district, 43.4° SL) which produced debris and mud flows that flooded Villa Santa Lucía, destroying half of the town's urban area. These mass wasting events covered an area of 3 square-kilometers on Rute 7 and 1 square-kilometer on Rute 235, which resulted in twenty-one fatalities and one person still missing. The rockslide was produced by an intense rainfall which took place on the 15th and 16th of December, same year. The rainfall's measured depth totaled 122.8 mm in only 24 hours, with a high isotherm of 0° (2.700 m asl). This event was preceded by a two-week-long period of high temperatures (22°C daily maximum) previously registered. The main playing factors were the presence of deeply altered volcanic rocks (clay-iron oxides) of the Cordón Yelcho Pleistocene Volcanic Range (SERNAGEOMIN-BRGM 1995) plus vertical fractures, open cracks and very steep slopes. The rockslide impacted a covered glacier and ice-cored moraine that resulted in a very high-speed blast, followed by large debris and mud flows that traveled a distance of 8 kilometers, deeply eroding the Burrito valley walls including its forest, soil and sediments (Duhart *et al.*, 2018). A 7.2×10^6 m³ total of sediments, water, ice and vegetal coverage were estimated and about 2×10^6 m³ were deposited on a 9×10^5 m² fan area, covering the northern area of Santa Lucía village. An average velocity of 72 km/h was estimated for the higher part of the flow (Fernandez *et al.*, 2018), although the initial blast was higher due to the trees that were uprooted and torn alongside the valley walls. As of today, the rockslide scar is still unstable with steep slopes, open cracks, a prominent hanging block and vertical fractures. A Laser Scan monitoring test was developed and is currently under assessment design. The implementation of permanent monitoring beneficial to the understanding of the rock's failure origins in the generation zone may enhance the development of an alert system for landslide hazard risk reduction.

Keywords: destructive landslide, rock fall, debris flow, covered glacier, triggered rainfall.

1. Introduction

This article is a report of the geology, velocity and volume estimations, of the Santa Lucía landslide, which occurred on 16 December 2017 that caused damage and fatalities in the homonymous village and the '7 way'. This landslide was generated in a periglacial environment with the conjugation of several conditioning factors and triggers.

* Corresponding author e-mail address: paul.duhart@sernageomin.cl

1.1. Location

The area is located in the Andean Main Range (43,413°S -72,367°W). The Santa Lucía village is located in the north-south oriented tectonic valley (Fig. 1), that corresponds to the Liquiñe-Ofqui Fault Zone. The valley has experienced erosion by glaciers and later filled by glacial, volcanic, alluvial and fluvial sediments. The Cordón Yelcho Mountain has northwest-southeast orientation with height above 2400 m asl, has covered by glaciers and is 8 km from the village.

1.2. Geology of the area

The Villa Santa Lucía area is composed of metamorphic, granitic, volcanic and limited sedimentary rocks (Fig. 1). The oldest rocks of the area are Paleozoic micaceous schist and amphibolites (PzTrbm). The intrusive basement is composed of Miocene diorites (Md) and tonalites (Mt), and Cretaceous tonalites (Kt), granites (Kg) and monzogranites (Kmg) (Fig. 1). As well as Jurassic-Cretaceous volcano sedimentary rocks (JKvs), Oligocene-Miocene sedimentary rocks (OIMvs), Pleistocene-Holocene volcanic rocks (Q(P)v) and unconsolidated sedimentary deposits (Fig. 1).

The landslide generation area corresponds to a Middle to Upper Pleistocene volcanic chain called 'Complejo Volcánico del Cordón Yelcho' (Moreno, 1995; in SERNAGEOMIN-BRGM, 1995) which is covered by glaciers and edified above 15 km-long metamorphic and granitic rocks with an N-S orientation and an average altitude of 2,100 m asl, its deep incisions forming radial valleys with virtually vertical walls. These rocks correspond mainly to lapilli and blocks tuffs, andesitic to dacitic, with fragments sub-rounded to angular, immersed in a matrix of fine ash with intense argillic alteration and the presence of iron oxides which are characterized by an orange-brown color.

The volcanic layers are displayed sub horizontally and exhibit marked sub-vertical fracturing. They overlay to an intrusive tonalite of amphibole and biotite (which is cut by basaltic dikes of metric width with a preferential east-west orientation) and a sub-vertical trend.

The outcrops exhibit streaks that represent an intense glacial polish. Glacial activity is also exhibited by the presence of subglacial rivers, subglacial lakes, 'U'-shaped valleys and debris-covered glaciers that exhibit thick and fine sediments, containing ice cores on their frontal part.

The main structural component region-wise is the Liquiñe-Ofqui Fault Zone (ZFLO) with an N-S orientation and a strike slip fault (Cembrano et al., 1996), whose primary trace corresponds to the Villa Santa Lucía valley.

2. Santa Lucía landslide

The landslide area amounts to a total length of 12 km of distance from the generation area up to the confluence of the Burrito and Frio rivers. Six indicative segments were recognized (Fig. 2).

2.1. Characterization of the triggering event

The landslide was triggered by the presence of warm rainfall during a two-weeks-long period in which the maximum daily temperatures exceeded 22°C, even reaching maximum temperatures above 27°C for two days which considerably aggravated the snowmelt (Rivera, 2017). During the 24 hours prior to the landslide event, rainfall reached a depth of 122.8 mm (www.dgastel.mop.cl, Table 1), with a maximum intensity of 10.6 mm/hr at 16:00 on 15.12.18. The rainfall event took place with a high isotherm of 0°C, above 2,700 m asl (Rivera, 2017), hence on 15.12.18 and 16.12.18 in Santa Lucía village, and on the Cordón Yelcho and its associated glaciers only liquid precipitations received.

2.2. Generation area

The generation area (number 1, Fig. 2) corresponds to the headwaters of the Burritos River, whose height ranges from 1,000 m to 1,400 m asl and whose main escarpment possesses a length of 900 meters long and 520 meters wide, covering an estimated area of 44 hectares. The northern wall's highest average slopes range between 77° and 81°. A rockslide originated from this area, which incorporated blocks of ice, snow, water, vegetation cover and variable grain

size sediments thus originating the debris flow that was channeled down the valley. Two lakes were generated as a result, with both of their frontal sections dammed by debris and ice blocks.

2.3. Channeled debris flow, Burritos river headwaters

The channelized debris flow followed a 2 km long course (number 2, Fig. 2) descended from elevation of 1,000m to 600m asl, had an approximated affectation width ranging from 200 to 400m wide and covered an approximate surface area of 54 hectares. From the Digital Surface Model (DSM) (SAF, 2017) and field observations, a wave height of 20m was estimated during the course of this path due the flow's incorporation of a large number of uprooted trees and vegetation cover, thus dramatically increasing its total mass, volume and energy.

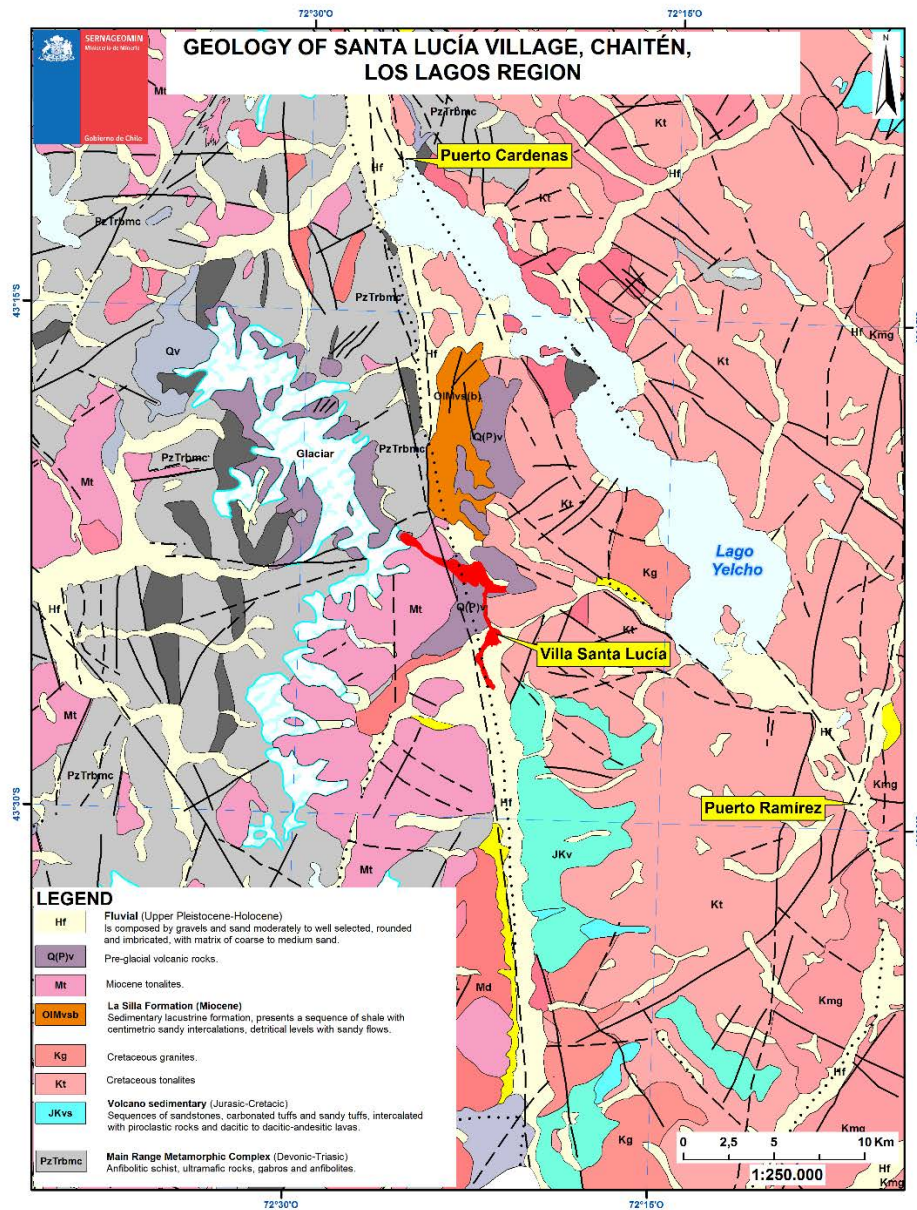


Fig. 1. Geological regional map (SERNAGEOMIN-BRGM, 1995) of Villa Santa Lucia and its surroundings. The area affected by the 16.12.17 landslide is marked in red.

2.4. Unchannelized debris flow

It corresponds to the piedmont (number 3, Fig. 2), where there is a noticeable decrease in the slope to 10°, causing the flow to lose its confinement and start spreading sideways, covering an approximate area of 274 hectares in the process. It descended from 600 to 380m asl, reaching a width of 1.4 km for 2.3 kilometer-long route in a west-east direction and going over ‘7 way’ at the 2 km mark, with a wave height of 40-50 m tall caused by the debris flow’s energy, evidenced by the razed vegetation.

2.5. Channeled debris flow, Burritos river’s northern-southern canyon

In this segment (number 4, Fig. 2), the debris flow entered to the canyon 20 m deep, of the Burritos river from 380 to 250 m asl, throughout a distance of 2 km. The affected area measures up to approximately 16 hectares. According to of the DSM (SAF, 2017), it is estimated that the flow’s wave would have reached a visual estimated height of 30 m tall.

Table 1. Rainfall on the triggering event

15-12-2017			16-12-2017		
Hour	Accumulation per hour (mm)	Cumulative precipitation (mm)	Hour	Accumulation per hour (mm)	Cumulative precipitation (mm)
8:00	0,8	0,8	1:00	3,4	104,8
9:00	1	1,8	2:00	4,4	109,2
10:00	4,6	6,4	3:00	3,8	113
11:00	5,6	12	4:00	4,4	117,4
12:00	6,8	18,8	5:00	3,2	120,6
13:00	5,2	24	6:00	1,4	122
14:00	8,4	32,4	7:00	0,8	122,8
15:00	7,4	39,8	8:00	0	122,8
16:00	10,6	50,4			
17:00	5,4	55,8			
18:00	8,2	64			
19:00	5,4	69,4			
20:00	6,8	76,2			
21:00	6,4	82,6			
22:00	7	89,6			
23:00	7	96,6			
0:00	4,8	101,4			
Total					122,8

2.6. Channeled debris flow, Burritos river’s northern-southern canyon

It corresponds to the area where most of the debris flow’s sediments were deposited in, thus resulting in the main affectation (number 5, Fig. 2) which covered about 50% of the total urban area of Villa Santa Lucía. The resulting deposit begins right at the apex of the fan, location where the flow loses its confinement and expands in a radius of 600 to 1,000 m to the southeast and southwest directions. The deposit is primarily composed of tree trunks and fragments of volcanic and intrusive rocks in a matrix of fine sand, silts and clays, thus forming a large, muddy mass of slow drainage that covered most of the low gradient topography to a thickness ranging from 1 to 7 m.

2.7. Deposit and flood in the lower course of the Burritos river

On the lower course of the Burritos river (number 6, Fig. 2) palisades that dammed the course were formed and resulted in the flooding of all the surrounding area. Meanwhile, fences (wired fences) held back, trapped branches and tree trunks that in turn caused water deviation, and more floods of the lowland areas.

2.8. Volume estimation involved in the generation area

The estimated volumes (of rock and ice) for the generation area were calculated by comparing the digital elevation models built prior to the event (INTERMAP, 2015; SRTM 30, 2000) with the digital elevation model (DSM) built by SAF on 19.12.2017 (Fig. 3). The estimated volume of the landslide was of 7,200,000 m³, out of which 2,200,000 m³ were deposited on the upper part of the river basin and the remaining 5,000,000 m³ were deposited on Santa Lucía village.

The area covered by the fan deposit at Villa Santa Lucia was estimated to be 900,100 m² as reported by the orthophotomosaic's interpretation (SAF, 2017). An average thickness of 2 m from excavations to search for missing persons, was taken into account, thus obtaining an estimated volume of 1,800,200 m³. Additionally, by using the digital elevation models DSM-SAF (2017) plus NEXTMAP World 10® DSM of INTERMAP (2015) for the fan deposit area in Villa Santa Lucía a volume of 2,130,192 m³ was further estimated. As a result, a total volume of 2,000,000 m³ is estimated for the fan deposit in Villa Santa Lucía.

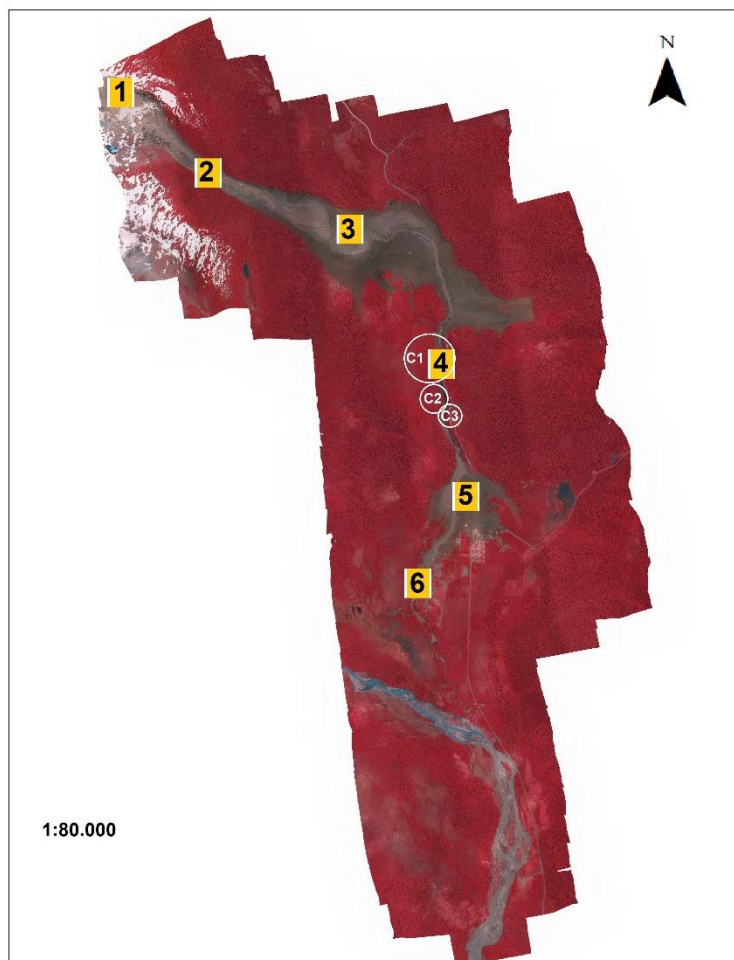


Fig. 2. Near infrared image (SAF, 2017). Red tones highlight the vegetation while gray tones delimit the affected area. Numbers indicate the segments described in this article. Circles indicate the curves used for velocity estimations.

2.9. Velocity estimation

By using the 'on inclination in curve' formula (Johnson, 1970), an average speed of the flow was estimated 72 km/hour for the Burritos River's confined channel (number 4, Fig. 2) (in a N-S direction).

$$V = \sqrt{\left(g * R * \cos \alpha * \frac{\Delta h}{\Delta x}\right)} \quad (1)$$

- V = median velocity (m/s)
- g = gravitational acceleration (m/s²)
- R = radius of curvature (m)
- α = channel slope (°)
- $\frac{\Delta h}{\Delta x}$ = cross-flow slope

The formula of Johnson (1970) was applied in 3 different curves (Fig. 2, Table 2) with the variables of the equation extracted from the surface model and the orthophotomosaic (SAF, 2017).

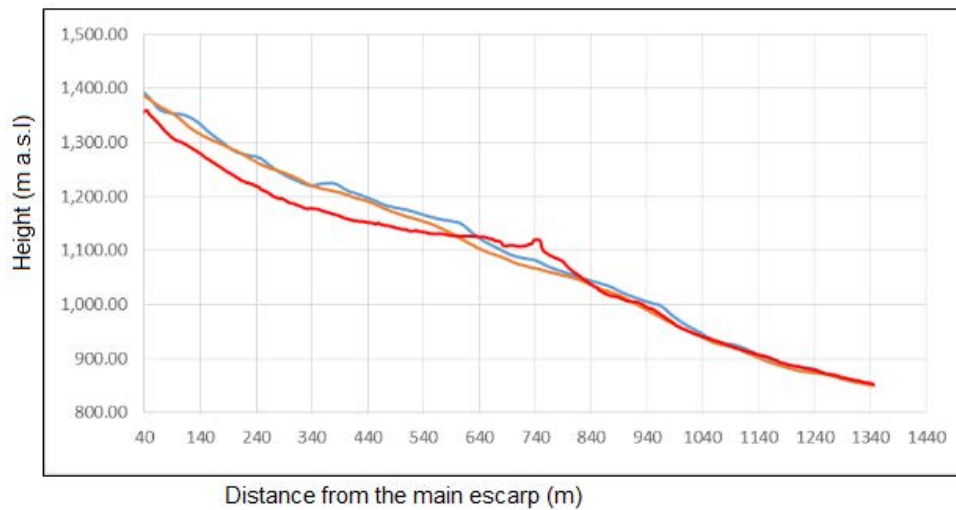


Fig. 3. DSM Profile. The red line corresponds to DSM SAF (2017), the orange line corresponds to NEXTMAP (2015) and the blue line corresponds to SRTM (2000).

Table 2. Variables and results of the equation (1)

Curve	C1	C2	C3	
R	460	210	225	
α	2.121	1.626	10	
Δx	145	55	57.4	
Δh	12	11	11	
$\frac{\Delta h}{\Delta x}$	0,082	0,2	0,191	
$\cos \alpha$	0,999	0,999	0,984	
V^2	372,820	411,434	416,141	
V (m/s)	19,308	20,283	20,399	Average
V (Km/hr.)	69,510	73,021	73,438	71,990

3. Conditioning factors and triggers

Photographs taken prior to the event (as of April 2017), field observations and analysis of satellite and GoogleEarth images, all allow the interpretation of the geomorphological and geological conditions were combined with the major trigger (intense rainfall with a high isotherm of 0°C) for generate the rockslide and debris and mud flows. The following are the factors that contributed to the debris flow event.

1. From 1985 up to 2017, the Yelcho Glacier (Rivera, 2017) receded approximately 1 km, according to the records.

2. Satellite images from GoogleEarth back in 2006 show the presence of a remnant glacier and a lateral moraine, both which are linked to a debris-covered glacier coming from the escarpment on the northwest and north directions of the Burritos River headwaters. The escarpment reveals orange and brown coloring representative of the action of argillic hydrothermal alterations (clays) on volcanic rocks of the 'Complejo Volcánico del Cordón Yelcho' which, consequently, contribute to the weakening of the rock mass. In addition, field observations also determined an intense sub-vertical fracturing of the volcanic rocks and the presence of abundant basaltic dikes.

3. The photographs from April 2017 and those taken after the events show an abundant presence of fractures, which are at least 1 m wide on the upper part of the north scar of the Burritos River headwaters. Furthermore, on the lower part of the generation area (corresponding to the basal outline of the escarpment) 350 m of the glacier covered by debris appears to have retreated. There is also evidence indicative of an incipient glacial lake, which would be partially clogged by debris and cryo-glacial morphologies (cavities in the ice) on the lateral moraine.

The conditions described above indicates the presence of water available (the glacial lake previously described) and an unstable retreating glacier (that would be melting) right beneath an active rockslide zone. The scarp of the active rockslide had steep slopes (approximately 80°), an intense fracturing, argillic alteration and open fractures in the volcanic rocks. Intense rains associated to a high isotherm of 0°C on 16 December 2017 triggered the rockslide and debris flow that would impact this covered glacier at the north-northwest orientation of the escarpment. The rockslide, in addition to water and sediments (debris) from the glacial lake, also forced the glacier down the Burritos River (Figure 4). This explains the formation of a debris flow with enough water to overtopped and eroded the banks of the Burritos River, stripping vegetation and entraining debris to create a cohesive flow (made of debris flow and mud) that included vegetation, soil, tree trunks, ice and detritus. This debris flow mobilized 8 km and eventually was deposited on the area of lower slope of the Burritos River valley, then was channeled down into the canyon where it would open as a fan, impacting Villa Santa Lucía. A less cohesive flow (debris flow) made of rocks and ice deposited on the intermediate zone of the mud flow as a result of the gravitational transport of the initial rockslide at the north-northwest escarpment.

4. Conclusions

The event that took place on 16.12.17 corresponds to a rockslide and debris-mud flow that impacted and partially covered the town of Villa Santa Lucia. This event was triggered by an hydrometeorological incident characterized by abnormally high and prolonged temperatures (registered beforehand) followed by intense rainfall with a high isotherm of 0°C on the day of the event. All the conditioning factors (including steep slopes, rock mass weakness, a retreating glacier, the presence of material ready to be dragged away) plus all the triggering factors (including intense rain and high isotherm of 0°C) culminated in an event of significant magnitude.

It was estimated through digital elevation models that the initial rockfall volume in its generation area was of 7,200,000 m³, out of which approximately 2,200,000 m³ worth of sediments were deposited on the upper part of the basin and the remaining 5,000,000 m³ mobilized towards Villa Santa Lucía. Regarding this last one, about 2,000,000 m³ constitute the fan deposit that hit Villa Santa Lucía and covered an area of 900,100 m². By using the 'on inclination in curve' formula (Johnson, 1970), it was estimated that the average flow velocity for the Burritos River canyon was 72 km/hour.

As of today, the rockslide generation area is still active increasing the possibility of similar events happening again. These events could be triggered again by an intense precipitation with a high isotherm of 0°C either by subduction earthquakes or by crustal earthquakes linked to the Liquiñe-Ofqui Fault Zone's activity.

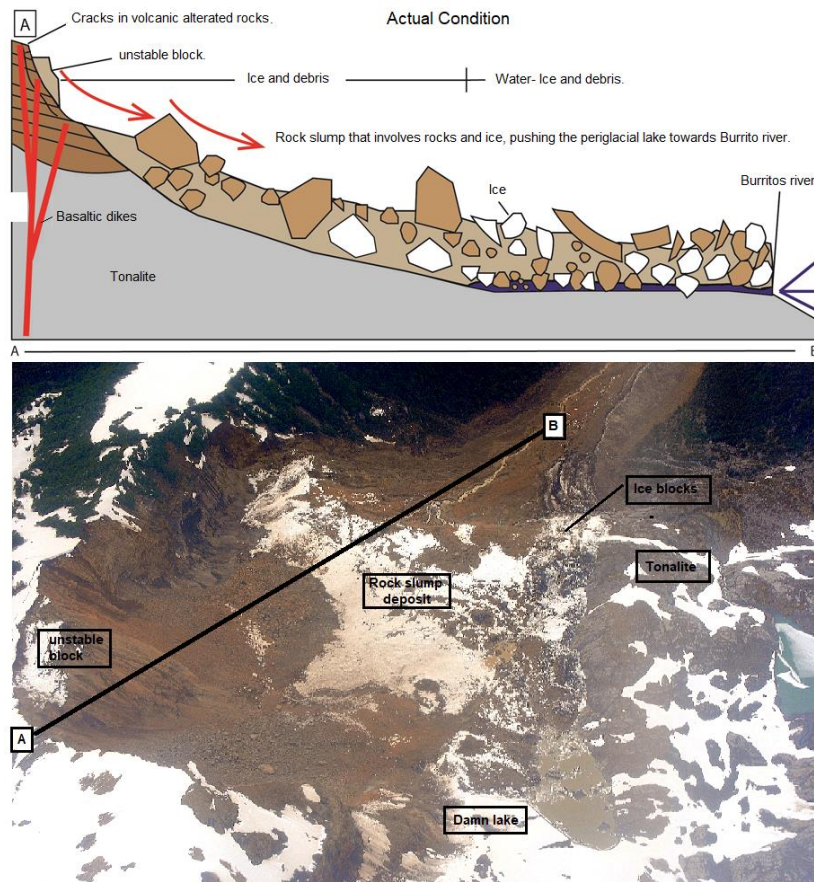


Fig. 4. Profile and sketch showing the current condition of the generation area. Picture was taken on 18.12.17, showing an unstable remnant blockstable; the current deposit of the landslide made of debris and ice blocks; the glacier, the dammed lake and the Burrito river headwaters.

References

- Rivera, A. 2017. Informe glaciológico sobre el flujo de detritos que afectó Villa Santa Lucía el 16 de diciembre del 2017. Laboratorio de Glaciología, Centro de Estudios Científicos.
- Cembrano, J.; Herve, F.; Lavenue, A., 1996. The Liquiñe-Ofqui Fault Zone: a long-lived intra-arc fault system in southern Chile. *Tectonophysics* 259: 55-66.
- DTM, 50cm, 19.12.17, DSM 50cm, 19.12.17 Aluvion NIR SAF Fuerza Aérea de Chile.
- Johnson, A. 1970. *Physical Processes in Geology: A Method for Interpretation of Natural Phenomena; Intrusions in Igneous Rocks, Fractures, and Folds, Flow of Debris and Ice*. Freeman, Cooper and Co, 577 p. San Francisco.
- Duhart, P., Garrido, N., Sepulveda, V., Mella, M., Fernandez, J., Quiroz, D., Hermosilla, G. 2018. Remoción en masa de Villa Santa Lucía (16.12.17), Chaitén-Chile: características e impactos. XV Congreso Geológico Chileno, actas, Concepción, Chile.
- Fernández, J. Garrido, N., Mella, M., Sepúlveda, V., Quiroz, D., Hermosilla, G., Duhart, P., Moreno, H. 2018. Estimación de volúmenes y velocidad del flujo de detritos que afectó a Villa Santa Lucía. XV Congreso Geológico Chileno, actas, Concepción, Chile.
- Moreno, H. 1995. Los Volcanes de la X Región Sur: estudio fotogeológico a escala 1:100.000. SERNAGEOMIN-BRGM (1995), Carta Metalogénica de la X Región Sur, Informe Registrado IR 95-05.
- NEXTMAP World 10® DSM de INTERMAP. 2015.
- Ortofotomosaico 12 cm, 19.12.17. Aluvión NIR SAF (2017). Fuerza Aérea de Chile.
- Online hidrometeorological stations of Dirección General de Aguas: <http://dgsatel.mop.cl/>.

Debris-flow risk management in practice: A New Zealand case study

Jeff Farrell^{a,*}, Tim Davies^b

^a Whakatane District Council, Private Bag 1002, Whakatane 3158 New Zealand

^b University of Canterbury, Private Bag 4800 Christchurch 8140, New Zealand

Abstract

In 2005 the settlement of Matatā on Awatarariki fan, Bay of Plenty, North Island, New Zealand was devastated by a $>3 \times 10^5 \text{ m}^3$ debris flow; several dwellings were destroyed and many damaged, but no fatalities occurred. In the 7 years following the event, design options for a debris-flow containment structure in the catchment were developed. Following a formal determination by the Government's building control agency in 2006, building consents were granted for a number of replacement dwellings on the fan. In 2012, the previously chosen containment structure project was cancelled due to effectiveness and cost concerns. Subsequent investigations confirmed there were no viable engineering solutions to manage debris-flow risk from this catchment, and risk analyses have demonstrated that no debris-flow management systems, warning and evacuation systems, or individual dwelling protection mitigation measures, independently or in combination, could deliver a residential environment with tolerable risk-to-life levels. Since 2013, Whakatāne District Council (the Council) has been working towards a non-legislated managed voluntary retreat from the area where the risk to life is greater than about 10^{-4} a^{-1} , which is also the area of boulder deposition in the 2005 event. This has involved many meetings with affected landowners, including legal counsel and experts, but the currently 13-year delay in resolving uncertainty about landowners' futures has generated considerable stress and even hostility. A parallel legislation-based workstream the Council has undertaken to fulfil its statutory responsibilities has exacerbated tension between the Council and some property owners. From a technical perspective, this study emphasises the danger of lay officials and consultants placing too much confidence in immature technologies to reliably modify debris-flow occurrence. From a public management perspective, it highlights the immaturity of New Zealand's natural hazard management policy framework, in particular the significant disconnect between policy intent and policy implementation and its polarising effects on a small provincial community.

Keywords: Debris-flow risk-to-life; risk reduction; national and local government responsibilities; engineered risk reduction; managed voluntary retreat; New Zealand.

1. Introduction

Although New Zealand is exposed to a wide range of natural hazards, use of formal risk management practices for low-frequency, high-consequence natural hazards is still an emerging field. New Zealand is one of 187 signatories to the 2015 Sendai Framework for Disaster Risk Reduction which refocused international policy direction for disaster reduction from disaster management to disaster risk management. In 2017, changes to New Zealand's Resource Management Act formally recognized the Sendai philosophy of proactively managing risks from natural hazards. However, the Act was changed with minimal consideration of how it might be applied in practice. And therein lies the problem. Some local authorities, in response to events, have identified situations where significant risk from natural hazards exists and for which no pragmatic and affordable engineering solution exists. In such cases, retreat from the high hazard area is the only option. For these scenarios, the legislative provisions of the Resource Management Act are proving to be not only woefully inadequate, but also polarizing to communities, driving a wedge between the

* Corresponding author e-mail address: Jeff.Farrell@whakatane.govt.nz

affected residents and the local authorities endeavoring to apply the legislation. We demonstrate the challenges involved in implementing a disaster risk reduction framework through a case study involving Matatā, a small rural township in the eastern Bay of Plenty of New Zealand that experienced debris flows in 5 catchments in and around the township in 2005. Matatā is part of the Whakatāne district which has a land area of 4,442 km² and a population of 32,691 (2013 Census). The Whakatāne District Council (the Council) is the governing territorial authority.

2. The Natural Hazard Event

In May 2005, extremely heavy rainfall in the steep catchments behind Matatā caused many slope failures that initiated debris flows and debris floods, devastating much of the coastal township (McSaveney et al, 2005). Twenty-seven homes were destroyed, 87 other properties damaged and major transport links cut, resulting in an estimated NZ\$20 million in damage. About 700,000 m³ of debris was deposited from 5 catchments. The most destructive debris flow was from the Awatarariki Stream, where about 300,000 m³ of debris was deposited throughout the fan. Boulders up to 7 metres diameter were mobilised in this debris flow. While there were no deaths or injuries, the nature of this event was such that deaths could easily have occurred.

The closest automatic rain gauge was at Awakaponga, 5km SSE of Matatā. This recorded 367.5 mm for the period 17-19 May, with a peak 1- and 24-hr rainfalls of 94.5 mm and 307.5 mm respectively. These are between 200-500 year recurrence intervals based on extreme value statistics – but may be more frequent. Blackwood (2005) regards them as ~20 percent greater than the 1% AEP estimated rainfall intensities. Morphological evidence at Matatā and the adjacent Manawahe area indicated that rainfall intensities in the storm centre were even higher (Ibid). Peak debris and water discharges in the streams flowing into Matatā are estimated to have been between five and twenty times the theoretical 100-year flood discharges, with water flows up to twice the estimated 100-year floods (Tonkin and Taylor Ltd, 2005). For the Awatarariki catchment, the subject of this case study, the 100-year design flow is 44 m³/s whereas the estimated peak debris-flow discharge for the May 2005 event was 700 m³/s (Tonkin and Taylor Ltd, 2015).

There is evidence that equally large and larger, debris flows have occurred many times over the last 7,000 years, with four smaller flows occurring since 1860 (McSaveney et al, 2005).

3. An Engineering Solution?

Following the 2005 debris flows, the Council engaged external experts to advise what options were available to manage the risk to the Matatā community from future debris-flow events. Considerable community engagement informed option selections. For all of the five catchments, cost-benefit analyses ranked engineering solutions higher than managed retreat (Walton and Clough, 2005).

The Awatarariki fan community wished to re-establish the residential environment through an engineered solution that reduced the risk from future debris flows to acceptable levels. The Council considered a range of mitigation options and settled on a debris dam to achieve this. Subsequent consultation with the community, however, identified that any option involving large scale earthworks would not be supported by tangata whenua (local people of Māori descent who exercise customary authority in an identified area) due to the presence of highly-valued burial caves in the planned location of the dam. The Council then investigated alternative, less intrusive options. A combination of active marketing and an appetite for innovation by key Council officers and Council advisors resulted in adoption of a flexible ring-net proposal as the preferred solution. As the detailed design process proceeded and the requirement to contain >3 x 10⁵ m³ of debris was established, significant design and construction challenges were identified, in particular the unprecedented 14 m high by 39 m wide size of the barrier required as well as the ability of the local bedrock to withstand the anchor forces involved. Ongoing maintenance costs were a separate community concern.

As a consequence of better understanding the design and maintenance parameters, external engineering experts eventually advised the Council that an engineered debris detention structure in the catchment was not viable. The Council then investigated engineering options for a fan solution. Despite a range of options being considered, no viable solution could be identified.

In December 2012 the Council resolved to not proceed with an engineered solution, and to investigate and develop a planning framework to manage the risk. This was a pivotal decision by the Council, not just for the affected landowners but also for the Council itself in its regulatory roles of building consent authority and resource consent authority. The Council decision formally recognised that the properties known to be at risk from the debris-flow hazard from the Awatarariki Stream catchment would continue to be exposed to that risk in the future.

4. Policy Framework for Natural Hazard Risk Management

In 2014 the New Zealand Insurance Council estimated that natural disasters can be expected to cost New Zealand just under 1% of its GDP (about NZ\$1.6B) in any year (Insurance Council of New Zealand, 2014). This ranked New Zealand as having the third most vulnerable economy in the world to the impact of natural disasters. However, a lot of natural hazard damage is uninsured and many of the consequences are difficult to monetize; a Government agency recently estimated the total annual cost of natural hazard events in New Zealand to be between NZ\$12B and NZ\$18B. Annual costs of this magnitude are not sustainable for a country with a population approaching 4.9 million (Stats NZ, 2018). Thus a policy shift away from disaster response to disaster risk management has wide-ranging support within New Zealand. Proactive risk reduction, strengthened community resilience, and reduced expenditure on disaster response are anticipated outcomes of the new policy direction. Current policies and legislation relevant to natural hazard management in New Zealand are summarised in the following table.

Table 1 Key legislation and policies relevant to natural hazard management in New Zealand

Strategic document	Description/Purpose	Relevance
Sendai Framework for Disaster Risk Reduction 2015-2030 (SFDRR)	SFDRR increases emphasis on disaster risk management and makes reduction of disaster risk a primary responsibility of signatory governments.	New Zealand is a signatory to the SFDRR. The nation has committed to reduce levels of risk that have been identified as being unacceptably high.
Civil Defence Emergency Management Act 2002 (CDEM)	To improve the sustainable management of hazards. Achieves acceptable levels of risk by identifying, assessing, and managing risks, consulting and communicating about risks, and identifying and implementing cost-effective risk reduction.	Both the Bay of Plenty Regional Council (BOPRC) and Council are part of the Bay of Plenty CDEM (Civil Defence Emergency Management) Group and contribute to the CDEM Group Plan. The Plan provides a framework for civil defence and emergency management decisions to be made across the Bay of Plenty. The Plan is linked to the Regional Policy Statement (RPS) which cascades to regional and district plans.
Local Government Act 2002 (LGA)	To meet the needs of communities for local infrastructure, local public services, and performance of regulatory functions in a way that is most cost-effective for households and businesses.	Section 11A(d) states that a core public service to be considered is the avoidance or mitigation of natural hazards
Resource Management Act 1991 (RMA)	Sets out how we should manage our environment, including the integrated management of natural and physical resources.	Natural hazard risk management is now a matter of national importance. Every RMA decision must take natural hazard risk into account. In this context regional authorities can extinguish existing use rights, without compensation.
Land Drainage Act 1908 and Soil Conservation and Rivers Control Act 1941	Provide for the conservation of soil resources, the prevention of damage by erosion and to make better provision for the protection of property from damage by floods.	Enable the regional council to undertake or maintain works to minimise flooding and damage in a catchment. Some mitigation measures have been carried out at Matatā under these Acts following the 2005 debris-flow event.
Local Government Official Meetings and Information Act (s 44A) 1987 (LGOIA)	Provides for Land Information Memoranda (LIM) - Council reports about a particular property or section or special features of the land, including hazard information. Their most common application is during the sale and purchase of properties.	Debris-flow risks within the hazard areas on the Awatarariki Stream fanhead are identified in Land Information Memorandum (LIM) reports.

Building Act 2004	Provides for Property Information Memoranda (PIM) - Council reports about a particular property or section or special features of the land, including hazard information that may impact upon a new development. Typically applied for before lodging a building consent application. Sections 71-74 relate to limitations and restrictions for the construction of buildings on land subject to natural hazards.	The Council applied to the Ministry of Business, Innovation and Employment (MBIE) for two determination under this Act during the Matatā process
Bay of Plenty Regional Policy Statement (RPS)	The NZ Building Code includes functional requirements and performance criteria for buildings. Code Clause B1 – Structure, includes requirements relating to building failure and references annual exceedance probabilities for some natural hazards that vary depending on occupancy and nature of activity undertaken.	In 2016, BOPRC introduced a risk management approach to natural hazards (Plan Change 2 – Natural Hazards). The RPS now requires both the Regional Council and District Council to take steps to reduce high natural hazard risk.
Whakatāne District Plan	Provides overarching policy for the Bay of Plenty which is given effect through regional and district plans. The RPS draws on long term plans, national policy statements and standards, and CDEM Group Plans (the latter being influenced by the National Civil Defence Emergency Management Strategy and National Civil Defence and Emergency Plan).	Identifies the important resource management issues in the District, and guides development in the district. Helps ensure Whakatāne is developing the way the community wants it to.
		Currently, the District Plan zones the Awatarariki Stream fanhead as Residential. The Council has commenced a process to re-zone the land to manage the debris flow and debris-flood risk to property and people. This will also fulfil the Council’s responsibilities under the new natural hazard provisions of the RPS for the debris-flow hazard from the Awatarariki Stream catchment.

The NZ Government’s adoption of the SFDRR signals the need for Government involvement in the development of national natural hazard risk management policies and frameworks, and in mitigation of risk from future (inevitable and foreseeable) high-impact natural hazard events that are beyond individual or community means to address.

Recognising the SFDRR commitment, recent changes to the Resource Management Act (RMA) have elevated the importance of managing natural hazard risk to now be a matter of national importance when statutory decisions are made. Additionally, the RMA provides for regional councils, under certain circumstances, to remove existing uses without payment of compensation; however, this contentious provision has yet to be tested through the judicial system.

A risk management approach to disaster reduction requires individual risks to be identified, quantified, and then managed according to priority. This introduces challenges for communities and regulatory decision-makers, including:

- developing an understanding of multiple (interacting and cascading) natural hazards;
- identifying the impacts associated with each hazard (alone and in combination with others);
- establishing a reasonable likelihood of the hazard event occurring;
- comparative analysis of different hazard impacts together with the levels of risk they present; and
- development and funding of risk reduction interventions.

It is already clear that these are formidable challenges. Firstly, the level of risk for many natural hazard events is being established on an ad-hoc basis with no guidance, support, or oversight by central Government. Second, risk quantification has proven costly and problematic due to the complex and uncertain nature and frequency of natural hazard events, particularly those of low probability where there are limited (if any) robust data from historical events. Also, and more importantly, no national framework has been established to guide communities on when risk reduction intervention is appropriate. Similarly, no national or regional funding framework exists to support risk reduction interventions. These challenges reflect the immature state of policy development for natural hazard risk management within New Zealand at the time this paper is authored.

The new risk management approach means management of natural hazards is prioritised by the risk they present. The policy intent of the recently introduced Bay of Plenty Regional Policy Statement (RPS) is to ensure that the consequences of natural hazard events, when they do occur, are as low as practicable. This recognises that under-acknowledgement of hazard risk in historical land use planning decisions has contributed to the high level of natural hazard vulnerability of many New Zealand communities.

Whereas the RMA focuses on environmental management, the Building Act (BA) focuses on building performance standards to ensure that buildings are safe for people to use. Specific provisions of the BA cover new building work on land that is potentially subject to natural hazards. In such cases, a building consent may be refused, or may be granted where the building construction won't accelerate or worsen the natural hazard on the site or other property; the owner is prepared to accept the risk from the unmitigated hazard; and the building consent authority can reasonably grant a waiver or modification of the building code. The BA requires the consenting authority to record this information on the property title at time of granting of the building consent. Building consent decisions can be challenged to the Ministry of Business, Innovation and Employment (MBIE) through a determination application.

5. Application of the Policy Framework to Management of Debris-Flow Risk on the Awatarariki Fan

In 2006, the year following the Matatā disaster, the Council applied for a BA determination from MBIE around whether it could issue dangerous building notices to prevent the Awatarariki fan properties being reoccupied. At the time it was considered that the 2005 debris flows were initiated by a rainfall event with a 0.005 to 0.002 AEP, and that if the event was replicated at any time in the future, similar consequences could be expected. The Council's position was that the area should not be reoccupied, however, MBIE concluded otherwise and determined that the Council should allow residents to reoccupy their homes (Department of Building and Housing, 2006). The decision was subsequently extended to those wishing to rebuild homes destroyed by the 2005 debris flow. As well as repairs to existing dwellings, six replacement dwellings were also constructed between 2007 and 2011.

Engineering works were completed on four of the five catchments affected by the 2005 event. The December 2012 Council resolution to not proceed with engineering works for the Awatarariki catchment, and to move to a planning solution instead, caused the Awatarariki residents to be (understandably) very upset.

In 2012, there was (and there still is) no national guidance on natural hazard risk management assessment methodologies, interpretation of assessments, or on tolerable/intolerable risk levels. The Council sought expert external advice to assist its decision-making processes. The Australian Geomechanics Society Landslide Risk Management Guidelines (AGS, 2007) were identified as an internationally well-respected framework. Debris flows can be considered a subset of landslides, providing justification for the use of the Guidelines for the Awatarariki debris-flow risk assessment. These assessments generated an annualised loss-of-life risk distribution across the fan that ranged from 10^{-2} to 10^{-6} (Tonkin and Taylor, 2013). International comparisons indicated that an annual loss-of-life risk greater than 10^{-4} for an existing environment was unacceptable for residential use. This criterion was also adopted for rockfall risk assessments on the Christchurch Port Hills following the 2010-2011 earthquakes (Massey et al., 2014). Similarly, societal risk plotted on a F-N chart presented in AGS (2007) confirmed the risk to be unacceptable.

Awatarariki fan residents were provided with the risk assessments conducted by Tonkin and Taylor Ltd and supporting information. A representative group of residents was invited to participate in a decision-making exercise to develop a way forward for the residents and the Council. A Consensus Development Group was subsequently established, including residents, a senior manager from the regional council, an elected representative and senior staff from the Council, expert technical and planning advisors, and independent facilitators. The Group met for four days over a two month period and explored a wide range of potential solutions. However not everything was agreed upon; for example, there was a significant gap between the Council and the landowners' views on where the line of tolerable/intolerable risk should be drawn or whether a line should be drawn at all. The group agreed that a high risk exists but individuals varied widely in their personal tolerance of this risk, with many prepared to take individual responsibility for accepting the risk. The group agreed that engineering options were likely to be unaffordable and accepted that the Council had legal responsibilities to manage natural hazard risk to all people in society including the young, the elderly, and visitors. At the end of the process, there was agreement on a roadmap to move things forward. This roadmap included a further review of the quantitative risk assessment; investigation of early warning systems; consideration of on-site mitigation options; and development of a settlement agreement for voluntary managed retreat, with funding provided by a number of agencies, if on-site mitigation of the risk is not possible.

A peer review of the risk assessment suggested that the modelled risk understated, by an order of magnitude, the risk-to-life during the 2005 debris-flow event, and consequently the area with loss-of-life risk greater than $10^{-4} a^{-1}$ was increased. The reviewers concluded that the risk in the expanded area (the "high risk area" hereafter) made residential use unsafe (McSaveney and Davies, 2015). This area includes 34 private properties of which 16 have dwellings, the rest being vacant sections. The other 11 publically-owned properties include transport infrastructure and reserves.

Early warning systems were investigated by GNS Science Ltd, a New Zealand Crown Research Institute, and it was concluded that they were unlikely to be effective due to the short time between event initiation in the catchment and impact on the fan. An escalating alert and warning system was also considered but discounted due to the lack of data on which to base reliable triggering, and the inevitable false warnings the system would produce. Capital and operational costs were additional factors, as was operational liability for system performance (Litchfield, 2015).

On-site mitigation options were explored through a second Building Act determination. Two property owners lodged building consent applications to build dwellings within the high risk area. With knowledge of the high level of natural hazard risk and the lack of any suitable risk mitigation option, the Council's building consent authority declined to issue a waiver or modification of the requirements of the New Zealand building code, and thereby declined to grant the building consents. The Council tested this decision by applying to MBIE for a determination. Two years after the application was lodged, the determination decision was finalised (Determination 2016/034). The decision confirmed that vacant sites in the high risk area should not be developed for residential use.

6. Voluntary Managed Retreat

Elimination of other possible solutions led to the final option identified by the Consensus Development Group, that of voluntary managed retreat; this would provide for acquisition of properties by the Government, BOPRC or the Council, on a 'willing buyer – willing seller' basis. One of the Government's responses to the devastating 2010 - 2011 Canterbury earthquake sequence was to enact special legislation which enabled large areas of badly-damaged land and buildings to be acquired and people relocated. Most of the acquisitions involved land that had been damaged in the earthquakes, whose loss-of-life risk was low. In a policy environment promoting disaster risk management, and where a high loss-of-life risk had been proven with no viable risk reduction mitigation intervention available, Awatarariki fan residents and the Council looked to the Government in the first instance, and BOPRC in the second instance, to support an outcome consistent with that provided to property owners in Canterbury.

To inform discussions with the Government and BOPRC an Acquisition Strategy was developed that would incentivise property owners to relocate away from the high risk area. Legal advice to the Council indicated that owners of all of the 34 properties in the high risk zone (i.e. vacant sites as well as sites with houses) needed to be offered the same process; final offers would reflect the difference in value of the land and assets obtained through a formal valuation process.

The Acquisition Strategy recognized the "chicken and egg" dilemma for the Council: it needed to establish financial parameters for meaningful engagement with potential funding partners through identifying indicative settlement offers, without confirmed funding arrangements being in place. Legislative provision exists in New Zealand for compulsory acquisition of private land under the Public Works Act, however voluntary managed retreat is not a public work and therefore these provisions do not apply. Experience of managed retreat in the United States indicated that unless residents were incentivized to relocate, take-up of a retreat package would be low (Freudenberg et al., 2016). Accepting that a significant proportion of property owners in the high risk area had limited capacity to repay additional debt, voluntary retreat proposals were developed to incentivise owners to relocate. The proposals were based on the current market value ignoring the natural hazard risk at the time of a formal offer, plus contributions towards legal expenses and relocation where the fan property was the primary residence of the owner. A valuation appeal procedure was also proposed. In sum, these provisions largely mirrored the acquisition provisions of the Public Works Act.

Individual property valuations were needed to establish the financial envelope for managed retreat of the 34 properties in the high risk zone. All but two owners gave consent for property valuers to visit their property. The valuation process assessed the potential cost of property purchases and clean-ups at NZ\$15M. Indicative voluntary retreat proposals were provided to individual property owners who were then asked to register their interest in exploring the managed retreat process further. Two property owners declined to participate, one of whom was a Maori family group who owned a large parcel of land on the fan and had plans to register that land as a Maori reservation with a reserve status to avoid further development; this group supported retreat from the area and wished to integrate the development of the reservation with the Council's broader plans for a coastal reserve for all of the high risk area. For a range of reasons including distrust of and lack of confidence in the Council, misunderstanding of the process, misunderstanding of the indicative offer, and different expectations of property values, 11 property owners did not return registrations of interest. The remaining 21 property owners wished to see the process continue.

Despite the shift in national policy direction towards DRR, little support for managed retreat from Government ministers, BOPRC elected representatives, and officials has been forthcoming. Feedback from the Minister of Local Government in mid-2017 included a statement that Government wished to see a more definite expression of intent by

the Council to pursue the formal legislative provisions of the Resource Management Act as provided for by Parliament, and to apply the recent changes to the RPS. The RMA provisions required a District Plan change to alter the zoning of the high risk area from 'Residential' to 'Coastal Reserve', and a change to a Regional Plan that would remove the occupancy rights of the 16 property owners with houses on their land, with no compensation. Whereas the change to the District Plan reflected the status quo arrived at following the 2016 BA determination, the change to the Regional Plan removed the 'voluntary' component of the Council's managed retreat strategy. This drastic change created a moral dilemma for several councilors who considered it one step too far. The subsequent Council resolution to progress along the RMA route was based on a majority vote rather than by consensus.

BOPRC introduced a risk management framework to the Bay of Plenty region through its change to the RPS. It will also be responsible for implementing and enforcing the change to the Regional Plan. The Council asked BOPRC to develop the Plan Change to the Regional Plan. This request was declined by BOPRC. As a consequence, the Council developed both plan changes. BOPRC was then asked to adopt the prepared Regional Plan Change, but again this request was rejected.

The lack of support from BOPRC and Central Government, combined with an absence of national and regional policy implementation direction and guidance, has required the Council, a provincial territorial authority with only 34,500 residents, to chart a course through unexplored and incomplete national and regional natural hazard risk management frameworks with relevant key public sector actors observing from the sidelines.

And what of the fan property owners, those most affected? The Council has maintained regular communication with all property owners throughout the process. For owners of vacant sites, the 2016 BA determination confirmed their inability to obtain a building consent to build on the land and their expectations largely reflected an acceptance of this. Unsurprisingly, a number of the owners of properties containing houses reacted angrily to the Council's decision to proceed with a Regional Plan Change that could see them forcibly removed from their homes without compensation. Their concerns were appropriately picked up by a sympathetic national media which resulted in Government Ministers taking a more active interest in engaging with the Council to pursue a managed retreat solution that is separate from the legislative RMA processes.

A change in Government in October 2017 has seen an holistic approach to public governance that includes wellbeing of citizens. The willingness by the current Government to engage with the Council over a managed retreat solution for the Awatarariki fan has had a moderating influence on BOPRC.

Now, 13 years after the event, and 6 years after a decision to not pursue an engineered solution, the level of risk is understood, and meaningful dialogue is occurring. This may not only lead to a solution for Awatarariki fan residents, but also result in a policy implementation template for managed retreat within New Zealand where unacceptable risk has been identified, no viable alternate solution to retreat exists, and the scale is such that local communities cannot afford to fund retreat on their own.

7. Conclusion

An initial proposal for an earth containment dam in the upper catchment reflected a traditional 'build back better' approach to management of debris-flow risk from the Awatarariki Stream and its tributaries. Community consultation resulted in an alternative construction proposal that was attractive to professionals and local authority officials for its innovation and cost. Unfortunately, the risk inherent in innovation went unrecognised and it wasn't until the detailed design phase that the inadequacies of the innovative design became apparent. Engineered fan solutions were also investigated and rejected.

Since all engineering options had been exhausted, a disaster risk management approach was adopted. Loss of life and property damage risks have been quantitatively assessed, with annualised loss-of-life risk ranging from 10^{-2} to $10^{-6}a^{-1}$ across the fan. 34 properties with an annual loss-of-life risk of $>10^{-4}a^{-1}$ were classified as being unsafe for residential use. Several risk reduction options were investigated including provision of early warning systems and active catchment management, but none proved to be viable. Having discounted all other risk reduction options, retreat from the risk was the only remaining option.

The journey the Council and property owners have gone through over the last six years has demonstrated significant failings in the national policy framework for disaster risk management.

- Although the policy vision is clear, the means to achieve it are lacking.
- No advice exists on how natural hazard risk should be assessed or what levels of risk require intervention.
- Intervention options are not enabled through supportive legislation, nor access to appropriate funding to implement risk reduction interventions.

- This lack of national policy guidance and support creates high levels of uncertainty, placing an unreasonable burden on local authorities and adversely influencing their ability to reduce natural hazard risk at the local level.
- Affected communities are seriously demoralised and polarised in the process.

Until these deficiencies are corrected, risk reduction initiatives will be resisted, inefficient practices will persist, and the New Zealand Government's natural hazard risk reduction objectives will not be realised – leaving people at unacceptable risk and personal hardship.

References

- Australian Geomechanics Society, 2007, Guideline for landslide susceptibility, hazard and risk zoning for land use planning: Extract from Australian Geomechanics Journal and News of the Australian Geomechanics Society, Volume 42, No 1, March 2007.
- Blackwood, P., 2005, Matatā Flooding 18 May 2005: Meteorology, Bay of Plenty Regional Council [New Zealand] Internal Memorandum 5810 03 2005-06-28.
- Department of Building and Housing, 2006, Determination 2006/119: Dangerous building notices for houses in Matatā, Bay of Plenty.
- Freudenberg, R., Calvin, E., Tolkoff, L., and Brawley, D., 2016, Buy-in for buy outs: the case for managed retreat: Lincoln Institute of Land Policy, Cambridge [Massachusetts].
- Insurance Council of New Zealand, 2014, Action required to protect New Zealand from natural hazards impact: Wellington, Retrieved November 11, 2014, from the World Wide Web: <http://icnz-staging.netco.nz.net/action-required-to-protect-new-zealand-from-natural-hazards-impact/>.
- Litchfield, N., 2015, Debris-flow risk, Awatarariki Catchment – Early warning system work stream, GNS Science.
- Massey, C.I., McSaveney, M.J., Taig, T., Richards, L., Litchfield, N.J., Rhoades, D.A., McVerry, G.H., Lukovic, B., Heron, D.W., Ries, W. and Van Dissen, R.J., 2014. Determining rockfall risk in Christchurch using rockfalls triggered by the 2010–2011 Canterbury earthquake sequence. *Earthquake Spectra*, 30(1), pp.155-181.
- McSaveney, M.J., Beetham, R.D., and Leonard, G.S., 2005, The 18 May 2005 debris-flow disaster at Matatā: Causes and mitigation suggestions, Institute of Geological and Nuclear Sciences for Whakatāne District Council, Client report 2005/71.
- McSaveney, M.J., Davies, T.R.H., 2015, Peer Review: Awatarariki debris-flow fan risk to life and retreat zone extent, Client report for the Whakatāne District Council.
- Ministry of Business Innovation and Employment, 2016, Determination 2016/034: Regarding the authority's refusal to grant a section 72 waiver for two building consents for proposed buildings on land subject to a natural hazard in Matatā, Bay of Plenty.
- Stats NZ, 2018, Population: Retrieved October 7, 2018, from the World Wide Web: <https://www.stats.govt.nz/topics/population>.
- Tonkin & Taylor Ltd, 2005, The Matatā debris flows preliminary infrastructure and planning options report, Client report for Whakatāne District Council, 22674.300.
- Tonkin & Taylor Ltd, 2013, Quantitative Landslide Risk Assessment, Matatā Escarpment, Client Report for Whakatāne District Council, 29115.
- Tonkin & Taylor Ltd, 2015, Supplementary risk assessment, debris-flow hazard, Matatā, Bay of Plenty, Client report for Whakatāne District Council, 29115.2000.
- Walton, M., and Clough, P., 2005, Matatā debris-flow mitigation: Cost benefit analysis of options: Wellington, NZIER Client report to Whakatāne District Council.

Post-fire debris-flow hazard analysis for Interstate 80, Truckee River Canyon, near the California-Nevada state line, USA.

Garrett Felling^a, Andrew Myers^a, Scott W. McCoy^{a,*}

^a Department of Geological Sciences and Engineering, University of Nevada, Reno, 89557, USA

Abstract

On July 9, 2017, west of the California-Nevada state line, USA, the 2.8 km² Farad fire burned steep slopes above Interstate 80. On the evening of August 18, 2017, a localized convective storm produced short-duration, moderate-intensity rain, which in turn triggered debris flows in a historically inactive basin. These flows impacted Interstate 80. At least four additional debris flows, not related to wildfire, have occurred along this section of road since 2013, but during much higher intensity rainfall. Here we utilize the history of pre- and post-fire debris flows along this section of Interstate 80 to explore the impacts of wildfire on debris flows. Specifically, we combine pre- and post-fire rainfall data and field measurements with empirical debris-flow models to quantify the impacts wildfire had on debris-flow generation and to estimate the likelihood and magnitude of future events. A characteristic pre-fire debris flow occurred on July 25, 2013 in a susceptible path ~30 minutes after rainfall began and during peak 15-minute intensities of ~50 mm/hr. This event closed both east and westbound lanes of Interstate 80. No other nearby paths had debris flows during this rainstorm. In contrast, one month post-fire, on August 18, 2017 a debris flow occurred in a historically inactive path, but within an area of high burn severity. Debris-flow initiation occurred ~30 minutes after the beginning of rainfall, but with peak 15-minute intensities of only ~26 mm/hr. This amplified rainfall-runoff response is consistent with fire-induced changes in soil hydraulic properties for which we measured post-fire decreases of a factor of 2 in field-saturated hydraulic conductivity and a factor of 4 in sorptivity. From field measurements, total volume estimates for the August 18, 2017 post-fire debris-flow event ranged between 1270 and 4700 m³ depending on assumptions regarding pre-event channel geometry and volume of hillslope sediment transported. A shallow landslide that liquefied and flowed into the channel contributed ~450 m³ of material and was apparently triggered by concentrated overland flow off an old road into the toe slope of a much older deep-seated landslide. Debris flows eroded most of the travel path above the fan to bedrock and contributed >850 m³ of debris, at a nearly uniform spatial rate, both of which suggest this event was likely limited by sediment availability. Just 100-150 m above Interstate 80 the flow transported boulders with maximum diameters in excess of 1 m, at peak velocities of ~2-5 m/s. We used the analysis of the August 18, 2017 debris-flow event to verify empirical equations developed by the USGS for predicting the probability, total volume, and runout distance of post-fire debris flows. We found good agreement between model output and observations and hence used these equations to predict characteristics of debris flows likely to occur in the near future.

Keywords: Wildfire; debris flow; hazard assessment; erosion

1. Introduction

Wildfire can dramatically change the hydrologic response of burned watersheds (Doerr et al., 2000; Ebel and Moody, 2017; Meyer and Wells, 1997; Moody and Martin, 2001). Debris flows that initiate within a burn scar and travel into populated areas are a severe hazard following fire (Cannon et al., 2010). Debris flows can grow dramatically through entrainment of sediment along the flow path and have discharges many times that of comparable water flows (Kean et al., 2016; McCoy et al., 2012; Santi et al., 2008). Post-fire debris flows represent a pervasive hazard that will likely become more prevalent in the future as intense rainfall and wildfire increase with a warming climate (IPCC, 2014; Westerling et al., 2006). Hence, there is a growing need for accurate debris-flow hazard assessments depicting the likelihood and magnitude of post-fire debris flows, as well as a mechanistic

* Corresponding author e-mail address: scottmccoy@unr.edu

understanding of the magnitude and recovery time of factors that change post-fire hydrologic response. Here we present a case study from the Interstate-80 corridor in the Truckee River canyon (Fig. 1) in which we document the changing hydrologic response following fire in steep debris-flow-prone basins, verify the predictions of a set of empirical equations that make up the USGS emergency post-fire hazard assessment (Gartner et al., 2014; Staley et al., 2016) and then apply these equations to explore the probability and magnitude of future post-fire debris flows.

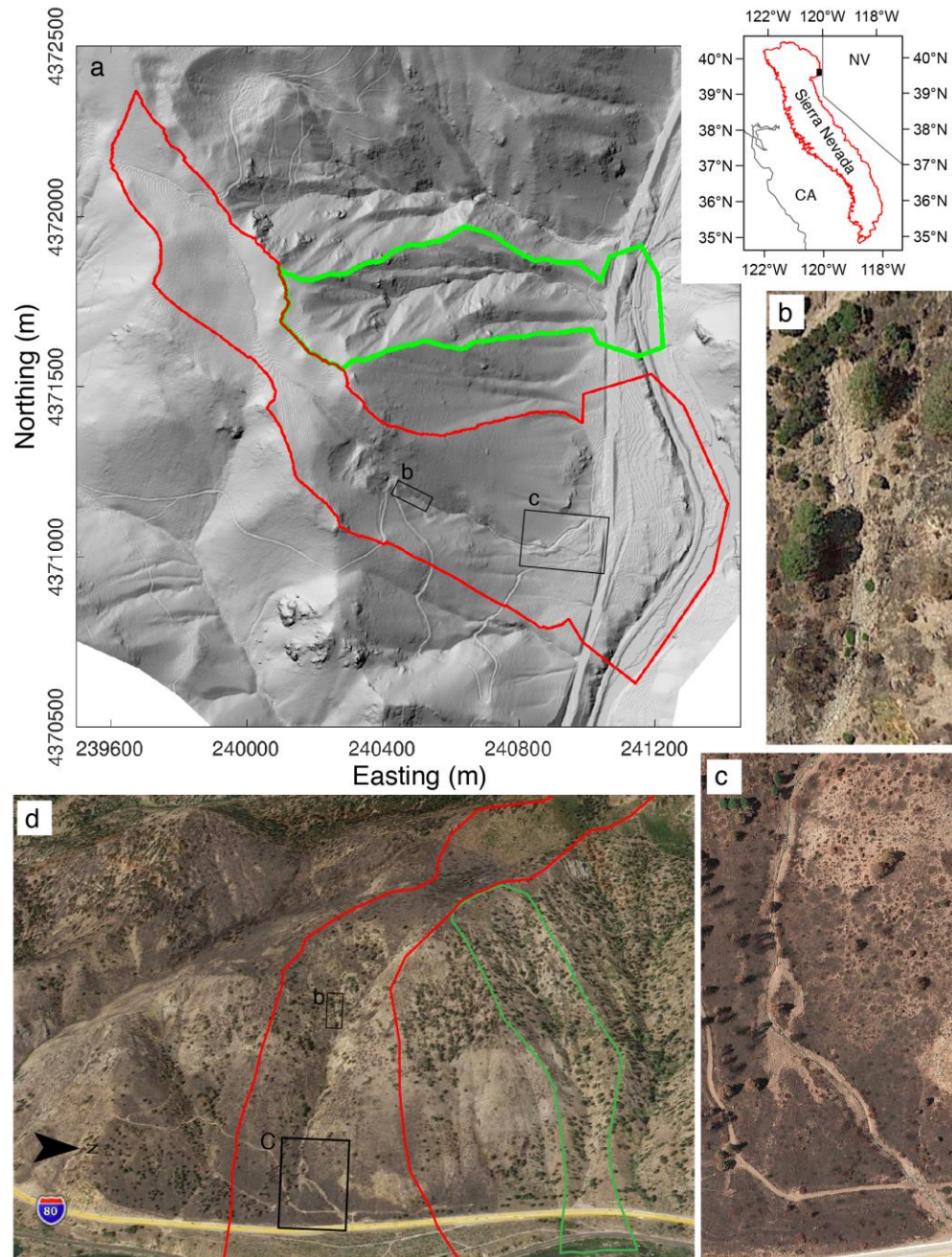


Fig. 1. Overview of study area in the Truckee River Canyon and site of the July 2017 Farad fire. (a) Bare-earth shaded-relief map derived from 0.5 m resolution lidar data. Red polygon outlines the basin that experienced a post-fire debris flow on August 18, 2017. The green polygon outlines the basin that has had multiple historic debris flows unrelated to wildfire; it was not burned or burned at low severity in the Farad fire, but had no debris flow in the August 18, 2017 storm. Inset: Location map showing study location (black square) on the eastern edge of the Sierra Nevada mountains (red line) and along the California and Nevada state line. (b) Close-up view of shallow landslide that occurred during the August 18, 2017 debris-flow event. (c) Close-up of debris-flow deposits (lighter colored) on the fan above Interstate 80 after the August 18, 2017 event. (d) Oblique view of Digital Globe Imagery from September 2017 draped over digital elevation model. Red and green boundaries as in (a).

2. Characterization of pre- and post-fire rainfall-runoff response

2.1. Characteristics of rainstorms triggering debris flow pre- and post-fire

Both pre- and post-fire debris flows in this portion of the Truckee River Canyon have been triggered predominantly by short-duration, moderate- to high-intensity rainstorms. We compare the pre-fire debris-flow event that occurred on July 25, 2013, for which we have the most complete rainfall and timing data, with the post-fire debris-flow event that occurred on August 18, 2017 to highlight the amplified rainfall-runoff response following fire. The nearest rain gauge that records 15-minute rainfall totals is located 4 km up river. On July 25, 2013 a convective storm tracked over this rain gauge, whereas on August 18, 2017 the rain gauge was almost completely missed. As an alternative to in situ rainfall measurements we used rainfall rates determined from radar reflectivity. Specifically, we used National Oceanic and Atmospheric Administration (NOAA), Next Generation Weather Radar (NEXRAD) stage-three precipitation intensity data product. This product incorporates gauge calibration and is collected at five-minute intervals (Kitzmilller et al., 2013). NEXRAD precipitation estimates have been used in hydrological modeling, and are generally found to compare favorably with gauge data (+/- 25 %), but with under or overestimation depending on site and storm characteristics (Cho and Engel, 2016; Habib et al., 2009; Kitzmilller David et al., 2013). We calculated a rainfall time series using the mean precipitation intensity of pixels within the burn perimeter for each radar image and then decimated the 5-minute resolution data to 15-minute intervals.

The results of this analysis are shown in Fig. 2. On July 25, 2013, peak 15-minute rainfall intensity was 50 mm/hr based on gauge data compared to 90 mm/hr based on radar returns. The July 25, 2013 storm appeared to track directly over the gauge so it is unclear why such an overestimation by the radar occurs, especially considering that radar-derived intensity commonly underestimates high-intensity rainfall (Habib et al., 2009). We have not looked extensively at other storms to see if this overestimation is systematic, but for this analysis we treat radar-derived precipitation intensities as maximums. This intense storm only triggered a debris flow in a steep, sparsely vegetated, and historically active basin (green outline in Fig. 1). No response was observed in the other more vegetated basins.

We lack gauge data for the post-fire August 18, 2017 storm, but radar data shows the storm had a peak 15-minute rainfall intensity of <26 mm/hr. In this storm, debris flows were triggered only in a severely burned basin (red outline in Fig. 1). Debris-flow paths that were not burned, but were historically more prone to debris flows had no response. Both storms were of short duration and only exceeded an intensity of 20 mm/hr for ~45 minutes. Post-fire peak rainfall intensities required to triggered debris flows were notably ~1/3 to 1/2 of intensities required pre-fire.

2.2. Soil infiltration properties pre- and post-fire

To quantify post-fire changes in runoff generation mechanisms potentially responsible for the amplified post-fire runoff response, we used a METER Minidisc tension infiltrometer with a radius of 2.25 cm set to a suction of 2 cm to make in situ measurements of field-saturated hydraulic conductivity, K_{fs} and sorptivity, S . We scraped away ash from the soil surface and then spread a thin layer of quartz sand to ensure uniform hydraulic contact with the

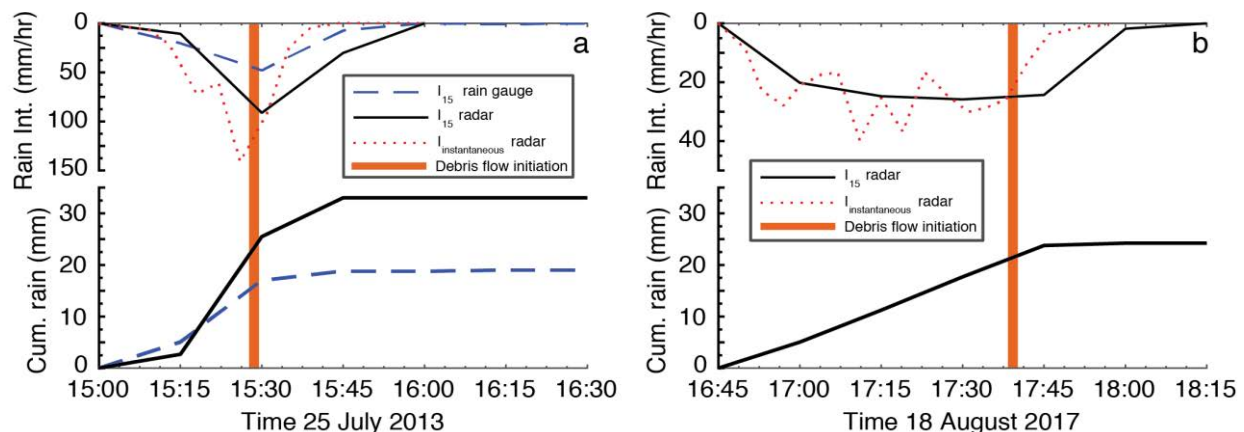


Fig. 2. Rainfall data and timing of debris-flow initiation for (a) July 25, 2013, which is characteristic of pre-fire events and for (b) post-fire August 18, 2017 event. Upper axis plots rainfall intensity, lower axis plots cumulative rainfall. On July 25, 2013 the storm tracked over a gauge recording 15-minute rainfall totals approximately 4 km from the debris-flow path, whereas on August 18, 2017 the storm missed this rain gauge.

infiltrometer disc. We recorded total volume of water infiltrated with time. We collected measurements at 10-second intervals during the first 60 seconds of the test, after which we decreased the sampling rate to every 15 to 30 seconds depending on infiltration rate. We analyzed these data using the methodology in Zhang (1997) and the derivative curve fitting technique suggested by Vandervaere et al. (2000) for two layer systems. The sand layer resulted in anomalously high infiltration rates for the first 10 to 20 seconds. These data points were discarded.

The Zhang (1997) methodology uses parameters of the van Genuchten soil water characteristic curve (SWCC) model to solve for K_{fs} and S . For both burned and unburned soils, we measured SWCCs using the simplified evaporation method (Fissel and Breitmeyer, 2017; Peters and Durner, 2008). We measured four SWCCs (two burned soils and two unburned soils) using a METER HYPROP apparatus as described in Fissel and Breitmeyer (2017). We estimated parameters for the van Genuchten SWCC model from the measured SWCC data using non-linear regression implemented in the proprietary HYPROP-FIT software package. We measured high suction (low water content) SWCC data using a METER environment WP4 chilled mirror hygrometer and appended these to the HYPROP data prior to fitting. These data were collected in general accordance with ASTM D6836 (ASTM International, 2016). Best-fit parameters for van Genuchten SWCC were different between the burned and unburned soils, as such, infiltration measurements were processed with parameters specific to burned or unburned soil.

We made a total of 50 infiltration measurements almost evenly split between soils that were burned at moderate to high severity in the Farad fire versus soils that were not burned. Measurements were made over a six-month period starting April 2018. Infiltration measurements were grouped into unburned and burned categories for subsequent analysis. Additionally, we calculated the wetting front suction head, h_f , defined in the Green-Ampt infiltration model, as a parameter incorporating the competing effects of K_{fs} and S (Ebel and Moody, 2017).

We found that burned soils had measurably lower K_{fs} , S , and h_f (Fig. 3). The geometric mean of K_{fs} for unburned soils (49 mm/hr) was a factor of 2.5 higher than for burned soils (19 mm/hr). The geometric mean of S for unburned soils (85 mm/hr^{0.5}) was a factor of 4 higher than for burned soils (20 mm/hr^{0.5}). The geometric mean of h_f for unburned soils (133 mm) was a factor of 7 higher than for burned soils (19 mm).

2.3. Initiation timing and initiation mechanisms of debris flows pre- and post-fire

The California Department of Transportation (Caltrans) reported that on July 25, 2013 at ~15:29, Interstate 80 was struck by a debris flow that closed both east and westbound lanes, which was ~30 minutes after the first rainfall and ~15 minutes after rainfall intensities increased above 20 mm/hr (Fig. 2a). Debris flows that impacted Interstate 80 only occurred in the basin outlined in green in Fig. 1. Post-event decimeter-resolution Digital Globe satellite imagery revealed extensive rill networks extending up to the drainage divide and debris-flow levees/deposits along the main travel path. No evidence of shallow landsliding was apparent and hence we interpret that this debris-flow event was triggered strictly by rainfall runoff and in-channel failure of debris (Kean et al., 2013).

On August 18, 2017, personal observation by S. McCoy revealed that by 17:40 Interstate 80 had been struck by debris flows. We assume that actual time of initiation was 5 to 10 minutes prior to 17:40 given the lack of first responders, which would put initiation ~30 minutes after rainfall intensities increased above 20 mm/hr (Fig. 2b). In contrast to pre-fire events that had generally been localized to the basin outlined in green, the post-fire event only triggered substantial debris flows in the basin outlined in red in Fig. 1, which had been historically inactive prior to

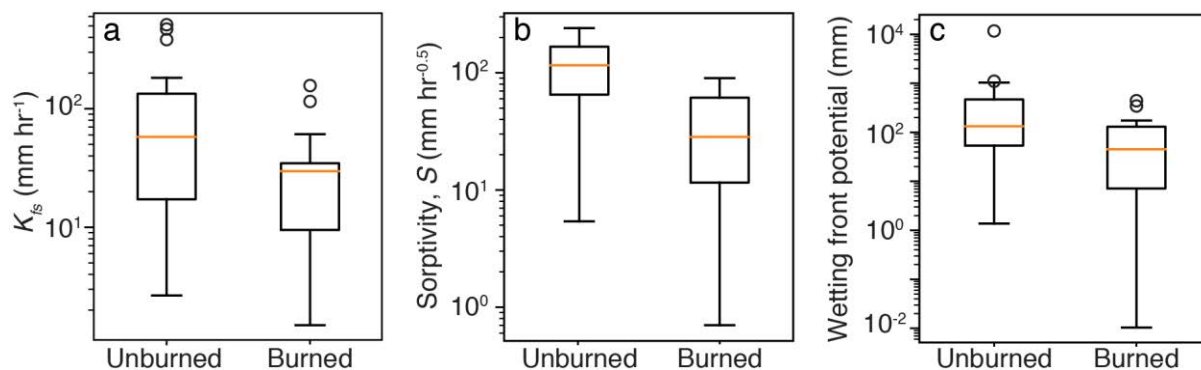


Fig. 3. Hydraulic properties of soils that were either unburned or burned at moderate to high severity in the Farad fire. (a) Field saturated hydraulic conductivity, K_{fs} . (b) Sorptivity. (c) Wetting front potential. On the box plots, the centerline shows the median, box edges mark the lower and upper quartiles, the whiskers extend 1.5 times the interquartile range, and circles show data that fall beyond the limits of the whiskers.

being burned. Post-event field surveys revealed high-density rill networks on burned hillslopes that fed into the main channel. These observations support an initiation mechanism by rainfall runoff (Kean et al., 2013). However, near the headwaters, a shallow translational landslide was found that had failed and entered the channel as a debris flow (Fig. 1b). This shallow landslide initiated within an old deep-seated landslide complex and occurred where runoff from an old road concentrated overland flow into the headscarp (Fig. 1). Levees were found upstream of the shallow landslide giving evidence that debris flows unrelated to the landslide were occurring upstream.

3. Characterization of the August 18, 2017 Post-Fire Debris Flow

To calculate maximum discharge of the largest debris-flow surge front, we estimated the maximum cross-sectional area of flow as the channel cross-sectional area beneath the maximum height of levee deposits and flow velocity using the forced vortex equation with the correction factor for viscosity and vertical sorting set to 1 (Prochaska et al., 2008). We assumed that minimal changes occurred in the channel after the passage of the peak surge that formed the levees. Channel and levee geometry were surveyed with a laser rangefinder, whereas radius of curvature of channel were measured on post-event satellite imagery (Fig. 1).

Channel cross-sectional area was measured at eight locations between the fan head and 30 m above Interstate 80, at which point channel cross-sectional area abruptly decreased. The mean cross-sectional area was 9.4 m^2 . Flow velocity was calculated at two locations corresponding to the tightest channel bends on the fan. Velocity estimated near the fan apex was $\sim 5 \text{ m/s}$ whereas the velocity $\sim 100 \text{ m}$ above Interstate 80 was $\sim 2.0 \text{ m/s}$. We used the mean velocity of flow on the fan and the mean cross-sectional area to estimate a peak discharge of $33.3 \text{ m}^3/\text{s}$.

We characterized composition of levee deposits on the fan through random-walk point measurements. Boulders greater than 25 cm in diameter and logs greater than 1 m long comprised $\sim 20\%$ of deposits. The average long axis length of boulders was 1.2 meters. The average log length measured was 3.4 m. The largest boulder was $2.4 \times 1.8 \times 1.5 \text{ m}$ and the largest log was 7.6 m long. All objects measured were located within 180 meters of Interstate 80.

To measure the total volume of material eroded along the flow path we followed the methods of Santi et al. (2008) and Gartner et al. (2014) in which eroded volume is estimated as the difference in cross-sectional area between post-event channel cross sections and projections of un-eroded hillslopes to the channel center line (Fig. 4). Channel shape prior to erosion was assumed to form a perfect V, but channel geometry in adjacent channels where limited erosion occurred showed that channels were more flat-bottomed to U-shaped. To test the sensitivity between a perfect V-shaped pre-event cross section and a more flat-bottomed one we raised the pre-event channel bottom at the centerline by 0.3 m and recalculated entrainment (Fig. 4a). Post-event channel geometry was surveyed with a laser rangefinder every $\sim 5 \text{ m}$ in areas of large scour and up to every $\sim 50 \text{ m}$ in areas of uniform scour. Link distances between cross-sections were measured with the laser rangefinder. Link volumes were found as the product of cross-sectional area eroded and link length, which were then summed to calculate total event volume.

The estimated volume of material eroded due to in-channel erosion was 820 m^3 for the V-shaped initial condition versus 1900 m^3 for a flat-bottom geometry. The cross-sectional area of scoured channel or spatial entrainment rate was nearly uniform along the flow path with a mean of 2.1 m^2 (Fig. 4b). These estimates are for the portion of channel from the base of the landslide to the point of transition from erosion to deposition at the fan head. Above the landslide, the channel did not show evidence of significant scour. The uniformity of entrainment rate was likely due to sediment-supply limitations. 80% of the channel length below the landslide headscarp eroded to bedrock at some

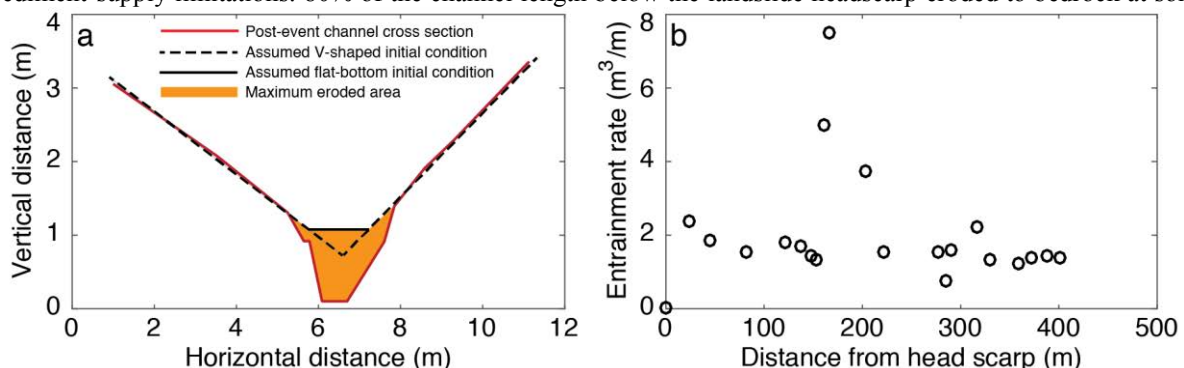


Fig. 4. Measurements of channel entrainment during the August 18, 2017 event. (a) Example of field-surveyed channel cross-section showing the two assumed geometries, V-shaped versus flat-bottomed, of the pre-event channel and the resulting area of eroded material (orange polygon shown for flat-bottom initial condition). (b) Spatial rate of channel entrainment as a function of distance from the landslide head scarp.

point in the channel cross section. The landslide contributed an additional volume of approximately 450 m³, resulting in a total debris-flow volume of 1270 m³ for V-shaped or 2350 m³ for flat-bottomed geometry. These estimates neglect any contribution of sediment eroded from hillslopes. Previous studies with high-resolution topographic differencing or modeling have shown hillslopes can contribute over half of the net eroded volume (Staley et al., 2014; McGuire et al., 2016). Significant hillslope contribution to total debris-flow volume is consistent with observations of significant hillslope erosion and extensive rill networks. We interpret a minimum debris-flow event volume as 1270 m³ with no hillslope contributions and V-shaped initial channel geometry versus a maximum event volume of 4700 m³ with 2350 m³ from channel entrainment and 2350 m³ from hillslope erosion.

3.1. Comparisons of field observations to empirical models of post-fire debris-flow probability, volume, and runoff

We used the empirical logistical regression equations of Cannon et al. (2010) as updated by Staley et al. (2016) in which the probability of post-fire debris flows is a function of the proportion of upslope area in burned area reflectance class (BARC) Class 3 or 4 with gradients $\geq 23^\circ$, the average differenced normalized burn ratio (dNBR) of the upslope area, soil erodibility factor (KF-Factor), and peak 15-minute rainfall intensity. To predict expected volumes of post-fire debris flows we used the multiple linear regression equation developed by Gartner et al. (2014) which is based on the elevation range of the basin, the upstream area that was burned at a high or moderate severity, and the peak 15-minute rainfall intensity. This set of equations for probability and volume comprise the core of the operational Emergency Assessment of Post-Fire Debris-Flow Hazard by the USGS. Our inputs vary slightly from that used in the operational USGS model. Instead of using the soil characteristics in US digital soil database STATSGO (Schwarz and Alexander, 1995) to calculate the KF-Factor we took two soil samples from the burn site and characterized soil structure as well as measured grains size distributions and organic content using standard sieve and hydrometer methods (ASTM D422-63; ASTM D1140-00) (ASTM International, 2017). The KF-Factor of the soil was then determined for each soil using the nomograph provided by the National Resources Conservation Service's National Soil Survey Handbook, Part 618, Subpart B. Our KF-Factor from in situ measurements was 0.075, which was substantially lower than the value calculated from the soil database parameters, ~ 0.25 , which in turn lowered our calculated probability of occurrence by ~ 10 to 20% as compared to the published USGS hazard forecast. Additionally, the geometry of the basin in which the August 18, 2017 event occurred (red outline in Fig. 1 and basin 67 in Fig. 5) is unique with an extremely low-gradient headwaters that transition to the steep debris-flow prone lower basin. The upper basin does not appear to contribute debris-flow sediment to the lower basin and was removed for the volume calculation. For probability and volume predictions, we selected a 15-minute rainfall intensity for a five-year storm (38 mm/hr) from the NOAA Atlas 14 precipitation frequency data server.

The basin in which the August 18, 2017 post-fire event occurred (red outline in Fig. 1 and basin 67 in Fig. 5) had a predicted probability of 30% for debris-flow occurrence in response to 15-minute rainfall intensity of 26 mm/hr. Basin 101 had an estimated 37% probability for the same precipitation intensity, and there was also a small debris flow that occurred in this basin, but it was intercepted by a dirt road before it could develop significantly. Nevertheless, the two drainages with the highest probability of occurrence for the August 18, 2017 precipitation intensity were the only ones that showed evidence of debris flows. The predicted volume for 26 mm/hr precipitation intensity in Basin 67 was 3950 m³, which is consistent with the upper range of our field-measured volume. The predicted volumes for a 5-year storm event for the basins most likely to experience a post-fire debris-flow event as numbered in Fig. 5 are 6500 m³, 4700 m³, 3900 m³, 6000 m³ for basins 67, 101, 20, and 139, respectively.

We estimated expected planimetric debris-flow inundation area using the USGS Laharz framework (Iverson et al., 1998). Rather than using the semi-empirical relationships that were developed for non-fire related debris flows, we used purely empirical equations that were developed by Bernard (2007) specifically for post-fire debris flows, $A=0.26V^{0.40}$ and $B=7.4V^{0.81}$, where A is the maximum cross-sectional area of the flow, B is the total planimetric area inundated by the flow, and V is the total volume of material produced by the debris flow. We selected the point of deposition onset to be the point at which channel slope decreased below 16 degrees, which was where deposition began in the August 18, 2017 event. This criterion resulted in onset of deposition proximal to fan heads. For basin 67, the predicted planimetric area inundated using the minimum of field-measured volume is much less than the observed, whereas the empirically estimated volume, which is consistent with the upper range of field-measured volume, matches observations well (Fig 5). Debris-flow inundation area was also estimated using volumes from the empirical volume model for a 5-year storm (38 mm/hr) for three drainages with 30% or greater probability of post-fire debris flow occurrence during a 5-year storm, as well as Basin 20, because its historical activity pre-fire. For all basins analyzed, debris flows are expected to impact Interstate 80 for a five-year storm event (Fig. 5).

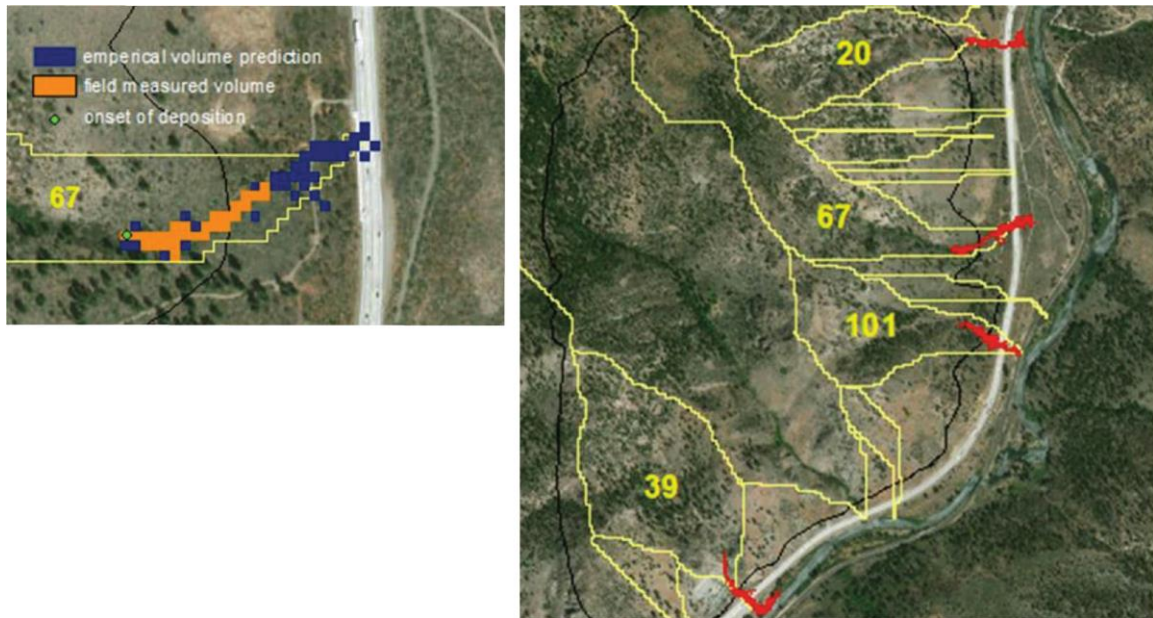


Fig. 5. Debris-flow basins (yellow outlines) within the Farad fire perimeter (thin black line). (Left) Comparison between predicted inundation area using minimum field-measured volume of channel erosion (orange) versus inundation area using volume predicted from empirical volume model, which is similar to maximum event volume estimated from field data (blue). Blue area matches observations. (Right) Extent of predicted debris-flow inundated area (red polygons) for each basin (yellow outlines with numbers) that has greater than a 30% chance of producing a post-fire debris flow given the occurrence of a 5-year precipitation event (basin 67 and 101) or has had a debris-flow event in the last 5 years.

4. Discussion and Conclusion

Analysis of pre- and post-fire rainfall runoff in the Farad fire burn scar revealed an amplified rainfall-runoff response following fire. Pre-fire, many moderately steep and moderately vegetated basins were historically inactive despite experiencing peak 15-minute rainfall intensities exceeding 50 mm/hr, and which triggered debris flows in adjacent more prone basins. Post-fire, one of these historically inactive basins that was almost completely burned at high to moderate severity, had a significant debris flow in response to peak 15-minute rainfall intensity of <26 mm/hr, whereas historically active basins that were not burned, or only burned at low severity, showed no response. This amplified rainfall-runoff response is consistent with fire-induced changes in soil hydraulic properties for which we measured post-fire decreases of a factor of 2 in field saturated hydraulic conductivity and post-fire decreases of a factor of 4 in sorptivity. Debris-flow initiation pre- and post-fire occurred within ~30 minutes of significant rainfall intensities and appeared to be related to rainfall-runoff initiation mechanisms described by Kean et al., 2013.

Field measurements of the August 18, 2017 post-fire debris-flow event showed it was moving quickly (greater than ~2 m/s), had a large peak discharge (~33 m³/s) and was transporting boulders just above Interstate 80; by all measures it was a flow that far exceeded a clear water flow out of such a small basin. Event-volume estimates from field measurements ranged between 1270 - 4700 m³ depending on assumptions made about pre-event channel geometry and volumes of hillslope sediment transported. Comparisons between post-event field observations and predictions from post-fire empirical models were favorable. Basins with the highest probability of debris-flow occurrence experienced debris flows, predicted debris-flow volumes were within the observed range, and predicted area inundated by debris flows closely matched that seen on post-event imagery. Predictions from these empirical models for a five-year rain event highlight the potential for post-fire debris flows to impact Interstate 80 in the future. Debris racks or nets, increasing channel conveyance capacity into existing debris basins and creating additional debris basins upstream of Interstate 80 would likely decrease debris-flow hazard.

Acknowledgements

This work was conducted as a senior design project by G. Felling and A. Myers in Geological Engineering at University of Nevada, Reno. We thank Tim Crosby of Caltrans for site visits and information regarding occurrence

of debris flows along Interstate 80. We thank Ronald Breitmeyer of UNR for conducting laboratory measurements of soil water characteristic curves and Scott Feehan and Jacob Greiner for help with infiltration measurements.

References

- ASTM International, 2017, Test methods for determining the amount of material finer than 75- μ m (No. 200) sieve in soils by washing: ASTM International, doi:10.1520/D1140-17.
- ASTM International, 2016, Test methods for determination of the soil water characteristic curve for desorption using hanging column, pressure extractor, chilled mirror hygrometer, or centrifuge: ASTM International, doi:10.1520/D6836-16.
- Bernard, D., 2007, Estimation of inundation areas of post-wildfire debris flows: Unpublished MS thesis, Department Geology Geological Engineering, Colorado School of Mines, Golden, CO.
- Cannon, S.H., Gartner, J.E., Rupert, M.G., Michael, J.A., Rea, A.H., and Parrett, C., 2010, Predicting the probability and volume of post-wildfire debris flows in the intermountain western United States: Geological Society of America Bulletin, v. 122, p. 127–144, doi:10.1130/B26459.1.
- Cho, Y., and Engel, B.A., 2016, NEXRAD quantitative precipitation estimations for hydrologic simulation using a hybrid hydrologic model: Journal of Hydrometeorology, v. 18, p. 25–47, doi:10.1175/JHM-D-16-0013.1.
- Doerr, S.H., Shakesby, R.A., and Walsh, R.P.D., 2000, Soil water repellency: its causes, characteristics and hydro-geomorphological significance: Earth Science Reviews, v. 51, p. 33–65, doi:10.1016/S0012-8252(00)00011-8.
- Ebel, B.A., and Moody, J.A., 2017, Synthesis of soil-hydraulic properties and infiltration timescales in wildfire-affected soils: Hydrological Processes, v. 31, p. 324–340, doi:10.1002/hyp.10998.
- Fissel, L., and Breitmeyer, R.J., 2017, Evaluation of uncertainty for soil water characteristic curve measurements and the implications for predicting the hydro-mechanical behavior of unsaturated soils: Geotechnical Frontiers, p. 579–588, doi:10.1061/9780784480472.061.
- Gartner, J.E., Cannon, S.H., and Santi, P.M., 2014, Empirical models for predicting volumes of sediment deposited by debris flows and sediment-laden floods in the transverse ranges of southern California: Engineering Geology, v. 176, p. 45–56, doi:10.1016/j.enggeo.2014.04.008.
- Habib, E., Larson, B.F., and Grascel, J., 2009, Validation of NEXRAD multisensor precipitation estimates using an experimental dense rain gauge network in south Louisiana: Journal of Hydrology, v. 373, p. 463–478, doi:10.1016/j.jhydrol.2009.05.010.
- IPCC, 2014, Climate Change 2014: Synthesis Report, Contribution of Working Groups I, II and III to the Fifth Assessment Report of the Intergovernmental Panel on Climate Change.
- Iverson, R.M., Schilling, S.P., and Vallance, J.W., 1998, Objective delineation of lahar-inundation hazard zones: Geological Society of America Bulletin, v. 110, p. 972–984, doi:10.1130/0016-7606.
- Kean, J.W., McCoy, S.W., Tucker, G.E., Staley, D.M., and Coe, J.A., 2013, Runoff-generated debris flows: Observations and modeling of surge initiation, magnitude, and frequency: Journal of Geophysical Research: Earth Surface, v. 118, p. 2190–2207, doi:10.1002/jgrf.20148.
- Kean, J.W., McGuire, L.A., Rengers, F.K., Smith, J.B., and Staley, D.M., 2016, Amplification of post-wildfire peak flow by debris: Geophysical Research Letters, 2016GL069661, doi:10.1002/2016GL069661.
- Kitzmilller D., Miller D., Fulton R., and Ding F., 2013, Radar and multisensor precipitation estimation techniques in national weather service hydrologic operations: Journal of Hydrological Engineering, v. 18, p. 133–142, doi:10.1061/(ASCE)HE.1943-5584.0000523.
- McCoy, S.W., Kean, J.W., Coe, J.A., Tucker, G.E., Staley, D.M., and Wasklewicz, T.A., 2012, Sediment entrainment by debris flows: In situ measurements from the headwaters of a steep catchment: Journal of Geophysical Research: Earth Surface, v. 117, F03016, doi:10.1029/2011JF002278.
- McGuire, L.A., Kean, J.W., Staley, D.M., Rengers, F.K., and Wasklewicz, T.A., 2016, Constraining the relative importance of raindrop- and flow-driven sediment transport mechanisms in post-wildfire environments and implications for recovery time scales: Journal of Geophysical Research: Earth Surface, v. 121, n. 11, p. 2211–2237, doi:10.1002/2016JF003867.
- Meyer, G.A., and Wells, S.G., 1997, Fire-related sedimentation events on alluvial fans, Yellowstone National Park, USA: Journal of Sedimentary Research, v. 67, n. 5, p. 776–791, doi:10.1306/D426863A.
- Moody, J.A., and Martin, D.A., 2001, Post-fire, rainfall intensity–peak discharge relations for three mountainous watersheds in the western USA: Hydrological Processes, v. 15, p. 2981–2993, doi:10.1002/hyp.386.
- Peters, A., and Durner, W., 2008, Simplified evaporation method for determining soil hydraulic properties: Journal of Hydrology, v. 356, p. 147–162, doi:10.1016/j.jhydrol.2008.04.016.
- Prochaska, A.B., Santi, P.M., Higgins, J.D., and Cannon, S.H., 2008, A study of methods to estimate debris flow velocity: Landslides, v. 5, p. 431–444, doi:10.1007/s10346-008-0137-0.
- Santi, P.M., deWolfe, V.G., Higgins, J.D., Cannon, S.H., and Gartner, J.E., 2008, Sources of debris flow material in burned areas: Geomorphology, v. 96, p. 310–321, doi:10.1016/j.geomorph.2007.02.022.
- Schwarz, G.E., and Alexander, R.B., 1995, Soils data for the conterminous United States derived from the NRCS State Soil Geographic (STATSGO) data base: US Geological Survey Open-File Report, 95–449.
- Staley, D.M., Negri, J.A., Kean, J.W., Laber, J.L., Tillery, A.C., and Youberg, A.M., 2016, Updated logistic regression equations for the calculation of post-fire debris-flow likelihood in the western United States: US Geological Survey Open-File Report, 2016–1106.
- Staley, D.M., Wasklewicz, T.A., and Kean, J.W., 2014, Characterizing the primary material sources and dominant erosional processes for post-fire debris-flow initiation in a headwater basin using multi-temporal terrestrial laser scanning data: Geomorphology, v. 214, p. 324–338, doi:10.1016/j.geomorph.2014.02.015.
- Vandervaere, J.P., Vauclin, M., and Elrick, D.E., 2000, Transient flow from tension infiltrometers: I. The two-parameter equation: Soil Society of America Journal, v. 64, p. 1263–1272, doi: 10.2136/sssaj2000.6441263x.
- Westerling, A.L., Hidalgo, H.G., Cayan, D.R., and Swetnam, T.W., 2006, Warming and earlier spring increase western U.S. forest wildfire activity: Science, v. 313, p. 940–943, doi:10.1126/science.1128834.
- Zhang, R., 1997, Determination of soil sorptivity and hydraulic conductivity from the disk infiltrometer: Soil Society of America Journal, v. 61, p. 1024–1030, doi:10.2136/sssaj1997.03615995006100040005x.

Debris-flow risk assessment and mitigation design for pipelines in British Columbia, Canada

Joseph E. Gartner^{a,*}, Matthias Jakob^b

^a*BGC Engineering Inc., Suite 211 - 701 12th Street, Golden, CO, 80401, USA*

^b*BGC Engineering Inc., 500 – 980 Howe Street, Vancouver, BC, V6Z0C8, Canada*

Abstract

Pipelines in mountainous terrain in British Columbia, Canada often cross debris-flow fans and channels along valley bottoms and can be susceptible to various geohazard impacts, including debris flows. The design of new pipeline infrastructure and maintenance of existing pipelines necessitates debris-flow risk assessments and appropriate mitigation design. A methodology is presented for assessing debris-flow risk along pipeline routes that consists of estimating the probability of a debris flow causing a pipeline loss of containment or disruption in service. The methodology consists of estimating debris-flow frequency, scour potential, and the vulnerability of the pipeline to break if impacted. Debris-flow frequency is estimated based on field observations of debris-flow deposits, degree of vegetative growth on debris-flow deposits, evidence of debris-flow impacts on trees near the pipeline crossing, documented debris-flow events, review of historical air photos and terrain mapping based on LiDAR-generated topography. Debris-flow scour potential is estimated based on channel morphology, presence of bedrock and grain size distribution of channel bed material. Vulnerability is estimated based on flow width and velocity and can be modified for different pipe diameters and wall thicknesses. Mitigation options for buried pipelines include those intended to decrease the likelihood of bed and bank scour (e.g. rip rap bed and bank protection), decrease the likelihood of the pipeline being exposed (increasing the burial depth of the pipeline) and to increase the resiliency of the pipeline to debris-flow impacts if exposed, (e.g. increasing pipeline wall thickness, adding concrete coating to the pipeline). The final option is to prevent debris flows from reaching the pipeline by designing and installing debris-flow deflection berms or sedimentation basins. The methodology presented is embedded in risk-informed thinking where pipeline owners and regulators can define probability thresholds to pipeline exposure or rupture and the pipeline designer needs to show that the proposed mitigation measures achieve these threshold criteria in ways that honor the ‘as low as reasonably practicable’ (ALARP) principle.

Keywords: Risk assessment; pipeline; vulnerability

1. Introduction

Pipelines in British Columbia, Canada (BC) as in many other nations travel throughout variable physiographic terrains that can include prairies, mountain ranges, upland plateaus, and lowlands occupied by floodplains. Since most fossil fuel reserves in western Canada lie either in Alberta or eastern BC, those needing to reach the ocean will have to cross mountainous terrain against its regional north-south grain; a legacy of BC’s tectonic history. The terrain between the BC coast and the western Canadian prairies is characterized by highly variable topography, climate and geology. As a result, a single pipeline may be exposed to numerous geohazards including landslides, rock avalanches, debris slides, rock falls, debris flows, debris floods, and scour and bank erosion from clear water floods.

Extreme environmental, economic and safety consequences can result from debris flows or other geohazards impacting and breaking a pipeline. An analysis of pipeline incident data in BC found geohazards to account for approximately 22% of failures (Porter et al., 2016). For example, a Pacific Northern Gas pipeline in BC was ruptured by a rock avalanche that transitioned to a debris flow and resulted in environmental damage to a pristine coastal ecosystem (Boulton et al. 2006; Jakob et al., 2004). Another recent example is a debris flow, initiated from the area burned by the Thomas Fire near Montecito, CA that impacted a high-pressure gas line in a residential area and caused a large explosion which impacted numerous houses (Kean et al., in print). Numerous other cases could be quoted worldwide. The potentially catastrophic safety or economic consequences emphasize the importance of accurately

* Corresponding author e-mail address: jgartner@bgcengineering.ca

characterizing the risks posed to a pipeline traversing rugged terrain, so that appropriate mitigation can be designed to minimize pipeline damages, loss of containment, and attendant consequences.

This paper describes methods for estimating debris-flow risks and selecting appropriate mitigation designs that have been applied to various pipelines throughout British Columbia, Canada.

2. Background

Due to the presence of existing right of ways and the logistical and geotechnically motivated desire to construct on shallow slopes, pipelines and other utilities are typically buried along valley bottoms. Where pipelines follow valleys, they will invariably intersect fans subjected by debris flows. Such fans are primarily depositional; however, channel scour is possible on parts of a fan during a debris flow. For example, a debris flow near the town of Hope, BC entrained most of its total volume in the colluvial channel extending through the debris-flow fan (Jakob et al., 1997) and Neff Creek near Pemberton, BC eroded approximately 80,000 m³ of material from its fan (Lau, 2017). At locations where the pipeline crosses a mountain pass or traverses steep terrain, the pipeline may cross debris-flow channels where massive channel scour is possible. In BC, yield rates in colluvial channels have been reported to range from 6 to 28 m³/m (Hung et al., 2005). More recent cases have shown yield rates up to 350 m³/m measured at Neff Creek (Lau, 2017). As highlighted by Jakob (2019, this conference), incorrect estimates of potential scour on fans prone to debris flow could lead to pipeline ruptures with highly disruptive outcomes to the environment, the pipeline owners and the design team. The question of when and by how much a debris flow can entrain versus deposit is highly complex and it appears that the mobilization of channel materials depends on pore water pressures of the channel base and banks (Iverson, 2011). Practically speaking, however, piezometers are not installed that could measure pore water pressures and antecedent moisture conditions to estimate if and how much debris flows could incise. Entrainment models have been proposed (Kang and Chan, 2018), but their practicality and application along pipeline corridors still needs to be tested.

Pipeline crossings of debris-flow channels are characterized as hydrotechnical hazards because the channel may have at least ephemeral clear water flows. However, debris flows in ephemeral channels pose a different hazard to a pipeline due to their potential to deeply incise channels during a single debris-flow event, transport large boulders many meters in diameter at high velocities and avulse and travel down paleochannels.

Pipeline design for watercourse crossings in BC is guided by the Government of British Columbia's Guidelines for Managements of Flood Protection Works in British Columbia (BC MoE, 1999), which state that the standard design flood is the flood having a 200-year recurrence period interval. Furthermore, a minimum depth of cover (DoC) of 1.2 m across watercourse crossings is typically adopted based on the Canadian Standards Association (CSA Z662-15). No such guidelines exist for debris flows which produce impact forces substantially higher than those exerted by hydrodynamic processes or by bedload mobilized through drag forces at the channel bed in rivers with alluvial beds. This realization necessitates a vastly different design approach for debris flows.

Some guidelines for assessing debris-flow hazards to pipelines are described in Jakob et al. (2004) and Porter et al. (2004). More recently, as part of the Trans Mountain Expansion Project, a pipeline proposed to connect Edmonton, Alberta to Vancouver, BC a plan has been developed to manage and mitigate geohazard sites that exceed specific risk tolerance criteria (Trans Mountain Pipeline ULC, 2017).

The design basis for protecting pipelines from debris-flow hazards can be hazard or risk-informed. In the former case, it consists of a design event scenario (e.g. to protect against a debris flow with a 200-year return period or probability of occurrence of 0.5% in any given year). In the latter case, a level of tolerable risk is identified by the owner or regulator. The pipeline designer is then to work towards achieving or exceeding such tolerable risk levels which is the focus of this contribution.

3. Risk Assessment Framework

Geohazard risk for pipelines can be calculated as the product of the annual probability of a geohazard, the spatial probability that the geohazard reaches the pipeline, the vulnerability of the pipeline to be damaged or broken by a geohazard and the consequence (CSA, 1997; AGS, 2000; Porter et al., 2004; 2017).

Total risk would include a systematic evaluation of the consequences of loss of containment such as health and environmental outcomes and may go as far as reputational loss to the pipeline operator, the entire industry and loss in share value. Evaluations of such consequences are outside the geotechnical realm and thus we focus on a narrower definition of pipeline risk which treats all pipeline failures as having equal consequence. Pipeline risk is defined here

as the frequency of a loss of containment (FLoC) at a debris-flow crossing (Baumgard et al., 2016). The FLoC can be expressed as:

$$F_{LoC(i)} = I_{(i)} \times F_{(i)} \times S_{H(i)} \times S_{V(i)} \times V_{(i)} \times M_{(I,F,SH,SV,V(i))}$$

where:

- $F_{LoC(i)}$ is the frequency of loss of containment due to a debris flow or debris flood at location i , expressed as an annual frequency.
- $I_{(i)}$ is the occurrence factor of 0 or 1 expressing whether a potential debris-flow or debris-flood hazard has credible opportunity to occur at location i .
- $F_{(i)}$ is the frequency of occurrence of the debris flow or debris flood at location i expressed as an annual frequency.
- $S_{H(i)}$ is the spatial probability of horizontal impact; expressed as a conditional probability that a debris flow or debris flood would horizontally reach the pipeline at location i , given its occurrence.
- $S_{V(i)}$ is the spatial probability of vertical impact; expressed as a conditional probability that a debris flow or debris flood would erode vertically to the pipeline at location i , given its occurrence.
- $V_{(i)}$ is the vulnerability of the pipeline expressed as a conditional probability that a debris flow or debris flood would result in loss of containment, given that it occurs and reaches the pipeline at location i . The unmitigated case assumes standard pipeline construction and operation conditions.
- $M_{(SH,SV,V(i))}$ is the mitigation reduction factor, ranging from 0 to 1, that is associated with various detailed design measures. This reduction factor accounts for the decreased spatial probability of a hazard reaching the centerline and eroding to the pipeline (identified by the SH and SV subscripts) or decreased vulnerability due to a specific mitigation applied at location i (identified by the $V(i)$ subscript).

Probability of Exposure (PoE) can be expressed as:

$$PoE = I_{(i)} \times F_{(i)} \times S_{H(i)} \times S_{V(i)}$$

To fully characterize the debris-flow risk at a pipeline crossing, estimates of FLoC should be completed for the active channel on a debris flow fan, potential avulsion paths and the fan surface (due to the possibility of a flow avulsing and reaching any part of the fan). Multiple calculations of FLoC at a single site may be required to evaluate risk associated with debris-flow scenarios at various frequencies and magnitudes. This is particularly important since it is the most frequent event leading to pipeline rupture that often provides the basis for total risk evaluations.

4. Methods for Estimating FLoC

FLoC can be estimated through combining desktop analysis, field investigations and data analysis. Desktop analyses of a debris-flow site may examine the following data sources, if available:

- Air photos and/or google earth imagery
- Digital Elevation Models (DEMs) derived from LiDAR data
- Geologic maps
- Documentation of previous debris flows at the site.

Field observations of debris flow channels may include:

- Grain size distributions in the debris-flow channel including maximum boulder size transported by previous debris flows
- Channel geometry, including channel width, channel depth, channel slope
- Observations of previous debris-flow deposits on the fan and along the channel
- Locations of previous avulsion channels
- The frequency of debris flows in the channel which may include:
 - presence and abundance of boulder impact tree scars
 - estimated ages of debris-flow deposits
 - estimated ages of vegetation in the channel and surrounding area

While detailed dendrogeomorphic methods or radiocarbon dating of organic sediments in natural outcrops or test trenches can be used to decipher accurate debris-flow frequencies, those are often not feasible to be conducted over hundreds of kilometers of pipelines within typical project development timelines. However, new methods have

emerged to approximate debris-flow frequencies and corresponding magnitudes from fan areas alone (Jakob et al. 2016). The following sections describe how this data can be incorporated into estimating the variables in the FLoC equation.

4.1. Occurrence, $I_{(i)}$

Occurrence ($I_{(i)}$) indicates whether a debris-flow hazard exists at a given site. A debris flow is considered a hazard if it has the potential to scour down to at least the crown of the pipeline at a given location. As most of the pipeline length is not subject to debris-flow or debris-flood hazards; in these locations, $I_{(i)} = 0$. Where past debris flows led to the formation of a debris-flow fan and/or evidence of debris flows persist, $I_{(i)} = 1$.

Geologic maps may identify alluvial fans which may have been formed primarily by debris-flow processes. Air photo analyses may reveal evidence of past debris flows. Literature searches of debris flows in the region may provide site specific information for the crossing. Field observations of debris-flow deposits, levees and tree impact scars can also be used to identify if there is a credible debris-flow hazard at the crossing. Watershed morphology can also help to identify watersheds dominated by debris-flow processes. Typically, small, steep watersheds are most susceptible to debris flows and can be differentiated from watersheds dominated by debris floods and clearwater floods by plotting Melton ratio (defined as the watershed relief divided by the square root of the watershed area) against watershed length (Wilford et al., 2004).

4.2. Frequency of Occurrence, $F_{(i)}$

Frequency of occurrence ($F_{(i)}$) is defined as the annual probability of occurrence of a debris flow (hazard probability) at location i . This frequency has a temporal and spatial component, i.e. how often does the debris flow both occur and reach the pipeline. Although most debris may deposit on the proximal or medial regions of a fan, the fluid afterflow should be assumed to reach the fan margins, and fine-grained channelized debris flows may transport most of their debris load to the fan's margins. Channel incision that lowers the fan's base level or artificial over-steepening of the fan (for example by a highway or railroad cut) may further influence fine-grained flows and fluid afterflow to travel to the fan margins. Many pipelines cross fans in their distal portion for logistical and constructability reasons.

Frequency can be expressed either as a return period or as an annual probability of occurrence. For example, if five debris flows have occurred within a 100-year period, the average return period is 20 years and the annual probability is 0.05 (or a 5% chance that a debris flow may occur in any given year assuming data stationarity). Given the uncertainty associated with estimating debris-flow frequency at a site, frequency classes with minimum and maximum bounds may be used (e.g. 0.03 to 0.1 for a 10 to 30-year return period).

Frequency classification can be based on existing site conditions and site conditions for the historic period for which air photos are available. Debris-flow activity on a fan and the availability of erodible sediment in the upstream catchment is related to the frequency of a debris flow that may reach and impact the pipeline. An important consideration is that estimated frequencies based on historical data may differ from frequencies in the future due to changes in sediment supply by forestry-related instabilities or forest fires, or by changing hydroclimatic environments associated with climate change. The past is no longer a key to the future as it pertains to debris flows and debris floods (Jakob and Lambert, 2009, Jakob et al. 2018). In cases where the science has advanced sufficiently to allow for future changes in debris flow frequency, it should be adjusted accordingly. Likewise, observations of existing site conditions may be influenced by a recent, rare debris-flow event that may create bias towards interpreting the site as being subject to frequent debris-flow occurrence.

4.3. Spatial Probability of Impact, $S_{H(i)}$ and $S_{V(i)}$

The spatial probability of horizontal impact ($S_{H(i)}$) is defined in the case of debris flows as the probability that a given event at location i will reach the pipeline alignment. For input into the FLoC equation, only debris flows that cross the pipeline may be evaluated which would make $S_{H(i)}$ equal to one. As an alternative, empirical modeling such as Flow-R (e.g. Horton et al., 2013) or numerical modeling such as DAN3D (McDougall and Hungr 2004), FLO-2D (FLO-2D, 2007), RAMMS (RAMMS, 2017) or D-Claw (George and Iverson, 2014) may be used to evaluate the spatial probability of impact along a pipeline crossing of a debris-flow fan.

The spatial probability of vertical impact ($S_{V(i)}$), is defined as the probability that a given event at location i will vertically expose at least the top of the pipeline (termed, the “crown”). Predicting debris-flow entrainment of channel material is challenging as previously noted, and there are no time-tested methodologies for reliably predicting scour depth of a debris flow. Therefore, estimates for $S_{V(i)}$ should be based on field observations, analyses of channel and fan morphology and professional judgement.

Debris flows tend to scour channels upstream of the debris-flow fan apex, oftentimes removing all colluvium in the channel and possibly exposing bedrock. As such, pipelines that cross a debris-flow channel upstream of the fan apex (which is rare, but possible) are particularly prone to be exposed by debris flows and would be assigned a high (between about 0.7 and 0.9) value for $S_{V(i)}$.

Although debris-flow fans are dominated by debris-flow depositional processes, pipeline crossings of debris-flow fans may be subject to channel scour. In some scenarios, extreme scour (greater than about 10 m depth) on a fan is possible. For example, a watershed that has produced several small debris flows may deposit material near the apex of the fan, which steepens the fan gradient and makes it susceptible to extreme scour during a subsequent debris flow or debris flood. Research on debris-flow and debris-flood fan scour has shown that the average fan gradient and watershed area can give a first indication of fans that could be prone to extreme scour (Lau, 2017). Flume studies in low gradient creeks (2-4%) have postulated that buried infrastructure on alluvial fans are not likely to be exposed if their depth is greater than 3.6 times the formative depth of a flood (Eaton et al., 2017). Although these studies are not directly applicable to estimating $S_{V(i)}$, they provide guidance for making appropriate estimates for the likelihood of channel scour on a fan to reach a pipeline at a given burial depth.

Figure 1 shows a pipeline crossing on a fan where material has been deposited on parts of the right of way, and channels have been eroded at other parts of the right of way. The erosion in this example, however, occurred likely due to fluvial material reworking, rather than due to the debris flow itself.

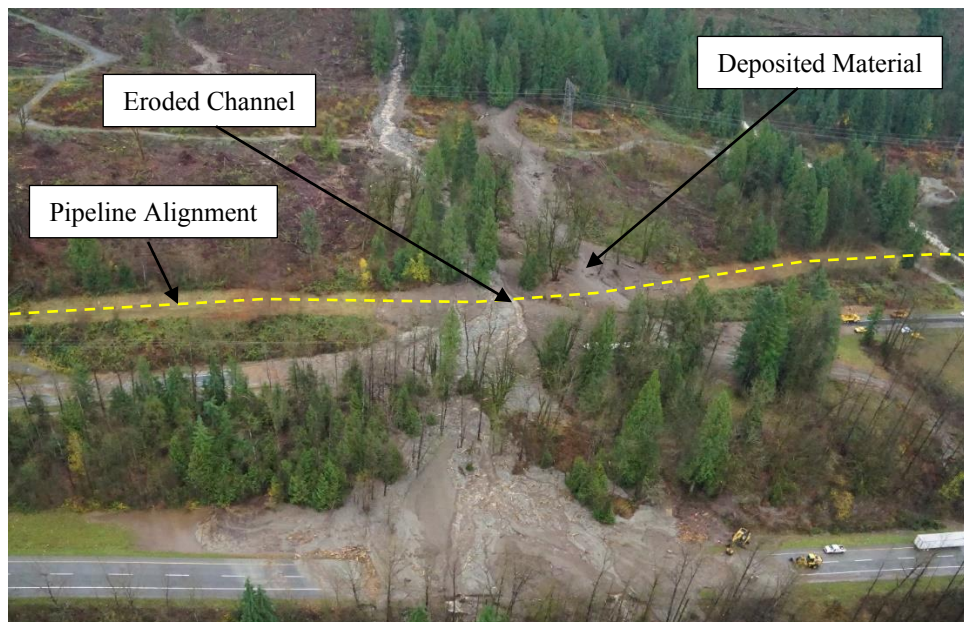


Fig. 1. A pipeline crossing of a debris-flow fan near Chilliwack, BC was both inundated with deposited debris-flow material and eroded by the debris flow or its hyperconcentrated flow phase. Vehicles and road near the bottom of the photo are visible for scale. Photo taken November 2017 by BGC Engineering Inc.

The observed depths of active and abandoned channels on a fan can provide an indication of the flow depth of past flows. However, it could be overly conservative to conclude that this incision is attributable to a single event, and it may indeed be the legacy of fluvial reworking rather than attributable to debris-flow scour. Irrespective, field measurements of channel scour depths and/or lidar measurements of channel depths on a fan, can be used to evaluate total scour potential at the active or avulsion channels and arrive at an estimate for $S_{V(i)}$. This method assumes that the presence of at least one deeply incised channel on a fan and the inference that other deeply incised channels could

form in previously unchanneled areas of the fan. These assumptions are conservative, which is justifiable due to the potentially high consequences associated with a loss of pipeline containment.

Some considerations for estimating scour potential on a fan include the position where the pipeline crosses the fan and the local channel geometry near the pipeline crossing. Scour depth can vary with respect to position on a fan with typically higher scour potential near the fan apex, where channel gradients are steeper, than at the distal part of the fan, where flows may be less confined by channel banks and travel over shallower gradients. Moreover, near the fan apex, there is less opportunity of streamflow to infiltrate into the coarse fan deposits. This implies higher degrees of channel bed saturation which enhances the likelihood of continued sediment entrainment and thus scour (Iverson, 2011). Therefore, higher estimates for $S_{V(i)}$ are likely for pipeline crossings at the fan apex than at the distal part of the fan.

Local channel geometry can lead to channel scour on fan when there is an abrupt increase in channel slope just downstream of the pipeline. At such locations, there is a possibility that a knickpoint (a sudden change in channel slope) may be exacerbated and migrate upstream and expose the pipeline. During construction of a pipeline, it is common for the right of way to be constructed with a cut and fill slope. The fill slope may create an over-steepened channel just downslope of the pipeline. As a result, future debris flows are likely to deposit material in the right of way cut and to erode the right of way fill material downslope. Figure 2 illustrates this scenario. Equally, when pipelines are constructed upstream of logging roads or highways, those have also been cut into the distal fan deposits, potentially leading to a knickpoint that is out of equilibrium with the natural channel slope.

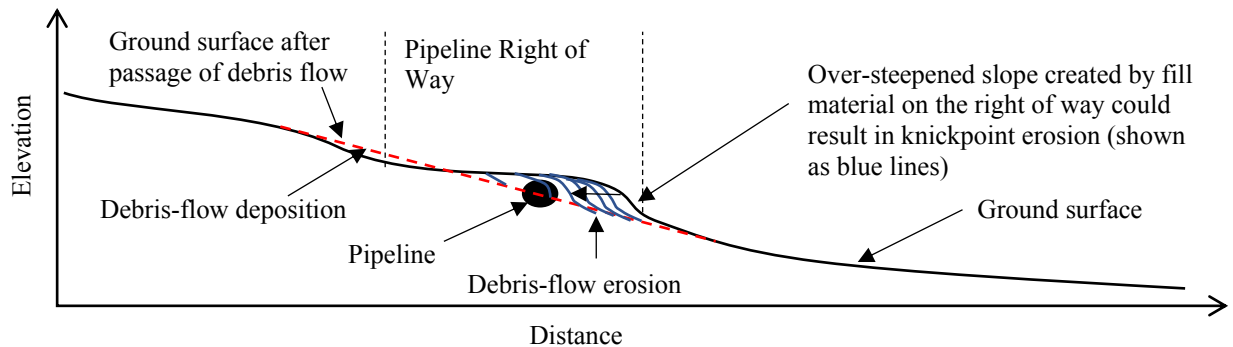


Fig. 2. Illustration of how knickpoint erosion during the passage of a debris flow may erode fill material of a pipeline right of way to expose the pipeline.

4.4. Pipeline Vulnerability, $V_{(i)}$

Pipeline vulnerability ($V_{(i)}$) is the vulnerability of the pipeline to loss of containment, given that the pipeline is exposed at location i . A loss of containment from a debris flow include may be caused by dynamic pressure on the pipeline or impact loading on the pipeline. For dynamic loading to break a pipeline, the passage of a debris flow exposes the pipeline and subsequent dynamic pressure of debris-flow material on the pipeline exceeds the resisting strength of the pipeline. For a pipeline to break due to impact loading, only the crown of the pipeline needs to be exposed for a boulder to impact the pipeline with a point load that exceeds the resisting strength of the pipeline.

Assessment of the vulnerability of a pipeline depends on the material strength of the pipeline which varies depending on pipeline wall thickness and pipeline diameter. Vulnerability can be assessed probabilistically using probability distributions of pipeline yield strength, debris-flow velocity, debris-flow density and grain size.

Debris-flow velocities can be estimated using superelevation of flow around a channel bend (Johnson, 1984) or runup against vertical barriers or adverse slopes (Iverson et al., 2016). However, sufficient field evidence for applying these methods may not be available and methods presented in Prochaska et al. (2008) may be applied with field estimates of debris-flow depth and measurements of channel slope. Grain size distributions can be estimated from field investigations of debris-flow deposits. Bulk density of debris flows in flume studies have ranged from 1400 – 2400 kg/m³ and bulk densities of natural debris flows typically range from 1800 to 2300 kg/m³ (Iverson, 1997).

4.5. Mitigation Reduction Factor, $M_{(S_H, S_V, V(i))}$

The mitigation reduction factor is a value from 0 to 1 that represents the reduction in the FLoC at a specific site due to a mitigation measure. Different mitigation measures could provide varying degrees of protection from impacts by changing either $S_{H(i)}$, $S_{V(i)}$, or $V(i)$ at location i . Mitigations that decrease $S_{H(i)}$ include debris retention basins and deflection berms. Mitigations that can decrease $S_{V(i)}$ include increasing the depth of cover, adding rip rap or grouted rip rap channel protection, grade control structures. Mitigations that decrease $V(i)$ include using pipeline with a thicker wall thickness or pipeline with a concrete coating.

Values for decreasing $M_{S_H, S_V, V(i)}$ range from zero to one and depend on the risk reduction the mitigation offers. For example, rerouting a pipeline or construction of a debris retention basin or deflection berm may have a significant reduction in the $S_{H(i)}$ variable and the associated mitigation reduction factor, $M_{S_H(i)}$ may be low (e.g. approaching 0.01). Increasing depth of cover may have varying effects on risk reduction depending on how deep the pipeline is buried and the associated mitigation reduction factor, $M_{S_V(i)}$ may have a broad range (e.g. from 0.1 to 0.9). Increasing pipeline wall thickness may have a marginal benefit to reducing risk at the pipeline and the associated mitigation reduction factor, $M_{V(i)}$ may be higher (e.g. approaching 0.9).

Accurate characterization of the mitigation reduction factors associated with different mitigation techniques allows for risk-informed design. A pipeline operator or regulatory body may choose a risk tolerance threshold for individual crossings, or a total FLoC for the entire pipeline. In the latter case, the sum of all geohazard FLoCs would need to be less than the total tolerable FLoC. At sites where the risk, as characterized by the estimated FLoC, exceeds such threshold the amount of risk reduction afforded by various mitigations can be quantified to demonstrate that risk has been reduced below that threshold. Alternatively, a PoE (probability of exposure) criteria may be chosen where the pipeline can have a given maximum annual probability of being exposed. Appropriate mitigations to reduce $S_{H(i)}$ and/or $S_{V(i)}$ could be applied until the PoE does not exceed this probability threshold.

If needed, a variety of mitigation techniques may be required to achieve the tolerable FLoC or PoE value. Figure 3 shows a site where channel erosion protection, grade control structures and increased depth of cover are present to protect the pipeline against an active debris flow channel. Where several mitigation methods are applied, multiple mitigation reduction factors can be integrated into the FLoC equation. Although complimentary mitigation measures provide greater risk reduction, engineering judgement needs to be applied to ensure that the combined mitigation reduction factors do not create an inflated level of risk reduction. Furthermore, detailed design of mitigation should incorporate detailed site-specific analysis of potential debris-flow magnitudes.

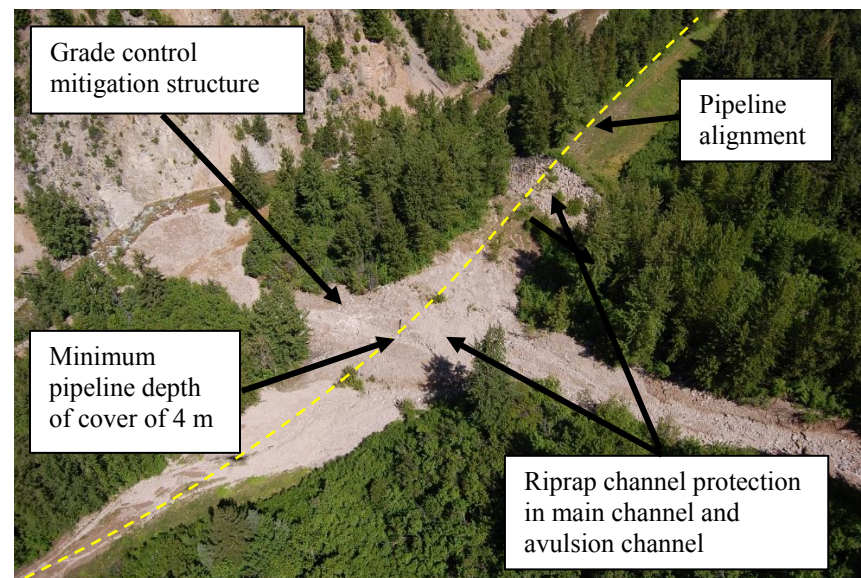


Fig. 3. Example of a combination of channel grade control and riprap erosion protection and increased depth of cover at a pipeline crossing of an active debris flow channel. Photo taken by BGC Engineering in May, 2016.

5. Summary

In this paper, a risk assessment methodology is presented suitable for quantifying debris-flow risk posed to pipelines. Risk is defined as the frequency of a loss of containment (FLoC). The method can also be applied to identify appropriate design measures to reduce FLoC or PoE to below a tolerable threshold set by either the pipeline owner or regulatory authority. Research is continuing to define best practices for quantifying debris-flow frequency-magnitude relationships, runout, scour and rheology as applicable to long linear infrastructure corridors. This methodology provides a framework that can be implemented with existing methods for debris-flow assessment and integrate scientific advancements in debris-flow research.

References

- Australian Geomechanics Society Subcommittee (AGS), 2000, Landslide Risk Management Concepts and Guidelines p 49-92.
- Baumgard, A., Beaupre, M., Leir, M., 2016, Implementing a quantitative geohazard frequency analysis framework as a component of risk assessment of new pipelines. *in* Proceedings of the 2016 11th International pipeline conference. September 26-30, 2016, Calgary, Alberta, Canada.
- Boulton, N., Stead, D., Schwab, J., Geertsema, M., 2006, The Zymoetz River rock avalanche, June 2002, British Columbia: Engineering Geology v. 83, no. 1-3, p. 76-93.
- British Columbia Ministry of Environment, Lands and Parks (BC MOE), 1999, Guidelines for Management of Flood Protection Works in British Columbia. Public Safety Section, Water Management Branch.
- Canadian Standards Association (CSA), 1997, Risk Management: Guidelines for Decision-Makers, CAN/CSAQ850-97. <https://www.scc.ca/en/standardsdb/standards/6777>.
- Canadian Standards Association (CSA). Oil and gas pipeline systems, Z662-15. <http://www.csagroup.org/ca/en/services/codes-and-standards>.
- Eaton, B., MacKenzie, L., Jakob, M., Weatherly, H., 2017, Assessing erosion hazards due to floods on fans: physical modeling and application to engineering challenges: *Journal of Hydraulic Engineering*, v. 143, no. 8, doi: 10.1061/(ASCE)HY.1943-7900.0001318.
- FLO-2D Software Inc., 2007, FLO-2D User's Manual Version 2007.10, October 2007.
- George D.L., Iverson R.M., 2014, A depth-averaged debris-flow model that includes the effects of evolving dilatancy. II. Numerical predictions and experimental tests: *Proceedings of the Royal Society A: Mathematical, Physical and Engineering Sciences*. <http://doi.org/10.1098/rspa.2013.0820>.
- Hungr, O., McDougall, S., Bovis, M., 2005, Entrainment of material by debris flows. *in* Jakob M., and Hungr, O., eds., *Debris flow Hazard and Related Phenomena*, Springer-praxis.
- Iverson, R.M., 1997, The physics of debris flows: *Reviews of Geophysics*, v. 35, p. 245-296.
- Iverson, R. M., George, D. L. and Logan M., 2016, Debris flow runup on vertical barriers and adverse slopes: *J. Geophys. Res. Earth Surf.*, v. 121, p. 2333–2357, doi:10.1002/2016JF003933.
- Iverson, R.M., Reid, M.E., Logan, M., LaHusen, R.G., Godt, J.W., Griswold, J.G., 2011, Positive feedback and momentum growth during debris-flow entrainment of wet bed sediment: *Nature Geoscience*. v. 4, no. 2, p. 116-121. doi: 10.1038/NGEO1040.
- Jakob, M., 2019. Debris-flow hazard and risk assessments – a practitioner's view, this volume.
- Jakob, M., Bale, S., McDougall, S., 2016. Regional debris-flow and debris-flood frequency-magnitude curves. *in* Proceedings of GeoVancouver 2016 conference, Vancouver, Canada, October 2016.
- Jakob, M., Porter, M., Savigny, W., 2004. Geomorphic approach vital to pipelines crossing mountain streams: *Oil and Gas Journal*, v. 102, i. 45.
- Johnson, A.M., 1984. Debris flow. *in* Brunsten D, Prior DB, eds. *Slope instability*. Wiley, Chichester, p. 257–361.
- Kang, C. and Chan, D., 2018. A progressive entrainment runout model for debris-flow analysis and its application: *Geomorphology*, v. 323, p. 25-40.
- Kean, J., Staley, D., Lancaster, J., Rengers, F., Swanson, B., Coe, J., Hernandez, J., Sigman, A., Allstadt, K., Linsay, D., 2018. Inundation, flow dynamics, and damage in the 9 January 2018 Montecito Debris Flow, California, USA: Opportunities and challenges for post-wildfire risk assessment. *Geosphere*. (in press).
- McDougall, S., Hungr, O., 2004, A model for the analysis of rapid landslide motion across three-dimensional terrain: *Canadian Geotechnical Journal*, v. 46, no. 6, p.1084-1097.
- Porter, M., Ferris, G., Leir, M., Leach, M., Haderspock, M., 2016, Updated estimates of frequencies of pipeline failures caused by geohazards. *in* proceedings of IPC 2016 International Pipeline Conference. September 26 – 30, 2016. Calgary, Alberta, Canada.
- Porter, M., Jakob, M., Holm, K., McDougall, S., 2017, Risk-based landslide safety assessments in Canada. *In* 3rd North American Symposium on Landslides, June 4-8, Roanoke, Virginia, U.S.
- Prochaska, A.B., Santi, P.M., Higgins, J.D., Cannon, S.H., 2008, A study of methods to estimate debris flow velocity: *Landslides*, v. 4, p. 431-444. doi:10.1007/s10346-008-0137-0.
- RAMMS, 2017, RAMMS: Debris Flow Users Manual v1.7.0, November 2017.
- Trans Mountain Pipeline ULC, 2017, Trans Mountain Expansion Project – Quantitative Geohazard Frequency Assessment – Post Mitigation. Final report February 28, 2017. Filed as part of NEB Condition 16.
- Wilford, D.J., Sakals, M.E., Innes, J.L., Sidle, R.C., Bergerud, W.A., 2004, Recognition of debris flow, debris flood and flood hazard through watershed morphometrics: *Landslides* v. 1, p. 61-66, doi: 10.1007/s10346-003-0002-0.

An overview of a decade of applied debris-flow runout modeling in Switzerland: challenges and recommendations

Christoph Graf^{a,*}, Marc Christen^b, Brian W. McArdell^a, Perry Bartelt^b

^aSwiss Federal Institute for Forest, Snow and Landscape Research WSL, Zuercherstr. 111, Birmensdorf 8903, Switzerland

^bWSL Institute for Snow and Avalanche Research SLF, Fluelastr. 11, Davos 7260, Switzerland

Abstract

Dynamic debris-flow runout models are applied by practitioners (1) to generate hazard maps, (2) to help design mitigation measures such as dams and warning systems, (3) to explore potential impacts of rare events such as pro-glacial lake failure, and (4) to illustrate the hazard process to local decision makers and stakeholders. Automated observations of debris flows in several torrents have shown a large degree of variability in the flow process, ranging from fast muddy debris floods to relatively slow debris flows with granular fronts, at any given torrent. It is not yet possible to predict with certainty which type of debris flow can be expected in any given catchment. The prediction problem is amplified by the fact that topographic data are generally coarse (2m horizontal resolution in Switzerland) compared with typical channel widths (1–10 m) and because channel topography changes with time. These challenges and their impact on hazard assessment is illustrated using recent examples of typical applied projects. Herein we use the RAMMS debris-flow runout model. However, the general procedures presented here are applicable to other similar runout models. Common points in these examples include the accurate assessment of potential erosion, deposition, and avulsion along the channel, as well as the systematic modification of the friction coefficients in the model to account for variations in water content, sediment size, channel-bed roughness, and other properties of the flow. We mention the main challenges in these steps, as the exact procedure is still not clearly regulated in Switzerland. In general, it is desirable to work with several scenarios to account for multiple flow surges and the erosion and deposition produced by each surge, and uncertainties in the expected debris-flow type (granular vs. muddy). Thus, for the generation of appropriate scenarios, experience in the field and with the use of runout models is essential.

Keywords: hazard assessment; debris-flow runout model; RAMMS; hazard maps

1. Introduction

Debris flows are a major natural hazard in alpine regions. They can cause significant damage along steep mountain torrents and especially on their fans due to their erosion potential, high impact forces and sudden occurrence. Because of their variable composition of coarse and fine rocks, mixed with water and other material, such as woody debris, their motion (speed, flow height, inundation area) are difficult to predict. When they develop, large solid masses can be transported within a short time inducing strong impact forces on structures. In addition, strong channel erosion and massive deposit of debris may occur outside the channel. They occur rarely and only in appropriate conditions, mostly triggered by meteorological factors.

In order to counteract this danger, great efforts have been made to define the affected area and to improve the protection of persons and infrastructure by means of measures (structural and organizational ones). The reduction of the area at risk remains a challenge for natural hazard experts. In addition to field assessments, comparative considerations based on analogous examples, the numerical calculation with runout-models is increasingly being applied in practice. This requires a comprehensive and accurate knowledge of the main characteristics of the expected debris-flow events. In many mountainous countries, automated observation stations (Hürlimann et al.,

* Corresponding author e-mail address: christoph.graf@wsl.ch

2003) and event databases (Lateltin et al., 2005) provide such information over longer time periods for a certain location. The data can be used with restrictions for comparable sites, if there is no other information available.

Computational dynamic debris-flow runout models are used to assess flow path, runout distance, velocity and flow depth (Crosta et al., 2003; Hürlimann et al., 2008; Hungr and McDougall, 2009; Christen et al., 2012) and they are a valuable tool for hazard assessment where predictions of flow intensity are required (e.g., Lateltin et al., 2005). The methods available for runout analysis can be divided into different classes, such as empirical, analytical, simple flow routing and numerical ones (Dai et al., 2002; Rickenmann, 2005). Besides defining the magnitude of an upcoming debris flow and the probability of occurrence, the determination of the debris-flow dynamics are the most important tasks for an in-depth hazard assessment (Jakob, 2005). It is important to emphasize that practitioners are increasingly basing (1) the generation of hazard maps, (2) the design of mitigation measures, (3) the exploration of potential impacts of rare events, and (4) the presentation of the hazardous process to local decision makers and stakeholders on results provided by numerical simulations. Therefore, the quality and accuracy of the input parameters is of utmost importance.

In the last decades, a series of different debris-flow runout models became available for scientific and practical use. Many of these models remained at an academic level and were not designed for practical use in the debris-flow engineering community. Often the models relied on a small development team (sometimes even a single person) and therefore lack extensive documentation for application by practitioners.

In recent years, practitioners have made frequent use of dynamic debris-flow runout models to generate hazard maps, to help design mitigation measures such as dams and warning systems, to explore potential impacts of rare events such as pro-glacial lake failure, and to illustrate the hazard process to local decision makers and stakeholders. Guidelines and standards for the minimal requirements are not yet regulated in Switzerland. Nevertheless, practitioners evaluate their field assessments, assess their design-event scenarios and visualize their study results to the authorities using numerical simulations. They have also extensively tested the existing tools, identified gaps and weaknesses, especially regarding existing flow theories, and formulated requirements for future models. The last point is quite important and useful for model development. Exchange of information e.g. by user workshops and knowledge exchange is very important. Because many of the numerical simulation tools need calibration and lack a strict calculation procedure e.g. by decision trees, only trained and experienced users will profit from the simulation results. Others might risk to produce questionable outcomes that show misleading or even wrong effects. The present situation in Switzerland can be summarized as a healthy skepticism of existing models, with a desire to improve both application guidelines as well as some of the underlying physics of numerical models, especially with regard to the constitutive modeling of granular/muddy mixtures.

The interpretation of numerical output by practitioners is considered an important problem. Output of simulation tools depends on two main factors: a) the capabilities of the mathematical representation of the very complex process and b) the quality of the input parameters. The first problem can be solved by the choice of the appropriate tool, or better, by the choice of a small number of tools that provide results that can be compared. Often, in practical application, the use and comparison of the results from two or more numerical simulation tools is not feasible because of lack of time, money and human power. Model result comparison implies that practitioners would have to invest much more time and effort to learn the use of different tools. Presently, they rely on the results of one tool only and the choice depends on the knowledge of the available personal.

In Switzerland, hazard assessment is part of the integral approach to natural hazards in Switzerland (PLANAT, 2005). The main product is a hazard map that provides information about the natural hazard process (Lateltin et al., 2005). The hazard is defined as the probability of a potentially damaging natural phenomenon within a specific period of time in a given area. For simplification, three levels of intensity are considered, high, medium and low. Regarding probability, the same three levels, high, medium and low, are used with the corresponding return periods 1–30, 30–100 and 100–300 years. The work to be done for a potential hazard is therefore to determine its intensity for the chosen levels of probability at selected points in a specified area. The federal law requires the cantons to establish hazard maps which have to be incorporated in regional master plans and local development plans. Each canton has drawn up a specification for its preparation, which is based on the legal foundations and the general recommendations and guidelines of the federal government. The use of debris-flow runout models is mentioned in these guidelines. However, detailed instructions are not specified on how to use them. Therefore, every engineering office has established its own approach. In most cases, the choice of a specific numerical model is left to the contractor. The degree that government agencies prescribe how to assess debris-flow hazard, therefore plays a role in how numerical models are applied in practice.

In this paper, we consider more than a decade of experience gained in the use, application and expert monitoring of hazard assessment projects in the Swiss Alps, where the use of the numerical simulation tools was the main or an important part of the project. Our goal is to communicate to the modeling and debris-flow engineering community how to improve, perhaps even simplify, existing tools. The discussions were in most cases about choosing the ideal friction parameters during the calibration process. Subordinate questions were repeatedly discussed about the starting conditions (Deubelbeiss and Graf, 2013) or the inclusion of constructional measures (Graf and McArdell, 2008, Hohermuth et al., 2016). These challenges and their impact on hazard assessment is illustrated using recent examples of typical applied projects. Common points in the examples include the accurate assessment of potential erosion, deposition, and possible avulsion along the channel, as well as the systematic modification of the friction coefficients in the model to account for variations in water content, sediment size, channel-bed roughness, and other properties of the flow. Another issue is the generalization process necessary to produce reliable hazard maps. This paper focuses on the application of exiting user-friendly debris-flow simulations tools. The runout model used herein is the well-known RAMMS 2D debris-flow runout model (Christen et al., 2010). However, the general procedures presented here are applicable to other similar runout models.

2. Materials and Method

We analyzed many different case studies of debris-flow hazard analysis in Switzerland that were performed ourselves using RAMMS (Christen et al., 2010) in the last decade or that we have advised during this period. Here we sum up the experiences made and point out the main topics. The evaluation is subject to a certain subjectivity. This is because the projects are not systematically evaluated in terms of the issues covered in this study.

2.1. Case studies, main questions and guidelines

We compare three different typical situations of hazard assessment using numerical simulation in debris-flow prone torrents in the Swiss Alps: Situation (1) shows only one important and well-documented event in the last century and several small, but not well documented events in the same period. The small events didn't cause significant damage and were therefore not analyzed in detail. The date of occurrence is sometimes known, but no data is available on initial starting point, volume, flow depth and discharge of the corresponding event. Situation (2) shows regular small events that do not cause any damage and a few larger events that caused minor damage and therefor are not well documented. Field survey and geomorphic field evidence suggests that there were much larger events in the past. In situation (3) a catchment with a high potential for large debris-flow events but with only a small number of well-known events of small size has to be assessed. To protect against future major events, protection structures have to be dimensioned. We compare the three typical situations asking the following questions:

- How important are well-documented events to determine the key parameters of different return periods?
- How does one single well-known event influence the determination of these key parameters?
- How does a potential situation of debris-flow susceptibility influence the determination of the key parameters?
- How many events are needed to determine trustful key parameters, and linked to this question:
- What series (mainly in terms of number, but also in terms of data quality) of documentation of debris-flow activity is necessary to achieve a well-based data set?
- Which kind of events in regard to volume, mixture, speed variability is necessary to achieve such a well-based data set?

Finally, we study the recommendations, guidelines and regulations in view of the use for numerical simulation programs. We then identify the best procedures to use and steps to follow to make a timely and accurate assessment of the debris-flow hazard.

2.2. RAMMS

The debris-flow module of RAMMS (Christen et al., 2010) requires a terrain model and a geo-referenced map or orthoimage. The user defines a region as study area. This calculation domain covers the area from the initiation to the potential deposition area. In addition, the start volume and the start location are defined, as well as the initiation mechanism. For a simple calculation, two friction parameters are defined for the design composition to be calculated. In RAMMS, a Voellmy-Salm approach is used, which splits the total basal friction into a velocity independent dry-Coulomb term which is proportional to the normal stress at the flow bottom (friction coefficient μ)

and a velocity dependent “viscous” or “turbulent” friction (friction coefficient ξ) (Salm, 1993). Both parameters need to be calibrated carefully based on a back-calculation of known events (Christen et al., 2012). No binding classification of typical parameter sets for debris flows is available until now. The user manual provides some examples and parameter suggestions for the two friction parameters. Additional model features like entrainment of sediment or erosion (Frank et al., 2017) are not discussed in this study.

2.3. Hazard assessment

The general procedure for hazard assessment in Switzerland (FOEN, 1997, FOEN, 2016) is well-defined, including input parameters and products. It is up to the contractor how to determine and specify the input parameters in detail. The same applies to the use of numerical simulation programs. Model use is not mandatory or recommended.

Figure 1 shows the general procedure to perform a hazard assessment using numerical simulation tools. In order to perform a hazard assessment and eventually to design protective measures against debris flows, it is necessary to determine basic parameters such as potential debris volume, mean flow velocity, peak discharge, and runout distance. In several studies, empirical relationships have been proposed to estimate these parameters (Rickenmann, 1999). Other approaches are now available to define the corresponding values for the input parameters, combining field and computer work (e.g. Jakob, 2005, Frick, 2008). Basic information is gained from field work, cadastral data and characterization of the catchment area. The data must be evaluated in terms of quality. The model shall be calibrated based on well-documented events in the catchment area to be investigated.

From basic information, scenarios for different recurrence times can be defined. These are evaluated either by expert opinion or by numerical modeling, or a combination of both. Further bases for the modeling are a digital elevation model, maps or orthoimage as well as possibly a mapping of envelopes of past events including deposition height information. Results need to be carefully interpreted. A validation and a plausibility check of the results is important and necessary. This is done first at the desk and then out in the field. In the field the potentially affected area, the expected intensity and possible weak spots are evaluated. The documentation of the work is done with intensity and hazard maps and a technical report, which comprehensibly describes their derivation and delineation.

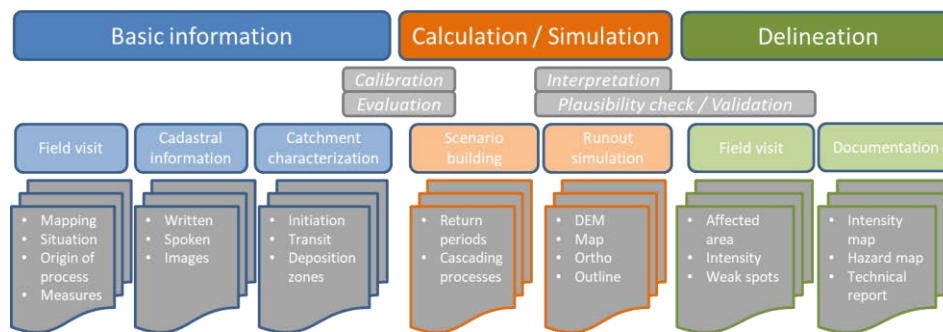


Fig. 1. Important steps in debris-flow hazard assessment using numerical runout simulation tools

2.4. Evaluation

The parameters for the input parameter in Fig. 2 are subjectively assessed on a scale (here from 1-10). The value 1 means a very poor data quality, and a corresponding high uncertainty. A value of 10 indicates a very high certainty and good data quality. The brackets, dashes and crosses indicate that scoring can be done within a bandwidth, e.g. by the assessment by several experts. The evaluation method presented here is not standardized. It merely suggests how the quality of the data could be assessed. Depending on the procedure, the category and elements may not be listed exhaustively. In this example (Fig. 2), the counter reaches 116 points or 68 % of possible score. This would mean a relatively good database and the result of the simulation would be promising. In case of less than 50% of the possible score, the result of the simulation must be considered with caution, and if less than 25 %, the result would have to be seriously doubted, since the input parameters show too much uncertainty. For such a case, the parameters would have to be varied within a bandwidth to display the uncertainty area.

Category	element	Rating Scale										Counter
		poor	medium						good			
		1	2	3	4	5	6	7	8	9	10	
DEM												
	resolution											9
	detailing											6
	topicality											4
Volume												
	initiation											4
	bulk											6
	deposition											9
Velocity												
	mean											7
	segment											3
Discharge												
	peak											7
	segment											3
Mixture												
	water content											8
	grain size distribution											7
	block size											9
	characteristics											7
Runout												
	distance											9
	affected area											9
	out-break zone											9
											116	68%

Fig. 2. Suggestion of a rating table for valuation of main input parameters of runout simulation tools

3. Results

In the following, statements about the three typical situations are presented in generalized form. Only the most important aspects are considered and only situation (3) is described in more detail.

Situation (1) with only one documented large event in the last century and many small events points out very well the difficulties in defining the parameters for a hazard assessment. We have no indication, if the large events was an extreme one, without any chance to be repeated in the future or if it's an event size that has a return period of about 100 years. The numerous small events could be used to calculate statistics regarding volume and return period but we are not sure if we miss large events. The conclusion of situation (1) is, that the time series is perhaps too short for the determination of the expected volumes for different return periods, especially the shorter ones. Therefore, the determination of the input parameters for volume, speed and discharge may be too high and too pessimistic. This result is reflected in the numerical simulations. The results indicate too large areas and too high intensities (as a product of flow height and flow velocity). Conversely, the description of the large event is an advantage for the calibration of the model. It allows the engineer to back-calculate a relevant debris-flow event and to better estimate important indications of the expected consequences, even for unknown, possibly larger events. The score using the proposed evaluation method for the different input parameters in such an example would be in the order of >50%. This is mainly due to good data on volume, runout and mixture, velocity and discharge of the large event. However, there are to make compromises in the spatial resolution of the terrain data. This is especially true if the event took place a long time ago.

Situation (2) with many small to mid-size debris-flow events is a slightly different problem. For small to mid-size debris flows, we have at least evidence, that events with a short return period happen regularly and we can approximate the return time. We miss data for larger events and have to estimate the parameters by the use of empirical relationships, estimates, and expert knowledge. The score using the proposed evaluation method for the different input parameters in such an example would be on the order of 75%. This is mainly due to statistically well-based data available for smaller events. Information on runout distances and weaknesses for out-break for large events is much more difficult to determine. The lack of information about damages also does not help the assessment.

For situation (3) we were able to calibrate the friction parameters based on one event that caused some damage and left the channel (Fig. 3a). The total volume of 30,000 m³ is at the top of the reasonably well-documented events. The values given in the event documentation were reduced by experts as it was considered too high. The volume was estimated from the available documents and set at a slightly lower value. The friction values were varied in such a way that resampling of the specific image simulated the main features of the deposit image as closely as possible (Fig. 3b). These were the runout distance, the break-out points and the area of the channel inundated by the event. The resulting parameter set is in the range found for other locations and was therefore assessed as plausible.

Subsequently, various structural measures could be checked by means of a numerical model for different scenarios. It was very challenging to estimate the possible volumes and the probable composition of significantly larger events. The estimation yielded very high values because of a generally high sediment availability in the catchment area. In addition, unstable rocky areas threatened to fall in the near future and the site is located in an area with high and sometimes heavy precipitation.

Since the drainage capacity of the channel on the fan is clearly too small for the assumed volumes, the out-break that happened in reality (Fig. 3a) became a model for an artificial deflection with a spillway (Fig. 3c). In the valley floor at the confluence with the receiving river there is insufficient room for deposition (Fig. 3b). For this reason, as much material as possible should be diverted in the case of a large event. The deposition is held back further down on the fan in a retention basin. If the volume deposited in it exceeds the retention capacity, the overflow returns to the main channel and flows to the receiving river. After action planning and implementation, numerical simulations proved the effects of the spillway for different event magnitudes, and have served to set the thresholds for a supplementary warning system.

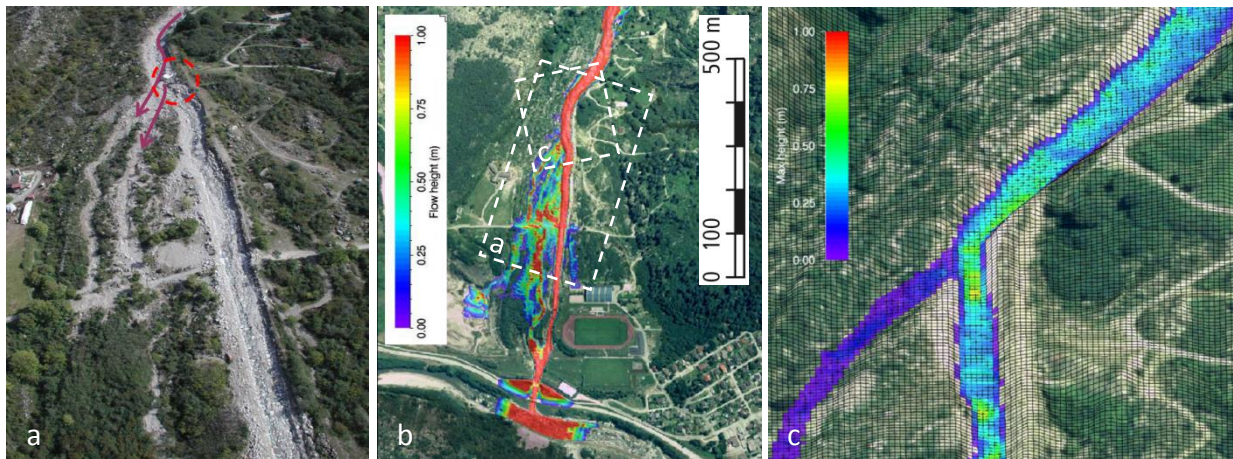


Fig. 3. (a) Aerial image of event traces with out-break (red circle) and flow direction highlighted by arrows; (b) back-calculation of documented event; approximate outline view figure a and figure c (white dashed lines); (c) oblique view of a scenario simulation evaluating new structural measure (spillway)

The score using the proposed evaluation method for the different input parameters in this example is on the order of >75%. This is mainly due to good data on volume, runout and intermediate-quality data on mixture, velocity and discharge of the well-documented events. Calibration of the model becomes easier. Thanks to detailed investigations and the planning of structural measures, good and up-to-date terrain data is available. Only when determining the parameters for large events limitations are to be expected. Generally, calibrated friction parameters are used for all event magnitudes.

4. Discussion and Conclusions

In general we found that debris-flow experts have little information on past debris-flow activity. There are exceptions; however, they are rare. Only large events, and events that caused major damage are analyzed in detail. They provide the most important parameters for the numerical modeling, such as deposited volume, run-out distance and eventually a description of the event series based on eye-witness. Additional parameters such as velocity, flow height, water content, particle size and distribution are more or less non-existent. Sometimes they are available in catchments where automated monitoring is present or in catchments of special interest after a major event. The first challenge in modeling debris flows starts with the definition of the adequate starting volume. Typically, no exact details of initiation volume of past events are known. While the initial debris-flow volumes are typically small, they can evolve to be a multiple thereof by entraining material along their flow paths (Berger et al., 2011), which means, the starting and ending volumes sometimes differ considerably. This challenge is due to the fact that debris flows tend to bulk, accumulating material from the torrential bed and the embankment, but sometimes also depositing sediment through levée formation and lateral out-breaks.

The prediction problem is amplified by the fact that topographic data are generally coarse (2m horizontal resolution in Switzerland) compared with typical channel widths (1–10 m) and because channel topography changes with time. Therefore, the data available for the representation of the terrain plays an important role, and the spatial resolution is critical. If relevant elements, such as side walls or blocks, are not given with sufficient accuracy, the simulation results are distorted. Terrain models therefore must be up-to-date. They have to reflect the condition of the channel and its surroundings for the investigation period. In addition, the geometry of protective structures, channel structures, surrounding buildings, and bridges are essential information that must be included in the terrain model. For buildings, the flow can usually be assumed during an event. This significantly influences the flow path. If, as discussed above, the grid mesh cannot provide a satisfactory and geometrically correct rendering, we recommend defining the buildings as impervious areas or no flux cells (Hohermuth et al., 2016). For structural safety measures and barriers, the question arises as to whether and when these factors are taken into account in the simulation. Investigations have shown that abrupt changes in inclination of artificial structures, such as dams or retention basins, represent major challenges for a numerical simulation model (e.g. Laigle and Labbé, 2016). If either the spatial resolution is too low or the grid size of the mesh does not optimally fit the object, incorrect effects will result, which are difficult to interpret by practitioners.

The flow properties of a debris flow (i.e. whether it is granular or low-viscosity) and the scenarios to define, must be clarified outside the application of a simulation program as part of the hazard assessment. It is not yet possible to predict with certainty which type of debris flow can be expected in any given catchment. For scenario building this is quite challenging (Jakob, 2005). If several scenarios are considered to be decisive, these can be investigated by means of numerical simulation tools. The flow properties of the debris flow to be simulated must be defined outside the application of a simulation program. If several scenarios are considered to be significant, this can be investigated by means of numerical simulation. Rare and unique events are the most difficult to classify and consider. It can be assumed that due to climate change several situations can arise that make events possible that have never occurred in the past. However, a serious hazard assessment must ask exactly this question about the conceivable extreme event and answer it meaningfully. Numerical models can assist with the answer and provide helpful results to preview infrequent and extreme situations. Cascading processes, such as rock slope failures, and more frequent debris flows involving soil masses released by permafrost play an important role in hazardous events in alpine regions as a potential impact by climate change. More than one process has to be judged, including the interaction between them.

Expert knowledge and experience continue to play an important role in the definition of input variables as well as in the interpretation of the simulation results. Very often, the basic data must be checked for plausibility and, if necessary, adapted. As a result, a lot of subjectivity comes into the choice of input data. It is therefore essential that the decisions are documented in technical reports in a comprehensible and detailed manner.

The computational power and performance of the models is still a challenge, especially if very high resolution results (sub meter) are expected. Parallelization and the exploitation of computer graphics processing units are accelerating the computations. Logical sequences and parameter variations can be automated, leaving the user time for other activities. Increasingly, automated evaluation methods are available to produce extensive results files. The effort for an accurate and transparent determination of the input parameters is not to be underestimated. The effort is worthwhile, however, because it gives one more defensible simulation results. It is often observed that under time pressure often little time is spent in the preparation of the input variables for the numerical simulation. Unfortunately, this approach is in most cases counterproductive because an inadequate exploration of input parameters will not yield trustworthy results. In addition, poor parameter selection can cause incorrect assessments of the situation. A second step, which is often overlooked, is the step of calibration. The calibration difficulty often lies in the fact that there is simply insufficient data for the location being examined. The calibration problem must therefore be remedied by analogy, assumptions, or rough estimates. Regrettably, practitioners frequently take incorrect approaches for calibrating friction parameters. Instead of an objective calibration process, the standard parameters are used, assuming that they yield an approximately correct result.

It must be noted that in the field of numerical modeling great progress has been made in recent years such that processes can be mathematically modeled with high precision. The model automates various tasks. On one hand, it delivers an independent expert opinion to the specialist. However, this requires the knowledge of the possibilities and limitations of the model and that the expert takes them into account when interpreting the results. On the other hand, in hazard assessment, the major challenge is not the model and its ability, but the adequate use of the model within the framework of the project.

We have found that the use of numerical simulation programs is desired by stakeholders and authorities. However, there are no clear guidelines for how to perform runout modeling. There are also no minimum

requirements for the choice of the input parameters. This concerns both the naming of the input parameters themselves, as well as the specification of the data quality. Because numerical modeling is becoming increasingly important, new guidelines must include the role of numerical simulations in hazard assessment in general.

We also need much more data on ongoing debris-flow activity. Therefore, we have to establish a well-structured data-base of debris-flow events including information of triggering conditions and parameters, the initial starting points, transit parameters such as super-elevation, bulking and levee deposits, deposition parameters such as break-out zones, levee formation, in-channel deposits, number and characteristic of surges and their run-out distance, information on composition, including water content, grain size distribution, etc.

Acknowledgements

We are very grateful to many different engineering companies throughout Switzerland, as well as to the relevant authorities who have worked on projects with RAMMS and have shared numerous examples with us and participated in exciting discussions about the difficulties in using a numerical tool in hazard assessment. Jason Kean and an anonymous reviewer provided helpful comments on the manuscript to improve the text significantly.

References

- Berger, C., McArdell, B.W., and Schlunegger, F., 2011, Direct measurement of channel erosion by debris flows, Illgraben, Switzerland: *Journal of Geophysical Research*, v. 116, iss. F1, F01002, doi:10.1029/2010JF001722.
- Christen, M., Kowalski, J., and Bartelt, P., 2010, RAMMS: Numerical simulation of dense snow avalanches in three-dimensional terrain: *Cold Regions Science and Technology*, v. 63, p. 1–14.
- Christen, M., Bühler, Y., Bartelt, P., Leine, R., Glover, J., Schweizer, A., Graf, C., McArdell, B.W., Gerber, W., Deubelbeiss, Y., Feistl, T. and Volkwein, A., 2012, Integral hazard management using a unified software environment: numerical simulation tool "RAMMS" for gravitational natural hazards, *in Proceedings, 12th Congress INTERPRAEVENT, Grenoble, v. 1: Klagenfurt, International Research Society INTERPRAEVENT, p. 77–86.*
- Crosta, G.B., Imposimato, S., and Roddeman, D.G., 2003, Numerical modeling of large landslides stability and runout: *Natural Hazards and Earth System Sciences*, v. 3, p. 523–538.
- Dai, F.C., Lee, C.F., Ngai, Y.Y., 2002, Landslide risk assessment and management: an overview: *Engineering Geology*, v. 64 p. 65–87.
- Deubelbeiss, Y., and Graf, C., 2013, Two different starting conditions in numerical debris-flow models - Case study at Dorfbach, Randa (Valais, Switzerland), *in Graf, C., ed., Mattertal - ein Tal in Bewegung. Publikation zur Jahrestagung der Schweizerischen Geomorphologischen Gesellschaft 29. Juni - 1. Juli 2011, St. Niklaus: Birmensdorf, Eidg. Forschungsanstalt WSL, p. 125–138.*
- FOEN, 1997, Consideration of Flood Hazards for Activities with Spatial Impact: Federal Office for Water Management, Federal Office for Spatial Planning, Federal Office for the Environment, Forests and Landscape: Berne, Recommendations, 32 p.
- FOEN, 2016, Protection against Mass Movement Hazards, Guideline for the integrated hazard management of landslides, rockfall and hillslope debris flows: Federal Office for the Environment, Berne, The environment in practice no. 1608, 97 p.
- Frank, F., McArdell, B.W., Oggier, N., Baer, P., Christen, M., Vieli, A., 2017, Debris-flow modeling at Meretschibach and Bondasca catchments, Switzerland: sensitivity testing of field-data-based entrainment model: *Natural Hazards and Earth System Science*, v. 17, iss. 5, doi: 10.5194/nhess-17-801-2017, p. 801–815.
- Frick, E., Kienholz, H. Roth, H., 2008, SEDEX - eine praxistaugliche Methodik zur Beurteilung der Feststofflieferung in Wildbächen, *in Proceedings, 11th Congress INTERPRAEVENT, Dornbirn: Klagenfurt, International Research Society INTERPRAEVENT, p. 319–330.*
- Graf, C., and McArdell, B.W., 2008, Simulation of debris flow runout before and after construction of mitigation measures: an example from the Swiss Alps, *in Chernomoretz, S.S., ed, Debris Flows: Disasters, Risk, Forecast, Protection: Pyatigorsk, International conference on debris flows: disasters, risk, forecast, protection, 22–29 September, 2008, p. 233–236.*
- Hohermuth, B., Graf, C., Heilig, J., 2016, Integrated natural hazards protection concept Vitznau LU - Case study Plattenbach, *in Proceedings, 13th congress INTERPRAEVENT, Lucerne: Klagenfurt, International Research Society INTERPRAEVENT, p. 535–543.*
- Hürlimann, M., Rickenmann, D., Graf, C., 2003, Field and monitoring data of debris-flow events in the Swiss Alps: *Canadian Geotechnical Journal*, v. 40, p. 161–175, doi: 10.1139/T02-087.
- Hürlimann, M., Rickenmann, D., Medina, V., and Bateman A., 2008, Evaluation of approaches to calculate debris-flow parameters for hazard assessment: *Engineering Geology*, v. 102, p. 152–163.
- Hungr, O., and McDougall, S., 2009, Two numerical models for landslide dynamic analysis: *Computers & Geosciences*, v. 35, p.978–992.
- Jakob, M., 2005, A size classification for debris flows: *Engineering Geology*, v. 79, iss. 3–4, p. 151-161.
- Laigle, D., Abbé, M., 2016, The impact of debris flows on structures: practice revisited in light of new scientific results, *in Proceedings, 13th congress INTERPRAEVENT, Lucerne: Klagenfurt, International Research Society INTERPRAEVENT, p. 782–790.*
- Lateltin, O., Haemmig, C., Raetzo, H., and Bonnard, C., 2005, Landslide risk management in Switzerland: *Landslides*, v. 2, p. 313–320. doi: 10.1007/s10346-005-0018-8.
- PLANAT, 2005, Hazard maps and related instruments, *Vademecum: Berne, 19 p.*
- Rickenmann, D., 1999, Empirical Relationships for Debris Flows: *Natural Hazards*, v. 19, p. 47–77.
- Rickenmann, D., 2005, Runout prediction methods, *in Jakob, M., Hungr, O., eds., Debris Flow Hazards and Related Phenomena: Chichester, Springer, p. 305–324.*
- Salm, B., 1993, Flow, flow transition and runout distances of flowing avalanches: *Annals of Glaciology*, v. 18, p. 221–226, doi:10.3189/S0260305500011551

Analysis of rainfall and runoff for debris flows at the Illgraben catchment, Switzerland

Jacob Hirschberg^{a,b,*}, Brian W. McArdell^a, Alexandre Badoux^a and Peter Molnar^b

^aSwiss Federal Institute for Forest, Snow and Landscape Research WSL, Zürcherstrasse 111, CH-8903 Birmensdorf, Switzerland

^bInstitute of Environmental Engineering ETH Zurich, John-von-Neumannweg 9, CH-8049 Zürich, Switzerland

Abstract

For hazard analysis, scenario design and mitigation there is a need to accurately and objectively predict the volume of debris flows. One approach is to base the calculation on rainfall properties. Herein we present an analysis of rainfall and debris-flow volume using data from the Illgraben catchment in Switzerland. The Illgraben debris-flow observation station, operated starting in the year 2000, has successfully recorded 75 debris flows and debris floods, with volume and bulk density estimates available for most of these events since 2000 and 2004, respectively. Here we describe results for 52 debris flows with sufficient data. Runoff coefficients determine the proportion of precipitation discharged from a catchment and support estimates on flow magnitudes. For each debris flow, runoff coefficients were determined by considering the event rainfall and the water contained in the debris flow. The events can further be characterized by the 14-day antecedent wetness. Runoff coefficients comprise a wide range from near 0 to close to 1. Clear trends are apparent, such as larger runoff coefficients during the snowmelt season. Furthermore, the debris-flow volumes are more sensitive to the antecedent rainfall than to the rainfall amount that triggered the event, likely because a wet channel bed enhances entraining. This study gives insights on which climate variables control the debris-flow volume. This will be further investigated and incorporated into the *SedCas* (Sediment Cascade) model (Bennett et al., 2014) to improve prediction of debris-flow activity.

Keywords: Runoff coefficient; Volume; Frequency

1. Introduction

Objectively quantifying debris-flow volumes and frequencies is unavoidable for the hazard analysis. The debris-flow volume indicates the severity of an event and can be a supportive parameter when planning mitigation measurements such as retention basins (Marchi and D'Agostino, 2004). Other magnitude parameters naturally also play a key role, such as the peak flow discharge for the planning of bridges crossing a torrent. Peak flow discharge is the most common parameter to assess flood magnitudes. For debris flows, however, volumes have shown to be a more robust measure. This is because there is more uncertainty in the friction parameter, which depends on the water-sediment proportions and grain sizes, and consequently affects the rheology of the flow (Pierson, 2005).

Several methods have been developed in the past to estimate debris-flow volumes. For example, Marchi and D'Agostino (2004) applied regression techniques and proposed a volume dependency on catchment area, mean gradient of the stream and a dimensionless geological index derived from the lithological classes present in the catchment. Their data set was not very sensitive to the latter parameter, which can be excluded (when the coefficients are adjusted). Stoffel (2010) reconstructed a debris-flow time series of the past ~140 years by performing tree-ring analysis and volume estimation on fan deposits. The added value of this technique is that time-series can be approximated for hazard assessment. In theory, once the volume has been estimated, it can be used to

* Corresponding author e-mail address: jacob.hirschberg@wsl.ch

infer parameters like peak discharge, velocity and cross-sectional area by applying empirical relations e.g. as presented by Rickenmann (1999).

Although empirical formulations overcome common limitations such as the lack of magnitude-frequency distributions, a range of factors affecting the geology, land use, geomorphology and hydrology play a role for debris-flow volumes and cannot easily be taken into account (Marchi and D'Agostino, 2004). Thus, debris flows can alter their composition, depending on the material they entrain from the bed (Takahashi, 2014). How much sediments are entrained, at which point in the channel entrainment starts and where it ends (i.e. stagnation or start of deposition) has not been uniquely defined and likely depends on parameters such as slope, sediment characteristics and discharge (Hung et al., 2005).

In the Illgraben catchment in the Swiss Alps, each year three to four debris flows have been observed on average in the most recent two decades. A world-wide unique debris-flow record including information on the time of occurrence and the volume, gives the opportunity to compute runoff coefficients and investigate how rainfall influences the debris-flow volume. Thereby, we intend to enhance the understanding of how climatic measures – primarily rainfall – control the debris-flow volume.

2. Study site

The Illgraben is located in the Rhône Valley in southwest Switzerland. The catchment spans from the Illhorn at 2716 m a.s.l in the south to the meeting point with the Rhône river at 610 m a.s.l in the north and covers an area of 9.6 km². The catchment can be divided into two sub-catchments, the Illgraben and the Illbach. whereas only the Illgraben (4.8 km²) is susceptible to debris flows and is the focus of this study. Little direct runoff from the Illbach has been observed, and the tributary channel is comparatively small. The Illsee is an artificial reservoir and hydrologically disconnected from the study site (Fig. 1).

The climate is comparatively dry and mild (Hürlimann et al., 2003). Yearly precipitation ranges from 600 mm in the valley to 1000 mm in the summit region (Hydrological Atlas of Switzerland). Precipitation can be twice as much in summer as in winter and often of a convective type, causing high-intensity rainfalls (Swiss Meteorological Service). In the catchment, rainfall is measured at three locations with tipping-bucket rain gauges at 10-minute and 0.2 mm resolution. Although, only one of them (RG1) is representative for the initiation zone (Badoux, 2009).

In the initiation zone, an area southeast above the channel mainly characterized by quartzites, mean hillslope erosion rates amount to 0.39 m/y mainly caused by landslides and rockfalls (Bennett et al. 2012). This material is transferred to the outlet primarily by debris flows. The sediment discharge when debris flows are excluded makes up less than 1% compared to the sediment discharge by debris flows (Schlunegger et al., 2009).

The debris-flow frequency increased in the years after a large rock avalanche in 1961. As a consequence, a large retention dam was built in the torrent followed by multiple smaller check dams. The large dam and the check dams are now backfilled and do not serve as retention basins anymore but stabilize the channel. The Illgraben differs from other catchments in terms of its sediment discharge which exceeds Alpine standards by two orders of magnitudes (Schlunegger et al., 2009). Therefore, the catchment has been subject to a variety of studies on sediment transfer patterns (e.g. Schlunegger et al. 2009; Berger et al., 2011b; Bennett et al., 2013; Bennett et al., 2014). Between 2 and 8 debris flows, 3 to 4 on average, have been observed per year (including debris floods) since the installation of a force plate in 2003 (McArdell et al., 2007). The force plate is located close to the catchment outlet.

The Illgrabenbach has no base flow and after rain storms, runoff is not necessarily observed in the lower part of the stream, indicating that large parts of the rainfall are stored. Only in spring substantial amounts of water from snowmelt contribute to continuous runoff.

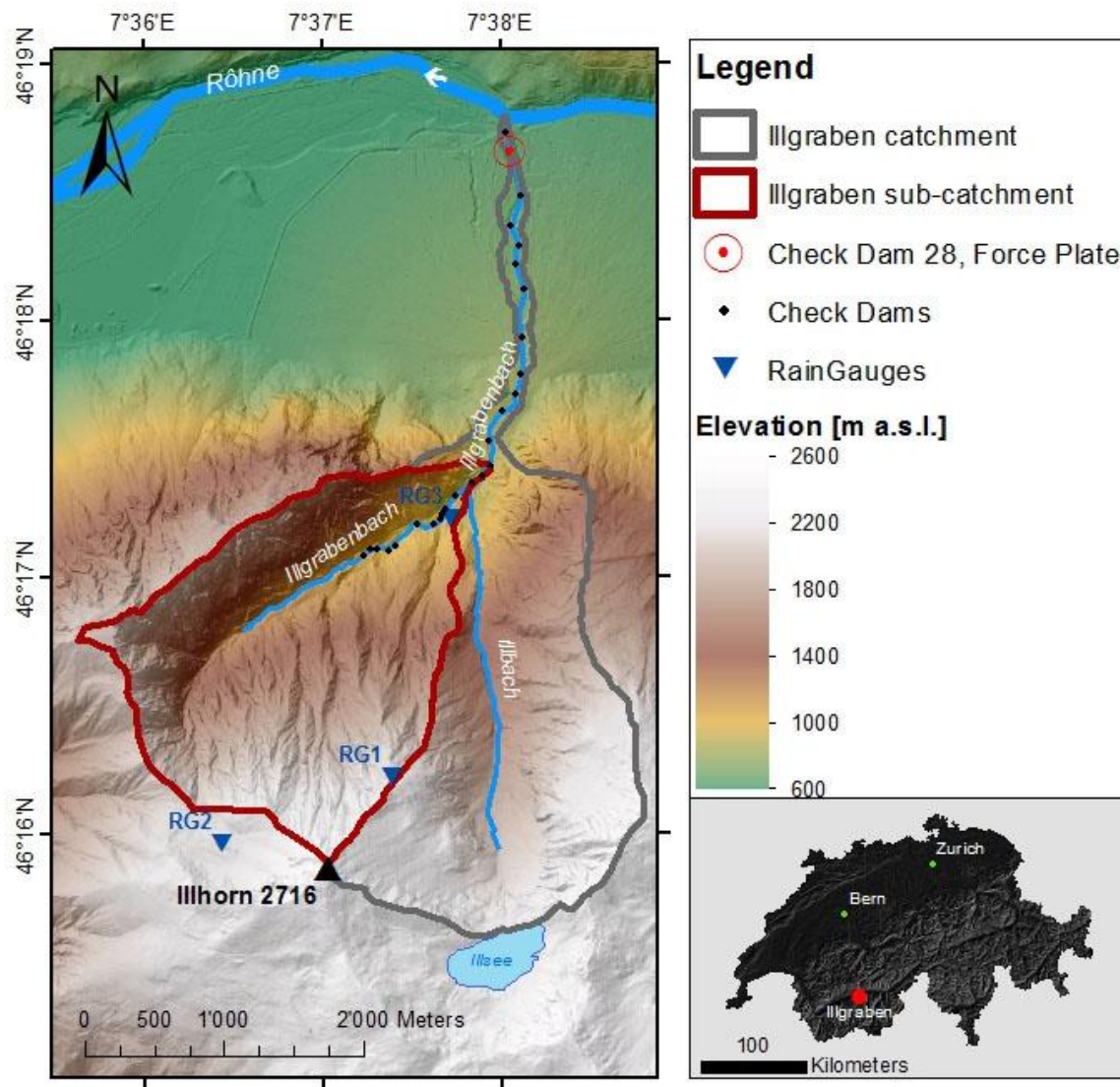


Fig. 1. Overview of the Illgraben catchment located in the Röhne valley in Switzerland. The hillshade image and the digital elevation model have a spatial resolution of 2 m (Federal Office of Topography Swisstopo). Only the western Illgraben sub-catchment is susceptible to debris flows and is covered by 44% exposed bedrock, 42% forest and 14% grassland (Schlunegger et al., 2009).

3. Methods

We determine runoff coefficients by defining the cumulated rainfall amount that triggered a debris flow (or debris flood) and comparing it to the amount of water present in the debris flow. The rainfall record for RG1 is consistent for the years 2002 to 2017 and for the months of May to October. We assume that RG1 is representative for the entire catchment. Considering the steep gradients in elevation and the convective nature of storms in the summer, this assumption rarely reflects reality. Nevertheless, RG1 is the most representative for debris-flow triggering since it is located only 1-2 km away from the initiation zone and at similar elevation (2210 m a.s.l.).

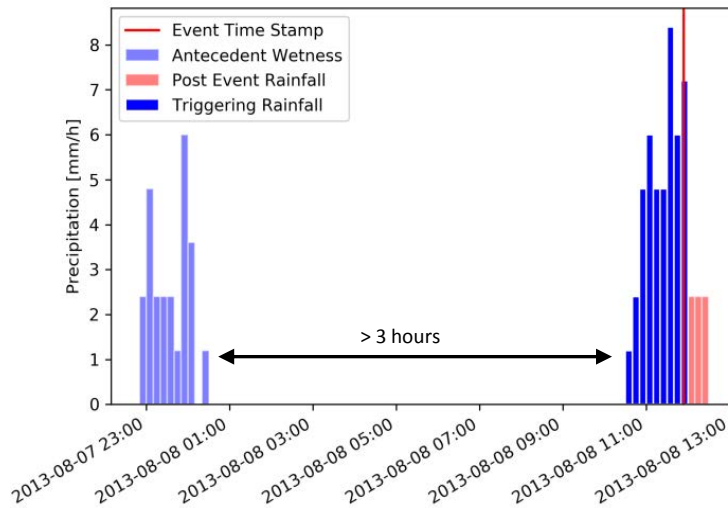


Fig. 2. Example of how an event is defined. Minimum-inter-event-time was set to 3 hours.

A rainfall event is defined by a minimum inter-event time of 3 hours (Fig. 2). In other words, if the gap between two rainfall pulses is less than three hours, they belong to the same rainfall event. If a debris flow occurred not immediately after but during a rainfall event, the instant of debris-flow occurrence was set as the last rainfall to be attributed to the particular debris flow.

The procedure for determining the debris-flow volumes was described in Schlunegger et al. (2009). The record in this study initially comprised 75 debris flows between 2000 and 2017. For some events, however, no volume could be determined and data on rainfall from RG1 is missing for large periods in 2000 and 2001. After excluding these cases the record consists of 52 debris flows.

To determine the amount of water per event, we assume that 50% of the total debris-flow volume consists of water, which corresponds to a bulk density of 1800 kg/m³. Schlunegger et al. (2009) quantified bulk densities in the Illgraben to be in the order of 1400-1800 kg/m³ for debris floods and 1800-2200 kg/m³ for debris flows. We do, however, not differentiate between flow types and assume 1800 kg/m³ to be the average bulk density. Hereafter, we will use the term *debris flow* for both types throughout the text. Finally, runoff coefficients (Ψ) are determined as follows:

$$\Psi = \frac{f \cdot V_{DF}}{\int_{t_0}^{t_e} p(t) dt} \quad (1)$$

where V_{DF} is the total debris-flow volume, f is the fraction of water (50%), $p(t)$ is the 10-minute rainfall at a given point in time t and t_0 and t_e mark the start and the end of the rainfall event which can be attributed to the triggering of the debris-flow event. In Fig. 2, t_0 and t_e would be defined by the first and the last rain pulse of the triggering rainfall.

4. Results and Discussion

Fifty-two debris flows which occurred in the Illgraben catchment were analyzed considering their volumes, triggering rainfalls, runoff coefficients and antecedent wetness conditions (Fig. 3). The debris flows occurred between May and October, with highest frequency in July (25) and fewer in the shoulder seasons in May (7) and September and October (6). Debris-flow volumes range between 4 000 and 90 000 m³ (median 25 000 m³). Runoff coefficients have a median value of 0.3 but vary between 0.003 and 4.6. Although, 50% of the values lie between 0.01 and 0.09. Four of the nine largest runoff coefficients were observed in May during the snowmelt period. Events with larger volumes have larger runoff coefficients and occur until the beginning of August. Triggering rainfall

amounts varied between 0.2 and 34.6 mm and have a median of 9.6 mm. For all events, the catchment experienced rainfall in the 14 days prior to the triggering event. Smaller events can have both high or low antecedent wetness during all seasons. While large events in May do not necessarily show increased antecedent wet conditions, large events occurring later into the year do.

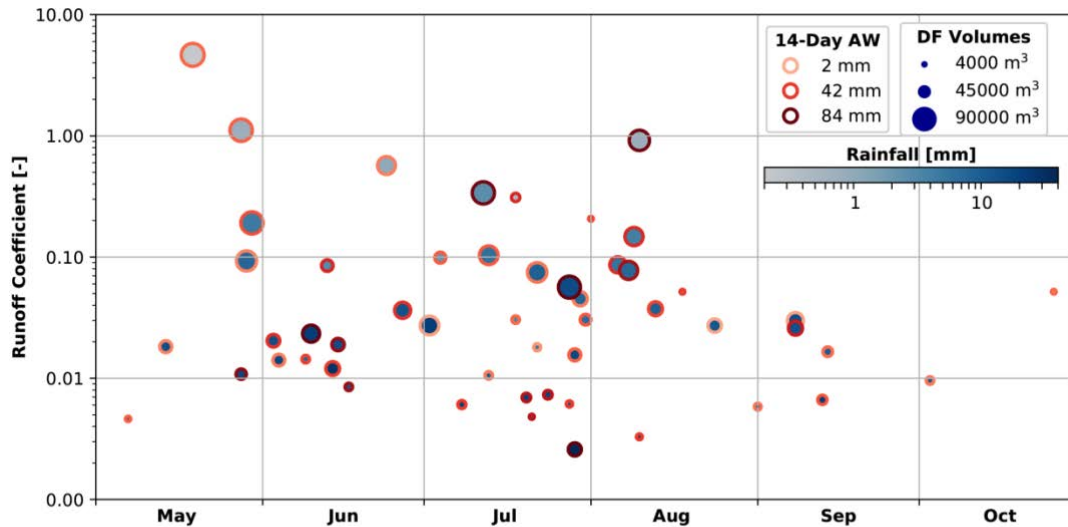


Fig. 3. Runoff coefficients (y-axis), debris-flow volumes (marker size), cumulated triggering rainfall (marker fill) and 14-day antecedent wetness (marker edge) of 52 debris flows (x-axis) that occurred in the Illgraben catchment between 2002 and 2017 in the period susceptible to debris flows between May and October.

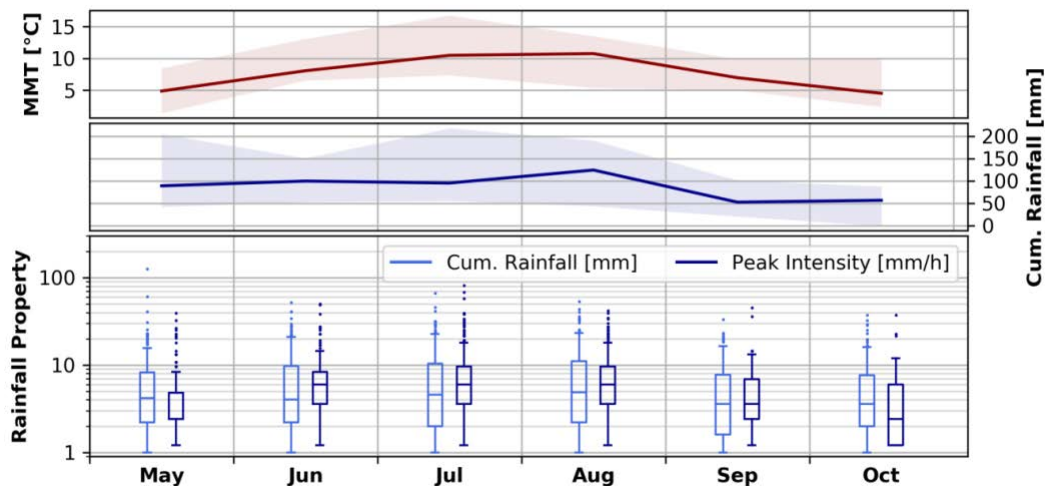


Fig. 4. Climate variables. Median, highest and lowest Mean Monthly Temperature (MMT) and cumulated monthly precipitation is shown in the upper two boxes. In the bottom, box plots for event cumulated rainfall (left) and rainfall peak intensity between 2002 and 2017 are presented.

The higher event frequencies during the summer months coincide with an increase in mean monthly temperatures and peak rainfall intensities (Fig. 4). In September and October, the decrease in debris-flow occurrence is accompanied by decreases in temperature, rainfall amounts and peak rainfall intensities.

In May, debris flows can be triggered by very small rainfall amounts, and runoff coefficients can even exceed 1. This strongly indicates that snowmelt plays a key role early in the season. Schneider et al. (2010) also evaluated snowmelt to be an important factor for debris flows triggered in a catchment of similar altitude as the Illgraben in the

Italian Dolomite Alps. Prenner et al. (2018) identified 6 of 41 debris flows where snowmelt fostered the triggering in an Austrian catchment also of similar altitude. Hence, our observation is consistent with others in similar catchments in terms of location and altitude.

In general, the Illgraben runoff coefficients increase with event volume. This is in line with the expectations, since we determine the water volume as 50% of the debris-flow volume. We also expect runoff coefficients of events with high cumulated rainfall amounts to be lower because of its definition (Eq. 1). A surprising result is that the largest debris flows were not initiated by the heaviest rainfalls (in terms of rainfall amounts). Rickenmann and Koschni (2010) highlighted that debris-flow volumes can have a large variability for a given runoff volume, in an analysis of a large storm event in Switzerland in 2005. Excluding catchments which were affected by landslides, this variability could be decreased. Consequently, it implies that there are other factors adding substantial uncertainty to the debris-flow magnitude, while rainfall and the resulting runoff only enhances the probability of triggering.

While the initial debris-flow volumes can be small, they can evolve to be a multiple thereof by entraining material along their flow paths (Berger et al., 2011a). Thereby, entrainment experiences positive feedback from the soil moisture in the flow path, because the pore water pressure increases as the debris-flow front approaches which can reduce the friction (Iverson et al., 2011; McCoy et al., 2012). Furthermore, the 14-day antecedent wetness can be considered as a proxy for the average soil moisture condition in the catchment. Debris flows in the Illgraben occur at all states of antecedent wetness, which therefore is not a good predictor for the actual event volume (Fig. 5). Nevertheless, out of the six largest debris flows, three occurred in May with modest antecedent wetness (~30 mm) while the other three took place later in the season under the highest observed antecedent wetness conditions (~80 mm). This exemplifies that there is a need to quantify the effects of snowmelt on the catchment, in order to make the climatic and hydrological conditions comparable. Furthermore, the results indicate that while events with smaller volumes can occur for the entire range of antecedent wetness, larger events with higher return periods are conditioned by antecedent wetness (except in May and June). Therefore, it is conceivable that there is an upper debris-flow volume limit for a given wetness condition (Fig. 5). These results are in line with McCoy et al. (2012) who observed substantially larger debris flows when the channel bed was wetter. It has also been noted that antecedent wetness is not necessarily required for debris-flow triggering (e.g. Coe et al., 2008; Abancó et al., 2016).

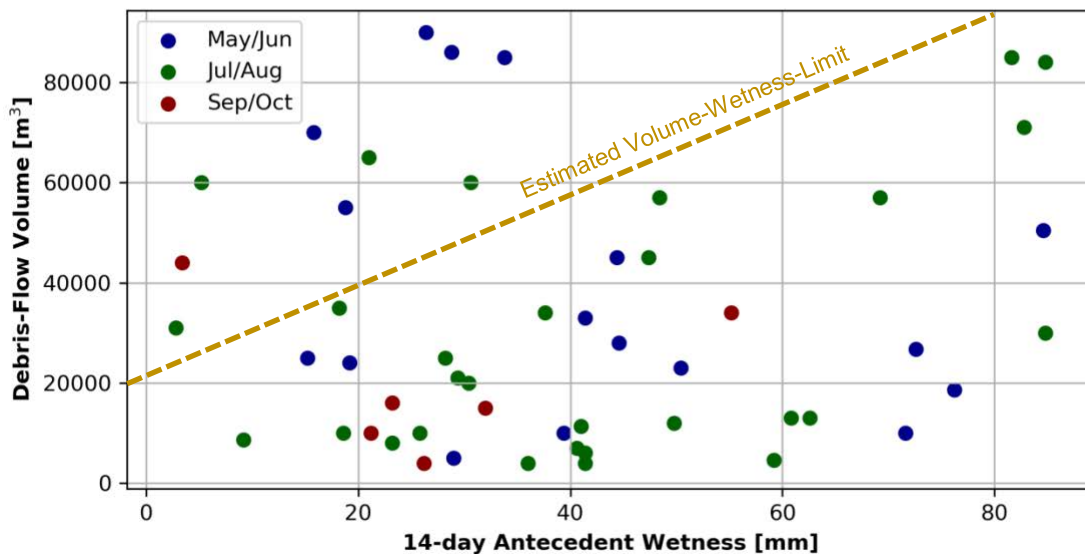


Fig. 5. Scatter plot of antecedent wetness, which corresponds to the cumulated rainfall in the 14 days before the event (excluding the triggering rainfall) and the debris-flow volumes for the 52 studied events. In color, the months during debris-flow season is indicated. There are indications that larger events are conditioned by antecedent wetness, which is exemplified by the dashed threshold line. The points above the line are likely due to snowmelt effects and uncertainties in the actual wetness conditions, among others.

In the case of sediment entrainment from the bed during an event, interstitial water stored in the soil is also entrained. This theory would explain the increased runoff coefficients for larger debris-flow volumes. In this study,

we are not able to determine runoff coefficients as usually defined in hydrology, because an unknown amount is added into the fluid component of debris flows. Therefore, the runoff coefficients illustrate that the amount of water exiting the catchment as discharge can be altered by debris flows.

Naturally, there are other factors enhancing the debris-flow volumes, which were not considered here. Even though the Illgraben catchment has indications of being transport-limited (Schlunegger et al., 2009), Bennett et al. (2014) modelled the long-term sediment output and only characterized 55% of the debris flows to be transport-limited. Therefore, it is likely that for a significant number of cases, the debris flows were supply-limited and sediment availability should also be considered as a variable controlling the debris-flow volume.

Finally, residual uncertainties remain in the rainfall measurements. Measuring precipitation with a rain gauge is a point measurement and upscaling to areal rainfall comes along with uncertainties. Nevertheless, the gauge RG1 is situated comparatively close to the initiation zone and at a representative altitude. Some uncertainty also exists in the synchronization in the timing of the force plate and the rain gauge, since the latter is operated by the cantonal authorities. An uncertainty assessment, however, revealed that even a time shift of two hours would not change the runoff coefficients significantly (p -value = 0.1). There is also uncertainty in the assumption of the bulk density. If variations in this parameter would be considered, the range of runoff coefficients would be squeezed, but not alter the general pattern.

5. Conclusions and Outlook

We determined volume, triggering rainfall, runoff coefficients and 14-day antecedent wetness for 52 debris flows in the Illgraben catchment. Runoff coefficients varied greatly and increase with increasing debris-flow volume. We conclude that the cumulated rainfall amount is not a proxy for the debris-flow volume. In fact, debris flows with the largest volumes were triggered by comparatively small rainfall amounts. Antecedent wetness, however, seems to be a key factor for the volume. Antecedent wetness has at least two effects. First, it enhances entrainment along the channel by increased pore-water pressure and second, in the process of entrainment, the interstitial water is also entrained, contributing to substantially larger runoff coefficients.

Furthermore, seasonal variations in the debris-flow volumes and frequencies are apparent. In spring, snowmelt likely enhances the triggering and entrainment of sediments, leading to some of the largest debris-flow volumes. In the summer months, the increased frequency of debris-flow occurrence is accompanied with an increase in high rainfall intensities. In autumn, only few and small debris flows happen because of lower rainfall amounts and intensities. Another reason is possibly the occurrence of supply-limited conditions in autumn because sediments have been washed out earlier in the season.

This study gives insights on which climate variables are likely to control debris-flow volume. Nevertheless, the variables discussed here are only indicators and do not replace the actual conditions which led to the formation of a debris-flow of a given volume. Therefore, it motivates future investigations on hydrological (snow, runoff, soil water content, etc.) and geomorphological variables (available sediments for mobilization) in more detail. Especially in a changing climate and for possible hazard mitigation adaptation, it would be interesting to explore debris-flow generation in a more quantitative approach. *SedCas*, a probabilistic sediment cascade model which has been developed for the Illgraben (Bennett et al., 2014), offers an ideal framework for the suggested investigations.

Acknowledgements

Funding for this project is from the WSL strategic initiative Climate Change Impacts on Alpine Mass Movements (CCAMM). We are very grateful to the canton of Valais and the municipality of Leuk for their support of the Illgraben research.

References

- Abancó, C., Hürlimann, M., Moya, J., and Berenguer, M., 2016, Critical rainfall conditions for the initiation of torrential flows. Results from the Rebaixader catchment (Central Pyrenees): *Journal of Hydrology*, v. 541, p. 218–229, doi:10.1016/j.jhydrol.2016.01.019.
- Badoux, A., Graf, C., Rhyner, J., Kuntner, R., and McArdell, B. W., 2009, A debris-flow alarm system for the Alpine Illgraben catchment: Design and performance: *Natural Hazards*, v. 49, p. 517–539, doi:10.1007/s11069-008-9303-x.

- Bennett, G. L., Molnar, P., Eisenbeiss, H., and Mcardell, B. W., 2012, Erosional power in the Swiss Alps: Characterization of slope failure in the Illgraben: *Earth Surface Processes and Landforms*, v. 37, p. 1627–1640, doi:10.1002/esp.3263.
- Bennett, G. L., Molnar, P., McArdell, B. W., and Burlando, P., 2014, A probabilistic sediment cascade model of sediment transfer in the Illgraben: *Water Resources Research*, v. 50, p. 1225–1244, doi:10.1002/2013WR013806.
- Bennett, G. L., Molnar, P., McArdell, B. W., Schlunegger, F., and Burlando, P., 2013, Patterns and controls of sediment production, transfer and yield in the Illgraben: *Geomorphology*, v. 188, p. 68–82, doi:10.1016/j.geomorph.2012.11.029.
- Berger, C., McArdell, B. W., and Schlunegger, F., 2011, Direct measurement of channel erosion by debris flows, Illgraben, Switzerland. *Journal of Geophysical Research: Earth Surface*, v. 116, p. 1–18, doi:10.1029/2010JF001722.
- Berger, C., McArdell, B. W., and Schlunegger, F. 2011, Sediment transfer patterns at the Illgraben catchment, Switzerland: Implications for the time scales of debris flow activities: *Geomorphology*, v. 125, p. 421–432, doi:10.1016/j.geomorph.2010.10.019.
- Coe, J. A., Kinner, D. A., and Godt, J. W., 2008, Initiation conditions for debris flows generated by runoff at Chalk Cliffs, central Colorado: *Geomorphology*, v. 96, p. 270–297, doi:10.1016/j.geomorph.2007.03.017.
- Hung, O., McDougall, S., and Bovis, M., 2005, Entrainment of material by debris flows, in *Debris-Flow Hazards and Related Phenomena*, p. 135–155, doi:10.1007/3-540-27129-5_7.
- Hürlimann, M., Rickenmann, D., and Graf, C., 2003, Field and monitoring data of debris-flow events in the Swiss Alps: *Canadian Geotechnical Journal*, v. 40, p. 161–175, doi:10.1139/t02-087.
- Iverson, R. M., Reid, M. E., Logan, M., LaHusen, R. G., Godt, J. W., and Griswold, J. P., 2011, Positive feedback and momentum growth during debris-flow entrainment of wet bed sediment: *Nature Geoscience*, v. 4, p. 116–121, doi:10.1038/ngeo1040.
- Marchi, L., and D'Agostino, V., 2004, Estimation of debris-flow magnitude in the Eastern Italian Alps: *Earth Surface Processes and Landforms*, v. 29, p. 207–220, doi:10.1002/esp.1027.
- McArdell, B. W., Bartelt, P., and Kowalski, J., 2007, Field observations of basal forces and fluid pore pressure in a debris flow: *Geophysical Research Letters*, v. 34, doi:10.1029/2006GL029183.
- McCoy, S. W., Kean, J. W., Coe, J. A., Tucker, G. E., Staley, D. M., and Wasklewicz, T. A., 2012, Sediment entrainment by debris flows: In situ measurements from the headwaters of a steep catchment: *Journal of Geophysical Research*, v. 117, doi:10.1029/2011JF002278.
- Pierson, T. (2005). Distinguishing between Debris Flows and Floods from Field Evidence in Small Watersheds: U.S. Geological Survey Fact Sheet, 2004-3142. 4 p.
- Prenner, D., Kaitna, R., Mostbauer, K., and Hrachowitz, M., 2018, The Value of Using Multiple Hydrometeorological Variables to Predict Debris Flow Susceptibility in an Alpine Environment: *Water Resources Research*, v. 54, p. 6822–6843, doi:10.1029/2018WR022985.
- Rickenmann, D., 1999, Empirical Relationships for Debris Flows: *Landscape*, v. 19, p. 47–77, doi:10.1023/A:1008064220727.
- Rickenmann, D., & Koschni, A., 2010, Sediment loads due to fluvial transport and debris flows during the 2005 flood events in Switzerland: *Hydrological Processes*, v. 24, p. 993–1007, doi:10.1002/hyp.7536.
- Schlunegger, F., Badoux, A., McArdell, B. W., Gwerder, C., Schnydrig, D., Rieke-Zapp, D., and Molnar, P., 2009, Limits of sediment transfer in an alpine debris-flow catchment, Illgraben, Switzerland: *Quaternary Science Reviews*, v. 28, p. 1097–1105, doi:10.1016/j.quascirev.2008.10.025.
- Schneider, H., Höfer, D., Irmeler, R., Daut, G., and Mäusbacher, R., 2010, Correlation between climate, man and debris flow events - A palynological approach: *Geomorphology*, v. 120, p. 48–55, doi:10.1016/j.geomorph.2009.09.014.
- Stoffel, M., 2010, Magnitude-frequency relationships of debris flows - A case study based on field surveys and tree-ring records: *Geomorphology*, v. 116, p. 67–76, doi:10.1016/j.geomorph.2009.10.009.
- Takahashi, T., 2014, *Debris flow: mechanics, predictions and countermeasures*. press CRC.

Debris-flow assessment from rainfall infiltration induced landslide

Yu-Charn Hsu ^{a,*}, Ko-Fei Liu ^a, Hung-Ming Shu ^b

^aDepartment of Civil Engineering National Taiwan University, No.1, Sec.4, Roosevelt Rd., Taipei 10617, Taiwan (R.O.C.)

^bTaitung Branch of Taiwan Soil and Water Conservation Bureau, No.665, Sec. 1, Zhonghua Rd., Taitung City 950, Taiwan (R.O.C.)

Abstract

In the study, debris flows induced by landslides are studied through physical models. TRIGRS and DEBRIS-2D models are integrated for simulation of rainfall infiltration induced shallow landslide and the subsequent debris flows. TRIGRS is used to estimate unstable mass on the hillslope and provide the initial volume for debris flow simulation, and DEBRIS-2D is applied to simulate mass motion and assess the hazard zone mapping. The method is applied to Daniao tribe's sediment disaster during Typhoon Morakot in Taiwan. The simulated final deposition zone and the disaster area in the real event are almost identical. All the geophysical parameters are obtained through official values and rheological parameters are obtained by in situ measurements.

Keywords: TRIGRS, DEBRIS-2D, estimate unstable mass, the hazard zone;

1. Introduction

Rainfall infiltration will increase soil moisture. As a result, shear strength is reduced and pore pressures and seepage forces are increased. Enough rainfall causes hillside failure, and the failure mass will slide down or turn into debris flows with enough water.

Many studies used empirical or statistical method to obtain landslide potential analysis and realize the hazard zone mapping for debris flow. But physical process combining landslide prediction and debris flow simulation is considered more precise in smaller scale.

Many researches have used coupled methodology to simulate a debris flow mobilization from a shallow landslide. Chiang et al. (2012) have combined a landslide susceptibility model in landslide prediction, an empirical model to select debris flow initiation points among predicted landslide area and a debris flow model to simulate the spread and inundated region of failed materials from the identified source areas. Gomes et al. (2013) have combined two physical models of SHALSTAB and FLO-2-D to model debris flow spreading area. Wang et al. (2013) have combined limit equilibrium theorem and 2-D depth-integral flow model to assess landslide and a debris flow processes.

In this study, TRIGRS (Baum et al., 2010) and DEBRIS-2D (Liu and Huang, 2006) models are coupled in an assessment with rainfall infiltration amount. TRIGRS is a well-known model used in estimating collapse region from rainfall infiltration. DEBRIS-2D has been successfully applied to a hazard zone simulation of debris flow, but DEBRIS-2D needs input for failure volume and location. Therefore, TRIGRS is used to estimate unstable mass on the hillslope and provide the initial volume for debris flow simulation, and DEBRIS-2D is applied to simulate mass motion and assess the hazard zone mapping. This way, TRIGRS and DEBRIS-2D models are integrated for simulation of rainfall infiltration induced shallow landslide and the subsequent debris flows.

* Corresponding author e-mail address: yucharnhsu@gmail.com

2. Fundamentals

2.1. Rainfall Infiltration

Rainfall infiltration causes soil water content to increase until saturation and then raise the water table. Therefore, the pore pressure in the saturated state needs to be calculated first. Consider a rectangular Cartesian coordinate system with its origin at an arbitrary point on the ground (see Fig.1), the x axis points to down slope, the y axis points to tangents the topographic contour, and the z axis is normal to $x - y$ plane and points into the slope. The fundamental of rainfall infiltration simulation is based on Iverson's (2000) linearized solution of Richard's equation. A generalized solution with an infinite basal boundary is expressed in equation (1), and an impermeable basal boundary at a finite depth is given by equation (2). The first term on the right hand side in equations (1) and (2) represents the steady solution and remaining terms on the right hand side represent the transient solution.

$$\begin{aligned} \varphi(Z,t) = & [Z-d]\beta \\ & + 2 \sum_{n=1}^N \frac{I_{nz}}{K_z} H(t-t_n) [D_1(t-t_n)]^{1/2} \operatorname{ierfc} \left[\frac{Z}{2[D_1(t-t_n)]^{1/2}} \right] \\ & - 2 \sum_{n=1}^N \frac{I_{nz}}{K_z} H(t-t_{n+1}) [D_1(t-t_{n+1})]^{1/2} \operatorname{ierfc} \left[\frac{Z}{2[D_1(t-t_{n+1})]^{1/2}} \right] \end{aligned} \quad (1)$$

$$\begin{aligned} \varphi(Z,t) = & [Z-d]\beta \\ & + 2 \sum_{n=1}^N \frac{I_{nz}}{K_z} H(t-t_n) [D_1(t-t_n)]^{1/2} \sum_{m=1}^{\infty} \left\{ \begin{aligned} & \operatorname{ierfc} \left[\frac{(2m-1)d_{LZ} - (d_{LZ} - Z)}{2[D_1(t-t_n)]^{1/2}} \right] \\ & + \operatorname{ierfc} \left[\frac{(2m-1)d_{LZ} + (d_{LZ} - Z)}{2[D_1(t-t_n)]^{1/2}} \right] \end{aligned} \right\} \\ & - 2 \sum_{n=1}^N \frac{I_{nz}}{K_z} H(t-t_{n+1}) [D_1(t-t_{n+1})]^{1/2} \sum_{m=1}^{\infty} \left\{ \begin{aligned} & \operatorname{ierfc} \left[\frac{(2m-1)d_{LZ} - (d_{LZ} - Z)}{2[D_1(t-t_{n+1})]^{1/2}} \right] \\ & + \operatorname{ierfc} \left[\frac{(2m-1)d_{LZ} + (d_{LZ} - Z)}{2[D_1(t-t_{n+1})]^{1/2}} \right] \end{aligned} \right\} \end{aligned} \quad (2)$$

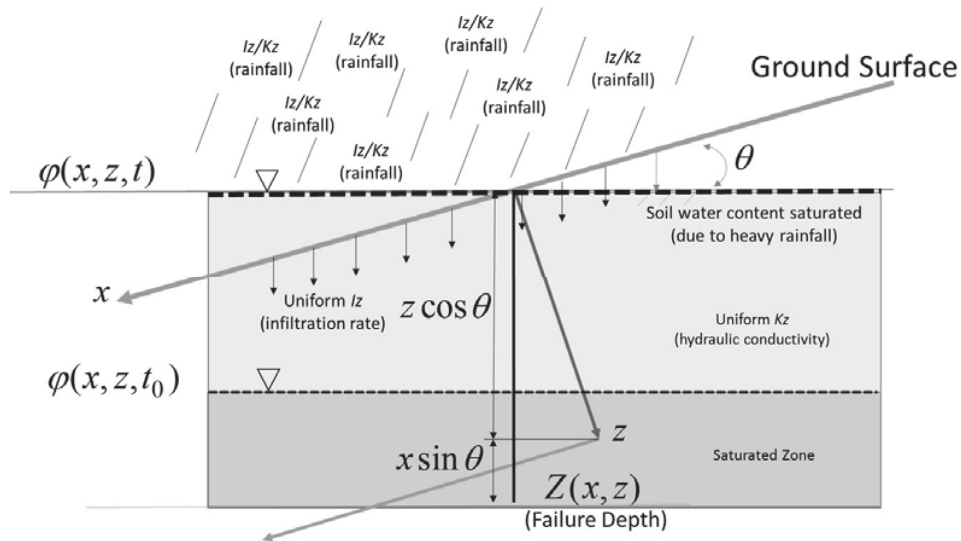


Fig.1 Coordinate system diagram of TRIGRS model.

Equation (1) applies where hydraulic properties are uniform and equation (2) applies where a well-defined decrease in hydraulic conductivity exists at a finite depth. In the equations φ is the groundwater pressure head, t is time, θ is the slope angle of x axis, $Z = z / \cos \theta$ is the failure depth, d is the initial depth of the water table measured in Z direction in steady state, d_{Lz} is a depth of impermeable basal boundary measured in Z direction, $\beta = \lambda \cos \theta$ [$\lambda = \cos \theta - (I_z - K_z)_{LT}$, with K_z the hydraulic conductivity in Z and I_z initial surface flux], I_{nz} means a surface flux of a given intensity in n^{th} time interval, $D_j = D_0 \cos^2 \theta$ with D_0 the saturated hydraulic diffusivity), $H(t - t_n)$ is Heaviside function. The function $ierfc$ is defined as

$$ierfc(\eta) = \frac{1}{\sqrt{\pi}} \exp(-\eta^2) - \mu erfc(\eta) \quad (3)$$

2.2. Slope Stability Analysis

Iverson (2000) used an infinite-slope stability analysis to model a hillslope stability. The ratio F_s called the factor of safety is calculated at Z depth by (4).

$$F_s = \frac{\tan \phi}{\tan \theta} + \frac{C - \varphi(Z, t) \gamma_w \tan \phi}{\gamma_s Z \sin \theta \cos \theta} \quad (4)$$

where ϕ is the friction angle, C is the cohesion of soil, both for effective stress, γ_w is specific gravity of water and γ_s is specific gravity of soil. Equation (4) expresses the failure of the infinite slope by the ratio between resisting from basal Coulomb friction to gravitationally induced downslope basal driving stress. The hillslope fails for $F_s < 1$. Therefore, the depth $H = z$ and area A of the hillside in unstable ($F_s < 1$) condition, the product H and A will provide volume for the mass motion simulation.

2.3. Debris flow

A hillside fails when $F_s < 1$, and this mass will mix with water and become debris flow as it moves down slope. A physical model, DEBRIS-2D (Liu and Hung, 2006) adopted depth integrated form of conservation law under long wave approximation in the plug flow region and has been successfully applied in debris flow simulation, which is original developed by Liu and Huang (2006). DEBRIS-2D with inclined coordinate system (see Fig. 2), x coincides with flow direction, y tangent to topographical contour direction and z normal to $x - y$ plane and points to depth direction. The velocity components in the x, y directions are u and v respectively, θ is the inclined angle, τ_0 is the yield stress, $H = h - B$ is the flow depth (where h is the free surface and B is the natural bottom of the debris flow). The momentum equations in conservative form are shown in equation (5) and (6), the continuity equation is shown in equation (7).

$$\frac{\partial uH}{\partial t} + \frac{\partial u^2 H}{\partial x} + \frac{\partial uvH}{\partial y} = -g \cos \theta H \frac{\partial (B+H)}{\partial x} + g \sin \theta H - \frac{1}{\rho} \frac{\tau_0 u}{\sqrt{u^2 + v^2}}, \quad (5)$$

$$\frac{\partial vH}{\partial t} + \frac{\partial uvH}{\partial x} + \frac{\partial v^2 H}{\partial y} = -g \cos \theta H \frac{\partial (B+H)}{\partial y} - \frac{1}{\rho} \frac{\tau_0 v}{\sqrt{u^2 + v^2}}, \quad (6)$$

$$\frac{\partial H}{\partial t} + \frac{\partial uH}{\partial x} + \frac{\partial vH}{\partial y} = 0, \quad (7)$$

The initial velocities when the hillslope just fails are $u = 0$ and $v = 0$, and the initial depth H is obtained from the slope stability analysis results under the instability condition $F_s < 1$ in equation (4). Three unknowns H, u and v could be solved from three independent equations (5), (6), and (7).

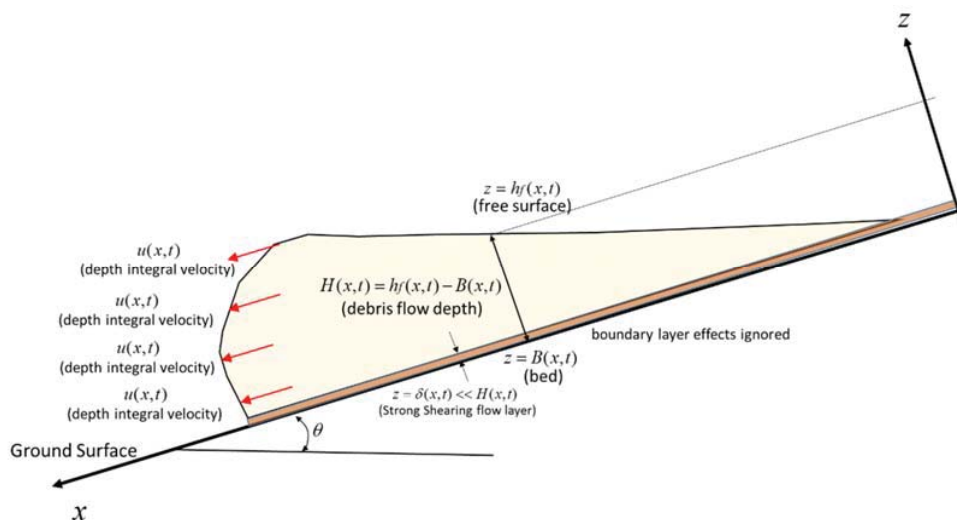


Fig.2 Coordinate system diagram of DEBRIS-2D model.

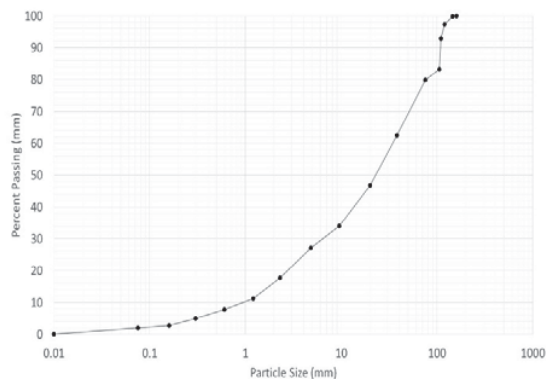
3. Descriptions of Environment and Modelling

3.1. Surface Survey

The landslide is located on the upper hillside of the Daniao tribe as in Fig. 3. The failure source on the ground was composed of slate, mudstone, sandstone and weathered gravel, which are all easily movable under external forces. The sieve analysis gives $D_{10} = 0.98$ mm, $D_m = 55.94$ mm and maximum is $D_{max} = 420$ mm.



(a) Photographs of Daniao tribe's landslide after Typhoon Morakot



(b) Particle distribution of Daniao tribe's landslide

Fig. 3 Surface survey results.

3.2. Topographical Analysis

The $2\text{ m} \times 2\text{ m}$ digital terrain model is used for the topographic analysis of the Daniao tribe's sediment disaster. The watershed area is approximately 52.38 ha, and the elevation changes from 60 m to 480 m, and the slope distribution is from 0° to 70° , the major stratigraphic trend is from the east to the west. The landslide occurred mostly within the steeper area (slope greater than 15°). The distributions of elevation, slope and flow direction of the hazard zone are shown in Fig. 4.

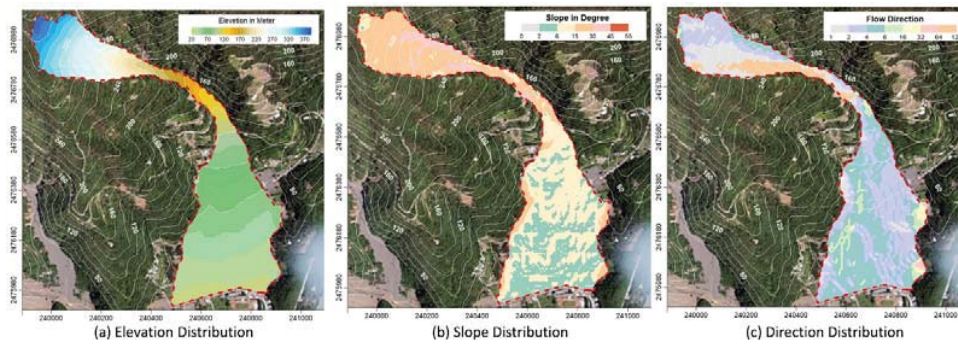


Fig. 4 Topographic analysis results.

3.3. Rainfall Event

During 2009 August, Typhoon Morakot struck Taiwan and induced sediment disasters throughout Taiwan. Daniao tribe watershed landslide is one of sediment disasters which is occurred in Eastern Taiwan. Typhoon Morakot produced heavy rainfall to Daniao tribe watershed from 2009/08/07 09:00 to 2009/08/10 03:00. The hyetograph is shown in Fig. 5. The rainstorm accumulated 759 mm in 65 hours, and maximal rainfall intensity reached 45.5 mm/hour on 2009/08/07 06:00. The rainstorm accumulation reached 740.5 mm at 2009/08/08 15:00, and induced landslides and debris flows.

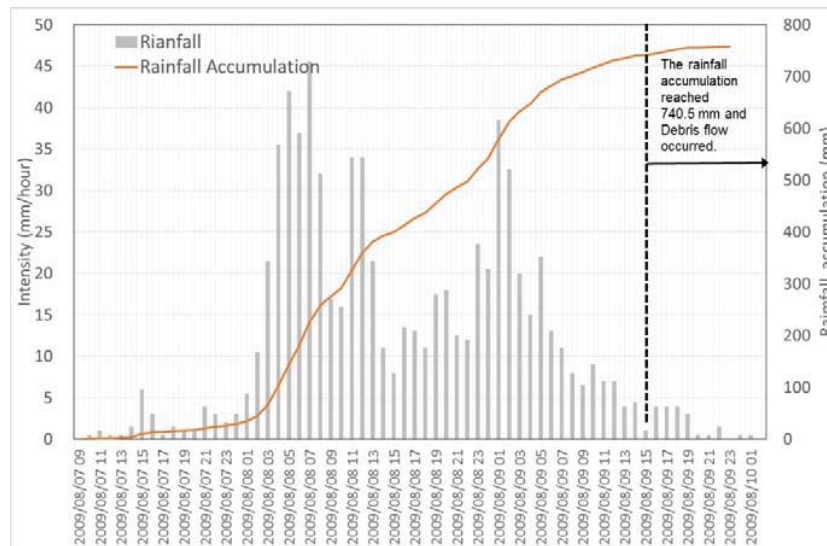


Fig. 5 Hyetograph during Typhoon Morakot struck Daniao tribe watershed.

3.4. Geological Properties

There were 10 boreholes drilled to understand the geological formation of the Daniao tribe's landslide after the disaster. The boreholes BH-1, BH-3, BH-5, BH-7, BH-9, and BH-10 were sampled using the Standard Penetration Test (SPT) every 1.5 m. The soil samples of the landslide were obtained from the split tube samplers, and all of the samples were tested for soil properties in a laboratory. According to the drilling results, there are two stratum underground. The first formation is composed of brown colluvial rock, concrete, backfill layer and gray sand, whose

depth ranged from 0 m to 0.75 ~ 12.65 m underground. The second formation is constituted by brown slate, gray slate, shear gouge, rust staining and quartz. The geological profiles of the boreholes and field particle distribution survey results are shown in Fig. 6.

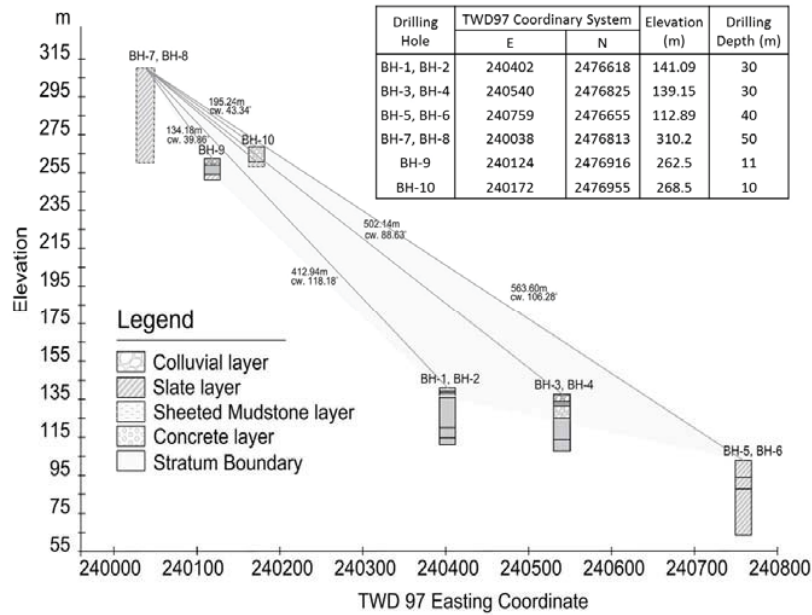


Fig. 6 Geological profiles of boreholes.

The remolded soil samples are used in the soil properties test, the soil properties of the Daniao tribe landslide region are shown in the Table 1. Direct Shear Test (DST) is applied to obtain the friction angle is 34.5° and cohesion is 1.6 ton/m³ of the remolded soil sample. According to the Plasticity Chart from Casagrande (1932), the stratum’s soil of Daniao tribe landslide could be classified as inorganic clays of low plasticity soil (CL-ML). The hydraulic conductivity K_s is about from 5.0×10^{-8} to 5.0×10^{-10} m/Sec. Liu and Wu (2008) found the diffusivity value D_0 of the colluvium soil is about 10 to 500 times that of the hydraulic conductivity K_s . Furthermore, if the soil is saturated that the steady infiltration rate I_z could be the same as the hydraulic conductivity K_s . Therefore, the diffusivity value selects 200 times of the K_s equals $D_0 = 1.0 \times 10^{-5}$ m²/Sec, and the steady infiltration rate I_z equals zero under fully saturated soil condition.

Table 1 Geological characteristics of soil samples in Daniao tribe landslide

Soil layer	Distributed Depth (m)	Material Constituted	Number of SPT (N)	Specific Gravity (ton/m ³)	Water Content (%)	Porosity Ratio	Liquid Limit LL (%)	Plasticity Index PI (%)
Brown elastic rock blocks of concrete or backfill layer with gray sand	From 0.00 m to 0.75 ~ 12.65 m underground	Collapse, Backfill layer	8 ~ >100.	2.11 ~ 2.28.	6.7 ~ 12.7.	0.26 ~ 0.43.	17.2 ~ 19.2.	6.8 ~ 8.7
			Average: 62.2	Average: 2.21	Average: 8.9	Average: 0.32	Average: 18.5	Average: 8.0
Brown, gray turn black and gray broken slate clip scissors mud and rust-strained quartz	From 0.75 ~ 12.65 m to 30~50 m underground	Broken Slate	50 ~ >100.	1.86 ~ 2.20.	8.5 ~ 9.8.	0.31 ~ 0.57.	17.6 ~ 19.5	6.8 ~ 9.5
			Average: 69.0	Average: 2.03	Average: 9.0	Average: 0.45	Average: 18.4	Average: 8.0

4. Results of Simulation and Discussion

The topographic data were from 2 m \times 2 m DTM. The hyetograph from Typhoon Morakot record is used to calculate infiltration. The geological parameters are obtained from boreholes and laboratory tests.

4.1. Estimation and Validation of Landslide Volumes

According to report of Soil and Water Conservation Bureau in 2011, the landslide volume is 319,875 m³ and failure area equals 51,873 m² using the DTM before and after the landslide disaster. The average depth is 5.2 m.

Assuming soil is already saturated just before the disaster, with the input information in Table. 1. TRIGRS model applied to assess the volume of the collapsed zone in the Daniao tribe's upstream hill, the infiltration model of TRIGRS equation (2) was used to calculate the total pressure head ϕ , we ran the TRIGRS model by increased the depth Z from 1 m to 6 m, the domain is almost the same as real event at $Z = 6$ m, then the area where $F_s < 1$ is shown in Fig.7. The corresponding failure depth is 6 m which is 1.15 times of the average failure depth from the report (SWCB, 2011). The landslide volume by TRIGRS is 367,085 m³. The TRIGRS's result is within 15% error of the report (SWCB, 2011). These values are inputs to DEBRIS-2D for calculate the hazard zone of debris flow.

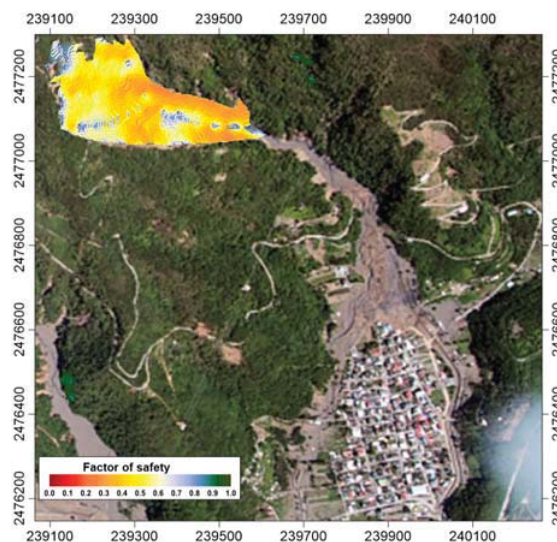


Fig.7 Factor of safety distribution due to failure depth equal to 6 m.

4.2. Simulation of Debris Flow

The yield stress was measured in the field as 256.8 dyne/cm². A time step of 0.005 seconds was set up, and the computational grid size was 2 m \times 2 m. The TRIGRS's results provide 367,085 m³ initial volume was distributed on the head of the Daniao tribe's hillslope as shown in Fig. 7.

The debris flow simulated results are shown in Fig. 8. The points P1, P2, P3 and P4 located at watershed gap, with maximal depths 12.99 m, 13.99 m, 13.09 m and 12.12 m, respectively. When the debris flow flows out of the watershed gap, at the positions P5 and P6, the maximal velocities equal 2.44 m/Sec and 1.48 m/Sec. Then debris flow begins to slow down, and the maximal flow depths reduced from 9.99 m to 7.46 m. The debris flow crossed the upstream of the Daniao tribe at the positions P7 and P10, then followed two diversion ditches on both sides Daniao tribe. Points P7 to P9 are a located on the left ditch and simulation indicated that debris flow arrived P7 at 334 Sec with maximal velocity 1.12 m/Sec and maximal flow depth 7.84 m at P8. And, the debris flow flows over Daniao tribe after crossing the P9 at 1008 Sec. The P10 to P11 is a right ditch, and simulation represented that debris flow arrived P10 at 488 Sec, which's maximal velocity reduced to 0.51 m/Sec and maximal flow depth of 6.37 m. And, the debris flow was stopped on P11 at 1200 Sec. We compared the final deposition zone for both of the simulation (colored contours) and the real event (purple line), the simulation results were nearly consistent with the field measurements.

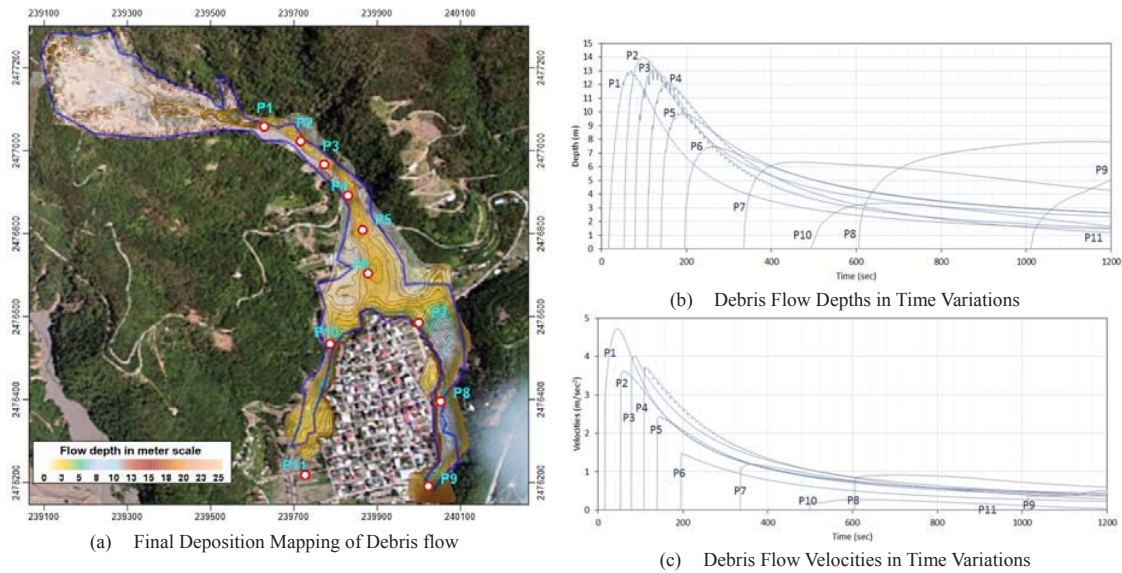


Fig.8 Final deposition mapping of debris flow and debris flow depths and velocities in time variations.

5. Conclusions

TRIGRS and DEBRIS-2D models are integrated for a rainfall infiltration inducing shallow landslide simulation. The result of the simulation is tested by Daniao tribe's landslide induced debris flow in 2009. All input parameters for the model are obtained from field measurements, no data fitting is involved. TRIGRS leads to a stability analysis of a hillslope and gives instability zone as well as failure depth. This provided the initial volumes for DEBRIS-2D in the simulation. The simulated hazard zone from DEBRIS-2D are nearly consistent to the aerial map measurements.

Acknowledgements

The authors wish to thank Soil and Water Conservation Bureau Taitung Branch for information providing.

References

- Baum, R. L., Godt, J. W., and Savage, W. Z., 2010, Estimation the timing and location of shallow rainfall-induced landslides using a model for transient, unsaturated infiltration: *Journal of Geophysical Research*, v. 115, F03013, doi:10.1029/2009JF00132.
- Chiang, S. H., Chang, K. T., Mondini, A. C., Tsai, B.W., and Chen, C. Y., 2012, Simulation of event-based landslides and debris flows at watershed level: *Geomorphology*, v. 138, p. 306–618, doi:10.1016/j.geomorph.2011.09.016.
- Casagrande, A., 1932, Research on the Atterberg limits of soils: *Public Roads*, v. 13, No. 8, p. 121-136.
- Gomes, R. A. T., Guimaraes, R. F., Carvalho Júnior, O. A., Fernandes, N. F., and Amaral Jr., E. V., 2013, Combining spatial models for shallow landslides and debris flows prediction: *Remote Sens.*, v. 5, p. 2219-2237, doi:10.3390/rs5052219.
- Iverson, R. M., 2000, Landslide triggering by rain infiltration: *Water Resour. Res.* v. 36, no. 7. p. 1897-1910, doi:10.1029/2000WR900090.
- Liu, C. N. and Wu, C. C., 2008, Mapping susceptibility of rainfall triggered shallow landslides using a probabilistic approach: *Environ Geol.*, v. 55, p. 907–915, doi:10.1007/s00254-007-1042-x.
- Liu, K. F. and Huang, M. Ch., 2006, Numerical simulation of debris flow with application on hazard area mapping: *Comput. Geosci.*, v. 10, p. 221–240, doi:10.1007/s10596-005-9020-4.
- Taitung Branch office of S.W.C.B., 2011, The planning report of conservation and investigation in the watershed of Daniao stream: Soil and Water Conservation Bureau in Taiwan, SWCB-100-005. (in Chinese)
- Wang, C., Marui, H, Furuya, G.,Watanabe, N., 2013, Two integrated models simulating dynamic process of landslide using GIS: *Landslide Sci. Practice*, v. 3, p. 389–395, doi:10.1007/978-3-642-31310-3_53.

Study of prediction methods of debris-flow peak discharge

Akihiko Ikeda^{a,*}, Takahisa Mizuyama^b, Takahiro Itoh^c

^a*Sabo & Landslide Technical Center (STC), 2-7-5 Hirakawacho, Chiyoda-ku, Tokyo 102-0093, Japan*

^b*Professor emeritus, Kyoto University, 3-14 Shinjocho, Ibaraki, Osaka 567-0884, Japan*

^c*Research and Development Center, Nippon Koei Co., Ltd., 2304 Inarihara, Tsukuba, Ibaraki 300-1259, Japan*

Abstract

Prediction of peak discharge of debris flow is one of the most important factors to mitigate debris-flow disasters. In general, peak discharge of debris flow has been either measured at the observation sites directly or estimated based on debris-flow velocity and cross-sections derived via field investigations (e.g., Mizuyama et al., 1992; Rickenmann, 1999, 2016). Based on these data, peak discharge of debris flow has been estimated from various aspects: (a) theoretical formulae, numerical simulations and laboratory flume experiments; (b) peak flood discharge using rational formulae; and (c) empirical methods based on the relationship between the peak discharge and total debris flow volume (magnitude) for many debris flow events (e.g., Takahashi, 1991; Mizuyama et al.; 1992, Ikeda et al., 2015). Peak discharge and magnitude of debris flow measured via direct observation are reliable. Although, while residual markings do not always accurately indicate riverbed and cross-sections during the debris flow, as revealed by field investigations. Also, no generally accepted prediction method of field investigation has been developed, therefore it is difficult to compare peak discharge and magnitude of debris flow among various sites. To date, to estimate peak discharge of debris flow, the focus has been on riverbed and cross-sections. The depth and length of riverbed deposits (riverbed sediment volume) between initiation zone of debris flow and downstream evaluation points cannot be used to accurately estimate magnitude. Here, we (i) improve the unified accurate prediction method of peak discharge and magnitude of debris flow via field investigations; (ii) compile and update data on numerous recent debris flows in Japan; (iii) analyze properties of peak discharge of debris flow in different occurrence type and the relationship between peak discharge and magnitude of debris flow; and (iv) offer the practical prediction method of peak discharge of debris flow.

Keywords: debris flow; peak discharge of debris flow; magnitude of debris flow; longitudinal changes of peak discharge

1. Introduction

Prediction of peak discharge of debris flow is one of the most important factors to mitigate debris-flow disasters. When designing debris-flow countermeasures, the peak discharge of debris flow determines the spillway sections of check dams and cross-sections of channel works, and is used to estimate check dam stability parameters such as overflow depth, and the impact and fluid dynamic forces. Also, data of peak discharge of debris flow is essential when planning non-structural countermeasures such as assessment of debris-flow hazard areas and warning and evacuation systems.

In general, peak discharge of debris flow has been either measured at the observation sites directly or estimated based on debris-flow velocity and cross-sections derived via field investigations (e.g., Mizuyama et al., 1992; Rickenmann, 1999, 2016). Peak discharge of debris flow has been estimated using (a) theoretical formulae based on debris flow characteristics derived via observations and field investigations, numerical simulations and laboratory flume experiments; (b) peak flood discharge using a rational formulae based on rainfall and sediment concentrations; and (c) empirical methods based on the relationship between peak discharge and total volume (magnitude) of debris flow for many debris flow events (e.g., Takahashi, 1991; Mizuyama et al., 1992; Ikeda et al., 2015). Currently, method (c) is used by the Ministry of Land, Infrastructure, Transport and Tourism (MLIT) of Japan to determine debris-flow

* Corresponding author e-mail address: ikeda@stc.or.jp

peak discharge because magnitude can be readily estimated in the field investigations; method (b) has served as a reference.

Direct measurements of peak discharge and magnitude of debris flow based on velocity and cross-section of debris flow at the observation sites are reliable, because that measured at the fixed cross-section. Although, while residual markings do not always accurately indicate riverbed and cross-sections during the debris flow and could possibly reflect the aftermath of several surges rather than a single surge of debris flow, as revealed by field investigations. Furthermore, few studies have used method (c) to consider the characteristics of catchments and debris flows when analyzing the relationship between peak discharge and magnitude of debris flow. For example, the magnitude of the landslide, sediment supply conditions, riverbed sediment volume between debris flow initiation zone and downstream evaluation points, and the occurrence type of the debris flow, or the slopes of the torrent channel and catchment. The occurrence type (initiation process) of debris flow are; i) debris flow generated by slope failure (landslide-type debris flow); ii) mobilization of riverbed deposits turning into debris flow (stream bed flow-type debris flow); and iii) debris flow generated by landslide dam-break failure (landslide dam-type debris flow). In addition, no generally accepted prediction method of field investigation has been developed, therefore it is difficult to compare peak discharge and magnitude of debris flow among various sites. To date, to estimate peak discharge and magnitude of debris flow based on field investigations, the focus has been on riverbed and cross-sections, and riverbed sediment volume between initiation zone of debris flow and downstream evaluation points.

Here, to improve the accuracy of field investigation data and accumulate that is easy to obtain, we (i) improve the unified accurate prediction method of peak discharge and magnitude of debris flow via field investigations; (ii) compile and update data on numerous recent debris flows in Japan; (iii) analyze properties of peak discharge of debris flow in different occurrence type and relationship between peak discharge and magnitude of debris flow; and (iv) offer the practical prediction method of peak discharge of debris flow.

2. Debris-flow data and analysis

2.1. Debris-flow data

Table 1 lists the debris-flow data analyzed herein; the data were derived via observation and field investigations during or after a debris flow [Mizuyama et. al. (1992), Ikeda et. al. (2015), MLIT Report, National Institute for Land and Infrastructure Management (NILIM) Disaster Investigation Report, and Disaster Committee Report].

2.2. Analysis of field investigation data

We extracted field data, including location of sites, photographs, showing cross-sections, residual markings, the depth and length, and thus sediment volume, of riverbed deposits between debris flow initiation zone and evaluation points, and riverbed gradients. We focused on flow paths that lacked tributary points to ensure continuity between the initiation zone and evaluation points. To compare different types of peak discharge of debris flow, we improved the unified accurate prediction method of cross-section (including riverbed) and debris-flow velocity (mean velocity), as shown in Figure 1 and described below:

- We identified riverbeds, including those at the bottom of check dam spillways, and solid basement rock;
- We measured water levels by reference to residual markings on both riverbanks;
- We measured cross-sections of peak discharges (A) around the above points;
- We determined mean depth of debris flow (the difference between riverbeds and water levels);
- We calculated mean width of debris flow (B) based on mean depth and cross-section;
- We measured riverbed gradient 200m upstream of evaluation points;
- We calculated mean velocity (m^3/s) using the above data and the Manning formula ($n=0.10$; as a guide of the main flow of debris flow).

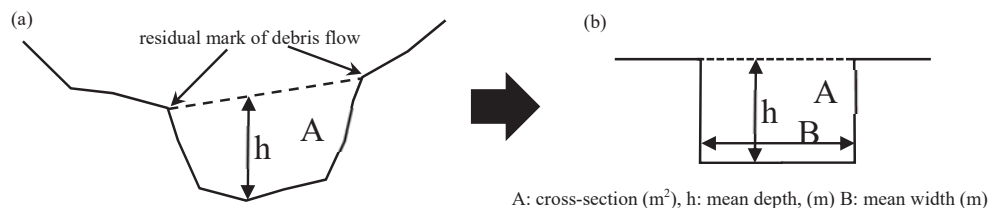


Fig. 1. (a) cross-section and mean depth of debris flow; (b) mean width of riverbed

Also, to estimate magnitude of debris flow, we extracted and measured riverbed sediment volume between debris flow initiation zone and evaluation points in view of Figure 1 based on topographic map, longitudinal profiles, photographs and cross-section of the field data, and LiDAR data before and after the debris flow, where the data exists and can be analyzed.

Table 1. Data of peak discharge, magnitude and property of each debris flow

Name	Location (Occurrence year of disaster)	Riverbed gradient	Peak Discharge Q_p (m ³ /s)	Magnitude (Total volume of Debris Flow) Q_T (m ³)	Type of Flow Property	Type of Occurrence (Initiation process)	Geological Condition	Analysis method	Source
Ishihara Creek	Yamaguchi, JAPAN (2009)	0.137	195	57,290	Granular	Landslide/Stream bed Flow-type	Granite	FI	NILIM Report
Wada River	Yamaguchi, JAPAN (2009)	0.251	336	3,427	Granular	Landslide/Stream bed Flow-type	Granite	FI	NILIM Report
		0.342	231	1,340					
Hiragi Creek	Yamaguchi, JAPAN (2009)	0.268	78	11,388	Granular	Landslide/Stream bed Flow-type	Granite	FI	NILIM Report
Matano River	Ehime, JAPAN (2004)	0.270	263	7,787	Granular	Landslide/Stream bed Flow-type	Metamorphic Sedimentary rock	FI	NILIM Report
Nishishirahama River	Ehime, JAPAN (2004)	0.207	21	6,149	Granular	Landslide/Stream bed Flow-type	Metamorphic Sedimentary rock	FI	NILIM Report
Higashikusuzaki River	Ehime, JAPAN (2004)	0.179	178	5,676	Granular	Landslide/Stream bed Flow-type	Metamorphic Sedimentary rock	FI	NILIM Report
		0.118	429	9,653					
Kusuzaki River	Ehime, JAPAN (2004)	0.332	90	409	Granular	Landslide/Stream bed Flow-type	Metamorphic Sedimentary rock	FI	NILIM Report
		0.469	28	199					
		0.357	56	757					
Moriyukihtani River	Kagawa, JAPAN (2004)	0.226	260	23,436	Granular	Landslide/Stream bed Flow-type	Metamorphic Sedimentary rock	FI	NILIM Report
Gamaharasawa Creek	Hime River, Nagano/Niigata, JAPAN (1996)	0.319	661	54,333	Granular	Large scale landslide	Sedimentary Rock	M	Committee REPORT, 1997
Atsumari River	Kumamoto, JAPAN (2003)	0.160	5037	296,173	Granular	Large scale landslide	Volcanic Rock	FI	Committee REPORT, 2004
Harihara River	Kagoshima, JAPAN (1997)	0.197	7705	322,812	Granular	Large scale landslide	Volcanic Rock	FI	Committee REPORT, 1998
Funaiishi River A B	Kagoshima, JAPAN (2007)	0.378	1526	21,915	Muddy	Large scale landslide	Granite	FI	NILIM Report
		0.283	5066	40,419					
Takesawa Creek	Mt.Fuji, JAPAN (2000)	0.290	403	13,728	Muddy	Stream bed Flow-type	Volcanic Rock	FI	Hanaoka, 2001
		0.273	239	18,035					
		0.194	325	33,229					
		0.195	190	32,378					
Nashizawa Creek	Kiso River, Nagano, JAPAN (2014)	0.061	543	635,376	Granular	Landslide/Stream bed Flow-type	Granite	FI	Hiramatsu, 2014 Kusano, 2016
		0.061	735	861,117					
Stava River	Trentino Alto Adige, ITALY (1985)	0.163	5341	597,346	Muddy	Dam Failure	Sedimentary Rock	FI	Muramoto, 1986
Nakakura River	Hiroshima, JAPAN (1999)	0.250	271	9,619	Granular	Landslide/Stream bed Flow-type	Granite	FI	NILIM Report
Omoji River	Hiroshima, JAPAN (1999)	0.285	110	3,541	Granular	Landslide/Stream bed Flow-type	Granite	FI	NILIM Report
Yasu River	Hiroshima, JAPAN (1999)	0.213	51	5,974	Granular	Landslide-type	Granite	FI	NILIM Report
Sarutaki River	Hiroshima, JAPAN (1999)	0.140	67	12,066	Granular	Landslide/Stream bed Flow-type	Granite	FI	NILIM Report
Kono River	Hiroshima, JAPAN (1999)	0.123	199	25,522	Granular	Landslide/Stream bed Flow-type	Granite	FI	NILIM Report
Doogahara River	Hiroshima, JAPAN (1999)	0.454	101	2,951	Granular	Landslide-type	Granite	FI	NILIM Report
Shimogasaki River	Hiroshima, JAPAN (1999)	0.666	209	6,363	Granular	Landslide/Stream bed Flow-type	Granite	FI	NILIM Report
Name River	Kiso River, Nagano, JAPAN	0.178	83-1556	23,900-110,000	Granular	Landslide/Stream bed Flow- type/Landslide dam failure	Granite	M	Ikeda, 2003
			737	28,519					
Nojiri River	Sakurajima Island, JAPAN	0.185	1-827	296-994,718	Muddy	Stream bed Flow-type	Volcanic Rock	M	Mizuyama, 1992
Mochiki River	Sakurajima Island, JAPAN	0.040	15.4-122.4	1,871-40,369	Muddy	Stream bed Flow-type	Volcanic Rock	M	Mizuyama, 1992
Harumatsu River	Sakurajima Island, JAPAN	0.040	5	2,165	Muddy	Stream bed Flow-type	Volcanic Rock	M	Mizuyama, 1992
Furusato No.1 River	Sakurajima Island, JAPAN	0.149	6.8-59.9	3,232-7,358	Muddy	Stream bed Flow-type	Volcanic Rock	M	Mizuyama, 1992
Arimura River	Sakurajima Island, JAPAN	0.020	19.6-335.3	9,832-70,145	Muddy	Stream bed Flow-type	Volcanic Rock	M	Mizuyama, 1992
Kurokami River	Sakurajima Island, JAPAN	0.015	8.9	9,614	Muddy	Stream bed Flow-type	Volcanic Rock	M	Mizuyama, 1992
Kamikamihorisawa Creek	Mt.Yakedake, Nagano, JAPAN	0.125	15.1-100	224.6-6,062	Granular	Stream bed Flow-type	Volcanic Rock	M	Mizuyama, 1992
Mt.Usuzan	Mt.Usuzan, Hokkaido, JAPAN	0.090	54.5-98.2	3,850-3,927	Muddy	Stream bed Flow-type	Volcanic Rock	M	Mizuyama, 1992
Mt.Tokachidake	Mt.Tokachidake, Hokkaido, JAPAN	—	1272	13,877,780	Muddy	Stream bed Flow-type	Volcanic Rock	FI	Mizuyama, 1992
Jiangjia Creek	Chang Jiāng River, Yunnan, CHINA	—	50.4-1142	7,826-1,120,495	Muddy	Stream bed Flow-type	Sedimentary Rock	M	Mizuyama, 1992
Hunshui Gully	Chang Jiāng River, Yunnan, CHINA	—	3.9-326.1	4,425-294,022	Muddy	Stream bed Flow-type	Granite	M	Mizuyama, 1992
Nojiri No.8 Sabo Dam	Sakurajima Island, JAPAN	0.128	25.3-233.4	9,579-129,619	Muddy	Stream bed Flow-type	Volcanic Rock	M	MLIT Report, 2015
Arimura No.3 Sabo Dam	Sakurajima Island, JAPAN	0.065	117	50,389	Muddy	Stream bed Flow-type	Volcanic Rock	M	MLIT Report, 2015
Mizunashi No.1 Sabo Dam	Mt.Uzen, Nagasaki, JAPAN	0.128	8-420	14,000-450,000	Muddy	Stream bed Flow-type	Volcanic Rock	M	MLIT Report, 2015
Alberta Creek	Alberta Province, CANADA	< 0.175	87.2-580.7	9,550-43,915	Muddy	Stream bed Flow-type	Sedimentary Rock	M	Mizuyama, 1992

*) Analysis method: FI: Field Investigation, M: Monitoring

3. Longitudinal changes in the debris-flow peak discharge of different occurrence types

Peak discharge of debris flow to vary longitudinally with changes in topographical features such as river width, riverbed gradient and meander. We used the field investigation data of Figure 1 to define initiation zones and the occurrence types of debris flow. We then tracked peak discharge debris flow longitudinally for 1) large-scale landslide flow-type; 2) stream bed flow-type; and 3) landslide/stream bed flow-type. We focused on data from Obaradani creek [case 1]; Fig. 2(a)], Takesawa creek [case 2]; Fig. 2(b)], and Nashizawa creek [case 3]; Fig. 2(c)]. Obaradani creek located in the left tributary of the Tostukawa River of Nara Prefecture, is 1.04 km in length, with an average riverbed gradient of 14.7°, and catchment area of 0.98 km². The base rock is formed by shale with blocks of chert and greenstone, and alternation of sandstone as an accretionary wedge. The source of debris flow was a large-scale landslide with a volume of approximately 2,500,000 m³ of which 1,300,000 m³ of sediment formed a debris flow (Ikeda et al., 2014). Takesawa creek located in Mt. Fuji in Shizuoka Prefecture, is 8.50 km in length, with an average riverbed gradient of 11.3°, and catchment area of 4.08 km². The base rock is formed by basaltic lava sheets and alternation of pyroclastic rock and lava. The source of debris flow was a riverbed deposit at an elevation of about 2,500 m where the boundary of lava sheet and pyroclastic rock. The debris flow continued for about 1,000 m (Hanaoka et al., 2001). Nashizawa creek located in the left tributary of the Kiso River of Nagano Prefecture, is 3.60 km in length, with an average riverbed gradient of 18.4°, and catchment area of 3.29 km². The base rock is formed by granite and granodiorite. The source of debris flow was an upstream landslide/riverbed deposit. Four check dams and one steel open check dam (the most downstream dam) have been installed (Hiramatsu et al., 2014; Kusano et al., 2016).

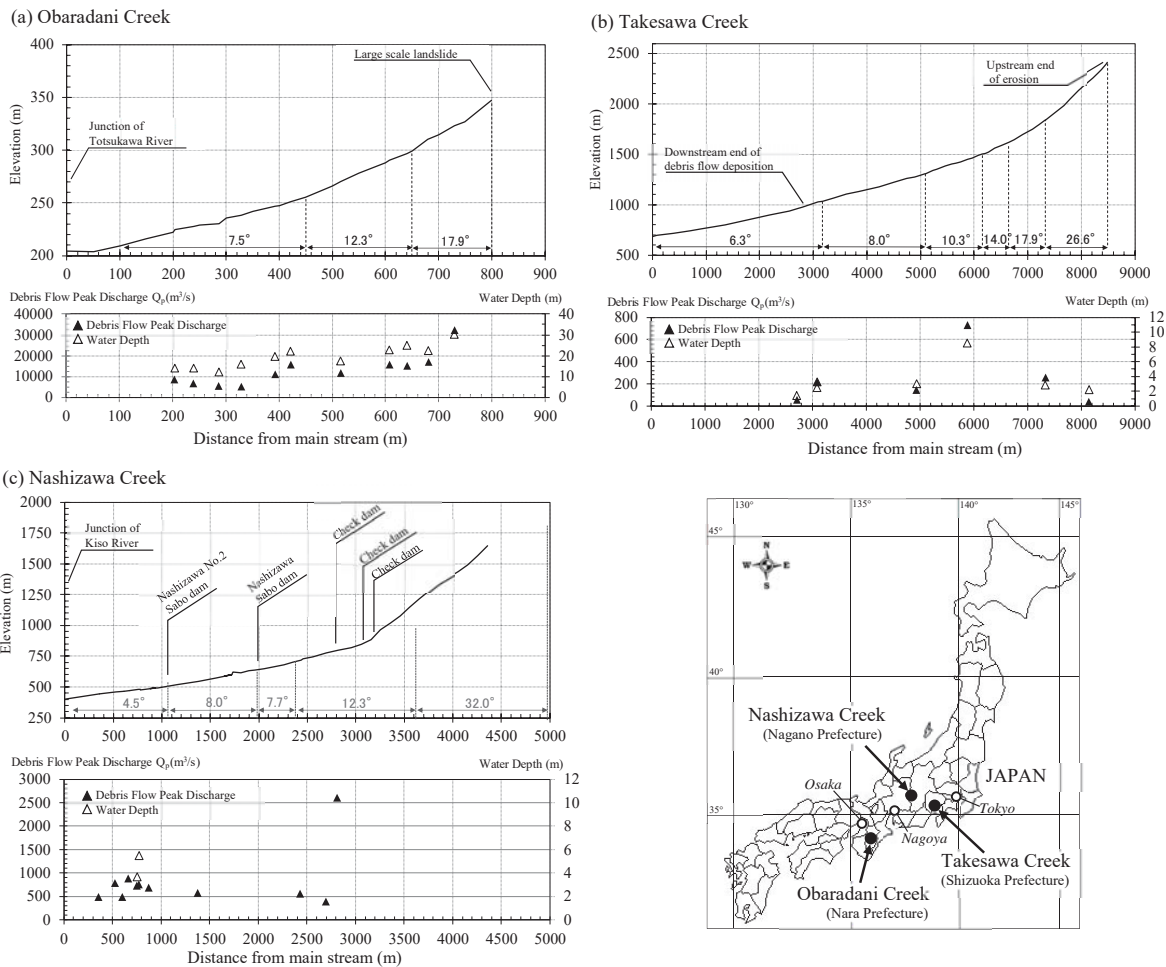


Fig. 2. Location and profiles of (a) Obaradani creek; (b) Takesawa creek; (c) Nashizawa creek

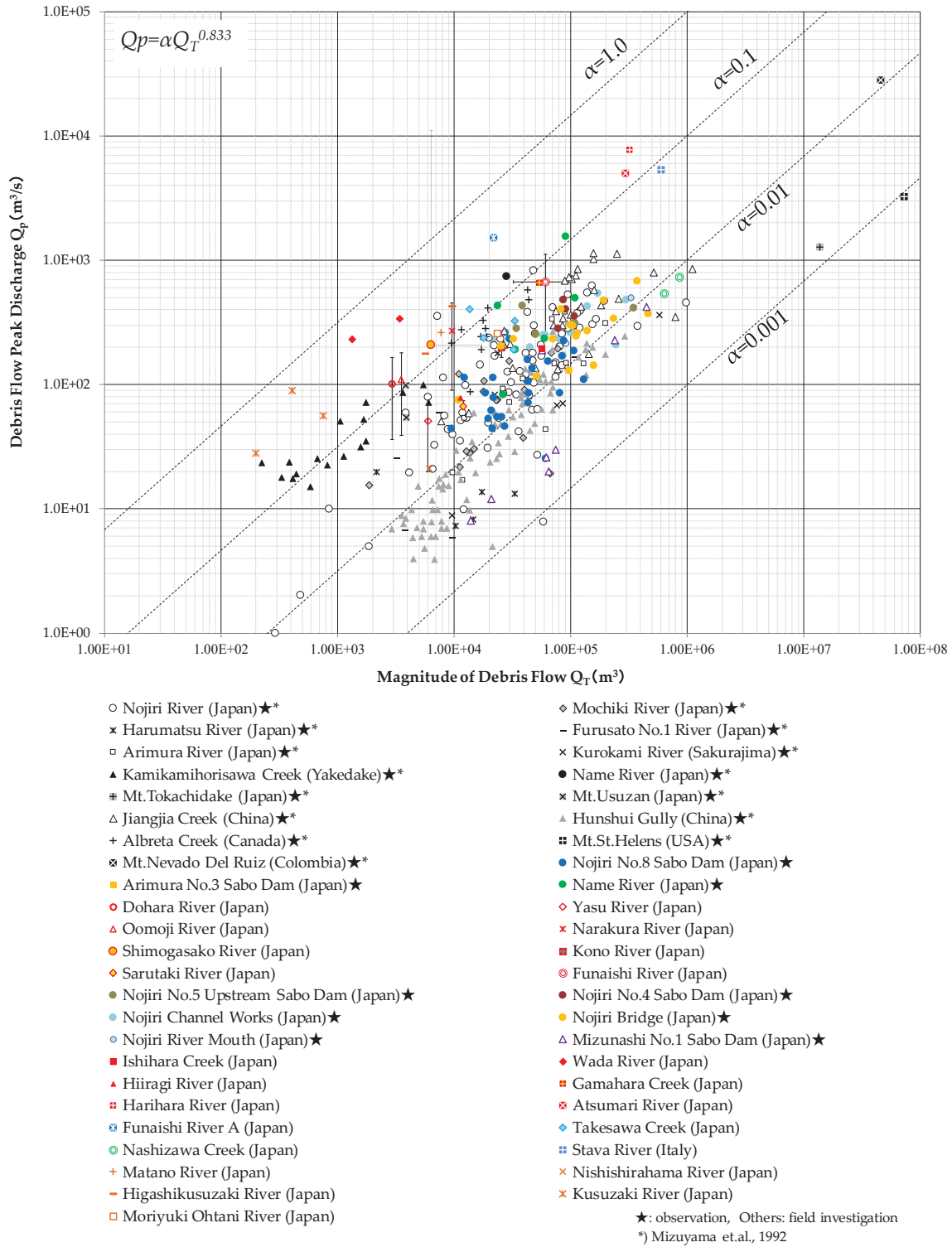


Fig. 3. Relationship between peak discharge and magnitude of debris flow

The peak discharge at the foot of the large-scale landslide in Obaradani creek was approximately 33,000 m³/s and gradually decreased as flow progressed toward the Totsukawa River. On the other hand, in Takesawa creek, the debris flow source was a riverbed deposit; the peak discharge increased gradually from the source to an elevation of about 1,450 m (approximately 730m³/s) and then decreased gradually to an elevation of about 1,000 m. In Nashizawa creek, at the upstream end of the debris flow caused by a landslide and riverbed deposit, the debris-flow peak discharge was approximately 2,600 m³/s, and the discharge across the entire section was similar (approximately 500–1,000 m³/s). Thus, longitudinal changes in peak discharge depend on the supply amount from the source and the type of occurrence.

4. Relationship between peak discharge and magnitude of debris flow

Figure 3 shows the relationship between peak discharge and magnitude of debris flow shown in Table 1. The line indicates the quasi-theoretical line relationship represented by the following equation:

$$Q_p = \alpha \cdot Q_T^{0.833} \quad (1)$$

where Q_p is the debris-flow peak discharge [m³/s], Q_T is the magnitude [m³], and $\alpha = 1.0-0.001$. The data shown in Figure 3 varies widely over the range of $\alpha = 0.1-0.001$, principally in the interval $\alpha = 0.1-0.01$. Monitoring data obtained near the initiation zone of debris flows from Kamikamihorisawa creek, the Nojiri River, the Mizunashi River, Jiangjia creek, the Hunshui gully and Alberta creek approximate the line (1). The α values tend to approximate $\alpha = 0.01$ if the debris flows are muddy (Nojiri River, Mizunashi River, Jiangjia creek and Hunshui gully) but approximate $\alpha = 0.1$ if the flows are granular (Kamikamihorisawa creek, Name River). Also, field investigation data approximate line (1), although the debris-flow peak discharges tend to be larger for events of similar magnitude, which is especially the case for the 2004 disasters of Hiroshima and Ehime, field investigation data approximates line (1). Relating to geological conditions such as volcanic and granite zone that account for the whole has no clear tendency of the α value, while in Kamikamihorisawa creek (volcanic zone) and Name River (granite zone) are both approximate $\alpha = 0.1$, it seems that type of debris flow property is dominant than geological conditions. Focus on slopes of torrent channel and catchment area, the α values tend to approximate $\alpha = 0.1$ if the slope is steep (more than 10°) or the catchment area is relatively small but in the interval $\alpha = 0.1-0.01$ if the slope is gentle (3°–10°) or the catchment area is relatively wide. In the upper/lower part of the same catchment (Nojiri River, Kamikamihori creek, Name River, Takesawa creek, and Nashizawa creek) that indicates the same α value in each catchment. The α values tend to in the interval $\alpha = 1.0-0.01$ if the occurrence type of debris flow is landslide/stream bed flow type (Nashizawa creek, Name River) but in the interval $\alpha = 0.1-0.001$ if the occurrence type of debris flow is stream bed flow type (Nojiri River, Kamikamihorisawa creek), this indicates the peak discharge of debris flow increase due to impact of landslide.

5. Conclusions

In conclusion, we have improved the unified accurate prediction method of peak discharge and magnitude of debris flow for field investigation, and updated (and enhanced the complication of) recent debris flow data from Japan. Depending on the occurrence type (initiation process) of debris flow, longitudinal changes in peak discharge depend on the supply amount of the source and type of occurrence. We confirmed that the relationships between peak discharge and magnitude of debris flow, and the α values of equation (1) depended heavily on catchment characteristics (sediment supply condition; riverbed sediment volume between debris flow initiation zone and evaluation points), type of debris flow property, and occurrence type of debris flow. More accumulating field investigations and analyzing along with observation data are required to validate our findings, that determining the α values of equation (1) and Manning's coefficient of roughness that determining the flow velocity to estimate peak discharge of debris flow.

Acknowledgements

Authors should be thankful for Ministry of Land, Infrastructure, Transport and Tourism (MLIT) and National Institute for Land and Infrastructure Management (NILIM) for providing monitoring and field investigation data and useful advice.

References

- Atsumari River Debris Flow Disaster Investigation Committee, 2004, Atsumari River Debris Flow Disaster Investigation Report, 84 p (In Japanese).
- Gamaharasawa Creek Debris Flow Disaster Investigation Committee, 1997, Gamaharasawa Creek Debris Flow Disaster Investigation Report, 70 p (In Japanese).
- Hanaoka, M., Tokita, K., Ikeda, A., and Suzuki, T., 2001, Property of debris flow occurred in the volcanic area –Case in Takesawa creek, Ashidori River, Mt. Fuji, on Dec. 21, 2001–: Outline collection of Erosion Control Engineering, p. 82–83 (In Japanese).
- Harihara River Debris Flow Disaster Investigation Committee, 1998, Harihara River Debris Flow Disaster Investigation Report, 70 p (In Japanese).
- Hiramatsu, S., Fukuyama, T., Yamada, T., Ohsaka, O., Nakatani, K., Matsumoto, N., Fujimura, N., Kato, N., Shimada, T., Kubo T., Matsuo, S., Nishio, Y., and Yoshino, K., 2014: Disaster report on the debris flow occurred on 9 July 2014 Nagiso, Nagano prefecture: Journal of the Japan Society of Erosion Control Engineering, v. 67, no. 4, p. 38–48 (In Japanese with English abstract)
- Hungr, O., Morgan, G.C., and Kellershals, R., 1984, Quantitative analysis of debris torrent hazards for design of remedial measures: Can. Geotechnical J., v. 21, p. 663–677.
- Ikeda, A., Monma, N., Horiuchi, S., and Yamada, T., 1998, Debris Flows Generated at Kitamata Valley of the Name River: Journal of the Japan Society of Erosion Control Engineering, v. 51, no. 2, p. 31–38 (In Japanese with English abstract).
- Ikeda, A., and Hara, Y., 2003, Flow properties of debris flows on the Kitamata Valley of the Name River, Japan: Debris-Flow Hazard Mitigation: Mechanics, Prediction, and Assessment, Rickenmann & Chen (eds), p. 851–862.
- Ikeda, A., Mizuyama, T., Uchida, T., and Ishizuka, T., 2015, Study of Factors Necessary for the Prediction of Debris Flow Peak Discharge: Proc. of 6th International Conference on Debris-Flow Hazard Mitigation: Mechanics, Prediction and Assessment (DFHM6).
- Ikeda, A., Mizuyama, T., Uchida, T., and Mizuno, H., 2017, Study of Property of Debris Flow Peak Discharge: Outline collection of Erosion Control Engineering, p. 112–113 (In Japanese).
- Ishikawa, Y., 1985, Debris Flows in the Name River: Journal of the Japan Society of Erosion Control Engineering, v. 37, no. 5, p. 24–29 (In Japanese).
- Knapp, R.T., 1951, Design of Channel Curves for Supercritical Flow: Trans, ASCE, v. 116, p. 296–301.
- Kusano, M., Kashino, M., Nishi, Y., Ikeshima, T., Nagarekawa, Y., Matsuda, S., Itoh, T., Nakayama, T., Kato, M., and Mizuyama, T., 2016, Prediction method of debris flow peak discharge using vibration sensor: Outline collection of Erosion Control Engineering, p. B90–B91 (In Japanese).
- Matsumoto Sabo Work Office, Ministry of Construction, 1979, Debris Flow Investigation of Mt.Yakedake and Ura River Part IV: p. 7–86 (In Japanese).
- Mizuno, H., 2004, Experimental study on an estimating method for velocity of debris flow in bending curves, Journal of the Japan Society of Erosion Control Engineering, 57(4), p. 56–59 (In Japanese with English abstract).
- Mizuno, H., et. al., 2003, The debris flow disasters caused by localized rainfall of seasonal rain front in Kyushu region in July, 2003 (prompt report): Journal of the Japan Society of Erosion Control Engineering, v. 56, no. 3, p. 36–43 (In Japanese with English abstract).
- Mizuyama, T., Kobashi, S., and Ou, G., 1992, Prediction of Debris Flow Peak Discharge: Proc. Int. Symp. INTERPRAEVENT, Bern, Switzerland, Bd. 4, p. 99–108.
- Mizuyama, T., and Uehara, S., 1984, Observed Data of the Depth and Velocity of Debris Flows: Journal of the Japan Society of Erosion Control Engineering, v. 37, no. 4, p. 23–26 (In Japanese).
- Muramoto, Y., Uno, T., and Takahashi, T., 1986, Investigation of the Collapse of the Tailings Dam at Stava in the Northern Italy: Scientific research expenses report of Ministry of Education, No.B–60–4, 64 p (In Japanese with English abstract).
- National Institute for Land and Infrastructure Management (NILIM), Ministry of Land, Infrastructure and Transport (MLIT), 2016, Manual of Technical Standard for establishing Sabo master plan for debris flow and driftwood: TECHNICAL NOTE of National Institute for Land and Infrastructure Management, No.904, 77 p (In Japanese).
- National Institute for Land and Infrastructure Management (NILIM), Ministry of Land, Infrastructure and Transport (MLIT), 1999–2009, Disaster Investigation Report of Debris Flow Disaster (field investigation data file).
- Okuda, S., Suwa, H., Okunishi, K., Nakano, M., and Yokoyama, K., 1977, Synthetic observation on debris flow Part 3: Annuals. Disaster Prevention Res. Inst., Kyoto Univ., No.20B-1, p. 237–263 (In Japanese with English abstract).
- Osumi River National Road Office, Ministry of Land, Infrastructure, Transport and Tourism (MLIT), Japan, 2015, Report of debris flow runoff analysis occurred in Sakurajima Island (In Japanese).
- Ou, G., Kobashi, S., and Mizuyama, T., 1991, Prediction of Debris Flow Peak Discharge: Journal of the Japan Society of Erosion Control Engineering, v. 44, no. 4, p. 24–29 (In Japanese with English abstract).
- Rickenmann, D., 1999, Empirical Relationships for Debris Flow: Natural Hazards 19, p. 47–77.
- Rickenmann, D., 2016, Methods for the Quantitative Assessment of Channel Processes in Torrents (Steep Streams): IAHR MONOGRAPH, 138 p.
- Suwa, H., and Okunishi, K., 1990, Motion, Debris Size and Scale of Debris Flows in a valley on Mount Yakedake Japan: Annuals. Disaster Prevention Res. Inst., Kyoto Univ., No.33B-1, p. 191–203 (In Japanese with English abstract).
- Takahashi, T., 1977, A Mechanism of Occurrence of Mud-Debris Flows and their Characteristics in Motion: Annuals. Disaster Prevention Res. Inst., Kyoto Univ., No.20B-2, p. 405–435 (In Japanese with English abstract).
- Takezawa, N., Uchida, T., Suzuki, R., and Tamura, K., 2009, Estimation of debris flow induced by a deep-seated landslide at the Funaishi river basin: Kagoshima prefecture in Japan, Journal of the Japan Society of Erosion Control Engineering, v. 62, no. 2, p. 21–28 (In Japanese with English abstract).
- Uehara, S., and Mizuyama, T., 1984, Peak Debris Flow Discharge Data: Journal of the Japan Society of Erosion Control Engineering, v. 37, no. 3, p. 23–24 (In Japanese).

Debris-flow hazard assessments – a practitioner’s view

Matthias Jakob

BGC Engineering, 500 – 980 Howe Street, Vancouver V6Z 0C8, Canada

Abstract

Substantial advances have been made in various aspects of debris-flow hazard and risk assessments over the past decade. These include sophisticated ways to date previous events, runout models including multi-phase flows and debris entrainment options, and applications of extreme value statistics to assemble frequency-magnitude analyses. Finally, quantitative risk management (QRM) has emerged as the most rational and defensible method to assess debris-flow risk and optimize mitigation efforts. Pertinent questions, of course, have remained the same: How often, how big, how fast, how deep, how intense, how far and how bad? Similarly, while major life loss attributable to debris flows can often, but not always, be avoided in developed nations, debris flows remain one of the principal geophysical killers in mountainous terrains. Substantial differences persist between nations in hazard or risk management. Some rely on a design magnitude associated with a specific return period, others use relationships between intensity and frequency, and some allow for, but do not mandate, in-depth quantitative risk assessments. The range in return periods considered in hazard and risk assessments varies over two orders of magnitude from 1:100 to 1:10,000. In many nations, access to funding and lack of at least regional prioritization provides the biggest obstacles to widespread safeguarding against debris flows. Two factors conspire to challenge future generations of debris flow researchers, practitioners and decision makers: Population growth and climate change. The former will invariably invite continued development in debris-flow prone areas, especially fans, floodplains and terraces subject to lahars or landslide/moraine dam/glacial outburst floods which, at times, assume debris-flow characteristics. As far as debris flows are concerned, climate change is manifesting itself increasingly by augmenting hydroclimatic extremes, especially a several-fold increase in the frequency of short-duration high-intensity rainfall that may soon exceed historical precedents. While researchers will undoubtedly finesse future remote sensing, dating and runout techniques and models and bring some of those to a degree of maturity, the practitioners will need to focus on translating those advances into practical cost-efficient tools and closely collaborate with clients to integrate those tools into meaningful long-term debris-flow risk management. Future debris flow disasters will not occur due to a lack of quantitative methods, but likely due to the lack of recognition, wilful ignorance of debris-flow hazards, lack of enforcement of risk management policies, or simply a lack of means to mitigate against known debris flow risks.

Keywords: debris flow; debris flood; hazard assessment; risk assessment;

1. Introduction

Adding some 70 million humans to Earth every year leaves a mark not only on ever-expanding urban centers and their suburban fringes as well as development of wildland interface, but a proportion of that growth will spill directly into mountainous terrain. Mountains consist of peaks and valleys, plateaus and ridges, ice-clad or bone-dry, covered with dense vegetation and entirely arid. Irrespective of their individual geomorphological or hydrological setting, water, however much or little there may be, drains from zero order barely noticeable depressions to higher order streams until those debouche onto floodplains or peneplains at the piedmont. If sufficiently steep and if loose, erodible sediment is available for transport, debris flows will form whenever sufficient rainfall exceeds some hydroclimatic threshold. With these defining criteria there are likely millions of debris-flow prone streams worldwide. Traditionally,

* Corresponding author e-mail address: msturzenegger@bgcengineering.ca

people have built homes and infrastructures on fans because in mountainous terrain these can be the areas with the shallowest gradients. The threat of debris flow may be recognized, but there can be a perception that riverine floods are the more damaging event because observable bank full flows may occur frequently and major overtopping of the flow channel at higher return periods may have been witnessed. Debris flows, in contrast, may occur at return periods of century scale, and thus outside the typical memory of residents or infrastructure owners. The longer the periods between events, the less obvious the signs of past destruction and geomorphic change. On top of that, the human trait of delusional thinking that such events are anomalous has led to continued urbanization of fans and cones in areas with high relief. None of this is new, and nations such as Japan, European countries adjoining the Alps, countries straddling the North and South American cordilleras, and other nations have developed systems to map, analyze and assess hazard and risk, and mitigate to the standard of the day. Hundreds of thousands of mitigation works have been constructed worldwide, ranging from make-shift log-crib structures, or masonry dams built entirely by hand to impressive mega-structures constructed with concrete capable of holding millions of cubic meters of sediment.

This contribution is not meant as an exhaustive review of debris-flow hazard assessments of which hundreds have been reported in the literature. Summaries of hazard assessments have been provided elsewhere (Jakob, 2005; Rickenmann, 2016; Chae et al., 2017). Rather, a few cases are highlighted to demonstrate the debris-flow risk assessments that have had a demonstrable effect of reducing risk to populations living amongst debris-flow hazards.

There is a bewildering plethora of papers that are being generated by the scientific community every year. An attempt was made in 2005 by Jakob and Hungr to summarize the state of knowledge through an edit volume of debris flows and related phenomena. Now, 13 years later, this volume hardly does justice to the key advances. This paper cannot address all significant new findings due to lack of space and the admission by this author of not being able to keep up with all relevant advances in debris flow science. Hence, personal bias is unavoidable.

2. Hazard Assessments

Debris-flow hazard assessments form the backbone of any plans to mitigate, if accompanied by a risk assessment or not. In simple speak, if the hazard assessment is faulty, so will be the risk assessment and, ultimately, the mitigation design to reduce hazard or risk. Of course, this can go both ways: An overestimated hazard will lead to an overestimated risk, which by extension results in overdesign of the mitigation works and the associated burden on funding agencies and/or the tax payer.

What does a thorough hazard assessment entail? The list is long but is separated, by and large, by two principal aspects: 1) assessment of the frequency and magnitude of events, and 2) assessment of the intensity of the respective debris-flow scenario. Breakthroughs have been made in the assessment of frequency analyses with the refinement of, for example, dendrochronological methods (Ballesteros-Canovas et al., 2015) and radiocarbon dating methods (Chiverrell and Jakob, 2013; Sewell et al., 2015). Magnitude analyses have been greatly enhanced and refined through empirical methods (e.g. Gartner et al., 2014) and numerical modeling that may allow event magnitudes to be reasonably estimated from known source area volumes and user-specified and/or theoretical entrainment rates (e.g. McDougall and Hungr, 2005; Iverson, 2012). Both methods can and ought to be used complementarily to decipher the “true” frequency-magnitude relationships. Unfortunately, it is literally impossible to characterize every known event, however, the statistical science has produced methods that are suited for a magnitude-limited truncation of datasets. Peak over threshold (POT) analyses can be applied to this problem set and statistical distributions such as the Generalized Pareto Distribution (GPD) are fit for application where fragmentary data exist but where one can be reasonably confident to have captured the biggest events (Jakob et al., 2017).

The degree of sophistication that is being applied to such hazard assessments differs widely from nation to nation, but also within nations with poorly developed or missing guidelines, and is strongly dependent on the practitioner’s background knowledge and that of his or her team. Many such assessments are conducted by consulting firms who may have to write competitive proposals. If all or most methods available to the practitioners are proposed, the costs of such studies may become non-competitive and a lower bid may win the job. This competitive process may put pressure on firms to win jobs with the lowest reasonable effort possible. But what does that mean and is it truly a problem?

Spectacular failures of debris-flow mitigation works are rarely reported in the scientific literature, presumably for reasons of embarrassment or potential ensuing legal action. Particularly in more litigative societies, legal action seems almost predictable and a thorough forensic analysis of a debris-flow mitigation system failure can be obscured through confidentiality clauses. This is lamentable, as the greatest advances in debris-flow mitigation may derive from an

analysis of past failures. In this sense, it is worthwhile to examine a few notable failure modes which have recently been summarized by Moase (2018).

2.1. Regional debris-flow studies

Most districts, states, provinces or even nations have limited funds for geohazard mitigation. This necessitates the allocation of existing funds to those sites with the highest risk potential. In reality, funds for studies and mitigation often get allocated because of particularly damaging events that result in focused public, media and political attention. Those sites, however, may not necessarily be the ones with highest risk. High risk sites are those that occur frequently and with a high economic or life loss potential. Only in the most affluent societies with long histories of debris-flow hazard recognition, quantification and management is it possible to systematically evaluate hazards and risks and prioritize mitigation accordingly (Sturzenegger et al., 2019, this volume, Kang and Lee, 2018). Even if possible, detailed fan and watershed studies for entire nations such as Switzerland, Austria or Japan take a very long time and hazard potential changes with land use, extreme events such as major landslides or volcanic eruptions and direct or indirect consequences of climate change. Therefore, it is advisable to devise methods in which debris-flow susceptibility can be adequately approximated and be readily compared to each other. Hazard frequencies can be assessed in classes with class boundaries being systematically defined and air photograph analysis allowing class designation. Debris-flow magnitude can be gleaned from regional debris-flow susceptibility models such as the empirically based Flow-R software. Flow-R model ("Flow-R" refers to "Flow path assessment of gravitational hazards at a Regional scale") was developed by Horton et al. (2008, 2013). It allows identification, at a preliminary level of detail, of potential debris flow or debris flood hazard and modeling of their runout susceptibility over large study areas. Unlike other numerical models suitable to simulate debris flows such as RAMMS, FLO-2D, DAN-3D and D-Claw, which may require substantial computer runtimes, depending on the model grid size and modelling domain, Flow-R runs very quickly and can be run on numerous debris-flow susceptible creeks at the same time. Sturzenegger et al. (2019, this volume), demonstrate the use of the model for a debris-flow risk-based prioritization study in British Columbia. Once magnitude and frequency have been approximated many creeks, the consequences can be evaluated either for fixed assets (homes, industries, linear infrastructure), or people in transit (on roads, by rail). An example of such regional prioritization has been provided by Holm et al. (2016, 2017). In this sense, debris-flow hazards and risks may not be estimated with any precision and susceptibility maps should not be interpreted as hazard maps. The importance lies in a systematic, replicable and transparent comparison of risks by using the same methodology for all sites investigated. Such prioritization studies cannot replace detailed fan hazard and risk assessments that would form the basis for mitigation design.

Future advances in this science could include a linkage between regional frequency-magnitude analysis and susceptibility models. This would allow a higher granularity in regional studies that have design frequency caps. Such added granularity would glean more confidence in risk quantifications as, often, the highest risk locations are those where debris-flow impact leads to life loss at the lowest return period (highest frequency).

2.2. Dating past debris-flow events

In terms of dating past debris-flow events, practitioners have a substantial variety of methods at their fingertips, and environmental conditions and budget are the key constraints. One of the most deeply researched methods that is also one of the most useful is dendrochronology (Stoffel and Bollschweiler, 2008; Stoffel, 2010; Stoffel et al., 2010; Schneuwly-Bollschweiler et al., 2012; Ballesteros-Canovas et al., 2015). Some key refinements are still outstanding, such as estimating the individual deposit volumes and intra-seasonal dating precision (Stoffel, pers. comm., 2018). Dendrochronological investigations are also used increasingly to identify possible climate change signals (van den Heuvel et al., 2016). Obviously, one does need trees on the fan or along the channel, and preferably old ones to obtain a reasonable record. Relative dating methods such as lichenometry (Innes, 1983; Andre, 1990, Rapp and Nyberg, 1981; Bull, 2018) provide a decent approximation, but without calibration of the lichen growth curve, translation into areas affected by debris flows and their respective date hampers establishment of detailed frequency-magnitude relationships. Radiocarbon dating (i.e. Chiverell and Jakob, 2013) remains a profoundly successful method and can be used not only to date debris flows, but by measuring the thickness of dated deposits allows approximations of debris-flow volumes.

2.3. Debris-flow magnitude analysis

Empirical relationships between flow volumes and inundated areas are highly useful (e.g. Griswold and Iverson, 2008), though local coefficients need to be established rather than blindly adopting reported ones, as was found in several of the author's and his colleagues unpublished studies. More work is needed here to differentiate hybrid events between coarse granular and fine-grained highly mobile events.

One aspect that is still rather challenging is to establish frequency-magnitude methods on a regional scale. For example, pipelines or other above-ground or buried linear infrastructure are still being built worldwide, some of which cross mountainous terrain. Oil and gas pipeline owners have a particularly low tolerance to pipeline rupture. Moreover, they wish to know the chance of pipeline impact for a range of return periods; in other words, a frequency-magnitude analysis is needed for tens if not hundreds of fans that their pipeline may cross. Detailed dendrogeomorphic studies, radiocarbon dating or even detailed mapping of previous deposits is very time and cost intensive and typically is not funded. Jakob et al. (2016) provided a simple, yet effective method to estimate frequency-magnitude relationships (Figure 1). However, this method is not particularly applicable if a high degree of precision is warranted. Using a series of well-researched debris-flow frequency-magnitude relationships, Jakob et al. (2016) were able to show that fan area or fan volume can well predict these relationships with quantifiable error. The underlying rationale is that the fan, unless truncated by a higher order stream, or obfuscated by a rapidly aggrading floodplain, reflects the sum of all fan-forming events. This method is particularly helpful in areas with late Pleistocene glaciation which means that the fan area or volume integrates all debris-flow events that occurred since deglaciation.

Fan areas, are very simple to measure in Google Earth or from orthorectified air photographs. However, caveats must be identified, such as abnormally large fans for their respective watersheds that may be attributable to previous large landslides that have now been overprinted by debris flows. In such cases, the method above may result in overly conservative results. Alternatively, river erosion at the toe of a fan may result in a fan area that is small in relation to the frequency-magnitude of debris flows in the upstream catchment.

The special case of debris-flow magnitude analysis in a post-fire setting has received much attention in the past 10 years and this paper can hardly do justice of the plethora of literature that has emerged. For the practitioner, general guidelines and simple applications are particularly useful, such as the recovery time for decreasing debris flow volumes to pre-fire situations (Santi and Morandi, 2013), or estimates of peak discharge in burned and unburned areas from bulked rational formulae and their limitations (Brunkal and Santi, 2017). Other highlights include probabilistic post-wildfire debris-flow modeling (Donovan and Santi, 2017) and studies on the timing of debris flows after fires (DeGraff, 2014; De Graff et al., 2015), which is key in triggering risk assessments, as debris flows may occur very quickly after fires are out (Kean et al., 2019).

Various statistical methods exist that help the practitioner with incomplete datasets that, in our science, are the rule rather than the exception. The application of simple magnitude-cumulative-frequency (MCF) methods or the GPD can lend credibility to the analysis and its extrapolation to annual probabilities outside the observed record. However, they come with a caveat, namely pronounced confidence bands. As has been shown by Jakob (2012), an honest reporting of such confidence bands may lead to a confidence loss with one's client or those potentially affected. The only remedy does remain expert judgement, which in itself is based on a thorough understanding of the entire debris flow system. Only a comprehension of potential point sources, entrainment rates, multiple debris-flow triggering mechanisms and runout behaviour will allow the practitioner or scholar to properly identify and quantify hazard zones.

2.4. Debris-flow scour and entrainment

On September 20, 2015 an anomalously erosive debris flow occurred on the fan of Neff Creek, north of Pemberton, British Columbia, Canada (Lau, 2017). The debris flow mobilized before reaching the fan apex. However, the total volume of the debris flow that was eventually deposited was 275,000 m³ with 83,000 m³ having been eroded from the fan. The discrepancy between these two volumes is due to the erosion of a small canyon-sized channel into the upper to mid alluvial fan, which at its maximum was 14 m lower than the original fan surface. Similar highly erosive debris flows have been observed in Switzerland (Scheuner et al., 2009; Frank et al., 2015) and elsewhere in British Columbia (Jakob et al., 1997; BGC Engineering Inc., 2018), but the causes for debris flow fans to "switch" between deposition and erosion are poorly understood and have only been recently researched (e.g. de Haas et al., 2017). Understanding when such highly erosive events occur on fans is crucial for practitioners tasked with specifying burial depth of pipelines or fiberoptic cables. In the case of Neff Creek, it is virtually certain, that even a professional with vast knowledge of debris-flow processes may have under-designed a buried crossing due to a severely underestimated

scour depth on the fan. In addition, clients may exert some pressure on the practitioners not to be overly conservative with the recommended burial depth because costs of construction and maintenance increase substantially with increasing burial depth. Had a pipeline been built, it would have very likely resulted in a fracture and spill of whatever substance the pipeline had carried. It is such events that give us reason to pause and stimulate further research.

Buried linear infrastructure that passes through mountainous terrain will invariably cross alluvial fans and colluvial cones. While fans and cones are generally regarded as depositional landforms, observations of progressive and catastrophic scour on such landforms indicate that this view is too simplistic. Fan and cone scour has exposed, and in the worst case, severed buried linear infrastructure. Continued expansion of buried linear infrastructure motivates a more detailed examination of fan scour to predict scour depth and manage the risk of buried infrastructure failure. Recent papers are split between physical-mathematical treatments of the problem, in large part supported by full-scale flume experiments, and papers reliant on case study and empiricism.

Iverson et al. (2011) conducted large-scale experiments at the USGS's debris-flow flume in Oregon to examine debris entrainment in steep channels. They addressed the pertinent question: How can flows that entrain bed material travel faster and further than those that do not, given that momentum conservation implies flow retardation? Iverson et al. (2011) found that debris-flow mass and momentum grows simultaneously when rapid debris loading over a wet alluvial channel surface produces large positive pore pressures. These elevated pore pressure fields encourage bed sediment scour, lead to friction reduction and unleash a positive feedback through further momentum increase. The key question is when the feedback becomes negative either due to deposition, avulsions or an increasingly dry bed, perhaps due to fan surface infiltration.

Four years after these initial findings, Iverson and Ouyang (2015) reviewed various models and suggested that many existing models are not suitable to predict debris entrainment as they are incorrectly applying depth-integrated conservation principles. They show that erosion or deposition rates at the interface between layers must, in general, satisfy three "jump" conditions, which is rarely the case.

A novel approach to debris-flow scour was suggested by Kang and Chan (2017), who proposed a model that accounts for surface erosional effects through progressive scouring and shear failure on the channel surface. By considering simple geometry and particle configurations, the authors developed equations for progressive scouring and considered rolling and sliding motion. In Kang and Chan's model, a probability-density function (PDF) is used to calculate the entrainment rate. The authors compared the model to flume experiments and found that the entrainment rate can be calculated using a normal-distribution PDF. It will be interesting to observe if real debris flows and associated scour can be accurately simulated by the model.

The importance of debris entrainment has also been highlighted in a recent paper by Frank et al. (2015), who provide instructive examples from the Swiss Alps. Theule et al. (2015) developed a functional relationship from a stepwise regression model as an empirical fit for the prediction of channel erosion by debris flows with a critical slope threshold at 0.19. The authors interpreted this slope threshold as the transition between the transport-limited and supply limited regimes, associated with the upstream decreasing erodible bed thickness. Finally, Haas and Woerkom (2016) experimentally investigated the effects of debris-flow composition on the amount and spatial patterns of bed scour and erosion downstream of a transition from bedrock to channel colluvium. The debris flows entrained bed particles grain by grain and en masse, and the majority of entrainment was observed to occur during passage of the flow front. Interestingly, the authors found that scour depth is largest slightly downstream of the bedrock to colluvium transition, except for clay-rich debris flows. The authors also found that basal scour depth increases with channel slope, flow velocity, flow depth, discharge and shear stress. From a practitioner's point of view, this highlights that debris-flow fans with comparatively large watersheds, such as hanging valleys that result in high peak discharges, are particularly susceptible near their apices, where the transition from bedrock to colluvium occurs. This is very much in line with observed scour depths near fan apices and indicates that those locations should be avoided in the design of linear infrastructure.

Using experiments from a 1:30 scale model, Eaton et al. (2017) were able to demonstrate that channel degradation due to floods on alluvial fans is dominated by lateral channel migration rather than vertical incision. However, experiments were conducted on a modeled fan of 4.5% gradient, and many debris flow fans are substantially steeper. Hence, it remains to be determined if the findings from Eaton et al. (2017) can be applied to steeper fans.

3. Concluding Remarks

Debris-flow hazard and risk assessments have considerably improved from when the design of debris-flow mitigation works were largely based on a practitioner's gut feel or some experience-based guidelines. The wealth of

methods, be they in dating past events, deciphering their magnitude, numerical models and measures of debris-flow intensities and vulnerabilities, has been bewildering and illuminating alike. Papers on one or another aspect of debris flows almost appear weekly, and only the most motivated may be staying abreast of absorbing this information tsunami. Rarely, however, can all or even several complimentary methods be applied to a specific problem. This is partially due to geographic constraints (i.e. dendrochronology is useless in treeless terrain, or radiocarbon dating is impossible in desert environments), and partially due to funding limitations in competitive bids for engineering/geoscientific studies.

Even in economically and socially advanced nations in Europe and North America, steep creek science has not advanced as rapidly as would have been desirable. A recent contribution (in German) by Rickenmann and Badoux (2018) identified deficits that are equally applicable to other nations: They include underfunding of process-based studies of mountain torrents, insufficient documentation of methods used for process characterization, missing transparency in debris-flow hazard assessments, and gaps in the systematic training of debris-flow specialists.

Only 10s of people (anecdotal data) die annually directly from debris flows in the US. However, indirect loss of life due to cutoff from health care, for example due to Hurricane Maria that affected Puerto Rico, can be much higher (Kishore et al., 2018). Globally, the total number of debris-flow-related deaths are more significant. Dowling and Santi (2014) estimated 77,779 fatalities have been recorded in academic publications, newspapers, and personal correspondence between 1950 and 2011, an average of approximately 1,250 fatalities per year.

While insignificant in terms of fatalities, the national economic costs are still substantial due to direct impact or infrastructure interruptions (Dowling and Santi, 2014; McCoy et al., 2016). Hence, complacency is certainly not warranted, nor morally justifiable. As with any science, it is valuable to occasionally take stock of the key accomplishments and ask the question: What else needs to be achieved until a science has matured to a degree where progress has slowed to a crawl or even stagnates, or where progress is largely academic with no direct or obvious connectivity to practical application?

One may argue that the quantitative methods available for debris-flow hazard quantification are approaching a level of maturity, as are the myriad of methods to mitigate hazard and associated risks. Clearly, refinements in numerical model capabilities, such as credible entrainment functions on channels and fans, are still necessary and welcome. There are potential pitfalls to widespread application of sophisticated debris-flow models by people with little modeling experience or a cursory understanding of the model being applied. Similarly, hazard intensity definition and mapping can still be homogenized and improved through existing tools that are well suited to deal with most, if not all, conditions adequately. National or regional databases are needed, as they allow a better statistical treatment of all components of hazard analysis. Setting tolerable risk thresholds will help to fine-tune and custom tailor mitigation measures while avoiding over-expenditure or underfunding. Finally, regional, or national-level debris flow risk prioritization is hugely helpful to allocate limited funding to the highest risk situations and to remove the arbitrariness of decisions on mitigation prioritization. None of the above will be useful unless a new generation of debris-flow experts is being trained in the science and art of debris-flow hazard and risk assessments. This needs to be complemented by the, formulation of detailed technical guidelines to homogenize approaches and enhancing research efforts including a systematic process documentation and its testing against existing methods.

Climate change is posing, and will continue to pose, a key challenge to institutions and practitioners alike, as the expected changes in climate and the associated higher order effects (glacial and permafrost changes, changes in wildfire activities, beetle infestations and associated tree mortality, all of which are known to influence debris-flow activity) in the ecosystems are becoming unprecedented in recent human history. While a fascinating global experiment, debris-flow researchers and practitioners will need to respond swiftly with amending their analytical arsenal in the attempt to predict and manage the effects of climate change as they pertain to debris-flow systems.

Despite all uncertainties clouding this science, future changes will require a new generation of experts who are knowledgeable in the ever-increasing subfields that feed into successful hazard and risk assessments. I hope that this contribution will inspire this debris-flow avant-garde and lead to ever more robust tools. It is also a call for funding agencies to provide academia with sufficient means to address pertinent outstanding questions so that science can be translated into practice with little delay. In conjunction with wise resource management and an acceptance of research-based decision making, there is reason for hope that debris flows may not become ubiquitous killer landslides. Future debris flow disasters will not occur due to imprecise science, rather due to the failure to fully recognize, nor quantify the debris-flow hazards and associated risks.

Acknowledgements

I would like to thank the conference organizers that allowed me to share my thoughts at this venue. I am also deeply indebted to all those who have put their brilliant minds to pursuing and advancing the knowledge in the broad field of debris flow science, instead of pursuing much more lucrative jobs elsewhere. Their work has inspired me and many such researchers have become friends. Many of my colleagues have greatly contributed to the work presented herein. Specific thanks for reviews, data, references and thought-provocative comments to Scott McDougall, Carie-Ann Lau, Kris Holm, Markus Stoffel, Dieter Rickenmann, Dick Iverson, Jon Major, Paul Santi, Akhiko Ikeda and Joseph Gartner. Thanks also to Lynn Forrest for finding many references that I was oblivious to.

References

- André, M.F., 1990. Frequency of debris flows and slush avalanches in Spitsbergen: a tentative evaluation from lichenometry. *Polish Polar Research*, 11(3-4), pp.345-363.
- de Haas, T., Densmore, A., Stoffel, M., Suwa, H., Imaizumi, F., Ballesteros Canovas, J.A., Wasklewicz, T., 2017. Avulsions and the spatio-temporal evolution of debris-flow fans. *Earth - Science Reviews* 177: 53 – 75.
- Ballesteros-Cánovas, J.A., Stoffel, M., St George, S., Hirschboeck, K. (2015): A review of flood records from tree rings. *Progress in Physical Geography* 39: 794–816
- BGC Engineering Inc. 2018. Seton Portage area integrated hydrogeomorphic risk assessment. Prepared for Squamish-Lillooet Regional District. <https://www.slrld.bc.ca/inside-slrld/current-projects-initiatives/seton-portage-area-integrated-hydrogeomorphic-risk-assessment-0>.
- Brunkal, H. and Santi, P., 2017. Consideration of the Validity of Debris-flow Bulking Factors. *Environmental and Engineering Geoscience*, 23(4), pp.291-298.
- Bull, W. B. (2018) “Accurate surface exposure dating with lichens,” *Quaternary Research*. Cambridge University Press, 90(1), pp. 1–9. doi: 10.1017/qua.2018.7
- Chiverrel, R. and Jakob, M. 2013. Radiocarbon dating: alluvial fan/debris cone evolution and hazards. In *Dating Torrential Processes on Fans and Cones*. Springer, Netherlands, pp. 265-282.
- De Graff, J.V., 2014. Improvement in quantifying debris flow risk for post-wildfire emergency response. *Geoenvironmental Disasters*, 1(1), p.5.
- De Graff, J.V., Cannon, S.H. and Gartner, J.E., 2015. The timing of susceptibility to post-fire debris flows in the Western United States. *Environmental & Engineering Geoscience*, 21(4), pp.277-292.
- Donovan, I.P. and Santi, P.M., 2017. A probabilistic approach to post-wildfire debris-flow volume modeling. *Landslides*, 14(4), pp.1345-1360.
- Dowling, C.A. and Santi, P.M., 2014. Debris flows and their toll on human life: a global analysis of debris-flow fatalities from 1950 to 2011. *Natural hazards*, 71(1), pp.203-227.
- Frank, F., McArdell, B.W., Huggel, C. and Vieli, A., 2015. The importance of entrainment and bulking on debris flow runout modeling: examples from the Swiss Alps. *Natural Hazards and Earth System Sciences*, 15(11), pp.2569-2583.
- Gartner, J.E., Cannon, S.H., Santi, P.M., 2014. Empirical models for predicting volumes of sediment deposited by debris flows and sediment-laden floods in the transverse ranges of southern California. *Engineering Geology*, 174:45-56.
- Griswold, J.P., and Iverson, R.M., 2008, Mobility statistics and automated hazard mapping for debris flows and rock avalanches (ver. 1.1, April 2014): U.S. Geological Survey Scientific Investigations Report 2007-5276, 59 p.
- Haas, T.D. and Woerkom, T.V., 2016. Bed scour by debris flows: experimental investigation of effects of debris-flow composition. *Earth Surface Processes and Landforms*, 41(13), pp.1951-1966.
- Holm, K., Jakob, M., Weatherly, H., Dercole, F., and Bridger, S., 2017. Quantitative Steep Creek Risk Assessment, District of North Vancouver, British Columbia. Canadian Society of Civil Engineering (CSCE) 23rd Canadian Hydrotechnical Conference. May 30-June 3, Vancouver, Canada.
- Holm, K., Jakob, M. and Scordo, S., 2016. An inventory and risk-based prioritization of steep creek fans in Alberta. 3rd European Conference on Flood Risk Management: Innovation, Implementation, Integration. 18-20 October 2016, Lyon France.
- Horton, P., Jaboyedoff, M., Rudaz, B.E.A. and Zimmermann, M., 2013. Flow-R, a model for susceptibility mapping of debris flows and other gravitational hazards at a regional scale. *Natural Hazards and Earth System Sciences*, 13(4), pp.869-885.
- Horton, P., Jaboyedoff, M. and Bardou, E., 2008. Debris flow susceptibility mapping at a regional scale. In *Proceedings of the 4th Canadian Conference on Geohazards: from causes to management* (pp. 399-406). Presse de l'Université Laval.
- Innes, John. (1983). Lichenometric dating of debris-flow deposits in the Scottish Highlands. *Earth Surface Processes and Landforms*. 8. 579 - 588. 10.1002/esp.3290080609.
- Iverson, R. M., and C. Ouyang (2015), Entrainment of bed material by Earth-surface mass flows: Review and reformulation of depth-integrated theory, *Rev. Geophys.*, 53, 27–58, doi:10.1002/2013RG000447
- Iverson, R.M., Reid, M.E., Logan, M., LaHusen, R.G., Godt, J.W. and Griswold, J.P. (2011). Positive feedback and momentum growth during debris-flow entrainment of wet bed sediment. *Nature Geoscience*, 4, doi: 10.1038/NCEO1040.
- Iverson, R.M., 2012. Elementary theory of bed-sediment entrainment by debris flows and avalanches. *Journal of Geophysical Research: Earth Surface*, 117(F3).
- Jakob, M., Hungr, O., Thomson, B., 1997. Two debris flows of anomalously high magnitude, in: Chen, C.-I. (Ed.), *Debris-Flow Hazards Mitigation: Mechanics, Prediction and Assessment*. American Society of Civil Engineers, San Francisco, California, pp. 382–394.
- Jakob, M. (2005): *Debris-flow hazard analysis*: Jakob, M. and Hungr, O. (eds.), *Debris-flow hazards and related phenomena*, Praxis and Springer, Heidelberg, pp. 411-443.
- Jakob, M., 2012, June. The fallacy of frequency. Statistical techniques for debris flow frequency magnitude analysis. In *Proceedings of the International Landslide Conference, Banff, Canada* (pp. 2-8).

- Jakob, M., Bale, S., McDougall, S., and Friele, P. 2016. Regional debris-flow and debris-flood frequency-magnitude curves. In Proceedings of the 69th Canadian Geotechnical Society Conference: history and innovation, GeoVancouver 2016, Vancouver, BC, 2-5 October 2016. Canadian Geotechnical Society, Richmond, BC. pp. 1-8.
- Jakob, M., Weatherly, H., Bale, S., Perkins, A. and MacDonald, B., 2017. A Multi-Faceted Debris-Flood Hazard Assessment for Cougar Creek, Alberta, Canada. *Hydrology*, 4(1), p.7.
- Kang, C., Chan, D., 2017. Modelling of entrainment in debris flow analysis for dry granular material. *Int. J. Geomech.* 17 (10), 1–20. [https://doi.org/10.1061/\(ASCE\)GM.1943-5622.0000981](https://doi.org/10.1061/(ASCE)GM.1943-5622.0000981).
- Kang, S. and Lee, S.R., 2018. Debris flow susceptibility assessment based on an empirical approach in the central region of South Korea. *Geomorphology*, 308, pp.1-12.
- Kean, JI, Staley, D., Lancaster, J., Regers, F., Swanson, B., Coe, J., Hernandez, J., Sigman, A., Allstadt, K., Linsay, D. 2018. Inundation, flow dynamics, and damage in the 9 January 2018 Montecito Debris Flow, California, USA: Opportunities and challenges for post-wildfire risk assessment. *Geosphere*. In print.
- Kishore, N. and 11 others. 2018. Mortality in Puerto Rico after Hurricane Maria. *New England Journal of Medicine*. 379:162-170.
- Lau, C.A. 2017. Channel scour on temperate alluvial fans in British Columbia. M.Sc. thesis. Simon Fraser University, Burnaby, Canada.
- Le Quéré et al. (2017) Global Carbon Budget 2017. *Earth System Science Data Discussions*. <https://doi.org/10.5194/essdd-2017-123>
- Lin, I.I., Chen, C.H., Pun, I.F., Liu, W.T. and Wu, C.C., 2009. Warm ocean anomaly, air sea fluxes, and the rapid intensification of tropical cyclone Nargis (2008). *Geophysical Research Letters*, 36(3).
- McCoy, K., Krasko, V., Santi, P., Kaffine, D. and Rebennack, S., 2016. Minimizing economic impacts from post-fire debris flows in the western United States. *Natural Hazards*, 83(1), pp.149-176.
- McDougall, S., and Hung, O. 2005. Dynamic modelling of entrainment in rapid landslides. *Canadian Geotechnical Journal*, 42(5): 1437–1448. doi:10.1139/t05-064.
- Moase, E., Strouth, A., Mitchell, A. 2018. A comparison of different approaches for modeling a fine-grained debris flow at Seton Portage, British Columbia, Canada. Second JTC1 Workshop on Triggering and Propagation of Rapid Flow-like Landslides, Hong Kong.
- Rapp, A. and Nyberg, R., 1981. Alpine debris flows in northern Scandinavia: morphology and dating by lichenometry. *Geografiska Annaler: Series A, Physical Geography*, 63(3-4), pp.183-196.
- Rickenmann, D., 2016. Debris-flow hazard assessment and methods applied in engineering practice. *International Journal of Erosion Control Engineering*, 9(3), pp.80-90.
- Rickenmann, D. and Badoux, A. 2018. Gefahrenbeurteilung von Wildbächen in der Schweiz – quo vadis? Standortbestimmung und kurzer Ausblick? *Agenda FAN 1/2018*.
- Santi, P.M. and Morandi, L., 2013. Comparison of debris-flow volumes from burned and unburned areas. *Landslides*, 10(6), pp.757-769.
- Schneuwly-Bollschweiler, M., Stoffel, M., Rudolf-Miklau, F. (2012): Dating torrential processes on fans and cones - Methods and their application for hazard and risk assessment. Springer, Berlin, Heidelberg, New York, 423 pp.
- Scheuner, T., Keusen, H., McArdell, B. W., and Huggel, C.: Murgangmodellierung mit dynamisch-physikalischen und GIS basierten Fließmodell, Fallbeispiel Rotlauhgraben, Guttannen, August 2005, *Wasser Energie Luft*, 101, 15–21, 2009 (in German.)
- Sewell, R.J., Parry, S., Millis, S.W., Wang, N., Rieser, U. and DeWitt, R., 2015. Dating of debris flow fan complexes from Lantau Island, Hong Kong, China: the potential relationship between landslide activity and climate change. *Geomorphology*, 248, pp.205-227.
- Staley, D.M., Kean, J.W., Cannon, S.H., Schmidt, K.M., Laber, J.L., 2013. Objective definition of rainfall intensity-duration thresholds for the initiation of post-fire debris flows in southern California. *Landslides* 10:547-562. DOI: 10.1007/s10346-012-0341-9. Second JTC1 Workshop. Hong Kong. 3 to 5 December 2018.
- Stoffel, M. 2018. Personal Communications.
- Stoffel, M., Bollschweiler, M. (2008): Tree-ring analysis in natural hazards research – an overview. *Natural Hazards and Earth System Sciences* 8: 187–202.
- Stoffel, M., Bollschweiler, M., Butler, D.R., Luckman, B.H. (2010): *Tree rings and natural hazards: A state-of-the-art*. Springer, Berlin, Heidelberg, New York, 505 pp.
- Sturzenegger, M., Holm, K., Lau, C.A., and Jakob, M., 2019. Semi-automated Regional Scale Debris Flow and Debris Flood Susceptibility Mapping based on Digital Elevation Model Metrics and Flow-R Software. 7th International Conference on Debris-Flow Hazards Mitigation, Golden, Colorado, June 2019.
- Theule, J.I., Liébault, F., Laigle, D., Loye, A. and Jaboyedoff, M., 2015. Channel scour and fill by debris flows and bedload transport. *Geomorphology*, 243, pp.92-105.
- van den Heuvel, F., Goyette, S., Rahman, K., Stoffel, M., 2016. Circulation patterns related to debris - flow triggering in the Zermatt valley in current and future climates. *Geomorphology* 272 , 127 – 136.

Evaluation of shallow landslide-triggering scenarios through a physically based approach: A case study from Bulathsinhala area, Kalutara in Sri Lanka

E.I. Jayasekara^{a,b*}, N.K. Weerasekara^b, H.A.G. Jayathissa^c, A.A.J.K. Gunatilake^d

^aPostgraduate Institute of Science, University of Peradeniya, Peradeniya (20400), Sri Lanka

^bNational Building Research Organization, Badulla (90000), Sri Lanka

^cNational Building Research Organization, Colombo (00500), Sri Lanka

^dDepartment of Geology, Faculty of Science, University of Peradeniya, Peradeniya (20400), Sri Lanka

Abstract

Transient Rainfall Infiltration and Grid-based Regional Slope-stability analysis (TRIGRS) is a regional, physically based stability model which could be applied to predict shallow landslides. It is important to evaluate the accuracy of TRIGRS for the prediction of landslide locations using actual events before use the TRIGRS model for further applications. This study presents the application of TRIGRS for Bulathsinhala area, Kaluthara in south western part of Sri Lanka where the number of shallow landslides occurred on 26th May 2017 and many of those events transitioned into damaging and killing debris flows. A back analysis of that landslide event was executed to authenticate the model by using different methods and techniques for the definition of the input parameters. Reliability of the model was evaluated through comparison with the 2017 landslide inventory in the particular area and it was revealed that most of the actual landslides were occurred in the predicted area ($FS < 1$) of the model. In order to quantify the effectiveness of the model, an index was proposed in the study called LR_{class} (landslide ratio for each predicted FS class). The obtained values of the LR_{class} index realize the trustworthiness of the model which indicates the considerably higher value (60%) for the lowest stability class. With this particular manner, the output of the study could be used to implement more reliable land use management and development plans and resettlement procedures. Further the TRIGRS model is advantageous for susceptibility mapping and landslide flow path analysis, particularly when linked with various advanced applications using GIS spatial functions.

Keywords: shallow landslide; factor of safety; transient pore pressure

1. Introduction

Landslides and debris flows are sources of severe natural disasters and societal hazards in mountainous regions in Sri Lanka. Hence, people meet a challenge to find a balance risk of natural hazards and the need for spatial development. Densely populated hillside regions in humid, subtropical or tropical climatic zones are often prone to various types of landslides. The socioeconomic impact, moreover, has become much higher than before because of the high population in hazardous zones. Accordingly, it is important to identify the areas prone to landslides and to categorize them in accordance with the risk level (i.e. high risk, moderate risk and low risk). Identification of lands, which have to be protected from human activities as well as to implement the stabilization measures in order to avoid possible mass movements, is also essential.

Landslides could be categorized mainly as “deep-seated” and “shallow” in terms of the mechanism of failure of the slope. Shallow landslides (especially debris flows) can pose a serious threat to life or property, in particular due to their high velocity, impact forces and long run-out, combined with poor temporal predictability (Jacob and Hungr, 2005). These phenomena consist of sudden mass movements of a mixture of water and granular material that rapidly develop downslope, eroding the soil cover and increasing their original volume (Iovine et al., 2003). Due to their high destructiveness, the study of these processes is an important research topic that can support decision makers in developing more detailed land-use maps and landslide hazard mitigation plans.

In Sri Lanka, shallow landslides are most common in the Middle Peneplane from 30-200m elevation, in areas with either colluvium or thin residual soil overburden. These shallow landslides often mobilize into destructive and even

* Corresponding author e-mail address: eranda.ij@gmail.com

deadly debris flows. Failure of rupture of shallow landslides are typically 1–3m deep and often occur at boundaries between the colluvium and the underlying more solid parent rock (Salciarini et al., 2008) and also occur at boundaries between two residual soil layers with different permeability values or boundaries between residual soil and the underlying parent rock.

The climate of Sri Lanka typical with South West (SW) monsoon (May-September), North East (NE) monsoon (December-February) and inter Monsoons (March-April and October-November) with pronounced seasonal precipitation. Therefore, rainfall-triggered landslides are a recurring problem in Sri Lanka. However, majorly the intense rainfalls occur with the SW monsoon especially to the south western part of the country where having generally less than 6m soil overburden because of the relatively shallow depth of the bedrock, and hence shallow landslides are frequent. Within the period of 25–26 May 2017, in particular, localized torrential heavy rainfall (419.25mm; 14 30 hrs on 25th – 07 00 hrs on 26th) occurred in Bulathsinhala area, amount approximately equal to 18% of the total annual rainfall for that region. Under these conditions, precipitation induced landslides caused translational mass movements that occurred suddenly. During the storm, shallow landslides were mostly triggered by heavy rainfall that increased the pore pressure of soil in the near-subsurface, with an attendant decrease in its shear strength. With that particular precipitation event, during the period of 02 30 – 03 30 hrs on 26th May in Bulathsinhala area, number of landslides occurred with causing significant damage and 8 of them were catastrophic. Most of the landslides were accompanied by debris flows, and these mixtures of debris flowed down in to the roads and surrounding human settlements. Seventy four people were killed and ten buildings were damaged by those debris flows (NBRO, 2017). Four of the major failures occurred with above mentioned event is given in figure 1.

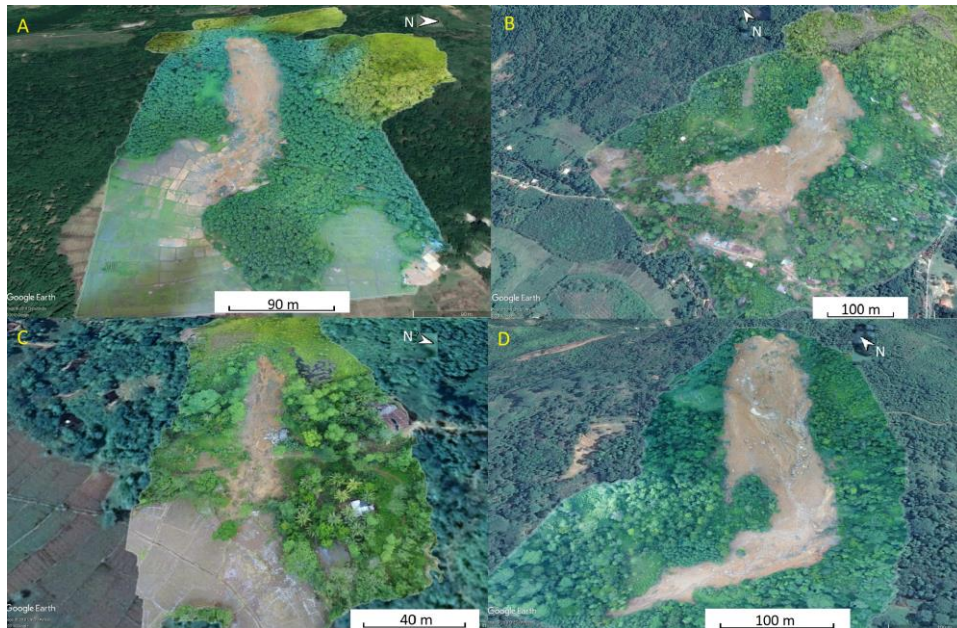


Fig. 1 Few major failures occurred on 26th May 2017; A - Kobowella, B - Niggaha, Pahiyangala, C - Paragoda, D – Thibbottawa. Locations of these landslides are marked in Figure 2.

It is not simple to predict the probability of the occurrence and magnitude of shallow landslides, considering the complexity of the phenomenon, mostly related to the variability of controlling factors (e.g., geology, topography, climate and hydraulic conditions). In this respect, a relationship between triggering events (i.e., rainfall) and landslide occurrences needs to be established.

In order to understand when and where rainfall-induced landslides have occurred in mountainous regions, and how topographic, geotechnical and hydraulic parameters affect the initiation of landslides and might be used to predict them, models adopting both empirical and deterministic approaches have been used.

In this study, it was taken an approach based on Transient Rainfall Infiltration and Grid-based Regional Slope-stability analysis (TRIGRS) (Baum et al., 2002), a physically based model that predicts the timing and distribution of shallow, rainfall-induced landslides combining an infinite slope stability calculation with a transient, one-dimensional analytic solution for pore pressure response to rainfall infiltration. This model has been used in order to define different

shallow landslide-triggering scenarios in the study area (Bulathsinhala) by varying the rainfall input on the basis of the results deriving from the analysis of the historical rainfall data.

The main objective of this study was to predict shallow, rainfall-triggered landslides using TRIGRS, in the region of Bulathsinhala. To evaluate accuracy of the predicted mode of initiation of shallow landslide comparative with the real situation (pre –failure mode) was also an objective. Results of the current study could be used for landslide early warning strategies, development of the mapping and development planning procedures as well as most importantly for further studies on landslide flow path analysis with the aid of models such as DAN 3D (Hung, 1995) and Flow-R (Horton et al., 2013)

2. Study Area

The study area is located in hilly terrain, which belongs to the Bulathsinhala DS Division of the Kalutara district in Western province of Sri Lanka (Figure 2). It is bounded by Colombo, Ratnapura and Galle Districts and by Indian Ocean from north, east, south, and west respectively. Geographically the study area belongs to the lower country Peneplane (Cooray, 1984). It is located between 06° 36' 40"- 06° 41' 15" N latitudes and 80° 08' 20" - 80° 14' 10" E longitudes (Kandawala Datum) and demarcated in Figure 2. The elevation of study area is generally 80m above mean sea level. Population is distributed hilly and flat terrains and this area measures 160 km².

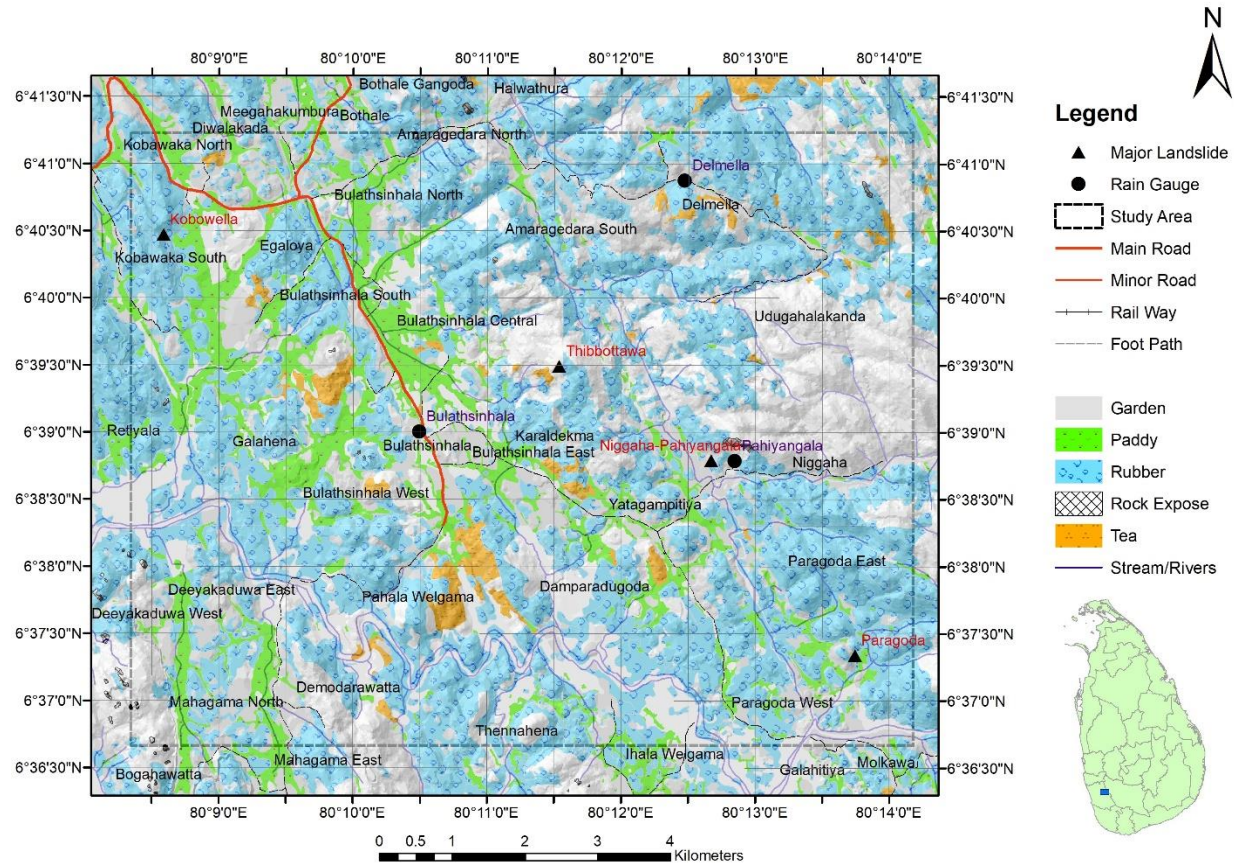


Fig. 2 Location Map of the Bulathsinhala area, Kaluthara District in Sri Lanka (Source: Survey Department of Sri Lanka)

3. Methodology

The approach proposed in this study consists of two stages. The first one is back analysis of the 26th May 2017 event occurred in Bulathsinhala area and the second one is evaluation of different triggering scenarios. With this regard the factor of safety (FS) map obtained by using TRIGRS, a well-known regional, physically based stability model was compared with the inventory map of the landslides triggered during the event. This model couples an infinite-slope stability analysis with a one-dimensional analytical solution to predict the transient pore pressure response to the infiltration of rainfall. The results predicted by the TRIGRS model are presented as factor of safety (FS) maps

corresponding to transient rainfall events. It also adopts the geographic information system (GIS) framework for determining the whole behaviour of a slope.

Reconnaissance field visit was done to obtain actual situation of the landslide locations and to identify landforms, physical factors such as soil type, overburden thickness, vegetation etc. and potentiality to further failures. Daily rainfall data and monthly rainfall in 2017 year were collected from Meteorological Department rain gauge stations and hourly rainfall data on 25th and 26th of May in 2017 was congregated from National Building Research Organization (NBRO) automated rain gauge located in the particular area.

The 2017 landslide incidents in Kaluthara district have been investigated by the Kaluthara district NBRO office. Information about occurred landslides in particular period such as landside incident time and date, width of the landside, length of the landslide, aspect, slope angel, overburden thickness etc. were collected from investigation data reports done by the Kaluthara NBRO office as well as by the field observations. After the occurrence of landslides on 26th May, subsurface geology as well as the properties of existing soils at the incident areas have been investigated by the Geotechnical Engineering and Testing Division (GETD) of the NBRO. All available data were obtained from the GETD and used in this analysis.

Input parameters of the TRIGRS such as the terrain DEM file, the raster files of flow direction and slope as well as the relevant maps were constructed using the Arc GIS 10.2. Then the further analysis part was done and the model was created using the TRIGRS to simulate areas of potential landslide initiation.

Many important parameters should be included to develop the model as topographic factors, soil thickness, as well as strength properties and hydraulic parameters of the soil. Accuracy and reliability of the results depend mainly on detailed knowledge of the study site, and on the quality of the input parameters.

Topographic analyses for elevation, slope angle and aspect were calculated from 1:10 000 maps developed by the Survey Department of Sri Lanka. Maps of No 7412, 7413, 7417 and 7418 were used for analyses. To create grids with 10m cells and to quantify the aforementioned information above for each cell of the DEM, ArcGIS was used.

Hydraulic parameters including saturated hydraulic conductivity (K_s), diffusivity (D_0) and steady infiltration rate (I_z) were obtained from laboratory tests and derived according to soil classes and empirical references. The values of D_0 and I_z were not well defined, since they had wide ranges according to the complex properties of soil (e.g. void, fine content, and soil density). These parameters are quite different for various samples, even though they were collected from the same site. Therefore, θ_s (saturated water content), θ_r (residual water content), diffusivity (D_0) and K_s are directly predicted using the ROSETTA pedotransfer functions (Schaap et al., 2001).

Information about the I_z rate, however, is rare in the literature. The I_z value is affected by soil characteristics including porosity, storage capacity, and transmission rate through the soil. The soil texture and structure, vegetation types and cover, water content of the soil and soil temperature also play a role in controlling the infiltration rate. If the soil is saturated, I_z can be the same as hydraulic conductivity, while it can be zero for dry soil. In this research, the reasonable value 0.01 of the K_s (Salciarini et al., 2008; Liu and Wu, 2008; Kim et al., 2010) was selected for I_z because of the hot, dry conditions during the dry season which was existed just before the heavy storm event.

In the simulations carried out in this study, a uniform soil depth of 4m was considered based on site investigation reports and overburden map created by the NBRO, and it conforms the several studies which show that most of shallow landslides in the mountainous regions of Bulathsinhala area are observed between 1 and 6m. The initial groundwater table was obtained from the piezometric data installed in bore holes and available water sources observed during the field visits. It was set at the same depth of soil thickness due to no heavy antecedent rainfall after the event.

Then using the created model, Zones of minimum FS ($FS < 1$) values were extracted and the variation of FS with the rainfall intensity was examined. After that the initiation area of real situation of landslide and values of the model were compared to evaluate the output of TRIGRS and to predict the landslide initiation area. Finally, the landslide ratio of each predicted FS class (LR_{class}) was employed to evaluate the performance of the landslide model. LR_{class} was based on the ratio of the percentage of landslide sites contained in each FS class in relation to the total number of actual landslide sites (total 40 locations) and the percentage of predicted landslide sites in each class of FS.

$$LR_{class} = \frac{\% \text{ of contained landslide sites in each class of FS}}{\% \text{ of predicted landslide sites in each class of FS}} \quad (1)$$

4. Results and Discussion

4.1 Rainfall characteristics

During May 2017 alone, Bulathsinhala area received about 18% of its total annual precipitation. Highest daily rain fall (419.25mm/day) was recorded in 26th May 2017(Figure 3). Hourly maximum rainfall was 68mmh^{-1} (02 30 – 03 30 hrs on 26th May). Figure 4 shows the rainfall distribution in the critical period of time on 25th and 26th May 2017. Shallow landslides were triggered by the localized torrential rainfall during this period, characterized by a cumulative rainfall of 419.25mm, of which 85% poured down during the last 8h (22 00 hrs on 25th – 06 00 hrs on 26th). The landslides started after the heavy rain occurred in first half of that 8 hours.

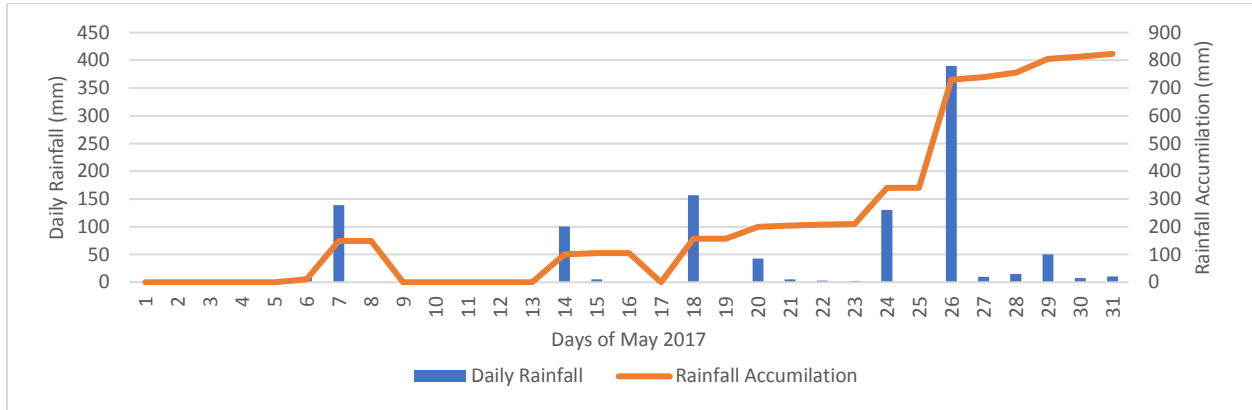


Fig. 3 Daily rainfall distribution in month of May with the rainfall accumulation

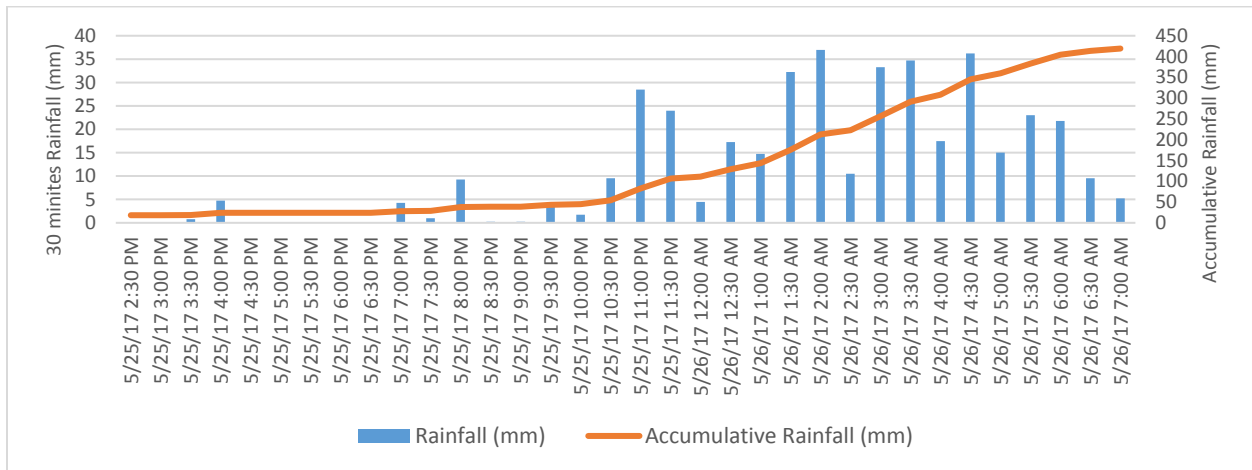


Fig. 4 Rainfall distribution in the critical period of time on 25th and 26th May 2017 with the rainfall accumulation

4.2 Prediction of the initiation area of landslides

One main objective of this research is to evaluate the spatiotemporal predictability of landslide events in Bulathsinhala area using the TRIGRS model for regional landslide hazard assessment. The factor of safety (hereafter FS) over the entire study area was calculated for each cell and plotted over time during this severe storm. Figure 4.3 shows the spatial distributions of FS in different periods of time. In other words, these depict the temporal and spatial dynamics of FS values induced by heavy rainfall during the duration of 12 hours (from 19 00, 25th May to 07 00, 26th May). The three FS maps are for 0, 3 and 12 hours, and 3h corresponded to the start of extraordinarily heavy rainfall for 8h. The areas characterized as having a factor of safety close to $FS=1.0$ progressively expanded when the rainfall became more intense. This implies that large numbers of the landslides were triggered by the intense rainfall. The study area has a lot of hillock and steep nature of mountainous terrain. This is why FS maps are very complex and tortuous. Nevertheless, the performance of the TRIGRS model for prediction, which has been evaluated by field investigation, can be considered reasonably applicable as indicated in Figure 5.

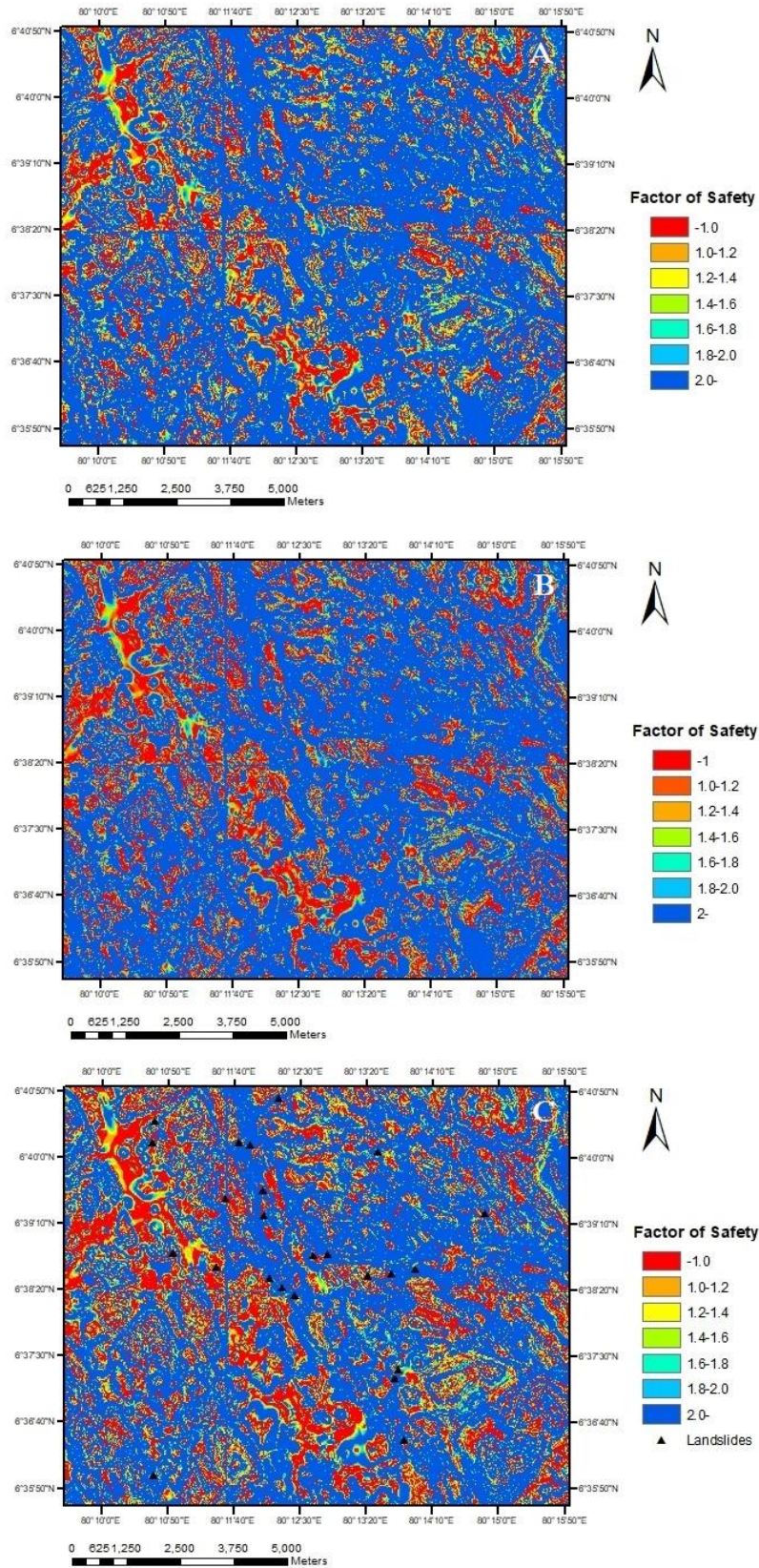


Fig. 5 Classes of topographic parameters (elevation, slope angle, aspect and curvature) for (A) 0 h (19 00 hrs., 25th May 2017), (B) 3 h (22 00 hrs., 25th May 2017), and (C) 12 h (07 00 hrs., 26th May 2017).

In the Bulathsinhala event, it is difficult to know the size of the landslides that occurred, therefore the number of the debris flows occurred after the landslides have been considered. Most landslides are connected with debris flow paths. This is the purpose why counting landslide sites, instead of calculating landslide area, was used in the equation (1) to calculate the LR_{class} .

In this study, in the numerator, the number of landslide sites, instead of the number of landslide cells, is used because of the difficulty in outlining boundaries between landslides and debris flows. The performance value derived by LR_{class} enables consideration of predicted stable areas as well as predicted unstable areas, and thus substantially reduces the overprediction of landslide potential. Disparate the numerator, the number of predicted and total cells is used in the denominator.

Table 1 Summary of TRIGRS results in landslide simulations

Factor of Safety Classes	Landslide site (a)	%of landslide sites (c)=a/b	% of predicted area (d)	$LR_{class}(e) =c/d$	% of $LR_{class} =e/f$
$FS \leq 1.0$	22	55.00	6.08	9.05	60.0
$1.0 < FS \leq 1.2$	6	15.00	9.92	1.51	10.0
$1.2 < FS \leq 1.4$	3	7.50	5.34	1.40	9.3
$1.4 < FS \leq 1.6$	3	7.50	5.38	1.39	9.2
$1.6 < FS \leq 1.8$	2	5.00	6.04	0.83	5.5
$1.8 < FS \leq 2.0$	2	5.00	6.12	0.82	5.4
$2.0 < FS$	2	5.00	61.13	0.08	0.5
Sum	40 (b)	100.00	100.00	13.61 (f)	100.00



Fig. 6 Results obtained by TRIGRS in each class; the graph of the Landslide percentage and the predicted FS percentage vs. factor of safety class.

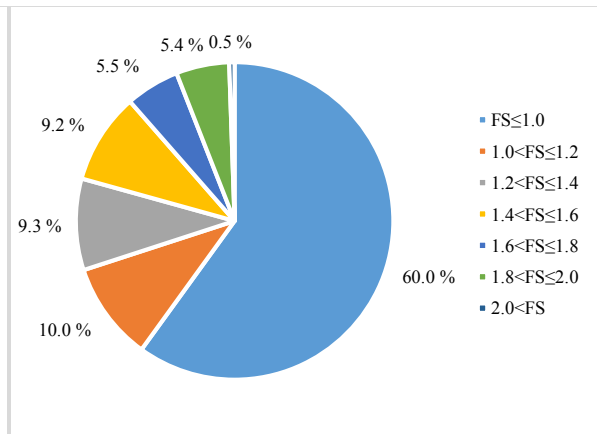


Fig. 7 Results obtained by TRIGRS in each class; the pie chart of LR_{class} with respect to the factor of safety class.

Table 1, Figure 6 and 7 show that 6.08% of the area was classified as unstable ($FS \leq 1.0$), and that 55% of the actual landslides were correctly localized within this predicted unstable area. $LR_{FS < 1}$ was about 9.05 with 55% over 6.08%. By calculating the % of LR_{class} , a quantitative result could be obtained. The percentage of $LR_{FS < 1}$ is 60%; in other words, if a landslide happens, then the predicted unstable area ($FS < 1$) has 60% (Figure 6) chance of including the landslide. Also, lower factor of safety classes showed higher values of LR_{class} percentages. The results show significant agreement between the simulated and known landslide occurrences from a quantitative point of view, despite missing information on landslide area (Figure 5).

5. Conclusions

In this study, an approach was introduced for the analysis of shallow landslide-triggering scenarios that uses the TRIGRS code, a physically based model which describes the stability conditions of natural slopes in response to specific rainfall events. As a first step, the model has been validated through the back analysis of a reference landslide event, i.e., the disaster that occurred in the Bulathsinhala area in May 2017.

Main purpose of this study was to suggest and verify an index LR_{class} (landslide ratio of each predicted FS class) for a pilot study. The biggest strength of this index is that it can estimate model performance quantitatively by

minimizing the overestimated area, even in landslide-debris flow regions where the area of landslide scars is unknown or ambiguous. According to the results, the percentage of LR_{class} of unstable area is 60%, and well reflects the effect of transient rainfall.

Comparing the results of the numerical simulation with the 2017 landslide inventory, it turns out that the model is able to reproduce the reference event quite well, both in terms of temporal evolution and spatial distribution of slope instability, identifying the areas most affected by shallow landslides. It is worth stressing that the model has been accurately parameterized through different methods and techniques, with specific focus on the evaluation of the spatial pattern of the triggering storm.

With regards to the proposed approach, the use of different techniques allows its application to different case studies, on the basis of the data availability. Furthermore, if we consider the possibility of depicting constantly updated triggering scenarios, this approach could be used to develop specific landslide early warning systems in order to support decision makers in both risk prevention and emergency response.

Acknowledgements

Special gratitude is given to the staff members of Badulla and Kaluthara NBRO district offices and staff of the Geotechnical Engineering and Testing Division of the NBRO for their enormous support as well as the data they provided to carry out this research.

References

- Baum, R.L., Savage, W.Z., and Godt, J.W., 2008, TRIGRS - A Fortran Program for Transient Rainfall Infiltration and Grid-Based Regional Slope-Stability Analysis, Version 2.0: Open-File Report, doi: 10.3133/ofr20081159.A model for run off analysis.pdf.
- Baum, R.L., Godt, J.W., and Savage, W.Z., 2010, Estimating the timing and location of shallow rainfall-induced landslides using a model for transient, unsaturated infiltration: *Journal of Geophysical Research: Earth Surface*, v. 115, doi:10.1029/2009JF001321.
- Berti, M., Martina, M.L.V., Franceschini, S., Pignone, S., Simoni, A., and Pizziolo, M., 2012, Probabilistic rainfall thresholds for landslide occurrence using a Bayesian approach: *Journal of Geophysical Research: Earth Surface*, v. 117, p. 1–20, doi:10.1029/2012JF002367.
- Highland, L.M., and Bobrowsky, P., 2008, *The Landslide Handbook - A Guide to Understanding Landslides*: Circular, doi: 10.3133/cir1325.
- Horton, P., Jaboyedoff, M., Rudaz, B., and Zimmermann, M., 2013, Flow-R, a model for susceptibility mapping of debris flows and other gravitational hazards at a regional scale: *Natural Hazards and Earth System Sciences*, v. 13, p. 869–885, doi:10.5194/nhess-13-869-2013.
- Hung, O., 1995, A model for the runout analysis of rapid flow slides, debris flows, and avalanches: *Canadian Geotechnical Journal*, v. 32, p. 610–623, doi: 10.1139/t95-063.
- Hung, O., Leroueil, S., and Picarelli, L., 2014, The Varnes classification of landslide types, an update: *Landslides*, v. 11, p. 167–194, doi:10.1007/s10346-013-0436-y.
- Iovine, G., Di Gregorio, S., and Lupiano, V., 2010, Debris-flow susceptibility assessment through cellular automata modeling: an example from 15–16 December 1999 disaster at Cervinara and San Martino Valle Caudina (Campania, southern Italy): *Natural Hazards and Earth System Science*, v. 3, p. 457–468, doi:10.5194/nhess-3-457-2003.
- Kim, D., Im, S., Lee, S.H., Hong, Y., and Cha, K.-S., 2010, Predicting the rainfall-triggered landslides in a forested mountain region using TRIGRS model: *Journal of Mountain Science*, v. 7, p. 83–91, doi: 10.1007/s11629-010-1072-9.
- Salciarini, D., Godt, J.W., Savage, W.Z., Conversini, P., Baum, R.L., and Michael, J.A., 2006, Modeling regional initiation of rainfall-induced shallow landslides in the eastern Umbria Region of central Italy: *Landslides*, v. 3, p. 181–194, doi:10.1007/s10346-006-0037-0.
- Schaap, M.G., Leij, F.J., and Van Genuchten, M.T., 2001, Rosetta: A computer program for estimating soil hydraulic parameters with hierarchical pedotransfer functions: *Journal of Hydrology*, v. 251, p. 163–176, doi:10.1016/S0022-1694(01)00466-8.
- Sorbino, G., Sica, C., and Cascini, L., 2009, Susceptibility analysis of shallow landslides source areas using physically based models: *Natural Hazards*, v. 53, p. 313–332, doi: 10.1007/s11069-009-9431-y.

Hydro-meteorological trigger conditions of debris flows in Austria

Roland Kaitna^{a,*}, David Prenner^a, Martin Braun^a, Markus Hrachowitz^b

^a University of Natural Resources and Life Sciences, Peter Jordanstr. 82, 1190 Vienna, Austria

^b Delft University of Technology, Building 23, Stevinweg 1, 2628 CN Delft, The Netherlands

Abstract

Different factors influence the disposition of a watershed for initiation of debris flows, including meteorological trigger conditions as well as the hydrologic and geomorphic disposition. The latter includes slowly changing factors like relief energy or sediment availability, whereas the hydrologic state of a watershed may vary over short time scales. This contribution summarizes the outcomes of a long term project to quantify meteorological and hydrological trigger conditions leading to debris flows at different temporal and spatial scales in the Austrian Alps. The analysis employs a database of more than 4,500 debris flows over the last 100+ years, which is the period for which systematic rainfall data is available. A Bayesian analysis was carried out for determining occurrence probabilities for all Austria. For selected regions, hydrological trigger conditions were assessed using a semi-distributed, conceptual rainfall-runoff model, which was calibrated to measured runoff data. As expected we find increasing trigger probabilities with increasing rainfall amounts and intensities. However, the additional information of regional hydrological parameters as well as their temporal evolution over days prior to a debris-flow event, enables to capture different trigger conditions, including short duration rainstorms, long lasting rainfall events, and snow melt. We also find that a trigger-type resolved prediction of debris-flow susceptibility based on the hydro-meteorological catchment information is superior to simple rainfall-only approaches. The results of this analysis shall improve our understanding of long-term trigger conditions and trends of extreme mass wasting processes in the Alps and aim to become a valuable tool in engineering hazard assessment.

Keywords: initiation conditions, probabilistic thresholds, hydrologic modeling, susceptibility

1. Introduction

Debris flows occurring in the European Alps are often triggered by rainfall events. Over the last decades a lot of work has been done to identify triggering rainfall amounts, intensity, or intensity-duration thresholds, mostly in conjunction with shallow landslides (see review by Guzzetti et al., 2007; 2008). To overcome the uncertainties that come with deterministic thresholds, Berti et al. (2012) outlined a probabilistic approach and derived conditional probabilities for shallow landslide initiation in the northern Apennine mountains. In the recent years also remote sensing techniques like radar or satellite data have been employed to derive rainfall thresholds at high spatial and temporal resolution (e.g. Marra et al., 2014; Salio et al., 2015). For the Austrian Alps the only published work is the case study of Moser and Hohensinn (1983).

Besides the triggering rainfall event also other factors, like sediment availability and hydrologic conditions within the watershed are expected to influence debris-flow initiation (Kienholz, 1995). As a proxy for the wetness state of a catchment the antecedent water was analyzed which consists of the rainfall inputs reduced by evapotranspiration and drainage losses within the last 10 days (e.g. Crozier, 1999; Wiczeorek and Glade, 2005). The sum of the antecedent water and the rainfall input at the actual day were considered to conclude whether to expect a landslide or not. A more complex model was provided by Ciavolella et al. (2016), who simulate the water cycle of a catchment by using a conceptual hydrological model that was calibrated to the catchments observed runoff. Result of the work was a threshold curve based on catchment water storage and precipitation as a tool to evaluate landslide susceptibility of the

* Corresponding author e-mail address: roland.kaitna@boku.ac.at

catchment. For events that were triggered in connection to snow melt, Meyer et al (2012) developed an intensity-duration threshold that considers two sources of critical water – melt water and rainfall water.

In this study we determined triggering rainfall events for more than 4,500 documented debris-flow events between 1901 and 2014 on a daily basis. Following the method of Berti et al. (2012) we also determined non-triggering rainfall events to calculate conditional probabilities for debris-flow triggering in Austria. At a regional scale we quantified the hydrological state of six contrasting regions when debris flows occur in the headwater catchments (Mostbauer et al., 2018; Prenner et al., 2018a,b). For that a semi-distributed rainfall-runoff model was setup covering periods of 40-60 years. Based on the temporal evolution of storage components and fluxes, we differentiated between three typical hydro-meteorological trigger conditions for debris-flow initiation in Austria.

2. Methods

2.1. Triggering rainfall

For 4,620 debris flows of the database of the Federal Ministry for Tourism and Sustainability (www.bmnt.gv.at/), the information of the data and the location (of damage) was available. In this database the definition of torrential processes follows the Austrian standard rules ONR 24800 (ONR, 2009) that separates between fluvial flows (floods and intensive bedload transport) and debris flow-like flows (debris floods and debris flows). Due to a sometimes unclear distinction between different processes (Bel et al., 2017), we only considered debris flows. The meteorological data was derived from the Hydrological Service (“HD”, ehyd.gv.at/) and the “Zentralanstalt für Meteorologie und Geodynamik” (“ZAMG”, www.zamg.ac.at). In total 790 time series of daily precipitation, daily temperature (mean, minimum and maximum), snow fall, and pressure were available. Here we used only the rainfall information.

For each observed debris-flow event the nearest active meteorological station was identified and the triggering event rainfall (TER) determined manually on a daily basis between 1901 and 2014 and on a sub-daily basis between 1993 and 2014. In the following we concentrate only on daily data. Events, for which meteo-station data exceeded a distance of 10 km and for which the determination of the rainfall event was unclear, were excluded from further analysis, reducing the number of TERs to 1,417. The database of TERs are (1) a direct result available for the community, but were (2) subsequently used to calibrate a detection algorithm for automatically identifying triggering and non-triggering rainfall events in all available time series from meteo-stations. For that we used an adapted algorithm provided by Matteo Berti (personal communication) and explained in Berti et al. (2012).

The probability Pr of a debris-flow event E conditional of a rainfall variable R in class $k = 1, 2, \dots, n$ was calculated with

$$Pr(E|R_k) = \frac{Pr(R_k|E) \times Pr(E)}{Pr(R_k)} \quad (1)$$

2.2. Hydro-meteorological trigger conditions

We setup a semi-distributed, process-based rainfall-runoff model for six contrasting regions in Austria (Fig 1) and analyzed the hydrological system state of the watershed on days where debris flows were observed in the steep headwater catchments and compared it to the days where no event was observed. The hydrologic model includes several storage components that represent snow and glaciers, unsaturated soil, interception, as well as fast and slow responding system components. Within a catchment different precipitation and elevation zones were modelled separately on a daily basis. For model calibration a likelihood-based differential evolution adaptive metropolis sampler (Vrugt, 2016) was used to derive posterior distributions of 43 calibration parameters. A detailed description of the model and the rigorous uncertainty assessment can be found in Prenner et al. (2018; 2019). A simplified analysis is described in Mostbauer et al. (2018). The modeling period for the six watersheds ranged from 46 to 71 years, including 3 to 43 days where debris flows were observed.

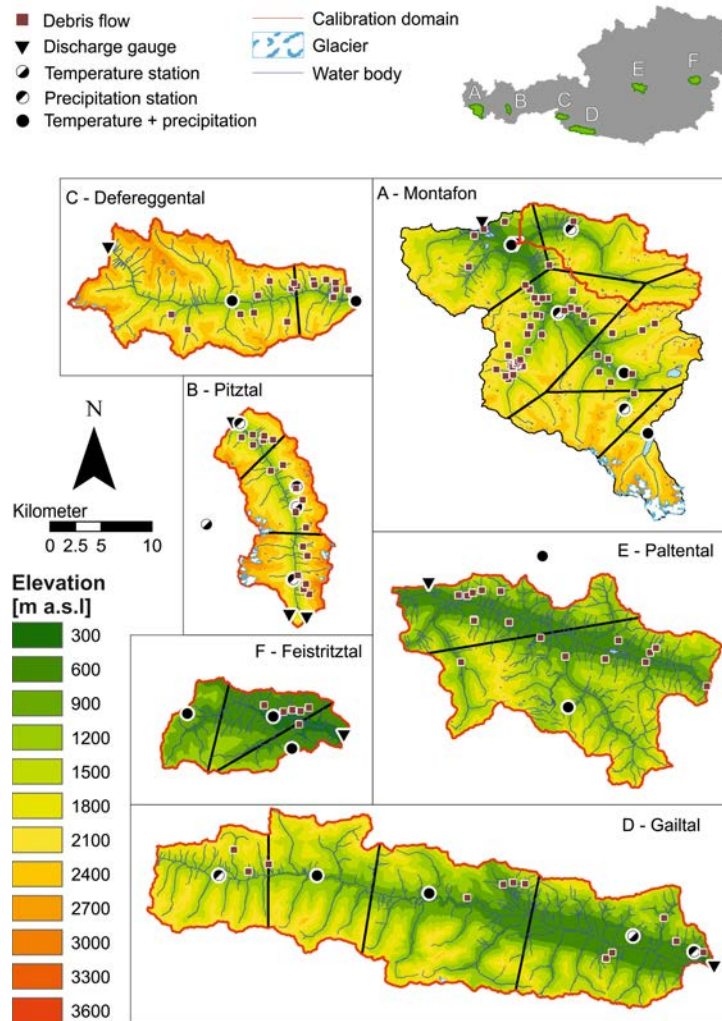


Fig. 1. Overview of the six study regions for the hydro-meteorological analysis

Table 1. Hydrological signals for identifying different trigger types for debris flows

Observation	Signal for LLR	Signal for SDS	Signal for SM
Increasing soil moisture in the prior days of event	X		
Decreasing potential evapotranspiration in the prior days of events	X		
Narrow air temperature span at the event day	X		
Decreasing soil moisture in the prior days of the event		X	
Constant high or increasing potential evapotranspiration in the prior days of events		X	
Large air temperature span at the event day		X	
Intense snow melt at the event day			X

Hydro-meteorological trigger conditions were analyzed for each watershed separately by comparing the distributions of modeled and measured variables like precipitation, soil moisture, (potential and actual) evapotranspiration, or runoff. Based on the notion that trigger conditions leave distinct signals in the hydrological time series, we ex-post differentiate between the trigger type long-lasting rainfall events (LLR), short-duration storms (SDS), and snow melt (SM). The hydrological signals for these simplified trigger types are given in Tab 1. Importantly, direct rainfall recordings were not used as criteria to avoid epistemic uncertainties from single point precipitation measurements. Here we try only to capture a general weather pattern, neglecting all different types of meteorological events. To also avoid a-priori definition of thresholds for these criteria, we sampled a 1000 times from a uniform distribution of plausible parameter values. Finally, the most frequent trigger type for each debris-flow event was selected (Prenner et al., 2018; 2019).

3. Results

3.1. Triggering rainfall

The median triggering rainfall amount for the analyzed debris-flow events was 40.0 mm, with a median intensity of 22.4 mm/d. Fig 2 compares derived triggering rainfalls and all automatically detected non-triggering rainfalls with the intensity-duration (I-D) thresholds for an Austrian case study of Moser and Hohensinn (1983), estimated by Guzzetti et al. (2007), and a global threshold for landslides and debris flows derived by Guzzetti et al. (2008, I-D threshold #6). Additionally we plot a quantile regression for the 5th percentile for the triggering rainfall. We see a wide range of measured trigger intensities. The 5% quantile regression plots below both thresholds. Especially for short triggering durations we expect that this daily analysis has limitations.

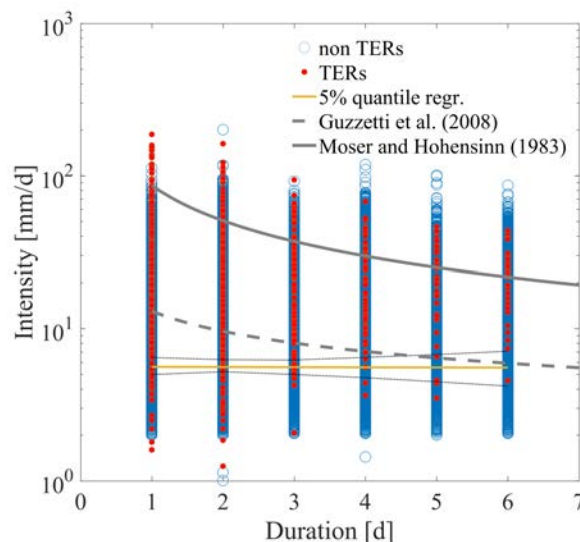


Fig. 2. Triggering and automatically detected non-triggering rainfalls for debris-flow events between 1901 and 2014 in Austria; the solid line represents the thresholds of Moser and Hohensinn (1983) as estimated by Guzzetti et al. (2007), the dashed line is a global threshold derived by Guzzetti et al. (2008).

As expected debris-flow occurrence probability increases with increasing precipitation. We find that the highest probabilities are associated with rainfall intensity, the total amount of rainfall, and the 3-day antecedent rainfall. The latter are shown in Fig 3. The two dimensional analysis of debris-flow probabilities in Austria conditional to the combination of rainfall intensity and duration shows that the highest probability emerges from high intensities > 24 mm/d.

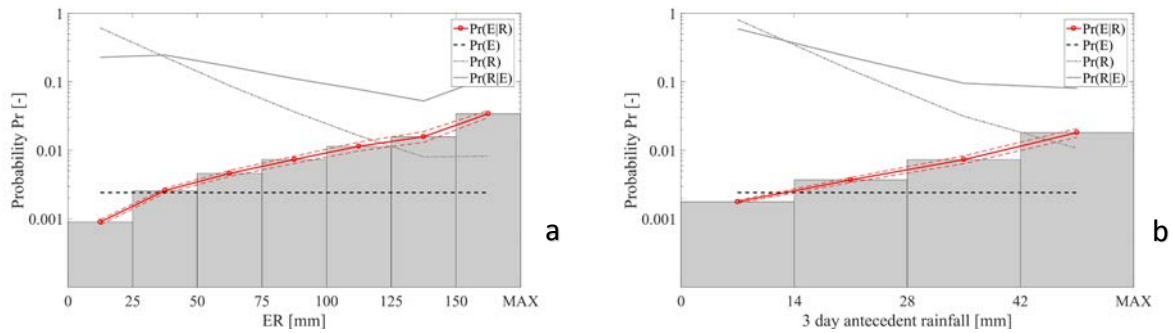


Fig. 3. (a) Probability of debris-flow occurrence conditional of total amount of rainfall (grey bars and red lines); (b) probability of debris-flow occurrence conditional of 3-day antecedent rainfall. In both plots dashed red lines refer to the 5th and 95th percentile of an assumed Poisson distributed counting error of debris-flow events; additionally the prior debris-flow probability $Pr(E)$ and prior rainfall probability $Pr(R)$ as well as conditional rainfall probability $Pr(R|E)$ are plotted.

It is important to note that our analysis is biased towards long rainfall event durations. Especially one-day intensities maybe strongly underestimated, as rainfall events may only last for few hours or minutes. Additionally, these mostly very local convective processes might not have been captured by the nation-wide rain-gauge network. In other words, we expect that our analysis does not capture debris-flow events that were triggered by short duration storms (SDS). As shown in the next section, our analysis might therefore be representative only for roughly 1/3 of the debris flows occurred in Austria.

3.2. Hydro-meteorological trigger conditions

Modeling performance after calibration of the six study regions were measured with different metrics and reached satisfying results (e.g. Nash-Sutcliffe efficiency indexes varying between 0.7 and 0.89). Fig 4 exemplarily shows modeling results for the study region Defreggental, a high alpine valley in the southern part of the alpine chain, for the year 2012. We see highest runoff during summer and a high fraction of melt water input into the soil and channel system during spring and late fall. Soil moisture gradually builds up during spring.

In the lower part of Fig 4 we show examples of the hydrologic state for three debris-flow event days. In the first example there is significant rainfall prior to the event day, leading to a continuous buildup of soil moisture. At the same time temperature and especially the difference between daily minimum and maximum temperature decreases, which is typically associated with a frontal rainfall of long duration (LLR). The second example shows a contrasting picture. Though some rainfall was measured on the days prior to the event, the temperature differences are high, indicating strong solar energy input during the day. Soil moisture slightly decreases. On the event day no significant rainfall was recorded. We classified this event trigger as a convective storm event of short duration (SDS). Finally, in the third example rainfall in conjunction with intensive snowmelt (SM) triggered the debris-flow event. We note that we also found debris-flow event days without any recorded rainfall but very intense snowmelt.

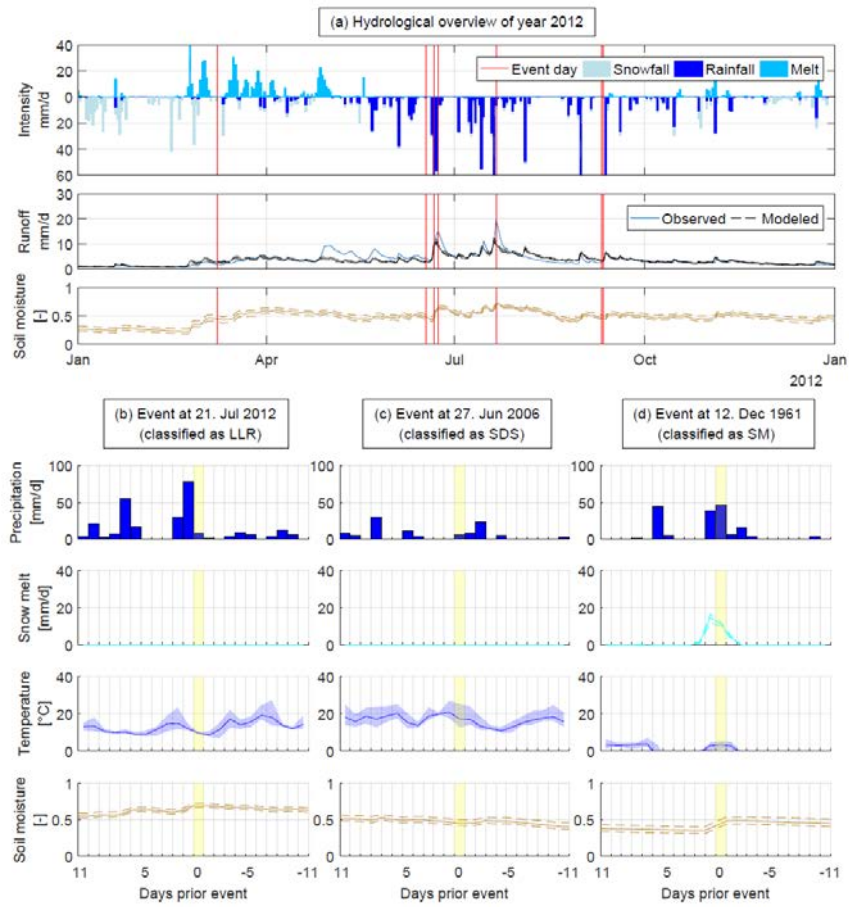


Fig. 4. (a) Example of selected modeling results for the study region Defreggental for the year 2012; (b) example of a debris-flow trigger that was classified as LLR, (c) as SDS, and (d) as an event were SM was important.

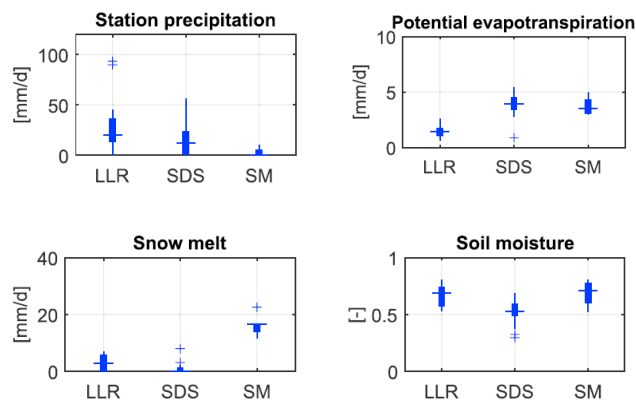


Fig. 5. Distribution of event day precipitation (which was not used for trigger classification), potential evapotranspiration, snow melt, and soil moisture at event days in the Montafon region (modified after Prenner et al., 2018).

Selected hydro-meteorological variables associated with the roughly separated trigger types are shown in Fig 5. We find that the registered event rainfall on the daily basis (which was not used for classification) supports our classification. LLR events have higher total rainfall sums than SDS events. (SDS events might have higher intensities, but this is probably not captured by the station network). For SM events sometimes no rainfall was measured. Similarly, also other variables are statistically different between the three groups (tested with the method of Kruskal and Wallis, 1952), which strongly supports the notion that different hydro-meteorological trigger types can be found in our study region.

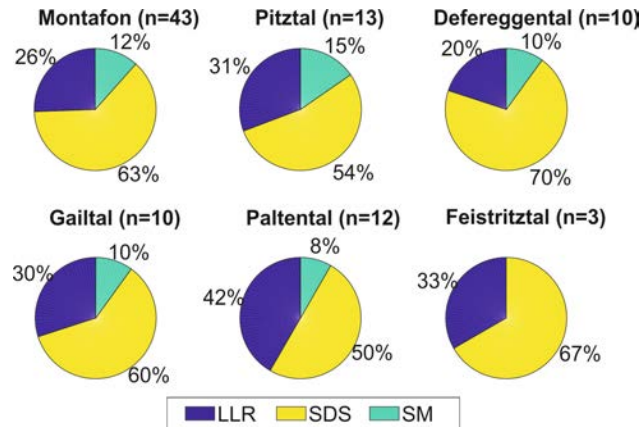


Fig. 6. Trigger of debris-flow events in the study regions.

In summary, we find the 50-70 % of the documented debris flows in the six study regions were triggered by SDS events, 20-44% due to LLR, and for up to 15 % snowmelt played a significant role (Fig 6). We think that for a better forecasting of debris-flow events, the combined information of rainfall forecasting and a real-time modeling of the hydro-meteorological history of a region, will be useful to capture these different trigger types.

4. Conclusions

A new database of triggering event rainfall for debris flows in Austria on a daily and sub-daily basis was created. The probabilistic analysis of triggering rainfall on a daily basis showed that probabilities for debris-flow occurrence increase with increasing rainfall amount, intensity and antecedent rainfall. The investigation of the hydro-meteorological trigger conditions in six contrasting study regions indicated a strong variability of hydro-meteorological trigger conditions of documented debris flows. The initial soil moisture as well as the rainfall on the event day, was higher for events associated with long-lasting rainfall events (LLR) than with short duration storms (SDS) across all study regions. Initial soil moisture and event day precipitation sums strongly vary across the regions for the same trigger type. Importantly, the temporal change of hydrological watershed state before events show similar signals across the regions and allows to draw more general conclusions about the susceptibility of regions to debris-flow release and might allow the development of a forecasting tool similar to the model suggested by Prenner et al. (2018). A major limitation of such a hydro-meteorological assessment, however, is the missing geomorphological component, e.g. temporal variation of sediment availability.

Acknowledgements

We thank Matteo Berti for sharing the detection algorithm for the rainfall events. Climatic and hydrologic datasets were provided by HD Austria including its subdivisions of Vorarlberg, Tyrol, Carinthia, Styria and Lower Austria, the ZAMG, TIWAG, Vorarlberger Illwerke AG. The model runs were performed on the Vienna Scientific Cluster

(vsc.ac.at), which we thankfully acknowledge. This project received financial support from the Austrian Climate and Energy Fund [grant number B464795] and was carried out within the framework of the ‘ACRP’ Programme.

References

- Bel, C., Liébault, F., Navratil, O., Eckert, N., Bellot, H., Fontaine, F., and Laigle, D., 2017, Rainfall control of debris-flow triggering in the Réal Torrent, Southern French Prealps: *Geomorphology*, v. 291, p. 17–32, doi:10.1016/j.geomorph.2016.04.004.
- Berti, M., Martina, M. L. V., Franceschini, S., Pignone, S., Simoni, A., and Pizziolo, M., 2012, Probabilistic rainfall thresholds for landslide occurrence using a Bayesian approach: *Journal of Geophysical Research: Earth Surface*, v. 117(F4), doi:10.1029/2012JF002367.
- Ciavolella, M., Bogaard, T., Gargano, R., and Greco, R., 2016, Is there Predictive Power in Hydrological Catchment Information for Regional Landslide Hazard Assessment? *Procedia Earth and Planetary Science*, v. 16, p. 195–203, doi:10.1016/j.proeps.2016.10.021.
- Crozier, M. J., 1999, Prediction of rainfall-triggered landslides: A test of the antecedent water status model: *Earth Surface Processes and Landforms*, v. 24(9), p. 825–833, doi:10.1002/(SICI)1096-9837(199908)24:9<825::AID-ESP14>3.0.CO;2-M.
- Guzzetti, F., Peruccacci, S., Rossi, M., and Stark, C. P., 2007, Rainfall thresholds for the initiation of landslides in central and southern Europe: *Meteorology and Atmospheric Physics*, v. 98(3–4), p. 239–267, doi:10.1007/s00703-007-0262-7.
- Guzzetti, F., Peruccacci, S., Rossi, M., and Stark, C. P., The rainfall intensity–duration control of shallow landslides and debris flows: an update: *Landslides*, v. 5(1), p. 3–17, doi:10.1007/s10346-007-0112-1.
- Kienholz, H., 1995, Gefahrenbeurteilung und -bewertung – auf dem Weg zu einem Gesamtkonzept: *Schweizerische Zeitschrift für Forstwesen*, v. 146, p. 701–725.
- Kruskal, W. H., and Wallis, W. A., 1952, Use of ranks in one-criterion variance analysis: *Journal of the American Statistical Association*, v. 47(260), p. 583, doi:10.2307/2280779.
- Wieczorek, G. F. and Glade, T., 2005, Climatic factors influencing occurrence of debris flows, in Jakob, M., and Hungr, O., eds., *Debris-flow Hazards and Related Phenomena*, Springer, Berlin, Heidelberg, p. 325–362, doi:10.1007/3-540-27129-5_14.
- Marra, F., Nikolopoulos, E. I., Creutin, J. D., and Borga, M., 2014, Radar rainfall estimation for the identification of debris-flow occurrence thresholds: *Journal of Hydrology*, v. 519, p. 1607–1619, doi:10.1016/j.jhydrol.2014.09.039.
- Meyer, N. K., Dyrddal, A. V., Frauenfelder, R., Etzelmüller, B., and Nadim, F., 2012, Hydrometeorological threshold conditions for debris flow initiation in Norway: *Natural Hazards and Earth System Sciences*, v. 12(10), p. 3059–3073, doi:10.5194/nhess-12-3059-2012.
- Moser, M. and Hohensinn, F., 1983, Geotechnical aspects of soil slips in Alpine regions: *Engineering Geology*, v. 19(3), p. 185–211.
- Mostbauer, K., Kaitna, R., Prenner, D., and Hrachowitz, M., 2018, The temporally varying roles of rainfall, snowmelt and soil moisture for debris flow initiation in a snow-dominated system: *Hydrology and Earth System Sciences*, v. 22(6), p. 3493–3513, doi:10.5194/hess-22-3493-2018
- Prenner, D., Kaitna, R., Mostbauer, K., & Hrachowitz, M., 2018, The Value of Using Multiple Hydro-meteorological Variables to Predict Temporal Debris Flow Susceptibility in an Alpine Environment: *Water Resources Research*, v. 54(9), p. 6822–6843, doi:10.1029/2018WR022985.
- Prenner, D., Hrachowitz, M., Kaitna, R., 2019, Trigger characteristics of torrential flows from high to low alpine regions in Austria: *Science of the Total Environment*, v. 658, p. 958–972, doi:10.1016/j.scitotenv.2018.12.206.
- Salio, P., Hobouchian, M. P., García Skabar, Y., and Vila, D., 2015, Evaluation of high-resolution satellite precipitation estimates over southern South America using a dense rain gauge network: *Atmospheric Research*, v. 163, p. 146–161, doi:10.1016/j.atmosres.2014.11.017.
- Vrugt, J. A., 2016, Markov chain Monte Carlo simulation using the DREAM software package: Theory, concepts, and MATLAB implementation: *Environmental Modelling & Software*, v. 75, p. 273–316, doi:10.1016/j.envsoft.2015.08.013.

Weather-radar inferred intensity and duration of rainfall that triggered the January 9, 2018, Montecito, California, disaster

Jeffrey R Keaton^{a,*}

^aWood, 6001 Rickenbacker Rd, Los Angeles 90040, USA

Abstract

Slopes above Montecito burned by the Thomas Fire in December 2017 produced disastrous debris flows in response to a short period of intense precipitation on January 9, 2018, killing 23 people, injuring many others, destroying and damaging residential buildings, and community infrastructure. The intense precipitation was in a narrow cold frontal rainband which obviously exceeded the intensity and duration threshold for post-wildfire debris flows. Rain gauges with self-activating radio transmitters reported by County of Santa Barbara Department of Public Works documented the precipitation in the Montecito area as it occurred, which allowed short-duration intensities to be calculated. Data from the rain gauge on Montecito Creek was used in this paper and showed that the rainband that produced the precipitation that generated the debris flows passed over Montecito in about one-half hour. Two weather radar stations operated by the National Weather Service are located within about 100 km of Montecito. Both stations were operational and recorded radar reflectivity on a frequency of about five minutes during the entire storm; data from the KVTX station located east of Montecito was used for this paper. Montecito is located on a coastal plain south of the Santa Ynez Mountains, which shield the lower elevations in the Montecito area from direct view of the radar stations. Composite radar reflectivity represents the amount of water droplets in the atmosphere in line-of-sight above the ground. The weather radar shows patterns similar to the precipitation documented by the rain gauges. Radar reflectivity at the coordinates of the rain gauge on Montecito Creek and at the coordinates of a point in the Santa Ynez Mountains on the west side of the Santa Ynez Creek watershed was extracted and converted to an approximate rainfall depth using a general National Weather Service relationship. The results are used to demonstrate the value of weather radar reflectivity for visualization and for developing approximate rainfall intensity and duration estimates at positions of interest remote from rain gauges for comparison with post-wildfire debris-flow thresholds. The analysis in this paper was developed as part of the Geotechnical Extreme Event Reconnaissance (GEER) Association response to the Montecito disaster.

Keywords: *Precipitation intensity and duration; Burned slopes; Weather radar; Debris flow*

1. Introduction

The Thomas Fire began in southwestern Ventura County on December 4, 2017, and was finally contained on January 12, 2018, after burning over 114,000 hectares in Ventura and Santa Barbara Counties (CalFire, 2018). The fire advanced into the watersheds above Montecito beginning on December 10, 2017, and stopped its westward progression on December 18, 2017 (EcoWest, 2017), but continued to burn northward into wildland areas until it was contained nearly four weeks later. The burned slopes above Montecito had soil burn severity of predominantly moderate, with some small areas of high burn severity (CalFire, 2018). Burned drainage basins north of Montecito were rated as high hazard of producing debris flows in response to a design rain storm producing a 15-minute rainfall intensity of 24 mm h⁻¹ (USGS, 2018, interactive preliminary hazard assessment map).

A flash flood watch was issued by the National Weather Service (NWS) in Los Angeles/Oxnard, California, on January 6, 2018, for regions of southwestern California that included Montecito (IEM, 2018a). The NWS flash flood watch indicated “A strong cold front will interact with a deep plume of subtropical moisture bringing a period of moderate to heavy rainfall to the region beginning Monday afternoon through Tuesday morning. Behind the front, scattered showers and isolated thunderstorms will continue through Tuesday evening. Rainfall rates in excess of one

* Corresponding author e-mail address: jeff.keaton@woodplc.com

half to an inch per hour [12.7 to 25.4 mm h⁻¹] are possible during the peak of the storm. This storm has the potential to create mud and debris flows in and around the recent burn areas. ...” (IEM, 2018a). Another NWS flash flood watch on Monday, January 8, 2018, forecast peak rainfall rates between 0.5 and 1.0 inch per hour (12.7 to 25.4 mm h⁻¹) with local rates up to 1.5 inch per hour (38.1 mm h⁻¹) (IEM, 2018b). The precipitation event that triggered devastating debris flows was associated with a weak atmospheric river that generated an intense convective precipitation band along a narrow zone that formed along a cold front, known as a narrow cold frontal rainband (Oakley et al., 2018). The short duration precipitation was not unprecedented for the region, but records for some stations were set by it.

The remaining sections of this paper describe the setting of Montecito in terms of weather radar and rain gauge locations, use selected NWS weather radar data and County of Santa Barbara rainfall records to estimate precipitation intensity and duration in the Montecito area on January 8 and 9, 2018, and compare the precipitation estimates to general thresholds for debris flows to be generated on burned slopes.

2. Setting of Montecito relative to weather radar and rainfall sensors

Montecito is located in southeast Santa Barbara County approximately 5 kilometers east of Santa Barbara. Two NEXRAD WSR-88D Doppler weather radar stations are located within 100 km of Montecito (Fig. 1), within the 230-km distance for short-range weather radar products (<https://www.ncdc.noaa.gov/data-access/radar-data/radar-map-tool>). Both weather radar stations were operating in precipitation mode, consisting of 16 360°-sweeps of 14 elevation angles in 5 or 6 minutes. Local mountains east and north of Montecito block the lowest elevation angles of both weather radar stations. Composite reflectivity data for the closer weather radar station, KVTX (-120.39583° Lon., 34.83806° Lat., 375.8 m elev.), were downloaded and used in this analysis. Composite reflectivity represents the maximum reflectivity for the volume coverage pattern of the radar at each azimuth and range position of the scan. Radar reflectance is reported in a scale specific to meteorology (decibels in the Z scale, dBZ). NEXRAD products are archived and available for no-cost online retrieval at <https://www.ncdc.noaa.gov/nexradinv/>. Reflectivity is a measure of size and number of water droplets in a volume of the atmosphere and is correlated to precipitation intensity, or rain rate, RR in mm h⁻¹. The correlation used in this study was calculated as equation (1) from a table of dBZ and RR values displayed on the NWS website (<https://www.weather.gov/jetstream/refl>), which corresponds exactly to the default $Z=300 RR^{1.4}$ but is easier to use in spreadsheet calculations. Reflectance higher than 51 dBZ may be an indicator of ice in the atmosphere contributing to overestimation of rain rates (Fulton, 1999).

$$RR = \exp(-4.073 + 0.1644 \times \text{dBZ}); 15 \leq \text{dBZ} \leq 55 \quad (1)$$

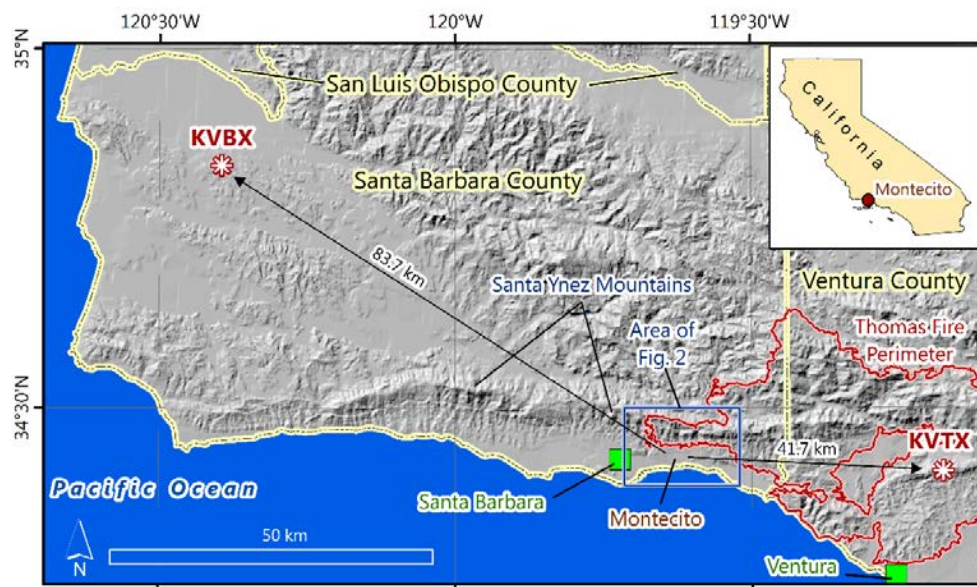


Fig. 1. Location map showing NWS weather radar station locations (NCEI, 2018). Thomas fire perimeter was obtained from GeoMAC (2018); shaded relief base map from U.S. Geological Survey bip file; county boundaries from ESRI basic data shape files. Projection: NAD 1927 California Teale Albers. Area of Fig. 2 (blue rectangle) encompasses western tip of Thomas Fire perimeter and the Montecito community.

The Montecito area has six automated rain gauges operated by the County of Santa Barbara Public Works Hydrology Section (Fig. 2). The Montecito gauge (#325; sensor 2547) is located on Montecito Creek and was selected for analysis in this paper. Data from the Montecito gauge for the storm of January 8-9, 2018, were obtained online (https://rain.cosbpw.net/site.php?site_id=47&site=d1f0d1f6-a251-4e7d-a036-927432472f28). The automated gauges record rainfall as it occurs and self-activating radio transmitters send data at variable intervals, ranging from as little as 2 seconds to as much as 12 hours; the median frequency of readings during the storm was about 3 minutes (0.05 hour). The frequency of readings was regularized to an interval of approximately 5 minutes for use in calculations.

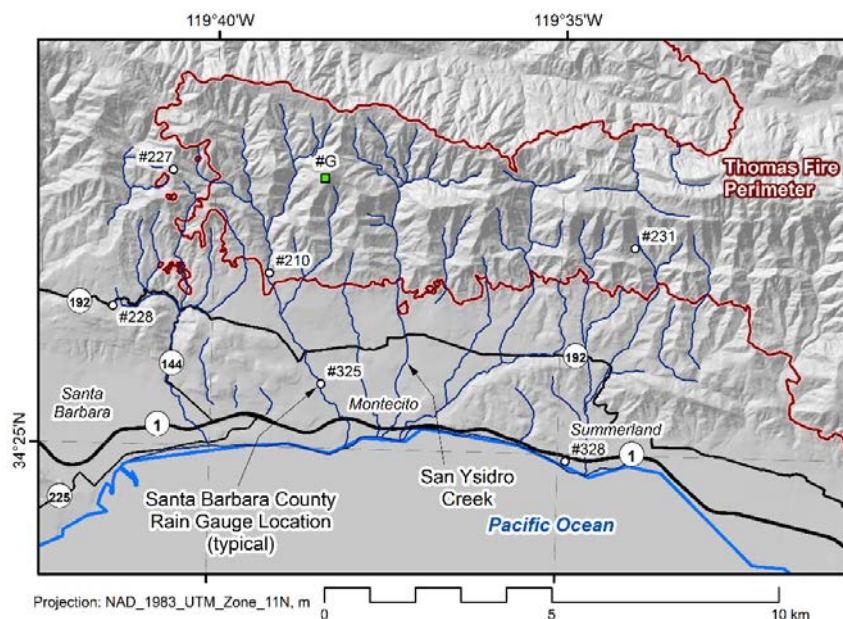


Fig. 2. Montecito area showing locations of Santa Barbara County rain gauges (COSBPW, 2018) and the Thomas Fire perimeter (GeoMAC, 2018). Location #G is the position where radar composite reflectivity was converted to rainfall. Base map hillshade calculated from 10-m DEM from National Elevation Dataset obtained from U.S. Department of Agriculture Natural Resources Conservation Service Geospatial Data Gateway. Stream channels from National Hydrography Dataset also obtained from Geospatial Data Gateway.

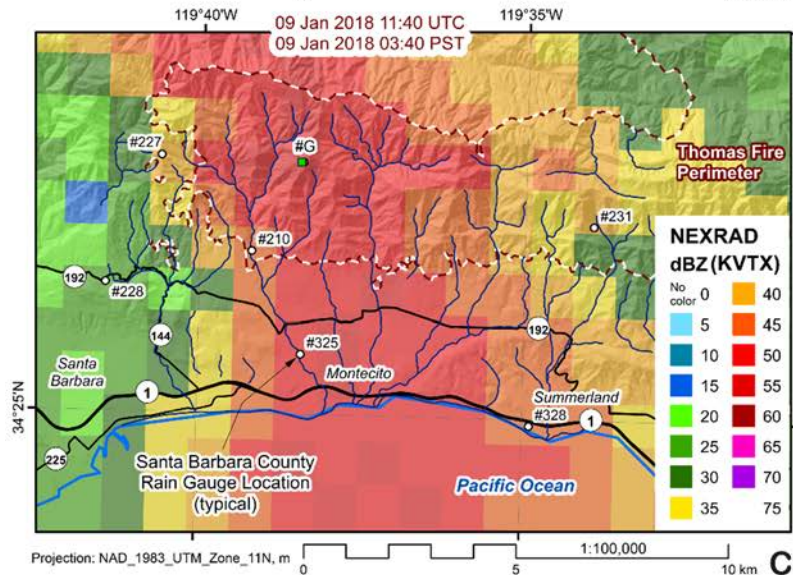
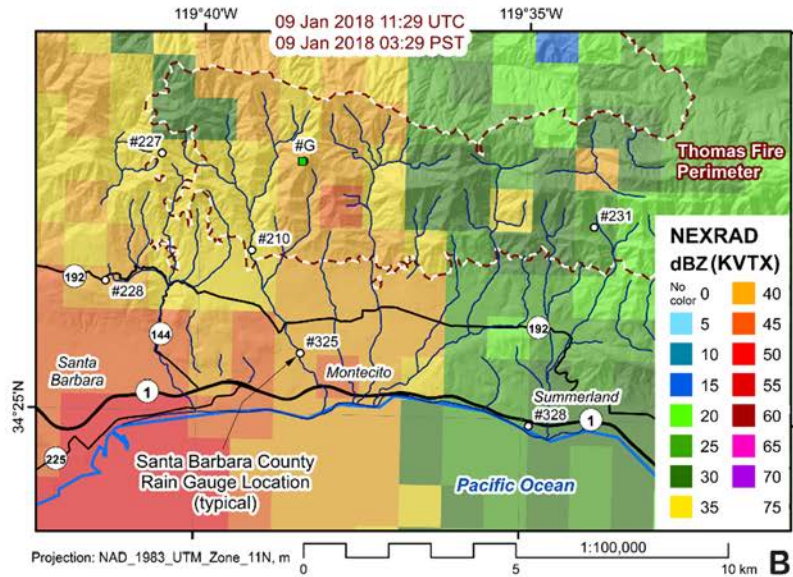
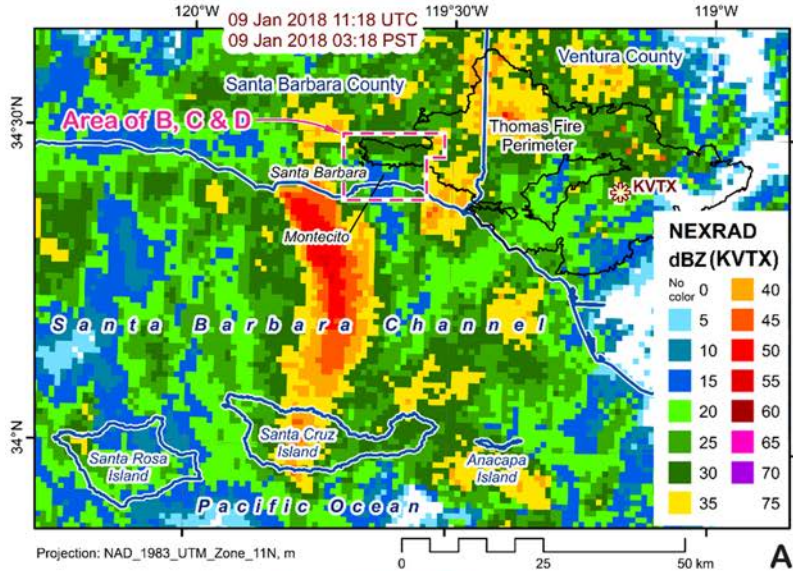
Location #G was selected as a point of interest because it is in the upper watersheds of San Ysidro Creek to the east and Montecito Creek to the west (Fig. 2). Sta #325 is on Montecito Creek; Location #G is approximately 4.5 km due north of Sta. #325. No rain gauges were located at positions other than those shown in Fig. 2 at the time of the January 8-9, 2018, storm; therefore, weather radar provides an opportunity for precipitation to be visualized, and estimated in a way that may be superior to interpolating or extrapolating from available rain gauges.

3. Weather radar reflectivity and automated rainfall

The downloaded reflectivity data for NEXRAD WSR-88D Doppler weather radar station KVTX for January 8 and 9, 2018, were processed using the Weather and Climate Toolkit (<https://www.ncdc.noaa.gov/wct/>) and exported for display and analysis using ESRI ArcGIS 10.4. The Weather and Climate Toolkit viewer allowed the relevant times of the storm in Montecito to be identified. The radar product selected for this analysis was the Level III, short-range, composite radar reflectivity (NCR), which had a complete dataset every 5 or 6 minutes. The composite reflectivity represents the maximum reflectance value in the scanned volume of atmosphere at each pixel. The pixel dimensions of the reflectivity data in the Montecito area were about 1 km square. Fast-moving storms can be represented by high reflectivity values, but the precipitation in the atmosphere at that pixel may fall to the ground in an adjacent pixel.

Four radar reflectivity scenes (Fig. 3), each 11 minutes apart, demonstrate that the strong narrow cold frontal rainband moved across Montecito in less than 30 minutes, with any one point receiving heavy precipitation for about 10 minutes (Fig. 3 and Fig. 4). A radar dataset was available between each pair of scenes selected for Fig. 3, and all scenes were used in the analysis, even though only selected scenes are displayed in this paper.

The radar data indicates that Montecito (Sta. #325) was experiencing light rain (15 dBZ) at 03:18 (Fig. 3A), as the main storm cell was making landfall on the west side of Santa Barbara. At 03:29 (Fig. 3B), 11 min later, Montecito



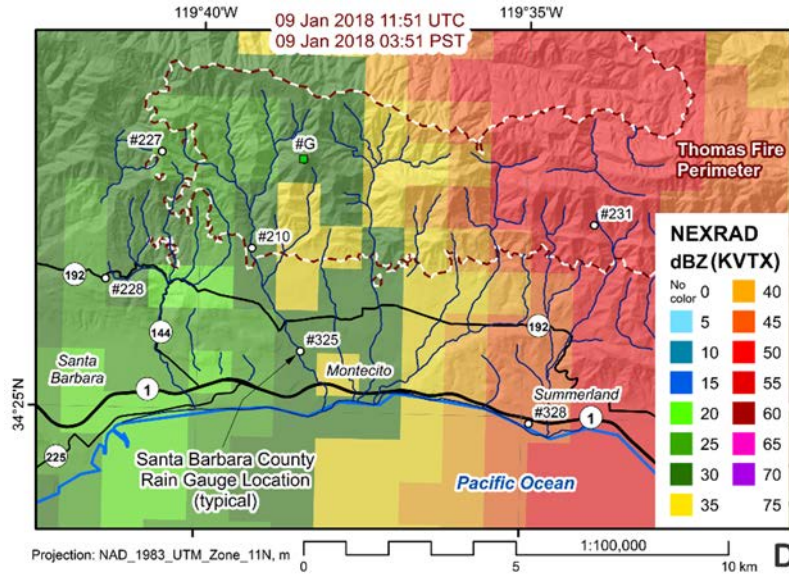


Fig. 3. Composite radar reflectivity of a narrow cold frontal rainband documented by KVTX on January 9, 2018. A. Radar scene at 03:18 PST with labels for the radar station, Thomas fire perimeter, Montecito, and area of Fig. 3B, 3C, and 3D; B. Radar scene at 03:29 PST with labels for rain gauges, point #G, Thomas fire perimeter, and Montecito; C. Radar scene at 03:40 PST; D. Radar scene at 03:51 PST.

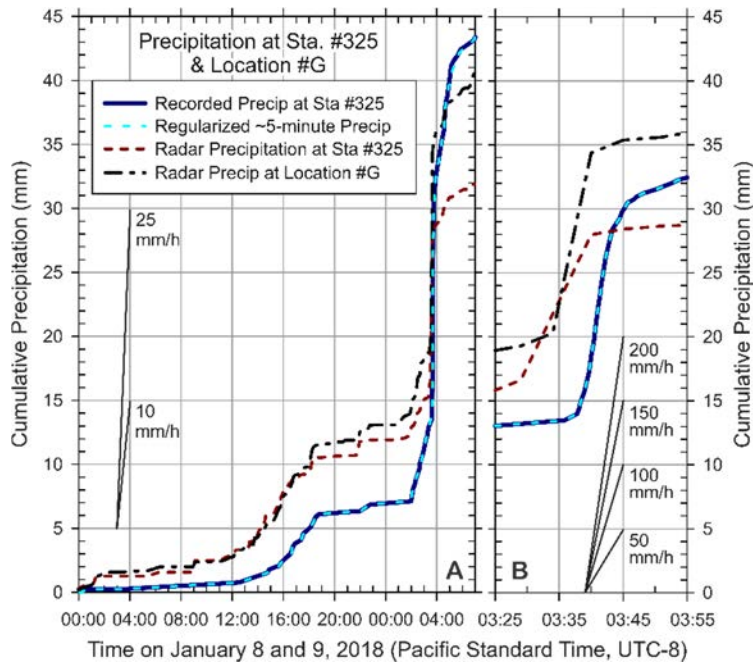


Fig. 4. Cumulative precipitation measured at Sta. #325 and calculated from radar reflectivity at Sta. #325 and Location #G. A. 31 hours of data from 00:00 Jan 8, 2018, to 07:00 Jan 9, 2018; B. 30 min of data from 03:25 to 03:55 Jan 9, 2018. Regularized line for precipitation has a 4- to 5-minute time interval (light blue dashed line) interpolated from variable frequency readings (dark blue line); the two lines are nearly superimposed.

Sta. #325 was receiving moderate to heavy rain (40 dBZ), while Location #G was receiving that same rate. At 03:40 (Fig. 3C), 11 min later, Montecito Sta. #325 was receiving very heavy rain (50 dBZ), while Location #G was receiving even heavier rain (55 dBZ). By 3:51 (Fig. 3D), 11 minutes later, Montecito Sta. #325 was receiving light rain (30 dBZ), while Location #G was receiving that same rate; the main storm cell had moved approximately 5 or 6 km east of the Montecito area by 03:51. Comparison of the main storm cell location in Fig. 3A with Fig. 3D indicates that it was moving east-northeast at a speed greater than 40 km h^{-1} .

A graph of cumulative precipitation (Fig. 4) displays both measured rainfall at Sta. #325 and estimated precipitation at location #G based on successive rain gauge and weather radar datasets covering the same period of time. The reflectivity values in each radar scene were converted to rain rate using equation (1) and then multiplied by the duration in hours since the previous radar scene to produce an equivalent precipitation depth for the time increment. Cumulative precipitation is the sum of the incremental precipitation depths. The measured rain at the Montecito gauge (Sta. #325) was reported in inches with a YYYY-MM-DD HH:MM:SS timestamp; the rain was converted to millimeters and the timestamp to converted to a serial number by copying Date-Time function data in Microsoft Excel and pasting it as unformatted numbers. The serial time and cumulative rain depth were converted to a regular time and corresponding rain depth, with the time step of 0.0035 days using a cubic spline interpolation in Mathcad. The resulting time step alternated between 0.003 and 0.004 days, which is equivalent to 4.32 and 5.76 minutes. Equivalent hourly precipitation intensity values for a range of duration intervals were calculated for both measured rainfall and estimated radar rain depths by successively summing estimated rain depths for different durations in spreadsheets and normalizing the results to a one-hour time duration.

Comparison of the rain gauge data for Sta. #325 (dark blue line in Fig. 4) with the calculated equivalent radar rain depth (red dotted line in Fig. 4) reveals that the radar-based rain at low intensity levels, before the main storm cell arrived at about 03:38 (Fig. 4B), exceeded the measured rain that reached the ground at that location. In contrast, by about 03:45 as the main storm cell departed Sta. #325 (Fig. 4B), the rain gauge data exceeded the calculated radar rain amount. The rain gauge data collected by Sta. #325 are the reference for its location. Rain depths estimated from radar reflectivity values are approximate and affected by at least three factors: 1) topography blocks the lowest elevation radar scans of Montecito from both weather radar stations, 2) the composite radar reflectivity values represent the maximum from all 14 elevation scans for the atmosphere volume above the Sta. #325 pixel, and 3) the correlation of rain rate from reflectivity is based on the default Z-R general relationship.

Radar-based cumulative precipitation at Location #G (black dot-dashed line in Fig. 4) matches the radar-based cumulative precipitation at Sta. #325 until about 18:00 on January 8. At the time the main storm cell moved into Montecito at approximately 03:30 on January 9, Location #G had 3 mm more estimated rain depth than the calculated radar rain depth at Sta. #325. However, by 03:40, the radar rainfall at Location #G was 7 mm greater than at Sta. #325. By 03:45, the measured rain depth at Sta. #325 exceeded the calculated radar rain depth by about 2 mm, and by 07:00, measured rain depth at Sta. #325 was 11 mm greater than the calculated rain depth.

The slope of cumulative precipitation plot is rainfall intensity, as indicated by the labeled thin black lines in Fig. 4. It is clear that the majority of the precipitation at the at Sta. #325 and location #G fell in a period less than 2 hours (Fig. 4A) and about 15 mm fell in less than 10 minutes (Fig. 4B). A graph of calculated precipitation intensity for the same 31-hour period in Fig. 4A is displayed in Fig. 5. The ~5-minute intensity values were calculated from the normalized measured rainfall data at Sta. #325 and the rain rate for individual weather radar scenes, which were collected at a 5- to 6-minute frequency. Therefore, each point plotted in Fig. 5 represents the rainfall amount over a period of about 5 minutes divided by the number of hours in the actual time interval. For example, a 5-minute precipitation amount of 11.67 mm divided by 0.0833 h = 140 mm h⁻¹, which is the precipitation intensity at Location #G estimated from radar reflectivity at 03:40 on January 9, 2018 (Fig. 3C; green triangle in Fig. 5). A 190 mm h⁻¹ intensity for Sta. 325 (red dot in Fig. 5) was based on a single regularized 4.32-minute interval (Fig. 6A).

4. Rainfall intensity and duration threshold for debris flows

Precipitation intensity and duration for Sta. #325 and Location #G (Fig. 6) were calculated from measured and regularized rainfall amounts (green diamond and black circle symbols in Fig. 6A) and weather radar reflectivity (variable symbols in Fig. 6A and 6B). The self-activating radio transmitter sensor at Sta. #325 sent rainfall data as it occurred, in intervals as short as 2 s for high-intensity rainfall. The intensity-duration values in Fig. 6 were calculated by summing the measured or calculated rain depth in mm over N successive measurements, where $1 \leq N \leq 95$ for the automated rain gauge and $1 \leq N \leq 8$ for weather radar reflectivity readings, and dividing by the corresponding duration in hours of the N measurements. The intensity-duration calculations were performed with spreadsheet functions in columns that allowed rows to be used in multiple, successive calculations. The large variety of duration values from measured rainfall (green diamond symbols in Fig. 6A) results from short intervals between data points. Plotting was arbitrarily cut off at intensities of about 2 to 7 mm h⁻¹.

The intensity-duration plots (Fig. 6) include two lines defining thresholds for post-fire debris flows on susceptible slopes (equations listed in Fig. 6B). The upper of the two lines (Staley et al., 2014) is an objective assessment of a database that includes the basis for the lower line (Cannon et al., 2008). It is clear from both rain gauge and weather

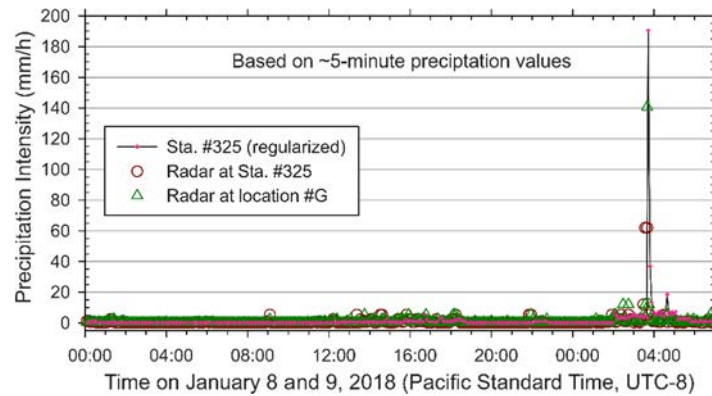


Fig. 5. Precipitation intensity at Sta. #325 and location #G based on approximately 5-minute increments. The irregular increments of rainfall measurements at Sta. #325 were regularized to 4- to 5-minute increments; weather radar in precipitation mode is in 5- to 6-minute increments.

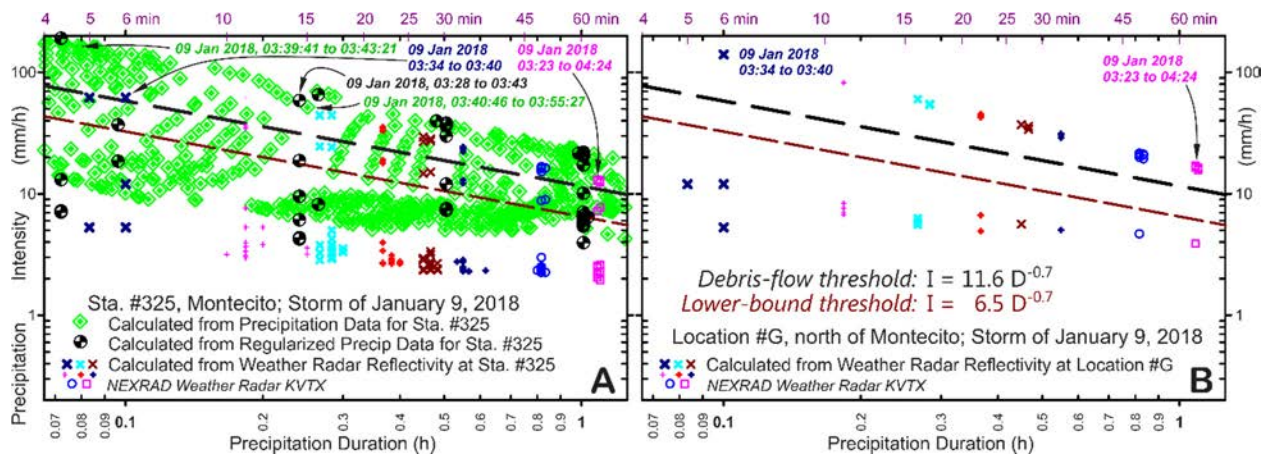


Fig. 6. Precipitation intensity and duration calculated at Sta. #325 and Location #G. A. Based on measured rainfall and radar reflectivity at Sta. #325; B. Based on radar reflectivity at Location #G. Thresholds from Cannon et al. (2008) and Staley et al. (2014) Calculated values are discussed in text.

radar data that the thresholds were surpassed at Sta. #325. However, the flash flood and debris flow sediments originated in the drainage basins north of Montecito that were burned by the Thomas Fire (Fig. 2). Comparison of the measured and estimated rainfall at Sta. #325 indicates that measured rainfall exceeded the amount and intensity of radar rainfall, but the timing and general trend of estimated rainfall were similar. The radar rainfall calculated for Location #G exceeded the amount and rate calculated for Sta. #325. Location #G was close to the crest of the Santa Ynez Mountains, indicating some orographic enhancement (Oakley et al., 2018). Calculated precipitation intensities exceed the debris-flow thresholds at Location #G (Fig. 6B) at durations ranging from 0.1 to over 1 h; the most intense part of the storm began at about 03:35 (Fig. 4) with debris-flow triggering intensities. Precipitation that followed the 10 minutes of highest short-duration intensity, suggested by estimates from radar rainfall, was sufficient to exceed the longer duration debris-flow thresholds for more than an hour.

5. Conclusions

The storm that caused the devastation in Montecito was a fast-moving ($>40 \text{ km h}^{-1}$) narrow cold frontal rainband event that dropped a modest amount of rain in 24 h (50-75 mm at lower elevations, including Sta. #325, and 100-125 mm at higher elevations), which were less than one-year return interval totals (Oakley et al., 2018). It was the strong rainband that passed over the Montecito area in about 30 minutes with precipitation intensities exceeding the threshold for triggering debris flows on susceptible slopes that did the damage. The Thomas Fire burned the upper watershed slopes less than one month prior to the storm. The County of Santa Barbara operates automated rain gauges that provided an excellent record of the storm across the Montecito area; no rain gauges were located in the upper parts of

primary canyons that produced the most damaging flash floods and debris flows (Montecito and San Ysidro Creeks). Actual rainfall rates in Montecito exceeded those included in the NWS flash flood watch on January 6, 2018.

Two National Weather Service NEXRAD WSR-88D Doppler radar stations recorded the storm from locations less than 100 km from Montecito; data from KTVX, the closer of the two stations, were used in this paper. Local mountains north and east of Montecito blocked the lowest of the precipitation-mode radar sweeps from each of the radar stations. Rainfall depths and intensities calculated from weather radar are approximate; however, comparison of calculated radar precipitation with measured rainfall at Sta. #325 indicates that radar rainfall was reasonable without over predicting. A few pixels in the main rainband had reflectivity values exceeding 51 dBZ, which typically is taken as the ice cap above which reflectivity values may not represent liquid water (Fulton, 1999). Precipitation intensity and duration values on January 9, 2018, clearly exceeded the threshold for triggering debris flows on susceptible slopes.

Despite its many limitations, weather radar provides essentially continuous, useful information suitable for visualizing and estimating precipitation amounts and intensities at any location of interest, including areas remote from rain gauges. Rain gauges that provide hourly precipitation values are not suitable for estimating intensity values at durations of interest, but may be supplemented by radar rainfall. Weather radar data are available online for no-cost download and include dozens of products, in addition to the composite reflectivity that was used in this analysis. GIS and other data analysis and visualization software are indispensable for manipulating weather radar and rainfall data.

Acknowledgements

The Geotechnical Extreme Events Reconnaissance (GEER) Association, supported by the U.S. National Science Foundation (NSF), organizes the response of the geoen지니어ing community to earthquakes and other natural disasters such as floods, landslides, tsunamis, etc. GEER members donate their time, talent, and resources to collect time-sensitive and potentially perishable field observations and data of the effects of extreme events. The GEER Association web site is www.geerassociation.org. This paper is based upon work supported by the National Science Foundation under Grant No. CMMI 1266418. Any opinions, findings, and conclusions or recommendations expressed in this material are those of the author and do not necessarily reflect the views of the National Science Foundation.

Comments by two anonymous reviewers were helpful in improving this paper.

References

- CalFire, 2018, Thomas fire incident information. Cal Fire website. http://www.fire.ca.gov/current_incidents/incidentdetails/Index/1922 accessed 21 Oct 2018.
- Cannon, S.H., Gartner, J.E., Wilson, R., Bowers, J., and Laber, J., 2008, Storm rainfall conditions for floods and debris flows from recently burned areas in southwestern Colorado and southern California. *Geomorphology* 96(3–4):250–269. doi.org/10.1016/j.geomorph.2007.03.019.
- COSBPW, 2018, Real-time rainfall, river-stream, and reservoir data: County of Santa Barbara Public Works website. <https://rain.cosbpw.net/map> accessed 21 Oct 2018.
- EcoWest, 2017, Thomas fire close up; U.S. Wildfires in 2017: EcoWest interactive website. <http://vis.ecowest.org/interactive/wildfires.php> accessed 21 Oct 2018.
- Fulton, R.A. 1999, Sensitivity of WSR-88D Rainfall Estimates to the Rain-Rate Threshold and Rain Gauge Adjustment: A Flash Flood Case Study: *Weather and Forecasting*, Vol. 14, pp. 604–624. doi.org/10.1175/1520-0434(1999)014<0604:SOWRET>2.0.CO;2
- GeoMAC, 2018, AZA3S-000205 THOMAS 03-09-2018 0000.kml: Google Earth file of the Thomas fire ultimate extent perimeter: Geospatial Multi-Agency Coordination. <https://www.geomac.gov/GeoMACKML/getKML.aspx> accessed 21 Oct 2018.
- IEM, 2018a, Flood watch: National Weather Service Los Angeles/Oxnard CA, 952 PM PST Sat Jan 6 2018. Iowa Environmental Mesonet, Iowa State University website. <https://mesonet.agron.iastate.edu/wx/afos/p.php?pil=FFALOX&e=201801070552> accessed 21 Oct 2018.
- IEM, 2018b, Flood watch: National Weather Service Los Angeles/Oxnard CA, 411 PM PST Mon Jan 8 2018. Iowa Environmental Mesonet, Iowa State University website. <https://mesonet.agron.iastate.edu/wx/afos/p.php?pil=FWLLOX&e=201801090011> accessed 21 Oct 2018.
- NCEI, 2018, WSR-88D stations KVBX and KVTX metadata: National Centers for Environmental Information, National Oceanic and Atmospheric Administration, U.S. Department of Commerce website: <https://www.ncdc.noaa.gov/nexradinv/chooseday.jsp?id=kvbx> and <https://www.ncdc.noaa.gov/nexradinv/chooseday.jsp?id=kvtx> accessed 21 Oct 2018.
- Oakley, N.S., Cannon, F., Munroe, R., Lancaster, J.T., Gomberg, D., and Ralph, F.M., 2018, Brief communication: Meteorological and climatological conditions associated with the 9 January 2018 post-fire debris flows in Montecito and Carpinteria, California, USA: *Natural Hazards Earth System Sciences* v. 18, 3037–3043, <https://doi.org/10.5194/nhess-18-3037-2018> accessed 12 Feb 2019.
- Staley, D.M., Gartner, J.E., and Kean, J.W., 2014, Objective definition of rainfall intensity-duration thresholds for post-fire flash floods and debris flows in the area burned by the Waldo Canyon Fire, Colorado, USA, in Lollino, G., Giordan, D., Crosta, G.B., Corominas, J., Azzam, R., Wasowski, J., Sciarra, N. (eds), *Engineering Geology for Society and Territory – Vol 2: Springer International Publishing Switzerland*, p. 621–624. doi.org/10.1007/978-3-319-09057-3.
- USGS, 2018, Emergency Assessment of Post-Fire Debris Flow Hazards: Thomas Fire (Ventura and Santa Barbara Counties, CA): https://landslides.usgs.gov/hazards/postfire_debrisflow/detail.php?objectid=178 accessed 12 Feb 2019.

Review of contemporary terminology for damaging surficial processes – Stream flow, hyperconcentrated sediment flow, debris flow, mud flow, mud flood, mudslide

Jeffrey R. Keaton^{a,*}

^aWood, 6001 Rickenbacker Road, Los Angeles 90040, USA

Abstract

The term "mudslide" seems to be favored by news media for all localized processes in which damage is caused by moving earth materials, regardless of whether the processes involved mud or sliding. The term came into prominence sixty years ago when an atmospheric river moved over southern California with disastrous landslides, debris flows, and floods. Very costly floodlike damage resulting from "mudslides" was added to the National Flood Insurance Program coverage as a result of the 1969 disaster. Landslides were, and still are, excluded from the flood insurance program and other insurance instruments. Because of lack of clarity in what range of phenomena was intended to be covered by the flood insurance program, a panel of experts assembled by the National Research Council (NRC) categorized the continuum of moving water to moving earth into (1) clear-water floods, (2) mud floods, (3) mud flows, and (4) other landslides. These categories recognize the lack of clear distinction between slope-movement classifications and floodlike damage caused by more fluid "landslides." Earth materials in the most recent landslide classification are subdivided into rock and soil; soil is further subdivided into debris and earth. Debris is composed of mineral fragments with 20 to 80 percent coarser than sand size, whereas earth is 80 percent sand and finer fragments. Mud was used in older geology-based classifications in a way similar to earth (e.g., mudstone). Mud is not a technical term in engineering usage. Sediment-water mixtures with sufficient water to behave hydraulically were called mud floods by the NRC. Mud flows differ from mud floods by having viscoplastic behavior, which allow mud flows to support fragments with densities greater than water during transportation and when the mass comes to rest. Mud flows and debris flows have a velocity-dependent strength (matrix viscosity) and a velocity-independent strength (shearing resistance of the mass). As a mud flow or debris flow slows to a stop, the velocity-dependent strength goes to zero; however, dense fragments do not sink or settle into the mass because of its static shearing resistance. The deposits of this spectrum of processes have distinctive sedimentary structures: clear-water flood deposits are stratified, graded, and fining upward; debris-flow deposits are unsorted, unstratified, and fully matrix supported; hyperconcentrated-flow deposits are fully clast supported. Debris-flow deposits may contain megaclasts, if they are available in the source area. Geoscientists and engineers need to understand contemporary terms used in the media to communicate with emergency managers and a variety of non-specialists, but also should recognize characteristics that are associated with specialized technical terms.

Keywords: *Sediment-water slurry; Streamflow; Debris flow; Mudflow; Landslide*

1. Introduction

This paper is intended to provide a limited review of terminology of sediment-water slurries and characteristics of resulting deposits. The processes of sediment-water slurry movement are complex, variable, and gradational, making descriptions of the processes challenging. This paper does not provide a comprehensive literature review or attempt in-depth discussion of process rheology. However, sediment-water slurries range from water-dominated to sediment-dominated, which results in deposits with distinctive characteristics.

This paper draws from a few publications, as well as results of searches using internet resources. Anderson et al. (1984) includes a concise appendix entitled "Debris flow, mud flow, mud flood, and mudslide terminology" (p. 90) that summarizes key aspects. Pierson (2004) wrote a four-page U.S. Geological Survey fact sheet entitled

* Corresponding author e-mail address: jeff.keaton@woodplc.com

“Distinguishing between debris flows and floods from field evidence in small watersheds.” The remaining sections provide comments on the history of some terminology and examples of the process phases and the resulting deposits.

2. History of ‘mud flow’ and related terminology

This section is an updated version of the appendix in Anderson et al. (1984), which was written by the author of this paper. The term "mudflow" has been used in geological literature since 1928 (Blackwelder, 1928). The term "mud" in geology refers to a wet material composed of clay and silt-rich sediment (USGS, 2017), and to a very fine-grained sedimentary rock formed from mud (e.g., mudstone). The term "mud" is not used in the Unified Soil Classification System (ASTM, 2017) and used only casually in engineering. However, it is a descriptive, commonly used word.

As a result of very costly floodlike damage in southern California in January 1969 (Campbell, 1975), damage resulting from "mudslides" was added to the National Flood Insurance Program at that time (Committee on Methodologies for Predicting Mudflow Areas, 1982). The legislative amendment that added mudslides to the program included the following wording:

“The Congress [of the United States] also finds that (1) the damage and loss which results from mudslides is related in cause and similar in effect to that which results directly from storms, deluges, overflowing waters, and other forms of flooding...”, and the following statement was added under “Definitions”:

“The term "flood" shall also include inundation by mudslides which are caused by accumulations of water on or under the ground; and all of the provisions of this title shall apply with respect to such mudslides in the same manner and to the same extent as with respect to floods.” (Committee on Methodologies for Predicting Mudflow Areas, 1982, p. 5 and 6).

Thus, although it might not have been clear what range of processes the word "mudslide" was intended to identify, the intent seemed to include floodlike damage. The term "landslide" is used widely for a spectrum of slope processes, including some that do not involve sliding. News media, particularly in southern California, seem to refer to a variety of slope movements collectively as "mudslides," perhaps because most damaging earth-related process occur during rainstorms and cause widespread disruption because of the “mud” that is deposited on roads and in communities, along with other landslide damage.

Damage from "landslides" was specifically excluded from the flood insurance program, but the program was intended provide the same range of provisions regarding protection from mudslides as from floods, including mapping mudslide zones along with floodplains. In its initial approach to implementing the mudslide provision, the Federal Insurance Administration defined a mudslide as “a general and temporary movement down a slope of a mass of rock, soil, artificial fill, or a combination of these materials, caused or precipitated by the accumulation of water on or under the ground” (Committee on Methodologies for Predicting Mudflow Areas, 1982). Aside from the last phrase of the mudslide definition, it was equivalent to the Highway Research Board (1958) definition of a landslide. Because "mudslides" seemed to be defined as a type of flood, a technical committee was formed by an advisory board of the National Research Council (NRC) in the United States to provide guidance to the administrators of the National Flood Insurance Program on delineation of ‘mudslide’ hazard areas that would be consistent with the national flood insurance policy requirements (Committee on Methodologies for Predicting Mudflow Areas, 1982).

A revision of the Standard Flood Insurance Policy in 1974 contained the phrase "mudslide (i.e., mudflow)." This phrase also appeared in the Code of Federal Regulations in 1976, and led to a general substitution of "mudflow" for "mudslide," but did not resolve the range of phenomena intended to be covered (Committee on Methodologies for Predicting Mudflow Areas, 1982, p. 8). The Federal Emergency Management Agency (FEMA) took over the Federal Insurance Administration in 1978 and in 1979 asked the National Academy of Sciences for guidance on identifying mudslide hazard areas. The National Academy of Sciences established the Committee on Methodologies for Predicting Mudflow Areas to identify and categorize the various phenomena that might be considered to be mudslides, as well as identify mudslide hazard areas, determine mudslide risk, and examine a mudslide hazard methodology that had been developed in Los Angeles County (Committee on Methodologies for Predicting Mudflow Areas, 1982).

The Committee understood that conventionally recognized flood effects included:

- Hydraulic forces associated with flowing water
- Inundation by flood water
- Impact from debris carried in a flooding stream and
- Deposition of sediment from a flooding stream.

The Committee also recognized that the legislative amendment to the flood insurance program suggested some additional set of phenomena were intended to be covered, because the flood effects were already covered. The

Committee considered that FEMA was responsible for defining phenomena intended to be included by "mudslide," and addressed processes triggered by heavy rains in mountain drainage basins in terms that reflect the nature of the physical aspects of the processes, locations where the processes occur, and the resulting kinds of damage.

Floodlike damage can result from processes classified as floods and landslides (Committee on Methodologies for Predicting Mudflow Areas, 1982, p. 17); therefore, processes ranging from water flooding to landsliding were subdivided into four categories that recognized the lack of distinction between slope movement classifications and floodlike damage caused by some "landslides:"

- Clear water floods
- Mud floods
- Mud flows
- Other landslides.

Under the heading "clear water floods and mud floods" in the Committee report, clear-water floods refer to inundation by water that is carrying little or no sediment, typically in response to a river or stream flowing over its banks and onto adjacent areas, usually parts of floodplains. Mud floods refer to floods carrying up to half sediment by volume, typically occurring in drainage channels and alluvial fans adjacent to mountains, although they may occur on floodplains (Committee on Methodologies for Predicting Mudflow Areas, 1982, p. 15 and 16). Both clear-water floods and mud floods are described as causing damage by inundation associated with rising water levels and deposition of fine-grained sediment, mud floods also can cause damage associated with impact of their heavy sediment load, which may include debris.

Under the heading "mud flows and other landslides" in the Committee report, mud flows refer to flow-type landslides that are able to support large boulders because of their viscous matrix. Mud flows may be confined to existing channels or be unconfined on hillslopes. Other landslides refer to non-flow type downslope movements of earth materials, including falling, toppling, sliding, and spreading. Other landslides may be wet or dry and can occur with or without heavy rainfall, although they may be triggered by such events and transition into mud flows as they move (Committee on Methodologies for Predicting Mudflow Areas, 1982, p. 16 and 17).

The currently accepted classification of slope movements considers five types: falls, topples, slides, lateral spreads, and flows (Cruden and Varnes, 1996). Most slope movements are complex combinations of two or more types, and slides can be either rotational or translational. The materials involved in slope movements can be divided into rock and soil (in the engineering sense) (Cruden and Varnes, 1996). The soil can be subdivided into debris and earth, with debris being generally coarse-grained and earth being generally fine-grained. Cruden and Varnes (1996) describe the rate at which slope movements occur, ranging from extremely slow (less than 16 mm per year) to extremely rapid (more than 5 m per second). Cruden and Varnes (1996) define water content of materials in slope movements as:

- Dry — no visible moisture
- Moist — some water but none free, may behave as a plastic material but not as a liquid
- Wet — contains sufficient water to behave in part as a liquid, has water flowing from it, or has significant standing water
- Very wet — contains sufficient water to flow as a liquid under low-gradient conditions.

The distinction between mud flow and debris flow in the classification systems of Cruden and Varnes (1996) would be on the basis of relative percentages of fine and coarse particles. Mud flows consist of material with more than 50 percent sand, silt, and clay; debris flows have more than 50 percent particles larger than sand. Processes including sufficient water to behave hydraulically are called mud floods (Committee on Methodologies for Predicting Mudflow Areas, 1982, p.16 footnote); no mention is made in this distinction of mud floods exceeding channel banks and causing inundation of adjacent areas. Mud flows or debris flows differ from mud floods by behaving in a viscoplastic manner to support fragments with densities greater than water (e.g., boulders) during transportation and when the mass comes to rest. As stated by the Committee on Methodologies for Predicting Mudflow Areas (1982, p. 16 footnote), the "ability to support [a dense] inclusion during transport stems from a velocity-dependent strength (the matrix viscosity), and a velocity-independent strength (the shearing resistance of the mass). When the flow comes to rest, the velocity-dependent strength goes to zero. However, the high density inclusion does not sink into the mass because it is supported by the static shearing resistance." Mud floods are capable of transporting heavy loads of sediment, including coarse debris; however, mud floods do not have static shearing resistance. Consequently, the coarse debris in mud floods settles as the velocity-dependent strength of mud floods decline in response to slowing fluid velocity.

The previous paragraphs demonstrate that slope movements consist of a range of processes involving a range of materials at a range of water contents moving at a range of rates. Distinctions between individual elements of each range typically are not sharp and clear, but gradational across any particular slope that may be moving. Furthermore,

the term flood is not restricted to a context of inundation beyond a normal channel and the term flow is not restricted to a context of containment within a normal channel.

3. Field observations and sedimentology

This section is based largely on Pierson's (2004) U.S. Geological Survey fact sheet, as well as descriptions and data in a 1985 paper by Pierson that related to some of the same debris flows and sediment-flood processes that were the subject of the Anderson et al. (1984) report. The relative concentration of sediment in discharges from steep watersheds controls the behavior of the flows into three process types that vary across indistinct boundaries based on the amount of silt and clay in the matrix:

- water flow, hyperconcentrated flow, and debris flow if the sediment contains material coarser than sand, or
- water flood, mud flood, and mud flow, if the sediment lacks coarse fragments and is generally fine grained.

Furthermore, different flow types can occur at different times during a single discharge event, and a discharge event can exhibit different flow types in different places along the channel at the same time.

In water flow or water flood, the amount of sediment is insufficient to induce behavior that differs from what is known as a Newtonian fluid, meaning that the capacity of the fluid to transport solid particles is dependent on the flow velocity. As a Newtonian fluid slows, its shear strength declines, and larger particles settle; a Newtonian fluid at rest has no capacity to keep coarse particles in suspension, and they settle as a function of fluid viscosity, particle diameter, and the density difference between the particle and the fluid. Normal streamflow (fluvial) deposits (Fig. 1) tend to have coarser particles at the bottom of a depositional unit and finer particles at the top that are described as "graded, fining upward." Normal streamflow deposits also commonly have cut-and-fill and other sedimentary structures.

Hyperconcentrated flow can transport substantial amounts of sand-size and coarser sediment by dynamic suspension, which distributes sediment through the fluid column in response to the velocity and turbulence of the flow. Mud flood could transport coarser sediment by the same hydrodynamic process if such sediment were available; of course, if sediment coarser than sand size were available and being transported, the process name would be hyperconcentrated flow. As the hyperconcentrated flow velocity slows, turbulence reduces and sediment drops out of suspension leaving unsorted deposits within the depositional unit (Fig. 2). A series of depositional units, some of which may be normal streamflow, gives the impression of overall stratification even though hyperconcentrated-flow deposits are unstratified.

Debris flow is a slurry condition similar to wet concrete that keeps gravel-sized and larger particles in suspension regardless of the flow velocity (Fig. 3). Mud flow, in this context, is a slurry condition similar to wet neat cement grout; if coarse rock fragments were available, they would have remained in suspension. Debris flows occurring in channels can attain high velocities; where debris flows lose the confinement of channels, they spread laterally, become thinner, possibly allowing some interaction of suspended sediment with the surface across which the flow is moving. Unchanneled slurries can lose water to the underlying material, which increases the sediment concentration and interaction between sediment particles and within the matrix, leading to energy dissipation between particles and within the matrix that exceeds the kinetic energy of the flowing slurry and causes the flow to come to a stop in a process known as frictional freezing or cohesive freezing (Lowe, 1982), depending on whether the flow type is dominated by particles or matrix.

A graph presented in Appendix A shows the relationships among sediment concentration by volume, sediment concentration by weight, gravimetric water content, and void ratio. Descriptions by O'Brien and Julien (1985) were based in part on laboratory experiments of mud (water, clay, silt, and fine sand) and focused on the fluid matrix. Designations in Appendix A labeled O1, O2, O3, and O4 are taken from O'Brien and Julien (1985); the long-term objective of their research was to develop a predictive mathematical model for hyperconcentrated sediment flow.

Descriptions by Pierson (1985) were based on phases of a channelized flow event in Rudd Canyon that occurred over a 22-minute period on June 5, 1983, and samples of the flow captured during the flow event. Images spanning about 3-1/2 minutes of the debris-flow surge (Fig. 4) show a boulder front (Fig. 4.A), the laminar flow trailing the boulder front (Fig. 4.B), a turbulent front of a surge without concentrated coarse particles (Fig. 4.C), and a laminar to turbulent trailing flow (Fig. 4.D). A short, steep riffle is reported to be the source of local turbulence at the right side the Fig. 4 photos. Estimated values of sediment concentration, flow velocity, and flow stage for the conditions depicted in Fig. 4 are listed in Table 1.

Table 1. Selected characteristics of June 5, 1985, sedimentation event in Rudd Canyon depicted in Fig. 4; estimated from Pierson (1985, Fig. 3).

<i>Element in Fig. 4</i>	<i>Sediment concentration (% by weight)</i>	<i>Flow velocity (m/s)</i>	<i>Flow stage (m)</i>
A. Boulder front	90	1.3	2.0
B. Trailing boulder front	88	3.0	2.2
C. Turbulent front	81	4.3	0.4
D. Trailing turbulent front	80	3.2	0.5



Fig. 1. Photograph of stratigraphy dominated by normal streamflow processes. Cut-and-fill sedimentary structures and fining upward grain size distribution. Furnace Creek Ranch, Death Valley National Park, California; photo taken by the author on December 20, 2013.



Fig. 2. Photograph of stratigraphy dominated by hyperconcentrated flow processes. Stratified sequence of mostly clast-supported, unsorted silty sand with gravel and cobbles with a few small boulders. Some units are matrix-supported debris-flow deposits. Cascade, Colorado; photo taken by the author on August 17, 2013.



Fig. 3. Photograph of stratigraphy dominated by debris flow processes. Matrix-supported, unsorted angular blocks of limestone in silty sand. Unchanneled depositional contact of debris-flow deposit on unsorted, unstratified hyperconcentrated deposits. Mosaic Canyon Trail, Death Valley National Park, California; photo taken by the author on December 22, 2013.

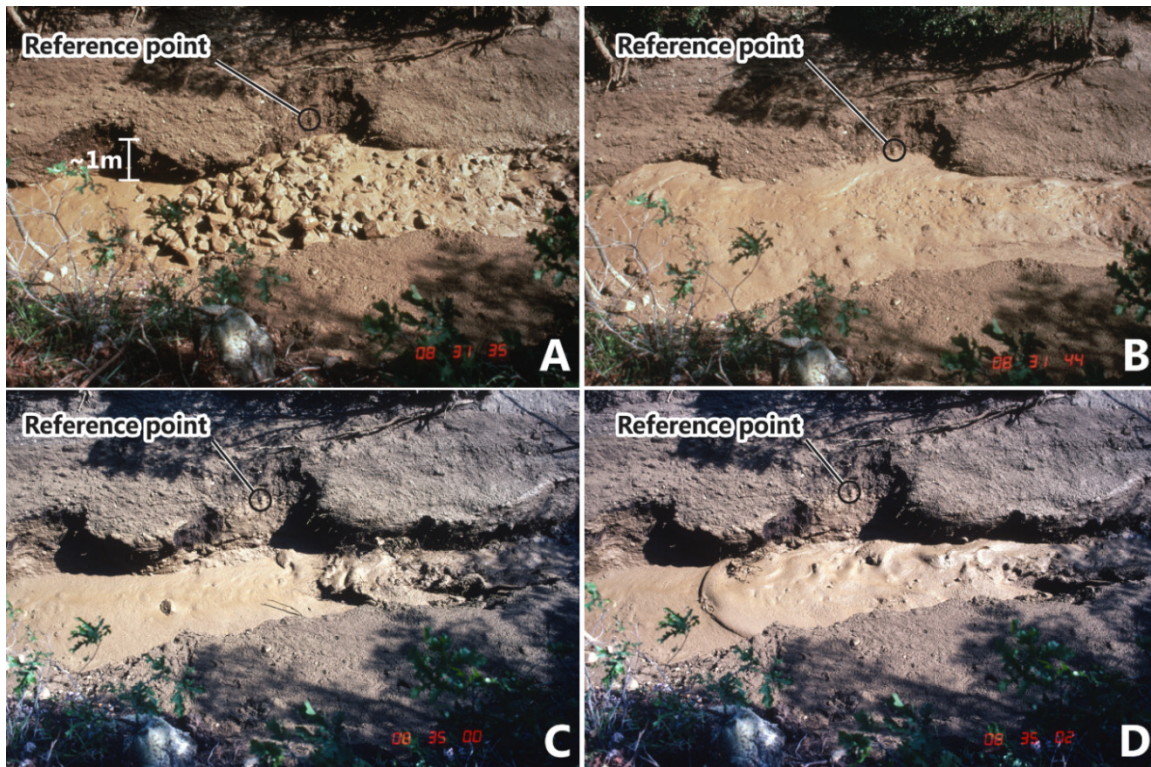


Fig. 4. Photographs of a June 5, 1985, sedimentation event in lower Rudd Canyon, Davis County, Utah. (A) boulder front of debris-flow surge approximately 1-1/2 minutes after initial surge; (B) debris-flow surge trailing boulder front by 9 seconds; (C) turbulent front of debris-flow surge without concentrated coarse clasts approximately 5 minutes after initial surge; and (D) laminar condition of turbulent front 2 seconds after photo in C. Flow is right to left. All photos courtesy of Thomas C. Pierson; annotations by the author. Scale in (A) is based on Pierson (2004).

4. Discussion and conclusions

Processes involving sediment-water slurries are complex and gradational. Modern or historic debris-flow deposits provide opportunities for understanding the context of the processes. Stream flow, hyperconcentrated flow, and debris flow can be phases of a single discharge event from small drainage basins, and the phases tend to have distinctive landforms and deposits have sedimentary structures and sediment characteristics (Pierson, 2004; Giraud, 2005). However, post-depositional processes, including storm events and damage cleanup, may modify deposits that mask original features or create unnatural features, such as matrix material on large boulders being washed away by storms or unstratified deposits created from originally stratified material by earthmoving equipment operators. Debris-flow deposits in the geologic record (e.g., Fig. 3) may not preserve evidence of the full process, making interpretation of stratigraphy in natural or excavated exposures problematic (e.g., Giraud, 2005).

A collection of terms is displayed in Fig. 5 in the context of the water-sediment-rock continuum and fluvial-landslide process continuum. Suggested terminology is in the process name row in Fig. 5. The term "sediment" is added to hyperconcentrated flow because it seems necessary for communication. The term "mud" is used in mud flow because the term "earth flow" is not useful for communicating what is intended. The term "mud" is not used by Cruden and Varnes (1996) in their chapter on landslide types, although they mention mudslide in their section 8.3.2 on Complex and Composite Slides, but dismiss it as imprecise. The term "mud" is used in other chapters in the same book in figure titles and in reference to drilling fluids (Turner and Schuster, 1996). The term "mud" in this context is herein defined as "very wet earth" in the Cruden and Varnes (1996) glossary for naming landslides. The term "mud flow" is simpler than "very rapid to extremely rapid, very wet earth flow" that would be consistent with the glossary for naming landslides. The terms "mass wasting" and "mass movements" are too vague to have value.

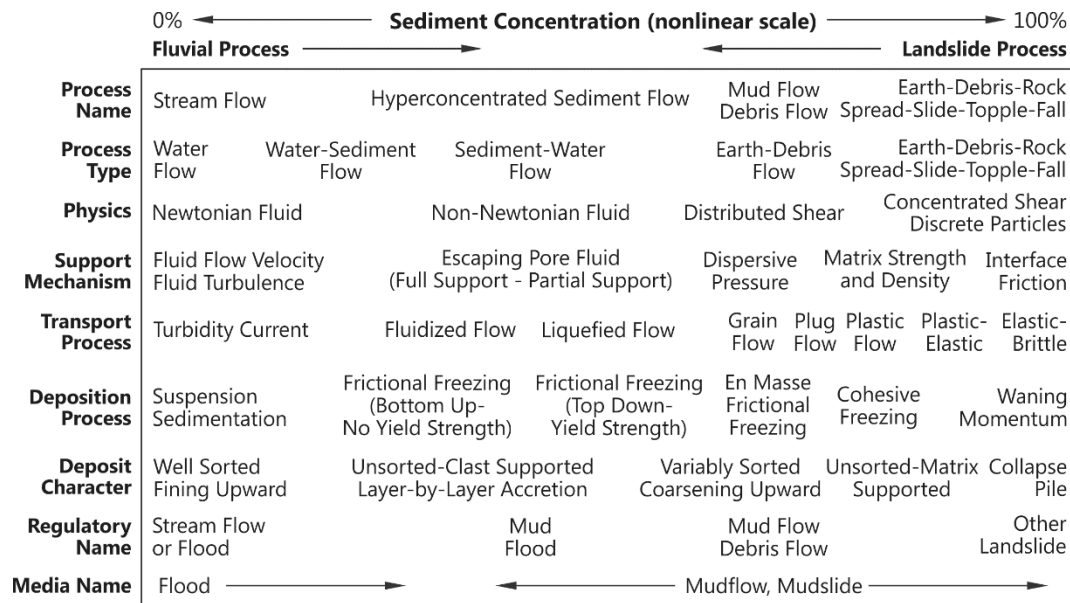


Fig. 5. Collection of relevant terms inspired by Blackwelder (1928), Nardin et al. (1979), Lowe (1982), the Committee on Methodologies for Predicting Mudflow Areas (1982), Pierson (1985, 2004), O'Brien and Julien (1985), Wieczorek (1986), and Gani (2004)

Sediment-water slurry processes are complex and gradational. Earth scientists need to be able to communicate with a variety of individuals using understandable terms appropriate for the discussion. Terms imply concepts of processes that can have perhaps higher meaning in technical discussions, whereas casual discussions can be effective with less precise terms. The process and deposit examples in this paper may help with terminology usage in the future. Depending on who is using the terms, "mudslide" and "mudflow" should be interpreted in their context by knowledgeable technical professionals, similar to the way the terms "cement" and "risk" are interpreted to refer to "concrete" and "hazard" when intended.

Acknowledgements

The author gratefully acknowledges discussions with Thomas C. Pierson, and use of his photographs.

References

- Anderson, L.R., Keaton, J.R., Saarinen, T.F., and Wells, W.G., II, 1984, The Utah landslides, debris flows, and floods of May and June 1983: Washington, D.C., National Academy Press, 104 p. <https://books.google.com/books?id=z14rAAAAAYAAJ> (accessed 7 Oct 2018).
- ASTM, 2017, Standard practice for classification of soils for engineering purposes (Unified Soil Classification System): West Conshohocken, PA, ASTM International, Standard D2487-17. DOI: 10.1520/D2487-17.
- Blackwelder, E., 1928, Mudflow as a geologic agent in semi-arid mountains: Geological Society of America Bulletin v. 39, no. 2, p. 465-484. DOI: 10.1130/GSAB-39-465.
- Campbell, R.H., 1975, Soil slips, debris flows, and rainstorms in the Santa Monica Mountains and vicinity, southern California: U.S. Geological Survey Professional Paper 851. DOI: 10.3133/pp851.
- Committee on Methodologies for Predicting Mudflow Areas, 1982, Selecting a methodology for delineating mudslide hazard areas for the national flood insurance program: Washington, D.C., National Academy Press, 35 p. <https://www.nap.edu/download/19560> (accessed 7 Oct 2018).
- Cruden, D.M. and Varnes, D.J., 1996, Landslide types and processes. In: Turner, A.K. and Shuster, R.L., Eds., Landslides: Investigation and mitigation: Washington, D.C., Transportation Research Board, Special Report No. 247, 36-75. ISBN: 0-309-06208-X. <http://www.trb.org/main/blurbs/153305.aspx> (accessed 7 Oct 2018).
- Gani, M.R., 2004, From turbid to lucid: A straightforward approach to sediment gravity flows and their deposits: The Sedimentary Record, v. 2, no. 3, p. 4-8. https://www.sepm.org/CM_Files/SedimentaryRecord/sedrecord2.3.pdf (accessed 10 Feb 2019).
- Giraud, R.E., 2005, Guidelines for the geologic evaluation of debris-flow hazards on alluvial fans in Utah: Utah Geological Survey Miscellaneous Publication 05-6, 16 pp. ISBN 1-55791-729-9. https://ugspub.nr.utah.gov/publications/misc_pubs/mp05-06.pdf (accessed 10 Feb 2019)
- Highway Research Board, 1958, Landslides and Engineering Practice: Highway Research Board Special Report 29, Washington, D.C., National Academy of Sciences. Predecessor volume to Turner, A.K. and Shuster, R.L., Eds., Landslides: Investigation and mitigation: Washington, D.C., Transportation Research Board, Special Report No. 247. <http://www.trb.org/main/blurbs/153305.aspx> (accessed 7 Oct 2018).
- Lowe, D.R., 1982, Sediment gravity flows II – Depositional models with special reference to the deposits of high-density turbidity currents: Journal of Sedimentary Petrology, v. 52, p. 279-297. <https://doi.org/10.1306/212F7F31-2B24-11D7-8648000102C1865D> (accessed 10 Feb 2019).
- Nardin, T.R., Hein, F.J., Gorsline, D.S., Edwards, B.D., 1979, A Review of Mass Movement Processes, Sediment and Acoustic Characteristics, and Contrasts in Slope and Base-of-Slope Systems Versus Canyon-Fan-Basin Floor Systems: Tulsa, OK, Society of Economic Paleontologists and Mineralogists Special Publication No. 27, p. 61-73. DOI: <https://doi.org/10.2110/pec.79.27.0061> (accessed 10 Feb 2019).
- O'Brien, J.S., and Julien, P.Y., 1985, Physical properties and mechanics of hyperconcentrated sediment flows, in Bowles, D.D., ed., Delineation of landslide, flash flood, and debris-flow hazards in Utah: Logan, Utah, Utah Water Research Laboratory, General Series UWRL/G-85/03, p.260-280. https://digitalcommons.usu.edu/water_rep/596 (accessed 7 Oct 2018).
- Pierson, T.C., 2004, Distinguishing between debris flows and floods from field evidence in small watersheds: U.S. Geological Survey Fact Sheet 2004-3142, 2 p. <https://pubs.usgs.gov/fs/2004/3142/> (accessed 7 Oct 2018).
- Pierson, T.C., 1985, Effects of slurry composition on debris-flow dynamics, Rudd Canyon, Utah, in Bowles, D.D., ed., Delineation of landslide, flash flood, and debris-flow hazards in Utah: Logan, Utah, Utah Water Research Laboratory, General Series UWRL/G-85/03, p.132-152. https://digitalcommons.usu.edu/water_rep/596 (accessed 7 Oct 2018).
- Turner, A.K. and Shuster, R.L., 1996, Eds., Landslides: Investigation and mitigation: Washington, D.C., Transportation Research Board, Special Report No. 247. <http://www.trb.org/main/blurbs/153305.aspx> (accessed 7 Oct 2018).
- USGS, 2017, Geologic Glossary: Geology and National Parks webpage, U.S. Geological Survey, U.S. Department of the Interior. <http://geomaps.wr.usgs.gov/parks/misc/glossarymn.html> (last updated 25 Apr 2017; accessed 10 Feb 2019).
- Wieczorek, G.F., 1986, Debris flows and hyperconcentrated streamflows. Proceedings, Water Forum '86: World Water Issues in Evolution: American Society of Civil Engineers, p. 219-226. ISBN: 0-872-625451.

Appendix A. Sediment concentration of earth-water mixtures

Flow or movement behavior is a function of the ratio of sediment to water with potential conditions ranging from nearly 100 percent sediment to 100 percent water. Sediment concentration can be described in terms of volume (C_v) or weight (C_w) and calculated based on a unit volume ($V = V_s + V_w + V_a$) comprised of the sum of the volumes of solids, water, and air. The corresponding weight ($W = W_s + W_w$) is the sum of the weights of solids and water. The specific gravity of solids (G_s) must be known or designated, and gravimetric water content ($w = W_w/W_s$) can be calculated. The void ratio (e) can be calculated from $G_s w = S e$ for assumed saturated conditions ($S=1$), or from the ratio of volumes of voids and solids ($e = V_v/V_s$).

$$C_w = W_s/W = W_s/(W_s + W_w) = W_s/(W_s + w W_s) = 1/(1 + w) \quad (A.1)$$

$$C_v = V_s/V = V_s/(V_s + V_w + V_a) = (W_s/G_s)/((W_s/G_s) + w W_s + V_a) \quad (A.2)$$

$$V = 1 = V_s + V_w + V_a; \therefore 1 - V_a = (W_s/G_s) + w W_s = W_s((1/G_s) + w) \quad (A.3)$$

$$W_s = G_s (1 - V_a) / (1 + w G_s) \quad (A.4)$$

$$C_v = W_s / G_s \quad (A.5)$$

$$e = (V_w + V_a) / V_s = (w W_s + V_a) / (W_s / G_s) = (G_s w) / S \quad (A.6)$$

The relationships among C_v , C_w , w , and e for $G_s = 2.65$ and three V_a values are plotted in Fig. A.1. Flow behavior fields are denoted with letter-number combinations; O denotes O'Brien and Julien (1985) for a laboratory fluid matrix consisting of silt, clay, and fine sand (i.e., mud) with $G_s = 2.72$, whereas P denotes Pierson (1985 and 2004) for data related to a sedimentation event on June 5, 1983, at Rudd Canyon, Davis County, Utah, and other debris-dominated events. Symbols plotted in Fig. A.1 are based on values tabulated in Pierson (1985) and assumed air content; square symbols represent $V_a = 0$, diamond symbols represent $V_a = 0.05$, and triangle symbols represent $V_a = 0.1$. Letter and letter-number designations in Fig. A.1 are described in Table A.1.

Table A.1. Letter and letter-number designations used in Fig. A.1.

Symbol	Meaning	Sediment Concentration by volume
N	Normal stream flow	--
H	Hyperconcentrated sediment flow	--
T	Transitional flow (subsequently included with hyperconcentrated sediment flow)	--
D	Debris flow	--
O1	Water flood	≤ 0.2
O2	Mud flood	0.2 to 0.45
O3	Mud flow	0.45 to 0.5
O4	Other landslide	0.5 to 0.9
P1	Normal stream flow	< 0.05 to 0.1
P2	Hyperconcentrated sediment flow	0.05 to 0.2 to 0.1 to 0.6
P3	Debris flow	>0.6

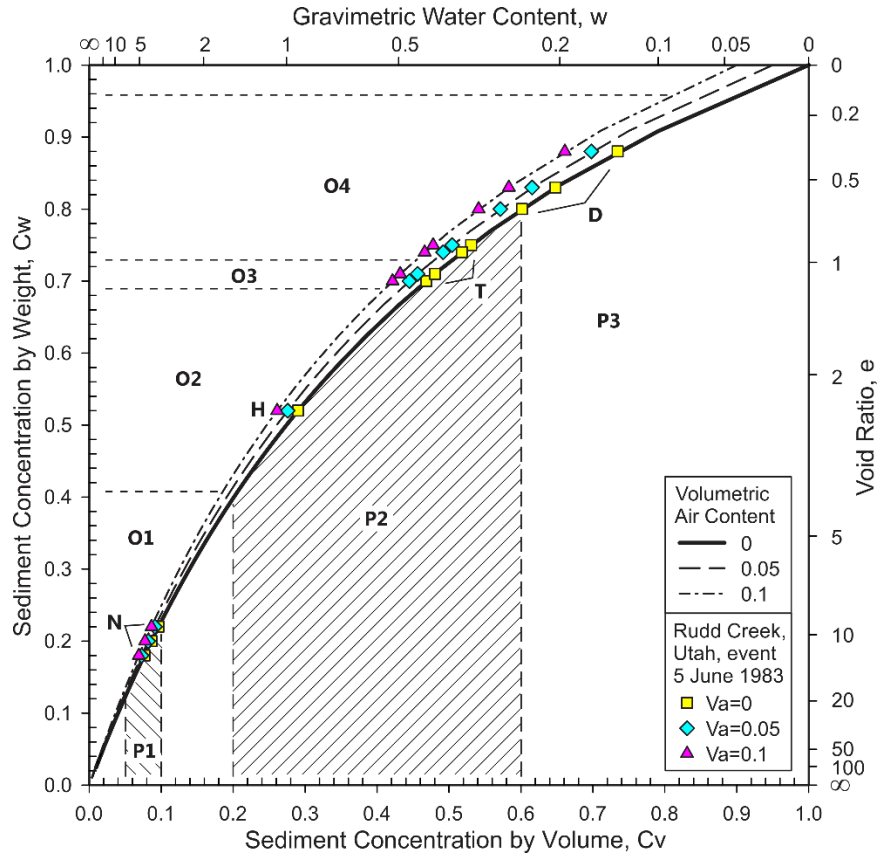


Fig. A.1. Graph of sediment concentration based on a unit volume and specific gravity of solids of 2.65. Notations are explained in Table A.1.

Evaluation of slope stability of Taebaeksan Mountain National Park using detailed soil map

Young-Hwan Kim^a, Kye-Won Jun^a, Byong-Hee Jun^a, Ho-Jin Lee^b, Soung-Doug Kim^b,
Chang-Deok Jang^c

^aGraduate School of Disaster Prevention, Kangwon National University, 346 Joongang-ro Samcheok-si Kangwon-do 25913, S. Korea

^bSchool of Civil Engineering, Chungbuk National University, 1 Chungdae-ro, Seowon-gu, Cheongju-si, Chungcheongbuk-do 28644, S. Korea

^cCreation & Development, 203, BI Center, 346 Joongang-ro Samcheok-si Kangwon-do 25913, S. Korea

Abstract

More than 64% of Korea's land is occupied by mountain regions, which have terrain characteristics that make it vulnerable to mountain disasters. The trails of Taebaeksan Mountain National Park—the region considered in this study—are located in the vicinity of steep slopes, and therefore, the region is vulnerable to landslides and debris flow during heavy storms. In this study, a slope stability model, which is a deterministic analysis method, was used to examine the potential occurrence of landslides. According to the soil classification of the detailed soil map, the specific weight of soil, effective cohesion, internal friction angle of soil, effective soil depth, and ground slope were used as the parameters of the model, and slope stability was evaluated based on the DEM of a 1 m grid. The results of the slope stability analysis showed that the more hazardous the area was, the closer the ratio of groundwater/effective soil depth is to 1.0. Further, many of the private houses and commercial facilities in the lower part of the national park were shown to be exposed to danger.

"Keywords: Slope stability; National park; Detailed soil map;"

1. Introduction

Currently, several natural disasters are occurring all over the world, which have not been frequently experienced in the past, owing to climate change. South Korea, where 64% of the land is occupied by mountain areas, is exposed to the risk of mountain disasters; this is also because the country experiences over 85% of annual average precipitation between April and September. For example, Typhoon Rusa (1,232 deaths and disappearances) in 2002 and Typhoon Maemi in 2003 (1,157 deaths and disappearances) occurred in the mountain areas and resulted in a great loss of life and property.

To prevent such landslides in advance and in turn reduce damage, appropriate preventive measures developed using landslide risk mapping are required. However, landslide risk maps also contain uncertainties, and landslide risk assessments based on topographic and geological characteristics have been made without considering rainfall, which is an important external factor determining the occurrence of landslides. In general, the mechanism of landslide occurrence includes unstable internal factors (cohesion, internal friction angle, etc.) caused by external factors (rainfall, etc.); change of soil saturation along with these factors should be considered for the slope stability analysis. To effectively cope with landslides, quantitative analysis techniques that consider rainfall are needed to simulate the saturation of soil.

Since 1990, it has become possible to estimate spatial distribution topography, geology, and climatic factors because of the rapid development of geographic information systems (GISs) and remote sensing (RS). Further, studies on an infinite slope stability analysis that considers these factors along with rainfall and soil saturation have been continuously carried out to better understand the regional landslide risk. Based on the concept of soil saturation

* Corresponding author e-mail address: kwjun@kangwon.ac.kr

proposed by O'loughlin (1986), Mont-Geomery and Dietrich (1994) verified that the simulated results for the Tennessee and Oregon regions of the United States using the infinite slope stability analysis technique are similar to the landslide initiation site. Van Westen and Terlien (1996) extracted the geological and geomorphic factors in the Manizales area in Colombia and analyzed the slope stability for each scenario of rainfall and earthquake; further, they introduced the concept of the overlay pressure of slope (distribution load of vegetation, building, etc.) to the infinite slope stability analysis. Borga et al. (2002) attempted to analyze the slope stability in Cordon and Vauz areas in Italy considering the wetting index, overburden pressure, and root cohesion, and introduced the concept of critical rainfall and wetness index to determine the failure probability through geographical characteristics of a watershed. Acharya et al. (2006) applied an infinite slope stability analysis to the Rasuwa area in Nepal by dividing the soil into dry ($m = 0$), semi-saturated ($m = 0.5$), and fully-saturated ($m = 1$); and the variability of safety factor was analyzed considering the dynamic characteristics of rainfall in the region. Ray and De Smedt (2009) distinguish the dry soil ($m = 0$), semi-saturated ($m = 0.5$), and fully saturated ($m = 1$) soil in the Dhaling area of Nepal similar to Acharya et al. (2006), and compared and analyzed the volatility of landslide-prone areas based on the specific yield calculated assuming a 2-year, 25-year rainfall and an initial saturation of 0.5.

However, in Korea, Oh et al. (2006) examined the applicability of a GIS-based mountain-terrain prediction model, SINMAP, to evaluate the applicability of a GIS-based debris flow prediction model. Through the risk analysis of the debris flow watershed using GIS, Jun (2011) developed a risk map of the disasters using various topographic, geological, and hydrological methods along with the SINMAP model analysis techniques that can be used in Korea. Jun (2012) examined the applicability of debris flow prediction in the regions of Umyeonsan Mountain, Seoul, damaged by debris flow using a slope stability model that considers the safety factor, which is a deterministic analysis method.

In this study, we considered Taebaeksan Mountain National Park as the field of study, which was recently designated as a national park, and analyzed the slope stability using the slope stability model proposed by Brunsdn and Prior (1984). The model can perform a simple and quick slope stability analysis in regions prone to mountain disasters.

2. Theory of Slope Stability Model

Landslides can be classified depending on the type of occurrence; however, the stability factor of the slope is typically evaluated using the concept of safety factors. The safety factor is expressed as the ratio of the force of collapse to that of support, and the factors that constitute each force are well known through various landslide studies. The model used in this study is proposed by Brunsdn and Prior, which is simple yet commonly used. This model is based on the assumption that the slope is an infinite slope as shown in Figure 1, and uses the ratio of rainfall to groundwater level, as in Equation (1). Infinite slopes measure the stability of the slope, and the slope that collapses is considered to be infinite.

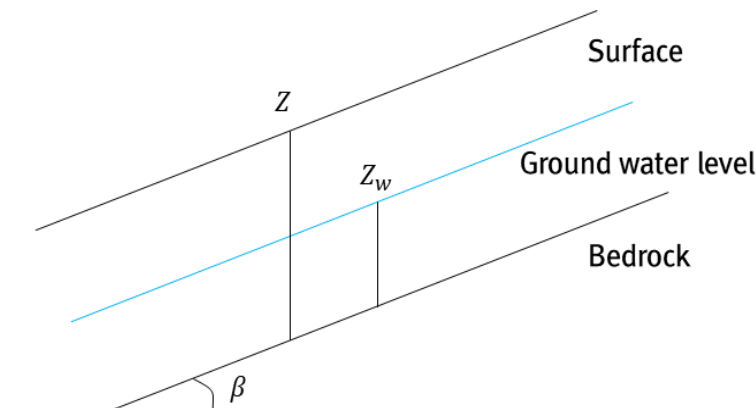


Fig. 1. Infinite slope stability analysis diagram

$$F = \frac{\text{Resistance force}}{\text{Driving force}} = \frac{C + (\gamma - m\gamma_w) z \cos^2 \beta \tan \varphi}{\gamma z \sin \beta \cos \beta} \quad (1)$$

Here, F is the safety factor, C is the effective cohesion ton/m^2 , γ is the soil specific weight ton/m^3 , m is the ratio of the groundwater level to effective soil depth (Z_w/Z), γ_w is the specific weight of water (ton/m^3), Z is the depth (m) of the soil from the surface of the earth, Z_w is the groundwater level (m), β is the ground slope ($^\circ$), and φ is the internal friction angle of soil ($^\circ$).

In Equation (1), if the safety factor is greater than 1, it is safe, and if the safety factor is less than 1, it is unstable, and the slope is taken at the time of collapse.

3. Application of Slope Stability Model

3.1 Study area

Since 2017, Taebaeksan Mountain National Park has been designated as a national park, and trail of the Danggol basin, which is the study area, is the most visited region in the national park (596,676 visitors to Taebaeksan Mountain National Park in 2017). In the downstream area, as there are private houses and many commercial facilities, there is a risk of personal injury and property damage. However, there are no such data regarding the disaster history because it was not until recently that the park was designated as a national park. Further, the result of the field survey shows that only a few risk areas are marked (6) and are being managed.

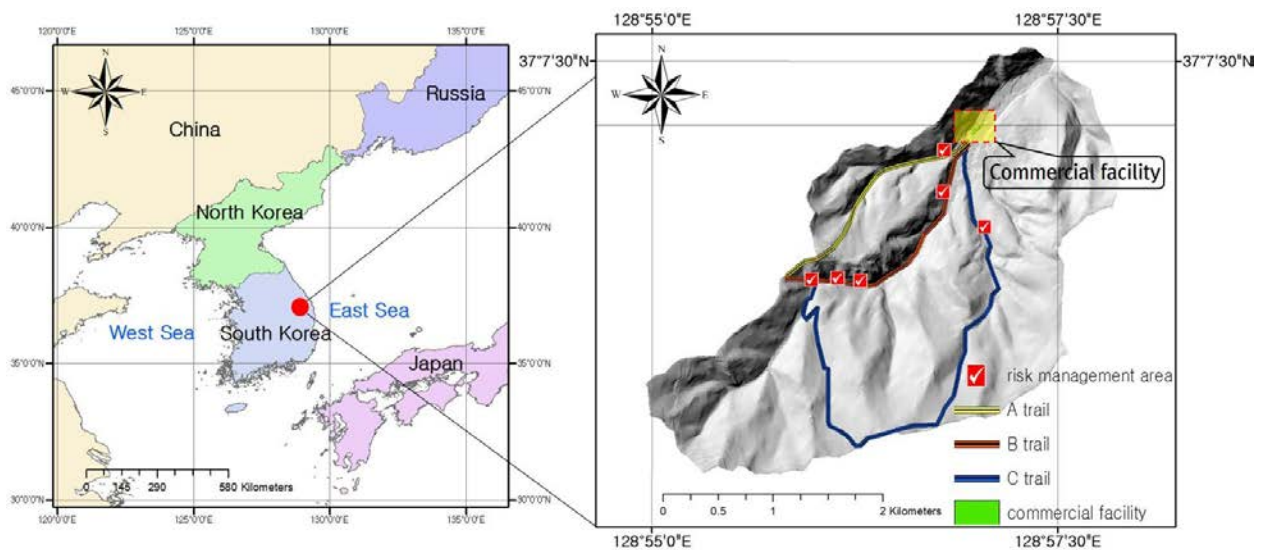


Fig. 1. Study area

3.2 Building database

To evaluate the slope stability, Lester data for the parameters given in Equation (1) are needed. In this study, to calculate the safety factor, ArcGIS 9.3.1 was used to extract DEM from a 1:5,000 digital topographic map provided by the National Geographic Information Institute with a 1 m resolution. A slope map was generated based on these data. In addition, to calculate the safety factor, effective cohesion, soil specific weight, and internal friction angle were constructed as a 1 m grid of Lester data from soil classification of the 1:25,000 detailed soil map provided by Korea Rural Development Administration.

3.3 Slope

The safety factor is calculated based on the slope map constructed from the DEM of a 1 m grid, and because the very low slope induces an excessively large safety factor (extremely safe), a slope of 5° or less was applied to the calculation as 5°, as shown in Figure 3.

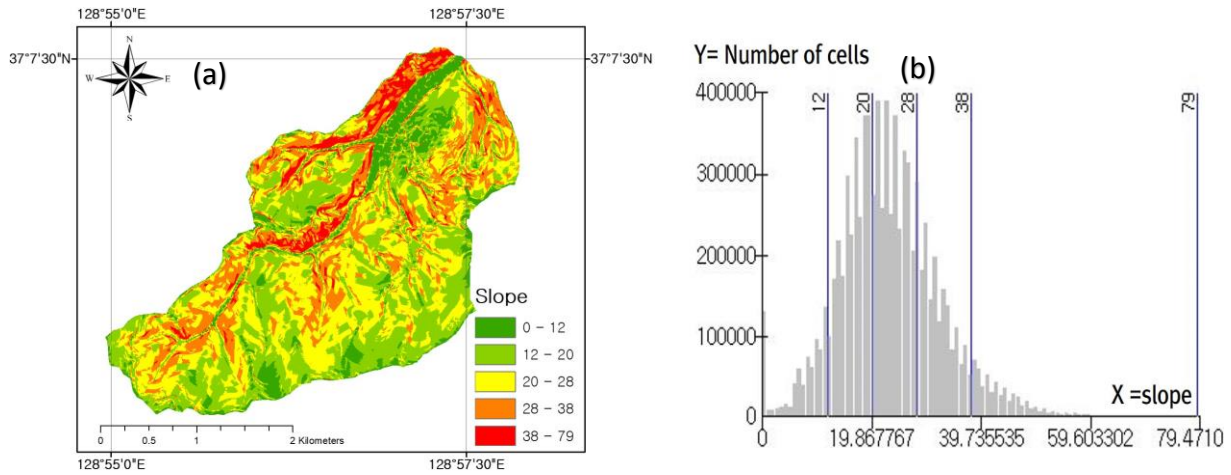


Fig. 3. Slope and histogram constructed from 1 m grid (a) slope; (b) slope histogram

3.4 Detailed soil map

The soil texture is divided into clay, silt, and sand according to the grain size of the soil. The soil texture is further divided into nine types—sandy loam soil, silt loam soil, sandy soil, etc. Table 1 lists the specific weight, cohesion, and internal friction angle of the soils provided by the National Disaster Management Institute of Korea (Korea National Disaster Management Institute).

Figure 3 is a 1:25,000 detailed soil map provided by the Rural Development Administration of Korea and shows the distribution of soil in the study area. A total of 16 soils are distributed in the study area—Danggol watershed. Among them, OsF, which occupies the southern part of the Danggol basin, and KIF2, which occupies the north, are the main components, which are classified as silt loam.

Table 1. Total soil content by surface soil, specific weight, cohesion, and internal friction angle

Soil type	Sand (%)	Silt (%)	Clay (%)	Specific Weight (t/m ³)	Cohesion	Internal Friction Angle (°)
Siliceous clay soil	10	55	35	1.73	1.15	22
Silt loam	15	70	15	1.75	0.96	27
Sandy loam	70	15	15	1.91	0.41	28
Fine sandy loam	70	15	15	1.91	0.41	27
Clay loam	30	30	40	1.79	0.98	20
Loamy sand	80	10	10	1.94	0.27	30
Loamy fine sand	100	0	0	2	0	30
Loamy coarse sand	100	0	0	2	0	30
Loam	40	4	20	1.82	0.74	25

Table 2. Area of different soils in the study area

Soil Type	Area (km ²)
Sandy loam (DEB, DEC, DbF2, DgF2, DpF2, MtE, SqE, StC, StD)	1.479
Silt loam (KdD2, KIF2, KzE2, OsF, RC)	6.883
Loam (OsE)	0.378
Total	8.740

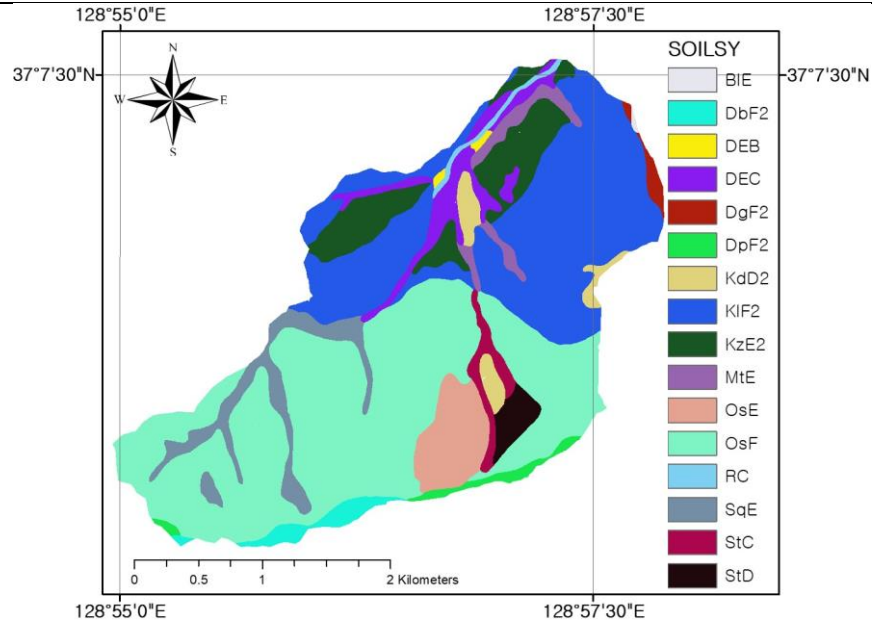
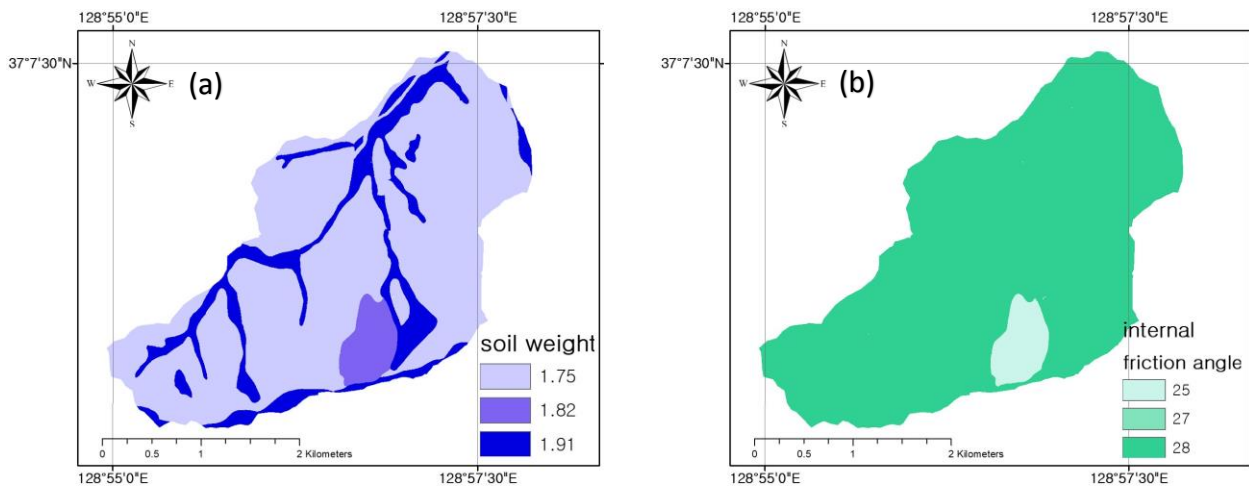


Fig. 4. Soil distribution in the study area

3.5 Soil parameters

The specific weight, internal friction angle, and effective cohesion of the soil required for stability evaluation were determined according to the type of soil in the detailed soil map, each of which was constructed with a 1 m grid of Lester data and used to evaluate slope stability. Figure 5 shows the distribution of the specific weight of the soil, internal friction angle, and effective cohesion.



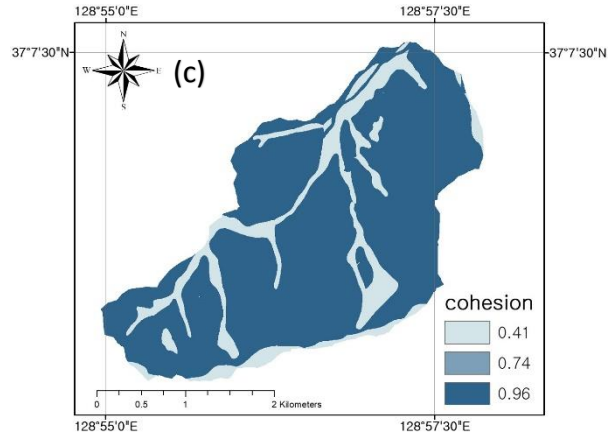
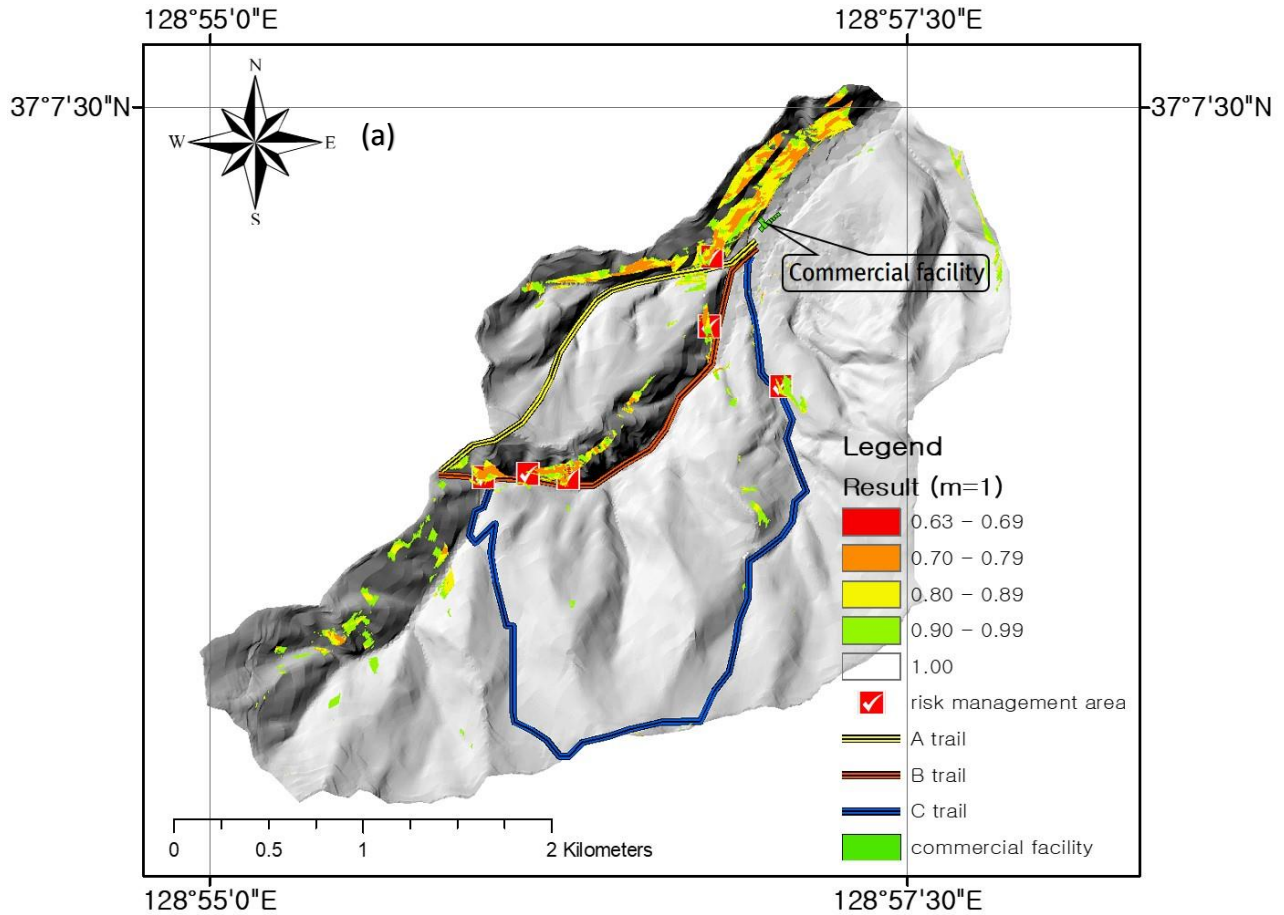


Fig. 5. (a) specific weight of soil; (b) internal friction angle; (c) effective cohesion

4. Evaluation of slope Stability

Figure 6 shows the evaluation of slope stability results calculated using each parameter constructed in Section 3. Stability factor of $F \geq 1.0$ is a safe condition and if $F < 1.0$, it is unsafe. Therefore, in this study, areas with a safety factor $F > 1.0$ were not shown in the results. Furthermore, the ratio of the groundwater level to the effective soil depth (m) was expressed as either the saturated area ($m = 1.0$) or wet area ($m = 0.5$) to show a dangerous area.



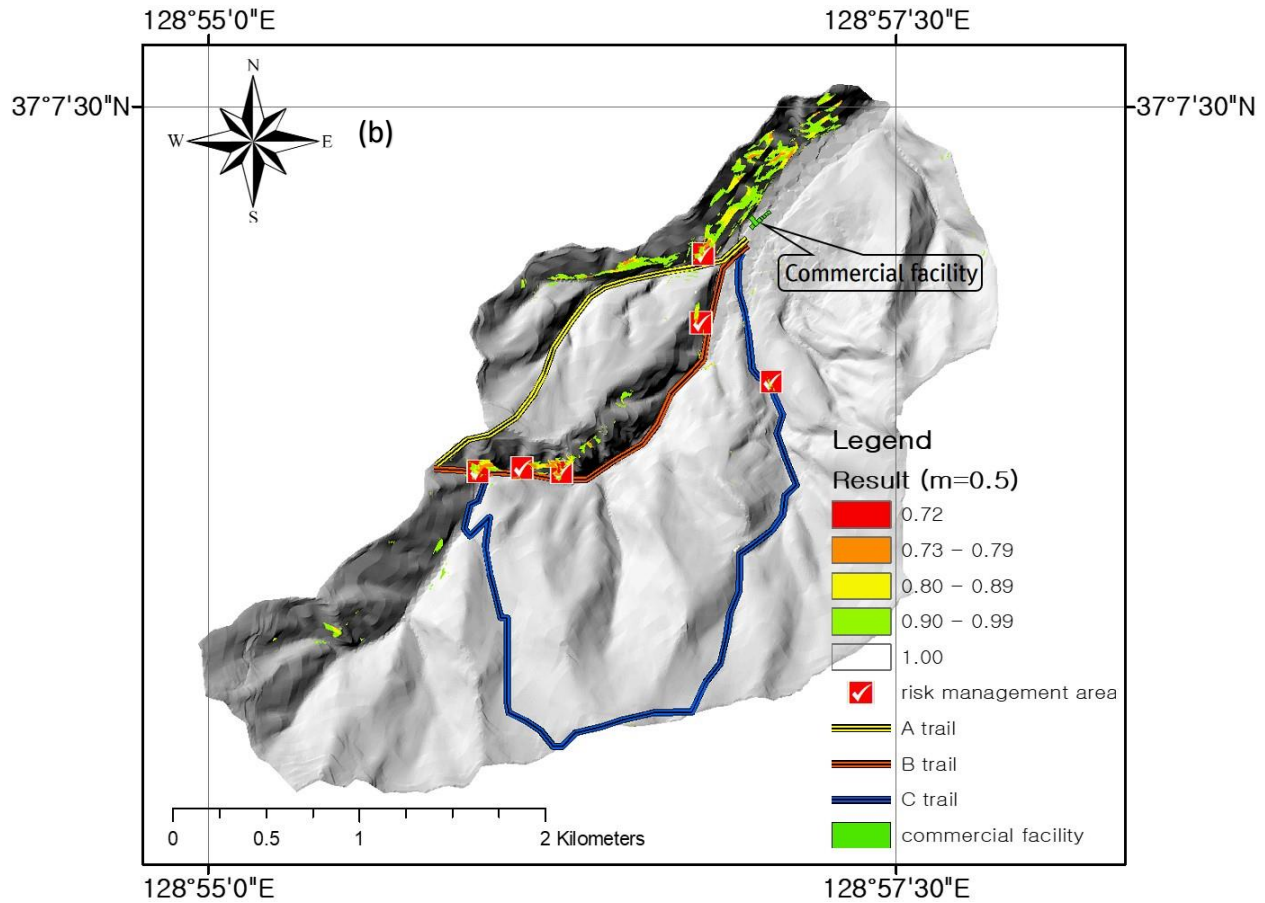


Fig. 6. Slope stability result (a) $m = 1.0$; (b) $m = 0.5$;

5. Conclusion

In this study, a slope stability model was applied to Taebaeksan Mountain National Park to analyze the regions prone to landslides. The input parameters of the model were estimated according to the soil characteristics classified in the detailed soil map. The results of the slope stability analysis of the target area showed an increase in the risk area with soil saturation. In particular, a few sections of the A–C trails and sites where downstream commercial facilities were located were analyzed as areas prone to landslides with a low safety factor. Currently, however, only 6 regions prone to landslides are managed by Taebaeksan Mountain National Park, the region considered for the study; therefore, additional management is needed in the future. Future studies will verify the applicability of the model by analyzing the rainfall when the soil is wet and saturated ($m = 0–1.0$) through a field investigation.

Acknowledgements

This research was supported by a grant(18CTAP-C141846-01) from Technology Advancement Research Program (TARP) funded by Ministry of Land, Infrastructure and Transport of Korean government.

References

- Acharya, G., De Smedt, F., and Long, N. T., 2006, Assessing landslide hazard in GIS: a case study from Rasuwa, Nepal, *Bulletin of Engineering Geology and the Environment*, v. 65, no. 1, p. 99-107.

- Borga, M., Dalla Fontana, G., and Cazorzi, F., 2002, Analysis of topographic and climatic control on rainfall-triggered shallow landsliding using a quasi-dynamic wetness index, *Journal of Hydrology*, v. 268, no. 1-4, p. 56-71.
- Brunsdon, D., and Prior, D. B. 1984. Slope instability.
- Jun, B. H., 2012, Evaluation of Slope Stability in Umyeon-san Area. *Journal of safety and crisis management*, v. 8, no. 5, p. 227-234
- Jun, K. W., and Oh, C. Y. 2011, Study on risk analysis of debris flow occurrence basin using GIS, *Journal of the Korean Society of Safety*, v. 26, no. 2, p. 83-88
- Montgomery, D.R. and Dietrich, W.E., 1994, A physically based model for the topographic control on shallow landsliding, *Water Resources Research*, v. 30, no. 4, p. 1153-1171.
- Oh, K. D., Hong, I. P., Jun, B. Ho., Ahn, W. S. and Lee, M. Y., 2006, Evaluation of GIS-based landslide hazard mapping, *Journal of Korea Water Resources Association*, v. 39, no. 1, p. 23-33
- O'loughlin, E.M., 1986, Prediction of surface saturation zones in natural catchments by topographic analysis, *Water Resources Research*, v. 22, no.5, p. 794-804.
- Park, D. G., Kim, T. H., & Oh, J. R. 2004, A study on the debris-flow and mitigation techniques (pp. 295-317). Research Report of National Institute for Disaster Prevention, National Institute for Disaster Prevention.
- Ray, R.L. and De Smedt, F., 2009, Slope stability analysis using GIS on a regional scale: a case study from Dhading, Nepal, *Environmental Geology*, v. 57, no. 7, p. 1603-1611.
- Van Westen, C.J. and Terlirn, T.J., 1996, An approach deterministic landslide hazard analysis in GIS: a case study Manizales (Colombia), *Earth Surface Processes Landforms*, v. 21, no. 9, p. 853-868.

Estimation of debris-flow volumes by an artificial neural network model

Deuk-Hwan Lee^a, Seung-Rae Lee^{a,*}, Jun-Seo Jeon^a, Joon-Young Park^a, and Yun-Tae Kim^b

^aDepartment of Civil and Environmental Engineering, KAIST, Daejeon, Republic of Korea

^bDepartment of Ocean Engineering, Pukyong National University, Pusan, Republic of Korea

Abstract

Estimating debris-flow volume is an essential requirement for hazard assessment in mountainous areas. A number of studies have been conducted on the estimation of debris-flow volumes using empirical, statistical, and physically-based methods. Despite such efforts, the prediction of erosion and deposition processes in mountainous terrain remains a challenging task due to the complexity of the issue and lack of data. In this study, data on a total of 30 debris-flow events observed in Mt. Umyeon, Seoul, Korea, which consist of eight GIS-based geomorphological and hydrological datasets, were collected from technical reports, scientific journals, aerial photographs, and DEM. The collected datasets were applied for a correlation analysis to ensure independency among the variables in a dataset and to avoid the over-fitting the data with a model. Using an Artificial Neural Network (ANN) technique, an estimation model of debris-flow volume was developed and tested by randomly selecting a validation dataset. The final ANN model consisted of one hidden layer with 5 neurons and exhibited training, and testing correlation coefficient (R) values, and mean square error (MSE) value of 0.92, 0.88 and 0.25, respectively. In order to verify the applicability of the suggested model, the performance of the model was compared with an existing regression equation. The results showed that the suggested ANN model possessed greater predictive capabilities and could serve as a reliable tool for estimating the debris-flow volume. However, additional factors that affect debris-flow volume should be studied for the development of a higher performance model.

Keywords: Landslide; Debris-flow; GIS; Artificial Neural Network; Volume estimation

1. Introduction

More than half of the territory of Korea consists of mountainous areas. In addition, heavy rainfall is concentrated during the summer season due to East Asian monsoon climates. As a result of such topographic and rainfall characteristics, landslides and debris-flows are of frequent occurrence, causing loss of life and damage to property. Statistical data reported by the Korea Forest Service on annual damage caused by landslides and debris-flows in Korea from 1990 to 2017 show that damage area and restoration costs have averaged over 450 ha and 45 million USD per year, respectively. Therefore, it is a necessity to mitigate and prevent debris-flow disasters.

The estimation of debris-flow volume is an essential requirement for hazard assessment in mountainous areas as it can be utilized as a major factor for indicators of the relative severity of future events in addition for the design of counter structures (Marchi and D'Agostino, 2004). Several researchers have conducted studies on the estimation of debris-flow volume through empirical, statistical, and physically-based methods, yet it remains a challenging task due to the complexity of predicting erosion and deposition processes in mountainous areas and a lack of data (Hung and Evans, 2004).

The objective of this study is to develop an ANN model for the estimation of debris-flow volumes without performing mathematical analyses on complicated debris-flow mechanisms. In order to develop a reliable and effective

* Corresponding author e-mail address: srlee@kaist.ac.kr

model, GIS-based geomorphological and hydrological datasets were collected from well-documented reports (KSCE, 2012) on historical debris-flow events that occurred at Mt. Umyeon in 2011. Eight conditioning factors built on GIS were selected through a correlation analysis and used as input parameters to operate the ANN model. The performance of the developed ANN model was verified by calculating the MSE value and correlation coefficients (R) of training and testing datasets. Lastly, comparisons were made with an existing conventional regression model.

2. Study Area and Data

2.1. Description of the study area

The study area was Mt. Umyeon, which is located in Seoul, South Korea (Fig. 1). The highest elevation of this area is 293 m above sea level. Areas with slopes greater than 15° cover 69% of the total area, and areas with slopes greater than 30° constitute 8%. The study area is part of the monsoon climate zone with hot and humid climates and intensive seasonal rainfall in the summer season.

On July 27th, 2011, a localized heavy rainfall event at Mt. Umyeon triggered approximately 151 shallow landslides. Most of the landslides were mobilized into debris-flows, which resulted in economic losses of approximately \$15 million USD as well as 16 fatalities and damage to 11 buildings (Park, 2014). As shown in Fig. 1, more than 30 debris-flow events were observed in this area and the area was partitioned into 30 watersheds based on the lowest pour points of the study area.

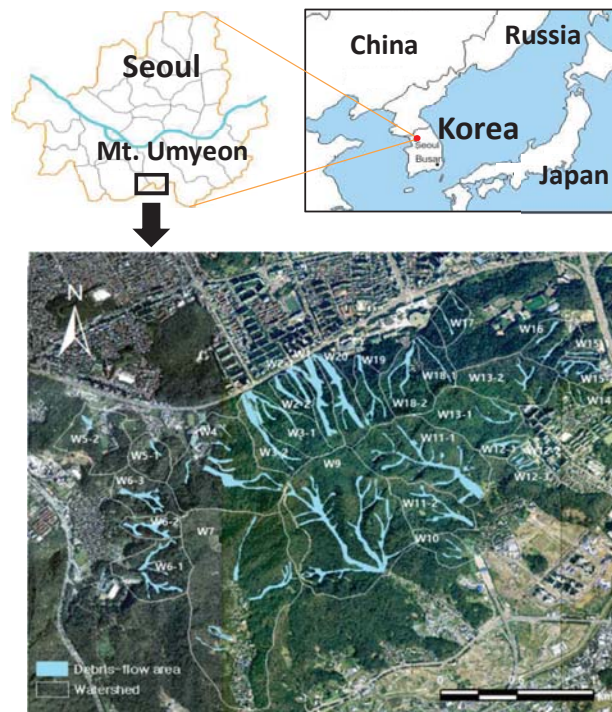


Fig. 1. Location of the study area and an aerial photograph showing the 32 debris-flows (blue colored polygons) in the 30 watersheds (outlined by white lines)

2.2. Debris-flow volume

The volumes of the debris-flows were measured based on field evidence. For detailed information of 15 debris-flow events, the volume data were calculated as the product of the average width, length, and erosion depth of the debris-flow path provided in a field survey report by the Korean Society of Civil Engineers (KSCE) in 2012. For the

remaining 15 cases, the volume data were conservatively estimated by identifying the scoured areas based on aerial photographs taken after debris-flow occurrence and multiplying the areas with the soil depth as erodible materials.

2.3. Debris-flow controlling factors

The selected geomorphological and hydrological controlling factors comprised of 8 types of features: the watershed area (A_w), the mean slope of stream (S), area with slopes greater than 15° (A_{15+}), area with slopes greater than 30° (A_{30}), area with slopes less than 15° (A_{15-}), the mean topographic roughness index (TRI), the mean sediment transportation index (STI), and the mean stream power index (SPI). All datasets were produced in 10m resolution.

The watershed area is one of the most essential and important factors of debris-flow amount, and has been considered in several studies (D’Agostino and Marchi, 2001; Chang et al., 2011). Larger watershed areas in steep mountainous terrain indicate greater capacities of water, which increase the possibility of debris-flow occurrence.

The mean slope of stream is another important factor that directly affects the slope stability. Considering the fact that most debris-flows in Korea occur as the channelized type (Jeong, 2013), the stream slope can greatly influence the erosion and deposition processes of debris materials.

Factors such as A_{15+} , A_{15-} , and A_{30} , which consider both watershed area and slope, are major factors in predicting the volume of debris-flow. According to studies by Takahashi (1981) and Kang (2017), debris-flow can occur if the slope is greater than 15°. Areas with slopes greater than 15° accounted for 69.2% of the total study area. Conversely, areas with a slope of less than 15° might be considered safe areas for the occurrence of debris-flow.

The TRI is a morphological index of the degree of surface ruggedness (Riley et al., 1999). Most of the debris-flow initiation points exhibited high TRI values. Therefore, it can be concluded that a high TRI value is required to generate the debris-flow. The index is given by Eq. (1).

$$TRI = \left[\sum (x_j - x_{00})^2 \right]^{1/2} \quad (1)$$

where x_j is the elevation of each neighboring cell.

STI and SPI are hydrological factors, which measure the erosive power of the flow and the transport capacity, respectively (Moore et al., 1992). High values of STI and SPI indicate that a surge increases with increasing specific catchment areas (A_s) and slope gradient (β) in degrees. The indices are given by Eq. (2) and (3).

$$SPI = h (A_s \tan \beta) \quad (2)$$

$$STI = 1.4 \left(\frac{A_s}{22.13} \right)^{0.4} \left(\frac{\sin \beta}{0.0896} \right)^{1.3} \quad (3)$$

2.4. Database establishment

Based on the aforementioned processes, data extraction was performed for each watershed, and a database was established (Table 1). Among the 30 debris-flow events, the volume ranged from a minimum of 685 m^3 to a maximum of 46,250 m^3 .

Table 1. Database of debris-flow volume and conditioning factors

Watershed ID	$V (m^3)$	$A_w (m^2)$	$A_{30} (m^2)$	$A_{15+} (m^2)$	$A_{15-} (m^2)$	$S (^\circ)$	TRI	SPI	STI
W1	46250	75600	27400	61200	16100	19	125.2	4.1	30.9
W2-1	4400	14700	5800	15400	4000	16.2	101.9	4.4	26.7
W2-2	3120	38400	9000	23900	15900	16.2	99.7	3.9	23.9
W3-1	22500	93600	5600	68000	29200	17.5	111.5	4.1	26.8
W3-2	26400	118000	26200	88000	26500	17.5	124.6	4.7	34.8
W4	30912	421400	69200	245200	69200	17.8	109.5	4.1	29.3
W5	878.8	74500	600	32900	25600	11.8	69.3	3.3	16.9
W5-2	685	158600	200	50400	42300	11.8	61.6	3.2	16.3
W6-1	14730	149400	25200	119700	33100	12	95.3	3.7	24.2

Table 1. Database of debris-flow volume and conditioning factors (continued)

Watershed ID	V (m^3)	A_w (m^2)	A_{30} (m^2)	A_{15+} (m^2)	A_{15-} (m^2)	S ($^\circ$)	TRI	SPI	STI
W6-2	6730	43500	18200	43000	8000	18	108.7	3.6	26.8
W6-3	5400	78100	20800	62700	23500	15.6	94.0	3.0	20.4
W7	18207	786400	95600	485000	147200	15.8	97.9	3.7	24.5
W9	39067	678900	176200	505900	136200	19.7	116.4	4.2	31.1
W10	3188	64200	3200	39700	15500	17.6	84.2	3.5	22.2
W11-1	18765	315000	161000	284200	34600	21.7	128.6	4.3	33.5
W11-2	14857.6	127800	18600	99800	34400	21.7	102.6	4.1	26.9
W12-1	3174.4	29200	8200	24900	5800	16.9	88.7	3.6	24.0
W12-2	2,307	5300	3400	10200	1500	16.9	84.9	3.2	22.2
W12-3	1630.7	7100	400	6700	1700	16.9	74.5	3.4	21.3
W13-1	6074.6	164100	71200	142000	31800	17.6	109.6	4.2	29.8
W13-2	5657.4	159900	24800	128000	28300	17.6	91.9	3.7	24.0
W14	1338.7	17700	3400	11500	6200	15	65.5	3.7	19.1
W15-1	7331.4	11400	2400	26500	13600	15.6	76.9	3.3	19.4
W15-2	2327	38400	0	7600	6900	15.6	60.9	3.1	16.2
W16	3176	90900	1200	44900	22400	13.3	73.8	3.1	17.0
W17	2552.3	57000	3800	39400	16500	15.9	79.9	4.0	22.6
W18-1	3710.1	65700	6400	47700	17600	19.4	103.8	4.3	26.2
W18-2	9870	119700	32200	92600	27000	19.4	120.9	4.4	31.3
W19	10465.5	76200	40000	65000	10200	20.9	130.5	4.3	34.4
W20	6960	90800	25400	76400	18200	20.1	125.4	4.3	32.3

3. Methodology

3.1. Correlation analysis for selecting controlling factors

In general, the more variables used in a developed estimation model, the better the prediction result. However, if the analysis is performed with the inclusion of meaningless factors, an over-fitting may occur even if the model is significant. In order to prevent this phenomenon, independent variable selection methods are used with consideration of the correlation with the dependent variable. In this study, the Pearson, Kendall and Spearman correlation analyses were performed.

3.2. Artificial Neural Network modeling

In this study, an ANN model was used to consider the non-linear relationships between debris-flow volume and the controlling factors. The ANN modeling mainly consists of a combination of various neurons in a multi-layer system. The output value of a certain neuron is the product of the weight prior to inputting the value to another neuron. The net is calculated as the sum of the products of each weight and the outputs from the previous neurons. The output is then used as the input value of the next neuron. The net and output can be calculated using transfer functions as shown in Eq. (4) and (5):

$$net = \sum_{i=1}^m W_i X_i \quad (4)$$

$$output = f(net - b) \quad (5)$$

where X_i is the input value to a certain neuron, W_i is the synaptic weight for the corresponding input value, b is the bias of each neuron, and f is the transfer functions such as sigmoid, tangent, and linear functions. In this study, the ANN model was trained using Bayesian regularization, which is commonly used for the error back-propagation algorithm (Kayri, 2016). For the performance evaluation of the ANN model, the R and MSE values were considered. The R has a value between -1 and 1, and the closer to 1, the better the predictive accuracy of the model. In the case of MSE, it can be evaluated as a good performance model when the value is closer to 0. The R and MSE are calculated as in the following Eq. (6) and (7):

$$R = \frac{\text{cov}(p,q)}{\sigma_p \sigma_q} \tag{6}$$

$$\text{MSE} = \frac{1}{n} \sum_{k=1}^n [p(k) - q(k)]^2 \tag{7}$$

where, cov is the covariance, σ is the standard deviation, p is the natural log of the estimated debris-flow volume, q is the natural log of the measured debris-flow volume, and n is the total number of dataset.

A total of 30 observed debris-flows were randomly selected for the training and testing phases, with 70% of the data being used for the training phase and 30% being used for the testing phase. The dependent variable, the debris-flow volume, is likely to have a large MSE value due to its wide range and large variance. In order to avoid this problem, the natural logarithm of debris-flow volume was used to reduce the data range and variance. In addition, in order to determine an optimal network structure, the number of neurons in the hidden layer varied from 1 to 7, with transfer function combinations shown in Fig 2. The ANN modeling of each transfer function combination was performed 1000 times, after which the average R-value was calculated to select the best transfer function combination. After selecting the best combination of transfer functions and neurons in the hidden layer with the highest average R-value, the ANN model with the lowest MSE was selected as the best predictive model.

3.3. Comparison with an existing regression model

In order to compare the performance of the proposed model with an existing model for estimating the debris-flow volume, a regression equation proposed by Marchi and D'Agostino (2004) was obtained using the database of the study area. Marchi and D'Agostino suggested the regression equation of the form of Eq. (8) for the Eastern Italian Alps, and used the mean stream gradient and watershed area as the two main factors.

$$V = \alpha \cdot A_w^b \cdot S^c \tag{8}$$

Here, A_w is the watershed area (m^2), S is the mean stream gradient ($^\circ$), and a , b , and c are fitting coefficients. The results of ANN model and the regression model were compared through the coefficient of determination (R^2).

4. Results

4.1. Correlation analysis result

The correlation of independent variables was confirmed by considering Pearson, Kendall, and Spearman correlation coefficients and significance probabilities (Table 2). The significance probability is considered to be significant for values of 0.05 or less, and the correlation coefficient indicates no correlation when the value is between -0.2 and 0.2. All controlling factors collected in this study are somewhat correlated with the determination of debris-flow volume. Therefore, all variables were used for the ANN model development.

Table 2. Correlation analysis results

Conditioning factors	Pearson's correlation		Spearman's correlation		Kendall's correlation	
	Coefficient	P-value	Coefficient	P-value	Coefficient	P-value
A_w	0.521	0.003	0.600	0.000	0.437	0.001
A_{30}	0.601	0.000	0.791	0.000	0.617	0.000
A_{15+}	0.594	0.001	0.764	0.000	0.568	0.000
A_{15-}	0.477	0.008	0.535	0.002	0.407	0.002
S	0.562	0.001	0.590	0.001	0.451	0.001
TRI	0.794	0.000	0.798	0.000	0.614	0.000
STI	0.602	0.000	0.795	0.000	0.618	0.000
SPI	0.590	0.000	0.595	0.001	0.384	0.003

4.2. Artificial Neural Network modeling

Fig 2. shows the correlation coefficient corresponding to the transfer function combination and the number of neurons in the hidden layer. The analysis results of the six transfer function combinations showed that the training R-values were approximately 0.8 and the testing R-values were approximately 0.7, regardless of the combination when the number of neurons was 3 or greater. Among the results, the model with 5 neurons showed the best performance (Training R-value=0.88, MSE=0.25, Testing R-value=0.81, MSE=0.55) with the combination of log-sigmoid and linear functions.

The determined artificial neural network structure consisted of eight input data, one hidden layer with five neurons, and one output layer, and the transfer function consisted of a combination of log-sigmoid and linear functions (Fig. 3). The ANN model using the selected transfer function and structure exhibited relatively high R-values, with 0.91 for training, 0.81 for testing, and 0.87 for the overall data (Fig. 4).

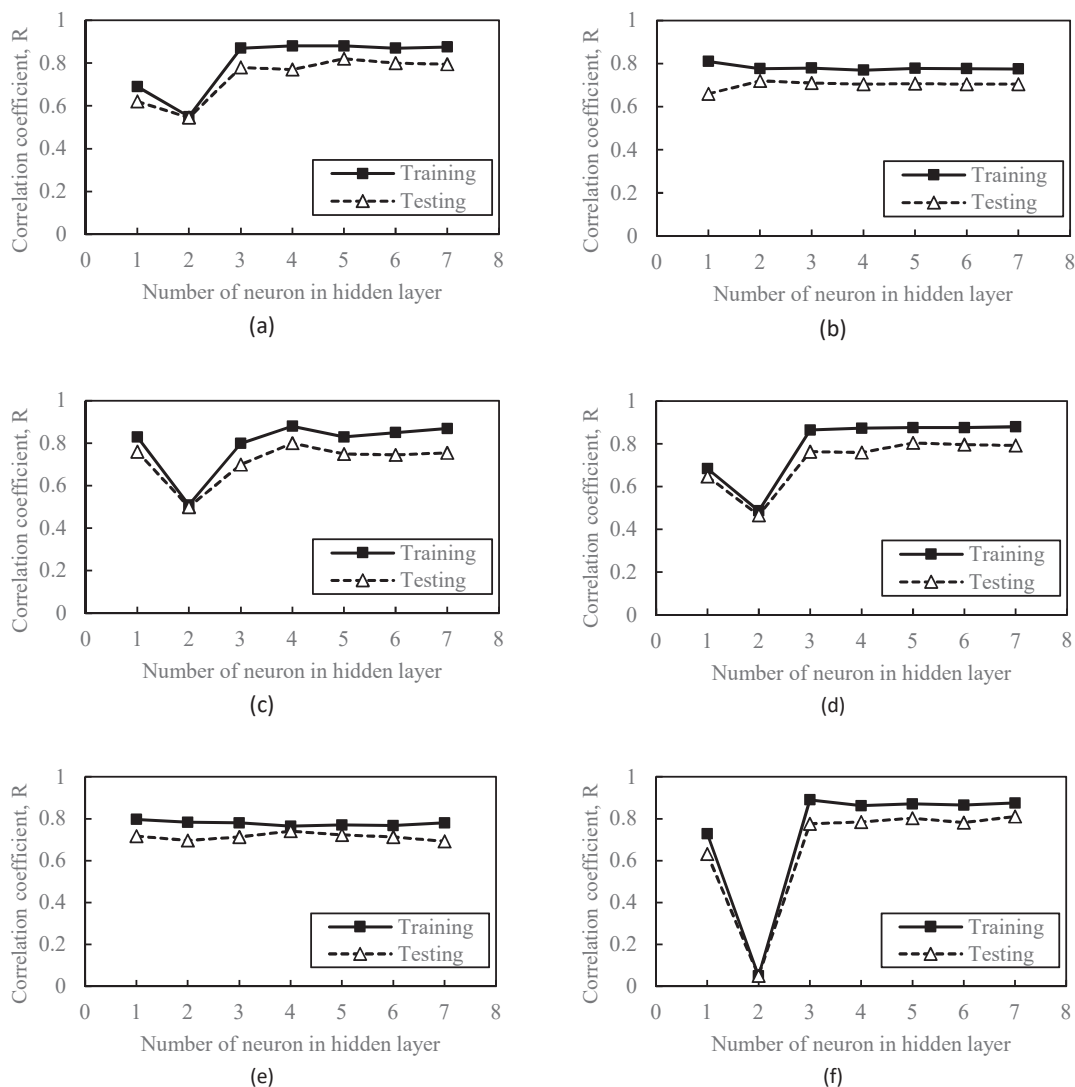


Fig. 2. Correlation coefficients of training and testing phases according to transfer function combination and the number of neurons; (a) log-sigmoid & linear function; (b) log-sigmoid & log-sigmoid function; (c) log-sigmoid & tangent-sigmoid function; (d) tangent-sigmoid & linear function; (e) tangent-sigmoid & log-sigmoid function; (f) tangent-sigmoid & tangent-sigmoid function

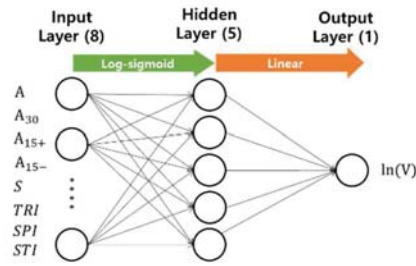


Fig. 3. ANN network (8-5-1) for estimating debris-flow volume

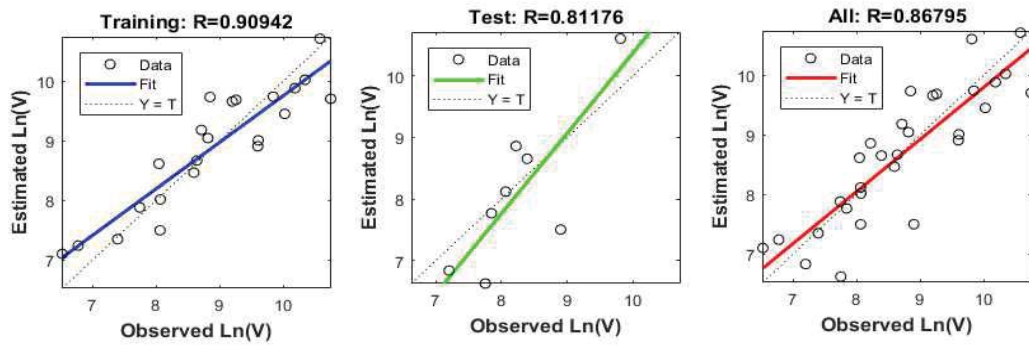


Fig. 4. ANN model performance results

4.3. Comparative analysis with an existing regression model

The fitting coefficients of Eq. (8) were derived using the MATLAB fitting curve tool. The regression equation using the data of the study area is as follows:

$$V = 0.3055 \cdot A_w^{0.4818} \cdot S^{1.721} \quad (9)$$

In order to evaluate the performance of the ANN model, this study compared the estimated debris-flow volumes with the observed debris-flow volumes based on the total data. As a result, the R^2 -values of the regression equation and the ANN model were 0.65 and 0.79, respectively (Fig. 5). The results show that the ANN model is a reliable and useful tool for estimating the debris-flow volumes.

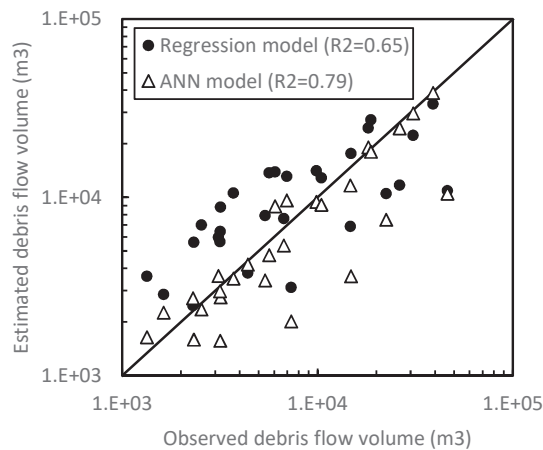


Fig. 5. Comparison of estimated and measured values using the ANN model and the regression equation

5. Conclusion

In this study, an ANN model was suggested for the reliable estimation of debris-flow volume. The model was developed based on 30 debris-flows events and 8 controlling factors including the A_w , S , A_{15+} , A_{15-} , A_{30} , TRI , STI , and SPI . The collected datasets were subjected to a correlation analysis to ensure independency among the variables and to avoid the over-fitting problem. An ANN network of 8-5-1 structure using sigmoid and linear transfer functions was adopted as the model exhibited reliable performance indicated by a high R-value of 0.91 for the training dataset. From the results of comparisons with an existing regression model, the ANN model exhibited greater predictive power and was a more reliable tool for estimating the debris-flow volume. However, the applicability of this model must be limited to local conditions similar to the study area. In addition, additional factors that affect debris-flow volume should be studied to develop a higher performance model.

Acknowledgements

This research was supported by the Basic Research Laboratory Program through the National Research Foundation of Korea funded by the Ministry of Science and ICT (NRF-2018R1A4A1025765), and the Technology Advancement Research Program (18CTAP-C143742-01) by Ministry of Land, Infrastructure and Transport of Korean government.

References

- Chang, C.W., Lin, P.S., Tsai, C.L., 2011, Estimation of sediment volume of debris flow caused by extreme rainfall in Taiwan, *Engineering Geology*, v.123, pp.83-90.
- D'Agostino, V., and Marchi, L., 2001, Debris flow magnitude in the Eastern Italian Alps: data collection and analysis, v.26, pp.657-663
- Jung, S.W., 2013, Debris Flow Mobility: A Comparison of Weathered Soils and Clay-rich Soils, *Journal of the Korean Geotechnical Society*, v.29, pp.23-37 (in Korean).
- Hungr, O., Evans, S.G., 2004, Entrainment of debris in rock avalanches: An analysis of a long run-out mechanism, *Geological Society of America, Bulletin*, pp.1-13.
- Kang, S., Lee, S.R., Nikhil, N.V., Park, J.Y., and Lee, D.H., 2017, Development of an initiation criterion for debris flows based on local topographic properties and applicability assessment at a regional scale, *Engineering Geology*, v.230, 65p.
- Korean Society of Civil Engineers, 2012, Research contract report: causes survey and restoration work of Mt. Umyeon landslide. Korean Society of Civil Engineers.
- Marchi, L. and D'Agostino, V., 2004, Estimation of debris-flow magnitude in the eastern Italian Alps Earth, *Surf. Process. Landforms*, 29, pp.207-220.
- Kayri, M., 2016, Predictive Ability of Bayesian Regularization and Levenberg-Marquardt Algorithms in Artificial Neural Networks: A Comparative Empirical Study on Social Data, *Mathematical and Computational Applications*, v.21, pp.1-11.
- Moore, I.D. and Wilson, J.P., 1992, Length-slope factors for the Revised Universal Soil Loss Equation: simplified method of estimation, *Journal of Soil and Water Conservation*, 47, pp.423-428.
- Takahashi, T., 1981, Estimation of potential debris flows and their hazardous zones: Soft countermeasures for a disaster, *Journal of Natural Disaster Science*, v.3, No. 1, pp. 57-89.
- Park, D.W., 2014, Simulation of landslides and debris-flows at regional scale using coupled model [M.S. Thesis], Korea Advanced Institute of Science and Technology, Daejeon, Republic of Korea.
- Riley, S.J., DeGloria, S.D., and Elliot, R., 1999, A terrain ruggedness index that quantifies topographic heterogeneity, *Intermountain Journal of Sciences*, v.5, pp.23-27.

Post-fire debris flows of 9 January 2018, Thomas Fire, southern California: Initiation areas, precipitation and impacts

Stefani G. Lukashov^{a,*}, Jeremy T. Lancaster^{a,*}, Nina S. Oakley^{b,c}, Brian J. Swanson^d

^aCalifornia Geological Survey, 801 K St, Sacramento, CA 95820, United States

^bWestern Regional Climate Center, Desert Research Institute, 2215 Raggio Parkway, Reno, NV 89512, United States

^cCenter for Western Weather and Water Extremes, Scripps Institution of Oceanography, 9500 Gilman Drive, La Jolla, CA 92093, United States

^dCalifornia Geological Survey, 320 West 4th St, Suite 850, Los Angeles, CA 90013, United States

Abstract

The post-fire debris flows of 9 January 2018 killed 23 people, destroyed over 130 homes, and caused severe damage to infrastructure in Montecito and Carpinteria, California. Highway 101 was closed for 13 days, significantly impacting transportation and commerce in the region. Collectively, debris flows from this event are comparable in magnitude to the largest documented post-fire debris flows in the state, inundating over 4 km² of land, and costing the Santa Barbara region over half a billion dollars in debris removal and damages to homes and infrastructure. Here, we document the extent and magnitude of inundation areas, debris-flow volumes, and source areas. Additionally, we describe the atmospheric conditions that generated intense rainfall and use precipitation data to compare debris-flow source areas with spatially associated peak 15-minute rainfall depths. We use a compilation of debris-flow damages to summarize economic impacts associated with the event.

Keywords: post-fire; debris flows; alluvial fan; NCFR; rainfall intensity; inundation; Montecito; Thomas Fire; loss estimate

1. Introduction

The Thomas Fire ignited on 4 December 2017 and burned steeply sloping terrain in the western portion of the Transverse Ranges in Santa Barbara and Ventura counties (CAL FIRE, 2018). The fire burned 114,078 ha (281,893 acres), with full containment declared on 12 January 2018. A total of 1,063 structures were destroyed across both counties and 280 additional structures were damaged. A Presidential Disaster Declaration was made on 8 December 2017.

Post-fire debris flows initiated at approximately 3:45 a.m. local time (PST) on 9 January 2018, starting first in the Santa Ynez Mountains and then spreading eastward to watersheds in the Topatopa Mountains. Within the Montecito and Carpinteria area, the debris flows travelled from the canyon mouths on to urbanized alluvial fan areas extending over four kilometers to the Pacific Ocean. The debris flows killed 23 people, destroyed over 130 homes, and caused severe damage to infrastructure. The Thomas Fire Presidential Disaster Declaration was amended on 10 January 2018 to include flooding, mudflows and debris flows.

As storm rainfall runs off on steep hillslopes burned by wildfire, sediment and debris are eroded from hillslopes and subsequently scoured from channels. As sediment and debris are entrained, progressive bulking of runoff may lead to the development of debris flows (Cannon et al., 2003). Debris flows commonly occur in steep watershed areas burned at moderate to high soil burn severity, with the largest events often triggered by the first significant post-fire rainstorm (Cannon et al., 2008; Parise and Cannon, 2012), and in response to short rainfall durations of high intensity (Moody et al., 2008; Kean et al., 2011). As debris flows travel down slope, they strip vegetation, entrain boulders, block drainages, damage structures, and flow in unpredictable directions (Lancaster et al., 2015). The destructive power of boulder-laden surge fronts magnifies the impacts of debris flows to life and property.

Post-fire debris flows have become a common threat to southern California communities due to urbanization of alluvial fans and floodplains downstream of the Transverse Ranges (Lancaster et al., 2015; Oakley et al., 2017). While

* Corresponding authors e-mail addresses: Stefani.Lukashov@Conservation.ca.gov and Jeremy.Lancaster@Conservation.ca.gov

many moderate- to large-sized destructive debris flows have occurred (Cannon et al., 2010; Gartner et al., 2014), documentation of runout distances, areal extent and depth, source areas, triggering rainfall, and damages and costs, are rare in published literature. Quantification of debris-flow damages and costs can be used for risk assessments, planning for future disasters, and in making decisions about allocating money for pre-disaster-mitigation mapping and prevention. However, assignment of post-fire debris-flow costs is challenging as there is no way to quantify the loss of human life and damage costs to physical structures can be difficult to compile where multiple entities are affected (Fleming and Taylor, 1980; Godt, 1999).

We document a large-magnitude, post-fire debris-flow event that occurred a month after the ignition of the Thomas Fire in the southern California counties of Santa Barbara and Ventura and significantly impacted the region. We focus on four aspects of the event: (1) atmospheric conditions and precipitation depth and durations that initiated the event, (2) the distribution of source areas that generated debris flows, (3) the extent of runout and inundation of the debris flows, including debris-flow depths, and (4) damage and costs associated with debris-flow impacts in Santa Barbara County.

2. Debris flow triggering storm event

2.1 Atmospheric conditions

The storm event that produced the high-intensity rainfall responsible for the debris flows featured a weak atmospheric river facilitating moisture transport into the area as well as a strong cold front (Oakley et al., 2018). A narrow band of high-intensity rainfall developed along the cold front (Fig. 1a), a feature referred to as a “narrow cold frontal rainband” (NCFR; Markowski and Richardson, 2010). Between 3:30 and 4:00 a.m. (PST) on January 9, the cold front and associated NCFR moved over the Thomas Fire burn area. One segment of the NCFR intensified within the Santa Barbara Channel as it moved towards Montecito (Fig. 1b). Subsequently, radar and surface-based precipitation observations show the NCFR began to weaken and dissipate to the east near the Santa Barbara-Ventura County line (Oakley et al., 2018).

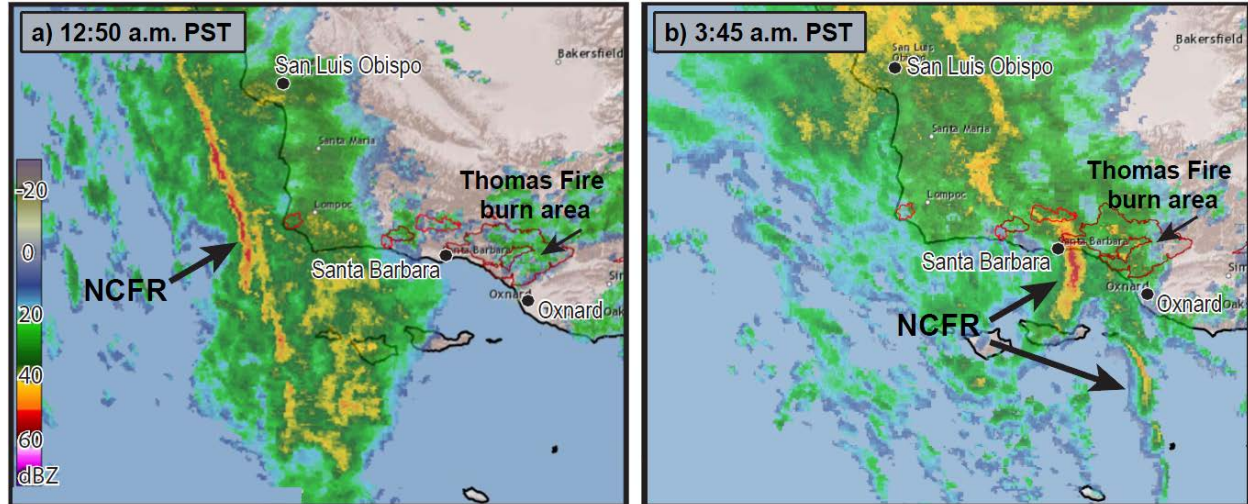


Fig. 1. Panels show radar imagery preceding (a) and at the time of (b) post-fire debris flows in the Thomas Fire burn area. Yellow to red colors indicate progressively higher storm intensity. Figure adapted from Oakley et al. (2018) Radar image source: CNRFC.

2.2 Precipitation observations

Observed rainfall data from Santa Barbara County Public Works Department show the 9 January 2018 storm broke station records but did not exceed the 15-min duration county record of 35.31 mm at San Marcos Pass in 2015, west of the burn area (not shown). Historical 15-min duration records are available for 36 rainfall stations in Santa Barbara County and four of these records were broken during the January 9 event (see Table 1 for summary of data). Two of these stations are within the burn area while two are just south in Montecito and Carpinteria (see Fig. 2 for locations).

Table 1. Summary of 15-min rainfall station records broken during 9 January 2018 storm

Station (abbreviations mark locations in Fig. 2)	15-min rainfall depth (mm)	Precipitation return event in years	Average return interval in years (90% confidence)	Record (start year – end)
Doulton Tunnel - DT	26.11	100	25 - 1,000	1965 - present
Jameson Dam - JD	25.15	25	10 - 500	1965 - present
Montecito - M	18.54	50	25 - 1,000	2009 - present
Carpinteria FS - CFS	21.84	50	25 – 1,000	1964 - present

Although 15-min rainfall intensities were not remarkable over Matilija Canyon, this area received the highest total storm precipitation, 164.85 mm, from 04:00 LST 8 January to 0:400 LST 10 January (Oakley et al., 2018; CNRFC, 2018). Peak 15-min rainfall depths from the storm were collected from 46 stations maintained by the Santa Barbara County Public Works Department and Ventura County Watershed Protection District, and depths were interpolated with the Inverse-Weighted Distance method in ArcGIS (Chen et al., 2017) and are shown as contours in Fig. 2.

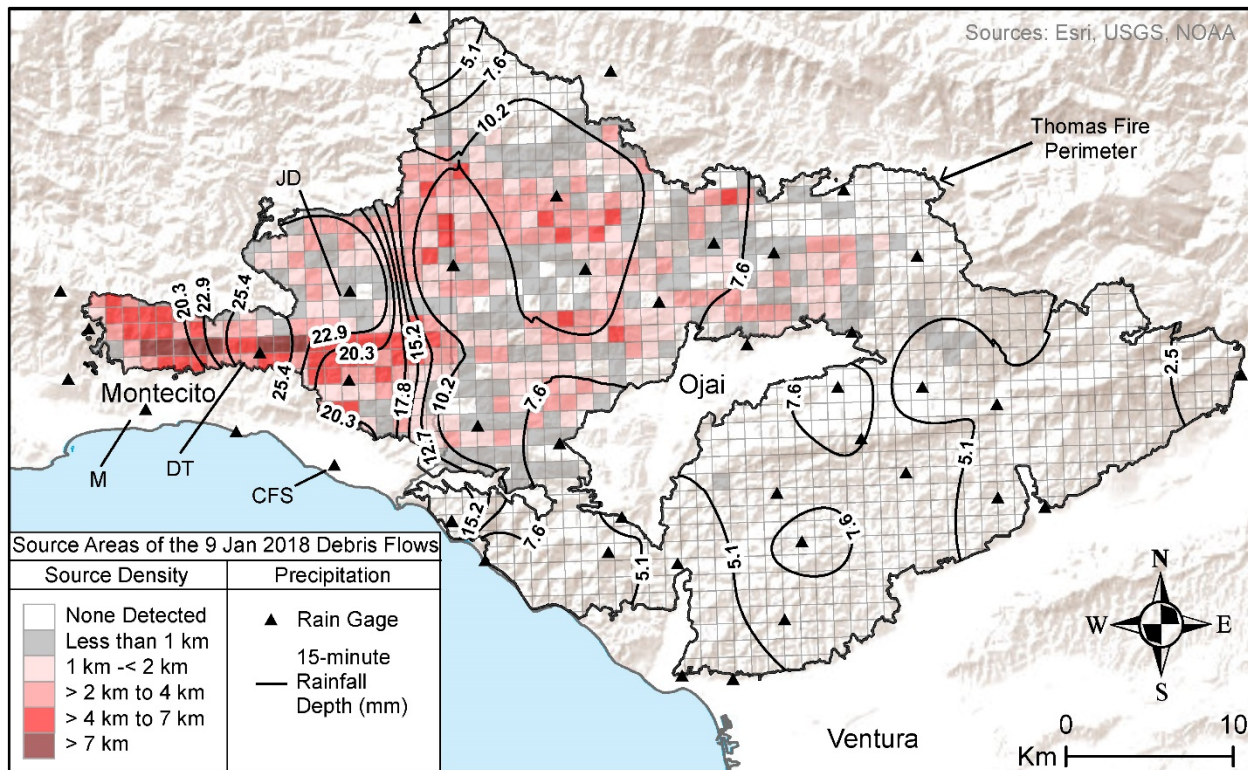


Fig. 2. Maximum 15-min rainfall depths (mm) over a 1 km² grid representing the cumulative lineal kilometers of debris-flow source gullies greater than 1.5 m in width; debris flows in gullies less than 1.5 m wide or those interpreted with questionable confidence, are not represented in this figure. The rain gages mentioned above are labeled as follows: DT- Doulton Tunnel, JD- Jameson Dam, M- Montecito, and CFS- Carpinteria.

3. Source areas

Large, destructive debris flows received widespread media coverage in the Montecito area and the extent of these flows and nearby rainfall data have been extensively documented (Kean et al., *in review*, and Oakley et al., 2018). However, identification of the distribution of flows across the rugged Thomas Fire burn area is a challenge owing to the large area impacted and limitations on access and personnel to map the entire area. Therefore, we conducted remote mapping with GIS and standardized identification protocols to assess the entire Thomas Fire area. The results of this mapping were spot checked in the field to validate interpretations and a simplified summary of this work is presented

on a 1 km grid in Fig. 2. Corresponding peak 15-min rainfall depths at the source-area grid cells can be interpolated from the contour lines.

3.1. Defining source areas

Debris-flow source areas were identified by interpreting erosional features expressed in post-event 1 m resolution Digital Globe imagery, lidar collected by Towill Inc. processed to a 0.5 m hillshade, and 5 cm resolution aerial photography. Geomorphic interpretation of hillslope and channel source areas was conducted by reviewing hillslope features at a screen scale of between 1:500 and 1:1,250. Geomorphic evidence for identification of source gullies that did or did not issue a debris flow included marginal levees, rills, gullies, extensive scour, mud drapes, boulder fields, and impacts, such as boulders deposited on roads. Marginal levees are considered to be a process unique to debris-flow surge fronts. Levees form along the paths of debris flows as shear stresses increase as slow moving, coarser-grained material is pushed aside at the lateral margins of the flow front by the advancing finer-grained slurry (Sharp and Noble, 1953; Johnson et al., 2012; Iverson, 2014). In contrast, the other geomorphic evidence may be associated with different processes. Progressive erosion and the development of debris flows within eroded gully networks with a minimum width of 1.5 m were determined as the minimum mappable feature, although we recognize debris flows having smaller widths occurred.

A confidence matrix following Wills et al. (2017), was used to classify source areas resulting from debris-flow generation, where, *definite* sources had marginal levees and/or were field verified, *probable* sources had more than one line of evidence, but did not have marginal levees, and *questionable* sources had one line of evidence, but where a process other than debris flow could not be precluded. Debris-flow sources were then intersected with a 1 km² grid and weighted by their confidence and summarized for each grid cell. Each confidence type was assigned a weight based on field validation of 184 source gullies across the study area, including 98% for *definite*, 69% for *probable*, and 22% for *questionable* sources (CGS, *in preparation*).

The accuracy of the debris-flow source area map is limited by the different sources and quality of data across the burn area. Lidar data was unavailable for approximately 10% of the burn area, primarily north of the Santa Ynez Mountains (see Fig. 3 for locations of geographic regions). Image quality also varies significantly across the entire burn area, with warping, shadows, and vegetation obscuring the identification and interpretation of erosional features. Confidence assignments are higher in the west where extensive field observations after 9 January validated the occurrence of debris-flow processes.

3.2. Source areas and rainfall

The source-area density map (Fig. 2) shows that the distribution of debris-flow sources varies greatly across the burn area. The highest concentration of source gullies is observed in the Santa Ynez Mountains north of Montecito and Summerland. There is a low-to-moderate concentration of source gullies in the Matilija Creek watershed and the area north and northeast of the Ojai Valley. There is little evidence to support initiation of sizeable debris flows in the southeast portion of the burn area, in Sulphur Mountain and Rincon Point (Fig. 3). Observed burn severity was commonly low in this area and bedrock sources are dominantly fine-grained and generate relatively few boulders for entrainment.

Contoured results of the 15-min duration data indicate the 10.2 mm rainfall contour generally encompasses debris-flow source areas with greater than 4 km/km² of source density, while the 5.1 and 7.6 mm contours define what appears to be a triggering precipitation boundary in the north and south of the burn area. The source areas originating at the base of the Topatopa Mountains did not receive rainfall rates as high as the rest of the burn area. The area south of Ojai has rainfall depths of >7.6 mm, but no geomorphic features suggestive of debris-flow generation were identified. The Rincon Point region, along the coast, had rainfall depths exceeding 15.2 mm, but did not have identifiable debris-flow source features. A relatively dense band of debris-flow source gullies in the Santa Ynez Mountains has an east-west trend and appears to correlate with high rainfall depths of up to 17.8 mm.

4. Mapping and evaluating inundated areas

Inundation mapping was conducted in two phases. The first phase was completed as a collaboration between the U.S. Geological Survey and the California Geological Survey in the first twelve days after the event to maximize the observation of perishable features (Kean et al., *in review*). In this phase, field observations were made along the five

primary runout paths through Montecito where damage occurred, including from west to east, Cold Spring, Hot Springs, Montecito, Oak, San Ysidro, Buena Vista, and Romero creeks (see Fig. 3). Observations include documentation of limits of inundation, maximum depth of inundation, scour depth, avulsion characteristics, local evidence of flow superelevation, and the distribution, thickness, and grain size of deposits within the inundation zone. In the second phase, additional inundation mapping was conducted using post-event satellite imagery, lidar and aerial photography, supplemented by general field observations (see Fig. 3).

4.1. Extent and depth of inundation

Post-event inundation mapping reveals over 4 km² of land was inundated in Santa Barbara and Ventura counties during the January 9 event, collectively. The built environment along the Santa Barbara coastal plain sustained the most inundation, with about 0.2 km² of inundation occurring in the canyons north of the Santa Ynez Mountains and west of the Topatopa Mountains. Of the 3.8 km² of inundation that occurred in the built environment, 0.6 km² of inundation impacted Carpinteria Creek and 3.2 km² of inundation impacted the Montecito and Summerland area, from Cold Spring Canyon Creek to Arroyo Paredon. Peak inundation depths of 10 m were recorded near the upper and middle portions of the piedmont, from the channel bottom to mud marks on a tree at Romero Creek at the edge of the burn perimeter, and from the bottom of Montecito Creek to a channel bank near the crossing at SR-192. The maximum debris runout distances, measured from each canyon mouth to the shore, were just over 4 km for Cold Spring Canyon, and 5 km for Romero Creek.

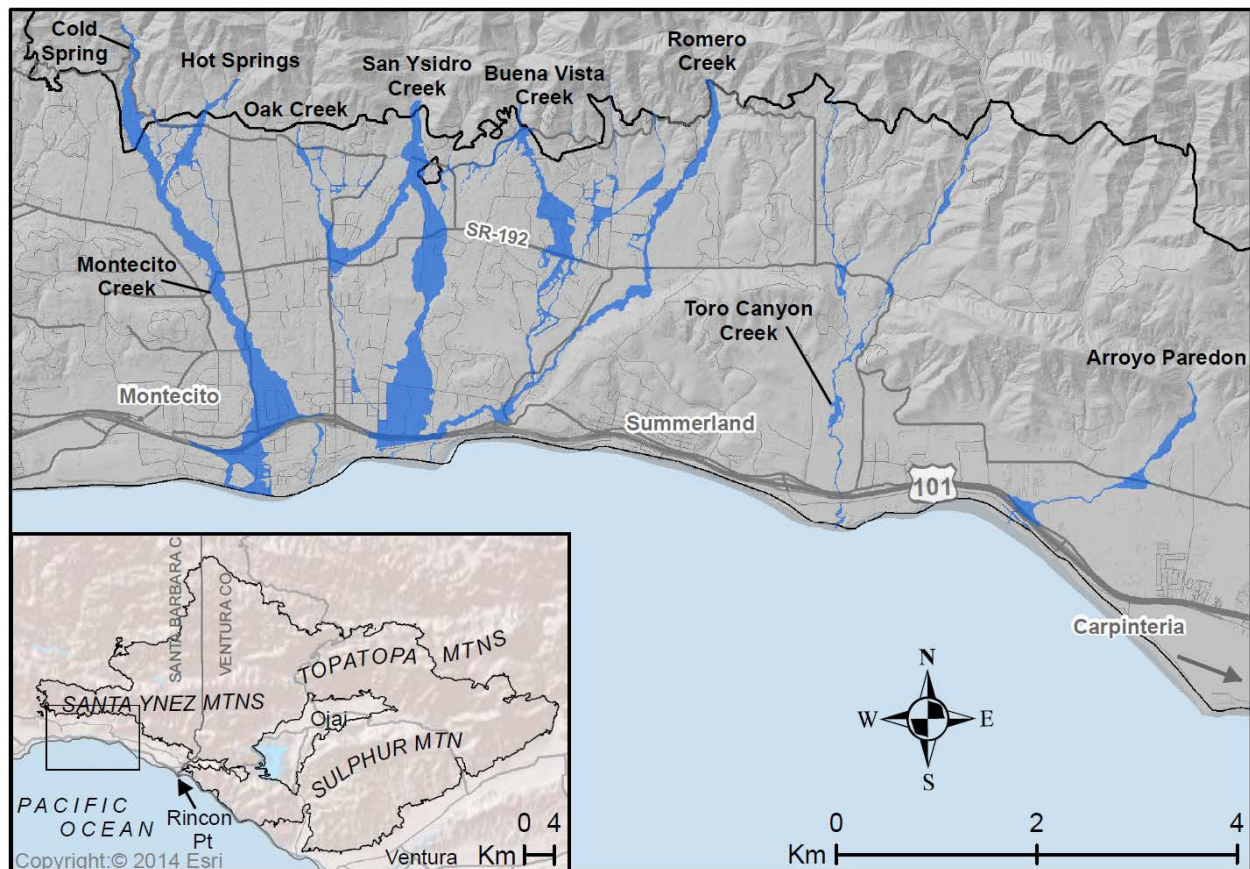


Fig. 3. Mapped inundation (blue) in the Montecito and Summerland region (shown at a 1: 125,000 scale) with an inset map of the Thomas Fire burn perimeter in the Santa Barbara and Ventura counties (shown at a 1: 1,000,000 scale). The primary map extent is shown on the inset map.

4.2. Debris-flow volume estimation

The reported total volume of 9 January 2018 storm material removed in Santa Barbara County from debris basins was 248,000 m³ and the volume removed from creek channels was 124,000 m³ (USACE 2018a and 2018b). Recorded sediment thickness at 373 locations, taken during field observations in the Montecito area, were used to estimate the possible debris volume over the inundation area in Montecito and Summerland. The total inundation extent in this area is 3,213,000 m². The average deposit depth is 0.3 m with a standard deviation of 0.53 m. Because the data does not have a normal distribution and is heavily skewed by large outliers, the median of 0.2 m is used to estimate deposit volumes (Schiff and D'Agostino, 1996). The median deposit depth multiplied by the inundation area of Montecito and Summerland, gives an estimated deposited debris volume of 643,000 m³. This estimated volume, combined with the debris volume removed from debris basins and channels amounts to about 1,014,000 m³.

The calculated inundation area and volume corresponds to a debris-flow magnitude 7 event according to Jakob (2005). Previous large magnitude events affecting similar areas to the January 9 event, include debris flows following the 1964 Coyote Fire and the 1971 Romero Fire; each impacted an estimated area of greater than 2 km² for a magnitude 5 classification (Lancaster, 2018; Jakob, 2005).

5. Damages

The compilation of damages and costs follows the general methodology of Fleming and Taylor (1980) and includes direct, indirect, and undetermined debris-flow damages within Santa Barbara County (damages were unavailable for Ventura County as of March 2019). Direct damages include repairs necessary to restore all structures and land sustaining physical damage immediately resulting from the debris flows. Indirect damages include secondary losses from the debris flows like loss of income or measures taken to mitigate additional debris-flow damages. Undetermined damages may be direct or indirect but are inseparable from damages due to the Thomas Fire based on available information. Cost information (Table 2) has been compiled from publicly available documents, such as press releases, presentations to board meetings, and news articles.

Table 2. Summary of damages related to direct and undetermined costs in Santa Barbara County

<i>Direct Damage Costs</i>		
Damage	Cost (USD 2018)	Data Source
U.S. 101 debris removal	\$11,250,000	CALTRANS, 2018a
bridge repairs; SR-192	\$55,000,000	CALTRANS, 2018b
Property insurance claims	\$422,000,000	California Insurance Commissioner, 2018
Debris basin and channel removal	\$110,400,000	O'Dell, 2018
Water district	\$5,500,000	Montecito Water District, 2019
<i>Indirect Damage Costs</i>		
Lost wages due to U.S. 101 closure	\$25,000,000	RDN, 2018
Installation of 6 debris ring nets	\$4,000,000	Magnoli, 2019
<i>Undetermined Damage Costs</i>		
County response and recovery	\$55,000,000	Santa Barbara County, 2018
Disaster assistance loans	\$50,000,000	Small Business Association, 2018

The total estimated cost of the debris flows alone, as of March 2019, is \$633,150,000, with possible additional costs of up to \$105,000,000 coming from undetermined costs (Table 2). About 64% of the direct costs come from residential property insurance claims. There were insured losses of \$388,000,000 from 1,415 residential personal property claims, \$27,200,000 from 235 commercial property claims, and \$6,700,000 from 388 auto and miscellaneous property claims. Potential damages and costs that cannot be quantified include impacts to the capacity of Gibraltar Reservoir, on the north side of the Santa Ynez Mountains (City of Santa Barbara, 2018), environmental repercussions to local beaches (Molina, 2018), and continued legal action against utility companies for alleged exacerbation of the fire and debris-flow damages (Okada, 2019).

6. Summary and discussion

Large magnitude, post-fire debris flows of 9 January 2018 took 23 lives as a result of extreme precipitation associated with a narrow band of high-intensity rainfall occurring in the vicinity of a cold front, known as a narrow cold frontal rainband (NCFR). The NCFR appears to have controlled the distribution of debris-flow initiation across the burn area. Collectively, the debris flows triggered by the 9 January 2018 event correlate to a magnitude 7 post-fire debris-flow event (Jakob, 2005), with a depositional volume of over 1,000,000 m³ in the Montecito and Summerland area. Costs associated with this event have exceeded a half billion dollars, as of January 2019.

NCFRs have been previously observed as a trigger for post-fire debris flows in southern California (Oakley et al., 2017), but there are no known studies on the frequency of the occurrence of these features in southern California. A similar damaging NCFR event in the region was the Springs Fire debris flow in Camarillo, CA on 12 December 2014 (Sukup et al., 2016) which also had unremarkable storm totals but high-intensity, short duration rainfall.

Several regions received precipitation in excess of post-fire debris flow triggering thresholds, yet debris flows were not identified as mappable based on our interpretive approach. These include the Sulphur Mountain region and the area around Rincon Point. The lack of debris flows in the Sulphur Mountain area is attributable to relatively lower watershed average slope values as well as generally low soil burn severity. Conversely, the Rincon Point area is typified by steeper sloping terrain and moderate to high soil burn severity, thus it is possible there were finer-scale erosional processes that triggered mudflows lacking levee features, as these areas are underlain by fine-grained sediment sources.

Jakob (2005) classifies boulder debris flows up to magnitude 6, where magnitudes 7-10 are used only for volcanic debris flows. He justified excluding boulder debris flows from larger magnitude classification because only volcanic debris flows were known for having large runouts due to their fluidized nature. The depositional overlap of these debris flows restricts the ability to separate material by watershed, so they are considered here as an aggregate event. The cumulative estimated volume for this event is greater than 1,000,000 m³, and the inundation area is over double the value used for the magnitude 6. Thus, based on the combined inundation areas, we classify the event as a magnitude 7 debris flow.

We anticipate that our compiled damage estimates will be further refined, but may ultimately underestimate the true cost of the debris flows, as there is no way to quantify the injuries or the loss of life, and documentation of damages to physical structures may never be comprehensive (Fleming and Taylor 1980; Godt, 1999; Taylor and Brabb, 1972). As documentation of economic losses improve with time, we speculate that the cost for this event may exceed \$1 billion dollars.

Acknowledgments

We would like to acknowledge the assistance of those who contributed information and data to this investigation: Yonni Schwartz (U.S. Forest Service); Jason Kean, Dennis Staley, Jeffrey Coe, and Francis Rengers (U.S. Geological Survey); Shawn Johnson and Jon Frye (Santa Barbara County Public Works); Jim O'Tousa (Ventura County Public Works Agency); Bruce Rindahl and Ron Marotto (Ventura County Watershed Protection District). Field reviews by Yonni Schwartz and Jim O'Tousa provided valuable feedback. We thank Jeff Keaton (WOOD Plc), Alex Strouth (BCG Engineering Inc.), and Jim O'Tousa for providing constructive reviews of this paper.

References

- California Department of Forestry and Fire Protection (CAL FIRE), 2018, *Thomas Fire Watershed Emergency Response Team – Final Report*: CA-VNC-103156, 172 p.
- California Insurance Commissioner, 2018, Montecito mudslide insurance claims top \$421 million: Press Release, available at <http://www.insurance.ca.gov/0400-news/0100-press-releases/2018/release033-18.cfm>
- California Geological Survey, *in preparation*, *Post-Fire Debris Flows of 9 January 2018, Thomas Fire, Southern California*: California Geological Survey Special Report 248.
- California Nevada River Forecast Center, 2018, Radar reflectivity, <https://cnrhc.noaa.gov/>, last access: 5 November 2018.
- Caltrans, 2018a, Caltrans Presentation of U.S. 101 recovery to SBCAG Board 2/15/18: County of Santa Barbara Access Television, CSBTV20.
- Caltrans, 2018b, News Release, Monday, October 8, 2018, available at <http://www.dot.ca.gov/dist05/paffairs/santabarbara/100818.pdf>
- Cannon, S.H., Gartner, J.E., Parrett, C., and Parise, M., 2003, Wildfire-related debris-flow generation through episodic progressive sediment-bulking processes, western USA. In *Debris-Flow Hazards Mitigation: Mechanics, Prediction, and Assessment*. Millpress, Rotterdam, 71-82.

- Cannon, S.H., Boldt, E.M., Kean, J.W., Laber, J., and Staley, D.M., 2010, *Relations between rainfall and postfire debris-flow and flood magnitudes for emergency-response planning, San Gabriel Mountains, southern California*: U.S. Geological Survey Open-File Report 2010-1039, 31 p.
- Cannon, S.H., Gartner, J.E., Wilson, R.C., Bowers, J.C., and Laber, J.L., 2008, Storm rainfall conditions for floods and debris flows from recently burned areas in southwestern Colorado and southern California: *Geomorphology*, Vol. 96, No. 3, pp. 250–269, doi:10.1016/j.geomorph.2007.03.019
- Chen, T., Ren, L., Yuan, F., Yang, X., Jiang, S., Tang, T., Liu, Y., Zhao, C., and Zhang, L., 2017, Comparison of Spatial Interpolation Schemes for Rainfall Data and Application in Hydrological Modeling: *Water*, v.9, 18 p, doi:10.3390/w9050342
- Fleming, R.W., and Taylor, F.A., 1980, *Estimating the costs of landslide damage in the United States*: U.S. Geological Survey Circular 832, 21 p.
- Gartner, J. E., Cannon, S. H., and Santi, P. M., 2014, Empirical models for predicting volumes of sediment deposited by debris flows and sediment-laden floods in the transverse ranges of southern California: *Engineering Geology*, Vol. 176, pp. 45-56, doi:10.1016/j.enggeo.2014.04.008
- Godt, J. W., 1999, *Maps showing locations of damaging landslides caused by El Niño rainstorms, winter season 1997-98, San Francisco Bay region, California: Pamphlet to accompany Miscellaneous Field Studies Maps MF-2325-A-J*: U.S. Geological Survey
- Iverson, R. M., 2014, Debris flows: behavior and hazard assessment: *Geology Today*, Vol. 30, No. 1, pp. 15-20, doi: 10.1111/gto.12037
- Jakob, M., 2005, A size classification for debris flows: *Engineering Geology*, Vol. 79, p. 151-161.
- Johnson, C. G., Kokelaar, B. P., Iverson, R. M., Lohan, M., LaHusen, R. G., Gray, J. M. N. T., 2012, Grain-size segregation and levee formation in geophysical mass flows, *Journal of Geophysical Resources*, Vol. 117, F01032, doi:10.1029/2011JF002185
- Kean, J.W., Staley, D. M., Lancaster, J.T., Rengers, F. K., Swanson, B. J., Coe, J. A., Hernandez, J. L., Sigman, A. J., Allstadt, K., and Lindsay, D. N., 2018, *in review*, Inundation, flow dynamics, and damage in the 1/9 Montecito Debris Flow, California, USA: Opportunities and challenges for post-wildfire risk assessment: Manuscript submitted for publication.
- Lancaster, J.T., Spittler, T.E., and Short, W.R., 2015, *Alluvial fan flooding hazards: an engineering geology approach to preliminary assessment*: California Geological Survey, Special Report 227, 46 p.
- Lancaster, J.T., 2018, The Santa Barbara County 1/9 Debris Flow of 2018 Extreme Runoff Response to Extreme Precipitation: unpublished presentation.
- Magnoli, G., 2019, Montecito Group Orders Debris Nets, Plans to Start Construction Soon: Noozhawk, available at https://www.noozhawk.com/article/montecito_group_orders_debris_nets_plans_to_start_construction_soon?
- Markowski, P., and Richardson, Y., 2010, *Mesoscale Meteorology in Midlatitudes*: Wiley-Blackwell, Barcelona, 430 p.
- Montecito Water District, 2019, Presentation to Montecito Association, February 12, 2019, available at <http://www.montecitowater.com/latest-news/presentation-to-montecito-association/>
- Molina, G., 2018, Water Off Goleta Beach Reopened After 6-Month Closure from Bacteria Contamination: Noozhawk, available at https://www.noozhawk.com/article/goleta_beach_ocean_waters_now_open_after_six_month_of_closure_20180707
- Moody, J. A., Martin, D. A., Haire, S. L., and Kinner, D. A., 2008, Linking Runoff response to burn severity after a wildfire: *Hydrological Processes*, Vol. 22, pp. 2063-2074, doi:10.1002/hyp.6806
- NOAA Atlas 14, 2017, 14 point precipitation frequency estimates: KS, available at https://hdsc.nws.noaa.gov/hdsc/pfds/pfds_map_cont.html
- Oakley, N. S., Lancaster, J. T., Kaplan, M. L., and Martin Ralph, F., 2017, Synoptic conditions associated with cool season post-fire debris flows in the Transverse ranges of southern California: *Natural Hazards*, Vol. 88, pp. 327-354, doi:10.1007/s11069-017-2867-6
- Oakley, N.S., Cannon, F., Munroe, R., Lancaster, J.T., Gomberg, D., and Ralph, R. M., 2018, Brief Communication: Meteorological and climatological conditions associated with the 9 January 2018 post-fire debris flows in Montecito and Carpinteria, California, USA. *Natural Hazards and Earth System Sciences*, 18, 3037-3043, doi: 10.5194/nhess-18-3037-2018
- O'Dell, D., 2018, Corps of Engineers completes debris removal from Santa Barbara basins following devastating mudslide: USACE News Stories, available at <https://www.spl.usace.army.mil/Media/News-Stories/Article/1522840/corps-of-engineers-completes-debris-removal-from-santa-barbara-basins-following/>
- Okada, S., 2019, SoCal Edison power lines sparked deadly Thomas Fire, investigators say: San Luis Obispo Tribune, available at: <https://www.sanluisobispo.com/news/local/article227982239.html>
- Parise, M., and Cannon, S., 2012, Wildfire impacts on the processes that generate debris flows in burned watersheds: *Natural Hazards*, Vol. 61, No. 1, pp. 217-227, doi:10.1007/s11069-011-9769-9
- Niehaus, Robert, D., Inc. (RDN), 2018, The Economic Impacts of the Montecito Mudslides: A Preliminary Assessment.
- Santa Barbara, City of, 2018, Council Agenda Report from Water Resources Division, Public Works Department, May 22, 2018.
- Santa Barbara County, 2018, Board of Supervisors Meeting- February 27, 2018, available at http://sbcounty.granicus.com/MediaPlayer.php?view_id=3&clip_id=3240
- Schiff, D., and D'Agostino, R. B., 1996, *Practical Engineering Statistics*: John Wiley & Sons, New York, NY, 309 p.
- Sharp, R. P., and Nobles, L., 1953, Mudflow of 1941 at Wrightwood, southern California, *Geological Society of America Bulletin*, Vol. 64, No. 5, p. 547–560, doi:10.1130/0016-7606(1953)64[547:MOAWSC]2.0.CO;2
- Small Business Administration (SBA), 2018, CA 15438-05 SBA Tops \$50 Million in Disaster Assistance Loans: Disaster Press Release, available at <https://www.sba.gov/offices/disaster/dfocw/resources/1624696>
- Sukup, S. J., Laber, J., Sweet, D., and Thompson, R., n.d., Analysis of an intense narrow cold frontal rainband and the Springs Fire debris flow of 12 December 2014: NWS technical attachment 1601, available at http://www.wrh.noaa.gov/media/wrh/online_publications/TAs/TA1601.pdf
- Taylor, F. A., and Brabb, E. E., 1972, *Maps showing distribution and cost by counties of structurally damaging landslides in the San Francisco Bay region, California, winter of 1968-69*: U.S. Geological Survey Miscellaneous Field Studies Map MF-327.
- United States Army Corps of Engineers Los Angeles District, 2018a, *Channel Clearing, Santa Barbara County, CA January 16, 2018*: Electronic document, available at <https://www.spl.usace.army.mil/Missions/Emergency-Management/Santa-Barbara-County-Debris-Removal/>
- United States Army Corps of Engineers Los Angeles District, 2018b, *Debris Basins, Santa Barbara County, CA January 16, 2018*: Electronic document, available at <https://www.spl.usace.army.mil/Missions/Emergency-Management/Santa-Barbara-County-Debris-Removal/>
- Wills, C. J.; Roth, N. E., McCrink, T. P., and Short, W. R., 2017, The California landslide inventory database. In *Proceedings Third North American Symposium on Landslides*. Association of Environmental and Engineering Geologists, Roanoke, VA, pp. 666–674.

Debris-flow susceptibility mapping in Colorado using Flow-R: calibration techniques and selected examples

Kevin M. McCoy^{a,*}

^aColorado Geological Survey, Colorado School of Mines, 1801 Moly Road., Golden, Colorado 80401, USA

Abstract

The Colorado Geological Survey (CGS) has been using ArcGIS in combination with Flow-R to prepare county-wide debris-flow susceptibility maps for 43 counties in 13 priority areas comprising the mountainous portions of the state. Limited personnel, site access, and limited records of recent events constrain the CGS's ability to calibrate models based on historical data or field observations. In response to these limitations, the CGS has developed methods to parameterize county-wide debris-flow source area and inundation area models in characteristic regions using recently available high-resolution (e.g., 1 m) digital elevation data. Method development has been continually evolving. The current process relies on an analyst who selects a subset of drainages of various sizes from unique regions within each county and manually identifies potential debris-flow source and deposition areas based on the digital terrain data or, if available, historical aerial imagery. The analyst records characteristics of identified source areas and initiates a series of test runs using a range of potential inundation area model parameters. The analyst visually interprets the source-area characteristics and inundation area model results and selects a single set of parameters to apply to similar drainages across the county. This paper presents current parameterization methods and discusses anticipated future improvements.

Keywords: Debris Flow; Model; Parameterization.

1. Introduction

An extreme rainfall event in September 2013 caused severe flooding and triggered over 1,000 debris flows in the Front Range of the Rocky Mountains in Colorado (Morgan et al., 2013b, 2013a; Coe et al., 2014; Godt et al., 2014; Anderson et al., 2015). Combined impacts from debris flows and water flooding included eight fatalities and extensive damage to roads and residences (Coe et al., 2014). In response to this event, the Colorado General Assembly passed Senate Bill 15-245 (Grantham and Young, 2015), which established funding for natural hazards mapping (updated flood plain maps, fluvial erosion zone maps, and debris-flow maps). The bill included the following tasks: (1) convene an interagency panel chaired by the Colorado Geological Survey (CGS) to establish priority areas and develop debris-flow mapping methodology; (2) conduct pilot projects to develop debris-flow susceptibility maps for the two highest-ranked priority areas (5 counties), and (3) develop a five-year implementation and funding plan to map the remainder of the priority areas. The maps are intended for use by planners and regulators to support review of site-specific geologic hazard reports submitted for development purposes as required by law, and by professional geologists planning detailed site-specific geologic hazard studies.

The CGS established 13 priority areas comprising 43 counties in the mountainous portions of the state (Fig. 1). Priority Areas 1 and 2 consist the three counties directly impacted by the September 2013 event and three additional counties along the Front Range Urban Corridor with either relatively high population density or high development pressure along the range front or in mountain valleys. Priority Areas 3 and 4 comprise counties along Interstate 70, an important transportation corridor. The remaining areas were prioritized by the CGS based on a combination of anticipated development pressures and availability of lidar data or plans for future lidar data collection. Due to the

* Corresponding author e-mail address: kemccoy@mines.edu

large geographic area (~183,000 km²), relatively short time frame (5 years), and desire for an objective process, the CGS chose a model-based mapping approach. The CGS selected Flow-R (Horton et al., 2013) because of its capability to produce regional-scale maps with relatively few input parameters and because of its successful application in other regions (e.g., Horton et al., 2011; Kappes et al., 2011; Fischer et al., 2012; Blais-Stevens and Behnia, 2016). For each county in Priority Area 1, model parameters were selected based on literature values (e.g., Horton et al., 2011; Jaboyedoff et al., 2011; Kappes et al., 2011; Michoud et al., 2012; Horton et al., 2013) and a single county-wide model was run. Parameters were not specifically calibrated to the local conditions; however, a CGS geologist with experience mapping debris-flow hazard areas in Colorado compared the model results to recent observations (Morgan et al., 2013b, 2013a; Coe et al., 2014; Godt et al., 2014) and manually revised the computer-generated outputs in a tedious and time-consuming process. The resulting maps were published as CGS Open-File Reports (Morgan et al., 2014; Wait et al., 2015) and the GIS polygons were made publicly available through the Colorado Hazard Mapping (CHAMP) web portal (coloradohazardmapping.com). For each of the first three pilot counties in Priority Area 2 (McCoy et al., 2018a, 2018b, 2018c), the CGS tested a small range of model parameters prior to running a single county-wide model, in an attempt to calibrate the model to local conditions and reduce the manual revision effort. However the computer-generated outputs were only slightly improved and significant manual revision based on records of recent events was again required to create a satisfactory map. Ongoing work described in this paper seeks to further improve the process to facilitate modeling in areas with minimal historical record and eventually eliminate the manual revision step.

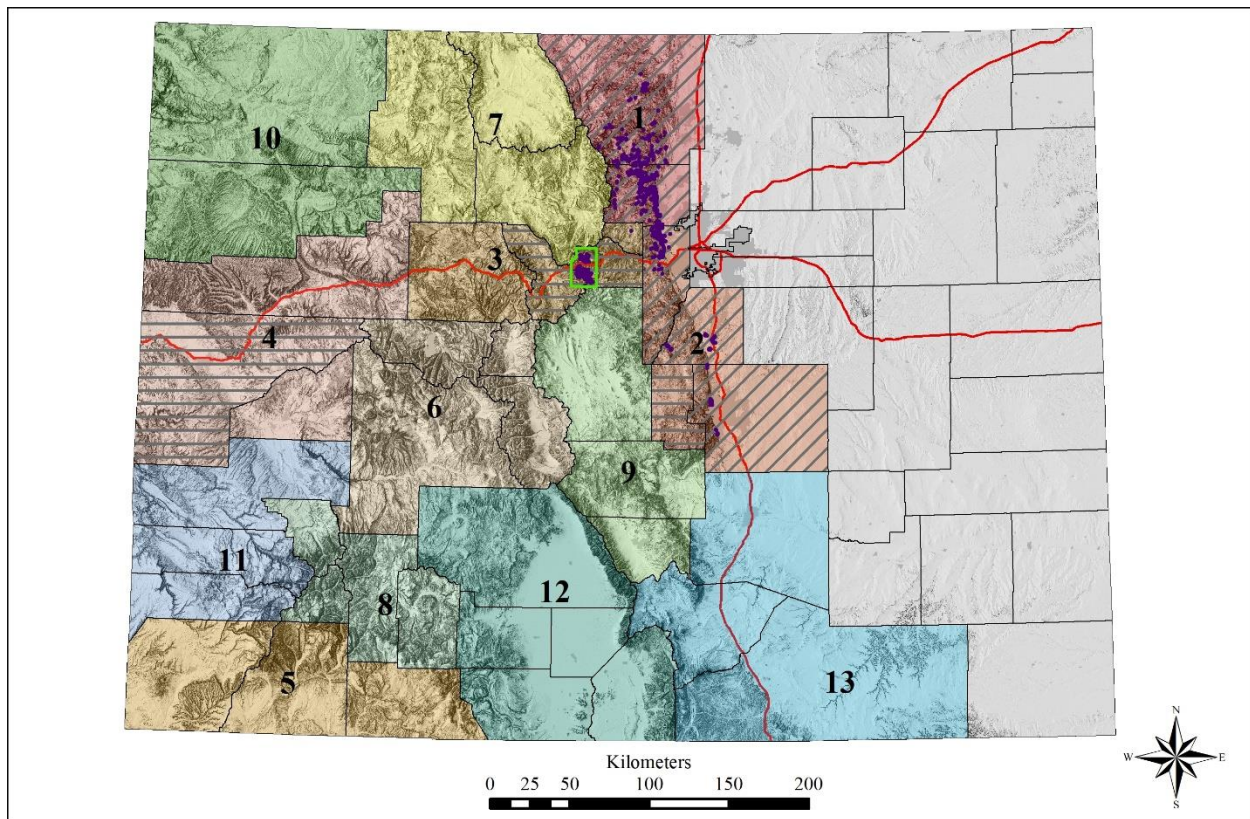


Fig. 1. The colored polygons illustrate the 13 debris-flow susceptibility mapping priority areas as delineated by the CGS; these priority areas comprise 43 counties (black outlines). Diagonal hachures show where debris-flow susceptibility maps have been published. Horizontal hachures show where debris-flow susceptibility mapping is in progress. Purple dots show debris-flow initiation points from the CGS debris-flow inventory. The green polygon outlines the study area discussed in this paper.

Fig. 1 shows points representing debris-flow source areas from a preliminary inventory of recorded debris-flow initiation locations and/or travel paths compiled by the CGS from previous CGS studies (Morgan et al., 2013a, 2013b), data provided by the United States Geological Survey (USGS) (from Coe et al., 2014; Godt et al., 2014), published

literature (Godt and Coe, 2007), and limited aerial image analysis recently performed by the CGS. Much of the currently available inventory occurs in Priority Areas 1 and 2, where debris-flow susceptibility maps have already been published by the CGS and geologic variability is relatively limited. Diverse geologic conditions and lack of historic records of initiation or transport conditions in most of the remaining priority areas create challenges for evaluating model calibration. Limited personnel and limited access to private land or remote areas impose further constraints. In response to these limitations, the CGS has developed methods to parameterize county-wide debris-flow source area and inundation area models in characteristic regions using recently available high-resolution (e.g., 1-m) digital elevation data. Method development has been continually evolving. This paper discusses current parameterization methods and goals for future improvements.

2. Methods

2.1. Overview

Methodology consists of (1) data preparation, visual interpretation of high-resolution terrain data, and selection of a subset of drainages for model parameterization; (2) parameterization and modeling of source areas in ArcGIS for each subset; (3) parameterization and modeling of transport and using Flow-R; (4) modeling source and inundation areas using the selected parameters, for each unique region in the county, and (5) visual review and any necessary manual editing of the outputs to produce the final susceptibility polygons. The following sections discuss each of these steps with examples from the study area shown on Fig. 1. The study area overlaps with the study area of Godt and Coe (2007). As a test of this methodology, the source area and inundation area models calibrated using this methodology were compared to the inventory of debris-flow source, transport, and deposition areas from Godt and Coe (2007).

2.2. Data Preparation and Visual Interpretation

The CGS has access to nominal 1-m horizontal resolution lidar data for Priority Areas 1, 2, 3, and 4, and portions of other priority areas in the state. This data was collected through various collaborative efforts with funding from the Colorado Geological Survey, the Colorado Water Conservation Board (CWCB), the USGS, and other state and federal agencies. The first step in the mapping process is to prepare GIS derivatives from the lidar-based digital elevation model (DEM). The raw DEM is used to prepare visualization aids. A downgraded DEM (typically 3- or 5-m resolution) is created from the lidar DEM for modeling to reduce noise in the data and improve computing performance (see discussions by Horton et al., 2013; Baum, 2017). Table 1 lists key GIS derivatives produced from the raw and downgraded DEMs and their respective uses. Most derivatives are prepared using ArcGIS geoprocessing tools, but some (e.g. Topographic Wetness Index, D-Infinity slope) are prepared using TauDEM Version 5 (<http://hydrology.usu.edu/taudem/taudem5>). Visual interpretation primarily relies on a classified slope map (based on values from VanDine, 1996; and Horton et al., 2013) and a classified synthetic stream network (based on values from Wilford et al., 2004) as shown in Fig. 2a, and 1-m interval elevation contours (not shown).

Table 1. List of key GIS derivatives created from lidar DEM.

Purpose	Lidar DEM (1 m typical)	Downgraded DEM (3 or 5 m typical)
Visual Interpretation	Multidirectional hillshade Slope map 1-m interval contour lines	Topographic Wetness Index (TWI) Plan curvature Distributed Melton ratio Distributed length to drainage divide Synthetic stream network
Source and Inundation Modeling	None	DEM Slope Plan curvature Topographic Wetness Index Flow accumulation

After the derivatives are prepared, an analyst (i.e. a CGS geologist or hazard analyst) visually examines the DEM derivatives and other digital data (e.g. digitized geologic maps, land use maps, climate maps, and/or aerial imagery) to identify potential debris-flow prone areas (i.e. fans, cones, alluvial wedges and/or steep, narrow gullies). During this process, the analyst selects regions with similar geology, regional elevation, fan size and slope, drainage size and slope, and/or synthetic stream network classification. For each region, the analyst selects a subset of drainages for parameterization and creates GIS points representing initiation (starts), onset of deposition (fan heads), and end of process (ends). Initiation points are typically placed where evidence of landslides or gully erosion is visible in the 1 m terrain data. Onset of deposition is typically assumed at fan heads; where evidence of fan incision is clearly visible, the “fan head” point is moved to the lower end of the incised portion of the fan. This is typically a judgement call by the analyst as the CGS has not defined a fan incision threshold. End points are typically placed where fan or cone angles decrease to less than 4 degrees, based on the description of composite fans by Lancaster et al. (2012), unless other evidence is available (e.g. records of previous events, knowledge of unique local conditions, clear fan edge visible with 1-m contours). Fig. 2b shows some interpreted start, fan head, and end points from the study area.

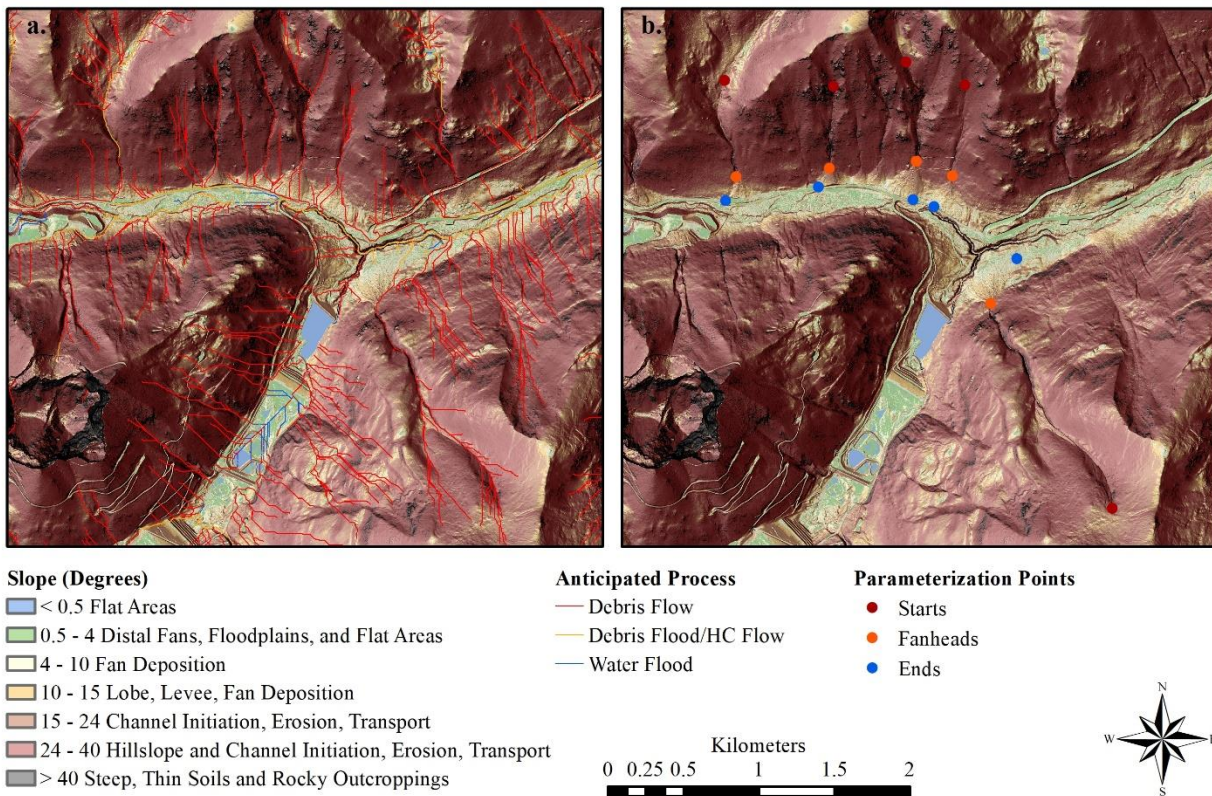


Fig. 2. (a) classified slope map (based on values from VanDine, 1996; and Lancaster et al., 2012) and classified synthetic stream network (streams defined by contributing area ≥ 0.01 km², classification based on values from Wilford et al., 2004) on 1 m hillshade; (b) subset of Start, Fan Head, and End points selected by visual analysis for parameterizing source area and inundation area models.

2.3. Parameterization and Modeling of Debris-Flow Source Areas

Source areas, defined by steep (typically $> 15^\circ$) channels and gullies, and/or colluvial hollows on steep (typically $> 24^\circ$) slopes, where debris-flow generating landslides, erosion, and transport may occur, are identified in ArcGIS. In general, the process involves classifying individual downgraded DEM derivatives (slope, plan curvature, topographic wetness index (TWI) and/or flow accumulation) into sources or non-sources using threshold values and overlaying the classified rasters to select the cells that are classified as “sources” in all raster layers. Fig. 3 shows the key derivatives typically used in the source area model. Specifically, parameterization involves extracting values from the key derivative rasters at each analyst-defined “Start” point, selecting initial threshold values for each raster based on these

extracted values, reclassifying each raster into sources and non-sources, iteratively reviewing and revising the threshold values until the analyst is satisfied with each classified component raster, and overlaying the final classified component rasters. The analyst then performs a manual cleanup step to remove clearly erroneous sources (i.e. on manmade objects or large, bare rock outcrops) or to add apparent sources that were missed by the computer model. The final source raster is exported from ArcGIS to a format compatible with Flow-R. The CGS performs classification and overlay in ArcGIS to facilitate visual evaluation and iterative revision of individual threshold values based on the analyst’s judgement. Aside from the ability to perform this review/revision step, the method is conceptually similar and produces similar results to the “Source areas” calculation available in the Flow-R software (Horton et al., 2013) and an analyst could just as easily use Flow-R for that purpose if they are confident in the applicability of their selected threshold values.

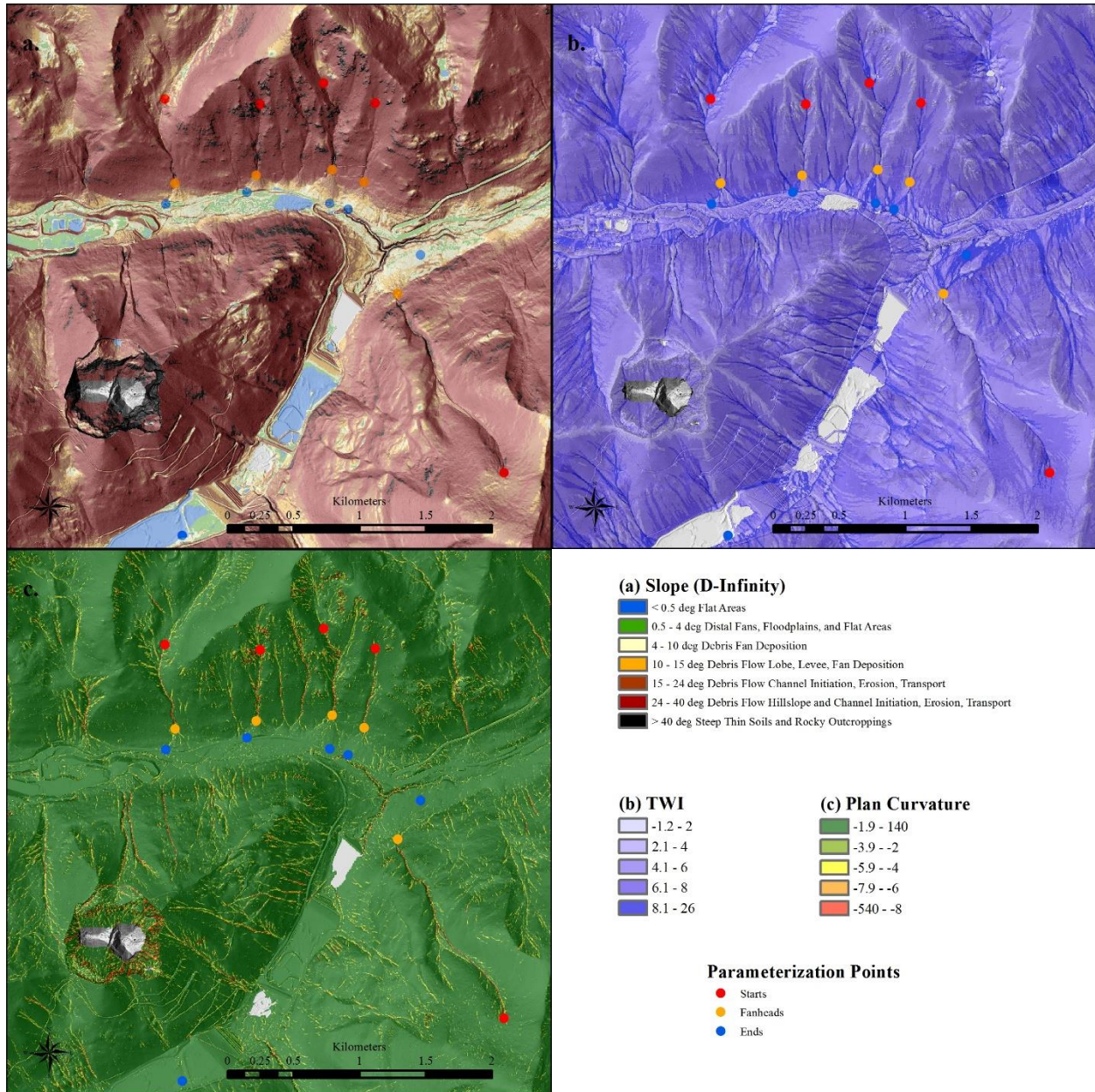


Fig. 3. Downgraded (3 m resolution) DEM derivatives for the debris-flow source area model: (a) D-infinity slope (degrees); (b) Topographic Wetness Index (TWI); (c) plan curvature.

2.4. Parameterization and Modeling of Debris-Flow Transport and Runout (Inundation Area Model)

Inundation areas are modeled with Flow-R. The governing equations and fundamental assumptions of the model are discussed by (Jaboyedoff et al., 2011; Horton et al., 2011, 2013), detailed discussion of the governing equations is beyond the scope of this paper. Guidelines for selecting parameters in areas with records of recent events or where site-specific geologic studies have been performed have been provided previously (e.g., Jaboyedoff et al., 2011; Horton et al., 2013). This section discusses methods used by the CGS to parameterize the inundation area model in areas with little to no records of recent events or site-specific geologic studies.

Parameterization involves: (1) energy model parameterization - selecting a friction loss function, selecting friction model parameters, and deciding whether to apply a velocity limitation; and (2) spreading model parameterization - selecting direction and inertial algorithms. For the County-Wide Debris-Flow Susceptibility Mapping Program, the goal is to identify a single set of energy and spreading model parameters for each unique analyst-defined region within the county. First, a series of energy model runs initiating at the analyst-defined Start points are run with friction parameters that vary within a range defined by literature values (e.g., Horton et al., 2011, 2013; Fischer et al., 2012; Blais-Stevens and Behnia, 2016) and no spreading (D-8 flow direction). The analyst compares the model results to the analyst-defined end points and selects the parameters that best fit the most drainages within the selected region based on visual interpretation. The CGS has used both the two-parameter friction model of Perla et al. (1980) and the simplified friction-limited model (SFLM) for previous maps. For the example discussed in this paper, the CGS chose the SFLM because it has fewer parameters to vary, and as discussed by (Jaboyedoff et al., 2011), it should provide similar travel distance to the more precise two-parameter friction model for a given drainage if an appropriate velocity limit is applied. For the example discussed in this paper, the CGS applied a velocity limitation of 15 m/s based following Horton et al. (2013).

Once the energy model parameters have been selected, they are held constant and a series of model runs with varying spreading parameters is performed. The analyst visually evaluates the results and selects the model that covers the most fan area without excessive spreading in source and steep transport areas. If the analyst cannot find an acceptable balance of runout and spreading parameters for all drainages in the region, the need for further sub-division into additional regions is evaluated and the process is repeated. Once parameters are selected, a single model is run for all source areas in each region. The resulting rasters are converted to simplified polygons in ArcGIS. The analyst then performs a final cleanup on the polygons to remove holes and adjust boundaries where needed.

3. Discussion and Goals for Future Improvement

Table 2 presents the selected model parameters. Fig. 4 shows examples of several inundation area runs and the final susceptibility polygons and Fig. 5 compares the final model results with debris flows mapped by Godt and Coe (2003 and 2007). Fig. 4 shows that the model does a fairly good job of identifying the prominent fans and Fig. 5 shows that it does a fairly good job predicting occurrence and inundation for the larger flows; however, the model under-estimates occurrence high in the drainages, over-estimates occurrence in general, and over-estimates travel distance for smaller flows. It's possible that some of these issues are caused by factors not considered in the Flow-R model (e.g. flow volume), or that distinguishing between channelized and open-slope flows is necessary to improve the results. Visual observations of the 1-m terrain data that suggest many areas identified by the model may be subject to debris flows even though they were not inundated in the mapped event, but additional field studies would be required to resolve this uncertainty. Given the goal of identifying areas for more detailed site-specific analysis, over-predictions of travel distance relative to a single observed event (where reasonable based on the terrain) may not be of significant concern.

Table 2. Selected model parameters.

Source Area Parameters	Energy Model Parameters	Spreading Model Parameters
Slope $\geq 15^\circ$	SFLM	Directions: Holmgren Modified
Slope $\leq 40^\circ$	Travel Angle = 10°	dh = 2.0
Plan Curvature ≤ -3	V _{Lim} = 15 m/s	exp = 4.0
TWI ≥ 7.5		Inertia: Gamma (2000)

The process described in this paper was developed to help the CGS apply a model-based approach to the county-wide debris-flow susceptibility-mapping project when moving outside of the areas covered by the inventory of recent

observations. The parameterization process described in this paper has generally improved the mapping process compared to the initial methods; however, there is still room for significant improvement. As of March, 2019, the CGS has partially completed development of a more objective process that still relies on an analyst to manually identify initial source and deposition areas, but enables significantly more model runs and uses a statistically based method of selecting the best model fits. It is anticipated that the updated process will improve on the methods described herein.

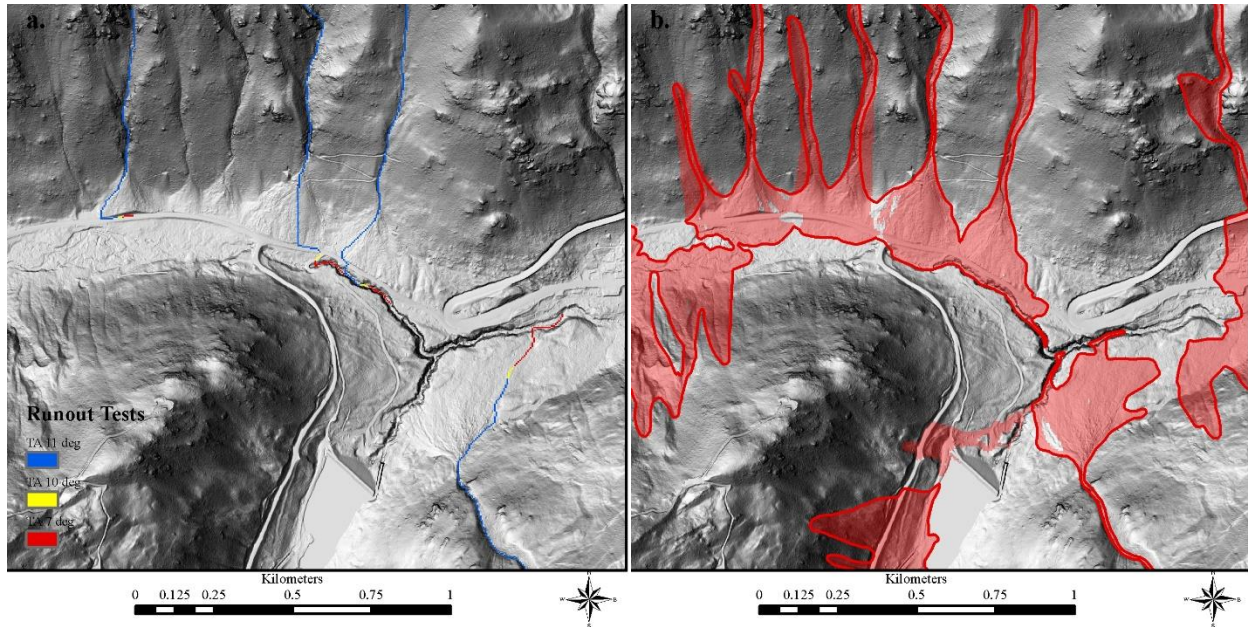


Fig. 4. (a) Examples of energy model tests for travel angles of 7 (red), 10 (yellow), and 11 (blue) degrees, respectively with a velocity limitation of 15 m/s for each. (b) Analyst-revised inundation area polygons (red outlines) and raw output of the regional inundation area model using the final selected parameters. The raw output is provided for illustrative purposes. Typically, only the final polygons are provided.

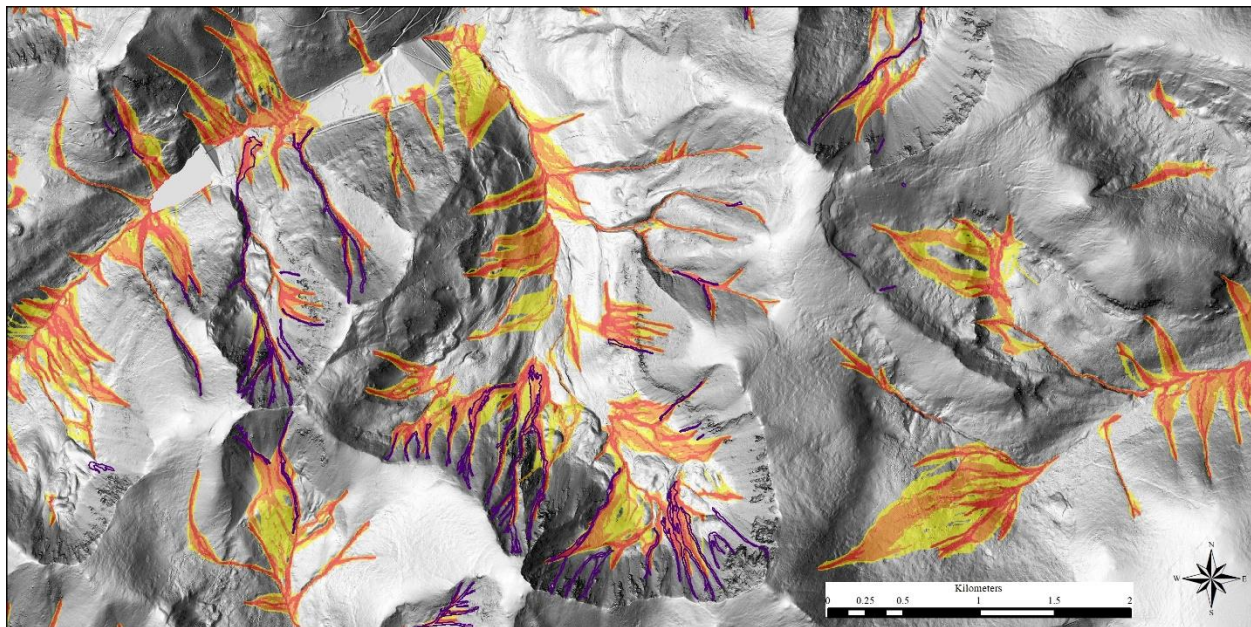


Fig. 5. Comparison of combined source and inundation area model results (yellow-red colored) with mapped debris flows (purple polygons) from Godt and Coe (2003 and 2007). The model does a fairly good job of predicting flow occurrence and inundation for large flows; however, it under-estimates occurrence high in the drainages, over-estimates occurrence in general, and over-estimates travel distance for smaller flows.

Acknowledgements

The work described in this paper utilized high-resolution digital terrain data collected with funding from the Colorado Geological Survey, the Colorado Water Conservation Board (CWCB), the USGS, and other state and federal agencies. The author would like to thank the organizing committee and the two anonymous reviewers whose comments and suggestions improved the quality and clarity of this paper.

References

- Anderson, S.W., Anderson, S.P., and Anderson, R.S., 2015, Exhumation by debris flows in the 2013 Colorado Front Range storm: *Geology*, v. 43, p. 391–394, doi:10.1130/G36507.1.
- Baum, R.L., 2017, Effects of Topographic Data Quality on Estimates of Shallow Slope Stability using Different Regolith Depth Models, in De Graff, J.V. and Shakoor, A. eds., *Landslides: Putting Experience, Knowledge and Emerging Technologies Into Practice*, Roanoke, Virginia, USA, Association of Environmental and Engineering Geologists (AEG), v. AEG Special Publication 27, p. 807–818.
- Blais-Stevens, A., and Behnia, P., 2016, Debris flow susceptibility mapping using a qualitative heuristic method and Flow-R along the Yukon Alaska Highway Corridor, Canada: *Natural Hazards and Earth System Sciences*, v. 16, p. 449–462, doi:10.5194/nhess-16-449-2016.
- Coe, J.A., Kean, J.W., Godt, J.W., Baum, R.L., Jones, E.S., Gochis, D.J., and Anderson, G.S., 2014, New insights into debris-flow hazards from an extraordinary event in the Colorado Front Range: *GSA Today*, v. 24, p. 4–10, doi:10.1130/GSATG214A.1.
- Fischer, L., Rubensdotter, K., Sletten, K., Stalsberg, K., Melchiorre, C., Horton, P., and Jaboyedoff, M., 2012, Debris flow modeling for susceptibility mapping at a regional to national scale in Norway, in Eberhardt, E., Froese, C., Turner, K., and Leroueil, S. eds., *Landslides and engineered slopes: protecting society through improved understanding*, Leiden, CRC Press/Balkema, p. 723–729.
- Godt, J.W., and Coe, J.A., 2007, Alpine debris flows triggered by a 28 July 1999 thunderstorm in the central Front Range, Colorado: *Geomorphology*, v. 84, p. 80–97, doi:10.1016/j.geomorph.2006.07.009.
- Godt, J.W., and Coe, J.A., 2003, OF-03-050 Map Showing Alpine Debris Flows Triggered by a July 28, 1999 Thunderstorm in the Central Front Range of Colorado: U.S. Geological Survey Open-File Report, scale Version 1.0, <https://pubs.usgs.gov/of/2003/ofr-03-050/>.
- Godt, J.W., Coe, J.A., Kean, J.W., Baum, R.L., Jones, E.S., Harp, E.L., Staley, D.M., and Barnhart, W.D., 2014, Landslides in the Northern Colorado Front Range Caused by Rainfall, September 11–13, 2013: Fact Sheet 2013-3114.
- Grantham, K., and Young, D., 2015, Concerning the provision of state funding for natural hazard mapping, Senate Bill 15-245, Seventieth General Assembly of the State of Colorado.
- Horton, P., Jaboyedoff, M., Rudaz, B., and Zimmermann, M., 2013, Flow-R, a model for susceptibility mapping of debris flows and other gravitational hazards at a regional scale: *Nat. Hazards Earth Syst. Sci.*, v. 13, p. 869–885, doi:10.5194/nhess-13-869-2013.
- Horton, P., Jaboyedoff, M., Zimmermann, M., Mazotti, B., and Longchamp, C., 2011, Flow-R, A Model for Debris Flow Susceptibility Mapping at a Regional Scale – Some Case Studies: *Italian Journal of Engineering Geology and Environment*, p. 875–884, doi:10.4408/IJEGE.2011-03.B-095.
- Jaboyedoff, M., Rudaz, B., and Horton, P., 2011, Concepts and parameterization of Perla and FLM model using Flow-R for debris flow, in Kelowna, British Columbia, doi:10.13140/RG.2.2.34884.94088.
- Kappes, M.S., Malet, J.-P., Remaitre, A., Horton, P., Jaboyedoff, M., and Bell, R., 2011, Assessment of debris-flow susceptibility at medium-scale in the Barcelonnette Basin, France: *Natural Hazards and Earth System Science*, v. 11, p. 627–641, doi:10.5194/nhess-11-627-2011.
- Lancaster, J.T., Spittler, T.E., and Short, W.R., 2012, Using Digital Geologic Maps to Assess Alluvial-Fan Flood Hazards, in Soller, D.R. ed., *Digital Mapping Techniques '10—Workshop Proceedings*, USGS, Open-File Report 2012–1171, https://pubs.usgs.gov/of/2012/1171/pdf/usgs_of2012-1171-Lancaster_p53-64.pdf.
- McCoy, K.M., Fitzgerald, F.S., Morgan, M.L., and Berry, K.A., 2018a, Debris Flow Susceptibility Map of Douglas County, Colorado: Colorado Geological Survey Open-File Report 18–08.
- McCoy, K.M., Morgan, M.L., and Berry, K.A., 2018b, Debris Flow Susceptibility Map of El Paso County, Colorado: Colorado Geological Survey Open-File Report 18–11.
- McCoy, K.M., Morgan, M.L., and Berry, K.A., 2018c, Debris Flow Susceptibility Map of Jefferson County, Colorado: Colorado Geological Survey Open-File Report 18–10.
- Michoud, C., Derron, M.-H., Horton, P., Jaboyedoff, M., Baillifard, F.-J., Loye, A., Nicolet, P., Pedrazzini, A., and Queyrel, A., 2012, Rockfall hazard and risk assessments along roads at a regional scale: example in Swiss Alps: *Natural Hazards and Earth System Sciences*, v. 12, p. 615–629, doi:10.5194/nhess-12-615-2012.
- Morgan, M.L., Fitzgerald, F.S., and Morgan, K.S., 2013a, Preliminary Survey of Debris Flow, Landslide, and Rockfall Deposits as a result of the September 11-14, 2013 Flooding Events, Boulder County, Colorado: <http://www.arcgis.com/home/item.html?id=39e6c721635f40c8add90112c9d1a646>.
- Morgan, M.L., Fitzgerald, F.S., and Morgan, K.S., 2013b, Preliminary Survey of Debris Flow, Landslide, and Rockfall Deposits as a result of the September 11-14, 2013 Flooding Events, Larimer County, Colorado: <http://www.arcgis.com/home/item.html?id=47fef299bc4a4a4c9e19cbb a8afe66f4>.
- Morgan, M.L., White, J.L., Fitzgerald, F.S., and Berry, K.A., 2014, Foothill and Mountainous Regions in Boulder County, Colorado that may be Susceptible to Earth and Debris/Mud Flows During Extreme Precipitation Events: Colorado Geological Survey Open File Reports OF-15-13, <https://doi.org/10.13140/2.1.3617.8246> (accessed September 2016).
- Perla, R., Cheng, T.T., and McClung, D.M., 1980, A Two-Parameter Model of Snow-Avalanche Motion: *Journal of Glaciology*, v. 26, p. 197–207, doi:10.1017/S002214300001073X.
- VanDine, D.F., 1996, Debris Flow Control Structures for Forest Engineering: B.C. Ministry of Forests Research Branch Working Paper 08/1996.
- Wait, T.C., Morgan, M.L., Fitzgerald, F.S., Morgan, K.S., Berry, K.A., and White, J.L., 2015, Debris flow Susceptibility Map of Larimer County, Colorado: Colorado Geological Survey Open File Reports OF-15-13.
- Wilford, D.J., Sakals, M.E., Innes, J.L., Sidle, R.C., and Bergerud, W.A., 2004, Recognition of debris flow, debris flood and flood hazard through watershed morphometrics: *Landslides*, v. 1, p. 61–66, doi:10.1007/s10346-003-0002-0.

Landslides and debris flows in volcanic rocks triggered by the 2017 Northern Kyushu heavy rain

Takehiro Ohta^{a,*}, Seiya Eguchi^a

^a Yamaguchi University, Yoshida 1677-1, Yamaguchi 753-8512, Japan

Abstract

About 200 landslides and debris flows occurred in Northern Kyushu during heavy rain at Asakura City, Toho Village, Hita City on July 5th to 6th, 2017. At Hita City, the total precipitation during this two-day event was 402.5 mm. At Asakura city, underlain by granitic rocks and schist, shallow landslides dominated. Whereas, at Toho Village and Hita City, which is underlain by volcanic rocks, the number of landslides and debris flows are fewer, are larger and deeper, than those at Asakura City.

We examined the geomorphology and geology at 19 landslides in volcanic rocks, 11 of which mobilized as debris flows. We studied the initiation mechanism of landslides underlain by volcanic rocks. The geology consists of pyroclastic rocks and lava flows in ascending order. The lava flows are distributed at ridges and contain vertical cooling joints. Scarps of landslides caused by the 2017 rain are located near the boundary of pyroclastic rocks and lava flows. The sliding surfaces of these landslides are at the contact between the lava flows and the pyroclastic rocks. We consider, therefore, that the trigger for these landslides was a decrease of strength at the contact caused by an increase in groundwater pressure caused by infiltration of rain water through the cooling joints in lava flows. Therefore, we conclude that the landslides caused by the 2017 heavy rain at volcanic rock fields are cap rock type landslide. Furthermore, the curvature of the hillsides downslope from landslides is concave, which may be a required condition for debris-flow mobilization.

Keywords: landslide ; heavy rain fall ; volcanic rocks ; cap rock

1. Introduction

About 200 landslides and debris flows occurred in Northern Kyushu during heavy rain at Asakura City, Toho Village, and Hita City on July 5th to 6th, 2017. The event, which was named “the 2017 Northern Kyushu heavy rain” by the Meteorological Agency of Japan, was induced by back building storms that caused heavy rain fall (Tsuguchi, 2017). The morphology of northern Kyushu Mountains including the Seburi Mountains and the Samgun Mountains, contributed to concentration and intensification of rains in the training (Tsuguchi, 2017). The training occurred at east end of the Seburi Mountains and traversed to the east into Asakura, Toho and Hita. Therefore, the amount of rainfall was greater at Asakura City than in Hita and Toho districts. The precipitation during the two days at Asakura area was 150% of that in the Hita and Toho districts.

At Asakura City in Fukuoka Prefecture, many debris flows, which initiated from landslides and contained a large quantity of fallen trees, occurred along rivers. These debris flows entered downstream town areas and caused huge damages. The source of debris flows at Asakura City was many small, shallow landslides with a few large landslides (Nishimura et al., 2018). In contrast, large landslides were the source of debris flows at the Hita and Toho districts (Nishimura et al., 2018). The geology of Asakura City area consists of metamorphic rocks and granitic rocks. On the other hand, volcanic rocks underlie the Hita and Toho areas. Therefore, at the Hita and Toho areas, large landslides occurred without small landslides in spite of only receiving two-thirds of the amount of rainfall of the Asakura area.

We examined the factors contributing to the occurrence of large landslides caused by a smaller amount of rainfall at Hita and Toho. This paper reports the characteristics of rainfall and the topographical and geologic conditions at

* Corresponding author e-mail address: takohta@yamaguchi-u.ac.jp

landslide sites in Hita City. We also discuss the initiation conditions for landslides that occur in areas underlain by volcanic rocks.

2. Regional Topography and Geological Settings at the Hita and Toho districts

The Chikugo River runs through the area where many landslides and debris flows occurred (Fig. 1). The Hita Basin and the Ryochiku Plain are adjacent to the river. The Samgun Mountains and the Hiko Mountains are on northern side of the river and contain some peaks of 1000 m in elevation. Tributary rivers such as the Oohi River and the Ono River join the Chikugo River from the north (Yada, 2018). The landslide and debris flow event occurred along the tributary rivers.

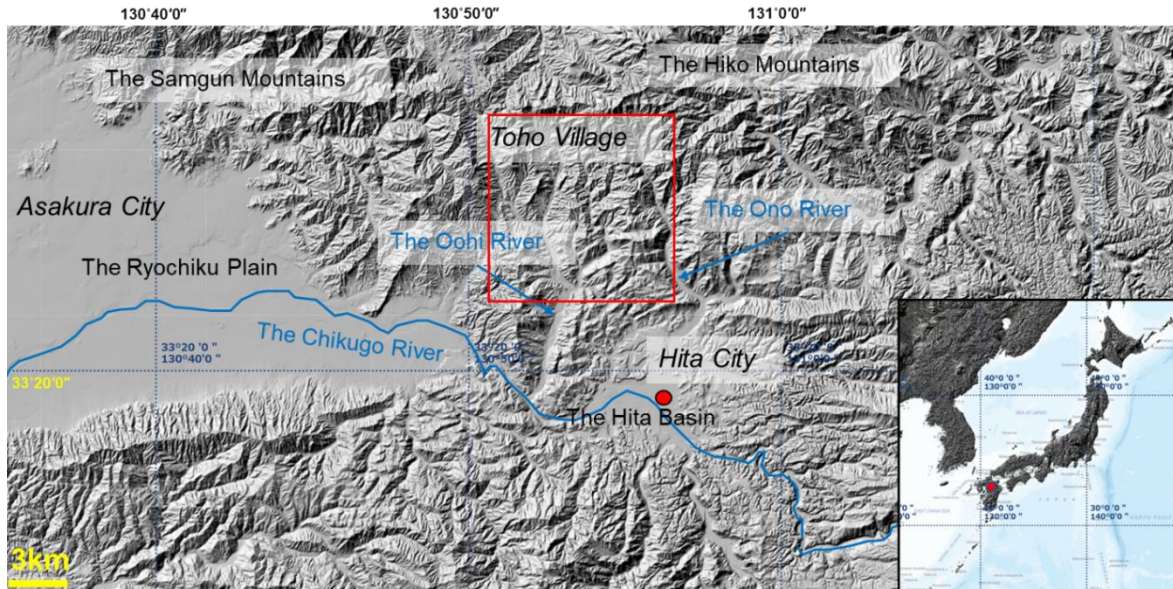


Fig. 1. Topographical map around the Hita, Toho, and Asakura area. This map is based on the digital map published by the Geospatial Information Authority of Japan. The red frame shows a field survey area of Fig. 6. Red point shows the Hita AMeDAS point.

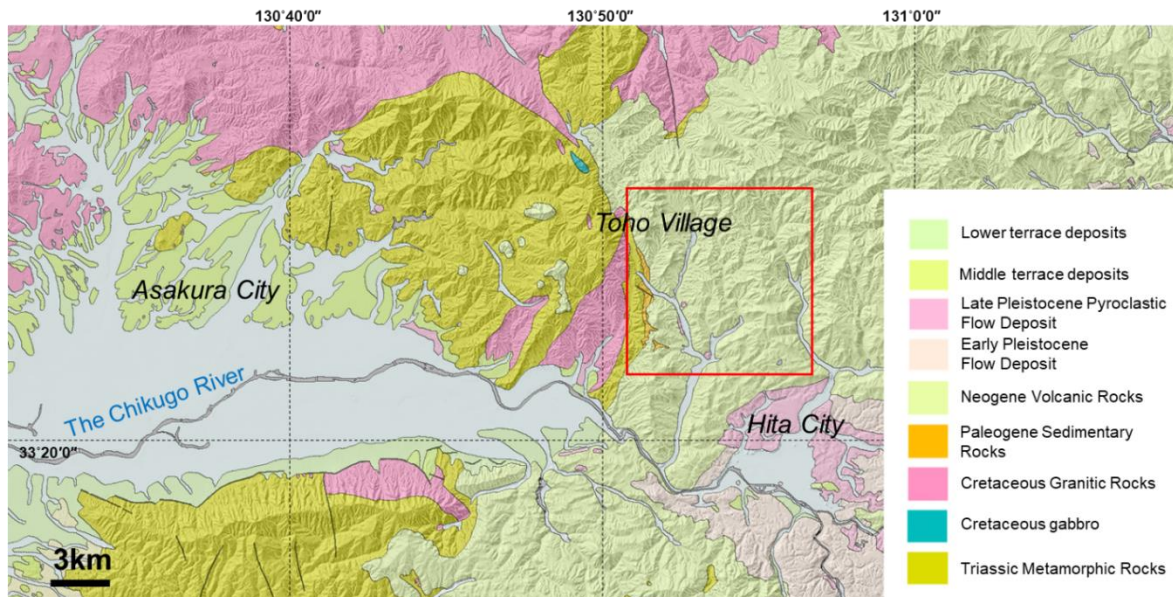


Fig. 2. Geological map around the Hita, Toho, and Asakura area (Geological Survey of Japan, AIST, 2015). The red frame shows a field survey area of Fig. 6.

Asakura City is underlain by metamorphic and granitic rocks (Fig. 2). The metamorphic rocks are part of the Samgun Metamorphic Belt and consist of pelitic schist and sandy schist with a small amount of green schist (Yada, 2018). The granitic rocks consist of mainly biotite hornblende granodiorite, which are part of the Soeda Granodiorite. The granitic rocks intruded into the metamorphic rocks, therefore the metamorphic rocks adjacent to the granitic rocks transformed to hornfels by contact metamorphism (Yada, 2018).

In the Hita and Toho districts on the eastern side of the Oohi River, Neogene and Quaternary volcanic rocks are distributed widely. The volcanic rocks consist of lavas, pyroclastic flows, and pyroclastic fall deposits. At the top of some peaks in Asakura City, there are also volcanic rocks (Yada, 2018).

3. Precipitation on July 5th to 6th at Hita City

At Hita City, the observed maximum hourly rainfall on July 5 and 6 at the AMeDAS (Automated Meteorological Data Acquisition System) point was 74 mm, the maximum 3 hour rainfall was 180.5 mm and the maximum 24 hour rainfall was 369.5 mm (Fig. 3). The total precipitation during this two-day event was 402.5 mm. The precipitation at Hita was smaller than that at the Asakura AMeDAS point, where the maximum hourly rainfall was 129.5 mm, the maximum 3 hour rainfall was 261 mm, and the maximum 24 hour rainfall was 545.5mm (Tsuguchi, 2017). However, the two days of precipitation at Hita was the most that had occurred there in the past seven decades, and the precipitation in two days exceeded 400mm that had occurred only two times during same seven decades.

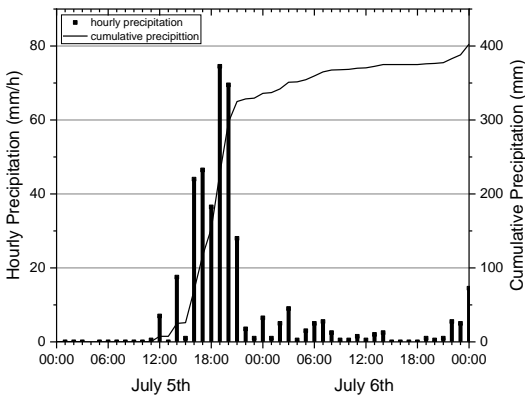


Fig. 3. Observed precipitation at Hita AMeDAS point.

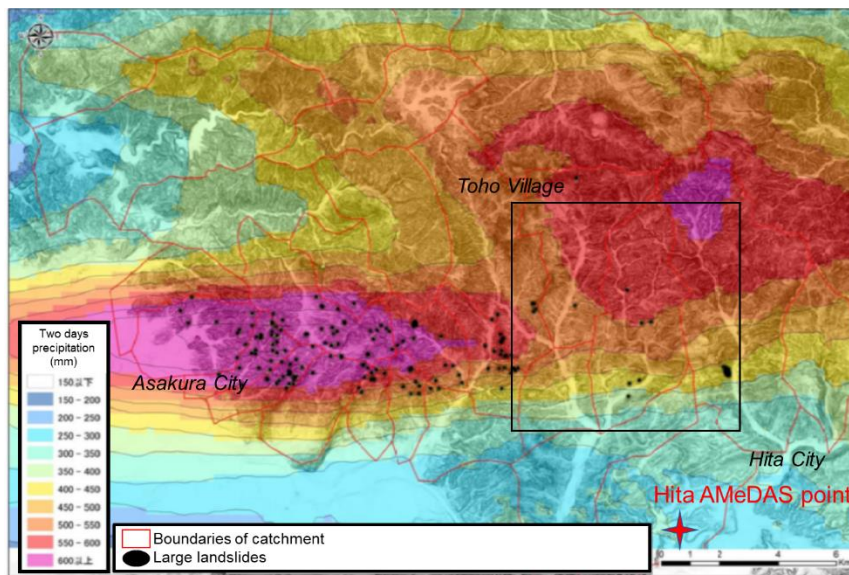


Fig. 4. Distribution of two days of precipitation and large landslides in the Hita, Toho, and Asakura area (Nishimura et al., 2018). The black frame shows a field survey area of Fig. 6.

Fig. 4 shows the distribution of two days precipitation in the Asakura, Toho, Hita districts, which was estimated by meteorological radar (Nishimura et al., 2018). In the mountainous areas, the radar estimated that precipitation during the two day period exceeded 550 mm. In areas near Asakura City, the distribution of landslides corresponded to a huge precipitation zone, whereas the landslide distribution in Hita City did not agree with the estimated precipitation (Fig. 5).

4. Distribution of Landslides and Debris Flows at Hita City

Fig. 5 shows the distribution of landslides and debris flows in the Asakura, Toho and Hita districts (Geographical Survey Institute, 2017). Numerous landslides and debris flows occurred in the mountainous area of Asakura City that coincides with the zone of high precipitation (Fig. 4) and the location of metamorphic and granitic rocks. In the Hita and Toho districts, where volcanic rocks are located, there were fewer landslides and debris flows than at Asakura City.

Nishimura et al. (2018) interpreted 189 landslides in Fig. 5, which had areas of 1,000 m² or more. Thirty-five landslides exceeded 6,000 m² in area. Six landslides with areas of 10,000 m² or more were detected (Nishimura et al., 2018), and two landslides of the six were in volcanic rocks. Furthermore, they said that twenty landslides were located in volcanic rocks, 142 landslides were located in metamorphic rocks, twenty-three landslides in granitic rocks and four landslides in sedimentary rocks. Nishimura et al. (2018) show that small landslides were dominant in areas underlain by metamorphic and granitic rocks, and that large landslides were dominant in areas underlain by volcanic rocks. In the volcanic rocks, there were 15 landslides with areas of 1,000 m² or more, and six landslides in volcanic rocks had areas of 6,000 m² or more. The median values of landslide areas in volcanic rocks, metamorphic rocks and granitic rocks are 4895 m², 3830 m² and 4081 m² respectively.

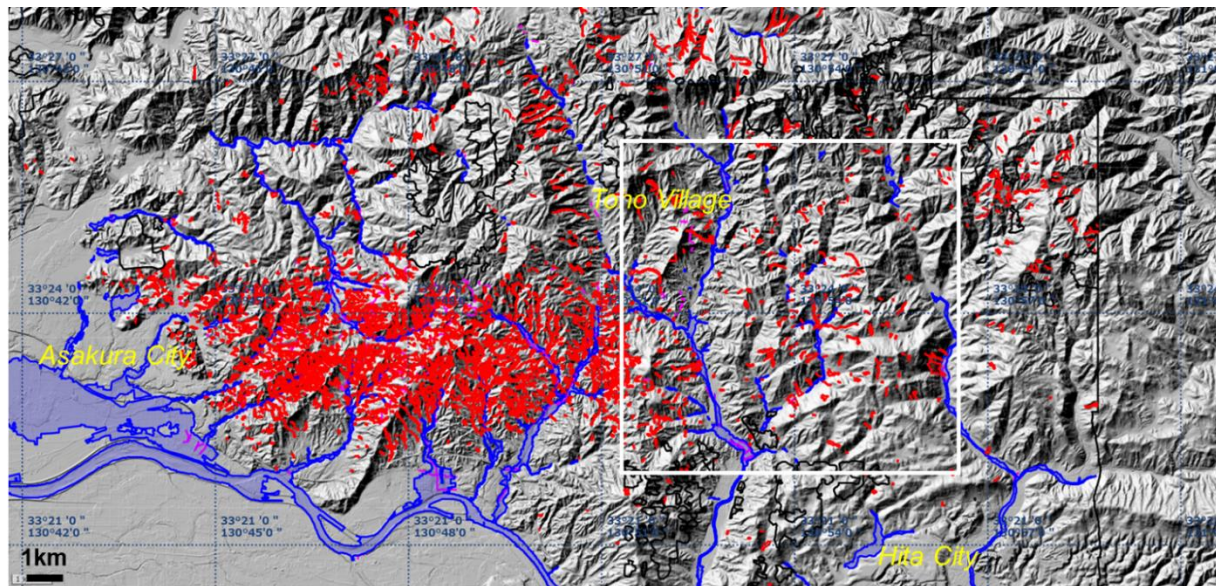


Fig. 5. Distribution of landslides, debris flows and floods in the Hita, Toho, and Asakura area (Geographical Survey Institute, 2017). Red: landslides and debris flows, Blue: flood area. The white frame shows a field survey area of Fig. 6.

5. Geomorphological and Geologic Features at landslide and debris flow sites in volcanic rocks

We interpreted the geomorphological features at 19 landslides in volcanic rocks with two days precipitation estimated by meteorological radar (Table 1). Eleven of 19 landslides triggered debris flow. It did not depend on a landslide area, the elevation of the scarp, the form at scarp and precipitation whether a landslide became the trigger of the debris flow. If landslides were followed by debris flow, the curvature of the hillsides downslope from landslides is concave. Occurrence of landslide were not controlled by geomorphology, because the form at scarp were various.

Table 1. The geomorphological features of landslides in volcanic rocks

No.	Landslide area (m ²)	Scarp elevation (m)	Two days precipitation (mm)	With or without debris flow	Form of at scarp		Form of the hillsides downslope from landslides	
					Vertical	horizontal	Vertical	horizontal
1	1,300	503	600	without	convex	straight	convex	straight
2	1,815	432	500	with	convex	ridge	concave	valley
3	3,214	334	550	without	convex	straight	rectilinear	straight
4	7,915	388	500	with	convex	valley	concave	valley
5	2,963	423	550	with	convex	ridge	concave	valley
6	6,381	252	400	without	convex	valley	convex	valley
7	67,600	379	400	without	concave	ridge	convex	ridge
8	12,732	236	350	without	convex	straight	rectilinear	straight
9	6,979	386	450	with	convex	valley	concave	valley
10	6,285	681	550	with	rectilinear	valley	concave	valley
11	5,479	544	600	with	convex	straight	concave	valley
12	4,942	526	600	with	convex	ridge	concave	valley
13	4,895	573	600	with	rectilinear	ridge	concave	valley
14	4,727	323	550	with	rectilinear	straight	concave	valley
15	4,701	652	550	with	convex	ridge	concave	valley
16	4,276	315	500	without	convex	straight	convex	straight
17	3,601	391	500	without	concave	valley	concave	valley
18	3,302	319	300	without	convex	straight	rectilinear	valley
19	1,072	575	500	with	rectilinear	valley	concave	valley

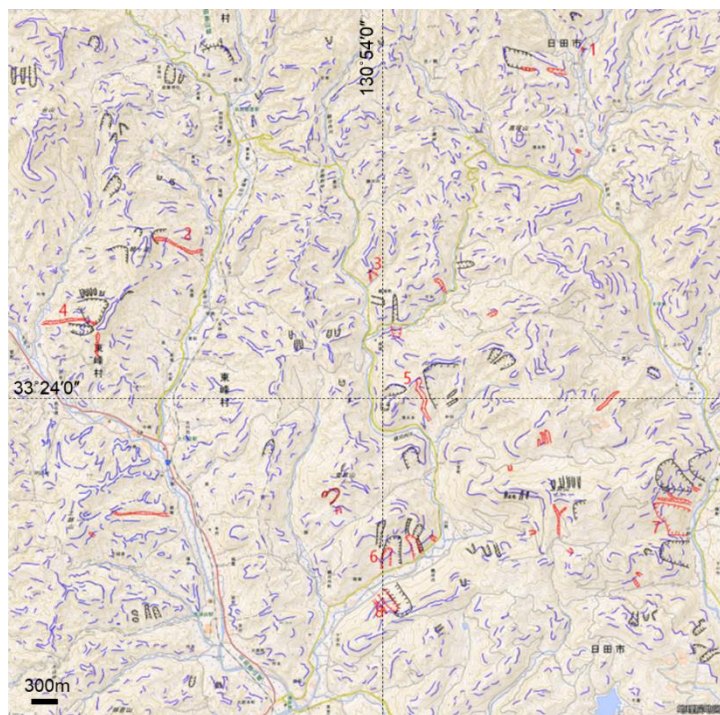


Fig. 6. Geomorphological features in the surveyed area. Red symbols are landslides by the 2017 event, black symbols are scarps recognized from aerial photographs taken before the 2017 event, and blue symbols are knick lines. Numbers are same as Tables 1, 2, and show representative landslides.

We analyzed the geomorphology and geology at eight landslides in detail. Detailed geomorphology at landslides was interpreted from aerial photographs which were taken before and after the event. Ground surveys were done to determine geologic units at representative 8 landslide sites. Fig. 6 shows the locations of analyzed landslides and results from the geomorphologic analysis. The geologic units at each landslide are shown in Fig. 7. The geomorphological features and geology are listed in Table 2. The results from these investigations suggest that;

1) Existing landslide morphology will influence the occurrence of new landslides, because 6 of 8 landslides investigated were situated near the older landslide scarps.

2) At 6 of 8 landslides investigated rigid lava flow with cooling joints cover pyroclastic flow deposits which have low permeability. Therefore, it is suggested that the geologic structure at scarp of landslides are cap rock structure. Furthermore, landslides occurrence did not be influenced by mineral assemblage of cap rock lava, because 2 of 6 lavas consist of hornblende-two-pyroxene andesite and other lavas consist of two-pyroxene andesite.

3) Hydrothermal alteration of rocks is prevalent in the northeastern part of the study area, because only few landslides were located in the northeastern part of the study area in spite of huge rainfall (Fig. 4).

4) The geomorphological features such as the elevation and slope angle at scarp, the slope angle at sliding surface, did not control whether a landslide triggered the debris flow.

Table 2. The geomorphological features and geology of representative eight landslides

Landslide No.	1	2	3	4	5	6	7	8
Landslide area (m ²)	1,300	1,815	3,214	7,915	2,963	6,381	67,600	12,732
Scarp elevation (m)	503	432	334	388	423	252	379	236
Slope angle at scarp (°)	37	41	38	49	17	21	21	37
Slope angle at sliding surface (°)	46	37	34	37	24	31	24	36
Running distance of debris flow (m)	non	900	non	800	1,000	non	non	non
Two days of precipitation (mm)	600	500	550	500	550	400	400	350
Geology	strongly hydrothermally altered andesite lava	bi-hb-2px andesite lava flow cap with pyroclastic flow deposits under layer	strongly hydrothermally altered andesite lava	2px andesite lava flow cap with pyroclastic flow deposits under layer	hb-2px andesite lava flow cap with pyroclastic flow deposits under layer	2px andesite lava flow cap with pyroclastic flow deposits under layer	2px andesite lava flow cap with pyroclastic flow deposits under layer	2px andesite lava flow cap with pyroclastic flow deposits under layer
Geomorphological feature	not close to an old scarp	close to an older scarp	rectilinear slope, not close to an old scarp	close to an older scarp	close to an older scarp	close to an older scarp	close to an older scarp	close to an older scarp

Landslide Numbers are same as Fig. 6. bi: biotite, hb: hornblende, px: pyroxene

6. Discussion

Landslides by 2017 event in volcanic rocks have some common features of geomorphology and geology (Table 1,2). Those are that the scarp of new landslides is located close to an older scarp and that the cap rock andesite lava covers low permeable pyroclastic flow deposits at the scarp. The width of joints in lavas near older scarp maybe spread due to slope instability caused by old landslide. It is easy to infiltrate rain water through the spread joints in lava. Therefore, we suggest that the cap rock structure might contribute to the occurrence of new landslides because rain water would infiltrate through the jointed lava flows and pool on top of the pyroclastic deposits, thus increasing pore pressure, and promoting landslide initiation and sliding at the contact.

There are only few landslides in the northeastern part of the study area in which hydrothermal altered volcanic rocks are distributed. At this area, the permeability of lavas maybe decreased by hydrothermal argillation. Therefore, at 2017 event rain water could not infiltrate into ground and ran off on slope surface, then only shallow and narrow landslides occurred.

Eleven debris flows were observed in volcanic rocks at 2017 event. From the interpretation of aerial photographs and ground surveys, we cannot find out the significant factors which will control to trigger a debris flow from a landslide (Fig. 8). However, if landslide had high elevation at scarp and high two-days precipitation, debris flow will

be easy to occur. At all hillsides downslope from landslides in volcanic rocks, at which debris flow ran down, form of the hillsides was concave-valley type. The curvature of the hillsides downslope from landslides is concave, which may be a required condition for debris-flow mobilization.

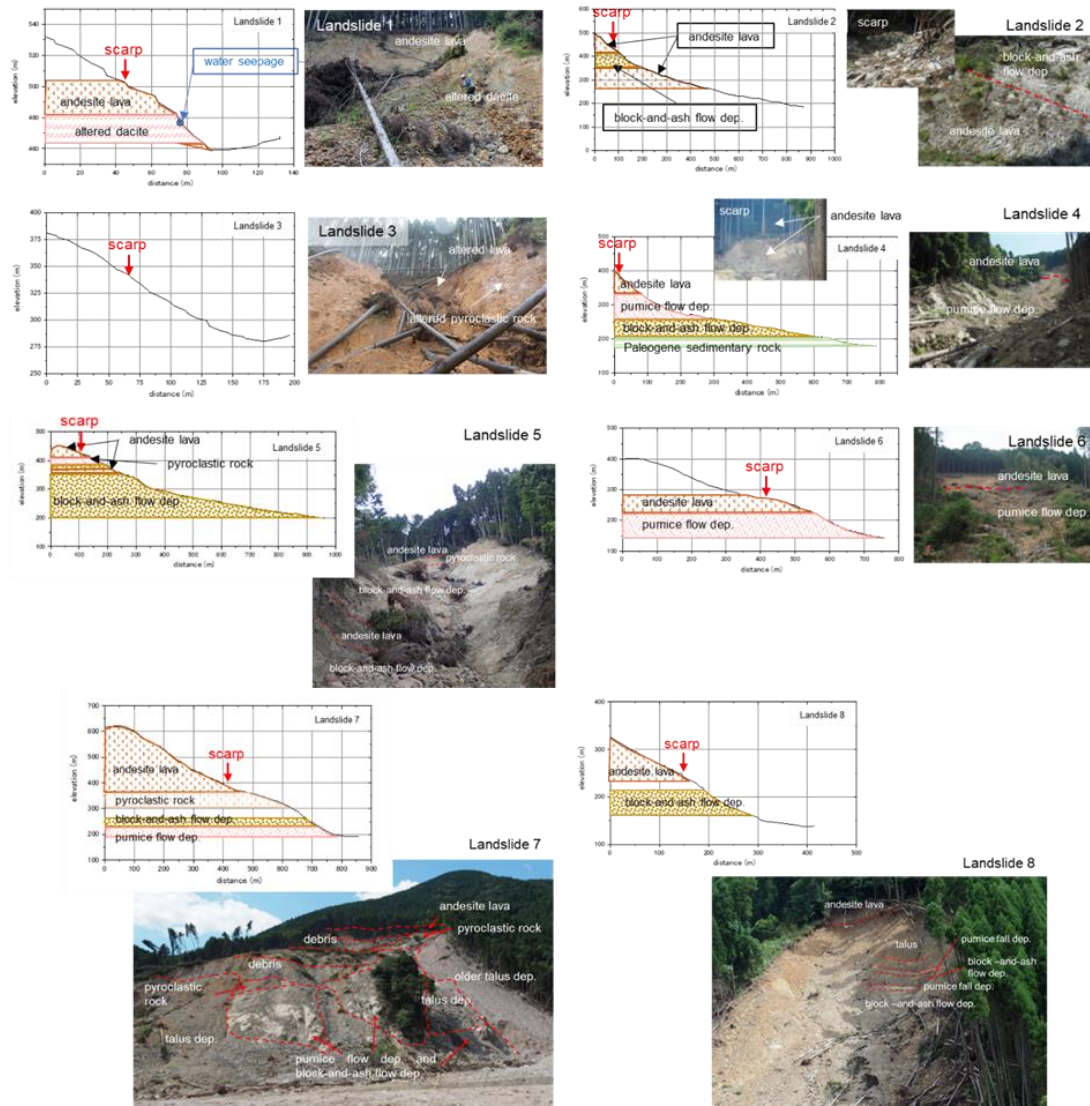


Fig. 7. Geology at each landslide.

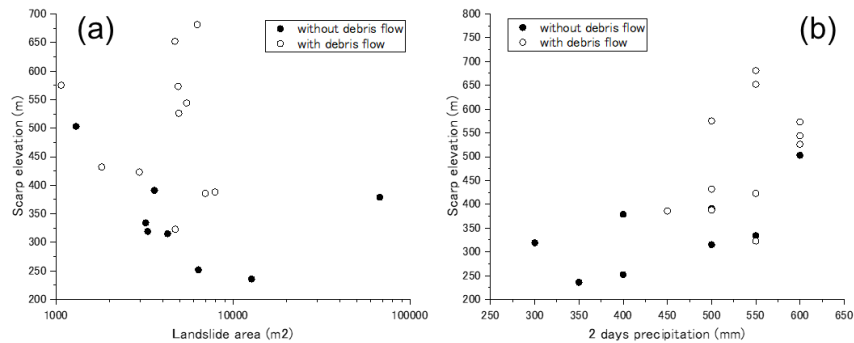


Fig. 8. Geomorphology and precipitation at landslides and debris flows. (a) the relationship between landslide area and scarp elevation, (b) the relationship between two days precipitation and scarp elevation.

7. Conclusions

We investigated landslides and debris flows which occurred in volcanic rocks in Hita and Toho districts in Northern Kyushu. These landslides and debris flows were triggered by heavy rain on July 5th and 6th, 2017. We mapped geomorphological and geological features of these land slide from aerial photointerpretation and ground surveys. The results from these investigations suggest that;

1) Existing landslide morphology will influence the occurrence of new landslides, because 6 of 8 landslides investigated were situated near the older landslide scarps.

2) At 7 of 8 landslides investigated rigid lava flow with cooling joints cover pyroclastic flow deposits which have low permeability. Therefore, we suggest that the cap rock structure might contribute to the occurrence of new landslides because rain water would infiltrate through the jointed lava flows and pool on top of the pyroclastic deposits, thus increasing pore pressure, and promoting landslide initiation and sliding at the contact.

3) Hydrothermal alteration of rocks is prevalent in the northeastern part of the study area. Only few landslides were located in the northeastern part of the study area. Therefore, it seems that altered rocks were minimally susceptible to land sliding during the 2017 rainfall event.

4) We cannot find out the significant factors which will control to trigger a debris flow from a landslide. However, the curvature of the hillsides downslope from landslides is concave, which may be a required condition for debris-flow mobilization.

Acknowledgements

We are deeply appreciation to members of the 2017 Northern Kyushu Heavy Rain Disaster Research Mission of JSEG for useful discussions about landslides. This work was supported partly by the Cabinet Office, Government of Japan, Cross-ministerial Strategic Innovation Promotion Program (SIP). This article was greatly improved by the comment of the reviewer.

References

- Geographical Survey Institute, 2017, Orthographic projection at Asakura and Toho Districts, GSI Web Site, <http://www.gsi.go.jp/>.
- Geological Survey of Japan, AIST (ed.), 2015, Seamless digital geological map of Japan 1: 200,000. May 29, 2015 version. Geological Survey of Japan, National Institute of Advanced Industrial Science and Technology.
- Nishimura, T., Takami, T. and Matsuzawa, M., 2018, Outline of the situation of Landslides and Collapses that occurred in the surveyed area, Report of the 2017 Northern Kyushu Heavy Rain Disaster Research Mission, JSEG, p. 15-27. in Japanese.
- Tajika, J., Ohta, T., Chida, K., Hasegawa, R., Usui, T., Tamaura, H., Nishimura, T., Matsuzaki, M., Nishiyama, K., Senda, K., Tobe, Y., Ikemi, H., Saeki, Y., Isobe, Y., Matsuo, T., Onoda, S., Kobayashi, H., Eguchi, T. and Inokuchi T., 2018, Characteristic landslides occurred in volcanic rock area induced by Kyushu-hokubu heavy rain-fall, July 2017: Ono Landslide, Hita City and some other slides, Report of the 2017 Northern Kyushu Heavy Rain Disaster Research Mission, JSEG, p. 34-42. in Japanese.
- Tsuguchi, H., 2017, About the outbreak factor of the July 2017 North Kyushu heavy rain, http://www3.u-toyama.ac.jp/climate/NHM_meeting/19_Tsuguti.pdf. in Japanese.
- Umezaki, N., Miyazaki, S., Tokuda, M., Usui, T. and JSEG Kyushu Branch Working Group, 2018, Landslide feature on the opposite bank of Nagino, Ono, Hita-city, Report of the 2017 Northern Kyushu Heavy Rain Disaster Research Mission, JSEG, p. 28-33. in Japanese.
- Yada, J., 2018, Topographical and geological overviews of damaged areas due to heavy rainfall on July, 2017, Report of the 2017 Northern Kyushu Heavy Rain Disaster Research Mission, JSEG, p. 3-6. in Japanese.

Debris-flow occurrence in granite landscape in south-southeast Brazil

Jefferson Picanço^{a,*}, Bianca Vieira^b, Tiago Martins^c, Marcelo Gramani^d, Gabriel Faccuri^{a,c}, Marcio Silva^a

^aGeosciences Institute, Unicamp, Rua Carlos Gomes, 250, Campinas, 13083-855, Brazil

^bDepto de Geografia, Faculdade de Filosofia Letras e Ciências Humanas, USP, Av. Professor Lineu Prestes, São Paulo 05508000, Brazil

^cCities Institute, Unifesp, Av. Jacu-Pessegue, 2630, Itaquera, São Paulo, 08260001 Brazil

^dInstitute for Technological Research, Av. Prof. Almeida Prado, 532, Sao Paulo, 05508-90,1 Brazil

^eCompanhia de Pesquisa de Recursos Minerais, SUREG-SP, Rua Costa, 55, São Paulo, 01304010, Brazil

Abstract

The widespread occurrence of Granite Massif landscapes in the Serra do Mar Range, south-southeast Brazil, is also connected with high incidence of debris-flow events. In recent years, the debris-flow events in Serra do Mar Range have caused many deaths and great infrastructure losses. These events occur in high gradient watersheds covered by a thin regolith. This paper intends to analyse the connection between debris-flows-prone watersheds and granitic regolith. These rocks, quite abundant along the mountain chain, are resistant to weathering, and present large vertical gradients. In addition, they generate porous and cohesive regoliths, which support infiltration to the rain water. When saturated, these regoliths can generate shallow landslides, which can liquefy and flow along channels, depositing this material in colluvial fans in piedmont areas. From this point of view, we analysed two watersheds in a granitic terrain, both of similar size and that recently suffered catastrophic events of debris-flows: 1) the Guarda-Mão creek watershed in Itaoca region, which had an intense meteorological event in January 2014; 2) the Gigante creek watershed, in Serra da Prata, which suffered an event with nucleation of debris-flows in March 2011. Both basins present themselves a thin regolith and rock outcrops in higher areas, grading to thicker regoliths and colluvium deposits in the foothills, where the gravels are deposited in the colluvionar fan. Both basins have soil densities (γ_s) between 2.4 and 2.7 g/cm³, reflecting the presence of primary (quartz, feldspar) and secondary minerals (illite, kaolinite, montmorillonite and iron oxides). Both materials are porous (32% to 44%), with plasticity indices (PI) between 1% and 17%. Most materials have low plasticity, although the Gigante creek watershed is even lower, between 1 and 5%. The analysed watersheds are typical of granite/granitoid terrains in Serra do Mar Range, and present great similarity. Further studies should consider the morphometric characteristics of these basins, the mechanisms of rupture and the regoliths liquefaction processes, besides modelling the deposition in fan areas. This understanding could bring improvements to disaster risk management strategies throughout the Serra do Mar region.

Keywords: debris-flow, granitic regolith, geotechnical properties

1. Introduction

Serra do Mar is mountainous landscape associated with escarpments fault that span for over 1,500km alongside the Brazilian south and south-eastern coast (**Fig. 1**), reaching an elevation of 2,000 m” (Vieira and Gramani, 2015). Most of that landscape is associated with granitic and/or gneissic rocks substrate. Because of these gradients, topography and slope materials, the Serra do Mar Range often presents flow-type slides, especially debris-flows, (Vieira and Gramani, 2015; Fernandes et al., 2004; Kanji et al., 2017), causing serious damages and loss of lives (**Table 1**). In recent years, a series of catastrophic events occurred throughout the region, forced the Brazilian government to change the legislation, besides promoting a more integrated disaster risk approach. Meanwhile this approach was progressing,

* Corresponding author e-mail address: jeffepi@unicamp.br

turned it out evident the relationships among debris-flow, Serra do Mar watersheds and granitic/gneissic regolith. Based on estimates, more than half of the debris-flows in the Serra do Mar range occur in granitoid or orthogneisses rocks of the same composition.

The abundant Archaean to Cambrian granitic and granitoid rock bodies in Serra do Mar Range are mostly situated in the hilltops, given their resistance to weathering (Modenesi-Gaultieri et al., 2002; Hiruma et al., 2008). The resultant granite-derived regolith has a generally silty-clayey to sandy-silty composition, with the common development of blocks (corestones) in deeper zones (Picanço et al. 2019; Scott and Pain, 2009). Understand these relationships could improve the mapping methods now in progress.

However, these connections are not easily perceived. Most of the watershed geomorphological and geotechnical data are geographically disperse and difficult to gather. To start the comprehension of these relationships between granitoid terrains and debris-flows in Serra do Mar range, we proposed the comparative discussion of two typical debris-flow occurrence areas.

The chosen areas where occurred flow slide events consist of sub-basins with more than 90% in granite substrate: the Gigante creek watershed in the Serra da Prata region (March/2011) and the Guarda-Mão creek watershed near the Itaoca town (January/2014) (Fig. 1).

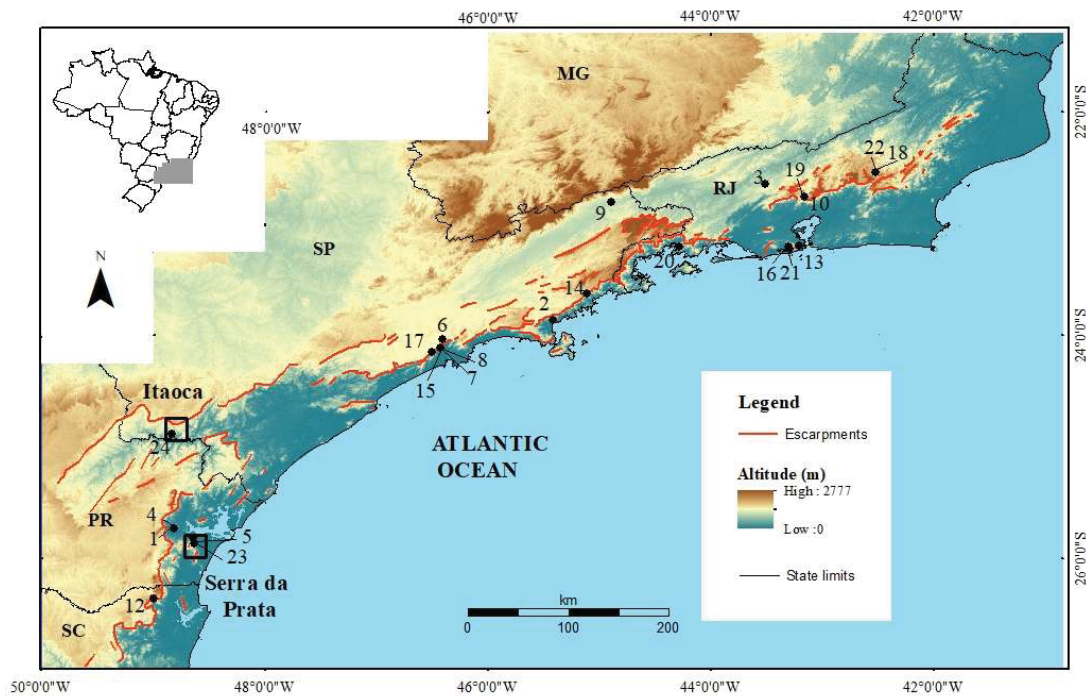


Fig. 1 - The Serra do Mar Range in south-southeast Brazil, showing the main escarpments. The investigated areas, Itaoca and Serra da Prata are localized in the map. The filled circles are related to main events associated to debris-flows recorded in the literature. Each number corresponds to events displayed in Table 1. SC: Santa Catarina State; PR: Paraná State; SP: São Paulo State; MG: Minas Gerais State, and RJ: Rio de Janeiro State.

Table 1. Selected debris-flow occurrences in the Serra do Mar range.

Nº	Year	Area, State	(Deceased People) and material losses	Lithotype	Ref.
1	1888	Morretes (PR)	(8) Floods and landslides	Granite, gneiss, schists	1
2	1967	Caraguatatuba (SP)	(120) 400 houses and highways destroyed,	Migmatite, granite-gneiss, mafic rocks	2
3	1967	Serra das Araras (RJ)	(>1,200) > 100 houses destroyed, highways damaged, destruction of hydroelectric plant	N/d	2
4	1969	Morretes (PR)	Floods and landslide	Granite, gneiss, schists	1
5	1975	Paranaguá	(3) Debris-flow occurrence	Granite, gneiss, schists	1
6	1975	Grota Funda (SP)	Damage to railway pillars	Gneiss	2
7	1976	Cubatão (SP)	N/d	Gneiss, granite, migmatite	2
8	1976	Cubatão (SP)	N/d	Gneiss, granite, migmatite	2
9	1986	Lavrinhas (SP)	(11) houses, bridges and highways destroyed	N/d	2
10	1988	Petropolis	(171) 5,000 displaced, 1,100 houses interdicted	Granite, gneiss, migmatite, schist, quartzite marble	2
11	1994	Cubatão (SP)	N/d	Gneiss, granite, migmatite	2
12	1995	Quiriri (SC)	Houses destroyed, highway interdicted	Granite, gneiss, schists	1
13	1996	Quitite/Papagaio (RJ)	(62) 200 houses destroyed	Gneiss, granite, tonalites, quartzite	2
14	1996	Ubatuba (SP)	Highway damaged, need for slope stabilization, water capture facility damaged	Schist, filonite/migmatite gneiss, foliated granite	2
15	1996	Cubatão (SP)	N/d	Gneiss, granite, migmatite	2
16	1996	Soberbo Highways, RJ	N/d	Gneiss, migmatite, granite	2
17	1999	Via Anchieta Km 42 (SP)	200 m of affected road, traffic stopped for several weeks, water capture facility affected	N/d	2
18	2001	Rio de Janeiro, Petropolis (RJ)	(40) 164 wounded people	N/d	2
19	2002	Petropolis (RJ)	(88) Houses destroyed	Granite, gneiss, migmatite, schist, quartzite, marble	2
20	2010	Angra dos Reis (RJ)	(53) 800 displaced people, houses destroyed	N/d	2
21	2010	Rio de Janeiro (RJ)	(253), 1,410 displaced people, and 338 dislodged	N/d	2
22	2011	Nova Friburgo (RJ)	(772) >300 disappeared, generalized destruction	Granite, gneiss, schists	2
23	2011	Serra da Prata (PR)	(3) 221 wounded, 33 dislodged, highway interrupted, houses and crops destroyed	Granite, gneiss, schists	3
24	2014	Itaoca (SP)	(27) 3 disappeared, houses destroyed	Granite, quartzite	4

Data sources: 1) Picanço et al., 2017; 2) Vieira and Gramani, 2015; 3) Picanço and Nunes, 2013; 4) Brollo et al., 2015.
N/d: non-available data.

2. Regolith profiles

The Guarda-Mão creek watershed in Itaoca area (**Fig. 2a**) has substrate constituted by Proterozoic granites, with a small portion in the highest hilly area capped by fine quartzites. The basin height is 657 m. The granitic rock is grey to pink, medium to coarse granulometry, homogeneous and massive texture, locally with porphyritic crystals. The granite has some portions with hydrothermal alteration. It presents a thin residual regolith in the regions of steeper slopes. This regolith is deep in the less inclined slopes and associated with colluvial material. Fluvial material occurs near the slope base. Locally, sand and gravel strings could be observed, derived from older debris-flows and debris floods.

In the Serra da Prata area, the Gigante creek watershed (**Fig. 2b**) has the largest part of its substrate formed by Proterozoic granitic rocks, with small occurrences of filonites, schists, and Mesozoic basic dykes (Cury, 2008). The granites vary from grey coarse-grained, porphyritic granites with biotite and hornblende to pinkish, medium- to fine-grained equigranular granites. The coarser granites are more weathering resistant and consist the highest part of the mountains. The watershed gradient is 665 m high. The residual regolith is a thin veneer in the upper portions of the watershed, with thicknesses of up to 5 m in the lower areas. Based on their geological and geotechnical characteristics, the residual regoliths (**Tab 2**) were separated in a) collapsed saprolith; b) saprolith; and c) saprock, in the transition to bedrock (Scott and Pain, 2011). The transported material was referred as colluvium.

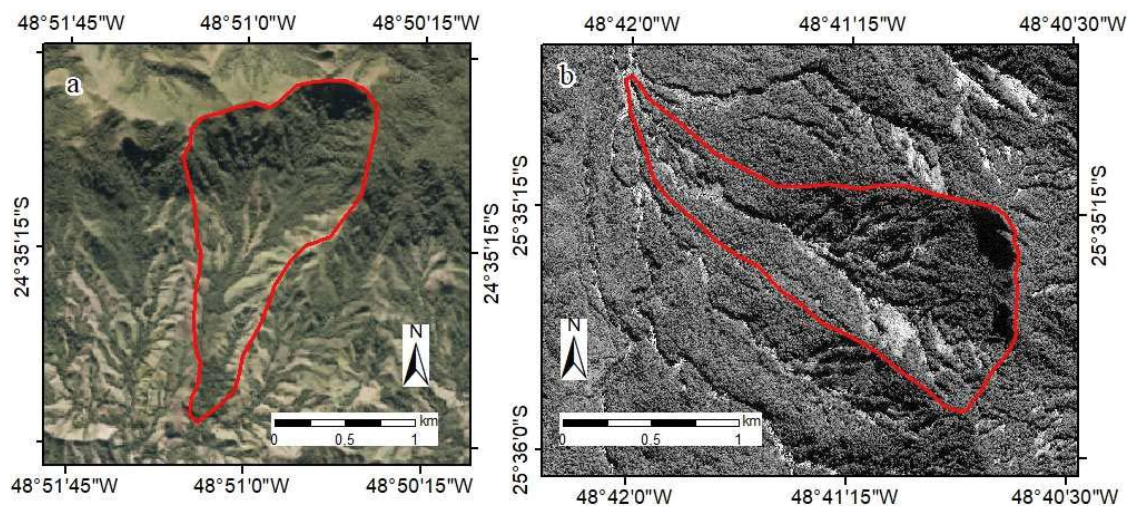


Fig. 2. (a) The Guarda-Mão creek watershed, in Itaoca region, before the debris-flow episode; (b) The Gigante creek watershed, in Serra da Prata area, with the main debris-flow zone areas.

The analysed regoliths in Guarda-mão creek watershed shows a sandier profile (**Fig. 3a**) than the regoliths from Serra da Prata watersheds. On the other hand, the weathering profile in the Gigante creek watershed (**Fig. 3b**) begins with a clayey-silty texture (sample 106A in the **Fig. 3b**), while the least weathered materials in depth are silty-sandy (sample 106D in the **Fig. 3b**). The presence of blocks and boulders increases in the transition from saprolite to altered rock. Colluvium materials in the watershed are more common downstream. Regolith materials also increase their thickness downstream. The colluvium material in these areas is very similar to the collapsed saprolith/regolith intermediate material (sample 108 in the **Fig. 3a**). This is due to the transport processes, which mixture materials during the colluvium formation (King, 1996).

The Guarda-Mão watershed regolith has liquid limits data (LL) between 38 and 44% (**Tab. 2**), whereas plasticity indices (PI) values fall between 12.4 and 17.5%. Colluvium materials from Guarda-Mão watershed have PI values slightly higher than the PI values of saprolith data. The LL data for the Gigante creek range from 32 to 37%, while the PI values vary from 1.5 to 5.0 %. The data of the granitic saprolite and the associated colluvium in the Guarda-Mão watershed fall close to the line A (CL field) in the plasticity chart (**Fig. 4**) (Bain 1970; Casagrande, 1948). The saprolite and colluvial data of the Gigante creek watershed regolith plot in the ML field near the boundary of the CL-ML field.

A saprolite sample fell further in the MH field.

The Guarda-Mão porosity data values range from 46% at the upper quartile and 42% at the lower quartile (**Fig. 5a**). The mean is 44.55% and the median is 45%. An outlier reached 40%. Gigante creek watershed regolith samples have porosity between 35 and 41%, with a 42% at the upper quartile and 28% at the lower quartile (Silva, 2017). The mean is 37.6% and the median is 38.5%.

The soil density data (γ) for both watersheds overlaps between 2.4 and 2.77 g/cm³. The Gigante creek watershed has γ values vary from 2.45 to 2.71 g/cm³, with the upper quartile of 2.6 g/cm³ and the lower quartile of 2.5 g/cm³. The mean is 2.53 g/cm³ and the median is 2.51 g/cm³. The values of γ of the Guarda-Mão creek regolith are between 2.77 and 2.45 g/cm³, with the upper quartile of 2.70 g/cm³ and the lower quartile of 2.55 g/cm³. The mean is 2.63 g/cm³ and the median is 2.65 g/cm³.

Table 2. Geotechnical data of selected samples in Guarda-Mão and Gigante watersheds.

sample	localization	material	Porosity (%)	γ_s (g/cm ³)	LL (%)	PI (%)	ref
01-P10	Guarda-Mão watershed	collapsed saprolith	42	2.7	39.4	12.4	1
02-P10	Guarda-Mão watershed	saprolith	61	2.7	-	-	1
03-P11	Guarda-Mão watershed	collapsed saprolith	37	2.8	-	-	1
04-P11	Guarda-Mão watershed	saprolith	35	2.6	-	-	1
05-P12	Guarda-Mão watershed	collapsed saprolith	41	2.7	-	-	1
06-P12	Guarda-Mão watershed	colluvium	39	2.7	44.1	17.5	1
07-P12	Guarda-Mão watershed	saprolith	37	2.7	-	-	1
08-P36	Guarda-Mão watershed	colluvium	42	2.8	-	-	1
09-P17	Guarda-Mão watershed	collapsed saprolith	38	2.6	-	-	1
10-P19	Guarda-Mão watershed	collapsed saprolith	61	2.7	-	-	1
11-P15	Guarda-Mão watershed	collapsed saprolith	38	2.5	40.9	13.2	1
14-P20	Guarda-Mão watershed	Colluvium	31	2.6	42.7	14.4	1
15-P21	Guarda-Mão watershed	collapsed saprolith	31	2.5	-	-	1
16-P37	Guarda-Mão watershed	collapsed saprolith	28	2.4	38.7	13.1	1
PF 001	Gigante watershed	saprolith	45	2.5	34.6	4	2
PF 010	Gigante watershed	collapsed saprolith	46	2.5	24.4	1.5	2
PF 033	Gigante watershed	collapsed saprolith	46	2.5	26.9	1	2
PF 96 A	Gigante watershed	saprolith	42	2.6	-	-	2
PF 96 B	Gigante watershed	saprolith	45	2.5	-	-	2
PF 97 B	Gigante watershed	saprolith	45	2.5	-	-	2
106 A	Gigante watershed	collapsed saprolith	46.0	2.5	46	4.86	3
106 B	Gigante watershed	saprolith	44.5	2.6	44.5	-	3
106 C	Gigante watershed	saprock	45.3	2.5	45.3	-	3
106 D	Gigante watershed	saprock	43.6	2.6	43.6	-	3
108	Gigante watershed	colluvium	45.8	2.5	45.8	4.38	3
109 A	Gigante watershed	collapsed saprolith	40.4	2.7	40.4	5.05	3
109 B	Gigante watershed	saprolith	45.0	2.5	45	4.87	3

References: 1) Silva, 2017; 2) Sturion et al., 2015; 3) Melo et al., 2015.

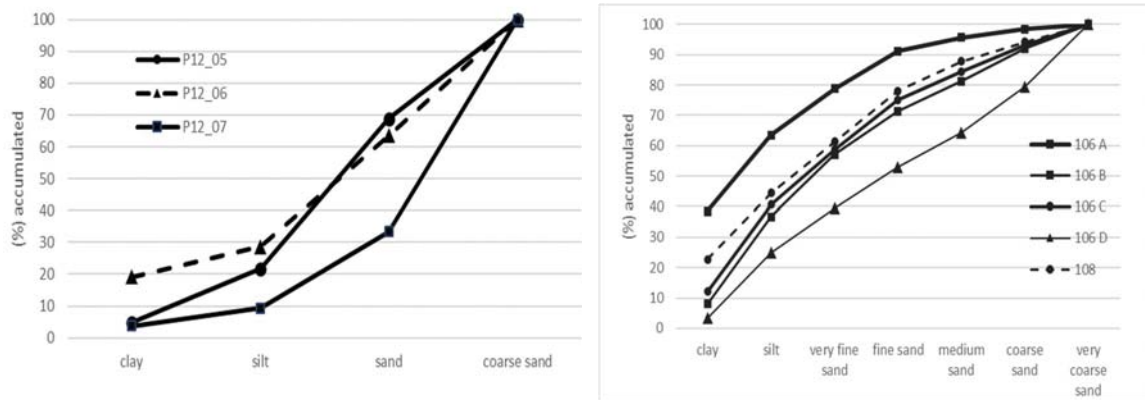


Fig. 3. (a) Granulometric chart of the regolitic profile of Guarda-Mão creek watershed; (b) Granulometric chart of the regolith profile in a landslide scar in the Gigante creek watershed. The samples 106 A-D are saprolite material and the sample 108 is a colluvium material.

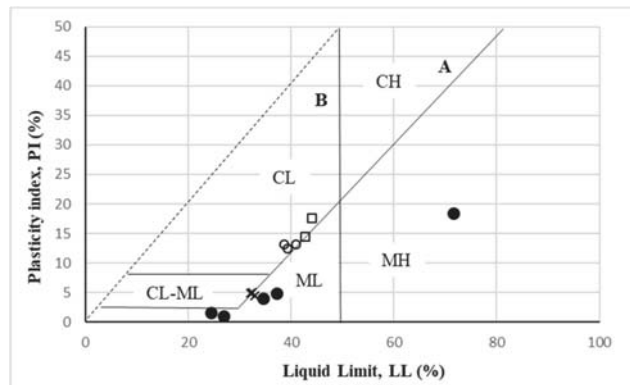


Fig. 4. Plasticity chart from Guarda-Mão watershed saprolites (open circles) and colluvium (open boxes), and samples from Gigante watershed saprolites (filled circles) and colluvium (X). Plasticity chart: CL – low strength clays; CH: high strength clays; ML: low strength. A-line: $PI=0.73LL-14.6$, B-line= $50\%LL$ (Casagrande, 1948; Bain, 1970)

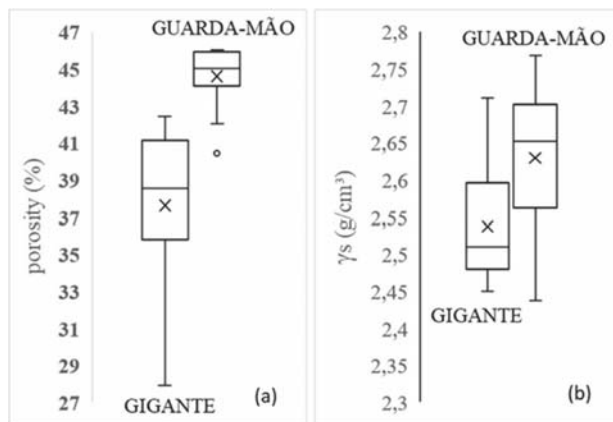


Fig. 5. (a) box and whisker plots of the porosity data; (b) box and whisker plots of the soil density data (γ_s).

3. Debris-flow events

The debris-flow in the Guarda-Mão watershed, São Paulo State, occurred on January 14th, 2014 after an intense rainfall episode, that recorded 200mm in 2 hours (Gramani and Arduin, 2015; Gramani and Martins, 2016). Shallow landslides began on the escarpment near the contact between granite and quartzite sequence (**Fig. 6a**). The slides on rock and soil had initially small volumes. However, the material must have increased due to small dams along the channel. The bursting of these dams raised the energy of the flow, which ran downstream eroding the channel margins and forming an extensive ravine (**Fig. 6b**). The Guarda-Mão creek ravine attain 50 meters wide and 15 meters high (**Fig. 6c**). The coarse material, with blocks up to 4m³, was deposited near the village (**Fig. 6d**) killing 23 people (Brollo et al., 2015).

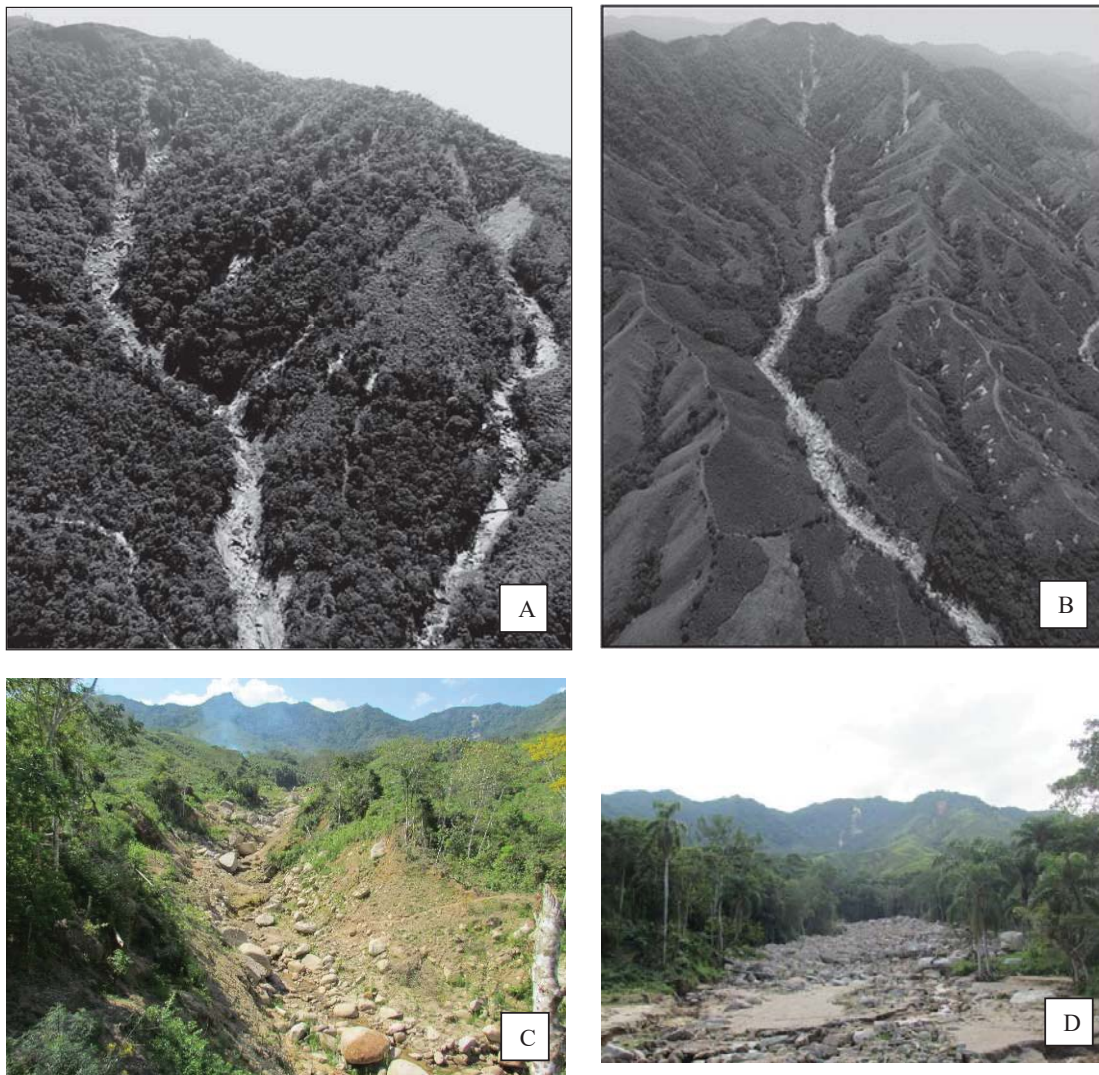


Fig. 6. (a) Panoramic view of Guarda-Mão creek. Observe the landslides scars and the severe river bank erosion. (b) View from the upper portion of the slopes of the Guarda-Mão stream basin. In this sector, predominated soil and rock slides with variable size and shape. (c) large ravine in debris-flow transport zone; (d) blocks and boulders in the deposit zone, Guarda-Mão creek.

The debris-flow of the Gigante creek occurred on March 11th, 2011 in Serra da Prata area, Paraná State. The 72h accumulated rain was 580 mm prior the onset (Picanço and Nunes, 2013). Almost all the ravines had the occurrence

of debris-flows in the Serra da Prata western slope, where is situated the Gigante creek watershed. The scars were on soil and rock (**Fig. 7a**), and the initial ruptures occurred in the saturated regolith related to slope inflexion points.

The scars in the Gigante creek watershed are 2 to 3 meters deep, where the biggest ones on the ground reached an area of up to 44,000 m². According to residents' reports, there were natural dam occurrence along the thalweg, which increased the flow discharge and its downstream energy (Melo et al., 2015). The debris-flow energy was raised, and eroded the regolith deepening the ravines (**Fig. 7b, c**). The coarse material deposit and aligned blocks in lateral bars extended to the entire alluvial fan area (**Fig. 7d**).

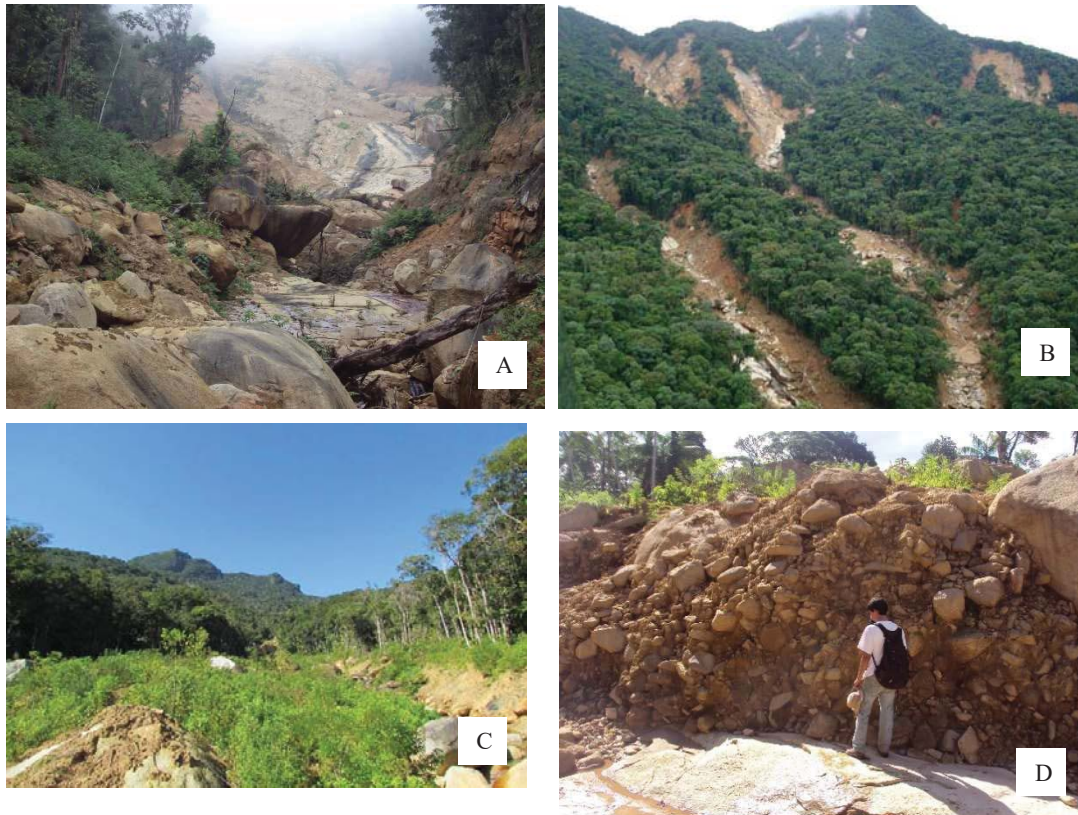


Fig. 7. (a) Scar in bedrock, Serra da Prata area; (b) Serra da Prata large scars and transport zone ravines, photo; Renato Lima; (c) Deposition zone, Gigante creek, in Serra da Prata area; (d) Debris-flow deposit, Serra da Prata, photo Flavio Sturion.

4. Discussion

The occurrence of debris-flows in Serra do Mar is not only related to granitic/gneissic substrate watersheds, but also there might be some relation with its typical landscape. Some of these links has a geomorphological signature, as basin shapes and vertical gradients. Other probable links come from geology and geotechnics that correspond to characteristics from parental rock and weathering profiles.

We could verify that both investigated areas have similar watershed shapes, gradients and lengths (**Fig. 2**). Not surprisingly, both debris-flows were similar in detritus type, block sizes and runout area (Sturion et al., 2015; Melo et al., 2015; Silva, 2017). Their analyses of morphometric parameters are quite analogous as well (Gramani and Martins, 2015; Picanço et al, 2016; Silva, op. cit.). Therefore, this kind of morphometric analyses could be useful to compare watersheds of similar features, but with no historical record events. This approach is necessary because the debris flow-prone watershed areas in Serra do Mar have low frequency of debris-flow occurrence (Picanço et al., 2017).

The frequency of these events is largely reliant on the presence of thick regolith in steep areas, and areas covered by dense vegetation, as both analysed watersheds. This condition could be attained in some areas when large meteorological events occur, generating the great episodes of debris-flow development, as shown in **Table 1**.

Areas with granitic substratum present a geomorphological evolution by shallow landslides rather than an erosion dominated runoff, as observed by Gaertner et al. (2004) in British Columbia. In contrast, the Gigante watershed samples present greater variation in terms of porosity than the samples of the Guarda-Mão watershed (**Fig. 5a**). While the former is lower and better distributed, the latter occur within a narrower range. In any case, the porosity differences are small and quite similar between the two areas.

The Gigante creek material presents low PI values. Some saprolite and colluvium samples are very close to the CL-ML field in the plasticity chart (**Fig. 3**). The LL values are very similar between the two areas. In the plasticity chart, the materials are very close to the beginning of the line A, and classified as CL or ML depending on its position relative to the line A.

The regolith of both areas have soil densities (γ) within the same range (**Fig. 5b**). The Gigante creek watershed regolith has an average density of 2.5 g/cm³, close to the density of primary minerals, as quartz and feldspar, and newly formed minerals, such as illite, kaolinite and gibbsite. The soil density of the regolith material from the Guarda-Mão creek watershed may suggest the additional presence of heavier mineral phases, such as iron oxides.

The occurrence of large rock blocks in the regolith is linked to translational landslides involving soil and rock, as observed in the analysed watersheds (**Fig. 6, 7**). The development of small landslides of this type may, however, trigger the liquefaction of more sandy and porous materials downstream as colluvium and talus deposits. The material able to be entrained in debris-flow path is highly dependent of the regolith formation rate (Jakob, 2005). These deposits could be then incorporated in the channel and increase the material volume to be deposited downslope (Sassa and Wang, 2005).

The general characteristics of granitic regolith, such as granulometry, porosity and mineral content, are obviously present in both Guarda-Mão and Gigante watersheds. All these characteristics suggest that granitic watersheds of similar type could generate very similar pebbly debris-flows. However, this assumption is not very well constrained, and the data are not enough to sound deductions. More comprehensive analyses must be done to prevail upon these initial propositions.

5. Conclusions

The analyses of regolitic material of the two discussed watersheds are important for the evaluation of the flow type movements occurred in granitic terrains of Serra do Mar Range. The characteristics of this granite regolith generate porous and low PI soils susceptible to rupture and liquefaction. In this way, the granite regolith is susceptible to an evolution marked by the translational landslide's occurrence. The fluidification of these materials and their entrainment in the gullies could give rise to debris-flows.

Notwithstanding, this relationship between debris-flows in granite-derived regolith is still poorly understood. The morphometric characteristic of some granite-related basins should be more developed. There is still a need for further studies in the Serra do Mar area concerning the rupture mechanisms of these materials beyond the Wolle and Hachich (1989) model. It is important, for example, the inclusion of dense vegetation in slope stability calculations. The understand of the behavior of these granitic regolith in the soil liquefaction and in the channel entrainment processes is another interesting topic.

As high slope terrain is largely supported by granite and granitoid rocks *lato sensu* as granitic gneisses, the Brazilian mountain range is a place where this type of flow movements is common in extreme weather events. The study of the characteristics of these lands can yield developments for many useful information to reduce the vulnerability of the population that lives in these areas.

Acknowledgments

The authors thank the Geosciences Institute-UNICAMP and the FAEPEX-UNICAMP for operational assistance in the various stages of the field work. We are also very grateful to Dr. Claudio Ferreira (Geological Institute of São Paulo) and Renato Lima (CENACID/Federal University of Paraná) to grant satellite images. The authors are also thankful to Mr. Jose Benedito Cipriano and Reinaldo Benedito Leite da Silva, from Soils Mechanics Lab of Faculty of Civil Engineering and Architecture of UNICAMP for the guidance of geotechnical analyses.

References

- Bain, J., 1971. A plasticity chart as an aid to the identification and assessment of industrial clays. *Clay Minerals*,9(1), 1-17. doi:10.1180/claymin.1971.009.1.01
- Brollo, M.J., Guedes, A., Ferreira, C., Rossini-Penteado, D., Andrade, E., Ribeiro, F., Santoro, J. Tominaga, L. Fernandes-Da-Silva, P.R.; Ribeiro, R., 2015, Mapeamento de riscos associados a escorregamentos, inundações e corridas de massa – Município de Itaoca, SP. São Paulo: Instituto Geológico, Secretaria do Meio Ambiente do Estado de São Paulo. Relatório Técnico, 2015. 3 volumes. Boletim do Instituto Geológico nº 64, http://www.sidec.sp.gov.br/producao/map_risco/pesqpdf3.php?id=417.
- Casagrande, A., 1948, Classification and identification of soils. *ASCE Trans.*,113(1948), pp.901-991.
- Cury, L. F., 2009, Geologia do Terreno Paranaguá. [Ph.D. thesis]: Geosciences Institute, Universidade de São Paulo, 210 p.
- Fernandes, N.F., Guimarães, R.F., Gomes, R.A., Vieira, B.C., Montgomery, D.R., Greenberg, H. 2004, Topographic controls of landslides in Rio de Janeiro: field evidence and modeling. *Catena*, v. 55(2), p.163-181.
- Gramani, M.F. & Arduin, D.H. 2015. Morfologia da Drenagem e dos Depósitos de Debris-flow em Itaoca, São Paulo. XV Congresso Brasileiro de Geologia de Engenharia e Ambiental, Proc., Bento Gonçalves, 18-21 october 2015. São Paulo: ABGE (in portuguese).
- Gramani, M.F. & Martins, V.T.S. Debris-flows Occurrence by Intense Rains on January 13, 2014 at Itaoca City, Sao Paulo, Brazil: Impacts and Field Observations. 12th International Symposium on Landslides ISL 2016, Napoli, June 12th-19th, 2016. 10p.
- Hiruma, S.T., Riccomini, C., Modenesi-Gauttieri, M.C., Hackspacher, P.C., Neto, J.C.H., Franco-Magalhães, A.O. (2010). Denudation history of the Bocaina Plateau, Serra do Mar, southeastern Brazil: Relationships to Gondwana breakup and passive margin development. *Gondwana Research*,18(4), pp.674-687.
- Kanji, M., Massad, F. Gramani, M., Cruz, P.T., 2017, Fluxo de detritos (fluxo de detritos). In: Ciccoti, L., Rodrigues, A. C., Günther, W. M. R., Desastres: Múltiplas Abordagens e Desafios, Elsevier Brazil, p. 183-210.
- King, J., 1996, Tsing Shan debris-flow (Special Project Report SPR 6/96). Geotechnical Engineering Office, Hong Kong Government, 133.
- Melo, L.L., Picanço, J., Mesquita, M.J., 2015, O estudo do regolito na sub-bacia do Córrego do Gigante (Morretes, PR): subsídios para a análise de nucleação de debris-flows. In: Proceedings of Brazilian Association of Engineering Geology and Environmental Congress, Bento Gonçalves, Out/2015.
- Modenesi-Gauttieri, M. C., Hiruma, S. T., Riccomini, C., 2002, Morphotectonics of a high plateau on the northwestern flank of the Continental Rift of southeastern Brazil. *Geomorphology*, v. 43(3), p. 257-271.
- Picanço, J. L., Nunes, L. H., 2013, A severe convective episode triggered by accumulated precipitation in the coast of Parana State, Brazil. In Proceedings of 7th European conference of severe storms, p. 4-14.
- Picanço, J., Mesquita, M. J., Soares, L. F., 2017, The Hydrological Disasters Through Historical Survey in the Serra do Mar Range, Southern Brazil. In: Workshop on World Landslide Forum, Springer, p. 1017-1026.
- Picanço, J.; Mesquita, M. J.; Melo, L.L., 2019., Geotechnical and Mineralogical Properties of Granite Regolith Related to Nucleation Mechanisms of Debris Flows in Tropical Areas. *International Journal of Erosion Control Engineering*, v.11, p.54 – 62. doi:10.13101/ijece.11.54
- Scott, K. and Pain, C., 2009, Regolith science. Csiro Publishing, 462 p.
- Silva, M.C. 2017, Caracterização Geológica e Geotécnica dos Debris-flow na Bacia do Córrego Guarda Mão (Itaoca-SP) no Desastre de Janeiro/2014. [MSc. Dissert.]: Geosciences Institute, Unicamp, 110 p.
- Vieira, B. C., Gramani, M. F., 2015, Serra do Mar: The Most “Tormented” Relief in Brazil. In: *Landscapes and Landforms of Brazil*, Springer Netherlands, p. 285-297.
- Wolle, C.M., 1989, Rain-induced landslides in southeastern Brazil. In Proc. 12th Internal. Conference on Soil Mechanics and Foundation Engng, v. 3, p. 1639-1642.

Hillslope evaluation in the vicinity of the Wolsong nuclear power plant after 12th September 2016 Gyeongju earthquake, South Korea

Ananta Man Singh Pradhan^a, Ji-Sung Lee^a, Seung-Rae Lee^b, Tae-Hyuk Kwon^b and Yun-Tae Kim^{a,*}

^a*Department of Ocean Engineering, Geo-systems Engineering Laboratory,*

Pukyong National University, Busan 48513, Republic of Korea

^b*Department of Civil and Environmental Engineering,*

Korea Advanced Institute of Science and Technology, Daejeon 34141, Republic of Korea

Abstract

Landslides result not only from the environmental background conditions of slopes but also from triggering factors, such as rainfall and earthquake. Severe landslides and debris flows are common natural disasters in South Korea since it is characterized by high rainfall and rugged topography. A secondary effect of an earthquake could be slope instability. A 5.8-magnitude (ML) earthquake, the most powerful seismic activity since the nation started measuring tremors, struck the historic city of Gyeongju, North Gyeongsan Province, at 20:32:54 KST. The Wolsong nuclear power plant is situated in the foothills of a mountainous area about 26 km SE of the earthquake epicenter. South Korea's biggest historical earthquake raised the nuclear safety concerns. To assess regional landslide hazard under the conditions of heavy rainfall and after 5.8 ML Gyeongju earthquake, this study, a coupled hydrological model with infinite slope model was used to find the hillslope stability under the roles of rainfall and earthquake.

Keywords: Gyeongju earthquake; hillslope evaluation; landslide

1. Introduction

Rainstorms are widely acknowledged as a significant landslide-triggering agent in hilly landscapes (Iverson, 2000). Often the landslides are a secondary effect of earthquakes, when the earthquake occurs on areas with steep terrain, the soil and rock falls causing landslides (Malamud et al., 2004; Keefer, 2011). In fact, destruction and fatalities due to earthquake-induced landslides may exceed damage directly related to a strong shaking of infrastructure. Landslide constitutes a major natural hazard in the Republic of Korea (hereafter Korea) due to high rates of weathering, abundant rainfall and infrastructure development (Pradhan and Kim, 2014). Korea is experiencing changes in climate. Due to these concentrated short duration and high-intensity rainfall from July to September has caused slope instability in Korea. The vulnerability of a nuclear power plant (NPP) subjected to an earthquake event is a major concern to the communities in many countries. Nuclear power plants are the main components of the electric grid in South Korea as well. Most of the currently operating NPPs are located close to terrain with moderate to steep slopes. Such a situation poses potential threats to the NPP safety from seismically-induced landslides where concentrated heavy rainfall in ample.

Two moderate-sized earthquakes with local magnitudes of ML 5.1 (19:44:30 KST) and 5.8 (20:32:54 KST) occurred within an interval of 48 min on 12th September 2016. The 2016 Gyeongju earthquakes have now become forceful reminders that such events have occurred in the past and can hit the region any time (Hee et al., 2016). Earthquakes are occurring in an area dense with nuclear power plants.

A large amount of research on slope stability has been carried out over the last 30 years for planning purposes. This research focuses on evaluating hillslope stability in the vicinity of the Wolsong NPP after the 2016 Gyeongju earthquake under historical heavy rainfall event which was responsible to landslide in Gyeongju in 2005. No surface

* Corresponding author e-mail address: yuntkim@pknu.ac.kr

ruptures were reported for the Gyeongju earthquake events and no landslides due to the sudden ground shaking were reported but in an earthquake prone area, susceptibility assessment of hillslope stability is very important around such nuclear plants for safety planning, disaster management, and hazard mitigation. The effect of natural hazards on this type of infrastructure is a crucial issue to be considered in order to prevent or mitigate damages to property and people.

Gyeongju is a coastal city in the far southeastern corner of North Gyeongsang Province. In this study, a catchment of Nasanchan river was selected as a model application site which covers 20.8 km² area as shown in Fig 1. The average elevation of the catchment is 100.3 m above mean sea level. The Wolsong NPP located on the coast near down reach of Nasanchan river and East sea. It is the only South Korean nuclear power plant operating pressurized heavy water reactors. It has 4 reactors, each of these reactors has a capacity of 700 MW. The Wolsong NPP supplies about 5% of South Korea's electricity.

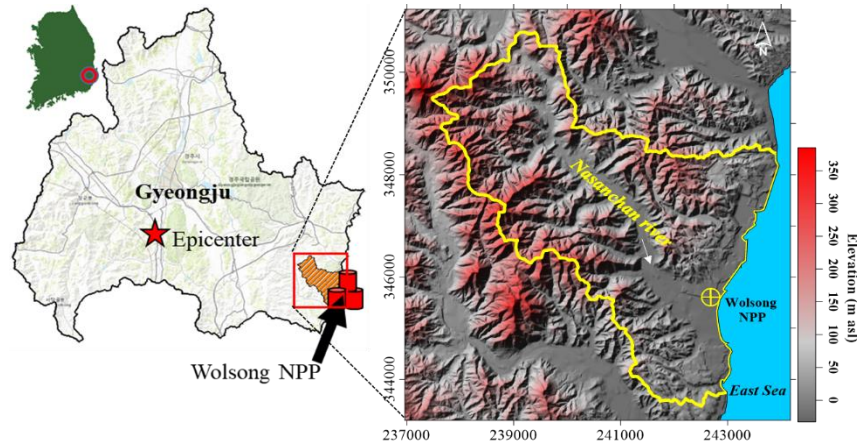


Fig. 1. Location map of study area

2. Methodology

This study was performed in three steps (Fig 2): (1) collection of database such as rainfall and landslide events from national catalog, LIDAR-based DEM (20×20m resolution), geotechnical data and seismic data during the Gyeongju earthquake; (2) FS was calculated using infinite slope model coupled with hydrological model considering unsaturated soil slope; and (3) preparation of warning model based on FS and rainfall thresholds.

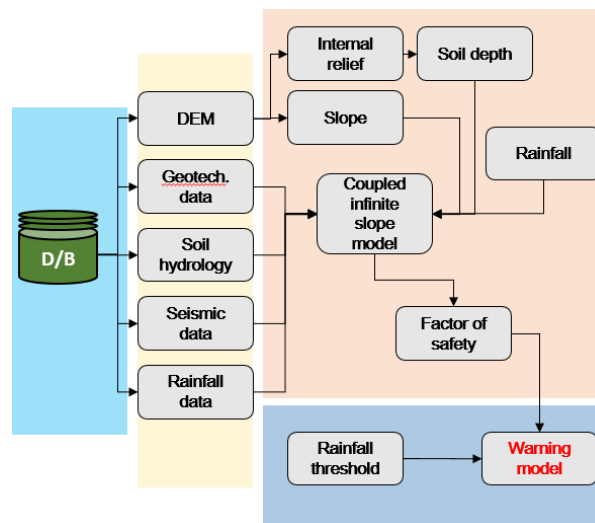


Fig. 2. Method adopted in this study

2.1. Infinite slope model

Recent efforts to extend the problem of slope stability to include unsaturated conditions have considered the slope instability from rainfall infiltration (Iverson, 2000). This study is to derive a mathematical model for an infinite slope subjected to unsaturated flow above a phreatic surface considering pseudo-static model. The driving force will increase in proportion with the seismic acceleration. The following equation (1) is derived for the static FS, neglecting acceleration normal to the slope. The expression is modified after (Iverson, 2000; Lu and Godt, 2008)

$$FS_{unsat} = \frac{c}{\gamma Z \cos \beta (\sin \beta + k_h \cos \beta)} + \frac{\tan \phi (\cos \beta - k_h \sin \beta)}{\sin \beta + k_h \cos \beta} - \frac{\psi \gamma_w S_e \tan \phi}{\gamma Z \cos \beta (\sin \beta + k_h \cos \beta)} \quad (1)$$

where c is cohesion, ϕ is friction angle, β is slope, ψ is pressure head, S_e is effective saturation, γ_s is soil unit weight, γ_w is unit weight of water, k_h represents horizontal seismic coefficient to present horizontal inertia forces from earthquake and Z is soil depth.

Despite the importance of soil depth most studies have used constant depth ignoring its spatial variability (Kuriakose et al., 2009). In this study soil depth was estimated by using internal-relief (IR) model (Pradhan et al., 2018). The IR corresponds to local height differences within a unit area and expressed as in equation (2)

$$\text{Soil depth } (Z) = \text{Depth}_{max} - \frac{IR_i - IR_{min}}{IR_{max} - IR_{min}} (\text{Depth}_{max} - \text{Depth}_{min}) \quad (2)$$

In this equation, Z is computed at each pixel (i), Depth_{max} and Depth_{min} are the maximum and minimum values of soil depth measured at the study area, and IR_{max} and IR_{min} are the maximum and minimum IR values at the study area, respectively.

2.2. 3D subsurface flow model

In this study, a 3D subsurface flow model was applied which was formulated by Richards (1931) as given in equation (3).

$$\frac{\partial \theta(\psi)}{\partial t} = \nabla (K(\psi) \nabla (\psi + z)) + q \quad (3)$$

where ψ is the pressure head (m), θ is volumetric moisture content (m^3/m^3), K is hydraulic conductivity (m/s), t is time (s), z is the vertical dimension (m), and q is general source including rainfall ($\text{m}^3/\text{m}^3/\text{s}$). Equation (3) is discretized within finite volume framework. An orthogonal horizontal and non-orthogonal vertical mesh.

A van Genuchten's soil water retention curve (van Genuchten, 1980) and Mualem's unsaturated hydraulic conductivity functions (Mualem, 1976) were used as follows:

$$S_e = \frac{\theta - \theta_r}{\theta_s - \theta_r} = \left\{ \frac{1}{1 + (\alpha |\psi|^{n_v})} \right\}^{1/n_v} \quad (4)$$

where θ_s and θ_r are saturated and residual moisture content.

$$K = K_s S_e^{1/2} \left\{ \left(1 - S_e^{n_v/(n_v-1)} \right)^{1/n_v} \right\}^2 \quad (5)$$

where α and n_v are van Genuchten parameters whose values depend on the soil properties, and K_s is the saturated hydraulic conductivity (m/s).

3. Results and discussion

3.1. Data preparation

The peak ground acceleration (PGA) data were collected from the Korea Meteorological Administration (KMA). For this purpose, seismograph from seismic stations namely ADO2, CSO, CHS, PHA2, YOCB, DAG2, and USN were used to calculate PGA and interpolated the real-time maximum acceleration during Gyeongju earthquake as presented in Fig 3. It is evident that it would be too conservative to use peak ground acceleration (PGA) because PGA lasts for a very short time and appears only once in the record. Therefore, instead of PGA, a fraction of it, $k_h = \zeta \times \text{PGA}/g$ is used. Different magnitudes of ζ between 0.2 (for sites near faults, violent and destructive earthquake)–0.65 (for intermediate slide mass) were proposed by Matasovic (1991). This study used 0.65 as ζ .

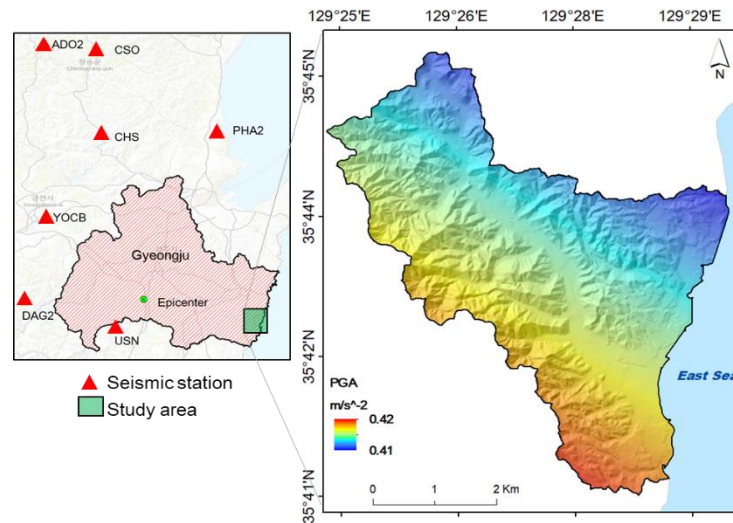


Fig. 3. PGA distribution during the Gyeongju earthquake

The soil depth is another important factor in an assessment of slope stability (Dietrich et al., 1995). The soil depth of the study area was estimated by using internal-relief model (Pradhan et al., 2018). The model showed that the soil depth is ranging from 0.1–3 m in the study area. From the national rainfall-induced landslide catalog, there was a landslide event in 2005 September 6 in Gyeongju area. The rainfall distribution during 2005 landslide event is presented in Fig (4a).

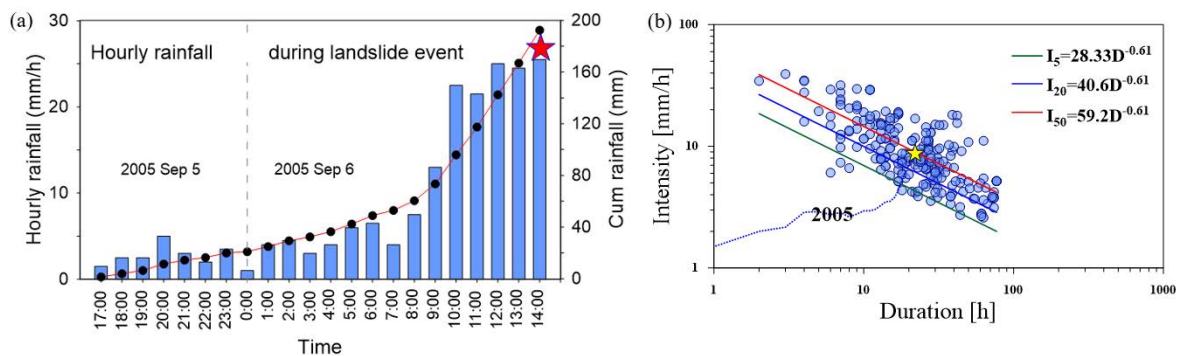


Fig. 4. (a) Hourly rainfall distribution during 2005 landslide event in Gyeongju (Red line is cumulative rainfall) and (b) ID rainfall threshold (broken line is rain path during the landslide event)

For this study, a national landslide inventory was prepared using data from the NDMI (National Disaster Management Institute), various reports, and newspapers. Rainfall data were collected from the Korea Meteorological Administration. A total of 255 landslide events occurring in 1999–2012 were collected; among them, only 224 events were identified as rainfall-triggered landslides in weathered soil in South Korea. We used a threshold curve in the form of $I = \alpha D^{-\beta}$, where α and β are constants, following the work of various researchers (Caine, 1980; Glade et al., 2000; Jakob and Weatherly, 2003; Aleotti, 2004; Chien-Yuan et al., 2005; Dahal and Hasegawa, 2008; Brunetti et al., 2010), to determine rainfall thresholds. The critical intensity (I) and duration (D) for each event were plotted on a log-log diagram (Fig. 4b) to define rainfall threshold with durations between 2 and 77 h. The critical duration of 2005 Gyeongju landslide event was calculated from the collected catalog and it was found to be 22 hrs and cumulative rainfall was calculated as 192.5 mm in 22 hrs. Warning levels were selected on the basis of the 5th percentile, 20th percentile, and 50th percentile. They were classified as ‘null’ (below the 5th percentile), ‘watch’ (5th–20th percentile), ‘attention’ (20th–50th percentile), and ‘alarm’ (above the 50th percentile) warning levels.

Table 1 represents the geotechnical parameters including friction angle, unit weight and cohesion for each geological units.

Table 1. Soil data

Lithology	ϕ (°)	γ (kg/m ³)	C (kg/m ²)
Shale	22	2501	2549
Alluvium	0	1600	0
Granite	33	2700	3161
Andesite	33	3000	3161
Diluvial	0	1600	0
Amphibolite granite	33	2700	3161
Granite porphyry	33	2700	3161
Marl and sandstone	40	2000	2651

Saturated hydraulic conductivity (K_s) was set as $1.3E^{-05}$. Saturated and residual moisture content are 0.5 and 0.18, adopted from Park et al. (2013). Van Genuchten parameters α and n_v were set as 20 (m⁻¹) and 1.4.

3.2. Model application

After preparing database, the model was applied to calculate FS using hourly rainfall data. The simulation time was set as 17:00 (KST) of 5th September 2005 (rainfall start) to 14:00 (KST) of 6th September 2005 (landslide event time). The FS maps were classified as $FS < 1$, $1-1.25$, $1.25-1.5$ and > 1.5 . From the simulation, a range of FS corresponding to hourly rainfall can be obtained as shown in Fig 5. The results shows, as the rainfall duration increases the corresponding hillslope instability also increases. Most of the areas were in a stable condition until the heavy rainfall on the 6th from 9 a.m. to 2 p.m. After 9 a.m. on 6th, the pore-water pressures in the bottom soil layer changed drastically, causing a rapid change in the FS. At 2 p.m., almost all the areas became saturated, and minimum FS values were estimated. The present study assumes the worst case condition considering pseudo-static seismic condition.

On the basis of hourly estimated FS, the rainfall threshold based FS can also be calculated. Figure 6 shows the warning level maps which are the cutoff rainfall path at 5th percentile, 20th percentile and 50th percentile rainfall thresholds following rainfall path. Dry condition yielded no unstable pixels (Fig. 6a). 5% exceedance probability, the unstable area increased to 0.28%. Under this particular condition, the area with $FS < 1$ can be considered a “watch” warning level (Fig. 6b). With 20% exceedance probability, the unstable area increased to 5.76%, and these unstable areas can be assigned to the “attention” warning level (Fig. 6c). Similarly, at a rainfall threshold of 50%, the unstable area was 20.52% (Fig. 6d); this area is assigned the “alarm” warning level. Table 2 shows the comparison between FS at four warning levels considering seismic coefficient and without considering seismic coefficient.

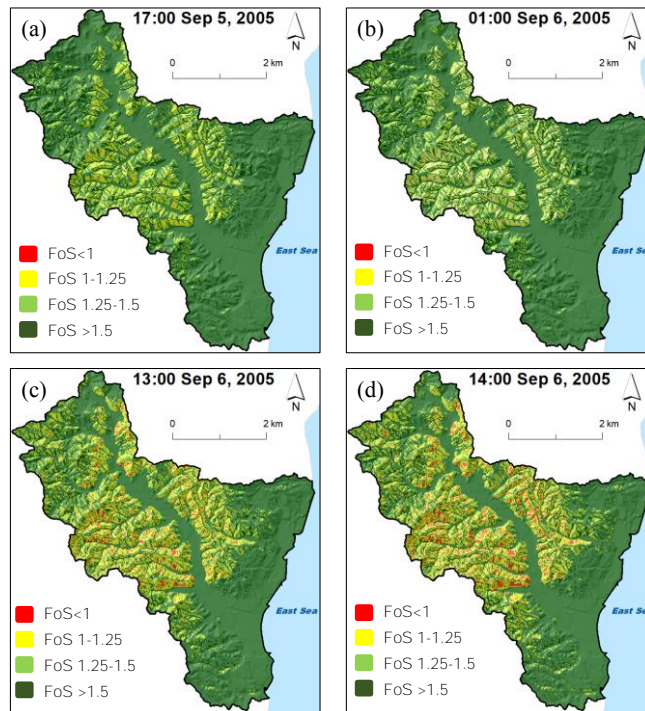


Fig. 5. Factor of safety distribution corresponding to hourly rainfall (only selected results are shown in this figure)

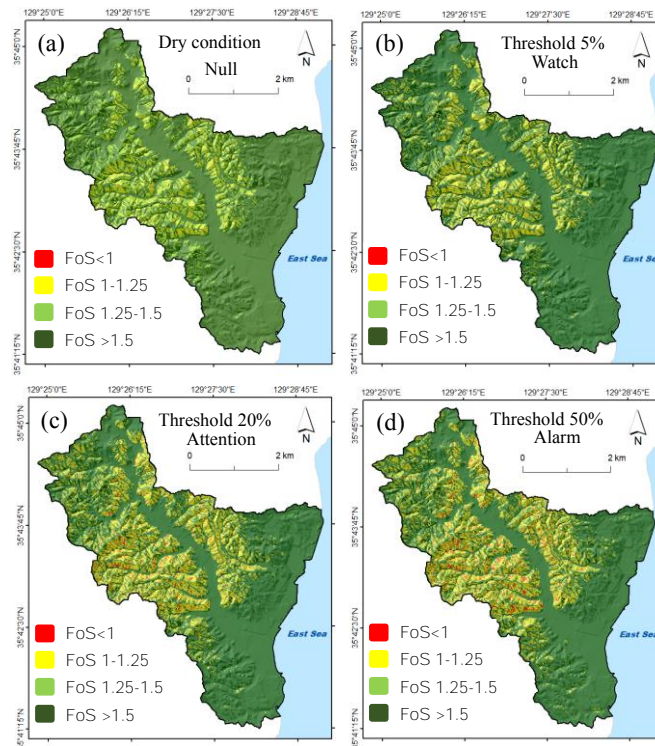


Fig. 6. Distribution of factor of safety in different rainfall scenarios: (a) dry condition, (b) watch, (c) attention, and (d) alarm

Table 2. Comparison between areas of FS

Factor of safety	Area % considering static seismic coefficient			Area % without considering seismic coefficient		
	5% threshold	20% threshold	50% threshold	5% threshold	20% threshold	50% threshold
FS <1	0.28	5.76	20.72	0.08	3.51	10.7
FS 1-1.25	6.12	20.8	33.8	2.62	19.1	25.8
FS 1.25-1.5	30.1	33.34	33.5	32.1	33.7	33.1
FS >1.5	63.5	40.1	11.98	65.2	43.69	30.4

From these calculations, two types of landslide warning can be issued in the catchment. First is using minimum FS and second is using rainfall threshold warnings. We assumed that FS 1.05 is critical level, in that case when minimum FS crosses the FS value 1, and then a warning can be issued. This warning can be issued 1h 30 min before the landslide event. Second type of warning is based on 5% percentile threshold value of national inventory. It shows, the 5th percentile threshold occurred at 1:00 PM 6th September. And considering FS 1.05 a critical level, in that case warning can be issued 2h 10 min before the landslide event.

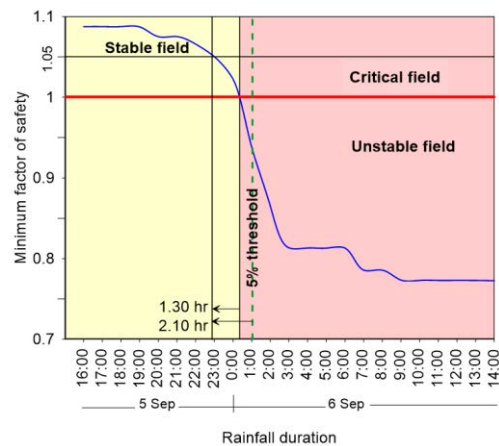


Fig. 7. Warning for landslide event

4. Conclusions

This research is based on a hypothesis “Past and present is key to the future.” Two extreme events were used in this research, one is 5.8 M_L Gyeongju earthquake and extreme rainfall event in 2005 September. Rainstorm and earthquake are significant landslide triggering agents in hilly landscape. The present model can be applied to calculate FS based on hourly rainfall in seismically affected hillslopes. The warning maps such as null, watch, attention and alarm maps were calculated on the basis of cutoff values of rainfall path and rainfall threshold warnings. The warning can be issued either 1h 30min (based on minimum FS) or 2h 10min (based on rainfall threshold warning levels) before landslide event. The outcome of the model can be used as a EWS to encourage local authorities and the population to monitor rainfall variation, such that the local population may be alerted to avoid or evacuate threatened area.

Acknowledgements

This work was supported by the Korean Institute of Energy Technology Evaluation and Planning (KETEP), the Ministry of Trade, Industry and Energy (MOTIE) of the Republic of Korea (No. 20171510101960) and the National Research Foundation of Korea (NRF) grant funded by the Korea government (2018R1A4A1025765).

References

- Aleotti, P., 2004, A warning system for rainfall-induced shallow failures: *Engineering Geology*, v. 73, p. 247–265, doi:10.1016/J.ENGGEOL.2004.01.007.
- Brunetti, M.T., Peruccacci, S., Rossi, M., Luciani, S., Valigi, D., and Guzzetti, F., 2010, Rainfall thresholds for the possible occurrence of landslides in Italy: *Natural Hazards and Earth System Science*, v. 10, p. 447–458, doi:10.5194/nhess-10-447-2010.
- Caine, N., 1980, The Rainfall Intensity - Duration Control of Shallow Landslides and Debris Flows: *Geografiska Annaler: Series A, Physical Geography*, v. 62, p. 23–27, doi:10.1080/04353676.1980.11879996.
- Chien-Yuan, C., Tien-Chien, C., Fan-Chieh, Y., Wen-Hui, Y., and Chun-Chieh, T., 2005, Rainfall duration and debris-flow initiated studies for real-time monitoring: *Environmental Geology*, v. 47, p. 715–724, doi:10.1007/s00254-004-1203-0.
- Dahal, R.K., and Hasegawa, S., 2008, Representative rainfall thresholds for landslides in the Nepal Himalaya: *Geomorphology*, v. 100, p. 429–443, doi:10.1016/J.GEOMORPH.2008.01.014.
- Dietrich, W.E., Reiss, R., Hsu, M. -L., and Montgomery, D.R., 1995, A process-based model for colluvial soil depth and shallow landsliding using digital elevation data: *Hydrological Processes*, v. 9, p. 383–400, doi:10.1002/hyp.3360090311.
- van Genuchten, M.T., 1980, A Closed-form Equation for Predicting the Hydraulic Conductivity of Unsaturated Soils1: *Soil Science Society of America Journal*, doi:10.2136/sssaj1980.03615995004400050002x.
- Glade, T., Crozier, M., and Smith, P., 2000, Applying Probability Determination to Refine Landslide-triggering Rainfall Thresholds Using an Empirical “Antecedent Daily Rainfall Model”: *Pure and Applied Geophysics*, v. 157, p. 1059–1079, doi:10.1007/s000240050017.
- Hee, K.Y., Kee, R.J., Tae-Seob, K., Minook, K., and Sang-Jun, L., 2016, The 12 September 2016 Gyeongju earthquakes: 1. Observation and remaining questions: v. 20, p. 747–752, doi:10.1007/s12303-016-0033-x.
- Iverson, R.M., 2000, Landslide triggering by rain infiltration: *Water Resources Research*, v. 36, p. 1897–1910, doi:10.1029/2000WR900090.
- Jakob, M., and Weatherly, H., 2003, A hydroclimatic threshold for landslide initiation on the North Shore Mountains of Vancouver, *British Columbia: Geomorphology*, v. 54, p. 137–156, doi:10.1016/S0169-555X(02)00339-2.
- Keefer, D.K., 2011, Toward the next generation of research on earthquake-induced landslides: Current issues and future challenges: *Engineering Geology*, v. 122, p. 1–8, doi:10.1016/J.ENGGEOL.2011.06.001.
- Kuriakose, S.L., Devkota, S., Rossiter, D.G., and Jetten, V.G., 2009, Prediction of soil depth using environmental variables in an anthropogenic landscape, a case study in the Western Ghats of Kerala, India: *Catena*, v. 79, p. 27–38, doi:10.1016/j.catena.2009.05.005.
- Lu, N., and Godt, J., 2008, Infinite slope stability under steady unsaturated seepage conditions: *Water Resources Research*, v. 44, doi:10.1029/2008WR006976.
- Malamud, B.D., Turcotte, D.L., Guzzetti, F., and Reichenbach, P., 2004, Landslides, earthquakes, and erosion: *Earth and Planetary Science Letters*, v. 229, p. 45–59, doi:10.1016/J.EPSL.2004.10.018.
- Matasovic, N., 1991, Selection of Method for Seismic Slope Stability Analysis, *in Proc., 2nd International Conference on Recent Advances in Geotechnical Earthquake Engineering and Soil Dynamics*, St. Louis, Missouri, University of Missouri--Rolla, p. 1057–1062.
- Mualem, Y., 1976, Hysteretical models for prediction of the hydraulic conductivity of unsaturated porous media: *Water Resources Research*, doi:10.1029/WR012i006p01248.
- Pradhan, A.M.S., and Kim, Y.T., 2014, Relative effect method of landslide susceptibility zonation in weathered granite soil: A case study in Deokjeok-ri Creek, South Korea: *Natural Hazards*, v. 72, p. 1189–1217, doi:10.1007/s11069-014-1065-z.
- Pradhan, A.M.S., Lee, J.-S., and Kim, Y.-T., 2018, Effect of spatial soil depth distribution model on shallow landslide prediction: a case study from Korean Mountain: 20th EGU General Assembly, EGU2018, Proceedings from the conference held 4-13 April, 2018 in Vienna, Austria, p.17502, v. 20, p. 17502, <http://adsabs.harvard.edu/abs/2018EGUGA..2017502S> (accessed September 2018).
- Richards, L.A., 1931, Capillary conduction of liquids through porous mediums: *Physics*, v. 1, p. 318–333, doi:10.1063/1.1745010.

Historical debris-flow occurrence in Rocky Mountain National Park, Colorado, USA

Sara L. Rathburn^{a,*}, Annette I. Patton^a, Eric L. Bilderback^b

^aDepartment of Geosciences, Colorado State University, Fort Collins, CO 80523-1482, USA

^bNational Park Service Geologic Resources Division, Lakewood, CO 80228, USA

Abstract

Debris-flow characteristics of initiation and runout are compared across the Continental Divide in Rocky Mountain National Park (RMNP), Colorado, USA to evaluate the influence of lithology, topography, and anthropogenic activities. Previous research indicates that 30 debris flows within the last century were large enough to transport sediment to valley bottoms and main stem channels and create new debris fans. Ten of the debris flows occurred on the east side of the Continental Divide and 20 on the west side. Those on the east side initiated after an extreme rainstorm in September 2013, whereas those on the west side occurred on the hillslope below an earthen ditch (12 flows) or on the natural hillslope (8 flows). Of those on the west side, four of the five largest debris flows initiated at the ditch. Comparing debris-fan area, transport distance, and elevation of initiation, we find greater variability in transport distance and elevation from east side debris flows, some of which entered alluvial channels and traveled >4 km under highly fluidized conditions. In contrast, the presence of the ditch on the west side limited the elevation of initiation, contributing area and hence, debris-flow transport distance. Lithologic differences between the east and west sides influences debris-supply conditions. On the east side, weathering-limited basins reduce source material and require a longer time to recharge convergent topographic source areas. Transport-limited hillslopes on the west side provide ample source material for debris flows, including till deposits and weathered volcanic rocks. Fan areas are comparable, and debris-flow morphology is generally similar across the Continental Divide. Recent anthropogenic and climatic disturbances, however, indicate that new patterns of debris-flow occurrence must be considered in the future. The increased occurrence of debris flows is an alert to park management who address hazards and risks to park staff, visitors and infrastructure. Furthermore, the high elevation of initiation for these modern debris flows expands the range of expected debris-flow hazards.

Keywords: Debris flows, sediment supply, anthropogenic disturbance

1. Introduction

Debris flows are part of the natural disturbance regime in mountainous landscapes that alter hillslopes and connect uplands to valley bottoms through processes of sediment transfer. In the semi-arid Rocky Mountains, large naturally occurring debris flows are primarily associated with wildfire (Cannon et al., 2001), surface runoff generated during extreme rainfall (Menounos, 2000; Godt and Coe, 2007; Coe et al., 2014), and rapid snowmelt (Brabb et al., 1989) that saturates hillslope materials. Anthropogenic causes of debris flows include overtopping or piping through earthen dams (Jarrett and Costa, 1984; Pitlick, 1993), and/or ditches (Clayton and Westbrook, 2008; Grimsley et al, 2016), and failures associated with road or building construction and maintenance (Highland, 2012). In Rocky Mountain National Park (RMNP), north central Colorado, USA (Fig. 1) both natural and anthropogenic debris flows have occurred historically and in the recent past. Research into debris-flow characteristics, both natural and human-induced

* Corresponding author e-mail address: sara.rathburn@colostate.edu

in RMNP, is important for an improved process-level understanding of debris flows and for hazard awareness and prediction.

Here we summarize the current literature on debris flows in RMNP and compare debris-flow characteristics across the Continental Divide in the park. Our main objective is to address how debris-flow attributes including fan area, transport distance, and elevation of initiation differ on east and west sides of the park. In addition, we address the management implications of debris flows in RMNP for hazard prediction in a changing climate, and with increasing annual visitors and mounting costs of maintaining park facilities and transportation infrastructure.

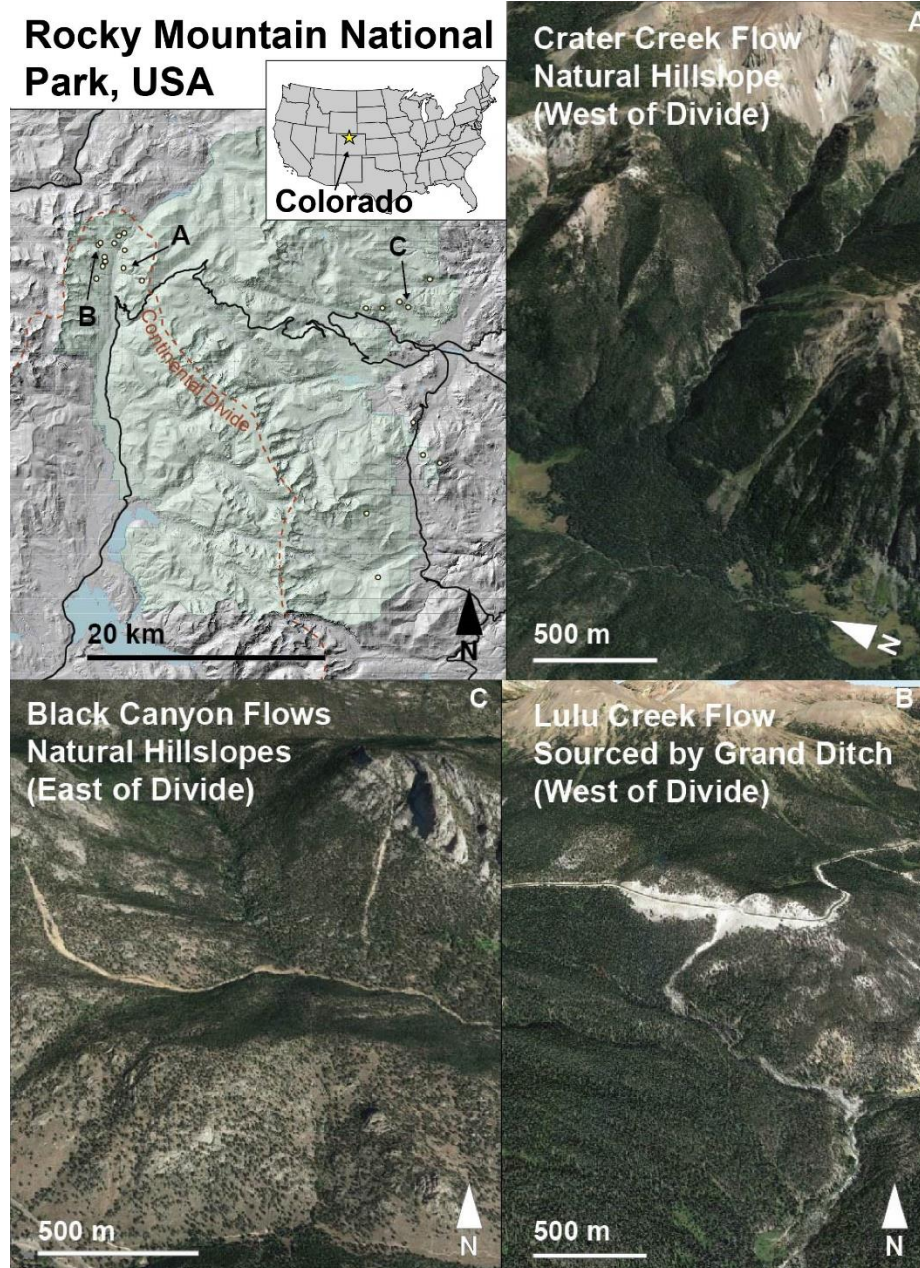


Fig. 1. Location map of the study sites on the east and west side of the Continental Divide in Rocky Mountain National Park, Colorado, USA (green shaded area). Dots indicate locations of historical debris flows addressed in this analysis. Google Earth images of debris flows within A) and B) the Upper Colorado River valley on the west side of the Continental Divide, and C) resulting from the September 2013 storms on the east side of the Continental Divide. Capital letters and arrows on the map show locations of debris flows in the Google Earth images and Grand Ditch on the west hillslope above the Colorado River.

1.1. Study Site

Rocky Mountain National Park in north central Colorado, is one of the top five-most visited parks in the US with over 4 million visitors annually (NPS; <https://irma.nps.gov/Stats/Reports/Park/ROMO>). Ranging in elevation from 2300 m in valley bottoms to >4000 m at the highest peaks, the park spans several geomorphic process domains (Montgomery, 1999; Wohl, 2010) and disturbance regimes that shape landscapes within the park. The Continental Divide bisects the park north to south (Fig. 1) and divides it into distinct geologic zones. The east side of the park is underlain primarily by Proterozoic Silver Plume Granite and biotite schist (Braddock and Cole, 1990). Quaternary surficial sediments include local alluvial, colluvial and glacial deposits. Pleistocene glaciation in the region contributed to over-steepened valley walls on both east and west sides of the Continental Divide (Madole et al., 1998). Active erosion by glacier ice was unlikely at the study sites on the east side; however, because they are outside of the maximum extent of Pleistocene glaciation (Madole et al., 1998). The Big Thompson and St. Vrain watersheds flow from mountainous regions in the park eastward to the plains of Colorado.

On the west side of the park, Tertiary volcanic rocks comprise a majority of the exposed bedrock with less biotite schist (Braddock and Cole, 1990). Within the headwaters of the Colorado River, the dominant lithologies are latite, rhyolite welded tuff, and undifferentiated volcanic rocks that are in places hydrothermally altered to bentonite. Till of Pinedale age mantles hillslopes below Grand Ditch, an unlined, earthen canal that brings water from the Colorado River basin across the Continental Divide to the Cache la Poudre basin (Fig. 1). Alluvial sediments fill the valley bottom of the Upper Colorado River basin.

2. Previous Debris-Flow Research

Some of the earliest work on debris flows in the Colorado Front Range is presented by Caine (1984) who qualitatively linked geomorphic processes to elevation. Working directly south of RMNP, Caine (1984) labeled the debris-flow hazard as “slight” at elevations between 2800 m and treeline (3350 m). In RMNP specifically, Menounos (2000) developed a Holocene debris-flow chronology from a high elevation lake (3320 m) on the east side of the Continental Divide. He used tephrochronology, radiocarbon dating, soil formation and lake cores to document 2800 years of debris-flow activity into Sky Pond. Also on the east side in RMNP, Patton et al. (2018) investigated the controls on debris-flow occurrence after an extreme storm in September 2013. The authors evaluated topographic properties, slope variables, and soil characteristics at 11 debris-flow sites and 30 undisturbed control hillslopes that received similar cumulative rainfall. On the west side of the divide, Grimsley et al. (2016) developed a debris-flow chronology for the Upper Colorado River valley to investigate the influence of failure of the 19th century earthen ditch on debris flow initiation, magnitude and frequency over the last century. A total of 20 debris flows were mapped and aged using dendrochronology, 12 on the hillslope below Grand Ditch, and 8 on the natural hillslope. In addition, Rubin et al. (2012) and Rathburn et al. (2013) assessed aggradation within the Upper Colorado River valley using shallow geophysics and radiocarbon dating, and channel response to a 2003 debris flow (Fig. 1), respectively, to understand the disturbance in the context of historical range of variability.

Herein, our summary of the current literature focuses on the work of Patton et al. (2018) and Grimsley et al. (2016) because both focused on inventorying debris flows large enough to descend to valley bottoms in RMNP (Table 1), affecting the geomorphology of trunk channels and valley floors in recurring patterns over the last century. In addition, their data provides sufficient sample sizes for a meaningful comparison east to west across the park. Finally, both studies evaluated the influence of lithology, topography, and anthropogenic disturbance, where possible.

We note that the time series of historical debris flows is biased toward high-frequency, low-magnitude events because large events tend to obliterate depositional evidence of earlier, smaller flows. In addition, the data set of historical debris deposits focuses on events that build fans which are preserved in the sedimentary record. We acknowledge that other debris flows have occurred for which we have no record. We present more specifics of the results on the east and west sides of the Continental Divide, and add a new analysis comparing debris-flow characteristics of fan surface area, transport distance, and elevation of initiation. Understanding the relative magnitudes, transport distances and initiation locations of debris flows will improve hazard expectations and mapping into the future.

2.1. East Side of Continental Divide in Rocky Mountain National Park

The field data collected by Patton et al. (2018) included measuring slope angle and categorizing slope morphology, mapping and surveying preserved surficial debris-flow deposits and erosional scars of flows that occurred during the September 2013 rainstorm in the Colorado Front Range. This study also evaluated exposure of previously buried stratigraphic layers, and analyzed ¹⁰Be in quartz from debris-flow boulders at one site to age the multiple levee-forming flows. Remote analyses included using raster data from a 10-m DEM and calculating contributing area and slope curvature. Results indicate that 10 debris flows large enough to transport sediment to valley bottoms resulted from the September 2013 storms. The authors found that 10 of the 11 mapped debris flows initiated from hillslopes that were south-, west- and east-facing. Patton et al. (2018) also noted that 8 of the 11 debris flows (73%) resulting from the September 2013 rainstorms initiated at sites of convergent topography and at >2800 m, unusually high elevation for debris flows in Colorado. This is contrasted against the >1100 debris flows that were triggered by the September 2013 storms, of which 95% initiated at elevations <2600 m (Coe et al., 2014). Additionally, the incidence of debris flows in areas of convergent topography, especially colluvial hollows, underscores the importance of local topographic controls on debris flow initiation on the east side of RMNP.

Table 1. Debris-flow study sites in Rocky Mountain National Park with measured geomorphic characteristics.

Site	Aspect	Contributing Area (km ²)	Lithology	Fan Area (m ²) ^a	Transport Distance (km) ^b	Elevation (m)	Source
East Side RMNP							
Mt. Meeker	East	0.05	Granite	13,339	4.35	3451	Patton et al. (2018)
North St. Vrain	East	0.46	Till; granite	0	0.74	2929	Patton et al. (2018)
Twin Sisters	West	0.01	Biotite schist	116,643	1.36	3081	Patton et al. (2018)
Cow Creek	South	0.002	Granite; biotite schist	10,355	0.45	2638	Patton et al. (2018)
Black Canyon North	South	0.001	Granite	8091	0.84	2903	Patton et al. (2018)
Black Canyon South	South-east	0.001	Granite	6252	1.09	2940	Patton et al. (2018)
Bighorn	South-east	0.001	Granite	4630	0.55	2747	Patton et al. (2018)
Lumpy Ridge	South-east	0.001	Granite	2156	0.42	2687	Patton et al. (2018)
Highway 7	East	0.002	Granite; biotite schist	0	0.38	2836	Patton et al. (2018)
Pierson Park	East	0.02	Biotite schist	30,363	3.81	3180	Patton et al. (2018)
Sky Pond	East	2.0	Biotite gneiss/schist	--	--	3320	Menounos (2000)
West Side RMNP^c							
<i>Below Grand Ditch</i>							
Specimen Cr West	East	0.30	Till; altered tuff	6813	0.28	3105	Grimsley et al. (2016)
Lady Creek	East	0.17	Altered tuff	3376	0.80	3105	Grimsley et al. (2016)
Lulu Creek	East	0.71	Altered tuff	5361	0.88	3105	Grimsley et al. (2016)
Sawmill Gulch	East	0.48	Till	4765	1.74	3105	Grimsley et al. (2016)
Little Dutch Creek	East		Till	6940	0.97	3105	Grimsley et al. (2016)
Misc. West	East	0.13	Till	2477-3993	0.77-0.87	3105	Grimsley et al. (2016)
Big Dutch Creek	East	0.35	Till	37,287	1.30	3105	Grimsley et al. (2016)
<i>Natural Hillslope</i>							
Little Yellow East	West	0.04	Altered tuff	12,131	0.39	3137	Grimsley et al. (2016)
Ellen's Tributary	West	0.63	Biotite schist	12,220	0.38	3048	Grimsley et al. (2016)
Misc. East	West	0.24	Biotite schist	2656-3873	--	--	Grimsley et al. (2016)
Crater Creek	West	3.67	Biotite schist	101,074	2.13	3296	Grimsley et al. (2016)

^a Ranges indicate the potential for multiple source areas contributing to fan deposition. All other fan areas represent single events.

^b Some transport distances and elevations on the west side of the Continental Divide are not available because initiation points on the natural hillslope were not readily identifiable in the field or in remote imagery.

^c 11 sites on the West Side of RMNP are listed, some of which show evidence of multiple debris flows, giving a total of 20 debris flows.

At one site with a 2013 debris flow (Bighorn, Table 1), evidence of multiple past events is preserved as linear debris-flow levees emanating from the same colluvial hollow. Although inheritance of ^{10}Be in debris-flow levee boulders was noted, Patton et al. (2018) concluded that four to seven debris flows occurred at that site within the last 75 ka, two of which occurred in the last 8 ka. Boulders sourced from adjacent rocky outcrops during periglacial processes associated with Quaternary glacial stages were likely transported via debris flow during subsequent wetter periods of the mid-Holocene.

2.2. West Side of Continental Divide in Rocky Mountain National Park

Field methods of Grimsley et al. (2016) included field mapping and surveying, using conifer dendrochronology to age debris flows, and aerial photographic interpretation. Results of that study indicate that 20 debris flows occurred on the west side of the Continental Divide in RMNP. Of these 20, 12 initiated on the east-facing hillslope below Grand Ditch, and the other 8 debris flows occurred on the west-facing natural hillslope. The authors found no substantial difference between debris flows on the hillslope below Grand Ditch versus the natural hillslope. Of the largest five debris flows; however, four originated on the hillslope below Grand Ditch, and all since 1937. Compared to previous work by Menounos (2000), who noted 1-5 debris flows on average in 16 centuries of record, the data on debris-flow frequencies from the west side suggest that the ditch has altered the debris-flow activity in the Colorado River headwaters. These findings are in agreement with Rubin et al. (2012) in an analysis of aggradation rates in an adjacent wetland. Ground penetrating radar surveys and radiocarbon analyses of sediment in the Lulu City wetland (Fig. 1) indicate increased aggradation through increased frequency of debris flows over the last two centuries of human intervention (Rubin et al., 2012).

Grimsley et al. (2016) concluded that valley bottom geometry of the Colorado River is the dominant control on response to debris flows, influencing sediment aggradation in debris fans and the persistence of debris-flow deposits. They found that sediment reaching the main stem Colorado River is transported through more confined valley reaches and retained forming persistent bars where valley geometry widens abruptly.

3. Controls on Debris-Flow Characteristics

Transport distances of debris-flow material are influenced by topography below the initiation site and downslope entrainment of sediment. For example, transport may be either halted or facilitated by entering existing channels. Where debris flows enter channels at acute angles they grow in size by entraining channel alluvium and following the path of the channel. Where debris flows enter channels at near-perpendicular angles or meet low-gradient valley bottoms, the flow path may be truncated (Guthrie et al., 2010, Patton et al., 2018). Debris sediment supply and the rate of hillslope and/or channel recharge also controls debris-flow magnitude and frequency (Bovis and Jakob, 1999). Here we use debris-fan surface area as a proxy for event magnitude, and couple it with transport distances and initiation site to address attributes of the 30 debris flows inventoried in RMNP.

Comparing east and west debris-flow fan areas, transport distances, and elevation of initiation (Fig. 2) indicates greater variability in transport distance and elevation for east side debris flows compared to west side ones. The longest transport distances, associated with debris flows from Mt. Meeker and Pierson Park, 4.3 and 3.8 km, respectively, were highly fluidized and entered existing channels, increasing the supply of sediment and providing a low-resistance flow path down the channel. In addition, east side debris flows initiated at elevations ranging from ~2700-3450 m. The much smaller transport distances and limited range of elevations (3105 m) on the west side are due to the presence of Grand Ditch on the hillslope above the Colorado River limiting the contributing area and hence, the transport distance. Twin Sisters on the east side was the largest fan area measured for all 30 debris flows. This debris-flow fan resulted from an abundance of fluidized sediment on the hillslope and formed as the steep, source hillslope transitioned to the lower-gradient valley bottom. Fan areas are similar, however, on the east and west side of the Continental Divide, with the largest exceeding 100,000 m².

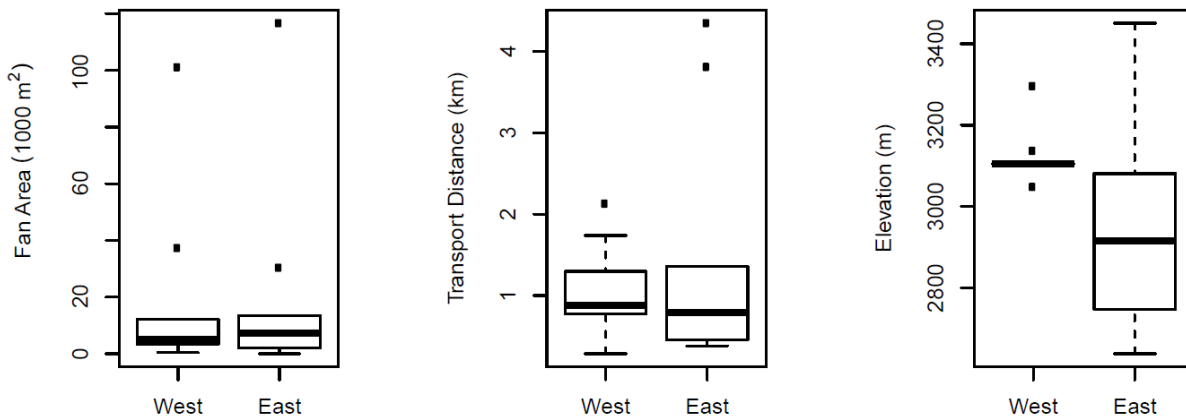


Fig. 2. Comparison between fan area, transport distance and elevation of debris flows on the east and west side of the Continental Divide in Rocky Mountain National Park. Heavy black horizontal line is the median value, end lines are the upper and lower quartiles, whiskers are maximum/minimum values in the population or the distance that is 1.5x the interquartile range, whichever is closest to the median. Dots represent values in the tail of the distribution beyond that distance.

4. Discussion

Clear differences exist between controls on debris-flow initiation east and west of the Continental Divide in RMNP including lithology, slope and channel morphology, and the presence of Grand Ditch. Lithologic differences influence the supply and erodibility of material available to be entrained in debris flows. The supply of sediment on the east side can be considered weathering limited due to the more resistant, unaltered crystalline bedrock, and slower sediment production rates on hillslopes. On the west side, debris-flow occurrence is transport limited due to rapid sediment production from the highly weathered volcanic rocks and thick deposits of till on hillslopes below Grand Ditch.

Differences in slope morphology on either side of the Continental Divide include the hillslope-valley bottom slope transition. This transition influences whether or not debris fans are deposited, and their size, at the base of hillslopes. In an analysis along an interstate corridor in Colorado, Coe et al. (2003) found that debris flows occur frequently on fans at the mouths of basins with steep slopes that transition to a low-slope channel. All of the debris flows evaluated in the Grimsley et al. (2016) study along the Colorado River demonstrated clear fan development where channels reached the low-gradient valley bottom. Hillslope morphology where debris flows occurred on the east side of the divide is more variable, with some flows delivering sediment to broad glacial valleys and some flows occurring entirely in steep fluvially incised valleys.

Despite these known differences in debris-flow initiation and deposition processes, debris-flow morphology is generally similar across the Continental Divide and varying levels of anthropogenic disturbance. Median fan area, transport distance, and elevation are not distinguishable for debris flows on the east and west sides of the Divide. Flows on the east side of the Divide; however, demonstrate a greater range of variability in both transport distance and elevation due to occurrence on hillslopes with diverse topography. Despite the abundance of till and highly weathered bedrock, fan area on the west side is comparable to the east side.

All of the 30 debris flows categorized here initiated at elevations greater than 2650 m. Including the region outside of RMNP, Coe et al. (2014) found that 95% of flows that occurred during the September 2013 storm initiated in canyons and on hogbacks at elevations lower than 2600 m. Flows with the largest scars and longest travel distances occurred at elevations above 2600 m on steep slopes with contributing areas >3300 m².

Although debris-flow regimes are likely to change in the upcoming decades, some aspects of the current and future debris-flow hazard in RMNP can be broadly characterized. On the east side of the Divide, colluvial hollows and channels that contributed sediment in 2013 have been deeply scoured, removing much of the loose material available for debris flows. Refilling of the same colluvial hollows may not take place on a human time scale unless the climate mechanisms that drive sediment sourcing and failure change. Thus, future debris flows may not initiate in the same locations or at high recurrence intervals. Other channels that did not scour; however, may show near-term activity.

Based on previous findings, debris flows of various magnitudes and frequencies are likely to continue to initiate at Grand Ditch, under the current ditch conditions, operation and management. Four of the five largest debris flows mapped on the west side initiated at Grand Ditch (Grimsley et al., 2016). The role of ditch operations and presence of hydrothermally altered rock on both sides of the valley is hard to separate, however. On the scale of recent geologic time, based on the last 4000 years of valley aggradation (Rubin et al., 2012), debris flows are frequent events. Even on a human scale, the debris flows might be considered typical, given that the last one occurred in 2003, with four additional large debris flows in the previous seven decades (2003-1937). Although the magnitude of flows on the west side is somewhat limited by the contributing area below Grand Ditch, the frequency of these events allows for significant impact to the morphology and ecology of the Upper Colorado River valley.

5. Implications for Future Management

On both sides of the Continental Divide, the increased incidence of debris flows over the last century in RMNP may be an alert to park staff who address hazards and risks posed to visitors. Even if widespread debris flows appear infrequent on human timescales, public awareness of debris flows is typically low so the consequences of debris flows may be greater than in areas with shorter return periods (Coe et al., 2014). As a federal agency with large holdings of land in the western US, awareness within the NPS of the infrastructure risk and risk to visitors in mass movement-prone areas appears to be growing. In some parts of the western US, the NPS is taking an active role in preparing for landslides as a result of climate change (Coe, 2016). Increased frequency of intense rainstorms (Klos et al., 2014), as well as increased fire intensity, frequency and extent (Abatzoglou and Williams, 2016) may increase landslide frequency in the coming decades. Active measures to respond to increased debris-flow risk include changes to new road construction to avoid areas of elevated landslide hazard, drainage improvements, visitor education, and planning for higher maintenance costs. Proposed changes for trails include managing drainage, stabilizing slopes, and restoring vegetation cover. Where possible, to mitigate debris-flow hazards, future construction should avoid existing debris fans. Where infrastructure already exists on debris fans, removal or protection of facilities should be considered.

Hazards to people and infrastructure are fundamentally similar on both sides of the Continental Divide, although some differences in process and setting may call for slightly different considerations. Specifically, higher population density and visitation on the east side of the park increases risk from debris flows, despite low event frequency. The east side of the park receives a majority of annual visitors and has the bulk of buildings and infrastructure. The town of Estes Park, (population >6,000), adjacent to the eastern RMNP boundary, is a primary center of tourism. Debris flows on the east side of the Divide therefore pose greater hazards to people, buildings, and highways.

On the west side of the Divide, debris fans will continue to be areas of sediment persistence in addition to large bars deposited in wide valley reaches of the Colorado River. The persistence of sediment poses the potential for ongoing remobilization, whereby subsequent high river flows will entrain and transport sediment into sensitive downstream ecosystems and receiving waters, causing renewed deposition, high sediment loads, and possibly impaired water quality.

6. Conclusions

An inventory of previous research on debris flows in RMNP reveals that 30 debris flows large enough to descend to valley bottoms occurred within the last century, affecting the geomorphology of main stem channels and valley floors in recurring patterns. Of the 30, ten debris flows initiated at high elevations on the east side of the Continental Divide, and 20 occurred on the west side. Those on the east side initiated after an extreme rainstorm in September 2013. Of the 20 on the west side, 12 initiated on the hillslope below Grand Ditch, with four of the five largest since 1937. The other 8 debris flows occurred on the natural hillslope. Debris-fan areas are comparable across the Divide, but transport distance and elevation of debris flows are more variable on the east side, where some flows entered alluvial channels and traveled >4 km under highly fluidized conditions. In contrast, the presence of the ditch on the west side constrains the elevation of initiation, contributing area and hence, debris-flow transport distance (<2 km). Thus, the key differences that influence debris-flow characteristics across the Continental Divide include lithology, which influences sediment supply, slope and channel morphology including the hillslope transition to valley bottoms, and the presence of the earthen ditch. On the east side, weathering-limited basins produce less debris supply and require a longer time to recharge convergent topographic source areas. Transport-limited hillslopes on the west side provide

ample source material for debris flows. Increased occurrence of debris flows in RMNP is an alert to park staff members who address risk. Increased knowledge of areas susceptible to debris flow will allow NPS to take an active role in preparing for debris flows to protect park visitors and infrastructure. Elevations that were once considered too high for debris-flow occurrence are now fully within the range of elevations with debris-flow hazards, as indicated by the elevations of initiation for all 30 of the debris flows characterized.

Acknowledgements

We thank numerous RMNP and NPS staff for their assistance. Funding was provided by RMNP, NPS, Colorado State University, Geological Society of America, and the Purdue University PRIME Lab. Joseph Mangano assisted with data analysis, and Jason Kean and Kevin Schmidt provided useful comments on an earlier version of this paper.

References

- Abatzoglou, J.T., and Williams, A.P., 2016, Impact of anthropogenic climate change on wildfire across western U.S. forests, *Proceeds of National Academy of Sciences*, v. 113, p. 11770-11775, doi.org/10.1073/pnas.1607171113.
- Bovis, M.J., and Jakob, J., 1999, The role of debris supply conditions in predicting debris flow activity, *Earth Surface Processes and Landforms*, v. 24, p. 1039-1054.
- Brabb, E.E., Wiecezorek, G.F., and Harp, E.L., 1989, Map showing 1983 landslides in Utah: U.S. Geological Survey Miscellaneous Field Studies Map MF-2085, scale 1:500,000.
- Braddock, W.A., and Cole, J.C., 1990, Geologic map of Rocky Mountain National Park and vicinity, Colorado: U.S. Geological Survey, Miscellaneous Investigations Series Map 1-1973, scale 1:50,000.
- Caine, N. 1984, Elevation contrasts in contemporary geomorphic activity in the Colorado Front Range: *Studia Geomorphologica Carpatho-Balcanica*, v. 18, p. 5-31.
- Cannon, S., Bigio, E., Mine, E., 2001, A process for fire-related debris flow initiation, Cerro Grande Fire, New Mexico, *Hydrologic Processes*, v. 15, p. 3011-3023.
- Clayton, J., and Westbrook, C., 2008, The effect of the Grand Ditch on the abundance of benthic invertebrates in the Colorado River, Rocky Mountain National Park, *River Research and Applications*, v. 24, p. 975-987.
- Coe, J.A., 2016, Landslide hazards and climate change: A perspective from the United States *in* Ho, K., Lacasse, S., Picarelli, L., eds., *Slope safety preparedness for impact of climate change*, p. 479-523, doi: 10.1201/9781315387789-16.
- Coe, J.A., and Godt, J.W., 2003, Historical debris flows along the Interstate-70 corridor in Clear Creek County, Central Colorado, *in* Boyer, D.D., Santi, P.M., and Rogers, W.P., eds, *Engineering Geology in Colorado: Contributions, Trends and Case Histories*: Denver, Colorado, Association of Engineering Geologists Special Publication No. 15 and Colorado Geological Survey Special Publication 55, not paginated.
- Coe, J.A., Kean, J.W., Godt, J.W., Baum, R.L., Jones, E.S., Gochis, D.J., and Anderson, G.S., 2014, New insights into debris-flow hazards from an extraordinary event in the Colorado Front Range, *GSA Today*, v. 24, p. 4-10, doi.org/10.1130/GSATG214A.1.
- Godt, J.W., and Coe, J.A., 2007, Alpine debris flows triggered by a 28 July 1999 thunderstorm in the central Front Range, Colorado, *Geomorphology*, v. 84, p. 80-97.
- Grimsley, K.J., Rathburn, S.L., Friedman, J.M., and Mangano, J.F., 2016, Debris flow occurrence and sediment persistence, Upper Colorado River Valley, CO, *Environmental Management*, v. 58, p. 76-92, doi:10.1007/s00267-016-0695-1.
- Guthrie, R. H., Hockin, A., Colquhoun, L., Nagy, T., Evans, S. G., 2010, An examination of controls on debris flow mobility: Evidence from coastal British Columbia, *Geomorphology*, v. 114, no. 4, doi:10.1016/j.geomorph.2009.09.021.
- Highland, L.M., 2012, Landslides in Colorado, USA-Impacts and loss estimation for 2010: U.S. Geological Survey Open-File Report 2012-1204, 49 p.
- Jarrett, R.D., and Costa, J.E., 1984, Hydrology, geomorphology, and dam-break modelling of the July 15, 1982, Lawn Lake Dam and Cascade Lake Dam failures, Larimer County, Colorado, U.S. Geological Survey Open File Report 84-612, 107 p.
- Klos, P., Link, T., Abatzoglou, J., 2014, Extent of the rain-snow transition zone in the western U.S. under historic and projected climate, *Geophysical Research Letters*, v. 41, p. 4560-4568, doi: 10.1002/2014GL060500.
- Madole, R.F., VanSistine, D.P., and Michael, J.A., 1998, Pleistocene glaciation in the Upper Platte River Drainage Basin, Colorado, U.S. Geological Survey Map Series 2644, scale 1:500,000, doi:10.3133/i2644.
- Menounos, B., 2000, A Holocene debris-flow chronology for an alpine catchment, Colorado Front Range, *in* Slaymaker, O., ed., *Geomorphology, Human Activity, and Global Environmental Change*, Wiley, p. 117-149.
- Montgomery, D., 1999, Process domains and the river continuum, *Journal of American Water Resources Association*, v. 35, p. 397-410.
- National Park Service Visitor Use Statistics, Rocky Mountain National Park, <https://irma.nps.gov/Stats/Reports/Park/ROMO>.
- Patton, A.I., Rathburn, S.L., Bilderback, E.L., and Lukens, C.E., 2018, Patterns of debris flow initiation and periglacial sediment sourcing in the Colorado Front Range, *Earth Surface Processes and Landforms*, v. 43, p. 2998-3008, doi:10.1002/esp.4463.
- Pitlick, J., 1993, Response and recovery of a subalpine stream following a catastrophic flood, *Geological Society of America Bulletin*, v. 105, p. 657-670.
- Rathburn, S.L., Rubin, Z.K., and Wohl, E.E., 2013, Evaluating channel response to an extreme sedimentation event in the context of historical range of variability: Upper Colorado River, USA, *Earth Surface Processes and Landforms* v. 36, p. 391-406.
- Rubin, Z.K., Rathburn, S.L., Wohl, E.E., and Harry, D.L., 2012, Historic range of variability in geomorphic processes as a context for restoration: Rocky Mountain National Park, Colorado, USA, *Earth Surface Processes and Landforms*, v. 37, p. 209-222, doi.org/10.1002/esp.2249.
- Wohl, E.E., 2010, A brief review of the process domain concept and its application to quantifying sediment dynamics in bedrock canyons, *Terra Nova*, v. 22, p. 411-416.

Debris-flow initiation promoted by extension within a slow-moving landslide

Mark E. Reid^{a,*}, Dianne L. Brien^a

^aU.S. Geological Survey, 345 Middlefield Road, MS 910, Menlo Park, CA, 94025, USA

Abstract

The dynamics of slow landslide motion can predispose oversteepened and extended slide regions to debris-flow initiation. For more than 20 years, our real-time monitoring, combined with repeat high-precision GPS surveys, of the Cleveland Corral landslide complex, California, USA, reveals that debris flows initiate from slow-moving kinematic elements of this complex. Different slide elements move in different wet years, and all remain dormant in dry years. To explore controls on landslide-element kinematics, we use triaxial testing to define the critical state behavior of the landslide material, and use a large-diameter sampling ring to determine *in situ* material porosities in both extensional and compressional regions of the slide complex. Regions undergoing extension contain materials looser than their critical state, potentially aiding liquefaction and debris-flow mobilization from shallow, secondary slides. Although intense rainfall serves as a trigger for debris-flow initiation, slow deformation of the larger landslide promotes debris-flow formation by oversteepening toe and lateral margins and by preferentially extending, and effectively loosening, material in these steep regions.

Keywords: debris-flow initiation; slow-moving landslide; critical state soil mechanics; porosity; GPS; California

1. Introduction

Debris flows initiate from a variety of sources, such as the mobilization of large or small landslides (Iverson et al., 1997; Geertsema et al., 2006; Crosta and Frattini, 2008) or progressive entrainment of sediment during surface runoff (Hungri et al., 1984; Takahashi, 1991; Cannon et al., 2001; Berti and Simoni, 2005; Coe et al., 2008). Within a geomorphic terrain, past movement behavior is often interpreted as forecasting future behavior, i.e. terrain may be prone to either rapid debris-flow initiation or slow-moving landslide deformation. Yet some debris flows initiate from parts of pre-existing, slow-moving landslides (Morton and Campbell, 1974; Reid et al., 2003; Malet et al., 2004; Jibson, 2005; Malet et al., 2005).

In a variety of terrains, locally steep slopes and intense rain can promote debris-flow initiation from landslides when widespread failure and partial or complete liquefaction occur (Iverson et al., 1997). Materials properties, such as porosity and grain-size distribution, can control the propensity for soil to liquefy when sheared during failure. Pervasive soil liquefaction greatly reduces shear strength and thereby enhances debris-flow formation. The application of critical state soil mechanics provides a framework to evaluate the predilection for soils to contract or dilate during shear, when they rearrange to achieve a critical void ratio as a function of the imposed stresses (Schofield and Wroth, 1968; Wood, 1990; Houlsby, 1991). Soils with an initial void ratio (or porosity) greater (looser) than their critical state void ratio contract during shear, increasing pore-fluid pressures and aiding liquefaction. In experimental studies, contractive behavior has been shown to aid debris-flow mobilization from landslides (Iverson et al., 2000; Okura et al., 2002; Olivares and Damiano, 2007).

Field investigations that have attempted to correlate locally contractive (loose) soils with debris-flow initiation sites have obtained mixed results (Fleming et al., 1989; Anderson and Sitar, 1995; Gabet and Mudd, 2006; McKenna

* Corresponding author e-mail address: mreid@usgs.gov

et al., 2012). Although some sites were associated with contractive soil behavior, others were, at least initially, dilative. As sizeable slow-moving landslides advance downslope, their persistent deformation commonly creates areas of extension (stretching) and compression (shortening) within the slide mass (Baum and Fleming, 1991). Such behavior may thereby modify landslide bulk porosities in specific locations and make general characterizations difficult.

Here, we investigate the hypothesis that the dynamics of a slow-moving landslide can precondition regions of the slide to debris-flow initiation. In particular, we ask whether landslide extension with concomitant increases in material porosities can promote localized debris-flow mobilization from shallow secondary failures. To address this issue, we examine possible linkages between active slide movement and debris-flow initiation using greater than 20 years of displacement monitoring at the slow-moving Cleveland Corral landslide complex, California, USA (Fig. 1). We then use geotechnical testing and critical state soil mechanics to assess whether extensional and compressional regions within the slide complex create localized areas with materials that might contract upon shear failure and preferentially mobilize into debris flows.

2. Cleveland Corral Landslide and Debris-flow Characteristics

2.1. Landslide setting

The toe of the Cleveland Corral landslide complex is perched about 50 m above U.S. Highway 50 in the Sierra Nevada mountain range of California (Fig. 1). It is situated in a landslide-rich, 14 km-long highway corridor where more than 600 landslides have been mapped (Spittler and Wagner, 1998); this corridor follows the steep-walled, conifer-covered canyon of the South Fork of the American River. In this region, a strongly seasonal precipitation pattern exists, with most rainfall occurring November through March; summers are dry. The Cleveland Corral landslide complex has an elevation of approximately 1200 m, and snowfall is typically minimal and transient. Movement of most of the larger slides in this corridor, including the Cleveland Corral landslide, is episodic with reactivation of previously established failures. The landslides are dormant in the dry summer season and move only during a very wet winter and spring (with cumulative precipitation greater than the long-term annual average) – not every year. During exceptionally wet winter seasons, several of these slides have failed catastrophically and blocked the highway for multiple weeks (Kuehn and Bedrosian, 1987; Sydnor, 1997).

With a sinuous form about 450 m in length, the Cleveland Corral landslide complex consists of colluvium and older slide debris underlain by quartz mica schist and gneiss, near a contact with Cretaceous diorite (Spittler and Wagner, 1998). The colluvium is a clayey, silty sand containing 10-15% cobble-sized clasts of bedrock. The slide is a complex of mass movements; overall it is a series of contiguous earth slides (Cruden and Varnes, 1996) with internal scarps and toes, as well as secondary shallow slides and debris flows at the steeper lateral margins and toes of various earth slide components. Despite the overall extent of the slide, it is relatively thin with slip surfaces located in surficial materials above bedrock. Several shallow seismic surveys indicate a depth to bedrock of 5-10 m (Reid et al., 2003); shear rods we installed in the slide reveal active slip in different elements at depths of 3-5 m. Ground surface slopes vary between 10° and 30°, but locally steepen to over 40°.

2.2. Landslide movement

Following the catastrophic failure of the nearby (about 2 km upstream) Mill Creek landslide in 1997 that buried Highway 50 and temporarily dammed the South Fork of the American River (Sydnor, 1997), the U.S. Geological Survey (USGS) installed radio-telemetered real-time monitoring equipment on the Cleveland Corral landslide complex (Reid and LaHusen, 1998), which also has the potential to fail and bury the highway. Since 1997, current precipitation, movement, and groundwater conditions at the site have been available to the public (<https://www.usgs.gov/natural-hazards/landslide-hazards/science/us-highway-50-california>). In addition, we have performed annual, campaign-style, Global Positioning System (GPS) surveys of monuments located both on and off the slide. We used our own nearby GPS base station for static differential processing and obtained repeat year-to-year standard deviations of < 2 cm for stable monument positions. These survey data and associated notes on data collection and processing are available in a supporting USGS data release publication (Reid et al., 2019). Following wet seasons with landslide movement, we used kinematic GPS techniques to map recently active structural features visible on the ground surface.

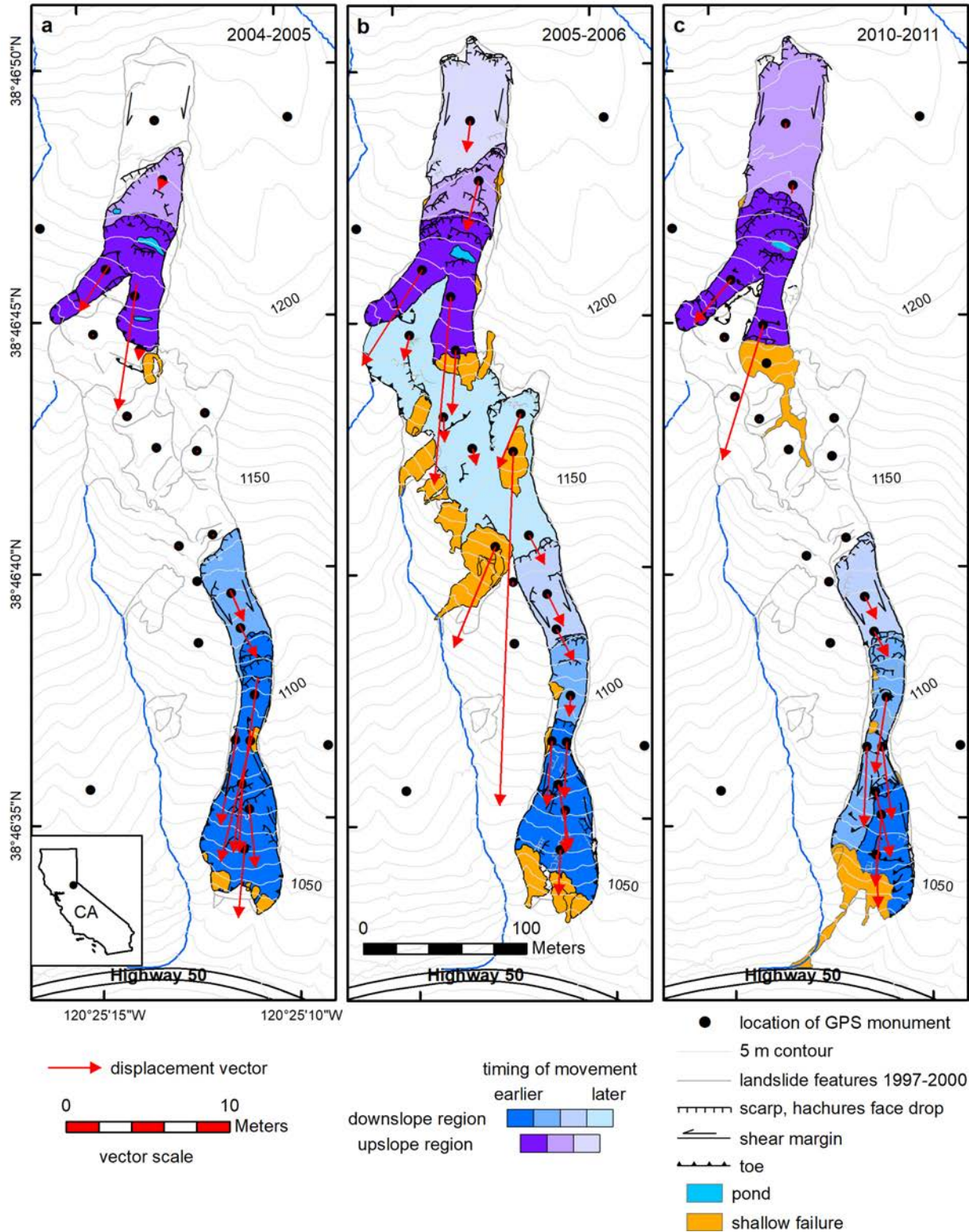


Fig. 1. Maps of the Cleveland Corral landslide complex showing active surface structures and kinematic elements during different wet years: (a) 2004-2005; (b) 2005-2006; (c) 2010-2011. Different elements are identified with different colors – blues for lower slide region, purples for upper. Elements with darker colors started moving earlier during the wet season, with movement typically progressing upslope into adjacent elements. Not all elements were active each year. Debris flows typically mobilized from shallow failures (orange) on the toes and margins of active elements. Displacement vector scale is 10X map scale.

Although the entire Cleveland Corral landslide complex has not failed catastrophically since our monitoring began in 1997, the combination of long-term real-time monitoring at specific locations with yearly overall displacement patterns has allowed us to correlate landslide movement with precipitation patterns. Various elements of the slide complex have moved during the wet seasons in 10 of the 21 years of monitoring. During the other years, all major slide elements remained dormant. Examples illustrating the differences in movement patterns for three water years when parts of the slide were active are shown in Figure 1. The slide complex consists of various kinematic elements that may move individually or in concert during a given wet year. In a wet season, certain elements typically move first – these include the overall toe (dark blue) and a mid-slide toe located in the upper section of the landslide (dark purple) (Fig. 1). Following initial movement, elements upslope and contiguous to the already moving elements may become active (lighter blues and purples), and additional activity may progress further upslope over several months. Depending on the wet season precipitation patterns, movement may be restricted to certain regions (Fig. 1a), although in a very wet season the entire slide complex can be active (Fig. 1b). When active, elements typically move at speeds of about 1-2 cm/day, but can range up to 20 cm/day. Even in active years, all elements cease motion by mid summer.

2.3. Debris-flow activity

Our monitoring has enabled us to identify conditions leading to debris-flow initiation from distinct parts of the overall slide complex. During above-average wet seasons, shallow (~0.5-1 m thick) debris slides (with typical volumes of about 5 to 400 m³) often occur at the margins and toes of active elements. These shallow slides originate along new failure surfaces, either within transported material forming the larger slide complex or at the lateral scarps in adjacent, previously unfailed materials. Intense rainstorms trigger these shallow slides, and the larger of these features occur within active elements of the main slide, either at the toes or debutressed margins (primarily on the western margin of the complex) – moreover, the larger of these shallow failures often mobilize into debris flows (Fig. 1). Smaller and less mobile slides may also occur along locally steep lateral margins in adjacent materials. Interestingly, minimal shallow sliding generally occurs at the toes or margins of dormant elements, even during relatively intense rainstorms.

Due to prolonged slide movement, the toes of the active slide elements become oversteepened compared to typical overall slopes of the larger landslide elements (Fig. 2). Although this oversteepening should predispose a toe region to shallow secondary failures, most of these shallow failures occur when the larger, encompassing slide element is also actively moving downslope.

3. Testing Methodology

To examine the hypothesis that an active landslide can selectively dilate slide materials and thus promote subsequent debris-flow initiation, we undertook a two-pronged approach. We first performed geotechnical testing to define the critical state line using materials from within the larger landslide. We obtained samples both in bulk and in thin-walled brass tubes (6.4 cm diameter by 15.2 cm tall) pushed into the floor of a shallow excavation of the lower toe in 2008 (see Fig. 2 for sample location 022808). These samples were collected at a depth of 0.65 m, similar to the depth of typical shallow debris slides that have occurred at the toe of the slide complex. The materials were subsequently tested in the University of California, Berkeley GeoEngineering Laboratories using both consolidated undrained (CU) and consolidated drained (CD) triaxial methods with saturated samples under a range of confining stresses (32-120 kPa) that represent shallow conditions. The seven CU tests used moist tamped specimens prepared to different porosities that were subsequently sheared to critical state. Our three CD tests used *in situ* specimens extruded from the thin-walled tubes. For both types of tests, we computed critical state porosities at 12% axial strain representing sheared conditions. In our results (Fig. 3), we present the critical state line relating principal stress to material porosity, rather than void ratio, to allow ready comparison with field-derived porosity values.

We then performed field characterization to determine *in situ* landslide porosities in regions exhibiting local compressional (e.g. internal thrusts) or extensional (e.g. tension cracks) surfaces features, all within the toe area of the overall slide (see Fig. 2 for locations). We were interested in bulk porosities representative of regions (on the scale of small, shallow landslides) that could mobilize into debris flows. Conventional geotechnical tube samples, however, cannot fully capture the larger-scale effects of localized thrusting or cracking. We opted for a protocol capable of assessing the porosity of a larger sample using a ring-excavation method (Grossman and Reinsch, 2002). At each sample site, we excavated surface material to a depth of approximately 10-30 cm and then carefully pushed

or lightly tapped a 24.8 cm diameter stainless steel ring into the underlying slide material. We used a micrometer to measure the depth (relative to a small shelf placed across the upper edge of the steel ring) of the exposed material surface, collecting 33 depth measurements in a radial grid pattern. Then, we excavated and retained material from within the ring (typically 3000-4000 cm³), and remeasured the post-excavation upper surface using the same grid pattern. From this, we could derive precise volumes for the excavated materials using radially weighted differences between surface measurements. The excavated materials were dried and weighed in the lab. Using dry weights and volumes, with a particle specific gravity of 2.7, we computed material porosities. We collected extensional samples (near surface tension cracks) during spring 2011, when the toe area had been recently active. Additional compressional samples (near thrusts) were collected in spring 2012, when the toe element was dormant.

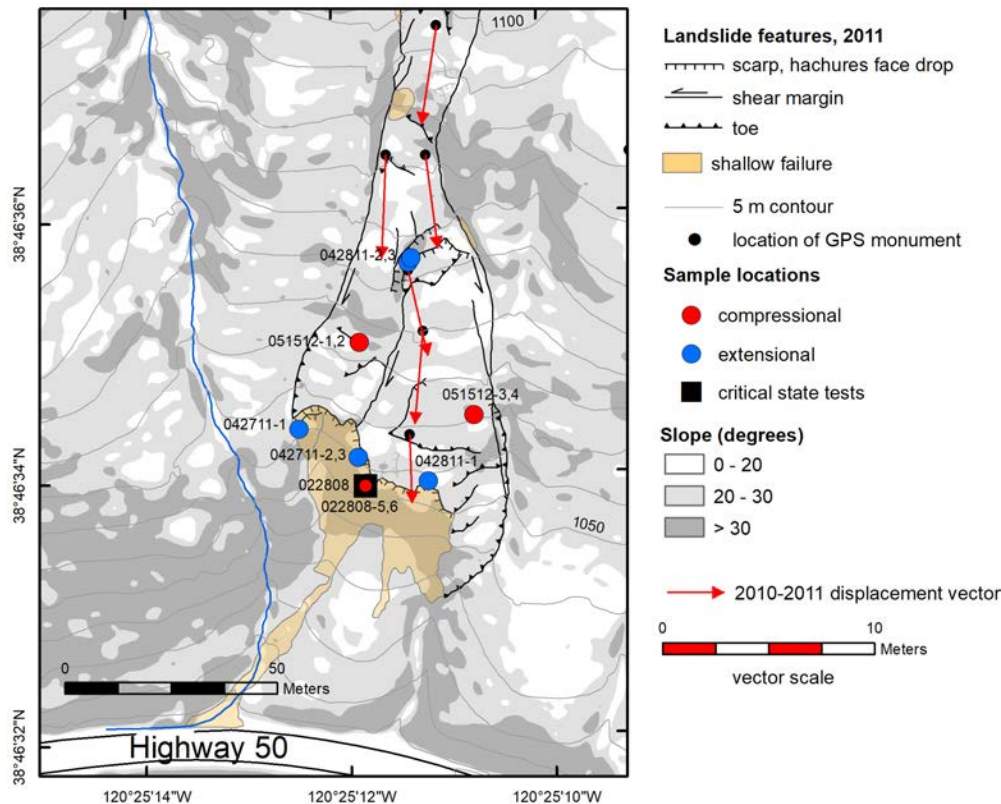


Fig. 2. *In situ* porosity locations at the toe of the Cleveland Corral landslide complex, categorized by nearby extensional or compressional surface structures. Surface structures shown as mapped during spring 2011; in some places, shallow failures mobilized into debris flows. Samples labeled with 022808 prefix were collected in 2008, prior to renewed activity in 2011. Vector displacement scale is 5X map scale.

4. Results

In Figure 3, we show our measured critical state line for toe landslide material using principal stress versus porosity during shear from both CU and CD triaxial tests. During our triaxial tests, materials with initial porosities higher (looser) than critical contracted during shear; those with initial porosities lower than critical (denser) dilated during shear. We also show *in situ* porosities determined by the ring-excavation method at different locations in the toe region (Fig. 2). For each location, we estimated likely *in situ* principal stress using sample depth, local slope, and saturated unit weight. Because sample depths were near the ground surface, we assumed that failure-appropriate principal stresses were oriented normal to the local ground slope.

The results for *in situ* porosities fall into three groups: looser than, near, and denser than the critical state line. The toe region is a complex of deforming landslide sub-elements with local surface expressions of extension (tension cracks) and compression (internal toes and thrusts) as shown in Figures 1 and 2. Sites with measured porosities greater (looser) than critical occurred near extensional features (Fig. 2), in particular these sites were located immediately upslope from the small headscarps of previous shallow slides. In preceding years, many of these

shallow slides mobilized into small debris flows (for examples, see Fig. 1). In contrast, sites with measured porosities lower (denser) than critical occurred near compressional features, in particular near the base of toes or just upslope of internal thrusts (Fig. 2). Nevertheless, some of these compressional sites, as well as several extensional sites had porosities near critical conditions for the given low principal-stress regime. Porosities near critical imply that minimal contraction or dilation would occur upon shearing; therefore, resultant pore-pressure increases or decreases that would enhance or impede motion would be less likely.

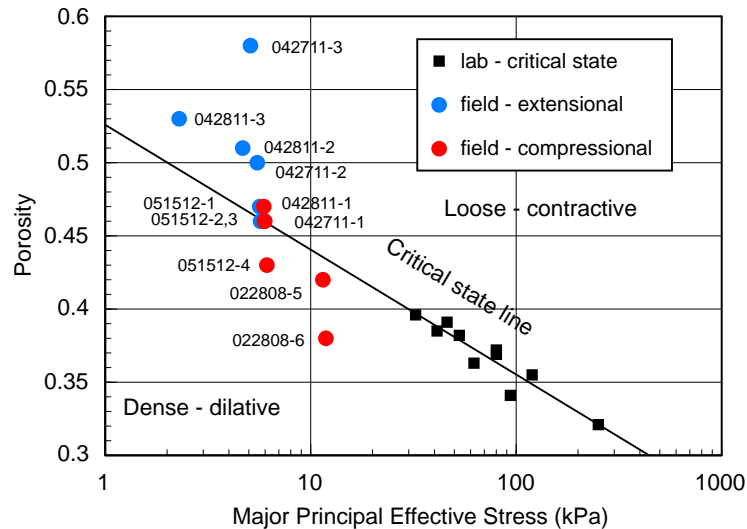


Fig. 3. Critical state line and *in situ* field porosities measured from the Cleveland Corral landslide complex toe region. Porosity values were collected near both extensional and compressional surface features. Materials looser than (above) the critical state line contract upon shearing and thus may aid liquefaction and reduce shear strength. Critical state line defined by CU and CD triaxial tests performed using low confining stresses readily achieved in the laboratory.

5. Concluding Discussion

Observations from 21 years of monitoring at the Cleveland Corral landslide complex indicated that debris flows mobilized from small, shallow, first-time failures on the topographically oversteepened toes and lateral margins during intense rainstorms (for examples, see Figs. 1 and 2). This association follows the precept that steep, wet ground promotes debris-flow mobilization from landslides (Iverson et al., 1997). However, not all shallow failures triggered during these rainstorms mobilized into flows – many small toe failures and those originating from scarps in adjacent areas on the lateral margins did not mobilize.

In addition to the spatial correlation with locally steep slopes, the largest shallow failures, with accompanying debris flows, occurred when encompassing kinematic elements of the Cleveland Corral landslide complex were actively moving downslope. This association implies that debris-flow mobilization from this slow-moving landslide complex required more than just steep and wet ground. Landslide movement can instigate spatial variations in stress patterns within slide materials, and thus may aid localized shallow failure. Our *in situ* porosity determinations indicated that looser materials occurred preferentially in regions of ground-surface extension, typically in the upper regions of steep active toes or lateral, debuttressed margins. These extensional regions resulted from dynamic slide movement and therefore could vary over time. Loose materials have the propensity to contract upon shear, generate elevated pore-water pressures, promote widespread liquefaction beyond an initial shear surface, and thereby potentially facilitate debris-flow mobilization.

Active slide motion can promote debris-flow initiation through several processes – oversteepening of toes and lateral margins, as well as stretching or extending materials (to an overall condition looser than critical state) within the slide. The topographic oversteepening promotes shallow failures, whereas the extension produces materials that can contract upon shear failure and thereby promote material liquefaction. These combined processes create select areas that are prone to debris-flow mobilization during intense rainstorms, even as the overall larger landslide maintains slow movement.

Acknowledgements

Monitoring of the Cleveland Corral landslide complex was conducted in cooperation with the Eldorado National Forest. Richard LaHusen (USGS) was instrumental in developing the real-time monitoring system deployed at the slide. We thank Michael Riemer (University of California, Berkeley) for performing the laboratory triaxial testing and Charlotte Wirion for field assistance in obtaining *in situ* porosities. Brian Collins (USGS), Nancy Calhoun (Oregon Department of Geology and Mineral Industries), and an anonymous reviewer helped improve the manuscript. Any use of trade, firm, or product names is for descriptive purposes only and does not imply endorsement by the U.S. Government.

References

- Anderson, S.A. and Sitar, N., 1995, Analysis of rainfall-induced debris flows, *Journal of Geotechnical Engineering*, v. 121, no. 7, p. 544-552, doi: 10.1061/(ASCE)0733-9410(1995)121:7(544).
- Baum, R.L. and Fleming, R.W., 1991, Use of longitudinal strain in identifying driving and resisting elements of landslides, *Geological Society of America Bulletin*, v. 103, no. 8, p. 1121-1132.
- Berti, M., and Simoni, A., 2005, Experimental evidences and numerical modelling of debris flow initiated by channel runoff, *Landslides*, v. 2, p. 171-182, doi: 10.1007/s10346-005-0062-4.
- Cannon, S.H., Kirkham, R.M., and Parise, M., 2001, Wildfire-related debris-flow initiation processes, Storm King Mountain, Colorado, *Geomorphology*, v. 39, p. 171-188, doi: 10.1016/S0169-555X(00)00108-2.
- Coe, J.A., Kinner, D.A., and Godt, J.W., 2008, Initiation conditions for debris flows generated by runoff at Chalk Cliffs, central Colorado, *Geomorphology*, v. 96, p. 270-297, doi: 10.1016/j.geomorph.2007.03.017.
- Crosta, G.B. and Frattini, P., 2008, Rainfall-induced landslides and debris flows, *Hydrological Processes*, v. 22, no. 4, p. 473-477.
- Cruden, D.M. and Varnes, D.J., 1996, Landslide types and processes, in Turner, A.K., and Schuster, R.L., eds., *Landslides: Investigation and Mitigation*, Volume Special Report 247: Washington, D. C., Transportation Research Board, p. 36-75.
- Fleming, R.W., Ellen, S.D., and Albus, M.A., 1989, Transformation of dilative and contractive landslide debris into debris flows - an example from Marin County, California, *Engineering Geology*, v. 27, p. 201-223.
- Gabet, E.J. and Mudd, S.M., 2006, The mobilization of debris flows from shallow landslides, *Geomorphology*, v. 74, p. 207-218, doi: 10.1016/j.geomorph.2005.08.013.
- Geertsema, M., Clague, J.J., Schwab, J.W., and Evans, S.G., 2006, An overview of recent large catastrophic landslides in northern British Columbia, Canada, *Engineering Geology*, v. 83, p. 120-143, doi: 10.1016/j.enggeo.2005.06.028.
- Grossman, R.B. and Reinsch, T.G., 2002, Bulk density and linear extensibility, in Dane, J. H., and Topp, G. C., eds., *Methods for Soil Analysis, Part 4, Physical Methods*: Madison, Wisconsin, Soil Society of America, p. 201-228.
- Houlsby, G.T., 1991, How the dilatancy of soils affects their behaviour, *Proceedings of the Tenth European Conference on Soil Mechanics and Foundation Engineering*, Florence, v. 4, p. 1189-1202.
- Hungr, O., Morgan, G.C., and Kellerhals, R., 1984, Quantitative analysis of debris torrent hazards for design of remedial measures, *Canadian Geotechnical Journal*, v. 21, no. 4, p. 663-677.
- Iverson, R.M., Reid, M.E., and LaHusen, R.G., 1997, Debris-flow mobilization from landslides, *Annual Review of Earth and Planetary Sciences*, v. 25, p. 85-138, doi: 10.1146/annurev.earth.25.1.85.
- Iverson, R.M., Reid, M.E., Iverson, N.R., LaHusen, R.G., Logan, M., Mann, J.E., and Brien, D.L., 2000, Acute sensitivity of landslide rates to initial soil porosity, *Science*, v. 290, no. 5491, p. 513-516, doi: 10.1126/science.290.5491.513.
- Jibson, R.W., 2005, *Landslide hazards at La Conchita, California*: U.S. Geological Survey, Open-File Report 2005-1067, 12 p.
- Kuehn, M.H. and Bedrosian, T.L., 1987, 1983 U.S. Highway 50 Landslide near Whitehall, El Dorado County, California, *California Geology*, v. 40, no. 11, p. 247-255.
- Malet, J.-P., Maquaire, O., Locat, J., and Rémaitre, A., 2004, Assessing debris flow hazards associated with slow moving landslides: methodology and numerical analyses, *Landslides*, v. 1, p. 83-90, doi: 10.1007/s10346-003-0005-x.
- Malet, J.-P., Laigle, D., Rémaitre, A., and Maquaire, O., 2005, Triggering conditions and mobility of debris flows associated to complex earthflows, *Geomorphology*, v. 66, p. 215-235, doi: 10.1016/j.geomorph.2004.09.014.
- McKenna, J.P., Santi, P.M., Amblard, X., and Negri, J., 2012, Effects of soil-engineering properties on the failure mode of shallow landslides, *Landslides*, v. 9, p. 215-228, doi: 10.1007/s10346-011-0295-3.
- Morton, D.M. and Campbell, R.H., 1974, Spring mudflows at Wrightwood, Southern California, *Quarterly Journal of Engineering Geology*, v. 7, no. 4, p. 377-384.
- Okura, Y., Kitahara, H., Ochiai, H., Sammori, T., and Kawanami, A., 2002, Landslide fluidization process by flume experiments, *Engineering Geology*, v. 66, no. 1-2, p. 65-78, doi: 10.1016/S0013-7952(02)00032-7.
- Olivares, L. and Damiano, E., 2007, Postfailure mechanics of landslides: Laboratory investigation of flowslides in pyroclastic soils, *Journal of Geotechnical and Geoenvironmental Engineering*, v. 133, no. 1, p. 51-62, doi: 10.1061/ASCE1090-0241(2007)133:1(51).
- Reid, M.E. and LaHusen, R.L., 1998, Real-time monitoring of active landslides along Highway 50, El Dorado County, California, *California Geology*, v. 51, no. 3, p. 17-20.
- Reid, M.E., Brien, D.L., LaHusen, R.L., Roering, J.J., de la Fuente, J., and Ellen, S.D., 2003, Debris-flow initiation from large slow-moving landslides, in Rickenmann, D., and Chen, C., eds., *Mechanics, Prediction and Assessment*: Proc. of the Third International DFHM Conference, Davos, Switzerland: Rotterdam, Millpress Science Publishers, p. 155-166.
- Reid, M.E., Brien, D.L., and Roering, J.J., 2019, Survey monument positions for the Cleveland Corral landslide near U.S. Highway 50, El Dorado County, California, U.S. Geological Survey data release, doi: 10.5066/P9X62EV3.
- Schofield, A.N. and Wroth, C.P., 1968, *Critical State Soil Mechanics*: New York, McGraw-Hill, 218 p.
- Spittler, T.E. and Wagner, D.L., 1998, Geology and slope stability along Highway 50, California, *California Geology*, v. 51, no. 3, p. 3-14.

- Sydnor, R.H., 1997, Reconnaissance engineering geology of the Mill Creek Landslide of January 24, 1997, *California Geology*, v. 50, no. 3, p. 74-83.
- Takahashi, T., 1991, *Debris Flow*: Rotterdam, A. A. Balkema, IAHR Monograph, 165 p.
- Wood, D.M., 1990, *Soil Behavior and Critical State Mechanics*: Cambridge, UK, Cambridge University Press, 462 p.

Regional level debris-flow hazard assessment for alpine infrastructure facilities using the 3D numerical high-performance simulation tool FIMT

Manfred Scheikl^{a,*}, David Powell^b

^{a,b}ALPINFRA/Canadian Hydrotech Corporation, 200 Burrard Street / P.O. Box 48600, Vancouver BC V7X 1T2, Canada

Abstract

Alpine infrastructure such as roads, railways, pipelines, powerlines and hydropower facilities, as well as alpine communities, are exposed to debris-flow hazards, rock-fall and snow avalanches. In most cases, debris-flows are rainfall induced and affect large areas, causing substantial financial and individual damages. Austrian infrastructure owners are maintaining approximately 5,000 km of railway tracks and at least 1,000 km of high priority highways which are exposed to debris-flow hazards. For assessing potential debris-flow impact along these infrastructure routes, the stand-alone physical-numerical based modeling tool **FIMT** (Flow Impact Modeling Tool) was developed in-house by ALPINFRA, which is applied on a 3D topography with a spatial resolution of 5x5m. The model is applied on a regional scale and areas with more than 3,000 km² were analyzed simultaneously. Debris-flows are highly dynamic, complex flow processes of multi-phase fluids with a constantly varying flow regime during single events and along flow paths. Many researchers, including Pudasaini et. al., 2005, Wang et. al., 2004 and Iverson, 1997, 2001, 2004 provide well developed physical approaches for single- and multi-phase fluids. The Mohr-Coulomb based friction model of Voellmy (1955) however, provides an acceptable and numerically implementable alternative, considering dry friction as well as hydraulic driven parameters. This approach was initially developed for snow avalanches and is now implemented in various debris flow and other rapid mass movement modeling software tools. Ahead of the implementation of the model for regional hazard assessments, ALPINFRA conducted calibration and parametric studies. These were done in test-regions and based on extensive field work, investigation of historical events and detailed numerical back analysis. Since 2013, all parts of the Austrian railway network exposed to debris-flow, major Austrian highways, as well as gas-pipelines and hydro power facilities have been analyzed with this tool as a basis for hazard and risk studies. For regional scales, simulation results have a comparatively high resolution (5x5m) and build a high-quality basis for hazard mapping, budgeting of mitigation measures and planning of detailed investigation projects.

"Keywords: debris-flows; infrastructure; high-resolution numerical modeling;"

1. Introduction

In Europe, the most important alpine infrastructures such as rail- and roadways were developed between the late 19th and the 20th century where the valuable valley floor was almost fully occupied by farmers for food production. Railroad and road routes were pushed to the valley flanks as far as possible. Limited space lead to a comparatively high development pressure and very remote areas were developed by roadways routed through very narrow valleys. The high relief energy from the steep topography throughout wide areas, as well as the climatic situation, resulted in a high hazard exposure of these structures. For several high alpine hydro-power facilities and the oil-pipelines crossing the Alps a similar hazard situation exists. For assessing the Austrian wide geo-hazard, steep-creek-hazard and snow-

* Corresponding author e-mail address: manfred.scheikl@alpinfra.com

avalanche-hazard exposure, an initial infrastructure hazard investigation program was started in 2010. This was mainly done by means of field investigation and analyzing event chronologies. Hazard maps were prepared on a super-regional level as well as at a rough scale of 1:25,000. In a second stage, more precise analyses were required for showing local hazard impact potential and deficits of protection. Therefore, high-performance hazard process modeling tools were developed for rock-fall, snow avalanches and debris-flows. The analyses were conducted on the 3D topography with a spatial resolution of 5x5m.

This paper describes this regional level debris-flow impact hazard assessment approach and the stand-alone 3D numerical debris-flow modeling tool **FIMT**, which was specifically developed in-house by ALPINFRA for investigations as described above.

2. Numerical Model Description

2.1. Rheology

For the rheological approximation of debris flows, the formulation of Voellmy (1955) was selected, which provides (a) the dry friction parameter μ , which rises with acting normal stresses according to $\rho \cdot g \cdot h$ and (b) a parameter for turbulence ξ , which lowers the overall flow resistance of a fluid particle linearly. The overall flow resistance according

to Voellmy (1955) is as follows:

$$S = \mu \rho H g \cos \phi + \frac{\rho g U^2}{\xi}$$

where:

- S = overall flow resistance [Pa]
- ρ = unite weight of the fluid [kg/m^3]
- g = gravitational acceleration [m/s^2]
- Φ = slope inclination [$^\circ$]
- H = flow depth [m]
- U = flow velocity [m/s]

2.2. Computation Model

The simulation tool FIMT computes the synchronous movement of single particles, each with a defined volume, by using the Voellmy rheology for calculating the flow resistance. The direction of movement is solved by means of a random walk algorithm (Révész, 1990) with side constraints. The release condition is that the most likely flow direction is oriented according to the topographic gradient. For computing the dynamic flow, the synchronous simulation of released debris flow particles allows for the consideration of temporary and spatially varying flow depth and flow velocity by means of the consideration of the momentum of the single particles at a discrete time step and location. The numerical solution fulfills the law of conservation of the mass, the momentum and energy. Deposition of particles is considered by means of a critical threshold value for the momentum for which a homogeneous fluid can be assumed. If the momentum falls below this yield value, decomposition of the fluid mix is assumed, and aggradation takes place. The release of particles is considered by means of a Mohr-Coulomb limit state stability approach. Output is generated as ASCII raster files for the maximum values, mean values, or selectable quantiles for the flow depth, flow velocity and dynamic pressure as well as for the deposition. Ahead of the calculation, a complex preprocessing procedure is required for generating the input files. The preprocessor uses a digital terrain model and preprocessing parameters such as the calculation domain, morphometric yield parameters and/or geologic mapping information for generating release areas. Single particles can be tracked for reproducing the traveling path when a particle impacts a section or point of interest, which can assist decisions requiring detailed investigations of release areas. Related release areas are highlighted according to their relevance. This is done based on a back-calculation or “back viewing” approach. The code was written in-house by ALPINFRA in C++ for usage on Linux platforms and optimized for computation performance that it can be used for very large areas.

2.3. Event Magnitudes

The release volume or magnitude is approached by means of morphometric parameters, hydrologic assessments, and is checked for plausibility based on empirical approaches provided by Zeller (1985), Takei (1980) and D'Agostino (1996). Investigated relationships between the size of hydrological catchments and debris-flow event magnitudes was summarized in IRASMOS (2011) as shown in Fig. 1. After a preprocessing stage the release map is visually checked by experts for plausibility based on LiDAR data.

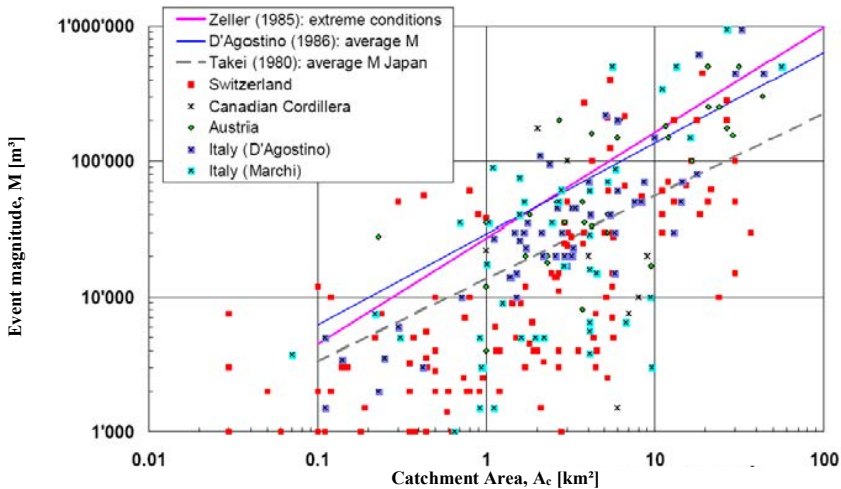


Fig. 1: Relationship between debris-flow magnitudes and size of hydrological catchments (IRASMOS 2011)

2.4. Parameterization

2.4.1. Discussion of Parameter Setting

Physical properties of entrained and released solids strongly influence the dynamical behavior of debris-flow and provides the basis for the selection of the rheological approach and its parameterization (Iverson, 1997, Rickenmann, 1999, Kaitna et al., 2007, Iverson et al., 2010). Fine-dominated solids will form fluids which can be reasonably described with a Bingham rheology compared to coarse-dominated source material which forms mixtures that can better be approached with a Voellmy rheology. The differential behavior of these mixtures is explained by the specific interaction of solid components with the fluid phase. The granular character of solids and the viscous behavior of the fluid-phase, as well as the influence of pore-water pressure, are approached by several rheological solutions (Wang et al., 2008, Bertolo und Wiczorek, 2005). However, implementation into a numerical model is sometimes not feasible and consequently, most of the available debris-flow models are based on the Voellmy approach (Wang et al., 2008).

Parameters discussed in the literature and listed in manuals of commercial software tools vary widely and match poorly with debris-flow characteristics. Therefore, a general test or bench mark test of every single simulation tool on a well-known example or synthetic topography should be conducted before application within hazard studies. It is also required to match parameter sets with sedimentological data from the source materials. Such assignments are normally not available in software tool manuals. The Swiss institute for snow and avalanche research (SLF) lists a general parameter range for debris-flow simulation using the Voellmy rheology as shown in Table 1.

Table 1: Voellmy parameter ranges for debris flows according to WSL 2012

Type of debris flow	Dry friction, μ	Turbulence, ξ
granular debris flows	0.05 - 0.40	100 - 200
muddy debris flows		200 - 1,000

Within a parametric study, Medina et. al. (2008) uses start parameters for back calculations in the Pyrenees which contain Cambrian and Ordovician marbles, phyllites and schists, as well as glacial deposits with $\mu = 0.065$ and $\xi = 100 \text{ m}^2/\text{s}$ and $400 \text{ m}^2/\text{s}$ respectively, which are within the range of the values provided by the SLF as listed in Table 1. Because these parameters did not give plausible results (Medina et. al., 2008), Medina et al. produced better matching results by using $\mu = 0.220$ and $\xi = 144 \text{ m}^2/\text{s}$. This selection gives a low turbulent flow at a considerably high portion of dry friction of approximately 12.5° . These parameters are roughly in line with those the SLF postulates for the back calculation of the Dorfbach (Randa, CH) debris-flow event (WSL, 2012).

2.4.2. Plausibility Test of Parameter Sets

Ahead of regional modelling, FIMT was tested for parameter settings and calibrated based on recorded events. Parameter sets were tested at well known debris-flow catchments in Ausserfern in Tyrol, Austria, between Reutte and the German border. The geological setting is limestone dominated and debris-flows have a comparatively granular appearance. The assignment of the magnitude volume for the parameter tests is based on D'Agostino (1996). The comparison of parameters demonstrated the plausibility of modeling results as well as the sensitivity for parameter variation. Fig. 2 to Fig. 7 show exemplary results for the maximum flow depth (h) maximum flow velocity (v) as well as the run out of modelled debris flows for different parameter sets.

The results show that the tool is generally producing reasonable results. As expected and according to the analytic check of the Voellmy term, a greater turbulence parameter reduces the overall flow resistance giving greater flow velocities. This effect would reflect a rising portion of fines in the fluid mix. A great number of other variations was checked for sensitivity and reasonable results were produced indicating the applicability of the introduced regional calculation tool.

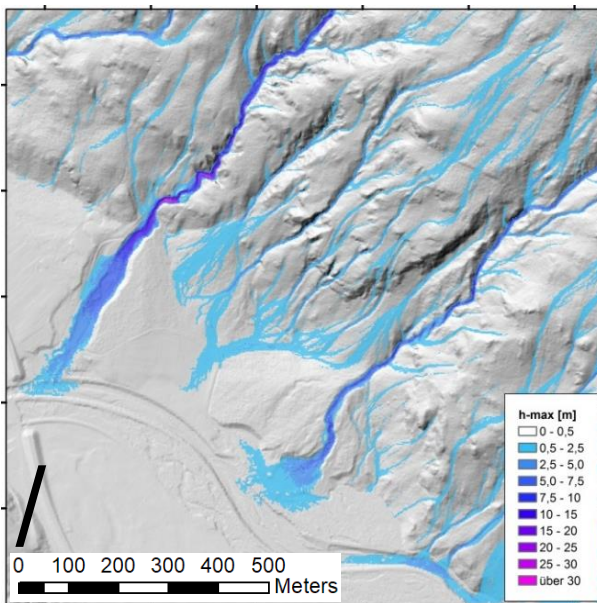


Fig. 2: Maximum flow depth for $\xi=250$ and $\mu=0.25$ in the test region in Ausserfern

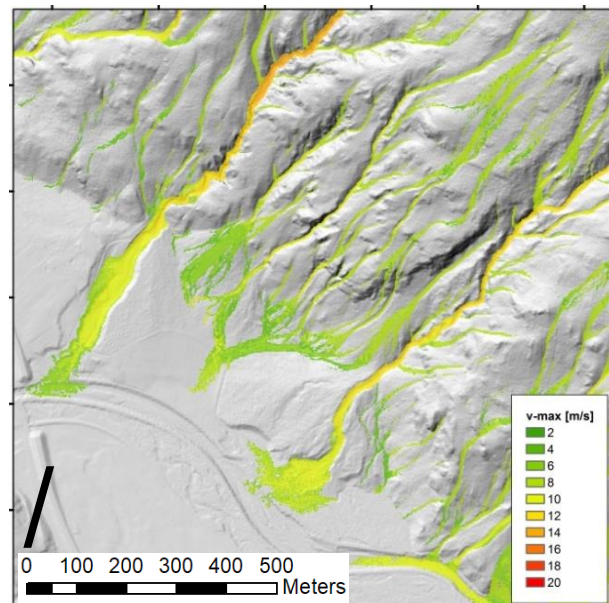


Fig. 3: Maximum flow velocity for $\xi=250$ and $\mu=0.25$ in the test region in Ausserfern

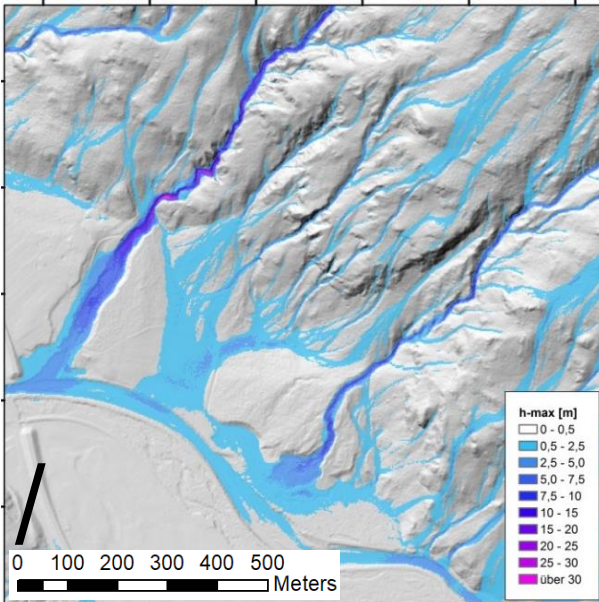


Fig. 4: Maximum flow depth for $\xi=600$ and $\mu=0.25$ in the test region in Auserfern

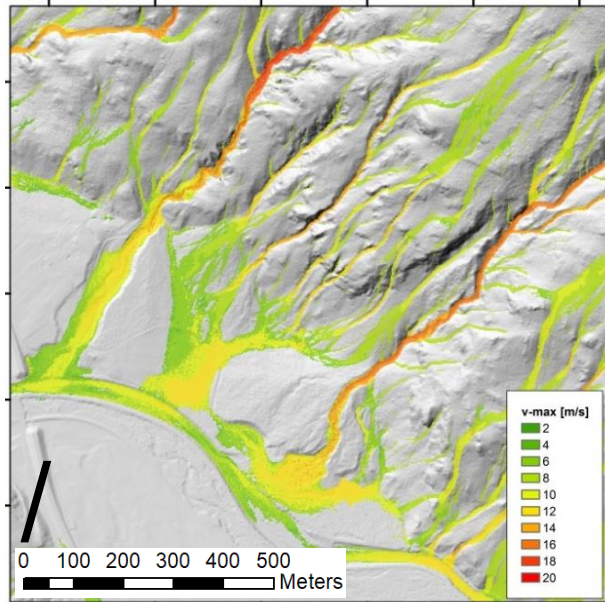


Fig. 5: Maximum flow velocity for $\xi=600$ and $\mu=0.25$ in the test region in Auserfern

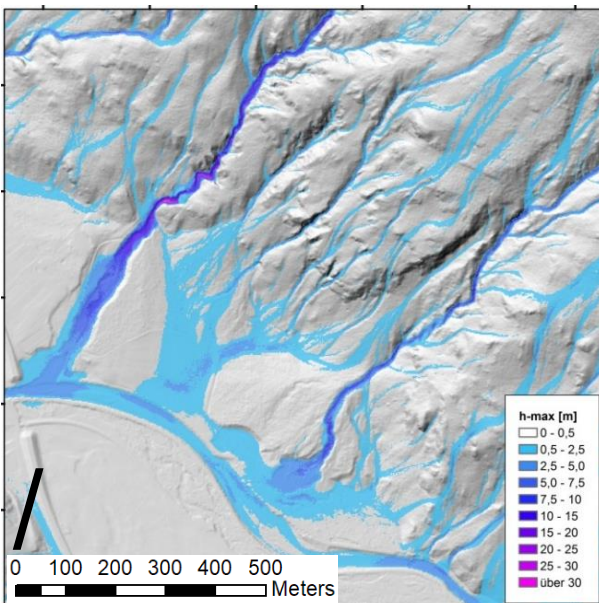


Fig. 6: Maximum flow depth for $\xi=1,000$ and $\mu=0.25$ in the test region in Auserfern

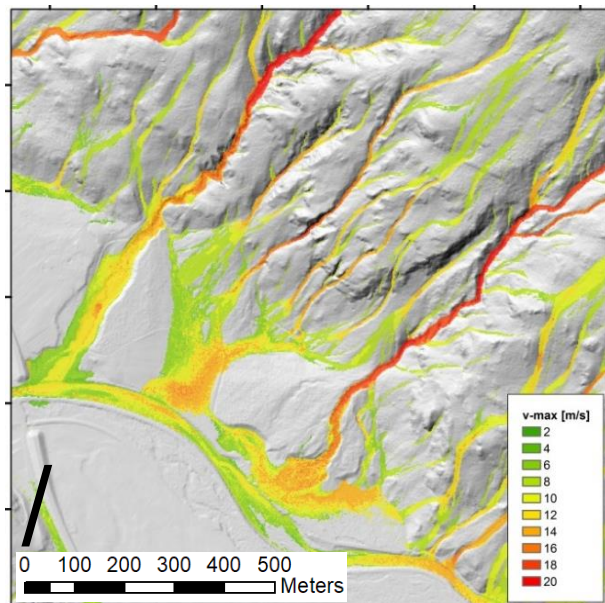


Fig. 7: Maximum flow velocity for $\xi=1,000$ and $\mu=0.25$ in the test region in Auserfern

3. Regional Application and Validation

For testing the applicability on the regional scale with relatively high spatial resolution of 5x5m, the entire alpine valleys Stanzertal and Klostersertal were analyzed simultaneously in 2012 with an overall extension of approximately 600 km². The overall computation time for 4 scenarios with annual exceedance probabilities (AEP) of 30 – 50 years, 50 -100 years, 100 – 300 years and a probable maximum debris-flow (PMDF) was approximately 24 hours on a multi-processor workstation normally used for 3D computational fluid dynamics (CFD) calculations. Calculation results were compared with data from event chronologies which have been investigated by the federal forest research center at the town of Innsbruck within the so-called Paramount research project in 2012. Fig. 8 shows the computed debris-

flow impact map of the Stanzertal valley. Fig. 9 shows details of a subset of the same region, where events occurred, and flow heights were recorded, are highlighted by red stars. Comparing the location of all recorded events with the computed map gives a 100% accordance in the sense that all documented events are correctly indicated by the computed debris flow impact locations. Comparing the computed event magnitudes, a good accordance regarding the maximum flow height calculated to measurements taken at culverts during debris-flow events is given. Events recorded in October 30 and 31, 2018 and on June 11, 2016 as shown in Fig. 10 and Fig. 11 demonstrate the very good accordance between computed impact locations and recently recorded impacts.

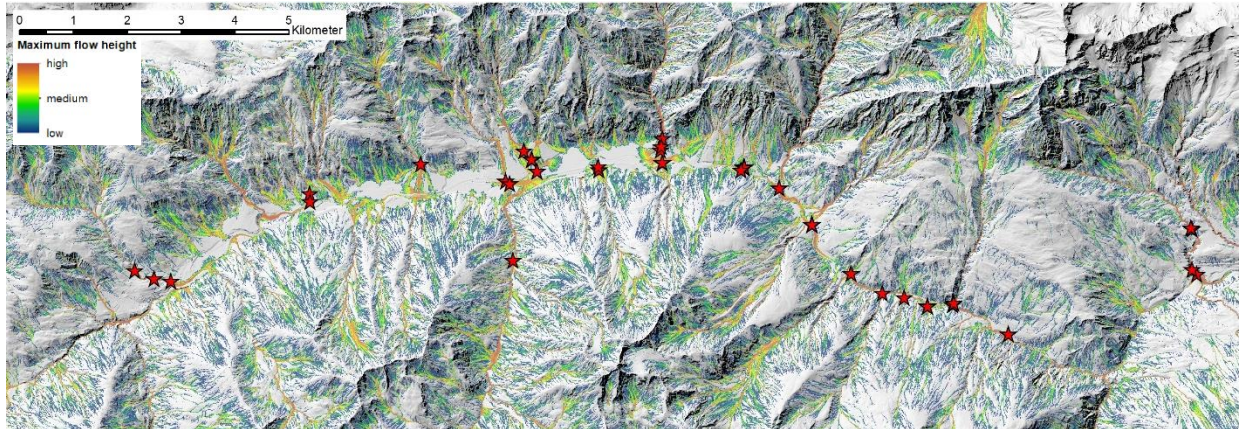


Fig. 8: Computed debris flow impact map (flow height) and recorded impact events which are indicated with red stars.

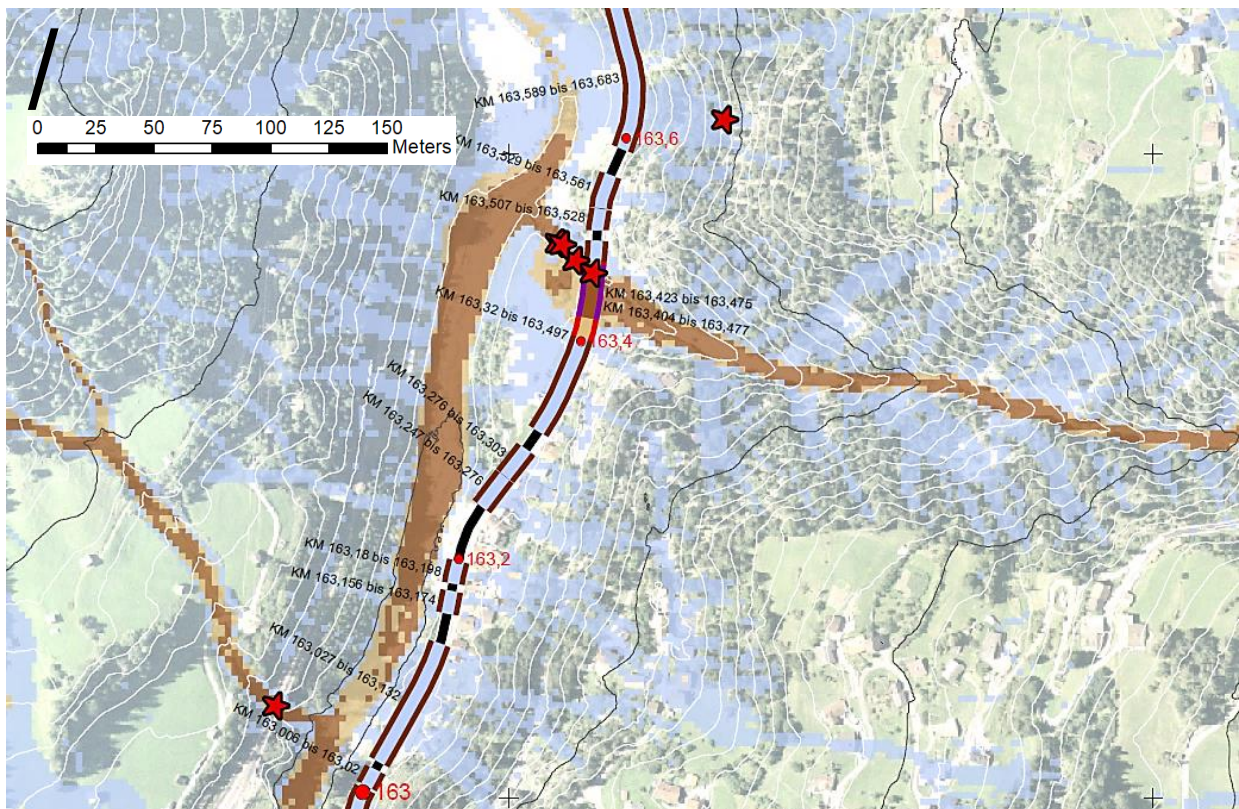


Fig. 9: Detail of computed debris flow impact map at the Stanzertal valley (brown indicates a debris flow, blue a flow with bed load content)

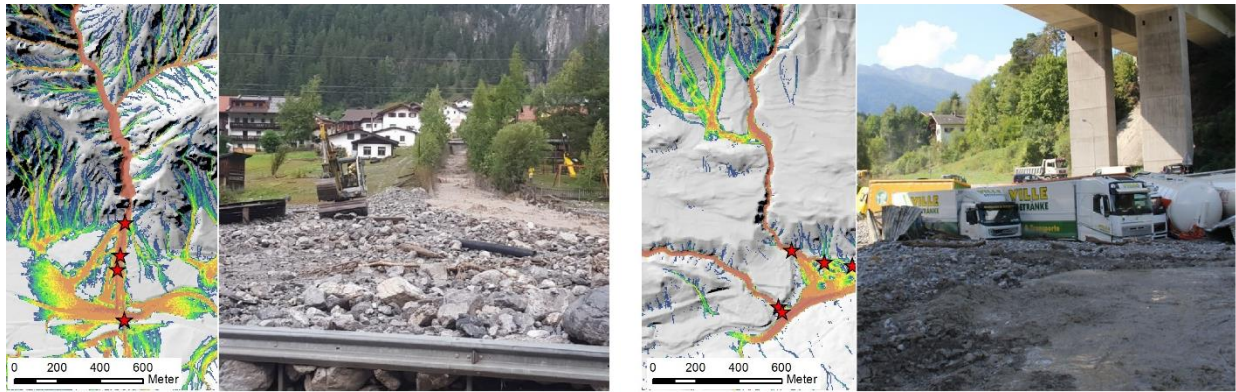


Fig. 10: Detail of computed debris flow impact map at the Stanzertal valley in 2016 and 2018 (blue: low flow depth; orange: high flow depth)

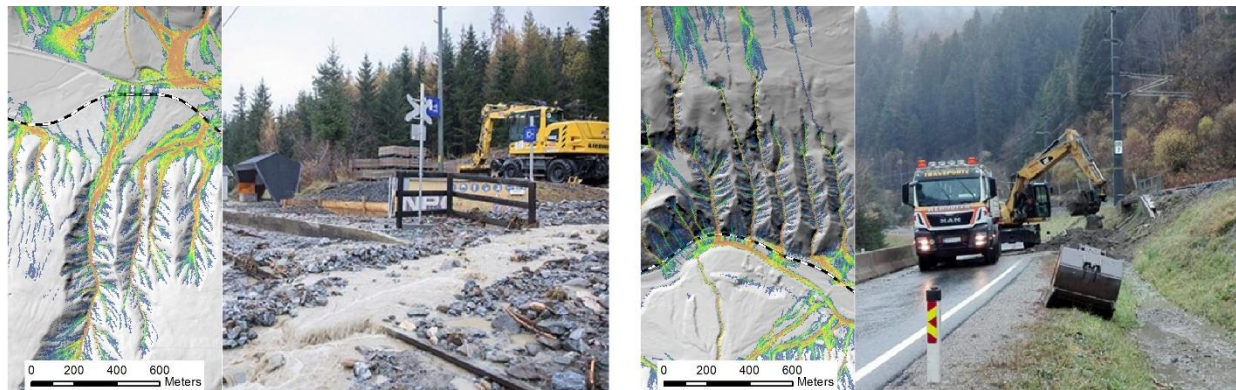


Fig. 11: Computed debris flow impact map and events from 2018 at the upper Drau valley (blue: low flow depth; orange: high flow depth)

After extensive testing, the **FIMP** debris-flow impact modelling tool was subsequently applied to the complete Austrian territory. Based on the modelling results, an Austrian wide debris-flow impact hazard map was compiled. For planning detail investigations and debris-flow mitigation projects, potentially affected railway sections were analyzed and highlighted in mitigation priority and protection deficit maps. For risk analyses, traffic frequency data for rail- and roadways were superimposed with regional annual exceedance probability (AEP) scenario related impact calculations and risk maps were produced. The Austrian wide data produced for railway lines was summarized in a hazard exposition priority map as shown in Fig. 12 and hazard classification and statistical analyses were conducted for budgeting of mitigation projects.

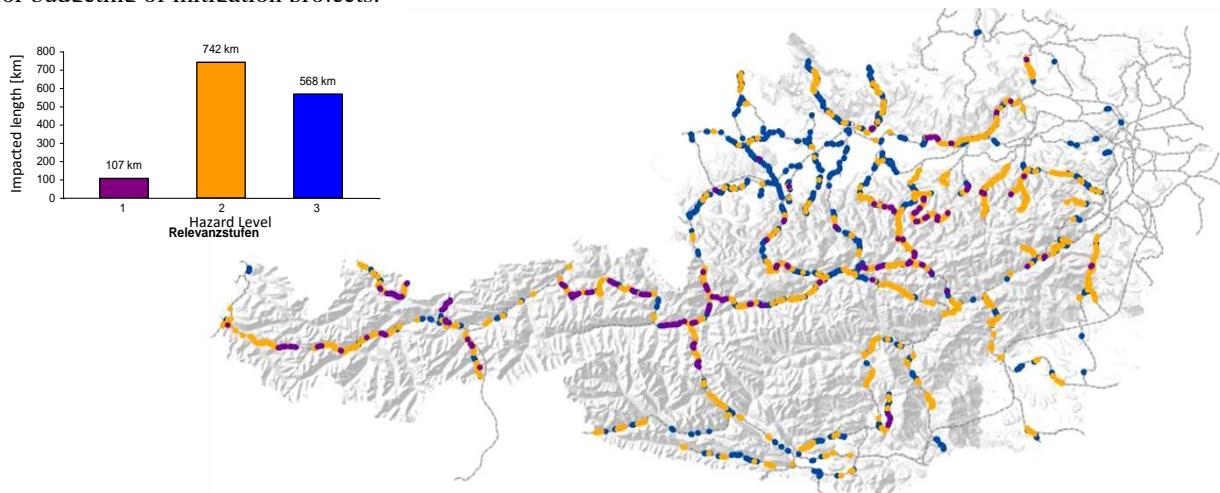


Fig. 12: Austrian wide debris impact hazard priority map with level 1 being most hazardous

For demonstrating that FIMP is applicable in other regions, a map which was computed on an indicational level for the Clear Creek Canyon west of Golden, Colorado, is shown in Fig. 13. The potential debris flow impact map was produced on a 5x5m terrain model, which does not consider bridges and culverts, as well as local debris-flow susceptibility. Plausibility checks were not done.

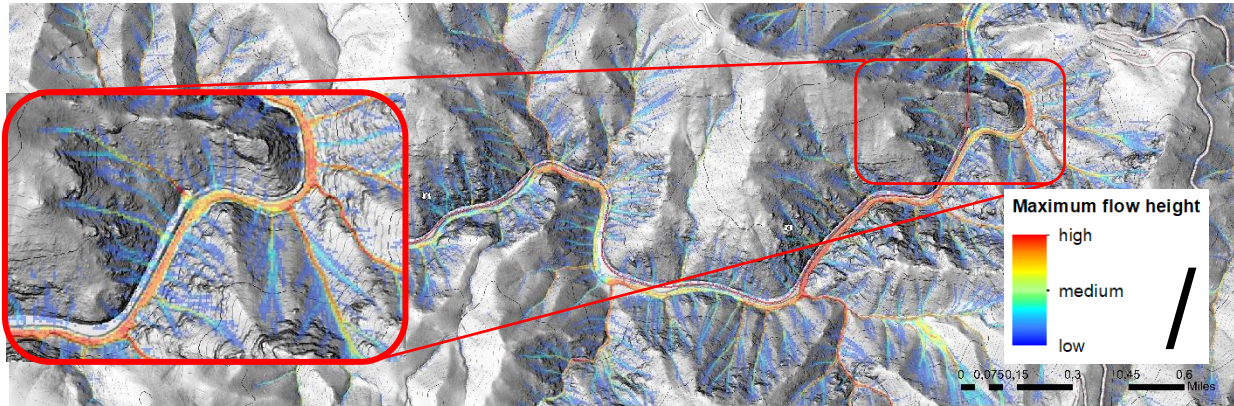


Fig. 13: Example map for the Clear Creek Canyon for demonstration purposes

References

- Scheikl M., and Powell D., 2012, Report of WP 5: Analysis of Economic Losses at the Stanzertal, Investigations on a regional danger analysis within the Alpine Space – Project imPROved Accessibility Reliability and security of Alpine transport infrastructure related to mountainous hazards in a changing climate.
- Tiefenthaler H., 1973, Innsbrucker geographische Studien. Bd. 1: Natur und Verkehr auf der Arlberg-Westseite. Hg. F. Fliri und A. Leidlmair. Innsbruck: Geographisches Institut der Universität Innsbruck.
- WSL, 2012, RAMMS User Manual v1.4 Debris Flow
- Bouchut, F., and Westdickenberg, M., 2004, Gravity driven shallow water models for arbitrary topography. *Communications in Mathematical Sciences* 2 (3), p. 359–389.
- Iverson, R. M., 1997, The physics of debris flows, *Rev. Geophys.*, 35, p. 245–296.
- Kaitna, R., Rickenmann, D., and Schatzmann, M., 2007, Experimental study on rheological behaviour of debris flow material, *Acta Geotech.*, 2, 71–85.
- Kuo, C.Y., Tai, Y.C., Bouchut, F., Mangeney, A., Pelanti, M., Chen, R.F., and Chang, K.J., 2009, Simulation of Tsaoling landslide, Taiwan, based on Saint Venant equations over general topography, *Eng. Geol.* 104, p. 181–189.
- Medina, V., Bateman, A., and Hurlimann, M., 2008, FLAT-Model: a 2-D finite volume code for debrisflow modeling, application to events occurred in the Eastern Pyrenees, *Int. J. Sediment Res.*, 23, p. 348–360.
- Patra, A., Bauer, A., Nichita, C., Pitman, E., Sheridan, M., Bursik, M., Rupp, B., Webber, A., Stinton, A., and Namikawa, L. et al., 2005, Parallel adaptive numerical simulation of dry avalanches over natural terrain. *Journal of Volcanology and Geothermal Research* 139 (1–2), p. 1–21.
- Pudasaini, S.P., Wang, Y., and Hutter, K., 2005, Rapid motions of free-surface avalanches down curved and twisted channels and their numerical simulation. *Philosophical Transactions of the Royal Society A: Mathematical, Physical and Engineering Sciences* 363 (1832), 1551.
- Révész, P., 1990, *Random Walk in Random and Non-Random Environments*, World Scientific, Singapore
- Rickenmann D., Laigle D., McArdeall B., and Hübl J., 2006, Comparison of 2D debris-flow-simulation models with field events. *Comput Geosci* 10(2), p. 241–264
- D’Agostino, V., 1996, *Analisi quantitativa e qualitativa del trasporto solido torrentizio nei bacini montani de Trentino Orientale [quantitative and qualitative analysis of sediment transport in torrents of mountainous catchments of eastern Trentino]*, Scritti dedicati a Giovanni Tournon, Associazione Idrotecnica Italiana, Sezione Liguria Piemonte e Valle d’Aosta (in Italian).
- Davies, T. R. H., 1990, Debris flow surges – experimental simulation, *J. Hydrology (N.Z.)* 29(1)

Using satellite radar interferometry to delineate burn area and detect sediment accumulation, 2018 Montecito disaster, California

Danielle Smilovsky^{a,*}, Jeffrey R. Keaton^b

^aWood, 4600 E. Washington Street, Phoenix 85034, USA

^bWood, 6001 Rickenbacker Road, Los Angeles 90040, USA

Abstract

The Thomas Fire burned slopes above Montecito, California in December 2017, setting the stage for debris flows and flash floods in response to precipitation that exceeded a threshold intensity and duration. A narrow cold frontal rainband storm occurred on January 9, 2018, that exceeded the threshold and caused a disaster in Montecito, killing 23 people, injuring many others, destroying residential buildings, and community infrastructure. The Geotechnical Extreme Event Reconnaissance (GEER) Association mobilized a team to document the damage and geomorphic effects. The potential value of the European Space Agency Copernicus Sentinel Synthetic Aperture Radar Satellite to detect and quantify erosion and deposition was recognized and an environmental scientist skilled with satellite radar interferometry therefore accompanied the GEER team. The Sentinel satellite data were obtained from satellite passes in late November, late December, and late January, which permitted constructions of interferograms that showed the effect of the fire before the January 9 storm and the effects of the storm. The interferometric results display an exact boundary compared to the burn perimeter determined by fire response teams. An interferometric change model constructed using post-fire pre-storm and post-storm Sentinel synthetic aperture radar scenes shows areas interpreted to be possible deposition and erosion. The immediate post-disaster search, rescue, and recovery activities resulted in substantial sediment removal from deposition areas which could not be captured by the available radar coverage.

Keywords: *Interferometry; Synthetic aperture radar; Burned slopes; Sediment flooding; Debris flow*

1. Introduction

This paper describes how satellite radar interferometry can be used to help characterize a burn area after a wild fire, and help locate debris accumulations after storm events. A burn area from a 2015 fire in Indonesia was identified using SAR C-Band data from Sentinel satellite in 2017. This information was found to be helpful with improving fire control management (Lohberger et al., 2017). Sentinel satellite data was also used to determine the burn scar during a study done to map the aftermath of a wildfire that occurred in the Western Cape, South Africa in January 2016 (Engelbrecht et al., 2017). The concepts surrounding interferometry are complex and the data available are robust. Many change detection studies have been performed globally using interferometry with synthetic aperture radar data (InSAR) for disaster monitoring and management. A series of change detection studies were done in Syria, Puerto Rico, California, and Iran. These studies demonstrate that SAR data can be used to monitor change from natural disasters (Washaya et al., 2018). This paper discusses the processes in which data were selected and how data were processed specifically for delineating a burn perimeter and locating debris accumulations in and around the city of Montecito, California. Since each satellite has its own line-of-sight and wavelength characteristics, product resolution helps point to areas of interest, but also has limitations. Quantification of debris deposits was not calculated in this study.

The present paper refers to a few publications and internet resources. However, most of the processes and results are original for this particular area and were developed specifically to discern if interferometry could be used to delineate the burn perimeter of the Thomas Fire and track debris deposits from the burned area after the narrow cold frontal rainband storm in early January 2018.

* Corresponding author e-mail address: danielle.smilovsky@woodplc.com

2. Background and need for interferometry

The Thomas Fire that burned the slopes above Montecito in Santa Barbara County, California started on December 4, 2017 approximately 50 kilometers to the east of Montecito, and north of Santa Paula in Ventura County, and continued to burn through January 12, 2018. This fire burned 114,078 hectares, making it the largest wildfire in California history at that time (CalFire, 2018). The destruction of the environment, infrastructure, and lives in and around the burn area will take years of mitigation and recovery. The damage to the watersheds within the burn area set the stage for even more destruction that became apparent after a heavy rainfall event on January 8 and 9, 2018. Precipitation intensities based on 5-minute precipitation values for this rainfall event are described by Keaton (2019, Fig. 5). This rain event produced flash floods and debris flows carrying large amounts of debris from the burned slopes toward the city of Montecito, damaging hundreds of structures and killing 23 people (CalFire, 2018).

This devastation prompted professionals from several technical and scientific realms to study this event to try to track the debris deposits after the narrow cold frontal rainband storm in early January. Since interferometry is performed to detect change, it became apparent that this event, despite the destruction, was well suited to use satellite radar interferometry to document where the ground had changed due to the fire, and then again after rainfall. Research was done to verify that satellite scenes could be obtained to calculate ground change after the Thomas fire, then again after the rain event. Once it was clear that data were available to track these changes, processing began for this study. The first objective was to verify that the burn delineation matched the boundary determined by the fire response team. The next objective was to verify changes in and near the channels located on the downward slopes toward Montecito. This was a big-picture attempt at trying to track the debris flow and see if the InSAR could help identify where the sediment traversed and landed.

Classically, interferometry is used to capture change on the ground surface by measuring the phase difference between at least two repeat passes of a fixed orbiting SAR satellite. It is a remote way of measuring relative distance. Since InSAR can detect millimeter change, a burn area and debris deposits should be detectable if the correct satellite, orbit, and acquisition dates are available for selection. The interferometric and change detection processing, as well as the interpretation in relation to the environmental events involving the Thomas Fire and the storm event, require critical attention to detail and an understanding of how to correct errors due to atmospheric effects (troposphere and ionosphere).

The level of error can be understood by checking the coherence of the satellite scenes after they are coregistered during the beginning stages of processing. Statistics can be calculated on the satellite scenes to determine how high the coherence percentage is between specific scenes. Olen and Bookhagen (2018) discuss calculating coherence, types of errors that cause loss of coherence, and methods to improve it. The statistical coherence calculation is built into most of the SAR processing applications, but users must choose to add that step into their computational processing models. Olen and Bookhagen (2018) use this statistical approach to understand coherence. Our study practices a similar step to check coherence; the scenes in this study hold 97% coherence or better after inspecting precipitation rates for the time frame of interest.

SAR methods have improved drastically over the last ten years or so as earth surface observation can now be effectively done independent of weather, cloud cover, and time of day. Natural hazards, such as, landslides and debris flows can be observed and studied better than ever with these radar observation improvements. However, Olen and Bookhagen (2018) discuss seasonality and how choosing satellite scenes during rainy or growing seasons is still an important consideration, since precipitation during a wet season can lower coherence and cause errors. Checking the daily precipitation amounts on the dates of SAR images can help make decisions on which satellite scenes to use. This background check is easy to skip, but using it will help lower error or noise and boost coherence.

3. Data selection and processing

In recent years, The European Space Agency (ESA) established the Copernicus Program to provide a satellite constellation which includes two newer satellites, Sentinel-1A and Sentinel-1B, which are in a near-polar, sun-synchronous orbit. These satellites share the same orbital plane with a 180° orbital phasing difference. These satellites carry a C-band synthetic aperture radar active sensor which was built for many scientific purposes, including the ability to collect data in all-weather during the day and night. The way these satellites collect data enable scientists to process data for many purposes, including radar interferometry. According to Paul Rosen at NASA JPL, radar interferometry can be broadly defined by use of phase measurements to precisely measure the relative distance to an object when imaged by synthetic aperture radar from two or more observations separated either in time or space (Rosen, 2014).

The ESA has made this data available free of charge and easily downloadable for quick turnaround during critical events such as the Thomas Fire (ESA, 2018).

The slopes that burned are above and north of the city of Montecito, California; therefore, a satellite with an ascending orbit would provide the best results since the line-of-sight (LOS) would capture the area of interest well as it ascends northward. Sentinel-1B offers 12-day repeat pass ascending orbits. Since Sentinel-1B has a frequent repeat pass orbit, the area of interest was captured in late November before the fire occurred, in late December after the fire had burned the slopes above Montecito, and in late January after the storm of 9 January 2018. Table 1 lists the satellite scenes used in this study.

Table 1. List of Sentinel-1B satellite scenes used to process two interferograms and deformation models.

Event	Acquisition date	Mission	Path	Frame	Orbit	Direction	Polarization
Before Thomas Fire	11/22/2018	S1B	137	109	8388	A	VV+VH
Late in Thomas Fire, before rain storm	12/28/2018	S1B	137	109	8913	A	VV+VH
After rain storm	1/21/2018	S1B	137	109	9263	A	VV+VH

The ESA not only offers data free of charge, but processing software, too. The software includes five Toolboxes that make up the Sentinel Application Platform (SNAP). In order to generate an interferogram, two scenes that have the same acquisition direction, path, and frame are required for the best possible result. In this case, each coregistered pair has at least 97% coherence, meaning that the interferometric processing will generate an interpretable result. An interferogram is considered a complex image, its magnitude is related to correlation. However, this technology has limits; in this case, its phase is related to geometry differences based on the capability of the synthetic aperture instrument the satellite carries. The Sentinel satellites carry C-band synthetic aperture radar instruments, meaning it has a 6-cm wavelength and the light from that will interact strongly with objects that are around the size of the wavelength. One cycle of LOS change is equal to half the physical wavelength, meaning the C-band instrument can detect about 3 centimeters of change per cycle (ESA, 2018).

Sometimes physical change occurs faster than can be detected by a single wavelength over the time difference between scenes or so much atmospheric interference is present that areas of decorrelation are in the InSAR scene. Radar is sensitive to the structure and scale of objects being captured relative to the radar wavelength. A massive area of burned forest imaged by a Sentinel satellite will return a decorrelated pattern in an interferogram calculated from radar scenes acquired before and after the burn. Decorrelated areas are important to recognize, especially in this study. Decorrelation is the basis used to identify land use, like agriculture and mining, or bodies of water, for example. Decorrelation areas can also help identify boundaries.

The general process for interferogram creation is shown in Fig. 1; however, additional steps may be required depending on the area of interest and data availability. Since the interferogram result is shown as color ramps or fringes that represent 2.8 cm of change per color cycle for Sentinel C-band SAR, it is best to unwrap the result to get the line of sight change in units that are easier to understand in terms of vertical displacement or elevation changes. Statistical-cost, network-flow algorithm for phase unwrapping (SNAPHU) is an ESA tool used for unwrapping interferometric information. This is separate from the ESA SNAP software and needs to be downloaded and configured (ESA, 2018). Once the interferogram has been unwrapped, the result needs to be imported back into SNAP to apply an equation to return values that reflect line of sight vertical elevation change in meters. The vertical displacement equation is

$$\text{Vertical Displacement} = (\text{unwrapped phase} \times \text{wavelength}) [-4\pi \times \cos(\text{incidence angle})]^{-1} \quad (1)$$

From there, the units can be easily converted appropriately. The result can now be geocoded and brought into a GIS (geographic information system) application for classification, quantification, profiling, and other mapping purposes.

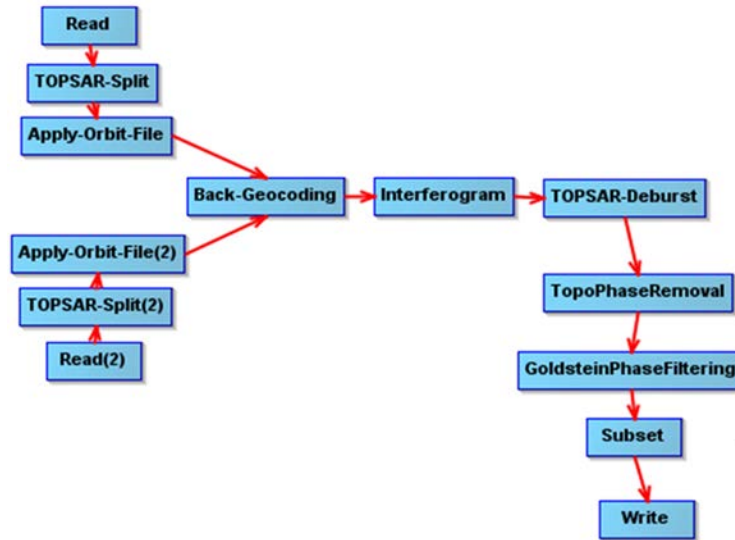


Fig. 1. Interferogram formation process tree, European Space Agency (ESA, 2018).

4. Discussion and conclusion

Two objectives were considered in the application of SAR technology to the Montecito disaster reconnaissance: 1) detection of the limits of the area that burned and 2) detection of the locations where sediment eroded or was deposited. The first notable characteristic regarding the pre-burn/post-burn interferogram is the delineated burn perimeter. The pre-burn satellite scene was acquired on November 22, 2017, and the late-stage burn satellite scene was captured on December 28, 2017 (the Thomas Fire was 100% contained on January 12, 2018). The area suffered such a major change from the fire that it appears as decorrelation in the interferogram (Fig. 2a). The ultimate burn perimeter determined by the fire response team matches the decorrelated area in the interferogram, except for the northernmost part circled in red, which burned after December 28, 2017 (Fig. 2b). The burn perimeter data that was determined by the fire response team was overlaid on top of the interferogram and compared to the drawn burn perimeter based on visual inspection of the decorrelated area. In this case, the interferometric results show the delineated burn perimeter between November 22, 2018 and December 28, 2018 clearly since it was expected to be decorrelated after the Thomas fire had just occurred (Fig. 2). This provides another indication that the interferometric results are reliable since both burn perimeters are very similar. Decorrelation in a result is typically the first sign to use different datasets or something major has happened on the ground surface between the two satellite passes. Since the occurrence of the Thomas Fire was known, decorrelation within the determined fire response burn perimeter was anticipated in the results, and in this case, a signal that the results are valuable (Fig 2c).

The second notable characteristic is the precise calculated distance from the satellite to the ground to detect change between two different satellite passes that can be interpreted. Since the winter storm event produced sediment deposition in the community of Montecito, reduction in the distance from the satellite to the ground can be interpreted generally as uplift, or in this case could be deposition (fig 3). Similarly, a distance increase can be interpreted as erosion or subsidence (3). Types or error are usually present and the quality of the data decreases if not corrected or removed. In this case, we have very strong coherence between the satellite scenes used for this study, which greatly reduces the presence of error. Additionally, finding a known zero within the overall satellite scene is another necessary method to reduce error. A given area within the satellite scene, which can be solid rock, for example, is assumed to be zero, meaning no difference should be detected in the results. Sometimes there is another value where it should be zero. This value represents a type of error that exists across the whole scene, which should be removed throughout the whole dataset to adjust the results to improve quality.

For the purposes of this study, a change model (Fig. 3) was created and classified to identify possible positive elevation change near channels where debris might have accumulated in channels and channel junctions. Classification of this change model also includes possible negative change due to erosion or subsidence. In this study, a relationship exists between areas of sediment deposition and erosion, and channels and channel junctions. It is possible that increases in elevation are due to debris flow deposition.

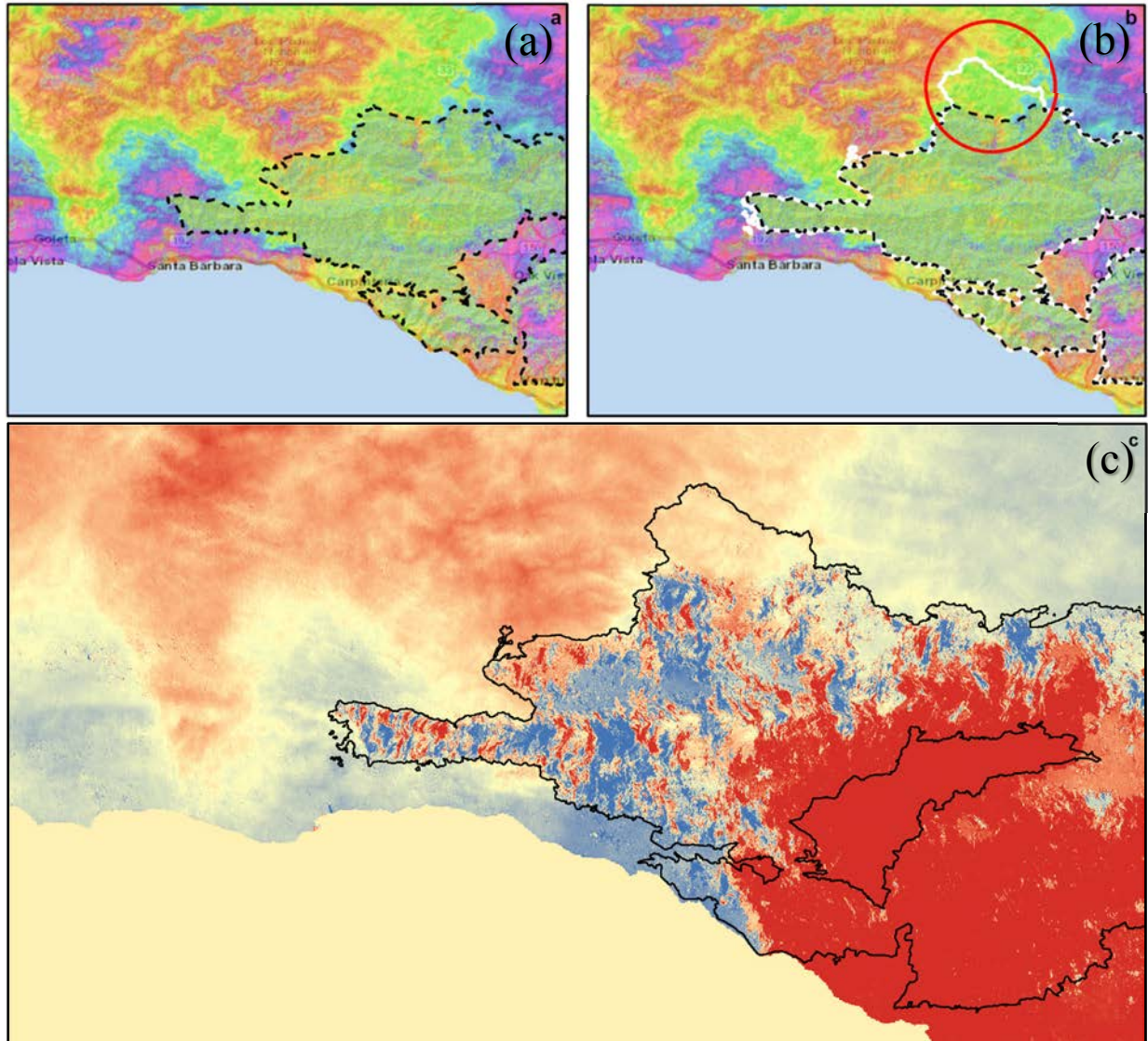


Fig. 2. (a) Decorrelated area (manually drawn black dashed line) generated during interferometry between November 22, 2018 and December 28, 2018; (b) Fire response team mapped burn perimeter (white solid line) for the ultimate burn ending on January 12, 2018 overlaid on top of interferogram for comparison; developed by first author, January 2018. The red circle in (b) denotes the northern extent of the Thomas Fire, which burned between December 28, 2017, and January 12, 2018. An interferogram constructed from radar scenes on November 22, 2017, and January 21, 2018, would have shown decorrelation corresponding to the total extent of the Thomas Fire. (c) Unwrapped displacement result. The area within the black solid line (CalFire, 2018) is another example of how results showing major change on the surface between two satellite scenes appear.

The change model (Fig. 3) shows elevation change areas, with red and dark red showing the most increase in elevation. The red and dark red areas are small clusters located in and around the channels and channel junctions. The center channel in Fig. 3 that leads straight into the city of Montecito is San Ysidro Creek. It has several red and dark red clusters that are interpreted to be sediment accumulation and possibly post-disaster cleanup prior to January 21, 2018. It is known that this channel carried a majority of debris into Montecito, so it is reasonable to interpret the interferogram as documenting sediment accumulation. An overview of geotechnical effects along San Ysidro Creek is presented in Keaton et al. (2019), including several photos of debris flow damage. Additionally, the change model (Fig. 3) shows blue and dark blue clusters which could represent areas where erosion or subsidence occurred sometime during and or after the rain event. SAR data has been used to detect surface change for over twenty years and, since the launch of the Sentinel missions in 2014 and 2016, change with millimeter accuracy can be evaluated every 6 to 12 days between two Sentinel satellite passes (ESA, 2018).

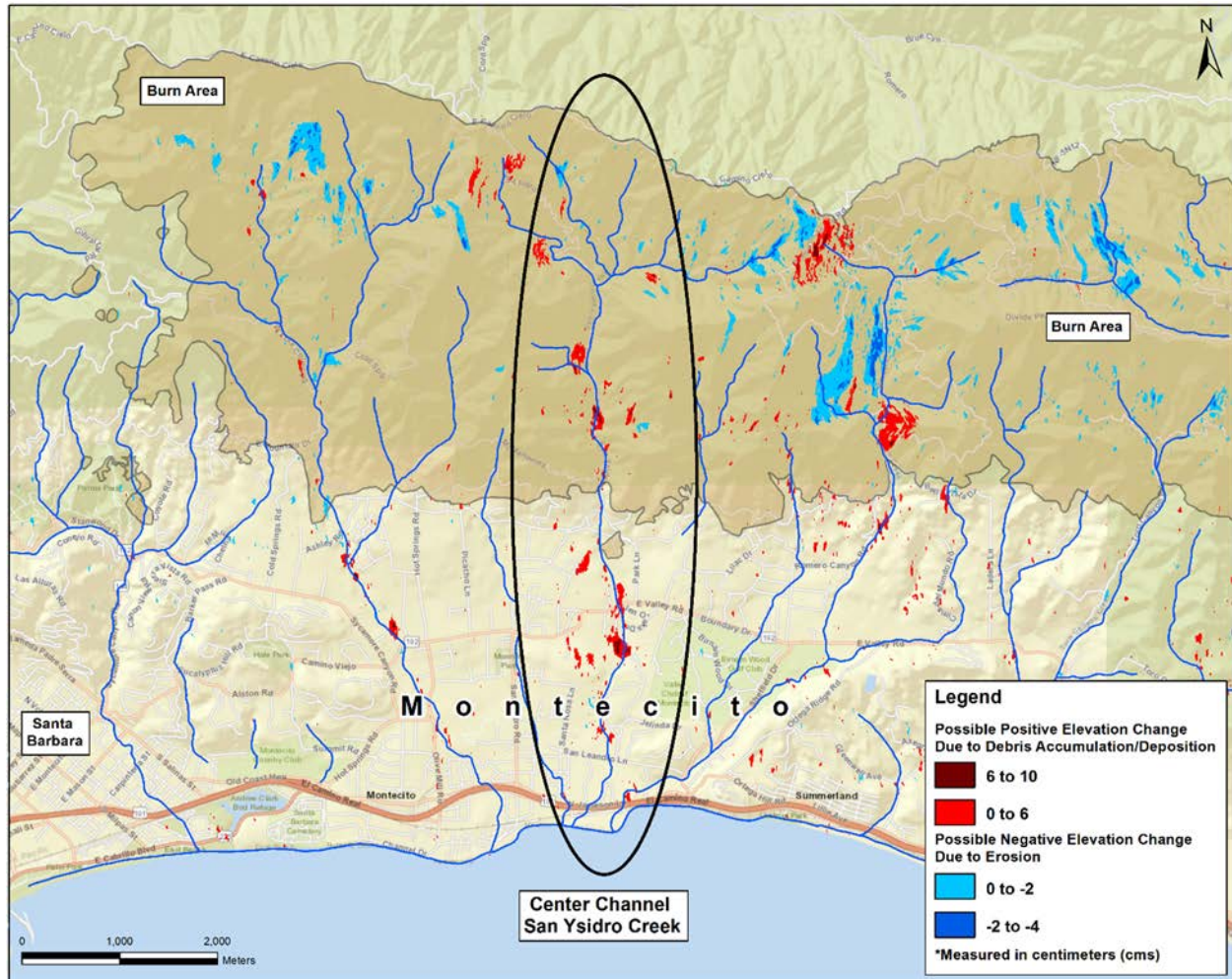


Fig. 3. Post-burn/post-rain event (December 28, 2017 to January 21, 2018) interferometric change model showing the most elevation change in and around channels within the burn area leading toward Montecito. Possible positive elevation change areas due to debris accumulation/deposition are shown in the red and dark red clusters. This could be debris deposits from the Thomas Fire flowing down slope into channel system with storm event in early January 2018. Possible negative elevation change areas due to erosion or maybe subsidence are shown in blue and dark blue clusters.

Acknowledgements

The Geotechnical Extreme Events Reconnaissance (GEER) Association, supported by the U.S. National Science Foundation (NSF), organizes the response of the geoenvironmental community to earthquakes and other natural disasters such as floods, landslides, tsunamis, etc. GEER members donate their time, talent, and resources to collect time-sensitive and potentially perishable field observations and data of the effects of extreme events.

This material is based upon work supported by the National Science Foundation under Grant No. CMMI 1266418. Any opinions, findings, and conclusions or recommendations expressed in this material are those of the authors and do not necessarily reflect the views of the National Science Foundation.

The European Space Agency made Sentinel data and SNAP software open source and free of charge. The Fire Response Team mapped the burn perimeter and shared it publicly for research purposes and public information.

References

- CalFire, 2018, Thomas fire incident information. Cal Fire website. http://www.fire.ca.gov/current_incidents/incidentdetails/Index/1922 (accessed September 2018).
- Engelbrecht, J., Theron, A., Vhengani, L., and Kemp, J., 2017 A Simple Normalized Difference Approach to Burnt Area Mapping Using Multi-Polarisation C-Band SAR: *Remote Sensing*, v. 9, no. 8, 764; <https://doi.org/10.3390/rs9080764> and <https://www.mdpi.com/2072-4292/9/8/764> (accessed February 2019).
- ESA, 2018, Sentinel Online. European Space Agency. <https://sentinel.esa.int>. (accessed October 2018).
- Keaton, J.R., 2019, Weather-radar inferred intensity and duration of rainfall that triggered the January 9, 2018, Montecito, California, disaster, in 7th International Conference on Debris-Flow Hazards Mitigation (in press; this volume).
- Keaton, J.R., Ortiz, R.M., Turner, B., Alessio, P., Gartner, J., Duffy, J., Parker, G., Smilovsky, D., and Watts, T., 2019, Overview of geotechnical effects of the January 9, 2018, debris-flow and flash-flood disaster in Montecito, California: in 7th International Conference on Debris-Flow Hazards Mitigation (in press; this volume).
- Lohberger, S., Stangel, M., Atwood, E.C., and Siegert, F., 2017, Spatial evaluation of Indonesia's 2015 fire-affected area and estimated carbon emissions using Sentinel-1: *Global Change Biology*. <https://onlinelibrary.wiley.com/doi/abs/10.1111/gcb.13841> (accessed 20 Feb 2019).
- Olen, S., and Bookhagen, B., 2018, Mapping Damage-Affected Areas after Natural Hazard Events Using Sentinel-1 Coherence Time Series: *Remote Sensing*, v. 10, no. 8, 1272; <https://doi.org/10.3390/rs10081272> (accessed February 2019).
- Rosen, P.A., 2014, Principles and Theory of Radar Interferometry, in UNAVCO Short Course: https://www.unavco.org/education/professional-development/short-courses/course-materials/insar/2014-insar-isce-course-materials/InSARPrinciplesTheory_UNAVCO_14.pdf (accessed February 2019).
- Washaya, P., Baiz, T., and Mohamadi, B., 2018, Coherence Change-Detection with Sentinel-1 for Natural and Anthropogenic Disaster Monitoring in Urban Areas: *Remote Sensing*, v. 10, no. 7, 1026; <https://doi.org/10.3390/rs10071026> (accessed February 2019).

Quantitative risk management process for debris flows and debris floods: lessons learned in Western Canada

Alex Strouth^{a,*}, Scott McDougall^b, Matthias Jakob^c, Kris Holm^c, Emily Moase^c

^aBGC Engineering Inc., Golden, Colorado, USA

^bUniversity of British Columbia, Vancouver, CANADA

^cBGC Engineering Inc., Vancouver, British Columbia, CANADA

Abstract

Debris flows and debris floods are common in mountainous regions of Western Canada, but there is no provincial or national standard for debris-flow/flood hazard or risk management. Instead, each local government manages hazards in its own way. Quantitative Risk Management (QRM) is being increasingly adopted, largely due to the effort of practitioners promoting its use. QRM uses numerical estimates of risk parameters to help risk managers within local government answer the following questions: Are present and future residents of my community safe enough? Is debris-flow/flood protection needed? How much should my community invest in debris-flow/flood protection? After roughly a decade of application, the benefits and challenges of QRM are emerging. This paper presents examples of the QRM process applied to debris-flow/flood risk management for communities, with a focus on debris-flow/flood mitigation decision making and remaining challenges.

Keywords: Risk assessment; hazard management; risk management; debris-flow mitigation; debris flood

1. Introduction

Debris flows and debris floods are widespread in mountainous regions of Western Canada, and numerous events have impacted residential areas in the past decade, resulting in fatalities and economic damage (Moase, 2017). Development on debris-flow and debris-flood prone fans has historically occurred without adequate recognition of the hazard, and few developments are effectively protected from these hazards. A variety of communities have been impacted, ranging from densely-developed, wealthy, urban settings to the sparsely-developed, rural settings that are prevalent in British Columbia and Alberta.

Typically, assessments are triggered following debris-flow or debris-flood events, often in areas that were not fully aware of the threat to their community. A provincial code, standard, or specification for debris-flow/flood hazard management does not exist, and there is no nationally or provincially-adopted level of debris-flow/flood safety. Hazard and risk management is delegated to the municipal level of government, and each municipal government manages hazards in its own way. Some guidance exists for assessing landslide hazards (including debris flow/flood) for proposed developments (e.g. EGBC, 2010; Cave 1993), but there is little guidance for existing developments.

A few municipal governments, such as District of North Vancouver (DNV) and Town of Canmore (TOC), have responded to landslide and debris-flow/flood events by developing local regulations for assessing hazards and managing risk using a Quantitative Risk Management (QRM) process. QRM is modelled after the process initially developed in Hong Kong for landslide hazards (GEO 1998, Malone 2004, VanDine 2018). Smaller municipal governments are now increasingly referencing the local regulations adopted by DNV and TOC.

With this evolving adoption of the QRM process there is a need to understand the benefits, challenges, and lessons learned from previous applications of QRM for debris flows/floods. This paper presents examples of the QRM process

* Corresponding author e-mail address: astrouth@bgcengineering.ca

applied to debris flows/floods that affect existing residential development, with a focus on the decision-making process for mitigation and remaining challenges of the QRM process.

The QRM process presented in this paper is designed for management of rapid-onset, highly-destructive hazards, where risk associated with direct impact is the controlling factor for decision making. Debris flows/floods are an ideal hazard type for this methodology. The process is distinct from those that manage slowly unfolding hazards (e.g. environmental contamination, flooding) where concepts of resilience and response as an event unfolds are relevant. The QRM process presented here is one of many tools for managing geologic hazards, each with its own strengths and weaknesses. This paper is not an argument for or against the QRM process, but rather an open discussion of its strengths and weaknesses.

2. Quantitative Risk Management

The QRM process described in Table 1 is well documented in literature (e.g. VanDine 2018, Holm et al. 2018, Hungr 2016, VanDine 2012, Fell et al. 2005, IUGS 1997, GEO 1995, Jakob 2019, this volume). It involves three overlapping phases: hazard assessment, risk assessment, and risk management. When applied to debris flows/floods, the hazard assessment phase involves estimating the frequency and magnitude of flows, typically in terms of total volume and peak discharge at the fan apex. Numerical modeling allows estimation of potential runout extent and impact intensity across the fan surface in terms of flow velocity and depth. Considerable experience and judgement is needed to calibrate the numerical models, interpret the raw model output, and create a comprehensive debris-flow/flood hazard map that considers a range of possible volumes, rheologies, and avulsion scenarios. Output of the hazard assessment is an estimated occurrence probability, spatial impact probability, and impact intensity, which varies across the hazard area, for each debris-flow/flood scenario.

Table 1. Quantitative risk management framework (adapted from Fell et al. 2005, VanDine 2012).

Hazard Assessment	Risk Assessment Risk Management Risk Communication and Consultation Informing stakeholders about the risk management process	1. Scope Definition a. Recognize the potential hazard b. Define the study area and level of effort c. Define roles of the client, regulator, stakeholders, and Qualified Registered Professional (QRP) d. Identify 'key' consequences to be considered for risk estimation	Monitoring and Review Ongoing review of risk scenarios and risk management process
		2. Geohazard Analysis a. Identify the geohazard process, characterize the geohazard in terms of factors such as mechanism, causal factors, and trigger factors; estimate frequency and magnitude; develop geohazard scenarios; and estimate extent and intensity of geohazard scenarios.	
		3. Elements at Risk Analysis a. Identify elements at risk b. Characterize elements at risk with parameters that can be used to estimate vulnerability to geohazard impact.	
		4. Geohazard Risk Estimation a. Develop geohazard risk scenarios b. Determine geohazard risk parameters c. Estimate geohazard risk	
		5. Geohazard Risk Evaluation a. Compare estimated risk against risk tolerance criteria adopted by the governing jurisdiction b. Prioritize risks for risk control and monitoring	
		6. Geohazard Risk Control Assessment a. Identify options to reduce risks to tolerable levels b. Select option(s) with the greatest risk reduction at least cost c. Estimate residual risk for preferred option(s)	
		7. Action a. Implement chosen risk control options b. Define and document ongoing monitoring and maintenance requirements	

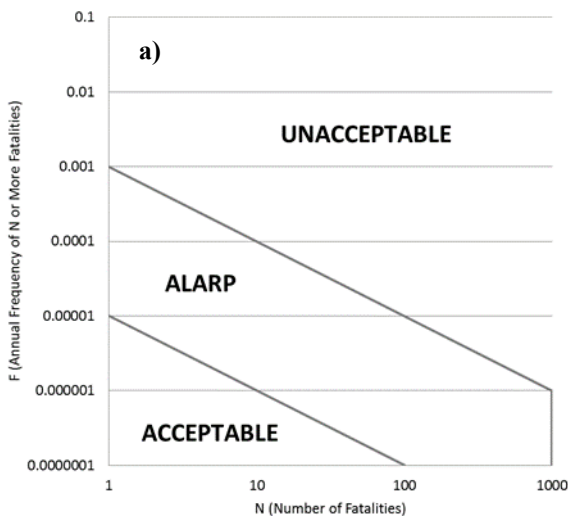
The risk assessment phase involves identifying elements (e.g. buildings, roads, bridges, pipelines) that could be impacted by a debris flow/flood, estimating risk, and comparing the estimated risk to risk tolerance criteria. The comparison of risk estimates with risk tolerance criteria addresses questions like: “Is my community safe enough?”, and “Is debris-flow/flood protection needed?”

Elements at risk are identified by overlaying the hazard map with a map of buildings and infrastructure. Risk of loss of life (safety risk) can be estimated for individuals or groups. Individual risk is an estimate of the annual likelihood that a specific person is killed by a debris flow/flood. Typically, individual risk is estimated at each building for the person most at risk, who is typically the person who spends the longest time per year within the hazard zone. Group risk (societal risk) is an estimate of the number of people who would be killed by each debris-flow/flood scenario. Risk is estimated using Equation 1. Individual risk is the sum of risks estimated for each debris-flow/flood scenario. Group risk considers the number of fatalities (N) that would be lost during each debris-flow/flood scenario. Group risk is typically represented graphically on an F-N plot, which displays the cumulative annual probability (F) of N or more lives being lost (Fell et al. 2005).

$$R = P(H) * P(S:H) * P(T:S) * V * E \tag{1}$$

In this equation, *R* (safety risk) is the probability that a person is killed by the specific debris-flow/flood scenario; *P(H)* is the probability per year that the debris-flow/flood scenario occurs; *P(S:H)* is the probability that the debris-flow/flood scenario reaches the element at risk; *P(T:S)* is the probability that the person is present, given the building or infrastructure is impacted; *V* is the probability that the person is killed, given they are impacted; and *E* is the number of people exposed to the hazard, taken as 1 for individual risk.

Risk tolerance is treated as a social, rather than a technical, question that is to be defined by decision makers who represent society’s interests. In practice, risk tolerance thresholds referenced in Western Canada (Fig. 1) have been introduced by landslide risk management professionals and adopted by municipal managers with varying degrees of public input. The thresholds are based on those developed in Hong Kong for landslide risk, and those developed in the UK, Australia, The Netherlands, and the United States for risk related to large industrial accidents and water retaining dams (Porter and Morgenstern 2013, Baecher 2015, Hungr et al. 2016). Risk tolerance thresholds adhere to principles described by IUGS (1997), including: landslide risk should not be significant compared to other risks to which a person is exposed in everyday life; society is intolerant to incidents that cause many simultaneous casualties; higher risks are tolerated for existing rather than planned projects; and risk should be reduced wherever reasonably practicable (ALARP principle).



- b) Individual risk tolerance thresholds**
 Annual probability of death to the individual most at risk
- New development**
 1:100,000 (1×10^{-5})
- Existing development**
 1: 10,000 (1×10^{-4})
 Similar to an individual’s risk of death in an automobile accident in the United States or Canada

Fig. 1. (a) Group (societal) risk tolerance criteria for landslides commonly referenced in Western Canada (GEO 1998); (b) Individual risk tolerance thresholds commonly referenced in Western Canada (Porter and Morgenstern 2013).

If the risk assessment identifies that debris-flow/flood risks are unacceptable, risk management may be pursued. The risk management phase refers to design and implementation of mitigation measures or non-structural options like monitoring and evacuation protocols, education, and land-use planning. The risk management assessment addresses questions like, “How much should my community invest in debris-flow/flood mitigation?” and “What impacts will debris-flow/flood mitigation have on my community?” The assessment involves identifying options to reduce risk and selecting a preferred option that optimizes cost and benefit. The preferred option often includes a combination of structural and non-structural measures.

The quantitative risk framework is used to select the location and size of the mitigation measures. Using an iterative process, the designer selects a combination of measures that reduces risk to tolerable levels, considering the full range of possible risk scenarios including different magnitude classes and avulsion scenarios. Structures are sized to manage a “design event” defined for the structure (i.e. the debris-flow/flood magnitude that controls sizing of the mitigation structure). Often the structure’s design event is the largest magnitude debris flow/flood that results in intolerable risk. Where it is not feasible to construct mitigation for large magnitude events, structures are sized for the maximum event that can feasibly be controlled, and larger, lower-probability scenarios are managed with non-structural measures like monitoring and evacuation.

The QRM process provides answers to basic risk management questions, identifies priorities, allows direct comparison of different hazard types, and can be used to demonstrate and communicate the decision-making process. However, for projects requiring some form of structural mitigation, a primary outcome of the QRM process is selection of the structure’s design event. When the QRM process is used, the structure’s design event is site-specific and corresponds to the number and distribution of people in the hazard zone. In general, smaller structures (e.g. designed for the 100-year return period event) are derived for areas that are infrequently occupied, while larger structures (e.g. designed for the 1,000 or even 10,000-year return period event) are derived where debris flows/floods have potential to impact an urban area (Fig. 2).

From a worldwide hazard management perspective, the QRM process is rare (Lateltin et al. 2005, ASI 2009, MOC 2000). Most geologic hazard types, including landslide and flood hazards in most countries, are managed using a prescriptive standards-based process. For example, in Canada flood control elements (e.g. dikes, conveyance structures) are commonly designed for 100-year to 200-year return period flood stages plus freeboard regardless of the number and distribution of elements at risk, and buildings are designed to resist the 2,475-year return period earthquake loads (NRC 2015). In Switzerland, the 100-year return period debris flow/flood is commonly taken as the design event for structural mitigation measures (Lateltin et al. 2005). This prescriptive standards-based process is much simpler to systematically apply, but it ignores the number of people at risk and is not flexible enough to consider site-specific conditions that would justify use of a larger or smaller mitigation design event. The standards-based approach also cannot be used to prioritize mitigation, which is a substantial limitation in Western Canada, where there currently are many developed fans without risk management measures, and limited funding available to allocate to such measures.



Fig 2. An undeveloped fan (left) and a highly-developed fan (right) in Alberta, Canada, both prone to debris floods. A prescriptive standards-based process would call for the same design event (100 or 150 years in the case of Switzerland, Japan or Austria) for mitigation for each fan. The QRM process would prescribe a relatively small structure for fan A, and a major structure or series of structures for fan B.

3. Application of the Quantitative Risk Management Process

The QRM process has been applied at more than 50 sites across British Columbia and Alberta for debris-flow/flood hazards during approximately the last ten years. Typically, where risk is found to be intolerable, the process is used to both inform and justify applications to government for mitigation funding, and to select the size of structural mitigation measures. However, the final, most-important step of risk management, which is construction or implementation of the mitigation design (item 7, Table 1), is often not completed. Local governments responsible for managing the hazards typically have a strong political mandate to protect their citizens, but they rarely have the financial resources to fund structural mitigation measures. Local governments compete for funding from a variety of provincial and federal grants, which can take years and for which there is no guarantee of success. Winning a grant is a function of many factors that may be unrelated to urgency of need for a particular community (e.g. number of applicants, knowledge of applicant, size of existing development and associated infrastructures, timing of submittal). While they wait for provincial and federal funding, local governments manage the situation as best they can with limited resources, often with strategies like educating residents about hazard and risk zones, empowering individuals to protect themselves, developing emergency response plans, and sometimes devising a warning system whose enforcement is largely voluntary and not associated with evacuation orders. Where the QRM process exposes levels of risk that are intolerable, but that cannot be managed under current policies and financial resources, it can lead to unintended hardships such as loss of property value. At the same time, avoiding assessment of identified geohazards can expose local governments to liability, leading to a ‘catch-22’ situation. QRM offers some solution to this conundrum in that it provides a defensible process for decision-making, even when solutions have yet to be realized.

In an ideal world, all hazard types affecting a province or nation would be characterized, prioritized, and managed using a single comprehensive framework that allocates resources based on need, so that resources and mitigation are provided to the communities exposed to highest risks. Unfortunately, although western Canada is beginning large scale efforts to prioritize areas based on risk to inform risk management decisions, the risk management process is not yet mature. Fig. 3 provides an indication of risk and estimated mitigation cost for ten debris-flow/flood hazard sites where the QRM process has been used by the authors. It demonstrates that funding is currently not preferentially allocated (or available) to the highest risk communities, and that there must be other factors that influence which communities acquire funding for debris-flow/flood mitigation.

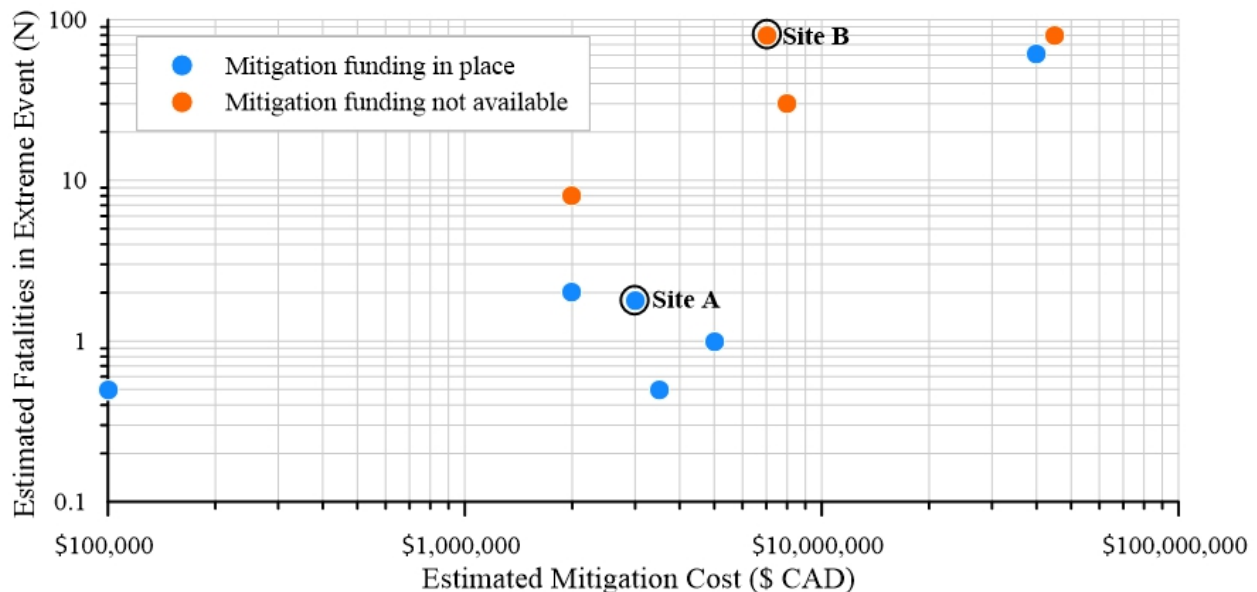


Fig 3. Each point is a debris-flow or debris-flood hazard site in Western Canada where the QRM process has been applied. Y-axis is the estimated number of fatalities that could occur during the most extreme event considered in the risk assessment (typically a 3,000-year or 10,000-year return period event) and is a proxy for risk. X-axis is the estimated mitigation cost in Canadian dollars, estimated based on a conceptual mitigation design that would reduce risk to a tolerable level.

The following two sites are each at extreme ends of the risk management spectrum, and while they may not illustrate ‘typical’ examples, they do highlight some of the issues:

Site A is a popular tourist destination in the Vancouver, British Columbia metropolitan area. The parking lot is in the distal region of a debris-flow fan. Small debris flows and floods that have eroded the fan surface have occurred during the past few decades, but a significant debris flow has not reached the parking lot in historical times. A debris-flow hazard and risk assessment identified that debris flows would rarely impact the parking lot (~3,000 year return period) and that parking lot impact could cause one to two fatalities (N 1 to 2). Individual risk at this site is acceptable (Fig. 1). Group risk plots in the As Low As Reasonably Practicable (ALARP) zone on the group risk tolerance diagram (Fig. 1), implying that risks should be reduced if the cost of mitigation is not disproportionate to the risk reduction achieved. The QRM process identified that debris-flow mitigation was not required, but indicated that the ALARP principle should be applied. The site is owned by a large and well-funded municipal government, who have applied the ALARP principle by designing flexible net debris-flow barriers to protect the parking lot. The proposed barriers are 4 m tall, more than 200 m long, and will cost several million dollars. Funding, provided by the municipality, is in place for the proposed mitigation, and construction is planned to begin in 2019.

Site B is a residential community in a rural area of Squamish-Lillooet Regional District, British Columbia. The community includes 114 occupied lots that are located on an active debris-flow fan (see Jakob 2019, this volume, for a summary of the risk profile). Debris flows have occurred frequently since the community was developed, including three debris flows between 2004 and 2013 that destroyed vehicles and buildings, but luckily did not result in loss of life. The QRM process identified that 76 residences exceeded the individual risk tolerance threshold of 1:10,000 (Fig. 1), and 18 residences exceeded 1:1,000 annual risk of fatality. Group risk plotted entirely within the unacceptable zone, including a scenario indicating that a 3,000-year to 10,000-year return period debris flow could result in up to 80 fatalities. The risk management phase of the QRM process identified that the 10,000-year return period debris flow would need to be addressed by structural and non-structural mitigation to move group risk into the ALARP zone on the group risk plot (Fig. 1). It was recognized that funding to protect against a 10,000-year event was unlikely to be available, so structural mitigation designs were developed for both a 1,000-year and 10,000-year design event. The preferred mitigation option was a debris-flow conveyance channel (which was possible due to the steep fan gradient), with estimated cost ranging from \$4 Million to \$9 Million, depending on the selected design event. The local government does not have resources to provide this mitigation, but has spent the past several years seeking funding from provincial and federal grants. Unfortunately, they have not yet been successful in acquiring mitigation funding.

4. Quantitative Risk Management Benefits and Challenges

At each site for which it has been applied, the risk management phase of the QRM process has consistently identified an appropriate design event and preferred mitigation option, but has not frequently led to implementation of structural or non-structural mitigation measures. Therefore, it can be questioned whether the recent adoption of the QRM process at individual sites has improved management of debris-flow/flood hazards and risks on a society-wide scale. The short-comings could be a result of Canada’s fragmentary system of managing and funding natural hazard mitigation. Alternatively, and as long as grants are being issued from provincial and federal sources, it may simply be a matter of time until funding reaches high-risk communities. At times, it appears that a systematic risk-based provincial debris-flow prioritization should have preceded application and refinement of the QRM process at specific sites. Irrespective, the past decade of experience has highlighted several important benefits and challenges associated with the QRM process, as described in the following paragraphs.

When compared to a prescriptive standards-based process for debris-flow/flood hazard management, the QRM process has the following benefits:

- **Prioritization** – The QRM process provides a way for local government to compare and prioritize different hazard types and sites, and to justify mitigation funding applications to higher orders of government. This is particularly helpful in large, sparsely populated areas where there are more hazard areas than can be feasibly managed by a standards-based process. Costs and benefits of hazard management can be optimized, which can reduce long-term hazard management costs.
- **Site-specific** – The QRM process is specific to the hazard, elements at risk, stakeholders, and objectives of the community at the particular site. This leads to debris-flow/flood risk management that is targeted for the local risk profile. Hazards and risks are typically well understood at the conclusion of the QRM process.
- **Consideration of non-structural measures** – Non-structural mitigation measures, such as public education, land use planning, warning and evacuation protocols, and emergency response planning can substantially reduce debris-

flow/flood risk in some cases. The QRM process is well suited to demonstrate the level of risk reduction achieved by these measures, allowing them to be considered alongside structural mitigation.

- **Communication** – The QRM process provides a clear language to define the factors that contribute to debris-flow/flood risk. This promotes informed discussion of risk and risk management options by community members and decision makers and promotes community resilience. QRM as a communication tool could be thought of as a by-product to the products described in this paper, but improved communication may be the most effective risk management step.

The following points describe challenges of the QRM process at achieving risk reduction:

- **Complication** – Due to its flexibility, the QRM process can be difficult and expensive to implement and it requires input from the full range of stakeholders and specialists to execute. Most processes that are intended to be applied by a wide range of people and environments (e.g. building codes) are intentionally designed to be simple and rigid to facilitate adoption and compliance. Experts are required to carry out the QRM process, and experts are rare and expensive.
- **Limited adoption** – Currently only a handful of geotechnical consulting firms are familiar with the QRM methods as they pertain to debris flows and debris floods. A more widespread adoption is desirable to promote homogenous application. Similarly, decision makers need to be educated about the advantages and disadvantages of the QRM process to allow adaptation at the local government level.
- **Lack of context** – In theory, the QRM process would allow multiple geohazard types to be directly compared to a consistent risk tolerance threshold. However, in practice, debris-flow/flood hazards are mostly assessed independently from other geohazard types. The risk tolerance thresholds that have been referenced lead to selection of mitigation structure design events (e.g. 300-year, 1,000-year, or even 10,000-year return periods) that are much more stringent than is applied for other geohazards (e.g. floods, snow avalanches). This could lead to inappropriate allocation of society's resources to debris-flow/flood hazard sites and away from other higher-risk sites or hazard types where risk tolerance thresholds have not yet been applied.
- **Communication challenges** – The QRM process is promoted as a tool for decision making, but it requires decision makers who are well-informed about the QRM process and the origin and implications of risk tolerance thresholds. The QRM process is more complex than prescriptive standards-based methods, and it frequently refers to complex mathematics (e.g. 1×10^{-4}) that is unfamiliar to many people. Improved tools are needed to provide context and explain the “real” meaning of the quantities referred to by the QRM process.
- **Promotes stagnation** – In its current application, the QRM process may lead to designs that are too expensive to be funded, which leads to stagnation and a lack of risk management implementation. This is primarily due to strict risk tolerance thresholds that have been adopted (Fig. 1) and because extreme events (e.g. 1,000-year and 10,000 year) tend to control group risk (Jakob et al. 2018).

5. Towards a More Effective Debris-Flow/Flood Risk Management Process

From a worldwide hazard management perspective, the QRM process is rare. However, it is increasingly being adopted by western Canadian municipalities for management of debris-flow/flood hazards and risks due to its important benefits, including flexibility to meet needs of a particular community, utility as a prioritization tool, consideration of event consequences, and ability to directly compare non-structural to structural risk management measures. Theoretically, the QRM process is an effective tool for managing debris-flow/flood risk on a societal level, but applications to date have highlighted practical challenges, such as lack of funding, expertise, and momentum to construct mitigation, that need to be overcome. The following could improve QRM practice in Western Canada, and facilitate adoption of the QRM process in other regions and for other hazard types:

- Shift responsibility for geohazard (including debris-flow/flood) risk management from the municipal to provincial level. This was the case prior to 2003 in British Columbia, and may soon be the case in Alberta as far as steep creek hazards are concerned. Higher levels of government have more resources and are better suited to view hazards at a particular site in context with other hazard sites and hazard types.
- Adoption of consistent risk assessment and risk tolerance guidelines by provincial or national government that are applicable to all geohazard types. This will help promote distribution of resources to the most critical locations and hazard types.
- Educate geoscientists and engineers about the QRM process and its application, to address the current shortage of qualified practitioners.

- Develop tools to improve communication of QRM concepts, allowing the public to understand debris-flow/flood risks in the context of other hazard types and risks faced in everyday life.
- Develop strategies to promote action and implementation of risk reduction measures (where mitigation investments are appropriate). For example, at existing developments, this may include a shift away from defining a risk tolerance threshold that must be met, towards quantifying the risk reduction that could be achieved by various economically-feasible mitigation options. This may also include adopting a risk-informed decision making approach, which considers risk evaluation as one of many decision inputs, rather than an approach focused on precisely meeting the strictly-defined risk tolerance threshold line.
- Develop funding mechanisms that encourage short-term action with available resources, and long-term action through a disaster prevention fund allocated according to risk-based regional geohazard prioritization. Note that large-scale, regional geohazard risk prioritization has begun in British Columbia, setting the stage for policy review within the next few years.

Acknowledgements

Staff of the District of North Vancouver, Town of Canmore, Squamish Lillooet Regional District, District of Squamish, Metro Vancouver, and BC Ministry of Transportation and Infrastructure contributed to the ideas in this paper through years of project meetings and higher-level discussions about the benefits and challenges of the QRM process.

References

- Engineers and Geoscientists of British Columbia (EGBC), 2010, Guidelines for legislated landslide assessments for proposed residential developments in BC.
- Austrian Standards Institute (ASI), 2009, ONR 24800 Protection works for torrent control – Terms and their definition as well as classification, in German.
- Baecher, G.B., Abedinsohi, F., and Patev, R.C., 2015, Societal Risk Criteria for Loss of Life Concepts, History, & Mathematics, Univ. of Maryland.
- Cave, P.W., 1993, Hazard Acceptability Thresholds for Development Approvals by Local Government, originally presented at the British Columbia Geologic Hazards Workshop, February 20 and 21, 1991, revised in 1993.
- Fell, R., Ho, K.K.S., LaCasse, S., Leroy, E., 2005, A framework for landslide risk assessment and management, *in* Proceedings, International Conference on Landslide Risk Management, May 31-June 3, 2005, Vancouver.
- Geotechnical Engineering Office (GEO), 1998, Landslides and boulder falls from natural terrain: Interim risk guidelines: GEO Report No. 75, The Government of Hong Kong Special Administrative Region.
- Geotechnical Engineering Office (GEO), 1995, Feasibility Study for QRA of Boulder Fall Hazard in Hong Kong: GEO Report No. 80, The Government of Hong Kong Special Administrative Region.
- Holm, K., Jakob, M., Kimball, S., Strouth, A., Esarte, A., and Camire, F., 2018, Steep Creek Geohazard Risk and Risk Control Assessment in the Town of Canmore, Alberta, *in* Proceedings, Geohazards 7 conference, June 2018, Canmore, Alberta.
- Hungr, O., 2016, A review of landslide hazard and risk assessment methodology. *in* Aversa et al, eds., Landslides and Engineered Slopes. Experience, Theory and Practice, Associazione Geotecnica Italiana, Rome, Italy, 25 p.
- Hungr, O., Clague, J., Morgenstern, N., VanDine, D., and Stadel, D., 2016, A review of landslide risk acceptability practices in various countries, *in* Aversa et al, eds., Landslides and Engineered Slopes. Experience, Theory and Practice, Associazione Geotecnica Italiana, Rome, Italy.
- IUGS Working Group on Landslides, Committee on Risk Assessment (IUGS), 1997, Quantitative risk assessment for slopes and landslides – the state of the art, *in* Cruden, D., and Fell, R., Landslide Risk Assessment, Proceedings of the International Workshop on Landslide Risk Assessment, Honolulu Hawaii, USA, 19-21 February 1997, Balkema, Rotterdam, pp. 3-12.
- Jakob, M., Friele, P., Porter, M., Hungr, O., McDougall, S., 2018, Should BC plan for the the 1:10,000-year probability landslide event? *Geotechnical News* 36(3): 34-38.
- Jakob, M., 2019, Debris-flow Hazard and Risk Assessments – A Practitioner’s View, *in* 7th Int. Conf. on Debris-Flow Hazards Management, Golden Colorado, USA, June 2019.
- Lateltin, O., Haemmig, C., Raetzo, H., Bonnard, C., 2005, Landslide risk management in Switzerland, *Landslides*, v. 2, p. 313-320.
- Malone, A.W., 2004, The Story of Quantified Risk and its Place in Slope Safety Policy in Hong Kong, *in* Glade, T., Anderson, M., and Crozier, M.J., *Landslide Hazard and Risk*, John Wiley & Sons, Ltd.
- Ministry of Construction Japan (MoC), 2000, Technical Guidelines for Debris Flow Control Measures, River bureau, sediment control department, sediment control division.
- Moase, E., 2017, Guidance for debris-flow and debris-flood mitigation design in Canada [Master’s Thesis]: Simon Fraser University, 169 p.
- National Research Council (NRC), 2015, National Building Code of Canada.
- Porter M., and Morgenstern N., 2013, Landslide Risk Evaluation – Canadian Technical Guidelines and Best Practices related to Landslides: a national initiative for loss reduction: Geological Survey of Canada, Open File 7312, 21 p.
- VanDine, D.F., 2012, Risk Management – Canadian Technical Guidelines and Best Practices Related to Landslides: Geological Survey of Canada, Open File 6996, 8 p.
- VanDine, D.F., 2018, Evolution of Landslide Hazard and Risk Assessments in Canada, Proceedings, Geohazards 7 conference, June 2018, Canmore, Alberta.

Semi-automated regional scale debris-flow and debris-flood susceptibility mapping based on digital elevation model metrics and Flow-R software

Matthieu Sturzenegger^{a,*}, Kris Holm^a, Carie-Ann Lau^a, Matthias Jakob^a

^a*BGC Engineering, 500 – 980 Howe Street, Vancouver V6Z 0C8, Canada*

Abstract

Regional scale debris-flow or debris-flood susceptibility mapping based on terrain analysis is limited by a high degree of effort and the availability of surface evidence for past events, which may be obfuscated by development or obscured by repeat erosion or debris inundation. This paper presents a semi-automated methodology for debris-flow and debris-flood susceptibility mapping at regional scale based on a combination of digital elevation model (DEM) metrics to identify potential source zones, and flow propagation simulations using the Flow-R code. The DEM metrics allow identification and preliminary, process-based classification of streams prone to debris flow and debris flood, respectively. Flow-R simulations are based on a combination of spreading and runout algorithms considering DEM topography and empirical runout parameters. The methodology was first tested in a region of the Canadian Rocky Mountains, where detailed debris-flood hazard assessments had been previously undertaken based on both field mapping and numerical modeling. It was then applied over two regions, with 22,000 km² and 55,000 km² areas, respectively, in central British Columbia, Canada. One important advantage of the presented methodology is the limited amount of data required to generate a preliminary susceptibility map over a large region. Once incorporated in a risk assessment framework, this map can be used to prioritize more detailed assessments. The methodology was also applied at a higher level of detail to an approximately 30 km long roadway corridor in Southwestern British Columbia. At the assessment level of this project, the methodology allowed generation of a susceptibility map which considered the cumulative contribution of several potential source zones within each debris-flow and debris-flood watershed. This map allowed risk-based prioritization and supported debris-flow risk reduction decision making.

Keywords: debris flow; debris flood; susceptibility mapping; digital elevation model; Flow-R; risk assessment

1. Introduction

Debris-flow and debris-flood susceptibility mapping based on terrain analysis is limited by the availability of surface evidence for past events, which may be obfuscated by development or obscured by progressive erosion or debris inundation. In addition, it can be limited by the relatively high level of effort to map large regions. To address these limitations, this paper presents a semi-automated methodology based on stream segments delineated from digital elevation models (DEMs), morphometric statistics on DEMs, and the Flow-R model ("Flow-R" refers to "Flow path assessment of gravitational hazards at a Regional scale") developed by Horton et al. (2008, 2013). This methodology allows identification, at a preliminary level of detail, of potential debris-flow or debris-flood hazard and modeling of their runout susceptibility over large study areas.

Using Flow-R, Horton et al. (2011) demonstrated the control of DEM topography on debris-flow propagation. Park et al. (2013) found good agreement between debris-flow paths predicted with Flow-R and an inventory of past events near Seoul, South Korea, despite the paucity of parameters for rheological properties and erosion rate required in the software. The software also provided reliable results within the framework of the development of a debris-flow susceptibility map at regional to national scale in Norway (Fisher et al., 2012). Blais-Stevens and Behnia (2016)

* Corresponding author e-mail address: msturzenegger@bgcengineering.ca

undertook susceptibility mapping with Flow-R in northwestern Canada, and their results highlighted debris-flow potential in a number of channels that had not been previously documented. These results are consistent with the objective of susceptibility mapping, which is to consider the largest credible area affected by geohazard in the process of prioritizing future, more refined work. Further validation of the Flow-R software has been documented by Pastorello et al. (2017) and Kang and Lee (2018).

A few authors attempted to integrate Flow-R into preliminary hazard assessments, which typically require definition of landslide magnitude and frequency. Based on the assumption that larger debris-flow events are less frequent and able to travel for longer distances than smaller, more frequent ones (e.g., Corominas and Moya, 2008), Blahut et al. (2010) and Kappes et al. (2011) defined three magnitude-frequency runout scenarios corresponding to low, moderate and high hazard by means of different angles of reach (the angle of reach being one of Flow-R main input parameters; see also Corominas, 1996). Blahut et al. (2010) simulations were coupled with ratings for debris-flow hazard initiation probability.

This paper presents four case studies using Flow-R for both debris-flow and debris-flood susceptibility mapping. The first case reports on a pilot study comparing Flow-R simulation results with detailed analysis of debris flood undertaken with the software FLO-2D. In the second and third ones, Flow-R results are integrated into regional scale debris-flow and debris-flood risk prioritization assessments, whose objective are to prioritize future detailed assessment on alluvial fans with higher risk potential. Finally, the fourth case study shows a similar example at a refined level of detail, where Flow-R was used to prioritize mitigation work on selected segments of roadway on a series of alluvial fans.

2. Methodology

2.1. Definitions

The term “landslide susceptibility” was defined by Fell et al. (2008) as “a quantitative or qualitative assessment of the classification, volume (or area), and spatial distribution of landslides which exist or potentially may occur in an area”. Susceptibility may be used for characterization of landslide potential both at the source and within the impact zone. In the two first case studies described in this paper, the term is primarily used to describe areas susceptible to geohazard impact, and no effort was made to classify source zones according to their likelihood of generating landslides. In the third example, classification and weighting of debris-flow source zones was incorporated based on experience and knowledge of the study area.

The proposed methodology required two main steps. The first one is the identification of steep creek geohazard sources, and the second one consists in the estimation of geohazard propagation and runout susceptibility. In this study, steep creek geohazards include both debris flow and debris flood. Debris flow is defined as a very rapid to extremely rapid surging flow of saturated debris in a steep channel, with strong entrainment of material and water from the flow path (Hungri et al., 2014). Debris floods correspond to very rapid flows of water, heavily charged with debris, in steep channels; their peak discharge is comparable to that of water floods (Hungri et al., 2014).

2.2. Identification of debris-flow and debris-flood sources

In this study, stream segments, generated based on DEMs, are used as “proxy” for steep creek geohazard source zones. This approach was chosen in part because it is computationally efficient across large regions. The segments need to be classified to differentiate the ones most likely to generate debris flows from the ones most likely to generate debris floods. In the proposed methodology, process types are classified using geomorphometric parameters such as the Melton ratio and watershed length. The former corresponds to the ratio between watershed relief and the square root of watershed area (Melton, 1957). The latter is calculated as the total channel length upstream of a given stream segment to the stream segment farthest from the fan apex. These terrain parameters are a good screening level indicator of the propensity of a creek to dominantly produce debris floods or debris flows (Holm et al., 2016). It should be noted that there is a continuum between debris flow and debris flood, which depends on factors such as velocity, sediment concentration and channel slope angle. As such some steep creek processes may present behavior in between typical debris flow or debris flood. In addition, both processes can occur within the same watersheds and consequently alluvial fans may not be completely assigned to one single process type.

2.3. Steep creek geohazard propagation and runout susceptibility modeling

FLOW-R simulates propagation of debris flows and debris floods through a DEM. In this study, sections of the freely available Canadian Digital Elevation Model (CDEM) at 20 m resolution were used. This resolution was selected, because it was the highest resolution available which covered the entire study areas. Propagation is modelled using spreading algorithms and simple frictional laws. Both spreading algorithms and friction parameters need to be calibrated by back-analysis of past events or based on geomorphological observations (e.g., alluvial fans).

FLOW-R can generate the maximum susceptibility that passes through each cell of the DEM, or the sum of all susceptibilities passing through each cell. The former is calculated using the “quick” calculation method and is used to identify the area susceptible to landslide processes. The “quick” method propagates the highest source segment, and iteratively checks the remaining source zones to determine if a higher energy or susceptibility value will be modelled. The latter is calculated in FLOW-R using the “complete” method and can be used to identify areas of highest relative regional susceptibility. The complete method triggers propagation from every cell in the source segments and then calculates the sum of susceptibilities at each cell of the DEM. It should be noted that the sum of susceptibilities has no physical meaning; rather it can be used as a regional comparison between sites to determine areas with higher hazard potential. Debris-flow and debris-flood propagations were modelled separately.

3. Case Studies

3.1. Pilot Study: Canmore Area

We simulated an initial set of debris floods in the Canmore area, where a number of debris-flood fans had been previously studied at a detailed level (Jakob et al., 2017; Holm et al., 2018). Canmore is located in the Front Range of the Canadian Rocky Mountains, approximately 90 km west of Calgary. The objective was to compare Flow-R propagation results with detailed numerical modeling results. The detailed numerical modeling had been undertaken for a spectrum of debris-flood scenarios on each creek, using the software FLO-2D (2004) and provided estimates of flow depth within and beyond alluvial fans.

Calibration of Flow-R propagation parameters focused on attempting to reproduce the extent of debris-flood potential inundation of the worst-case scenario, corresponding to a 1000-3000-year return period event. The “quick” method was used for this purpose, as we were mostly interested in the maximum extent of potential inundation areas. The results were satisfying, as illustrated in Fig. 1, and provided confidence that Flow-R is able to delineate potential areas susceptible to debris flood at regional scale. Calibrated parameters in this pilot study are shown in Table 1. It should be noted that the FLO-2D model used a 10-m DEM resolution, while the DEM resolution used in Flow-R was 20 m.

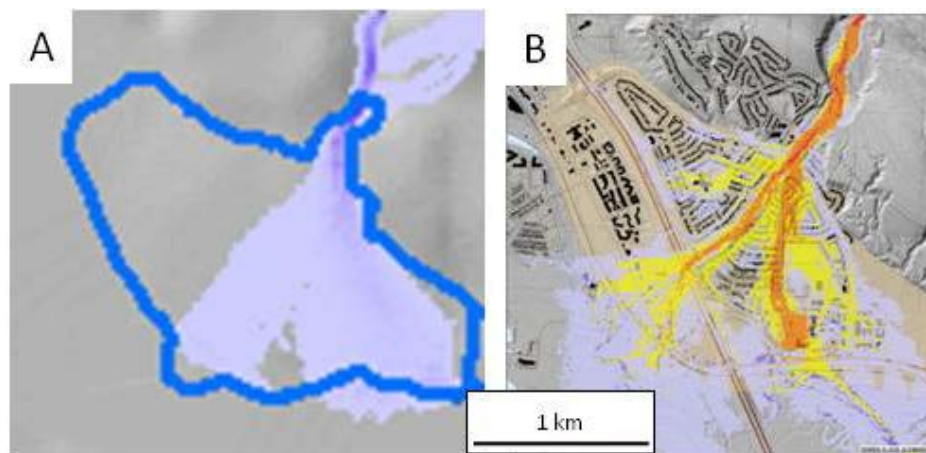


Fig. 1. Comparison between Flow-R propagation extent (A) and FLO-2D modeling results (B) at one of the alluvial fans of the Canmore area. The blue polygon in A and beige background in B outline a mapped alluvial fan. The purple color in B shows the extent of flow simulated with FLO-2D (yellow to red zone correspond to various flow impact intensities). The scenario shown in (B) is the largest modelled debris-flood scenario on this creek, corresponding to an estimated 1000-3000-year return period event.

Table 1. Calibrated debris-flood parameters used in Flow-R (Canmore)

Selection	Flow-R Parameter	Value
Directions algorithm	Holmgren (1994) modified	dh = 2, exponent = 1
Inertial algorithm	Weights	Gamma (2000) - Cosinus
Friction loss function	Travel angle	2-3°
Energy limitation	Velocity	< 15 m/s

Note that Flow-R could not model avulsions that are likely at culverts and bridges and which could send flow towards the western portion of the fan as shown on Fig. 1. Flow-R also cannot simulate bank erosion, channel scour and aggradation, all of which can affect flow behavior and thus risk. These limitations need to be considered in any site-specific application.

3.2. Regional scale assessments: Central British Columbia

The two case studies in Central British Columbia were part of regional scale steep creek geohazard risk prioritization studies. The study areas covered the entire Regional District of Central Kootenay (RDCK, 22,000 km²) and the entire Thompson River Watershed (TRW, 55,000 km²), British Columbia. The objective of the prioritization studies was to characterize and prioritize steep creek hazards that might impact developed properties. The studies focused on alluvial fans, as these are the landforms commonly occupied by elements at risk. Relative ratings of the likelihood that events occur and impact elements at risk were combined with consequence ratings to assign priority ratings to each fan. The results supported risk management decisions, policymaking, and prioritization of further assessment.

Flow-R modelling focused on one component of the prioritization studies, the assignment of impact likelihood ratings. An impact likelihood rating was assigned to each fan of the study areas considering the relative spatial likelihood that geohazard events result in uncontrolled flows that could impact elements at risk. Uncontrolled flows were assumed to result from avulsions, whose potential depends of characteristics such as channel confinement and surface evidence for previous avulsions. Flow-R propagation parameters were calibrated based on typical parameters from the literature, experience with calibrated case studies (e.g., Section 3.1), and using the extent of mapped alluvial fans within the study areas. Table 2 and Table 3 show the calibrated debris-flow and debris-flood parameters, respectively, for the RDCK case study.

Table 2. Calibrated debris-flow parameters used in Flow-R for the RDCK assessment.

Selection	Flow-R Parameter	Value
Directions algorithm	Holmgren (1994) modified	dh = 2, exponent = 1
Inertial algorithm	Weights	Gamma (2000)
Friction loss function	Travel angle	5°
Energy limitation	Velocity	< 15 m/s

Table 3. Calibrated debris-flood parameters used in Flow-R for the RDCK assessment.

Selection	Flow-R Parameter	Value
Directions algorithm	Holmgren (1994) modified	dh = 2, exponent = 1
Inertial algorithm	Weights	Cosinus
Friction loss function	Travel angle	4°
Energy limitation	Velocity	< 15 m/s

The Flow-R “complete” method with sum of susceptibilities was used. The summed susceptibility values followed a negative exponential distribution (Fig. 2). They were classified into zones of very low, low, moderate, and high relative susceptibility based on comparison to fans with the clearest evidence of the extent of previous

events, including avulsion channels and deposits visible on LiDAR imagery. Zones of the DEM with summed susceptibility values lower than a threshold corresponding to the 70th percentile were attributed ‘very low’ regional susceptibility (i.e., ‘very low’ susceptibility include the majority of areas covered by Flow-R simulations). Zones of ‘low’ regional susceptibility were defined between the 70th and 85th percentile (the 85th percentile corresponding approximately to the mean susceptibility value); ‘moderate’ and ‘high’ susceptibility were defined between the 85th and 95th percentile, and greater than the 95th percentile, respectively (Fig. 2). Portions of alluvial fans not encompassed by susceptibility modelling were interpreted as having “very low” regional susceptibility where modern fan morphometry encouraged flow away from the unaffected area, or not affected by debris flows/floods where deep channel incision indicated paleofans.

Because the study objective was to compare relative risk at a fan level of detail, the analysis did not include estimation of spatial impact likelihood for individual elements at risk on a fan. However, average impact likelihood ratings were assigned to compare fans, based on the proportion of each mapped fan area covered by moderate and high Flow-R susceptibilities. The initial impact likelihood ratings (based on the Flow-R “complete” method with sum of susceptibilities) were adjusted to consider avulsion susceptibility or recorded evidence, as Flow-R susceptibility modeling does not account for recent activity on the fans. Although impact likelihood ratings were assigned only to mapped alluvial fans, Flow-R simulations extending beyond the fan boundary were also considered when evaluating sites for potential future assessment. Impact likelihood ratings were verified based on both geomorphic mapping and records of past events.

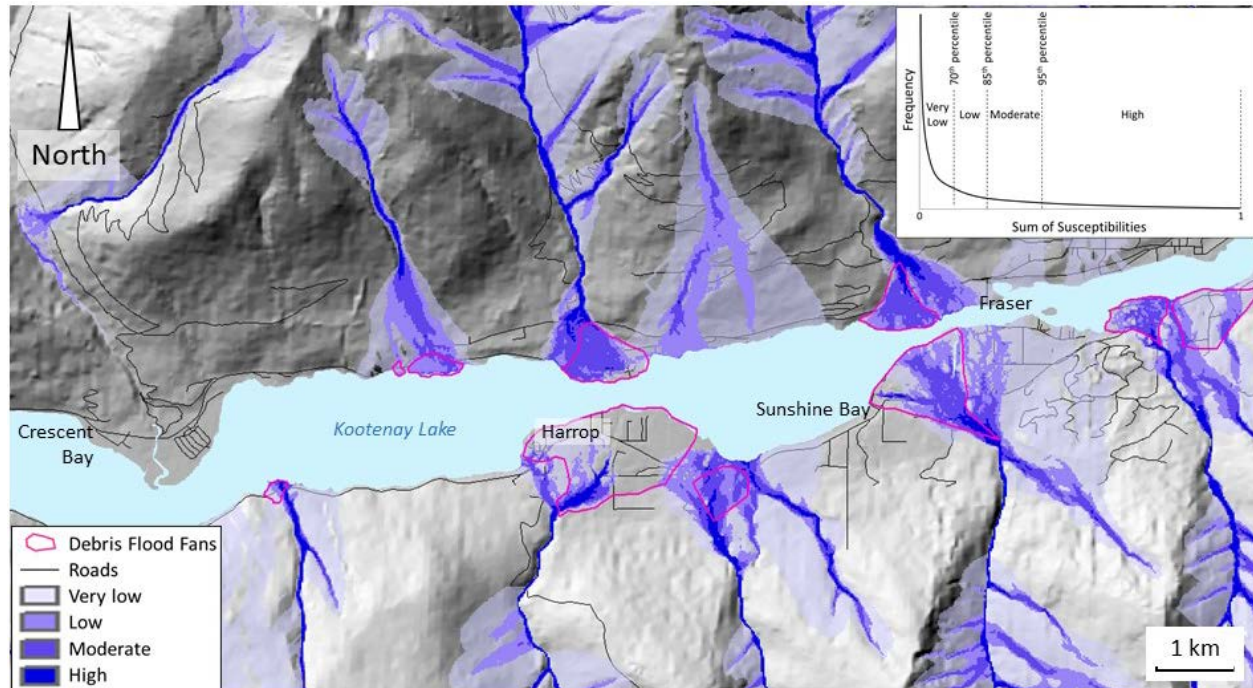


Fig. 2. Debris-flood susceptibility map for a section of the RDCK study area showing the spatial distribution of very low, low, moderate and high susceptibility. The inset figure shows a sketch illustrating the negative exponential distribution of summed susceptibilities and the percentiles used to define zones of very low, low, moderate and high susceptibility.

3.3. Refined regional scale assessment: roadway corridor in southwestern British Columbia

This study aimed to risk-prioritize creeks subject to both debris flows and debris floods along a 30 km long roadway corridor in southwestern British Columbia. The goal of creek prioritization was to facilitate objective and science-based allocation of resources for mitigation along a roadway located at the toe of steep creeks, without requiring detailed and costly hazard frequency-magnitude analysis and scenario modelling at each creek. Debris-flow and debris-flood hazards were categorized based on both relative frequency of initiation (rating of source areas) and their susceptibility to impact and cover the roadway.

FLOW-R was used to develop susceptibility zones within each fan of the entire study area, allowing comparison of relative susceptibility throughout the corridor. For this purpose, the “complete” method with sum of susceptibilities was used after calibration of propagation parameters. The summed susceptibility values were classified into areas of low, moderate, and high susceptibility in a similar manner as described in Section 3.2. Areas within alluvial fans not inundated by Flow-R modelling represent inactive zones, considering the present-day morphometry of the DEM.

The results suggest that the methodology allows direct comparison of the relative debris-flow/debris-flood runoff susceptibility for the alluvial fans within the study area. Areas of higher relative regional runoff susceptibility corresponded to watersheds with higher susceptibility of the source zones (i.e., higher number of potential debris flows/floods that can reach an alluvial fan), as well as increased control of topographic features (i.e., incised channels or avulsion paths within alluvial fan). Fig. 3 compares the calculated susceptibility values with the extent of debris-flow deposits from past events. As explained in Section 2.3, the susceptibility values calculated in this study have no physical meaning, rather were used for comparison between sites within the roadway corridor to determine higher relative hazard potential.

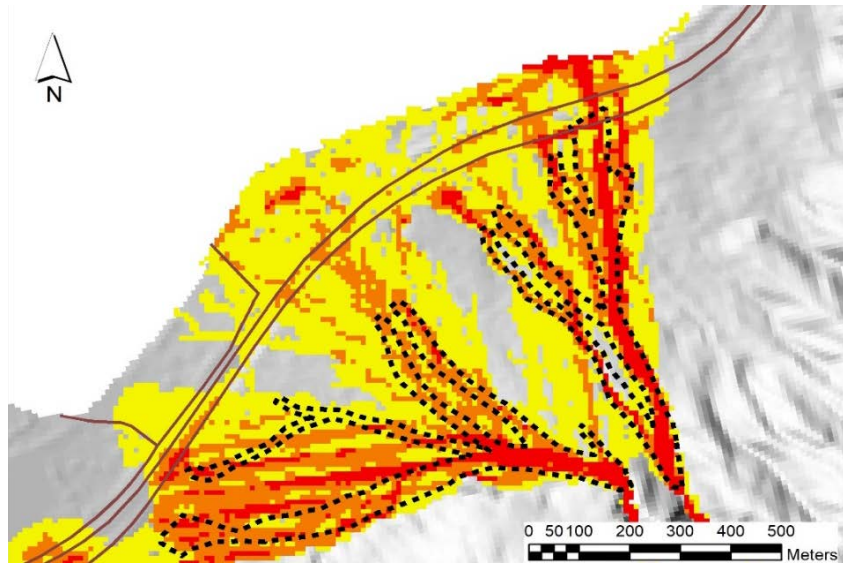


Fig. 3. Map comparing the extent of recent debris-flow deposits (black, dashed lines) on an alluvial fan of the roadway corridor with the results of Flow-R modeled susceptibility, where yellow = low susceptibility, orange = moderate susceptibility, and red = high susceptibility. The alignment of the roadway is shown with brown lines.

4. Discussion

This paper presents a semi-automated methodology for debris-flow and debris-flood susceptibility mapping at regional scale, which combines GIS-based identification of geohazard sources with geohazard propagation modeled using the software Flow-R. Four case studies show that modeled susceptibility includes areas inundated by known debris-flow or debris-flood events and match active alluvial fan boundaries. This provides a basis to evaluate relative hazards in cases where detailed frequency-magnitude analyses and scenario modelling is not feasible.

4.1. Semi-automated steep creek geohazard source identification

Steep creek geohazard source zones were identified as stream segments automatically generated from DEMs. It is possible that stream segments were not generated for very small watersheds. At the scale of the regional studies, we consider that very small watersheds are unlikely to represent a significant steep creek geohazard risk. Another potential limitation of using stream segments as source zones is that steep creek geohazards rarely initiate exactly in stream channels and are more commonly triggered by landslides initiating on channel side slopes. Consequently, defining debris-flow source zones based on stream segments should be considered an empirically-based proxy for actual source areas, because it can be efficiently completed and calibrated for large regions. This simplification does not affect propagation results significantly.

The methodology for source identification applied to the Canmore, RDCK and TRW case studies answered the question, “given debris-flow/flood occurrence, what is the runout/spreading?”. Watersheds can exist where debris-flow source zones are mapped but no actual debris source exists (e.g., bare rock channels with insufficient sediment supply), or where limited source areas result in lower runout susceptibility. This simplification was necessary due to the limited data concerning sediment availability at regional scale. For more refined studies, such as the roadway case study, where more detailed information was available about steep creek source zones, rating of source segments can be integrated.

The proposed semi-automated approach for steep creek process type classification (based on Melton ratio and watershed length) systematically identifies stream segments as debris-flow or debris-flood sources. In reality, steep creek processes may behave transitionally between debris flows and debris floods, and the two processes may occur alternatively on the same alluvial fan. In the proposed methodology, both debris-flow and debris-flood stream segments can exist within the same watershed and consequently, alluvial fans may be inundated by Flow-R simulations from both debris-flow and debris-flood segments. To account for this limitation, expert judgement was applied to classify each alluvial fan as the most likely process type.

4.2. Susceptibility mapping with Flow-R

Propagation parameters in Flow-R are empirical and require calibration. In the case studies presented in this paper, debris-flow and debris-flood propagation parameters were calibrated so that the extent of the simulations reproduces as closely as possible the extent of mapped alluvial fans. In terms of frequency-magnitude relationship, the susceptibility mapping corresponds to the affected fan areas of rare and large events, and in many cases the modelled extent could be viewed as the largest credible event.

The RDCK case study illustrates the applicability of susceptibility mapping at regional scale using Flow-R. It is important to note that for larger study areas (e.g., TRW case study), application of a single set of model parameters per process may not be appropriate; the study area may need to be subdivided into sub-regions based on their physiographic, geological and/or climatic conditions, and model parameters calibrated independently for each sub-region. It is also interesting to note that two of the studied watersheds in the Canmore area contain dams. Such watersheds can be expected to require specific model parameters for susceptibility mapping. This is consistent with previous work by Pastorello et al. (2017).

Calculation of the sum of susceptibilities in Flow-R allows subdivision of alluvial fans in zones with various susceptibility levels, as illustrated in Sections 3.2 and 3.3. In the case study presented in Section 3.3, this approach allows consideration of individual elements at risk within the fans of a studied region.

Flow-R propagation is controlled by present-day topography of alluvial fans, as provided by DEMs. The summed susceptibilities allow consideration of watershed size and associated cumulative potential source zones. In addition, if source zones are weighted (e.g., Section 3.3), modelled susceptibility accounts for initiation frequency implicitly and in a relative way. However, the software does not fully take into consideration evidence for past avulsions in the assessment of fan activity and potential for uncontrolled flows.

5. Perspective

The case studies presented in this paper illustrate a methodology for steep creek geohazard susceptibility mapping combining semi-automated identification of geohazard sources with propagation simulations modeled using the software Flow-R. The reported case studies are characterized by different assessment levels, depending on the scale of the study area and the degree of understanding and knowledge of steep creek geohazards. The following is an attempt to define three levels of detail for debris-flow/flood hazard incorporating the proposed methodology:

- High/screening level assessment: Flow-R simulations are run from stream segments using the “quick” method to generate susceptibility maps corresponding to the maximum expected extent of steep creek geohazards. These maps allow identification of locations where elements at risk intersect zones susceptible to debris-flow or debris-flood hazards.
- Regional scale assessment: in the RDCK and TRW case studies, Flow-R simulations are run from stream segments using the “complete” method to generate susceptibility maps corresponding to the maximum credible extent of steep creek geohazards, and allowing rating each fan using an impact likelihood value. Combined with estimates of hazard likelihood and potential consequences, the rating provides an objective, practical approach

to prioritize hundreds to thousands of steep creek fans across many thousands of square kilometers. It should be noted that impact likelihood ratings are for entire fans and therefore not estimates of spatial probability of impact for specific elements at risk, which would vary depending on their location on the fans.

- Refined regional scale assessment: in the roadway case study, a similar approach as in the RDCK and TRW case studies was used, but the relative susceptibility rating was used to identify zones of higher susceptibility within alluvial fans to prioritize allocation of funds for mitigation work. This is a first step towards estimation of the spatial probability of impact for specific elements at risk (sections of the roadway in this case). However, the approach does not replace quantitative estimates of the spatial probability of impact for specific element at risk, as would be completed in a detailed study. Since susceptibility modelling does not consider volume or flow peak discharge, it is not suited for detailed risk analyses or risk control design, which require numerical modeling of flow extent, depth and velocity for specific hazard scenarios.

Acknowledgements

We would like to thank the Town of Canmore, the Regional District of Central Kootenay, and the British Columbia Ministry of Transportation and Infrastructure for granting permission to use project data in this paper.

References

- Blahut, J., Horton, P., Sterlacchini, S., and Jaboyedoff, M., 2010, Debris-flow hazard modelling on medium scale: Valtellina di Tirano, Italy: *Natural Hazards Earth System Sciences*, v. 10, p. 2379–2390.
- Blais-Stevens, A., and Behnia, P., 2016, Debris-flow susceptibility mapping using a qualitative heuristic method and Flow-R along the Yukon Alaska Highway Corridor, Canada: *Natural Hazards Earth System Sciences*, v. 16, p. 449–462.
- Corominas, J., 1996, The angle of reach as a mobility index for small and large landslides: *Canadian Geotechnical Journal*, v. 33, p. 260–271.
- Corominas, J., and Moya, J., 2008, A review of assessing landslide frequency for hazard zoning purposes: *Engineering Geology*, v.102, p. 193–213.
- Fell, R., Corominas, J., Bonnard, C., Cascini, L., Leroy, E., and Savage, W. Z., 2008, Guidelines for landslide susceptibility, hazard and risk zoning for land use planning: *Engineering Geology*, v. 102, p. 85–98.
- Fischer, L., Rubensdotter, L., Sletten, K., Stalsberg, K., Melchiorre, C., Horton, P., and Jaboyedoff, M., 2012, Debris-flow modeling for susceptibility mapping at regional to national scale in Norway, *in Proceedings, 11th International and 2nd North American Symposium on Landslides*, Banff, Canada, June 2012.
- FLO-2D Software Inc., 2004, FLO-2D User's manual version 2004.10, October 2004.
- Gamma, P., 2000, Dfwalk – Ein Murgang-Simulationsprogramm zur Gefahrenzonierung: Geographisches Institut der Universität Bern.
- Holm, K., Jakob, M., Scordo, E., Strouth, A., Wang, R., and Adhikari, R., 2016, Identification, prioritization, and risk reduction: steep creek fans crossed by highways in Alberta, *in Proceedings, GeoVancouver 2016 Conference*, Vancouver, Canada, October 2016.
- Holm, K., Jakob, M., Kimball, S., Strouth, S., Esarte, A., Camire, F., 2018, Steep creek risk and risk control assessment in the Town of Canmore, Alberta, *in Proceedings, Geohazards 7 Conference*, Canmore, Canada, June 2018.
- Holmgren, P., 1994, Multiple flow direction algorithms for runoff modelling in grid-based elevation models: an empirical evaluation: *Hydrological Processes*, v. 8, p. 327–334.
- Horton, P., Jaboyedoff, M., and Bardou, E., 2008, Debris-flow susceptibility mapping at a regional scale, *in Locat, J., Perret, D., Turmel, D., Demers, D., and Leroueil, S., eds, 4th Canadian Conference on Geohazards*, Quebec, Canada, May 2008, p. 339–406.
- Horton, P., Jaboyedoff, M., Zimmermann, M., Mazotti, B., and Longchamp, C., 2011, Flow-R, a model for debris-flow susceptibility mapping at a regional scale – some case studies, *in Proceedings, 5th International Conference on Debris-Flow Hazards Mitigation*, Padua, Italy; *Italian Journal of Engineering Geology and Environment*, p. 875–884.
- Horton, P., Jaboyedoff, M., Rudaz, B., and Zimmermann, M., 2013, Flow-R, a model for susceptibility mapping of debris-flows and other gravitational hazards at regional scale: *Natural Hazards Earth System Sciences*, v. 13, 869–885.
- Hungr, O., Leroueil, S., and Picarelli, L., 2014, The Varnes classification of landslide types, an update: *Landslide*, v. 11, p. 167–194.
- Jakob, M., Weatherly, H., Bale, S., Perkins, A., and MacDonald, B., 2017, A multi-faceted debris-flood hazard assessment for Cougar Creek, Alberta, Canada: *Hydrology*, v. 4 (7), 33 p.
- Kang, S., and Lee, S.-R., 2018, Debris-flow susceptibility assessment based on an empirical approach in the central region of South Korea: *Geomorphology*, v. 308, p. 1–12.
- Kappes, M. S., Malet, J.-P., Remaitre, A., Horton, P., Jaboyedoff, M., and Bell, R., 2011, Assessment of debris-flow susceptibility at medium-scale in the Barcelonnette Basin, France. *Natural Hazards Earth System Sciences*, v. 11, p. 627–641.
- Melton, M.A., 1957, An analysis of the relation among elements of climate, surface properties and geomorphology: Department of Geology, Columbia University, New York, Technical Report 11.
- Park, D.W., Nikhil, N.V., and Lee, S.R., 2013, Landslide and debris-flow susceptibility zonation using TRIGRS for the 2011 Seoul landslide event: *Natural Hazards Earth System Sciences*, v. 13, p. 2833–2849.
- Pastorello, R., Michelini, T., and D'Agostino, V., 2017, On the criteria to create a susceptibility map to debris flow at a regional scale using Flow-R: *Journal of Mountain Sciences*, v. 14 (4), p. 621–635.

Study on methods for assessing sediment disaster inundation zone in regions with insufficient data: Case study of the Aranayake disaster in Sri Lanka

Kiyotaka Suzuki^a, Taro Uchida^b, Naoki Matsumoto^b, Kana Nakatani^c, and Gamini Jayathissa^d

^aPASCO Corporation, 1-1-2 Higashiyama Meguro-ku, Tokyo 153-0043, Japan

^bNational Institute for Land and Infrastructure Management, 1 Asahi Tsukuba, Ibaraki 305-0804, Japan

^cKyoto University, Kitashirakawaoiwakecho Kyoto Sakyo-ku, Kyoto 606-8502, Japan

^dLandslide Research and Risk Management Division, National Building Research Organization, 99/1, Jawattha Road Colombo -05, Sri Lanka

Abstract

In Sri Lanka, landslide disasters and floods occur frequently and have caused much damage. So, landslide susceptibility has been mapped and published as the Landslide Hazard Zonation Map (LHZM). Although the LHZM shows the susceptibility of landslide initiation, it does not show the potential inundation zone of landslides. As a characteristic of land use in Sri Lanka, plantation farms for cultivating Ceylon tea, natural rubber and other products are located on slopes. And, many people live on slopes. Therefore, it is necessary to assess the potential inundation zone not only in the deposited area but also the runout area below hillslopes. Recently, diverse numerical simulation models have been developed for describing landslides and debris flows. These numerical simulations are effective tools for addressing landslide problems in Sri Lanka. However, to use numerical simulation, we have to input and validate a variety of environmental variables and, unfortunately, adequate information on past disasters and environmental conditions is still lacking. Therefore, we studied methods for assessing the potential sediment disaster inundation zone in regions where empirical methods cannot be applied due to insufficient past disaster records. We applied the "HyperKANAKO" debris-flow model for describing inundated zone due to recent debris flow in Sri Lanka. We tested the sensitivity of input conditions such as the (1) percentage of fine grains (fluid density and sediment concentration), (2) landslide volume, (3) input hydrograph (peak flow rate and duration), and (4) representative sediment particle diameter. We confirmed that, for regions with insufficient disaster records, the potential inundation zone due to debris flow can be assessed using numerical simulation. However, we also found that the calculation result is strongly controlled by (1), (2), and (4), so it is necessary to set these parameters appropriately.

Keywords: debris flow; numerical simulation; input condition; hazard map; Aranayake disaster

1. Introduction

1.1. Background and study objective

In Sri Lanka, landslide disasters and floods occur frequently and have caused much damage. Moreover, these landslides often turned into debris flows and run out long distance. Landslide susceptibility has been mapped and published as the Landslide Hazard Zonation Map (LHZM) by the National Building Research Organization (NBRO, Sri Lanka). Although the LHZM shows the susceptibility of landslide initiation, it does not show the potential inundation zone caused by landslides. In Sri Lanka, it is considered that disasters risk is increasing as lowland development and slope excavation are carried out without conscious of disasters. Furthermore, there is a characteristic that farmland for cultivating Ceylon tea, natural rubber and other products is on the slope. And, many

* Corresponding author e-mail address: kiky6523@pasco.co.jp

people live on slopes. Therefore, it is necessary to assess the potential inundation zone not only in the deposited area but also the runoff area on hillslopes. Recently, diverse numerical simulation models have been developed for describing landslide and debris flow (e.g., O'Brien et al., 1993; Iverson and Denlinger, 2001; Rickenmann et al., 2006; Frank et al., 2015; Suzuki et al., 2016). These numerical simulations are effective tools for addressing landslide problems in Sri Lanka. To use numerical simulation, we have to input and validate a variety of environmental variables. However, unfortunately, adequate information on past disasters and environmental conditions is still lacking. Therefore, we tested the applicability of numerical simulation using "HyperKANAKO" to assessing the potential sediment disaster inundation zone due to debris flow in regions where empirical methods cannot be applied due to insufficient records of past disaster.

2. Study site

A large-scale landslide occurred in Aranayake, Kegalle District, Sri Lanka, on May 17, 2016 (Fig. 1). This landslide occurred due to heavy rain caused by tropical cyclone. In terms of human loss, 31 people died and 96 went missing in Aranayake (Handa et al., 2018). Fig. 1a is an aerial photograph taken during a helicopter survey on May 22, while Fig. 1b shows a spatial pattern of elevation change due to landslide. The elevation change was calculated by subtracting the elevation value of the topography model of the LiDAR survey before the disaster from the elevation value of the DSM (Digital Surface Model) created by the SfM (Structure from Motion) method from the photograph taken from the helicopter after the disaster (Handa et al., 2018). The landslide occurred in the upper part of the hillslope. The width of the landslide was about 200 m, the length of the landslide was about 200 m, and the landslide sediment volume was roughly estimated to be about 200,000 m³. The landslide sediment turned into a debris flow, and the debris flow branched to the east and west just below the landslide initiation area and flowed down. The sediment deposits were approximately 1 to 5 m thick on the middle reaches of the hillslope (under exposed rock). At the lower reaches of the hillslope (Narrow part), the deposited sediment was about 2 to 5 m thick. At the valley exit, the thickness of the sediment deposit was about 10 m, and the maximum particle diameter was about 5 m. At the lower flat part of the inundation zone, the sediment was mainly composed of fine grains, and the deposit was about 0.5 to 1.5 m thick (Handa et al., 2018).

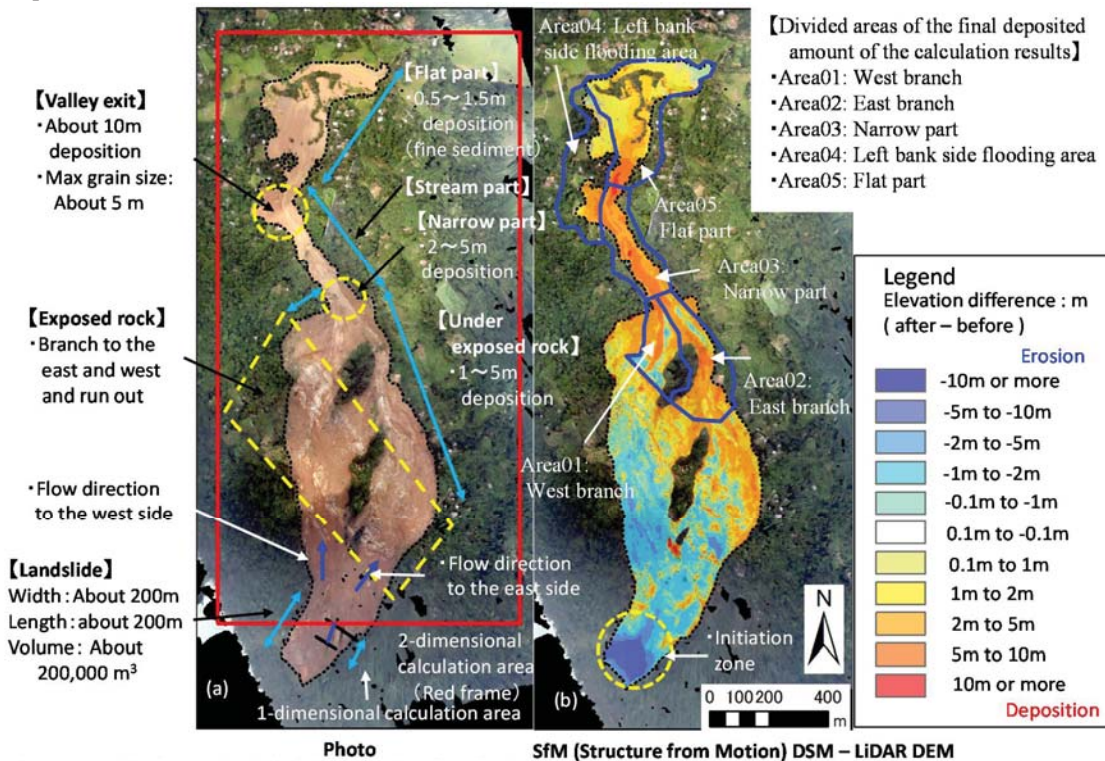


Fig. 1. Aranayake disaster (a) Aerial photograph just after disaster; (b) Elevation change due to landslide

3. Numerical methods

In this study, we applied the “HyperKANAKO” debris-flow model to describe the inundated zone due to the Aranayake disaster. The “HyperKANAKO” is a two-dimensional debris-flow model, developed by Horiuchi et al (2012). It is based on the concept of stony debris flow, sediment sheet flow and bedload proposed by Takahashi and his colleagues (Takahashi et al, 2009). The “HyperKANAKO” can use LiDAR data. We prepared the terrain model using LiDAR survey data (measured in December 2015 before the disaster occurrence, 2m*2m grid size).

We assumed that the potential landslide initiation area was identified by the existing LHZM. Then, we addressed a situation in which information other than the landslide position and topography data could not be obtained sufficiently before debris-flow occurrence. Additionally, we examined how to set various input conditions and how much the difference in input conditions affects the predicted inundation zone. Specifically, we examined the influence of the (1) percentage of fine grains (fluid density and sediment concentration), (2) landslide volume, (3) input hydrograph (peak flow rate and duration), and (4) representative sediment particle diameter (Table 1).

3.1. Percentage of fine grains (Fluid density and sediment concentration)

It is thought that fine grains together with the pore water in the debris flow constitute the pore fluids, because fine grains can be suspended in the fluid (Fig. 2a). Furthermore, it has been shown that the percentage of fine grains constituting the pore fluid has a large influence on the calculation result (e.g. distance to the end of deposit zone, distance to the end of erosion zone of the river bed) (Nishiguchi et al., 2011). However, as information on the percentage of fine grains constituting the pore fluid is insufficient, in many cases, it is based on past disaster records (e.g., Nakatani et al, 2018). Therefore, we changed the percentage of fine grains constituting the pore fluid to 0%, 20%, and 30%, to evaluate the influence of the percentage of fine grains constituting the pore fluid on the calculation results.

3.2. Landslide volume

The landslide volume should greatly influence not only the deposited area but also the runout area. However, it is difficult to accurately predict the landslide volume before a landslide occurs. So, we tested the influence of the landslide volume on the calculation results, by halving and doubling the landslide volume. The landslide volume was based on the 200,000 m³ actually measured by Handa et al. (2018).

3.3. Input hydrograph

The input hydrograph (water and sediment supply situation) is a parameter that affects the calculation result. Therefore, we set three different input hydrographs at the upper end of calculation section (Fig. 2b). In these cases, the total input water and sediment volume were the same. The shape of the input hydrograph was assumed to be an isosceles triangle with a peak flow rate at 1/2 of the duration, which is based on Public Works Research Institute (2012).

3.4. Representative particle diameter

The representative sediment particle diameter is also a parameter that affects the calculation result. Although information on the representative particle diameter of landslide sediment can be set by field survey, etc., perhaps sufficient information might be difficult to obtain in advance due to problems, such as investigation cost. We measured the sediment particle diameter by field survey on January 25, 2018 (Fig. 3a). Unfortunately, the date of the survey was about 1 year and 8 months after the Aranayake disaster. We measured the coarse sediment particle diameter at 0.5 m intervals, and we obtained data from 82 points. Also, we sampled the fine sediment for laboratory tests. In addition, we confirmed the sedimentary condition, and we quantified the ratio of fine sediment (< 30mm) in a cross-section of deposited sediments (Fig. 3a) and found that the ratio was 31%. From these survey results, we obtained the particle diameter distribution diagram (Fig. 3b). And, we set the representative particle diameter to 13.6 cm as the average value of coarse sediment diameter (Fig. 3b). Therefore, we changed the representative sediment particle diameter by 1/3 times and triple. We tested the influence of the representative sediment particle diameter on the calculation results.

3.5. Other input conditions

Other input conditions are as shown in Table 2. The one-dimensional calculation area was set as the landslide portion, and the river width of the one-dimensional calculation area was set to 200 m, which is the actual landslide width. The two-dimensional calculation area was set as a rectangle on the downstream side of the landslide (red frame in Fig. 1a). The unstable sediment thickness in the two-dimensional calculation area was set as 5 meters depth.

3.6. Evaluation of calculation results

To compare measured and calculated elevation changes, we divided the lower part of the hillslope into five sections (blue frame in Fig. 1b) by erosion deposition pattern. We accumulated the final deposited amount of the calculation result in each divided area. The grid size was 10 m², and we included grid cells that had a final deposition depth of 0.1 m or more.

Table 1. Changed input conditions

Case No.	Percentage of fine grains (%)	Fluid density (kg/m ³)	Sediment concentration	Landslide volume (m ³)	Duration of debris flow (s)	Peak flow rate (m ³ /s)	Representative sediment particle diameter (m)
01	30	1,625	0.469	232,000	8	58,000	0.137
02	0	1,000	0.585	232,000	8	58,000	0.137
03	20	1,477	0.536	232,000	8	58,000	0.137
04	30	1,625	0.469	116,000	8	29,000	0.137
05	30	1,625	0.469	464,000	8	116,000	0.137
06	30	1,625	0.469	232,000	80	5,800	0.137
07	30	1,625	0.469	232,000	300	1,547	0.137
08	30	1,625	0.469	232,000	8	58,000	0.046
09	30	1,625	0.469	232,000	8	58,000	0.413

Table 2. Fixed input conditions

Item	Unit	Value
Calculation time	Sec	1,440
Time interval of calculation	Sec	0.005
Mass density of sediment	kg/m ³	2,650
Gravity acceleration	m/s ²	9.8
Minimum flow depth	m	0.01
Concentration of movable bed	-	0.65
Manning's roughness coefficient	-	0.1
Coefficient of erosion velocity	-	0.0007
Coefficient of deposition velocity considering inertial force	-	0.05
Internal friction angle	deg	35
Thickness of 2-D plane unstable sediment	m	5.0
Interval of 1-D calculation points	m	5.0
Interval of 2-D calculation points	m	10.0

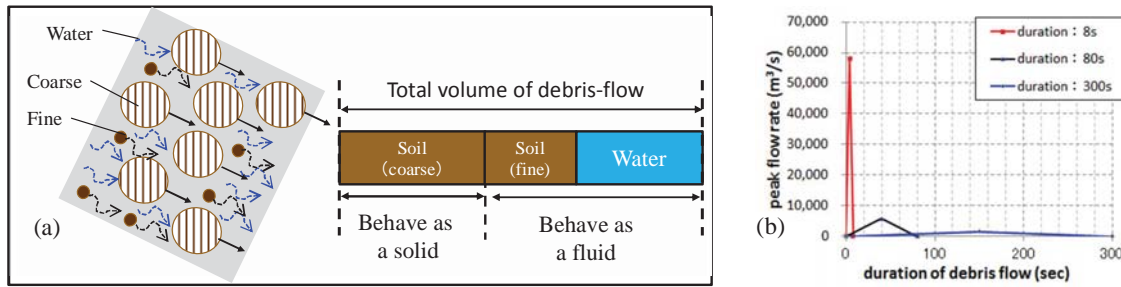


Fig. 2. Model framework, (a) Concept of pore fluid; (b) Input hydrograph

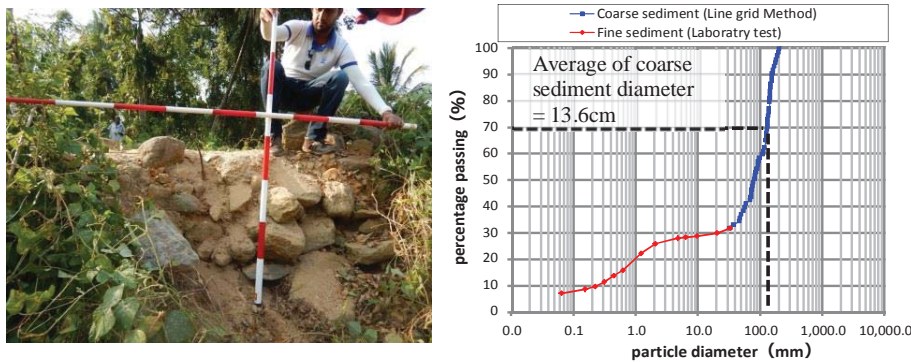


Fig. 3. Survey of the representative particle diameter, (a) Photograph of field survey; (b) Particle diameter distribution diagram

4. Comparison of measured and modeled deposits

Fig. 4 shows the calculation results with varying the percentage of fine grains, that is, Case No. 01 to 03 in Table 1. Fig. 5 shows the calculation results with varying the landslide volume, that is, Case No. 01, 04, and 05 in Table 1. Fig. 6 shows the calculation results with varying the input hydrograph, that is, Case No. 01, 06, and 07 in Table 1. Fig. 7 shows the calculation results with varying the representative sediment particle diameter, that is, Case No. 01, 08, and 09 in Table 1. Figs. 4a-7a show the deposition depth at the end of the calculation in each calculation case. Also, Figs. 4b-7b show the total deposited amount of sediment at the end of the calculation in each divided area indicated by the blue frame in Fig. 1b. And, "Measured" in Figs. 4-7 is the difference of the elevation values before and after the disaster by Handa et al. (2018). The direction of the debris flow of the calculation results shown in Figs. 4a-7a describe the downward flowing process where the debris flow branches to the east and west flow path, similar to disaster. On the other hand, since the debris flow erodes the hillside slope, the total deposited amount in Figs. 4b-7b is generally larger than the landslide volume in each case of Table 1. In a few cases (e.g., Case 02 in Fig. 4b), the total deposited amount is smaller than the supplied amount, because collapsed sediment is accumulated just below the landslide initiation area. The disaster record ("Measured") and each sensitivity analysis results were compared based on Figs. 4-7. The calculation result of Case 01 in Fig. 4 is most suitable result for the disaster record in terms of the downward flow range, the deposition range, and the deposited amount of sediment. However, the total deposited amount in the divided area 01 and area 02 in Case 01 is smaller than the measured amount of sediment.

5. Sensitivity analysis results

5.1. Influence of the percentage of fine grains (Fluid density and sediment concentration)

Fig. 4 shows the calculation results with varying the percentage of fine grains, that is, Case No. 01 to 03 in Table 1. In Case 02 where the percentage of fine grains constituting the pore fluid is 0%, most of the sediment deposit is on the hillslope, and the amount of sediment reaching downstream (especially the divided areas 03-05) is extremely small. In Case 03 where the percentage of fine grains constituting the pore fluid is 20%, the deposited sediment

amount in the divided area 01 and area 02 is about the same as the measured amount. However, the deposited sediment amount in the divided areas 03-05 is smaller than that of the measured. In addition, the deposited sediment amount in the divided areas 01–05 in Case 02 is about 20% that of Case 01, and the deposited sediment amount in the divided areas 01–05 in Case 03 is about 60% that of Case 01. From the above, we found that the percentage of fine grains (fluid density and sediment concentration) greatly influences the calculation result.

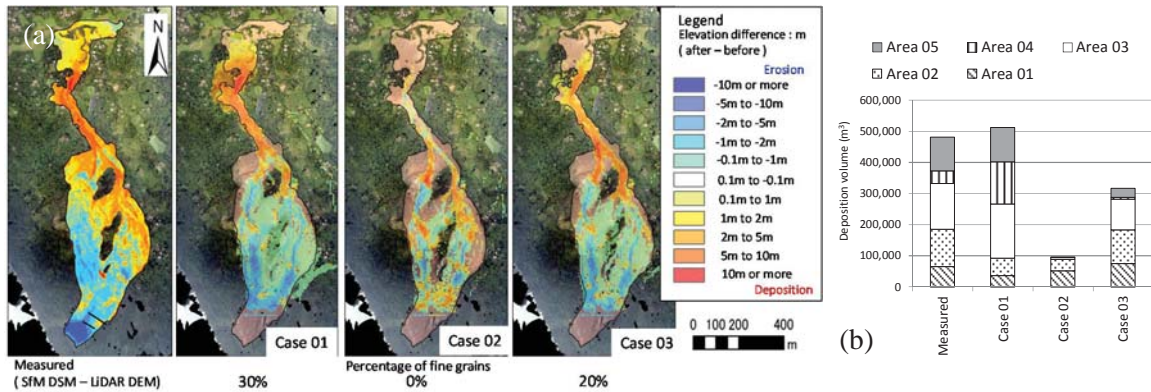


Fig. 4 Calculation results with varying the percentage of fine grains, (a) The deposition depth; (b) Quantitative evaluation of calculation results

5.2. Influence of landslide volume

Fig. 5 shows the calculation results with varying the landslide volume, that is, Case No. 01, 04, and 05 in Table 1. Comparing Cases 01, 04, and 05, both the width and distance of the debris flow area become greater and the deposition depth increases, as the amount of landslide volume increases. In Case 04 (landslide volume set to 1/2 that of Case 01), the deposited sediment amount in the divided areas 01 and 02 is not so different than that of Case 01, but the deposited sediment amount in the divided areas 03-05 is smaller than the corresponding data in Case 01. In addition, the deposited sediment amount in the divided areas 01–05 in Case 04 is about half the corresponding data in Case 01. In Case 05 (landslide volume set to 2 times that of Case 01), the deposited sediment amount in the divided areas 01 and 02 is not so different than that of Case 01, but the deposited sediment amount in the divided areas 03-05 is larger than the corresponding data in Case 01. In addition, the deposited sediment amount in the divided areas 01–05 in Case 05 is about twice the corresponding data in Case 01. Thus, the sediment deposited amount changes according to the set amount of landslide volume. The variation in the deposited sediment amount in the divided area 04 is especially large.

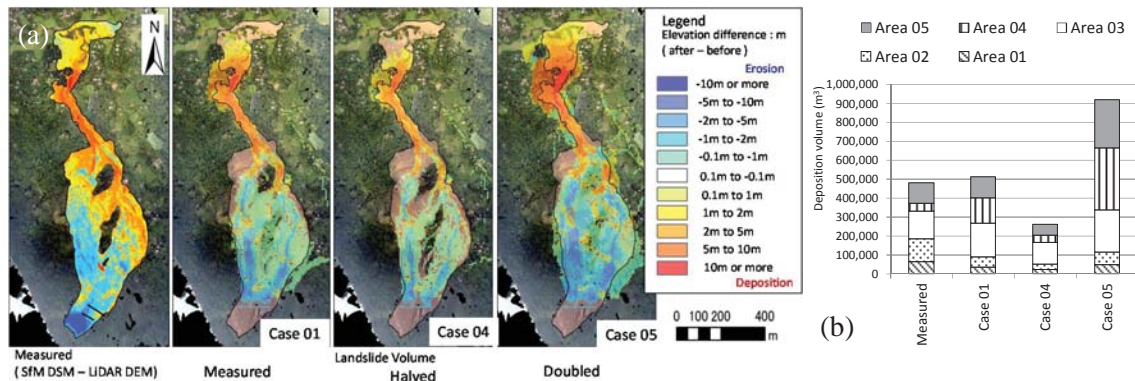


Fig. 5 Calculation results with varying the landslide volume, (a) The deposition depth; (b) Quantitative evaluation of calculation results

5.3. Influence of the input hydrograph

Fig. 6 shows the calculation results with varying the input hydrograph, that is, Case No. 01, 06, and 07 in Table 1. In Case 06, the duration of the input hydrograph was set to 10 times that of Case 01, and the peak flow rate was set to 1/10 that of Case 01. In Case 07, the duration of the input hydrograph was set to 37 times that of Case 01, and the peak flow rate was set to 1/37 that of Case 01. Comparing Cases 01, 06, and 07, the larger the peak flow rate, the larger the debris flow area. However, the deposited sediment amount in each divided area is little different than that of Case 01.

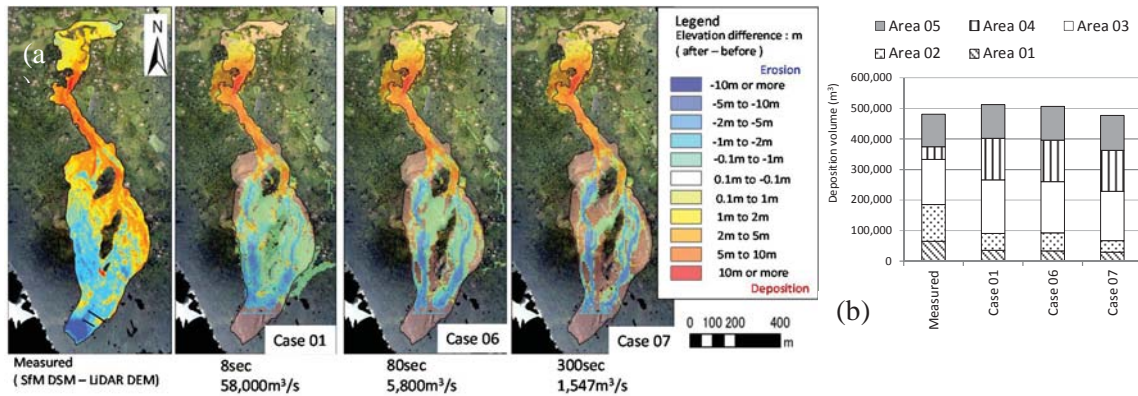


Fig. 6 Calculation results with varying the input hydrograph, (a) The deposition depth; (b) Quantitative evaluation of calculation results

5.4. Influence of the representative sediment particle diameter

Fig. 7 shows the calculation results with varying the representative sediment particle diameter, that is, Case No. 01, 08, and 09 in Table 1. In Case 08, the representative sediment particle diameter was set to 1/3 times that of Case 01, and in Case 09, the representative sediment particle diameter was set to 3 times that of Case 01. Comparing Cases 01, 08, and 09, both width and distance of flow area of debris flow become greater, as the representative particle diameter decreases. Also, the larger the representative particle diameter, the smaller the deposited sediment amount in each divided area. The deposited sediment amount in the divided areas 01–05 of Case 08 is about 130% that of Case 01. The deposited sediment amount in the divided areas 01–05 of Case 09 is about 60% that of Case 01. Therefore, we found that the representative particle diameter has a large influence on calculation results.

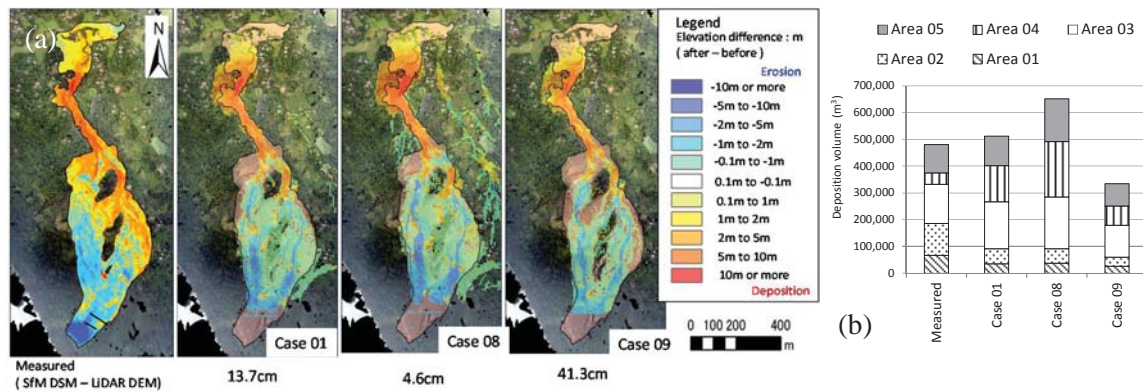


Fig. 7 Calculation results with varying the representative sediment diameter, (a) The deposition depth; (b) Quantitative evaluation of calculation results

6. Discussion and Conclusion

In this study, we used the "HyperKANAKO" debris-flow model to describe area inundated by a recent debris flow in Sri Lanka and propose a method for assessing sediment disaster inundation zone in regions where empirical methods cannot be applied due to insufficient records of past disasters. As a result, we found that it is possible to describe sediment disaster inundation zone with a certain degree of accuracy, based on the limited information, i.e., topographical data and landslide location. However, the calculation result is strongly controlled by the percentage of fine grains, landslide volume, and representative particle diameter. Therefore, when assessing the sediment disaster inundation zone in Sri Lanka, it is necessary to pay attention so as not to underestimate the inundation zone. According to the results of this study, setting the percentage of fine grains between 20% and 30% was generally consistent with the disaster record. However, we need to test another data about disasters and grasp the suitable value range for the percentage of fine grains. Also, we need to set the amount of landslide volume appropriately. Previous studies show a variety of empirical relationships between landslide area and landslide volume (e.g., Guzzetti et al, 2009; Larsen et al, 2010). So, landslide volume might be roughly predicted according to the LHZM and area-volume relationship. Moreover, since particle diameter had a large effect on the simulation results, it is important to revise our information based on it. Therefore, it is desirable that we conduct particle diameter surveys at many disaster sites, and accumulate survey results. Since the particle diameter might be affected by the bedrock geology, we can set the probable range of particle diameter for bedrock geology based on accumulated survey results.

Acknowledgements

The LiDAR survey data before the disaster occurred was provided by JICA's 'Capacity Development Project for Creating Digital Elevation Model Enabling Disaster Resilience'. Also, Terrain data after the occurrence of the disaster was provided by JICA's 'Technical Cooperation for Landslide Mitigation Project' this data is DSM (Digital Surface Model) data created by SfM (Structure from Motion) using aerial photographs obtained by a helicopter just after the disaster. And, we are also grateful to the unidentified reviewers.

References

- Frank, F., McArdell, B.W., Huggel, C., and Vieli, A., 2015, The importance of entrainment and bulking on debris flow runoff modelling: examples from the Swiss Alps: *Natural Hazards and Earth System Sciences*, v. 15, p.2569-2583, doi: 10.5194/nhess-15-2569-2015.
- Guzzetti, F., Ardigzone, F., Cardinali, M., Rossi, M., and Valigi, D., 2009, Landslide volumes and landslide mobilization rates in Umbria, central Italy: *Earth and Planetary Science Letters*, v. 279, p.222-229, doi: 10.1016/j.epsl.2009.01.005.
- Handa, K., Okawara, A., Sasaki, A., Okamura, M., Ishihara, M., Nakano, R., Matsumoto, N., Uchida, T., Suzuki, K., and Washio, Y., 2018, Survey report of sediment disaster in Aranayake, Sri Lanka, on May, 2016: *International Journal of Erosion Control Engineering*, v. 11, no. 1, p.28-35, doi: 10.13101/ijece.11.28.
- Horiuchi, S., Iwanami, E., Nakatani, K., Satofuka, Y., and Mizuyama, T., 2012, Development of "Hyper KANAKO", a debris flow simulation system using with laser profiler data: *Journal of the Japan Society of Erosion Control Engineering*, v. 64, no. 6, p.25-31, doi: 10.11475/sabo.64.6_25.
- Iverson, R.M. and Denlinger, R.P., 2001, Flow of variably fluidized granular masses across three-dimensional terrain, 1. Coulomb mixture theory: *Journal of Geophysical Research*, v. 106, no. B1, p.537-552, doi: 10.1029/2000JB900329
- Larsen, I.J., Montgomery, D.R., and Korup, O., 2010, Landslide erosion controlled by hillslope material, *Nature Geoscience*, v. 3, p.247-251 doi: 10.1038/ngeo776.
- Nakatani, K., Furuya, T., Hasegawa, Y., Kosugi, K., and Satofuka, Y., 2018, Study on fine sediment phase change factors and influence on debris flow behavior: *Journal of the Japan Society of Erosion Control Engineering*, v. 70, no. 6, p.3-11.
- Nishiguchi, Y., Uchida, T., Ishizuka, T., Satofuka, Y., and Nakatani, K., 2011, Numerical simulation for run out process of large-scale debris flow focused on fine sediments behaviors: application for debris flow triggered by a deep catastrophic landslide: *Journal of the Japan Society of Erosion Control Engineering*, v. 64, no. 3, p.11-20.
- O'Brien, J.S., Julien, P.Y., and Fullerton, W.T., 1993, Two-dimensional water flood and mudflow simulation: *Journal of Hydraulic Engineering*, v. 119, no. 2, p.244-264, doi: 10.1061/(ASCE)0733-9429(1993)119:2(244)
- Public Works Research Institute., 2012, Technical note of Public Works Research Institute, Japan, no. 4260, 29p.
- Rickenmann, D., Laigle, D., McArdell, B.W., and Hubl, J., 2006, Comparison of 2D debris-flow simulation models with field events: *Computational Geosciences*, v. 10, p.241-264, doi: 10.1007/s10596-005-9021-3.
- Suzuki, T., and Hotta, N., 2016, Development of modified particles method for simulation of debris flow using constitutive equations: *International Journal of Erosion Control Engineering*, v. 9, no. 4, p.165-173, doi: 10.13101/ijece.9.165.
- Takahashi, T., 2009, A review of Japanese debris flow research: *International Journal of Erosion Control Engineering*, v. 2, no. 1, p.1-14, doi: 10.13101/ijece.2.1.

Application of an MPS-based model to the process of debris-flow deposition on alluvial fans

Takuro Suzuki^{a,*}, Norifumi Hotta^b, Haruka Tsunetaka^a, Yuichi Sakai^b

^aForestry and Forest Products Research Institute, Japan, 1 Matsunosato, Tsukuba-shi, Ibaraki 3058687, Japan

^bThe University of Tokyo, 1-1-1 Yayoi, Bunkyo-ku, Tokyo 1138657, Japan

Abstract

A modified moving particles simulation model (MPS-DF) to simulate inundation and sediment deposition of debris flows is presented. This model is based on the moving particles semi-implicit (MPS) method, which was originally used for incompressible viscous fluid flows with free surfaces. In the MPS-DF model, the constitutive equations of Egashira is introduced to the MPS method. In Egashira's theory, debris flows are treated as a continuum and sand grains are expressed using sediment concentration. Thus, each particle has a variable sediment concentration value. In this study, we tested the applicability of the MPS-DF model for the formation process of alluvial fans. For this purpose, flume experiment was conducted. The experimental flume consisted of a straight channel 6.0m long and 0.1m wide, with an inclination of 15°, connected to an outflow plain. The inclination of the outflow plain decreased gradually from 12° to 3°. At the straight channel, 5.0m long erodible bed with a thickness of 0.2m was present. Water was supplied from upper end for 60 s. at the rate of 3,000 cm³/s and debris flow was generated by entraining the erodible bed. Debris flow inundated and deposited sediment at the outflow plain and an alluvial fan was formed. Numerical simulations were also performed with the MPS-DF as well as a depth-integrated method based on the shallow water equations (2D simulation). 2D Simulation results of alluvial fan shape and flooding area were laterally spread and significantly different from those of experiment. The results of the MPS-DF were more similar to experimental results. Natural channels and lateral levees were formed as well as experiment. However, the alluvial fan shape of MPS-DF was slightly wider than that created during the experiment. This is thought to be due to the behavior of pore water of deposited layer, such as the seepage of water out of the deposited layer once the deposition process has been completed.

Keywords: numerical simulation; particles method; alluvial fan formation process

1. Introduction

Debris flows cause enormous damage. To mitigate the damage, it is important to predict their range of influence. Numerical simulation is an effective tool for predicting debris-flow inundation (e.g., Liu et al., 2012; Pastor et al., 2014). In Japan, residential areas are sometimes built on alluvial fans at valley exits of steep mountain rivers. An example that illustrates this situation is a debris-flow disaster that occurred in Hiroshima in August 2014 (Nakatani et al., 2017). In this disaster, it was suggested that houses and other structures that existed in the alluvial fan area at the exit of the valley impeded the flood and deposit of debris flow. It is also shown that when debris flow occurs continuously in multiple streams, the fan formed by preceding debris flows affects the fan formation process of subsequent debris flows (Chen et al., 2016). In numerical simulations based on shallow water equations, it is necessary to average flow velocity distribution and sediment concentration distribution in the vertical direction, and it is therefore considered difficult to reproduce such complicated behaviors (Suzuki and Hotta., 2015, 2016).

In recent years, there have been advances made in research on particle simulation methods for debris flow based on Smoothed Particle Hydrodynamics (SPH) (Monaghan, 1988) or Moving Particle Simulation method (MPS) (Koshizuka and Oka, 1996). Most of these studies treat debris flow as one viscous fluid (e.g., Laigle et al., 2007; Wang et al., 2016). With these methods, separation of sand grains and water is not reproduced. Suzuki and Hotta (2015,

* Corresponding author e-mail address: takurosuzuki@ffpri.affrc.go.jp

2016) developed a particles simulation method for debris flow (hereinafter referred to as MPS-DF) that introduced the constitutive law for flow resistance and sediment concentration of debris flow (Egashira et al., 1989, 1997) to the MPS method. With this method, it has been shown that the erosion and deposition process can be reproduced in constant width flumes (Suzuki and Hotta, 2015, 2016). Conversely, the process of debris-flow deposition on alluvial fans involves transverse spreading. In this study, we tested the applicability of the MPS-DF model for the deposition process on alluvial fans. For this purpose, flume experiments were carried out using gravel of uniform grain size and numerical simulations were also performed. The numerical simulations were performed using the MPS-DF method as well as a method based on the shallow water equation, and the results of both methods were then compared.

2. Experiment

2.1. Experimental flume and materials

The experimental flume consisted of a 6.0 m long and 0.1 m wide straight channel, with an inclination of 15°, connected to an outflow plain (Fig. 1). The gradient of the outflow plain changes by 3 degrees every 1 m, and the 3-degree area only has a length of 2 m. The transverse direction is horizontal. In the straight channel part, sand grains with a depth of 20 cm were deposited in the 5 m downstream part. The height of the sediment surface was equal to the height of the connecting outflow plain. The average grain diameter was 0.265 cm while the specific gravity was 2.6.

2.2. Method and measurement

Water was supplied at 3,000 cm³/s from the upstream end for 60 sec, while debris flow was generated through the erosion of sediment in the straight channel. The sediment concentration was about 32% at the beginning and about 16% at the time of 60 sec, when it was measured using the erosion depth roughly estimated from the side-view videos of the flow. The debris flow separated into water and sand grains at the outflow plain, forming an alluvial fan. The formation process was photographed using three digital cameras from the top of the outflow plain. The photographed images were analyzed using SfM software (Photoscan Professional, Agisoft LLC) to create point clouds. Elevation data was then created by processing the point clouds and known coordinates, while the deposition depth was calculated as the difference from the original altitude data (De Haas et al., 2014).

3. Numerical Simulation

3.1. Outline of MPS-DF method

Suzuki and Hotta (2015, 2016) developed the MPS-DF method by introducing the constitutive equations developed by Egashira et al. (1989, 1997) into the MPS method (Koshizuka and Oka, 1996). The outline is as follows.

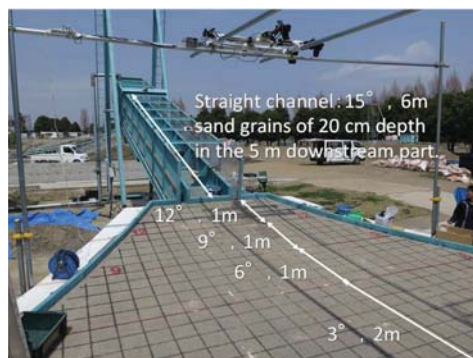


Fig. 1. Experimental flume

In the MPS-DF method, in order to treat the debris flow as a one-fluid model, the debris flow itself is divided into aggregates of particles that possess parameters of sediment concentration. First, Suzuki and Hotta (2015, 2016) modified the resistance law of debris flow as follows, so that it can be introduced into the framework of the MPS method.

$$\tau_c = \tau_{cy} + \rho_w \frac{\partial f(c)}{\partial c} \frac{\partial c}{\partial z} \left| \frac{\partial u}{\partial z} \right| \left(\frac{\partial u}{\partial z} \right) + 2\rho_w f(c) \left| \frac{\partial u}{\partial z} \right| \left(\frac{\partial^2 u}{\partial z^2} \right) \quad (1)$$

$$\tau_{cy} = \left[\frac{1}{5} \left(\frac{c}{c_*} \right)^{-\frac{4}{5}} \frac{\partial c}{\partial z} \int_z^h c(z) dz - \left(\frac{c}{c_*} \right)^{\frac{1}{3}} c \right] \rho_w \left(\frac{\sigma}{\rho_w} - 1 \right) g \cos \theta \tan \phi_s \quad (2)$$

$$f(c) = (K_d + K_f) d^2, \quad K_d = k_g (1 - e^2) \left(\frac{\sigma}{\rho_w} \right)^{\frac{1}{3}} c^{\frac{1}{3}}, \quad K_f = k_f \frac{(1-c)^{\frac{5}{2}}}{c^{\frac{3}{2}}} \quad (3)$$

where τ_c represents the shear stress, τ_{cy} represents the yield stress, $\rho_w = 1.0$ is the density of water, c represents the sediment concentration, u represents the flow velocity, z represents the axis in the depth direction perpendicular to the flow direction of the debris flow, K_d is the coefficient of particle collision, K_f is the coefficient of pore water turbulence, c_* is the sediment concentration in the bed, $\sigma = 2.65$ is the gravel density, $\phi_s = 38.5^\circ$ is the friction angle, d is the diameter of the sediment particles, $e = 0.775$ is the coefficient of restitution, and where $k_g = 0.0828$ and $k_f = 0.16$ are empirical constants (Egashira et al., 1989, 1997). The first term of Eq. (1) is the yield stress, and the second and third terms show the dynamic stress for each differential order. θ is an angle formed by the flow velocity vector of the particle and the horizontal vector. τ_c that was obtained by converting τ_c into a vector in the rectangular coordinate system was introduced instead of the viscous term used in the MPS method.

Next, a model was constructed in which the value of the sediment concentration moves among neighboring particles. First, the equilibrium concentration gradient, gc_e is calculated by substituting the above parameters of a focused particle (its number is defined as i) into the concentration distribution formula developed by Egashira et al. (1989, 1997). Then, a concentration gradient with neighboring particles, gc is calculated. Fig. 2 shows the concept of the variable sediment concentration model. The change in the sediment concentration of a focused particle was calculated for the underlying particles, because the concentration distribution was obtained by integrating the concentration gradient from the riverbed to the water surface. The particle shown in Fig. 2 tends to result in an increase in c because $gc_e > gc$. Therefore, $ccp(i)$, which expresses the magnitude and direction of the change in c , is defined as follows:

$$ccp(i) = l_0 (gc_e - gc) \quad (4)$$

Here, l_0 is the standard particle distance. The time-derivative of c is derived using the kernel function, $w(r)$, assuming that c changes in proportion to the difference in $ccp(i)$ between neighboring particles. Here, $w(r)$ is defined by Koshizuka and Oka (1996).

$$\left(\frac{\partial c}{\partial t} \right)_i = \frac{1}{T} \frac{1}{n_0} \sum_{i \neq j} w(r) \frac{1}{2} (ccp(i) - ccp(j)) \quad (5)$$

Here, n_0 is the standard particle number density and is a constant parameter of the MPS method (Koshizuka and Oka, 1996), r is the inter-particle distance, and T is the relaxation time. Notably, T needs to be small enough to satisfy the local equilibrium of sediment concentration (Suzuki and Hotta, 2015, 2016). Therefore, we adopted the method proposed by Suzuki et al. (2016) to link the relaxation time with the increment time.

With the MPS-DF method, for example, when debris flow moves from a steep slope to a gradual slope, the sediment concentration for the upper layer particles moves to the lower layer particles. This is because the equilibrium concentration, calculated using a low gradient, is lower than the current value. The sediment concentration moves to reduce the difference between the current high sediment concentration and equilibrium concentration. When the sediment concentration of the lower layer particles exceeds a certain level, the yield stress term represented by Eq. (2) becomes larger than the shearing force, and the particles are in an immovable state; that is, they become deposited particles (a state in which vibration is slightly repeated). This process corresponds to a deposition process, while the opposite process corresponds to an erosion process.

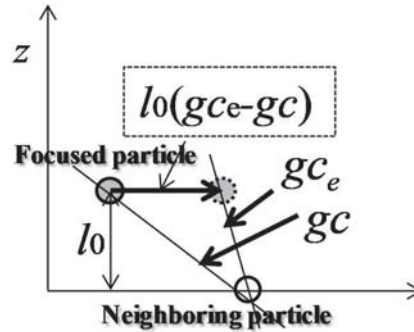


Fig. 2. A schematic diagram illustrating the concept of the variable sediment concentration model (Suzuki and Hotta, 2016).

3.2. Treatment of momentum in the concentration change model

Moving the sediment concentration is equivalent to exchanging gravel with water. Because gravel and water have different specific gravities, moving the sediment concentration alone cannot satisfy the momentum conservation law. In previous studies, the influence on the calculation result was small, so we ignored the non-conservation of momentum. However, there is a possibility that it may affect the planar deposition process. Therefore, when calculating the change in sediment concentration using Eq. (5), the change in momentum corresponding to a movement in sediment concentration was calculated simultaneously (hereafter it is called the modified MPS-DF). In this study, numerical simulations were performed using a method that does not consider the change in the momentum (called MPS-DF in this study) and the influence of momentum conservation was verified.

3.3. Two-dimensional simulation based on shallow water equations

For comparison, a two-dimensional simulation based on the standard shallow water flow equations (Hereafter, it is called the two-dimensional simulation) was also performed. This method adopted Egashira's constitutive law for flow resistance (Egashira et al., 1989, 1997). Eq. (1) - (3) are obtained by differentiating the resistance law used in this method with z . This method also adopted erosion rate formula as follows (Miyamoto and Ito, 2002).

$$E = \tan(\theta - \theta_e)|u| \quad (6)$$

$$\tan\theta_e = \frac{c(\sigma/\rho_w - 1)}{c(\sigma/\rho_w - 1) + 1} \tan\phi_s \quad (7)$$

Here, E is the erosion rate, and θ_e is the equilibrium gradient corresponding to the sediment concentration. According to Eq. (6) and Eq. (7), erosion and deposition are determined only by the relationship between the equilibrium gradient corresponding to the average sediment concentration in the vertical direction and the bed gradient.

3.4. Calculation condition

In the MPS-DF method, the particle diameter was 0.5 cm. In the two-dimensional simulation, an orthogonal grid with a width of 5 cm was used. These values were determined from the relationship between resolution and calculation time. The other parameters mentioned above are material properties or empirical constants.

4. Results

4.1. Alluvial fan formation process

The experimental results and calculation results of the alluvial fan formation process are shown in Fig. 3, while the final deposition depth is shown in Fig. 4. In Fig. 3 and 4, the outlet of the straight channel was set as the 0 m point.

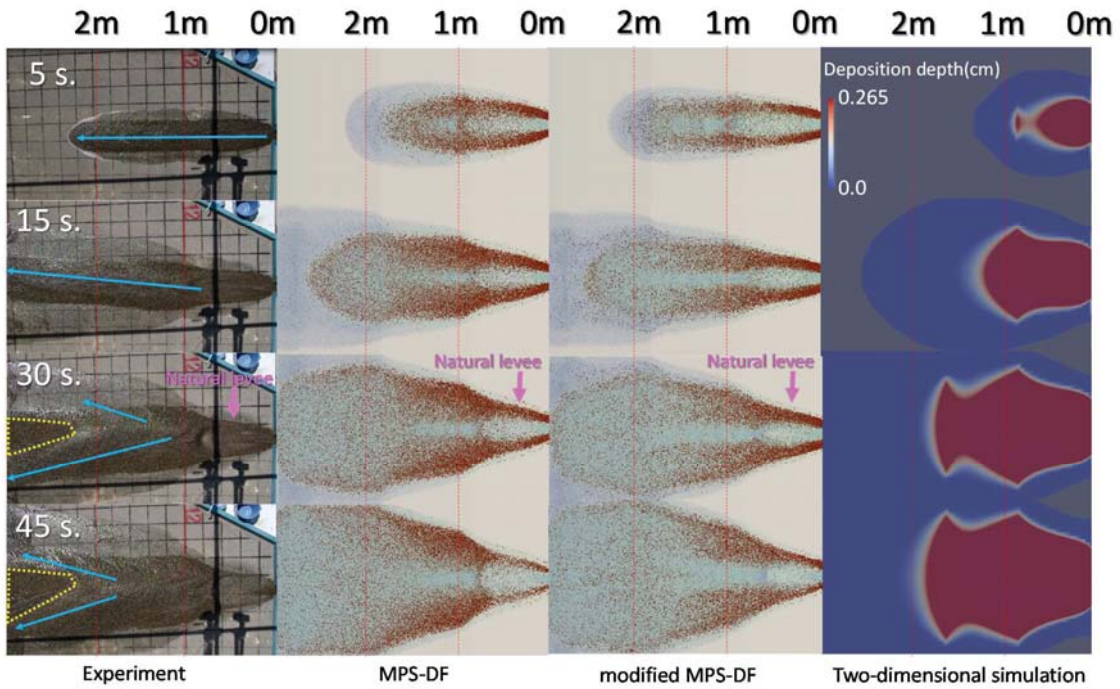


Fig. 3. Alluvial fan formation process. The yellow broken line indicates a region with no surface flow.

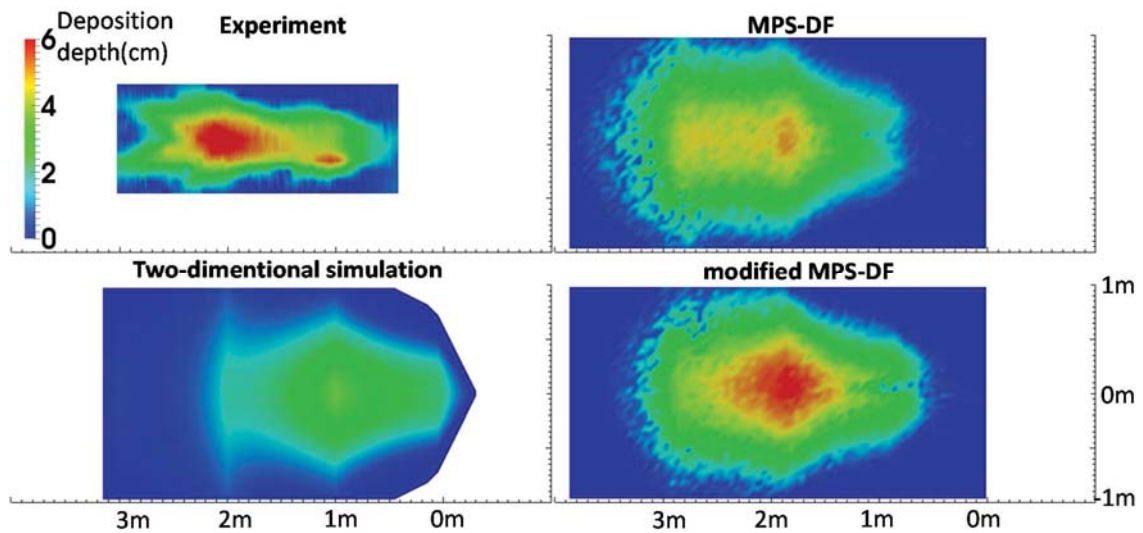


Fig. 4. Final deposition depth

The time at which the front of the debris flow arrives at the outlet of the straight channel was set to 0 sec, and the results are shown every 15 sec.

In the experiment, the deposit expanded linearly in the downslope direction for approximately 3 m without spreading horizontally. After that, the flow direction changed to the right side. Then, when the deposition on the right side progressed to a certain extent, the flow changed to the left side direction. The final result was the formation of an almost symmetrical alluvial fan. A waterway was formed near the outlet of the straight waterway. A waterway was formed near the outlet of the straight waterway, similar to the result obtained by De Haas et al, in which a waterway and a natural levee were formed near the outlet of the straight waterway (De Haas et al., 2015).

In the result obtained from the two-dimensional simulation, deposition began immediately from the outlet of the straight channel that gradually spread in the downstream side and transverse direction. Compared to the experimental results, the spread in the transverse direction was large and the distance covered in the downward flow direction was short. It can be said that the deposition process/shape from the two-dimensional simulation was significantly different from that obtained from the experimental results.

In the result obtained using the MPS-DF method, a linear deposition shape was formed in the initial process, but it expanded in the transverse direction from around the point beyond the 1 m point. The flow direction did not change and a symmetrical fan was formed. Similar to the experimental results, a waterway and natural levee were also formed. The final fan shape spread in the transverse direction, in contrast to the trend obtained from the experimental results.

In the result of the modified MPS-DF, the lateral spread was suppressed to some extent due to the movement of the momentum. However, as time passed, it expanded in the lateral direction, and its deviation from the experimental results increased.

4.2. Final deposition depth

Fig. 4 shows the result of the final deposition depth and Fig. 5 shows the longitudinal section of the final deposition depth at the center of the outflow plain. The experimental result shows only the region analyzed using the SfM software. Comparing the results of the MPS-DF and modified MPS-DF models, it was observed that the result of MPS-DF model showed a slight downstream deposition. Regarding the point with the largest deposition depth, the results obtained from the two-dimensional simulation were significantly different from the experimental results. Conversely, the MPS-DF and modified MPS-DF results generally agreed with the experimental results. In particular, the result of the modified MPS-DF was nearly quantitatively consistent with the experimental results.

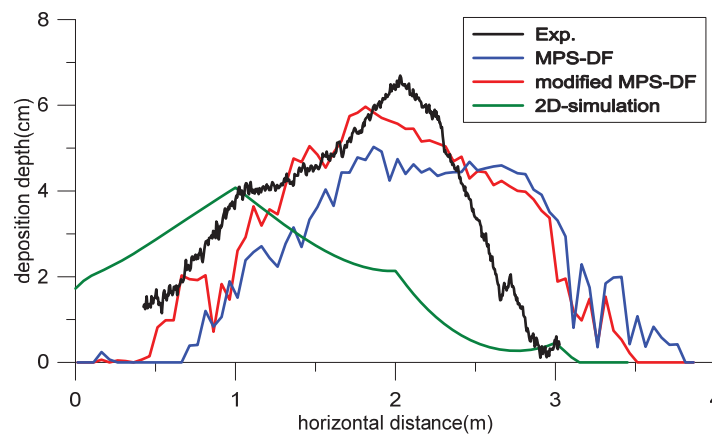


Fig. 5. A longitudinal section of the final deposition depth at the center of the outflow plain

5. Discussions and Conclusions

In the two-dimensional simulation, deposition occurred immediately near the outlet of the straight channel and spread laterally. In the experiment, deposition gradually progressed linearly from the straight channel outlet. Only the water in the upper layer of the flow spread sideways. In the two-dimensional simulation, the movement of sand grains between meshes was calculated using the sediment discharge, obtained by multiplying the flow rate by the transport concentration (Miyamoto and Ito, 2002). The flux sediment concentration which is obtained by dividing sediment discharge by total discharge is a mesh-specific value; that is, it is the same value in the downward flow direction and the lateral direction in the two-dimensional simulation. Therefore, it is believed that the situation in which the upper layer of water selectively spreads sideways was not reproduced, and instead, that the deposition widely spread in the lateral direction. In the MPS-DF and modified MPS-DF methods, since the direction of movement and sediment concentration of each particle was calculated, it is possible to automatically evaluate sediment transport in the downward flow and lateral directions. Therefore, the evaluation was greatly improved from the two-dimensional simulation.

Furthermore, in the two-dimensional simulation, the deposition distance in the downward flow direction was short. Additionally, in the two-dimensional simulation, an erosion/deposition rate equation was used, but the momentum change process was not considered. Therefore, the fact that the deposition occurs suddenly corresponds to the sudden loss of momentum by the sand grains. The absurdity of momentum accompanying erosion/deposition in the calculation using shallow water flow equations was pointed out by Iverson and Ouyang (2015), and is a difficult problem to solve. Since the motion equation was solved for each particle in the MPS-DF method, the deviation from the experimental results was small. However, the non-conservation of momentum occurs when the momentum transfer accompanying concentration movement is ignored. In the case of the deposition process, the concentration moved from the upper layer with a large momentum to the lower layer with low momentum, implying that the momentum was gradually lost. As a result, this may have allowed for the easier deposition of sediment. The modified MPS-DF that solved this problem yielded results that more closely matched the experimental results, especially in the early stage of deposition.

In the early stage, the deposition was formed in the upper stream in the MPS-DF model, more so than in the modified MPS-DF model, while final deposition was formed in the most downstream side. This is considered to be the effect of sediment re-erosion by subsequent debris flow with low concentration, because the eroded sediment becomes easy to move for the reason opposite that of the deposition process. However, the longitudinal deposition results of the modified MPS-DF model were almost in agreement with the experimental results.

As described above, the modified MPS-DF model has the highest reproducibility for the longitudinal deposition results. To accurately reproduce the erosion/deposition process, it is important to strictly evaluate the sediment concentration distribution, flow velocity distribution, and momentum conservation law. The particle method is effective for conducting this evaluation. However, in the later process, the results obtained using the modified MPS-DF model deviated from the experimental results in terms of lateral spreading. One of the reasons for this was that bedload was generated from the edge of the deposit and continued to flow downstream. As the size of the calculation particles was larger than the average particle size of the sand grains, it proved impossible to represent the movement of individual sediment particles. Although reducing the size of the calculation particles could solve this problem, it is not realistic in terms of the calculation load. Therefore, other solutions need to be considered.

Another reason for the deviation of the results is due to the behavior of seepage flow in the deposited sediment. Fig. 3 shows the region where surface flow did not occur. The vicinity of the surface in this region is unsaturated. In other words, water moves differently than sand grains. Even in the saturated region, seepage flow seemed to occur in the deposited sediment. Since water selectively flowed out from the pore, it was believed that sand grains were difficult to spread laterally. It is difficult to reproduce the behavior of seepage flow using the particles method based on the one-fluid model. However, it is possible to reproduce unsaturated seepage flow by giving parameters of water content ratio to particles and moving them among neighboring particles. Based on this model, it is necessary to improve the calculation model so as to reproduce the seepage of water out of the deposited layer.

Acknowledgements

This work was supported by JSPS KAKENHI Grant Number JP16K16375 and 18H03957.

References

- Chen, H.X., Zhang, L.M., Gao, L., Yuan, Q., Lu, T., Xiang, B., Zhuang, W.L., 2016, Simulation of interactions among multiple debris flows: *Landslides*, v. 14, p. 595-615.
- De Haas, Ventra, D., Carbonneau, P. E., Kleinhans, M. G., 2014, Debris-flow dominance of alluvial fans masked by runoff reworking and weathering: *Geomorphology*, v. 217, p. 165-181.
- De Haas, T., Braat, L., Leuven, J.R.F.W., Lokhorst, I.R., Kleinhans, M.G., 2015, Effects of debris flow composition on runout, depositional mechanisms, and deposit morphology in laboratory experiments: *Journal of Geophysical Research: Earth Surface*, v. 120, no. 9, p. 1949-1972.
- Egashira, S., Ashida K., Yajima H. and Takahama J., 1989, Constitutive equations of debris flow: *Disaster Prevention Research Institute Annuals*, Kyoto University, no. 32 B-2, p. 487-501.
- Egashira, S., Miyamoto, K., Ito, H., 1997, Constitutive equations of debris flow and their applicability: *Proc. 1st International Conference on Debris-Flow Hazards Mitigation*, ASCE, p. 340-349.
- Iverson, R. M. and Ouyang, C., 2015, Entrainment of bed material by Earth-surface mass flows: review and reformulation of depth-integrated theory, *Reviews of Geophysics*, v. 53, p. 27-58.
- Koshizuka, S. and Oka, Y., 1996, Moving Particle Semi-implicit Method for Fragmentation of Incompressible Fluid: *Nuclear Science and Engineering*, v. 123, p. 421-434.
- Laigle, D., Lachamp, P., Naaim, M., 2007, SPH-based numerical investigation of mudflow and other complex fluid flow interactions with structures: *Computational Geoscience*, v. 11, p. 297-306.
- Liu, J., Nakatani, K., Mizuyama, T., 2012, Hazard Mitigation Planning for Debris flow Based on Numerical Simulation Using Kanako Simulator: *Journal of Mountain Science*, v. 9, p. 529-537.
- Miyamoto K. and Ito T., 2002, Numerical simulation method of debris flow introducing the erosion rate equation: *Journal of the Japan Society of Erosion Control Engineering*, v. 55, no. 2, p.24-35.
- Monaghan J. J., 1988, An introduction to SPH: *Computer Physics Communications*, Volume 48, Issue 1, p. 89-96.
- Nakatani, N., Kosugi, M., Satofuka, Y., Mizuyama, T., 2017, Influence of housing and roads on debris flow flooding and deposition in alluvial fan areas : Case study on debris flows in Hiroshima, Japan, in August 2014: *Journal of the Japan Society of Erosion Control Engineering*, v. 69, no. 5, p. 3-10.
- Pastor, M., Blanc, T., Haddad, B., Petrone, S., Sanchez Morles, M., Drempevic, V., Issler, D., Crosta, G. B., Cascini, L., Sorbino, G., Cuomo, S., 2014, Application of a SPH depth-integrated model to landslide run-out analysis: *Landslides*, v. 11, p. 793-812.
- Suzuki T. and Hotta N., 2015, Development of modified particles method for simulations of debris flows based on constitutive equations and its application to deposition process: *Journal of the Japan Society of Erosion Control Engineering*, v. 68, no. 1, p. 13-24
- Suzuki, T. and Hotta, N., 2016, Development of Modified Particles Method for Simulation of Debris Flow Using Constitutive Equations: *International Journal of Erosion Control Engineering*, v. 9, no. 4, p. 165-173.
- Suzuki, T., Hotta, N., Iwata, T., 2016, Accelerating methods for particle model of debris flows and its application to entrainment process: *Proceedings of the 8th Symposium on Sediment-Related Disasters*, p.193-198.
- Wang, W., Chen, G., Han, Z., Zhou, S., Zhang, H., Jing, P., 2016, 3D numerical simulation of debris-flow motion using SPH method incorporating non-Newtonian fluid behaviour: *Natural Hazards*, v. 81, p. 1981-1998.

Numerical modeling of debris flows and landslides triggered by an extreme rainfall event

Yuan-Jung Tsai ^{a,*}, Fang-Tsz Syu ^a, Shin-Pin Lee ^a, Chjeng-Lun Shieh ^{a,b}

^aDisaster Prevention Research Center, National Cheng Kung University, 3F, No500, An-Ming Rd., Annan Dist, Tainan City 709, ROC

^bDept. of Hydraulic and Ocean Engineering, National Cheng Kung University, No.1, University Road, Tainan City 701, ROC

Abstract

The frequency of extreme rainfall corresponding with debris flows and large-scale landslides is increasing in the Taiwan. The traveling distance of debris flows get longer with increased sediment supply, and the hazard area is also larger than regular disaster situation. The debris flows can be considering as a mixture with solid phase and liquid phase. With a larger sediment supply in the dynamic process, the volume of fine sediment separating from solid phase is also larger, and so the state of liquid phase is change after fine sediment mix with water. This phenomenon contributes a significant effect on the mobility of debris flows and large-scale landslides. The composition of the mixture plays an important role in the analysis of the hazard area. In the present study, a two-dimensional numerical model is proposed to simulate the dynamic process of debris flows and landslides under different compositions of the mixture. The proposed was applied to simulate a case of extreme rainfall event, and the topographic data after disaster was used for verification. When the composition of the mixture included with fine sediment, the simulation of affected area had a good agreement with the real situation. The present study pointed out that the simulation of debris and landslide under extreme rainfall condition should consider the effect of fine sediment in the simulation condition.

Keywords: Debris flow, Landslide, Numerical modeling, Extreme rainfall

1. Introduction

In Taiwan, the effects of climate change have resulted in more frequently, extreme rainfall events, having higher intensity and shorten duration than in the past (Hsu and Chen, 2002). With the increased rainfall, landslide and debris flow disasters are becoming more common (Chen et al, 2011). Unexpected disasters occur even with mitigation works installed to reduce the sediment movement. Fig.1a shows the debris flow case occurred during Typhoon Morakot in 2009 with 32 fatalities (Shieh et al, 2010). In fact, there were evacuation plans prepared for the villages based on empirical formulas to identify the fan as a dangerous area (SWCB, 2013). However, the consideration of empirical formulas did not involve scenario of a large sediment supply in an extreme rainfall event (Fig.1b).

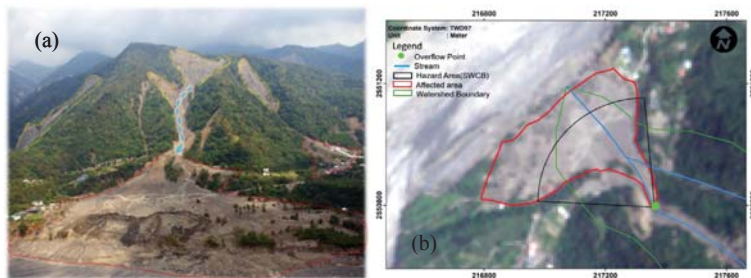


Fig. 1. Disasters during Typhoon Mocarot (a) aero photo; (b) Comparison between hazard area and affected area.

* Corresponding author e-mail address: rongtsai@dprc.ncku.edu.tw

With a larger volume debris material, the water flow will mix with more volume of fine sediment, the density of liquid phase in the mixture flow will increase, and so the mobility of debris flow and landslide become higher. Hence, the original evacuation plan using empirical formulas is not able to avoid the debris flows and large-scale landslides in an extreme rainfall (Lee et al, 2016). After disastrous event, it is important to review and revise the existing evacuation plans. This requires a suitable tool for delineating the hazardous areas during extreme rainfall. Here, we outline a process for setting the parameters of a numerical model that can be used to identify debris-flow hazard zones.

2. The effect of extreme rainfall during debris-flow movement

The conditions for debris-flow movement condition can be described by equation (1), such as the constitutive equation developed by Egashira et al. (1989).

$$\frac{h_s}{h_t} = \frac{1}{\left(\frac{\sigma}{\rho_w} - 1\right) \bar{c}_s} \cdot \frac{\tan \theta}{(\tan \varphi - \tan \theta)} \quad (1)$$

where \bar{c}_s is the depth-averaged concentration of the moving sediment layer, σ is the density of sediment, ρ_w is the density of water, and φ is the friction angle of sediment. These results have been applied to a wide range of mass flows from debris flows to water flow and bedload transport. Fig. 2 presents a schematic model of such a debris flow.

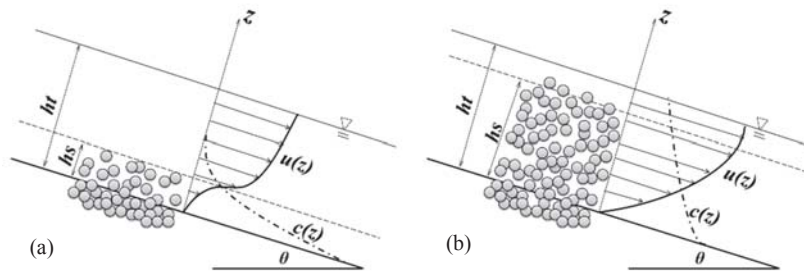


Fig. 2 Schematic model (a) when sediment transport is dominantly bed load; (b) when sediment transport is a debris flow

In Fig. 2, h_s is the sediment layer depth, h_t is total depth, $u(z)$ is the velocity profile along the z -axis, $c(z)$ is the concentration profile, and θ is the slope of the river bed. The depth ratio of the moving sediment layer to depth of flow h_s/h_t is indicative of the type of sediment movement on or above the bed. When h_s/h_t is similar to the diameter of the particles, sediment is transported predominately as bed load. Conversely, when h_s/h_t is greater than 0.8, the water and sediment are almost completely mixed, which indicates the occurrence of a debris flow. Between these two types, it is a type of motion referred to as sediment-laden flow (Egashira, 1989, 1991, 1992 & 1997).

Equation (1) can be applied to the continuum between debris flow and water flow with bed load. According to the post Chi-Chi-earthquake monitoring, multiple landslides contributed new sediments to the drainage network (Lin et al, 2004). The new sediment contained a greater proportion of fine particles and therefore the density of flow increased rapidly because of the fine particles in suspension. So, in the above relationship, the density of water including the suspended matter, ρ_m can be used instead of ρ_w . Therefore, the original equation can be modified as follow:

$$\frac{h_s}{h_t} = \frac{1}{\left(\frac{\sigma}{\rho_m} - 1\right) \bar{c}_s} \cdot \frac{\tan \theta}{(\tan \varphi - \tan \theta)} \quad (2)$$

$$\rho_m = \rho_s \cdot C_v + \rho_w \cdot (1 - C_v) \quad (3)$$

where C_v is the fine particle concentration in the runoff.

The relationship between the depth ratio and riverbed gradient is plotted in Fig.3. The figure shows that when the density of flow increases, the depth-ratio of the moving sediment layer to the flow depth also increases.

For example, when ρ_m is 1.0 and the riverbed gradient is 6° , the depth ratio is 0.4. In this situation, the flow type can be classified as a sediment-laden flow. When ρ_m increases to 1.3, however, the depth-ratio reaches 0.8 and the type of flow is a debris flow. Furthermore, note that the lowest possible riverbed gradient for debris flow decreases as the density of flow increases. In Fig.3, when ρ_m increases to 1.5, a debris flow can occur with a gradient as low as 5 degrees, on the other, the debris flow could occur at more downstream.

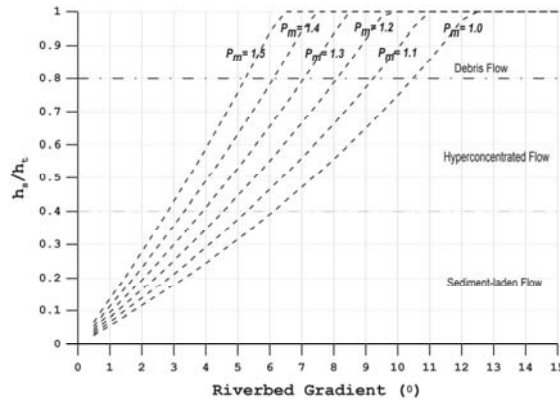


Fig. 3 The relationship between depth-ratio and riverbed gradient

3. Numerical model of debris-flow movement

3.1 Government equations

Based on the same idea, the theory of Egashira et al. (1992, 1997) was used to simulate this movement. The mass conservation for the mixture flow and sediment transport are

$$\frac{\partial h}{\partial t} + \frac{\partial M_i}{\partial x_i} = \frac{E}{c_*} \quad (4)$$

$$\frac{\partial \bar{c}h}{\partial t} + \frac{\partial \gamma \bar{c}M_i}{\partial x_i} = E \quad (5)$$

The momentum conservation for the flow is

$$\frac{\partial M_i}{\partial t} + \frac{\partial \bar{u}_j M_i}{\partial x_i} = -gh \frac{\partial H}{\partial x_i} - \frac{\partial \tau_{oi}}{\partial x_i} \quad (6)$$

where h is flow depth, M_i is the flux vector, E is the erosion rate of bed sediment, and \bar{u}_j is depth-averaged velocity. g is gravity acceleration, H is the surface level of the flow, τ_{oi} is the shear stress acting on the bed, ρ_m is the mass density of a hyper-concentrated sediment-water mixture. c_* is the concentration of stationary layer, \bar{c} is the averaged concentration, γ is the specific gravities of soil.

The erosion and deposition at the river bed were calculated using the equation of bed surface elevation which can be expressed as:

$$\frac{\partial z_b}{\partial t} = -\frac{E}{c_* \cos \theta_r} \quad (7)$$

where z_b is the elevation of river bed, and θ_r is the slope of the river channel.

The shear stress acting on the slip surface can be expressed as:

$$\mathbf{T} = \mathbf{T}_s + \mathbf{T}_d + \mathbf{T}_f \tag{8}$$

where \mathbf{T}_s is the static inter-granular contact, \mathbf{T}_d is the particle-to-particle collision, and \mathbf{T}_f is the interstitial liquid phase, which were shown as

$$\mathbf{T}_s = \alpha c(\sigma - \eta\rho)gh \cos \theta \tan \varphi_s \cdot \mathbf{u}/|\mathbf{u}|, \alpha = (c/c^*)^{1/5} \tag{9}$$

$$\mathbf{T}_d = 25/4 \cdot k_d \sigma (1 - e^2) c^{1/3} (d/h)^2 |\mathbf{u}| \mathbf{u} \tag{10}$$

$$\mathbf{T}_f = 25/4 \cdot k_f \rho (1 - c)^{5/3} / c^{-2/3} (d/h)^2 |\mathbf{u}| \mathbf{u} \tag{11}$$

where φ_s is the friction angle, e is the restitution coefficient; c^* obtained from the field investigation, are the concentrations of the solid phase in volume in the flow and at a packed state; d is the diameter of particles of the solid phase; k_d and k_f are constants ($k_g=0.0828$ and $k_f=0.16$ to 0.25); θ is the gradient of the slip surface; $\eta=0.808$ is the coefficient of the effect of buoyancy and takes a value from 0 to 1. In this study, η which is suggested by Miyamoto (2002). \mathbf{T}_s and \mathbf{T}_d will change according to the speed of the sediment movement. When the sediment is moving slow, \mathbf{T}_s has larger impact than \mathbf{T}_d . Otherwise, it will be the other way around. The internal friction angle is constant. The static inter-granular contact \mathbf{T}_s is updated automatically with the movement.

The above-mentioned equations including the constitutive equation, the mass conservation equations, and the momentum equation can be integrated to handle the interface between any two movement mechanisms. For example, the interface between landslide and debris flow or the interface between debris flow and sediment transportation in a river channel (Chen et al, 2011). Therefore, this assumption makes the simulation of compound disaster possible. In applications, however, definition of the parameter values is the biggest challenge.

3.2 Modification of parameters for numerical simulation

According to the theory, the fine sediment plays an important role during debris-flow movement. The concentration of the solid phase is constrained by field data. The fine sediment content is obtained from sieve analysis. The specific gravity of the liquid phase is obtained from Fig. 4. It shows the deposition situation before and after the debris-flow event. After the debris-flow event, water and fine sediments mix together to form a hyper-concentrated water that could remain in the “liquid phase” The density of fluid would increase with fine sediment. In addition, the concentration of sediment is reduced due to the non-calculated fine sand.

Before the event, the concentration of material is c , the porosity is $1 - c$, the specific weight of sediment is σ , and the specific weight of water is ρ_w . After moving, fine sediment (p) was suspended in water. The concentration of sediment would decrease to $p \times c$. The density of fluid ρ_m would increase from unit to $\sigma \times c \times (1 - p) + \rho_w \times (1 - c)$. The largest size of particle that can be suspended in water can be estimated by the particle settling velocity and the fluid shear velocity.

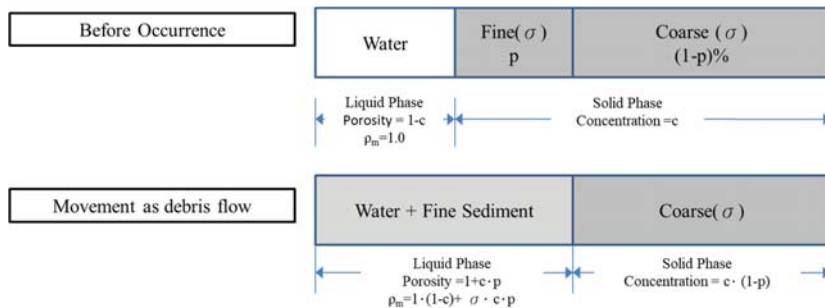


Fig. 4. The parameter condition before and after event

4. Case study

4.1 Study area

The Xinkai landslide, occurred during typhoon Morakot, was located upstream of the potential debris-flow torrent known as Kaohsiung DF078. The area of this watershed is approximately 52 ha. According to the major landslide disaster report provided by the Soil and Water Conservation Bureau, the landslide occurred on the upstream slopes of a natural stream, behind the village, forming a debris flow that caused 32 deaths and damaged 38 buildings(Fig.5).



Fig 5. The photo of study area (a) before typhoon Morakot; (b) after typhoon Morakot

4.2 Parameter setting

Input data include the terrain before and after the landslide for identifying the location of the landslide. Model parameters include particle diameter, friction angle, specific gravity of solid, concentration of solid phase, and specific gravity of the liquid phase. These parameters are derived based on field investigation and laboratory experiment. The particle diameter is based on the surface characteristic particle size.

- Terrain Data

To clarify the lost of typhoon, aero photos were taken after the event (August 2009), and high-resolution digital elevation model (DEM) were produced with the photos by Aerial Survey Office, Forestry Bureau. The resolution of DEM is 2-meter square. The DEM for initial terrain were produced in 2006 by same office. For the simulation, 10-meter square grid were made from 2-meter square DEM data.

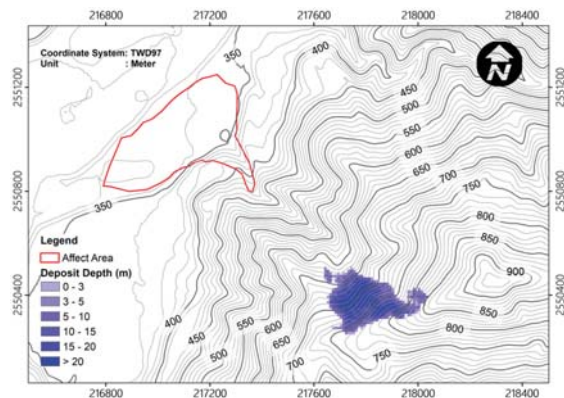


Fig 6. The initial of the unstable material

- Simulation Parameters

In this study, particles with size of 3 cm in diameter can be suspended when the flow depth is 0.1m or deeper. Fine sediment, smaller than 3 cm, is estimated as 30 % of sediment particles, and about 35.2% of liquid phase of hyper-

concentration fluid. The value of concentration of coarse sediment reduced from 0.65 to 0.46. The density of fluid increased from 1 to 1.59. All parameters were listed in Table 1.

Table 1. Parameters used in the simulation

Parameter	Angle of repose	Average particle diameter	Specific weight of particle	Concentration	Specific weight of fluid
Without modification	35	0.2	2.65	0.65	1.0
with modification	35	0.5	2.65	0.46	1.59

4.3 Results

Fig.6 and Fig.7 shows simulation of debris-flow movement with/without parameter modification from 20 seconds to 120 seconds. According the results, at 20 seconds, the material already filled the natural stream. At 40 seconds, debris flow already reach the village and start to deposit. From 40 to 80 seconds, the debris fan getting increase. After 100 seconds, the movement of material start get slow and stop at 120 seconds.

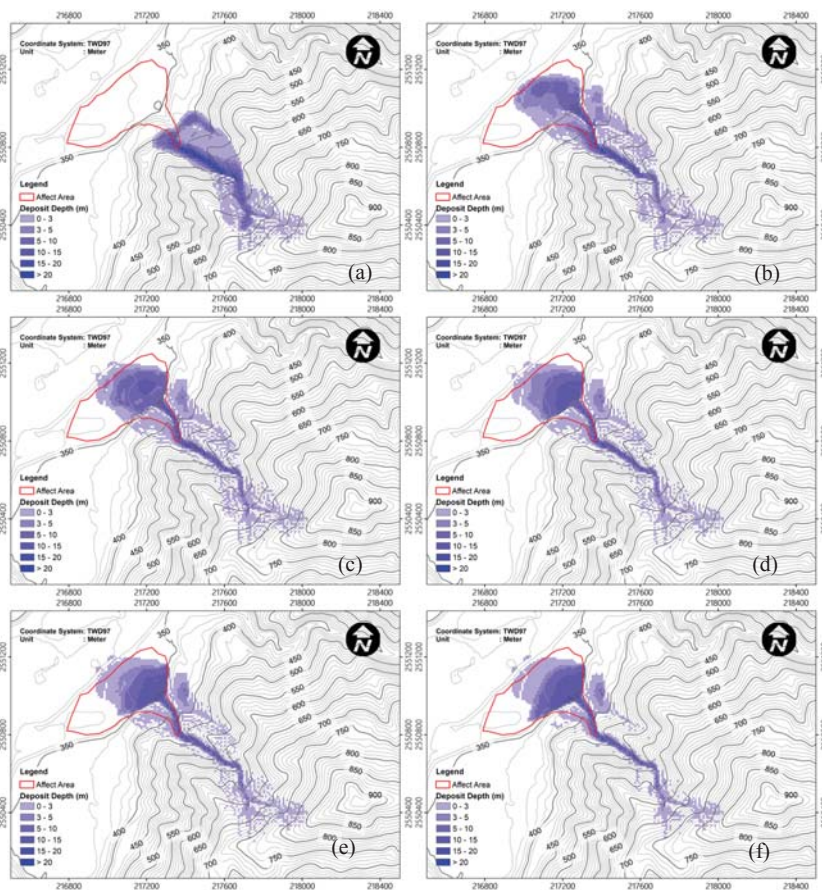


Fig 7. Simulation results without modification (a) 20 second; (b) 40 second; (c) 60 second; (d) 80 second; (e) 100 second; (f)120 second.

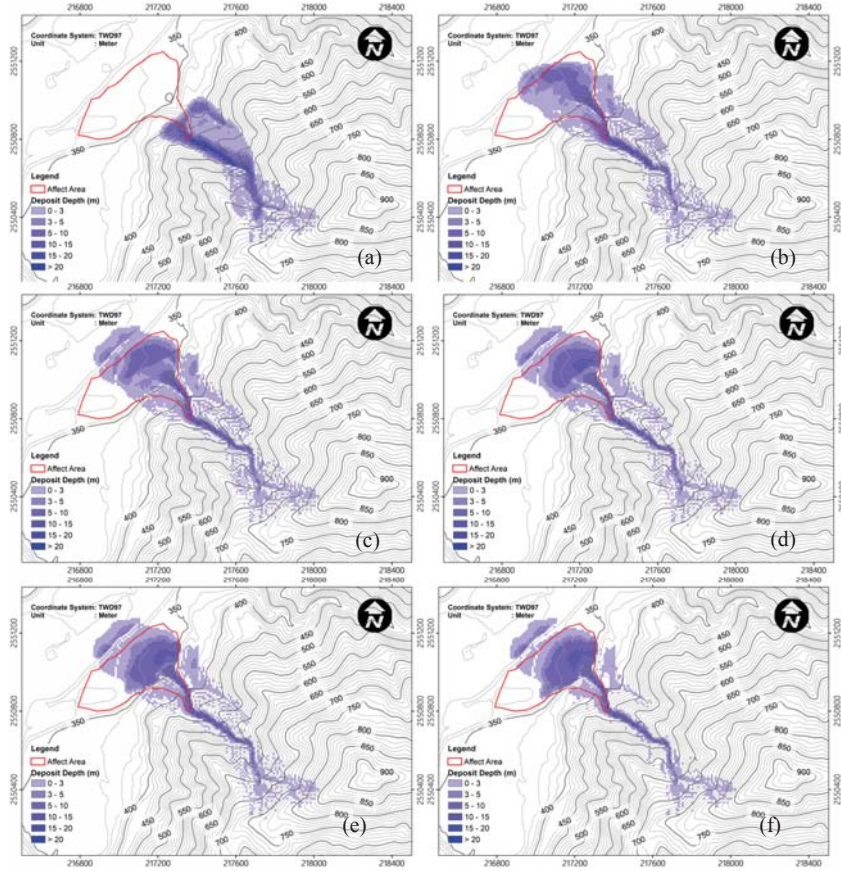


Fig 8. Simulation results with modification (a) 20 second; (b) 40 second; (c) 60 second; (d) 80 second; (e) 100 second; (f)120 second.

Without parameter modification, all the martial hit the village, but the deposition zone did not reach the main channel. The result didn't well describe affected area well (Fig.9). After the parameter modification, it shows more compliant with the real affected area. The maximum deposition is 15-20 meters, the result was verified with field investigation data.

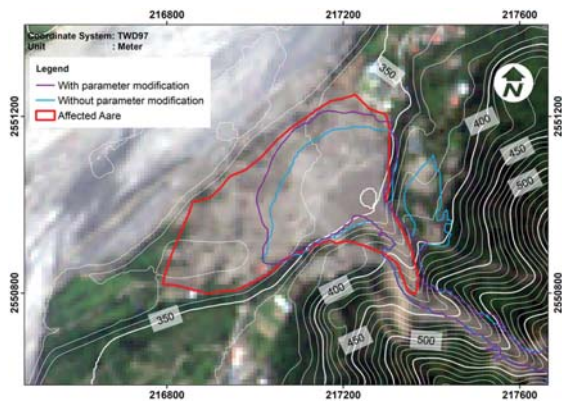


Fig 9. Comparison between with/without parameter modification

Conclusion

The present study confirmed that the effect of fine sediment plays an important factor in the simulation of debris flow and landslide under extreme rainfall conditions. A two-dimensional depth-integrated model was proposed to simulate dynamic process of debris flow and landslide with different composition of the mixture. By the proposed model, the differences of affected area of debris flow and landslide corresponding with concertation of fine sediment can be investigated. A case study of extreme rainfall event was represented using the proposed model with/without consideration of fine sediment, and the topographic data after disaster was used to verify the simulation result. Under the consideration of fine sediment, the simulation of affected area had a good agreement with the real situation. Conversely, the affected area without the effect of fine sediment was small than real situation. This present study pointed out that the hazard mapping for debris flow and landslide under extreme rainfall condition has to include with parameter of concertation of fine sediment and the prediction will be more reasonable.

References

- Chen, Y. S., Kuo, Y. S., Lai, W. C., Tsai, Y. J., Lee, S. P., Chen, K. T., & Shieh, C. L. (2011). Reflection of typhoon Morakot - the challenge of compound disaster simulation. *Journal of mountain science*, 8(4), 571-581.
- Egashira, S., & Ashida, K. (1992). Unified view of the mechanics of debris flow and bed-load. In *Studies in Applied Mechanics* (Vol. 31, pp. 391-400). Elsevier.
- Egashira, S. (1997). Constitutive equations of debris flow and their applicability. In *Proc. 1st Int. Conf. on Debris-Flow Hazards Mitigation, 1997* (pp. 340-349).
- Egashira, S., Miyamoto, K., & Itoh, T. (1997) Constitutive equations of debris flow and their applicability, debris-flow hazards mitigation. *Water Resour Eng Div/ASCE*, pp 340-349
- Hsu, H. H., & Chen, C. T. (2002). Observed and projected climate change in Taiwan. *Meteorology and Atmospheric Physics*, 79(1-2), 87-104.
- Lee, S. P., Shieh, C. L., Tsai, Y. J., Hsu, T. C., & Wong, H. K. (2016) The Study for Debris Flow Hazard Zone that caused by Deep-Seated Landslide. 2016 International Debris-Flow Workshop, Kyoto, Japan
- Lin, C. W., Shieh, C. L., Yuan, B. D., Shieh, Y. C., Liu, S. H., & Lee, S. Y. (2004). Impact of Chi-Chi earthquake on the occurrence of landslides and debris flows: example from the Chenyulan River watershed, Nantou, Taiwan. *Engineering geology*, 71(1-2), 49-61.
- Miyamoto, K. (2002). Two dimensional numerical simulation of landslide mass movement. *J Jpn Soc Eros Control Eng*, 55(2), 5-13. (In Japanese)
- Miyamoto, K. (2010). Numerical simulation of landslide movement and Unzen-Mayuyama disaster in 1792, Japan. *Journal of Disaster Research*, 5(3), 280-287.
- Mizuyama, T., Satofuka, Y., Ogawa, K., & Mori, T. (2006). Estimating the outflow discharge rate from landslide dam outbursts. In *Proceedings of the interpraevent international symposium on disaster mitigation of debris flows, slope failures and landslides* (Vol. 1, No. 2, pp. 365-377).
- Shieh, C. L., Wang, C. M., Chen, Y. S., Tsai, Y. J., & Tseng, W. H. (2010). An overview of disasters resulted from Typhoon Morakot in Taiwan. *Journal of Disaster Research*, 5(3), 236-244.
- Soil and Water Conservation Bureau (2013) Hazard mapping of potential debris flow torrent.
- Tsai, Y. J., Wang, K. C., Chen, Y. C., & Shieh, C. L. (2011). The Variability in Time of the Occurrence Conditions of Debris Flow after Catastrophic Typhoons and Earthquakes: A Theoretical Explanation with Experimental Tests. The 5th Int. Conf. on Debris-Flow Hazards Mitigation: Mechanics, Prediction, and Assessment. *Italian J. Engng. Geo. Envir. (IJEGE)*, B-017.

Debris-flow building damage level and vulnerability curve – A case study of a 2015 Typhoon event in northern Taiwan

Ting-Chi Tsao^{a,*}, Chih-Hao Hsu^a, Hsiao-Yuan Yin^b, and Keng-Ping Cheng^b

^aDisaster Prevention Technology Research Center, Sinotech Engineering Consultants, INC., 280 Xinhua 2nd Rd., Neihu Dist., Taipei 11494, Taiwan

^bDebris Flow Disaster Prevention Center, Soil and Water Conservation Bureau, Council of Agriculture, 6 Guanghua Rd., Nantou 54044, Taiwan

Abstract

Physical vulnerability of the building is the key element for debris-flow hazard Quantitative Risk Analysis (QRA). Most vulnerability curves were related to the deposition height (Fuchs et al., 2007; Lo et al., 2012), or the combination of deposition height, velocity, and impact force (Quan Luna et al., 2011; Jakob et al., 2012; Kang and Kim, 2016). This study uses datasets obtained from a debris-flow hazard caught on video in northern Taiwan during a 2015 Typhoon event and compare with the existing building damage classes and vulnerability curves. The deposition heights, ranging from 0.1 to 5-m, and damage levels of the 15 houses were carefully documented. Of these 15 reinforced-concrete, reinforced-brick, and brick houses, 7 were considered as totally destroyed judging by their actual damage level, others sustained various damages. The debris-flow velocity and impact force were simulated with RAMMS::DebrisFlow module using inputs of the event and compared with the aftermath inundation range and velocity captured in a live video. It shows that when the information of velocity is unavailable, using deposition height alone could also lead to a reasonable result.

Keywords: Vulnerability; debris-flow; Taiwan; damage classification

1. Introduction

Debris flow has been one of the most devastating sediment disasters in mountainous area; the direct and indirect damages caused by debris flow have cost tremendous economic losses and great casualties worldwide, statistical analysis indicates that debris flow is responsible for 165 fatalities annually around the world (Dowling and Santi, 2014). In Taiwan, the steep terrain, frequent occurrence of earthquake and heavy rainfall has made debris flow a major natural hazard in the mountains (Cheng et al., 2005; Lo et al., 2012; Tsao et al., 2018). To reduce and mitigate hazard risks to the society, the understanding of vulnerability to the elements at risk become an important issue (Fuchs et al., 2012).

1.1. Natural hazard risk and vulnerability

In the conceptual natural hazard risk equation $Risk=Hazard \times Exposure \times Vulnerability$ the vulnerability representing one of the key components, and for debris flow the risk is usually expressed as the loss of life or economic (Jakob et al., 2012). In UNDRO's definition, vulnerability is defined as "materialized in natural sciences as the degree of loss of a given element at risk or set of such elements resulting from the occurrence of a natural phenomenon of a given magnitude and is expressed on a scale from 0 (no damage) to 1 (total loss)" (UNDRO, 1979), and could be evaluated as "the interaction between the intensity of the hazard and the type of elements at risk" (Corominas et al., 2014; Blahut et al., 2014).

In this study we focused on the physical vulnerability of debris flow, which was stated by Fuchs et al. (2007) as the damage ratio between the losses of the individual reinstatement value for each element at risk and its original

* Corresponding author e-mail address: tctsa@sinotech.org.tw

value under given debris-flow deposition height. Detailed field survey and aftermath loss monetary value, either from official estimation or insurance claims, were required to generate the vulnerability curve. However, in many regions around the world the insured losses are not available (Jakob et al., 2012; Lo et al., 2012), using damage level or damage classes by expert judgment to define the corresponding vulnerability under different damage conditions provided a surrogate solution (Jakob et al., 2012; Guillard-Gonçalves et al., 2016; Kang and Kim, 2016).

Several studies focused on developing vulnerability curve under the corresponding value of deposition height, flow velocity, or flow pressure in different region (Quan Luna et al., 2011; Lo et al., 2012; Jakob et al., 2012; Totschnig and Fuchs, 2013; Kang and Kim, 2016; Prieto et al., 2018). This study conducted field survey of a debris-flow event which destroyed and damaged several houses in northern Taiwan to determine the building damage levels and deposition height, also the analysis of the live video made the comparison of numerical simulation result with actual event available.

1.2. Purpose

The applicability of vulnerability curves was verified from post-disaster datasets (Papathoma-Köhle et al., 2017), with the curves available, the result could be applied to other regions which do not have complete dataset or not yet struck by debris flow. Using numerical simulation could provide a designated disaster scenario for disaster risk reduction planning, however a validation of the simulation parameters need to be setup. With the above mentioned information available, the quantitative risk analysis of debris flow hazard could be achieved.

2. Study Area

Heliu Community is located in Fuxing Township of Taoyuan County, northern Taiwan. The small community with 30~40 residents is located at the mouth of a potential debris-flow torrent (enlisted as Taoyuan DF034) (Fig 1(a)). Of the 15 residential houses in the community, 4 were built of reinforced concrete, 7 reinforced brick, 2 were brick, and 2 were metal sheet structure. Regarding the storey of the buildings, 12 out of 15 were one-storey and 3 were two-storey buildings, the percentage of building structure and number of storey are in consistent with the findings in Lo et al. (2012). The distribution of these 15 houses is shown in Fig 1(b).

Between 1996 and 2004 three debris-flow events with minor damage were recorded in Heliu Community. The basic information of Taoyuan DF034 is shown in Table 1. In the early morning (approx. 07:45) of Aug. 8, 2015 when Typhoon Soudelor strike Taiwan, the heavy rainfall triggered a landslide in the torrent catchment, the debris were transported down and became debris flow, which damaged 15 residential houses in the community. It is estimated that 13,000 m³ of debris was transported down and deposited in the community, the debris covers almost 8,000 m² with maximum deposition height exceed 5 meters (Lee et al., 2016). The pre and post event views of the deposition zone are shown in Fig 2.

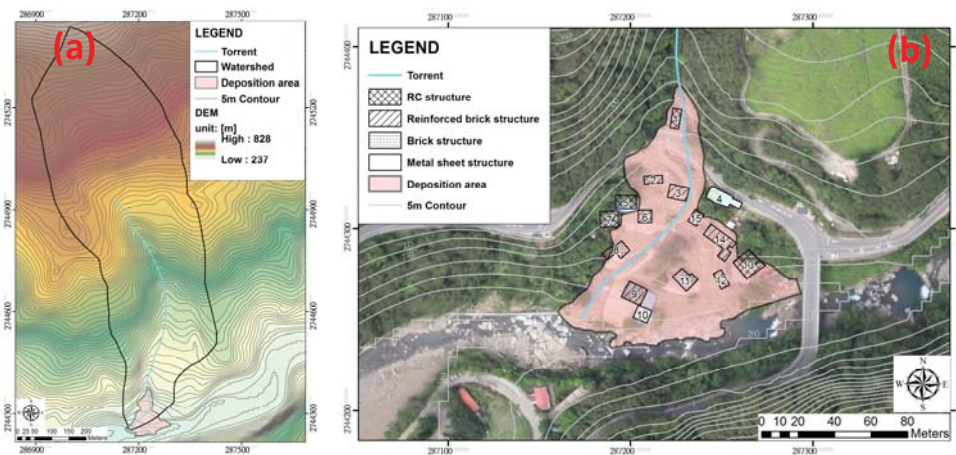


Fig. 1. (a) Catchment topographic map of the study area; (b) Classification and distribution of the 15 houses in the Heliu Community

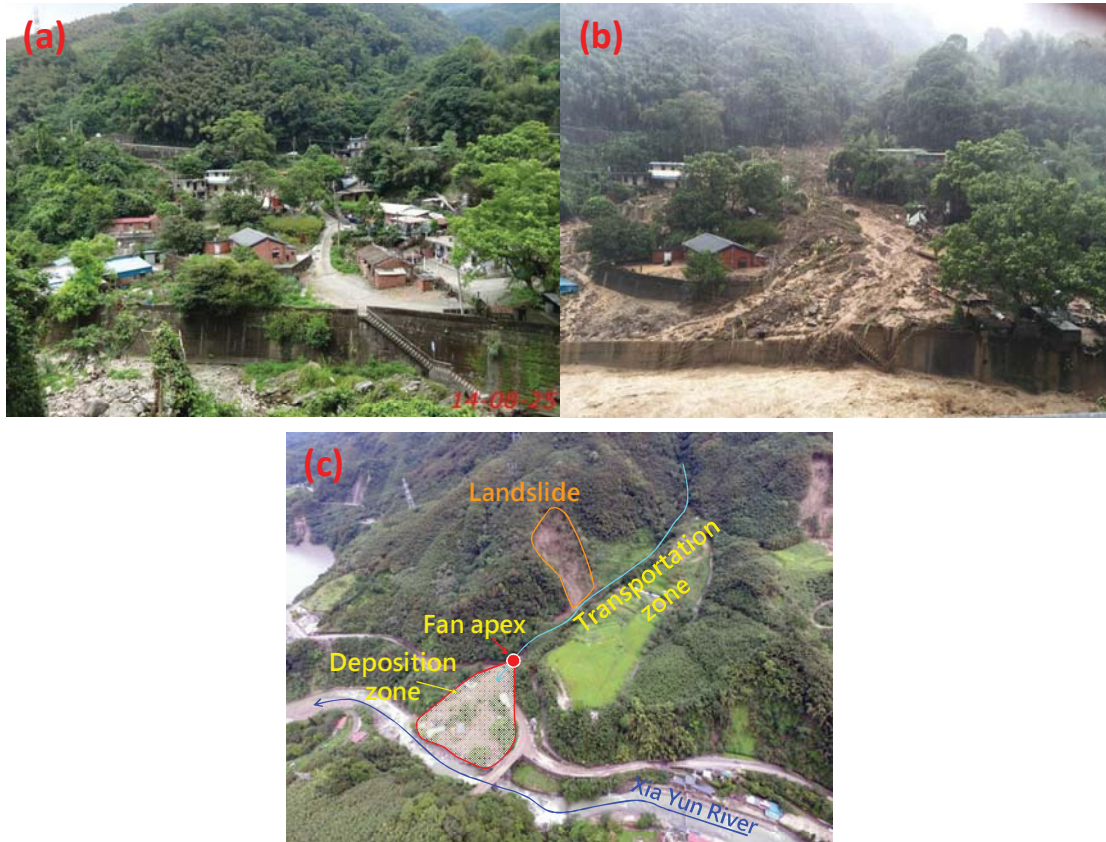


Fig. 2. View of the Heliu Community (a) before the event; (b) during the event; (c) UAV photo after the event (photo: Tsao, T.C. and SWCB)

Table 1. Basic information of Taoyuan DF034 potential debris-flow torrent

Name	Length (m)	Catchment area (ha)	Average slope (°)	Head slope (°)
Taoyuan DF034	759	34	18	30~50

3. Methodology and results

3.1. Damage classification

The damage degree of the 15 buildings in Heliu Community were determined from the field survey two days after the event, the types of building structure, interior and external damage status were carefully checked and documented (Fig 3). As the actual monetary or insured losses were unavailable, this study applies the damage classification to further analysis the vulnerability of the building.

Two methods to determine building damage level were applied in this study. Based on previous studies Guillard-Gonçalves et al. (2016) divided the damage level of the building into 5 classes: negligible damage, slight damage, significant damage, severe damage, and very severe damage, each class with a corresponding range of loss ratio. The estimated loss ratio of buildings in Heliu Community applying this method is shown in Table 2 and Fig 4.

Jakob et al. (2012) classified the damage of buildings into 4 categories (some sedimentation, some structural damage, major structure damage, and complete destruction), with damage description in each category. The result of applying this method is shown in Table 2. In total 7 buildings were considered as complete destruction (IV), 1 as

major structural damage (III), 5 as some structural damage (II), and 2 with some sedimentation (I), some of the damaged buildings and their corresponding damage classes were shown in Fig 3.

The loss ratio of the 15 buildings were plotted on Fig 5 together with vulnerability curves from Fuchs et al. (2007) and Lo et al. (2012), of the 15 plots on Fig 5, more than half of the data sets fall within or close to these 3 curves. In a closer look, reinforced brick and reinforced concrete (R.C.) building were destroyed (loss ratio 1.0) when deposition height is greater than 3.5 m, data sets from reinforced brick buildings fits best to the existing curves, indicates that using deposition height to estimate loss ratio is still a robust but feasible approach.

Table 2. Helio Community building structure information and damage class

Building ID	Building structure	Storey(s)	Loss ratio	Damage class (Guillard-Gonçalves et al., 2016)	Damage class (Jakob et al., 2012)
#1	R.C.	2	1	5	IV
#2	Rein. brick	1	1	5	IV
#3	Rein. brick	1	1	5	IV
#4	Metal sheet	1	0.1	1	I
#5	R.C.	2	0.3	2	II
#6	Rein. brick	1	0.7	4	II
#7	R.C.	2	0.2	1	I
#8	Brick	1	0.5	3	II
#9	Rein. brick	1	0.4	2	II
#10	Metal sheet	1	1	5	IV
#11	Brick	1	0.4	2	II
#12	Rein. brick	1	1	5	IV
#13	R.C.	1	0.8	4	III
#14	Rein. brick	1	1	5	IV
#15	Rein. brick	1	1	5	IV



Fig. 3. Damaged building and damage class applying Jakob et al. (2012) method: (a) #4, metal sheet structure with damage class I; (b) #11, brick structure with damage class II; (c) #13, reinforced concrete structure with damage class III (photo: Hsu, C.H.)

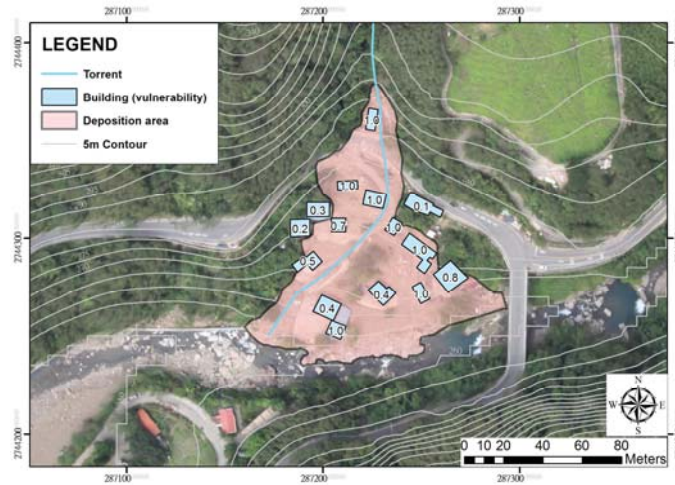


Fig. 4. Loss ratio of the 15 residential houses in the Heliu Community

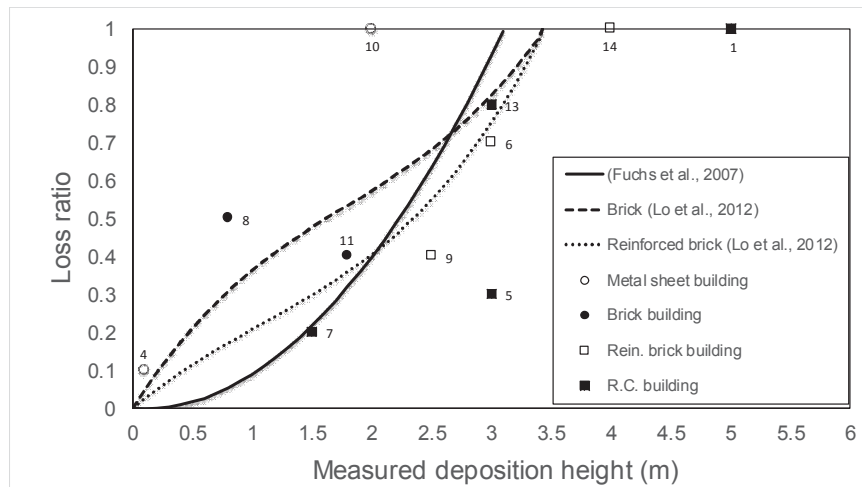


Fig. 5. Comparison of loss ratio with previous studies using deposition height

3.2. Debris-flow numerical simulation

In this study the RAMMS module was applied for debris-flow numerical simulation. The RAMMS (Rapid Mass Movement Simulation) software was developed by WSL (Swiss Federal Institute for Forest, Snow and Landscape Research) for avalanche, rockfall, and debris-flow numerical simulation (Bartelt et al., 2012; Hussin et al., 2012; Leine et al., 2013). The RAMMS::DebrisFlow module is designed for flow phenomena containing fast moving particulate debris. The model is based on 2-D depth-averaged shallow-water equations for granular flows in three dimensions given by the coordinates of the topographic surface of the digital elevation model in a (x,y,z) coordinate system and at time (t), for more information about the module one could refer to WSL (2017) or Frank et al. (2017).

The debris-flow numerical simulation and back calculation of Heliu Community debris-flow event were conducted by Lee et al. (2016) and Huang et al. (2018), using RAMMS::DebrisFlow and compared with the live video captured during the event. Through comparing with the actual event shows that in debris coverage area, deposition height, and flow velocity good result could be observed, with average deviation around 24%, 2 to 10%,

and 3 to 12% respectively (Lee et al., 2016), the simulated deposition height compared with field measurement is shown in Fig 7, The input parameters of the RAMMS simulation are listed in Table 3.

The simulation result, include flow height (Fig 6a) and flow velocity (Fig 6b), was extracted and stored in each cell, with this information available, the intensity index (I_{DF}) and damage probability (P_{DF}) proposed by Jakob et al. (2012) could be calculated. I_{DF} is the product of maximum expected flow height (d) and the square of the maximum flow velocity (v), in some studies I_{DF} is also refer as momentum flux (Jakob et al., 2012; Prieto et al., 2018).

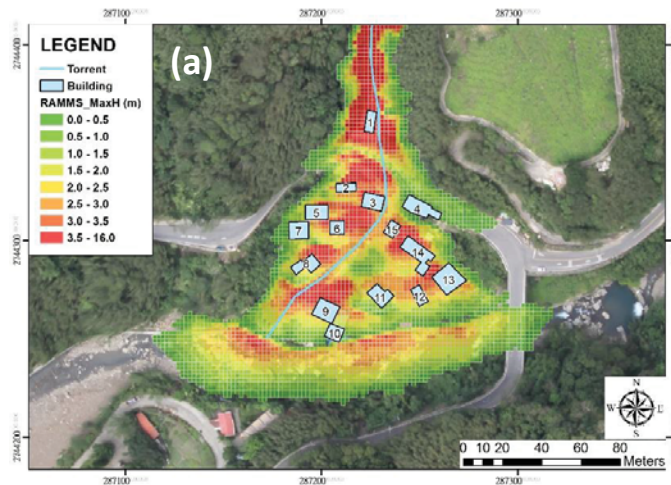
Using the abovementioned simulation result and adopting statistic result of damage probability from Jakob et al. (2012), the estimated number of houses in each damage class is calculated and listed next to the actual losses, as shown in Table 4. The differences in I, II, III, and IV classes were 0% (match), 20%, 75%, and 29% respectively.

Table 3. The input parameters for RAMMS simulation (after Lee et al., 2016; Huang et al., 2018)

Parameter	Input
Terrain (DEM)	2m*2m
Landslide area (m ²)	5,736
Average thickness of landslide (m)	4.7
Block release volume (m ³)	26,966.7
Density (kg/m ³)	1,920
Dry-Coulomb type friction (dimensionless)	0.24
Viscous-turbulent friction (m/s ²)	300
Simulation duration (hr)	3

Table 4. Damage probabilities for Heliu Community and the total number of houses affected

I_{DF}	Number of houses affected	I(%)	II(%)	III(%)	IV(%)
0~1	2	70	30	0	0
1~10	3	22	50	22	6
10~100	4	0	37	38	25
100~1,000	6	0	5	28	67
>1,000	0	0	0	0	100
Calculated result (round to integer)	2.06 (2)	3.88 (4)	3.86 (4)	5.20 (5)	
Actual damage class (from Table 2)	2	5	1	7	



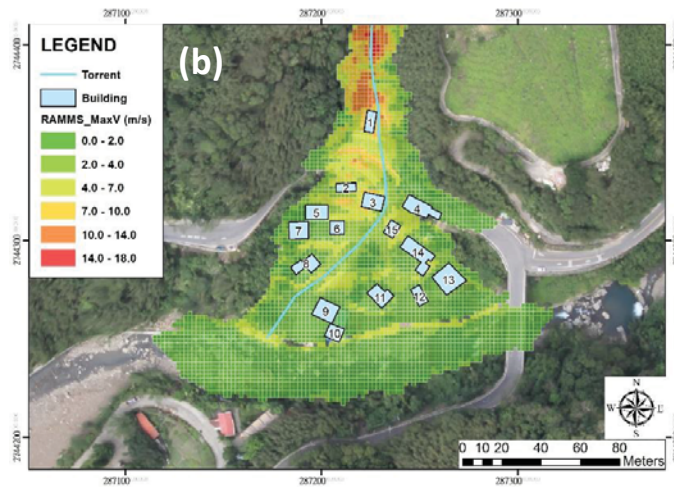


Fig. 6. (a) Maximum flow height of RAMMS simulation; (b) Maximum flow velocity of RAMMS simulation (modified from Huang et al., 2018)

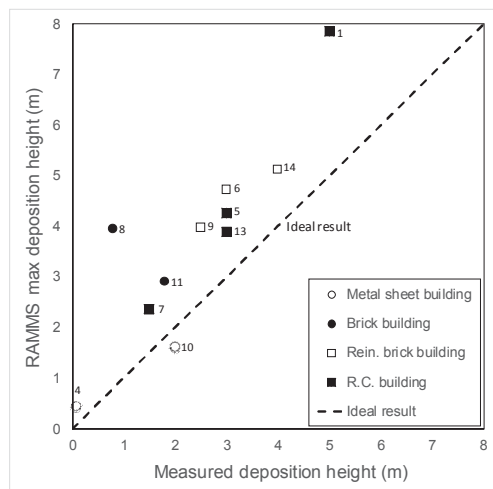


Fig. 7. Comparison of RAMMS simulation result with field measured deposition height

4. Conclusion

Two types of damage classes from debris-flow impact were utilized in a detailed-documented and simulated debris-flow event in northern Taiwan, the result was compared with existing vulnerability curves and intensity index. It shows that alone using deposition height to estimate the loss ratio through existing vulnerability still remain as a simple but feasible method. Also considering flow velocity or impact force might be a promising solution when data were available.

However, users should keep in mind that all vulnerability curves, matrices and indicators, or numerical simulation models have their limitations according to their assumptions, original datasets, inputs and parameters (Nakatani et al., 2013; Papathoma-Köhle, 2016; Papathoma-Köhle et al., 2017), thus more understanding about the characteristic of vulnerability is needed (Fuchs et al., 2012).

Acknowledgements

The authors give their greatest thanks to the Soil and Water Conservation Bureau of Taiwan, which provided part of the research funding. The authors also thank Dr. Ching-Fang Lee and Mr. Chuan-Yi Huang for providing the simulation result, and Prof. Hsien-Ter Chou for the field survey and discussion of the case.

References

- Bartelt, P., Bühler, Y., Buser, O., Christen M., and Meier, L., 2012, Modeling mass-dependent flow regime transitions to predict the stopping and depositional behavior of snow avalanches: *Journal of Geophysical Research*, 117, F01015, doi: 10.1029/2010JF001957.
- Blahut, J., Glade, T., and Sterlacchini, S., 2014, Debris flows risk analysis and direct loss estimation: the case study of Valtellina di Tirano, Italy: *J. Mt. Sci.*, 11(2), p. 288-307, doi: doi.org/10.1007/s11629-013-2806-2.
- Cheng, J.D., Huang, Y.C., Wu, H.L., Yeh, J.L., and Chang, C.H., 2005, Hydrometeorological and landuse attributes of debris flows and debris floods during typhoon Toraji, July 29–30, 2001 in central Taiwan: *Journal of Hydrology*, 306(1-4), p.161-173, doi: doi.org/10.1016/j.jhydrol.2004.09.007
- Corominas, J., van Westen, C., Frattini, P., Cascini, L., Malet, J.-P., Fotopoulou, S., Catani, F., Van Den Eeckhaut, M., Mavrouli, O., Agliardi, F., Pitilakis, K., Winter, M. G., Pastor, M., Ferlisi, S., Tofani, V., Hervás, J., and Smith, J. T., 2014, Recommendations for the quantitative analysis of landslide risk: *Bull Eng Geol Environ*, 73(2), p. 209-263, doi: doi.org/10.1007/s10064-013-0538-8.
- Dowling, C.A. and Santi, P.M., 2014, Debris flows and their toll on human life: a global analysis of debris-flow fatalities from 1950 to 2011: *Nat Hazards*, 71(1), p. 203-227, doi: doi.org/10.1007/s11069-013-0907-4.
- Frank, F., McArdell, B.W., Oggier, N., Baer, P., Christen, M., and Vieti, A., 2017, Debris-flow modeling at Meretschibach and Bondasca catchments, Switzerland: sensitivity testing of field-data-based entrainment model: *Nat. Hazards Earth Syst. Sci.*, 17, p. 801-815, doi: doi.org/10.5194/nhess-17-801-2017.
- Fuchs, S., Heiss, K., and Hübl, J., 2007, Towards an empirical vulnerability function for use in debris flow risk assessment: *Nat. Hazards Earth Syst. Sci.*, 7(5), p. 495–506, doi: doi.org/10.5194/nhess-7-495-2007.
- Fuchs, S., Birkmann, J., and Glade, T., 2012, Vulnerability assessment in natural hazard and risk analysis: current approaches and future challenges: *Nat Hazards* 64(3), p. 1969-1975, doi: doi.org/10.1007/s11069-012-0352-9
- Guillard-Gonçalves, C., Zêzere, J. L., Pereira, S., and Garcia, R. A. C., 2016, Assessment of physical vulnerability of buildings and analysis of landslide risk at the municipal scale: application to the Loures municipality, Portugal: *Nat. Hazards Earth Syst. Sci.*, 16, 311-331, doi: doi.org/10.5194/nhess-16-311-2016.
- Huang, C.Y., Hsu, C.H., and Tsao, T.C., 2018, Analysis and comparison of two debris flow numerical simulation models – A case study of a debris flow hazard event: *Sinotech Engineering*, 141, p. 45-55 (in Chinese).
- Hussin, H.Y., Quan Luna, B., van Westen, C.J., Christen, M., Malet, J.P., and van Asch, Th. W.J., 2012, Parameterization of a numerical 2-D debris flow model with entrainment: a case study of the Faucon catchment, Southern French Alps: *Nat. Hazards Earth Syst. Sci.*, 12, p. 3075-3090, doi: doi.org/10.5194/nhess-12-3075-2012.
- Jakob, M., Stein, D., and Ulmi, M., 2012, Vulnerability of buildings to debris flow impact: *Natural Hazards*, 60(2), p. 241-261, doi: doi.org/10.1007/s11069-011-0007-2.
- Kang, H. and Kim, Y., 2016, The physical vulnerability of different types of building structure to debris flow events: *Nat Hazards*, 80(3), p. 1475-1493, doi: doi.org/10.1007/s11069-015-2032-z.
- Lee, C.F., Chou, H.T., Tsao, T.C., Hsu, C.H., Huang, C.H., and Liao, W.S., 2016, Helium debris flow induced by Typhoon Soudelor: Failure mechanism and numerical simulation: *Journal of Chinese Soil and Water Conservation*, 47 (4), p. 171-184 (in Chinese).
- Leine, R.I., Schweizer, A., Christen, M., Glover, J., Bartelt, P., and Gerber, W., 2013, Simulation of rockfall trajectories with consideration of rock shape: *Multibody System Dynamics*, 32(2), p. 241-271, doi: doi.org/10.1007/s11044-013-9393-4.
- Lo, W.C., Tsao, T.C. and Hsu, C.H., 2012, Building vulnerability to debris flows in Taiwan - a preliminary study: *Natural Hazards*, 64(3), p. 2107-2128, doi: doi.org/10.1007/s11069-012-0124-6.
- Nakatani, K., Okuyama, Y., Hasegawa, Y., Satofuka, Y., and Mizuyama, T., 2013, Influence of housing and urban development on debris flow flooding and deposition: *J. Mt. Sci.*, 10(2), p. 273-280, doi: doi.org/10.1007/S11629-013-2507-x.
- Papathoma-Köhle, M., 2016, Vulnerability curves vs. vulnerability indicators: application of an indicator-based methodology for debris-flow hazards: *Nat. Hazards Earth Syst. Sci.*, 16, p. 1771-1790, doi: doi.org/10.5194/nhess-16-1771-2016.
- Papathoma-Köhle, M., Gembis, B., Sturm, M., and Fuchs, S., 2017, Matrices, curves and indicators: A review of approaches to assess physical vulnerability to debris flows: *Earth-Science Reviews*, 171, p. 272-288, doi: doi.org/10.1016/j.earscirev.2017.06.007.
- Prieto, J.A., Journeay, M., Acevedo, A.B., Arbelaez, J.D., and Ulmi, M., 2018, Development of structural debris flow fragility curves (debris flow buildings resistance) using momentum flux rate as a hazard parameter: *Eng. Geol.*, 239, p. 144-157, doi: doi.org/10.1016/j.enggeo.2018.03.014
- Quan Luna, B., Blahut, J., van Westen, C. J., Sterlacchini, S., van Asch, T. W. J., and Akbas, S. O., 2011, The application of numerical debris flow modelling for the generation of physical vulnerability curves: *Nat. Hazards Earth Syst. Sci.*, 11, p. 2047-2060, doi: doi.org/10.5194/nhess-11-2047-2011.
- Totschnig, R. and Fuchs, S., 2013, Mountain torrents: quantifying vulnerability and assessing uncertainties: *Eng. Geol.*, 155, p. 31-44, doi: doi.org/10.1016/j.enggeo.2012.12.019.
- Tsao, T.C., Huang, C.Y., Chien, J.H., Yin, H.Y., and Chen, C.Y., 2018, Comparison of debris flow hazard mapping between empirical function and numerical simulation - a case study in Taiwan: In: Yamada, T. et al. (eds.): *Symposium Proceedings of INTERPRAEVENT 2018 in the Pacific Rim*, Toyama, Japan, Oct. 1–Oct.4, 2018, pp. 349-354.
- UNDRO (United Nations Disaster Relief Coordinator), 1979, *Natural disasters and vulnerability analysis in report of expert group meeting*. UNDRO, Geneva, Switzerland.
- WSL, 2017, *RAMMS::DEBRISFLOW User Manual v1.7.0*, Switzerland.

Estimating mechanical slope stability to predict the regions and ranges of deep-seated catastrophic landslides

Kousuke Yoshino^{a,*}, Taro Uchida^b

^aAsia Air Survey co.,Ltd., 3-15-58,Ozone, Kita-ku, Nagoya-city, Aichi, 462-0825, Japan

^bNational Institute for Land and Infrastructure Management, Ministry of Land, Infrastructure and Transport and Tourism.,Asahi 1, Tsukuba-city, Ibaraki, 305-0804, Japan

Abstract

In Japan, Typhoon Talas (T1112) induced many rapid deep-seated landslides in the Kii Peninsula. A landslide is one of main processes associated with debris flow initiation. In particular, deep-seated catastrophic landslides can lead to large-scale debris flows that seriously impact human welfare. Previous studies have explored the roles played by geology and geological structure. However, no single, widely used physical model is employed to analyze such landslides. Here, we focus on slope scale and gradient, and explore the relationship between height and gradient for several slopes. We found that the height of slopes exhibiting various gradients was limited, where the greater the gradient, the lower the height; the relationship was amenable to slope stability analysis. We developed a physical model of deep-seated landslides and identified regions at risk. We focused on slopes where typhoon Talas caused such landslides and used detailed topological (LiDAR) data collected before and after the typhoon to measure slope gradients and relative heights. Our model effectively localized deep-seated landslides, although we assumed that the strength of weathered rock was uniform throughout the study area, based on data on the side-slope gradients and relative heights of land abutting the Totsugawa River.

Keywords: deep-seated catastrophic landslides, slope stability analysis, Typhoon Talas, Kii peninsula

1. Introduction

In Japan, typhoon Talas caused many large-scale, deep-seated catastrophic landslides in 2011, principally in the Kii Peninsula. The Shimanto Belt (a paleo-accretionary prism) is widely distributed throughout the Kii Peninsula and is well known for its deep-seated landslide events. In addition, many of the deep-seated landslides caused by Typhoon Talas occurred in “dip slope” formations; this type of geological structure is considered to be a precursor to that responsible for deep-seated landslide occurrences.

Shallow landslides have been physically modeled by combining slope stability analysis with a model of underground water flow; many previous studies have evaluated landslide risks (e.g., Montgomery and Dietrich, 1994). However, only a few models of deep-seated catastrophic landslides are available, although slope risk evaluation methods based on geological structure and small-scale slope deformations have been suggested to be important in this context.

Schmidt and Montgomery (1995) focused on slope size, height, and inclination, and explored the relationship between the latter two variables. For a particular inclination, slope height is limited, where the steeper the slope, the smaller the limit; this relationship is amenable to slope stability analysis. Matsushi et al. (2014) used detailed topographical data collected pre- and post-landslide to estimate soil parameters; it was possible to explain landslides by reference to height limits for slopes of various inclinations, as proposed by Schmidt and Montgomery (1995). Korup and Schlunegger (2007) similarly analyzed bedrock collapse in the Swiss Alps. Previously, we assumed that widening of water channels caused by erosion when landslides were triggered by dam overflows reflected repetitive side-bank collapse triggered by changes in the soil mechanical balance attributable to riverbed erosion; we

* Corresponding author e-mail address: ksk.yoshino@ajiko.co.jp

formalized this balance by reference to the internal soil stress and strength (Yoshino et al., 2013). Thus, we explored changes in soil mechanical balance when the relative height of a slope increased because the riverbed was lowered by erosion, using the method of Schmidt and Montgomery (1995). However, other studies considered that deep-seated catastrophic landslides occurring near rivers were attributable to loss of soil and rock mechanical balance when the relative height was increased by elevation of the slope (e.g., Matsukura, 1987a and 1987b). On the one hand, landslides caused by dam overflows trigger erosion that widens water channels, while on the other hand deep-seated catastrophic landslides create valleys. The processes involved differ in terms of both genesis (riverbed lowering and ridge upheaval, respectively) and speed. However, if Matsukura (1987a and 1987b) is correct, both processes could be described using a model similar to that of Yoshino et al. (2013). Therefore, we explored the relative heights of slopes that participated in deep-seated catastrophic landslides after typhoon Talas (2011), and of slopes that remained stable. We used detailed topographical data collected both before and after the event. We then determined whether the side-bank collapse model that we had earlier developed could be realistically applied to typhoon-triggered landslides. We suggest that our approach can be used to predict the location, scale, and shape of deep-seated catastrophic landslides, and the challenges they pose.

2. Methods

2.1. Working hypothesis

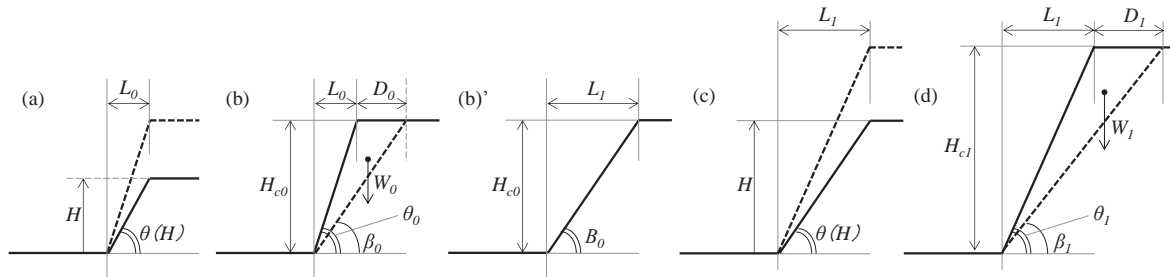
Previous works on the development of mountain topography considered that the rates of upheaval and erosion of channels with large drainage areas were generally uniform, thus varying little with elevation (e.g., Kaizuka, 1978). However, in mountain streams with shallow slopes and small drainage areas, the rate of erosion is lower than the upheaval rate, and elevation will thus increase. Specifically, for ridges, erosion caused by running water is zero. If the valley and ridge positions are considered to remain constant, the valley elevation does not change but both the slope relative height and inclination increase over time. Yoshino et al. (2013) formalized the collapse of water channel side-banks, which sometimes occurs when landslides caused by overflowing dams trigger erosion. The analysis was based on the relationship between slope inclination and the relative height limit developed by Schmidt and Montgomery (1995). Although the time scales of landslides triggered by dam overflow erosion and mountain topographic development vary greatly, they share the feature that the valley and ridge, corresponding to the side-bank shoulder of a landslide caused by dam overflow, do not change. Both the inclination and relative slope height, i.e., the slope and relative height of the side-bank, increase with time, and the slope (side-bank) ultimately becomes physically unstable, collapsing when the relationship between the relative height and inclination reaches a critical point. Therefore, we assumed that, considering that the horizontal positions of the valleys and ridges does not change, deep-seated catastrophic landslides are more likely to occur in a slope that became unstable due to a time-dependent elevation of the ridge, even though the elevation of the valley remains constant. We verified this hypothesis using the concept of water channel side-bank collapse, as caused by erosion when dam overflow triggers a landslide [Yoshino et al. (2013)]. It can be thought that the underground structures, likes bedding angle and so on, should be affected heterogeneity of bedrock strength and groundwater movement. However, in this study, we did not consider heterogeneity of underground condition. So here we tested effects of topography on deep-seated catastrophic landslide occurrence.

2.2. The model

Figure 1 shows a schematic diagram of the landslides studied. The model assumes that the relative slope height (H) increases because of slope upheaval and valley bottom erosion, while L remains constant; when the slope becomes unstable, it collapses over width D_i , creating a wedge-shaped landslide front of inclination β_i , thus increasing the slope width (L). The slope safety ratio is derived via stability analysis:

$$F_s = \frac{C_i + (W_i \cos \beta_i - U_i) \tan \phi}{W_i \sin \beta_i} \quad (1)$$

Here, $W_i = H_i D_i \gamma / 2$, $C_i = c \{(L_i + D_i)^2 + H_i^2\}^{1/2}$, $U_i = u \{(L_i + D_i)^2 + H_i^2\}^{1/2}$, $\beta_i = \arctan\{H_i / (L_i + D_i)\}$, where c , ϕ , γ and u are the adhesiveness of soil, internal friction angle, unit weight, and pore water pressure, respectively. The subscript



- (a): The relative height of the slope H increases because of slope upheaval and valley bottom erosion. As L_0 remains constant, the slope inclination ($\tan \theta$) is H/L_0 .
- (b),(b)': When $H = H_{c0}$, the slope collapses over a width D_0 and a wedge-shaped landslide front of inclination β_0 forms.
- (c) As in (a): When $H = H_{c0}$, the relative height of the slope (H) increases because of slope upheaval and valley bottom erosion. As L_1 remains constant, the slope inclination $\tan \theta$ is H/L_1 .
- (d) When $H = H_{c1}$, the slope collapses over a width D_1 and a wedge-shaped landslide front of inclination β_1 develops.

Fig. 1. Schematic of side-slope collapse.

i refers to the number of landslides, and is thus initially zero. The minimum relative height H_C yielding $F_S = 1$ can be expressed by the relationship between the limit of the relative slope height and the inclination, as determined by Culmann (1875); this is Eq. (2):

$$H_C = \frac{4c}{\gamma} \frac{\sin \theta \cos \phi}{[1 - \cos(\theta - \phi)]} \quad (2)$$

where θ is the slope inclination. Assume that the conditions prevailing when the first landslide is triggered are as shown in Figure 1(b). Then, the relative height of the slope at collapse, H_C , and the landslide width D_i , are given by Eqs. (3) and (4):

$$H_{C_i}(L_i) = \frac{(4c + \gamma \cdot L_i) \sin \phi + \sqrt{16c^2 + 8c \cdot \gamma \cdot L_i}}{\gamma \cdot \cos \phi} \quad (3)$$

$$D_i = \frac{\gamma \cdot H_{C_i}^2 - \gamma \cdot H_{C_i} L_i \tan \phi - 4c L_i + H_{C_i} \sqrt{A_i}}{4c + 2\gamma \cdot H_{C_i} \cdot \tan \phi} \quad (4)$$

where

$$A_i = \gamma^2 \cdot H_{C_i}^2 - 2 \cdot \gamma \tan \phi (\gamma \cdot L_i + 4c) H_{C_i} + \gamma^2 \cdot \tan^2 \phi \cdot L_i^2 - 8c \cdot \gamma \cdot L_i - 16c^2 \quad (5)$$

Thus, the slope shape after the first landslide is shown in Figure 1(b)', and L_{i+1} can be expressed as:

$$L_{i+1} = L_i + D_i \quad (6)$$

We assume that, as long as the slope continues to satisfy the stable conditions ($F_S > 1$) of Eq. (1), L_i does not change; only H increases. The relationship between θ and H is:

$$\tan \theta = \frac{H}{L_i} \quad (7)$$

When L_0 , c , ϕ , and γ are defined as above, the relationship between H and $\theta(H)$ can be calculated. Figure 2 shows the process in graphical form. If the slope relative height, H , increases because of slope upheaval, θ also increases when L_i is held constant (thick solid line). Later, when H attains H_{c0} , the first landslide occurs, causing θ to decrease as shown in Figure 1. Later, if upheaval continues, H and θ increase once more [Eq. (7)], and a second landslide develops similarly. We assume that the width of the riverbed does not change either when the relative height of the slope increases or when the slope collapses.

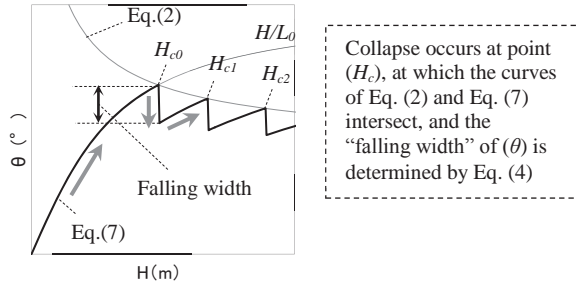


Fig. 2. Graphical presentation.

3. Sites and methodology

3.1. Deep-seated catastrophic landslide sites

We selected three (among many) deep-seated catastrophic landslides that occurred in the Kii Peninsula after typhoon Talas in 2011, i.e., those at Akadani, Akadani-higashi, and Nagatono (Figure 3). All three slopes have “dip slope” type configurations.

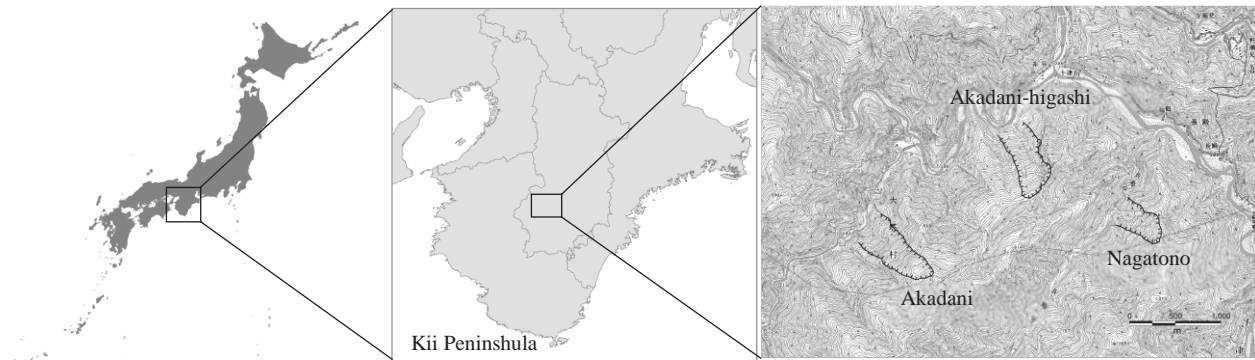


Fig. 3. The study area

3.2. Data

We used 1-m digital elevation model (DEM) data collected by airborne lasers. The pre- and post-landslide data were obtained in 2009 and between December 2011 and February 2012, respectively. For Akadani, a few re-slides and landslide expansions occurred after the deep-seated catastrophic event (Sakurai et al., 2015); the data did not encompass these later events.

3.3. Analysis

We evaluated areas to 500 m up- and down-stream from each landslide, as follows. First, using pre-landslide data, we set reference points at 20-m intervals along the ridges. Then, we drew lines from these points toward the points in the region of the slope toes (where the slope bottoms and the flats between the banks intersect) where the inclinations were steepest. We then divided the cross-sections into those associated with landslides (termed CSLs below) and not associated with landslides (termed NCSLs below) (Figure 4). When at least 66% of the lines were included in the landslide, the cross-sections were considered to be CSLs, and the relationship between relative height (H) and slope inclination (θ), from the slope foot to the ridge, was examined with respect to all lines. Then, ground strength parameters (c , ϕ , and γ) were repeatedly varied within specific ranges (c : 5 to 300 kN/m², ϕ : 10 to 40°, γ : 15 to 25 kN/m³) and entered into Eq. (2) to optimize landslide prediction by H_c (the percentage of cross-sections correctly identified as landslide sections among the actual CSLs) and the cover rate (the percentage of actual CSLs among cross-sections with $F_S < 1$.) We then derived the combination of parameters that optimally predicted landslide occurrence/non-occurrence.

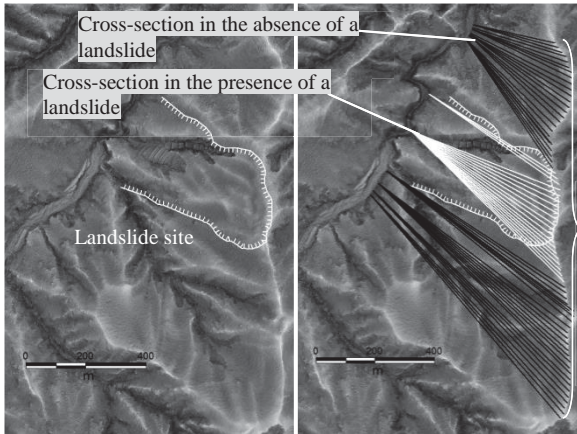


Fig. 4. Examples of when collapse did and did not develop. Occurrence/non-occurrence setting of collapse

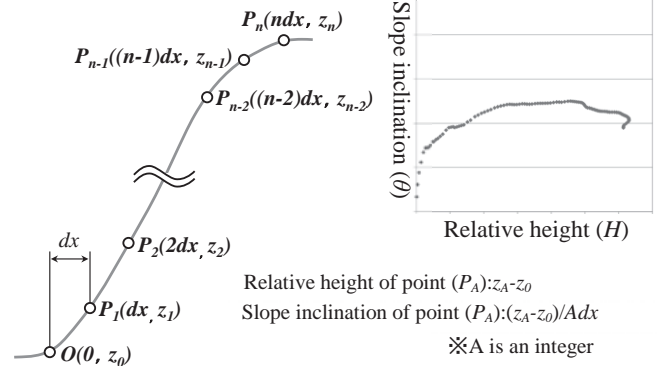


Fig.5. Topographical features of a slope

Although many landslides commenced from the slope foot, the entire slope did not necessarily collapse. Thus, using pre-landslide data, we set measurement points every 10 m along each line running horizontally from the slope foot, and explored the relationship between the relative height and inclination according to those of the slope foot (Figure 5). We thus extracted unstable regions in the middle of slopes, and not only in the ridges; this was especially important when the slope was convex. Next, using the post-landslide data, we performed a similar analysis to determine whether the landslides had eliminated unstable slopes. If our hypothesis was correct, it would be possible to calculate the decrease in slope inclination caused by a landslide (arrows in Figure 2), in turn allowing calculation of the size and shape of the wedge-shaped landslide front. We compared the shape before and after a landslide; we now show how to estimate the shape and the front size.

4. Result

4.1. Longitudinal slope shapes

The longitudinal lines drawn in the three landslide sites are shown in Figure 6. Figure 7 shows the shape of the principal longitudinal line of each slope, i.e., that located in the central CSL. In the longitudinal direction, the slope of the Akadani-higashi terrain prior to the landslide [Fig. 7(b)] is linear or (downward) convex. However, the pre-landslide terrains of Akadani [Fig. 7(a)] and Nagatono [Fig. 7(c)] are steepest from the bottom to the middle of the slope, gradually becoming gentler from the middle to the top, and trending (upward) convex. In Figure 7, the Akadani-higashi trend differs from those of Akadani and Nagatono, attributable to the fact that the 2011 landslide at Akadani-higashi was a re-slide of the internal region (at the top of the slope) of the landslide produced by the major Totsugawa flood of 1889.

4.2. Relationship between slope relative height and inclination

Figure 8 shows the pre-landslide relationship between the relative slope height (H) and inclination ($\tan\theta$) (from the foot to the ridge) relative to the longitudinal lines drawn at the three sites (Fig. 6). In the graph, CSLs and NCSLs are represented by + and \circ , respectively. At Akadani [Fig. 8(a)] and Nagatono [Fig. 8(c)], the NCSLs downstream from the landslide, i.e., those within the dashed frames were in areas of low relative height but with large inclinations; the upstream NCSLs were in areas of large relative height and small inclinations. For Akadani-higashi [Fig. 8(b)], the CSLs were in areas of large relative height and pronounced inclination. Thus, although the Nagatono data are not as clear as those from the two other sites, most CSLs are in the upper right corner of the graphs, i.e., in areas with large relative heights and slope inclinations). Also, as indicated in Table 1 and Figure 8, the calculated ground strength parameters were relatively high (ϕ : 10 to 15°, γ : 18 to 22 kN/m³, c : \geq 200 kN/m² in all cases), and the sites were similar. There are differences in best-fitted ground strength parameters although these three landslides underlain by same bedrock geology. While, Schmidt and Montgomery (1995). evaluated ground strength in the Chuckanut Formation in the northern United States as ϕ of 17 to 21° and c of 120 to 150 kN/m²

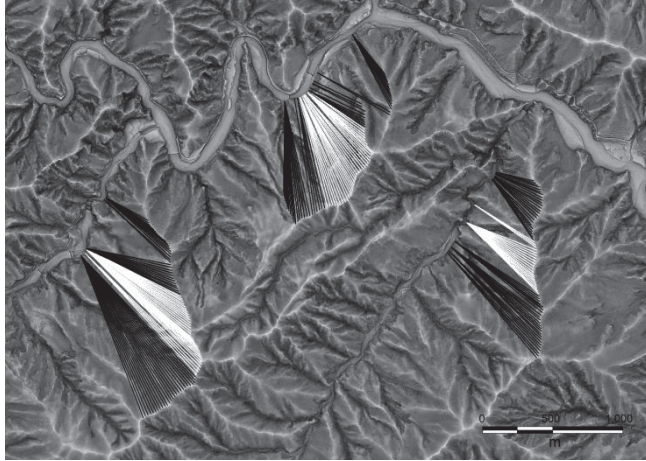


Fig.6. Longitudinal profiles (white: cross-section in the presence of a landslide, black: cross-section in the absence of a landslide)

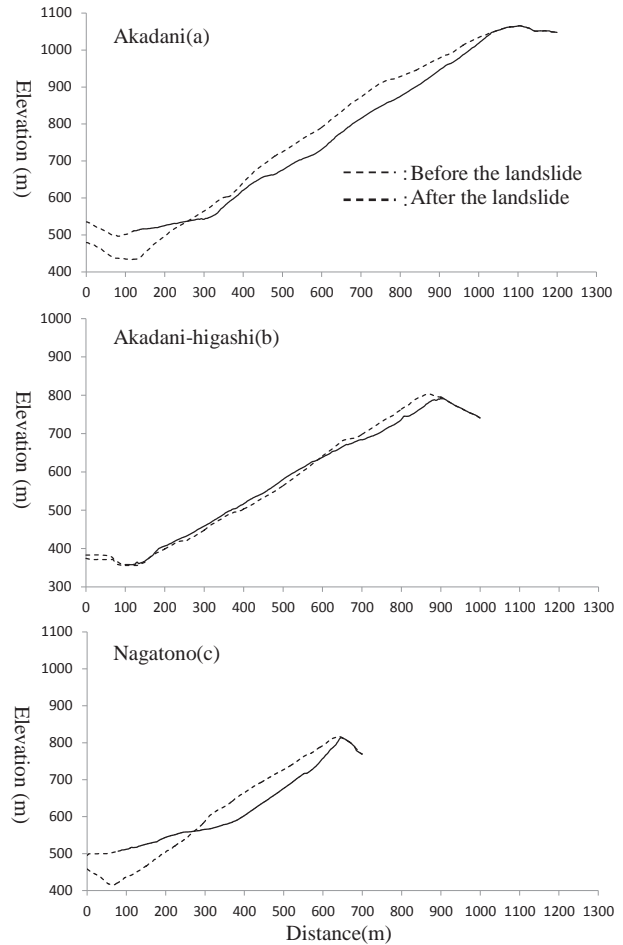


Fig.7. Longitudinal profile

Table.1. The most appropriate values for parameters predicting landslide occurrence/non-occurrence

	Parameters			cover rate	Correct prediction (1=100%)
	c (kN/m ²)	ϕ (°)	γ (kN/m ³)		
Akadani	250	15	18	0.58	1.00
Akadani-higashi	263	10	20	0.92	0.70
Nagatono	230	15	22	0.65	0.68

using similar method. The degree of variation of this study is similar to that of Chuckanut Formation, suggesting that ground strength controls landslide occurrence might be varied in space even in the same bedrock type

5. Discussion

5.1. Estimation of landslide slope

As shown in Section 4.2, in most upstream and downstream slopes, landslides developed in the upper right corners of Figure 8, i.e., in areas with large relative height and slope inclination. Hence, our method identifies slopes located along high-risk mountain streams that are at relatively high risk of landslides. It was possible to distinguish landslide from non-landslide slopes by the bedrock strength. In Akadani, one point in an area of large relative height slightly exceeded the relationship described by Eq. (2). Akadani noted multiple re-slides and landslide expansions after the landslide caused by typhoon Talas but, as our data were obtained prior to these events, and as an expanding landslide later developed in the upper region of the landslide site, it is possible that this was a component of the

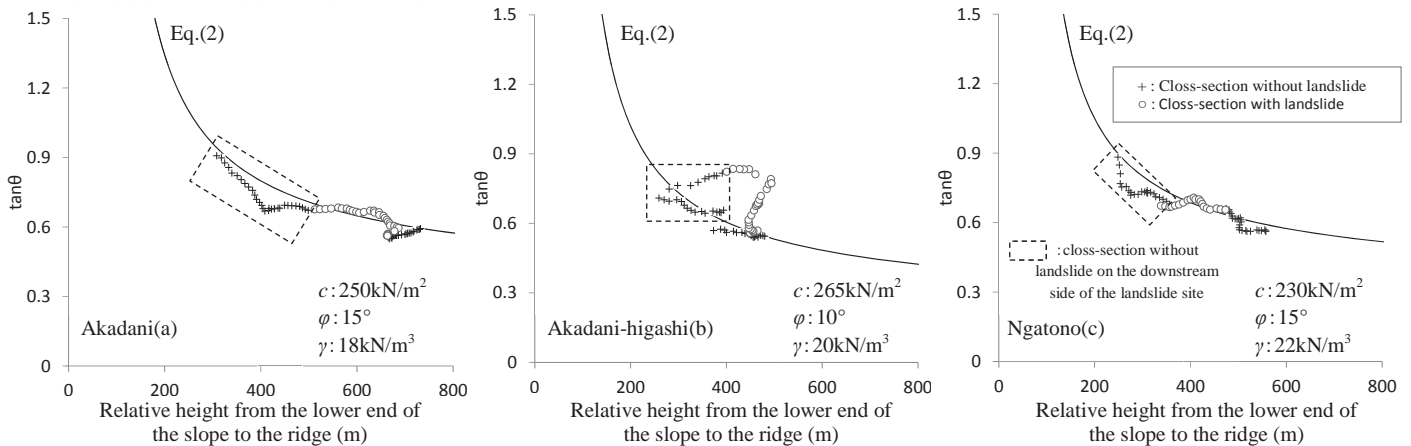


Fig.8. Relationships between relative height and slope gradient (from the lower to the upper end of the slope).

5.2. Estimation of landslide scale and shape

Here, we discuss landslide scale in terms of the relationships between the real and calculated data. Figure 9 shows the relationship between the relative height and inclination of the principal slope cross-section, calculated every 20 m horizontally from the slope foot; we used both pre- and post-landslide data in this analysis. Except for a few points with steep inclinations in areas of low relative height, the pre-landslide Akadani inclination was maximally $\tan\theta = 0.79$ ($H = 380$ m), but became relatively uniform after the landslide, ranging from $H = 200$ – 600 m with $\tan\theta = 0.6$. Similarly, at Akadani-higashi, the post-landslide inclination became near-uniform at $H \geq 300$ m and $\tan\theta = 0.6$. At Nagatono, the maximum inclination pre-landslide was $\tan\theta = 0.75$ ($H = 200$ m), but reduced markedly post-landslide, to $\tan\theta = 0.56$ ($H = 180$ m); the relative height increased, as did the slope inclination. The shape differences post-landslide are evident in Figure 7; at Akadani and Nagatono, the inclinations fell particularly sharply. However, the actual decreases were about 40–60% of the calculated values. In other words, the actual falls were smaller than those calculated. The region that we analyzed experienced multiple deep-seated catastrophic landslides after the heavy rains of 2011; many originated on northwest-oriented “dip slope-type” slopes, indicating that geological structure plays a major role in the development of such landslides (Hiraishi and Chigira, 2011). Thus, it is possible that landslides develop over structurally soft surfaces, such as bedding planes. In addition, recent studies suggest that such soft surfaces may have been earlier deformed by the long-term effects of gravity; the extent of deformation may determine the landslide scale (Chigira et al., 2013). It is also possible that such geological structures are associated with high local pore water pressures (Jitozono et al., 2004). Our model assumes that geological strength is uniform and does not consider underground water. This may be why the model did not accurately predict post-landslide decreases in inclination; thus, further refinement is required.

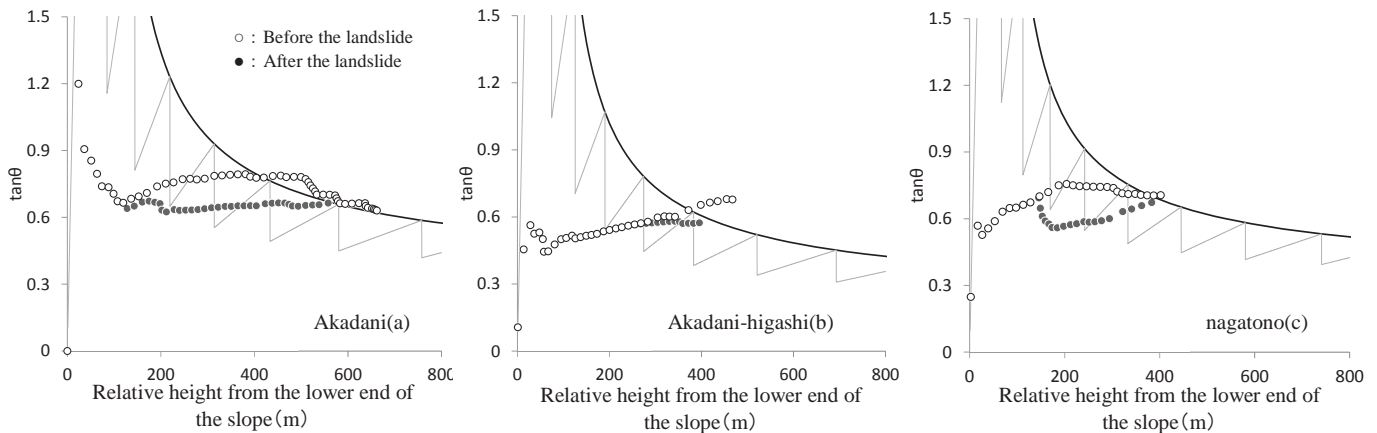


Fig.9. Relationship between the relative height and the gradient of the lower and upper ends of slopes (representative sections).

6. Summary and future tasks

In areas with similar geological structure and soil strength, our model successfully reproduced the relationship between the side slopes and their relative height along the course of the Totsugawa River. This does not contradict the hypothesis wherein, considering that the horizontal positions of the valleys and ridges does not change, deep-seated catastrophic landslides are more likely to occur in a slope that became unstable due to the time-dependent elevation of the ridge, even though the elevation of valley remains constant. Thus, we used measurable physical parameters to identify slopes that might trigger deep-seated catastrophic landslides. However, when we explored whether the model estimated landslide shape and scale in slope cross-sections, we found that, for Akadani and Nagatono, although inclinations were significantly reduced after the landslides, the extent of the reduction was less than predicted.

We modeled slope shape and landslide formation in a relatively simple manner. However, although many landslides commence at the slope foot, the entire slope does not necessarily collapse. Therefore, when our model is further applied to actual phenomena, such as landslides developing in the mid-sections of uniform or concave slopes, inconsistencies are to be expected.

In this study, we only focused on dip-slope. Thus, to use this method as "a predictive tool in other locations or at a larger scale", it would be necessary to consider roles of underground characteristics, such as underground structure and spatial variability of ground strength controls landslide occurrence. Thus, further work is needed. In future, we will analyze slope topographical characteristics in greater detail and underground condition and evaluate more actual landslide sites; we will also consider terrain changes caused by the Totsugawa disaster of the Meiji era.

References

- Chigira, M., Tsou, C.Y., Matsushi, Y., Hiraishi, N., Matsuzawa M., 2013, Topographic precursors and geological structures of deep-seated catastrophic landslides caused by Typhoon Talas: *Geomorphology*, 201, p.479-493.
- Culmann, C., 1875, *Die Graphische Statik*: Meyer and Zeller, Zurich, Switzerland.
- Hiraishi, N., Chigira, M., 2011, Formation of Inner Gorge and Occurrence of Gravitational Slope Deformation in the Central Kii Mountains: *Transactions, Japanese Geomorphological Union*, 32(4), p.389-409.(in Japanese)
- Jitozono, T., Shimokawa, E., Sako, M., Teramoto, Y., 2004, Hydrogeomorphological characteristics of a deep-seated Landslide in the Harihara river basin, Izumi city, Kagoshima prefecture, Japan: *Journal of the Japan Society of Erosion Control Engineering*, Vol.56, No.5, p.15-26.(in Japanese)
- Kaizuka, S., 1978, *Topography of Japan – characteristics and origin*: Iwanami Shoten, Publishers, 234pp. (in Japanese)
- Korup, O. and Schlunegger, F., 2007, Bedrock landsliding, river incision, and transience of geomorphic hillslope-channel coupling: Evidence from inner gorges in the Swiss Alps, *Jornal of Geophysical Research*, Vol. 112, F3027, p.1-19.
- Matsukura, Y., 1987a, Critical height of cliff made of loosely consolidated materials: *Annual Report of the Institute of Geoscience, Univ. Tsukuba*, 13, p.68-70.
- Matsukura, Y (1987b) : Evolution of valley side slopes in the “Shirasu” ignimbrite plateau, *Transactions of the Japanese Geomorphological Union*, 8, p.41-49.
- Matsushi, Y., Chigira, M. and Kosugi, K., 2014, Orographic Rainfall, Deep-seated Catastrophic Landslides, and Landscape Evolution: *Geomorphic Hazard Assessment in Active Orogens, INTERPRAEVENT International Symposium 2014 Natural Disaster Mitigation to Establish Society with the Resilience*, o-4.
- Montgomery, D.R. and Dietrich, W.E., 1994, A physically- based model for the topographic control on shallow landsliding: *Water Resources Research*, Vol.30, p.1153-1171.
- Sakurai, W., Sakai, R., Goto, H., Ogawauchi, Y., Tatsumi, H., Kaihara, D., Uto, T., Fujiwara, Y., 2014, A large re-slide occurred on a deep-seated landslide slope on September 21, 2013, 5 days after Typhoon No. 18: *Journal of the Japan Society of Erosion Control Engineering*, Vol.67, No.3, p.29-35.(in Japanese)
- Schmidt, K.M., and Montgomery, D.R., 1995: Limits to Relief: *SCIENCE*, Vol.270, No.27, p.617-620.
- Yoshino, K., Uchida, T., Ishizuka, T., Mizuyama, T., 2013, Study on developing process of water channel by landslide dam overtopping erosion,: *Journal of the Japan Society of Erosion Control Engineering*, Vol.66, No.2, p.3-9.(in Japanese)

Multi-scale hazard assessment of debris flows in eastern Qinghai-Tibet Plateau area

Qiang Zou^{a,b,*}, Peng Cui^{a,b}, Guangze Zhang^c, Dong Wang^c

^a Key Laboratory of Mountain Hazards and Earth Surface Process/Institute of Mountain Hazards and Environment, Chinese Academy of Sciences (CAS), #9, Block 4, Renminnanlu Road, Chengdu and 610041, China

^b The Center for Excellence in Tibetan Plateau Earth Sciences (CETES) of the Chinese Academy of Sciences (CAS), Beijing, China

^c China Railway Eryuan Engineering Group CO. LTD, Chengdu, China

Abstract

Process analysis and hazard assessment are essential for the prevention and mitigation of debris-flow hazards in mountainous areas. Many villages and ongoing infrastructure projects in China are vulnerable to large debris flows during heavy rainfall or glacier lake outbursts. Without emergency management planning, such contingencies can lead to extensive loss of life and egregious property damage. In the eastern Qinghai-Tibet Plateau area, debris-flow disasters are a common phenomenon. In this article, we analyzed the spatial distribution, activity and hazard characteristics of debris flows and established a debris-flow database by using geographic information technology. Moreover, we comprehensively analyzed the dynamic process of debris flow at a local scale, the compound effects of debris flows along riverside section and the disaster environment factors of debris flows overall scale of Sichuan-Tibet highway respectively. Accordingly, we built an applicable factor system and a comprehensive framework to quantitatively evaluate debris-flow hazard degree, and then proposed a multi-scale debris-flow hazard assessment method by analyzing typical large-scale debris-flow hazard, debris flows along riverside highway and debris flows in whole traffic corridor, respectively. Especially, with respect to typical large-scale debris-flow disaster, we proposed a dynamic process-based method to analyze debris-flow hazard by using numerical simulation of debris flow, flood analysis, RS and GIS technology. In view of debris flows along riverside highway, we analyzed debris flow process and determined the hazard evaluation indexes and proposed a quantitative method of hazard assessment for debris flow along riverside highways. Regarding to debris flows along whole road, we proposed a quantitative method to analyze the hazard of debris flows and classified hazard levels in the debris-flow prone area along highways. Finally, these proposed methods were applied in case studies in a local scale (K3404 of G318), Xiqu river section and Sichuan-Tibet highway respectively. The results showed that the calculated risk zones consist with the actual distribution and severity of damage of the debris-flow events, which can provide scientific reference for debris-flow risk management and disaster prevention and mitigation of arterial traffic lines.

Keywords: Debris flow; Dynamic process; Hazard prediction; Multi-scale assessment; Qinghai-Tibet Plateau

1. Introduction

The Qinghai-Tibet Plateau, with an average elevation of over 4000 m a.s.l. is often referred to as the roof of our earth, and its mystic and beautiful landscapes have attracted worldwide attention. However, in this region, strong uplift of the Earth's crust creates a complex natural environment, which presents active crustal stress, tremendous elevation difference and dramatic climate change (Dhital, 2015). Large-scale natural disasters commonly occur in the eastern area of the Qinghai-Tibet Plateau. In particular, the formation conditions of debris flows are prevalent, including appropriate lithologic structures and loose materials, and water resource conditions; thus, an increasing number of debris flows seriously devastate local villages and lifeline engineering projects. Therefore, it is vital to develop an accurate evaluation method of debris-flow process and associated hazard in the eastern Qinghai-Tibet Plateau area.

Hazard assessment of debris flow is one of the hottest topics in disaster forecast and disaster prevention, which has gradually being got worldwide attention. Scholars recently have explored various models and methods to

* Corresponding author e-mail address: zouqiang@imde.ac.cn

prevent or reduce debris-flow hazard. In 1957, Scientist C.M. Fowlie Cashman analyzed the jacking force of viscous debris flow body and the relations between initial shear strength and the viscosity in his book *Debris Flow and Road Design in Debris Flow-affected Area*. He did deep research about dynamic experiment and movement mechanism of debris flow (C.M. Fowlie Cashman, 1957). From 1977 to 1988, Scientists in the United States did a cataloging work about road debris flow in California Saratoga, Switzedard area and its northern forest logging area (Ellen and Wieczorek, 1988). Since the 1990's, spatial information technology and computer science provide a powerful technical support in collecting transportation network debris-flow data, which greatly improved the efficiency of analyzing debris flow information and mapping (Carrara et al., 1991). To date, the debris flow investigation and cataloging statistics (Hollingsworth and Kovacs, 1981; Zhong et al., 1988), formation mechanism and experimental observations (Saito, 1969), debris flow physics (Iverson, 1997), the mechanism of debris-flow movement (Takahashi, 1988; Chen, 1988), debris-flow evaluation (Hunger, 1987) and the control technology have made great progress. Some scientists mainly focused on analyzing parameters of debris-flow watershed, which is suitable for hazard analysis of regional debris flow (Hollingsworth and Kovacs, 1981; Smith, 1988; Olivier, 1998). This method has advantages of convenience and strong operation, but is difficult in determining accurate hazardous range of debris flow. Some analyzed debris-flow hazard based on actual field investigation and model test, relationships between debris-flow deposition area and its characteristic parameters, e.g. debris-flow volume, disturbance area of debris-flow watershed (Hunger, 1987; Adachi et al., 1977; Takahashi, 1980; Liu, 1995). This is suitable to analyze debris-flow hazard in areas with the same or similar environmental conditions. Furthermore, through a detailed survey of terrain conditions and physical parameters of debris flow in a debris-flow watershed, scholars simulated movement process of debris flow and identified risk zoning of debris flow (Cui et al., 2011; Hu and Wei, 2005). This method has a better practicability and veracity, but several precise parameters are hardly acquired for determining the debris-flow process. However, the multi-scale hazard assessment of debris flows has not established due to the lack of comprehensive debris-flow theory and method.

In this article, we analyzed complicated debris-flow formation conditions in eastern Qinghai-Tibet Plateau area, and proposed a systematic hazard assessment method of debris flows by combine GIS technologies, mathematics and geosciences models in analyzing the debris-flow hazards at different scales.

2. Methods for regional hazard assessment along Sichuan-Tibet transportation corridor

Debris flow hazard assessment is an important step in debris-flow prevention and risk management. We analyzed the hazard of debris flows on basis of systematic indexes including hill slopes, elevation difference, rocks' shear strength, angle of internal friction, weathering degree of rock stratum, distances to faults, earthquake magnitude, land use types, annual mean temperature, and maximum daily rainfall. Through adopting information acquisition analysis method for the above selected factors, we evaluated the hazard degree of debris flow, and completed debris-flow hazard mapping of Sichuan-Tibet highway with support of GIS technique.

According to the definition of information quantity (Aldo et al., 2002), the occurrence of disaster (Y) is affected by various factors ($X_i, i=1, 2, \dots, n$), which can be expressed as:

$$I(Y, x_1 x_2 \dots x_n) = I_n \frac{P(Y|x_1 x_2 \dots x_n)}{P(Y)} \quad (1)$$

$$I(Y, x_1 x_2 \dots x_n) = I(Y, x_1) + I_{x_1}(Y, x_2) + \dots + I_{x_1 x_2 \dots x_{n-1}}(Y, x_n) \quad (2)$$

where, $I(Y, X_1 X_2, \dots, X_n)$: the amount of information provided by the disaster (Y) is determined by a combination of factors $X_1 X_2 \dots X_n$;

$P(Y, X_1 X_2, \dots, X_n)$: the probability of disaster occurrence under the condition of factor combination;

$P(Y)$: the probability of disaster occurrence.

In the study of mountain disasters, the simplified single factor information model is adopted (Ding, 2013):

$$I = \sum_{i=1}^n I_i = \sum_{i=1}^n \ln \left[\frac{A_i / A}{S_i / S} \right] \quad (3)$$

where, I : the prediction value of one unit information in the study area;

I_i : Factor X_i provides information on disaster occurrence (km^2);

A : the total area of the study area (km^2); A_i : the total area of the unit containing factor X_i (km^2);

S : the total area of disaster unit has occurred (km^2);

S_i : the sum of the unit area of the disaster that occurs in the unit of factor X_i (km^2).

3. Methods for sub-regional hazard assessment along riverside section of highway

Through analyzing the hazard effect modes and damage process along highways, we developed three key indexes, scale of debris flows, deposits on highways and river blockage, to describe the highway disasters quantitatively. These three indexes can be easily quantified and divided into four grades respectively: extreme low hazard, low hazard, middle hazard, and high hazard. Moreover, each grade can be evaluated between 0 and 1 based on their characteristics and survey data from historical events (Table 1).

Table 1 Hazard indexes and hazard grading of highway damage caused by debris flows

Grade	Values of each index	Indexes			
		The total runoff of debris flow (10^4m^3)	Deposit extent of debris flow		River blockage due to debris flow
			Subgrade deposition	bridge headroom deposition	
I	0.0-0.25	<1	0-1/3	0-1/3	<0
II	0.25-0.50	1-10	1/3-2/3	1/3-2/3	0-1/2
III	0.50-0.75	10-100	2/3-1	2/3-1	1/2-1
IV	0.75-1.0	>100	>1	>1	>1

Accordingly, we developed a new method to determine the hazard degree and mapping of debris flow. And the hazard degree of debris flow can be calculated

$$H = H_1 + H_2 + H_3 \quad (4)$$

where, H is the total hazard degree of debris flow, H_1 is the total runoff of debris flow, H_2 is the deposit extent of debris flow, H_3 is the river-blockage due to debris flow.

3.1. Scale of debris flow

The Scale of debris flow is usually indexed by total runoff of a single debris flow which can be calculated by the peak discharge of the water flow and the peak discharge of debris flow.

The peak discharge of the water flow (Q_B) in debris flow gully is calculated through the Eq.(5) which is widely used in Sichuan province (Water Resources Department of Sichuan Province 1984):

$$Q_B = 0.278\varphi \frac{S}{T^n} F \quad (5)$$

where, Q_B is peak discharge of the water flow (m^3/s); Ψ is the runoff coefficient; s is the rainstorm intensity (mm/s); τ is flow concentration time (h); n is the rainstorm attenuation coefficient; F is the catchment area (km^2).

The peak discharge of debris flow is calculated by combining the peak discharge of water flow and the soil supplement, especially channel blockage by debris, as following equation (Zhou et al.1991):

$$Q_c = (1 + \varphi_c) \times Q_B \times D_U \quad (6)$$

where, Q_c is the peak discharge of debris flow (m^3/s); Q_B is the peak discharge of the water low (m^3/s); D_U is the blockage coefficient, shows the quantity of landslide deposits in the channels, normally taken 1~3; φ_c is correction coefficient of debris-flow peak discharge, $\varphi_c = (\gamma_c - \gamma_w) / (\gamma_s - \gamma_c)$, and γ_c is debris-flow density (t/m^3); γ_w is water density (t/m^3); γ_s is solid matter density (t/m^3).

The total runoff of a single debris flow is calculated by applying the empirical Eq.(7) (Ou et al.2006).

$$Q_t = 152.97 Q_c^{1.266} \quad (7)$$

where, Q_t is total runoff of a single debris flow (m^3) and Q_c is peak discharge of debris flow (m^3/s).

3.2. Debris-flow deposition parameters

The mud depth and deposition range of debris flow are critical parameters to identify debris-flow hazard. Applying debris-flow hazard prediction method (Liu, 1995), the parameters the deposition area, the maximum deposition length, and the maximum deposition depth can be calculated by using the following models (Liu, 1995; Chen et al. 2011):

$$\begin{aligned} S_d &= 38.41(V_c G \gamma_c / \ln \gamma_c)^{2/3} \\ L_d &= 8.71(V_c G \gamma_c / \ln \gamma_c)^{1/3} \\ h_d &= 0.017[V_c \gamma_c / (G^2 \ln \gamma_c)]^{1/3} \\ V_c &= (\gamma_c \gamma_w) Q_c / (\gamma_s \gamma_w) \end{aligned} \quad (8)$$

where, S_d is the deposition area of single debris flow (m^2), L_d is the maximum deposition length(m), h_d is the maximum deposition depth (m), V_c is the maximum volume of supplementary loose debris(m^3), Q_c is the peak discharge of debris flow (m^3/s), G is the deposition slope($^\circ$), γ_c is the density of debris flow (t/m^3), γ_w is water density (t/m^3); γ_s is solid material density (t/m^3)

3.3. Degree of river blockage

According to deposition parameters of a single debris flow, river blockage degree can be calculated by the following equation:

$$H_3 = (L - l) / B \quad (9)$$

where, H_3 is the river blockage degree of debris flow, if $H_3 \geq 1$, debris flow completely blocks the river, H_3 is equal to 1. L is the maximum deposition length of debris flow (m), l is the distance between river bank and the mouth of debris flow gully(m), B is the river width (m), the parameters B , l can be calculated from topographic data.

4. Methods for local hazard assessment of debris-flow inundation

4.1. Numerical approach for modeling debris-flow processes

Flow velocity is a key parameter for identifying the impact force of a debris flow, while the flow depth can reflect the silting hazard (O'Brien et al., 1993; Kienholz, 1999; Rickenmann, 2001; Wei et al., 2006). When discussing debris-flow deposits, the debris-flow motion equation includes three important variables: mud depth, the x -velocity component, and the y -velocity component,

$$\begin{aligned} \frac{Du}{Dt} &= gS_{sx} - gS_{fx} \\ \frac{Dv}{Dt} &= gS_{sy} - gS_{fy} \end{aligned} \quad (10)$$

where, u and v are x -component and y -component velocities respectively (m/s), g is acceleration due to gravity(m/s^2), S_{sx} is the bottom slope of the deposition area in the x -direction ($^\circ$), S_{sy} is the bottom slope of the deposition area in the y -direction($^\circ$), S_{fx} is the friction gradient of the debris flow in the x -direction ($^\circ$) and S_{fy} is the friction gradient of the debris flow in the y -direction($^\circ$).

The model treats debris-flow masses as aggregates of many small particles, each of which has its own mass and velocity. To solve Eq. (2) numerically, Hu et al. (2005) improved the particle model originally developed by Wang et al. (1997), while Cui et al (2011b) discussed the method and approximated the debris-flow movement by using the forward difference for each particle. The difference equations can thus be expressed as

$$\begin{aligned}\frac{u_k^{n+1} - u_k^n}{\Delta t} &= gS_{sx}^{n,k} - gS_{fx}^{n,k} \\ \frac{v_k^{n+1} - v_k^n}{\Delta t} &= gS_{sy}^{n,k} - gS_{fy}^{n,k}\end{aligned}\quad (11)$$

where, u_k^{n+1} , v_k^{n+1} are the values of u and v for the k -th particle at time $n + 1$, respectively, and u_k^n , v_k^n , $S_{sx}^{n,k}$, $S_{sy}^{n,k}$, $S_{fx}^{n,k}$, and $S_{fy}^{n,k}$ are the values of u , v , S_{sx} , S_{sy} , S_{fx} , and S_{fy} for the k -th particle at time n .

4.2. Method for local hazard analysis

Hazard analyses of debris flows provide information on the hazard activity. This analysis assesses the debris-flow hazard degree which is useful in land utilization, urban planning, road-line selection and disaster mitigation management. With the development of debris flow motion equations and computer technology, numerical simulation provides an efficient and quantitative approach for such hazard analysis.

Besides the impact and silting hazards caused by individual debris flows, large-scale debris flows also have the following particular characteristics: a) Debris flows occurring upstream of a township may cause a river blockage, resulting in a dam-breaking flood. b) A debris flow blocking a river downstream area will create a barrier lake that will cause inundation loss.

In order to analyze the hazard characteristics of debris flows, we propose a systematic and quantitative hazard analysis method supported by numerical simulation of debris-flow movement.

Considering the compound characteristics of debris flow and its following hazards including burying hazard by debris flows, inundating hazard by dammed lakes and scouring hazard by outburst flood and torrent flow, the model of hazard assessment was established and the proposed model is expressed as

In order to analyze the hazard characteristics of debris flows occurring in a group around mountain townships, we propose a systematic and quantitative hazard analysis method supported by numerical simulation of debris-flow movement and flood analysis. The proposed model is expressed as

$$H = H_e + H_h + H_i + H_f \quad (12)$$

where, H is the total hazard degree, H_e is the hazard caused by the impact force of the debris flow indexed to the maximum kinetic energy value in each grid during the whole debris-flow movement process, H_h is the hazard caused by debris flow silting indexed to flow depth, H_i is the inundating hazard of the barrier lake indexed to the inundated backwater depth, and H_f is the dam-breaking flood hazard indexed to the highest water level of the flooding.

5. Results

5.1. Study site

In this article, the Sichuan-Tibet transportation corridor, which is the most significant transportation corridor in the western mountain areas of China and connects the provincial capital cities of Sichuan and Tibet, is severely affected by debris flows. The Xiqu River section of the Sichuan-Tibet Highway is located in the Hengduan Mountain area of the eastern Qinghai-Tibet Plateau and is taken as a study area to analyse the hazard characteristics of debris flows. In this section, Haitong Watershed is located at right bank of Xiqu River. The highway from Chengdu to Lhasa is situated at the left bank of Xiqu River in this site. Haitong Watershed is characterized by the shape of quasi-rectangle and has 5 major gullies with V-shape and the mountain slope of 20~40°.

5.2. Regional hazard assessment along the Sichuan-Tibet transportation corridor

Through adopting information acquisition analysis method in session 2.1, the hazard degree of debris flow was evaluated, and debris-flow hard mapping of Sichuan-Tibet highway was completed with support of GIS technique (Figure 1). The proposed method divides the hazard degree along the highway into 5 levels: very low, low, medium, high and very high. The high hazardous areas along G318 Sichuan-Tibet highway are mainly located in the medium,

high, very high levels, which account for 71.99% of the whole highway area. They are located in the canyon area of Dadu River, Jinsha River, Lanchang River, Nu River and Palongzangbu River. Referring to these areas, the debris - flow prevention project should be strengthened in road construction and land designing. While the very low hazardous areas are relatively small, accounting for only 4.21%, which are located in the sections of Chengdu plain area and Tibetan plateau area. The analyzed results above are consistent with results from the actual debris flows situation along Sichuan-Tibet highway. Thus, this hazard evaluation results are suitable for providing debris-flow risk analysis and line selection for new road.

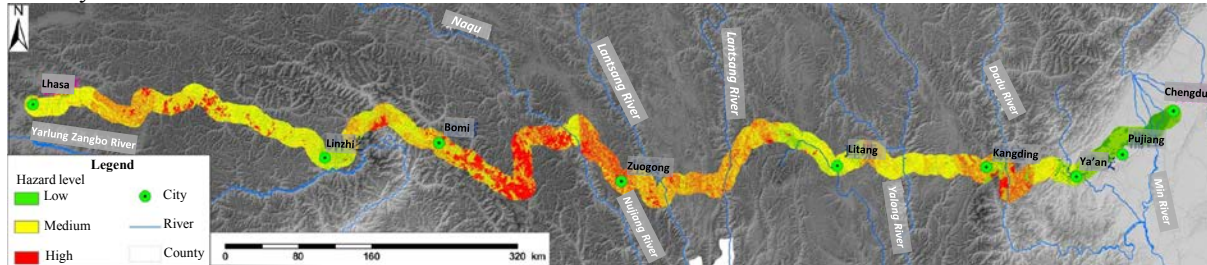


Figure 1 Hazard zonation map of debris flows along G318 Sichuan-Tibet Highway

5.3. Sub-regional hazard assessment along the Xiqu section of the Sichuan-Tibet highway

Applying Eq.(4), hazard degree is calculated in Xiqu section of Sichuan-Tibet highway. The calculated hazard values fall in the range of 0.75 ~2.75. According to the natural divided points as data analysis for zonation mapping with support of natural breakpoint method, the hazard degrees are graded into 3 grades as low hazard, medium hazard and high hazard. The results are shown in Figure 2. After analyzing debris-flow hazard for the whole highway, the total length of highway in high hazard area is 11.35 km, 24.34 km in medium risk area, 21.91 km in low hazard area, respectively. Furthermore, the length of highway in high hazard area is accounted for 19.7% of total length of highway, located in the No.6 highway maintenance squad and the section from the No.4 highway maintenance squad to Haitong army service station where the advantageous conditions (major faults pass through, loose mass and large longitude) give privilege to form large-scale debris flows; the total length of highway in low low area is located in the west section of the No.6 highway maintenance squad, the section between Xiqu River power station and Dongla Mountain, and the exit area of Xiqu River, where debris flows bring little damages for highway.

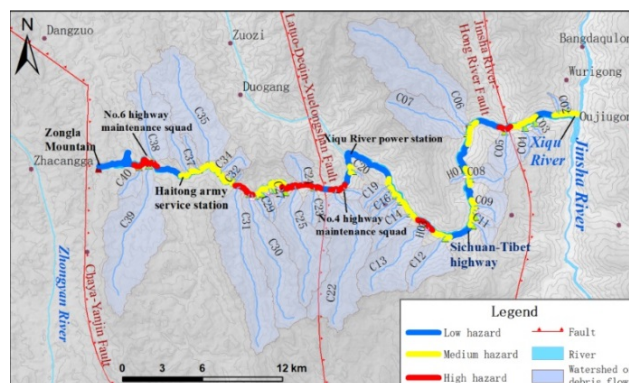


Figure 2 The hazard map of the Xiqu section of Sichuan-Tibet highway

5.4. Local hazard assessment of debris flow in the Haitong watershed

The large-scale debris flow occurs on June 23th, 2012 and its following hazards seriously destructed G318 Highway. Debris flows delivered about 10,000m³ sediments and formed a deposition fan with the length of 230m along river, the width of 100m and the average depth of 7~8m, the peak depth of 11m. The highway at the opposite bank was directly buried about 230m by debris-flow deposits. Moreover, debris flow blocked Xiqu River and produced a dammed lake of 100 000 m³ reservoir volume with the length of 300m, the average width of 60m and the mean depth of water 8-10m. The water of dammed lake submerged about 160m highway at the upper of the dam.



Figure 3 Landscape of Haitong Watershed after 6.23 large-scale debris flows
(a. Taken in June 2012, Deposition dam:200m length, 100m width and 6-8m depth; b. Taken in Sept. 2013)

The parameters of the debris flow on June 23, including velocity and discharge which were obtained from the cross-section at the outlet and material components from deposit sample test, were input into a dynamic movement model of debris flow to simulate and analyze deposition process and result(Figure 4). Then hazard of debris flow was implemented using the formulae (12). The result showed that the influenced and endangered highway was about 820m, and 380m, 330m and 110m was in high-danger zone, middle-danger zone and low-- danger zone, respectively (Figure 5), and those in middle--danger zone and high--danger zone covered 86.5%. The destructed highway on site was about 860m and the total of the buried and submerged highway was about 650 m, which agreed with those from simulated model. Therefore, the models for movement simulating and risk assessment strongly benefits to prediction and prevention and reduction of risk and mitigation of debris-flow hazards.

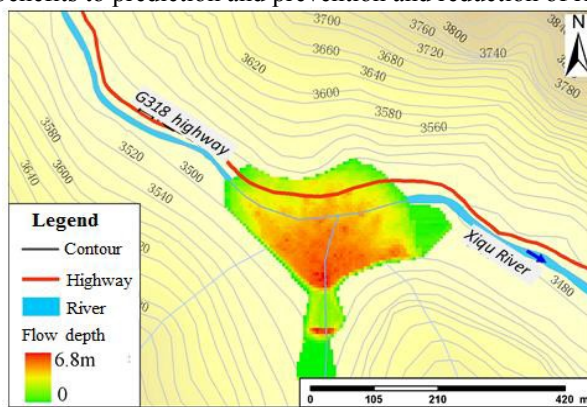


Figure 4 Dynamic simulation result of debris flow in the outlet

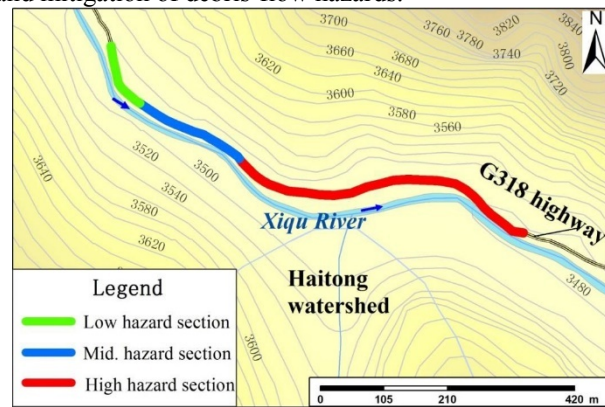


Figure 5 Risk map of debris flow in Haitong Watershed

6. Summary and Conclusions

The Sichuan-Tibet highway and railway are the main traffic trunks line in the western mountain areas of China. Unfortunately, this road has long been severely affected by debris flows. The steep terrain, numerous unconsolidated soil produced by complex lithology and hydrologic meteorological, and the high intensity rainfall are very conducive to the formation of large scale debris flow. Various types of debris flow are widely spread along the major road, which strongly affect road safety.

We have analyzed the spatial distribution, activity and hazard characteristics of debris flows. Moreover, we comprehensively analyzed the dynamic process of debris flow at a local scale, the compound effects of debris flows along riverside section and the disaster environment factors of debris flows overall scale of Sichuan-Tibet highway respectively. Accordingly, we built an applicable factor system and a comprehensive framework to quantitatively evaluate debris-flow hazard degree, and then proposed a multi-scale debris-flow hazard assessment method.

The high hazardous areas along G318 Sichuan-Tibet highway are mainly located in the canyon area of Dadu River, Jinsha River, Lanchang River, Nu River and Palongzangbu River. Referring to these areas, the debris-flow prevention project should be strengthened in road construction and land designing. Among them, the Xiqu River section of Sichuan-Tibet highway was seriously affected by debris flow. The large-scale debris flow on June 23, 2012 at Haitong Watershed was composed by the hazard chain including flash flood, debris flow, dammed lake and outburst flood. The risk assessment based on dynamic model indicated that the high-danger zone and middle-danger

zone occupied 86.5%, where were buried by debris-flow deposits or submerged by the following dammed lake, which agreed with the actual. According to the characteristics, hazards and risk of 6.23 debris flows, the protection measures, including dangerous debris-flow identification, risk assessment, rational route, highway protection, integrated control and emergency plan, were recommended to reduce highway hazards.

Acknowledgements

This work was supported by the National Nature Science Foundation of China (Grant No. 41790432), the Research Program of China Railway Eryuan Engineering Group CO. LTD (Grant No. KYY2018015(18-20)) and the Key Research Program of Frontier Sciences of Chinese Academy of Sciences (Grant No. QYZDY-SSW-DQC006).

References

- Adachi K., Tokuyama K., Nakasuji A., et al, 1977, Study on judgment of outbreak ability of debris flow: SHIN - SABO, v.33, p. 7-16.
- Aldo C., Susanna P., Claudio T., et al., 2002, A procedure for landslide susceptibility zonation by the conditional analysis method: *Geomorphology*, v.48, p.349-364.
- Carrara A., Cardinali M., Detti R., et al., 1991, GIS techniques and statistical models in evaluating landslide hazard: *Earth surface processes and landforms*, v.16, p. 427-445, doi: 10.1002/esp.3290160505.
- Chen N. S., 2011, *Exploration technology of debris flow*: Beijing, Science Press.
- Cui P., Hu K. H., Zhang J. Q., et al., 2011, Prediction of the debris flow area by combing hydrological and inundation simulation methods: *Journal of Mountain Science*, v.8, p. 1-9.
- Dhital, M. R., 2015, *Geology of the Nepal Himalaya: Regional perspective of the classic collided orogeny*, USA, Springer International Publishing.
- Ellen S.D., Wieczorek G. F., 1988, Landslides, Floods, and Marine Effects of the Storm of January 3-5, 1982, in the San Francisco Bay Region, California. California: US Geological Survey Professional Paper, 1434, doi:10.3133/pp1434.
- Fowlie Cashman. C. M., 1957, *Debris flow and road design in debris flow-affected area*: Beijing, China Communications Press.
- Hollingsworth R. and Kovacs. G.S., 1981, Soil slumps and debris flows: prediction and protection: *Bulletin of the Association of Engineering Geologists*, v.38, p.17-28.
- Hu K.H. and Wei F.Q., 2005, Numerical-simulation-based Debris Flow Risk Zoning: *Journal of Natural Disasters*, v.14, p.10-14.
- Hunger O., Morgan C.G., Van Dine D.F., et al., 1987, Debris flow defenses in British Columbia: *Geological Society of America Reviews in Engineering Geology*, v.7, p.201-222.
- Kienholz H, 1999, Anmerkungen zur Beurteilung von Naturgefahren in den Alpen: Relief, Boden, Paläoklima, v.14, p.165-184.
- Liu X. L. and Tang C., 1995, *Debris flow hazard assessment*: Beijing, Science Press.
- O'Brien JS, Julien PY, Fullerton WT, 1993, Two-Dimensional Water Flood and Mudflow Simulation: *Journal of Hydraulic Engineering*, v.119, p.244-261.
- Olivier L., 1998, Example of hazard assessment and landuse planning in Switzerland for snow avalanches, floods and landslides: Bern, Swiss national hydrological and geological survey.
- Ou G. Q., You Y., Lu J., et al., 2006, A study on the scale forecast and the influence of debris flow on the water diversion project in the west line project of water diversion from upper Yangtze River into upper Yellow River: *Journal of Mountain Science*, v.24, p.580-584.
- Rickenmann D, 2001, Methoden zur Gefahrenbeurteilung von Murgängen. In: Projekt CADNAV, Etablissement d'une méthodologie de mise en oeuvre des cartes de dangers naturels du canton de Vaud: Switzerland, 2eme rapport intermédiaire, Ecole Polytechnique Federal de Lausanne.
- Saito M., 1969, Forecasting time of slope failure by tertiary creep: *Proceedings of the 7th International Conference on Soil Mechanics and Foundation Engineering*, v.2, p.677-683.
- Iverson. R. M., 1997, The physics of debris flow: *Review of Geophysics*, v.35(3), p.245-296.
- Smith T. C., 1988, A method for mapping relative susceptibility to debris flows, with an example from San Mateo County, California. In: Ellen, S.D., Wieczorek, G.F. (Eds.), *Landslides, Floods, and Marine Effects of the Storm of January 3-5, 1982, in San Francisco Bay Region, California*: US Geological Survey Professional Paper, 1434, p.185-194.
- Takahashi T., 1980, Debris flow on prismatic open channel: *Journal of the Hydraulics Division, Proc. ASCE*, 106(HY3), p.381-396.
- Takahashi T., Hajime N., Sato H., 1988, Hazard assessment of debris flow alluvial fan: *Annuals, DPRI*, 31 (B-2), p. 655 - 676.
- Chen. C.L., 1988, General solution for visoplastic of debris flow: *Journal of Hydraulic Engineering, ASCE*, 114(3), p. 259-282.
- Water Resources Department of Sichuan Province., 1984, *Storm flood Computation Handbook of small watershed in Sichuan Province*: Chengdu, China, The books press of hydrological terminus in Sichuan province water resources and power authority.
- Wei F.Q., Hu K.H., Lopez J.L., et al., 2006, Model and method of debris flow risk zoning based on momentum analysis: *Wuhan University Journal of Natural Sciences*, v.11, p. 835-839.
- Zhong Z.L., Wang C.H., Xie H., et al., 1988, *The catalog database and regional law of debris flow and landslide of China*: Chengdu, Sichuan Science Technology Press.
- Zhou B.F., Li D.J., Luo D.F., et al., 1991, *Guidebook for Debris Flow Prevention and Control*: Beijing, Science Press, p.87-92.

Preliminary calibration of a numerical runout model for debris flows in Southwestern British Columbia

Sophia Zubrycky^{a,*}, Andrew Mitchell^a, Jordan Aaron^b, Scott McDougall^a

^a Department of Earth, Ocean and Atmospheric Sciences – University of British Columbia, Vancouver, British Columbia, Canada

^b Department of Engineering Geology – ETH Zürich, Zürich, Switzerland

Abstract

Debris-flow hazard and risk assessments require reliable estimates of inundation area, velocity and flow depth to evaluate spatial impact and impact intensity. Semi-empirical numerical runout models that simulate bulk flow behavior with simple rheological models are useful in forecasting these parameters, however, they require calibration by back-analyzing past events. This paper presents the back-analysis of six debris flows in southwestern British Columbia using a novel automated calibration approach that systematically optimizes the Dan3D runout model to fit field observations. The calibration method yielded good simulations of runout length, but under-predicted flow depths in some cases, and over-predicted velocities in all cases. The best-fit Voellmy rheology parameters for the studied cases ranged from 46 to 531 m/s² for the turbulence coefficient and 0.08 to 0.18 for the friction coefficient. There is a potential inverse correlation between friction coefficient and event volume. Calibrated parameters were compared to morphometric parameters for the study sites, which may be useful for guiding parameter selection once a larger dataset is calibrated. Ongoing work is focused on refining the calibration technique, including standardization of input parameters more relevant to debris flows. The long-term goal is to apply the technique to a larger dataset of debris-flow cases and provide practitioners with better guidance on the selection of model input parameters for forecasting purposes.

Keywords: debris flows; runout analysis; numerical modeling; automated calibration; rheology parameter selection

1. Introduction

Estimating the spatial impact of debris flows is an important part of hazard mapping, risk assessment and mitigation design. A variety of tools and techniques have been developed for estimating potential inundation areas and flow velocities, including semi-empirical numerical models that simulate bulk flow behavior using simple rheological relationships (e.g. O'Brien et al., 1993; Hungr, 1995; McDougall and Hungr, 2004; Pirulli, 2005; Kwan and Sun, 2007; Pastor et al., 2009). Although these models do not necessarily simulate the complex mechanics of debris flows, they can capture the bulk behavior required for runout forecasting (McDougall, 2017). One of the main challenges with applying these types of models is the selection of appropriate rheologies and rheological input parameters. These inputs must be calibrated by back-analyzing past events, which requires sufficiently detailed documentation of a number of debris flows that have already occurred, as well as reliable pre-event topographic data. Further, an objective, efficient, and repeatable calibration method is needed.

In this study, we applied a recently developed automated calibration technique to systematically back-analyze six debris flows in southwestern British Columbia using the semi-empirical runout model Dan3D. We examine the performance of this calibration technique in the context of debris-flow behavior and discuss ways it could be refined prior to more extensive calibration efforts. Potential useful links between observable morphometric parameters and rheological input parameters are also briefly discussed.

* Corresponding author e-mail address: szubrycky@eoas.ubc.ca

2. Methodology

2.1. Data Collection

Geomorphic mapping was conducted at six case study locations (Fig. 1) to collect event-specific field observations for back-analysis. Historical airphotos, orthophotos and satellite images were used to identify source areas, delineate inundation areas and constrain the event date for undocumented events. Planet (2018) provided access to an archive of satellite imagery dating back to 2016 for PlanetScope (3 m resolution) and 2009 for RapidEye (5 m resolution).

Field work was conducted by the authors over the period of July to September, 2018, for all locations except Bear Creek, which was studied by BGC Engineering Inc. in 2017. The objective of the field work was to map the deposit extents, delineate the active channel, take deposit and flow depth measurements, measure superelevation at channel bends for velocity estimates (Prochaska et al., 2008), measure channel cross-section areas at bedrock controlled reaches for peak discharge estimates, and collect information about debris composition (grain size, sorting and lithology).

Likely source areas were identified using pre- and post-event Planet (2018) satellite imagery, however, initial volumes were not known. Deposit volumes were mostly estimated by multiplying a range of representative estimated deposit depths from field observations by the mapped impact area. At Neff Creek, Lau (2017, Chapter 5) used pre- and post-event LiDAR data provided by BC Hydro to estimate erosion and deposition volumes within the transmission corridor.

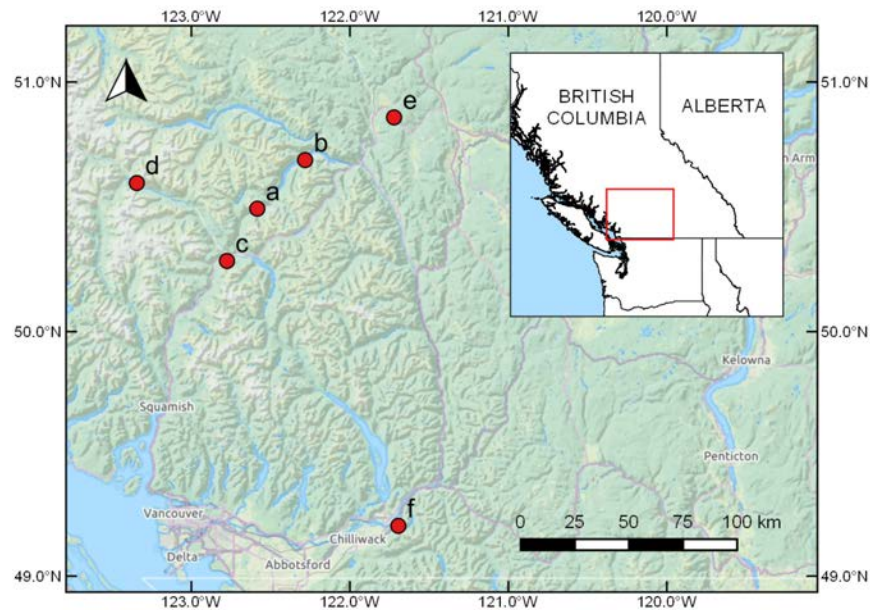


Fig. 1. Case study locations. (a) Neff Creek; (b) Bear Creek; (c) Mt. Currie B; (d) Middle Lillooet Fan; (e) Pavilion Lake Fan; (f) Cheam Fan E.

2.2. Numerical Modeling

The numerical model used in this study was Dan3D, a semi-empirical, depth-averaged, Lagrangian model that simulates landslide motion over 3D terrain (McDougall and Hungr, 2004 and 2005). The model is based on the Smoothed Particle Hydrodynamics (SPH) numerical technique, in which the moving mass is discretized into particles that interact with each other and are free to split apart to simulate flow around obstacles. The model treats the landslide as an “equivalent fluid”, whose behavior is governed by simple internal and basal rheologies (Hungr, 1995). The model features an open rheological kernel, and the parameters that govern these rheologies must be calibrated. Calibration typically relies on well-described past events at the study site, or cases that are deemed to be similar based on professional judgement. In this preliminary study, the Voellmy rheology (Hungr, 1995) was used for all cases.

The goal of model calibration is to determine the set of model parameters that best reproduce field observations for a case history of interest, and ultimately identify patterns within a set of calibrated cases that can be applied to prediction.

We used a method developed by Aaron et al. (2019) originally for rock avalanches, to calibrate the model. The method treats model calibration as an optimization problem, where the following least squares objective function is minimized:

$$\Phi = \sum_{i=1}^n (w_i \cdot r_i)^2 \quad (1)$$

$$r_i = c_i - o_i \quad (2)$$

where Φ is the value of the objective function, w_i is a user-specified weight given to observation i , r_i is the difference between the simulated and actual value of observation i (e.g. the difference between simulated and observed velocities at a point), c_i is the simulated value of observation i , o_i is the measured value of observation i , and n is the number of simulation constraints. The user-specified weight is selected based on the standard deviation of the simulated feature (Aaron et al., 2019).

Equation 1 is minimized using the Gauss-Marguart-Levenberg (GML) algorithm (Nocedal and Wright, 2006). This algorithm uses the derivative of Equation 1, taken with respect to the calibrated parameters, in order to minimize the misfit between observed and simulated landslide features. The main advantages of the GML algorithm are that it is computationally efficient and can be used to calibrate more than two parameters. The GML optimization analyses were implemented using the Parameter Estimation Package (PEST) (Watermark Numerical Computing, 2010).

The following model constraints were used: trimline, runout length, deposit volume, and point estimates of velocity, maximum flow depth and deposit depth. For the trimline constraint, the modelled maximum depth greater than 0.3 m (a cutoff value is necessary due to the SPH method used in Dan3D) is compared to a gridded representation of the impact area, where a value of 1 in a cell indicates that the debris flow has impacted that location, and a value of zero indicates otherwise. The runout length is defined as the furthest straight-line distance from a user specified origin point (fan apex used this study), and the fitness is calculated by comparing this constraint to the median final position of a user-specified number of particles (25 used in this study). Due to uncertainty with estimating the initial volumes and entrainment rates (McDougall and Hungr, 2005), the initial volume was estimated, and the entrainment rate was included as a calibration parameter to simulate the final deposit volume constraint.

Four of the six cases had pre-event LiDAR coverage of the fan area, except Mount Currie B and portions of Neff Creek with post-event LiDAR available. The Neff Creek grid was merged with pre-event grid and manually adjusted to represent pre-event conditions, while Mount Currie B was left unaltered. Five-meter gridded topography with Gaussian smoothing was used for all cases.

3. Case Studies

The case studies consist of six recent debris flows in southwestern British Columbia (Fig. 1) with reasonably well-preserved field evidence and LiDAR coverage of the fan area. Fig. 2 shows Google Earth imagery of the fan and watershed areas, and Fig. 3 shows representative field photographs of the deposits. Table 1 provides a summary of morphometrics and event characteristics. A brief summary of each case study is provided below.

Neff Creek is located in the Birken-D'Arcy Valley, 25 km northeast of Pemberton, BC. The watershed is underlain by Jurassic to Cretaceous sedimentary rocks of the Cayoosh Assemblage, consisting of siltstone, sandstone, shale and argillite (Cui et al., 2015). On September 20, 2015, a large debris flow occurred at Neff Creek during a high intensity rainstorm, likely initiating as a rockfall or rockslide from the steep bedrock cliffs in the western part of the upper watershed. This event is well described by Lau (2017, Chapter 5). The debris flow eroded a channel up to 14 m deep through the upper portion of the fan. The debris avulsed upstream of the highway bridge and inundated the distal reach of the fan, depositing material up to 10 m thick. It is estimated about 40% of the deposit volume is sourced from the upper fan (Lau 2017, Chapter 5). Eyewitness reports suggest that the debris flow occurred as multiple surges.

Bear Creek is located at Seton Portage between Anderson and Seton Lakes. Bedrock geology consists of marine sedimentary and volcanic rocks of the Bridge River Complex, including chert, argillite, and basalt (Cui et al., 2015). Bear Creek is one of two creeks that form a large half cone fan. The channel is deeply incised at the upper portion of the fan, losing confinement by mid-fan. The fan complex has a legacy of fine-grained debris flows with high mobility (BGC, 2018b). On July 30, 2016, a thunderstorm triggered a debris flow that travelled past the fan toe.

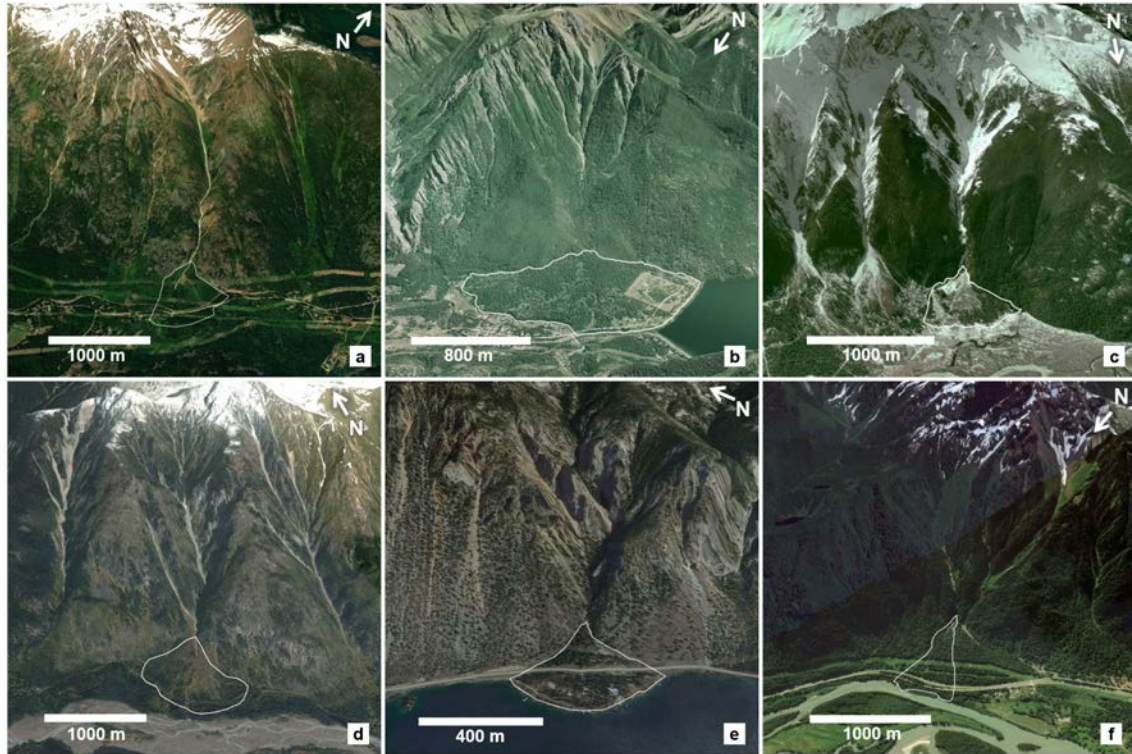


Fig. 2. Google Earth satellite images of the six case study locations. White line delineates the fan boundary. (a) Neff Creek; (b) Bear Creek; (c) Mount Currie B; (d) Middle Lillooet Fan; (e) Pavilion Lake Fan; (f) Cheam Fan E.



Fig. 3. Photographs of debris-flow deposits for the six case studies. (a) Neff Creek; (b) Bear Creek (photo courtesy of Matthias Jakob); (c) Mount Currie B; (d) Middle Lillooet Fan; (e) Pavilion Lake Fan; (f) Cheam Fan E.

Table 1. Summary of case study morphometrics and event details.

Site	Bedrock Geology	Watershed			Fan		Fan Channel		Event	
		Area (km ²)	Relief (km)	Melton Ratio	Area (km ²)	Average Gradient (°)	Length (km)	Average Gradient (°)	Estimated Deposit Volume (m ³)	Impact Area (m ²)
(a) Neff Creek ^{1,2}	Sedimentary	3.29	1.87	1	0.36	15	0.83	11	220,000 ± 30,000	136,300
(b) Bear Creek ³	Marine sedimentary and volcanic	2.18	1.81	1.2	1.27	12	1.03	10	60,000 ± 10,000	98,000
(c) Mount Currie B ¹	Intrusive	2.69	2.14	1.3	0.32	13	0.85	9	500,000 ± 150,000	269,100
(d) Middle Lillooet Fan ²	Intrusive	2.69	1.81	1.1	0.55	15	0.84	14	45,000 ± 10,000	25,400
(e) Pavilion Lake Fan ²	Marine sedimentary and volcanic	1.45	1.02	0.9	0.11	13	0.37	14	7,500 ± 1,500	9,200
(f) Cheam Fan E	Sedimentary	1.87	1.9	1.4	0.27	14	1.1	10	45,000 ± 15,000	49,800

¹Average gradient measurements derived from post-event LiDAR data.

²Watershed measurements derived from the TRIM Digital Elevation Model for British Columbia (1:250,000)

³Geomorphic mapping and deposit volume provided by BGC Engineering Inc.

Mount Currie B is the western-most of three active debris-flow fans from the steep north facing slopes of Mount Currie, a mountain range immediately south of Pemberton, BC. The Pemberton Diorite Complex forms the bedrock of the upper watershed (Cui et al., 2015) and is subject to frequent rockfalls, rock slides and debris slides that fill the watershed gullies with colluvium (BGC, 2018a). A debris-flow deposit of approximately 500,000 m³ is visible in satellite imagery, occurring sometime during the late fall of 2016. This debris flow traveled along a gully in the western part of the upper watershed, flowed down through the channelized bedrock reach at the fan apex, and spread out well beyond the previous fan limits to the Green River floodplain. Part of the flow avulsed from the main channel at the channel bend downslope of the apex. Debris from this event varied in size from boulders and cobbles at the upper portion of the fan, boulders and cobbles in a sandy matrix in the lower half of the deposit, and a finer-grained sediment plume at the distal end visible in the Green River.

The Middle Lillooet Fan is a small and steep fan on the left bank of the Lillooet River downstream of Meager Creek approximately 50 km northeast of Pemberton. The bedrock consists of granodiorite and debris flows on this fan are characteristically coarse-grained (Jordan, 1994). Upstream of the fan apex, massive rockfall boulders >10 m in diameter fill the bedrock-controlled channel. Sometime in September or October of 2015, a coarse debris avalanche/debris flow ran out past the forest service road. The bulk of the material deposited on the mid fan as bouldery levees.

Pavilion Lake Fan is a small half cone fan on Pavilion Lake 25 km northeast of Lillooet. The Marble Canyon Formation (limestone, marble) and the Cache Creek Complex (chert, argillite, limestone, basalt) form the upper and lower parts of the watershed, respectively (Cui et al., 2015). On August 20, 2014, a series of debris flows along Highway 99 were triggered by an intense storm, forcing road closure and evacuations. The debris flow at Pavilion Lake deposited levees at bedrock-controlled channel reaches near the apex, flowed through knickpoints in the paleofan surface at the top of the fan, and ran out past the highway reaching the lake.

Cheam Fan E is located in the Cheam Range of the Cascade Mountains near Bridal Falls and about 20 km northeast of Chilliwack. Bedrock consists of folded and faulted rocks of the Chilliwack Group (pelite, sandstone, conglomerate, mafic and felsic volcanics, carbonates) (Cui et al., 2015). The site is adjacent to the 5,000 year-old Cheam rock avalanche deposit (Orwin et al., 2004). The Cheam fan complex is formed by material from two separate watersheds. Following several days of heavy rain and snowmelt, a series of debris flows and floods occurred on November 23, 2017, temporarily closing the Trans-Canada Highway between Bridal Falls and Hope. The debris flow on the east channel at Cheam Fan was used in this study. Material was eroded from talus slopes in the upper east side of the watershed. On the fan, the flow avulsed the main channel to the west at three locations occupying paleochannels and inundated the highway with mud and debris.

4. Results

Model results using optimized parameter values for each complete set of calibration back-analyses are shown in Fig. 4. A summary of the calibrated parameters and optimized fitness metrics is provided in Table 2. The best-fit parameter combinations are shown graphically in Fig. 5, along with information about the source geology and total volume of each event. Relationships between the calibrated friction coefficients and fan channel gradients are shown in Fig. 6, for further discussion below.

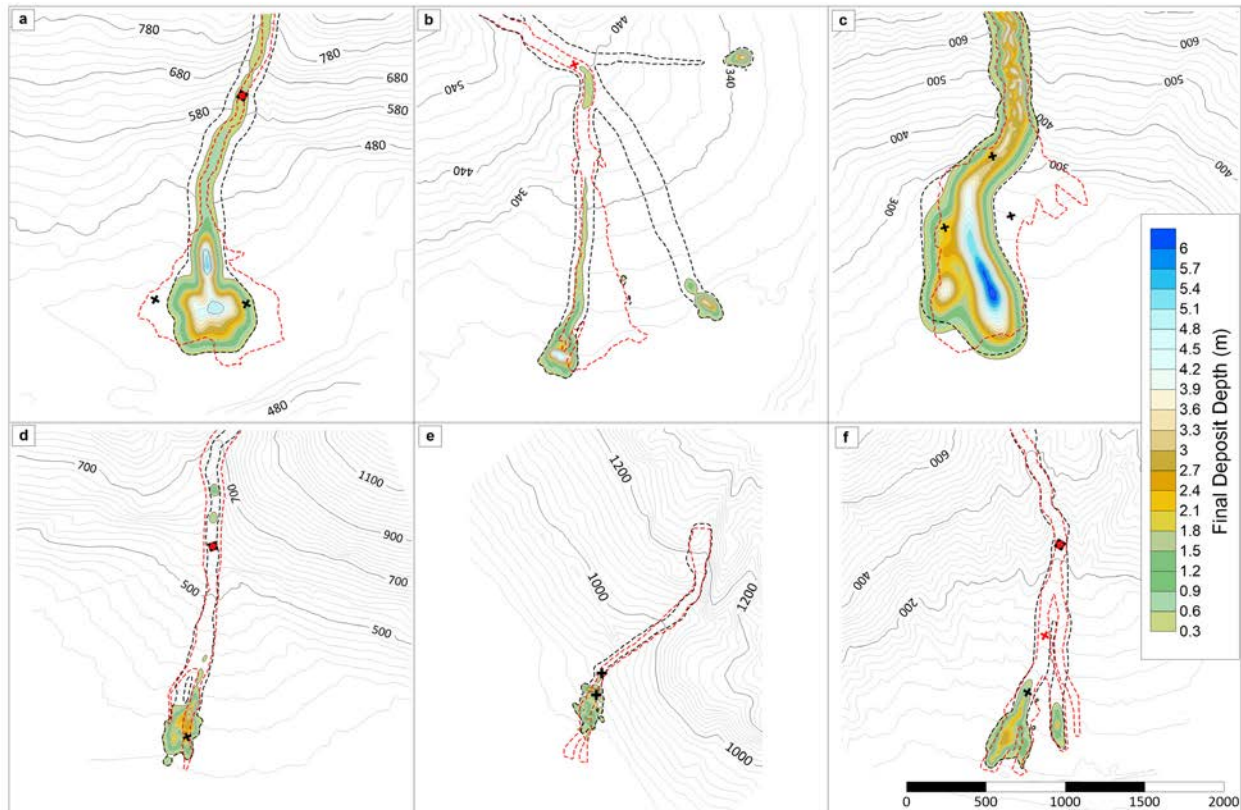


Fig. 4. Model results using optimized parameter values for (a) Neff Creek; (b) Bear Creek; (c) Mount Currie B; (d) Middle Lillooet Fan; (e) Pavilion Lake Fan; (f) Cheam Fan E. Modeled and observed deposit trimlines are shown by the black and red dashed lines, respectively. The locations of depth and velocity observations used in the calibration are indicated by black and red crosses, respectively. All units are in meters.

Table 2. Calibrated rheological parameters for the six case studies.

Site	Friction Coeff.	Turbulence Coeff. (m/s ²)	Calibration Constraint Performance ¹			
			Runout Distance from Fan Apex	Deposit Depth	Maximum Flow Depth	Velocity
(a) Neff Creek	0.10	365	<5%	-74% to -100%	-71%	+83%
(b) Bear Creek	0.11	531	<5%	N/A	N/A	+72%
(c) Mount Currie B	0.08	46	<5%	<5% to -100%	-42%	N/A
(d) Middle Lillooet Fan	0.16	203	<5%	+143%	-48%	+36%
(e) Pavilion Lake Fan	0.18	105	-25%	-56%	+30%	N/A
(f) Cheam Fan E	0.15	473	<5%	-18%	-7%	+130% to +186%

¹Calibration performance calculated as (modelled – observed)/observed × 100%

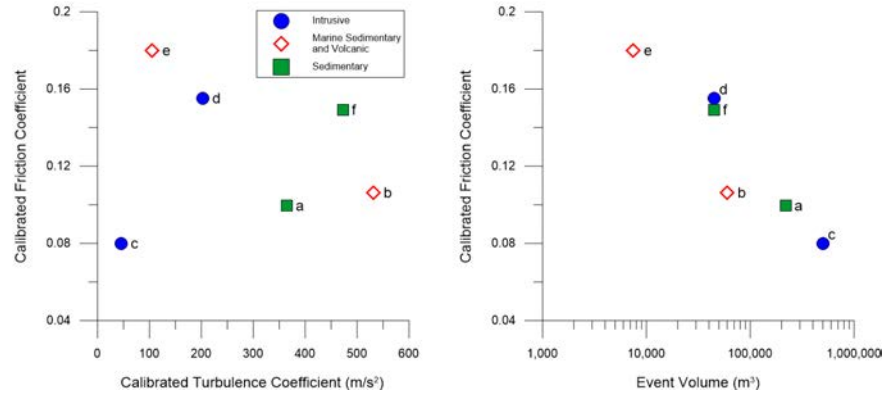


Fig. 5. Left: Calibrated best-fit parameter combinations. Right: Event volume vs. calibrated friction coefficient.

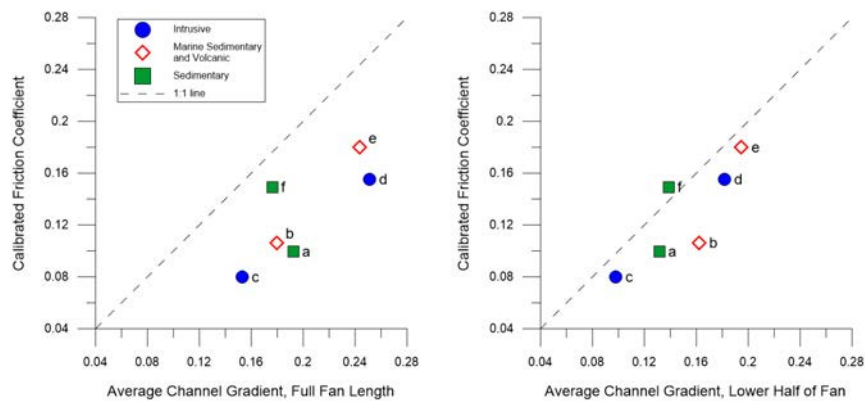


Fig. 6. Left: Relationship between calibrated friction coefficient and average channel gradient for the full length of the fan. Right: Relationship between calibrated friction coefficient and average channel gradient for the lower half of the fan.

5. Discussion

The calibrated parameter values summarized in Table 2 are in the same range as values reported by others based on similar debris-flow back-analyses (e.g. Ayotte and Hungr, 2000; Revellino et al., 2004). As shown in Fig. 4 and Table 2, the best-fit parameter combinations resulted in relatively good simulations of total runout length in every case, reflecting the relative weighting/importance assigned to runout length as an input calibration constraint.

In general, deposit width was under-predicted in cases where significant spreading occurred on the fan. All events in the present study were modeled as single surges, which is not realistic in several cases. For debris flows with multiple surges, erosion/deposition by earlier surges may significantly alter the topography affecting subsequent surges, which could lead to avulsions. Further, heterogeneity within each debris flow was not explicitly modeled, so avulsions caused by channel plugging from frictional boulder fronts were not captured either.

Although the present sample of calibrated cases is very small, some interesting potential trends warrant further consideration as the dataset expands. Fig. 5 Right suggests a potential inverse correlation between event volume and calibrated friction coefficient. This trend mirrors the inverse correlation between event volume and travel angle (“fahrböschung”) observed by others (e.g. Corominas, 1996). A potentially useful relationship between fan channel gradient and calibrated friction coefficient is also suggested in Fig. 6. The calibrated friction coefficients for the six cases in this study are very close to, or slightly lower than, the average fan channel gradient for the lower half of each fan, suggesting that local fan gradient may be a useful metric for selecting friction coefficients for forecasting purposes.

One of the goals of automated calibration is to make the calibration process more objective and repeatable. However, subjective judgement on the part of the modeler is still required to prepare the model inputs. The present study has highlighted the importance of standardizing such input as much as possible before expanding the study to include other cases. For example, model results were found to be relatively sensitive to down-sampling and smoothing of input topographic data (e.g. 5 m vs. 3 m grid spacing) and the number of particles used in the simulation.

6. Conclusion

This study has demonstrated the usefulness of a recently developed automated calibration technique for the numerical analysis of debris-flow runout. Preliminary relationships between morphometric parameters and rheological input parameters have been developed. Ongoing work is focused on refinement of the technique and standardization of input. The long-term goal is to apply the technique to a larger dataset of debris-flow cases to examine the relationships between morphometric and rheological parameters. The variability in these relationships will provide practitioners with better guidance on the ranges of model input parameters used for forecasting purposes.

Acknowledgements

We would like to thank the British Columbia Ministry of Transportation and Infrastructure, Squamish-Lillooet Regional District and BC Hydro for permission to use LiDAR data. Thank you to Brian Menounos from the University of Northern British Columbia, and John Clague and Gioachino Roberti from Simon Fraser University for providing LiDAR coverage at the Middle Lillooet Fan, and to BGC Engineering Inc. for sharing Bear Creek field mapping data. We would like to acknowledge Erin and Rob Elliott and the Ts'kw'aylaxw First Nation for land access permissions. Special thank you to José Pullarello, Stephanie Tarnai, Carie-Ann Lau and Bea Collier-Pandya for assistance in the field, and David Bonneau for compiling the original case study database that served as a catalyst for the present work. Funding for this research was provided in part by the Natural Sciences and Engineering Research Council of Canada (NSERC).

References

- Aaron, J., McDougall, S., Nolde, N., 2019, Two methodologies to calibrate landslide runout models: *Landslides*, p. 1–14, doi: 10.1007/s10346-018-1116-8.
- Ayotte, D. and Hungr, O., 2000, Calibration of a runout prediction model for debris-flows and avalanches, *in* Proceedings, Second International Conference on Debris-Flow Hazards Mitigation, Taipei, Taiwan, p. 505–514.
- BGC Engineering Inc. (BGC), 2018a, Mount Currie Landslide Risk Assessment. Final report prepared for Squamish-Lillooet Regional District dated January 16, 2018, Project No. 1358004, 195 p.
- BGC Engineering Inc. (BGC), 2018b, Seton Portage Integrated Hydrogeomorphic Assessment: Final report prepared for Squamish-Lillooet Regional District dated April 6, 2018, Project No. 1358005, 355 p.
- Corominas, J., 1996, The angle of reach as a mobility index for small and large landslides: *Canadian Geotechnical Journal*, v. 33, p. 260–271.
- Cui, Y., Miller, D., Schiarizza, P., and Diakow, L.J., 2017, British Columbia digital geology: British Columbia Ministry of Energy, Mines and Petroleum Resources, British Columbia Geological Survey Open File 2017-8, 9 p. Data version 2018-04-05.
- Hungr, O., 1995, A model for the runout analysis of rapid flow slides, debris flows and avalanches: *Canadian Geotechnical Journal*, v. 32(4), p. 610–623.
- Jordan, P., 1994, Debris Flows in the Southern Coast Mountains, British Columbia: Dynamic Behavior and Physical Properties [PhD Thesis]: University of British Columbia, 272 p.
- Kwan, J.S.H. and Sun, H.W., 2007, Benchmarking exercise on landslide mobility modelling - runout analyses using 3dDMM, *in* Proceedings of the 2007 International Forum on Landslide Disaster Management, Hong Kong, p. 945–966.
- Lau, C.A., 2017, Channel Scour on Temperate Alluvial Fans in British Columbia [MSc Thesis]: Simon Fraser University, 200 p.
- McDougall, S., 2017, 2014 Canadian Geotechnical Colloquium: Landslide runout analysis - current practice and challenges: *Canadian Geotechnical Journal*, v. 54, p. 605–620, doi: 10.1139/cgj-2016-0104.
- McDougall, S. and Hungr, O., 2004, A model for the analysis of rapid landslide motion across three-dimensional terrain: *Canadian Geotechnical Journal*, v. 41, p.1084-1097, doi: 10.1139/t04-052.
- McDougall, S., and Hungr, O., 2005, Dynamic modelling of entrainment in rapid landslides: *Canadian Geotechnical Journal*, v. 42, p. 1437–1448, doi: 10.1139/t05-064.
- Nocedal, J., and Wright, S.J., 2006, Numerical Optimization (Second Edition): New York, Springer, 664 p.
- O'Brien, J. S., Julien, P. Y., and Fullerton, W. T., 1993, Two-dimensional water flood and mudflow simulation: *Journal of Hydraulic Engineering*, v. 119(2), p. 244–261.
- Orwin, J., Clague, J., and Gerath, R.F., 2004, The Cheam rock avalanche, Fraser Valley, British Columbia, Canada: *Landslides*, v. 1, p. 289–298, doi: 10.1007/s10346-004-0036-y.
- Pastor, M., Haddad, B., Sorbino, G., Cuomo, S. and Drempetic, V., 2009, A depth-integrated, coupled SPH model for flow-like landslides and related phenomena: *International Journal for Numerical and Analytical Methods in Geomechanics*, v. 33, p. 143–172.
- Pirulli, M., 2005, Numerical Modelling of Landslide Runout: A Continuum Mechanics Approach [PhD Thesis]: Politecnico di Torino, 204 p.
- Planet Team, 2018, Planet Application Program Interface: In Space for Life on Earth. San Francisco, California (available at <https://api.planet.com>).
- Prochaska, A.B., Santi, P.M., Higgins, J.D., and Cannon, S.H., 2008, A study of methods to estimate debris flow velocity: *Landslides*, v. 5, p. 431–444, doi: 10.1007/s10346-008-0137-0.
- Revellino, P., Hungr, O., Guadagno, F.M., and Evans, S.G., 2004, Velocity and runout simulation of destructive debris flows and debris avalanches in pyroclastic deposits, Campania region, Italy: *Environmental Geology*, v. 45, p. 295–311.
- Watermark Numerical Computing, 2010, PEST Model Independent Parameter Estimation User Manual, 5th Edition, 336 p.

Engineering and Mitigation

Predicting debris-flow scour depth downstream from a check dam

Hua-Yong Chen^{a,b,c,*}, Xiao-Qing Chen^{a,b,c}, Jian-Gang Chen^{a,b,c}, and Jin-Bo Tang^{a,b}

^a Key Laboratory of Mountain Hazards and Earth Surface Process/Institute of Mountain Hazards and Environment, Chinese Academy of Sciences, Chengdu 610041, China

^b University of Chinese Academy of Sciences, Beijing 100049, China

^c CAS Center for Excellence in Tibetan Plateau Earth Sciences, Chinese Academy of Sciences (CAS), Beijing, 100101, China

Abstract

Debris flows often pose great threats to people's lives and property in mountainous regions. For example on August 8, 2010, a debris flow with a volume of $220 \times 10^4 \text{ m}^3$ occurred in ZhouQu county, Gansu province, China. The debris flow resulted in not only significant loss of farmlands, but also in 1,248 deaths and 496 people missing. The construction of check dams in debris-flow valleys is a useful way to mitigate deaths and damages. Herein, we investigate scour downstream from check dam spillway structures. We propose that the main parameters which determine scour depth of a scour hole downstream from check dams, include flow density, flow depth, flow discharge per unit width, and acceleration due to gravity. Physical experiments were also carried out to investigate debris flow movement and scour characteristics. In addition, a theoretical expression was deduced to predict the maximum scour depth downstream from check dams. There was a good correlation between experimental data and results predicted from theory. The results obtained in this paper can provide constraints for the design of check dams in mountainous areas.

Keywords: Check dam, Debris flow; Energy dissipation; Scour depth prediction, Discharge per unit width

1. Introduction

Debris flows are poorly sorted, fast-moving mixtures of sediment and water that mobilize in upstream region of a valley, surge down slopes in response to gravity (Iverson, 1997). Excessive rainfall (Chen et al., 2014; Zhou et al., 2015; Melo et al., 2018), snowmelt (Decaulne et al., 2008; Decaulne et al., 2010), or glacier lake outburst floods (GLOF) (Breien et al., 2008) can all generate debris flows. When abundant loose soil particles are available along a valley, they can be eroded and entrained by flood waters and transformed into large debris flows. In China, debris flows are considered one of the most serious natural hazards in mountainous areas, especially after the occurrence of the May 12, 2008 Wenchuan Earthquake. Many large scale debris flows were triggered by intensive rainfall following the earthquake, such as September 24, 2008 Wenchuan debris flow (Huang, 2011), and the August 13, 2010 Qingping debris flow (Xu et al., 2012; Ma et al., 2013). Additionally, on 8 August, 2010, a large debris flow occurred in the Sanyanyu and Luojiayu gullies, north of ZhouQu county, Gansu province. This debris flow blocked the Bailongjiang River, resulting in the formation of a lake that inundated over half of ZhouQu (Cui et al., 2013). Many countermeasures have been applied to mitigate debris-flow hazards and reduce the risk to people and structures. Counter structures include check dams, discharge drainages or debris basins. A closed-type check dam with a rectangular or trapezoid spillway is one of the most effective structural countermeasures for debris-flow control. These dams are commonly installed to stabilize channel side-slopes, to reduce scour, to capture sediments, and to reduce debris-flow velocities (Shrestha et al., 2008; Shrestha et al., 2009; Zeng et al., 2009; Hsieh et al., 2013).

Experimental and theoretical studies have been carried out to investigate local scour under different conditions. Sheppard and Miller (2006) conducted pier scour experiments and compared their results with local scour equations. Ballio et al. (2010) studied the temporal scales for scour at abutments. Local scour experiments were performed with four different uniform cohesionless sediment diameters, then a design equation is proposed based experimental data

* Corresponding author e-mail address: hychen@imde.ac.cn

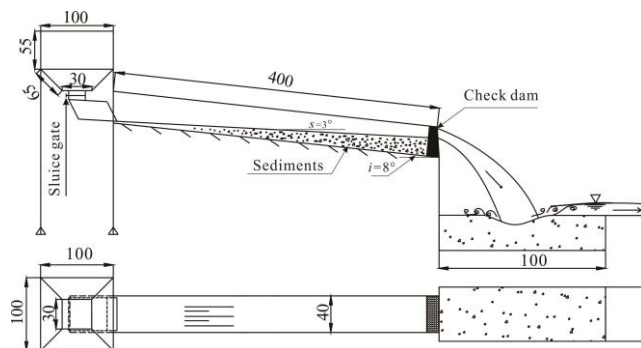
and existing live-bed scour data (Barbhuiya and Mazumder, 1997). Manes and Brocchini (2015) derived a new predictive formula to calculate the scour depth at piers, which merges the theory of turbulence with empirical observations. The validity of the proposed approach for local scour around bridge piers was tested for vertical-wall bridge abutments (Coscarella et al., 2018). Much previous attention was paid to the clear-water scour and sediment-laden water scour. However, relatively little attention has been focused on debris-flow scour, especially, the local scour downstream from check dams. Lenzi and Comiti (2003) examined local scouring characteristics downstream from 29 drop structures in a steep mountain river. Their results indicated that drop height, flow depth, and step spacing affect scouring dynamics in a complex way. Pan et al. (2013a) conducted flume experiments to investigate the laws governing a scour hole's shape downstream of a debris-flow check dam under different circumstances. Results demonstrated that the position of the maximum depth point moved downstream with an increase in flume-slope angle. Pan et al. (2013b) gave a theoretical formula to calculate the depth of a scour hole downstream of a debris-flow check dam in 2D physical experiments. Results indicated that the scour hole mainly depended on channel slope, flow density, flow depth, mud and sand characteristic coefficients, and a scour-hole formation coefficient. Chen et al. (2016) investigated four different lateral contraction ratios of spillways and proposed an empirical model to predict the scour depth downstream of a check dam.

In this paper, experiments were conducted to investigate the characteristics of a debris-flow nappes downstream a check dam. For each experimental test, video cameras were employed to record the trajectory of debris-flow nappes from the spillway to the debris-flow surface downstream. The characteristics of scour holes downstream from different spillway structures were analyzed in relation to nappe characteristics. Additionally, we employed momentum conservation theory to predict the depth of scour holes formed by debris flows. The results presented in this paper can provide information for the structure design of check dams in mountainous areas.

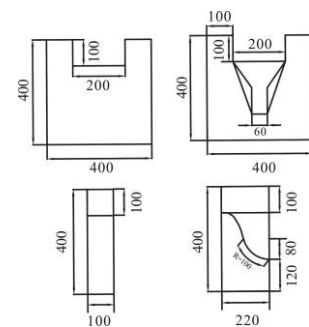
Our experimental flume consisted of a hopper, a sluice gate, a rectangular channel, a check dam with a spillway, and a downstream erodible bed composed of the loose soil material with the maximum diameter no more than 20.0 mm (Fig.1a). The gate was used to control the discharge of debris flows passing through the spillway. In each experimental run, a volume of debris flow was held in the hopper. The sudden remove of the sluice gate was used to simulate a debris-flow event. The rectangular channel was about 4.0 m long, 0.4 m wide and 0.4 m high, with a slope of $i=8^\circ$ (Fig.1b). The mean velocity of the flow front in the channel was estimated by video after it ran out from the hopper. The spillway shapes of the check dam in our experiments are rectangular and Y-type, respectively. The check dam was made of steel material was set at the end of the rectangular channel (Fig.1).



(a) Photograph of the experimental setup



(b) Schematic diagram (unit: cm)



(c) The rectangular and Y-type spillway of check dams

Fig.1. The experimental setup

The hopper of the check dam was filled with the sediment from Jiangjia ravine, with a slope of $s=3^\circ$ (Fig.1b). Particle size distribution of sediment may affect the debris-flow density and flow motion along the channel. In the prototype, the particle sizes of the debris flows change from clay to boulder. In the experimental model, the particle sizes of the debris flows should be relative small due to the limited model dimensions. The sediment used in this experiment was equivalent to a sample of typical debris flows and excluded particles larger than 20.0mm. The diameter of the sediments in the erodible bed was also smaller than 20.0 mm. In addition, the clay and fine particles (smaller than 1.0 mm) were excluded to avoid the effects of matric suction on the development of the scour hole. The particle size distribution of sediments for both debris flows and erodible bed is shown in Fig.2. In our experiments, the flow rate can be obtained by monitoring the flow velocities and flow depths at the outlet of spillway. Debris flow density can also be measured by monitoring the weight and volume of debris-flow samples taken at the end of the spillway. Although the experimental setup and sediments used in experiments were not strictly follow the similarity theory, dimensions of our physical model, debris flow volume, and particle sizes were roughly set based on the natural debris-flow events. Therefore, the results obtained in our experiments can reflect the dynamic evolution process and basic mechanism in prototype.

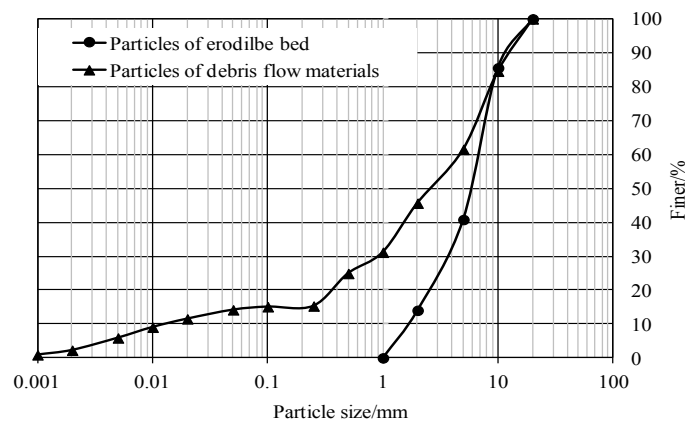


Fig. 2. The particle size distribution of the sediments

2. Experimental results and analysis

2.1. Typical flow pattern downstream from the check dam

When debris flows pass a check dam a lot of debris flow materials are retained in the channel, forming an obvious elevation difference downstream and upstream from check dam site. In our experiments, we saw that debris flows overflowed the spillway of check dams and then plunged into the dissipation pool with erodible bed (Fig.1). A debris flow nappe, which represented the debris flows from spillway outlet to downstream water level, was observed downstream from the check dam under different spillway structures. However, for different spillway structures, the profiles of the debris-flow nappe can be different. For example, when debris flows overflow the spillway of the rectangular cross-section, the flow nappe is relatively thin (no more than 60.0 mm) and the flow turbulence is relatively weak. But when debris flows overflow the spillway of the lateral contraction (Y-type spillway), the flow nappe is relatively thick and the flow turbulence is relatively strong, as shown in Fig.3.



(a) Debris flows passing through spillway with rectangular cross-section



(b) Debris flows passing through spillway with "Y-type" cross-section

Fig. 3. Typical debris flow patterns downstream from the check dam with different types of spillway

2.2. Plunging velocity analysis

During the plunging process of the debris-flow nappe, the debris-flow velocity increases when it plunges to the downstream flow surface due to gravity. Actually, the spillway velocity, v_1 , is easily estimated by a float method (testing the average velocity covering certain distance by floating a marker on flow surface) but this method cannot be used to estimate the plunging velocity due to strong turbulence at the end of the flow nappe. Fortunately, we can predict the plunging velocity based on the projectile motion theory as shown in Fig.4 (Hayen, 2003).

If we suppose debris flows overflow the spillway at velocity, v_1 (v_1 is composed of v_{x1} and v_{z1} components, Fig.4) and debris flows plunge into the dissipation pool at v_2 (v_2 is composed of v_{2x} and v_{2z} components), where x means the movement distance of the debris flow mass in the horizontal direction and z means the movement distance in the vertical direction, then we have

$$x = v_1 \cos \alpha \cdot t \quad (1)$$

$$z = v_1 \sin \alpha \cdot t + \frac{1}{2} g t^2 \quad (2)$$

Combined (1) with (2), then

$$z = x \tan \alpha + \frac{1}{2} g \frac{x^2}{v_1^2 \cos^2 \alpha} \quad (3)$$

So x can be expressed as

$$x = \frac{v_1^2}{g} \left(-\sin \alpha \cos \alpha + \cos \alpha \sqrt{\sin^2 \alpha + \frac{2gz}{v_1^2}} \right) \quad (4)$$

According Equation. (1), then

$$t = \frac{x}{v_1 \cos \alpha} = \frac{v_1}{g} \left(-\sin \alpha + \sqrt{\sin^2 \alpha + \frac{2gz}{v_1^2}} \right) \quad (5)$$

where x is distance in the x direction, z is distance in the z direction, v_1 is flow velocity at spillway outlet, v_{x1} is flow velocity in the x direction, v_{z1} is flow velocity in the z direction, α is flow direction at the spillway outlet, t is time, and g is the acceleration gravity.

Plunging velocity v_2 of debris flows can be expressed as

$$v_2 = \sqrt{v_1^2 + g^2 t^2 + 2v_1 \sin \alpha g t} \quad (6)$$

θ , shown in Fig.4 can be expressed as

$$\theta = \arctg\left(\frac{v_1 \sin \alpha + g t}{v_1 \cos \alpha}\right) \quad (7)$$

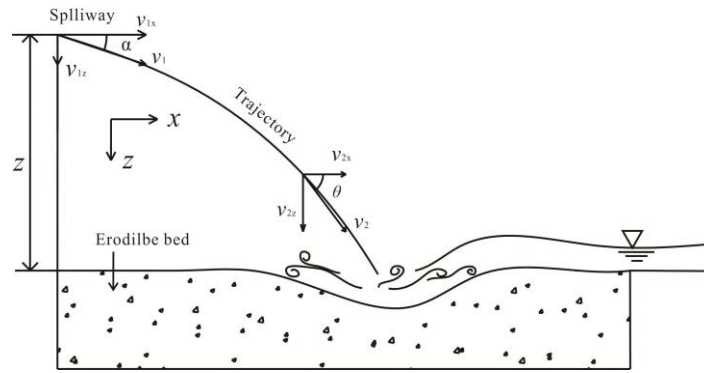


Fig. 4. Diagram of debris flow trajectory

2.3. Debris-flow scour downstream from a check dam

When debris flows plunge into the dissipation pool at relatively high speeds, the debris flows can mobilize sediments in the erodible bed and transport them downstream. A scour hole can be found in the erodible bed as shown in Fig.5. When the impact stress of the debris flows which flow over the erodible bed is greater than the resistance of the erodible bed, the scour hole will develop further. The scour hole will reach an equilibrium status when the debris flows can't initialize and transport the particles in the erodible bed. When the scour hole reaches its equilibrium status the slope of the scour hole is equal to the angle of repose because the erodible bed is formed by the non-cohesive particles. Debris flows can mobilize and transport much more sediments from the erodible bed with increasing flow velocity at spillway. Meanwhile, according to Equation (4) and Equation (6), the movement distance of the debris-flow mass in the horizontal direction and the plunging velocity will also increase. Therefore, with increasing the debris-flow volume, not only the maximum scour depth, but also the distance between the check dam site and deepest scour location will increase as shown in Fig.6.

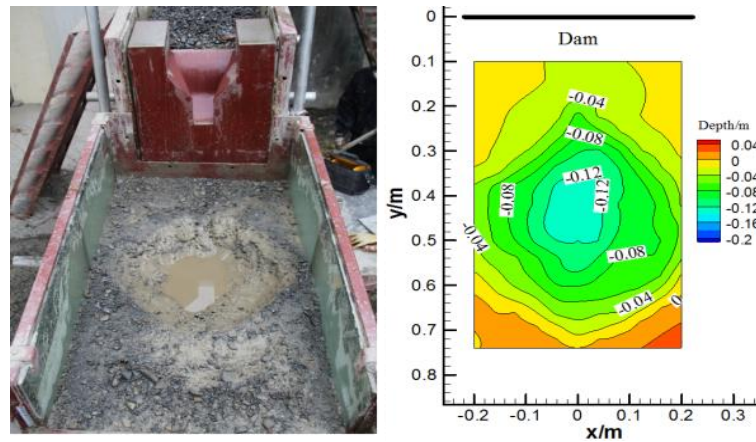


Fig. 5. The shapes of scour hole downstream from the check dam

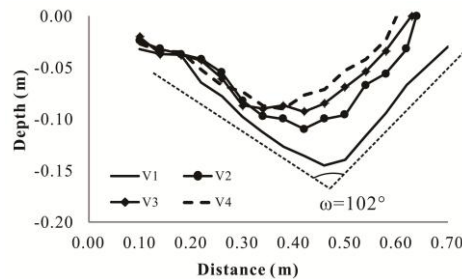


Fig. 6. The profiles of scour hole at different debris flow volumes: $V_1=0.16 \text{ m}^3$; $V_2=0.10 \text{ m}^3$; $V_3=0.06 \text{ m}^3$; $V_4=0.03 \text{ m}^3$.

3. Prediction of debris-flow scour depth

Definitely, besides the debris flow volumes, the scour depth can be determined by some other factors such as the sediment concentration or debris-flow density, debris-flow velocity, particle-size distribution, and the maximum diameter of sediments. Obviously if all the factors are considered in our study, it will become very complex. So we fix the particle-size distribution and maximum diameter of sediments, and pay more attention to the dynamic parameters of debris flows such as flow density, velocity, and volumes. The diagram of scour dynamic processes in the erodible bed is shown in Fig.7. Herein, we considered a spillway with rectangular cross-section and a "Y"-type spillway. For each spillway structure, four different discharges were considered to measure the key parameters of debris flows and predict the maximum scour depth in the erodible bed. The values of key parameters measured are shown in Table 1.

The study area is chosen as shown in Fig.7. The momentum equation between section 1 and 2 is expressed as follows

$$P_1 - P_2 - G \sin \varphi - \tau_0 L = \rho q (V_{m2} - V_{m1}) \quad (8)$$

where P_1 and P_2 are the hydrostatic forces at section 1 and section 2 respectively, G is the gravity force of the debris flow, θ is downstream slope angle of the scour hole, τ_0 is the shear stress, ρ is debris flow density, q is unit flow discharge, V_1 and V_2 are the average velocity at section 1 and section 2 (Fig.7), respectively.

P_1 can be expressed as

$$P_1 = \int_0^{(h_c+h_t)/\cos\varphi} \rho g h \cos \varphi dh = \frac{1}{2} \rho g (h_c + h_t)^2 / \cos \varphi \quad (9)$$

P_2 can be expressed as

$$P_2 = \int_0^{h_t/\cos\varphi} \rho g h \cos \varphi dh = \frac{1}{2} \rho g h_t^2 / \cos \varphi \quad (10)$$

G can be expressed as

$$G = \frac{\rho g}{2} ((h_c + 2h_t) / \cos \varphi) \cdot (h_c / \cos \varphi) \cdot ctg \varphi \quad (11)$$

where φ , h are the angle of repose and the water depth downstream, respectively.

When a debris-flow nappe reaches the bottom of the scour hole, the flow velocity changes its direction roughly parallel with the erodible bed. We assumed that the flow velocity V_1 was the average velocity and also considered it as the boundary velocity which caused the shear stress τ_0 .

Drag force F can be expressed as

$$F = \tau_0 L = \rho g V_{m1}^2 / C^2 \cdot L = \rho g \left(\delta \sqrt{\frac{d_0 \sin \theta}{h_c + h_t}} \right)^2 / C^2 \cdot (h_c / \cos \varphi) \cdot ctg \varphi \quad (12)$$

where, C is the Chezy parameter ($C=60.0$), L is the downstream slope length of the scour hole, δ is constant ($\delta = 2.28$), d_0 is the thickness of the debris flow nappe, θ is the recipient angle of the debris flow nappe.

From Equation (7) to Equation (11), then we have

$$g \left(\delta v_2 \sqrt{\frac{d_0 \sin \theta}{h_c + h_t}} \right)^2 / C^2 \cdot (h_c / \sin \varphi) = q (\delta v_2 \sqrt{\frac{d_0 \sin \theta}{h_c + h_t}} - V_{m2}) \quad (13)$$

In Equation (13), every parameter can be obtained based on the experiments except the erosion depth h_c . Therefore, we can calculate the erosion depth by trial and error method. The value of each parameter and the results of the erosion depth h_c are shown in Table 1. Fig.8 showed the results of the predicted scour depth and the experimental data. It indicated that the scour depth calculated by Equation (13) was in good agreement with the experimentally calculated scour depth.

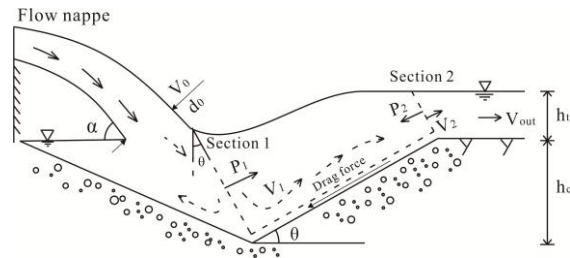


Fig. 7. Diagram of scour dynamic process

Table 1. The values of key parameters under different spillway operating conditions

Spillway types	Parameters										Error	
	ρ (kg/m ³)	q (m ³ /s)	ϕ (°)	V_0 (m/s)	d_0 (m)	θ (°)	h_t (m)	h_{ce} (m)	h_c (m)	V_1 (m/s)		V_2 (m/s)
Spillway with Rectangular cross-section	1500	0.0893	40	3.30	0.025	71.54	0.035	0.164	0.142	1.02	1.80	-13.41%
	1500	0.0735	40	3.27	0.022	72.60	0.030	0.145	0.164	0.98	1.73	4.88%
	1500	0.0592	40	3.23	0.017	73.56	0.025	0.123	0.129	0.92	1.55	-2.78%
	1500	0.0484	40	3.00	0.015	74.50	0.020	0.110	0.138	0.85	1.46	18.52%
	1500	0.0893	40	3.30	0.05	51.85	0.035	0.145	0.164	1.50	1.90	13.10%
"Y"-type Spillway	1500	0.0735	40	3.27	0.042	53.00	0.030	0.123	0.129	1.48	1.80	25.45%
	1500	0.0592	40	3.23	0.035	53.40	0.025	0.110	0.138	1.43	1.74	27.96%
	1500	0.0484	40	3.00	0.030	52.30	0.020	0.108	0.105	1.30	1.53	-1.08%

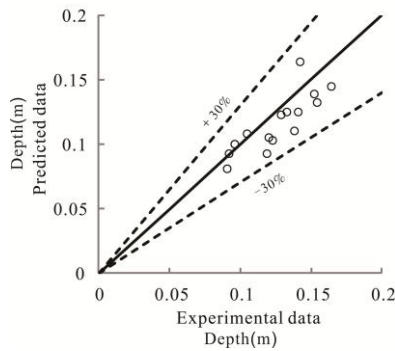


Fig. 8. Comparison of predicted data and experimental scour depths

4. Conclusion

In this paper, we described experiments that we conducted to investigate the characteristics of debris-flow nappe downstream from a check dam. A theoretical analysis for predicting the maximum scour depth is also presented. The following conclusions were drawn from this analysis:

- 1) The geometry of debris-flow nappes are mainly determined by the type of spillway. For rectangular spillways, debris flows overflow with shallow flow depths, and the nappe is wide and thin. However, for Y-type spillways with lateral contraction, the nappe is relatively narrow and thick.
- 2) Scour holes formed when the debris-flow nappe plunged into the erodible bed and the deepest point of the scour hole occurred at the tip of the debris-flow nappe. With increasing debris-flow volume, the maximum scour depth increased and the deepest position of the scour hole extended further downstream.
- 3) Based on the momentum conservation law, a theoretical expression was proposed to predict the maximum scour depth downstream from the check dam. The predicted results exhibited good agreement with the experimental results. The maximum relative error of the predicted results was always smaller than 27.96%.

Acknowledgements

The study presented in this paper was supported by the 135 Strategic Program of the Institute of Mountain Hazards and Environment, CAS, NO. SDS-135-1701, the National Natural Science Foundation of China (Grant No. 41661144028; 41372331), the Science and technology research project of China railway corporation (2017G008-F), and Foundation of Youth Innovation Promotion Association, Chinese Academy of Sciences (Grant No. 2017425).

References

- Ballio, F., Radice, A., and Dey, S., 2010, Temporal scales for live-bed scour at abutments, *Journal of Hydraulic Engineering*, v.136, no.7, p.395-402.
- Barbhuiya A K, and Mazumder M H., 2014, Live-bed local scour around vertical-wall abutments, *Journal of Hydraulic Engineering*, v.20, no.3, p.339-351.
- Breien, H., Blasio, F. V. D., Elverhøi, A., and Høeg K., 2008, Erosion and morphology of a debris flow caused by a glacial lake outburst flood, *Western Norway. Landslides*, v. 5, no. 3, p. 271-280.
- Chen, H. Y., Cui, P., Zhou, G. G. D., Zhu, X., H., and Tang, J. B., 2014, Experimental study of debris flow caused by domino failures of landslide dams, *International Journal of Sediment Research*, v. 29, no. 3, p. 414-422.
- Chen, H.Y., Liu, J.F., and Zhao, W.Y., 2016, Effects of Y-type spillway lateral contraction ratios on debris flow patterns and scour features behind a check dam, *Natural Hazards & Earth System Sciences*, v.16, no. 11, p. 2433-2442.
- Coscarella, F., Gaudio, R., and Manes, C., 2018, Local scour around long vertical wall abutments and the phenomenology of turbulence[C]// *Iahr Europe Congress -New Challenges in Hydraulic Research and Engineering*.
- Cui, P., Zhou, G. G.D., Zhu, X.H., and Zhang, J.Q., 2013, Scale amplification of natural debris flows caused by cascading landslide dam failures, *Geomorphology*, no.182, p.173-189.
- Decaulne, A., Porsteinn O., SÁmundsson. And Aorsteinn, 2008, Debris-flow characteristics in the Gleidarhjalli area, North-western Iceland, *Debris-Flow Hazards Mitigation: Mechanics, Prediction, and Assessment*.
- Decaulne, A, SÁmundsson. Aorsteinn, and Petursson, O., 2010, Debris flow triggered by rapid snowmelt: a case study in the glei. arhjalli area, northwestern iceland, *Geografiska Annaler*, v.87, no. 4, p. 487-500.
- Dey, S., and Barbhuiya, A.K., 2004, Clear-water scour at abutments in thinly armored beds, *Journal of Hydraulic Engineering*,v.130, no. 7, p. 622-634.
- Iverson, R. M., 1997, The physics of debris flows, *Reviews of Geophysics*, v. 3, no. 35, p. 245-296.
- Hayen, J. C., 2003, Projectile motion in a resistant medium. II. Approximate solution and estimates, *International Journal of Non-Linear Mechanics*, v. 38, no. 3, p. 371-380.
- Hsieh, H. M., Luo, C.R., Yang, J.C., and Chen R.F., 2013, Numerical study of the effects of sabo dams on erosion and sedimentation in the Pachang River, *International Journal of Sediment Research*, v. 28, p. 304-315.
- Huang, R. Q., 2011, Geo-engineering Lessons Learned from the 2008 Wenchuan Earthquake in Sichuan and Their Significance to Reconstruction, *Journal of Mountain Science*, no. 8, p. 176-189.
- Lenzi, M.A., and Comiti F., 2003, Local scouring and morphological adjustments in steep channels with check-dam sequences, *Geomorphology*, v. 55, p. 97-109.
- Ma, C. Hu, K.H. and Tian, M., 2013, Comparison of debris-flow volume and activity under different formation conditions, *Nat Hazards*, no.67 , p. 261-273.
- Manes, C., and Brocchini, M., 2015, Local scour around structures and the phenomenology of turbulence, *Journal of Fluid Mechanics*, no.779: 309-324
- Melo, R, Asch, T. V., and Zêzere, J. L., 2018, Debris flow run-out simulation and analysis using a dynamic model. v.18, no.2:1-35.
- Pan, H. L., Yang, S., Ou, G. Q., and Huang, J.C., 2013a, Local scour and the laws of scour pit's shape of debris flow sabo dam downstream, *Journal of Mountain Science*, v. 10, no. 6, p. 1063-1073.
- Pan, H. L., Wang, R., Huang, J. C., and Ou G. Q., 2013b, Study on the ultimate depth of scour pit downstream of debris flow sabo dam based on the energy method, *Engineering Geology*, v. 160, p. 103-109.
- Sheppard, D. M., and Miller Jr, W., 2006, Live-bed local pier scour experiments. *Journal of Hydraulic Engineering*, v. 132, no.7, p. 635-642.
- Shrestha, B.B., Nakagawa, H., Kawaike, K., and Baba Y., 2008, Numerical and experimental study on debris-flow deposition and erosion upstream of a check dam, *Annual Journal of Hydraulic Engineering, JSCE*, no. 52, p. 139-144.
- Shrestha, B.B., Nakagawa, H., Kawaike, K., Baba Y., and Zhang H., 2009, Capturing Process of Debris Flow with Driftwood by an Open Type Check Dam. *Annuals of Disaster Prevention Research Institute, Kyoto University*, no. 52 B, p. 697-715.
- Xu, Q., Zhang, S., and Li, W.L., 2012, The 13 August 2010 catastrophic debris flows after the 2008 Wenchuan earthquake, China, *Natural Hazards and Earth System Sciences*, v.12, p. 201-216.
- Zeng, Q.L., Yue, Z.Q., Yang, Z.F., and Zhang X.J., 2009, A case study of long-term field performance of check-dams in mitigation of soil erosion in Jiangjia stream, China, *Environmental Geology*, no. 58, p. 897-911.
- Zhou, G. G., Cui, P, Zhu, X.H., Tang, J. B., Chen, H.Y., and Sun, Q. C., 2015, A preliminary study of the failure mechanisms of cascading landslide dams, *International Journal of Sediment Research*, v. 30, no. 3, p. 223-234.

Debris-flow mitigation measures and an application case in a small-scale watershed in China

Jiangang Chen, Xiaoqing Chen^{*}, Wanyu Zhao, Yong You

Key Laboratory of Mountain Hazards and Earth Surface Process, Institute of Mountain Hazards and Environment, Chinese Academy of Sciences (CAS), Chengdu, 610041, China

Abstract

The Wenchuan earthquake in China (May 12, 2008) triggered numerous debris flows, some of which caused serious secondary disasters, such as in Wenjia gully (Sichuan Province) and Sanyanyu gully (Gansu Province). To solve this problem, a planning method for debris-flow mitigation engineering measures was proposed based on watershed and river sediment transport characteristics. This method aids in the selection of engineering measures to effectively prevent secondary disasters and control unconsolidated soil and debris-flow movement from upstream to downstream. Several measures are considered in the proposed method, including check dams and transverse structures built across gullies, which are important engineering measures in debris-flow hazard mitigation. Based on the developed planning method, new types of check dams were proposed, the regulation effect of sediment particle size in slit check dams was qualitatively analyzed, and the design parameters (e.g., deposition slope, deposition length, and dam height) of the check dams were deduced. Moreover, a series of drainage channels was proposed to cross highways and discharge debris flows into the river or debris-flow deposition basin below. Finally, an engineering application case in Xiaogangjian gully, Sichuan Province, China, was examined using the proposed watershed planning method, in which a series of check dams with different orifices sizes was constructed. The engineering application results provide useful data for developing check dams as a restoration tool and hazard mitigation technology in small watersheds.

Keywords: Debris flow; mitigation measures; small-scale watershed; check dam; drainage channel

1. Introduction

Debris flows are sediment movements that can travel several kilometers as a series of surges; they are common on steep terrain and in deep gullies within mountainous areas (Iverson, 1997; Hungr et al., 2001; VanDine and Bovis, 2002; Godt and Coe, 2007; Cui et al., 2013). They can scour channel banks and gully beds, enhancing the debris-flow discharge due to the effects of the blockage and subsequent outbreak process in watersheds (Cui et al., 2013). The Wenchuan earthquake in China (May 12, 2008, Sichuan Province) triggered numerous debris flows, some of which caused serious secondary disasters, such as in Wenjia gully (Sichuan Province) and Sanyanyu gully (Gansu Province) (Zhou et al., 2013; Zhang and Matsushima, 2018). Subsequently, numerous large-scale debris flows occurred during the rainy season from 2008 to 2018, when portions of hillslope deposits were transferred to channel deposits, and the source materials in the channel were carried to the outlet of the watershed. Based on a study of the debris-flow activities along a highway in China, the debris flow volume, runout distance, and deposition width decrease over time due to the decreasing source material volume and a possible change in debris-flow type (Zhang and Zhang, 2017). Whereas 665 debris-flow events per year occurred from 2001 to 2008, the average number of debris-flow events per year reached 1153 from 2009 to 2016 in China (Fig. 1). This trend suggests that debris-flow hazard prevention and mitigation will remain an urgent issue in the coming decades, as stated by Stoffel et al. (2014).

Debris-flow mitigation measures can be classified as structural measures (e.g., check dams, drainage systems, flexible barriers, and debris-flow basins) or nonstructural measures (e.g., warning and evacuation systems, appropriate land use, and building improvements) (Armanini and Larcher, 2001; Takahisa, 2008; Hassanli et al.,

^{*} Corresponding author e-mail address: xqchen@imde.ac.cn

2009; You et al., 2011; Canelli et al., 2012; Chen et al., 2014; Chen et al., 2015; Liu et al., 2017; Wang et al., 2017; Chen et al., 2018; Wang et al., 2018). Although debris-flow mitigation measures have been constructed in a few watersheds in the Wenchuan earthquake area, China, large-scale debris flows have still occurred, proving that existing mitigation measures are inadequate (Wang et al., 2012; Wang et al., 2013). In addition, the dual impacts of the Lushan earthquake (April 20, 2013, Sichuan Province, China) and the Jiuzhaigou earthquake (August 8, 2017, Sichuan Province, China) are expected to further increase the incidence of debris-flow disasters (Cui et al., 2014; Chen et al., 2018). Therefore, developing new planning methods and techniques based on debris-flow characteristics in this earthquake-stricken region is a critical issue.

This paper presents a new planning method for debris-flow hazard prevention and mitigation measures, and describes several corresponding engineering technologies. The proposed debris-flow hazard prevention and mitigation method was tested based on several medium-sized debris flows, and a related case study of a small, steep watershed is described. The results indicate that this method is effective in regulating debris-flow hazards; therefore, this planning method and related engineering technologies may provide a new process for debris-flow hazard mitigation.

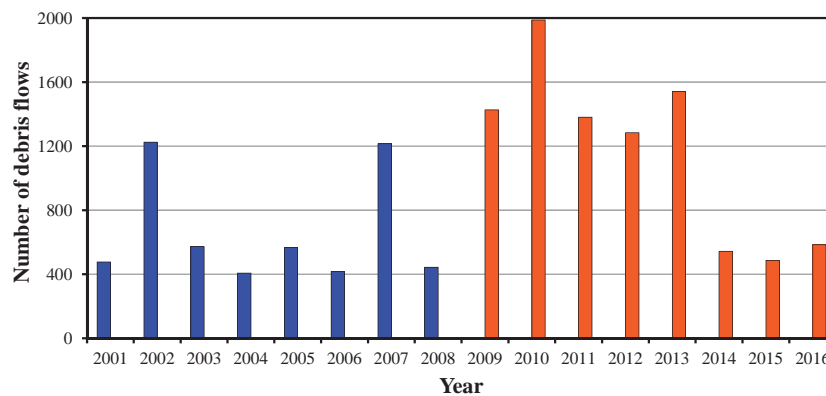


Fig. 1 Debris-flow events in China from 2001 to 2016

2. Debris-flow hazard mitigation engineering planning method and new technologies

2.1. Planning method

The early planning method for debris-flow hazard mitigation engineering, in 1980s in China, is primarily based on the target objects intended to be protected, which is effective for small debris flows, but not large debris flows. For instance, several large debris flows have exited the gully in which they originated and blocked the river below, such as in Wenjia gully (Sichuan Province) and Sanyanyu gully (Gansu Province). Therefore, the planning method requires reconsideration for large debris flows. Based on the calculation method of the debris flow block the main river (He, 2003) and to make full use of the sediment transport capacity of rivers, Chen et al. (2015) proposed the use of cascade check dams and deposition basins to regulate the scale of debris flows in gullies. Figure 2 shows the specific implementation process of the new planning method for debris-flow mitigation engineering measures, which includes consideration of the debris-flow peak discharge with a design standard (Q_{Total}), the debris-flow peak discharge through the drainage channel ($Q_{Drainage}$), the debris-flow peak discharge requiring blockage by check dams (Q_{Block}), and the debris-flow peak discharge that must be accommodated by the deposition basin ($Q_{Deposition}$). The primary steps in designing a mitigation system include the determination of Q_{Total} based on the design standard and rainfall data, as well as the transport capacity of nearby rivers based on river discharge data, followed by the determination of $Q_{Drainage}$. Why we consider the drainage channel discharge capacity and the sediment transport capacity of the river, the reason is that the river can be blocked when the debris flow discharge into the river is large than the sediment transport capacity of the river. Based on the block condition of the river, the better process can be selected according to the flow chart in Figure 2. The relation between the debris-flow peak discharge with a design standard and the total volume Q of a debris flow is $Q = 19TQ_p/72$, T stands for the debris flow duration time and Q_p stands for the debris-flow peak discharge.

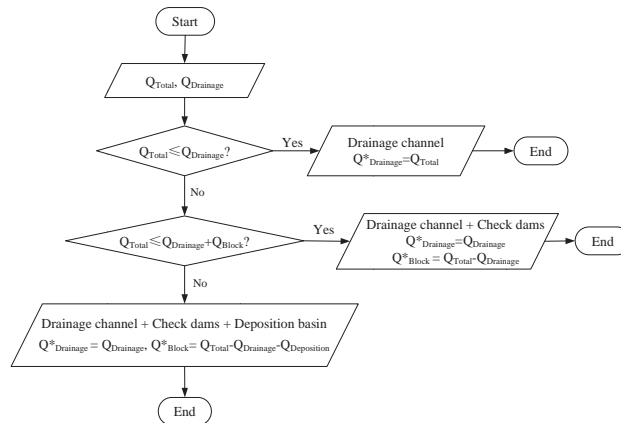


Fig. 2 The implementation process of the proposed planning method

2.2. New debris-flow hazard-mitigation technologies

To better apply the proposed planning method, a large number of check dams and drainage channels were researched and developed. Several types of structures are described in the following sections.

2.2.1 Cascade check dams with orifices of various sizes

A series of open check dams with rectangular orifices with various sizes can be used to block and separation debris particles and the interval spaces of the orifices was calculated by the debris flow impact force. When debris flows enter the circulation area, water and stones are separated. The mean particle size gradually becomes smaller further downstream, thereby decreasing the impact forces of large stones. Such structures can achieve a uniform distribution of debris flow materials along the length of the debris flow. As such, this method makes use of both the siltation and hazard mitigation functions of check dams. Cascade check dams have completely prevented debris flows (Liu et al., 2017); therefore, they have an important hazard mitigation function. Since cascade check dams have the advantage of reducing debris flow particles with sequentially decreasing orifice sizes, regulating the debris-flow peak discharge, this method is expected to have major impacts on the mitigation and treatment of large-scale debris flows.



Fig. 3 Cascade check dams with orifices of various sizes in Shaofang gully, China

2.2.2 Debris-flow blocking structure with piles

Blocking structures can be constructed from both rectangular and T-shaped piles arranged in a staggered formation (shown in Fig. 4). In these structures, the horizontal coupling beam is made of reinforced concrete with a rectangular cross-section. Such structures can block stones, while having minimal effects on flow efficiency. The rectangular pile structure in the first row is relatively strong, and mainly blocks large stones; the T-shaped piles in

the second row are used to form a soil arch effect. Overall, this enables the pile structure to block debris and form a dam. Debris-flow blocking structures with two rows of piles at equal intervals can block large stones while discharging smaller particles, protecting downstream buildings from the impact forces of large debris. Meanwhile, the T-shaped piles improve the stability of the structure. Compared with gravity retaining check dams, the pile spacing can be easily adjusted, reducing the project budget without affecting the function. Finally, the structure is relatively convenient, economical, and practical to construct in the poverty-stricken area.

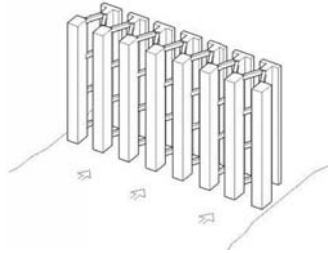


Fig. 4 Debris-flow blocking structure with piles

2.2.3 Drainage channel with prefabricated reinforced concrete boxes

The drainage channel with prefabricated reinforced concrete boxes described herein represents a new type of debris flow drainage channel, which is shown in Fig. 5. In this design, the prefabricated reinforced concrete boxes can be used to construct the sidewall or as an energy dissipation section by filling with stones. The side walls, which can be either vertical or inclined, can be constructed from masonry, concrete, reinforced concrete, or prefabricated, reinforced concrete boxes. The ground sill was constructed by reinforced concrete. The energy dissipation section is located between the upstream and downstream sections of the channel slab, and stones are used to fill the structure. Different structural forms, such as a steel cable network can be used to avoid scouring damage, can be used as the slab of the energy dissipation section, and a concrete lining layer can be used to protect the bottom from scouring. Debris flows can flow through the top open surface as they pass through the structure. Some of the energy is dissipated via strong interactions between the debris flow and stones. In addition, the impact energy of the debris flow can be absorbed by the soft foundation, and exchange between the debris flow and bottom soil can be inhibited, controlling the erosion of the channel slab by the debris flow. Ultimately, this structure can achieve a balance between the reduction in the potential energy and the dissipated energy.

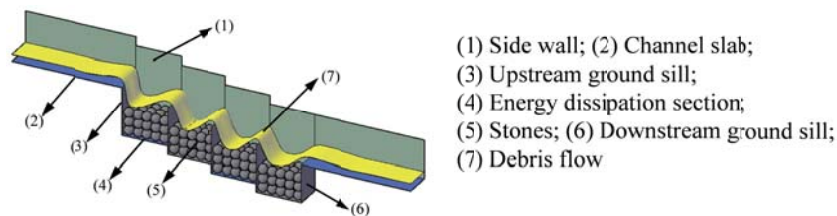


Fig. 5 Schematic diagram of a drainage channel with prefabricated reinforced concrete boxes

2.2.4 Drainage channel with a step-pool configuration

Drainage channels with a step-pool configuration are composed of sidewalls, a channel slab (i.e., step section), upstream and downstream ground sills, and a pool section (Fig. 6). The step section includes the upstream ground-sill, the downstream ground-sill, and a concrete slab that connects the upstream and downstream ground-sills. The pool section is located between two adjacent ground-sills and is filled with stones. Debris-flow energy can be dissipated via interactions between the debris flow and stones. In addition, debris-flow impact energy can be absorbed by the soft foundation, and exchange between the debris flow and bottom soil can be prevented to control erosion of the channel slab. Figure 6 shows the structural

characteristics of a drainage channel with a step-pool configuration. The sidewalls can be vertical or inclined, and different structural forms can be used in the pool sections. Additionally, steel cable networks, soft foundations, or concrete lining layers can be used in the pool bottom to protect against bottom scouring.

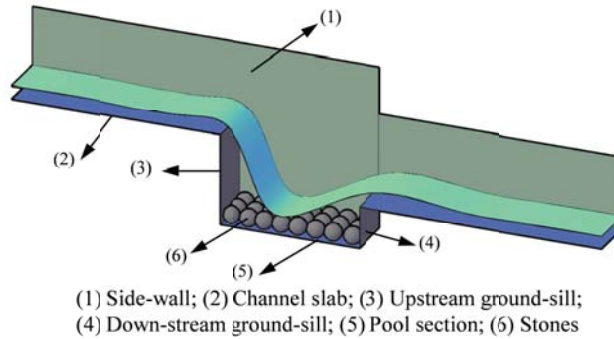


Fig. 6 Schematic diagram of a drainage channel with a step-pool

3. Engineering application case

3.1. Research area

The small-scale watershed of Xiaogangjian gully is located in the central Longmen Mountains area (31°02'N, 104°07'E). The area of this gully is 1.36 km², the main channel of the gully is 2,590 m long, and the longitudinal gradient is 412‰. The altitude of the catchment ranges from 810 to 1,987 m, representing an elevation difference of 1,177 m. The area with slope gradients equal to or greater than 25° measures approximately 1.16 km². The slopes in this catchment are mostly steep with large longitudinal gradients, favoring the concentration of stormwater runoff, making the area prone to debris flows.

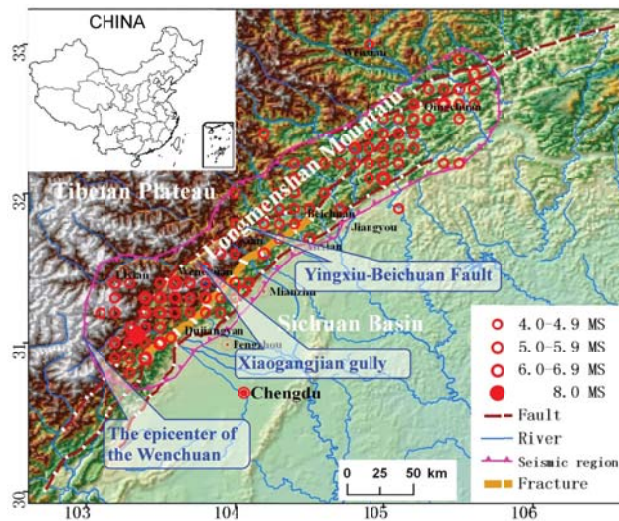


Fig. 7 Location of Xiaogangjian gully (source: China Earthquake Administration; MS stands for the Richter scale)

The Wenchuan earthquake induced numerous landslides and avalanches in this gully, with total deposits of $80 \times 10^4 \text{ m}^3$. Ten debris flows occurred between May 12, 2008, and September 5, 2011, and caused a radical change to the landscape, particularly the outlet of the gully. The total volume of solid materials that exited the gully was estimated to be $50 \times 10^4 \text{ m}^3$, including materials from the old accumulation platform ($40 \times 10^4 \text{ m}^3$) and those from

the collapse upstream ($10 \times 10^4 \text{ m}^3$). An area of $3 \times 10^4 \text{ m}^2$ was directly affected by the debris flow in the gully outlet, including the road below the gully. Major hazards included the blockage and siltation of the main road and river channel, the formation of a dammed lake, the inundation of the upstream road, and the rise in the downstream river bed due to high-intensity sedimentation, which resulted in the burial of the road downstream. For example, the road was buried by a debris flow that occurred on July 26, 2010, interrupting traffic for 18 days. Another larger-scale debris flow occurred on August 13, 2010, and blocked the road at the gully outlet to form a dammed lake that flooded the upstream road, interrupting traffic until August 20, 2010.

3.2. Debris-flow mitigation engineering measures in Xiaogangjian gully

To protect lives, properties, and the road, as well as create favorable conditions for a healthy economy and environment and for construction and development in the nearby town, a debris-flow mitigation project in Xiaogangjian gully was carried out in 2011. The design standard of the debris flow mitigation measure was to resist rainstorm-induced debris flows with a 20-year return period. Geological, geomorphological, hydrological, and meteorological conditions were considered in the project design.

3.2.1 Systematic planning of the debris flow mitigation project

Based on the planning method for debris-flow hazard mitigation engineering, the debris-flow discharge into the river through the drainage channel is large than the sediment transport capacity of the main river, then the river can be blocked by the debris flow. Thus, the maximum debris-flow discharge into the river through the drainage channel should not exceed the threshold of $Q_{\text{Drainage}} > 17.5 \text{ m}^3/\text{s}$. Based on the hydrology of the small basin, the debris-flow peak discharge with a 20-year return period, Q_{Total} , was $90.3 \text{ m}^3/\text{s}$. Because $Q_{\text{Total}} > Q_{\text{Drainage}}$, a drainage channel alone would be insufficient in this gully.

A series of check dams with orifices of various sizes was used to raise the erosion base level and stabilize the inner bank slope. Based on an analysis of the geological and geomorphological conditions, it was determined that three check dams should be built in the gully. Based on a slope stability analysis, these dams could mitigate a peak discharge of $Q_{\text{Block}} = 31.3 \text{ m}^3/\text{s}$. Because $Q_{\text{Total}} > Q_{\text{Drainage}} + Q_{\text{Block}}$, a debris flow basin was added to accommodate additional debris flow peak discharge. To avoid blocking the river, the debris flow basin should be capable of accepting a peak discharge of $Q_{\text{Deposit}} = Q_{\text{Total}} - Q_{\text{Drainage}} - Q_{\text{Block}} = 90.3 - 17.5 - 31.1 = 41.7 \text{ m}^3/\text{s}$.

In summary, the design of the engineering project based on the debris flow peak discharge and the total volume of a single debris flow event is as follows: the peak discharge, Q_{Drainage} , of the debris flow that can drain into the main river is $17.5 \text{ m}^3/\text{s}$; the reduction in peak discharge, Q_{Block} , that can be produced by check dams is $31.1 \text{ m}^3/\text{s}$; the peak discharge, Q_{Deposit} , that can be accepted by the debris flow basin is $41.7 \text{ m}^3/\text{s}$, with a minimum volume of $26,414 \text{ m}^3$, which can be calculated by the empirical formula $Q = 19TQ_p/72$, T stands for the debris flow duration time and Q_p stands for the debris-flow peak discharge.

3.2.2 Application of the drainage channel

Three check dams with orifices of various sizes were constructed in Xiaogangjian gully to mitigate debris flows (Fig. 8). In downstream succession, the sequence of dams is as follows: the first dam is 12.5 m high with 7 orifices, the sizes of the orifices are $0.8 \times 5.0 \text{ m}$ and $0.8 \times 3.5 \text{ m}$ (width \times height); the second dam is 11.5 m high with 7 orifices, the sizes of the orifices are $0.8 \times 4.5 \text{ m}$ and $0.8 \times 3.0 \text{ m}$ (width \times height); the third dam is 12.5 m high with 10 orifices, the sizes of the orifices are $0.8 \times 3.0 \text{ m}$, $0.8 \times 2.5 \text{ m}$ and $0.8 \times 1.0 \text{ m}$ (width \times height). To protect the highway at the gully outlet, a drainage channel with prefabricated reinforced concrete boxes was constructed to enable discharge of the debris flow into a debris flow basin (Chen et al., 2015). The steps in designing the drainage channel are as follows.

(1) Based on field measurements, the drainage channel slope is approximately $i = 35\%$, and the length of the channel is 105 m. The cross-section is rectangular, the width of the channel is $B = 6 \text{ m}$, and the height of the sidewall is 3.5 m. According to the construction material, the roughness coefficient is approximately $n_0 = 0.02$. Based on the velocity characteristics of the scour resistance of the reinforced concrete materials, the admissible velocity in the drainage channel ranges from 2.7 to 8 m/s.

(2) Assuming that the width and length of the energy dissipation section are $b = 3.0 \text{ m}$ and $L = 15 \text{ m}$, respectively, the mean diameter of the filled stones is $D = 0.4 \text{ m}$. The roughness coefficient of the energy dissipation structure section can be calculated using the equation proposed by Chen et al. (2018).

(3) The debris-flow velocity can be obtained by substituting the parameters into the Manning equation. During

the design process, the relationship between the debris flow depth and the mean diameter of the filled stones is $h = 4D$.

(4) The calculated debris-flow velocity and the admissible velocity in the first step are compared to determine whether the parameters are reasonable. If not, the design parameters can be adjusted, and the computational process repeated.

Ultimately, for design parameters of $i = 0.35$, $b = B = 6.0$ m, $L = 25.0$ m, and $D = 0.3$ m, the roughness coefficient of the energy dissipation structure section is $n = 0.109$. The calculated debris flow velocity is 4.9 m/s, which meets the permissible velocity limit for the drainage channel.

3.3. Effect of the debris flow mitigation project in Xiaogangjian gully

The debris-flow mitigation project was completed in May 2012. From August 13 to 18, 2012, seven debris flows were triggered in the gully with a total flow volume to $23.2 \times 10^4 \text{ m}^3$. The mitigation project was designed by the rainstorm with a 20-year return period in this steep and rich source materials gully, thus, the highway was effectively protected by the mitigation engineering and the debris flows did not cause a disaster. This outcome indicates that the debris flow mitigation strategy used in this gully is effective and that the construction of the mitigation system is feasible. In general, strategies for controlling debris flows using a combination of check dams, drainage channels, and debris flow deposition basins are effective (Chen et al., 2015). However, the design standard of the mitigation measures should be improved if the areas to be protected are particularly important. To ensure the longevity of the debris flow mitigation system, the following measures must be taken. During the construction, the construction quality should be inspected. After the debris flow mitigation measures are installed, their operation and maintenance, such as dredging to maintain the capacity of the check dams and repairing abrasion of the drainage channel, must be performed in a timely fashion.



Fig. 8 Application of the debris-flow mitigation structures in Xiaogangjian gully, Sichuan Province, China

4. Conclusion

Avalanches and landslides caused by the Wenchuan earthquake in the Longmen Mountains region provided an abundant source of loose slope material for debris flows. Based on the large-scale debris-flow characteristics of the Wenchuan earthquake, a new planning method for debris-flow mitigation measures in small-scale watersheds was proposed, and new techniques for the planning and designing were suggested. A drainage channel constructed of prefabricated reinforced concrete boxes was developed and applied in a practical engineering case. In the case application in Xiaogangjian gully, a series of check dams with orifices with various sizes was constructed to promote the settling of debris-flow particles of various sizes and separate water from stone along the length of the gully channel. The impact forces of debris flows can be effectively reduced using this method. Moreover, this method can uniformly distribute debris flow materials among the group of check dams, more fully enabling the siltation and hazard mitigation functions of check dams. The results support the application of the new debris-flow

mitigation measure and new planning method to small-scale watersheds, which can not only effectively protect roadways and minimize losses by debris flows in China, but also it can apply to debris-flow-prone regions worldwide.

Acknowledgements

This study was supported by the National Science Foundation of China (Grant Nos. 41661144028, 41790434, and 51709259), and the CAS “Light of West China” Program and Youth Innovation Promotion Association of the CAS (2017426).

References

- Armanini, A., and Larcher, M., 2001, Rational criterion for designing opening of slit-check dam. *J. Hydraul. Eng.*, v.127, no. 2, 94–104, doi: 10.1061/(ASCE)0733-9429(2001)127:2(94).
- Canelli, L., Ferrero, M., Migliazza, M., and Segalini, A., 2012, Debris flow risk mitigation by the means of rigid and flexible barriers – experimental tests and impact analysis. *Nat. Hazards Earth Syst. Sci.*, v. 12, 1693–1699, doi:10.5194/nhess-12-1693-2012.
- Chen, J.G., Chen, X.Q., Wang, T., Zou, Y.H., and Zhong, W., 2014, Types and causes of debris flow damage to drainage channels in the Wenchuan earthquake area. *J. Mt. Sci.*, v.11, no. 6, 1406–1419, doi: 10.1007/s11629-014-3045-x.
- Chen, J.G., Chen, X.Q., Zhao, W.Y., and You, Y., 2018, Debris flow drainage channel with energy dissipation structures: experimental study and engineering application. *J. Hydraul. Eng.*, v. 144, no. 10, 06018012, doi: 10.1061/(ASCE)HY.1943-7900.0001523.
- Chen, X.Q., Chen, J.G., Cui, P., You, Y., Hu, K.H., Yang, Z.J., Zhang, W.F., Li, X.P., and Wu, Y., 2018, Assessment of prospective hazards resulting from the 2017 earthquake at the world heritage site Jiuzhaigou Valley, Sichuan, China. *J. Mt. Sci.*, v. 15, no. 4, 779–792, <https://doi.org/10.1007/s11629-017-4785-1>.
- Chen, X.Q., Cui, P., You, Y., Chen, J.G., and Li, D.J., 2015, Engineering measures for debris flow hazard mitigation in the Wenchuan earthquake area. *Eng. Geol.*, v. 194, 73–85, doi: 10.1016/j.enggeo.2014.10.002.
- Cui, P., Zhang, J.Q., Yang, Z.J., Chen, X.Q., You, Y., and Li, Y., 2014, Activity and distribution of geohazards induced by the Lushan earthquake, April 20, 2013. *Nat. Hazards*, v. 73, 711–726, doi: 10.1007/s11069-014-1100-0.
- Cui, P., Zhou, G.G.D., Zhu, X.H., et al., 2013, Scale amplification of natural debris flows caused by cascading landslide dam failures. *Geomorphology*, v. 182, 173–189, doi: 10.1016/j.geomorph.2012.11.009.
- Godt, J.W., and Coe, J.A., 2007, Alpine debris-flows triggered by a 28 July 1999 thunderstorm in the Central Front Range, Colorado. *Geomorphology*, v. 84, 80–97, doi:10.1016/j.geomorph.2006.07.009.
- Hassanli, A.M., Nameghi, A.E., and Beecham, S., 2009, Evaluation of the effect of porous check dam location on fine sediment retention (a case study). *Environ. Monit. Assess.*, v. 152, no. 14, 319–326, <https://doi.org/10.1007/s10661-008-0318-2>.
- He, Y.P., 2003, Influence of debris flow on the evolution of river bed in mountain areas, Graduate School of Chinese Academy of Sciences, pp. 102–107, (in Chinese).
- Hungri, O., Evans, S.G., Bovis, M.J., and Hutchinson, J.N., 2001, A review of the classification of landslides of the flow type, *Environ. Eng. Geosci.*, 7: 221–238, DOI: 10.2113/gseengeosci.7.3.221.
- Iverson, R.M., 1997, The physics of debris flows. *Rev. Geophys.*, v. 35, 245–296, doi: 10.1029/97RG00426.
- Liu, F.Z., Xu, Q., Dong, X.J., Yu, B., Frost, J.D., and Li, H.J., 2017, Design and performance of a novel multi-function debris flow mitigation system in Wenjia gully, Sichuan. *Landslides*, v. 14, 2089–2104, doi: 10.1007/s10346-017-0849-0.
- Stoffel, M., Mendlik, T., Schneuwly-Bollschweiler, M., and Gobiet, A., 2014, Possible impacts of climate change on debris-flow activity in the Swiss Alps. *Climatic Change*, v. 122, 141–155, doi: 10.1007/s10584-013-0993-z.
- Takahisa, M., 2008, Structural countermeasures for debris flow disasters. *Int. J. Eros. Control Eng.*, v.1, no. 2, 8–43, doi: 10.13101/ijece.1.38.
- VanDine, D.F., and Bovis, M., 2002, History and goals of Canadian debris-flow research. *Nat. Hazards*, v. 26, no. 1, 67–80, doi: 10.1023/A:1015220811211.
- Wang, F., Chen, X.Q., Chen, J.G., and You, Y., 2017, Experimental study on a debris-flow drainage channel with different types of energy dissipation baffles. *Eng. Geol.*, v. 220, 43–51, <https://doi.org/10.1016/j.enggeo.2017.01.014>.
- Wang, T., Chen, X.Q., Li, K., Chen, J.G., and You, Y., 2018, Experimental study of viscous debris flow characteristics in drainage channel with oblique symmetrical sills. *Eng. Geol.*, v. 233, 55–62, <https://doi.org/10.1016/j.enggeo.2017.11.024>.
- Wang, Z.Y., Qi, L.J., and Wang, X.Z., 2012, A prototype experiment of debris flow control with energy dissipation structures. *Nat. Hazards*, v. 60, 971–989, doi: <https://doi.org/10.1007/s11069-011-9878-5>.
- Wang, Z.Y., Qi, L.J., and Wang, X.Z., 2013, Debris flow control with energy dissipation structures-experiences from Wenjiagou. *J. Hydraul. Eng.*, v. 43, no. 3, 253–263. (in Chinese).
- You, Y., Pan, H.L., Liu, J.F., and Ou, G.Q., 2011, The optimal cross-section design of the ‘Trapezoid-V’ shaped drainage channel of viscous debris flow. *J. Mt. Sci.*, v.8, 103–107, doi: 10.1007/s11629-011-1023-0.
- Zhang, N., and Matsushima, T., 2018, Numerical investigation of debris materials prior to debris flow hazards using satellite images. *Geomorphology*, v. 308, 54–63, <https://doi.org/10.1016/j.geomorph.2018.02.008>.
- Zhang, S., and Zhang, L.M., 2017, Impact of the 2008 Wenchuan earthquake in China on subsequent long-term debris flow activities in the epicentral area. *Geomorphology*, v. 276, 86–103, <http://dx.doi.org/10.1016/j.geomorph.2016.10.009>.
- Zhou, J.W., Cui, P., Yang, X.G., Su, Z.M., and Guo, X.J., 2013, Debris flows introduced in landslide deposits under rainfall conditions: The case of Wenjiagou gully. *J. Mt. Sci.*, v.10, no. 2: 249–260, doi: <https://doi.org/10.1007/s11629-013-2492-0>.

Roles of barrier location for effective debris-flow mitigation: assessment using DAN3D

Shin-Kyu Choi^a, Tae-Hyuk Kwon^{a,*}, Seung-Rae Lee^a, and Joon-Young Park^b

^a*Dept. of Civil and Environmental Engineering, Korea Advanced Institute of Science and Technology, 291 Daehak-ro, Daejeon 305701, KOREA*

^b*Geo-Environmental Hazards Research Center, Korea Institute of Geoscience and Mineral Resources, 124 Gwahak-ro, Daejeon 34132, KOREA*

Abstract

Debris flows can travel at rapid velocities and can cause economic and societal damages. Accordingly, barriers that can dissipate the energy of debris flows are frequently installed as a mitigation measure. However, the effect of barriers on debris-flow behavior is not fully understood. In this study, we used DAN3D to investigate the interactions between a debris flow and barriers, and evaluate the effect of barrier location on debris-flow velocity and volume. We chose a study site in Seoul, Korea, where a debris-flow event occurred in 2011. At the site, we numerically installed a closed-type barrier at four different locations along the flow path in the watershed. We then simulated the debris flow while monitoring debris-flow velocity and volume. The barriers decreased the velocity and volume of the debris flow compared to a simulation with no barrier. In particular, installation of the barrier at the upstream portions of watersheds resulted in the greatest reduction in velocity. Installation of the barrier at downstream portions of watersheds resulted in the greatest deposition of volume. These results contribute to a better understanding of debris-flow behavior associated with the installed barriers as a mitigation measure, and can be used for optimum and efficient design of the debris-flow barriers.

Debris flows; Debris-flow barrier; Location; Velocity; Volume; Entrainment

1. Introduction

Recently, damage caused by landslides has increased due to heavy rainfall. Debris flows, a flow-like type of landslides can travel at extremely rapid velocities and entrain basal channel materials with scouring. Installing debris-flow barriers that can dissipate the energy of debris flows is one of the frequently used methods for preventing damages.

Many researches have conducted small-scale experiments to verify the effect of debris-flow barriers (Wenbing and Guoqiang, 2006; Lim et al., 2008; Takahara and Matsumura, 2008; Canelli et al., 2012; Kim et al., 2013; Xie et al., 2014; Ng et al., 2015; Choi et al. 2018). Also, research on flow patterns of debris flows using numerical analysis has been carried out (Remaître et al., 2008; Kwan et al., 2014), but only a little research has been done on analyzing the influence debris-flow barriers on debris-flow characteristics (Remaître et al., 2008; Jeong et al., 2015). Therefore, there is a need for research on this topic.

In this study, we explored the influence of a debris-flow barrier on characteristics of a debris flow that occurred during heavy rainfall in Woomyeon Mountain, Korea in 2011. A closed-type barrier that traps all of the debris-flow sediment and water was numerically installed separately at four locations along the debris-flow channel, and 2011 debris flow was then simulated. The effect of the closed-type barrier on characteristics of the debris flow was evaluated with respect to velocity and volume. In all cases, the closed-type barrier significantly reduced velocity and volume compared to the 2011 debris flow without the barrier. Our results contribute to a better understanding of debris-flow behavior associated with installed barriers as a mitigation measure, and can be used to determine an optimum and efficient design for debris-flow barriers.

* Corresponding author e-mail address: t.kwon@kaist.ac.kr

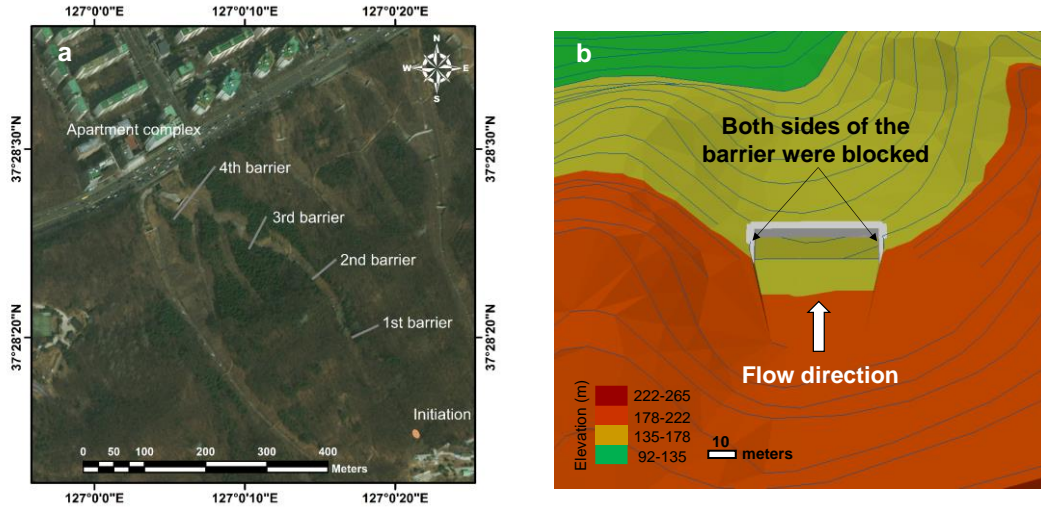


Fig. 1. (a) Locations of the numerical barriers and debris-flow initiation area; (b) Schematic description of barrier installation

2. Numerical code

2.1. Governing equation

DAN3D (Dynamic Analysis of Landslides in Three Dimensions; McDougall and Hungr, 2004, 2005) is a commercially available code that simulates the flow dynamics of viscous, liquid-like debris. This numerical code is based on a smoothed particle hydrodynamics (SPH) method that was first developed by Hungr (1995). Changes in a complex 3D terrain cause non-hydrostatic, anisotropic internal stresses, which strongly affect landslide dynamics. The governing equations of DAN3D are composed of mass conservation equation and momentum conservation equations.

$$\frac{\partial h}{\partial t} + h \left(\frac{\partial v_x}{\partial x} + \frac{\partial v_y}{\partial y} \right) = \frac{\partial b}{\partial t} \quad (1)$$

$$\rho h \frac{\partial v_x}{\partial t} = \rho h g_x + k_x \sigma_z \left(-\frac{\partial h}{\partial x} \right) + k_{yx} \sigma_z \left(-\frac{\partial h}{\partial y} \right) + \tau_{zx} - \rho v_x \frac{\partial b}{\partial t} \quad (2)$$

$$\rho h \frac{\partial v_y}{\partial t} = \rho h g_y + k_y \sigma_z \left(-\frac{\partial h}{\partial y} \right) + k_{xy} \sigma_z \left(-\frac{\partial h}{\partial x} \right) + \tau_{zy} - \rho v_y \frac{\partial b}{\partial t} \quad (3)$$

Where, h is the bed-normal flow depth, ρ is the material bulk density, t is time, v is flow velocity, b is the bed-normal erosion-entrainment depth, g is the acceleration due to gravity, k is the stress coefficients.

DAN3D simulates the local divergence (or convergence) of landslides flowing over complex 3D topography by using Rankine's earth-pressure theory (Rankine, 1857). The DAN3D code can incorporate the increase in debris-flow volume based on the effect of momentum transfer between the main flow and the bed materials, assuming that the exponential growth in volume is correlated with the displacement of the debris flow. This code can utilize any of five different rheology models: Newtonian, Plastic, Bingham, Frictional, or Voellmy.

2.2. Rheological model

The volume increases due to entrainment phenomenon at the bottom of the channel can be considered with erosion rate and the flow characteristics (velocity and deposition) can be controlled by the rheological models. Among the rheology models, many researchers have used the Voellmy model for analysis of the debris flows. The voellmy model was originally developed to analysis snow avalanches (Voellmy, 1955; McDougall, 2017). However, the model began

to be used for landslide analyses because ranges in the velocity and thickness of snow avalanches are similar to landslides (Korner, 1976; McDougall, 2017). The Voellmy model requires frictional and turbulence coefficient values as input parameters. The frictional coefficient is related to the deposition characteristics of debris flows, and the turbulence parameter is related to the velocity of debris flows (McDougall, 2017). For debris flows, the frictional coefficient previously used was in the range of 0 to 0.3 and the turbulence parameter was in the range of 0 to 1000 m/s². Most debris flows in Korea have extremely rapid velocity (measured maximum velocity was 28 m/s) due to high water content from heavy rainfall. In order to satisfy these high-velocity characteristics, a low frictional coefficient and a high turbulence parameter were used in this study.

3. Case study

3.1. Research area

The study area was Mt. Woomyeon, located in Seoul, South Korea. Mt. Woomyeon has a maximum elevation of 293 m above sea level and is surrounded by buildings and roads within an area of 5,104,162 m² (Park, 2014). Korean Society of Civil Engineers (KSCE) reported that 33 debris flows occurred from ~150 landslides on July 26–27, 2011. The estimated financial loss was approximately US\$15 million, with sixteen lives lost (KSCE, 2012).

One of the debris-flow events occurred in the Sindonga watershed, Mt. Woomyeon was chosen for this study. This event has been previously investigated by KSCE (2012). For the Sindonga debris flow case, the watershed area, runoff length, average slope angle of the channel were 214,400 m², 633.6 m, and 17.5°, respectively. The event consisted of three debris flow that coalesced in the main watershed channel and had a total combined volume of 45000 m³. All input parameters used for the back-analysis were based on the field investigation (KSCE, 2012). The debris flow reproduced by the back-analysis had the frictional coefficient of 0.03, the turbulence parameter of 800 m/s² and the erosion rate of 0.0078 m⁻¹. A debris flow that flowed out to the Sindonga apartment complex was selected as a reference case (Case REF) for numerical modeling in this study (Fig. 1a).

3.2. Condition of debris flow barriers

The effect of location of barrier installation was examined numerically. The distance (L) between the debris source and the roadway near to the Sindonga apartment was 596 m (Fig. 1a). Four locations along the debris-flow channel were determined; thereby, a barrier was placed at 0.3L (i.e., 179 m far from the debris source; Case 1), 0.5L (i.e., 298 m far from the debris source; Case 2), 0.7L (i.e., 417 m far from the debris source; Case 3), or 0.9L (i.e., 537 m far from the debris source; Case 4). The barriers were created by numerically increasing elevation values in the topography file to achieve the desired shape and size using ArcGIS 10.5 (Fig. 1b). The barrier was installed to be perpendicular to the debris flow direction. The barrier width was determined to be two times wider than the width of the front part of the reference debris flow occurred in 2011; it resulted in 48 m wide (Case 1), 50 m wide (Case 2), 60 m wide (Case 3), and 110 m wide (Case 4). The height and thickness of all barriers were set to be 7 m and 3 m, respectively (Table 1). Surface erosion near the barrier was prevented by setting the no erosion zone which was 50 m long and 50 m wide in the upstream and downstream sides of the barrier. Total five simulations, one without the barrier (or reference case; REF) and four with the barrier (Cases 1-to-4), were conducted, as shown in Table 1.

4. Results

Figure 2a shows temporal changes in velocities of the modeled debris flow with respect to the barrier locations, respectively. Herein, as the SPH method was used, the velocity of moving debris flows was determined from the average velocity of all moving particles. When any overflow was observed in some cases, the velocity represented the average velocity of the overflowed particles. The results indicate that debris-flow velocity gradually increased to approximately 7 m/s due to the steep slope angle in the upper part of the flow path, then gradually decreased as the debris flowed downslope. Each time that the debris collided with a barrier, the velocity decreased over time compared to the actual debris flow. Particularly, debris flows were not transferred to downstream in Case 1. In Case 4, debris flows were almost entirely deposited and only about 131 m³ of material was transferred to downstream locations. Immediately after the collision of barriers, velocities decreased to zero in the front part, but debris flows continuously come in. When volume of debris flows exceeded allowable deposition of the barrier, overflow was generated and velocities increased as it passed downstream due to the steep slope. This tendency occurred frequently in the

downstream locations because volume of the debris flow grow further by entrainment to the downstream. In Cases 2 and 3, the overflowed debris slightly gained their velocities, mainly due to the steep slope after the barriers, and their volumes also increased due to the entrainment as those flowed downslope along the flow path. If there was no entrainment effect, the overflowed volume is expected to stay constant while the velocity is primarily determined by the slope of the channel.

Table 1. Barrier conditions

Case name	Number of barriers	Width of the reference debris flow (m)	Width of the barrier (m)	Height of the barrier (m)	Thickness of the barrier (m)	Distance from the source (m)
1	1	24	48	5	3	179
2		25	50			298
3		30	60			417
4		55	110			537
REF	0			-		

Figure 2b shows the volume of the moving segments (or particles). The debris reached a volume of 4100 m³ as it approached the downstream roadway at 85 s in Case REF. Upon the barrier installation, the debris volume was significantly reduced to less than 1000 m³ in all cases with the barrier. As the debris overflowed the barrier in Cases 2, 3, and 4, the volume slightly increased.

Toward the downstream area, the barrier became huge because of the increased debris volume and the widened channel width. The volume of the deposited debris (e.g., 200 m³ for Case 1, 600 m³ for Case 2, 1200 m³ for Case 3, and 2800 m³ for Case 4) progressively increased as the barrier location became more distant from the source area. These results implies that it is better to install a barrier near the source location, if it is predictable, before the debris grow further by entrainment. However, it is a daunting task to predict the source location, and thus, either multiple barriers along a debris flow channel or one gigantic barrier at the downstream is expectedly required, when the large-scale debris flow is predicted.

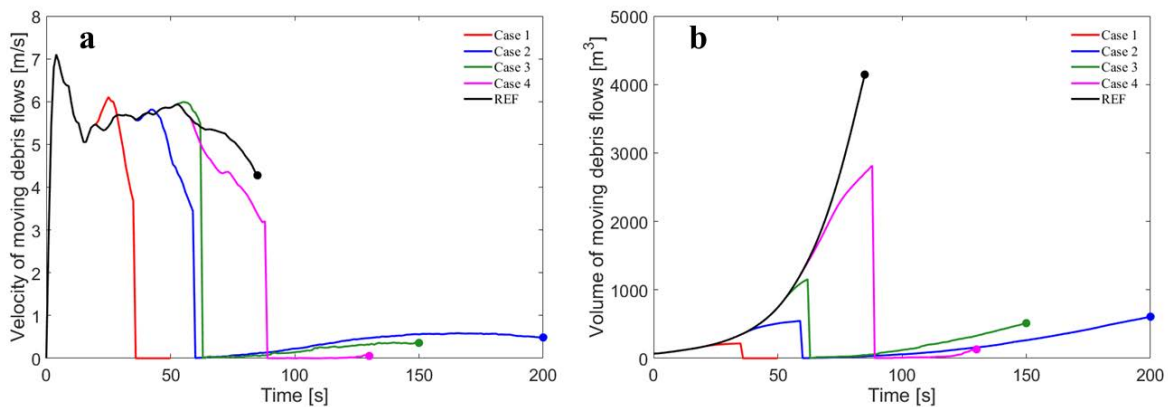


Fig. 2. (a) Changes of the average velocity; (b) Distribution of the volume of moving debris flows. Dots indicate the time of access to the village

5. Conclusion

The effects that barrier locations along a channel have on debris-flow behavior have been explored using the DAN3D numerical code. Temporal changes in debris-flow velocity and volume were observed for scenarios with and without barriers. The velocity of the debris flow significantly decreased at barriers and small volume (< 600 m³ in Case 4) of the debris flow was transferred to downstream locations. After collision with the barrier, the velocity of the overflowed debris flow increased again due to the steep slope after the barrier. Our work shows that it is possible to

prevent debris flows from being transferred downstream by installing one barrier in a proper location when the scale of debris flow is small ($< 200 \text{ m}^3$ in Case 1). Because volume of debris flows around the source and the width of the channel are small, the debris flow can be adequately blocked by small-sized barrier. However, it is difficult to install due to problems with the access road. Large-sized barrier should be installed because the volume increases by entrainment and the width of the channel grows as progressed downstream. For this reason, optimum location is required. These results can be used for optimum and efficient design of the debris-flow barriers.

Acknowledgements

This research was supported by the (BRL, Basic Research Laboratory) Program through the National Research Foundation of Korea (NRF) funded by the MSIT (NRF-2018R1A4A1025765).

References

- Canelli, L., Ferrero, A. M., Migliazza, M., and Segalini, A., 2012, Debris flow risk mitigation by the means of rigid and flexible barriers-experimental tests and impact analysis. *Natural Hazards and Earth System Sciences*, v. 12, n.5, p. 1693.
- Hungr, O., 1995, A model for the runout analysis of rapid flow slides, debris flows, and avalanches. *Canadian Geotechnical Journal*, v. 32, n. 4, p. 610–623.
- Jeong, S. S., Lee, K. W., and Ko, J. Y., 2015, A study on the 3D analysis of debris flow based on large deformation technique (Coupled Eulerian-Lagrangian). *Journal of the Korean Geotechnical Society*, v. 31, n. 12, p. 45–57.
- Kim, Y., Nakagawa, H., Kawaike, K., and Zhang, H., 2013, Study on Characteristic Analysis of Closed-type Sabo Dam with a Flap due to Dynamic Force of Debris Flow. *Annals of the Disaster Prevention Research Institute, Kyoto University*, n. 56.
- Korean Society of Civil Engineers, 2012, Research contract report: causes survey and restoration work of Mt. Woomyeon landslide. Korean Society of Civil Engineers.
- Körner, H.J. 1976, Reichweite und Geschwindigkeit von Bergstürzen und Flieβschneelawinen. *Rock Mechanics*, v. 8, p. 225–256.
- Kwan, J. S. H., Chan, S. L., Cheuk, J. C. Y., and Koo, R. C. H., 2014, A case study on an open hillside landslide impacting on a flexible rockfall barrier at Jordan Valley, Hong Kong. *Landslides*, v. 11, n. 6, p. 1037–1050.
- Lim, Y. H., Jeon, G. U., Kim, M. S., Yeom G. J., Lee, J. H., 2008, Capture effect of slit dam for debris flow and woody debris with hydraulic model experiment -Focusing on A and D type. In 2008 Summer conference of Korean Forest Society, Korean Forest Society, p. 343–344
- McDougall, S., and Hungr, O., 2004, A model for the analysis of rapid landslide motion across three-dimensional terrain. *Canadian Geotechnical Journal*, v. 41, n. 6, p. 1084–1097.
- McDougall, S., and Hungr, O., 2005, Dynamic modelling of entrainment in rapid landslides. *Canadian Geotechnical Journal*, v. 42, n. 5, p. 1437–1448.
- McDougall, S., 2016, 2014 Canadian Geotechnical Colloquium: Landslide runout analysis—current practice and challenges. *Canadian Geotechnical Journal*, v. 54, n. 5, p. 605–620.
- Ng, C. W., Choi, C. E., Song, D., Kwan, J. H. S., Koo, R. C. H., Shiu, H. Y. K., and Ho, K. K., 2015, Physical modeling of baffles influence on landslide debris mobility. *Landslides*, v. 12, n. 1, p. 1–18.
- Park, D. W., 2014, Simulation of landslides and debris flows at regional scale using coupled model. Master's Thesis, Korea Advanced Institute of Science and Technology, Daejeon, Republic of Korea.
- Rankine, W. M., 1857, On the stability of loose earth. *Philosophical Transactions of the Royal Society of London*, v. 147, p. 9–27.
- Remaître, A., Van Asch, T. W., Malet, J. P., and Maquaire, O., 2008, Influence of check dams on debris-flow run-out intensity. *Natural Hazards and Earth System Sciences*, v. 8, n. 6, p. 1403–1416.
- Takahara, T., and Matsumura, K., 2008, Experimental study of the sediment trap effect of steel grid-type sabo dams, *International Journal of Erosion Control Engineering*, v. 1, n. 2, p. 73–78
- Voellmy, A., 1955, Über die Zerstörungskraft von Lawinen. *Schweizerische Bauzeitung*, v. 73, p. 212–285.
- Wenbing, H., and Guoqiang, O., 2006, Efficiency of slit dam prevention against non-viscous debris flow, *Wuhan University Journal of Natural Sciences*, v. 11, n. 4, p. 865–869.
- Xie, T., Yang, H., Wei, F., Gardner, J. S., Dai, Z., and Xie, X., 2014, A new water-sediment separation structure for debris flow defense and its model test. *Bulletin of Engineering Geology and the Environment*, v. 73, n. 4, p. 947–958.

Scour and erosion experience with flexible debris-flow nets

Nadine Feiger^{a,*}, Corinna Wendeler^b

^a*Department of Civil, Environmental and Geomatic Engineering ETH Zurich, Stefano-Franscini-Platz 5, Zürich 8093, Switzerland*

^b*Geobrugg AG, Achstrasse 11, Romanshorn 8590, Switzerland*

Abstract

Flexible debris-flow nets were developed in the frame of a three-year PhD thesis by Wendeler in 2008. Since then, they have been used all over the world for debris-flow protection or slope/riverbed stabilization. Some of these installed flexible debris-flow nets have already been filled a couple of times and verified the developed load model. Nevertheless, depending on soil properties, most problems with debris-flow nets appear to be related to construction, such as channel flank erosion, which exposes anchors, or undermines supporting foundations. Both cases lead to instability of the entire system and to increased maintenance costs and should therefore be avoided. In this contribution, we present a service ability method for scour and erosion issues on flexible debris-flow nets. In this context, “service ability method” means a design tool that should help to suggest construction possibilities to avoid erosion problems along the barrier in order to guarantee a lifetime of more than 25 years. The results are based on an analysis of existing barriers to determine occurring scour and erosion problems. Hence, an approach to calculate scour and erosion length and depth respectively around the barrier construction is developed. To validate this approach, a debris-flow simulation with the software RAMMS, or equivalent software, is used. In terms of economic efficiency, different construction measures for riverbed and flank stabilization are analyzed and implemented into the service ability. This tool will help designers and planning engineers to design and calculate their debris-flow protection system in a more economic and safe way. Further, maintenance costs will be minimized and a longer lifetime of the entire barrier system, including the anchors as the most cost-intensive parts, can be provided. Since the project is still ongoing, the final design tool with its equations cannot yet be discussed in detail in the following paper.

"Keywords: Flexible ring net, Debris flow, Service ability"

1. Introduction

Floods, debris flows, and slope failures are the most common natural hazards in Switzerland. In inhabited areas, material and personal damages occur from time to time. Therefore, investigations about debris-flow dynamics and protective structures have been a research topic for many years (e.g. Böll, 1997; Bergmeister, 2009). To increase knowledge about debris-flow behavior, several small- to large-scale flume experiments were recently conducted (e.g. Weber, 2003; de Haas et al., 2015; Major, 1997) and described (e.g. Iverson, 1997; Kowalski, 2008) worldwide. Nowadays, various mitigation structures are available against natural hazards, but erosion around them is a notable problem.

One possible mitigation structure against debris flows is flexible ring nets. Until 2005, flexible nets were mainly used for rockfall barriers. Retained slides in these nets were observed, but there was no existing dimensioning concept which proved that these nets are capable of retaining large slides. As a result, real-scale experiments with flexible ring nets were performed at Illgraben test site in Switzerland between 2005 and 2008 (Wendeler, 2008). At least once per year a middle ($10'000 - 20'000\text{m}^3$) to large ($> 50'000\text{m}^3$) debris flow naturally occurs in the Illgraben and is suitable to test and improve flexible ring nets. Tests showed that a single barrier can retain debris-flow material until its retaining capacity is reached, depending on the channel geometry. Afterwards the material can overflow the barrier without damaging the system. Therefore, a so-called multi-level system, with several barriers in a row, can be planned and constructed. Such a multi-level system was tested at Hasliberg and Merdenson (Switzerland) (Wendeler et al., 2008).

* Corresponding author e-mail address: nadine_feiger@hotmail.com

Based on these tests, a dimensioning concept was developed by Wendeler (2008) and led with load distribution and simulation with the finite-element software FARO (Volkwein, 2004) to standardized flexible ring net barriers. Since then, flexible ring net barriers have been installed worldwide. Some of them have already been filled a couple of times. Experiences over the past ten years showed that most problems with ring nets appear to be related to construction, such as channel flank erosion, which exposes anchors or undermines supporting foundations.

We present an initial progress on developing a service ability method based on an analysis of existing barriers, 1:1 field test, an intermediate-scale flume experiment and a debris flow simulation with Rapid Mass Movement Simulation (RAMMS) (WSL Institute for Snow and Avalanche Research SLF) to help designers and planning engineers to design and calculate their debris flow protection systems in a more economic and safe way. Furthermore, the lifetime of these flexible net systems can be optimized by protecting them against erosion and scour processes.

2. Study site and data

To develop an appropriate service ability method, scour and erosion problems on existing flexible ring nets have been analyzed. The main database provides 80 installed flexible ring net barriers in Switzerland since 2005 by Geobruigg AG. Few debris-flow events occurred in Switzerland since then, and therefore, data from filled barriers in Italy, Spain and Peru were additionally used. All installed flexible ring nets in Switzerland will be found on Geobruigg's web page with information about installation year, barrier type, occurred events and problems beginning in May 2019.

Calculation of possible erosion scenarios are based on commonly used equations in river and hydraulic engineering. Developed erosion scenarios are validated by new erosion data collected in an intermediate-scale flume experiment in 2018/2019. Within the same data set, behavior of a slope stabilization mesh (TECCO[®]) as erosion protection was tested. In addition, 1:1 field data with slope stabilization meshes are collected at Illgraben, Switzerland from December 2018 until June 2019. Experimental small-scale data from (Speerli, 2009), large-scale data from (Bugnion et al., 2012) and observations at Illgraben by WSL were used for comparison. Further data were required to simulate and verify the developed service ability with the Rapid Mass Movement Simulation (RAMMS) debris-flow module. These included (a) a digital elevation model (DEM), (b) a hydrograph or (c) a release area.

3. Methods

To develop a service ability concept, major problems have to be identified and their corresponding solutions designed. First, erosion in a mountain torrent can be triggered by a debris-flow event or normal water flow, for example due to rain. The design should cover both cases. Second, important parameters such as channel geometry, barrier type, soil properties and soil mechanical properties must be detected. Hence, possible scour areas related to flexible ring net barriers were identified upstream and downstream of a barrier construction (Fig. 1). In practice, a barrier overflow can lead to erosion and scours downstream of the barrier (Fig. 1c), whereas a construction post behaves as a pile scour and can lead to undermining of the foundation (Fig. 1d). In case of the barrier filling process or depending on the flow depth, flank erosion occurs at the anchors (Fig. 1a).

To quantify these erosion and scours, different calculation formulas can be found in the literature. However, none of them are directly suitable for mountain torrents. To verify an appropriate approach, 1:1 field test (Section 3.1) and an intermediate-scale flume experiment was conducted (Section 3.2). Comparison with experimental data by Speerli (2009), Bugnion (2012), natural Illgraben events and RAMMS simulation led to the final design.

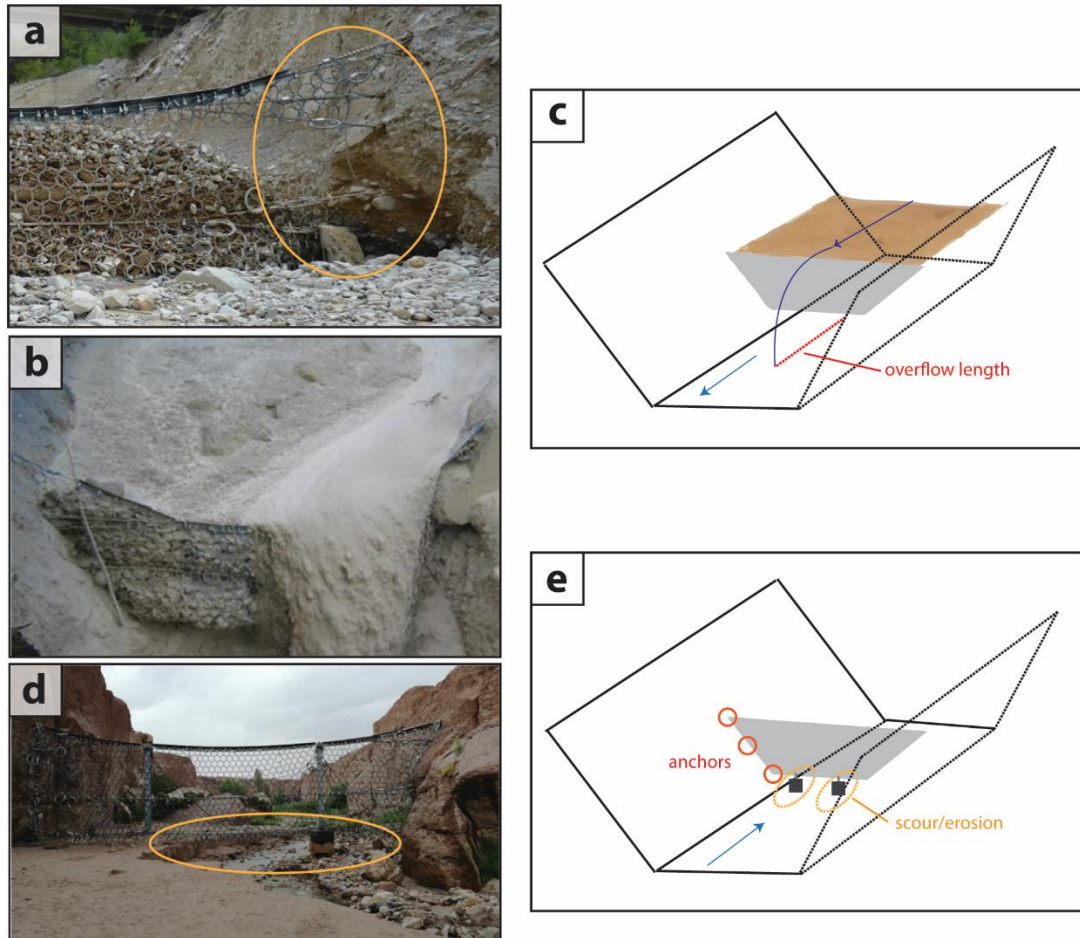


Fig. 1. Examples of erosion/scour problems on flexible ring net and schematic overview. (a) Eroded anchors; (b) Filled barrier with an overflow; (c) schematic overview of erosion problem in case of an overflow; (d) undermined foundations due to riverbed erosion; (e) Schematic overview upstream erosion problem of the barrier (anchors due to flank erosion, and foundation due to riverbed erosion).

3.1. 1:1 field installation

In rivers, riprap or concrete bolts are commonly used for erosion protection; however, a slope stabilization mesh with or without a geotextile layer is another possible option. There are no data or experiences of such a mesh in a mountain torrent. To evaluate the effectiveness of stabilization mesh on erosion control, a Geobrug AG slope stabilization mesh was installed at Illgraben (Switzerland) from December 2018 until June 2019 (Fig. 2). Two different mesh types G65/3 and G45/2 were chosen and installed. One only the mesh and one with the corresponding geotextile. In total, four meshes with a 3.9 m width were anchored with ramming nails (Fig. 2a and 2b). Based on the torrent topography, it was not possible to install the mesh in the middle of the torrent bed as well as to cover the mesh edges by a rope (Fig. 2a and 2b). In general, the mesh is anchored by a raster system and on all edges by a top, bottom and lateral boundary rope to fix the mesh as tightly as possible onto the slope (Fig. 2c).

Erosion and mesh behavior were observed by a time series of pictures, which were mostly taken after rain events. After a significant event, estimation of acting shear force (τ) was carried out by a RAMMS simulation and calculation according to Equation 1:

$$\tau = \rho \cdot g \cdot h \cdot J \quad (1)$$

where ρ = density, g = gravitational acceleration, h = flow depth, and J = channel inclination.

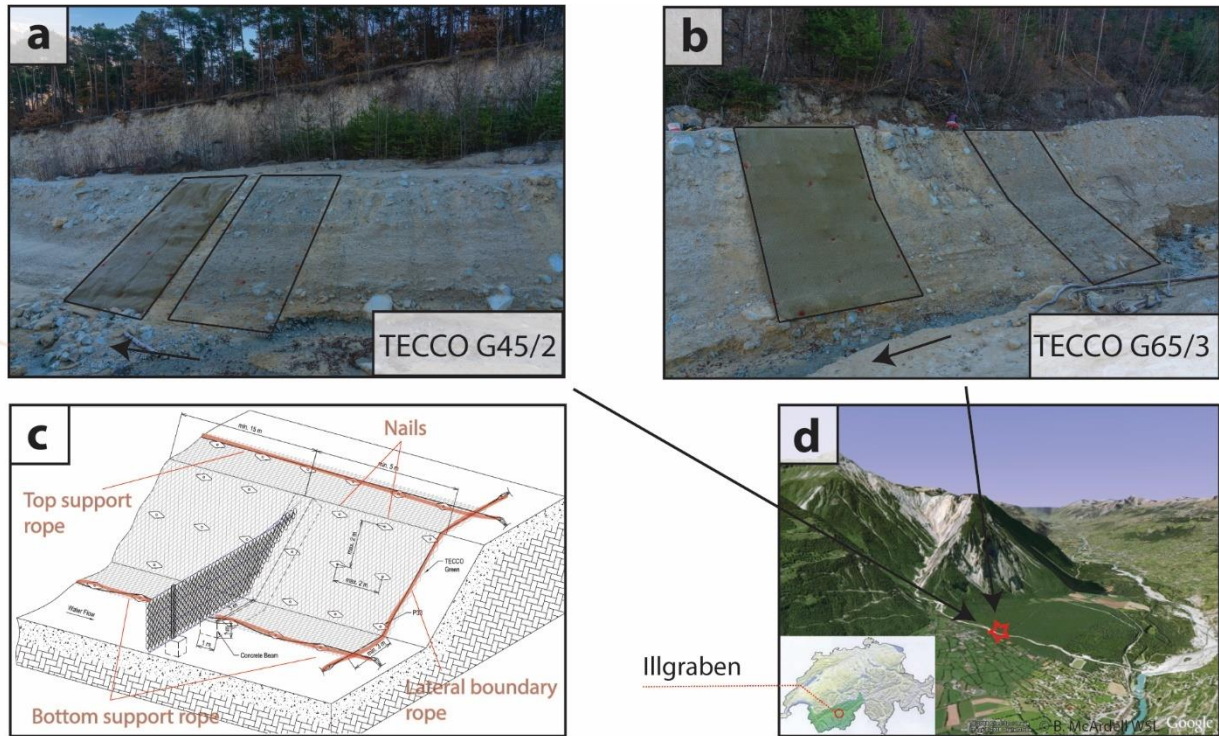


Fig. 2. (a) TECCO G45/2 with TECMAT (brown) and without (grey); (b) TECCO G65/3 with TECMAT (brown) and without (grey), Arrow indicates flow direction; (c) Schematic TECCO erosion protection (d) Study site overview.

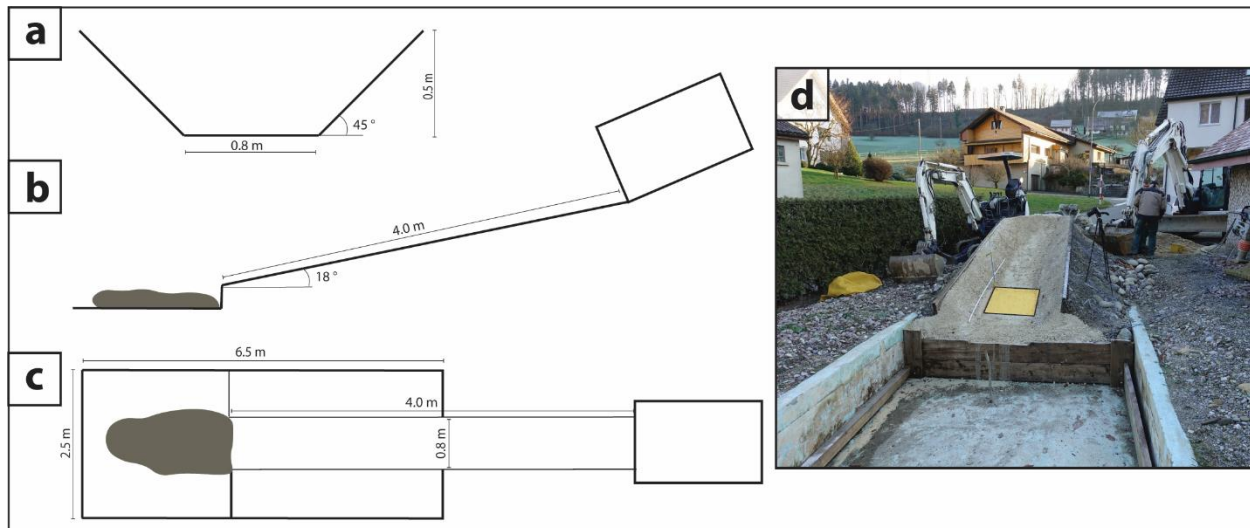


Fig. 3. Schematic flume experiment view. (a) Channel cross section; (b) Side view; (c) Plan view; (d) Flume with force plate (yellow).

3.2. Flume experiment

To obtain data on overflow length - distance from the net to the impact of the discharge jet - (Fig. 1c), shear force, and erosion behavior of a slope stabilization mesh, an intermediate-scale flume was constructed as shown in Fig. 3. Flume geometry was determined by the available space and to be on a scale of around 1:10 to 1:15 (Fig. 3a-c). No laser sensors were available, therefore, flow velocity (u) and flow depth (h) were estimated by a high-speed camera. Shear (τ) and pressure force (N) were measured with a force plate (Fig. 3d), which was already used by Bugnion

(2012). The shear and force plates were calibrated and sampled at a rate of 1 kHz. One flume flank is covered with the slope stabilization mesh (G45/2). The used slope material was taken from the Illgraben. The original Illgraben material was used for the debris-flow mud mixture. The release of smaller mud mixture amount (0.05-0.2 m³) was done by an excavator shovel, and larger amounts by a concrete mixer.

In the first experiment series, different material volumes were released to identify the relation between measured shear force and Froude numbers (Fr). During that, erosion underneath the slope stabilization mesh was observed with images. In a second experiment series, overflow length of flows past a ring net barrier that was installed in the flume 2.5 meters downstream of the release point were evaluated. In these experiments, a single debris-flow release filled the net. Additional flows were released and the length of overflow past the net was measured.

Collected shear force data were transformed from kg into kN/m^2 and for each experiment its Froude number (Fr) was calculated according to Equation 2:

$$Fr = \frac{u}{\sqrt{g \frac{A}{b}}} \quad (2)$$

where u = flow velocity, g = gravitational acceleration, A = cross-sectional area, and b = water level width.

To be able to compare our measured shear forces with the measurements made at different scales by Bugnion (2012) and measured at Illgraben (McArdell, 2016), the shear stress is converted to be a dimensionless number alpha (α) as shown in Equation 3:

$$\alpha = \frac{\tau_{characteristic}}{\frac{\tau_{measured}}{\mu}} = \frac{\frac{u}{h}}{\frac{\tau_{measured}}{\mu}} \quad (3)$$

where τ_{char} = characteristic shear force defined as u/h = flow velocity over flow depth (shear rate), $\tau_{measured}$ = measured shear force, and μ = viscosity.

Overflow length (Fig. 1c) calculation was done according to Equations 4-6 for each overflow event, as well as for existing data from Speerli (2009) and video recorded Illgraben events. Calculated lengths were then compared with the measured ones in the experiment. The most fulfilling equations were used for the design tool to determine the overflow length.

Equation 4 is used for dimensioning stilling basin length (Bergmeister, 2009):

$$L_T = (u + \sqrt{2 \cdot g \cdot h}) \cdot \sqrt{\frac{H}{g}} + h \quad (4)$$

where L_T = stilling basin length, u = flow velocity, g = gravitational acceleration, h = flow depth, and H = construction height.

Equation 5 determines the overflow length based on the trajectory parabola with inclination:

$$L_P = (H + h) \cdot \tan(\alpha) + u \sqrt{\frac{2(H+h)}{g \cdot \cos(\alpha)}} \quad (5)$$

where L_P = trajectory length, α = slope inclination, g = gravitational acceleration, h = flow depth, and H = construction height.

Equation 6 is used to calculate hydraulic jump length for inclined channels (Jirka et al., 2009):

$$L_w = (6.1 + 4.0 J) \cdot h_2 \quad (6)$$

where L_w = hydraulic jump length, J = channel inclination, h_2 = flow depth downstream the barrier and $h_2 = \frac{h_1}{2} (\sqrt{1 + 8 Fr^2} - 1)$ with h_1 = flow depth upstream the barrier, and Fr = Froude number.

Further, other equations can be found in literature such as from Smetana, Rouse, and others (Bollich, 2013) that are used for stilling basin length dimensioning. All of them are based on an empirical number and the h_2 term. Therefore, an empirical number was determined for the taken flume experiment data to improve the equation.

3.3. Service ability design

The service ability design works as a decision-making tool (Fig. 4). First, parameters, such as channel geometry, barrier type, soil properties and soil mechanical properties are added. Based on this input information and the most suitable equation identified in Section 3.2, a recommendation according to erosion can be made. Based on that a possible mitigation system (slope stabilization mesh, concrete bolts, riprap or a combination of them) can be suggested to ensure a long lifetime of the barrier.

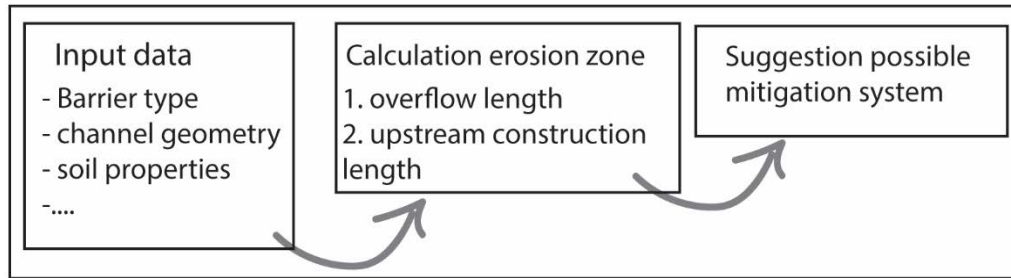


Fig. 4. Schematic overview of service ability tool.

4. Results and Discussion

Since the project is still ongoing, some first results will be presented here. Note that they are not completed yet.

4.1. Field observation

Two weeks after slope stabilization mesh installation (3 December 2018) either a debris flow or flood event with significant sediment transport occurred at Illgraben. Unfortunately, all installed observation measurement devices (geophones, laser sensor etc.) from WSL (Swiss Federal Institute for Forest, Snow and Landscape Research) were not operating in December 2018. Figure 5 shows the slope stabilization meshes after the event. Flow depth is clearly visible, as well as erosion on the upstream and downstream side of the mesh. Upstream side mesh erosion could be expected due to the lack of a lateral boundary rope and the fact that the mesh is not as tight to the slope as it normally is when it gets anchored. However, ramming nails were not displaced by the event.

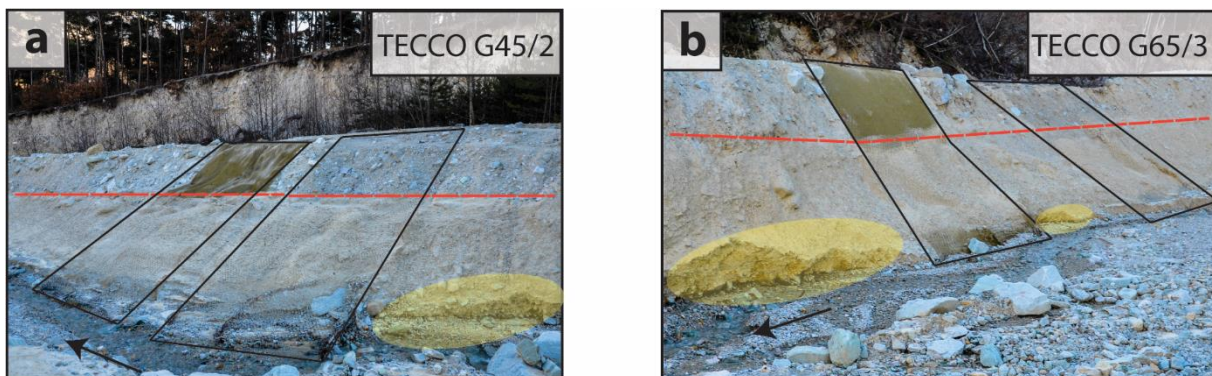


Fig. 5. Installed slope stabilization mesh (rectangular) after debris flow event of 3 December 2018. Red dashed line shows flow depth, yellow ellipse indicates erosion up- and downstream the mesh. Flow direction is indicated by the arrow.

Table 1 shows calculated shear force for the event on 3 December 2018 based on Equation 1, for granular flow as well as mud flow at two Illgraben locations. One at the mesh location with $J=0.05$, $h=3$ m and the other at the measurement device location with $J=0.09$, $h=1.5$ m. Comparison with 2006 recorded data, one can assume that the event was approximately the size of $10'000-18'000\text{m}^3$. A comparison with a RAMMS simulation is ongoing.

Table 1. Shear force results at Illgraben.

	Shear force (kN/m^2) mesh location	Shear force (kN/m^2) measurement device location
Granular flow ($\rho=2150 \text{ kg/m}^3$)	3.2	2.8
Mud flow ($\rho=1900 \text{ kg/m}^3$)	2.8	2.5

4.2. Flume experiment

Reliable overflow length determination based on actual overflow events at Illgraben is almost impossible. Some overflow events are larger than the recorded video section. Therefore, one can only approximately say the overflow is larger than ten meters or smaller than ten meters. However, a first overflow length estimation based on recorded videos from Speerli (2009) experiments can be done as well as from our first flume experiments. Besides, overflow length according to Equation 4-6 can be calculated for this data as well as for Smetana. Percentage deviation for each trial from the calculated value (trajectory parabola with inclination, stilling basin, hydraulic jump, and Smetana) are shown in Figure 6. Trial 1-5 are data from Speerli (2009) and 6-15 from realized flume experiments.

As expected, the length results for the stilling basin (orange dots) underestimate the measured results due to the lack of a slope correction factor within the equation. The trajectory parabola (blue dots) fluctuates around the measured values and has the lowest deviation from measured lengths. The expectation was that the hydraulic jump (green dots) would deviate most. The equation according to Smetana ($L_S = 3 \cdot (\sqrt{1 + 8Fr_1^2} - 3)$) (yellow dots) is basically the hydraulic jump with additional empirical values and one can see that it already deviates less. However, all of these equations have their limitations and are designed for water. Since all of them depend on the flow depth, flow velocity and hence, the Froude number, a sensitivity analysis was conducted (not shown in this paper). So far one can state that the flow depth uncertainty with respect to measurement error does not account as much as the velocity for the deviation from the measured value. To identify the optimal domain to use the equation, the results for each equation will be correlated with the Froude number. Consequently, the equations to use for the service ability tool will result out of that analysis. These results will be presented at the presentation.

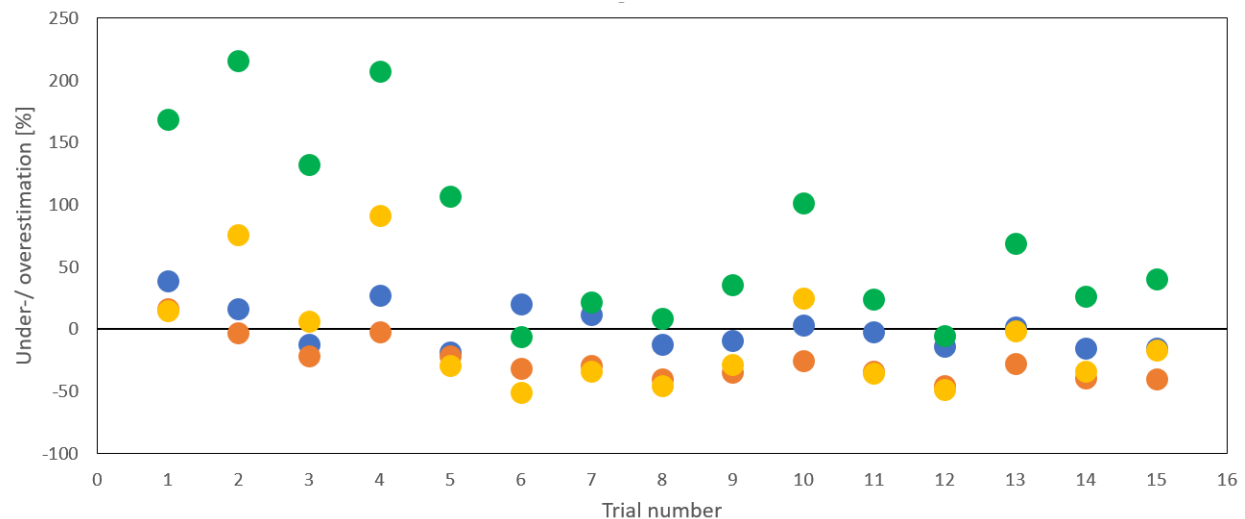


Fig. 6. Percentage deviation from measured Trial (zero line) to calculated trajectory parabola with inclination (blue), stilling basin (orange), hydraulic jump (green), and Smetana (yellow).

Some first results of dimensionless numbers (α) and Froude number (Fr) were calculated from available Illgraben data. The regression indicates a quadratic behavior, but a final statement cannot be made, since the results from the flume experiments are not fully analyzed.

5. Conclusion and Outlook

So far, no finalized conclusion can be made. The 1:1 field installation is under observation and during the winter months no significant event is expected. RAMMS simulation of the observed event is running. Flume experiments to determine overflow length are completed and shear force experiments are ongoing. Afterwards, interpretation of the data will allow the determination of equations to describe a lower and upper bound for the construction length. Measured shear forces will be analyzed and compared with the measured Illgraben data. Finally, the service ability design can be programmed and tested. The tool will be presented at the presentation.

The eventual creation of the tool describes an overall start for guidelines and help to design a sustainable flexible ring net barrier. Further tests, experiments and especially experience are necessary to improve service ability on flexible ring net barriers.

Acknowledgements

This project was done within a master thesis frame at the Swiss Federal Institute of Technology in Zurich, Switzerland (ETHZ) in collaboration with Geobru gg AG, Switzerland. A grateful acknowledgement to Geobru gg AG for the opportunity to realize such a project and for all the assistance and helpful discussions. Especially, A. Lanter, S. Karrer and R. Wyss for helping in the field. Thanks to B. McArde ll for sharing Illgraben knowledge and data from Swiss Federal Institute for Forest, Snow and Landscape Research (WSL).

References

- Bergmeister, K., 2009, Schutzbauwerke gegen Wildbachgefahren: Grundlagen, Entwurf und Bemessung, Beispiele: John Wiley and Sons, 121 p.
- Bollrich, G., 2013, Technische Hydromechanik 1: Grundlagen, Berlin: Beuth Verlag GmbH, 289.
- Böll, A., 1997, Wildbach- und Hangverbau: Berichte der Eidgenössischen Forschungsanstalt für Wald, Schnee und Landschaft, Nr. 343.
- Bugnion, L., McArde ll, B. W., Bartelt, P., and Wendeler, C., 2012, Measurements of hillslope debris flow impact pressure on obstacles: Landslides, v 9(2), p. 179-187, doi: 10.1007/s10346-011-0294-4.
- Haas, T., Braat, L., Leuven, J. R., Lokhorst, I. R., and Kleinhans, M. G., 2015, Effects of debris flow composition on runout, depositional mechanisms, and deposit morphology in laboratory experiments. Journal of Geophysical Research: Earth Surface, p. 1949-1972, doi: 10.1002/2015JF003525.
- Iverson, R. M., 1997, The physics of debris flows. Reviews of geophysics, p. 245-296.
- Jirka, G. H., and Lang, C., 2009, Einführung in die Gerinnehydraulik. Karlsruhe: Universitätsverlag Karlsruhe, 69 p.
- Kowalski, J., 2008, Two-phase modeling of debris flows [Ph.D. thesis]: Zurich, ETH Zurich.
- Major, J. J., 1997, Depositional Processes in Large-Scale Debris-Flow Experiments: The Journal of Geology, p. 345-366, doi: 10.1086/515930.
- McArde ll, B. W., 2016, Field Measurements of Forces in Debris Flows at the Illgraben: Implications for Channel-Bed Erosion: International Journal of Erosion Control Engineering, p. 194-198, doi: 10.13101/ijece.9.194.
- Speerli, J., 2009, Murgang Modellierung. Rapperswil: Institut für Bau und Umwelt (unpublished).
- Volkwein, A., 2004, Flexible Murgangbarrieren: Bemessung und Verwendung. Birmensdorf: Berichte der Eidgenössischen Forschungsanstalt für Wald, Schnee und Landschaft, v. 8.
- Weber, D., 2003, Untersuchungen zum Fliess- und Erosionsverhalten granularer Murgänge [Ph.D. thesis]: Zurich, ETH Zurich.
- Wendeler, C. S., 2008, Murgangrückhalt in Wildbächen: Grundlagen zu Planung und Berechnung von flexiblen Barrieren [Ph.D. thesis]: Zurich, ETH Zurich.
- Wendeler, C., Volkwein, A., Roth, A., Herzog, B., Hahlen, N., and Wenger, M., 2008, Hazard prevention using flexible multi-level debris flow barrier, on Proceedings, Interpraevent, 11th, Dornbirn: Voralberg, Austria, p. 547-554.

Steel stakes to capture woody debris on an impermeable Sabo-type dam

Norio Harada^{a,*} and Yoshifumi Satofuka^b

^aMitsui Consultants Co., Ltd., 1-2-1, 1000, Benten Minatoku Osaka, 552-0007, Japan

^bRitsumeikan University, 1-1-1 Noji-higashi, Kusatu-city, Shiga, 525-8577, Japan

Abstract

It is important to capture driftwood, namely, woody debris, in upstream areas to prevent debris flows from blocking downstream bridges. Specific details of the conditions of dams in Japan must be taken into consideration when investigating this issue. There have been recent proposals to use steel stakes as countermeasures to woody debris blockage at impermeable Sabo-type dams. To design such a countermeasure effectively, it is necessary to clarify the woody debris capture mechanisms implemented by the countermeasure. We proposed a structure composed of steel stakes for use at impermeable Sabo-type dams. This proposal is based on experiments that take into consideration the rotation of woody debris at Sabo dams and the mechanism by which woody debris is captured at the stakes.

Keywords: Impermeable Sabo-type dam; woody debris; experiment; steel stake; debris flow

1. Introduction

There have been many reports of experiments and simulations (Ishikawa et al., 1989; Matsumura et al.; 1990; Doi et al., 1999; Horiguchi et al., 2015) to identify the mechanisms for capturing woody debris at open-type and impermeable Sabo-type dams, and thus prevent blockages by woody debris found beneath debris flows caused by land-slides (Taniguchi et al., 1999). The Japanese government has published newly revised design standards that require the installation of steel stakes at impermeable dams, to act as countermeasures against blockages caused by woody debris, as shown in Figure 1 (Japanese Government, 2016). The design standards have been updated in this manner because the current countermeasures are not effective at impermeable dams, although these countermeasures are very important in streams that do not contain large stones (Japanese Government, 2016). There have been proposals for other improvements to countermeasures for capturing woody debris at impermeable the dams, such as sub-dams with steel stakes near the feet of Sabo dams, as shown in Figure 2. The distance between the main Sabo dam and the sub dam is determined based on the criteria such as the water flow and the amount of woody

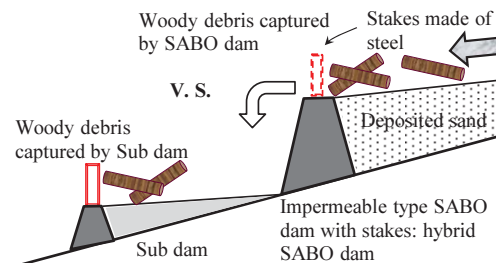


Fig. 1. Stakes installed as countermeasures against woody debris accumulation on an impermeable dam

* Corresponding author e-mail address: harada@mcnet.co.jp



Fig. 2. Sub-dam with stakes installed near the foot of the Sabo dam

debris. However, these structures are based on technologies for rivers with small gradients, not rivers with steep slopes. Furthermore, there have been reported a few reports of large amount of driftwood being captured by secondary dams, as shown in Figure 2. Hence, it is necessary to validate the applicability of these structures for capturing woody debris, taking into consideration the effect of woody debris rotation caused by the influence of water flow. As there are few constructions of this type, there is an urgent need to establish new design standards that are suitable for the hybrid structure.

To elucidate the woody debris capture mechanisms at hybrid Sabo dams and sub-dams with steel stakes near the feet of the dams, experiments were conducted to investigate the key properties of counter-measures against woody debris accumulation, in particular woody debris rotation and capture mechanisms.

2. Woody debris capture experiment

2.1. Method

Figures 3 and 4 show the experimental apparatus for comparing woody debris capture at the sub-dam and hybrid Sabo dam shown in Figure. 1. An experimental channel, which was 300 cm long and 20 cm wide, was installed in a flume. The experimental dimensions were scaled to a ratio of approximately 1/100. The small pieces of woody debris captured by the stakes, which were installed at the down-stream edge of the flume, were counted. Woody debris (n_w), sand (V_s), and water (Q_1) were supplied to the upper end of the flume. The woody debris was ϕ_2 mm in diameter, 8 cm in length, and had a dry density of 0.75 g/cm³. The flume was inclined at the angle of 10 degrees (Japanese standards for Sabo plan, 2016). The riverbed was covered in gravel to stabilize the flow, as in a real river. The stake interval, l_2 (4 cm), was set at the half length of the woody debris, l_1 , which was 8 cm. Ishikawa et al., 1989 reported that the spaces between stakes can easily become blocked when the woody debris is half as long as the distance between the stakes. We confirmed the effect of differences in channel distance (1–5 m) in a pre-experiment.

We ensured that our experimental conditions matched those at impermeable Sabo dams by depositing sand at the back of the dam. The sand supply rate, V_s , was set to maximize the concentration of sediment transported by running water. The woody debris supply time was the same as the sediment supply time, in consideration of the variation in woody debris input direction. The water-throughway width, l_3 , of the Sabo dam was 0.77 (1/1.3) times the length of the pieces of woody debris, l_1 (Japanese Government, 2016).

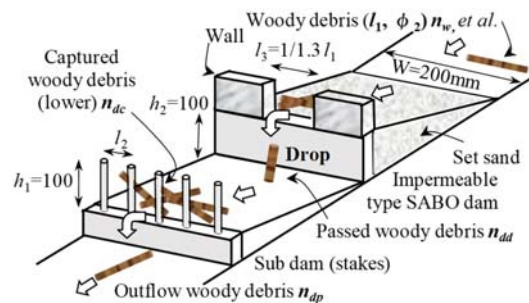


Fig. 3. Impermeable Sabo dam and sub-dam with stakes for capturing woody debris

The hybrid Sabo dam shown in Figure 4 did not have a channel for comparison of the difference in woody debris rotation due to falling water (Figure 3). The height of the steel stakes, h_2 and h_3 , was the same as the head height, h_1 . We observed the effect of varying the inclination of the flume, θ_1 ; upstream water supply rate, Q_1 ; number of woody debris pieces, n_w ; sand type, silica sand no. 1–4; stake interval, l_2 ; and woody debris diameter Φ_2 , on the stake woody debris capture efficiency, referring to pre-experimental results and previous research. The Froude (Hubert, 2004) numbers for water discharge (1.0, 1.7, 2.4 l/s) through the channel were 1.0 – 1.5, 1.3 – 2.0, and 1.6 – 2.2, respectively, and were affected by differences in the inclination of the flume, θ_1 (10, 15, 20 degrees). Here, each parameter was varied independently while the others were held constant. The experiments were repeated three times under the same hydraulic conditions and we varied the manual supply of woody debris. The results were recorded using a video camera.

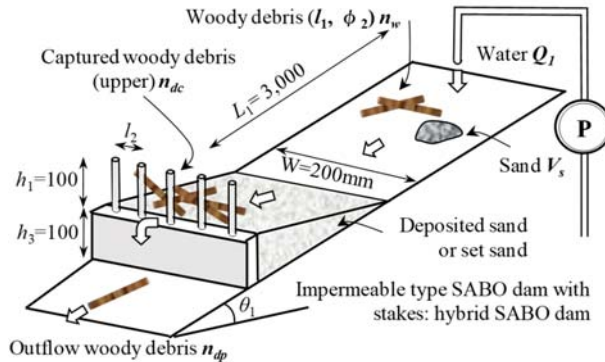


Fig. 4. Combination of hybrid Sabo dam, impermeable Sabo dam, and stakes

2.2. Effect of varying the stake installation positions

The woody debris capture rate of the hybrid Sabo dam shown in Figure 4, f_{c1} , that of the sub-dam shown in Figure 3, f_{c2} , and the non-capture rate, f_{dp} , which is the rate at which woody debris passes between the stakes, are defined as follows:

$$f_{c1} = n_{dc} / n_w \quad (1)$$

$$f_{c2} = n_{dc} / n_{dd} \quad (2)$$

$$f_{dp} = n_{dp} / n_w \quad (3)$$

where n_{dc} is the number of woody debris pieces captured by each stake, n_{dp} is the number of woody debris pieces that pass between stakes, n_{dd} is the number that pass through the channel (Figure 3), and n_w is the number of woody debris pieces supplied. Later, we consider the effect of changing these conditions on the woody debris capture function.

Figure 5 shows the relationship between the stake installation positions at the hybrid Sabo dam shown in Figure 4, f_{c1} , and those at the sub-dam shown in Figure 3, f_{c2} , for each channel inclination θ_1 and f_c . The graph shows the numbers of woody debris pieces calculated by Equations (1) and (2) in parentheses.

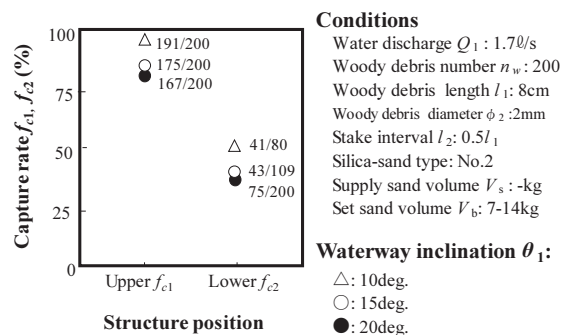


Fig. 5. Effect of channel inclination and stake position on the capture rate, f_c

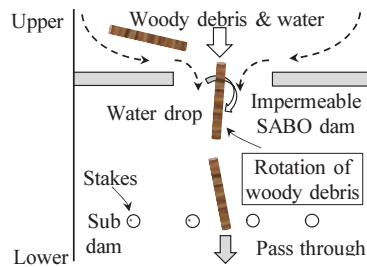


Fig. 6. Behavior of woody debris in the sub-dam, planar view

The hybrid Sabo dam captured more woody debris than the sub-dam shown in Figure 5. The woody debris pieces rotated in the flow direction as they proceeded along the water-throughway, having passed between the stakes at the sub-dam shown in Figure 6. The value of f_c decreased as the gradient θ_1 became steeper. The Froude (Hubert, 2004) number increased as woody debris at the upstream end of the channel rotated in the flow direction.

Figure 7 shows the relationship between the stake installation positions for each channel inclination θ_1 and f_{dp} . f_{dp} increased as the gradient θ_1 became steeper. Figure 8 shows the relationship between the dam type with each water discharge Q_1 and f_c . The trends in Figures 7 and 8 are the same: the flow velocity increased with both θ_1 and Q_1 .

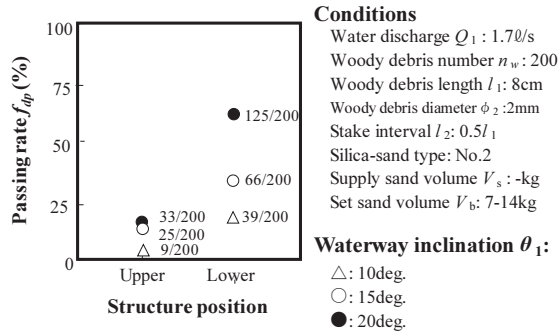


Fig. 7. Effect waterway of inclination and stake positions on the non-capture rate, f_{dp}

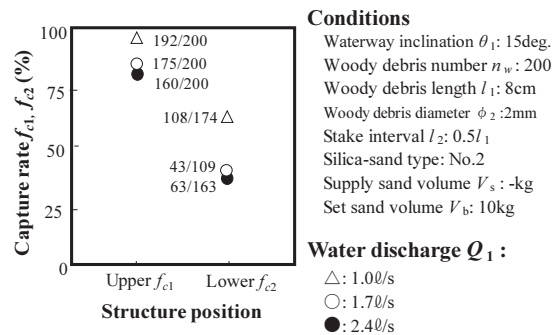


Fig. 8. Effect of water discharge rate and stake positions on the capture rate, f_c

Figure 9 shows the relationship between the diameter of the woody debris Φ_2 and f_c . The water flow has little effect on the rotation of driftwood, because the inertial force of the driftwood increases with the diameter of the driftwood. Hence, it appears that the blockage rate of the driftwood increased in the piles.

Figure 10 shows the relationship between the horizontal spacing between the stakes l_2 and f_{c2} , which increased as the woody debris diameter and l_2 decreased. Varying l_2 made little difference to f_c , when the woody debris diameter was large. One possible explanation for these results is that the rotational motion of the woody debris as it was transported through the channel varied with its diameter. Hence, these results and those shown in Figure 9 could be caused by the same mechanism, *i.e.*, the effect of the rotational motion of the woody debris.

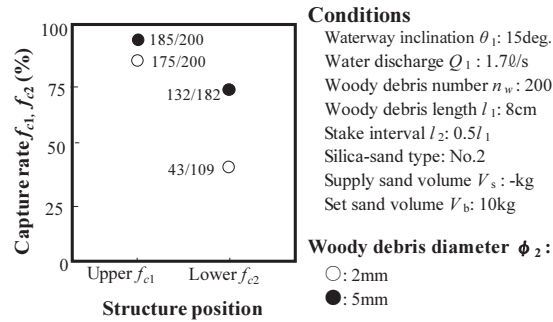


Fig. 9. Effect of woody debris diameter and stake position on the capture rate, f_c

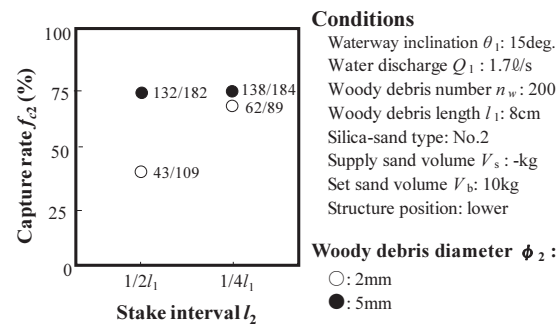


Fig. 10. Effect of horizontal spacing and positions of the stakes on the capture rate, f_c

Figure 11 shows the relationship between the number of pieces of woody debris supplied, n_w , and f_c , which increased with n_w . More woody debris tended to be captured once some woody debris had already been captured at the stakes.

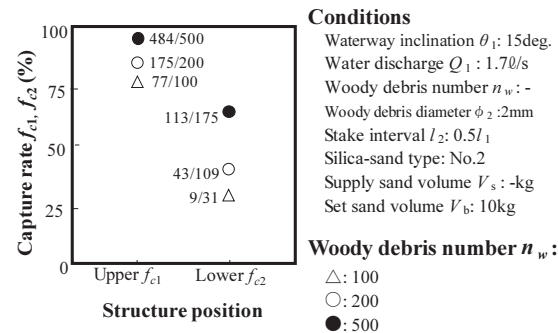


Fig. 11. Effect of the number of pieces of woody debris supplied and stake positions on the capture rate, f_c

3. Quantification of woody debris captured at a hybrid Sabo dam using steel stakes

3.1. Method

The channel shown in Figure 4 is similar to that used in the experiment conducted at the hybrid Sabo dam. We observed the effect of varying the inclination of the flume, θ_1 ; the upstream water supply rate, Q_1 ; the number of woody debris pieces, n_w ; the sand type, silica sand no. 1–4; the stake interval, l_2 ; and the woody debris diameter Φ_2 , on the stake woody debris capture efficiency. We found that the deposited inclination θ_d at the impermeable Sabo dam was

affected by differences in the supply sand conditions; θ_d was estimated using riverbed inclination θ_1 . Finally, we focused on differences in woody debris shape and input density.

3.2. Mechanisms of woody debris capture by the hybrid Sabo dam

Figure 12 shows the relationship between the sand conditions at the back of the hybrid Sabo dam (removed sand) and f_{dp} , which is smaller when sand is removed, such as at a managed dam, than when sand is not removed. We observed the effect of the secondary (vertical) flow in the water at the back of the dam on the woody debris rotation. The woody debris was gradually incorporated into the sand delta at the managed dam, preventing woody debris out flow, as shown in Figure 13. In contrast, the woody debris-rotated in the flow direction as it passed between the stakes at the unmanaged dam. f_{dp} was presumed to be similarly affected by woody debris rotation.

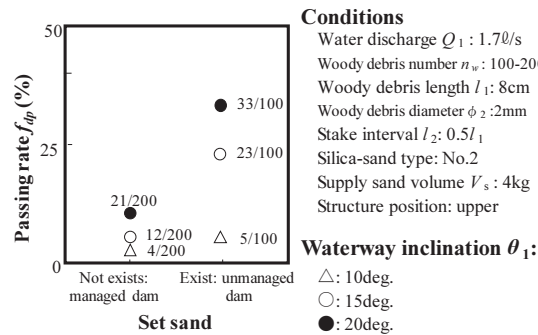


Fig. 12. Effect of sand at the back of the dam on the rate of woody debris passing between stakes, f_{dp}

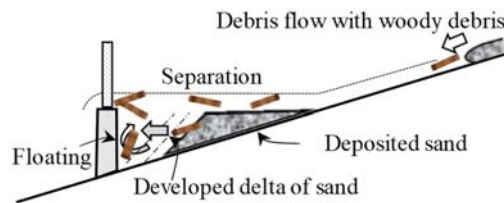


Fig. 13. Woody debris and sediment capture in the managed dam

Figure 14 shows the relationship between the inclination of the channel and f_{c1} for the case of the unmanaged dam, as shown in Figure 15. Many pieces of woody debris were captured by the stakes (a), and about 2% of the woody debris was deposited in the sediment. Sediment was deposited (b) at the location of the gradient change and the woody debris continued to flow down the channel, separating from the starting position.

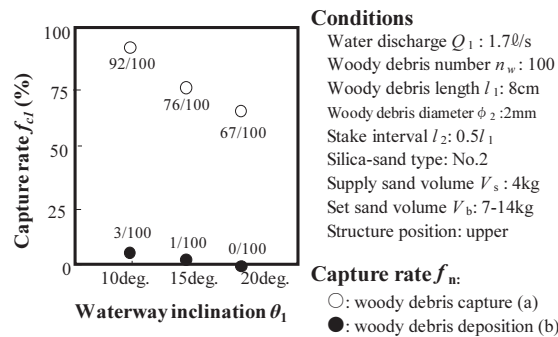


Fig. 14. Effect of channel inclination on the capture rate, f_c , at the unmanaged dam

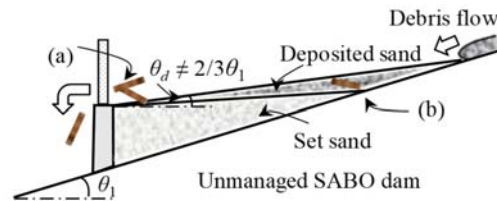


Fig. 15. Woody debris and sediment capture in the unmanaged dam

Figure 16 shows the relationship between the woody debris deposition rate and the number of woody debris pieces supplied, where woody debris deposition rate refers to the ratio of the maximum woody debris capture height to the water depth. The results (Figure 17) show little evidence that the woody debris capture height depended on the number of woody debris pieces supplied or the water discharge rate. Woody debris was captured at the water depth ($h_{dmax}=1.0-1.2h_w$) due to the permeability of the captured woody debris deposits.

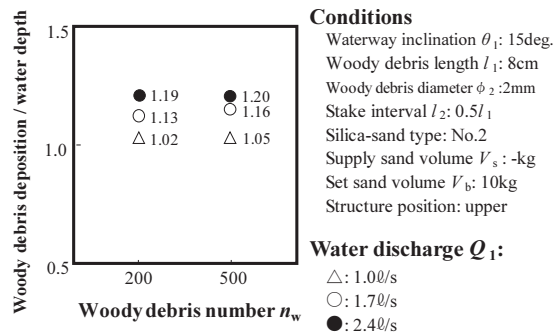


Fig. 16. Relationship between the woody debris deposition rate and the number of woody debris pieces supplied

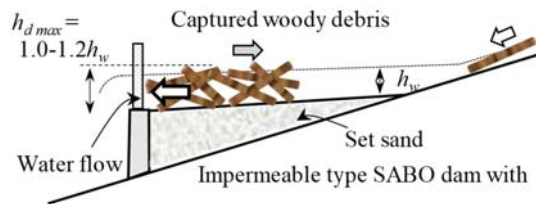


Fig. 17. The woody debris capture mechanism

Figure 18 shows the relationship between the silica type (mean sand particle diameter) and deposition inclination, θ_d (Figure 5). The deposited inclination depended on the gradient of the channel and the silica type.

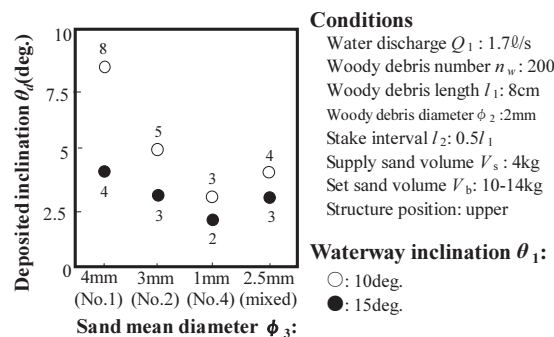


Fig. 18. Relationship between mean sand particle diameter and deposition inclination

To further improve the efficiency of the woody debris capture, experiments should be carried out in the future to investigate the effect of varying the sand particle-size, woody debris length, riverbed roughness, and interval between stakes in detail.

Conclusions

The aim of this study was to elucidate the woody debris capture mechanisms of hybrid Sabo dams and sub-dams with steel stakes near the feet of the dams. We carried out experiments investigate the key properties of countermeasures against the accumulation of woody debris. A basic channel experiment was conducted to inform the planning and design of countermeasures against woody debris blockage, taking the mechanisms for woody debris rotation and sedimentation into consideration. The hybrid Sabo dam captured more woody debris than the sub-dam, because woody debris pieces rotated into the flow direction as they proceeded through the channel, having passed between the stakes at the sub-dam. The capture rate at the stakes increased as the woody debris diameter increased. One possible explanation for this result is that the rotational motion of the woody debris varied in diameter as it was transported through the channel. Further study of this aspect of woody debris flow is needed. Finally, we observed that woody debris was captured at the water depth ($h_{dmax} = 1.0-1.2h_w$) due to the permeability of the deposits of captured woody debris. We will analyze the properties of the woody debris in further detail in future studies.

References

- Doi, Y., Minami, N., Yamada, T. and Amada, T., 1999, Experimental analysis of woody debris trapping by impermeable type sabo dam, filled with Sediment: Journal of the Japan Society of Erosion Control Engineering, v. 52, p.49-55.
- Fujimura, N., Kuroiwa, T., Izumiyama, H., Akazawa, Y. and Mizuno, H., 2016, Report on experimental analysis of debris-wood release and trapping by closed type sabo dam: Memorandum of PWRI, v. 4331.
- Taniguchi, F., Ogawa, T., Mizuyama, T., Fujita, M., Kosuct, K. and Ougi, K., 1999, Tees damaged by typhoon 9807 in southern Nara: Journal of the Japan Society of Erosion Control Engineering, v. 52, p.27-30.
- Horiguchi, T., Shibuya, H., Katsuki, S., Ishikawa, N. and Mizuyama, T., 2015, A basic study on protective steel structures against wooden debris hazards: International Journal of Protective Structures, v. 6-2, p. 191-215.
- Hubert, C., 2004, Hydraulics of Open Channel Flow: An Introduction (2nd ed.), Butterworth-Heinemann, v. 650.
- Ishikawa, Y., Mizuyama, T. and Fukuzawa, M., 1989, Generation and flow mechanisms of floating logs associated with debris flow: Journal of the Japan Society of Erosion Control Engineering, v. 42, p.5-10.
- Matsumura, K., Hashida, Y. and Kasai, S., 1990, Effect of trapping flood wood by grid type sabo dam: Journal of the Japan Society of Erosion Control Engineering, v. 43, p.9-12.
- Nationality institute for land and infrastructure management ministry of land, infrastructure and transport, Japan., 2016, Manual of technical standard for establishing Sabo master plan debris flow and debris-wood: Technical note of national institute for land infrastructure management, v. 364.

Debris-flow mitigation – research and practice in Hong

Kong Ken K.S. Ho^{a,*}, Raymond C.H. Koo^a, Julian S.H. Kwan^a

^a *Geotechnical Engineering Office, Civil Engineering and Development Department, Hong Kong SAR Government, China*

Abstract

Dense urban development on a hilly terrain, coupled with intense seasonal rainfall and heterogeneous weathered profiles, gives rise to acute debris flow problems in Hong Kong. The Geotechnical Engineering Office (GEO) of the Hong Kong SAR Government has launched a holistic R&D programme and collaborated with various tertiary institutes and professional bodies to support the development of a comprehensive technical framework for managing landslide risk and designing debris flow mitigation measures. The scope of the technical development work includes compilation of landslide inventories, field studies of debris flows, development and calibration of tools for landslide runout modelling, back analysis of notable debris flows, physical and numerical modelling of the interaction of debris flow and mitigation measures, formulation of a technical framework for evaluating debris flow hazards, and development of pragmatic mitigation strategies and design methodologies for debris flow countermeasures. The work has advanced the technical understanding of debris flow hazards and transformed the natural terrain landslide risk management practice in Hong Kong. New analytical tools and improved design methodologies are being applied in routine geotechnical engineering practice.

Keywords: Debris flow mitigation; landslide risk management

1. Introduction

Starting in 2010, systematic study and mitigation of natural terrain landslide risk has become a core component of the Hong Kong Government's Landslip Prevention and Mitigation (LPMit) Programme, which is managed by the Geotechnical Engineering Office (GEO). In order to tackle natural terrain landslide hazards, technical development work has been in progress by GEO since the late-1990s. Through systematic mapping and studies of notable landslides, advances have been made in the understanding of the mechanisms and classification of natural terrain landslides and debris movement, together with the formulation of risk management and hazard mitigation strategies.

Based on the state-of-the-art knowledge, GEO developed a technical framework for evaluating landslide hazards (Ho et al., 2015), and implemented R&D studies to advance the strategy and design of mitigation measures in order to reduce landslide risk to an as low as reasonably practicable (ALARP) level.

This paper presents the progressive development of the natural terrain risk mitigation practice in Hong Kong, and the advances made by the R&D work. The practical challenges in relation to the design, construction and maintenance of landslide mitigation measures are discussed.

2. Nature of Natural Terrain Landslides

Hong Kong has a population of over 7 million and a small land area of 1,100 km², only 15% of which is developed land. The terrain is hilly, with 75% of the land being steeper than 15° and 30% steeper than 30°. Rainfall intensities exceeding 70 mm/hour and 300 mm/day are not uncommon. The dense urban development on a hilly terrain, together with intense seasonal rainfall and variable weathered profiles, gives rises to acute slope safety problems in Hong Kong. This is reflected by a death toll of over 470 fatalities due to landslides since the 1940s.

* Corresponding author e-mail address: kenho@cedd.gov.hk

Hong Kong comprises a hilly terrain with dense urban development close to steep hillsides. The natural terrain is typically mantled by weak and heterogeneous saprolite or colluvium, which is susceptible to shallow, small to medium-scale landslides (see Figure 1), usually several hundreds cubic metres, or occasionally more sizeable, due to loss of suction or build up of local perched water pressure as a result of intense rainstorms. This can be further complicated by ongoing progressive deterioration of the condition of the natural hillside due to successive heavy rainstorms. These landslides can develop into debris flows where debris reaches drainage lines with surface water flow resulting in increased mobility (i.e. larger velocity and greater runout distance). Based on the landslide inventory, on average about one landslide occurs each year for every 2 km² of natural hillside in Hong Kong. Occasionally, larger scale debris flows (see Figure 2) can occur given adverse site setting and intense rainfall. The inventory, compiled using aerial photographs, contains records of more than 100,000 past failures on the natural hillsides in Hong Kong.

Apart from structural, geological and hydrogeological factors, unfavourable topographical factors can also contribute to increased susceptibility to landslide initiation, such as breaks in slope, topographic depression, head of drainage line, and presence of regolith downslope of a rock outcrop.

Channelised debris flows along incised drainage lines or pronounced topographic depressions with concentrated surface water flow tend to be more mobile (as compared to landslides on a planar hillslope) with notable velocities (in the order of 10 m/s or more). Due cognizance needs to be taken of the nature of channelised debris flows in the design of mitigation measures. Debris flows can occur in pulses and may entrain loose materials due to erosion along the flowpath. They can also engulf large boulders, which can be isolated or in clusters occurring as a bouldery front, typically with an inverse grading due to reverse segregation (see Figure 3). The complex and transient nature of such surge two-phase flows can be further complicated by the presence of large broken tree trunks. Additionally, there is the possibility of dam break pulses occurring along the drainage line due to build-up of a temporary debris dam.



Fig. 1. Landslide-prone natural terrain of Hong Kong



Fig. 2. The 1990 channelised debris flow at Tsing Shan



Shek Mun Kap



Yi O Village



Nam Chung Tsuen

Fig. 3. Bouldery front of channelised debris flows observed in June 2008 in Hong Kong

3. Natural Terrain Landslide Risk Management

The Geotechnical Engineering Office (GEO) has launched a holistic R&D programme and collaborated with various tertiary institutes and professional bodies to support the development of a comprehensive technical framework for managing landslide risk and designing debris flow mitigation measures with more scientific rigour. The scope of the technical development work includes compilation of landslide inventories, field studies of debris flows, development and calibration of tools for landslide mobility modelling, back analysis of notable debris flows, physical and numerical modelling of the interaction of debris flow and mitigation measures, formulation of a technical framework for evaluating debris flow hazards, and development of pragmatic mitigation strategies and design methodologies for debris flow countermeasures. The work, which spans the last two decades, has advanced the technical understanding of debris flow hazards and transformed the natural terrain landslide risk management practice

in Hong Kong. New analytical tools and improved design methodologies are being applied in routine geotechnical engineering practice by local practitioners including geotechnical engineers and engineering geologists.

One of these new tools is an emphasis on risk-based management. Landslide risk can be quantified as follows:

$$\text{Risk} = P_i \times C_i \quad (1)$$

where P_i is probability of occurrence of landslide hazard and C_i is landslide consequence.

The risk posed to a given facility can be managed by reducing P_i by means of stabilisation works or by reducing C_i through mitigation measures, or by doing both. For existing facilities such as buildings or roads subjected to natural terrain hazards, slope stabilisation on the steep hillside is often neither practically nor economically and environmentally justifiable. Instead, an active mitigation strategy involving the implementation of mitigation measures (such as debris-resisting rigid barriers, steel flexible barriers, or boulder fences) is more practicable (Ho, et al., 2015). In view of the complexities and uncertainties associated with debris flows, emphasis has been given by GEO in developing and adopting pragmatic and suitably simplified barrier design methods. An overview of the advances in geotechnology for slope stabilisation and landslide mitigation was given by Ho (2005).

4. Evolution of Barrier Design Practice

4.1. Phase 1 – Development of Barrier Design Guidelines

Traditionally, the assessment of natural terrain landslide hazards was undertaken by engineering geologists through an engineering geological approach, with a qualitative risk assessment and the necessary risk mitigation measures determined largely by experience and judgement. The process was typically not particularly transparent.

Starting in the late 1990s, significant advances have been made by GEO in developing practical numerical tools for debris mobility assessment and calibrating the rheological models and input parameters through systematic back analysis of local case histories of the more mobile landslides (Kwan & Sun, 2007). GEO also promulgated guidance on the assessment of debris discharge, flow velocity and thickness, debris run-up, retention capacity of barriers, and surface drainage provisions (GEO, 2014).

The technical guidance on mitigation measures promulgated by GEO at that time covers primarily the design of rigid barriers against debris and boulder impact. In developing the guidance, a holistic approach was adopted including benchmarking against international practice and reviewing relevant laboratory and field studies, back analysis of instrumented field data, performance review of barriers upon impact by landslides, etc. In essence, the basis of the guidance promulgated at this early stage was largely empirical, supported by literature review and limited field studies.

4.2. Phase 2 – Rationalisation and Enhancement of Barrier Design Guidelines

From about 2010 onwards, GEO initiated further R&D work focusing on the use of flexible and rigid barriers to arrest natural terrain landslides.

The advances have led to an improved understanding which enables the guidance on barrier design to be rationalised and expanded. The basis of the enhanced design approaches is multi-pronged, including back analysis of field observations, use of physical models (laboratory flume), numerical techniques, analytical solutions, etc. A key consideration is to build in sufficient robustness to cater for the uncertainties in the field associated with the complex characteristics and variable composition of debris flows. The work culminated in the promulgation of new or improved design guidance covering the following areas:

- (a) a design methodology for the impact of debris and boulders on rigid and flexible barriers using a force approach (Kwan & Cheung, 2012);
- (b) a design methodology for debris impact on flexible barriers using the energy approach based on insight from Discrete Element Model (DEM) analysis and a simplified analytical framework (Sun & Law, 2012);
- (c) a design methodology for debris impact on rigid or flexible barriers using the force approach, including a multiple-phase debris impact model which accounts for dynamic impact pressure and static earth pressure of the deposited debris, with due allowance made for the variation in debris velocities at different phases of debris impact as computed from debris mobility analysis (GEO, 2015), together with allowance for the additional drag force in the event the debris overtops the barrier;

- (d) an analytical framework for the design of multiple barriers (with the upstream barriers acting as check dams) based on a newly developed staged mobility analysis (Kwan et al., 2015); and
- (e) a design framework for the use of prescribed flexible barriers in mitigating open hillslope landslides in order to streamline the design process (GEO, 2014).

The current design approaches adopted in Hong Kong are summarised in Figures 4 and 5.

Step 1

<p>(i) Calculate energy loading for pile-up mechanism (E_p)</p> $E_p = \frac{\alpha \rho Q_0 (U_0)^3}{4(\mu \cos \theta - \sin \theta) g}$	<p>(ii) Calculate energy loading for run-up mechanism (E_r)</p> $E_r = \frac{\rho Q_0 (U_0)^5 \cos(\theta + \gamma) \sin(\theta + \gamma)}{48 h_0 g^2 (\mu \cos \theta - \sin \theta)^2}$
---	--

where α is dynamic coefficient (taken to be 2.0 for flexible barrier); ρ is debris density; Q_0 is discharge rate; U_0 is debris impact velocity; μ is basal friction coefficient (i.e. $\tan \phi$); ϕ is debris friction angle; θ is inclination of channel base; γ is inclination of ramp formed by debris behind the barrier; and g is gravity

Step 2

<p>(i) Calculate kinetic energy of landslide debris when the debris front reaches the design location of flexible barrier (E_{k1})</p>	<p>(ii) Calculate kinetic energy of landslide debris that pass through the design location of flexible barrier (E_{k2})</p>
---	--

Step 3

Design energy loading $E = \min \{ \max(E_p, E_r), \max(E_{k1}, E_{k2}) \}$

Step 4

Check if design energy loading $\leq 0.75 \times$ energy rating of flexible barrier certified by ETA full-scale rockfall test.

Notes: (1) For other design checks, see (ii), (iii) & (iv) of Figure 5.
 (2) If Step 4 cannot be satisfied, then use force approach for design.

Fig. 4. Summary of the energy approach for design of flexible barriers

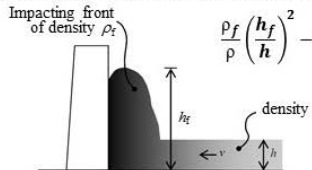
(i) Calculate dynamic load of debris and boulder impact

Debris impact pressure $p = \alpha \rho v^2$ where α is dynamic coefficient, ρ is debris density & v is impact velocity

Rigid barriers - assume $\alpha = 2.5$ for debris with boulders up to 0.5 m in size
 Flexible barriers - assume $\alpha = 2.0$ for debris with boulders up to 2.0 m in size

Boulder impact force $F = 4000 K_c v_b^{1.2} r_b^2$ (for rigid barriers)
 where K_c is reduction coefficient (taken = 0.1), v_b is impact velocity and r_b is boulder diameter

(ii) Check run up height (same for both flexible and rigid barriers)



$$\frac{\rho_f}{\rho} \left(\frac{h_f}{h} \right)^2 - \frac{h_f}{h} - 1 + \left(\frac{\rho_f h_f}{\rho h} \right)^{-1} - 2 \frac{v^2}{gh} = 0$$

(Kwan & Cheung, 2012)

where ρ is debris density, v is impact velocity, g is gravity and h is debris thickness

(iii) Check static load from debris deposited behind the barrier (same for both flexible and rigid barriers)

Debris static pressure $p_s = K \rho g h$ where K is lateral pressure coefficient (taken = 1), g is gravity & h is deposited debris height

(iv) Check retention capacity based on gradient of the deposition area (i.e. $\tan \gamma$) and gradient of the slope channel (i.e. $\tan \theta$)

$\tan \gamma = 1/2$ to $3/4 \times \tan \theta$ (for rigid barriers)
 $\tan \gamma = 0$ (for flexible barriers)

For flexible barriers, the residual barrier height should be considered after final barrier deformation upon debris impact.

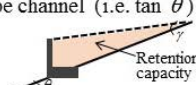


Fig. 5. Summary of the force approach and key design checks for flexible and rigid barriers

The concepts of a composite structure comprising a rigid barrier with baffles to dissipate the energy of landslide debris and arrest some of the boulders, together with a cushioning layer on the rigid barrier front face to help reduce boulder impact load, are promoted to enhance robustness.

Apart from the promulgation of technical design guidelines, GEO has also published guidance on other related design and construction issues as follows:

- (a) suitable detailing of rigid and flexible barriers (e.g. avoiding damage of posts in flexible barrier due to boulder impact, improving drainage provisions, and enhancing resilience against scouring of the substrate of the barrier foundation, detailing of a deflector at the crest of a rigid barrier to avoid spillage of debris due to debris run-up upon impact, etc.);
- (b) improvement of contract specification for new flexible barriers to enhance durability based on a performance review of about 100 local barriers, together with retrofitting of deteriorated steel components of existing barriers; and

(c) guidance on slope landscaping and use of bioengineering techniques to improve the aesthetics and biodiversity of the plants on or close to the barriers (GEO, 2011).

GEO is currently also using Building Information Modelling (BIM) model to examine buildability issues and construction sequencing in order to optimise the design layout of barriers and minimise cut and fill operations.

4.3. Phase 3 – Optimisation of Barrier Design

To validate or calibrate the various design approaches and improve the understanding of barrier behaviour with a view to optimising barrier design, GEO has continued to undertake in-house development work and collaborate with practitioners and with local tertiary institutes and overseas experts in pursuing various R&D initiatives. These include the use of state-of-the-art physical modelling (centrifuge as well as laboratory and field flume tests) to study mechanisms, application of advanced numerical modelling, and development of new analytical approaches.

i. Displacement-based approach for assessing geotechnical stability and flexural response of rigid barriers

Conventional force-based design approaches often result in over-design of rigid barriers subject to debris impact which is transient in nature. The newly proposed displacement-based approach could provide a more realistic evaluation of the performance of rigid barriers subject to boulder impact. Based on fundamental principles of dynamic analysis, Lam & Kwan (2016) developed closed-form formulae for estimating the translational and rotational movements, as well as the flexural deflection and tensile reinforcement strain of rigid barriers, due to boulder impact. A series of small scale impact tests were carried out to verify the predictions using this displacement-based approach (Lam et al., 2017) and good agreement was obtained. A comparison was made between the displacement-based approach and the conventional limit equilibrium analysis. Based on the impact scenarios that are typically encountered in routine design (i.e. a 1 m diameter boulder with a velocity of 10 m/s impacting onto a typical 6 m high, 10 m long rigid barrier), the predicted translational and rotational movements of the barrier were found to be insignificant based on the displacement-based approach. Large-scale tests were also carried out to investigate the structural response of a rigid barrier subject to impact by a solid steel impactor, which successfully validated the enhanced flexural stiffness method. The above have demonstrated that substantial cost savings could potentially be achieved in barrier designs by accounting for the inertia effect of a rigid barrier.

ii. Field testing of cushioning materials for reducing boulder impact load on rigid barriers

Field monitoring and observations together with recent centrifuge tests indicate that impacts due to hard inclusions (i.e. boulder front) of a debris flow can result in high magnitude and transient loads on a rigid barrier. With a view to damping out these force spikes, a systematic study on the use of different cushioning materials to shield the barrier was initiated by the GEO. In general, the cushioning materials are deformable and thus capable of prolonging the impact process and attenuating the impulsive forces due to the hard inclusions. A large-scale instrumented pendulum impact test facility involving a 1.16 m diameter concrete ball (2,000 kg in weight) with a maximum impact velocity of 8.4 m/s and a kinetic energy of up to 70 kJ was set up. Four types of cushioning materials, namely rock-filled gabions, recycled glass cullet, ethylene-vinyl acetate (EVA) foam, and cellular glass, were tested. The results show that the cushion layer could effectively reduce the maximum impact forces although it would become less effective after successive impacts (Ng et al., 2018). The test data were also used to calibrate numerical models for further parametric studies.

Recent large-scale impact tests have also shown the effectiveness of a gabion cushioning layer in preventing localized structural damage (such as cracking, penetration, perforation and scabbing) in a reinforced concrete barrier, and in substantially reducing the flexural deflection at barrier crest (by 67% to 90%).

iii. Study on use of baffles to dissipate energy of debris flow

Baffles are flow-impeding structures installed along the flow path to dissipate the energy of debris flows and screen out large boulders. A series of instrumented flume tests and back analyses were carried out to investigate dry sand flow impact on an array of baffles (Choi et al., 2014). The influence of baffle height, number of rows, and transverse and longitudinal spacing of baffles was systematically examined. These small-scale tests with dry sand indicate that increasing the baffle height from 0.75 to 1.5 times the approaching flow depth would lead to a more effective development of subcritical flow condition which promotes energy dissipation of the debris. Increasing the number of rows from a single row to a staggered three-row array results in about 70% additional energy loss. Energy loss is attributed to the deflection of granular jets and backwater effects.

iv. Advanced coupled analysis of debris-barrier interaction

Advanced numerical modelling has been adopted to simulate debris-barrier interaction using the computer program LS-DYNA. Various researchers (e.g. Kwan et al., 2015, Koo et al., 2018) have demonstrated that the use of Arbitrary Lagrangian-Eulerian method in LS-DYNA appears to be a promising tool for modelling debris flow and debris-barrier interaction. Such modelling has been benchmarked against laboratory flume tests and actual landslide cases in terms of debris runout characteristics. In the conventional approach, landslide mobility analyses and structural analyses of the barrier are carried out separately. The landslide mobility is first simulated under a free-field condition to obtain design parameters such as flow velocity and depth (e.g. 3d-DMM by Kwan & Sun, 2007), which are then converted into a pseudo-static impact force as input to a separate structural model (e.g. computer program NIDA-MNN by Sze et al., 2018). This latter approach however neglects the dynamics of debris-barrier interaction.

Coupled analyses can be carried out using LS-DYNA, with the landslide mass modelled as a continuum in a finite element formulation (see Figure 6). The results successfully reproduced the deformation and forces in various structural components as observed in instrumented case studies (Cheung et al., 2018). The coupled analyses also provided insight on the energy dissipation of landslide debris in the debris-barrier interaction process. The preliminary findings are that the overall strain energy absorbed by the flexible barrier upon debris impact only amounted to a fairly small portion (generally less than 35% based on parametric studies) of the total debris impact energy, as due to internal distortion of the debris and changes in momentum flux direction under a debris run-up mechanism upon impact. It is noteworthy that the continuum model adopted in LS-DYNA has certain limitations as it may not fully simulate particle-fluid interaction and the presence of hard inclusions at the debris front. Other research tools such as coupled analysis using discrete element models and computational fluid dynamics models are being used to examine the potential effects of particle-fluid interaction (Li & Zhao, 2018).

v. Parametric study of varied debris composition and different barrier configurations using physical tests

Centrifuge and/or flume tests were conducted for various types of mitigation structures (e.g. flexible barrier, curved rigid barrier, slit barrier, etc.) to examine the effects of impact mechanisms and influence of different debris composition under controlled conditions (Choi et al., 2016; Ng et al., 2016; Song et al., 2017). During the frontal impact of a two-phase debris flow without hard inclusions, the measured dynamic pressure coefficient in the hydrodynamic approach is close to unity (which confirms the principle of conservation of momentum), for both rigid and flexible barriers that are upright (note that the coefficient is less than unity for a curved rigid barrier subject to impact by coarse granular flow). Increasing the solid fraction of a debris flow was found to promote transition from run-up to pile-up mechanisms. Furthermore, test results indicate that the presence of large hard inclusions (boulders) in the debris flow are liable to induce transient force spikes reflecting significant impulse loading on a rigid barrier.

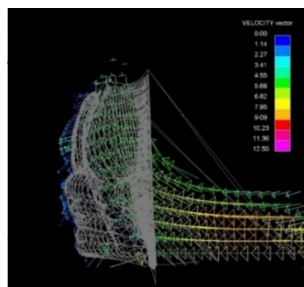


Fig. 6. LS-DYNA simulation of debris impact on flexible barrier

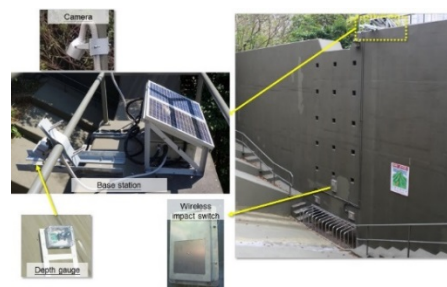


Fig. 7. Smart rigid barrier system

5. Way Forward

The above studies have provided useful yardsticks for calibrating or bracketing existing design approaches. They further highlight that there is potential scope for further rationalising and optimising the design, e.g. the numerical coupled analyses suggest that the impact energy transmitted to a flexible barrier could be much lower than that assessed by the current design approach because of internal distortion of the debris and change in momentum flux direction. Similarly, the displacement approach, corroborated by laboratory model tests, suggests that the dynamic

force exerted on a rigid barrier would be much lower than conventional elastic theory taking due account of the inertia effect. Notwithstanding the above, it should be borne in mind that the physical models are constrained by the use of idealised materials as compared to real life debris flows, and potentially by uncertainties involved in scaling up the observed behaviour. As a basis for validation of the observed insights from the latest R&D work with a view to optimising the design methods, large-scale field tests are planned with a failure volume up to about 500 m³. Class A predictions could be made, which would be calibrated by large-scale field tests using a material composition that resembles real debris flows as much as possible.

6. Ongoing Challenges

Some ongoing challenges and pertinent issues faced by the practitioners are highlighted below:

(a) Behaviour of energy dissipation (or brake) elements – brake elements are an essential component of a flexible barrier in dissipating the impact energy. However, there is as yet no internationally recognised testing standard to check their stress strain characteristics at an appropriate strain rate and assess their degree of variability. Based on limited site observations following debris impact (e.g. Kwan et al., 2014), there is an element of uncertainty regarding the actual behaviour of different types of brake elements, particularly when they become buried by landslide debris (as some of them apparently were not activated following debris impact and barrier deformation).

(b) Potential for under-estimation of landslide hazards due to climate change – recent local experience with extreme rainfall events has shown that the response of natural hillsides in Hong Kong is highly sensitive to more severe rainfall in that the number, scale and mobility of landslides are much elevated. The assessment of the landslide hazard to be designed for during the design life of the mitigation measure is fraught with considerable uncertainty and difficulty, given that the relatively short time window available for compiling the landslide inventory may not have captured the extreme rainfall events. This is exacerbated by the increased likelihood of occurrence of more frequent and intense weather events associated with potential climate change. The possibility of barriers being under-designed and overwhelmed by more sizeable and/or more mobile landslide hazards than those anticipated by designers based on prior knowledge and experience calls for a paradigm shift in the strategy for managing the associated landslide risk. A recent initiative by the GEO is the development of smart barriers incorporating the use of real time wireless sensors and Internet of Things (IoT) and cloud computing technology to provide early warning of landslide impact and facilitate timely emergency response (see Figure 7). Other recent advances in the management of landslide risk associated with extreme weather events in Hong Kong entailed refinement of the landslide warning system (Ho et al., 2017), development of rainfall-based landslide susceptibility zoning (Ko & Lo, 2018), and innovative approaches in enhanced public education. The above are some of the non-structural measures of landslide risk management under a systems approach in addressing landslide risk in a holistic manner.

(c) Durability and long-term maintenance of flexible barriers – a cost effective long term strategy for maintenance of flexible barriers is needed, given that the steel components are subject to progressive deterioration in hot and humid climates like Hong Kong. It is also necessary to have improved knowledge on the rate of corrosion of steel components and various forms of treatment in corrosive environments.

7. Concluding Remarks

The design of landslide risk mitigation measures for debris flows and other flow-like landslides is highly challenging in light of the many uncertainties involved. A holistic and progressive approach has been adopted in Hong Kong to improve our fundamental knowledge of debris flows and to provide scientific insight into the behaviour of debris-resisting landslide barriers as a result of debris-structure interaction (e.g. effect of Froude number of debris flows on impact behaviour, influence of debris impact mechanisms, presence of a dead zone associated with debris deposition upon initial impact, effect of varied debris composition including solid fraction, postulated effect of suction on debris mobility and impact behaviour, influence of compressibility of debris flow on impact behaviour, etc.). The systematic technical development work carried out on landslide mitigation measures has led to an improved understanding of the related mechanisms and the controlling parameters. Nevertheless, it is important to remain pragmatic and to strike a suitable balance in translating research findings into practice with due account taken of the simplifications made in the model testing and computational analyses as opposed to the complex and random nature of real debris flows in the field. Due allowance should also be made in the design for enhanced robustness and redundancy in managing the uncertainties.

Apart from the consideration of appropriate technical standards and improved design methodologies, it should be borne in mind that there are other pertinent issues that are of relevance to practitioners, including guidance on proper detailing of the works, consideration of buildability, the structural form to be adopted (e.g. post-supported flexible barrier versus side-anchored flexible barriers), an appropriate acceptance system for flexible barrier products for quality assurance and quality control, landscaping works, etc.

8. Acknowledgements

This paper is published with the permission of the Head of Geotechnical Engineering Office and Director of Civil Engineering and Development, Hong Kong SAR Government, China.

References

- Cheung, A.K.C., Yiu, J., Lam, H.W.K. & Sze, E.H.Y., 2018, Advanced numerical analysis of landslide debris mobility and barrier interaction, HKIE Transactions, v. 25(2), in press.
- Choi, C.E., Goodwin, G., Ng, C.W.W., Cheung, D.K.H., Kwan, J.S.H., and Pun, W.K., 2016, Coarse granular flow interaction with slit structures, Géotechnique Letters, v. 6(4), p. 267–274.
- Choi, C.E., Ng, C.W.W., Song, D., Law, R.P.H., Kwan, J.S.H. and Ho, K.K.S., 2014, A computational investigation of baffle configuration on the impedance of channelized debris flow, Canadian Geotechnical Journal, v. 52(2), p. 182–197.
- GEO, 2011, Technical Guidelines on Landscape Treatment for Slopes, GEO Publication No. 1/2011. Geotechnical Engineering Office, Civil Engineering and Development Department, Hong Kong SAR Government, China, 217 p.
- GEO, 2014, Guidelines on Empirical Design of Flexible Barriers for Mitigating Natural Terrain Open Hillslope Landslide Hazards, GEO Technical Guidance Note No. 37. Geotechnical Engineering Office, Civil Engineering and Development Department, Hong Kong SAR Government, China, 18 p.
- GEO, 2015, Assessment of Landslide Debris Impact Velocity for Design of Debris-resisting Barriers, GEO Technical Guidance Note No. 44. Geotechnical Engineering Office, Civil Engineering and Development Department, Hong Kong SAR Government, China, 4 p.
- Ho, K.K.S., 2005, Keynote paper: Recent advances recent in geotechnology for slope stabilization and landslide mitigation – perspective from Hong Kong. Proc. Ninth Int. Sym. On Landslides, Rio de Janeiro, v. 2, p. 1507–1560.
- Ho, K.K.S., Cheung, R.W.M. & Kwan, J.S.H., 2015, Advances in urban landslide risk management. In Proceedings of the International Conference on Geotechnical Engineering – Geotechnics for Sustainable Development. Sri Lankan Geotechnical Society, Sri Lanka, p. 67–93.
- Ho, H.Y. & Roberts, K.J., 2016, Guidelines for Natural Terrain Hazard Studies, Second Edition, GEO Report No. 138. Geotechnical Engineering Office, Civil Engineering and Development Department, Hong Kong SAR Government, China, 173 p.
- Ko, F.W.Y. & Lo, F.L.C., 2018, From landslide susceptibility to landslide frequency: A territory-wide study in Hong Kong. Engineering Geology, v. 242, p. 12–22.
- Ho, K.K.S., Sun, H.W., Wong, A.C.W., Yam, C.F. & Lee, S.M., 2017, Enhancing slope safety preparedness for extreme rainfall and potential climate change impacts in Hong Kong, Slope Safety Preparedness for Impact of Climate Change, CRC Press, The Netherlands, p.105–150.
- Ko, F.W.Y. & Lo, F.L.C., 2018, From landslide susceptibility to landslide frequency: A territory-wide study in Hong Kong. Engineering Geology, v. 242, p. 12–22.
- Koo, R.C.H., Kwan, J.S.H., Lam, C., Goodwin, G.R., Choi, C.E., Ng, C.W.W., Yiu, J., Ho, K.K.S., and W.K., Pun., 2018, Back-analyses of geophysical flows using 3-dimensional runout model. Canadian Geotechnical Journal, v. 55, p. 1081–1094.
- Kwan, J.S.H., Chan, S.L., Cheuk, J.C.Y., Koo, R.C.H., 2014, A case study on an open hillside landslide impacting on a flexible rockfall barrier at Jordan Valley, Hong Kong, Landslides 2014, v. 11(6), p. 1037–1050.
- Kwan, J.S.H. & Cheung, R.W.M., 2012, Suggestions on Design Approaches for Flexible Debris-resisting Barriers, Discussion Note No. DN 1/2012. Geotechnical Engineering Office, Civil Engineering and Development Department, Hong Kong SAR Government, China, 91 p.
- Kwan, J.S.H., Koo, R.C.H. & Ng, C.W.W., 2015, Landslide mobility analysis for design of multiple debris-resisting barriers. Canadian Geotechnical Journal, v. 52 (9), p. 1345–1359.
- Kwan, J.S.H. & Cheung, R.W.M., 2012, Suggestions on Design Approaches for Flexible Debris-resisting Barriers, GEO Discussion Note No. DN 1/2012. Geotechnical Engineering Office, Civil Engineering and Development Department, Hong Kong SAR Government, China, 91 p.
- Kwan, J.S.H. & Sun, H.W., 2007, Benchmarking exercise on landslide mobility modelling - runout analysis using 3dDMM. Proceedings of the 2007 International Forum on Landslide Disaster Management, v. 2, p. 945–966.
- Li, X.Y. and Zhao, J.D., 2018, Dam-break of mixtures consisting of non-Newtonian liquids and granular particles, Power Technology, v. 338, p. 493–505.
- Lam, N.T.K., Yong, A.C.Y., Lam, C., Kwan, J.S.H., Perera, J.S., Disfani, M.M., and Gad, E., 2017, Displacement-based approach for the assessment of overturning stability of rectangular rigid barriers subjected to point impact, Journal of Engineering Mechanics, in press.
- Lam, C. & Kwan, J.S.H., 2016, Displacement-based Assessment of Boulder Impacts on Rigid Debris-resisting Barriers - A Pilot Study, GEO Technical Note No. TN 5/2016. Geotechnical Engineering Office, Civil Engineering and Development Department, Hong Kong SAR Government, China, 67 p.
- Ng, C.W.W., Song, D., Choi, C.E., Kwan, J.S.H., Shiu, H.Y.K., and Koo, R.C.H., 2016, Impact mechanisms of granular and viscous flows on rigid and flexible barriers, Canadian Geotechnical Journal, v. 54(2), p. 188–206.
- Ng, C.W.W., Su, A.Y., Choi, C. E., Lam, C., Kwan, J.S.H., Chen, R., and Liu, H., 2018, Comparison of cushion mechanisms between cellular glass and gabions subjected to successive boulder impacts. Journal of Geotechnical and Geoenvironmental Engineering, (accepted).
- Song, D., Ng, C. W. W., and Choi, C.E., Kwan, J.S.H., and Koo, R.C.H., 2017, Influence of debris flow solid fraction on rigid barrier impact, Canadian Geotechnical Journal, v. 54(10), p. 1421–1434.
- Sun, H.W. and Law, R.P.H., 2012, A Preliminary Study on Impact of Landslide Debris on Flexible Barriers, GEO Technical Note No. TN 1/2012. Geotechnical Engineering Office, Civil Engineering and Development Department, Hong Kong SAR Government, China, 43 p.
- Sze, E.H.Y., Koo, R.C.H., Leung, J.M.Y. & Ho, K.K.S., 2018, Design of flexible barriers against sizeable landslides in Hong Kong, HKIE Transactions, v. 25(2), p.115–128.

Flume investigation of the interaction mechanisms between debris flows and slit dams

H. S. Hu^{a,b*}, Gordon G. D. Zhou^{a,b}, D. Song^{a,b}

^a Key Laboratory of Mountain Hazards and Earth Surface Process/Institute of Mountain Hazards and Environment, Chinese Academy of Sciences (CAS), #.9, Block 4, Renminnanlu Road, Chengdu, 610041, China

^b University of Chinese Academy of Sciences, No.19(A) Yuquan Road, Shijingshan District, Beijing, 100049, China

Abstract

Slit dams are designed to mitigate debris-flow hazards. However, according to field surveys and past experimental studies, slit dams constructed using currently prescribed design methods usually become blocked, which then leads to the loss of capacities of the slit dam's capability to mitigate debris-flow hazards. In this study, a series of flume tests were conducted to investigate the interaction mechanisms between debris flows and slit dams. This work aims to contribute to the design of slit dams more reliable. The influence of debris-flow water content (w) and the slit-dam relative post spacing b/d_{\max} (b : post spacing; d_{\max} : maximum particle diameter) were examined. Experimental results reveal that when $w < 22\%$, dead zones and pile-ups occur during the interaction processes. When $w \geq 22\%$ and $b/d_{\max} \leq 2.3$, run-up, overtopping, and backwater effects can be observed, and with no apparent formation of dead zones. Moreover, when $w \geq 26\%$ and $b/d_{\max} > 2.3$, majority of the granular-water mixtures pass through the slit dam in the form of jet flows with no obvious overtopping.

Keywords: Debris flow; slit dam; interaction mechanisms; flume tests;

1. Introduction

Slit dams, as one type of open-type dams, designed with one or several vertical opening(s) (Chanson, 2004), are initially designed to retain large particles and weaken the peak discharge (Lien et al., 2000; Choi et al., 2018). The relative post spacing (b/d_{\max} , b : post spacing, d_{\max} : maximum particle diameter) is the key parameter (Johnson and McCuen, 1989; Lien et al., 2003), which directly affects the trapping or regulation function of a slit dam. Mizuyama et al. (1988) and MLR (2004) recommended that b/d_{\max} should be between 1.5 and 2.0 for design of slit dams.

However, experimental results from Lin et al. (1988) revealed that slit dams have notable effect on trapping debris materials when $b/d_{\max} \leq 1.7$. Furthermore, Han and Ou (2006) reported that when $b/d_{\max} < 1.5$, the slit dams become prone to blockage. In addition, field investigations (Shima et al., 2016) showed that slit dams are more likely to be filled up by granular materials contained in debris flows when the relative post spacing is narrower ($b/d_{\max} \approx 1.5$). This effectively diminishes the trapping capacity of a slit dam (Fig. 1a and Fig. 1b). The results from both engineering practice and past experimental studies have shown that slit dams will be blocked with condition of $b/d_{\max} \leq 1.5 \sim 2.0$, and it will trap granular materials contained in debris flows until the trapping capacity is lost. Ideal behavior of slit dams is to weak the peak discharge of debris flow while is not to be blocked rapidly. Accordingly, the interaction mechanisms between debris flows (with different water contents) and slit dams (with different post spacings) are investigated, which contributes to improving the reliability of slit dams designing.



Fig. 1 Slit dam filled up by granular materials (the pictures from Shima et al., taken in Rishiri island, Japan, 2016)

* Corresponding author e-mail address: huhongsen15@mails.ucas.ac.cn

2. Flume model tests

2.1. Scaling

Small-scale flume modelling is widely adopted to investigate the complex flow interaction between mass movement and structures (Choi et al., 2014; Ng et al., 2015), since it can provide a controlled and systematic manner to study mechanisms of flow-structure interaction (Choi et al., 2015). The Froude number (Fr), which macroscopically quantifies the ratio of the inertial to gravitational forces, is widely adopted to characterize the dynamic similarity between channelized granular flows (Chehata et al., 2003; Hauksson et al., 2007) and geophysical flows (Hübl et al., 2009; Choi et al., 2015). It can be expressed as (Choi et al., 2015):

$$Fr = \frac{v}{\sqrt{gh \cos \theta}} \quad (1)$$

where v is the frontal velocity, g is the gravitational acceleration, h is the maximum approaching flow depth (because the damage of structures usually appeared when debris flows approach with maximum flow depth), and θ is the inclination of the channel.

2.2. Model setup and instrumentation

The experiments were carried out using a flume model with an overall length of 7.0 m, a channel width of 0.3 m, and depth of 0.35 m. Figure 2a shows the flume, which consists of a storage tank, a channel with two different inclinations, and a deposition section. The upper part of the channel with has a steeper angle and is usually regarded as the transportation zone. The lower part is the deposition zone. A model of the slit dam was installed 2.8 m upstream of the outflow plain (Fig. 2b). The slit dam consists of three posts. The post spacing of the modelled slit dam varies from 27 mm to 72 mm by decreasing thickness of the posts.

To measure the flow depth of the debris flows, three laser sensors (Leuze, ODSL 30/V-30M-S12, named Lasers A to C) with a resolution of 1 mm were used at the monitoring sections A, B, and C. Meanwhile, three cameras (SONY FDR-AX40, named camera A to C) with a resolution of 1440×1080 pixels and a frame rate of 25 frames per second (fps) were fixed to capture the kinematics of the tests. Three grid lines, with intervals of 0.01 m, were drawn at the base of the channel at sections A, B, and C to approximate the frontal velocity of the flow using the high-speed cameras. In addition, a fourth camera (Nikon D 610, named camera D), with a resolution of 1280×720 pixels and a frame rate of 60 fps, was positioned at the side of the flume to capture the interaction process between debris flows and slit dams. One differential strain-gauge pore pressure transducer (PPT, model KPSI 735, 0 ~ 18 kPa) was used to record the variation in the pore water pressure of debris flows.

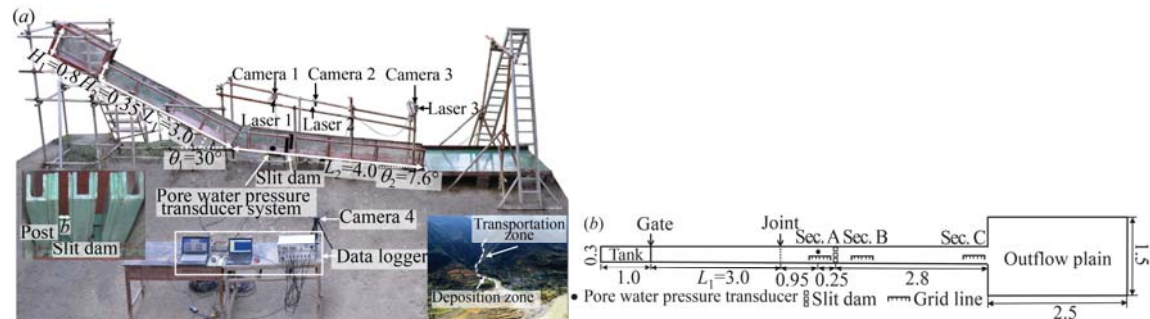


Fig. 2 Setup of flume model tests. (a) side view of flume model; inset on the left: model slit dam; inset on the right: a natural debris flow channel in Kangding county, Sichuan, China; (b) plan view of flume model; (all dimensions in m)

2.3. Experimental materials and program

The granular materials used in the tests were obtained from the debris-flow deposition fan of the Jiangjia Ravine, in the Dongchuan District of Yunnan Province, China. The granular material with diameters larger than 20 mm were removed to make sure that all particles flow smoothly in the flume (Cui et al., 2015). Figure 3 shows the topographic

map of Jiangjia Ravine, the sample collecting site, and the grain-size distribution of the granular material used for the tests. The bulk density of the granular materials was measured to be 2680 kg/m³ in the laboratory. Sixty-five kg dry granular material was used in each test.

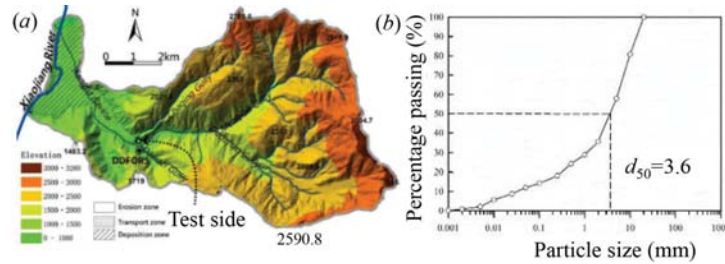


Fig. 3 (a) The topographic map of Jiangjia Ravine in Yunnan province and the sample collecting site; (b) particle size distribution of the granular material

The water content of the debris flows and the relative post spacing were varied to discern their influence on the flow-dam interaction. The range of water contents that were used in the experiments was selected based on trial and error. When the water content of debris flow is less than 18% (15% adopted), the granular-water mixture is not yet considered to be saturated. The velocity of the flow is very low and the debris stops upslope of the slit dam. On the other hand, when the water content of debris flow is greater than 38% (40% adopted), the *Fr* of the approaching flow becomes higher than 8.5, exceeding the common *Fr* range of natural debris flows. Therefore, the water content is varied from 18% to 38% with an interval of 4%. Narrow relative post spacings were set to be $b/d_{max} < 2.0$ (i.e., $b/d_{max} = 1.4$ and 1.8) while wide relative post spacings varying from 2.3 to 3.6. Details of the modelling tests were summarized in Table 1.

Table 1. Test program of debris flow-slit dam interaction

Test ID	Relative post spacing b/d_{max}	Water content W (%)	Bulk density (kg/m ³)	Solid concentration (C_s)	Degree of liquefaction σ_w/α	Approach velocity (m/s)	Flow depth (m)	Froude number Fr
w18-1.4	1.4	18	2160	0.69	0.17	1.56	0.056	2.11
w18-1.8	1.8					1.62	0.056	2.19
w18-2.3	2.3					1.42	0.070	1.72
w18-2.7	2.7					1.39	0.073	1.65
w18-3.1	3.1					1.70	0.061	2.21
w18-3.6	3.6					1.65	0.070	2.00
w22-1.4	1.4	22	2010	0.63	0.45	3.00	0.045	4.53
w22-1.8	1.8					3.25	0.035	5.57
w22-2.3	2.3					3.25	0.035	5.57
w22-2.7	2.7					3.00	0.039	4.87
w22-3.1	3.1					3.00	0.040	4.81
w22-3.6	3.6					3.08	0.043	4.76
w26-1.4	1.4	26	1970	0.59	0.55	3.25	0.043	5.02
w26-1.8	1.8					3.38	0.040	5.42
w26-2.3	2.3					3.50	0.036	5.92
w26-2.7	2.7					3.38	0.036	5.71
w26-3.1	3.1					3.38	0.040	5.42
w26-3.6	3.6					3.33	0.040	5.34
w30-1.4	1.4	30	1920	0.56	0.59	3.50	0.049	5.07
w30-1.8	1.8					3.62	0.050	5.19
w30-2.3	2.3					3.88	0.044	5.93
w30-2.7	2.7					3.75	0.041	5.94
w30-3.1	3.1					3.88	0.040	6.22
w30-3.6	3.6					3.50	0.046	5.23
w34-1.4	1.4	34	1880	0.53	0.65	4.00	0.040	6.41
w34-1.8	1.8					3.88	0.046	5.80
w34-2.3	2.3					4.00	0.043	6.18
w34-2.7	2.7					4.00	0.044	6.11
w34-3.1	3.1					4.12	0.036	6.96
w34-3.6	3.6					4.00	0.046	5.98
w38-1.4	1.4	38	1830	0.50	0.83	4.12	0.049	5.97
w38-1.8	1.8					4.25	0.045	6.42
w38-2.3	2.3					4.12	0.036	6.96
w38-2.7	2.7					4.25	0.039	6.90
w38-3.1	3.1					4.25	0.042	6.65
w38-3.6	3.6					4.00	0.043	6.18

3. Observed interaction process between debris flow and slit dam

In this study, two typical water contents (i.e., $w=18\%$, $w=30\%$) and two typical relative post spacings (i.e., $b/d_{\max}=1.4$, $b/d_{\max}=3.1$) were chosen to illustrate the interaction processes between debris flows and slit dams, which contributes to the understanding of the interaction mechanisms between slit dams and debris flows.

3.1. Interaction process between slit dam and debris flows with low water content

Debris flows with low water contents (low Fr condition), such as those in $w18-1.4$, approach the slit dam with narrow relative post spacing. The debris-flow front is thin and wedge-shaped. It approaches slit dam at $t=0$ s (Fig. 4a) and impacts the slit dam at $t=0.22$ s. The measured frontal velocity is 1.56 m/s (Fig. 4b). When the front of the debris flow impacts the slit dam, few debris are observed to pass through while the majority of the debris are retained. Sediments depositing behind the slit dam form a dead zone (a region in which the debris are static). At $t=0.35$ s, the trajectory of the flow started to change as a thin layer of run-up (the debris layer keep running while its height increasing) develops before the slit dam (Figs. 4c&d). As the interaction proceeds, more debris pile up (debris accumulation) on top of the dead zone (Fig. 4e). The pile-up stops when the sediments reach the highest point of the flow (Fig. 4f). Afterwards, the deposited mass begins to propagate upstream along the surface of dead zone (Fig. 4g). The deposits eventually reach a static state at $t=1.33$ s (Fig. 4h).

Figure 5 shows the interaction between debris flows with a low water content $w=18\%$ (low Fr condition) and a slit dam with wide relative post spacing $b/d_{\max}=3.1$. The interaction process observed in this test was similar to that observed in test $w18-1.4$ (Fig. 4) as previously discussed, including the tapered approaching debris flow with a measured frontal velocity of 1.70 m/s, impacting on the slit dam (Fig. 5a&b), runs-up (Fig. 5c&d), and piles-up on top of the dead zone (Fig. 5e), backflows (Fig. 5f), and eventually assumes a static state (Fig. 5h). When the debris flow impacts on the slit dam, much more of granular material-water mixture pass through the posts of slit dam. In addition, a weaker backflow was observed in this test as compared to that of $w18-1.4$.

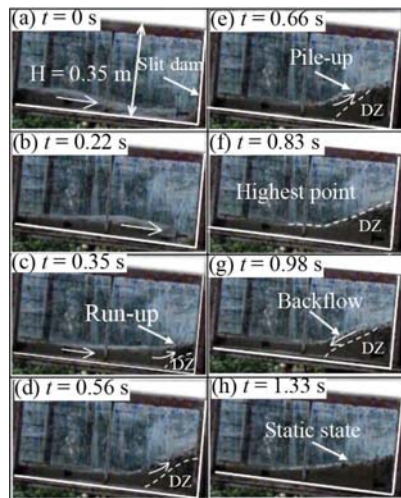


Fig. 4 Interaction process between debris flow with low water content ($w=18\%$) and slit dam with narrow relative post spacing ($b/d_{\max}=1.4$): test $w18-1.4$. DZ represents “dead zone”.

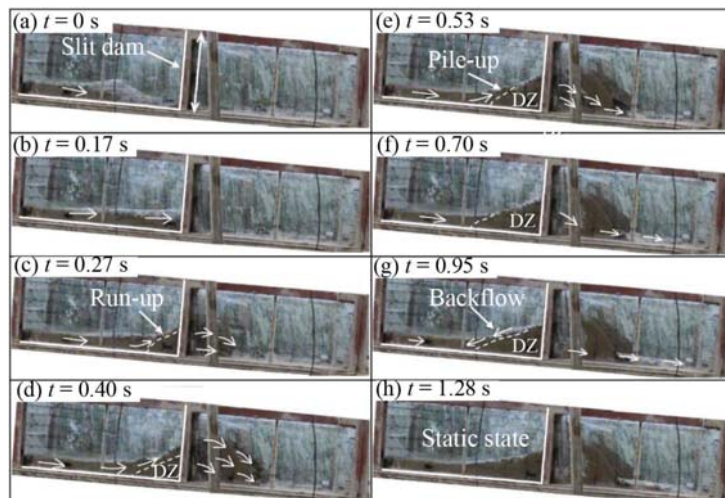


Fig. 5 Interaction process between debris flow with low water content ($w=18\%$) and slit dam with wide relative post spacing ($b/d_{\max}=3.1$): test $w18-3.1$. DZ represents “dead zone”.

3.2. Interaction process between slit dam and debris flows with high water content

Debris flows with high water contents (high Fr condition) were set to impact the slit dams with narrow relative post spacings. Taking the test $w30-1.4$ as an example, a thinner debris-flow front with a larger velocity of 3.5 m/s approaches the slit dam at $t=0$ s (Fig. 6a). Upon impacting the slit dam, part of the debris flow, the main of the slurry, passes through the slit dam and develops a distinct run-up along the face of the slit dam (Figs. 6b&c). Overtopping is observed at $t=0.26$ s (Fig. 6c) and $t=0.43$ s (Fig. 6d). Run-up continues to overtop the slit dam and the run-up region becomes thicker (Fig. 6d). Meanwhile, backward rolling occurs in the run-up region, where part of

debris flow hits the posts of the slit dam and is bounced backward (Fig. 6d). The vertical jet begins to fall down towards the channel base (Fig. 6e). At $t = 0.93$ s, more distinct falling towards the channel base is observed, as well as a bouncing phenomenon which happens when the granular-water mixtures splatter against the channel base (Fig. 6f). Then the granular material-water mixtures upstream of the slit dam start to flow back, increasing the flow's depth (Fig. 6g). Finally, the slit dam retains the sediments, and the slurry contained in the granular material-water mixtures flows through the slit dam (Fig. 6h).

Debris flows with high water contents (high Fr condition) were also set to impact on the slit dam with wide relative post spacings. Taking the test w30-3.1 for example, the measured frontal velocity of a thin debris flow was 3.9 m/s (Fig. 7a). The debris flow makes impact on the slit dam and more of the granular material-water mixture flow through the post spacing. Meanwhile, run-up is observed to develop (Fig. 7b), but was not distinctly thicker than that observed in test w30-1.4 (Figs. 7c&d). No apparent overtopping was observed. At $t = 0.67$ s, backward rolling occurs (Fig. 7e), which leads to a bouncing phenomenon upstream of the slit dam and is accompanied by the falling of the debris flow down into the channel base downstream of the slit dam (Fig. 7f). Then, the granular material-water mixture upstream of the slit dam start to flow back (Fig. 7g). Finally, majority of the sediment flow through the post spacing, leaving behind a relatively low fraction of its volume behind the slit dam (Fig. 7h).

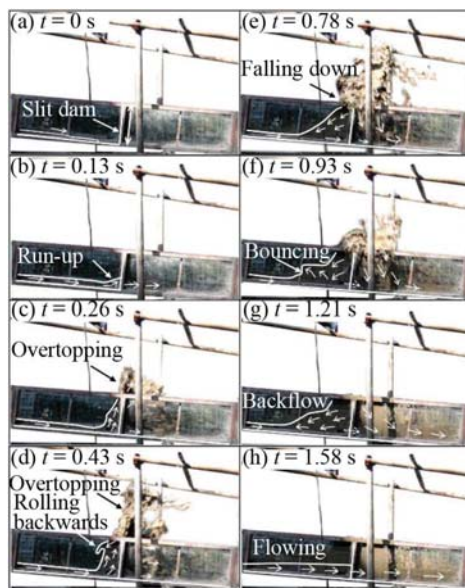


Fig. 6 Interaction process between debris flow with high water content ($w=30\%$) and slit dam with narrow relative post spacing ($b/d_{\max}=1.4$): test w30-1.4.

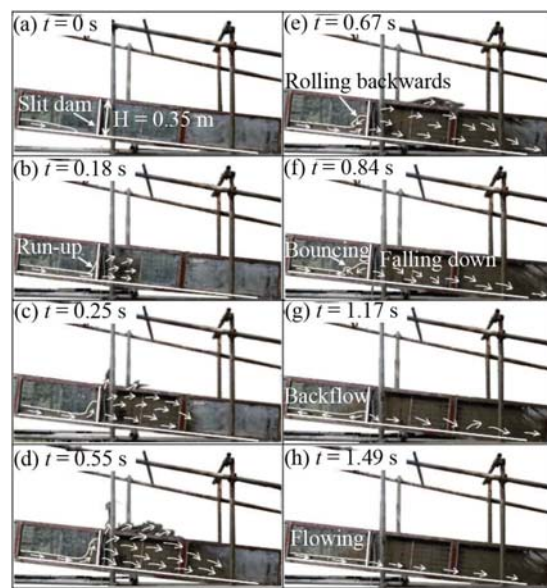


Fig. 7 Interaction process between debris flow with high water content ($w=30\%$) and slit dam with wide relative post spacing ($b/d_{\max}=3.1$): test w30-3.1.

4. Interaction process influenced by water content and relative post spacing

4.1. Influence of water content on interaction process

Comparing Fig. 4 with Fig. 6, with the same $b/d_{\max}=1.4$, the difference in the interaction process is obvious. With a water content of 18%, debris flow-slit dam interaction phenomena such as run-up, dead zone, pipe-up, and backflow are observed. However, when the water content is increased to 30%, additional interaction processes such as overtopping, backwater effect, and bouncing (happens in the form of sediments splash down to the base of the flume) are observed. It is also noted that there is no formation of dead zones. Similarly, set-ups with water contents of 18% (Figs. 5) and 30% (Figs. 7) with relative post spacing of 3.1 are compared. The main interaction processes observed in Fig. 5 are very much similar to those in Fig. 4. The case in Fig. 7 however, shows a much more violent interaction process as debris flows impact the slit dam. Most of its content fly through the slit dam with only a small portion of the debris flow running up along the posts of slit dam and then falling back down to the base of the flume, causing a bouncing phenomenon (Fig. 7f).

Figure 8 show the different interaction processes caused by different water contents that are varied from 18% to 38% and the relative post spacing is 1.8. Here it is observed, that overtopping or run-up are at their highest points. It is noted that when the water content of debris flow is 18% (Fig. 8a), no overtopping phenomenon is observed. However, when $w \geq 26\%$, there is distinct overtopping. Moreover, the height of overtopping increases with the increasing water content.

4.2. Influence of relative post spacing on interaction process

Cases where the debris-flow water contents are both kept at 18%, while the b/d_{\max} is increased from 1.4 (Figs. 4) to 3.1 (Figs. 5) are compared to isolate the influence of the relative post spacing. The interaction processes are almost identical, except that more debris passes through the slit dam when b/d_{\max} is wider. Similarly, comparing Fig. 6 with Fig. 7, the water contents of debris flow are kept at 30% and the b/d_{\max} also increases from 1.4 to 3.1. The differences in these two tests are obvious. In test w30-1.4, apparent run-up, overtopping, backwater effect, and bouncing after the debris flow falls down to the base of the flume are observed. In contrast, in test w30-3.1, due to the wider b/d_{\max} , more debris pass through the slit dam in a jet flow manner, and no overtopping phenomenon is observed. The run-up and bouncing phenomena are still observed but are not as obvious as compared with those in test w30-1.4.

The different interaction processes caused by different b/d_{\max} are also shown in Fig. 9, where the water contents are kept at 30% and the b/d_{\max} is increased from 1.4 to 3.1. In these cases, overtopping or jet flow are at their highest. When $b/d_{\max} \leq 2.3$, overtopping after the debris flow makes impact on the slit dam dominates. Increasing b/d_{\max} , decreases the height of the run-up (h_c). However, when $b/d_{\max} > 2.3$, majority of the granular material-water mixture pass through the slit dam as a jet flow and no obvious overtopping is observed.

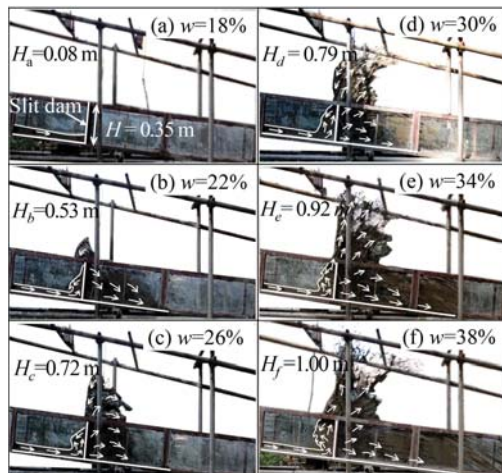


Fig. 8 Snapshots of each test when the overtopping or run-up is at its highest point. Relative post spacing is kept at 1.8 while the water content is varied from 18% to 38% at an interval of 4%.

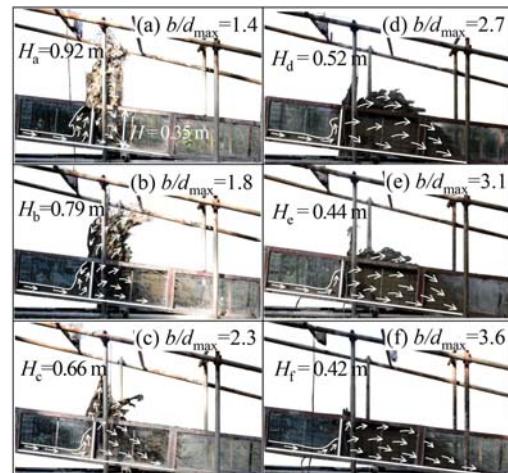


Fig. 9 Influence of the relative post spacing on the interaction process between debris flow and slit dam. Water content is kept at 30% and the relative post spacing ranges from 1.4 to 3.6.

5. Influence of water content and relative post spacing on the height of run-up

Overtopping phenomenon occurs after the interaction between debris flows and slit dams. This potentially causes the foundation of dams to be eroded and result in structural instability (Pan et al., 2013). The degree of overtopping is determined by the height of run-up. Accordingly, it is imperative to ascertain the height of run-up after the interaction between debris flow and slit dam. In this study, the influence of water content and relative post spacing on the height of run-up is investigated. The height of the run-up (h_c) is normalized by the depth of approaching flow (h). This value is named the relative run-up height (h_c/h).

Figure 10 shows the relationship between the relative run-up height (varying water contents) and the relative post spacing. When the relative post spacing is constant, the relative height of run-up increases with the water content. When $w \geq 22\%$, the relative run-up height decreases with the increasing relative post spacing. Indeed, the relative run-

up height reaches its maximum value (about 30) when $w=38\%$ and $b/d_{\max}=1.4$. For debris flow with $w=18\%$, the relative run-up height is obviously lower than those with $w \geq 22\%$, and the influence of the relative post spacing on the relative run-up height is negligible. It is also noticed that the overtopping phenomenon is more likely to occur when $w \geq 22\%$ than when $w=18\%$.

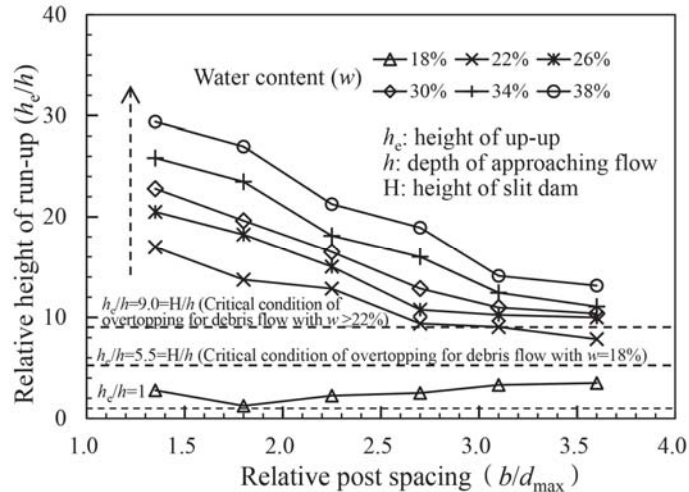


Fig. 10 The relationships between relative run-up height (h_c/h) and relative post spacing (b/d_{\max}) for different water contents; h_c : height of run-up.

6. Interaction mechanisms between debris flows and slit dams

Based on the analysis of the interaction processes between debris flows and slit dams, it is evident that water content w and relative post spacing b/d_{\max} are two key variables influencing the interaction mechanisms. Hürlimann et al. (2015) demonstrated, through laboratory experiments, that water content strongly influences the run-out distance of debris flows. In fact, water content essentially reflects the degree of liquefaction of debris flows. The degree of liquefaction, which is defined as the ratio of pore water pressure (σ_w) to the total normal stress of debris flow (σ), is used to represent the normalized influence of basal pore pressure on Coulomb resistance (Iverson et al., 2010). The total normal stress (σ_t) was estimated by the bulk density and approaching flow depth, that is $\sigma_t \approx \rho g h \cos \theta$, where g is the gravitational acceleration; and θ is the inclination of the channel (Iverson et al., 2010). Both flume experiments (Iverson, 1997; 2010) and field observation (McArdell et al., 2007) suggested that the basal fluid water pressure (proportional to the degree of liquefaction) contributes to the mobility of debris flows.

With lower degree of liquefaction, the grain-contact effective stress dominates. Force chains form much easier and the internal shearing of solid grains is enhanced. From the energy point of view, energy dissipation efficiency of the grain-contact effective stress is much higher than the viscous stress of the liquid phase. Accordingly, debris flows approach the slit dam with a lower velocity. This explains why, when $w < 26\%$, the debris flow with a lower velocity impacts on the slit dam, no distinct overtopping is observed, and the trapping capacity of slit dam is obviously influenced by b/d_{\max} .

On the contrary, with high degree of liquefaction, the effective stress of debris flows decreases, and debris flows are more fluid-like. Thus the basal resistance becomes minor, leading to higher mobility of debris flows. In addition, solid inertial force dominates during the movement, resulting in highly energetic debris flows. Accordingly, when $w \geq 26\%$, debris flows with higher velocities impact the slit dam. When b/d_{\max} is narrow, the granular-water mixtures can run up and overtop the slit dam. This further explains why when water content $w \geq 26\%$, the influence of relative post spacing b/d_{\max} on the trapping capacity is less obvious.

7. Conclusions

A set of flume experiments were carried out to study the interaction mechanisms between slit dams and debris flows. The key findings that can be drawn from this study are:

- (1) The relative post spacing and water content govern the interaction mechanisms of slit dams and debris flows. When water content $w < 22\%$, pile-up occurs and no distinct overtopping is observed, showing that the

trapping capacity of the slit dam is obviously influenced by b/d_{\max} . When $w \geq 22\%$ and the relative post spacing $b/d_{\max} \leq 2.3$, run-up, overtopping, and backwater effects are apparent, and dead zones do not form. The trapping capacity of slit dam is obviously influenced by water content. Moreover, when $w \geq 26\%$ and $b/d_{\max} > 2.3$, majority of the granular material-water mixtures pass through the slit dam in the form of a jet flow and no obvious overtopping phenomenon is observed.

- (2) The run-up height reaches its maximum value (about 30) when $w = 38\%$ and $b/d_{\max} = 1.4$. The relative run-up height is obviously lower for debris flows with $w = 18\%$, than those with $w \geq 22\%$, and the influence of the relative post spacing on the relative height of run-up is negligible.
- (3) The degree of liquefaction (σ_w/σ_t) dominates the interaction mechanisms between debris flows and slit dams are when the relative post spacing is kept constant. With a lower degree of liquefaction, the grain-contact effective stress dominates. Force chains are much easier to be formed and the internal shearing of solid grains is enhanced. On the contrary, with a high degree of liquefaction, the effective stress of debris flows decreases. Thus the basal resistance becomes minor, leading to highly mobile of debris flow.

Acknowledgements

The authors acknowledge the financial support from the National Natural Science Foundation of China (grant No. 11672318), the Youth Innovation Promotion Association, CAS, and the Chinese Academy of Sciences (CAS) Pioneer Hundred Talents Program. The financial support from research grant T22-603/15-N provided by the Research Grants Council of the Government of Hong Kong SAR, China is also greatly appreciated.

References

- Chanson, H., 2004, Sabo check dams-mountain protection systems in Japan: *Internal Journal of River Basin Management*, v. 2, no. 4, p. 301-307, doi: 10.1080/15715124.2004.9635240.
- Chehata, D., Zenit, R., and Wassgren, C.R., 2003, Dense granular flow around an immersed cylinder: *Physics of Fluids (1994-present)* v. 15, no. 6, p. 1622-1631, doi: 10.1063/1.1571826.
- Choi, C.E., Ng, C.W.W., Song, D., Kwan, J.H.S., Shiu, H.Y.K., Ho, K.K.S., and Koo, R.C.H., 2014, Flume investigation of landslide debris-resisting baffles: *Canadian Geotechnical Journal*, v. 51, no. 5, p. 540-553, doi: 10.1139/cgj-2013-0115.
- Choi, C.E., Ng, C.W.W., Au-Yeung, S.C.H., and Goodwin, G., 2015, Froude characteristics of both dense granular and water flows in flume modelling: *Landslides*, v. 12, no. 6, p. 1197-1206.
- Choi, S.K., Lee, J.M., and Kwon, T.H., 2018, Effect of slit-type barrier on characteristics of water-dominant debris flows: small-scale physical modelling: *Landslides*, v. 12, no. 6, p. 111-122.
- Cui, P., Zeng, C., and Lei, Y., 2015, Experimental analysis on the impact force of viscous debris flow: *Earth Surface Processes and Landforms*, v. 40, no. 12, p. 1644-1655, doi: 10.1002/esp.3744.
- Han, W., and Ou, G., 2006, Efficiency of slit dam prevention against non-viscous debris flow: *Wuhan University Journal of Natural Sciences*, v. 11, no. 4, p. 865-869.
- Hauksson, S., Pagliardi, M., Barbolini, M., and Jóhannesson, T., 2007, Laboratory measurements of impact forces of supercritical granular flow against mast-like obstacles: *Cold Regions Science and Technology*, v. 49, no. 1, p. 54-63, doi: 10.1016/j.coldregions.2007.01.007.
- Hübl, J., Suda, J., and Proske, D., 2009, Debris flow impact estimation, in *Proceedings, The 11th international symposium on water management and hydraulic engineering*, Ohrid, Macedonia, September 2009, Volume WMHE2009, p. 137-148.
- Hürlimann, M., McArdell, B.W., and Rickli, C., 2015, Field and laboratory analysis of the runout characteristics of hillslope debris flows in Switzerland: *Geomorphology*, v. 232, p. 20-32, doi: 10.1016/j.geomorph.2014.11.030.
- Iverson, R.M., 1997, The physics of debris flows: *Reviews of geophysics*, v. 34, no. 3, p. 244-296, doi: 10.1029/97RG00426.
- Iverson, R.M., Logan, M., LaHusen, R.G., and Berti, M., 2010, The perfect debris flow? Aggregated results from 28 large-scale experiments: *Journal of Geophysical Research: Earth Surface*, v. 115, no. F03005, doi: 10.1029/2009JF001514.
- Johnson, P.A., and McCuen, R.H., 1989, Slit dam design for debris flow mitigation: *Journal of Hydraulic Engineering*, v. 115, no. 9, p. 1293-1296, doi: 10.1061/(ASCE)0733-9429(1989)115:9(1293).
- Lien, H.P., and Tsai, F.W., 2000, Debris flow control by using slit dams: *International Journal of Sediment Research*, v. 15, no. 4, p. 391-409.
- Lien, H.P., 2003, Design of slit dams for controlling stony debris flows: *International Journal of Sediment Research*, v. 18, no. 1, p. 74-87.
- Lin, Y.Y., and Jiang, Y.Z., 1988, Experimental study on the effectiveness of slit dam on debris flow: *Journal of Chinese soil and water conservation*, v. 19, no. 1, p. 40-57 (in Chinese).
- Mizuyama, T., Suzuki, H., Oikaka, Y., and Morita, A., 1988, Experimental study on permeable sabo dam: *Journal of Japan erosion control engineering society*, v. 41, no. 2, p. 21-25 (in Japanese).
- MLR (Ministry of Land and Resources), 2004, Design standards for debris flow hazard mitigation measures (DZ/T0239-2004), Beijing, China: Chinese Geological Survey, Ministry of Land and Resources (in Chinese).
- McArdell, B.W., Bartelt, P., and Kowalski, J., 2007, Field observations of basal forces and fluid pore pressure in a debris flow: *Geophysical Research Letters*, v. 34, no. 7, doi: 10.1029/2006GL029183.
- Ng, C.W.W., Choi, C.E., Song, D., Kwan, J.H.S., Koo, R.C.H., Shiu, H.Y.K., and Ho, K.K.S., 2015, Physical modelling of baffles influence on landslide debris mobility: *Landslides*, v. 12, no. 1, p. 1-18.
- Pan, H., Wang, R., Huang, J., 2013, Study on the ultimate depth of scour pit downstream of debris flow sabo dam based on the energy method: *Engineering Geology*, v. 160 p. 103-109, doi: 10.1016/j.enggeo.2013.03.026.
- Shima, J., Moriyama, H., Kokuryo, H., Ishikawa, N., and Mizuyama, T., 2016, Prevention and Mitigation of Debris Flow Hazards by Using Steel Open-Type Sabo Dams: *International Journal of Erosion Control Engineering*, v. 9, no. 3, p. 135-144, doi: 10.13101/ijece.9.135.

Empirical model for assessing dynamic susceptibility of post-earthquake debris flows

Kaiheng Hu^{a,b*}, Zhang Wang^{a,b,c}, Cheng Chen^{a,b,c}, Xiuzhen Li^{a,b}

^aKey Laboratory of Mountain Hazards and Earth Surface Processes, Chinese Academy of Sciences, Chengdu, Sichuan 610041, China

^bInstitute of Mountain Hazards and Environment, Chinese Academy of Sciences & Ministry of Water Conservancy, Chengdu, Sichuan 610041, China

^cUniversity of Chinese Academy of Sciences, Beijing 100049, China

Abstract:

Debris-flow susceptibility is controlled not only by static effective factors such as topography and lithology, but also by dynamic effective factors such as earthquake, rainfall and human activity. In this paper, a simple model of calculating the dynamic susceptibility is developed based on the assumption of linear relationship between the static and dynamic susceptibilities. The influence of earthquake and rainfall events is represent by two coefficients. The earthquake coefficient is considered as an exponential function of intensity, and a negative power function of elapsed time. The rainfall coefficient is proportional to the occurrence days of heavy rainfall. This model is applied to assess the debris-flow susceptibility of Hengduan mountainous area from 2000 to 2015. Four static effective factors including relative relief, slope, lithology and fault density are used to calculate the static susceptibility by ARCGIS grid toolbox. There are six earthquake events since 1995 whose intensity zones of $\geq VI$ are intersected with the Hengduan area. The earthquake coefficient is calculated with the intensity zoning data of each of the six events and then is accumulated to get the final earthquake coefficient in each year. TRMM satellite rainfall data from 2000 to 2015 are collected to extract the occurrence days of heavy rainfall which is used to calculate the rainfall coefficient. The dynamic susceptibilities from 2000 to 2015 are obtained by multiplying the static susceptibility with the earthquake and rainfall coefficients in respective year. The 2015 susceptibility map shows a qualitative agreement with the distribution map of disasters in 2015.

Keywords: Debris flow; Susceptibility; earthquake; rainfall; dynamic assessment;

1. Introduction

Risk assessment is one of the most important non-engineering countermeasures against debris-flow hazards. The risk assessment models have evolved from qualitative evaluation into quantitative evaluation, and from geological statistical methods into physical models and numerical simulation methods since the 19th century (Wei et al., 2003). There are three different levels of risk assessment: susceptibility, hazard and risk assessment (Hu et al., 2013). The susceptibility can be considered as a kind of occurrence probability of hazards at a place. Most of susceptibility assessing methods relate it to effective environmental factors such as rainfall, slope, slope direction, lithology, etc. by geological and statistical models (Carrara, 1991; Jade, 1993; Dai, 2002; Carrara, 2008; Tang, 1994; Wei, 2000; Liu, 2004; Hu, 2012; Cheng, 2015).

Debris-flow susceptibility is controlled not only by static effective factors such as topography and lithology, but also by dynamic effective factors such as earthquake, rainfall and human activity. So the susceptibility varies with dynamic factors. For example, the magnitude and frequency of debris-flow events increased largely in Longmeng mountain after the 2008 Wenchuan earthquake (Cui et al, 2011). However, the present susceptibility assessing models are based on static effective factors such as slope, relative elevation, lithology etc., and cannot reflect such a variation. Due to lack of awareness of such susceptibility changes, reconstructions such as residential buildings and tourist facilities were built in the areas with highly increasing susceptibility, and suffered a great deal of damages. In order to assessing varying susceptibility resulted from earthquakes and rainfalls, a simple model is developed based on the assumption of linear relationship between the static and dynamic susceptibilities. The influence of earthquake and rainfall events represent by two coefficients. The

* Corresponding author e-mail address: khhu@imde.ac.cn

earthquake coefficient is considered as an exponential function of intensity, and a negative power function of elapsed time. Hengduan mountainous area in the southwestern China is chosen as the study case (Fig 1).

2. Dynamic model and method

2.1. Dynamic model

The susceptibility is determined by two factors: static and dynamic. Static factors are determined by background conditions, such as relative relief, slope, lithology, fault density, etc., which vary very little over hundreds of years and can be considered as unchanged. Other factors such as earthquakes, rainfalls and human activities can result in the rapid change of water and soil supplies and are considered as dynamic factors (Fig 2).

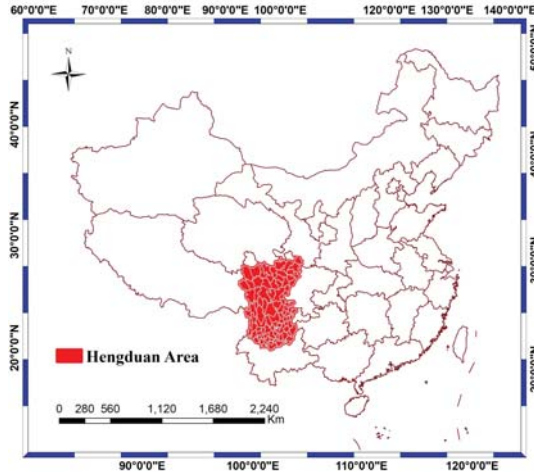


Fig.1 The location map of Hengduan mountainous area

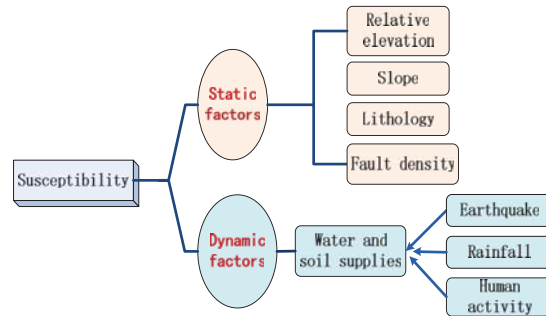


Fig.2 Static and dynamic effective factors with geo-hazard susceptibility

Due to the complexity of human activities, we only consider the effects of earthquake and rainfall. It is assumed that the static factors, the effects of earthquake and rainfall are independent statistically. The time unit of assessing is simplified to one year, and the annual susceptibility is assumed to be proportional to the static susceptibility under the influence of earthquakes and rainfalls. Then the dynamic susceptibility can be expressed as the product of static susceptibility, earthquake and rainfall influence coefficients:

$$H(t) = S \times E_k(t) \times R_k(t) \tag{1}$$

where, H is the annual susceptibility of debris flows; S is the susceptibility caused by static factors (i.e. background value of susceptibility); E_k and R_k are annual influence coefficients of earthquake and rainfall.

2.2. Static evaluation method

The static susceptibility assessment is evaluated by factors that remain unchanged or change slowly, such as topography, geology, vegetation, soil and other underlying surface factors. The following conditional probability model is adopted:

$$S = \sum_{i=1}^n \omega_i P_i(x) \tag{2}$$

where, ω_i is the weight coefficient of the i factor, $P_i(x)$ is the probability of debris-flow occurrence when the i factor is equal to x , i.e. the conditional probability of the i factor. Usually x takes some interval or some category. If a square grid cell is used as evaluation unit, then

$$P_i(x) = \frac{n_i(x)}{N_i(x)} \tag{3}$$

where, $N_i(x)$ is the total number of grid cells at which the value of the i factor = x , and $n_i(x)$ is the total number of grid cells where the value of the i factor = x and debris flows occurred. The weights of static factors

are determined by statistical methods, such as Grey Relational Degree or Analytic Hierarchy Process (Li et al., 2010).

Based on the debris-flow inventory data in Hengduan area, the principal component analysis method found that relative relief, slope, lithology and fault density had the closest relation with disasters (Wei et al., 2008). The relative relief is defined as the difference between the maximum and the minimum elevation within a certain radius. It represents the energy condition of soil and water migration and reflects the energy of local terrain. The slope is the height difference of unit length, reflecting the energy gradient. The lithology is divided into quaternary deposits, soft rock, intercalated soft and hard rock, and hard rock. The fault density is defined as the total length (km) of faults per unit area (km²). The conditional probability of the four factors is calculated respectively in ARCGIS according to Eq.(3) (Fig 3).

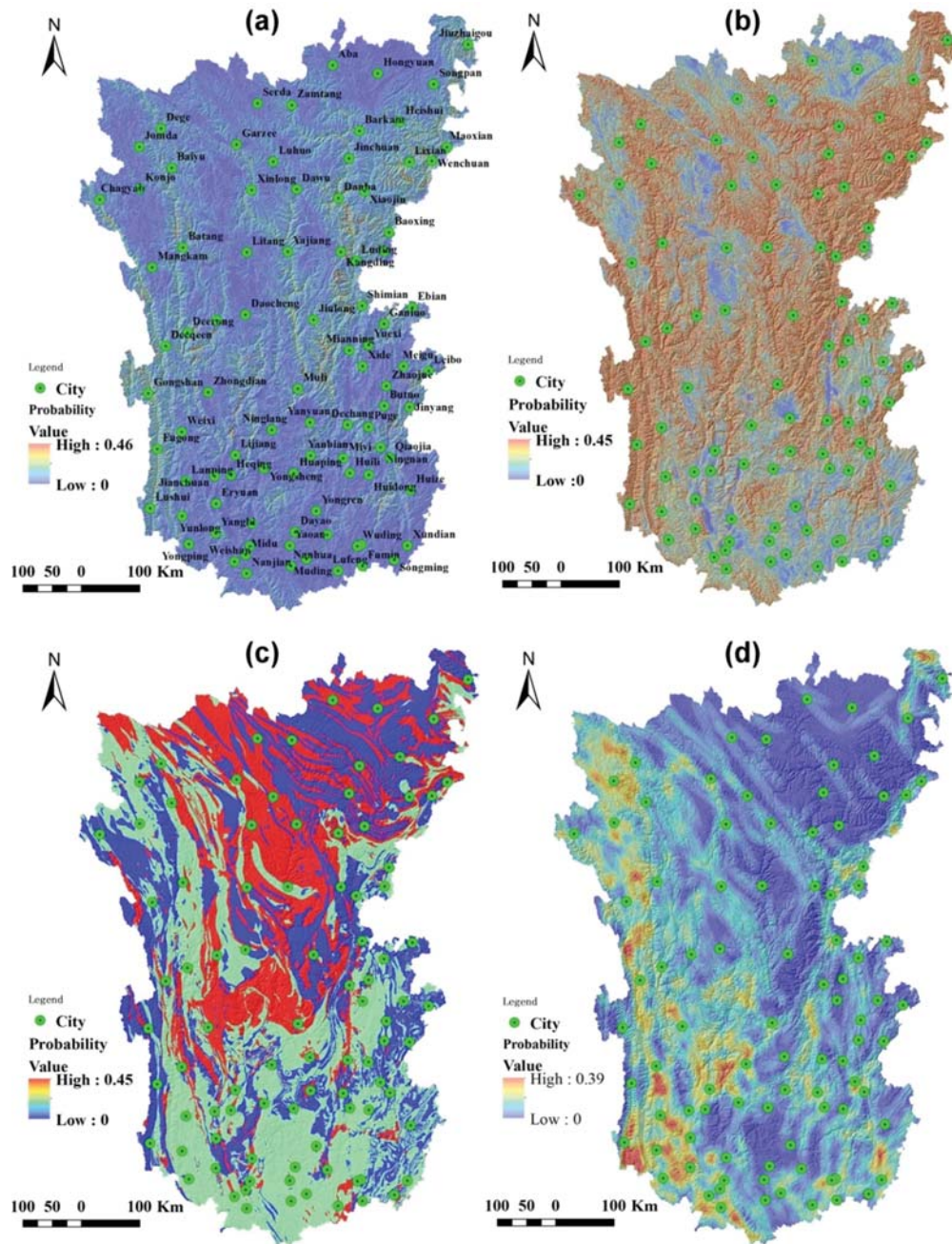


Fig.3 Occurrence probabilities of the hazard in different background factors in Hengduan mountainous region (a. relative elevation, b. slope, c. lithology, d. fault density)

The Grey Relational Degree and GIS are used to determine the weight values of relative relief, slope, lithology and fault density in the susceptibility, respectively (Li et al., 2010): relative relief=0.2048, slope=0.1969, lithology = 0.1836, fault density = 0.2196. The static susceptibility of the Hengduan area is obtained by summing the weighted conditional probability of each factor (Fig 4).

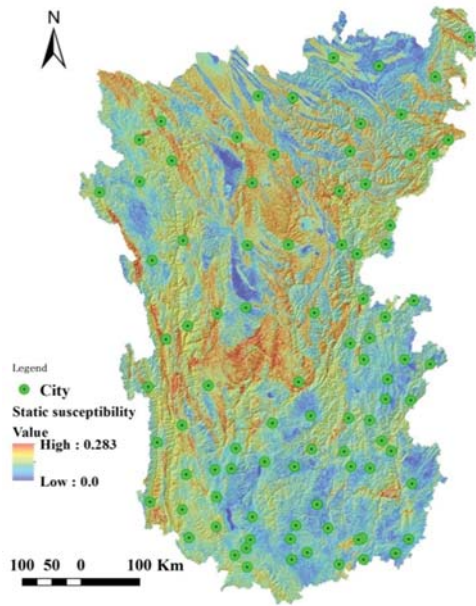


Fig.4 Static susceptibility of the hazard in in Hengduan mountainous region

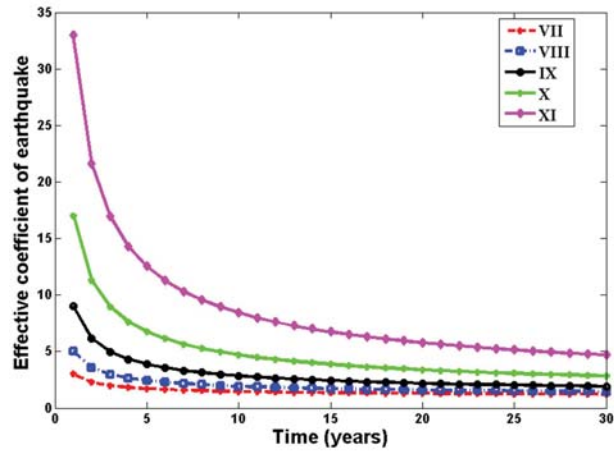


Fig.5 Decaying curve of effective coefficient of earthquake Ek for different seismic intensities according to Eq(4)

3. Seismic effect coefficient

Strong earthquakes often trigger a large number of landslides. Lots of loose material caused by seismic landslides, avalanches and rockfalls accumulates at hillslopes or upstream of catchments, providing abundant material for debris flow, which can easily occur eroded by rainstorms. Large earthquakes in mountainous area at home and abroad (such as the Great Kanto Earthquake in Japan, the Chi-Chi earthquake in Taiwan, the Chayu Earthquake in Tibet, the Wenchuan Earthquake in Sichuan, etc.) indicate that the activity of debris-flow disaster is obviously enhanced, namely the number, scale and frequency are increased after the earthquake (Nakamura, 2000; Lin, 2004; Lin, 2006; Cui, 2008; Bao, 2004). Relevant studies have shown that the number of landslide initiated by earthquake in intensity region of V and below is very small (Xin and Wang, 1999). The number of landslide below VI degree in Wenchuan Earthquake is only 0.18% of the total (Cui et al., 2011). Moreover, the numbers of the landslides show an exponentially decreasing trend with the distances to epicenters or seismogenic faults (Prestininzi and Romeo, 2000; Chen and Hu, 2017). The seismic intensity has a close positive relationship with the epicentral or fault distances. Therefore, it is assumed that the influence coefficient of earthquake is a power law function of seismic intensity.

On the other hand, the debris flow triggered by earthquakes is a type of limited loose material supply (Bovis and Jakob, 1999). As time goes by, the loose materials are transported to the downstream channel or the deposition fan, or consolidate gradually and strengthen, which reduces their volume and erodibility. The activity of debris flows after the earthquake will decrease along with the reducing loose materials. As a result, the susceptibility decreases over time. According to the observation data of debris flows at Guxiang catchment after the Chayu Earthquake in Tibet in 1950, an empirical power function describes well the decay process of the debris-flow activity. The power function exponent is about -0.63 by linear regression method (Hu et al., 2011).

Based on the above analysis, the susceptibility is equal to the static one if the seismic intensity is below VI, and the susceptibility doubles when the intensity is one level higher. Meanwhile, the susceptibility will decrease exponentially along with time. Therefore, it can be expressed by the following formula for a single earthquake event:

$$E_k = \begin{cases} 1.0, & x < 6 \\ 1.0 + 2^{x-6} N^{-0.63}, & x \geq 6 \end{cases} \quad (4)$$

where, x is the intensity value ($=6.0\sim 11.0$ from VI to XI), and N is the total number of years after the earthquake. E_k is set to 1.0 when $x < VI$, indicating that the earthquake has no effect on the susceptibility. According to Eq.4, the influence coefficients in seismic area of VII, VIII and IX approximate to 1.0 after about 30 years from the curve, where is still very high after 30 years of XI seismic area, about 4.8 (Fig 5). In order to analyze the impact of the earthquake on the debris-flow susceptibility, all of earthquake events whose the area of $> VI$ intensity overlaps with the Hengduan region are collected since 1995 ($M_s > 6.5$) (Table 1). Then, according to the intensity range of each event, Eq.4 is used to calculate the total influence coefficient of seismic events from 1995 to 2015 in the Hengduan area (Hu et al., 2018).

Table 1. Historical earthquakes in Hengduan mountainous area since 1995

Date	Time (Beijing time)	Latitude (Degree)	Longitude (Degree)	Depth(km)	Magnitude	Maximum Intensity	Location
1995.10.24	6:46:49	25.9	102.2	15	6.5	IX	Wuding, Yunnan
1996.2.3	19:14:20	27.2	100.3	10	7.0	IX	Ljiang, Yunnan
2000.1.15	7:31:02	25.5	101.1	30	6.5	VIII	Yaoan, Yunnan
2008.5.12	14:28:01	31.0	103.4	14	8.0	XI	Wenchuan, Sichuan
2013.4.20	8:02:46	30.3	103.0	13	7.0	IX	Lushan, Sichuan
2014.8.3	16:30:10	27.1	103.3	12	6.5	IX	Ludian, yunan

4. Rainfall event effect coefficient

Debris flows in Hengduan area is mainly caused by heavy rain and storm. In general, if topographic and geological conditions are same, then the more heavy rain events happen, the more disasters can occur. Therefore, the influence coefficient of rainfall can be represented by occurrence days of heavy rain:

$$R_k = b \times I_{>25mm} \quad (5)$$

where, $I_{>25mm}$ is days of heavy rain, b is the proportion coefficient. By using TRMM satellites data, we calculate occurrence days of heavy rain at each grid cell in the area from 2000 to 2015 (Table 2). The cell size is 0.25° by 0.25° . There are 84497.13 days of heavy rains with an average daily rainfall of more than 25 mm per year added up for all of cells in China. At the same time, the average annual number of disasters is 23980.6 according to the National Geological Disaster Bulletin from 2001 to 2015. Some of the disasters were related to earthquakes, and most of them were triggered by rainfalls. The ratio of the disaster number to the day•cell number is 0.284. That means a heavy rain event can cause about 0.284 disasters on average per year in China. The occurrence probability of disasters in Hengduan area should be higher than the national average. However, there is no historical data of disasters in the area. Therefore, the value of b is considered as 0.284.

Table 2. Occurrence days of heavy rainfall and storm from 2000 to 2015 in the Hengduan

Year	Number of Day•Cell of rainfalls (> 25mm)		Year	Number of Day•Cell of rainfalls (> 25mm)	
	In Hengduan	In China		In Hengduan	In China
2000	5243	80913	2008	4975	88308
2001	6755	77337	2009	5344	78796
2002	5299	89154	2010	5198	94035
2003	5059	81621	2011	3737	72396
2004	5452	75345	2012	5501	95659
2005	4753	83898	2013	4733	89546
2006	4280	79684	2014	5505	85036
2007	5322	81314	2015	6123	95328

5. Dynamic evaluation result

Combining the static susceptibility, seismic influence coefficient and rainfall influence coefficient, the dynamic susceptibility is calculated by Eq.1 in Hengduan area from 2000 to 2015. The susceptibility is divided

into four levels: very high, high, moderate and low (Fig 6). By comparing the distribution of disaster events with the susceptibility map in 2015, it is found that they are spatially consistent by and large (Fig 7). The disasters mainly occurred on the west side of Longmen mountain, the lower reaches of Jinsha river and the northwest of Yunnan where the susceptibility is relatively high.

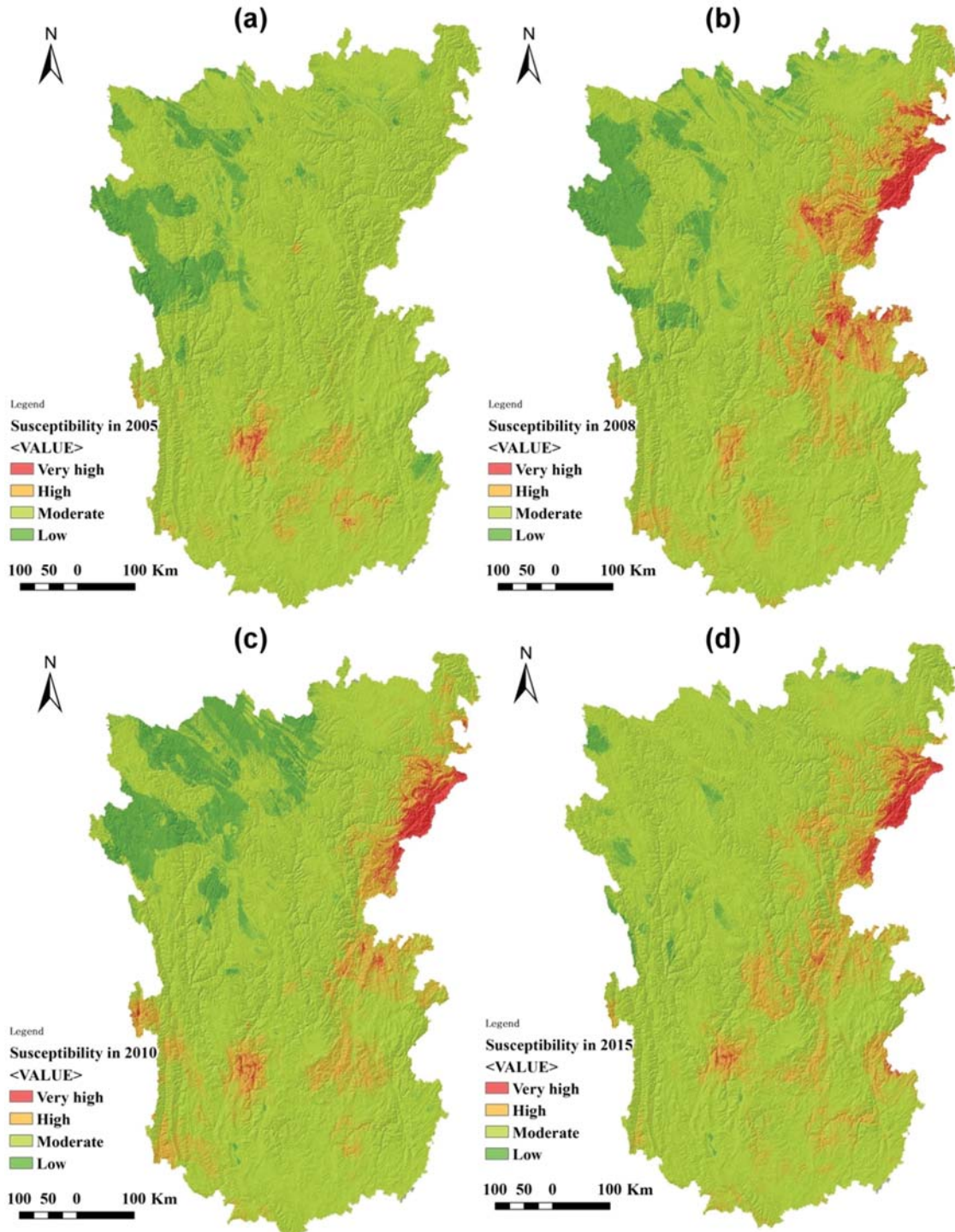


Fig.6 Maps of the dynamic susceptibility in 2005 (a), 2008 (b), 2010 (c) and 2015 (d) in the Hengduan

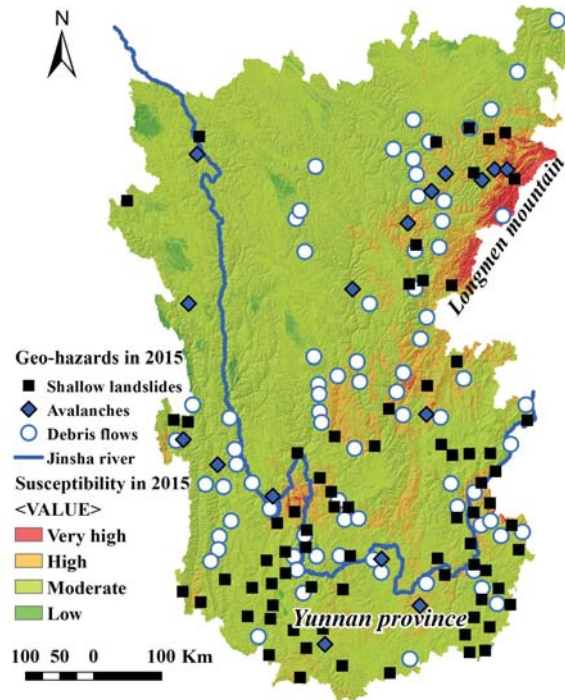


Fig.7 Maps of the hazard susceptibility and inventory in 2015 in the Hengduan

6. Conclusions

The susceptibility of debris-flow disaster is a dynamic process affected by earthquake, rainfall and human activities. The paper classifies the influencing factors of debris-flow susceptibility into static and dynamic factors, and analyzes the impact of earthquake intensity and its decay effect and heavy rain event on disasters. The method and model are used to calculate the seismic influence coefficient of debris-flow susceptibility and annual susceptibility from 2000 to 2015 in the Hengduan area. The results showed that the susceptibility in meizoseismal areas is still four times higher than that before the earthquake even though the quake happened 30 years ago. From 2000 to 2015, days of heavy rain in the Hengduan mountainous area varied greatly, and the maximum year was 1.81 times that of the minimum year. The actual distribution of disaster events is consistent with the results of susceptibility zoning in 2015.

The dynamic assessment model and method of disaster susceptibility is acceptable qualitatively, but more disaster event data are necessary for verification and improvement. The lack of disaster event data, errors of rainfall, geology and other data may lead to deviation in statistical calculation. In addition, there is no widely accepted model for the quantitative relationship between earthquake and debris flows. The linear hypothesis of dynamic susceptibility and the decaying model of seismic influence coefficient need more tests with real monitoring and study data.

Acknowledgements

This work has been supported by the National Basic Research Program of China (973 Program) (Grant No. 2015CB452704), and the National Natural Science Foundation of China (Grant No. 41790434 and 41601011).

References

- Bao, Y.J., 2004, Probability analysis and first-step predict of earthquake-induced landslides[Master thesis]: Institute of Geophysics, China Earthquake Administration.
- Bovis, M.J., and Jakob, M., 1999, The role of debris supply conditions in predicting debris flow activity: Earth Surf. Process. Landforms, v.24, p.1039-1054.

- Carrara, A., Cardinali, M., Detti R., Guzzetti, F., Pasqui, V., and Reichenbach, P., 1991, Gis techniques and statistical-models in evaluating landslide hazard: *Earth Surface Processes and Landforms*, v.16, p.427-445.
- Carrara, A., Crosta, G., and Frattini, P., 2008, Comparing models of debris-flow susceptibility in the alpine environment: *Geomorphology*, v.94, p.353-378.
- Chen, C., and Hu, K.H., 2017, Comparison of distribution of landslides triggered by Wenchuan, Lushan and Ludian earthquakes: *Journal of Engineering Geology*, v.25, p.806-814.
- Cui, P., He, S.M., Yao, L.K., Wang Z.Y. et al., 2011, Formation Mechanism and Risk Control in Wenchuan earthquake of Mountain Disasters: Science Press, Beijing.
- Cui, P., Chen, X.Q., Zhu, Y.Y. et al., 2011, The Wenchuan earthquake (May 12, 2008), Sichuan province, China, and resulting geohazards: *Nat Hazards*, v.56, p.19-36.
- Cui, P., Wei, F.Q., Chen, X.Q., and He, S.M., 2008, Geo-hazards in Wenchuan earthquake area and countermeasures for disaster reduction: *Bulletin of the Chinese Academy of Sciences*, v.23, p.317-323.
- Dai, F.C., and Lee, C.F., 2002, Landslide characteristics and slope instability modeling using GIS, Lantau Island, Hong Kong: *Geomorphology*, v.42, p.213-228.
- Hu, K.H., Cui, P., Han, Y.S., and You, Y., 2012, Susceptibility mapping of landslides and debris flows in 2008 Wenchuan earthquake by using cluster analysis and maximum likelihood classification methods: *Science of Soil and Water Conservation*, v.10, p. 12-18.
- Hu, K.H., Cui, P., You, Y., and Chen, X.Q., 2011, Influence of debris supply on the activity of post-quake debris flows: *The Chinese Journal of Geological Hazard and Control*, v.22, p.1-6.
- Hu, K.H., and Ding, M.T., 2013, Discussion on framework of landslide and debris-flow risk assessments: *The Chinese Journal of Geological Hazard and Control*, v.24, p.26-30.
- Hu, K.H., Chen, C., Li, X.Z, and Li, P., 2018, Dynamic assessment of debris-flow susceptibility under the influence of earthquake and rainfall events: *The Chinese Journal of Geological Hazard and Control*, v.29, no.2, p.1-8.
- Jade, S., and Sarkar, S., 1993, Statistical-models for slope instability classification: *Eng Geol*, v.36, p.91-98.
- Li, X.Z., Wang, C.H., and Deng, H.Y., 2010, Application of grey relation analysis and distance discrimination analysis methods in discriminating potential landslides of Xiluodu Reservoir area: *The Chinese Journal of Geological Hazard and Control*, v.21, p.77-81.
- Lin, C.W., Shieh, C.L., Yuan, B.D., et al., 2004, Impact of Chi-Chi earthquake on the occurrence of landslides and debris flows: example from the Chenyulan River watershed, Nantou, Taiwan: *Engineering Geology*, v.71, p.49-61.
- Lin, C.W., Liu, S.H., Lee, S.Y., et al., 2006, Impacts on the Chi-Chi earthquake on subsequent rainfall-induced landslides in central Taiwan: *Engineering Geology*, v.86, p.87-101.
- Liu, X.L., Wang, Q.C., Kong, J.M., et al., 2004, Hazard assessment of debris flows and their developing trend along Dujiangyan-Wenchuan highway: *Journal of Disaster Prevention and Mitigation Engineering*, v.24, p.41-46.
- Nakamura, H., Tsuchiya, S., Inoue, K., et al., 2000, Sabo against Earthquakes: Kokon Shoin, Tokyo, Japan, p.190-220.
- Prestininzi, A., and Romeo, R., 2000, Earthquake-induced ground failures in Italy: *Engineering Geology*, v.58, p.3-4.
- Tang, C., and Liu, Q.Z., 1994, A study on hazardous intensity and risk regionalization in china: *The Chinese Journal of Geological Hazard and Control*, v.5, p.30 -36.
- Wei, F.Q., Gao, K., Hu, K., Li, Y., and Gardner, J. S., 2008, Relationships between debris flows and earth surface factors in Southwest China: *Environmental Geology*, v.55, p.619-627.
- Wei, F.Q., Hu, K.H., Lopez, J. L., et al., 2003, Method and its application of the momentum model for debris flow risk zoning: *Chinese Science Bulletin*, v.48, p.298-301.
- Wei, F.Q., Xie, H., and Zhong, D.L., 2000, Risk factors zoning of debris flow in Sichuan Province: *Journal of Soil and Water Conservation*, v.14, p.59-63.
- Xin, H.B., and Wang, Y.Q., 1999, Criteria for earthquake-induced landslide and avalanche: *Chinese Journal of Geotechnical Engineering*, v.21, no.5, p.591-594.

From practical experience to national guidelines for debris-flow mitigation measures in Austria

Johannes Huebl ^{a*}, Georg Nagl ^a

^aUniversity of Natural Resources and Life Sciences, Peter Jordan Straße 82, Vienna 1190, Austria

Abstract

In the second half of the 19th century a lot of torrential disasters occurred in the Alps causing substantial damage. These catastrophes may be traced back to non-sustainable land-use management with inadequate alpin pasture farming, leading to forests in a poor condition, large denuded areas and steep incised channels. Starting with an analysis of these disasters, political decisions were made to implement mitigations measures, including forestry, agricultural and structural measures. Additional financial regulations were established to facilitate mitigations measures even for poor rural communities. The technological background for the design of structural measures was founded in forestry, because of the experience with construction of log driving. Basic hydraulic models were used for designs, sometimes empirical values were added to consider bedload or the impact of point loads. The structures served to stabilize the channel bed, to deposit bedload upstream of settlements, to restrict sedimentation or inundation on the fan or to redirect the flow to areas of low interest. In the early years of torrent control in the Alps, structures were usually built as dry masonry walls, later cement mortar masonry walls and concrete gravity walls were favoured. New static concepts and the use of reinforced concrete formed the basis of a colloquium in Vienna (1973), where load models and static concepts were discussed. In practice, the multiplier of the static load of the Lichtenhahn-model was used within a broad range, leading to different structural design of check-dams. In the beginning of the 21st century, based on the design concept of EUROCODE, new technical guidelines for barrier design (ONR-Series 248xx) were developed. The load cases include flood and debris-flow and combination of events for all kind of torrential structures. The experience in the application of these guidelines is currently being evaluated and will lead to a new national standard.

Keywords: Mitigation measures; Debris-flow; Design Standards; Torrent control service; Austria;

1. Introduction

There is a long tradition of natural disaster mitigation in Alpine regions. In the 18th century, Joseph Walcher (1719-1830), an Austrian Jesuit, physicist and mathematician, worked on the topic of hydraulic and glacier lakes. In his work *”Nachrichten von den Eisbergen in Tyrol”* (Walcher, 1773), he investigated the Vernagt glacier, Gugler glacier and especially the Rofner glacier lake, which threatened the Ötz valley by repeated glacial lake outburst floods (Fig 1). These outburst floods had catastrophic consequences for the province of Tyrol in the years 1600, 1678, 1680 and at 1845. In the year 1788, an edict promulgated by Wenzel Graf von Sauer, incited working-groups to establish mitigation measures (Graf von Sauer, 1788). Franz Seraphin von Zallinger zum Thurn (1743-1828), priest and physicist, worked on this edict and addressed the issue of inundation in Tyrol in his work *“Abhandlung von den Überschwemmungen in Tyrol”* in the year 1779 (Zallinger zum Thurn, 1778;1779).

* Corresponding author e-mail address: Johannes.huebl@boku.ac.at



Fig. 1. Glacier lakes illustration of (Walcher, 1773); (a) Rofner glacier lake; (b) Passyer lake

One of the first technical drawings can be found in this publication. Also in France, Jean Antoine Fabre (1748-1834) was involved in the topic of mitigation measures in Alpine regions with his book “*Essai sur la théorie des torrens et des rivères*” (Fabre, 1797). In the next decades, the topic gained interest, but most work remained theoretical (Aretin, 1808; Streffleur, 1852; Müller, 1857). It was the work of Josef Duile (1776-1863), that started practical implementation of mitigation measures (Duile, 1826). He was an engineer, primarily in the field of hydraulics and road construction with a keen interest in torrent control. Due to his leading role in this field, he was called to Switzerland and applied his knowledge there. He can be considered as father of the European torrent control (Fig 2). In this time, two technical domains characterized the progression of the torrent control: one part was hydraulic engineering and the other part was forest engineering.

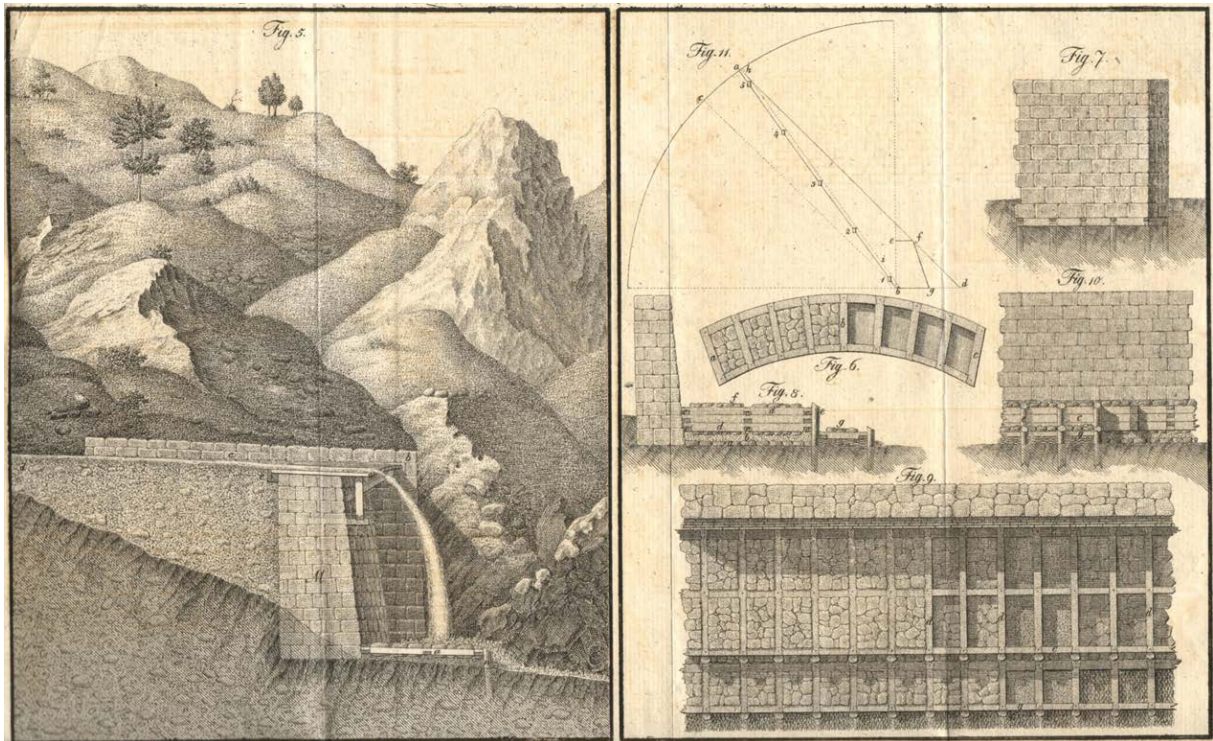


Fig. 2. Technical illustration of mitigation measures; (Duile, 1826)

Hydraulic engineering was mainly applied to the lower part of the torrent while forest engineering addressed the headwaters. The political question who should further be responsible for torrent control works led to a controversy between Arthur Freiherrn von Seckendorff (forest engineering) and Weber von Ebenhof (hydraulic engineering) (Länger, 2003). During this time, Seckendorff started to study the methods developed in France, especially the works of Demontzey, (1880).



Fig. 3. These drawing originate from a report of an eyewitness (forester) of a debris-flow near Faucon (Barcelonette, France) in (Demontzey, 1880). The longitudinal section shows the accumulation of coarse boulders at the debris-flow front and the right picture displays the debris-flow cross section during the passage of the front.

Owing to the major catastrophes in the years 1846 and 1856 along the rivers Loire and Rhone in France (Fig 3), increasing knowledge developed in this field and public support started and led to a legal foundation of mitigation works in the years 1860 and 1864, especially related to reforestation.

The severe floods in Tyrol and Carinthia in the year 1882 initiated, as in France, a rethinking. Julius Graf Falkenhayn travelled to France in the year 1883 to learn of the methods used, and to implement them in Austria (Wang, 1901). The emperor of Austrian-Hungarian monarchy passed the torrent control act in 1884, stating that torrent control works have to be executed on a national level, with public funding and with a systematic approach. Seckendorff introduced the forest engineering background from France successfully. The government implemented a legal basis for financing and organizing the torrent control service to ensure further development. Educational courses were established at the University of Natural Resources and Life Sciences, Vienna (BOKU) for students and the staff of the new established service.

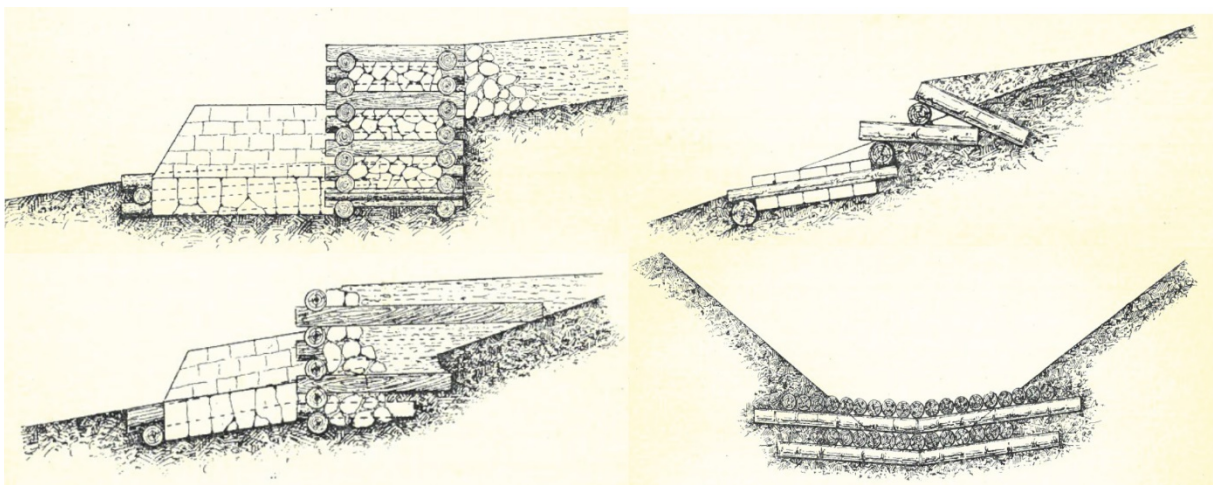


Fig. 4. Example of technical structure of (Wang, 1901)

2. Empirical design approaches

The construction materials used at this period consisted of the locally available construction materials near the torrents, see Fig 4 (Wang, 1901). Wood and dry-stone masonry were used for mitigation measures. Progress was achieved through dissemination of experience and not by research because no research facilities existed at the time. Nonetheless, first innovative experimental structures were raised, for example:

- Barrier with a self-cleaning function (dosing) was installed in the Fischbach, Tyrol (1924-1928) (Fig 5)
- A cement mortar arch dam was built in the years 1951/52 in the Finsingbach, Tyrol, to study the failing conditions of this construction type.
- Prefabricated construction of a barrier of reinforced concrete in the Winklergraben, Upper Austria (1929-1931).



Fig. 5. Barrier with a self-cleaning function (dosing); “Strele-Sperre”, Fischbach, Längenfeld, Tyrol (IAN-Archive)

Due to the improvement of materials and mechanization on building sites in the second half of the 20th century, new methods were established in the torrent control service. Increasing usage of heavy machinery in the steep regions enhanced construction efficiency.

Depending on the two main types of structures used, the arch dam and the gravity wall, different formulas were used for design. The focus of the gravity wall was external stability (safety against tilting, sliding and bearing capacity failure) and the dimensions of the bottom width of the structure. Arch dams reduce the construction volumes by using the arching effect for stability. The arch dam designed by Hampel (1960) in the Finsingbach set a trend for the dimension of arch dam with a simple formula based on the ring tension. The formula reads

$$d = \frac{(h + u) \cdot r \cdot \gamma}{\sigma_d} \quad (1)$$

with the thickness of the dam d , the height h , flow depth u , radius of the arch dam r , allowable pressure loading of the material σ_d and the density of water γ with 1 metric ton/m³ (Leys, 1968).

The Austrian Centre for Forest Research (BFW) held an international colloquium on check-dams in Vienna in the year 1972. Lichtenhahn presented at this colloquium the often-used load model for design (Lichtenhahn, 1972). He proposed an empirical multiplier k to increase the hydrostatic pressure p_{st} to include load of debris-flow pressure. In practice, this multiplier ranges significantly and led to different structural designs of check-dams.

$$p_{st} = k \cdot \rho \cdot g \cdot h \quad (2)$$

3. Adaptation to EUROCODE concept

Due to this long tradition in torrent control works in the Austrian Alps, numerous different types of protection works were designed in different regions in Austria. The design of technical structures is now based on the EUROCODE concept, that specifies how structural design should be conducted within the European Union (EU). Based on this, the ONR Series 248xx was established, encompassing torrential processes, snow avalanches and rock fall. An interdisciplinary working group (ON-K-256) developed the new standards for the load models, design, construction and life cycle assessment of torrent control works (technical standard series ONR 24800). The following national documents have been developed:

- ONR 24800: 2009 02 15 (Austrian Standards, 2009), Protection works for torrent control - Terms, definitions and classification; Contains the terminology and classifications of torrent control including the terms concerning the design and function of torrential barriers. An important classification is the definition of functional barrier types.
- ONR 24801: 2013 08 15 (Austrian Standards, 2013), Protection works for torrent control - Impacts on structures; stresses on torrential barriers result from water (hydrostatic, dynamic), earth and debris-flow impacts. In special cases effects from avalanches, falling rocks and earthquakes must also be considered.
- ONR 24802: 2011 01 01 (Austrian Standards, 2011), Protection works for torrent control - Design of structures; for the design of torrential barriers, the Ultimate Limit States (ULS) and the Serviceability Limit States (SLS) must be considered. The concept gives specific design rules (e.g. stress combinations) for torrential barriers.
- ONR 24803, 2008 02 01 (Austrian Standards, 2008), Protection works for torrent control - Operation, monitoring, maintenance; a fundamental requirement to guarantee a minimum safety level of the protection works is periodic monitoring of their condition and effectiveness. The monitoring concept, in the *ONR 24803*, is divided in two parts, the inspection and the measurement or intervention part.

By these technical standards, the “traditional” assessment and construction concepts for torrent control structures were adapted to the EUROCODE standards. The documents are based on and interact with EN 1990 (basic of structural design), EN 1992-1-1 (design of concrete structures), EN 1997-7 (geotechnical design) and the related documents for the Austrian national specifications.

Torrential barriers with the functions energy-dissipating, dosing, filtering or deflecting (Hübl, 2018) are subject to extreme dynamic stress that presupposes the application of high safety standards for design, construction and maintenance. The Austrian Standard ONR 248xx provides a standardized model for the design of torrent barriers under debris-flow impact, which has been developed from comparative calculation of common debris-flow models from engineering practice in torrent control and calibrated by impact measurements of debris-flow events.

The proposed method should enable practitioners to properly design debris-flow countermeasures with the restriction that usually only little data are available. Naturally, simplifications and assumptions are necessary. Therefore, the process “debris-flow” and the interaction with the structure itself are separated. At the interface of the barrier and the debris-flow process the process parameters are transferred to impact parameters that act on a specified load area. The design basis is the load distribution and the force of the stress model (Fig 6).

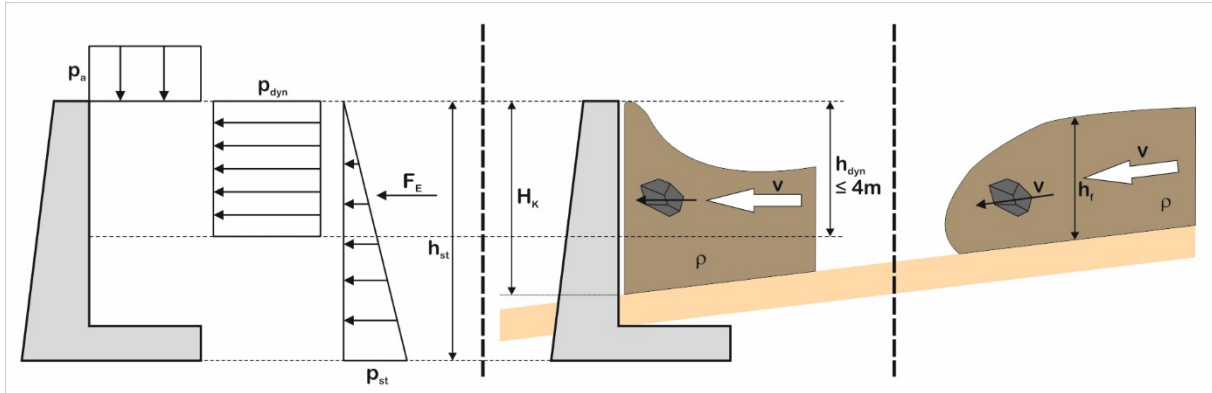


Fig. 6. Schematic illustration of the distinction between load and process model. The standard distinguishes between the process part (right section) the moment of impact (middle section) and the load model for the design (left section), where v is the velocity, h the flow depth, ρ the density, H_k the barrier height, p_{st} the static pressure, p_{dyn} the dynamic pressure, p_a the self-weight of the overtopping material and the impact force of a single element F_E .

For the assessment of impact by channel processes on structures, a process model and a stress model are combined. The process model represents the behavior of a debris-flow process according to its physical properties. At the interface characteristic parameters of the debris-flow process (e.g. energy, density, flow height, flow velocity) are transferred to the impact model, which simulates the interaction of the process with the structure and comprises the representative stress (areal or single load) and the related load distribution. For the design of torrent barriers for engineering purposes, simplifications concerning the model parameters, the stress model and the load distribution are required. A revised version, based on the gained experience with the ONR-Series within the last years, will be published in 2019 as ÖNORM B4800.

4. Conclusion

The challenge in developing national guidelines was to connect the experience of the practitioners with scientific research results and to derive a state of the art, starting with terminology, definitions, construction rules and design procedures. On the one hand the guidelines should provide a standardized method for the design of torrent control structures, on the other hand a degree of freedom must be left to adjust the design according to the peculiarity of the torrent. In Fig.7 is shown a recently completed debris-flow barrier, designed according to the ONR National Guidelines.



Fig. 7. Recently completed debris-flow barrier with the sediment retention basin (Schallerbach, Tyrol), designed according to the ONR National Guidelines.

References

- Aretin, G., 1808, Über Bergfälle und die Mittel, denselben vorzubeugen oder wenigstens ihre Schädlichkeit zu vermindern: Innsbruck.
- Austrian Standards, 2008, Protection works for torrent control - Operation, monitoring, maintenance, (ONR 24803: 2008 02 01)
- Austrian Standards, 2009, Protection works for torrent control - Terms and their definitions as well as classification, (ONR 24800: 2009 02 15)
- Austrian Standards, 2011, Protection works for torrent control - Design of structures, (ONR 24802: 2011 01 01)
- Austrian Standards, 2013, Protection works for torrent control - Static and dynamic actions on structures, (ONR 24801: 2013 08 15)
- Demontzey, P., 1880, Studien über die Arbeiten der Wiederbewaldung und Berasung der Gebirge. [translated by Seckendorff-Gudent, A.], Vienna: C. Gerold's sohn.
- Duile, J. 1826, Ueber Verbauung der Wildbäche in Gebirgs-Ländern, Zum Gebrauche für Bau- und Forstbeamte, Obrigkeiten, Seelsorger und Gemeinds-Vorstände: Innsbruck, Wagner, p. 179, <http://doi.org/10.3931/e-rara-19671>
- Fabre, J.A., 1797, Essai sur la théorie des torrens et des rivières: chez Bidault, Libraire, An VI 1797, p. 284, <http://dx.doi.org/10.3931/e-rara-44675>
- Graf von Sauer, W., 1788, Gubernialverordnung
- Hampel, R., 1960, Bruchversuch an einer Bogensperre der Wildbachverbauung. In *Österreichische Wasserwirtschaft* (12 Heft 8/9), p. 187.
- Hübl, J., 2018, Conceptual Framework for Sediment Management in Torrents: *Water*, 10(12), 1718, p.13, <https://doi.org/10.3390/w10121718>
- Länger, E., 2003, Der forsttechnische Dienst für Wildbach- und Lawinerverbauung in Österreich und seine Tätigkeit seit der Gründung im Jahre 1884. Die Grundlagen für die Aufgabenerfüllung der Dienststellen der Wildbach- und Lawinerverbauung im Bereich der heutigen Republik Österreich, sowie Die Grundlagen für die Aufgabenerfüllung der Dienststellen der Wildbach- und Lawinerverbauung im Bereich der heutigen Republik Österreich, sowie die allgemeine Entwicklung der Tätigkeiten der Dienststellen, insbesondere im Bundesland Kärnten. [Ph.D. thesis]: Vienna, Universität für Bodenkultur
- Leys, E., 1968, Zum Bau von Gewölbesperren in der Wildbachverbauung: In J. Kar (Ed.): *Oesterreichische Wasserwirtschaft*. 20. Jahrgang. Wien, New York: Springer, p. 243–249.
- Lichtenhahn, C., 1972, Berechnung von Sperren in Beton und Eisenbeton: In Forstlichen Bundesversuchsanstalt in Wien (Ed.): *Kolloquium über Wildbachsperren*. 1 Volume. Wien: Österreichischer Agrarverlag, p. 91–118.
- Müller, F., 1857, Die Gebirgs-Bäche und ihre Verheerungen wie die Mittel zur Abwendung der Letzteren: Krüll'sche Universitäts-Buchhandlung, p. 44
- Streffleur, V. R. v., 1852, Über die Natur und die Wirkung der Wildbäche: In *Sitzungsberichte der Akademie der Wissenschaften mathematisch-naturwissenschaftliche Klasse 08* 1852, p. 248–261.
- Walcher, J., 1773, Nachrichten von den Eisbergen in Tyrol: Kurzböck.
- Wang, F., 1901, Grundriss der Wildbachverbauung. Leipzig: S. Hirzel.
- Zallinger zum Thurn, F. S., 1778, De causis et remediis inundationum in Tyroli. Innsbruck.
- Zallinger zum Thurn, F. S., 1779, Abhandlung von den Ueberschwemmungen in Tyrol. Innsbruck.

Flexible debris-flow nets for post-wildfire debris mitigation in the western United States

William F. Kane^{a*}, Mallory A. Jones^b

^{a,b}KANE GeoTech, Inc., 7400 Shoreline Drive, Suite 6, Stockton, California 95219 USA

Abstract

Wildfires are a continual threat in the western United States. Post-fire debris flows annually cause millions of dollars in damage and often result in loss of life. Rapid post-fire response is essential to prevent additional hazards in terms of debris-flow damages. Flexible systems utilizing high-strength steel ring nets have proven to be reliable and cost effective. These systems can be installed rapidly to minimize or eliminate the dangers caused by post-fire debris flows. Wildfires in the western United States generally occur during the dry season in late summer and fall. Although monsoonal storms can cause debris flows in the summer months, seasonal rain storm events occur in fall and winter, often resulting in devastating debris flows. In the Rocky Mountain states debris flows occur during the summer monsoon season. In both areas, storm cells can remain stationary over mountain peaks for hours dropping large amounts of rain in a very short time. The resulting runoff and erosion can cause damaging debris flows miles away from the rain event. Debris impacts differ significantly from rockfall impacts. The debris nets must withstand both a surge in pressure on impact, and a static load once the flow has dissipated. Tested and engineered, flexible nets can be rapidly deployed in strategic locations to lessen or eliminate the threat. Compared to large, rigid structures and debris basins, these nets are cost-effective, rapidly constructed, environmentally friendly, and approval by regulatory agencies can be relatively quick. This study focuses on current mitigation and protection practices using flexible debris-flow nets as developed in Switzerland and used in the United States. Case studies of projects in Colorado, New Mexico, and California detailing site investigations, engineering, and construction of flexible debris-flow nets are described. Of special interest are the steps and protocols taken as a result of debris flows following the Thomas Fire in California.

Keywords: debris flow; ring nets; protection; wild fire

1. Introduction

Each year, across the globe debris flows cause substantial damage and loss of life. Torrential rains from typhoons and hurricanes, or post-wildfire rain events can trigger large masses of vegetation, soil, and rock to flow catastrophically from mountain valleys and canyons out into inhabited areas. To date, the majority developmental work on debris-flow nets has been conducted by the Swiss government in conjunction with the Swiss company Geobrugg, AG, Romanshorn, Switzerland. This paper describes design and projects using the Swiss/Geobrugg debris mitigation products. Other manufacturers also provide debris nets. These nets were not used in the projects described.

The principle behind debris nets is to catch debris flows close to the source, usually in mountain canyons, stop the massive flow, and then, if desired, allow the material to be placed back in the channel to allow natural process to return to normal sediment transport conditions.

Flexible debris nets have been installed in hundreds of locations around the world to protect people and infrastructure in a low-impact, environmentally sound way.

The basic debris-flow protection system consists of a custom ring net engineered to resist the velocities and dynamic and static pressures unique to debris flows. Support ropes are installed into channel banks and transfer debris impact and pressure loads from ring nets to the ground. Excessive energy is absorbed by net braking elements in the support ropes. In addition, the rings in the system allow the passage of water and fine sediment beneath and through the net.

*Corresponding author e-mail address: william.kane@kanegeotech.com

1.1 Development from rockfall barriers

European countries pioneered the development of rockfall protection barriers in the mid 20th Century. Rockfall barriers were the logical extension of snownets already installed in mountainous regions. Early snownets were composed of wire rope nets which held snowfall until spring melting thereby preventing avalanche formation. Post-thaw inspection of the nets showed them to have caught boulders which had fallen from above. This led to research and development of rockfall barriers on a full scale by Brugg Cable (now Geobrugg), Maccaferri, and other wire and wire rope manufacturers.

The California Department of Transportation (Caltrans), an early American adopter of rockfall barriers, observed that the barriers were effective in stopping small debris flows. This led to increased interest and research in the use of flexible nets to stop debris events.

2. Research

2.1 Theory

Existing methods for determining debris-flow protection were meant for large watersheds and large-scale structures such as basins and check dams (Bradley, et al., 2005). Early research on debris nets, including the use of anti-submarine ring nets, was conducted by the California Department of Transportation (Caltrans) and the United States Geological Survey (USGS). They installed a flexible ring net at the base a small flume (De Natale, et al., 1996). Other researchers were also conducting research on flexible nets in Japan, Europe and other countries. Conventional debris-flow net design is based on field observations and full-scale testing in controlled situations (Muraishi and Sano, 1997). Other publications related to the design of debris-flow protection systems includes Mitzuyama, et al. (1992), Rickenmann (1999, 2001), and PWRI (1988).

2.2 Illgraben research

After catastrophic debris flows in Switzerland in 2005, the Swiss government partnered with Geobrugg to conduct a major research program to determine if the nets could be used as lightweight, low-cost, environmentally sound replacements for concrete check dams and debris basins. The goal was to develop a standardized approach to debris-flow mitigation using flexible high-strength steel ring nets (Wendeler, 2017)

The main focus of the Swiss research was a full-scale test site on the Illgraben near Leuk, Switzerland. The Illgraben usually produces five to six debris-flow events per year. A fully instrumented debris net was installed, Fig 1. Geophones installed upstream signaled the instrumentation at the net site to begin collecting data. They also turned on floodlights for nighttime events. Instruments monitored flow height, net rope forces, flow velocity, and weight. The channel dimensions were well known so volume and density could be determined.

2.3 Mechanics of debris flow impacting flexible barrier

Geobrugg examined the forces involved in the impact of debris material into a flexible net. They found that flows occur in pulses or waves. The first pulse was stopped at the base of the net. Subsequent pulses flow up and over the previous pulses. Nets were designed using this information with the maximum forces at the base of the net. In addition, the flexing and deformation of the net and net ropes will also absorb the dynamic impact pressures. Once the debris material is stopped the net must then support the static load of the material.

It should be noted that debris flows tend to be sequential events so that after an initial dynamic impact, additional surges add only a quasi-static load to the net, instead of a fully dynamic load. In addition, the debris material already impacted and de-watered on the net serves to absorb some of the energy of the subsequent surges. The result is that much of the debris-flow material is not against the net, resulting in decreased energy absorption and height requirements, Fig 2.

2.4 Design concept

As a result of its research, Geobrigg (2003) developed a methodology suitable for the design of its debris-flow net systems. Existing research results allow a peak discharge to be calculated and the flow velocity estimated. Once the mass and velocity are known, the design pressures can be determined. Finally, the design height is calculated.



Fig 1. Instrumented test net in the Illbraben, Leuk, Switzerland.

2.4.1 DEBFLOW software

This methodology is incorporated into the software program, DEBFLOW, which determines the appropriate Geobrigg debris-flow system as a function of the characteristics of a given debris-flow basin and channel. The DEBFLOW program is based on the full scale testing in controlled situations at Illgraben, solutions of the rope equation, and finite element modeling.

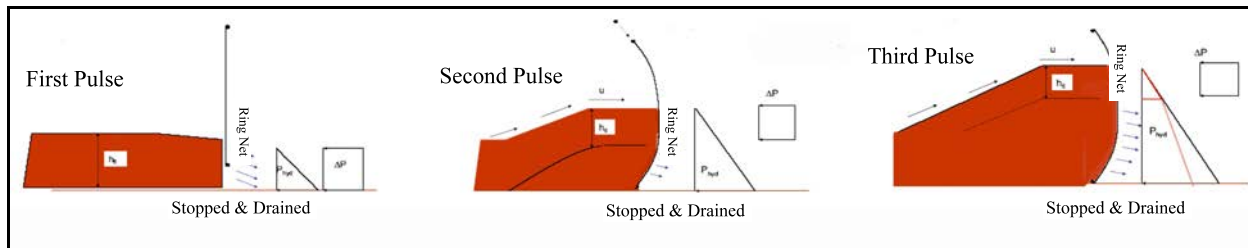


Fig 2. Schematic showing successive impact pressures from a debris flow being applied to a net. The net and its anchorages must be designed to withstand dynamic and static (Rankine) pressures. Note that successive debris impacts after the first flow lose energy by having to go up the previous flow and also stop debris material back up in the channel.

Given input parameters such as debris material, channel dimensions, number of pulses, etc. DEBFLOW provides the user with recommended Geobrigg nets. The type of net specified depends on the width of the channel and the calculated dynamic and static pressures.

There are two basic versions of the Geobrigg debris net systems. The VX net is intended for relatively narrow channels up to 40-ft (15-m) wide, Fig 3. The UX net is installed in wider channels up to 90-ft (25-m) wide and has posts to keep the top net support rope from sagging, Fig 4.

2.4.2 Debris-flow Volumes

In the United States, initial volumes can be estimated following debris flows using WERT and BAER Reports. However, these estimated total debris-flow volumes will frequently exceed the one-event capacity of the available flexible net designs. Therefore, for design purposes, nets can be assumed to fill completely.

Debris-flow volume storage area can be based on field observations, previous flow volumes, and measurements of channel geometry (Gartner, et al., 2008, and others,). For DEBFLOW analyses, the calculated volume of sediment detained by each net is based primarily on a uniform



Fig 3. Post-fire VX net installed above running stream in Nambé, New Mexico. Note basal opening allowing water and fish passage beneath. Animals can pass either underneath or through rings.

geometry of each net and channel gradient. This assumes the storage area is a trapezoidal prism extending upstream from the net. This volume estimate does not take into account changes in channel shape upstream from each net location. However, sites are chosen to maximize storage area, so the volume estimates should be considered minimum values of sediment retained. Optimum locations are where channel geometry is constricted and upstream geometry widens to provide maximum storage capacity.

3. Design and Construction

In order to produce installation plans for the nets, it is necessary to consider strength of the anchoring rock and, if required, the design of foundations for the posts. Design loads are supplied to the engineer by the manufacturer as a result of their testing and modeling. Rock and soil properties are determined during the field investigation at each installation site.

Flexible debris nets can be constructed rapidly with minimal environmental impact and can be combined with the existing debris basins to maximize material storage in the canyons. They have a small construction footprint and do not change channel flow unless a debris-flow event occurs.

3.1 Anchor Design and Testing

Anchor design for UX and VX nets consists of determining the depth required to support the loads on the wire ropes. Previous work by the Post Tension Institute (PTI) (2014) gives a methodology for anchor design that is used for soil walls, tie-back walls, slope post-tensioning, slope stabilization system design, and rockfall and debris net anchor design. The PTI provides design charts with a recommended shear, or bond, strength for a particular rock/grout combination as determined by the geologist. The data comes from thousands of actual installations.

For example, from PTI tabulated data, a weathered and fractured sandstone will have a bond strength of 100-psi to 120-psi. The maximum test load, as provided by Geobrugg, for a debris net anchor is about 80,000-lbs. Using the PTI criteria and assuming a 4-in drill hole and minimum bond strength of 100-psi, the necessary depth to hold the anchor in the fractured sandstone is 10.6-ft. This is well within the capability of a small rock drill.

Rather than using estimates of bond strength material type, it is preferable when possible to perform actual field pull-out tests on anchors to determine the site-specific bond-strength characteristics. Verification anchors are sacrificial anchors installed in typical sections of colluvium or rock. The anchors are drilled to various depths and tested. The load at pullout can then be back-calculated to determine the actual bond strength for the particular rock in the field. Tabulated data is often very conservative and time and money can be saved by performing verification tests prior to net installation.

3.2 Foundation Design

UX nets require the construction of post foundations. Early practice involved using a large block of reinforced concrete about 1-m x 1-m. These blocks were not engineered and consisted of reinforced threaded bars inserted in the concrete to anchor the post base plate. Although easy and inexpensive to construct, they were prone to large foundation displacements and cracking on impact.

Subsequently, engineered shallow foundations were used. These foundations are designed using concrete and building codes for steel reinforcement. In general they are designed to use the passive pressure of the soil as the soil resistance. Since lateral loading on post foundations can exceed 80,000-lbs, foundation dimensions can become quite large and introduce additional complications during construction.

Because of the high loads and large foundation blocks, cast-in-drilled-hole (CDIH) foundations are considered economical alternatives to large concrete blocks. These foundations resist the loads by deformation and changing soil



Fig 4. UX net with posts for wider channels Camarillo, California.

resistance. The design approach was developed by Reese & O'Neill (1988). Developed for laterally loaded pile foundations, the method utilizes the finite difference method and p - y curves (Reese & O'Neill, 1988). These curves model the soil or rock as systems of springs which push back on the foundation as it deforms from the bending of the foundation. Design consists of comparing the maximum moment developed in foundation with foundation strength. Displacement of various depths on the foundation can be calculated. Controlling factors in design are foundation size and displacement. The approach involves significant computational effort. Generally, lateral foundation loads are too great to use shallow foundations.

4. Construction

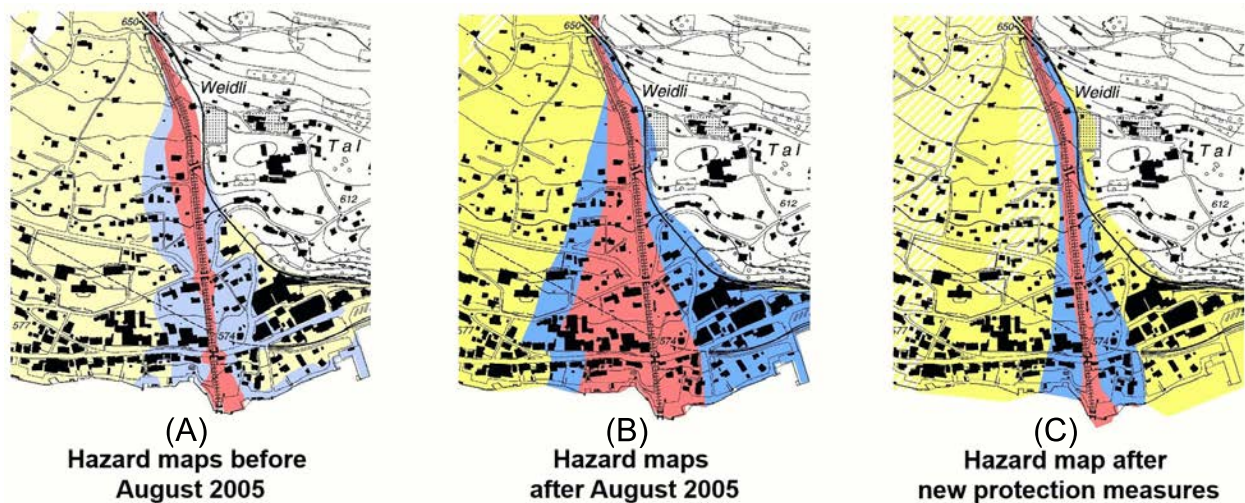


Fig 5. Changes in risk in the town of Brienz, Switzerland before (A), after the catastrophic debris flows of 2005 (B), and after the installation of a system of Geobrigg debris nets in the Alpine drainages above the town (Geobrigg, 2017).

Debris net construction initially consists of drilling anchor holes and grouting wire rope anchors. Drilling equipment varies but in general downhole hammers are used. Sometimes these are hand operated but can be equipment mounted. Specialized equipment that can negotiate narrow canyons like the Kaiser SL2 are versatile and can drill quickly.

For UX nets and SLBs, foundations are constructed and posts erected. Because debris channels often contain loose sand and rock, foundation usually require an excavation. A reinforcing bar cage is fabricated and placed in the hole, concrete is then poured into the excavation. If the excavation is large, a sonotube or form is necessary. Backfill around the form must be compacted to perform as the material used in the design. Alternatively, a controlled density fill (CDF) or soilcrete can be used.

Support ropes are installed between the anchors. Then the ring nets are hung and secured with shackles. If a backing mesh is used, it is installed at this time. Finally, the overtopping plates are installed to the top rope.

5. Risk Reduction

After the flooding of August 2005 in Switzerland, the Swiss government and Geobrigg worked to reduce the debris risk to residents living in high risk zones by using environmentally sound debris nets. Fig 5 shows the changes in risk in the town of Brienz, Switzerland along the Trachtbach River after two catastrophic debris flows in summer 2005.

6. Case Studies

6.1 Glen Eyrie Conference Center, Colorado Springs, Colorado

In the summer of 2012, the Waldo Canyon Fire destroyed 11-mi² of mountainous land above the city. Debris flows following the fire created substantial damage. Glen Eyrie Conference Center at the base of Queen's Canyon installed three flexible debris nets. To protect the structures, a VX net was installed in the channel near the Center with a UX net directly above it. These nets were meant to be cleaned out. Further up the Canyon, a UX net was installed to protect a small water supply dam. It was not intended for clean out.

The lower UX net was a unique design. The channel was too wide to install a stock UX net. In addition, the Center required access to the back of the net. An engineered fill embankment was designed and constructed to allow the support ropes to pass through the embankment and be anchored directly in the bedrock, Fig 6. This design allowed the net to deform as intended since none of the actual debris net was embedded in the embankment.

6.2 Santa Clara Pueblo, New Mexico

The Jemez Mountains portion of the New Mexico lands of the Santa Clara Band of Pueblo Indians was devastated by the Las Conchas Fire in the summer of 2011. Initially nine sites were selected for flexible debris nets. Funding delays led to further degradation of the channels resulting in the construction of only five nets in the fall of 2014.

Equipment to construct the CIDH foundations for the UX nets could not be obtained so the contractor excavated the foundations and formed the shafts using sonotube tubes. A mixture of colluvium and cement was used to backfill around the tubes, resulting in higher strength than the native material originally there.

The following summer the nets experienced an impact. The resulting cost savings to the Pueblo from not having the material impact their road was significant, Fig 7.

6.3 Nambé Pueblo, New Mexico

The Pacheco Fire of 2011 burned Sangre de Cristo mountains above the Nambé Pueblo. Subsequent debris flows impacted the Nambé Rio and Nambé Reservoir. The Pueblo installed three debris nets along the water to prevent further degradation of the reservoir. The nets were designed with a relatively large basal opening to allow wildlife and small debris to pass beneath, Fig 3.

6.4 Camarillo Springs, California

The Springs Fire of May 2013 burned a large swath of the Santa Monica Mountains. A debris-flow event consisting of mostly ash occurred in October 2014. During cleanup, a second debris flow occurred in December 2014 doing significant damage to a number of homes in the community, Fig 8.

Several types of debris mitigation structures were constructed including shallow landslide barriers, UX and VX debris nets and berms to conduct surface runoff into the channels. The short time frame in which to construct the mitigation led to the use of soilcrete as backfill around excavations. Instead of a sonotube, a corrugated metal pipe was used for the foundation form. This added stiffness also enabled the shafts to be shortened, which in turn, allowed the construction time to be reduced.

Two days after construction was completed, the first major rainfall of the season occurred filling several of the nets, Fig 9.



Fig 6. VX net (below) and UX net (above) with armored access abutment, Glen Eyrie Conference Center, Colorado Springs, Colorado.

6.5 Montecito, California

In December and January, 2018, the Thomas Fire became the largest fire in California history. In early January 2018, torrential rains pounded the Santa Ynez Mountains above the coastal community of Montecito. The ensuing debris flows killed 23 people, destroyed 10% of the housing in the community, blocked the U.S. Highway 101 Freeway interrupting commerce, Fig 10.

A preliminary risk assessment of the mountain canyons and the community was made to determine the need for debris-flow mitigation prior to the upcoming rainy season (BGC, 2018). BGC concluded that a large supply of fine-grained sediment, boulders, tree-trunks, and branches remain in the canyons and is readily available for future debris-flow events in the coming rainy season. They also pointed out that the existing sediment basins in Montecito are inadequate to catch and store the volume of debris likely to be mobilized during a debris-flow event similar to the January 9, 2018 event.

BGC recommended that immediate mitigation action be taken and that an instrumentation and warning system be installed. They recommended that flexible debris nets be placed in the canyons to help protect against large-scale debris-flow events.

Seventy-one sites in the five canyons that drain into Montecito were identified as potential flexible debris net sites. Of those, 16 were to be constructed the first summer. However, delays caused by environmental permitting issues resulted in construction being scaled back to 12 debris nets. Another outcome of the environmental community concern was that no foundation construction could occur in the channels. This eliminated the consideration of UX nets. A “Super VX” net has been engineered to span the larger sites that conventional VX nets cannot span.

6.6 Conclusions

Flexible debris nets have been shown to be effective measures in the protection of people and property in post-fire debris events. Among the advantages are:

- Lightweight - easily deployed
- Rapid construction
- Economical
- Significant risk reduction
- Environmentally sound

With the size and frequency of wildfires in the American southwest increasing, the use of these nets has demonstrated that it is a proven technology for protecting people and infrastructure.



Fig 7. Filled Geobrugg UX debris net in Santa Clara Pueblo, New Mexico.



Fig 8. Aftermath of post-fire debris flow in Camarillo Springs, California.



Fig 9. Filled VX debris net in Camarillo, California.



Fig 10. Aerial view of debris-flow damage in Montecito, California, January 13, 2018.

References

- BGC Engineering, 2018, Letter to Suzanne Elledge: “Montecito Debris-Flow Risk Management – Urgent Action Needed.” BGC Project No. 1890-001, August 31, 2018.
- Bradley, J. B., Bahner, C. D., Richards, D. L., Bahner, C. D., 2005, “Debris Control Structures – Evaluation and Countermeasures.” Hydraulic Engineering Circular 9, 3rd Edition, Federal Highway Administration, FHWA-IF-04-016 HEC-9.
- Cannon, S. H., Gartner, J. E., Santi, P. M., and Dewolfe, V. G., 2008, Empirical models to predict the volumes of debris flows generated by recently burned basins in the western U.S.: *Geomorphology*, v. 96, p. 339-354.
- De Natale, J. S. et al. 1996, “Response of the Geobrug Cable Net System to Debris Flow Loading.” Report, California Polytechnic State University, San Luis Obispo, California.
- Denk, M., Roth, A., Volkwein, A., Wartmann, S., & Wendeler, C., 2007, Field measurements and numerical modeling of flexible debris flow nets. *Debris-Flow Hazards Mitig. Mech. Predict. Assess.* Millpress, Rotterdam, 681-687.
- Denk, M., Gröner, E., Wendeler, C., 2017, “Zehn Jahre Erfahrung mit flexiblen Murgangbarrieren.” (“Ten years of experience with flexible debris barriers.”) *Austrian Journal of Engineers and Architects*, v. 162, p. 209-214. (In German).
- Geobrug, 2003, “Design Concept, VX/UX Protection System Against Debris Flow.” Fatzler AG, Geobrug Protections Systems, Switzerland.
- Geobrug, 2013, “Product Manual for VX/UX Debris Flow Barriers.” Geobrug North America, 22 Centro Algodones, Algodones, New Mexico.
- Geobrug, 2017, “DEBFLOW for advanced users.” Design Academy HYDRO, August 29-31, 2017, Romanshorn, Switzerland.
- O’Neill, M.W., Reese, L.C., 1988, “Drilled Shafts: Construction and Design”. FHWA Publication No. HI-88-042.
- Post-Tensioning Institute (PTI), 2014, Recommendations for Prestressed Rock and Soil Anchors. Post-Tensioning Institute.
- PWRI, 1988, “Technical Standard for Measures Against Debris Flows (Draft).” Ministry of Construction, Japan.
- Rickenmann, D., 1999, “Empirical Relationships for Debris Flows.” *Natural Hazards*, 19(1), 47-77.
- Rickenmann, D., 2001, “Estimation of Debris Flow Impact on Flexible Wire Rope Barriers.” Birmensdorf, interner Bericht, unver ffentlicht.

Application of an innovative, low-maintenance weir to protect against debris flows and floods in Ottone, Italy

Chiara Morstabilini^{a,*}, Ilaria Boschini^b, Federica Zambrini^b, Giovanni Menduni^b, Marco Luigi Deana^c, Nadia Zorzi^a

^aMaccaferri Innovation Center, Via Volta 13/a, 39100 Bolzano, Italy

^bPolitecnico di Milano, piazza Leonardo da Vinci 32, 20133 Milano, Italy

^cOfficine Maccaferri S.p.A., via Kennedy 10, 40069 Zola Predosa (BO), Italy

Abstract

The need of a low-maintenance and easy-applicable apparatus against debris flow led Maccaferri Innovation Center and the Politecnico of Milan to a new hydraulic-based approach that was focused on the application of a special weir called Mini Skirt Check Dam (MSCD). After a three-years research on applicable equations, a construction site in Ottone (Italy) was identified to have been affected by destructive debris flow in the past years. The site is characterized by the presence of an underground pipe that collects the stream flow rate flowing under the village square. The purpose of this work is to design a MSCD, able to prevent a pressure driven flow in the underground pipe and to avoid the related risk for the inhabitant of the village. MSCD is a special weir, which consists in large wings to slow the flow and a ring net to block boulders and logs, as to become a sifting filter of the debris. As to design the best performing apparatus, materials and type of anchoring are crucial; for this reason, an analysis of the impact pressure was performed. The case study has considered several different aspects: hydrology, size of the material and its characteristics and previous events to have a complete analysis of what could happen in the next events. The result of this collaboration is the complete design of a MSCD, ready to be installed.

Keywords: debris flow; management of the hydraulic risk;

1. Introduction

Ottone is a town in the province of Piacenza, in the Emilia-Romagna region of northern Italy, with an important extension (98.96 km²) which is compared to a small resident population of only 495 inhabitants (ISTAT, 2017). The town is capital of the municipality and it is located at an elevation of 510 m above sea level, while the hamlets are located at higher altitudes and they are a major tourist destination especially in the summer.

The village of Ottone is located in the Alta Val Trebbia, on the Ligurian Apennines. Some of the numerous hamlets that make up the territory are in the Val Boreca. The territory includes the Trebbia and Aveto basins, the main tributary of the Trebbia. The main course of the Trebbia river develops in SW-NE direction for 116 km, from the source on Mount Prelà on the Ligurian Apennines (1406 m), up to the outlet in the river Po near Piacenza. The portion of the basin close to Ottone drains approximately 207 km². The municipal territory develops from a minimum elevation of 344 m to a maximum of 1667 m above sea level, and the average slope of the area is 53%. The inhabited nucleus of the Capital is set on an alluvial fan that has stabilized over time and overlooks the river bed of the Trebbia on the hydrographic right.

The hydrology of Ottone town is characterized by the waters of Rio del Montone and Rio della Ghiossa flow underneath the old town (see Fig. 1), in particular they join below Piazza Vittoria and then continue flowing towards

* Corresponding author e-mail address: c.morstabilini@maccaferri.com

the river Trebbia, draining a total area of about 40 hectares. This peculiarity has caused several problems to the population and the purpose of this project is to permanently solve this problem with a lower maintenance weir.

1.1. Problems occurred in Ottone

The main risk for the municipality of Ottone is given by the hydraulic security of Piazza Vittoria. Originally, in the urban plan, the inhabited nucleus was placed outside the path of the two streams Rio della Ghiossa and Rio del Montone. Around the second half of the 1800's, the two streams started to be covered because in the urban planning the area was intended as a market square.

The covering of the last segments of the two streams was completed between 1873 and 2000. The sewer is in masonry with sections of 1.30×1.40 m or 2.00×1.50 m and with vaulted roof. The drainage disposal capacity, assessed with a maximum filling level of the sections equal to $2/3$ of the available height and considering clear water, is $8 \text{ m}^3/\text{s}$, equivalent to a multisecular flow rate. However, the flood events regarding the two streams are characterized by a strong presence of solid transport that can plug the sewer system. This scenario of occlusion made by massive solid transport has occurred more than once in recent history and the events of considerable importance are:

- 19 September 1953
- 13-16 October 2000
- 13-14 September 2015

The most recent event had a particularly high intensity that led to the complete obstruction of the eastern channel of the sewer of Rio del Ghiossa and the current situation of inadequacy of the network that puts at risk the appurtenances of the square. In the period immediately following the September 2015 event, works were carried out to try to restore the flow of Rio del Ghiossa by bypassing the blocked section to canalize the waters up to Trebbia through the western channel. The image in Fig. 1 makes it possible to appreciate the situation following the first interventions for restoring the transport capacity: the black section is out of service due to the clogging caused by the debris carried by the flood, while the green section is the bypass.

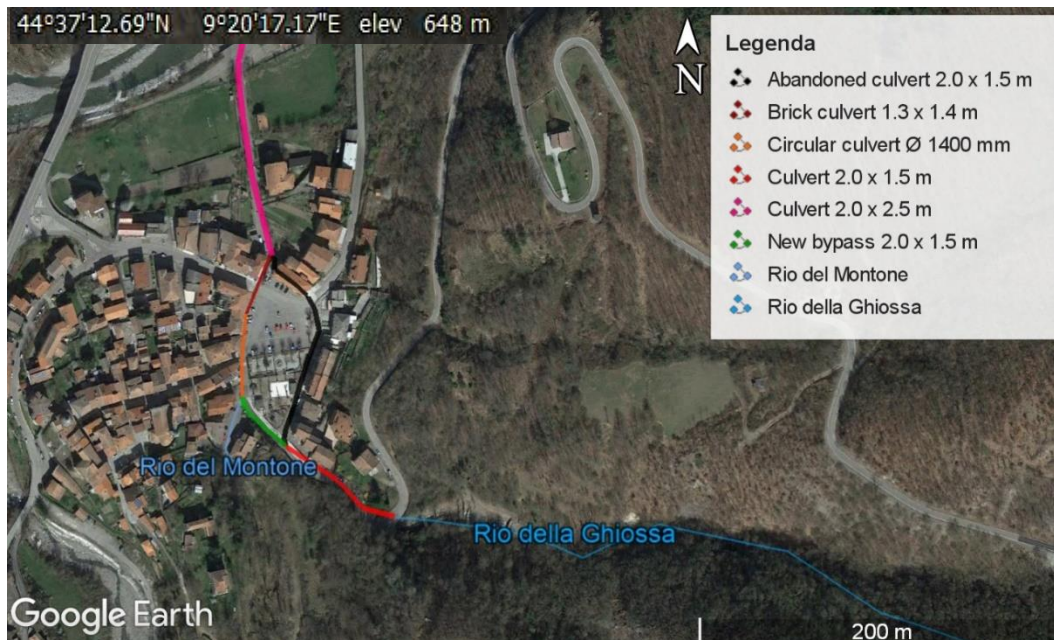


Fig. 1 Representation of the channel system of Rio della Ghiossa and Rio del Montone below Piazza Vittoria after the first restoration: the black section is out of service due to the clogging made by the September 2015 event, while the green section is the bypass made to allow the flow of the waters of Rio della Ghiossa up to Trebbia, following the West channel.

The slopes of the square exceeding 5% allow a good drainage capacity to the underlying sewer. The system is not specifically affected by a possible regurgitation of the Trebbia. To protect the inhabited area, there are four weirs installed upstream of the sewer entrance, at a distance of about 30 meters one to the other (Fig. 2). The structural reliability of these structures should be verified, together with the state of consistency and maintenance.



Fig. 2 Photos of the last two weirs.

1.2. How to reduce the risk

From the past events and from the geomorphological and hydraulic studies of the basin it was noticed that the biggest problem in the case of debris flow comes from Rio del Ghiossa. The measures to reduce the risk of debris flow on Piazza Vittoria are divided into two categories: structural and non-structural.

For the non-structural part, the installation of a monitoring and alerting system designed by CAE S.p.A. in collaboration with the Politecnico di Milano, financed by the Emilia-Romagna region, is about to be completed. Thanks to the study of the precursors to the calamitous event, it is possible to alert the population in advance in order to follow predefined emergency procedures that increase security and reduce material damage. The system logic is based on the correlation between precipitation duration and intensity and the occurrence of debris flow (Guzzetti et al., 2007; Pizziolo et al., 2005).

The structural interventions in the project can be distinguished in interventions for the changing layout of the square and mitigation measures for “debris-flow hazard”. After the September 2015 event, concrete barriers with a jersey profile were laid along the western side of the square in order to preserve the entrance to the shops and create a safe walkway for pedestrians who unfortunately had to be in the area at the time of the manifestation of the landslide event. This floodproofing intervention should be developed in the square renewal project. The hydraulic restoration works in the square were entrusted to a local engineering company, which defined a technological solution that provides the adjustment of the West channel and of the sewage system. The choice to refer to this setting was made on the basis of operational and economic evaluations.

On the other side, the installation of an apparatus called Mini Skirt Check Dam upstream of the entrance of the sewer is planned. It is a slit weir with a central net that is raised with respect to the riverbed, see Fig. 3. This product allows the lowering of the debris discharge, reducing substantially the speed and the highest discharge. The advantage over the traditional weirs is that, with the addition of the net, larger debris and timber that are often the most destructive part of the debris flow can be retained more effectively. Moreover, the presence of the net guarantees the need for a wider slot, which entails a lower expenditure of materials and, in particular, a lower impact on the structure that can be designed with smaller anchorages and greater durability. This weir does not need maintenance at the end of each event and for this reason it is optimal in all contexts where the accessibility of the site is problematic and linked to weather conditions.

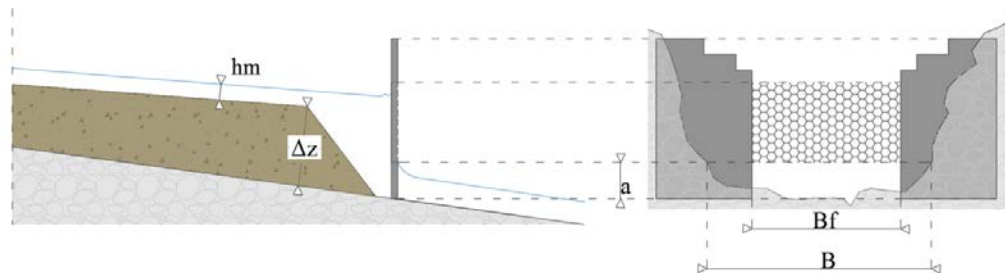


Fig. 3 General hydraulic scheme of a MSCD (University of Trento, 2016). The wings could be made in gabions or concrete and are designed with a specific $R=B/B_f$ for each Froude number and volume of debris. The net in the middle is designed with a specific hm/a parameter, where hm is the flow level in the upper part of the weir.

2. Hydraulic and hydrological modelling

In order to properly design the MSCD, a hydraulic model and hydrological study was implemented. While creating the models, the reference setting has been the “project scenario”, with the new configuration of the sewer that will be completed soon.

2.1. Hydraulic modelling

1D hydraulic modelling has been carried out applying the HEC-RAS model (US Department of Defense, Army Corps of Engineers, 2016), to a series of cross-section, with the aim of identifying the critical section, which is obviously the one with worst debris accumulation. The definition of the geometry has been simple to implement since 88% of the channel is artificial and was constructed using a precast concrete box of defined size. For the remaining part, the reference was to a topographic evaluation received from the technical service of the municipality and to an in situ evaluation carried out with a geologist.

The technical service department of Ottone Municipality had also provided information regarding the elevation of the submerged channel in correspondence to manholes for inspections so that an accurate reconstruction of the submerged part was possible. Since no data was available regarding the elevation of the riverbed upstream of the covered part, an assumption of constant slope (5%) was made.

Considering all the obtained data, the available sections were 41; due to the model structure and function, some of the sections need to be doubled, so that a total of 64 sections were introduced into the model. The junctions among the channels composing the sewer were solved using the momentum equation.

The roughness factor has been kept constant along the whole transverse section, adopting 3 reference values for the main characteristics of sections (precast concrete box, natural open sky section, and open sky section with concrete).

The adopted values of discharge were taken by the previous work from Politecnico di Milano (Menduni, 2016), imposing as an input value that the whole Rio della Ghiossa contribution is channeled in the East segment, as planned in the restoration project. The selected upstream boundary condition was due to the hydraulic jump on the weir. From the output, it has been possible to compute the transport capacity, whose profile is shown in Fig. 4, and identify the critical section.

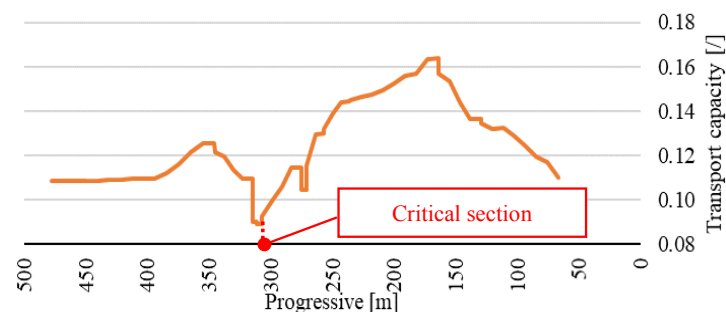


Fig. 4 Transport capacity along the sewer channels based on Hec Ras.

2.2. Hydrological study

Since no hydrometer and rain gauges are present in the basin, calibrating and predicting the peak of flow rate for each return period chosen in the analysis was not a simple task. The total surface of the hazardous basin is less than 0.5 km², so it was extremely inaccurate to use the measuring apparatus installed on Trebbia river to calibrate the model. A simulation based on a GIS tool was preferred to find the water discharge for each return period. A calibration was possible with the data from the previous study (Menduni, 2016), that was calibrated on the amount of rain near the basin and the amount of material accumulated in the village.

The procedure followed consists in different steps:

- GIS analysis to identify the basin and its feature
- Hydraulic manipulation using the Peak Flow model (Rigon et al., 2011) to obtain hydrograph
- Amplification of the obtained curve according to the previous studies (Menduni, 2016)
- Calculation of the solid flow rate

It was fundamental to perform a complete GIS hydrological analysis to identify the basin and some hydraulic characteristic supplied as input data to the Stage tool implementing Peak Flow model and obtain the complete shape of the liquid discharge in time (as it is fully explained in Rigon et al., 2011) an example of the GIS analysis could be found in Fig. 5.

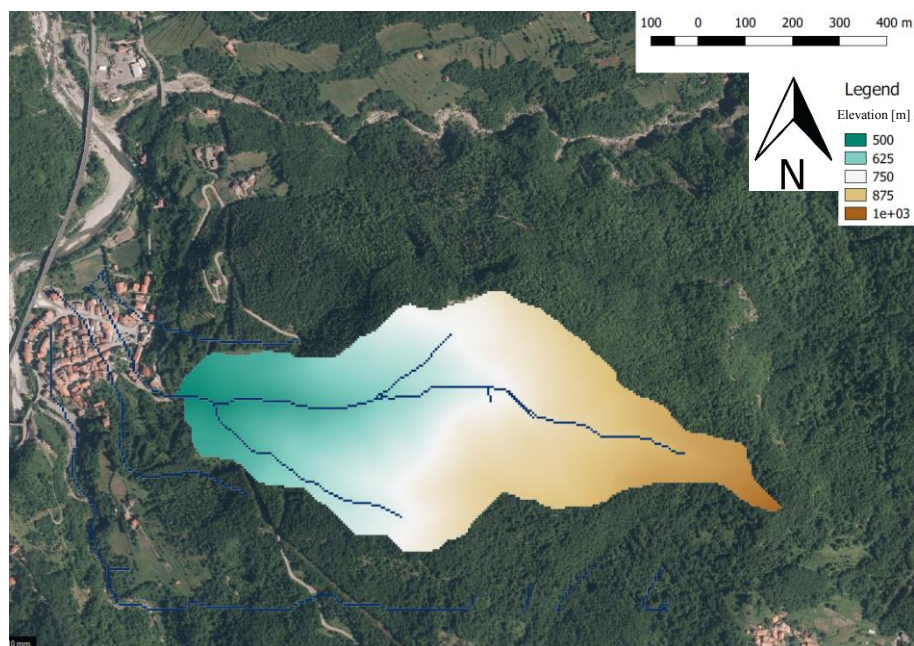


Fig. 5 DTM applied on the reference basin and direction of the main flow carried out with QGIS, each colour correspond to an elevation (in m) above the sea level.

Starting from the output of the GIS study, it was possible to perform a further step of analysis using the software Peak flow. The calibration took into account the peak of the flow rate found in the previous studies (Menduni, 2016), so all the curve was multiplied for a factor that gives the same peak. The resulting discharge was amplified to accomplish the values found in previous studies, as shown in Fig. 6.

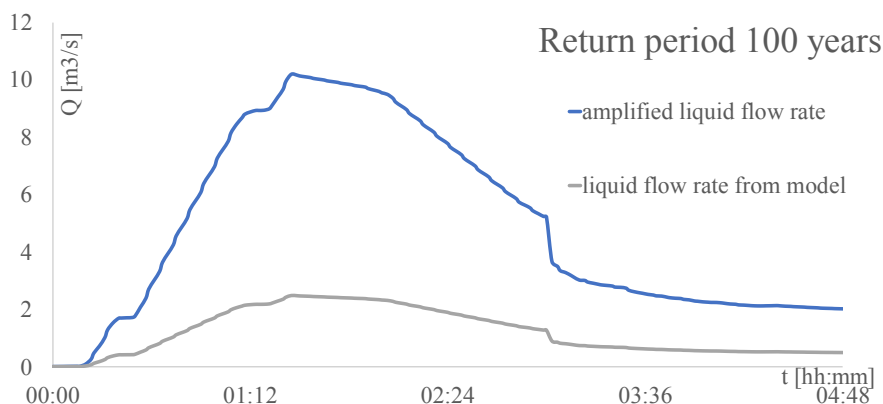


Fig. 6 Example of the amplification of the resulting discharge from the application of the Peak Flow model. For the return period of 100 years the factor of amplification is 4.12, similar factor has been used for the other return periods.

A series of four curves was obtained for four reference return periods. Starting from these curves, the Takahashi criterion (Takahashi, 1978; Lanzoni, 1993) was chosen to obtain the complete curve of the solid and liquid flow rate. An example of the application on the obtained curves is provided in Fig. 7.

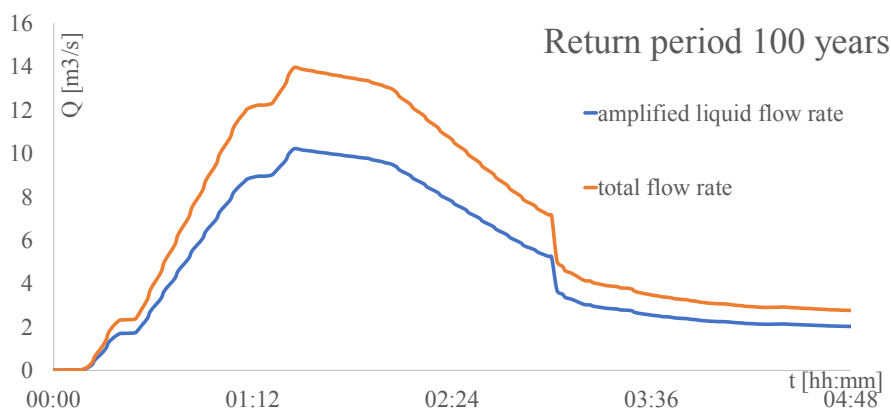


Fig. 7 Example of the amplification of the resulting return period of 100 years event, using the Takahashi (1978) criterion.

Errore. L'autoriferimento non è valido per un segnalibro. shows c and n parameters defining the depth-duration-frequency curves for each return period that were fixed from the local administration and which play an important role in the Peak Flow model (Rigon et al., 2012); $Q_{L,max}$ is the maximum flow rate for each return period and was fixed by Menduni (2016). We call “scale parameter” the coefficient applied to adapt the discharge from the Peak Flow elaboration, to the Peak imposed by the previous studies. V_L represents the total volume of water during the flood event, calculated as an integral of the amplified curve. V_{tot} represents the calculation of the total volume of both sediment and water that flows during the event and is calculated with the Takahashi criterion.

Table 1 Final results of the hydrological study

		Tr 20 yrs	Tr 100 yrs	Tr 200 yrs	Tr 500 yrs
c	mm/h	35.99	70.68	77.81	87.2
n	-	0.348	0.335	0.332	0.328
$Q_{L,max}$	m ³ /s	7.55	10.12	11.2	12.64
Scale parameter	-	3.88	4.12	4.14	4.21
V_L	10 ³ m ³	17	23	24	27
V_{tot}	10 ³ m ³	23	32	33	37

3. Design of MSCD

The characteristics of the basin and the presence of a sewer portion of the stream, forced the design procedure to install an apparatus like the MSCD, that could dilute the amount of water and sediment but also requiring less maintenance. A section for the installation that is near to the road and easy to access was chosen and at the same time far enough from the bridge to avoid problems related to the pressure in that section. This job site is a part of the whole works in the County to improve safety against debris flow that will occur in the future. This installation, in particular, will ensure a constant amount of flow rate in the channel and thus, avoiding the pressure inside the sewer.

To avoid the sediment to overflow the hydraulic obstacle, all the volume of the debris moved by the 500 years return period flood must be contained in the chosen section in the space upstream, so a check on the available storage capacity was necessary while choosing the position.

With reference to Fig. 3, the design parameters to be determined were:

- a, how much the net is uplifted from the ground: this parameter could be found in the abacus of the design (Morstabilini & Deana, 2018)
- R what is the ratio between B (the width of the undisturbed section) and Bf (the distance between the wings of the MSCD), see Fig. 3.

The considered base section is 4.7 m wide, so two possible Bf: Bf = 3 m and Bf = 3.5 m were chosen leading to two design options: R = 1.57 and R = 1.34. one of the resulting graphics for these options is reported in Fig. 8.

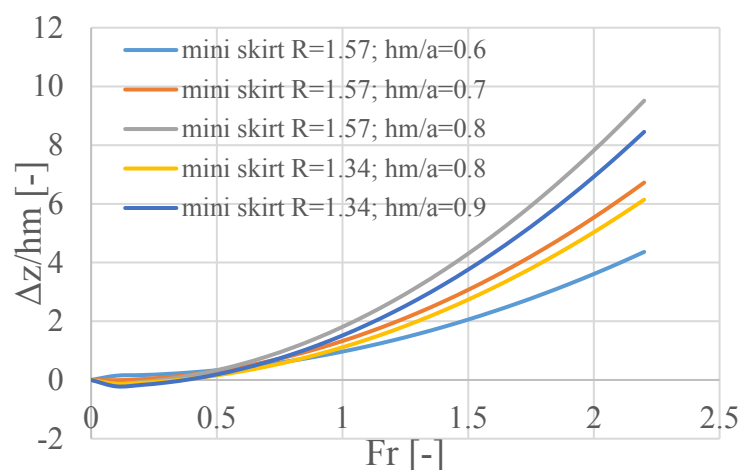


Fig. 8 Example of a resulting design abacus for R=1.57 and R=1.34 and different hm/a parameters

The ability of the MSCD to dilute the debris flow is determined by the ratio $\Delta z/h_m$ which is a non-dimensional parameter that expressed the maximum amount of material that is temporarily blocked by the apparatus. Considering that the maximum height of the weir should be 2 m, the options for the design are in Table 2 the chosen solution is the third, with final drawing of Fig. 9.

Table 2 Final results of the hydraulic model

R	a	h_m/a	h_m	dz/h_m	dz	dz + h_m	Fr	U	Q
[-]	[m]	[-]	[m]	[-]	[m]	[m]	[-]	[m/s]	[m ³ /s]
1.57	0.35	0.70	0.25	6.72	1.65	1.89	2.20	3.41	3.42
1.57	0.30	0.80	0.24	7.04	1.69	1.93	1.90	2.92	2.50
1.57	0.70	0.60	0.42	3.61	1.52	1.94	2.00	4.06	8.14
1.34	0.35	0.80	0.28	6.14	1.72	2.00	2.20	3.65	3.66
1.34	0.30	0.90	0.27	6.22	1.68	1.95	1.90	3.09	2.66

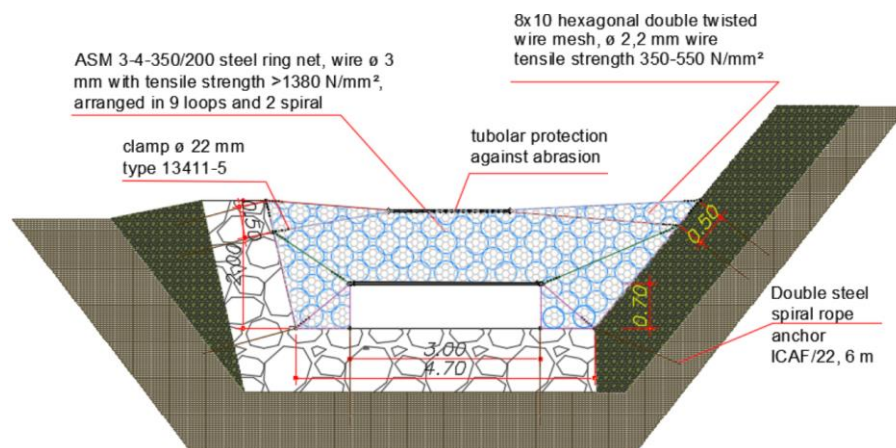


Fig. 9 Final design of the MSCD: in order to be easy to apply, the particular asset of the wire ensure the hole to stay open during the event.

4. Conclusions and future development

The Ottone research was an interesting case study to apply the results of the research on MSCD. In addition, the creation of a work team that involved Maccaferri Innovation Center and the Politecnico of Milano was fundamental in finding the best design solution for this site. During 2019 data load cells will be installed in the clamps which will communicate the tensile strength on anchoring. Combing this information with data coming from the sensor already installed for the early warning system, it will be possible to find a correlation between the rain and the pressure on the barrier, enlarging the knowledge on the phenomena occurring in the area.

Acknowledgements

This research was possible thanks to a collaboration between Maccaferri Innovation Center and the Hydraulic department of the Università degli Studi di Trento, in the person of Prof. Aronne Armanini, as part of a research project to study innovative apparatus for the control of debris flow phenomenon.

References

- Brunner, G. W., 2016, HEC-RAS: River Analysis System: Hydraulic Reference Manual (5.0 ed.): US Department of Defense, Army Corps of Engineers.
- Guzzetti, F., Peruccacci, S., Rossi, M., and Stark, C., 2007, Rainfall thresholds for the initiation of landslides in central and southern Europe: *Meteorology and Atmospheric Physics*, v. 98, p. 239–267, doi: 10.1007/s00703-007-0262-7.
- Rigon, R., d'Odorico, P. and Bertoldi, G., 2011, The geomorphology structure of the runoff peak: *Hydrogeology and Earth System Science*, doi:10.5194/hess-15-1853-2011.
- Takahashi, T., 1978, Mechanical characteristics of debris flow: *Journal of the Hydraulics Division* 104 HY8, 1153 - 1169.
- Arpa, 2005, Evaluation of the risk of landslides in Appennines in Emilia Romagna [translated from Valutazione del rischio da frana nell'Appennino Emiliano-Romagnolo].
https://ambiente.regione.emiliaromagna.it/it/geologia/temi/dissestoidrogeologico/pdf/soglie_pluviometriche.pdf@@download/file/soglie_pluviometriche.pdf
- Menduni, G., 2016, Analysis of the hydrogeologic risk in Ottone related to the events of 13-14 september 2015 and residual risk [translated from Analisi del rischio idrogeologico nel Capoluogo del Comune di Ottone con particolare riguardo agli effetti calamitosi del 13-14 settembre 2015, ai conseguenti scenari di intervento e alla gestione del rischio residuo], Milan.
- Morstabilini, C. and Deana, M. L., 2018, Debris Flow: a new design approach: *Geomechanics and Geodynamics of Rock Masses*. European Rock Mechanics Symposium, vol 2.
- Lanzoni, S., 1993, *Meccanica di miscugli solido-liquido in regime granulo inerziale*. [ph. D thesis] Padova, University of Padova.

Laboratory tests of an innovative check dam

Chiara Morstabilini^{a,*}, Marco Luigi Deana^b

^aMaccaferri Innovation Center, Via Volta 13/a 39100 Bolzano, Italy

^bOfficine Maccaferri S.p.A., via Kennedy 10 40069 Zola Predosa (BO), Italy

Abstract

The flow of both solid and liquid particles, especially in mountain basins, is impulsive, not easily predictable and for this reason extremely dangerous. As to avoid the damages caused by this phenomenon, barriers are usually used. They are easy to install but are high maintenance and, in addition, they are aimed at blocking all the sediment, running the risk of under-designing the volume to be collected. Starting from this assumption, the need of a maintenance-friendly approach was investigated by Maccaferri Innovation Center with an innovative apparatus called Mini Skirt Check Dam (MSCD). This is a special dam which is made up of two parts: solid wings that have a vertical fissure in which a ring net is applied. The net is uplifted from the ground as to leave a part of the debris flowing and blocking only the top part of it. The research analyzed the design procedure of a standard weir and several laboratory tests were performed in cooperation with the University of Trento (Italy) that ended with the creation of a new approach against debris flow. The MSCD permits the cutting of the peak of the flow rate and, at the same time, blocking tree trunks and boulders. Laboratory tests conducted showed that the combination of weir and net slows down the debris and collects only the most dangerous part of the flow with a lower maintenance requirement and a good hydraulic performance.

Keywords: debris flow; on scale laboratory tests on weirs; hydraulic design procedure

1. Introduction

According to Takahashi (1991), debris flow is a phenomenon of transport of both liquid and solid particles that occurs in mountain areas characterized by a severe slope where the motion of the solid phase is driven by gravity. The shape of the sieve curve of the solid phase is usually various, from a few centimeters to diameters of over one meter and it is transported by a water and mud matrix (Armanini et al, 2005). One of the more relevant factors of the phenomenon is that boulders and big stones usually float over the debris. The triggering factors of debris could be related to the presence of solid material and a fixed range of slope, between 15°9' and 23°5', as indicated by Takahashi (1978). One other possible cause is the rain, generally the event that causes the debris comes after a continuous light rain that is sufficiently able to saturate the soil.

This phenomenon is not constant in time and space and, in addition, is extremely violent and impulsive; this last characteristic makes forecasting and design extremely difficult because the rheology of the flow and its motion has not been fully explained yet.

1.1. Solutions in use for debris flow and their problems

The solution normally applied for debris flows are barriers. The principle application of this product is to block all the material that is flowing up to a certain prefixed retain volume and to leave all the other material overpassing the barrier. The threshold for the determination of the typology of barrier is a function of the recharge basin and its shape (so by the total amount of the material that could potentially be moved) and by the return period of design (in this case the amount of the material must be estimated for the design return period).

* Corresponding author e-mail address: c.morstabilini@maccaferri.com

As shown in Fig.1. there are two typical barrier applications: Fig. 1. (a) shows a typical barrier application on an open hill, this application is commonly used for both debris flow and landslides; Fig. 1. (b) shows the debris flow barrier application in a channel, in this case the barrier is a hydraulic structure that represents an obstacle for the material flow of the whole basin up to the install section.

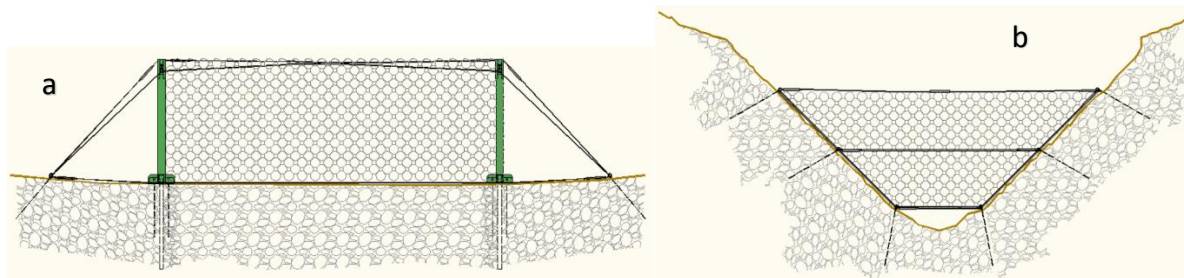


Fig. 1. (a) typical barrier for open hills; (b) typical barrier for channel (Courtesy of Maccaferri)

Based on existing knowledge of the phenomenon, the principle of blocking all the sediment that is flowing seemed to be the only solution against the violence and the destructive power of the flow. The cost of these types of nets is reduced because they are light and easy to install. However, the cost is extremely increased when taking the maintenance costs into account. As it is shown in Fig. 2. Barriers in general get clogged and the material in the upper section that has been successfully blocked, needs to be cleaned. In most cases, apart from the cost of the work and the related risk to this type of job the cleaning of the objects must also be considered as it is not possible in every site of installation due to the slope or the presence of unstable boulders.



Fig. 2. Barrier clogged by rocks installed in the Alps (Courtesy of Maccaferri)

2. New approach

Starting from the hydraulic approach normally in use for weirs, a new apparatus called Mini Skirt Check Dam (MSCD), designed for debris flow, was studied. The main idea, as shown in Fig. 3 is not to block all the sediment as done in regular barriers but to dilute the debris, to cut the maximum amount of discharge and to release it in a second

part of the event. This approach is environmentally-friendly because the discharge is reduced and could be designed according to the return period of the reference event and, in addition, effectively reduces the damage of the debris, ensuring a constant flow rate during the event that could be acceptable for the basin.

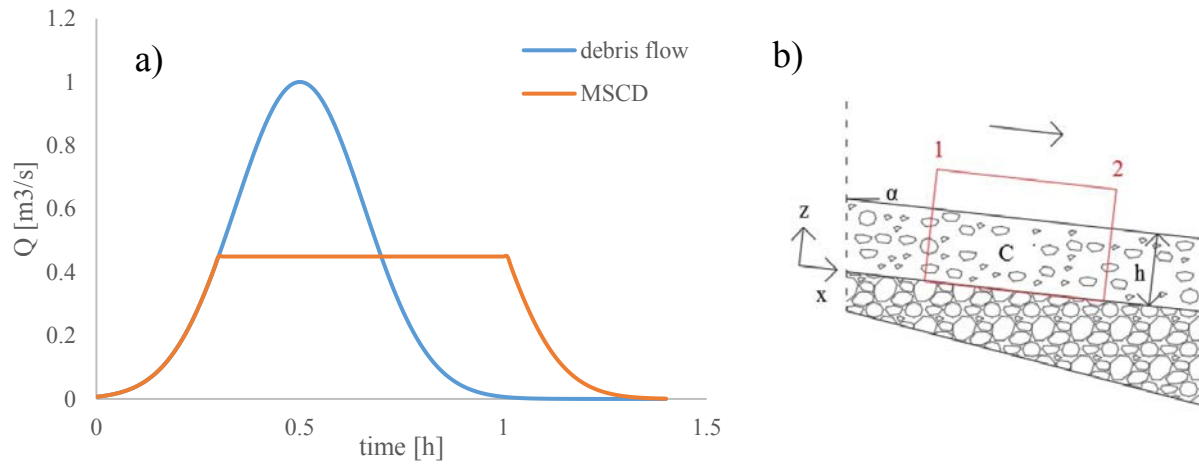


Fig. 3. (a) Performance of MSCD in comparison to the natural event in term of flow rate in the section after the apparatus; (b) the picture shows the control volume to which all the balance of energy and flow rate are referred to. The balance could be written between two generic sections 1 and 2, taking into account the direction of the flow rate. The picture on the right shows the different concentration in flow depth and the α angle.

The main goal of the research was to study and identify a new approach, based on the performance of the apparatus, that could be suitable for both weirs and MSCD, applicable for rivers and small basins ($<10 \text{ km}^2$) with intense sediment transport.

The general procedure studied for the design started from the application of the Navier-Stokes set equation in the direction of the flow, x , for both liquid and solid phase. The application of this approach on two general sections, 1 and 2, allows a system of three equations to be written: the conservation of the solid mass, the conservation of the liquid mass and the momentum, as done in Eq.1.

$$\begin{cases} (C\rho_s B U h)_1 = (C\rho_s B U h)_2 \\ ((1 - C)\rho_w B U h)_1 = ((1 - C)\rho_w B U h)_2 \\ \frac{\partial}{\partial x} \int_A (p + \rho_w g z + \rho_w u^2 / 2) (u dA) = -i_E \rho_w g Q \end{cases} \quad (1)$$

Where C is the concentration of solid material in the control volume, ρ_s is the density of the solid phase, B is the width of the channel, U is the medium velocity, h is the flow depth, ρ_w is the density of the water, p is the pressure, g is gravity, u is the local velocity, A is area, i_E is the loss of energy, Q is the flow rate, x is the coordinate of the flow (supposed mono directional) and z is a vertical coordinate, defined in the opposite direction from the application of the vector g .

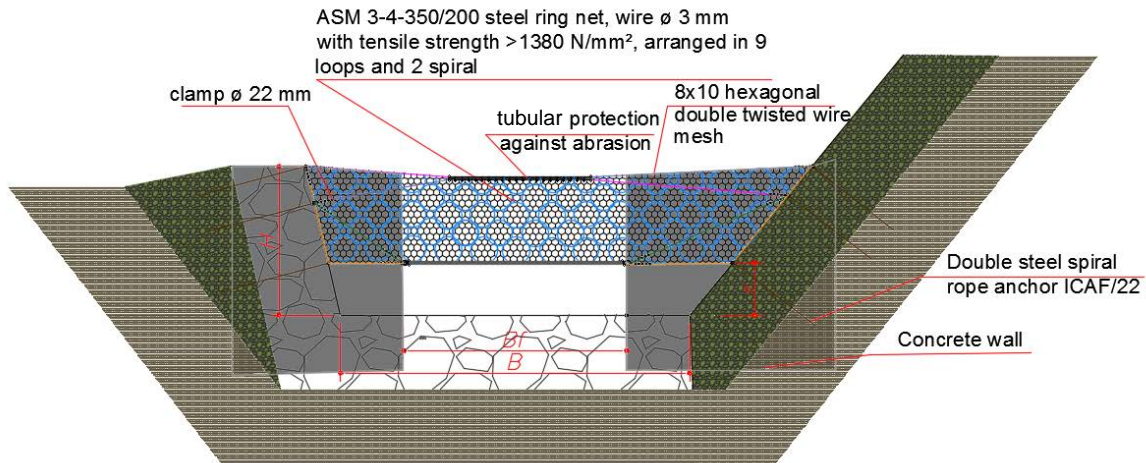


Fig. 4. General scheme of a MSCD: wings could be made by concrete or gabion, the nets, located downstream from the wall, is made by two layer of nets; the ring net for the structural function of transferring the force of the debris to the ropes and the anchoring, the double torsion net ensures a thin filter for the lower part of the sieve curve of the material.

The main goal of the project was to apply Eq. (1) on a new apparatus called Mini Skirt Check Dam. A general hydraulic scheme can be found in Fig. 4. The apparatus is composed of wings that are designed according to the hydraulic criteria used for weirs and a ring net (diameter 35 cm) with an optional double torsion net (Morstabilini et al., 2018). The advantage of the net is to block boulders and logs and at the same time to reduce the quantity of concrete needed for the wings. This reduction of material, if compared to a regular weir, allows for an easier installation procedure, so less time and cost. The presence of the concrete, that could be substituted by gabions, is necessary to force the accumulation of the material before the apparatus. The lower part of the net is void, this means that the net is uplifted from the ground, so that a certain amount of flow discharge is being left free to flow. The design of a parameter (with reference to Fig. 4) is a function of the regular flow rate of the channel, the maximum space available before the MSCD and the threshold of the return period in which the MSCD should be active.

3. Experiments on weirs

The simplification of this system was fully explained in Morstabilini et al. (2018) and resulted in a final design equation expressed in Eq. (2):

$$\Delta z + h_m \cos \alpha + \alpha_3 \frac{U_m^2}{2g} = h_f \cos \beta_f + \alpha_3 \frac{U_f^2}{2g} + \frac{(U_m - U_{or})^2}{2g} \quad (2)$$

where: α_3 is a hydraulic coefficient that should be calibrated on the characteristics of the flow, U_i are velocities in each section and the other variables are expressed in Fig. 5. The coefficient is defined below and the quantity indicated with the capital letter is the average on the section volume and the lowercase letter is the punctual quantity:

$$\alpha_3 = \frac{\int_h cudy}{CUh} \quad (3)$$

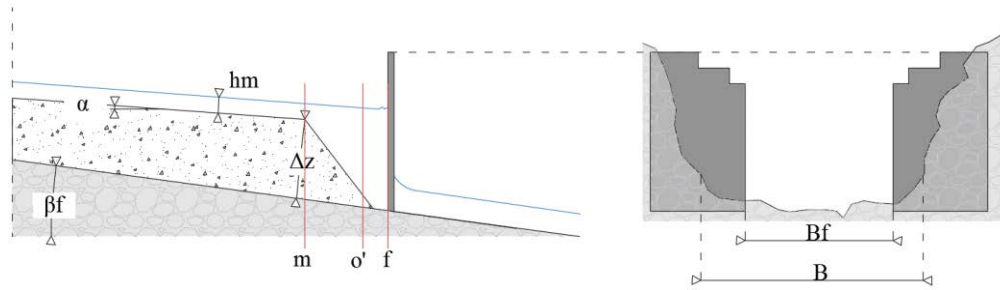


Fig. 5. Hydraulic scheme of a weir.

The application of Eq. (2) on weirs give the possibility of writing a design procedure focused on the Δz parameter (see Fig. 5), the weir considered for the application is reported in Fig. 5. The hypothesis of the method is that inside the weir the condition of $Fr=1$ is reached and that the weir is completely impermeable, so no filtration motion is allowed. This procedure could be extremely effective in defining the capacity of the weir to temporary block the flowing material, as a function of the Froude number and was fully explained in Morstabilini et al. (2018). In the case of a normal weir, Eq. (2) is applied between sections m and f and needs to define two different α_3 coefficients because the local velocity U_i is different in the two sections. The design parameter is represented by the R number, which is the ratio between B and B_f (see Fig. 5). In this case the design equation is:

$$\frac{\Delta z}{h_m} = R^{2/3} Fr_m^{1/3} \cos \beta_f + \frac{Fr_m^2}{2} \left[\left(\frac{R}{Fr_m^2} \right)^2 \alpha_{3f} - \alpha_{3m} \right] - \cos \alpha + \frac{Fr_m^2}{2} \left[1 - \frac{2}{3} (Fr_m R)^{-2/3} \right]^2 \quad (4)$$

Eq. (4) was calibrated by a series of on scale experiments, conducted in the CUDAM laboratory of the Università degli Studi di Trento (Armanini et al., 2017). These experiments were conducted on a steady flow channel 0.3 m width for several categories of R parameters. Eq. (4) was simplified to be no-dimensional, as to have a reasonable comparison between the on-scale results and the real parameters on a full scale. In Fig. 6 and 7 the calibration for $R=6.3$ in two experiment settings is reported. In Fig. 6 the theoretical curve is compared to simulated debris flow with different d_{50} of the material. In Fig. 7 the theoretical curve is calibrated with different types of mixture by varying the concentration of the solid particles. Both the approaches of calibration show that there is a good correspondence between data and curve; moreover, it seems that the approach is independent to the sieve curve of the material.

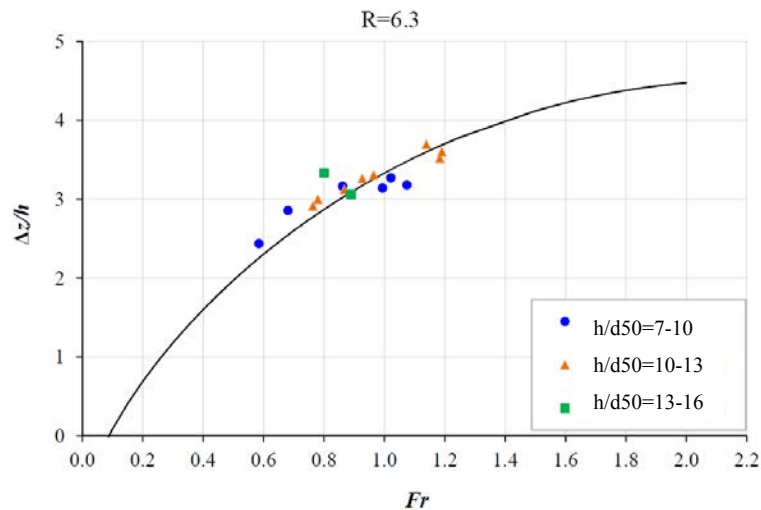


Fig. 6. Calibration of Eq. (4) for different sieve curve, as a function of d_{50} of the material and the flow depth.

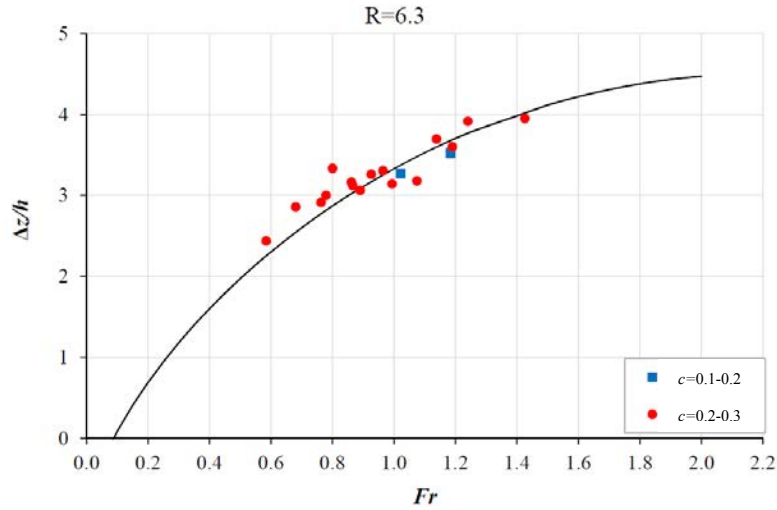


Fig. 7. Calibration of Eq. (4) for different concentrations of the mixture.

4. Experiments on MSCD

The application of Eq. (2) on MSCD required defining a new coefficient related to the occlusion of the mesh, C_f . This is a dimensionless coefficient that accounts for the degree of occlusion of the net, in case of total occlusion (safer hypothesis) $C_f=1$, otherwise $C_f > 1$. In this case, the application of Eq. (2) could be expressed as:

$$\frac{\Delta z}{h_m} = \frac{\alpha C_{cv} C_f}{h_m} \cos \beta_f - \cos \alpha + \frac{Fr_m^2}{2} \left[R^2 \left(\frac{h_m}{\alpha C_{cv} C_{co} C_f} \right)^2 - \alpha_{3m} \right] + \frac{Fr_m^2}{2} \left(\frac{\Delta z/h_m}{1 + \Delta z/h_m} \right)^2 \quad (5)$$

Where C_{ci} are coefficients related to the reduction of the horizontal and vertical flow depth, normally considered constant and equal to 0.61. Eq. (5) was calibrated with a series of on scale experiments conducted in the CUDAM laboratory of the Università degli Studi di Trento (Armanini et al., 2017). These experiments were conducted on a steady flow channel 0.3 m width for several categories of R and h_m/a parameters.

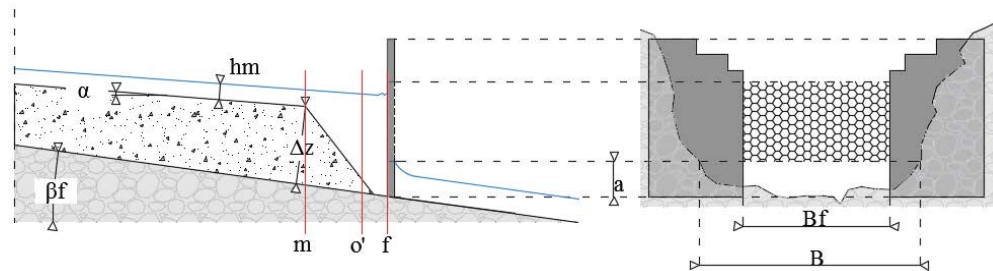


Fig. 8. Hydraulic scheme of a MSCD.

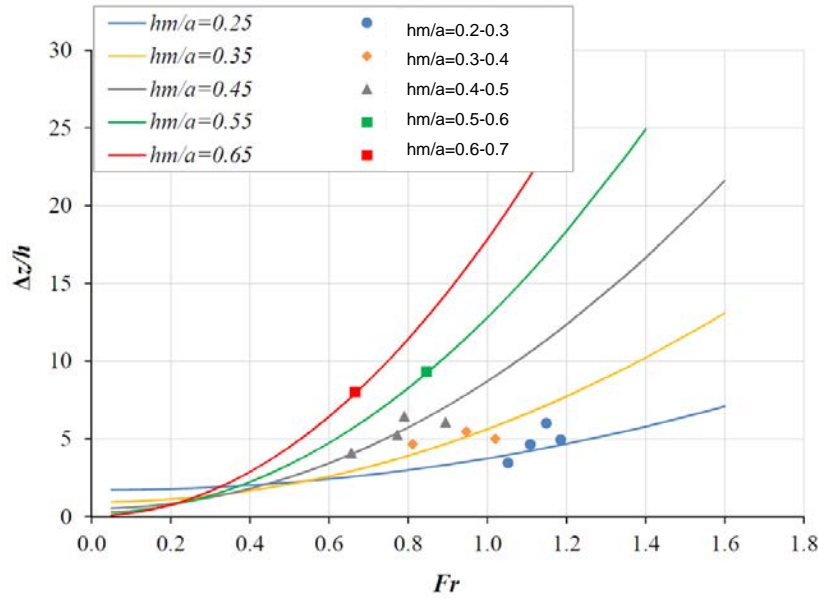


Fig. 9. Calibration of Eq. (5) for $R=6.3$, $C_{co} = 1$, $C_{cv} = 0,61$ and $C_f = 1,1$, different types of h_m/a curves were investigated.

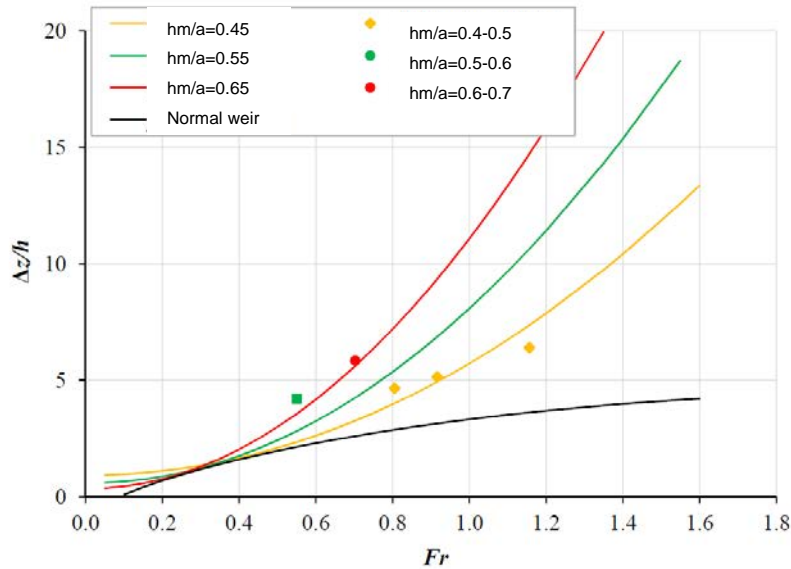


Fig. 10. Calibration of Eq. (5) for $R=6.3$, $C_{co} = 1$, $C_{cv} = 0,61$ and $C_f = 1,4$, different types of h_m/a curves were investigated.

Fig. 9 shows the calibrating result for $R=6.3$ and for several values of h_m/a parameters. In Fig. 9 this calibration involved a complete occluded mesh, with $C_f=1.1$. On the other hand, Fig. 10 represent the calibration for a partially occluded mesh, with $C_f=1.4$. The data shows a good correspondence between Eq. (5) and the on-scale experiments.

It seems that this correspondence is better for $C_f=1.1$, which suggests that the design equation is more effective with a completely occluded mesh. This fact is related to the issue that, the partial occlusion of the mesh does not block all the material on the net but leaves some part of this material flowing through it. This suggests that another equation set should be studied in order to have a specific shape of the net for a filtering use and to lower the pressure of impact on anchoring.

The calibrating process was successfully done and showed that, if Eq. (5) is applied for the design, C_f should be considered equal to 1 for safety.

5. Conclusions and future development

A new approach for the characterization of the hydraulic apparatus has been defined by this research. This project investigated a new apparatus and its performances in diluting the discharge of a debris flow. Data used for the calibration of Eq. (3) suggests a no-correlation to the sieve curve of the material, which should be investigated by later experiments. Data used for the calibration of Eq. (5) suggests the need of investigating the filtering properties of the net to apply a more realistic coefficient that will express these properties and will be useful in reducing the pressure on the net.

The whole research investigated the innovative hydraulic design criteria for MSCD. The full-scale design of this apparatus requires further investigation of the impact pressure on a partially open obstacle. In addition, the filtering properties of the net should be correlated to the potential reduction of the pressure, as to have a more realistic design procedure for anchoring.

Acknowledgements

This research was possible thanks to a collaboration between Maccaferri Innovation Center and the Hydraulic department of the Università degli Studi di Trento, in the person of Prof. Aronne Armanini, as part of a research project to study innovative apparatus for the control of debris-flow phenomenon.

References

- Armanini, A., Fraccarollo L., and Larcher M., 2005, Debris Flow: Encyclopedia of Hydrological Sciences, v. 4(12), p. 2173-2186.
Takahashi, T., 1991, Debris Flow: International Association for Hydraulic Research.
Takahashi, T., 1978, Mechanical characteristics of debris flow: Journal of the Hydraulics Division v. 104, no. HY8, p. 1153–1169.
Morstabilini, C., and Deana, M. L., 2018, Debris Flow: a new design approach: Geomechanics and Geodynamics of Rock Masses. European Rock Mechanics Symposium, v. 2.
Morstabilini, C., Ferraiolo, F., and Armanini, A., 2018, Mini Skirt Check Dam: an innovative apparatus against debris flow: IAHR, doi: 10.3850/978-981-11-2731-1_251-cd.

Numerical study of debris flows in presence of obstacles and retaining structures: A case study in the Italian Alps

Marina Pirulli^{a*}, Mario Manassero^{a,b}, Carmine Terriotti^b, Alessandro Leonardi^a, Giulia La Porta^a

^aPolitecnico di Torino, Corso Duca degli Abruzzi 24, Torino 10129, Italy

^bGeotechnical Engineering, Corso Duca degli Abruzzi 42, Torino 10129, Italy

Abstract

Debris flows are one of the most frequent mass movement processes and occur in all regions with steep relief and at least occasional rainfall. Their high flow velocity, impact forces, and long runout, combined with poor temporal predictability, cause debris flows to be one of the most hazardous landslide types. An essential aspect of debris-flow risk management is the design of mitigation measures, which reduce the existing risk to an accepted level of residual risk, by reducing the potential damage that the moving mass can produce in terms of loss of human life and destruction of structures and infrastructures. Among these mitigation measures, transverse retention structures are used to delimit storage basins and prevent dangerous debris flows from reaching high-consequence areas. Due to the enormous impact forces that debris flows can exert on obstacles in their path, a reasonable planning requires that dynamic stresses are taken into account during the structural designing process, regardless of the complete (solid body barrier) or partial (open barrier) retention function that the type of selected structure can exert on the flowing mass. Since the village of Cancia, close to Cortina d'Ampezzo (Italian Dolomites), is hit by destructive debris flows for a long time, a storage basin delimited by natural and gabion barriers was built in 2000. In 2009 a severe event caused the partial collapse of the gabions and the overflow of the flowing mass. The present paper analyses through numerical modelling the dynamics of the flow and the influence of an abandoned building, existing inside the storage basin, on the occurred event.

Keywords: Debris flow; Retention barriers; Numerical modelling; Risk mitigation

1. Introduction

Debris flows are fast-flowing mass movements composed of a mixture of water, mud and debris, discharging through steep and confined channels (Iverson, 1997). This natural process represents a widespread threat to villages and infrastructures in mountain areas. Therefore, countermeasures have to be adopted by the local governments to mitigate the risk related to these phenomena.

In order to protect elements at risk and to reduce expected losses, different passive (e.g. land-use management, hazard delimitation) as well as active (e.g. structural measurement, protection forest) mitigation strategies are available (Holub and Fuchs, 2008). In particular active structural measures, such as retention basins, check dams and channelization are established in the management of mountain hazards. But, knowledge of debris-flow dynamics, impact forces and loads is needed to design these engineered structures strong enough to withstand the forces of the impacting mass.

A contribution to this knowledge can to a certain extent be obtained through numerical modelling (e.g., Iverson and Denlinger 2001; Pitman and Le 2005; Pudasaini et al. 2005; Pirulli 2005), if measures and observations for the model validation and calibration are available. Data from real events would allow one to completely bypass any possible scale effects affecting laboratory-scale results, but available data are usually limited.

* Corresponding author e-mail address: marina.pirulli@polito.it

In the present paper, the numerical code RASH^{3D} (Pirulli, 2005) has been used to back-analyse the debris-flow event that affected the village of Cancia (Italian Dolomites) in July 2009.

Since destructive debris flows have long impacted this area, a storage basin delimited by a compacted soil embankment surrounded by gabions was built in 2000 as temporary mitigation structure. This barrier was partially destroyed by the July 18th, 2009 event. The collapse allowed the flowing mass to impact a house located downstream of the retention structure, where two people died.

Numerical modelling carried out with RASH^{3D} was aimed to investigate the dynamics of the flow and the influence on the event on an abandoned building located inside the storage basin.

2. Study area

The investigated area is the sector of the Boite river valley that is located at the foot of the Antelao Mountain, where the Cancia hamlet is (Fig. 1a). This hamlet is part of the Borca di Cadore municipality, which is located a few kilometers from Cortina d'Ampezzo (North-Eastern Italian Alps).

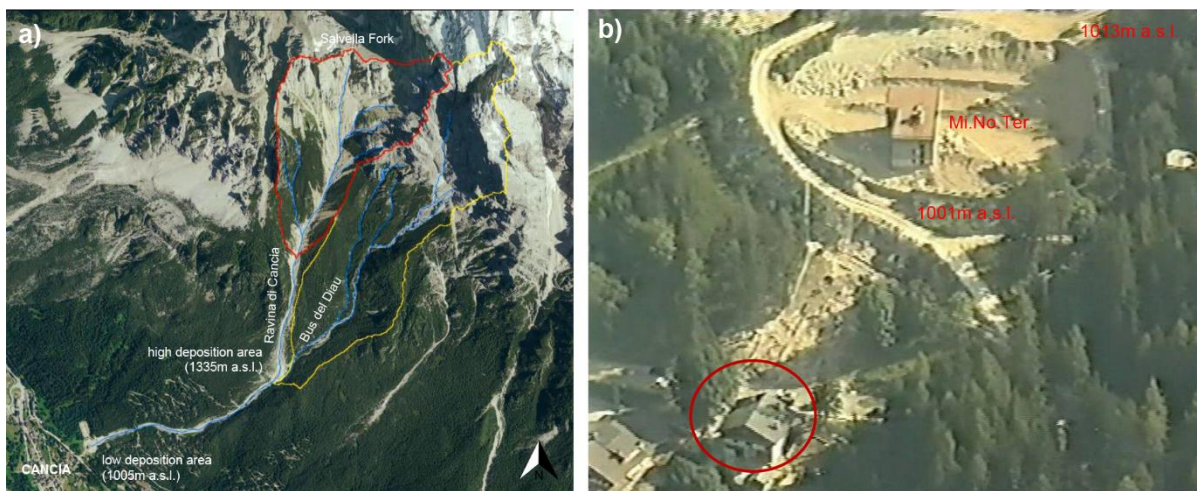


Fig. 1. (a) The Cancia study area (modified after Boreggio 2014); (b) the low deposition area where the partially destroyed storage basin is located. The red circle indicates the house impacted by the July 18th 2009 debris flow (image modified after Boreggio, 2014).

From a geological and structural point of view, the Antelao mountain range is between two important south-verging thrust faults: the Antelao line to the North and the Pieve di Cadore line to the South. The segmentation of the regional structure is further enhanced by movements along the faults and some existing paleotectonic fractures with NW-SE and NNW-SSW orientation. Cataclastic processes due to the above dislocations have originated the thick debris layer that characterizes the area (Turconi and Tuberga, 2010).

From a geomorphological point of view, the western side of the Antelao mountains presents an extremely irregular profile, because of the existing geological structure but also due to the intense modifications that occurred during the Würm glaciation. The retreat of glaciers made numerous mountainsides unstable and prone to collapse (Turconi and Tuberga, 2010).

Over the last few decades, the Antelao slope overhanging the Cancia hamlet has been object of periodic and intense instability phenomena in the form of debris flows.

The source area of these events extends from 1005 m a.s.l. at the terminus to 3264 m a.s.l. (Antelao Mountain), comprising a drainage area of about 1.8 km². Its main channel, namely Ravina di Cancia, has a length of about 2400m with a mean slope of about 20°. It originates at the feet of the Salvella Fork (2500 m a.s.l.) and ends at 1005m a.s.l. in a storage basin (low deposition area), which was built in 2000 to protect the Cancia village. At the confluence with the Bus del Diau torrent (1335 m a.s.l.), the Ravina di Cancia pattern intersects a flat area (high deposition area) that was specifically built to divert and slow down flow events (Manassero et al., 2018).

The debris flow occurred on July 18th, 2009 was triggered by heavy but not exceptional rainfall; nevertheless, it was the most catastrophic of the historically occurred events, causing the loss of two human lives. The event, which

triggered from the upper part of the Ravina di Cancia channel and the Bus del Diau (Fig. 1a), mobilized about 30.000 m³ of material. This volume estimation is based on on-site surveys and comparison between pre- and post- event digital topography data and is defined as a function of the material eroded and deposited from the high deposition area up to the low deposition area and the Cancia hamlet (Fig. 1a).

During its propagation, it impacted and caused the partial collapse of some gabion barriers located upstream (1013m a.s.l.) and at the end (1001m a.s.l.) of the above mentioned storage basin (Fig. 1b). The partial collapse of the 1001m a.s.l. gabions allowed the mass to continue its running downstream and impact against a house located along its main flow trajectory, where two people were killed by the flowing mass (Fig. 1b).

The flowing mass entered the impacted house through windows and doors facing upstream and splashed up to the ceiling of the rooms. Immediately after, the mass fell through the floor into the downstairs garage and then exited the house from openings and pointed downstream.

After the event it was observed that gabions were not joined together, thus preventing the structure to act as a monolithic mass against the flow. Furthermore, a large quantity of fine size aggregates filled the inner part of the gabions, thus preventing the water to flow through the wall and not minimizing the build-up of pressure behind. The collapsed gabions were found emptied by confirming the washing away of fines by the moving mass.

3. RASH^{3D} model

The back analysis of the aforementioned event was carried out using the RASH^{3D} numerical code (Pirulli, 2005; Pirulli et al., 2007). RASH^{3D} is based on a single-phase continuum mechanics approach and on depth-averaged St. Venant equations. This implies that both the depth and length of analysed flowing masses are assumed large, if compared to the characteristic dimension of the particles involved in the movement. The real moving mixture of the solid and fluid phases can therefore be replaced with a homogeneous continuum, whose rheological properties are intended to approximate the bulk behaviour of the real mixture, and the motion can be described using a model that consists of the balances of mass and momentum (Pirulli and Marco, 2010). Furthermore, assuming that the vertical structure of the flow (i.e depth) is much smaller than its characteristic length allows one to integrate the balance equations in depth and to obtain the so-called depth-averaged continuum flow model (Savage and Hutter, 1989):

$$\left\{ \begin{array}{l} \frac{\partial h}{\partial t} + \frac{\partial(\overline{v_x}h)}{\partial x} + \frac{\partial(\overline{v_y}h)}{\partial y} = 0 \\ \rho \left(\frac{\partial(\overline{v_x}h)}{\partial t} + \frac{\partial(\overline{v_x^2}h)}{\partial x} + \frac{\partial(\overline{v_x v_y}h)}{\partial y} \right) = -\frac{\partial(\overline{\sigma_{xx}}h)}{\partial x} - \tau_{zx} + \rho g_x h \\ \rho \left(\frac{\partial(\overline{v_y}h)}{\partial t} + \frac{\partial(\overline{v_y v_x}h)}{\partial x} + \frac{\partial(\overline{v_y^2}h)}{\partial y} \right) = -\frac{\partial(\overline{\sigma_{yy}}h)}{\partial y} - \tau_{zy} + \rho g_y h \end{array} \right. \quad (1)$$

where $\overline{v_x}$, $\overline{v_y}$ denote the depth-averaged flow velocities in the x and y directions (z is normal to the topography), h is the fluid depth, τ_{zx} , τ_{zy} the shear resistance stress (transverse shear stresses τ_{xy} are neglected), $\overline{\sigma_{xx}}$, $\overline{\sigma_{yy}}$ the depth-averaged normal stress and g_x , g_y the projection of the gravity vector.

Different rheologies exist to describe the basal shear that develops at the interface between the flowing material and the rough surface and are implemented in RASH^{3D}. As far as the Voellmy rheology is concerned, Rickenmann and Koch (1997) and Revellino et al. (2004) showed that this model, originally developed for snow avalanches (Voellmy, 1955), offers a good simulation of velocities for debris flows and debris avalanches. According to these authors and our experience, the Voellmy rheology was selected for the numerical back analysis of the July 18th event.

The Voellmy model combines a frictional term, which includes the friction coefficient μ ($= \tan \varphi$, where φ is the friction angle) and a turbulent term, which includes the turbulence coefficient ξ :

$$\tau_{zi} = - \left(\rho g h \mu + \frac{\rho g v_i^{-2}}{\xi} \right) \text{sgn}(v_i) \quad (\text{where } i=x,y) \quad (2)$$

4. Dynamic analysis of the July 18th debris flow

The analysis of the July 18th debris flow is here presented. An attempt was made to investigate the influence of an abandoned building (Mi.No.Ter. in Fig. 1b), located inside the storage basin, on the flow trajectory and dynamics. A set of numerical analyses in presence and absence of the Mi.No.Ter. building have been then carried out.

Both a Digital Surface Model (DSM) and a Digital Terrain Model (DTM) generated from LiDAR, with a 1m grid spacing of the pre-event topography, were provided by the Ministry for the Environment and Protection of the Territory and the Sea. The starting position of the 30,000 m³ mass was the confluence of Ravina di Cancia with Bus del Diau torrent at 1335m a.s.l (Fig. 2). The Voellmy resistance model shown in Eq. (2) was used. The two Voellmy parameters were systematically adjusted until simulations approximately reproduced the observed distribution of deposits in the storage basin.

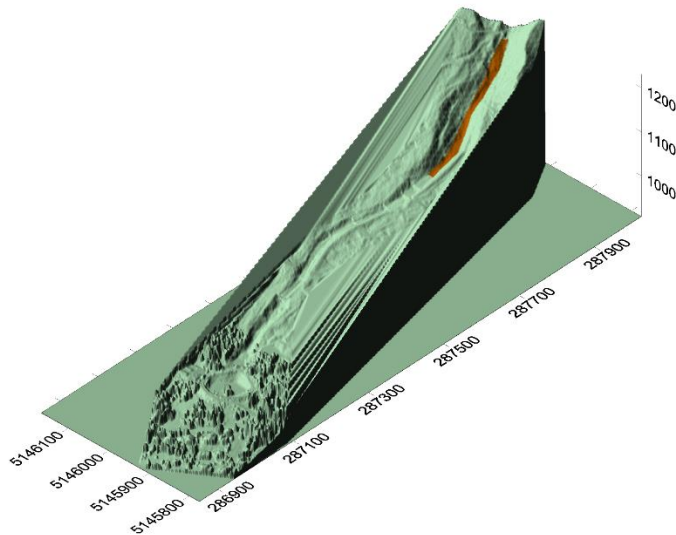


Fig. 2. RASH^{3D} numerical simulation: starting position of the released mass on the topography.

The model provided a good match of the general extent and distribution of the storage basin deposit using a friction coefficient (μ) equal to 0.1 and a turbulence coefficient (ξ) equal to 300 m/s². A comparison between numerical simulations with the above calibrated parameters (Fig. 3b) and survey data collection (Fig. 3a) shows that the model reasonably simulates the event in terms of distribution of the final deposit.

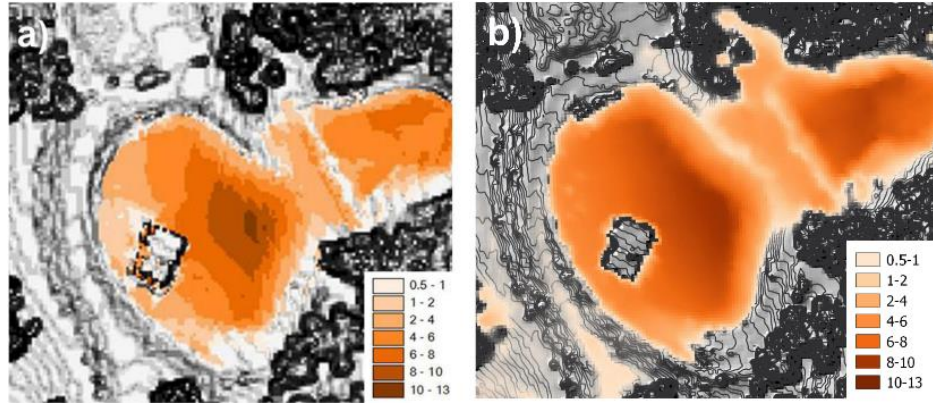


Fig. 3. Comparison between deposit depth as obtained processing pre- and post-event available digital topographic data (a) and RASH^{3D} numerical results (b).

Regarding the flow velocity (Fig. 4), it is observed that the flow reaches high velocity (>10 m/s) along the channel and in the upper part of the retention basin. The velocity decreases downstream of the gabion barrier to 5-6m/s.

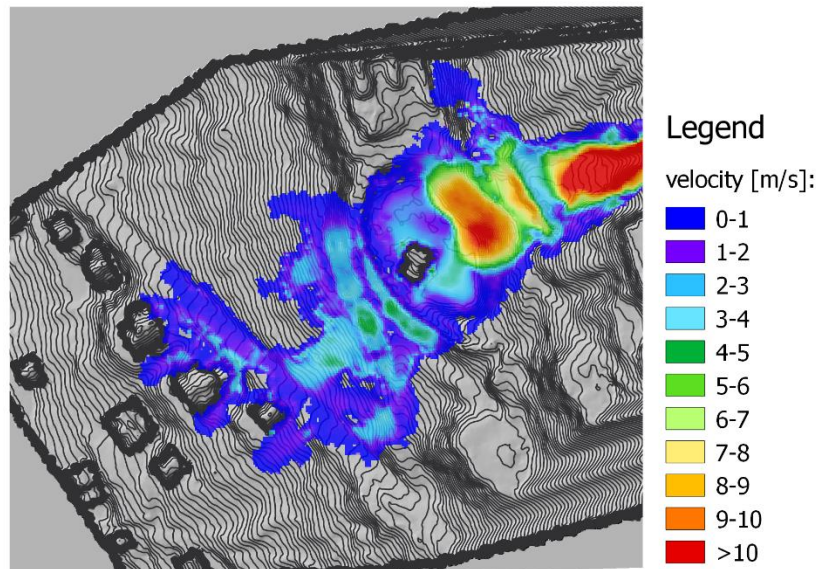


Fig. 4 RASH^{3D} numerical results: maximum computed flow velocity.

To highlight the role of the Mi.No.Ter building (Fig. 1b) on flow dynamics, we modeled the flow with (Fig. 5a) and without (Fig. 5b) the building in the sediment basin. The results show that without the Mi.No.Ter. building, the flow would still have overflowed the storage basin (Fig. 5b, Scenario B). Nevertheless, a smaller quantity of material would have escaped from the storage basin and affected the downstream area. In particular, a lower height flow would have impacted the house below the debris basin where two people died. Based on the height of the windows, a lower flow height would have reduced the amount of flow into the house (highlighted with red squares in the legend of Fig. 5a and 5b). In particular, numerical results indicate a decrease of the flow thickness from a maximum value of 2 m (Fig. 5a, Scenario A in the presence of Mi.No.Ter.) to a maximum value of 1.4 m (Fig. 5b, Scenario B in the absence of Mi.No.Ter.). Results are justified by the fact that with the building, a larger quantity of material overflow the gabion barrier. While, without the house, the storage capacity of the basin increases and a minor quantity of material overflow the gabion barrier.

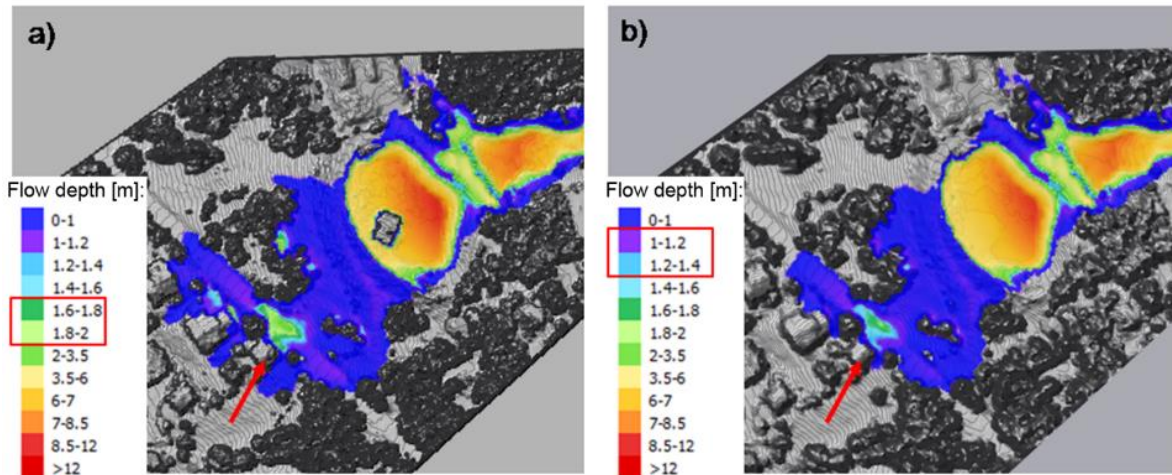


Fig. 5. RASH^{3D} numerical simulation: deposit depth distribution with (a) and without (b) the Mi.No.Ter. building. Red arrow indicate the position of the mainly impacted house during the July 18th event.

5. Conclusions

The design of countermeasures and the hazard zoning in debris-flow prone basins need an estimation of the debris-flow magnitude and require the understanding of the flow dynamic characteristics. With this in mind, the continuum mechanics based numerical code RASH^{3D} was used to investigate the role of a storage basin, built to protect the village of Cancia from regularly occurring debris flows, and of an abandoned building, located inside the above storage basin, on the dynamics and trajectory of the event here occurred on July 18th 2009. First, the calibration of the model parameters was made on the basis of the deposit shape and depth distribution surveyed on site. Simulations in presence and absence of the abandoned building were carried out and results compared. We found that removal of the building would not have prevented the mass from exiting the storage basin. But, without the abandoned building, the impact depth of the flowing mass would have decreased from about 2 m to 1.4 m. This would have reduced the flow of material into the house. Our results show that the RASH3D model can adequately simulate the complex flow dynamics of this event and, therefore, can be used quantify potential debris-flow impacts to infrastructure and inform the design of mitigation structures. Specific numerical analyses to investigate the partial collapse of the gabion barrier are foreseen in future.

References

- Boreggio, M., 2014, Simulazione degli eventi di colata detritica avvenuti nei bacini del Rio Lazer (TN), Fiammes (BL) e Cancia (BL) mediante i codici di calcolo "D.F.R.M." e "T.R.E.N.T.2D-df" [Master thesis]: Università degli Studi di Padova, 284 p.
- Denlinger, R.P., and Iverson, R.M., 2001, Flow of variably fluidized granular masses across three-dimensional terrain: 2. Numerical predictions and experimental tests: *J. Geophys. Res.*, no. 106(B1), p. 553–566.
- Holub, M., and Fuchs, S., 2008, Benefits of local structural protection to mitigate torrent-related hazards: *WIT Transactions on Information and Communication Technologies*, no. 39, p. 401–411.
- Iverson, R.M., 1997, The physics of debris flows: *Rev. Geophys.*, no. 35, p. 245–296.
- Manassero, M., Pirulli, M., and Terrioti, C., 2018, The influence of obstacles in debris-flow dynamics: the case study of Cancia (Italian Dolomites), *in* Proceedings, Congresso Nacional de Geotecnia, 16th, Acores: Portugal, 27-30 May 2018, p. 1-9.
- Pitman, E., and Le, L., 2005, A two-fluid model for avalanche and debris flows: *Royal Society of London Transactions Series A - Mathematical, Physical and Engineering Sciences*, no. 363 (1832), p. 1573–1601.
- Pirulli, M., 2005, Numerical modelling of landslide runout, a continuum mechanics approach [Ph.D. thesis]: Italy, Politecnico di Torino, 204 p.
- Pirulli, M., Bristeau, M.O., Mangeney, A., and Scavia, C., 2007, The effect of the earth pressure coefficients on the runout of granular material: *Environmental Modelling and Software*, no. 22(10), p. 1437-1454.
- Pirulli, M., Marco, F., 2010, Description and numerical modelling of the October 2000 Nora debris flow, Northwestern Italian Alps: *Canadian Geotechnical Journal*, no. 47, p. 135-146.
- Pudasaini, S., Wang, Y., and Hutter, K., 2005, Modelling debris flows down general channels: *Natural Hazards and Earth System Sciences*, no. 5(6), p. 799–819.
- Revellino, P., Hungr, O., Guadagno, F.M., and Evans, S.G., 2004, Velocity and runout simulation of destructive debris flows and debris avalanches in pyroclastic deposits, Campania region, Italy: *Environmental Geology*, no. 45, p. 295-311.

- Rickenmann, D., and Koch, T., 1997, Comparison of debris flow modelling approaches, *in* Proceedings, Int. Conf. on Debris Flow Hazards Mitigation: Mechanics, Prediction, and Assessment, 1st, Chen, C.L., ASCE, Reston, Va., p. 576-585.
- Savage, S.B., and Hutter, K., 1989, The motion of a finite mass of granular material down a rough incline: *Journal of Fluid Mechanics*, no. 199, p. 177-215.
- Turconi, L., and Tuberga, S., 2010, *Relazione tecnica su incarico per consulenza evento 18.07.2009, Cancia (Borca di Cadore)*. Report, 90 p.
- Voellmy, A., 1955, *Über die Zerstörungskraft von Lawinen*, Schweiz: *Bauzeitung*, no. 73, p. 212-285.

Design of a debris retention basin enabling sediment continuity for small events: the Combe de Lancey case study (France)

Guillaume Piton^{a,*}, Vincent Mano^b, Didier Richard^a, Guillaume Evin^a, Dominique Laigle^a, Jean-Marc Tacnet^a, Pierre-Alain Rielland^b

^a Univ. Grenoble Alpes, IRSTEA, ETNA, Grenoble, 38402, France

^b ARTELIA Eaux Et Environnement, Echirolles, 38130, France

Abstract

The Combe de Lancey stream is a relatively calm tributary of the Isère River flowing through the city of Villard-Bonnot near Grenoble (France). In 2005, a long-lasting extreme rainfall event triggered dramatic erosion processes in this 18 km² granitic catchment. A volume of 20,000 m³ of sediment and logs deposited in the paper factory located near the fan apex. This paper focuses on the definition of a new protection system, namely a debris retention structure made of an excavated basin and an open check dam. The design is based on expert knowledge and tested by physical small scale modelling. The particularity of this case study relies on two points: (i) its design scenarios and (ii) the structure capacity to transfer small events. Attention was paid to define several 100-year return period events used as “design events” for which the structure must have its best effectiveness. Extreme events with higher return periods called “safety check events”, for which the structure must still withstand the event without failure but with acceptable marginal damages, were also modeled. The definition of the scenarios is described in the paper. Secondly, the debris retention basin should have the capacity to transfer small debris floods without trapping sediment in order to prevent downstream incision and heavy maintenance costs. It must however trap nearly totally the sediment and large woods that are erratically supplied by the catchment during extreme events. Classical debris retention basins are usually not able to achieve such a dual objective. Here, two concepts developed in past works, namely a guiding channel and a hybrid open check dam with mechanical – hydraulic control were successfully tested. The paper presents the design and testing procedure of this case study exemplifying the next generation of debris retention structures.

Keywords: debris flood, hazard scenario, open check dam, guiding channel

1. Introduction

Steep mountain streams erratically experience debris-flows and debris-flood events releasing massive amounts of sediment and large woods on fans. The municipality of Villard-Bonnot is partially built on the Ruisseau de la Combe de Lancey alluvial fan and aims at removing here a closed paper factory to create new residential areas. Before doing so, the French state requested a torrential hazard mitigation plan to protect the whole fan. Past studies demonstrated that a debris retention basin was part of the best option (SOGREAH 2010). The best location to build it is at the slope break between the upstream gorges and the alluvial fan (Fig. 1). Indeed, massive deposition was observed in the last extreme event at this location.

Designing a debris retention basin in a city center deserved a detailed analysis which has been performed using expert assessment along with numerical and small scale physical modelling. This case study had two particular challenges so far poorly addressed in the literature and worthy of publication: (i) determination of the debris-flood multiple scenarios and (ii) solutions to enable sediment transport in normal conditions while trapping all gravels and large woods for events overloading the quite low channel capacity. This paper synthesizes these points after a short presentation of the catchment and before to briefly describe the structure behavior in physical small scale model subjected to various scenarios. All details may be found in the technical report by ARTELIA and IRSTEA (2018).

* Corresponding author e-mail address: guillaume.piton@irstea.fr

2. Catchment short presentation

The Ruisseau de la Combe de Lancey is a steep stream flowing from a 18 km² catchment in the Belledonne mountain range, north-east to Grenoble. Its confluence with the Isère River is located on the Villard-Bonnot municipality that occupies its alluvial fan. The torrent passes through four geomorphic units along its path (Fig. 1a & b). The steep headwaters experience erratic debris-flow activity. Along the 6 km of 12%-steep mid-mountain range, the torrent has a very stable, about 4 m wide steep-pool pattern with a wider paleo-bed. A very steep gorge with a bedrock and cascade bed connects the mid-range with the alluvial fan. The fan is almost entirely occupied by a huge 19th century paper factory now closed, the village center, a regional road and the railway to Italy (Fig. 1c). The final torrent section is 1.5% steep before its confluence with the Isère River. It is worth being stressed that where the river channel crosses a deep ditch dug to drain the Isère floodplain a long time ago (Fig. 1c), the torrent has only the capacity to carry 7 m³/s, so that any additional discharge supplied by the catchment is lost in the drainage ditch.

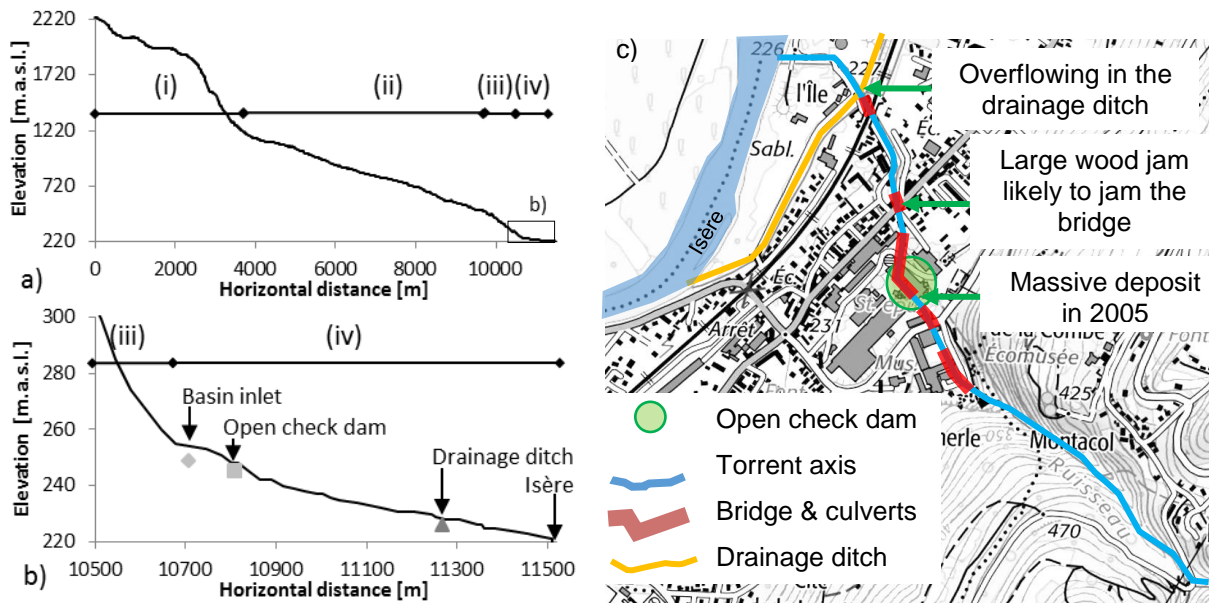


Fig. 1: a) full longitudinal profile of the Combe de Lancey torrent, split in four sections (i) headwater, debris-flow reaches, (ii) mid-range 12%-steep section, (iii) 28%-steep final gorges and (iv) alluvial fan; b) zoom on the fan section with location of the debris deposition basin, drainage ditch and confluence with the Isère River; c) map of final gorge and alluvial fan areas, location of bottleneck sections with deposition, jamming and overflowing issues (©IGN BD Alti 25m and Scan25).

The granitic geology of the catchment makes primary sediment production quite low; consequently, bedload sediment transport is supply-limited under normal conditions. Large sediment supplied to the fan is in any case limited by the mid-mountain range 12%-slope, except in the case of landslide in the final gorges which has been considered possible but very improbable and consequently not studied further in detail.

On Aug. 21st and 22nd, 2005, a long lasting extreme rainfall event hit the Belledonne mountain range (IRMA 2006). Most torrents with sources located close to the summits experienced flood events with high intensity lasting at least 24 h, triggering massive geomorphic adjustments and debris releases on fans. The Combe de Lancey experienced debris flows in the headwaters and debris floods further downstream. Bridge clogging and bed widening in the mid-range occurred and 20,000 m³ of gravels deposited under and around the paper factory at the slope break between fan and gorges. Water peak discharges were not extreme ($Q \sim 22$ m³/s, return period ~ 30 yrs, SOGREAH 2010) but the high flows lasted about 24 h, much longer than under usual thunderstorm conditions. The multivariate nature of this event, i.e., peak flows, duration, sediment transport, large wood recruitment or resulting damages, makes a direct estimation of a return period difficult but it can certainly be considered as exceptional. If considering simply damages, the historical records let us think that the return period of such events is closer to centuries than to decades. Not all details could be provided here for the sake of conciseness. The paper rather aims at conceptually explaining the coupled historical – geomorphic – physical appraisal used to fine-tune the structure to the torrent.

3. Design scenarios for debris-flood events

3.1. Event status in design scenarios

Debris retention basins fundamentally aim at partially changing the sediment cascade processes but should optimally (i) only influence events likely to create hazardous problems, (ii) fully cope with a certain range and variability of events and (iii) not aggravate hazards when overloaded beyond their capacities. Several event magnitudes were consequently studied. (Fig. 2 and Table 1):

- As mentioned above, the torrent has the capacity to convey down to the Isère River only discharges up to 7 m³/s, i.e., about the annual peak flows. Trapping the bedload transport occurring below those conditions would increase cleanout costs for the structure, trigger sediment starvation downstream and should therefore be prevented with a suitable design. Several short runs on the physical small scale model with low sediment supply were tested to verify this point and are hereafter referred to as “*routine events*”.
- The structure should be able to cope with a similar event than the one experienced in 2005, which is assumed to have a return period of damages of about 100 years, these damage being mostly related to the volume of sediment transport. Assuming that sediment transport is mostly related to the hydrograph (see below for a discussion on this point), one must consider that a 1:100 years return period event could also have other features, e.g., a shorter duration but higher peak discharge. Two events with exceedance probability of about 1:100 years were tested and are hereafter referred to as “*project design events*”. Under these various harsh conditions, the structure must fully protect the area, i.e., with a certain safety factor taken as a 1 m-high freeboard on the flow level.
- A protection structure should not fail and aggravate the hazards even under a certain range of events with magnitudes higher than these project design events or more rare events with extraordinary features, e.g., massive armor breaking in the stable step-pool systems or cascading hazards of landslide and strong thunderstorm triggering an abnormally sediment-laden flood. Such events were tested as “*safety check events*” to control the structure robustness and reliability. For these events, a null freeboard is considered acceptable but full structure failures are not. They aim at understanding possible failure modes and at raising stakeholder awareness that structures protect up to a certain limit.

Table 1: Synthesis of event scenarios

Name	Event status	Sediment main source	Return period [yr]	Peak discharge [m ³ /s]	Event* duration [h]	Solid volume [m ³]	Structure objective for this event
Small events	<i>Routine events</i>	Armored torrent bed	<<10	3-7	3-7	<<1,000	Sediment transport transfer downstream, no trapping
Type 2005	<i>Project event</i>	Debris flows in the headwaters	~100	22	30	20,000	Maximum effectiveness with 1m freeboard and without large woods releases to the downstream channel
Long thunderstorm	<i>Project event</i>	Debris flows in the headwaters	~100	35	18	20,000	
Armor breaking	<i>Safety check</i>	Large scale armor breaking	>100	35	18	20,000	Observation of potential failure modes for safety check: the structure should not aggravate the hazards but may be overloaded and not able to cope with such events. Freeboard may be null
Short & Hyper-concentrated	<i>Safety check</i>	Landslides or massive bank erosion in the catchment inter range	>100	22	14	20,000	
Volume overloading	<i>Safety check</i>	Larges debris flows in the headwaters	>>100	35	36	40,000	
Debris flows	<i>Extreme</i>	Landslide in the steep gorges just above the fan	>>100	?	?	?	Considered too unlikely to be studied.

* Event duration: full hydrograph duration, assumed to be four times longer than the rainfall and two times longer than the flood high stages as displayed in Fig. 2.

3.2. Computation of event hydrographs

The first step was to reconstruct the 2005 event. Analyzing historical data, crisis management reports, *ex-post* technical reports and rainfall data, a hydrograph has been proposed to model the event with the following features:

peak discharge $Q_p=22 \text{ m}^3/\text{s}$, high flow stage duration, i.e., with $Q>Q_p/2$, $t=10 \text{ h}$, a full duration of 36 h and a water volume of 760,000 m^3 .

The other ~ 1:100 years flood event was considered to have a hydrograph with maximum value $Q_p=35 \text{ m}^3/\text{s}$ (SOGREAH 2010), a high flow stage shorter duration $t_1=5 \text{ h}$, a full duration of 18 h and a volume of 560,000 m^3 of water as a response to a 5 h rainfall event.

To the best of authors’ knowledge, recommendations based on the determination of discharges – durations, of given exceedance probability, in the context of debris flood-prone ungauged mountain streams – have never been tried or tested. To estimate longer hydrologic events of similar exceedance probabilities, a straightforward technique has been used: assuming that peak discharges are proportional to the rainfall intensities - the so-called “rational method” in discharge estimation - one can express peak discharges as a power equation on time:

$$Q_p(T, t) = \frac{C(T).A.I(T,t)}{3.6} = \frac{C(T).A.a_T.t^{1-b_T}}{3.6} \Leftrightarrow \frac{Q_p(T,t_1)}{Q_p(T,t_2)} = \left(\frac{t_1}{t_2}\right)^{1-b_T} \quad (1)$$

with event time return T [years]; peak discharge Q_p [m^3/s]; runoff coefficient C [-]; rainfall intensity I [mm/h], catchment area A [km^2], rainfall intensity-duration coefficients a_T [mm/h] and b_T [-], and rainfall durations t , t_1 and t_2 [h]. Fig. 2 displays the peak discharge reduction against rainfall duration using $b_T=0.37$, mean value of the frequency-intensity-duration curves measured at the rain gauges located on or near the Belledonne massif (Alleverd, Fond de France, Saint Martin d’Hères, according to Djerboua 2011). The longer project design event, corresponding to the 2005 disaster, falls in the $\pm 20\%$ uncertainty range around this 1:100 year exceedance probability domain (Fig. 2, light blue area). The same method has been used to estimate other exceedance probability domains based on discharge knowledge for 1:10 years and extrapolating using daily rainfall extreme values and discharge-rainfall relationships according to Carré and Fretti (2010) for 1:1,000 years.

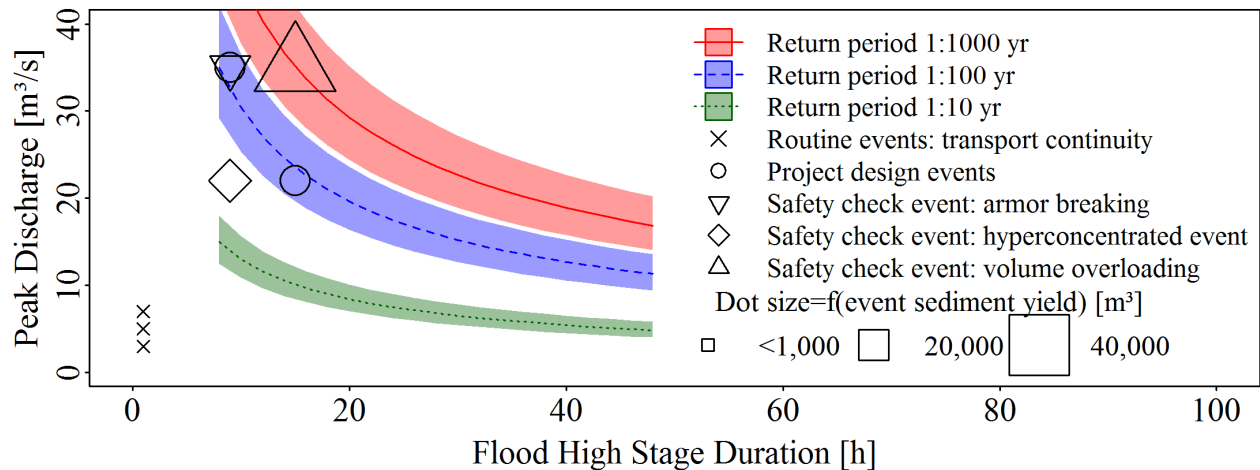


Fig. 2: Theoretical peak discharge – flood high stage duration for both routine, project and safety check events; exceedance probabilities of event magnitudes are based on rainfall intensity and peak discharge – rainfall relationships; sediment yields are computed with a bedload transport formula.

3.3. Computation of sediment yield and geomorphic scenarios

Bedload transport has been computed in a second step according to the “travelling bedload” framework specifically suitable for heavily armored bed experiencing colluvial sediment inputs, e.g., debris flows and landslides (Piton and Recking 2017). All the fan being urbanized and mostly covered, no alluvial material could be found near the structure location to assess the fan apex grain size distribution representative of debris-flood events. Measurements were thus realized upstream in the mid-mountain range ($D_{84}=332 \text{ mm}$) and downstream on the fan distal part close to the Isère confluence ($D_{84}=98 \text{ mm}$). Based on evidences of 2005’s disaster pictures, debris-flood events were assumed to supply grain sizes finer than the first sample but coarser than the latter. Project design events were tested with a mixture of 40% of the coarse gorge sample and 60% of the fine fan one. It has additionally been

observed that cobbles of approximately 400 mm of diameter tended to deposit in the fan channel and hardly to be transported until the Isère confluence.

Using this grain sizes with the aforementioned 2005's hydrograph and the mid-mountain range 12% slope resulted in a sediment yield estimation of 58,000 m³, nearly three times the 20,000 m³ observed in 2005. This is consistent with the supply-limited state observed in normal condition: only rare triggering of massive debris flows in the headwaters can supply the material to generate debris floods. As often done in practice, the slope has been artificially lowered to 6.8% in order to model this supply-limitation and obtain the 20,000 m³ transport under the reconstructed hydrology.

Several hypotheses had to be done on hydrology and sediment sizes and availability as described above. Scenarios testing the occurrence of events different than expected were used as safety check events (Fig. 2, Table 1):

- A safety check test was performed using coarser grain sizes corresponding to 60% of the gorge sample and only 40% of the fan sample. This event is assumed to correspond to a large scale armor breaking event. This test aimed at verifying the structure capacity to cope with the supply of sediment coarser than usual.
- Another possible geomorphic scenario is the occurrence of landslides and mass wasting processes into the torrent bed and the occurrence of a flood event of moderate magnitude, e.g., exceedance probability 30 years, before that channel cleaning with earth moving machinery could be performed. Such an event would trigger sediment laden flows loaded at full transport capacity, i.e., with the geometrical slope of 12%. This test aimed at verifying the structure capacity to cope with the supply of sediment with a solid concentration much higher than usual.
- Performing hydrology studies of ungauged high mountain catchments is highly uncertain. In addition to the two project design events which vary mostly in term of hydrograph, another safety check event aimed at testing how the structure respond to both a long (38 h) and intense event ($Q_p=35 \text{ m}^3/\text{s}$) supplying 40,000 m³ of sediment, thus strongly overloading the debris basin volume capacity. Its hydrological exceedance probability is assumed to be about 1:1,000 years (Fig. 2).

3.4. Large wood recruitment

In addition to sediment and water, extreme debris-flood events recruit large woods, i.e., logs longer than 1 m and diameter higher than 0.1 m, on banks and from mass wasting processes. During the 2005 disaster, a cumulated volume of 600 m³ of large wood jams was measured in the catchment (ONF-RTM 2005). This value is close to the lower envelope of values estimated from empirical formulas (400 m³-3,000 m³) as reviewed in Piton and Recking (2016a). Large wood jams in retention basins increase obstruction ratio and trapping performances but are also likely to be released aggravating downstream hazards. They should consequently be considered cautiously during the design procedure (Bezzola et al. 2004). Based on historical evidences and observations of large wood pieces in the final gorges, a total absence of large wood pieces was considered really unlikely. However, in order to prevent an overestimation of trapping capacity, a relatively small volume of 100 m³ of large wood pieces were introduced during the raising limb of the hydrograph during all events tested in the laboratory. Close attention was paid to observe large wood accumulation and abrupt releases by overflowing possibly generating jamming problems further downstream (Fig. 1).

4. Debris retention basin design: basic and optimized

The basin has a diamond shape adjusted to the area available in the current and future urban fabric. It is roughly 100 m wide and long. The design is inspired by the state-of-the-art reviewed by Piton and Recking (2016a, 2016b) and by Schwindt et al. (2017, 2018) for the adaptations to enable sediment transport continuity during routine events while fully trapping sediment transport for larger events.

- The basin bottom slope has been chosen at precisely 1.5%, i.e., value of the bottleneck downstream reach, from the drainage ditch to the Isère River (Fig. 1). In essence, the structure should be able to transfer precisely the amount of sediment that the most constrained part of the whole downstream torrent system is able to export. This bottleneck reach has a hydraulic capacity of 7 m³/s. A guiding of channel of precisely the same capacity was dug in the basin to enable the continuity: the slope is not sufficient to transfer the sediment load if flows spread in the basin, flows must also be laterally constrained to keep their transport capacity (Piton et al. 2018a).
- Designing an open check dam able to transfer all sediment transport for routine events and trapping nearly all higher sediment supplies was an unresolved challenge until recently. The recent works by Schwindt et al. (2017) and Roth et al. (2018) provided clear recommendations to do so with so-called "hybrid" open check dams. Such

structures have a bottom outlet that takes advantage of (i) a orifice hydraulic functioning to rapidly increase head losses and trapping capacity when discharges overpass the guiding channel capacity, along with (ii) a preceding grill with bottom clearance that prevent self-flushing during flow recession. The grill bottom clearance was 0.4 m high, the space between bars was 0.2 m and the bottom orifice was 4 m wide and 0.5 m high in the first option, adjusted to 0.8 m after preliminary tests (Fig. 3).

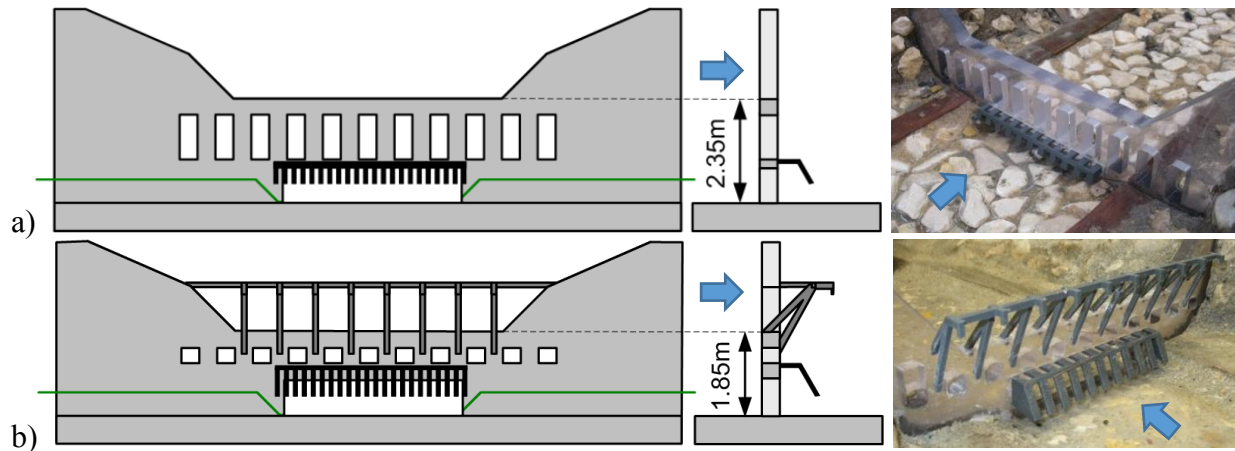


Fig. 3: a) Basic and b) optimized versions of the open check dam: upstream and left side views at prototype scale and pictures of the 1:40 scaled physical model. Blue arrows display the flow direction. The bottom slot was equipped with an inclined grill according to the hybrid mechanical-hydraulic controlled described by Schwindt et al. (2017); optimization consisted in increasing the bottom slot height of 0.3 m, lowering the spillway level by 0.5 m and adding a rack on the spillway to retain large woods in the basin

Above this outlet dedicated to the routine event management, eleven vertical slits were added to enable flows from routine events up to project design events to pass through the dam. They were 1.0 m high, adjusted to 0.35 m in a second round and 0.4 m wide. The slits' width was narrow enough to rely on their clogging by the cobbles of the same size observed in the channel. Additionally empirical evidences from other catchments let us think that mixtures of large wood pieces and even finer gravels will very likely lead to the clogging of the whole dam for heavy solid supply.

Finally a typical 6 m-wide trapezoidal spillway was added at a height of 2.35 m above the river bed, decreased to 1.85 m after optimization. This crest feature should prevent structure by-passing and guide extreme event flows or design event flows when outlets' clogging occurs. After a few tests, the following observation made clear some slight optimization needs as illustrated by difference between Fig. 3a & b:

- The 4 m-wide, 0.5 m-high bottom slot and inclined grill triggered a head loss a bit higher than expected likely to trap sediment for discharge in the range 4-7 m³/s. The bottom slot height was consequently increased to 0.8 m.
- The structure was able to trap all of the project design events' sediment supplies; some room even remained in the basin distal part due to the quite steep deposits (see later). Lowering the water level would enable the deposit front to prograde faster in the basin and optimize its filling. The spillway level strongly controlling the water level, the structure crest had consequently been lowered by 0.5 m, thus lowering too the vertical slit height.
- Large wood accumulated against the open check dam, clogged the bottom slot and some slits, thus increased head losses and water levels. No abrupt and massive release of large woods was observed for discharges up to 28 m³/s, while nearly full large wood overtopping was observed for discharge approaching 34 m³/s. A rack dedicated to retain large woods in the basin was added on the spillway crest to prevent it.

5. Short description of structure behavior on the physical small scale under various event scenarios

The optimization proved to have satisfactory results: (i) flows up to 7 m³/s were only marginally influenced by the basin and new dam and (ii) large woods were mostly retained upstream of the rack, only a few pieces passed in uncongested transport. The prevention of wood release maintained however higher head losses and the basin filling did not significantly change between the basic and the optimized designs. Safety check events were then tested to check failure modes and structure functioning robustness.

In addition to those empirical observations, classic measurements methods were used on the small scale model: photogrammetric analysis and surface velocity measurements by image analysis (Piton et al. 2018b). All events followed similar geomorphic trajectories although with various celerity and slight random variations. In essence: some bedload transport occurred in the guiding channel, however most of the supplies massively deposited near the basin inlet as soon as water discharge overpassed the 7 m³/s threshold. A small fan-like pattern grew and progressively prograded in the basin, the active channels wandered, split and merged on the depositional form. Since basin bottom slope was low and head losses rapidly grew, most of the basin was flooded and deposition actually occurred under a delta shape rather than a pure alluvial fan shape. The delta eventually reached the open check dam and large wood accumulation only occurred near the end of the events. The basin thus trapped all of the sediment supply, except for the volume overloading event. During this particular event, the bedload transport continuity was recovered near half of the run and 13,000 m³ out of the 40,000 m³ supplied were transferred in the channel downstream. The basin was thus capable to store 27,000 m³ at most, i.e., with null freeboard.

Maximum deposit elevations were measured to design the lateral embankments (Fig. 4). The project design event deposits plus the 1 m freeboard, as well as the safety check events (volume overloading and hyperconcentrated) with null freeboard, were measured above the ground level on a length of about 50 m from the basin inlet. Embankments suitably protected from erosion are required in this section. Conversely the simple excavation of the current ground is sufficient to contain the flows and depositions further downstream. Depositions slopes are relatively constant between events, around 5-6%, except for the hyperconcentrated and armor breaking events, which naturally resulted in steeper deposits with slopes around 7-8%.

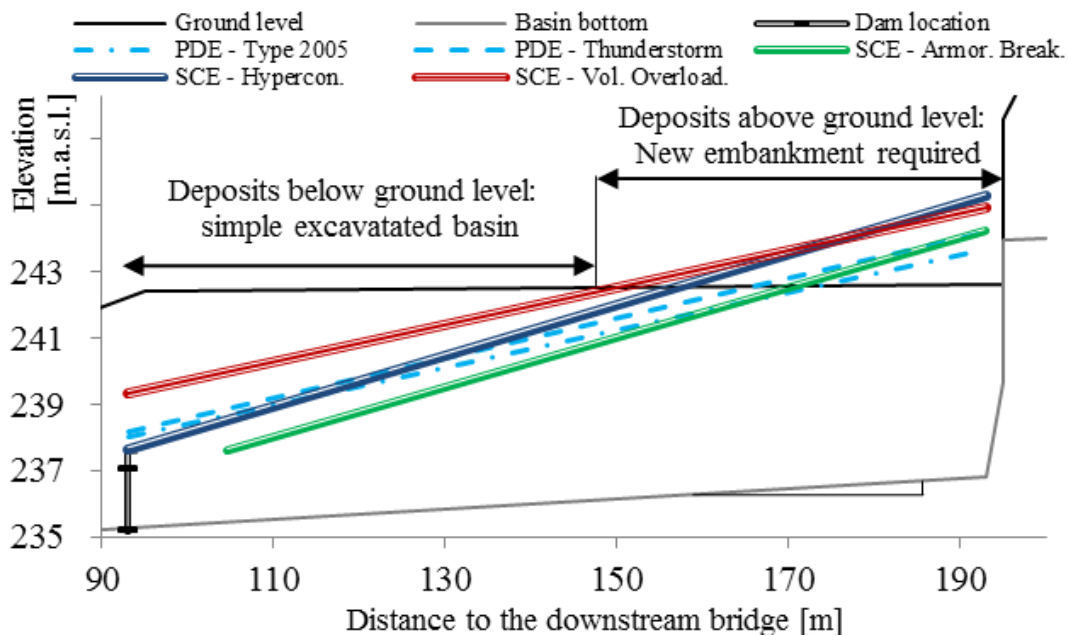


Fig. 4: Longitudinal synthetic profiles of ground level, i.e., current terrain in the area, basin bottom level, i.e., excavation to be performed to dig the basin, and deposit maximum elevations for the various scenarios: either project design events (PDE) or safety check events (SCE). Both project design events have very similar deposit maxima despite their different dynamics; both the hyperconcentrated and the volume overloading safety check events were necessary to determine the deposit maxima for extreme events enabling to check the embankment length.

6. Discussion and conclusion

Debris retention basins are complex structures whose filling and responses to the natural variety of processes have been seldom directly observed (Piton et al. 2018a). The deposition process complexity (Piton and Recking 2016a) and interactions between structures and large woods (Piton and Recking 2016b) are consequently not fully understood. To the best of the authors' knowledge, numerical models are not yet considered to be fully reliable tools to model debris-flood events, i.e., gravel, water and large wood mixtures flowing on slope of 5-15%. Small scale physical modelling was and is still a powerful tool to perform comprehensive analysis of such processes. But

performing each run is costly in labor force and time, typical case-studies can consequently afford only a handful of runs. Ensuring the necessary representativeness of those runs and not missing a likely surprising behavior resulting in the structure failure is thus of utmost importance. Testing the great variability of torrential flows observed in Nature by clearly highlighting the hydrologic and geomorphic scenarios likely to occur is thus a key preliminary study of any expensive small-scale physical model campaign.

Based on a recent case study of the Ruisseau de la Combe de Lancey in France, this paper shortly describes how the authors chose to deal with historical, geomorphic and physical data and methods to fine tune a debris retention basin. Three types of events were modeled:

- *Routine events* enabled to test and optimize the design so that small magnitude events, not threatening the village, could be transferred with marginal trapping to prevent maintenance effort and environmental degradation.
- *Project design events*, of various peak discharges and durations but globally having a $\sim 1:100$ years return period, enabled to verify the structure capacity to cope with such events with a reasonable freeboard.
- *Safety check events*, less probable though without specified exceedance probability due to the lack of data, enabled to test a greater variability of hydrological and geomorphic events and to make sure that no failure mode would appear for those magnitudes that remain possible although quite rare.

We hope that this example of applied research will help practitioners in other case studies or researchers in connecting scientific challenges in hydrology, sediment transport and extreme value theory with the challenges posed by the application data-scarce context.

Acknowledgements

The work of G.P. was funded by the H2020 project NAIAD [grant no. 730497] from the European Union's Horizon 2020 research and innovation program. The authors would like to thank the Villard-Bonnot municipality for allowing re-using the study results in this paper. The authors gratefully thank Kevin McCoy and an anonymous reviewer for numerous suggestions that helped us to improve the paper content.

References

- ARTELIA and IRSTEA. 2018. Etude de l'Aménagement d'une Plage de Dépôt sur le Torrent de la Combe De Lancey - Site des Anciennes Papeteries de Villard Bonnot - Rapport de Modélisation Physique. Ville de Villard-Bonnot. 69p.
- Bezzola, G. R., H. Sigg, and D. Lange. 2004. Driftwood retention works in Switzerland [translated from Schwemmholzurückhalt in der Schweiz]. INTERPRAEVENT Conference Proceedings. VII:29-40.
- Carré, J., and B. Fretti. 2010. Analyse et critique de la méthode Speed (Système probabiliste d'étude par événements discrets). SOGREAH. Technical report. 107p.
- Djerboua, A. 2001. Prédétermination des pluies et crues extrêmes dans les Alpes franco-italiennes: prévision quantitative des pluies journalières par la méthode des analogues. [PhD thesis] Grenoble, INPG, 214p.
- IRMA. 2006. On n'a jamais vu ça ! ou l'incorrigible nature... Institut des Risques Majeurs. Grenoble. 24p.
- ONF-RTM. 2005. Evènements des 22 et 23 août 2005 dans le massif de Belledonne. Préfecture de l'Isère. Technical report. 10p.
- Piton, G., F. Fontaine, H. Bellot, F. Liébault, C. Bel, A. Recking, and T. Hugerot. 2018a. Direct field observations of massive bedload and debris flow depositions in open check dams. Pages 1–8 Riverflow conf. Proc. E3S Web of Conferences. doi: 10.1051/e3sconf/20184003003
- Piton, G., and A. Recking. 2016a. Design of sediment traps with open check dams. II: woody debris. Journal of Hydraulic Engineering 142:1–17, doi:10.1061/(ASCE)HY.1943-7900.0001049
- Piton, G., and A. Recking. 2016b. Design of sediment traps with open check dams. I: hydraulic and deposition processes. Journal of Hydraulic Engineering 142:1–23. doi:10.1061/(ASCE)HY.1943-7900.0001048
- Piton, G., and A. Recking. 2017. The concept of travelling bedload and its consequences for bedload computation of mountain streams. Earth Surface Processes and Landforms, 42(10):1505-1019. doi:10.1002/esp.4105
- Piton, G., A. Recking, J. Le Coz, H. Bellot, A. Hauet, and M. Jodeau. 2018b. Reconstructing Depth-Averaged Open-Channel Flows Using Image Velocimetry and Photogrammetry. Water Resources Research 54:4164–4179. doi:10.1029/2017WR021314
- Roth, A., M. Jafarnejad, S. Schwindt, and A. Schleiss. 2018. Design optimization of permeable sediment traps for fluvial bed load transport. E3S Web of Conferences 40:03009. doi:10.1051/e3sconf/20184003009
- Schwindt, S., M. Franca, G. De Cesare, and A. Schleiss. 2017. Analysis of mechanical-hydraulic bedload deposition control measures. Geomorphology. 295:467-479, doi:10.1016/j.geomorph.2017.07.020
- Schwindt, S., M. J. Franca, A. Reffo, and A. J. Schleiss. 2018. Sediment traps with guiding channel and hybrid check dams improve controlled sediment retention. Natural Hazards and Earth System Science 18(2):647–668. doi:10.5194/nhess-18-647-2018
- SOGREAH. 2010. Plage De Dépôt Sur Le Torrent De La Combe De Lancey Sur Le Site Des Papeteries - Etude De Faisabilité. Commune De Villard Bonnot. Technical report. 26p.

Review of the mechanisms of debris-flow impact against barriers

S. Poudyal^{a,*}, C.E. Choi^{a,b}, D. Song^{c,d}, G.G.D. Zhou^d, C.Y. Yune^e, Y. Cui^a, A. Leonardif,
M. Busslinger^g, C. Wendeler^h, G. Pitonⁱ, E. Moase^j & A. Strouth^j

^a Department of Civil and Environmental Engineering, The Hong Kong University of Science and Technology, Hong Kong

^b HKUST Jockey Club Institute for Advanced Study, The Hong Kong University of Science and Technology, Hong Kong

^c University of Chinese Academy of Sciences, Beijing, China

^d Institute of Mountain Hazards and Environment, Chinese Academy of Sciences & Ministry of Water Conservancy, Chengdu, China

^e Gangneung-Wonju National University, South Korea

^f Politecnico di Torino, Turin, Italy

^g Tetra Tech Canada Inc, Vancouver Geotechnical Engineering, Vancouver, Canada

^h Geobrugg AG, Switzerland

ⁱ Institut national de recherche en sciences et technologies pour l'environnement et l'agriculture (IRSTEA), France

^j BGC Engineering, Vancouver

Abstract

Our limited understanding of the mechanisms pertaining to the force exerted by debris flows on barriers makes it difficult to ascertain whether a design is inadequate, adequate, or over-designed. The main scientific challenge is because flow-type landslides impacting a rigid barrier is rarely captured in the field, and no systematic, physical experimental data is available to reveal the impact mechanisms. An important consideration in flow-structure interaction is that the impact dynamics can differ radically depending on the composition of the flow. Currently, no framework exists that can characterize the impact behavior for a wide range of flow compositions. This review paper examines recent works on debris-flow structure interactions and the limitations of commonly used approaches to estimate the impact load for the design of barriers. Key challenges faced in this area and outlook for further research are discussed.

Keywords: Debris flows, barriers, impact mechanisms, flow compositions,

1. Background

The Association of Geohazard Professionals (AGHP) is an industry association that was created in 2013 to support the development of standards, specifications, and best practices for the design and implementation of geohazard-related technologies and products; and to provide education to the geohazard community. The AGHP Debris Flow and Steep Creek Hazards Mitigation Committee (Committee) was formed in 2017 and currently includes members from North America, Asia, and Europe. The first committee workshop was held on June 3, 2018 in Canmore Alberta, Canada and included a discussion of the wide range of design guidelines that are available. The Committee recognized that design practices for debris-flow mitigation structures vary between different world regions, and some aspects of practice are not well described in the existing guidelines. This paper is a collective effort by AGHP members and focuses specifically on current understanding of debris-flow impact mechanism against barriers.

Steep creek flows made of mixtures of soil, rock and water, surge downslope at high velocities. These flows include floods, hyper-concentrated flows, debris flows, and rock avalanches (Hung et al., 2014). To mitigate these hazardous flows, rigid barriers (e.g., Takahashi, 2014) and flexible barriers (e.g., DeNatale et al., 1999; Wendeler, 2008; Bugnion et al., 2012) are commonly installed in the predicted flow paths. Correspondingly, a reliable estimate of impact load is required to design these barriers. However, current design approaches for estimating impact loads relies heavily on empiricism and do not explicitly consider the composition of the flow, including the particle size and the ratio of solids

* Corresponding author e-mail address: spoudyal@connect.ust.hk

to fluids. Such approaches make it difficult to ascertain whether a barrier design is robust, inadequate, or over-designed.

Our present knowledge in this area is deficient for three main reasons. First, debris flows impacting structures are rarely captured in the field. Second, debris flows are scale-dependent phenomena (Iverson, 1997; Zhou and Ng, 2010). More specifically, small-scale physical experiments (e.g., Canelli et al., 2012; Scheidl et al., 2013) cannot holistically model the absolute stress state in a granular assembly, the timescale for pore pressure dissipation, and the degree of viscous shearing observed in prototype flows (Iverson, 2015). To capture the granular and fluid stresses in real flows more holistically, centrifuge model tests (Bowman et al., 2010) or large-scale physical experiments are necessary (Iverson, 2015). Third, depending on flow composition, specifically the ratio of solids to fluids (Iverson, 1997; Iverson and George, 2014) and particle size (Faug, 2015; Song, 2016; Song et al., 2017a and 2017b), the impact dynamics of debris flows can vary drastically. A framework that characterizes the impact mechanism of debris flows by considering a wide range of flow compositions—solid-fluid interaction and particle size effects—is necessary to make reliable estimations of the impact load.

2. Impact Models

Current opportunities for advancing our understanding of the impact mechanism of debris flows are reflected in international guidelines (VanDine, 1996; MLR, 2006; NILIM, 2007; Kwan, 2012). An estimate of impact force exerted by debris flows, assuming continuum-like behavior, is based on force equilibrium in hydrostatic models and momentum conservation in hydrodynamic models. Another type of loading that needs to be considered is discrete loading, which is created by short duration impulses from large particles (Ng et al., 2018). Existing approaches for estimating loading are discussed below.

2.1. Continuum loading

Continuum-based approaches adopt empirical coefficients to account for various uncertainties, including unknown impact mechanisms and flow composition. For example, the momentum-based equation for estimating impact (Hungri et al., 1984; Kwan, 2012; Volkwein et al., 2014) is given as follows:

$$F = \alpha \rho v^2 h w \tag{1}$$

where α is the empirical pressure coefficient, ρ is the bulk density, v is the impact velocity, h is the flow thickness and w is the channel width. Clearly, flow composition is not explicitly considered in equation 1, and α accounts for the complexity of variables involved in natural geological material and natural settings. To highlight the empiricism of equation 1, a literature review shows that α values are not consistent (Table 1). For example, α of 3.5 is recommended for less viscous flows and 1.0 to 5.3 for more viscous flows (Scotton and Deganutti, 1997). Thurber Consultants Ltd. (1984) recommended α value of 3 to 5 for flow compositions in Austria and Switzerland. Kwan (2012) recommended α values from 2.0 to 2.5, depending on the type of structural countermeasure. Sovilla et al. (2016) demonstrates that the dimensions of the structure also fundamentally influence the impact pressure. Clearly, a scientifically based approach is urgently required to characterize the impact behavior for a wide range of debris flows.

Table 1. Summary of hydrodynamic models for estimating debris flow impact on a rigid barrier

Pressure coefficient (α)	Reference
$\alpha = 1.0$	VanDine (1996)
$\alpha = 3.0$ to 5.0	Zhang (1993)
$\alpha = 1.0$ for circular structure	MLR (2004)
$\alpha = 1.3$ for rectangular structure	
$\alpha = 1.5$ for square structure	
$\alpha = 2.5$ to 3.0	Lo (2000), Kwan (2012)
$\alpha = 2.0$	Vagnon and Segalini (2016)
$\alpha = 1.5$ to 5.5	Canelli et al., (2012)
$\alpha = 2.0$ to 4.0	Hübl and Holzinger (2003)
$\alpha = 1.0$	NILIM (2007)
$\alpha = 1.0$	SWCB (2005)

Ancey and Bain (2015), Faug (2015), Ashwood and Hungr (2016), and Song (2016) all suggest that to more appropriately characterize impact, both static and dynamic loading must be explicitly considered as follows:

$$F = 0.5k\rho g(\beta h)^2 w + \alpha' \rho v^2 h w \tag{2}$$

where α' is the coefficient for dynamic effect only, k is the coefficient for static effect only, and β is the ratio between the height of the static deposit and flow thickness before impact. Song et al. (2017b) further characterized the pressure coefficient to represent both dynamic and static loading with clearer physical meaning as portrayed by the following relationship:

$$\alpha = \frac{\kappa' \beta^2}{2} \frac{1}{F_r^2} + \alpha' \tag{3}$$

where F_r is the Froude number (v/\sqrt{gh}). The F_r is characterised by the ratio of inertial to gravitational forces of flow-type landslides in an open channel flow (Hübl et al., 2009; Choi et al., 2015a).

2.2. Discrete loading

Discrete loading is generated from large particles entrained in debris flows. These particles exert a concentrated impulse that can destroy structures in the flow path. To capture discrete loads exerted by these large particles, the Hertz equation is often used in design guidelines (Lo, 2000; NILIM, 2007; Swiss Federal Road Authority, 2008). The impact force calculated based on the Hertz contact theory (Johnson, 1985) assumes an elastic impact scenario which is given as follows:

$$F = \frac{4E}{3} R^{\frac{1}{2}} x^{\frac{3}{5}} \tag{4}$$

where E is the effective modulus of elasticity, which is given as $1/E = (1 - \nu_1^2)/E_1 + (1 - \nu_2^2)/E_2$ (subscripts 1 and 2 denote parameters relating to the barrier and boulder, respectively) and ν is the Poisson's ratio. R is the equivalent radius, which is given as $1/R = 1/R_1 + 1/R_2$, (R_1, R_2 are the radius of curvature of contacting bodies) and x is the deformation, which is given as follows:

$$x = \frac{15mv^2}{16ER^{\frac{1}{2}}} \tag{5}$$

where, m is the mass of boulder and v is the impact velocity.

Kwan (2012) introduced a modified version of Eqn. 4 for design to estimate the impact force between a granite boulder and a reinforced concrete rigid barrier. The equation is given as follows:

$$F = K_c 4000 v^{1.2} R^2 \tag{6}$$

where, K_c is a load-reduction factor, v is the velocity of the boulder and R is the radius of the boulder.

A fully elastic solution is generally believed to be over conservative (Hungr et al., 1984; Lo, 2000; Sun et al., 2005). Therefore, a load-reduction factor K_c was introduced. This factor is empirical and recommended values vary in the literature (Table 2). Equation 6 is for a single boulder and an equation that can capture the mechanics of a cluster of boulders impacting a surface simultaneously remains a crucial scientific challenge that needs to be addressed.

Table 2. Summary of Hertz equations for estimating boulder impact load on rigid barrier

Load reduction factor K_c	Reference
$K_c = 0.1$	Lo (2000)
$K_c < 0.1$	NILIM (2007)
$0.2 < K_c < 0.5$	SWCB (2005)

3. Impact Mechanisms

Equation 2 is convenient for engineering design, but fails to explicitly capture the key mechanisms of impact observed in physical experiments. These key mechanisms include the accumulation of static deposits called ‘dead zones’ (Chanut et al., 2010; Faug et al., 2009, 2011, 2012 and 2015; Choi et al., 2017), the pile-up of highly frictional flows (Koo et al., 2016) or the vertical-jet-like behavior of viscous flows (Choi et al., 2015a). Physical experiments have demonstrated that the impact mechanism strongly influences the impact load, and consequently the load distribution along a structure (Song et al., 2017a). As such, more details pertaining to impact mechanisms in two most extreme types of geophysical flows: dry granular flow and water flow are discussed below.

3.1. Pileup and vertical-jet mechanisms

To illustrate how the impact mechanism is governed by flow composition, let us consider two of the most extreme types of geophysical flows, specifically dry granular flow and water, impacting a rigid barrier. A dry granular flow is highly frictional with air as the interstitial fluid, which has a low viscosity and plays a relatively insignificant role in regulating the flow dynamics. Instead, frictional and inertial grain stresses dominate. Choi et al., (2015a) demonstrated that when a dry granular flow composed of Leighton Buzzard (LB) fraction C sand with uniform grain diameters of about 0.6 mm, impacts a rigid barrier, a pileup mechanism develops (Fig. 1a).

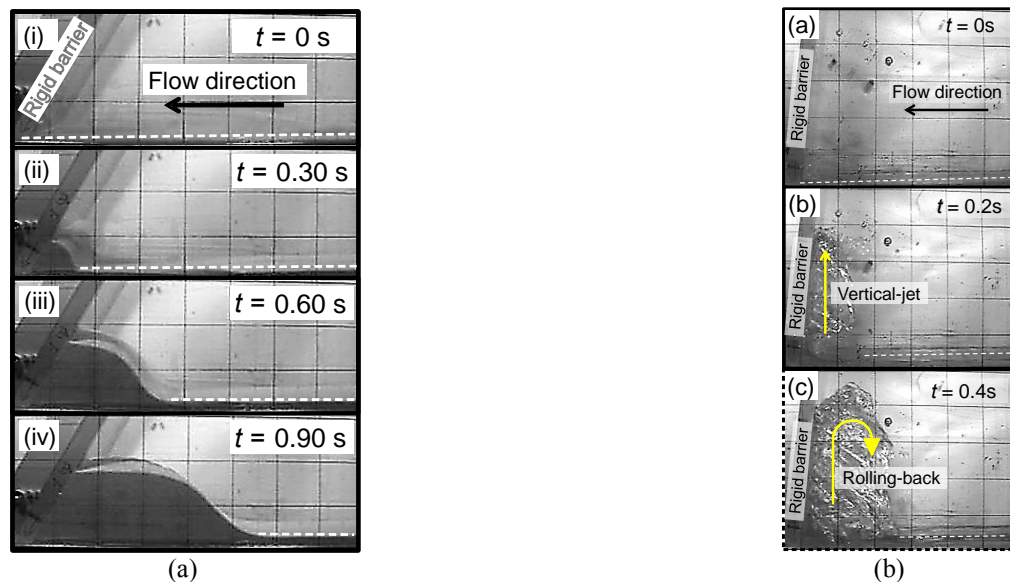


Fig. 1 (a) Observed pileup impact mechanism for supercritical dry sand impacting an orthogonal barrier (b) Observed vertical-jet mechanism for supercritical water flow impacting a vertical barrier installed along a channel inclined at 5° (redrawn from Choi et al., 2015a)

This mechanism exhibits a rapid attenuation of flow kinetic energy from the high degree of enduring frictional contacts between grains and their boundaries. Furthermore, a granular material with angular grains, such as sand, exhibits a high degree of bulk compressibility, assuming fragmentation does not occur. This feature is controlled by the changes in void ratio from elastic shear distortions of angular grain contacts (Iverson, 2015). High compressibility leads to bulk deformation during impact through shearing between grains, which is a very effective dissipater of flow kinetic energy compared to viscous shearing contributed by the interstitial fluid (Choi et al., 2015b). The properties of dry sand therefore inherently limit accretion along the free surface upon impacting a barrier. Instead, bulk deformation, for F_r within the transitional range (Faug, 2015), leads to the development of a granular bore that propagates or piles-up along the upstream direction in the channel.

Compared to dry granular flow, water exhibits a vertical-jet mechanism upon impact if the initial F_r conditions are supercritical (Armanini, 1997; Choi et al., 2015a). This impact mechanism is characterized by the redirection of flow vertically along the barrier (Fig. 1b). A vertical-jet mechanism develops because the inertia of the flow is significantly

larger than the restoring gravitational field, which is responsible for ‘pulling’ the flow towards the channel. The obvious transfer of flow momentum in the vertical direction for water, compared to dry sand, is because less flow kinetic energy is lost during the impact process. The energy loss is only limited to viscous shearing of the fluid and shearing along its boundaries (Choi et al., 2015b). The effects of viscous shearing in the dissipation of flow kinetic energy is less significant compared to enduring frictional-grain stresses in dry sand. Furthermore, water, has a relatively low bulk compressibility compared to that of dry sand. This lower bulk compressibility promotes run-up upon impact in the only unconfined boundary within a channel, and that is the free surface. By contrast, dry granular flow can compress along the slope-parallel direction during impact and can also pileup towards the free surface of the channel.

Aside from the flow composition, the dynamics of channelized flow, specifically the F_r before impact also strongly influences the resulting impact mechanism (c.f., equation 3). Physical model tests have already demonstrated that water in supercritical flows exhibit a vertical-jet mechanism. By contrast, water in subcritical flow exhibits a reflective-wave mechanism upon impacting a rigid barrier. This mechanism can be characterized by limited transfer of momentum along the vertical direction or free-surface of the channel, the flow impacts the barriers and is allowed to reflect back upstream. Any disturbance to the flow in the channel, such as the barrier, will transfer energy as a wave. The flow inertia for subcritical flows is less than the restoring gravitational field. Therefore, a reflective-wave mechanism is exhibited for subcritical flows. For granular flows, the F_r of the flow before impact strongly influences whether gravitational or inertial effects are dominant (Faug, 2015; Sovilla et al., 2016).

4. Flow composition effects on dynamic response

4.1. Solid-fluid interaction

The complex flow dynamics of debris flows are governed by the interaction between the solid and the fluid phases. Solid-fluid interactions control the changes in the pore fluid pressure, which in turn regulates the Coulomb friction within and at the boundaries of a landslide (McArdell et al., 2007; Iverson and George, 2014; George and Iverson, 2014). The degree of interaction between the solid and fluid phases in the flow can be represented by the solid fraction, or the proportion of solids to fluids by volume (Cui et al., 2015). Flows with a higher solid fraction more readily dissipate flow energy by shearing between grains (Choi et al., 2015b).

Although a great foundation has been established for the structural response of different types of barriers (DeNatale et al., 1999; Wendeler et al., 2006; 2007; Kwan et al., 2014), there remains a knowledge gap on how different flow types can result in very different impact loads. To remedy this gap in the literature, Ng et al., (2016a; 2016b) and Song et al., (2017a; 2017b) carried out a set of centrifuge tests to model the impact mechanisms of debris flows, dry sand and viscous flows, with varying flow composition, on rigid and flexible barriers. Depending on the flow composition, the impact behavior differed drastically. For dry granular flows, the dissipation of the flow kinetic energy was significantly enhanced via stress-dependent friction, unlike viscous flows, which dissipated the flow kinetic energy less readily.

As discussed, a dead zone is useful for attenuating the impact load on an obstacle or barrier, but it can also contribute to the overall load acting on a structure. Song et al., (2017b) carried out a series of centrifuge experiments modelling the impact of two-phase flows on a rigid barrier. In these experiments, the solid fraction was progressively increased from 0 to 0.5. As expected, as the solid fraction increased, particle image velocimetry analysis (White et al., 2003) showed large dead zones. The larger the dead zone observed, the higher the resulting peak impact load measured on the barrier. These findings confirmed that the impact process for two-phase flows is as much a dynamic process as it is a static process. The higher the solid-fraction in the flow, the more pronounced the dead zones. These deposits in turn augment the overall load acting on the orthogonally-configured barrier (Fig. 2a).

4.2. Influence of particle size

Another important feature that adds to the complexity of investigating the impact mechanisms of debris flows is the effects of particle size. Song (2016), Song et al., (2017b), and Song et al., (2018) demonstrated that as the particle size increases, more discrete loads with higher magnitudes are generated. The impact dynamics resulting from large glass spheres differ significantly from dry sand or a two-phase mixture, with the same equivalent volume and F_r conditions before impact. Dry sand exhibits a progressive loading pattern to its static state without an obvious dynamic peak or sharp impulses. The two-phase mixture, however, exhibits a continuous loading behavior, which reaches its

peak load before softening towards a static state. The two-phase mixture is fluidized and takes a longer time to reach a static state because of a lack of shear resistance in the flow. Clearly, a comparison of the different flow types highlight the distinct loading pattern exerted by a cluster of large particles compared to dry sand and two-phase flows.

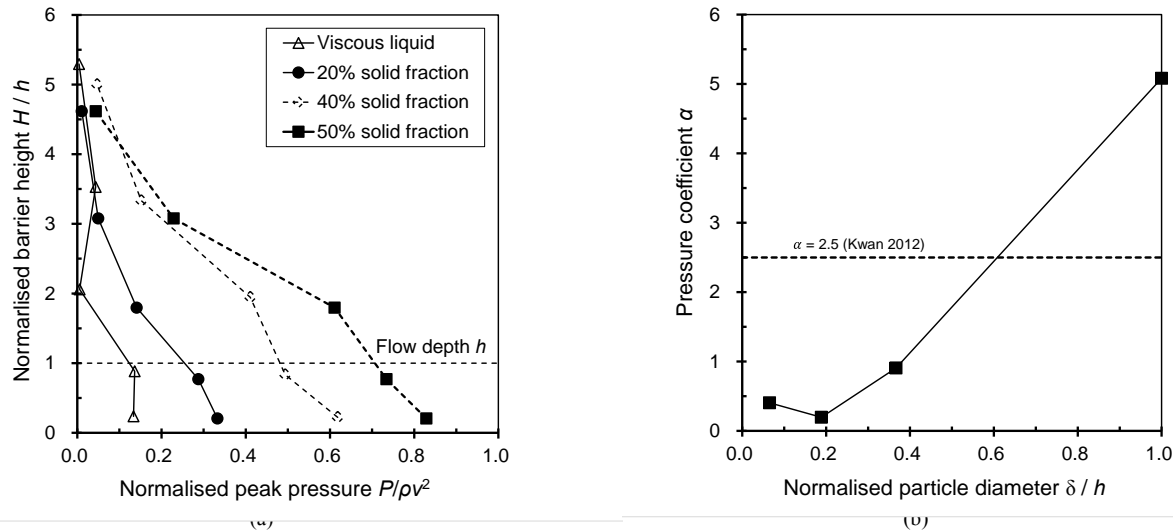


Fig. 2 (a) Influence of solid fraction on dynamic response of rigid barrier (redrawn from Song et al., 2017b) (b) Effects of particle size on dynamic response of rigid barrier (redrawn from Song et al., 2018)

A comparison of the loading time-histories with existing impact models show that both the dry sand and two-phase mixture are bounded by the superposition of both equations 2 and 3. However, the cluster of glass sphere, resembling a bouldery flow, generates sharp impulses that exceed the superposition of equations 2 and 3. These results indicate that the entrainment of large and hard inclusions in debris flows warrants consideration in the design of structural countermeasures, to safeguard against local damage.

To further investigate the effects of particle size, the performance of the hydrodynamic approach, based on different normalized particle sizes was investigated (Song, 2016). The peak loads were compared (Fig. 2b), and results showed that continuum-based mechanics (equation 3) fail to capture sharp impulse loads at a normalized particle size of 22 mm, based on the recommended dynamic coefficient of 2.5 (Kwan, 2012). Although a solution for capturing the impulse loads for a cluster of large particles was not provided, test results help to evaluate the current impact models for discerning the effects of particle size. A crucial challenge remains to account for impulse loads from a cluster of large particles and to distinguish what particle size is generating impulses that cannot be captured using continuum mechanics (equation 3).

Sharp impulses can be attenuated by increasing the contact time between a particle and a surface. Depending on overall stiffness of a structure, the effects of particle size can diminish. For instance, flexible barriers were originally adopted for capturing rock fall and have been adopted for resisting debris flows in the past decade (Kwan et al., 2014). Another approach for attenuating sharp impulses is to install cushioning materials in front of rigid barriers to diminish these loads (Ng et al., 2017).

5. Summary

Examination of the current state of research on the impact mechanisms of debris flows is presented in this paper. This study highlights the importance of considering the composition of a debris flow to assess the resulting dynamic response and impact mechanisms induced on a rigid barrier. Some key aspects from this review paper is summarized as follows:

- 1) The effects of the particle size are manifested in the inertial grain stresses of the flow during impact. As the particle size increases, the debris-flow transitions from contact-dominated (continuum) to inertial-dominated (discrete) grain stresses. The larger the particle size, the higher the magnitude and number of sharp impulses that are induced on a barrier.
- 2) The effects of solid-fluid interaction, specifically the ratio of solids to fluids dictates the force exerted on a barrier.

The higher the solid fraction, the more predominant grain-contact stresses are, thereby inducing higher static loads on the barrier during impact.

- 3) The flow type governs the mechanism of impact on rigid barriers. Granular flow, which consist of angular grains, readily dissipate flow kinetic energy through enduring shear contacts between grains and deformation from its high bulk compressibility. By contrast, inviscid flow does not readily dissipate flow kinetic energy from internal viscous shearing and viscous shearing along its boundaries. The ratio of inertial to gravitational forces before impact dictate the impact mechanism. These mechanisms are critical for discerning the design load and distribution on barriers.

Acknowledgements

Members of the Association of Geohazard Professionals provided valuable input to this paper during and after the June 2018 workshop organized by the Debris Flow and Steep Creek Hazards Mitigation Committee. The authors are grateful for the financial sponsorship from the National Natural Science Foundation of China (51709052), the theme-based research grant T22-603/15-N and the General Research Fund 16209717 provided by the Research Grants Council of the Government of Hong Kong Special Administrative Region, China, by the H2020 project NAIAD [grant no. 730497] from the European Union's Horizon 2020 research and innovation program. The authors would like to gratefully acknowledge the support of the HKUST Jockey Club Institute for Advanced Study and the Hong Kong Club Charities Trust and the Hong Kong Jockey Club Disaster Preparedness and Response Institute (HKJCDPRI18EG01). The first author gratefully acknowledges generous support from Hong Kong PhD Fellowship for his PhD study. Support from Tetra Tech Canada Inc. for preparation of this manuscript is gratefully acknowledged.

References

- Ancey, C., and Bain, V., 2015, Dynamics of glide avalanches and snow gliding: *Reviews of Geophysics*, v. 53, no. 3, p. 745-784.
- Armanini, A., 1997, On the dynamic impact of debris flows. In *recent developments on debris flows*: Springer Berlin Heidelberg, p. 208–226.
- Ashwood, W., and Hungr, O., 2016, Estimating total resisting force in flexible barrier impacted by a granular avalanche using physical and numerical modelling: *Canadian Geotechnical Journal*, v. 53, no. 10, p. 1700–1717.
- Bowman, E.T., Laue, J., Imre, B., and Springman, S.M., 2010, Experimental modelling of debris flow behaviour using a geotechnical centrifuge: *Canadian Geotechnical Journal*, v. 47, no. 7, p. 742–762.
- Bugnon, L., McArdell, B.W., Bartelt, P., and Wendeler, C., 2012, Measurements of hillslope debris flow impact pressure on obstacles: *Landslides*, v. 9, no. 2, p. 179–187.
- Canelli, L., Ferrero, A.M., Migliazza, M., and Segalini, A., 2012, Debris flow risk mitigation by the means of rigid and flexible barriers—experimental tests and impact analysis: *Natural Hazards Earth System Sciences*, v. 12, no. 5, p. 1693–1699.
- Chanut, B., Faug, T., and Naaim, M., 2010, Time-varying force from dense granular avalanches on a wall: *Physical Review E*, v. 82, no. 4, 041302.
- Choi, C. E., Cui, Y., Liu, L. H. D., Ng, C. W. W., and Lourenço, S. D. N., 2017, Impact mechanisms of granular flow against curved barriers: *Géotechnique Letters*, v. 7, n. 4, p. 330-338.
- Choi, C.E., Au-Yeung, S.C.H. and Ng, C.W.W., 2015a, Flume investigation of landslide granular debris and water run-up mechanisms: *Géotechnique Letters*, v. 5, n. 1, p. 28–32.
- Choi, C.E., Ng, C.W.W., Au-Yeung, S.C.H. and Goodwin, G., 2015b, Froude scaling of landslide debris in flume modelling: *Landslides*, v. 12, no. 6, p. 1197–1206.
- Cui, P., Zeng, C. and Lei, Y., 2015, Experimental analysis on the impact forces of viscous debris flow: *Earth Surface Processes Landform*, v. 40, no. 12, p. 1644–1655.
- DeNatale, J.S., Iverson, R.M., Major, J.J., LaHusen, R.G., Fiegel, G.L. and Duffy, J.D., 1999, Experimental testing of flexible barriers for containment of debris flows: US Department of the Interior, US Geological Survey, p. 45.
- Faug, T., 2015, Macroscopic force experienced by extended objects in granular flows over a very broad Froude-number range: *European Physical Journal E*, v. 38, no. 24, p. 1–10.
- Faug, T., Beguin, R. and Chanut, B., 2009, Mean steady granular force on a wall overflowed by free-surface gravity-driven dense flows. *Physical Review E*, v. 80, no. 2, p. 021305.
- Faug, T., Caccamo, P. and Chanut B., 2011, Equation for the force experienced by a wall overflowed by a granular avalanche: experimental verification: *Physical Review E*, v. 84, no. 5, p. 051301.
- Faug, T., Caccamo, P. and Chanut, B., 2012, A scaling law for impact force of a granular avalanche flowing past a wall. *Geophysics Research Letters*, v. 39, no. 23, L23401.
- George D.L. and Iverson R.M., 2014, A depth-averaged debris-flow model that include the effects of evolving dilatancy. II. Numerical predictions and experimental tests: *Proceedings of Royal Society A: Mathematical, Physical and Engineering Sciences*, v. 470, no. 2170.
- Hübl, J. & Holzinger, G., 2003, Entwicklung von Grundlagen zur Dimensionierung kronenoffener Bauwerke für die Geschiebemanagement in Wildbächen: Klassifikation von Wildbachsperrern: WLS Report 50. Im Auftrag des BMLFUW VC 7a (unveröffentlicht). Wien: Institut für Alpine Naturgefahren, Universität für Bodenkultur.
- Hübl, J., Suda, J., Proske, D., Kaitna, R. and Scheidl, C., 2009, Debris flow impact estimation. In *Proceedings of the 11th international symposium on water management and hydraulic engineering*, Ohrid, Macedonia (eds. C. Popovska and M. Jovanovski), Skopje, Macedonia: University of Ss. Cyril and Methodius, p. 1–5.

- Hungr, O., Leroueil, S., Picarelli, L., 2014, The Varnes Classification of Landslide Types, an Update: *Landslides*, v. 11, no. 2, p. 167-194.
- Hungr, O., Morgan, G.C. and Kellerhals, R., 1984, Quantitative analysis of debris torrent hazards for design of remedial measures: *Canadian Geotechnical Journal*, v. 21, no. 4, p. 663-677.
- Iverson, R.M., 2015, Scaling and design of landslide and debris-flow experiments: *Geomorphology*, v. 244, p. 9-20.
- Iverson, R.M., 1997, The physics of debris flows: *Reviews of Geophysics*, v. 35, no. 3, p. 245-296.
- Iverson, R. M., and George, D. L., 2014, A depth-averaged debris-flow model that includes the effects of evolving dilatancy. I. Physical basis: *Proceedings of the Royal Society A: Mathematical, Physical and Engineering Sciences*, v. 470, no. 2170, 20130819.
- Johnson, K.L., 1985, *Contact mechanics*: Cambridge University Press, London, UK.
- Koo, R.C.H., Kwan, J.S.H., Ng, C.W.W., Lam, C., Choi, C.E. and Song D., 2016, Velocity attenuation of debris flows and a new momentum-based load model for rigid barriers: *Landslides*, v. 14, no. 2, p. 617-629.
- Kwan, J.H.S., Chan, S.L., Cheuk, J.Y.C. and Koo, R.C.H., 2014, A case study on an open hillside landslide impacting on a flexible rockfall barrier at Jordan Valley, Hong Kong: *Landslides*, v. 11, no. 6, p. 1037-1050.
- Kwan, J.S.H., 2012, Supplementary technical guidance on design of rigid debris-resisting barriers, Report No. 270. Kowloon, Hong Kong: Geotechnical Engineering Office.
- Lo, D.O.K., 2000, Review of natural terrain landslide debris resisting barrier design, Report No. 104. Kowloon, Hong Kong: Geotechnical Engineering Office.
- McArdell, B.W., Bartelt, P. and Kowalski, J., 2007, Field observations of basal forces and fluid pore pressure in a debris flow: *Geophysics Research Letters*, v. 34, no. L07406, p. 1-4.
- Ministry of Land and Resources, 2004, Design standards for debris flow hazard mitigation measures (DZ/T0239-2004). Beijing, China: Chinese Geological Survey, Ministry of Land and Resources (in Chinese).
- Ng, C.W.W., Choi, C.E., Su, A.Y., Kwan, J.S.H. and Lam, C., 2016a, Large-scale successive impacts on a rigid barrier shielded by gabions: *Canadian Geotechnical Journal*, v. 53, no.10, p. 1688-1699.
- Ng, C.W.W., Song, D., Choi, C.E., Kwan, J.S.H., Shiu, H.Y.K. and Koo, R.C.H., 2016b, Centrifuge modelling of dry granular and viscous impact on rigid and flexible barriers: *Canadian Geotechnical Journal*, v. 54, no. 2, p. 188-206.
- Ng, C.W.W., Song, D., Choi, C.E., Koo, C.H., and Kwan, J.S.H., 2016c, A flexible barrier for landslide impact in centrifuge: *Géotechnique Letters* v. 6, no. 3, p. 221-225.
- National Institute for Land and Infrastructure Management, 2007, Manual of technical standards for designing Sabo facilities against debris flow and Driftwood, Technical Note of NILIM No. 365. Tsukuba, Japan: National Institute for Land and Infrastructure Management, Ministry of Land, Infrastructure and Transport (in Japanese).
- Scheidt, C., Chiari, M., Kaitna, R., Müllegger, M., Krawtschuk, A., Zimmermann, T. and Proske, D., 2013, Analyzing debris-flow impact models, based on a small-scale modelling approach: *Surveys in Geophysics*, v. 34, no. 1, p. 121-140.
- Scotton, P. and Deganutti, A.M., 1997, Phreatic line and dynamic impact in laboratory debris flow experiments: *Proceedings of the 1st International Conference on Debris Flow Hazards Mitigation: Mechanics, Prediction and Assessment*, San Francisco, USA.
- Soil and Water Conservation Bureau, 2005, Soil and water conservation handbook. Nantou, Taiwan: Soil and Water Conservation Bureau of the Council of Agriculture, Executive Yuan and Chinese Soil and Water Conservation Society (in Chinese).
- Song, D., 2016, Mechanisms of debris flow impact on rigid and flexible barriers [PhD Thesis]: HKUST, HKSAR.
- Song, D., Choi, C. E., Zhou, G. G. D., Kwan, J. S. H., and Sze, H. Y., 2018, Impulse Load Characteristics of Boulderly Debris Flow Impact: *Géotechnique Letters*, v. 8, no. 2, p. 111-117.
- Song, D., Choi, C.E., Ng, C.W.W. and Zhou, G.G.D., 2017a, Geophysical flows impacting a flexible barrier: effects of solid-fluid Interaction: *Landslides*, v. 15, no. 1, p. 99-110, <https://doi.org/10.1007/s10346-017-0856-1>
- Song, D., Ng, C.W.W., Choi, C.E., Kwan, J.S.H. and Koo, R.C.H., 2017b, Influence of debris flow solid fraction on rigid barrier impact: *Canadian Geotechnical Journal*, v. 54, no.10, p. 1421-1434.
- Sovilla, B., Faug, T., Kohler, A., Baroudi, D., Fischer, J., and Thibert, E., 2016, Gravitational wet avalanche pressure on pylon-like structures: *Cold Regions Science and Technology*, v. 126, p. 66-75.
- Sun, H.W., Lam, T.T.M. and Tsui, H.M., 2005, Design basis for standardized modules of landslide debris-resisting barriers. GEO Report No. 174. Geotechnical Engineering Office, HKSAR.
- Swiss Federal Road Authority, 2008, Effects of rockfall protection galleries. Federal Roads Office. Switzerland.
- Takahashi, T., 2014, *Debris Flow: Mechanics, Prediction and Countermeasures* (2nd edition). London, UK, Taylor & Francis Group.
- Thurber Consultants Ltd., 1984, Debris torrents: a review of mitigation measures: report to ministry of transportation & highways, British Columbia, Canada.
- VanDine, D.F., 1996, Debris flow control structures for forest engineering. (Ministry of Forests Research Program, Working Paper 22/1996). Vancouver, Canada: Government of the Province of British Columbia.
- Vagnon, F. and Segalini, A., 2016, Debris flow impact estimation on a rigid barrier: *Natural Hazards Earth System Sciences*, v. 16, no. 7, p. 1691-1697.
- Volkwein, A., 2014, Flexible Debris Flow Barriers: Design and Application, Swiss Federal Institute for Forest, Snow and Landscape Research, WSL Berichte 18, p. 32.
- Wendeler C., 2008, Murgangrückhalt in Wildbächen - Grundlagen zu Planung und Berechnung von flexiblen Barrieren, [Dissertation]. ETH Nr. 17916, Schweiz.
- Wendeler, C., McArdell, B.W., Rickenmann, D., Volkwein, A., Roth, A. and Denk, M., 2006a, Field testing and numerical modeling of flexible debris flow barriers. In *Proceedings of the sixth international conference of physical modelling in geotechnics* (eds. C.W.W. Ng, Y.H. Wang and L.M. Zhang), Boca Raton, FL, USA: CRC Press, p. 4-6.
- Wendeler, C., Volkwein, A., Denk, M., Roth, A. and Wartmann, S., 2007, Field measurements used for numerical modelling of flexible debris flow barriers. In *Proceedings of fourth international conference on debris flow hazards mitigation: mechanics, prediction, and assessment* (eds. C. L. Chen and J. J. Major), Rotterdam, the Netherlands: Millpress, p. 681-687.
- White, D.J., Take, W.A. & Bolton, M.D., 2003, Soil deformation measurement using particle image velocimetry (PIV) and photogrammetry: *Géotechnique*, v. 53, no.7, p. 619-63.
- Zhang, S., 1993, A comprehensive approach to the observation and prevention of debris flows in China: *Natural Hazards*, v. 7, no. 1, p. 1-23.
- Zhou, G.G.D. & Ng, C.W.W., 2010, Dimensional analysis of natural debris flow. *Canadian Geotechnical Journal*, v. 47, no. 7, p. 719-729.

Small scale impact on rigid barrier using transparent debris-flow models

Nicoletta Sanvitale^{a,*}, Elisabeth Bowman^a, Miguel Angel Cabrera^b

^aUniversity of Sheffield, Sir Frederick Mappin Building, Mappin St., Sheffield, S1 3JD, UK

^bUniversidad de los Andes, Carrera 1 Este No. 19^a-40, Bogotá, 111711, Colombia

Abstract

Fast landslides, such as debris flows, involve high speed downslope motion of rocks, soil and water. Their high flow velocity, high degree of runout and potential for impact make them one of the most hazardous gravitational mass flows. While the estimation of the pressure generated by the impact of debris flows on civil engineering structures has been widely investigated, the state of the knowledge is still insufficient to accurately describe the dynamics and load evolution of the impact process. Both fluid and solid forces influence the dynamics of debris flows but existing design approaches for barrier or mitigation structures tend to treat these geophysical flows as a single continuum, neglecting the solid fluid-interactions. Hence in the literature, impact models are yet largely semi-empirical. This paper presents the first results of experiments using transparent debris flows in a small-scale flume aiming at investigating the mechanism of impact on rigid barriers. The use of a transparent debris-flow model allows the movements of particles and fluid within the medium to be probed. We examine flows consisting of uniform and well graded particle size gradings at two different fluid contents. The evolution of the impact load, bed normal pressure and fluid pore pressure for the different flows are measured and analysed in order to gain a quantitative comparison of their behaviour before and after impact.

Keywords: Debris flows; Barriers; Physical modelling; Transparent soil

1. Introduction

A debris flow is a rapid surging flow of saturated-debris and soil in a steep channel that may present high impact load and long runout (Iverson, 1997; Takahashi, 2007; Hung et al., 2013). A common method to prevent these flows from reaching vulnerable areas is by obstructing their channelized paths with barriers, dampening the overall flow inertia, trapping most of the transported debris, and, therefore, decreasing their expected runout. These barriers can be rigid walls or flexible nets, with a main goal of withstanding the impact forces from the transported debris and suspended material.

Rigid barriers, also called catch dams, are the most common mitigation structure against debris flows, due to the minimal technical skills required in their construction and easiness in the supply of building materials for reinforced concrete. These barriers sustain the lateral impact forces by self-weight, consisting of a debris-flow breaking structure, a retention basin and a pre-structure (Hübl et al., 2009). While the estimation of the pressure generated by the impact of debris flows on civil engineering structures has been widely investigated (Moriguci et al., 2009, Armanini et al., 2011; Bugnion et al., 2011; Hu et al., 2011; Scheidl et al., 2012; Cui et al., 2015; Zhou et al., 2018.), the state of knowledge is still insufficient to accurately describe the dynamics and load evolution of the impact process.

The current paper presents the first results of experiments using transparent analogue debris flows in a small-scale flume, aiming at investigating the bulk impact forces on rigid barriers. The experimental variables are the initial particle size distribution and fluid content while measuring the impact forces against the obstacle, the basal total- and fluid-pressures, flow height, and the cross-sectional flow dynamics at impact observed via Planar Laser Induced Fluorescence, PLIF (Sanvitale & Bowman, 2012). Section 2 presents details on the experimental setup and its

* Corresponding author e-mail address: n.sanvitale@sheffield.ac.uk

instrumentation, describing the materials employed and experimental protocol. Section 3 focuses on the direct measurements and discusses the impact mechanisms. Finally, Section 4 presents the main conclusions of the current work and provides insights into ongoing research.

2. Methods

2.1. Experimental set up

The material is stored in a rectangular tank, at the top of the channel. A slice gate, fitted between acrylic seals, releases the material by hand pull. The material flows down a rectangular flume 2.57 m long and 0.15 m wide, at an adjustable angle (see Fig. 1). Experiments reported in this paper are performed for a flume inclination of 20°. The lateral walls are made of borosilicate glass and the flume's bottom is roughened with 3D-printed PLA plates with a hexagonal packing of 3 mm semi-spheres. The roughened bed is instrumented along its base with three pore pressure transducers, PPT2, 3 and 4 (PDCR 810 Druck) placed at 175 mm centres along the flume at 30 mm from the centerline with PPT2 placed closest to the barrier at 8.5cm distance and PPT3 and PPT4 placed 175mm and 350mm further upslope. One load cell (LUX-B-ID Kyowa) with a circular sensing plate of 23mm diameter is mounted flush with the flume across from PPT2 (at 30 mm on the other side of the centerline). All basal sensors have 3D printed disk headings, equivalent to the roughness of the rest of the base.

The barrier model is made of a PMMA plate 10 mm thick, 150 mm wide and 190 mm tall (Fig. 1). The plate is connected to an aluminum support, connected at one end, on its mid-width, to an axial load cell (U9C, HBM) and fixed on its base to a linear bearing (LZMHS12-37T2P1, SKF). The barrier model is fixed to the flume bed at 2.25 m from the gate release, and is orientated normal to the flow direction (see inset in Fig. 1).

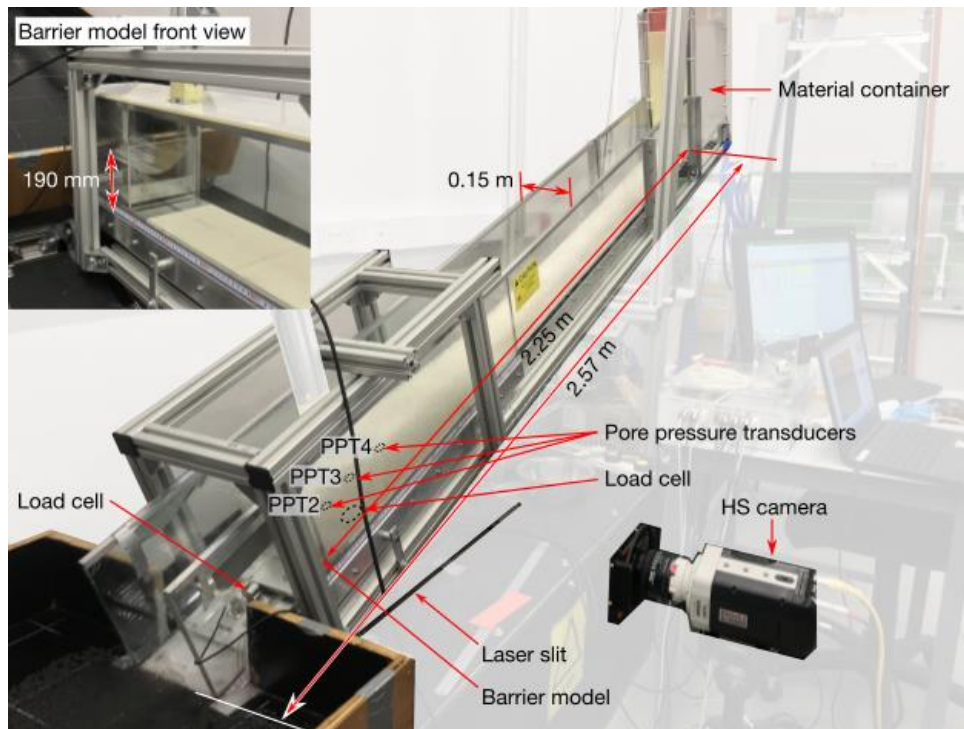


Fig. 1. Experimental setup after test. (Inset) Barrier model front view.

A 0.5 mm thick 532 nm laser light sheet is allowed to pass through the roughened bed and barrier model base, illuminating the flowing material at the flume's mid-width. The illuminated plane is located about in front of the barrier lighting the material from the flume's bottom (Fig. 1). The longitudinal motion is recorded with a Phantom high speed camera at a frame rate of 2000 fps. For more details on the PLIF technique please refer to Sanvitale and Bowman (2012).

2.2. Materials

In order for the PLIF technique to work under optimum conditions, the fluid and solid should present a match of their refractive indices. The current experiments are performed with hydrocarbon oil (Cargille laboratories) dyed with a fluorescent powder, and mixed with borosilicate glass beads (Sigmund Lindner GmbH). The fluid has a viscosity that is higher than water and a density that is lower, such that particle / fluid consolidation behaviour is equivalent to that using quartz particles that are four times smaller in water (Sanvitale & Bowman, 2012). Three particle size distributions (PSD) are employed in experiments; two uniform samples with glass beads of 3 mm and 7.5 mm, and a well graded sample (coefficient of uniformity $C_U=6$) with mean particle size of 7.5 mm (see Fig. 2). These samples are intended to provide an insight on the potential effects of particle size distribution on the impact mechanism.

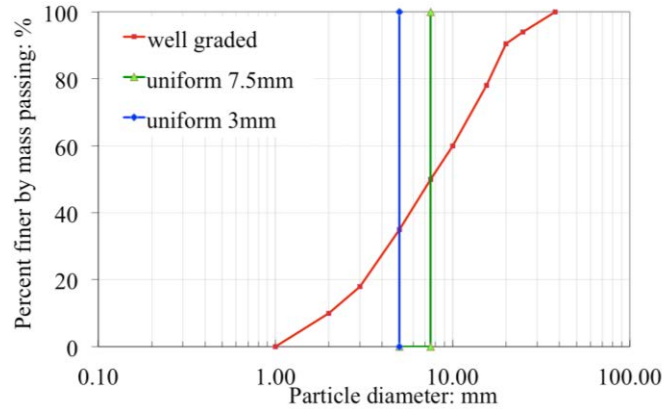


Fig. 2. Glass beads samples particle size distribution.

2.3. Test procedure

Experiments explore the effects of 28% and 32% fluid content f_c , defined as $\text{mass}_{\text{fluid}}/\text{mass}_{\text{solid}}$, impacting a rigid barrier model. Prior to experiment, the flume is cleaned, avoiding the presence of oil films on the roughened bed and lateral walls. For each experiment 10 kg of glass beads are used. Oil is gently poured into the container and mixed with the glass beads, paying special attention to the removal of air bubbles inside the mixture. Once the desired amount of fluid is added into the container, the laser beam is set-on, the high-speed camera is activated, and the slice gate is opened. At release, a triggering shutter connected to the gate activates the sensor recording at a sampling rate of 36 kHz, for a duration of 9 s.

3. Results and discussion

Qualitative features of flow impact can be revealed by the analysis of the video images. Figure 3 presents a sequence of images for each PSD at the fluid content, f_c 28% (images for f_c 32% are not shown for brevity). Fig. 4 shows the runup height at the barrier measured on the video footage for all the tests except the well graded flow with 32% of fluid content, for which the movie was not available. The images show different instants during the impact of the mixture against the barrier with respect to the time $t=0$ at which the slice gate was opened. Images on the left column show the initial phase of the impact, the middle image is taken when the runup of the material occurs and the image on the right shows the final phase of each test. All the tests displayed similar dynamics during the impact, with preliminary collisions of dry bouncing particles against the barrier prior the arrival of the flow front. Only in the test with 3mm beads and f_c 28% could we observe the arrival of a first small frontal surge before the impact of the main flow surge.

The impact of the leading surge led to a runup that exceeded for a few centimeters the height of the barrier for all the experiments except for the 3mm mixture at f_c 28% (Figure 4). However during runup only a small quantity of mixture was able to override the barrier because the vertical wave produced rapidly broke backward, resulting in an upstreaming propagating shock wave. The same behavior was observed by Iverson et al. (2016) in large scale flume tests using soil and water mixtures.

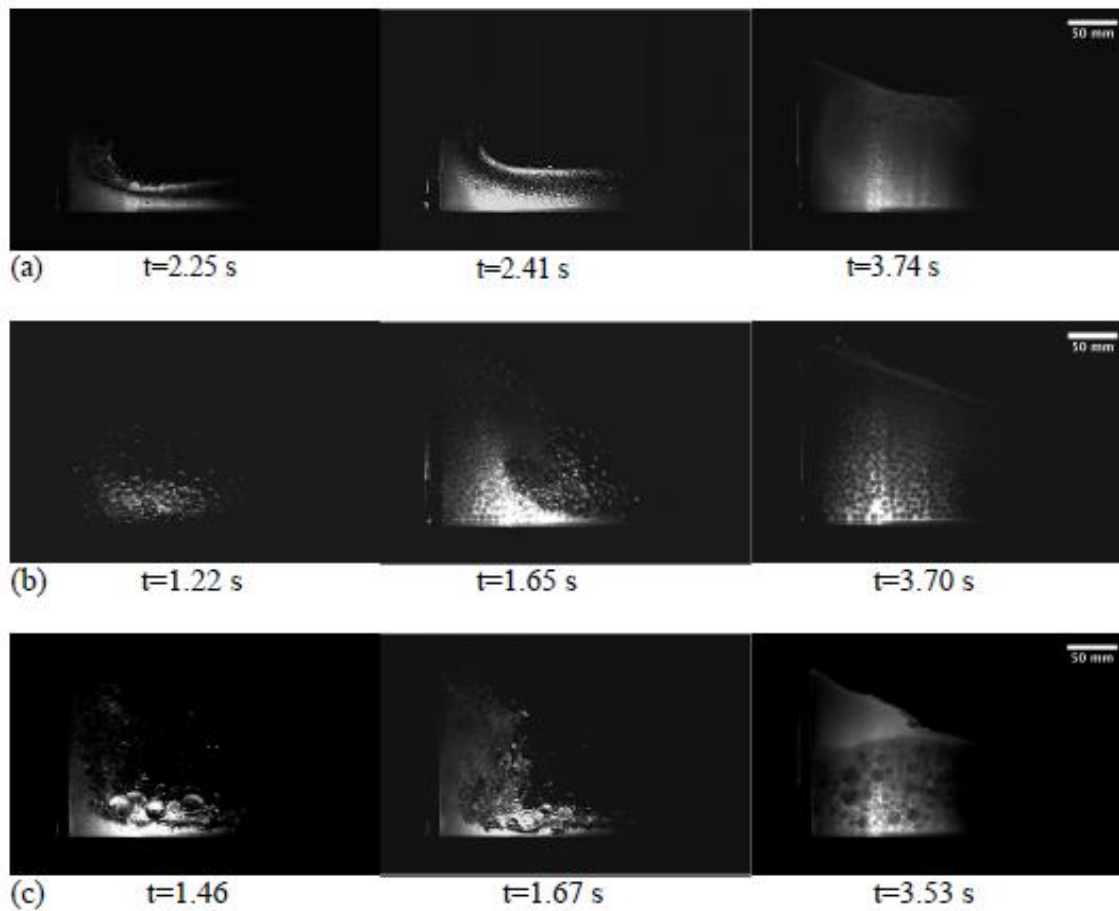


Fig. 3. Illuminated section at centerline of flume during impact (a) 3mm uniform, (b) 7.5mm uniform, (c) well-graded with $D_{50} = 7.5\text{mm}$, $C_U = 6$

The velocity of the tests is generally larger at higher fluid content. The front velocity of the tests at f_c 28%, estimated using the instant at which the flow front arrive at the barrier, is approximately 1.1 m/s, 1.9 m/s and 1.8 m/s \pm 0.2 m/s for the 3mm, 7.5mm and well graded PSDs, respectively. When the fluid content is 32% the estimated front velocity is 1.6m/s, 2.1m/s, 1.9 m/s \pm 0.2 m/s for the 3mm, 7.5mm and well graded PSDs, respectively. The estimate of the instant in which the flow arrives at the barrier is not an easy task due to the fact that the tests are run in a dark environment to avoid any light except that produced by the fluorescent dye excited by the laser being recorded by the high speed camera. As the flow front is usually unsaturated, we can only track the position of the flow front from the reflected light coming from the reflections of the laser with the surface of the beads. Further work is ongoing to obtain the field velocity during impact using particle image velocimetry analyses on the flow images.

3.1. Basal pressure development

Figs 5 and 6 shows the responses of the pore pressure transducers using a running filtering window of 300 Hz. The PPT responses are dominated by the increase in the height of the fluid-saturated debris behind the barrier (which is effectively impermeable) after impact. Therefore, although flows initially pass over PPT4, then PPT3 and then PPT2 in succession on their descent (resulting in relatively small recorded pressures of the order of 0.2 kPa), PPT2 (closest to the barrier) then produces the largest and earliest response to this impact with recorded pressures ranging between 1 and 2 kPa.

There is a considerable difference in pore pressure behaviour after impact between flows at f_c 28% and 32%, particularly for the 3mm flows which, considering the ratio of pore pressure to total stress, appears to be close to hydrostatic for f_c 28% but above this immediately post impact for f_c 32%. For the well graded flows, it is clear that the

pore pressures are much greater than hydrostatic upon and post impact at both fluid contents. For the 7.5mm flows, the picture is mixed – appearing slightly above hydrostatic for the 28% and considerably above for f_c 32%. These results point to several things: excess pore pressures do not necessarily generate within uniform flows of spheres, except where sufficient fluid is present and sufficient agitation is generated (e.g. during an impact event).

The 7.5 mm flows generate large forces at impact, higher velocities and greater agitation than the 3mm flows, although otherwise it would be expected from consolidation theory the finer material should both generate and maintain higher pore pressure. This only occurs for the 3mm flow at f_c 32%, showing that the fluid content plays a role in developing excess pore pressure which is necessary for enhanced mobility. Conversely, for well-graded flows (at least for the chosen grading and same fluid contents) excess pore pressures are both generated and maintained at impact. This is likely due to there being both larger particles to agitate the flow upon impact and fines to reduce permeability and hence maintain the excess pore pressure for longer.

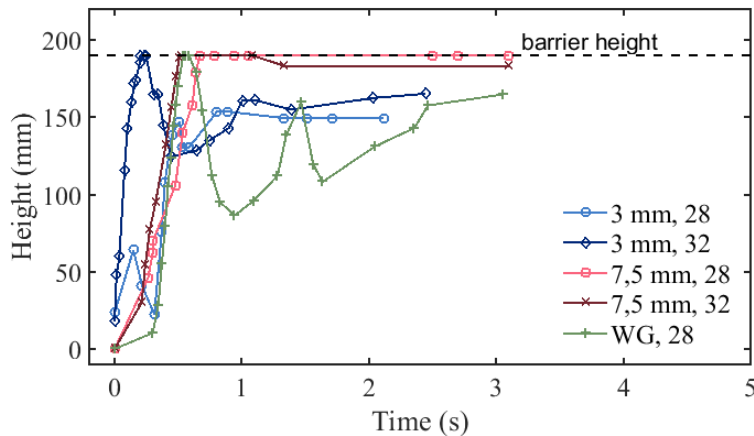


Fig. 4. Measured run-up height at the barrier (time $t=0$ is the time of the flow front arrival)

3.2. Impact load

The recorded raw impact signals present high frequency spikes that can be due to random effects depending on the resonance frequency of the load cell and on single instantaneous impact of large particles. In order to filter the data we followed the procedure proposed by Scheidl et al. (2012), applying a low pass filter with a maximum high frequency estimated considering the average maximum front velocity v_f and the maximum particle diameter, as follows $f_i = v_f / d_{max}$. For the uniform tests with 3 mm and 7.5 mm particles this produced a low pass frequency of 450 Hz and 270 Hz respectively. For the well graded material we decided to assume as d_{max} the value of $d_{90} = 20$ mm and obtained a low pass frequency of 100 Hz.

Figures 5 and 6 present the impact load measured during tests after filtering. The influence of the particle size on the response of the barrier is clear. The uniform flows with the 7.5 mm particles generate the greatest initial impact load, while that of the well graded flow (with d_{50} of 7.5 mm and d_{90} of 20 mm) is intermediate to that of the 3 mm and 7.5 mm for both fluid content series.

The well graded tests such as those with 7.5 mm show a number of spikes in the impact signal recorded from the load cell, representing collisions of large particles against the barrier, however, both the peak force during and after the impact reach values similar to those of 3 mm mixtures. This indicates the dampening influence of the fine particles within this flow material, considering that it has larger particles than the uniform 7.5 mm flows.

Comparing the videos with the development of the impact load it is possible to recognize common dynamics for all the tests. We observe an initial dynamic impact characterized by the rapid increase of the load due to the front surge arrival and the subsequent material runup hitting the barrier. The impact force peak is followed by a quick drop when the runup wave breaks backward down, suppressing the action of the incoming flow for a subsequent runup. From this point on, the increase of the impact force can be considered as a result of the progressive deposition of the mixture behind the material already settled in front of the barrier.

The peak load due to the initial dynamic impact of the flows appears to be enhanced by the presence of a larger quantity of fluid for the 7.5 mm and well graded tests. The 3 mm tests do not show a greater initial impact at larger fluid content but instead it is possible to observe a slight increase in the load exerted from the flow after the impact,

probably due to the fact that the more fluidised mixture results in a faster flow and hence most of the particles within the mixture are able to travel till the end of the channel, increasing the weight of the material behind the barrier (see Fig. 4).

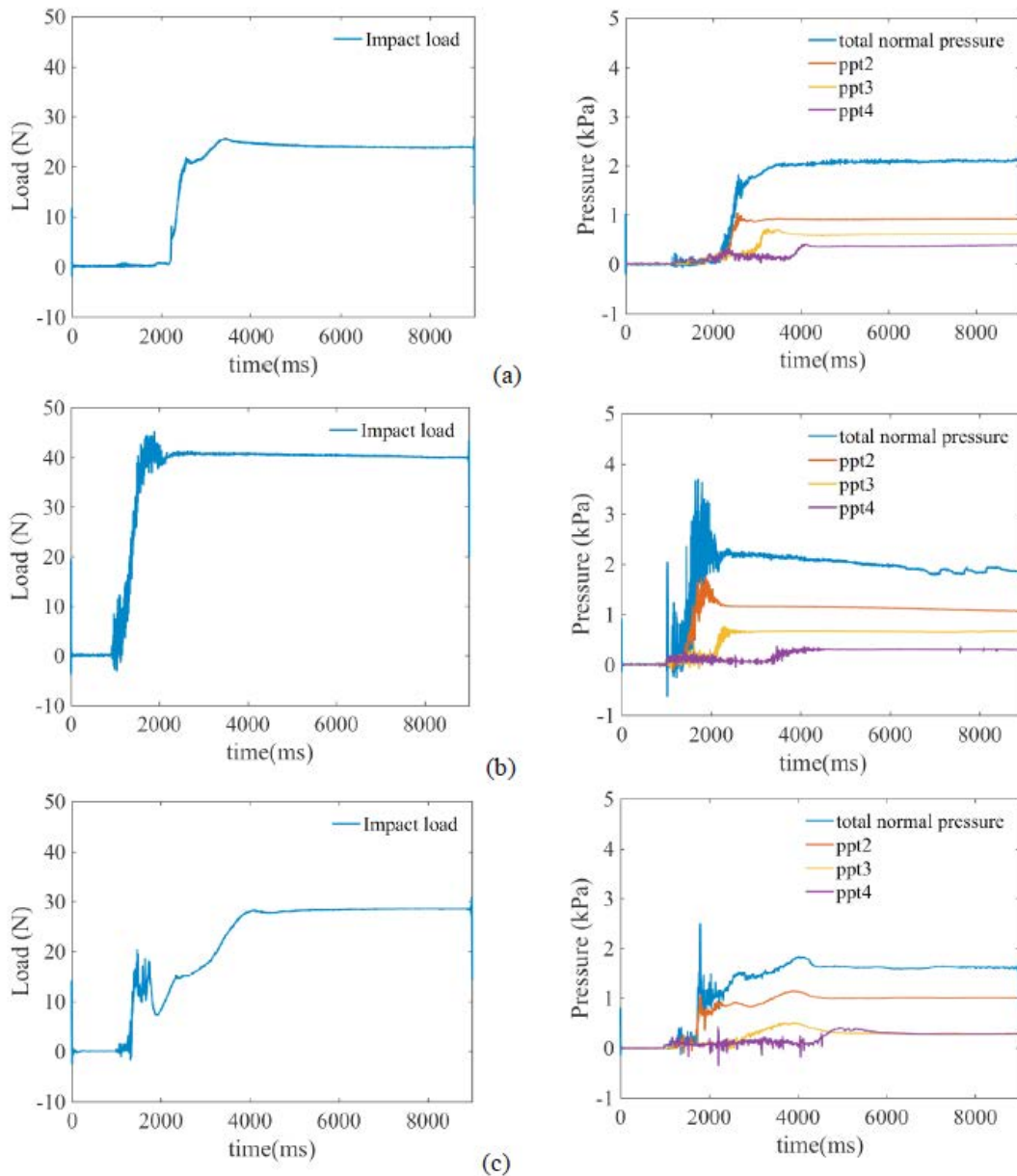


Fig. 5. Fluid content 28% (Left) Load on barrier (Right) Basal pressures (a) 3mm uniform, (b) 7.5mm uniform, (c) well-graded with $D_{50} = 7.5\text{mm}$, $C_U = 6$

Closer examination shows that the flow at f_c 28% for the 3 mm particles behaves similarly to that of the 7.5 mm flows with a near constant pressure response after impact, however at f_c 32%, it is more similar to that of the well graded flows where the impact pressure initially rises then falls then rises again. Coupled with the pore pressure response for 3 mm, this suggests that the behaviour of this uniform flow strongly depends on the fluid content.

Only the 7.5mm tests exhibited a peak load generated by the initial dynamic impact on the barrier that is higher than that exerted from the material deposited behind. The reason for that is that such fast mixtures, once they hit the

barrier, can produce a high and large runup wave with large particles that, despite their size, can be easily mobilized and pushed upward and against the barrier exerting high pressure.

In contrast, it is clearly visible from the high speed camera video, that for the f_c 28% well graded test, most of the top part of the runup wave is comprised of fluid as the large particles at the flow front are too heavy to be pushed any higher than approximately the middle height of the barrier (Fig. 3). Furthermore, the presence of finer material can also have a damping effect on the large particle collisions. The combination of these factors can explain the similar value of the impact load between the 3 mm and the well graded tests.

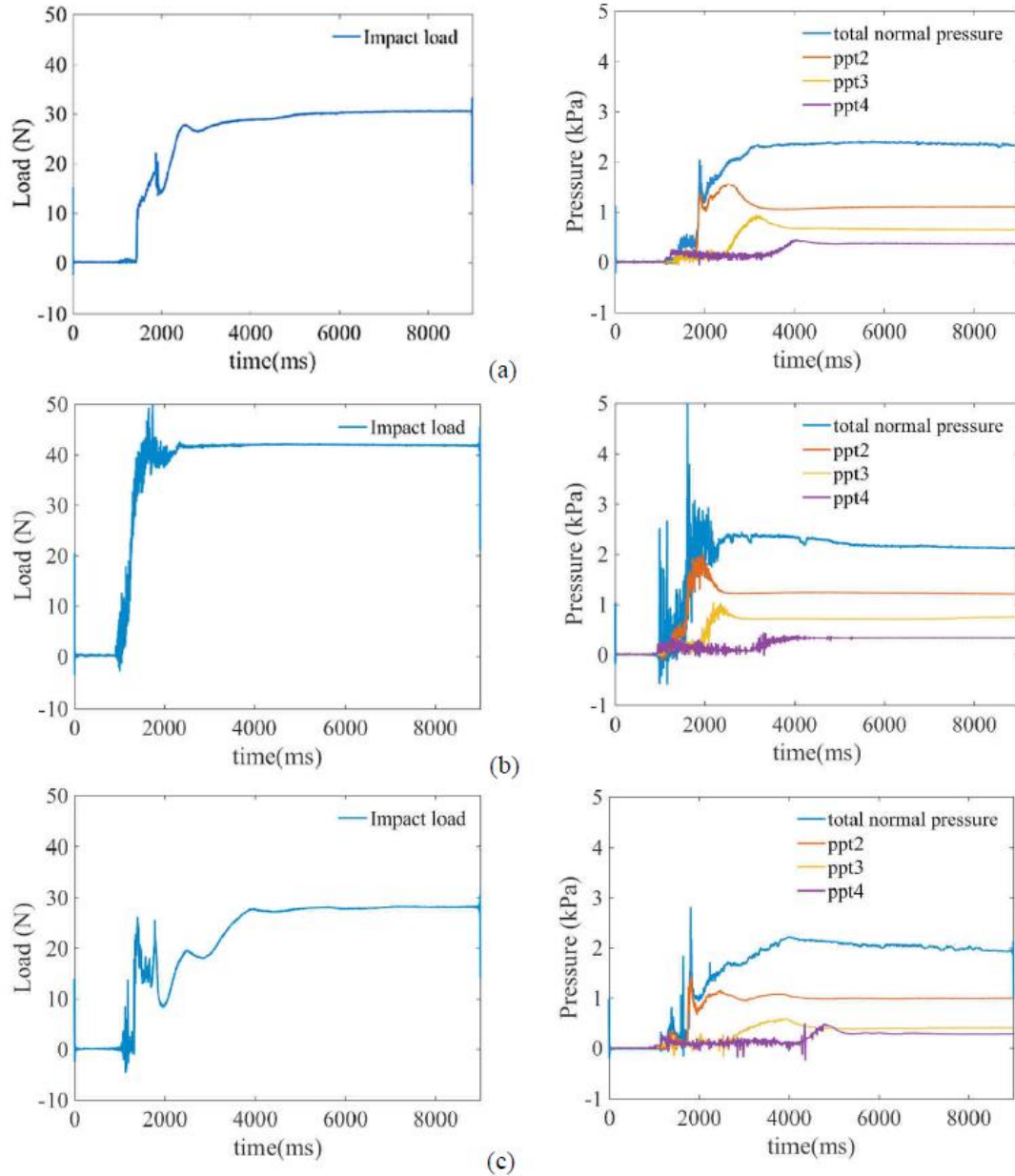


Fig. 6. Fluid content 32% - (Left) Load on barrier (Right); Basal pressures (a) 3mm uniform, (b) 7.5mm uniform, (c) well-graded with D_{50} 7.5mm, $C_u = 6$

4. Conclusions

The paper presents the results of tests performed using a small-scale flume in which the impact of a transparent debris-flow model on rigid barrier is investigated. The roughened base of the channel is instrumented along its base with three pore pressure transducers and a load cell for the measure of the total normal stress. The barrier is fixed to the flume bed at 2.25 m from the gate release and is orientated normal to the flow direction.

The evolution of the impact load, bed normal pressure and fluid pore pressure for flows consisting of uniform and well graded particle size gradings at two different fluid contents, 28% and 32%, is measured and analyzed before and after impact. It has been found that excess of pore pressures do not necessarily generate within uniform flows of spheres, except where sufficient fluid is present and sufficient agitation is generated (e.g. during an impact event). The particle size of the material has an effect on impact. The uniform flows with the larger particles generate the greatest initial impact load while for the well graded mixture the presence of fine particles within the flow can provide a dampening influence. Further work is ongoing to obtain the field velocity during impact using particle image velocimetry analysis on the flow images in order to investigate the impact kinematics in detail.

Acknowledgements

This research was supported through the Engineering and Physical Sciences Research Council (EPSRC), UK project no. EP/M017427/1 “High speed granular debris flows: new paradigms and interactions in geomechanics”. The authors would like to acknowledge the assistance of technicians at the University of Sheffield in the construction of the apparatus. MAC was partly funded by the Early-stage Researcher fund (FAPA) from the Universidad de los Andes, under the Grant agreement No. PR.3.2016.3667.

References

- Armanini, A., Larcher, M., and Odorizzi, M., 2011, Dynamic impact of a debris flow front against a vertical wall, in Proceedings, 5th international conference on debris-flow hazards, Mitigation, mechanics, prediction and assessment, Padua, p. 1041–1049.
- Bugnon, L., McArdell, B., Bartelt, P., and Wendeler, C., 2011, Measurements of hillslope debris-flow impact pressure on obstacles: Landslides, p. 1–9, doi:10.1007/s10346-011-0294-4.
- Cui, P., Zeng, C., and Lei, Y., 2015, Experimental analysis on the impact force of viscous debris flow: Earth Surf. Processes Landforms, v.40, p. 1644–1655, doi:10.1002/esp.3744.
- Hu, K., Wei, F., and Li, Y., 2011, Real-time measurement and preliminary analysis of debris-flow impact force at jiangjia ravine, china: Earth Surf Process Landf., v. 36, p. 1268–1278, doi:10.1002/esp.2155 .
- Hubl, J., Suda, J., Proske, D., Kaitna, R., and Scheidl, C., 2009, Debris-flow impact estimation, in Proceedings of the 11th International Symposium on Water Management and Hydraulic Engineering, Ohrid, Macedonia.
- Hungr, O., Leroueil, S., and Picarelli, L., 2013, The Varnes classification of landslide types, an update: Landslides, v. 11, p. 167-194.
- Iverson, R.M., 1997, The physics of debris flows: Reviews of Geophysics, v. 35, no. 3, p. 245-296.
- Iverson, R.M., George, D.L., and Logan, M., 2016, Debris-flow run-up on vertical barriers and adverse slopes: Journal of Geophysical Research-Earth Surface, v. 121, p. 2333–2357, doi:10.1002/2016JF003933.
- Moriguchi, S., Borja, R., Yashima, A., and Sawada, K., 2009, Estimating the impact force generated by granular flow on a rigid obstruction: Acta Geotech., v. 4, no. 1, p. 57–71.
- Sanvitale, N., and Bowman, E.T., 2012, Internal imaging of saturated granular free-surface flows: International Journal of Physical Modelling in Geotechnics, v. 12, no. 4, p. 129-142.
- Scheidl, C., Chiari, M., Kaitna, R., Mullegger, M., Krawtschuk, A., Zimmermann, T. and Proske, D., 2012, Analysing debris-flow impact models, based on a small scale modelling approach: Surveys in Geophysics, v. 34, no. 1, 121–40.
- Takahashi, T. 2007. Debris flow: Mechanics, prediction and countermeasures. Taylor & Francis.
- Zhou, G.G.D., Song, D., Choi, C.E., Pasuto, A., Sun, Q.C., and Dai, D.F., 2018, Surge impact behavior of granular flows: effects of water content: Landslides, v. 15, no. 4, p. 695-709.

Estimation of temporal changes of debris flows and hydraulic model tests of channel works with multi-drop structures

Haruki Watabe ^{a,*}, Tsuyoshi Ikeshima ^a, Yotaro Nishi ^a, Yohei Nagarekawa ^a,
Satoru Matsuda ^a, Takashi Nakayama ^b, Takahiro Itoh ^a, Takahisa Mizuyama ^c

^a*Nippon Koei Co., Ltd., 5-1-43, Ekinishihonmachi, Kanazawa-shi, Ishikawa, 920-0025, Japan*

^b*Tamano Consultants Co., Ltd., 2-17-14, Higashisakura, Higashi-ku, Nagoya, Aichi, 461-0005, Japan*

^c*National Graduate Institute for Policy Studies, 7-22-1, Roppongi, Minato-ku, Tokyo, 106-8677, Japan*

Abstract

A debris-flow disaster took place in the Nashizawa creek in Kiso River catchment, Nagano Prefecture, Japan on 9th July 2014 due to intensive rainfall from the typhoon Neoguri. There were few data available for estimation of debris-flow discharge in the catchment. A CCTV camera and a high sensitivity seismometer were installed along Nashizawa creek prior to the debris flows. Surges of debris flows were recorded by CCTV camera, though the camera was eventually destroyed by those surges during debris flows. The shape of debris-flow surges was estimated using the discharge analysed by CCTV camera data and fitting curve of relations between debris-flow discharge and acceleration of vibration. Peak discharge was extrapolated from peak acceleration of the vibration, and was estimated about 756 m³/s. At the Nashizawa creek, channel works with multi-drop structures were planned for construction after the debris-flow disaster. Some research was conducted experimentally for planning and design of channel works such as multi-drop structures. This research pointed out several problems for multi-drop structures in supercritical flow such as scouring and flow depth increases due to shock waves. We investigated characteristics of shockwaves and countermeasures using multi-drop structures in a steep channel with supercritical flow experimentally to design the channel works. We found that stair-type dissipaters are effective for mitigating shockwaves from multi-drop structures.

Keywords: Debris-flow discharge; cctv camera; vibration meter; hydraulic model test; channel work; shockwave; stair-type dissipater

1. Introduction

A debris flow with boulders and driftwoods triggered by rainfall from typhoon Neogri took place in Nagiso-Town, Nagano Pref., Japan on July 9, 2014. The Nashizawa catchment (area =3.28 km²) where the debris flows occurred contains two basins of Onashizawa (A=2.55 km²) and Konashizawa (A=0.73 km²) (Fig. 1). The onashizawa basin had two sabo dams (1. Nashizawa sabo dam, Closed-type, dam height=20.0m, 2. Nashizawa No.2 sabo dam, Partial slit dam, H=14.5m). The konashizawa basin had a sabo dam (Nashizawa No.1 sabo dam, Slit dam with iron grid, H=12.5m), and some groundsills were installed along the creek. Groundsill is one of crossing structures for protecting from bed erosion, and these are set in channel works. Debris flows took place in both these creeks, and part of a debris flow was trapped by some sabo dams, but the debris flow caused a disaster including the human damage by overflowing channel works even though some sabo structures caught some debris-flow sediments. For the design discharge of the Nashizawa debris flow, we estimated temporal changes of debris-flow discharge from images recorded by CCTV camera and ground vibration recorded by a vibration meter, and a hydrograph estimated from verifying free surface trace that it was obtained in field surveys.

At Nashizawa creek, channel works with multi-drop structures were to be constructed after events. Multi-drop structures are installed continuously in channel works, and those are one of crossing structures for the decrease of water energy by drops. There was some research conducted experimentally for the planning and design of multi-drop structures on steep slopes (e.g., Ashida et. al., 1975; Mizuyama et. al., 1989). This research pointed out several

* Corresponding author e-mail address: a6809@n-koei.co.jp

problems for multi-drop structures in area with supercritical flow. One is local scouring caused by drop flow, and another is the increase in flow depth due to the shock waves caused by the multi-drop structures and the increase of velocity at downstream end (e.g., Mizuyama et al., 1989). There is little research on countermeasures for shockwaves in multi-drop structures in supercritical flow.

In this study, we evaluate 1) debris-flow discharge is estimated from analyzing the relationship between the acceleration of vibrations and discharge measured at a field site, and 2) the increase in flow depth caused by shock waves, and 3) countermeasures for shock waves caused by supercritical flow through multi-drop structures in the steep.

2. Study Area

Nashizawa catchment contains Onashizawa and Konashizawa creeks which are right and left side of tributaries, and those are confluent at around 650m from downstream of Kiso River. The average bed slope of the Onashizawa and Konashizawa creeks is $1/4.4$ (12.8 degrees) and $1/3.8$ (14.7 degrees), respectively (Fig. 1(b)). The bedrock underlying the Nashizawa watershed is granite. After the 2014 debris flow, there were many boulders over 2 m in diameter on the creek beds. A CCTV camera is located at the confluence of Onashizawa and Konashizawa creeks. A vibration meter (High Sensitivity Seismograph Network Japan, Hi-net) is installed under the ground about 104 m in depth, 10 m from center of the river, and 500 m from the confluence. Channel works with multi-drops are installed downstream from the confluence of Nashizawa and Konashizawa creeks, and are constructed from the confluence area to Kiso River over a total distance of 625 m (Fig.1(a)).

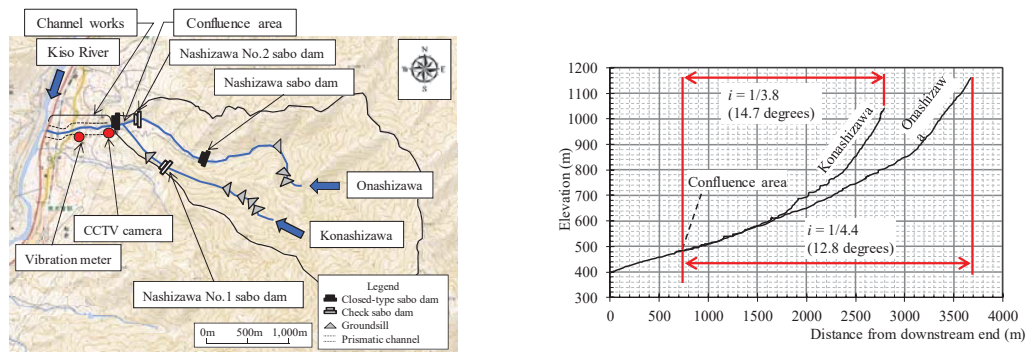


Fig. 1. (a) Plan map of the Nashizawa catchment; (b) Longitudinal bed profiles of Onashizawa and Konashizawa creeks

3. Estimation of Debris-Flow Hydrograph

3.1. Estimation of debris-flow discharge by camera image

Surges of debris flows were recorded by the CCTV camera, even though the camera was eventually destroyed by those surges. Water level and surface velocity were measured from camera images. Mean velocity was calculated using the relationship of 3/5 times of surface velocity (e.g., Mizuyama et al., 1984) during the debris flow passed at a dam. Estimated discharges ranged from $79 \text{ m}^3/\text{s}$ to $428.4 \text{ m}^3/\text{s}$.

3.2. Synchronizing between discharge and acceleration of vibration

Vertical component of vibration acceleration calculated using root mean square (RMS) was two remarkable peaks when debris flow took place. Some testimonies were obtained by hearing survey from local inhabitants, and there was debris deposit in Kiso River before the large scale of debris flow occurs twice. Debris flows were recorded by CCTV camera before two remarkable peaks. The peak time of acceleration and discharge obtained by camera images is synchronized the time when the pattern of increase and decrease is almost equal before two remarkable peaks because CCTV camera and vibration meter are installed separately. Fig. 2 shows temporal changes of the acceleration of the vibration and time synchronization with the acceleration of the vibration and discharge obtained

by CCTV images. Temporal changes of acceleration of vibration is compared with analyzed discharge using CCTV before the peak stage.

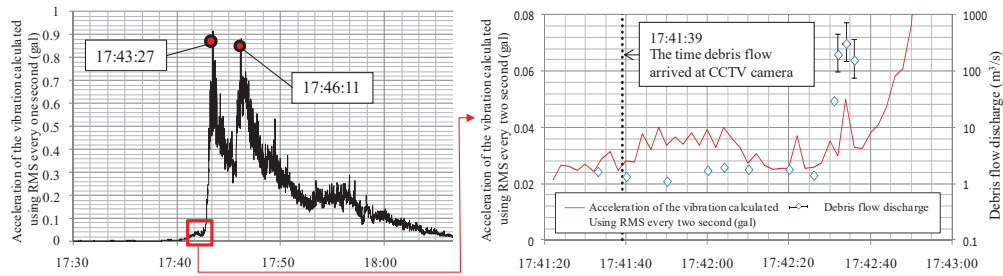


Fig. 2. Temporal changes of the acceleration of the vibration and time synchronization with the acceleration of the vibration and discharge obtained by CCTV images

3.3. Estimation of debris-flow peak discharge and hydrograph

Debris flow with bolder is known to generate strong ground vibration (e.g., Suwa et al., 1999). Referring to previous study of high correlations between peak discharge of the surge and peak acceleration of the vibration, a fitting curve is proposed by the form of $Q = a(G - b)^{25/42}$. Q is the discharge, G is the acceleration of vibration (gal). Coefficient a and b are determined by least-squares method. Fig. 3 (a) shows relation between discharge and acceleration calculated in every two seconds, and those relation is shown as quadratic curve by extrapolated using the data over $10 \text{ m}^3/\text{s}$. Peak discharge extrapolated from peak acceleration of the vibration is calculated about $756 \text{ m}^3/\text{s}$. Fig. 3 (b) shows estimation hydrograph of debris flow. Estimated peak discharge and hydrograph were inspected by discharge estimated by free surface trace supposing uniform flow.

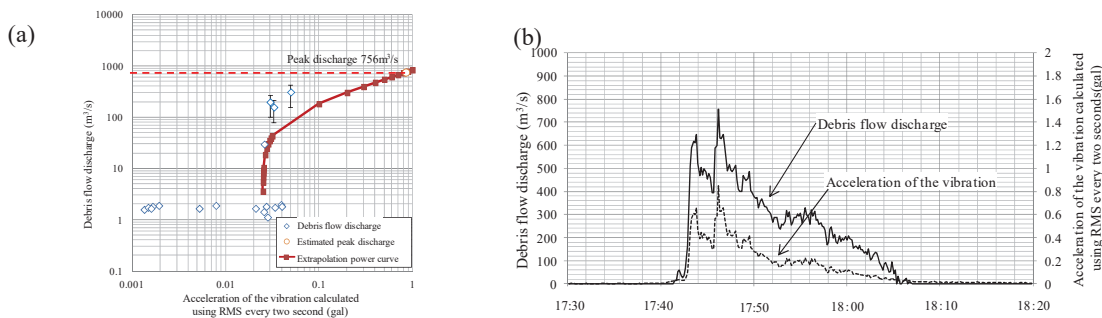


Fig. 3. (a) Relation between discharge and acceleration calculated in every two seconds; (b) Estimated hydrograph shapes of debris flow

4. Hydraulic Model Test for Channel Works

4.1. Hydraulic model

Figure 4 (a) shows the plan view map of channel works in Nashizawa creek. Fig. 4 (b) shows hydraulic model. Plan shape and values for channel works in prototype are divided by model scale of $1/100$ with froude similarity, and values of model length and width are 6.5m and 3.0m, respectively. Water supplied from water tank set at upstream of model, and it flows to downstream end through the channel works with multi-drops. Channel works confluent at downstream end of the model (Kiso River) with having some curvature sections. Houses and public facilities are also modelled on the fan. Photos and movies are obtained from digital camera at the position as shown in Fig. 4 (b). Servo-type meter is set at downstream of the flume to measure automatically temporal changes of flow depth by every 1 second in model. Discharge is measured by bucket at downstream end.

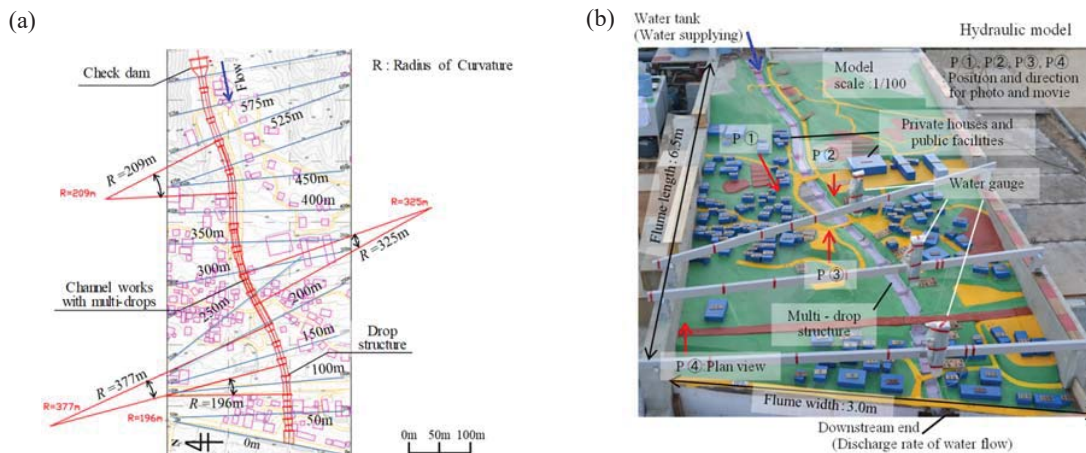


Fig. 4. (a) Plan view map of channel works; (b) Hydraulic model

4.2. Experimental conditions

Figure 5 shows longitudinal bed profiles of channel works in Nashizawa creek in prototype value. All figures and tables related to the experiment are showed in prototype value. Bed slope is 1/10 (5.7 degrees) in upstream area, and those are steeper as going downstream area. Fig. 6 shows cross sectional of channel works in prototype value. Bottom width and height of channel works are 8.0 m and 1.3m with side bank slope of 1:0.5. Flow discharge is set at 100m³/s in steady flow, and the values are calculated in uniform flow condition for maximum flow capacity of cross sectional shape. Hydraulic condition is shown in Table 1. Froude similarity is applied for setting of hydraulic parameters, and bed roughness of multi-drop structure is 0.040(m^{-1/3}s). The model scale is 1/100. Froude number is 2.26, and supercritical flow is formed in channel works. Supercritical flow is determined in case that Froude number is over 1.0, and influence of flow disturbance is not transmitted to upstream area. Experimental runs are as follows: Run 1 is the experiment for present shape of multi-drop structure (without countermeasure), and Run 2 is experiment for installation of the countermeasure for shockwave.

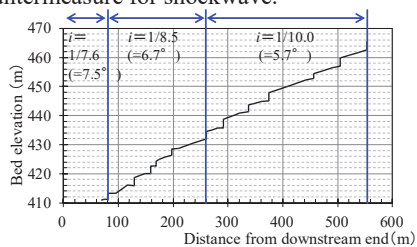


Fig. 5. Longitudinal bed profiles of channel work in Nashizawa creek (prototype value)

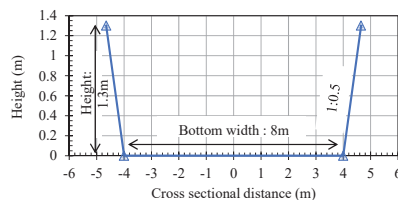


Fig. 6. Cross section of channel works in Nashizawa creek (prototype value)

Table 1. Hydraulic conditions (prototype value)

	Unit	Value
λ	-	1/100
θ	(degree)	5.73
n	(m ^{-1/3} s)	0.040
B	(m)	9.38
A	(m ²)	12.0
R	(m)	1.08
Q	(m ³ /s)	100
h_0	(m)	1.38
V	(m/s)	8.33
Fr	-	2.26
Re	-	7.58×10 ⁶

Herein, λ :model scale, θ :bed slope at upstream area, n :bed roughness, B :free surface width, A :flow area, R :hydraulic radius, Q :water discharge, h_0 :uniform flow depth, v :cross sectional average flow velocity, Fr :Froude number, Re :Reynolds number

4.3. Shock waves in supercritical flow

Figure 7 shows the flow patterns in Run 1 (without countermeasure), and the overflow occurs at right side bank in multi-drop structure. Shock waves yielded at side bank are transported downstream diagonally, and overflow is caused by increasing of flow depth at side bank due to the concentration of shock waves. Shock wave shows flow pattern, and it is formed from structure such as side bank and changing point of plan view in supercritical flow.

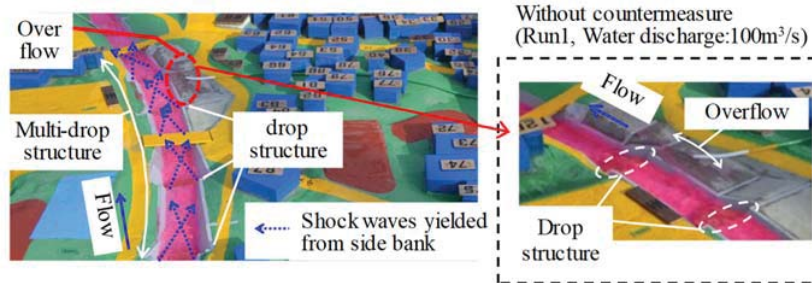


Fig. 7. Flow patterns in Run1 (without countermeasure)

Figure 8 shows schematics of multi-drop structure. There are the changing points in plan view such as expansion section and contraction section at downstream of drop structure, and napping flows with sediments prevent from colliding to side bank of multi-drop structure (Fig.8). Those plan view causes increasing of flow depth, and previous study also showed the effect of plan view on increasing of flow depth. Plan view of multi-drop structure produces vena contracta at downstream of drop structure. Vena contracta is formed during changing section from contraction to expansion section in plan view. Flow depth increases because vena contracta collides to side bank of downstream of expansion sections. Contraction section also results in increasing of velocity due to decreasing of flow area. Figure 9 (a) shows cross sectional free surface distributions in Run1 and Run2. The data shows increasing of flow depth in right side bank. Water jump is defined that water splashes out at drop sections such as just downstream of structure. This is also reason why increasing of flow depth occurs in multi-drop structure. Consequently, one is shock wave yielded at side bank, and the others are water jump at downstream of drop structure and vena contracta caused by plan view of multi-drop structure. Fig. 9 (b) shows longitudinal free surface and flow depth profiles in Run1. Free surface is measured at the center of cross section of the training channel. Fig. 10 shows longitudinal velocity distributions in Run1. Velocity is calculated by water discharge and flow depth each section. Velocity

increases gradually as going downstream, and value of velocity fluctuates in downstream reach of the channel.

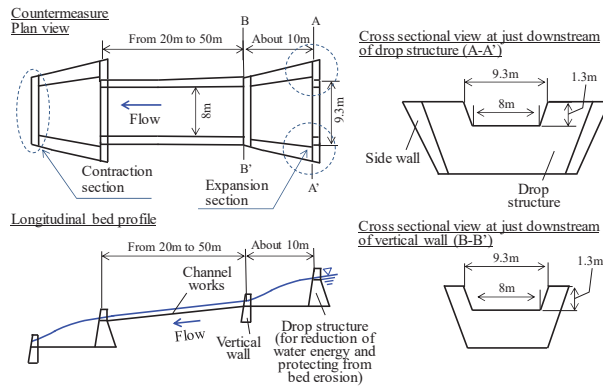


Fig. 8. Schematics of multi-drop structure in Run1

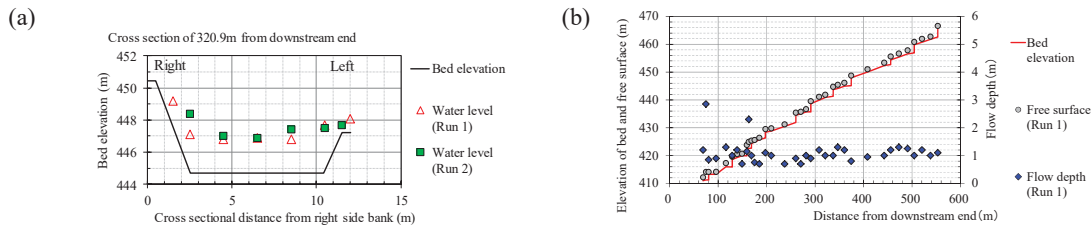


Fig. 9. (a) Cross sectional free surface distribution in Run1 and Run2 (prototype); (b) Longitudinal free surface and flow depth in Run1 (prototype)

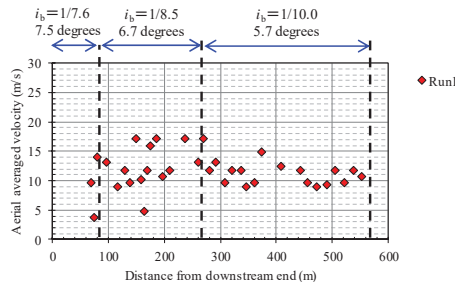


Fig. 10. Longitudinal velocity distribution in Run1 (prototype value)

4.4. Countermeasure for shock waves

Countermeasure for shock wave is focused in present study on increasing of water depth. Stair type dissipater is installed at just downstream of drop structure of channel works as countermeasure of shock wave. Fig. 11 shows schematics of multi-drop structure with countermeasure, and it also makes expansion and contraction sections be straight in plan view. Downstream of drop structure is stair types in longitudinal shape of channel works. The surface of stair type dissipater is covered by boulders.

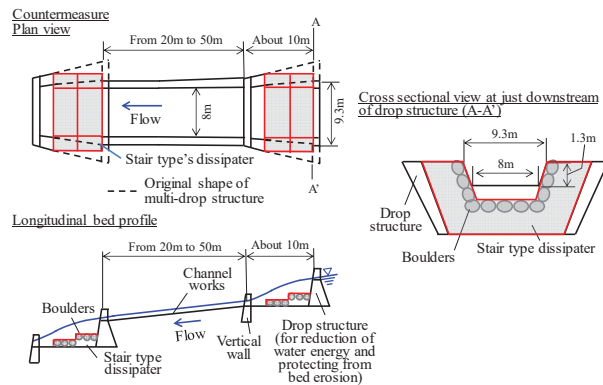


Fig. 11. Schematics of multi-drop structure and countermeasure using stair type dissipater in Run2

Figure 12 shows flow patterns in Run 2 (with countermeasure). Overflow does not occur in the outer reach of curved parts at right side bank. There are some reasons why overflow is not occurred. Vena contracta is not easy to be produced due to linearization of plan shape at downstream of drop structures. Influence of concentration of shock wave on increasing of flow depth are mitigated due to the boulders at surface of stair type dissipater, and shockwave is not produced during the channel. Some steps of stair type dissipater are effective for water jump at drops because energy of flow is dissipated by some steps.

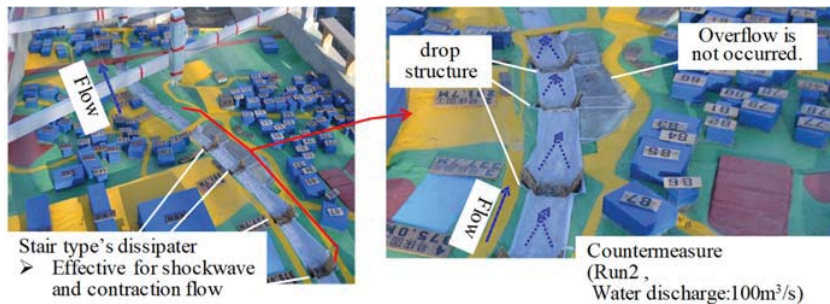


Fig. 12. Flow patterns in Run2 with countermeasure

Flow depth at right side bank in case of Run2 decreases in comparison to that of Run1. Fig. 13 shows longitudinal free surface and flow depth profiles in Run 1 and Run 2. Stair-type dissipater can have roles for smoothing of longitudinal and transverse free surface profiles in comparison to Run 1 (Fig. 13). Fig. 14 shows longitudinal velocity distributions in comparison to Run1 and Run2. Velocity in case of Run2 increases because plan shape of multi-drop structure is more straight compared with Run1. If the space for stairs can be prepared just downstream of the drops considering flow magnitude, the stair-type dissipater might be one of effective structures for flow smoothing because flow area is not reduced there. Installation of stair type dissipater is needs to be considered design flow discharge so as not to reduce the flow area of drops.

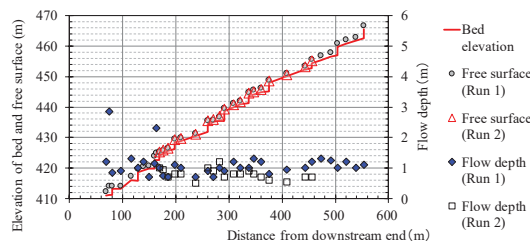


Fig. 13. Longitudinal free surface and flow depth profiles in Run1 and Run2 (prototype value)

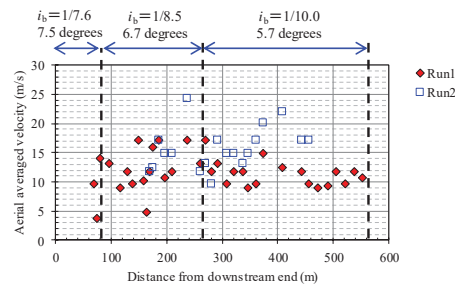


Fig. 14. Longitudinal velocity distributions in Run1 and Run2 (prototype value)

5. Conclusions

A debris flow triggered by rainfall from typhoon Neogri took place in Nagiso-Town, Nagano Pref., Japan on July 9, 2014. There were few data available for estimation of debris-flow discharge for analyzing of debris flow occurred in Nashizawa creek. For the design discharge of the Nashizawa debris flow, we estimated temporal changes of debris-flow discharge from images recorded by CCTV camera and ground vibration recorded by a vibration meter, and a hydrograph estimated from verifying free surface trace that it was obtained in field surveys. At Nashizawa creek, channel works with multi-drop structures were to be constructed after the disaster. We evaluated the characteristics of flow patterns in channel works with multi-drop structures experimentally, and proposed the countermeasure for some problems such as shock wave. For estimation of temporal changes of debris flow and hydraulic model tests focused on countermeasures using channel works with multi-drops, the results obtained in present study are summarized as follows,

Estimated peak discharge is about $756 \text{ m}^3/\text{s}$, and it is extrapolated by the fitting curve analyzed using by the relationship between discharges estimated by image of CCTV camera and acceleration of the vibration calculated using root mean square (RMS). The value is confirmed by discharge estimated using free surface traces in the field survey just after disaster.

Concentration of shock waves in the channel and plain shape of the channel cause increasing of flow depth near the drop structure, and result in overflow at the outer bank of the channel. It is better for flow smoothing to set stair-type dissipater just downstream of drop structure, and the stair-type dissipater is effective to reduce increasing of flow depth caused by shock waves.

Stair type dissipater is desirable to set at just downstream of drop structures not to change the flow area in corresponding to design flow discharge. The knowledge can be included for new design and tools for multi-drop structure in a channel works in steep slope. There are some problems to be solved, that countermeasures for water velocity in downstream end of multi-drop structure, the influence of height of drops on water jump and so on.

Acknowledgements

This study is supported by Tajimi office of Sabo and National Highway, Ministry of Land, Infrastructure, Transport and Tourism. We would like to express appreciation to the office for providing data in the field.

References

- Suwa, H., Yamakoshi, T., and Sato, K., 1999, Estimation of debris-flow discharge by monitoring ground tremor, *Journal of the Japan Society of Erosion Control Engineering*, v. 52, no. 2, p. 5-13 (in Japanese).
- Mizuyama, T., and Uehara, S., 1984, Observed data of the depth and velocity of debris flow, *Journal of the Japan Society of Erosion Control Engineering*, v. 37, no. 4, p. 23-26 (in Japanese).
- Erosion and Sediment Control Division, River Bureau, Ministry of Construction, Japan, 2000, A draft of the guideline for driftwood countermeasures (in Japanese).
- Ashida, K., Takahashi, T., and Mizuyama, T., 1975, Some Discussions on Hydraulic Design of Waterway Stabilization Structures: *Journal of the Japan Society of Erosion Control Engineering*, v. 97, p. 9-16 (in Japanese).
- Mizuyama, T., and Kurihara, J., 1989, Hydraulics of Multi-Drop Structures and Prevention Methods of Super Elevation: *Journal of the Japan Society of Erosion Control Engineering*, v. 42, no. 2 (163), p. 11-15 (in Japanese).

Author Index

- Aaron, J., 911-918
Abancó, C., 131-137
Adams, K., 231-238
Akita, H., 207-213
Alberti, R., 573-580
Alcalde, A.L., 597-604
Alessio, P., 500-507
Allstadt, K.E., 77-84, 154-161, 192-198
Arai, M., 124-130, 239-248
Arattano, M., 103-110
Asano, Y., 385-392
Badoux, A., 693-700
Baillet, L., 146-153
Barnhart, K., 85-92
Bartelt, P., 685-692
Bateira, C., 597-604
Bauer, J.B., 549-556
Baum, R.L., 249-256
Bazai, N.A., 38-45
Beason, S.R., 93-102
Berenguer, M., 184-191
Bernard, M., 557-564, 573-580
Berti, M., 557-564
Bessette-Kirton, E.K., 257-264, 613-620
Bilderback, E.L., 816-823
Blankenship, B.T., 10-17
Bonneau, D.A., 565-572
Bonnefoy-Demongeot, M., 146-153
Boreggio, M., 573-580
Borgniet, L., 146-153
Boschini, I., 996-1003
Bowman, E., 1035-1042
Braun, M., 732-739
Brien, D.L., 824-831
Brito, H.D., 265-272
Bunn, M., 192-198
Burns, W.J., 581-588
Buscarnera, G., 369-376
Busslinger, M., 1027-1034
Cabral, V.C., 265-272
Cabrera, M.A., 407-413, 1035-1042
Calcagno, E., 354-360
Calhoun, N.C., 581-588
Camiré, F., 589-596
Cannon, C.M., 287-293
Carleo, L., 131-137
Carmo Giordano, L., 265-272
Cato, K., 605-612
Cattanach, B.L., 549-556
Cavalli, M., 103-110
Chen, C., 973-980
Chen, H., 920-927
Chen, J., 920-927, 928-935
Chen, X., 361-368, 920-927, 928-935
Cheng, K., 887-894
Choi, C.E., 38-45, 1027-1034
Choi, S., 936-940
Christen, M., 685-692
Coe, J.A., 85-92, 154-161, 199-206, 257-264,
613-620
Coelho, R.D., 645-652
Comiti, F., 103-110
Contreras, T.A., 613-620
Corrêa, C.V.S., 265-272
Coviello, V., 103-110
Crema, S., 103-110
Crucil, G., 557-564
Cui, K., 2-9
Cui, P., 476-483, 903-910
Cui, Y., 38-45, 1027-1034
Curran, J.C., 621-628
Das, R., 629-636
Davies, T., 661-668
de Haas, T., 10-17, 231-238, 637-644
de Souza, L.M., 597-604
Deana, M.L., 996-1003, 1004-1011
Densmore, A., 10-17, 637-644
Dey, L., 323-329
Dias, H.C., 645-652
Dias, V.C., 597-604, 645-652
Du, J., 273-279
Duffy, J., 500-507
Duhart, P., 653-660
Ebel, B.A., 524-531

Egashira, S., 459-466
 Eguchi, S., 790-797
 Eu, S., 111-115
 Evin, G., 1019-1026
 Faccuri, G., 798-807
 Fang, Y., 116-123
 Farin, M., 77-84
 Farinotti, D., 222-229
 Farrell, J., 661-668
 Feiger, N., 941-948
 Felling, G., 669-676
 Feng, Q., 10-17
 Fernández, J., 653-660
 Flanagan, P., 621-628
 Fontaine, F., 146-153
 Friedman, E.Q., 484-491
 Fritton, P., 10-17
 Frost, J.D., 508-515
 Fuemmeler, S.J., 549-556
 Fujimura, N., 138-145, 207-213
 Fujita, M., 170-176, 280-286
 Furuya, T., 170-176
 Gares, P., 231-238
 Garrido, N., 653-660
 Gartner, J.E., 500-507, 677-684
 George, D.L., 25-32, 77-84, 287-293
 Ghasemi, A., 10-17
 Ghent, J.N., 85-92
 Goforth, B., 605-612
 Gomes Vieira Reis, F.A., 265-272
 Graf, C., 685-692
 Gramani, M.F., 645-652, 798-807
 Gregoretti, C., 557-564, 573-580
 Gunatilake, A.A.J.K., 724-731
 Hanson, M.A., 613-620
 Harada, N., 949-956
 Hasegawa, Y., 294-300, 385-392
 Hay, S., 581-588
 Haydon, S., 532-538
 Hermosilla, G., 653-660
 Hill, K.M., 10-17
 Hina, J., 301-306, 377-384, 443-450
 Hirschberg, J., 693-700
 Ho, K.K.S., 957-964
 Holm, K., 847-854, 855-862
 Hotta, N., 18-24, 421-428, 443-450, 871-878
 Hrachowitz, M., 732-739
 Hsiao, D., 307-314
 Hsu, Chih-Hao, 887-894
 Hsu, Ciao-Kai, 323-329
 Hsu, Y., 701-708
 Hu, H.S., 965-972
 Hu, K., 973-980
 Huang, L., 307-314
 Huang, R., 508-515
 Huebl, J., 124-130, 177-183, 981-987
 Hürlimann, M., 131-137, 184-191
 Hutschinson, D.J., 565-572
 Ikeda, A., 315-322, 709-715
 Ikeshima, T., 1043-1050
 Im, S., 111-115
 Imaizumi, F., 162-168, 492-499
 Itoh, T., 46-53, 138-145, 170-176, 315-322,
 709-715, 1043-1050
 Iverson, R.M., 25-32, 77-84, 192-198, 287-293
 Iwao, M., 330-337
 Iwata, T., 18-24
 Jacobacci, K.E., 613-620
 Jakob, M., 677-684, 716-723, 847-854, 855-862
 Jan, C., 323-329
 Jang, C., 758-765
 Jayasekara, E.I., 724-731
 Jayathissa, G., 863-870
 Jayathissa, E.I., 724-731
 Jeon, J., 766-773
 Jeong, S., 346-353
 Jia, Y., 476-483
 Jones, E.S., 249-256
 Jones, M.A., 988-995
 Jongmans, D., 146-453
 Jost, R.P., 93-102
 Jun, B., 758-765
 Jun, K., 758-765
 Kaitna, R., 10-17, 124-130, 177-183, 732-739
 Kane, W.F., 988-995
 Karrer, T., 414-420
 Katou, H., 138-145
 Kean, J.W., 77-84, 85-92, 154-161, 192-198
 199-206, 257-564, 516-523,
 524-531, 581-588, 613-620

Keaton, J., 500-507, 740-747, 748-757
 840-846
 Kennard, P.M., 93-102
 Kenyon, T.R., 93-102
 Kim, H., 346-353
 Kim, S., 758-765
 Kim, Young-Hwan., 758-765
 Kim, Yun-Tae., 393-400, 766-773, 808-815
 Kisa, H., 46-53, 330-337
 Kleiber, W., 85-92
 Kobiyama, M., 338-345
 Koo, R.C.H., 957-964
 Kudo, T., 33-37
 Kwan, J.S.H., 957-964
 Kwon, T., 393-400, 808-815, 936-940
 Laigle, D., 146-153, 1019-1026
 Lancaster, J.T., 774-781
 Lane, P.N.J., 532-538
 Langhans, C., 532-538
 Lau, C., 855-862
 Lecce, S., 231-238
 Lee, D., 766-773
 Lee, H., 758-765
 Lee, J., 393-400, 808-815
 Lee, K., 346-353
 Lee, Seung-Rae, 393-400, 766-773, 808-815,
 936-940,
 Lee, Shin-Pin, 879-886
 Legg, N.T., 93-102
 Lei, M., 38-45
 Leonardi, A., 354-360, 1012-1018, 1027-1034
 Leshchinsky, B., 192-198
 Li, S., 361-368
 Li, Xiang, 369-376
 Li, Xiuzhen, 973-980
 Liebault, F., 146-153
 Liu, D., 38-45, 476-483
 Liu, F., 508-515
 Liu, K., 701-708
 Lizárraga, J.J., 369-376
 Lockhart, A.B., 77-84
 Logan, M., 77-84, 192-198
 Lucía, A., 103-110
 Lukashov, S.G., 774-781
 MacAulay, B., 539-547
 Macconi, P., 103-110
 Manassero, M., 1012-1018
 Mano, V., 1019-1026
 Marchi, L., 103-110
 Martins, T., 597-604, 645-652, 798-807
 Matsubara, T., 377-384
 Matsuda, S., 170-176, 1043-1050
 Matsumoto, N., 301-306, 377-384, 863-870
 McArdell, B., 222-229, 414-420, 437-442,
 451-458, 637-644, 685-692
 693-700
 McBride, S.K., 77-84
 McCoy, K.M., 782-789
 McCoy, S.W., 669-676
 McDougall, S., 565-572, 847-854, 911-918
 McGuire, L.A., 467-474, 516-523, 524-531
 Mella, M., 653-660
 Menduni, G., 996-1003
 Michel, A., 154-161
 Michel, R.D.L., 338-345
 Mickelson, K.A., 613-620
 Mirus, B.B., 524-531
 Mitchell, A., 911-918
 Miyamoto, K., 46-53
 Mizuno, M., 207-213
 Mizuyama, T., 61-68, 138-145, 170-176,
 315-322, 709-715, 1043-1050
 1043-1050
 Moase, E., 847-854, 1027-1034
 Molnar, P., 693-700
 Moreno, H., 653-660
 Morstabilini, C., 996-1003, 1004-1011
 Moss, R.E.S., 54-60
 Moya, J., 131-137
 Murakami, M., 301-306
 Murasawa, M., 162-169
 Myers, A., 669-676
 Nagarekawa, Y., 1043-1050
 Nagayama, T., 170-176
 Nagl, G., 177-183, 437-442, 981-987
 Nakatani, K., 294-300, 385-392, 863-870
 Nakayama, T., 1043-1050
 Nandi, A., 629-636
 Nguyen, B., 393-400
 Nishi, Y., 1043-1050

Nishiguchi, Y., 301-306, 401-406, 443-450
 451-458
 Noske, P.J., 532-538
 Nyman, P., 532-538
 Oakley, N.S., 774-781
 Obryk, M., 192-198
 Ohta, T., 790-797
 Okuyama, R., 377-384
 Olsen, M., 192-198
 Oorthuis, R., 131-137
 Ortiz, R.M., 500-507
 Ou, G., 69-75
 Ousset, F., 146-153
 Palau, R.M., 184-191
 Pan, H., 69-75
 Papa, M.N., 429-436
 Park, J., 766-773, 936-940
 Parker, G., 500-507
 Patton, A.I., 816-823
 Picanço, J., 798-807
 Pinzón, G., 407-413
 Pirulli, M., 354-360, 1012-1018
 Piton, G., 589-596, 1019-1026, 1027-1036
 Porta, G.L., 1012-1018
 Poudyal, S., 1027-1034
 Powell, D., 832-839
 Pradhan, A.M.S., 808-815
 Prenner, D., 832-839
 Qiao, J., 214-221
 Quiroz, D., 653-660
 Rapstine, T.D., 192-198
 Rathburn, S.L., 816-823
 Reid, M.E., 824-831
 Rengers, F.K., 85-92, 192-198, 257-564,
 516-523, 613-620
 Rey, E., 146-153
 Richard, D., 1019-1026
 Rickenmann, D., 414-420, 437-442
 Rielland, P., 1019-1026
 Sakai, Y., 421-428, 443-450, 871-878
 Sakurai, W., 33-37, 301-306, 377-384
 Santi, P.M., 484-491, 539-547
 Sanvitale, N., 1035-1042
 Sarno, L., 429-436
 Satofuka, Y., 294-300, 377-384, 385-392,
 451-458, 949-956
 Schärer, C., 532-538
 Scheevel, C.R., 249-256
 Scheidl, C., 414-420, 437-442
 Scheikl, M., 832-839
 Schuerch, P., 637-644
 Schwindt, S., 589-596
 Sempere-Torres, D., 184-191
 Sepúlveda, V., 653-660
 Sharifi-Mood, M., 192-198
 Sheridan, G.J., 532-538
 Shi, L., 214-221
 Shieh, C., 879-886
 Shu, H., 701-708
 Silva, M., 798-807
 Simoni, A., 557-564
 Slaughter, S.L., 613-620
 Smilovsky, D., 500-507, 840-846
 Smith, Joel B., 77-84, 85-92, 154-161,
 192-198, 199-206, 524-231
 Song, D., 361-368, 965-972, 1027-1034
 Song, Z., 369-376
 Staley, D.M., 85-92, 257-264, 516-523,
 524-531, 581-588
 Strouth, A., 847-854, 1027-1034
 Sturzenegger, M., 855-862
 Suzuki, G., 280-286
 Suzuki, K., 863-870
 Suzuki, T., 18-24, 871-878
 Swanson, B.J., 774-781
 Syu, F., 879-886
 Tacnet, J., 1019-1026
 Tagata, S., 138-145
 Takahashi, Y., 207-213
 Tang, H., 516-523
 Tang, J., 920-927
 Targa, D.A., 265-272
 Taylor, E.M., 613-620
 Terriotti, C., 1012-1018
 Theule, J.I., 103-110
 Tian, H., 214-221
 Tsai, V.C., 77-84
 Tsai, Y., 879-886

Tsao, T., 887-894
Tsunetaka, H., 443-450, 871-878
Tucker, G.E., 85-92
Turner, B., 500-507
Uchida, T., 33-37, 301-306, 377-384, 401-406
451-458, 863-870, 895-902
Usuki, N., 61-68
Vieira, B.C., 597-604, 645-652, 798-807
Villani, P., 429-436
Walter, F., 222-229
Wang, D., 903-910
Wang, Z., 973-980
Wasklewicz, T., 231-238
Watabe, H., 1043-1050
Watts, T., 500-507
Weerasekara, N.K., 724-731
Wendeler, C., 941-948, 1027-1034
Wennder, M., 222-229
Wiens, A.M., 85-92
Wooten, R.M. 549-556
Wooten, R., 524-531
Xie, Z., 69-75
Xu, Q., 508-515
Yamanoi, K., 280-286
Yang, C., 323-329
Yang, D., 69-75
Yang, S., 69-75
Yang, Z., 214-221
Yeates, P., 532-538
Yin, H., 116-123, 887-894
Yin, Y., 38-45
Yokota, Y., 162-169
Yoshino, K., 61-68, 895-902
You, Y., 928-935
Youberg, A.M., 467-474, 516-523
Yu, Z., 38-45
Yune, C.Y., 1027-1034
Zambrini, F., 996-1003
Zhang, G., 903-910
Zhao, W., 928-935
Zhou, G.G.D., 2-9, 273-279, 361-368,
965-972, 1027-1034
Zorzi, N., 996-1003
Zou, Q., 903-910
Zubrycky, S., 911-918